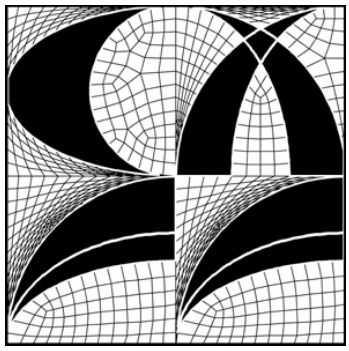

Conference on
Modelling Fluid Flow
CMFF'06
September 6-9, 2006

The 13th Event of international Conference Series
on Fluid Flow Technologies Held in Budapest

CONFERENCE PROCEEDINGS

Edited by
T. Lajos, J. Vad

Department of Fluid Mechanics
Budapest University of Technology and Economics

2006

Proceedings of the Conference on Modelling Fluid Flow
Budapest University of Technology and Economics, Hungary 2006

Edited by T. Lajos, J. Vad

ISBN 963 420 872 X

Published by Department of Fluid Mechanics
Budapest University of Technology and Economics
H–1111 Budapest, Bertalan L. u. 4–6, Hungary
Tel: +36 1 463 40 72
Fax: +36 1 463 34 64
e-mail: lajos@ara.bme.hu
www.ara.bme.hu

Local Organising Comittee

Chairman: Prof. T. Lajos, Budapest
Secretary: Ms. T. Lőrinc, Budapest
Members: Dr. L. Kullman, Budapest
Prof. Sz. Szabó, Miskolc
Dr. J. Vad, Budapest

Orginising Institution

Department of Fluid Mechanics, Budapest University of Technology and Economics

Co-operating Organizations

Department of Hydrodynamic Systems
Budapest University of Technology and Economics
Department of Fluid and Heat Engineering, University of Miskolc
Scientific Society of Mechanical Engineers (Flow Technology Section)
Committee of Fluid Mechanics and Thermodynamics of the Hungarian Academy of Sciences
The Japan Society of Mechanical Engineers
Visualization Society of Japan
FLUENT Europe

Editors

Prof. Tamás Lajos, DSc.
Associate Prof. János Vad, PhD.
Department of Fluid Mechanics, Budapest University of Tecnology and Economics

Conference Organisation

International Scientific and Programme Committee (ISPC)

Chairman: Univ. Prof. Dr.-Ing. habil. R. Schilling, Munich (D)
Co-Chairman: Prof. T. Czibere, Miskolc (H)
Secretary: Dr. J. Vad, Budapest (H)
Members:

Prof. R. S. Abhari, Zürich (CH)
Dr. L. Baranyi, Miskolc (H)
Prof. A. R. J. Borges, Lisbon (P)
Prof. R. A. Van den Braembussche, Sint-Genesius-Rode (B)
Prof. Dr. Dr. h.c. F. Durst, Erlangen (D)
Dr. B. P. M. van Esch, Eindhoven (NL)
Dr. Á. Fáy, Miskolc (H)
Prof. L. Fuchs, Lund (S)
Dr. T. Gausz, Budapest (H)
Prof. V. Goriatchev, Tver (RUS)
Prof. R. Grundmann, Dresden (D)
Prof. G. Halász, Budapest (H)
Prof. H. Jaberg, Graz (A)
Dr. L. Kalmár, Miskolc (H)
Prof. G. Kosyna, Braunschweig (D)
Prof. K. Kozel, Prague (CZ)
Dr. G. Kristóf, Budapest (H)
Prof. Dr. H. Kuhlmann, Vienna (A)
Prof. J. Kumicak, Kosice (SK)
Prof. M. Leschziner, London (UK)
Prof. I. R. Lewis, Newcastle-upon-Tyne (UK)
Prof. N. C. Markatos, Athens (GR)
Prof. M. Nedeljkovic, Belgrade (YU)
Prof. H. Nørstrud, Trondheim (N)
Prof. A. Okajima, Kanazawa (J)
Dr. E. Pap, Magdeburg (D)
Prof. M. L. Riethmuller, Sint-Genesius-Rode (B)
Dr. F. Rispoli, Rome (I)
Prof. A. Rivas, San Sebastián (E)
Prof. R. Rohatynski, Zielona Góra (PL)
Prof. W. Schneider, Vienna (A)
Prof. M. Shirakashi, Nagaoka (J)
Prof. S. J. Song, Seoul (KR)
Prof. R. Susan-Resiga, Timisoara (RO)
Prof. D. Thevenin, Magdeburg (D)

Table of Contents
Volume I.

Invited Lectures

Workshop
Modelling of Turbomachinery Aerodynamics

Workshop
Coupling CFD with Optimisation

Atmospheric Flows

External Fluid Dynamics

Flow and Acoustics

Fluid Power

Internal Flows

Volume II.

Multiple Fluid Phases and Components

Turbulence Modelling, Numerical Methods

Reactive Flows

Turbomachinery

Author's Index

Preface

The present conference is the next event in a successful series of conferences establishing and maintaining relationships among experts all over the world working in research and development related to fluid machinery for decades. The host institution for this conference is the Budapest University of Technology and Economics (BUTE), its organiser is the Department of Fluid Mechanics at BUTE, supported by the Department of Hydrodynamic Systems at the same University, and by the Department of Heat and Fluid Engineering at the University of Miskolc. Co-operating organisations are: the Scientific Society of Mechanical Engineers (Flow Technology Section), Committee of Fluid Mechanics and Thermodynamics of the Hungarian Academy of Sciences, The Japan Society of Mechanical Engineers, the Visualisation Society of Japan, and FLUENT Europe.

When organising the last Conference CMFF'03 in 2003, the main topic of the conference was shifted from fluid machinery towards the most dynamically developing areas of computational fluid dynamics and advanced flow measurements. The integration of these two areas into one international conference was very successful: the presentations delivered by experts from more than 30 countries gave a plentiful overview of research and application related to flow simulation and measurements. In the past decades, the events of the Conference series were held in every fourth year. Because of the success of the Conference, the International Scientific and Programme Committee decided to hold the next Conference in three years, in 2006. The expectations were justified: authors from more than 40 countries submitted more than 150 papers. After careful reviewing, 139 session papers have been published in the Proceedings. The review of the papers has been carried out by the members of the International Scientific and Programme Committee as well as by invited experts, thus guaranteeing the high level of publications in the Proceedings. The Proceedings contains the Invited Lectures and the Workshop papers as well.

A considerable portion of the publications reports the concerted application of CFD and modern experimental techniques. It is our pleasure that despite the extension of conference profile, the traditional topic appears again as a focal point: a large portion of the sessions deal with fluid machinery.

The editors thank the authors for their valuable contribution.

Budapest, on 7 September 2006

Prof. Tamás Lajos
Dr. János Vad

Invited Lectures

Conference on Modelling Fluid Flow (CMFF'06)
The 13th International Conference on Fluid Flow Technologies
Budapest, Hungary, September 6-9, 2006

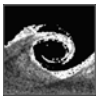

LUDWIG PRANDTL, LIFE AND WORK

Prof. Dr.-Ing., Dr. techn. E. h., Dr. h. c. Jürgen ZIEREP

Institute of Fluid Mechanics, University of Karlsruhe,
76131 Karlsruhe, Germany

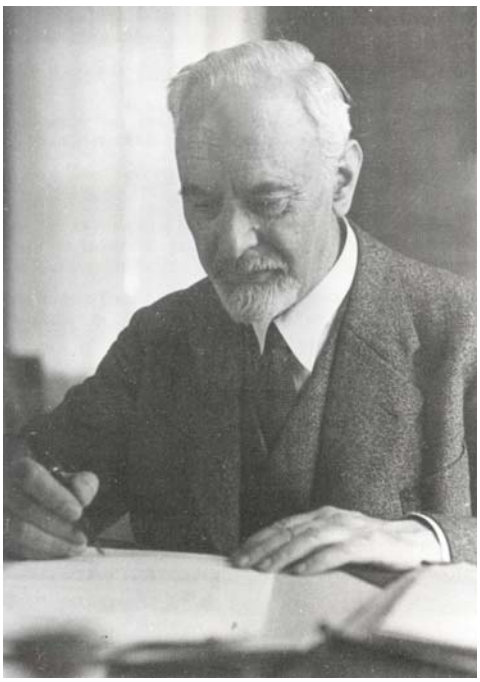

Figure 1. Ludwig Prandtl 1943

The 100. birthday of Boundary Layer Theory (1904/2004) of *Ludwig Prandtl* (1875 – 1953) was a good occasion to remember this famous Fluiddynamic Scientist of the 20. century. The IUTAM (International Union of Theoretical and Applied Mechanics) took this opportunity to organize a meeting in Göttingen, where Prandtl lived about 50 years and built up a famous centre for fluid dynamic research [1,2].

There exists an extensive literature concerning his scientific work and his live. His collected scientific – technical papers, published 1961, fill three volumes of 1620 pages [3]. All of his publications and important remarks are recorded there in detail. Now as before we have here a real mine for the expert. Anything is of historical interest, because we understand by reading the fast development of modern fluid mechanics in all disciplines written by first hand. Two fundamental discoveries, given in publications of completely different size: the one "On Fluid motion with very small friction" (Über Flüssigkeitsbewegung bei sehr kleiner Reibung) [4], the other one "Wing theory I, II" (Tragflügeltheorie) [5] can be named with full right as fateful hours of modern new fluid mechanics. Both investigations opened a closed door. The first is concerned with the friction drag of a body in a fluid flow. Prandtl showed that the important process can be understood and calculated in a "Boundary Layer" in the immediate neighbourhood of the wall. In the second case he studied the fluid flow around "Wings". The different vortex systems lead quantitatively to an integral equation for the circulation, that means for the lift and for the

induced drag. Both investigations lead to developments that remain to be actual till today and are strongly connected with Prandtl´s name for all time. But not to forget, the idea of boundary layer was not an initial ignition accepted everywhere. We know that boundary layer theory was studied in the first twenty years (1904 – 1924) nearly only in Göttingen, connected with the names: Blasius [6], Boltze [7], Hiemenz [8] and Pohlhausen [9]. After that the boundary layer-virus spread world wide – and no end is to be seen [10,11]. In the following we give a short vita of Ludwig Prandtl. After that we discuss some fundamental discoveries that are connected with his name. This is only a short survey of the work of Ludwig Prandtl. But we will see, that there is no representative of fluid mechanics whose name is so often connected with fundamental discoveries.

Ludwig Prandtl was born 1875 in Freising, Bavaria. He studied mechanical engineering 1894 – 1898 at the Technical University in Munich. The great expert in mechanics, *August Föppl* (1854 – 1924), was his scientific and personal admired teacher, later on he became his father in law. 1900 Ludwig Prandtl promoted to Ph. D. at the University of Munich with a remarkable dissertation. After that he was one year engineer in the well known factory MAN at Nürnberg. There he was confronted with viscous fluid flow in diffusors with separation. This leads him to the idea of boundary layer flow. He presented his theoretical and experimental results in a lecture at the III. Int. Math. Congr. in Heidelberg at the 12. August 1904. This was the birthday of boundary layer theory. The famous mathematician from Göttingen, *Felix Klein* (1849 – 1925), judged this lecture to the best of this international congress. Ludwig Prandtl was Professor at the Technical University of Hannover 1901 – 1904. Due to the activity of Felix Klein, Ludwig Prandtl became Professor in Göttingen 1904. He remained thereuntil he retired 1947. In that long time he built up in Göttingen a centre for fluid dynamic research and development. 1907 – 1937 he was Director of the Aerodyn. Versuchsanstalt, Göttingen, (AVA) [12], 1925 – 1946 he was besides this Director of the Kaiser – Wilhelm – Institut für Strömungsforschung, Göttingen [13]. 1912 he was one of the founder of DGLR (Deutsche Gesellschaft für Luft- und Raumfahrt) and 1922 of the GAMM (Gesellschaft für Angewandte Mathematik und Mechanik).

Ludwig Prandtl received many high awards, for instance 7 Drs h. c.: TH Danzig (1920), ETH Zürich (1930), TH Prag (1932), TH Trondheim (1935), University of Cambridge (1936), Univ. Bukarest (1942), Univ. Istanbul (1952).

He was member or honorary member of about 20 Academies or scientific Societies. 1951 he received a high award of the Federal Republic of Germany (Großes Bundesverdienstkreuz). He had 83 PhD – students, the name of these and other scientific coworkers of Germany and foreign countries read like a “who is who” in Fluidmechanics of the first half of the 20. century.

We discuss now some discoveries that are strongly connected with Prandtl´s name with corresponding dates and citations.

1. Prandtl-boundary layer theory (1904) [4],
2. Prandtl-wing theory I (1918), II (1919) [5],
3. Prandtl-mixing length concept (1925) [14],
4. Prandtl-rule (1930) [15], Prandtl-Glauert analogy (1928) [16],
5 . Prandtl-Meyer expansion (1907) [17], (1908) [18],
6. Prandtl-Busemann characteristics method (1929) [19],
7. Prandtl-relation for normal shock (1905) [21],
8. Prandtl-number (1910) [22],
9. Prandtl- pressure tube (1913) [23],
10. Prandtl-transition wire (1914) [24],
11. Prandtl-wind tunnel (Göttingen type) (1908) [25],
12. Prandtl-formula in rheology (1950) [26,27].

All these discoveries, conceptions and technical mechanisms connected with Prandtl´s name belong today to the classical substance of fluid mechanics or even to routine. They show the wide spectrum of Prandtl´s contributions. We will explain in a few sentences the very new idea of everything especially for those readers who had not the opportunity to meet Prandtl personal in Göttingen.

Concerning the idea of *boundary layer*- [4] and *wing theory* [5] we gave already some sentences in the introduction. On *eight* pages [4] we find the conception, the differential eqs and suggestions for future developments including separation. Sketches and photographs illustrate the fundamental concept. The study of this concentrated paper can even after 100 years recommended to everybody (**Fig. 2, 3, 4**).

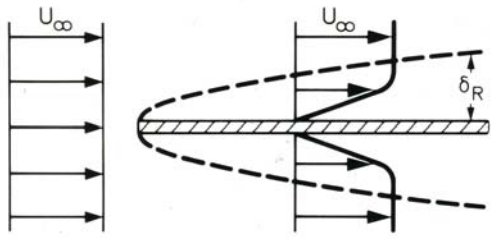

Figure 2. Boundary layer for flat plate, u_∞ = Velocity at infinity, δ_R = boundary layer thickness

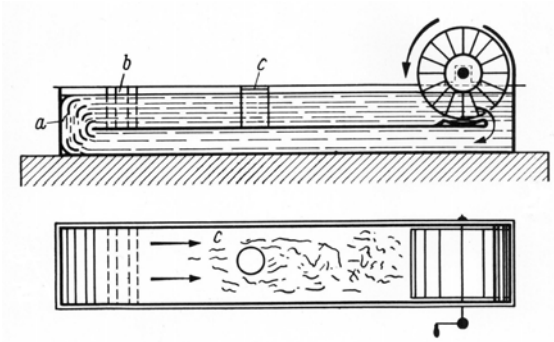

Figure 3. Prandtls water tunnel for investigation of boundary layers 1903 [4].

The small water tunnel is a very simple one. *Jakob Ackeret* (1898 – 1981) (**Fig. 17**), one of Prandtls scholars, coming from Swiss, told us that this small hand driven water tunnel had only a value of about 40 SF.

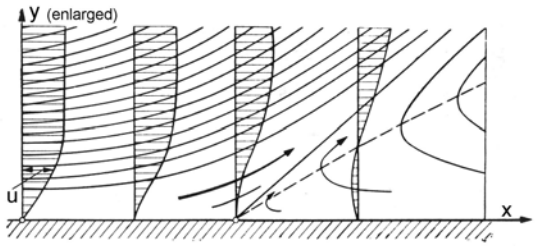

Figure 4. Boundary layer with separation [4].

The wing theory based upon different types of vortices. We have the bound vortex fixed at the airfoil and the free vortices coming from the airfoil tips. They build together the horseshoe vortex (**Fig. 5, 6**). The starting vortex rounds up the vortex system. The flow around a 3 D airfoil is described primarily by a suitable distribution of the circulation in spanwise direction. Vortex systems around an airfoil had been already qualitatively considered by *Lanchester* (1878 – 1946) [28]. It was Prandtls merit however to transform this model in mathematical form of the airfoil theory. By this lift and induced drag

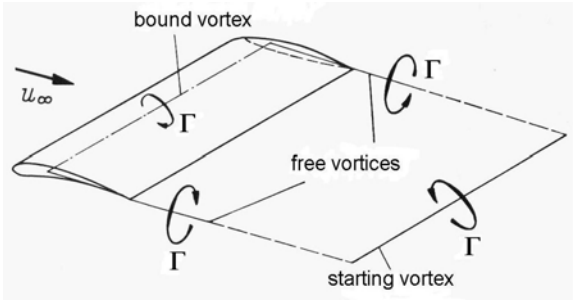

Figure 5. Vortex system of airfoil theory [5, 31, 42].

Figure 6. Free vortices from airfoil tips [29].

are finally given in integral form or respectively by an integral eq.. *Von Kármán* (1881 – 1963) (**Fig. 7**), a famous scholar of Prandtl, described in impressive form [29] two limits, the airfoil

Figure 7. Theodore von Kármán (1881 – 1963)

with large and small stretching in spanwise

direction (**Fig. 8**). In the first case we use the lifting line theory [5], but in the second case [30] we need the complete airfoil theory [31,32]. The two limits lead respectively to a two dimensional consideration. In the first case (large aspect ratio) in a plane normal to the spanwise direction, in the second case (small aspect ratio) normal to the fluid flow [33], in the so called Trefftz-plane.

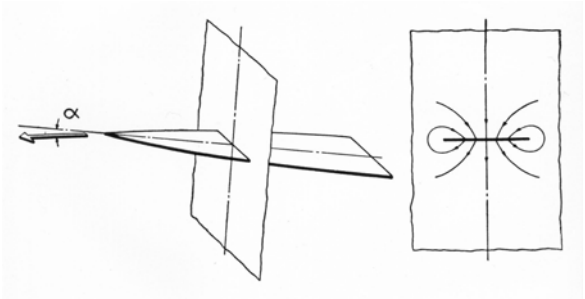

Figure 8. Flow around airfoil of small aspect ratio [29,33].

The *mixing length concept* [14] leads for the first time to a description of the turbulent velocity fluctuations in the Reynolds model. The fundamental idea is the analogy to the mean free path in gaskinetics (**Fig. 9**). The Reynolds apparent shear stress comes out to be proportional to the square of the gradient of the mean velocity. A consequence of this is the logarithmic velocity profile near the wall. This concept has been widely used and was starting point for many investigations.

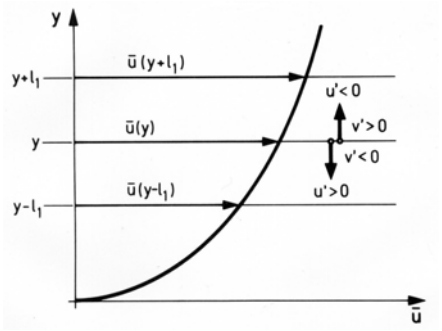

Figure 9. Prandtls mixing length concept,
$\bar{u}$ = mean velocity, (u', v') = velocity fluctuations,
l_1 = mixing length

The *Prandtl rule* [15] or the *Prandtl-Glauer-analogy* [16] are the starting points for *all* similarity laws of the gasdynamics (**Fig. 10**). The compressibility leads to the influence of Mach-number on lift and drag of slender affine

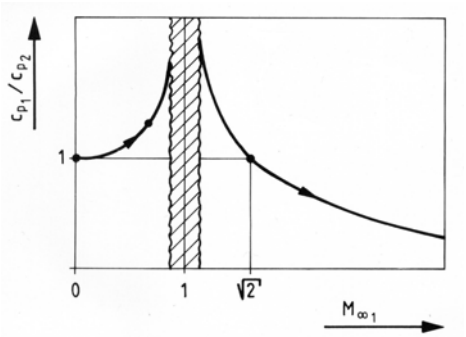

Figure 10. Prandtl rule. Pressure coefficient c_p as function of Mach number

profiles. These investigations start from *linear* differential eqs of 2nd order for the disturbances in sub- and supersonic flow. They were important for aerodynamics of airplanes. Later on similar considerations were successfully used for transonic and hypersonic flow. Nevertheless here we have *nonlinear* differential eqs. The solutions are now as before of great interest either for commercial flight (transonic) or for space aircraft (hypersonic).

The *Prandtl-Meyer expansion* [17,18] describes for sonic- or supersonic flow the turn around a corner (**Fig. 11, 12**).

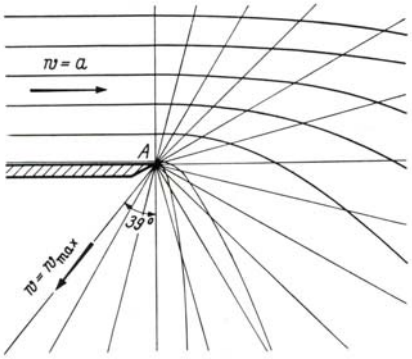

Figure 11. Prandtl-Meyer Expansion of sonic parallel flow (w = a) to maximum speed

Figure 12. Interferogram of Prandtl-Meyer Expansion. Fluid flow counterclockwise [43].

It is an exact solution of the nonlinear eqs of motion. Pressure, density, velocity,… are constant along straight radial lines from the edge. This solution shows typical behaviour of supersonic flow in contrast to subsonic flow.

The *Prandtl-Busemann characteristics method* [19] is a mixed numerical-graphic differences method to calculate supersonic flow around airfoils and in Laval-nozzles. In addition to the fluid-flow-plane we need the hodograph-plane, with the velocity components as axes. In the hodograph steady expansion and compression are given in form of an epicycloide (**Fig. 13**). This describes the Prandtl-Meyer expansion again. If there exists a shock wave, we have to use additionally the Busemann shock polar (Cartesian leaf) [20].

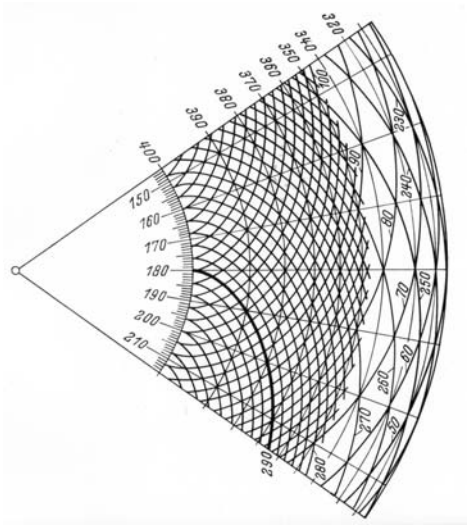

Figure 13. Epicycloid-diagram for Prandtl-Busemann characteristics method

The *Prandtl-relation* for normal shock [21] means that the product of the velocity in front of and behind the shock is the square of the critical sonic velocity. Because we have supersonic flow ahead of the shock, we get subsonic flow behind. That is a fundamental statement in gasdynamics.

The *Prandtl-number* [22] is the ratio of the molecular quantities for transport of momentum and heat (cinematic viscosity/temperature conductivity). This quantity is important for heat transport and fixes for instance the ratio of boundary layer thickness for friction and temperature.

The *Prandtl-pressure-tube* [23] is a very usefully combination of pitot-tube and static pressure probe (**Fig. 14**). We measure the dynamic pressure and by this the flow velocity. An indispensable measuring device!

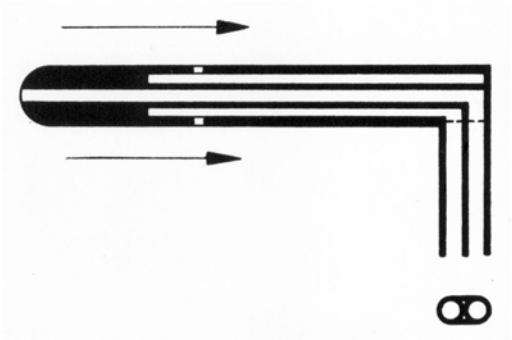

Figure 14. Prandtl-pressure tube

The *Prandtl transition wire* (stumbling wire) [24] plays an important role as experimentum crucis to understand the strong drag reduction for a sphere due to transition from laminar to turbulent boundary layer flow (**Fig. 15a,b**)

a

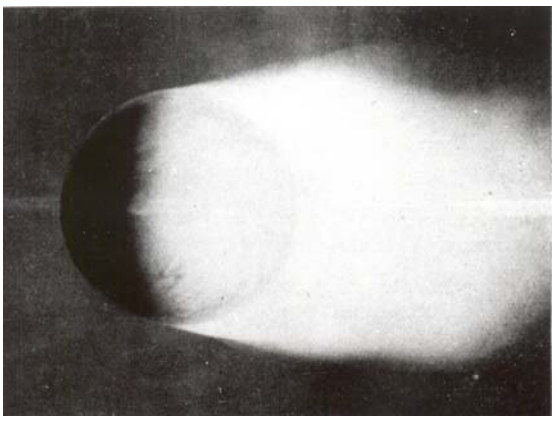

b

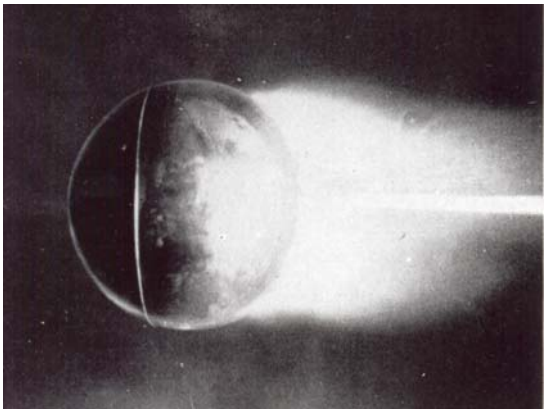

Figure 15. a, b Prandtl transition wire for flow around a sphere. a) laminar flow, b) turbulent flow

If the Reynolds-number $\mathrm{Re} \approx 5 \cdot 10^5$ we have for laminar flow a strong separation in front of maximum thickness with high pressure drag (**Fig. 15a**). Prandtl fixed a wire ahead of that maximum which makes the flow turbulent (**Fig. 15b**). The separation was shifted to the backside with a considerable reduction of the total drag. The reason for that is, that the strong *decrease* of pressure drag overcompensates the *increase* of friction drag. That leads to a strong reduction of total drag, an effect often used in aerodynamics and fluid flow machines.

The *Prandtl wind tunnel* (Göttingen type) [25]. This is a widely used construction, a channel with closed circulation. The air is driven by an axial fan. The test section may be closed or be an open free jet (**Fig. 16**). Besides this there are wind tunnels without circulation (Eiffel type) with suction from and blowing to the atmosphere.

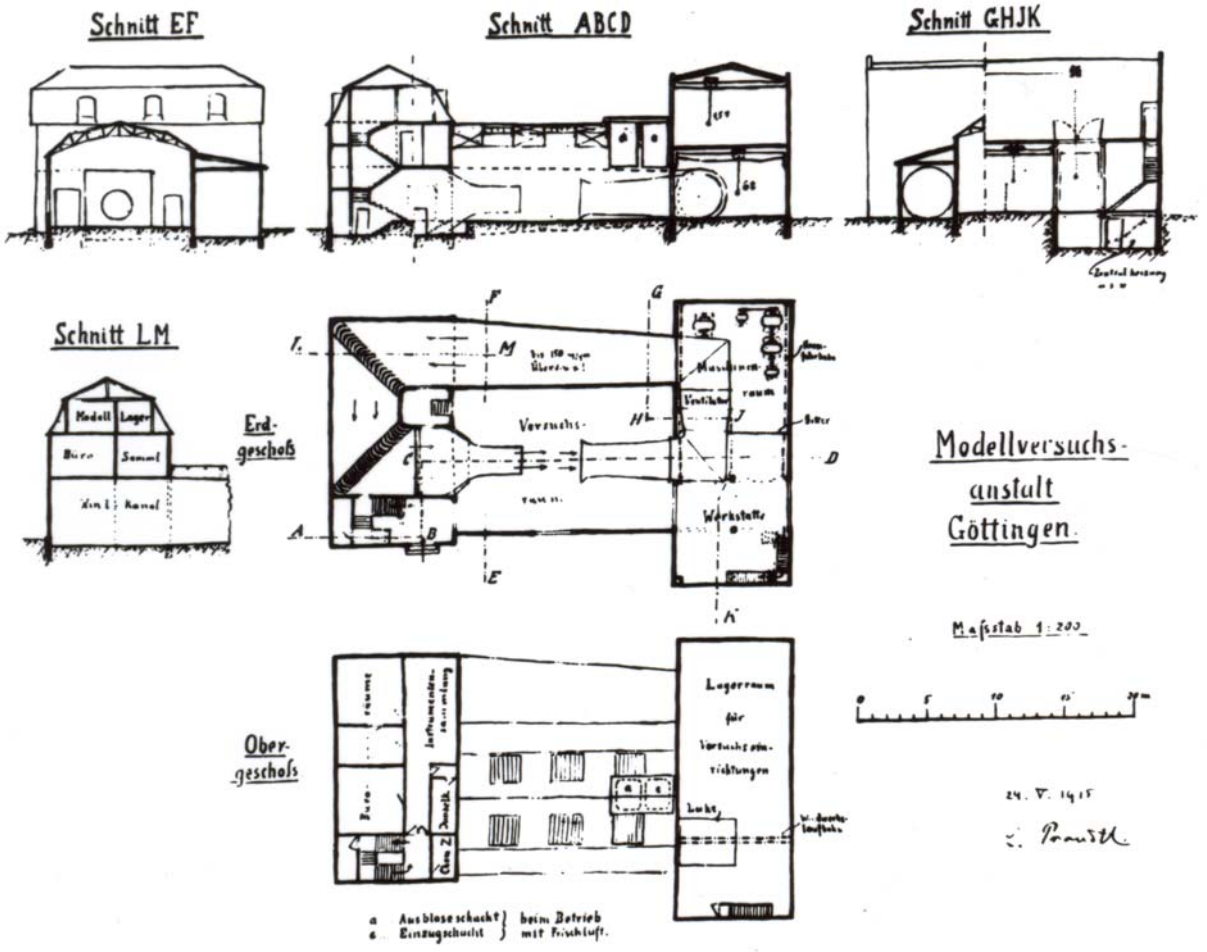

Figure 16. Firsthand sketch by Prandtl for a building with wind tunnel 1915 [12].

For higher velocities there is a great number of different conceptions. Of special interest is the pioneer development of Jakob Ackeret (**Fig. 17**). He built the first continuous running supersonic tunnel at ETH in Zürich [34] (**Fig. 18**).

The *Prandt formulas in rheology* [26]. Prandtl studied over a long time the microstructure of solid bodies [27] and that of general viscous fluids. The results are known as Prandtl- or Prandtl-Vandrey-rules [26].

Besides these directly with Prandtl´s name connected discoveries, there are many suggestions due to him, important for the development of the modern-so called-new fluiddynamics.

We mention in this connection only the famous Volta-congress in Rome 1935 [34]. The most important aerodynamicists of that time discussed theory, experiment and future developments in high speed flow (**Fig. 19**).

Figure 17. Jakob Ackeret (1898–1981)

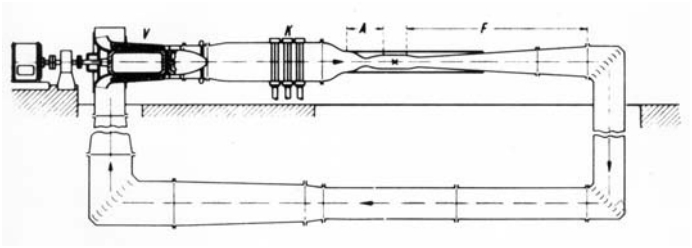

Figure 18. Ackerets supersonic tunnel in Zürich
x: Testsection, V: Compressor,
K: Cooler, A: Nozzle, F: Diffusor

Figure 19. Auditorium of Volta-congress in Rome. We see among others: Prandtl, Bénard, Crocco, Wieselsberger, Busemann, Carlo Ferrari, Maurice Roy,… [34].

The Proceedings of that congress are now as before of great interest. Among others the congress was the birthday of the study of condensation phenomena of humid air in gasdynamics. Prandtl showed a schlieren-picture of a condensation shock – a so called ghost shock – in a Laval nozzle (**Fig. 20**). By this he started an intense investigation in that field actual till to day. A pioneer contribution was given by *Klaus Oswatitsch* (1910 – 1993) (**Fig. 21**) [35] – another international well known scholar of Ludwig Prandtl -. The further development of these fluid flows with energy addition reads like a crime novel [36, 37].

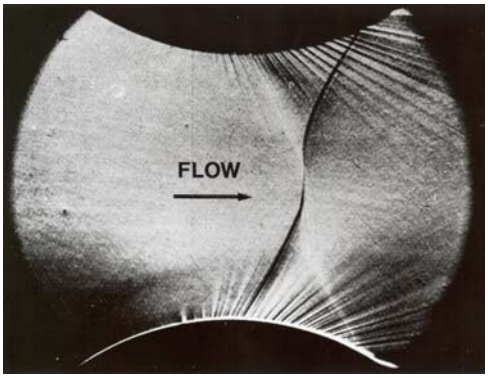

Figure 20. Schlieren picture of condensation shock [34].

These are some fundamental contributions connected with Prandtls name. It is surprising that he made his most important discoveries with simple experiments and by physical considerations. He described this in one of his last papers: " My way to hydrodynamic theories" [38]. His famous collegue, *Werner Heisenberg*, told: " Prandtl solves the fundamental differential- or integral eqs more or less by physical consideration and not alone by mathematics". We all admire this, but we know how difficult it is.

Ludwig Prandtl was active in science and technology for a very long time. He discussed applications in rheology and meteorology and last not least again for turbulent flows. He proposed a new system of formulas for this complex phenomenon.

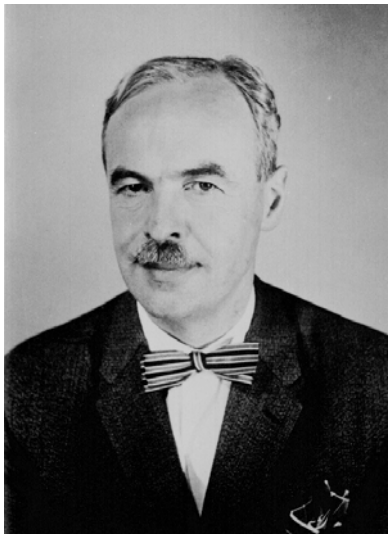

Figure 21. Klaus Oswatitsch (1910 – 1993)

But besides this he enjoys classical problems like fluid flow by shaking of vessels [39] or he discusses the nature of surface tension [40]. The result corrects many statements in textbooks of physics.

Ludwig Prandtl has founded in Göttingen a famous school whose scholars carried his way of thinking around the world in second and even now in the third generation. His daughter, Mrs Johanna Vogel-Prandtl [41] has given a live picture of her father with many remembrances and documents that show us this unforgettable personality of Ludwig Prandtl (**Fig. 22**).

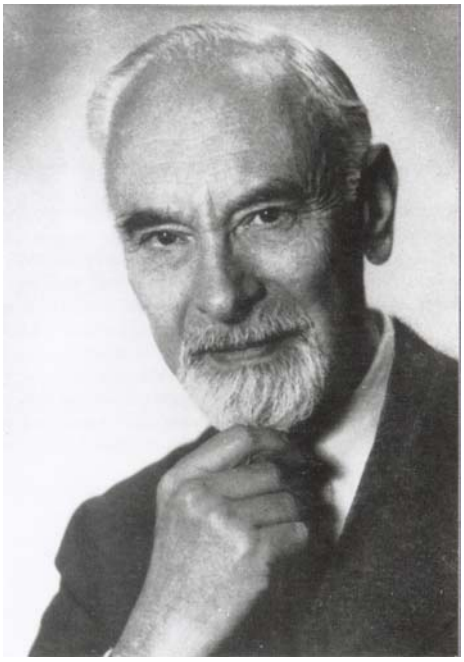

Figure 22. Ludwig Prandtl.

REFERENCES

[1] Meier, G. E. A. (Hrsg.): IUTAM Symp.: 100 years Boundary Layer Theory (12. Aug. 2004), *Kluwer Academic Publishers 2005*

[2] Meier, G. E. A. (Hrsg.): Ludwig Prandtl, ein Führer in der Strömungslehre (Biographische Artikel zum Werk Ludwig Prandtls). *Verlag Vieweg, Braunschweig/Wiesbaden, 330 S., 2000*

[3] Prandtl, L.: Gesammelte Abhandlungen zur angewandten Mechanik, Hydro- und Aerodynamik. 3 Bde. Herausgegeben von W. Tollmien, H. Schlichting und H. Görtler, *Springer – Verlag Berlin, Göttingen, Heidelberg 1961*

[4] Prandtl, L.: Über Flüssigkeitsbewegung bei sehr kleiner Reibung.Verhandlungen des III. Internat. Math. – Kongr. Heidelberg, 8. – 13. Aug. 1904 Leipzig: *Teubner 1905, S. 484-491*

[5] Prandtl, L.: Tragflügeltheorie I. Mitteilg. Nachr. Ges. Wiss. Göttingen, Math-phys. Kl., 1918, S. 151-177; sowie: Tragflügeltheorie II. Mitteilg. Nachr. Ges. Wiss. Göttingen, *Math.-phys. Kl., 1919, S. 107-137*

[6] Blasius, H.: Grenzschichten in Flüssigkeiten mit kleiner Reibung. *Diss. Göttingen 1907. Z. Math. Phys. Bd. 57 (1908), S. 1*

[7] Boltze, E.: Grenzschichten an Rotationskörpern in Flüssigkeiten mit kleiner Reibung. Diss. Göttingen 1909

[8] Hiemenz, K.: Die Grenzschicht an einem in den gleichförmigen Flüssigkeitsstrom eingetauchten geraden Kreiszylinder. Diss. Göttingen 1911; *Dinglers polytechn. J. Bd. 326 (1911), S. 321*

[9] Pohlhausen, K.: Zur näherungsweisen Integration der Differentialgleichung der laminaren Grenzschicht. Diss. Göttingen 1921 [1922]; *ZAMM Bd. 1 (1921), S. 252*

[10] Tani, I.: History of boundary-layer theory. *Ann. Rev. Fluid Mech. 9 (1977), p. 87-111*

[11] Gersten, K.: Die Bedeutung der Prandtlschen Grenzschichttheorie nach 85 Jahren. *Z. Flugwiss. und Weltraumforschung 13 (1989),S. 209-218*

[12] Rotta, J. C.: Die Aerodynamische Versuchsanstalt in Göttingen, ein Werk Ludwig Prandtls. *Verlag Vandenhoeck u. Rupprecht, Göttingen 1990*

[13] Oswatitsch, K. und K. Wieghardt: Ludwig Prandtl and his Kaiser- Wilhelm-Institut, *Ann. Rev. Fluid Mech. 19 (1987), S. 1-25*

[14] Prandtl, L.: Bericht über Untersuchungen zur ausgebildeten Turbulenz. Zeitschr. Angew. *Math. Mech.5 (1925), S. 136-139*

[15] Prandtl, L.: Über Strömungen, deren Geschwindigkeiten mit der Schallgeschwindigkeit vergleichbar sind. *J. aeronaut. Res. Inst., Tokyo Imp. Univ. Bd. 5, Nr. 65 (1930) S. 25-34*

[16] Glauert, H.: The Effect of Compressibility on the Lift of an Aerofoil. *Proc. Roy. Soc. A, Bd 118 (1929), S. 113*

[17] Prandtl, L.: Neue Untersuchungen über die strömende Bewegung der Gase und Dämpfe. *Phys. Z. 8. Jg. (1907), S. 23-30*

[18] Meyer, Th. : Über zweidimensionale Bewegungsvorgänge in einem Gas, das mit Überschallgeschwindigkeit strömt. *Diss. Göttingen 1908. Mitt. Forsch. Ing.-Wes. H. 62 (1908)*

[19] Prandtl. L. und A. Busemann: Näherungsverfahren zur zeichnerischen Ermittlung von ebenen Strömungen mit Überschallgeschwindigkeit. Festschrift zum 70. *Geburtstag von Prof. Dr. A. Stodola. Zürich: Füssli 1929, S. 499-509*

[20] Busemann, A.: Vorträge aus dem Gebiet der Aerodynamik. *Aachen 1929*

[21] Prandtl. L.: Strömende Bewegung der Gase und Dämpfe. *Enzyklopädie der mathematischen Wissenschaften Bd. V, Art. 5b (1905) Nr. 15-23, S. 287-319*

[22] Prandtl. L.: Eine Beziehung zwischen Wärmeaustausch und Strömungswiderstand der Flüssigkeiten. *Phys. Z. 11 Jg. (1910), S. 1072-1078*

[23] Prandtl, L.: Regeln für Leistungsversuche für Ventilatoren und Kompressoren. Aufgestellt vom Verein Deutscher Ingenieure...(1912), *S. 35-68. 2. Aufl.: VDI-Verlag 1926, S. 13-18*

[24] Prandtl, L.: Der Luftwiderstand von Kugeln. Nachr. Der Gesellschaft der Wiss. Zu Göttingen, *Math.-physikalische Klasse (1914), S. 177-190*

[25] Prandtl, L.: Die Bedeutung von Modellversuchen für die Luftschiffahrt und Flugtechnik und die Einrichtung für solche Versuche in Göttingen. *Z. VDI Bd. 53 (1909). S. 1711-1719*

[26] Prandtl, L. und Fr. Vandrey: Fließgesetze normalzäher *Stoffe im Rohr. ZAMM Bd. 30 (1950), S. 169-174*

[27] Prandtl, L.: Contribution to the Mechanics of Solids. *Timoshenko 60th Anniversary Volume, p.184-196. New York: Macmillan 1939*

[28] Lanchester, F. W.: Aerial Flight, Bd. I (Aerodynamics). Constable, London 1907, deutsch von C. u. A. Runge, Teubner, *Leipzig 1909*

[29] Kármán, Th.: Aerodynamik, ausgewählte Themen im Lichte der historischen Entwicklung. Interavia Genf 1956

[30] Weißinger, J.: Über eine Erweiterung der Prandtlschen Theorie der tragenden Linie. *Math. Nachrichten 2 (1949), S. 45. Zuerst veröffentlicht als F.B. 1553 (1942)*

[31] Truckenbrodt, E.: Tragflächentheorie bei inkompressibler Strömung. *Jb. Wiss. Ges. Luftfahrt 1953, S. 40-65*

[32] Weißinger, J.: Tragflügeltheorie. *Handb. Phys. (Hrsg. S. Flügge) VIII/2, S. 385-437 Berlin, Göttingen, Heidelberg: Springer 1963*

[33] Jones, R. T.: Properties of Low-Aspect-Ratio Pointed Wings at Speeds below and above the Speed of Sound. *NACA Report No. 835 (1946)*

[34] Volta, 1935, Reale Accademia D´Italia, Fondazione Alessandro Volta. Atti die Convegni 5. Le Alte Velocita in Aviazione. Sept. 30 – Oct. 6, *1935 – XIII Roma. 1st ed 1936 – XIV; 2nd ed, 1940 – XIX*

[35] Oswatitsch, K.: Kondensationserscheinungen in Überschalldüsen. Z. angew. *Math. Mech. 22, 1-14, (1942)*

[36] Wegener, P. P.: Nonequilibrium flow with condensation. *Acta Mechanica (1975), S. 65-91*

[37] Zierep, J.: Strömungen mit Energiezufuhr, Verlag G. Braun, Karlsruhe, 2. *Aufl., 104 S., 1990*

[38] Prandtl, L.: Mein Weg zu hydrodynamischen Theorien. Physikalische Blätter, *4. Jg. (1948), S. 89-92*

[39] Prandtl, L.: Erzeugung von Zirkulationen beim Schütteln von Gefäßen. *ZAMM Bd.:29 (1949), S. 8-9*

[40] Prandtl, L.: Zum Wesen der Oberflächenspannung. Vervielfältigt (1944). *Ann. Phys. 6. Folge, Bd. 1 (1947), S. 59-64*

[41] Vogel- Prandtl, J.: Ludwig Prandtl. Ein Lebensbild, Erinnerungen, Dokumente. Mitt. Max-Planck-Institut für Strömungsforschung, *Nr. 107, Göttingen 1993*

[42] Truckenbrodt, E.: Fluidmechanik Bd. 2. *Berlin, Heidelberg, New York (1980)*

[43] Frank, W.: Stationäre und instationäre Kondensationsvorgänge bei einer Prandtl-Meyer Expansion. Hab. schrift Univ. Karlsruhe 1979, Strömungsmech. und Strömungsmasch. 25 (1978) 61-87. See also: Frank, W.: Condensation Phenomena in Supersonic Nozzles, *Acta Mech., 54, 135 – 156, 1985*

Conference on Modelling Fluid Flow (CMFF'06)
The 13th International Conference on Fluid Flow Technologies
Budapest, Hungary, September 6-9, 2006

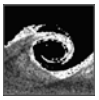

MODELLING INTERNAL REACTING FLOWS

Dominique THÉVENIN

Lab. of Fluid Dynamics and Technical Flows, University of Magdeburg "Otto von Guericke", Universitätsplatz 2, D-39106 Magdeburg, Germany. Tel.: +49 391 67 18 570, Fax: +49 391 67 12 840, E-mail: Dominique.Thevenin@vst.uni-magdeburg.de

ABSTRACT

Internal reacting flows are essential for a wealth of practical applications (car engines, domestic boilers, nano-particle production, electricity generation by a power plant…). Most applications involving such flows take place in the turbulent regime, but new developments like for example micro-reactors are based on laminar flows. In both cases the non-linear coupling between the flow and the reaction phenomena completely determines the behaviour of the full system. Due to this complex coupling truly predictive numerical models are not really available at present time, but they are of course deeply needed to improve existing devices and develop new configurations. In order to increase the understanding of the phenomena controlling chemical reactions in a complex flow, numerical simulations of simple, model configurations are essential. These simulations can be used to compute fundamental quantities, for example space- and time-correlations between different physical parameters, in order to test existing physical models or to develop new modelling approaches. In what follows, different issues related to the numerical simulation of internal reacting flows are considered in more details: Direct Numerical Simulations (DNS) and the post-processing of DNS results, acoustic emissions, process engineering applications and finally the numerical optimization of combustion installations.

Keywords: reacting flows, CFD, combustion.

1. INTRODUCTION

Internal reacting flows are used in many practical systems and in several areas of technological importance, in particular for energy generation (about 80% of the needed energy worldwide is still produced through combustion), transportation (internal combustion engines, aeronautical gas turbines), process engineering (precipitation, micro-reactors…). It is also of central concern in many security issues (fires, explosions) and has a considerable indirect impact on air quality. Since these systems are so widespread it is important to improve their performance and reliability and diminish resulting pollutant emissions. Stability augmentation and more generally safety of operation of combustors and processes is of fundamental importance in many applications. Solution of these questions requires a deep understanding of the basic phenomena and mechanisms and may be greatly helped by numerical simulation.

Recent developments in Computational Fluid Dynamics for Reactive Systems (CFD-RS) have had a great impact on the present understanding of such flows by allowing studies of many problems that could not be tackled by more classical analytical or experimental methods. It has for example been possible to consider the full complexity of combustion phenomena and to calculate the detailed structure of flames including complex kinetics, multi-species thermodynamics and molecular transport. Such calculations first became possible in the 80's with the development of computational science and computer technology. Numerical combustion thus constitutes a relatively new field, the domain explored by scientists and engineers is still limited but its boundaries are rapidly expanding. For combustion applications [1] as well as for general internal reacting flows, results obtained through CFD-RS have had a considerable impact on general scientific understanding and technological design methods.

The broad range of problems underlying internal reacting flows cannot be solved with a unique method. It is therefore useful to identify different levels of modelling, describe their domain of application and some characteristic features. One may conveniently distinguish four modelling classes:

- Detailed Numerical Modelling (DNM): in that case the objective is to take into account complex reaction models as well as multi-species transport and to describe thermodynamic properties with a high accuracy, in order to study the structure of reaction zones, pollutant formation, catalysis,

ignition and extinction conditions, or flame response to external perturbations. In general the flow configuration is relatively simple, the complexity arising from the physical mechanisms. Detailed numerical modelling is essentially limited to laminar and low-Reynolds number reactive flows, and will be mostly considered in what follows, since it is essential to increase the basic understanding of the underlying coupling processes. It has been initially carried out in one-dimensional situations (plane, cylindrical or spherical symmetry) but has been later on extended to multidimensional situations [2]. Section 6 considers specifically a corresponding application for the optimization of a laminar burner.

- Direct Numerical Simulations (DNS) constitute a very important component of Detailed Numerical Modelling. DNS are specifically used to compute reacting flows at low Reynolds numbers by solving directly and as exactly as possible the corresponding conservation equations, without relying on any approximate model to describe turbulence properties. One essential objective is to obtain information on processes which govern turbulent reacting flows. Models devised by analyzing direct simulation results may then be used to improve physical modelling methods [3]. Due to the complexity of turbulent flows, DNS generally rely on slightly simplified physical models compared to generic DNM [4]. At the beginning many DNS even used to rely on simple chemistry and elementary models for diffusive transport and thermodynamics. Direct simulations now use more detailed models but the requirements for computational resources increase of course rapidly with model complexity. Sections 2 and 4 consider specifically DNS applications in more details. In Section 3 an essential side issue of DNS is considered: how is it possible to extract the information needed for model improvement from the wealth of data delivered by DNS, considered as a "numerical experiment"?
- Physical modelling methods (PMM). Physical modelling is required if one wishes to simulate internal reacting flows with complex three-dimensional geometries, as found in practical devices. The balance equations are averaged in time with respect to the turbulent fluctuations of the flow variables. This averaging introduces higher-order moments and mean reaction rate terms which cannot be computed without closure schemes. Basic work in this area focuses on the development and validation of improved closure models while calculations are being made in a variety of applications [1]. These methods are often referred to as Reynolds-Averaged Navier-Stokes (RANS) modelling. Section 5 will consider one typical application for process engineering. The interested reader is referred for example to [3] for a recent, excellent review concerning combustion flows.
- Large-Eddy Simulations lie between DNS and PMM. The large structures of the flow are calculated exactly while the fine-grain turbulent motion is modelled. While LES methods are now fairly well established for non-reacting flows, there are many specific difficulties when applying LES for reactive situations [1]. As a consequence LES are not yet fully established for internal reacting flows and will not be considered in detail in what follows. For a recent review, the interested reader can refer to [5].

After this brief classification of the four description levels which are presently being used for CFD-RS a few illustrative examples and computational implications will now be considered:

- Section 2 describes DNS of turbulent flames;
- Section 3 deals with the post-processing issue, in order to extract useful information from the resulting DNS data;
- Section 4 presents a numerical study to investigate the acoustic emission of reacting flows;
- Section 5 deals specifically with internal reacting flows found in process engineering applications;
- Finally, section 6 considers a DNM application for the optimization of a laminar burner.

This work is certainly not intended to be exhaustive. It complements previous articles of the author on related topics and a wealth of further publications can be found on these different subjects.

2. DIRECT NUMERICAL SIMULATIONS OF TURBULENT FLAMES

Direct numerical simulation methods, originally developed to investigate turbulent non reactive flows, have found important applications in combustion. In DNS all scales are calculated without resorting to a closure model. Direct simulations may thus be used to analyze problems which are otherwise intractable and should be considered as a "numerical experiment" [6].

Among other applications DNS have allowed detailed studies of regimes of combustion, structures of flames wrinkled or corrugated by turbulence and vortical structures, local extinctions and pocket generation, ignition in turbulent flows and flame/wall interactions [7, 8], just to mention a few. Fundamental problems treated with DNS yield results which may be used to improve physical

submodels [3]. This method has been used e.g. in several occasions to analyze the different terms of a model, e.g. the transport equation for flame surface density, and suggest modifications, improvements or even new modelling approaches [1].

Direct simulations of the compressible Navier-Stokes equations are carried out by solving five conservation equations. Reacting flows require N_s supplementary equations, where N_s stands for the number of reacting species considered. For realistic reaction schemes, the value of N_s varies typically between 9 for hydrogen-oxygen flames, around 35 for methane-air flames and at least 100 for higher hydrocarbons. This leads of course to huge computing time requirements, but is in principle the only possibility to investigate for example pollutant formation in an exact, quantitative manner [4].

The tremendous computational costs of such three-dimensional simulations with realistic chemistry explain why almost no really detailed 3D simulation has been carried out up to present time. It is necessary to reduce the complexity in some way in order to come back to an acceptable computational cost. This can be done by following different routes, depending on the most important physical phenomena in the configuration of interest. Classical methods consist in [4]: (a) reducing the physical complexity, for example by considering only incompressible flows, or chemical reactions without heat release; (b) reducing the spatial dimensions by working only in two dimensions; (c) diminishing the cost of the chemistry by using simplified reaction schemes. Several methods are frequently combined to further reduce the cost. It is also important to maximize the available computing power, which means working with the most powerful available computer architectures (at present time parallel computers, possibly with vector processors).

First, some results obtained with full chemistry and transport, but limited to 2D, are presented. Although turbulence is known to be a fundamentally three-dimensional phenomenon, direct simulations have been frequently carried out in two dimensions to reduce the computational cost. Physically, it is known that the influence of heat release can tend to reduce the growth of three-dimensional instabilities in some configurations. Turbulence with more or less organized 2D structures is also observed in some important cases (mixing layers, wakes, jets), which partly justifies this choice from a physical point of view. Results obtained through two-dimensional DNS have greatly helped in understanding basic features of turbulent combustion [7, 8]. Nevertheless, it is clear that the main reason for limiting computations to 2D is of course the induced tremendous reduction in computing times and memory.

In Figure 1 a non-premixed, initially planar hydrogen-air flame is placed in a field of two-dimensional isotropic homogeneous turbulence. The chemical scheme used to describe hydrogen combustion consists of 9 species and 37 reactions. Such complete chemistry computations are used to study the interaction between turbulence and chemical species and identify the differences between the chemical radicals. These simulations may be particularly useful for the investigation of pollutant formation in turbulent flames. Full chemistry computations are also required in order to compare numerical results with experimental measurement of important intermediate species, like for example CH or OH. As usual for DNS, the simulations must be repeated several times in order to get rid of the influence of initial conditions and to calculate meaningful statistical results and moments [9]. The case shown in Fig.1 has been for example computed five other times in order to realize a later ensemble averaging. The corresponding Reynolds number associated with the integral scale of turbulence is 210.

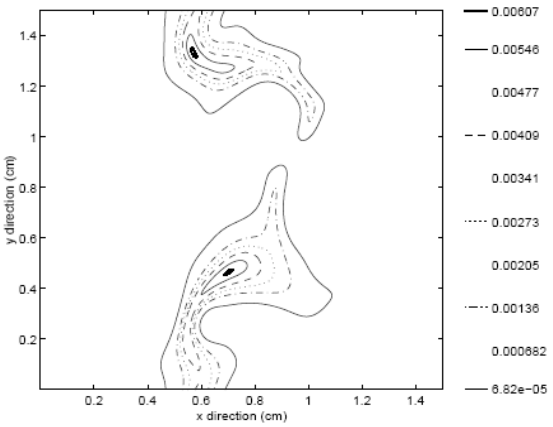

Figure 1. Instantaneous OH mass fractions for a non-premixed hydrogen-air flame evolving in 2D homogeneous isotropic turbulence.

When using detailed chemistry models to represent the chemical reaction, as in this example, the supplementary cost incurred represents over 70% of the total computational cost. This includes the time spent to determine complex multispecies transport properties, thermodynamic coefficients and reaction rates. In other words, the cost of solving the fluid dynamics balance equations is almost negligible when compared with the cost of treating the chemistry. Even if corresponding three-dimensional simulations are now possible on very high-end supercomputers, systematic studies are still impossible in 3D. In Figure 2 a corresponding three-dimensional flame structure is shown, illustrating the complexity of the problem. Such three-dimensional computations have become recently possible in our group through a collaboration with Dr. Alain Laverdant (ONERA, France), who computed this case on a NEC SX6.

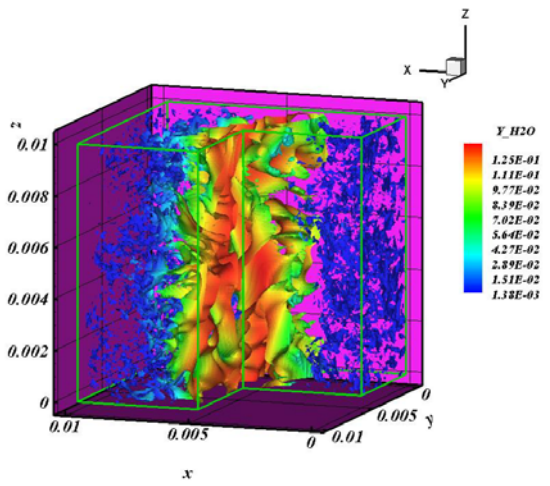

Figure 2. Instantaneous water mass fraction in a turbulent, non-premixed, three-dimensional hydrogen/air flame, plotted on top of isosurfaces of flame index, used to describe the combustion regime. These three-dimensional results have been obtained through a collaboration with Dr. Alain Laverdant (ONERA, France).

In spite of the great interest of these three-dimensional results, it is still almost impossible today to incorporate directly such full chemistry models in three-dimensional solvers running on broadly available computing systems. Thus, alternative solutions must be found.

A new-generation three-dimensional DNS code, called π^3 and written in Fortran 95 has been developed for this purpose. A considerable reduction of the needed computing times is obtained by combining a low-Mach number approach, well suited for most configurations involving combustion, with an accurate and efficient reduction technique for the chemistry, called FPI. Thanks to these two methods it is possible to obtain acceptable computing times for three-dimensional direct simulations of turbulent flames using an accurate description of reaction processes.

For most applications of interest, like for example furnaces and boilers, but also inside the combustion chambers for automotive or aeronautical and aerospace applications, the maximum Mach number is generally quite small, at least in the region where combustion takes place. It is then unnecessary and inefficient to employ a fully compressible formulation to investigate numerically such configurations. The low-Mach number approximation allows an important speed-up, since the stability restrictions associated in particular with the Courant-Friedrichs-Lewy (CFL) condition are practically released. Moreover, the equations are considerably simplified since several viscous terms become negligible, in particular in the energy equation [10].

A pressure-projection method is used to implement the low-Mach number formulation in our DNS code. The pressure is thus splitted into a mean thermodynamic pressure, depending only on time and in practice constant and equal to the atmospheric pressure for the applications considered here, and a fluctuating part, varying in space and time. Through a prediction/correction procedure, it is in this case easy to describe the pressure/velocity coupling, as demonstrated in [11]. Using this low-Mach number approximation, a possible coupling with acoustics cannot be taken into account. This approximation had therefore to be checked for direct simulations of turbulent flames, and a detailed validation procedure has been carried out using full reaction schemes. Simulations of decaying turbulence without chemical reactions, of turbulent ozone decomposition flames and of turbulent premixed hydrogen/air flames have been carried out. In all cases, local as well as global properties of the flow and of the reaction zone are reproduced with less than 5% difference using the low-Mach number approximation compared to the fully compressible formulation, all other models being identical [11, 12]. These slight differences appear first near the boundaries of the numerical domain. The boundary conditions are necessarily different for the low-Mach number approximation and for the fully compressible formulation, since acoustic waves are suppressed in the low-Mach number limit, while they play a major role in the Navier-Stokes Characteristic Boundary Conditions [13] used for the compressible formulation. Inside the numerical domain the agreement is excellent. A low-Mach number approximation can therefore be used to perform direct simulations of turbulent flame structures when the coupling with acoustic waves is not of central interest. Computing times are typically reduced by an order of magnitude, showing that the low-Mach number formulation leads to a considerable speed-up. Readers interested by acoustic/flame interactions should be satisfied later on in Section 4.

In order to further reduce the computing times, it is now necessary to develop an alternative to complete reaction schemes. Specifically for this purpose a tabulated-chemistry approach, called FPI, has been developed within the last 8 years. The theory underlying the FPI method and the practical computation of corresponding look-up tables would lead us too far. Many articles are available on this subject and the interested reader is referred in particular to [14-16]. For the original birth of FPI and its relation with the older, mathematically exact ILDM method [17], see [18, 19]. In order just to understand slightly how FPI works, let us say that, after identifying a few (typically one to four) appropriate coordinates (usually mass fraction(s), enthalpy, possibly pressure), many computations of (for example) laminar premixed flames relying on a

complete reaction scheme are combined together in a look-up table. Afterwards, only transport equations for the table coordinates are implemented in the DNS computation. Knowing these coordinates, the values of all other variables of interest are directly retrieved from the pre-computed look-up table.

At the difference of the ILDM method, there is no rigorous mathematical explanation to justify the accuracy of the FPI approximation. On the other hand, this procedure takes into account exactly the correct boundary conditions both on the high- and low-temperature boundaries, and of course relies on a physically-exact flame structure to relate the species. Many tests have been carried out to check the accuracy of the FPI method within the last years, demonstrating an impressive agreement with complete chemistry models. Flame speed, extinction limits and radical profiles are predicted almost exactly when compared to the full reaction scheme [14-16, 18, 19]. Furthermore, the FPI method leads to a reduction in computing times up to a factor 30. Combining the low-Mach number approach and the chemistry reduction using FPI leads to a typical speed-up of two orders of magnitude compared to a fully compressible DNS formulation employing complete reaction schemes. Thanks to this tremendous acceleration, three-dimensional DNS of turbulent reacting flows become feasible, even on a standard PC. As an example, a turbulent premixed flame computed with π^3 is now considered.

For this, time integration is performed using a fourth-order Runge-Kutta procedure. Spatial derivatives are computed using a sixth-order centered approximation. The pressure perturbation is determined by solving a Poisson equation using a spectral method in the associated Fourier space. The time-derivative of density needed in this equation is approximated by a third-order backward derivative. The grid spacing is constant and uniform, equal to 55 μm. This relatively coarse grid-step (for DNS of flames) is possible thanks to the FPI approximation, since only the two non-stiff FPI-coordinates must be solved to determine all the chemical species. Minor, stiff radicals like HCO or CH_2O are not directly solved, but deduced from the FPI look-up table. It is therefore possible to use coarser grids compared to simulations relying on complete reaction schemes.

Since the DNS code π^3 relies simultaneously on the low-Mach number approximation of the reactive Navier-Stokes equations and on the FPI technique to describe chemical reactions, 3D DNS computations are carried out on a small Linux-PC-cluster or even on a single, standard PC, as here. Typical computation time for a three-dimensional case at low Reynolds number is about one week on a single PC. In Fig. 3 an example is shown for the instantaneous turbulent velocity field (showing 3 different isosurfaces) and the corresponding flame position, represented by a selected isosurface of the reaction product CO_2.

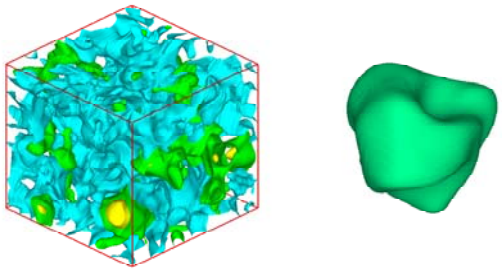

Figure 3. Instantaneous turbulent velocity field (left), represented by three isosurfaces, and corresponding position of the turbulent flame, represented by an isosurface of the reaction product CO_2.

Thanks to such efficient computations, it becomes possible to investigate in great detail the structure of the turbulent flames, for example here a rich premixed methane/air flame, by repeating systematically such computations and carrying out a statistical averaging procedure. But understanding such complex coupled processes requires also a very detailed post-processing.

3. POST-PROCESSING DNS RESULTS

As illustrated on a DNS example in the previous section, both numerical and experimental investigations of internal reacting flows lead in general to a tremendous amount of raw data (time- and space-dependent results for many variables, see for example Figures 2 and 3), which have to be post-processed carefully in order to get useful information for the physical understanding of such flows. This post-processing is essential to test and improve simplified models and to validate numerical methods based on RANS or LES approaches, for example to develop appropriate subgrid-scale models.

For this purpose a specific toolbox has been developed in our group based on the broadly available commercial program MatLab. This add-on toolbox consists of three different kinds of routines: tools for geometrical treatments, tools for statistical investigations and tools to investigate in detail the flame structure. The corresponding routines have been first developed for two-dimensional results but have been in the meantime extended to deal with three-dimensional geometries as well.

In many cases the first suitable way to analyze results (for example DNS data) is through graphic visualization by appropriate plots. MatLab already provides many basic graphical functions to create such plots (contour plots to visualize scalars, vector

graphs for example to investigate gradients or to display velocity fields, plots for data statistics like for example histograms or scatter-plots).

As an example, the most important steps for post-processing DNS results for a non-premixed hydrogen/air flame are illustrated in what follows. The computation relies on 9 chemical species and 37 individual chemical reactions, is only two-dimensional to simplify visualization, with 401 grid points in each direction (similar to Fig. 1).

Using the first group of tools it is possible to analyze the raw data geometrically. First, the flame front is extracted, using a definition freely given by the user. In the present case a mixture fraction is first computed, as usually done for non-premixed flames [3, 20], and the isolevel associated to stoichiometric conditions is retained as the location of the flame front (Figure 4).

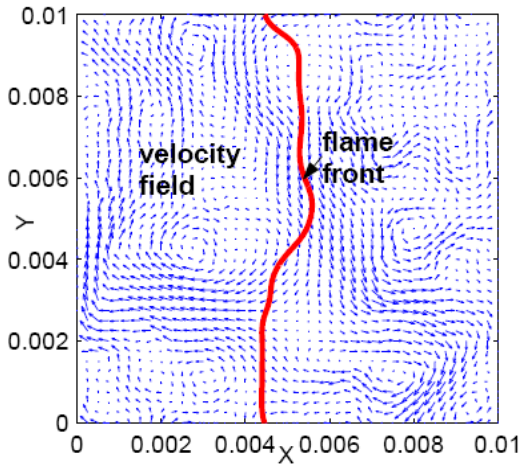

Figure 4. Extracted instantaneous flame front together with turbulent velocity field.

After this step it is easily possible through direct calls to the corresponding functions of the developed toolbox to obtain for example the flame length, the distribution of flame thickness, of strain-rate (Figure 5) and of curvature along this flame front. Vector variables like velocities or gradients can be computed and displayed as well.

For modelling purposes the distribution of all variables along the flame front is essential, together with correlations between these quantities. As an example Figure 6 shows the temperature variation along the flame front, demonstrating that the developed routines also deliver automatically minimum, maximum and mean values as well as r.m.s. variations.

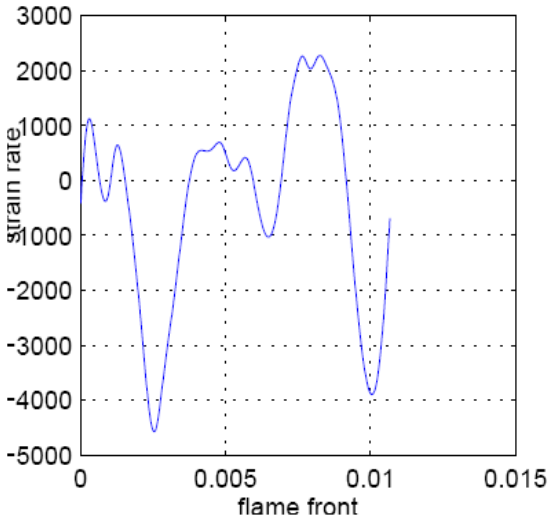

Figure 5. Strain-rate variation (1/s) along the flame front (in m) shown in Fig.4.

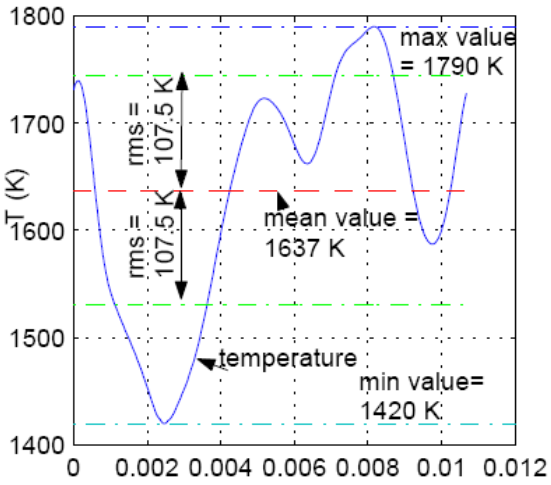

Figure 6. Temperature variation (in K) along the flame front shown in Fig.4.

Figure 7 illustrates a tentative correlation between the local temperature (Fig.6) and the local strain-rate (Fig.5) along the flame front, in the form of a scatter-plot. A non-negligible positive correlation is found for this case. Should this be confirmed by a more systematic investigation, this information should for example be used to validate/invalidate or improve existing turbulent combustion models for non-premixed flames.

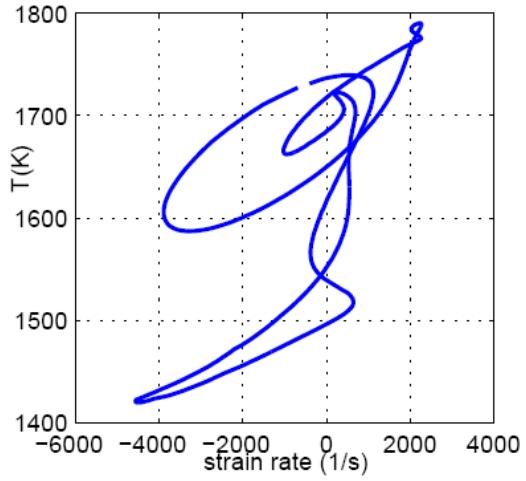

Figure 7. Tentative correlation between local temperature and local strain-rate along the flame front shown in Fig.4.

Presently, the available toolbox is being extended to compute automatically all source terms associated with the acoustic properties of reacting flows, since DNS is now being used extensively to investigate combustion noise, as shown in the next section.

4. ACOUSTIC EMISSIONS OF REACTING FLOWS

The results presented in this section have been obtained with the DNS code *parcomb* [9, 21, 22]. It is a finite-difference DNS code solving the compressible Navier-Stokes equations for multi-component reacting flows. Derivatives are computed using centered explicit schemes of order six except at boundaries where the order is four. Temporal integration is realized with a Runge-Kutta algorithm of order four. Boundary conditions are treated with the help of the Navier-Stokes Characteristic Boundary Condition (NSCBC) technique, extended to take into account multi-component thermodynamic properties [13]. Transport coefficients and chemical kinetics are treated following methods similar to those used in CHEMKIN II and TRANSPORT [23, 24]. This DNS code has been parallelized and widely used over the last ten years to investigate various kinds of turbulent flames.

Parcomb is used here to investigate the interaction of a Gaussian acoustic wave with a CO/H_2/Air turbulent premixed flame in two-dimensions, with a spatial resolution of 40 µm, necessary to resolve intermediate radicals playing a key role for oxidation. The left-hand boundary condition is a subsonic inlet with imposed values, while the right-hand boundary condition is a non-reflecting subsonic outlet. A complete reaction scheme with 13 species (CO, HCO, CH_2O, CO_2, H_2O, O_2, O, H, OH, HO_2, H_2O_2, H_2, N_2) and 67 individual reactions is taken into account. A one-dimensional laminar flame is first computed and then transposed to a 2-D flow, with fresh gases on the left side and burnt gases on the right side. An isotropic 2-D turbulent velocity field is superposed on top of it using a von Kármán spectrum coupled with Pao correction [25, 26]. The interaction of the initially planar flame with the turbulent field is then computed during a time equivalent to one turbulent time, in order to obtain a flame wrinkled by the turbulence (Figure 8).

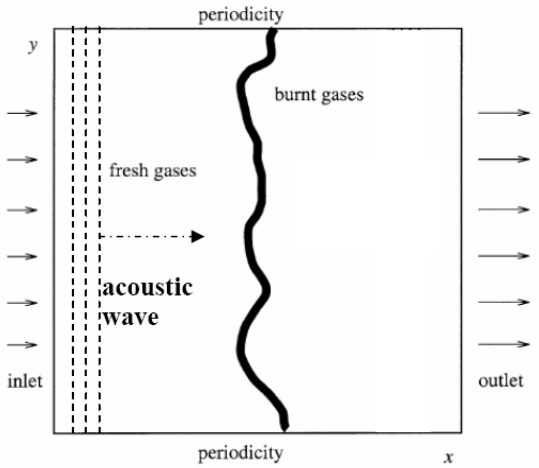

Figure 8. Starting numerical configuration for flame/acoustic wave interactions.

Choosing this time as new origin of time, $t' = 0$, a Gaussian acoustic wave may then be initialized instantaneously as a straight wave across the y-direction inside the fresh gases near the left boundary and propagates naturally towards the flame, crossing it a short time later.

It is now possible to use these results in order to investigate the influence of the reactive flow on the acoustic wave: neutral, leading to amplification or to damping? For this, the well-known stability criterion of Lord Rayleigh has been recently revisited [27] in order to develop a local, instantaneous version of it. Using these results, the influence of the flame on acoustic processes is directly obtained by multiplying the pressure fluctuation Π' (Figure 9) with the corresponding heat release fluctuation Q' (Figure 10). Therefore, Figure 11 can simply be seen as the "product" of Fig.9 with Fig.10. The resulting picture illustrates the complexity of the coupling process. While both pressure fluctuation and variation of heat release exist on a large scale, the product between both quantities only leads to considerable values for very small regions within the reaction zone, due to the fact that the profiles of Π' and Q' are very different, with relatively little overlap.

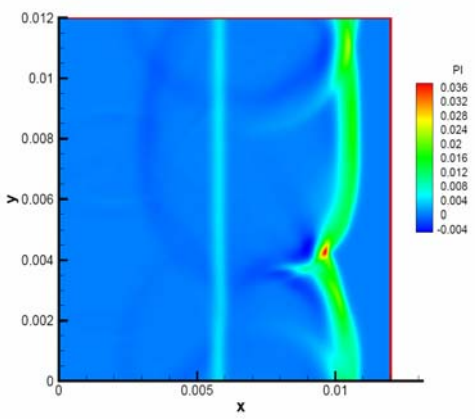

Figure 9. Instantaneous pressure fluctuation at *t'*=10 μs after acoustic wave initialization.

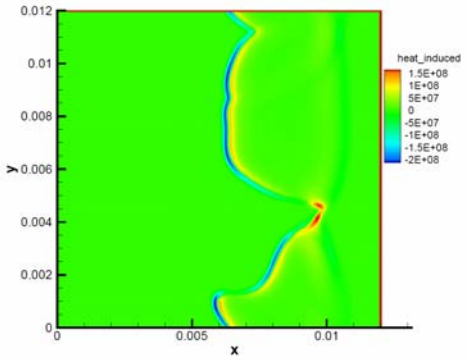

Figure 10. Instantaneous heat release rate fluctuation at *t'*=10 μs after acoustic wave initialization.

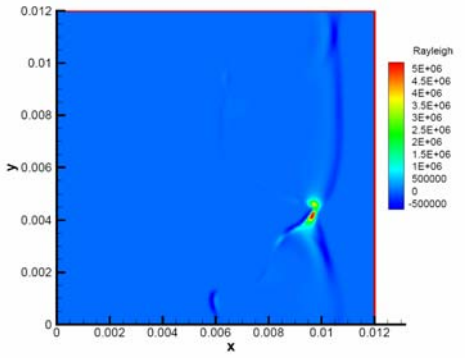

Figure 11. Instantaneous stability criterion of Lord Rayleigh (local instantaneous version) at *t'*=10 μs after acoustic wave initialization.

This explains the difficulty associated with the development of quantitative models to predict combustion noise emissions: the resulting far-field acoustics are dominated by complex processes occurring at the micro-scale and not homogeneous throughout the reaction zone, so that it is almost impossible to carry out a single numerical simulation covering all aspects from the smallest to the largest scales in an accurate manner.

In the next section, applications of internal reacting flows for process engineering are considered to illustrate other, complementary problems and challenges associated with CFD-RS.

5. PROCESS ENGINEERING

For process engineering applications practical flows generally involve complex three-dimensional geometries. Furthermore, moving parts (e.g. mixers) must often be considered. Therefore, robust CFD codes, able to consider three-dimensional moving geometries are needed for such simulations. Several such codes are nowadays available on the commercial market. Nevertheless, supplementary physical models and/or equations must usually be implemented in these codes in order to really be able to solve fundamental issues. This can be realized through user-defined functions and variables, which are then integrated within the industrial CFD code, as illustrated afterwards.

In the previous sections of this paper, only homogeneous gas-phase reactions have been considered. But many practical applications involve other kinds of internal reacting flows. For process engineering, turbulent flows within crystallization or precipitation reactors are of particular importance and are now considered.

For this purpose, a Rushton tank has been simulated with a 6-blade impeller rotating at 300 rpm in the clockwise direction (corresponding Reynolds number Re = 4 500). Near the wall, 18 baffles are implemented. The geometry and the grid for this reactor are shown in Fig. 12. A total number of 79 776 volume elements are used for the full three-dimensional domain.

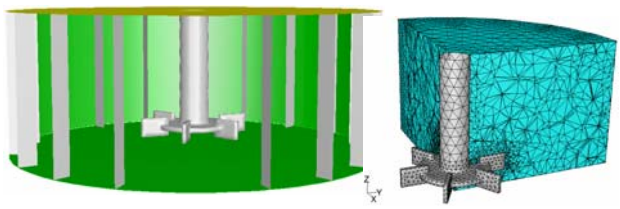

Figure 12. Geometry (left) and part of the numerical grid (right) for the precipitation reactor.

In the numerical simulation this reactor is filled with a suspension of droplets, initially containing SO_4^{2-} ions. Droplets containing Ba^{2+} ions are fed into the reactor through an injection vessel ending near the impeller with a constant feed rate, during a period of 257.14 s. Through coalescence and re-dispersion processes, the Ba^{2+} and SO_4^{2-} ions can be exchanged between droplets and react together to form barium sulphate particles, a classical product for many applications and fundamental studies in

the field of process engineering. By reducing the size of the droplets using appropriate products to modify surface tension, it is possible to obtain a micro-emulsion, in which the same reaction process takes place. Due to the small size of the droplets, the production of nano-scale barium sulphate particles becomes feasible in this manner. Here, a water-in-oil-microemulsion consisting of water, cyclohexane and the non-ionic technical surfactant Marlipal O13/40 is used to synthesise such $BaSO_4$ nano-particles. The reaction is initiated by the mixing of two microemulsions, one containing the first reactant $BaCl_2$ (feed) and the other containing the second reactant K_2SO_4 (initially present in the droplets within the reactor) occurring in a standard Rushton tank (volume: 300 ml).

The three-dimensional simulations in the reactor have been performed in two stages by assuming a batch system (the liquid volume is not changing): first the flow field has been simulated without the reaction process, until fully time-periodic hydrodynamic conditions are achieved; secondly the whole reaction process has been simulated by switching off the flow and the turbulence model (i.e. using frozen-flow conditions) while activating chemical reactions. By this way, the computations have been considerably accelerated compared to the fully coupled simulation of the reacting flow. The computing times are respectively 24 h and 3 h for the first and the second stage employing a single Pentium-IV Linux PC (2.7 GHz/2 GB memory). By repeating this simulation and solving flow, turbulence and chemical reaction in a fully coupled manner, we have checked during a physical time of 100 s that the obtained results are not changed. But the computing time is increased by more than an order of magnitude.

In order to simulate the motion of the impeller, the multiple reference frames (MRF) model has initially been applied, yielding an approximate flow estimation at steady-state. Afterwards, the obtained MRF-solution has been used as an initial guess for the further unsteady state simulation applying the sliding mesh model (SMM). Unlike the MRF model, the SMM is capable of reflecting the impeller-baffle coupling effects taking the time-dependent location of the impeller into consideration. Therefore the SMM delivers much more accurate results for an unsteady calculation. During these flow field simulations a 2nd-order discretization has been used in space and a 2nd-order implicit time formulation has been chosen for the unsteady solution.

The standard k-ε approach has been retained for the turbulence model, since this model delivers a reasonable accuracy and short computing times for such baffled tanks in which no strong, swirling flow occurs. Time-periodic flow conditions have been achieved after 100 full rotations of the impeller (i.e. 20 s real time) during the unsteady simulation employing SMM. The velocity vectors on the middle cross-sectional surface of the reactor and the turbulent kinetic energy contours around the impeller at the end of the first-stage simulations are shown in Figures 13 and 14.

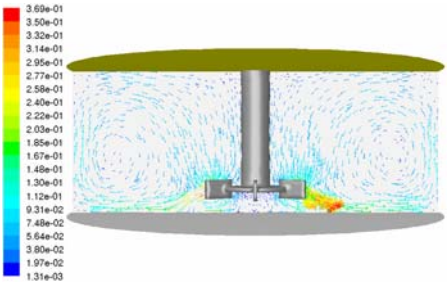

Figure 13. Instantaneous velocity field in m/s obtained at the end of Stage 1.

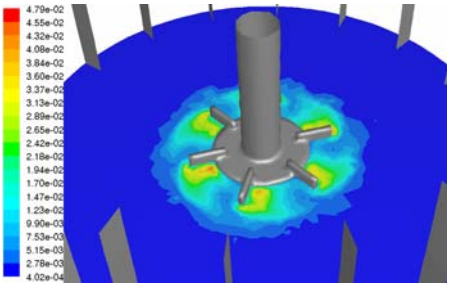

Figure 14. Instantaneous field of turbulent kinetic energy obtained at the end of Stage 1.

In order to describe the physical processes leading to the production of barium sulphate particles, User-Defined Functions and Scalars have been added into the industrial CFD code Fluent. The four equations of the corresponding supplementary system of Ordinary Differential Equations are only valid in the case that only one particle can exist within one droplet. This assumption is reasonable due to the fact that the droplet size is here very small (around 5 nm), so that only a few dissolved ions are present inside. Taking into account droplets with several particles would make the model considerably more complex, so that this point is not considered in the present formulation. The total number of droplets without particles consists of a sink term for droplets in which nucleation takes place and a source term for the feeding of new droplets. The total number of molecules in solid phase is calculated by the addition of dissolved molecules which undergo a nucleation process and the addition of dissolved molecules which contribute to particle growth. The total number of droplets is only changed by the feeding of new droplets, due to the fact that microemulsions are thermodynamically stable. Therefore, the fusion of two droplets directly leads after a very short time to the redispersion into two

equally-sized droplets. Further necessary variables, e.g. the mean numbers of reactant ions in one droplet needed for the determination of the Poisson distribution, are calculated by a few simple algebraic equations. All details of the models can be found in [28].

The time-dependent evolution of the mean number of dissolved Ba^{2+} and SO_4^{2-} ions per droplet and the mean particle diameter with respect to time according to the second-stage simulation (including only the inhomogeneous precipitation on top of the frozen flow) are represented in Figure 15 for both zero- and full three-dimensional analysis. Zero-dimensional computations consider the process as unsteady, but fully homogeneous in space, so that no geometry must be considered. Referring to this comparison, it can be concluded that an almost homogeneous reaction process is observed in the present reactor. This proves that the mixing conditions inside the reactor are almost perfect so that three-dimensional effects are quite negligible in this first configuration. But it is also possible to find cases where this is not true any more, for example when considering a very short injection time for the feed.

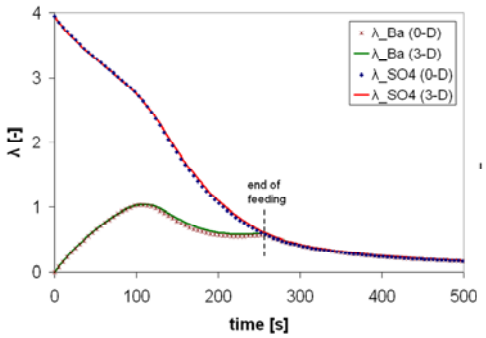

Figure 15. Time-dependent evolution of the mean number λ of dissolved Ba^{2+} and SO_4^{2-} ions per droplet of the suspension.

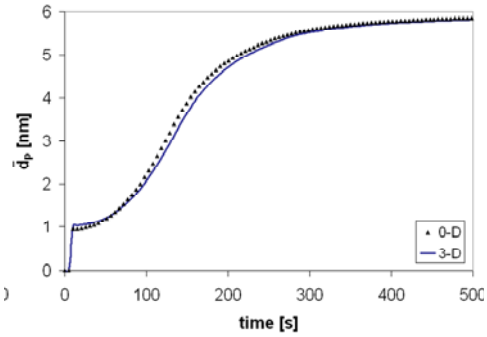

Figure 16. Time-dependent evolution of the mean size (in nm) of barium sulphate particles produced by the reaction of Ba^{2+} with SO_4^{2-} within the droplets of the suspension.

Figure 16 demonstrates that nano-scale particles can indeed be obtained with this process. First comparisons with experimental measurements show a good agreement [28].

When accurate CFD models are finally available for a practical application, it is possible to further consider the automatic optimization of such configurations, as demonstrated in the last section of this paper.

6. OPTIMIZATION OF A LAMINAR BURNER

In this section the optimization of the shape of the flame within a laminar household burner is investigated using the Simplex method, when varying the fuel/air ratio in a primary and a secondary inlet. The objective is to obtain a homogeneous temperature profile at a prescribed distance from the injection plane, which is in practice of high importance before entering the heat exchanger. An in-house computer package, called *Opal*, controls the full optimization process in an automatic manner. The flow involving chemical reactions is solved using the dedicated in-house CFD code *UGC+* [29, 30].

A two-dimensional configuration is considered to illustrate the procedure, involving a primary inlet in the centre of the computational domain and a secondary inlet at the periphery. The optimization problem consists in finding a temperature field as homogeneous (“flat”) as possible at a prescribed distance from the inlet. The single objective is in this case the variation of the temperature solution along the corresponding horizontal cut through the solution. The parameters modified by the optimization procedure are the fuel and oxidizer mass flows of the primary inlet, while the total amount of fuel and oxidizer injected through both inlets is of course kept constant. There are therefore two parameters, that may freely vary between a lower bound (0: no fuel or no oxidizer injected through this inlet) and an upper bound (all the available fuel or all the available oxidizer injected through this inlet). For this burner the computational geometry is fixed for all computations, but the boundary conditions (composition of the mixture for the primary and the secondary inlets) are varied during the optimization procedure. Since the optimization problem is here relatively simple (a single objective), the Simplex method [31] is employed to obtain a fast computational procedure. For more complex problems involving several concurrent objectives, other computational methods, for example evolutionary algorithms, are usually more efficient [32]. Many different optimization algorithms are already available in the employed optimization software, *OPAL*, which is an object-oriented C++ code for Linux systems [29, 32]. A Tcl script is used for coupling *OPAL* with other computer codes, and is employed in the present case to call a C interfacing program responsible for the evaluation

of the objective functions. For computing the burner, both the mesh generation and the flow computations are carried out inside the in-house software *UGC+*. The evaluation of an individual set of parameters for the optimization finally requires three steps [33]:

1. the computation of the composition of the mixture in the primary and secondary inlet, knowing the specific design variables;
2. the CFD simulation, i.e. the resolution of the governing coupled equations for the flow variables, the energy and the species conservation equations;
3. post-processing the obtained results to extract the value of the objective function (temperature variation along a line) for these design variables.

Since the geometry is fixed in the present case, the initial, coarse computational grid is generated once and for all before starting the optimization procedure. The CFD software *UGC+* uses a dynamic grid adaptation to increase the accuracy of the solution, so that the final grid may differ depending on the specific parameters considered. Further possibilities for optimization when the geometry and or grid must be modified for each computation can be found for example in [32].

The temperature field obtained for the two-dimensional burner considered here with the initial (arbitrarily chosen) values for the composition of the two inlets is shown in Figure 17. A very inhomogeneous temperature field is found in the combustion chamber for this set of compositions.

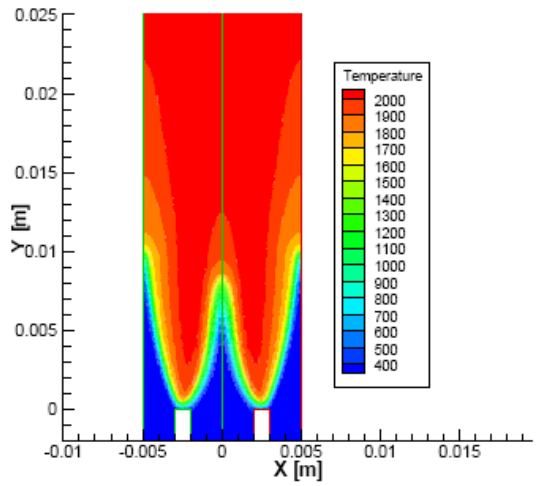

Figure 17. Temperature distribution at Iteration 1 (initial guess for the optimization parameters).

The automatic optimization procedure is now started, with the objective of reducing as much as possible the temperature variation along the horizontal cut through the solution at a height y=1 cm above injection exit.

The evolution of the obtained temperature difference with the number of iterations of the optimization procedure is shown in Table 1, demonstrating the high efficiency of the computational method employed here. Within 7 iterations, the temperature difference has been reduced by a factor of roughly 100.

Table 1. Results for the optimization procedure, with all temperature values in K.

Iteration number	Maximum temperature	Minimum temperature	Temperature difference
1	2078.6	1292.7	785.9
2	2018.9	357.2	1661.7
3	2134.7	1957.9	176.8
4	2050.8	474.5	1576.3
5	2168.7	2127.2	41.5
6	2105.3	1925.8	179.5
7	2156.1	2148.6	7.5

As might have been expected for this simple test problem, the optimal configuration corresponds to two almost identical fully premixed and nearly stoichiometric mixtures, injected through the primary and the secondary inlet and leading to the shortest possible flame. In this case, it would probably have been easy for a human being to guess spontaneously this optimal solution, but this is not true in general!

Considerable variations have been tested by the optimization procedure, corresponding to about 25 % of variations for the fuel and 60% for the air inflow rate, before identifying the optimal solution. The obtained optimal temperature distribution is depicted in Figure 18. The progress compared to the initial guess (Fig.17) is so tremendous that it should not be necessary to comment further on this point.

To quantify in a more precise way the progress of the iteration procedure, the optimization result (i.e. the horizontal temperature profile at a height y=1 cm above the burner) is shown in Figure 19 for all seven computed configurations. As usual for an optimization procedure, the process temporarily leads to solutions much worse than the starting (arbitrary) guess (for example at iteration 2). This is expected since the initial guess is a random choice and thus should not be associated to a particularly bad (or good) solution. But the Simplex method leads to a very fast improvement of the objective function and reaches an optimal solution in a small number of iterations.

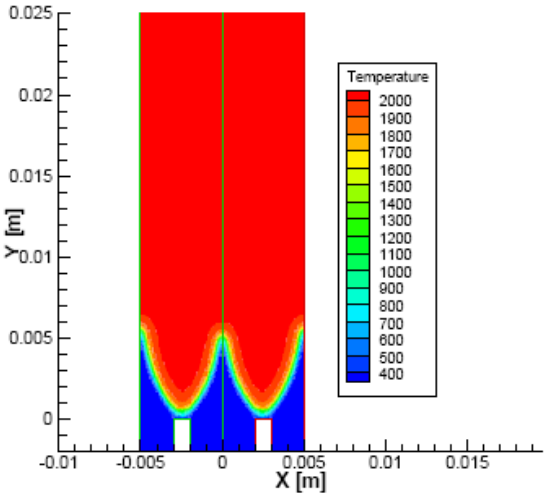

Figure 18. Temperature distribution at Iteration 7 of the optimization procedure (optimum).

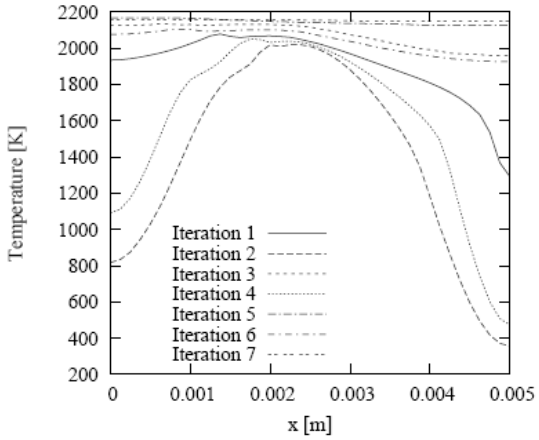

Figure 19. Temperature profiles of all computed configurations 1 cm above injection exit plane.

This case study demonstrates that optimization of internal reacting flows involving heat transfer and chemical reactions is possible, provided very efficient numerical methods are used for the optimization process (here *OPAL*) as well as for the CFD procedure (here *UGC+*). In this case, optimal solutions can be obtained with a small number of iterations and acceptable computing times. This remains true for much more complex multi-objective problems [32]. Further investigations are presently conducted to decrease the needed computing time and therefore have access to even more realistic, three-dimensional configurations, described with more refined models and using a higher number of parameters.

7. CONCLUSIONS

In this paper different important aspects for the numerical simulation of internal reacting flows have been reviewed, in order to illustrate what is currently possible with the available computational resources, numerical methods and physical models. First, results obtained for turbulent configurations with the most exact numerical treatment (Direct Numerical Simulations) have been shown. Such simulations allow a very accurate study of fundamental problems associated with internal reacting flows, for example to determine the structure of the reaction zones (Section 2) or the resulting acoustic emissions (Section 4). In general for CFD simulations and in particular for DNS results, which can be considered as a "numerical experiment", post-processing the wealth of data produced by the computations (Section 3) often takes more time than the simulation itself, if meaningful and relevant quantities shall be obtained to test modelling issues or improve the understanding of the process. In Section 5, an example pertaining to chemical engineering applications has been proposed, before illustrating in Section 6 one of the possible main directions for the future of CFD: the coupling with an automatic optimization procedure.

ACKNOWLEDGEMENTS

The results presented in this paper have been obtained over several years in collaboration with several Ph.D. students, post-doctoral fellows and colleagues, in particular G. Janiga, A. Laverdant, R. Hilbert, H. Shalaby, A. Öncül, O. Gicquel and C. Zistl. The results pertaining to combustion noise have been obtained with the support of the Deutsche Forschungsgemeinschaft (DFG) through Research Unit 486.

REFERENCES

[1] Poinsot, T. and Veynante, D., 2001, *Theoretical and numerical combustion*, Edwards Publishing, PA.

[2] Candel, S., Thévenin, D., Darabiha, N. and Veynante, D., 1999, "Progress in numerical combustion", *Combust. Sci. Tech.*, Vol.149, pp.297-337.

[3] Veynante, D. and Vervisch, L., 2002, "Turbulent combustion modeling", *Prog. Energy Combust. Sci.*, Vol.28 (3), pp.193-266.

[4] Hilbert, R., Tap, F., El-Rabii, H. and Thévenin, D., 2004, "Impact of detailed chemistry and transport models on turbulent combustion simulations", *Prog. Energy Combust. Sci.*, Vol.30, pp.61-117.

[5] Pitsch, H., 2006, "Large-Eddy Simulation of turbulent combustion", *Ann. Rev. Fluid Mech.*, Vol.38, pp.453-482.

[6] Poinsot, T., 1996, "Using direct numerical simulations to understand premixed turbulent

combustion", *Proc. Combust. Inst.*, Vol.26, pp.219-232.

[7] Poinsot, T., Candel, S. and Trouvé, A., 1996, "Applications of direct numerical simulation to premixed turbulent combustion", *Prog. Energy Combust. Sci.*, Vol.21, pp.531-576.

[8] Vervisch, L. and Poinsot, T., 1998, "Direct numerical simulation of non-premixed turbulent combustion", *Ann. Rev. Fluid Mech.*, Vol.30, pp.655-692.

[9] Hilbert, R. and Thévenin, D., 2002, "Autoignition of turbulent non-premixed flames investigated using direct numerical simulations", *Combust. Flame*, Vol.128 (1-2), pp.22-37.

[10] Giovangigli, V., 1999, *Multicomponent flow modeling*, Birkhäuser, Boston.

[11] de Charentenay, J., Thévenin, D. and Zamuner, B., 2002, "Comparison of direct simulations of turbulent flames using compressible or low-Mach number simulations", *Int. J. Numer. Meth. Fluids*, Vol.39 (6), pp.497-516.

[12] de Charentenay, J., Thevenin, D. and Zamuner, B., 2001, "Direct numerical simulation of turbulent H2/O2 premixed flames using compressible and low-Mach formulations", in *Direct and Large-Eddy Simulation IV*, B.J. Geurts, R. Friedrich, O. Metais (Eds.), Kluwer Academic Publishers, Amsterdam, pp.129-136.

[13] Baum, M., Poinsot, T. and Thévenin, D., 1995, "Accurate boundary conditions for multicomponent reactive flows", *J. Comput. Phys.*, Vol.116, pp.247-261.

[14] Fiorina, B., Baron, R., Gicquel, O., Thévenin, D., Carpentier, S. and Darabiha, N., 2003, "Modelling non-adiabatic partially premixed flames using flame-prolongation of ILDM", *Combust. Theory Modelling*, Vol.7, pp.449-470.

[15] Fiorina, B., Gicquel, O., Carpentier, S. and Darabiha, N., 2004, "Validation of the FPI chemistry reduction method for diluted nonadiabatic premixed flames", *Combust. Sci. Tech.*, Vol.176, pp.785-797.

[16] Fiorina, B., Gicquel, O., Vervisch, L., Carpentier, S. and Darabiha, N., 2005, "Approximating the chemical structure of partially premixed and diffusion counterflow flames using FPI flamelet tabulation", *Combust. Flame*, Vol.140, pp.147-160.

[17] Maas, U. and Pope, S. B., 1992, "Simplifying chemical kinetics: intrinsic low-dimensional manifolds in composition space", *Combust. Flame*, Vol.88, pp.239-264.

[18] Gicquel, O., Thévenin, D., Hilka, M. and Darabiha, N., 1999, "Direct numerical simulation of turbulent premixed flames using intrinsic low-dimensional manifolds", *Combust. Theory Modelling*, Vol.3 (3), pp.479-502.

[19] Gicquel, O., Darabiha, N. and Thévenin, D., 2000, "Laminar premixed hydrogen/air counterflow flame simulations using Flame Prolongation of ILDM with differential diffusion", *Proc. Combust. Inst.*, Vol.28, pp.1901-1908.

[20] Peters, N., 2000, *Turbulent combustion*, Cambridge University Press.

[21] Thévenin, D., Behrendt, F., Maas, U., Przywara, B. and Warnatz, J., 1996, "Development of a parallel direct simulation code to investigate reactive flows", *Comput. Fluids*, Vol.25 (5), pp.485-496.

[22] Thévenin, D. and Baron, R., 1999, "Investigation of turbulent non-premixed flames using Direct Simulations with detailed chemistry", in *Direct and Large-Eddy Simulation II*, (Voke, P.R., Sandham, N.D. and Kleiser, L., Eds.), Kluwer Academic Publishers, pp.323-334.

[23] Kee, R. J., Miller, J. A. and Jefferson, T. H., 1980, "CHEMKIN: a general purpose, problem-independent, transportable, FORTRAN chemical kinetics code package", *Technical Report*, SANDIA Rpt. SAND80-8003.

[24] Kee, R. J., Warnatz, J. and Miller, J. A., 1983, "A FORTRAN computer code package for the evaluation of gas-phase viscosities, conductivities and diffusion coefficients", *Technical Report*, SANDIA Rpt. SAND83-8209.

[25] Thévenin, D., van Kalmthout, E. and Candel, S., 1997, "Two-dimensional direct numerical simulations of turbulent diffusion flames using detailed chemistry", in *Direct and Large-Eddy Simulation II*, (Chollet, J.P., Voke, P.R. and Kleiser, L., Eds.), Kluwer Academic Publishers, pp.343-354.

[26] Hinze, J. O., 1975, *Turbulence*, McGraw Hill Book Company, 2nd Edition.

[27] Laverdant, A. and Thévenin, D., 2003, "Interaction of a gaussian acoustic wave with a turbulent premixed flame", *Combust. Flame*, Vol.134 (1-2), pp.11-19.

[28] Öncül, A., Niemann, B., Thévenin, D. and Sundmacher, K., 2006, *"CDF model of a semi-batch reactor for the precipitation of nanoparticles in the droplets of a*

microemulsion", Proc. *16th International Symposium on Computer-Aided Process Engineering ESCAPE16*, DECHEMA, Garmisch, Germany, accepted for presentation.

[29] Baron, R., 2002, "Calcul et optimisation de brûleurs laminaires industriels", *PhD Thesis 2002-37*, *Ecole Centrale Paris*.

[30] Janiga, G., Gordner, A., Shalaby, H. and Thévenin, D., 2006, *"Simulation of laminar burners using detailed chemistry on parallel computers"*, Proc. *ECCOMAS CFD*, Egmond aan Zee, The Netherlands, accepted for presentation.

[31] Nelder, J. A. and Mead, R., 1965, "A Simplex method for function minimization", *Computer J.*, Vol.7, pp.308-313.

[32] Hilbert, R., Janiga, G., Baron, R. and Thévenin, D., 2006, "Multi-objective shape optimization of a heat exchanger using parallel genetic algorithms", *Int. J. Heat Mass Trans.*, Vol.49 (15-16), pp.2567-2577.

[33] Thévenin, D., Zähringer, K. and Janiga, G., 2005, *"Automatic optimization of two-dimensional burners"*, Proc. *European Combustion Meeting ECM05*, Louvain, Belgium, pp.240/1-240/6.

Conference on Modelling Fluid Flow (CMFF'06)
The 13th International Conference on Fluid Flow Technologies
Budapest, Hungary, September 6-9, 2006

INDUSTRIAL DEMANDS ON FLOW MODELLING

Stephan Bross[1], Jochen Fritz[2]

[1] Corresponding Author. KSB Aktiengesellschaft, Product Management / Development Engineered Pumps, Johann-Klein-Straße 9, 67227 Frankenthal,, Germany. Tel.: +49 6233 86-3771, Fax: +49 6233 86-3400, E-mail: stephan.bross@KSB.com
[2]KSB Aktiengesellschaft, Hydraulics & Structural Analysis, Johann-Klein-Straße 9, 67227 Frankenthal, Germany. E-mail: jochen.fritz@KSB.com

Abstract

Flow modelling in an industrial context is not – as is often assumed – something that is carried out for its own sake by development units, but rather, it is employed to satisfy the ever-increasing demands of (internal and external) customers. As this always involves the eternal triangle of "Time – Cost – Quality", the industrial demands on flow modelling are also weighted accordingly.

Therefore industrial demands are understood to be more than just defining new applications for simulation tools or needs for advanced solvers but clarifying the requirements for using flow modelling effectively in industrial processes.

In the present paper, this will be explained using the example of a boiler feed pump, and illustrated using applications from the areas of day-to-day operations, product development, and pre-development.

Keywords: CFD, Flow Modelling, Industrial Process, Eternal Triangle

NOMENCLATURE

H	[m]	head
n	[min^{-1}]	speed
NPSH	[m]	suction head
P	[kW]	power
Q	[m^3/h]	flow rate
η	[-]	efficiency

Subscripts and Abbreviations

A	plant conditions
i	incipient
BEP	best efficiency point
CFD	computational fluid dynamics
CSM	computational structural mechanics
3%	head loss

1. Introduction

Modelling of flow processes has long been an integral part of the work flow in various branches of industry. The demands on the modelling of specific flow phenomena are as varied as the technical applications involving fluid flows – ranging from vehicle and aircraft construction, to process and plant engineering, and the building industry.

Any attempt to specify these demands more exactly and to provide a comprehensive review in a general paper is doomed to failure from the outset – the applications are too varied and the problem areas involved are too complex.

The aim of this paper is rather to take a closer look at the general demands which are made on the modelling of flow processes in the context of industrial work flows and to illustrate these using examples from the pump industry.

2. Definitions

Before having a closer look onto the 'Industrial Demands' of 'Flow Modelling', both expressions should be specified more precisely:

2.1 Flow Modelling

As used here, the term Flow Modelling is to be understood as including all forms of modelling which help to examine relevant flow processes and describe these in a suitable form.

This may involve the use of knowledge databases, correlations, simple (e.g. one-dimensional) modelling methods or complex computational fluid dynamics simulations (CFD).

Strictly speaking, in addition to theoretical or numerical methods, this also includes experimental investigation. However, the importance of experiment has definitely shifted over the past

decades. In the 80s, modelling was mainly based on the results of extensive experimental investigation. Today, a few targeted experiments serve to verify or calibrate the theoretically developed conceptual models.

This trend is also reflected in the personnel structure of development departments, as is shown, for example, in Figure 1 for the hydraulic development department of KSB AG. While in 1980, 45% of the capacity were employed in experimentation and testing, and only 5% in computation and modelling (Fig 1a), today this relationship has almost been reversed, Fig. 1b. But this does not mean, of course, that experiment and testing are of lesser merit. Now, as ever, the customer demands experimental proof of the performance of the product purchased – and this is provided by using increasingly sophisticated measuring methods.

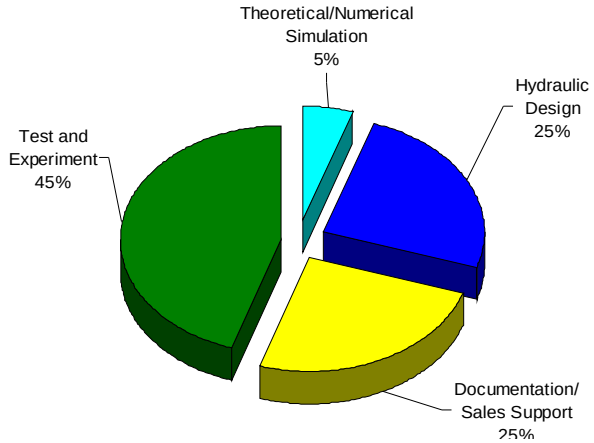

Figure 1a: **Personal Structure of Hydraulic Department 1980**

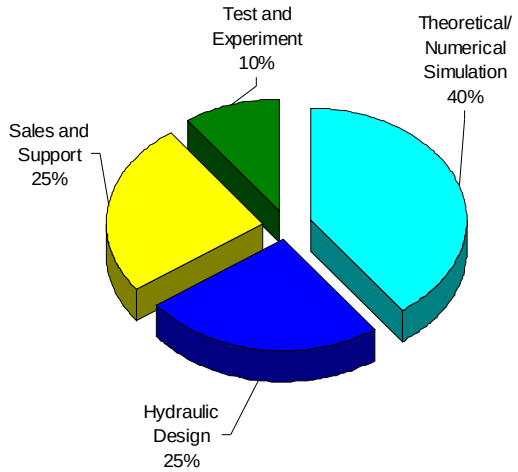

Figure 1b: **Personal Structure of Hydraulic Department 2005**

Even though, as outlined, experimentation is a significant part of flow modelling, the following comments focus mainly on the requirements for the development or application of theoretical / numerical methods.

2.2 Industrial Demand

Basically, all activities of an industrial company should serve the purposes of the company. If we follow the definition given by Professor Malik [1],

"The purpose of a company should therefore be seen as creating satisfied customers. Customer value must consistently and continuously be the guiding principle of Management. This – and only this – maximises the chances (not the certainty) of making the right long-term decisions and ultimately, also to have satisfied shareholders and stockholders",

the requirements to be met by flow modelling must also be geared to the (internal or external) customer.

Flow modelling is therefore not an end in itself for the development departments, but a tool employed to meet customer needs while balancing the Time – Quality – Cost requirements triangle [2], Figure 2.

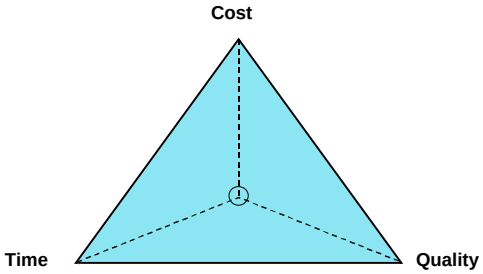

Figure 2: **Eternal Triangle of „Time-Quality-Cost"**

3. Flow Modelling Requirements for Boiler Feed Pump Design

The following explanations describe the use of, and the differing demands on, modelling approaches in the work flow of day-to-day operations, type series development, or the definition of fundamentals (pre-development). In the following chapters, the design process for a boiler feed pump like it is shown in Figure 3 serves mostly as an example. In cases for which other pumps are treated, it is named explicitly.

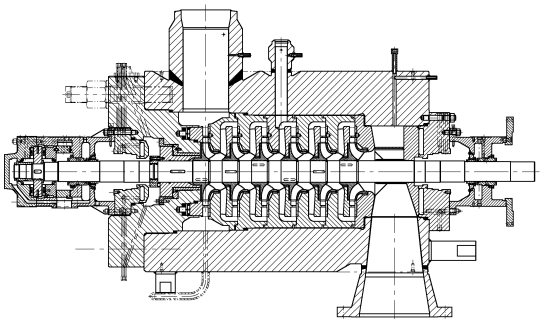

Figure 3: **Boiler Feed Pump**

For the work flows stated above, the time, cost and quality criteria of Fig. 2 are weighted differently in terms of priority. Accordingly, the demands on the flow modelling methods and their applications also change.

The following examples deliberately exaggerate one of the three criteria, in the full knowledge that these do not exist independently of one another.

3.1 Day-to-day Operations: Time-Cost-Quality

Day-to-day operations are characterised by the requirement for rapid response and high informational value. Regardless of whether a particular case involves the initial design of a machine in the early phase of a project, a satisfactory solution to the case of an imminent complaint, or the determination of the final impeller geometry in the context of a trimming test – the time available is always the decisive factor.

In this case the focus is not on recording the last detail of the flow, but rather on arriving at an integral statement quickly.

What is essential is that the necessary knowledge, e.g. in the form of databases, combined with simple but rapid design programs is available to a large number of users within the framework of a continuous process.

Important is the interlinking of different "data sources" to build a continuous design process. In case of the above mentioned pump design, flow modelling is limited to formulating correlations between certain design parameters (e.g. flow rate, discharge head, speed of rotation, suction characteristics etc.) and the design dimensions of the machine geometry (number of vanes, pressure coefficient, delivery coefficient, geometry etc.). Two main different approaches are in use. The first one tries to correlate the in and output data based on approximation formulae (sometimes including physical laws and conditions), while the second one is related to pure data processing methods (e.g. neural networks). An essential prerequisite for both of them is, that the databases are always kept up to date, and the correlation parameters are updated "off-line". By this, the process is carried out avoiding the handling of (large) data quantities and with rapid access to the underlying correlation parameters.

Figure 4 illustrates the use of neuronal networks for choosing the initial impeller geometry. Flow parameters like the flow rate Q, the Pump Head H, the hydraulic efficiency η etc. are stored together with the impeller geometry data (diameter, width, number of vanes, angle distribution etc.) in a statistical data bank. Special concepts of multi-layer neuronal networks are trained in the learning phase, which may be significant time consuming [3]. Once the network is trained, processing input data into the required geometry output is very fast. The advantage of this process is, that the databank can be extended using data from different sources, whether experimental or theoretical/numerical.

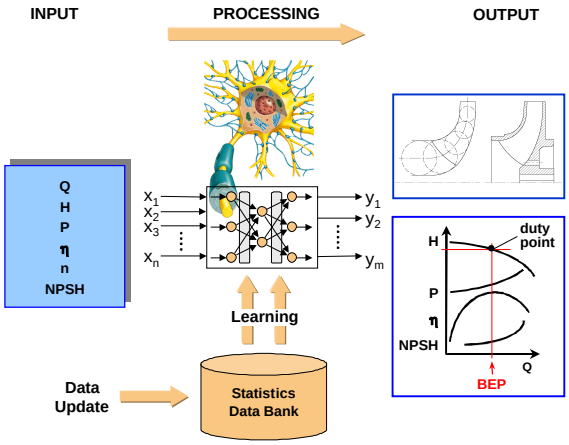

Figure 4: **Impeller Design Process based on Neuronal Networks**

Equal to the human being, the learning phase is the more effective, the more learning friendly the data base concept is. Therefore, a lot of efforts have to be spent to create smart concepts of low parameter geometry descriptions without loosing the required flexibility [4].

In this context, the industrial demands on flow modelling focus on the intelligent evaluation and description of existing databases and their intelligent processing rather than on the modelling of complex flow processes. Even if this field of application is sometimes perceived to be a (rather unspectacular) marginal area of flow modelling, it does have a special importance for industrial application. At no other point in the "business process" is so much money gained or lost than at the start of order processing. General arrangement drawings or specifications supplied to the customer

(and these are demanded by the customer very soon after the order has been placed – long before the pump has been designed in detail) can only be revised with great difficulty and great (financial) effort.

Meeting the industrial demands must therefore be aimed at improving these data processing procedures and their handling.

3.2 Type Series Development: Cost -Time - Quality

In the context of type series development, the technical and economic product requirements described in the functional and technical specification must be implemented within the allocated budgets of cost and time.

Design and development of a boiler feed pump are initially based on the provision of a suitable hydraulic system for generating the required operating data (flow rate, discharge head, performance and efficiency). According to the progress of the development phase, ever more complex tools are used, but these are always calibrated for the case of application for which they are in use.

While at the start the main dimensions are determined on the basis of exemplary hydraulics, correlations or underlying databases, increasingly sophisticated modelling tools are used in the further stages of the process for the detailed design of the hydraulic contours. This ultimately involves the complete three-dimensional simulation of transient flows in one or more pump stages by solution of the Reynolds-averaged Navier-Stokes equations.

Although the optimisation of high-performance machines hinges on the knowledge about and the interpretation of flow details and their effect on the performance of the machine (see Figure 5), the industrial demands on flow modelling neither focus on the generation of extended turbulence models nor on the provision of LES (Large-Eddy Simulation). Rather, product development uses flow simulation as a certified, i.e. calibrated, reliable and “rapid” working tool in its field of application, which must be integrated into the relevant overall process, in particular into the company's IT and software architecture.

If one bears in mind that the optimisation of a hydraulic system design goes through several iterations, it becomes clear that this can only be managed economically within a synchronized chain of processes.

Interfacing to the company's CAD system, simplified and automated mesh generation, industry-geared or application-centred pre- and post-processing, overriding optimisation algorithms, and standardised interfaces for the transfer of data to additional, or even integrated, modelling processes (e.g. fluid / structure interaction as shown in Figure 6) are the major criteria of interest for the industrial application of flow modelling within the context of product development.

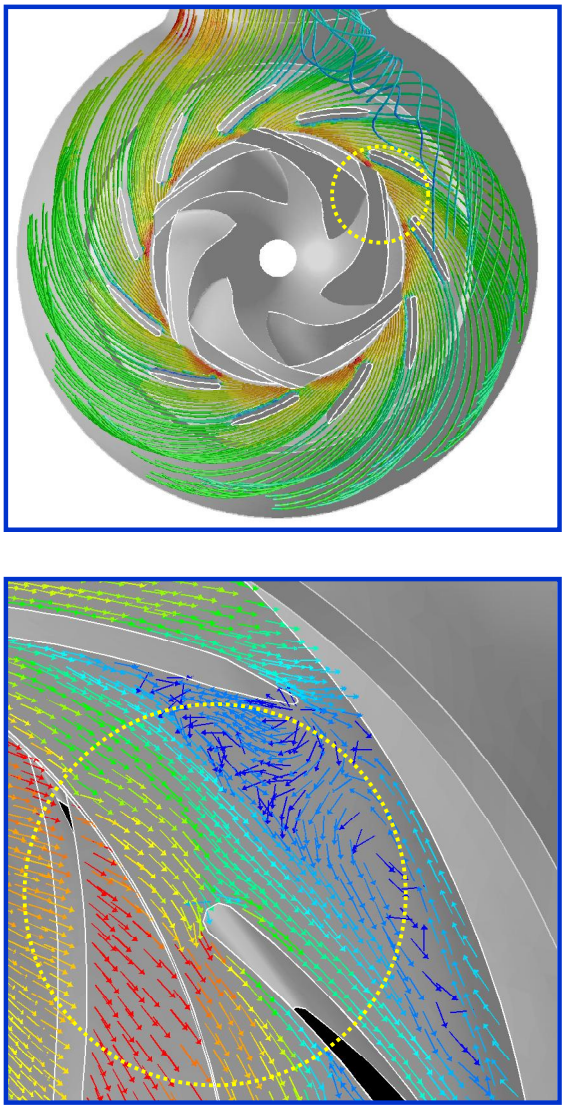

Figure 5: **Calculated Path Lines for an Impeller/ Diffuser/Stage Bowl Configuration using the Software Package FLUENT (above). Analysis of detailed Flow Structures indicates Blockage in one of the Diffuser Channels (below).**

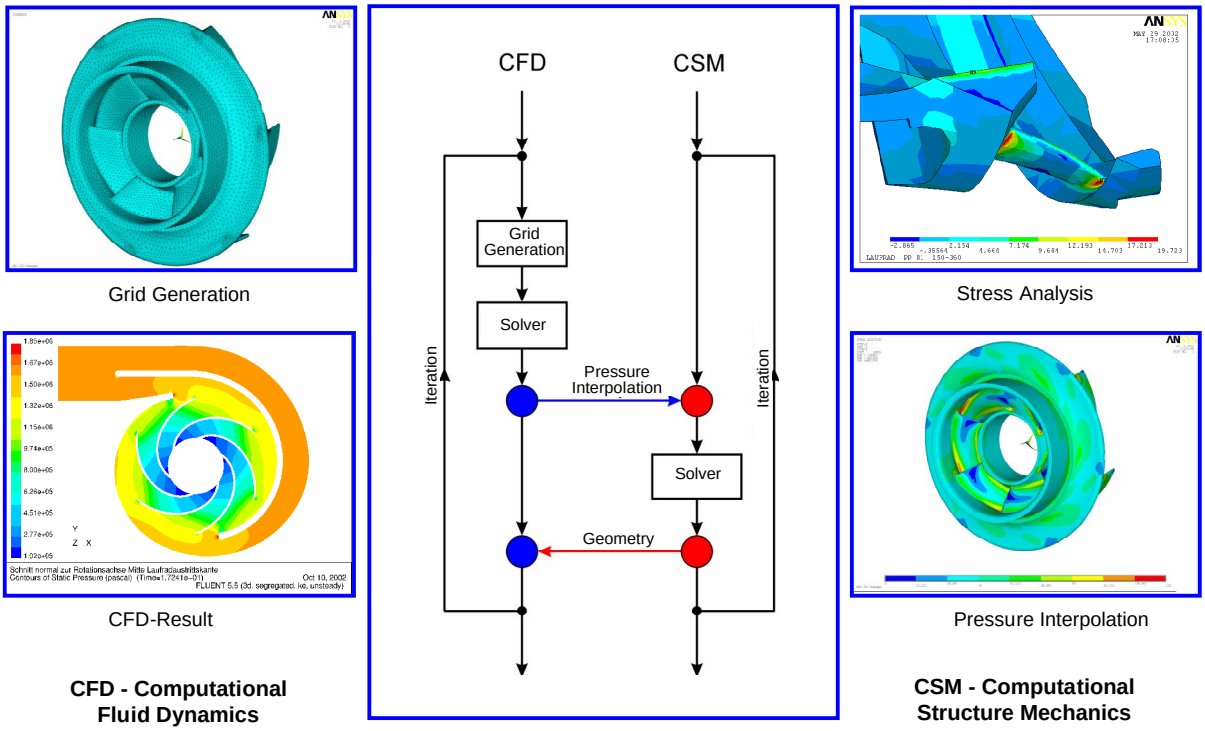

Figure 6: Simulation of Fluid-Structure Interaction of a Pump Impeller using integrated Processes and Interfaces

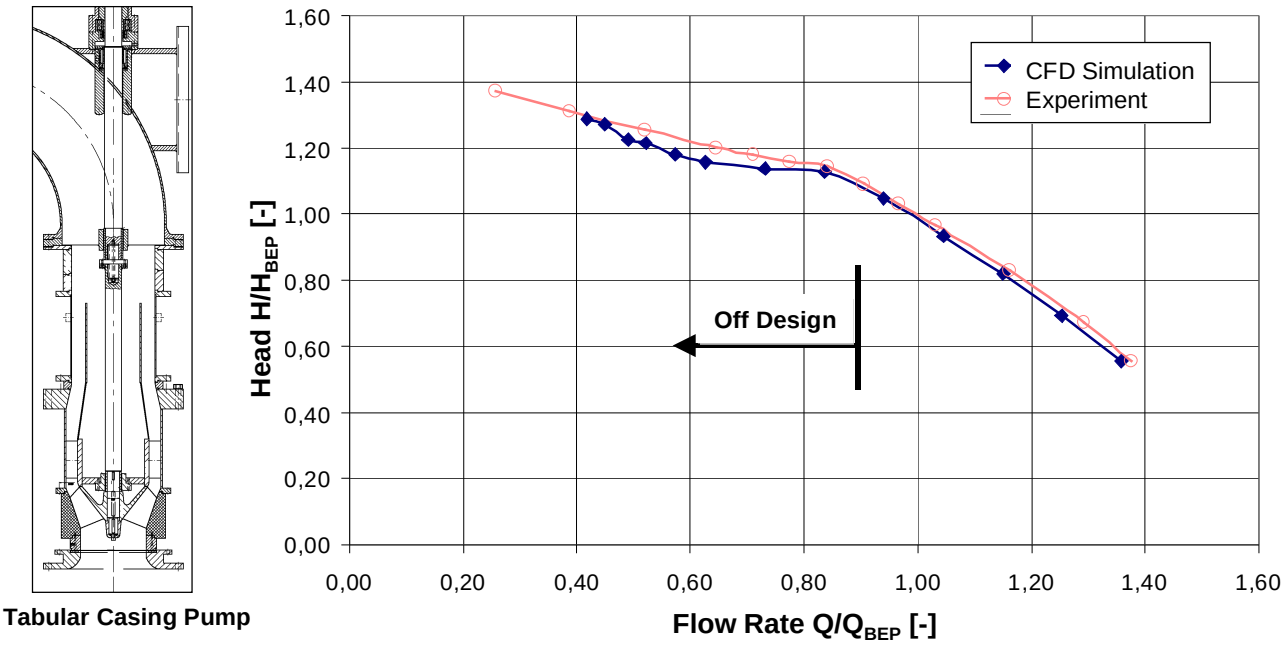

Figure 7: Comparison of Experimental and Calculated Head Curve for a Tabular Casing Pump

3.3 Pre-Development: Quality-Time-Cost

In the field of pre-development fundamentals are established, which are later integrated into type series development as well-proven sub-concepts, or serve to improve, extend and accelerate the application of modelling tools used in day-to-day operations or product development.

A major part of this work is the testing and adaptation of the computation models for new or extended cases of application, the evaluation of the results, as well as the determination of the validation limits. It is obvious that the demands on flow modelling are primarily focused on the performance of the modelling methods and the quality of the results. Naturally, this area also involves approaches dealing with the optimisation of running time, as well as the possibility of future process integration.

Ever-increasing competition, but also the rising demands of customers drive an ever faster cycle of matching the scope of flow modelling to the needs of industry.

Starting from the modelling of flow at the operating point in earlier times, transient flow analysis and parallel computer architectures allows forecasting the off-design behaviour today. In Figure 7, the head curve of a tubular casing pump is shown, comparing theoretical and numerical results. Even at part load conditions, at which the so call part load recirculation at the impeller inlet dominates the flow behaviour, a remarkable matching between experimental and numerical results is visible.

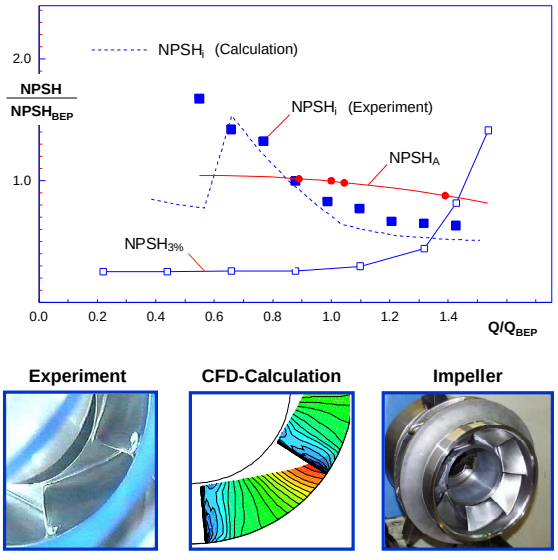

Figure 8: Cavitation-free Operation of a highly loaded Boiler Feed Pump for 900MW Power Plant

Moreover, new, and above all, validated numerical simulation models for multi-phase flow enable to determine the cavitation characteristics of pumps with sufficient accuracy [5]. In Figure 8, the comparison of predicted and measured incipient cavitation flow regime is illustrated for the above mentioned boiler feed pump. Again, the measured data are matching the predicted ones more than sufficient.

Hence, fluid / structure interaction in the mechanical and thermal areas, as well as the analysis of noise generation, transmission and propagation in pumps form the focus of further efforts. Apart from the purely qualitative demands on flow modelling, this field makes very special demands on the collaboration between industry and the institutes who specialise in the development of modelling tools.

These institutes are well advised to look into the processes commonly used in industry, and to assimilate the rules of project management (specification of content, time, budget) and not lose sight of the true industrial purpose of flow modelling (ultimately to earn money).

For its part, industry must accept that a collaboration of this kind cannot be undertaken for the solution of problems of day-to-day operations, but primarily for the implementation of medium- to long-term strategies. In this context, the provision of precise technical specifications is just as necessary as the commitment to long-term financing.

4. Summary

The present paper has attempted to illustrate the industrial demands on flow modelling in the light of the "Time – Quality – Cost" requirements triangle, using the example of a boiler feed pump.

One conclusion that emerged is that the weighting of the time, quality and cost factors differs for the various fields of application.

Hence in day-to-day operations, or in the early phase of a project, the rapid accumulation (time) of information from various systems and databases is the focus of attention. In the field of product development, the spotlight is on the integration of proven modelling methods in the design process. Particular attention must be paid to the issues of pre- and post-processing, as well as the creation of suitable interfaces, in order to be able to integrate numerical flow simulation into the company's internal IT and software architecture. Only if this is achieved is it possible to work not only effectively (costs), but also efficiently (time).

The classic demands on flow modelling are made in the definition of fundamentals (quality) in the field of pre-development. Extension of the areas of application, validation in industrially relevant test cases, running time optimisation etc. are the focus of attention here. These tasks can not be carried out by small to medium-sized companies on their own, but only by strategic alliances, with appropriate investments.

References

[1] Malik, Ferdinand, "Malik on Management", 11. Jahrgang Januar 2003, MoM Letter 1/2003, S. 5.

[2] Gerboth, Thomas, "Das Magische Dreieck: Kosten - Zeit - Qualität", Controlling, Heft 7/2002, S. 417.

[3] Zell, A., "Simulation Neuronaler Netze". R. Oldenburg Verlag, 2003.

[4] Krämer, S., "Entwurf von Beschaufelungen hydraulischer Maschinen mit Hilfe Künstlicher Neuronaler Netze", Technische Universität München, Lehrstuhl für Fluidmechanik, Abteilung Hydraulische Maschinen und Anlagen, Dissertation 2005.

[5] Stoffel, B., Schaad, C., "Entwicklung und experimentelle Validierung eines Codes zur numerischen Berechnung kavitierender Strömungen in anderen Flüssigkeiten als Wasser in Kreiselpumpen", AIF Forschungs-vorhaben Nr. 13759, 2. Zwischenbericht, Darmstadt, 2005.

Conference on Modelling Fluid Flow (CMFF'06)
The 13th International Conference on Fluid Flow Technologies
Budapest, Hungary, September 6-9, 2006

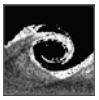

MODERN TURBOMACHINERY COMPONENT DESIGN

René A. VAN DEN BRAEMBUSSCHE

von Karman Institute for Fluid Dynamics, Turbomachinery and Propulsion Department, Waterloose steenweg, 72, 1640 Sint-Genesius-Rode, Belgium. E-mail:vdb@vki.ac.be

ABSTRACT

An overview of the different inverse techniques that are available for the design of turbomachinery components is followed by a more detailed discussion of the optimization techniques based on gradient methods, and evolutionary theories. Special attention is given to a hybrid method combining Artificial Neural Network, Genetic Algorithms, Design of Experiments and a Navier-Stokes solver. Merits and problems encountered with the different methods are discussed and illustrated with examples.

Keywords: Artificial Neural Network, Design of Experiment, Genetic Algorithm, Inverse Design, Optimization, Turbomachinery.

NOMENCLATURE

b	[m]	impeller outlet width
I	[m^3]	moment of inertia
q	[m/s]	velocity or solution quality
l	[-]	substring length
N	[-]	number of design variables
n	[-]	population of a generation
OF	[-]	objective function
P	[Pa]	pressure or penalty
R	[m]	radius
T	[K]	temperature
t	[-]	number of generations
w	[-]	penalty weight factor
u	[-]	non-dimensional length
X	[-]	axial coordinate
x,y	[m]	blade coordinates
β	[o]	flow or blade angle
θ	[rad]	blade camberline angular position
η	[-]	efficiency
Φ	[m^2/s]	potential function
Ψ	[m^2/s]	stream function

Subscripts and Superscripts

h	hub
t	tip
0	impeller inlet
3	impeller outlet
x, y	axial, tangential coordinate

1. INTRODUCTION

CFD has seen a very important development over the last 30 years and has reached a high level of reliability. Navier Stokes solvers are routinely used to study fluid flows in the same way Finite Element Analysis is used for stress predictions. They provide detailed information about the flow around existing blade shapes in a relatively short time and as such constitute an attractive alternative for detailed flow measurements. Complex flow phenomena are now studied in what is called "Numerical Laboratories". Although this has resulted in a drastic decrease of the number of prototype testing, there are still two problems that prevent a more efficient use of CFD in the turbomachinery design process.

The first one results from the difficulty to visualize 3D flows on 2D screens or drawings. 2D Vector plots are only a poor presentation of the reality. They can be very misleading as they may suggest that the flow is penetrating the solid walls. (Fig. 1).

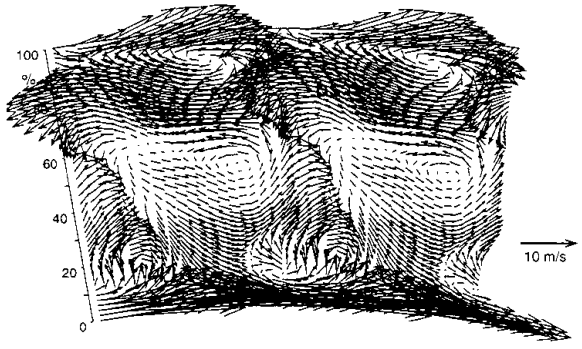

Fig. 1 - 2D view of the 3D flow at the exit of a turbine stage

Synthetic environments, also called virtual reality, are very promising in this respect. These techniques will not remain restricted to computer games but will become part of the everyday reality for engineers in the next decade [1]. Designers will walk inside blade rows and diffusers to inspect the complex 3D flow structures by following 3D streamlines and to verify the effect of geometrical changes.

The second problem relates to the abundance of information provided by the Navier Stokes solvers. Three velocity components, pressure and temperature in typically 10 000. points (2D flow) or in more than 1 000 000. points (3D flow) is more than what the human brain is able to grasp and fully exploit in new designs. The output of a Navier Stokes solver contains all the information needed to improve the performance. However these methods do not provide any information on what modifications are needed to reach that goal. Most of the information remains unused as the designer will often calculate a global parameter to find out if one geometry is better than an other one.

The traditional design procedures in which standard 2D blade sections are selected and scaled up or down to adapt them to the requirements is no longer acceptable. The designer is now faced with the development of new blade shapes [2].

One needs new tools to use the available information in a more efficient way than with the traditional trial and error procedure in which the systematic testing of blade shapes has only been replaced by Navier Stokes calculations. The outcome of this procedure strongly depends on the expertise of the designer. This may become problematic since experienced designers are replaced by young engineers, who may be highly skilled computer- and CFD experts but may have limited knowledge about turbomachinery flows. Designers can hardly be expert in all disciplines that interfere with a design (aerodynamics, mechanics, manufacturing etc). Hence the need for automated and computerized design systems.

The main goal when designing turbines or compressors is to achieve light, compact and highly efficient systems while reducing the cost and the duration of the design cycle. Many designs are stopped because the deadline is reached, not because the target was obtained. The new design systems should therefore be "**fast"** and affordable.

Turbomachines are often operating outside the nominal- or design conditions. Compressors for air-conditioning applications must be able to operate efficiently at all seasons i.e. at different mass flows. Low Solidity Diffusers (LSD) are specially designed to perform well at a large variety of inlet flow conditions. Optimizing those geometries for one operating condition is only part of the job. **"Multipoint"** design is needed to find the global optimum i.e. satisfying the performance requirements at all operating points with minimum power consumption over the whole lifetime of the machine.

Optimum performance is of no use if the mechanical integrity of the turbomachine cannot be guaranteed. This requires a stress or heat transfer analysis to verify that the maximum allowable constraints are not violated. Lower material- and manufacturing cost are also important design criteria. Designing a turbomachinery is therefore a complex exercise requiring a **"multidisciplinary"** approach.

These design targets can be achieved by means of inverse methods, in which the geometry, corresponding to a prescribed pressure or velocity distribution, is defined by a computer program. An alternative are the optimization systems searching for the geometry that best satisfies more global requirements in terms of performance, mechanical constraints or any other design criterion.

In what follows one will give a short overview of both approaches. A short description of the methods is followed by a discussion of the advantages and disadvantages. The most promising methods are illustrated by an example.

2. INVERSE DESIGN METHODS

Inverse design methods directly define the geometry (blade shape) required to achieve a prescribed velocity or pressure distribution. They are very powerful and well suited for cases where the "optimum" pressure or velocity is known.

The optimum pressure distribution can be defined in most 2D flows but it is still unknown for 3D blades taking into account the secondary flow effects. An important contribution to a better understanding of the optimum pressure distribution on compressor blades was made by Lefoll [3] and worked out by Papailiou [4]. The outcome of such a design is what is commonly called controlled diffusion blades. The suction side velocity distribution is characterized by a continuous acceleration up to the point of maximum velocity where a controlled deceleration starts. The latter one is the maximum diffusion that can take place over the remaining blade length without flow separation.

Fig. 2 shows the possible compressor blade suction side pressure coefficients with controlled diffusion downstream of the transition point. Optimum is the one with maximum lift coefficient [5].

Optimum turbine blade velocity distributions are discussed by Sieverding [6]. The pressure side has a continuous acceleration up to the trailing edge whereas the suction side shows a limited deceleration over a short distance upstream of the trailing edge.

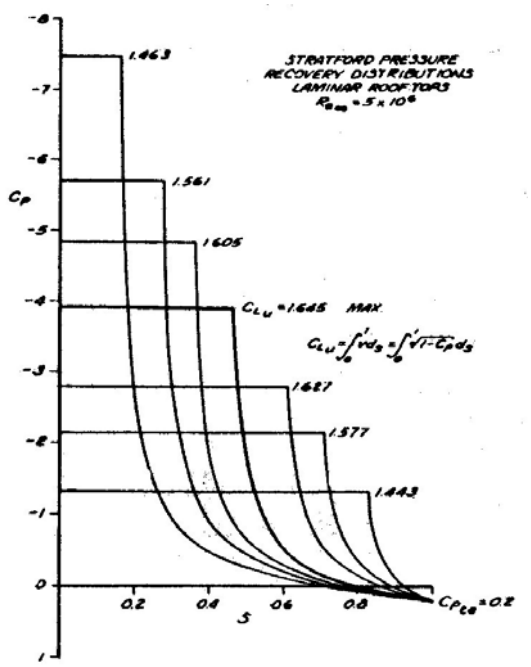

Fig. 2 Controlled diffusion suction side velocity distribution.

A major difficulty is the definition of a velocity or pressure distribution that, at the same time, is optimum one in terms of performance (turning and losses), and corresponds to a blade that is feasible (closed contour with positive thickness) and respects the mechanical constraints (minimum and maximum blade thickness).

The existency problem or respect of mechanical constraints has been theoretically studied by Lighthill [7]. A discussion of some necessary conditions for 2D Turbomachinery applications can be found in [8].

An inherent problem of inverse design methods are the undefined limits of the numerical domain. As long as the blade is not defined one does not know where to impose the boundary conditions. Inverse methods distinguish by the way they handle this problem:

* direct inverse methods, are the oldest ones and based on analytical flow solvers. They avoid the problem of unknown boundaries by changing independent variables.
* iterative methods start from a first guess of the geometry on which the flow solver is applied. This provides input to an "automated" geometry modification system.

An alternative approach [9], which has also been extended to 3D geometries [10], prescribes only the blade loading. A possible link to previous inverse methods is described in [11]

2.1 Direct inverse design methods

Direct inverse design methods use analytical solvers and are limited to 2D inviscid flow. This constitutes serious limitations in terms of applicability.

The hodograph method no longer calculates the flow in the physical (x,y) plane but in the q, β plane of which the boundaries are defined in function of the prescribed velocity distribution. [12]. This method does not allow designing rounded leading edges and rounding-off the leading edge, often leads to unwanted velocity peaks in that area. [13].

Very simple boundaries are obtained when solving the equations in the Φ,Ψ plane. The flow field between 2 successive blades transforms into a trapezium in which the constant Φ,Ψ lines are parallel to the x and y axis . (Fig. 3) [14].

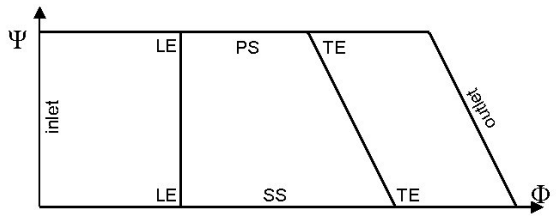

Fig. 3 Projection of a blade to blade flow passage on the Φ,Ψ plane.

The prescribed velocity distribution allows defining Φ and Ψ on the walls. The nonlinear flow equations are solved to find q and β on the boundary of the numerical domain so that the blade contour or streamlines can be defined by

$$x = \int_{\Psi=Cte} \frac{\cos\beta}{q} d\Phi \qquad y = \int_{\Psi=Cte} \frac{\sin\beta}{q} d\Phi$$

A third group of methods establishes the relation between a geometry (a circle) for which the flow-field is known and the required blade geometry. This conformal mapping method is at the origin of the well known Joukowski profiles and has been used by Lighthill [7], Papailiou [4].

Besides the limitations to 2D potential flow solvers the main drawback of the inverse methods is the difficulty to respect geometrical constraints, because the physical blade shape is available only in the very last step of the design procedure.

2.2 Iterative inverse design methods

A second group of inverse methods uses a procedure in which the numerical domain (and thus also the solution) is defined in an iterative way. These methods make use of existing numerical methods such as 2D and 3D Euler or Navier Stokes solvers or modified versions of them. Hence they cover a large group of applications including rotational- and viscous flows.

Iterative methods have been developed by [15,16] combining existing solvers with a shape modification routine based on the flow equations.

The classical boundary conditions used in flow analysis programs are inverted. Instead of

calculating the pressure distribution corresponding to zero normal velocity on the blade, they calculate the normal velocity corresponding to a prescribed velocity distribution. The resulting normal velocity distribution is then used to calculate a new blade shape by means of a transpiration technique.

This procedure is repeated until the analysis shows that the target is reached i.e. when the flow solver predicts a zero normal velocity. The method has been extended to compressible and viscous flows by [17,18,19]. The main advantages of this approach are that one can make use of existing numerical methods such as Euler or Navier Stokes solvers and that the same method can be used for design and off-design analysis by adapting the inlet or outlet conditions

An other advantage of this approach is that one can follow the evolution of the geometry changes and interfere when the geometry starts violating the mechanical constraints. In that case one can obtain a geometry that is as close as possible to the optimum one without violating the constraints.

Volpe [20] and Demeulenaere [21] describe iterative procedures in which the target is modified during the procedure until the mechanical constraints are satisfied. An other way out is the use of an hybrid method whereby the optimum velocity distribution is imposed on one side only together with a prescribed blade thickness distribution.

Inverse methods allow a detailed definition of the local flow and have shown to lead to improved blade shapes [22,23].

Figure 4 shows a comparison between the initial Mach number distribution and the shock free one obtained by inverse design. The less optimal pressure side distribution is a consequence of the hybrid method in which only the suction side Mach number and the blade thickness distribution are imposed.

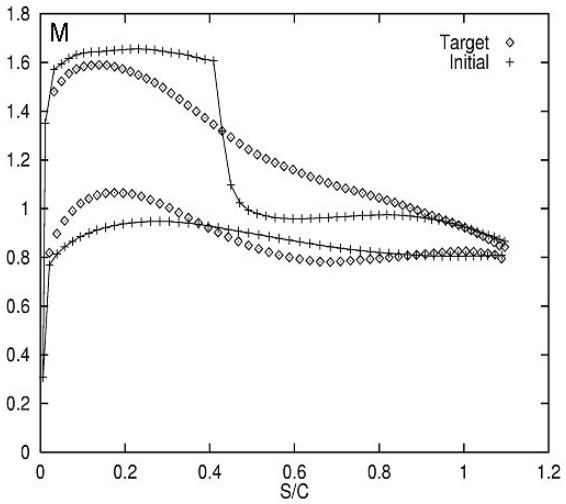

Fig. 4 Mach number distribution on shock free transonic blade with controlled blade thickness versus original Mach number distribution.

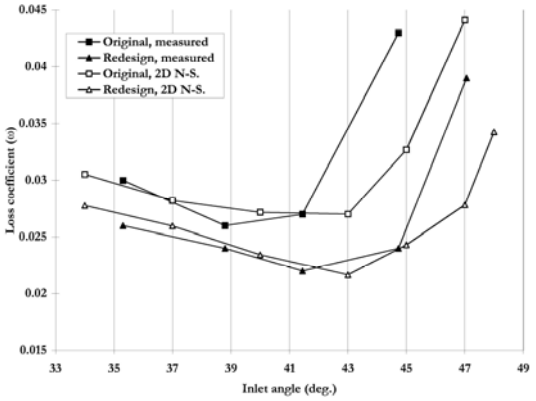

Fig. 5 Total pressure losses with original and redesigned controlled diffusion blade.

Fig. 5 compares the total pressure losses of a low speed compressor blade before and after redesign by an inverse method. [22]

Iterative inverse methods are very well suited to make a first definition of the blade section before stacking them into a 3D geometry for further optimization.

3. OPTIMIZATION METHODS

Optimization methods attempt to determine the design variables X_i^* $(i=1,N)$ that minimize an object function $OF(U(X_i),X_i)$ where $U(X_i)$ is the solution of the flow equations $R(U(X_i),X_{i.})=0$ and subject to the aerodynamic constraints $A_j(U(X_i),X_{i.}) \leq 0$ $(j=1,N_A)$ and geometrical constraints $G_k(X_{i.}) \leq 0$ $(k=1,N_g)$.

Specifying as objective function the difference between a prescribed and calculated pressure distribution, results in an inverse method. Aiming to improve a global performance parameter such as efficiency or work output, results in a global optimization technique.

Numerical optimization procedures consist following items, described in next paragraphs:

* Choice of independent design parameters, definition of constraints and limitation of the addressable part of the design space
* Choice of an objective function (lift, drag, velocity error function, cost, ..)
* Search mechanism to find the optimum combination of the design parameters.

3.1 Parameterization

The number of coordinates needed to completely define an arbitrary geometry is infinite and a direct definition of all of them by a numerical optimization procedure is not feasible. It is required to reduce the number of variables by an adequate parameterization of the geometry. This parameterization should be sufficiently general, not to impose unwanted restrictions on the geometry, but also sufficiently simple, to limit the number of variables to be defined.

Most optimization methods make use of Bézier curves to describe the geometry. This assures smoothness of the surface and facilitates the transfer of the data to CAD-CAM systems. It is important not to exclude any physical acceptable geometry. Any blade shape that can not be generated can also not be found by the optimizer even if it is the optimum one. Pierret [24] shows that between 15 and 20 parameters are needed to simulate all possible turbine blade shapes. A selection of them is shown on Fig. 6.

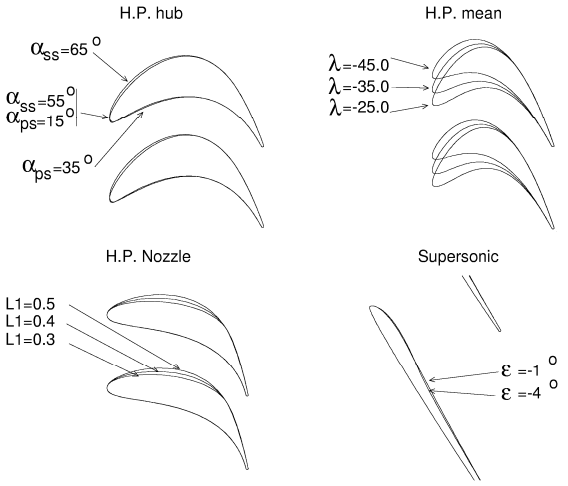

Fig. 6 Turbine blade sections generated by a 17 parameter model.

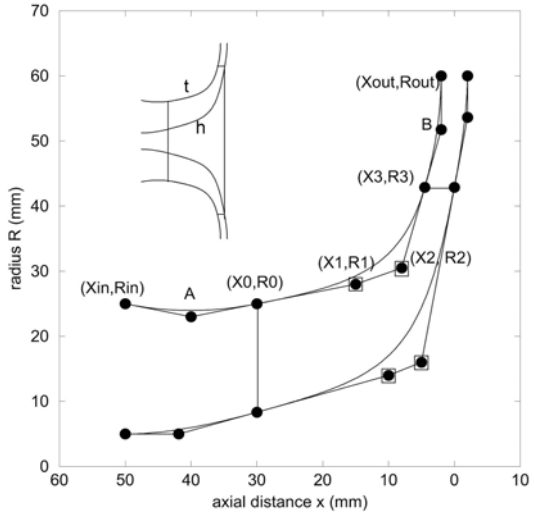

Fig. 7 Parameterization of meridional contour.

The 3D geometry parameterization of Alsalihi et al., [25] requires up to 27 parameters for a 3D radial impeller with splitter vanes.

The hub and tip meridional contours are defined by third order Bézier curves, between the leading edge and trailing edge section with second-order extensions upstream and downstream (Fig. 7). The points (X0,R0) and (X3,R3) are prescribed. They are the result of a preliminary 1D design where one may also account for the off-design operation. The unknown that need to be defined during the optimization process are the values of (X1,R1) and (X2,R2) at hub and tip.

The blade camber line at hub and tip are defined by cubic Bézier curves in Bernstein polynomial form $\beta=\beta_0+\beta_1.u+\beta_2.u^2+\beta_3.u^3$

β_0 is the blade metal angle at the leading edge (u=0.). β_3 is the blade trailing edge metal angle (u=1).

Extra curves may be needed for the splitter vanes

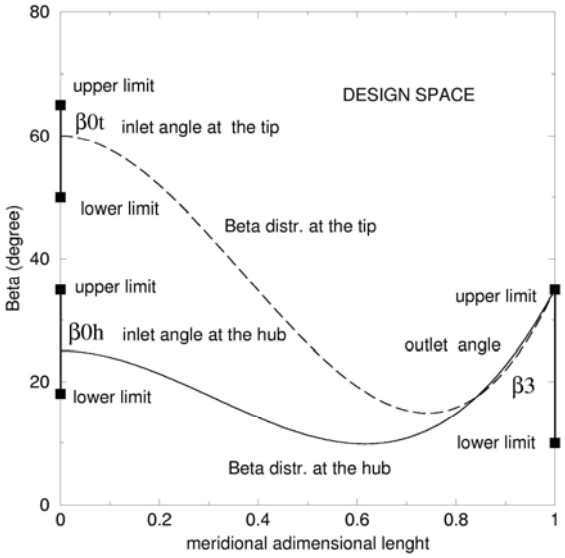

Fig**. 8 Blade angle variation at hub and shroud.**

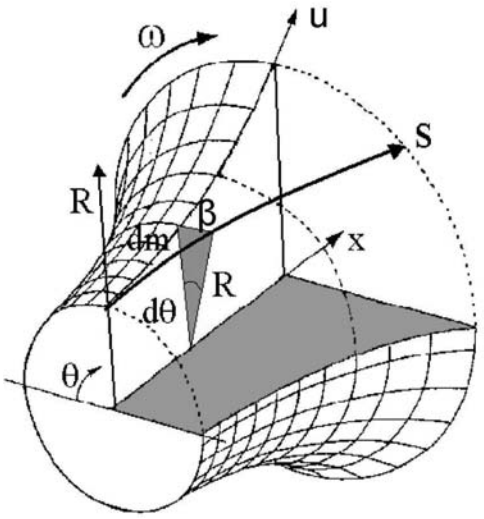

Fig. 9 Parameterization of meridional contour and blade angle β distribution.

The coordinate θ of the blade camber line is computed from the optimized distribution of the blade angle β (Fig. 9).

The impeller geometry definition is completed by a thickness distribution, number of blades and parameters defining the diffuser geometry.

The design parameters can be constrained to realistic values which also accelerates the convergence. The shroud radius (Fig.7) must be larger than R0t because otherwise the impeller can not be mounted. In order to avoid that the impeller exit bends forward, one imposes that X2t and X2h are smaller than or equal to X3t and X3h. The leading and trailing edge blade angles β_0 and β_3 can vary over $\pm 5.^o$ around a first estimate of the optimum value (Fig. 8). Values of β_1 and β_2 are not limited but the values of θ_3, obtained by integrating β along hub and shroud, should not be too different, i.e. the corresponding trailing edge rake angle defined by atan(R3(θ_{3h}-θ_{3t})/b3 should be less than $45.^o$.

3.2 Search mechanisms

There are two groups of search mechanisms:

* Analytical ones, calculating the geometry changes in a deterministic way from the output of the performance evaluator. They are mostly based on gradient calculations.
* Zero order or stochastic procedures, simulating the evolution of a physical process such as the surviving of the fittest in nature or the solidification of molten metal.

3.2.1 Gradient method

These optimization algorithms define the steps $dX_i=X_i^{m+1}- X_i^m$ $i=1,N$ leading to the optimum design parameters X_i^* $(i=1,N)$ i.e. the set of variables for which the objective function $OF(U(X_i),X_i)$ is minimum. *A* comprehensive overview of gradient based optimization techniques is given by Vanderplaats [26]. A common one is the steepest descend method simulating the descend towards a valley in the dark by following the path with the steepest downward slope (Fig. 10).

It requires of following steps

* Definition of the direction of the steepest descend for the objective function.
* Definition of the step length leading to the minimum of the objective function in that direction.
* Evaluation of the performance in the new position and verification of convergence.

These three steps are repeated until the minimum objective function or the limit of a design parameter is reached.

The procedure may get stuck in a local minimum where all the derivatives of the objective function are zero. Hence there is no logical way to proceed. This situation can be avoided/remediated by restarting the procedure from different initial geometries.

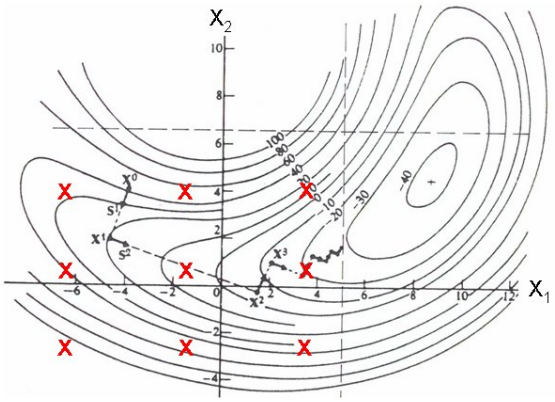

Fig. 10 Graphical presentation of an objective function of two parameters.

Since U is a function of X, the flow governing equation $U(X)$ must be solved each time a design parameter is changed. Hence the calculation of the gradient by finite differences

$$\nabla OF_i = \frac{OF\left(U(X_i + \Delta X_i), X_i + \Delta X_i\right) - OF(U(X_i), X_i)}{\Delta X_i}$$

requires $N+1$ evaluations at each step. This is feasible only if the evaluation is sufficiently fast. The number of evaluations is N_{steps}*(N+1) and the required computer effort may become prohibitive if the performance evaluations require a 3D Navier Stokes analysis on a large number of grid points.

An attractive alternative is the use of the adjoint variables method [27]. It allows calculating the gradient by a single calculation requiring the same effort as one Navier-Stokes calculation. The Taylor series development of the flow equation

$$R(U + \varepsilon\tilde{U}, X + \varepsilon\tilde{X}) = R(U, X) + \frac{\partial R(U, X)}{\partial X}\varepsilon\tilde{X} + \frac{\partial R(U, X)}{\partial U}\varepsilon\tilde{U} + O(\varepsilon^2) = 0$$

reduces to

$$\frac{\partial R}{\partial X}\varepsilon\tilde{X} + \frac{\partial R}{\partial U}\varepsilon\tilde{U} + O(\varepsilon^2) = 0$$

Further

$$\nabla_X^T OF . \varepsilon X = \frac{\partial OF}{\partial X}\varepsilon\tilde{X} + \frac{\partial OF}{\partial U}\varepsilon\tilde{U}$$

Combining both equations results in:

$$\nabla_X^T OF . \varepsilon\tilde{X} = \left(\frac{\partial OF}{\partial X} - \psi^T\frac{\partial R}{\partial X}\right)\varepsilon\tilde{X} + \left(\frac{\partial OF}{\partial U} - \psi^T\frac{\partial R}{\partial U}\right)\varepsilon\tilde{U}$$

Imposing that:

$$\frac{\partial OF}{\partial U} - \psi^T\frac{\partial R}{\partial U} = 0$$

allows calculating ψ^T for which the gradient can be calculated as a function of X only

$$\nabla_X^T OF = \left(\frac{\partial OF}{\partial X} - \psi^T\frac{\partial R}{\partial X}\right)\varepsilon\tilde{X}$$

This mathematically rather complex method is of interest only in combination with implicit solvers. It still requires a full solution at each optimisation step and at least a similar amount of

computational effort, using the transpose of the Jacobian of the implicit solver, to calculate the gradient.

This approach has first been developed for single airfoil design. The main difference with turbomachinery component designs is that the objective function is no longer depending on the flow characteristics on the wing surface but on the losses and flow characteristics far downstream the impeller [27].

3.2.2 Zero order search

The use of numerical algorithms to minimize the object function requires a large number of flowfield analyses and does not favor an optimum use of computer resources. An alternative are zero order optimization methods requiring only function evaluations and no derivatives. They do a random- or systematic sweep or use genetic algorithms and simulated annealing.

A systematic sweep, defining v values between the maximum and minimum limits of each of the N design variable requires v^N function evaluations. Fig. 10 illustrates how such a sweep of the design space by calculating the OF for 3 different values of X_1 and X_2 provides a very good estimation of where the optimum geometries with only 9 function evaluations. This is a valid alternative for gradient methods when N is small but requires more than 14. 10^6 calculations for $N=15$.

Evolutionary strategies such as Genetic Algorithms and Simulated Annealing may allow a drastic acceleration of the procedure by replacing the systematic sweep by a more intelligent selection of new geometries using information obtained during previous calculations.

Simutated Annealing is derived from the annealing of solids. At a given temperature, the state of the system varies randomly. If a state results in a lower energy level, it is immediately accepted. If however, a higher state results from the variation, it is only accepted with the probability Pr that is function of the temperature.

$$Pr = exp\frac{(E_{opt} - E_{act})}{T}$$

As the temperature decreases, the probability of accepting a higher state becomes lower. In a simulated annealing algorithm, the design parameters characterise the state of the system whereas the objective function characterises the energy level.

Genetic Algorithm (GA)

A Genetic Algorithm (GA) is a numerical technique, simulating Darwin's evolutionary theory, to find the optimum. According to this theory, an individual (a geometry) with favorable genetic characteristics (design variables) will most likely produce more performant offsprings. By selecting them as parent, the next generation will have better individuals than the previous one.

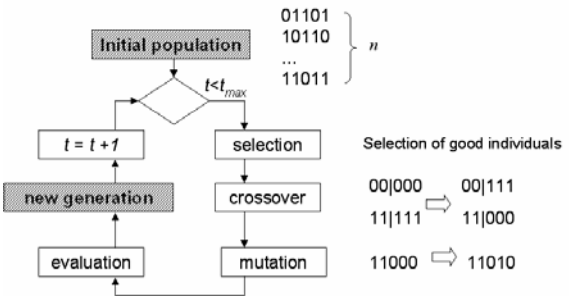

Fig. 11 Working principle of a GA.

The operational principle of a standard GA is shown in Fig. 11 . Pairs of individuals (parents) are selected from an initially random population of n designs, each represented by a binary coded string of length l. Genetic material is subsequently exchanged between them (crossover) and altered within the child (mutation). This process is repeated to create the n individuals of the new generation. This is repeated for t generations.

The quality of the GA optimizer depends on:

* the required computational effort i.e. the number of performance evaluations that are needed to find that optimum (GA efficiency).
* the value of the optimum (GA effectiveness).

A correct setting of the GA parameters is therefore very important to reach the real optimum with minimum effort.

The GA software used in the VKI design system is the one developed by David L. Carroll [28]. The "optimum parameter settings" proposed by the author have been verified and adapted by means of a systematic study on two typical design cases: one defined by 7 parameters and one defined by 27 parameters [29]. Conclusions are based on the solution quality q, measuring the degree to what the GA optimum approaches the real one within a given effort (5000 function evaluations). It is defined by:

$$q = \frac{OF_{AV} - OF_{GA}}{OF_{AV} - OF_{min}} \cdot 100$$

where:

OF_{AV} is the average of the objective function over the complete design space.

OF_{min} is the global minimum value of the objective function obtained from a systematic (numerically very expensive) scanning of the whole design space.

OF_{GA} is the minimum obtained from the GA optimization.

A q value of 100% indicates that the global minimum value has been found. The function evaluations for the numerical experiments are made by means of a metafunction (approximation of the NS solver based on ANN (explained in section 4.1).

Optimum substring length:

In a standard binary-coded GA, the N real-valued design parameters X_1, defining a geometry, are jointly represented by one binary string:

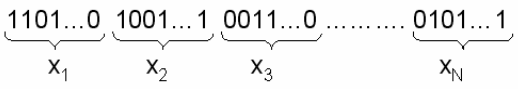

The substring length, denoted by l (number of bits per variable), determines the total number of values (2^l) each design parameter can take.

The minimum substring length l_i for the i^{th} design variable depends on the upper and lower bound respectively x_{imin} and x_{imax}, as well as on the desired resolution (ε_i) for this variable:

$$l_i = \log_2 \frac{x_i^{min} - x_i^{max}}{\varepsilon_i}$$

Very short substrings ($l < 3$) result in a very low resolution and the GA is not able to accurately approach the global minimum. Longer substrings ($3 < l < 10$) enable a sufficiently high resolution but cause a larger search space and make it difficult to find the complete optimal binary string. It is concluded that $l = 8$ is the optimum substring length independent of the number of unknown parameters.

Selection scheme

Different selection schemes can be used. One is the roulette: a system in which the chance that a individual is selected increases proportional with its fitness ($1/OF$). This scheme favors the best individuals

In the tournament selection, "s" individuals are chosen randomly from the population and the individual with the highest fitness (lowest OF) is selected as parent. The same process is repeated to find the second parent. The parameter s is called the tournament size and can take values between 1 and n (population size). Large values of s give more chances to the best samples to create off-springs and favor a rapid, but maybe premature, convergence to a local optimum. Too small values of s result in a random selection of parents. The standard value of s=2 turns out to be the best.

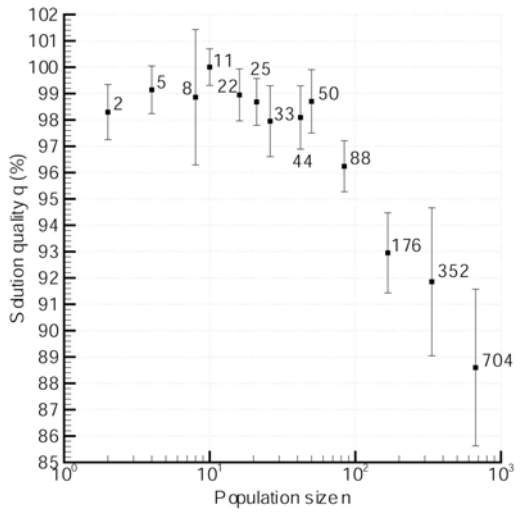

Fig. 12 Dependence of GA solution quality on population size for the 27 parameter test case.

Population size

Fixing the total number of function evaluations to 5000, the number of generations t is a consequence of the population size n (n.t=5000). Fig. 12 shows the solution quality at the end of the GA run of the test case. The solution quality is maximum for n = 11 to 20. Small populations (n<10) converge prematurely to suboptimal solutions, due to a lack of high performing samples in the initial population. Larger populations (n>25) have a sluggish convergence to the optimal geometry because less generations are allowed

Crossover probability

In a single-point crossover operator, both parent strings are cut at a random place and the right-side portions of both strings are swapped with the probability p_c (Fig. 11). In case of uniform crossover, the value of p_c defines the probability that crossover is applied per bit of the parent strings. High values of p_c increase mixing of string parts and at the same time, increase disruption of good string parts. Experiments confirm that a single point crossover with probability p_c=0.5 is optimal.

Mutation probability

The mutation operator creates new individuals by changing a "1" to a "0" or vice versa in the child strings. The mutation probability p_m is defined as the probability a bit of a child string is flipped. Systematic numerical experiments confirm that the optimum setting for the mutation probability is $p_m = 1/(n.l)$ for all optimizations This corresponds to changing on average one bit at every generation.

Creep mutation and Gray coding

Changing one digit in binary coding may result in a large variation of the digital value: i.e. the small difference between 0111 and 1111 corresponds to a doubling of the digital value. Small variations of the digital value may require a large number of binary digits to be changed: i.e. 0111 and 1000 are adjacent digital values but all four digits are different. This discontinuous relation between the digital value and binary string may confuse the GA optimizer. Creep mutation tries to avoid this by limiting the change of the real value to a binary step length.

Gray coding uses an algorithm in which similar binary strings correspond to adjacent digital values. In contrast to what was expected, the previous methods showed slower convergence for all test cases.

Fig. 13 shows how the optimization of the GA parameter settings has lead to an improved and smoother GA convergence.

3.3 Objective function

The objective function measures in how far the geometry satisfies the aero-requirements and reaches the performance goals that have been set forward

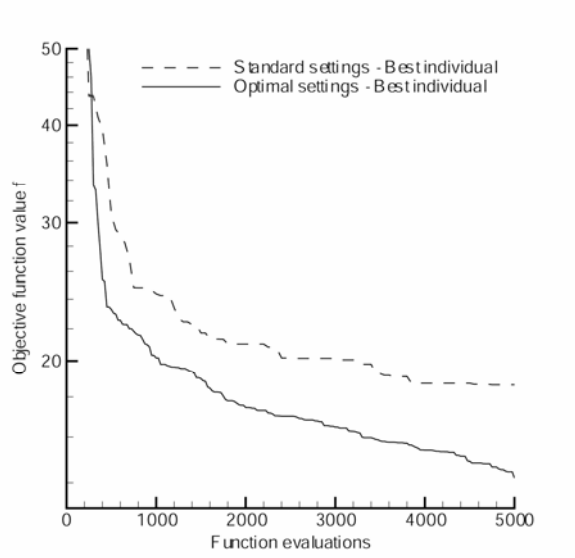

Fig. 13 GA convergence for a for the 27 parameter test case (standard versus optimized parameter setting).

High aero performance is not the only design objective of an optimization. A good design must also provide good off-design performance (multipoint optimization) and respect the mechanical and manufacturing constraints (multidisciplinary optimization). Some constraints must be satisfied without any compromise (i.e. maximum stress level) whereas others tolerate some margin (i.e. cost or weight) or can be corrected for after the design is finished (adjusting the blade height to achieve the required mass flow).

The first type of constraints will be discussed in section 6. A possible approach to the second group is the definition of a pseudo-objective function (OF) by summing up penalty terms that are increasing when the constraints are violated [24]. Each term is multiplied by a weight factor to change its relative importance in the optimization procedure.

Following lists some contributions to the global objective function that one has been using in different applications:

$$OF_{2D} = w_a \cdot P_{aeroBC} + w_M \cdot P_{Mach} + w_d \cdot P_{discharge} + w_G \cdot P_{Geom} + w_S \cdot P_{Side}$$

$\boldsymbol{P_{perf}}$ is the penalty for non optimum performance i.e. it increases for lower efficiency (η)

$$P_{perf} = \boldsymbol{max}\left[|1-\eta|, 0.0\right]$$

$\boldsymbol{P_{AeroBC}}$ is the penalty for violating the aerodynamic boundary conditions. The purpose of this penalty is to enforce the boundary conditions or requirements at the inlet and outlet of the computational domain, that cannot be imposed such as the outlet flow angle (β_2), the mass flow, etc. The penalties for not respecting boundary conditions start increasing when the actual values differ from the target values by more than a predefined tolerance. For mass flow one often uses following expression:

$$P_{mass} = w_i \cdot \left[\max\left(\left|\dot{m}_{act} - \dot{m}_{req}\right| / \dot{m}_{req} - .02\ ,\ 0.\right)\right]^2$$

resulting in an increasing penalty when the mass flow error exceeds 2% .

This formulation does not guarantee that the constraints will be satisfied in a strict way. An increase of the *OF* because of violating a constraint could be compensated by a decrease of another penalty term. However it has the advantage that the geometries violating the constraints are still available to drive the geometry back to the feasible domain.

$\boldsymbol{P_{Mach}}$ is the penalty for non-optimum Mach number distribution. Analyzing the Mach number distribution may help to rank blades that have nearly the same loss coefficient. Navier Stokes solvers are not always reliable in terms of transition modeling and large discontinuous variations of penalty function may occur when the location of the transition point is changing. Transition criteria based on Mach number distribution may help to relieve this uncertainty.

One must avoid designing blades that have very good performance at design point but are likely to separate (with high losses) at slightly off design conditions. One way of achieving this is discussed in section 5. A simpler approach accounts for the changes on the Mach number distribution that can be expected at off-design. This increases the chances for good performance of the blade over a wide range of operating conditions without the cost of extra Navier-Stokes computations.

Different Mach number penalties have been formulated for turbine blade optimizations [24]. They tend to achieve a continuous flow acceleration with a minimum of deceleration

$\boldsymbol{P_{discharge}}$ penalizes the spanwise distortion of the flow at the exit because a more uniform flow has a favorable effect on the downstream diffuser or next blade row inlet flow angle and hence on stage efficiency.

$\boldsymbol{P_{Geom}}$ is the penalty for violating the geometrical constraints. These are the constraints that do not influence the mechanical integrity but assure dimensional agreement with other components.

$\boldsymbol{P_{Side}}$ is the penalty for violating the side constraints. Depending on the application, weight, manufacturing and maintenance cost may be important issues and some geometries can be favored by formulating an appropriate penalty.

The balance between the different objectives may not be clear from the beginning. The different *OF* can then be plotted in the fitness space (Fig. 14) on which the Pareto curve allows a tradeoff between the two goals. This approach is useful for 2D or 3D problems where the Pareto front can be visualized. It is much more cumbersome in higher order problems or when the Pareto front is not convex.

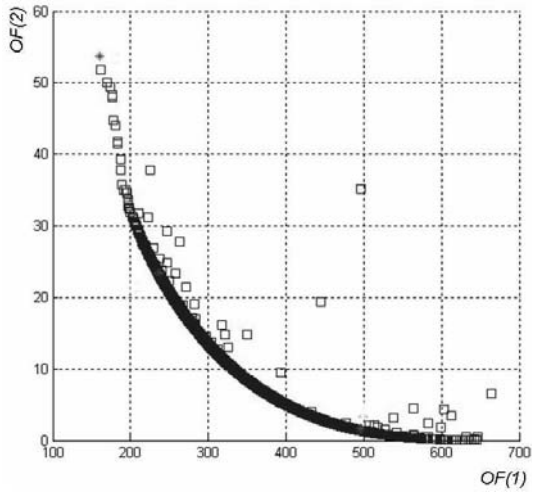

Fig. 14 Convex Pareto front.

4. TWO LEVEL OPTIMIZATION

Genetic algorithms require a large number of function evaluations and it may be prohitive expensive to us a Navier-Stokes solver for function evaluations.

One way to speed up the convergence is by working on different levels of sophistication and by using of the knowledge, gained during previous designs, for subsequent ones. Fast but approximate prediction methods are used to find a near optimum geometry, which is then further verified and refined by a more sophisticated but also more expensive solver. Approximations of the Navier Stokes solver, called meta-functions, are used for the first level optimization.

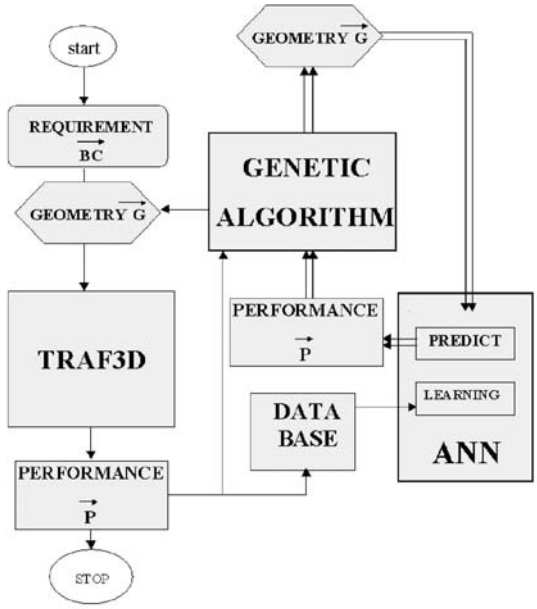

Fig. 15 Flowchart of optimization system.

The system developed and used at the von Karman Institute [24]. (Fig. 15) makes use of a Genetic Algorithm (GA) to minimize the objective function (*OF*). The input for the *OF* is predicted by means of an Artificial Neural Network (ANN). This interpolator uses the information contained in the DATABASE to correlate the performance to the geometry, similar to what is done by a Navier Stokes solver (NS). An ANN is a very fast predictor and allows evaluation of the *OF* of the many geometries generated by the GA with much less effort than a NS solver. Unfortunately the prediction is not always very accurate and the optimized geometry must be verified by means of a more accurate but time consuming NS solver TRAF3D [30]. The results of this verification are added to the DATABASE and a new optimization cycle is started. It is expected that the new learning on an extended DATABASE will result in a more accurate ANN. The optimization cycle is stopped once the ANN predictions are in agreement with the NS calculations i.e. once the GA optimization has been made with an accurate performance predictor. The main advantage of this method is the fact that, once the system is converged, there will be no discrepancy between the ANN prediction and the one obtained by a Navier Stokes calculation.

4.1 Artificial Neural Networks (ANN)

Artificial Neural Networks (ANN) are used to predict the performance of a new geometry by means of the information contained in the DATABASE. This requires the learning of the relation between the input data (geometry) of a process (Navier Stokes solver) and the output of the process (mass flow, efficiency, local pressures and temperatures, velocities, etc.). An exact ANN prediction would even reduce the effort to one design cycle. Hence a more accurate ANN will shorten the design procedure.

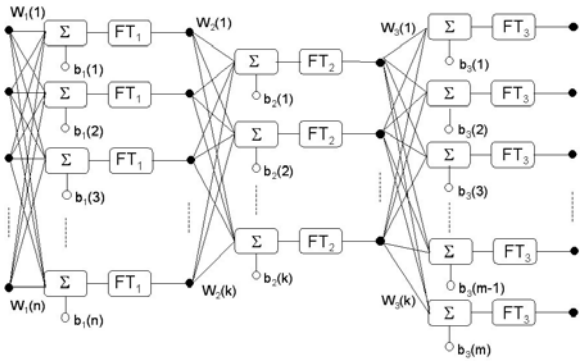

Fig. 16 Artificial Neural Network architecture.

An Artificial Neural Network (ANN) (Fig. 16) is composed of several elementary processing units called neurons or nodes. These nodes are organized in layers and joined with connections (synapses) of different intensity, called the connection weight (W) to form a parallel architecture. Each node performs two operations: the first one is the summation of all

the incoming signals and the second one is the transformation of the signal by using a transfer function.

$$a_1(i) = FT_1\left(\sum_{j=1}^{n} W_1(i,j)p(j) + b_1(i)\right)$$

A network is generally composed of several layers; an input layer, zero, one or more hidden layers and one output layer. The coefficients are defined by a LEARNING procedure relating the output to the input data

The purpose of ANN is not to reproduce the existing database with maximum accuracy but to predict the performance of new geometries it has not seen before i.e. to generalize. Three conditions are necessary, although not sufficient, for good generalization:

The first one is that the inputs to the ANN contain sufficient information pertaining to the target, so that one can define a mathematical function relating correctly outputs to inputs with the desired degree of accuracy. The designer should select design parameters that are relevant, i.e. that have an influence on performance

The second one is that the function to be learned (relating inputs to the correct outputs) is smooth. In other words, a small change in the inputs should, produce a small change in the outputs. Most physical problems are well defined in this respect.

The third one requires that the training set is a sufficiently large and a representative sample of all cases that one wants to generalize (the "population" in statistical terminology).

The standard back propagation is the most widely used and criticized learning algorithm in the Artificial Neural Network literature.

In ANN learning the available samples are normally subdivided into "training", "test" and "validation" sets. Each of them has its own purpose.

* The Training set contains the samples used for learning; that is to fit the parameters (i.e., weights) of the classifier.
* The Test set contains the samples used only to assess the performance (generalization) of a fully-specified ANN (given weights and architecture).
* The Validation set contains the samples used to tune the parameters (i.e., architecture, not the weights) of a classifier, for example to choose the number of hidden units in a neural network.

4.2 DATABASE

The main purpose of the DATABASE is to provide information about the relation between the geometry and performance. The more general and complete this information, the more accurate may be the ANN and the closer the first optimized geometry will be to the real optimum. Hence a good database may considerably speed up the convergence to the optimum.

Making a database is an expensive operation because it requires a large number of 3D Navier Stokes calculations. One is interested in making the smallest possible database containing the maximum amount of information about the whole design domain. This means relevant information with a minimum of redundancy i.e. the impact of every design parameter is included but only once.

Any information missing in the database may introduce an erroneous ANN that could drive the GA into a geometry that is not optimum. This is not a problem because the Navier Stokes analysis of that geometry will provide the missing information when it is added to the database. However the worst case is when an incomplete database results in an erroneous extrapolation by the ANN predicting a low performance (large *OF*) in that part of the design domain where in reality the *OF* is low. As a consequence, the corresponding geometry will never be selected by the GA and the error may never been corrected. It is therefore important to assure that the initial database covers the whole design domain.

Design Of Experiment (DOE) refers to the process of planning an experiment so that the appropriate data, when analyzed by statistical methods, result in valid and objective conclusions. It is used in the optimization process to select the most significant geometries that will be stored in the database. The theory of DOE is explained in many excellent textbooks [31]. The advantages of using DOE, to construct the database for the VKI optimization program, has been evaluated in detail by [32]

Factorial designs are widely used in experiments where it is necessary to study the effect of different factors on a response. The most important one is where each of the k factors has only two values corresponding to the “high” or “low” levels of a design variable. A complete replicate of such a design requires 2^k observation and is called full factorial design.

Following illustrates the loss of information by comparing the ANN predictions, based on different fractional factorial designed databases with the exact values for the following test function with 6 variables:

$$R=1-0{,}001(A-D)^3 + 0{,}002(C+E)(F-B) - 0{,}06(A-F)^2 (F+C)(E+A)$$

The results of the databases defined by DOE are compared to those of databases in which the geometrical parameters are randomly generated between the prescribed boundaries.

The full factorial design requires $2^6 = 64$ runs to estimate all possible parameter combinations. The loss of information is measured by the following error term,

$$error = \sum_{i=1}^{n-samples} \frac{exact\ \ value - predicted\ \ value}{exact\ \ value}.100$$

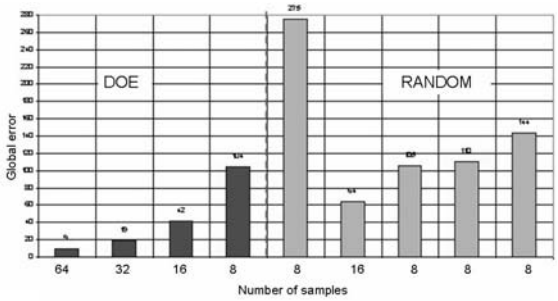

Fig. 17 ANN's global error in function of Database samples.

Comparing the error obtained by means of the DOE technique and by means of randomly selected samples (Fig. 17), it becomes clear that the DOE based predictions are consistently more accurate for the same number of samples in the database.

Randomly generated databases are all different and so is the accuracy of the results. The four randomly generated cases with 8 samples in the database, show an error that varies between 105 (what is the same as the DOE defined database) up to an error that is almost 3 times larger (first randomly generated 8 sample database).

Only 2-level designs (every variable can take two values) and one central-point run (every value is at the center of the allowed range) are considered.

The high and low value of each design variable are located at 75 and 25% of the parameter's range. The central point is the mid value (50%). The range is defined by the designer, based on his experience about feasible geometries and mechanical constraints.

5. MUTLTIPOINT OPTIMIZATION OF LOW SOLIDITY DIFFUSER

The radial compressor vaned diffusers provide high pressure recovery and efficiency but the operating range is limited by stall, at positive incidence and diffuser throat choking, at negative incidence. Low Solidity Diffusers (LSD) are characterized by a small number of short vanes and do not show a well defined throat section. They intend to stabilize the flow at low mass flow (avoiding diffuser stall) without limiting the maximum mass flow by choking. The solidity (chord/pitch) is typically of the order of 1 or less (Fig. 18). A multipoint optimization is mandatory for the LSD design because a wide operating range is the major target.

Table 1 Inlet conditions at the 3 operating points

	Low m	Medium m	Large m
β (°)	68.	60.	54.
P^o_2 (Pa)	218395.	213447.	187666.
P_3/P^o_2	.9157	.9276	.9430
T^o_2 (K)	365.4	360.3	350.4

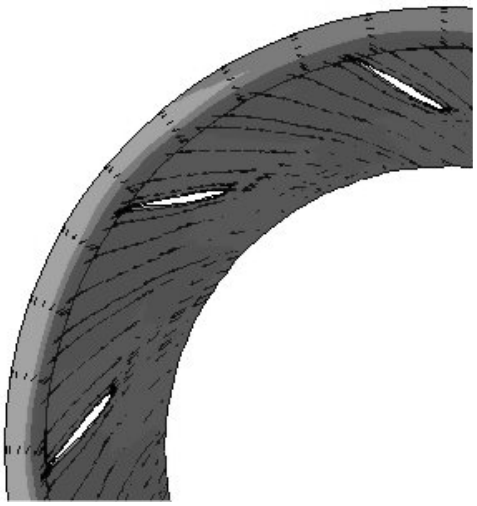

Fig. 18 Low Solidity Diffuser.

The optimization of the LSD is done for the 3 operating points listed in table 1 . Inlet conditions are different for each operating point because they result from a different operation point of the impeller. Hence the mass flow will be different for every geometry.

The blade geometry is defined by a NACA thickness distribution superposed on a camber line defined by a 4 parameter Bézier curve. The 5th design parameter is a scale factor for the NACA thickness distribution (between .7 and 1.3). The 6th parameter is the number of blades (between 6 and 21).

The main performance parameters are the static pressure rise- and total pressure loss coefficient

$$Cp = \frac{\overline{P}_3 - \overline{P}_2}{\overline{P}^o{}_2 - \overline{P}_2} \qquad \omega = \frac{\overline{P}^o{}_2 - \overline{P}^o{}_3}{\overline{P}^o{}_2 - \overline{P}_2}$$

They are calculated from the 3D Navier Stokes results obtained by means of the TRAF3D solver on a grid with 400 000. cells (Fig. 19)

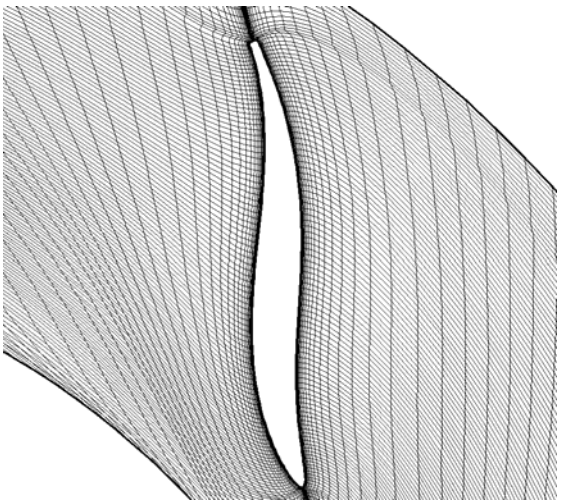

Fig.19 Typical LSD vane and grid.

Making the DATABASE is quite costly because it requires to analyze each geometry at three operating points. The initial DATABASE is therefore limited to only 10 randomly generated samples requiring 30 Navier Stokes calculations.

Cp is imposed and cannot be used as a criterion for the optimization. One must also take into account the losses that are generated to reach that pressure rise. Taking into account that

$$Cp + \omega = Cp_{isentropic}$$

it is clear that the losses are a measure of the degree to which *Cp* approximates the isentropic *Cp*. One wants to achieve the pressure rise with minimum loss to keep the maximum kinetic energy available for the downstream components.

The best results have been obtained with following objective function

$$OF = \left(1 - \left(w_{low}.Cp_{low} + w_{med}.Cp_{med} + w_{high}.Cp_{high} \right)\right) + w_{low}.\omega_{low} + w_{med}.\omega_{med} + w_{high}.\omega_{high}$$

$$w_{low} = .25 \qquad w_{med} = .5 \qquad w_{high} = .25$$

The fastest convergence has been obtained by using three different ANN to predict separately the performance at the three operating points.

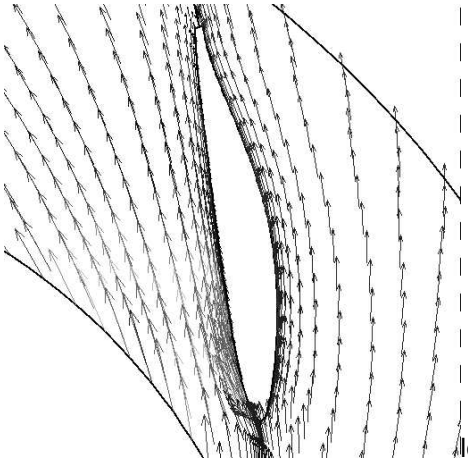

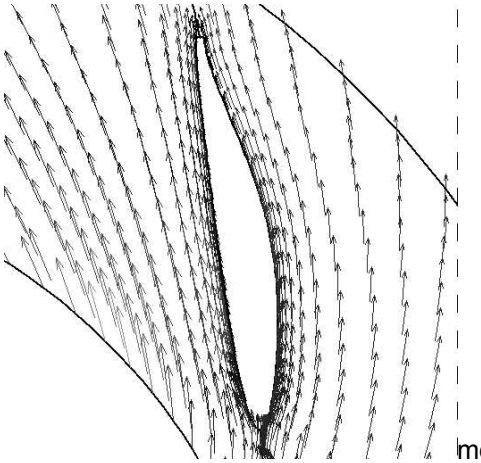

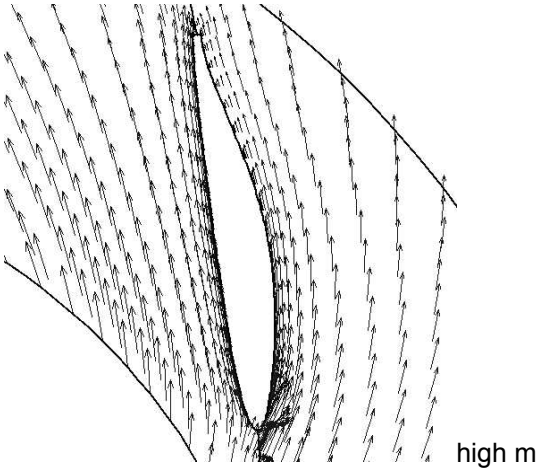

Fig. 20 Midspan velocity vector of optimized diffuser.

The velocity vectors at midspan, shown on Fig. 20, indicate attached flow at the 3 operating points and hence stable operation at low mass flow and large pressure rise at high mass flow.

6. MULTIDISCIPLINARY OPTIMIZATION.

Most mechanical constraints such as maximum stress and deformation have a direct impact on the turbomachinery integrity and must therefore be rigorously respected. Hence they cannot be imposed by a weak formulation as done for the geometrical constraints. The geometries that are violating them arre eliminated from the optimization process by associating a very large *OF* to them.

Some of those constraints can be respected by a simple limitation of a design parameter and do not create problems. Bird ingestion resistance defines a minimum leading edge radius (R_{LE}) . Corrosion may define the minimum trailing edge radius (R_{TE}) and blade thickness.

However most of the mechanically unacceptable geometries result from a combination of different parameters and cannot be avoided by reducing the feasible range of the individual design parameters. A possible approach is a verification of the mechanical constraints by a Finite Element Analysis (FEA) before starting the aero analysis on every geometry proposed by the GA. This sequential analysis is very time consuming and is being replaced by a parallel analysis shown on Fig. 21. It is an extension of the flow chart shown in Fig. 15. The GA, searching for the optimum geometry, gets its input from the Finite Element stress Analysis (FEA) as well as from the Navier Stokes flow analysis. The same type of extension could also be used to verify the other constraints related to acoustic or weight limitations.

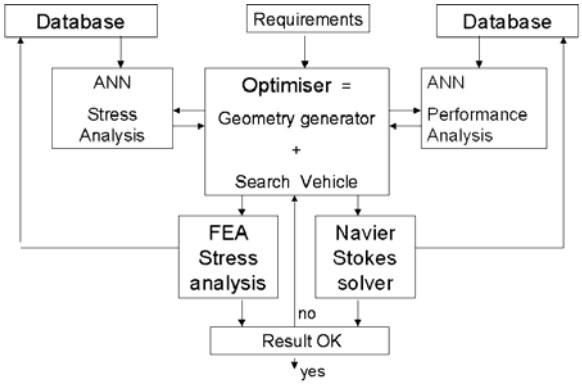

Fig.21 Multidisciplinary optimization flow chart.

The main advantages of such an approach are:

* The existence of only one "master" geometry i.e. the one defined by the geometrical parameters used in the GA optimizer. This eliminates all possible approximations and errors when transmitting the geometry from one discipline to an other.
* The existence of one objective function accounting for all disciplines. This allows a more direct convergence to the optimum geometry without iterations between the aerodynamically optimum geometry and the mechanically acceptable one.
* The possibility to do parallel calculations. The different analyses can be made in parallel if each discipline is independent i.e. if stress calculations do not need the pressure distribution on the vanes or flow calculations are not influenced by geometry deformations.

The computational effort increases proportional with the number of different analyses that are needed for the performance evaluation of the GA proposed geometries. It can be drastically reduced if one can eliminate the unfeasible geometries before any expensive flow analysis is started i.e. if, in analogy with the Aero analysis, one can formulate an approximate prediction model for mechanical characteristics. In practical applications the mechanical constraints can often be expressed as simple geometrical constraints. The parameters of primary importance in controlling the static and dynamic load on the axial compressor or turbine blade are: the 2D cross section area (Surface), the minimum momentum of inertia (I_{min}), the maximum momentum of inertia (I_{max}), the angle between the axis of minimum momentum of inertia and the axial direction (α_I).

The explicit FEA can also be replaced by simpler correlations. Analyzing some representative geometries it is possible to build a correlation defining the limits of the mechanically acceptable design space.

An important parameter in radial compressor and turbine design is the blade lean angle in the axial or radial part. The centrifugal forces create large stresses in the blade root section of non radial

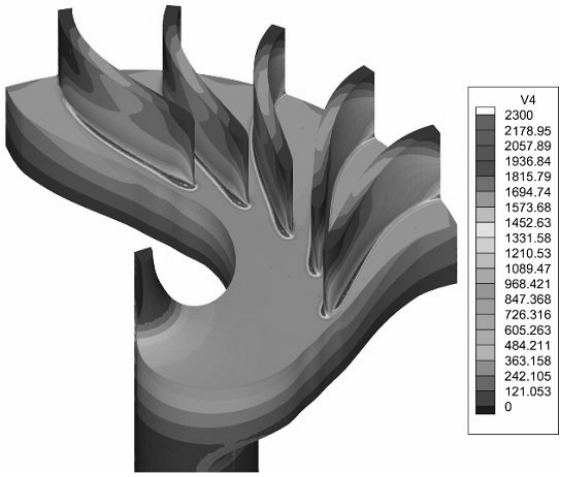

Fig. 22 2D rotor stress distribution (reference blade height and thickness).

blades and deformations that can reduce the tip clearance to zero which means the destruction of the optimized geometry.

The use of a simple stress correlation is illustrated for the 2D radial turbine impeller for micro-gasturbine applications shown on Fig. 22. Blade height and blade metal angle are two important parameters. The stress levels are highest at the turbine trailing edge where the centrifugal forces are almost perpendicular to the blades.

Fig. 23 shows the results of a systematic FEA study of the stresses in a turbine impeller for micro-gasturbine operating at 500 000. RPM. The material is Kersit (Silicium Nitride) For a given blade thickness, maximum stresses vary in function of the blade height and blade trailing edge angle β_{TE} . One observes an increase of stresses with increasing trailing edge angle because the centrifugal forces become more perpendicular to the blade. Larger blade height increases the stresses in the hub region because the blades have a larger overhang.

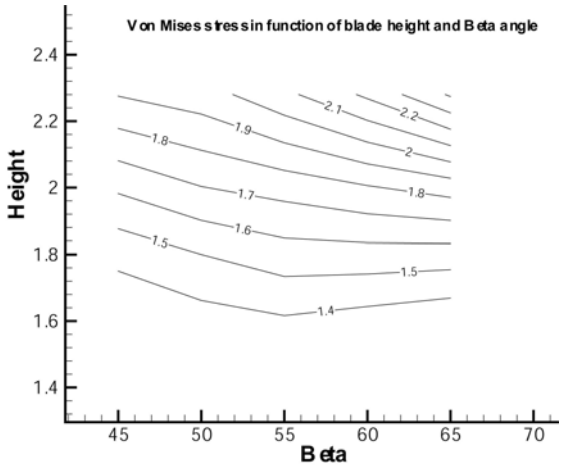

Fig.23 Variation of maximum stress as function of blade height and trailing edge angle β_{TE} .

Impellers with larger blade height are likely to perform better because of smaller clearance and friction losses. They need a larger trailing edge angles to control the mass flow and exit swirl. Hence geometrical changes have a direct impact on both the stresses and performance. Using this information in a way similar to the DATABASE for Aero-performance allows a rapid elimination of unfeasible geometries and drastically reduces the computational effort for the optimization.

7. CONCLUSIONS

The overview of the different methods illustrates the long history and large progress that has already been made in the domain of computerized Turbomachinery design. The following list of references is only a small selection from the available literature.

Inverse methods and the different optimization techniques are complementary.

Inverse design methods require a lot of input from the designer to guarantee good and realistic blades. However they allow very detailed interference in the flow.

The large improvements in computer capacity favour the more recent trend towards optimization techniques based on gradient methods or on evolutionary theories. They still require a huge amount of computer effort and present research is oriented towards

* more efficient techniques i.e. better convergence leading to less computer effort.
* more complete techniques allowing multipoint and multi-objective optimizations
* better integrated techniques i.e. multidisciplinary methods that are linked to the whole production process.

Optimization techniques already constitute a valuable support to designers but are useless without the input of the designer in terms of definition of objectives and constraints, as well as validation of results.

REFERENCES

[1] Thilmany J., 2000, Walkabout in another world, Mechanical Engineering revue, November.

[2] Lichtfuss H.J., 2004, "Customized Profiles – the Beginning of an Area", ASME GT2004-53742

[3] Lefoll J., 1965, " A Theory of representing the Properties of Boundary Layers on a Plane", Proc. Seminar on Advanced Problems in Turbomachinery, VKI.

[4] Papailiou K.D., 1971, "Boundary layer Optimization for the Design of High Turning Axial Flow Compressor Blades", Journal of Engineering for Power, pp. 147-155.

[5] Stratford B.S., 1959, "An Experimental Flow with zero Skin Friction throughout its Region of Pressure Rise" Journal of Fluid Mechanics, Vol. 5, pp. 17-35

[6] Sieverding C., 1985, "Subsonic Blading Design", VKI CN 124.

[7] Lighthill J.M., 1945, "A New Method of two dimensional Aerodynamic Design", ARC R&M 2112.

[8] Van den Braembussche R.A., 1964, "Inverse Design Methods for Axial and Radial Turbomachines", in: Numerical methods for Flow Calculation in Turbomachines, VKI-LS 1994-06.

[9] Hawthorne W.R., Than C.S., Wang C. and McCure J.E., 1984, "Theory of Blade Design for Large Deflections, Two-dimensional Cascades", ASME Journal for Gas-Turbines and Power, Vol. 106, pp. 346-353.

[10] Goto A. and Zangeneh M., 2002, "Hydrodynamic design of Pump Diffuser Using Inverse Design Method and CFD", ASME Journal Fluids Engineering, Vol. 124, pp.319-335.

[11] Van den Braembussche R.A., Demeulenaere and J. Borges, 1993, "Inverse Design of Radial Flow Impellers with prescribed Velocity at Hub and Shroud", AGARD CP 537, paper 18.

[12] Cantrell H.N. and Fowler J.E., 1958, "The aerodynamic Design of two-dimensional Turbine Cascades for Compressible Flow with High Speed Computer", ASME 58A141

[13] Sanz J.M., 1988, "Automated Design of Controlled Diffusion Blades", ASME Journal of Turbomachinery, Vol. 110, pp. 540-544.

[14] Schmidt E. 1980, "Computation of Supercritical Compressor and Turbine Cascades with a Design method for Transonic Flow", ASME Journal Engineering for Power, Vol. 102, pp 68-74.

[15] Murugesan, K and Railly J.W., 1969, "Pure method of two dimensional aerodynamic design", Journal Mechanical Engineering Science, Vol. 11, No5, pp. 454-464.

[16] Van den Braembussche, Leonard O. and Nekmouch L., 1989, "Subsonic and Transonic Blade Design by Means of Analysis Methods", AGARD CP 463, paper 9.

[17] Leonard O. and Van den Braembussche R.A., 1993, "Design Method for Subsonic and Transonic Cascade with Prescribed Mach Number Distribution", ASME Journal of Turbomachinery, Vol. 114, pp. 553-560.

[18]Demeulenaere A. and Van den Braembussche R.A., 1998, "Three Dimensional Inverse Design Methods for Turbomachinery Blading Design", ASME Journal of Turbomachinery, Vol. 120, pp.247-255.

[19]De Vito L., Van den Braembussche R.A. and Deconinck H., 2003, "A Novel Two-Dimensional Viscous Inverse Design Method fort Turbomachinery Blading", ASME Journal of Turbomachinery, pp. 310-316

[20]Volpe G., 1990, "Inverse Design of Airfoil Contours: Constraints, Numerical Method and Application", AGARD R 780, paper 4 and 5.

[21]Demeulenaere A. and Van den Braembussche R.A., 1999, "A New Compressor and Turbine Blade Design Method Based on Three-dimensional Euler Computations with Moving Boundaries", Intl. Journal on Inverse Problems in Engineering, Vol. 7 pp 235-266.

[22]Bogers P.F., Van den Braembussche R.A. and Breugelmans F.A.E., 1998, "Design and Experimental Verification of an Optimized Compressor Blade", ASME 98-GT-193.

[23]Starken H., 1989, "Design Criteria for Optimal Blading design", AGARD LS 167, paper 2.

[24]Pierret S. and Van den Braembussche R.A., 1999, "Turbomachinery Blading Design Using Navier Stokes Solver and Artificial Neural Network", ASME Journal of Turbomachinery, Vol. 121 pp. 326-332.

[25]Alsalihi Z. and Van den Braembussche R.A., 2002, "Evaluation of a Design Method for Radial Impellers based on Artificial Neural Network and Genetic Algorithm", Proc. of ESDA 2002, 6th Biennial Conference on Engineering Systems Design and Analysis, Istanbul,

[26]Vanderplaats G.N., 1984, "Numerical Optimization Techniques for Engineering Design", McGraw-Hill.

[27]Gauger N. and Mauss M., 2001, "Das Adjugiertenverfahren in der aerodynamischen Optimierung von Turbomaschinen", DLR bericht 129-2001/22.

[28]Carroll D.L. 2001, "FORTRAN Genetic Algorithm (GA) Driver version 1.7.1a ". available at URL:http:/cuaerospace.com/carroll/ga.html

[29]Harinck J., Alsalihi Z., Van Buytenen J.P. and Van den Braembussche R.A., 2005, "Optimization of a 3D Radial Turbine by means of an improved Genetic Algorithm", Proceedings of European Turbomachinery Conference, Lille.

[30]Arnone A., 1994, "Viscous Analysis of Three-dimensional Rotor low Using a Multigrid Method", ASME Journal of Turbomachinery, Vol. 116, pp. 435-445.

[31]Montgomery D.C., 1997, "Design of Experiments", John Willey & sons Inc.

[32]Kostrewa K., Van den Braembussche R.A. and Alsalihi Z., 2003, "Optimization of Radial Turbines by means of Design of Experiment", VKI PR 2003-17.

Workshop
Modelling of Turbomachinery Aerodynamics

presented at ***Conference on Modelling Fluid Flow (CMFF'06)***
The 13th International Conference on Fluid Flow Technologies
Budapest, Hungary, September 6-9, 2006

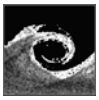

DEVELOPMENT OF IMPROVED BLADE TIP END-PLATE CONCEPTS FOR LOW-NOISE OPERATION IN INDUSTRIAL FANS

Alessandro CORSINI[1], Franco RISPOLI[2], A. Geoff SHEARD[3]

[1] Corresponding Author. Dipartimento di Meccanica e Aeronautica, University of Rome "La Sapienza". Via Eudossiana 18, I00184 Rome, Italy. Tel.: +39 06 44585231, Fax: +39 06 4881759, E-mail: alessandro.corsini@uniroma1.it
[2] Dipartimento di Meccanica e Aeronautica, University of Rome "La Sapienza". E-mail: franco.rispoli@uniroma1.it
[3] Fläkt Woods Ltd. E-mail: geoff.sheard@flaktwoods.com

ABSTRACT

The use of improved blade tip geometries is addressed as an effective design concept for passive noise control in industrial fans. These concepts, based on geometrical modifications of datum blade by means of profiled end-plates at the tip, are shown to reduce fan noise in its tonal and broadband components by changing the tip leakage flow behaviour. The three dimensional structures of tip vortical flow fields are discussed for a family of axial fans in fully-ducted configuration, to investigate on the aerodynamics of the proposed blade tip concepts. The study has been carried-out using an accurate in-house developed parallel finite element RANS solver, with the adoption of non-isotropic two-equation turbulence closure. The nature of the flow mechanisms in the fan tip region is correlated to the specific blade design features that promote reduced aerodynamic noise. It was found that the tip geometrical modifications markedly affect the multiple vortex leakage flow behaviours, by altering the turbulence and velocity fluctuations in the near-wall region as well along the blade span. The tip end-plates were demonstrated to influence also the rotor loss behaviour, in the blade tip region. The improvement of rotor efficiency curves were assessed and correlated to the control of tip leakage flows exploited by the tip end-plates.

Keywords: industrial fans, end-plates, tip leakage flow, noise

NOMENCLATURE

Latin letters

k	[m^2/s^2]	turbulent kinetic energy
l.e.		leading edge
PS		pressure side
P	[Pa]	static pressure
r	[mm]	radius
SS		suction side
t.e.		trailing edge
U_c	[m/s]	casing relative peripheral velocity
v, w	[m/s]	absolute and relative velocities
x, y, z		Cartesian coordinates

Greek letters

γ	[deg]	stagger angle
ε	[m^2/s^3]	turbulent dissipation rate
ζ	[-]	total loss coefficient, $\bar{p}_{0in} - p_0 \big/ 0.5\rho\bar{w}_{in}^2$
η	[-]	efficiency
ν	[-]	hub-to-casing diameter ratio
ν_t	[m s^{-2}]	turbulent viscosity
ξ_i	[s^{-1}]	absolute vorticity vector
ξ_s	[-]	absolute streamwise vorticity, $\xi_s = (\xi_i \cdot w_i)/(2\omega\lvert w\rvert)$
σ	[-]	blade solidity
Φ	[-]	global flow coefficient (annulus area-averaged axial velocity normalised by U_c)
χ	[-]	rotor tip clearance
Ψ	[-]	pressure rise coefficient ($\Delta p/(\rho\, 0.5\, U_c^2)$)
ω	[rad/s]	rotor angular velocity

Subscripts and superscripts

a, p, r	axial, peripheral and radial
c	casing wall
h	hub wall
i	Cartesian component index
in	inlet section
s	streamwise component
$\bar{}$	pitch-averaged value

1. INTRODUCTION

Often in axial flow fans the design specifications demand large tip gap according to the requirements of operating with variable stagger or pitch angles, e.g. cooling fans, or in some cases for emergency operation at up to 400°C for two hours to extract smoke in the event of a fire, e.g.

ventilating fans. As well known, the tip clearance plays a detrimental role affecting the rotor aero-dynamics [1-3], significantly contributing to the aero-acoustic signature of impeller in low speed ventilating equipments. In this pictures the tip clearance flow is recognized to inflence the rotor noise spectra by discrete frequency noise, due to periodic velocity fluctuation, and a broadband or high-frequency noise, due to velocity fluctuation in the blade passage [4-6]. To this end there is a strong motivation to look for deliberate aerodynamic design in order to minimize the negative effects of tip gap and to manage the fan or compressor tip clearance flow to minimize its impact on performance. Thus techniques and concepts that help to reduce tip clearance noise without sacrificing aerodynamic efficiency are highly desired and needed.

By surveying the techniques for noise control in fans and compressors, it was found that the solutions proposed could be grouped into active and passive noise control techniques, conceptually designed to accomplish this goal by reducing the leakage flow rate or by enhancing the primary-secondary flow momentum transfer.

In the ambit of active control techniques for fans and compressors, recently a number of experimental studies reconsider the control of tip clearance flow by means of fluid injection on the casing wall in axial compressor [7], and low-speed axial flow fan [8].

As far as the passive control techniques are concerned, the literature review puts in evidence the role of three approaches respectively focused on three-dimensional blade design and on geometrical modifications of the equipments in the gap region. The first concept makes use of sweep technique in blade design, recognized as a remedial strategy to improve the aerodynamic limits in compressor and low-speed axial fan rotors owing to the capability of affecting the rotor stall margin by reducing secondary flows effects and the flow leakage by unloading the blade tip [9-11].

A second family of control technique is based on gap geometrical manipulation and makes use of casing treatments in the shroud portion, over the blade tip, which is reported since the early 70s to improve the stable flow range by weakening the tip leakage vortex. Noticeable contributions deal with the use of grooves and slots [12-13], or stepped tip gaps [14]. Furthermore, in the ambit of fan technologies recirculating vanes, and annular rings have been proposed as anti-stall devices [15].

A final technique, appeared during the last decade, proposed the blade tip modifications by means of anti-vortex appendices such as the end-plates investigated by Quinlan and Bent [6], or the solutions recently proposed by industrial patents for ventilating fans [16-19].

In this ambit, the present paper aims to investigate on the use of profiled end-plates at the blade tip [20]. The study focuses on a family of commercially available fans and compares the aerodynamic and aeroacoustic performance of the datum blade against two improved tip geometries, respectively with constant or variable thickness end-plate [21]. The paper reports on the experimental and numerical assessment of the pay-off derived from the blade tip concept developed at Fläkt Woods Ltd with respect to the aerodynamic performance of a class of low noise level industrial fans.

The single rotor investigations are carried out at design operating condition for three configurations of the six-blade axial flow fan under investigation, namely: the datum fan, coded AC90/6; two fans modified by the adoption of tip features, respectively coded AC90/6/TF and AC90/6/TFvte. The studies have been carried in ducted configuration, adopting a high tip pitch angle configuration, i.e. 28 degrees, where the fan provides the higher static pressure and flow rate of its operational range.

The comparative aerodynamic performance experiments have been carried out according to ISO 5801 for type D fully ducted configuration set-up. The noise performance test have been carried out in accordance with the British Standard BS484, Part 2 for outlet noise hemispeherical measurement. The fans have been tested employing a type A configuration, in the Fläkt Woods Ltd anechoic chamber at the design operating conditions.

The tip flow characteristics are analysed by using a three-dimensional (3D) steady Reynolds-Averaged Navier-Stokes (RANS) formulation, with use of first order non-isotropic turbulence closure successfully validated for fan rotor flows [22-23]. Despite the steady-state condition, the RANS is considered an effective investigation tool for vortical structure detection [24]. The authors adopt a parallel multi-grid (MG) scheme developed for the in-house finite element method (FEM) code [25]. The FEM formulation is based on a highly accurate stabilized Petrov-Galerkin (PG) scheme, modified for application to 3D with equal-order spaces of approximation.

By means of such a numerical investigation, the tip leakage flow structures of the fans are analysed in terms of vortical structures detection, leakage flow energy and loss behaviours. Emphasis is laid on the assessment of the benefits related to the improved tip geometry in terms of efficiency and operating margin gains. The overall objective is to investigate, via steady computational simulations, the technical merits of a passive control strategy for controlling the leakage flow and reducing tip clearance vortex/stator interaction noise and rotor-tip self noise.

2. TEST APPARATUS AND PROCEDURES

2.1. Test fans

The present study was performed on a family of commercially available highly efficient cooling fans. The in-service experiences indicated that this family of fans gives good acoustic performance with respect to the state-of-the-art configurations. The investigated fans have six-blade unswept rotor, with blade profiles of modified ARA-D geometry type originally designed for propeller applications. The blade profiles geometry is given in Table 1, for the datum fan AC90/6 at the hub, and tip sections respectively.

Table 1 AC90/6 fan family specifications. Blade profile geometry and rotor specifications.

blade geometry	*AC90/6 fans*	
	hub	*tip*
ℓ / t	1.32	0.31
pitch angle (deg)	36	28
camber angle (deg)	46	41
fan rotor		
blade number	6	
blade tip pitch angle (deg)	28	
hub-to-casing diameter ratio ν	0.22	
tip diameter (mm)	900.0	
rotor tip clearance τ (% span)	1.0	
rated rotational frequency (rpm)	900 – 935	

The studied blade configurations, for datum and modified rotors, feature a high tip stagger angle, i.e. 28 degrees, measured, as is customary in industrial fan practice, from the peripheral direction. This rotor angular setting has been chosen in order to exploit operating points where the vortical flow near the rotor tip dramatically affects the aerodynamic performance and noise characteristics of the fans under investigation.

The fan blades are drawn in Figure 1, together with a detailed view of blade tip for the datum rotor, and the improved rotors developed for low noise emission labeled: AC90/6/TF and AC90/6/TFvte. Fig. 1 compares, in a qualitative view not to scale, the thickness distributions of the developed improved tip concepts against the datum base-line.

The improved blade tip geometry, for AC90/6/TF fans, was originally inspired by the technique developed for tip vortex control and induced drag reduction by preventing 3D flows in aircraft wings, also used as anti-vortex devices for catamaran hulls.

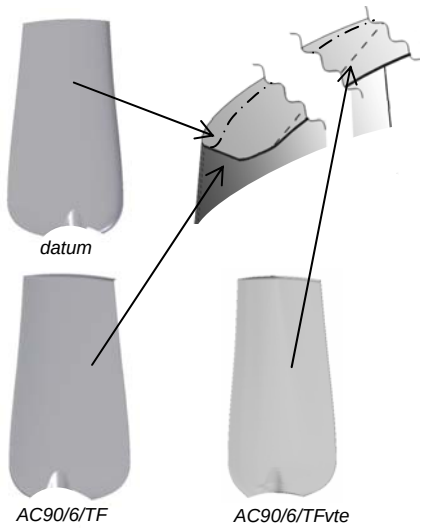

Fig. 1 Test fans and rotor blades (not to scale)

The tip blade section was modified by adding an end-plate along the blade pressure surface that ends on the blade trailing edge with a square tail. By means of the introduction of the end-plate, the blade section is locally thickened of a factor 3:1 with respect to the maximum thickness at the tip of datum blade. According to the theory behind the end-plate design, this dimension was chosen as the reference radial dimension of leakage vortex to be controlled that could be estimated in the range 0.2 ÷ 0.1 blade span, as shown by former studies on rotors of axial compressor [26] and fan [11]. A recent investigation, carried out by Corsini and co-workers [20], assessed the aerodynamics and aeroacoustics gains of rotor AC90/6/TF with respect to the datum one. The numerical simulation founded the evidences of a tip leakage vortex breakdown that affect the rotor AC90/6/TF at the design operating condition. In order to correct this negative feature, responsible for a loss in fan efficiency, Corsini in [21] recently proposed a blade tip geometry that exploits a variable thickness distribution of the end-plate according to safe rotation number chord-wise gradient concept, here labeled AC90/6/TFvte.

2.2. Numerical procedure and axial fan modeling

The Reynolds-averaged Navier-Stokes equations are solved by an original parallel Multi-Grid Finite Element flow solver [25]. The physics involved in the fluid dynamics of incompressible 3D turbulent flows in rotating frame of reference, was modelled with a non-linear k-ε model [27], here used in its topology-free low-Reynolds variant. This turbulence closure has been successfully validated on transitional compressor cascade flows, as well as high-pressure industrial fan rotors [10, 23].

The numerical integration of PDEs is based on a consistent stabilised Petrov-Galerkin formulation developed and applied to control the instability origins that affect the advective-diffusive incompressible flow limits, and the reaction of momentum and turbulent scale determining equations. The latter ones, respectively, related to the Coriolis acceleration or to the dissipation/destruction terms in the turbulent scale determining equations [22]. Equal-order linear interpolation spaces (Q1-Q1) are used for primary-turbulent and constrained variables, implicitly eliminating the undesirable pressure-checkerboarding effects. Concerning the solution strategy, a hybrid full linear MG accelerator was built-in the in-house made overlapping parallel solver. The Krylov iterations in the smoothing/solving MG phases are parallelized using an original additive domain decomposition algorithm. The message passing operations were managed using the MPI libraries. By that way, the fully coupled solution of sub-domain problem involves an efficient non-conventional use of Krylov sub-space methods. The preconditioned GMRes(5) and GMRes(50) algorithms were respectively used as smoother and core solver.

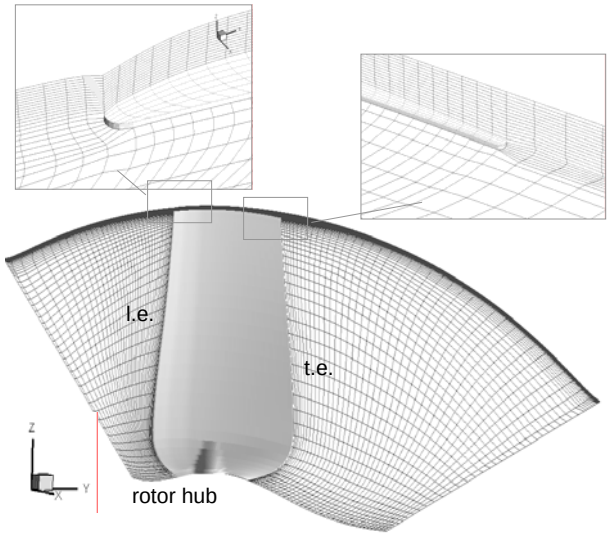

Fig. 2 Computational grid of fan rotor, mesh details in the tip gap region

The mesh has been built according to a non-orthogonal body fitted coordinate system, by merging two structured H-type grid systems. The mesh in the main flow region, surrounding the blade, and an embedded mesh in the tip gap region. The mesh has 154×68×58 nodes, respectively in the axial, pitch, and span wise directions. In the axial direction the node distribution consists of 20%, 50% and 30% of nodes respectively upstream the leading edge, in the blade passage and downstream of it. Moreover, there are 14 grid nodes to model the tip-clearance along the span. The computational grid is illustrated, in Figure 2, providing detailed view at the tip of the mesh in meridional and blade-to-blade surfaces.

The mesh has an adequate stretch toward solid boundaries, with the ratio of minimum grid spacing on solid walls to mid-span blade chord set as 2×10^{-3} on the blade tip, casing wall, and blade surfaces. The adopted grid refinement towards the solid surfaces controls the dimensionless distance δ^+ value about 1 on the first nodes row.

2.3. Boundary conditions and investigated flow conditions

Standard boundary condition set has been adopted, already used in recent numerical studies on high performance fans [10-11].

The Dirichlet conditions for the relative velocity components are imposed at the inflow section half a mid-span chord far upstream the leading edge. The velocity profile has been obtained from flow simulation in an annular passage of identical hub-to-casing diameter ratio that includes an upstream spinner cone. The inlet distribution of the turbulent kinetic energy k is obtained from axi-symmetric turbulence intensity (TI) profile derived on the basis of former studies on ducted industrial fans [10]. The TI profile features a nearly uniform value in the core region (about *6* percent) and it grows markedly approaching the endwalls (about *10* percent). The inlet profile of turbulence energy dissipation rate is basedon the characteristic length scale l_ε set to *0.01* of rotor pitch at mid-span. Flow periodicity upstream and downstream the blading, and Neumann outflow conditions (homogeneous for k and ε and non-homogeneous for the static pressure) complete the set of boundary data.

The numerical investigation compares fan leakage flow patterns for datum, AC90/6/TF and AC90/6/TFvte fan rotors operated in near-design condition (D) with volume flow rate 7 m^3/s and global flow coefficient Φ = 0.278. The Reynolds number based on tip diameter and rotor tip speed is 8.3×10^5, for normal air condition.

3. PERFORMANCE EXPERIMENTS

The aerodynamic and noise performance tests were carried out at Fläkt Woods Ltd laboratory in Colchester.

3.1. Aerodynamic tests

The aerodynamic tests were conducted according to ISO 5801 set up, for fully ducted configuration and installation type D. This installation features ducted inlet and outlet regions and the fan is supplied with a properly-shaped inlet bell mouth. The primary performance parameters measured were the fan static pressure and the efficiency. Figure 3 compares the static pressure and efficiency characteristic curves for datum, AC90/6/TF and AC90/6/TFvte rotors. The analysis

of static pressure curves of Fig. 3, gives the evidence of a small performance reduction in rotor AC90/6/TF with improved tip concept, e.g. about 2% at 6m^3/s, according to the interaction between the tip clearance flow and the suction side near surface fluid [28]. This performance penalty is, on the contrary, partially receovered by rotor AC90/6/TFvte whose static pressure rise increases remarkably by throttling the rotor toward the peak pressure.

Concerning the efficiency curves it is evident that both the modified rotors feature an efficiency improvement in the range of volume flow rate higher than the design one. Moreover the efficiency curve comparison shows that the adoption of the tip end-plates results always in the appearance of a clear efficiency plateau, that shift the peak η volume flow rate towards the rotor stall margin.

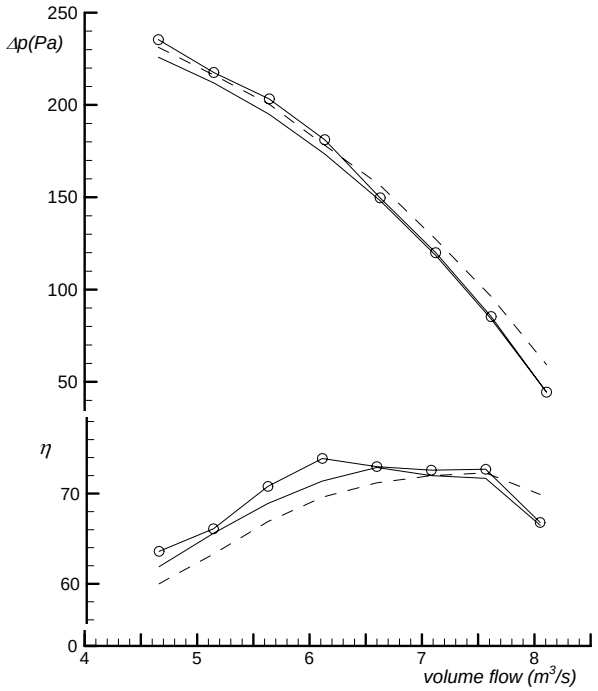

Fig. 3 Static pressure and efficiency characteristic curves (dashed lines: datum fan; solid lines: AC90/6/TF fan; line-symbols: AC90/6/TFvte fan)

The rotor performance were assessed along the operating line. The predicted overall performance for 900 rpm rotational frequency are compared in Table 2 to the experimental data measured at Fläkt Woods Ltd measurements according to the fan performance test standards ISO5801:1997 for installations type D with inlet bell-mouth. Efficiency η is computed in terms of static pressure rise. The comparison confirms the validity of the predicted performance at the chosen setting angle, where the blades of this fan are the most loaded and more readily prone to flow separation.

It is also worth noting that the prediction of performance parameters have been referred to axial sections respectively located at the inlet of the domain, and 1.2 midspan chord downstream the blade trailing edge. The comparison confirms the validity of the predicted performance.

Table 2 Predicted and measured fan overall performance @ 7 m^3/s

	Measurements		*Predictions*	
	Δp_{stat} (Pa)	η	Δp_{stat} (Pa)	η
datum	134.8	0.490	133.3	0.510
AC90/6/TF	126.2	0.510	126.1	0.504
AC90/6/TFvte	129.0	0.519	128.2	0.516

3.2. Noise tests

The noise performance test have been carried out in accordance with the British Standard BS484, employing a type A testing configuration.

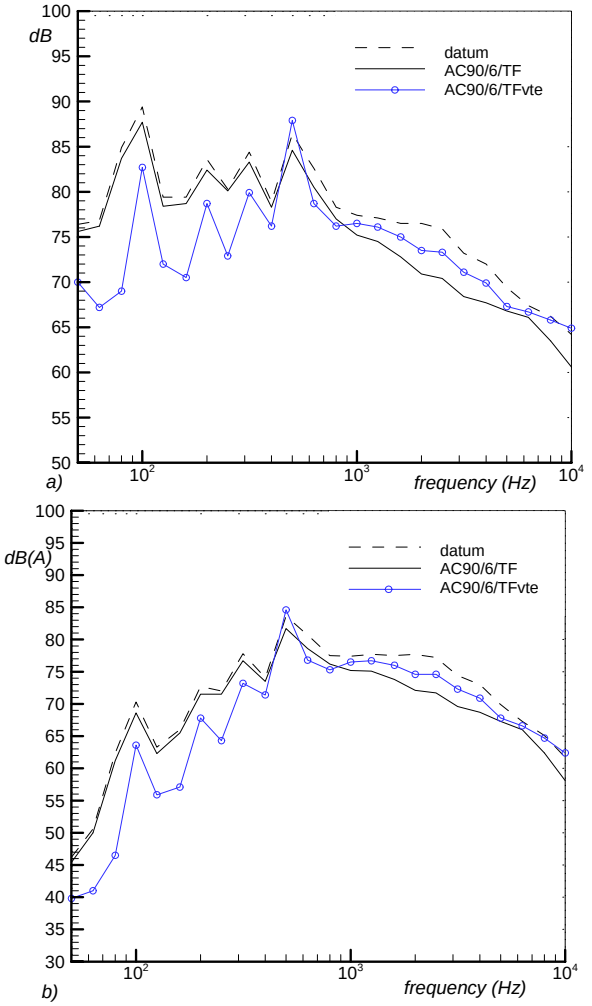

Fig. 4 Sound power level spectra in one-third-octave band. a) un-weighted spectra and b) A-weighted spectra (dashed lines: datum fan; solid lines: AC90/6/TF fan; line-symbols: AC90/6/TFvte fan)

In this method the fan is placed downstream of a plenum chamber with a free outlet, in an arrangement similar to that used for compact cooling fans.

Figure 4 compares the measured power spectra in one-third-octave band. Fig. 4.a and Fig. 4.b respectively show the measured sound power level and the A-weighted sound power level spectra for the frequency-dependent human audition. The noise tests have been done in order to compare the rotors aeroacoustic signature for identical static pressure rise, e.g. 190 Pa close to the peak pressure operation. As shown in Fig. 4, the effectiveness of the improved tip concepts, with constant and variable thickness end-plates, is demonstrated by the reduction of the rotor aeroacoustic signature both in terms of tonal noise and broad-band noise. These noise components are related to the main recognized tip noise generation mechanisms in axial decelerating turbomachinery. The convection of the primary tip vortex and its interaction with the statoric structures produces mainly tonal noise, while the oscillating tip vortex behaviour could be linked to the production of broadband self-generated noise [29].

Finally, Table 3 compares the overall sound power levels for the family of fans under investigation.

Table 3 Overall sound power levels @ 190 Pa

	un-weighted SWL dB	*A-weighted SWL dB(A)*
datum	94.6	88.7
AC90/6/TF	93.0	86.3
AC90/6/TFvte	91.5	88.1

4. INNER WORKINGS OF END-PLATES

The improved blade tip concepts, developed with constant thickness and variable thickness end-plates, has been shown to control the aeroacoustic signature of the family of fans under investigations and this pay-off is correlated to a large efficiency improvement in the peak pressure operating range. These experimental evidences prompted a comparative investigation, for the datum fan and the fan with blade tip features, onto the inner workings of the passive control device used to influence the structure of the tip leakage vortex and other systems of secondary vorticities. The effectiveness of the passive tip devices is analysed by comparing the normalized streamwise vorticity map evolution along the chord, and the tip vortex core paths. These analyses are complemented with the evaluation of tip leakage flow energy contents, affecting the rotor aeroacoustic signatures, and with the presentation of loss coefficient map evolution within the blade passage to assess the influence of the geometrical modification at the blade tip and the rotor aerodynamic efficiency along in operating range of the fans.

4.1. Helicity distributions and vortex cores

The tip leakage vortical structures are now investigated by using the normalized helicity H_n based on the absolute vorticity [3, 24] as the detection tool. H_n is defined and normalized as: $H_n = (\xi_i \cdot w_i)/(|\xi||w|)$ with i = 1, 3, where ξ_i and w_i are the Cartesian components of the absolute vorticity and relative velocity vectors, $|\xi|$ and $|w|$ their norms. Figure 5 shows the normalized helicity distribution in the blade tip region by comparing the contours on cross flow planes in near-design operating condition. The probing planes are located, respectively, at 0.25, 0.43, 0.65, 0.89 and 1.2 blade chord ℓ from the tip section leading edge. The normalized helicity distribution is plotted with the vortex cores colored by the its local magnitude.

For the investigated fan rotors, a clear vortex cores identification is only observed for the leakage flow structures emerging in the front portion of the tip blade sections. In the multiple vortex behaviour of datum fan rotor, Fig. 5.a, the helicity field shows that a main clock-wise vortical structure (*TLV1*) develops through the passage with high skewing angle with respect to the blade surface.

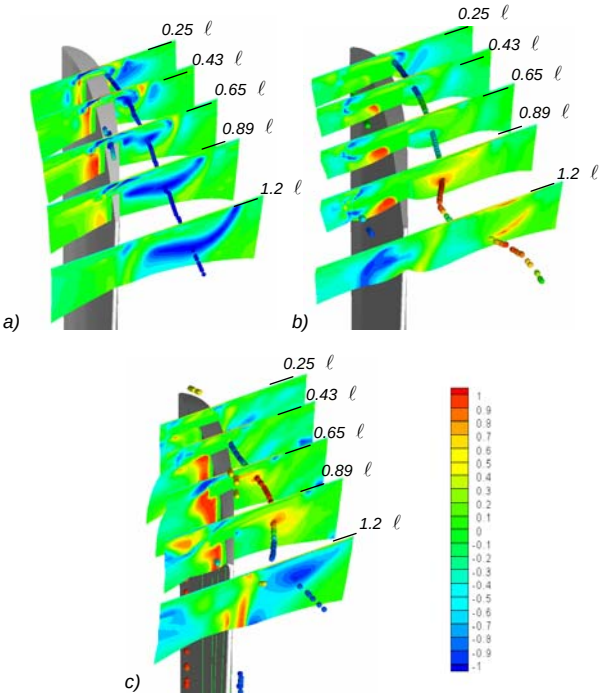

Fig. 5 Normalized helicity H_n contours on cross sections and vortex cores at the tip, *D* operating point: a) datum rotor, b) AC90/6/TF rotor, and c) AC90/6/TFvte

Moreover Fig. 5.a shows the existence of a weak tip secondary vortex, co-rotating with *TLV1*, in the vicinity of the suction surface, as clearly shown on 0.65 ℓ plane by the streamwise vorticity distribution. In the front portion of the blade, 0.25 ℓ downstream the leading edge, the helicity map shows also the presence of a third vortical structure spreading from the leading edge of the blade. In the blade aft region, the leakage flow is mainly characterized by the merging of tip separation vortex *TLV2* and leading edge vortex with *TLV1*

one, resulting in a unique clock-wise vortical structure able to affect a large share of the blade pitch on the casing annulus.

As far as the AC90/6/TF rotor is concerned, Fig. 5.b gives evidence of a clear modification in the tip leakage phenomenon. First of all, Fig. 5.b shows the existence of a vortex limiting the mass leakage along the blade pressure surface, and recognized as the evidence of the pressure side leg of a horse-shoe like structure. In the first quarter of the blade chord, it is evident the trace of an additional leading edge vortex co-rotating with *TLV1*, in a similar way to datum rotor.

Both the *TLV1* and the leading edge vortices feature, since their appearance on 0.25 ℓ plane, a smaller in-passage extension coupled with a reduced helicity magnitude when compared to the datum rotor field. Furthermore, the leading edge vortex never collapses into the *TLV1*, but it decays as indicated on 0.43 ℓ plane. Moving downstream, about mid-chord, the *TLV1* features a gradual H_n reduction owing to the weakening of flow vorticity and to the deflection of vortex core.

This circumstance agrees with the hypothesis of mass leaking reduction along the chord, that gives rise to a leakage flow structures nearly adjacent to the blade suction surface (i.e. *TLV2* structure). In the aft portion of the blade, due to the leakage flow un-feeding the *TLV1* collapses, producing a bubble-type separation recognized as the evidence of a vortex breakdown by Corsini and co-workers [20].

The separated flow turns into a counter-clock wise vortex under the influence of trailing edge leakage flow streams, rapidly washing-out the vortex behind the rotor so that on 1.2 ℓ plane no coherent vortical structure is evident.

Finally, Fig. 5.c shows that the use of variable thickness concept markedly influences the tip flow features. The origin position of the main vortical structure *TLV1* moves downstream with respect to datum and AC90/6/TF blades, e.g. about 0.3 ℓ, and, as shown by the vortex core path, it develops closer to the blade suction surface. At mid-chord the weakened *TLV1* vortex interacts with highly energetic leakage jet that causes the inversion of vortex rotation. In the aft chord fraction, the tip vortex finally merges with a rotating cell and exits the blade passage appearing as a coherent clock-wise vortical structure.

The helicity maps confirms, for this end-plate configuration, that a driving role is played by the pressure side vortical structures as given by the horse-shoe vortex leg and by the corner vortex developing under the end-plate.

Figure 6 compares the TLV1 vortex core trajectories within the blade passage.

As shown in Fig. 6, the vortex core path analysis gives further information about the inner working of the developed end-plates for leakage flow control.

Except from the location of vortex origins, both the end-plates feature *TLV1* core trajectories developing along paths which are less skewed than the blade tip section.

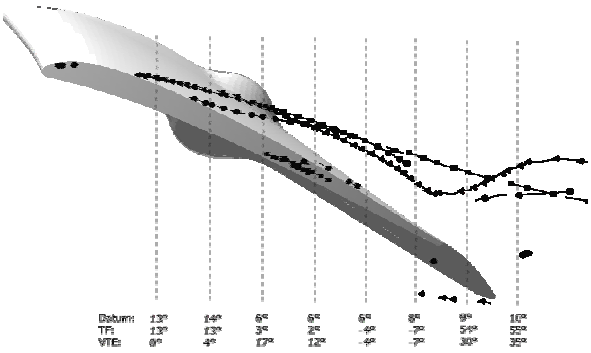

Fig. 6 Tip leakage vortex TLV1 trajectories (line-squares: datum, line-circles: AC90/6/TF; line-triangles: AC90/6/TFvte)

Moreover, due to the anti-vortex action exerted by the end-plates, both the improved tip rotors feature a *TLV1* core sudden deviation due to the interaction between the low energy leakage vortices and the passage flow exiting from the rotor.

4.2. Leakage flow energy

The analysis of primary tip vortex structures, detected by means of the helicity distributions, is now completed by investigating on their energy contents. The rotational kinetic energy, defined on the basis of crosswise relative velocity components, and the resolved isotropic turbulence intensity are considered as the bench-mark quantities.

The sound sources, tonal in nature, are related to the energy contents of the tip leakage vortices moving in the axial direction and interacting with any stationary surfaces (i.e. struts or outlet guide vanes). Figure 7 compares the rotational kinetic energy isolines within the tip gap, i.e. R = 0.998. In Fig. 7 the rotational energy is normalized by the bulk kinetic energy.

The datum rotor, as shown in Fig. 7.a, features the highest rotational kinetic energy magnitude located at the onset of *TLV1*, where the vortical structure origins with an energy content comparable to the bulk one. Moreover, the datum rotor map shows the evidence of a second highly rotating core tracing the tip separation vortex *TLV2*, already found in Fig. 5.a. In view of this picture, both the improved rotors, Fig. 7.b and Fig. 7.c, provide the evidence that the end-plates markedly affects the leakage flow rotational kinetic energy. Their actions implements twofold beneficial mechanisms: first, the reduction of the momentum transfer *via* leakage jet, is able to control the rotational energy at the *TLV1* onset; second, as shown by the reduction of the vortex energy, below the 50% of bulk kinetic energy across the blade passage, the designed anti-

vortex devices act as rotational energy damper in that unfeeding the mass leaking they are able to weaken the peripheral momentum transfer to tip vortices along the chord.

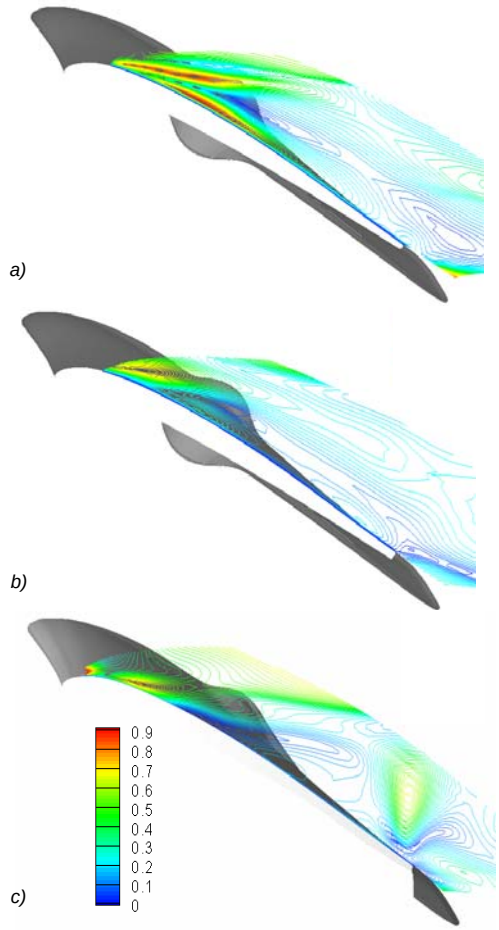

Fig. 7 Rotational kinetic energy isolines in the rotor tip gap @ *R* = 0.998, *D* operating point: a) datum rotor, b) AC90/6/TF rotor, and c) AC90/6/TFvte

As a second energy marker the turbulence level maps are here discussed by comparing the 3D chord-wise tip flow evolution on probing sections at 0.25, 0.43, 0.65, 0.89 and 1.2 blade chord from the tip section leading edge. Figure 8 compares the turbulence intensity *TI* maps for the investigated fans. These figures also include the simulated tip leakage stream-paths.

As shown in Fig. 8, the chordwise evolution of turbulence level maps gives evidence of significant differences between the rotors under investigation, mainly concentrated in the vicinity of the casing annulus end-walls. As a general observation, in presence of the anti-vortex device the attenuation of leakage flow results also in an attenuation of the local turbulence level that reduces the peak turbulent kinetic energy within the leakage vortex cores. This circumstance is particularly evident in Fig. 8.b and Fig. 8.c, where the primary tip vortex rolls-up into a low turbulence level core. While the peak *TI* values remain concentrated in the interaction cores between the suction side near-surface fluid and the leakage flow. In Fig. 8.b it is also worth noting that the AC90/6/TF rotor streamlines confirms that the primary tip vortex collapses giving rise to a separation bubble structure, similar to the time-averaged evidence of leakage flow vortex breakdown shown by Inoue and Furukawa [24].

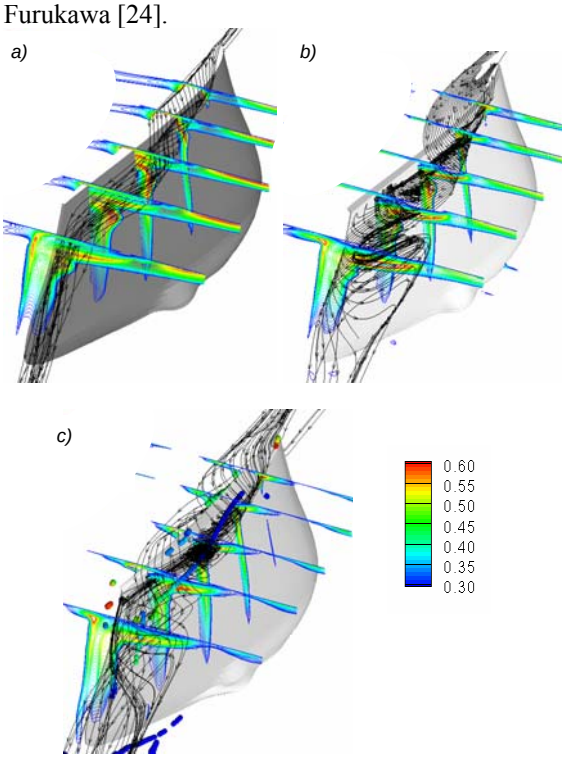

Fig. 8 Turbulence intensity *TI* contours on cross sections and tip vortex streamlines, *D* operating point: a) datum rotor, b) AC90/6/TF rotor, and c) AC90/6/TFvte

While in Fig. 8.c, is clearly evident that the end-plate variable thickness distribution is able to correct the *TLV1* breakdown acting locally on the vortex rotation number on the basis of the end-plate thickness distribution in the chord direction [21].

4.3. Loss at the rotor tip

Rotor loss behaviors at the blade tip is discussed with reference to the local total loss coefficient defined ζ. The loss behaviour is, finally, investigated with reference to the local total loss coefficient defined as: $\zeta = \overline{p}_{0in} - p_0 \big/ 0.5\rho\overline{w}_{in}^2$, where p_0 is the local total pressure, $\overline{p}_{0in}$ and $0.5\rho\overline{w}_{in}^2$ are respectively the reference pitch-averaged relative total and dynamic pressures computed at the inlet mid-span plane.

Figure 9 shows the total loss coefficient distribution within the blade passage, probing the flow fields in the vicinity of the blade leading edge, about mid-chord and in the region behind the blade (i.e. respectively about 0.25 and 0.65 and 1.2 chord

from the leading edge). In the design operating condition, Fig.s 9.a, 9.b and 9.c, the predicted loss evolutions agree with the evidences found in literature for low-speed rotors. At the rotor inlet, all rotor distributions feature loss cores mainly concentrated on the hub annulus walls. Moving toward the blade aft, the loss maps are characterized by loss core directly related to the development of primary tip vortices crossing the blade vane. As shown in Fig. 9.b, the improved tip concept rotor AC90/6/TF, owing to the vortex breakdown, is affected by a larger peak loss core. Nonetheless, by comparing the loss map on 1.2 ℓ plane with the datum rotor one, it is clearly evident that the improved tip rotor presents a spanwise beneficial loss distribution, outperforming the datum one within the wake and on the hub end-wall on pressure and suction side corners.

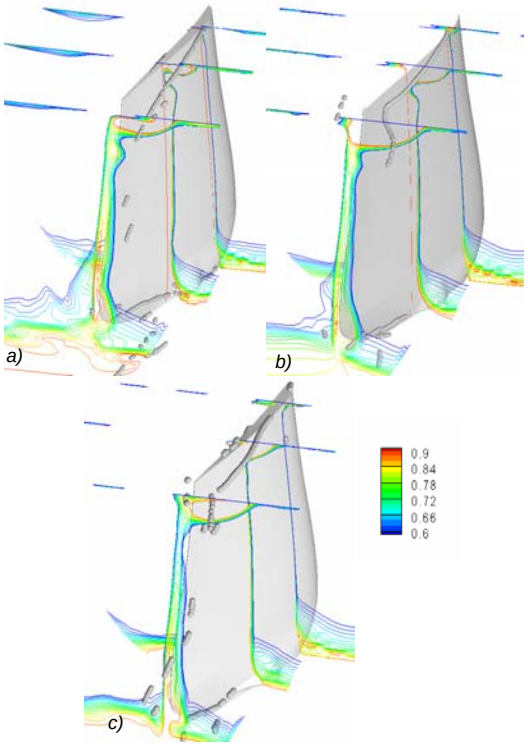

Fig. 9 Evolution of total pressure loss coefficient ζ inside the blade passage: a) datum rotor, b) AC90/6/TF rotor, and c) AC90/6/TFvte

As far as the AC90/6/TFvte fan rotor is concerned, Fig. 9.c gives the evidence that the end-plate design concept [21], by controlling the appearance of leakage vortex breakdown is able to reduce the high loss core at the tip, behind the rotor and along the blade suction side within the interaction region between leakage and near surface flows. This comparative behaviour, in agreement with the aerodynamic test results, could be considered as a consequence of the reduced 3-D flow re-arrangement consequent to the reduction in the mass leaking through the tip gap. The limited radial migration of near-wall surface fluid, induces smaller hub loss core and the contraction of suction/corner stall (shown by the hub corner stall core in Fig. 9.b and Fig. 9.c).

5. CONCLUSIONS ON END-PLATES NOISE CONTROL

Sound is a weak by-product of a subsonic turbulent flow, and noise generation control in fans is challenging because turbulence is remarkably inefficient as an acoustic source. The analysis of leakage flow was intended to provide evidences of the aerodynamic mechanisms realized by the end-plate based tip concepts for passive noise control. To this end, the phenomenological viewpoints, given in Section 4, must be complemented by hints on the influence that end-plates exert on the rotor aeroacoustic by altering the turbulent flow in the tip region.

The end-plates work as mixing enhancement devices, altering by that way the turbulence statistics and the time- and length-scales of noise generating eddies. These flow modifications directly impact the sound field by modifying the low- and high-frequency noise components.

In this respect the effectiveness of tip end-plates, in AC90/6/TF and AC90/6/TFvte, is first assessed by comparing the turbulence level iso-surfaces in the vicinity of the tip. In Figure 10 two turbulence intensity levels have been taken, respectively $TI = 0.3$ and $TI = 0.6$.

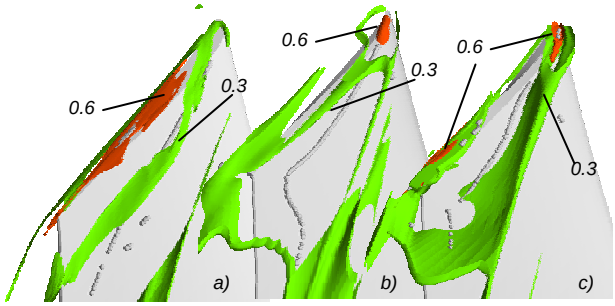

Fig. 10 Turbulence intensity iso-surfaces at the tip: a) datum rotor, b) AC90/6/TF rotor, and c) AC90/6/TFvte

It is worth noting that the datum rotor features, Fig. 10.a, a high turbulence level core concentrated about the tip blade that develops over a large share of the chord. Concerning the vortex core path, it is furthermore evident that it entirely evolves within a conical iso-surfaces at $TI = 0.3$. With respect to this baseline, both the rotors exploiting the improved tip concepts share common features such as: the peak TI cores are located near the leading edge at the onset of the main leakage vortex, e.g. *TLV1*; moreover, the vortex core trajectories remain inside wide low turbulence volumes bounded by the $TI = 0.3$ iso-surface, shifted at the periphery of vortical regions remarkably larger than the one detected in the datum rotor.

Furthermore, Figure 11 compares the turbulent viscosity ($\nu_t = c_\mu k^2/\varepsilon$, normalized by the molecular viscosity) distribution in vicinity of the blade tip. As shown in Fig. 11.b and Fig. 11.c, it is confirmed that the improved tip rotors handle the leakage flow by enhancing the turbulent diffusivity within the leakage vortices.

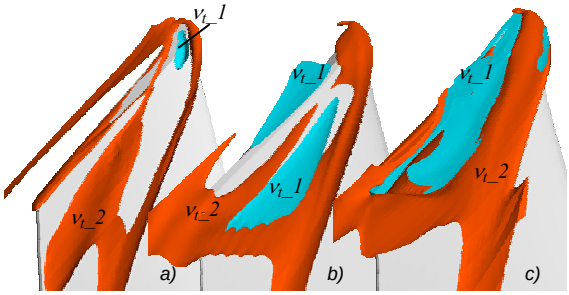

Fig. 11 Normalized turbulent viscosity ν_t iso-surfaces at the tip: a) datum rotor, b) AC90/6/TF rotor, and c) AC90/6/Tfvte (ν_t_2: 10^2 ν_{mol}; ν_t_1: 5×10 ν_{mol})

On the contrary in Fig. 11.a, the datum rotor features lower diffusivity level in correspondence with the *TLV1* path, and reaches the peak viscosity level behind the blade where the vortex interacts with primary and secondary flows.

As far as the broadband noise is concerned, in the subsonic range, it could be related to primary tip vortices that once formed are responsible for the convection of large-scale fluctuations downwind the trailing edge that gives rise to scattering and broadband noise [29]. Moreover, observations drawn from flow visualization experiments and fluid dynamic measurements complete this picture by indicating that also secondary flows contribute to the broadband noise generated by small cooling axial flow fans.

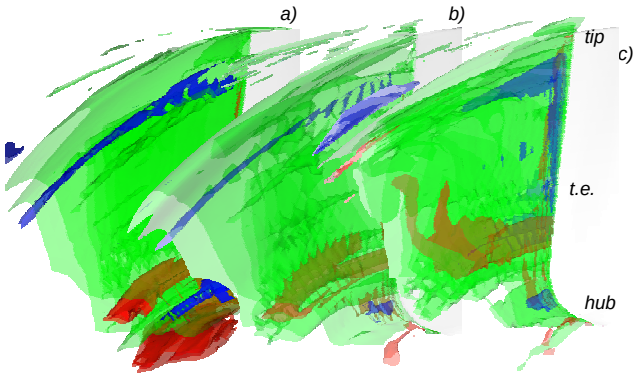

Fig. 12 Normalized helicity H_n iso-surfaces behind the fan rotors: a) datum rotor, b) AC90/6/TF rotor, and c) AC90/6/TFvte

Figure 12 shows the normalized helicity distribution behind the rotors under investigation, in order to compare how the wake behaviour is affected by the end-plates adoption.

As a general comment it could be concluded that the application of the improved tip concepts extends its beneficial effect on the blade passage secondary flows. As clearly shown in Fig. 12.b and 12.c, the helicity maps give the evidence of the magnitude reduction of the secondary phenomena related to the wake and to the hub corner vortices.

6. SUMMARY

We have carried out a study on the structure of tip leakage flow and its influence on the fluid dynamical behaviour in a family of axial flow fans. The aim of the paper has been to speculate on the effectiveness of improved blade tip concepts to control the leakage flow phenomena and rotor aeroacoustic signatures. Two end-plate geometries have been developed the first one with constant thickness, and the second one with a variable thickness distribution according to safe rotation number chord-wise gradient concept.

The aerodynamic tests have shown that the improved tip concepts are affected by a small performance de-rating, but the efficiency curves give evidence of an improvement with increased peak performance and wider high efficiency plateau towards the rotor stall margin. The noise test, furthermore, demonstrated a reduction of the rotor aeroacoustic signature both in terms of tonal noise and broad-band noise.

The investigation was based on an in-house developed parallel finite element Navier-Stokes solver. The physical interpretation of the detailed 3D flow field predictions were discussed by means of streamlines, streamwise vorticity, or leakage flow kinetic energy and loss maps. The following conclusions are drawn on the basis of the found fluid dynamical behaviours.

The comparison of the detected leakage vortical structure evolutions showed that the datum rotor features a multiple vortex behaviour characterized by a dominant leading edge vortical structure, highly skewed with respect to the local relative flow direction, and a weak tip secondary vortex in the vicinity of the suction surface. The presence of the end-plates influence the leakage flows structure at the leading edge by changing its orientation with respect to the local relative streamlines that govern the secondary flow advection in the rotor frame. Both the rotors designed with the improved tip geometries appear to be characterized by two vortical structures at the tip, respectively the trace of the pressure side leg of an incoming horse-shoe vortex like structure and the suction side trace of the main leakage flow. In this viewpoint the existence of this pressure side vortex, peculiar of the improved tip concepts rotor, is recognized as one of the factor contributing to the control of the leakage phenomenon promoting a *vena contracta* effect. By that way the mass leaking is un-fed close to the leading edge and the gained control on leakage flow

onset turns into potentially improved aeroacoustic performance.

The analysis of the leakage flow energy contents, indirectly related to the recognized tip leakage noise mechanisms, has given the evidence of a reduction in the rotational kinetic energy and turbulence level on the casing owing to the presence of the anti-vortex device.

The loss coefficient distributions confirm that the highest loss regions were always observed in coincidence with the leakage vortex core with a nearly constant peak loss value. The comparative analysis of mechanical energy loss within the gap showed that the presence of the anti-vortex device at the tip leads to a reduction of mechanical energy loss within the gap, suggesting that the loss level within the tip gap is mainly controlled by the mass leaking.

ACKNOWLEDGEMENTS

The present research was done in the context of the contract FW-DMA03, between *Flakt Woods Ltd* and *Dipartimento di Meccanica e Aeronautica University of Rome "La Sapienza"*. The authors gratefully acknowledge Mr. I. Kinghorn and Mr. B. Perugini for their contribution to the experiments.

REFERENCES

[1] Fukano, T., Takamatsu, Y, 1986, "The effects of tip clearance on the noise of low-pressure axial and mixed flow fans", *J. of Sound and Vibration*, Vol. 105, pp. 291-308.

[2] Storer, J.A., Cumpsty N.A., 1991, "Tip leakage flow in axial compressors", *J. of Turbomachinery*, Vol. 113, pp. 252-259.

[3] Furukawa, M, Inoue, M., Saiki, K., Yamada, K., 1999, "The role of the tip leakage vortex breakdown in compressor rotor aerodynamics", *J. of Turbomachinery*, Vol. 121, pp. 469-480.

[4] Fukano, T., Jang, C., 2004, "Tip clearance noise of axial flow fans operating at design and off-design condition", *J. of Sound and Vibration*, Vol. 275, pp. 1027-1050.

[5] Jang, C., Fukano, T.,Furukawa, M., 2003, "Effects of the tip clearance on vortical flow and its relation to noise in an axial flow fan", *JSME Transaction Series B*, Vol. 46, pp. 356-365.

[6] Quinlan, D., A., Bent, P., H., 1998, "High frequency noise generation in small axial flow fans", *J. of Sound and Vibration*, Vol. 218, pp. 177-204.

[7] Bae, J.W., Breuer, K.S., Tan, C.S., 2005, "Active control of tip clearance flow in axial compressors", *J. Turbomachinery*, Vol. 127, pp. 352-362.

[8] Roy, B., Chouhan, M., Kaundinya, K.V., 2005, "Experimental study of boundary layer control through tip injection on straight and swept compressor blades", ASME paper GT2005-68304.

[9] Wadia, A., R., Szucs, P.,N., Crall, D., W., 1998, "Inner workings of aerodynamic sweep", *J. of Turbomachinery*, Vol. 120.

[10] Corsini, A., Rispoli, F., 2004, "Using sweep to extend stall-free operational range in axial fan rotors", *J. of Power and Energy*, Vol. 218, pp. 129-139.

[11] Corsini, A., Rispoli, F., Kinghorn I., Sheard A. G., 2004, "The aerodynamic interaction of tip leakage and mainstream flows in a fully-ducted axial fan", ASME Paper GT2004 -53408.

[12] Takata, H., Tsukuda, Y., 1977, "Stall margin improvement by casing treatment – its mechanism and effectiveness", *J. Eng. Power*, Vol. 99, pp. 121-133.

[13] Smith, G..D.J., Cumpsty N.A., 1984, "Flow phenomena in compressor casing treatment", *J. Eng. Gas Turbines Power*, Vol. 106, pp. 532-541.

[14] Thompson, D.W., King, P.I., Rabe, D.C., 1998, "Experimental and computational investigation on stepped tip gap effects on the flowfield of a transonic axial-flow compressor rotor", *J. Turbomachinery*, Vol. 120, pp. 477-486.

[15] Jensen, C., E., 1986, *Axial-flow fan*, US Patent No. 4,630,993.

[16] Longet, C., M., L., 2003, *Axial flow fan with noise reducing means*, US Patent 2003/0123987 A1.

[17] Mimura, M., *Axial flow fan*, 2003, US Patent 6,648,598 B2.

[18] Belady, C., L., 2004, *Winglet-Enhanced Fan*, US Patent 6,776,578 B2.

[19] Uselton, R., B., Cook, L., J., Wright, T., 2005, Fan with reduced noise generation, US Patent 2005/0147496 A1.

[20] Corsini, A., Rispoli, F., Kinghorn I., Sheard A. G., 2006, "Investigation on improved blade tip concept", ASME Paper GT2004-90592.

[21] Corsini, A., 2006, "Safe Rotation number tip end-plate design concept", *Technical Report* TMRG-DMA-06/FW1, to be published.

[22] Corsini, A., Rispoli, F., Santoriello, A., 2003, "A new stabilized finite element method for advection-diffusion-reaction equations using quadratic elements", in: *Modelling Fluid Flow*, Ed. by T. Lajos et al., Springer Verlag.

[23]Corsini, A., Rispoli, F., 2005, “Flow analyses in a high-pressure axial ventilation fan with a non-linear eddy-viscosity closure”, *Int. J. of Heat and Fluid Flow*, Vol. 26, pp. 349-361.

[24]Inoue, M., Furukawa, M., 2002, “Physics of tip clearance flow in turbomachinery”, ASME paper FEDSM2002-31184.

[25]Borello, D., Corsini, A., Rispoli, F., 2003, “A finite element overlapping scheme for turbomachinery flows on parallel platforms”, *Computers and Fluids*, Vol. 32/7, pp. 1017-1047.

[26]Inoue, M., Kuroumaru, M., Furukawa, M, 1986, “Behavior of tip leakage flow behind an axial compressor rotor”, *J. of Gas Turbine and Power*, Vol. 108, pp. 7-14.

[27]Craft, T.J., Launder, B.E., Suga, K., 1996, “Development and application of a cubic eddy-viscosity model of turbulence”, *Int. J. of Heat and Fluid Flow*, Vol. 17, pp. 108-155.

[28]Gbadebo, S., A., Cumpsty, N., A., Hynes, T., P., 2006, “Interaction of tip clearance flow and three-dimensional separations in axial compressors”, *ASME paper GT2006-90071*.

[29]Khourrami, M., R., Choudari, M., 2001, “A novel approach for reducing rotor tip-clearance induced noise in turbofan engines”, AIAA paper 2001-2148.

Conference on Modelling Fluid Flow (CMFF'06)
The 13th International Conference on Fluid Flow Technologies
Budapest, Hungary, September 6-9, 2006

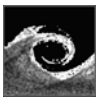

GRID-INSENSITIVE TREATMENT OF WALL BOUNDARY CONDITIONS FOR RANS MODELS

Kemal HANJALIC[1], Mirza POPOVAC[2]

[1] Corresponding Author. Department of Multi-scale Physics, Delft University of Technology. Lorentzweg, 2628 CJ Delft, The Netherlands. Tel.: +31152781448, Fax: +31 15 2781204, E-mail: hanjalic@ws.tn.tudelft.nl
[2] Department of Multi-scale Physics, Delft University of Technology. Lorentzweg, 2628 CJ Delft, The Netherlands. Tel.: +31152781448, Fax: +31 15 2781204, E-mail: mirza@ws.tn.tudelft.nl

ABSTRACT

The treatment of wall boundary conditions in RANS computations of wall friction and heat transfer in complex turbulent flows has long been a major challenge. Because of the need for very fine grid clustering, integration up to the wall (ItW) has never appealed to industry, whereas the conventional and widely popular wall functions (WF) approach has been known to be inadequate in flows that significantly depart from local energy equilibrium. Developments in computer power have encouraged industry to use denser grids, but - especially with automatic gridding - it is difficult to fulfil a priori the fine-grid ItW prerequisite in the whole flow domain. Instead, the first grid point often lies in the buffer layer ($5<y^+<30$ in the wall attached flows), making neither ItW nor WF applicable.

We propose here a compound wall treatment (CWT), which reduces either to the ItW when the first near-wall cell is in the viscous sublayer, or to the appropriate WF when it lies in the fully turbulent region. When the first grid node is in the buffer region, the boundary conditions are provided from blending the viscous and fully turbulent limits using exponential blending functions. This blending is based on a generalization of the expressions for the mean velocity and temperature profiles of Kader (1981) that approximate reasonably well the whole wall region of a boundary layer, including its viscous/conductive and fully turbulent wall layers. This makes the model insensitive to the precise positioning of the first grid point and - within reasonable limits - to the quality of the mesh in the near-wall region. The CWT can be applied in conjunction with any turbulence model that permits ItW, with any wall functions. However, it is advisable to use a well-tuned, physically well-justified and robust ItW model, preferably without empirical damping functions, which has been proved to successfully reproduce properties of a minimum set of generic flows exhibiting various non-equilibrium effects (strong pressure gradients, separation, impingement, and others). Here we use the robust elliptic relaxation ζ-f model proposed by Hanjalić et al. (2004) for the ItW. Likewise, no compound treatment will lead to success in computing non-equilibrium wall bounded flows with a relatively coarse grid, if the conventional wall functions are used. For that reasons, we also present the newly developed generalized wall functions (GWF) that account for non-equilibrium effects and yet preserve the simple standard form making its implementation into the existing CFD codes very easy and straightforward. It is noted that the GWF formulation proposed here is applicable to any high-Re-number model, ranging from the standard k-ε to the second-moment (Reynolds stress) closures. Of course, depending on the model used, the stress components appearing in the wall functions will be evaluated either from the kinetic energy or from the corresponding eddy-viscosity expression, or from the solution of the (algebraic or differential) stress equations.

The computations with fine and coarse meshes of a steady and pulsating flow in a plane channel, in flow behind a backward-facing step and in a round impinging jet using the proposed *compound wall treatment* (CWT) are all in satisfactory agreement with the available experiments and DNS data. The method is recommended for computations of industrial flows in complex domains where it is difficult to generate a computational grid that will satisfy a priori either the ItW or WF prerequisites.

Conference on Modelling Fluid Flow (CMFF'06)
The 13th International Conference on Fluid Flow Technologies
Budapest, Hungary, September 6-9, 2006

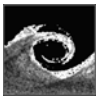

LARGE EDDY SIMULATION OF SEPARATED FLOW USING A NEAR-WALL EDDY-VISCOSITY FORMULATION

Georgi KALITZIN[1], Gorazd MEDIC[2]

[1] Corresponding Author. Department of Mechanical Engineering, Stanford University. 488 Escondido Mall, Stanford, CA 94305-3030, USA. Tel.: +1 650 723 8476, Fax: +1 650 725 3525, E-mail: kalitzin@stanford.edu
[2] Department of Mechanical Engineering, Stanford University. 488 Escondido Mall, Stanford, CA 94305-3030, USA. Tel.: +1 650 723 8476, Fax: +1 650 725 3525, E-mail: gmedic@stanford.edu

ABSTRACT

A novel concept for the near-wall treatment of LES has been proposed and applied successfully to channel flow with both a wall model and wall-parallel coarsening. In that formulation, the LES subgrid-scale eddy-viscosity is replaced in the near-wall region with a RANS eddy-viscosity which is dynamically corrected with the resolved turbulent stress. The RANS eddy-viscosity can either be precomputed using various RANS turbulence models or computed from RANS equations solved simultaneously with the LES.

The aim of this work is to apply the proposed approach to separated flow in a channel with one wall forming a hill-shaped periodic constriction. The proposed near-wall treatment for LES is evaluated for both coarse grids with a wall stress model and with wall-resolved grids coarsened in wall-parallel directions.

Keywords: LES, near-wall eddy-viscosity, separated flow, wall modeling, wall-parallel coarsening

NOMENCLATURE

u^+	[-]	velocity, u/u_τ
u_τ	[m/s]	friction velocity
y^+	[-]	wall distance, $y\,u_\tau / \nu$
p	[Pa]	static pressure
ν	[m^2/s]	kinematic viscosity
ν_t^+	[-]	eddy-viscosity, ν_t / ν
C_p^+	[-]	pressure gradient, $\mathrm{d}p/\mathrm{d}x\,(\nu / u_\tau)$
S	[$1/s$]	strain rate, $1/2\,(\partial_j u_i + \partial_i u_j)$

Subscripts and Superscripts

1	wall-adjacent cells
rms	root mean square
SGS	subgrid-scale
NW	near-wall
^	instantaneous
−	averaged

1. INTRODUCTION

LES resolves the large-scale structures of the flow while modeling the small-scale phenomena. This allows many of the important flow features to be captured without the expense of resolving the smaller scales, whose effects on the large scales are accounted for by sub-grid scale (SGS) models. Unfortunately, the full promise of LES has not yet been realized for wall-bounded flows because current SGS models do not properly account for the small, dynamically important features near a wall. As a consequence, these features must be resolved, resulting in the grid resolution scaling as Re_τ^2 [1]. Such a scaling is almost as expensive as DNS, effectively limiting LES to low to moderate Reynolds numbers.

In an effort to allow LES to be efficiently applied to high Reynolds number flows, many techniques have been proposed. One such technique involves the use of grids coarsened in the wall-parallel direction, while leaving the wall-normal resolution unchanged; this reduces the computational cost for at least one order of magnitude. Not all turbulent scales can be resolved with such grids and additional modeling is required. RANS equations are well suited for this type of grids because only the mean wall-normal gradients must be resolved while the entire turbulence spectrum is modeled. A well known approach in this category is detached-eddy simulation (DES) which was designed to simulate massively separated aerodynamic flows, where RANS is used in the boundary layer and LES resolves the separated region [2]. However, the coupling of RANS and LES regions is not formulated in a satisfactory manner; in the pressure-driven channel this causes significantly overpredicted mass flow rate [3].

Another approach to reducing the computational cost of LES is wall modeling [4]. These models are designed to be used with coarse

grids that do not resolve the wall-layer, allowing LES at a fraction of the cost when compared to wall-resolved grids. Traditional wall models provide wall stresses to the LES as boundary conditions; a successful application of that approach is not trivial, as discussed in [5].

The aim of this work is to apply the eddy-viscosity based near-wall treatment for LES proposed in [6-8] to complex flows such as the flow in a channel with one wall forming a hill-shaped periodic constriction [9]. The near-wall treatment is evaluated for both coarse grids with a wall stress model and with wall-resolved grids coarsened in wall-parallel directions.

2. NEAR-WALL FORMULATION

We have proposed a novel concept for the near-wall treatment of LES which has been successfully applied to various flows with both a wall model and wall-parallel coarsening. In that formulation, a RANS eddy-viscosity corrected dynamically using the resolved turbulent stress is imposed near the wall (while the dynamic Smagorinsky model is used elsewhere):

$$\nu_t^{SGS,NW} = \nu_t^{RANS} + \overline{\hat{u}\hat{v}} \Big/ \frac{d\bar{\hat{u}}}{dy} \qquad (1)$$

where $\hat{u}$ and $\hat{v}$ are the streamwise and wall-normal velocity components. Since $\overline{\hat{u}\hat{v}}$ and $d\bar{\hat{u}}/dy$ have opposite signs, the second term on the right hand side of (1) is negative. Thus, in the presence of turbulent fluctuations, the near-wall LES viscosity, $\nu_t^{SGS,NW}$, is always less than the RANS viscosity, ν_t^{RANS}, with the difference being a dynamic correction for the resolved fluctuations. The RANS eddy-viscosity can either be precomputed and stored in a look-up table or obtained from a simultaneous solution of RANS turbulence model equations. When the latter approach is used, the LES provides the averaged velocity $\bar{\hat{u}}$ for the turbulence model equations, see [10] and [11].

For the wall modeling computations presented in this paper, the LES equations are solved with the wall stress boundary condition and the near-wall subgrid-scale eddy-viscosity, $\nu_t^{SGS,NW}$, in the wall-adjacent cells. The wall stress, $\tau_w = \rho u_\tau^2$, is obtained using a look-up table $u^+ = f(y^+)$ and the RANS eddy-viscosity is also computed from a similar look-up table $(\nu_t^{RANS})^+ = f(y^+)$.

The LES code used in the computations is a second-order finite-volume method for solving the time-dependent three-dimensional incompressible Navier-Stokes equations in a generalized coordinate system [12]. The approach uses volume flux variables with the traditional time-splitting fractional step method. The equations are discretized using a staggered mesh system: the pressure is defined at the cell center and the volume flux across each face. The dynamic Smagorinsky model [13] is adopted as the subgrid scale model.

3. CHANNEL FLOW

3.1. Wall-parallel coarsening

If the no-slip boundary conditions are to be used, only limited coarsening in the wall-normal direction can be applied and, thus, savings must be achieved through wall-parallel coarsening. The results for both the proposed near-wall treatment for LES dynamically coupled with the k-ω model and the traditional LES are presented for the computations of channel flow at $Re_\tau = 950$ on a grid with 64 x 64 x 64 cells (Figure 1). The near-wall region, where $\nu_t^{SGS,NW}$ is applied, extends up to y / h = 0.05. The mean velocity is significantly overpredicted when the traditional LES is used on a grid this coarse. DES also fails for channel flow. In contrast, the results with the near-wall treatment agree much better with the DNS presented in [14].

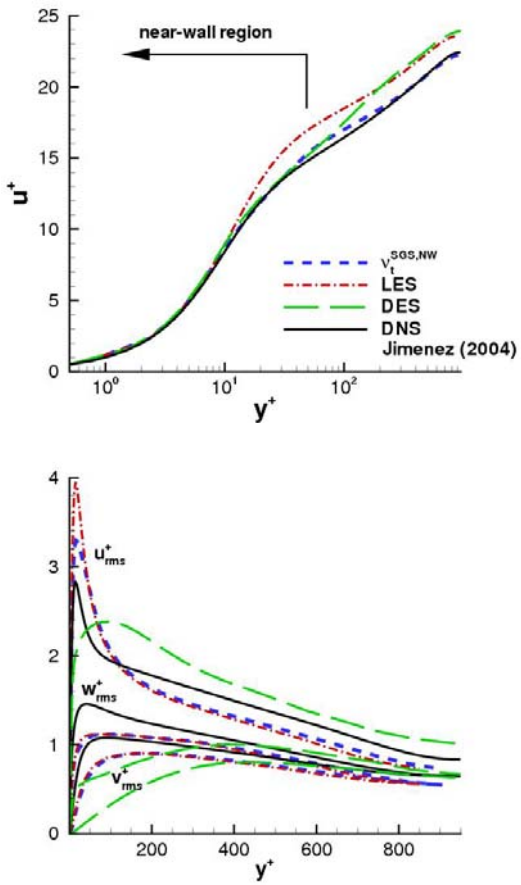

Figure 1. Channel flow, Re_τ = 950, wall-parallel coarsening, computational grid, 64 x 64 x 64 cells. Mean (top) and rms (bottom) velocities.

At these Reynolds numbers, the savings in CPU time for wall-parallel coarsening are about one order of magnitude, when compared to full LES. This indicates that wall-parallel coarsening used with the proposed near-wall treatment may be a viable technique for performing LES at lower cost.

3.2. Wall modeling using $\nu_t^{SGS,NW}$

Applying the proposed approach with a wall stress model to LES on coarse grids effectively allows the computations of high Reynolds flows at a fraction of a cost of a full-blown LES. Here, $\nu_t^{SGS,NW}$ is applied only in the wall-adjacent cells. We have obtained results for a range of high Reynolds numbers on coarse grids with 32 x 33 x 32 cells which show that the logarithmic mean velocity profile is consistently predicted very well (Figure 2).

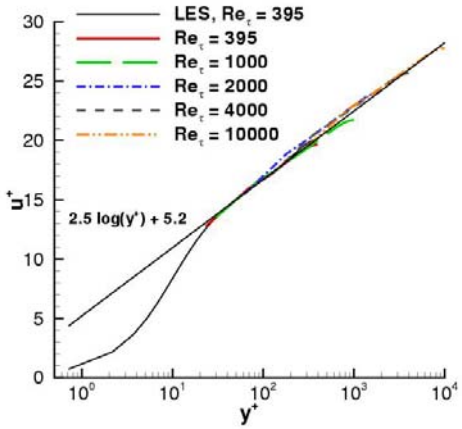

Figure 2. Channel flow, wall modeling for LES, mean velocity for various Reynolds numbers, computational grid, 32 x 33 x 32 cells.

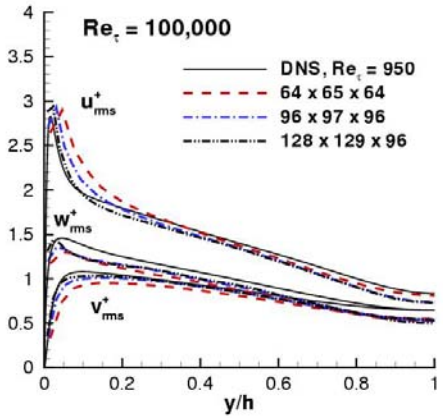

Figure 3. Channel flow, Re_τ = 100,000, wall modeling for LES, rms velocities for various computational grids

Even for channel flow at Re_τ = 100,000, the finest grid used in a computations is relatively coarse (barely exceeding one million gridpoints, with 128 x 129 x 96 cells). The question that such computations raise is the following: What turbulence information is retained on grids this coarse? The profiles for rms velocities agree well with DNS results [14] at Re_τ = 950 (Figure 3). In addition, a detailed analysis of energy spectra indicates that large structures qualitatively agree to the DNS which is at a much lower Re_τ.

4. FLOW OVER A PERIODIC HILL

For the periodic hill, the equation (1) can still be applied as long as the quantities $\overline{\hat{u}'\hat{v}'}$ and $d\overline{\hat{u}}/dy$ are defined in a local coordinate system aligned with the wall. In practice, $\overline{\hat{S}}_{ij}$ and $\overline{\hat{u}_i'\hat{u}_j'}$ are computed in the general coordinate system and are then expressed in the local coordinate system.

The flow over a periodic hill [9] has been computed using the grids coarsened in the wall-parallel directions as well as with a wall-stress model on a coarse grid. The Reynolds number based on the channel height H (and bulk velocity) is 21,560 (which corresponds to 10595 if Re is based on the hill height h). The streamwise length of the channel is 9 h, and the spanwise width is equal to 4.5 h. First, a wall-resolved LES was performed on a grid that contains 256 x 128 x 128 cells and the results were compared to similar computations presented in [9] where a wall-resolved grid with 4.7 million cells was used. The location of the reattachment point in our computations agrees very well with [9]; x_r = 4.75 vs. 4.72. The isosurfaces of instantaneous streamwise vorticity and the contours of the time- and spanwise-averaged eddy-viscosity, as well as two-dimensional streamlines are shown in Figures 4a and 4b, respectively.

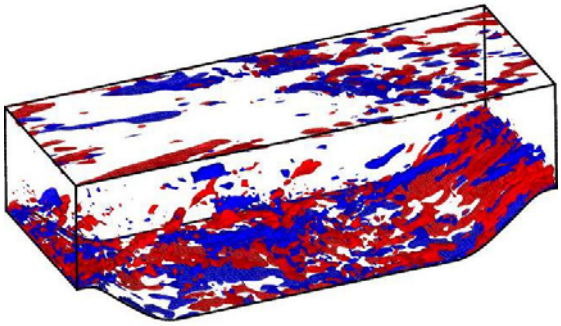

Figure 4a. Flow over a periodic hill , wall-resolved LES, computational grid: 256 x 128 x 128 cells, isosurfaces of instantaneous stream-wise vorticity.

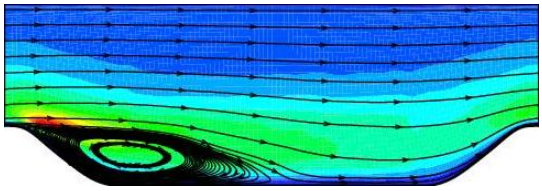

Figure 4b. Flow over a periodic hill, wall-resolved LES, location of the reattachment point, x_r = 4.75; contours of averaged eddy-viscosity and the corresponding streamlines.

4.1. Wall-parallel coarsening

Next, a grid coarsened in the wall-parallel directions (with 128 x 64 x 32 cells, shown in Figure 5) is used to assess the performance of the proposed approach. The near-wall formulation has been tested using a look-up table for ν_t^{RANS}, as well as the dynamic coupling with both k-ω and Spalart-Allmaras turbulence models. The near-wall eddy-viscosity $\nu_t^{SGS,NW}$ was applied up to y / h = 0.05, where h is the hill height.

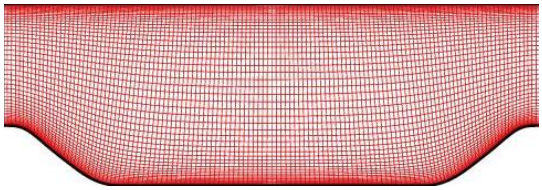

Figure 5. Wall-parallel coarsening: computational grid, 128 x 96 x 32 cells

The prediction of the location of the reattachment point computed using traditional LES, DES and the proposed near-wall treatment for LES dynamically coupled with the k-ω model is compared to the result from the wall-resolved LES in Table 1. The superiority of the near-wall treatment is evident.

Table 1. Location of reattachment point, x_r

LES[9]	under-resolved LES	DES	near-wall treatment
4.72	3.8	4.05	4.7

The corresponding contours of the time- and spanwise-averaged eddy-viscosity, as well as two-dimensional streamlines are shown in Figures 6-8.

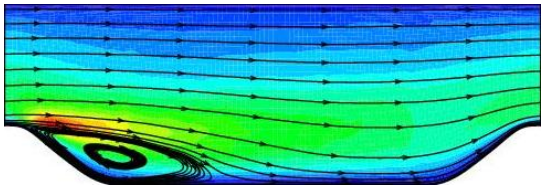

Figure 6. Wall-parallel coarsening: traditional LES, x_r = 3.8

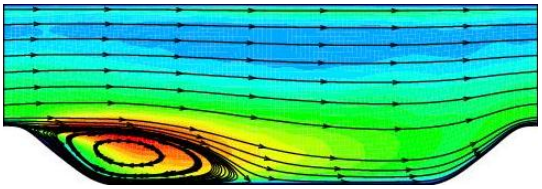

Figure 7. Wall-parallel coarsening: DES, x_r = 4.05

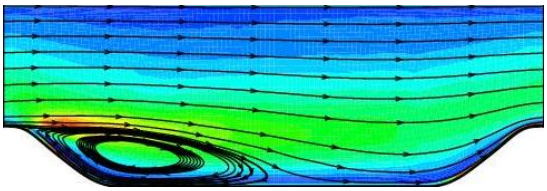

Figure 8. Wall-parallel coarsening: near-wall treatment for eddy-viscosity, x_r = 4.7

A detail of the near-wall distribution of eddy-viscosity computed on the grid containing 128 x 64 x 32 cells is shown in Figure 9 for the traditional (under-resolved) LES and the computation that employs the proposed near-wall treatment for LES. The increased near-wall eddy-viscosity increases the momentum flux near the wall leading to a larger separation.

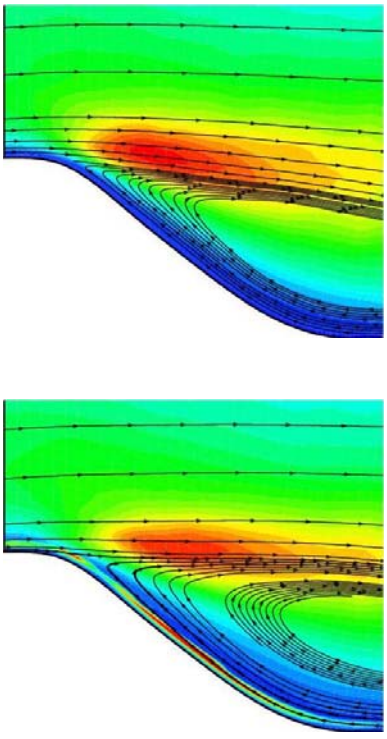

Figure 9. Detail of the near-wall eddy-viscosity distribution on the grid with 128 x 64 x 32 cells computed using the traditional LES (top) and the proposed near-wall formulation (bottom).

Finally, the profiles of averaged streamwise velocity computed using the grid coarsened in the wall-parallel directions are compared to the results from the wall-resolved LES. Two profiles, computed at x/h = 0.0 and 4.5, are presented in Figure 10. Clearly, consistent with the streamlines plots, the near-wall treatment for the eddy-viscosity yields velocity profiles which are in a better agreement with the resolved LES, than the results from the under-resolved LES or DES.

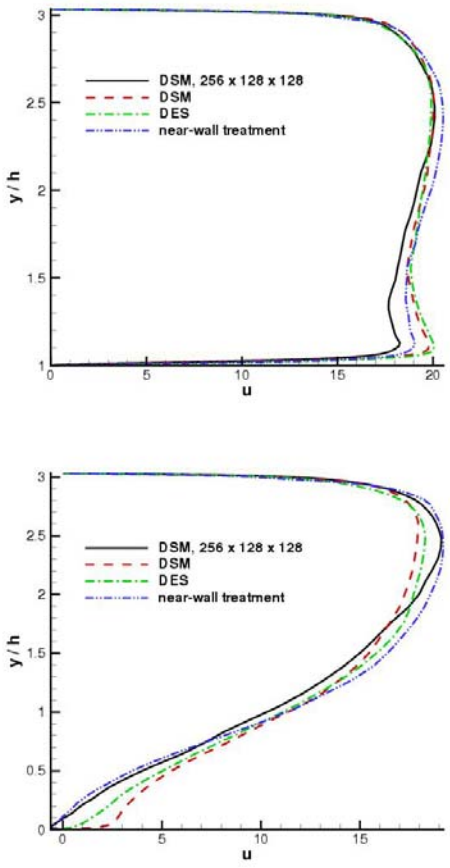

Figure 10. Wall-parallel coarsening, computational grid 128 x 64 x 32 cells: profiles of mean streamwise velocity, at x / h = 0.0 (top) and x / h = 4.5 (bottom).

4.2. Wall modeling using $\nu_t^{SGS,NW}$

Here, a wall-stress model is used with the proposed near-wall treatment for eddy-viscosity to compute the flow over a periodic hill on a coarse grid that does not resolve the near-wall region. The computational grid contains 64 x 32 x 32 cells and is shown in Figure 11. The values of y_1^+ for these computations are in the range of $0 < y_1^+ < 15$.

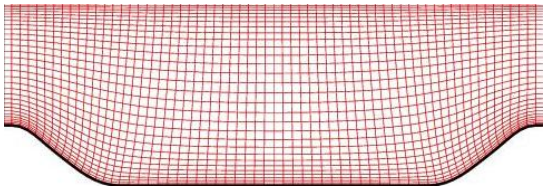

Figure 11. Wall modeling: computational grid, 64 x 32 x 32 cells

First, we apply the wall-stress model described in Section 2, formulated for zero-pressure gradient, to compute τ_w. The reattachment point is at about $x_r = 3.3$; the contours of the averaged eddy-viscosity and streamlines are shown in Figure 12.

The zero-pressure gradient wall–stress model fails to capture the pressure gradient effects. A significant improvement can be achieved by taking the pressure gradient into account when computing the wall stress τ_w. This was proposed for RANS in [15]; i.e the pressure gradient is accounted for explicitly via:

$$\frac{d}{dy^+}\left(\left(1+\nu_t^+\right)\frac{du^+}{dy^+}\right)=\frac{dp^+}{dx^+}=C_p^+ \qquad (2)$$

By applying the van Driest formula for eddy-viscosity, ν_t^+, equation (2) can be integrated resulting in the equation for u_τ:

$$u^+ = f_0\left(y^+\right)+ f_C\left(y^+, C_p^+\right) \qquad (3)$$

where f_0 defines the standard zero-pressure gradient velocity profile and f_c accounts for the pressure gradient effects.

In the context of LES, this formulation can be applied similarly to the zero-pressure gradient wall stress model; the instantaneous velocity $\hat{u}$ and pressure gradient $d\hat{p}/dy$ from LES are used in (3) to compute the friction velocity u_τ. The computations with this procedure and the proposed near-wall treatment for eddy-viscosity yielded a bigger separation with the reattachment location $x_r = 3.75$. The corresponding contours of the averaged eddy-viscosity and streamlines are shown in Figure 13. The isosurfaces of instantaneous streamwise vorticity are shown in Figure 14 to illustrate the unsteady nature of the flow. Note how the resolved structures computed on this coarse grid (64 x 32 x 32 cells) differ from those presented in Figure 4a computed on a much finer, wall-resolved grid (256 x 128 x 128 cells).

As for the computations on grids coarsened in the wall-parallel directions, the profiles of averaged streamwise velocity computed using the wall model are compared to wall-resolved LES in Figure 15; the agreement is surprisingly good (obviously, the reattachment occurs to early).

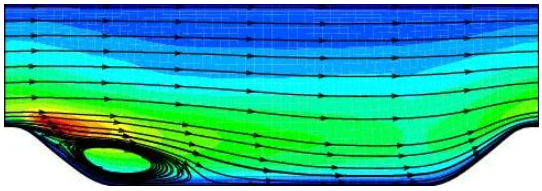

Figure 12. Wall modeling: wall-stress model with the near-wall treatment for eddy-viscosity, x_r = 3.3

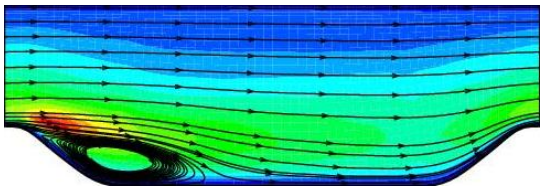

Figure 13. Wall modeling: pressure-gradient sensitive wall-stress model with the near-wall treatment for eddy-viscosity, x_r = 3.75

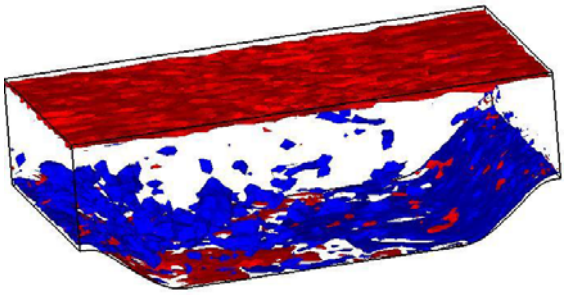

Figure 14. Wall modeling: isosurfaces of instantaneous streamwise vorticity.

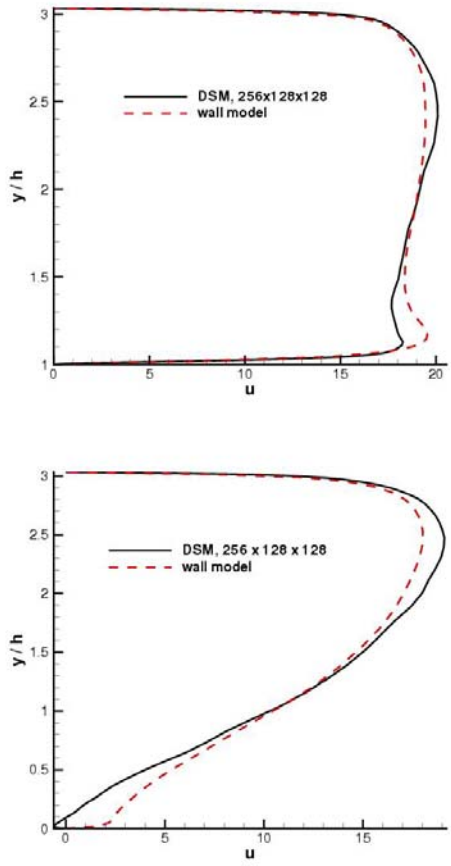

Figure 15. Wall modeling, computational grid 64 x 32 x 32 cells: profiles of mean streamwise velocity, at x / h = 0.0 (top) and x / h = 4.5 (bottom).

5. CONCLUSIONS

The flow problems presented in this paper show the ability of the proposed approach to handle complex geometries, flow separation, as well as adverse and favorable pressure gradient. The results for the flow over a periodic hill for the grids coarsened in the wall-parallel directions clearly show the superiority of the proposed approach over traditional under-resolved LES and detached eddy simulation (DES). It has also been observed that when the wall modeling approach is used, the wall stress model has to account properly for the pressure gradient effects.

The successful application of the near-wall treatment for these test cases showed the feasibility of near-wall treatment for LES as well as the expected computational savings for aerospace flows, such as the flow over an airfoil.

REFERENCES

[1] Baggett, J.S., Jimenez, J, and Kravchenko, A.G., 1997, "Resolution requirements in large-eddy simulation of shear flows", *CTR Annual Research Briefs*, pp. 51–66.

[2] Spalart, P.R., Jou, W.-H., Strelets, M., and Allmaras, S.R., 1997, "Comments on the feasibility of LES for wings, and on a hybrid RANS/LES approach," *First AFOSR International Conference on DNS/LES*, Ruston, LA, pp. 4-8.

[3] Nikitin, N.V., Nicoud, F., Wasistho, B., Squires, K.D., and Spalart, P.R., 2000, "An approach to wall modeling in large-eddy simulations," *Phys. Fluids*, Vol. 12 (7), pp.1629.

[4] Piomelli, U., and Balaras, E., 2002, "Wall-layer models for large-eddy simulations", *Ann. Rev. Fluid Mech.*, Vol. 34, pp. 349–374.

[5] Cabot, W., 1997, "Wall models in large eddy simulation of separated flow," *CTR Annual Research Briefs*, pp. 97–106.

[6] Kalitzin, G., Templeton, J.A., and Medic, G., 2005, "A near-wall eddy-viscosity formulation for LES", *Proceedings of Symposium on Complex Effects in LES*, *Limassol, Cyprus, September 20-24, 2005*, Springer-Verlag, Heidelberg.

[7] Medic, G., Templeton, J.A., and Kalitzin, G., 2006, "A formulation for near-wall RANS/LES coupling", *Int. Journal of Engineering Science* (accepted).

[8] Templeton, J.A., Medic, G., and Kalitzin, G., 2005, "An eddy-viscosity based near-wall treatment for coarse grid LES", *Phys. Fluids*, Vol. 17(10).

[9] Temmerman, L., Leschziner, M.A., Mellen, C.P., and Frohlich, J., 2004, "Investigation of wall functions and SGS models in LES of separated flow in a channel with streamwise periodic constrictions", *Int'l. J. Heat & Fluid Flow*, Vol. 24, pp. 157-180.

[10] Medic, G., Daeninck, G., Templeton, J.A., and Kalitzin, G., 2005, "A framework for near-wall RANS/LES coupling", *CTR Annual Research Briefs*.

[11] Daeninck, G., Medic, G., Templeton, J.A., and Kalitzin, G., 2006, "On near-wall dynamic coupling of LES with RANS turbulence models", *ASME Paper* GT2006-91234.

[12] Wu, X., and Durbin, P. A., 2001. "Evidence of longitudinal vortices evolved from distorted wakes in a turbine passage". *J. Fluid Mech.*, Vol. 446, pp. 199–228.

[13] Germano, M., Piomelli, U., Moin, P., and Cabot, W., 1991, "A dynamic subgrid-scale eddy-viscosity model", *Phys. Fluids*, Vol. 3, pp. 1760–1765.

[14] Hoyas, S., and Jimenez, J., 2005, "Scaling of the velocity fluctuations in turbulent channels up to Re = 2003", *CTR Annual Research Briefs*.

[15] Medic, G., and Mohammadi, B., 1998, "A critical evaluation of the classical k-epsilon model and wall-laws for unsteady flows over bluff bodies", *Int'l J. Computational Fluid Dynamics*, Vol. 10(1), pp. 1-12.

Conference on Modelling Fluid Flow (CMFF'06)
The 13th International Conference on Fluid Flow Technologies
Budapest, Hungary, September 6-9, 2006

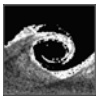

TRANSITION MODELLING IN TURBOMACHINERY

Witold ELSNER[1]

[1] Corresponding Author. Department of Mechanical Engineering and Computer Science, Czestochowa University of Technology. Al. Armii Krajowej 21, 42-200 Czestochowa, Poland: Tel. +48 34 32 50 507, Fax: +48 34 32 50 555, E-mail: welsner@imc.pcz.czest.pl

ABSTRACT

The paper deals with the problems of boundary layer modeling in turbomachinery applications, where various mechanisms are present especially under the conditions of upstream wakes. The paper presents the review of recent achievements in interpretation of by-pass, wake induced and separation induced transition processes. It discusses the most important aspects of transition modeling. This review is complemented by physical explanation of those phenomena based on the recent literature data as well as on the results of numerical and experimental investigations.

Keywords: transition modelling, boundary layer, by-pass and wake induced transition, turbomachinery

1. INTRODUCTION

Laminar-turbulent transition in boundary layers influences performance of many technical devices. The location of the onset and the extension of transition are of major importance since they determine drag and lift forces and heat fluxes that are crucial for an overall efficiency and performance of a variety of machinery and devices. One the most common examples of the machinery, where the laminar-turbulent transition is of particular importance are the turbomachinery and gas and aero-engine turbines in particular. Despite a technical maturity of gas turbines the research optimisation and development concerning this technology still continues, as increasing the engine's performance by a fraction of a percent or improving the turbine cooling in face of ever-increasing turbine inlet temperature provides enormous economic benefits. Hence the understanding of the laminar-turbulent transition in gas turbine cascades plays very important role in their optimisation [1].

In general there are three important transition regimes. The first is called natural transition. This transition regime can appear in practice only if free stream turbulence is very low that happens only occasionally in technical applications. Such a mode of transition begins with a weak instability in the laminar boundary layer as described first by Tollmien and Schlichting (see Schlichting, 1979) and proceeds through various stages of amplified instability to fully turbulent flow. The linear stability theory plays an important role in research and understanding of this transition regime. Because of increased level of turbulent intensity this type of transition is not present in turbomachinery.

The second mode, frequently called "bypass" transition after Morkovin (1969), is caused by interaction of the vortex structures in the free stream and the boundary layer and completely bypasses the Tollmien-Schlichting waves. This is a common mode of transition in the case of turbomachinery flows.

The third mode, called "separated-flow" transition following Mayle (1991), occurs in a separated boundary layer and may or may not involve the mechanism of Tollmien-Schlichting waves. This mode of transition appears in the boundary layers with strong adverse pressure gradient particularly in the compressors and low-pressure turbines [3].

In technical applications due to high turbulence level of the incoming flow especially under the wake impact the bypass transition is the dominant mode and hence its modelling is crucial for practice. On the other hand, the wakes also influence the separation behaviour of boundary layer and have a large effect on the performance of airfoils as well as turbine and compressor blades.

2. WAKE INDUCED TRANSITION – THE EFFECT OF TURBULENCE

As a consequence of high turbulence level of background flow, turbulent spots are created in

boundary layer as a direct result of turbulence fluctuations of outer stream, and this type of l-t transition is known as a bypass one. The viscous wakes present in turbomachinery flows, which transport additional turbulence towards the blade surface, trigger the turbulent spot production and finally shift the location of l-t transition upstream.

According to the latest evidence [4] the bypass transition is initiated by the interaction of freestream disturbances and this mechanism is usually denoted as receptivity mechanism. Initially, the small scales from the freestream are prevented to perturb the boundary layer by the mean shear (it is known as sheltering mechanism). Then the low-frequency fluctuations mainly caused by irregular motion of long structures with narrow spanwise scales (greater usually than 15-20 boundary layer thickness) appear inside the boundary layer and they were denoted by Kendall [4] as Klebanoff mode. In fact, the Klebanoff mode is ensemble-averaged view of streaky structures as it was observed in numerous experimental works [4]. The streaky structures are then disturbed by small-scale eddies from freestream and irregularities similar to Kelvin-Helmholtz instability are triggered. Finally, they develop into turbulent spots, which spread laterally and intensively propagate downstream the flow. As a result, spots originating from different locations merge to form a completely turbulent boundary layer.

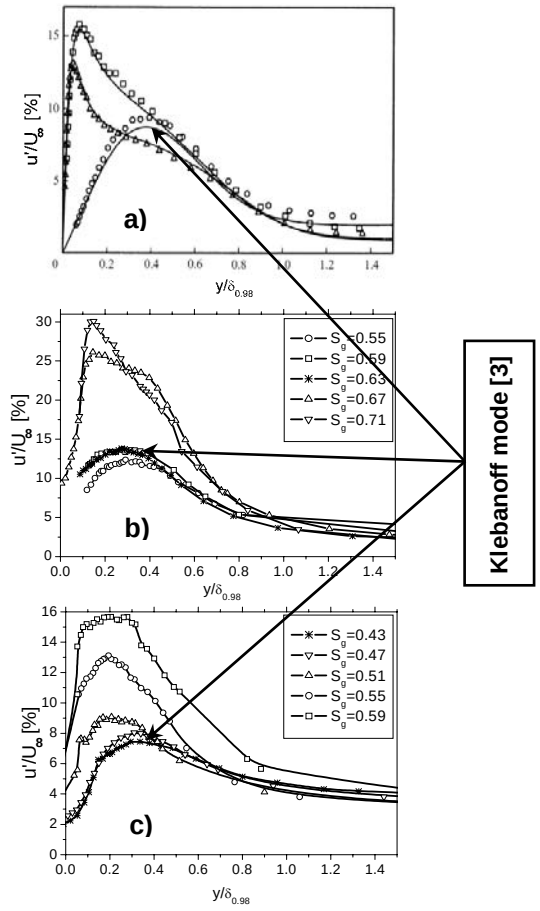

Fig.1 Velocity fluctuation profiles u' versus y/δ, according to Jacobs, Durbin [6] (a), for steady case (b), for unsteady case (c)

Growth and merging of spots are the crucial features of the bypass mechanism. One of the basic concepts was the Narasimha's concentrated breakdown hypothesis, stating that spot production rate could be represented by Dirac delta function. This is due to the fact, that upstream of the start of transition, spots are unable to form while downstream of the start, the formation of spots is inhibited by calmed regions following spots which were formed earlier. Somewhat later Shulte and Hodson [5] proposed continuous breakdown concept, which is more appropriate especially for wake induced transition.

Because of the high turbulence level in the wake, the physical mechanism of unsteady transition should be the same as in the case of bypass transition. The confirmation of this suggestion was given initially in the paper of Wu at al [6], who performed DNS analysis of the wake interaction with boundary layer on the flat plate. Wu et al [6] proved, that inlet wake disturbances inside the boundary layer evolved rapidly into longitudinal puffs during an initial receptivity phase. Small scale freestream vortices interacted with boundary layer edge (longitudinal streaks) also in this case, through a local Kelvin-Helmholtz instability and then negative streamwise fluctuations associated with the inflectional profiles evolved into strong forward eddying motions, producing young spots.

The evidence that in the boundary layer the mechanism of wake induced transition is the same as in the case of the bypass transition, was recently given by Elsner [7]. In the experiment performed for the turbine blade cascade disturbed by the wakes generated by the wheel with cylindrical bars rotating upstream the cascade, the existence of Klebanoff mode in the pre-transitional phase was proved. It is commonly assumed nowadays [4], that the Klebanoff mode is the ensemble-averaged signature of the longitudinal streaky structures. Fig. 1 shows the comparison of the streamwise velocity fluctuation profiles in the boundary layer taken from Jacobs and Durbin [3] (a), from Elsner [7] for steady (undisturbed) case (b), and for the unsteady case with upstream wakes (c). It is seen that in both steady and unsteady cases the rms distribution has the same characteristic *"smooth"* shape with maximum at $y/\delta \approx 0.4$, which is seen also for the reference data. One can also notice that the first appearance of turbulent spot, seen as increase of rms level accompanied with shift of the maximum towards the blade surface is observed at various streamwise locations in each case. For the steady case the increase of energy of fluctuations appears for streamwise non-dimensional coordinate S_s=0.67, while for the unsteady case it is shifted upstream

i.e. it is observed for S_s=0.55. This behavior may be regarded as a proof of strong wake impact on the boundary layer development.

3. WAKE INDUCED TRANSITION – THE JET EFFECT

As it was already mentioned heavily loaded blades used in modern turbine aero-engines are subjected to strong adverse pressure gradient. Such conditions together with relatively low Reynolds number lead to development of separation on a suction side of the blade and as a consequence increased profile losses. Presence of upstream wakes, transporting high energy medium, has a positive effect visible as a reduction of the area covered by separated boundary layer.

However, as it was shown by Stiger and Hodson [8] the transition to turbulence in such geometrical configurations could not only be due to increased turbulence level, but also due to the negative jet of the wake. The jet effect results from the velocity deficit in the wake, which forces the relative movement of the fluid from the pressure side the suction side of the turbine blade profile. Close to the suction side in the front of the wake one may observed the acceleration of the flow followed by its deceleration in reference to the mean velocity. It was experimentally confirmed [8] that such a kinematic wake impact, by forcing inflectional velocity profiles, causes breakdown of the separated shear layer as a result of Kelvin-Helmholtz instability, which then develops into roll-up vortices of a scale of separation bubble. The roll-up vortices produce high level of turbulent kinetic energy what leads to the transition development. The authors also pointed out that for quasi-steady flow the mechanism could be similar, although in this case the roll-up vortices have much smaller scale. These observations were lately confirmed by Opoka and Hodson [9], who discovered additionally that higher freestream turbulence delayed appearance of inflexional velocity profiles and reduced the chance for forming of roll-up vortices.

The evidence of the way how the wake interacts with the separation bubble and the description of the new transition mechanism is crucial for the development of transition models applied especially for highly decelerated boundary layers.

4. TRANSITION MODELING

The variety of possible transition mechanisms in turbomachinery makes it difficult to propose the general strategy for numerical simulation. Intuitively, the best solution for modeling transitional boundary layer is application of Direct Eddy Simulation (DES) or Large Eddy Simulation (LES). However, in LES which unlike DNS resolves only dynamically important (large) scales the effect of unresolved small scales is modelled. One question that arises when applying LES to transition problem regards its capability to predict the development of shear layer and vortices whose scale is close to the numerical filter [11]. A subgrid scale model should not dissipate the energy of the low level perturbations during the initial stages of transition, but should reproduce the energy transfer to the unresolved scales during the non-linear stages when these marginally resolved structures are generated. LES was already successfully used in simulating bypass transition on the flat plate, among the others by Voke and Yang [10], and Huai at al [11] who were able to show the pretransitional linear instability modes, the secondary instability Λ-vortex structures and the streaky like structures. However, application of LES for modelling transition is still limited to the low Reynolds number flows as for higher Reynolds numbers the difference between the largest and the smallest eddies increases and progressively wider range of scales needs to be resolved by the subgrid scales model. The second limitation is the required numerical mesh and resulting high computational time, because approaching the wall, the scales diminishes their dimension so finer and finer grid is required.

Hence the RANS methods and for unsteady calculations URANS with appropriately modelled transitional boundary layer remain the only presently applicable engineering tools to study the transitional flows. It means that it is worth to make effort to improve and look for the new RANS or URANS modelling approaches especially because of strong interest of industry.

Application of existing low-Re turbulence models for laminar-turbulent transition boundary layer, as reviewed by Savill [12] and recently by Menter et al. [13] are highly empirical and require experimental data for the proper calibration. In these methods to determine the onset of transition usually various experimental correlations are used. According to Menter et al. [13] the ability of a low-Reynolds turbulence model to predict transition seems to be coincidental, as the calibration of the damping functions is based on the viscous sublayer behaviour and not on transition from laminar to turbulent flow.

Transition process could be described by intermittency parameter γ, which gives information about the fraction of time, when the flow is turbulent. That is why the coupling with intermittency seems to be the best way to take into account the physical mechanism of transitional flow and model transition in proper way. The estimated intermittency factor at the current location and in time (for the unsteady calculations) is usually used as a multiplier of the production term in the

turbulence model. In the pretransitional regime γ is set to zero, and when it attains the positive value the transition is initiated.

Recently, some new methods were developed, from which all rely on the intermittency parameter. The first one is the Prescribed Unsteady Intermittency Model (PUIM) developed at Cambridge University [14] which solely relies on empirical correlations. PUIM calculates a distance-time intermittency distribution as a function of space and time field (constant in time in the case of steady flow simulation). To have this information PUIM employs Mayle [1] and Abu-Ghannam and Shaw (1980) correlations for transition onset and also Mayle or Gostelow and Walker (1992) correlations for spot production rate. The spreading of the turbulent spots is prescribed using functions of the edge velocity and the pressure gradient parameter. For separated flow, the other Mayle correlation gives the spot production rate from the momentum-thickness Reynolds number at separation. The detection of the separation arises from the skin friction and Thwaites criterion. Such a solution ensures that not only attached flow transition onsets but also separated onsets could be identified. The high quality of this approach was confirmed among the others in T106 [14] and on N3-60 test cases [15].

Two other methods involve transport equations of intermittency, the first was developed by Lodefier and Dick at Ghent University [16] and the second is a result of the work performed by Menter and co-authors [17]. According to the first approaches two dynamic equations for intermittency: one for near-wall intermittency γ and one for free-stream-intermittency ζ were proposed. The near wall intermittency takes into account the fraction of time during which the near-wall velocity fluctuations caused by transition have a turbulent character and tend to zero in the free stream region while on the wall attains unity. The free-stream factor ζ describes the intermittent behavior of the turbulent eddies, coming from the free stream and impacting into the underlying pseudo-laminar boundary layer. Near the wall, the eddies are damped and the free-stream factor goes to zero while in the free-stream reaches unity. For onset detection in case of bypass and turbulence wake induced transition the model employs Mayle [1] correlation. For quasi-steady separation transition a criterion proposed for such type of flows by Mayle [1] is applied. Additional criterion is used in case of wake induced transition over a separation bubble.

This method shows to be a efficient tool for prediction of wake interaction with the separation bubble and especially for wake interaction with the attached flow [18].

A different strategy is proposed by Menter at all [17].In this method, only local information is used to activate the production term in the intermittency equation, and the link between the correlations and the intermittency equation is achieved through the use of the vorticity Reynolds number. The proposed model is based on the SST turbulence model and two transport equations. The first one is an intermittency equation used to trigger the transition process. The second transport equation of momentum thickness Reynolds number $Re_{\theta t}$ was implemented for avoiding non-local operations introduced by experimental correlations. Outside the boundary layer the transport variable is forced to follow the value of $Re_{\theta t}$ given by the correlations. For this purpose the standard and in-house correlations are used for natural, bypass and separation induced transition. This information is then diffused into boundary layer with the use of standard diffusion term. Due to this methodology the strong variation of the turbulence intensity and pressure gradient, which are typical for turbomachinery can be taken into account. The local information used to trigger the onset of the transition in this model, is the vorticity Reynolds number Re_v. This quantity depends only on density, viscosity, wall distance and the vorticity, so it could be easily computed at each grid point. It is the main advantage of this methodology which could be applied for a parallel calculations on unstructured grids. Our own experience [19] shows that this model, in spite of lack of physics in the proposed additional equation for $Re_{\theta t}$, is able to predict properly the periodical evolution of the boundary layer under the influence of impinging wake with adequate quality. One should noticed however, that some tuning of the correlation for length of the transition should be done.

All the above transition models are used in connection with the linear turbulence model. Another approach is proposed by Lardeau and Leshziner [20], where the intermittency based formulation is coupled with low-Re algebraic Reynolds–stress model. From this assumption it results that this model should return properly all the Reynolds-stress components, what is especially important for the near wall flows where strong turbulence anisotropy is present. The advantage of this modeling approach the ability to model the pretransitional rise of turbulence intensity, which was experimentally confirmed, among the others by Elsner at all. [15]. This ability is achieved mainly due to the introduction of parameters modifying dumping functions, which control its cross-flow and streamwise variations by taking into account Klebanoff mode properties observed in the pretransitional phase of boundary layer development. The experimental verification of this methodology based mainly on ERCOFTAC data base shows improvement in the prediction of onset transition and its length [20].

6. CONCLUSIONS

The paper proves, that the accurate modeling of complex geometries in turbomachines is of primary importance. The experimental results discussed in the paper show the complexity of the process of the transition from laminar to turbulent state, especially under the condition of wake impact. It is concluded, that this process induced by freestream turbulence consists of the formation and growth of a streaky structures, followed by the development of secondary instabilities, formation of spots which coalescence into fully developed turbulent boundary layer. Another mechanism is present when wake interacts with separation bubble, where kinematic forcing by Kelvin-Helmholtz instability, induce development of roll-up vorticies.

The paper reveals, that currently only the mechanisms of generation, amplification and convection of isolated turbulent spots could be modelled, while the pretransitional phase is only mimiced by various experimental correlations for transition onset. The exception is the Lardeau and Leshziner model which attempts to model the pretransitional Klebanoff mode fluctuations.

It is also shown that currently the only feasible way to take into account the physical mechanism of transitional flow and to model transition in a proper way is to couple the turbulence model with intermittency.

The problem, which should be also considered during the unsteady computations in the URANS framework is the proper modeling of a unsteady movement of the upstream wake. In this context the grid quality in the blade passage, the number of time steps per one wake period and methods of wake parameters prescription at the inlet to the computational domain, is important.

ACKNOWLEDGEMENTS

The research was supported by the Polish State Committee for Scientific Research under the research grant No. 3T10B 08426.

REFERENCES

[1] Mayle R., 1991, “The role of laminar-turbulent transition in gas turbine engines”. ASME J. of Turbomachinery, vol. 113, pp. 509-537

[2] Jacobs, R.G. and Durbin, P.A., 2001, “Simulations of bypass transition”, J. Fluid Mech., Vol. 428, pp. 185-212

[3] Howell R.J, E., Hodson H.P, Shulte V., Stiger R.D., Schiffer H.P., Haselbach F., Harvey N.W., 2002 “Boundary Layer Development in the BR710 and BR715 LP Turbines—The Implementation of High-Lift and Ultra-High-Lift Concepts”, ASME J. of Turbomachinery, vol. 124, pp. 385-392

[4] Kendall J.M., 1985, „Experimental study of disturbances produced in a pre-transitional laminar boundary layer by week free stream turbulence”, AIAA Paper 85-1695

[5] Schulte V., Hodson H. (1998); Prediction of the becalmed region for LP turbine profile design, Trans. ASME, J. of Turbomachinery, vol. 120, pp.839-846

[6] Wu X., Jacobs R.G., Hunt J.C.R., Durbin P.A., 1999, ”Simulation of boundary layer transition induced by periodically passing wakes”, J. Fluid Mech., Vol. 398, pp.109-153

[7] Elsner W., 2004, “Influence of nonstationary interactions on laminar-turbulent transition process on a turbine blade profile”, CzUT Publishing, Ser. Monographs, vol. 103, Czestochowa

[8] Stieger R. D. and Hodson H. P. (2003), The transition mechanism of highly-loaded LP turbine blades. ASME GT-2003-38304, Atlanta, USA

[9] Opoka, M.M., Hodson, H.P, 2005, “An Experimental Investigation on the Unsteady Transition Process on the High Lift T106A Turbine Blade”, Paper No 1277 ISABE Munich

[10] Voke P.R., Yang Z., 1995, “Numerical Study of Bypass Transition”, Phys. Fluids, 7, pp.2256-2264

[11] Huai X., Joslin R., Piomelli U., 1997, „Large-Eddy Simulation of Transition to Turbulence in Boundary Layers“, Theoret. Comput. Fluid Dynamics 9, pp.149-163

[12] Savill M., New strategies in Modelling By-Pass Transition, Ed. Launder B.E., Sandham N. „Closure Strategies for Turbulent Transitional Flows”, Cambridge University Press, 2002

[13] Menter F.R., Esch T., Kubacki S., 2002, „Transition modelling based on local variables“,In: W. Rodi and N. Fueyo, Eds., Engineering Turbulence Modeling and Measurements 5, pp..555-564

[14] Vilmin, S., Savill, M.A., Hodson, H.P., Dawes, W.N., 2003, “Predicting Wake–Passing Transition In Turbomachinery Using a Intermittency-Conditioned Modelling Approach”, 33rd AIAA Fluid Dynamics Conference and Exhibit, Orlando, June

[15] Elsner W., Vilmin S., Drobniak S., Piotrowski W., 2004, “Experimental analysis and prediction of wake-induced transition in turbomachinery”, ASME paper no. GT2004-53757, ASME TURBO EXPO 2004, Vienna

[16] Lodefier K. and Dick E., 2003, “Transition modeling with the SST turbulence model and

an intermittency transport equation", ASME GT-2003-38282, Atlanta, USA

[17]Menter F.R., Langtry R.B., Likki S.R., Suzen Y.B., Huang P.G., Völher S., (2004), A correlation – based transition model using local variables P.I – Model formation, ASME paper GT2004-53452, ASME TURBO EXPO 2004, Vienna

[18]Lodefier K., Dick E., Piotrowski W., Elsner W., 2005, „Modelling of wake induced transition with dynamic description of intermittency", 6th European Turbomachinery Conference., Paper No. 071_05/66, Lille

[19]Piotrowski W., Elsner W., 2005, „Modeling of boundary layer with an Intermittency transport methodology, Proc. of Colloquium Fluid Dynamic, 2005, Praha, pp. 113-116

[20]Lardeau S., Leshziner M., 2004, „Modelling bypass transition with Low-Reynolds-number nonlinear eddy-viscosity closure", Flow, Turbulence and Combastion, 73(1); pp.49-76

Conference on Modelling Fluid Flow (CMFF'06)
The 13th International Conference on Fluid Flow Technologies
Budapest, Hungary, September 6-9, 2006

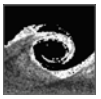

SMC ANALYSIS OF TURBULENT STRUCTURES IN THE TIP LEAKAGE OF A LINEAR COMPRESSOR CASCADE

Domenico BORELLO[1], Kemal HANJALIC[2], Franco RISPOLI[3]

[1] Corresponding Author. Department of Mechanics and Aeronautics, Università di Roma 'La Sapienza'. Via Eudossiana, 18, I-00184 Rome, Italy. Tel.: +39-06-44585233, Fax: +39-06-4881759, E-mail: borello@dma.ing.uniroma1.it
[2] Department of Multi Scale Physics, Delft University of Technology. E-mail: hanjalic@ws.tn.tudelft.nl
[3] Department of Mechanics and Aeronautics, Università di Roma 'La Sapienza'. E-mail: rispoli@dma.ing.uniroma1.it

ABSTRACT

An innovative analysis based on second-moment closure (SMC), incorporating proper modelling of low-Re-number and wall proximity effects is adopted in conjunction with numerical model based on an in-house parallel finite element code for the prediction of a 3D linear compressor cascade flow with tip clearance.

The strong interaction between the tip leakage vortex, the mainstream, the passage vortex and the other turbulent structures causes important portion of energy losses and it influences the overall performance of the compressors.

A systematic comparison among predictions of the proposed SMC with respect to a linear eddy viscosity closure (standard k-ε) and experiments is carried out.

In the blade passage, near the casing, the tip leakage flow interacts with the passage vortex creating complex turbulence structures (e.g. tip leakage vortex).

In the tip clearance the turbulent flow is characterized by an high level of anisotropy induced by complex shear effects. Here, experiments can hardly reproduce the flow details between the blade tip and the casing due to the difficult to obtain accurate measurement in narrow spaces.

The present predictions demonstrates that second moment closures feature a superior capability to reproduce all the phenomenological features related to tip leakage flows and can be considered a powerful tool for the investigation of turbulent structures.

Keywords: axial flow compressors, CFD, Second Moment Closures, tip gap analysis

NOMENCLATURE

c	[mm]	blade chord
C_p	[-]	static pressure coefficient
H	[-]	shape factor
k	[m^2/s^2]	turbulent kinetic energy
l	[m]	dissipation scale lenght
p	[Pa]	pressure
Re	[-]	Reynolds number
U_i	[m/s]	velocity components
$\overline{u_i u_j}$	[m^2/s^2]	Reynolds stress tensor component
x, y, z	[m]	coordinate directions
ε	[m^2/s^3]	dissipation
$\tilde{\varepsilon}$	[m^2/s^3]	homogeneous dissipation
ν	[m^2/s]	kinematic Viscosity

Subscripts and Superscripts

$\bar{}$	Reynolds averaging
i,j,k,l	vector indices

1. INTRODUCTION

The need to increase the efficiency of the compressors stages requires a continuous advancement of the design methodologies and an accurate prediction of the loss phenomena in turbomachines. The reduction of efficiency has to be related to the loss mechanism originated by the presence of complex turbulent phenomena associated with flow separation and reattachment, tip leakage flows, streamline curvature, strong favourable or adverse pressure gradient, laminar-to-turbulent transition, secondary flows [1]. The correct reproduction of tip leakage flows proves to be of strategic importance. The prediction of tip vortex core size, center position, vorticity, as well as the details of tip gap velocity and turbulence3 field, represents a quite severe challenge for the

present CFD codes in terms of modeling and computational capabilities. In recent years the availability of High Performance Computing tools [e.g. 2] has relaxed the numerical constraints in terms of run-time and computational resources requirements. These advances encouraged the development of complex physical modeling able to reproduce the main phenomena in turbomachinery flows [3-8] and particularly in tip leakage region [9-15]. The choice of turbulence modeling remains a critical item for the prediction of turbomachinery efficiency. Despite the world-wide success of Reynolds Averaged Navier Stokes (RANS) models coupled with a first-order low-Reynolds eddy-viscosity models (Low-Re EVM), featuring both linear and non-linear stress-strain relationship [16-17], many drawbacks remain to be resolved, mainly related to the excessive diffusivity introduced in the solution by the eddy viscosity concept, the simplified approach (in linear closures) assuming an overlap between principal axes of rate-of-strain tensor and Reynolds-stress tensor and the difficult calibration of the empirical coefficients introduced in non-linear closures. With all these inconvenient circumstances, papers claiming satisfying results in predicting compressor cascade flows with EVM in both 2D [18, 2], and 3D [19-20] turbulent flows have been recently published.

A decisive improvement in the prediction of turbomachinery flows is expected by the adoption of second-moment closures (SMC) with incorporated low-Re-number and wall proximity effects. Despite the computational load associated to this approach is higher (about twice) respect to simpler EVMs, SMCs are able to take in account properly for turbulence anisotropy in the near wall region and vorticity distribution. Many authors (e.g. [21-22]) published extended analysis of several complex turbomachinery flows with Reynolds Stress Modelling. Despite some contrasting results, the superior capabilities of SMC in predicting turbomachinery flows make it possible to argue that industrial application of SMC in turbomachinery should be considered a target of the next generation of CFD solvers. The adoption of an accurate SMCs already established for different flow configurations has to be considered for an extensive analysis of 3D turbomachinery flows. Recently, Borello *et al*. [23] have successfully simulated 2D cascade flows by adopting Hanjalic and Jakirlic model (HJ – [24]) and Elliptic Blending Model - EBM [25]. As a result of the computations, full validation of both models in predicting separation-induced and transitional and separated flows has been obtained. An improved version of EBM extended the field of application of that model and very promising results in the prediction of turbulent flows subjected to the mechanism of by-pass transition have been obtained [26]. In the same time, a successful assessment of HJ on 3D cascade flow has been carried out [27-28].

The aim of this paper is to discuss the prediction capabilities of the HJ model in a 3D linear compressor cascade with 4 mm tip-clearance in design conditions [11,12,29]. The HJ predictions have been assessed by comparisons with an isotropic EVM and experiments. The analysis has been focused on flow features in the blade passage with particular reference to tip leakage flow.

2. PHYSICAL MODELLING

The physics describing the flow field of incompressible turbulent flows is modeled by adopting a RANS approach (1-2). As a result of Reynolds averaging, non closed terms requiring the introduction of turbulence model (Reynolds stresses gradients) appear in the momentum equation (box in (2)).

$$\frac{\partial \overline{U_i}}{\partial x_i} = 0 \tag{1}$$

$$\frac{D\overline{U_i}}{Dt} = -\frac{\partial \overline{p}}{\partial x_i} + \nu \frac{\partial^2 \overline{U_i}}{\partial x_j \partial x_j} - \boxed{\frac{\partial \overline{u_i u_j}}{\partial x_j}} \tag{2}$$

Turbulent flows arising in turbomachines are characterized by an high level of anisotropy, resulting from several effects like tip leakage flows, presence of solid walls, rotational effects, streamlines curvature and pressure gradients. Nevertheless, a large amount of numerical investigation on 3D compressor cascade flows is based on simplified turbulence models as mixing length or isotropic eddy viscosity models (EVM) featuring both wall function and low-Reynolds (low-Re) treatment of solid boundaries [30-16]. In the framework of low-Reynolds EVM, a more physical route available for approximating the Reynolds stresses is founded on the adoption of a non-linear algebraic connection between Reynolds-stress and rate-of-strain. Nevertheless, their effectiveness in the solution of 3D complex flows is not completely assessed yet [13,19].

On the other hand, adoption of low-Re SMCs should result in improved prediction capabilities compared to those of EVMs. The main advantages of SMC could be summarized as follows: a) the Reynolds tensor components obtained by the solution of Reynolds stress transport equations are used to close the momentum equation, dispensing with the need to introduce any momentum diffusion hypothesis (related to turbulent viscosity) in the Navier-Stokes equations; b) the solution of a transport equation for each Reynolds stress component allows to evaluate directly the anisotropy of turbulent stress field; c) production, convective and viscous diffusion terms are solved in closed forms allowing to reduce substantially the

modelling uncertainties. Modelling of non-closed term constitutes a crucial item for obtaining credible representation of turbomachinery flows. Indeed, many SMC have been assessed in simpler 2D flows, but applications to complex flows of turbomachinery interest are scarce [21-22]. In recent works, Hanjalic and Jakirlic SMC [24] has demonstrated to be a powerful tool for the prediction of 2D and 3D turbomachinery flows [23, 27, 28].

SMC closure

The general form of the second moment closure equations system in terms of Reynolds Stress ($\overline{u_i u_j}$) and scalar dissipation (ε) reads:

$$\frac{D\overline{u_i u_j}}{Dt} = P_{ij} + D_{ij}{}^{\nu} + D_{ij}{}^{t} + \Phi_{ij} - \varepsilon_{ij} \qquad (3)$$

$$\frac{D\varepsilon}{Dt} = D_{\varepsilon}{}^{\nu} + D_{\varepsilon}{}^{t} + P_{\varepsilon} - \varepsilon_{\varepsilon} + \psi \qquad (4)$$

the term on the left hand side denotes the material derivative of the current variable, P_ϕ production ($P_{ij} = -\overline{u_i u_k}\partial\overline{U_j}/\partial x_k - \overline{u_j u_k}\partial\overline{U_j}/\partial x_k$), $D_\phi{}^{\nu}$ and $D_\phi{}^{t}$ molecular and turbulent diffusion respectively, Φ_{ij} is the pressure-strain term, ε_ϕ molecular destruction, and ψ is the gradient production term in ε equation. The details of current implementation of HJ low-Reynolds number second-moment closure are reported on previous works (e.g. [23]).

3. NUMERICAL TECHNIQUE

The numerical solution of the RANS equations set and the turbulence model is based on a implicit stabilised FEM discretisation [31] featuring a consistent Petrov-Galerkin Q1-Q1 scheme to control the instability effects arising in the advective-diffusive discretised equations in presence of incompressible constraint [2], and reaction terms [30]. The linearization of the equations system is solved by adopting a Fixed-Point strategy. The equations of motion and continuity are solved in a fully coupled fashion. The Reynolds stresses gradients have been directly implemented in the momentum equation as a source term. A parallel MPI scheme is employed for the solution of the computational domain, partitioned by using a block structured domain decomposer [2]. A Flexible-GMRes solver [32-33] is adopted for the solution of the fully coupled linearized equations system.

In all the presented simulations the convergence threshold parameters are defined as:

$$\| r \| / \| r^0 \| < rtol \; ; \; \| \bar{F}_i^n - \bar{F}_i^{n-1} \| / \| \bar{F}_i^n \| < stol$$

where $\| r \|$ and $\| r^0 \|$ are, respectively, actual and initial residual quadratic norms, while $\bar{F}_i$ is the generic unknown quantity and the superscripts refer to the non linear iteration. Both the prescribed threshold parameters *rtol* and *stol* are set to 10^{-4}. It is worth to note that, in SMC simulations this constraint is more coercive, being relative to a number of equations (11 degrees of freedom - dof - per node) greater than EVM (6 dof per node).

To prevent the occurrence of non-physical values of turbulent variables during the solution procedure, a lower positive bound (*clipping*) has been placed for the turbulent terms that are positive definite ($\overline{u_i u_i}$, ε).

4. LINEAR COMPRESSOR CASCADE

The tip leakage flow for the VUB linear compressor cascade has been experimentally analyzed and discussed by Kang and Hirsch [11,12,29] and numerically by the authors [28]. An experimental database is available on line for benchmarking (Kang and Lacor, [34]) . Here we analyze the design configuration with a tip clearance equal to 2% of chord.

The main blade design parameter are specified in Table 1.

Table 1. VUB cascade profile details

Profile Type	NACA 65-1810
Chord	200 mm
Pitch	180 mm
Tip-clearance size	4 mm
Aspect Ratio	1.0
Solidity	1.111
Stagger angle	10°
Blade inlet angle	32.5°
blade outlet angle	-12.5°
Flow inlet angle	29.3°
Mach Number	< 0.1

A comparison of results obtained with both the HJ SMC and the standard low-Re-number k-ε turbulence model (Launder and Sharma, [16] – in the following dubbed EVM) with experiments is carried out. The flow is incompressible and steady. Flow specification are obtained from experiments and they are briefly sketched in Table 2.

Table 2. Flow specifications

Re	300,000
Inlet TI	3.4%
Inlet H	1.22 mm
Dissipation scale length l	5% of chord

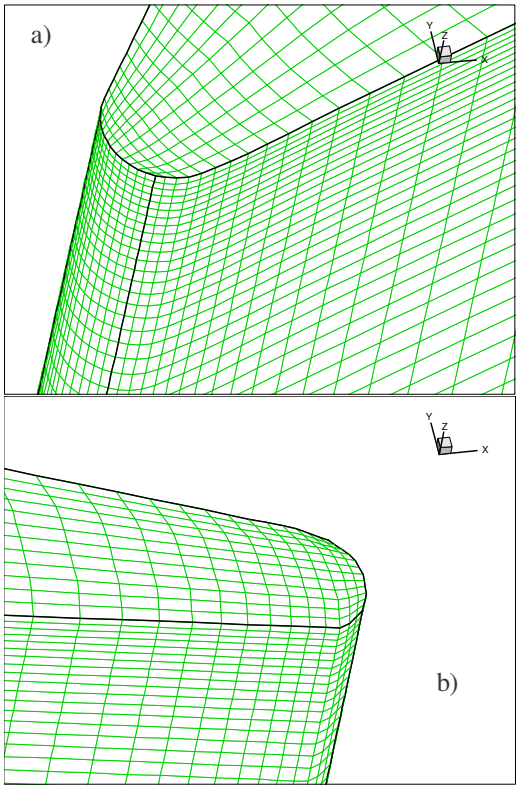

Figure 1. Blade discretisation: a) leading edge; b) trailing edge

Because of the flow symmetry in spanwise direction, the mesh reproduces only the upper part of the cascade (i.e. 104 mm from casing to mid-span). An embedded *H*-shape mesh is adopted (imposing zero values of flow variables inside the blade) to obtain good quality grid without distortion in the leading edge, trailing edge and the tip leakage regions. Simulations have been carried out on three grids with different refinements up to 1.15 M grid points (141x73x81, 141x81x87, 141x85x97, in streamwise, pitchwise and spanwise directions respectively) to obtain a mesh-independent solution. The grids feature y+ values in the first nodes row close to the solid boundary lower than 1.6. An uniform discretisation (featuring 21 points) is used to discretize the tip gap. Figure 1 shows the details of blade leading and trailing edge discretisation (Figures refer to intermediate grid of about 1M nodes).

The inlet section is placed 40% *c* upstream the leading edge where Kang and Lacor [34] measured the mass-averaged air inlet angle. In the experiments at this location the boundary layer was turbulent. The outlet section is located one-chord length downstream the trailing edge to obtain a turbulent flow field in the blade to blade and wake region not affected by the outlet boundary conditions.

Experimental data are used to obtain inflow boundary conditions. A non-uniform velocity profile, obtained by interpolating the experimental data, is imposed in inlet. The calculated shape factor in the inlet section is equal to 1.22. The turbulent variables are set on the basis of an anisotropic distribution of Reynolds stresses $\overline{u_i u_j}$, obtained by the solution of a turbulent channel flow at the same Re number and extrapolating the values in the section where the shape factor is equal to 1.22. For the EVM simulation the *k* values distribution is set as the half-trace of Reynolds stress tensor. The inlet scalar dissipation (ε) is obtained by imposing the following relation (for SMC):

$$\varepsilon_{in} = \left((k)^{3/2} / l \right) + 2\nu \left(\partial \sqrt{k} / \partial x_j \right)^2 \qquad (5)$$

Neumann conditions are set for all the variables in the outflow boundaries. On the walls, no slip conditions have been used for all the variables but dissipation (equal to $\varepsilon = \left(\partial \sqrt{k} / \partial x_j \right)^2$) and pressure. Flow periodicity is strictly imposed at the permeable boundaries, while symmetry is assumed in the mid-span section. It is worth to note that the EVM assumes $\tilde{\varepsilon}$ rather than ε as dissipation-like variable ($\tilde{\varepsilon} = \varepsilon - 2\nu \left(\partial \sqrt{k} / \partial x_j \right)^2$).

The pressure coefficient distribution C_p ($C_p = \left(p - p_{ref} \right) / (1/2) \rho U^2$) in three reference section (mid-span, 15% and 1.5% blade spa from the tip) is presented in Figure 2.

The EVM predictions here shown refer to the finer and the intermediate grids. For HJ only the intermediate grid results are reported. The results on the finest grid show no appreciable difference respect to the intermediate one.

At mid-span (Figure 2.a), on the pressure side, the experimental results show a rapid acceleration up to 5% of chord followed by a region featuring a strong adverse pressure gradient (APG) and then a plateau extending more than 50% of chord. This suggests the occurrence of laminarisation and successive transition of the boundary layer. Downstream a region featuring an moderate adverse pressure gradient is noticed. Along the suction side, an acceleration zone is present up to 15% of chord, followed by a pressure plateau up to 40% *c*. Again, this behavior indicates the occurrence of laminarisation and transition of boundary layer. Finally, a region of adverse pressure gradient is noticed. It is important to point out that at mid-span the measured pressure coefficient with and without tip clearance return similar values due to the marginal influence of tip-leakage flows in the middle of the blade [27, 29].

EVM results show similar features using both grids. On the pressure side the slight ADP (after transition) in the aft region of the blade is well reproduces only by HJ.

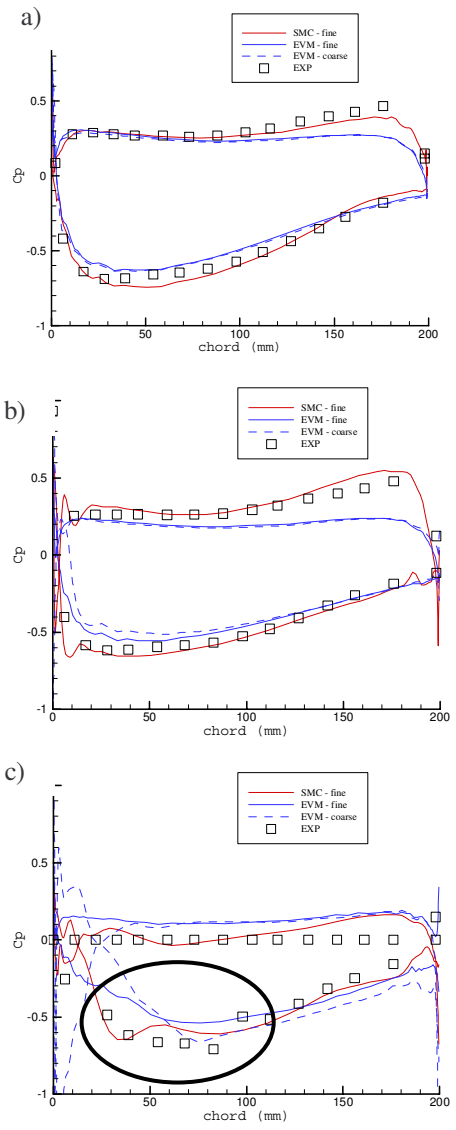

Figure 2. C_p along the blade surface : a) mid-span; b) 15% span from the tip; c) 1.5% span from the tip

On the suction side, only HJ reproduce accurately the experimental results.

At 15% span from the blade tip (Figure 2.b) similar features to mid-span could be noted for both measurements and simulations. The reduction of blade loading is small indicating reduced influence of tip leakage flow in this spanwise location. Moreover the EVM coarse grid predictions show deteriorate results in the suction side leading edge.

Moving towards the tip at 1.5% span (Figure 2.c), the experiments show a small blade unloading followed by successive reloading. This behavior should be related to the generation of tip-leakage flow and the successive rolling up of the tip-leakage vortex (TLV) (put in evidence by the black ellipse). The passage of fluid across the tip gap from pressure side leads to a pressure increase on the suction side near the leading edge. This circumstance causes the shift of minimum of *Cp* downstream (after 40% of chord). Also in this case the HJ simulations returns a clear improvements respect to EVM along the suction side in the APG zone, where the second moments closure confirms its good attitude in predicting the pressure growth moving towards the trailing edges. The experimental APG located at about 50% of the chord indicate transition. HJ returns similar phenomena (not noticed by EVM) but it occurs at 25% of chord.

Due to the grid independent results obtained on the intermediate grid, only these class of results is reported in the following.

In Figure 3 the isolines of pitchwise velocity in selected sections in the blade passage are presented. Figure 3.a shows the experimental results of Kang and Lacor at Sections 3,4,7 and 10 (placed respectively at 12.5%, 25%, 57.5% and 90% of chord). Dashed lines indicate negative values and the isolines have a constant pitch equal to 10% of the bulk velocity. Unfortunately, the data regarding the tip region are not sufficiently detailed. Nevertheless, useful comparisons with EVM (Figure 3.b) and HJ (Figure 3.c) can be carried out. With reference to the Section n.7, strongly influenced by the TLV, it is possible to argue that the EVM model features an excessive diffusivity (related to the limits of Boussinesq hypothesis). Actually, under the effect of diffusivity and the interaction with the passage vortex (PV – put in evidence by the large zone with negative pitchwise velocity near the casing), the tip leakage flow is rapidly convected in the TLV remaining close to the blade suction side. On the other hand, HJ simulation features a less diffusive velocity profile extending the tip leakage jet along the pitch and turning the TLV farther from the blade in very good agreement with experimental results. Furthermore, the HJ simulation shows the presence of a region of negative pitchwise velocity near the casing thinner than the one predicted by EVM with a better agreement with experimental evidences (Figure 3.a). Similar features can be noted in the section placed near the trailing edge (Section 10). Reverse flow takes place in the tip clearance very near the blade (see also Figure 4.c). Kang and Hirsch [29] noted a similar flow pattern and they supposed the presence of a saddle point on the blade tip near to the present measurement section. That saddle point is the main cause of a separation vortex in the tip moving towards the suction side and rolling up downstream. Again the HJ returns results in very good agreement with experiments. This behavior is confirmed in Figure 4 where the details of the tip leakage flow in section 10 are plotted. The presence of tip recirculation region is clearly predicted by the HJ (Figure 4.c) and not by EVM. Kang and Hirsch states that this is the cause of the generation of the tip separation vortex. Moreover, a pitchwise

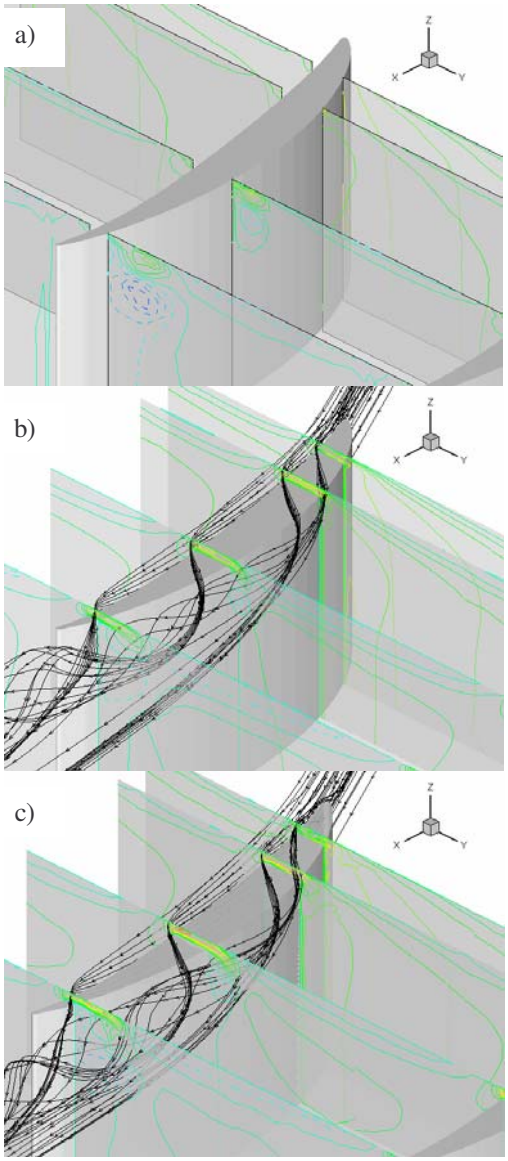

Figure 3. Isolines of pitchwise velocity and streamlines in the blade passage: a) experiments; b) EVM; c) HJ

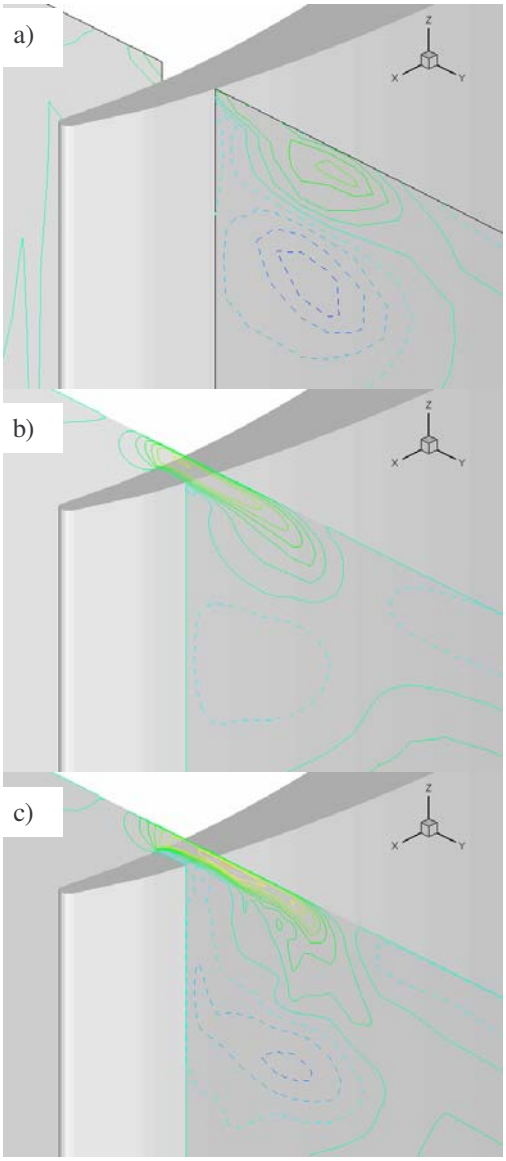

Figure 4. Isolines of pitchwise velocity and streamlines near the trailing edge: a) experiments; b) EVM; c) HJ

velocity acceleration (stronger respect to EVM) is noticed in the tip leakage leading to a pronounced flow ejection on the suction side. The pitchwise velocity isolines confirm the capabilities of HJ in predicting TLV and PV.

In order to investigate the nature of the turbulence in the blade to blade passage, in Figure 5 the isolines of turbulent kinetic energy are plotted for EVM (Figure 5.a) and for HJ – in this case obtained as the semi-trace of Reynolds stress tensor (Figure 5.b). For ake of clarity the number and the limits of isolines are maintained constant for both models. In all the sections, the turbulence level induced by EVM is greater respect to HJ case, in particular, near the casing where the region featuring an high level of k (i.e. greater than 0.01) is thicker due to the interaction of a stronger PV with the main flow and on the suction surface subjected to a strong APG. Further it could be noted that, especially in HJ, the TLV core rolls into a low turbulent energy region.

In Figure 6 the normal Reynolds stresses predicted by HJ are compared. They feature a large anisotropy confirming the requirement of an anisotropic model for the prediction of complex 3D flows.

With reference to the tip leakage region, it could be noted that: a) in the second reference section the HJ simulation suggests the presence of a small recirculation region close the blade in proximity of the pressure side; b) in the last section the different jet length generated by the tip leakage flow leads to a strong difference in the turbulence levels.

In Figure 7 the velocity distribution in the tip gap relative to Section 10 are reported for both EVM and HJ (dubbed SMC here). Three profiles

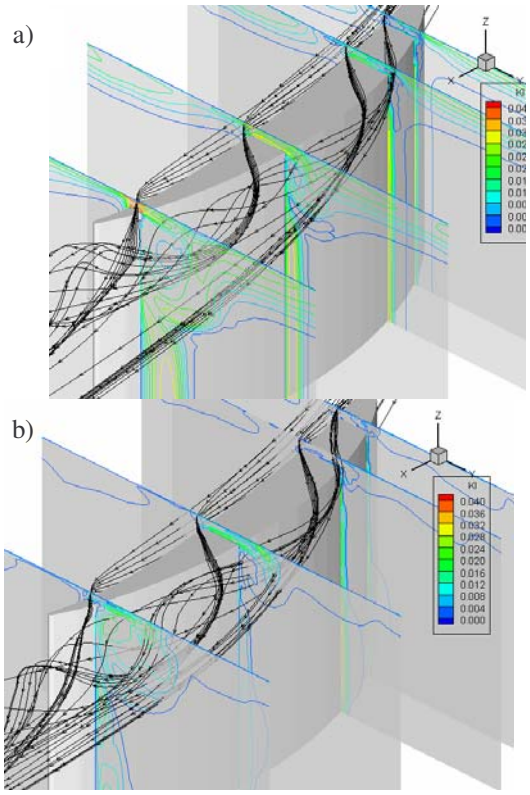

Figure 5. Isolines of turbulent kinetic energy and streamlines in the blade passage: a) EVM; b) HJ

have been analyzed: near the pressure side (prs), near the suction side (sus) and in the mid of the passage (mid).

Starting from the mid passage and up to the suction side, HJ predicts the presence of the TSV recirculation (Figure 7.a). EVM simulation feature a too high turbulence level (Figure 7.b) and this circumstance avoids the occurrence of TSV. In Figure 7.c the $\overline{uw}$ Reynolds Stress distribution is shown.

5. CONCLUSIONS

The present paper is focused on the computational analysis of three-dimensional flow features arising inside a linear 3D compressor cascade with 4 mm tip clearance and in design conditions.

A parallel finite element code featuring advanced turbulence (up to Second Moment Closure) and numerical models is used for numerical simulations.

Comparisons with available experimental results have shown that a clear improvement in the prediction of complex turbulent phenomenology is obtained when an appropriate SMC closure has been adopted respect to a standard Eddy Viscosity Model approach.

In particular, the improved SMC solution is:

a) not affected by turbulent diffusivity;
b) sensitive to turbulent anisotropy;
c) able to reproduce accurately the flow field in the blade passage;
d) appropriate to predict the velocity and turbulence inside the tip clearance.

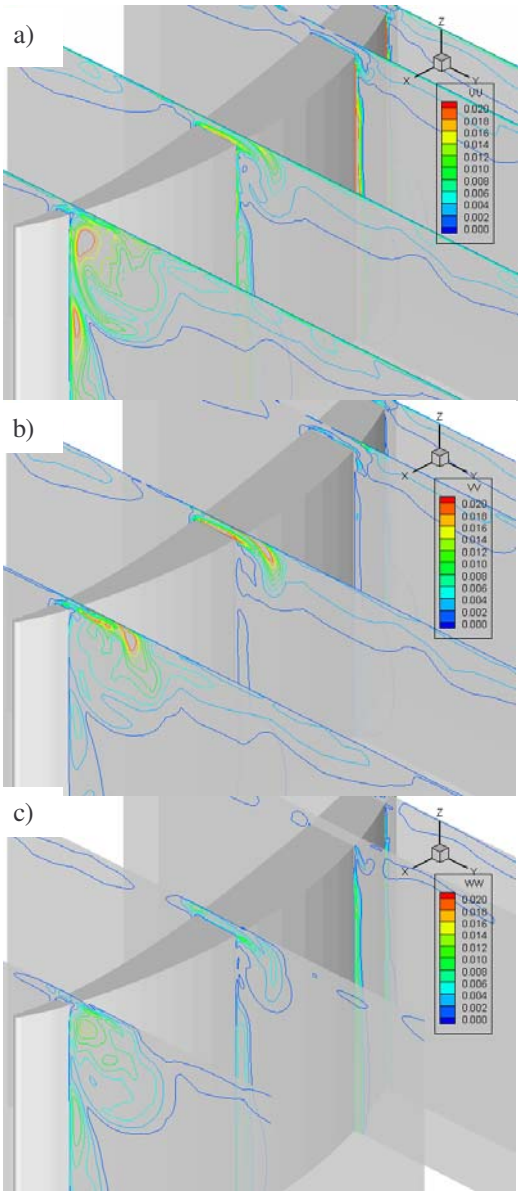

Figure 6. Isolines of normal Reynolds Stresses and streamlines in the blade passage: a) $\overline{uu}$; b) $\overline{vv}$; c) $\overline{ww}$

REFERENCES

[1] Denton, J.D., 1993, "Loss Mechanisms in Turbomachinery", the 1993 IGTI Scholar Lecture, *ASME J. of Turbomachinery*, Vol.115, pp.621-656.

[2] Borello, D., Corsini, A. and Rispoli, F., 2003, "A finite element overlapping scheme for flows

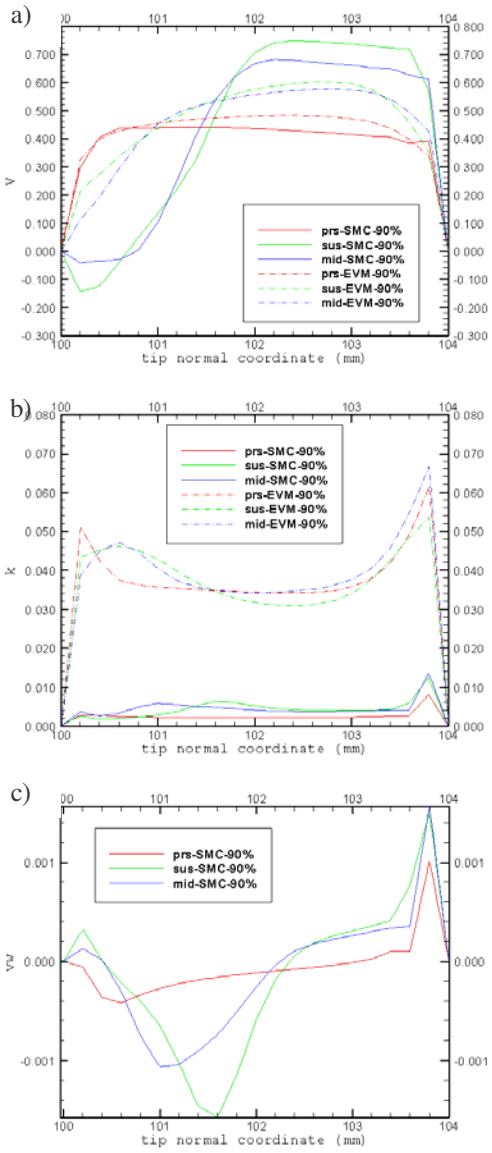

Figure 7. Tip gap analysis in Section 10: a) pitchwise velocity, b) turbulent kinetic energy, c) vw Reynolds Stress (only SMC)

on parallel platform", *Computer and Fluids*, Vol. 32, pp. 1017-1047.

[3] Kang S. and Hirsch C., 1991, "Three dimensional flow in a linear compressor cascade at design conditions", *ASME IGTI 91-GT-114*, Orlando, Florida.

[4] Cleack, J.G.E. and Gregory-Smith D.G., 1992, "Turbulence modeling for secondary flow prediction in a turbine cascade", *ASME J. of Turbomachinery*, Vol. 114, pp. 590-598.

[5] Suryavamshi, N. and Lakshminarayana, B., 1992a, "Numerical prediction of wakes in cascade and compressor rotors including the effects of mixing: Part 1 – Cascade wakes including the effects of incidence and free-stream turbulence", *ASME J. of Turbomachinery*, Vol. 114, pp.607-616.

[6] Suryavamshi, N. and Lakshminarayana, B., 1992b, "Numerical prediction of wakes in cascade and compressor rotors including the effects of mixing: Part 2 – Rotor passage flow and wakes including the effects of spanwise mixing", *ASME J. of Turbomachinery*, Vol. 114, pp. 617-626.

[7] Kunz, R.F., and Lakshminarayana, B., 1992, "Three-dimensional Navier-Stokes computation of turbomachinery flows using an explicit numerical procedure and a coupled k-ε turbulence model", *ASME J. Of Turbomachinery* , Vol. 114, pp. 627-642.

[8] Gbadebo, S. A., Cumpsty, N., Hynes, T. P., 2004, "Three dimensional separations in axial compressors", *ASME Turbo Expo 2004*, GT2004-53617, Wien.

[9] Crook, A. J., Greitzer, E. M., Tan, C. S., Adamczyk, J.J., 1993, "Numerical simulation of compressor endwall and casing treatment flow phenomena", *ASME J. of Turbomachinery*, Vol. 115, pp. 501-512.

[10] Kunz, R.F., Lakshminarayana, B., and Basson, A.H., 1993, "Investigation of tip clearance phenomena in an axial compressor cascade using Euler and Navier-Stokes procedures", *ASME J. of Turbomachinery*, Vol. 115, pp. 453-467.

[11] Kang, S., and Hirsch, C., 1993a, "Experimental study on three dimensional flow within a compressor cascade with tip clearance: Part I: velocity and pressure fields", *ASME J. of Turbomachinery*, Vol. 115, pp. 435-443.

[12] Kang, S., and Hirsch, C., 1993a, "Experimental study on three dimensional flow within a compressor cascade with tip clearance: Part II: the tip leakage vortex", *ASME J. of Turbomachinery*, Vol. 115, pp. 444-452.

[13] Corsini, A., Rispoli,, F., 2005, "Flow analyses in a high-pressure axial ventilation fan with a non-linear eddy-viscosity closure", *Int.J. of Heat and Fluid Flows*, Vol. 26.3, pp. 349-361.

[14] Gbadebo, S. A., Cumpsty, N., Hynes, T. P., 2004, "Iteraction of tip-clearance flow and three-dimensional separation in axial compressors", GT2006-90071, *ASME Turbo Expo 2006,* Barcelona, Spain.

[15] Tang, G., Simpson, R.L., Tian, Q., 2006, "Experimental study of tip-gap turbulent flow structure", GT2006-90359, *ASME Turbo Expo 2006,* Barcelona, Spain.

[16] Launder B.E., and Sharma B.I., 1974, "Application of the energy dissipation model of turbulence to the calculation of flow near a

spinning disc", *Letters in Heat and Mass Transfer*, Vol. 1, pp. 131-138.

[17]Craft T.J., Launder B.E., Suga K., 1996, "Development and application of a cubic eddy-viscosity model of turbulence", *Int. J. of Heat and Fluid Flow*, Vol. 17, pp. 108-155.

[18]Chen W.L., Lien F.S., Leschziner M.A., 1998, "Computational prediction of flow around highly loaded compressor – cascade blades with non-linear eddy-viscosity modes", *Int. J. of Heat and Fluid Flow*, Vol. 19, pp. 307-319.

[19]Borello, D. and Rispoli, F., 2003, "Improved non-equilibrium turbulence closure modeling for axial flow compressors simulation", *IGTI03*, Atlanta, GA, June 2003.

[20]Corsini, A., Rispoli, F. , 2004, "Using sweep to extend stall-free operational range in sub-sonic axial fan rotors", *Proc. Instn Mech. Engrs*, Vol. 218 Part A: J. of Power and Energy, pp. 129-139.

[21]Chen, W.L., Leschziner M.A., 1999, "Modelling turbomachine-blade flows with non-linear eddy-viscosity models and second moment closure", *IMechE Paper C557/131/99*, Vol. A, pp. 189-199.

[22]Gerolymos, G.A., Neubauer, J., Sharma, V.C., Vallet, I., 2002, "Improved prediction of turbomachinery flows using near-wall Reynolds –stress model", *ASME J. of Turbomachinery*, 124, pp. 86-99.

[23]Borello, D., Rispoli, F. and Hanjalic, K., 2005, "Prediction of cascade flows with innovative Second Moment Closures", *ASME J. of Fluids Engineering*, Vol. 127, pp.1059-1070.

[24]Hanjalic, K. and Jakirlic, S., 1998, "Contribution towards the second moment closure modelling of separating turbulent flows", *Computers and Fluids*, Vol. 27, 2, pp.137-156.

[25]Manceau, R. and Hanjalic, K., 2002, "Elliptic blending model: a new near-wall Reynolds-stress turbulence closure", *Physics of Fluids*, Vol. 14, 3, pp. 1-11.

[26]Borello, D., Orisni, P. and Rispoli, F., 2006, "Elliptic blending SMC model for transitional flows", Paper A-168, *Int. Conf. on Heat and Mass Tr. 2006*, Dubrovnik, Croatia

[27]Borello, D., Rispoli, F. and Hanjalic, K., 2005, "Numerical simulation of turbulent flows in 3D decelerating cascade using Second Moment closure modelling", *6th European Turbomachinery Conference (ETC6)*, Lille, France.

[28]Borello, D., Rispoli, F. and Hanjalic, K., 2006, "Prediction of tip-leakage flow in axial flow compressor with Second Moment Closure", GT2006-90535, IGTI 2006, Barcellona.

[29]Kang, S., and Hirsch, C., 1994, "Tip leakage flow in linear compressor cascade", *ASME J. of Turbomachinery*, Vol. 116, pp. 657-664.

[30]Jones, W.P., and Launder, B.E., 1972, "The prediction of laminarization with a two-equation model of turbulence", *Int. J. Heat Mass Transfer*, Vol. 15, pp. 301-314.

[31]Corsini, A., Rispoli, F. and Santoriello, A., 2003, "A new stabilized finite element method for advection-diffusion-reaction equations using quadratic elements", *CMFF'03*, Budapest Hungary.

[32]Borello, D., Borrelli, P., Quagliata, E., and Rispoli, F., 2001, "A multigrid additive and distributive parallel algorithm for FEM turbomachinery CFD", *ECCOMAS CFD 2001*, Swansea, UK.

[33]Borello D., Migliarese M. and Rispoli F., 2002, "A parallel multilevel solver for axial compressor CFD", *Parallel Computation Fluid Dynamics 2002*, Elsevier Science, Kyoto, Japan.

[34]Kang, S., and Lacor, D., 2000, available on the net at http:// dataserv.inria.fr/flownet/

Workshop
Coupling CFD with Optimisation

Conference on Modelling Fluid Flow (CMFF'06)
The 13th International Conference on Fluid Flow Technologies
Budapest, Hungary, September 6-9, 2006

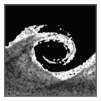

ON DEVELOPING CFD-BASED OPTIMIZATION TOOLS FOR PAPERMAKING

Jari HÄMÄLÄINEN[1], Taija SAIKKONEN[2],
Elina MADETOJA[2], Henri RUOTSALAINEN[2]

[1] Corresponding Author. Department of Physics, University of Kuopio, P.O.B. 1627, FI-70211 Kuopio, Finland. Tel.: +358 17 162 279, Fax: +358 17 162 585, E-mail: jari.hamalainen@uku.fi
[2] Department of Physics, University of Kuopio. E-mails: taija.saikkonen@uku.fi, elina.madetoja@uku.fi, henri.ruotsalainen@uku.fi

ABSTRACT

Development of tailored software tools based on coupling of CFD with optimization is presented in this paper. Industrial applications are in papermaking dealing with fluid dynamics at the wet-end of a paper machine where the paper web is formed. The tools are developed for optimal shape design and optimal control problems. Different level of complexity of CFD modelling as well as a dimension reduction technique are also considered in this paper. The reduced CFD model is validated with a complete model. Furthermore, multiobjective optimization and multiphysical modelling are introduced as they are a basis for decision support systems of large industrial systems in near future.

Keywords: CFD, modelling, model reduction, multiobjective optimization, papermaking

NOMENCLATURE

$C(m)$	[-]	depth-averaging coefficient
D	$[m]$	depth of the slice channel
p	$[Pa]$	static pressure in 3D
$\mathcal{P}$	$[Pa]$	depth-averaged static pressure
$\underline{\mathcal{U}}$	$[m/s]$	velocity vector in 3D
$\underline{\mathcal{V}}$	$[m/s]$	depth-averaged velocity vector
$\underline{\underline{\varepsilon}}$	$[1/s]$	strain tensor
ρ	$[kg/m^3]$	density
μ	$[Pa \cdot s]$	dynamic viscosity

1. INTRODUCTION

Optimal shape design is the most well-known example of model-based optimization in which the model is described as a system of partial differential equations. Optimal shape design is a kind of an inverse problem, that is, the shape of a domain is not known a-priori. Instead, it is searched such that a cost function is minimized (or maximized), and a state equation and possible constraints are fulfilled. The cost function, also known as objective function, measures quality of the shape. Typically it is formulated such that its minimum (or maximum) value corresponds to the best possible shape called as an optimal shape. The state equation is a model describing physical phenomenon to be studied, the Navier-Stokes equations, for example. The constraints takes care that the optimal shape is reasonable. For instance, they give limits to total material usage in solid mechanical problems, minimum and maximum material thicknesses and so on. Optimal control is a special case of shape optimization. Instead of the shape of a domain, boundary data, for example, is now a-priori unknown. A typical optimal control problem related to Computational Fluid Dynamics (CFD) is searching of an optimal velocity profile at an inlet or optimal heat flux through a wall.

Optimal shape design is said to be started from Hadamard in 1910 [1] who first gave a formula for a partial differential equation in order to evaluate the change due to a boundary modification of the domain. First engineering applications were in solid mechanics. It emerged to CFD through potential flows, Euler equations, and finally to viscous Navier-Stokes equations including turbulence models. For further information, see [2-4] and bibliographical studies therein.

In traditional optimal shape design or optimal control problems there are only one objective (cost function) to be optimized. However, every-day engineering problems typically involve several conflicting objectives that should simultaneously be achieved. A single objective function can be derived from multiple ones, as a weighted sum, for example, but then practical relevance of cost function values may be lost. Instead, it is more reasonable to handle multiple objectives as they naturally arise from engineering problems and by

using methods of multiobjective optimization [5, 6]. Importance of multiobjective optimization will even be more emphasized when dealing with large industrial processes taking into account consecutive unit-processes, raw material, energy consumption, as well as end-product quality and price, each of them having their own objectives. Applications of multiobjective optimization are not necessary only in engineering problems, but they are getting important role also in decision support systems in future.

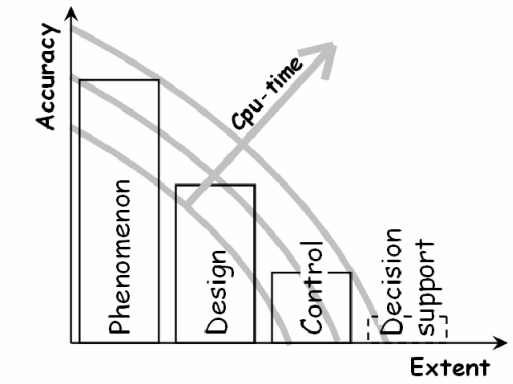

Figure 1. Compromise between accuracy and extent of CFD when coupled with optimization.

Computing capacity is always limited and it leads to compromises between accuracy, scope and computing time as illustrated in Figure 1. Naturally there are needs for detailed small-scale modelling like DNS (Direct Numerical Simulation) which requires high performance computing even without any optimization. The detailed models cannot be coupled with optimization if total cpu-time is kept reasonable. When a new product is designed, relatively long cpu-time, days or even weeks, can be accepted. Therefore, optimal shape design can be used based on a complex CFD model. But, when a fast response, seconds or minutes, is demanded, one cost function evaluation has to be done extremely quickly. It is possible only by using reduced CFD models. Furthermore, when the scope extends to a large system consisting of numerous unit-process models, coupled with multiobjective optimization, models need to be reduced even more. This is the case when modelling the whole papermaking process. Evidently, CFD and different CFD-based optimization applications have different demands for accuracy, complexity and cpu-time.

CFD-based optimization tools developed for paper industry are discussed in this paper. Applications vary from optimal shape design (Chapter 2) and optimal control (Chapter 3) of a so-called headbox to multiobjective optimization (Chapter 4) and decision support systems (Chapter 5) designed for the whole paper machine, all having basis in reduced CFD models. Validation of one such model, the depth-averaged Navier-Stokes equations, in a contracting channel is also studied in this paper.

2. OPTIMAL SHAPE DESIGN OF THE TAPERED HEADER

A traditional designing problem in a paper machine headbox is the tapering of a header such that the outlet flow rate distribution is even across the full width of a paper machine [7-9]. The header is the first flow passage in the headbox (see Figure 2). Fibre-water mixture coming from a pump is turned 90 degrees into the machine direction and distributed in the header as illustrated in Figure 3. For example, an uneven flow rate distribution may cause an uneven basis weight profile in the produced paper web. Non-optimal header is also one potential source for cross-directional flows inside the headbox which in turn, causes misaligned fibres in the paper as fibres approximately follow the velocity vectors at the outlet jet of the headbox. Optimization is utilized to minimize these disturbances.

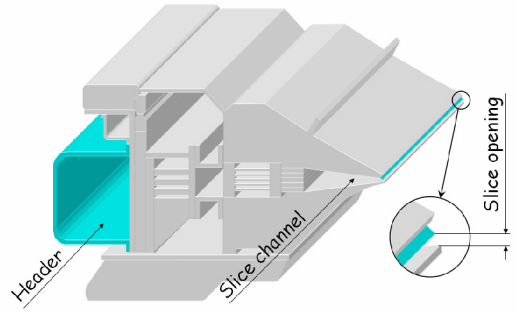

Figure 2. Paper machine headbox.

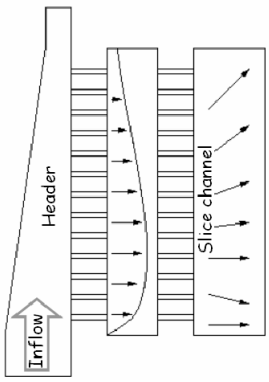

Figure 3. Cross-directional flows inside a headbox due to uneven flow distribution coming from the tapered header.

Designing of the tapered header has been formulated as an optimal shape design problem. A cost function describes how even the flow rate distribution after the header is (or should be), and design variables define location of the back wall of the header. The first numerical experiments of the

header optimization were reported in early 1990's [10, 11].

Modelling of the headbox flows includes some special features. First, the tube bundles (see Figures 2 and 3) consist of hundreds of small tubes. They cannot be included in detail in CFD but are taken into account as an effective porous medium. A three-dimensional (3D) CFD model would also be too time-consuming in optimization. That is why specific two-dimensional (2D) models have been developed for the headbox applications [12]. The header model is derived from a 3D, incompressible, k-ε turbulence model by averaging them in the vertical direction resulting in a non-standard 2D flow model. Similar approach has also been studied in [13] for open-channel problems.

In addition to model reductions, optimization methods have also remarkable influence on computing efficiency. In general, gradient-based methods have proven to be more efficient than gradient-free methods for the optimization problems introduced in this paper. The most critical step in gradient-based optimization algorithms is the evaluation of the cost function gradient. Finite difference approximation is easy to obtain even for complex models, but on the other hand, it is inefficient. The so-called adjoint state technique has also been studied for the tapered header [14] but only for laminar or algebraic turbulence models. Evaluation of the cost function gradient can be avoided by using genetic algorithms [15, 16], but at least in papermaking applications, gradient-based methods are much faster than genetic algorithms, even when the gradient is approximated by finite differences.

The designing software tool for optimization of the tapered header was taken into use in industry in 1995. Designing procedure takes place only once a week. Therefore, several hours cpu-time is accepted, and it is justified to utilize a two-equation turbulence model together with finite difference approximation of the cost function gradient instead of a fast solver based on an algebraic turbulence model and the adjoint state technique.

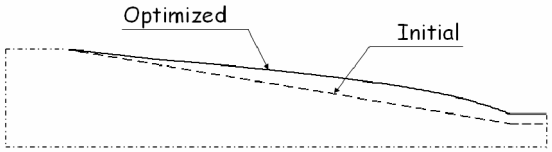

Figure 4. Initial and optimized back wall of the tapered header.

Optimal shape design of the header has been utilized in design process for a decade in industry [17]. One example of the initial and optimized shape of the header and resulting outflow velocity profiles are illustrated in Figures 4 and 5, respectively. As seen, the optimized velocity profile is very even across the width of a machine except some minor boundary layer effects at the edges.

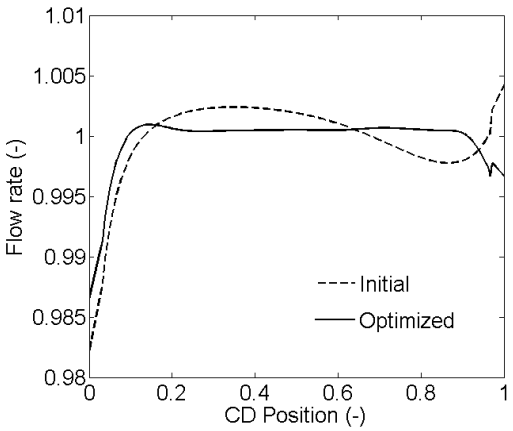

Figure 5. Initial and optimized flow rate distribution of the header.

In design processes relatively complex and computationally expensive models can be coupled with optimization, as shown in this example. In the header optimization tool, a 2D turbulence model has been used, but when faster response times are required, more reduced models are needed. This kind of example for a control problem is presented in the next chapter.

3. OPTIMAL CONTROL OF THE SLICE CHANNEL FLOWS AND RESULTING FIBRE ORIENTATION ANGLES

3.1. On Modelling Fibre Orientation

Modelling of fibre suspension flows includes plenty of challenges. Wood fibres are non-spherical particles with length-to-diameter aspect ratio typically in order of 100. Having approximately the same density as water, they tend to align with the velocity direction, but due to their flexibility they also form accumulations called as fibre flocs. Moreover, fibres interact with the carrying phase and turbulence as well. Thus, we are facing contradictory modelling challenges: the CFD model should be as simple as possible when coupled with optimization meanwhile even the complete 3D turbulence model is not accurate enough to predict all detailed fluid flow phenomena occurring in the headbox. Therefore, the basic phenomena affecting fibre orientation need to be studied by developing elaborated fluid flow models, and thereafter, separate reduced models are used in optimization.

In the designing case of the header (Chapter 2), several hours cpu-time was accepted. But, when developing tools for engineers having an assignment to go round the paper mills and optimize the papermaking process, a much faster

CFD-based optimization tool is desired. To fulfil these demands a simulator called HOCS Fibre has been developed (HOCS=Headbox Optimization Control Simulator). It solves an optimal control problem in order of a minute. Efficiency is obtained by a reduced CFD model, that is, a laminar depth-averaged Navier-Stokes equations, and by using adjoint state technique in a gradient-based optimization algorithm. Yet, simplifying the flow field simulation is not enough, but we need to reduce also the fibre orientation model.

Fibre orientation angle is not just a scalar depending on the fluid velocity. To be precise, in any location (or, in a small volume) there are plenty of fibres oriented more or less randomly in different directions, hence forming a distribution of fibre orientation angles. Modelling of the fibre orientation probability distribution (FOPD) leads to a four-dimensional equation for a 3D geometry, and to a three-dimensional equation for a 2D geometry. The detailed modelling of FOPD in the headbox and its free jet is considered in [18]. However, when aiming to optimize the fibre orientation profile over the width of a real paper machine, there are significant model reductions to be done. Consequently, the fibre orientation is considered simply as a misalignment angle with respect to the machine direction (MD), having a profile in the cross-machine direction (CD). On the other words, in HOCS Fibre simulator only the expected value of the FOPD model is considered in each CD position. It is also assumed that the orientation angle is fully determined by the velocity components in MD and CD.

3.2. HOCS Fibre – A Trouble Shooting Tool

The last component in the headbox is the slice channel (see Figures 2 and 3). The channel outflow is controlled by the height of the outlet boundary, called as a slice opening.

Basically, HOCS Fibre [19] makes two CFD-model based optimizations: Step 1 solves a diagnostics problem in order to find out what defects in the headbox cause the fibre orientation misalignment. Hence, the measured orientation angle profile determines the cost function, and the inlet flow speed is used as the control variable. After that, Step 2 searches for an optimal control for the slice opening profile to obtain an even fibre orientation angle, that is, the angles equal to zero. When the optimal slice opening profile is found, it can be fed to actual slice opening control system of the paper machine.

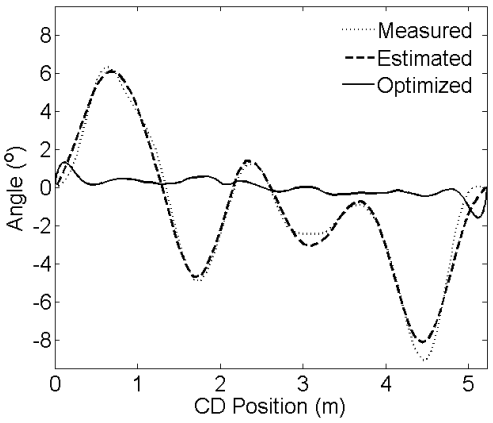

Figure 6. Measured, estimated (step 1) and optimized (step 2) fibre orientation profiles.

Nowadays, HOCS Fibre simulator is installed on a paper making engineer's laptop and, hence, the necessary control corrections can be calculated and made at a paper mill. Despite of the model reductions done HOCS Fibre has confirmed its accuracy; typically for the first paper machine start-up, only one slice opening tuning proposed by the software is needed. HOCS Fibre has been successfully used at tens of paper mills and one example of a real trouble shooting case is given in Figure 6. As seen in the figure, the fibre orientation angle is much better after optimization than the original one measured at a mill. The original fibre orientation profile may cause problems in printing machines but the optimized one fulfils all the market demands.

3.3. Depth-averaged Navier-Stokes Equations

To be able to optimize the fibre orientation in trouble shooting purposes, some model simplifications have to be done. First of all, the fibre orientation probability distribution (FOPD) model cannot be used. Instead, expect value of the FOPD is assumed to be determined by mean velocity field. Furthermore, instead of using the 3D geometry of the headbox slice channel, the depth-averaged Navier-Stokes equations are used. They are introduced next.

Let the velocity vector $\underline{\mathcal{U}} = (u, v, w)$ and the static pressure p be a solution of the 3D Navier-Stokes equations. The depth-averaged pressure $\mathcal{P}$ and the velocity components U and V are defined as averaged values in the vertical direction over the depth of the slice channel as follows

$$U(x,z)=\frac{1}{D(x,z)}\int_0^{D(x,z)}u(x,y,z)dy,$$
$$V(x,z)=\frac{1}{D(x,z)}\int_0^{D(x,z)}v(x,y,z)dy, \quad (1)$$
$$\mathcal{P}(x,z)=\frac{1}{D(x,z)}\int_0^{D(x,z)}p(x,y,z)dy,$$

where $D=(x,z)$ is the depth of the slice channel depending on a position (x,z). Then, by integrating the 3D continuity equation over the depth and by using the definitions (1), the following depth-averaged continuity equation is obtained

$$\nabla\cdot(D\underline{\mathcal{V}})=0, \quad (2)$$

where $\underline{\mathcal{V}}=(U,V)$ is the reduced 2D velocity vector. The depth-averaged momentum equation is derived similarly, and it is

$$-(1/D)\nabla\cdot(2\mu D\underline{\underline{\varepsilon}}(\underline{\mathcal{V}}))+\rho C(m)\underline{\mathcal{V}}\cdot\nabla(D\underline{\mathcal{V}}) +\left[4(m+1)\mu/D^2\right]\underline{\mathcal{V}}+\nabla\mathcal{P}=0, \quad (3)$$

where

$$C(m)=(2m+2)/(2m+1), \quad m\geq 2, \quad (4)$$

is a coefficient associated with the velocity profile in the depth direction. For example, $m=2$ corresponds to a parabolic velocity profile, and $m=7$ to a turbulent plug flow profile. See also [13] for depth-averaging of the *k*-ε turbulence model.

3.4. Validation of the Depth-averaged Navier-Stokes Equations

The reduced model, that is, the depth-averaged Navier-Stokes equations, has been validated by comparing the results to a complete CFD model which includes the headbox slice channel and its free jet in 3D. The coordinate frame of the model is described with the sketch in Figure 7. The x-axis follows the main flow direction meanwhile the z-axis lies at the span-wise direction. The utilised 3D CFD model has been validated with wind tunnel experiments [20].

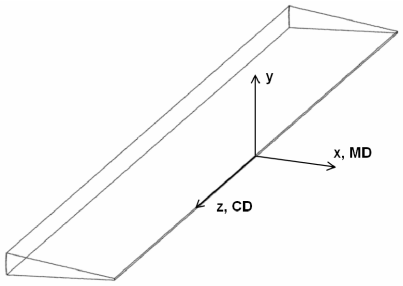

Figure 7. The coordinate frame of the full 3D model.

The fibre orientation angle profile is mostly determined by the cross directional (CD) velocity component, because variations in the machine directional (MD) velocity are only order of one per mille. Thus, the CD velocity component is the most important in the validation. The CD velocity profiles at the slice opening for the step 1 are presented in Figure 8. That is the diagnostics step determining flow rate profiles inside the headbox which causes the measured fibre orientation profile. The prediction given by HOCS Fibre agrees well with the result calculated with the whole 3D model even though the reduced model does not take into account the effect of the jet.

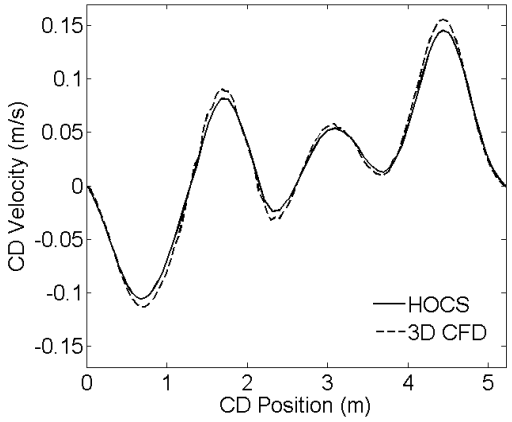

Figure 8. Comparison of CD velocity for the diagnostics (step 1) between HOCS Fibre and the three-dimensional CFD model

After the diagnostics step, the fibre orientation is optimized. The CD profiles obtained from step 2 are presented in Figure 9. As can be noticed, the difference between the reduced model and the full one is now slightly bigger than in step 1, but both the models predict very small CD velocities resulting in optimal fibre orientation angle profile.

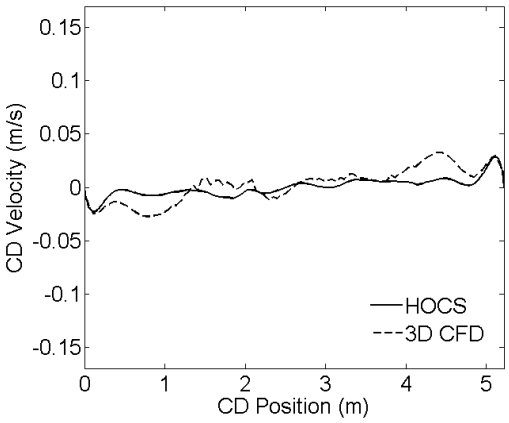

Figure 9. Comparison of CD velocity for the optimal control (step 2) between HOCS Fibre and the three-dimensional CFD model.

The validation shows that the depth-averaged equations are accurate enough for industrial fibre orientation trouble-shooting problems. The reduced 2D model is solved by using a stabilized, upwinding Petrov-Galerkin finite element method [21, 22]. One CFD solution takes only a few seconds on a lap-top computer for a typical finite-element mesh consisting of 5,000 elements. The cpu-time is only 1/1000 compared to the full 3D model (2-3 million elements, turbulence model and free jet). HOCS Fibre can even perform the both optimization steps, that is, the diagnostics and optimal control steps, in couple of minutes. If the full 3D model had been coupled with optimization by using finite difference approximation for the cost function gradient, it would lead to days or weeks computing times, which is unreasonable. As illustrated in Figure 1, compromises need to be done and CFD models need to be reduced when developing tools for controlling purposes.

4. MULTIOBJECTIVE OPTIMIZATION OF PAPERMAKING LINE

When the scope of the optimization problem is extended or more than one unit-process is needed to be optimized together, the elaborateness and the accuracy of the CFD models have to be remarkably reduced. One might even need to replace the CFD model with a statistical or stochastic one in order to decrease the cpu-time used. Moreover, when handling multiphysical or multidisciplinary problems, more efficient and intelligent optimization procedures are needed. Like presented in the previous chapters, the unit-processes of the paper machine have been individually modelled and optimized for more than ten years, but there is an increasing demand to be able to handle larger ensembles, even the whole papermaking process. This is a real challenge, because the paper machine consists of a number of consecutive sub-ensembles, where the output of one unit-process is an input for the following unit-process. Figure 10 shows an example of a paper machine construction, where the process starts from the headbox, then continues from right to left and ends-up as a ready paper on the roll.

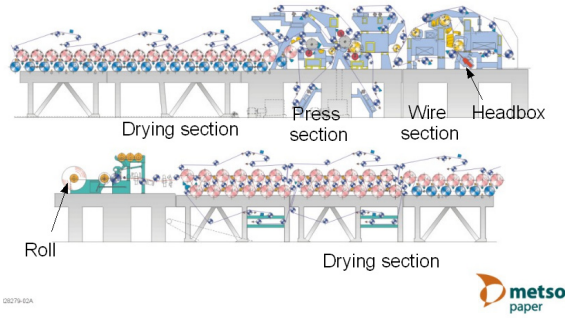

Figure 10. Layout of a paper machine. Courtesy of Metso Paper, Inc.

In papermaking process there are always several requirements for the end product that should be simultaneously achieved. These targets are often conflicting; for example, by accelerating the machine speed in order to increase production amount, probability of web breaks may increase resulting in more downtime, which in turn, decreases the production amount. Better runnability could be obtained by making stronger paper from more expensive raw material, but it affects economy. Therefore, numerous criteria need to be taken into account simultaneously.

Although accurate simulation of the whole paper machine is still far in the future, a multiobjective optimisation tool, called virtual papermaking line, has been developed [23, 24]. It combines dissimilar unit-process models from different disciplines, for example, mathematical formulas ranging from simple algebraic equations to CFD models. It also includes models for moisture and heat transfer, and for paper quality properties. Simplifications of computationally expensive models are used for water removal, for instance. That is, an accurate multi-phase flow model of the dewatering phenomena is replaced with a statistical model based on data produced by the accurate model. The last mentioned models are useful especially in optimization when tens, hundreds or even thousands simulation model evaluations are needed.

The following example in Figure 11 illustrates advantages of multiobjective optimization compared to trial-and-error simulations. It also shows a conflict between two paper quality properties, formation and tensile strength ratio. Formation is a small scale weight variation and tensile strength ratio is the machine-directional tensile strength divided by the cross-directional one.

Both of them are to be minimized in this example. By doing trial-and-error simulations, a bunch of solutions are obtained. But, by letting a multiobjective optimization routine to search the control variable values, much better solutions are found as they are located in the left-bottom corner of the graph. The clear advantage of optimization is that all the solutions it founds are so-called Pareto-optimal, mathematically best possible compromises.

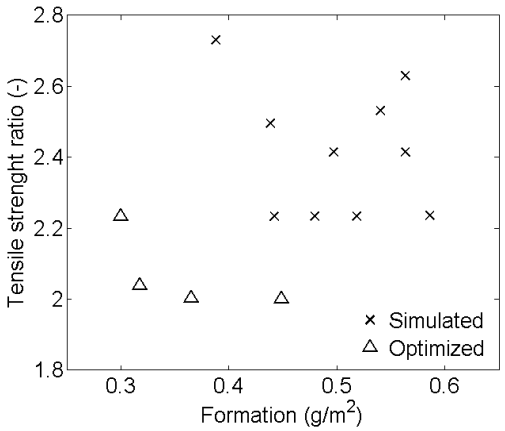

Figure 11. Simulated and optimized conflicting paper quality properties.

A more complicated example of four papermaking targets is studied next. Table 1 shows the desired values and six optimal compromise solutions calculated with the virtual papermaking line. When comparing the values, it can be seen that the chosen targets are conflicting, and hence cannot be reached simultaneously. For example, strength and weight are the best in Compromise 2, but formation is better in Compromise 4.

Table 1. Six optimal compromise solutions.

Target	Tensile strenght ratio (-)	Formation (g/m2)	Basis weight (g/m2)	Dry solids content (%)
Desired value	3.00	0.30...0.35	54.00	92.00
Compr.1	2.80	0.43	54.03	92.48
Compr.2	3.00	0.40	54.00	92.14
Compr.3	2.34	0.39	54.33	92.30
Compr.4	4.91	0.35	54.35	92.27
Compr.5	3.90	0.38	53.74	92.27
Compr.6	3.38	0.41	53.92	92.12

Handling even a few conflicting targets at the same time is too complex for human mind and therefore multiobjective optimization routines are needed. Furthermore, the papermaking process can be controlled as a whole and relationships between the targets can be seen more clearly.

5. TOWARDS DECISION-SUPPORT SYSTEMS

The virtual papermaking line integrates mathematical modeling with multiobjective optimization, thus giving a basis for a development of an intelligent decision-support system [24]. By means of such a system, a paper making expert can take into account not only the separate requirements of the produced paper but all the related aspects beginning from choice of raw materials and control of wood fibre preprocessing till market situation and customer demands – all the facts affecting decision making in real life.

A decision-making tool is required to be flexible for different types of usage and for users varying from research and development engineers till managers of a paper mill. Moreover, the system must include interactive interfaces to automation and control softwares as well as direct connections to on-line measurements. This trend of development sets new challenges to modelling and optimization. At its best the decision support system is able to provide new knowledge on physical and economical mechanisms affecting papermaking and finally lead to remarkable financial benefits.

6. CONCLUSIONS

Depending on requirements of the software tool to be developed, choice of appropriate modelling approach is essential. It means making compromises between accuracy and extent of CFD, especially when coupled with optimization. In phenomenological research the road leads towards more detailed and accurate modelling, like DNS, but when aiming to control larger ensembles, there is a need for decision-support systems.

In this paper some examples of coupling optimization with CFD have been presented. They are chosen to represent different categories of modelling extent and accuracy. Decision-support systems are coming in near future, but optimal shape design and optimal control are possible today, and in fact, in every-day use in industry. The examples presented here all are from paper industry. Nevertheless, independently of industrial sector (car or aeroplane industries, for example) CFD-related optimization problems face everywhere same challenges. As a matter a fact, industrial application in question is described by a state equation, that is, the CFD model. All the other aspects are common including optimization methods, needs for model reductions, and handling multiple criteria.

ACKNOWLEDGEMENTS

Many colleagues of the authors have contributed results discussed in this paper, especially Dr. Pasi Tarvainen and M.Sc. Eeva-Kaisa Rouhiainen from Numerola Oy (Ltd). We are also

thankful to National Technology Agency of Finland (Tekes) and Metso Paper, Inc. for financial support of this work.

REFERENCES

[1] Hadamard, J., 1910, *Leçons sur le calcul des variations*, Gauthier-Villars.

[2] Pironneau, O., 1984, *Optimal Shape Design for Elliptic Systems,* Springer-Verlag.

[3] Haslinger, J., Neittaanmäki, P., 1996, *Finite Element Approximation for Optimal Shape, Material and Topology Design,* John Wiley & Sons.

[4] Mohammadi, B., Pironneau, O., 2001, *Applied Optimal Shape Optimization for Fluids*, Oxford University Press.

[5] Miettinen, K., 1999, *Nonlinear Multiobjective Optimization*, Kluwer Academic Publishers.

[6] Steuer, R., 1986, *Multiple Criteria optimization: Theory, Computations, and Applications*, John Wiley & Sons Inc.

[7] Baines, W., Nicholl, C., Cook, R., Mardon, J., 1956, "The Taper-Flow Headboxes (A New Design Concept)", *Pulp and Paper Magazine of Canada,* pp. 139-148.

[8] Mardon, J., Manson, D., Wilder, J., Monahan, R., Trufitt, A., Brown, E., 1963, "The Design of Manifold Systems for Paper Machine Headboxes, Part II - Taper Flow Manifolds", *TAPPI*, vol. 46.

[9] Trufitt, A., 1975, "Design Aspect of Manifold Type Flowspreaders", *Pulp and Paper Technology Series, Joint Textbook Committee of the Paper Industry, C.P.P.A. and TAPPI.*

[10] Hämäläinen, J., 1990, "The Optimal Shape Design of the Header", Proc. *Finite Element Method in Simulation*, Jyväskylä, Finland, CSC Research Reports, R07/90, pp 18-23.

[11] Hämäläinen, J., 1991, "Numerical Modelling and Simulation of Fluid Flow in Headboxes of Paper Machines", *Reports on Applied Mathematics and Computing 5/91, University of Jyväskylä.*

[12] Hämäläinen, J., 1993, "Mathematical Modelling and Simulation of Fluid Flows in the Headbox of a Paper Machine", *Doctoral dissertation, University of Jyväskylä, Department of Mathematics.*

[13] Rodi, W., 1984, "Turbulence Models and Their Application in Hydraulics", *International Association for Hydraulic Research*, Delft.

[14] Hämäläinen, J., Mäkinen, R., Tarvainen, P., 2000, "Optimal Design of Paper Machine Headboxes", *International Journal for Numerical Methods in Fluids*, 34, pp. 685-700.

[15] Deb, K., 2001, *Multi-Objective Optimization using Evolutionary Algorithms,* Wiley.

[16] Hämäläinen, J., Malkamäki, T., Toivanen, J., 1999, "Genetic Algorithms in Shape Optimization of a Paper Machine Headbox", Proc. *Evolutionary Algorithms in Engineering and Computer Science, EUROGEN 99*, Jyväskylä, Finland, pp. 435-443.

[17] Hämäläinen, J., Tarvainen, P., 2002, "CFD-optimized Headbox Flows", *Pulp & Paper Canada,* 103:1, pp. 39-41.

[18] Saikkonen, T., Hämäläinen, J., 2006, "Modelling of fibre orientation in the headbox jet", Proc. *92nd annual meeting of Pulp and Paper Technical Association of Canada, PAPTAC 2006*, Montreal, Canada, pp. B95-B99.

[19] Hämäläinen, J., Tarvainen, P., Aspholm, P., 2005, "HOCS FIBRE – New tool for optimized fibre orientation angles", CD-Rom Proc. *91st annual meeting of Pulp and Paper Technical Association of Canada, PAPTAC 2005*, Montreal, Canada.

[20] Parsheh, M., 2001, "Flow in Contractions with Applications to Headboxes", *Doctoral dissertation, Royal Institute of Technology (KTH), Department of Mechanics.*

[21] Brooks, A., Hughes, T., 1982, "Streamline upwind/Petrov-Galerkin Formulations for Convection Dominated Flows with Particular Emphasis on the Incompressible Navier-Stokes Equations", *Computer Methods Applied in Mechanics and Engineering*, 32, pp. 199-259.

[22] Franca, L., Frey, S., 1992, "Stabilized Finite Element Methods: II. The Incompressible Navier-Stokes Equations", *Computer Methods Applied in Mechanics and Engineering*, 99, pp. 209-233.

[23] Madetoja, E., Rouhiainen, E.-K., Tarvainen, P., 2005, "Making Higher Quality Paper: Case Study of Optimizing a Multidisciplinary System", CD-Rom Proc. *of Computational Methods for Coupled Problems in Science and Engineering*, Santorini, Greece.

[24] Karlsson, M., Hämäläinen, J., 2004, "A Model-based Decision-aid System to Add Value to Papermaking", CD-Rom Proc. *4th European Congress on Computational Methods in Applied Sciences and Engineering, ECCOMAS 2004*, Jyväskylä, Finland.

Conference on Modelling Fluid Flow (CMFF'06)
The 13th International Conference on Fluid Flow Technologies
Budapest, Hungary, September 6-9, 2006

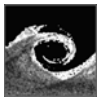

MULTI-OBJECTIVE SHAPE OPTIMIZATION FOR HEAT EXCHANGER MODULES

M. Manzan, E. Nobile[1], S. Pieri, F. Pinto

{manzan, nobile, stpieri, fpinto}@units.it
Dipartimento di Ingegneria Navale, del Mare e per l'Ambiente – DINMA, Sezione di Fisica Tecnica, Università di Trieste, Trieste, ITALY
[1] Corresponding author

ABSTRACT

In this article we present our approach for the multi-objective shape optimization of heat exchanger modules. The first problem, of fundamental nature, describes a procedure for the geometric parameterization and multi-objective shape optimization of two-dimensional periodic wavy channels. The geometry of the channel is parameterized either by means of linear-piecewise profiles, or by nonuniform rational B-splines. The second case, of industrial interest, illustrates the development of an automatic method for the design of small gas turbine recuperators. For both problems the two objectives considered are the maximization of heat transfer rate and the minimization of friction factor, with the additional objective of minimization of heat transfer surface for the recuperator module. Since there is no single optimum to be found, we use a multi-objective genetic algorithm and the so-called Pareto dominance concept, both readily available in the *modeFRONTIER* optimization package. The results obtained are very encouraging, and the procedure described can be applied, in principle, to even more complex problems.

Keywords: CFD, MDO, genetic algorithm, heat exchanger, recuperator.

NOMENCLATURE

a	[m]	plate corrugation amplitude
A	[m^2]	module heat exchange area
b	[m]	channel height
c_p	[$J/(kg\ K)$]	specific heat
f	[-]	friction factor, $f = \beta\ 2\ b\ /\ (2\ \rho\ u^2)$
h	[m]	height of 2D protuberance
H	[m]	module length *and* 2D channel height
L	[m]	wavelength of the corrugation *and* 2D channel length
$\boldsymbol{n}$	[-]	unit vector normal to a surface
Nu	[-]	Nusselt number $Nu = h\ 2\ b/\lambda$
p	[Pa]	pressure
Pr	[-]	Prandtl number $Pr = c_p\ \mu/\lambda$
Re	[-]	Reynolds number $Re = (\rho \bar{u}\ 2b)\ /\ \mu$
S	[m^2]	surface
T	[K]	temperature
u	[m/s]	velocity in flow direction
U	[W/(m^2 K)]	global heat transfer coefficient
$\boldsymbol{W}$	[m/s]	velocity vector
x,y,z	[m]	Cartesian coordinates
β	[Pa/m]	overall pressure gradient in the flow direction
γ	[K/m]	temperature gradient in the flow direction
ϕ	[W]	heat flux
θ	[°]	corrugation angle
λ	[W/(m K)]	thermal conductivity
μ	[kg/(m s)]	dynamic viscosity
ρ	[kg/m^3]	density
φ	[°]	inclination angle for the 2D linear-piecewise channel

Subscripts and Superscripts

b	bulk
c	cold
h	hot
i	inlet
o	outlet
w	wall
~	periodic component

1. INTRODUCTION

The standard approach, when solving thermo fluids problems numerically, is to prescribe the geometry, boundary conditions, and thermophysical properties, and solve the governing equations for velocity, pressure, temperature, turbulent kinetic energy, etc. Problems of this type are referred to here as analysis problems. In design practice, the

engineer usually tries different geometries, chooses other materials with different properties, etc., until satisfactory performance is obtained. Such cut-and-try method relies on the experience and skill of the designer to obtain any improvement, and optimal performance is rarely achieved. This simple approach, however, becomes impractical when the number of design variables is large, when there is more than one objective, and there are several constraints to be satisfied. Therefore it is mandatory in such cases to adopt an optimization strategy. However, the integration of numerical optimization techniques as part of the design process is still not very common today, particularly in the heat transfer community. With reference to shape optimization, a basic requirement, in order to proceed in a systematic way, is to define the shape of the system to be optimized in terms of (known) functions and (unknown) parameters. This task is typically accomplished by means of a parametric computer-aided design (CAD) system, and by making use of an optimization procedure, automatic variations of the parameters associated with the geometric model lead to the creation of a variety of feasible shapes, which are then subjected to numerical analysis.

The aim of this article is to describe a general strategy for automatic, multi-objective shape optimization of heat exchangers modules. This represent a truly multi-objective optimization problem, since it is desired, from a design point of view, to maximize the heat transfer rate, in order to, for example, reduce the volume of the equipment, and to minimize the friction losses, which are proportional to the pumping power required. These two goals are clearly conflicting, and therefore there is no a single optimum to be found. For this reason we use a MOGA (Multi-Objective Genetic Algorithm), and the so-called Pareto dominance, which allows us to obtain a design set rather than a single design.

The optimization of two-dimensional wavy channels is obtained by means of an unstructured finite-element (FE) solver, for a fluid of Prandtl number Pr= 0.7, representative of air, assuming fully developed velocity and temperature fields, and steady laminar conditions. The geometry of the channels is parameterized by means of NURBS (Non-Uniform Rational B-Splines), and their control points represent the design variables. An alternative, and simpler, geometry is described by means of piecewise-linear profiles.

A similar strategy has been adopted for the multi-objective optimization of the periodic module of Cross-Corrugated (CC hereafter) compact recuperator. However, in this case, several widespread industrial codes are linked sequentially to obtain an automatic procedure for the recuperator design and optimization. The utilized software tools are CATIA for the geometric parameterization, ANSYS ICEM-CFD for the grid generation, and ANSYS-CFX for pre-processing, solution and post-processing. The present research has the aim to propose an advanced calculation methodology of the thermo-fluid-dynamical aspects of a recuperator design. Such a methodology correlates all the phases throughout the design process, i.e. the different mechanical, thermal and fluid dynamical aspects, according to the concept of Multi Disciplinary Optimization (MDO). The final objective is to find optimum configurations for high effectiveness and high compactness recuperators.

The optimization procedure described is robust and efficient, and the results obtained are very encouraging. There are no fundamental reasons, apart from computational costs and modelling accuracy issues, which prevent the application of the methodology to more complex geometries, and more complex physics, such as, for example, unsteady or turbulent flow regimes.

2. PROBLEM STATEMENT

The problems considered in this paper are: I - the multi-objective shape optimization of two-dimensional convective wavy channels; II – the multi-objective optimization of cross-corrugated channels. The study is limited to a single module at fully developed flow and heat transfer conditions. In this case, channels of periodic cross section form can be considered periodic in the flow and thermal fields, as well. Therefore the computational domain of interest becomes a single periodic module of the entire geometry, as depicted in figure 1 for the two-dimensional channel.

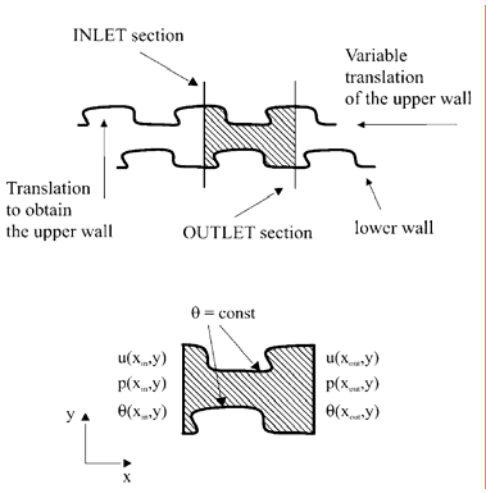

Figure 1. Repeating module of the two-dimensional wavy channel.

For the case of the cross-corrugated (CC hereafter) heat exchanger, the repeating module considered is depicted in figure 2, and it can be noticed that, differently than other authors, both hot and cold fluids are included [1, 2].

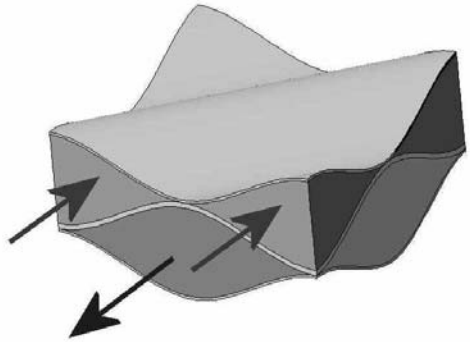

Figure 2. Computational domain for the Cross-Corrugated heat exchanger.

We have limited the study to the steady, laminar flow regime, which is found in many practical circumstances. The Reynolds number chosen for the simulation is Re = 200 for both two-dimensional channel and CC module, which corresponds to the typical value found in microturbine recuperators, while the Prandtl number is assumed as Pr = 0.7, representative of air and other gases.

2.1. Governing equations

The flow is assumed to be incompressible, Newtonian, and of constant thermophysical properties. Moreover, we refer to a stationary and laminar forced convection with negligible viscous dissipation and buoyancy contribution.

2.2 Boundary conditions

The velocity field is periodic in the mean flow direction, so pressure can be expressed as the sum of a linear term β, depending on the pressure gradient, and a periodic pressure field $\tilde{p}$ [3]

$$p(x,y,z) = -\beta x + \tilde{p}(x,y,z) \tag{1}$$

Therefore velocity and the periodic pressure $\tilde{p}$ on periodic interfaces assume the same value

$$\begin{aligned} \tilde{p}_i(y,z) &= \tilde{p}_o(y,z) \\ u_i(y,z) &= u_o(y,z) \\ v_i(y,z) &= v_o(y,z) \\ z_i\ (y,z) &= z_o(y,z) \end{aligned} \tag{2}$$

while standard zero velocity condition has been assumed on solid walls. The pressure gradient term β can be added to the x moment equation as a source term. During the computation this value is constantly updated to obtain the desired value of Reynolds number.

The temperature field in a heat exchanger or in a regenerator is not periodic, since it changes continuously along the channel in the mean flow direction. Periodic heat analysis encountered in literature requires only the cold or hot domain to be solved, since suitable boundary condition must be applied on the walls.

For fully developed periodic flow with uniform temperature at the walls, the periodicity is attained for the *non-dimensional temperature* defined as

$$\tilde{T}_{nd} = \frac{T - T_w}{T_b - T_w} \tag{3}$$

where T_w is the wall temperature and T_b the bulk one defined as:

$$T_b = \frac{\int |\mathbf{W}\cdot\mathbf{n}|\, T\, dS}{\int |\mathbf{W}\cdot\mathbf{n}|\, dS} \tag{4}$$

and S is the area of a surface normal to the mean flow direction. This boundary condition has been used for the 2D wavy channels, and is representative of, for example, automotive radiators at high liquid flow rates, with negligible wall thermal resistance.

If the heat flux is prescribed on the boundary, temperature and pressure can be treated in a similar way. The temperature is expressed as the sum of a periodic and a linear component driven by the gradient in the mean flow direction γ

$$T(x,y,z,t) = \gamma x + \tilde{T}(x,y,z,t) \tag{5}$$

$$\tilde{T}(x = H, y, z, t) = \tilde{T}(x = 0, y, z, t) \tag{6}$$

Eq.(5) can be substituted into the energy equation

$$\frac{\partial(\rho c_p T)}{\partial t} + \nabla\cdot\left(\rho c_p T\, \mathbf{W}\right) = \nabla\cdot\left(\lambda \nabla T\right) \tag{7}$$

to obtain the transport equation for the periodic component:

$$\begin{aligned} \frac{\partial(\rho c_p \tilde{T})}{\partial t} + \nabla\cdot\left(\rho c_p \tilde{T}\, \mathbf{W}\right) = \\ = \nabla\cdot\left(\lambda \nabla \tilde{T}\right) + \gamma u \rho c_p \end{aligned} \tag{8}$$

Eq. (8) can be solved with appropriate boundary conditions as in [4], were a uniform wall flux was imposed and, to satisfy the energy balance, the temperature gradient was computed as:

$$\gamma = \frac{\phi}{\dot{m} c_p H} \tag{9}$$

where H is the length of the periodic module in the mean flow direction, and ϕ is the overall thermal flux specified at the walls. While the uniform flux is a practical solution for imposing a thermal boundary condition, it does not correctly describe the heat transfer in a recuperator module. Indeed the fluid flows in the furrows of the CC ducts with complicated three-dimensional patterns, strongly affecting the local heat transfer rates.

In this work the elementary periodic module is doubled to take into account both cold and hot fluids as shown in Fig. 2. Eq. (8) is applied to both domains and no boundary condition has to be imposed at the interface wall. To satisfy the global energy balance the same flux has been applied to the hot and cold domains

$$\phi_h = -\phi_c \tag{10}$$

using Eq. (9) to compute the source term of Eq. (8). Temperatures of the hot and cold domains are automatically adjusted during the iterative computation to satisfy automatically the overall energy balance

$$\phi = U\, A\, \Delta T \tag{11}$$

where ΔT is the constant temperature difference between hot and cold fluid

$$\Delta T = (T_{bi})_h - (T_{bo})_c = (T_{bo})_h - (T_{bi})_c \tag{12}$$

and U is the global heat transfer coefficient.

3. NUMERICAL METHODS

The numerical solution of the 2D wavy channels case was carried out by means of the FEMLAB software package [5]. Full details of the methodology are reported in [6], and are not repeated here. A grid independence study was performed for different geometric configurations of the channel (designs), in order to ensure the accuracy of the results presented.

For the CC heat exchanger module, the ANSYS-CFX CFD package has been employed. Hexahedral structured grids have been generated by means of the ICEM-CFD grid generation package. In order to validate the calculation procedure, a comparison of our results with those obtained by different authors have been performed. The analysed geometry was defined by standard sinusoidal profiles as in [7], using values of L/a = 12, channel height $b = 2a$ and the inclination angle θ = 90°. The structured grid presented in Fig. 3 is composed by 154800 hexahedral cells, and has been selected as a trade-off between accuracy and computational costs. Computations with refined grids up to 371124 elements have been carried out to check for grid independence. It has been verified that the coarser mesh used in this work involves an estimated error of 1% for the Nusselt number and 0.4% for the friction factor.

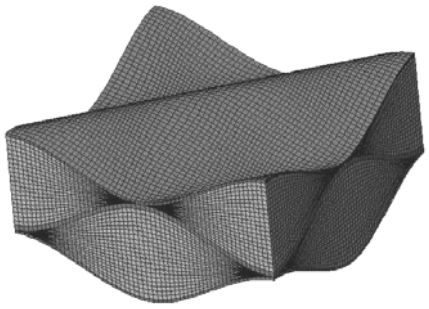

Figure 3. Structured grid for the CC module generated in ICEM-CFD.

4. GEOMETRY PARAMETERIZATION

Different geometry parameterizations have been used for the two-dimensional channels and the CC module, respectively, and are described next.

4.1 Two-dimensional channels

The shape of two-dimensional convective channel is represented either by linear-piecewise profiles, or by NURBS. The two different geometric profiles, the linear-piecewise and the NURBS, are depicted in Figures 4a and 4b, respectively.

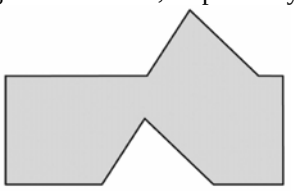

(a)

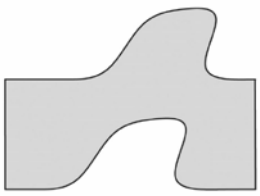

(b)

Figure 4. Periodic 2D channels: (a) linear-piecewise channel; (b) NURBS channel.

We recall that parameterization means describing a system using a discrete set of variables, and that the number of degrees of freedom (DOFs) of the system and number of design variables are equivalent concepts.

4.1.1 Linear-Piecewise Parameterization

The linear-piecewise wall profile of the channel is characterized by a small number of design variables, and these are shown in Figure 5a. Four DOFs are requested for describing the wall profile.

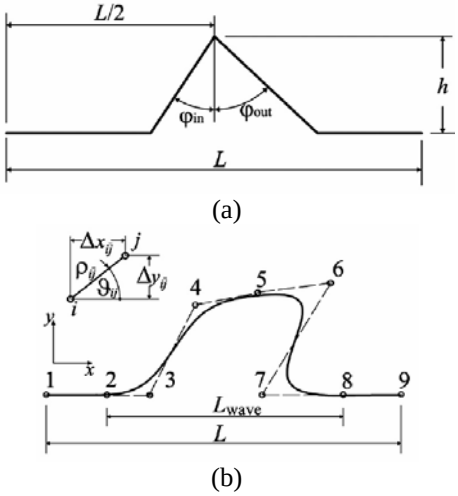

Figure 5. Geometric parameterizations for the 2D channels: (a) linear-piecewise parameterization; (b) NURBS parameterization and control points.

4.1.2 NURBS Parameterization

As a good compromise between the number of DOFs and the geometric complexity, we have chosen a 9-control-points periodic cubic NURBS, to ensure the periodicity of the channel itself. As depicted in Figure 5b, both the first and the last three aligned control points are needed to maintain the entrance and the exit of the profile parallel to the x direction. The remaining ones give freedom to the wavy section. The parameters required for the definition of the lower profile are numbered as in Figure 5b. The number of DOFs is now 10.

4.1.3 Channel construction

In Figures 4a and 4b both types of channel are depicted, i.e., linear-piecewise channel and NURBS channel, and they are constructed in the same way. Once the lower wall profile has been obtained, the upper one, as illustrated in Figure 1, is made by a simple translation in y direction of the former, in order to obtain the height of the channel, followed by a translation in the *x* direction. This guarantees the realistic desire to construct the channels of, *e.g.*, a finned heat exchanger, by simple juxtaposition of identical wavy plates. This action introduces in both cases another DOF, which defines the *x* translation of the upper profile. The *y* translation is instead fixed: in this way the average height of the channel is set to 0.5. Finally, the periodic duct module is cut by two straight lines, representing the inlet and the outlet section, as sketched in Figure 1. Overall, we are left with 5 DOFs for the linear-piecewise model, and 11 DOFs for the NURBS channel.

4.2 Cross-Corrugated module

As already mentioned, the CAD package CATIA [8] has been utilized to develop the heat transfer surface geometry, thanks to its key feature of allowing the generation of parametric drawings. In Fig. 6 the parameters required to describe the geometry of a cross corrugated surface are presented. Points *P1*, *P2*, *P3* and *P4* defines the Bezier curves which give the shape of both the extruded virtual profiles forming the flow channel. The half height of the channel is given by parameter *a*, while its width is defined by parameter *L*. The corrugation angle between upper and lower plates is given by θ. Changing the parameter values, various different geometries can be easily produced.

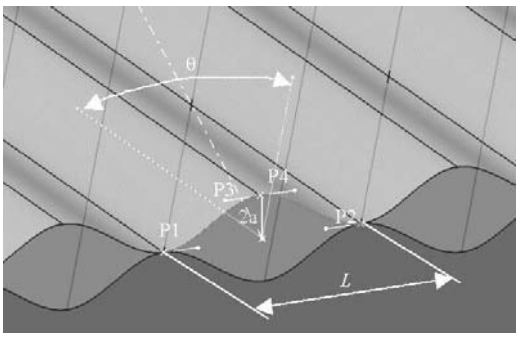

Figure 6. Geometric parameterization for the CC module using *Catia*.

The geometry generated for a set of the parameters can be exported and subsequently loaded by the software ANSYS *ICEM-CFD* [9], which generates the grid. In this work, because of their superior accuracy for Finite Volume discretization, only structured hexahedral grids have been used, but alternative possibilities exist for more complicated geometries. The generated grid is imported into the pre-processor *cfx5pre* of ANSYS-*CFX* [10] were fluid characteristics and boundary conditions are automatically defined. The case file exported by the *cfx5pre* module is processed by the *cfx5solve*, that solves fluid and thermal equations. Finally the results are post-processed by the *cfx5post* code to obtain the not-dimensional synthetic data for performance evaluation.

5. OPTIMIZATION METHODS

Optimization can be described as the task of obtaining the best configuration for a system having a defined number of DOFs, and subjected to certain constraints on both inputs and outputs. The goal desired is the so-called *objective function*, in some

cases called *fitness*, which can be a single parameter O or a certain set O_1, O_2, …,O_m. The objective is a function of some other decisional parameters, X_1, X_2,…,X_n, called design variables

$$\mathbf{O} = \begin{Bmatrix} O_1 \\ \cdots \\ O_m \end{Bmatrix} = f(\mathbf{X}) = f \begin{Bmatrix} X_1 \\ \cdots \\ X_m \end{Bmatrix} \qquad (13)$$

The constraints can either affect design, i.e., *design constraints*, or system behaviour, i.e., *functional constraints*. They are respectively translated in mathematical terms as

$$g(\mathbf{X}) < 0 \qquad (14a)$$

$$f = m[g(\mathbf{X})] < 0 \qquad (14b)$$

where g and m are two general applications, and f is their compound application.

Optimization algorithms can be divided into classical and evolutionary ones. Limiting our attention to problems in which the objectives of the optimization are implicit (or unknown) functions of the design variables, from a numerical point of view, the majority of the classical techniques are based on gradient evaluation. Since in our case the range of variability of the design variables is quite large, there is the well known risk that the optimization algorithm remains trapped in a local extreme. However, the most important issue in the present CFD-based optimization is that, due to possible inconsistency in the geometry definition, or in the mesh generation, or due to lack of numerical convergence, we cannot guarantee the absence of failed designs. This means undefined derivatives and the impossibility of determining a gradient. Finally, our problem is a multi-objective one. Classical techniques are not able to deal with multi-objective optimizations except by means of so-called utility functions.

Evolutionary algorithms allow one to maximize a function without any restriction imposed by functional constraints, as gradient-based algorithms do. Moreover, they can perform truly multi-objective optimization. Their shortcoming is the reduced convergence rate. In this work we used the genetic algorithms (GAs), which mimic the evolution of living organisms in nature.

To perform the optimization task, the software *modeFRONTIER* [11] has been chosen. The optimization process follows these tasks: the optimization software automatically generates a set of numbers, *i.e.*, the geometric design variables, representing the shape of a channel. These variables are written in an input file, which is either sent to the CAD package, for the CC module, or sent to the CFD solver. Once the geometry is defined and deemed feasible, the mesh is generated, followed by a pre-processing stage for definition of boundary conditions, setting of material properties and simulation parameters etc. Finally, the CFD solver computes the flow and thermal fields, and from these, the post-processor evaluates the objective functions. For this study, we used an efficient version of multi-objective GA, *MOGAII*, available in *modeFRONTIER*. It includes *directional crossover* and *elitism*. [6].

5.1 Design of Experiments

The *Design of Experiments* (DOE) is a structured, organized method for defining the relationship between factors affecting a process and the output of that process. The initial sampling of the design space is an important step in every optimization process. The *modeFRONTIER* package includes several algorithms for the DOE selection [11].

5.2 Definition of the Best Solutions

As soon as there are many, possibly conflicting, objectives to be optimized simultaneously, there is no longer a single optimal solution, but rather a whole set of possible solutions of equivalent quality. This can be the case for heat exchangers: the desired objectives might be to maximize heat transfer rate per unit volume, to minimize the pumping power, and to minimize cost and weight. These goals are conflicting, and therefore there is no single optimum to be found. For this reason, the so-called *Pareto dominance* must be used, according to which *design a dominates design b* if and only if

$$(\forall i \; f_i(a) \geq f_i(b)) \cap (\exists j : f_j(a) > f_j(b)) \qquad (15)$$

where f_i is the ith objective function, and for simplicity it is assumed that we are considering the maximization of the m objectives. Expression (15) means that at least for one purpose design a is better than design b, while for the others they might be equal.

6. RESULTS AND DISCUSSION

6.1 Two-dimensional channels

The objectives taken into account are the Nusselt number Nu, to be maximized, and the friction factor f, to be minimized. They will be expressed as ratios to the reference case of a constant-wall-temperature parallel-plate channel in fully developed flow and heat transfer condition, in which case their values are, respectively, $Nu_0 = 7.5407$ and $f_0 = 24/\mathrm{Re}$.

6.1.1 Linear-piecewise channels

In an evolutionary optimization process it is important to choose a well-distributed set of initial individuals (DOE). For the linear-piecewise chan-

nels we used the Full Factorial algorithm with three levels to achieve the task. After having performed the numerical simulation on this set, we have chosen its Pareto front as the initial population of multi-objective optimization with the GA. The optimization has been performed with MOGAII along 30 generations of 20 individuals each, so the total number of designs evaluated is 600. The results are sketched in Figure 7, where the Pareto front is highlighted. Analyzing the shape of the channels along the Pareto front, sketched for convenience in the same figure, it results that there is no sensible fluctuation for variables such as φi_n and h, which remain close to 60° and 0.4, respectively. What makes the difference is the translation of the upper profile in the streamwise direction, responsible for the length of the separation bubble induced by the corrugation.

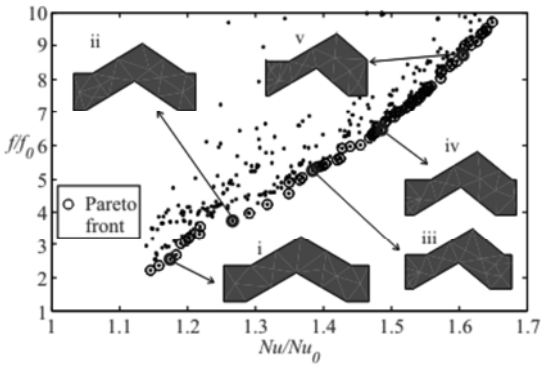

Figure 7. Pareto front after the optimization of linear-piecewise two-dimensional channels.

6.1.2 NURBS-based channels

In contrast with linear-piecewise optimization, for NURBS-based channels, where the number of design variables is very large, we have used the Sobol algorithm [11] to define a smaller initial population of 50 individuals. The optimization algorithm chosen was again MOGAII. Once a high-quality Pareto front has been obtained, one can choose slightly different strategies in order to improve the fitness of channels. One way is to transform the multi-objective problem into a single-objective one by means of a weighted function, involving objectives. The modeFRONTIER software package combines several different objectives into a unique monotone function using preference relations between designs, which can be set by the user. The mono-objective optimization, performed using MOGAII and SIMPLEX [12] algorithms, makes the process faster. After about 2,500 designs were evaluated, we obtained the results summarized in Figure 8.

In the same figure, two sequences of three channels, each having almost the same performance metrics, are marked. Although various kinds of corrugations are present, there are two main types, and they differ by the length of the module. This is an important feature of the optimization, because it shows the non-univocity of the solution, *i.e.*, similar performances can be reached by different geometries [13].

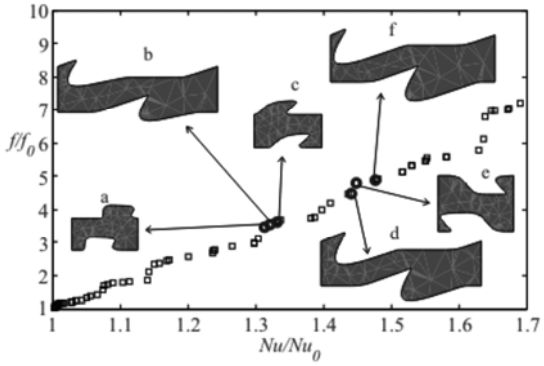

Figure 8. Pareto front after the optimization of NURBS-based two-dimensional channels.

6.2 Cross-Corrugated module

For this problem, the results presented are somehow preliminary, and further investigation is needed. At first the optimization was attempted, again using MOGA II, using for the DOE an original design with sinusoidal wall profile, *design 0*, characterized by a corrugation angle θ = 60°, and 35 designs chosen with sobol method. The value of the angle θ has been chosen, following Stasiek *et al*. [14], as a good compromise in terms of heat transfer rate and friction factor. The six design variables were, with reference to figure 6, *P1*, *P2*, *P3*, *P4*, *L* and θ. The three objectives, to be minimized, were the pressure gradient, β, the temperature difference between the two fluids, ΔT, eq. (15), and the heat transfer surface. In addition, all three objectives were constrained to be smaller or at least equal than those for the reference design *0*. This attempt, however, was quite unsuccessfull, with most of the computed designs considered *unfeasible* (outside the constraints domain).

Therefore a second, simpler optimization has been carried out using 5 design variables, by fixing *L*. Moreover the objective ΔT has been transformed to a constraint, in order to simplify the optimization and to favour module geometries with lower surface area and lower pressure drop. The optimization has been carried out for 332 designs, when the process was practically converged. Among the designs that belong to the Pareto front, the *design 134* has been chosen for illustrative purposes. In fact it has less than 19% pressure gradient β, and a surface area lower than 2% compared to the original one, while maintaining the same ΔT. This result have been duly verified by running grid-independence tests at several grid resolutions, up to 5×10^5 cells. The new optimized geometry has a sharper shape of the walls

and a lower value of the corrugation angle, *i.e.* θ = 42°, which means a major length of the repeating module. The original and optimized profiles are given in figure 9, together with the heat flux on the wall for the *hot fluid*.

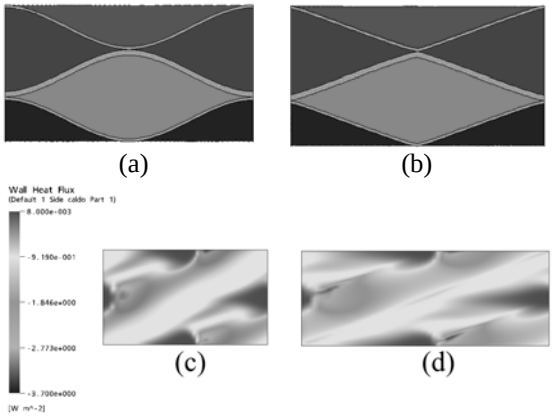

Figure 9. (a) Original design 0, with θ = 60°; (b) optimized design 134, with θ = 42°; (c) heat flux on the wall for the original design; (d) heat flux on the wall for the optimized design.

7. CONCLUDING REMARKS

In this article we have described our approach for the multi-objective shape optimization of convective periodic channels, which represent a fundamental building block of many heat exchangers.

We considered first the optimization of two-dimensional channels, described either by linear-piecewise corrugated walls, or by wavy NURBS-based profiles. It has been shown that, as in similar studies, very different channel shapes offer almost the same flow and heat transfer performance, *i.e.*, non-uniqueness of the shape optimization problem.

The optimization of the Cross-Corrugated periodic module, has been carried out considering both hot and cold fluid streams, without the necessity of imposing artificial constant-temperature or constant-flux boundary conditions. In this case, a major effort was the proper linking of the different software packages and additional utilities. The first results are very encouraging, since one of the optimized geometries leads to almost the same heat transfer performance of the original design, but with a significant pressure drop reduction of about 20% and without increase of the heat transfer surface.

The procedure described has been proved robust and efficient, and could be applied, in principle, to even more complex problems.

ACKNOWLEDGEMENTS

Financial support for this research is provided by MIUR, PRIN 2004, *Surface Optimization for Heat Transfer Problems*, and PRIN 2005, *Study and Optimization of Buoyancy-controlled Thermal Systems*, and is gratefully acknowledged.

REFERENCES

[1] Manzan, M., Micheli, D., and Pieri, S., 2006, "Automatic Integration in the Design of a Microturbine Compact Recuperator", GT2006-90529, Procs.GT2006 ASME Turbo Expo 2006, Barcelona, Spain.

[2] Manzan, M., Pieri, S., and Nobile, E., 2006, "Thermal Periodic Boundary Conditions for Automatic Design Process of Cross Corrugated Channels", Proc. XXIV UIT Conf., June 21-23 2006, Napoli, Italy.

[3] Patankar, S.V., Liu, C. H., and Sparrow, E. M., 1977, "Fully Developed Flow and Heat Transfer in Ducts Having Streamwise-Periodic Variations of Cross-Sectional Area", *ASME J. Heat Transfer*, vol 99, pp 180-186.

[4] Nobile, E., and Stalio, E., 2003, "Direct numerical simulation of heat transfer over riblets", *Int. J. Heat Fluid Flow*, vol. 24, pp. 356-371.

[5] FEMLAB 3 Documentation. www.comsol.com.

[6] E. Nobile, E., Pinto, F., and Rizzetto, G., 2006, "Multiobjective shape optimization of two-dimensional convective periodic channels", to appear on *Numer. Heat Transfer, part A – Fundamentals*.

[7] Croce, G., and D'Agaro, P., 2002, "Numerical analysis of forced convection in plate and frame heat exchangers", *Int. J. Numer. Meth. Heat & Fluid Flow*, Vol. 12, No. 6, pp. 756-771.

[8] CATIA Documentation. www.3ds.com/products-solutions/plm-solutions/catia/overview/.

[9] ANSYS ICEM-CFD Documentation. http://www.ansys.com/products/icemcfd.asp

[10] ANSYS-CFX Documentation, http://www.ansys.com/products/cfx.asp

[11] modeFRONTIER version 3 Documentation. www.esteco.com.

[12] Rao, S., 1996, *Engineering Optimization, Theory and Practice*, Wiley, New York.

[13] Poloni, C. and Pediroda, V., 1996, "GA Coupled with Computationally Expensive Simulations: Tools to Improve Efficiency", in *Genetic Algorithms and Evolution Strategy in Engineering and Computer Science: Recent Advances and Industrial Applications*, chap. 13, pp. 267–288, Wiley, Chichester UK.

[14] Stasiek, J., Collins, M. W., and Ciofalo, M., 1996, "Investigation of flow and heat transfer in corrugated passages – I. Experimental results", *Int. J. Heat Mass Transfer*, Vol. 39, n. 1, pp 149-164.

Conference on Modelling Fluid Flow (CMFF'06)
The 13th International Conference on Fluid Flow Technologies
Budapest, Hungary, September 6-9, 2006

EVOLUTIONARY DESIGN OPTIMISATION OF A TURBINE STATOR BLADE USING FREE FORM DEFORMATION TECHNIQUES

Stefan MENZEL, Markus OLHOFER, Bernhard SENDHOFF

Honda Research Institute Europe GmbH. Carl-Legien-Strasse 30, D-63073 Offenbach/Main, Germany. Tel.: +49 (0)69 890 11-750, Fax: +49 (0)69 890 11-749. E-mail: stefan.menzel@honda-ri.de, markus.olhofer@honda-ri.de, bs@honda-ri.de

ABSTRACT

Design optimisation methods are applied in various applications where the shape of an object has to be adapted with respect to aerodynamic properties. However, the description and parameterization of the often three dimensional shapes subject to the optimisation is a crucial point and often the key to a successful optimisation.

In the present paper a representation based on the method of free form deformation is proposed and combined with evolutionary computation methods in order to generate a system for the design optimization.

It is demonstrated that free form deformation methods are well suited for the optimisation of aerodynamic properties because of several reasons. One of these reasons is that they provide a highly efficient way of representing arbitrary shapes, while the complexity of the shape is decoupled from the dimensionality of the optimisation problem. Another reason is that it holds the advantage of a fast automatic mesh generation which is needed for automized CFD calculations.

To illustrate the efficient combination of FFD with evolutionary optimisation a test scenario has been set up in which a stator blade of a gas turbine is optimized.

Keywords: Computational Fluid Dynamics, Evolutionary Design Optimisation, Free Form Deformation, Representation, Turbine Blade

NOMENCLATURE

f	[ds]	performance index = fitness
t_1	[-]	pressure loss = 1- P_{out}/P_{in}
t_2	[°]	difference to target outflow angle
t_3	[-]	difference to target solidity
t_4	[mm]	difference to target minimum blade thickness
t_5	[mm]	difference to target minimum trailing edge thickness
w_i	[-]	weights for the different input data t_1, t_2, … t_5
x, y, z	[m]	global coordinate system
x', y', z'	[m]	local cylinder coordinate system

1. INTRODUCTION

In order to apply evolutionary design optimisation methods, it is necessary to generate a fully autonomous system of optimiser driven design modification, calculation and quality evaluation.

Therefore, a representation is needed which produces valid designs and as far as Computational Fluid Dynamic (CFD) is involved for a flow simulation an automatic meshing process is of high importance.

Due to the stochastic components and the use of a population of solutions evolutionary algorithms need generally a higher number of quality evaluations than e.g. gradient based optimisation algorithms. At the same time, they allow a global search, are able to overcome local optima and are robust against noise in the quality evaluations. Generally, evolutionary algorithms show a good trade-off between convergence speed and global optimisation. In the present paper, an evolutionary strategy, more precisely the special variant using the covariance matrix adaptation (CMA-ES) [1] is applied as it has shown to be able to cope with a small population size while having a high convergence speed for real valued parameter optimisation problems. Its features are explained in more detail in Section 2.

In the present paper this variant of Evolution Strategy is combined with free form deformation (FFD) techniques as a representation as it provides several advantages for the optimisation of complex systems. While more classical representations such as spline descriptions define the geometry itself, FFD uses transformation equations to manipulate a given initial geometry. FFD allows a decoupling of a complex design description from the optimisation parameters because the parameters of the

deformation functions are encoded instead of the geometry itself.

Therefore, the number of parameters is determined by the shape flexibility instead of the complexity of the represented shape.

Furthermore, FFD deforms a part of the design space instead of describing the shape directly. Therefore, it allows the deformation of the shape and simultaneously of the CFD mesh, which represents the design in the CFD simulation. As a consequence, no remeshing of the design is required which normally involves human interaction for complex geometries. The concept of FFD and its impact on an evolutionary design optimisation are described in more detail in Section 3.

To illustrate the combination of FFD and evolutionary optimisation a first test scenario has been built in which a stator blade of a gas turbine is optimized. The optimisation is outlined in Section 4 & 5. We draw some conclusions in the last section.

2. EVOLUTIONARY DESIGN OPTIMISATION

Evolutionary algorithms belong to the group of stochastic optimisation algorithms. They mimic the principles of Neo-Darwinian evolution, see e.g. [2], by applying operators for reproduction, mutation and/or recombination and selection to a population of possible solutions (e.g. a vector of continuous parameters, the objective variables). Adaptation of solutions is realized by variation and by selection of the best solutions for the next generation. The variations can be classified as purely stochastic (usually called mutation) and combinatoric/ stochastic (usually called recombination or in the context of genetic algorithms crossover). Schematically, the evolutionary cycle is depicted in Figure 1, already with respect to the present turbine blade optimisation.

Examples for evolutionary algorithms are Evolution Strategies (ES), Genetic Algorithms (GA) or Genetic Programming (GP), respectively.

Among the advantages of evolutionary algorithms are robustness against noisy or discontinuous quality functions, the ability to escape from local optima and to enable global search.

In this paper, a special variant of Evolution Strategies, the Covariance Matrix Adaptation (CMA-ES), is applied which has the advantage of a high convergence rate for real-valued problems while requiring only a small population size. This is particularly advantageous for problems that require very time consuming fitness evaluations like CFD simulations. The successful application of the CMA-ES to CFD shape design has been shown previously e.g. for a two-dimensional turbine blade optimisation [4]. Mainly three features distinguish the CMA-ES from standard evolutionary strategies.

Firstly, the stochastic influence in the mutation step is reduced by introducing only one stochastic source which is used for modifying both, the object as well as the strategy parameters. Secondly, the so-called cumulative step-size adaptation is applied which extracts information from past generations to speed up and stabilize the adaptation of the strategy parameter. Thirdly, an adaptation of the full covariance matrix of the probability density vector of the normally distributed mutations takes place. Therefore, correlated mutations can be realized which can significantly increase the convergence speed of the algorithm [1], [4], [5].

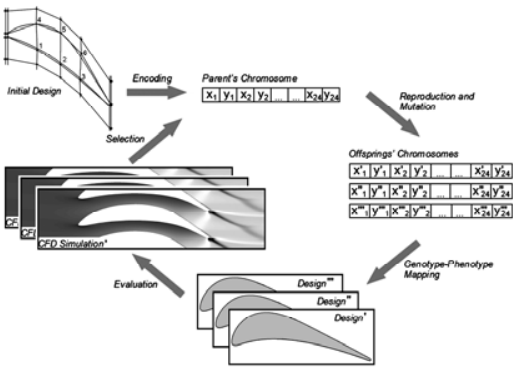

Figure 1. The generation cycle in evolutionary design optimisation [3]

3. FREE FORM DEFORMATION (FFD)

3.1. FFD in computer graphics

Free Form Deformation has been introduced initially in the field of soft object animation (SOA) in computer graphics. The special feature of FFD is that it uses transformation equations to apply modifications on a given geometry instead of a direct definition of the shape. Hence, not the geometry itself is parameterized but spline equations are formulated to realize the deformations. This is especially advantageous if the geometric description is very complex. An FFD system comprises in general a lattice of control points, the so called control volume, spline knot vectors and spline degrees. The altering of the geometry is then realized by a modification of the control points. Different FFD systems have been developed in the past three decades which differ mainly in the underlying spline functions and the shape of the control volumes.

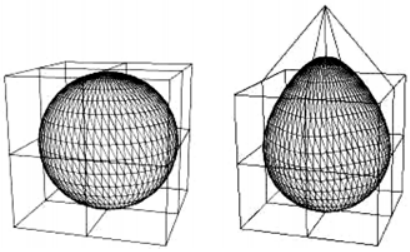

Figure 2. Free Form Deformation [6]

A basic FFD system has been introduced in the 80s by Sederberg and Parry [7]. They used trivariate Bernstein polynomials in combination with parallelepiped control volumes which enable a very efficient formulation of the transformation equations. It allows to neglect a complicated calculation of the geometry in spline parameter space which can be a costly process if e.g. B-splines are used. To achieve more flexibility Coquillart [8] extended the FFD system to arbitrarily shaped control volumes which consequently require B-splines as basis functions because of their local definitions. Additionally, more local modifications of the design are achieved which is advantageous for the object designer and for the optimisation algorithm in a design optimisation because the influence of a control point on a local region of the design is increased.

The usual workflow of such an FFD system is outlined as follows. At first a control volume has to be constructed which encloses either the whole object or the specific part of the object which is modified in the deformation step. In the second step the geometry has to be transferred into the parameter space of the control volume, a procedure which is also called “freezing”. When an object is frozen the u, v and w coordinates of the geometry in spline parameter space are calculated. This is usually done by Newton approximation which is regarded to be the fastest approach but it can also be done by similar gradient based methods [8], [9]. Finally, the object is deformed by moving a single or several control points to new positions and evaluating the spline functions to calculate the modified geometry.

3.2. FFD in evolutionary design optimisation

The choice of an adequate representation in evolutionary design optimisation depends on various requirements. It is important to keep the number of optimisation parameters as low as possible because a smaller parameter set implies usually a faster convergence of the optimisation process. In most cases this conflicts with the flexibility of the representation. An adequate and efficient representation finds a good trade-off between minimality and completeness. A second aspect is the strong causality which is frequently quoted in this context [10]. The representation defines the properties of the map from the genotype space (the object parameter space) to the phenotype space (the space of possible designs). These properties are important because they influence the structure of the search space and therefore the search process. In this context, strong causality refers to the property that similar causes (in our case small mutations on the genotype space) lead to similar effects (in our case small differences of the designs in phenotype space). Especially for evolutionary algorithms this property is meaningful since it supports the self-adaptation of the step sizes which is one reason for the high performance of Evolution Strategy for the optimization of continuous parameters.

For the present problem FFD has been chosen. Since these methods are based on transfer functions instead of defining the geometry explicitly, the optimisation parameters are decoupled from the geometric description of the design in opposite to representations based e.g. on surfaces or splines.

When dealing with a CFD or FE solver for performance evaluation there is one additional constraint on the representation. In this case in every generation for each offspring a computational grid has to be computed which is the basis for each CFD simulation. With respect to a fully automized environment this can be a very time consuming (or even impossible) process if the geometry is highly complex. FFD provides the advantage of generating the geometry and the CFD mesh simultaneously [6]. Since everything within the control volume is deformed, also the grid points of a CFD mesh are modified. Since the structure of the grid is kept, the mesh is directly available for simulation.

4. 3D TURBINE BLADE OPTIMISATION

Subject of the optimization is a turbine stator blade which is part of a gas turbine developed for the propulsion of a small business jet. An illustration of the turbine is shown in Figure 3. In order to reduce the weight of the engine only one turbine stage is used with a ultra-low-aspect-ratio (ULAR) stator with only 8 blades. The blades have been already target of design optimization. For more detailed information on the turbine functionality and on a design optimization approach using spline representation the reader is referred to [11], [12] and [13].

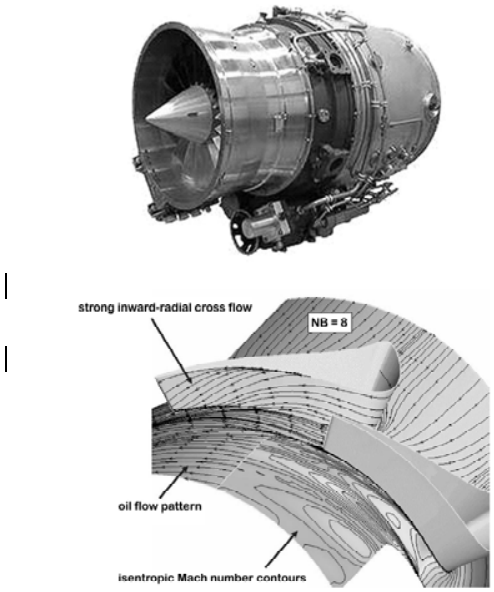

Figure 3. Gas Turbine and its fluid dynamics in one blade section [12]

In order to optimize the blade shape using FFD a lattice of control points has to be constructed in which the target geometry is embedded. Due to the rotational symmetry of the turbine only one of the eight turbine blade sections is encoded.

It is important to note that not only the blade geometry itself but the mesh necessary for the CFD simulation is deformed. Therefore, the control volume is constructed in such a way that it includes the grid which is in the passage between two blades, i.e. it spans from the suction side to the pressure side of two neighboring blades. As mentioned above, in this way the CFD mesh can be directly gained from the deformation and a remeshing is omitted. In the present example, the re-meshing costs would have not been crucial for the optimization because of the 'simple' structured grid consisting of parallelepiped volumes but if the grid structure is more complex containing edges and ridges the omission of a costly remeshing procedure is very advantageous.

The design evaluation of a blade consists of two steps. At first geometric constraints are tested such as blade thickness. In a second step, the flow is simulated by CFD to determine the flow characteristics.

The distribution of control points is depicted in Figure 4.

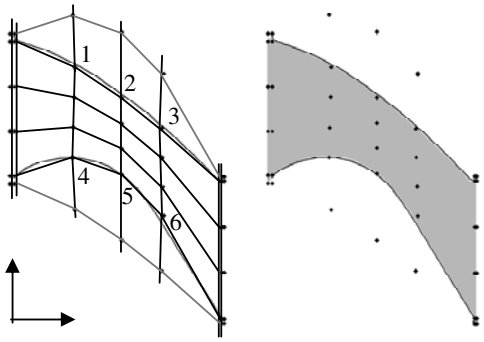

Figure 4. Blade geometry embedded in a lattice of control points [3]

Twelve control points have been taken from the lattice as optimization parameters. Six control points are on the hub section and six are on the casing section. All remaining control point positions are linear interpolated. To simplify the calculations and because of the bending of the turbine blade the global x, y and z coordinates of the design and of the knots of the CFD grid have been transferred to a local cylinder coordinate system x', y' and z' which is depicted in Figure 5.

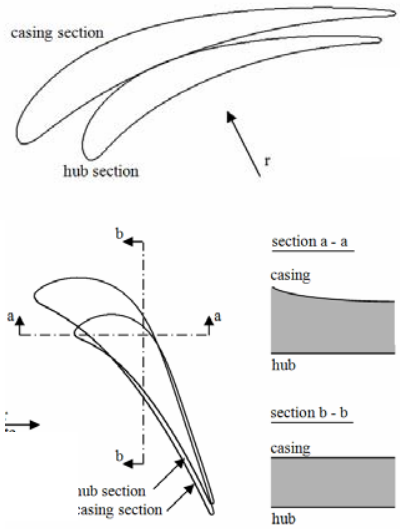

Figure 5. Transformation of global coordinate system to cylinder coordinates (a-a and b-b denote the positions of the cross sections a - a and b - b respectively)

4.1. Definition of optimisation parameter

The lattice is fully three dimensional and an example of the cross-section is depicted in Figure 6.

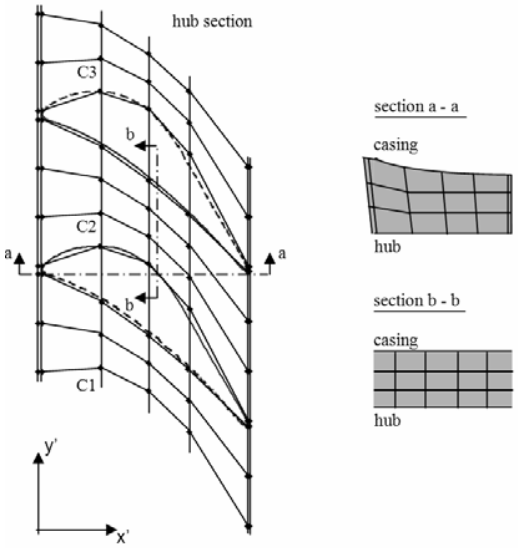

Figure 6. Illustration of the three-dimensional control volume

The continuous lines in Figure 4 and 6 illustrate the blade shape: the continuous upper line is the pressure side and the continuous lower one the suction side of two neighbouring turbine blades. The grey regions in the right part of Figure 6 mark the area of the knots and volume cells of the CFD grid. In Figure 6 two blade contours are depicted to show the position of the blades with respect to the control volume. In this test scenario, the number of optimization parameters is kept as low as possible because here the target is to demonstrate the feasibility of the representation via free form deformation. As a consequence the movements of the chosen control points effect more or less global design changes of the blade which can also be seen in Figure 8. A higher degree of local changes can easily be realized by refining the control point lattice but with all its consequences on the optimizer, e.g. the increasing number of parameters.

In local x'-direction seven control points have been set. In local y'-direction six control points are introduced. Due to the rotational symmetry of the design additional points are introduced to realize periodic boundary conditions for the splines which results in 10 control points for that direction. For a detailed description the reader is referred to [3]. In z'-direction four control points have been positioned which resulted in a total number of 7x10x4 = 280 control points.

Although all of these control points are important for freezing and deforming the geometry and the CFD mesh, only 12 points had to be considered for optimization. Six of these points are shown in Figure 6 for the hub section and another six points have been chosen analogously at the casing section. In total 24 parameters (x and y coordinates of the 12 points) have been considered in the evolutionary optimization and were encoded in the chromosome. To maximize the influence of these control points on the blade geometry they have been positioned as close as possible to the boundary layers of the blade so that the mutation of the control points provides a high impact on the design. The present optimization was motivated to analyze in how far these global design changes influence the performance.

Based on these control point settings the initial CFD grid and the blade geometry have been frozen, i.e. the coordinates of the grid knots have been calculated in spline parameter space.

4.1. Performance evaluation

The quality of each blade is evaluated using the 3D Navier-Stokes flow solver HSTAR3D [11]. The used CFD grid is restricted to 175 x 52 x 64 = 582400 cells which allowed an estimation of the quality of one generation of individuals on a cluster of 32 CPUs in a reasonable time of about five to six hours.

In each generation the parameter that are stored in the chromosome of each of the eight individual of a population are decoded and used for a transformation of the initial CFD mesh.

After deforming the initial CFD grid for all eight individuals numerical solutions for the flow patterns are calculated based on the resulting CFD grids and the overall quality is estimated based on the fitness function described in the following.

$$f = w_1 t_1 + \sum_{i=2}^{5} w_i t_i^2 \rightarrow \min \qquad (1)$$

The main optimization criterion is the minimization of the pressure loss w_1. To keep the blade geometry within feasible constraints four additional values w_2 to w_5 have been extracted from the CFD calculation and blade geometry respectively The quality of the blade are calculated according to (1). Instead of hard constraints which would exclude illegal designs the constraints define penalty terms in the formulation of the fitness function which are determined by the outflow angle, a maximum solidity, a minimum blade thickness and a trailing edge thickness. The weighting coefficients were chosen like in [12], [13].

4.1. Results of the optimisation

The course of the fitness (note: in a minimization problem like equation (1) fitness values are minimized) and the step size are depicted in Figure 7. A total number of 134 generations has been calculated resulting in an overall optimization time of approx. six weeks. In the first ten generations a (1,6)-strategy has been used but was extended to a (1,8)-strategy starting with generation

11 because of the high variance of the fitness values. Generally, a population size of 10 is recommended for the used strategy but could not be realized due to restrictions of the computational resources. The fitness value of the initial blade is about 10.69 and is marked by the dashed line in the fitness graphs.

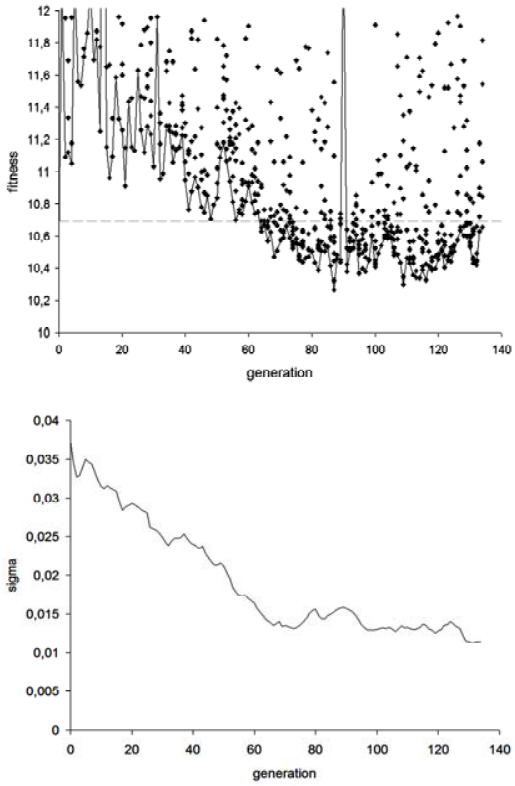

Figure 7. Result of the optimisation run. Upper figure: Fitness values of single evaluations (note: minimization problem). The best individuals in each generation are connected by a line. Lower figure: mutation step size.

It can be seen that in the beginning the fitness values of the designs are higher than that of the initial design (baseline). During the optimization the initial fitness value is recovered by generation 60. The reason is likely to be a sub-optimal choice of the initial step size. This is not a principle problem because the step size is adapted during optimization. However, it delays the convergence and basically wastes computational resources during the early stages of optimization. This is supported by the fast decrease of the step size until generation 60, thereafter it is kept nearly constant. In general the initial step size depends on the experience gathered for the problem at hand. However it can be observed that the step size adaptation in the CMA-ES algorithm finds a proper setting.

The best value of 10.27 is found in generation 87, which corresponds to a performance gain of 4%.

The initial blade and the shape of the best design of generation 87 are depicted in Figure 8 to visualize the changes which occurred.

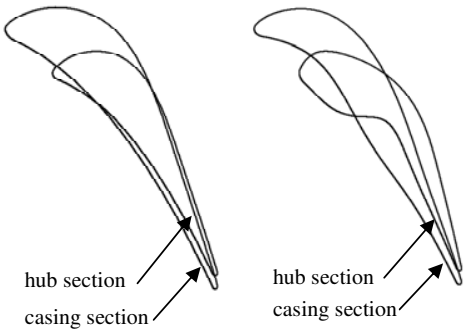

Figure 8. Initial and optimized shape of the turbine blades [3]

5. CONCLUSIONS

In the present paper the techniques of free form deformation have been combined with evolutionary design optimization. This combination is especially promising if coupled with CFD or FEM simulators for calculating the performance of the designs under realistic conditions. In contrast to a direct definition of the shape geometry, e.g. with the help of splines or spline surfaces, for free form deformation the geometry is embedded in a control volume and the shape modifications are calculated via transformation equations. Hence, for many complex systems the number of optimization parameters can be reduced drastically. The additional possibility of deforming the shape geometry and the CFD/FEM mesh simultaneously is highly advantageous because the grid structure is kept and a re-meshing procedure is avoided. The easy and successful applicability of this representation and the comfortable integration in autonomous evolutionary design optimization has been illustrated by the example of a turbine blade development.

ACKNOWLEDGEMENTS

The authors would like to thank M. Hasenjäger, T. Arima and T. Sonoda cordially for their support and advice on the turbine blade scenario.

REFERENCES

[1] Hansen, N., Ostermeier, A., 2001, “Completely Derandomized Self-adaptation in Evolution Strategies”, *Evolutionary Computation*, vol. 9, no. 2, pp. 159-196.

[2] Fogel, D B., 1995, “Evolutionary Computation: toward a new philosophy of machine learning”, New York, NY: IEEE Press.

[3] Menzel, S., Olhofer, M., and Sendhoff, B., 2005, “Application of Free Form Deformation Techniques in Evolutionary Design Optimisation”, *6th World Congress on Multidisciplinary and Structural Optimisation*, Rio de Janeiro.

[4] Sonoda, T., Yamaguchi, Y., Arima, T., Olhofer, M., Sendhoff, B., and Schreiber, H-A., 2004, “Advanced High Turning Compressor Airfoils for Low Reynolds Number Condition, Part 1: Design and Optimization”, *Journal of Turbomachinery*, 126: 350-359.

[5] Jin, Y., Olhofer, M., and Sendhoff, B., 2001, “Managing Approximate Models in Evolutionary Aerodynamic Design Optimization”, *Congress on Evolutionary Computation (CEC)*, vol. 2, pp. 592-599.

[6] Perry, E. C., Benzley, S. E., Landon, M., and Johnson, R., 2000, “Shape Optimization of Fluid Flow Systems“, *Proceedings of ASME FEDSM'00*, *2000 ASME Fluids Engineering Summer Conference*, Boston, Massachusetts.

[7] Sederberg, T. W., and Parry, S. R., 1986, “Free-Form Deformation of Solid Geometric Models”, *Computer Graphics*, 20(4):151-160.

[8] Coquillart, S., 1990, “Extended Free-Form Deformation: A Sculpturing Tool for 3D Geometric Modeling”, *Computer Graphics*, 24(4):187-196.

[9] Piegl, L., and Tiller, W., 1995 and 1997, “The NURBS Book”, *Springer-Verlag Berlin Heidelberg.*

[10] Sendhoff, B., Kreutz, M. and von Seelen, W. A condition for the genotype-phenotype mapping: Causality. *Proceedings of the Seventh International Conference on Genetic Algorithms (ICGA'97)*, pages 73-80, Morgan Kauffmann, San Francisco, 1997.

[11] Arima, T., Sonoda, T., Shirotori, M., Tamura, A., and Kikuchi K., 1999, “A numerical investigation of transonic axial compressor rotor flow using a low-Reynolds-number k-ε turbulence model”, *ASME Journal of Turbomachinery*, 121(1), pp.44-58.

[12] Hasenjäger, M., Sendhoff, B., Sonoda, T. and Arima, T., 2005, “Three dimensional Aerodynamic Optimization for an ultra-low aspect ratio transonic Turbine Stator Blade”, *Proceedings of the ASME Turbo Expo*, ASME GT2005-68680.

[13] Hasenjäger, M., Sendhoff, B., Sonoda, T. and Arima, T., 2005, “Single and Multi-Objective Approaches to 3D Evolutionary Aerodynamic Design Optimisation”, *6th World Congress on Structural and Multidisciplinary Optimization*, Rio de Janeiro, Brazil.

,

Conference on Modelling Fluid Flow (CMFF'06)
The 13th International Conference on Fluid Flow Technologies
Budapest, Hungary, September 6-9, 2006

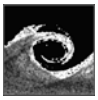

NUMERICAL OPTIMISATION OF A LAMINAR BURNER TO REDUCE CO EMISSIONS

Gábor JANIGA[1], Dominique THÉVENIN[2]

[1] Corresponding Author. Lab. of Fluid Dynamics and Technical Flows, University of Magdeburg "Otto-von-Guericke", Germany. Tel.: +49 391 67 18196, Fax: +49 391 67 12840, E-mail: Gabor.Janiga@vst.uni-magdeburg.de
[2] Lab. of Fluid Dynamics and Technical Flows, University of Magdeburg "Otto-von-Guericke", Germany.

ABSTRACT

In this work the optimisation of the flame shape of a laminar burner is investigated using different optimisation methods when varying the fuel/air ratio in a primary and a secondary inlet. The objective is to reduce the CO emission at a prescribed distance from the injection plane. An in-house computer package, called *Opal*, controls the optimisation process in a fully automatic manner. The flow involving chemical reactions is solved using the in-house CFD code *UGC+*.

Keywords: laminar burner, numerical simulation, optimisation

NOMENCLATURE

h	[J/kg]	enthalpy
p	[Pa]	pressure
T	[K]	temperature
v	[m/s]	velocity
Y	[-]	mass fraction
ρ	[kg/m^3]	density
μ	[Pa·s]	dynamic viscosity
$\dot{\omega}$	[kg/m^{3}s]	reaction rate

Subscript

k	species index

1. INTRODUCTION

Designing optimal shapes for practical engineering applications has been the subject of numerous publications during the last decade. Generic and robust search methods inside the design shape, such as genetic algorithms (GA), offer several attractive features for such problems [1]. The basic idea associated with the GA approach is to search for optimal solutions using an analogy to the evolution theory. During the iteration (or "evolution" using GA terminology) procedure, the decision variables or genes are manipulated using various operators (selection, combination, crossover or mutation) to create new design populations, i.e., new sets of decision variables.

For simpler optimisation problems, more classical optimisation methods, like the Simplex approach, are often better adapted to find the optimal solution within a small number of iterations [2].

The main goal of this work is to achieve cost-efficient design optimisation of problems involving complex flows with heat transfer and chemical reactions, using computational fluid dynamics (CFD) codes for practical configurations, while keeping reasonable overall computing times.

Laminar flows involving chemical reactions play an important role in many practical applications. In this work a two-dimensional simulation dedicated to solving the Navier-Stokes equations in the low-Mach number limit is presented, using accurate models for chemistry, diffusion and thermodynamics.

Optimisation involving CFD computations is an intensive field of research. In aerodynamics an optimal shape geometry is often needed. Thus, the design of an airfoil shape was for example optimised in [3] and [4]. The wall shapes of incompressible diffusers have been investigated by CFD and optimised in [5]. Han and Maeng [6] have presented a shape optimisation of cut-off in a multi-blade fan/scroll system analyzed using two-dimensional CFD.

In the same way, heat transfer problems often involve optimisation. Heat exchange through smooth and corrugated walls has been investigated in [7]. Shape design of a cylinder with heat transfer was carried out in [8]. The optimal shapes of fins and pins inside heat exchangers are examined by various authors [9-13]. Foli et al. [14] have obtained optimal results for a micro heat exchanger based on different multi-objective optimisation methods.

There is also a great interest at present to optimise complex flows involving chemical

reactions. A detailed description of the chemical kinetics is generally needed to fully understand the chemical processes in such cases. Multi-objective evolutionary algorithms are often employed for determining and adjusting the reaction parameters or for reducing the number of reactions [15-17]. Furthermore, the reduction of pollutant emission (NOx, CO, soot…) is of major practical interest. Evolutionary Algorithms have been applied in gas turbines for minimizing NOx emissions and/or for reducing combustion noise [18-20]. Mono-objective optimisation of a laminar burner was investigated in [2], where the objective was to obtain a homogeneous temperature profile at a prescribed distance from the injection plane.

As a whole, optimisation of configurations involving the coupled simulation of flows and heat transfer, especially with combustion, remains a fairly new field of research.

On the other hand, many methods can be found in the literature for optimisation problems, based on different strategies, most of the time developed for a specific class of models. In a previous project a multi-objective optimisation problem has been considered, since it covers many interesting application fields [1]. As a matter of fact, most of the time, engineers responsible for the design of installations have to face configurations with more than one objective to fulfil at the same time. But the optimisation problem considered here involves only a single objective and should thus be more efficiently solved using a Simplex-based optimisation technique.

A two-dimensional configuration is considered, involving a primary inlet in the centre of the computational domain and a secondary inlet at the periphery. The optimisation problem consists in finding the minimal mass-flow rate of the pollutant species CO; the corresponding integral value is computed at a prescribed distance from the inlet. The single objective is in this case the minimal concentration of CO along the corresponding horizontal cut through the solution. The parameters modified by the optimisation procedure are the fuel and oxidizer mass flows of the primary inlet, while the total amount of fuel and oxidizer injected through both inlets is of course kept constant. There are therefore two parameters that may freely vary between a lower bound (0: no fuel or no oxidizer injected through this inlet) and an upper bound (all the available fuel or all the available oxidizer injected through this inlet).

In this paper it will be shown that it is possible using CFD to reach an optimal configuration for a problem involving coupled fluid flow and heat transfer as well as chemical reactions, within a reasonable computing time, even for configurations close to practical ones. In the present work laminar flows are considered, since it corresponds to realistic engineering problems, for example domestic burners. A laminar gas flame is thus considered, as found in practice in such low-power domestic boilers.

2. GOVERNING EQUATIONS

Laminar flows involving chemical reactions are considered in this paper. In the presented application Mach numbers M are very low. It is observed that pressure variations through laminar flames at low Mach numbers are always of the order of magnitude of a few Pascal and stem mainly from hydrodynamical and not from compressibility effects. Stated differently, density variations only result from heat release due to chemical reactions and from changes in the mixture composition, but not from local fluid compression. Temperature and density vary in opposite directions, such that their effects within the ideal gas law compensate. These physical observations motivate the decomposition of pressure into a bulk background uniform thermodynamic pressure p_u and a hydrodynamic fluctuation term $\tilde{p}$ [21; 22]:

$$p(\boldsymbol{x},t) = p_u(t) + \tilde{p}(\boldsymbol{x},t) \quad (1)$$

For the presented application (a domestic gas burner), the numerical domain is considered open, hence p_u equals the atmospheric pressure and is constant. If acoustic waves may propagate in the gas mixture, then an additional acoustic pressure term has to be considered. Since acoustic/flame interactions are not addressed here, it is assumed from now on that acoustic waves are either inexistent or of negligible effect on the flame structure and on the flow. Readers particularly interested in flame/acoustic interactions may e.g. refer to [23; 24] for further specific details.

Within the low-Mach number approximation, the density appears as a function of temperature T and mean molar weight W. When the numerical domain is opened to the atmosphere the influence of the hydrodynamic pressure $\tilde{p}$ on the density must be neglected. The full problem is then described by the following set of balance equations, written in conservative form for mass, momentum, mass fractions and enthalpy, solved in the present case:

$$\frac{\partial \rho}{\partial t} + \nabla \cdot (\rho v) = 0 \quad (2)$$

$$\frac{\partial (\rho v)}{\partial t} + \nabla \cdot (\rho v v) = \\ = -\nabla \tilde{p} + \nabla \cdot \left\{ \mu \left(\nabla v + (\nabla v)^T \right) \right\} \quad (3)$$

$$\frac{\partial (\rho Y_k)}{\partial t} + \nabla \cdot (\rho Y_k v) = -\nabla \cdot (\rho Y_k V_k) + W_k \dot{\omega}_k \\ 1 \le k \le K-1 \quad (4)$$

$$\frac{\partial(\rho h)}{\partial t} + \nabla \cdot (\rho h v) = \nabla \cdot \left(\lambda \nabla T - \rho \sum_{k=1}^{K} h_k Y_k V_k \right) \quad (5)$$

Using a unity Lewis number assumption for the diffusion model, Equations (4) and (5) become much simpler:

$$\frac{\partial(\rho Y_k)}{\partial t} + \nabla \cdot (\rho Y_k v) = \nabla \cdot \left(\frac{\lambda}{c_p} \nabla Y_k \right) + W_k \dot{\omega}_k \quad (6)$$

$$\frac{\partial(\rho h)}{\partial t} + \nabla \cdot (\rho h v) = \nabla \cdot \left(\frac{\lambda}{c_p} \nabla h \right) \quad (7)$$

Equation (6) is solved for $K - 1$ species, because the last species (the nitrogen) is a non-reacting species, simply determined using:

$$Y_{N_2} = 1 - \sum_{k=1}^{K-1} Y_k \quad . \quad (8)$$

For all computations presented in this paper, the complete set of chemical species and elementary reactions, with their Arrhenius coefficients A_i (pre-exponential factor), β_i (temperature exponent) and E_i (activation energy), is taken for methane/air flames from [25]. This detailed reaction scheme involves 29 species and 141 elementary reactions.

3. NUMERICAL SOLUTION

The numerical simulation is performed using *UGC+*. This code has been optimised for the computation of steady laminar low-Mach number flows with chemical reactions [26; 27]. It is designed as an application of the multi-purpose *UG* library [28]. *UG* is a modular numerical toolbox originally aimed at investigations of multigrid methods on various model problems described by sets of partial differential equations.

UGC+ is based on two main modules: a low-Mach Navier-Stokes solver and a thermo-reactive solver. A joint module has been developed to achieve the full coupling of the two sub-modules into one single PDE system. The two solvers are in charge of their own diagonal block of the Jacobian matrix and there is an information interchange between them (mass fluxes, density and viscosity).

The *UGC+* code attempts to find steady solutions through time-marching. Time discretisation is of first-order implicit type. The value of the time-step can be adapted at each iteration, according to convergence or any user-defined condition. The unsteady equations are solved by fixed-point or approximate-Newton iterations and the user can freely specify how often the Jacobian matrix has to be assembled. The linearised equations are then solved by a Bi-CGSTAB algorithm, preconditioned by multigrid V-cycles with an ILU smoother. An adaptive grid is used to increase resolution for such multi-scale problems (thin reaction zones, large geometries).

The smallest grid spacing obtained in the present computations is 31 µm. This resolution is needed for very stiff intermediate radicals like HCO and C_2H_2. The numerical grid is refined adaptively according to a predefined criterion, here the mass fraction of HCO. During these computations the numerical grid contains between 7000 and 22 000 finite-volume cells after reaching the third level of grid refinement (see Figure 1).

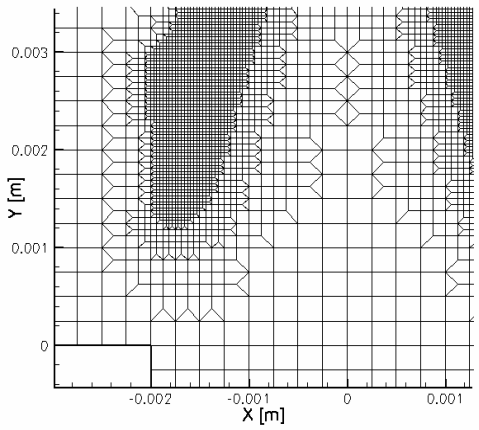

Figure 1. Part of the numerical grid at the flame front.

The numerical simulation of a physical problem can be performed using various geometries and/or boundary conditions. For the present burner the computational geometry is fixed for all computations, but the boundary conditions (composition of the mixture for the primary and the secondary inlets) are varied during the optimisation procedure. To perform the CFD simulation, we rely on the in-house code *UGC+* [27; 29]. Since the optimisation problem is here simple (single objective), the Simplex method is used to speed-up the computational procedure [30]. This method cannot be described here due to lack of space, all details can be found in other publications, for example [27; 31]. In a further step a Genetic Algorithm is employed to investigate more completely the allowed optimisation domain for the retained input parameters.

Another possibility to decrease the simulation time is to perform every numerical simulation on parallel computers [32] or to use simplified methods to describe the chemistry (e.g. the flamelet approach [33; 34] or tabulated chemistry [35-38]). These issues are not further discussed in the present paper.

All the simulations are carried out on a single Pentium-IV PC with 2.6 GHz/2 GB-RAM running under Red Hat 9 Linux. Typical computations times for the CFD evaluation vary between 3 and 10 hours depending on the conditions.

4. DISCUSSION

4.1. OPAL (OPtimization ALgorithms) package

Opal [1; 27] is an object-oriented C++ code for Unix/Linux systems, using a Tcl script interpreter. A Tcl script is used for coupling *Opal* with other computer codes, and is employed in our case to call a C interfacing program responsible for the evaluation of the objective functions. For computing the burner, both the adaptive mesh generation and the flow computations are carried out inside the in-house CFD-software *UGC+*.

To illustrate the full computational procedure, the evaluation of an individual set of parameters requires three steps:

- the computation of the composition of the mixture in the primary and secondary inlet, knowing the specific design variables;
- the CFD simulation, i.e. the resolution of the governing coupled equations for the flow variables, the energy and the species conservation equations;
- the post-processing of the obtained results to extract the value of the objective function (average mass flow rate of CO along a horizontal cut) for these design variables.

For the case considered here the configuration is two-dimensional and can be optimised on a single PC with a reasonable computing time, provided a CFD software as efficient as *UGC+* is employed. Nevertheless, this will not always be the case. Therefore a parallel version of this optimisation procedure has been developed. Due to lack of space, corresponding results cannot be shown here, but supplementary information can be found in [1].

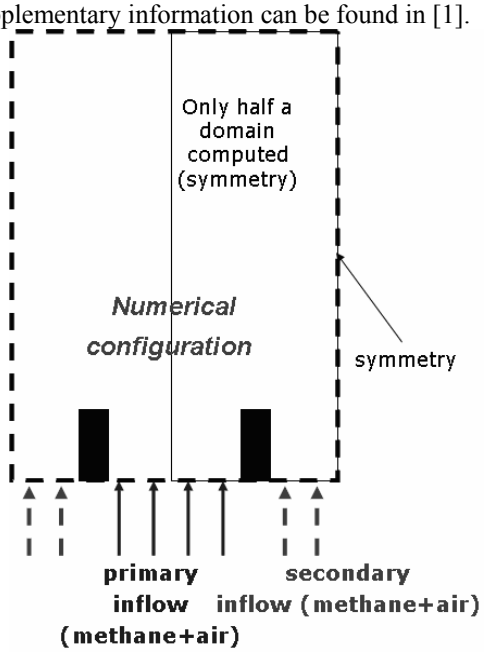

Figure 2. General configuration of the laminar burner. A methane/air mixture enters through the primary and secondary inlets with a varying composition.

The investigated configuration is depicted in Figure 2. Due to the symmetry only the right half of the domain is considered in the computation. Depending on the input parameters methane/air mixtures with different compositions enter the domain through the primary and secondary inlets, with a fresh gas temperature of 298 K. Atmospheric pressure is imposed at the outlet. The inlet wall temperature is constant and equal to 298 K.

The optimisation procedure can now be started, with the objective of reducing as much as possible the average mass flow rate of CO along a horizontal cut through the solution at y=0.025 m, near the outlet. The trajectory followed by the optimal point of the Simplex inside the optimisation space controlled, as explained before, by two parameters, is shown in Figure 3 to exemplify the search procedure. The top left part of the figure contains no results. Since the corresponding input parameters would yield a configuration in contradiction with the concept of a central primary inlet with a surrounding secondary inlet, they are considered as infeasible configurations and are not computed.

The evolution of the CO mass flow rate with the number of iterations of the optimisation procedure is shown in Figure 4, demonstrating the high efficiency of the computational method employed here. Within a few iterations, the mass fraction of CO has been reduced by a factor of roughly 4 using Simplex (Case1).

To quantify in a more precise way the progress of the iteration procedure, all computed feasible configurations are shown in Figure 4. As usual for an optimisation procedure, the process temporarily leads to solutions much worse than the starting guess. This is expected since the initial guess is a random choice and thus should not be associated to a particularly bad (or good) solution.

The Simplex optimisation was performed using different initial guess values. Two of these results are presented (see Figs. 3 and 4). It was observed that this method often finds only a local optimum. Therefore, a Genetic Algorithm was employed to explore the complete optimisation domain. The corresponding results are also shown in Figures 3 and 4. All GA parameters are listed in Table 1.

Table 1. Parameters of the Genetic Algorithm

Parameter	*Value*
Population size	20
Generations	20
Survival probability	0.5
Average probability	0.3
Crossover probability	0.2
Mutation probability	1.0
Mutation magnitude	70 %* (± 35 %)

* This value is multiplied by 0.8 at each generation. Mutation magnitude should be decreased during the optimization process to stabilize the population.

Additionally, the evaluation results are also depicted in Figure 5 using a contour plot representation. The darker values correspond to a lower mass flow rate of CO. This figure explains why the Simplex method in Case 1, at the difference of Case 2, can not come near to the global optimum, because the algorithm can never jump over the "hill" represented with light colours. Depending on the initial guess, the Simplex solution is thus constrained to a subpart of the accessible domain, leading to a local optimum.

The mass fraction field of CO obtained for the two-dimensional burner considered here with a few chosen compositions of the two inlets are presented in Figures 6-9. In all figures the mass fraction of the radical HCO is also shown to visualise the shape and position of the active reaction zone. Fig. 6 corresponds to a non-optimal solution of the Genetic Algorithm. Comparing with Figures 7 to 9 a large CO mass fraction and thus mass-flow rate is found at the outlet of the combustion chamber for this set of compositions.

A much better configuration is achieved with the Simplex method (Case 1), presented in Fig. 7. Examples of optimal mass fraction distributions for CO can be seen in Figures 8 and 9 for the GA.

Table 2. Primary inlet flow-rates for the selected simulations

Figure number	Injector1 Methane mass flow rate [*g/s*]	Injector1 Air mass flow rate [*g/s*]
6	$8.31 \cdot 10^{-2}$	$9.01 \cdot 10^{-1}$
7	$5.51 \cdot 10^{-2}$	$9.18 \cdot 10^{-1}$
8	$8.92 \cdot 10^{-2}$	$7.43 \cdot 10^{-2}$
9	$8.71 \cdot 10^{-2}$	$1.03 \cdot 10^{-1}$

The values chosen by the optimisation procedure for the primary inlet for the Cases corresponding to Fig.6 to 9 are listed in Table 2. Considerable variations have been tested by the optimisation procedure, corresponding to more than 40 % of variations for the fuel and more than 50 % for the air inflow rate, before identifying the best solution. Such large variations would certainly not have been considered by a human being carrying out a "manual" optimization.

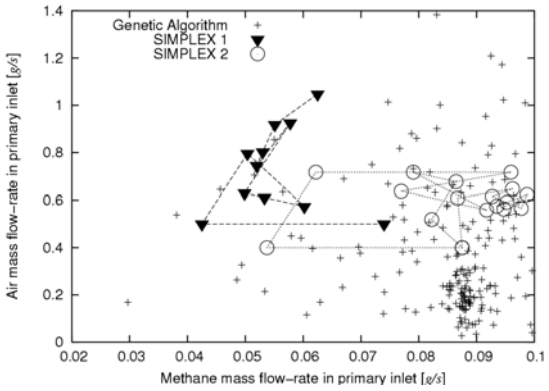

Figure 3. Input parameters of the optimisation using Simplex and Genetic Algorithms

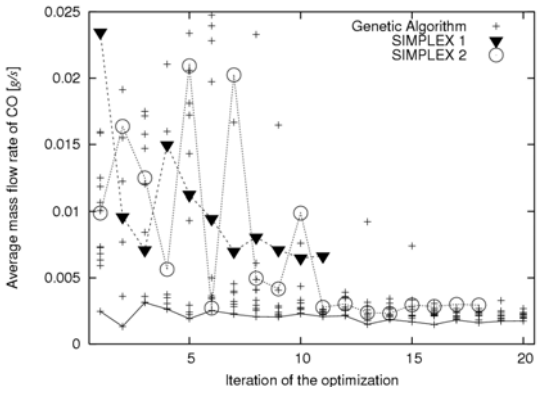

Figure 4. Results of the optimisation using Simplex and Genetic Algorithms

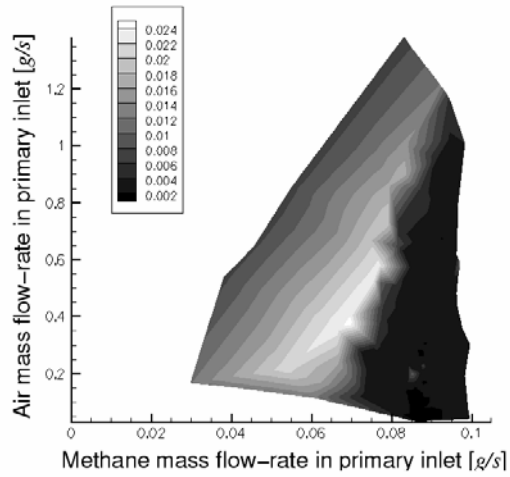

Figure 5. Contour plot of the average mass fraction of CO as a function of the input parameters.

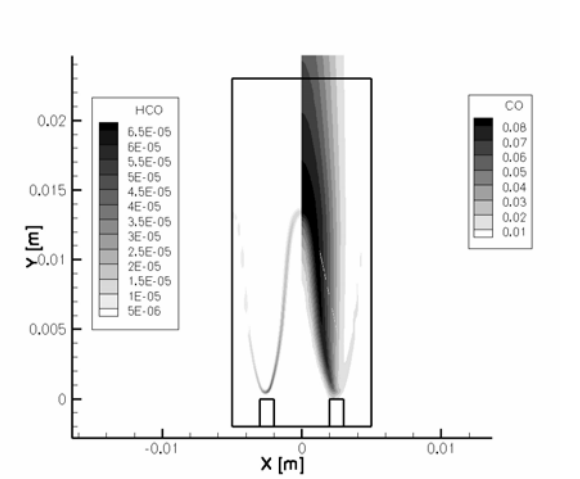

Figure 6. Mass fraction field of HCO (left) and CO (right) in one of the worst case for the Genetic Algorithm optimisation

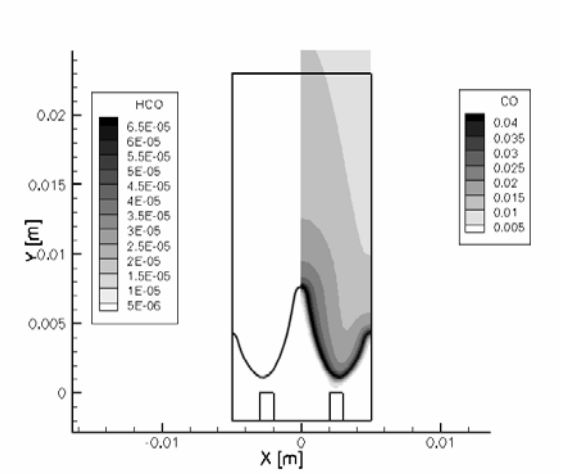

Figure 7. Mass fraction field of HCO (left) and CO (right) in the last Simplex (Case 1) iteration

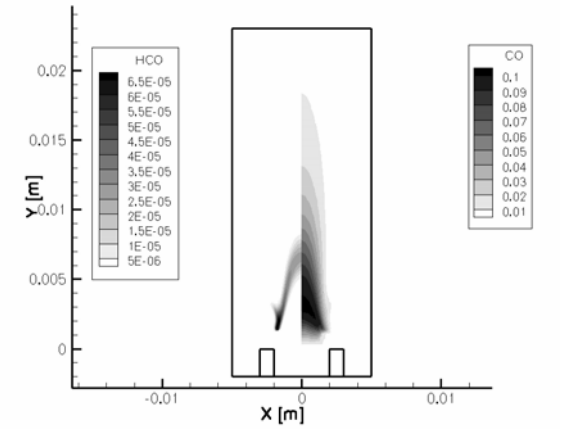

Figure 8. Mass fraction field of HCO (left) and CO (right) in one of the optimum cases for the Genetic Algorithm optimisation

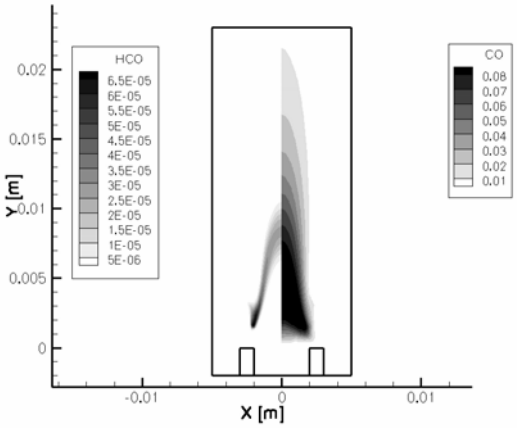

Figure 9. Mass fraction field of HCO (left) and CO (right) in another optimum case for the Genetic Algorithm optimisation

5. SUMMARY

This study has demonstrated that optimisation of complex flows involving heat transfer and chemical reactions is possible, provided very efficient numerical methods are used for the optimisation process (here the in-house *Opal* library) as well as for the CFD procedure (here the in-house *UGC+* code). In this case, optimal solutions can be obtained with a small number of iterations and acceptable computing times. This remains true for much more complex multi-objective problems, as demonstrated in other publications. In the present case the Simplex method has found several but only local optimal configurations depending on the starting point. The optimisation domain has been explored using Genetic Algorithm with more success, but with a considerably higher computational effort. Further investigations are presently being conducted to decrease even more the needed computing time and therefore have access to more realistic, three-dimensional configurations, described with more refined models using a higher number of parameters.

ACKNOWLEDGEMENTS

The library *Opal* has been first developed by Romain Baron during his Ph.D. The development of the program *UGC+* would not have been possible without the work presented in the Ph.D. of S. Paxion and R. Baron. This project has been initially supported by different French organizations and companies, including DGA, ADEME and CETIAT.

REFERENCES

[1] Hilbert, R., Janiga, G., Baron, R., and Thévenin, D., 2006, "Multiobjective shape optimization of a heat exchanger using

parallel genetic algorithms", *International Journal of Heat and Mass Transfer*, Vol. 49, pp. 2567-2577.

[2] Janiga, G., Zähringer, K., and Thévenin, D., 2005, "Automatic optimization of two-dimensional burners", *Proceedings of the European Combustion Meeting ECM05*, Louvain-la-Neuve, Belgium, pp. 240/1-240/6.

[3] Falco, I. D., 1997, "An introduction to Evolutionary Algorithms and their application to the Aerofoil Design Problem - Part I: the Algorithms", *von Kármán Lecture Series on Fluid Dynamics, Bruxelles, Belgium, April 1997*.

[4] Mäkinen, R., Neittaanmäki, P., Périaux, J., and Toivanen, J., 1998, "A Genetic Algorithm for Multiobjective Design Optimization in Aerodynamics and Electromagnetics", Computational Fluid Dynamics '98, Proceedings of the ECCOMAS 98 Conference, K. D. Papailiou, D. Tsahalis, J. Périaux, and D. Knörzer, eds., Wiley, Athens, Greece, 418-422.

[5] Madsen, J. I., Shyy, W., and Haftka, R. T., 2000, "Response surface techniques for diffuser shape optimization", *AIAA Journal*, Vol. 38, pp. 1512-1518.

[6] Han, S. Y., and Maeng, J. S., 2003, "Shape optimization of cut-off in a multi-blade fan/scroll system using neural network", *International Journal of Heat and Mass Transfer*, Vol. 46, pp. 2833-2839.

[7] Fabbri, G., 2000, "Heat transfer optimization in corrugated wall channels", *International Journal of Heat and Mass Transfer*, Vol. 43, pp. 4299-4310.

[8] Cheng, C. H., and Chang, M. H., 2003, "Shape design for a cylinder with uniform temperature distribution on the outer surface by inverse heat transfer method", *International Journal of Heat and Mass Transfer*, Vol. 46, pp. 101-111.

[9] Lee, K. S., Kim, W. S., and Si, J. M., 2001, "Optimal shape and arrangement of staggered pins in the channel of a plate heat exchanger", *International Journal of Heat and Mass Transfer*, Vol. 44, pp. 3223-3231.

[10] Fabbri, G., 1998, "Heat transfer optimization in internally finned tubes under laminar flow conditions", *International Journal of Heat and Mass Transfer*, Vol. 41, pp. 1243-1253.

[11] Balagangadhar, D., and Roy, S., 2001, "Design sensitivity analysis of steady fluid-thermal systems", *Computer Methods in Applied Mechanics and Engineering*, Vol. 190, pp. 5465-5479.

[12] Bonjour, J., Rocha, L. A. O., Bejan, A., and Meunier, F., 2004, "Dendritic fins optimization for a coaxial two-stream heat exchanger", *International Journal of Heat and Mass Transfer*, Vol. 47, pp. 111-124.

[13] Fabbri, G., 2004, "Effect of viscous dissipation on the optimization of the heat transfer in internally finned tubes", *International Journal of Heat and Mass Transfer*, Vol. 47, pp. 3003-3015.

[14] Foli, K., Okabe, T., Olhofer, M., Jin, Y., and Sendhoff, B., 2006, "Optimization of micro heat exchanger: CFD, analytical approach and multi-objective evolutionary algorithms", *International Journal of Heat and Mass Transfer*, Vol. 49, pp. 1090-1099.

[15] Edwards, K., Edgar, T. F., and Manousiouthakis, V. I., 1998, "Kinetic model reduction using genetic algorithms", *Computers and Chemical Engineering*, Vol. 22, pp. 239-246.

[16] Elliott, L., Ingham, D. B., Kyne, A. G., Mera, N. S., Pourkashanian, M., and Wilson, C. W., 2003, "Multiobjective genetic algorithm optimization for calculating the reaction rate coefficients for hydrogen combustion", *Industrial and Engineering Chemistry Research*, Vol. 42, pp. 1215-1224.

[17] Elliott, L., Ingham, D. B., Kyne, A. G., Mera, N. S., Pourkashanian, M., and Wilson, C. W., 2005, "Reaction mechanism reduction and optimization using genetic algorithms", *Industrial and Engineering Chemistry Research*, Vol. 44, pp. 658-667.

[18] Büche, D., Stoll, P., and Koumoutsakos, P., 2001, "An evolutionary algorithm for multi-objective optimization of combustion processes", *Center for Turbulence Research Annual Research Briefs 2001*, Vol. pp. 231-239.

[19] Büche, D., Stoll, P., Dornberger, R., and Koumoutsakos, P., 2002, "Multiobjective evolutionary algorithm for the optimization of noisy combustion processes", *IEEE Transactions on Systems, Man and Cybernetics Part C: Applications and Reviews*, Vol. 32, pp. 460-473.

[20] Pascherelt, C. O., Schuermans, B., and Büche, D., 2003, "Combustion process optimization using evolutionary algorithm", *American Society of Mechanical Engineers, International Gas Turbine Institute, Turbo Expo (Publication) IGTI*, pp. 281-291.

[21] Giovangigli, V., 1999, *Multicomponent flow modeling*, Birkhäuser, Boston.

[22] Majda, A., and Sethian, J., 1985, "The derivation and numerical solution of the equations for zero Mach number combustion", *Combustion Science and Technology*, Vol. 42, pp. 185-205.

[23] Laverdant, A., and Thévenin, D., 2003, "Interaction of a gaussian acoustic wave with a turbulent premixed flame", *Combustion and Flame*, Vol. 134, pp. 11-19.

[24] Gordner, A., 2005, "Numerische Simulation nichtlinearer Aeroakustik bei kleinen Machzahlen", PhD Thesis, Universität Heidelberg, Germany.

[25] Lindstedt, P., 1998, "Modelling of the chemical complexities of flames", *Proceedings of the Combustion Institute*, Vol. 27, pp. 269-285.

[26] Paxion, S., 1999, "Développement d'un solveur multigrille non-structuré paralléle pour la simulation de flammes laminaires en chimie et transport complexes", PhD Thesis, École Centrale Paris, France, 1999-40.

[27] Baron, R., 2002, "Calcul et Optimisation de Brûleurs Laminaires Industriels", PhD Thesis, École Centrale Paris, France, 2002-37.

[28] Bastian, P., Birken, K., Johannsen, K., Lang, S., Neuß, N., Rentz-Reichert, H., and Wieners, C., 1997, "UG - A flexible software toolbox for solving partial differential equations", *Computing and Visualization in Science*, Vol. 1, pp. 27-40.

[29] Baron, R., Paxion, S., Gicquel, O., Simous, N., Bastian, P., and Thévenin, D., 2003, "Development of a 3D parallel multigrid solver for fast and accurate laminar steady flame computations", Numerical Flow Simulation III, E. H. Hirschel, ed., Springer-Verlag, 115-128.

[30] Nelder, J. A., and Mead, R., 1965, "A Simplex Method for Function Minimization", *Computer Journal*, Vol. 7, pp. 308-313.

[31] Fletcher, R., 1987, *Practical Methods of Optimization*, John Wiley & Sons, New York.

[32] Janiga, G., Gordner, A., Shalaby, H., and Thévenin, D., 2006, "Simulation of laminar burners using detailed chemistry on parallel computers", *European Conference on Computational Fluid Dynamics, ECCOMAS CFD 2006*, TU Delft, The Netherlands, pp. to be appeared.

[33] Oijen, J. A. v., and Goey, L. P. H. d., 2000, "Modelling of premixed laminar flames using flamelet-generated manifolds", *Combustion Science and Technology*, Vol. 161, pp. 113-137.

[34] Bongers, H., van Oijen, J. A., Somers, L. M. T., and de Goey, L. P. H., 2005, "The Flamelet-Generated Manifold Method applied to steady planar partially premixed counterflow flames", *Combustion Science and Technology*, Vol. 177, pp. 2373-2393.

[35] Maas, U., and Pope, S. B., 1992, "Simplifying chemical kinetics: Intrinsic low-dimensional manifolds in composition space", *Combustion and Flame*, Vol. 88, pp. 239-264.

[36] Fiorina, B., Baron, R., Gicquel, O., Thévenin, D., Carpentier, S., and Darabiha, N., 2003, "Modelling non-adiabatic partially premixed flames using flame-prolongation of ILDM", *Combustion Theory and Modelling*, Vol. 7, pp. 449-470.

[37] Fiorina, B., Gicquel, O., Carpentier, S., and Darabiha, N., 2004, "Validation of the FPI chemistry reduction method for diluted nonadiabatic premixed flames", *Combustion Science and Technology*, Vol. 176, pp. 785-797.

[38] Fiorina, B., Gicquel, O., Vervisch, L., Carpentier, S., and Darabiha, N., 2005, "Approximating the chemical structure of partially premixed and diffusion counterflow flames using FPI flamelet tabulation", *Combustion and Flame*, Vol. 140, pp. 147-160.

Atmospheric Flows

Conference on Modelling Fluid Flow (CMFF'06)
The 13th International Conference on Fluid Flow Technologies
Budapest, Hungary, September 6-9, 2006

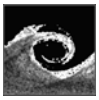

NOVEL ESTIMATION OF THE SPEED UP OVER 2D ESCARPMENT WITH VARIOUS ANGLES OF INCLINATION

István GORICSÁN

Corresponding Author. Department of Fluid Mechanics, Budapest University of Technology and Economics. Bertalan Lajos u. 4 – 6., H-1111 Budapest, Hungary. Tel.: +36 1 463 3465, Fax: +36 1 463 3464, E-mail: goricsan@ara.bme.hu

ABSTRACT

Nowadays, the growing importance of renewable energy sources especially of the wind power indicates the necessity of understanding, describing and predicting the flow field around the planned site of wind power plants.

The wind tunnel investigations on flow field over an escarpment with various angles of inclination provide data base for e.g. installation, structural sizing and operation of wind power plants. Hot wire measurements are carried out in atmospheric boundary layer flow upstream and over the escarpment. Due to the speed up this type of topographical elements is especially appropriate for installation wind power plants. The applied measurement technique (hot wire) and the adequately large number of measuring points allow investigation on the fine structure of turbulence besides definition of mean flow field.

The experimental results have ensured wide range data base respecting flow and turbulence field over simple model escarpment. The data base is applicable to wind energy or CFD validation investigations, or model development.

This paper presents that applicability of the formulas for fractional speed up (ΔS) found in literature is limited on the investigated range of angle. Based on experimental investigations using hot wire technique on flow over model escarpment with various angles of inclination ($5° \le \gamma \le 20°$, $0{,}175 \le H/L_1 \le 0{,}728$) situated in atmospheric boundary layer, the fractional speed up and so the specific wind power distribution over the investigated topographic elements have been determined. This paper presents modified formulas to define spatial distribution of speed up and the integral length scale variations caused by the simple model escarpment are proposed.

Keywords: fractional speed up over escarpment, hot wire anemometry, wind tunnel test

NOMENCLATURE

Examples:

ΔS	[-]	fractional speed up ratio
ΔU	[*m/s*]	perturbation velocity
γ	[°]	slope
H	[*m*]	height of the escarpment
L_1	[*m*]	half-length of the escarpment
S	[-]	speed up factor
A_z	[-]	amplification factor
d_0	[*m*]	displacement height
α	[-]	profile exponent
δ	[*m*]	boundary layer height
Tu	[-]	turbulence intensity
Lu_x	[*m*]	integral length scale
R	[-]	curve fitting error
U	[*m/s*]	mean velocity, u component
C	[-]	constant

Subscripts and Superscripts

ref	reference
x, *z*	downstream, vertical (coordinate)

1. INTRODUCTION

The atmospheric boundary layer flow has been affected by non-homogenous terrain. Several changing have been come into existence in boundary layer properties compared with boundary layer flow over homogenous terrain. Considering only the surface elevation neglecting the surface temperature and roughness modifications and the effect of thermal stability, one of the most important effects the velocity variance caused by the obstacle (hill, escarpment, etc.). Generally, the flow accelerates over a 2D simple hill model and a speed up occurs above the surface of the hill (see Figure 1.). The typical distribution of perturbation velocity (ΔU) is shown in Fig. 1. A most important feature of the wind profile over a hill is that it increases with height much more rapidly than over level ground. Several possibilities can be found in

literature for quantitative determination of speed up. For use in wind energy or wind load predictions two useful ways of characterizing the increase in perturbation velocity, ΔU over a hill have been spread. These are the "fractional speed up ratio", ΔS and the "speed up factor", S.

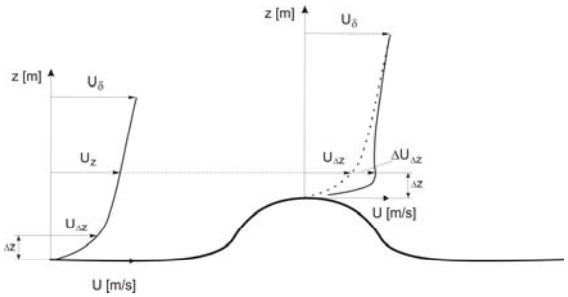

Figure 1. Speed up over a 2D hill

The first is the ratio of the increase in velocity a distance Δz above the surface to the upwind velocity at the same displacement (1).

$$\Delta S(x,\Delta z) = \frac{\Delta U(x,\Delta z)}{U(\Delta z)} \quad (1)$$

where Δz is the height above the surface of hill, x is the distance in downstream direction.

The speed up factor is the ratio of the speed relative to the wind speed at the same absolute elevation z (2).

$$S = \frac{U(\Delta z) + \Delta U(x,\Delta z)}{U(z)} \quad (2)$$

The disadvantage of using S near the surface of the hill is that it is highly dependent on the value of Δz whereas ΔS vary much less with Δz over the surface. Consequently, S is only useful near the hill top or above the inner region (the inner region is defined by the region from surface to the height of maximum of speed up) [1].

Besides, the "amplification factor", A_z is used which is the ratio of the absolute or increased velocity at the height of Δz above the surface of the hill to the upwind velocity at height of Δz [2]. Actually this factor is equal to the fractional speed up added to 1.

Determination of speed up is based on theoretical assumptions validated by wind tunnel and full-scale experiments [3, 4] and of course measured wind data [5 to 8]. The latter empirical formulas are widely used in engineering practice while the others based on theoretical assumptions used in numerical codes. Cook [6] suggests the topographic speed increment coefficient, s_L for calculating the topography factor, which is identical to the speed up ratio or amplification factor. The topographic speed increment coefficient is given for different types of obstacles (hill, escarpment, cliff, etc.) in nomograms. For example the flows over escarpment have been divided flows up shallow and steep escarpment. The border upwind slope is 17° which mean that above this slope the flows similar to the flows over escarpment with slope of 17°, hence the maximum speed up occurs at 17° slope. Hereby Cook [6] states that the speed up irrespective of the slope (naturally just for the slopes which are larger than the critical slope) because the upwind separation bubble adjusts itself to maintain an effective slope about 17° to the external flow.

Weng et al. [8] and Utsunomiya et al. [7] propose formulas for determination of fractional speed up over the crest of escarpment. In order to be precise Utsunomiya et al. [7] suggest formulas for speed up at height z/H=0.1 which height is approximately equal to the height of the maximum speed up. Contrarily to this the formula proposed by Weng et al. [8] describes the whole speed up profile over the crest.

Simple approximation proposed by Lemelin et al. [6] appropriate for describing the speed up upwind and over an escarpment. This assumption is denoted with abbreviation of LSD in followings.

In several cases i.e. the investigated escarpments neither LSD [6] nor Weng et al. formulas offers adequate speed up values for the entire range. The necessity of development a new formula has been justified by this fact. The wind data and the novel estimation presented in this paper are compared with LSD [6] and Weng et al. [8] formulas.

2. EXPERIMENTAL SET-UP

The experiments have been carried out in the horizontal wind tunnel of Institute of Aerospace Engineering at Dresden University of Technology. It is a low-speed close circuit tunnel with an open test section 4.5 *m* long and 3 *m* in diameter (see Figure 2.). The main dimensions of the wind tunnel have been shown in Fig.2. The detailed description of the wind tunnel and the method of atmospheric boundary layer generation can be found in [9].

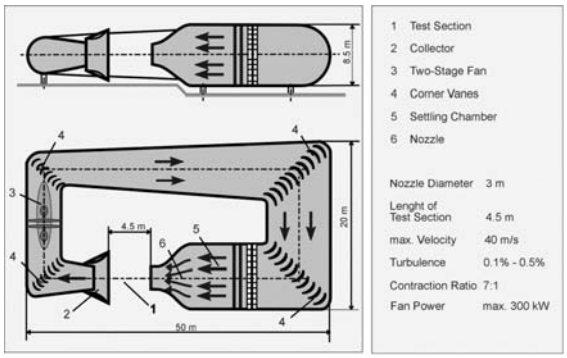

Figure 2. Sketch of the low speed wind tunnel of Dresden University of Technology

The ground was situated 0.8 *m* below the centre and was made aerodynamically rough by covering it

whit uniformly spaced roughness elements to simulate the lower part of a suburban atmospheric boundary layer. In order to produce a thicker boundary layer, a differently spaced horizontal grid was placed at the beginning of the test section.

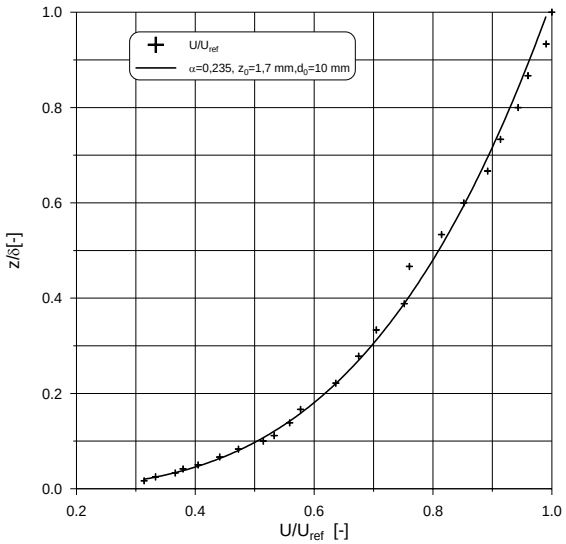

Figure 3. Mean velocity profile of approaching flow

The combination of the grid and the surface roughness simulate a suburban neutral boundary layer whose properties have been shown in Figure 3. to 6.

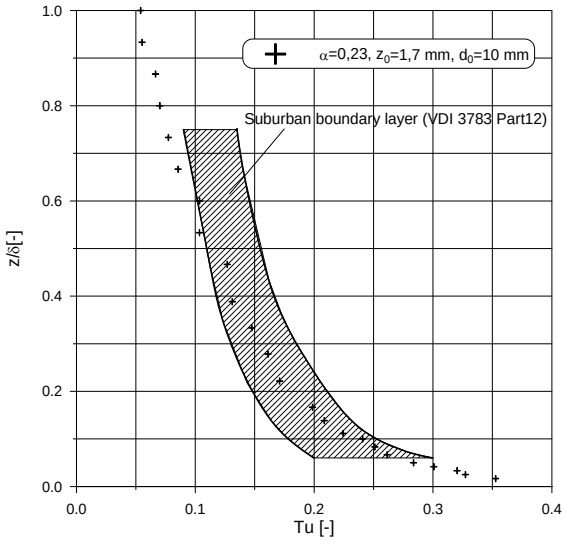

Figure 4. Turbulence intensity profile of approaching flow

The vertical velocity distribution in fully developed boundary layer can be described by the power law,

$$\frac{U_z}{U_\delta} = \left(\frac{z - d_0}{\delta - d_0} \right)^{\alpha} \qquad (3)$$

where U_δ is the mean velocity at the boundary layer height δ, U_z is the mean velocity at the height z, d_0 is the displacement height, and the wind profile exponent α was 0.235.

The wind velocity is continuously recorded using both a Pitot-static tube and a hot-wire, DANTEC P11 probe, connected to a constant temperature anemometer, DISA model M51.

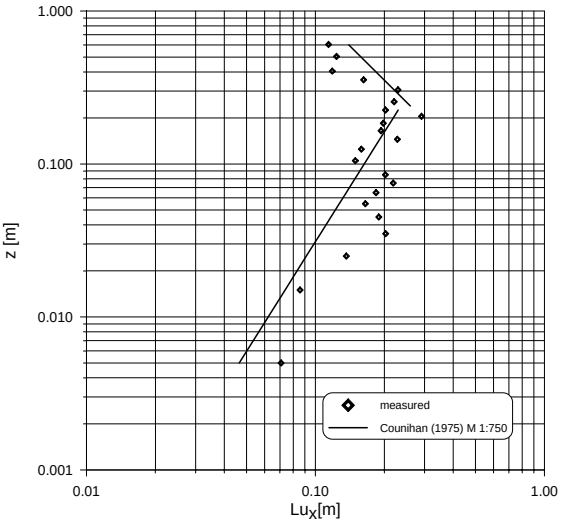

Figure 5. Integral length scale profile of approaching flow

Exact modelling of turbulence parameters like integral length scale and power spectra are necessary for adequate modelling of atmospheric boundary layer flow. The integral length scale is scaled down by the model scale in this case 1:750 (see Fig. 5.). The power spectra calculated at various heights has been compared with dimensionless Kármán-spectra. The agreement to Kármán-spectra is quite satisfactory (see Fig. 6.).

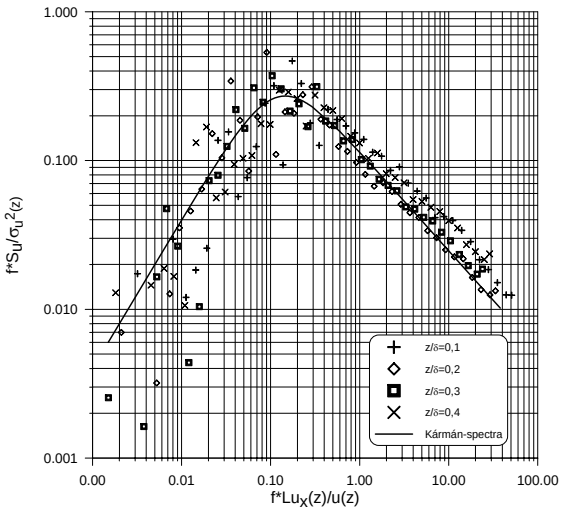

Figure 6. Power spectra in various heights versus Kármán-spectra in approaching flow

The model escarpment has been placed at the ground of test section far from the wind tunnel outlet in a fully developed boundary layer flow. The places where the velocity profiles have been measured are shown in Figure 7.

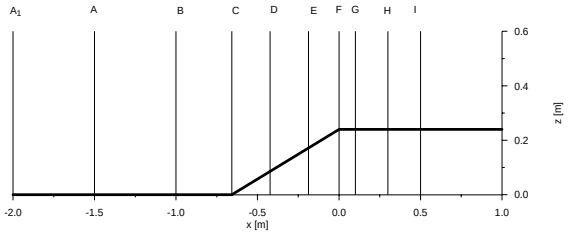

Figure 7. Place of the velocity measurements

The slope of the escarpment has been varied between 5° and 20° in 5° steps. The origin of the coordinate system has been fixed at the crest of the escarpment (see Fig. 7.).

3. NOVEL ESTIMATION OF SPEED UP OVER A 2D ESCARPMENT

The novel estimation of fractional speed up ratio based on wind data obtained from wind tunnel experiments. In data fitting procedure a nonlinear least-squares data fitting by Gauss-Newton method has been used. This method finds the coefficient of a nonlinear user defined function. The code has been written in MATLAB. The error of the fitted curves has been defined as the follows:

$$R = \frac{1}{n_{data}} \sqrt{\sum_{i}^{n_{data}} \left(\frac{m_i - f_i}{f_i} \right)^2} \tag{4}$$

where n_{data} means the numbers of data used in fitting procedure, m_i means the measured while f_i the fitted value. R tends to zero means better fitting and R=0 marks the perfect fitting.

More than 700 data has been used in fitting procedure. The proposed estimation for the fractional speed up has been shown in (5) to (8). The validity of presented formulas has been limited by the measured range. First this is valid in case of suburban type atmospheric boundary layer approaching flow (characteristics of the approaching flow can be seen in Fig. 3. to 6.). The validity range has been covered in downstream direction $-2.5 \le x/\delta \le 0.8$ (note the crest of the escarpment is located at x=0 position) and $0.025 \le z/\delta \le 1$ in vertical direction. The slope can be varied between 5° and 20° ($0.175 \le H/L_1 \le 0.73$).

$$\Delta S\left(\frac{x}{\delta}, \frac{z}{\delta}, \frac{H}{L_1} \right) = \sum_{i=0}^{2} C_i \left(\frac{x}{\delta}, \frac{H}{L_1} \right) \cdot \left(\frac{\delta}{z} \right)^i \tag{5}$$

if $i \le 1$

$$C_i = \frac{\left(\frac{x}{\delta} - C_{i3} \right)}{\sum_{j=0}^{2} C_{ij} \cdot \left(\frac{x}{\delta} - C_{i3} \right)^j} \tag{6}$$

if i=2

$$C_2 = C_{21} \cdot \sin\left(\frac{x}{\delta} - C_{22} \right) + C_{23} \tag{7}$$

where

$$C_{ij} = C_{ij_1} \cdot \ln\left(\frac{H}{L_1} \right) + C_{ij_2} \tag{8}$$

where x, z denote the downstream and vertical direction respectively, H is the height of the escarpment and L_1 the half-length of slope (the distance from the hill top to where the elevation is half its maximum), δ is the boundary layer height (here δ=0.6 m corresponds to 450 m is full scale), C denotes the constants.

Table 1. Constants for the equations (5) to (8)

C_{001}	C_{002}	C_{011}	C_{012}
-28,03	4,6531	27,468	-2,5591
C_{021}	C_{022}	C_{031}	C_{032}
-20,01	0,1016	0,0885	-1,0101
C_{101}	C_{102}	C_{111}	C_{112}
-22,437	3,3368	8,2753	-19,276
C_{121}	C_{122}	C_{131}	C_{132}
-2,6964	32,474	0,24	-0,4381
C_{211}	C_{212}	C_{221}	C_{222}
-0,0003	-0,0008	-0,2936	-0,0174
C_{231}	C_{232}		
-0,0001	-0,0002		

Table 1. contains the constants for the equations (5) to (8).

4. RESUTLS

The measured wind data and fractional speed up ratio obtained by LSD [6], Weng et al. [8] and the proposed formula (5) to (8) have been shown in Figure 9. to 12. In case of the smallest investigated slope over the crest the LSD [6] formula provide good agreement with the measured data, however down- and upstream the error has been increased (see Fig. 9.). The gap has been grown extremely wide especially in case of higher slopes and far upstream from the crest (see Fig. 11. and 12.). Generally upstream from the crest near the ground the LSD [6] gives no adequate values. In the near-ground region over the crest and downstream the LSD formula overestimates the measured value except at the lowest position where the maximum of the speed up has been measured (see Fig. 9. to 12.). As regards the maximum of ΔS the LSD values over the crest are close to the measured values, downstream this tendency changes, the predicted values are lower than the measured. Contrarily to this trends the formula proposed by Weng et al. [8]

underestimates the measured values particularly in near wall region. This trend can be observable in case of all investigated slope although in decreasing degree with increasing slope. The reason of this behaviour can be found in the way of determination of the maximum speed up. This method underestimates the maximum speed up because of neglecting the effect of approaching flow. The Weng formula takes into account only the shapes of hills.

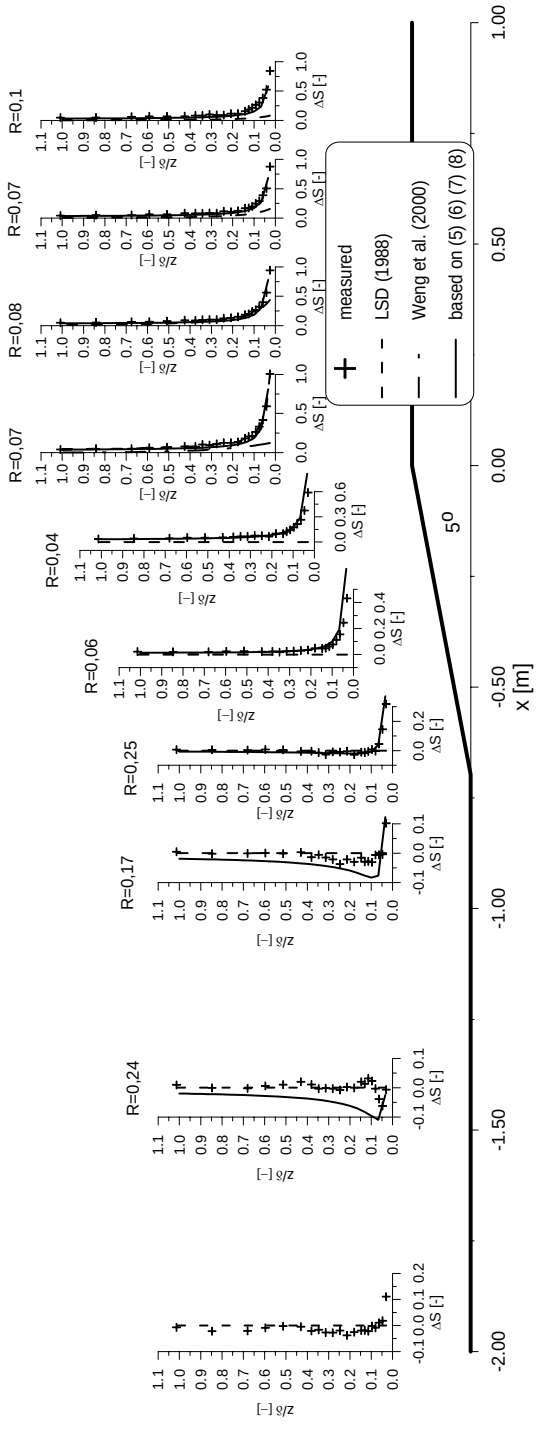

Figure 9. Fractional speed up ratio in case of 5° escarpment, measured, fitted and literature data

Since neither the LSD nor the Weng formula give adequate value for fractional speed up ratio in whole investigated region, novel estimation of speed up has been developed. This method provides good approximations for speed up for the entire range either the speed loss in front of the slope. The best approximations have been found in the region near the crest and above the plateau.

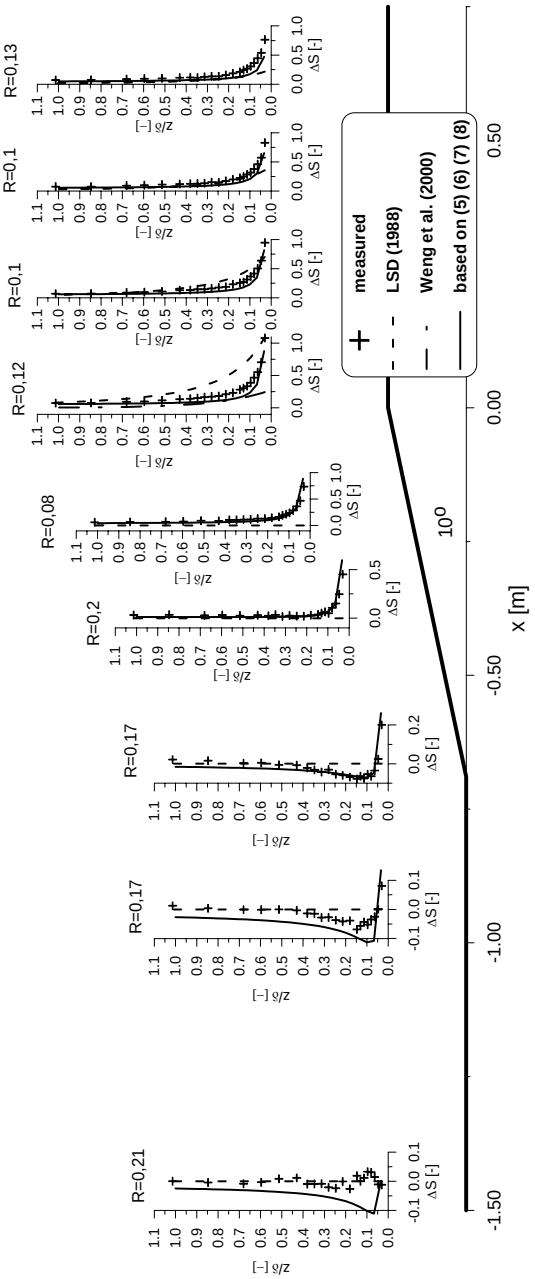

Figure 10. Fractional speed up ratio in case of 10° escarpment, measured, fitted and literature data

These results provides basis for model development and structural sizing or operation of wind power plants. For example the specific wind power can be easily determined from the fractional speed up ratio.

$$\left(\frac{U}{U_{ref}}\right)^3 = \left((\Delta S + 1)\cdot\left(\frac{z}{z_{ref}}\right)^{\alpha}\right)^3 \qquad (9)$$

where U_{ref} is the reference velocity measured at height of z_{ref}, α is the profile exponent. Naturally using the proposed formulas (equations (5) to (8) presented in this paper) the value of profile exponent is limited to the typical value of suburban type atmospheric boundary layer flow. Besides the slopes and the places of a planned wind power plant has to be in the validity range of the proposed formula.

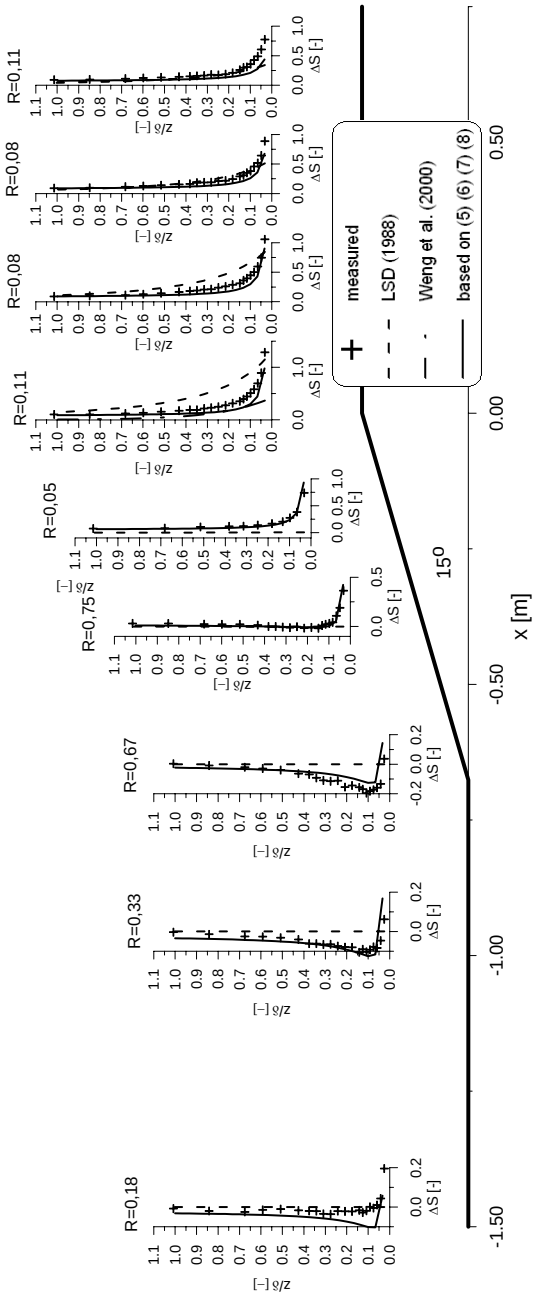

Figure 11. Fractional speed up ratio in case of 15° escarpment, measured, fitted and literature data

Whereas the investigated slopes and places of velocity measurement cover the most cases occurred in nature.

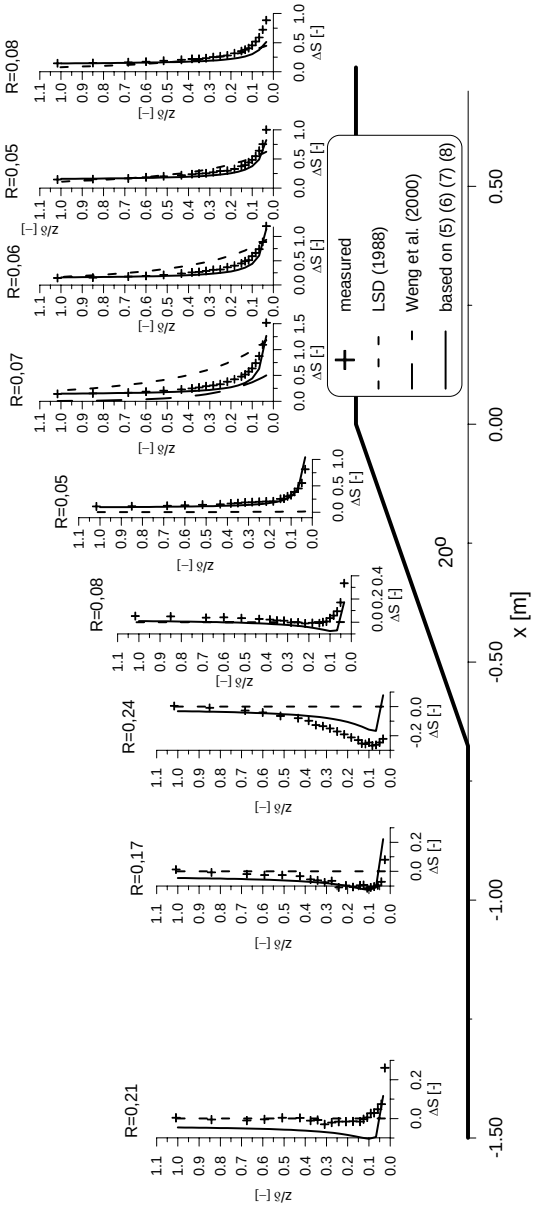

Figure 12. Fractional speed up ratio in case of 20° escarpment, measured, fitted and literature data

The simple geometry used in the presented investigations clearly affects the turbulence characteristics. The applied measurement technique and the adequately large number of measuring points also allow the investigation on the fine structure of turbulence beside the definition of mean flow field. The limitations of this paper do not allow to describe this effects.

5. SUMMARY

The wind tunnel investigations on flow field over an escarpment with various angles of inclination provide data base for (e.g.) the installation, structural sizing and operation of wind power plants. Due to the speed up, these types of topographic elements are especially suitable for the installation of wind power plants. Hot wire measurements have been carried out in atmospheric boundary layer flow upstream and over the escarpment. Based on wind data obtained by wind tunnel investigation the fractional speed up and so the specific wind power distribution over the investigated topographic elements have been determined. Due to the weakness of the formulas found in literature this paper presents a novel formula for estimation of fractional speed up ratio. The applicability and validity of the proposed formula have been shown through comparison with measured wind data.

The experimental results offer a wide-range data base concerning flow field over simple model escarpment. The data base is applicable either to wind energy and CFD validation investigations, or to model development.

REFERENCES

[1] Hunt, J.C.R., Simpson, J.E. (1982) Atmospheric boundary layers over non-homogeneous terrain, *Engineering Meteorology ed. E.J. Plate, Elsevier Scientific Publishing Company, pp. 269-318*

[2] Bowen, A.J., Lindley, D. (1977) A Wind-tunnel Investigation of the Wind Speed and Turbulence Characteristics Close to the Ground over Various Escarpment Shapes, *Boundary-Layer Meteorology, vol. 12., pp. 259-271*

[3] Jensen, N.O., Peterson, E.W. (1978) On the escarpment wind profile, *Quart. J. R. Met. Soc. 104, p. 719*

[4] Taylor. P.A., Gent, P.R. (1974) A model of atmospheric boundary layer flow above an isolated two-dimensional hill; an example of flow above „gentle topography", *Boundary Layer Meteorology, 7, pp. 349-362*

[5] Lemelin, D.R., Surry, D., Davenport, A.G. (1988) Simple Approximations for Wind Speed up over Hills, *Journal of Wind Engineering and Industrial Aerodynamics, Vol. 28, pp. 117-127*

[6] Cook N.J. (1985) The designer's guide to wind loading of building structures, ISBN 0 408 00870 9

[7] Utsunomiya, H., Nagao, F., Noda, M., Yamada, M. (1999) Effects of a roughness change on wind properties around two-dimensional hills, *Wind Engineering into the 21st Century, ed. Larsen, Larose, Livesey, Balkema, Rotterdam, pp. 369-376*

[8] Weng, W., Taylor, P.A., Walmsley, J.L. (2000) Guidelines for airflow over complex terrain: model developments, *Journal of Wind Engineering and Industrial Aerodynamics, vol. 86, pp. 169-186*

[9] Buckisch, R., Brechling, J., (2001) "The influence of the model scale on wind tunnel tests with regard to environmental aerodynamics", *Proc. of International. Workshop on Physical Modeling of Flow and Dispersion Phenomena*

[10] Counihan, J. (1975) Adiabatic atmospheric boundary layers: A review and analysis of data from the period 1880-1972, *Atmospheric Environment, vol 9. pp. 871-905*

[11]VDI 3783 Part 12. Environmental meteorology, Physical modelling of flow and dispersion processes in the atmospheric boundary layer, Application of wind tunnels

Conference on Modelling Fluid Flow (CMFF'06)
The 13th International Conference on Fluid Flow Technologies
Budapest, Hungary, September 6-9, 2006

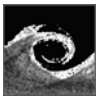

NUMERICAL SIMULATIONS OF TURBULENT FLOWS OVER HILLS AND COMPLEX URBAN AREAS WITH DISPERSION OF POLLUTANTS

S. Kenjeres[1], R. Hagenzieker, K. Hanjalic

[1] Corresponding Author. Department of Multi Scale Physics, Faculty of Applied Sciences, Delft University of Technology, 2628 CJ Delft, The Netherlands. Tel.: +31 15 2783649, Fax: +36 15 2781204, E-mail: kenjeres@ws.tn.tudelft.nl;

ABSTRACT

The paper reports on numerical simulations of turbulent flows over real hills and urban street canyons with dispersion of passive pollutants. Several extensions of the standard k-ε eddy-viscosity turbulence model have been investigated expected to remove some few well-known deficiencies of the standard model that are potentially relevant for accurate predictions of environmental flows. These include effects of surface roughness, generalized wall-functions, a redefined production of turbulence kinetic energy, a time-scale limiter and a RANS/LES merging approach. The accuracy and the numerical robustness of these models implemented in Navier-Stokes solver for structured non-orthogonal geometries are investigated. Another novelty is a simple and efficient representation of blocked flow regions (passive elements approach) used for mimicking entire buildings or their segments. The following configurations are simulated: flow over a realistic orography (Askervein Hill, U.K.), idealised 2D and 3D urban street canyons at laboratory- and full scale (Goettinger Strasse, Hanover, Germany) with traffic pollution sources. For all cases simulated, good agreement with the available field/laboratory measurements and with previously performed numerical studies has been obtained demonstrating acceptable accuracy and numerical robustness of the approach presented.

Keywords: numerical simulations, turbulent flows, complex urban areas and hills, dispersion of pollutant;

1. INTRODUCTION

The 18 months long observations by the European Space Agency (ESA) satellite ENVISAT – launched in February 2002 – revealed that the traffic, industry and energy utilities in urban areas in Europe, North and South America as well as in Asia are the world's main producers of nitrogen dioxide (NO_2) pollution (http://www.esa.int). It is believed that excessive exposure to this mainly man-made gas can cause lung damage and respiratory problems. As such, it is one of the main contributors to urban pollution in big cities. In addition, this gas is known to be the main precursor of ozone production in the troposphere and thus an important parameter in atmospheric chemistry. Obviously, reduced emissions can have significant positive impacts on public health. Severe air pollution of urban areas is usually associated with intensive traffic/industrial emissions and critical meteorological conditions (windless days, strong stratification, temperature inversion capping, etc.). Local wind conditions and time dependent intensity of pollutant emission determine the air quality, Britter and Hanna [1]. In many urban centres with environmental pollution problems monitoring systems have been established in order to provide proper data which can be used as an input to computer models and as a basis for the decision-making by authorities in order to reduce further increase of pollution. Since the origin of environmental pollution is in complex spatial and temporal flow, turbulence and dispersion interactions, computer simulations can be powerful tools for estimating the impacts of different parameters on pollution. Air flow and pollutant dispersion at environmental scales are characterized by high values of Reynolds numbers (indicating highly turbulent flows) and with complex geometries (topography of terrain simulated, arrays of buildings and streets). Obviously, direct numerical resolving of all flow and turbulence scales is beyond the reach of present computational power – so mathematical models for scales not resolved by underlying numerical grid (subgrid/subscale contributions) must be introduced. These models are based on the solutions

of conservative transport equations of mass, momentum, energy and species concentration. In this paper, we will address several extensions of the eddy-viscosity based models that are usually used for simulations of environmental flows.

2. MATHEMATICAL MODEL

The problem of turbulent flow and dispersion of the passive pollutant is mathematically described by conservation laws for mass, momentum, concentration, turbulent kinetic energy and its dissipation rate:

$$\frac{\partial U_i}{\partial t}+U_j\frac{\partial U_i}{\partial x_j}=-\frac{1}{\rho}\frac{\partial P}{\partial x_i}+\frac{\partial}{\partial x_j}\left[\nu\left(\frac{\partial U_i}{\partial x_j}+\frac{\partial U_j}{\partial x_i}\right)-\overline{u_iu_j}\right] \quad (1)$$

$$\frac{\partial C}{\partial t}+U_j\frac{\partial C}{\partial x_j}=\frac{\partial}{\partial x_j}\left[\frac{\nu}{Sc}\left(\frac{\partial C}{\partial x_j}\right)-\overline{cu_j}\right] \quad (2)$$

$$\frac{\partial k}{\partial t}+U_j\frac{\partial k}{\partial x_j}=\frac{\partial}{\partial x_j}\left[\left(\nu+\frac{\nu_t}{\sigma_k}\right)\frac{\partial k}{\partial x_j}\right]+P_k-\varepsilon \quad (3)$$

$$\frac{\partial \varepsilon}{\partial t}+U_j\frac{\partial \varepsilon}{\partial x_j}=\frac{\partial}{\partial x_j}\left[\left(\nu+\frac{\nu_t}{\sigma_\varepsilon}\right)\frac{\partial \varepsilon}{\partial x_j}\right]+\frac{C_{\varepsilon 1}P_k-C_{\varepsilon 2}\varepsilon}{T} \quad (4)$$

where Reynolds stresses and turbulent mass/concentration fluxes are calculated from:

$$\overline{u_iu_j}=\frac{2}{3}k\delta_{ij}-\nu_t\left(\frac{\partial U_i}{\partial x_j}+\frac{\partial U_j}{\partial x_i}\right) \quad (5)$$

$$\overline{cu_j}=-C_\Phi\frac{k}{\varepsilon}\overline{u_iu_j}\frac{\partial C}{\partial x_j} \quad (6)$$

Following model variants are applied and tested:

- Standard model, $T=k/\varepsilon, P_k=2\nu_t|S|^2$
- Kato-Launder Modification (Kato and Launder [2]): $P_k=2\nu_t S\Omega$
- Durbin time-scale limiter (Durbin [3]):

$$T=min\left[\frac{k}{\varepsilon},\frac{0.6}{\sqrt{6}C_\mu|S|}\right]$$

In addition to the standard Reynolds-Averaged-Navier-Stokes (RANS), we considered also a recently proposed hybrid RANS/LES approach, Kenjeres and Hanjalic [4]. The underlying idea is to sensitise the coefficient(s) in the turbulence-model equations to the mesh size, relative to the characteristic length-scale and thus to make them sensible to flow instabilities and unsteadiness:

$$C_{\varepsilon 2}=C_{\varepsilon 1}+\frac{0.48}{\alpha},\alpha=max\left(1,\frac{L_{RANS}}{L_{LES}}\right)$$

$$L_{RANS}=\frac{k^{3/2}}{\varepsilon},L_{LES}=\left(\Delta x\cdot\Delta y\cdot\Delta z\right)^{1/3} \quad (7)$$

It can be seen that this approach asymptotically returns the standard RANS when mesh is coarse ($\alpha=1$) and with mesh refinements, modelled contributions are approaching zero making it finally pure DNS ($\alpha\to\infty$). We report here on several (though preliminary) attempts in using this hybrid approach for simulations of environmental flows. For flows at realistic environmental scales, two additional important issues need to be taken into account: surface roughness and generalised treatment of the wall boundary conditions that depart from the conventional equilibrium wall functions. The surface roughness has significant impact on levels of turbulence created in the proximity of the surface. Since the high Reynolds numbers associated with high velocities and large physical dimensions prevent the use of the low-Re-number models (due to enormous grid requirements) – the use of wall functions is the only viable way of defining the wall boundary conditions. The velocity wall-functions with surface roughness imply calculation of the wall-friction as follows:

$$\tau_w=\rho C_\mu^{1/4}k_P^{1/2}\kappa\frac{U_P^t}{\ln\left(\frac{E_Ry_P^*}{e^*}\right)} \quad (8)$$

In order to make it possible to deal (at least partially) with the non-equilibrium effects, which are common in environmental flows, a generalised form of the wall function is used:

$$\tau_w^G=\tau_w\Psi \quad (9)$$

where the correction term is calculated from:

$$\Psi=1-\frac{C_Uy_P}{U_P\kappa U_\tau} \quad (10)$$

and the correction parameter C is evaluated from the combination of time-dependent, convective and source (pressure gradient) terms of momentum equations, evaluated at the previous time step or iteration. For this particular expression, it is assumed that the flow is mainly oriented in the tangential direction (U) i.e.:

$$C=\frac{\partial U}{\partial t}+U\frac{\partial U}{\partial x}+V\frac{\partial U}{\partial y}+W\frac{\partial U}{\partial z}+\frac{1}{\rho}\frac{\partial P}{\partial x} \quad (11)$$

Table 1. Model Coefficients

$C_{\varepsilon 1}$	$C_{\varepsilon 2}$	C_Φ	σ_C	σ_k	σ_ε
1.44	1.92	0.1	0.71	1	1.3

3. NUMERICAL METHOD

The equations set given in Section 2 is solved numerically using a finite volume Navier-Stokes solver in structured general non-orthogonal geometries. Cartesian vector and tensor components

are used in collocated variable arrangement. The second-order central difference scheme (CDS) is applied for discretisation of the diffusive terms of conservative variables. The second-order quadratic upwind scheme (QUICK) is applied for all convective terms. In order to keep the numerical stability when QUICK scheme is used, deferred correction with first-order upwind scheme (UDS) is applied. The coupling between the velocity and pressure fields is provided trough the SIMPLE algorithm. The fully implicit second order three-time-levels marching scheme is used for the time integration.

An important issue is how to treat the geometrically complex domain occupied with many buildings in the simulated domain and yet to provide a numerically efficient meshing tool for parametric studies. In this work we adopted the passive elements approach, Kenjeres et al. [5]. In contrast to the conventional multi-block approach in structured geometries where the building-blocks strategy is applied for fluid-flow regions, here the blocks representing complete building or parts of buildings are simply excluded from the basic underlying numerical mesh (mesh covering the empty-fluid flow domain) and treated as a new solid boundaries (walls). We proved earlier (in numerical simulations of occupied and furnished indoor-climate configurations) and reconfirmed again in this study that this method is computationally very efficient and numerically robust – reducing drastically time usually needed for re-generation of new sets of numerical grids.

4. RESULTS

4.1. Flow over realistic complex orography: Askervein hill

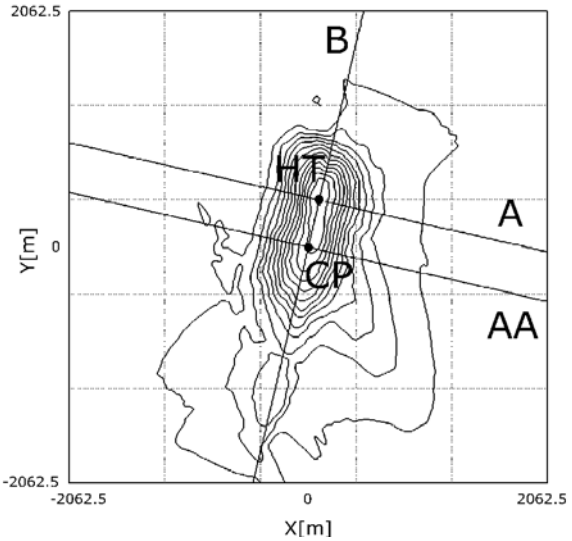

Figure 1. Topographic map of the Askervein Hill and characteristic experimental locations.

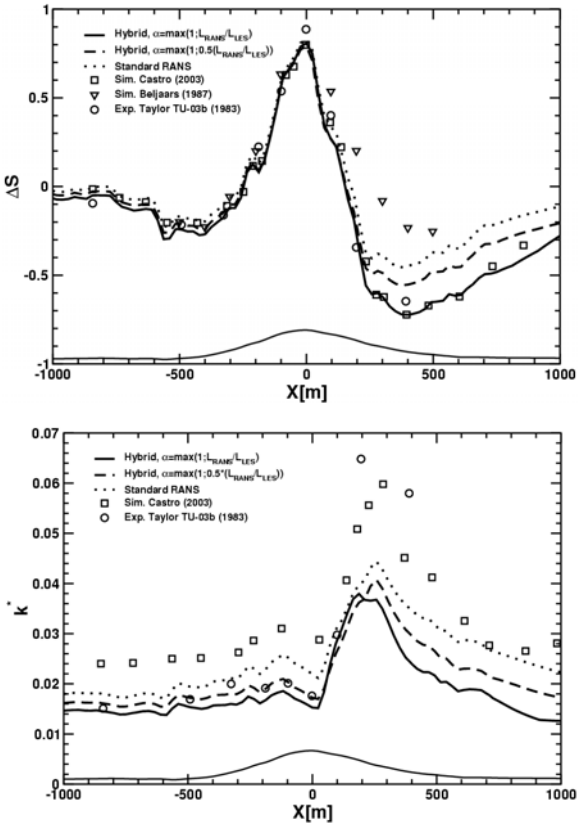

Figure 2. Comparison of the horizontal velocity and turbulence kinetic energy along the A-A line: experiments of Taylor et al. (1983), previous simulations of Castro (2003) and present simulations;

Extensive experimental investigations of Taylor et al. [6] for flow over realistic hill with a height of 116 m and moderate slope (Askervein Hill, U.K.) formed a basis for numerous benchmark studies of different numerical codes for the environmental flow simulations, Raithby et al [7], Beljaars et al. [8], Castro et al. [9]. Field measurements (based on the use of Gill UVW, sonic and cup anemometers) were mostly conducted along lines parallel to the major and minor hill axes (at 10 m above the hill surface, A, AA and B lines), Fig.1. In addition, two 50 m high towers were placed at the hilltop (HT) and at the hill-central point (CP) to collect vertical profiles of mean velocity and turbulent stresses. Additional reference site (RS) located upstream from the hill was constructed in order to provide flow and turbulence parameters of an undisturbed approaching flow. The flow is characterized by very large Reynolds number, $Re \sim 10^{9.}$ In order to accommodate the approaching wind direction of 210^0 the numerical mesh is created by rotating and interpolating hill coordinates from the available maps. This is done in order to impose simple inlet-outlet boundary conditions for simulated flow domain. The terrain-following (boundary-fitted coordinates) numerical grid consisted from 176^2x

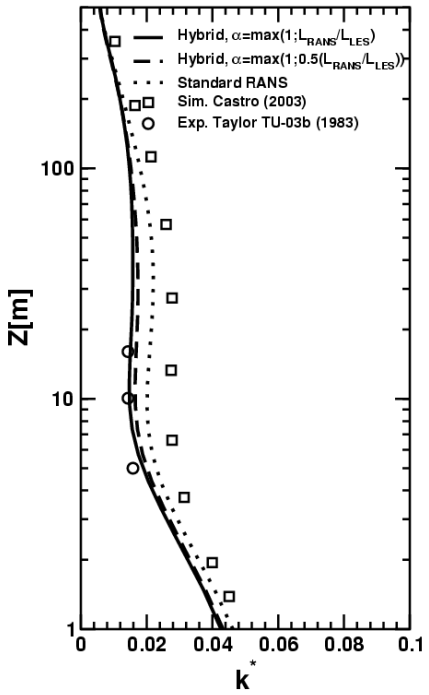

Figure 3. Vertical profiles of turbulence kinetic energy at the CP location; (See caption in Fig.2)

36 control volumes, which together with the applied QUICK discretization scheme for the convective terms of momentum equations should provide grid-independent solutions. Effects of the surface-roughness have been proved to be very influential for the final results, so typical roughness of z_0=0.03 m (mimicking the grass over hill surface) is specified. The inflow conditions are provided from the separately performed simulation of the fully-developed turbulent boundary layer flow with identical specification of the roughness parameter. Distribution of relative-speed-up (defined as $\Delta S(x, y, \Delta z) = [U(x, y, \Delta z) - U_0(\Delta z)] / U_0(\Delta z)$) of the horizontal velocity and of the scaled turbulent kinetic energy (defined as $k^*(x, y, \Delta z) = k(x, y, \Delta z) / U_{10}^2$) along the A-line are shown in Fig. 2. (here $U_0(\Delta z)$ is value of the undisturbed/approaching horizontal velocity and U_{10} is the inlet/approaching horizontal velocity at 10 m above the surface). It can be seen that the velocity distribution shows very good agreement with experimental data of Taylor et al. [6]. The wake region is particularly well captured with the newly proposed hybrid RANS/LES approach – showing significant improvements in comparison to the standard RANS approach. The origin of this improvement is in the reduced levels of turbulent kinetic energy of the approaching flow (up-hill region), which can be seen in Fig.2-below. The profiles of turbulent kinetic energy show under-prediction in respect to experiments (especially characteristic peak at the location just after the hill-top is not well captured) but generally qualitatively good agreement is obtained. The vertical profiles of the scaled turbulent kinetic energy at the central peak (CP) location are shown in Fig.3. Again, good agreement with experiments is observed. This first stage of numerical validation of few variants of eddy-viscosity based turbulence models for real-scale environmental flows in complex geometries demonstrated numerical robustness and good agreement with available experimental and numerical simulations of other authors.

4.2. Simulations of simplified 2D urban street canyons at laboratory scale

Flow over an array of 2D obstacles at laboratory scale is simulated next. Because of its geometrical simplicity, this flow configuration was extensively studied in literature – both experimentally and numerically. In this paper, we selected experimental studies of Brown et al. [10] as the most recent one for comparison of velocity and turbulence parameters. The configuration consists from 7 rectangular blocks fully occupying the span-wise dimension – so the entire problem can be considered as two-dimensional. Experiments are performed for different values of approaching horizontal velocity - ranging from 0.3 to 8 m/s. In this paper we simulated flow situation which corresponds to Re=$4x10^4$. It is important to note that all blocks should be taken into simulations since experiments clearly demonstrated different flow patterns at particular locations between obstacles – indicating still developing phase of flow. For this purpose, the passive element approach is used for definitions of blocked flow regions. Finally, the numerical mesh consisted of 420x2x80 control volumes – stretched in proximity of horizontal bottom walls and levels of obstacles heights. In order to provide proper inlet profiles of simulated variables, a separate simulation of fully-developed channel with roughness specification identical to height of obstacles are performed. This approach resulted in inlet velocity profiles in excellent agreement with experiments, but unfortunately, turbulent kinetic energy was under-predicted (for approximately 50%). This difference is probably caused by the spires along the bottom wall used in experiments – which were not taken into account in simulations. Instead of simulating all flow details, the inlet profiles of turbulent kinetic energy are approximated from experimental data. The results of the simulation in the centre of the second canyon are shown in Fig.4. The vertical profile of the horizontal velocity shows good agreement – apart the region close to the bottom wall – where the velocity shows significantly smaller levels of recirculation - compared to experimental data of Brown et al. [10], Fig.4-above. It is remarkable that velocity profile does not show

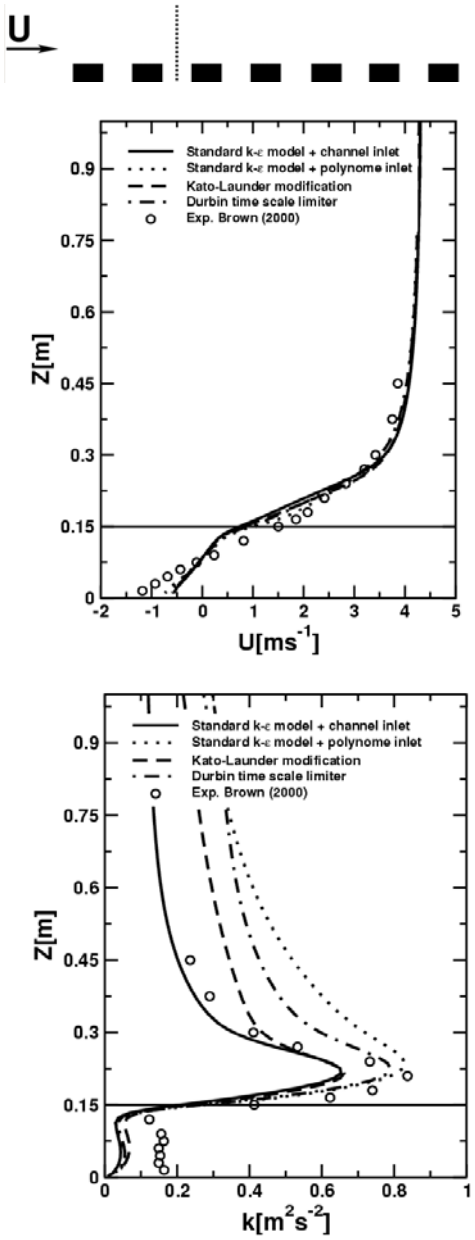

Figure 4. Vertical profiles of the horizontal velocity and turbulent kinetic energy in the second canyon in flow over array of 2D obstacles; Comparison with experiments of Brown et al. [10]

any significant dependence on the model used or different types of inlet specifications. In contrast to that, the vertical profile of turbulent kinetic energy shows bigger sensitivity to models of turbulence used as well as to specification of inlet conditions. In general, models which underpredict the peak value, show good agreement in the region further away from the obstacle. The concentration measurements of a passive tracer gas (ethane) emitted from the centre of the sixth street canyon are available. Contours of the non-dimensional concentration K (defined as $K = CU_{ref} HL / Q_e$) are shown in Fig.5. It can be seen that good

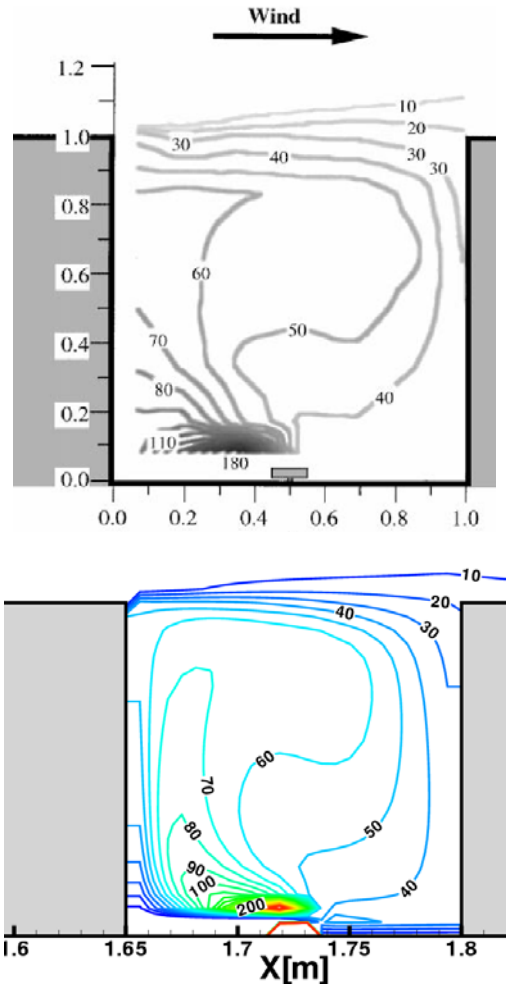

Figure 5. Contours of concentration emitted from the centre of the second - comparison with experiments of Pavageau and Schatzman [11]

agreement between experimental distributions and numerically simulated values is obtained.

4.3. Flow and concentration distribution in idealised 3D urban street canyons

The following test case replaces the previously simulated idealised 2D situations with more realistic 3D obstacles – making the flow patterns significantly different (now numerical mesh consists of 420x100x80 control volumes and in total 21 cubical obstacles are placed in the simulation domain). Identical inlet and boundary conditions are used as for the case with 2D obstacles. The horizontal velocity profile in the centre of the second canyon shows very good agreement with experiments, Fig. 6-above. The recirculation length is now better predicted than in the previously studied 2D case. The turbulent kinetic energy profile show two characteristics peaks – as observed in measurements – but levels of TKE are under-predicted in region below obstacle height and over-predicted in free-stream region, Fig.6-below. It is

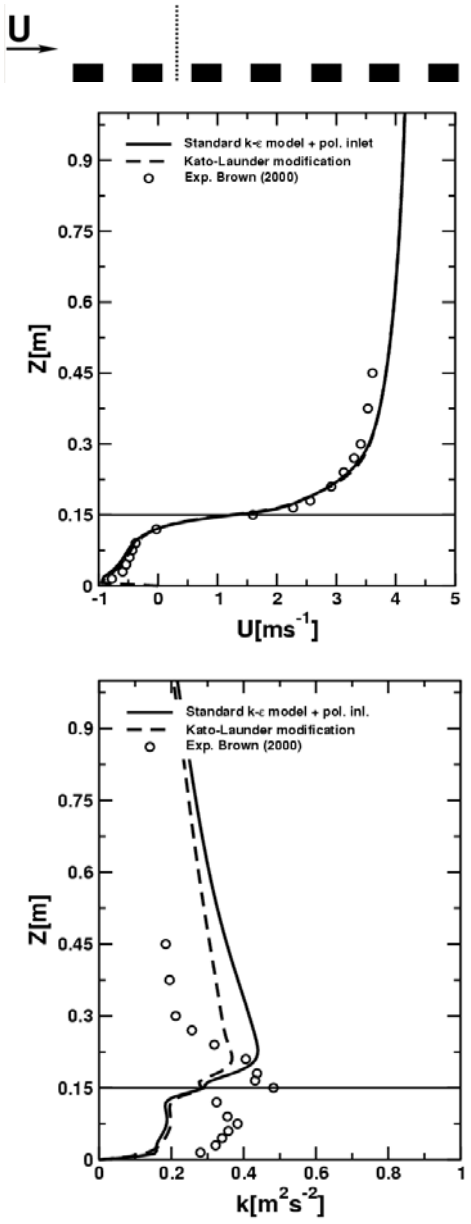

Figure 6. Vertical profiles of horizontal velocity and turbulent kinetic energy for flow over array of 3D obstacles, experiments of Brown et al. [10]

interesting to note that because of 3D effects, levels of TKE in lower part of simulated domain is twice higher than in 2D case and in upper part (above the obstacle height) its peak value is significantly reduced. Simulations accurately reproduced these main features of flow but exact levels are still different when compared to measurements. Despite these deficiencies, the predictions of non-dimensional concentration levels show excellent agreement with experiments, Fig.7. Here the concentration profiles in the centre of second (Fig.7-above) and sixth (Fig.7-below) street canyons are plotted. It can be seen that the wall-emission values, the peak values and values in the upper free-stream zone are all very well predicted.

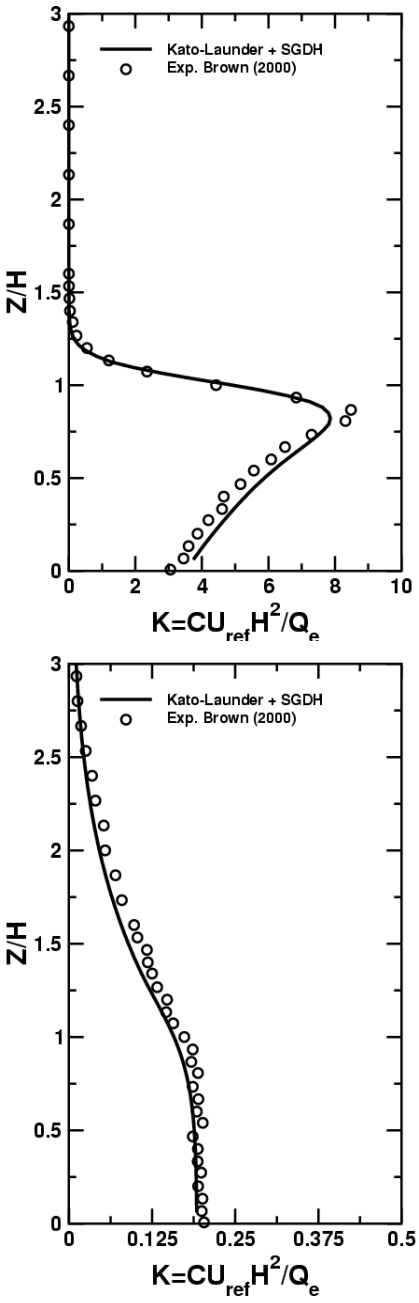

Figure 7. Vertical profiles of non-dimensional concentration, experiments of Brown et al. [10]

Now, after detailed benchmarking and validations on laboratory scale, we move to realistic (full-scale) urban street canyon situations.

4.4. Simulations of realistic urban street canyons: case of Goettinger Strasse in Hannover, Germany

The selected case is the "Goettinger Strasse" in Hannover, Germany, Fig.8. This particular cite is selected since it served as a benchmark case for validation of CFD codes in framework of the European research network (TRAPOS-Optimisation of Modelling Methods for Traffic Pollution in

Streets) and for which extensive experimental database is available. The experimental data are provided by permanent monitoring station of Environmental Agency of Lower Saxony in four-line street canyon with a traffic load of approximately $3x10^3$ vehicles per day including about 16% of heavy vehicles. The characteristic street canyon width is 25 m surrounded with both sides with complex buildings which are approximately 20 m high. In addition to field measurements, the laboratory scale measurements of the scale-down setup are available too. The numerical mesh representing the slightly simplified geometry of the considered location (in order to have identical geometry representation as previously done in the TRAPOS benchmark studies, Theodoridis et al. [12]) consists of 146x138x50 control volumes and approximately 35 passive elements (obstacles), Fig.9. Since the original orientation of the street is 163^0 with respect to North – numerical mesh is rotated for the same angle in order to provide simple inlet-outlet boundary conditions along the entire inlet- and outlet-planes, respectively. Different wind directions are simulated together with their impacts on pollutant dispersion. The emission of pollutants is mimicked though two line sources located at 220<X<225m, 100<Y<280m and 230<X<235m, 100<Y<280m positions, respectively. The velocity vectors and contours of vertical velocity and turbulent kinetic energy at plane 10m above street are shown in Fig.10 (for East-West approaching inflow direction). The resulting flow pattern is very

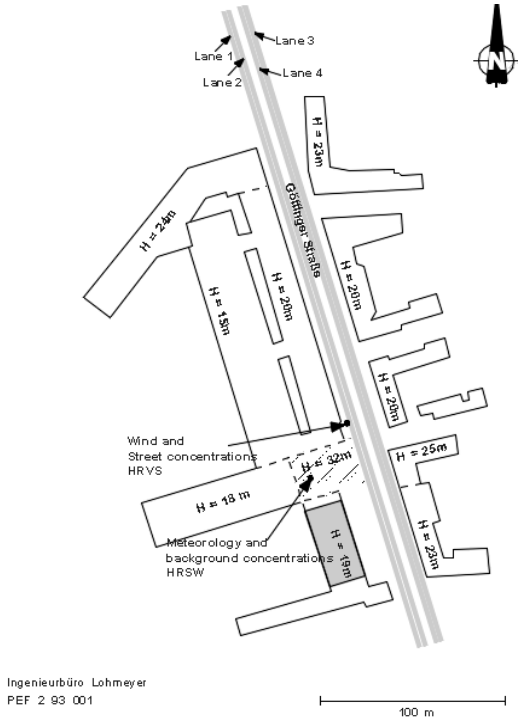

Figure 8. Sketch of the 'Goettinger Strasse' location: specifications of surrounding buildings and four-line emissions sources.

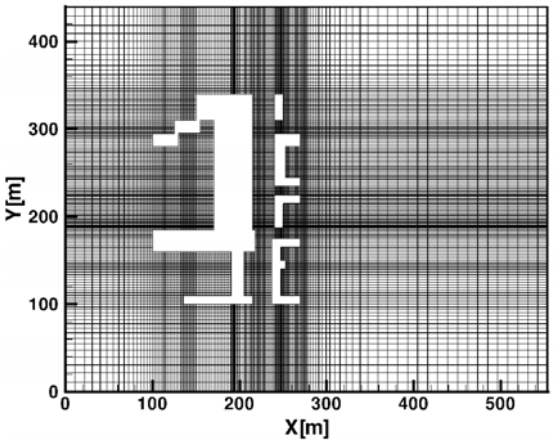

Figure 9. Top view of the numerical mesh used for series of simulations.

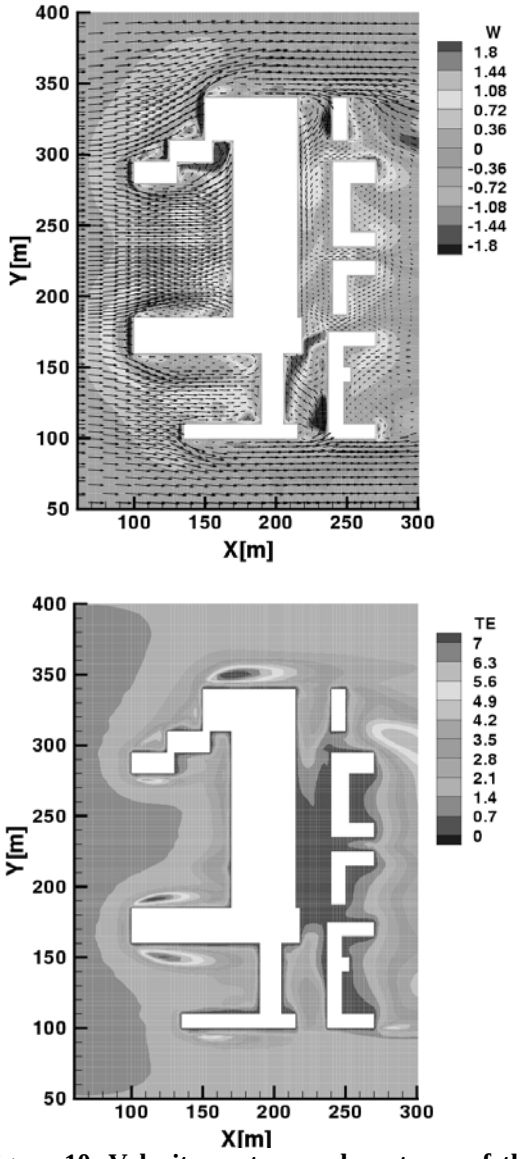

Figure 10. Velocity vectors and contours of the vertical velocity (W) and of turbulent kinetic energy at 10 m above the street for West-East wind direction;

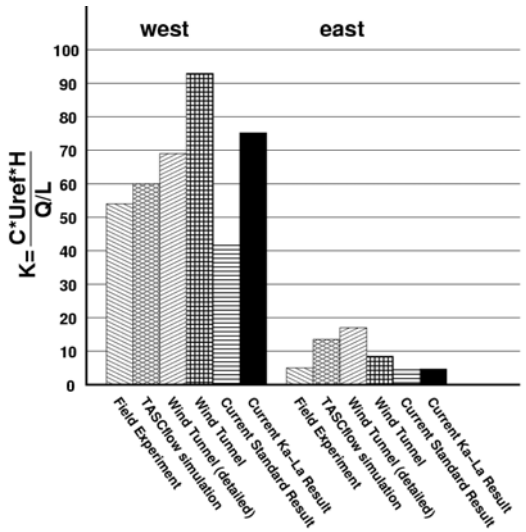

Figure 11. Summary of performed simulations (different wind directions) and predicted values of pollution levels with field-measurements, laboratory-scale measurements and previous simulations of Theodoridis et al. [12].

complex – produced by local configuration of surrounding buildings. Patches of local extremes of vertical velocity (strong flow acceleration or de-acceleration) and turbulent kinetic energy (reattachment and recirculation regions) can be easily located. Finally, an overview of performed simulations and comparison of predicted levels of concentration at monitoring point (indicated in Fig.8) are shown in Fig.11. It can be seen that presented simulations gave qualitatively good agreement with field-measurements for all directions of approaching flow, making it possible to fully replace laboratory scale measurements of this configuration.

5. SUMMARY

In this paper we addressed applications of numerical simulations of turbulent fluid flow and pollutant dispersion over complex geometries – on both laboratory and full-scale applications. The numerical simulations are based on finite-volume approach in non-orthogonal geometries with possibility to activate efficient blockage of parts of flow ('passive elements approach'). Numerical algorithm with different extensions of standard two-equations eddy-viscosity models is extensively tested and validated on series of cases including: flow over arrays of 2D and 3D obstacles at laboratory scale, flow over full-scale realistic orography ("Askervein Hill") and realistic urban street canyon ("Goettinger Strasse") with different orientations of approaching wind and street emissions. It is shown that surface roughness and reduced production played important role in obtaining good agreement with experimental results. Finally, it is demonstrated that numerical simulations can be powerful tools for prediction of pollutant dispersion in complex urban areas.

REFERENCES

[1] Britter R. E. and Hanna S. R., 2003,"Flow and dispersion in urban areas", *Annual Review of Fluid Mechanics*, Vol.35, pp.469-496.

[2] Kato M. and Launder B. E., 1993, "The modelling of turbulent flow around stationary and vibrating square cylinders", Proceedings of the 9th Symposium on Turbulent Shear Flows, Kyoto, Japan, pp.10.4.1-10.4.6.

[3] Durbin P., 1995, "Separated flow computations with the k-e-v2 model", AIAA Journal, Vol. 33. pp.659-664.

[4] Kenjeres S. and Hanjalic K., 2005,"LES, T-RANS and hybrid simulations of thermal convection at high Rayleigh numbers", *Proceedings of ERCOFTAC International Symposium on Engineering Turbulence Modelling and Measurement ETMM6*, Sardinia, Italy, pp.1-10.

[5] Kenjeres S., Hanjalic K. and Gunarjo S. B., 2002, "A T-RANS/VLES approach to indoor climate simulations", Paper No: FEDSM20002-31400, *Proceedings of ASME Fluids Engineering Division, Summer Meeting*, July 14-18, 2002, Montreal, Quebec, Canada, pp.1-9.

[6] Taylor P. A. and Teunissen H. W., 1987, "The Askervein Hill project: overview and background data", *Boundary Layer Meteorology*, Vol.39, pp.15-39.

[7] Raithby G. D., Stubley G. D. and Taylor P. A., 1987, "The Askervein Hill project: a finite control volume prediction of three-dimensional flows over the hill", *Boundary Layer Meteorology*, Vol.39, pp.247-267.

[8] Beljaars A. C. M., Walmsley J. L. and Taylor P. A., 1986, "A mixed spectral finite-difference model for neutrally stratified boundary-layer flow over roughness changes and topography", *Boundary Layer Meteorology*, Vol.38, pp.273-303.

[9] Castro F. A., Palma J. M. L. M., Silva Lopez A., 2003,"Simulation of the Askervein flow: Part I: Reynolds-Averaged Navier-Stokes equations", *Boundary Layer Meteorology,*, Vol.107, pp.501-530.

[10] Brown M. J., Lawson R. E., De Croix D. S. and Lee R. L., 2000,"Comparison of centreline velocity measurements obtained around 2D and 3D building arrays in a wind tunnel", *Conference of International Society of Environmental Hydraulics*, Tempe, Arizona, U.S.A.

[11] Pavageau M. and Schatzman M., 1999,"Wind tunnel measurements of concentration fluctuations in an urban street canyon", *Atmospheric Environment*, Vol.33, pp.3961-3971.

[12] Theodoridis G., Karagiannis V. and Valougeorgis D., 2002, "Numerical prediction of dispersion characteristics in an urban area based on grid refinement and various turbulence models", *Water, Air and Soil Pollution: Focus*, Vol.2, pp.525-539.

Conference on Modelling Fluid Flow (CMFF'06)
The 13th International Conference on Fluid Flow Technologies
Budapest, Hungary, September 6-9, 2006

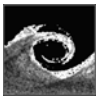

SENSITIVITY STUDIES OF THE COUPLED AERMOD/ETA ATMOSPHERIC DISPERSION MODELLING SYSTEM

Tamás WEIDINGER, András Zénó GYÖNGYÖSI[1],Enikő SASS[2]

[1]Department of Meteorology, Eötvös Loránd University, H-1117, Budapest, Pázmány Péter sétány 1/A., E-mail: weidi@ludens.elte.hu
[2]Meteorological Service of the Hungarian Defence Forces, P.O. Box 1885, Budapest

ABSTRACT

The AERMOD model is a steady-state plume model, developed by the American Meteorological Society (AMS) and the US Environmental Protection Agency (EPA). It has been designed to describe the transport of pollutants over both flat and complex terrains in local scale (~ 30 x 30 km^2). Dispersion of different passive pollutants emitted by industrial sources is calculated by a hybrid Gaussian scheme using the Monin-Obukhov similarity theory. Hourly meteorological dataset for model calculation has been derived either from the ALADIN model of the Hungarian Meteorological Service (HMS) or the NCEP/ETA model. The latter is a limited area numerical weather prediction model developed by the National Centers for Environmental Prediction (NCEP) and adapted for the Carpathian Basin being run operationally at the Eötvös University. In addition to the description of the coupled AERMOD/ETA modelling system, a sensitivity study of the AERMOD model for surface parameters and mixing layer height is presented in this paper.

Keywords: plume model, dispersion, mixing layer, sensitivity study

1. INTRODUCTION

Regulatory air pollution modelling is being carried out since the early 1960's in Hungary. First, Gaussian puff models were used. Instability and boundary layer depth were calculated [1]. For the uniform application of transmission schemes, the standardization of air quality models is crucial. This work ended in the early 1980's [2]. Pollution of point, line and areal sources were modelled. The parameterization of dispersion and the calculation of effective source height (plum rise) were emphasized. Next step was the development of the Hungarian Standardized Model (HNS-TRANSMISSION) in the 1990's. This Gaussian transmission model can consider the contribution of up to 50 sources. It is suitable to describe the transmission processes from local scale to regional scale including orographical effects [3].

Modernization of transmission standards became actual at the end of the 90's. Surface layer characteristics and the profiles of meteorological fields were calculated with the Monin-Obukhov Similarity Theory. The assessment of the surface energy budget components was also standardized. The depth of stable and unstable Planetary Boundary Layer (mixing layer depth) were obtained [4,5] according to the recommendation of the COST Action 710 [6]. In order to perform sensitivity studies, the EPA AERMOD system has been implemented at the Hungarian Meteorological Service [7,8]. This system is suitable for the estimation of concentration of pollutants above both plane and complex terrains. The applied system is a result of a multi year development. It is a descendant of the earlier EPA models as ISC3 (Industrial Source Complex) or the CALPUFF [9]. All above mentioned models are non-steady-state dispersion models for the estimation of dispersion of gaseous pollutant from different type of sources (point, line, area, etc.) using time and space-varying meteorological conditions on the pollutant transport, removal by transformation. These models are widely used in many countries of the world. Earlier model versions were implemented in Slovakia [10,11] and in Hungary as well. Meteorological pre-processors based on numerical model results were developed. Graphical software for the visualization of the results was also implemented. The AERMOD is integrated into the Hungarian Air Quality Regulatory System. In the framework of the COST-728/732 program, international validation studies are being performed [12].

Applied research, related to the AERMOD model, is being processed at the Department of Meteorology at the Eötvös Loránd University. Our goals are (i) to couple the model to the NCEP/ETA limited area Numerical Weather Prediction model,

which yields the input for the meteorological pre-processor unit, (ii) to perform sensitivity studies to test the effects of orography, surface and planetary boundary layer (PBL) characteristics, (iii) to test the dispersion processes over complex terrain (iv) and the adaptation of the model into the Environmental Education at the University. Some results of this work are given below. We demonstrate the structure of the coupled system, the effect of orography on the structure of the concentration field and some results from the sensitivity studies on mixing layer depth.

2. THE AERMOD SYSTEM

The AERMOD dispersion model (AMS/EPA Regulatory Model), which has been developed in the United States, is a multi layer regulatory, Gaussian plume model. Atmospheric concentration of industrial contaminants, emitted by line, area and volumetric sources, can be calculated [13,14]. The AERMOD system consists of a main unit (AERMOD) and two pre-processor units (AERMET and AERMAP) (Figure 1).

The AERMET unit performs meteorological data assimilation and the estimation of PBL parameters is also necessary for the calculation of dispersion.

The AERMAP unit characterizes the terrain and generates the receptor grid network needed by the model. It is suitable for the handling of all types of terrain (including simple, moderate and complex) and able to handle both discrete receptors and a grid of receptors.

The main unit (AERMOD) performs the prediction of concentration values, output results are given in tabular form for unlimited number of receptors and for unlimited number of sources.

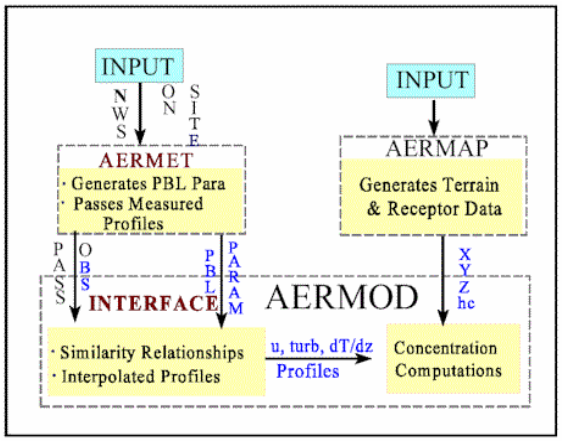

Figure 1. The structure of the AERMOD system.
NWS: Numerical Weather System
OBS: Meteorological observations
PBL PARAM: Planetary Boundary Layer (PBL) characteristics. (Illustration taken from the Lakes Environmental Web page [15].)

2.1. The input dataset

Systematic assimilation of the available meteorological data and estimation of the necessary PBL characteristics for the calculation of dispersion by AERMOD are performed by the AERMET meteorological pre-processor. Hourly surface observations and rawinsonde measurements twice a day of National Meteorological Services as well as on-site field measurement data (e.g., tower measurements, remote sensing data) can be processed. The latter is optional, while the first two should be given. Measured data can be replaced by numerical model output (e.g., yielded by the ALADIN and MM5 models from the HMS, or by the NCEP/ETA model from the Department of Meteorology at the Eötvös University).

The input dataset for the calculation of transmission includes calculated PBL characteristics besides standard meteorological measurements. According to investigations using various models we know that the model integration is more sensitive to the data assimilation technique than to the model formulation itself: output results of different dispersion models on the same meteorological input show small variation while different input fields obtained by different assimilation techniques applied to the same model results in large variation in the output fields [16,17]. Inaccuracy in the initial fields carries large errors, so quality control of meteorological datasets is crucial. This implies standardization of measurements and calculation processes. As a consequence of the great importance of the meteorological pre-processor, a detailed description of the calculation process applied by the AERMET is given below.

The main function of the AERMET is to calculate necessary boundary layer characteristics for the AERMOD, using meteorological dataset and surface characteristics representative for the considered area and period. These parameters are used by the meteorological unit INTERFACE in the generation of the profiles of the necessary meteorological variables (wind, turbulence, temperature). All observations besides are yielded by the AERMET for AERMOD.

Note that an important difference between AERMOD and the earlier ISC3 model is the way of handling surface effects. While in ISC3 an open land surface is assumed by default, in AERMET surface characteristics define the state the PBL aloft. This dependence is based on the fact that the structure and evolution of the PBL is governed by heat and momentum fluxes. Boundary layer depth and dispersion of contaminants are affected by surface characteristics. These characteristics are the following: (i) surface roughness (z_0) i.e., height over surface (or over the replacement height (d) where wind speed becomes zero; (ii) albedo (α) i.e., the measure of reflectivity of a surface body; (iii) and

Bowen ratio (B_0) i.e., the ratio of sensible and latent heat flux, representing the available moisture content of the surface. All above parameters depend on landcover-landuse (e.g., urban area, deciduous or coniferous forest, agricultural area, water bodies, etc) and show seasonal variation and variation with wind speed, for example.

Input variables of AERMET are standard meteorological data (wind speed, wind direction, temperature and cloud amount) and surface characteristics (albedo, roughness length and Bowen ratio). The next PBL parameters are calculated on these inputs by this unit: friction velocity (u_*), Monin-Obukhov length scale (L_*), convective velocity (w_*), dynamical temperature (T_*), mixing layer depth (z_i) and sensible heat flux (H). The above parameters are taken to the unit INTERFACE, and vertical profiles of the following variables are calculated using similarity considerations: horizontal wind velocity (u), deviation of horizontal and vertical wind (σ_v and σ_w), potential temperature (θ) and potential temperature gradient ($\partial\theta / \partial z$).

3. THE NCEP/ETA MODEL

The National Centers for Environmental Prediction (NCEP) "Early" Eta analysis and forecasting system was operationally implemented in June 1993, replacing the Limited-area Fine Mesh model in providing early forecast guidance over North America. The current version of the model is being run at Eötvös Loránd University with a horizontal resolution of approximately 10 km. The vertical grid network of the model is a modified sigma coordinate (which is a terrain following pressure coordinate) that ensures quasi-horizontal planes in the vicinity of mountain slopes avoiding lee flow instabilities that usually arises from terrain following sigma coordinates. The implementation of the ETA model was made at the Eötvös University in early April, 2005, and operational run of the model is performed for a domain including the Carpathian Basin in the Central European region on daily basis. The initial and boundary conditions of the limited area model is taken from NCEP via anonymous FTP from the Global Forecasting Model datasets. The output fields are stored on backup DVD-s for further analysis and research purposes. Currently, these input datasets are used for coupled model integration with a mesoscale dispersion model. From the input fields of the ETA model, suitable input meteorological conditions for the AERMOD model can also be generated. Our future plans include the coupled model integration of the AERMOD/ETA modelling system.

4. SENSITIVITY TEST OF THE AERMOD

Two cases of the test runs are presented here: the first presents the effect of orography and the length of the averaging interval on the distribution of surface concentration, the second example demonstrates the nonlinear effects of the uncertainty of PBL height.

4.1. Orography effect

In the planning process of industrial facilities and for the calculation of surface concentration, it is essential to take into account the effect of the most common meteorological conditions and the orography. The influence of orography on concentration has been investigated for different point sources with different height (H) and emission (E). During the sensitivity study, analyses for four different types of orography have been calculated (flat terrain, valley, hill and mountain) using 3 different averaging intervals (1 hour, 24 hours and a 10 days period). At surface a grid of receptor points has been considered.

Concentration at a hilly terrain is presented. In case of an averaging interval of 1 hour, distribution of concentration represents atmospheric stratification of the considered time interval. In unstable case, when plume touches orographic obstacles, it deflects vertically following surface, and a lateral diffusion can be observed. In a stable case, plume deflects laterally as it touches orography, and separate polluted districts can be generated. For this reason a larger deviation can be observed by stable stratification. Figures 2-4 are demonstrating the above mentioned features.

24 hours average contains the effect of both stable and unstable periods besides diurnal variation of wind direction. Concentrations are lower and the angle of the area affected by the plume is larger. One can visualize some area where plume is lifted and others where it is deflected by orography. Distribution of concentration illustrated on Figure 5 corresponds to hilly terrain for 24 hours average.

240 hours average represents dominant winds of the given period and a larger area is affected by pollution. Of course average concentrations are the smallest in this case. Results representing the whole 10 days period are shown on Figure 6.

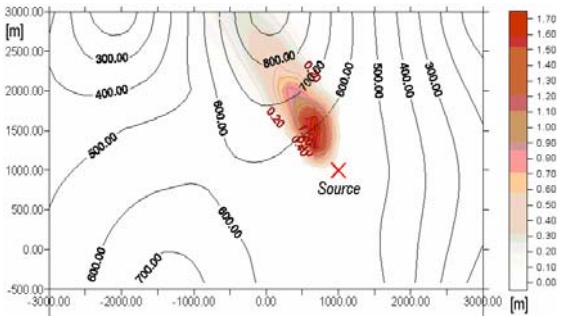

Figure 2. Plume shape in case of hilly terrain, 1 hour averaging interval and unstable stratification. E = 1 g/s, H = 35 m.

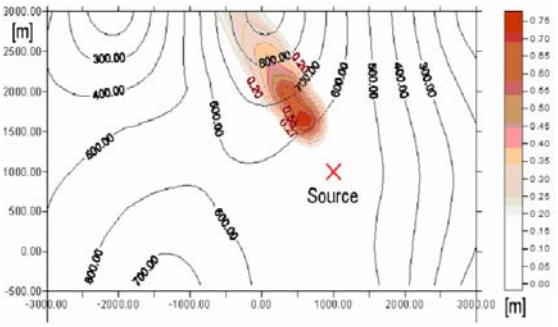

Figure 3. Plume shape in case of hilly terrain, 1 hour averaging interval and stable stratification. E = 1 g/s, H = 100 m.

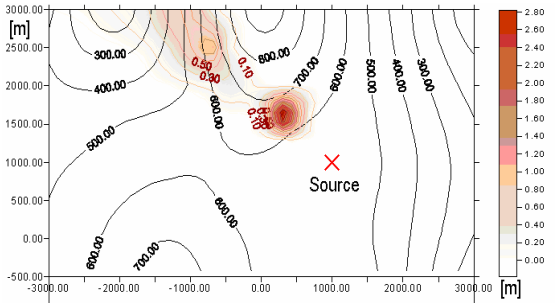

Figure 4. Plume shape in case of hilly terrain, 1 hour averaging interval and stable stratification. E = 1 g/s, H = 35 m.

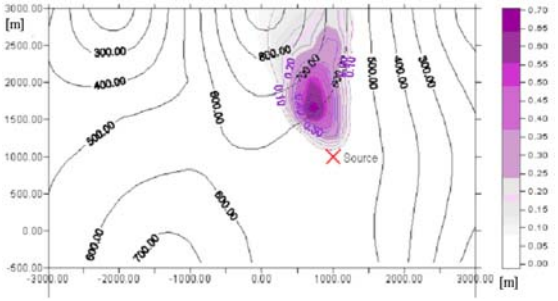

Figure 5. Plume shape in case of hilly terrain, 24 hours averaging interval. E = 1 g/s, H = 35 m.

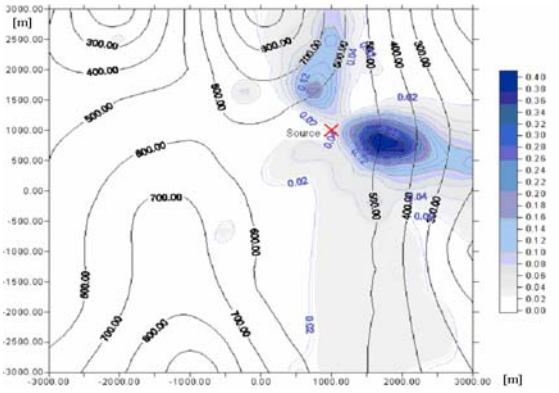

Figure 6. Plume shape. Hilly terrain, 240 hours averaging interval. E = 1 g/s, H = 35 m.

4.2. Sensitivity of the model to the mixing layer depth

The new generation AERMOD-PRIME version has been used in this study. This version contains algorithms for dry and wet deposition. Our goal was to investigate the effect of a change in the depth of PBL (i.e., the mixing layer depth) on the concentration of a contaminant. PBL is the lower 0.2 km to 2 km deep layer of the atmosphere, which separates surface from the free atmosphere. Transport processes of mass and atmospheric properties (e.g., momentum, sensible and latent heat flux) take place in the PBL. Depth of the PBL varies in space and time, having a typical diurnal variation governed by the thermal forcing of the surface. AERMOD contains different methods for the treatment of stable and convective boundary layer.

Investigation has been performed for the oil refiner in Százhalombatta for a one week period in winter for the next input data:

Meteorological input data: ALADIN output for the period from the 1st till 7th of January, 2005

Source data: type: point source

Emission: E = 20 g s^{-1}

Emission height: H = 80 m

Temperature of emitted gas: 300 K

Vertical velocity of emitted gas: 10 m s^{-1}

Internal diameter of source: 5 m

Contaminant: NO_x

Orography: Terrain of the neighborhood of the refiner in Százhalombatta, an area of about 30 x 30 km^2 (Fiugre 7)

Grid receptors: The considered area covered by a Cartesian coordinate-system of 55 x 55 receptor points

Surface characteristics: Typical winter values of albedo, Bowen ratio and roughness length for each sector.

Average concentrations for 1 hour, 24 hours and 168 hours period have been investigated. Mechanical and convective mixing layer depth has been modified compared to the values given by AERMET. A change by 5, 10, 15 and 20% has been introduced.

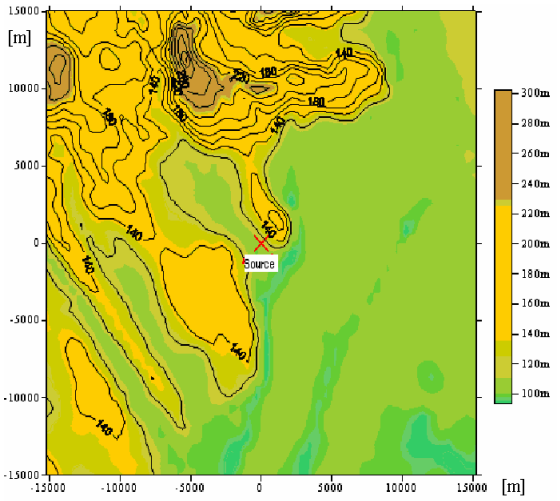

Figure 7. Terrain of Százhalombatta with the large stack point source of the refiner.

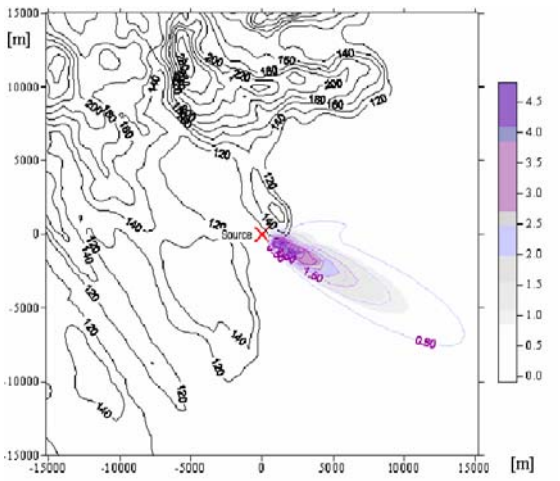

Figure 8. Plume shape for a 24 hours averaging interval at 4 January, 2005.

The 1 hour averages were the highest while 168 hours averages were the lowest in general.

In case of 1 hour averages distribution of concentration represents the stratification (stable or unstable) of the considered time interval. 24-hour averages contain both the effects of stable and unstable stratification and the diurnal variation of wind speed and direction. So concentration values are smaller while angle of the area affected by the plume is larger. Figure 8 illustrates the shape of plume for a 24 hours averaging period. Average concentration of a time interval of 168 hours represents typical winds of the considered period, affecting even larger area.

Variation of the PBL depth has larger impact in case of larger concentrations, so we considered the largest values for all averaging periods. Figure 9 demonstrates the maximum concentration of contaminants as a function of PBL height. Figure 9 upper panel corresponds to a stably stratified nocturnal case while the lower panel to an unstably stratified case in the midday.

While unstable stratification improves dilution (due to thermal and mechanical turbulence), concentrations are smaller in that case than in stable case (only mechanical turbulence). So the variation is much larger in stable case. Note that for meteorological conditions of the considered period orography did not influence dispersion, but in general, due to an obstacle in the prevailing wind direction, contaminants can accumulate significantly. It can be seen that an increase in the mixing layer depth results in a decrease in the maximal concentration, because it allows larger scale mixing of contaminants. Similarly, decrease in the depth of mixing layer results in an increase in the concentration.

10% change of mixing layer depth results in a 5-6% variation in the concentration in stable case. 20% change modifies maximal concentrations by 10-12%. The order of magnitude of decrease of

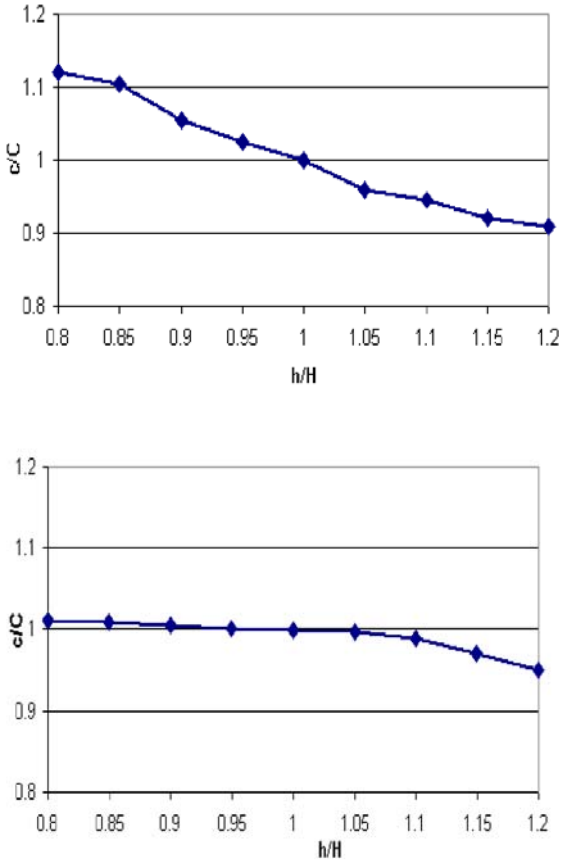

Figure 9: Maximal relative concentration by 1 hour averaging in stable case (top) and in unstable case (bottom) as a function of relative PBL height.

concentration resulted from an increase in mixing layer depth is smaller than the increase of concentration by decrease of depth. This is due to

smaller intensity of mixing processes by stable conditions.

On Figure 10 upper panel maximal surface concentration of the contaminant is presented as a function of boundary layer depth in a certain receptor point for 24 hours averaging. It can be seen that an increase in the boundary layer depth results in a decrease in maximal concentration values, while a decrease in the boundary layer depth results in an increase in maximal concentration. 10% change in the depth results in a negligible 0.13-0.14% variation in the maximal concentrations and 20% change modifies concentration by only 0.26-0.29%.

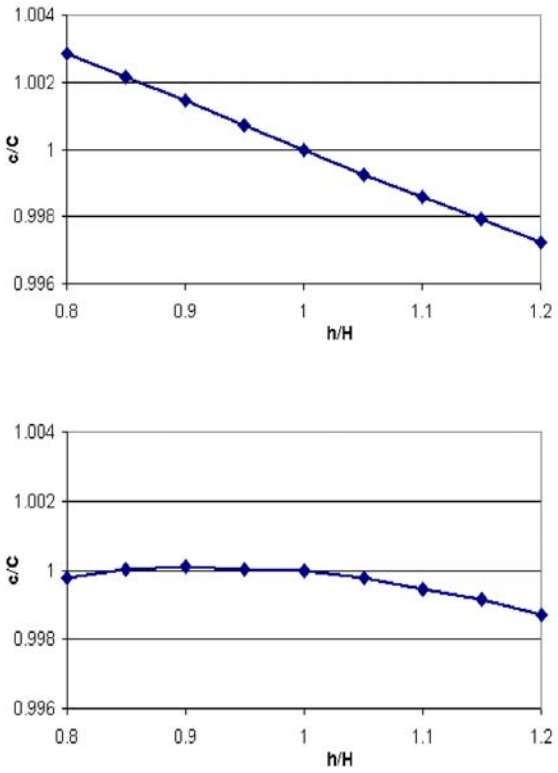

Figure 10: Maximal relative concentration by 24 hours (top) and 168 hours (bottom) averaging as a function of relative PBL height.

Figure 10 lower panel demonstrates the concentration of the contaminant as a function of boundary layer depth in a certain receptor point by 168 hours averaging. The effect of a change in the boundary layer depth is the less pronounced in this case. Variation of 0.13% at 20% change in PBL depth is the largest impact among the investigated cases. An interesting feature of this case is that similar to the previous cases concentration decreases with increasing boundary layer depth, but a decrease of the mixing layer does not imply necessarily definite increase in the maximal concentrations. In case of 20% decrease in the mixing layer depth for example, concentration is smaller than in the original case. This is probably a consequence of a smoother distribution of the concentration for a longer averaging period around the point of maximum concentration. Due to the variation of wind speed and direction, one certain point is not always in the direction of maximum concentration in the plume. This is a logical explanation to the week correlation between maximal concentration and variation in mixing layer depth for longer averaging intervals.

5. CONCLUSION

We have demonstrated the development of the ETA/AERMOD system at the Department of Meteorology at Eötvös University. The effect of complex terrain on the diffusion of contaminants has been analyzed. We investigated the uncertainty of maximal surface concentrations due to variation of mixing layer depth in stable and unstable cases. According to our expectations, in stable cases (thin layer), hourly surface concentrations are more sensitive to the mixing layer depth than in deep convective cases. With the increase of averaging period the importance of mixing layer depth decreases. This is a consequence of a variation in the shape and direction of the plume with varying wind speed and direction.

Among our plans are further sensitivity studies including the investigation of the effect of surface characteristics (albedo, Bowen ratio and roughness length) on the distribution of concentration.

Surface – as a thermal and mechanical constraint – induces turbulent exchange processes influencing transport of contaminants. Because the model the structure of the PBL is a function of the surface characteristics beneath, our further investigations are towards the analyses of the PBL itself.

ACKNOWLEDGEMENTS

The financial support of the Agency for Research Fund Management and Research Exploitation (KPI) for the program “Development and testing of a multi-range atmospheric transport model system for the estimation of air quality expected up to 2010 in Hungary (3A/088/2004)” is gratefully acknowledged.

REFERENCES

[1] Szepesi, D., 1967: “Meteorological conditions of the turbulent diffusion of atmospheric pollutants in Hungary” (in Hungarian), *Hungarian Meteorological Institute, XXXII, Budapest*.

[2] Fekete, K., Popovics, M. and Szepesi, D., 1983: “Guide to Estimate the Transmission of Air

Pollutions" (in Hungarian), *Hungarian Meteorological Service, LV, Budapest*.

[3] Szepesi, D., Fekete, K., Büki, R., Koncsos, L. and Kovács, E, 2005: "Development of regulatory transmission modelling in Hungary", *Időjárás*, Vol. 109, pp. 257-279.

[4] Baranka, Gy., Weidinger, T., Mészáros, R., Mikó, R., and Kovács, R., 2001: "Wind speed and temperature profiles and structure of planetary boundary layer" (in Hungarian), *Scientific Days of Meteorology, 2001. (Edited by: Mika, J.) Hungarian Meteorological Sservice*, pp. 109-119.

[5] Baranka, Gy., Weidinger, T. and Mészáros, R., 2001: "Renewal of methodology for regulation of transmission in Hungary" (in Hungarian), *Energiagazdálkodás*, Vol. 42, No. 5, 4–9.

[6] Fisher, B. E. A., Erbrink, J. J., Finardi, S., Jeannet, P., Joffre, S., Morsellini, M. G., Pechinger, U., Seibert, P. and Thomson, D. J. (Editors), 1998: "COST Action 710 – Final report. Harmonization of the pre-processing of meteorological data for atmospheric dispersion models", *EUR 18195 EN*.

[7] Steib, R., 2005: "Regulatory modelling activity in Hungary", I. Faragó et al. (eds.) *Advances in Air Pollution Modelling for Environmental Security, Springer, Printed in the Netherlands*, pp. 337-347.

[8] Bozó, L., Labancz, K. and Steib, R., 2006: "Estimation of expected air pollution level for 2010 using a dynamical model approach" (in Hungarian), *Scientific Days of Meteorology, 2005 (Edited by Weidinger, T.), Hungarian Meteorological Service*, pp. 207-215.

[9] EPA, 1998: "A comparison of CALPUFF with ISC3 (EPA-454/R-98-020)", *U.S. Environment Protection Agency. Research Triangle Park NY.*

[10] Zavodsky, D., 2000: "Air pollution model quality assurance – some remarks", *Meteorologicky casopis*, Vol. 3, No. 4, pp. 21-27.

[11] Krajcovicova, J., 2003: "CALPUFF dispersion model and its implementation for Bratislava", *Meteorologicky casopis*, Vol. 6, No. 1, pp. 15-25.

[12] Steib, R., and Labancz, K., 2005: "Regulatory modelling in Hungary – the AERMOD model", Part I. Description and application. *Időjárás*, Vol. 109, pp. 157-172.

[13] Cimorelli, A. J., Perry, S. G., Venkatram, A., Weil, J. C., Paine, R. J., Wilson, R. B. Lee, R. F., Peters, W. D., Brode, R. W. and Paumier, J. O., 2002: "AERMOD: Description of Model Formulation (Version 02222)", *EPA 454/R-02-002d. U. S. Environmental Protection Agency, Research Triangle Park, NC.*

[14] Daberrot, W. F., Carroll, M. A., Baumgardner, D., Carmichael, G., Cohen, R., Dye, T., Ellis, J., Grell, G., Grimmond, S., Hanna, S., Irwin, J., Lamb, B., Madronich, S., McQueen, J., Meagher, J., Odman, T., Pleim, J., Schmid, H. P., and Westpal, D. L., 2004: "Meteorological research needs for improved air quality forecasting", *Report of the 11th prospectus development team of the U.S. Weather Research Program, American Meteorological Society, BAMS*, pp. 563-586.

[15] Lakes Environmetal Web page: http://www.weblakes.com/aermodvol1/2.html

[16] Baranka, Gy., 2002: "Modelling of air pollution from industrial sources" (in Hungarian), *Energiagazdálkodás*, Vol. 43. No. 3.

[17] Gács, I. and Bihari, P., 2002: "Uncertainty of input data for air pollution transport" (in Hungarian), *Energiagazdálkodás*, Vol. 43. No. 2.

Conference on Modelling Fluid Flow (CMFF'06)
The 13th International Conference on Fluid Flow Technologies
Budapest, Hungary, September 6-9, 2006

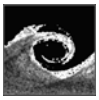

WIND TUNNEL STUDY OF FENCE SHELTER ON CONTINUOUS RELEASE OF HEAVY GAS IN THE TURBULENT BOUNDARY LAYER FLOW

Bao-Shi SHIAU[1] , Hwui-Shang CHIOU[2]

[1] Corresponding Author. Institute of Physics, Academia Sinica, Taipei, 115 Taiwan; Department of Harbor and River Engineering, National Taiwan Ocean University, Keelung, 202 Taiwan. Tel.: +886 2 27896749, Fax: +886 2 27889829, E-mail: bsshiau@gate.sinica.edu.tw
[2] Department of Harbor and River Engineering, National Taiwan Ocean University, Keelung, 202 Taiwan. E-mail: b0085@mail.ntou.edu.tw

ABSTRACT

The wind tunnel modeling experiments were conducted to examine the shelter effect of the fence on the dispersion characteristics of horizontally continuous release of heavy gas from an elevated source. In the experiments, carbon dioxide was adopted as the tracer of heavy gas. The scaled rural terrain type of neutral atmospheric turbulent boundary layer flow was simulated and used as the approaching flow. Measured results show that with setting fence behind the elevated source, the significant shelter effect for reducing heavy gas concentration has been exhibited. The ground-level concentration along the downstream distance in the leeside of the fence comes to a larger value as increasing the released heavy gas densemetric Froude number. When the fence porosity reduces, the ground-level concentration along the downstream distance behind the fence decreases.

Keywords: wind tunnel modelling, heavy gas, ground-level concentration, densimetric Froude number, fence, shelter effect, turbulent boundary layer

NOMENCLATURE

C	[*ppm*]	concentration
Cs	[*ppm*]	initial source concentration
D_s	[*mm*]	source diameter
g	[m/s^2]	gravity acceleration
H	[*cm*]	fence height
hs	[*cm*]	elevated source height
n	[--]	power exponent of velocity profile
Re	[--]	ambient Reynolds number
Re_s	[--]	source Reynolds number
U_{ref}	[*m/s*]	free stream velocity
u_{rms}	[m/s]	root mean square of turbulent velocity fluctuation
Z_{ref}	[*m*]	boundary layer thickness
X	[cm]	downstream coordinates
Y	[cm]	lateral coordinate
Z	[cm]	vertical coordinate
φ	[--]	fence porosity
ρ_s	[g/cm^3]	heavy gas density
ρ_a	[g/cm^3]	ambient air density
μ_a	[$N\text{-}s/m^2$]	ambient air viscosity

1. INTRODUCTION

In the industrial park, there are many kinds of chemical gases storage tanks. Most of the chemical gases are toxic and heavier than the air. Usually these kinds of gas are called heavy gases or dense gases. Accidents of continuous release of heavy gas form the storage tank will cause a strong impact on the industrial park environment.

Schatzmann [1,2] indicated that the dispersion of the heavy gas is quite different from that of the airborne pollutants. Britter [3] had make a review on the atmospheric dispersion of heavy gas. Zhu et al. [4] investigated experimentally on the flow structure within a Dense Gas Plume. Robin et al. [5] conducted the wind tunnel study on the dense gas dispersion in a neutral boundary layer over a rough surface. Donat and Schatzmann [6] had conducted experiments on the one single-phase heavy gas jets released in the turbulent boundary layer. Nielsen et al. [7] made the field tests on the dispersion of pressure liquefied ammonia. Khan and Abbasi [8] developed the numerical model to simulate the heavy gas dispersion on the basis of modification in plume path theory. Duijm et al. [9] made a review and on the evaluation protocol for heavy gas diapersion models.

To reduce the heavy gas release impacts on the environment, fence is one kind of the wind barrier which is commonly used to prevent the dispersion of the heavy gas. The numerical model developed by the Khan and Abbasi [8] did not account for the

fence shelter effect. Wind tunnel test made by Donat and Schatzmann [5,6] were also in absence of fence in their experiments. In the present study, measurements of the concentration distribution of heavy gas (carbon dioxide) in the turbulent boundary layer flows with fence were carried out. The urban types of neutral atmospheric turbulent boundary layers were simulated as the approaching flows. Sheletr effects on the heavy gas dispersion for the solid and porous fences under various release of densimetric Froude numbers were investigated.

2. EXPERIMENTAL SET-UP AND INSTRUMENTS

The experiments were carried out in the National Taiwan Ocean University's Environmental Wind Tunnel. The wind tunnel test section has a cross section of 2 m wide, 1.4 m high, and 12.5 m long. The tunnel is an open suction type and it contracts to the test section with an area ratio of 4:1. The turbulence intensity of empty tunnel in test section is less than 0.5 % at the mean velocity of 5 m/s.

Four spires of 100 cm height and roughness elements (2 cm x 2 cm x 2cm) are properly arranged at the entrance of test section to generate a thick turbulent boundary layer which is used as the approaching flow. The turbulent boundary layer flow is approximated by the power law.

An X-type hot-wire incorporating with the TSI IFA-300 constant temperature anemometer was employed to measure the turbulent flow signals. Output of the analog signals for turbulent flow was digitized at a rate of 4 K Hz each channel through the 12 bit Analog-to–Digital converter. Since none of the analog signals containing significant energy or noise above 1 K Hz, with the Nyquist criteria, a digitizing rate of 2 K Hz was sufficient. The low pass frequency for the analog signals is set as 1 K Hz in all runs of the experiments.

We choose carbon dioxide (CO_2) as tracer of heavy gas, which is with a molecular weight of 44 (1.52 times molecular weight of air). Dispersion experiments were undertaken by continuously releasing heavy gas, carbon dioxide (CO_2) at a controlled flow rate from an elevated point source. Sampling tracer of the heavy gas was carried out for various spilling flow rates and wind barrier downstream distances away from source at different downstream stations. For concentration measurements, tracer gas sampling system was developed. It is composed of 15 sampling tubes that arranged in a rake. The 15 tubes attach to 15 air bags and suck the tracer gas by pumps. In order to obtain sufficient tracer concentration analysis, 5 minutes of sampling time was executed in every downstream station. Mean concentrations of the sampled tracer gas in air bags were obtained by using the analyzer of Cole-Parmer carbon dioxide detector. The detector has the concentration range of 0~100000 ppm with a resolution of 10 ppm.

The solid and porous thin plates of 6 cm high and 180 cm long with sharp leading edge were used as fences. The porosity of the thin plate is 0% (solid) and 26 % (porous).

The experimental arrangement for approaching flow, release of heavy gas, and placement of fence in the wind tunnel is shown in Fig.1.

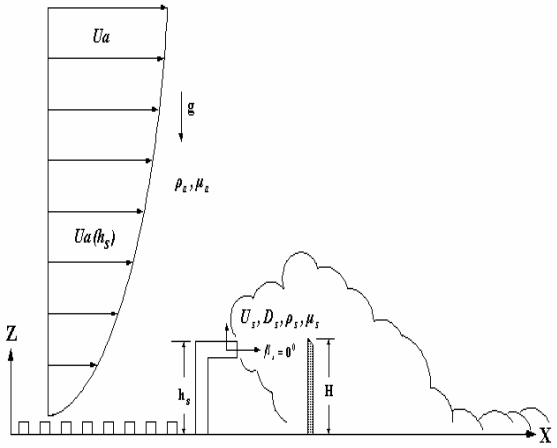

Figure 1. The schematic diagram of the experimental arrangements for releasing heavy gas and fence locating

3. SIMILARITY ANALYSIS OF CONCENTRATION

From fluid flow modelling laws, some similarity requirements have to be performed for transferring small scales of wind tunnel model results to prototype scales. The similarity laws are obtained by dimensional analysis. The sketch of the continuously release of the heavy gas and fence location is shown as in Fig.1. The local heavy gas concentration downstream of the spill source can be expressed as the following function:

$$\frac{C}{C_s} = F_1\left\{\begin{matrix} X, Y, Z, g, h_s, D_s, H, \beta_s, \varphi, U_s, \\ \rho_s, U_a(h_s), n, Z_{ref}, \rho_a, \mu_a \end{matrix}\right\} \quad (1)$$

where cooordinates : X is the downstream direcrion, Y is the lateral direction, and Z is the vertical direction. h_s: elevated height of source; D_s: diameter of source, H: fence height, φ: fence porosity, β_s : heavy gas release angle, *Us*: release velocity of heavy gas, ρ_s :density of spilled heavy gas; $U_a(h_s)$:cross mean wind velocity at the height h_s; n: exponent of power law for approachig flow velocity profile; Z_{ref} :boundary layer thickness; ρ_a :

ambient air density; μ_a :viscosity of the air; C is heavy gas concentration at ($x,y.z$), and C_s is the concentration at source.

After the dimensional analysis, some dimensionless groups were obtained, and equation (1) can be transoformed into the following non-dimensionlized form as shown in eqaution (2).

$$\frac{C}{C_s} = F_2\left\{\begin{matrix}\frac{X}{H},\frac{Y}{H},\frac{Z}{H},\frac{h_s}{H},\beta_s,\varphi,n,\frac{Z_{ref}}{H},\\ \frac{\rho_s}{\rho_a},Fr_s,\frac{U_s^{\Delta}}{U_a(h_s)},\mathrm{Re}_s,\mathrm{Re}\end{matrix}\right\} \qquad (2)$$

where (h_s/H): dimensionless source height; Z_{ref}/D_s : dimensionless boundary layer height; ρ_s/ρ_a : density ratio; where $Fr_s = U_s^{\Delta}/\sqrt{gD_s(\rho_s-\rho_a)/\rho_s}$: densimetric Froude number; $U_s^{\Delta} = U_s - U_a(h_s)\cos\beta_s$:excess velocity; $U_s^{\Delta}/U_a(h_s)$: velocity ratio; $\mathrm{Re}_s = D_s U_s \rho_s/\mu_s$: Reynolds numberof of source; $\mathrm{Re} = L_0 U_0 \rho_a/\mu_a$: Reynold numeber of ambient.

As shown in equation 2, it indicates that the local concentration *C/Cs* in both of the model and prototype is the same at the locations X/D_s, Y/D_s, Z/D_s, provided that all the remaining dimensionless parameters on the right hand side of equation can be matched in the wind tunnel experiments. In the present study, all the parameters are set the same for model and prototype except two parameters, such as: ambient Reynolds number, *Re* and spill source Reynolds number, Re_s. The ambient Reynolds numbers kept exceeding the critical number (10^4) for ensuring flow becomes turbulent in the experiments. A cross wire was placed at the exit of the elevated source to trip the outflow. This is to ensure it become turbulent flow.

The experiments carried out in the present study were run for the following dimensionless parameters which make sure of both safe experimental operating conditions and a variation of the similarity parameters dominating the heavy gas dispersion. Elevated height of source h_s/D_s =0.075; Fence height h_s/H =1; Release angle β_s =0°; Approaching flow profile exponent n=0.27; Density ratio ρ_s/ρ_a =1.52; Densimetric Froude number Fr_s = 8; 14, 20; Velocity ratio $U_s^{\Delta}/U_a(h_s)$ =1, 1.725, 2.464; Ambient Reynolds number $\mathrm{Re} = Z_{ref}U_{ref}\rho_a/\mu_a$ =1.29x10^5; Fence porosity φ=0%, 26 %.

4. RESULTS

4.1. Approaching Flow

The urban terrain type of neutral turbulent boundary layer was generated as the approaching flow. Mean velocity profile of the simulated turbulent boundary layer flow is approximated by the power law shown as equation (3).

$$\frac{U(Z)}{U_{ref}} = \left(\frac{Z}{Z_{ref}}\right)^n \qquad (3)$$

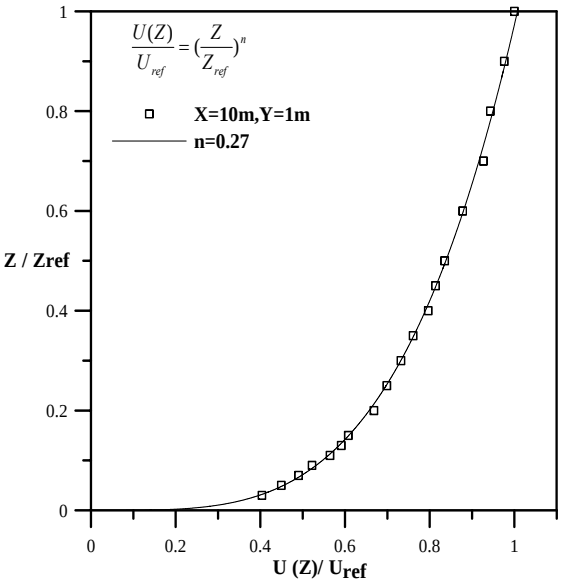

Figure 2. Mean velocity profile of approaching flow

where *U(Z)* is the mean velocity at height of Z , U_{ref} is the free stream velocity, and Z_{ref} is the boundary layer thickness. In the present study, a rural terrain type of neutral atmospheric boundary layer was simulated with a model scale of 1/500. The free stream velocity is U_{ref} =2 m/s; and the boundary layer thickness, Z_{ref} is about 100 cm. The measured mean velocity profile is shown in Figure 2. Results indicate that the power exponent *n* is 0.27. This value lies in the range of 0.23 to 0.40 as proposed by Counihan [10] for the urban terrain type of neural atmospheric boundary layer flow.

The simulated turbulence intensity profile is shown in Figure 3. Here u_{rms} is the root mean square of turbulent velocityy fluctuation. It is seen that the simulated longitudinal turbulence intensity close to the wall is about 23%. Counihan [10] had indicated that the longitudinal turbulence intensity close to the ground-level in the urban terrain areas fell in the range of 20% to 35 %.

The Reynolds stress profile of the simulated approaching flow is shown in Fig.4. Here $\overline{u'w'}$ is the Reynolds stress, and U is the local mean velocity. As seen in the figure, a constant stress layer exists near the ground of the boundary layer. This agrees with the results of field observations reviewed by Counihan [10].

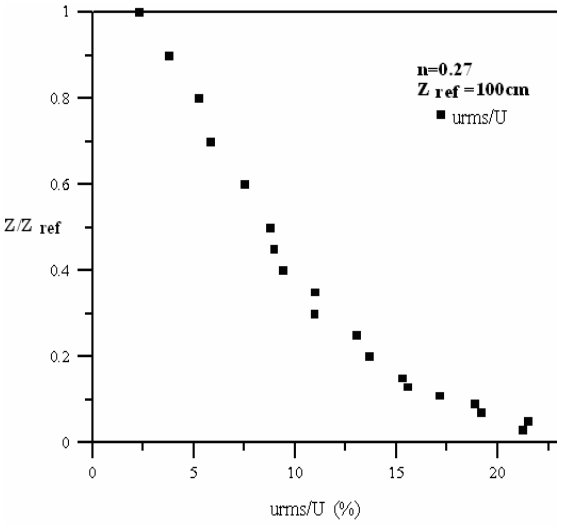

Figure 3. Turbulence intensity profile of approaching flow

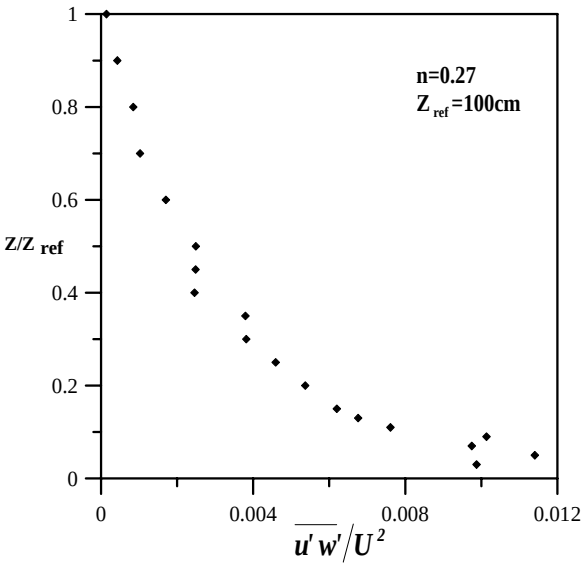

Figure 4. Reynolds stress profile of approaching flow

4.2. Shelter effect of solid fence on the concentration of heavy gas cloud

To examine the solid fence shelter effect on the heavy gas cloud dispersion, we carried out five cases of experiments to measure without and with solid fence located at downstream source distances of X/H=1, 8, 15, and 24. Fig.5 shows the isolines of concentration in x-z plane along the centreline of the heavy gas cloud without and with fence for Fr_s=14. As comparing these figures, it is shown that solid fence significantly deflects the isolines of concentration. The concentration of heavy gas cloud accumulates behind the fence due to the shelter effect of the solid fence. The accumulated concentration of the heavy gas cloud becomes higher when the fence is located as closer as to the source. The shelter effect is not significant when fence located at a far downstream distance, like X/H=24.

Vertical concentration profiles of the heavy gas cloud along the downstream distance for without and with solid fence located behind the source of X/H=8 are shown in Fig.6. The fence shelter effect on the change of concentration profiles are pronounced especially for the profiles of the location ahead of the fence.

The function of maximum value of vertical concentration profile in each downstream station versus the downstream distance of the source for different locations of solid fence are plotted and shown in Fig.7. Results reveal that at X/H=10, the maximum concentration reduces 40% and 20% of concentration with no fence for fence located at X/H=1 and X/H=8, respectively.

Ground-level concentration decay with the downstream distance for solid fence located at different downstream distances of the source is shown in Fig.8. To estimate the dangerous reach of the hazardous heavy gas cloud, Schatzmann [2] has proposed two parameters, Lower Flammability Concentration (LFC) and Lower Flammability Distance (LFD). Here we define LFC as C/Cs=0.1%, and LFD is defined as the distance from the source within which ignitable gas concentrations (i.e. LFC) occur. Fig.8 exhibits that ground-level concentration is less than LFC for X/H>20 as the fence located at X/H=1 downstream of the source. When the solid fence is located at a distance of X/H=8 behind the source, the ground-level concentrations at all downstream distances of source are lower than LFC. The ground-level concentration is less than LFC for X/H>12 and 20 as the fence located at X/H=15, and 24 downstream of the source, respectively.

Results of Fig.8 also exhibit that the closer the fence is to the source, the shorter the LFD becomes. It is noted that when the fence is put at a moderate distances from the source, like X/H=8, 15, the ground-level concentrations of these cases are all lower than the LFC.

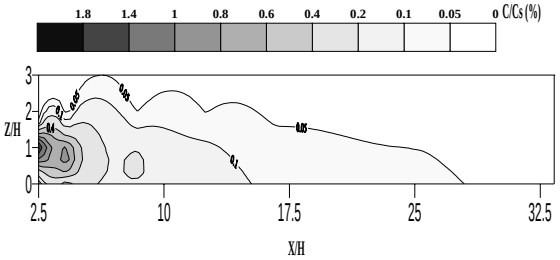

(a) without fence

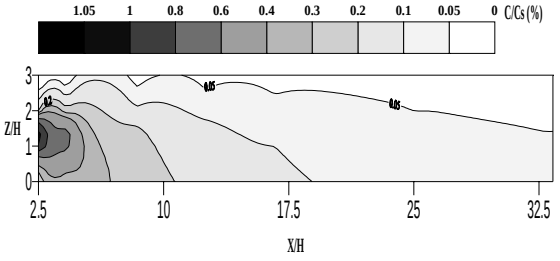

(b) solid fence set at X/H=1

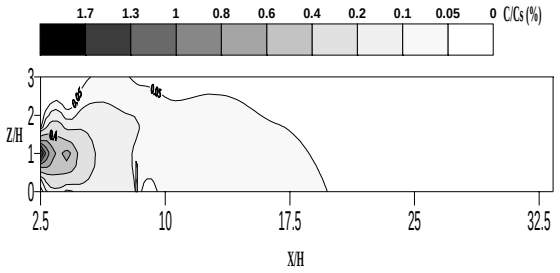

(c) solid fence set at X/H=8

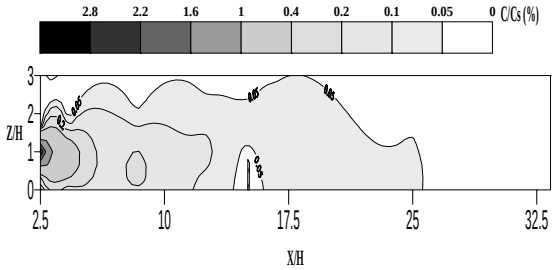

(d) solid fence set at X/H=15

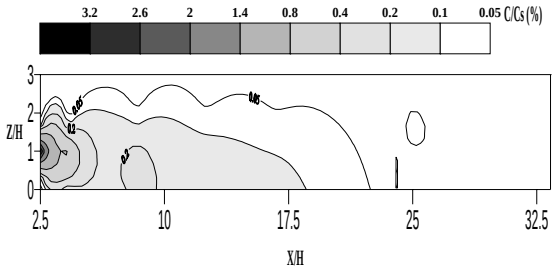

(e) solid fence set at X/H=24

Figure 5. Isolines of concentration in x-z plane along the centreline of the heavy gas cloud; Fr_s=14 . (a) without fence, (b) solid fence set at X/H=1 downstream of the elevated source, (c) solid fence set at X/H=8 downstream of the elevated source, (d) solid fence set at X/H=15 downstream of the elevated source, (e) solid fence set at X/H=24 downstream of the elevated source

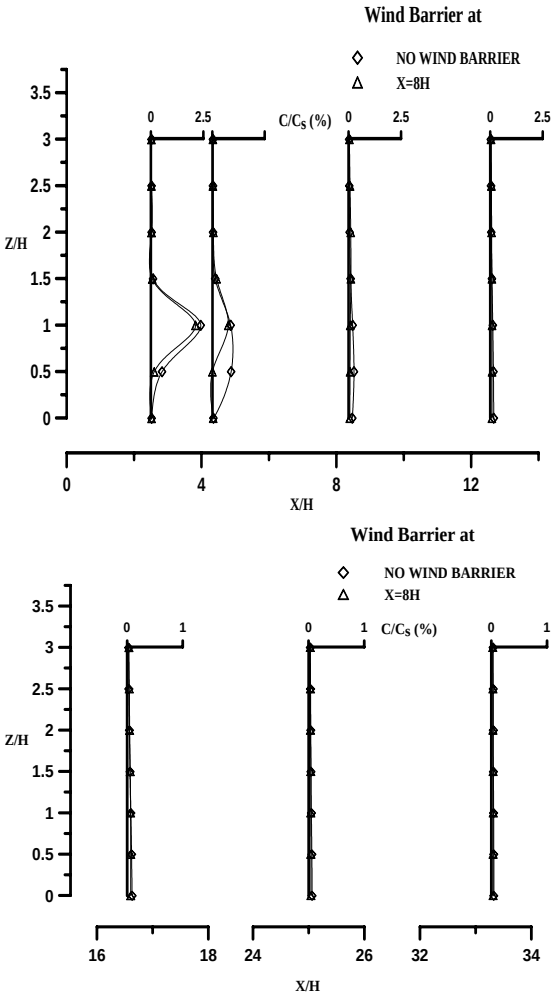

Figure 6. Vertical concentration profiles of the heavy gas cloud along the downstream distance; y/H=0, Fr_s=14 .

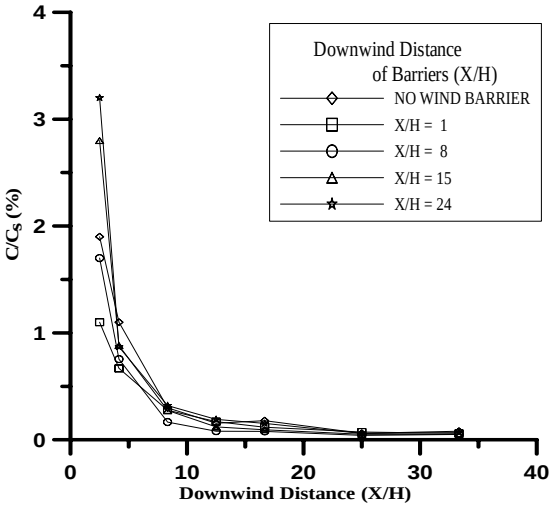

Figure 7. Maximum concentrations decay with the downstream distance for solid fence located at different downstream distances of the elevated source

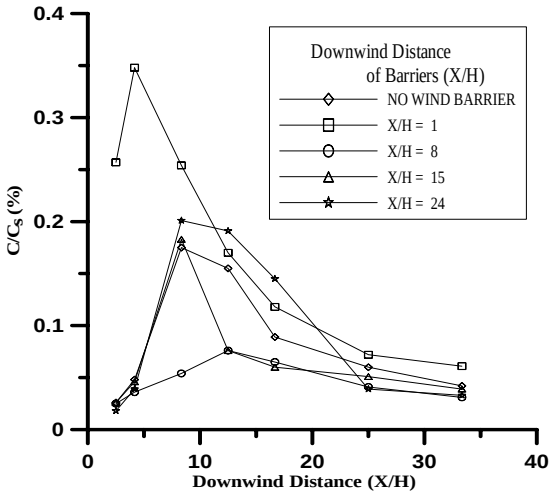

Figure 8. Ground-level concentration versus the downstream distance as a function of solid fence location

4.3. Densimetric Froude number on the variation of concentration

In practical cases, accidental release of heavy gas may happen in different release velocities, flow rates, or source diameters. To probe all of these variables effect on dispersion of heavy gas cloud, the densimetric Froude number as seen in equation (2) is an appropriate scaling dimensionless parameter to account for all of these variables.

Fig.9 is the function of maximum value of vertical concentration profile in each downstream station versus the downstream distance of the solid fence for different densimetric Froude numbers. Here the solid fence was located at X/H=1. For lower value of densimetric Froude number (eg. Fr_s =8), the maximum concentration is shown to be smaller than that of for higher value of densimetric Froude number (eg. Fr_s =14, Fr_s =20). But the maximum concentrations seem to be a small difference for higher value of densimetric Froude number from Fr_s =14 to Fr_s =20.

The estimation of the influence reach for heavy gas cloud can be inferred from the ground-level concentration. LFC and LFD adopted in the present study is followed the definition proposed by Schatzmann [2]. Fig.10 shows the results of the ground-level concentration versus the downstream distance for solid fence located at different downstream distances of the source. Shown is the fence located at X/H=1. Results indicate that LFD becomes longer as increasing Fr_s. It appears that LFD shows no dramatic increase when increasing the densimetric Froude number from Fr_s =14 to Fr_s =20.

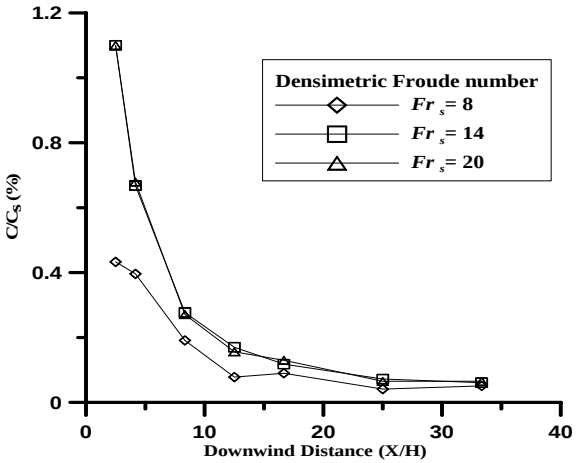

Figure 9. Maximum concentrations decay with the downstream distance for different densimetric Froude numbers; solid fence located at X/H=1 downstream of the elevated source

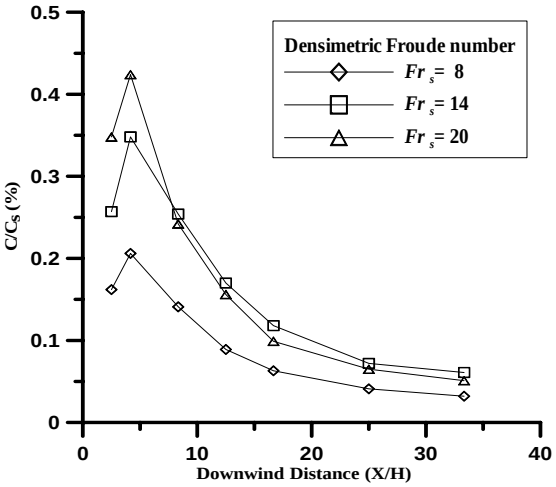

Figure 10. Ground-level concentration variation along the downstream distance as a function of densimetric Froude number; solid fence located at X/H=1 downstream of the elevated source

4.4. Fence porosity effect on the variation of concentration

The isolines of concentration in x-z plane along the centreline of the heavy gas cloud for different porosity of the fence are shown in Fig.11. Shown is the fence located at X/H=8.

The vertical concentration profiles along the downstream distance of source for different fence porosities are plotted in Fig.12. Here the fence are located at X=8H downstream of the source. A change of the fence porosity from 0% (solid) to 26% appeared to have no significant variation on the vertical concentration profiles for the distance X/H>8 downstream of the source.

The maximum concentration as a function of downstream distance for various fence porosities is shown in Fig.13. Here the fence is located at X/H=8,

and Fr_s=14. In the leeward side of the fence (i.e. X/H>8), the difference of the maximum concentration is slightly as changing of the fence porosity.

The ground-level concentration along the downstream distance for various fence porosities is plotted in Fig.14. Here the fence is placed at X/H=8 and Fr_s=14. Results reveal that the ground-level concentration value has a great decrease as the fence porosity reduces. In Fig.14, the ground-level concentration along the downstream distance for no fence is also shown for comparison. The ground-level concentration of fence porosity 26% (fence is placed at X/H=8), is larger than that of without fence existing for the distance X/H>8 downstream of the source. In the meanwhile, the ground-level concentration of solid fence (porosity = 0%, fence is placed at X/H=8), is smaller than that of no fence existing for the downstream distance X/H>8.

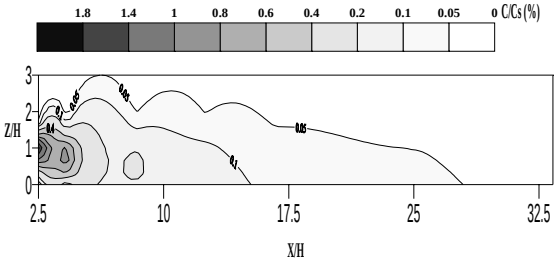

(a) without fence

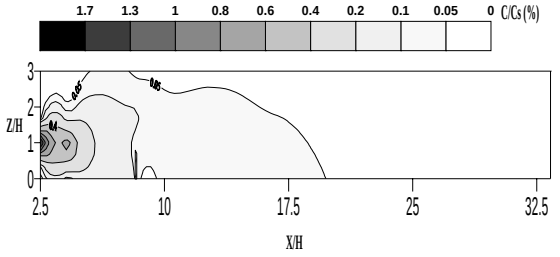

(b) Porosity 0%

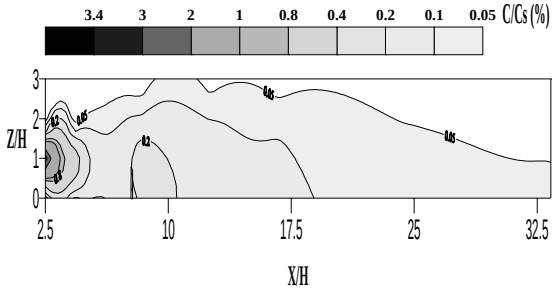

(c) Porosity 26%

Figure 11. Isolines of concentration in x-z plane along the centreline of the heavy gas cloud; Fr_s=14 . (a) without fence, (b) fence porosity 0 % and located at X/H=8 downstream of elevated source, (c) fence porosity 26 % and located at X/H=8 downstream of elevated source

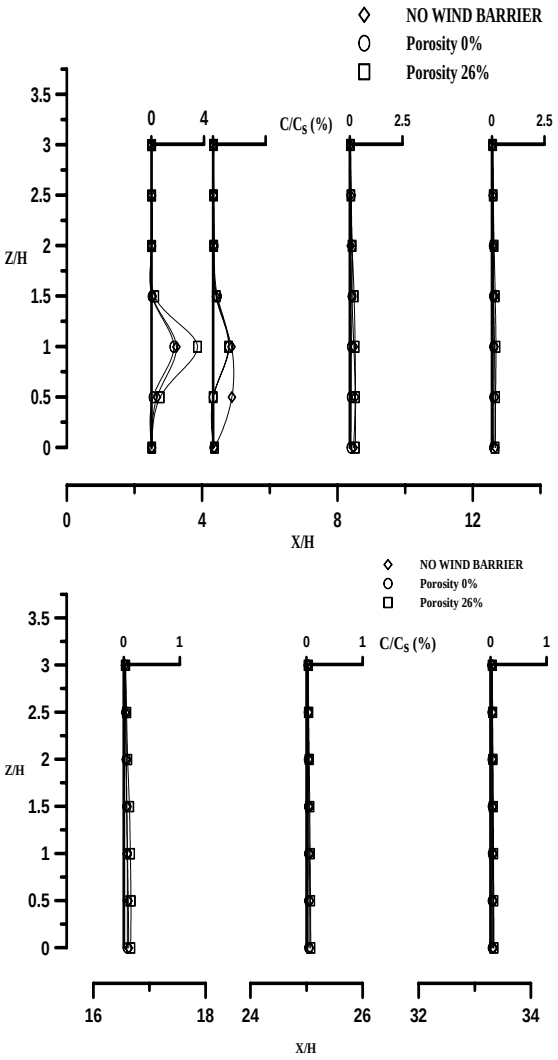

Figure 12. Vertical concentration profiles of the heavy gas cloud along the downstream distance for different fence porosity; y/H=0, Fr_s=14

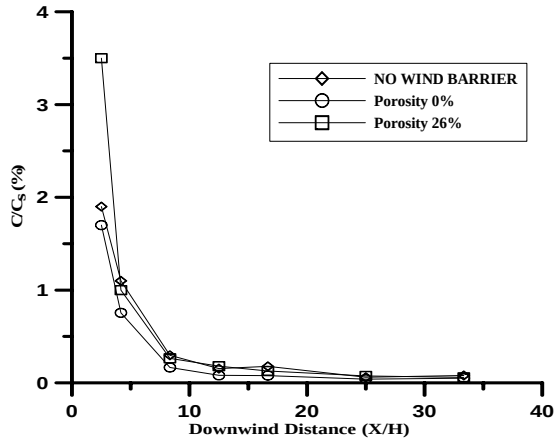

Figure 13. Maximum concentration as a function of downstream distance for various fence porosities; fence located at X/H=8 downstream of the elevated source and Fr_s=14

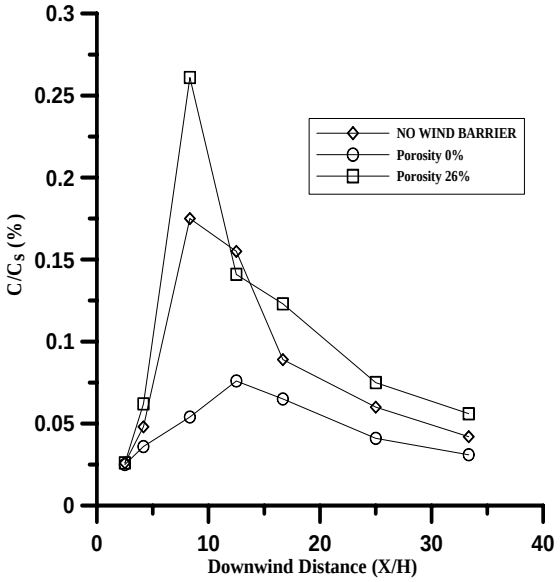

Figure 14. Ground-level concentration versus the downstream distance as a function of fence porosities; wind barrier located at X/H=8 downstream of the source and Fr_s=14

5. CONCLUSION

Study of the fence shelter effects on the dispersion of horizontally continuous release of heavy gas (carbon dioxide) from an elevated source were carried out in wind tunnel. The scaled rural terrain type of neutral atmospheric turbulent boundary layer flow was properly simulated and used as the approaching flow. Measured results show that fence was set at where the location closer to the elevated source, it could creat a better shelter effect for reducing heavy gas concentration. The ground-level concentration along the downstream distance in the leeside of the fence comes to a larger value as increasing the released heavy gas densemetric Froude number. When the fence porosity reduces, the ground-level concentration along the downstream distance behind the fence decreases.

ACKNOWLEDGEMENTS

The authors express their thanks for the partial financial support of the National Science Council, Taiwan under the grant NSC93-2611-E019-001.

REFERENCES

[1] Schatzmann, M., 1993, ”Experiments with Heavy Gas Jets in Laminar and Turbulent Cross-Flows”, *Atmospheric Environment*, Vol. 27A, pp. 1105-1116.

[2] Schatzmann, M., 1995, ”Accidental Release of Heavy Gases in Urban Areas”, *Wind Climate in Cities, Cermak, J.E., et al. (Eds.)*, pp. 555-574.

[3] Britter, R.E., 1989, ”Atmospheric Dispersion of Dense Gases,” *Annual Review of Fluid Mechancis*, Vol.21, pp.317-344.

[4] Robins, A., Castro, I., Hayden, P., Steggel, N., Contini, D., and Heist, D., 2001, ”A Wind Tunnel Study of Dense Gas Dispersionin a Neutral Boundary Layer over a Rough Surface,” *Atmospheric Environment*, Vol.35, pp. 2243-2252.

[5] Zhu, G., Arya, S.P., and Snyder, W.H., 1998, ”An Experimental Study of the Flow Structure within a Dense Gas Plume,” *Journal of Hazardous Materials*, Vol.62, pp. 161-186.

[6] Donat, J. And Schatzmann, M., 1999, ”Wind Tunnel Experiments of Single-phase Heavy Gas Jets Released under Various Angles into Turbulent Cross Flows”, *Journal of Wind Engineering and Industrial Aerodynamics*, Vol. 83, pp. 361-370.

[7] Nielsen, M., Ott, S., Jorgensen, H.E., Bengtsson, R., Nyren, K., Winter, S., Ride, D., and Jones, C. 1997, ”Field Experiments with Dispersion of Pressure Liquefied Ammonia”, *Journal of Hazardous Materials*, Vol. 56, pp. 59-105.

[8] Khan, F. and Abbasi, S.A., 2000, ”Modeling and Simulation of Heavy Gas Dispersion on the Basis of Modification in Plume Path Theory”, *Journal of Hazardous Materials*, Vol. 80, pp. 15-30.

[9] Duijm, N. J, Carssimo, B., Mercer, A., Bartholome, C., and Giesbrecht, H., 1997, “Development and Test of an Evaluation Protocol for Heavy Gas Dispersion Models”, *Journal of Hazardous Materials*, Vol. 56, pp. 273-285.

[10] Counihan, J., 1975, ”Adiabatic Atmospheric Boundary Layers: A Review and Analysis of the Data from the Period 1880-1972”, *Atmospheric Environment*, Vol. 9, pp. 871-905.

Conference on Modelling Fluid Flow (CMFF'06)
The 13th International Conference on Fluid Flow Technologies
Budapest, Hungary, September 6-9, 2006

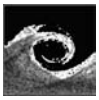

NUMERICAL AND EXPERIMENTAL INVESTIGATION OF WIND INDUCED PRESSURES ON A TALL BUILDING IN BUCHAREST

Andrei GEORGESCU[1], Liviu HASEGAN[2], Costin COSOIU[3], Mircea DEGERATU[4], Lucian SANDU[5]

[1] Corresponding Author. Hydraulic and Environmental Protection Department, Technical University of Civil Engineering Bucharest. Blvd. Lacul Tei 124, sect. 2, 020396 Bucharest, Romania. Tel.: +40 21 243 3660, Fax: +40 21 243 3660, E-mail: andreig@hidraulica.utcb.ro
[2] Hydraulic and Environmental Protection Department, Technical University of Civil Engineering Bucharest. E-mail: hasegan@hidraulica.utcb.ro
[3] Hydraulic and Environmental Protection Department, Technical University of Civil Engineering Bucharest. E-mail: costin@hidraulica.utcb.ro
[4] Hydraulic and Environmental Protection Department, Technical University of Civil Engineering Bucharest. E-mail: mircead@hidraulica.utcb.ro
[5] Hydraulic and Environmental Protection Department, Technical University of Civil Engineering Bucharest. E-mail: slucian@hidraulica.utcb.ro

ABSTRACT

In the last few years the number of tall buildings constructed in Bucharest has increased dramatically. New buildings have lighter and more flexible structures and their envelopes are more continuous and fragile, easily damageable by winds. In this respect, the civil engineers became more attentive and began to demand wind engineering tests on the buildings when the envelope shape is more complicated. Our laboratory performed numerical and experimental tests for a 110 *m* tall building that is to be erected in the suburban area. Numerical tests were performed using the FLUENT CFD code while experimental ones were conducted on a 1/100 model of the building in our boundary layer wind tunnel. Both numerical and experimental investigations aimed at the determination of wind loads on the envelope (which is important for the determination of the way in which the envelope will be anchored on the structure) as well as on the quasi-steady forces induced by wind on the structure. At the express demand of the civil engineers, forces were calculated for all the tested wind directions with respect to the axes of the building. The results of the experimental investigation are in good agreement with the results obtained by numerical modelling.

Keywords: boundary layer wind tunnel, CFD, quasi-steady forces induced by wind, wind engineering

NOMENCLATURE

A	$[m^2]$	area assigned to a pressure value
A_C	$[m^2]$	characteristic area of the building
A_x	$[m^2]$	projection of A on the yOz plane
A_y	$[m^2]$	projection of A on the xOz plane
A_z	$[m^2]$	projection of A on the xOy plane
C	[-]	force coefficient
C_M	[-]	moment coefficient
C_p	[-]	local pressure coefficient
F_x	$[N]$	force along the Ox axis
F_y	$[N]$	force along the Oy axis
F_z	$[N]$	force along the Oz axis
h	$[m]$	height above the ground
M_x	$[Nm]$	moment around the Ox axis
M_y	$[Nm]$	moment around the Oy axis
M_z	$[Nm]$	moment around the Oz axis
TI	[-]	turbulent intensity
U	$[m/s]$	velocity
U_{10}	$[m/s]$	standard velocity at 10 m above the ground
l_C	$[m]$	characteristic length
p	$[Pa]$	local pressure on model
x	$[m]$	coordinate along the Ox axis
y	$[m]$	coordinate along the Oy axis
z	$[m]$	coordinate along the Oz axis
α	[−]	power law coefficient
ρ	$[kg/m^3]$	air density
θ	$[grd]$	angle between wind direction and the Ox axis of the building

Subscripts and Superscripts

i	denotes discrete values
max	maximal value
M, N	on the model, in nature
ref	reference
t	total
x, y, z	related to the coordinates of the building

1. INTRODUCTION

In the last few years the number of tall buildings constructed in Bucharest has increased. New buildings have lighter and more flexible structures and their envelopes are more continuous and fragile, easily damageable by winds. In this respect, the civil engineers became more attentive (although in our country the main loads are supposed to be induced by earthquakes) and began to demand wind engineering tests on the buildings when the envelope shape is more complicated. Our laboratory performed numerical and experimental tests for a 110 *m* tall building with a metallic structure that is to be erected in the suburban area of the town.

Numerical tests are cost effective and relatively easier to perform than experimental ones, which are difficult and expensive. The disadvantage of numerical tests is that they have to be validated by experimental measurements in order to ascertain their accuracy. That is the main reason why the approach used in our study comprises both numerical and experimental tests. Wind tunnel tests allowed to validate the numerical model, which is used in the sequel, to yield more complete results (i.e. greater number of discrete values). The numerical model was also used to compute results for different conditions than the initial experimental ones.

Numerical tests were performed using the FLUENT v.6.02 Computational Fluid Dynamics (CFD) code, while experimental ones were conducted on a 1/100 model of the building in our Boundary Layer Wind Tunnel (BLWT). Both numerical and experimental investigations aimed at the determination of wind loads on the envelope (which is important for the determination of the way in which the envelope will be anchored to the structure), as well as on the quasi-steady forces induced by wind on the structure.

At the express demand of the civil engineers, forces were calculated for all the tested wind directions with respect to the axes of the building (standard values are usually calculated with respect to the wind direction [1]). The results of the experimental investigation are in good agreement with the results obtained by numerical modelling.

2. EQUATIONS OVERVIEW

Both experimental and numerical tests aimed primarily at determining discrete local pressure ($p_{i,M}$) distributions on the models.

Experiments were performed in each of the studied cases for 8 wind directions (i.e. North, North-East, East, South-East, South, South-West, West and North-West) and results were all reduced with respect to the axes of the building. The relationship between wind directions and building axes is presented in Figure 1.

The shape of the envelope, axes and positive directions of forces and moments are presented in Figure 2.

The building consists of 2 major parts (see Fig. 2): the base part that is strongly developed in the horizontal plane but has a reduced height, and the tower that is slim and tall, asymmetrically positioned on the base part.

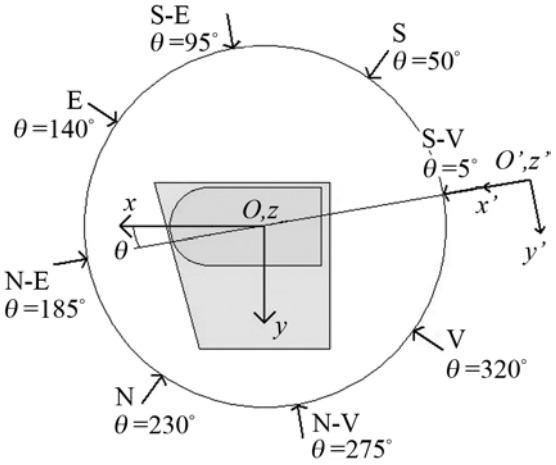

Figure 1. Relation between wind directions and building axes

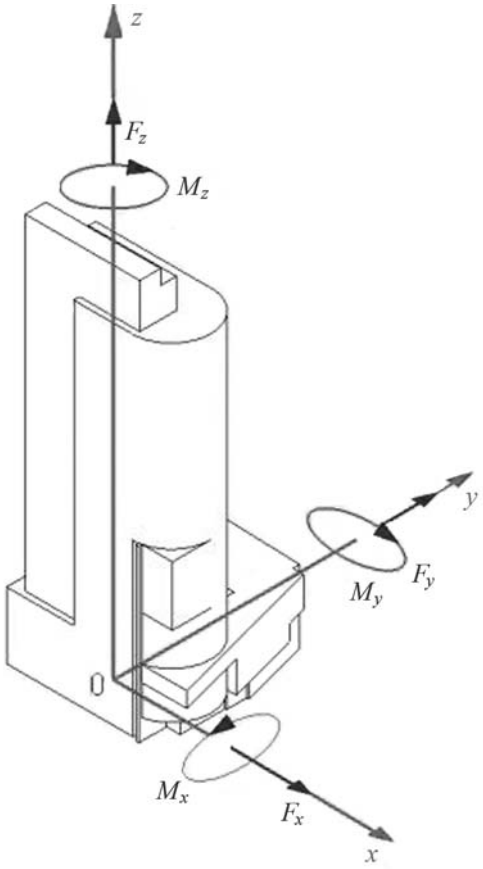

Figure 2. Axes system of the modelled building and positive directions for forces and moments

Local pressure coefficients were computed as:

$$C_{p_i} = \frac{p_{i,\mathrm{M}} - p_{ref,\mathrm{M}}}{\frac{\rho U_{\mathrm{ref,M}}^2}{2}} \quad (1)$$

Reference values on the experimental model were chosen at 0.94 *m* above the bottom of the BLWT.

From those values of the local coefficients, civil engineers can compute values of the pressures exerted on the real building in the same analogous points where the pressure coefficients are defined, with the following equation:

$$p_{i,\mathrm{N}} = C_{p_i} \frac{\rho U_{\mathrm{ref,N}}^2}{2} \quad (2)$$

Reference velocity values in nature can be computed form the standard velocity at 10 *m* above the ground, provided by the Romanian National Meteorological Institute, by taking into account the power law mean velocity profile of the suburban area [2] and the corresponding reference height (i.e. 94 *m* above the ground), with the following equation:

$$U_{\mathrm{ref,N}} = U_{10,\mathrm{N}} \left(\frac{z_{\mathrm{ref,N}}}{10} \right)^{\alpha} \quad (3)$$

A specific area from the lateral surface of the envelope was allocated to each point with available pressure values. The areas were projected on normal planes formed by the axes of the building (e.g. the projection of the area $A_{i,\mathrm{M}}$ on the plane formed by the O*z* and *Oy* axes will be denoted $A_{x_{i,\mathrm{M}}}$ in the sequel) by taking into account the angle formed between the axis and the normal direction to the surface .

With this notations, global force coefficients on the entire building were calculated with the following equation:

$$\begin{cases} C_x = \frac{1}{A_{\mathrm{C,M}}} \sum_i C_{p_i} \cdot A_{x_{i,\mathrm{M}}} \\ C_y = \frac{1}{A_{\mathrm{C,M}}} \sum_i C_{p_i} \cdot A_{y_{i,\mathrm{M}}} \\ C_z = \frac{1}{A_{\mathrm{C,M}}} \sum_i C_{p_i} \cdot A_{z_{i,\mathrm{M}}} \end{cases} \quad (4)$$

In Eqs. 4 to 7, A_{C} represents a reference area (in our study it is the horizontal cross-section of the tower) and l_{C} represents a reference length (in our case the height of the building). The values corresponding to the experimental model are used to determine coefficients while values in nature are used in the sequel to compute forces and moments on the building. Global moment coefficients with respect to the axes of the building were computed with the following equation:

$$\begin{cases} C_{M_x} = \frac{1}{A_{\mathrm{C,M}} l_{\mathrm{C,M}}} \sum_i C_{p_i} \left(A_{y_{i,\mathrm{M}}} z_{i,\mathrm{M}} - A_{z_{i,\mathrm{M}}} y_{i,\mathrm{M}} \right) \\ C_{M_y} = \frac{1}{A_{\mathrm{C,M}} l_{\mathrm{C,M}}} \sum_i C_{p_i} \left(A_{z_{i,\mathrm{M}}} x_{i,\mathrm{M}} - A_{x_{i,\mathrm{M}}} z_{i,\mathrm{M}} \right) \\ C_{M_z} = \frac{1}{A_{\mathrm{C,M}} l_{\mathrm{C,M}}} \sum_i C_{p_i} \left(A_{x_{i,\mathrm{M}}} y_{i,\mathrm{M}} - A_{y_{i,\mathrm{M}}} x_{i,\mathrm{M}} \right) \end{cases} \quad (5)$$

With those values of the global coefficients, civil engineers can compute forces exerted on the real building with the following equation:

$$\begin{cases} F_{x\mathrm{N}} = C_x \frac{\rho U_{\mathrm{ref,N}}^2}{2} A_{\mathrm{C,N}} \\ F_{y\mathrm{N}} = C_y \frac{\rho U_{\mathrm{ref,N}}^2}{2} A_{\mathrm{C,N}} \\ F_{z\mathrm{N}} = C_z \frac{\rho U_{\mathrm{ref,N}}^2}{2} A_{\mathrm{C,N}} \end{cases} \quad (6)$$

The global moment coefficients acting around the building axes are computed with the following equation:

$$\begin{cases} M_{x\mathrm{N}} = C_{M_x} \frac{\rho U_{\mathrm{ref,N}}^2}{2} A_{\mathrm{C,N}} \cdot l_{\mathrm{C,N}} \\ M_{y\mathrm{N}} = C_{M_y} \frac{\rho U_{\mathrm{ref,N}}^2}{2} A_{\mathrm{C,N}} \cdot l_{\mathrm{C,N}} \\ M_{z\mathrm{N}} = C_{M_z} \frac{\rho U_{\mathrm{ref,N}}^2}{2} A_{\mathrm{C,N}} \cdot l_{\mathrm{C,N}} \end{cases} \quad (7)$$

3. EXPERIMENTAL SETUP

The BLWT used for the experiments is 27 *m* long, with a cross section of 1.80 $m \times 1.80$ *m*. It is an opened circuit wind tunnel in which air flow is obtained with a fan, driven by a 75 *kW* electric engine with adjustable rotation speed (continuous from 0 to 100%) [3].

This facility is different from wind tunnels used in aerodynamics. The length of the BLWT is imposed by the natural development, in the experimental zone, of a boundary layer similar to the atmospheric one. Aerodynamic wind tunnels are built with the purpose of achieving a constant velocity distribution in the experimental zone.

On the bottom of the BLWT we have disposed concrete bricks in order to obtain the desired roughness needed for the suburban mean velocity profile [4]. Velocity measurements for the calibration of the BLWT were performed with a T.S.I. thermo anemometer, and digitized at a 100 *Hz* frequency [5]. The α coefficient obtained for the power law describing the best fit (in the least

squares sense) on the experimental velocity data was of 0.23 (see Figure 3.a – the continuous curve), which is a normal value for the suburban area [2] in which the modelled building will be erected.

The Reynolds number computed with the reference velocity and the reference height (94 *m* above the ground in nature, i.e. 0.94 *m* above the bottom of the BLWT in our study) was of about 7.8 10^5, which insures the auto modelling with respect to that criteria.

The turbulent intensity *TI* profile variation with height was also computed and is presented in Figure 3.b.

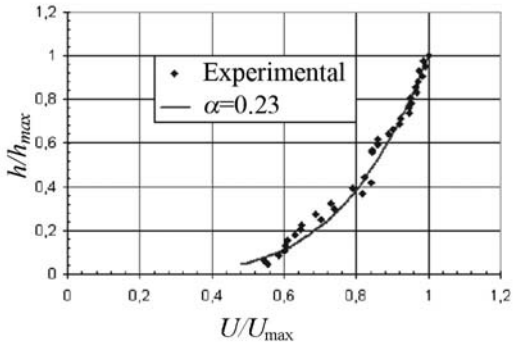

a.

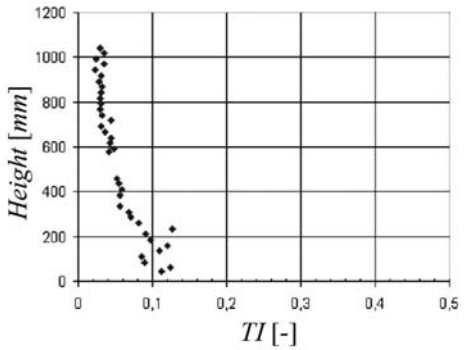

b.

Figure 3. Mean velocity profile (a) and turbulent intensity profile (b) used in the experimental investigation

The model of the building was built in Plexiglas. The length scale of 1/100 was chosen so that the model would not produce significant blockage in the experimental zone of the BLWT.

On the model, 114 pressure taps were placed on the tower and none on the base part although this part was also modelled in order to ensure a similar flow around the tower (see Figure 4). We considered that for the experimental model, the base part is not that important due on one hand to it's small height and on the other to the relatively small wind velocities appearing near the ground. The tower proved enough for the calibration of the complete numerical model that took also into consideration the base part.

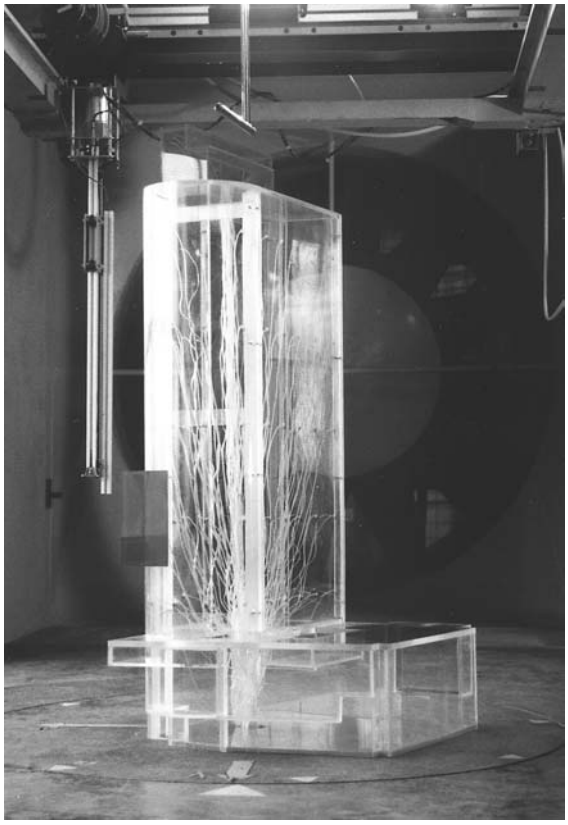

Figure 4. Experimental model in the BLWT

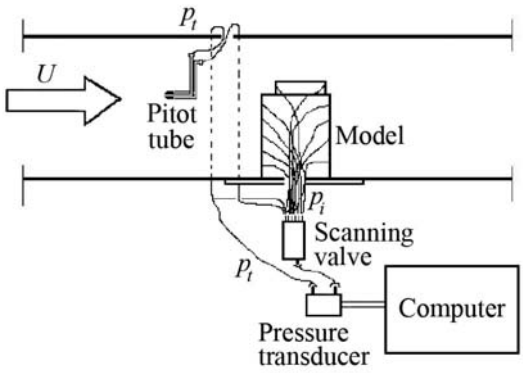

Figure 5. The experimental setup

Pressure taps were 0.6 *mm* in diameter and were divided into 3 groups that lead pressure values to the 48 gates scanning valve used during the experiments (i.e. 3 passes of the scanning valve were needed for each studied wind direction) Pressure measurements were performed with an AutoTran Model 600D-011 differential pressure transducer with the measuring range between 0 and 256 *Pa*. Two of the gates of the scanning valve were reserved to the Pitot tube situated in front of

the model. As the tunnel is on the suction side of the fan, pressures measured on the building were connected to the low pressure tap of the transducer, while the high pressure tap was connected to the total pressure tap of the Pitot tube p_t (see Figure 5).

The pressures measured on the model were acquired via an acquisition board directly into a computer. Pressure, force and moment coefficients were computed in an M.S. Excel spread sheet and the results were presented with the use of the MATLAB code that permits similar representations to the ones given by the FLUENT code [6].

4. NUMERICAL SETUP

For the numerical modelling we used the FLUENT v.6.0.12 CFD code. The building was modelled at its natural geometrical size. The mesh was generated using the GAMBIT v. 2.0.4 code that is part of the FLUENT CFD code.

The flow domain was considered rectangular, 600 *m* long, 200 *m* wide and 200 *m* high. The origin of the axis system of the building was placed in the flow domain, at 200 *m* from the inlet. We used tetrahedral elements with different sizes varying from 2.5 *m* (near the building) up to 10 *m* (on the boundaries of the flow domain). The sizes of the elements were computed by the program and the matrix associated to the flow domain resulted of 300000 elements, which is a suitable size for our computational capabilities (see Figure 6).

The inlet into the flow domain is a square vertical surface positioned relatively close to the building. Velocity distribution is considered constant along the *Oy* model axis, while it varies along the *Oz* axis as a Davenport mean velocity profile (see Fig. 6) [7].

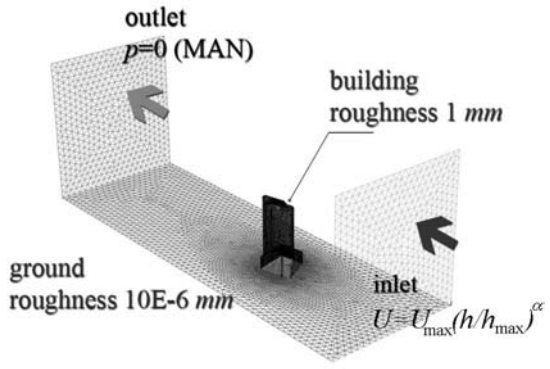

Figure 6. The numerical model with boundary conditions

The outlet of the flow domain is also a square vertical surface positioned farther to the building than the inlet. It has a boundary condition of zero gage scale pressure.

The bottom of the flow domain is a rigid wall, which doesn't permit mass or energy transfer. The roughness of this surface was set to 10^{-6} *mm*. Such an extremely small value is due to the fact that the velocity distribution at the inlet must not be altered by the roughness. Using this approach we were able to reduce the distance between the inlet and the building and subsequently to magnify the distance between the building and the outlet. This allowed us to observe boundary layer separation on the obstacle without increasing the flow domain and the number of cells used in the computations.

On the lateral and upper sides, the flow regime is bounded by walls permeable to mass and energy, which represent in fact an infinite space [8].

The turbulence model used with this numerical model was the k-ε standard model implemented in FLUENT, as long as we were not interested in temporal pressure fluctuations.

Numerical tests were firstly performed for the same mean velocity profile as the one used in experimental modelling. The results were compared (for the tower) to the experimental ones and the numerical model proved to yield consistent results. The values obtained on the numerical model (more numerous than the experimental ones and distributed over the whole surface of the building, tower as well as base part) were then processed in order to obtain the force and moment coefficients, we presented to the beneficiaries of the study.

Additional tests were also performed for the case in which the configuration of the surrounding buildings will change in the near future. In this respect the inlet velocity profile was changed in order to meet the values corresponding to the city centre [7].

5. RESULTS

In order to give a global image of the pressures acting on the envelope, pressure coefficients obtained experimentally were mapped on a 3D representation of the tower. As there were no pressure taps on the horizontal part of the roof, all the values corresponding to the nodes in that area were set to 0 and interpolation between successive values was only performed between adjacent horizontal nodes. The results for wind blowing from the N-E (which is the dominant wind direction for Bucharest) are presented in Figure 7.

Pressure coefficients obtained numerically on the complete model of the building are presented in Figure 8 for wind blowing from the N-E.

The differences that may appear between Figs. 7 and 8 are due, on one hand, to a different perspective view applied by FLUENT to the 3D numerical model and on the other, to the differences that exist between FLUENT and MATLAB in the way colours are interpolated between values.

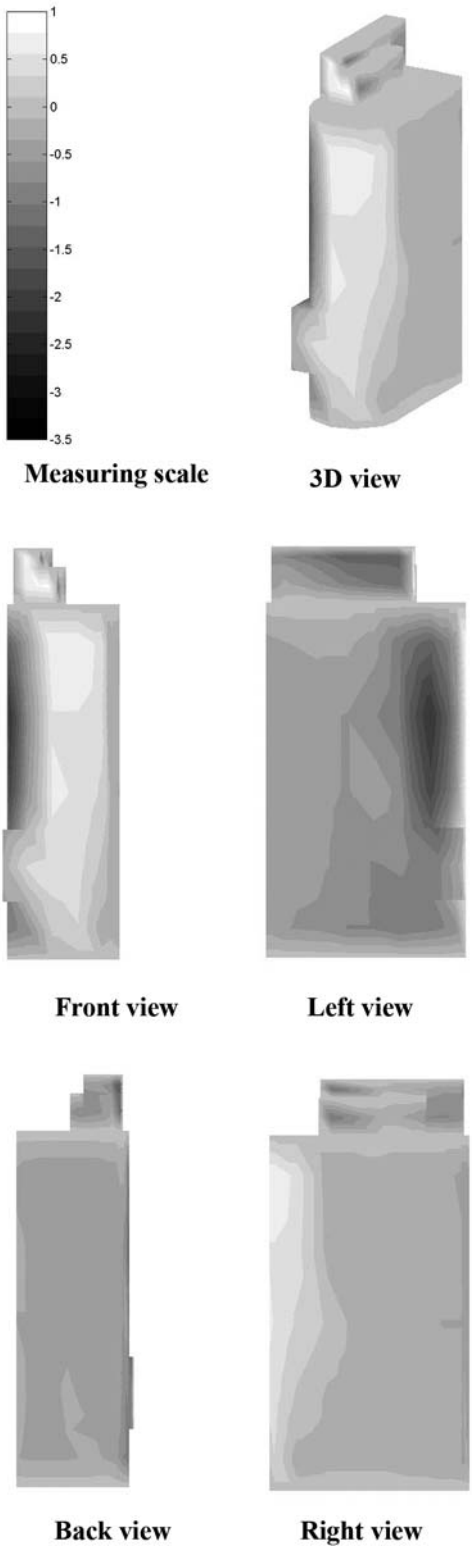

Figure 7. Experimentally obtained values of the pressure coefficients for the N-E wind direction

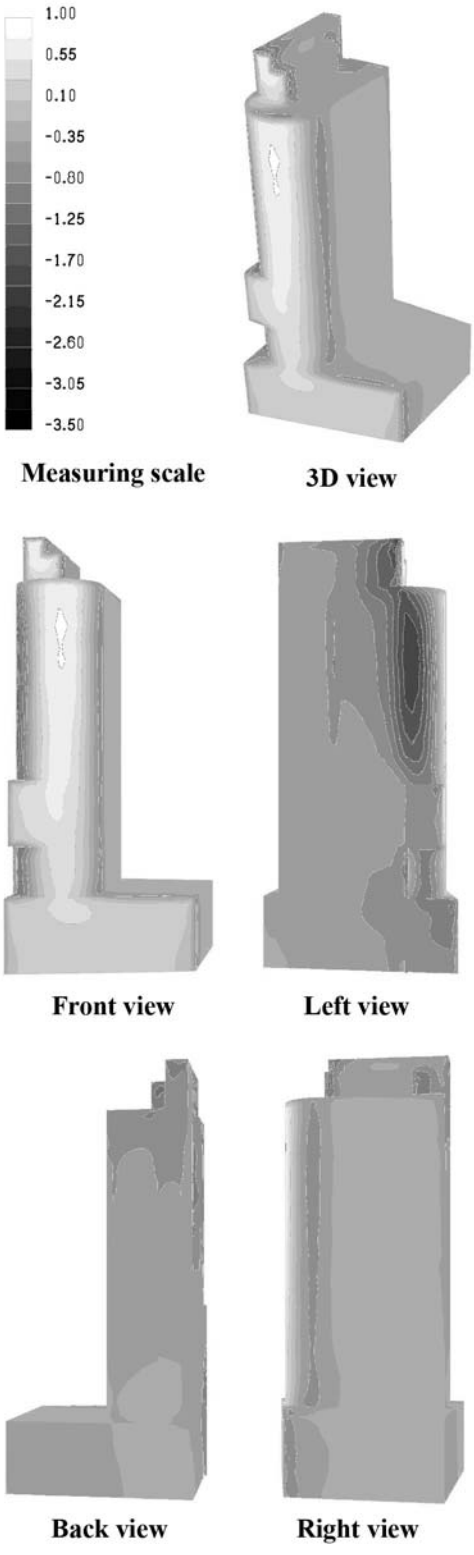

Figure 8. Numerically obtained values of the pressure coefficients for N-E wind direction

For this paper we were obliged to perform manual changes of colours in order to be able to match the same palette on both MATLAB and FLUENT representations.

As already mentioned above, the general rule is that for the experimental results (where the number of discrete values is relatively small with respect to the ones obtained in FLUENT) the interpolation is less accurate between adjacent values.

That is why the results computed with MATLAB present more ample zones of high as well as low pressures in comparison with the relatively sharper ones obtained from FLUENT.

In Figure 9.a, we present the variation of force coefficients. In Figure 9.b we present the variation of moment coefficients with respect to the studied wind directions.

Forces on the *Oz* axis of the building were very small and thus were not plotted in Fig. 9.a.

Pressure, force and moment coefficients have significant values for this building, especially C_y, which is important for the cross-section structural design.

Values of the moment coefficients (C_{M_x} and C_{M_y}) are relatively high, especially C_{M_x}, which is important for the dimensioning of structural elements of the building.

In spite of the asymmetry of the tower, its shape leads to a relatively constant torque (C_{M_z} has moderately high values) with respect to all studied wind directions.

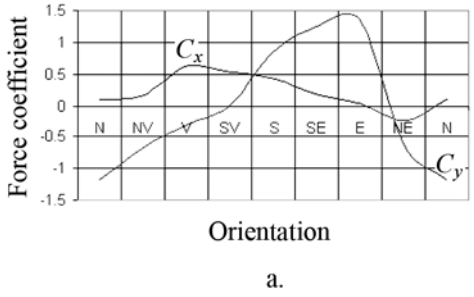

a.

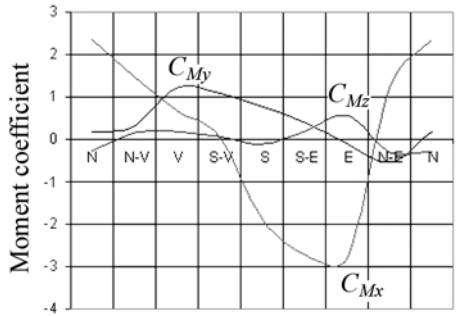

b.

Figure 9. Global force (a) and moment (b) coefficient variation with respect to the wind direction

Figure 10 presents the stream lines formed around the building for wind blowing from the N-E (views from the front, as well as from behind the numerical model of the building).

With the use of such representation, ground zones that could eventually present discomfort for the pedestrians or that can be subjected to excessive snow deposits were identified around the building.

6. CONCLUSIONS

The present paper presents the methodology used to determine quasi-static wind loads on one of the tallest buildings that is to be erected in Bucharest, Romania. The obtained values for this tall (110 *m* high) and slim building, with flexible metallic structure proved useful to the civil engineers in the design process of the envelope, as well as of the structure itself.

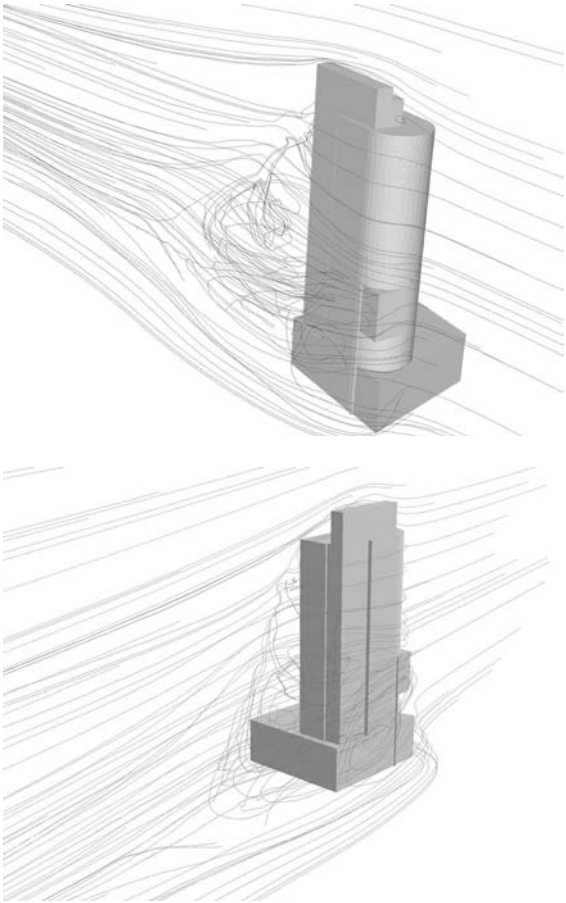

Figure 10. Stream lines around the building for wind blowing from the N-E direction

The procedure used to perform this study (i.e. extended numerical modelling validated by experimental results) has also proven useful by the significant reduction in the amount of time necessary to complete the study, as well as by reducing the costs that were allocated to this project.

ACKNOWLEDGEMENTS

Part of this work has been supported by the Romanian National University Research Council (CNCSIS), under the Consortium Grant 33/2005, entitled “Vortex Hydrodynamics and Applications”.

REFERENCES

[1] Romanian Standard Institute, 1990, "Loads due to wind", *STAS 10101/20*.

[2] Degeratu, M., 2002, *Stratul limită atmosferic*, Ed. Orizonturi Universitare, Timişoara, ISBN 973-8109-89-2.

[3] Sandu, L., Degeratu, M., Hasegan, L., Georgescu, A., Stefan, R., Cosoiu, C., 2005, "Actual and Perspective Research in Wind Engineering", Trans. on Mechanics, Sci. Bull. Politehnica University of Timisoara, Romania, Vol. 50 (64), pp. 23-32.

[4] Iamandi, C., Georgescu, A., Erbasu, C., 2003, "Experimental Modelling of a Four Steel Tanks Battery", Proc. *11th International Conference on Wind Engineering*, (T21), Lubbock, Texas, USA.

[5] Iamandi, C., Georgescu, A., Erbaşu, C., 2002, "Atmospheric Boundary Layer Change", *Int. J. of Fluid Mechanics Research*, Begell House Inc, New York, Vol. 29, ISSN 1064-2277

[6] Nakamura, S., 1996, *Numerical analysis and graphic visualization with MATLAB*, Prentice Hall.

[7] Davenport, A., Mackey, S., Melbourne, W., 1973, "Wind Loading and Wind Effects", Proc. *International Conference Lehigh University*, Bethlehem, USA.

[8] FLUENT Incorporated, 2001, *FLUENT user's guide*.

External Fluid Dynamics

Conference on Modelling Fluid Flow (CMFF'06)
The 13th International Conference on Fluid Flow Technologies
Budapest, Hungary, September 6-9, 2006

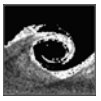

APPLICATION OF VORTEX CLOUD FLOW MODELLING TO CYLINDERS IN ORBITAL MOTION AT LOW REYNOLDS NUMBERS AND COMPARISONS WITH SOME PUBLISHED GRID-BASED CFD PREDICTIONS.

R. Ivan LEWIS[1]

[1] Corresponding Author. 2-16 Bruce Building, University of Newcastle upon Tyne, Newcastle upon Tyne, NE1 7RU, U.K. Tel: +44 (0)191 2226201, E-mail: r.i.lewis@ncl.ac.uk

ABSTRACT

Cylinders in elliptical orbital motion at low Reynolds numbers have been fairly extensively researched by grid-based Computational Fluid Dynamic (CFD) methods, revealing discontinuous behaviour of the rms lift coefficient from positive to negative values for low transverse amplitudes and orbital periodicity close to the Strouhal number. Following published grid-based analyses, this paper studies a few flows for Reynolds numbers of 130, 160 and 180 with orbital periodicity set at 85% of the Strouhal frequency. The orbital amplitude in the mainstream flow direction *Ax* is fixed at 0.3 of the cylinder diameter, while the transverse amplitude is varied over the range $0<Ay<0.3$. A brief outline of the vortex cloud analysis is first given followed by a presentation of predicted lift and drag coefficients for this range of flow conditions plus selected flow patterns for regions of main interest. While the detailed predicted *CLrms* results are not identical to the published grid-based analysis, similar proneness to this switching phenomenon is found to occur. The flow mechanism underlying this is shown to be that of vortex pair formation in the downstream wake and is illustrated by predicted vortex-cloud patterns.

Keywords: CFD, Cylinder orbital motion, vortex shedding, vortex cloud model, vortex wakes.

NOMENCLATURE

Ax, Ay	Amplitudes of orbital oscillation in the *x, y* directions
C_D	Drag coefficient, $C_L = L/(\frac{1}{2}\rho U^2 d)$
C_L	Lift coefficient, $C_D = D/(\frac{1}{2}\rho U^2 d)$
d	Cylinder diameter
f, f_x, f_y	Frequency of orbital oscillations
f_v	Vortex shedding frequency
$K(s_m,s_n)$, $k(s_m,s_n)$	Coupling coefficients linking body points *m* & *n*
L,D	Lift and drag forces
Re	Reynolds number, $Re = U_\infty d/\nu$
s	Distance along the body profile measured from the leading edge
St	Strouhal number, $St = f_v d/U_\infty$
u_o, v_o	Orbital velocity components in the *x,y* directions
U_∞, V_∞	Components of W_∞ in the *x,y* directions
v_s	Surface slip velocity
W_∞	Uniform stream
x,y	Cartesian coordinates
x_o, y_o	Orbital coordinates
Z	Number of discrete vortex elements $\Delta\Gamma_j$
α_∞	Angle of inclination of W_∞ to the x axis
$\gamma(s_n)$	Surface vorticity sheet strength at point s_n
Γ_b	Cylinder bound vorticity
$\Delta\Gamma_j$	Strength of the discrete shed vortex *j*
Δt	Time step
ν	Kinematic viscosity
ρ	Fluid density

1. INTRODUCTION

Formation of vortex streets behind bluff bodies has fascinated large numbers of researchers since the early experiments of Strouhal [1] in 1878 concerning the generation of 'Aeolean tones' and the famous 1911 paper by Theodore von Kármán [2] bequeathing his name to the 'von Kármán vortex street'. Vortex streets are created as the outcome of periodic shedding of vorticity created initially at the suface and subsequently diffused and convected within the body boundary layer. The consequent fluctuations result in large periodic variation of the lift and drag forces and their associated lift and drag coefficients C_L and C_D defined as follows.

$$C_L = L/(\tfrac{1}{2}\rho U_\infty^2 d), \quad C_D = D/(\tfrac{1}{2}\rho U_\infty^2 d) \qquad (1)$$

Shedding frequency f_v is categorised by the dimensionless Strouhal number defined by

$$St = \frac{f_v d}{U_\infty} \qquad (2)$$

As discussed elsewhere [3-5], the onset of regular vortex street shedding occurs above $Re \approx 47$ and remains two-dimensional in character until $Re \approx 190$, above which, as convective processes gain ascendency over viscous diffusion, three-dimensional instabilities begin to occur as proven theoretically by Barkley & Henderson [6] and Posdziech & Grundmann [7] and experimentally by Williamson [8]. The present studies using two-dimensional modelling are thus restricted to this range but towards the upper end for the three values Re=130, 160 & 180 for which convective processes begin to dominate.

Because of vortex wake periodicity, flexibly mounted bodies such as struts, heat exchanger tubes, chimney stacks etc. may deflect and oscillate in response to these forces, possibly in linear or orbital motion. In such cases the vortex shedding properties will change resulting in quite different lift and drag variations with time. The main aim of this paper is to simulate these conditions for a cylinder in elliptical orbital motion at low Reynolds numbers. Studies of this type were previously undertaken by Baranyi [3,4] employing a very precise grid based Eulerian type method of CFD for solving the two-dimensional Navier Stokes equations. Vortex cloud modelling provides a quite different CFD method based on Lagrangian modelling of the same situation and the second aim of this paper is to compare results obtained by these two techniques of fluid-flow simulation. Such comparisons of the now well established CFD codes for classical datum cases are crucial at this stage of increasingly wide engineering design/analysis application and one such paper has already been published by Baranyi and Lewis [5] for low Re flow past a stationary cylinder. The present paper extends these cross-checks to cylinders in orbital motion.

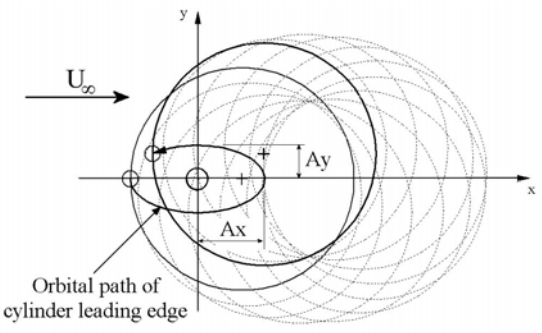

Figure 1. Elliptical path for a cylinder in orbital motion

The main advantage of the vortex cloud model is its ability to keep account of all the vorticity in the downstream wake without the restriction of any reference grid and the consequent ease for obtaining simulated wake patterns. A full account of the fundamentals of vortex cloud analysis have been given by Lewis [9] and of its application to moving bodies and cascades [10,11]. Thus only a brief summary of the underlying theory will be given here in section (2) followed in section (3) by comparisons of predicted lift and drag coefficients and presentation of selected wake patterns. Before proceeding with this we begin with a presentation of the underlying geometrical definitions of the proposed orbital motion as illustrated in Figure 1.

As shown here the cylinder is located in a uniform stream U_∞ but subjected to an orbital motion following an elliptical path with semi-major and minor axes A_x , A_y where the cylinder leading edge point O is taken here to define this path. In practice oscillations might occur with different frequencies f_x and f_y parallel to the x and y axes. For elliptical motion however we will impose equal values $f=f_x=f_y$ and adopt anticlockwise motion beginning in the downstream direction for which the cylinder displacements x_o, y_o at time t become

$$x_0 = -A_x \cos(2\pi ft),\ y_0 = -A_y \sin(2\pi ft) \qquad (3)$$

and its velocity components u_0 and v_0 in the x,y directions are thus

$$u_0 = 2\pi f A_x \sin(2\pi ft),\ v_0 = -2\pi f A_y \cos(2\pi ft) \qquad (4)$$

2. THE VORTEX CLOUD METHOD.

(a) Vortex cloud wake flow simulation.

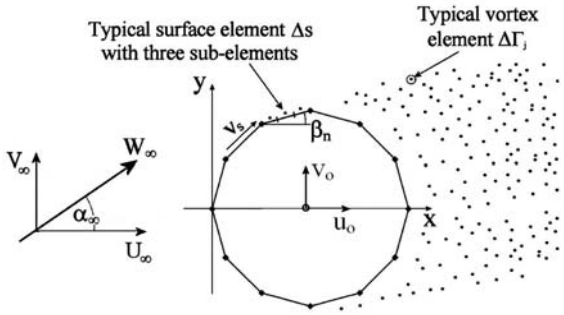

(b) Numerical model

Figure 2. Numerical model for vortex cloud analysis

The flow model for vortex cloud analysis is illustrated in Figure 2. At any instant the flow past the cylinder generates a surface vorticity sheet of local strength $\gamma(s)=v_s$ equal in magnitude to the surface slip-velocity v_s. If the cylinder is represented by M surface elements, the vorticity at element n is assumed to be shed as a discrete vortex element of strength $\Delta\Gamma_n = \gamma(s_n)\Delta s_n$. Although only 12 elements are shown in Fig 2, typically fifty surface elements would be adopted for acceptable resolution as in the present project. For further accuracy sub-elements may be used as illustrated in Fig 2(b), where the line vortex element $\gamma(s_n)\Delta s_n$ has been modelled by three sub-elements of strength $\Delta\Gamma_n = \frac{1}{3}\gamma(s_n)\Delta s_n$. The governing integral equation is then given by [6]

$$\frac{1}{2}\gamma(s_m) + \oint k(s_m,s_n)\gamma(s_n)ds_n + (U_\infty - u_0)\cos\beta_m + (V_\infty - v_0)\sin\beta_m + \sum_{j=1}^{Z}\Delta\Gamma_j(U_{mj}\cos\beta_m + V_{mj}\sin\beta_m) = 0 \quad (5)$$

which states that the velocity on and parallel to the body surface of point m is zero. This equation may be represented numerically by the following set of M linear equations,

$$\sum_{n=1}^{M} K(s_m,s_n)\gamma(s_n) = -(U_\infty - u_0)\cos\beta_m - (V_\infty - v_0)\sin\beta_m - \sum_{j=1}^{Z}\Delta\Gamma_j(U_{mj}\cos\beta_m + V_{mj}\sin\beta_m) \quad (6)$$

where the cylinder is located in the uniform stream W_∞ and Z discrete vortex elements $\Delta\Gamma_j$ have been shed into the fluid since initiation of the motion.

The vortex cloud computations are undertaken in a time-stepping sequence, in the present case for 3000 steps of size Δt=0.05, with a uniform stream U_∞=1.0 and a cylinder diameter d=1.0. A summary of the computations undertaken for each time step is as follows:

Vortex Cloud analysis time-stepping procedure.

1. Potential flow analysis by equation (6), to calculate the body surface slip flow and the newly created surface vorticity $\gamma(s_j)$.
2. The shedding of discrete vortices $\Delta\Gamma_j = \gamma(s_j)\Delta s_j$ from each surface element, thus creating a cloud of vortex elements.
3. Use of the random walk procedure [9] for each discrete vortex $\Delta\Gamma_j$ to simulate viscous diffusion over the time step Δt.
4. Mutual convection of all members of the vortex cloud for this time step.
5. Recombination of any vorticies which become excessively close due to the random walk. This has the beneficial side effect of reducing the total volume of the vortex cloud.
6. Deletion of any discrete vortices which stray inside the body profile during diffusion and imposition of the circulation theorem to ensure that the equivalent loss is restored during the subsequent potential flow analysis (step 1 above) in order to ensure overall conservation of vorticity.

Output data of importance to categorise the resulting motions are the predicted vortex wake motions and the lift and drag coefficients C_L, C_D. In view of the oscillatory nature of the latter, helpful practice is to evaluate their average values and their rms fluctuations, defined as follows.

$$CLmean = \frac{1}{t_2 - t_1}\int_{t_1}^{t_2} C_L\, dt$$
$$CLrms = \sqrt{\frac{1}{t_2 - t_1}\int_{t_1}^{t_2}[C_L - CLmean]^2\, dt} \quad (7)$$

and similarly for *CDmean* and *CDrms*, where the interval t_1 to t_2 includes a large number of completed oscillations.

3. PREDICTED RESULTS FOR THREE TEST CASES

Baranyi [3] published results predicted by his grid CFD method for the three configurations given in Table 1 below, which will be the focus of the present studies. The orbital semi-major axis *Ax* is fixed at 0.3 for all cases and the semi-minor axis is varied over the range $0.0 \le Ax \le 0.3$. For each *Re* value the orbital frequency *f* is set at 85% of the Strouhal number for the fixed cylinder.

Table 1. parameters for test cases

Case	Re	*f*	Ax	Ay range
1	130	0.1521	0.3	0.0 to 0.3
2	160	0.1598	0.3	0.0 to 0.3
3	180	0.165665	0.3	0.0 to 0.3

Vortex cloud calculations were undertaken for these three test cases for a cylinder modelled by 50 elements, with two sub-elements. Further to this, to reduce the "numerical noise" inherent in the random walk model for viscous diffusion, it was also decided to undertake the viscous diffusion in three sub-steps of value $\frac{1}{3}\Delta t$. Vortex cloud predictions will now be presented for these three cases in comparison with Baranyi [3].

3.1 Case 1 - Re = 130, f = 0.1521

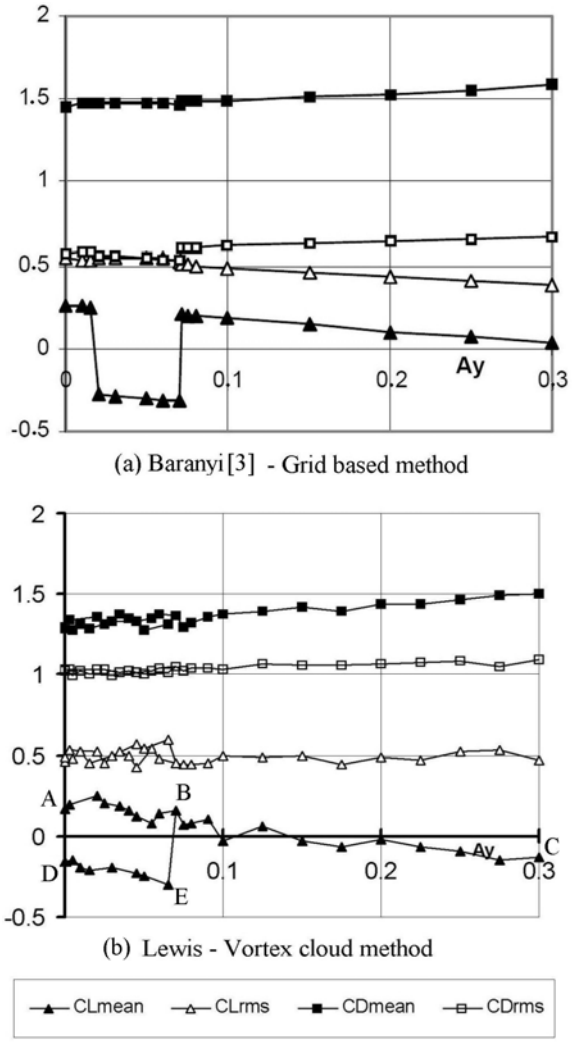

Figure 3. Comparison of predicted force coefficients for *Re* = 130, *f*=0.1521, *Ax* = 0.3

The mean and rms lift and drag coefficients are compared in Figure 3, where, of particular interest, are the predicted *CLmean* values. As previously predicted by Baranyi, Fig 3(a), these resolve into two distinct envelopes which show a major discontinuity in the lower range of *Ay* values. His results shift discontinuously from the upper envelope to the lower one at $Ay \approx 0.02$ and revert to the upper at $Ay \approx 0.07$.

The present vortex dynamics predictions, Fig 3(b), show good general agreement of *CLmean* with Baranyi's results but with some very interesting variations in the lower range $Ay < 0.07$ for which results fell on either the upper envelope ABC or the lower one DEB. The immediate deduction to be drawn from this is the likelihood of some major instability between two possible stable vortex wake regimes and we will return to this later. Good agreement was also obtained between the two methods for the predicted values of *CLrms* and *CDmean* but less so for *CDrms* for which vortex cloud modelling shows much higher values. Next we will take a look at the actual variations of C_L and C_D with time, Figure 4.

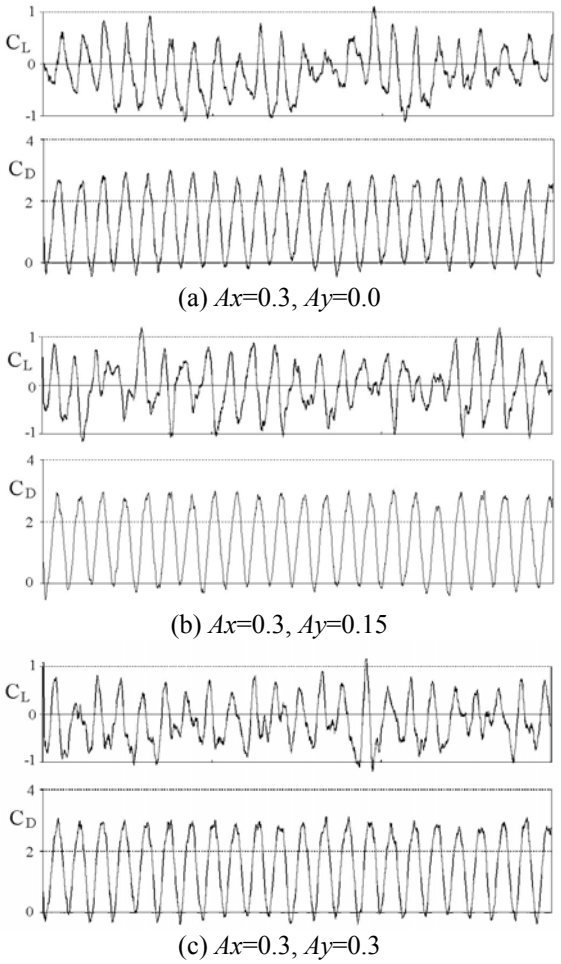

Figure 4. Predicted lift and drag coefficients for *Re* = 130, *f*=0.1521

The predicted variations with time of C_L and C_D are shown in Fig 4 for Ax=0.3 for three values of Ay spanning the orbital range from purely horizontal motion Ay=0.0, on to elliptical motion Ay=0.15 and finally for circular motion Ay=0.3. The C_D curves are remarkably similar which explains the fairly constant values for *CDmean* and *CDrms* in Fig 3 and it is of some interest to note that this wide variation in orbital motion should have such little impact on the magnitude and character of the drag coefficient. On the other hand much more variation can be observed in the predicted lift coefficient C_L. There are fluctuations in the amplitude and variations in the predicted wave pattern for all three cases but increasingly so as the vertical orbital displacement Ay is increased. The most regular of these is for horizontal motion Ay=0.0, Fig 4(a), particularly over the first half of the time sequence. Attention should be drawn to the

general wave shape which has sharp maxima and more rounded minima, a characteristic discovered by Baranyi[3,4]. This same feature in conspicuous in Fig 4(c) for circular motion, *Ay*=0.3, if less conspicuously so for the elliptical orbit, Fig 4(b).

For further insight into some of these characteristics we will now focus attention on predicted wake patterns for these three orbital cases, Figure 5.

(a) Motionless cylinder with zero orbital motion, *f*=*Ax*=*Ay*=0.0

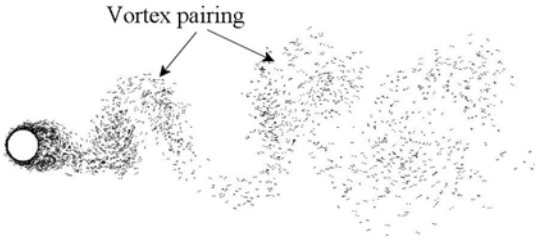

(b) Cylinder in orbital (horizontal) motion with *f*=0.1521, *Ax*=0.3, *Ay*=0.0.

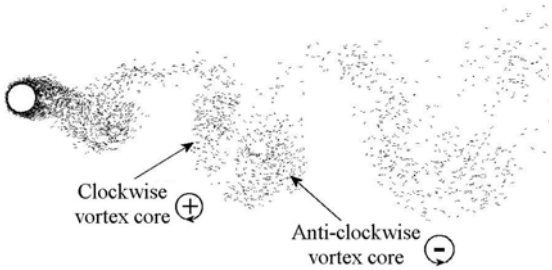

(c) Cylinder in orbital (elliptical) motion with *f*=0.1521, *Ax*=0.3, *Ay*=0.15.

(d) Cylinder in orbital (circular) motion with *f*=0.1521, Ax=0.3, Ay=0.3.

Figure 5. Predicted wake flow for *Re*=130 for various orbits.

Figure 5 portrays the predicted wake patterns for these three cases in comparison with that for the motionless cylinder with its typical von Kármán vortex street, Fig 5(a). Here the cylinder in practice sheds vortices of alternate sign and equal magnitude into the wake at regular intervals, namely the Strouhal frequency *St*, as borne out here by vortex cloud simulation. The predicted flow pattern for purely horizontal motion, Fig 5(b), is quite similar to this but with some evidence of vortex pairing of the two +ve and -ve vortices shed during each orbit. For the cylinder in orbital motion however, Figs 5(c) and 5(d), much more development of this phenomenon is observed, namely the formation in the wake of very distinct vortex pairs. Thus in Fig 5(c), attention is drawn to the pairing of a clockwise +ve vortex shed from the upper surface with an anticlockwise -ve vortex shed slightly previously from the lower surface and we observe also a new vortex pair being shed just downstream of the cylinder as it completes it's upstream orbiting motion. These +/− vortex pairs have a natural self-convection effect in the downwards direction resulting in a general net downward drift of the cylinder wake. The same phenomenon can be observed in Fig 5(d) for the circular orbit. Once again the vortex pairing is of +/− type as for the elliptical orbit, Fig 5(c). It is of particular interest to observe however that the opposite −/+ vortex pairing occurred for the case of purely horizontal motion *Ay*=0.0 shown here in Fig 5(b). In this case, Fig 3(b), the related *CLmean* value was at point D located on the lower envelope whereas the *CLmean* values for the elliptical and circular orbiting cases *Ay*=0.15&0.3 actually lie on the upper envelope. There thus seems to be a direct connection between the sign of vortex pairing and the particular envelope on which the *CLmean* results lie.

3.2 Case 2 - Re = 160, f = 0.1598

Results for the higher Reynolds number of Re=160 are shown in Figure 6 where the behavioural trends of *CLmean* are again similar for the two CFD methods, with good agreement for the wider orbiting range 0.15<*Ay*<0.3. As before Baranyi discovered the switching of *CLmean* between upper and lower envelopes, in this case for *Ay*>0.07. However it is of considerable interest to note that his predicted *CLmean* curve is an inversion of that for *Re*=130, Fig 5(a). Vortex cloud predictions here suggest a more progressive switch over the range 0.09<*Ay*<0.15 and many more points were obtained on the lower envelope than the upper for *Ay*<0.08. The reason for the greater stability of the *CLmean* curves for the higher *Ay* values is probably due to the stronger stirring effect of the wider elliptical orbit shedding large amounts of clockwise vorticity. This leads here to anticlockwise bound vorticity and large negative lift. However

one stray point A was found for *Ay*=0.21 seeming to lie on the extended upper envelope, Fig 6(b).

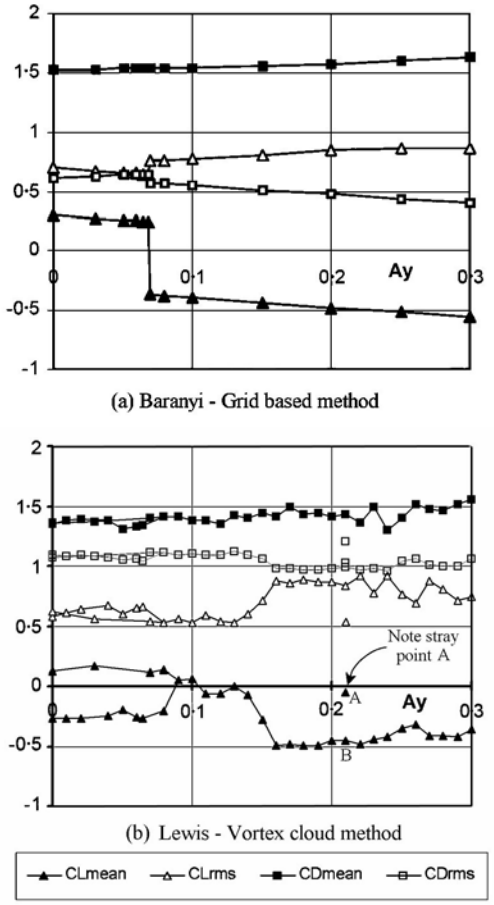

Figure 6. Comparison of predicted force coefficients for Re=160, fx=fy=0.1598, Ax=0.3

A re-run of this situation resulted in the *CLmean* value B lying on the lower envelope having the normal vortex pairing, as can be seen from Figure 7 below.

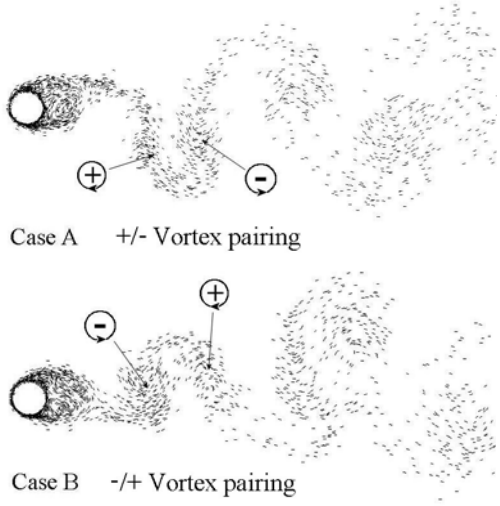

Figure 7. Opposite vortex pairing of points A & B in Fig 6.

As can be seen from Figure 7 the stray point A has +/− vortex pairing which is opposite to the normal more stable −/+ pairing of Case B. What is of particular importance to note here however is that at the higher *Re* of 160 the vortex pairing for the wider *y* orbital range of 0.07<*Ay*<0.3 of stable vortex motion is of Case B −/+ type which is quite contrary to that exhibited for *Re*=130 orbital motion where the stable vortex pairings were of +/− type, a remarkable switch of behaviour for such a small Reynolds number rise. Comparing Baranyi's results for these two Reynolds numbers, Figs 5(a) and 6(a), the same shift of vortex pairing between the +/− and −/+ types was in all probability also occurring, judging by the shift from the upper envelope to the lower for *Ay*>0.07. We now consider results for a further increase to *Re* = 180 for the same orbital motions.

3.3 Case 3 - Re = 180, f = 0.165665

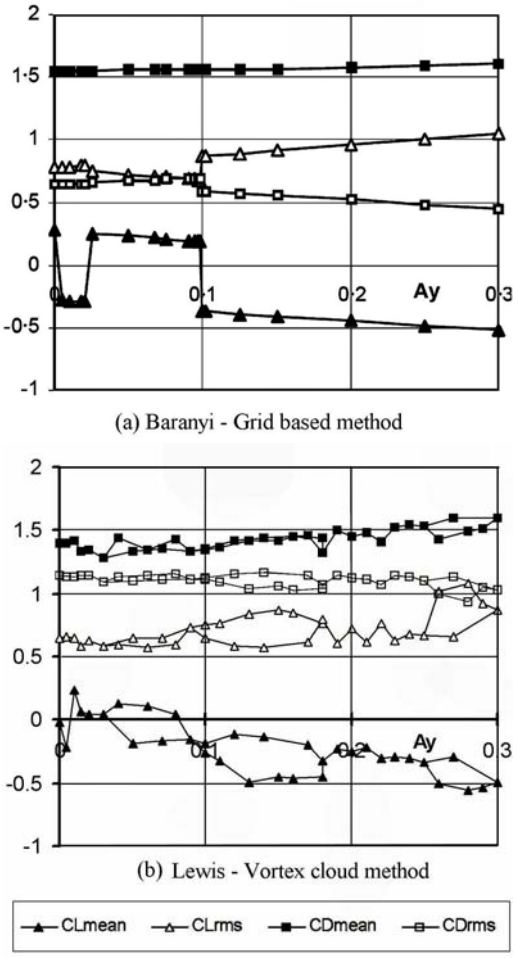

Figure 8. Comparison of predicted force coefficients for Re=180, fx=fy=0.165665, Ax=0.3

Predicted results for the third case at the highest Reynolds number *Re*=180 with orbital

frequency f=0.165665 are shown in Figure 8. As before Baranyi[3], Fig 8a, found there to be two envelopes, with a fairly similar distribution of *CLmean*. Thus all *CLmean* values for Ay>0.1 are lying on the lower envelope following the same trend as the Re=160 results. For Ay<0.1 on the other hand his predicted values lay mainly on the upper envelope with deviations from this in the very low y amplitude range $Ay \approx 0.004$ to 0.02.

Vortex cloud analysis predicted similar overall trends for the lower envelope for Ay>0.1 but also, surprisingly, the presence of the an upper envelope over most of this wider orbiting range. The strategy adopted here on the evidence of section 3.2 was to plot points with $+/-$ vortex pairing on the upper envelope and $-/+$ pairs on the lower one. Within the small range $0.18<Ay<0.25$ however no points were found on the lower envelope. It is difficult to escape the conclusion, comparing Figs 3, 6 & 8, that these developments of the upper envelope for the range Ay>0.1 at the increasing Reynolds number are caused by the progressive dominance of convection over viscous diffusion. At the lower orbital range of Ay<0.1 the same indeterminacy of vortex pairing type is present and the upper envelope is in good agreement between the two CFD methods. A couple of points were however still found on the lower envelope by vortex cloud modelling.

Another feature of test runs for Re=180 was the tendency so switch occasionally between the $+/-$ and $-/+$ vortex pairing modes for some of the Ay values. Similar switching occurred to a very limited extent at Re=160 in the lower Ay range. At these lower Re values of 130 and 160 however stable locking of the vortex pairs generally occurred as the norm for each test run.

4. CONCLUSIONS

The following conclusions may be drawn from this study:

1. Reasonable agreement has been obtained between a high resolution grid based CFD method and vortex cloud modelling of cylinders in orbital motion within the low Re range 130 to 180, with special focus on the time averaged lift coefficient *CLmean*. Best agreement was obtained at the lower Reynolds number Re=130.
2. Although vortex shedding is dependent ultimately upon boundary layer formation and separation, which is more rigorously modelled in the grid-based method of Baranyi, for bluff body flows periodic vorticity shedding is also strongly dominated by the formation of large scale vortex structures within the downstream wake and their upstream influence. Both CFD methods are well adapted to predict these strongly convective motions.
3. Both methods revealed the presence of upper and lower envelopes of the *CLmean* curves. For Re=130 results for the larger y orbits over the range $0.1<Ay<0.3$ lay on the upper envelope. For Re=160 & 180 however *CLmean* values predicted by Baranyi lay on the lower envelope over this range.
4. For the higher Reynolds number Re=180 however, the present method predicted the presence of *CLmean* values lying on both upper and lower envelopes over almost the entire y orbiting range $0.023<Ay<0.3$ which can be attributed to the greater influence of convective motions as one approaches the upper limit of $Re\approx190$ below which the flow locks into two-dimensional motion and above which three-dimensional instabilities begin to set in.
5. The present studies have revealed that the orbital motion results in regular vortex pairing in the downstream wake. These are shown to be of the two possible types, namely $+/-$ and $-/+$. Points on the upper envelope are found to be of $+/-$ type and those on the lower envelope are of $-/+$ type.
6. Wake patterns at the higher Re=180 were sometimes found to switch between $+/-$ and $-/+$ type, whereas at the lower Reynolds numbers much more stable locking of the vortex pairs was occurring as the norm.

REFERENCES

1. Strouhal, V. Über eine besondere Art der Tonerregung. *Ann. Phys. und Chemie. Nav. Series*, 1878, **5**, pp 216-251.

2. Kármán T. von. Über ein Mechanismus des Widerstandes, den ein bewegter Körper in einer Flüssigkeit erfährt. *Göttingen Nachrichten Maths, -Phys*., 1911, **KI**., pp 509-517.

3. Baranyi, L. Numerical simulation of flow past a cylinder in orbital motion. *J. Comp. App. Mech.*, 2004, **5**(2), pp 209-222.

4. Baranyi, L. Lift and drag evaluation in translating and rotating non-inertial systems, *J. of Fluids & Structures,* 2005, **20**, pp 25-34.

5. Baranyi, L. and Lewis, R.I. Comparison of a grid-based CFD method and vortex dynamics predictions of low Reynolds number cylinder flows. *Paper accepted for publication in J. Aero. Sc.,(2006).*

6. Barkley, D. and Henderson, R.D. Three-dimensional Floquet stability analysis of the wake of a circular cylinder. *Journal of Fluid Mechanics,* **332**, (1996), pp. 215-241.

7. Posdziech, O. and Grundmann, R. Numerical simulation of the flow around an infinitely long circular cylinder in the transition regime. *Theoretical and Computational Fluid Dynamics,* **15**, (2001), pp. 121-141.

8. Williamson, C.H.K. Vortex dynamics in the cylinder wake. *Annual Review of Fluid Mechanics*, **28**, (1996), pp. 477-539.

9. Lewis, R.I. Vortex Element Methods for Fluid Dynamic Analysis of Engineering Systems, *Cambridge University Press*, 1991.

10. Lewis, R.I., Development of Vortex Dynamics for Simulation of Turbomachine Cascades and Blade Rows. *J. Comp. App. Mech.*, 2001, Vol. 2, No. 1, pp. 73-85.

11. Lewis, R.I., Study of blade to blade flows and circumferential stall propagation in radial diffusers and radial fans by vortex cloud analylsis. *J. Comp. App. Mech.*, 2004, Vol. 5, No. 2, pp. 323-335.

Conference on Modelling Fluid Flow (CMFF'06)
The 13th International Conference on Fluid Flow Technologies
Budapest, Hungary, September 6-9, 2006

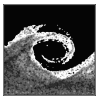

NUMERICAL PREDICTIONS OF LOW REYNOLDS NUMBER FLOW OVER AN OSCILLATING CIRCULAR CYLINDER

Eric DIDIER[1], António R.J. BORGES[2]

[1] Corresponding Author. Departamento de Engenharia Mecânica e Industrial, Faculdade de Ciências e Tecnologia, Universidade Nova de Lisboa. Monte de Caparica, 2829-516 Caparica, Portugal. Tel.: +351 212 948 567, Fax: +351 212 948 542, E-mail: deric@fct.unl.pt
[2] Departamento de Engenharia Mecânica e Industrial, Faculdade de Ciências e Tecnologia, Universidade Nova de Lisboa. Monte de Caparica, 2829-516 Caparica, Portugal. E-mail: ajb@fct.unl.pt

ABSTRACT

Unsteady two dimensional incompressible viscous uniform flow over an oscillating cylinder at Reynolds number 300 is simulated using an implicit second order fully coupled resolution method, an original and interesting alternative approach to classical segregated method. The cylinder is forced to oscillate in both transverse and longitudinal directions, that can result in an orbital motion. Computations are carried out for different values of frequency and amplitude of the oscillation. The flow field changes significantly as a result of the cylinder oscillations and manifests in the forces experienced by the body and the Strouhal number for the vortex-shedding frequencies. The cylinder exhibits the phenomenon of lock-in in a range of frequency. For longitudinal oscillations, the vortex-shedding frequency locks-on the cylinder frequency in a wide frequency band, around twice the natural vortex-shedding frequency observed for a stationary cylinder. For cross-flow oscillations, lock-in is observed in a narrow frequency band around the natural frequency and the vortex-shedding frequency matches the cylinder oscillations. For an orbital motion the same phenomena occur, but the two bandwidths of lock-in frequency are slightly different than those observed for in-line or transverse oscillation.

Keywords: finite volume method, fully coupled resolution method, lock-in, orbital motion of a circular cylinder, unsteady flow, vortex shedding

NOMENCLATURE

C_D, C_L	[-]	drag and lift coefficient
C_p	[-]	pressure coefficient
D	[m]	cylinder diameter
Re	[-]	Reynolds number, $U_\infty D/\nu$
S	[-]	non-dimensional cell surface
St	[-]	Strouhal number, fD/U_∞
U_∞	[m/s]	free stream velocity
V	[-]	non-dimensional cell volume
a	[-]	discretised equation coefficient
b	[-]	source term
f	[Hz]	frequency
n	[-]	interface normal vector
p	[-]	pressure
t	[-]	time
u	[-]	velocity
u^*	[-]	pseudo-velocity
u_b	[-]	cylinder velocity
x_i	[-]	Cartesian co-ordinates
ν	[m^2/s]	viscosity

Subscripts and Superscripts

c	central cell of discretised molecule
e	amplitude of velocity oscillation and frequency of cylinder
f	interface of two adjacent cells
i	i=1,2; horizontal and vertical directions
nb	neighbour cell of a central cell
o	reference values for a stationary cylinder
p	coefficient of pressure scheme
u_i	coefficient of convection-diffusion scheme
rms	root-mean-square value
–	temporal mean

1. INTRODUCTION

Study of flow past a circular cylinder is of special interest for basic understanding of the aerodynamics of aeroelastic phenomena. Despite the simplicity of geometry the flow around a cylinder is very complicated and of particular importance, since it may induce unsteady forces on structures associated with vortex shedding. Unsteady forces acting in both directions, in-line and cross-flow, respectively represented by drag and lift coefficients, can induce structure vibrations. These oscillations result in a general orbital motion. These types of flow have been extensively studied: oscillatory flows [1], oscillating cylinder in uniform flow [2] [3], and particularly the case where the

cylinder oscillates in the cross flow direction in an uniform stream. More recently, Baranyi [4] investigated the orbital motion of a circular cylinder in an uniform flow.

This paper focuses on the case where cylinder oscillations, in a uniform flow, occur in-line, cross-flow and both in-line and cross-flow directions that can result in an orbital motion. Computations are carried out for various values of the structural frequency, including the natural shedding frequency, and velocity amplitude of cylinder, 10 to 30% of the free stream velocity. The flow field changes significantly and manifests in the forces experimented by the cylinder and the related Strouhal number.

Computational investigations are performed considering unsteady two-dimensional flow for an incompressible viscous fluid. An implicit second order fully coupled resolution method [5] [6] [7], developed for structured and unstructured meshes with a finite volume framework for cell-centered collocated grids is presented. This approach is an alternative to classical segregated method, like SIMPLE [8] or PISO [9]. Whereas the segregated methods lead to a sequential resolution of discrete equations, with the fully coupled resolution method only one linear system in velocity-pressure is solved. This approach does not require correction steps, relaxation parameters or other special treatment to ensure convergence and reduces the number of non-linear iterations needed to converge.

1. GOVERNING EQUATIONS

The unsteady bidimensional Navier-Stokes equations for incompressible viscous fluid are considered in conservative dimensionless integral form and written in the referential of the cylinder.

$$\int_S u_j \, n_j \, dA = 0 \tag{1}$$

$$\int_V \frac{\partial u_i}{\partial t} dV + \int_S u_i \, (u_j \, n_j) dS = -\int_V \frac{\partial p}{\partial x_i} dV + \frac{1}{Re} \int_S \frac{\partial u_i}{\partial x_j} n_j dS + \int_V \frac{\partial u_{bi}}{\partial t} dV \tag{2}$$

These equations involve the fluid viscosity ν, the Cartesian components u_i of the velocity, the pressure p. V is the volume of the element, S is its area and n_i the components of the outward unit vector normal to the surface.

The motion of the centre of the cylinder is specified as follows:

$$u_{b1}(t)=u_{e1} \cos(2\pi f_{e1} t)$$
$$u_{b2}(t)=u_{e2} \sin(2\pi f_{e2} t) \tag{3}$$

where u_{e1}, u_{e2} and f_{e1}, f_{e2} are the non-dimensional amplitude velocity and frequency of cylinder oscillatory motion in longitudinal and transversal direction. When the two amplitudes and frequencies are equals, $f_{e1}=f_{e2}$ and $u_{e1}=u_{e2}$, the orbital path becomes a circle. If one of the amplitudes is zero, longitudinal or transverse oscillation is obtained. When both amplitudes are zero the cylinder is stationary.

2. FULLY COUPLED RESOLUTION METHOD

The fully coupled resolution method is developed for structured and unstructured grids and unsteady flow within a finite volume framework. This method defers from segregated formulations by the implicit treatment of pressure-velocity coupling. Only one linear system is solved and no relaxation parameters or special operations are required to ensure convergence.

2.1. Finite volume mesh convention

Finite volume discretization schemes are used with collocated cell-centered unknowns. The central control volume is denoted by c and the neighbouring control volumes, around the central one, are denoted by nb. M_{nb} is the face midpoint of two adjacent cells. For non-orthogonal grid, the face midpoint may be different from the intersection point defined by the cell-centroids line and the face. Therefore a correction is required to transfer the values from the cell center c and nb to the points c' and nb' (Figure 1).

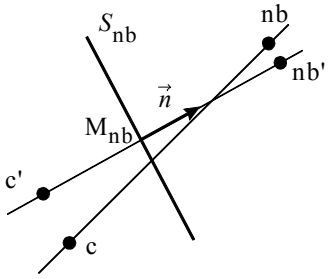

Figure 1. Interface between two adjacent cells and notations used for discretization

2.2. Discrete schemes

The fully coupled resolution method involves solving a complex linear system of algebraic equations. It is thus necessary to consider compact implicit schemes, based only on the adjacent cells, conserving in the same time a precision of second order.

An implicit three-level second order scheme is used to discretize the transient term. Central differencing scheme, that involves only the values

of adjacent cells, is used to evaluate the viscous term. The pressure term is calculated using a linear interpolation. The advection term is calculated using the deferred correction approach [10], combining a first-order UDS and a higher-order scheme, WACEB [11], with the factor ω_{DC} set to 1. The ith component velocity at the interface f of the control volume can be written as follows:

$$\left(u_i\right)_f = \left(u_i^{UDS}\right)_f^{Imp} + \omega_{DC}\left(u_i^{WACEB} - u_i^{UDS}\right)_f^{Expl} \quad (4)$$

Corrections are required to estimate pressure and velocity at the face midpoint when the grid is non-orthogonal. These corrections are added explicitly to the source term of discrete equations.

2.3. Fully coupled system

The momentum equation can be written as follows

$$(u_i)_c = b^{u_i} + \frac{1}{a_c^{u_i}}\sum_{nb} a_{nb}^{u_i}\,(u_i)_{nb} - \frac{1}{a_c^{u_i}}\left(a_c^p\,p_c + \sum_{nb} a_{nb}^p\,p_{nb}\right) \quad (5)$$

The source term b^{u_i} gathers contributions of explicit part of discretization schemes.

Following Prakash and Patankar [12], the convected velocity $(u_i)_c$ can be considered as the sum of a pseudo-velocity $(u_i^*)_c$ and a pressure gradient term.

$$(u_i)_c = (u_i^*)_c - \left(\frac{a_c^p}{a_c^{u_i}}\,p_c + \sum_{nb}\frac{a_{nb}^p}{a_c^{u_i}}\,p_{nb}\right) \quad (6)$$

The pseudo-velocity gathers all contributions of discrete momentum equations, except the pressure gradient contribution.

$$(u_i^*)_c = b^{u_i} + \frac{1}{a_c^{u_i}}\sum_{nb} a_{nb}^{u_i}\,(u_i)_{nb} \quad (7)$$

The velocity in the discrete continuity equation can be substituted using the discrete velocity Eq. (6). The continuity equation, expressed in terms of pseudo-velocity and reconstructed pressure [13], allows to obtain a pressure equation.

$$\sum_{nb}\left(\left((u_i^*)_c - \frac{1}{a_c^{u_i}}\left(a_c^p\,p_c + \sum_{nb} a_{nb}^p\,p_{nb}\right)\right)n_i\right)_{nb} s_{nb} = b^p \quad (8)$$

2.4. Resolution strategy

The fully coupled system is constructed gathering Eqs. (6) to (8).

$$\begin{bmatrix} \underline{\underline{I}} & -\underline{\underline{I}} & \underline{\underline{G}} \\ \underline{\underline{C}} & \underline{\underline{I}} & 0 \\ 0 & \underline{\underline{D}} & \underline{\underline{DG}} \end{bmatrix}\begin{pmatrix} \underline{U} \\ \underline{U^*} \\ \underline{P} \end{pmatrix} = \begin{pmatrix} 0 \\ \underline{B}_u \\ \underline{B}_P \end{pmatrix} \quad (9)$$

The matrix of this linear system is sparse, non-symmetrical, with large dimension and an ill-conditioned pressure block. The linear system is solved using the iterative algorithm BiCGSTAB-ω [14], in conjunction with a LU preconditioner.

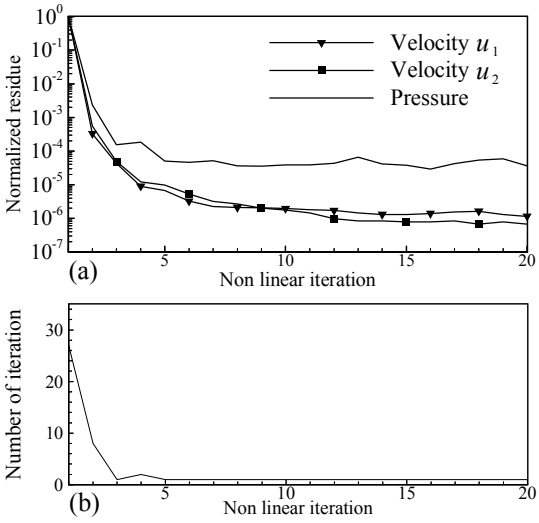

Figure 2. Convergence history for a stationary cylinder, Re=300, at t=100: (a) non-linear normalised residue, (b) number of iterations to solve the fully coupled linear system

In opposition to segregated methods, like SIMPLE [8] or PISO [9], that lead to a sequential resolution of discrete equations, the fully coupled resolution method allows to solve only one single linear system, gathering pressure and velocity, to obtain the solution.

The residual convergence is fast due to velocity-pressure coupling. A residual reduction of six to seven orders is obtained in a few number of non-linear iterations (Figure 2). At the beginning of the non-linear process, a rather high number of iterations is mandatory and a severe variations of normalised residual is observed. This step corresponds to the main non-linear reduction phase.

3. CFD RESULTS AND DISCUSSION

CFD results at *Re*=300 are presented for motions with various velocity amplitudes and frequencies, respectively: 10, 20 and 30% of the free stream velocity and normalised frequencies between 0.2 to 3.0. Before simulating the flow past

an oscillating cylinder the flow around a stationary one is considered. It serves as a reference to analyse forces and flow topology when oscillations occur. These reference values are represented in all figures by a solid line.

3.1. Stationary cylinder and mesh

Let us therefore first consider the flow around a stationary cylinder. Not only is this good to test the accuracy of the fully coupled resolution method, it also serves as reference. A grid refinement study made revealed that an O-grid with 200 and 155 nodes respectively in angular and radial direction, with a first grid-point near to the wall situated at $5.10^{-4}D$ is well adapted to the present simulation. A radius equal to $30D$ ensures that external boundary effects are sufficiently minimised (Figure 3). The time step is equal to 10^{-2}.

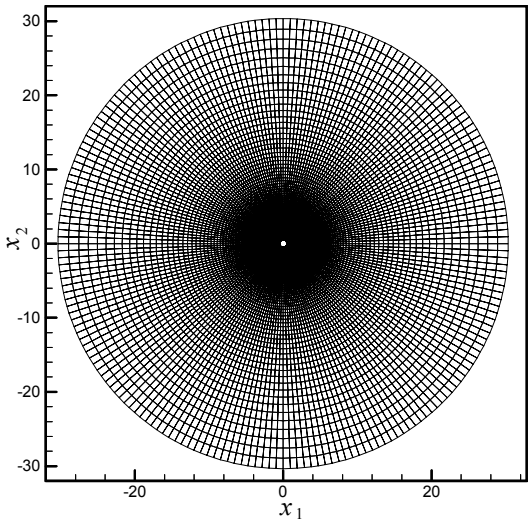

Figure 3. O-grid around the cylinder

Table 1 shows good agreement obtained for the shedding frequency and the drag coefficient, if compared with results of Singh et al. [15] and Henderson, from Williamson [16]. The *rms* drag and lift coefficients are equal to $5.3.10^{-2}$ and 0.62. Efficiency and accuracy of the present resolution method were demonstrated by the authors [7] [17].

Table 1. Comparison of present results with literature data

	Present method	Singh et al. [15]	Henderson from [16]
$\overline{C}_{D,o}$	1.352	1.357	1.360
St_o	0.214	0.210	0.212

3.2. In-line oscillation

When in-line oscillation occurs, the cylinder oscillates only in the direction of the free stream velocity. Calculated Strouhal number and drag coefficient are presented in Figures 4a and 4b. Figures 5a and 5b show the *rms* drag and lift coefficients versus the normalized in-line excitation frequency f_{e1}/f_o, with f_o the natural frequency of vortex shedding for a stationary cylinder in an uniform flow.

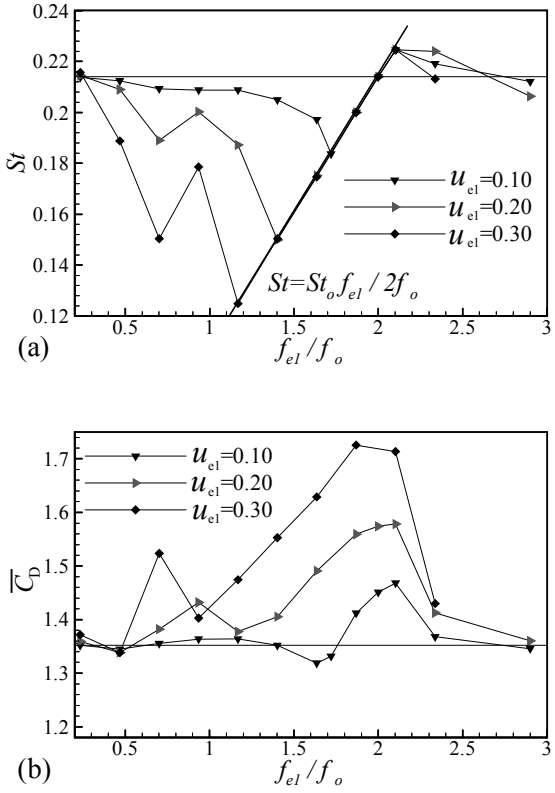

Figure 4. In-line oscillation: (a) Strouhal number and (b) mean drag coefficient

It can be observed that, as has been reported by various authors, the in-line oscillation alters the flow field significantly. These effects manifest themselves in the forces experienced by the cylinder and the related Strouhal numbers for the vortex-shedding frequencies.

As can be seen, in-line cylinder oscillations cause a global diminution of the shedding frequency. This is not true for frequencies higher than $2f_o$, where the Strouhal number is either higher or equal than St_o. The minimum shedding frequency decreases when velocity amplitude of the cylinder increase. The shedding frequency locks-on the excitation frequency, in a large frequency band for frequencies lower or slightly higher than $2f_o$, with the following relation: $St/St_o=f_{e1}/2f_o$. The bandwidth of lock-in increases with the amplitude of velocity oscillation. For $f_{e1}=2f_o$ the lock-in is strong, the shedding frequency is equal to the natural shedding frequency. It is the so-called synchronization.

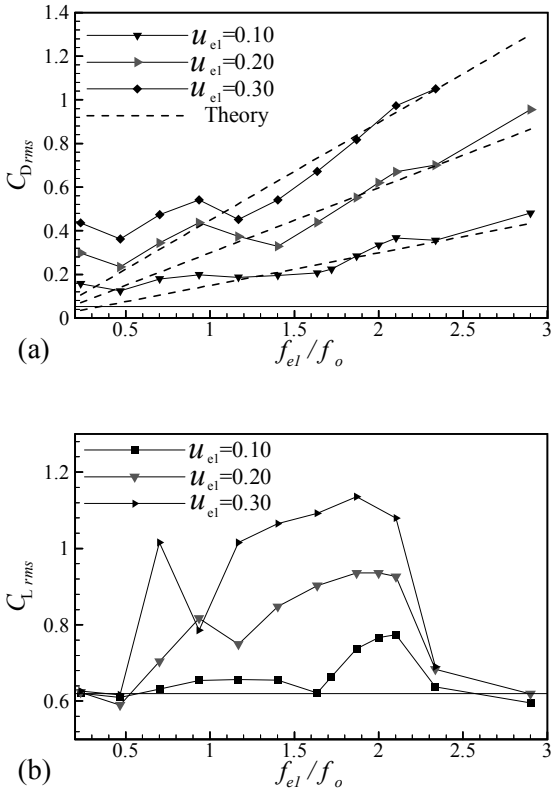

Figure 5. In-line oscillation: (a) *rms* drag and (b) lift coefficients

The longitudinal and transversal forces acting on the cylinder globally increase if compared to the values calculated for stationary uniform flow. Mean drag and *rms* lift coefficients are larger when lock-in occurs. Maximum of mean drag and *rms* lift coefficients take place for synchronization, i.e. $f_{e1}=2f_o$. However, another smaller peak appears when $f_{e1}\sim f_o$ for the larger amplitude velocity fluctuation. For normalised frequency f_{e1} under 0.3 or above 2.7, mean drag and *rms* lift coefficients converge to stationary ones. The *rms* drag coefficient does not follow this behaviour and increases with frequency. This is connected with inertial effects. Effectively, numerical values well agree with theoretic formulation, considering the added mass and neglecting viscous effects, more especially at high frequencies where the inertial effects dominate the viscous non-linear phenomenon, as shown previously [18].

Figures 6a and 7a show the time history of drag and lift coefficients for an uniform flow and for an in-line cylinder oscillation in an uniform flow, with u_{e1}=0.20 and f_{e1}=0.30. Figures 6b and 7b show the vorticity field at the non-dimensional time 0.1/*St*, considering the temporally periodic solution for the two cases. As can be seen, the *rms* lift coefficient is larger than the natural one. The C_L temporal signal becomes asymmetric, while the uniform flow lift coefficient is harmonic. This is a characteristic feature of lock-in phenomena. As can be seen in Figs. 6b and 7b, the near vorticity field is rather affected by the cylinder oscillations. The structure of positive and negative vorticity is significantly modified.

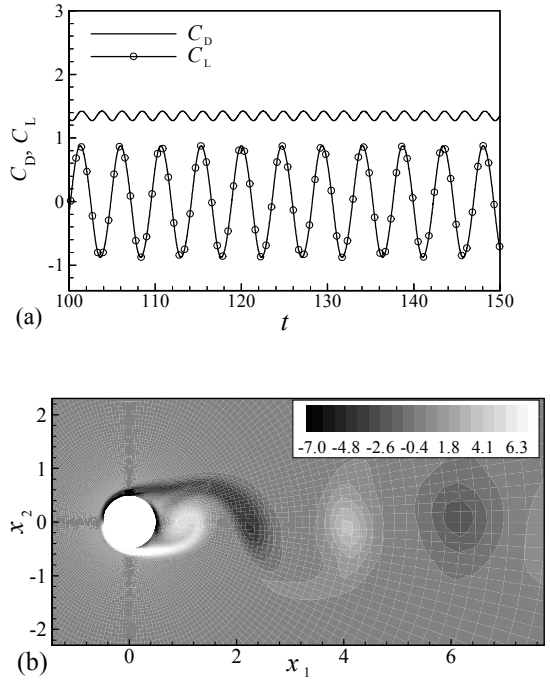

Figure 6. Uniform flow: (a) drag and lift coefficient and (b) vorticity field

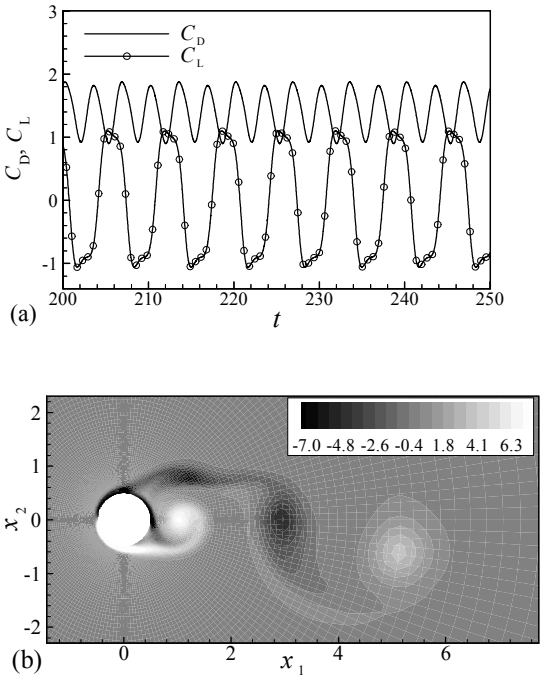

Figure 7. In-line oscillation: (a) drag and lift coefficient and (b) vorticity field

3.3. Cross-flow oscillation

Figures 8a, 8b and 8c show the Strouhal number, the mean and *rms* drag coefficients versus the normalized cross flow excitation frequency f_{e2}/f_o.

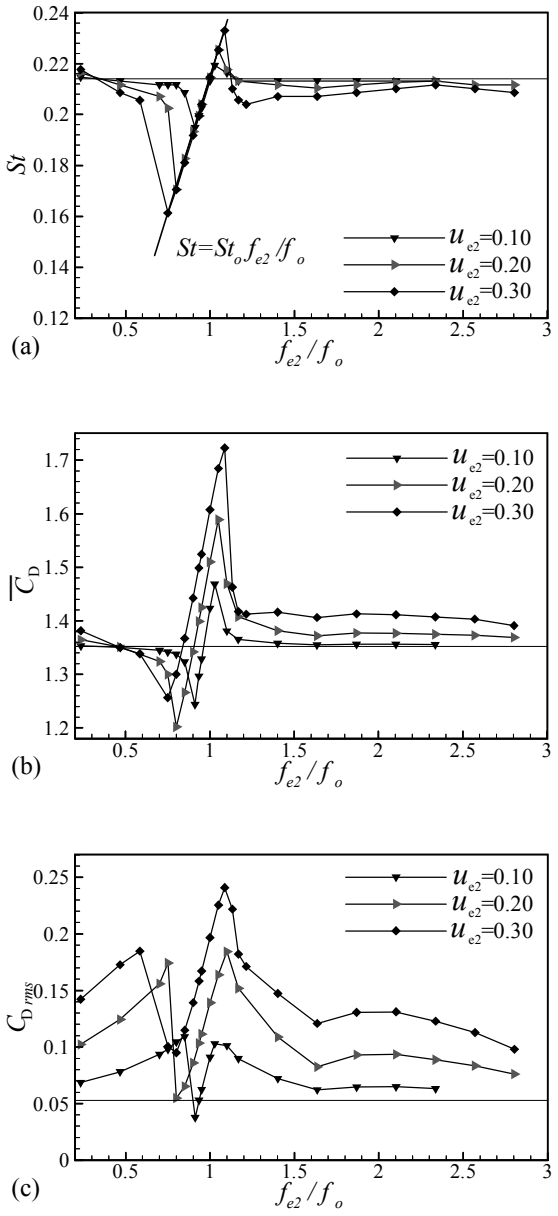

Figure 8. Cross-flow oscillation: (a) Strouhal number, (b) mean drag coefficient and (c) *rms* drag coefficient

Cross-flow oscillations cause only a significant variation of the shedding frequency in a band around the natural shedding frequency f_o. This frequency band is reduced compared with that obtained for an in-line oscillation. The shedding frequency locks-on the excitation frequency, with the following relation: $St/St_o=f_{e2}/f_o$. For $f_{e2}=f_o$ the shedding frequency is equal to the natural one. It is the synchronization. The lock-in frequency band increases with amplitude velocity of cylinder motion. For higher frequencies it can be seen that the frequency is slightly lower than the natural frequency. However, it seems to tend toward the natural frequency, like mean drag and *rms* drag coefficients tend toward mean natural $C_{D,o}$ and $C_{Drms,o}$.

For each amplitude the mean drag coefficient presents a linear variation in the lock-in zone, like the *rms* drag. For low lock-in frequencies the mean drag is slightly lower than the natural one. For the higher lock-in frequency the mean drag is maximum and much higher than the natural drag. The *rms* drag coefficient presents a type of crisis before the lock-in zone. The C_{Drms} decrease brutally to reach its minimum value. It increases again linearly in the lock-in band until its maximum value and decrease slowly, tending to the natural $C_{Drms,o}$.

3.4. Orbital oscillation

Computations are carried out for cylinder velocity u_{e1} and u_{e2} equal and set to 10% of the free stream velocity. In-line and cross-flow frequencies motion are equal and denoted f_e. Results are compared with reference values and with results obtained for in-line and cross-flow motion.

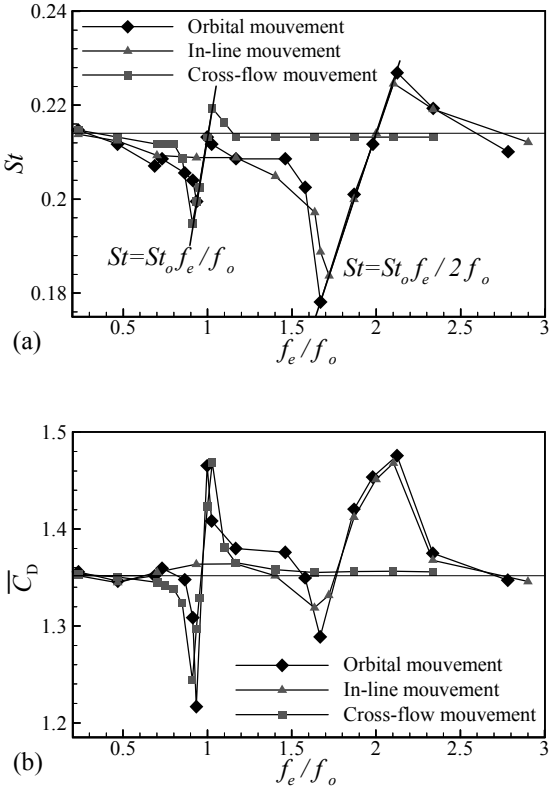

Figure 9. Orbital oscillation: (a) Strouhal number and (b) mean drag coefficient

Figures 9a and 9b show the Strouhal number and the mean drag coefficient vs the normalised frequency. The lock-in occurs in two frequency

bands around $f_e=f_o$ and $f_e=2f_o$. However, frequency lock-in bands are different than those obtained for in-line or cross-flow oscillating cylinder. The first one is located in the frequency interval 0.200 to 0.214 and can be defined by the relation $St=St_o f_e/f_o$. The lock-in occurs in a restricted bandwidth, narrower than the frequency band associated to the cross-flow oscillation cylinder motion. The second one, defined by $St=St_o f_e/2f_o$, appears between 0.348 to 0.456. The lock-in bandwidth is slightly broader than the frequency band defined for an in-line oscillating cylinder.

In Fig. 9b, it can be seen that mean drag variation in the first lock-in band, around $f_e/f_o=1$, is not equal to mean drag evolution obtained for cross flow cylinder motion. Firstly, the band frequency is smaller. Secondly, minimum and maximum mean drag coefficient values in the lock-in band are larger. The jump of mean drag coefficient in this lock-in zone presented a slightly larger intensity than that occurring for transversal motion.

Figure 10 shows the mean and *rms* pressure coefficient on the cylinder in transversal and orbital motion, compared with a stationary one. Mean C_p is similar between the mean front stagnation point and 60 degrees. Beyond 80 degrees, the mean C_p for orbital motion is larger than the others, like the $C_{p,rms}$, and minimum mean drag coefficient is smaller than for the other motions. Flow topology analysis shows that separation points, for orbital motion, moved further downstream. So, the variation of mean drag coefficient is larger than that obtained for the cross-flow cylinder motion. The line slope defined by $d\overline{C}_D/d(f_e/f_o)$ is twice the line slope obtained for only cross-flow oscillation. For high frequencies, around $f_e/f_o=2$, the mean drag coefficient is similar for both cases.

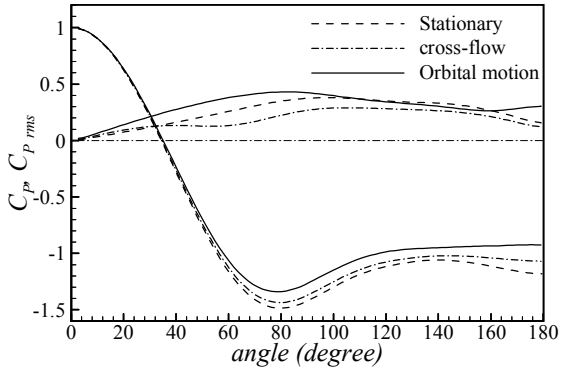

Figure 10. Mean and *rms* coefficient pressure for f_e=0.20

Figures 11a and 11b show the *rms* drag and lift coefficients. Inertial effects are observed for both coefficients at higher frequencies. As can be seen in Fig. 11a, the *rms* drag coefficients for orbital cylinder motion and in-line motion present a similar evolution. Only small lock-in effects are observed around $f_e/f_o=1$ and $f_e/f_o=2$. In Fig. 11b, evolution of *rms* lift coefficient is similar than that obtained for cross-flow motion of cylinder: inertial effects are observed like the influence of the lock-in in the band frequency around $f_e/f_o=2$. The jump of *rms* lift coefficient in the lock-in zone, around $f_e/f_o=1$, presented a slightly larger intensity than that obtained for cross-flow oscillating cylinder. Particularly, the *rms* lift coefficient is almost half than the reference value. Like the mean drag coefficient, the line slope variation $d\overline{C}_{L,rms}/d(f_e/f_o)$ is twice the line slope obtained for only cross-flow oscillation. This effect is clearly induced by the longitudinal component of the orbital motion of the cylinder.

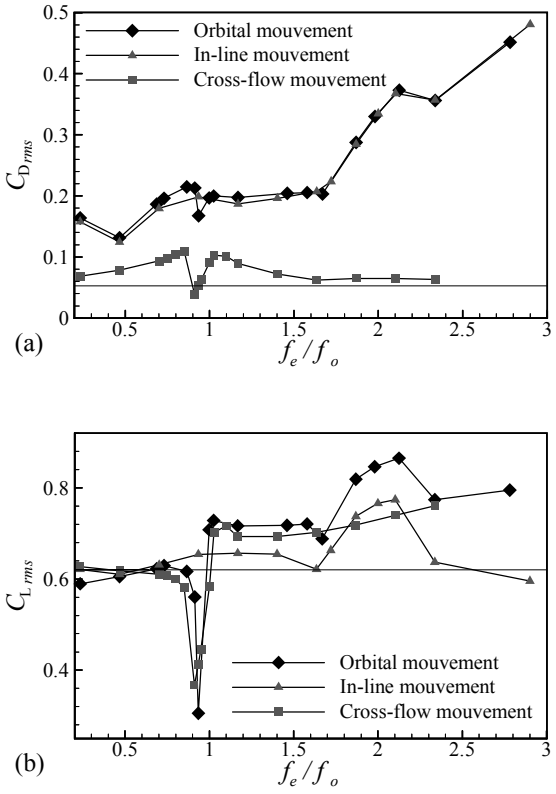

Figure 11. Orbital oscillation: (a) *rms* drag and (b) lift coefficients

5. CONCLUSIONS

Numerical simulation of flow past an oscillating cylinder was done using an implicit fully coupled second order resolution method, developed by the first author, an original approach to solve Navier-Stokes equations. Lock-in and synchronisation were observed for all cases studied: for in-line and cross-flow cylinder oscillation and for the various amplitudes of cylinder motion. It can be observed that in-line and cross-flow oscillating cylinder in an uniform flow alter the flow field significantly.

For in-line oscillation, the shedding frequency locks-on the excitation frequency, in a large frequency band for frequencies lower and slightly higher than $2f_o$, with the following relation: $St/St_o=f_{e1}/2f_o$. The flow is perturbed, in comparison with the uniform flow, in a large band of normalised frequencies, between 0.3 to 2.6. Mean drag and lift *rms* coefficients are both larger than natural values when lock-in occurs and also for the normalised frequency band 0.25 to 2.6.

For cross-flow oscillation, the flow is disturbed in a much reduced frequency band. The shedding frequency locks-on the cross-flow oscillation around the natural frequency f_o, with the following relation: $St/St_o=f_{e2}/f_o$. Mean drag and drag and lift *rms* coefficients present a sharp variation in this narrow band. The lock-in bandwidth is narrower than the in-line oscillation case.

The analysis of the orbital motion of the cylinder shows that aerodynamical coefficients and the related Strouhal number are equivalent to an addition between the in-line and cross-flow results. However, differences are observed: first, lock-in bandwidth is narrower than the cross-flow one; second, lock-in zone is broader than the in-line one; the slope of mean drag and *rms* lift coefficients in lock-in around $f_e/f_o=1$ is twice the slope obtained for the cross-flow oscillation. Those differences are clearly due to the cylinder orbital motion. Around $f_e/f_o=2$, mean drag and *rms* lift coefficient are not significantly affected by the orbital motion if compared with the in-line ones. The *rms* drag coefficient is not modified.

REFERENCES

[1] Bearman, P.W., Downie, M.J., Graham, J.M.R., and Obasaju, E.D., 1985, "Forces on cylinders in viscous oscillatory flow at low Keulegan-Carpenter number", *J Fluids Mechanics*, Vol. 154, pp. 337-356.

[2] Okajima, A., 1995, "Numerical analysis of the flow around an oscillating cylinder", Proc. *Sixth International Conference on flow-Induced Vibration*, London, pp. 159-166.

[3] Mittal, S., and Kumar, V., 1999, "Finite element study of vortex-induced cross-flow and in-line oscillations of a circular cylinder at low Reynolds numbers", *Int J Numer Meth Fluids*, Vol; 31, pp. 1087-1120.

[4] Baranyi, L., 2003, "Numerical simulation of flow past a cylinder in orbital motion", Proc. *Conference on Modelling Fluid Flow*, Budapest, pp. 365-372.

[5] Deng, G.B., Piquet, J., Vasseur, X., and Visonneau, M., 2001, "A new fully coupled method for computing turbulent flows", *Comput Fluids*, Vol. 30, pp. 445-472.

[6] Ammara, I., and Masson, C., 2004, "Development of a fully coupled control-volume finite element method for incompressible Navier-Stokes equations", *Int J Numer Meth Fluids*, Vol. 44, pp. 621-644.

[7] Didier, E., and Borges, A.R.J., 2003, "Unsteady Navier-Stokes equations: A fully coupled method for unstructured mesh", Proc. *Conference on Modelling Fluid Flow*, Budapest, pp. 814-821.

[8] Issa, R.I., 1985, "Solution of the implicit discretized fluid flow equations by operator-splitting", *J Comp Physics*, pp. 40-65.

[9] Patankar, S.V., 1980, *Numerical Heat Transfer and Fluid Flow*, McGraw Hill.

[10] Khosla, P., and Rubin, S., 1974, "A diagonally dominant second-order accurate implicit scheme", *Computers Fluids*, Vol. 2, pp. 207-209.

[11] Song, B., Liu, G.R., Lam, K.Y., and Amano, R.S., 2000, "On a higher-order bounded discretization scheme", *Int J Numer Meth Fluids*, Vol. 32, pp. 881-897.

[12] Prakash, C., and Patankar, S.V., 1985, "A control-volume-based finite-element method for solving the Navier-Stokes equations using equal-order velocity-pressure interpolation", *Num Heat Transfer*, Vol. 8, pp. 259-280.

[13] Rhie, C.M., and Chow, W.L., 1983, "A numerical study of turbulent flow past an isolated airfoil with trailing edge separation", *AIAA Journal*, Vol. 21, pp. 1525-1532.

[14] Sleijpen, G.L.G., and Van der Vorst, H.A., 1995, "Maintaining convergence properties of BiCGSTAB methods in finite precision arithmetic", *Numer Algorithms,* pp. 203- 223.

[15] Singh, S.P., and Mittal, S., 2005, "Flow past a cylinder: Shear layer instability and drag crisis", *Int J Numer Meth Fluids*, Vol. 47, pp. 75-98.

[16] Williamson, C.H.K., 1996, "Vortex dynamics in the cylinder wake", *Annu Rev Fluid Mech*, Vol. 28, pp. 477-539.

[17] Didier, E., and Borges, A.R.J., 2005, "Numerical simulation of two-dimensional cross-flow past a cylinder using an unstructured mesh based fully implicit second order coupled method", Proc. *4th European & African Conference on Wind Engineering*, Praha, article 243.

[18] Didier, E., and Borges, A.R.J., 2005, "A fully coupled method for computing uniform fluctuating flow around bluff bodies", Proc. *4th European & African Conference on Wind Engineering*, Praha, article 127.

Conference on Modelling Fluid Flow (CMFF'06)
The 13th International Conference on Fluid Flow Technologies
Budapest, Hungary, September 6-9, 2006

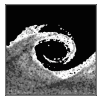

INFLUENCE OF A CRUCIFORM ARRANGEMENT DOWNSTREAM STRIP-PLATE ON CROSSFLOW VIBRATION OF A SQUARE CYLINDER

Mizuyasu KOIDE[1], Naoto KATO[2], Shuichi YAMADA[2], Tsutomu TAKAHASHI[2] and Masataka SHIRAKASHI[3]

[1] Niigata Sangyo University, 4730 Karuigawa, Kashiwazaki, 945-1393, Japan.
[2] Nagaoka University of Technology, 1603-1 Kamitomioka, Nagaoka, 940-2188, Japan.
[3] Corresponding Author. Department of Mechanical Engineering, Nagaoka University of Technology, 1603-1 Kamitomioka, Nagaoka, 940-2188, Japan. Tel.: 81-258-47-9730, Fax: 81-258-47-9770, E-mail: kashi@mech.nagaokaut.ac.jp

ABSTRACT

In earlier works, the present authors found that the Kármán vortex excitation of a circular cylinder is effectively suppressed by setting another cylinder in cruciform arrangement downstream with a gap-to-diameter ratio s/d less than 0.5, and that new vortex excitations are induced by two types of longitudinal vortices shedding periodically near the cross in higher velocity ranges. In this work, influence of a strip-plate set downstream in cruciform arrangement on the vibration of a square cylinder is investigated by wind tunnel experiment. The Kármán vortex excitation is well suppressed by the strip-plate with a width w equal to the side of square d when $s/d<2$. The galloping is also completely suppressed by the plate when $s/d<4$, except the range of $1<s/d<2$. In the latter range of s/d, a new vibration occurs and its maximum amplitude at s/d around 1.3 is double the original galloping. Flow visualization by tuft grid and velocity measurement show that this vibration is caused by the longitudinal vortex shedding periodically near the cross which synchronizes with the cylinder motion, similar to the case of two-circular-cylinder system.

Keywords: Flow induced vibration, Galloping, Longitudinal vortex, Vibration control, Vortex excitation

NOMENCLATURE

d	[mm]	side-length of square cylinder, =26mm
f_n	[1/s]	system natural frequency
f_v	[1/s]	vortex shedding frequency
f_{v0}	[1/s]	vortex shedding frequency for fixed systems
f_z	[1/s]	vibration frequency
Re	[-]	Reynolds number (= Ud/ν)
s	[mm]	gap between bodies
St	[-]	Strouhal number (= $f_v d/U$)
St_0	[-]	Strouhal number for fixed systems (= $f_{v0} d/U$)
Su	[-]	spectrum of velocity u
U	[m/s]	free stream velocity
u	[m/s]	velocity component in the x-direction
w	[mm]	width of downstream strip-plate
Z	[mm]	z-displacement of upstream cylinder
Z_{rms}	[mm]	root-mean-square value of Z
Z_{rms}*	[-]	Z_{rms} divided by Z_{rms} of single cylinder
δ	[-]	logarithmic damping factor
ν	[m^2/s]	kinematic viscosity of fluid

1. INTRODUCTION

Since vibrations of cylindrical bodies in fluid flow have caused many serious accidents in mechanical and structure engineerings, various methods for controlling of flow-induced vibration of a cylindrical body have been proposed so far, such as suction holes on the surface of the body, tripping wires near separation points, a splitter plate in the wake, and so on [1]. The innumerable number of such techniques shows the practical importance of the phenomenon.

Tomita et al. [2] reported that the acoustic noise from a circular cylinder can be suppressed by setting another cylinder downstream in cruciform arrangement with a certain gap between them as shown in Figure 1. Inspired by Tomita's work, the present authors investigated effect of the downstream cylinder on the Kármán vortex excitation of the upstream cylinder, and found that the vibration is effectively suppressed when the gap-to-diameter ratio s/d is less than around 0.5. However, it was also found that two types of longitudinal vortices, i.e. necklace vortex (Figure 1(a)) or trailing vortex (Figure 1(b)), shed periodically depending on the gap-to-diameter ratio and that these longitudinal vortices induce resonant excitation similar to the Kármán vortex excitation

over respective velocity regions, several times higher than that of the latter [3, 4].

In the case of a square cylinder, it is well known that another crossflow vibration called a "galloping" occurs at velocities higher than the Kármán vortex excitation caused by flow-elastic instability [1].

The specific aim of this work is to investigate if a cylindrical downstream body in cruciform arrangement is effective also to suppress the galloping, and if the longitudinal vortex excitation is induced with it also for the case of a square cylinder.

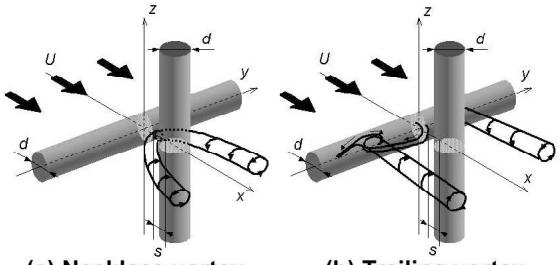

Figure 1. Longitudinal vortices from cruciform two-circular-cylinder system

2. EXPERIMENTAL APPARATUS AND MEASUREMENT

Arrangement of the experimental apparatus and the coordinate system used in this paper are shown in Figure 2. The test section of the wind tunnel has a 0.32 m square cross-section (the upper and lower walls of the test section are not drawn in Figure 2) and a 1 m length.

A rigid rod passes through slots on the side walls of the measuring section and is fixed rigidly or supported elastically at both ends outside the measuring section. In the latter setup, two twin-plate-springs are used as shown in Figure 2 so as to make its motion pure crossflow mode [5]. A square cross section cylinder with side-length d=26 mm and spanwise length l_e=318mm is fixed to the rod. End plates are attached to the cylinder to remove influence of flow through the slots [6].

A strip-plate is mounted rigidly on a traversing table set beneath the measuring section, which enables to adjust the gap s within a preciseness of 0.05mm. The downstream strip-plate is spanned over the whole height of the measuring section. The width of the downstream strip-plate w is varied from 10mm to 26mm, while its thickness is fixed at 5mm. Preliminary experiments have shown that the influence of the plate thickness is insignificant.

The natural frequency f_n and logarithmic damping factor δ are obtained by free damping oscillation in air otherwise at rest. The effective mass m_e is calculated from f_n thus determined and the spring constant k measured separately. The free flow velocity U is measured by the ring-type velocimeter [7]. The vortex shedding frequency f_v is determined from a spectrum Su of x-component velocity u, measured by using a hot-wire probe placed at an appropriate location to detect the periodic shedding of vortices.

The vertical displacement of the square cylinder, Z, is defined as the average of values measured by laser displacement sensors at the both ends of the supporting rod outside the measuring section (Figure 2). The tuft grid method is applied to observe the cross section of the longitudinal vortex in the wind tunnel.

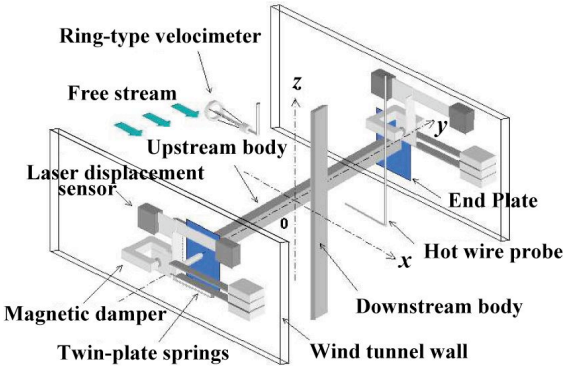

Figure 2. Arrangement of the experimental apparatus and the coordinate system

3. RESULTS AND DISCUSSIONS

3.1. Kármán vortex excitation and galloping of an isolated square cylinder

Vibration of the isolated square cylinder (i.e. without downstream strip-plate) and the vortex shedding frequency were measured with an increasing and then decreasing flow velocity.

In Figure 3, the oscillation amplitude expressed by the RMS value of z-displacement, Z_{rms}, and the vortex shedding frequency f_v are plotted against the flow velocity U. As well known for the case of a single square cylinder, the Kármán vortex excitation and the galloping are clearly observed in separated velocity regions in the figure. The former is observed over a range of U, where the spectra of displacement Z and velocity u have a sharp peak at the frequency f_n, showing occurrence of the lock-in phenomenon. While, the latter vibration increases with velocity and f_v is much higher than f_n. The spectra of displacement Z show that vibration frequency f_z is fixed at f_n over the whole velocity range of galloping, being much lower than the Kármán vortex shedding frequency f_v.

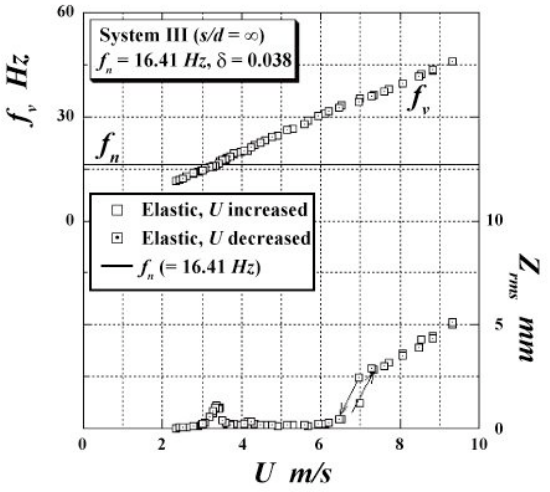

Figure 3. Vibration behavior of an isolated square cylinder (Hot-wire probe position: x/d = 1.5, y/d = 0, z/d = 0.4)

3.2. Suppression of Kármán vortex excitation

To see the suppression effect of the downstream strip-plate on the Kármán vortex excitation, the flow velocity was set constant at the value where the Kármán vortex excitation is maximum in Figure 3, and then the downstream plate was made to approach from s/d = 6.0. The vibration amplitude Z_{rms} is normalized by the value for the isolated cylinder.

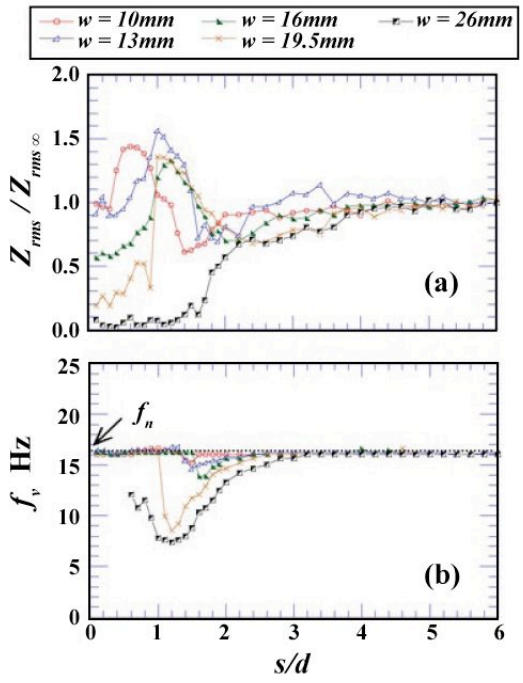

Figure 4. Effect of downstream strip-plate on the Kármán vortex excitation (U = 3.4 m/s)

(a) Vibration amplitude normalized by its value of isolated cylinder

(b) Vortex shedding frequency (Hot-wire probe position: x/d=1.5, y/d=1.25, z/d=0.4)

The results thus obtained are plotted against s/d in Figure 4 for five strip-plates with different widths, together with the vortex shedding frequency. By approaching the w=26mm plate (w/d=1), the vibration begins to decrease when s/d=4 and almost completely suppressed when s/d<1.5. However, this effect becomes weaker for narrower plates and it is paradoxical that the vibration amplitude becomes considerably larger than the original Kármán vortex excitation by the plates with w≤19.5mm over a certain region of s/d<1.5. The vortex shedding frequency f_v in Figure 4 (b) is seen to be considerably lower than f_n or to vanish, when the vibration is small.

In Figure 5, the suppression of Kármán vortex excitation is compared for the cases of three different configuration cruciform systems with w/d=1, i.e. System I : two circular cylinders, System II : circular cylinder and strip-plate, and, System III : square cylinder and strip-plate (the present setting but supported by single plate springs) [8] . In this figure, Z_{rms}* begins to decrease around s/d = 2~3 for all the systems. Compared with the other two systems, i.e. the two-circular-cylinder and the circular-cylinder/strip-plate systems, the effect is strongest for the square-cylinder/strip-plate system in the sense that the maximum value of s/d to suppress the vibration is largest among the three.

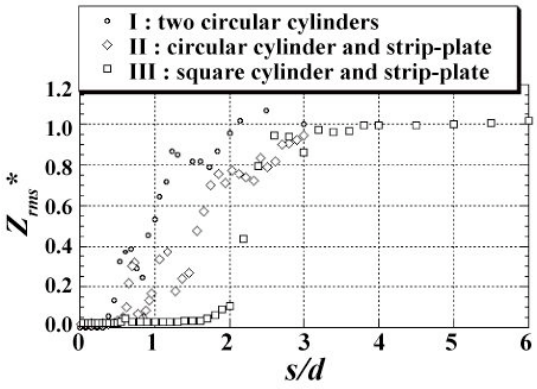

Figure 5. Suppression of Kármán vortex excitation for three systems with different configurations (w/d = 1) [8]

3.3. Suppression of galloping

The suppression effect of the strip-plate on the galloping was observed in the same way as for the Kármán vortex excitation described above. The velocity was set constant at 7.6 m/s selected as the representative value (see Figure 3) and the results are presented in Figure 6. Compared with the case of Kármán vortex in Figure 4, the effect is more remarkable in that the vibration is completely suppressed with s/d as large as around four when w/d=1. The maximum value of s/d where the vibration begins to become lower is smaller with the smaller width strip-plates. However, there

appears again a large vibration when s/d is made still smaller, in the cases of w=10 *mm*, 13 *mm* and 26 *mm*. This second vibration peak is indefinite for the plates with intermediate width plates (w=16 *mm* and 19.5 *mm*). In the case of the w=26 *mm* plate, the peak value of the second vibration in the range of s/d=1.2 ~ 1.5 is double the original galloping. The vortex shedding frequency f_v in this range of s/d is equal to f_n for the w=26 *mm* plate, while f_v for the second vibration peak is a slightly higher than the value of single cylinder for the w=10 *mm* and 13 *mm* plates. Note that the vibration frequency f_z is fixed at f_n for all the measurements shown in Figure 6.

The results shown in Figure 6 infer that the origin of the second vibration peak for the w=26 *mm* plate is the longitudinal vortex similar to those observed in the two-circular-cylinder system as shown in Figure 1. In contrast, the second vibration of the w=10 *mm* and 13 *mm* plates are not attributed to the longitudinal vortex but may be to the galloping.

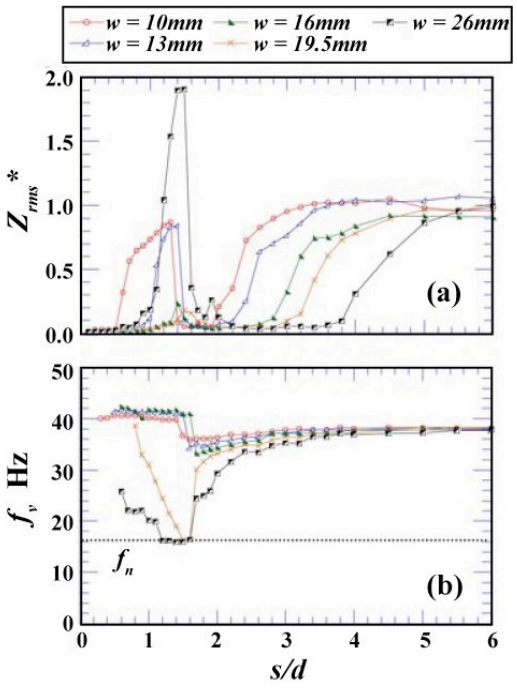

Figure 6. Effect of downstream strip-plate on galloping (U=7.6 *m/s*)

(a) Vibration amplitude normalized by its value of isolated cylinder

(b) Vortex shedding frequency (Hot-wire probe position: x/d=1.5, y/d=1.25, z/d=0.4)

3.4. Longitudinal vortex excitation

The w=26*mm* plate was set at s/d = 1.2, the gap at which the second vibration is clearly observed in Figure 6, and the flow veloicity was increased and then decreased. As seen in Figure 7, both the Kármán vortex excitation and the galloping in Figure 3 disappear and a new vibration is induced instead over a velocity range of U = 6.5 ~ 8 *m/s*, where the peak frequency f_v in velocity spectrum remains fixed on f_z=f_n. Except this range of U, f_v increases proportionally with U and is much lower than that of an isolated cylinder. Therefore, the new vibration is inferred to be caused by the longitudinal vortices.

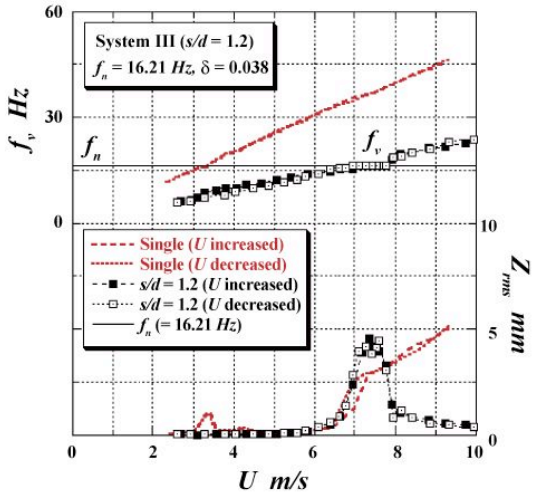

Figure 7. f_v and Z_{rms} vs. U of square cylinder with w/d = 1 and s/d= 1.2 (Hot-wire probe position: x/d=1.5, y/d=1.25, z/d=0.4)

To assure it, the flow downstream the cross of the vibrating square cylinder was visualized by tuft-grid method as shown in Figure 8. There, the cross section of longitudinal vortex is clearly observed at the two antiphase instants, (a) and (b), in a period of cylinder displacement Z. It is clearly seen that the pattern is symmetric about the x-z plane both in photos (a) and (b), and that the vortex pattern is observed only one side of positive or negative z region. However, it cannot be discerned whether the longitudinal vortex in Figure 8 is the necklace or the trailing vortex shown in Figure 1.

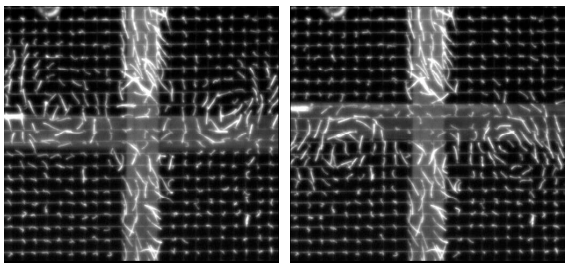

(a) $\phi = \pi/4$ **(b) $\phi = 5\pi/4$**

(ϕ is the phase angle in a cycle of the cylinder displacement Z)

Figure 8. Longitudinal vortices synchronizing with the square cylinder oscillation in wind tunnel (w/d = 1, s/d = 1.2, δ = 0.069, single-plate-springs, Re = 13200, Grid position : x/d =2.7)

3.5. Characteristics of longitudinal vortex from fixed system

The square cylinder in the same setting as in Figure 8 was fixed rigidly and the hot-wire probe was traversed towards the side wall parallel to the y-axis. Figure 9 shows velocity spectra for various spanwise position thus obtained. A sharp peak appears in Su when $y/d < 3$ and no peak is observed beyond this position, showing that the Kármán vortex shedding is removed by the downstream plate.

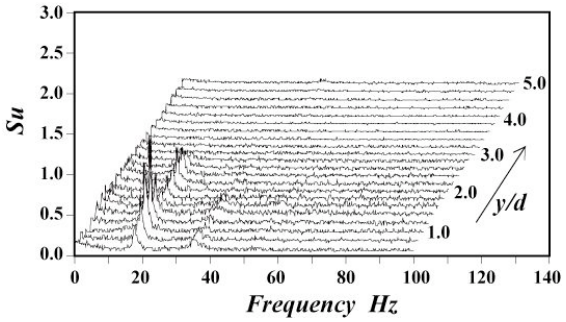

Figure 9. Velocity spectra for various spanwise position (w=26 *mm*, s/d=1.2, U=7.6*m/s*, probe position x/d=1.5, y/d=0.8 ~ 5.0, z/d =0.4)

The hot-wire probe was set at the position where the peak in spectrum Su is most clearly observed in Figure 9, and the gap s was varied while the velocity U was set constant. The spectra and the peak frequency f_{v0} thus obtained are shown in Figure 10, the latter being normalized by its single-cylinder value and compared with the results by Fox [9] on a two-square-cylinder system. The peak in Su in the region s/d>5 is caused by the Kármán vortex with a frequency essentially equal to that of the isolated cylinder. The continuous nature of the changes in the shape and peak frequency of Su in the region 2<s/d<6 inferrs that the Kármán vortex sheds there and that its frequency and regularity become lower by the interference of the downstream plate.

The abrupt changes in Su and f_{v0} at around s/d=1.7 show that the vortex structure becomes different from that of Kármán vortex when s/d is smaller than this value. The observation of flow as seen in Figure 8, and also by Fox [9], may suggest that the low frequency vortex in the region s/d<1.7 is the necklace vortex as shown in Figure 1 (a). The peak frequency f_{v0} in Su near the cross of the fixed system is reduced to the Strouhal number St_0 and plotted against the Reynolds number Re as shown in Figure 11, together with results for the other two configuration systems. Figures 9 ~ 11 verify that the periodic shedding of the longitudinal vortex is inherent to this boundary condition but not induced by the cylinder vibration, and show that the Strouhal number of the longitudinal vortex is 0.05 ~ 0.06, while that of the Kármán vortex is around 0.13.

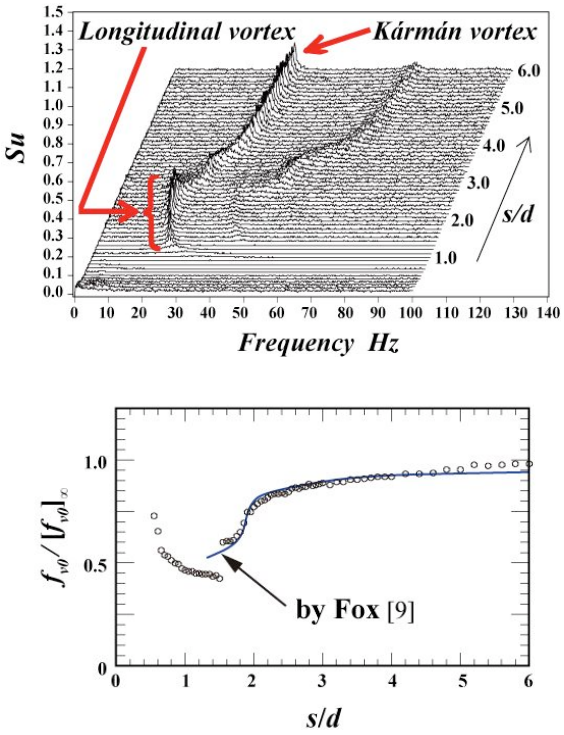

Figure 10. Variation of velocity spectrum and its peak frequency with gap for fixed system (w=26 *mm*, U=7.6 *m/s*, Probe position: x/d=1.5, y/d=1.25, z/d=0.4)

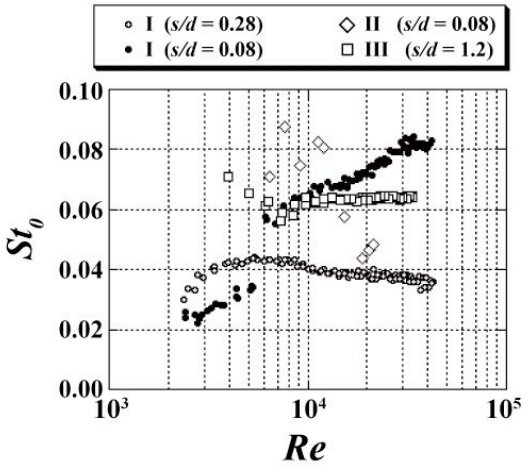

Figure 11. Strouhal number of longitudinal vortices vs. Reynolds number for fixed system

I : Two Circular-cylinder,

II : Circular-cylinder / Strip-plate,

III: Squqre-cylinder / Strip-plate (present system)

CONCLUSIONS

Wind tunnel experiment was carried out to investigate interference effect of a strip-plate set downstream in cruciform arrangement on the crossflow vibration behavior of a square cylinder in uniform flow. The results are compared with differnt configuration systems, i.e. cruciform two-circular-cylinder and circular-cylinder/strip-plate systems. The conclusions are summarized as follows.

1. Both the Kármán vortex excitation and the galloping of the square cylinder are effectively suppressed by the downstream strip-plate in spite of the fact that the mechanisms of the two vibrations are absolutely different.

2. A longitudinal vortex excitation similar to that observed for the two-circular-cylinder system is induced by the downstream strip-plate over a range of non-dimensional gap s/d considerably larger compared with the latter.

Generally speaking, effect of a cruciform downstream strip-plate is stronger in the square-cylinder/strip-plate configuration in the sense that the range of s/d to influence the vibration is much larger than in the other two cases. Most remarkable effect is that the galloping is completely suppressed by the w/d=1 strip-plate even when the gap is as large as four times the side length of square.

However, the above effects of the downstream plate are largely different when the width of the plate is smaller. Since the flow around the cross is of highly three dimensional nature accompanied with periodic vortex shedding of longitudinal vortices superimposed by turbulence, mechanisms to cause the influences on vibration are left for further investigations.

ACKNOWLEDGEMENTS

The authors would like to thank Mr. Ohta, M. for his experimental supports.

REFERENCES

[1] Blevins, R. D., Flow-Induced Vibration, 2nd Ed., Van Nostrand, 1990.

[2] Tomita, Y., Inagaki, S., Suzuki, S. and Muramatsu, H., 1987, "Acoustic characteristics of two circular cylinders forming a cross in uniform flow." JSME International Journal, 30, pp. 1069-1079.

[3] Shirakashi, M., Bae, H. M., Sano, M., Takahashi, T., 1994, "Characteristics of periodic vortex shedding from two cylinders in cruciform arrangement." J. Fluids and Structures, 8, pp. 239-256.

[4] Takahashi, T., Baranyi, L., Shirakashi, M., 1999, "Configuration and frequency of longitudinal vortices shedding from two cylinders in cruciform arrangement." Journal of the Visualization Society of Japan, 19, No. 75, pp. 328-336.

[5] Kamimura, Y., Koide, M. Takahashi, T. and Shirakashi, M., 2001, "Effect of slenderness on cross-flow oscillation of a rectangular cylinder supported by cantilever in uniform flow." CMFF'03, The 12th International Conference on Fluid Flow Technologies, pp. 399-406.

[6] Shirakashi, M., Ishida, Y. and Wakiya, S., 1986, "Higher velocity Resonance of Circular Cylinder in Crossflow." Journal of Fluids Engineering, 108, pp.392-396.

[7] Koide, M. Takahashi, T. and Shirakashi, M., 2001, "Development of a Ring-Type Vortex Anemometer for Low-Velocity Wind Tunnel Experiments." Bulletin of JSME, (in Japanese), 67, No. 657, B, pp. 1105-1111.

[8] Kato, N. Koide, M. Takahashi, T. and Shirakashi, M., 2005, "Interference of downstream body on the oscillation behavior of a circular and a square cylinder in uniform flow." Proc. PVP 2005, PVP2005-71517, July 17-21, Denver, Colorado USA.

[9] Fox, T. A., 1992, "Interference in the wake of two square-section cylinders arranged perpendicular to each other." Journal of Wind Engineering and Industrial Aerodynamics, 40, 1, pp. 75-92.

Conference on Modelling Fluid Flow (CMFF'06)
The 13th International Conference on Fluid Flow Technologies
Budapest, Hungary, September 6-9, 2006

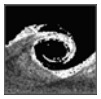

REDUCING THE ATHLETE'S AERODYNAMICAL RESISTANCE

Luca OGGIANO[1], Lars SAETRAN[2], Sveinung LOSET[3], Ronny WINTHER[4]

[1] Corresponding Author. Norwegian University of Science and Technology, Faculty of Engineering Science and Technology, N-7491 Trondheim, Norway Tel.: +47 45691711 , E-mail: luca.oggiano@ntnu.no
[2] Norwegian University of Science and Technology, Faculty of Engineering Science and Technology, N-7491 Trondheim, Norway Tel. +47 91897999 E-mail: Lars Satran@ntnu.no
[3] Norwegian University of Science and Technology, Faculty of Engineering Science and Technology, N-7491 Trondheim, Norway Tel. +47 73594629E-mail: sveinung.loset@ntnu.no
[4] Norwegian University of Science and Technology, Faculty of Engineering Science and Technology, N-7491 Trondheim, Norway Tel. +47 73594629E-mail: ronny.winther@ntnu.no

ABSTRACT

This paper presents an experimental investigation on the effect of surface roughness on legs and arms of an athlete. Because of their cylindrical shape, arms and legs of an athlete can be approximately studied as flow over circular bodies. The variation of roughness has been obtained using three different textiles and changing the diameter of the cylinder. To evaluate the results, two textiles from two alpine suits used by the Norwegian alpine ski team have been tested. All the results have been compared with a cylinder with a smooth surface. The critical Reynolds number for a significant drop in the drag coefficient decreases by increasing surface roughness.

Keywords: Aerodynamic, Bluff bodies, Cylinder, Drag, Roughness, Sport.

NOMENCLATURE

A	[m^2]	Projected area normal to the wind
$Diam$	[m]	Diameter of the cylinder
υ	[m^2/s]	Dynamic viscosity
D	[N]	Drag
ρ	[kg/m^2]	Density
C_d	[-]	Drag coefficient
w,d	[m]	Roughness width, depth
k	[µm]	Roughness parameter
r	[-]	Roughness coefficient
V	[m/s]	Free stream velocity

1. INTRODUCTION

In many sports the aerodynamical resistance (drag – D) is of primary importance for the athlete's performance – e.g. in speed-skating where D is about 80% of the physical forces acting against the athlete's speed; and in a ski-jumper's in-run where the velocity at take-off is determined by 60% for the ski/snow friction and 40% by D. Estimates using these figures show that a speed-skater will reduce his lap-time by one tenth of a second per % reduced D, and that a ski-jumper significantly can increase the velocity at take-off by a modest reduction in D.

The drag D is proportional to the square of the velocity V, $(D=\rho V^2 C_d A/2)$,where $C_d A$ is the product of the Drag coefficient and a characteristic cross sectional area – and is an important parameter to evaluate and work on to minimize. One can work on this parameter by either 1)reducing A and 'streamlining' the body, and/or 2) by manipulating the flow close to the body such that flow separation from the body is delayed – producing a smaller wake zone and thereby less drag force.

The athletes themselves normally have no quantitative feedback on how effective their body posture and equipment is minimizing D. The wind tunnel equipped with instrumentation for measurement of physical forces represents an efficient way of quantitatively optimizing body posture and develop aerodynamically clothing and equipment for the athletes.

For a speed-skater the leg, from the skate and up to the knee, represent about 1/3 of the skater's total air resistance. By tripping the airflow boundary layer on the leg, using certain material textures, separation can be delayed and the leg's D significantly reduced.

Working on body postures for ski-jumpers (in-run) resulted in an increased speed of 1 km/h at take-off for the Norwegian national team (in average) In the experiments carried out it has been chosen to focus the attention on the reduction of drag in legs and arms using different textiles with different surface roughness (or dimples).
Using the approximation that legs and arms are cylindrically shaped the textiles has been tested on cylinders with different diameters.
For smooth cylinders in a cross flow the critical Reynolds number (when transition is happening and the drag coefficient fall) is around $3x10^5$.

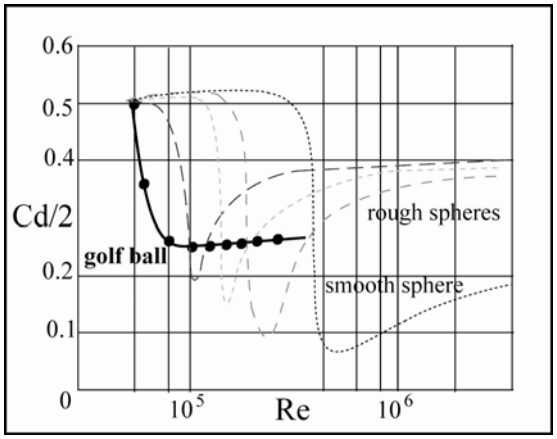

Figure 1. Variation of C_d with Reynolds number for smooth and rough sphere and golf ball. (3)

The introduction of surface roughness on the cylinder surface can shift the transition to lower Reynolds number.
Usually the larger the roughness parameter, the lower is the value of the critical Reynolds number, but the smaller will be the fall in C_d. That has been shown by Achenbach (1) for spheres and by Bearman and Harvey (2) for cylinders. From Achenbach's experiments(1), for the post-critical regime, to increase the roughness on a sphere means increasing the drag coefficient if it is compared with a smooth surface sphere (see Fig.1).
Flows around spheres and cylinders are very similar so it can expected that the results carried on from the experiments done will be close to the results what Achenbach and Bearman-Harvey found(1). The target is to obtain the same drag reduction for a cylinder as obtained for a golf ball (Fig 1) by covering the cylinder surface with clothing of different textures thereby varying the roughness coefficient.
This will permit to estimate the drag reduction in the cylindrical parts of the athlete's body.

2. EFFECTS OF TRANSITION AND SEPARATION

The total drag can be split in two different parts. A part of drag is due to skin friction and is called friction drag and another part is due to the difference between the high pressure in the front part of the body (close to the stagnation point) and the low pressure on the rear region (separated region) and is called pressure drag.

$$Cd_{TOT} = Cd_{FRICTION} + Cd_{PRESSURE} \quad (1)$$

The relative contribution of friction and pressure drag depends on the body shape, especially its thickness. The cylinder is a bluff body and most of the drag, even with a rough surface, will be contributed to by the pressure drag.
For cylinders (and in general for bluff bodies) the transition from laminar to turbulent increases the skin friction because of the Reynolds stress but, on the other hand, the pressure drag decreases by a large margin by moving the separation point to the back of the cylinder and diminishing the width of the wake.

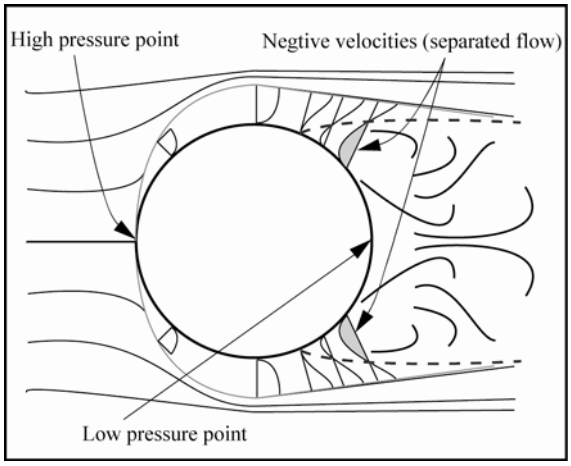

Figure 2. Flow around cylinder

3. EXPERIMENTAL SETUP

3.1 Wind tunnel

For the experiments, the wind tunnel of NTNU (Norwegian University of Science and Technology) in Trondheim has been used. (Fig.3). The contraction ratio is 1:4.23, and the test section of the wind tunnel is 12.5 meters long, 1.8 m high, and 2.7 m wide. The wind tunnel is equipped with a 220KW fan that can produce a variation of speed between 0 - 30 m/s.

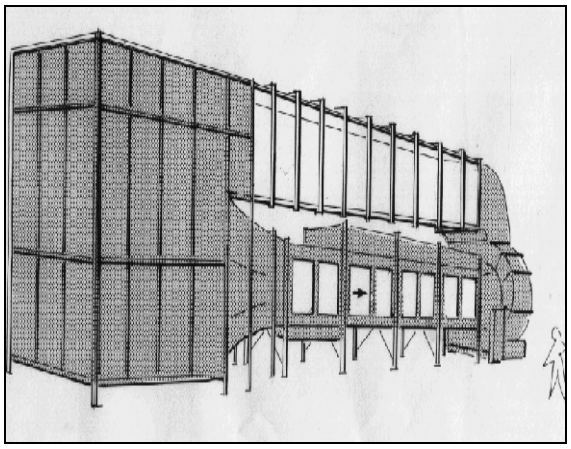

Figure 3. Wind tunnel

3.2 Cylinder position in the wind tunnel

The cylinder is mounted as shown in Fig 4 and it is connected to a balance positioned under the wind tunnel floor. The cylinder is mounted in the wind tunnel on a support and two dummy cylinders are connected to the wall but not to the balance to reduce the finite cylinder length effect. This solution permits a comparison of the results with an infinitely long cylinder. . The cylinder length is 120cm (for all the 3 cases: 11cm, 20 cm, 31cm diameter.)

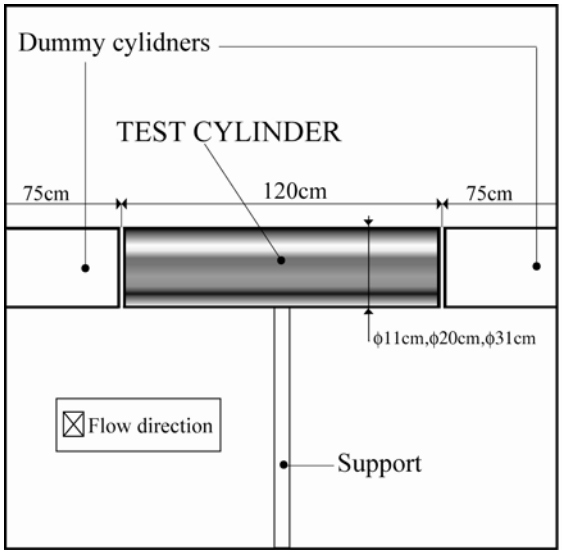

Figure 4. Cylinder in the wind tunnel

3.3 Six components balance

The balance (Carl Schenck AG) used is a six components balance capable of measuring the three forces and the three momentums around the three axes. Variations of forces and momentum are measured using strain gauges glued to the balance body.

The voltage outputs are measured by a LabVIEW based PC program.

3.4 Textiles

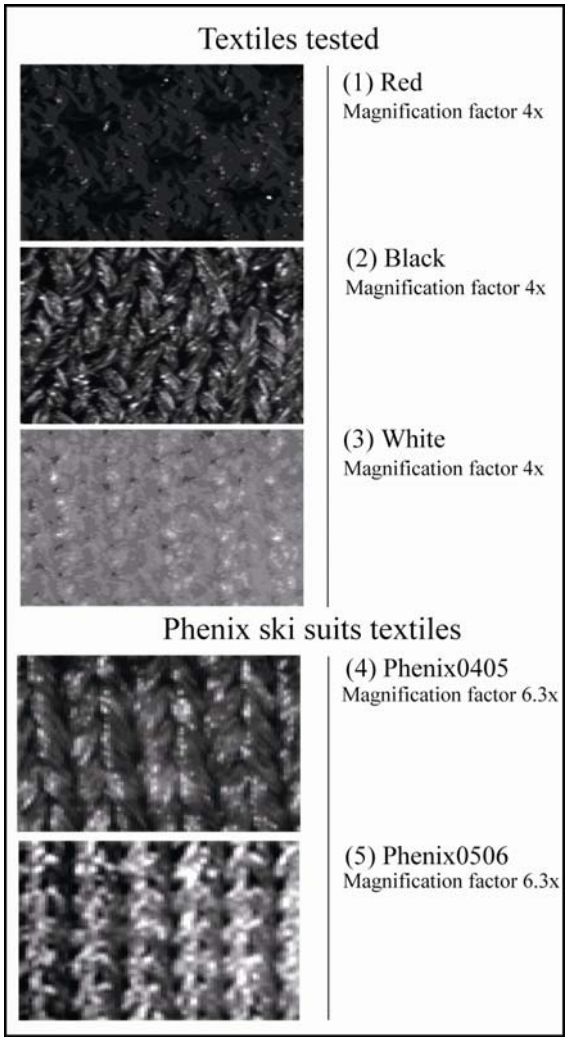

Figure 5. The five different textiles used

The following chapter shows the different textiles used to change the surface roughness on the cylinders. The five textiles have all different surface roughness (Table 1).
Different roughness has been obtained manufacturing each textile in a different way and with a different pattern. (See Table 1).
The roughness factor for each textile was found using an electronic microscope with a magnification factor of 20X. Based on structure width and depth a surface parameter can be defined as:

$$k_{surface} = \sqrt{w \cdot d} \qquad (2)$$

Only for the black textile it has been chosen to use a different surface because of the different structure of this textile. The black textile presents in fact an inner-seam and an outer-seam. The roughness

calculated is the average between inner and outer roughness.

$$k_{surfaceTOT} = \frac{k_{inner} + k_{outer}}{2} \qquad (3)$$

Fig.5 represents five pictures of the textiles. The first three (1), (2) ,(3), are obtained using a magnification factor of 4X.

Table 1. Roughness parameters of the different textiles used

	k	*r*
11cm Red (1)	642	5.84E-03
11cm Black (2)	386	3.51E-03
20cm Red (1)	642	3.21E-03
20cm Black (2)	386	1.93E-03
31cm Red (1)	642	2.07E-03
31cm Black (2)	386	1.25E-03
11cm White (3)	108	9.82E-04
20cm White (3)	108	5.40E-04
31cm White (3)	108	3.48E-04
20cm 0405 (4)	273	1.37E-03
20cm 0506 (5)	335	1.68E-03

The red textile is the roughest and some dimples are present on the structure. The black structure presents a roughness parameter *k* between the red and the white textile. Some dimples are presents also in the black textile structure but it is not possible to localize them in the picture shown
Fig. 5(4) and 5(5) shows the pictures obtained with a magnification factor of 6.3 of the two textiles used in the alpine suits.
The roughness parameter *k* is a surface length scale that will influence on the flow close to the cylinder surface.
The surface curvature (given by the cylinder diameter) determines the pressure gradient that influences on the flow separation conditions. Then combining these two parameters in a dimensionless roughness coefficient *r* :

$$r = \frac{k}{Diam} \qquad (4)$$

4.RESULTS

4.1 Cd-Re curves

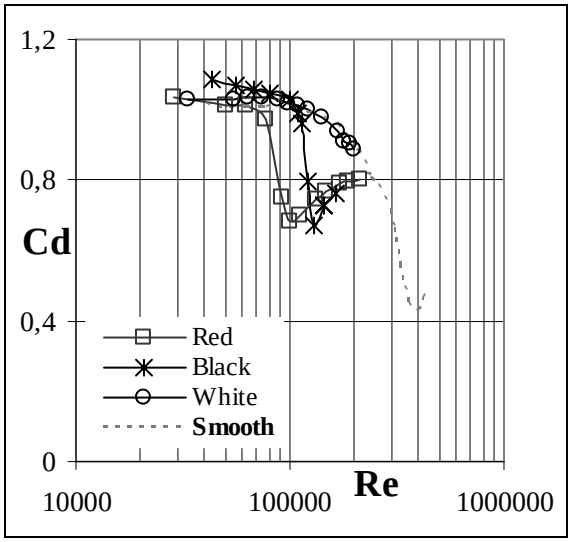

Figure 7. 11cm cylinder

The four curves in fig 7 represent the *Cd-Re* curves for the 11cm diameter cylinder. The transition for the black (r=3,51·10^{-3}) and the red (r=5,84·10^{-3}) textile happens at lower Reynolds number than for the smooth cylinder and for the white (r=9,82·10^{-4}) material.
The results are conform to the literature: increasing the roughness, the transition to turbulent start at a lower Reynolds numbers which means that it is possible to reduce the drag of about 40%. Over a certain Reynolds number range the white textile has a *Cd-Re* curve similar to the *Cd-Re* curve for the smooth cylinder.
Choosing the correct material for the correct speed makes it possible to reduce the drag coefficient of 40-45%.

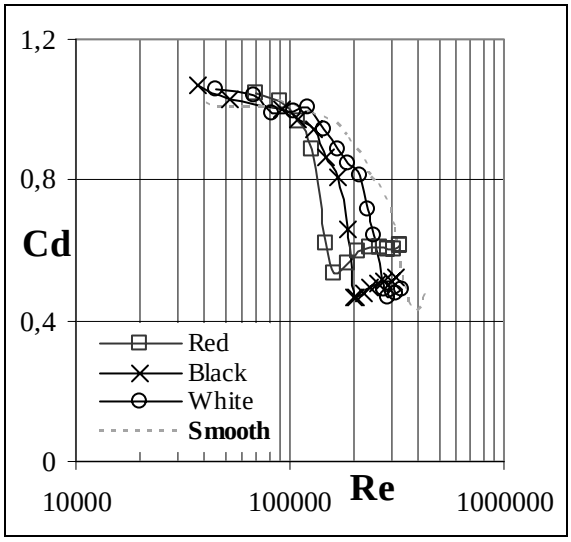

Figure 8. 20cm cylinder

Comparing the 20 cm diameter cylinder results (Fig 8) with the same graph for the 11cm diameter (Fig 7) it is easy to recognize the same trend (increase roughness means shift the transition to lower Reynolds number).

Until a certain Reynolds number (Re=1.75·10^5) the red textile (r=3.21·10^{-3} minimizes the drag coefficient most. Between Re=1.85·10^5 and Re=2.7·10^5 the black (r=1.93·10^{-3}) and for a Re>2.7·10^5 the white textile (r=5.40·10^{-4}) produce the lowest drag coefficient. Increasing the Reynolds number (Re>3.2·10^5), the cylinder with the red textile has a C_d higher than the C_d measured for the smooth cylinder.

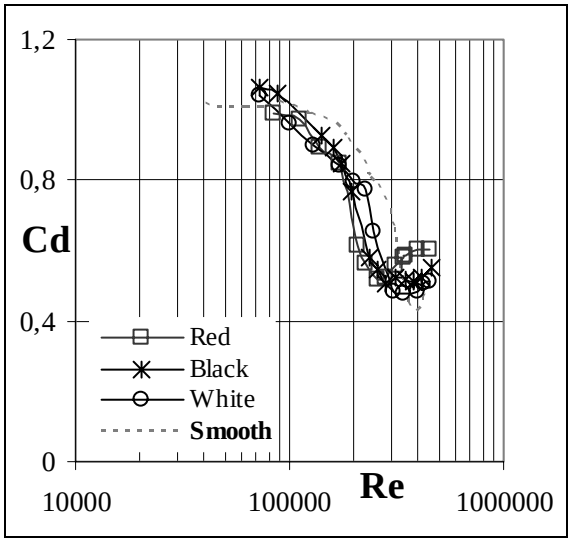

Figure 9. 31cm cylinder

The *Cd-Re* curves trend for the 31cm diameter cylinder is comparable to the tendency shown in Fig.7 and Fig 8 for the 11cm and 20cm diameter cylinders.

For the lower Reynolds number region the cylinder dressed with the red textile (r=2.07·10^{-3}) is the one with the lowest C_d, for the middle region the black textile (r=1.25·10^{-3}) minimizes the drag coefficient and for high Reynolds number the material that minimizes the drag coefficient more than the others is the white textile (r=3.48·10^{-4}). It is also easy to see, that now the drag coefficient reduction is about 20-30% less than the 40-45% found for the other cylinders (11cm and 20 cm diameter).

4.2 Roughness coefficient correlation

The correlation between the roughness parameter r and the trend of the *Cd-Re* curves has been analyzed defining a specific Reynolds number Re_{trans}. This specific Reynolds number has been chose to give an approximate description of where transition occurs. Defining Re_{trans} as the Reynolds number where the C_d curve has gone through half its drop (ΔC_d /2), Re_{trans} can be correlated with the roughness coefficient r (Fig 10), and the results can be expressed by the correlation

$$r = A + B\ln(\mathrm{Re}_{trans}) \qquad (5)$$

where the best fit for our limited data base is for A=0.0594, B=-0.0048

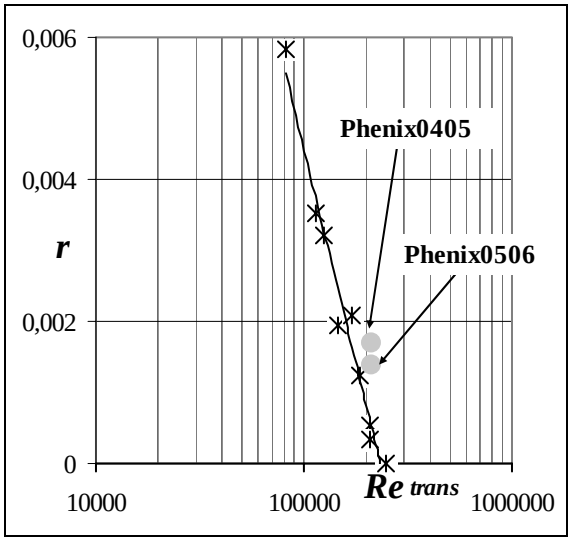

Figure 10. Correlation between r and Re_{trans}. The 2 round marks present in the figure are relatives to the data acquired for 2 textiles from 2 different ski suits used by the Norwegian national team.

6. CONCLUSIONS

Experiments carried out on cylinders dressed with different textiles show that the introduction of surface roughness (dimples), cause the critical regime to occur at lower Reynolds numbers than that for smooth cylinders. For increasing roughness, the experiments show that transition occurs at lower Reynolds. An explicit correlation the roughness factor r and the typical Reynolds number Re_{trans} has been suggested

The results for drag reduction presented here can be used for choosing the right textiles when designing suits for athletes, thereby reducing the athlete's aerodynamical resistance.

AKNOWLEDGEMENTS

The project is supported by the Norwegian Olympic Committee

REFERENCES

(1) Achenbach E. *"The effects of surface roughness and tunnel blockage on the flow past spheres"* Journal of fluid mechanics Vol. 65 Pt.1 1964

(2) P.W. Bearman and J.K. Harvey, *"Control of Circular Cylinder flow by the use of dimples"* AIAA-Journal Vol.31 No.10 October 1993

(3) P.W. Bearman and J.K. Harvey, *"Golf ball Aerodynamics"* Aeronautical Quarterly May 1976

(4) Frank M. White *"Viscous fluid flow (second edition"* Mc.Graw-Hill international editions 1991

Conference on Modelling Fluid Flow (CMFF'06)
The 13th International Conference on Fluid Flow Technologies
Budapest, Hungary, September 6-9, 2006

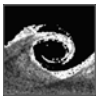

VORTEX DYNAMICS AND GRID-BASED SIMULATIONS FOR LOW REYNOLDS NUMBER FLOW PAST A CYLINDER

R. Ivan LEWIS[1], László BARANYI[2]

[1] School of Mechanical and Systems Engineering, University of Newcastle upon Tyne, UK, E-mail: r.i.lewis@ncl.ac.uk
[2] Corresponding Author. Department of Fluid and Heat Engineering, University of Miskolc, H-3515 Miskolc-Egyetemváros, Hungary. Tel.: +36 46 565 154, Fax: +36 46 565 471, E-mail: arambl@uni-miskolc.hu

ABSTRACT

Computational Fluid Dynamics models range from the Lagrangian style vortex cloud simulation technique to the finite difference type grid-based method for solving the Navier-Stokes equations. This paper undertakes a comparison of these two methods for the classical datum case of flow past a stationary circular cylinder at low Reynolds numbers in the range 10 to 220. Comparisons include time-history, time-mean and root-mean-square values of oscillating drag and lift coefficients, frequency of vortex shedding and related vortex street wake flow patterns. Particularly close agreement was obtained for Strouhal number versus Reynolds number, and good agreement for time-mean value of drag coefficients; comparison was also made with experimental results. Attempts are also made to calculate the skin friction and surface pressure components of the cylinder drag, revealing the significance of skin friction drag within this range and its relative insignificance above a Reynolds number of 220.

Keywords: CFD, grid-based method, stationary circular cylinder, Strouhal number, vortex cloud method

NOMENCLATURE

C_D [-] drag coefficient, $2D/\left(\rho U^2 d\right)$
C_{Df} [-] drag coefficient due to skin friction
C_L [-] lift coefficient, $2L/\left(\rho U^2 d\right)$
d [m] cylinder diameter, length scale
D [-,N] dilation, drag force
f_v [1/s] vortex shedding frequency
$k(s_m,s_n)$, $K(s_m,s_n)$ [1/m,-] coupling coefficients linking points m and n on a body
L [N] lift force
p [-] pressure, non-dimensionalised by ρU^2
Re [-] Reynolds number, Ud/ν
St [-] Strouhal number, $f_v d/U$
t [-] time, non-dimensionalised by d/U
u,v [-] velocities in x,y directions, non-dimensionalised by U
U [m/s] free stream velocity, velocity scale
U_∞ [m/s] free stream velocity in the x directions
U_{mj}, V_{mj} [m/s] velocity components at m due to a unit strength vortex element at j
v_{sn} [m/s] body surface velocity at point n
x,y [-] Cartesian coordinates, (grid-based method), non-dimensionalised by d
β_m [-] body profile slope at point m
γ [m/s] surface sheet vorticity strength
$\Delta\Gamma_j$ [m^2/s] discrete vortex element strength
Δt [-] time step (non-dimensionalised by d/U)
□ [kg/m^3] fluid density
ν [m^2/s] kinematic viscosity
ω [1/s] vorticity

Subscripts

c critical
D drag
f skin friction
L lift
m, n points on a body surface
mean time-mean value
rms root-mean-square value

1. INTRODUCTION

An interest in the formation of vortex streets behind bluff bodies has fascinated large numbers of researchers since the early experiments of Strouhal [1] in 1878 concerning the generation of 'Aeolean tones' and the famous 1911 paper by Theodore von Kármán [2] on the phenomenon later called the 'Kármán vortex street'. Serious early attempts at discrete vortex modelling were made by Rosenhead [3], who studied the related phenomenon of the Kelvin-Helmholtz instability of vortex sheets. Abernathy and Kronauer [4] extended Rosenhead's model to simulate instabilities of a parallel pair of

vortex sheets of equal and opposite strength subjected to an initial sinusoidal perturbation along their length, a flow akin to two separating vortex sheets released by a bluff body. Also asserted by these authors was the constancy of mean drag coefficient and Strouhal number for a circular cylinder over a wide range of Reynolds numbers, Re=300 to 100,000, demonstrating the negligible influence of viscosity upon these flows. Below $Re \approx 300$ viscosity is very important, while above this range three-dimensional instabilities due to convection set in. Within this range however there are considerable variations of both Strouhal number and cylinder drag coefficients, which are one interest of the present study.

This problem is of such practical importance that there are numerous studies dealing with flow past cylinders that are fixed, oscillating, rotating, or in orbital motion. Among these, the fixed cylinder is usually the starting point of investigations, as it is relatively simple to carry out experiments, and thus also for numerical studies it is favoured because comparison with experimental data is possible to confirm validity of the computer method used.

A huge number of researchers have investigated flow around a single circular cylinder through experimental, theoretical, and numerical approaches. Despite its simple geometry, the problem is not only extremely complex but also one with many applications. Knowledge of flow patterns around bluff bodies is important in the design of large structures such as smokestacks or bridges, which in winds are often subjected to large amplitude oscillation due to alternating vortex shedding, sometimes causing collapse of the structure. Slender struts or tubes are likewise subject to vibration due to vortex shedding, which can also cause noise generation in both external aerodynamics and internal aerodynamic. Roshko [5], Norberg [6], and Bearman [7] are among those who have provided invaluable experimental data on flow around a fixed cylinder. Computations on the same problem have been performed by many researchers [8,9].

The main purpose of this study is to compare two very different CFD methods against the important datum case of flow past a stationary circular cylinder at low Reynolds numbers. The first author has developed a vortex cloud analysis that follows the creation and diffusion from the body surface in Lagrangian fashion, Lewis [10], and that is well suited for modelling separated flows where boundary layer modelling is less key. This analysis is reviewed briefly in section 2.1. The second author on the other hand has developed a finite difference method based on Eulerian description with grid transformation that facilitates simulation of the flow of a viscous fluid past a cylinder. This was developed to study the flow past a cylinder in oscillating or orbital motion, Baranyi [11], and his method is reviewed briefly in section 2.2 for application to a stationary cylinder. Both methods deliver solutions of the Navier-Stokes equations for two-dimensional flow and are thus suited to simulation of cylinder wake studies in the low Reynolds number range 10 to 220.

2. OVERVIEW OF THE TWO METHODS OF ANALYSIS

This section gives an overview of the vortex cloud and grid-based methods for simulating a low Reynolds number flow around a circular cylinder placed in a uniform stream.

2.1. Overview of the present vortex cloud CFD method

The fundamental basis of vortex element representation of the Navier-Stokes equations has been given by the first author [10]. According to this method the entire flow is controlled by vorticity continuously being created at the body surface, diffused by viscosity and convected. The numerical method is Lagrangian in character and involves discretisation of the surface vorticity into discrete free-vortex elements which are released from the body surface at successive small time steps and subjected to convection and viscous diffusion, the latter being undertaken by random walks as defined by Chorin [12], and Porthouse [13].

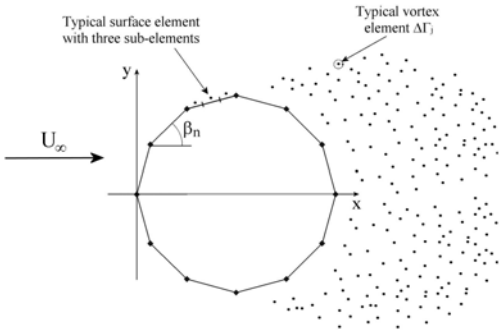

Figure 1. Numerical model for vortex cloud analysis

Central to the vorticity creation process is the boundary integral equation for potential flow past an arbitrary body in the presence of a uniform stream U_∞ and a surrounding cloud of vortex elements $\Delta\Gamma_j$, Figure 1, namely

$$\frac{1}{2}\gamma(s_m) + \oint k(s_m, s_n)\gamma(s_n)ds_n + U_\infty \cos\beta_m + \sum_{j=1}^{Z} \Delta\Gamma_j \left(U_{mj}\cos\beta_m + V_{mj}\sin\beta_m\right) = 0 \quad . \qquad (1)$$

The slip flow at the body surface is created by the vorticity sheet $\gamma(s)$ where, for the boundary condition of zero internal velocity inside the body,

the surface velocity v_{sn} is equal to the local surface vorticity $v_{sn}=\gamma(s_n)$.

In a viscous fluid the surface vorticity $\gamma(s)$ is being continuously created in the boundary sub-layer and diffused away from the surface where it is also subject to convective processes. For practical computations Eq. (1) may be expressed in the following equivalent numerical form

$$\sum_{1}^{M} K(s_m, s_n)\gamma(s_n) = -U_\infty \cos\beta_m - \sum_{j=1}^{Z} \Delta\Gamma_j \left(U_{mj}\cos\beta_m + V_{mj}\sin\beta_m\right) \quad , \qquad (2)$$

where, as illustrated in Fig. 1, the body surface is represented by M elements.

Over a sequence of small time steps Δt vortex cloud theory assumes that these vortex sheets are shed as discrete vortex elements of strength $\Delta\Gamma_n=\gamma(s_n)\Delta s_n$. As indicated in Fig. 1, greater resolution may be achieved by shedding this vorticity from n_{sub} sub-elements, where, for the example of three illustrated, the discrete vortex strengths would be $\Delta\Gamma_n = \gamma(s_n)\Delta s_n/3$. In addition to this vorticity creation and shedding process for each time step Δt and in accordance with the Navier-Stokes equations, the vortex cloud is subject to convection and diffusion, the latter being accomplished by imposing random walks.

2.1.1. Lift and drag forces

Lift and drag forces comprise two components due to surface pressure and shear stresses. As shown elsewhere [10], the pressure distribution on the cylinder surface at any instant may be calculated from the equation

$$\Delta p_n = -\rho\gamma(s_n)\Delta s_n / \Delta t = -\rho\, n_{sub}\Delta\Gamma_n / \Delta t \ , \qquad (3)$$

where Δp_n is the pressure change along the surface of element Δs_n during the time step Δt. Pressure forces P_x and P_y on the cylinder in the x and y directions then follow from

$$P_x = \sum_{n=1}^{M} \Delta p_n \sin(\beta_n), \quad P_y = -\sum_{n=1}^{M} \Delta p_n \cos(\beta_n) \ . \qquad (4)$$

Frictional shear stresses may be estimated for each surface element by considering the shear stress after time t on a plane wall parallel to the x axis shedding surface vorticity $\gamma(s_n) = U$ at time t=0. As shown elsewhere [10,14], the frictional forces F_x and F_y on the cylinder may then be approximated by

$$F_x = \rho\sqrt{\frac{\nu}{\pi\Delta t}} \sum_{n=1}^{M} \gamma(s_n)\Delta s_n \cos(\beta_n),$$

$$F_y = \rho\sqrt{\frac{\nu}{\pi\Delta t}} \sum_{n=1}^{M} \gamma(s_n)\Delta s_n \sin(\beta_n). \qquad (5)$$

The lift and drag forces then follow from

$$L = P_y + F_y \ , \qquad D = P_x + F_x \ . \qquad (6)$$

One problem of vortex cloud analysis is the presence of significant numerical noise due to the use of random walks for simulation of viscous diffusion. Smoothing can be achieved by using a running average of say three time steps before and after the current one when evaluating lift and drag, the practice adopted here.

2.2. Overview of the grid-based method of CFD analysis

The second author's earlier studies dealt with computation of the flow around a fixed circular cylinder at different Reynolds numbers, from Re = 10 to 1000, and up to Re = 180 for an oscillating cylinder, e.g. Baranyi and Shirakashi [15], and good agreement was obtained with experimental data for the variation of Strouhal number and time-mean drag coefficient with Reynolds number, especially up to Re = 190 above which three-dimensional instabilities occur. Further features of flow are investigated for a fixed cylinder in Baranyi [16], and the time-mean value of base pressure coefficient, which influences the near-wake structure, compares well with the experimental data of Roshko [17]. In [16] the energy equation for a stationary circular cylinder with constant surface temperature placed in a uniform flow is also solved from Re= 50 to 180 and the predicted dimensionless heat transfer coefficient or Nusselt number agrees well with available experimental results. In Baranyi and Lakatos [18], computational results obtained by this method are compared in the Reynolds number domain of Re = 50 - 180 with existing experimental results for the root-mean-square value of lift coefficients shown in Norberg [19], and a very good agreement is observed. Additional evidence for the reliability of the method has been given by comparison with other computational methods. De Sampaio [20], reports that his results for time-mean drag coefficient, obtained by the finite element method, agree well with those in [16].

At the time [15] was published the computing power of computers was more limited. In this paper some of the earlier computations are repeated with much finer temporal and spatial resolution, and new computations have also been added and compared with those of the vortex cloud method.

2.2.1. Governing equations

Constant property incompressible Newtonian fluid flow is assumed. When deriving the governing equations, which in non-dimensional forms are the

Navier-Stokes equations, the equation of continuity and a Poisson equation for pressure:

$$\frac{\partial u}{\partial t}+u\frac{\partial u}{\partial x}+v\frac{\partial u}{\partial y}=-\frac{\partial p}{\partial x}+\frac{1}{Re}\left(\frac{\partial^2 u}{\partial x^2}+\frac{\partial^2 u}{\partial y^2}\right); \quad (7)$$

$$\frac{\partial v}{\partial t}+u\frac{\partial v}{\partial x}+v\frac{\partial v}{\partial y}=-\frac{\partial p}{\partial y}+\frac{1}{Re}\left(\frac{\partial^2 v}{\partial x^2}+\frac{\partial^2 v}{\partial y^2}\right); \quad (8)$$

$$D=\frac{\partial u}{\partial x}+\frac{\partial v}{\partial y}=0; \quad (9)$$

$$\nabla^2 p=\frac{\partial^2 p}{\partial x^2}+\frac{\partial^2 p}{\partial y^2}=2\left[\frac{\partial u}{\partial x}\frac{\partial v}{\partial y}-\frac{\partial u}{\partial y}\frac{\partial v}{\partial x}\right]-\frac{\partial D}{\partial t}. \quad (10)$$

The gravity force is included in the pressure terms in Eqs. (7) and (8). Although the dilation D is theoretically zero by continuity (9), it is advisable to retain the term $\partial D/\partial t$ to avoid computational instability.

On the cylinder surface, no-slip boundary condition is used for the velocity and a Neumann type boundary condition is used for the pressure. At the far region, potential flow is assumed.

2.2.2. Transformation of domain and applied numerical methods

To be able to impose the boundary conditions precisely, a boundary-fitted coordinate system is used. The physical domain and the governing equations with boundary conditions are all transformed to the computational plane with an equidistant mesh, see [16]. This mapping (see Figure 2) provides a very fine mesh near the cylinder surface to capture the fluid-structure interaction in the near wake, but is gradually reduced to a coarse mesh in the far field to reduce computational cost. The equidistant mesh for the computational plane is beneficial for computational ease. The transformed equations are solved by finite difference method, [16]. 4th order central difference is used for the diffusion term and pressure derivatives, and the convective term is handled by a 3rd order upwind scheme [8]. Equations of motion (7) and (8) are integrated explicitly in time, and the S.O.R. method is used for solution of the pressure Poisson equation. Continuity (9) is satisfied at every time step. The code has been extensively tested against experimental results for stationary cylinders and good agreement has been found.

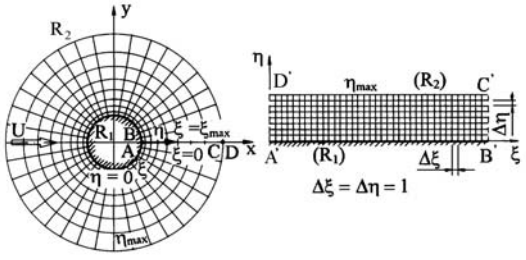

Figure 2. Physical and computational planes

For this study of flow around stationary cylinders the non-dimensional time step was 0.0005 and the number of grid points for the majority of runs was 301x177, but at the lowest three *Re* numbers 201x118, 251x148, and 270x159 were used, respectively, for convergence reasons. Even for the highest *Re* investigated, the solution was mesh independent. The computational domain shown in Fig. 2 is characterised by R_2/R_1=40. For further details see [15,16].

3. COMPARISON OF C_L/C_D, STROUHAL NUMBER AND WAKE FLOW PATTERN VERSUS REYNOLDS NUMBER

As we shall see, over the chosen range of Reynolds number *Re* there are considerable variations of both lift coefficient C_L and drag coefficient C_D. Vortex street development is associated with large oscillations of C_L as *Re* increases above a value of about 47. A summary of the variations in amplitude of C_D and Strouhal number *St* predicted by the two analyses is given in section 3.1

The drag on a circular cylinder originates from two sources, namely pressure forces normal to the body surface or "form drag", and viscous shear stresses parallel to the surface or "skin friction drag" C_{Df}. For this low *Re* range there are also considerable variations of these and comparisons of the predicted values are given in section 3.2. As a consequence of this the fluid motion is dominated by viscous effects at the low values *Re* in this range and by convective effects at high *Re*. This has considerable influence over the wake flow patterns and will be illustrated in section 3.3.

3.1. Comparison of lift and drag coefficients and of Strouhal number versus Reynolds number

In this section comparisons are given of predicted lift coefficient and Strouhal number for the two CFD methods. To begin with in Figure 3, comparisons are given of the predicted lift and drag coefficients for a sample mid-range value of *Re*=120, assuming a uniform stream *U*=1.0, a cylinder diameter of unity and an overall elapse time of *t*=400, ample to establish periodic motion.

As may be seen from Fig. 3, the lift coefficient settles down quickly into oscillating von Kármán vortex shedding with a mean value of zero. The predicted Strouhal number for *Re*=120 is of value 0.173 from the vortex cloud analysis and 0.175 from the grid-based method which compare well. As is well known, the frequency of the drag coefficient signal is double that of the lift coefficient as predicted by both methods. There are, however, considerable differences in the predicted time-history curves obtained by the two methods.

The grid-based analysis predicts that the motion settles down into a very regular periodic motion in which both C_L and C_D oscillate with constant amplitudes. The vortex cloud method on the other hand, exhibits some randomness in these amplitudes, although the mean values are in reasonable agreement as can be seen from the dashed curves in Fig. 3a. The predicted variations of amplitude of C_L and C_D are probably due to the random walk method for simulation of viscous diffusion in vortex dynamics. However, good agreement between the methods was obtained for the two performance parameters that most affect the excitation characteristics of cylinder wake flows, the Strouhal number and the root-mean-square value of the lift coefficient fluctuations C_{Lrms}. As further evidence of this, comparisons of the predicted values of St, C_{Drm} and C_{Lrms} versus Re for the two methods are given below in Figures 4 & 5.

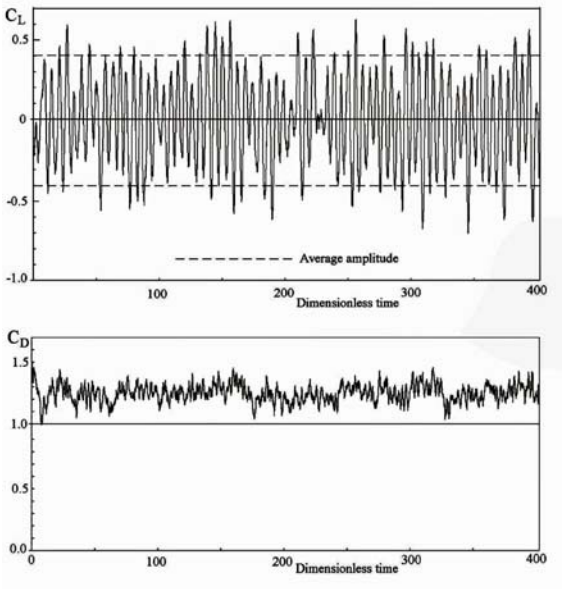

(a) Vortex cloud method

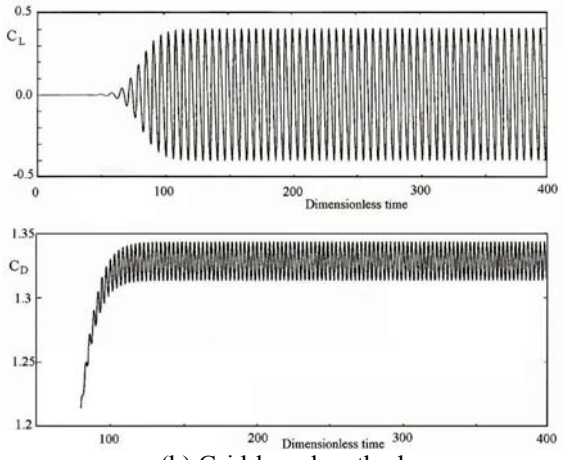

(b) Grid-based method

Figure 3. Comparison of the time histories of the lift and drag coefficients predicted by the vortex cloud and grid-based methods for Re=120

Fig. 4 shows excellent agreement between the two methods of analysis for the predicted value of St up to Re= 190. The grid-based analysis illustrated clearly that the onset of a von Kármán type vortex wake occurs at $Re \approx 47$, below which the influence of viscous diffusion predominates over that of vortex convection (bearing in mind that vortex street formation is fundamentally a convective process). Vortex cloud simulations are in general agreement with this although it was just about possible to detect slight wake fluctuation from seven diameters downstream of the cylinder for Re = 40 and an intermittent fluctuation of C_L. Above Re = 47, however, the Strouhal number rises steadily from 0.12 to about 0.2 for Re=210, in very good agreement. However, note that grid method computations were carried out from Re = 10 to only 190. This is because of experimental evidence from Williamson [21], and Floquet stability analysis by Barkley and Henderson [22], proving that a three-dimensional instability (mode A) begins to appear at around Re = 190. Above this Re number the application of a three-dimensional code is needed to capture the three-dimensional instabilities.

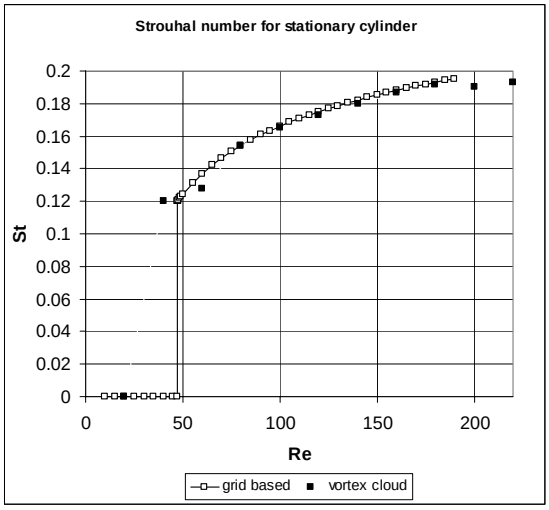

Figure 4. Comparison of predicted Strouhal numbers

The second author investigated the critical Reynolds number for the onset of vortex shedding. However, grid method computations in the vicinity of this critical Re require a lot of CPU time to reach the quasi-steady state of vortex shedding (although the possibility exists that introducing turbulence into the free stream may reduce the time needed for the establishment of vortex shedding). That is why in this study the case pertaining to Re = 47.2 was the nearest Reynolds number investigated above the critical one. By extrapolating the present C_{Lrms} values to zero the critical Reynolds number is about $Re_c \approx 46.8$. Other studies have found similar values. For sufficiently large aspect ratios Norberg [23] found experimentally that the critical value of

Reynolds number where periodic vortex shedding starts is about $Re = 47$. By using the Stuart-Landau model Thompson and Le Gal [24] found that the supercritical Hopf bifurcation characterising the onset of periodic vortex shedding is at $Re = 46.4$.

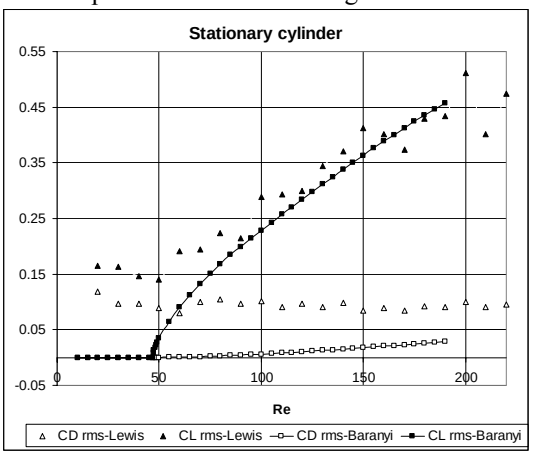

Figure 5. Variation of rms lift and drag coefficient fluctuations with Reynolds numbers

Fig. 5 shows the variation of the *rms* values of lift and drag coefficient over the chosen *Re* range, comparing the two CFD methods. It can easily be seen that predicted C_{Lrms} values are much larger than C_{Drms} values above the critical Reynolds number of $Re \approx 47$, especially for the grid-based method. There is a good measure of agreement in C_{Lrms} between the two CFD methods in the supercritical region, albeit with a scatter in the vortex cloud results. On the other hand the predicted C_{Drms} values are excessively high for the vortex cloud method.

3.2. Comparison of predicted form and skin friction drag coefficients

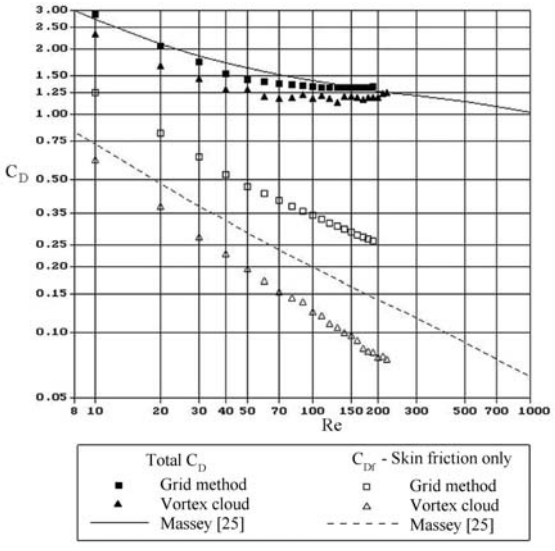

Figure 6. Comparison of predicted total and skin friction drag coefficients with published experimental values

The final comparison of the two CFD methods is shown in Figure 6, namely predicted values of both the total drag coefficient C_D and the skin friction component of this C_{Df} compared also with experimental results published by Massey [25] for the selected *Re* range.

As Massey's results show (Fig. 6) the total drag coefficient drops considerably over the range $10<Re<200$ from about 2.75 to 1.25 (a ratio of 2.2) and both methods predict this trend well, the grid method particularly so. It is encouraging to see this mutual agreement over such an important widely varying *Re* range of twenty to one, within which the shift transfers from the dominance of viscous effects to those of convective processes (as will be illustrated by other considerations in Section 3.3 and Table 1 below). Thus also from Massey's data the skin friction drag component falls from roughly $C_{Df} = 0.75$ to 0.14 over this *Re* range (a ratio of 5.4!) and is thus only a small fraction of the total drag, decreasing to negligible values at the top end of the *Re* range. The two CFD methods here produce predictions that lie on either side of Massey's experimental results, reflecting the general dramatic trends while not in such good agreement with each other.

3.3. Selected flow patterns for low Re predicted by the vortex cloud method

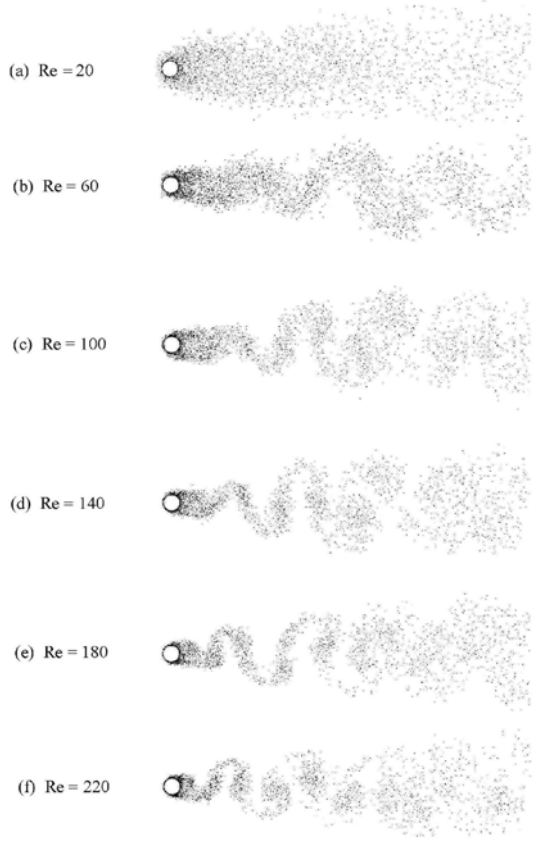

Figure 7. Predicted vortex shedding flow patterns for Re range 20 to 220

One advantage of the vortex cloud method is the economy in modelling wake patterns by the cloud of discrete vortices, which can then also be viewed in movie style. Application of this method for the selected *Re* range produced the comparisons presented in Figure 7 revealing the developing significant changes in wake pattern.

As shown by these results, the onset of periodic vortex shedding only begins to appear above *Re*=20, below which viscous diffusion dominates sufficiently over convection to avert this. At the higher value of *Re*=60 however a very regular wake periodicity is established which continues right through the higher *Re* range up to *Re*=220. Through *Re*=100-140 the actual vorticity wake sheet thins down to a fairly constant thickness in the near wake oscillations. At the higher range of *Re* =180-220 however, one observes that as convection begins to dominate, the near wake oscillations begin to roll up into distinct vortex cores while remaining still in a regular vortex street pattern.

A simple analysis that bears up this expectation follows from a comparison of the average convective and diffusive displacements of a typical vortex element as a function of *Re*. Assuming an average convective velocity of say ½*U*, the average convective displacement Δx_{av} of a vortex cloud element during a time step Δt would thus be $\Delta x_{av}=\frac{1}{2}U\Delta t$. As also shown elsewhere [10,14], the diffusion average random walk may be expressed

$$\Delta r_{av} = \sqrt{4\nu\Delta t \ln 2} \;=\; 2\sqrt{(Ud\Delta t \ln 2)/Re} \qquad (11)$$

Table 1. Vortex cloud average convective and diffusive shifts for U=1.0, d=1.0, Δt=0.05

Re	Ave. convective shift Δx_{av}	Ave. diffusive shift Δr_{av}
10	0.025	0.117741
20	0.025	0.083255
60	0.025	0.048068
100	0.025	0.037230
140	0.025	0.031468
180	0.025	0.027752
220	**0.025**	**0.025101**
260	0.025	0.023091
300	0.025	0.021496

Table 1 compares these predicted average convective and diffusive shifts Δx_{av} and Δr_{av} for $10\le Re\le 300$. The extremely interesting observation to be made here is that for a typical vortex element Δx_{av} and Δr_{av} are equal when $Re\approx 220$. Thus convective processes may be expected to dominate above this *Re* value and diffusive processes below it, in agreement with the vortex wake motions presented in Fig. 7. For the lowest value *Re*=10 tabulated here however, the average diffusive shift of the vortex cloud random walk process is almost 5 times the average convective shift. It should be mentioned that for this Reynolds number the numerical vortex cloud scheme arranges for the random walk simulation of viscous diffusion to be undertaken in five sub-steps to maintain equal resolution with the convective process.

4. CONCLUSIONS

Two completely different CFD simulation techniques based on vortex dynamics and a grid-based method have been compared for the classic datum case of flow past a stationary circular cylinder over the low Reynolds number range $10\le Re\le 220$ with the following conclusions:

1. Good agreement was obtained in prediction of the Strouhal number which varies between $0.12<St<0.2$ over the *Re* range considered, and both methods predict the formation of a von Kármán vortex street above $Re \approx 47$. Using the grid method and extrapolating the C_{Lrms} values to zero, the critical *Re* for the onset of vortex shedding was found to be $Re_c\approx 46.8$.
2. Both methods are in reasonable agreement with the experimental measurements published by Massey [25] and with one another for the total drag coefficient C_D. Predictions of the contribution to this due to skin friction C_{Df} are in less good agreement but show similar trends.
3. Predictions of the *rms* fluctuations C_{Lrms} and C_{Drms} are in less good agreement. The grid CFD method predicts zero values of these below the critical level *Re*=47 due to the total absence of a vortex street and rapidly rising values $0.0<C_{Lrms}<0.46$ for $47<Re<190$. Vortex cloud results agree with the latter reasonably well but predict excessive values of both C_{Lrms} and C_{Drms} for subcritical Reynolds numbers $Re<47$.
4. With regard to the last mentioned item, it is noted that the grid CFD method used extremely small time steps Δt=0.0005 resulting in tight control of the discretisation errors in this time sensitive motion. The vortex cloud method on the other hand used time steps 100 times bigger, namely Δt=0.05 resulting in a much greater scale of "numerical turbulence". The main impact of this is felt within the body boundary layer due to the random walk method for simulation of viscous diffusion and its resulting impact on surface vorticity creation.
5. The average convective and diffusive shifts of a typical vortex element during a time step become equal at about *Re*=220. Above this, convective processes become more dominant.
6. Vortex dynamics handles heavily convective wake motions extremely well providing easy graphical presentation of the vortex street wake patterns. Furthermore the method has proved extremely flexible for adaptation to any other stationary or moving body flow and has been useful for simulating such other phenomena as rotating stall in turbomachinery blade rows.

ACKNOWLEDGEMENTS

The support provided by the Hungarian Research Foundation (OTKA, project No. T 42961) is gratefully acknowledged by the second author. We also thank Mr. S. Ujvárosi for preparing Fig. 6.

REFERENCES

[1] Strouhal, V., 1878, "Über eine besondere Art der Tonerregung", *Ann. Phys. und Chemie. Nav. Series*, **5**, pp. 216-251.

[2] Kármán T. von, 1911, "Über ein Mechanismus des Widerstandes, den ein bewegter Körper in einer Flüssigkeit erfährt", *Göttingen Nachrichten Maths, -Phys*., **KI**, pp. 509-517.

[3] Rosenhead, L., 1931, "The formation of vortices from a surface of discontinuity", *Proc. Roy. Soc. A*., **134**, pp. 170-192.

[4] Abernathy, F.H. and Kronauer, R.E., 1962, "The formation of vortex streets", *J. Fluid Mech.*, **13**, pp. 1-20.

[5] Roshko, A., 1954, "On the development of turbulent wakes from vortex streets", *NACA Rep.* 1191

[6] Norberg, C., 2001, "Flow around a circular cylinder: aspects of fluctuating lift", *J. Fluid Struct.*, **15**, pp. 459-469.

[7] Bearman, P.W., 1997, "Developments in the understanding of bluff body flows", *Proc. JSME Centennial Grand Congress, Int. Conf. on Fluid Eng.*, Tokyo, **1**, pp. 53-61.

[8] Kawamura, T. and Kuwahara, K., 1984, "Computation of high Reynolds number flow around a circular cylinder with surface roughness", *Proc. 22nd Aerospace Sci. Meeting*, Reno, Nevada, AIAA-84-0340, pp. 1-11.

[9] Karniadakis, G.E. and Triantafyllou, D.S., 1989, "Frequency selection and asymptotic states in laminar wakes", *J. Fluid Mech.*, **199**, pp. 441-469.

[10] Lewis, R.I., 1991, Vortex Element Methods for Fluid Dynamic Analysis of Engineering Systems. *Cambridge University Press*.

[11] Baranyi, L., 2004, "Numerical simulation of flow past a cylinder in orbital motion", *J. Comp. App. Mech.*, **5**(2), pp. 209-222.

[12] Chorin, A.J., 1973, "Numerical study of slightly viscous flow", *J. Fluid Mech.*, **57**, pp. 785-796.

[13] Porthouse, D.T.C. and Lewis, R.I., 1981, "Simulation of viscous diffusion for extension of the surface vorticity method to boundary layer and separated flows", *J. Mech. Eng. Sci., I. Mech. E.*, **23**(3), pp. 157-167.

[14] Baranyi, L. and Lewis, R.I., 2006, "Comparison of grid-based and vortex dynamics predictions of low Reynolds number cylinder flows", *Aeronaut. J.,* **110**, pp. 63-71.

[15]Baranyi, L. and Shirakashi, M., 1999, "Numerical solution for laminar unsteady flow about fixed and oscillating cylinders", *Comp. Assisted Mech. and Eng. Sci.*, **6**, pp. 263-277.

[16] Baranyi, L., 2003, "Computation of unsteady momentum and heat transfer from a fixed circular cylinder in laminar flow", *J. Comp. App. Mech.*, **4**(1), pp. 13-25.

[17] Roshko, A., 1993, "Perspectives on Bluff Body Aerodynamics" *J. Wind Eng. Ind. Aerod.*, **49**, pp. 79-100.

[18] Baranyi, L., and Lakatos, K., 2004, "Computational fluid dynamics analysis of low Reynolds number flow around stationary and oscillating cylinders", *Proc. 4th Int. Eng. Conf.*, Mansoura-Sharm El-Shiekh, **1**, pp. 459-465.

[19] Norberg, C., 2003, "Fluctuating lift on a circular cylinder: review and new measurements", *J. Fluid Struct.*, **17**, pp. 57-96.

[20] de Sampaio, P.A.B., 2005, "A finite element formulation for transient incompressible viscous flows stabilized by local time-steps", *Comput. Methods Appl. Mech. Engrg.*, **194**, pp. 2095-2108.

[21] Williamson, C.H.K., 1996, "Vortex dynamics in the cylinder wake", *Annu. Rev. Fluid Mech.*, **28**, pp 477-539.

[22] Barkley, D. and Henderson, R.D., 1996, "Three-dimensional Floquet stability analysis of the wake of a circular cylinder", *J. Fluid Mech.*, **322**, pp. 215-241.

[23] Norberg, C., 1994, "An experimental investigation of the flow around a circular cylinder: influence of aspect ratio", *J. Fluid Mech.*, **256**, pp. 287-326.

[24] Thompson, M. C. and Le Gal, P., 2004, "The Stuart-Landau model applied to wake transition revisited", *Eur. J. Mech. B-Fluid*, **23**, pp. 219-228.

[25] Massey, B.S., 1989, *Mechanics of Fluids*, 6th ed., Van Nostrand Reinhold, London

Conference on Modelling Fluid Flow (CMFF'06)
The 13th International Conference on Fluid Flow Technologies
Budapest, Hungary, September 6-9, 2006

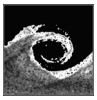

LARGE EDDY SIMULATION OF FLOW OVER A VERTICALLY MOUNTED FINITE CYLINDER ON A FLAT PLATE

Imran Afgan[1], Charles Moulinec[2], Dominique Laurence[3]

[1] Corresponding Author. C16, George Begg Bldg, Sackville St., School of MACE, University of Manchester. PO box 88, M601QD, UK. Tel.: +44 161 306 3736, Fax: +44 161 306 3723, E-mail: I.Afgan@postgrad.manchester.ac.uk
[2] University of Manchester. E-mail: C.Moulinec@manchester.ac.uk
[3] University of Manchester. E-mail: Dominique.Laurence@manchester.ac.uk

ABSTRACT

Flow structure around circular cylinders of various finite heights has been numerically investigated by Large Eddy Simulation (LES) with local refinement using *STAR-CD V4* software. The two aspect ratios tested are 6 and 10 and the Reynolds number (*Re*) based on cylinder diameter and free stream velocity is kept at 20,000 for both the cases. A Cantilever cylinder mounted on a flat plate was chosen since it gives insight into two entirely different flow phenomena; the end tip effects of the cantilever cylinder which shows strong three-dimensional wake structures and the base effects due to interaction of flow between the cylinder and the flat plate. Regular vortex shedding was found in the wake of the higher aspect ratio case as was anticipated, along with a strong downwash originating from the flow over the free end of the cylinder, whereas irregular and intermittent vortex shedding was found in the lower aspect ratio case. Pressure distributions were computed all along the length of the cylinder and compared to experimental results. Lift, drag and their root mean square values were also computed along with Strouhal numbers.

Keywords: aspect ratio, CFD, finite cylinder, hanging nodes, large eddy simulation, vortex shedding

NOMENCLATURE

C_P	[-]	pressure coefficient
C_S	[-]	Smagorinsky coefficient
D	[m]	diameter of cylinder
P	[N/m^2]	pressure
P_{ref}	[N/m^2]	reference pressure
Re	[-]	Reynolds number
SGS	[-]	Subgrid-scale
$\|\bar{S}\|$	[$1/s$]	filtered strain rate magnitude
$\bar{S}_{ij}$	[$1/s$]	filtered strain rate tensor
St	[-]	Strouhal number
U_0	[m/s]	inlet velocity
Y^+	[-]	non dimensional cell distance from wall
$\bar{\Delta}$	[m]	filter length
ν	[m^2/s]	kinematic viscosity
ν_t	[m^2/s]	turbulent SGS eddy viscosity
Ω	[m^3]	cell volume
ρ	[kg/m^3]	density of fluid
τ_w	[N/m^2]	wall shear stress
τ_{ij}	[N/m^2]	stress tensor

Subscripts and Superscripts

$'$	fluctuating component
$\bar{}$	filtered quantity

1. INTRODUCTION

A cantilever cylinder with one end fixed and the other free to vibrate has been numerically simulated to study the dynamics of flow around cylinder bodies. The long-term objective of this study is to apply LES to Flow Induced Vibrations (FIV). The present fixed cylinder case is intended to serve as validation and analysis of the flow-physics. It has been observed in the past that the flow over a finite cylinder's free end has a complicated three dimensional wake structure: the free end plays a direct and significant factor for the flow three dimensionality. In fact a finite cylinder has 3D flow characteristics over all Reynolds number ranges [1]. It has also been reported earlier that the three dimensionality of the flow around a finite cylinder is due to the counter rotating vortices generated by the free end itself. In cylinders with both ends fixed however the scenario is somewhat different where the fluid must first be accelerated and then

displaced sideways in order to pass over the cylinder body and enter the wake region.

The applications of finite cylinders are vast and numerous, including tall rising buildings in city centres and nuclear cooling towers. At lower *Re* numbers one finds applications to internal structures of nuclear plants such as fuel or control rods and various instrumentation. Notable papers containing extensive experimental data are those of Park and lee [1-3] and that of Okajima et al. [4]. In this study flow over such configurations is numerically simulated. Two aspect ratio cases are tested and then compared to experimental results. Non conforming local mesh refinement is implemented in all three directions to reduce the size of the computational grid since the finite cylinder poses a huge computational grid requirement.

2. GEOMETRY

The geometry consists of a finite cylinder vertically mounted on a flat plate with one end fixed and the other free (and in later cases also allowed to vibrate). Due to vortices being shed from the cylinder and a strong downwash from its free end a fairly long computational domain had to be used. The downstream length was kept at 20 diameters whereas the upstream length was taken as 12 diameters. Complete geometry is shown in Figure 1 where a uniform flow enters from the left.

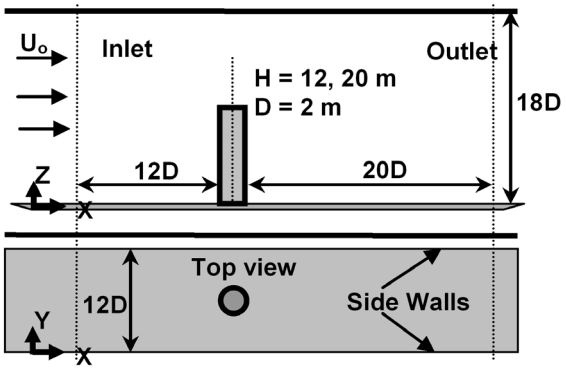

Figure 1. Geometry under consideration

3. NUMERICS

A finite volume code for complex geometries, *STAR-CD V4*, is used to solve 3D Navier-Stokes equations on unstructured grid. The flow is assumed Newtonian and incompressible (density ρ is constant). For LES the filtered Navier-Stokes equation is shown in Eq. (1). For Subgrid-scale modelling (SGS) standard Smagorinsky model is used which is shown in Eq. (2). $\overline{S}_{ij}$ is the filtered strain rate tensor ($\|S\| = \sqrt{2\overline{S}_{ij}\overline{S}_{ij}}$), ν_t the turbulent viscosity and $\overline{\Delta}$ the filter length. As the cells used in the present work are hexahedral one can take $\overline{\Delta} = 2\Omega^{1/3}$, where Ω is the cell volume. The Smagorinsky constant, C_S, is set to 0.065 .

$$\begin{cases} \dfrac{\partial \overline{u}_i}{\partial t} + \dfrac{\partial \overline{u}_i \overline{u}_j}{\partial x_j} = \\ -\dfrac{1}{\rho}\dfrac{\partial \overline{p}}{\partial x_i} + \nu \dfrac{\partial^2 \overline{u}_i}{\partial x_j \partial x_j} - \dfrac{\partial \tau_{ij}}{\partial x_j}, \\ \dfrac{\partial \overline{u}_i}{\partial x_i} = 0, \; i \in \{1,2,3\} \end{cases} \tag{1}$$

$$\begin{aligned} \tau_{ij} - \frac{1}{3}\tau_{kk}\delta_{ij} &= -2\nu_t \overline{S}_{ij} \\ &= -2(C_S\overline{\Delta})^2 \|S\| \overline{S}_{ij} \end{aligned} \tag{2}$$

In the collocated finite volume approach used here, all variables are located at the centres of the cells (which can be of any shape). The momentum equations are solved by considering an explicit mass flux and a fully cantered convection scheme. Velocity and pressure coupling is insured by a prediction/correction method with a SIMPLEC algorithm [5]. The Poisson equation is solved with a conjugate gradient method. The collocated discretization requires a [6] interpolation in the correction step to avoid oscillatory solutions.

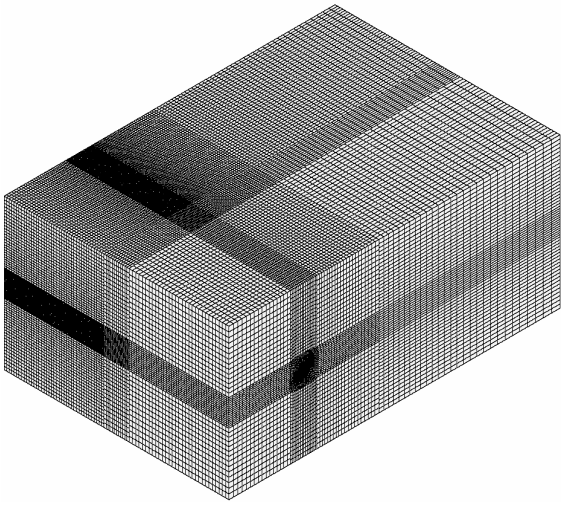

Figure 2. 3D view of the entire grid

The three time level implicit time advancing scheme (TTLM), [5], is used for time discretization in *STAR-CD V4*. This scheme performs the integration over an interval cantered on the new time level which makes the scheme a 2nd order approximation. The non-orthogonalities are taken into account with a reconstruction technique explained in [5, 7-8]. When a non-orthogonal grid is used, the matrix contains the orthogonal

contribution only and the non-orthogonal part is included in the right hand side of the equation. This is known as the deferred correction (the non-orthogonal part is explicit), however one can iterate on the system to make it implicit.

Suitability of this commercial code for LES has been extensively tested at Manchester, on homogeneous grid turbulence and channel flows [9-11]. In Moulinec et al. [10] conservation of kinetic energy with collocated unstructured finite volumes is discussed, and it is recommended to use polyhedral cells or Cartesian cells with localized refinement. Conserving kinetic energy not only eliminates numerical diffusion, but it also ensures a bounded solution even with pure central differencing as herein. Indeed it is well known that upwinding, even in small quantity or via higher order terms is not suitable for LES; see e.g. Grotzbach and Worner [12], Kravchenko and Moin [13].

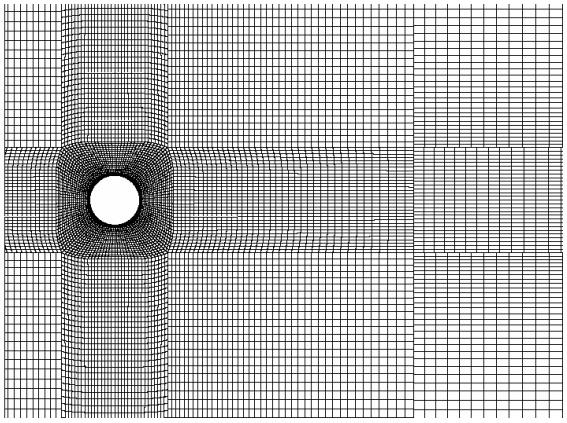

Figure 3. 2D cross sectional view of grid in XY plane

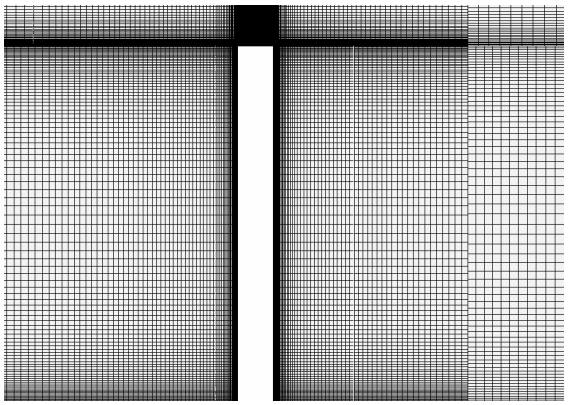

Figure 4. 2D cross section of grid in XZ plane showing the cylinder

Grid generation was thus carefully controlled rather than automatic with moreover economy concerns as the complex finite cylinder geometry poses a huge computational resource requirement. Thus the biggest constraint was of limiting the grid to be less than 2.6 million cells in line with limited computational resources (8 CPU's of an in house Beowulf cluster). The numerical results from private communications (contributions of M. Strelets and S. Krajnovic to the DESider database) will be used for comparison only. The first (Strelets) results are based on a grid of 2 million cells for detached eddy simulation (DES). However the present LES grid in comparison is of the same fineness level near the cylinder surface and flat plate, significantly finer at the tip of the cylinder, but fairly coarse in the far field. This was achieved by use of non-conforming refinement in all directions. The interface cells are not treated as "hanging nodes", but as polyhedral cells with more than 6 faces. In fact a total of 9 levels of local refinements have been used with the cell size change ratio limited to a maximum of 33% in every case (i.e. 3 cells matching with 2 cells rather than 2 facing 1 as this latter case has been observed to lead to oscillations in some cases, see Laurence [11]). Thus for every direction the grid has three levels of non-conforming refinements. Figures 2 to 4 show the various views of the computational grid with hanging nodes in different directions. The cell next to the cylinder is fixed at around 1, viscous unit (Y^+=1) in both azimuthal and normal directions whereas the Y^+ value for the flat plate is around 5 which is reasonable enough to model the near wall damping effect (admittedly not fine enough for an accurate reproduction of BL development, but the latter is very short in the experiment).

For the numerical simulations all side and top domains are kept as slip planes to reduce the size of the computational mesh. The solid cylinder surface and the flat bottom plate however are kept as no slip adiabatic walls. The LES simulations were run for around 15 complete flow cycles with time averaging of results done over the last 10 cycles.

4. DISCUSSION OF RESULTS

4.1. Pressure Distribution

For the finite cylinder one notices that the mean pressure on the cylinder surface is a direct result of the free end interference. From Fig. 5 it is seen that the mean pressure upstream the windward side increases as one moves towards the fixed end due to the blockage effect of the cylinder, while near the free end the mean pressure is significantly reduced.

Looking at the pressure distributions in Figs. 6 to 7 one sees that the LES results are in close agreement with the experimental values of Park and Lee [2]. These figures show the pressure coefficient (C_P) distributions around the cylinder at Z/L = 0.5 and 0.75 location respectively for aspect ratio 6 case. It is observed that the peak values almost overlap each other, the local pressure minima is also predicted decently by all simulations but the biggest discrepancy is in the wake of the cylinder at 180

degrees where one sees a gradual increase in mean pressure values. Experimental findings of Park and Lee [1-3] report such phenomenon but for the aspect ratio 10 case. In fact as we move closer to the free end of the cylinder the prediction of pressure rise becomes steeper and more abrupt.

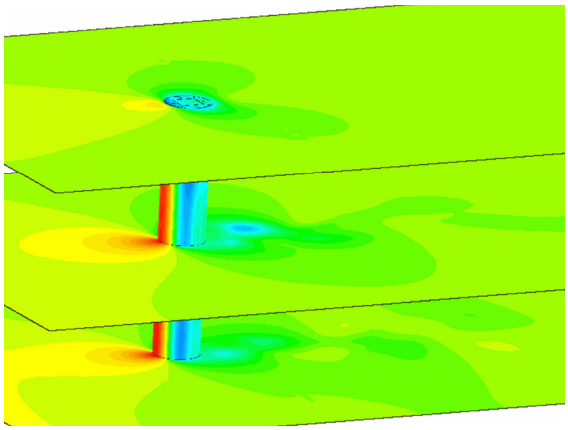

Figure 5. Instantaneous pressure distribution along the height of the cylinder for aspect ratio 6 case

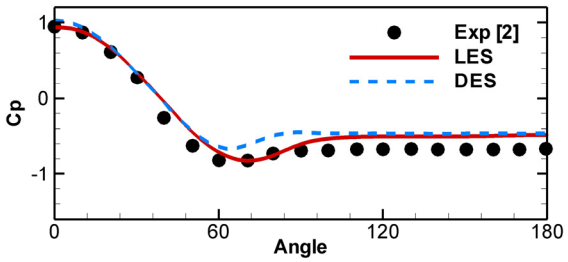

Figure 6. C_P distribution along the cylinder surface for aspect ratio 6 case at Z/L=0.5

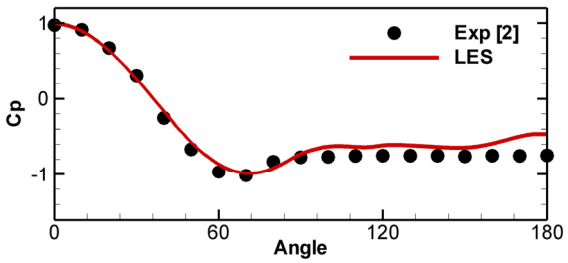

Figure 7. C_P distribution along the cylinder surface for aspect ratio 6 case at Z/L=0.75

In Figs. 6 to 9 the C_P was obtained by dividing the difference between surface pressure (P) and a reference pressure (P_{ref}) by the dynamic pressure to get $C_P = 2(P - P_{ref}) / \rho U_0^2$.

However the pressure is variable along the vertical stagnation line, hence data has been rescaled with a variable pressure $P_{ref}(Z)$ such that C_P=1 for each altitude.

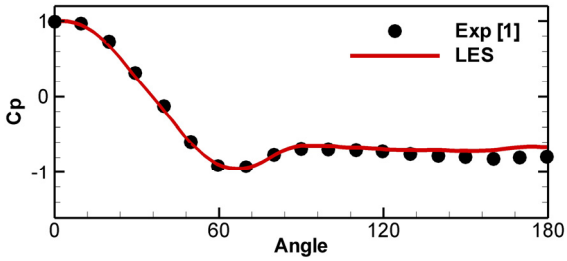

Figure 8. C_P distribution along the cylinder surface for aspect ratio 10 case at Z/L=0.883

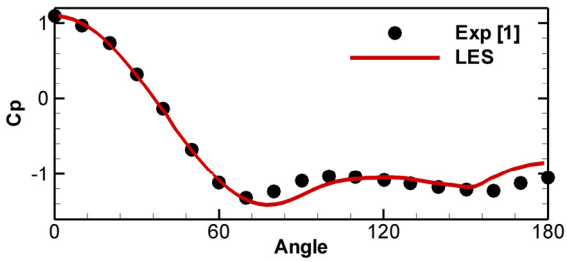

Figure 9. C_P distribution along the cylinder surface for aspect ratio 10 case at Z/L=0.950

At Z/L=0.5 the DES (Strelets), the present LES and the ongoing (hence not shown here) fine LES by S. Krajnovic tend to show somewhat a higher plateau than the experimental in the leeward side of the cylinder. In any case the plateau for all data is significantly higher than that found for infinite cylinder at similar *Re* (which is around -1.2 to -1.5). This pressure recovery (gradual pressure rise) is accompanied by suppression of vortex shedding behind the cylinder. Experimental findings of [1] report irregular and weak vortex shedding in aspect ratio 6 case. Numerical simulations on the other hand predict intermittent yet visible vortex shedding where the downwash effect is strong but not enough to totally eliminate the vortex shedding. The pressure recovery behind the cylinder (at 180 degrees) is better seen in the larger aspect ratio case, where both experimental and numerical results show this sharp pressure rise in the wake of the cylinder (see Fig. 9). It is also noted that the down-wash effect which was very strong in the smaller aspect ratio case is now some what reduced leading to regular vortex shedding in the lower half of the aspect ratio 10 case.

It is established that as the aspect ratio decreases the vortex shedding frequency also decreases. But classification of vortex shedding behind the cylinder depending on the aspect ratio is a debatable issue. Various experimental and numerical sightings report differently. According to Farivar [14] the regular vortex shedding disappears for cylinders with aspect ratios lower than 7.5, Zdravkovich et al. [15] on the other hand found regular vortex shedding behind a cantilevered cylinder with an aspect ratio of 4. Hence drawing a

clear limiting value of aspect ratio where vortex shedding is suppressed is not possible at present.

4.2. Velocity Distribution

Due to the strong downwash near the free end of the cylinder in the wake there is a sharp and sudden increase in the velocity magnitude. The maximum velocity which at the inlet was 10 m/s goes as high as 14 m/s.

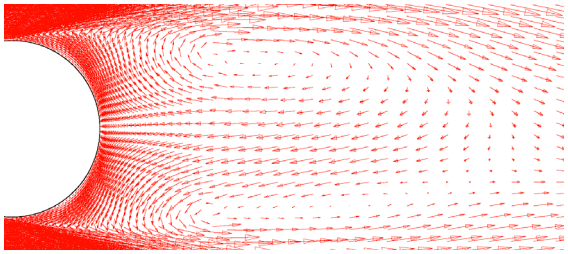

Figure 10. Mean velocity vector plot in the wake of the cylinder at Z/L=0.6 for aspect ratio 6 case

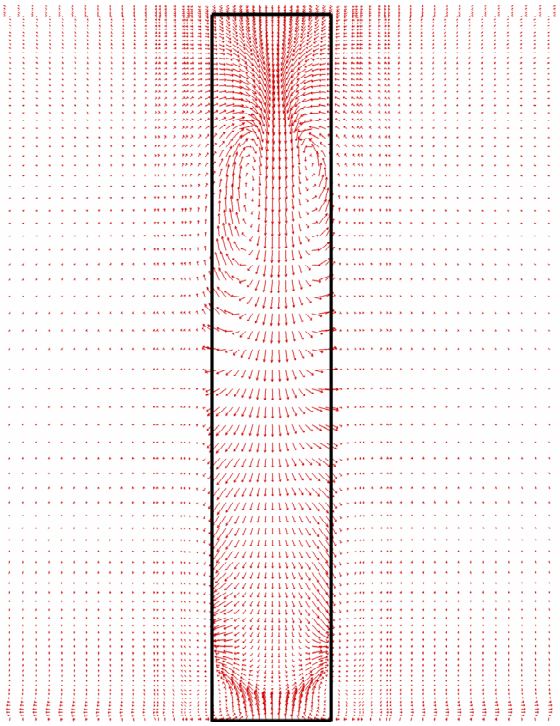

Figure 11. Mean velocity vectors in YZ plane in the wake of the cylinder at X/D=2 for aspect ratio 6 case

Fig. 10 shows the mean velocity vector plot in XY plane at Z/L=0.6 location for smaller aspect ratio case. It is interesting to note that the pair of narrow recirculation bubbles in the wake is generating a strong and wide back-flow (towards the cylinder), a significantly different pattern from the infinite cylinder case which can explain the higher C_P plateau. Fig. 11 shows the mean velocity vector plot for the same case in YZ plane at X/D=2 location. One sees another elliptical vortex pair below the top which can emanate from the tip as Figs. 12-13 tend to show down flow at 45 degrees. For a much smaller aspect ratio of H/D=2.5 Frohlich et al. [16] observed an arch vortex structure in the cylinder wake, which is consistent with the well separated vortex pair in Fig. 10, but the top arch is not so clear in Fig.13. Near the base in Fig.11, an opposite sense vortex pair can be attributed to the classical horseshoe vortex around pillar-plate junctions, however the one seen here is quite weak as the incoming boundary layer is nearly uniform.

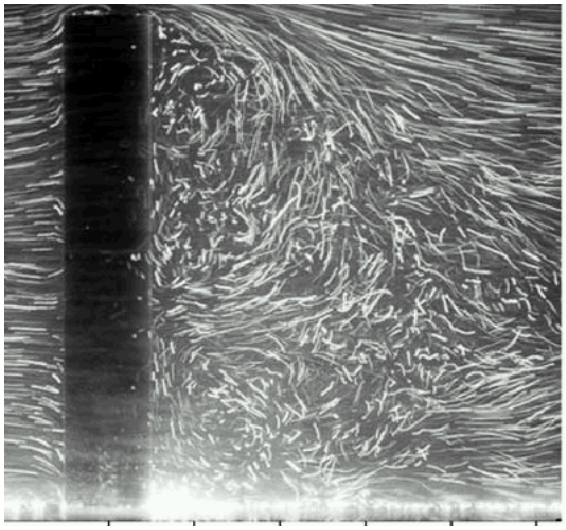

Figure 12. Experimentally obtained velocity vectors in XZ plane at Y/D=0 for aspect ratio 6 case

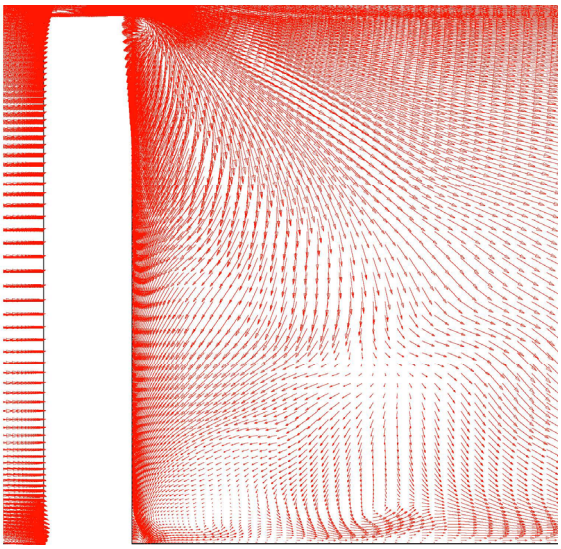

Figure 13. Numerically obtained mean velocity vectors in XZ plane at Y/D=0 for aspect ratio 6 case

Figs. 12 to 13 show a comparison between experimentally and numerically predicted velocity

vectors respectively in XZ plane at Y/D=0. It is seen that the effect of the down wash almost reaches the base plate. In fact the downwash is so strong that it suppresses the vortex shedding from the sides of the cylinder and becomes the dominant factor in the wake of the cylinder.

Fig. 14 shows the zoomed in velocity vectors near the free end of the cylinder in YZ plane at X/D=0 location. These counter rotating vortices are in fact perfectly symmetrical but oppositely directed. It is believed that the roll up of the shear flow separation from the free end gives birth to this counter rotating pair of vortices in Fig. 11. These counter rotating vortices then cause strong downwash which interfere with the cylinder vortex shedding. Fig. 15 shows the velocity magnitude plot in XZ plane at Y/L=0 behind the cylinder for higher aspect ratio case. One can see the vortex columns behind the cylinder which are distorted over 2/3 of the height and even suppressed by the downwash near the tip.

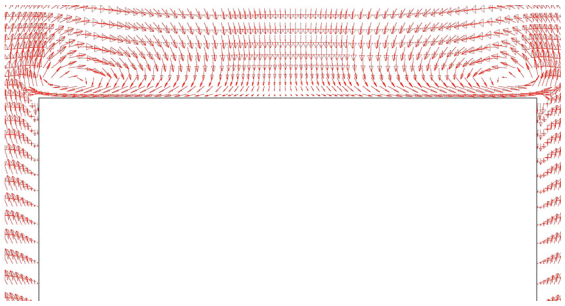

Figure 14. Mean velocity vectors in YZ plane at X/L=0 for aspect ratio 6 case showing counter rotating vortices near the top surface

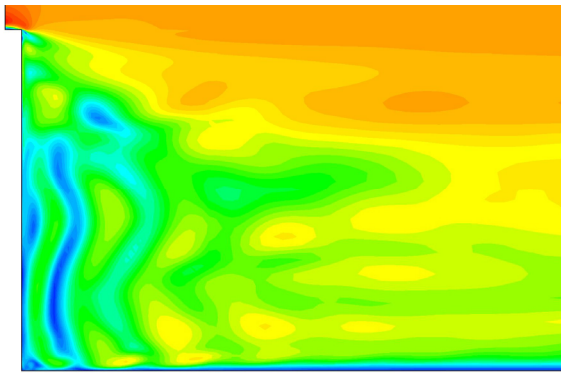

Figure 15. Instantaneous Velocity magnitude behind the cylinder for aspect ratio 10 case in XZ plane at Y/L=0

Fig. 16 shows a comparison of velocity magnitudes at various Z/L locations for both the numerical cases. For the smaller aspect ratio case at both Z/L=0.3 and Z/L=0.8 locations one sees a peculiar flow behaviour where the wake seems to be split into two tongues. These tongues behave as though they are independent of each other unlike for a 2D or infinite cylinder. However the bottom two pictures in the same figure which are for the higher aspect ratio case at the same Z/L locations show a different phenomenon. Here one sees that near the base (at Z/L=0.3) the cylinder wake behaves just like a 2D cylinder with regular vortex shedding from the upper and lower surfaces, however near the tip (at Z/L=0.8) the behaviour is similar to smaller aspect ratio case. Hence it is concluded that a finite cylinder with aspect ratio 10 shows both finite tip effects and base effects (2D cylinder behaviour) where the aspect ratio 6 cylinder does not show any infinite cylinder behaviour.

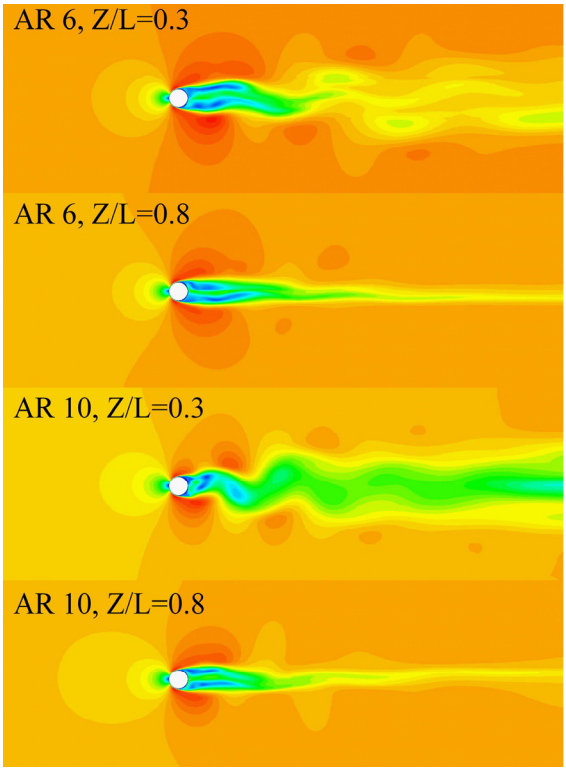

Figure 16. Instantaneous velocity magnitude for aspect ratio 6 and 10 case at various Z/L locations

4.3. Turbulence Intensity

A comparison between numerically and experimentally obtained turbulence intensities at Z/L=0.5 location in the wake of the cylinder (X/D=5) for the lower aspect ratio cases is shown in Fig. 17. The experimental data taken from Park and Lee [2] shows a peak value of 28% whereas the LES simulation shows a double peak of 23% (as well as DES by Strelets). Findings of Park and Lee [1,2] report that the vortex shedding frequency decreases as the aspect ratio of the cylinder decreases where a 2D cylinder has a Strouhal number of 0.198. Similar trend is seen in the numerical computations where the Power Spectrum Density analysis (PSD) is shown in Fig. 18. A

comparison between experimental [1-3] and numerical Strouhal numbers is given in Table 1.

A comparison of $< u'u' >$ at various Z/L locations for the higher aspect ratio case is shown in Fig. 19. One notices that the streamwise turbulence intensities are slightly under-predicted even though the pressure and velocity comparisons were decent. However the general trend and the length of the vortex formation region are still being predicted accurately. The slight under prediction in numerical results comes from a number of sources, one of them being the grid fineness level. The grid has been resolved to the wall in the wake of the cylinder but in doing so the grid distribution downstream becomes some what coarse. Secondly the change in the wake of the cylinder from laminar to fully turbulent is sudden and abrupt causing the model to return slightly under predicted values. It is anticipated that the use of dynamic model here would perhaps yield better results.

Table 1. Strouhal number comparison

St	Park and Lee [1-3]	Numerical
AR 6	0.135	0.132
AR 10	0.159	0.167

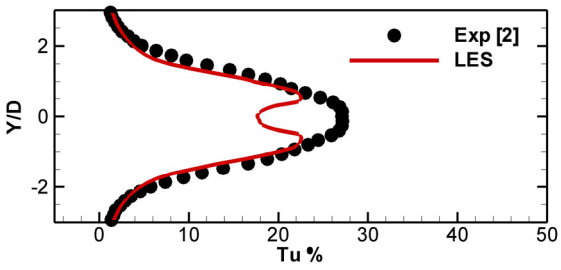

Figure 17. Stream wise turbulence intensity at Z/L=0.5 and X/D=5 for aspect ratio 6 case

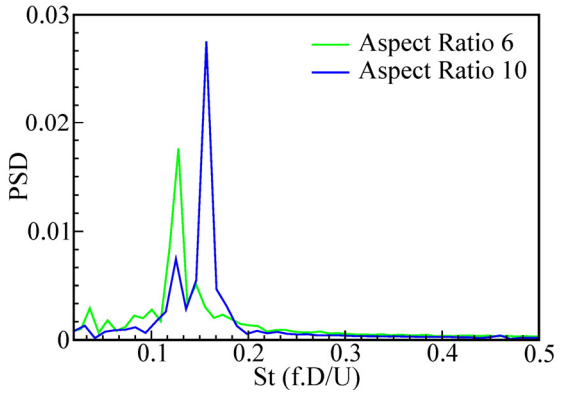

Figure 18. DSP of lift coefficient for numerical computations

Coming back to the flow physics one notice that the streamwise turbulence intensities increase as we move towards the fixed end of the cylinder, where the maximum values are in the lower half of the cylinder (bottom graph, Fig. 19). This confirms the initial observation that the effect of the strong down wash is in fact reducing the turbulence intensity and vortex formation region in the upper half of the cylinder where the $< u'u' >$ is being reduced to almost one third in magnitude (top graph, Fig. 19). This is confirmed in the experiments and is similar to Frohlich et al. [16] results.

Further PIV data is available from [1,2], but could not be fully reconciled with the 3 simulations by DESider partners which on the other hand are in closer agreement, in particular wake velocity profiles. Further analysis is needed before presenting these results.

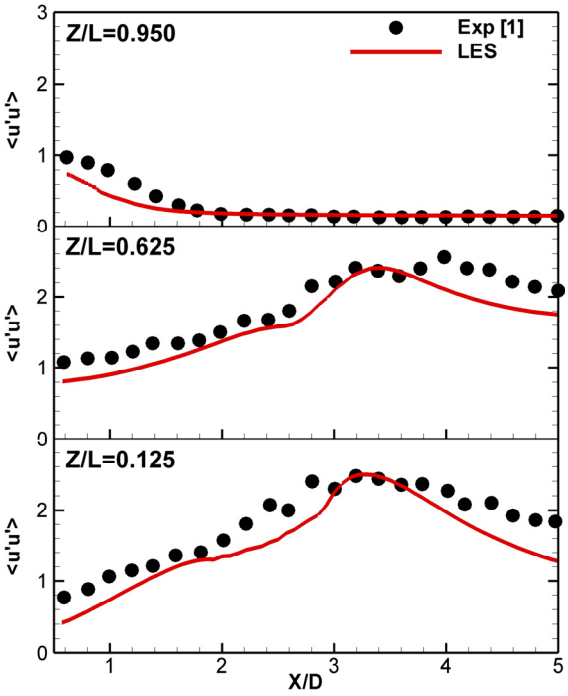

Figure 19. $< u'u' >$ at various Z/L locations for aspect ratio 10 case, top; Z/L=0.950, centre; Z/L=0.625, bottom; Z/L=0.125

5. CONCLUSIONS

Flow over a cantilever cylinder mounted vertically on a flat plate was numerically simulated by LES. The two cases tested were of aspect ratio 6 and 10. Numerical results were then compared to experimental data of Park and Lee [1-3]. Use of multiple levels of local refinements enabled the *STAR-CD V4* LES simulation of such a complex geometry using only 2.6 million cells where with a regular grid LES requirement is around 50 million cells. Flow over both the cylinders was found to be 3 dimensional and fully turbulent especially in the lower half of the wake of the cylinder. It was found that the roll up of shear layer separation from the free end causes two counter rotating vortices near the free end of the cylinder leading to a strong

downwash extending nearly to the base. This downwash completely changes the flow physics by interacting with the regular vortices being shed from the sides of the cylinder. This interaction causes a change on the pressure distribution in the wake of the cylinder. Not only this, the interaction also causes damping of the vortex formation with a decrease in turbulence intensities.

For the smaller aspect ratio case the effect of the downwash is stronger where the effect is felt all along the cylinder height, hence weak and intermittent vortex shedding is observed. For the higher aspect ratio case the effect of the downwash is limited to the top half of the cylinder and hence the interaction is weaker causing pressure recovery in the wake of the cylinder with regular vortex shedding.

Aspect ratio 6 case shows a peculiar flow behaviour which is quite different from an infinite cylinder especially in the wake region, where the wake is split into two halves. Aspect ratio 10 case on the other hand shows both tip and base effects, where the former is similar to the aspect ratio 6 case and the later similar to a 2D or infinite cylinder.

In the next part of this study a cantilever cylinder free to vibrate will be numerically simulated using LES. Same two aspect ratios will be tested and the experimental data of Okajima et al. [4] will be used for comparison. This complex fluid structure interaction problem will be solved with dynamic structural loading coming from fluid structure interaction at every time step which will dictate the movement of the mesh around the cylinder thus causing it to oscillate.

ACKNOWLEDGEMENTS

Authors are grateful to C. W. Park and S. J. Lee for provision of experimental data and clarification of its use, as well as discussions with M. Strelets and S. Krajnovic.

This work has been partly supported by DESider project funded by European Union under Contract No. AST3-CT-2003-502842. (http://cfd.me.umist.ac.uk/desider)

REFERENCES

[1] Park, C. W., and Lee, S. J., 2000, "Free End Effect on the Wake Flow Structure Behind a Finite Circular Cylinder", *J of Wind Engineering and Industrial Aerodynamics*, Vol. 88, pp. 231-246.

[2] Park, C. W., and Lee, S. J., 2002, "Flow Structure around a Finite Circular Cylinder Embedded in Various Atmospheric Boundary Layers", *fluid Dynamics Research*, Vol. 30, pp. 197-215.

[3] Park, C. W., and Lee, S. J., 2004, "Effects of Free-End Corner Shape on Flow Structure around a Finite Cylinder", *J of Fluids and Structures*, Vol. 19, pp. 141-158.

[4] Okajima, A., Kosugi, T., and Nakamura, A., 2002, "Flow-Induced In-Line Oscillation of a Circular Cylinder in a Water Tunnel", *J of Pressure Vessel Technology,* ASME, Vol. 124, pp. 89-96.

[5] Ferziger, J. H., and Peric, M., 2002, "Computational Methods for Fluid Dynamics", *Springer*, 3rd edition, ISBN-3-540-42074-6.

[6] Rhie, C., and Chow, W., 1982, "A Numerical Study of the Flow past an Isolated Airfoil with Trailing Edge Separation", *J* AIAA-21:1525–1532.

[7] Benhamadouche, S., Laurence, D., 2003, "LES, Coarse LES, and Transient RANS Comparisons on the Flow across Tube Bundle", *Int. J. Heat and Fluid Flow*, Vol. 4, pp 470-479.

[8] Bouris, D., Bergeles, G., 1999, "Two Dimensional Time Dependent Simulation of the Subcritical Flow in a Staggered Tube Bundle using a Subgrid scale Model", *I. J. Heat and Fluid Flow*, Vol. 20, Issue 2, pp. 105-114.

[9] Laurence, D., 2006 (to appear), "Industrial LES with Unstructured Finite Volumes, in Direct & Large Eddy Simulation", *6, J-P Bonnet, E. Lambalais Edts, Springer ERCOFTAC series*.

[10] Moulinec, C., Benhamadouche, S., Laurence, D., Peric, M., 2005, "LES in a U-bend Pipe Meshed by Polyhedral Cells", *ERCOFTAC ETMM-6 conference, Sardinia, Elsevier.*

[11] Benhamadouche, S., Laurence, D., Jarrin, N., Afgan, I., Moulinec, C., 2005, "Large Eddy Simulation of Flow Across in-line Tube Bundles", *NURETH-11, Avignon, France.*

[12] Grotzbach, G., and Worner, M., 1999, "Direct Numerical and Large Eddy Simulations in Nuclear Applications", *J of Heat and Fluid Flow,* Vol. 20, pp. 222-240.

[13] Kravchenko, A. G., and Moin, P., 1997, "On the Effect of Numerical Errors in Large Eddy Simulation of Turbulent Flows", *J of Computational Physics,* Vol. 131, pp. 310-322.

[14] Farivar, D., 1981, "Turbulent uniform flow around cylinders of finite length", *J of AIAA*, Vol. 19, pp. 275-281.

[15] Zdravkovich, M. M., Brand, V. P., Mathew, G., and Weston, A., 1989, "Flow past short circular cylinders with two ends free", *J of Fluid Mechanics*, Vol. 203, pp. 557-575.

[16] Frohlich, J., Rodi, W., 2004, "LES of Flow around a Circular Cylinder of Finite Height", *J of Heat and Fluid Flow,* Vol. 25, pp. 537-548.

Conference on Modelling Fluid Flow (CMFF'06)
The 13th International Conference on Fluid Flow Technologies
Budapest, Hungary, September 6-9, 2006

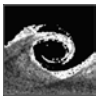

LARGE EDDY SIMULATION OF MIXED CONVECTION AROUND A VERTICAL HEATED CYLINDER COOLED BY A CROSS-FLOW AIR CIRCULATION

Sofiane BENHAMADOUCHE[1], Sophie BOURNAUD[1], Philippe CLEMENT[2], Bernard DURET[2], Yannick LECOCQ[1]

[1] EDF R&D, Dept. MFEE, 6 Quai Watier BP 49, F-78401 Chatou Cedex – France, sophie.bournaud@edf.fr - Phone: (33) 1 30 87 86 61 - Fax (33) 1 30 87 74 61

[2] CEA DEN 17, Rue des Martyrs, F-38054 Grenoble Cedex – France, philippe.clementh@cea.fr - Phone: 33 (0)4 38 78 31 76 - Fax: 33 (0)4 76 38 78 52 90

ABSTRACT

VALIDA experiments [1] were carried out within the framework of radioactive waste management to improve the understanding of mixed-convection flow and more particularly the interaction between a global cross-flow circulation and local natural convection effects around a vertical heated cylinder. The VALIDA loop implements a cylinder of 3.1 height to diameter ratio, mounted vertically in an insulated tunnel cooled by a cross-flow air circulation.

The air flow and the temperature fields on the cylinder and in the plume behind it have been studied numerically using Large Eddy Simulation (LES) and compared to available experimental data. Although several tests have been carried out, changing experimental parameters, one will focus on one test case. Two CFD codes have been used: EDF in-house code, *Code_Saturne* [*CS*] [5] on the one hand and CEA in-house code, *Trio_U* [11], [13] on the other hand. For the present test-case - air input bulk velocity of 1 m/s and heat flux density of 600 W/m^2 imposed along the cylinder - the Reynolds number based on the cylinder diameter, the bulk air velocity and the reference viscosity is Re ~ 40 000, inducing a sub-critical flow regime with laminar boundary layers around the cylinder and turbulent wake in the plume behind. From the transient downstream air calculations, the thermal fluctuations at several locations and the plume behind the container are analysed and compared to experimental data. The results show satisfactory qualitative and quantitative behaviour.

Keywords : finite circular cylinder, cross-flow cooling, heat transfer, LES, mixed-convection

NOMENCLATURE

h	$[W/m^2°C]$	Heat transfer coefficient
Φ	$[W/m^2]$	Heat flux density
Φ_v	$[W/m^3]$	Total power (source or sink)
$\vec{U}$	$[m.s^{-1}]$	Air velocity
$\vec{u}$	$[m.s^{-1}]$	Filtered air velocity
$\vec{g}$	$[m.s^{-2}]$	Gravity vector
D	$[m]$	Cylinder diameter
H	$[m]$	Cylinder height
P	$[Pa]$	Air pressure
t	$[s]$	Time
T	$[°C]$	Temperature
T_0	$[°C]$	Reference temperature
ρ	$[kg/m^3]$	Density
β	$[1/K]$	Thermal expansion coefficient
μ	$[kg/(m.s)]$	Dynamic viscosity
ν	$[m^2.s^{-1}]$	Kinematic viscosity
C_p	$[J/(kg.K)]$	Specific heat
λ	$[W/m/K]$	Thermal conductivity
Gr*	[–]	Grashof number: $g \beta H^4 \Phi /(\nu^2\lambda)$
St	[–]	Strouhal number
Re	[–]	Reynolds number

Subscripts and Superscripts

[*CS*] relating to *Code_Saturne* computations

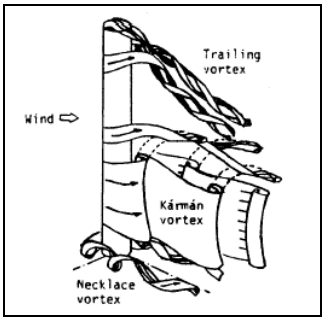

Figure 1 : Typical flow configuration studied

1. INTRODUCTION

Within the framework of radioactive waste management, the VALIDA program started to provide reliable experimental data for the validation of numerical tools utilized to model the cooling of spent nuclear fuel containers in dry storage facilities. The design of such facilities implies thermal-aeraulic calculations in order to predict containers and wall temperatures. These temperatures must never exceed critical values. The understanding of mixed-convection flow and more particularly the interaction between a global cross-flow circulation and local natural convection effects is a key point of these design studies. VALIDA experiments [1] were carried out for this purpose at CEA on a finite circular heated cylinder of 3.1 height to diameter ratio, mounted vertically in an insulated tunnel cooled by a cross-flow air circulation.

The purpose of this paper is to present the results of Large Eddy Simulation on the following test case: an air input bulk velocity of 1 m/s and a heat flux density of 600 W/m^2. The CFD tools used herein - *Code_Saturne* (thereafter called [*CS*]) and *Trio_U* Code [6] – are both based on a finite volume approach for unstructured meshes.

2. NUMERICAL APPROACHES

The characteristics of the flows around cylinders cooled by air usually involve a high level of turbulence. Hence, Direct Numerical Simulation is totally out of reach of the most powerful computers, even at low to moderate Reynolds numbers. On the other hand, Reynolds Averaged Navier Stokes models (such as the k-ε model or more advanced ones) might deal with such flows rather easily. However, they lack accuracy in specific complex areas of the flow, and most of all, they can only yield to average quantities and low frequencies, which is not suitable in heat transfer studies. In the last few years, the growing of computers power has made large size configurations accessible to a third and intermediate technique: Large Eddy Simulation. In LES, only the smaller scales of turbulence are modeled, whereas the large energy carrying structures are computed directly. Thus, LES provides 3D time dependent solutions, on which any kind of signal processing can be done, at much higher Reynolds numbers than DNS.

2.1. Basic equations

Conservation equations for mass (1), momentum (2) and energy (3) of the fluid flow are given in differential form by using the vector notation.

$$\nabla.(\vec{U}) = 0 \tag{1}$$

$$\frac{\partial \vec{U}}{\partial t} + \vec{\nabla}.\left(\vec{U} \otimes \vec{U}\right) = \vec{\nabla}.\left(\nu_{air}\left[\vec{\nabla}\vec{U} + \vec{\nabla}^{T}\vec{U}\right]\right) - \vec{\nabla}\left(\frac{P}{\rho_{air}}\right) + \beta\left(\mathrm{T} - \mathrm{T}_0\right)\vec{\mathrm{g}} \tag{2}$$

$$\frac{\partial T}{\partial t} + \vec{\nabla}.\left(T \cdot \vec{U}\right) = \vec{\nabla}.\left(\alpha_{air} \cdot \vec{\nabla}T\right) + \frac{\Phi_v}{\left(\rho C_p\right)_{air}} \tag{3}$$

where $\alpha_{air} = \lambda_{air} / (\rho C_p)_{air}$

The general heat equation to solved in the cylinder is given by the following:

$$\left(\rho C_p\right)_{\mathrm{cyl}} \frac{\partial \mathrm{T}}{\partial t} = \vec{\nabla}.\left(\lambda_{\mathrm{cyl}} \cdot \vec{\nabla}\mathrm{T}\right) + \Phi_v \tag{4}$$

2.2. Filtered fluid flow equations

In order to separate the large-scale motions from the small-scale fluctuations, a filter operation [15], [20] is applied on the conservation equations (1), (2) and (3), assuming that the filtering operation commutes with the derivative. In this operation, only the non-linear terms lead to contributions of the unresolved scales to the resolved ones. In analogy with the Boussinesq's eddy viscosity concept, this operation leads to the filtered momentum equation for turbulent flow where in the equation (5) and (6), the special notations of the filtered quantities and the air fluid flow are omitted:

$$\frac{\partial \vec{\mathrm{u}}}{\partial t} + \vec{\nabla}.\left(\vec{\mathrm{u}} \otimes \vec{\mathrm{u}}\right) = \vec{\nabla}.\left(\left[\nu + \nu_{\mathrm{t}}\right] \cdot \left[\vec{\nabla}\vec{\mathrm{u}} + \vec{\nabla}^{\mathrm{T}}\vec{\mathrm{u}}\right]\right) - \vec{\nabla}\left(\frac{P}{\rho}\right) + \beta \cdot \left(\mathrm{T} - \mathrm{T}_0\right)\vec{\mathrm{g}} \tag{5}$$

The turbulent heat flux in the energy equation of the fluid flow is evaluated using a turbulent conductivity $\lambda_t = (\rho\ \nu_t\ C_p) / Pr_t$ where Pr_t is the turbulent Prandtl number (Pr_t=0.9 in the present case). Finally, the filtered energy equation can be expressed in the form:

$$\frac{\partial \mathrm{T}}{\partial t} + \vec{\nabla}.\left(\mathrm{T}.\vec{U}\right) = \nabla.\left(\left[\alpha + \alpha_{\mathrm{t}}\right] \cdot \vec{\nabla}\mathrm{T}\right) + \frac{\Phi_v}{\rho C_p} \tag{6}$$

where $\alpha_t = \lambda_t / (\rho\ C_p)$

It should be noted that in k-ε approaches, the turbulent viscosity represents the dissipation of the whole energy spectrum, whereas in LES the subgrid viscosity only represents the effects of small scale structures (high frequencies).

Turbulent viscosity ν_t can be calculated with different models. In *Code_Saturne*, both the standard [7] and the dynamic [10] Smagorinsky models are available but only the standard one is used in the present work with the Smagorinsky constant set to 0.065. As it is known, this model may overestimate the turbulent viscosity in the boundary layer near walls. *Trio_U* calculation has been performed with the WALE model [12] that has been developed especially to treat correctly wall bounded flows.

Concerning the near-wall modeling, [*CS*] computations rely on a standard logarithmic wall

function if the non-dimensional distance to the wall exceeds 11.8 with Van Driest dumping for the viscosity SGS. Near-wall modeling functions may also used in *Trio_U* but none in this calculation thanks to satisfactory wall mesh size.

2.3. Numerical tools description

2.3.1. CEA CFD tool *Trio_U*

Trio_U is the CFD reference code of the CEA [13], which is especially designed for incompressible, turbulent flows with scalar transport in complex geometries, such as industrial Large Eddy Simulations (LES) on structured and unstructured grids of several tens of millions of nodes [4], [6]. Boussinesq's approximation is used to account for density effects. Conduction phenomenon into solid domains can be coupled in order to resolve thermal interactions between thermalhydraulic and heating solid components.

The *Trio_U* discretisation method has been developed as a finite volume / finite element approach (VEF): the 3D domain is discretised in tetrahedral elements, and the differential equations, written in the conservative form, are integrated over control volumes associated to those elements. Velocity and temperature unknowns are located in the centre of the faces whereas pressure unknowns are located in both, the centre and the vertices of the element. This arrangement leads to a so-called staggered grid approach. The unknown continuous variable is expressed as a combination of a base of shape functions that is assigned to each element and that depends on the nodal values. The *Trio_U* discretisation is characterized as P_1-non-conforming for velocity and temperature (P1-NC), and P_0-P_1 for pressure [21]:

- P_1-NC: the unknown variable is calculated at the midpoints of the element faces, and is assumed to be a linear function of coordinates (its gradient is constant); it is discontinuous at the interfaces, but the fluxes continuity is respected.
- P_0-P_1: the unknown variable is the sum of a constant and a linear function over the element. The variable is discontinuous at the interfaces.

The implemented solution method to solve the non-linear algebraic equations system obtained is a pressure matrix projection scheme derived from the SOLA method originally developed in 1975 by Hirt [14]. In this method, the pressure is taken implicitly in the momentum equations and the velocities are taken implicitly in the continuity equation. All other terms are taken explicitly. The pressure is then used in combination with a time marching scheme to project at each time step the velocity field into the divergence free space. A conjugated gradient method with SSOR preconditioning technique is used to calculate this pressure field. The user has to verify that the mass conservation is satisfied.

Specific second order schemes for space discretised equations (centered EF for the velocity [16], MUSCL with slope test [17] for the temperature) and an iterative implicit second order Crank-Nicholson time marching scheme are used to perform the LES simulation presented here. In the case of 3D convection/diffusion and conduction problems, the stability conditions are evaluated for each cell and at each time step with classical CFL and Fourier criteria. The overall time step is 5 times the time step imposed by the overall flow stability criterion, which is calculated in analogy to parallel resistances in an electrical network. The user only defines a convergence criterion for the recursion loop of the Jacobi method to implicitly solve the convection/diffusion problem for each time step.

Once fluid velocity field is known, the fluid energy convection/diffusion problem and the conduction problem in the meshed cylinder may be resolved using an explicit first order Euler time marching scheme, taking into account a stability criterion being the minimum between Fourier stability criterion calculated for the cylinder and the overall flow stability criterion. Every time step, the thermal coupling between air and solid domains is performed considering the equality of calculated heat flux ($\lambda \vec{\nabla} T$) for each cell that membership of the solid/air interface.

For the present calculations, this process leads here to a time−step about 0.0025 s.

2.3.2. EDF numerical tools

The EDF in-house finite volume CFD code, *Code_Saturne* [*CS*] [5], is used to solve Navier-Stokes equations on unstructured meshes. The code is based on a collocated approach that handles cells of any shape. The flow is assumed incompressible and Newtonian and the density is only a function of temperature (Boussinesq's approximation).

Several computations using LES have been carried out with *Code_Saturne* on academic and industrial configurations, among them [2], [3].

For LES calculations, second order schemes are used in space (fully centered scheme for the velocity components, centered scheme with slope test for the temperature) and time (Crank-Nicholson with linearised convection). A second order Adams-Bashforth method is used for the part of the diffusion involving the transposed velocity gradient, to keep the velocity components uncoupled.

The momentum equations are solved by considering an explicit mass flux (the three components of the velocity are thus uncoupled). Velocity and pressure coupling is insured by a SIMPLEC prediction/correction method with outer-iterations [8]. The Poisson equation is solved with a conjugate gradient method with diagonal preconditioning. The collocated discretisation requires a Rhie and Chow interpolation in the correction step to avoid oscillatory solutions. This

interpolation has been used in the present application, although it doesn't seem essential for unstructured meshes.

For the present calculations, the time-step is set to 0.0005 s, giving a maximum CFL number of 2.

The solid code *Syrthes* is coupled with *Code_Saturne* to compute the cylinder temperature. It uses finite element technique to solve the general heat equation where all properties can be time, space, or temperature dependent. More details on the possibilities of the finite element code *Syrthes* can be found in [9].

The thermal coupling between each code at each cell of the air/solid interface is based, every time step, on the exchange of the wall temperature from *Syrthes* to [*CS*]. The exchange coefficient h defining the heat flux at the wall is thus calculated by [*CS*] and returned to *Syrthes*. Then, the two codes work separately and calculate their own temperature implicitly considering the same heat flux. Time-step for *Syrthes* computations can be taken different from *Code_Saturne*'s

3. VALIDA CONFIGURATION

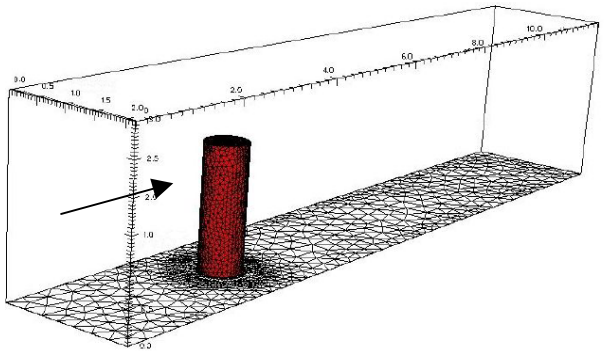

Figure 2 : View of VALIDA configuration

3.1. Experimental set-up

The heated cylinder investigated in the present work is that from the experiments by Duret et al. [1]. The geometry of the computational domain is given in Figure 2. Located in CEA, the VALIDA loop implements a cylinder of 3.1 height to diameter ratio: 2 m high and a 0.64 m diameter, mounted vertically in an insulated tunnel cooled by a cross-flow air circulation. The wind tunnel is a cube–shaped channel with a 2.4 m width, 3 m height, and a 12 m length from inlet to outlet. The cylinder axis is placed in the middle of the channel width, at 3 m from the inlet (see Figure 2). The two lateral walls are therefore at a distance of 0.88 m from the cylinder wall. The cylinder is made up of 5 mm thick steel. It is thermally insulated on the inside and heated by a uniform heat flux density imposed on the inner wall and on the top. Table 1 gives the experimental input data simulated in the present paper.

Air and cylinder temperature measurements are described in details in [1]. The air temperature is measured behind the cylinder, using a movable frame with 77 thermocouples. The cylinder wall temperatures are measured along an instrumented vertical line in rotation.

A temperature measurements accuracy of ±0.5°C can be considered.

Cylinder heating Power (W)	Inlet air velocity (m/s)	Height to diameter ratio	Re	Gr*
2615[1]	1	3.1	43000	$2.7.\ 10^{13}$

Table 1 : Experimental input parameters

3.2. Numerical parameters

3.2.1. Meshes

The calculation presented here is used to qualify both *Trio_U* and *Code_Saturne* calculations for the cooling of spent nuclear fuel containers in dry storage facilities. The investigated phenomena are occurring around and behind the cylinder, in the plume. Due to the coupled resolution of heat conduction in the heating cylinder with the high Re number convection of cooling air around it, fine meshes are required in and around the cylinder to simulate such thermal interactions and mixing phenomena which are affected by the processes in the boundary layers. For LES calculations, millimetric mesh sizes are thus used in and close to the cylinder to resolve the boundary layers.

The *Trio_U* VEF module requires a conforming tetrahedral meshing, which has been generated using the commercial mesh generator ICEM™. The mesh contains about 1.1 million tetras in the aeraulic domain, i.e. about 2.2 million nodes when using the *Trio_U* discretisation, and 20 000 tetras in the 5 mm thickness of the cylinder for the coupled heat conduction problem. *Trio_U* mesh is shown in Figure 3. It gives a maximum non-dimensional distance to the wall of 8.

The [*CS*] fluid mesh is presented in Figure 4. It contains 1 million cells and gives a maximum non-dimensional distance to the wall of 5. The *Syrthes* solid mesh contains 70 000 tetras.

3.2.2. Input data and boundary conditions

In this specific study, the inlet air velocity is $1 ms^{-1}$ with uniform profile in space and constant in time. No inlet turbulent intensity is taken into account in *Trio_U* calculation whereas 10% is used in [*CS*] computation but with a random generation method that does not really sustain turbulence.

[1] Corresponding heating flux density imposed on the inner wall: $\Phi = 600\ W/m^2$

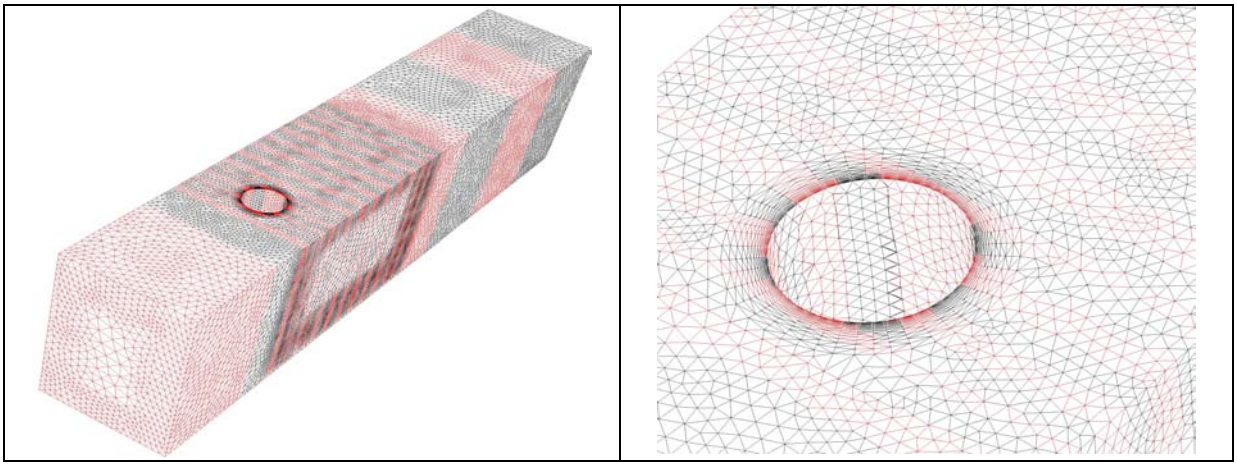

Figure 3 : Meshing of the VALIDA test facility (ICEM™) used for *Trio_U*

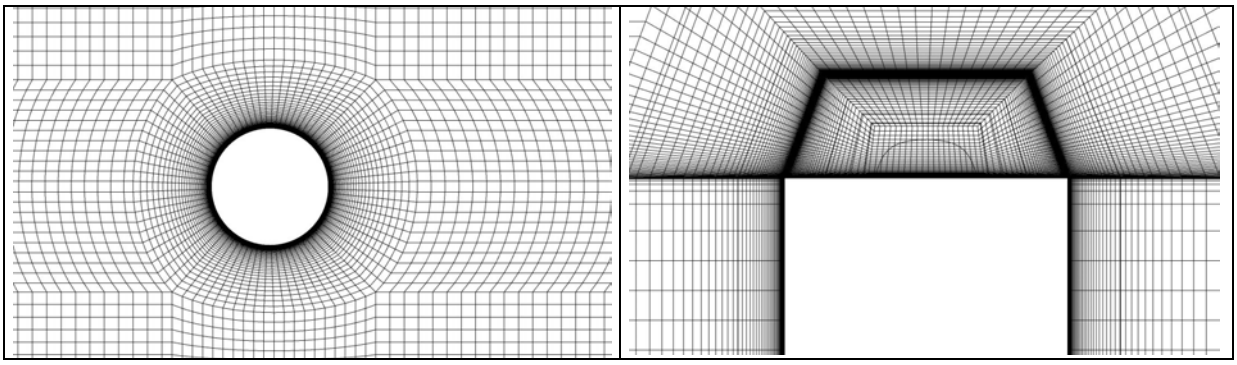

Figure 4 : Meshing of the VALIDA test facility used for *Code_Saturne*

The physical properties of the air fluid and steel cylinder are evaluated at reference temperature T_0=20°C that is the inlet temperature.

The uniform heat flux density imposed on the inner wall's cylinder, including cover, is 600 Wm^{-2}.

Zero gradients are imposed as free boundary conditions at the channel outlet for temperature (*CS* and *Trio_U*), velocity (*CS*), and pressure (*Trio_U*). Adiabatic and frictional conditions are used for ground, roof, and lateral channel walls.

Symmetrical conditions are taken into consideration in [*CS*] calculation on lateral walls, as the discretization is poor.

3.2.3. Initial thermal calculation process

Due to the weighty thermal inertia of the solid cylinder compared to thermal air evolutions, a specific pre–calculation process is needed to accelerate the thermal solid convergence. This process is carried out in two steps:

- A first adiabatic calculation of the air around the cylinder is made in order to achieve a typical steady average air velocity field,

- Then, a coupled calculation is done thanks to *Syrthes* for [*CS*]. For *Trio_U*, it is done while maintaining, during this entire first fluid/solid calculation, the previous average air velocity field.

As no velocity/pressure system has to be solved, a corresponding steady temperature field in the cylinder can be reached quickly enough. This temperature field becomes the first guess of the real coupled fluid/solid calculation.

It should be noted that during the real fluid/solid calculation, cylinder's temperature field is not significantly modified.

4. GENERAL COMPUTATIONAL RESULTS

4.1. Qualitative observations

The field covered in VALIDA is characteristic of a sub-critical transverse convection regime (see Figure 1). Its Reynolds number, based on the cylinder diameter, the bulk air velocity, and the reference viscosity, is Re ~ 40 000, therefore between 10^3 and 2.10^5. In such regimes, laminar boundary layer, laminar flow separation, and regular alternate vortex shedding are pointed out by Zukauskas [18], and Williamson [19].

Laminar boundary layers appear at the stop front stagnation point of the cylinder and then thicken. Inside these boundary layers, pressure is constant along the radius of the cylinder.

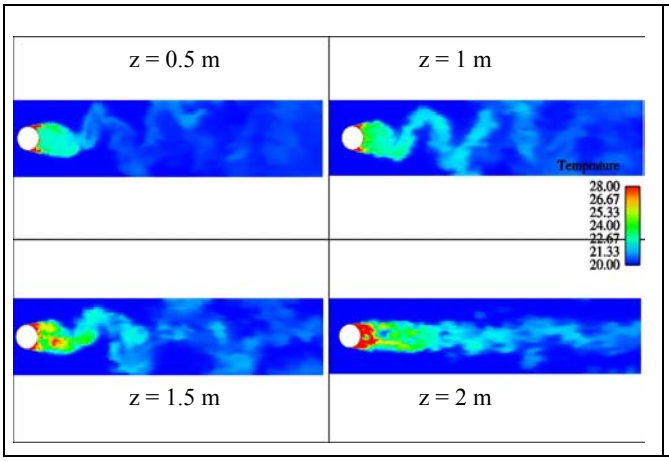

Figure 5 : Example of instantaneous air temperature at various z elevations [*CS*]

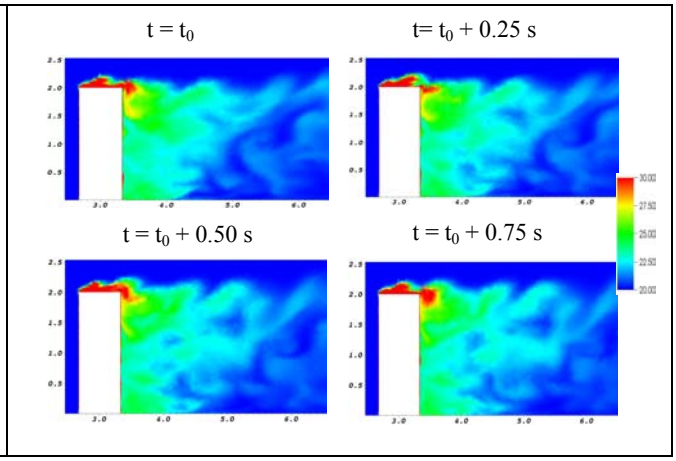

Figure 6 : Example of air temperature time evolution in the longitudinal middle cut–plane [*Trio_U*]

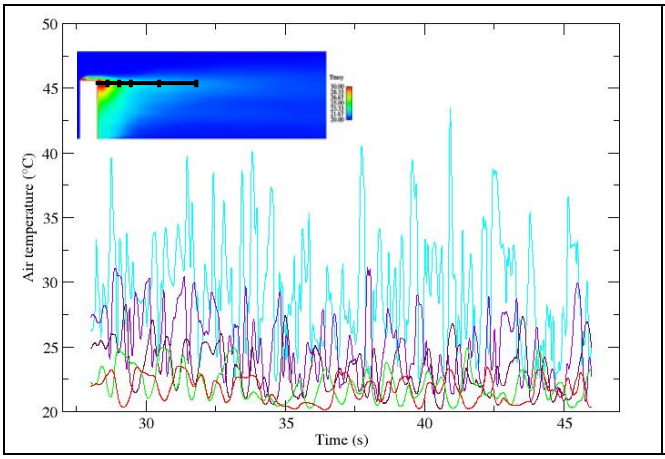

Figure 7 : Instantaneous air temperature [*CS*]

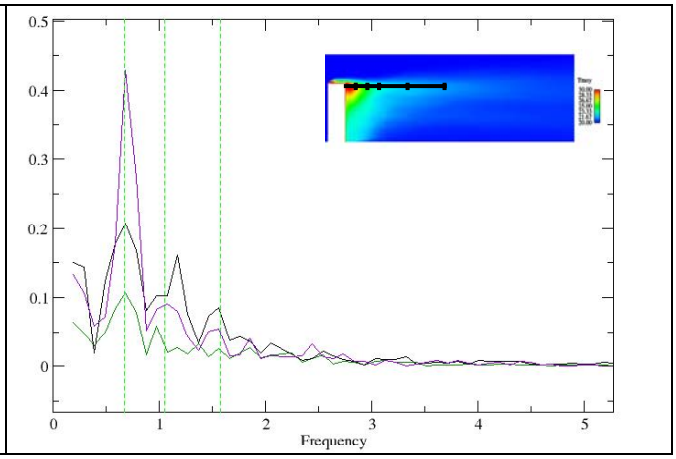

Figure 8 : Air temperature DFT [*CS*]

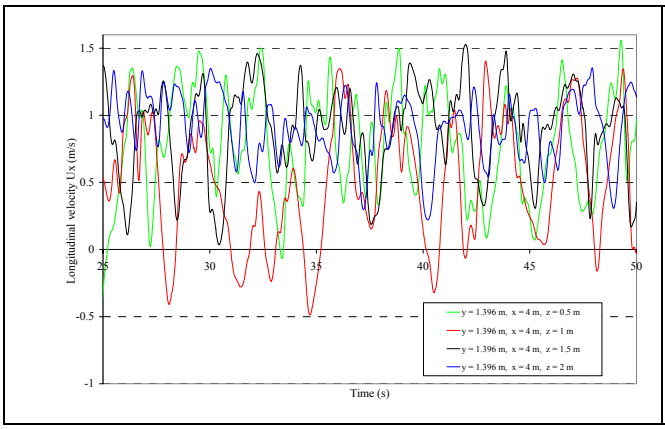

Figure 9 : Instantaneous air velocity [*Trio_U*]

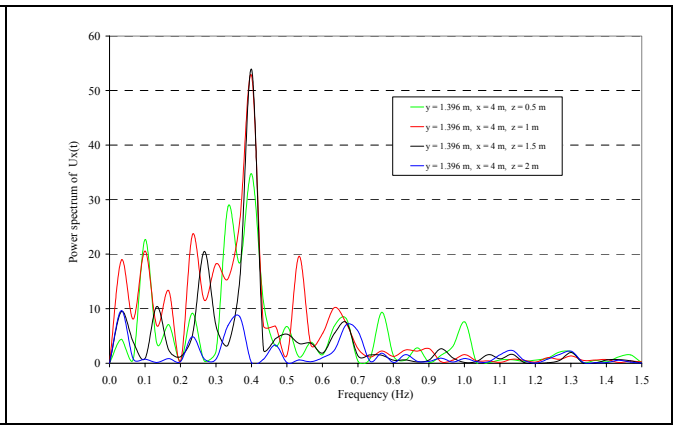

Figure 10 : Air velocity DFT [*Trio_U*]

On the contrary, tangentially to the wall, air velocity increases along the front face from the attack point, and then decreases along the rear face. When velocity gradient equals zero, the boundary layer separates from the wall and convection heat exchanges reach a minimum. The separated flow area at the back of the cylinder appears to be turbulent. These general flow behaviours are well observed in both computations. Examples are given in Figure 5 and Figure 6. They show instantaneous and time evolution temperature fields in different cut-planes. Karman vortices appear very significantly in both cut-planes at 1m and 1.5m, whereas the effect of the upper separation predominates at 2m and that of the bottom wall appears at 0.5m. The effect of natural convection behind and very close to the wall cylinder may also be pointed out through these figures.

4.2. *Instantaneous signals analyses*

One can observe on Figure 8, three characteristic temperature frequencies: f_1 = 0.6 Hz, f_2 = 1 Hz, f_3 = 1.5 Hz. The same characteristic frequencies also appear in *Trio_U* air temperature Fourier transformations (not presented herein).

On Figure 10, the characteristic velocity frequency observed is f_0 = 0.4 Hz. It is obtained from Fourier transformations of longitudinal air velocity in the plume cylinder (Figure 9). The same characteristic frequency f_0 also appears in [*CS*] velocity Fourier transformations (not presented herein). This characteristic frequency corresponds to a Strouhal number St of 0.2 if St = f_0.D/U with D the cylinder diameter and U the bulk air velocity (1ms^{-1}). This Strouhal number is related to the Strouhal number of shedding vortices commonly observed [22] for a circular cylinder immersed in a steady cross flow in the range 10^4 < Re < 10^5. The frequency of Karman vortices appears quite significantly at 1m and 1.5m on Figure 10 whereas the upper separation shows its effects at 2m and the bottom wall's influence appears at 0.5m.

5. TEMPERATURES COMPARISON WITH EXPERIMENTS

Statistics have been collected during 22 s for [*CS*], corresponding to 44 000 time-steps. The averaging starts at t = 30 s. For *Trio_U*, average values are obtained between 20 and 50 s.

Figures 11 compares qualitatively experimental and computed results for air temperature behind the cylinder. Figure 14 compares them quantitatively. Figure 12 compares qualitatively experimental and computed results for cylinder temperatures. Figure 13 compares them quantitatively.

6. CONCLUSION AND PERSPECTIVES

The field covered in the present VALIDA test case is characteristic of a sub-critical transverse convection regime (Re ~ 40 000). Comparisons between experimental and LES computed results show very good agreement for both EDF and CEA CFD codes even though they are based on different numerical approaches and models.

Karman vortices appear very significantly in both computational results. Their characteristic frequency corresponds to the Strouhal number of shedding vortices commonly observed for a circular cylinder immersed in a steady cross flow.

Other test cases, with varied Reynolds and Grashof numbers, are being simulated at the moment on the same configuration. They are relevant to other experimental inputs (air velocity and cylinder heat flux) and show different flow regimes. They will lead to heat transfer estimations and could open out into the establishment of correlations for heat transfer coefficient in mixed convection.

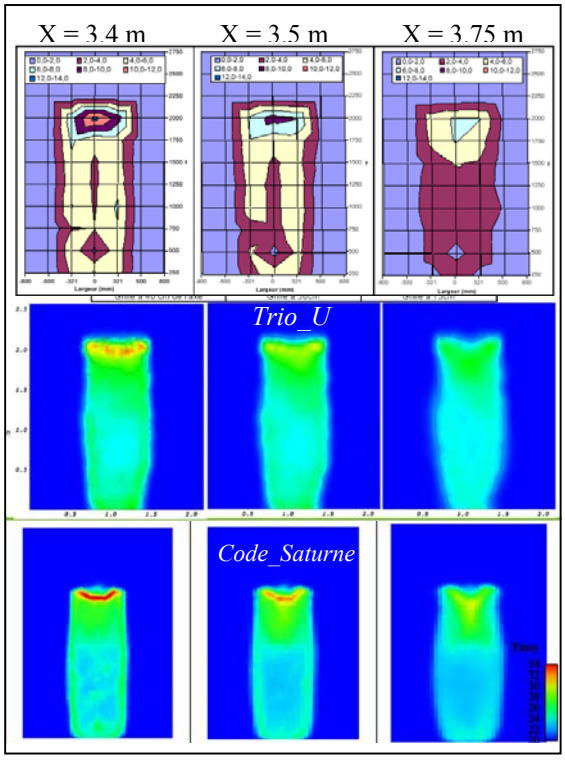

Figure 11 : Experimental and computed air temperature behind the cylinder [*CS* / *Trio_U*]

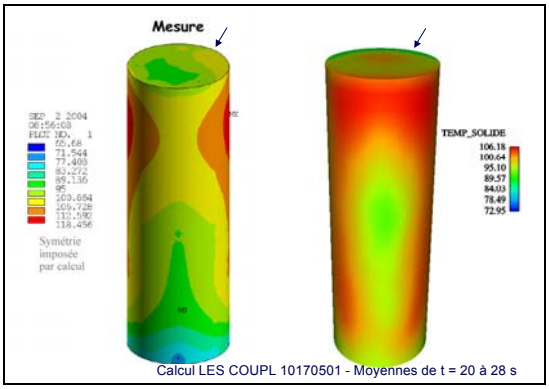

Figure 12 : Experimental and computed cylinder temperatures [*CS*]

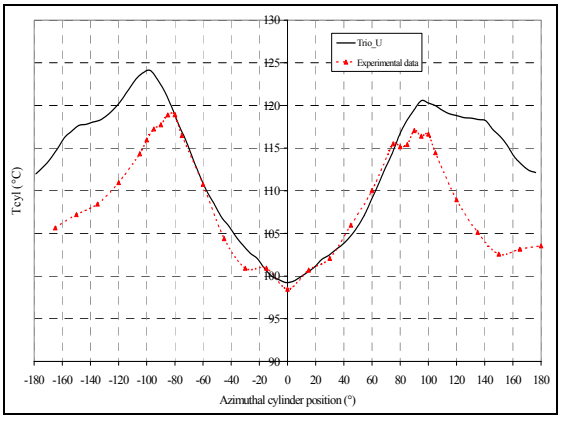

Figure 13 : Experimental and computed cylinder temperatures at z = 1.75 m [*Trio_U*]

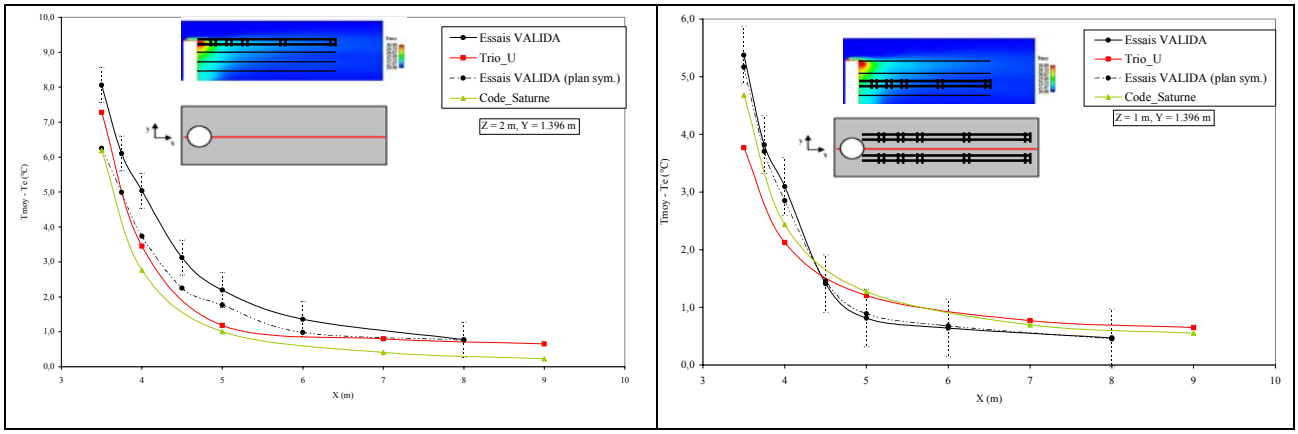

Figure 14 : Experimental and computed average air temperature profiles in the plume [*CS* / *Trio_U*]

REFERENCES

[1] Duret, B., Bonnard, J.,C., Colmont, D., VALIDA MOCK-UP - Experimental results on turbulent heat transfer in mixed-convection for one large vertical heating cylinder in air cross-flow, submitted to *International Heat Transfer, 2006.*

[2] Benhamadouche, S., and Laurence, D., LES, Coarse LES, and Transient RANS Comparisons on The Flow Across Tube Bundle, *Int. J. Heat and Fluid Flow*, 4, pp 470-479, 2003.

[3] Benhamadouche S., Laurence D., Jarrin N., Afgan I. and Moulinec C., Large Eddy Simulation of Flow across in-line tube bundles, *The 11th International Topical Meeting on Nuclear Reactor Thermal-Hydraulics (NURETH-11) paper 405, Popes' Palace Conference Center, Avignon, France, October 2-6, 2005.*

[4] Bieder, U., Höhne, T., Prasser, H.–M., Kliem, S., Validation of Trio_U – Numerical Simulations Of ROCOM Buoyancy Driven Test Case, *12th Int. Conference on Nuclear Engineering, Washington D.C., USA, April 25–29, 2004.*

[5] Archambeau, Fr., Méchitoua, N., Sakiz, M. *Code_Saturne*: A Finite Volume Code for the Computation of Turbulent Incompressible Flows - Industrial Applications - *International Journal of Finite Volumes 2004 (electronic).*

[6] Bieder, U., Calvin, C., Mutuelle, H., Detailed Thermal Hydraulic Analysis Of Induces Break Sever Accidents Using The Massively Parallel Code Trio_U, *Supercomputing in Nuclear Applications, Paris, September 22–24, 2003.*

[7] Smagorinsky, J., General circulation experiments with the primitive equations, part I: the basic experiment, *Monthly Weather Rev., 91, 99-164 (1963).*

[8] Ferziger, J.H., Peric, M., Computational Methods for Fluid Dynamics, *Springer, third edition (2002).*

[9] Rupp, I., Peniguel, Ch., Coupling Heat Conduction, Radiation and Convection in Complex Geometries, *Int Journal of Numerical Methods for Heat and Fluid Flow*, **9** (1999).

[10] M. Germano, U. Piomelli, P. Moin and W. Cabot, A dynamic subgrid-scale eddy viscosity model, *Phys. Fluids*, 3(7):1760–1765 (1991).

[11] Bieder, U., Calvin, C., Emonot, P., "PRICELES: An Object Oriented Code for Industrial LES" , Proc. 8th Ann. Conf. of the CFD Soc. of Canada, Montreal, 11-13 June 2000.

[12] Nicoud, F., Ducros, F., Subgrid scale modelling based on the square of the velocity gradient tensor. Flow, *Turbulence and Combustion, 62(3) 183-200, 1999.*

[13] Calvin, Ch., Cueto, O., Emonot, P., An object-oriented approach to the design of fluid mechanics software. *Mathematical Modelling and Numerical Analysis, Vol. 36, No. 5, 2002.*

[14] Hirt, C. V., Nichols, B.D., Romero, N.C., SOLA - A numerical solution algorithm for transient flow. *Los Alamos National Lab., Report LA-5852, 1975.*

[15] Lesieur, M., "Turbulence in fluids", Kluwers, Third edition.

[16] Quemere P., Nouvelle approche VEF pour la réalisation de Simulations des Grandes Echelles (LES) en non structuré, Technical note CEA/DEN/SMTH/LDTA/2003–010, 2003.

[17] Van Leer, B., Toward the ultimate conservative difference schemes, a second order sequel to Godunov's method, *Journal of Computational Physics, 32, 1979.*

[18] Zukauskas, A., Heat Transfer From Tubes In Crossflow, *Advances In Heat Transfer*, 18, pp. 87-159, 1987.

[19] Williamson, C.H.K., Vortex Dynamics In The Wake, *Annu. Rev. Fluid. Mech.*, 28, pp. 477-539, 1996.

[20] Pope, S., "Turbulent Flows", Cambridge University Press.

[21] Heib, S., "Nouvelles discrétisations non structurées pour des écoulements de fluides à incompressibilité renforcée", *PhD, Pierre et Marie Curie University (Paris), 2003.*

[22] White, F.M., Fluid Mechanics, 2nd Edition, McGraw-Hill, New York, pp. 253–268, 1986.

Conference on Modelling Fluid Flow (CMFF'06)
The 13th International Conference on Fluid Flow Technologies
Budapest, Hungary, September 6-9, 2006

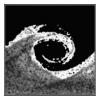

FLOW-INDUCED IN-LINE OSCILLATION OF TWO CIRCULAR CYLINDERS IN TANDEM ARRANGEMENT

Atsushi OKAJIMA[1], Satoru YASUI[2], Takahiro KIWATA[2], Shigeo KIMURA[2]

[1] Professor, Kanazawa-Gakuin Tanki University, 10 Sue-Machi, Kanazawa, 920-1392, Japan, Phone: 81-76-229-8816, Fax: 81-76-229-8968,
E-mail: a-okaji@kanazawa-gu.ac.jp
[2] School of Graduate Natural Science and Technology, Kanazawa University, Kakuma-machi, Kanazawa, 920-1192, Japan

ABSTRACT

Flow-induced in-line oscillation of two tandem circular cylinders has been experimentally studied by free-oscillation tests in a wind tunnel. Only one cylinder of either upstream or downstream cylinder was elastically supported easily to move in the in-line direction for reduced mass-damping parameter $Cn \approx 1$; the other of the tandem cylinders was fixed to the tunnel sidewalls. The gap between upstream and downstream cylinders was changed from $s = 0.3$ to 3. The response amplitudes of the oscillatory cylinder in the in-line direction and the vortex-shedding frequency in the wake were measured. The flow around the tandem cylinders was visualized by the smoke-wire method.

As results of the upstream cylinder free to undergo in-line oscillation, there was a wide excitation region of reduced velocity, $Vr = 1.5$ to 2.5 in all ranges of gap ratios of $s = 0.3$ to 3. This excitation was mainly induced by symmetrical vortex shedding; the other excitation of $Vr = 3$ to 3.5 at wide gap ratios of $s = 2$ to 3, was induced by alternate Karman vortex shedding, as with the in-line oscillation of a single cylinder. Next, the downstream cylinder free to move in the in-line direction had an excitation region in a wide range of $Vr = 2$ to 4 for the narrow gap distance of $s = 0.3$ to 0.75, which seems to be induced by alternate Karman vortex shedding. The other excitation regions due to symmetrical vortices were limited to the regions of gap distances of $s = 0.75$ to 2. Furthermore, the downstream cylinder oscillated as a buffeting phenomenon influenced by wake turbulence and fluctuation of the upstream cylinder, when gap distance was greater than $s = 2.5$.

Keywords: flow-induced vibration, in-line oscillation, two circular cylinders, tandem arrangement, flow visualization

1. INTRODUCTION

Flow-induced vibration of multi-tube banks occurs in industry plants such as nuclear power plants, heat exchangers, offshore platforms and so on, and it has been of great interest for many decades. If the working fluid is a liquid, structures with extremely small mass ratios may be easily induced to oscillate in the in-line direction at relatively low reduced velocities. As a typical example, a flow-induced vibration in the in-line direction caused damage to a thermocouple in the fast breeder reactor "Monju" of the Japan Nuclear Cycle Development Institute in 1995 [1].

Vortex shedding from an elastically supported cylinder can cause the cylinder to oscillate in the cross-flow (transverse) and in-line (streamwise) directions, if system damping is small. In addition, the value of mass ratio M ($= m/\rho D^2$, m being mass per unit span length, ρ being fluid density and D being cylinder diameter) is small in liquid flows such as water, oil or metal sodium at high temperature. The in-line oscillation of the cylinder occurs easily at low reduced velocity, because reduced mass-damping parameter Cn ($= 2M\delta$; δ being the logarithmic decrement of the structure damping parameter) is extremely small.

Some studies have been done on in-line oscillation of circular cylinders, for example, King et al.[2] carried out experiments on in-line oscillation of a flexible cantilevered circular cylinder beam in a water channel. Those authors observed that in-line oscillation of the cylinder occurs with large amplitude, when the Cn number is less than 1. The velocity-regions with in-line oscillation comprise two regions near half the resonance velocity, that is, the first excitation region occurs at lower velocities, the second at higher velocities. Recently, many experimental studies have been done on in-line oscillation in wind tunnel [3] and water tunnel [4], in addition to computational simulations [5,6], to evaluate the critical values of the reduced mass-damping parameter for in-line oscillations under the same oscillation conditions as the free-oscillation tests

by Scruton [7] in the cross-flow direction.

Therefore the flow-induced in-line oscillation of multiple cylinders in a tandem arrangement was measured by free-oscillation tests in a wind tunnel. Either the upstream or downstream of the two tandem cylinders was elastically supported to move in the in-line direction, while the other cylinder was fixed. Gap distance S between the upstream and downstream cylinders was changed from $s = S/D = 0.3$ to 3. The response amplitudes of a cylinder oscillating in the in-line direction and the vortex-shedding frequency in a wake were measured as functions of the gap distance between two cylinders. The flow around tandem cylinders was visualized by the smoke-wire method.

This paper consist of 6 sections. Section 1 is an introduction about this study. Section 2 presents an outline of the experimental rig and the leading equations. In section 3 the results of tandem fixed cylinders are compared with the previous results. Section 4 presents the excitation results of the upstream cylinder free to undergo in-line oscillation. In section 5 the results are given for the reverse situation of the downstream cylinder free for in-line oscillation and the fixed upstream cylinder. Finally section 6 is a conclusion of this paper.

NOMENCLATURE

Cn Reduced mass-damping parameter, $2M\delta$
D Cylinder diameter
f_c Characteristic frequency of a cylinder
f_n Natural vortex shedding frequency for a stationary cylinder
f_w Frequency of a wake
L Span length of a cylinder
M Mass ratio, $m/\rho D^2$
m Mass of a cylinder per unit span length
Re Reynolds number, UD/ν
S Gap distance between two cylinders
St_c Non-dimensional characteristic frequency of a cylinder, $f_c d/U$
St_n Strouhal Number of a wake for a stationary cylinder, $f_n D/U$
St_w Strouhal Number of a wake, $f_w D/U$
s Non-dimensional gap distance between two cylinders, S/D
U Uniform flow velocity
Vr Reduced velocity, $U/f_c D$
Vr_{cr} Critical reduced velocity, $U/f_n D = 1/St_n$
x_{rms} Root-mean square response amplitude of a cylinder

δ Logarithmic decrement of the structure damping parameter of a cylinder
ν Kinematic viscosity of working fluid
ρ Fluid mass density
ξ_{rms} Non-dimensional response amplitude of a cylinder, x_{rms}/D

2. EXPERIMENTAL ARRANGEMENTS

The experiments were performed in a low-speed wind tunnel with a rectangular working section of 300mm × 1200mm, as shown in Fig. 1. The turbulence level in the working section was less than 0.5%. The circular cylinder model with diameter of $D = 120$ mm was made of styroform with smooth surfaces covered by aluminum foil. The span-length of the cylinder models was 293mm. The circular end plates, approximately 120mm in diameter and 0.5mm thick were fixed to both sides of an oscillatory model, to reduce the influence of any end-effects. The oscillatory model of either upstream or downstream cylinder was supported by eight coil

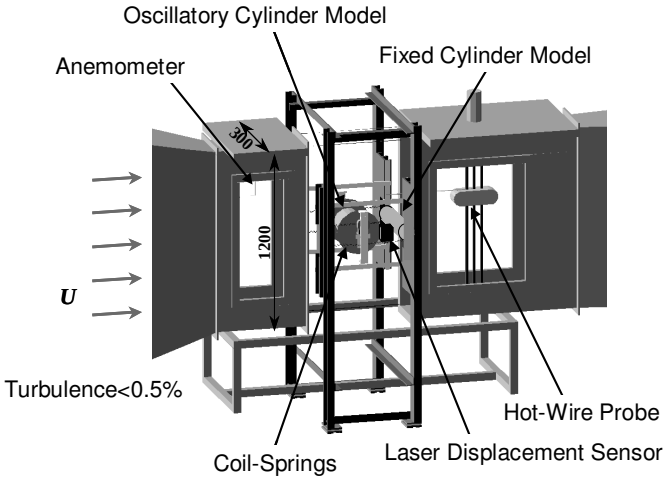

Fig.1 Wind tunnel and test section for experiments.

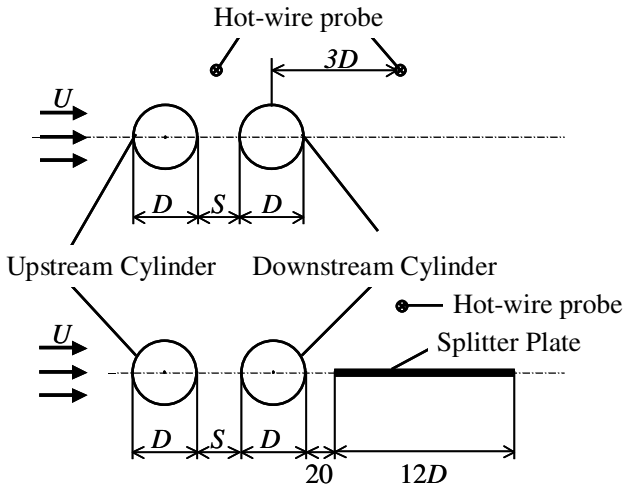

Fig.2 Arrangement of multiple tandem models.

springs to move in the in-line direction. The system natural frequency f_n of a tested model was 3.85 Hz, whereby non-dimensional value of the system natural frequency St_n was evaluated as f_nD/U, where U is the wind speed. The reduced mass-damping parameter (Scruton number) is defined by

$$C_n = \frac{2m\delta}{\rho D^2},$$

where m is the equivalent mass of the model per unit span, ρ is air density and δ is the logarithmic damping parameter of the oscillation system. An oscillatory cylinder model of two tandem cylinders was elastically supported to move in the in-line direction, with the other cylinder fixed to the tunnel sidewalls. The ratio $s = S/D$ of gap distance S between the upstream and downstream cylinders was changed from $s = 0.3$ to 3, as illustrated in Fig. 2.

The response amplitudes of a cylinder under in-line oscillation and the vortex-shedding frequency in a wake were measured as functions of the gap distance. The responses of an oscillatory model were measured by Laser displacement detectors, and the root-mean-square amplitudes of the in-line oscillation were non-dimensionalized by cylinder diameter D. The reduced velocity Vr and the wake Strouhal number St_W are respectively defined by

$$Vr = \frac{U}{f_n D} \quad \text{and} \quad St_w = \frac{f_w D}{U},$$

where f_W is the vortex-shedding frequency measured by the hot-wire probe located in a wake as shown in Fig.2.

Thus the flow-induced in-line oscillation of two circular cylinders in a tandem arrangement was experimentally studied in a wind tunnel. The flow around the tandem cylinders was visualized by the smoke-wire method, using liquid paraffin smoke.

3. STROUHAL NUMBERS OF TWO CIRCULAR CYLINDERS IN TANDEM ARRANGEMENT

Fig. 3 shows the measured values of the Strouhal number of a wake behind two tandem circular cylinders St_W against different values of gap distance ratio s between two cylinders at Reynolds numbers of $Re = (1–2)\times10^4$, in comparison with the results of reference [8] of $Re = 1.7\times10^5$ and reference [9] of $Re = (0.15–1)\times10^4$, respectively. The present values of the Strouhal

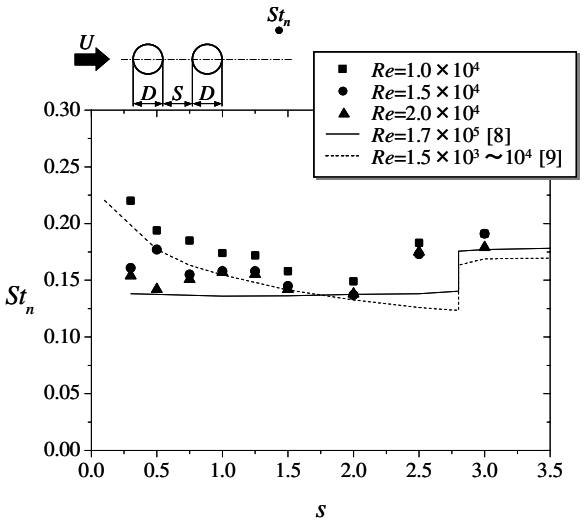

Fig.3 Strouhal number St_n versus gap ratio s of two tandem cylinders.

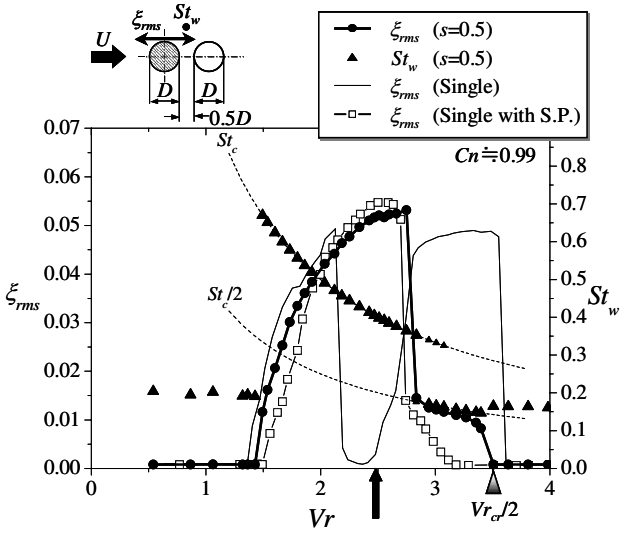

(a) The response amplitude and Strouhal number

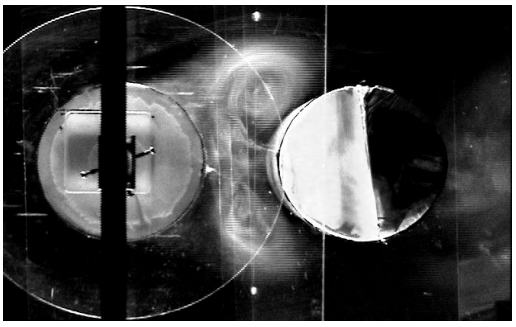

(b) Visualized flow-patters (Vr= 2.49)

Fig.4 (a) Response amplitude of upstream cylinder and Strouhal number against reduced velocity and (b) Visualized flow-pattern (Vr = 2.49) for reduced mass-damping parameter Cn = 0.99 with gap ratio s = 0.5.

number seem to be close to those obtained at lower Reynolds numbers [9].

4. FLOW-INDUCED IN-LINE OSCILLATION OF THE UPSTREAM CYLINDER

When the ratio $s = S/D$ of gap distance S between the upstream and downstream cylinders was changed from $s = 0.3$ to 3, the fluid-elastic characteristics of the upstream cylinder of two tandem cylinders are examined, and the typical results for cases of gap distance ratios $s = 0.5$ (narrow) and 2 (wide) are shown.

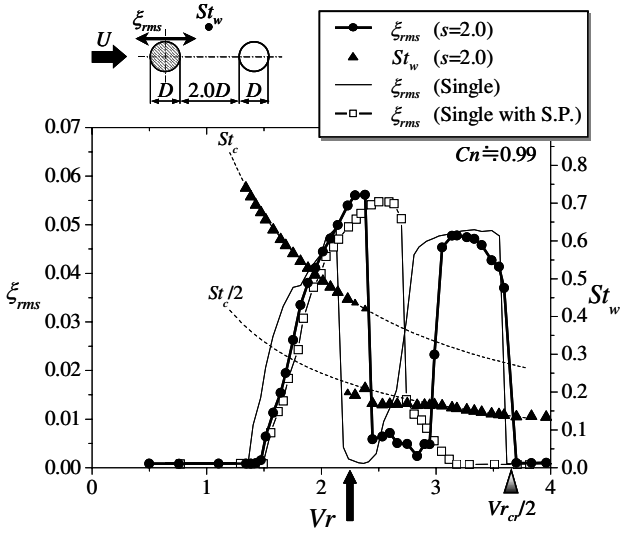

(a) The response amplitude and Strouhal number

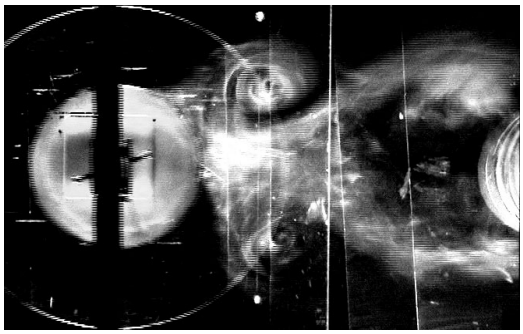

(b) Visualized flow-patter (Vr= 2.23)

Fig.5 (a) Response amplitude of upstream cylinder and Strouhal number against reduced velocity and (b) Visualized flow-pattern (Vr = 2.23) for reduced mass-damping parameter Cn = 0.99 with gap ratio s = 2.

4.1. Gap distance ratio of s = 0.5

Fig. 4a shows an example of the response curve of the in-line oscillation of the upstream circular cylinder for the narrow gap distance ratio s = 0.5. These figures show non-dimensional response amplitude ξ_{rms} and the Strouhal number St_w of a wake against reduced velocity Vr for the reduced mass-damping parameter Cn = 0.99, in comparison with the results for a single cylinder and

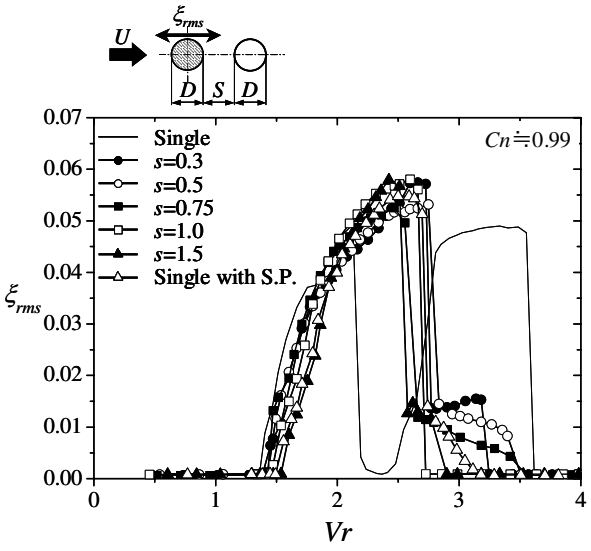

Fig.6 (a) Response amplitude of upstream cylinder against reduced velocity for reduced mass-damping parameter Cn = 0.99 with gap ratios s = 0.3 to 1.5.

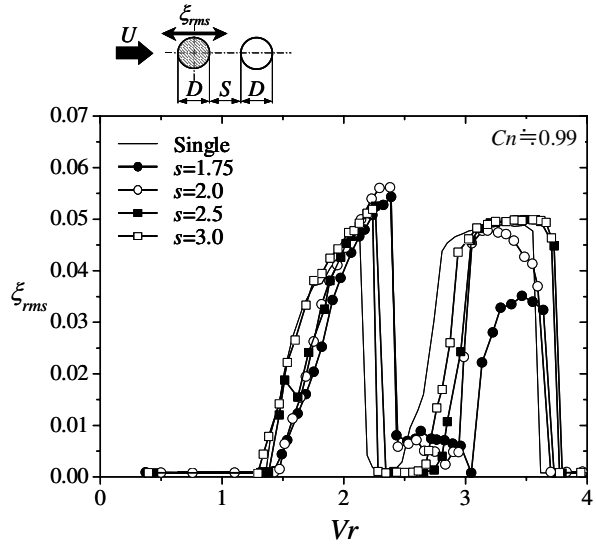

Fig.6 (b) Response amplitude of upstream cylinder against reduced velocity for reduced mass-damping parameter Cn = 0.99 with gap ratios s = 1.75 to 3.

a cylinder with a splitter plate (abbreviated to S.P. in Fig. 4a). In this figure, the in-line oscillation occurs near $Vr = 1.4$, while amplitude ξ_{rms} gets a rise up to $\xi_{rms} = 0.053$ with the increase of Vr, cylinder oscillation suddenly damping near $Vr = 2.8$ and stopping at $Vr = 3.5$. The lock-in phenomenon is found in the range $Vr = 1.4$ to 3.8, whose frequency is equal to the non-dimensional characteristic frequency of a cylinder St_c.

Fig. 4b presents a visualized picture for the upstream cylinder oscillating in the in-line direction at $Vr = 2.49$. In this figure, the shear layer separating from the upstream cylinder clearly rolls up into symmetrical vortices in the gap-field between the upstream and downstream cylinders. It is evident that this in-line oscillation is induced by the symmetrical vortices formed in the gap-field with the Strouhal frequency St_c.

4.2. Gap distance ratio of *s* = 2

Fig. 5a shows the results of the in-line oscillation of the upstream cylinder when the gap distance becomes relatively wide, $s = 2$. In this figure, two excitation regions remarkably appear in the regions $Vr = 1.5$ to 2.4 (the first excitation region) and 2.9 to 3.6 (the second excitation region) , while cylinder oscillation is suppressed less than 0.005 in the range $Vr = 2.4$ to 2.9, which appears to be very similar to the response characteristics of a single cylinder. It is certified in Fig.5(a) that Strouhal frequency of the first region equals to St_c, although the frequency value of the second region is $St_c/2$.

Fig. 5b presents a smoke picture for the upstream cylinder oscillating in the in-line direction at $Vr = 2.23$ and $s = 2$. In this figure, it can be observed apparently two pairs of symmetrical vortices arranged in the gap-field between two tandem cylinders.

4.3. Narrow gap distance ratios of *s* = 0.3 to 1.5

Fig. 6a summarizes the response curves of the in-line oscillation of the upstream cylinder for the narrow gap distance ratios of $s = 0.3$ to 1.5. All response curves of the narrow gap distance appear to be similar to the response characteristics of a cylinder with a splitter plate (plotted by the symbol Δ). It implies that this excitation is induced by the symmetrical vortices formed in the gap before the downstream cylinder.

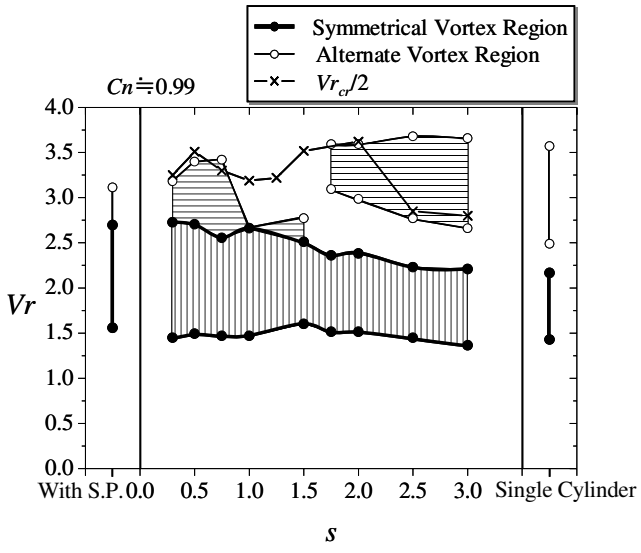

Fig.7 Excitation regions of upstream cylinder as functions of gap distance s and reduced velocity *Vr*.

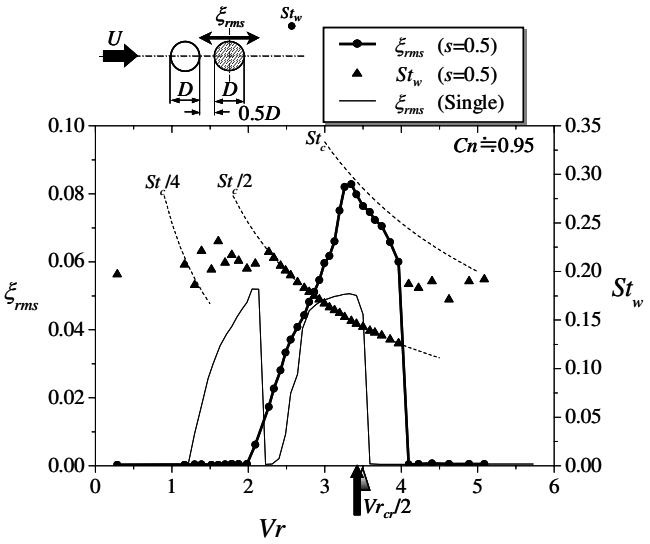

(a) The response amplitude and Strouhal number

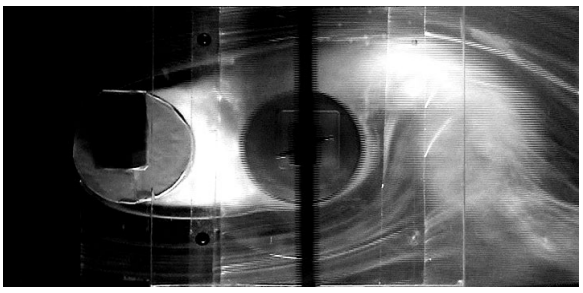

(b) Visualized flow-patter (*Vr*= 3.34)

Fig.8 (a) Response amplitude of downstream cylinder and Strouhal number against reduced velocity and (b) Visualized flow-pattern ($Vr = 3.34$) for reduced mass-damping parameter $Cn = 0.95$ with gap ratio $s = 0.5$

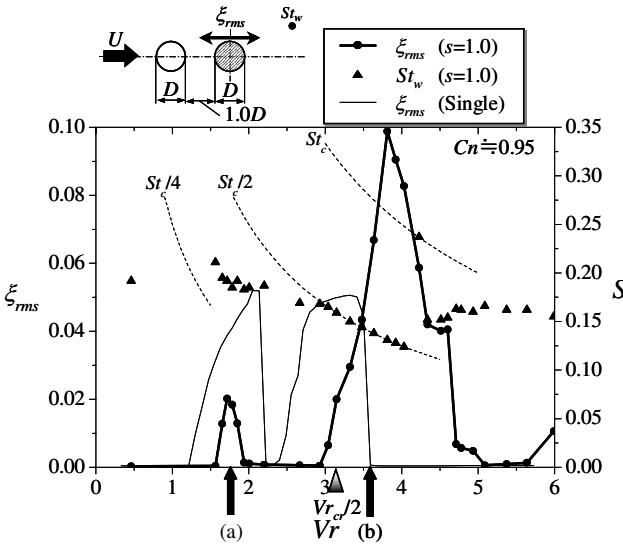

Fig.9 Response amplitude of downstream cylinder and Strouhal number against reduced velocity

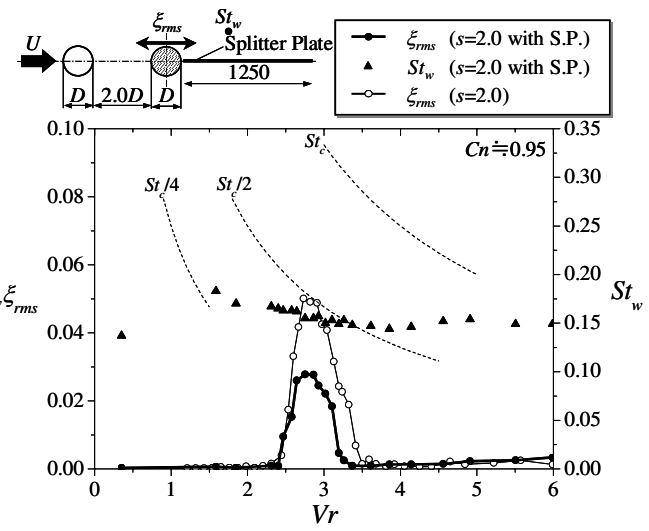

Fig.11 Comparison between response amplitudes of downstream cylinders without and with splitter plate against reduced velocity for reduced mass-damping parameter of *Cn* = 0.97 with gap ratio *s* = 0.3.

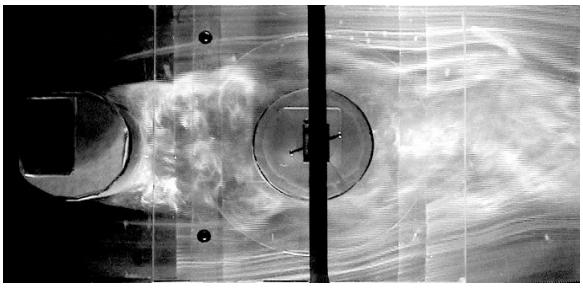

(a) Visualized flow-patter (*Vr*= 1.71)

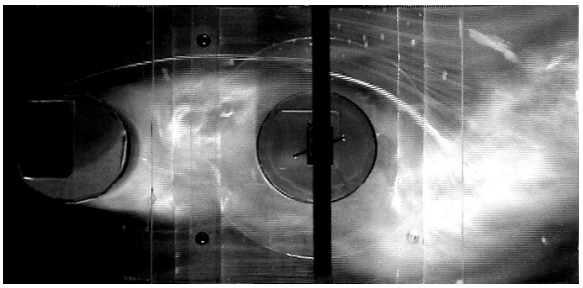

(b) Visualized flow-patter (*Vr*= 3.56)

Fig.10 Visualized flow-pattern((a)*Vr* = 1.71, (b)*Vr* = 1.71) for reduced mass-damping parameter *Cn* = 0.95 with gap ratio *s* = 1.0

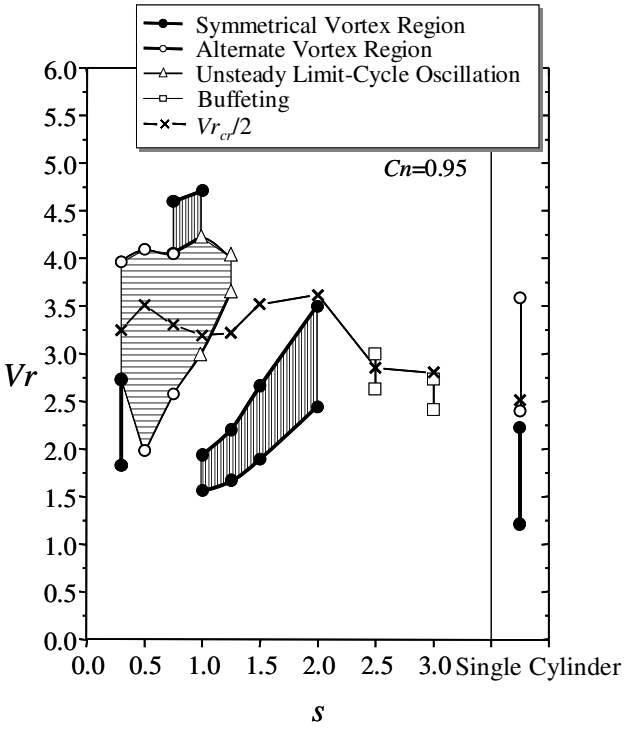

Fig.12 Excitation regions of downstream cylinder as functions of gap distance s and reduced velocity *Vr*.

4.4. Wide gap distance ratio of *s* = 1.75 to 3

The response curves for the wide gap distance ratios of $s = 1.75$ to 3 are plotted in Fig. 6b. It is evident that all the response curve shapes are increasingly like that of a single cylinder with spreading of gap distance.

4.5. Excitation regions of upstream cylinder

Excitation regions of the upstream cylinder were mapped as functions of gap distance s and reduced velocity Vr as shown in Fig. 7, where the values of half the reduced resonance velocity $Vr_{cr}/2$ are also plotted by the symbol x. We can see two kinds of excitation ranges due to different oscillation mechanisms; that is, symmetrical vortices (the first excitation region) and alternate vortices (the second excitation region); excitation induced by symmetrical vortex shedding appears at all gap ratios of $s = 0.3$ to 3. The fluid-elastic characteristics of the upstream cylinder with wide gap ratios of $s = 2$ to 3 have two kinds of exciting oscillation mechanisms; that is, movement-induced excitation and vortex-excitation[10], similar to that of the single cylinder.

5. IN-LINE OSCILLATION OF THE DOWNSTREAM CYLINDER

Next the fluid-elastic characteristics of the downstream cylinder of two tandem cylinders are examined, and it is shown typical results for cases of gap distance ratios $s = 0.5$ (narrow), 1(middle) and 2 (wide).

5.1. Gap distance ratio of *s*=0.5

Fig. 8(a) shows the response curve and Strouhal numbers of the downstream cylinder with narrow gap distance ratio $s = 0.5$, for damping parameter $Cn = 0.95$, together with the results of a single cylinder. The response characteristics of only one excitation region with half the Strouhal frequency $St_c/2$ are quit different from those of a single cylinder having two excitation regions, so Fig. 8(b) shows a visualized picture for the downstream cylinder oscillating in the in-line direction at $Vr = 3.34$. In this figure, a downstream cylinder oscillates with half the Strouhal frequency $St_c/2$, locking to alternate Karman vortex shedded from the upstream cylinder.

5.2. Gap distance ratio of s=1

It is noted that the response curve and Strouhal numbers of the downstream cylinder with middle gap distance ratio $s = 1$ has two excitation regions; that is, $Vr = 1.5$ to 2 and 3 to 5, as shown in Fig.9. It is found in this figure that the excitation of small amplitude begins to grow at low reduced velocity, and this oscillation is due to the movement-induced excitation, accompanied with symmetrical vortices in a wake, as shown in the visualized flow-pattern of Fig.10(a) ($Vr = 1.71$). It is apparent in the visualized pattern of Fig. 10(b) ($Vr = 3.56$) that the other excitation of large amplitude is induced by alternate Karman vortex shedding.

5.3. Gap distance ratio of s=2

Fig. 11 shows the response ξ_{rms} and St_w of the downstream cylinder against Vr for a wide gap distance of 2, in comparison with the results for two tandem cylinders with a splitter plate. The damping parameter values of the two cases differ slightly $Cn = 0.95$ and 0.97, respectively. The exciting regions are in the same range $Vr = 2.4$ to 3.5, while the oscillation amplitude of the latter cylinder is slightly suppressed.

5.4. Excitation regions of downstream cylinder

Excitation regions of the downstream cylinder of two tandem cylinders are mapped against gap distance s and reduced velocity Vr, as shown in Fig. 12. The excitation region of very narrow gap distance $s = 0.3$ to 0.75 is induced by alternate Karman vortex shedding, while the excitation regions due to symmetrical vortices are limited to the regions of gap distance $s = 0.75$ to 2. When the gap distances are greater than $s = 2.5$, it is clear that the downstream cylinder oscillates as a buffeting phenomenon influenced by wake turbulence and fluctuation of the upstream cylinder.

6. CONCLUSIONS

Flow-induced in-line oscillation of two tandem circular cylinders was experimentally studied by free-oscillation testing in a wind tunnel for small reduced mass-damping parameter $Cn \approx 1$. Only one cylinder of the two cylinders was elastically supported easily to move in the in-line direction; the other cylinder was fixed. The gap between them was varied from $s = 0.3$ to 3. The response amplitudes of the oscillatory cylinder in in-line oscillation and the vortex-shedding frequency in the wake were measured in a wind tunnel. The flow around the cylinders was visualized by the smoke-wire method.

The results for the upstream cylinder free to undergo in-line oscillation showed a wide excitation region of reduced velocity $Vr = 1.5$ to 2.5 in all gap ratio ranges $s = 0.3$ to 3. This excitation was mainly induced by symmetrical vortex shedding; the other excitation of $Vr = 3$ to 3.5 at wide gap ratios $s = 2$ to 3 was induced by alternate Karman vortex shedding, like the in-line oscillation of a single cylinder.

The in-line excitation region of downstream cylinder free to move in the in-line direction was in a wide range

of Vr = 2 to 4 for the narrow gap distance s = 0.3 to 0.75, the excitation apparently induced by alternate Karman vortex shedding.

The other excitation regions attributable to symmetrical vortices were limited to gap distance ratios s = 0.75 to 2. Furthermore, downstream cylinder oscillation in the in-line direction was a buffeting phenomenon influenced by wake fluctuation of the upstream cylinder, when the gap distance values were greater than s = 2.5.

The part of this work has been supported by the Grants-in-Aid for Scientific Research of JSPS.

REFERENCES

[1] JSME, JSME Int. J., Ser. B, Fluids &Thermal Eng., 44-4 (2001.11), pp.681-687, and Okajima, A., Morishita, M., Nishihara, T., Nakamura, The 6th International Conference on Nuclear Thermal Hydraulics, Operations and Safety (NUTHOS-6) Nara, (2004.10), N6P160.

[2] King, R., Prosser, M. J., and Johns, D. J., J. Sound & Vibration, 29(2), (1973), pp.169-188.

[3] Okajima, A., Yasuda, T. and Iwasaki, T., Proc. FLUCOME 2000, Fl048, Sherbrooke (Qc), Canada,(2000.8), pp.13-17

[4] Okajima, A., Nakamura, A., Kosugi, T., Uchida, H., Tamaki, R., European Journal of Mechanics, B (2004.2) 23, pp.115-125.

[5] Nakamura, A., and Okajima, A., Proc. ASME-PVP Flow-Induced Vibration Symposium, Atlanta, Georgia, (2001.7)

[6] Tamura,T. and Okada,R., Proc. ASME FED SM, 98-5162, 1998.

[7] Scruton, C., 1963, Proc., Int. Conf. Wind Effects on Build & Struct. (Teddington), Her Majesty's Stationery Office.

[8] Okajima, A., Trans. JSME, 44-384 (1978), pp.2663-2671.

[9] Imaiti, K., et al., Proc. Kansai Branch JSME, 734-5 (1973), pp.104-106.

[10] Naudasher, E. and Wang, Y., J. Fluids and Structures, **7**(1993), pp.341-373.

Conference on Modelling Fluid Flow (CMFF'06)
The 13th International Conference on Fluid Flow Technologies
Budapest, Hungary, September 6-9, 2006

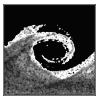

NUMERICAL SIMULATIONS OF FLOW OVER TWO CIRCULAR CYLINDERS IN TANDEM

Eric DIDIER[1], António R.J. BORGES[2]

[1] Corresponding Author. Departamento de Engenharia Mecânica e Industrial, Faculdade de Ciências e Tecnologia, Universidade Nova de Lisboa. Monte de Caparica, 2829-516 Caparica, Portugal. Tel.: +351 212 948 567, Fax: +351 212 948 542, E-mail: deric@fct.unl.pt
[2] Departamento de Engenharia Mecânica e Industrial, Faculdade de Ciências e Tecnologia, Universidade Nova de Lisboa. Monte de Caparica, 2829-516 Caparica, Portugal. E-mail: ajb@fct.unl.pt

ABSTRACT

Flow interference between two identical circular cylinders in a tandem arrangement is investigated numerically. Computations are carried out using a fully coupled resolution method developed in a finite volume framework for unstructured grids. The flow is assumed two-dimensional and laminar since the Reynolds number, based on cylinder diameter, is equal to 100. Consequently two-dimensional Navier-Stokes equations are adapted for simulations. The mean drag coefficient, the Strouhal number and the fluctuating drag and lift coefficients are recorded for centre-to-centre cylinder spacing between 1.5 and 10 diameters. The results are compared with flow past a single cylinder and with numerical and experimental data. A grid convergence study showed that solution is easily reached with medium grid for cylinder spacing smaller than the critical spacing. However, for cylinder spacing near or above the critical spacing, solution require a fine grid. A critical cylinder spacing was found between 4.1 and 4.2 diameters. At this critical spacing, the fluctuating forces jumped appreciably, the same happens with shedding frequencies. The downstream cylinder, which lies in the wake of the upstream one, may experience very large unsteady forces.

Keywords: finite volume, fully coupled resolution method, two tandem circular cylinders, unsteady flow, unstructured grid, vortex shedding

NOMENCLATURE

C_D	[-]	drag coefficient
C_L	[-]	lift coefficient
C_p	[-]	pressure coefficient
D	[m]	cylinder diameter
h	[m]	cylinder length
L	[m]	centre-to-centre distance between two cylinders
Re	[-]	Reynolds number, $U_\infty D/\nu$
S	[-]	non-dimensional cell surface
St	[-]	Strouhal number, fD/U_∞
U_∞	[m/s]	free stream velocity
V	[-]	non-dimensional cell volume
f	[Hz]	frequency
n	[-]	interface normal vector
p	[-]	non-dimensionalised pressure
t	[-]	non-dimensionalised time
u	[-]	non-dimensionalised velocity
x_i	[-]	non-dimensionalised Cartesian co-ordinates
ν	[m^2/s]	viscosity
θ	[degree]	angle from the front stagnation point

Subscripts and Superscripts

1	upstream cylinder
2	downstream cylinder
i	i=1,2; horizontal and vertical directions
o	reference values for a single cylinder
rms	root-mean-square
−	temporal mean

1. INTRODUCTION

The flow past groups of bluff bodies is of great practical interest for wind engineering and off-shore technology, because strong unsteady aerodynamic forces may act on the structures. Examples include groupings of electrical transmission lines, bridge piers and cables, skyscrapers in a city and pipes from offshore oil platforms. Cylindrical circular geometries often appear in those engineering structures forming a large separated wakes with origin in separating points not known a priori. The difficulty to predict flow around circular cylinders increases when two or more cylinders are placed in proximity to each other. The large separated wakes from the cylinders interact with each other generating a flow field much different than the flow past a single cylinder. The interaction is highly

dependent on the cylinder spacing and the Reynolds number of the flow.

Zdravkovich [1] summarised a variety of measurements of drag forces on two circular cylinders in a tandem arrangement. Ohya et al. [2] considered a vast range of Reynolds numbers, from 80 to 2.3×10^5, and cylinder gaps of up to 30 diameters. They found that the drag coefficient is dependent on both Reynolds number and cylinder spacing. For the two cylinders, a sudden increase of drag coefficient occurs at the critical spacing. Igarashi [3] conducted a detailed examination of flow structure. Following Zdravkovich [4], the flow past two circular cylinders in tandem arrangement presents three possible regimes. When centre-to-centre cylinder spacing is less than about 1.2*D*-1.8*D* (depending on Reynolds number), only one wake is formed due to the free shear layers issuing from the upstream cylinder engulf the second one. For gaps in the range of $1.2<L/D<3.4$-3.8, there is a reattachment of the shear layers emanating from the first cylinder on the wall of the second one. In both cases the wake is formed behind the downstream cylinder. In the third regime, $L/D>4.0$, vortices shed off the front cylinder roll up before striking the rear cylinder. The vortices, that shed off the front cylinder, interact strongly with the vortices shed off the rear cylinder, causing the vortices shed off the rear cylinder to become extremely powerful. The wake behind the downstream cylinder is called binary, because each vortex is formed by the combination of one vortex shed from the first cylinder and another by the downstream cylinder.

It is already known that vortex shedding is a three-dimensional phenomenon. However, two-dimensional simulations at low Reynolds number can be used to give some insight about the vortex dynamics, particularly when very few numerical studies can be found in the literature. Numerical study have been conducted by Mittal et al. [5], Meneghini et al. [6], Li et al. [7] and Sharman et al. [8]. The current results are compared to those of Li et al., in spite of the limited computer power that forced them to use coarse meshes and with the more recent results obtained by Sharman et al. on unstructured grid. Results are not compared with Mittal et al. since they only presented data for two cylinder spacings. Also, Meneghini et al. carried out simulations for different Reynolds number.

Flow interference between two identical circular cylinders, of equal diameter, in tandem arrangement are investigated numerically. Computations are carried out using a fully coupled resolution method developed in a finite volume framework for unstructured grids [9]. A Reynolds number of 100, based on cylinder diameter, was used to ensure that the flow remained laminar as showed by Huhe-Aode et al. [10].

2. EQUATIONS

The governing equations for a Newtonian, incompressible viscous flow are the conservation of mass and the Navier-Stokes equations. In two-dimensions and without body forces, they may be written as follows:

$$\frac{\partial u_i}{\partial x_i} = 0 \quad \text{with i=1, 2} \tag{1}$$

$$\frac{\partial u_i}{\partial t} + u_j \frac{\partial u_i}{\partial x_j} = -\frac{\partial p}{\partial x_i} + \frac{1}{Re} \frac{\partial^2 u_i}{\partial x_j^2} \tag{2}$$

where u_i are the non-dimensional velocity components, p is the non-dimensional pressure, Re the Reynolds number.

On the circular cylinder surface a no-slip condition is applied, which implies that the fluid velocity is zero.

With the present formulation the velocity field is applied on the external boundary situated far from the cylinder.

$$u_1 = U_\infty , \; u_2 = 0 \tag{3}$$

No pressure condition is needed at the external boundary.

3. FULLY COUPLED METHOD

Finite volume discretization is used with a collocated cell-centered unknowns. The present formulation is adapted to unstructured grids and allows to simulate flows past complex geometries.

Equations are written in conservative dimensionless integral form, as follows:

$$\int_S u_j \, n_j \, dS = 0 \tag{4}$$

$$\int_V \frac{\partial u_i}{\partial t} dV + \int_S u_i \, (u_j \, n_j) dS = -\int_V \frac{\partial p}{\partial x_i} dV + \frac{1}{Re} \int_S \frac{\partial u_i}{\partial x_j} n_j dS \tag{5}$$

where V is the volume of the cell, S is its area and n_i the outward unit vector normal to the area.

The fully coupled resolution method involves solving a complex linear system. Thus it is necessary to consider compact implicit schemes, based on adjacent cells, conserving in the same time a global precision of second order.

Time integration is realised using an implicit three-level second order scheme.

Central differencing scheme allows evaluation of the viscous part of Navier-Stokes equations.

The pressure at interface cell is calculated using a linear interpolation.

Convection flux needs particular attention. The deferred correction approach [11], combining a first order UDS and third-order scheme WACEB [12], is adopted. The ith velocity component at the cell interface is written as follows:

$$u_i = \left(u_i^{UDS}\right)^{Imp} + \left(u_i^{WACEB} - u_i^{UDS}\right)^{Expl} \qquad (6)$$

For non-orthogonal grids, the face midpoint may be different from the intersection point between the cell-centroids and the face. Hence corrections are required to estimate velocity components and pressure to the face midpoint. These explicit corrections are added to the source term of discrete equations.

From the discrete momentum equation, one can write the discrete convected velocity associated to the control volume. Following Prakash and Patankar [13], the convected velocity can be considered as the sum of a pseudo-velocity and a pressure gradient term. Thus, the pseudo-velocity gathers all contribution of discrete momentum equation, except the pressure part. Finally, the pressure equation is obtained using the Rhie and Chow reconstruction [14], substituting in the discrete mass equation, the velocity by the discrete convected velocity. A detailed description of the numerical method is available in [9, 15].

The fully coupled linear system is constructed gathering the discrete momentum equations, the pseudo-velocity definition and the pressure equation. Only one linear system is solved and no relaxation parameters or special treatment are required to ensure convergence, whereas the segregated methods, like SIMPLE [16] or PISO [17], lead to a sequential resolution of discrete equations. The key element in guaranteeing successful fully coupled solutions lies in the use of an efficient linear equation solver and preconditioner. The fully coupled linear system is solved using a LU preconditioned BiCGSTAB-ω algorithm [18]. Previous studies have shown [9] that this algorithm is efficient and robust for solving non-symmetrical sparse matrix, such as the present matrix structure. Fully coupled method is second order accuracy and previous simulations have demonstrated the ability of the technique to predict accurately unsteady separating flows. The method also allows fast non-linear convergence due to the implicit velocity-pressure coupling.

4. SINGLE CIRCULAR CYLINDER

Before simulating the flow over two circular cylinders in tandem, the flow past a single cylinder is simulated at *Re*=100. At this Reynolds number the flow is laminar. Results serve as a reference to evaluate the effects of adding the second cylinder and allow us to define the best grid for simulation.

The unstructured mesh consists of two parts: a structured grid close to the cylinder and an unstructured one in the remaining domain. The structured mesh allows for having adequate control on the resolution of the boundary layer. It consists of *N* nodes on the cylinder surface, with a thickness of the first layer element, *e*. The unstructured mesh is generated via the Delaunay's triangulation technique. This type of hybrid mesh is useful in handling complex geometries by providing adequate resolution close to the body without requiring the same distribution of grid nodes in the remaining domain.

The details of the four grids are given in Table 1. The non-dimensional time step is equal to 0.01 and a radius equal to 35*D* ensures that external boundary effects are sufficiently minimised.

Table 1. Mesh details for a single cylinder

Mesh	N	*e/D*	elements
M1	60	0.002	5777
M2	90	0.001	11877
M3	140	0.0008	26675
M4	200	0.0005	33811

The *rms* drag and lift coefficients, the mean drag coefficients and Strouhal numbers are presented for four grids and compared with literature data in Table 2. Mean drag coefficient, Strouhal number and *rms* lift coefficient became independent of the mesh M3. It is found that numerical errors, based on the fine grid solution, are lower than 1%. The *rms* drag coefficient presents a numerical error of 2.5%.

Good agreement is obtained with numerical results of Mittal [19], Henderson (from Williamson) [20] and Park et al. [21].

Table 2. Comparison of present results with literature data for a single cylinder, *Re*=100

Mesh	*St*	$\overline{C}_D$	$C_{D,\,rms}$	$C_{L,\,rms}$
M1	0.165	1.31	0.0073	0.222
M2	0.165	1.32	0.0072	0.226
M3	0.164	1.31	0.0066	0.226
M4	0.163	1.31	0.0068	0.225
[19]	0.164	1.32	0.0064	0.226
[20]	0.164	1.32	-	-
[21]	0.165	1.33	0.0064	0.230

5. TWO CIRCULAR CYLINDERS IN TANDEM

Figure 1 shows the notation for flow over two tandem cylinders. Simulations were performed at *Re*=100. At this Reynolds number the flow over two tandem cylinders is laminar, according to the observations of Huhe-Aode et al. [10].

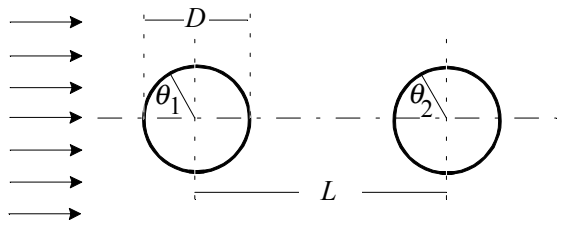

Figure 1. Two circular cylinders in tandem

5.1. Domain and mesh

The domain is similar to that used for flow over a single cylinder. The circular external boundary is placed at 35 diameters from the centre of the downstream cylinder. Figure 2 shows the medium mesh for *L/D*=4.5.

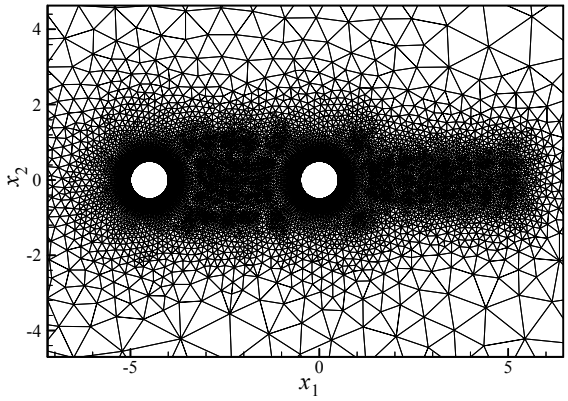

Figure 2. Medium grid for two cylinders in tandem, *L/D*=4.5

5.2. Grid dependence study

It is very important to verify that the mesh between the two cylinders in tandem is adequate to obtain accurate results. Grid convergence is analysed for five meshes with centre-to-centre distance *L/D*=4.0 and *L/D*=4.5.

Mesh details are given in Table 3. Results for mean drag, *rms* drag and lift coefficient and Strouhal numbers for the upstream and downstream cylinders are shown in Table 4 for *L/D*=4.5 and Table 5 for *L/D*=4.0.

Table 3. Mesh details for *L/D*=4.0 and *L/D*=4.5

Mesh *L/D*=4.0	elements	Mesh *L/D*=4.5	Elements
P1	13496	N1	13674
P2	20475	N2	21435
P3	37613	N3	47137
P4	57195	N4	-
P5	66913	N5	69663

Table 4. Mesh comparisons for *L/D*=4.5

Cylinder 1	*St*	$\overline{C}_{\mathrm{D}}$	$C_{\mathrm{D,\,rms}}$	$C_{\mathrm{L,\,rms}}$
N1	0.150	1.23	0.0100	0.28
N2	0.152	1.25	0.0098	0.29
N3	0.152	1.26	0.0097	0.29
N4	0.151	1.26	0.0105	0.29
Cylinder 2				
N1	0.150	0.73	0.125	1.02
N2	0.152	0.77	0.129	1.04
N3	0.152	0.76	0.128	1.05
N4	0.151	0.75	0.129	1.06

Table 5. Mesh comparisons for *L/D*=4.0

Cylinder 1	*St*	$\overline{C}_{\mathrm{D}}$	$C_{\mathrm{D,\,rms}}$	$C_{\mathrm{L,\,rms}}$
P1	0.147	1.241	0.0150	0.290
P2	0.146	1.242	0.0168	0.289
P3	0.146	1.243	0.0156	0.291
P4	0.113	1.089	0.0014	0.023
P5	0.114	1.090	0.0018	0.022
Cylinder 2				
P1	0.147	0.705	0.1397	0.935
P2	0.146	0.702	0.1422	0.956
P3	0.146	0.702	0.1410	0.942
P4	0.113	0.110	0.0085	0.255
P5	0.114	0.102	0.0081	0.235

It can be observed in Table 4 that grid convergence is obtained for the medium mesh N3, with numerical errors lower than 1%, compared with the fine grid. The *rms* drag coefficient presents a numerical error of 5%, larger than for the single cylinder (see Table 2). Medium mesh N2 presents similar results.

However, grid dependence study was also carried out for a cylinder spacing close to the classic critical spacing, *L/D*=4.0. In Table 5, an unexpected result can be seen: whereas the convergence seems reached with the previous medium grid P3, the fine grid P5 led to another solution. Simulation performed with a very fine grid P5, with 66913 control volumes, demonstrate that grid independency is only obtained for a fine grid. The jump observed in the grid convergence process is directly connected with the flow interference between the two circular cylinders in tandem and, particularly, with the instability zone associated to the critical cylinder spacing.

Figure 3 shows the Strouhal number vs the cylinder spacing. Present results, for medium and fine meshes, are compared with the numerical ones of Li et al. [7] and the more recent of Sharman et al. [8]. The present medium grid, based on mesh N2 and N3, is similar to the mesh used by Sharman et al. The global results will be discussed later, in the next section.

The results of Li et al. suffered from an insufficient domain, coarse grid and large time step

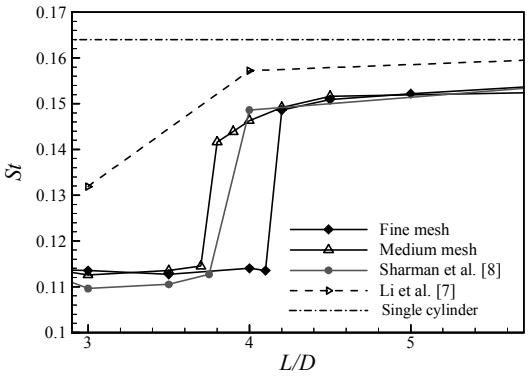

Figure 3. Strouhal number vs cylinder spacing: comparison of numerical results

due to the lack of computational power available. They calculated that the critical cylinder spacing is $3<L/D<4$. But their results did not agree well, even with recent accepted benchmark data for a single cylinder. Sharman et al. identified the critical spacing as being between 3.75 to 4. Their results agree well with current results obtained with the present medium mesh, with $3.7<L/D<3.8$. Effectively, one can note that the mesh used by Sharman et al., an unstructured mesh composed by 24000 control volumes, is similar to the medium mesh of the present study. However, using the fine mesh, for which grid solution independence is guaranteed, the critical spacing is located between L/D=4.1 and 4.2. That is a significant difference compared to the solution reported by Sharman et al.

5.3. Results and discussion

The Strouhal number, calculated using the dominant frequency of the lift force, happens to be equal for both cylinders and all spacings. Figure 4a compares the Strouhal number against the experimental data of Huhe-Aode et al. [10] and the numerical results of Li et al. [7], in spite of the limited computer power that forced them to use coarse meshes, and with the more recent results obtained by Sharman et al. on unstructured grids [8].

One observation of the results for Huhe-Aode et al., in Fig. 4a, is that for Re=100, and cylinder spacing between 5 to 10, the Strouhal number stays equal to 0.14. However, the Strouhal number should approach that of a single cylinder, St=0.163, when the cylinder spacing increases. Huhe-Aode et al. used a h=30cm long cylinder with a diameter of 1cm cantilevered from one of the walls. Norberg [22] and Williamson [23] showed that the Strouhal number is St=0.14 for aspect ratio below 30 and around 0.16 for higher aspect ratios. These results confirm that Huhe-Aode et al. conducted their experiments under two conditions. For small cylinder spacing, the aspect ratio, defined by h/L, is near to 30 and the flow is two-dimensional.

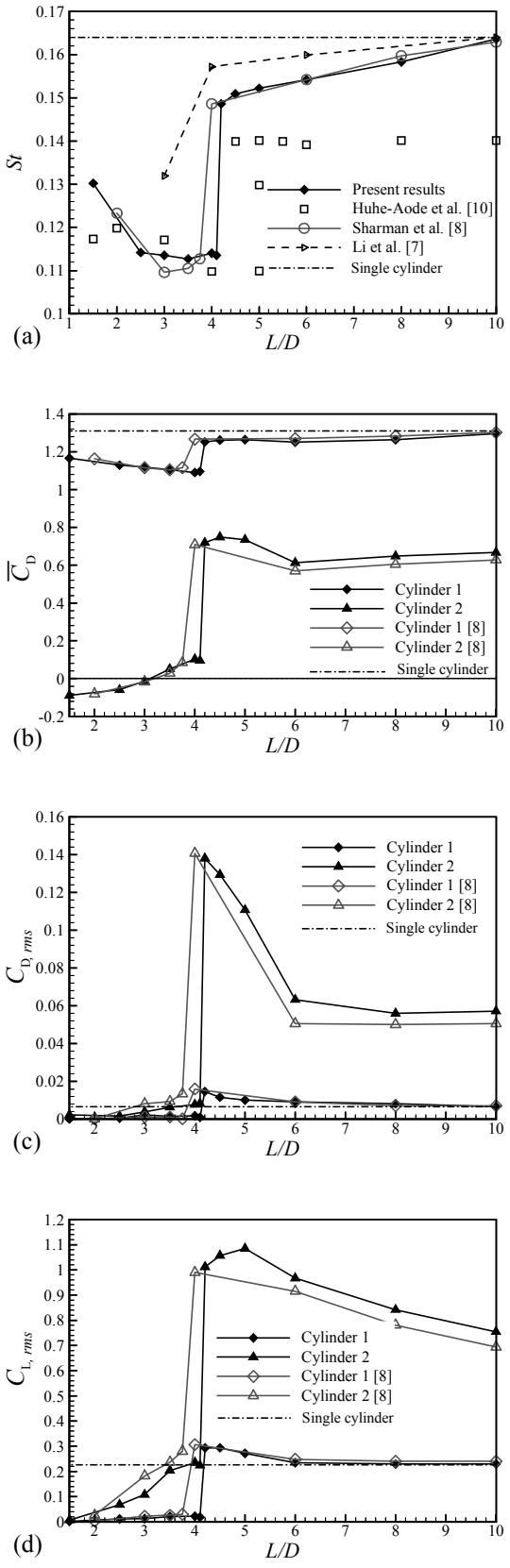

Figure 4. Strouhal number (a), mean drag coefficient (b), *rms* drag coefficient (c), and *rms* lift coefficient (d), vs cylinder spacing

However, when the cylinder spacing increases, the aspect ratio *h/L* decreases and becomes insufficient to ensure that the flow remains two-dimensional. Three-dimensional phenomena alter the flow. Thus their results, up to *L/D*<4, can be used to compare the present numerical results. One can see a global good agreement.

The Fig. 4a shows that the cylinder spacing has a large effect on the Strouhal number. The critical spacing is apparent, with a large and sudden jump in the Strouhal number. The present results are similar with those obtained by Sharman et al., particularly before and after the critical spacing. However, Sharman et al. found a critical spacing between 3.75 to 4.0, whereas in the current study critical spacing is found to be between 4.1 and 4.2. This discrepancy seems to be due to the mesh, as was shown in the previous section. It is interesting to mention that the change in Strouhal number is due to the change of interference type between the two cylinders. For small gaps, the Strouhal number is considerably lower than the one found in the case of an isolated cylinder. A minimum value of *St*=0.114 is reached for a gap between 2.5 and 4.1. For gaps higher than the critical, the Strouhal number tends asymptotically to the reference value obtained for a single cylinder, *St*=0.164. The variation of Strouhal number is explained by the very two different types of interference between the cylinders. This is discussed further in this section.

Figures 4b to 4d show the mean drag coefficient, the fluctuating *rms* drag and lift coefficients vs cylinder spacing and for the two cylinders. The critical spacing is very apparent in all figures and for the two cylinders. The mean drag coefficient is positive for the upstream cylinder and negative for the downstream cylinder for small spacings, less than 3.0. The effect is the manifestation of an attraction force between the cylinders. These results are in accordance with the observation of Zdravkovich, in which a negative mean drag is observed for the same range of cylinder spacing. The mean drag coefficient on the downstream cylinder turns out to be less negative as the gap increases, and increases to small positive values and then jumps markedly at the critical spacing. The drag of cylinder 2 does not approach that of a single cylinder, even for large cylinder separations. Effectively, the downstream cylinder is immersed in the wake of the upstream cylinder, on a low momentum region. The presence of cylinder 2 also reduces the mean drag of cylinder 1, since it induces an increase in pressure in the separated wake behind the first cylinder.

The fluctuating drag and lift coefficients, in Figs. 4c and 4d, follow similar trends to that of the mean drag coefficient as the cylinder spacing is increased. However, all fluctuations are small for sub-critical gap values. One can see that fluctuations on cylinder 1 remain extremely low. The fluctuations become extreme as the cylinder spacing increases to *L/D*=4.2. For the upstream cylinder, the fluctuations become slightly larger than that of a single cylinder. However, for the downstream cylinder, the fluctuations becomes extreme, 4.6 and 21 times higher than that of a single cylinder for *rms* lift and drag coefficients respectively. The fluctuations are slowly reduced as the cylinder spacing is increased beyond the critical spacing. However, the maximum of fluctuating lift coefficient for the downstream cylinder is reached after the critical spacing, for *L/D*=5.0, and decreases slowly beyond.

Comparing the current results with those obtained by Sharman et al., in Figs. 4a to 4d, one can conclude that they present an overall similar behaviour. Only a discrepancy for gaps near and higher than the critical spacing are observed, certainly due to the use by Sharman et al. of a medium mesh.

Figure 5 shows the total mean drag coefficient resulting from the sum of the upstream and downstream cylinder mean drag coefficient. This figure allows to identify clearly two modes. The first one happens before the critical spacing. The total mean drag coefficient is smaller than the mean drag coefficient of a single cylinder and the cylinders function like one body. The interaction between the cylinders is strong. The second mode corresponds to a weak interaction and happens at the critical spacing and for *L/D*>4.2. The total mean drag coefficient is larger than that of a single cylinder and asymptotically tends to twice the mean drag coefficient of a single cylinder.

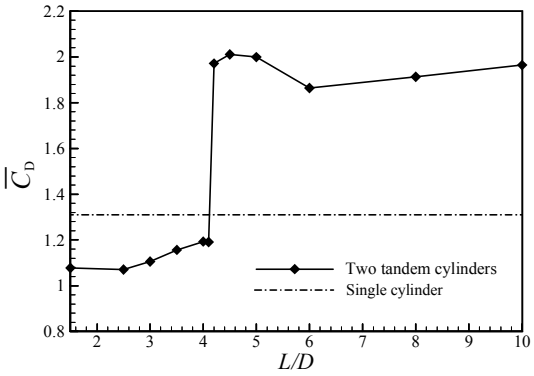

Figure 5. Total mean drag coefficient vs cylinder gap

5.4. Topology of flow

The advantage of applying numerical methods to such problems is that the flow can be studied in fine detail. The location of separation and reattachment points on a body are analysed since they have a large effect on the forces acting upon it.

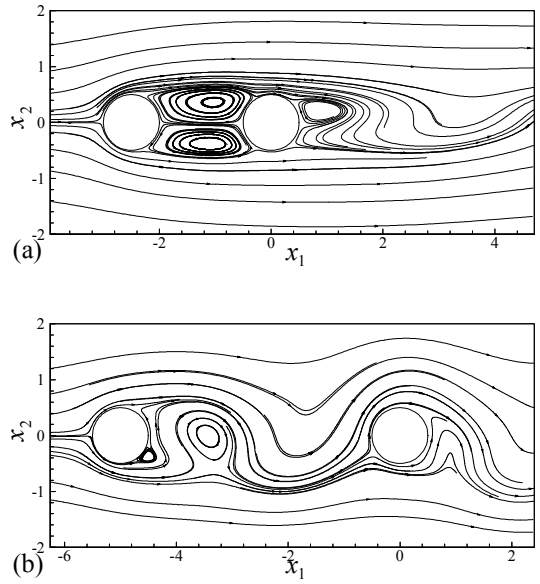

Figure 6. Streamlines for *L/D*=2.5 and *L/D*=5.0

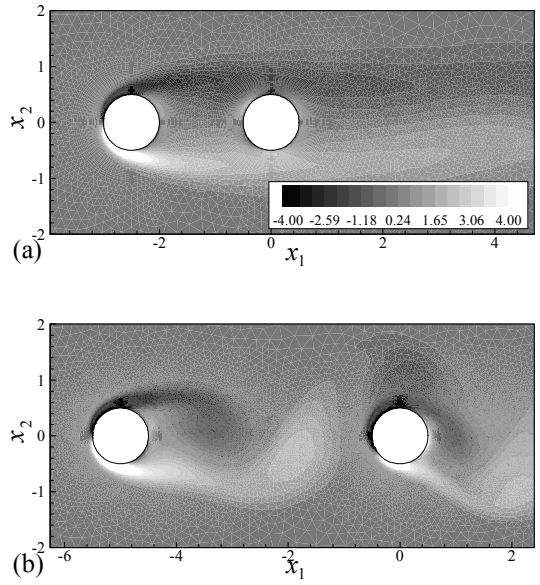

Figure 7. Vorticity field for *L/D*=2.5 and *L/D*=5.0

Figure 6 shows the instantaneous streamlines for cylinder spacing *L/D*=2.5 and 5.0, respectively before and after the critical spacing. Figure 7 shows close-up views of vorticity contours, also for *L/D*=2.5 and 5.0. It can be seen from Figs. 6 and 7 that the flow changes radically between these two cylinder spacings.

In Fig. 6a, for *L/D*=2.5, the free shear layers issuing from cylinder 1 reattach to cylinder 2. A symmetrical flow pattern is observed between the two cylinders. The wake is formed behind the downstream cylinder due to the separation occurring on the surface. Long vortices are shed off cylinder 2 which explains the lower Strouhal number reported in Fig. 4a.

In Fig. 6b, one can see that vortex shedding occurs from both cylinders. The vortices move the reattachment point and energise the fluid so that it flows completely around the downstream cylinder. The wake behind cylinder 2 is called binary because each vortex is formed by the combination of one vortex shed from cylinder 1 and another by cylinder 2. This effect contributes to the large lift forces observed on the downstream cylinder and reported in Fig. 4d.

The location of separation and reattachment points on the cylinder have a large effect on the forces acting upon it. The position of these points also explains the surface pressure distributions. Fig. 7 shows the vorticity field for *L/D*=2.5 and 5.0. Separation and reattachment points occur when the vorticity is equal to zero at the surface.

Cylinder 1 does not have any reattachment points, but there are two separation points. For *L/D*=2.5, the separation points are found around 115° from the stagnation point and they move very little. For *L/D*=5.0, the separation points moved between 113° and 121°.

The flow around the downstream cylinder radically changes between *L/D*=2.5 and *L/D*=5.0. In the first case, two separation and reattachment points exist. The reattachment points are found between 57° and 60° while the separation ones vary between 130° and 135°. For *L/D*=5.0, there exist only one reattachment and one separation point. The reattachment and separation points flip from side to side during a flow period cycle. The reattachment point moves between -38° and 38°. The separation point varied between 98° and 262°. One can see in Figs. 6b and 7b that the flow remains attached on both sides of the cylinder.

6. SUMMARY

A convergence study for flow past a single circular cylinder at *Re*=100 shows that the numerical fully coupled resolution method is accurate since the results agree well with recent benchmarks.

Simulations are performed for bidimensional laminar flow over two tandem circular cylinders of equal diameter at *Re*=100. The spacing between the two cylinders varies between 1.5 and 10 diameters.

The present results demonstrate that, for a cylinder spacing near to the critical one, grid convergence is obtained only with a very fine grid. The Strouhal number, the mean drag, the *rms* drag and lift coefficients show very clearly the existence of a critical spacing.

A large jump is observed in fluctuating and mean forces and Strouhal number. The critical spacing is found between 4.1 and 4.2, in accordance with the literature data, even if Sharman et al. defined a critical spacing between 3.75 and 4.0. Current results present a similar behaviour to those obtained by Sharman et al., with, however, a

discrepancy for gaps near and higher than the critical spacing, certainly due to the mesh quality and the sensitivity of the flow.

Two separation points are found on the upstream cylinder. This is an expected result. For a cylinder spacing L/D=2.5, two reattachment points and two separation points exist on the downstream cylinder. But for L/D=5.0, only one reattachment and one separation point was found on the downstream cylinder. These points fluctuate with large amplitudes: 76° and 164° for the reattachment point and separation point respectively.

REFERENCES

[1] Zdravkovich, M.M., 1997, *Flow around circular cylinders - Volume 1: fundamentals*, Oxford University Press, Oxford.

[2] Ohya, Y.O., Okajima, A., and Hayashi, M., 1989, "Wake interference and vortex shedding", *Aerodynamics and compressible Flow*, Vol. 8, pp. 322-389.

[3] Igarashi, T., 1981, "Characteristics of the flow around two interfering circular cylinders", *Bulletin of the JSME*, Vol. 24, pp. 323-331.

[4] Zdravkovich, M.M., 1985, "Flow-induced oscillations of two interfering circular cylinders", *Journal of sound and vibration*, Vol. 101, pp. 511-521.

[5] Mittal, S., Kumar, V., and Raghuvanshi, A., 1997, "Unsteady incompressible flows past two cylinders in tandem and staggered arrangements", *Int J Numer Meth Fluids*, Vol. 25, pp. 1315-1344.

[6] Meneghini, J.R., Saltara, F., Siqueira, C.L., and Ferrari, J.A., 2001, "Numerical simulation of flow interference between two circular cylinders in tandem and side-by-side arrangements", *J Fluids and Structures*, Vol. 15, pp. 327-350.

[7] Li, J., Chambarel, A., Donneaud, M., and Martin, R., 1991, "Numerical study of laminar flow past one and two circular cylinders", *Computers and Fluids*, Vol. 19, pp. 155-170.

[8] Sharman, B., Lien, F.S., Davidson, L., and Norberg, C., 2005, "Numerical predictions of low Reynolds number flows over two tandem circular cylinders", *Int J Numer Meth Fluids*, Vol. 47, pp. 423-447.

[9] Didier, E., and Borges, A.R.J., 2003, "Unsteady Navier-Stokes equations: A fully coupled method for unstructured mesh", *Proc. Conference on Modelling Fluid Flow*, Budapest, pp. 814-821.

[10] Huhe-Aode, Tatsumo, M., and Taneda, S., 1985, "Visual studies on wake structure behind two cylinders in tandem arrangement", *Reports of Research Institute for Applied Mechanics*, Vol. 32.

[11] Khosla, P., and Rubin, S., 1974, "A diagonally dominant second-order accurate implicit scheme", *Comput Fluids*, Vol. 2, pp. 207-209.

[12] Song, B., Liu, G.R., Lam, K.Y., and Amano, R.S., 2000, "On a higher-order bounded discretization scheme", *Int J Numer Meth Fluids*, Vol. 32, pp. 881-897.

[13] Prakash, C., and Patankar, S.V., 1985, "A control-volume-based finite-element method for solving the Navier-Stokes equations using equal-order velocity-pressure interpolation", *Num Heat Transfer*, Vol. 8, pp. 259-280.

[14] Rhie, C.M., and Chow, W.L., 1983, "A numerical study of turbulent flow past an isolated airfoil with trailing edge separation", *AIAA Journal*, Vol. 21, pp. 1525-1532.

[15] Didier, E., and Borges, A.R.J., 2005, "Numerical simulation of two-dimensional cross-flow past a cylinder using an unstructured mesh based fully implicit second order coupled method", Proc. *4th European & African Conference on Wind Engineering*, Praha, article 243.

[16] Issa, R.I., 1985, "Solution of the implicit discretized fluid flow equations by operator-splitting", *J Comp Physics*, pp. 40-65.

[17] Patankar, S.V., 1980, *Numerical Heat Transfer and Fluid Flow*, McGraw Hill.

[18] Sleijpen, G.L.G., and Van der Vorst, H.A., 1995, "Maintaining convergence properties of BiCGSTAB methods in finite precision arithmetic", *Numer Algorithms,* pp. 203- 223.

[19] Mittal, S., 2005, "Excitation of shear layer instability in flow pas a cylinder at low Reynolds number", *Int J Numer Meth Fluids*, Vol. 49, pp. 1147-1167.

[20] Williamson, C.H.K., 1996, "Vortex dynamics in the cylinder wake", *Annu Rev Fluid Mech*, Vol. 28, pp. 477-539.

[21] Park, J., Kwon, K., and Choi, H., 1998, "Numerical solutions of flow past a circular cylinder at Reynolds numbers up to 160", *KSME Int Journal*, Vol. 12, pp. 1200-1205.

[22] Norberg, C., 1994, "An experimental investigation of the flow around a circular cylinder: influence of aspect ratio", *J Fluid Mech*, Vol. 258, pp. 287-316.

[23] Williamson, C.H.K., 1989, "Oblique and parallel modes of vortex shedding in the wake of a circular cylinders at low Reynolds numbers", *J Fluid Mech*, Vol. 206, pp. 579-627.

Conference on Modelling Fluid Flow (CMFF'06)
The 13th International Conference on Fluid Flow Technologies
Budapest, Hungary, September 6-9, 2006

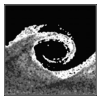

INVESTIGATION OF THE CHARACTERISTICS OF TURBULENT BOUNDARY LAYER OVER AN AIRFOIL

Tamás RÉGERT[1], László NAGY[2], Márton BALCZÓ[3], Balázs MOLNÁR[4]

[1] Corresponding Author. Department of Fluid Mechanics, Budapest University of Technology and Economics. Bertalan Lajos u. 4 – 6, H-1111 Budapest, Hungary. Tel.: +36 1 463 2464, Fax: +36 1 463 3464, E-mail: regert@ara.bme.hu
[2] Department of Fluid Mechanics, Budapest University of Technology and Economics. E-mail: nagy@ara.bme.hu
[3] Department of Fluid Mechanics, Budapest University of Technology and Economics. E-mail: balczo@ara.bme.hu
[4] Undergraduate student, Budapest University of Technology and Economics

ABSTRACT

The paper deals with a sub-part of a extensive research program on the effect of leading edge sweep on the characteristics of wings or fan blades. Experiments were carried out in a closed section NPL (Eiffel) type wind tunnel at a Re_c = 1.3E+05 based on the chord length of the RAF 6 type airfoil. The wing span was 2.5*c* long (*c*: chord length) of constant cross section geometry and the angle of attack was set to 8° and 15°. The mean and RMS velocity profiles are mapped as well as the turbulent characteristics like length scales, skewness, flatness, turbulence 1D spectrum along several locations of the suction side of the RAF 6 type airfoil by means of single component hot-wire measurements, and Laser Doppler Velocimetry. The same case is computed by means of CFD (Computational Fluid Dynamics) from the point of validation and that of understanding the phenomena proceeding on the suction side of the wing.

Keywords: turbulence, hotwire, CFD, LDA, airfoil

NOMENCLATURE

c	$[m]$	chord length
E	$[V]$	electric tension, voltage
E_{11}	$[m^3/s^2]$	streamwise 1D turbulence spectral kinetic energy
k	$[m^2/s^2]$	turbulent kinetic energy
L	$[m]$	integral length scale
Sk	[-]	skewness (kurtosis)
t	$[s]$	time
Tu	[%]	turbulence intensity
u	$[m/s]$	instantaneous velocity in x-direction
$\bar{u}$	$[m/s]$	average velocity
u'	$[m/s]$	fluctuation of x-velocity
U_∞	$[m/s]$	free stream velocity
U_{RMS}	$[m/s]$	root mean square of velocity
x	$[m]$	streamwise coordinate
y	$[m]$	vertical coordinate
y^+	[-]	dimensionless vertical coordinate
ε	$[m^2/s^3]$	dissipation rate of k
ω	$[1/s]$	specific dissipation rate of k
η	$[m]$	Kolmogorov scale
κ	$[1/m]$	sreamwise wave number
$\rho(\tau)$	[-]	auto correlation coefficient
τ	$[s]$	time shift for correlation

1. INTRODUCTION

The Department of Fluid Mechanics at Budapest University of Technology and Economics (BME) has recently started the investigation on the aerodynamic characteristics of wings of swept leading edge [1, 2]. Sweeping of the leading edges of wings or blades of fans leads to the decrease of losses and to the reduction of the noise generated [3]. Investigation on the effect of forward and backward sweep have already been fully investigated from the point of view of integral characteristics, pressure distributions and transition phenomena [4]. Expectably the turbulent boundary layer will contain 3-dimensional structures which can only be visualized by means of numerical simulation.

The research group has chosen the "old fashioned" Royal Air Force airscrew profile, which is typical for industrial fans. Due to the fact that this airfoil has been developed before the introduction of advanced measurement techniques, its turbulence characteristics have not been mapped yet. The frame work in which this article is also embedded, aims to determine the missing properties of the flow around the RAF 6E airfoil for the purpose of the validation of results obtained via Computational Fluid Dynamics (CFD). To strengthen the basis of the experimental results, the velocity profile measurements have been carried out independently

by means of two different measurement techniques: Laser Doppler Velocimetry and Hot-wire anemometry.

2. DESCRIPTION OF THE EXPERIMENT

The experiments were planned according to the needs of the upcoming Large Eddy Simulation, thus well defined boundary conditions and relatively low Reynolds number flow were prescribed.

2.1. The RAF6 E airfoil

The RAF6 E airfoil was designed by the Royal Air Force of the United Kingdom around 1930. However, the RAF X series were developed continuously during World War II and several modifications were done.

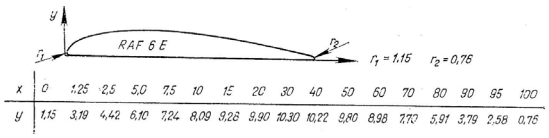

Figure 1. The geometry of the RAF6 E airfoil [5]

This airfoil was applied for airscrew blades due mainly to its relatively simple geometry. The geometry of the RAF 6E airfoil is represented in Figure 1. The pressure side of the airfoil is flat and thus easy to produce and only the suction side has to be manufactured carefully. The choice of the authors was made on this airfoil mainly for this reason. In case of our experiments, the chord of the airfoil was 200mm.

2.2. Experimental facility

The experiments were carried out on the Eiffel type wind tunnel in the laboratory of the Department of Fluid Mechanics at the Budapest Univ. of Technology and Economics. This wind tunnel has a square shaped 0.5m x 0.5m cross section and the test section is closed. The air is drawn through the wind tunnel from the ambience, providing very low, 0.4% turbulence intensity (measured by hot-wire and LDV independently) and a uniform inlet velocity profile.

The length of the wind tunnel section between the convergent nozzle and the leading edge of the wing was 8c where c is the chord length, the distance of the fan from the trailing edge of the wing is 12.5c. These sizes ensured developed inflow conditions and low backward effect of the suction fan. Due to reasons from the CFD computations the inflow velocity was set to 10m/s which resulted in a Reynolds number of $1.33 \cdot 10^5$ based on the chord length.

The uniformity of the inlet velocity profile was checked by means of Prandtl tube measurements at several locations, where the dynamic pressure was measured by a Betz manometer and the profile was regarded to be uniform.

2.3. Hot-wire measurement system

The turbulence characteristics of the airfoil were determined on one hand by using hot-wire measurement technique. At this stage of the research authors used a one-component hot-wire of type DISA 55P11. This hot-wire probe is equipped with a platinum coated tungsten wire of 5μm diameter and 1.3mm of length. The bridge was a type of DISA 55M and 1.8 overheating ratio was applied. Due to surrounding electric noises, a filter was connected between the bridge and the data acquisition system in low-pass operational mode with a cut-off frequency of 2 kHz.

The measured data were collected by an analogue/digital data acquisition card of type NI DAQCard AI 16XE50 through a BNC connector multi-channel board.

According to the cut-off frequency, the sampling frequency was set to 6 kHz to avoid aliasing effect.

The dynamic calibration of the hot-wire system was carried out by supplying square-wave signal onto the bridge and was carried out at the maximal velocity (17 m/s) that would be expected during the measurement session. According to the suggestion of DANTEC [6] the maximal response frequency of the hot-wire measurement system was found to be 28 kHz, high above the cut-off frequency of the filter.

Static calibration of the hot-wire was carried out in-situ inside the wind tunnel. This was possible due to the very low turbulence intensity of the flow upstream the wing. The exact velocity was monitored by using a Prandtl tube at a given location of the test section upstream the wing. Because of the significant disturbance of the Prandtl tube, the calibration was carried out on two stages: a round tube connected to the end of the convergent nozzle of the wind tunnel (introducing no disturbance in the flow) was calibrated to the Prandtl tube, and then the Prandtl tube was removed and the hot-wire system was calibrated to the round tube's signal while the hot-wire probe was placed in the same location where the Prandtl tube was present. For the calibration King's law [12] was used in the form of:

$$E^2 = A + Bu^n \qquad (1)$$

where E [V] is the voltage measured on the bridge, A, B and n are constants depending on the calibration. In case of these experiments these constants were determined by an iterative regression process using least-squares method. The evaluation of the signals from the hot-wire system was fully digital and no linearization devices were applied. For the evaluation of the results, in-house

software were developed and used. The uncertainty of the measurements is dominated by the uncertainty of the calibration and the curve fitting quality. As King's law performs an average curve fitting error of 0.5% [6], the main source of uncertainty is the calibrator system, which was, in our case, the wind tunnel. Thus at the lowest measured velocity (1 m/s) the relative error was over 60%, while in faster parts of the flow (over 3m/s) it was below 6%. The number of independent samples was very low in the laminar region due to the large time scale of the flow, but in the turbulent boundary layer it was always higher than 3000, that means the largest error in higher statistical moments was around 1%.

The hot-wire was supported by an L shaped stem which aligned the prongs of the probe parallel to the direction of flow. The positioning of the probe was solved by a traversing system the uncertainty of which was 0.02mm.

2.4. LDV measurement system

The LDV (Laser Doppler Velocimetry) system was a type of ILA fp50fus equipped with a He-Ne laser of 10mW. This system measures one component of the velocity vector and not sensitive to the direction of flow. However, in the present case the direction of flow over the wing is known a-priori. The optical unit of the LDV system was placed onto the same traversing system as that of the hot-wire system.

The processing unit was connected to a computer and the software provided by ILA were applied. Due to the low rate of bursts the measurements were not applicable for length scale determination, the data was sampled by 16 MHz frequency. The determination of the accuracy of the measurement was based on the documentation of the system, i.e. the velocity was measured with an accuracy of 0.2%.

2.5 Numerical simulation

The flow field around the airfoil was computed via a 2D RANS (Reynolds Averaged Navier Stokes equations) approach. The Reynolds stresses appearing in the RANS equations were approximated by the isotropic eddy viscosity type turbulence models, like 'realizable' k-ε [7], the Spalart-Allmaras [8] model and the more sophisticated SST k-ω [9] turbulence models. For the computations, Fluent commercial software was used. The numerical mesh was block structured and contained quadrilateral cells only. The boundary layer and the wake were fully resolved, providing values of $y^+ \approx 1$ for the wall-neighbouring cells and fine in the near wake region. Both turbulence models use a one-equation turbulence model for regions where $Re_y < 200$, which is specially tuned for near-wall, anisotropic regions.

3. RESULTS AND DISCUSSION

3.1 Profiles of statistical quantities at an angle of attack of 8°

The aim of the measurements was to map the fine details of the flow to obtain the sufficient information for the validation of CFD results from Large Eddy Simulation technique. Velocity, turbulence intensity, length scale and skewness (kurtosis) profiles were measured at the following distances measured from the leading edge of the airfoil (c is the chord length): 0.19*c*, 0.29*c*, 0.4*c*, 0.52*c*, 0.62*c*, 0.98*c* along the suction side of the airfoil. Also, measurements were taken in the wake of the airfoil at locations: 1.1*c*, 1.25*c* and 1.5*c*.

In this document, authors define root-mean-square, turbulence intensity, length scale and skewness in the following ways:

$$U_{RMS} = \sqrt{\frac{1}{N}\sum_{i=1}^{N}(u_i - \bar{u})^2} \tag{2}$$

$$Tu = \frac{U_{RMS}}{U_\infty} \tag{3}$$

$$L = \bar{u} \cdot \int_0^\infty \rho(\tau) d\tau \tag{4}$$

$$Sk = \frac{1}{N}\sum_{i=1}^{N}\frac{(u_i - \bar{u})^3}{U_{RMS}^3} \tag{5}$$

In eq.(2) N denotes the number of samples. For the length scale in eq.(4) Taylor's frozen turbulence hypothesis and the autocorrelation function were applied. The autocorrelation function is defined here as follows.

$$\rho(\tau) = \frac{\overline{u(t) \cdot u(t+\tau)}}{U_{RMS}^2} \tag{6}$$

The over-line in Eq.(6) denotes Reynolds averaging, or, in the present case, time averaging. Note that length scale and skewness are based on local quantities while turbulence intensity is referred to the free stream velocity which was 10m/s in the investigated cases. The length scale characterizes the fine structure of the turbulent flow, while Skewness indicates the spatial range over which turbulence exerts its effect to the outer (mainly potential) flow region. Both these statistical quantities serve for validation of Large Eddy Simulation results on a higher level of computational quality.

To decrease the uncertainty in positioning the profiles were measured along lines perpendicular to the direction of free stream and not to the surface of the airfoil. The measured and computed velocity profiles are represented in Figure 2 where one can follow the development of the boundary layer and

the wake. At location $x = 0.19c$ the boundary layer is characterized by small turbulence intensities of around 1-2% (see Figure 5). From the low values of turbulence intensity and the value of the local Reynolds number of $3 \cdot 10^4$ based on the distance from the leading edge, the boundary layer is regarded to be laminar.

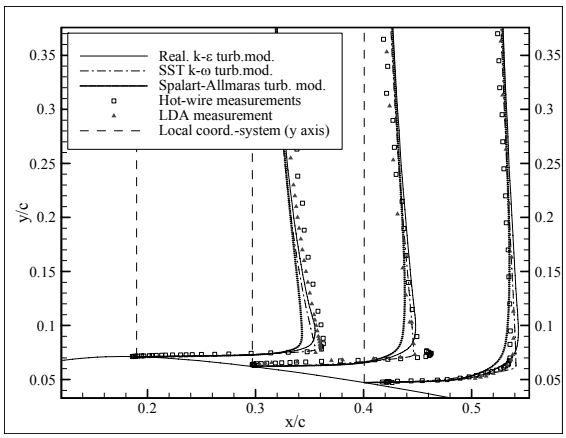

a)

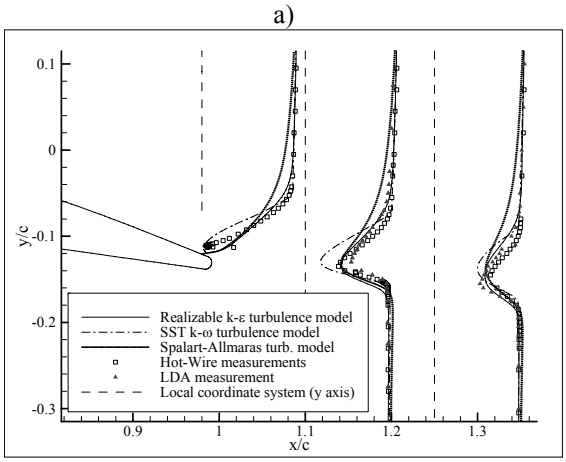

b)

Figure 2. Measured and computed mean non-dimensional velocity (U/U_∞)profiles at a) 0.19*c*, 0.29*c*, 0.4*c* and b) 0.98*c*, 1.1*c*, 1.25*c* streamwise locations for 8° angle of attack. In the figure, one x/c unit indicates $U/U_\infty = 0.1$.

The velocity measured by means of hot-wire and by LDV are in a good agreement with each other in all locations, except at location 0.29*c* where hot-wire measurements indicate a small peak of high velocity right at the outer edge of the boundary layer, on which authors have no exact explanation, however, LDV measurements did not indicate that peak at the same place. Both measurement techniques show relatively sharp change of velocity from the viscous affected region to the outer potential region. Numerical simulation gave best approximation when 'realizable' k-ε turbulence model was used. SST k-ω turbulence model performed worse, although boundary layer transition effects were taken into account. The Spalart-Allmaras turbulence model performs well, however its more dissipative character points out at the prediction of more smooth velocity profiles. The measured profiles at 0.98*c* are in good agreement but the computation with Spalart-Allmaras shows a much thicker region affected by the boundary layer. SST k-ω model predicts a velocity profile having an inflection point close to the wall, indicating a tendency of the boundary layer to separate.

In the wake of the airfoil the velocity distribution shows narrower deficit region than that predicted by the Spalart-Allmaras model. The SST k-ω model predicts the width of the wake at different locations well, but the minimal velocity is smaller than that, measured by the two different experimental techniques. The 'realizable' k-ε agrees with the results of the two measurement techniques far below their uncertainty. In case of an angle of attack of 8° best performance is clearly dedicated to the 'realizable' k-ε turbulence model.

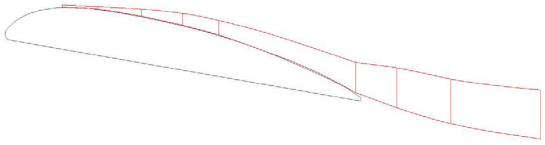

Figure 3. Boundary of the region affected by the boundary layer over the suction side of the airfoil at 8° angle of attack. Proportionally correct representation.

Skewness (*Sk*, see eq.(5)) indicates the deflection of the probability density function of the velocity fluctuations from the Gaussian distribution. These deflections are highest at the edges of mixing layers, i.e. zones of high velocity gradients. At the outer edge of the boundary layer, where the character of the flow is intermittent, skewness takes its minimal value. Inside the boundary layer, where the fully turbulent core is present, skewness tends to zero. When the viscous sub-layer is approached and turbulent fluctuations begin to be damped by the viscous effects, skewness takes its maximum. So, the region between the minimal and maximal values of skewness contains the region where most of the turbulent momentum transfer is present. The upper lines in Figure 3 are fitted to the minimum values, the lines closest to the suction surface of the airfoil are fitted to the maximum values of the skewness, respectively, for both angles of attack. However, in the wake of the airfoil skewness does not exhibit any maximum, so the lines are fitted to the upper minimum and lower minimum of the skewness profiles how it is represented schematically on Figure 7.

Authors have observed that the values of the length scale were very large in regions characterized by low turbulence intensity. This is due to the shape of the autocorrelation function.

When the process, i.e. the flow has non-stochastic feature then the integral of the autocorrelation coefficient in eq.(4) tends to infinity. The length scale values decreased orders of magnitudes where the turbulence intensity reached values above 5%, according to our experiences. Figure 4 shows that the length scales close to the leading edge are of the order of 1% of the cord length and increasing as the outer region of the boundary layer is approached. One can observe that length scales increase at the profile 0.4*c* to a value of 1.5% of the cord length and slightly increase farther downstream along the locations x = 0.52*c*, 0.62*c*, 0.98*c* to a maximum of 20% of cord length. The length scale profiles show an almost constant value between *y*/*c* = 1% and 2.5% of cord length in case of profiles from 0.29*c* to 0.52*c*, while the constant region expands up to *y*/*c* = 3% and 5% cord length at profiles 0.62*c* and 0.98*c*, respectively. In the wake of the airfoil, length scale seems to increase towards downstream from an average value of 2% to 3%. It can be also observed that the wake drifts downwards and spreads wider as the flow moves downstream.

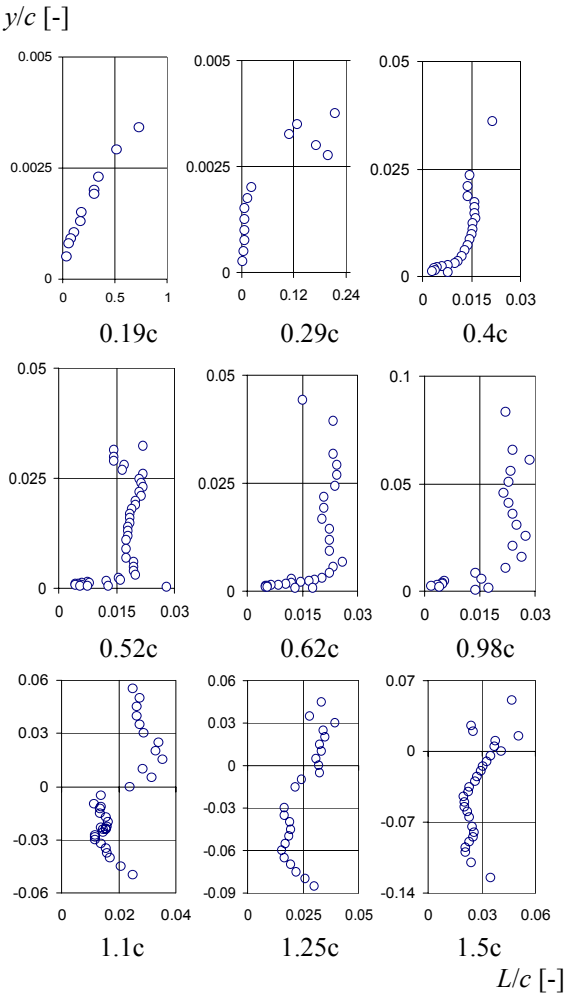

Figure 4. Distribution of integral length scale over the suction side and in the wake of the airfoil at 8° angle of attack.

Turbulence intensity distributions for the airfoil at 8° angle of attack can be seen in Figure 5. The free stream turbulence intensity is below 1% and remains low along the profile at 0.19*c* location. The maximum value is below 3% which is rather an uncertainty of the measurements but not due to turbulence. The boundary layer at this location is predominantly laminar. At location 0.29*c* the maximum of turbulence intensity is around 9% and shifts further from the wall. However, the boundary layer here is rather transitional. The profiles from location 0.4*c* to 0.98*c* are concluded to be turbulent, based on the character of the distribution and values of turbulence intensity across them.

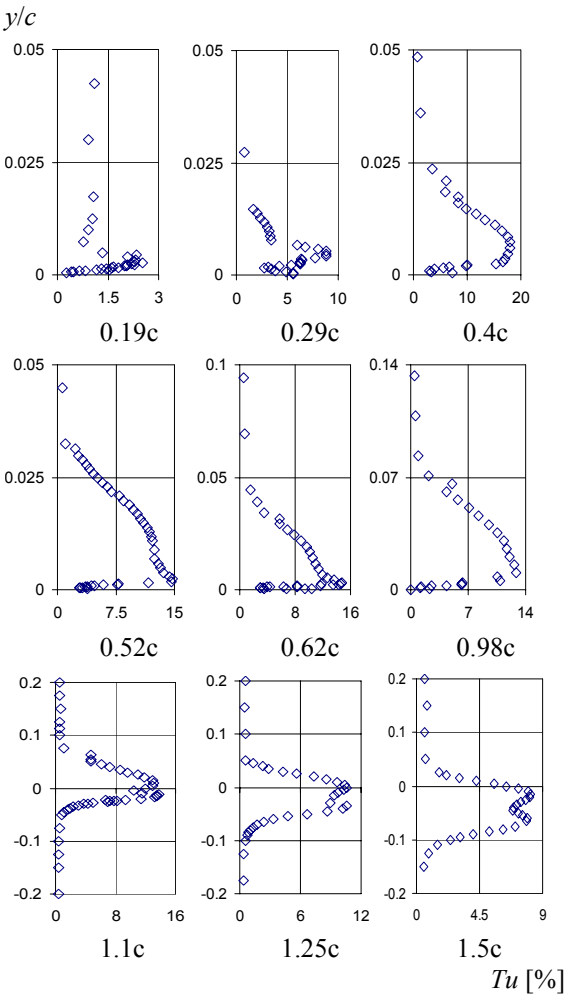

Figure 5. Distribution of turbulence intensity over the suction side and in the wake of the airfoil at 8° angle of attack.

Comparing Figure 5 to Figure 4 one can observe that the integral length scale is constant independently from the intensive decrease of turbulence intensity at the outer regions of the boundary layer.

In the wake of the airfoil, when investigating it along a *y* = const. line towards negative *y* direction, turbulence intensity increases from the outer

potential flow towards the edge of the wake region. Inside the wake, turbulence intensity decreases, exhibits a minimum and increases again until its peak value on the lower edge of the wake. Further along the y = const. line towards negative y direction, turbulence intensity decreases back to its free stream value. The minimum value in the center of the wake is probably a consequence of the viscous sub-layers when they join after separating from the trailing edge.

3.2 Profiles of statistical quantities at an angle of attack of 15°

The velocity profiles measured in case of 15° angle of attack can be seen in Figure 6.

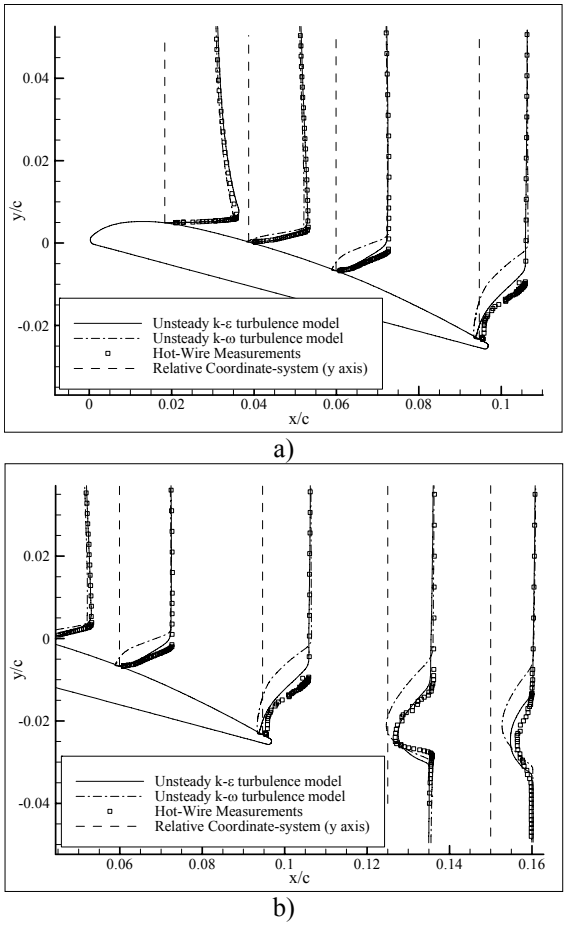

Figure 6. Measured and computed mean non-dimensional velocity (U/U_∞)profiles at a) 0.19c, 0.4c, 0.62c, 0.98c and b) 0.98c, 1.25c, 1.5c, streamwise locations for 15° angle of attack. In the figure, one x/c unit indicates U/U_∞ = 0.1.

In this case LDV measurements were not taken, so computations are compared to hot-wire measurements only. At this angle of attack, separation of boundary layer is expected.

Based on the present and previous results, it can be concluded that computations by the 'realizable' k-ε turbulence model via the technique of time marching [10] gave the best approximation to the measurement results.

By means of hot-wire measurements it is not possible to determine the direction of flow but in this case results from measurements and those from computations complete each other and provide a tool for the understanding and description of the flow field.

The boundary layer remains attached until the location of 0.62c. Upstream this location the agreement between experiments and 'realizable' k-ε based computations is good. The profile at 0.98c already shows the difference due to the directional problems of hot-wire technique. Computations show a small separation zone close to the trailing edge. The agreement between experiments and 'realizable' k-ε based computations in the upper region of the profile at 0.98c certifies the validity of the lower region, as well. The computations using SST k-ω turbulence model show large domain of boundary layer separation already starting between 0.4c and 0.62c. This separation is now experienced to be not real.

The wake behind the airfoil shows also good agreement between computations and experiments. However, SST k-ω model resulted in a different flow field.

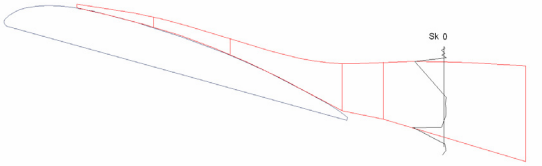

Figure 7. Boundary of the region affected by the boundary layer over the suction side of the airfoil at 15° angle of attack. Proportionally correct representation.

Length scales occurring at this angle of attack, are much larger than in the 8° case. Already at 0.19c location, the characteristic eddy size is growing almost linearly from 0.01c to a value of 0.05c of chord length from where it remains constant along the y axis. The same character but spreading of the region in y direction can be observed at location 0.4c, the length scale does not differ much from that measured at 0.19c. Above the trailing edge and in the wake, eddy size ranges between 0.05c and 0.07c beside some large values appearing due to the intermittent characteristic of the flow at this Reynolds number.

Turbulence intensity plots show that the boundary layer is likely separated at 0.98c but signs of separation in the distributions can not be discovered at upstream locations. The distributions in the wake are asymmetric to the y/c = 0 centerline showing a wider turbulent upper region and a thin lower turbulent region.

The separation of the boundary layer is also confirmed from the observation, that the centerline of the wake does not deflect downwards as it did for the case of 8° angle of attack.

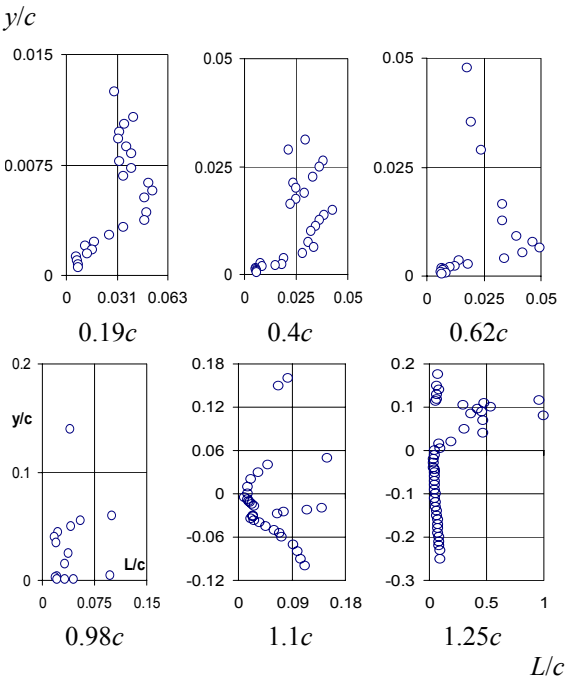

Figure 8. Distribution of integral length scale over the suction side and in the wake of the airfoil at 15° angle of attack.

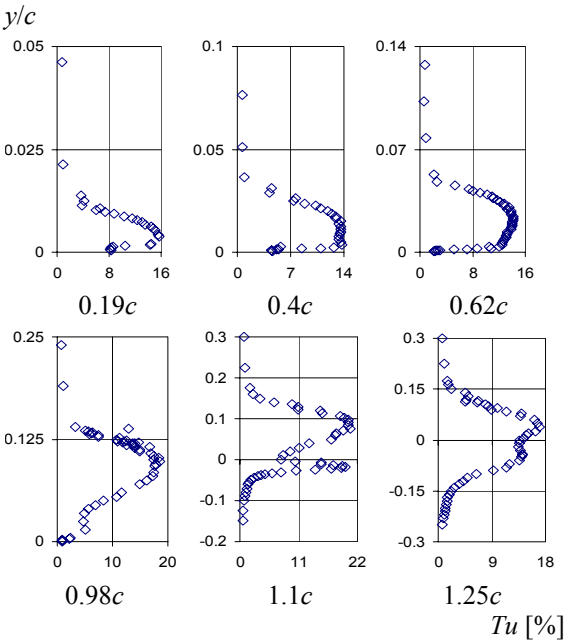

Figure 9. Distribution of turbulence intensity over the suction side and in the wake of the airfoil at 15° angle of attack.

3.3 Spectrum of turbulence

Spectrum of turbulence shows the kinetic energy distribution among the broad range of vortex-scales of turbulent flows [11]. Generally speaking, the three-dimensional spectrum of turbulence would be aimed to compute. However, by means of single-hot-wire and one-component LDV measurements, only one-dimensional spectrum of turbulence can be computed, which is the square of the Fourier transform of the velocity fluctuations [10, 11] (eq. (7)).

$$E_{11} = \left(\int_{-\infty}^{\infty} u'(x) \cdot e^{-2\pi i \kappa} dx \right)^2 \qquad (7)$$

In eq.(7), x denotes streamwise coordinate and u' is the streamwise velocity fluctuation, κ is the streamwise wave number. As authors have carried out only single-point measurements, the obtained time series were transformed into spatial data via Taylor's „frozen turbulence" hypothesis ($x = \overline{u} \cdot t$). The transformation of f frequency into wave number is thus hand-forward $\kappa = 2\pi f / \overline{u}$.

The profiles at 0.19c were found to be laminar for both angle of attacks, thus turbulence spectrum is not evaluated there. In addition, the profile at 0.29c for the case of 8° angle of attack was also determined to be laminar. All spectra are evaluated below the "validity limit" of the statistical quantities, i.e. from where integral length scales fall into reasonable range.

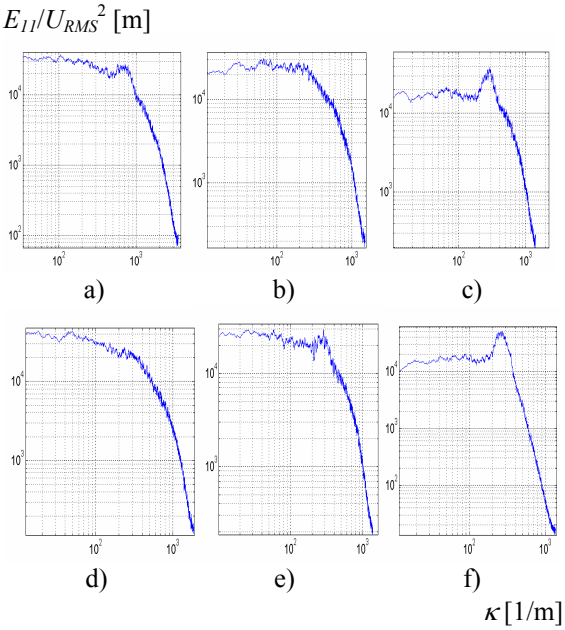

Figure 10. 1-dimensional spectra of turbulence at 8° angle of attack for two profiles: 1.) x = 0.4c, y = 0.0025c (a)), 0.0135c (b)), 0.021c (c)); 2.) x = 0.52c, y = 0.00485c (d)), 0.027c (e)), 0.032c (f)).

In all cases where spectrum was analyzed, the turbulent cascade, i.e. the range of vortex scales was between 10^2-10^3 1/m that means length scales between $(3\cdot10^{-4})c$ and $(3\cdot10^{-5})c$ in chord length units. The Kolmogorov scale was estimated to be $10^{-4}c$ in the most turbulent regions which is $8\cdot10^4$ 1/m in terms of wave number via eq. (8) [11].

$$\eta = L \cdot \sqrt[4]{15}\left(\mathrm{Re}_L\right)^{-3/4} \qquad (8)$$

The minimum scale resolvable by the hot-wire was limited by the length of the wire of 1.3mm, which is $5\cdot10^3$ 1/m in terms of wave number. One can observe peaks in Figure 10. c and f at a wave number of 250 1/m that corresponds to a length of $0.12c$ at the outer edge of the boundary layer. At the profile located at $x = 0.62c$ this peak still appears but with much weaker contrast comparing to the previously mentioned two profiles. This relatively long wavelength disturbance is not likely a vortex, but a wavy motion of the fluid that decays as the fluid moves further downstream. At the profile $x = 0.98c$ the spectrum shows the "classic" character (see Figure 11.), showing an inertial sub-range between wave numbers of 200 and 1000 1/m well below the limits determined by the hot-wire system with a slope of -5/3 indicating Kolmogorov's relation as $E_{11} \sim \kappa^{-5/3}$.

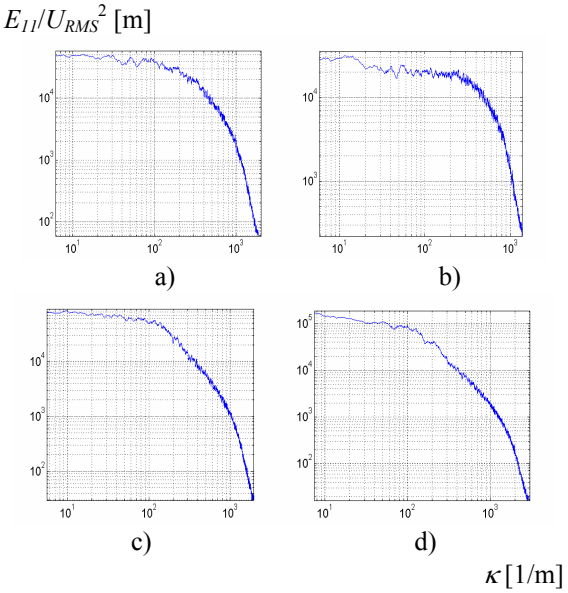

Figure 11. 1-dimensional spectra of turbulence at a) 8° and b) 15° angle of attack for the profile at location a) $x = 0.98c$ at a height of $y = 0.06c$ and b) $x = 0.4c$ at $y = 0.024c$. Spectra in the centre of the wake for the case c) 8°, d) 15° angle of attack, respectively

In case of 15° angle of attack the previously mentioned long-wavelength peak at a wave number of 250 1/m does not appear. In all cases at this angle of attack, the spectrum has the same characteristics as in Figure 11.a, although the inertial sub-range shifts towards higher wave numbers, i.e. smaller vortices (see Figure 11.b).

In the wake region, turbulence decays, the inertial sub-range expands to a wider range of wave-numbers as shown in Figure 11.c and d. The turbulence characteristics of the wakes do not change with respect to each other when the angle of attack changes. This is probably due to the self similar character of the wakes of bodies.

4. CONCLUSIONS

In this work, authors mapped the characteristics of the boundary layer over the suction side of the RAF 6E airfoil by means of measuring profiles of velocity and its statistical derivatives. Measurements were carried out independently by hot-wire and LDV measurements. The flow field was also determined by 2-dimensional CFD computations based on RANS approach with several turbulence models, out of which, 'realizable' k-ε model performed best. Length scale distributions and turbulence 1D spectra were analyzed and the range of scales, as well as, their E_{11} spectral kinetic energy appearing in case of the present flow fields were determined.

ACKNOWLEDGEMENTS

Authors wish to thank for OTKA T 043493, T 037651, T 037730, K 63704 and SZEFH Foundation for the financial support.

REFERENCES

[1] Vad, J. (2004), „Effects of Sweep and Spanwise Changing Circulation Applied to Airfoils: A Case Study", Journal of Computational and Applied Mechanics, Vol. 5, No. 2. pp. 383-400.

[2] Vad, J., Koscsó, G., Gutermuth, M., Kasza, Zs., Tábi, T., Csörgő, T. (2005), „Reduction of Flow Generated Noise of Airfoils by Means of Acoustically Soft Coating", Proc. VSTech 2005, The First International Symposium on Advanced Technology of Vibration and Sound, Hiroshima, Japan, Paper No. 050606, pp. 29-34.

[3] Beiler, M. G., and Carolus, T.H., 1999, "Computation and Measurement of the Flow in Axial Flow Fans with Skewed Blades", ASME J Turbomachinery, Vol. 121, pp. 59-66.

[4] Wassermann, P., Kloker, M., 2005, "Transition mechanisms in a three-dimensional boundary-layer flow with pressure-gradient changeover", *J. Fluid. Mech. vol. 530,* pp. 265-293

[5] Gruber, J., 1966, "Ventilátorok", *Műszaki Könyvkiadó*, Budapest

[6] Jorgensen, F. E., 2002, "How to measure turbulence with hot-wire anemometers", DANTEC Dynamics A/S

[7] Shih, T. -H., Liou, W.W., Shabbir, A., Yang, Z. and Zhu J., "A New k-ε Eddy-Viscosity Model for High Reynolds Number Turbulent Flows - Model Development and Validation", Computers Fluids, 24(3): 227-238, 1995.

[8] Spalart, P., and Allmaras, S., 1992, "A One-Equation Turbulence Model for Aerodynamic Flows", *Technical Report* AIAA-92-0439.

[9] Menter, F. R., 1994, "Two-Equation Eddy-Viscosity Turbulence Models for Engineering Applications", AIAA Journal, 32(8):1598-1605

[10] Ferziger, J.H., Peric, M., 2002, "Computational methods for fluid dynamics", Springer Verlag, Berlin Heidelberg New York, 3rd edition

[11] Pope, S.B., 2000, "Turbulent flows", Cambridge University Press

[12] Bruun, H. H., 1995, "Hot-wire anemometry", Oxford University Press

Conference on Modelling Fluid Flow (CMFF'06)
The 13th International Conference on Fluid Flow Technologies
Budapest, Hungary, September 6-9, 2006

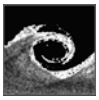

NUMERICAL SOLUTION OF 2D INCOMPRESSIBLE FLOW OVER A VIBRATING AIRFOIL

Radek HONZÁTKO[1], Karel KOZEL[2], Jaromír HORÁČEK[3]

[1] Corresponding Author. Department of Technical Mathematics, Czech Technical University in Prague. Karlovo náměstí 13, Praha 2 – Nové Město, 121 35, Czech Republic. Tel.: +420 2 2435 7215, Fax: +420 2 2491 1406, E-mail: Radek.Honzatko@fs.cvut.cz
[2] Department of Technical Mathematics, Czech Technical University in Prague. E-mail: Karel.Kozel@fs.cvut.cz
[3] Institute of Thermomechanics, Czech Academy of Sciences. E-mail: jaromirh@it.cas.cz

ABSTRACT

The work deals with a numerical solution of 2D steady and unsteady inviscid incompressible flow over profiles NACA 0012 and DCA 8% in a channel. Several cases of an unsteady behaviour are simulated - a prescribed oscillation and a flow induced vibration of the profile in a channel. One degree of freedom is considered. Governing system of equations is the system of incompressible Euler equations.

The finite volume method (FVM) in a form of cell-centered explicit scheme with an added artificial viscosity is applied. With respect to the profile shape a quadrilateral C-mesh is used in the case of NACA 0012 profile, which allows to capture the blunt leading edge of the profile in an appropriate way. An H-mesh is used in the case of the DCA 8% profile.

Two approaches to the numerical treatment of the moving profile are considered. At first, the small disturbance theory (SDT) is chosen as a simple method for modeling of a profile rotation. The main restriction of this method is that only small angles of attack of the profile are allowed. At second, the Arbitrary (Semi) Lagrangian-Eulerian (ALE) method on moving meshes is employed. This method allows more complex motion of the profile with large displacements.

Some numerical results of steady and unsteady inviscid incompressible flows over the profile in a channel are presented. Numerical results of unsteady flows over the vibrating profile fixed in an elastic axis achieved by both SDT and ALE method are presented and compared.

Keywords: aeroelasticity, Arbitrary Lagrangian-Eulerian method, cell-centered scheme, Euler equations, finite-volume method

NOMENCLATURE

A		continuous bijective operator
C_p	[-]	static pressure coefficient
D		finite volume cell
$\underline{F}$		inviscid physical flux vector in x direction
$\underline{G}$		inviscid physical flux vector in y direction
$\underline{\widetilde{F}}$		inviscid numerical flux vector in x direction
$\underline{\widetilde{G}}$		inviscid numerical flux vector in y direction
K	[-]	constant
M	[Nm]	aerodynamic momentum
P	[-]	non-dimensional pressure
$\underline{\underline{R}}$		diagonal matrix
T	[-]	non-dimensional time
U	[-]	x component of non-dimensional velocity vector
V	[-]	y component of non-dimensional velocity vector
Vol		finite volume domain
$\underline{W}$		vector of conservative variables
a	[-]	constant
c	[kgm^2/s^2]	torsional stiffness
f	[Hz]	frequency
k	[kgm^2/s]	coefficient of torsional damping
l	[m]	length
$\underline{n}$		normal vector to the boundary
p	[Pa]	static pressure
q	[m/s]	velocity value
t	[s]	time
Δt	[s]	time step
u	[m/s]	x component of velocity vector
v	[m/s]	y component of velocity vector
w	[m/s]	domain velocity vector
θ	[$kg\ m^2$]	momentum of inertia
μ	[m^3]	volume of a finite volume cell
ρ	[kg/m^3]	density
φ	[rad]	angle of rotation

Subscripts and Superscripts

i	cell index
k	summation index

ref	reference dimensional value
t	torsional
t, x, y	partial derivative with respect to time and spatial coordinates
T, X, Y	partial derivative with respect to time and spatial coordinates (non-dimensional)
t	time dependent
0	amplitude
∞	upstream reference value
A	aerodynamic
n	time level
m	number of neighbouring cells

1. INTRODUCTION

A mathematical model of the flow is represented by a system of incompressible Euler equations in conservation form.

The explicit cell-centered Lax-Wendroff scheme in Richtmyer form with added artificial viscosity is used for the numerical solution of steady and unsteady flows over a profile in a channel.

The method of artificial compressibility in a conjunction with the time dependent method is applied to steady computations.

Prescribed oscillation and flow induced vibration of a profile is considered. Flow induced vibration of a profile is described by an ordinary differential equation (ODE) of second order.

2. MATHEMATICAL MODEL

The behaviour of a flow is described by the system of incompressible Euler equations Eq. (1) in conservation form:

$$\underline{\underline{R}}\,\underline{W}_t + \underline{F}_x + \underline{G}_y = \underline{0}, \qquad (1)$$

where

$$\underline{W} = \begin{pmatrix} \frac{p}{\rho} \\ u \\ v \end{pmatrix}, \quad \underline{F} = \begin{pmatrix} u \\ u^2 + \frac{p}{\rho} \\ uv \end{pmatrix}, \quad \underline{G} = \begin{pmatrix} v \\ uv \\ v^2 + \frac{p}{\rho} \end{pmatrix}$$

and

$$\underline{\underline{R}} = \mathrm{diag}\|0,1,1\|.$$

The system Eq. (1) is solved with the diagonal matrix $\underline{\underline{R}} = \mathrm{diag}\left\|\frac{1}{a^2},1,1\right\|$, $a \in R$, which represents the method of artificial compressibility used for steady state solutions.

Here ρ [kg/m^3] is a density (constant), p [Pa] is a pressure and (u, v) [m/s] is a velocity vector.

Upstream conditions are given by two prescribed values, a third one is extrapolated. Downstream conditions are given by a prescribed pressure. Wall conditions are impermeability conditions $(u,v)\underline{n} = 0$ ($\underline{n}$ represents normal vector to the boundary).

The method of artificial compressibility (see, e. g., [1]) and the time dependent method are used for computations of steady state solutions. In the case of unsteady solution it is necessary to consider $a \to \infty$ or a»K, where K is a given (large) positive number. To avoid an influence of a value of the paremeter a on numerical results a dual time stepping method or an implicit method can be used, see, e. g., [2].

2.1. Prescribed Profile Oscillation

A rotation of the profile fixed in a point of an elastic axis is given by the Eq. (2).

$$\varphi = \varphi_0 \sin(2\pi f t) \qquad (2)$$

Here φ [rad] is an angle of rotation of the profile from an equilibrium position, φ_0 [rad] is an amplitude of oscillations, f [Hz] is a frequency of oscillations and t [s] is time.

2.2. Dynamical Effects of the Flow Field on the Profile

Dynamical effects (changes of a position of the profile fixed in a point of an elastic axis) are considered by the behaviour of the ODE

$$\theta\ddot{\varphi} + k_t\dot{\varphi} + c_t\varphi = M_A(t), \qquad (3)$$

where φ [rad] is an angle of rotation of the profile from the position of equilibrium, θ [$kg\ m^2$] is a momentum of inertia, k_t [$kg\ m^2/s$] is a coefficient of torsional damping, c_t [$kg\ m^2/s^2$] is a torsional stiffness, $M_A(t)$ [Nm] is an aerodynamic momentum.

3. NUMERICAL SOLUTION

3.1. Non-dimensional Variables

The non-dimensional variables U, V, P, T are used for the numerical solution. The relations between dimensional and non-dimensional variables are given by the normalization of the dimensional variables u, v, p, ρ, t with reference (dimensional) values u_∞, v_∞, l_{ref} in the following way:

$$X = \frac{x}{l_{ref}}, Y = \frac{y}{l_{ref}}, P = \frac{p}{\rho q_{ref}^2},$$
$$U = \frac{u}{q_{ref}}, V = \frac{v}{q_{ref}}, T = \frac{t q_{ref}}{l_{ref}}, \quad (4)$$

where $q_{ref} = \sqrt{u_\infty^2 + v_\infty^2}$ represents a reference velocity value. Here u_∞, v_∞ are components of a reference velocity vector, l_{ref} is a reference length.

The system Eq. (1) has in the non-dimensional variables Eq. (4) the following form

$$\underline{\underline{R}}\,\underline{W}_T + \underline{F}_X + \underline{G}_Y = \underline{0}, \quad (5)$$

where

$$\underline{W} = \begin{pmatrix} P \\ U \\ V \end{pmatrix}, \quad \underline{F} = \begin{pmatrix} U \\ U^2 + P \\ UV \end{pmatrix}, \quad \underline{G} = \begin{pmatrix} V \\ UV \\ V^2 + P \end{pmatrix}$$

and

$$\underline{\underline{R}} = \mathrm{diag}\|0,1,1\|.$$

The system Eq. (5) is solved with the diagonal matrix $\underline{\underline{R}} = \mathrm{diag}\left\|\frac{q_{ref}^2}{a^2},1,1\right\|$, $a \in R$, which represents the method of artificial compressibility used for steady state solutions.

3.2. Numerical Scheme in FVM

The cell-centered explicit Lax-Wendroff (LW) (Richtmyer form) scheme in a form of predictor-corrector with an added artificial viscosity is used at a quadrilateral C-mesh (m=4).

- LW Richtmyer predictor:

$$\underline{W}_i^{n+1/2} = \underline{W}_i^n - \frac{1}{2}\frac{\Delta t}{\mu_i}\sum_{k=1}^{m}\left(\underline{\widetilde{F}}_{ik}^n \Delta y_k - \underline{\widetilde{G}}_{ik}^n \Delta x_k\right) +$$
$$+ \frac{\varepsilon}{m}\sum_{k=1}^{m}\left(\underline{W}_k^n - \underline{W}_i^n\right)$$

- LW Richtmyer corrector:

$$\underline{\widetilde{W}}_i^{n+1} = \underline{W}_i^n - \frac{\Delta t}{\mu_i}\sum_{k=1}^{m}\left(\underline{\widetilde{F}}_{ik}^{n+1/2} \Delta y_k - \underline{\widetilde{G}}_{ik}^{n+1/2} \Delta x_k\right)$$

$$\underline{W}_i^{n+1} = \underline{\widetilde{W}}_i^{n+1} + AD\underline{W}_i^n,$$

where $\mathrm{AD}\,\underline{W}_i^n$ is an artificial viscosity and

$$\underline{\widetilde{F}}_{ik} = \frac{(\underline{F}_i + \underline{F}_k)}{2}, \underline{\widetilde{G}}_{ik} = \frac{(\underline{G}_i + \underline{G}_k)}{2}, \varepsilon \in \langle 0,1 \rangle.$$

3.3. Boundary Conditions

The upstream conditions are realized by the specification of upstream velocity vector values $U = U_\infty$, $V = V_\infty$ and pressure P is extrapolated. In the case of the downstream conditions a pressure value $P = P_2$ is specified and the other values of the vector of conservative variables are extrapolated. Wall conditions are realized by using of "reflection principle", i. e. there are ghost cells in the wall created by a reflection on the wall. The velocity vector (u, v) is also reflected on the wall.

3.4. Oscillating Profile

Two approaches are applied to treating a vibrating profile. At first, the small disturbance theory is considered. Under the assumption of a small angle of attack ($|\varphi| \le 6^o$) the rotation of the profile can be approximated by the rotation of a normal vector to the profile surface (see Figure 1), i. e. there is no real movement of the profile and no change of the finite volume mesh. At second, the ALE method is used. The mesh is deformed with respect to the profile rotation. Larger angles of attack are allowed in conjunction with this method.

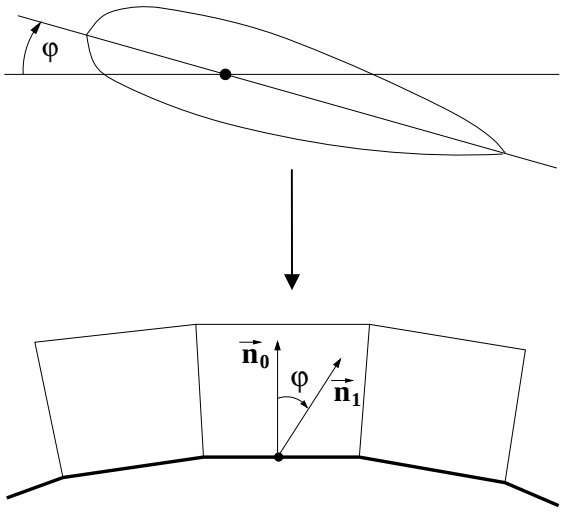

Figure 1. Small disturbance theory, rotation of a normal vector to the profile surface

3.5. Aeroelastic Effects

At first, the system of Euler equations is solved. At second, a new angle of attack φ is computed using Eq. (3). A pressure field solved in the first step determines the aerodynamic momentum $M_A(t)$ acting on the profile and appearing on the right hand side of Eq. (3). The profile position is changed with respect to the new value of the angle φ, i. e.

either the normal vector to the boundary is rotated in the case of SDT or the mesh is changed in the case of the ALE method. Then again the first step follows and this two-step procedure repeats.

The ODE Eq. (3) is solved by the Runge-Kutta method of 4th order.

3.6 FVM in ALE Formulation

The integration over the time dependent finite volume cell denoted $D_i(t)$ is demanded in FVM used on moving meshes

$$\int_{D_i(t)} \left(\underline{W}_t + \underline{F}_x + \underline{G}_y\right) dxdy = \underline{0}. \tag{6}$$

Therefore a continuous bijective transformation (operator) A_t satisfying

$$A_t : D_i^0 \mapsto D_i^{A_t} \equiv D_i(t)$$

is considered. Here D_i^0 is the finite volume cell in an reference (original) domain and $D_i(t)$ is this finite volume cell in the computational domain at time t (current configuration), see Fig. 2.

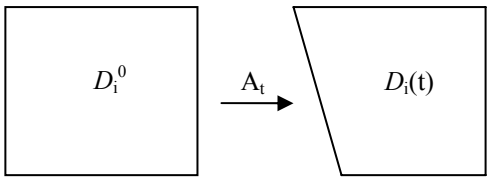

Figure 2. Time dependent transormation A_t of reference finite volume cell D_i^0

By the integration over the time dependent domain $D_i(t)$ the following **transport theorem in ALE formulation** is applied

$$\frac{d}{dt}\int_{Vol^{A_t}} f\, dVol = \int_{Vol^{A_t}} \frac{D^{A_t} f}{Dt} + f\left(\nabla \cdot \underline{w}\right) dVol =$$
$$= \int_{Vol^{A_t}} \frac{\partial f}{\partial t} + \nabla \cdot \left(f\,\underline{w}\right) dVol\,,$$

especially the relationship

$$\frac{d}{dt}\int_{Vol^{A_t}} f\, dVol = \int_{Vol^{A_t}} \frac{\partial f}{\partial t} + \nabla \cdot \left(f\,\underline{w}\right) dVol\,, \tag{7}$$

where Vol^{A_t} denotes a time dependent domain with respect to the mapping A_t and f represent a function of time and spatial variables. If the symbol Vol^{A_t} is replaced by $D_i(t)$ and f by the vector $\underline{W}$, the formula Eq. (7) can be applied directly to the equation Eq. (6) after a not complicated adjustment. The integration is considered for all components of the vector $\underline{W}$. The vector $\underline{w}$ represents a domain velocity, sometimes also called a grid velocity.

If the term $\nabla \cdot \left(\underline{w}\underline{W}\right) = \left(w_1 \underline{W}\right)_x + \left(w_2 \underline{W}\right)_y$ is added and contemporaneously subtracted to the integrand in Eq. (6) it results to

$$\int_{D_i(t)} \left[\underline{W}_t + \left(w_1 \underline{W}\right)_x + \left(w_2 \underline{W}\right)_y + \hat{\underline{F}}_x + \hat{\underline{G}}_y\right] dxdy =$$
$$= \int_{D_i(t)} \left[\underline{W}_t + \left(w_1 \underline{W}\right)_x + \left(w_2 \underline{W}\right)_y\right] dxdy +$$
$$+ \int_{D_i(t)} \left(\hat{\underline{F}}_x + \hat{\underline{G}}_y\right) dxdy = \underline{0}, \tag{8}$$

where

$$\hat{\underline{F}} = \underline{F} - w_1 \underline{W},\ \hat{\underline{G}} = \underline{G} - w_2 \underline{W}\,. \tag{9}$$

To the first integral of the last equation in Eq. (8) the formula Eq. (7) is applied and to the second term the Green formula is applied.

Finally, the ALE formulation of finite volume method applied to the system of Euler equations is given by the following formula

$$\frac{d}{dt}\left(\int_{D_i(t)} \underline{W}\, dxdy\right) + \oint_{\partial D_i(t)} \left(\hat{\underline{F}} dy - \hat{\underline{G}} dx\right) = \underline{0},$$

where $\hat{\underline{F}}, \hat{\underline{G}}$ are given in Eq. (9).

For more details on the ALE method used in aeroelasticity problems, see, e. g., [3, 4].

4. NUMERICAL RESULTS

Results of a numerical solution of flow over the vibrating profile NACA 0012 and DCA 8% in the channel are presented. Steady state results and their comparison with experimental data are presented, e. g., in [5].

Some numerical results of a steady state solution computed by the use of the SDT and over a rotated profile with rotated mesh for the angle of attack $\varphi = 2^o$ are presented and compared respectively.

Furthermore, some numerical results of unsteady flow over a vibrating profile in a channel achieved by both SDT and ALE method are presented and compared respectively.

Unsteady flow is either caused by prescribed oscillations of the profile fixed in an elastic axis given by the formula Eq. (2) or by flow induced vibrations (Eq. (3)).

Particularly, isolines of pressure coefficient C_p close to the profile are presented.

Figures Fig. 3 and Fig. 4 show a good agreement of pressure coefficient isolines computed by the use of the SDT (Fig. 3) and with the use of rotated mesh (Fig. 4). Therefore, it seems that the SDT can be considered as a suitable method how to compute numerical solution of flow over a profile with sufficiently small nonzero angle of attack in a simple way.

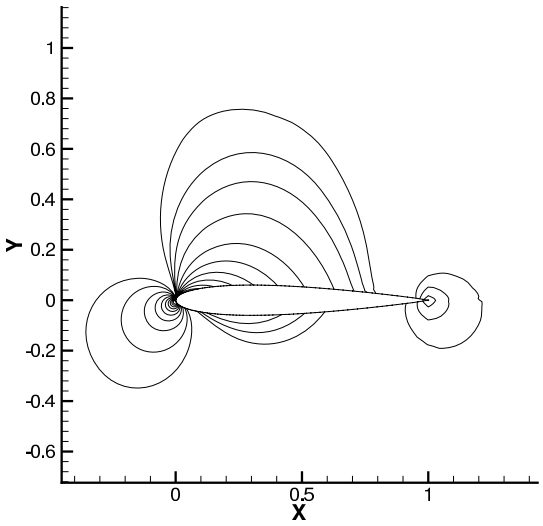

Figure 3. Pressure coefficient isolines, steady state solution, $\varphi = 2^o$, small disturbance theory

In the case of unsteady solution the amplitude is $\varphi = 3^o$ and f = 30 Hz. Three significant positions (angles of attack) of the profile within one time period are shown in Figures 5 to 7 and Figures 8 to 10. Figures 5 to 7 concern the small disturbance theory and Figures 8 to 10 concern the ALE method. Figures Fig. 5 and Fig. 7 demonstrate the symmetry of pressure coefficient isolines at two extreme positions of the profile in the case of the SDT. The same demonstration is represented by figures Fig. 8 and Fig. 10 in the case of the ALE method.

Good agreement of the numerical results achieved by the two presented methods can be observed in the comparison of corresponding figures in figure series Figures 5 to 7 and Figures 8 to 10.

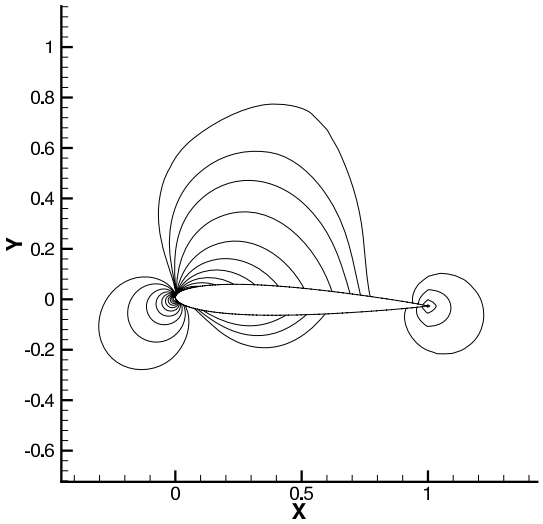

Figure 4. Pressure coefficient isolines, steady state solution, $\varphi = 2^o$, rotated mesh

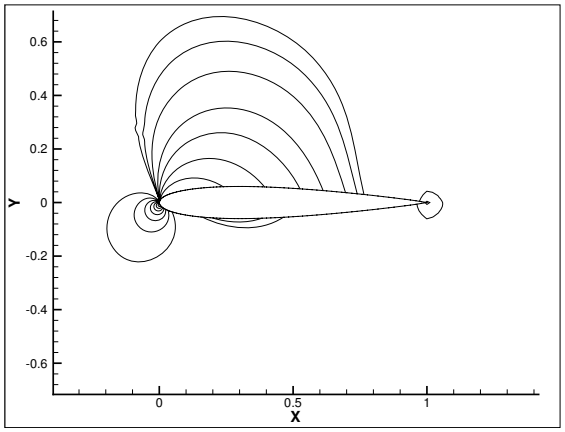

Figure 5. Pressure coefficient isolines, $\varphi = 3^o$, small disturbance theory

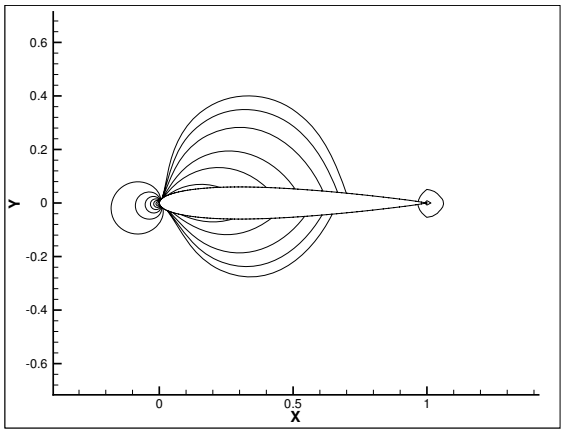

Figure 6. Pressure coefficient isolines, $\varphi = 0^o$, small disturbance theory

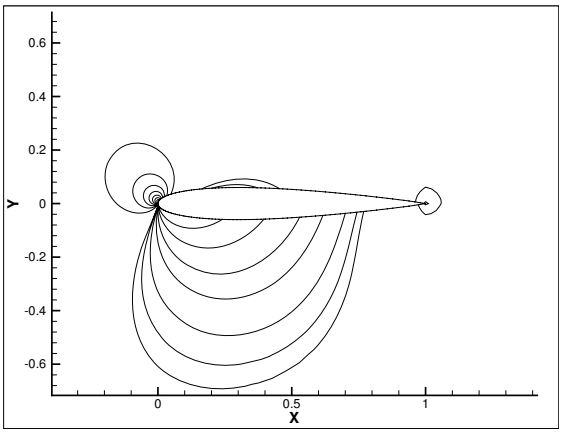

Figure 7. Pressure coefficient isolines, $\varphi = -3^o$, small disturbance theory

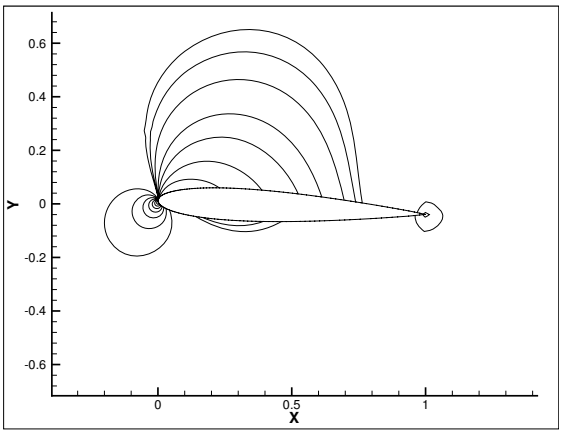

Figure 8. Pressure coefficient isolines, $\varphi = 3^o$, ALE method

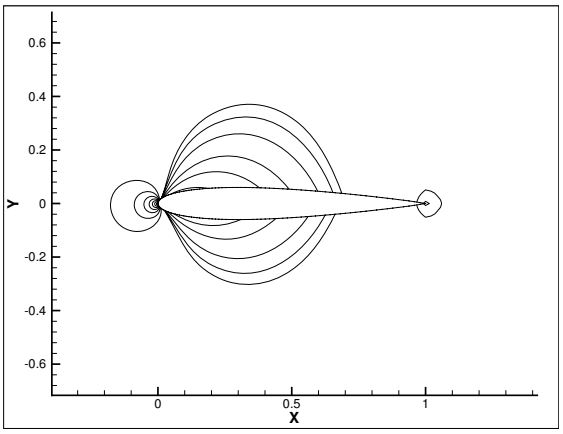

Figure 9. Pressure coefficient isolines, $\varphi = 0^o$, ALE method

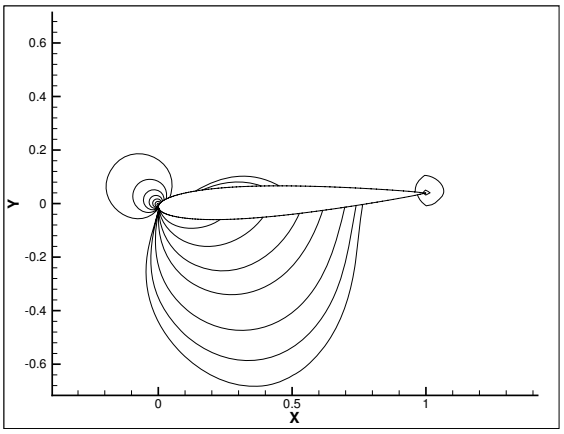

Figure 10. Pressure coefficient isolines, $\varphi = -3^o$, ALE method

Figure Fig. 11 shows comparison of pressure coefficient distribution in dimensionless time *T* for the SDT and the ALE method. Thin lines concern ALE method and thick lines concern SDT. Small differences may be observed. The distribution is only captured in short time period. Figure Fig. 12 sketches the profile with points on the profile surface in which the pressure coefficient is computed.

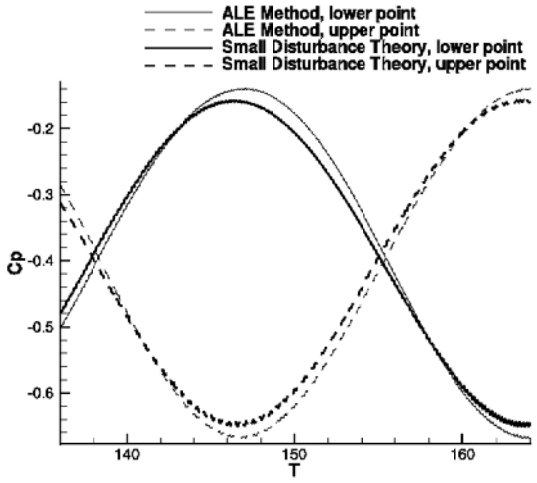

Figure 11. Pressure coefficient distribution in points on the profile surface with respect to the dimensionless time (h=20% of L, see Fig. 12)

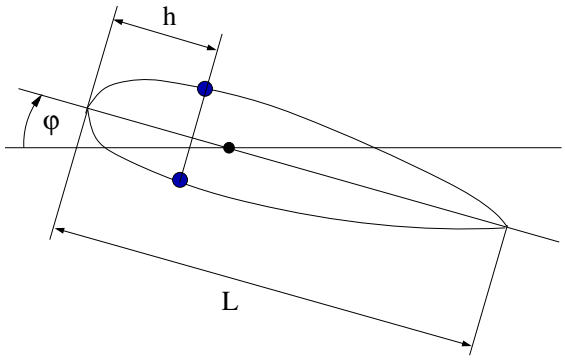

Figure 12. Points on the profile surface in which the pressure coefficient is computed

Figures Fig. 13 to 19 present oscillation of the profile DCA 8% described by the equation Eq. (3) for different upstream velocities u_∞ (1, 5, 7, 9, 10, 12 and 20 m/s line by line). The profile is positioned at 58% of the channel height from the lower channel wall. A moderate damping of oscillation can be observed for upstream velocities 1, 5 and 7 m/s. For the upstream velocity 9 m/s the amplitude of oscillation is increasing, while it is almost constant for u_∞=10 m/s. Finally, when the upstream velocity is increased further to 20 m/s the damping of oscillation is more pronounced.

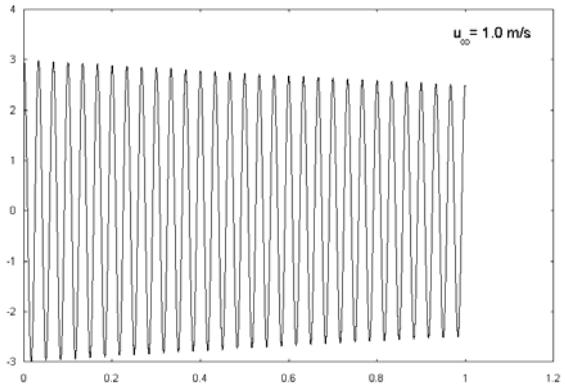

Figure 13. Oscillation of the profile for the upstream velocity u_∞=1 m/s

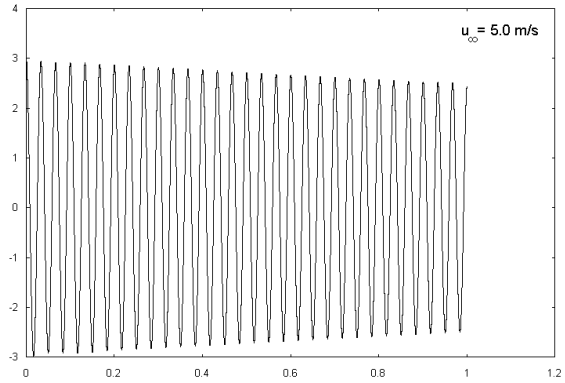

Figure 14. Oscillation of the profile for the upstream velocity u_∞=5 m/s

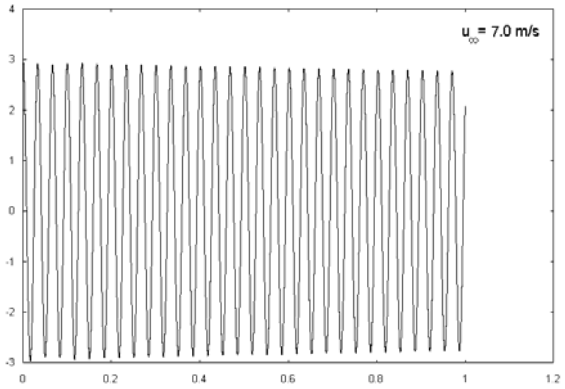

Figure 15. Oscillation of the profile for the upstream velocity u_∞=7 m/s

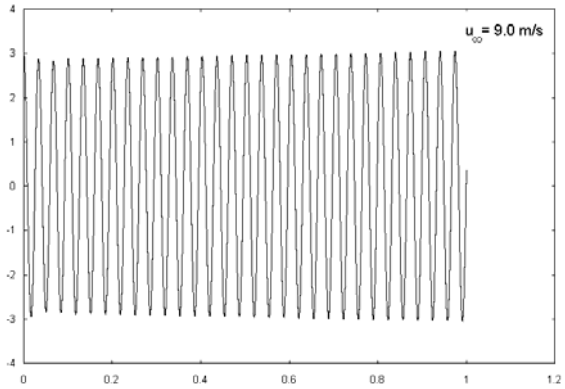

Figure 16. Oscillation of the profile for the upstream velocity u_∞=9 m/s

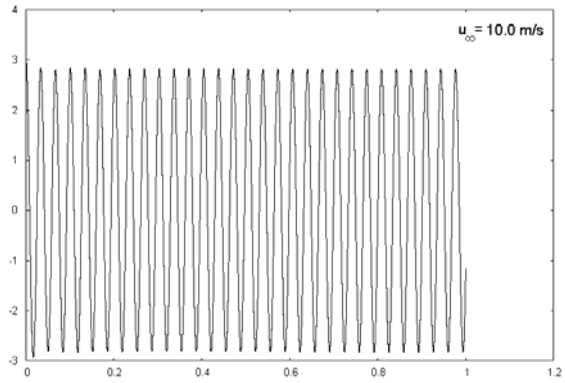

Figure 17. Oscillation of the profile for the upstream velocity u_∞=10 m/s

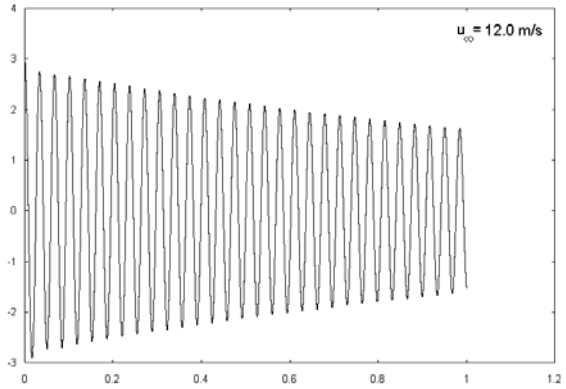

Figure 18. Oscillation of the profile for the upstream velocity u_∞=12 m/s

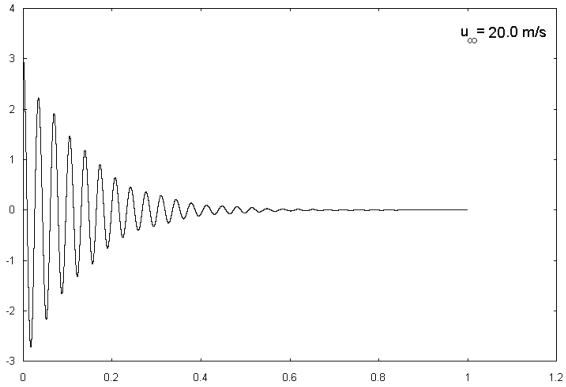

Figure 19. Oscillation of the profile for the upstream velocity u_∞=20 m/s

5. CONCLUSIONS

The numerical solver of a steady and an unsteady inviscid incompressible flow over a profile in a channel was developed. The explicit scheme with an added artificial viscosity in FVM was used.

In the case of steady a state solution a good agreement of numerical results achieved by the use of the SDT and with rotated mesh is observed.

In the case of unsteady solution of flow over a vibrating profile a good agreement of numerical results achieved by the use of the SDT and the ALE method can be observed.

The future steps intended are an implementation of an implicit numerical scheme and two degrees of freedom of the profile for inviscid flow and extension of this method to viscous flows.

ACKNOWLEDGEMENTS

This work has partly been supported by the Research Plan of the Ministry of Education of the Czech Republic No 6840770010 and project of the Grant Agency of the Academy of Science of the Czech Republic No IAA200760613 “Computer modelling of aeroelastic phenomena for real fluid flowing past vibrating airfoils particularly after the loss of system stability”.

REFERENCES

[1] Chorin, A. J., 1967, “A numerical Method for Solving Incompressible Viscous Flow Problems”, *Journal of Computational Physics*, 2(1):12-26.

[2] Kozel, K., Louda, P., and Příhoda, P., 2001, “Numerical Solution of 2d and 3d Incompressible Viscous Flow Problems”, Proc. *Proceedings of 5th ISAIF Symposium*, Gdańsk, Poland.

[3] Sváček, P., and Feistauer, M., 2003, “Application of a Stabilized FEM to Problems of Aeroelasticity”, Proc. *Numerical Mathematics and Advanced Applications (ENUMATH 2003)*, Heidelberg, pp. 796-805.

[4] Nomura, T., and Hughes, T. J. R., 1992, “An Arbitrary Lagrangian-Eulerian Finite Element Method for Interaction of Fluid and a Rigid Body”, Proc. *Computer Methods in Applied Mechanics and Engineering 95*, pp. 115-138.

[5] Honzátko, R., Kozel, K., and Horáček, J., 2004, “Numerical Solution of Flow through a Cascade and over a Profile with Dynamical and Aeroelastic Effects”, Proc. *Proceedings of the 8th International Conference on Flow-Induced Vibration*, Paris, pp. 377-382.

[6] Shmilovich, A., and Caughey, D. A., 1985, “Grid Generation for Wing-tail-fuselage Configurations”, *Journal of Aircraft*, 22(6):467-472.

[7] Fűrst, J., Honzátko, R., Horáček, J., and Kozel, K., 2004, “Flow over a Given Profile in a Channel with Dynamical Effects”, Proc. *Proceedings of Czech-Japanese Seminar in Applied Mathematics 2004*, Prague, pp. 63-72.

Conference on Modelling Fluid Flow (CMFF'06)
The 13th International Conference on Fluid Flow Technologies
Budapest, Hungary, September 6-9, 2006

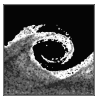

AN UNSTEADY LIFTING LINE APPROACH FOR CURVED AND SWEPT WINGS AERODYNAMIC COMPUTATION

Sébastien MULLER[1], Annie LEROY[2], Philippe DEVINANT[2]

[1] Corresponding Author. Laboratoire de Mécanique et d'Energétique, Université d'Orléans. 8 rue Léonard de Vinci, 45 072 Orléans Cedex 2, France. Tel.: +33 2 38 49 43 87, Fax : +33 2 38 41 73 83, E-mail: sebastien.muller@univ-orleans.fr
[2] Laboratoire de Mécanique et d'Energétique, Université d'Orléans

ABSTRACT

An unsteady lifting line method is developed for curved and swept wings of high aspect ratio. Using the matched asymptotic expansion in terms of the inverse of the aspect ratio performed by Guermond and Sellier [1], an implicit Prandtl-like approach is completed by unsteady as well as curvature and sweep effects. More precisely, in this time marching computational approach, the inner domain is calculated thanks to the unsteady two-dimensional Theodorsen theory. This theory allows to take into account compressibility and viscous effects by the use of experimental 2D airfoil data tables. In the outer domain, the wing is represented by a lifting line and the wake by a surface doublet distribution. The velocity induced by the wake on the wing is calculated thanks to Hadamard finite part integrals requiring no regularisation. Moreover the unsteady free wake is calculated using a rigorous emission and convection formulation. Comparisons of our approach with lifting surface results show very good agreements for different curved wings even for highly unsteady motions.

Keywords : curved and swept wings, lifting line, potential theory, three dimensional flow, unsteady flow.

NOMENCLATURE

AR	[-]	aspect ratio
C_z	[-]	lift coefficient
PV	[-]	principal value (of an integral)
FP	[-]	finite part (of an integral)
U_∞	[*m/s*]	velocity of the free stream
b	[*m*]	span
d	[*m*]	half chord
$c(y)$	[*m*]	chord distribution
$l(y)$	[*m*]	quarter chord equation
$w(y,t)$	[*m/s*]	induced velocity
$\alpha(y)$	[-]	geometric incidence distribution
$\Gamma_0(y,t)$	[*m²/s*]	two-dimensional steady circulation
$\Gamma(y,t)$	[*m²/s*]	circulation
$\underline{\gamma}(P,t)$	[*m/s*]	strength of the vortex distribution
$\Lambda(y)$	[-]	sweep angle
$\rho(y)$	[*m*]	radius of curvature

Subscripts and Superscripts

z, N	lift, normal
$\dot{f}$	derivative (of *f*)

1. INTRODUCTION

Helicopter generates a very complex wake geometry that still is a hard challenge for modern aerodynamicists. Besides, many industrial applications of aerodynamic calculations such as aero acoustics, aero elasticity or flight mechanics require fast flow modelling tools. This is why an unsteady lifting line method for curved and swept wings is developed in collaboration with ONERA in order to simulate the flow around a helicopter rotor. Many previous studies have been done on applying different lifting line methods to helicopter rotors. The first ones [2] extend Prandtl lifting line theory to helicopter by solving a quasi steady formulation of the problem, considering the flow field to be periodic in time. Then, Le Bouar [3] introduced unsteady effects by using a time-marching approach based on a rigorous matched asymptotic expansion valid for straight unswept lifting lines. A weak point of this work was the treatment of the Hadamard finite part integration that was done using a regularisation process instead of a rigorous calculus. Furthermore, this work is theoretically not valid for curved and/or swept wings. The aim of the work presented in this paper is then to overcome these geometric limitations and to treat the Hadamard finite part integrals properly.

This work is based on the matched asymptotic expansion in terms of the inverse of the aspect ratio made by Guermond and Sellier [1]. They exhibited two domains of influence: the near domain that will

here be modeled using the Theodorsen unsteady two-dimensional theory and the far domain in which the wing is assimilated to a lifting line shedding a wake that is considered as a vortex sheet and represented by a double layer distribution. The wake evolution is then calculated using a rigorous formulation established in the general framework of potential flows by Mudry [4].

The unknown of the problem which is the circulation around the wing is determinated using a time marching algorithm in which a Prandtl-like implicit equation is solved by an iterative process.

The last part of this paper is a validation of this approach using comparisons with a lifting surface method [5]. Results are shown for an incidence step movement and for a pitch ramp for swept as well as curved wings.

2. THE GENERAL LIFTING LINE THEORY

2.1. Physical problem

Consider a wing relatively to a cartesian coordinate system (O, x, y, z). This wing is defined by its span b and for all y in $[-b/2; b/2]$, its quarter chord line equation $l(y)$, its chord distribution $c(y)$ and its geometrical incidence $\alpha(y)$ (see Figure 1). From the quarter chord line equation, the local sweep angle and the local radius of curvature are defined by :

$$\Lambda(y) = \arctan l'(y) \text{ and } \rho(y) = \frac{\left(1 + l'(y)^2\right)^{3/2}}{l''(y)}$$

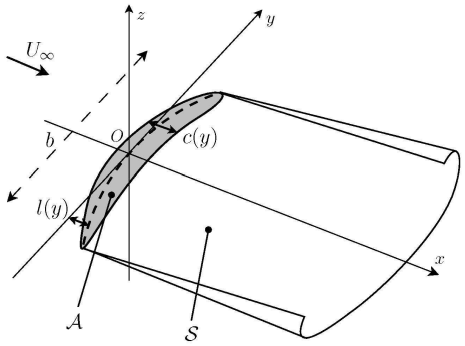

Figure 1. The wing and its wake

This wing is placed in a uniform flow so that the velocity of the free stream is given by $\underline{U} = U_\infty \underline{u_x}$ and its movement, due to heave and pitch motions, is supposed to have small amplitude and, in this paper, a wave length of the order of the span.

2.2.Hypothesis made and modelling

The flow is supposed to be incompressible and irrotational almost everywhere and the fluid inviscid. The wake is then a surface S, attached to the trailing edge of the wing. The velocity normal to S is continuous across this surface and the tangential velocity is discontinuous having a finite jump. Moreover, this surface is supposed to stay close to the (O, x, y) plan. The wing is supposed to be thin and the aspect ratio, defined here by $\mathrm{AR} = \frac{b}{c(0)}$, is supposed high. It is also supposed that the disturbances induced by the wing are small enough so that at every point of the domain the velocity is not very different from the free stream one. From the velocity U, the acceleration perturbation potential Ψ can be introduced (see [1]) so that the fluid mechanics equations lead to $\Delta\Psi = 0$ outside A and S. The boundary conditions are :

- tangential flow to the airfoil surface,
- undisturbed flow at infinity,
- Kutta Jukowsky condition at the trailing edge,
- continuous normal velocity across S.

This equation can be simplified by the use of Green theorem applied at every point M of the domain Ω to Ψ and to the Newton potential.

It leads to :

$$\Psi(M) = \frac{1}{4\pi} \iint_A [[\Psi]](P) \frac{\overline{PM}.\underline{n}}{PM^3} dS_P \qquad (1)$$

Introducing the acceleration perturbation potential allows the integral to be only on A. The intensity of the potential jump is calculated so that the tangency condition is satisfied. But, for field points M on the boundary, the right hand of (1) is a singular integral due to the presence of PM^3 in the denominator. It can be evaluated using the concept of finite part of an integral in the sense of Hadamard [6]. From this is derived the classical numerical panel method which solves a similar equation for the velocity perturbation potential.

2.3. The general lifting line theory

Prandtl and Van Dyke approaches

In the early twentieth century without any computer help, prediction of the flow field produced by a finite lifting wing was already one of the most attractive problems in aerodynamic. Prandtl developed the first rational attempt at predicting loads on subsonic, three dimensional wings [7]. This work was principally done on intuitive basis and still is now referred to as the Prandtl lifting line theory. The circulation is given by the integro-differential equation :

$$\Gamma(y) = \pi c(y) U_\infty \left(\alpha - \frac{1}{4\pi U_\infty} \mathrm{PV} \int_{-b/2}^{+b/2} \frac{\dot{\Gamma}(\eta)}{y - \eta} d\eta \right) \qquad (2)$$

The 2D term $\Gamma_0(y) = \pi c(y) U_\infty \alpha$ is modified by a three dimensional induced velocity term.

Later on, in the 1960's, Van Dyke justified this theory in the case of a straight and unswept wing operating in a non viscous, incompressible, irrotational and steady flow by the use of matched asymptotic expansions (M. A. E.) in terms of the inverse of the aspect ratio [8]. He found, at order $\varepsilon = \frac{1}{\mathrm{AR}}$ the same equation as the Prandtl integro-differential equation except that the $\Gamma(y)$ term is replaced by a $\Gamma_0(y)$ term on the right hand side of (2). Thus, the solution at order ε is an explicit function of the geometrical terms and of $\Gamma_0(y)$ (which is the solution at order 1) while Prandtl approach leads to an implicit equation of the same form.

Guermond and Sellier general approach :

The same M. A. E. approach was used by Guermond and Sellier to obtain a complete unsteady lifting theory for curved and swept wings [1]. In their linearized approach, for every point M of the lifting line they consider different influence domains (see figure 2) :

- The inner domain I is defined by the points whose distance to M is of order $c(0)$,
- The outer domain O is defined by the points whose distance to M is of order b,
- The domain O_{wi} is the part of O that is located downstream of I.

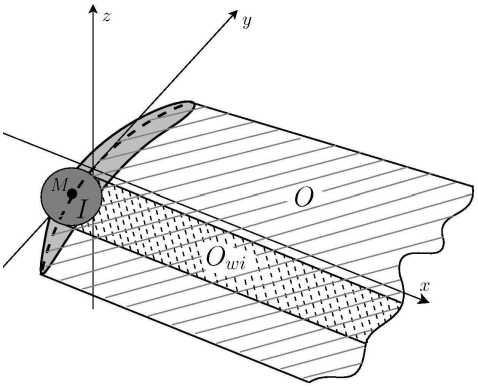

Figure 2. The influence domains

Thus, the matched asymptotic expansion in terms of the inverse of the aspect ratio $\varepsilon = \frac{1}{AR}$ leads at order ε to :

$$\Gamma(M,t) = \pi c \cos\Lambda \left(U_\infty \alpha + w_I(M,t) + w_O(M,t) + w_c(M,t) \right) \quad (3)$$

As in Prandtl equation, the two-dimensional steady or quasi-steady term $\Gamma_0(M,t) = \pi c U_\infty \cos\Lambda \, \alpha$ is corrected by three-dimensional and unsteady effects coming from the velocities induced by the inner domain $w_I(M,t)$ and the outer domain $w_O(M,t)$.

An additional $w_c(M,t)$ term appears in the matched asymptotic expansion computation. It can be written as :

$$w_c(M,t) = a_1 \Gamma_0(M,t) + a_2 \frac{\partial \Gamma_0(M,t)}{\partial y}$$

$$\text{where : } a_1 = \frac{1}{4\pi\rho}\left(1 - \tan^2\Lambda + K\right) \qquad a_2 = \frac{1}{2\pi}\left(K \sin\Lambda + \ln\left|\frac{1+\sin\Lambda}{\cos\Lambda}\right|\right) \quad (4)$$

$$\text{with } K = \frac{1}{2} + \ln\frac{c\cos^2\Lambda}{4\,\mathrm{AR}\,c(0)}$$

This term vanishes when the wing is straight and unswept ($\Lambda = \rho = 0$) so it is a term specific of curved and swept wings that is logically not present in Prandtl or Van Dyke theories.

Gallois and Devinant showed that, using an implicit Prandtl like approach i.e. replacing all $\Gamma_0(M,t)$ terms with $\Gamma(M,t)$ leads to results closer to lifting surface panel method results in the steady case [9]. The same Prandtl-like approach will then be used in this unsteady study as this approach also seems physically more intuitive. $w_I(M,t)$, $w_O(M,t)$ and $w_c(M,t)$ will then be computed using $\Gamma(M,t)$ instead of $\Gamma_0(M,t)$. Details are given in the next section.

3. THE MODEL:

3.1. The inner problem :

To compute the velocity induced by the inner domain $w_I(M,t)$, domains O_{wi} and I are grouped together so that a two-dimensional theory can be used for this calculus. The Theodorsen airfoil model [10] has been retained in the present work because it is a complete analytical model and also because it possible to extend it to the case of real fluids (i.e. with compressibility and viscous effects) by means of experimental 2D airfoil data (see [2] or [3]).

Let us consider a two-dimensional airfoil undergoing unsteady motion.

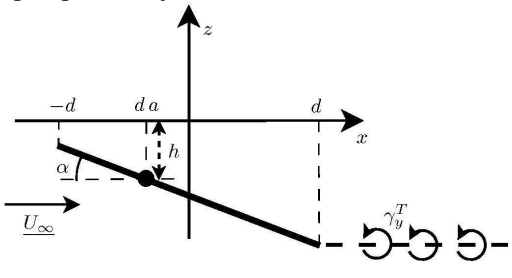

Figure 3. 2D airfoil characteristics

The flow is incompressible, irrotational and non-viscous so that the linearization theory can be applied and the solution for the thickness loads can be separated from the solution of the lifting problem (see [11]). Only the last one is taken into account here so that the airfoil is assimilated to a flat plate. Airfoil motion is then described by its heaving motion $h(t)$ and its pitch angle $\alpha(t)$ about an axis perpendicular to the (x,z) plane going through $x = d\,a$ and $z = -h$ where $d = c/2$ (see Figure 3).

Theodorsen introduces the upwash velocity of the three quarter chord point due to the movement of the airfoil that can be calculated by :

$$Q(t) = \dot{h}(t) + U_\infty \alpha(t) + d\left(1/2 - a\right)\dot{\alpha}(t) \qquad (5)$$

He then models the airfoil by a sources and sinks distribution to satisfy the boundary conditions completed by a vortices distribution to satisfy the Kutta Jukowsky condition and the wake is modelled by a counter vortices distribution γ_y^T to satisfy Kelvin's circulation conservation theorem. He uses conformal mapping to solve the problem on a circle and find that the circulation around the airfoil can be described by :

$$\Gamma_{2D}(t) = 2\pi d\, Q(t) + \int_d^{+\infty} \left(\sqrt{\frac{\xi + d}{\xi - d}} - 1 \right) \gamma_y^T(\xi, t)\, d\xi \qquad (6)$$

Then, by integrating the pressure distribution along the airfoil, lift can be written as :

$$C_z^{2D}(t) = C_z^Q(t) + C_z^{NC}(t) + C_z^w(t)$$

where:

$$\begin{aligned} C_z^Q(t) &= 2\pi \frac{Q(t)}{U_\infty} \\ C_z^{NC}(t) &= \frac{\pi d}{U_\infty^2} \frac{\partial}{\partial t}\left(Q(t) - \frac{1}{2} d\dot{\alpha}(t) \right) \\ C_z^w(t) &= \frac{1}{U_\infty} \int_d^{+\infty} \frac{1}{\sqrt{\xi^2 - d^2}}\, \gamma_y^T(\xi, t)\, d\xi \end{aligned} \qquad (7)$$

A similar decomposition can also be made for moments (see [3] for example). Theodorsen theory presented here was adapted to the case of an infinite swept wing (see [12] for more details). (6) becomes:

$$\Gamma_{2D}(t) = \pi c \cos\Lambda\; Q(t) + \int_d^{+\infty} \left(\sqrt{\frac{\xi + d}{\xi - d}} - 1 \right) \gamma_y^T(\xi, t)\, d\xi \qquad (8)$$

3.2. The outer problem :

In the outer problem, the characteristic scale is b and c is considered as small compared to b so that the wing degenerates into a lifting line placed for example, at the line of quarter chord. In the M. A. E. made by Guermond and Sellier, the velocity induced by the wake on a point M of the lifting line can be written as :

$$w_O(M,t) = \frac{1}{4\pi} \underline{z}.\mathrm{FP} \iint_S \Gamma(P,t) \underline{\nabla_M} \left(\underline{n}.\frac{\underline{r}}{r^3} \right) dS_P \qquad (9)$$

where $\underline{r} = \underline{PM}$ and $\underline{n}$ is the unit vector normal to S at P.

This can be physically interpreted as the velocity induced by a surface doublet distribution.

It can be shown (for example [11]) that this distribution is equivalent to a line and surface vortex distribution :

$$\begin{aligned} \iint_S \Gamma(P) \underline{\nabla_M} \left(\underline{n}. \right) \frac{\underline{r}}{r^3} dS_P = & \iint_S \frac{\underline{\gamma(P)} \wedge \underline{r}}{r^3} dS_P \\ & + \int_{\partial S} \Gamma(P) \frac{\underline{r} \wedge \underline{dl}}{r^3} \end{aligned} \qquad (10)$$

where $\underline{\gamma(P)} = \underline{n} \wedge \underline{\nabla_P}\left(\Gamma(P)\right)$ is the surface vortex strength.

In this study, the wake is supposed to be free and is calculated using a rigorous emission and convection formulation explained in [4] and summarized here.

The unsteady wake is considered as a vortex sheet S and characterised by :

- ω the median parameterisation which gives the geometric position of the vortex sheet (a tangential velocity discontinuity surface) by giving the position at instant t of the particle emitted at position q at instant τ :

$$\underline{\underline{\omega}}: \begin{cases} \mathbb{R}^3 \to \mathbb{R}^3 \\ (q, \tau, t) \mapsto (x_1, x_2, x_3) \end{cases}$$

- γ the associated median vortex density that gives the vortex sheet strength in the parameterisation coordinates :

$$\underline{\underline{\gamma}}: \begin{cases} \mathbb{R}^3 \to \mathbb{R}^2 \\ (q, \tau, t) \mapsto (\gamma^1, \gamma^2) \end{cases}$$

So that :

$$\underline{\gamma}(q,\tau,t) = \gamma^1 \frac{\partial \underline{\underline{\omega}}}{\partial q}(q,\tau,t) + \gamma^2 \frac{\partial \underline{\underline{\omega}}}{\partial \tau}(q,\tau,t) \qquad (11)$$

The velocity of the surface is then given at every point by :

$$\frac{\partial \underline{\underline{\omega}}}{\partial t}(q,\tau,t) = \frac{\underline{\underline{U}}^+ + \underline{\underline{U}}^-}{2} \qquad (12)$$

Where $\underline{\underline{U}}^+$ and $\underline{\underline{U}}^-$ are the fluid velocity on the upper and the lower surface.

A main interest of introducing this parameterisation is the time conservation of the two contravariant components γ^1 and γ^2 (see [4]) that can then be determined once for all at the emission of the particle.

$$\begin{aligned} \gamma^1(q,\tau,t) &= \frac{\partial \Gamma}{\partial q}(q,\tau) \\ \gamma^2(q,\tau,t) &= \frac{1}{U_\infty} \frac{\partial \Gamma}{\partial \tau}(q,\tau) \end{aligned} \qquad (13)$$

The velocity induced by the surface on a point P of this surface is then:

$$\underline{U}(P,t)=\frac{1}{4\pi}\iint_S \frac{\underline{\gamma(P',t)\wedge P'P}}{P'P^3}dS_{P'} + \frac{1}{4\pi}\int_L \Gamma(P',t)\frac{\underline{P'P\wedge dl_{P'}}}{P'P^3} \quad (14)$$

The position and the intensity of the vortex particles can then be computed by solving equation (12) together with (14), (13) and (11).

3.3 Final formulation :

The velocity induced by the O_{wi} domain called w_{Owi} is calculated twice : once in the Theodorsen theory and once in w_O, so, as explained in [1], it has to be removed once.

$$w_{Owi}(y,t)=\frac{1}{2\pi}\mathrm{FP}\int_0^{\infty}\frac{\gamma_y(\xi,y,t)}{\xi}d\xi \quad (15)$$

Thus the general equation for circulation distribution can be written :

$$\Gamma(y,t)=\pi c\cos\Lambda\left(Q+w_O(y,t)+w_c(y,t)\right) + \int_d^{+\infty}\left(\sqrt{\frac{\xi+d}{\xi-d}}-1\right)\gamma_y^T(\xi,t)\,d\xi - d\ \mathrm{FP}\int_0^{\infty}\frac{\gamma_y(\xi,y,t)}{\xi}d\xi \quad (16)$$

By defining a near and a far wake respectively, it can be shown (see [3]) that the far wake effect of the two-dimensional unsteady inner problem and the negative contribution of w_{Owi} cancel each other. The inner and outer domains are matched by saying that the two-dimensional term γ_y^T is equal to the corresponding term γ_y from the outer domain : at section *y* :

$$\gamma_y^T(\xi,t)=\gamma_y(\xi-d,y,t) \quad (17)$$

Using Le Bouar decomposition (see [3]), circulation can then be rewritten :

$$\Gamma(y,t)=\Gamma_{1/4}+d\Gamma+\Gamma_{2D\ inst}+\Gamma_{2D\ 3D}$$

where :

$$\Gamma_{1/4}(y,t)=\pi c\cos\Lambda\left(Q-d\dot{\alpha}+w_O+w_c\right)$$

$$d\Gamma(y,t)=\pi c\cos\Lambda\left(d\dot{\alpha}\right)$$

$$\Gamma_{2D\ inst}(y,t)=\int_d^{X+d}\left(\sqrt{\frac{\xi+d}{\xi-d}}-1\right)\gamma_y^T(\xi,t)\,d\xi \quad (18)$$

$$\Gamma_{2D\ 3D}(y,t)=-d\,\mathrm{FP}\int_0^{X}\frac{\gamma_y(\xi,y,t)}{\xi}d\xi$$

$\Gamma_{1/4}(y,t)$ can be interpreted as the circulation of a two-dimensional airfoil at a relative incidence of $\alpha_{tot}=\cos\Lambda\dfrac{Q-\dot{\alpha}+w_O+w_c}{U_\infty}$ at the quarter chord. This expression of $\Gamma_{1/4}(y,t)$ supposes a linear relation between lift and angle of attack. As in [2], rewriting :

$$\Gamma_{1/4}=bU_\infty C_z^t\left(\frac{Q-d\dot{\alpha}+w_O+w_c}{U_\infty}\cos\Lambda\right) \quad (19)$$

allows to replace this linear relation between C_z^t and the angle of attack with values issued from experimental 2D airfoil tables in order to include viscous and compressibility effects to the model :

3.4. Loads calculation :

A similar decomposition can be done for loads and moment. For the lift coefficient, it leads to :

$$C_z(y,t)=C_z^{QS}+dC_z+C_z^{NC}+C_z^{3D}$$

where :

$$C_z^{QS}(y,t)=C_z^t\left(\frac{Q-d\dot{\alpha}+w_O+w_c}{U_\infty}\cos\Lambda\right)$$

$$dC_z(y,t)=2\pi\left(\frac{d\dot{\alpha}}{U_\infty}\right)\cos\Lambda$$

$$C_z^{NC}(y,t)=\frac{\pi d}{U_\infty^2}\frac{\partial}{\partial t}\left(Q-\frac{1}{2}d\dot{\alpha}\right)\cos\Lambda \quad (20)$$

$$C_z^{3D}(y,t)=\frac{1}{U_\infty}\left(\int_d^{d+X}\frac{\gamma_y^T(\xi,t)}{\sqrt{\xi^2-d^2}}d\xi - \mathrm{FP}\int_0^{X}\frac{\gamma_y^T(\xi,y,t)}{\xi}d\xi\right)$$

3.5. Numerical implementation and algorithm:

The problem is solved using a time marching approach in which the time step δt is constant. The lifting line is divided in small curved lines for which the projection on axis Oy is constant and equal to δy. This introduces a wake discretisation in which for every panel $\Gamma(P,t)$ varies linearly that is to say that $\underline{\gamma}$ is constant on a panel. Thus at each time step, equation (17) is solved using an iterative process at every collocation points (called *M* on figure 4) that are placed in the middle of the curved lines. Then, the intensity of the wake that is emitted is calculated by deriving the circulation obtained and the wake is convected by moving the corners of the panels using equation (12).

For this study, considering a point of the lifting line, the near wake is the first panel so that $X=U_\infty\delta t$ and thus :

$$\Gamma_{2D\ 3D}(M,t)=-\frac{c}{2}\gamma_y(M,t)\ln\left(\frac{2U_\infty\delta t}{b}\right) \quad (21)$$

and

$$\Gamma_{2D\ inst}(M,t)=\frac{c}{2}\gamma_y(M,t)\times\left(\frac{2}{u^*+1}-\ln\left(\frac{u^*-1}{u^*+1}\right)\right) \quad (22)$$

where $u^*=\sqrt{1+\frac{c}{U_\infty\,\delta t}}$

The last term that presents some difficulties is the w_O term which has to be calculated as a finite part. In [3], Le Bouar avoided these difficulties by using a Gauss-type numerical integration.

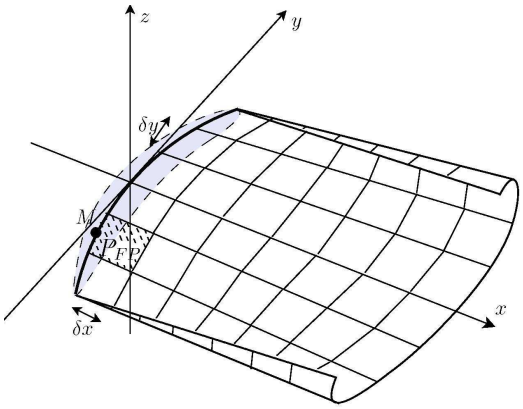

Figure 4. The discretisation and the singular panel

Once the wake is discretised (see figure 4), at a point M of the lifting line only the first panel P_{FP} is singular and needs a finite part calculation. Using the indications given in [1] and the fact that on the singular panel :

$$\Gamma(P,t)=\Gamma(M,t)+(x_P-x_M)\gamma_y(M,t)-(y_P-y_M)\gamma_x(M,t) \quad (23)$$

after some calculations it can be shown that :

$$w_O^{pf}(M,t)=\frac{1}{4\pi}\mathrm{FP}\iint_{P_{FP}}\frac{\Gamma(P,t)}{PM^3}\,dS_P=\frac{1}{4\pi}\left(-\Gamma(M,t)\rho(M)\ln\frac{\delta y}{b}+s_x(M)\gamma_y(M,t)-s_y(M)\gamma_x(M,t)-\frac{4\Gamma(M,t)}{\delta y}\right) \quad (24)$$

Where :

$$s_x(M)=2\cos\Lambda\,\ln\frac{\delta y}{b}-\int_{-\frac{\delta y}{2}}^{\frac{\delta y}{2}}\frac{ds}{\sqrt{\frac{s^2}{\cos^2\Lambda}+2\,\delta x\,s\tan\Lambda+\delta x^2}} \quad (25)$$

$$s_y(M)=2\sin\Lambda\,\ln\frac{\delta y}{b}-\int_{-\frac{\delta y}{2}}^{\frac{\delta y}{2}}\frac{s\tan\Lambda+\delta x}{s\sqrt{\frac{s^2}{\cos^2\Lambda}+2\,\delta x\,s\tan\Lambda+\delta x^2}}ds \quad (26)$$

Thus $w_o(M,t)=w_o^{FP}(M,t)+w_o^{reg}(M,t)$ (27)

Where

$$w_o^{reg}(M,t)=\frac{1}{4\pi}\left(\iint_{S-P_{FP}}\frac{\underline{\gamma(P,t)}\wedge\underline{r}}{r^3}dS_P+\int_{\partial(S-P_{FP})}\Gamma(P,t)\frac{\underline{r}\wedge\underline{dl}}{r^3}\right).\underline{z} \quad (28)$$

As the circulation is continuous on the wake, the vortex line term of a panel cancels each other with the vortex line term of its neighbour (except when the neighbour panel is the singular one). Thus, only the vortex line terms of the edges of the wake need to be computed. $w_o^{reg}(M,t)$ is then calculated using numerical integration as in [3].

Finally, the velocity induced by the wake is :

$$w_O(M,t)=\frac{1}{4\pi}\left(-\Gamma(M,t)\rho(M)\ln\frac{\delta y}{b}+s_x(M)\gamma_y(M,t)-s_y(M)\gamma_x(M,t)-\frac{4\Gamma(M,t)}{\delta y}+\int_{\partial S-\partial P_{FP}}\Gamma(P,t)\frac{\underline{r}\wedge\underline{dl}}{r^3}.\underline{z}+\iint_{S-P_{FP}}\frac{\underline{\gamma(P,t)}\wedge\underline{r}}{r^3}dS_P.\underline{z}\right) \quad (29)$$

4. RESULTS AND COMPARISONS

The lifting line model derives from the lifting surface one and is valid for high aspect ratio wings. Results are then compared with results obtained with a lifting surface computation on various wings of high aspect ratio (AR=10).

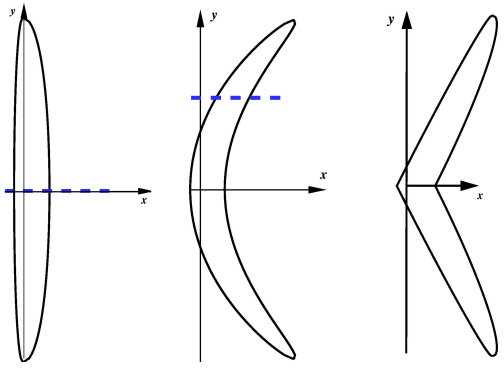

Figure 5. The wings tested (straight, curved and swept)

The first results concern a straight wing with an elliptic chord distribution ($c(y)=c_0\sqrt{1-y^2}$) (see figure 5) for a sinusoidal pitch ramp :

$$\alpha(t) = \alpha_{\max}\left(1-\cos\frac{\pi t}{t_0}\right) \quad \text{for } t \le t_0$$
$$\alpha(t) = \alpha_{\max} \quad \text{for } t \ge t_0 \qquad (30)$$

For this computation, $c_0 = 0.2$ m and $b = 2$ m so that $\mathrm{AR} = 10$, $U_\infty = 1\,\mathrm{m/s}$, $\alpha_{\max} = 10°$ and $t_0 = 0.6\,\mathrm{s}$. All the following results consider a non dimensional time $\tilde{t} = \frac{U_\infty}{c_0}t$ and are obtained with discretisation assuring spatial and temporal convergency. Computation was here done using a discretisation of 40 points on the lifting line and a time step of 0.05 s and it took just a few minutes on a personal computer. Figure 6 shows the evolution of the non dimensional circulation $\Gamma(y)/\Gamma_0(0)$ and the evolution of the lift coefficient (or the normal coefficient for the VLM) on the middle section of the wing. It shows good agreement with the VLM results and improvement compared to results obtained by Le Bouar. These improvements come from the better numerical treatment of the finite-part integrals.

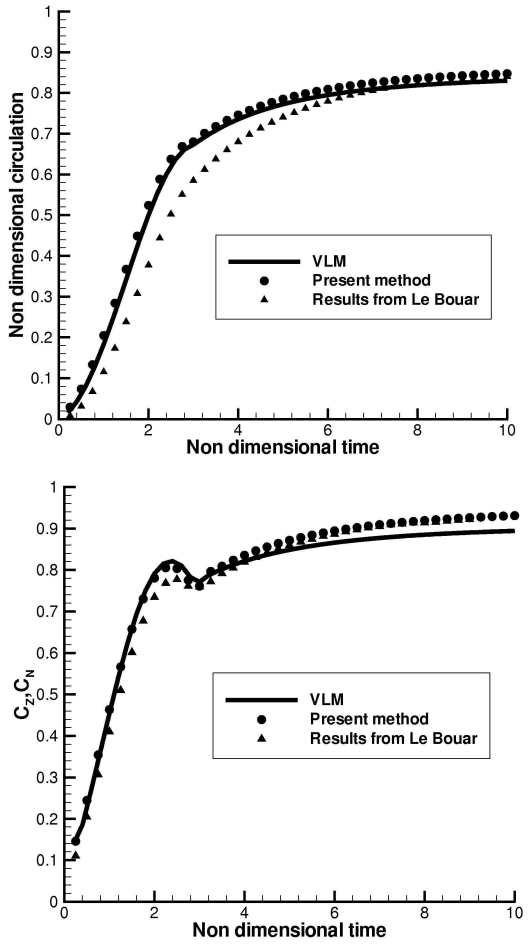

Figure 6. Circulation and lift evolution for a straight wing

Circulation distribution for this elliptic wing after 20 chords is also very close to the classical results in the steady case obtained with the Glauert-Carafoli analytical solution. The wake shed during the pitch ramp is shown in figure 7. It presents smooth rolling up of the tip vortices.

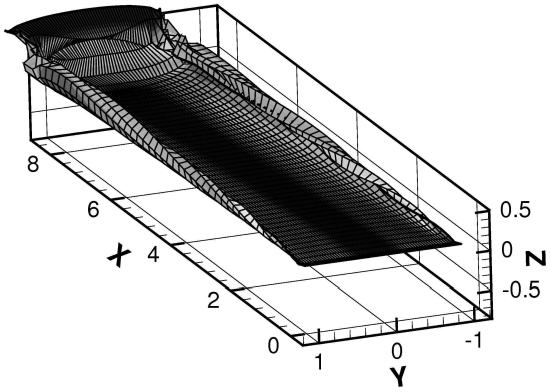

Figure 7. The wake distortion

To validate this approach for more critical cases, a computation is done for a more curved and swept wing and for an incidence step of 10°. The quarter chord equation is given by $l(y) = 0.5\,y^2$ (see figure 5). Circulation evolution at $y = 0.5\,\mathrm{m}$ still is in good agreement with the lifting surface results.

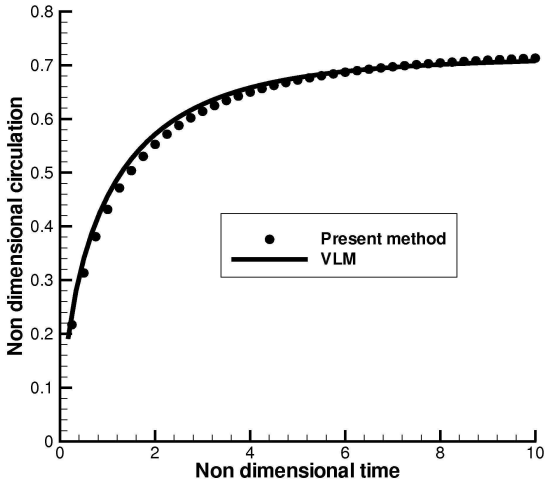

Figure 8. Circulation evolution for a curved wing

Finally, a computation is done for the swept wing presented in figure 5. This wing is out of the frame of the theory as curvature tends to 0 at the apex of the wing. This problem is overcome by regularising the apex on a region that represents here 15% of the total span. Figure 9 shows the non dimensional circulation distribution for $t = 4\,\mathrm{s}$ after a pitch ramp of t_0 = 0.6 s.

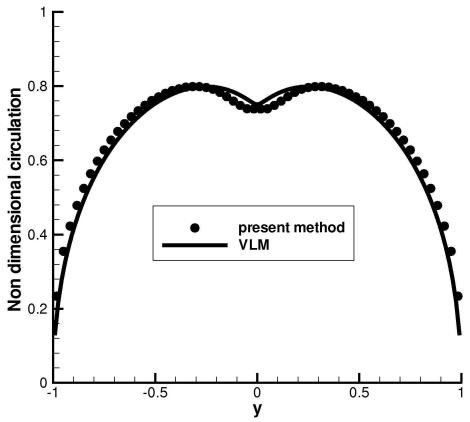

Figure 9. Circulation distribution for a swept wing

5. CONCLUSIONS AND PERSPECTIVES

An unsteady lifting line approach for computing curved and swept wings was described. This work derives from the matched asymptotic expansion done by Guermond and Sellier and also includes a rigorous free wake model.

Comparisons of our approach with lifting surface results show very good agreements for different curved wings even for highly unsteady motions.

Furthermore, the advantage of our approach is that it is much faster than CDF computations and compared with lifting surface method, it also offers the possibility to take into account real fluid effects such as compressibility or viscous effects. This is now being incorporated in a helicopter rotor simulation tool that is used, for instance, to perform aero acoustic or flight mechanics computations and that was based on the previous study done by Le Bouar [3].

ACKNOWLEDGEMENTS

This work has been supported by O.N.E.R.A. and the French Centre regional authorities. The authors also wish to express their sincere thanks to M. Costes and F Breme for their judicious comments on this manuscript.

REFERENCES

[1] Guermond, J.L. and Sellier, A. 1991 “A unified unsteady lifting-line theory”, *J. Fluid. Mech.* 229, 427-451.

[2] Michéa, B., Desopper, A. and Costes, M., 1992, “Aerodynamics rotor loads prediction method with free wake for low speed descent flight”, *18th European Rotorcraft Forum.*

[3] Le Bouar, G., Costes, M., Leroy-Chesneau, A. and Devinant, P., 2004, “Numerical simulations of unsteady aerodynamics of helicopter rotor in manoeuvring flight conditions”, *Aerospace Science and Technology*, 8 :11–25.

[4] Mudry, M., 1982, “La théorie générale des nappes et filaments tourbillonnaires et ses application à l’aérodynamique instationnaire”, *PhD thesis, Université Paris 6*.

[5] Leroy, A., Devinant, P; 1999, “A general approach for computing 3D unsteady lifting and/or propulsive systems derived from a complete theory”, *International Journal for Numerical Methods in Fluids*, 29, 75–95.

[6] Hadamard, J., 1932, *Le problème de Cauchy et les équations aux dérivées partielles linéaires hyperboliques.*

[7] Prandtl, L., 1920, “Applications of modern hydrodynamics to Aeronautics”, *NACA Tech. Notes* 9.

[8] Van Dyke, M., 1964, *Perturbation methods in fluid mechanics.* Academic Press, New York.

[9] Devinant, P. and Gallois, T., 2002, “Swept and curved wings : a numerical approach based on generalized lifting-line theory”, *Comp. Mech*. 29, 322-331.

[10] Theodorsen, T., 1945, “General theory of aerodynamic instability and the mechanism of flutter”, *NASA Tech. Report 496*.

[11] Ashley, H., Landhal, L., 1965, *Aerodynamics of wings and bodies.* Addison-Wesley.

[12] Muller, S., 2006, “Développement d’une méthode de ligne portante courbe et instationnaire pour l’étude de l’aérodynamique du rotor d’hélicoptère”, PhD Thesis, Université d’Orléans.

Conference on Modelling Fluid Flow (CMFF'06)
The 13th International Conference on Fluid Flow Technologies
Budapest, Hungary, September 6-9, 2006

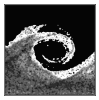

NUMERICAL SOLUTION OF TRANSONIC FLOWS OVER AN AIRFOIL AND A WING

P. Furmánek[1], J. Dobeš[2], J. Fořt[3], J. Fürst[4], M. Kladrubský[5], K. Kozel[6]

[1] Corresponding Author. Department of Technical Mathematics, Czech Technical University in Prague. Karlovo náměstí 13, Praha 2 – Nové Město, 121 35, Tel.: +420 2 2435 7447, E-mail: Petr.Furmanek@fs.cvut.cz
[2] Department of Technical Mathematics, Czech Technical University in Prague. E-mail: Jiri.Dobes@fs.cvut.cz
[3] Department of Technical Mathematics, Czech Technical University in Prague. E-mail: Jaroslav.Fort@fs.cvut.cz
[4] Department of Technical Mathematics, Czech Technical University in Prague. E-mail: Jiri.Furst@fs.cvut.cz
[5] Aeronautical Research and Test Institute in Prague Letňany, E-mail: kladrubsky@vzlu.cz
[6] Department of Technical Mathematics, Czech Technical University in Prague. E-mail: kozelk@fsik.cvut.cz

ABSTRACT

This work deals with numerical solution of transonic flow past a 2D profile (steady viscous turbulent flow) and a 3D swept wing (steady inviscid flow). In this work we use several types of finite volume schemes. Firstly explicit schemes based on Lax-Wendroff type schemes in the cell-centered (MacCormack) and cell-vertex (Ron-Ho-Ni) form are used. For 2D steady and turbulent flows over RAE 2822 authors used implicit scheme based on modern ENO and ROE schemes. For all computational results authors used solver developed at our department and in Aeronautical Research and Test Institute in Prague Letňany during long term research work in this field.

Keywords: cell-centered scheme, cell-vertex scheme, Euler equations, RANS, transonic flows, turbulence modelling

NOMENCLATURE

F		inviscid physical flux vector in x direction
G		inviscid physical flux vector in y direction
Pr	[-]	Prandtl number
R		viscous physical flux vector in x direction
S		viscous physical flux vector in y direction
T	[-]	non-dimensional temperature
W		vector of conservative variable
c_p	[-]	static pressure coefficient
c_V	[-]	static volume coefficient
e	[-]	total energy per unit volume
k	[-]	heat conductivity coefficient
p	[Pa]	static pressure
u	[m/s]	x component of velocity vector
v	[m/s]	y component of velocity vector
w	[m/s]	z component of velocity vector
η	[-]	dynamical viscosity
κ	[-]	constant
ρ	[kg/m^3]	density
τ	[-]	viscosity tensor

Subscripts and Superscripts

t, x, y, z	partial derivative with respect to spatial coordinate and time
1	inlet conditions

1. INTRODUCTION

A mathematical model of viscous turbulent flow is represented by a system of Navier-Stokes equations. Several types of schemes (ENO/WENO, Roe, MacCormack, Ron-Ho-Ni) are used for numerical solution of steady flows around RAE 2822 profile (2D) and over a wing (modified NACA profile, L-AS28).

2. MATHEMATICAL MODEL

To describe compressible viscous flow over a profile the system of the Navier-Stokes equations is used.

$$W_t + F_x + G_y = R_x + S_y, \tag{1}$$

where

$$W = \begin{pmatrix} \rho \\ \rho u \\ \rho v \\ e \end{pmatrix}, \; F = \begin{pmatrix} \rho u \\ \rho u^2 + p \\ \rho uv \\ (e+p)u \end{pmatrix}, G = \begin{pmatrix} \rho u \\ \rho uv \\ \rho v^2 + p \\ (e+p)v \end{pmatrix}$$

and

$$R = \begin{pmatrix} 0 \\ \tau_{xx} \\ \tau_{xy} \\ u\tau_{xx} + v\tau_{xy} + kT_x \end{pmatrix}, S = . \begin{pmatrix} 0 \\ \tau_{xy} \\ \tau_{yy} \\ v\tau_{yy} + u\tau_{xy} + kT_y \end{pmatrix},$$

while

$$\tau_{xx} = \frac{2}{3}(2u_x - v_y), \; \tau_{xy} = (u_x - v_y),$$

$$\tau_{yy} = \frac{2}{3}(-u_x + 2v_y).$$

To solve this system, also the following relation has to be added

$$p = (\kappa - 1)[e - \frac{1}{2}\rho(u^2 + v^2)], \; \kappa = \frac{c_p}{c_v}.$$

For the computation of the heat flux could be used

$$kT_x = \frac{\eta}{\Pr}\frac{\kappa}{\kappa - 1}\left(\frac{p}{\rho}\right)_x, \; kT_y = \frac{\eta}{\Pr}\frac{\kappa}{\kappa - 1}\left(\frac{p}{\rho}\right)_y.$$

For turbulent flows RANS computation (Reynolds Average Navier-Stokes Equation) are used [8]. In two dimensional inviscid case the viscous fluxes in (1) are neglected and the system of Euler equations is has the form

$$W_t + F_x + G_y = 0. \qquad (2)$$

For 3D inviscid computation the system (2) is simply extended into three dimensions, then the velocity vector will have three components (*u, v, w*) and we will get the system of Euler equation as follow:

$$W_t + F_x + G_y + H_z = 0. \qquad (3)$$

3. NUMERICAL SOLUTION

3.1. Grid generation

Authors have used several types of finite volumes grids. For 2D case of flow over RAE 2822 C-type grid refined near the profile was used. Similarly for 3D transonic flows over a swept wing L-AS28 an extended 2D C-type mesh was used. For 3D swept wing with modified 2D NACA 0012 profile H-type finite volumes mesh was used see Figure 1.

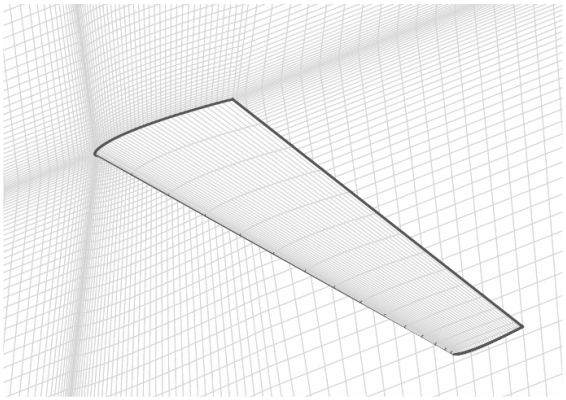

Figure 1. H-mesh for 3D computation of steady inviscid flow over a swept wing (modified NACA 0012).

3.2. Numerical schemes

Several types of finite volume schemes were used.

3.2.1 2D viscous steady turbulent flow over a Rae 2822 profile

For viscous steady turbulent flow over RAE 2822 profile two independently developed methods based on the finite volume method (FVM) with piecewise linear reconstruction of solution with the second order of accuracy were developed. The first was an ENO/WENO scheme (implicit, solved by GMRES with ILU preconditioning). In this case the least square reconstruction (WSLSQR – see [1]) was used. Numerical fluxes were computed by AUSMPW+ method [2] and as a turbulence model the Kok TNT model mentioned in [3] was used.

In the second case authors have used the ROE method with Barth limiter [4] and Menter SST turbulence model [5] . Both methods use for time integration first order implicit scheme which is suitable for stationary problems. For results see the Figures No. 2 – No. 9.

3.2.2. 3D inviscid steady flow around a swept wing with modified NACA 0012 profile

For computation an extension of 2D predictor-corrector MacCormack scheme [6] into three

dimensions with 2nd order Jameson artificial dissipation was used.

3.2.3 3D inviscid steady flow around a swept wing L-AS28

The second case of 3D flow that was considered is flow around the L-AS28 wing (used in the Czech advanced light combat aircraft L-159). For the computation the simple configuration of wing fixed in a wall has been used (as in the previous case). The used method is based on cell-vertex Ron-Ho-Ni scheme and described completely in [7]. Obtained results are compared to the experimental data of Research and Test Aeronautical Institute in Prague Letňany. Differences between the numerical solution and experimental results are above all in the intensity of the shock wave (Figures No. 14 – No. 17).

3. SOME NUMERICAL RESULTS

3.1. 2D model, RAE 2822

Flow over RAE 2822 was computed for two regimes: subsonic (M_1 = 0.604, α_1 = 2.12°) and transonic (M_1 = 0.729, α_1 = 2.31°). Fig. 2 – Fig. 9 show isolines of Mach number and distribution of c_p and c_f compared with experimental results for both cases. It is possible to see that both numerical results using different schemes and also turbulent models achieved practically the same results and comparison with experiment seems to be also satisfactory.

3.1.1. Subsonic regime, M_1 = 0.604, α_1 = 2.12°

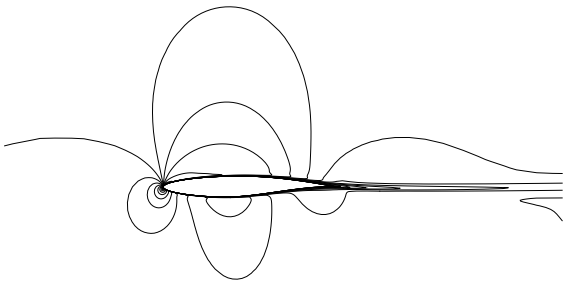

Figure 2. Isolines of Mach number, RAE 2822, ΔM = 0.05, Roe scheme, SST model.

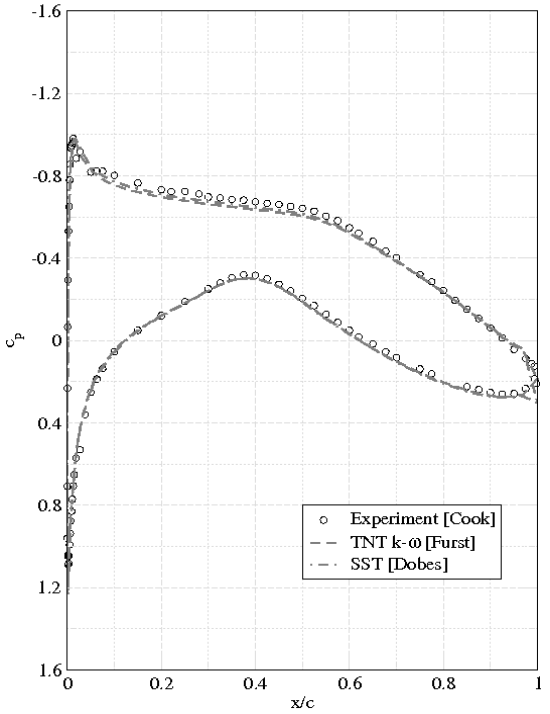

Figure 3. Behaviour of c_p on the upper and lower side of the profile.

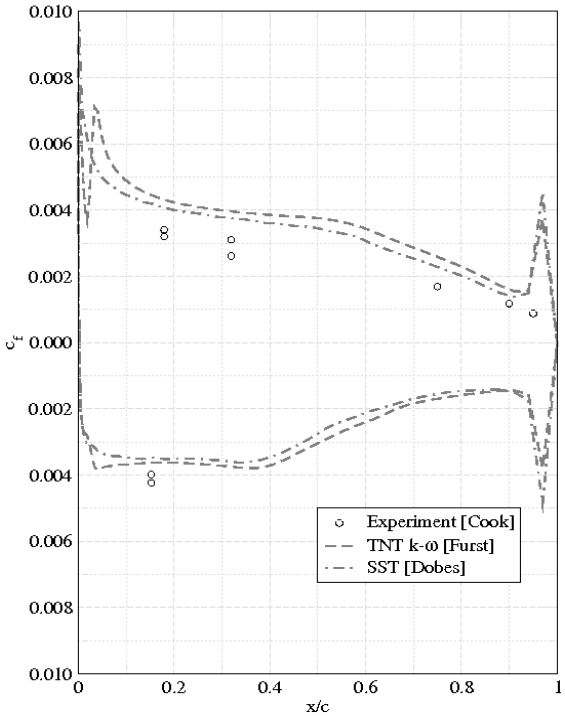

Figure 4. Behaviour of c_p on the upper and lower side of the profile.

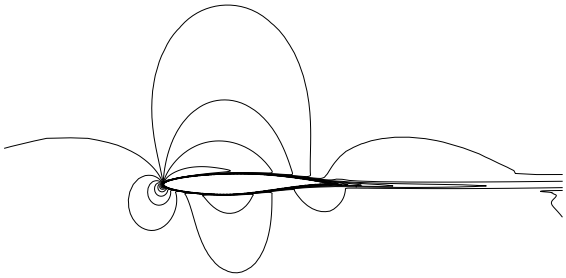

Figure 5. Isolines of Mach number, RAE 2822, ΔM = 0.05, WLSQR scheme, TNT k-ω model.

3.1.2. Transonic regime, M_1 = 0.729, α_1 = 2.31°

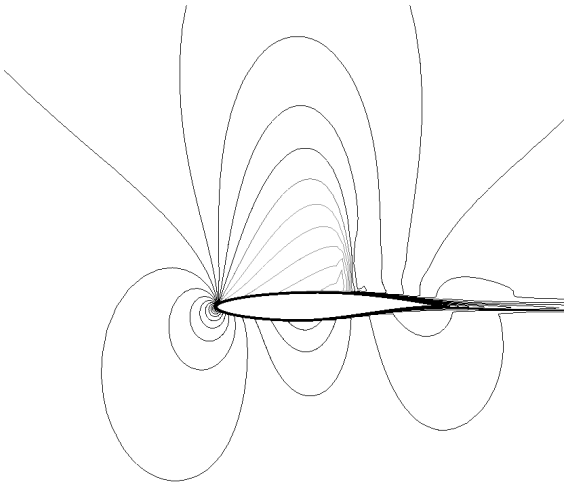

Figure 6. Isolines of Mach number, RAE 2822, ΔM = 0.05, WLSQR scheme, TNT k-ω model.

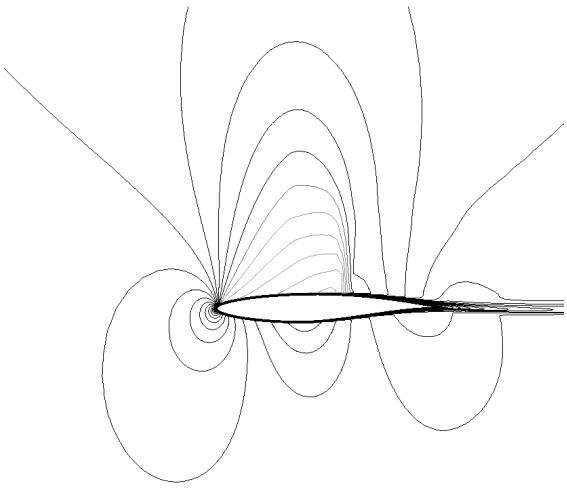

Figure 7. Isolines of Mach number, RAE 2822, ΔM = 0.05, Roe scheme, SST model.

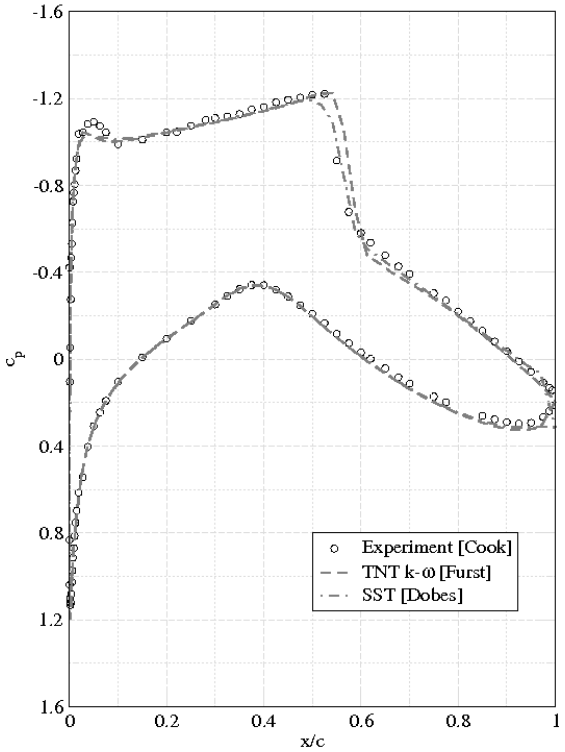

Figure 8. Behaviour of c_p on the upper and lower side of the profile.

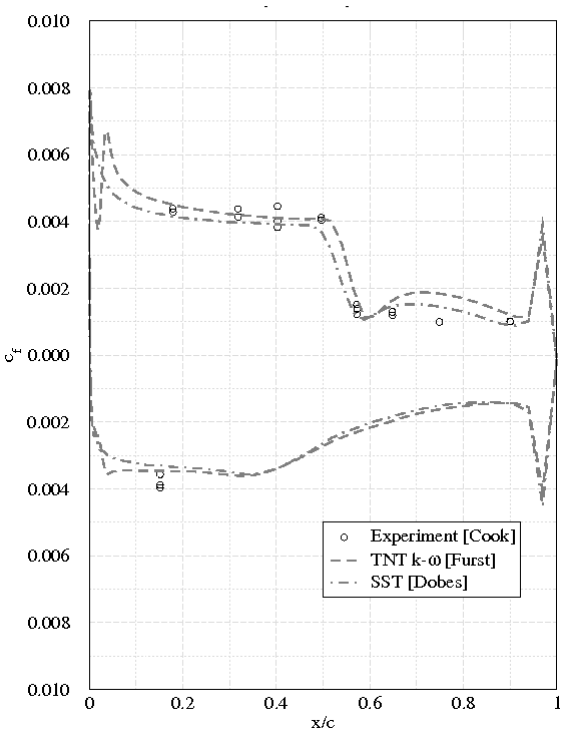

Figure 9. Behaviour of c_p on the upper and lower side of the profile.

3.2. 3D model, modified NACA 0012.

In this case authors show first numerical results of flow over 3D wing developed by extension of 2D NACA 0012 profile. Two cases of the same M_1 =

0.85 and different angles of attack are considered and computed. Results are presented in form of the isolines of Mach number on the wing and the wall and its behaviour on the upper and lower side of the wing in four cuts for z = *const.* (Figures No. 10 – No. 13).

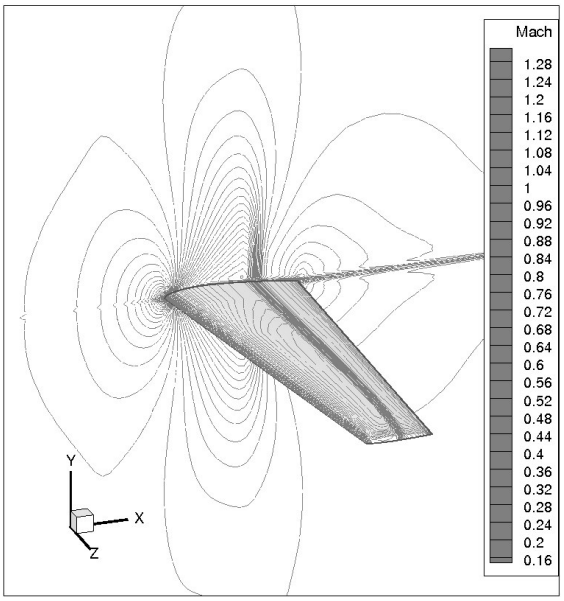

Figure 10. Isolines of Mach number, $M_1 = 0.85$, $\alpha_1 = 0°$.

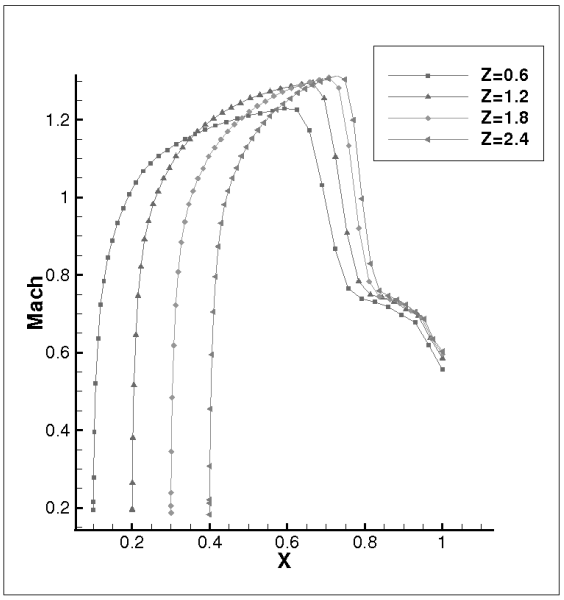

Figure 11. Behaviour of Mach number on the profile $M_1 = 0.85$, $\alpha_1 = 0°$.

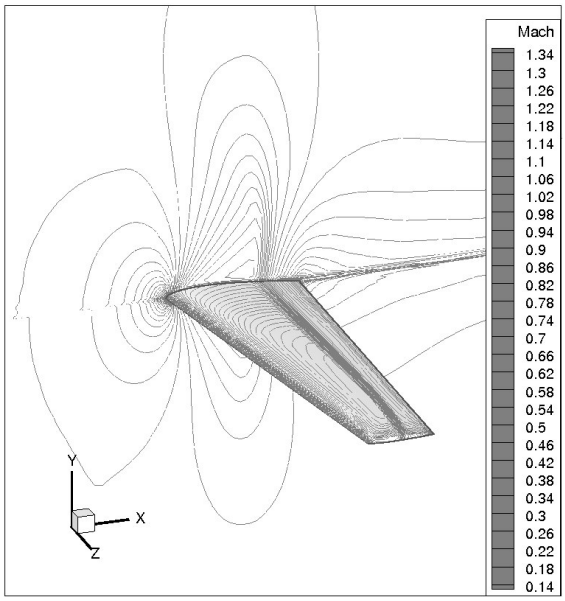

Figure 12. Isolines of Mach number, $M_1 = 0.85$, $\alpha_1 = 1.25°$.

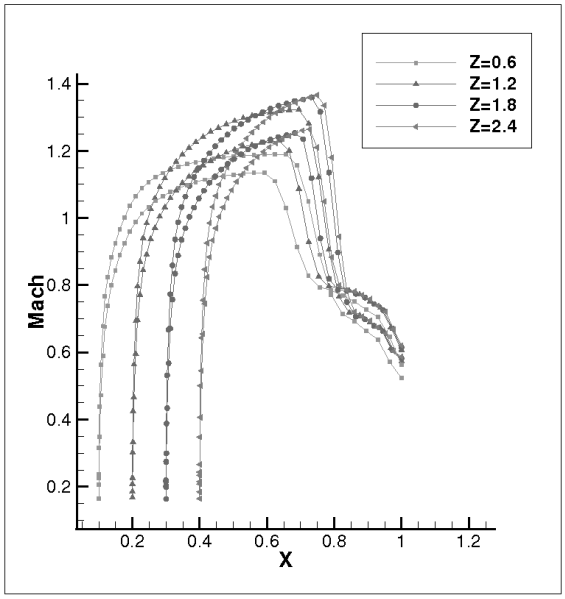

Figure 13. Behaviour of Mach number on the upper and lower side of the profile $M_1 = 0.85$, $\alpha_1 = 1.25°$.

3.3. 3D model, L-AS28 wing.

The last case considers 3D wing (L-AS28) of Czech production. Here numerical results of inviscid model are compared with experimental results (distribution of c_p) of Research and Test Aeronautical Institute in Prague Letňany.

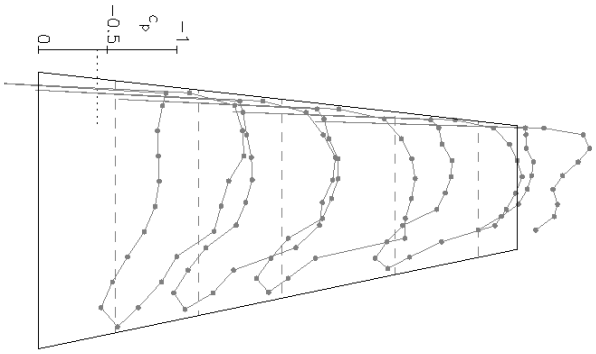

Figure 14. Behaviour of c_p on the wing, $M_1 = 0.8$, $\alpha_1 = 2°$, experimental result.

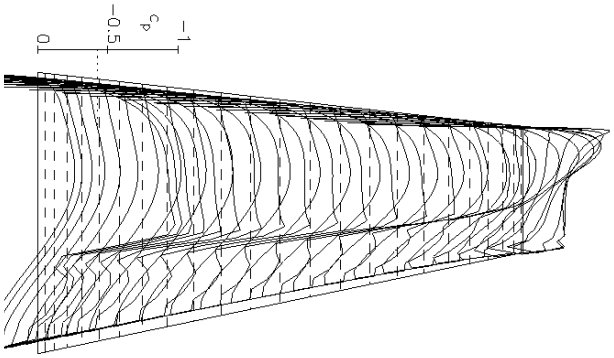

Figure 15. Behaviour of c_p on the wing, $M_1 = 0.8$, $\alpha_1 = 2°$, numerical result.

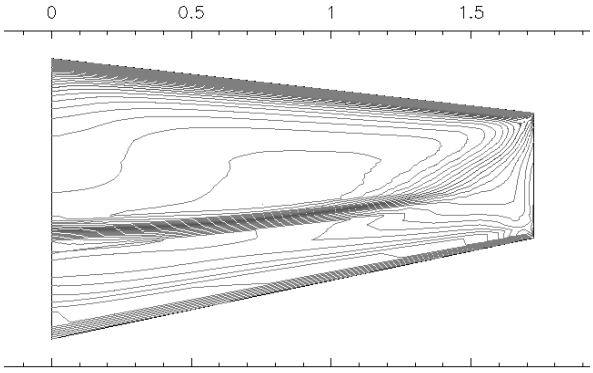

Figure 16. Numerical result – isobars on the wing, $M_1 = 0.8$, $\alpha_1 = 2°$.

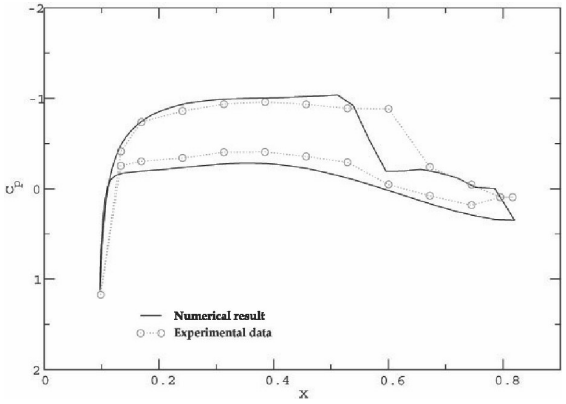

Figure 17. Comparison of c_p in the central cut, $M_1 = 0.8$, $\alpha_1 = 2°$, experimental result.

4. CONCLUSIONS

The numerical methods for solving following problems were developed:

a) 2D steady viscous turbulent flow. In this case, two different implicit schemes were used and compared.
b) A simple test case of 3D steady inviscid flow (swept wing with modified NACA 0012 profile fixed in the wall). In order to obtain first results an explicit 2nd order scheme with added artificial viscosity was used.
c) 3D steady inviscid flow around a real wing L-AS28 solved by a cell-vertex Ron-Ho-Ni FVM scheme and compared to experimental data.

In future the work will continue with implementation of an implicit schemes suitable for solving 3D viscous turbulent flows (in case of current 3D inviscid schemes) and extension of mentioned methods to nonstationary problems.

ACKNOWLEDGEMENTS

This work has partly been supported by the Research Plan of the Ministry of Education of the Czech Republic No. 6840770010 and grant GACR 201/05/0005.

REFERENCES

[1] Fürst, J., A finite volume scheme with weighted least square reconstruction. In S. Raghay, F. Benkhauldoun, D. Ouazar, edito, *Finite Volumes for Complex Applications IV*, pages 345-354. Hermes Science, 2005. ISBN 1-905209-48-7

[2] Kyu Hong Kim, Chongam Kim, Oh-Hyun Rho. Methods for the accurate computations of hypersonic flows I. AUSMPW+ scheme.

Journal of Computational Physics, (174):38-80. 2001.

[3] Kok, J. C. Resolving the dependence onfree stream values for the k-omega turbulence model. Technical Report NLR-TP-99295, NLR, 1999.

[4] Dobeš, J., Fořt, J., Halama, J., Numerical solution of single and Multiplephase internal transonic flow probléme. *International Journal for Numerical Methods in Fluids,* (48):91-97, 2005.

[5] Dobeš, J., Fořt, J., Fürst, J., Kladrubský, M., Kozel, K., Louda, P.. Numerical Solution of Transonical Flow around a Profile and a Wing. Research report V-1814/04, VZLU a.s. 2004

[6] Furmánek, P., Numerical Solution of Transonical Flow around an Isolated Profile, diploma thesis, CTU in Prague, FNSPE, 2004.

[7] Pelant J., Kyncl M., Kladrubský M., *Project of CFD methods for the three-dimensional inviscid compressible flow around wings and cascades.* Research report V-1728/01, VZLU a.s. 2001.

[8] Dobeš, J., Fořt, J., Fürst J., Furmánek P., Kladrubský, M., Kozel, K., Louda, P.. Numerical Solution of Transonical Flow around a Profile and a Wing II. Research report V-1850/05, VZLU a.s. 2005

Conference on Modelling Fluid Flow (CMFF'06)
The 13th International Conference on Fluid Flow Technologies
Budapest, Hungary, September 6-9, 2006

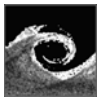

DEVELOPMENT OF NEW A HANG-GLIDER WING CONCEPT USING CFD

Péter PANDAZIS[2], Tamás GAUSZ[3], Attila KISS[4], György PAÁL[1]

[1] Corresponding author, Department of Hydrodynamic Systems, Budapest University of Technology and Economics, P.O. Box 91, 1521 Budapest, HUNGARY, Tel.: +36 1 463 2991, Fax: +36 1 463 3091, E-mail: paal@vizgep.bme.hu
[2] Siemens Power Generation , Budapest, peter.pandazis@siemens.com
[3] Department of Aircraft and Ships, Budapest University of Technology and Economics, gausz@rht.bme.hu
[4] Final year student, Budapest University of Technology and Economics, attila-kiss@freemail.hu

ABSTRACT

Hang-gliders are ultralight gliding planes used for leisure purposes. They can be with or without engine but its wing is similar in both cases. The wing has the following characteristics: delta-wing, S-profile, and its shape changes flexibly and elastically under wind load. In this paper as a first step the flow around two commercial hang-glider wings is simulated, and a very good agreement with experimental results is obtained. Several well-known features of the flow are reproduced. The flight characteristics experienced by pilots are also reflected in the CFD results. As a second step a new concept is proposed. Based upon the observation that large predator birds use separately standing strong feathers at the trailing edge of the wing during gliding (probably to save energy) a so-called wing-grid theory has been developed. This theory has been already successfully tried in small conventional airplanes and the tests resulted in a significant fuel saving. Here a commercial wing geometry has been modified by replacing the last fifth of the wing by "feathers" – small winglets attached to the rest of the wing body. The purpose of the modifications is to get a better glide ratio while keeping the other flight parameters constant. The geometrical characteristics of the winglets have been systematically varied and the optimum searched for. The improvement in the glide ratio compared with the original wing seems to be encouraging.

Keywords : Hang-glider, wing, wing-grid.

NOMENCLATURE

c	[-]	force coefficient
F	[N]	force
H	[-]	averaged quadratic error
l	[mm]	chord length of the feathers
N	[-]	number of the data points
r	[mm]	slit size between feathers
v	[m/s]	relative velocity
y^+	[-]	wall coordinate
γ_i	[-]	setting angles of the feathers
ε	[-]	glide ratio
ρ	[kg/m^3]	air density

Subscripts and Superscripts

calc	data from the CFD simulations
L, D	lift, drag
measured	data from the measurements
min, max	

1. INTRODUCTION

Hang-gliding is one of the most popular aviation sports. There are hang-gliders with or without engine but their wings are similar in both cases.

The hang-glider has several specific features as opposed to traditional aircraft:

- steering by centre of gravity control;
- delta-wing;
- the wing shape changes flexibly and elastically under wind load;

Since there is no control surface and stabilizer in the hang-glider, the wing is swept and has an S-profile. For these reasons, the detailed measurement and calculation of its aerodynamic characteristics is very difficult [1]. Wind tunnel experiments are prohibitively expensive, because the span of a typical hang-glider is 10 *m* or more. Building a physical model which reproduces the flexible and elastic features as well is great challenge.

Another experimental method is to measure with a special measuring car [2]. This method has been standardized by the DHV (Deutscher Hänge-gleiterverband) for the international certification of hang-gliders.

Nowadays, there is no easy, cheap, and sufficiently reliable method to characterize a hang-glider wing. In these days, just as in the heroic age

of hang-gliding, the designers rely mainly on test-pilots' reports during the development process.

The fast improvement of computer capacity, as well as of the numerical solving algorithms of the 3-dimensional Navier-Stokes equations has opened the door to an alternative approach of the wing development. Although the coupled elasticity-fluid mechanics problem is at the moment still too complicated [3, 4, 5], by ignoring the flexible and elastic changes, assuming a rigid wing and solving only the flow equations provides also valuable insights into the aerodynamic behaviour of the wings. To this end, commercial "Computational Fluid Dynamics" (CFD) software was used to check the influence of certain geometrical changes. In this paper two existing hang-glider types have been investigated and on the basis of the second a new concept was tried.

2. CFD MODELLING OF A HANG-GLIDER

2.1 The modelled hang-glider types

The first modelled type is called *Magic III* (Figure 1.). Although it was developed in 1984 it is still in use and its flying parameters are perfectly all right.

The basic parameters of *Magic III* are:

- wing span: 10.7 *m*
- wing area: 16 m^2
- sweep angle: 30°
- v_{min}: 25 *km/h*
- v_{max}: 80 *km/h*

Figure 1. Photo of the *Magic III*

The second modelled wing geometry is called *Süsü II* (Figure 2.). This is a new hang-glider type with a small engine. It was developed by the Danubian Aircraft Company Hungary in 1996 but it is not yet in serial production, only one prototype exists. The design philosophy of Süsü II. was to create a wing with a higher glide ratio at the price of a more complicated structure and larger instability.

The basic parameters of *Süsü II*:

- Wing span: 10.4 *m*
- Wing area: 16.5 m^2
- Sweep angle: 34°
- v_{min}: 35 *km/h*
- v_{max}: 135 *km/h*

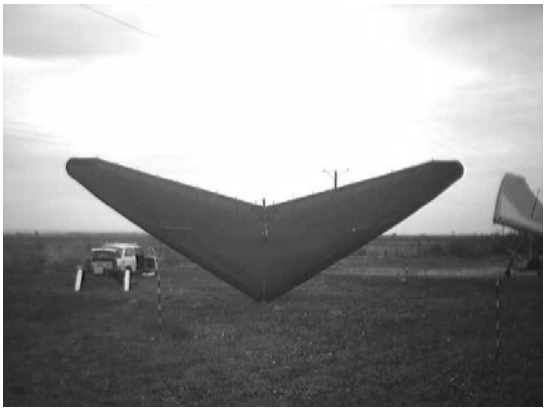

Figure 2. Photo of the *Süsü II*

2.2 Model building

2.2.1 The geometrical model

The geometrical model and the mesh was prepared with the software ANSYS ICEM 4.8. Since the hang-glider wing is symmetrical, and it is assumed that the flow is also symmetrical only the half of the wing-model was used.

The geometry was recorded by point by point measurements. Ten profile sections were selected parallel to the keel tube and each profile was covered by a reasonable number of points. In order to achieve the same form as during normal flight, the wing was loaded by sand. At the end the wing was reproduced by 140 points. The point coordinates were read into ICEM by a custom-made code automatically. First the profile sections were reproduced using spline fitting and then the surface was formed from the curve array using 2D spline fitting.

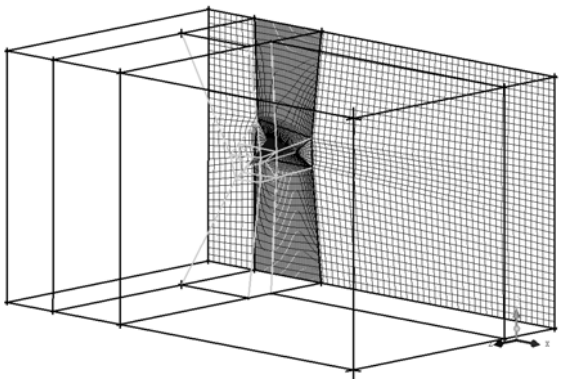

Figure 3. The block-structure and the grid

The half wing was enclosed into a significantly larger hexagon (Figure 3.) It had to be ensured that the boundaries are far enough that they do not disturb the flow.

For this model block-structured hexagonal mesh was used, because the accuracy and convergence properties are clearly advantageous over an unstructured mesh. The price to be paid is the larger effort to prepare the mesh. The final grid in each case included approximately 900000 elements. A significantly denser mesh was used in the vicinity of solid surfaces, the first element high being typically 5 *mm* corresponding to an y^+ of 200.

2.2.2 The physical model

The physical model was built using the commercial CFD software ANSYS CFX 5.7.

The flow was assumed to be steady, incompressible, isothermal and turbulent. The fluid used was air at 25 *°C*, with a density of 1.185 kg/m^3 and a dynamic viscosity of $1.831*10^{-5}$ *kg/ms*.

Two turbulence models were tried: the k-ε and the SST (Shear Stress Transport). In one selected case a comparison between the two models were made. Although the k-ε model converges significantly faster, the results of the SST model, especially the vortex structure corresponds more to the expectations. Therefore the SST turbulence model was selected.

The boundary conditions are shown in Fig.4. The inlet boundary condition was uniform velocity entry. On the wing surface no slip condition was used. The symmetry plane was used because of the assumed symmetry of the flow and on the rest of the surfaces the so-called opening boundary condition was used meaning a constant static pressure but not specifying the flow direction. A second order spatial discretisation scheme was used.

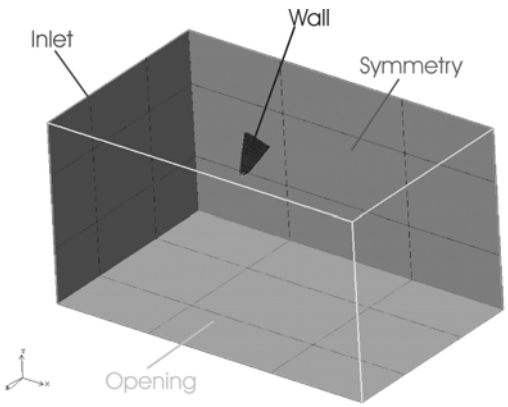

Figure 4. The location of the boundary conditions

2.3 Validation

Since the shape of hang-glider wing changes flexibly and elastically under wind load, which is neglected here, the flow is highly complex and to the best knowledge of the authors there is no other CFD simulation, on hang-glider this simulation must be validated. For this purpose the measured data of Cook and Kilkenny [2] are used.

2.3.1 Description of the experiment of [2]

Three hang-glider wings were the subject of aerodynamic investigation. The experimental equipment was the British mobile test facility designed for full-scale measurements on hang-glider wings, with a microcomputer for the analysis of the recorded test data. This is a car with an 8 *m* high beam structure (the higher the wing hangs, the less it is affected by disturbances from the ground) where the wing is hung and equipped by a six-component force and moment measurement device. The test rig also includes an air speed anemometer and a direction indicator. Three different hang-glider types were measured with this facility in a wide angle of attack range (-15°÷40°) and for various velocities one of which was *Magic III.* The lift, drag and pitching moment coefficients were determined in this experiment as well as flow visualisations have been made. These values are used for the validation of our calculations.

2.3.2 Results of validation

The model of *Magic III* was simulated with 10.9 *m/s* inlet velocity (in accordance with the experiments) and with eight different angles of attack (-5°, 0°, 5°, 10°, 15°, 21°, 25°, 30°). The comparison of the measured and calculated drag and lift coefficients, defined by Eq. (1) [6], are presented in Fig.5.

$$c_{\mathrm{L,D}} = \frac{F_{\mathrm{L,D}}}{A\left(\frac{\rho}{2}\right)v^2} \qquad (1)$$

Considering the difficulties both in the measurements and in the simulations the agreement is excellent. This means a large boost of confidence to believe in the accuracy of the further simulations. It has to be noted that at 25° and 30° the simulation does not converge to a steady state probably indicating transient periodic flow. Therefore the values are not as certain as in the previous points. For a quantitative description of the deviation of the experimental data from the calculated ones the averaged quadratic error H, defined by Eq. (2), is used.

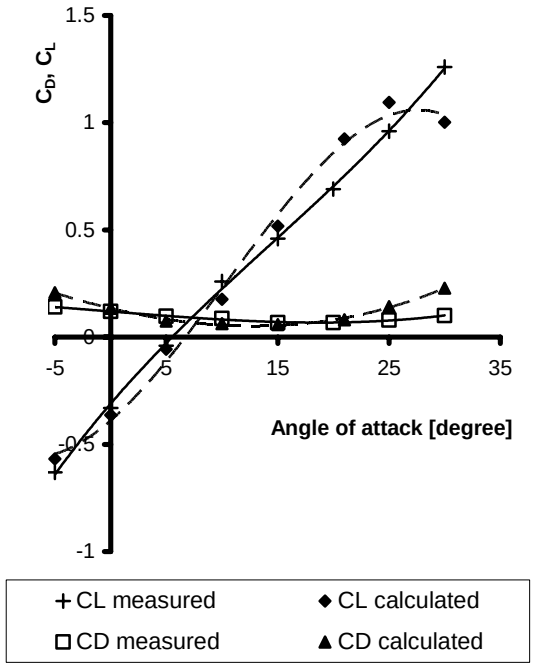

Figure 5. Measured and calculated values of c_D and c_L of *Magic III*, as a function of the angle of attack

$$H = \sqrt{\frac{\sum_{i=1}^{N}(c_{L,D,measured} - c_{L,D,calc})^2}{N}} \qquad (2)$$

The value of H is non-dimensionalised by the maximum values of C_L and C_D. This value is 24% for C_D and 8% for C_L. Nevertheless in many points the agreement is much better than that. Particularly encouraging is the fact that the best agreement is obtained at 15º which is the normal flying position at the given velocity. The measured shape also belongs to this flying angle. At other angles the larger disagreement is not surprising since the wing shape flexible and elastically deforms away from the normal flying position.

A marked difference between measured and simulated values can be seen in the angle of stall. The simulations predict the appearance of stall at about 25º as compared to about 35º for the measurements (not shown in the figure). This can again be attributed to the uncertainties in the shape of the wing at various loads.

The results of the flow visualisation in [2] are also well reproduced by the simulation, such as streamlines or separation zones.

The forgoing results provide a basis of trust for the coming simulations with other geometries.

2.4 Investigation of the new wing prototype

The new concept was a hang-glider wing prototype, the *Süsü II*. This wing is a most profile-true and a tight concept, and it has a different, rounded wingtip. This wing is modelled and simulated under similar conditions as *Magic III*.

2.4.1 Results of the comparison

The purpose of the comparison was to determine the advantages and disadvantages of the new wing type. The comparison included the drag and lift coefficient, the force distribution, glide ratio (Eq.(3)) and the Trefftz-planes.

Figure 6 shows the drag and the lift coefficients plotted against the angles of attack by the two cases. The designers expected that the wing produced more lift force at the price of a larger instability. This means among other things a better climbing ability (shorter runway). This property was confirmed by the test pilot. The simulations are in complete agreement with the expectations. The lift force is higher in the whole investigated range of angles than that of *Magic III*, while even the drag force is lower up to 15º in the case of *Süsü II* and becomes higher only at larger angles.

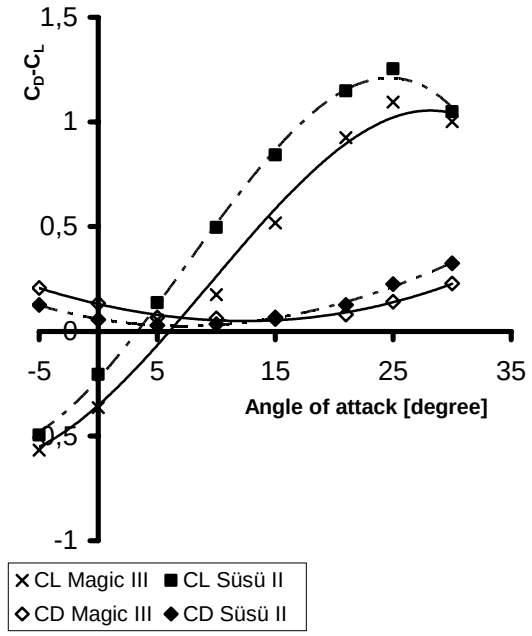

Figure 6. c_D and c_L obtained from the simulation of Magic III and Süsü II

The glide ratio is used to express the ratio of drag force and lift force. The smaller this value, the better is the wing.

$$\varepsilon = \frac{c_D}{c_L} \qquad (3)$$

Table 1. The glide ratios

Angle of attack	Magic III	Süsü II
5	1.212	0.207
10	0.357	0.070
15	0.113	0.079
21	0.087	0.110
25	0.129	0.180
30	0.228	0.310

The best glide ratio is associated with *Süsü II* at 10° (shows in table 1). The optimum glide ratio is reached at different angles by different types. The reason for this is that the two types are designed for different velocities.

The two types have different wingtips; *Magic III.* has an edgy one, whereas *Süsü II* has a rounded one. Therefore the established flow fields and the vortices are different. To examine the influence of wingtip design on the vortices and the drag force, the vortices can be visually compared with the help of the so-called Trefftz-plane (a plane behind the wing perpendicular to the symmetry-plane and the plane of the wing), 20 *m* from the inlet.

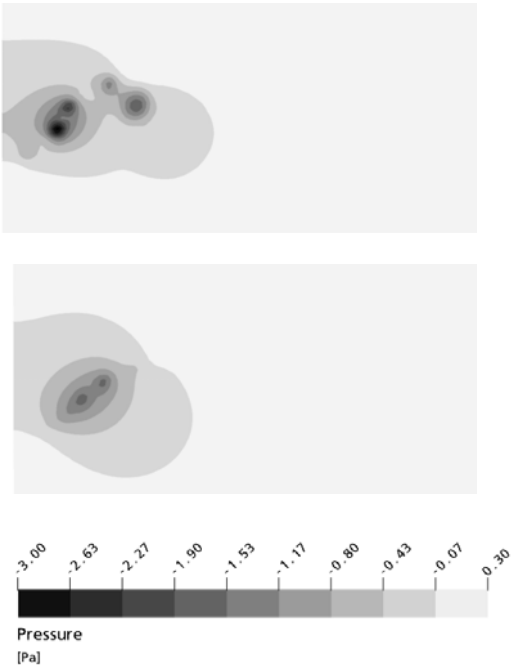

Figure 7. Pressures on the Trefftz-plane (top: *MagicIII*, bottom: *Süsü II*)

These plots indicate that the rounded wingtip (*Süsü II*) produced smoother, less intensive pressure trace. Hence, this rounded wingtip produced less induced drag force so that is one reason for the decreased drag force by *Süsü II*.

In the case of a swept wing, the effective angle of attack grows in the direction of the trailing edge. Therefore the form of the force distribution on the wing deviates from the ideal (half-parabola) form. This gives an advantage regarding stability in the vicinity of stall but the glide ratio is worse than that of an ideal wing [6, 7].

Figure 8. shows the force distribution on the wings. The distribution on the Süsü II wing is more uniform; hence, from the viewpoint of load this is advantageous.

Of course these calculations are far from a full aerodynamic analysis, but demonstrate well that the *Süsü II* type has good flying parameters. In the next chapter an attempt is made to improve the characteristics even further using a new concept.

3. THE WING-GRID

The hang-glider is a relatively new flying device (since ~1970), but it has been developing continuously. The improvements have focussed on efficiency and safety (stability, good manoeuvrability). The new concept is aimed at improving both properties at the same time.

The wing-grid is a specially designed wingtip device. The basic idea is stolen from nature. It has been observed that large birds have large feathers at the end of their wings which they simply spread and keep steady while they glide. With this device some large birds can make up for the disadvantage of their small aspect ratio wings and can achieve the same glide ratios as birds with large aspect ratio wings [8]. In our case this means a sectioning of the wing-tip perpendicular to the keel tube (symmetry plane) [1]. It has been hoped that with this geometry change the drag force would be reduced.

3.1 The wing-grid theory

The theoretical reasoning behind this idea is the following. One of the most important components of the drag force is the induced drag. The induced drag is due to a vortex attached to the wing. According to the second vortex-law of Helmholtz a vortex-tube can't close in a flow field, it can create only a closed vortex-loop [9, 10].

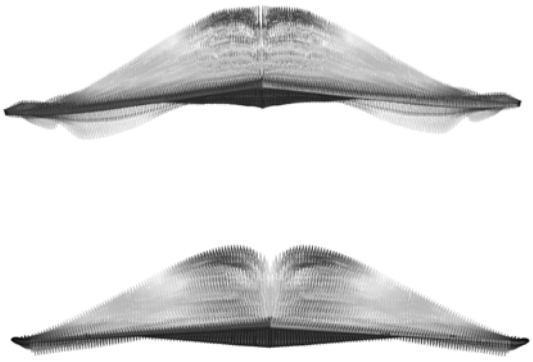

Figure 8. Force distribution (above: *Magic III*, below: *Süsü II*)

Therefore the starting vortex is bundled with the bound vortex on the wing. Those bundled vortices are called trailing vortices. On account of the pressure-difference between the upper and lower side of the wing, the fluid moves towards the trailing edges. As a consequence a vortex system rolls up onto the trailing edges [6, 7]. Those vortices are called induced vortices, and this vortex is created at each wingtip. The induced drag is caused by this vortex. The dimensioning and design of the vortex is an important part of the design of a wing.

The wing-grid is supposed to cut up the induced vortex thereby creating many smaller vortices. The smaller vortices change the velocity direction around the airfoil less than the large vortices and also dissipate faster thereby reducing the induced drag [8].

3.2 Implementation in the hang-glider

The goals of the hang-glider with wing-grid configuration are to reduce the glide ratio by reducing the induced drag, and to improve the stability and the manoeuvrability of the hang-glider with a possible reduction of wing span and chord length.

3.2.1 The basic design

For the design of the first modified geometry the bird's wing-design and the results of the La Roche Consultants [8] are used. Based on the investigation of the bird wings, the last 20 % of the hang-glider wing was cut off and "feather" wings were attached.

In order to keep the calculations and the possible later manufacturing simple only three feathers per side were used.

For the profile of the feathers a NACA1412 type was selected in *Designs I.* and *II.* This profile-type produced a small drag and lift force for the investigated angles of attack. That was important to separate the effect of wing-grid from the individual properties of the feather wings. In addition, in *Design III.*, a Gö647 profile was used. This is the same profile as the original one.

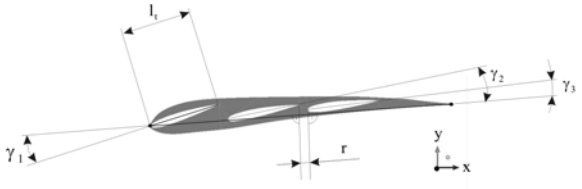

Figure 9. The main parameters of the wing-grid

In this structure a lot of parameters could be varied but the number of versions for the CFD study had to be limited. Therefore three feather designs and three main parameters were selected. The three main parameters were (Fig. 9.):

- Chord length of the feathers (l)
- The setting angles of the feathers (γ_i)
- The slit size between feathers (r);

Significant difference exists only between *Design I.* and *Design III. Design II.* is only a rounded version of *Design I.* These parameters are changed in a systematic way and the geometries tested by CFD. All the geometries were solved with a 10˚ angle of attack, with the same velocity, 10.9 *m/s* and with the same boundary conditions, only the geometry and thus the numerical grid differed.

3.3 Results of the wing-grid

From the 15 versions simulated, 11 had the same feather design. The investigation focused on the drag and the lift coefficients and the glide ratio, so primarily the performance parameters and not the stability was examined.

All the results are summarized in Table 2. Some of the results are shown in Fig. 10. There are two cases in which the glide ratio has a better value than the original *Süsü II* wing. These two values are associated with *Design III.* at -5˚ and 25˚ angle of attack. Therefore the concept of *Design III.* is better than the others for extreme flying positions. Maybe the profile of the feathers is good but the setting angles aren't perfect.

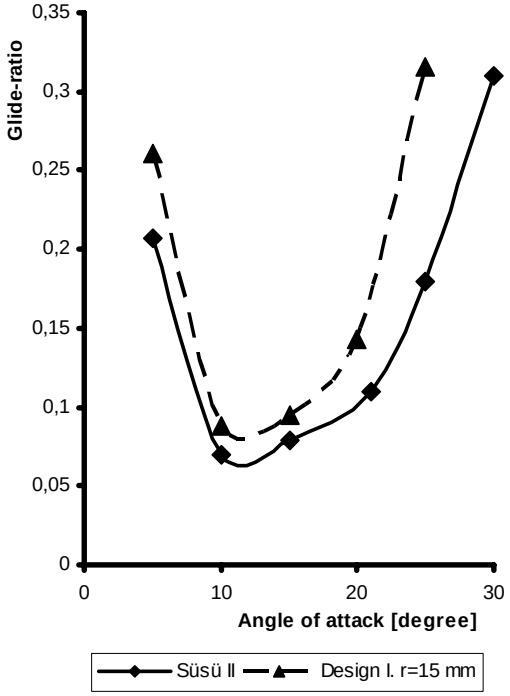

Figure 10. The glide-ratios of the wings with and without wing-grid as a function of the angle of attack

The other designs (I. and II.) produced worse glide ratios. Probably the selected profile-type is not optimum because the feathers produced only drag

forces with less lift force than in the original *Süsü* design.

Table 2. The glide-ratios of wing-grid designs.

Design	r	Angle of attack	Glide ratio
I.	0	15	0.1
I.	15	-5	-0.24
I.	15	5	0.26
I.	15	10	0.09
I.	15	15	0.1
I.	15	20	0.14
I.	15	25	0.32
I.	21.1	10	0.085
I.	37.3	10	0.084
I.	52.4	10	0.084
I.	70.5	10	0.087
II.	37.3	10	0.09
III.	13.5	-5	-0.27
III.	13.5	10	0.07
III.	13.5	25	0.17

On the basis of the results of *Design I.* it is clear that a slit size over about 20 *mm* has no significant effect on the glide ratio in this Reynolds number range. Therefore, this is the minimum feather distance above which there is no interaction between the flows around neighbouring feathers (with l = 24.2 *mm*).

Another remarkable result is, that *Design II.* produces a higher glide ratio than *Design I.* If the forces are compared for these two geometries, it is found that *Design II.* reached a smaller drag and a smaller lift either. The rounded form reduces the drag force of the wing-grid by rounding off the sharp edges but at the same time the presence of the transition between the main wing and feather reduces the effective wing-span and thus the lift force too.

The wing-grid has other effects which are not reflected in the glide ratios. These effects can be studied with the help of the streamlines and of the Trefftz-planes, shown in Figs. 11.

The Trefftz-planes show that the wing with wing-grid (*Design III.*) produces a smoother pressure track, and the pressure values in the vortex core are larger. Therefore this wing-grid reduced the intensity of the wingtip vortex.

In summary, the concrete wing grid geometry used in this paper has not fulfilled the expectations. Nevertheless it can be explained by the fact that the basis of comparison with the old design was not quite correct. There are several encouraging signs showing that the concept has a future.

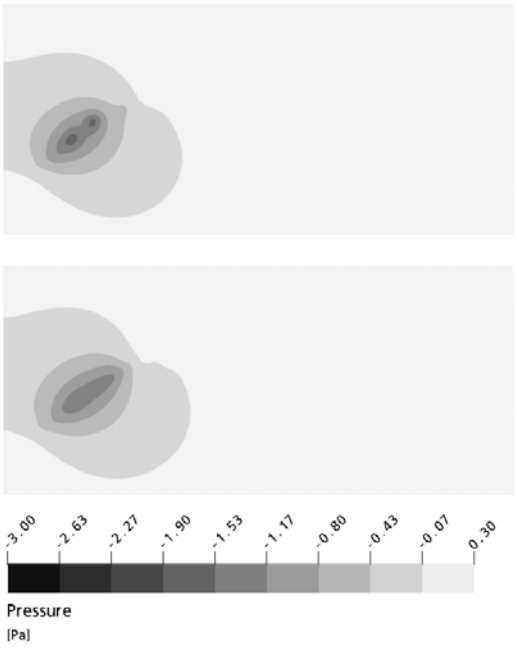

Figure 11. Trefftz-planes (above: Süsü II, bottom: Design III.)

4. SUMMARY

In this paper several hang-glider designs have been numerically simulated using a commercial code. A simulation on an existing design has shown that it is a suitable tool to estimate the flying parameters without building expensive prototypes and performing expensive and not infrequently dangerous experiments. The agreement with experimental results was excellent. In a second step a new design was simulated for which no experimental data are available but the aim of the designer was known. The results again confirmed all the expectations: in most of the flying parameters the new design proved to be superior over the old one. The limitation of the simulation in this moment is that the flexible and elastic deformation of the wing is not taken into account. In a future work a coupled simulation could be performed on the wing-flow interaction.

In the last step a new concept, the wing grid design was tried. The flying parameters have not improved to the extent originally expected but there are encouraging signs that the concept is correct. Many further parameter studies are necessary to reach an optimum design.

REFERENCES

[1] Fáy, P., Gausz, T., Seregély, L., Takáts, Zs., Varga, L., 1989, ”Siklórepülőgépek terheléseinek elméleti és statisztikai vizsgálata”, *LRI, Budapest* (in Hungarian)

[2] M.V.Cook, and E.A. Kilkenny, 1991, ”An experimental Investigation of The Hang-

Glider", *NASA IAA Conference Paper 88A11200*

[3] Altmann, H., Sahs, G., 1994 „Aeroelastic Characteristics and Static Stability of Hang Gliders in Longitudinal Flight", *4th Mini Conf. on Vehicle System Dynamics Identification and Anomalies,* Budapest

[4] Boer, G., 1982, „Numerical and Experimental Investigation of the Aerodynamics of Double Membrane Sailwing Airfoil Sections", *Rep. LR-345, Delft University of Technology*, February

[5] Jackson, P.S., Christine, G.W., 1987, „Numerical Analysis of Thre-Dimensional Elastic Membrane Wings", *AIAA Journal*, Vol. 25, No. 5, pp. 676-682

[6] Oertel jr., H. 2002, "Prandtl – Führer durch die Strömungslehre", *Vieweg & Sohn Verlaggesellschaft mbH, Braunschweig / Wiesbaden*

[7] Jereb Gábor, 1977, "Vitorlázó Repülőgépek", *Műszaki könyvkiadó, Budapest*

[8] La Roche Consulting, www.winggrid.ch

[9] Katz, J., Plotkin, A., 1991, „Low Speed Aerodynamics", *McGraw-Hill New-York*

[10] Nickel, K. E., 1987, „A Theory of Sail-Wings, Zeitschrift für Flugwissenschaften und Weltraumforschung", Vol. 11 pp. 321-328

Conference on Modelling Fluid Flow (CMFF'06)
The 13th International Conference on Fluid Flow Technologies
Budapest, Hungary, September 6-9, 2006

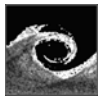

NEAR-WALL, REYNOLDS-STRESS MODEL CALCULATIONS OF TRANSONIC FLOW CONFIGURATIONS RELEVANT TO AIRCRAFT AERODYNAMICS

Roland JESTER-ZÜRKER[1], Suad JAKIRLIĆ[1,2], Bernhard EISFELD[3]

[1] Chair of Fluid Mechanics and Aerodynamics, Department of Mechanical Engineering, Darmstadt University of Technology, Petersenstr. 30, D-64287 Darmstadt, Germany. E-mail: roland@sla.tu-darmstadt.de
[2] Corresponding Author. Tel.: +49 6151 163554, Fax: +43 6151 164754, E-mail: s.jakirlic@sla.tu-darmstadt.de
[3] Institute of Aerodynamics and Flow Technology, DLR - German Aerospace Center, Lilienthalplatz 7, D-38108 Braunschweig, Germany. E-mail: bernhard.eisfeld@dlr.de

ABSTRACT

The present work focuses on the application of a near-wall, wall-normal free, second-moment closure (SMC) model in the RANS (*Reynolds-Averaged Navier-Stokes*) framework in computing the (compressible) transonic flow past aircraft configurations and their elements (airfoils and wings). The flow geometries primarily considered in this work include the transonic RAE 2822 profiles (cases 9 and 10), the ONERA M6 wing and the ALVAST wing-body configuration. The SMC predictions show encouraging results with respect to the shock position and its structure and the strength of the wing-tip vortex.

Keywords: RANS, Reynolds-stress models, near-wall treatment, transonic flow configurations, aircraft aerodynamics

1. INTRODUCTION

Computational Fluid Dynamics (CFD) is nowadays regarded as an indispensable tool in aerodynamic design and optimization. The application of efficient CFD methods in aircraft aerodynamics and related disciplines enables reduction of costs and shortens substantially the time for development in aircraft industry. Furthermore, the employment of CFD methods supports to a large extent a detailed evaluation of new technologies and concepts as well as alternative configurations with respect to security, environmental (e.g., noise pollution) and economic aspects of transport and passenger aircrafts. Together with the high-lift configurations corresponding to the take-off and landing regimes, the high-speed, cruise-flight configurations play important role in the entire operational range of an aircraft. The transport and passenger aircrafts operate at the cruise flight velocities corresponding to the Mach number ranging in interval $Ma = 0.75 - 0.85$. The associated flow regime past an aircraft wing is of transonic nature. It is characterized by development of a closed, wall-bounded supersonic flow region at the upper wing surface, Fig. 1 (its appearance at the lower wing surface is also possible depending on its curvature and the angle of attack).

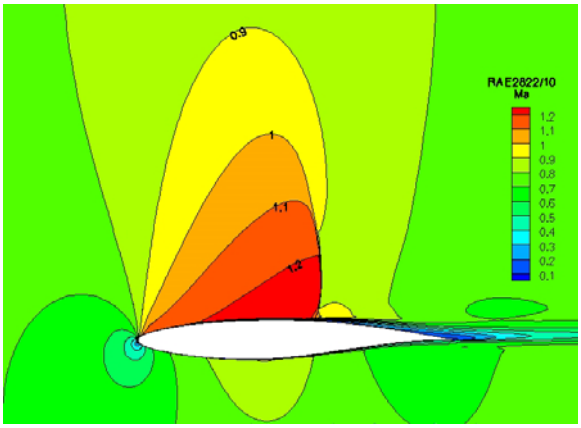

Figure 1. Mach-number contours in the transonic flow around RAE2822/10 profile

The flow is strongly accelerated reaching the sound velocity at the leading edge of the wing. The supersonic region spreads behind the so-called sound line, denoting the isoline with $Ma = 1.0$. The pressure increase behind the maximum profile thickness causes the formation of a shock wave which closes the supersonic region. The shock front proceeds almost orthogonally to the wing profile contour. Transonic flows are further featured by the boundary layer-shock interaction with respect to the boundary layer thickening due to adverse pressure gradient and in some cases the shock-induced

separation occurs. The change of the flow regime – from subsonic regime to supersonic one and opposite – implies the solving of a combined elliptic/hyperbolic flow problem. These features as well as the compressible properties of the flow in general pose a special challenge not only for the numerical treatment but also for turbulence models. The work focuses on the application of a near-wall second-moment closure (SMC) model, which accounts separately for both viscous effects and kinematic wall blockage with respect to the anisotropic nature of the Reynolds-stress and stress dissipation fields.

2. COMPUTATIONAL METHOD

The continuity, momentum and energy equations governing the compressible flow with relevance to the aircraft aerodynamics are given in differential form in the *Reynolds-Averaged Navier-Stokes* framework as follows:

$$\frac{\partial \overline{\rho}}{\partial t} + \frac{\partial}{\partial x_j}\left(\overline{\rho}\tilde{U}_j\right) = 0 \tag{1}$$

$$\frac{\partial(\overline{\rho}\tilde{U}_i)}{\partial t} + \frac{\partial}{\partial x_k}(\overline{\rho}\tilde{U}_i\tilde{U}_k + \overline{\rho}\widetilde{u_i''u_k''}) = -\frac{\partial \overline{P}}{\partial x_i} + \frac{\partial \overline{\tau}_{ik}}{\partial x_k} \tag{2}$$

$$\frac{\partial(\overline{\rho}\tilde{E})}{\partial t} + \frac{\partial}{\partial x_k}(\overline{\rho}\tilde{H}\tilde{U}_k + \overline{\rho}\widetilde{u_i''u_k''}\tilde{U}_i) = \frac{\partial}{\partial x_k}(\overline{\tau}_{ik}\tilde{U}_i) - \frac{\partial}{\partial x_k}(q_k + q_k^{(t)}) + \overline{\rho}D_{kk} \tag{3}$$

Where, a Newtonian fluid with the stress tensor and a Fourier type heat flux

$$\overline{\tau}_{ij} = 2\overline{\mu}\tilde{S}_{ij};\ \tilde{S}_{ij} = \frac{1}{2}\left(\frac{\partial \tilde{U}_i}{\partial x_j} + \frac{\partial \tilde{U}_j}{\partial x_i} - \frac{2}{3}\frac{\partial \tilde{U}_k}{\partial x_k}\delta_{ij}\right) \tag{4}$$

$$q_i = -\overline{\lambda}\frac{\partial \tilde{T}}{\partial x_i} \tag{5}$$

is assumed. In these material laws the dynamic viscosity follows from Sutherland's formula and the heat conductivity is related to the dynamic viscosity via a constant Prandtl number. Thermodynamic closure is achieved by the assumption of an ideal, calorically perfect gas. Note, that the contribution of turbulent diffusion ρD_{kk} to the total energy equation and the contribution of the kinetic turbulence energy to the total energy E and total enthalpy H are usually neglected.

The following sections outline the description of the turbulence model used and numerical method applied.

2.1. Turbulence Modelling

All computations were performed with a wall-normal free version of the low-Re number Second-Moment (Reynolds stress) closure model (RSM) due to Hanjalic and Jakirlic (1998). The model satisfies all important requirements, with a specific emphasis on limiting states of turbulence (vanishing and very high turbulence Re numbers, two-component limit,...), reproducing the laminar-to-turbulent and reverse transition (by-pass and shear-generated transition with minimum background turbulence), appropriate reproduction of effects of extra strain rates (transverse shear, skew-induced three-dimensionality), high acceleration (including laminarization), high deceleration (approaching separation), swirl effects, mean compression, flow separation, recirculation and reattachment, see e.g. Hanjalic and Jakirlic (2002). The best illustration for the model's ability to account properly for a large deviation from the equilibrium conditions is given in Fig. 2, where semi-log plots of the mean velocity are presented for several boundary layer flows subjected to different pressure gradients (favourable and adverse) featuring the flow phenomena pertinent to aircraft aerodynamics.

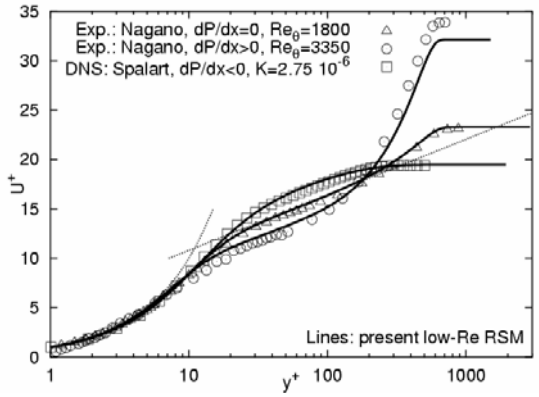

Figure 2. Semi-log plots of the mean axial velocity in the boundary layers subjected to different pressure gradients

Another interesting model feature accounts separately for the wall effects on anisotropy of stress bearing and dissipative scales by introducing both the turbulent stress and dissipation rate anisotropy (A and E; $A = 1 - 9(A_2 - A_3)/8$, $A_2 = a_{ij}a_{ji}$, $A_3 = a_{ij}a_{jk}a_{ki}$; $E = 1 - 9(E_2 - E_3)/8$, $E_2 = e_{ij}e_{ji}$, $E_3 = e_{ij}e_{jk}e_{ki}$) in addition to viscosity effects taken into account via $\mathrm{Re}_t = k^2/(\nu\varepsilon)$ The

strong difference in the anisotropy rates of both tensors ($a_{ij} = \overline{u_i u_j}/k - 2\delta_{ij}/3$ and $e_{ij} = \varepsilon_{ij}/\varepsilon - 2\delta_{ij}/3$) expressed in terms of their two-componentality factors A and E and the turbulence model capability to capture them correctly is shown in Fig. 3.

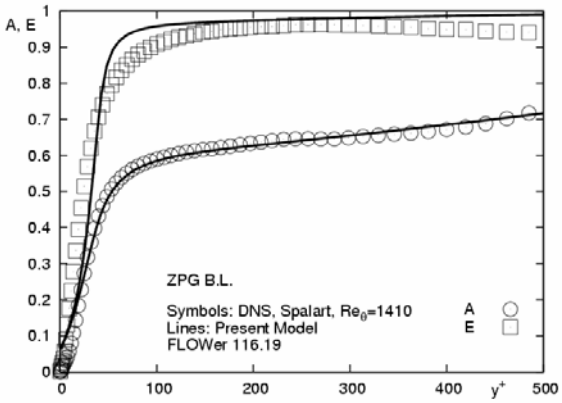

Figure 3. Two-componentality parameters A and E in a zero-pressure gradient boundary layer

The precise specification of the entire turbulence model is given below. The present near-wall, second-moment closure model is based on the model equations governing the Reynolds stress tensor and the dissipation rate of the kinetic energy of turbulence:

$$\frac{\partial\left(\overline{\rho}\tilde{U}_k\widetilde{u_i''u_j''}\right)}{\partial x_k} = D_{ij}^{v} + D_{ij}^{k} + \overline{\rho}P_{ij} - \overline{\rho}\varepsilon_{ij} + \overline{\rho}\Phi_{ij} + \overline{\rho}\Phi_{ij}^{w} \tag{6}$$

$$\frac{\partial\left(\overline{\rho}\tilde{U}_k\varepsilon\right)}{\partial x_k} = D_{\varepsilon}^{v} + D_{\varepsilon}^{t} + \overline{\rho}\left(C_{\varepsilon,1}P_k - C_{\varepsilon,2}\varepsilon\right)\frac{\varepsilon}{k} + C_{\varepsilon,3}\overline{\eta}\frac{k}{\varepsilon}\widetilde{u_j''u_k''}\frac{\partial^2\tilde{U}_i}{\partial x_j\partial x_l}\frac{\partial^2\tilde{U}_i}{\partial x_k\partial x_l} \tag{7}$$

with the following anisotropic formulation of the dissipation correlation

$$\varepsilon_{ij} = f_s\widetilde{u_i''u_j''}\frac{k}{\varepsilon} + \left(1-f_s\right)\frac{2}{3}\varepsilon\delta_{ij} \tag{8}$$

and a quadratic formulation of the pressure strain model

$$\begin{aligned}\Phi_{ij} = &-\varepsilon\left[C_1 a_{ij} + C_1'\left(a_{ik}a_{jk} - \frac{1}{3}A_2\delta_{ij}\right)\right] \\ &-C_2' a_{ij}P_k + C_3 k\tilde{S}_{ij} \\ &+C_4 k\left(a_{ip}\tilde{S}_{pj} + a_{jp}\tilde{S}_{pi} - \frac{2}{3}a_{pq}\tilde{S}_{pq}\delta_{ij}\right) \\ &+C_5 k\left(a_{ip}\tilde{W}_{pj} + a_{jp}\tilde{W}_{pi}\right)\end{aligned} \tag{9}$$

with $\tilde{W}_{ij} = 0.5\left(\partial\tilde{U}_i/\partial x_j - \partial\tilde{U}_j/\partial x_i\right)$ being the mean vorticity tensor. The wall reflexion term model

$$\begin{aligned}\Phi_{ij}^{w} = &C_1^{w} f_w\frac{\varepsilon}{k}\left(\widetilde{u_k''u_m''}n_k n_m\delta_{ij} - \frac{3}{2}\widetilde{u_i''u_k''}n_k n_j - \frac{3}{2}\widetilde{u_k''u_j''}n_k n_i\right) \\ &+C_2^{w} f_w\frac{\varepsilon}{k}\left(\Phi_{km,2}^{IP}n_k n_m\delta_{ij} - \frac{3}{2}\Phi_{ik,2}^{IP}n_k n_j - \frac{3}{2}\Phi_{kj,2}^{IP}n_k n_i\right)\end{aligned} \tag{10}$$

$$\Phi_{ij,2}^{IP} = -C_2\left(P_{ij} - \frac{2}{3}P_k\delta_{ij}\right) \tag{11}$$

was made wall-normal free by introducing a unit vector pointing into the direction of the non-homogeneity of the turbulence field, in line with the proposal of Gerolymos and Vallet (2002): $n_i = \nabla(Ak^{3/2}/\varepsilon)\big/\left|\nabla(Ak^{3/2}/\varepsilon)\right|$.

The model coefficients are summarized as follows

$$\begin{aligned}&C_1 = 2.5AF^{1/4}f + \sqrt{A}E^2 \\ &C_1' = -max\left[0.8A_2; 0.5\right] \\ &C_2 = 0.6A^{1/2};\ C_3 = \frac{4}{3}C_2;\ C_4 = C_2 \\ &C_5 = -C_2;\ C_2' = 0;\ F = min\left[0.6; A_2\right] \\ &f = min\left[\left(\frac{Re_t}{150}\right)^{3/2}; 1\right]\end{aligned} \tag{12}$$

$$\begin{aligned}&C_1^{w} = max\left[0.9 - 0.7C; 0.3\right] \\ &C_2^{w} = min\left[A; 0.3\right] \\ &f_w = min\left[\frac{k^{3/2}}{C_l\varepsilon y_n}; 1.4\right]\end{aligned} \tag{13}$$

$$C = 2.5AF^{1/2}f;\ C_2 = 0.6A^{1/2};\ C_l = 2.5$$

$$C_{\varepsilon,1} = 1.44;\quad C_{\varepsilon,2} = 1.8;\quad C_{\varepsilon,3} = 0.3 \tag{14}$$

with y_n representing the wall closest distance.

The turbulent heat flux is modelled in analogy to Fourier type heat conduction

$$q_i^{(t)} = -\lambda^{(t)} \frac{\partial T}{\partial x_i} \tag{15}$$

where the eddy conductivity is computed from an equivalent eddy viscosity via the definition of the turbulent Prandtl number, i.e.

$$\lambda^{(t)} = \frac{C_p \mu^{(t)}}{\mathrm{Pr}_t} = \frac{C_p \rho k}{\mathrm{Pr}_t\, \omega} \tag{16}$$

2.2. Numerical Method

All computations were performed by using the DLR FLOWer code, which is well established in the academic research and aeronautical industry. It employs a variety of turbulence models, ranging from eddy viscosity models (Baldwin-Lomax, Spalart-Allmaras type, *k*-ω type) to full Reynolds stress models (Wilcox stress-ω, SSG/LRR-ω), which have been validated in a large number of test cases, ranging from baseline to complete aircraft flow configurations, Kroll et al. (2002) and Eisfeld (2004).

The DLR FLOWer code is a Finite Volume method for block-structured meshes, solving the afore-specified compressible RANS equations with any of the above turbulence models. The code is density based, i.e. it solves the coupled system of continuity, momentum, total energy and turbulence equations. For the RANS equations different spatial discretization schemes are available, where the most common one is a second order central scheme with artificial dissipation. An explicit hybrid five-stage Runge-Kutta scheme is used for integration that is accelerated by local time stepping, implicit residual smoothing and a multigrid algorithm (Jameson et al., 1981). The convective terms in the equations governing the turbulence quantities are discretized by a first order upwind scheme, whereas the diffusion terms are discretized by a second order central scheme. The turbulence equations are integrated by an implicit method on the finest level only, which has shown to be a highly efficient and robust approach (Fassbender, 2004).

3. RESULTS AND DISCUSSION

The performances of the turbulence model presented are illustrated by computing three transonic flow cases: 2-D flow over the RAE2822 airfoil (Cook et al., 1979), 3-D flow past the ONERA M6 wing (Schmitt and Charpin, 1979) and the flow over the DLR-ALVAST wing-body configuration representing a generic transport aircraft model, Burgsmüller and Hoheisel (2000). Selected results concerning the wall pressure distribution and mean velocity and turbulence fields are displayed and discussed in the following subsections.

3.1. RAE2822

The first example is the transonic flow around a RAE2822 airfoil, Cook et al. (1979). A fairly strong shock is created near the mid chord ($x/c = 0.55$). Two cases, denoted by Case 9 and 10, characterized by $Ma_\infty = 0.73$, $\mathrm{Re}_\infty = 6.5 \cdot 10^6$ and $Ma_\infty = 0.75$, $\mathrm{Re}_\infty = 6.2 \cdot 10^6$ respectively, were considered. Both airfoil configurations are at an incidence angle of $\alpha = 2.8^o$. Important difference between the two flows is a local, post-shock separation occurring in the case 10. Calculations were performed on a C-type grid consisting of 737*x*177 grid cells, Fig. 4.

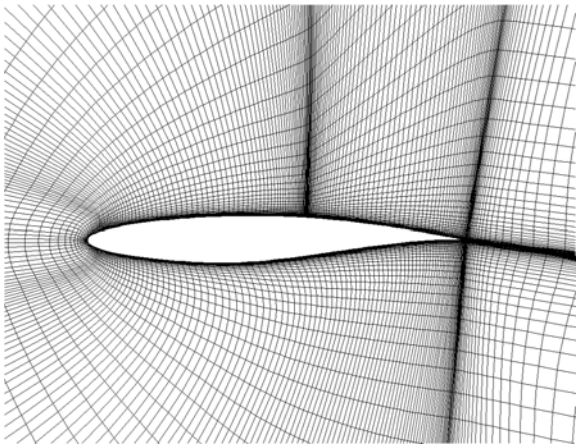

Figure 4. Blow-up of the C-type grid (737*x*177 cells) used for the computation of the flow past RAE2822 airfoils (every second grid line is shown)

The solution domain is extended to 20 chord lengths in all directions. At the solution domain boundaries the far-field boundary conditions based on the theory of characteristics were applied. Transition to turbulence in the experiment was induced by tripping the flow near the leading edge at $x/c = 0.03$ on both upper and lower surfaces of the airfoil. The computational treatment of this transition location was accounted for by multiplying the entire source term (production, redistribution and dissipation) in the equations governing the Reynolds stresses and dissipation rate by an appropriate function providing its zero value in the laminar flow part and a unit value in the fully turbulent flow region. Furthermore, it should be noted that the corrections of the computational results obtained under the free-flight conditions with respect to the wind tunnel confinement (experimental conditions) were introduced in line with the proposal of Haase et al. (1993).

Fig. 5 shows the comparison of the computed pressure coefficient distribution with available

experimental data for both flow configurations considered. The overall agreement is satisfactory.

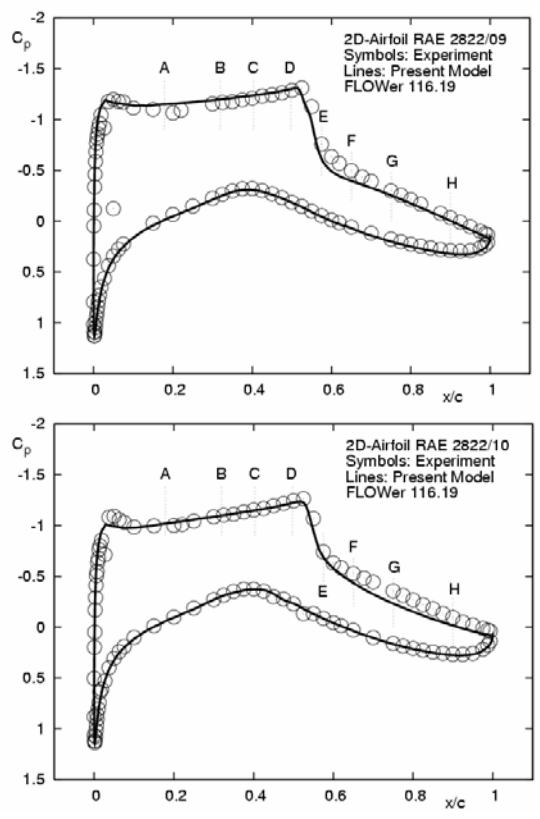

Figure 5. Pressure coefficient distribution for RAE2822 airfoil: case 9 (upper) and case 10 (lower)

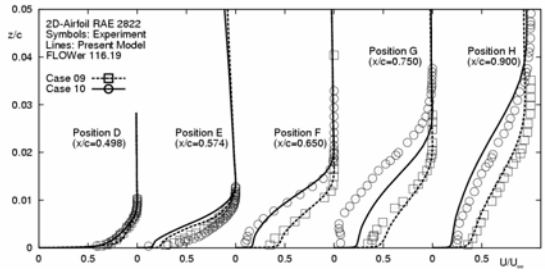

Figure 6. Mean axial velocity profile evolution in the transonic flow over the upper RAE2822-profile surface for the cases 9 and 10

Slight discrepancy with respect to the premature shock location in the case 9 is noticeable in the mean velocity field, Fig. 6. The velocity profile at the location *E* corresponding to the shock position indicates a somewhat stronger momentum loss. Interestingly, these circumstances don't influence the correct capturing of the flow recovery in the post-shock region. The evolution of the mean velocity field indicating clearly the boundary layer thickening is obtained in good agreement with experiment. Both the pre-shock suction pressure and the velocity profile immediately after the shock wave (location *F*) were captured well in the case 10. However, important discrepancies concerning the post-shock region with respect to the local, low-intensity flow reversal situated around the location *G* were revealed. It should be noted that the present near-wall, Reynolds-stress model has never been tested before in the flows influenced by compressibility. The computations with the model modified appropriately to account for the compressibility effects are in progress. The boundary layer structure is strongly influenced by the sudden pressure increase. Fig. 7 shows the profiles of the normal Reynolds stress components at two streamwise locations corresponding to the positions *D* and *F*, with the shock wave occurring in between. The effects of the increasingly varying adverse pressure gradient in the region of shock are demonstrated through the intensive turbulence production (all stress components experienced strong increase) due to strongly enhanced irrotational straining with respect to the rapid flow deceleration.

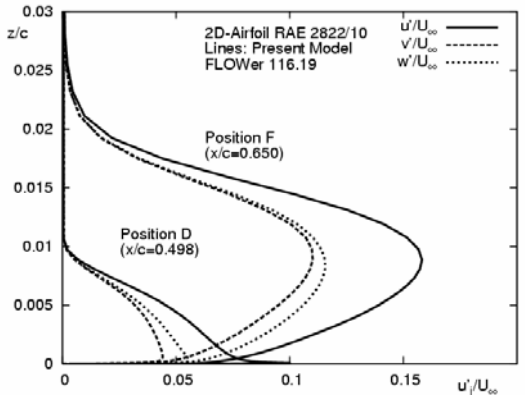

Figure 7. RMS of the normal components of the Reynolds stress tensor at two selected locations at the RAE2822/10-profile before and after the shock

3.2. ONERA M6 Wing

Flow over the ONERA M6 semi-span wing (Schmitt and Charpin, 1979) is calculated at $Ma_\infty = 0.84$, $\mathrm{Re}_\infty = 11.0 \cdot 10^6$ and $\alpha = 2.8^o$ angle of incidence, Fig. 8. The fully-turbulent calculations were performed at the C-C-type grid comprising 241*x*65*x*53 cells, Fig. 9. The solution domain was extended to 7.5 chord lengths in the *x* and *y* directions and 9.5 chord lengths in the *z* direction. Similar as in the previous case, the far-field boundary conditions were applied at the solution domain boundaries. The symmetry boundary conditions were imposed at the *x-y* (*z=0*) plane, Fig. 9.

The wall pressure contours displayed in Fig. 8 as well as the Mach-number contours (Fig. 10) and the pressure coefficient distribution (Fig. 11) illustrate the region of alternating favourable and adverse pressure gradients causing local acceleration and deceleration within the supersonic part of the flow.

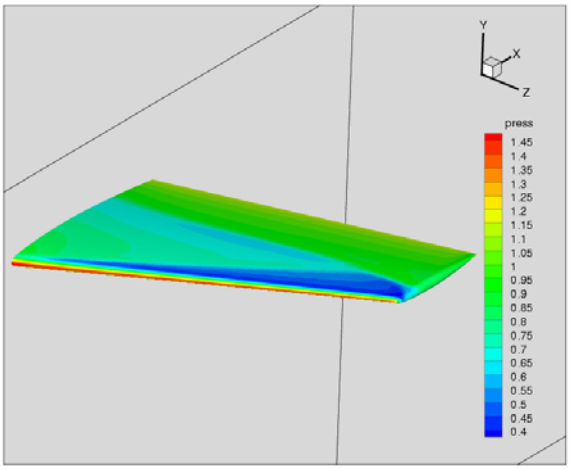

Figure 8. ONERA M6 wing: wall pressure contours

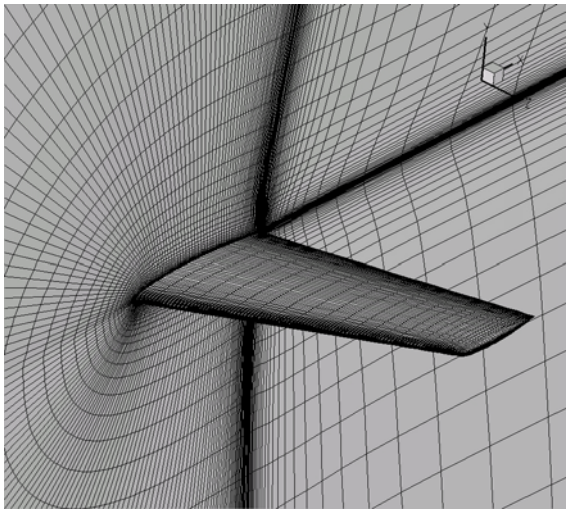

Figure 9. Computational grid (241*x*65*x*53 cells) used for the computation of the flow past ONERA M6 wing

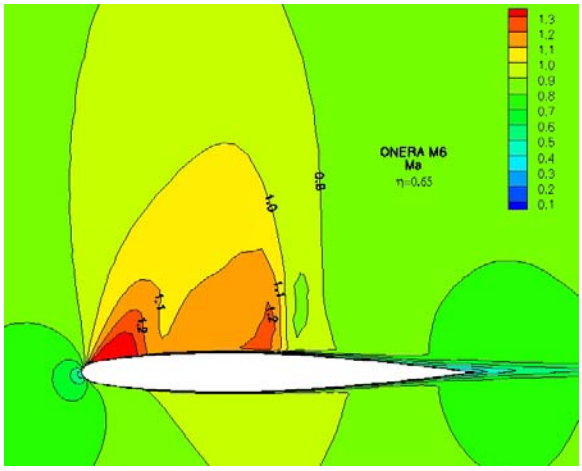

Figure 10. Mach-number contours in the transonic flow around ONERA M6 wing at 65% span.

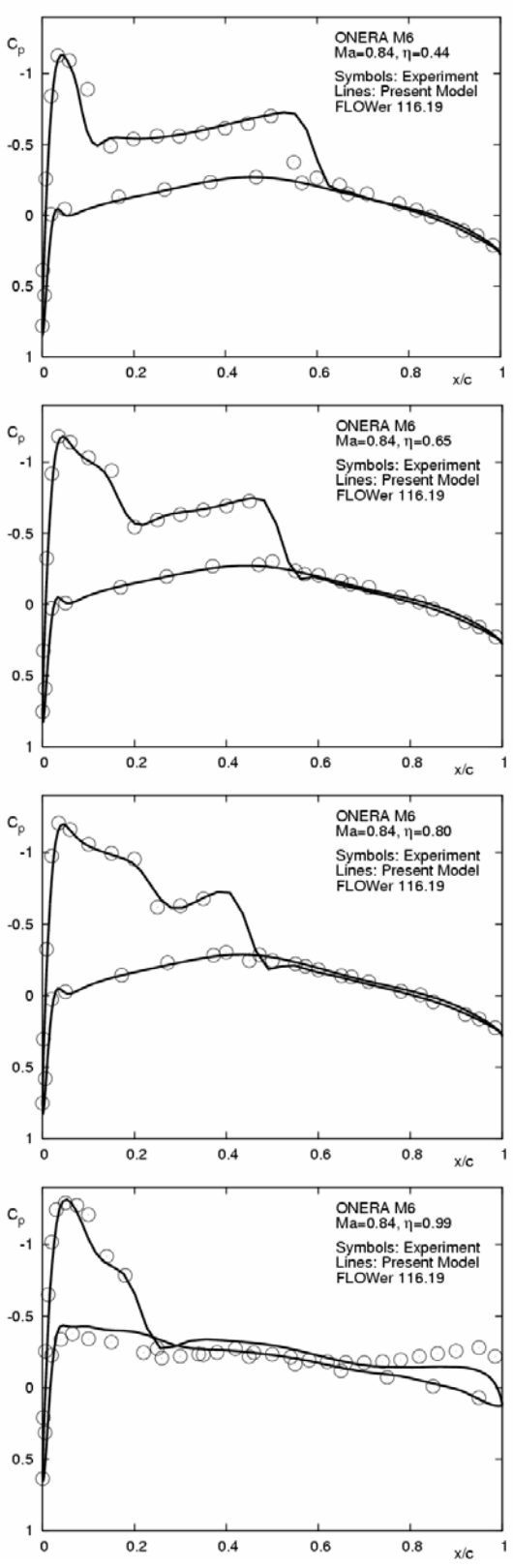

Figure 11. ONERA M6 wing: pressure coefficient distribution at selected spanwise location.

The consequence of such flow behaviour is its double-shock-like structure representing a double expansion into the supersonic regime. The flow experiences a rapid acceleration in the leading edge

region of the wing ($x/c = 0.1 - 0.2$) up to $Ma \approx 1.4$, Figs. 10 and 11 (upper). A prompt deceleration of the flow down to $Ma \approx 1.1$ follows creating consequently a weak, unstable shock, whose front propagates within the supersonic region towards the second, fairly strong shock. The second shock changes its position depending on the span location. The coalescence of the shocks occurs in the final 15-20% of the wing span in the wing-tip region, Fig. 11. The varying positions of both shocks with respect to the spanwise location as well as the wall pressure magnitude over the entire wing surface are reasonably well captured by the present model. The pressure coefficient distribution illustrates the equality of the wall pressure values at both wing surfaces over the whole wing span corresponding to the second half of the chord. The only exception is the last spanwise position situated directly at the wing tip, $\eta = 0.99$. Here, the influence of the tip vortex created by the flow from the lower wing surface upwards the upper wing surface around the tip itself on the pressure distribution is clearly visible. This feature is reasonably well returned by the present model.

3.3. DLR-ALVAST

The DLR-ALVAST is a generic transport aircraft model that can be equipped with turbine-driven engine simulators (Kiock, 1996). It has been used, e.g. in the EU-project ENIFAIR, for studying engine interference effects (Burgsmüller and Hoheisel, 2000).

In the present paper numerical simulations have been performed for the clean wing configuration (Fig. 12) at a free stream Mach number of $Ma_\infty = 0.75$ and a Reynolds number of $\mathrm{Re} = 4.3 \cdot 10^6$ based on the mean chord length. The incidence has been varied to achieve a lift coefficient of $C_L = 0.500$, which is the design point.

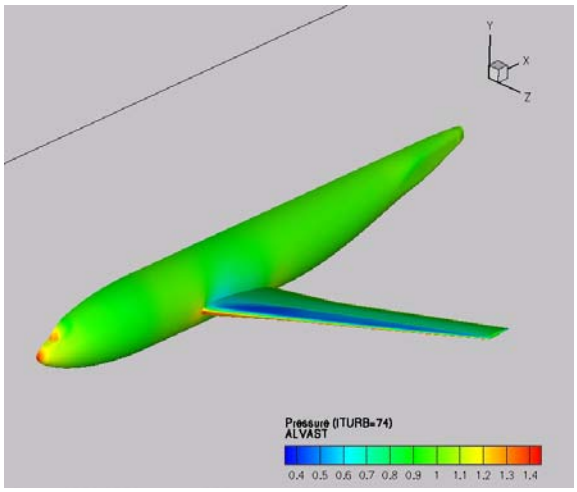

Figure 12. DLR-ALVAST wing-body configuration: wall pressure contours

The computations have been carried out on a grid consisting of $4.1 \cdot 10^6$ cells, where the near wall grid lines have a wall distance well below $y_1^+ = 1$ all over the geometry, except a small portion at the fuselage tail. The artificial dissipation coefficients have been set to $k^{(2)} = 1/2$ for first order accuracy at shocks and to $k^{(4)} = 1/32$ for second order in regions where the solution is smooth. The relatively high value of the latter has been necessary in order to damp oscillations that are generated by a separation zone at the wing-body junction. Nevertheless a rather low value of the Martinelli coefficient (Martinelli and Jameson, 1988) of $\zeta = 0.3$ could have been used, avoiding excessive artificial dissipation in highly stretched cells.

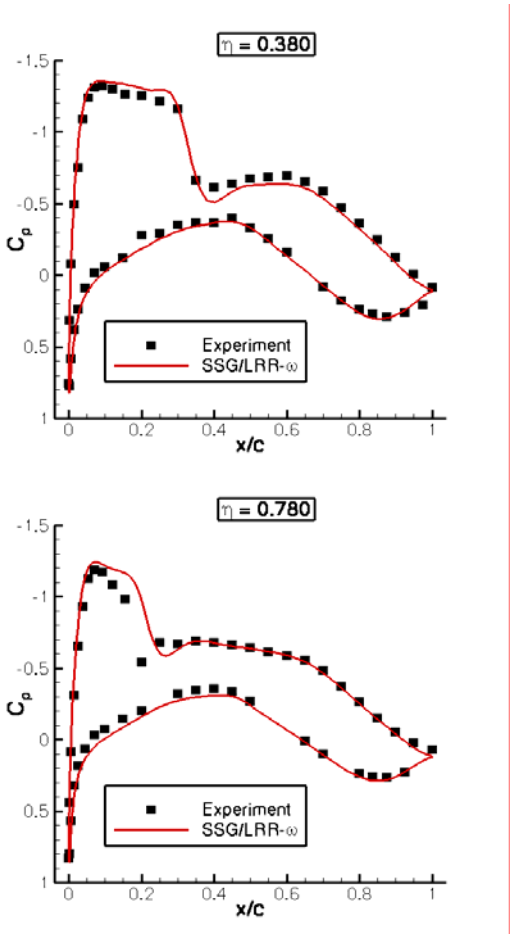

Figure 13. DLR-ALVAST generic aricraft: experimental and numerical pressure distribution at 38% and 78% span.

Figs. 13 show the pressure distributions in two span-wise wing sections obtained with the SSG/LRR-ω SMC[1] (Eisfeld and Brodersen, 2005) in comparison with experimental data from the EU-

[1]The computations of the DLR-ALVAST configuration with the present near-wall RSM are in progress.

project ENIFAIR in the ONERA S1MA wind tunnel (Burgsmüller and Hoheisel, 2000). While the overall agreement is fairly good, some deviations occur with respect to the shock position. It is observed that in the inboard part of the wing the shock is predicted upstream the measured position, while it is predicted downstream the measured position towards the wing tip. These deviations can be attributed to the fact that the model heated up and hence deformed during the experiments.

4. CONCLUSIONS

The performances of a near-wall, Reynolds-stress turbulence model accounting separately for the viscous effects and the effects of Reynolds-stress and dissipation anisotropy are investigated under the transonic flow conditions characterized by the shock formation and strong shock/boundary layer interaction. The overall agreement with the available experimental data for the surface pressure distribution with respect to the shock position is satisfactory in all flow configurations computed. A double-shock-like structure of the flow over the ONERA-M6 wing was captured in good agreement with the experimental findings. Important departures are revealed concerning the shock-induced separation at the RAE2822/10 airfoil which was not captured by the present model. Despite correctly predicted shock position, the departure from the experimentally obtained post-shock pressure level caused attached flow. Further analysis of these phenomena with respect to the specific model features that requires special consideration concerning the compressibility effects and the conditions of strong property variation is in progress.

ACKNOWLEDGEMENTS

The present work is performed in the framework of the German project MEGADESIGN dealing with the aerodynamic simulation and optimisation in the aircraft design. The financial support of the German Ministry for Economy and Technology (BMWi) through the grant 20A0302K for R. Jester-Zürker is gratefully acknowledged.

REFERENCES

[1] 2nd AIAA CFD Prediction Workshop (2003): Orlando, Florida June 21-22, 2003

[2] Burgsmüller, W., Hoheisel, H. (2000): ENIFAIR – EU Research into Engine Integration on Future Transport Aircraft, *Air & Space Europe*, Vol. 2, No. 2, pp. 81-85

[3] Cook, P.H., M.A. McDonald, M.C.P. Firmin (1979): Aerofoil RAE 2822 - Pressure Distributions, and Boundary Layer and Wake Measurements: Experimental Data Base for Computer Program Assessment. *Report of the Fluid Dynamics Panel Working Group 04, AGARD AR 138*

[4] Eisfeld, B. (2004): Numerische Simulation aerodynamischer Probleme mit Reynolds-Spannungsmodellen. *14. DGLR-Fach-Symposium der AG STAB*, University of Bremen, November 16-18

[5] Eisfeld, B., Brodersen, O. (2005): Advanced Turbulence Modelling and Stress Analysis for the DLR-F6 Configuration, *AIAA-Paper 2005-4727*

[6] Fassbender, J.K. (2004): Improved Robustness for Numerical Simulation of Turbulent Flows around Civil Transport Aircraft at Flight Reynolds Numbers, *DLR-Forschungsbericht 2003-09*

[7] Gerolymos, G.A. and Vallet, I. (2002) Wall-normal-free near-wall Reynolds-stress model for 3-D turbomachinery flows. *AIAA Journal*, Vol. 40, No. 2 pp. 199–208

[8] Hanjalic, K., and Jakirlic, S. (1998): Contribution Towards the Second-Moment Closure Modelling of Separating Turbulent Flows. *Computers and Fluids*, Vol. 22, No. 2, pp. 137-156

[9] Hanjalić, K. and Jakirlić, S. (2002): Second-Moment Turbulence Closure Modelling. In *Closure Strategies for Turbulent and Transitional Flows*, B.E. Launder and N.H. Sandham (Eds.), Cambridge University Press, Cambridge, UK, pp. 47-101

[10] Haase, W., Brandsma, F., Elsholz, E., and Leschziner, M.A., and Schwamborn, D. (1993): EUROVAL – A European Initiative on Validation CFD Codes. *Notes on Numerical Fluid Mechanics*, Vol. 42, Vieweg Verlag, Braunschweig

[11] Jameson, A., Schmidt, W., and Turkel, E. (1981): Numerical solutions of the Euler equations by finite volume methods using Runge-Kutta time-stepping schemes, *AIAA-Paper 81-1259*

[12] Kiock, R. (1996): *The ALVAST Model of DLR, DLR-Institutsbericht 129-96/22*

[13] Kroll, N., Rossow, C.C., Schwamborn, D., Becker, K., Heller, G. (2002): MEGAFLOW – A Numerical Simulation Tool for Transport Aircraft Design, *ICAS Congress 2002, Paper No. 1.10.5*

[14] Martinelli, L., Jameson, A. (1988): Validation of a Multigrid Method for the Reynolds Averaged Equations, *AIAA-Paper 88-0414*

[15] Schmitt, V. and F. Charpin (1979): Pressure Distributions on the ONERA-M6-Wing at Transonic Mach Numbers: Experimental Data Base for Computer Program Assessment. *Report of the Fluid Dynamics Panel Working Group 04, AGARD AR 138*

Conference on Modelling Fluid Flow (CMFF'06)
The 13th International Conference on Fluid Flow Technologies
Budapest, Hungary, September 6-9, 2006

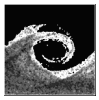

MODELING THE CONDENSATION CLOUD OVER AN AIRCRAFT UNDER VARIOUS FLIGHT CONDITIONS

S.J. KARABELAS[1], N.C.MARKATOS[2]

[1] Corresponding Author. Department of Chemical Engineering, Computational Fluid Dynamics Unit, National Technical University of Athens (N.T.U.A.), Iroon Politexniou 9, 15780, Athens, Greece. Tel +30-210-8030879, e-mail: stkarabelas@hotmail.com
[2] Department of Chemical Engineering,, Computational Fluid Dynamics Unit, National Technical University of Athens (N.T.U.A.).E-mail: N.Markatos@ntua.gr

ABSTRACT

The present study investigates the process of condensation of water vapor to water liquid substance in highly convective flow conditions. An aircraft (model) geometry was chosen to simulate the condensation effects, since this application is of real interest worldwide. The flow is considered subsonic and compressible at high Reynolds number. The contribution of turbulence effects is accounted for by the Spalart-Allmaras model, which is suitable for such type applications. The study of condensation is based on a mixture two- phase model, which allows the substances to be interpenetrating, while following the economical single fluid approach. Furthermore, both phases move at different velocities (slip velocity) in a manner that is described by conservation equations. Results are presented for several flight conditions, concerning the flow Mach number and the ambient air humidity levels. Since the condensation effects are investigated on an aircraft configuration, emphasis has been given to the liquid mass-fraction distribution in several critical areas, where considerable formation of liquid droplets is observed. Results show that for humidity levels higher than 0.8, high liquid concentration areas are indicated onto the rear part of the wings near their roots. For lower relative humidity values, those areas are situated at the rear part of the cockpit. Attention is focused on the dispersion of the condensation cloud and on the areas of mass-transfer interaction. Results are presented here by means of grayscale figures and numerical diagrams.

Keywords: aircraft, condensation cloud, co-trails, humidity, water vapour

NOMENCLATURE

E	$[Joule/m^3]$	total energy
G_v	$[N/m^2]$	production of turbulent viscosity
M	[-]	mach number
P	$[Pa]$	static pressure
S_M	$[Kg/m^3\text{-}s]$	mass source
S_h	$[Joule/m^3]$	latent heat rate release by mass transfer between two phases
T	$[K]$	static temperature
Y_v	$[N/m^2]$	destruction of turbulent
d	$[m]$	distance from the wall
h_{fg}	$[Joule/Kg]$	reference latent heat of condensation
k	$[W/m\text{-}K]$	thermal conductivity
m	$[Kg]$	fluid mass
$\dot{m}$	$[Kg/m^3\text{-}s]$	fluid mass rate
t	$[s]$	time
u	$[m/s]$	velocity component
$\vec{\upsilon}_{dr}$	$[m/s]$	drift velocity vector
$\vec{\upsilon}$	$[m/s]$	velocity vector
v	$[m^2/s]$	eddy viscosity
x_1	$[m]$	x axial coordinate
x_2	$[m]$	y axial coordinate
α	[-]	mass fraction viscosity
μ	$[Kg/m\text{-}s]$	molecular viscosity
ρ	$[Kg/m^3]$	fluid density
τ_{ij}	[-]	stress tensor

Subscripts

c	control volume
eff	effective value
k	index for phases
m	mixture value
sat	variable value in saturation conditions
w.v.	water vapour
1	first phase (air and water vapor)
2	second phase (liquid water)

1. INTRODUCTION

Heat- and mass-transfer processes among phases in multiphase flow systems usually affect considerably the overall flow structure in many engineering applications. Some examples are windy day evaporation, vaporization of moisture and fog,

distillation of a volatile component from a mixture of involatiles, cryogenic pumping and gas cooling and many more.

Humidity conditions affect flight conditions, especially at high altitudes. It is well known that at these altitudes, there is snow formation on the wings, which of course affects the boundary layer flow and changes the values of the aerodynamic forces (different aeroelasticity behaviour). At low and medium altitudes, co-trails are observed near the body of the aircraft, usually near the root of the wing and above the cockpit, which form in high manoeuvrability turns or in direct flight under intense humidity conditions (flight above the sea, humid day, e.t.c).

For forced convection flows, there exist a few references in literature studying heat and mass transfer for multiphase processes but concern mainly laminar flows [1], [18], shock wave flows [7], [15] or industrial flows [10].

The simplest physical model for condensation flows considers the secondary phase as species, which are diffused through the flowfield. A species diffusion equation is solved for the transport of this phase. In this simulation a two phase 'mixture model' was adopted, where the mixture of air and water vapor (moist air) is considered as the primary phase and the liquid water as the secondary. Both faces will exchange momentum and energy, but the dominant term here is the mass transfer due to the ambient humidity conditions.

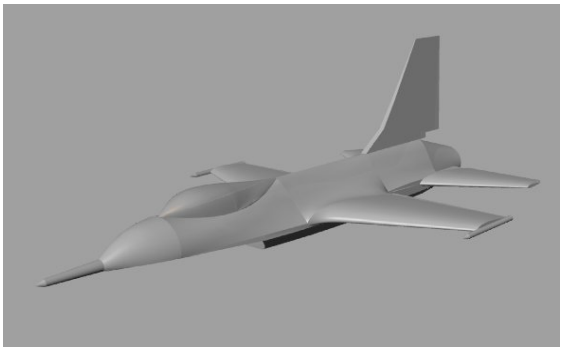

Figure 1. Isometric view of the model

1.1. Geometrical Model

In the present study the geometry examined is that of an aircraft, which was designed based on a simple model. Computer-Aided-Design programs were used to construct the faces. Nurbs modeling was adopted for the design process. Figure 1 represents an isometric view of the model. The computational domain is bounded by four wall regions and another two pressure type boundary conditions (inlet-outlet, figure 2). For computational cases of this type, when turbulence is a significant factor contributing to the flow development, the Spalart-Allmaras one-equation model is a suitable and economical one, as it was specifically designed for aerospace applications with wall bounded areas [16, 17].

Interesting results of volume-fraction and mass diffusion of condensation cloud (consisting of water droplets), have been obtained for various humidity ambient conditions. Particular attention is paid to the critical areas of water vapor condensation.

2. MATHEMATICAL MODEL

2.1. Governing equations

The present modeling is based on the two-phase "mixture model" conservation equations, where the primary phase (moist air) is treated as a compressible fluid and the secondary as incompressible. The conservation equations of mass, momentum and energy are derived by summing the individual corresponding equations for all phases. Also the volumetric constraint has to be applied, which demands the total volume fraction to be equal to 1.0. This model allows for slip velocity formulation, e.g. the two phases may move at different speeds. The flow can be described by the following governing equations:

Continuity:

$$\frac{\partial \rho_m}{\partial t} + \nabla \cdot (\rho_m \underline{\upsilon}_m) = S_M \tag{1}$$

$$\underline{\upsilon}_m = (\sum_{k=1}^{k=2} a_k \rho_k \underline{\upsilon}_k) / \rho_m$$

and $\rho_m = \sum_{k=1}^{k=2} a_k \rho_k$

Momentum:

$$\frac{\partial}{\partial t}(\rho_m \underline{\upsilon}_{mi}) + \underline{\upsilon}_m \nabla \underline{\upsilon}_{mi} = -\nabla p + \nabla \cdot \tau_{ij} + \underline{\upsilon}_{dr,k} \nabla \cdot (\sum_{k=1}^{k=2} a_k \rho_k \underline{\upsilon}_{dr,ki}) \tag{2}$$

where τ_{ij} represents the viscous stress tensor given by $\tau_{ij} = (\mu(\frac{\partial u_i}{\partial x_j} + \frac{\partial u_j}{\partial x_i}) - \frac{2}{3}\delta_{ij}\mu \frac{\partial u_k}{\partial x_k})$ for *i,j*=1,2,3 and $\mu_m = \sum_{k=1}^{k=2} a_k \mu_k$ and $\underline{\upsilon}_{dr,k}$ the drift velocity for phase *k*, which is defined as:

$$\underline{\upsilon}_{dr,k} = \underline{\upsilon}_k - \underline{\upsilon}_m$$

Energy:

$$\frac{\partial}{\partial t}(\sum_{k=1}^{k=2} a_k \rho_\kappa E_k) + \nabla \cdot (\sum_{k=1}^{k=2} a_k \underline{\upsilon}_k (\rho_k E_k + p)) = \nabla \cdot (k_{eff} \nabla T) + S_h \tag{3}$$

where the effective thermal conductivity coefficient

k_{eff} is computed according to the turbulence model used.

Finally, the volumetric constraint has to be applied, which means that the volume fraction of the second phase has to be specified by another equation:

$$\frac{\partial(a_k \rho_k)}{\partial \mathbf{t}} + \nabla \cdot (a_k \rho_k \underline{\upsilon}_m) = -\nabla \cdot (a_k \rho_k \underline{\upsilon}_{dr,k}) \quad (4)$$

In equations (1)-(4), the density of air is assumed to follow the perfect gas law and water is treated as an incompressible fluid. Moreover, laminar viscosity is modeled by Sutherland's equation [4], to account for sharp temperature differences. The properties of the primary phase, which is a mixture (air and water vapor) have to be evaluated. Details for the properties of moist air are given in [6].

Turbulence effects have been examined by Spalart-Allmaras' one-equation model, since it is suitable for aerospace applications. Eq. (5) is the transport equation for eddy viscosity, applied in this model:

$$\frac{\partial}{\partial t}(\rho v) + \frac{\partial}{\partial x_i}(\rho v u_i) = G_v + \frac{1}{\sigma_v}[\frac{\partial}{\partial x_j}\{(\mu + \rho v)\frac{\partial v}{\partial x_j}\} + C_{b2}\rho(\frac{\partial v}{\partial x_j})^2] - Y_v \quad (5)$$

The model involves low computatinal costs, since it is not necessary to calculate a length scale related to the local shear layer thickness. Details for this model may be found in [4], [16] and [17].

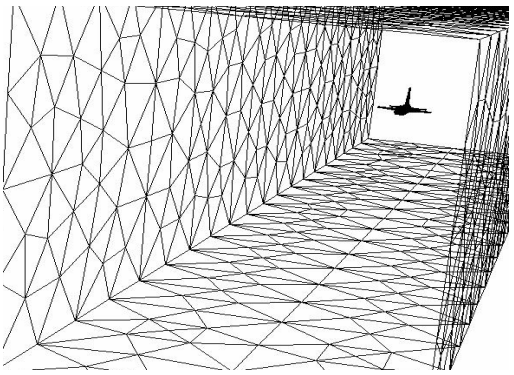

Figure 2. Computational domain for flow calculations

2.2. Multiphase mass and heat transfer

The present model incorporates mass transfer from the primary to the secondary phase (water droplets). We assume that the rate of mass transfer between the two phases is thermodynamically related to the saturation of the water vapor, which is a process dependent upon the ambient humidity conditions. We consider also that the droplets formed by condensation are of diameter 0.01 *mm*. The saturation mass is given by empirical correlations as a function of temperature. The empirical formulation used here is:

$$m_{sat} = 0.001 * (5.018 + 0.3232T + 0.0081847 \cdot T^2 + 0.00031243 \cdot T^3) \quad (6)$$

Eq. (6) predicts quite accurately the saturation mass per cubic meter of air for the usual flight temperature fields. Assuming homogeneous condensation, mass transfer from phase 1 to phase 2 is related to the temperature distribution. The rate of mass exchange between water vapor and liquid can be described by the following state equation:

$$\dot{m} = (u_2 + v_2 + w_2)(m_2) A_c / V_c = (u_2 + v_2 + w_2)(m_{w.v.} - m_{sat}) A_c / V_c \quad (7)$$

Therefore, $m_{w.v.} - m_{sat}$ gives the total water mass. The main contribution at every computational cell is defined according to the local velocity vector and temperature. The total mass rate is considered as a mass source S_M and it contributes to the continuity equation.

The second process, which has to be simulated, coupled with the condensation effect is the latent heat, released to the ambient fluid. This heat rate is also related to the temperature field and contributes as a heat source to the energy equation:

$$S_h = h_{fg} * m_2 \quad (8)$$

2.3. Fluid properties and boundary conditions

The mixture is assumed to be at a given ambient relative humidity. From the moist air properties [6], we compute the volume fraction of water vapor.

At the inflow boundary (fig.2) we impose a given dynamic pressure boundary condition, which means that the total pressure is specified at 130000 *Pascal* and the static at 101325 *Pascal* for moist air. The total temperature at inlet is specified at 315 *K*. At the outlet a fixed pressure of 101325 *Pascal* is applied and the total temperature is specified at 315 *K*. The volume-fraction for the water liquid (secondary phase) is given at both boundaries. Zero-gradient conditions for the energy equation (adiabatic conditions) are applied at the walls and no-slip conditions for velocities. Details for the above types of boundary conditions are given in ref. [19].

3. NUMERICAL SOLUTION PROCEDURE

The mathematical model presented above was implemented in the commercial computational fluid dynamics program FLUENT. The GAMBIT mesh generator was used to create the grid. The solution method for the discretization of the partial differential equations is the finite volume

formulation. The discrete equations are solved by the SIMPLE algorithm of Patankar and Spalding [13]. The equations are solved by an iterative Gauss-Seidel method in conjunction with an algebraic multigrid solver. The second-order upwind scheme is used for the convective fluxes and the classical second order central scheme for the diffusion terms.

The contribution of the extra terms, described above (heat and mass transfer rates) proceeds as follows:

When the mixture temperature is less or equal to the dew point for the specific relative humidity, then activate the heat and mass rate terms described by eqs. (7), (8). In this case the continuity and energy equations are adapted correspondingly. Otherwise, set the two transfer rates at zero and do not account for these terms in the conservation equations. This occurs far away from the aircraft, where the primary phase dominates and the temperature is relatively high (ambient temperature, in our case is 293 *K*).

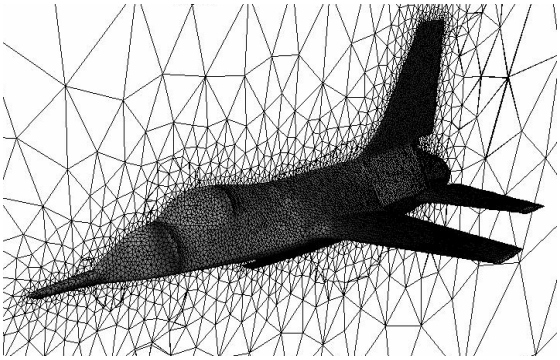

Figure 3. Computational grid on the aircraft's boundaries

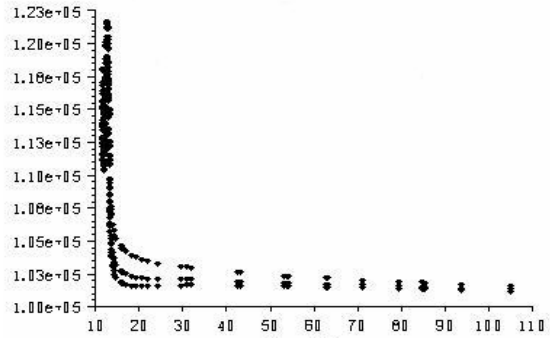

Figure 4. Pressure distribution behind the aircraft. The curves of 410000 and 590000 cells are close together

Figure 3 illustrates the computational domain near the aircraft. For reasons of saving computational time, only half of the aircraft was simulated because of symmetry along the longitudinal axis. To test grid-independency of the results, three unstructured grids were used. The velocity distribution above the main lift-area and near its' root, and the pressure behind the aircraft at the symmetry axis are presented in Figures 4, 5. It is shown that the results obtained with the grid of 410000 cells do not significantly differ from those obtained with 590000 cells (Figs. 4, 5). Accordingly the choice of 495000 cells appears a good compromise between economy and accuracy.

Computational results were obtained on a Pentium IV Machine with a cpu time of about 9 hours for full convergence, when using the 495000 cells grid. Convergence is deemed to occur when the scaled residuals fall below 10e-5.

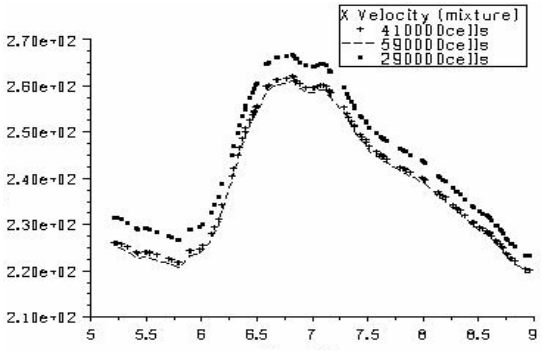

Figure 5. Velocity profiles at a slice near the root of the wings

4. RESULTS AND DISCUSSION

In the present study calculations are performed for flow of moist air over a model aircraft. As it has been already mentioned the temperature distribution on the aircraft is the most significant factor for this simulation, since it affects the mass transfer interaction between water vapor and liquid water. Figure 6 clearly indicates the critical regions, which are dominated by low temperatures. In those areas, a considerable amount of water vapor mass is converted to liquid droplets, changing the balance between both phases. After that transition the liquid mass generated, diffuses towards all directions, as it will be discussed later in detail. The formation of liquid droplets is usually called 'condensation cloud' or 'co-trails' in aeronautical terminology. Some times, depending on the humidity levels and the aircraft's manoeuvres this cloud is visible. Another factor affecting the visibility of the cloud is the diffraction of the sun rays through the sky. Mass fraction profiles depicting this cloud in two and three dimensions are presented in figures 7 and 8, respectively, for relative humidity 70%. The relative humidity of the ambient air is the most important aspect of this process. Higher humidity levels allow condensation at higher temperature levels, since the saturation point is relatively high, while low humidity levels restrict condensation, since the dew point is at lower temperature.

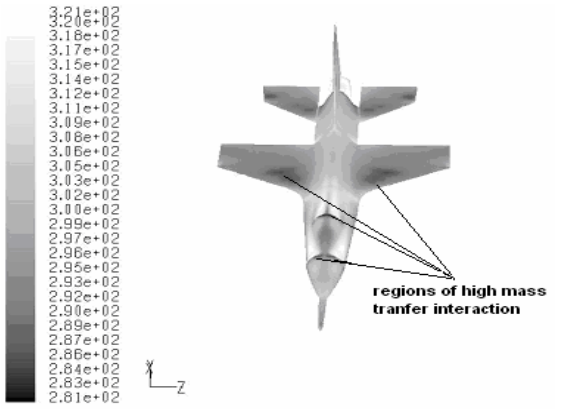

Figure 6. Temperature distribution on aircraft's surface

In this simulation, assuming that the aircraft travels at sea level, the Mach number is about 0.7. This velocity causes a wide temperature distribution as is has been already shown in fig.6. According to water vapor data, for relative humidity levels (0.7, 0.8, 0.9 and 1.0), there is always condensation. Figure 9 demonstrates the effect of humidity level on the water volume-fraction profile along the symmetry plane of the aircraft. It is clearly seen that a 10% increase of relative humidity causes a really impressive increase of the mass fraction distribution.

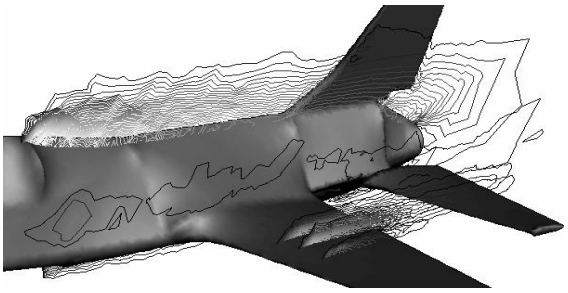

Figure 7. Contours of water volume fraction for 70% relative humidity (slices across the fuselage and the wings of the aircraft)

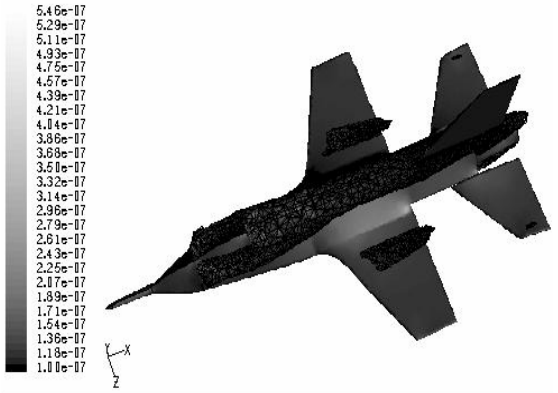

Figure 8. Three dimensional volume fraction distribution-'condensation cloud' (water *gr/Kg* of moist air)

Careful inspection of the above figures, shows that water concentration spreads in regions, where the temperature levels are high. For example, at the rear part of the cockpit, despite the fact that the temperatures are high, there is considerable concentration of water (fig. 7).

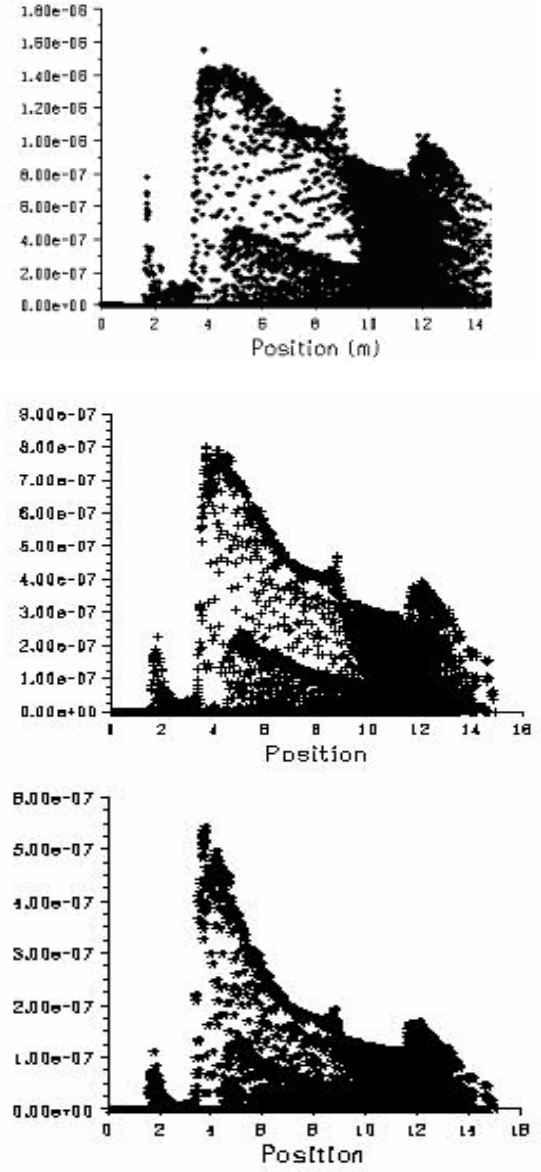

Figure 9. Plots of Volume fraction distribution along symmetry plane. (top 90%, middle 80% bottom 70% rel. humidity)

In those regions no condensation happens, since the dew point is clearly below those temperatures. The existence of the water droplets there, is explained by their transport from elsewhere, as they carry the momentum and energy of the water vapor that generated them. When they enter in regions with no condensation they lose their momentum and energy, because there is no contribution from new droplets generation. The above mechanism explains why there is a significant amount of droplets in

regions of high temperatures. This result is more pronounced in transonic flows. Another interesting result regarding the water concentration is that for low humidity levels we also have maximum droplet concentration behind the cockpit, while for higher values the maximum mass fraction occurs at the rear parts of the wing near the roots. This is because the regions of low temperature at the wings are much wider than those at the cockpit, although the latter one is at lower temperature values. As relative humidity reaches 70% the mass-transfer rate is relatively low and occurs in regions of temperatures below the dew point, which include mainly small areas at the cockpit. On the other hand, observing the mass- fraction profiles at the wings, mass transfer there is low (because of higher temperatures) and there are no circumstances for the development of a dense condensation cloud. However, these circumstances are met at humidity levels higher than 80%, where there exists a wide surface of low temperatures, below the dew point, contributing to high water mass-fraction values. Figure 10 illustrates the water volume-fraction at the aircraft's skin.

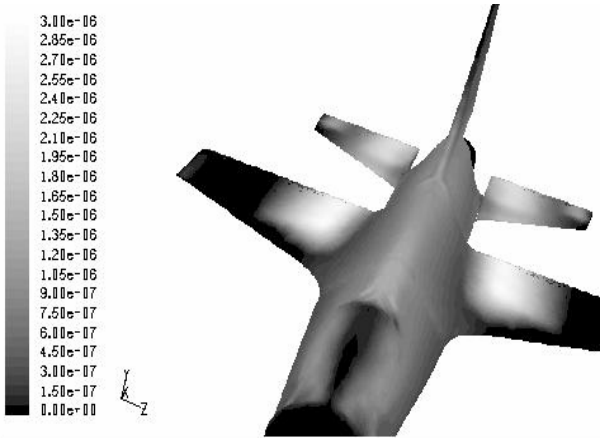

Figure 10. Volume fraction contours onto the wings and fuselage for 80% rel. humidity

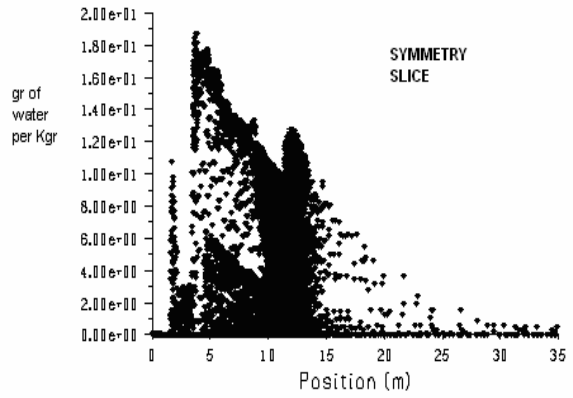

Figure 11. Concentration along symmetry plane. large values correspond to regions near the aircraft

It is of real interest to indicate the point of zero concentration at symmetry plane behind the aircraft in a straight flight at constant velocity and low flight altitude. This point is located according to figure 11, at about 20 meters behind the aircraft. The water velocity field is given in figure 12.

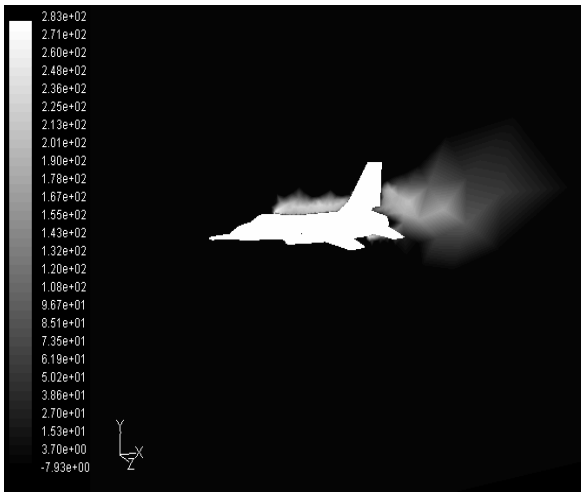

Figure 12. Water velocity field along symmetry plane

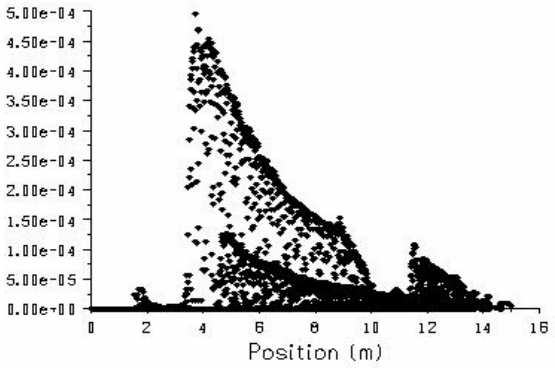

Figure 13. Mass fraction distribution for *M*=0.61

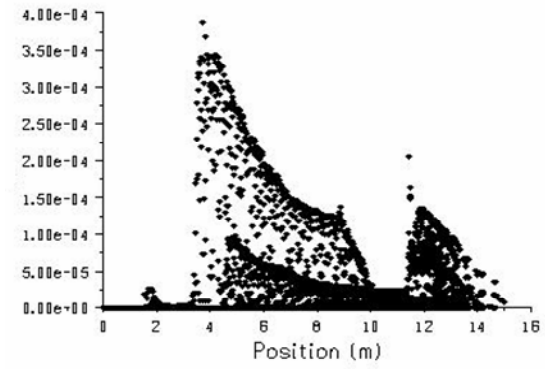

Figure 14. Mass fraction distribution along symmetry plane for *M*=0.55 (*Kg* of water/*Kg* of moist air)

Investigation of the effect of convection on condensation cloud formation also gives interesting results. The convection terms are dominant in the momentum equations at the Mach numbers considered. Three cases are examined with Mach numbers 0.55, 0.61 and 0.7 for ambient relative humidity of 80%. Figures 13,14 and 9 (middle diagram) compare the concentration of water droplets for M=0.55 M=0.61 and M=0.7. It is seen that concentration increases non linearly with Mach number. When M increases by 10% the mean mass fraction distribution is 20-25% higher.

5. CONCLUSIONS

Turbulent flow over an aircraft under the simultaneous influence of thermal and mass transfer due to phase change has been investigated. The effects of humidity conditions and flight Mach number was the motivation for this work. A two phase 'mixture model' approach was used, accounting for the exchange of mass, momentum and energy between both phases. It is satisfying to note that complex fluid-flow problems like the present one can be simulated today within reasonable computer resources. The results appear physically plausible. It may be concluded that:

1. In forced convection flows, the flow is influenced by the mass transfer between the phases and the release of latent heat. The first factor is more significant than the energy release and affects the momentum of both phases.
2. When the humidity levels rise the water mass fraction at the symmetry plane and the wings increases nonlinearly. Furthermore, the regions of maximum liquid concentration are removed from the cockpit area to wings areas.
3. The increase in Mach number reduces the static pressure and temperature at the upper part of the aircraft and simultaneously enriches the water phase with vertical and longitudinal momentum, contributing to a much wider condensation cloud, due to the considerable mass diffusion rates.

More work is required to validate the results by applying the model to realistic flight conditions for which reliable observations exist.

ACKNOWLEDGEMENTS

The contribution of Assistant Professor P.Koytmo (University of Patras), by providing the license for using the commercial software FLUENT and GAMBIT for the numerical implementation is gratefully acknowledged.

REFERENCES

[1] Chow, L. C. and Chung, J.N. "Evaporation of water into a laminar stream of air and superheated steam". Int. J. Heat Mass Transfer, 1982, 25, 499-511.

[2] W. J. Chang, C. I. Weng, "An analytical solution to coupled heat and moisture diffusion in porous materials", International Journal of Heat and Mass Transfer 43 (2000) 3621-3632.

[3] M. K. Choudhary, K. C. Karki, S. V. Patankar, "Mathematical modeling of heat transfer, condensation, and capillary flow in porous insulation on a cold pipe", *International Journal of Heat and Mass Transfer* 47 (2004) 5629-5638.

[4] Sebastian Deck, Philippe Duvaeu, Paulo d'Espincy, Philippe Guillen, "Development and application of Spalart-Allmaras one equation turbulence model to three dimensional supersonic complex configurations", Aerospace Science and Technology pp. 171-183, January 2002.

[5] Eckert, E. R. G. and Drake, R. M., Jr. Analysis of Heat and Mass Transfer. Chapters 20, 22, McGraw-Hill, New York, 1972.

[6] Fujii, T., Kato, Y., and Mihara, K. "Expressions of transport and thermodynamic properties of air, steam and water". Sei. San Ka Gaku Ken Kyu Jo, Report No. 66, Kyu Shu Dai Gaku, Kyu Shu, Japan, 1977.

[7] Jang-Chang Lee; Zvi Rusak, "Transonic Flow of Moist Air Around a Thin Airfoil with Equilibrium Condensation", Journal of Aircraft 2001 0021-8669 vol.38 no.4 (693-702).

[8] M. Kaviany, "Principles of Heat Transfer in Porous Media", Springer, Berlin, 1991.

[9] Manganaro, J. L. and Hanna, O. T. "Simultaneous energy and mass transfer in the laminar boundary layer with large mass transfer rates toward the surface". A.I.Ch.EJ., 1970,16, 204-211.

[10] N.C.Markatos, "Modelling of two-phase transient flow and combustion of granular propellants", Int.J.Multiphase flow, Volume 12, 6, pp.913-933, 1986

[11] N. C. Markatos, "Mathematical modelling of single and two phase flow problems in the process industries", Revue de l' Institute Francais du Petrole, Vol. 48, No.6, pp 631-632, 1993.

[12] N. C. Markatos, "On numerical modelling of embedded subsonic flows", Int. J. Num. Methods in Fluids, Vol.6, pp 103-112, 1986

[13] Patankar, S. V. and Spalding, D. B., (1972), "A Calculation Procedure for Heat, Mass and Momentum Transfer in Three-dimensional Parabolic Flows". International Journal for Heat

and Mass Transfer, 15, 1787-1806.

[14] John C. Tannehill, Dale A. Anderson, Richard H. Pletcher, “Computational Fluid Mechanics and Heat Transfer”, Taylor & Francis Inc, 1997.

[15] Smith, L. T./Yale U., NEW HAVEN, CONN./, “Experimental investigation of the expansion of around a sharp corner”, AIAA Journal 1971 0001-1452 vol. 9 No. 10 (2035-2037).

[16] P. R. Spalart, S. R. Allmaras, “A one equation turbulence model for aerodynamic flows”, AIAA, 1999.

[17] P. R. Spalart and S. R. Allmaras, “A one-equation turbulence model for aerodynamic flows”, Technical Report AIAA-92-0439, American Institute of Aeronautics and Astronautics, 1992.

[18] Wu, C. H., Davis, D. C.,Chung. J. N., and Chow, L. C. “Simulation of wedge-shaped product dehydration using mixtures of superheated steam”.

[19] W. M. Yan, Y. L. Tsay, and T. F. Lin, “Simultaneous heat and mass transfer in laminar mixed convection flows between vertical parallel plates with asymmetric heating”, International Journal *of Heat and Mass Transfer*, Vol. 10, 262-269.

Conference on Modelling Fluid Flow (CMFF'06)
The 13th International Conference on Fluid Flow Technologies
Budapest, Hungary, September 6-9, 2006

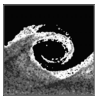

ON THE APPEARANCE OF OSCILLATING FLOW IN ROCKET NOZZLES

José Antonio MORÍÑIGO

Department of Space Programmes, National Institute for Aerospace Technology. Madrid, Spain
Tel.: +34 91 520.1351, Fax: +34 91 520.1384, E-mail: morignigoja@inta.es

ABSTRACT

Cold gas testing of subscale Thrust-Optimized Contour (TOC) rocket nozzles have provided valuable information of the role the characteristic flow structures play on the full-scale (hot-gas) TOC nozzles performances in over-expansion. Given that this class of nozzles thrust space launchers during their early ascent, appearance of strong side-loads and unsteadiness arises as a paramount operational concern as they may compromise the vehicle integrity. From its first time reported evidence [1] to the present, more and more involved research has been undertaken within the aerospace community. Nevertheless, fundamental aspects concerning underlying physical mechanisms remain unclear, so further investigation is needed.

Recent data recorded with pressure transducers in cold gas specimens [2-4] have emphasized an interesting behaviour concerning the flow unsteadiness: a low-frequency band, say under 100 to 200Hz, holds the greater part of the spectral power, hence indicating a trend of the over-expanded flow to oscillate for stable supply chamber conditions. In addition, axisymmetric and 3D time-accurate simulations [5,9] agree with this pheno-menon. The present study focuses the appearance of oscillating flow in TOC nozzles by means of numerical simulation, carried out using an unsteady Reynolds averaged Navier-Stokes (URANS) solver. Results stress the development of sustained osci-llations at definite tones for prescribed Nozzle Pressure Ratios (NPRs).

Keywords: optimized contour nozzles, over-expanded flow, self-sustained oscillations

NOMENCLATURE

f	$[Hz]$	frequency
k	$[m^2/s^2]$	turbulent kinetic energy
p	$[Pa]$	pressure
r, x	$[m]$	radial, axial coordinate
t	$[s]$	time
L	$[m]$	nozzle length
M	[-]	Mach number
NPR	[-]	nozzle pressure ratio, p_c/p_{amb}
T	$[^oK]$	temperature
γ	[-]	specific heats ratio
θ	[º]	azimuthal coordinate
μ	$[m^2/s]$	dynamic viscosity
Δ	[-]	increment

Subscripts and Superscripts

amb	ambient
avg	temporal average
c	chamber conditions
div	divergent of the nozzle
imp	impingement
jet	jet (inflow) conditions
l	laminar
n	nozzle
p	*plateau*
r	reattachment
sep	separation
st	steady
t	turbulent, stagnation
w	wall
–	spatial mean

1. INTRODUCTION

Various experimental and numerical studies have appeared in the literature concerning the TOC nozzles phenomenology. The first work on this topic is attributed to Nave & Coffey [1], who reported an hysteresis loop to occur for the subscale J-2S nozzle and the development of two different flow regimes, the so-called separation modes: the Free Shock Separation (FSS), where the flow experiences shock-induced separation and does not reattaches to the wall; and the Restricted Shock Separation (RSS), where flow reattaches to the wall after separation. FSS and RSS terminology is due to Frey & Hagemann [10,11] and of commonly use at present. More than two decades separate this work from the numerical investigation of Chen et al. [12] on the steady and transient operation of the subscale

J-2S nozzle, and computed using RANS and a modified Baldwin-Lomax closure. The goal of Chen *et al.* was to capture both branches of the hysteresis loop and, as a result, the duality of the flowfield (FSS and RSS modes) for a range of NPRs; in addition, they reported for the first time the formation of a large region of reverse flow anchored inmediately after the shock pattern. This recirculation region has been laterly obtained in simulations carried out with different TOC nozzles [2,13-15]; in particular, for the subscale J-2S nozzle [6,7]. Controversy on its real existence disappeared after its empirical confirmation [16].

Unsteadiness has been investigated in TOC nozzles with experimental techniques and numerical simulation. Hence, separation modes transition has been analyzed by Alziary (both experimental and numerical, [2]) and Nguyen et al. (experimental, [3,4]). Furthermore, bursting of separation bubbles during startup and shutdown transients was focused by Tomita et al. [17]. Main conclusions of these works state a major implication of separation bubble bursting and modes transition in triggering side-loads. Additionally, recent tests with TOCs have revealed that pressure fluctuations exhibit much of their energy in the low-frequency band, below 200Hz [2-4]. To some extend, similar low-frequency response has been also reported in over-expanded planar nozzles by Reijasse et al. [18].

From the numerical standpoint, the axisymmetric URANS simulations conducted by Alziary [2] and the author [6,7] with TOC nozzles, are in agreement with the oscillations evidence, and periodic low-frequency fluctuations develop at prescribed NPRs. Statistical correlations of pressure data given by Nguyen et al., suggest that the recompression shocks experience a quasi-axial pulsating motion. Regarding unsteady 3D RANS simulations Deck & Guillen [19] have pointed out an asymmetrical separation pattern and low-frequency pressure pulsations emanating from the separation line in a truncated ideal contour (TIC) nozzle. For TOCs, Moríñigo & Salvá [8,9] have shown for the subscale J-2S nozzle the development of self-oscillating flow and what seems to be a synchronized response of the flow, which generates a coupling between the side-loads and the thrust oscillations.

This paper is organized as follows. Section 2 summarizes the experimental data concerning flow unsteadiness and fluctuations reported to occur in subscale TOC nozzles. In section 3, prediction of the separation point in over-expanded rocket nozzles is addressed in the frame of available data and solver. Numerical results of the development of sustained oscillating flow with time-accurate axi-symmetric and three-dimensional (3D) modelling are provided. Section 4 presents the analysis of an annular-jet, which constitutes a testcase to investigate the sustainment of oscillations. Section 5 discusses shocks fluctuations. Finally, section 6 summarizes the results.

2. FLOW IN TOC NOZZLES

2.1. Flow Structure

The flowfield structures corresponding to the two attainable stable flow regimes in TOCs for the same NPR are outlined in Figure 1. FSS separation mode constitutes the standard shock-induced separation extensively visualized in planar nozzles, where fluid from the outside is entrained and a small recirculation bubble anchores near the nozzle lip. The FSS mode is typically associated to low-NPRs in the startup of rocket nozzles. During the startup, at some NPR, say NPR_2, the flow suddenly evolves from FSS to RSS (denoted FSS→RSS).

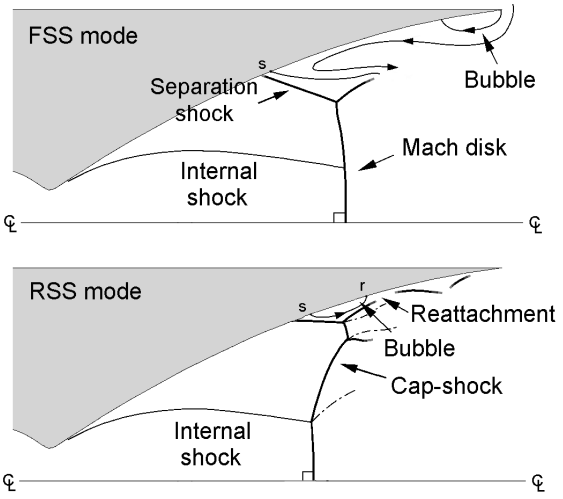

Figure 1. Sketch of a nozzle meridional section, with the FSS and RSS modes at a given NPR.

Conversely, in the shutdown phase the flow passes from RSS to FSS at certain $NPR_1<NPR_2$ (RSS→FSS transition). Therefore, the range [NPR_1, NPR_2] determines the TOCs hysteresis regime where both separation modes may be observed. The shock pattern that appears in the RSS mode depicted in Fig.1, is called 'cap-shock' in the literature due to its characteristic form. The formation of the cap-shock obeys to the interference of the recompression shock (Mach-disk) with the internal shock which emerges from the nozzle throat vicinity. A discussion on the transition from the Mach-disk structure to the cap-shock pattern formation is provided in [7].

Furthermore, a large reverse flow region arises in the RSS mode, downstream the cap-shock pattern. Figure 4 shows the recirculation bubble structure for the RSS mode in the J-2S TOC nozzle at NPR=43 (from [6]); flow reattachment is inferred out of the jet-diverging outflow exiting the nozzle.

2.2 Low-frequency Unsteadiness

Recent experimental studies on subscale TOC nozzles support the development of low-frequency fluctuations in the flow. In this respect, Alziary [2] has reported large-scale self-oscillations in a TIC nozzle from the spectral analysis of the pressure data at multiple wall locations (moreover, his time-accurate axisymmetric simulations in a TOC nozzle have shown a pseudo-periodic displacement of the cap-shock).

Additionally, Nguyen et al. [3,4] report very low-frequency pressure fluctuations to occur in a TOC nozzle at the vicinity of the separation line, for both FSS and RSS modes. Examination of the power spectral density (PSD) has pointed out that the increase of the fluctuations level with NPR is due to the increase of the low-frequency contribution. No azimuthal phase shift is observed in the range <100Hz, and the low-frequency unsteadiness persists far away in the separated flow region.

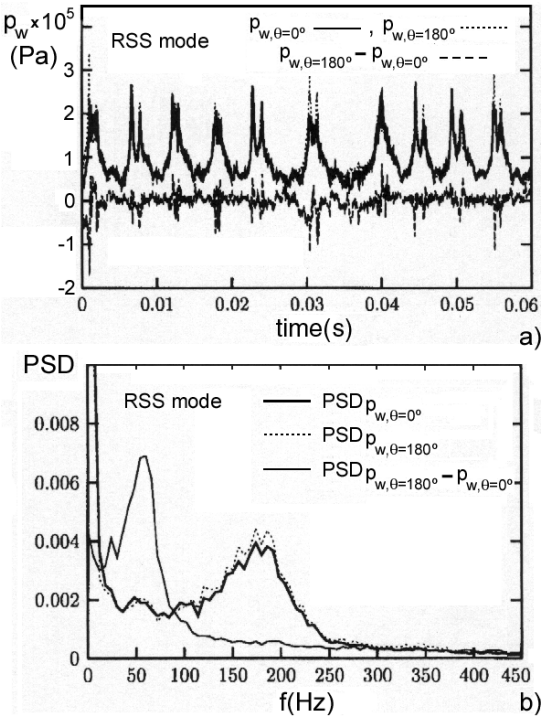

Figure 2. Wall pressure: a) Fluctuations; and b) PSDs at NPR=42.6 in a TOC nozzle with RSS mode. Pressure measured at two opposite points ($\theta=0^o$ & 180^o) in a cross section at $x/L_{div}=0.975$, and their difference (data from [4]).

For the RSS mode, they have suggested the existence of a quasi-axial pulsation of the cap-shock which induces very intense pressure fluctuations, as it is visible in Figure 2a (p_w peaks over 2bar). The PSD plotted in Fig. 2b reveals that the spectral content of the side-loads presents a bump centered at ~50Hz, in agreement with the frequency data registered by Nave & Coffey. This pseudo-periodic pulsating nature of the flow was already advanced by Frey & Hagemann [20] in the context of the so-called 'end-effects' regime (when the separation shock is close to the lip), but it remains unclear, in part motivated by the difficulties regarding the direct visualization of the flow structures.

The work of Verma & Ciezki [21] confirms that in the RSS mode the separation line experiences asymmetry and oscillates in a wavy pattern. The experiments of Tomita et al. [17] with a compressed contour nozzle have verified this behaviour. Their visualizations capture the asymmetrical movement of the separation line during the FSS↔RSS transitions and it is concluded that the bursting and formation of separation bubbles near the nozzle lip provokes high levels of side-loads. Also Alziary reports peaks of side-loads during the RSS mode and incresasing NPR, linked to the strong unsteadiness of the flow that appears when the separation bubbles open to the ambient when the reattachment point of the RSS mode reaches the nozzle lip. It is noted that side-loads are not limited to TOCs, but they appear in over-expanded planar, conical and TIC nozzles, since separated flow exhibits a certain degree of asymmetry which implies side-loads, but with a much lesser intensity than in TOCs.

3. NUMERICAL RESULTS

3.1. Solver and Turbulence Modelling

The code [22] solves the 3D RANS equations on multiblock structured grids. Gas is assumed ideal and Newtonian; laminar viscosity follows the Sutherland´s law. The algorithm implements a semidiscrete cell-centred finite volume formulation with 2nd order discretization in space and time. Turbulence is modelled with two-equation k-τ linear eddy viscosity closure of Speziale et al. [23] ($\tau=k/\varepsilon$: turbulence timescale) and $y^+\sim1$ condition is satisfied by y^+-grid adaptations in the simulations. Eddy viscosity μ_t is modified with a turbulent stress limiter [24] to ensure the realizability condition. Time-accurate simulations have been carried out using the dual time stepping scheme with time step of 1ms.

3.2. Prediction of the Flow Structure

Separation prediction is an important topic to check for the assessment of the solver results. In a previous work [6], it has been shown that the computed meridional wall pressure distributions match remarkably well their experimental counterpart for a set of NPRs; unfortunately, the reduce number of available pressure data for the J-2S impedes the precise determination of the separation station in tests. Hence, this section extends the comparison to the correlation of Schmucker [25], which constitutes a method of widespread use to

predict separation in over-expanded rocket nozzle flows. Schmucker criterion relies on correlating the pressure and Mach number upstream the separation shock, at the boundary layer edge

$$\frac{p_{sep}}{p_{amb}} = NPR \cdot \frac{p_{sep}}{p_c} = \left(1.88 \cdot M_{sep} - 1\right)^{-0.64} \qquad (1)$$

where

$$M_{sep} = \sqrt{\frac{2}{\gamma - 1}\left[\left(p_c / p_{sep}\right)^{\frac{\gamma-1}{\gamma}} - 1\right]} \qquad (2)$$

In strict sense, Eq. (1) is only applicable to separated-non-reattached flows (that is, FSS mode). Figure 3a presents this situation for a wide range of NPRs, exhibiting a close fitting to the simulations trend.

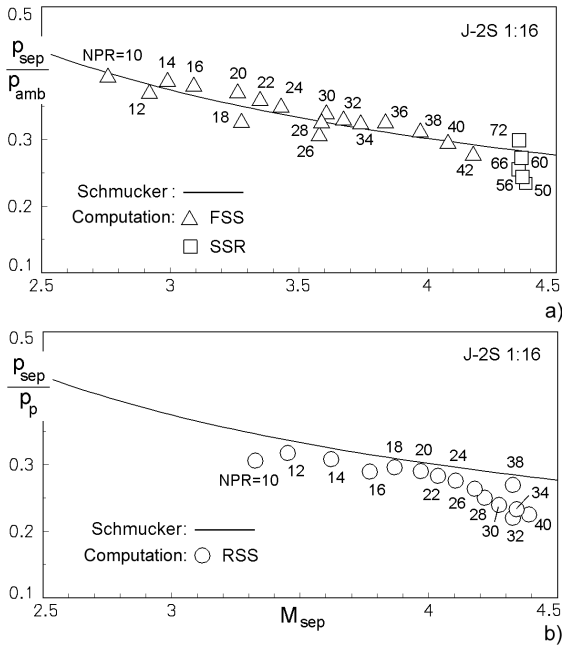

Figure 3. Separation location predicted by the Schmucker criterion; and computed NPRs for: a) FSS mode; and b) RSS mode.

For completion, Schmucker formulae has been re-written using the *plateau* pressure p_p instead of p_{amb} to test it with the RSS mode results. From the ratio p_{sep}/p_{amb} expressed as $(p_{sep}/p_p)\cdot(p_p/p_{amb})$, the term p_{sep}/p_p is then plotted in Figure 3b. It is seen that its prediction is acceptably good for NPR<~26, but it deteriorates as NPR approaches NPR~43, value at which the reattachment line reaches the nozzle lip and transition RSS→FSS occurs.

Figure 4 depicts a flow snapshot at NPR=43, where the cap-shock and large recirculation bubble are apparent. Side-by-side comparison with the Schlieren picture stresses the quite similar structure obtained in the exiting outer-jet. The density and Mach gradients clearly delimit the crosswise extension of the two jets that constitute the flow topology of the RSS mode: the subsonic inner-jet, and the supersonic outer-jet (see Fig.4a).

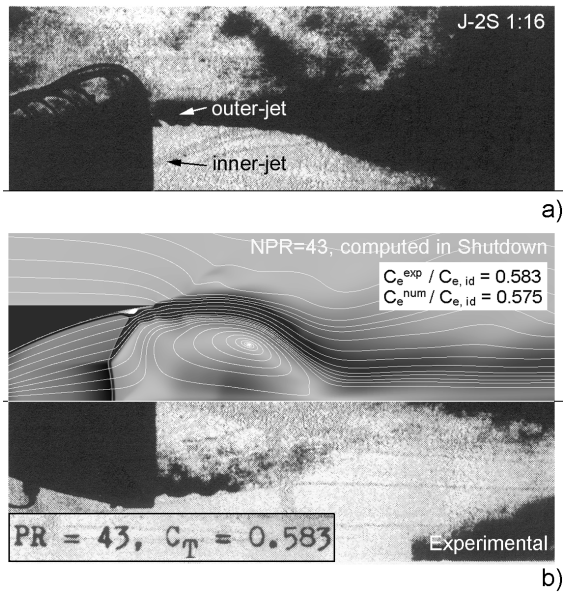

Figure 4. Subscale J-2S nozzle with RSS mode at NPR=43: a) Schlieren image; and b) Numerical-experimental comparison (upper half: computed Mach plot & streamlines; lower half: Schlieren). Thrust efficiency ($C_e/C_{e,id}$) is also compared.

3.3. Self-oscillations in TOCs

This section gathers together the frequency data obtained from the time-accurate axisymmetric and 3D simulations of the subscale J-2S nozzle [6-9]. The results indicate that the flow exhibits defined sustained oscillations at dominant tones for all the NPRs. Frequencies are given in Tables (1) and (2). For convenience, a third SSR (Shock Separation with Recirculation) mode is added to the FSS / RSS clasification, which refers to the case of separated-non-reattached flow with a recirculation bubble downstream the shock pattern (attained at large NPRs in the J-2S nozzle).

Table 1. Sustained oscillations in the J-2S nozzle obtained with axisymmetric simulation.

NPR	30, FSS	30, RSS	50, SSR	65, SSR
f(Hz)	63.2	41.8	45.0	58.2

Table 2. Sustained oscillations in the J-2S nozzle obtained with 3D simulation.

NPR	24, RSS	27, RSS	30, RSS	43
f_a(Hz)	24.1	33.6	28.6	22.9
f_t(Hz)	12.0	16.6	14.3	11.4

Periodic oscillations develop for separated-non-reattached and reattached flow, in consonance with the observations in TOCs [1,3,4]. Their amplitude turns out to be quite dependent on the separation mode; whereas the fluctuations amplitude remains small in the FSS & SSR modes, the RSS mode exhibits large-amplitude axial displacements of the shock pattern, which lead to significant oscillations of the nozzle thrust and peaks of side-loads. Particularly, the 3D simulation at NPR=43 has revealed very strong axial flow pulsations at ~23Hz, in close agreement with the experiments.

Flow structure into the nozzle and in the plume computed with axisymmetric and 3D modelling is laid out in Figure 5. In terms of spectral content, axisymmetric simulations exhibit one major tone, while the 3D results evidence two major tones f_a, f_t~ $f_a/2$, corresponding to the leading longitudinal (thrust) and transverse (side-loads) oscillating modes. Further details suggesting synchronization of thrust with the side-loads are given in [8,9].

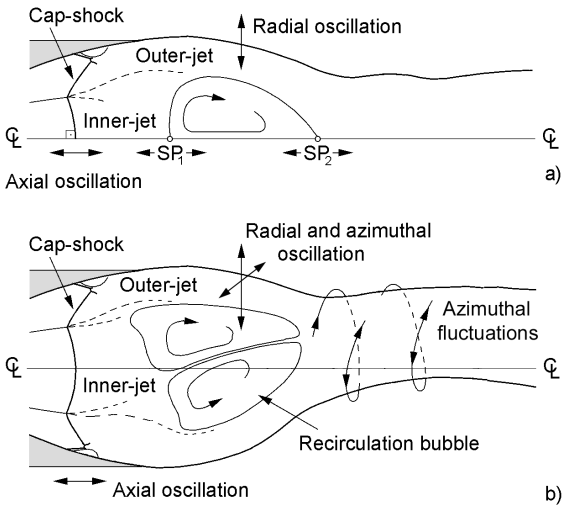

Figure 5. Layout of the coaxial jets structure and large recirculation bubble for the RSS mode, computed with: a) Axisymmetric modelling (SP: stagnation point); and b) 3D simulation.

4. ANNULAR-JET RESPONSE

4.1. Simulation Setup with Coupling

The complex interactions among strong shocks, co-flowing jets and recirculating flow in TOCs, makes difficult to identify the mechanisms that sustain low-frequency fluctuations by means of axisymmetric and 3D modelling. Thus, lack of understanding may be attributed to the intrinsic complexity, difficulties regarding the direct visualization of structures and demanding cost of time-accurate simulations.

Such aspects have motivated to analyze the simpler case of an annular-jet of air discharging into the ambient, in an attempt to gain additional understanding on how oscillations may be or not sustained when the jet experiences some kind of coupling with the downstream fluctuations. In this sense, the turbulent mixing and jet impingement at the rear part of the recirculation bubble resemble the interaction that occurs with the outer-jet in the TOC nozzle, as can be seen in Figure 6. Testcase geometry, grid and flowing conditions are specified in Appendix A. Radial width of the annular-jet is similar to the nozzle outer-jet extension. Besides, uniform radial profiles have been set for stagnation and turbulence magnitudes (M_{jet}~0.48).

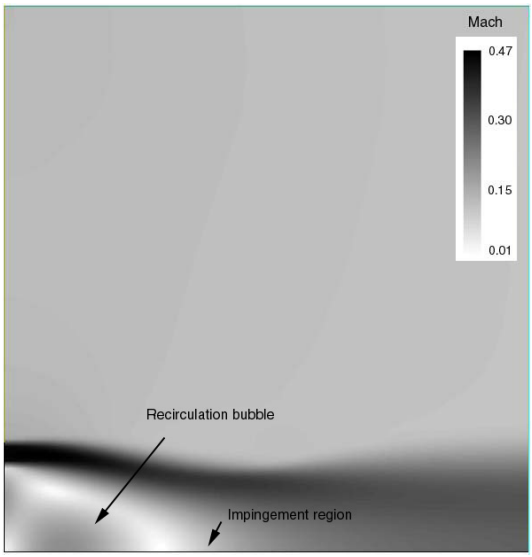

Figure 6. Snapshot of the subsonic Mach field, where jet spreads due to turbulent mixing.

Time-accurate axisymmetric simulations have been carried out to explore the appearance of flow oscillations. Coupling effects on driving oscillations are here analyzed by means of imposing a coupling relationship in one of the BC_{jet} variables (p_t, T_t or $\mu_{t,jet}$). Therefore, coupling of a generic variable σ at BC_{jet} to the downstream pressure level behind the recirculation bubble (Fig. 6) is enforced by the expression

$$\sigma = \bar{\sigma} \cdot \left(1 + \alpha_c \frac{\Delta \bar{p}_{imp}}{\bar{p}_{imp,st}}\right) \qquad (3)$$
$$\text{with } \Delta \bar{p}_{imp} = \bar{p}_{imp}(t) - \bar{p}_{imp,st}$$

which updates the jet boundary condition at each time step (σ stands for $p_{t,jet}$, $T_{t,jet}$ or $\mu_{t,jet}$ depending on the coupling considered). Coupling parameter α_c introduces amplification upon the jet inlet response to the impingement pressure p_{imp} fluctuation,

averaged over the axis segment ab (see Fig. 11). Simulations have been conducted for various coupling factor in the range [10^2, 10^4] and accomplished in two stages: a first stage to initialize the flowfield, where convergence is attained with time-marching; and a second stage that corresponds to time-accurate integration out of the initialized flowfield and using the same numerical schemes and eddy viscosity modelling as in the TOC nozzle simulations. A perturbation $\delta p_t \sim 0.05 p_{t,\mathrm{jet}}$ is added to $p_{t,\mathrm{jet}}$ at $\mathrm{BC_{jet}}$ at the starting time. Plots of time response are given in the next section.

4.2. Sustained Oscillations

Results indicate that sustained flow oscillations may arise when coupling according to Eq. (3) is established. Specifically, simulations with coupling in $\sigma=p_{t,\mathrm{jet}}$ or $T_{t,\mathrm{jet}}$ reveal damping to rest in a short time. An example of this situation is illustrated in Figure 7 for α_c=1000, where the plot of the time-varying spatial averaged static pressure at the jet impingement region, indicates that the initially developed oscillations (triggered by δp_t) decay in amplitude until they disappear. On the contrary, simulations performed with coupling in $\sigma=\mu_{t,\mathrm{jet}}$ exhibit sustained oscillations.

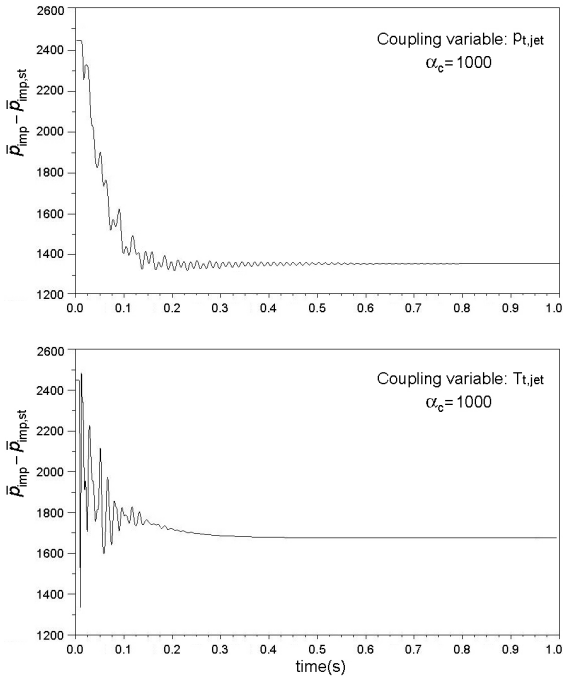

Figure 7. History of static pressure (p_{imp}) at axis impingement region for simulations with strong coupling (α_c=1000) in stagnation pressure (upper plot) & temperature (bottom plot).

A set of simulations with varying α_c for $\sigma=\mu_{t,\mathrm{jet}}$ has shown that sustained oscillating flow appears at large enough coupling parameter α_c in the coupling relationship. Pressure at the impingement region for the non-oscillating (low α_c) and oscillating flow (high α_c) is plotted in Figure 8, where the different behaviour is visible. A map with the regions of non-oscillating and oscillating flow is depicted in Fig. 8; transition between both is determined to occur at $\alpha_c \sim 700$. Sustained oscillations imply pressure fluctuations of 1-3% regarding $p_{\mathrm{imp,st}}$ at the jet impingement region (of increasing amplitude with the coupling parameter).

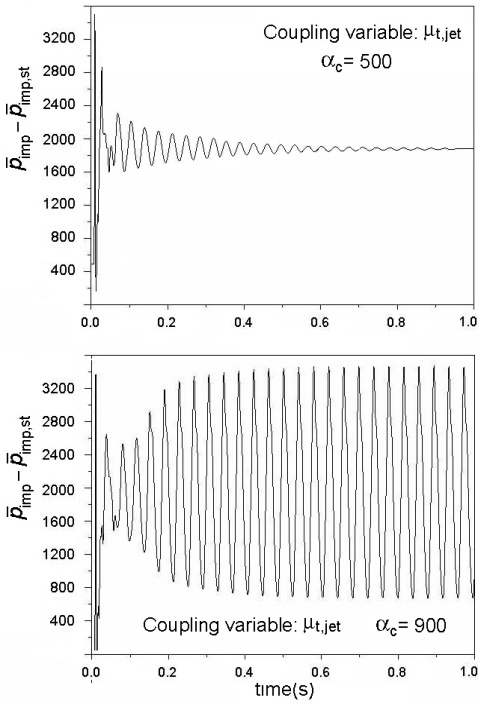

Figure 8. History of static pressure (p_{imp}) at axis impingement zone obtained for α_c=500: damped oscillations (upper plot); and α_c=900: sustained oscillations at ~32Hz (bottom).

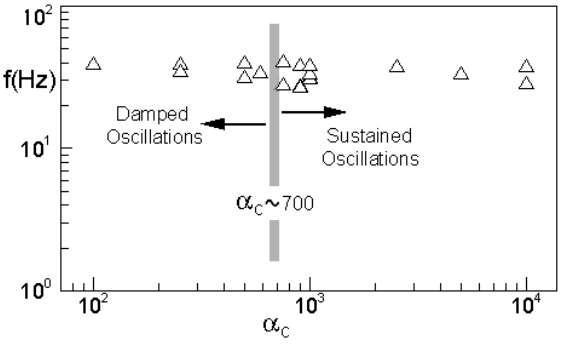

Figure 9. Annular-jet response to α_c (coupling variable: eddy viscosity).

5. SHOCK FLUCTUATIONS

In over-expanded nozzles and diffusers, shocks adjust their location to adapt the flow in pressure. Thus, oscillating shocks for fixed NPRs impose a

time-dependent pressure distribution near the shock pattern. Experiments have shown all components of the velocity fluctuations are amplified across a shock and turbulent kinetic energy (TKE) tends to saturate for upstream shock Mach number beyond M~3 [26,27]. In the present URANS computations accomplished for the J-2S nozzle with the eddy viscosity closure k-τ of Speziale et al., turbulent viscosity experiences an abrupt increase across the shocks (dependent on the shock strenght), reduced in part by means of the realizability constraint implemented in the TKE equation, according to Moore and Moore [24].

Table 3. TKE jump across the shock and eddy viscosity fluctuation per oscillation cycle at the J-2S nozzle axis for selected NPRs (station 1: upstream / 2: downstream the shock)

NPR	TKE_2/TKE_1		$\Delta\mu_t/\mu_{t,avg,2}$
	max	min	in %
64,SSR	4.3	3.3	19
50,SSR	4.2	2.9	24
40,RSS	4.5	2.6	34
30,RSS (FSS)	3.8 (3.6)	2.6 (2.9)	29 (18)
20,RSS (FSS)	3.7 (3.3)	2.7 (2.8)	26 (14)

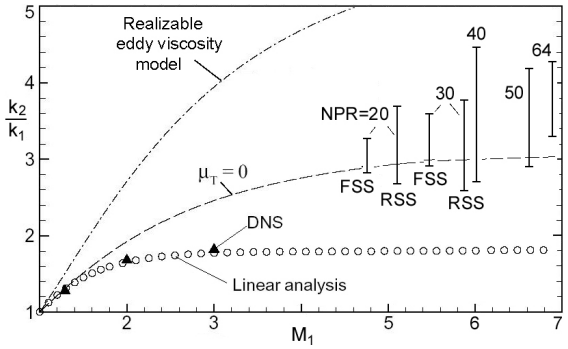

Figure 10. TKE amplification across a shock as a function of the upstream Mach. Simulated nozzle NPRs are compared with the results of eddy viscosity assumption and direct numerical simulation (DNS) data [26].

In addition to obtain the correct trend in eddy viscosity, realizability yields k-τ values independent of the grid resolution. The jump experienced by the TKE and eddy viscosity across the shock pattern in the J-2S nozzle is shown in Table (3) for the simulated NPRs (shock location at the nozzle centerline is selected for properties evaluation). In comparison with the k-production reported across strong shocks [26,27], the results exhibit over-prediction of the amount of TKE amplification caused by the shock, as it is seen in Figure 10. This graph shows that the use of a realizability constrain yields much lower TKE amplification, so provides an improved prediction compared with the one obtained using the original k-τ formulation.

The large fluctuation of μ_t downstream the shock, up to ~35% for the analyzed NPRs, confirms that the shock pattern drives the eddy viscosity level left by the shock front. Hence, as a shock moves, the eddy viscosity varies. This coupled response holds similarities with the coupling mechanism analyzed in the annular-jet case, albeit it is known that shock displacement due to low-frequency downstream perturbations occurs with a phase shift dependent on the oscillation frequency [28], not encompassed in the preceding annular-jet study.

6. SUMMARY

Unsteady axisymmetric and 3D RANS simulations with eddy-viscosity modelling have shown the development of sustained oscillations in subscale TOC rocket nozzles in over-expansion at prescribed NPRs. Appearance of low-frequency tones exhibit close agreement with the spectral energy content reported in experiments.

To investigate this periodic nature and feedback mechanisms that participate, the simpler testcase of a compressible subsonic annular-jet of cold gas has been focused. Here, the oscillations due to upstream feedback of downstream flow fluctuations appear when a coupling condition is enforced. Preliminary results of the annular-jet time response point out to the interaction of the inflow turbulent viscosity with the downstream pressure fluctuations (by the rear end of the recirculation bubble) as one possible cause of self-oscillations sustainment. In TOC nozzle, the shock pattern oscillations leads the eddy viscosity to vary accordingly across it. Then, the cyclic displacement of the shock pattern as the downstream pressure fluctuates, implies a cyclic change of the TKE production and, therefore, of the turbulent viscosity left by the shock front, which mimics the effect analyzed in the annular-jet case.

It is emphasized that the annular-jet study has permitted to isolate the cyclic behaviour of the eddy viscosity to the downstream flow perturbations. In particular, the jet inflow response due to pressure feedback arises as a plausible cause of the low-frequency energetic fluctuations that develop, in consonance with the TOC nozzle simulations. A further investigation on this topic is in progress.

ACKNOWLEDGMENTS

The author expresses his gratitude for the contribution to this work made by José J. Salvá of the Polytechnic University of Madrid; and thanks Franco Magagnato of the Technical University of Karlsruhe for making available his solver.

Access to computing resources at the Centro de Investigaciones Energéticas, Medioambientales y Tecnológicas (CIEMAT, Madrid) is acknowledged.

APPENDIX A: CASE OF ANNULAR-JET

A layout of the annular-jet testcase discharging into air near to rest and domain extension used in the simulations is shown in Figure 11. Jet blockage ratio corresponds to 48/60=0.8 (ratio of disk wall to upper jet-lip radial extension).

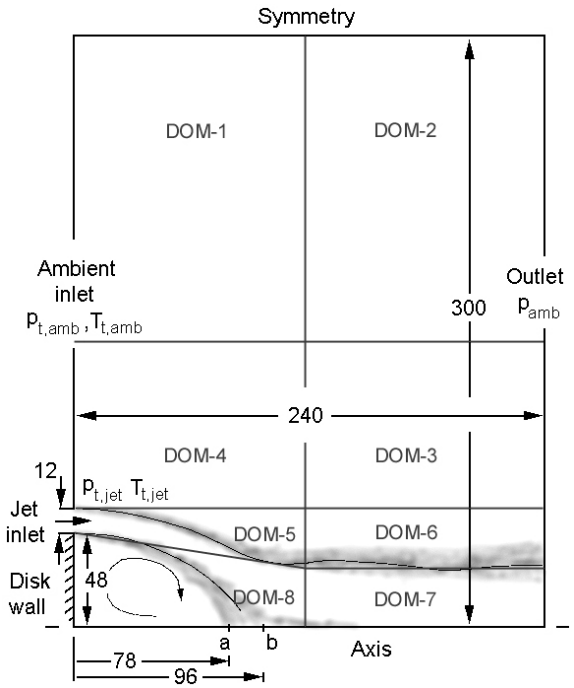

Figure 11. Annular-jet geometry, grid blocking (DOM-1 to -8) and boundary conditions setup (dimensions in mm).

Air inlet and outlet Boundary Conditions (BCs) implement 1D-Riemann invariants. Jet and ambient thermodynamic state is given in Table (4).

Table 4. Boundary conditions at inlets & outlet.

BC	Jet	Ambient	Outlet
p_t (Pa)	$1.14 \cdot 10^5$	$1.01 \cdot 10^5$	10^5 (p_{amb})
T_t (ºK)	300	300	—
μ_t/μ_l	10^4	1	—

A structured grid that comprises 8 blocks of 96(axial)x48(radial) cells each, has been generated. Radial clustering of the nodes is set at the jet-inlet edges and shear layers regions.

REFERENCES

[1] Nave, L.H., and Coffey, G.A., 1973, "Sea Level Side Loads in High-Area-Ratio Rocket Engines", AIAA *Paper* 73-1284.

[2] Alziary de Roquefort, T., 2001, "Unsteadiness and Side Loads in Over-expanded Supersonic Nozzles", *Proc. 4th European Symp. Aerothermodynamics for Space Vehicles*, ESA SP-487, Capua, Italy.

[3] Nguyen, A.T., Deniau, H., Girard, S., Alziary de Roquefort, T., 2002, "Wall Pressure Fluctuations in an Over-Expanded Rocket Nozzle", AIAA *Paper* 2002-4001.

[4] Nguyen, A.T., Deniau, H., Girard, H., Girard, Alziary de Roquefort, T., 2003, "Unsteadiness of Flow Separation and End-effects Regime in a Thrust-optimized Contour Rocket Nozzle", *Flow, Turbulence and Combustion*, Vol. 71, pp.161-181.

[5] Deck, S. and Nguyen, A.T., 2004, "Unsteady Side Loads in a Thrust-optimized Contour Nozzle at Hysteresis Regime", *AIAA J.*, Vol. 42, N^{er} 9, pp. 1878-1888.

[6] Moríñigo, J.A and Salvá, J.J, 2002 "Numerical Investigation of the Separation Modes Transition and Hysteresis in the Sub-scale J2S Rocket Engine Nozzle", *Proc. 4th Int. Conference on Launcher Technology*, Liège, Belgium.

[7] Moriñigo, J.A., 2003, "Numerical Study of the J-2S Rocket Nozzle Contour Effect on the Cap-shock Pattern Formation", Proc. 12th *Int. Conference on Modelling Fluid Flow*, Budapest, Hungary, pp. I.327-I.334.

[8] Moríñigo, J.A., 2004, "Numerical Study of the Hysteresis and Side-Loads in Thrust Optimized Rocket Nozzles in Over-expansion", (in Spanish), Doctoral Thesis, Polytech. University of Madrid.

[9] Moríñigo, J.A., and Salvá, J.J., 2006, "Three-dimensional Simulation of Self-Oscillating Flow and Side-Loads in an Over-expanded Subscale Rocket Nozzle", *J. Aerospace Engineering*, accepted, to appear.

[10] Frey, M., Hagemann, G., 1998, "Status of Flow Separation Prediction in Rocket Nozzles", AIAA *Paper* 98-3619.

[11] Frey, M., Hagemann, G., 2000, "Restricted Shock Separation in Rocket Nozzles", *J. Propulsion and Power*, Vol. 16, N^{er} 3, pp. 478-484.

[12] Chen, C.L., Chakravarthy, S.R., Hung, C.M., 1996, "Numerical Investigation of Separated Nozzle Flow", *AIAA J.*, Vol. 32, N^{er} 9, pp. 1836-1843.

[13] Onofri, M., Nasuti, F., 1998, "Viscous and Inviscid Vortex Generation During Nozzle Flow Transients", *AIAA J.*, Vol. 36, N^{er} 5, pp. 809-815.

[14] Östlung, J., Jaran, M., 1999, "Assessment of Turbulence Models in Overexpanded Rocket Flow Simulations", AIAA *Paper* 99-2583.

[15] Takahashi, M., Ueda, S., Tomita, T., Tamura, H., Aoki, K., 2001, "Transient Flow Simulation of a Compressed Truncated Perfect Nozzle", AIAA *Paper* 2001-3681.

[16] Stark, R., Kwan, W., Quessard, F., Hagemann, G., Terhardt, M., 2001,"Rocket Nozzle Cold-Gas Test Campaigns for Plumes Investigations", *Proc. 4th European Symp. Aerothermodynamics for Space Vehicles*, ESA SP-487, Capua, Italy.

[17] Tomita, T., Takahashi, M., Ueda S., Tamura, H., Aoki, K., 2001, "Visualization of the Formation of Separation Bubbles on Bell-shaped Nozzle Surface in Relation to Serious Side-load", AIAA *Paper* 2001-3559.

[18] Reijasse, Ph., Corbel, B., Soulevant, D., 1999, "Unsteadiness and Asymmetry of Shock-induced Separation in a Planar Two-dimensional Nozzle: a Flow Description", AIAA *Paper* 99-3694.

[19] Deck, S. and Guillen, Ph., 2002, "Numerical Simulation of Side Loads in an Ideal Truncated Nozzle", *J. Propulsion and Power*, Vol. 18, Ner 2, pp. 261-269.

[20] Frey, M. and Hagemann, G., 1999, "Flow Separation an Side Loads in Rocket Nozzles", AIAA *Paper* 99-2815.

[21] Verma, S.B., Ciezki, H.K., 2003, "Unsteady Nature of Flow Separation Inside a Thrust Optimized Parabolic Nozzle", AIAA *Paper* 2003-1139.

[22] Magagnato, F., 1998, "KAPPA - Karlsruhe Parallel Program for Aerodynamics", *Task Quarterly*, Ner 2, pp. 215-270.

[23] Speziale, C.G., Abid, R., Anderson, E.C.,1990, "A Critical Evaluation of Two-equation models for Near Wall Turbulence", ICASE *Report* Ner 90-46.

[24] Moore, J.G., Moore, J., 1999, "Realizability in Two-equation Turbulence Models", AIAA *Paper* 99-3779.

[25] Schmucker, R.H., 1974, "Status of Flow Separation Prediction in Liquid Propellant Rocket Nozzles", NASA TM X-64890.

[26] Lee, S., Lele, S.K., Moin, P., 1997, "Interation of Isotropic Turbulence with Shock Waves: Effect of Shock Strength", *J. Fluid Mechanics*, Vol. 340, pp. 225-247.

[27] Sinha, K., Mahesh, K., Candler, G.V., 2003, "Modeling Shock Unsteadiness in Shock/Turbulence Interaction", *Physics of Fluids*, Vol. 15, Ner 8, pp. 2290-2297.

[28] Sajben, M., 1985, "The Response of Normal Shocks in Diffusers", *AIAA J.*, Vol. 23 Ner 3, pp. 477-478.

Conference on Modelling Fluid Flow (CMFF'06)
The 13th International Conference on Fluid Flow Technologies
Budapest, Hungary, September 6-9, 2006

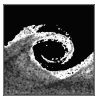

LARGE-EDDY SIMULATION OF A TURBULENT JET AND WAKE VORTEX INTERACTION

Odile Labbé

ONERA, Computational Fluid Dynamics and Aeroacoustics Department, BP 72, 29 avenue de la Division Leclerc, F-92322 Châtillon France. Tel.: +33 1 46 73 42 50, Fax: +33 1 46 73 41 66, E-mail: labbe@onera.fr

ABSTRACT

Temporal Large-Eddy Simulations of the interaction between a turbulent jet flow and a trailing vortex are described in this study. Three cases are analysed: in the first one, the jet and the vortex axes are sufficiently well separated to not interact immediately, while in the second case the distance between the jet and the vortex is reduced to the half. In the last case the jet blows in the vortex core. In the two first cases, as the jet spreads, it is progressively deflected by the continuous input of crossflow momentum, so that it acquires azimuthal and radial component of velocity, causing the emergence of three-dimensional structures of azimuthal vorticity around it. When the jet and the vortex are superimposed, the turbulent kinetic energy does not increase, the vortex core is extremely buffeted. Results of the numerical simulation of the convection-diffusion of a passive scalar show that its distribution (initially in the jet) cannot penetrate inside the vortex core, due to its solid rotation, for the cases where the jet is initially outside the vortex and when it is injected in the vortex wake, its value remains very high and cannot get out of the vortex core.

Keywords: Lamb-Oseen vortex, Large-Eddy Simulation, low subsonic, subgrid scale models, turbulent jet, wake vortex.

NOMENCLATURE

b	[m]	wingspan of experimental model
R	[m]	jet radius
S	[-]	swirl parameter
t	[-]	jet time
t_v	[-]	vortex time
U_y	[m/s]	streamwise velocity
U_θ	[m/s]	azimuthal velocity
U_c	[m/s]	centre jet velocity
V_0	[m/s]	initial jet velocity
V_j	[m/s]	jet velocity
Γ	[m^2/s]	circulation
θ	[m]	momentum boundary layer thickness
Ω_y, Ω_θ	[-]	Non-dimensional streamwise and azimuthal vorticity

Subscripts

j	jet
r , θ, y	radial, azimuthal and axial directions
x, y, z	spanwise, streamwise and transversal directions.
v	vortex
$'$	fluctuation

1. INTRODUCTION

In the near field of the aircraft wake the exhaust jets of the turbines are entrained into the two counter-rotating wingtip vortices which at the same time roll up from the sheet of vorticity induced by the wings. First of all, the jets rapidly mix with ambient air while the vorticity shed from the wings rolls up into a pair of trailing vortices. Then, the dynamics is dominated by the entrainment of the jets into the vortex flow, it is the interaction regime.

In 1999 Brunet *et al*. [1] presented experimental results of a hot jet behind a generic wing planform NACA0012 equipped with two jets beneath the airfoil. Laser Doppler Velocimetry and thermocouples were used to survey the jet at four locations, ranging from one-half to eight wing spans downstream. Based on this wind-tunnel experiment, Ferreira Gago *et al*. [2] used a three-dimensional temporal numerical simulation to study the interaction between a jet and a vortex wake in order to contribute to the understanding of engine jet dispersion of an aircraft in cruise condition. After the computation of the jet development, a Lamb-Oseen vortex is imposed in the vicinity of the jet. Large-scale structures appear as counter-rotating vortex rings visualized by azimuthal vorticity, which lose rapidly coherence, while the vortex core maintains its axial vorticity. Besides the studies mentioned previously, the computation of this

complex flow has been undertaken by various authors. Gerz and Ehret [3], Paoli *et al.* [4] simulate the jet/vortex interaction with Large-Eddy Simulation (LES), while Fares *et al.* [5] used a Reynolds Averaged Navier-Stokes solver. Huppertz *et al.* [6] investigated experimentally and numerically the very near wake up to five chords behind the trailing edge of a rectangular wing and analysed different engine positions and jet speeds. Holzäpfel *et al*. [7] analysed the wake vortex decay mechanisms. However, in spite of the progresses made in the understanding of the turbulence mechanism in a wake vortex, essential dearth of information still exists, especially dealing with the role of large-scale structures on a scalar field distribution. The passive scalar helps in explaining the entrainment and mixing processes of the engine emissions in the vortex.

The work presented here is the continuation of the work performed by Ferreira-Gago *et al.* [2]. The study attempts to give a physical insight into how the mixing of the engine jet is affected by the three-dimensional turbulence and the vortex flowfield. The Reynolds number of flows of aeronautic and environment interest is often very high, however many physical phenomena are also observed in flows at lower Reynolds number. Temporal Large-Eddy simulations with an Mixed-Scale Model on a moderate refined mesh have been carried out for three positions of the hot jet. The first one coincides with the experimental set-up, in the second one, the jet is closer to the vortex, the distance between them is reduced of a factor 2. In the last case, the jet is located in the centre of the vortex. The computation is advanced in two steps: the first step is stopped when it provides an estimation of the end of the jet regime, in the second step interaction with a Lamb-Oseen vortex field is accounted for.

2. MATHEMATICAL MODEL AND NUMERICAL METHODS

In the LES approach the fully compressible Navier-Stokes equations (mass, momentum and total energy) are filtered spatially with the Favre filter, so that any variable may be decomposed into a resolved (or large scale) part and a non resolved (or subgrid scale) part. The subgrid terms represent the effects of unresolved scales of motion on the large scales and need to be modelled. The subgrid scale viscosity is provided by the Mixed-Scale Model proposed by Sagaut [8]. Mixing phenomenon is studied through the passive scalar, which is initially assumed to have a value of zero in the external flow, and reaches a maximum of unit at the centre of the jet.

In convective terms, spatial derivatives are approximated with sixth-order compact finite-differences [9]. To minimize the aliasing error, we follow the procedure applied by Boersma and Lele [10]. The non-linear terms have been rewritten in the skew symmetric form. Diffusive terms are discretized by using a second-order accurate finite difference scheme. The time integration is carried out with a third-order Runge-Kutta method [11]. In the present study, in the streamwise direction (y), periodic conditions are applied on boundaries and non-reflexive conditions introduced by Thompson [12] are used at the lateral boundaries (x, z) of the computational domain. The computations are split in two parts: the jet phase and the interaction phase. The equations are non-dimensionalized by scaling the velocities with the centreline velocity of the jet V_j and the length scale is equal to the radius R. The Reynolds and Mach numbers are respectively equal to 5 000 and 0.2.

2.1. Jet phase

In a first step the jet development is computed, without accounting for the vortex field. The computational domain is rectangular and the grid is uniform in all directions. The cross plane extends from x, z =-5.1R to x, z =5.1R and the streamwise length of the computational domain is L_y=6R, which corresponds to twice the wavelength of the maximum growth rate of the first azimuthal instability of a spatially evolving jet. The LES is carried out on a $(69\times61\times69)$ grid corresponding to a mesh of $\Delta y=0.1R$ and $\Delta x,z = 0.15R$, which is probably a coarse grid, but enough to obtain a fully turbulent region. The Courant-Friedrichs-Lewy number is 0.6 resulting from a time step Δt=0.01. The jet axial velocity is initialized as $V = V_0(1+\varepsilon\tilde{V})$ where V_0 is a tanh profile, $\varepsilon\tilde{V}$ is a white noise random perturbation with a maximum amplitude 1% of V_0 and $\left\|\tilde{V}\right\| \le 1$.

In the following, we use the initial velocity profile: $V_0(r) = \frac{V_j}{2}(1-\tanh\left\{\frac{1}{4}\frac{R}{\theta}(\frac{r}{R}-\frac{R}{r})\right\})$ r being the radial coordinate in a cross-section. The momentum boundary layer thickness θ is defined as: $\theta = \int_0^\infty \{V(r)/V_0\}\{1-V(r)/V_0\}dr$

We restrict the present investigation to one value of the jet parameter, namely $R/\theta = 10$. Among the cases studied by Michalke and Hermann [13] , this value corresponds to the most unstable jet velocity profile. The initial mean temperature is provided by the Crocco-Busemann relation and the jet temperature ratio is T_j/T_0=2.

The end of the jet regime is chosen when the maximum of turbulent kinetic energy is reached, around an adimensional time $t = t^*/t_j$ =50, t_j being R/V_j, this time corresponds to y/b=0.5, b being the wingspan of the experimental model, the first cross section measured downstream in the experiments [14]. At this time, the temperature jet has reduced to

the half. In a first phase, this energy is increasing linearly, it reaches a peak around t=50 and decreases. An important feature to characterize the jet is given with the turbulent intensities plotted in Fig. 1. In the case of round jet flow simulations, profiles of turbulent stresses are formulated in cylindrical coordinates. These latter are computed as follows. First, the instantaneous field ϕ_i (velocity) is interpolated into a polar grid. Second, the Fourier transform of each velocity component is computed. The turbulent intensities are defined as: $|\phi_i'\phi_i'| = \hat{\phi}_i(x,z,k_y,t)\hat{\phi}_i^t(x,z,k_y,t)$. Here $\hat{\phi}_i$, $\hat{\phi}_j^t$ and k_y denote respectively the Fourier transform of the velocity component, the complex conjugate of the Fourier transform velocity component and the wave number in the axial direction. Finally $\langle\phi_i'\phi_i'\rangle$ is computed by taking simple average over all points in the homogeneous direction. The mean turbulent intensities (azimuthal, radial and axial) are normalized by the mean axial velocity in the jet centre (U_c) at time t=50. The level of azimuthal and radial velocity components of turbulent intensities are of same level (8%), but the axial component is lower and more spread out.

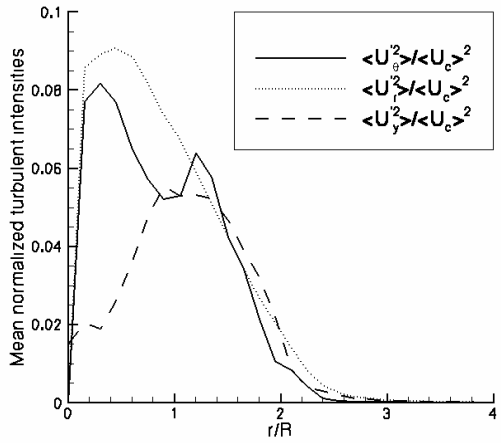

Figure 1. Profiles of mean normalized turbulent intensities of the jet at t=50.

2.2 Interaction phase

Then the interaction with the vortex wake is taken into account and a Lamb-Oseen vortex, is fitted on the transverse part of the experimental velocity field, given by:

$U_\theta / U_{\theta\max} = (1 - \exp(-\beta (r/R)^2)/(r/R)$

where β=2.5 and $\partial\rho/\partial r = \rho U_\theta^2 / r$. The computational domain is enlarged to 169x169 nodes, in the cross planes. It is uniform in the domain –11.1R< x, z <11.1R, with a mesh of 0.15R and stretched using a monotonic tanh law outside this domain. The reference velocity $U_{\theta\max}$ corresponds to the viscous radius r_c, with r_c /R=.7 and at the beginning of the interaction phase the initial jet to vortex velocity ratio is V_j / $U_{\theta\max}$ =0.75. The non-dimensional time t_v is introduced as t_v=t*/(R/ $U_{\theta\max}$) and its origin is reset to zero.

For computing the mean flow profiles, the simulated data, which are in Cartesian coordinates (x,y,z), are transformed to cylindrical coordinates (r, θ, y) using a high order cubic spline interpolation formula. All the results presented as a function of the radius r/R are obtained in the following way: the instantaneous quantity is averaged in the axial direction y. Secondly, the averaged quantity is interpolated into a polar grid and third averaged in the azimuthal direction, to obtain a profile depending on r. No averaging in time is performed; therefore, the mean profile is time depending.

3. RESULTS AND DISCUSSION

In order to study the interaction of the jet turbulence on the vortex with respect to their initial relative locations, three different jet positions have been tested. In the two first cases, the jet is located outside the vortex and in the last case the jet is superimposed to the vortex core and will be studied separately. The first one, case A coincides with the experimental set-up cited above, in which the distance between the jet and the vortex centre at time t_v=0 is equal to 7.2R. In the second one, case B the jet is closer to the vortex and the distance is reduced to the half of the one of experimental set-up, i.e. 3.6R. The last case C is quite different, because the jet is blowing in the vortex core making the flow similar to a q-vortex (Batchelor).

To illustrate the relative jet position with respect to the vortex, Figure 2 shows the longitudinal component of vorticity Ω_y (min =-2.9, max =4.9 ; Δ=.2) at time t_v= 0, in the median plane normal to the axial direction. The vortex core is concentrated at the centre of the computational domain (i.e. x/R=0 and z/R=0), positive and concentric contours represent the vorticity distribution of the vortex core, while the jet patterns consist in positive and negative coherent fields.

The analysis of the results is performed in terms of turbulent kinetic energy, the azimuthal and longitudinal vorticity components, the passive scalar and the scalar flux for the mixing characteristics.

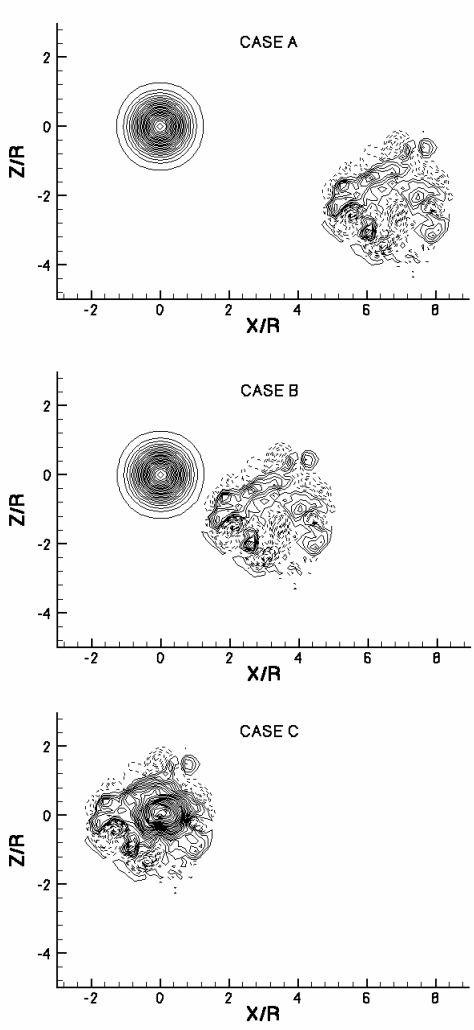

Figure 2. Longitudinal component of vorticity Ω_y, (-2.9, 4.9 ; Δ=.2) at t_v= 0 in a median plane, dashed/solid lines correspond to negative/positive values.

In this paragraph the both cases A and B are analysed and compared in order to evaluate the jet/vortex interaction dynamics and the jet mixing characteristics as well. The evolution of the mean kinetic energy is shown in Figure 3 for the two configurations. First a spectrum is obtained by performing the Fourier transform of the velocity field in the periodic direction and integrating the Fourier coefficients in the (x, z) plane. Then the turbulent kinetic energy is obtained by integrating the values of the one-dimensional spectrum for all wave numbers. The comparison of the two curves exhibits a different behaviour of the interaction process. For the case A, the energy is first decreasing due to jet diffusion process. Then the jet is sufficiently close (t_v= 56) to the vortex to interact with the latter and due to amplification of the instability waves, the energy increases to a maximum 0.41 at t_v= 180 which corresponds to an energy increase of 0.3. Then the energy slowly decreases. For the case B, the jet is sufficiently near the vortex to interact immediately (t_v= 2.5) and the turbulent energy saturates and a peak (0.52) is reached at t_v= 32.5, the increase of energy 0.3 is the same as case A. Then, the energy is quickly decaying.

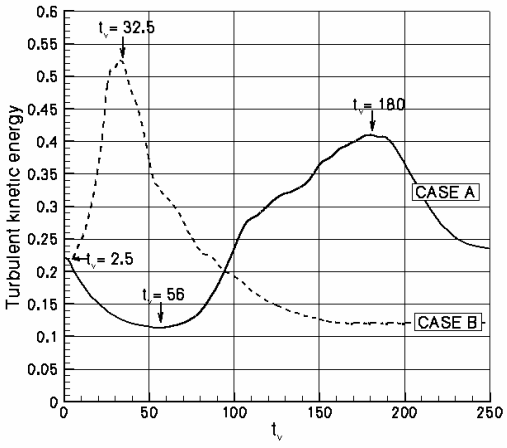

Figure 3. Evolution of the turbulent kinetic energy (Case A: full line, CASE B: dashed line).

To illustrate the dynamics phenomena, three characteristic times corresponding to growth, saturation and decay of the turbulent kinetic energy have been chosen for each case. At the beginning of the interaction (case A: t_v= 56 ; case B: t_v= 2.5), the turbulent kinetic energy is growing to reach a maximum (case A: t_v= 180 ; case B: t_v= 32.5) followed by a period of decay called dissipation regime (case A: t_v= 250 ; case B: t_v= 200).

In Figure 4, the helical structures surrounding the core are surfaces of azimuthal vorticity for the times mentioned previously. These large-scale helical structures are counter rotating vortices where the dark grey surface indicates a positive value (+0.4) and the fair grey a negative one (-0.4). The position of the vortex is plotted with an iso-surface of vorticity Ω_y (+2) in black. The dynamics of the interaction is first dominated by the entrainment and the capture of the jet by the vortex, as the jet spreads, it is progressively deflected by the continuous input of crossflow momentum so that it acquires azimuthal and radial components of velocity. The deflection regime corresponds to the emergence of three-dimensional structures of azimuthal vorticity around it. The vorticity of the jet is progressively stretched and generates spiral-shaped vorticity structures. At the maximum of turbulent kinetic energy, the large-scale vortical structures seem more coherent in case A than in the case B. In the dissipation zone, the jet is more rapidly annihilated when it is injected closer to the vortex. In case B, the jet interacts immediately with the vortex due to the short distance between them and the jet axial velocity is higher than in case A,

because this velocity component is decreasing with the time as commonly observed in the literature. As the increase of turbulent kinetic energy is identical for both cases, this augmentation seems more related to the vortex, than the jet itself. As observed in the figure the break-up of these large-scale structures takes place, however in both cases the jet does not perturb irremediably the vortex core.

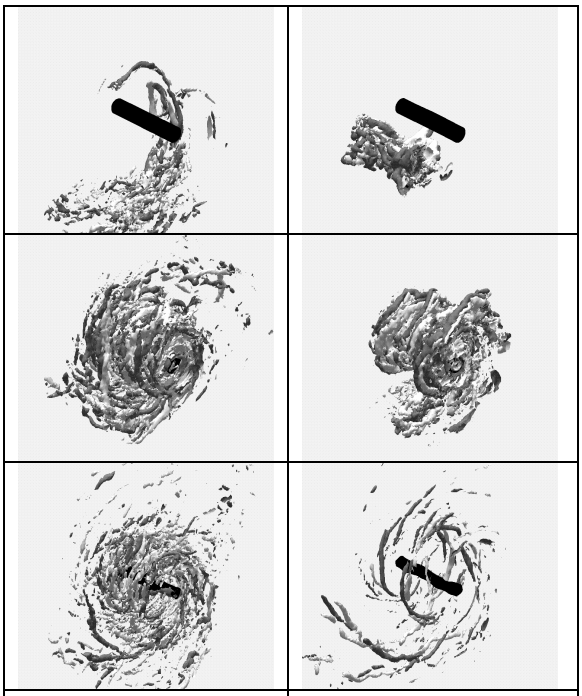

CASE A: top to bottom t_v=56, 180 and 250	CASE B: top to bottom t_v=2.5, 32.5 and 200

Figure 4: 3-D view of the azimuthal vorticity Ω_θ (fair -0.4, dark 0.4); the vortex position is plotted with an iso-surface of vorticity Ω_y in black.

It is also interesting to study the influence of jet turbulence on the vortex through the passive scalar. To quantify the mixing process, the computational passive scalar Z as function of the radius r/*R*, at different times, referenced previously, is plotted in Figure 5**.** Results of the numerical simulation of the convection-diffusion of a passive scalar show that its distribution initially immersed in the jet, is very spread out and remains constant but weak for the case A. In the case B the scalar passive is closer and closer to the vortex but cannot enter into the core. In addition to the investigation of the scalar field distribution, the turbulent flux $\langle Z'u_2' \rangle$ calculated as explained previously for the jet, are displayed in the following figures. The three components (axial, azimuthal and radial) $\langle Z'u_2' \rangle$, $\langle Z'u_\theta' \rangle$ and $\langle Z'u_r' \rangle$ of the turbulent flux are of the same level. Moreover the structure of isolines of turbulent flux $\langle Z'u_2' \rangle$ in Figure 6 for the both jet positions at their respective maximum of turbulent kinetic energy, at t_v= 180 for case A and at t_v= 32.5 for case B are correlated to the large helical structures described in Fig. 4.

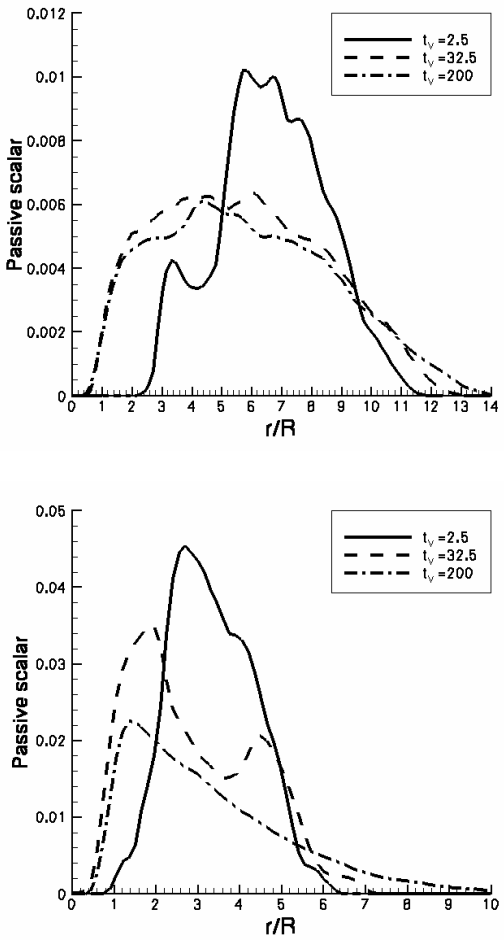

Figure 5. Evolution of the passive scalar, (top: case A, bottom: case B).

Finally, the results of these both cases, where the jet is initially located outside the vortex, reveal a similar behaviour. The fully turbulent jet is deflected and entrained by the vortex velocity field and starts to wrap around it. During that process the jet vorticity is progressively stretched and leads to the production of large structures in the shape of helical sheets of vorticity. Due to the strong rigid-body-like flow field, theses structures break up and drives the vortex to a laminar configuration, all the more because the jet is close to the vortex.

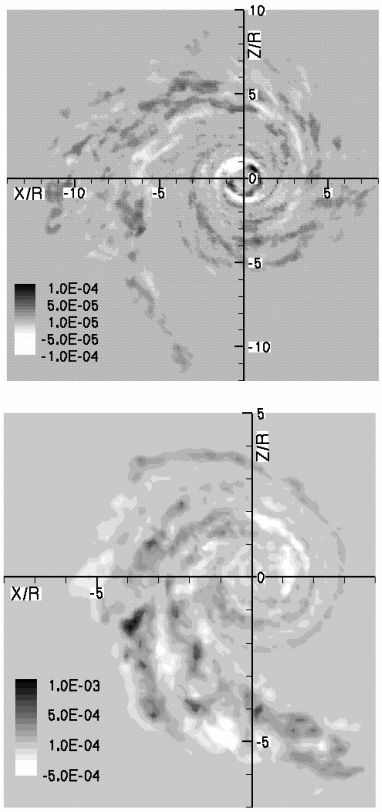

Figure 6. Turbulent flux $\langle Z'u_2' \rangle$ (top: case A at t_v=180, bottom: case B at t_v=32.5).

In case C, the jet is superimposed to the Lamb-Oseen vortex yielding the interaction strong enough which could lead to a destabilization of the vortex core. As previously, the jet turbulence is already developed and injected in the vortex core, therefore the case studied is similar to a q-vortex configuration, but in the present configuration the jet is fully turbulent.

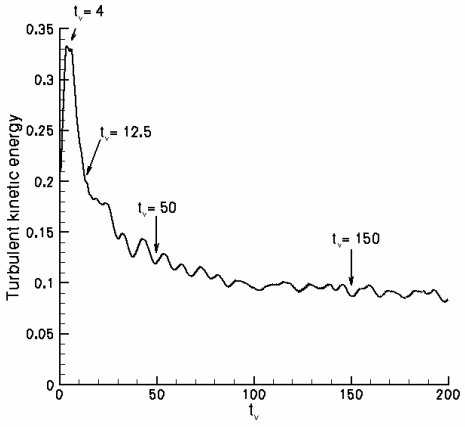

Figure 7. Case C, evolution of the turbulent kinetic energy.

The evolution of turbulent kinetic energy is presented in Figure 7. After a very short increase, the curve exhibits a peak (0.33) at t_v= 4, then decreases with oscillations. In order to analyse the different phenomena, four characteristic times have been chosen in order to describe the unsteady dynamics. The first characteristic time coincides with the maximum of turbulent kinetic energy t_v= 4, the second time t_v= 12.5 when the energy rates .2 , t_v= 50 has been chosen when the energy is reduced and the last time t_v= 150 when the energy has reached a minimum level (0.08).

The contours of azimuthal Ω_θ and streamwise Ω_y vorticity components are presented in Figure 8 (left) top to bottom for the four times previously defined with the same contours levels. At time t_v=4 (top), the dynamics of the interaction is dominated by both positive and negative vorticity embedded within each other and very concentrated around the core, which progressively expand at time t_v=25 (middle), then the flow rotation suppresses the small-scale motions of turbulence, at time t_v= 150 (bottom) the structures have almost disappeared.

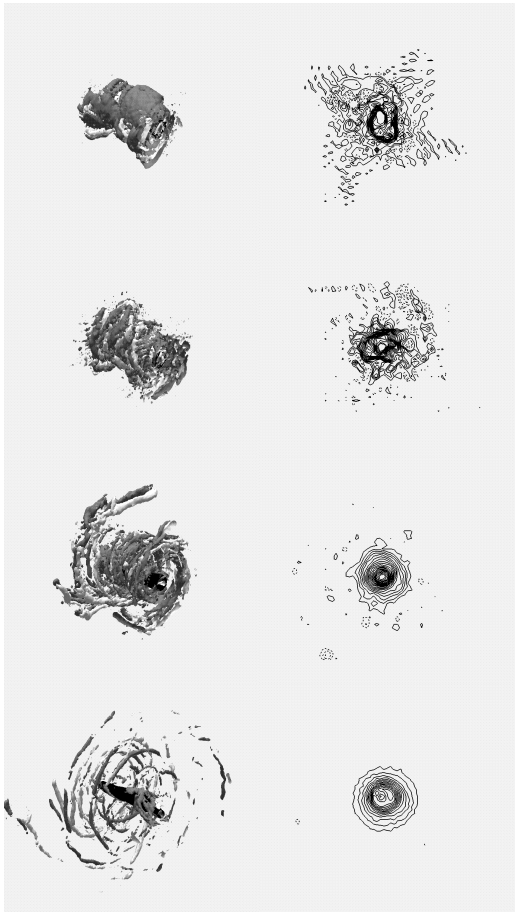

Figure 8. Case C, left: 3-D view of the azimuthal vorticity Ω_θ (fair -0.4, dark 0.4); the vortex position is plotted with an iso-surface of vorticity Ω_y in black. Right: longitudinal component of vorticity Ω_y. From top to bottom at t_v=4, 12.5, 50 and 150.

As previously the interaction of the jet with the vortex is analysed through the longitudinal

component of vorticity Ω_y, see Fig. 8 (right) at the four characteristic times in a median plane normal to the axial direction. Examining the iso-contours, the shape of the vortex is very altered by the jet. At time t_v= 4 (top), the longitudinal component of vorticity Ω_y is concentrated, the negative vorticity (dashed lines) are already located outside of the core. At time t_v= 50 the vortex core starts to recover a standard shape. At the last stage t_v= 150 (bottom) the jet seems to be eliminated and the vortex core slowly retrieves its initial shape with spurious oscillations. An animation in time of these results, shows that the vortex core is extremely buffeted by the jet and is oscillating in the cross planes, where the displacement core can reach 0.3*R*. This phenomenon is due to the meandering. Two phenomena are superposed, the first one which is high frequency, corresponds to the meandering of the vortex and the second one, low frequency, which coincides with the oscillations of the turbulent kinetic energy of fig. 7 would be identify as a pulsation of the set jet and vortex.

The case C corresponds to a Batchelor q-vortex. The stability of this vortex is controlled by the value of the swirl parameter *S*, defined as : $S \approx 1.56 \max(U_\theta)/\max(U_y)$ which measures the relative tangential and axial velocity intensity. The critical value of *S*, given for example by Fabre and Jacquin [15] is approximately 1.5. For larger values, rotation stabilizes all perturbations, and these latter are transformed into a regime of inertial waves. In case C, as U_θ is always greater than U_y means that the swirl parameter is in the present case, greater than 1.5 and therefore the instability saturates and a laminarization of the flow is reached. In Paoli *et al.* [4], the Swirl number have a low value, which leads to the deformation of the vortex structure.

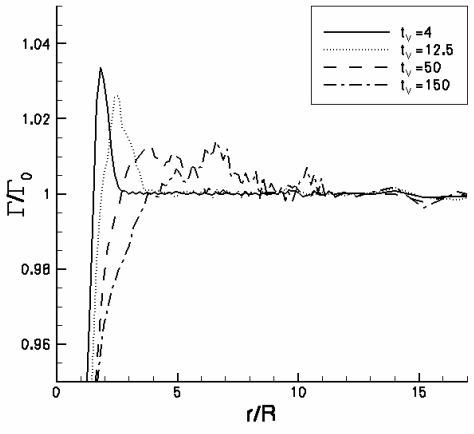

Figure 9. Case C, evolution of the circulation at the different characteristic times.

The circulation profiles plotted in versus r/*R* in Figure 9 at the four characteristic times shows the emergence of a circulation overshoot of small magnitude at the interaction peak t_v=4 also obtained from DNS of Pantano and Jacquin [16]. The propagation of the circulation overshoot is the diffusion process by which angular momentum may be finally transported outward, albeit at a small rate.

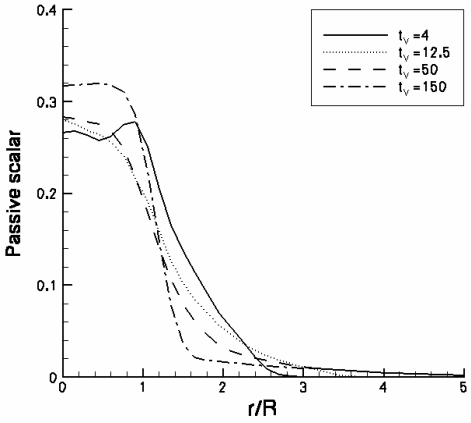

Figure 10. Case C, evolution of the passive scalar at the different characteristic times.

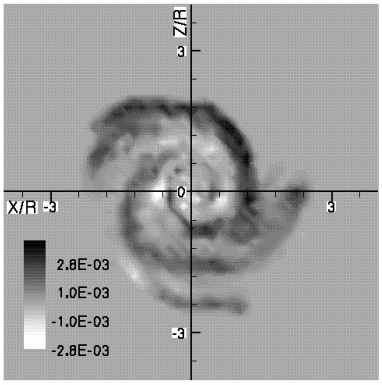

Figure 11. Case C, turbulent flux $\langle Z' u_2' \rangle$ at t_v=4.

In order to study the mixing process, Figure 10 displays the computational passive scalar Z with respect to the radius r, at the different referenced times. When the jet is injected in the vortex, the maximum is increasing with the time and the passive scalar is confined in the vortex core and is trapped in it. The turbulent flux $\langle Z' u_2' \rangle$ at t_v=4 are plotted in Figure 11, where the high values are concentrated around the vortex core. This would be related to the existence of a "dispersion buffer" region discussed by Jacquin and Pantano [17], adjacent to the core, which prevents perturbations and turbulence generated inside the core from being amplified when reaching the vortex periphery zone. Compared to the case B, the peak level is much more high.

Even injected in the vortex, the present jet does not destabilize the vortex. Three-dimensional

structures progressively expand around the vortex and lose coherence. The vortex is extremely buffeted and undulations appear, the passive scalar seems trapped in the core.

4. CONCLUSION

Large Eddy simulations of the interaction between a turbulent jet and a wake vortex have been performed for three configurations. Initially, the jet simulation is carried out until the maximum of turbulent kinetic is reached. Then, the resulting jet data are injected outside of the vortex in the cases A and B, while the last case C the jet is blowing in the vortex core. According to the cases, the jet is located at a distance of 7.2*R* (case A), 3.6*R* (case B) or in the Lamb-Oseen centre (case C). For cases A and B, when the jet interacts with the vortex, the turbulent kinetic energy increases and large-scale structures around the vortex core appear as counter-rotating vortex rings, due to the longitudinal jet velocity. As the downstream distance increases, the large-scale vortical structures disappear, and kinetic energy decays. The vortical structures rapidly lose coherence and stabilizing effect of the flow rotation suppresses the small-scale motions of turbulence. For all simulations the vortex core maintains its positive axial vorticity. In case C, the jet is superimposed to the vortex and the longitudinal vorticity shows the meandering of the vortex. For the three jet positions simulated in the present study, the vortex recovers its initial shape.

The evolution of the passive scalar clearly shows that the distribution initially included in the jet decreases rapidly and does not enter the vortex core for the cases A and B. When the jet is injected in the vortex core, the passive scalar is concentrated in it and seems not be able to escape of this region, that is conform to the existence of a region adjacent to the core, called the "dispersion buffer" discussed by Jacquin and Pantano [17]. In case C, the value of the Swirl number is sufficiently high to allow the vortex to evolve toward an equilibrium state and becoming persistent.

REFERENCES

[1] Brunet, S. Garnier, F. and Loraud J. C., 1999, "Three dimensional direct numerical simulation of plume entrainment and mixing in trailing vortices", *Computational Fluid Dynamics Journal,* Vol. 8, No. 3, pp. 410-418.

[2] Ferreira-Gago, C. Brunet, S. and Garnier, F., 2002, "Numerical investigation of turbulent mixing in a jet/wake vortex interaction", *AIAA Journal,* Vol. 40, No. 2, pp. 276-284.

[3] Gerz, T. and Ehret T., 1997, "Wingtip vortices and exhaust jets during the jet regime of aircraft wakes", *Aerospace Science and Technology* 1, pp. 1468-1477.

[4] Paoli, R. Laporte, F. and Cuenot B., 2003, "Dynamics and mixing in jet/vortex interactions", *Physics of Fluids*, Vol. 15, No. 7, pp. 1843-1860.

[5] Fares, E. Meinke, M. and Schroeder, W., 2000, "Numerical simulation of the interaction of wingtip vortices and engine jets in the near field", *AIAA Paper* pp. 2000-2222.

[6] Holzäpfel, F. Hofbauer, T. Darracq, D. Moet, H. Garnier, F. and Ferreira-Gago, C., 2003, "Analysis of wake vortex decay mechanisms in the atmosphere", *Aerospace Science and Technology*, 7 pp. 263-275.

[7] Huppertz, G. Fares, E. Abstiens, R. and Schroder W. 2004, "Investigation of engine jet/wing-tip vortex interference", *Aerospace Science and Technology* 8, pp. 175-183.

[8] Sagaut, P., 2005, *Large Eddy Simulation for Incompressible Flows : An Introduction.* Third Edition, Springer .

[9] Lele, S. K., 1992, "Compact finite difference scheme with spectral-like resolution". *Journal of Computational Physics,* Vol. 103 , pp. 16-42.

[10] Boersma, B. J. and Lele, S. K., 1999, "Large eddy simulation of a Mach 0.9 turbulent jet", *AIAA Paper* 99-1874.

[11] Lowery, P.S. and Reynolds, W.C., 1986, "Numerical simulation of a spatially developing forced mixing layer", *Report n°TF-26, Stanford University*.

[12] Thompson, K.W, 1990, "Time dependent boundary conditions for hyperbolic system II", *Journal of Computational Physics,* Vol. 89, pp. 439-461.

[13] Michalke, A. and Hermann, G., 1982, "On the inviscid instability of a circular jet with external flow". *Journal of Fluid Mechanics*, Vol. 114, pp. 343-359.

[14] Brunet, S. Garnier, F. and Jacquin, L., 1999, "Numerical/experimental simulation of exhaust jet mixing in wake vortex", *30th AIAA Fluid Dynamics Conference* Norfolk (USA), June 28-July 01.

[15] Fabre, D. and Jacquin, L., 2004, "Viscous instabilities in trailing vortices at large swirl numbers", *Journal of Fluid Mechanics*, Vol. 500, pp. 239-262.

[16] Pantano, C and Jacquin, L., 2001, "Differential rotation effects on a turbulent Batchelor vortex". *In DLES-IV Workshop*, Enschede, The Netherlands, July 18-20, Kluwer.

[17] Jacquin, L. and Pantano, C., 2002, "On the persistence of trailing vortices", *Journal of Fluid Mechanic*s, Vol. 471, pp. 159-168.

Conference on Modelling Fluid Flow (CMFF'06)
The 13th International Conference on Fluid Flow Technologies
Budapest, Hungary, September 6-9, 2006

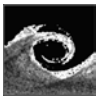

THE SPREADING OF A CARBON DIOXIDE GAS ROUND JET INTO A COLLATERAL AIR FLOW

Pavel JONÁŠ[1], Oton MAZUR[2], Elzbieta MORYŃ-KUCHARCZYK[3], Maciej PODOLSKI[3]

[1] Corresponding Author. Institute of Thermomechanics, Academy of Sciences of the Czech Republic, Dolejškova 5, 182 00 Prague, Czech Republic. Tel.: +420°266052025, Fax: +420286584695, E-mail: jonas@it.cas.cz
[2] Institute of Thermomechanics, AS CR. E-mail: mazur@it.cas.cz
[3] Institute of Thermal Machinery, TU of Czestochowa. E-mail: moryn@imc.pcz.czest.pl; podolski@imc.pcz.czest.pl

ABSTRACT

The paper deals with the velocity and concentration measurement in homogeneous low turbulence air flow with round CO_2 jet outgoing in the main flow direction from a tube output d = 3 *mm* on a cylindrical support perpendicular to the flow direction. To compare the jet spreading into a low turbulence flow with the spreading into a wake of the support we used constant temperature anemometer method (CTA). This method employs two parallel wires of different diameters and heated on considerably different temperatures. Due to this experimental arrangement we are able to measure simultaneously instant CO_2 concentration and the longitudinal velocity component. Measurement results, i.e. distribution and profiles of mean velocity and concentration are in very good agreement with measurement using Pitot-static tube and concentration analyser. Moreover, the CTA measurement gives data on variances and co-variances of concentration and longitudinal velocity fluctuations. From our measurements follows that the jet penetrates into the support wake faster then into the undisturbed outer stream. The covariance of concentration and velocity fluctuations is negative and increases with moving downstream from the jet outlet and from the jet axis. Our experimentation with the constant temperature anemometer method suggests that this method may serve to investigate the turbulent diffusion in complex conditions.

Keywords: carbon dioxide jet in air flow, CTA, simultaneous velocity and concentration measurement turbulent diffusion

NOMENCLATURE

A_j	[-]	a parameter in Eq. (3)
B_j	[-]	a parameter in Eq. (3)
C	[-]	molar concentration of CO_2 in the mixture with air
E_j	[V]	CTA output voltage
M_j	[-]	a parameter in Eq. (3)
N_j	[-]	a parameter in Eq. (3)
Nu_j	[-]	Nusselt number (4)
P	[Pa]	static pressure
Re_j	[-]	Reynolds number (4)
R_j	[Ω]	resistance of wire heated at T_j
R_D	[Ω]	resistance in series with the wire
S_{Cj}	[V]	concentration sensitivity (14)
S_{Uj}	[$m^{-1}sV$]	velocity sensitivity (14)
T	[K]	fluid temperature
T_{fj}	[K]	film temperature (2)
T_j	[K]	hot-wire temperature
U	[$m\ s^{-1}$]	fluid velocity
a_{jk}	[-]	coefficients in Eq. (6) for A_j (6)
b_{jk}	[-]	coefficients in Eq. (6) for B_j (6)
c	[-]	fluctuating component of C
d	[m]	diameter of the jet outlet
d_j	[m]	diameter of wire labelled j
e_j	[V]	fluctuating component of E_j voltage
l_j	[m]	length of the wire labelled j
m_{jk}	[-]	coefficients in Eq. (6) for M_j
n_{jk}	[-]	coefficients in Eq. (6) for N_j (6)
u	[$m\ s^{-1}$]	fluctuating component of U
x	[m]	Cartesian coordinate, in the undisturbed flow direction
y	[m]	Cartesian coordinate, opposite to the direction of gravity
z	[m]	Cartesian coordinate
$\lambda\ (C, T_m)$	[$J\ K^{-1}m^{-1}s^{-1}$]	thermal conductivity
$\mu\ (C, T_m)$	[$kg\ m^{-1}s^{-1}$]	molecular viscosity
$\rho\ (C, T_m)$	[$kg\ m^{-3}$]	density of the fluid

SUBSCRIPTS

j	label of wire, (j=1, 2)
k	subscript of coefficients of a quadratic equations (6) (k=0, 1, 2)

OPERATORS

$Mean\ F \equiv \overline{F}$ time-mean value of quantity F

Var $f = \overline{\left(F - \overline{F}\right)^2} = \overline{f^2}$ variance of fluctuating component of F

Covar $fg = \overline{f\,g}$ covariance(correlation) of fluctuations f and g

1. INTRODUCTION

Many problems of environmental aerodynamics and wind engineering are joint with turbulent air-flow in atmospheric boundary layer. Processes in this layer are more complex than in a Prandtl boundary layer because e.g. of complexness and diversity of the earth surface, the earth rotation, Archimedes (buoyancy) force, sunshine and variability of conditions. Therefore similarly as in the case of general turbulent flow a solely theoretical solution is not possible yet and problems are studied by means of experiments in wind-tunnels and mathematical modelling. Experiments in wind-tunnels inspire in making crucial assumptions for the improvement of computational methods and for their testing. Namely the diffusion of fluid particles is the important problem. Examining the diffusion it is very useful to stream some gas (e.g. Ar, CO_2, Freon 12) into the main air-flow as a tracer. Then simultaneously with the velocity field the concentration field originates. The most basic descriptions of these fields, e.g. [1] are distributions of the mean velocity vector and the mean concentration (scalar). The vector of the velocity and concentration covariance in the conservation equation for the mean concentration plays an analogous role to that of the Reynolds stresses tensor in the Reynolds equations. So far accumulated experimental evidence on Reynolds stresses at various circumstances contributed to improvement of turbulence models applicable on single fluid flows.

A lack of experimental data on statistical characteristics including concentration fluctuations inhibits the development of mathematical models considering flow of a gas with an admixture of another gas. This lack is a result of missing an appropriate method for simultaneous measurement of unsteady velocity and concentration.

Hot wire anemometer (HWA) is capable to follow rapid changes of the investigated quantities and to change its sensitivities to the observed quantities by means of the wire orientation and the wire temperature. Corrsin [2] derived that a single heated sensor (wire, filament, cone) operated at several temperatures, or few sensors of different dimensions, could be used for measurements of mixed statistical moments of gas mixture concentration and flow velocity. Elaborated surveys on HWA application onto the velocity and concentration measurement were compiled in [3, 4]. Way and Libby [5, 6] were among the first who applied this technique to the simultaneous measurements of concentration and velocity. They developed a combined hot-wire/hot-film probe with thermally interfering crossed sensors. Probes of similar construction were used later also by Favre-Marinet [7] and Mazur et al. [8]. These probes were applied to measurements in helium-air flows. Measurements in the air-CO_2 flow cause bigger problem due to high similarity of thermo-physical characteristics of the above gases. For such flows Chassaing [9] suggested a composite probe consisting of two parallel hot-wire sensors with different overheat ratios, so that one of the sensors was almost insensitive to the concentration owing to an appropriate adjustment of overheat ratio.

The possibility of simultaneous measurement of velocity and concentration results from the relationship of heat loss of the heated element to the velocity and physical properties of flow. This dependence is given by e.g. a modified version of Collis and Williams equation – cooling law [10]

$$Nu = \left(\frac{T_f}{T}\right)^{0.17}\left[\begin{array}{l} 0.24\left(\dfrac{Pr}{Pr_{air}}\right)^{0.2} + \\ +0.56\left(\dfrac{Pr}{Pr_{air}}\right)^{0.33} Re^{0.45} \end{array}\right] \quad (1)$$

commonly applied for two-component mixtures, where Pr and $(Pr)_{air}$ denote the Prandtl number for the gas and air at the mean film temperature

$$T_f = \left(T + T_j\right)/2 \quad (2)$$

Sakai et al. [11] noticed that Chassaing's method leads to some practical difficulties and proposed a method with two parallel hot-wire sensors: tungsten wire with small overheat ratio and platinum wire with large overheat ratio. A probe of similar design has been developed and made in the Institute of Thermal Machinery of Częstochowa, University of Technology (ITM), calibrated in the Institute of Thermomechanics, AS CR (IT) and applied for the preliminary study of the spreading of a CO_2 round jet into a collateral air flow.

2. DUAL SENSORS HOT-WIRE PROBE AND ITS CALIBRATION

The probe is a modification of the DANTEC probe of 55P71 type. It is composed from two parallel heated wires: the first one, subscript j =1 (Pt-Rh alloy, d_1 = 10E-06 m, l_1 = 2.2E-03 m) is thicker and the second thinner wire, j = 2 is made from wolfram, d_2 = 5E-06 m, l_2 = 2.25E-03 m. The dimensional scheme of the probe is shown in Figure 1. Temperature dependences of electric

resistance of each wire were determined and then applied for the evaluation of working wire resistances. They were chosen hot-wire temperatures T_1 = 855 *K* and T_2 = 525 *K* which corresponds to the operating resistance settings R_1 = 9.12 Ω and R_2 = 13.71 Ω.

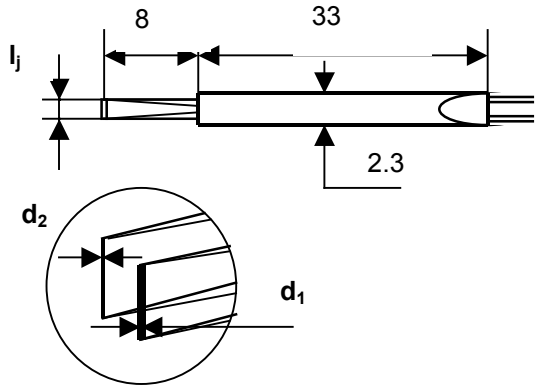

Figure 1. Dimensional scheme of the dual sensors hot-wire probe (dimensions in *mm*)

Calibration of the probe was performed in a small variable density close-circuit wind tunnel (VDT). The test section has circular cross section (dia = 14 *mm* and 14 *mm* in length). It is possible to fill up the tunnel with a non-explosive gas mixture using the weigh-batching device. Then the error of determination of the admixture concentration is less than ± 0.005. VDT allows adjustment of the absolute pressure level from 5 *kPa* up to 1.6 *MPa* and the flow velocity from 0.05 *m/s* up to 120 *m/s* with the accuracy better than ± 0.5%.
More details on the calibration facility and on the procedure of an air/gas admixture formation are given e.g. in Mazur et al. [8, 12].
The two channel CTA system DISA type 55M with LP filters 10 *kHz* on the outputs is usually used for heating both wires in the IT. The output signals are then digitalized using the A/D transducer (National Instruments data acquisition system, sampling frequency 25 *kHz*, 16 *bit*). Together with each record of length 10 *s* are stored time mean values of flow temperature, pressure etc. in the controlling PC, using the LabVIEW software.
Each heated sensor of the dual probe was calibrated against velocity *U* (control of the bulk flow inside VDT) and changes of the fluid temperature *T* at a series of molar concentrations *C*. Results of the calibration of the forced heat convection from the hot-wire into flow were interpolated by means of the formula

$$Nu_j \left(\frac{T_f}{T} \right)_j^{M_j} = A_j + B_j \, Re_j^{N_j}; \; j = 1,2 \qquad (3)$$

where subscript *j* denotes which wire is considered (*j* = 1 or 2). The formula was well proved at measurements with heated wires of finite length in pure airflow. The Nusselt and Reynolds numbers are defined as follows

$$Nu_j = \frac{Q_j}{\pi l_j \lambda_j \left(T_j - T \right)} \; ; \; Re_j = \frac{d_j U \rho_j}{\mu_j} \qquad (4)$$

The physical features of the fluid, λ, μ, ρ are taken at the given molar concentration *C* and at the film temperature T_{fj} relevant to the wire labelled j. Complex formulas for the evaluation of physical features of a gas mixture can be found in [12]. The heat rate Q_j generated by an electric current $I_j = E_j / R_j$ is calculated according to the formula

$$Q_j = \frac{R_j E_j^2}{\left(R_D + R_j \right)^2} \qquad (5)$$

The calibration procedure has been done as follows. Just after the mixing of the selected mole fraction of CO_2 i.e. the concentration *C*, an array of observations of the output voltages E_j (*j* = 1,2) has been done at adjusted velocity U_k = 0,5÷16 *m/s* (k = 1, 2,..,12) and at the prescribed set of wire temperatures T_{js} (*s* = 1, 2,…,9):

T_{1s} = 650 ÷ 875 *K* ; T_2 = 525 *K*
T_1 = 855 *K*; T_{2s} = 350 ÷ 545 *K*

Statistical estimates of the coefficients A_j, B_j and exponents M_j, N_j appearing in the cooling law (3) were calculated from the set of measurement at the given concentration *C*, using the same procedures as are those common for air-flow experiments.

Table 1. Summary of the dual probe calibration coefficients

k	0	1	2	r
a_{1k}	0.366	0.325	-0.155	0.99
b_{1k}	0.371	0.933	-0.0688	1
m_{1k}	-0.0716	0.165	0	0.98
n_{1k}	0.482	0	0	*s* = ±0.016
a_{2k}	0.355	0.450	-0.225	0.99
b_{2k}	0.501	1.148	-0.142	1
m_{2k}	0.357	0.137	0	0.98
n_{2k}	0.449	0	0	*s* = ±0.02

Then the analysis of correlations of these statistical estimates with concentration was done. It was recognized that proper regression functions are following

$$A_j = \sum_{k=0}^{2} a_{jk} C^k ;\ B_j = \sum_{k=0}^{2} b_{jk} C^k ;$$
$$M_j = m_{j0} + m_{j1} C;\ N_j = n_{j0} \qquad (6)$$

The statistical estimates of coefficients appearing in formulas (6) together with relevant sample correlation coefficients r or standard deviations s are presented in Table 1.

3. EXPERIMENTAL APPARATUS

The experiments were performed in an open-circuit blower driven wind tunnel in ITM at Czestochowa. The closed working section has square section 0.4 x 0.4 m^2 and length 4 m inclusive a honeycomb and an array of damping screens. Free stream velocity can be adjusted between 3 *m/s* and 13 *m/s* by means of choking at the exit of the working section. Natural turbulence level is about 0.8 % in the undisturbed stream. Pitot-static tube connected to an inclined-tube ethyl alcohol manometer was used for the measurement of free stream velocity (accuracy about ±1 %). The experiment was performed at a free stream velocity of (11.5 ± 0.6) *m/s* and at atmospheric total pressure (98.6 *kPa* ÷ 99.5 *kPa*) and temperature (24 °*C* ÷ 25 °*C*).
The jet of carbon dioxide was blown out from a circular nozzle (d = 3 *mm*) of a brass tube (outer dia = 5 *mm*). The centre of the nozzle is in the centre of Cartesian coordinate system $x = y = z = 0$. The temperature of the jet at the outlet was broadly equal to the ambient temperature. The volume flux was controlled by means of a reducer for CO_2 with heater and rotameter (±2%). It was kept at 8 *l/min* during experiments. Experimental geometry and the Cartesian co-ordinate system are shown in Figure 2.
The total pressure distribution along the x-axis and the reference static pressure were acquired using a Pitot tube (outer diameter 1.6 *mm*) and wall static pressure tap. Two inclined-tube ethyl alcohol manometers measured pressure differences. The common procedure, based on the Bernoulli's equation and on the concentration distribution, was applied for the evaluation of the mean velocity distribution $U(x, 0, 0)$.

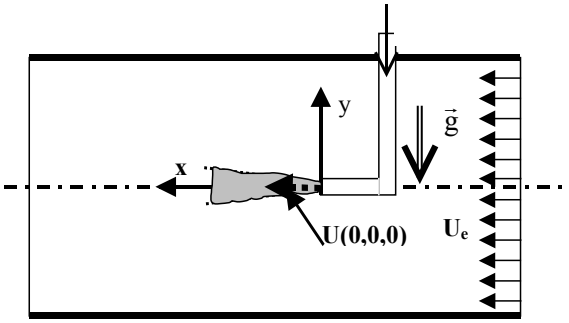

Figure 2. Experimental geometry and the Cartesian co-ordinate system

The distribution of time mean molar concentration C (x, 0, 0) was measured using Carbon Dioxide Monitor Guardian Plus (Edinburgh Instruments and Sensors). The bore of the sampling tube has diameter 2.6 *mm*. So some art of concentration averaging in space and time was made. The value *Mean C* was calculated according to the manual.
The simultaneous measurement of the longitudinal unsteady velocity and concentration was acquired by the dual HW-probe (2nd chapter) and a two channel CTA system DISA type 55M with LP filters 10 *kHz* (DISA 55D26) and DC-voltmeters (METEX MXD-4460A and multimeter HP 34401A). The digital analyse system (HP 3567A, HP 35651B, HP 35652B) was connected in parallel with the DC voltmeters. The CTA system was operating at the same conditions as described in the chapter 2. Wire labelled with subscripts 1 (Pt/Rh material) was heated on temperature T_1 = 855 K and the wire 2 (wolfram) was heated on T_2 = 525 K. Thus the system is giving primary statistical characteristics of the output signals E_1 and E_2 relevant to the CTA channels heating both wires:

$$\overline{E}_1;\ \overline{E}_2;\ \overline{\left(E_1 - \overline{E}_1\right)^2} = \overline{e_1^2};$$
$$\overline{\left(E_2 - \overline{E}_2\right)^2} = \overline{e_2^2};\ \overline{e_1 e_2} \qquad (7)$$

These characteristics together with the mean temperature T and static pressure P of the flow are sufficient for the evaluation of statistical characteristics of the unsteady molar concentration C and the unsteady longitudinal component of the flow velocity U.

4. EVALUATION OF RESULTS

The conversion of the acquired anemometer voltages E_1 and E_2 into the related concentration C and velocity U is the topic of this chapter.
The expressions of the instantaneous voltages E_j can be obtained by substituting relations (4) and (5) into the equations (3) and rearranging

$$E_j = \sqrt{\Phi_j(C) + \Psi_j(C) U^{N_j}} \qquad (8)$$

where j = 1,2 and the substitutions are introduced as follows

$$\Phi_j = A_j F_j\left(C, T, T_j\right),$$
$$\Psi_j = B_j(C) G_j\left(C, T, T_j\right),$$
$$F_j = \frac{\pi l_j \lambda_j \left(T_j - T\right)\left(R_D + R_j\right)^2}{R_j}\left(\frac{T_{fj}}{T}\right)^{-M_j}, \qquad (9)$$
$$G_j = F_j\left(\frac{d_j \rho_j}{\mu_j}\right)^{N_j}.$$

The linearized Taylor expansion of (8) leads to the expressions

$$E_j\left(\bar{C}+c,\bar{U}+u\right)=\bar{E}_j+e_j=$$
$$=\bar{E}_j+c\left\{\frac{\partial E_j}{\partial C}\right\}_{\bar{C},\bar{U}}+u\left\{\frac{\partial E_j}{\partial U}\right\}_{\bar{C},\bar{U}} \quad (10)$$

The formulas for the mean velocity $\bar{U}$ can be obtain by inverting the equation (8) adapted for the mean values $\bar{E}_j$

$$\bar{U}_j=\left[\frac{\bar{E}_j^2-\Phi_j}{\Psi_j}\right]^{1/N_j} \quad (11)$$

Both signals labelled $\bar{E}_1$ and $\bar{E}_2$ must give the same (within the limits of the measurement accuracy) value of the mean velocity

$$\bar{U}=\bar{U}_1=\bar{U}_2 \quad (12)$$

after inserting the correct value $\bar{C}$ into calculations of functions and parameters appearing in (11). The applied solver was working with the requirement

$$\frac{\left|\bar{U}_1-\bar{U}_2\right|}{\bar{U}_1+\bar{U}_2}<0.005 \quad (13)$$

The interpretation of variances $\overline{e_1^2},\overline{e_2^2}$ and covariance $\overline{e_1e_2}$ of the fluctuating components of the output signals follows from the series expansion (10). The desired statistical characteristic of fluctuations of concentration and velocity are solution of the system of equations (14)

$$\begin{aligned}\overline{e_1^2}&=S_{C1}^2\overline{c^2}+2S_{C1}S_{U1}\overline{cu}+S_{U1}^2\overline{u^2},\\ \overline{e_2^2}&=S_{C2}^2\overline{c^2}+2S_{C2}S_{U2}\overline{cu}+S_{U2}^2\overline{u^2},\\ \overline{e_1e_2}&=S_{C1}S_{C2}\overline{c^2}+\left(S_{C1}S_{U2}+S_{C2}S_{U1}\right)*\\ &\quad *\overline{cu}+S_{U1}S_{U2}\overline{u^2}.\end{aligned} \quad (14)$$

here the nomenclature was introduced

$$\left\{\frac{\partial E_j}{\partial C}\right\}_{\bar{C},\bar{U}}\equiv S_{Cj},\quad \left\{\frac{\partial E_j}{\partial U}\right\}_{\bar{C},\bar{U}}\equiv S_{Uj} \quad (15)$$

the necessary derivations are a triviality.

5. RESULTS

Figure 3 and Figure 4 show the axial variations of the time mean values of concentration and velocity determined by means of CTA measurement and by the solver outlined in (12) and (13). Values C(CTA+) were worked out from the empirical formula

$$C(CTA+)=0.1155\overline{E_1}^2-0.476\overline{E_2}^2-0.908; \quad (16)$$

Simultaneously results of measurement using the carbon dioxide analyser Guardian Plus and Pitot tube are plotted in relevant figures.

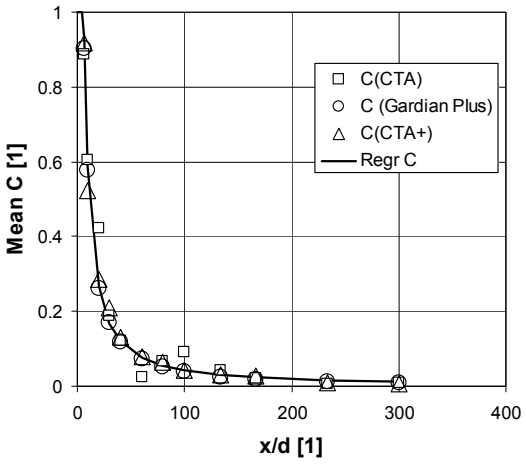

Figure 3. Variation of the mean concentration of CO_2 along the jet axis

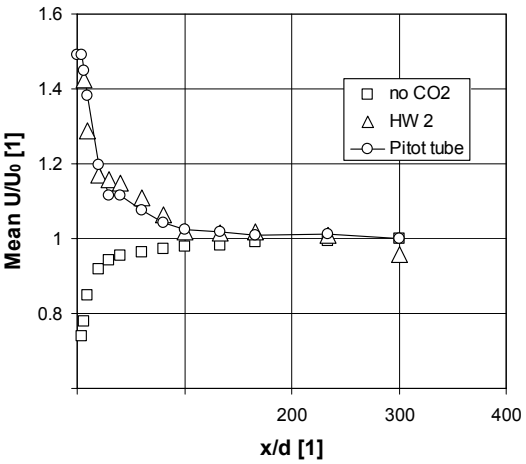

Figure 4. Variation of the normalized mean velocity along the jet axis

The local mean velocity is related to the free/undisturbed stream mean velocity U_0 (11.5 *m/s* ± 0.6 *m/s*). The mean velocity distribution measured in case without blowing of CO_2 (squares) is also plotted in Fig. 4. It displays the effect of the blowing CO_2 on the mean velocity field in the given experimental layout.

The mean concentration distributions against lateral direction *y/d* in three cross sections *x/d* are shown in Figure 5. Asymmetry of profiles indicates that the CO_2-jet penetrates deeper into the wake downstream from the nozzle-holder than into the undisturbed flow ($y<0$). It appears that a higher level of *Mean C* is stabilized below the jet-axis and also peaks on the distributions of *C* are shifted in the gravity direction. Probably these observations result from the action of Archimedes force.

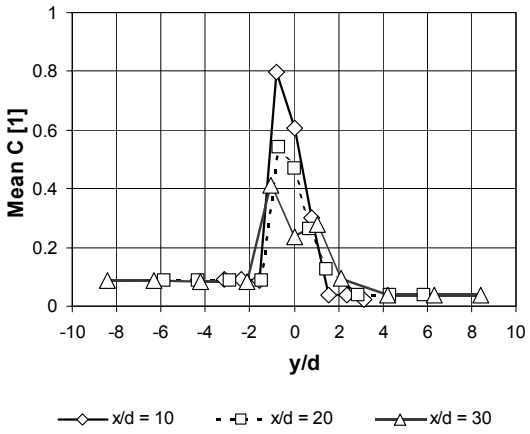

Figure 5. Radial profiles of the mean concentration of CO_2

Figure 6 shows the normalized mean velocity plotted against *y/d* at conditions with CO_2 blowing (empty marks) and without blowing (black marks). It is evident from Fig. 6 that the flow deceleration arises inside the wake of the nozzle-holder, asymmetry of distributions indicates faster turbulent diffusion into wake then into free stream and that the peaks are located on the jet axis.

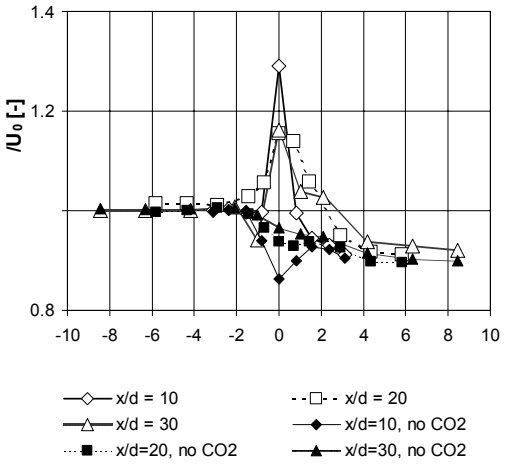

Figure 6. Radial profiles of normalized mean velocity

The comparison of location of *Mean C* and *Mean* U/U_0 peaks is supporting a concept on the Archimedes force action on the jet spreading.

The decay of concentration and velocity fluctuations in stream wise direction along the jet axis is obvious from the Figure 7. It is evident from Fig. 7 that the covariance $\overline{cu}$ of concentration and velocity fluctuations increases with decaying $\overline{c^2}$ i.e. the correlation between *c* and *u* decreases with the distance *x*.

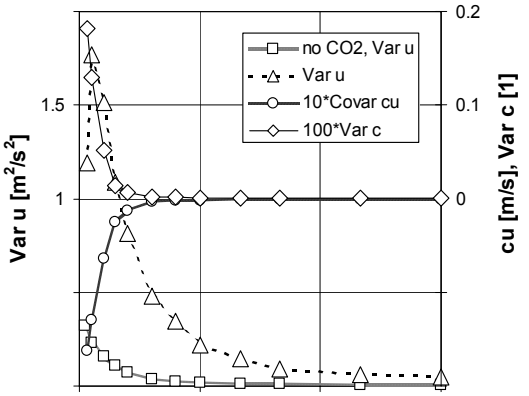

Figure 7. Variation of CO_2 concentration and velocity fluctuations characteristics along the jet axis

Variance of the velocity fluctuations $\overline{u^2}$ decreases with the distance *x/d* more slowly than $\overline{c^2}$ anywhere owing to the shear flow (Fig. 6) supporting the turbulence production. The comparison of *Var u* distributions at conditions with CO_2 blowing (triangles) and without blowing (squares) demonstrates large effect of blowing on the velocity field.

The profiles of 2nd order central moments $\overline{c^2}, \overline{cu}, \overline{u^2}$ across the CO_2 jet and $\overline{u^2}$ in case without blowing in the same direction *y* are shown in Figures 8a,b and c. It follows from the figures that the levels of both concentration and velocity fluctuations are higher on the wake side than in the free stream far beside the jet. Furthermore disturbances produced by blowing CO_2 spread deeper into wake than in the opposite direction far beside the jet.

6. CONCLUSIONS

It was proved that the developed procedure of the simultaneous measurement of concentration and velocity by means of a CTA works satisfactory. The differences of the CTA data from those measured by the specialized devices i.e. analyser Guardian plus and Pitot tube with manometer are sufficiently small, particularly with regard that CTA can moreover provide data on the statistical moments of concentration and velocity fluctuations.

The described experiments revealed that the CO_2 jet diffuses into wake faster than into low turbulence flow and Archimedes force influences the jet spreading remarkably.

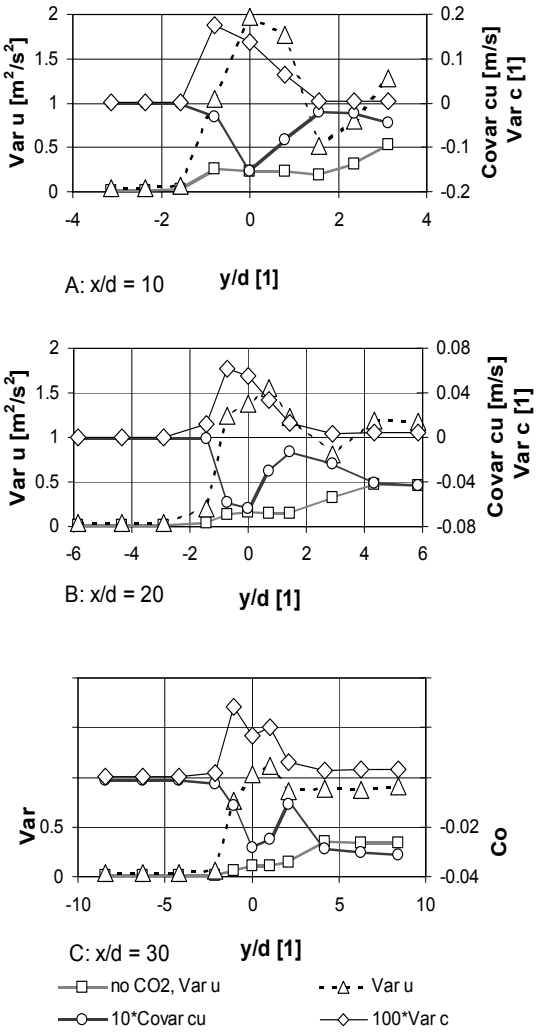

Figure 8. Radial profiles of concentration and velocity fluctuations characteristics

7. PROSPECTS

It is meaningful continue in development of CTA measuring method for measurement in air with a gas admixture above all other with regard for simultaneous measurement of concentration and lateral components of flow velocity. As had been shown by Uruba et al. [14] this method can contribute to the improvement and further development of the wind-tunnel modelling of environmental aerodynamics and wind engineering problems.

ACKNOWLEDGEMENTS

This work was supported by the Ministry of Education, Youth and Sports of the CR through COST Action 114 No. OC 114 in IT CAS and through Polish projects No. BW-1-103-209/2003/P and No. BS-1-103-301/2004/P in ITM.

REFERENCES

[1] Pope, S.B., 2000, *Turbulent Flows,* University Press, Cambridge.

[2] Corrsin, S., 1947, "Extended Applications of the hot-wire anemometer", *Rev. Sci. Instr.* 18, 469-471.

[3] Lomas, C.G., 1986, *Fundamentals of hot-wire anemometry*, University Press, Cambridge.

[4] Brunn, H.H., 1995, *Hot-wire anemometry*, Oxford University Press.

[5] Way J., Libby P.A., 1971, "Application of hot-wire anemometry and digital techniques to measurements in a turbulent helium jet", *AIAA Journal*, Vol.9, no.8, 1567-1573.

[6] Way J., Libby P.A., 1970, "Hot-wire probes for measuring velocity and concentration in helium – air mixtures", *AIAA Journal*, Vol.8, no.5, 976-978.

[7] Favre-Marinet M., 1998, "Experimental techniques in gas mixtures applications to boundary layers and jets", *Turbulence*, Vol.4, 83-95.

[8] Mazur O., Uruba V., Jonáš P., 2003, "Simultaneous measurement of velocity and molar concentration in a gas-mixture turbulent flow using a dual heated-sensor probe", (in Czech), Proc. *18th Symposium on Anemometry*, Úvaly u Prahy, 92-99.

[9] Chassaing P., 1977, "Heat transfer from cylindrical anemometer probes in CO_2-air mixtures", *Physics of Fluids*, Vol.20, no.8, 1260-1262.

[10] Simpson R.L., Wyatt W.G., 1973, "The behavior of hot-film anemometers in gas mixtures", *J. Phys. E.: Sci. Instrum.* 6, 981-987.

[11] Sakai Y., Watanabe T., Kamohara S., Kushida, T., Nakamura I., 2001, "Simultaneous measurements of concentration and velocity in a CO_2 jet issuing into a grid turbulence by two-sensor hot-wire probe", *Int. J. of Heat and Fluid Flow*, 22, 227-236.

[12] Mazur, O., Jonáš, P., Uruba, V., Šarboch, J., 2002, "Improved calibration method of the conjunct hot-wire/ hot-film probe for simultaneous measurement of velocity and concentration in a stream of two gases mixtures", (in Czech), In: Proc. *Coll. Fluid Dynamics* (P. Jonas, V. Uruba eds.), IT AS CR Prague (ISBN 80-85918-77-3), 121-124.

[13] Mazur, O., Jonáš, P., Šarboch, J., Uruba, V., 2003, "Calculation of the physical properties of some gases mixtures", (in Czech), In: Proc. *Topical Problems of Fluid Mechanics* (J. Příhoda, K. Kozel eds.), IT AS CR Prague (ISBN 80-85918-82-X), 67-72.

[14] Uruba, V., Jonáš, P., Mazur, O., Bezpalcová, K., 2004, "Physical modelling of point source dispersion inside atmospheric boundary layer", *PAMM – Proc. Appl. Math. Mech.* **4**, 498-499.

Conference on Modelling Fluid Flow (CMFF'06)
The 13th International Conference on Fluid Flow Technologies
Budapest, Hungary, September 6-9, 2006

Predictions of Structure of Jet in Crossflow Flow Field Using Different Turbulence Models

Aku KARVINEN[1], Hannu AHLSTEDT[2]

[1] Corresponding Author. Institute of Energy and Process Engineering Tampere University of Technology P.O. Box 589, FI-33101 Tampere, Finland. Tel.: +358 3 3115 2953, Fax: +358 3 3115 3751, E-mail: aku.karvinen@tut.fi
[2] Institute of Energy and Process Engineering Tampere University of Technology. E-mail: hannu.ahlstedt@tut.fi

ABSTRACT

Numerical simulations of a turbulent flow in a jet in crossflow are conducted using commercial computational fluid dynamics code. A grid resolution study is carried out to find a grid that yields grid-independent results. In total, six turbulent models are compared: standard k-ε model, RNG k-ε model, realizable k-ε model, standard k-ω model, SST k-ω model and one version of the Reynolds stress model. In all calculations, the near-wall regions are resolved all the way down to the wall and no wall functions are used. Jet to crossflow velocity ratio is 3.3. The Reynolds numbers of the crossflow and the jet are 317,000 and 8,130, respectively. The grid independence test shows that accurate calculation of the jet in a crossflow requires a very fine grid. Results of the turbulence model comparison show that predicted turbulence intensities of both k-ω models are too low on the boundary layer approaching the jet. This deviation reverberates to the whole structure of the flow field of these models. Other models capture the structure of the flow field fairly well. All models used predict streamline trajectory quite well.

Keywords: CFD, jet in crossflow, k-ε turbulence model, k-ω turbulence model, Reynolds stress model

NOMENCLATURE

C	[-]	constant
D	[m]	pipe diameter
Re	[-]	Reynolds number
a	[-]	constant
k	[m^2/s^2]	turbulence kinetic energy
ℓ	[m]	length scale
p	[Pa]	mean pressure
u	[m/s]	mean velocity
x, y, z	[m]	space coordinates
α	[-]	constant
β	[-]	constant
ε	[m^2/s^3]	turbulence kinetic energy dissipation
η	[-]	constant
μ	[Ns/m^2]	dynamic viscosity
ν	[m^2/s]	kinematic viscosity
ω	[1/s]	specific dissipation rate
ρ	[kg/m^3]	density
σ	[-]	constant
τ	[Pa]	shear stress

Subscripts and Superscripts

D	pipe diameter
j	jet
k	turbulence kinetic energy
t	turbulent
ε	turbulence kinetic energy dissipation
ω	specific dissipation rate
∞	free stream of crossflow
$'$	fluctuating component
$\bar{}$	mean value

1. INTRODUCTION

A jet in crossflow occurs in many applications, e.g. in combustion chambers, in vertical and/or short take-off and landing (V/STOL) aircraft, in oil or gas flow into a container, in chemical industry, and in waste discharge into water bodies and into the atmosphere. Jet in crossflow is a challenging simulation case, because flow field around the jet is extremely complex; it includes a counterrotating vortex pair (CVP), horseshoe vortices, wake vortices, boundary vortices, and jet shear-layer vortices.

Jet in crossflow has been under intensive study for over fifty years. The first studies focused on determining the place of the core of the jet, i.e. the jet trajectory [1, 2]. In the articles [3], [4], [5], [6], [7], and [8] the shape and the structure of the jet have been studied experimentally. Numerical studies have been done e.g. in [9], [10], [11], [12], and [13]. A more extensive review can be found in [14] and [15].

The objective of this study is to investigate the structure of the flow field of a jet in a crossflow us-

ing different turbulent models and commercial computational fluid dynamics (CFD) code. In total six turbulent models are compared: standard k-ε model, RNG k-ε model, realizable k-ε model, standard k-ω model, SST k-ω model, and one version of the Reynolds stress model.

2. GOVERNING EQUATIONS AND THEIR NUMERICAL SOLUTION

In this work, buoyancy has not been taken into account. Assuming incompressible steady-state flow, the Reynolds-averaged Navier-Stokes equations (RANS) are

$$\frac{\partial u_i}{\partial x_i} = 0, \tag{1}$$

$$u_j \frac{\partial u_i}{\partial x_j} = -\frac{1}{\rho}\frac{\partial p}{\partial x_i} + \nu \frac{\partial^2 u_i}{\partial x_j \partial x_j} + \frac{\partial}{\partial x_j}\left(-\overline{u_i' u_j'}\right), \tag{2}$$

where u_i is the mean velocity component in x_i direction, ρ is the density, p is the mean pressure, ν is the kinematic viscosity, the overbar denotes time averaging, and the prime denotes the fluctuating part.

2.1. Turbulence Models

In the k-ε models and the k-ω models, the Boussinesq hypothesis is used in which the Reynolds stresses, $-\overline{u_i' u_j'}$, are approximated with

$$-\overline{u_i' u_j'} = 2\nu_t S_{ij} - \frac{2}{3}k\delta_{ij}, \quad S_{ij} = \frac{1}{2}\left(\frac{\partial u_i}{\partial x_j} + \frac{\partial u_j}{\partial x_i}\right), \tag{3}$$

where ν_t is the turbulent, or eddy, viscosity.

In **the standard k-ε model** [16], the turbulence kinetic energy, k, and its dissipation rate, ε, are obtained from the modeled transport equations, which are as follows

$$u_j \frac{\partial k}{\partial x_j} = \frac{\partial}{\partial x_j}\left[\left(\nu + \frac{\nu_t}{\sigma_k}\right)\frac{\partial k}{\partial x_j}\right] + \nu_t S^2 - \varepsilon, \tag{4}$$

$$u_j \frac{\partial \varepsilon}{\partial x_j} = \frac{\partial}{\partial x_j}\left[\left(\nu + \frac{\nu_t}{\sigma_\varepsilon}\right)\frac{\partial \varepsilon}{\partial x_j}\right] + C_{1\varepsilon}\frac{\varepsilon}{k}\nu_t S^2 - C_{2\varepsilon}\frac{\varepsilon^2}{k}, \tag{5}$$

where the modulus of the mean rate-of-strain tensor $S \equiv \sqrt{2 S_{ij} S_{ij}}$. The turbulent viscosity is computed from $\nu_t = C_\mu k^2/\varepsilon$, where C_μ is a constant. Model constants used have the following values: $C_\mu = 0.09$, $C_{1\varepsilon} = 1.44$, $C_{2\varepsilon} = 1.92$, $\sigma_k = 1.0$, and $\sigma_\varepsilon = 1.3$.

The transport equations for k and ε in **the RNG k-ε model** [17] are

$$u_j \frac{\partial k}{\partial x_j} = \frac{\partial}{\partial x_j}\left(\alpha_k \nu_t \frac{\partial k}{\partial x_j}\right) + \nu_t S^2 - \varepsilon, \tag{6}$$

$$u_j \frac{\partial \varepsilon}{\partial x_j} = \frac{\partial}{\partial x_j}\left(\alpha_\varepsilon \nu_t \frac{\partial \varepsilon}{\partial x_j}\right) + C_{1\varepsilon}\frac{\varepsilon}{k}\nu_t S^2 - C_{2\varepsilon}\frac{\varepsilon^2}{k} - \frac{C_\mu \eta^3 (1 - \eta/\eta_0)}{1 + \beta\eta^3}\frac{\varepsilon^2}{k}, \tag{7}$$

where $\eta \equiv Sk/\varepsilon$, $\eta_0 = 4.38$, $\beta = 0.012$, and ν_t is obtained in a similar way as in the standard k-ε model. The quantities α_k and α_ε are inverse effective Prandtl numbers (not constants as in [17]), see [18] for more details. The model constants are: $C_\mu = 0.0845$, $C_{1\varepsilon} = 1.42$, and $C_{2\varepsilon} = 1.68$.

The transport equations for k and ε in **the realizable k-ε model** [19, 18] are

$$u_j \frac{\partial k}{\partial x_j} = \frac{\partial}{\partial x_j}\left[\left(\nu + \frac{\nu_t}{\sigma_k}\right)\frac{\partial k}{\partial x_j}\right] + \nu_t S^2 - \varepsilon, \tag{8}$$

$$u_j \frac{\partial \varepsilon}{\partial x_j} = \frac{\partial}{\partial x_j}\left[\left(\nu + \frac{\nu_t}{\sigma_\varepsilon}\right)\frac{\partial \varepsilon}{\partial x_j}\right] + C_{1\varepsilon} S \varepsilon - C_{2\varepsilon}\frac{\varepsilon^2}{k + \sqrt{\nu\varepsilon}}, \tag{9}$$

where $C_{1\varepsilon}$ is not a constant. The turbulent viscosity is obtained in a similar way as in the standard k-ε model, but C_μ is no longer constant. The model constants are: $C_{2\varepsilon} = 1.9$, $\sigma_k = 1.0$, and $\sigma_\varepsilon = 1.2$.

In **the standard k-ω model** [20], the turbulence kinetic energy, k, and the specific dissipation rate, ω, are obtained from the following transport equations:

$$u_j \frac{\partial k}{\partial x_j} = \frac{\partial}{\partial x_j}\left[\left(\nu + \frac{\nu_t}{\sigma_k}\right)\frac{\partial k}{\partial x_j}\right] + \nu_t S^2 - \beta^*_\infty f_{\beta^*_\infty} k\omega, \tag{10}$$

$$u_j \frac{\partial \omega}{\partial x_j} = \frac{\partial}{\partial x_j}\left[\left(\nu + \frac{\nu_t}{\sigma_\omega}\right)\frac{\partial \omega}{\partial x_j}\right] + \frac{\omega}{k}\nu_t S^2 - \beta_i f_{\beta_i}\omega^2, \tag{11}$$

and the turbulent viscosity is obtained from $\nu_t = k/\omega$. The functions $f_{\beta^*_\infty}$ and f_{β_i} are auxiliary functions, see [18] for more details. The model constants are: $\beta_i = 0.072$, $\beta^*_\infty = 0.09$, $\sigma_k = 2.0$, and $\sigma_\omega = 2.0$. In this work, the low-Reynolds-number version of the k-ω model is used [20].

The SST k-ω model [21] has a form similar to that of the standard k-ω model. The transport equations are as follows

$$u_j \frac{\partial k}{\partial x_j} = \frac{\partial}{\partial x_j}\left[\left(\nu + \frac{\nu_t}{\sigma_k}\right)\frac{\partial k}{\partial x_j}\right] + \nu_t S^2 - \beta^*_\infty k\omega, \tag{12}$$

$$u_j \frac{\partial \omega}{\partial x_j} = \frac{\partial}{\partial x_j}\left[\left(\nu + \frac{\nu_t}{\sigma_\omega}\right)\frac{\partial \omega}{\partial x_j}\right] + S^2 - \beta_i \omega^2 + D_\omega, \tag{13}$$

where $\beta_i = F_1\beta_{i,1} + (1 - F_1)\beta_{i,2}$ and the turbulent viscosity is obtained from $\nu_t = k/\omega \max[1, \Omega F_2/a_1\omega]$. The quantity Ω is the mean rate-of-rotation, F_1 and F_2 are the blending functions, and σ_k and σ_ω are the auxiliary functions. The term D_ω is the cross-diffusion term. See [18] for more details. The model constants are: $a_1 = 0.31$, $\beta^*_\infty = 0.09$, $\beta_{i,1} = 0.075$, $\beta_{i,2} = 0.0828$, $\sigma_{k,1} = 1.176$, $\sigma_{\omega,1} = 2.0$, $\sigma_{k,2} = 1.0$, and $\sigma_{\omega,2} = 1.168$. See [18] for details of the low-Reynolds-number correction to the turbulent viscosity which is enabled in this work.

In **the Reynolds stress model (RSM)**, there are the exact transport equations for the transport of Reynolds stresses, $-\overline{u_i' u_j'}$ [22, 23]:

$$\frac{\partial}{\partial x_k}\left(u_k \overline{u_i' u_j'}\right) = \underbrace{-\frac{\partial}{\partial x_k}\left[\overline{u_i' u_j' u_k'} + \overline{\frac{p'}{\rho}\left(\delta_{kj} u_i' + \delta_{ik} u_j'\right)}\right]}_{D_{ij}^{\mathrm{t}}} - \left(\overline{u_i' u_k'}\frac{\partial u_j}{\partial x_k} + \overline{u_j' u_k'}\frac{\partial u_i}{\partial x_k}\right) + \frac{\partial}{\partial x_k}\left[\nu \frac{\partial}{\partial x_k}\left(\overline{u_i' u_j'}\right)\right] + \underbrace{\overline{\frac{p'}{\rho}\left(\frac{\partial u_i'}{\partial x_j} + \frac{\partial u_j'}{\partial x_i}\right)}}_{\phi_{ij}} - \underbrace{2\nu \overline{\frac{\partial u_i'}{\partial x_k}\frac{\partial u_j'}{\partial x_k}}}_{\varepsilon_{ij}}, \tag{14}$$

where D_{ij}^{t} is the turbulent diffusive transport, ϕ_{ij} is the pressure-strain term, and ε_{ij} is the dissipation tensor. See [18] for details on how these terms are modeled. The model constants are: $C_1 = 1.8$, $C_2 = 0.60$, $C_{1\varepsilon} = 1.44$, $C_{2\varepsilon} = 1.92$, $C_\mu = 0.9$, $\sigma_k = 1.0$, and $\sigma_\varepsilon = 1.3$.

2.2. Calculation of Near-Wall Area

When using some of the k-ε models or the RSM, the model should be modified in the vicinity of the no-slip walls. In this work, the method is used in which the whole domain is subdivided into two regions, based on the Reynolds number $\mathrm{Re}_y = y\sqrt{k}/\nu$, where y is the normal distance from the wall. In the fully turbulent region, i.e. where $\mathrm{Re}_y > 200$, the k-ε model or the RSM is used. In the region where $\mathrm{Re}_y < 200$, basic model equations are retained, but [24, 25]

$$\nu_{\mathrm{t}} = C_\mu \sqrt{k}\ell_\mu, \qquad \ell_\mu = C_\ell y\left(1 - e^{-\mathrm{Re}_y/A_\mu}\right), \tag{15}$$

$$\varepsilon = \frac{k^{3/2}}{\ell_\varepsilon}, \qquad \ell_\varepsilon = C_\ell y\left(1 - e^{-\mathrm{Re}_y/A_\varepsilon}\right), \tag{16}$$

where $A_\mu = 70$ and $A_\varepsilon = 2C_\ell$ [25]. Between the inner ($\mathrm{Re}_y < 200$) and outer ($\mathrm{Re}_y > 200$) region, ν_{t} and ε are blended to ensure a smooth transition [18].

2.3. Calculation Procedure

All the calculations have been done using FLUENT 6.1.22 [18], a commercial software based on the finite volume method. All terms in all equations are discretized in space using second-order central differencing, apart from the convection term, which is discretized using a second-order upwind scheme. Pressure-velocity coupling has been done using the traditional SIMPLE algorithm.

Default values of all constants of software are used. All options which are enabled by default are used. In addition, a differential formula for effective viscosity $\mu_{\mathrm{eff}} = \mu + \mu_{\mathrm{t}}$ (μ is a molecular viscosity) is used in the RNG k-ε model to take into account low-Reynolds-number effects. Also a low-Reynolds-number correction to the turbulent viscosity is enabled when using either of the k-ω models. All iterations are continued until residuals approach the machine number and therefore it can be assumed that iteration error is negligible. Relaxation parameters are reduced when needed.

3. DOMAIN AND MESH

The schematic of the problem is shown in Figure 1. The arrangement of the problem is exactly the same as in article [26] and is based on the experiments of [7]. The Reynolds number based on the crossflow free stream velocity (u_∞) and the distance from the leading edge of the flat plate to the jet axis is $\mathrm{Re}_x \approx 317{,}000$, whereas, the Reynolds number based on the jet average velocity (w_{j}) and the jet diameter is $\mathrm{Re}_D \approx 8{,}130$. The working fluid is air with density $\rho = 1.225\ \mathrm{kg/m^3}$ and dynamic viscosity $\mu = 1.7894 \times 10^{-5}\ \mathrm{kg/ms}$ ($\nu = \mu/\rho$).

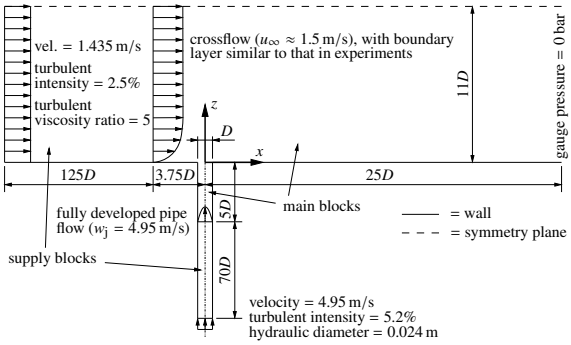

Figure 1. Computational domain, boundary conditions, and schematic of velocity profiles in block interfaces. Domain width is $25D$ (modeled half $12.5D$) and as sidewall boundary condition symmetry plane is used. Pipe diameter $D = 24$ mm.

In the experiments [7], special consideration was given to establishing the fully developed incoming flow conditions on the flat plate and in the pipe. The boundary layer of the flat plate was turbulent. In the simulation, this is achieved using a long enough development distance of the boundary layer ($128.75D$) so that the boundary layer velocity and Reynolds stress profiles close to the jet axis ($x = -3.75D$) are similar to their measured values when the RSM is used. In the measurements, turbulent boundary layer is produced using a vortex generator and a shorter development distance. In the experiments, pipe flow was fully developed. Also in the simulation, a long enough pipe ($75D$) is used to produce a fully developed pipe flow.

The computational grid consists of four blocks (Fig. 1 and Figure 2). Only one half of the domain is modeled because of symmetry. The pipe consists of a so-called supply block and of a so-called main block, where 11,800 and 11,040 control volumes have been

used, respectively. Also the crossflow consists of two blocks, i.e. the supply block (117,000 control volumes) and the main block where six different grid resolutions have been used such that the total number of control volumes used is 267,640, 387,340, 549,340, 910,840, 1,405,240, or 2,302,990. Grids in all blocks have been constructed so that the dimensionless wall unit, $y^+ = u_\tau y/\nu$ ($u_\tau = \sqrt{\tau_w/\rho}$, where τ_w is the surface shear stress), is close to unity at the wall-adjacent cells of all no-slip walls. All grids are constructed so that grid is finer in the vicinity of the jet than elsewhere.

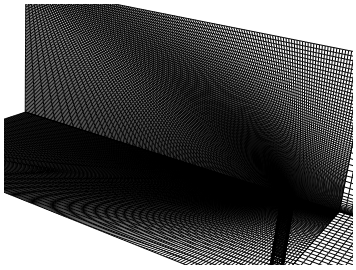

Figure 2. Grid consisting of 1,405,240 **cells.**

4. RESULTS

It can been seen from the streamlines of the jet and the crossflow (Figure 3) how complex flow structure is in the vicinity of the jet, especially in the downstream side of the jet.

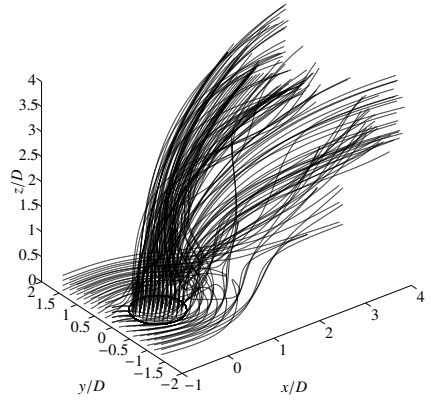

Figure 3. Streamlines of jet and crossflow.

4.1. Grid Independency Test

A grid independency test has been done using the standard k-ε model. According to Figure 4, grid should be very fine to attain a grid-independent solution. This is in close agreement with the article [27].Velocity profiles of the standard k-ε model do not change significantly when grid has been made finer than 549,340 control volumes. However, we can see slight changes in the turbulent kinetic energy. If only a trajectory of the jet is considered, grid resolution needed is lower than in the case where the whole velocity field is desired to be solved accurately (Figure 5). The grid consisting of 1,405,240 control volumes is used exclusively from here onwards.

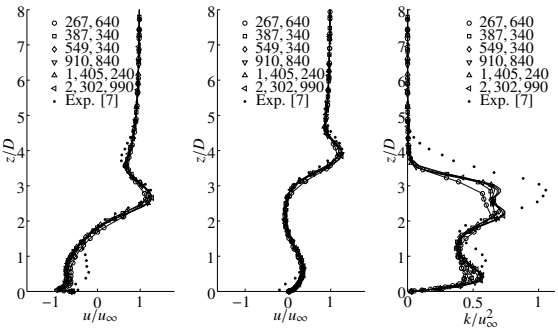

(a) $x/D = 0.67$ (b) $x/D = 1.83$ (c) $x/D = 0.67$

Figure 4. Normalized horizontal mean velocity and turbulent kinetic energy in symmetry plane.

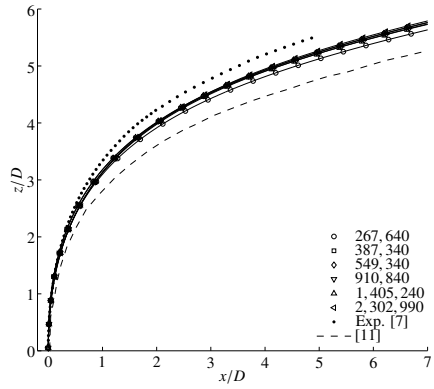

Figure 5. Streamline trajectories, effect of grid.

4.2. Turbulence Model Comparison

Deviations of the streamline trajectories calculated using different turbulence models from the measured streamline are quite notable (Figure 6). All k-ε models give a streamline trajectory which is too close to the flat plate, RNG k-ε giving the best compatibility with experiments. Both k-ω models give a trajectory which is too far from the flat plate. The trajectory of the Reynolds stress model is too close to the flat plate in the vicinity of the jet exit, but the model captures results of the experiments quite well farther from the jet exit.

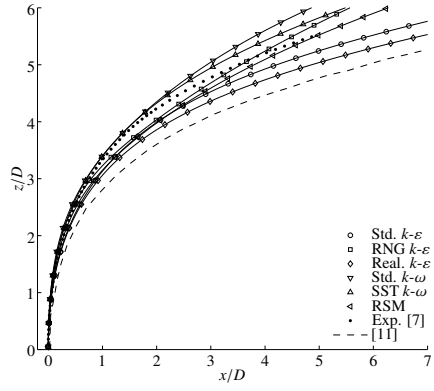

Figure 6. Streamline trajectories, effect of turbulence model.

In Figure 7, mean velocity field in symmetry plane is represented. There exists a node in the downstream side of the jet, near the wall. The measured node is shown in every figure by a cross to help the comparison between modeled and measured flow fields. All models predict velocity field quite well.

The counterrotating vortex pair is shown in Figure 8. The measured core of the CVP is located in every figure. Some models predict the shape of the CVP and the place of the core accurately, but there are notable deviations in results.

The greatest differences between modeled velocity fields can be seen from the velocity field in the plane $z/D = 0.17$ (Figure 9). Both of the k-ω models predict a velocity field which is considerably different from the measured field.

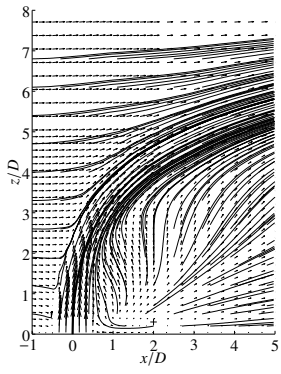

(a) Exp. [7]

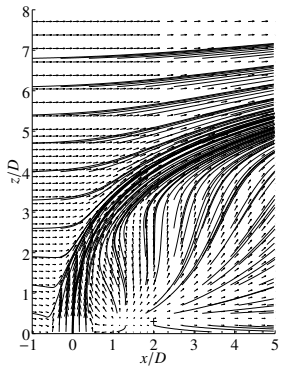

(b) Std. k-ε

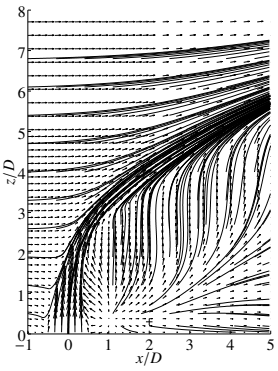

(c) RNG k-ε

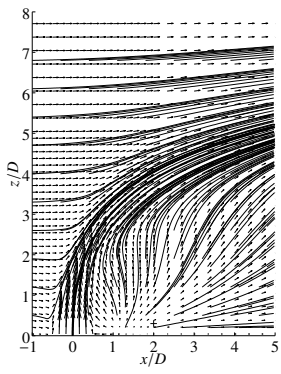

(d) Real. k-ε

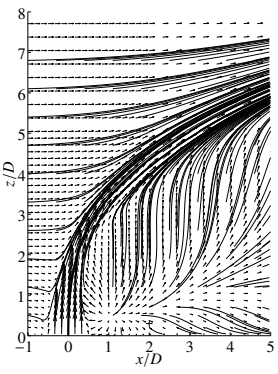

(e) Std. k-ω

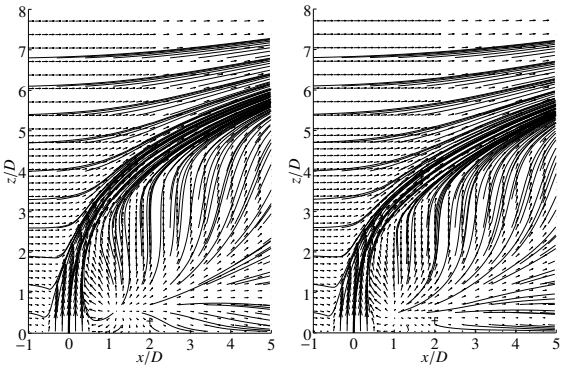

(f) SST k-ω (g) RSM

Figure 7. Mean velocity vector maps and sectional streamlines in symmetry plane.

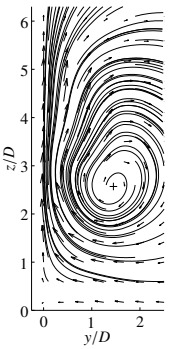

(a) Exp. [7]

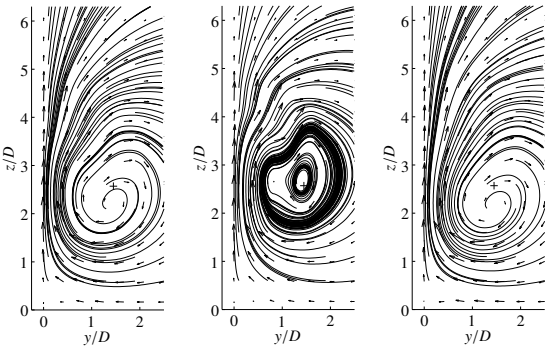

(b) Std. k-ε (c) RNG k-ε (d) Real. k-ε

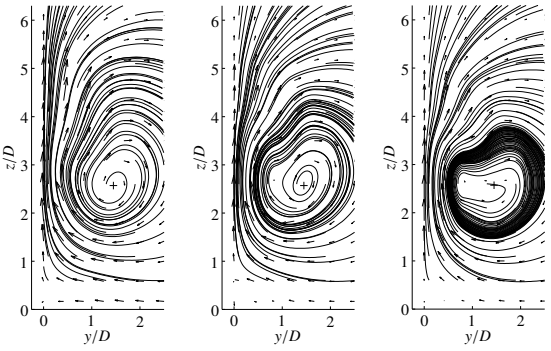

(e) Std. k-ω (f) SST k-ω (g) RSM

Figure 8. Mean velocity vector maps and sectional streamlines in plane $x/D = 2.4$.

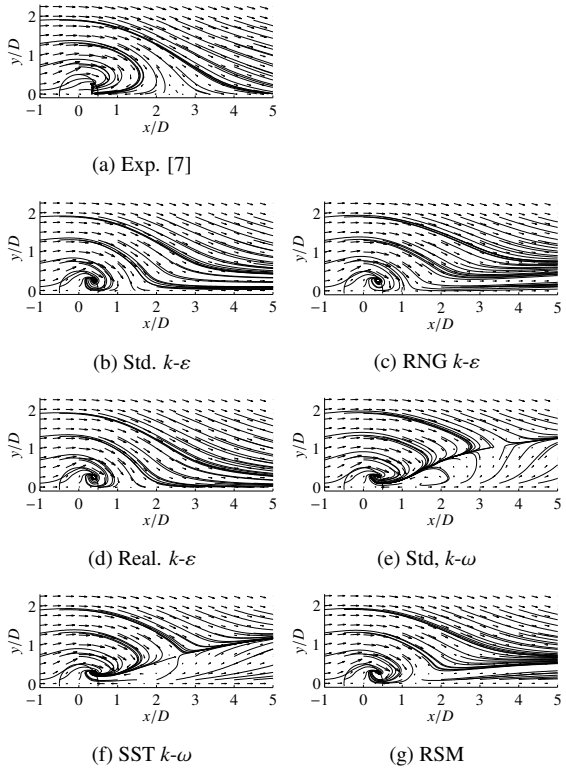

(a) Exp. [7]

(b) Std. k-ε (c) RNG k-ε

(d) Real. k-ε (e) Std, k-ω

(f) SST k-ω (g) RSM

Figure 9. Mean velocity vector maps and sectional streamlines in plane $z/D = 0.17$.

All models predict too great a reverse flow velocity value in the downstream side of the jet, some models giving the value $u/u_\infty \approx -1$, whereas the measured value is about -0.45, as can be seen from Figure 10.

In the plane $z/D = 2.4$, the measured maximum vertical velocity is in the upper part of the jet (Figure 11). In contrast, all models give a maximum in the side part of the jet, near the CVP.

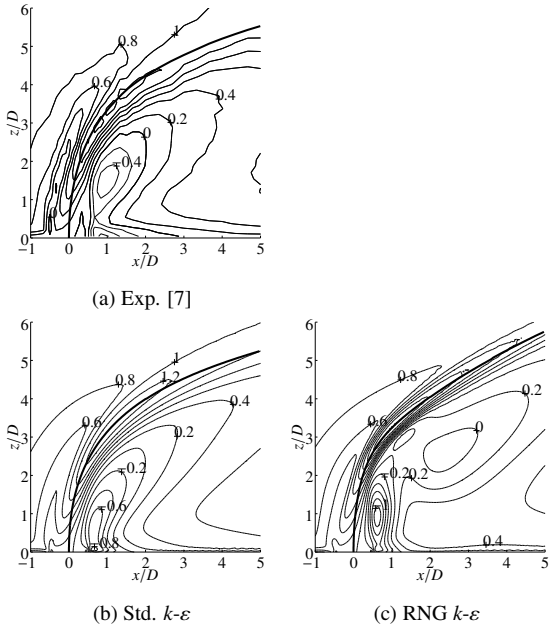

(a) Exp. [7]

(b) Std. k-ε (c) RNG k-ε

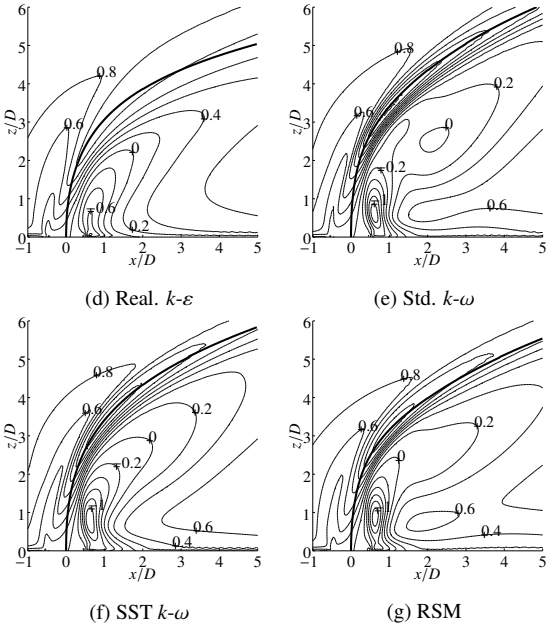

(d) Real. k-ε (e) Std. k-ω

(f) SST k-ω (g) RSM

Figure 10. Contour plot of normalized horizontal mean velocity in symmetry plane.

The reason for peculiar behavior of both k-ω models can be seen in Figure 12. These models give turbulence kinetic energy levels in the vicinity of the jet which are much too low.

Velocity values in five different locations are compared in Figure 13.

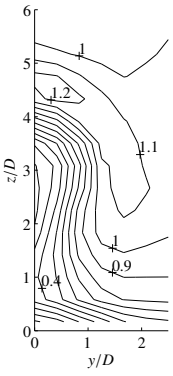

(a) Exp. [7]

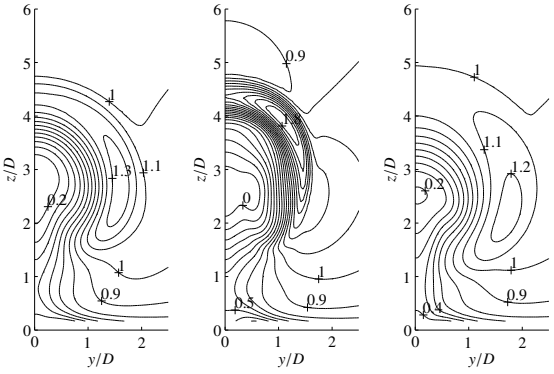

(b) Std. k-ε (c) RNG k-ε (d) Real. k-ε

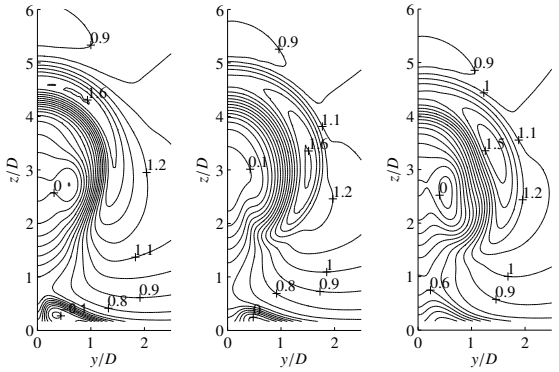

(e) Std. k-ω (f) SST k-ω (g) RSM

Figure 11. Contour plot of normalized horizontal mean velocity in plane $x/D = 2.4$.

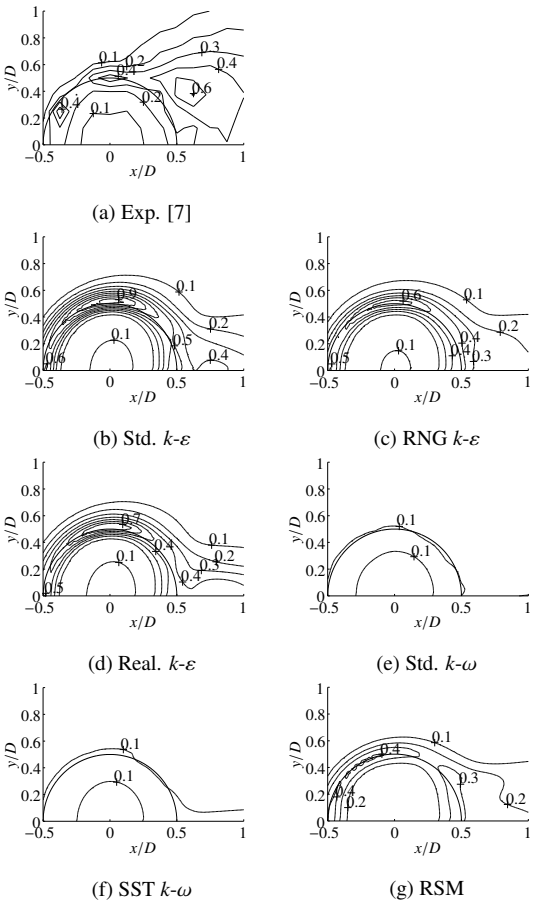

(a) Exp. [7]

(b) Std. k-ε (c) RNG k-ε

(d) Real. k-ε (e) Std. k-ω

(f) SST k-ω (g) RSM

Figure 12. Contour plot of normalized turbulent kinetic energy in plane $z/D = 0.17$.

5. CONCLUSIONS

Results of the grid independence test showed that accurate calculation of the jet in a crossflow requires a very fine grid. Results of the turbulence model comparison showed that predicted turbulence intensities of both k-ω models are two low in the boundary layer approaching the jet. This deviation reverberates to the whole structure of the flow field of these models. Other models captured the structure

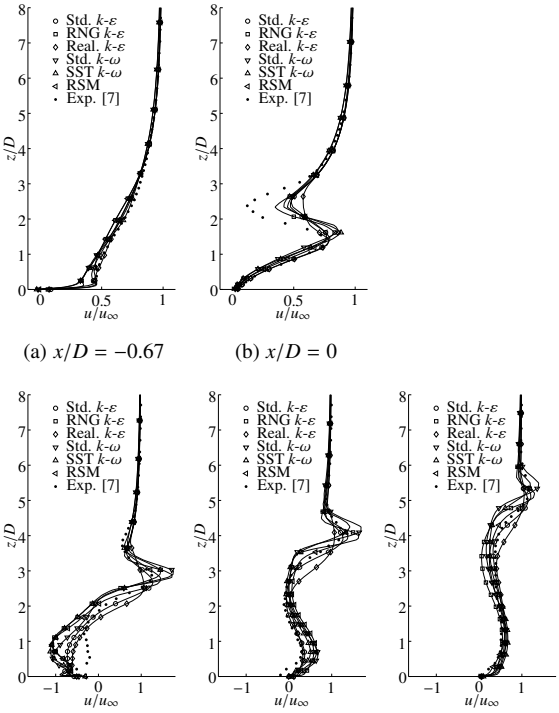

(a) $x/D = -0.67$ (b) $x/D = 0$

(c) $x/D = 0.67$ (d) $x/D = 1.83$ (e) $x/D = 3.67$

Figure 13. Normalized horizontal mean velocity in different locations in symmetry plane.

of the flow field fairly well. All models used predicted streamline trajectory reasonable well, but there exist some deviations from measured values. All k-ε models gave a streamline trajectory which is slightly too close to the flat plate, RNG k-ε giving the best compatibility with experiments. Both k-ω models gave a trajectory which is slightly too far from the flat plate. The trajectory of the Reynolds stress model is too close to the flat plate in the vicinity of the jet exit, but the model captures results of the experiments quite well farther from the jet exit.

ACKNOWLEDGMENTS

The authors gratefully acknowledge the support from Tekes - The National Technology Agency of Finland, Andritz Oy, Enprima Oy, Fortum Nuclear Services Oy, Kværner Power Oy, Metso Paper Oy, Nokia Oy, Numerola Oy, Patria Aviation Oy, and Process Flow Ltd Oy.

REFERENCES

[1] Jordinson, R., 1956, *Flow in a Jet Directed Normal to the Wind.*, R & M No. 3074, British A.R.C.

[2] Margason, R. J., 1968, "The Path of a Jet Directed at Large Angles to a Subsonic Free Stream", *Technical Report* NASA TN D-4919.

[3] Ramsey, J. W., and Goldstein, R. J., 1971, "Interaction of a Heated Jet With a Deflecting

Stream", *Journal of Heat Transfer*, Vol. 94, pp. 365–372.

[4] Andreopoulos, J., and Rodi, W., 1984, "Experimental Investigation of Jets in a Crossflow", *Journal of Fluid Mechanics*, Vol. 138, pp. 93–127.

[5] Kim, K. C., Kim, S. K., and Yoon, S. Y., 2000, "PIV Measurements of the Flow and Turbulent Characteristics of a Round Jet in Crossflow", *Journal of Visualization*, Vol. 3, pp. 157–164.

[6] Cortelezzi, L., and Karagozian, A. R., 2001, "On the Formation of the Counter-Rotating Vortex Pair in Transverse Jets", *Journal of Fluid Mechanics*, Vol. 446, pp. 347–373.

[7] Özcan, O., and Larsen, P. S., 2001, "An Experimental Study of a Turbulent Jet in Cross-Flow by Using LDA" *Technical Report* MEK-FM 2001-02, Technical University of Denmark.

[8] Meyer, K. E., Özcan, O., and Westergaard, C. H., 2002, "Flow Mapping of a Jet in Crossflow with Stereoscopic PIV", *Journal of Visualization*, Vol. 5, pp. 225–231.

[9] Patankar, S. V., Basu, D. K., and Alpay, S. A., 1977, "Prediction of the Three-Dimensional Velocity Field of a Deflected Turbulent Jet", *Journal of Fluids Engineering*, Vol. 99, pp. 758–762.

[10] Alvarez, J., Jones, W. P., and Seoud, R., 1993, "Predictions of Momentum and Scalar Fields in a Jet in Cross-Flow Using First and Second Order Turbulence Closures", In *Computational and Experimental Assessment of Jets in Cross Flow*, AGARD-CP-534, pp. 24–1...24–10.

[11] Yuan, L. L., 1997, "Large Eddy Simulations of a Jet in Crossflow", *Ph.D Thesis, Department of Mechanical Engineering, Stanford University.*

[12] Yuan, L. L., Street, R. L., and Ferziger, J. H., 1999, "Large-Eddy Simulations of a Round Jet in Crossflow", *Journal of Fluids Engineering*, Vol. 379, pp. 71–104.

[13] Muppidi, S., and Mahesh, K., 2005, "Direct Numerical Simulation of Turbulent Jets in Crossflow", Proc. *34rd AIAA Aerospace Sciences Meeting and Exhibit*, Reno, Nevada.

[14] Schetz, J. A., 1980, "Injection and Mixing in Turbulent Flow", volume 68 of *Progress in Astronautics and Aeronautics*, AIAA, New York.

[15] Margason, R. J., 1993, "Fifty Years of Jet in Cross Flow Research" In *Computational and Experimental Assessment of Jets in Cross Flow, AGARD-CP-534*, pp. 1–1...1–33.

[16] Launder, B. E., and Spalding, D. B., 1972, *Lectures in Mathematical Models of Turbulence*, Academic Press, London.

[17] Yakhot, V., and Orszag, S. A., 1986, "Renormalization Group Analysis of Turbulence: 1. Basic Theory", *Journal of Scientific Computing*, Vol. 1, pp. 3–51.

[18] Fluent Inc., 2003, *FLUENT 6.1 User's Guide*, Lebanon.

[19] Shih, T. -H., Liou, W. W., Shabbir, A., Yang, Z., and Zhu, J., 1995, "A New k-ε Eddy Viscosity Model for High Reynolds Number Turbulent Flows", *Computers Fluids*, Vol. 24, pp. 227–238.

[20] Wilcox, D. C., 1998, *Turbulence Modeling for CFD*, DCW Industries, Inc., La Canada, California.

[21] Menter, F. R., 1994, "Two-Equation Eddy-Viscosity Turbulence Models for Engineering Applications", *AIAA Journal*, Vol. 32, pp. 1598–1605.

[22] Gibson, M. M., and Launder, B. E., 1978, "Ground Effects on Pressure Fluctuations in the Atmospheric Boundary Layer", *Journal of Fluid Mechanics*, Vol. 86, pp. 491–511.

[23] Launder, B. E., Reece, G. J., and Rodi, W., 1975, "Progress in the Development of a Reynolds-Stress Turbulence Closure", *Journal of Fluid Mechanics*, Vol. 68, pp. 537–566.

[24] Wolfshtein, M., 1969, "The velocity and temperature distribution of one-dimensional flow with turbulence augmentation and pressure gradient", *International Journal of Heat and Mass Transfer*, Vol. 12, pp. 301–318.

[25] Chen, H. C., and Patel, V. C., 1988, "Near-Wall Turbulence Models for Complex Flows Including Separation", *AIAA Journal*, Vol. 26, pp. 641–648.

[26] Karvinen, A., and Ahlstedt, H., 2005, "Comparison of Turbulence Models in Case of Jet in Crossflow Using Commercial CFD Code", Proc. *Engineering Turbulence Modelling and Measurement – ETMM6*, Sardinia, Italy, pp. 399–408.

[27] Karvinen, A., and Ahlstedt, H., 2003, "A Comparison of Turbulence Models and the Calculation of the Near-Wall Area in the Case of a Jet in a Crossflow", Proc. *VIII Finnish Mechanics Days*, Helsinki, Finland, pp. 99–110.

Conference on Modelling Fluid Flow (CMFF'06)
The 13th International Conference on Fluid Flow Technologies
Budapest, Hungary, September 6-9, 2006

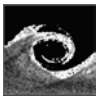

LES OF THE FLOW AROUND A ROTATING SPHERE AT RE_D=10000

Thomas GORA[1], Jörg FRANKE[2], Wolfram FRANK[3]

[1] Corresponding Author. Department of Fluid- and Thermodynamics, University of Siegen. Paul-Bonatz-Str. 9-11, D-57076 Siegen, Germany. Tel.: +49 271 740 4675, Fax: +49 271 2666, E-mail: gora@ift.mb.uni-siegen.de
[2] Department of Fluid- and Thermodynamics, University of Siegen. E-mail: franke@ift.mb.uni-siegen.de
[3] Department of Fluid- and Thermodynamics, University of Siegen. E-mail: frank@ift.mb.uni-siegen.de

ABSTRACT

Large Eddy Simulation (LES) of the flow over a sphere rotating perpendicular to the streamwise direction is performed in order to investigate the effect of the rotation on the flow parameters at Re_D=10^4, where Re_D is the Reynolds number based on the free-stream velocity, sphere diameter and kinematic viscosity of the fluid. The rotational speeds considered are in the range of $0 \le \omega^* \le 0.72$ where the spin parameter ω^* is defined as the ratio of the maximum circumferential velocity on the sphere surface to the free-stream velocity. The Smagorinsky-Lilly eddy viscosity model is applied to model the impact of the subgrid-scales on the resolved ones.

The simulations are performed with the commercial flow solver FLUENT 6.1 [1] which was first validated by computing the flow around a non-rotating sphere and comparing the results with other data available from the literature. With rotation the magnitude of the mean force coefficients is continuously increasing with ω^*, which can be attributed to the altered pressure distribution with rotation. The change in pressure is a result of the change in boundary layer separation and shear layer transition. These changes also lead to wake zones with reduced size and increased turbulent kinetic energy with increasing spin parameter.

Keywords : boundary layer, computational fluid dynamics, large eddy simulation, drag force, lift force, rotating sphere

NOMENCLATURE

C_p	[-]	static pressure coefficient
C_S	[-]	Smagorinsky constant
D	[m]	sphere diameter
F	[N]	force
K_R	[m^2/s^2]	resolved turbulent kinetic energy
L	[m]	mixing length for subgrid scales
L_R	[m]	recirculation length
Re_D	[-]	Reynolds number
S_{ij}	[N/m^2]	resolved rate of strain tensor
St	[-]	Strouhal number
T	[-]	non-dimensional time
V	[m^3]	volume of computational cell
c	[-]	force coefficient
d	[m]	distance to the nearest wall
p	[Pa]	pressure
t	[s]	physical time
u	[m/s]	velocity
u'	[m/s]	velocity fluctuation
u_τ	[m/s]	friction velocity
x,y,z	[m]	Cartesian coordinates
Δr^+	[-]	non-dimensional wall distance
Δt	[s]	time step
δ	[-]	Kronecker delta function
φ	[°]	angle
κ	[-]	von Kármán constant
ν	[m^2/s]	kinematic viscosity
ν_{SGS}	[m^2/s]	subgrid-scale viscosity
ρ	[kg/m^3]	density of the fluid
τ_{ij}	[N/m^2]	subgrid stress tensor
ω^*	[-]	spin parameter

Subscripts and Superscripts

–	filtered quantity
⟨…⟩	time averaged quantity
b	base
d	drag
l	lift
S	static
∞	free stream

1. INTRODUCTION

It is well known that besides the Reynolds number the rotation of the sphere has a substantial influence on the flow field around the sphere and therefore on the forces which are needed for the calculation of sports ball trajectories. That is why this topic has recently received much attention so it is important to know and understand the effect of rotation on the flow characteristics.

There are many experimental and numerical simulations of the flow around non-rotating spheres [2-5], but there are only a few examinations of the flow over rotating spheres and only at low $Re_D \leq 500$ [6-9]. The Reynolds numbers encountered in ball sports are however much larger. The objective of this work is therefore to numerically investigate the flow around a smooth sphere at a Reynolds number of $Re_D = 10^4$, rotating perpendicular to the streamwise direction at spin parameters ω^*=0, 0.18, 0.36, 0.54 and 0.72. First the flow solver FLUENT 6.1 is validated for the non-rotating case by comparing the results with data available from the literature. Then the results of the rotating sphere are shown and the effect of rotation on the flow characteristics is analysed.

2. SIMULATION OVERVIEW

2.1. Computational mesh

The computational domain around the sphere consists of two hemispheres with diameter 15D of which the first is defined as inflow and the second as outflow. The investigated sphere is located at the centre of the computational domain, see Figure 1. This dimension of the computational domain has been chosen to reduce the influence of the approximation of the boundary conditions on the results.

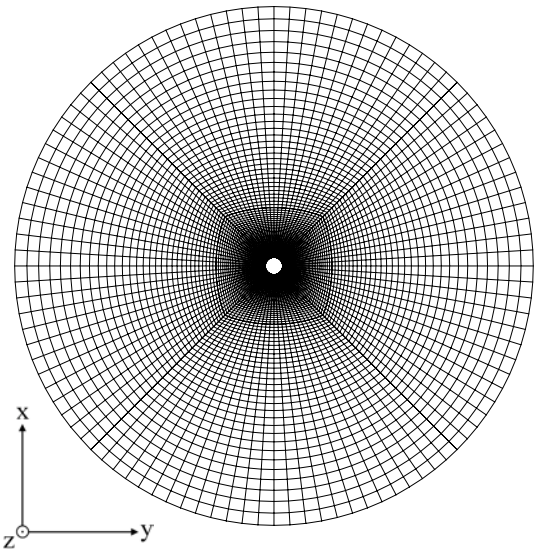

Figure 1. Computational mesh (xy-plane, z=0). The origin of the coordinate system is in the sphere's centre.

A block-structured mesh of O-type is used within the computational domain. Corresponding to the recommendation of Constantinescu et al. [2] the centre of the first cell is located at $\Delta r^+ = u_\tau r / \nu \leq 1$, where $u_\tau = 0.04 u_\infty$ is used as a conservative estimate of the friction velocity. The grid point spacing in radial direction then grows with a geometric meshing law with maximum ratio of 1.05 . In polar and azimuthal direction the grid points are uniformly distributed. The mesh consists of approximately 430000 control volumes. A cut through the mesh in the xy-plane at z=0m is shown in Figure 1.

2.2. Governing equations and numerical details

In this study the flow field is solved by means of LES in which the eddies that can be resolved by the grid are computed directly and only the unresolved subgrid-scales (SGS) need to be modelled. The basic equations for the LES are obtained by applying an implicit spatial filter to the incompressible Navier-Stokes-Equations.

$$\frac{\partial \overline{u}_\mathrm{i}}{\partial x_\mathrm{i}} = 0 \tag{1}$$

$$\frac{\partial \overline{u}_\mathrm{i}}{\partial t} + \frac{\partial \left(\overline{u}_\mathrm{i}\overline{u}_\mathrm{j}\right)}{\partial \mathrm{x}_\mathrm{j}} = -\frac{\partial \overline{p}}{\partial x_\mathrm{i}} + \nu \frac{\partial}{\partial x_\mathrm{j}}\left(\frac{\partial \overline{u}_\mathrm{i}}{\partial \mathrm{x}_\mathrm{j}} + \frac{\partial \overline{u}_\mathrm{j}}{\partial \mathrm{x}_\mathrm{i}}\right) - \frac{\partial \tau_\mathrm{ij}}{\partial x_\mathrm{j}} \tag{2}$$

The spatially resolved quantities are indicated with an overbar. From the unresolved scales only the subgrid stress tensor τ_{ij} has been retained. The commutation errors which result when applying a spatial filter with variable width have been omitted. These commutation errors are of second order in the filter width and can be neglected (see Ghosal et al. [10]) if like in this work a second order scheme is used for the numerical solution of equations (1) and (2). Therefore the closure problem manifests itself solely in the appearance of the subgrid stress tensor,

$$\tau_\mathrm{ij} = \overline{u_\mathrm{i} u_\mathrm{j}} - \overline{u}_\mathrm{i}\overline{u}_\mathrm{j} \tag{3}$$

τ_ij is modelled with the Smagorinsky-Lilly model which uses the eddy viscosity assumption

$$\tau_\mathrm{ij} - \frac{1}{3}\tau_\mathrm{kk}\delta_\mathrm{ij} = -2\nu_\mathrm{SGS} S_\mathrm{ij} \tag{4}$$

where ν_SGS is the subgrid-scale eddy viscosity and S_ij is the resolved rate of strain tensor. ν_SGS is modelled as

$$\nu_\mathrm{SGS} = L^2 \sqrt{2 S_\mathrm{ij} S_\mathrm{ij}} \tag{5}$$

with the length scale

$$L = \min\left(\kappa\, d, \mathrm{C_S}\, V^{\frac{1}{3}}\right) \tag{6}$$

Here C_S is the Smagorinsky constant set to C_S=0.1, which is the default value in FLUENT, κ=0.4187 is the von Karman constant and d is the radial distance from the sphere's surface.

A Dirichlet boundary condition, which consists of a uniform velocity $u_x = u_\infty$ is used at the inflow whereas a Neumann boundary condition with zero normal gradient for all variables is assumed at the downstream boundary. The sphere's surface is a solid wall at which no slip conditions are imposed i.e. the relative velocity between the flow and the sphere is zero on the sphere's surface.

For time integration a second order implicit method is used. The approximation of pressure is carried out with a second-order upwind scheme whereas momentum is discretised with a second order central-differencing scheme. The pressure-velocity coupling is done with the SIMPLE method. The stopping criterion for iterative convergence is set to 10^{-4} for continuity and the velocity components. Approximately 25 iterations per time step were necessary to achieve a converged solution.

A constant time step of Δt = 0,04 D / u_∞ has been used for all the simulations, which corresponds to about 110 steps per period of the vortex shedding of the non-rotating sphere.

The histories of the force-coefficients, which are defined by Eqs. (7) and (8)

$$c_\mathrm{d} = \frac{F_\mathrm{d}}{\frac{\rho}{2} u_\infty{}^2 \frac{\pi D^2}{4}} \tag{7}$$

$$c_\mathrm{l} = \frac{F_\mathrm{l}}{\frac{\rho}{2} u_\infty{}^2 \frac{\pi D^2}{4}} \tag{8}$$

have been monitored and a moving average has been used to judge how many time steps are needed to obtain a converged time average. After a statistically steady state of the force coefficients was reached the statistics of the flow field have been accumulated over time intervals of at least $T = t\, u_\infty / D$ = 270 non-dimensional times, depending on ω^*.

3. CODE VALIDATION

To validate the numerical code and for comparison with the flow around the rotating sphere at Re_D=10^4 the turbulent flow of the non rotating case was simulated first. For this Reynolds number the flow is subcritical, i.e. the boundary layer is laminar until separation. Transition to turbulence occurs in the separated shear layers due to the Kelvin-Helmholtz instability, leading to a turbulent wake.

The results for the characteristic integral parameters of the flow are shown in Table 1 together with corresponding results from other numerical and experimental simulations. The mean drag coefficient compares well with the one reported by Kim [5] who calculated the flow with FLUENT 6.2. However both values are larger than the results of Constantinescu et al. [2] and of Yun et al. [4], both predicting a value which is only slightly smaller than the experimental result of Achenbach [3]. The reason for the difference in the mean drag between these simulations and the present one is the substantially shorter recirculation length which is the distance from the base point of the sphere to the point where the mean streamwise velocity is zero along the centreline. The reason for the differences can be attributed to the different numerical approximations used for the convective terms. Constantinescu et al. [2] used a hybrid scheme that consists of a fifth-order upwind scheme which is used until separation and for the first part of the separated shear layers. Elsewhere second-order central differences are used. Yun et al. [4] employed a third-order upwind scheme only until separation and then switched to central differences. Hence their shear layers are resolved with less numerical viscosity, leading to an earlier transition and therefore to a shorter recirculation length. The use of second-order central differences in the present work in the entire domain then leads to an even earlier transition and a shorter recirculation length. The higher suction pressure on the sphere's base is consistent with the higher drag and the smaller recirculation length. The pressure coefficient is computed from

$$C_p = \frac{\langle p_\mathrm{S} \rangle - p_\infty}{\frac{\rho}{2} u_\infty{}^2} \tag{9}$$

where the maximum pressure at the inlet boundary is used as reference pressure p_∞.

Table 1. Flow parameters for the flow around a non rotating sphere. $St=fD/u_\infty$ obtained from c_d spectra except in [4] from radial velocity spectra.

	$\langle c_\mathrm{d} \rangle$	C_{pb}	St	$\langle L_R \rangle / D$
present	0.434	-0.286	0.196	1.134
Constantinescu et al. [2] (LES)	0.393	-0.25	0.195	-
Constantinescu et al. [2] (DES)	0.397	-0.275	0.2	1.7
Yun et al. [4]	0.393	-0.274	0.17	1.364
Kim [5]	0.438	-	0.182	-
Achenbach (exp.) [3]	0.40	-0.25 (Re_D= $1.65 \cdot 10^5$)	0.195	-

The present result for the Strouhal number agrees very well with the other simulations and the experiment. The Strouhal number has been obtained from the power spectrum of the drag coefficient following the method proposed by Choi et al. [11]. The entire time series is divided into eleven intervals with 50% overlap, each interval containing 1024 data points. For every interval the power spectrum is computed and these spectra are then averaged. This procedure was necessary to clearly identify the dominant frequency as the time series of lift and drag are known to contain high energy at small frequencies due to a large scale modulation [2,4]. Furthermore our simulations suffer from dispersion errors well known for second-order approximations and the reflectivity of the inflow and outflow boundary conditions. The influence of these numerical errors on the results is further investigated at the moment. The computed Strouhal number represents the characteristic frequency of the vortex shedding in the wake. The characteristic higher frequency of the shear layer instability could not be detected in the spectra, i.e. there was no second peak or range with increased energy [4].

4. RESULTS FOR THE FLOW AROUND THE ROTATING SPHERE

Finally the results for the sphere rotating with spin parameters ω^*=0.18, 0.36, 0.54 and 0.72 are presented in this section and compared with the results of the non rotating case. In Fig. 2 the computed non dimensional mean streamwise velocity component is shown in the xy plane at z=0m for all spin parameters. Without rotation a nearly symmetric recirculation region results. With rotation the wake is lifted becoming more and more asymmetric. Due to the rotation in anti clockwise direction the flow on the upper half is decelerated while it is accelerated on the lower half. This leads to a reduction of the size of the region with the maximum negative velocities. The deceleration and acceleration of the flow has a pronounced effect on the boundary layer separation and shear layer transition which are the main processes determining the flow characteristics. These effects can be very well seen from the contours of K_R,

$$K_R = 0.5(<\overline{u}'^2_x> + <\overline{u}'^2_y> + <\overline{u}'^2_z>) \qquad (10)$$

which is shown in Fig. 3 in the same xy plane. For all spin parameters the flow is laminar with negligible K_R up to the transition to turbulence in the separated shear layers. At ω^*=0 this transition takes place at the same x-coordinate on the upper and lower half of the sphere. The asymmetry of K_R in the wake is due to the insufficient averaging time. At ω^*=0.18 the boundary layer on the lower half stays longer attached due to the acceleration. The shear layer transition is therefore moved further in flow direction. On the upper half the shear layer transition occurs further away from the sphere with no visible change in the x position when compared with the non rotating case. This process is enhanced with increasing rotation. At ω^*=0.36 and ω^*=0.54 it can also be seen well that the shear layers on the upper half are getting thinner due to the increasing difference between the velocity on the sphere's surface and the velocity of the displaced approach flow. The shear layers on the lower half are no longer very well visible from ω^*≥0.54. Besides the change in the form of the wake zone the intensity of the turbulence is increasing with the highest values appearing at ω^*=0.72. For this spin parameter the region of non negligible K_R is also maximum and the highest values very close to the sphere's back are obtained. These fluctuations are first reduced for ω^*=0.18 and ω^*=0.32 to substantially increase again from ω^*≥0.54.

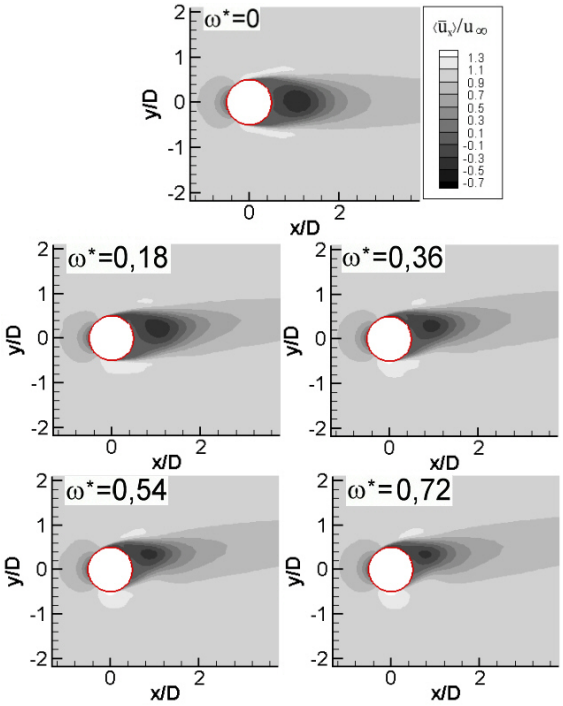

Figure 2. Non dimensional time averaged velocity component in streamwise direction.

The change of the flow field also leads to a change in the pressure distribution on the sphere. In Fig. 4 the azimuthally averaged mean pressure coefficients defined in equation (9) are shown for all spin parameters. The angle φ is measured from the front of the sphere. From 0° to 180° therefore represents the upper half of the sphere and from 180° to 360° the lower half. For the non rotating case the pressure distribution is symmetric showing even the experimentally obtained pressure increase towards the base [3]. The base pressure coefficient is then continuously decreasing with increasing spin parameter. While the pressure distribution on the

frontal part of the sphere is nearly unaltered the suction peaks change substantially due to the deceleration and acceleration of the flow. On the upper half the suction is reduced due to the earlier separation of the boundary layers. For $\omega^* \geq 0.54$ it completely disappears. The opposite can be observed on the lower half of the sphere where the flow is accelerated and the boundary layer separation delayed. The pressure therefore continuously decreases. Furthermore the minima are shifted towards the apex corresponding to the fact that the highest velocities are reached earlier with increasing ω^*, see Fig. 2.

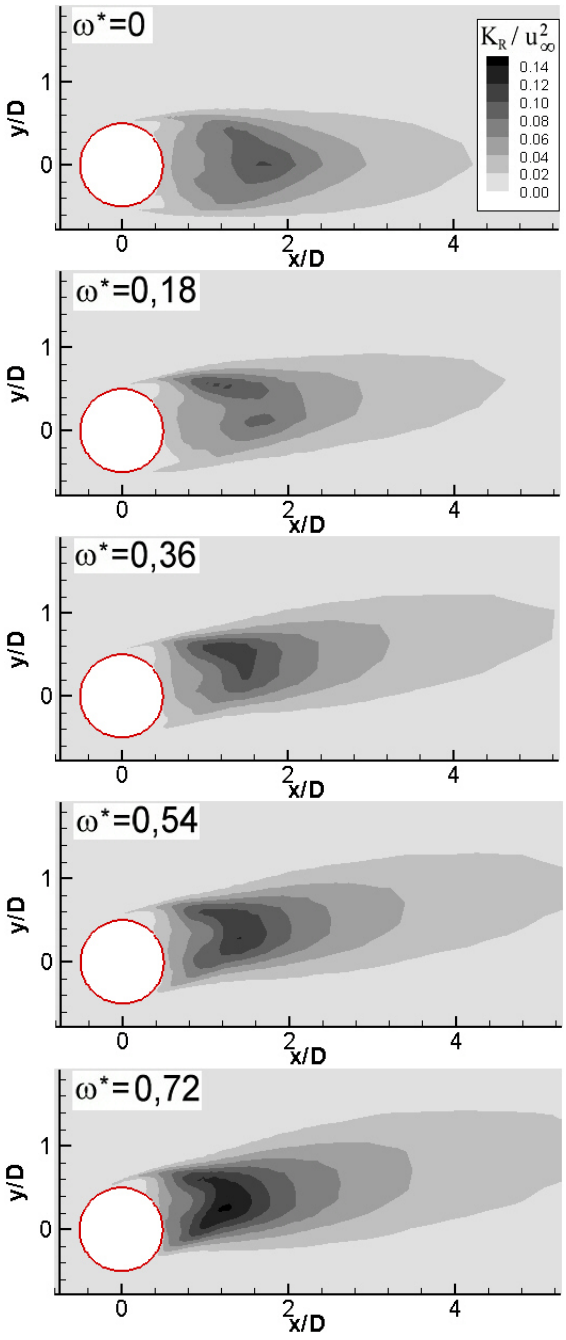

Figure 3. Non dimensional time averaged turbulent kinetic energy

From the pressure distribution the change of the force coefficients with spin parameter can be anticipated. The decrease of the pressure below the sphere together with the pressure increase on the upper half leads to a negative lift force. As the changes occur in front of the upper and behind the lower apex they also contribute to the drag force. The pressure rise on the front and the pressure decrease on the back lead to an increase in the drag coefficient. The main reason for the increase in the drag force is however the decrease of the pressure over the sphere's back.

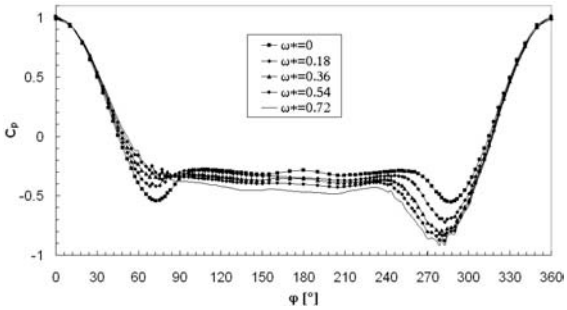

Figure 4. Mean pressure coefficient distribution on the sphere averaged in azimuthal direction. $0° < \varphi < 180°$: upper half, $180° < \varphi < 360°$: lower half of the sphere.

In Fig. 5 the mean force coefficients are shown as function of Reynolds number.

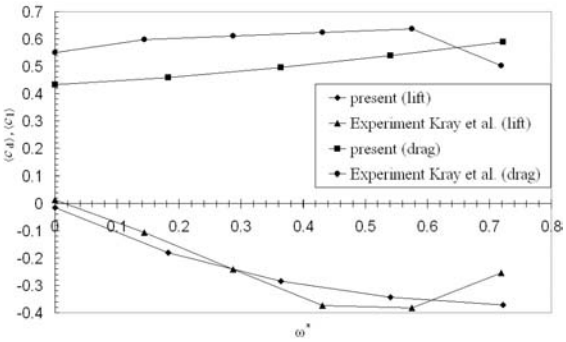

Figure 5. Mean force coefficients as function of spin parameter. Experimental data of Kray et al. [12] for $Re_D = 7 \cdot 10^4$.

Also included are the experimental results of Kray et al. [12] which have been obtained for $Re_D = 7 \cdot 10^4$. At this Reynolds number a decrease of the magnitude of the force coefficients for high spin parameters can be already observed. This phenomenon is known as negative Magnus effect and is absent in our results due to the lower Reynolds number. The other noticeable discrepancy between the measurements and the simulations is the large difference in the drag coefficients for $\omega^*=0$ which can be attributed to the mounting used in the

experiments [12]. Due to these differences the comparison of the data is only qualitative.

The simulation results show a constant increase of the magnitudes of the force coefficients. While the drag increase is nearly linear the negative lift force is increasing less with increasing spin parameter. To assess the question whether it will approach a constant value requires further simulations with even higher spin parameters. Comparing the present results with the measurements of Kray et al. [12] it can be stated that the slope of the drag coefficient curve is well predicted until the onset of the negative Magnus effect. For the lift coefficient curve the agreement is also good but only for small spin parameters.

5. CONCLUSIONS

In this paper results of the large eddy simulations of the flow around a sphere at $Re_D = 10^4$ with and without rotation of the sphere were presented. The results of the non rotating case showed a reasonable agreement with experimental and numerical data from the literature. LES of the flow around a rotating sphere with FLUENT V6.1 was therefore considered as feasible. The results of the cases with rotation perpendicular to the approach flow showed that the wake is lifted with increasing rotational speed because of the earlier separation of the boundary layer on the upper half and the delayed separation of the boundary layer on the lower half of the sphere. Shear layer transition is also modified by the rotation leading to higher turbulence in the wake with increasing spin parameter. The pressure distribution on the sphere does no longer show a suction peak on the upper half of the sphere due to the deceleration of the flow. At the lower half the suction increases with spin parameter. Both effects lead to an increasing negative lift force with increasing spin parameter. The drag force also increases as the base pressure is reduced. The computed force coefficients showed a reasonable qualitative agreement with available measurements at $Re_D = 7 \cdot 10^4$. The quantitative differences can be attributed to the experimental support of the sphere. The qualitative differences at large spin parameters are due to the negative Magnus effect not present at $Re_D = 10^4$. Therefore further simulations are planned at Reynolds numbers high enough for the negative Magnus effect to appear.

REFERENCES

[1] Fluent, 2003, "Fluent 6.1 User's guide", Fluent Inc., Lebanon, New Hampshire, USA

[2] Constantinescu, G.S., Squires, K.D., 2003, "LES and DES Investigations of Turbulent Flow over a Sphere at Re=10000", *Flow, Turbul. Combust.*, Vol. 70, pp. 267-297

[3] Achenbach, E., 1972, "Experiments on the flow past spheres at very high Reynolds numbers", *J. Fluid Mech.*, Vol. 54, pp. 565-575

[4] Yun, G., 2006, "Vortical structures behind a sphere at subcritical Reynolds numbers", *Phys. Fluids*, Vol. 18, 1

[5] Kim, S.-E., 2004, "Large-Eddy Simulation Using Unstructured Meshes and Dynamic Subgrid-Scale Turbulence Models", *AIAA Paper*, 2004-2548

[6] You, C., Qi, H., Xu, X., 2003, "Lift force on rotating sphere at low Reynolds numbers and high rotational speeds", *Acta Mech. Sin.*, Vol. 19, No.4, pp. 300-307

[7] Kim, D., Choi, H., 2002, "Laminar flow past a sphere rotating in the streamwise direction", *J. Fluid Mech.*, Vol. 461, pp. 365-386

[8] Kurose, R., Komori, S., 1999, "Drag and lift forces on a rotating sphere in a linear shear flow", *J. Fluid Mech.*, Vol. 384, pp. 183-206

[9] Niazmand, H., Renksizbulut, M., 2003, "Surface effects on transient three-dimensional flows around rotating spheres at moderate Reynolds numbers", *Comp. Fluids*, Vol. 32, pp. 1405-1433

[10] Ghosal, S. Moin, P., 1995, "The basic equations for the large eddy simulation of turbulent flows in complex geometry", *J. Comput. Phys.*, Vol. 118, pp. 24-37

[11] Choi, H., Moin, P., 1990, "On the space-time characteristics of wall-pressure fluctuations", *Phys. Fluids A*, Vol. 2, 8, pp. 1450-1460

[12] Kray, T., Frank, W., 2006, "Investigations on the flow around non-rotating and rotating spheres", Proc. *International Scientific Conference microCAD 2006 - Section F: Fluid and Heat Engineering*, University of Miskolc, Hungary

Conference on Modelling Fluid Flow (CMFF'06)
The 13th International Conference on Fluid Flow Technologies
Budapest, Hungary, September 6-9, 2006

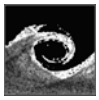

VORTEX IDENTIFICATION: NEW REQUIREMENTS AND LIMITATIONS

Václav KOLÁŘ

Institute of Hydrodynamics, Academy of Sciences of the Czech Republic, 166 12 Prague 6, Czech Republic. Tel.: +420-233109095, Fax: +420-233324361, E-mail: kolar@ih.cas.cz

ABSTRACT

Flow modelling and numerical simulation of turbulent and/or complex vortical flows still lack a generally acceptable definition of a vortex though understanding of vortex dynamics (i.e. generation, evolution, interaction, and decay of vortical structures) should be based on objective and unambiguous detection schemes. There is no doubt that the physical reasoning for these schemes plays a crucial role.

Firstly, a brief survey dealing with popular vortex-identification methods is presented. The most widely used local criteria (applied point by point) — sharing a basis in the velocity-gradient tensor $\nabla \mathbf{u}$ — are treated more thoroughly to recall the underlying requirements and to emphasize both their positive and negative aspects. A large number of recent papers have pointed out various applicability limitations of these most popular schemes for vortex identification and formulated (explicitly or implicitly) new general requirements, for example: validity for compressible flows, vortex-axis identification, allowance for an arbitrary axial strain, determination of the local intensity of swirling motion, non-local properties, and ability to provide the same results in different rotating frames. Some other, quite natural, requirements are pointed out and added to those already mentioned.

Secondly, the vortex-identification outcome of the proposed triple decomposition of the local relative motion near a point is briefly reviewed. The triple decomposition of motion has been motivated by the fact that vorticity cannot distinguish between pure shearing motions and the actual swirling motion of a vortex. The new vortex-identification method — based on the extraction of a so-called "effective" pure shearing motion — is discussed on the background of previous methods and general vortex-identification requirements (illustrative examples are included).

Keywords: decomposition of motion, vortex identification, vortex-identification criteria, vortical structures, vorticity decomposition

1. INTRODUCTION

What is a vortex? Though a vortex intuitively represents a distinct flow phenomenon, the answer to this question is neither simple nor unique, e.g. Lugt [1]. He presents one of the intuitive definitions of a vortex as follows: "A vortex is the rotating motion of a multitude of material particles around a common centre". These intuitive definitions are often depicting a vortex in terms of closed or spiralling streamlines or pathlines, local pressure minima, and isovorticity contours and surfaces. However, spiralling streamlines or pathlines are obtained just for an observer moving with the vortex to be identified, and the existence of a local pressure minimum does not guarantee the existence of a vortex (and vice versa).

Vorticity tensor, as a Galilean invariant quantity expressing an average angular velocity of fluid elements, appears as one of the most natural choices for a vortex-identification criterial measure. However, it has been recently emphasized by many authors that vorticity is not suitable for the identification of a vortex as it cannot distinguish between pure shearing motions and the actual swirling motion of a vortex (Jeong and Hussain [2], Kida and Miura [3], Cucitore et al. [4]). This property of vorticity leads to the misrepresentation of vortex geometry. Moreover, the vortex geometry depends on the vorticity threshold applied.

The most widely used local methods for vortex identification are based on the analysis of the velocity-gradient tensor $\nabla \mathbf{u}$, its symmetric and antisymmetric components, strain-rate tensor $\mathbf{S}$ and vorticity tensor $\mathbf{\Omega}$, $\nabla \mathbf{u} = \mathbf{S} + \mathbf{\Omega}$, and the three invariants of $\nabla \mathbf{u}$. The application of complex measures derived from $\nabla \mathbf{u}$ has already revealed their importance for the description of large-scale vortical structures in turbulent free-shear flows as well as turbulent boundary-layer flows. These measures provide a rational basis for vortex identification and for the general classification of 3D flow fields. In the following section the most popular vortex-identification criteria are shortly described. Needless to say, these criteria are

Galilean invariant (i.e. independent of the translational velocity of an observer).

In Section 3, some other — more recent — identification methods and discussions about vortex definition are surveyed with a particular emphasis put on the applicability limitations of various schemes. New general requirements for vortex identification are summarized and other natural requirements are pointed out.

In Sections 4 and 5, the vortex-identification outcome of the proposed triple decomposition of the local relative motion near a point is presented and reviewed on the background of previous methods and general identification requirements. Illustrative examples of this novel approach are included.

2. THE MOST WIDELY USED LOCAL VORTEX-IDENTIFICATION CRITERIA

A vortex represents obviously a non-local flow phenomenon in space and time. However, as noted by Chakraborty et al. [5], the presence of viscosity in real fluids results in continuity in the kinematic features of the flow field. Consequently, a reasonable estimate of some non-local vortical features can be inferred from the local (pointwise, applied point by point) methods and characteristics.

2.1. *Q*-criterion

Hunt et al. [6] identify vortices of an incompressible flow as connected fluid regions with positive second invariant of $\nabla \mathbf{u}$ (in tensor notation below the subscript /*j* denotes differentiation)

$$Q = -\frac{1}{2} u_{i/j} u_{i/j} = \frac{1}{2}\left(\|\mathbf{\Omega}\|^2 - \|\mathbf{S}\|^2 \right) > 0 , \qquad (1)$$

that is, as the regions where the vorticity magnitude prevails the strain-rate magnitude. The norm (or absolute tensor value) $\|\mathbf{G}\|$ of any tensor $\mathbf{G}$ is defined by $\|\mathbf{G}\| = \left[\mathrm{tr}\left(\mathbf{G} \cdot \mathbf{G}^{\mathrm{T}} \right) \right]^{1/2}$. In addition, the pressure in the vortex region is required to be lower than the ambient pressure.

2.2. Δ-criterion

Dallman [7] and Chong et al. [8] define vortices as the regions in which the eigenvalues of $\nabla \mathbf{u}$ are complex (a pair of complex-conjugate eigenvalues occurs) and the streamline pattern is spiralling or closed in a local reference frame moving with the point. Such points can be viewed within the critical-point theory — on a plane spanned by the complex eigenvectors — as elliptic ones (focus or centre). For incompressible flows, this requirement reads

$$\Delta = \left(\frac{Q}{3} \right)^3 + \left(\frac{R}{2} \right)^2 > 0 \qquad (2)$$

where Q and R are the invariants of $\nabla \mathbf{u}$, Q is given by (1), $R = \mathrm{Det}\left(u_{i/j} \right)$. Q and R play a crucial role in the reduced (due to incompressibility) characteristic equation for the eigenvalues λ of $\nabla \mathbf{u}$

$$\lambda^3 + Q\lambda - R = 0 . \qquad (3)$$

2.3. λ_2-criterion

The approach of Jeong and Hussain [2] is formulated on dynamic considerations, namely on the search for a pressure minimum across the vortex. Their general requirements for a vortex are: a vortex must have a net circulation and the vortex geometry should be Galilean invariant. Taking the gradient of the Navier-Stokes equations they find

$$a_{i/j} = -\frac{1}{\rho} p_{/ij} + \nu u_{i/jkk} \qquad (4)$$

where $a_{i/j}$ is the acceleration gradient, the symmetric tensor $p_{/ij}$ is the pressure Hessian. By decomposing (4) into symmetric and antisymmetric parts they derive the well-known vorticity transport equation, the antisymmetric part of (4), and the strain-rate transport equation, the symmetric part of (4). The latter reads

$$\frac{\mathrm{D}S_{ij}}{\mathrm{D}t} - \nu S_{ij/kk} + \Omega_{ik}\Omega_{kj} + S_{ik}S_{kj} = -\frac{1}{\rho} p_{/ij} \qquad (5)$$

where the pressure Hessian $p_{/ij}$ contains information on local pressure extrema. The occurrence of a local pressure minimum in a plane across the vortex requires two positive eigenvalues of the tensor $p_{/ij}$.

By removing the unsteady irrotational straining and viscous effects from the strain-rate transport equation (5) one yields the vortex identification criterion for incompressible fluids in terms of two negative eigenvalues of $\mathbf{S}^2 + \mathbf{\Omega}^2$. The reason for discarding these terms lies in the fact that the existence of a local pressure minimum is neither a sufficient nor a necessary condition for the presence of a vortex in general, and the two removed terms from the equation (5) are found to be the main cause of this inaccuracy.

Finally, a vortex is defined as a connected fluid domain with two negative eigenvalues of $\mathbf{S}^2 + \mathbf{\Omega}^2$. Since the tensor $\mathbf{S}^2 + \mathbf{\Omega}^2$ is symmetric, it has real eigenvalues only. If these eigenvalues are ordered as follows, $\lambda_1 \geq \lambda_2 \geq \lambda_3$, the vortex-identification criterion is equivalent to the resulting condition $\lambda_2 < 0$.

3. OTHER VORTEX-IDENTIFICATION APPROACHES, NEW REQUIREMENTS AND LIMITATIONS

The papers mentioned in the preceding section have stimulated new and significant research activity. In this section some other recent vortex-identification methods and discussions on vortex definition are briefly surveyed.

Kida and Miura [3], similarly as Jeong and Hussain [2], point out that a swirling motion is not always associated with a sectional pressure minimum. This aspect has motivated these authors to improve the pressure-minimum scheme by imposing a kinematic swirl condition, and they have constructed the central axes of vortices by the sectional-swirl-and-pressure-minimum scheme for the identification of the low-pressure vortices in freely decaying homogeneous turbulence. As noted by Wu et al. [9] an extremal condition adopted by Kida and Miura [3] for low-pressure vortices is necessary for identifying a single line as the vortex axis.

In the eduction of longitudinal vortices in wall-turbulence, Jeong et al. [10] employ a non-zero threshold for λ_2 contrary to the λ_2-criterion. This practical aspect is emphasized by Kida and Miura [3], as well as by Lin et al. [11] in their study of a neutrally stratified planetary boundary-layer flow.

The Q-criterion and λ_2-criterion are limited to incompressible flows. In the case of compressible fluids additional terms occur on the LHS of Eq. (5) as shown by Cucitore et al. [4]. The use of $\mathbf{S}^2+\mathbf{\Omega}^2$ as an approximation of the pressure Hessian $p_{,ij}$ for compressible fluids requires discarding other terms besides the unsteady irrotational straining and viscous effects removed originally from the strain-rate transport equation (5) valid for incompressible flows only.

Another aspect worth mentioning is that all the methods based on the analysis of $\nabla\mathbf{u}$ are pointwise providing local vortex-identification criteria. This aspect has led Cucitore et al. [4] to introducing the concept of non-locality for determining the vortices as structures. They suggest a non-local, Galilean-invariant identification technique. The reason is that the use of local procedures often selects a particular privileged direction which is considered as the vortex axis. For example, the λ_2-criterion captures the pressure minimum in a plane across the vortex but not along it. The non-local criterion of Cucitore et al. [4] is based on the intuitive notion that the particles inside a vortical structure show small variations in their relative distance even when following completely different trajectories.

Zhou et al. [12] use the imaginary part of the complex eigenvalue of $\nabla\mathbf{u}$ to visualize vortices and to quantify the strength of the local swirling motion inside the vortex (the so-called swirling-strength criterion). Their method is based on the Δ-criterion, however, it identifies not only the vortex region (equivalently as Δ-criterion), but also the local strength and the local plane of swirling. For a similar approach based on complex eigenvalues see Berdahl and Thompson [13]. The associated instantaneous-streamline analysis is further developed in Chakraborty et al. [5]. Their criterion enhances the swirling-strength criterion by including a local approximation of the non-local property proposed by Cucitore et al. [4] requiring that the swirling material points inside a vortex have bounded separation remaining small. Moreover, Chakraborty et al. [5] study the relationship between local identification schemes. They show that all these local criteria, given the proposed usage of threshold, result in a remarkable vortex similarity.

The evaluation of vortex-identification criteria by comparing the resulting vortex patterns in numerically simulated complex vortical flows cannot lead to a final choice for the correct criterion as the judgment depends on the adopted intuitive and subjective concept on what should be called a vortex, as pointed out by Wu et al. [9]. Instead of numerical examples they make an analytical diagnosis of four local criteria, demonstrated by the Burgers and Sullivan vortex, indicating that Q-criterion and λ_2-criterion may cut a connected vortex into broken segments at locations with strong axial stretching. Consequently, the following requirements are emphasized: a generally applicable vortex definition should be able to identify the vortex axis and allow for an arbitrary axial strain. Note that all the local criteria described in Section 2 identify just a vortex region through criterial inequalities without specifying the vortex axis inside this region. Wu et al. [9] state that an equality is necessary for identifying a single line as the vortex axis. Recall that the extremal condition of Kida and Miura [3] enables to find the vortex skeleton by tracing the lines of sectional pressure minimum provided that a swirl condition is satisfied.

Xiong et al. [14] define a vortex as follows: if all the fluid particles within the area in the plane normal to the vorticity direction have the rotational velocity components in the same direction around any point in the area, the area is identified as a part of a vortex. They clearly state that the validation of the vortex definition using flow examples is not rigorous because of a prejudice of expecting what is a vortex a priori. Examples are only sufficient to invalidate but not support an idea. Xiong et al. [14] emphasize that a method to identify a vortex should be evaluated by whether there is a clear physical meaning in the vortex definition and that the vortex-identification method should be chosen by which characteristics the definition focuses on.

The fact that all the most widely used vortex definitions are not objective relative to an arbitrarily

rotating reference frame has motivated Haller [15] to develop an objective frame-independent definition of a vortex based on Lagrangian stability considerations. Accordingly, a vortex is defined as a set of fluid trajectories along which the strain acceleration tensor is indefinite over directions of zero strain. This definition should help in the situations of an unclear choice for a reference frame (for example, vortical flows in rotating tanks).

The above mentioned new requirements for vortex-identification schemes and their underlying criterial quantities can be summarized as follows:

- validity for compressible flows
- to avoid the subjective choice of threshold in the vortex-boundary identification
- determination of the local intensity of swirling motion (to describe inner vortex structure)
- vortex-axis identification
- allowance for an arbitrary axial strain
- non-local properties
- ability to provide the same results in different rotating frames

Though most of these requirements are intuitively clear, some of them may need further justification.

As to the local intensity of swirling motion, engineering practice may frequently need this local quantity to be integrable across the vortex region to obtain the integral strength of a vortex (this may be considered not only in planar cross-section sense but even in volumetric sense). However, the application of conventional circulation Γ for this purpose is in fact misleading as the vorticity is misrepresenting the local intensity of actual swirling motion of a vortex. For example, one obtains a net circulation for the region of a pure shearing motion due to a net vorticity of this motion.

Further, another requirement — much more trivially looking than the integral strength of a vortex — is the swirl orientation. The local angle between the vortex-axis tangent and the vorticity vector may reach almost 90° due to a strong shearing aligned with the vortex axis. A nice theoretical example in this regard is represented by an inviscid streamwise vortex in a homogeneous shear flow (see §5.2.1 of Jeong and Hussain [2]). This requirement becomes particularly important in complex 3D vortical flows subjected to high shear.

These additional requirements are quite natural and, therefore, added to those already mentioned:

- swirl orientation
- determination of the (integral) vortex strength

4. TRIPLE DECOMPOSITION OF THE RELATIVE MOTION NEAR A POINT AND VORTEX IDENTIFICATION

The triple decomposition of the local relative motion near a point (TDM) has been motivated by the fact that vorticity cannot distinguish between pure shearing motions and the actual swirling motion of a vortex. Therefore, this decomposition method is — including its vortex-identification outcome — based on the extraction of a so-called "effective" pure shearing motion. The TDM is expressed through the corresponding triple decomposition of $\nabla \mathbf{u}$ introduced in [16].

To discuss all the main aspects of the TDM in 3D flows is far beyond the scope of this short contribution and the research is in this regard incomplete due to its complexity. However, its planar version — including the application to vortex identification — is very illustrative. Particularly, a straightforward qualitative comparison with the most widely used vortex-identification methods is provided in Section 5.

Although we focus below on planar flows, it is convenient to introduce the TDM algorithm using 3D formalism. The TDM reads

$$\nabla \mathbf{u} = (\nabla \mathbf{u})_{\mathrm{EL}} + (\nabla \mathbf{u})_{\mathrm{RR}} + (\nabla \mathbf{u})_{\mathrm{SH}} \qquad (6)$$

where an irrotational straining motion is given by the symmetric tensor $(\nabla \mathbf{u})_{\mathrm{EL}}$ (subscript EL denotes elongation), a rigid-body rotation is given by the antisymmetric tensor $(\nabla \mathbf{u})_{\mathrm{RR}}$, and an *effective* pure shearing motion $(\nabla \mathbf{u})_{\mathrm{SH}}$ is described by the "purely asymmetric tensor form" of $\nabla \mathbf{u}$ with components fulfilling *in a suitable reference frame*

$$u_{i/j} = 0 \quad OR \quad u_{j/i} = 0 \quad (\text{for all } i, j)\,. \qquad (7)$$

The above requirements are apparently insufficient. What we really need is a physically well-justified algorithm leading to a unique decomposition. The "shear tensor" satisfying the condition (7) can be easily generated by the natural and straightforward decomposition scheme which is applicable to an arbitrary reference frame

$$\nabla \mathbf{u} = \begin{pmatrix} residual \\ tensor \end{pmatrix} + \begin{pmatrix} shear \\ tensor \end{pmatrix} \qquad (8a)$$

where the residual tensor is given by

$$\begin{pmatrix} residual \\ tensor \end{pmatrix} = \begin{pmatrix} u_x & (\operatorname{sgn} u_y)\,\mathrm{MIN}\left(|u_y|, |v_x|\right) & \bullet \\ (\operatorname{sgn} v_x)\,\mathrm{MIN}\left(|u_y|, |v_x|\right) & v_y & \bullet \\ \bullet & \bullet & w_z \end{pmatrix} \qquad (8b)$$

In (8a, b) the following simplified notation is employed: u, v, w are velocity components, subscripts x, y, z stand for partial derivatives. The remaining two non-specified pairs of off-diagonal

terms of the residual tensor in (8b) are constructed strictly analogously as the specified one, each pair being either symmetric or antisymmetric.

If considered separately, an arbitrary shearing motion should be, by (7), recognized *in a suitable reference frame* as a third elementary part of the TDM. Finding a minimum of the norm of the residual tensor within the scheme (8a, b) by changing the reference frame under an orthogonal transformation guarantees to satisfy this necessary requirement and leads to the correct frame choice (to perform the desired decomposition). This condition says that the effect of extraction of the shear tensor from $\nabla\mathbf{u}$ is maximized.

The TDM is closely associated with the so-called *basic reference frame* (BRF) where it is performed. In this frame, an *effective* pure shearing motion is shown in a clearly visible manner described by the form (7) on condition that the norm of the residual tensor in (8a, b) is minimized. That is, consistently with the limiting case mentioned in the preceding paragraph, on condition that the effect of extraction of the shear tensor is maximized. Considering the following relation expressed in terms of strain-rate and vorticity tensors, **S** and **Ω**, and valid in an arbitrary reference frame,

$$\left\| \begin{pmatrix} residual \\ tensor \end{pmatrix} \right\|^2 + 4\left(\left|S_{12}\Omega_{12}\right| + \left|S_{23}\Omega_{23}\right| + \left|S_{31}\Omega_{31}\right| \right) = \left\|\nabla\mathbf{u}\right\|^2 \qquad (9)$$

the definition condition of the BRF takes the form

$$\left[\left|S_{12}\Omega_{12}\right| + \left|S_{23}\Omega_{23}\right| + \left|S_{31}\Omega_{31}\right| \right]^{\mathrm{BRF}} = \mathrm{MAX\ over\ all\ frames}\,. \qquad (10)$$

Note that the BRF, unlike the system of principal axes of **S**, is determined *simultaneously* on the basis of **S** and **Ω**.

The decomposition algorithm consists of the following three steps (a uniform dilatation can be removed prior to further analysis of $\nabla\mathbf{u}$ without loss of generality and applicability to compressible flows)

Step 1: Determination of the BRF satisfying the condition (10).

Step 2: Decomposition of $\nabla\mathbf{u}$ following the scheme (8a, b); according to the initial scheme (6), the residual tensor represents the sum $(\nabla\mathbf{u})_{\mathrm{EL}} + (\nabla\mathbf{u})_{\mathrm{RR}}$, and the shear tensor represents $(\nabla\mathbf{u})_{\mathrm{SH}}$.

Step 3: Return to the original (e.g. laboratory) reference frame: any additive part **A** of $\nabla\mathbf{u}$ is described in an arbitrary reference frame rotated with respect to the BRF under an orthogonal transformation **Q** by $\mathbf{QAQ}^{\mathrm{T}}$ as

$$\mathbf{Q}\left(\sum_i \mathbf{A}_i\right)\mathbf{Q}^{\mathrm{T}} = \sum_i \mathbf{Q}\mathbf{A}_i\mathbf{Q}^{\mathrm{T}}\,. \qquad (11)$$

In the planar case treated below in detail, the uniqueness of this decomposition is obvious.

From the viewpoint of the double decomposition, the TDM components of $\nabla\mathbf{u}$ are certain products of interaction between **S** and **Ω**. The term $(\nabla\mathbf{u})_{\mathrm{SH}}$ is responsible for a specific portion of vorticity labelled "*shear* vorticity" and for a specific portion of strain rate labelled "*shear* strain rate". The remaining portions are called "*residual* vorticity" and "*residual* strain rate".

In planar flows, the velocity-gradient tensor $\nabla\mathbf{u}$ can be described in an arbitrary reference frame, in the system of principal axes, and in the above mentioned BRF as follows

$$\begin{pmatrix} u_x & u_y & 0 \\ v_x & -u_x & 0 \\ 0 & 0 & 0 \end{pmatrix} \rightarrow \begin{pmatrix} s & -\omega & 0 \\ \omega & -s & 0 \\ 0 & 0 & 0 \end{pmatrix}^{\mathrm{PRINCIPAL\ AXES}} \rightarrow \begin{pmatrix} 0 & s-\omega & 0 \\ s+\omega & 0 & 0 \\ 0 & 0 & 0 \end{pmatrix}^{\mathrm{BRF}} \qquad (12)$$

where s and ω fulfil the relations

$$\left|s\right| = \left(\sqrt{4u_x^2 + \left(u_y + v_x\right)^2} \right)/2\,, \qquad (13)$$

$$\omega = \left(v_x - u_y\right)/2\,. \qquad (14)$$

In the BRF, there are two different relative rotational orientations of $u_y\mathrm{d}y$ and $v_x\mathrm{d}x$, the same and the opposite, see Fig. 1. In Fig. 1(a) vorticity dominates strain rate. The characteristic angles, α_1 and α_2, correspond to the *residual* vorticity ω_{RES} (associated with the rigid-body rotation) and *shear* vorticity ω_{SH} (associated with the pure shearing motion) while their sum is proportional to the *total* vorticity ω. In Fig. 1(b) strain rate dominates vorticity. The characteristic angles, β_1 and β_2, correspond to the *residual* strain rate s_{RES} and *shear* strain rate s_{SH} while their sum is proportional to the *total* strain rate s. Note that ω_{RES} and ω_{SH} have the same signs in the BRF due to the algebraic structure of (8a, b). The same holds for s_{RES} and s_{SH}. The superimposing geometrical construction in Fig. 1 is of virtual nature and applicable to infinitesimal motional changes only. For both rotational orientations, the magnitude of the superimposed shearing motion is given by the

difference of absolute values of u_y and v_x. In planar flows, a non-zero ω_{RES} apparently existing only for the same rotational orientation of $u_y \mathrm{d}y$ and $v_x \mathrm{d}x$, see Fig. 1, excludes the existence of a non-zero s_{RES} existing only for the opposite rotational orientation of $u_y \mathrm{d}y$ and $v_x \mathrm{d}x$.

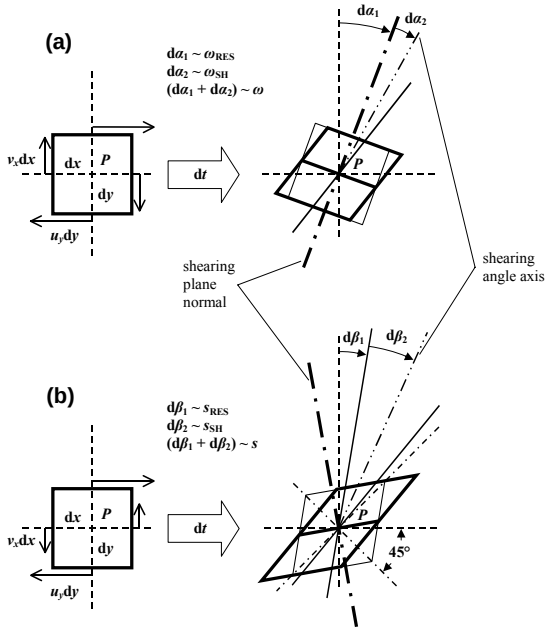

Figure 1. Geometrical interpretation of 2D fluid motion: (a) vorticity components, (b) strain-rate components.

With respect to the algebraic structure of (8a, b) the following set of relations can be derived for *s* and *ω*, and their *residual* and *shear* components (not stated case $|s| = |\omega|$ represents a simple shear)

$$s = s_{\mathrm{RES}} + s_{\mathrm{SH}}, \tag{15}$$

$$|s| = |s_{\mathrm{RES}}| + |s_{\mathrm{SH}}|, \tag{16}$$

$$s_{\mathrm{SH}} = (\mathrm{sgn}\, s)|\omega| \quad for \quad |s| > |\omega|, \tag{17}$$

$$s_{\mathrm{SH}} = s \quad for \quad |s| < |\omega|, \tag{18}$$

$$\begin{aligned} s_{\mathrm{RES}} &= s - s_{\mathrm{SH}} \\ &= (\mathrm{sgn}\, s)\left[|s| - |\omega|\right] \quad for \quad |s| > |\omega|, \end{aligned} \tag{19}$$

$$s_{\mathrm{RES}} = s - s_{\mathrm{SH}} = 0 \quad for \quad |s| < |\omega|, \tag{20}$$

$$\omega = \omega_{\mathrm{RES}} + \omega_{\mathrm{SH}}, \tag{21}$$

$$|\omega| = |\omega_{\mathrm{RES}}| + |\omega_{\mathrm{SH}}|, \tag{22}$$

$$\omega_{\mathrm{SH}} = \omega \quad for \quad |s| > |\omega|, \tag{23}$$

$$\omega_{\mathrm{SH}} = (\mathrm{sgn}\, \omega)|s| \quad for \quad |s| < |\omega|, \tag{24}$$

$$\omega_{\mathrm{RES}} = \omega - \omega_{\mathrm{SH}} = 0 \quad for \quad |s| > |\omega|, \tag{25}$$

$$\begin{aligned} \omega_{\mathrm{RES}} &= \omega - \omega_{\mathrm{SH}} \\ &= (\mathrm{sgn}\, \omega)\left[|\omega| - |s|\right] \quad for \quad |s| < |\omega|. \end{aligned} \tag{26}$$

The vortex-identification outcome of the TDM reads: a vortex is defined as a connected fluid domain with a non-zero magnitude of the *residual* vorticity. In the present context, the planar-vortex regions are characterized by the non-zero *residual* vorticity for $|s| < |\omega|$ using (24) and (26), see preliminary results [16] for the plane turbulent wake of two side-by-side square cylinders [17]. The planar analysis may be applied as quasi-2D method provided that the velocity gradients in the third direction are negligible. Fig. 2 shows the quasi-2D secondary-flow vortex geometry in two downstream cross-sections of a single jet in crossflow (JICF), data [18], which is nearly circular in terms of ω_{RES}.

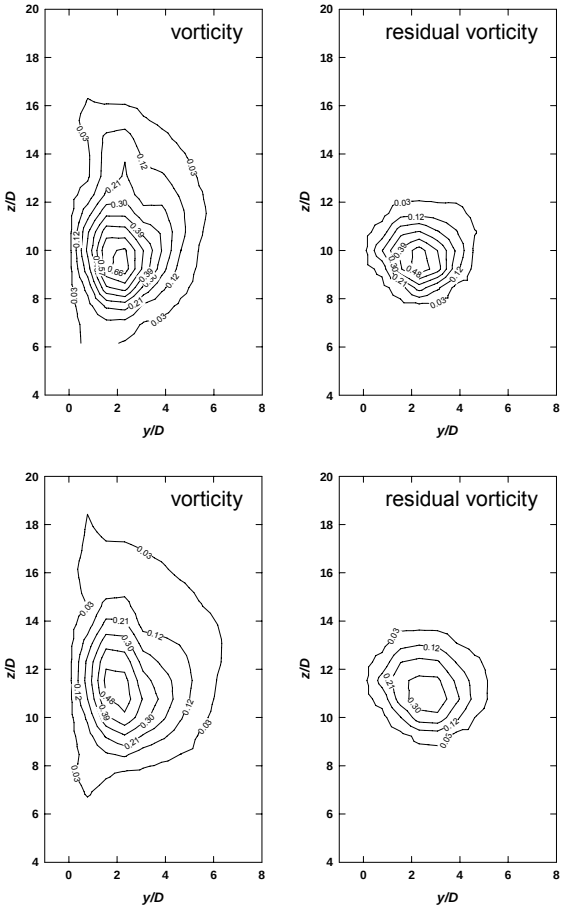

Figure 2. Secondary-flow vortex geometry of the JICF in terms of (negative) vorticity and *residual* vorticity at *x/D* = 10 (above), *x/D* = 15 (below).

5. DISCUSSION

It should be emphasized that the identification method based on the *residual* vorticity represents a certain qualitative "comeback" of vorticity, namely its specific portion associated with the local *residual* rigid-body rotation obtained after the removal of pure shearing motion. In view of the requirements summarized in Section 3, note that all very useful vorticity features — vectorial character (direction and orientation), applicability to compressible flows, easy integrability across an arbitrary surface area, etc. — are retained. On the other hand, it is still a local quantity, moreover, not invariant with respect to rotating reference frames.

In planar flows, all the local criteria described in Section 2 degenerate to the same one [2, 9] identifying the vortex region by the condition $\omega^2 - s^2 > 0$ implying that vorticity dominates strain rate. This criterion corresponds to the Weiss criterion [19, 20] for elliptic flow regions and can be geometrically interpreted as the region of positive unnormalized Gaussian curvature of the stream function [21].

The kinematically consistent model of a planar vortex-shear interaction employed below provides a fair basis to obtain correct qualitative results on vortex identification. The examined planar $\nabla\mathbf{u}$-field is formed by superimposing of two linear shearing effects of a Gaussian distribution located symmetrically at $y = \pm 0.5$ onto the $\nabla\mathbf{u}$-field of an ideal axisymmetric Taylor vortex centred at (0, 0).

The distribution of positive $\omega^2 - s^2$ exhibits the formation of a double peak quite similar to that of vorticity distribution, see Fig. 3 (for the same strength of "flow components" in terms of vorticity peaks). For large shearing values the peak magnitudes of both vorticity and $\omega^2 - s^2 > 0$ are adequately large and the locations of peak values are ultimately attaining the locations of shearing maxima at $y = \pm 0.5$. This is causing an inevitable ambiguity in defining the vortex axis in terms of vorticity as well as $\omega^2 - s^2$ by using the natural extremal condition, as discussed in Section 3. In Fig. 3 it is shown that the conventional criterial quantity, positive $\omega^2 - s^2$, identifying satisfactorily the overall vortex region fails — unlike ω_{RES} — in describing the vortex axis correctly (in terms of the location and magnitude of the peak value) provided that a pure shearing motion superimposed onto an ideal vortex is not negligible. This quantity cannot represent the local intensity of a vortex due to the strong inherent bias towards $\left[|\omega| + |s|\right]$ expressed by

$$\begin{aligned} \omega^2 - s^2 &= \omega_{\mathrm{RES}} \cdot (\omega + \omega_{\mathrm{SH}}) \\ &= (\operatorname{sgn}\omega)\left[|\omega| - |s|\right] \cdot (\operatorname{sgn}\omega)\left[|\omega| + |s|\right] \qquad (27) \\ &\qquad for \quad |s| < |\omega| . \end{aligned}$$

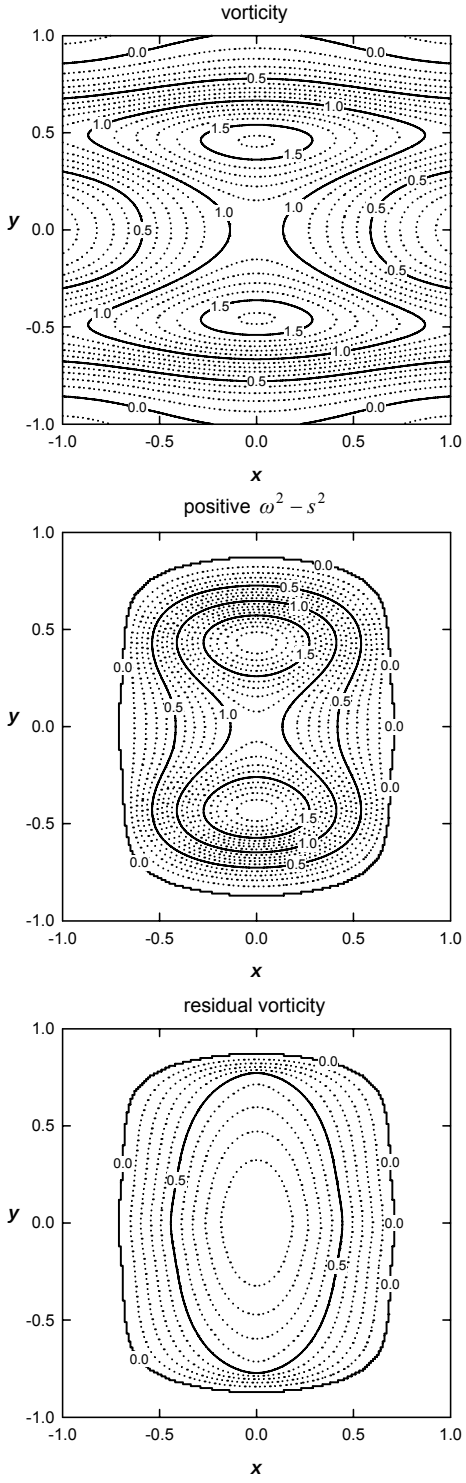

Figure 3. Description of vortex-shear interaction.

The expression (27) explains the coincidence of the zero contour for $\omega^2 - s^2$ with that for ω_{RES} (Fig. 3). In both cases, this contour represents the identified vortex boundary, however, only roughly matching the original axisymmetric boundary of an isolated Taylor vortex. The reason is that any *local* schemes based on pointwise analysis can hardly reveal any virtual *non-local* flow components or features exactly.

6. CONCLUSIONS

A brief survey of popular vortex-identification methods is presented. The most widely used local criteria are critically reviewed on the background of other vortex definitions and relevant discussions. A particular emphasis is put on the summary of new general requirements for any vortex-identification schemes and their underlying criterial quantities.

Further, the present paper suggests that a specific portion of vorticity provides a proper physical quantity for the *kinematic* identification of a vortex. On the basis of the triple decomposition of the local relative motion near a point, the vorticity is decomposed into two parts, *shear* vorticity and *residual* vorticity. The latter is associated with the local *residual* rigid-body rotation obtained after the extraction of an *effective* pure shearing motion. The *residual* vorticity retains all very useful vorticity features and, consequently, satisfies most of the general requirements for vortex identification.

ACKNOWLEDGEMENTS

This work was financially supported by the Grant Agency of the Acad. of Sci. of the Czech Rep. through grant IAA2060302, and by the Acad. of Sci. of the Czech Rep. through Inst. Res. Plan AV0Z20600510.

REFERENCES

[1] Lugt, H.J., 1983, *Vortex Flow in Nature and Technology*, Wiley.

[2] Jeong, J., and Hussain, F., 1995, "On the identification of a vortex", *J Fluid Mech*, Vol. 285, pp. 69-94.

[3] Kida, S., and Miura, H., 1998, "Identification and analysis of vortical structures", *Eur J Mech B/Fluids*, Vol. 17, pp. 471-488.

[4] Cucitore, R., Quadrio, M., and Baron, A., 1999, "On the effectiveness and limitations of local criteria for the identification of a vortex", *Eur J Mech B/Fluids*, Vol. 18, pp. 261-282.

[5] Chakraborty, P., Balachandar, S., and Adrian, R. J., 2005, "On the relationships between local vortex identification schemes", *J Fluid Mech*, Vol. 535, pp. 189-214.

[6] Hunt, J.C.R., Wray, A.A., and Moin, P., 1988, "Eddies, stream, and convergence zones in turbulent flows", *Center for Turbulence Research Report* CTR-S88, pp. 193-208.

[7] Dallmann, U., 1983, "Topological structures of three-dimensional flow separation", *DFVLR Report* No.221-82-A07.

[8] Chong, M.S., Perry, A.E., and Cantwell, B.J., 1990, "A general classification of three-dimensional flow fields", *Phys Fluids A*, Vol. 2, pp. 765-777.

[9] Wu, J.-Z., Xiong, A.-K., and Yang, Y.-T., 2005, "Axial stretching and vortex definition", *Phys Fluids*, Vol. 17, pp. 038108-1-038108-4.

[10] Jeong, J., Hussain, F., Schoppa, W., Kim, J., 1997, "Coherent structures near the wall in a turbulent channel flow", *J Fluid Mech*, Vol. 332, pp. 185-214.

[11] Lin, C.-L., McWilliams, J.C., Moeng, C.-H., Sullivan, P.P., 1996, "Coherent structures and dynamics in a neutrally stratified planetary boundary layer flow", *Phys Fluids*, Vol. 8, pp. 2626-2639.

[12] Zhou, J., Adrian, R.J., Balachandar, S., and Kendall, T.M., 1999, "Mechanisms for generating coherent packets of hairpin vortices in channel flow", *J Fluid Mech*, Vol. 387, pp. 353-396.

[13] Berdahl, C., and Thompson, D., 1993, "Eduction of swirling structure using the velocity gradient tensor", *AIAA J*, Vol. 31, pp. 97-103.

[14] Xiong, A.-K., Kobayashi, K., Izawa, S., Fukunishi, Y., 2004, "Discussions on the methods for vortex identification", Proc. *IUTAM Symposium on Elementary Vortices and Coherent Structures: Significance in Turbulence Dynamics*, Kyoto, Japan, pp. 90-91.

[15] Haller, G., 2005, "An objective definition of a vortex", *J Fluid Mech*, Vol. 525, pp. 1-26.

[16] Kolář, V., 2004, "2D velocity-field analysis using triple decomposition of motion", Proc. *15th Australasian Fluid Mechanics Conference*, Sydney, Australia, Paper AFMC00017, http://www.aeromech.usyd.edu.au/15afmc.

[17] Kolář, V., Lyn, D.A., Rodi, W., 1997, "Ensemble-averaged measurements in the turbulent near wake of two side-by-side square cylinders", *J Fluid Mech*, Vol. 346, pp. 201-237.

[18] Kolář, V., Savory, E., Toy, N., 2000, "Centerline vorticity transport within a jet in crossflow", *AIAA J*, Vol. 38, pp. 1763-1765.

[19] Weiss, J., 1991, "The dynamics of enstrophy transfer in two-dimensional hydrodynamics", *Physica D*, Vol. 48, pp. 273-294.

[20] Basdevant, C., and Philipovitch, T., 1994, "On the validity of the "Weiss criterion" in two-dimensional turbulence", *Physica D*, Vol. 73, pp. 17-30.

[21] Dresselhaus, E., and Tabor, M., 1989 "The persistence of strain in dynamical systems", *J Phys A Math Gen*, Vol. 22, pp. 971-984.

Conference on Modelling Fluid Flow (CMFF'06)
The 13th International Conference on Fluid Flow Technologies
Budapest, Hungary, September 6-9, 2006

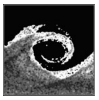

NUMERICAL STUDY OF THE VORTEX STRUCTURE IN PERIODICALLY FLUCTUATED TURBULENT SEPARATED FLOW

Masaki YAMAGISHI[1], Shinichi TASHIRO[2]

[1] Corresponding Author. Department of Mechanical Engineering, Nagaoka National College of Technology. 888 Nishikatakai, Nagaoka, Niigata 940-8532, Japan. Tel.: +81 258 34 9206, Fax: +81 258 34 9206, E-mail: yamagisi@nagaoka-ct.ac.jp
[2] Department of Mechanical Engineering, Graduate School of Science and Technology, Tokyo Metropolitan University. E-mail: tasiro@tmit.ac.jp

ABSTRACT

Introduction of an external fluctuation into the flow is one of the promising methods to control and/or reduce the flow separation. There are effective fluctuation frequencies for the reduction of separated region. The mechanism of the reduction in the flow around the inclined flat plate was investigated by numerical simulation. The artificial periodic velocity fluctuations with various frequencies were introduced into the mean upstream flow of the separated region. The vortex structure in a separated region changes to that of various patterns when the fluctuation is introduced into the separated region. It was found that the vortices of some scale are formed in the separated shear layer. With the effective frequency, these vortices generate periodically and shed from the reattachment point in frequency of fluctuation.

Keywords: separation, reattachment, shear layer, velocity fluctuation, vortex, CFD

NOMENCLATURE

In this study, all of the values are non-dimensionalized by the mean flow velocity U_0 and flat plate length L.

A	[m/s]	Amplitude of external fluctuation velocity
a	[m/s]	Maximum amplitude of external fluctuation velocity
f	[Hz]	frequency of velocity fluctuation
L	[m]	flat plate length
p	[Pa]	pressure
t	[s]	time
U_0	[m/s]	mean flow velocity
$\underline{u}$	[m/s]	velocity vector
u, v	[m/s]	velocity
u', v'	[m/s]	fluctuation component of velocity
x, y	[m]	coordinate axes (parallel and normal to the mean flow direction)
λ	[m]	wavelength
ξ, η	[m]	coordinate axes (parallel and normal to the flat plate direction)

Subscripts and Superscripts

e	external fluctuation
shed	on the vortex shedding
R	on the reattachment point
Z	component along the mean flow axis

1. INTRODUCTION

Separation phenomena in a flow become the source of oscillation and noise which lead to the crucial damage of the performance of machines. Consequently the control and the reduction of flow separation are the most important subjects in engineering. An external fluctuation is one of the promising methods to control and/or reduce the flow separation. The fluctuation also causes the rolling up of separated shear layer which leads to the generation of vortices and the promotion of reattachment.

Sigurdson [1] and Kiya *et al.* [2] investigated the influences of the external fluctuation on the reduction of flow separation and on the mechanism. In their study the separated flow was formed on the front face of a blunt circular cylinder whose axis is aligned along the mean flow. The velocity fluctuation was generated from the edge of front face of cylinder in which the woofer is installed. They investigated experimentally the mechanism of the velocity fluctuation with various frequencies and amplitudes. The previous studies concluded that reattachment length attains a broad minimum at a particular frequency. Sigurdson suggests that the effective frequency for reduction of separated region relates to the frequency of shedding of vortices from the reattachment region. He also showed that the most effective frequency was found to be two to five times the shedding frequency. Yoshioka et al. [3] investigated the effect of frequency on the reduction of separated region in

perturbed backward facing step flow. The wavy streamline patterns were observed behind the step, and vortices developed with these wavy patterns. The spatial interval of the vortices was correlated to the wavelength of the wavy patterns caused by the external perturbation. In the effective frequencies, the number of vortices per unit time generated in the recirculation region has the maximum owing to the frequency condition.

The vortex structures caused in the separated region by introducing the fluctuation are important for the reduction of separated region as described above. In the present study, numerical simulations for the flow around the inclined flat plate were conducted. The external periodic velocity fluctuations with various frequencies were introduced in the upstream along the flat plate. We focused the changes of the vortex structures on the flat plate. The vortex scale due to the introduced external fluctuation is discussed.

The remainder of this paper is organized as follows. Section 2 outlines the numerical method. The following Section 3 presents and discusses the results. Finally, Section 4 includes the concluding remarks of this work.

2. NUMERICAL METHOD

2.1. Method of Numerical Calculation

The calculation model is our previous experiments [4]. In this study, regular interval rectangular grid system was used in the calculation. The basic equations are the two-dimensional incompressible Navier-Stokes equation and the equation of continuity shown in vector form as follows;

$$\frac{\partial \underline{u}}{\partial t} + (\underline{u} \cdot \nabla)\underline{u} = -\nabla p + \frac{1}{\mathrm{Re}} \nabla^2 \underline{u} \tag{1}$$

$$\nabla \cdot \underline{u} = 0 \tag{2}$$

These equations are non-dimensionalized by both the mean flow velocity U_0 and the flat plate length L. All of the values are non-dimensional in this paper. Hyper Simplified Marker and Cell (HSMAC) method is employed to solve those equations. Two order Adams-Bashforth method is used for the time integration in Eq.(1). For the spatial derivatives, fifth order upwind difference, fourth order central difference and second order central difference are employed for the nonlinear term, the viscous term and pressure term respectively. In Eq.(2) all the spatial derivatives are approximated by second order central difference.

In this study, the flow field around the flat plate with the inclination angle of 5 degrees is calculated numerically. Schematic figure of calculation region is shown in Fig.1. The grid points are 400×300, and the interval of grid point is 0.01 in both directions. The origin of axes is set at the leading edge of the flat plate. In the mean flow x is parallel and y is normal to the mean flow. On the other hand, ξ and η are the parallel and normal axes to the flat plate respectively. Equations (1), (2) are solved in the field of the axes of ξ and η. Calculation region is in the ranges of $-1.0L < \xi < 3.0L$ and $-1.5L < \eta < 1.5L$. Flat plate is given by imposing non-slip condition on the grid at $0.0 < \xi < 1.0$, $\eta = 0.0$. The main flow is introduced into the calculation region with inclination angle of 5 degrees. At the first, the potential flow is given on the whole calculation field. Reynolds number Re based on the mean flow velocity U_0 and on the flat plate length L is 3.0×10^4.

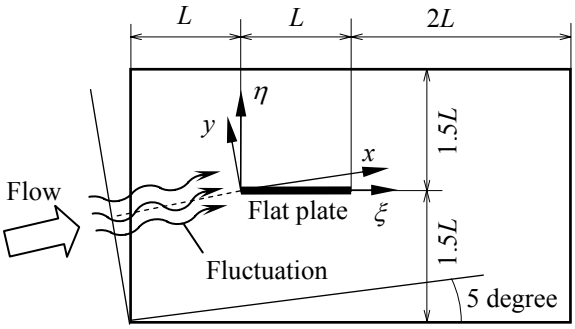

Figure 1. Coordinate system

2.2. Introduction of the Periodic Fluctuation

Periodic fluctuation is introduced into the limited region by being fluctuated the velocity components at the inflow boundary condition. If the fluctuations are simply added on the velocity components, they do not satisfy the equation of continuity. Fluctuation component of v'_Z which is normal to the mean flow is determined first. Fluctuation component of u'_Z is then calculated by substituting that of v'_Z for the equation of continuity. These components of velocity fluctuation are determined as follows;

$$u'_Z = \frac{U_0}{2\pi f_e}\frac{dA}{dy}\cos\left\{2\pi f_e\left(\frac{x}{U_0} - t\right)\right\} \tag{3}$$

$$v'_Z = A\sin\left\{2\pi f_e\left(\frac{x}{U_0} - t\right)\right\} \tag{4}$$

In this study, the phase difference in y-direction is neglected. To introduce the velocity fluctuation into the limited region, as shown in Fig.2, amplitude of fluctuation velocity A is given in the y-direction by

Gaussian function as follows;

$$A(y) = a\exp\left\{-(hy)^2\right\} \tag{5}$$

Where a is the maximum amplitude of external fluctuation velocity and h is the control parameter that decides the width of the given fluctuation. The maximum in the Gaussian profile is set in the upstream of the leading edge of the flat plate. The fluctuation intensity varies by changing the maximum amplitude a. As the effect of the frequency of the external periodic fluctuation is main subject in this study, the maximum amplitude a is assumed to 0.1 times mean flow velocity U_0 for introducing the fluctuation with the single fixed frequency. The parameter h means the length between the inflection points of the Gaussian function, and depends on h_0 which is a half the spatial wavelength λ (see Fig.2). Namely h_0 is determined by the fluctuation frequency f_e and the mean flow velocity U_0 as follow;

$$h_0 = \frac{2\sqrt{2}f_e}{U_0} \tag{6}$$

In this study, h is determined as equal to h_0.

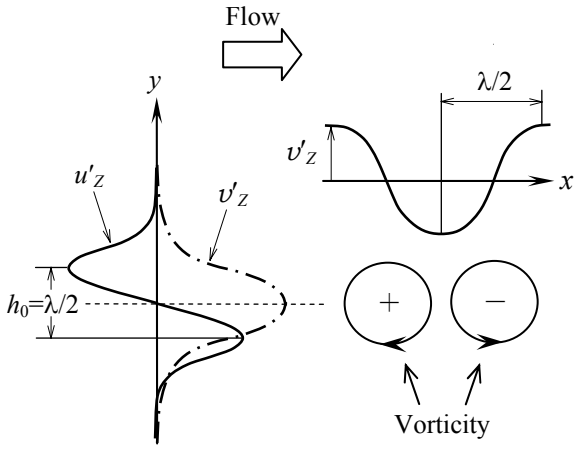

Figure 2. Fluctuation velocity condition

3. RESULTS AND DISCUSSION

3.1. Separated flow on the flat plate

Figure.3 shows the instantaneous vorticity contours on the flat plate without external fluctuation. The triangle mark indicates the time-averaged reattachment point. Reattachment point is determined by reverse-flow intermittency [2] on the flat plate. The flow separates at the leading edge, and thus the separated shear layer is formed. The shear layer rolls up to form vortices, then reattaches on the wall after a few times of merging. In the actual flow, disturbances involved in the mean flow grow, in itself, in the selected frequencies under Kelvin-Helmholtz instability. In the numerical calculation, however, the disturbances do not grow, and shear layer does not roll up to form vortices, which is due to the mean flow without disturbances. Vortices shown in Fig.3 are therefore not due to Kelvin-Helmholtz instability.

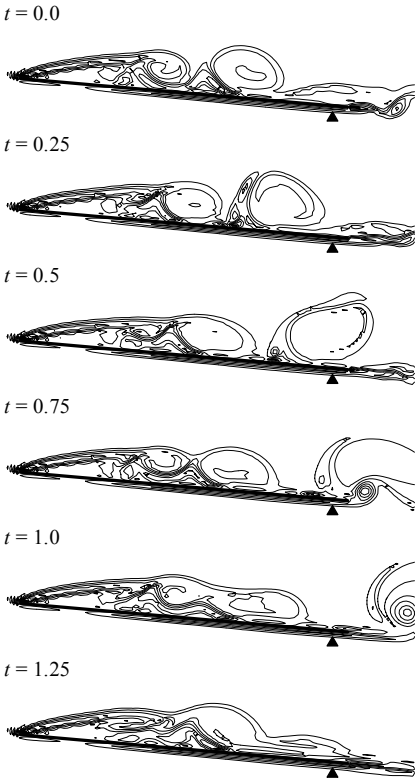

Figure 3. Vorticity contours (without fluctuation)

The frequencies of the external periodic fluctuation, f_e, were referred to the dominant frequency in the separated region. To determine this dominant frequency, the characteristics of frequency in the separated region were examined. Figure.4 shows the power spectra with the time series of velocities measured in the separated region ((a) ~ (d)) and in the wake of the flat plate ((f)). The effective frequencies which decay the separated region relates to f_{shed}; the vortex shedding frequency [1,2]. In the calculation results, the vortex shedding frequency f_{shed} is assumed about 1.1, which was selected for the base frequency. In Fig.4(b), another spectrum peak is shown at $f \approx 2.3$. This frequency indicates the scale of vortices that first roll up. In the downstream, these vortices merge to form the vortex structures with frequency $f = 1.1$.

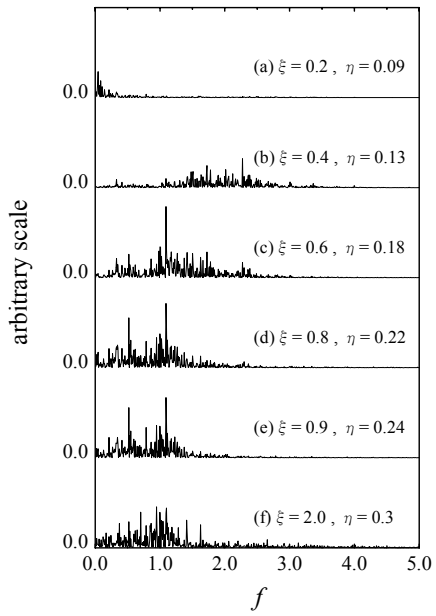

Figure 4. Power spectrum

3.2. The changes of the separated flow field by introducing the periodic fluctuation

The schematic pattern of vortex structures generated by the external fluctuation is divided into four patterns shown in Fig.5 ~ 8. In these figures, the time is set as zero when the time series of velocity at the point ξ = 0.0, η = 0.05 reach the maximum amplitude.

As seen Fig.5, the separated shear layer flutters periodically by the external fluctuation in the mean flow. During a unit period of fluttering, shear layer rolls up to plural vortices with a several scales. These vortices are merged into a large vortex, which reattaches on the wall. This reattached vortex is shed from reattachment point to the downstream with the frequency of fluctuation. It indicates that vortex shedding is controlled by the introducing fluctuation while it does not control the rolling up of shear layer to the vortex of the scale in frequency of fluctuation.

Fluttering motion of the shear layer is clearly shown in Fig.6. Vortices are formed nearer the leading edge than that shown in Fig.5. In this pattern, one vortex is formed and shed in a unit period of the fluttering motion. Vortex reattaches without merging, and the same scale vortices are lined up in regular interval on the flat plate. The separated region is reduced the most in all patterns. From these results it is inferred that the effective frequency on the reduction of the separated region will form the vortex street on the flat plate in stable.

As shown in Fig.7 the vortices in the shear layer are formed at the nearest point on the leading edge of the flat plate in all patterns. These vortices, however, travel to the direction away from the wall. These vortices merge once or twice, grow large one, and reattaches. If the numbers of merging times until reattachment are constant, reattachment length is reduced. The scale of shedding vortex is similar to that shown in Fig.6. In Fig.7, however, separated region are not smaller than that in Fig.6.

As shown in Fig.8, separated shear layer in high frequency condition rolls up to the scale independent of the frequency of fluctuation. These vortices grow and merge into the large vortices, and then reattach on the wall. The vorticity contours are similar qualitatively to those without fluctuation. Extremely high frequencies have less effect on the reduction of the separated region.

Figure.9 shows the relation between the fluctuation frequency f_e and the reattachment length ξ_R. The reattachment lengths are normalized by that without fluctuation; ξ_{R0}. In the frequency range 1.2 < f_e < 2.5, the reattachment length becomes extremely short. In this frequency range, shedding vortices lined up on the wall in regular interval. Around the frequency $f_e \approx 1.8$, however, the effect of the reduction of the separated region decreases due to merging next one. In the frequencies between about 2.5 and 5.5, the reattachment length decreases again. If the frequency is over about 5.5, the effect of the reduction decreases. Furthermore, if frequency is the harmonic of f_{shed}, the effect gets large. The variation of the reattachment length corresponds to the vortex structure patterns showed in Fig.5~8. The effective frequencies reducing the separated region therefore form the periodic vortex structures.

3.3. The critical frequency and the specific vortex

There are differences among the vortex structures formed by different frequencies. It is inferred that the formed vortex structures relate to the effect of reduction. Especially, seen in Fig.9, there is the critical value around frequency $f_e \approx 2.5$ in variation of the reattachment length. Figure.10 shows vortex structures under the critical frequency. As shown in Fig.10, vortices of a certain scale, circled in figures, are formed. This vortex will be called “specific vortex” in follows. In the frequency range 1.2 < f_e < 2.5, one specific vortex is formed in a unit period of the shear layer fluttering. The specific vortices reattach on the wall without merging and these line up in the regular interval. If the frequency of the external fluctuation gets high, interval of these vortices gets narrow. Vortices are merged of the neighboring vortices if the interval smaller than a certain value. In this interval, namely frequency, the effect of the reduction extremely decreases because the vortices merge near the wall and induce backward flow. This frequency to cause merging is the critical frequency $f_e \approx 2.5$. Same

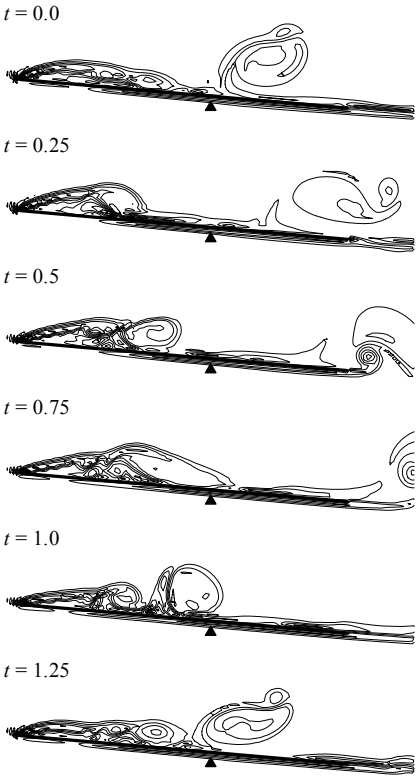

Figure 5. Vorticity contours (f_e = 0.7)

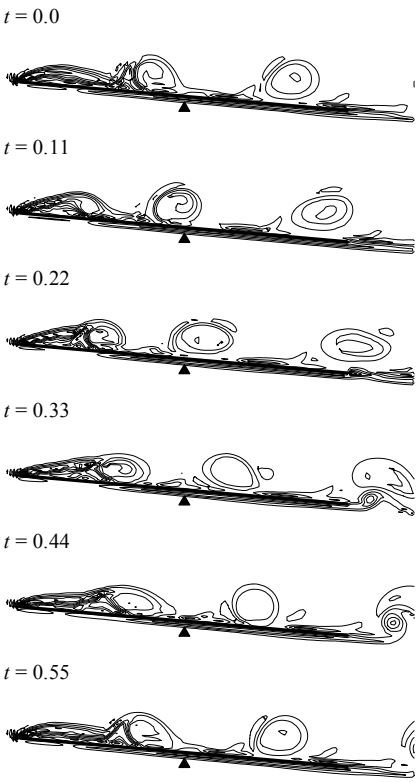

Figure 6. Vorticity contours (f_e = 1.4)

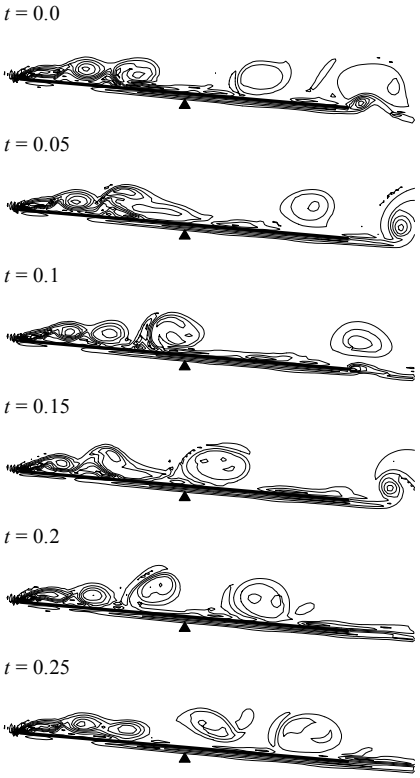

Figure 7. Vorticity contours (f_e = 3.5)

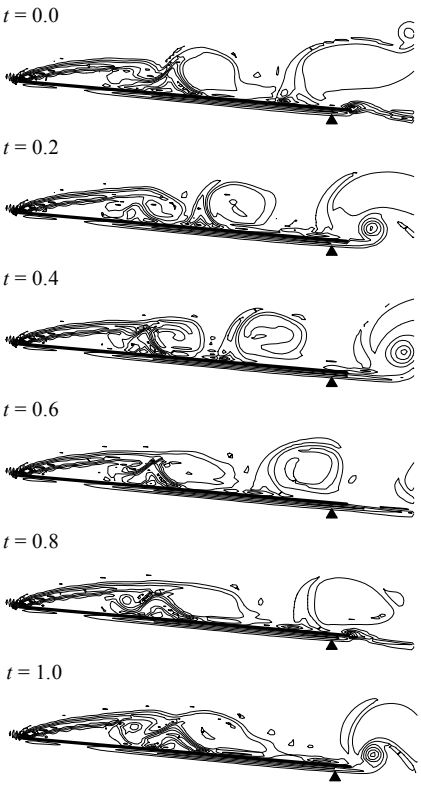

Figure 8. Vorticity contours (f_e = 10.0)

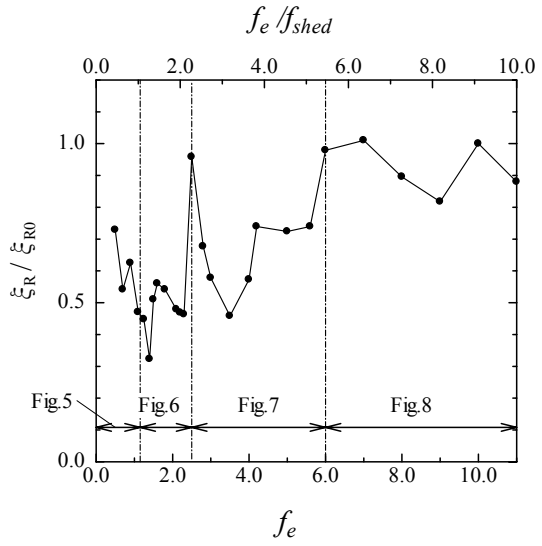

Figure 9. Variation of reattachment length

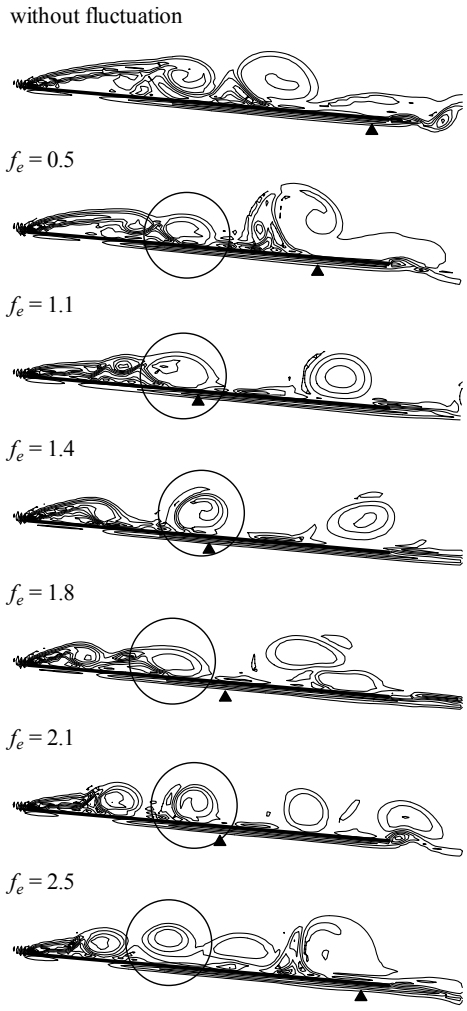

Figure 10. Vorticity contours of the frequency under the critical

decreases of the effect on the reduction are seen around the frequency $f_e \approx 1.8$.

Vortices shed from the reattachment point do not merge with neighboring one. The reason is that vortices satisfy the stable condition like Kármán vortex street. This is an interaction with vorticity of the opposite sign, the image vorticity resulting from the presence of the wall [1,2]. Among the frequency range $1.2 < f_e < 2.5$, the specific vortices line up periodically on the wall. This vortex street formed by introducing external fluctuation satisfies the stable condition as described above. And the interval of these vortices, namely shedding frequency is corresponding to the external frequency. The effective frequency is therefore the frequency which satisfies the stable condition of vortex street on the specific vortex scale.

4. CONCLUDING REMARKS

Numerical calculations in the flow around the inclined flat plate were conducted. The influence of the external fluctuation frequency on vortex structure on the flat plate was focused, and following results are obtained:

(1) Separated shear layer get fluttering by external periodic velocity fluctuation in the mean flow. And shear layer is promoted to rolling up vortices by this fluttering motion.

(2) Changes of vortex structure on the flat plate are divided four patterns. The separated region is decay if the specific scale vortices are formed periodically.

(3) The specific scale is inherent in the separated region. The effective frequencies promote rolling up the specific scale vortices and make them line up in regular interval.

REFERENCES

[1] Sigurdson, L. W., 1995, "The structure and control of a turbulent reattaching flow", *J.Fluid Mech.*, Vol. 298, pp. 139-165.

[2] Kiya, M., Shimizu, M., Mochizuki, O., 1997, "Sinusoidal forcing of a turbulent separation bubble", *J.Fluid Mech.*, Vol. 342, pp. 119-139.

[3] Yoshioka, S., Obi, S., Masuda, S., 2001, "Organized vortex motion in periodically perturbed turbulent separated flow over a backward-facing step", *International Journal of Heat and Fluid Flow*, Vol. 22, pp. 301-307.

[4] Yamagishi, M., Tashiro, S., 2002, "Effect of external fluctuation frequency introduced in the mean-flow on the characteristic frequency of separated flow", *JSME International Journal*, Series B, Vol.45, No.4, pp.796-803.

Conference on Modelling Fluid Flow (CMFF'06)
The 13th International Conference on Fluid Flow Technologies
Budapest, Hungary, September 6-9, 2006

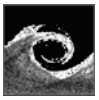

UNSTEADY FLOW PHENOMENA IN THE EDGE TONE

István VAIK[1], György PAÁL[2]

[1] Corresponding Author. Department of Hydrodynamic Systems, Budapest University of Technology and Economics. Stoczek u. 2 – 4, H-1111 Budapest, Hungary. Tel.: +36 1 463 1111, Fax: +36 1 463 3091, E-mail: vaik@hds.bme.hu
[2] Department of Hydrodynamic Systems, Budapest University of Technology and Economics. Stoczek u. 2 – 4, H-1111 Budapest, Hungary. Tel.: +36 1 463 1111, Fax: +36 1 463 3091, E-mail: paal@hds.bme.hu

ABSTRACT

Despite its geometrical simplicity, the edge tone displays a remarkably complex behaviour. The plane jet oscillates around the edge with a relatively stable frequency and under certain circumstances emits an audible tone. This configuration plays a central role in the sound production of organ pipes and recorders but has also industrial applications including Y-shaped pipe branches or the tongue of turbomachines. The flow exhibits various interesting nonlinear phenomena reported in the literature which are not entirely explained. In this paper detailed high precision numerical simulations of the edge tone are reported under various parameters. Several phenomena are reproduced in agreement with the literature such as the existence of "stages", the linear dependence of frequency on the outflow velocity within one stage, the pressure distribution on the edge surface, etc. The parallel existence of two stages can happen in two ways: either as a superposition of two different frequencies or the switching of one pure stage into the next. At the same time some disagreement with the literature seems to arise for example in the dependence of the frequency on the jet exit – edge tip distance or in the spatial development of higher harmonics.

Another presentation in the same conference is focussed on acoustic simulation based on this and on another flow simulation in another simple geometry.

Keywords: edge tone, oscillating flow, numerical simulation, hydrodynamic modes

NOMENCLATURE

C	[$m^{1/2}$]	constant in Eq. (1)
F	[N]	force
$H1$	[mm]	length of the nozzle
$H2$	[mm]	length of the wedge
M	[Nmm]	torque
Re	[-]	Reynolds number
St	[-]	Strouhal number
$V1$	[mm]	notation in Fig. 2
$V2$	[mm]	notation in Fig. 2
f	[Hz]	frequency
h	[mm]	jet-edge distance
u	[m/s]	inlet velocity
x_F	[mm]	distance of the point of force action from the edge tip
α	[deg]	angle of the wedge
δ	[mm]	width of the slit
Δf	[Hz]	frequency resolution of spectra
μ	[kg/ms]	kinematic viscosity of air@25°C
ν	[m^2/s]	dynamic viscosity of air@25°C
ρ	[kg/m^3]	density of air@25°C
τ	[s]	time step

Subscripts and Superscripts

u	upper surface of the wedge
l	lower surface of the wedge
x, y, z	length coordinates
rms	root mean square

1. INTRODUCTION

The edge tone consists of a plane jet and a wedge-shaped object, opposite of the jet exit. It has been observed for a long time that the jet oscillates around the wedge (also called edge) in a more or less periodic manner. Many unusual and nonlinear phenomena have been observed such as the existence of different "hydrodynamic modes" or "stages" or hysteresis effects. Under certain conditions the configuration can emit an audible tone at the oscillation frequency. The edge tone is thought to be responsible for the feeding of acoustic energy into the resonator in the case of a flue organ pipe or a recorder but it appears also in a number of industrial situations such as the Y-shaped pipe branch or the tongue of radial turbomachines. A semianalytical treatment of the phenomenon goes back to Powell [1] and until today this is the most widely accepted model for the edge tone. He explains the edge tone as a feedback loop. The various elements of the feedback loop have to have a certain phase relationship with each other in order

to have a stable oscillation. The basic configuration can be schematically seen in Figure 1, the main parameters being the exit velocity u and the jet exit-edge tip distance h. The widely accepted relationship between the main parameters and the oscillation frequency [2, 3]:

$$f = C\frac{u}{h^{3/2}} \quad (1)$$

where C is a stage- and geometry-dependent constant.

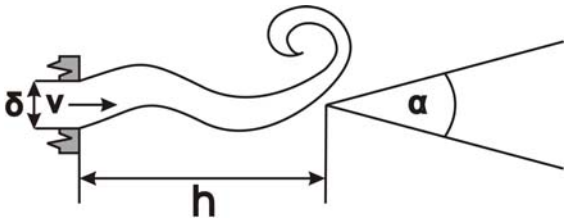

Figure 1. The edge tone configuration

Various aspects of the edge tone have been investigated with careful experimental work [4, 5, 6] which are attempted to reproduce in this paper. Numerical simulations have been carried out by [7], and [8] nevertheless the present work covers a wider range of parameters and allows broader conclusions. The paper is a further improvement of a previous conference publication by the same authors [9]. After very careful preparatory work the simulations can be considered as a reliable tool to gain physical insights into the fluid mechanics of the edge tone.

2. FLOW SIMULATION

2.1. Flow domain and numerical mesh

The geometry and the mesh were generated with the software ANSYS ICEM.

The domain of the simulation can be seen in Figure 2. The geometrical measures are the following: $V1 = V2 = H2 = 75$ *mm*; $H1 = 12.5$ *mm;* $\alpha = 30^{o}$; $\delta = 1$ *mm*. The distance h is varied in the paper; the values will be given later.

The velocity profile was top hat; the jet exit was sharp edged. It is conjectured that these parameters would also influence the oscillation; for example using a parabolic profile or a rounded nozzle exit. The flow was assumed to be two-dimensional, and since the used software is three-dimensional, a one cell thick layer was used for the simulations.

The boundaries were far enough from the region interest not to have a disturbing effect on the flow. Our experience showed that it is advantageous for the flow development if the back boundary is placed somewhat behind the nozzle exit (*H1*).

In order to increase the simulation accuracy a block-structured hexagonal mesh was used (Figure 3). Extensive mesh convergence studies have been performed in one geometry ($h = 10$ *mm* and $Re = \delta u/\nu = 200$) and in this case the mesh finally used contained 36300 hexahedral elements. Here the nozzle exit-wedge tip distance was covered by 32 elements. When the distance h was varied, the number of elements in this region was increased proportionally.

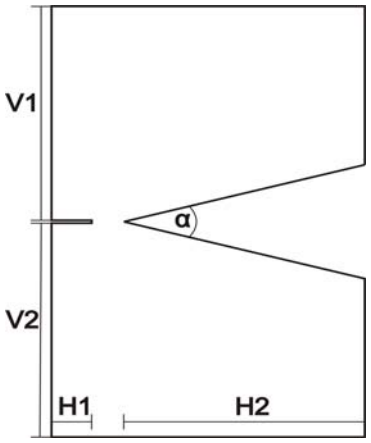

Figure 2. Fluid solver domain

2.2. Boundary conditions, flow and simulation parameters

On the two planes bordering the 2D slice symmetry boundary conditions were prescribed. At the solid walls of the wedge no slip boundary conditions whereas at the outer nozzle wall free slip conditions were given. At the back wall a small (about 1% of the exit velocity) inflow was prescribed. This has been done in order to stabilize the flow, while not influencing the parameters studied. Without this experience shows that there is an increased risk that non-physical vortices appear and remain in the domain. As mentioned at the nozzle exit uniform velocity distribution was assumed. All other boundaries were set to opening boundary condition i.e. prescribed static pressure with no prescribed flow direction.

Air at 25 C° ($\rho = 1.185$ *kg/m*^{3}, $\mu = 1.831\cdot10^{-5}$ *kg/ms*) was used as the material of the flow. The flow was assumed to be incompressible and laminar, so no turbulence model was used. Second order accurate spatial and temporal discretisations were used.

It has been tested to what extent the initial condition influences the result. To this end simulations with initially quiescent fluid and initially steady state flow have been performed. It turned out that the initial condition has no influence on the final character of the flow. No special measures had to be taken to initiate the oscillation;

the oscillation set in spontaneously after a short transient period.

Great care was taken to determine the optimum temporal resolution. Having determined the optimum time step for a reference case, an analytical criterion was derived. This states that the discretisation error remains constant if the time step decreases inversely proportionally with $f^{3/2}$, where f is the expected frequency. The details of this derivation will be given in a later publication.

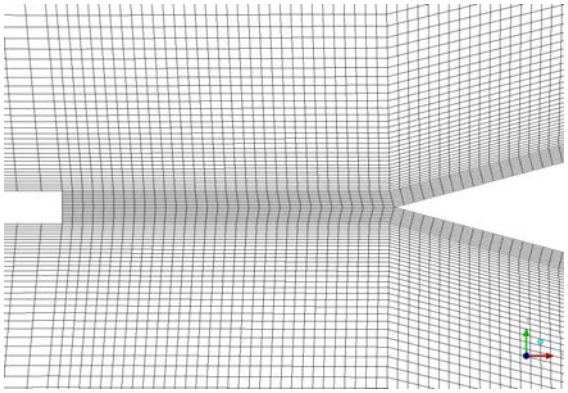

Figure 3. Mesh around the nozzle and the wedge, h/δ = 10

The duration of the simulations (in simulated time) was mainly determined by the required frequency resolution of the spectra made from the temporal signals. Of course, when the time step becomes very small, it becomes increasingly difficult to get the same frequency resolution in a reasonable time. It was decided that the duration of the simulation ensures a frequency resolution of 1-2% of the expected maximum frequency. One simulation typically took over a week of CPU time.

Table 1. Timestep information

Re [-]	f_{max} [*Hz*]	Stage	τ [*ms*]	Δf [*Hz*]	Nr. of timesteps
200	112	I.	0.2	2	3000
225	130	I.	0.15625	2	3841
250	328	II.	0.04	2	15002
300	417	II.	0.029	2	20688
350	504	II.	0.023	2	26081
400	563	II.	0.018	2	33333
450	665	II.	0.014	2	42841
500	751	II.	0.0115	2	52159
550	819	II.	0.0095	8	23678
600	882	II.	0.008	8	28121
700	1115	II.	0.007	10	28562
800	1265	II.	0.006	12	25667
900	1381	II.	0.00475	12	37878
1000	1546	II.	0.004	12	42514
1200	1864	II.	0.00285	12	52618
1400	3600	III.	0.0023	17	30439
1600	4082	III.	0.00175	20	34274
1800	4604	III.	0.0015	22	36657

Table 1 shows detailed information about the timestep which was used in the simulations for the h/δ = 10 case.

3. SIMULATION RESULTS

The first remarkable result is that the existence of three stages has been reproduced by simulation, to the best knowledge of the authors, for the first time. To provide a qualitative picture, vector diagrams of the three modes are displayed in Figures 4 to 6. It is clearly seen that the mode (or stage) order number corresponds to the number of waves between jet exit and wedge. The periodic vortex shedding can be very nicely observed in these figures.

Two kinds of systematic parameter studies were performed:

i) the h/δ value was kept fixed at 10 and the Reynolds number was varied between 200 and 1800 with increasing step size. (The Reynolds number was changed by changing the exit velocity);

ii) the Reynolds number was kept fixed at 350 and the h/δ value was varied (h/δ = 3, 4, 5, 6.25, 7.5, 8.75, 10 and 15)

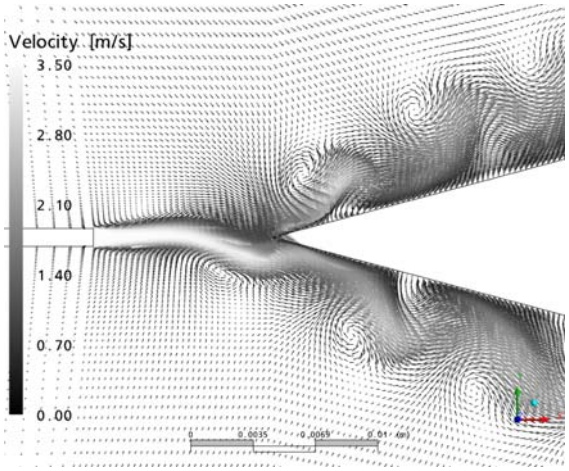

Figure 4. Stage I., h/δ = 10, *Re* = 225

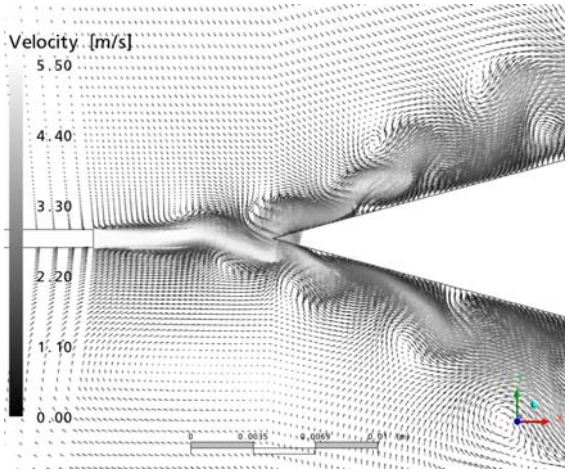

Figure 5. Stage II., h/δ = 10, *Re* = 350

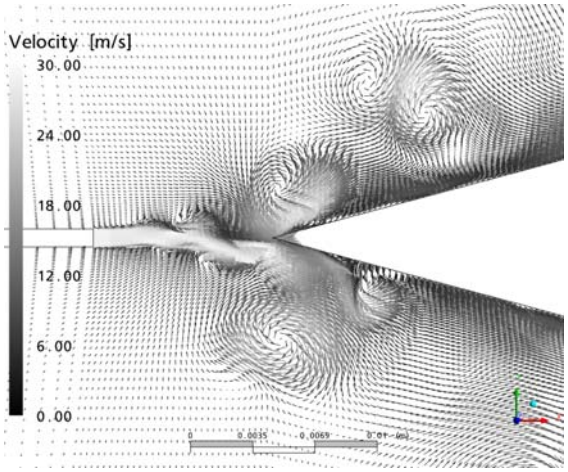

Figure 6. Stage III., h/δ = 10, Re = 1800

For quantitative analysis of the results several points had been defined to obtain pressure and velocity values from. Pressure signals had been read out from points from the upper and lower side of the wedge and also from the symmetry axis between the orifice and the wedge. Transversal velocity values were read out only from the symmetry axis in the same points as for the pressure signals (See Figure 7).

From these signals the dominant frequency components and their amplitudes had been calculated with FFT using MatLab R13 and also other parameters determined.

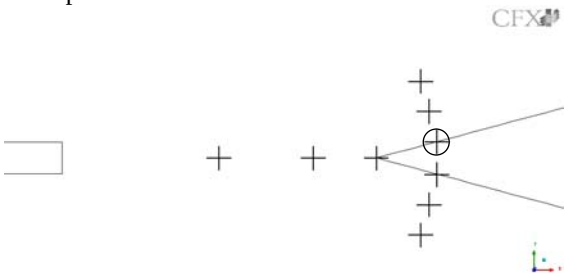

Figure 7. Monitoring points

3.1. Frequency analysis

The frequency – as expected – does not really depend on the position of the point. It should be noted that in some – but not in every – simulations the dominant frequency of the pressure signal at the symmetry axis is the twice the oscillation frequency because the pressure is insensitive to the direction of the jet deflection. Hence the oscillation frequency of the jet was calculated from the pressure signals at upper and lower side of the wedge or the transversal velocity signals from the symmetry axis.

3.1.1. Reynolds number dependence

In Figures 8 and 9 the frequency and the Strouhal number ($St = f\delta/u$) is presented as a function of the Reynolds number, respectively. The bars in the figures represent the width of the spectral peak. Agreeing well with the literature, (e. g. Powell [1]), it can be seen, that the frequency is a linear function of the Reynolds number within one stage but with different slopes in different stages, and the Strouhal number is nearly constant in each stage. One big difference relative to Powell's findings is that when the Reynolds number is increased the first stage does not disappear here but coexists further with the higher stages. Whereas at lower Reynolds numbers the pure stages jump from one to the other at higher Reynolds numbers the various stages are superposed to each other. Since at the third stage three independent frequencies are superposed the motion becomes very complicated and strictly speaking not periodic

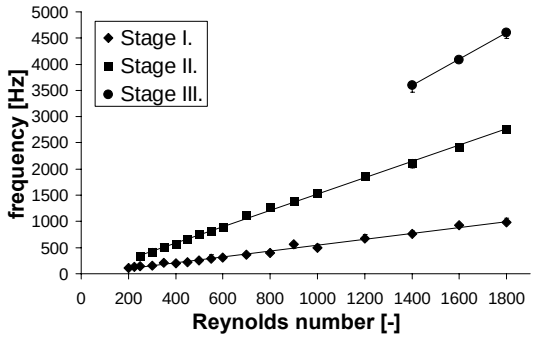

Figure 8. Frequency as a function of Reynolds number

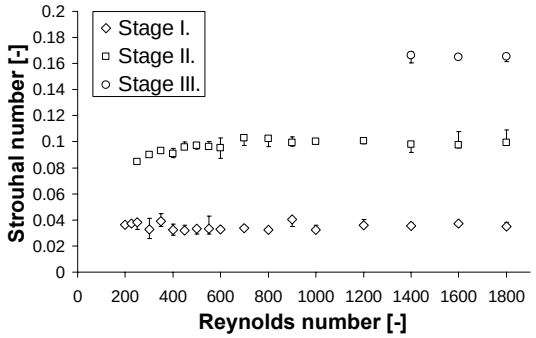

Figure 9. Strouhal number as a function of Reynolds number

3.1.2. *h* – dependence

The Reynolds number was kept constant at 350. For h/δ = 3 there was no edge tone activity, the flow remained steady. The first stage of the edge tone appeared at h/δ = 4 and till h/δ = 7.5 only the first stage was present. From h/δ = 7.5 the second mode appeared but the first mode was still present. For the h/δ = 15 case only the second mode evolved.

From the results of the simulations with Re = 350 it was found out that the relationship between the oscillation frequency and the nozzle-wedge

distance not the generally accepted relationship $f \sim h^{-3/2}$ but $f \sim h^{-1}$. A similar result was reported recently by Bamberger et al. [8]. For both stages the result was the similar (Figures 10 and 11). Simulations for other Reynolds numbers confirmed this relationship.

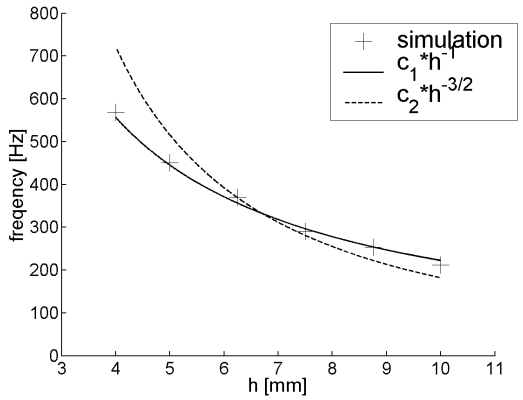

Figure 10. *h*-dependence of the frequency, *Re* = 350, Stage I.

For comparison a best fit $h^{-3/2}$ curve was included to show to what extent this relationship is incorrect.

In Figure 12 the amplitude of the various stages is plotted against the Reynolds number. In the range of the investigated Reynolds numbers basically the amplitudes of all stages increase showing no sign that one of the lower stages is bound to disappear. Even higher Reynolds numbers will be investigated whether this trend changes.

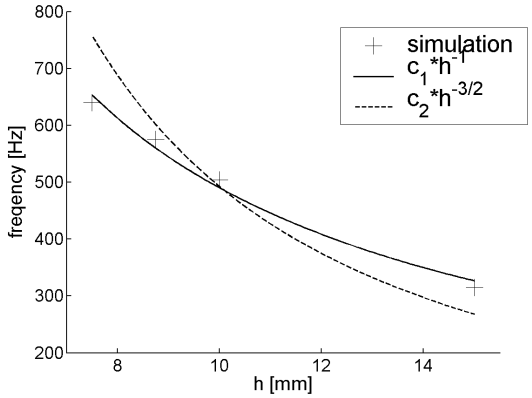

Figure 11. *h*-dependence of the frequency, *Re* = 350, Stage II.

3.2. Pressure distribution on the wedge and location of force action

In Figure 13 the rms pressure distribution along the wedge can be seen. All Reynolds numbers display a similar distribution except for the magnitude of the pressure. The sharp peak in the immediate vicinity of the wedge tip is followed by gradual drop, a second, flatter peak and finally a slowly decreasing long region. The distribution is basically similar to that of [4] but our spatial resolution and particularly the length of the wedge is much larger. Therefore the calculated mean point of force action (x_F) is much further behind the tip than found in [4]. This point has an importance because this should indicate the effective location of the acoustic dipole.

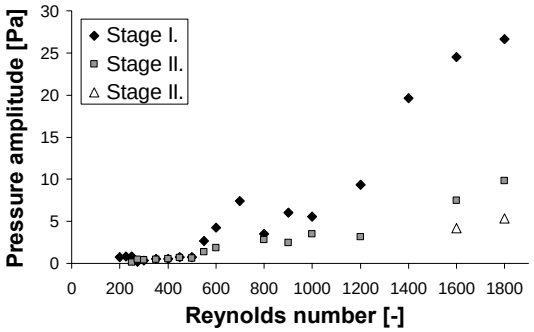

Figure 12. Amplitude of the various stages in the pressure signal at the point indicated with a circle in Fig. 7

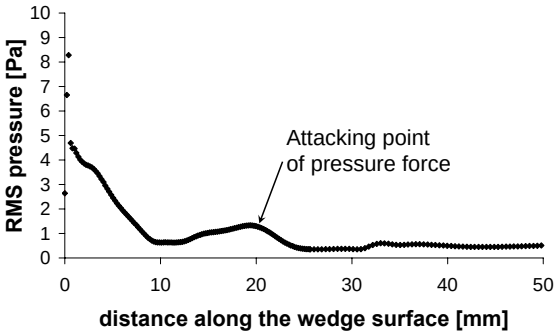

Figure 13. Pressure distribution along the wedge surface

For comparison: in [4] it was roughly 1 mm whereas here it is 16-20 mm from the tip. The temporal history of x_F is shown in Figure 14 and we can see that there is a slight difference between the location of the attack in the two half cycles. This can be simply attributed to a slight flow asymmetry. Between the two values the singularities are physically not realistic; they indicate that the y component of the force gets zero twice in a cycle. The mean x_F is calculated as

$$x_F = \frac{M_{zrms}}{F_{yrms}} \qquad (2)$$

(Both the torque and the force are meant per unit length.)

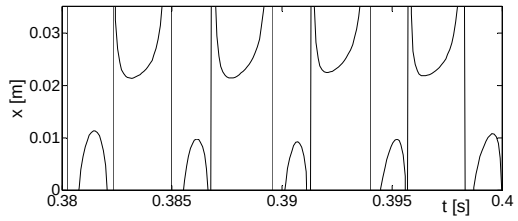

Figure 14. Point of force action varying in time; h/δ = 10, Re = 350

The value of x_F is remarkably stable (between 16 and 20 *mm* almost everywhere) both as a function of the Reynolds number and as a function of h, see Figures 15 and 16 This means that the effective sound source should be largely independent of the details of the flow as long as the wedge geometry is constant.

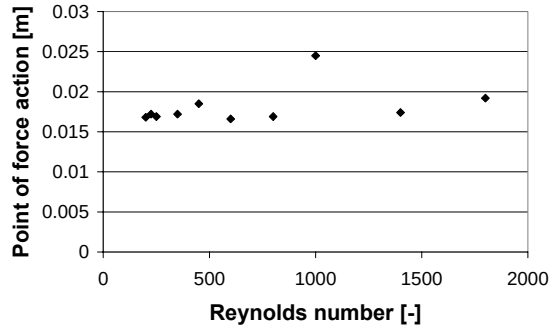

Figure 15. Mean point of force action as a function of Reynolds number, h/δ = 10

The one point at Re = 1000 in Figure 16 deviating from the rest, should not have any importance.

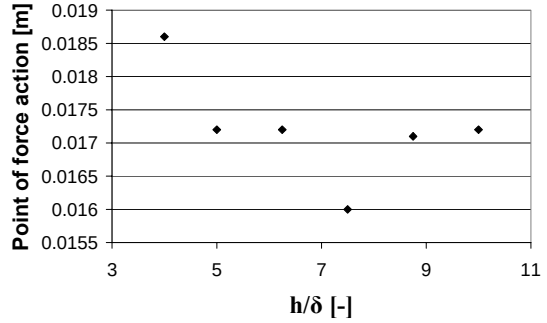

Figure 16. Mean point of force action as a function of h/δ, Re = 350

In Figure 17 the two components of the force per unit length can be seen as a function of the inlet velocity. The force is calculated by integrating the static pressure over the whole wedge surface. The dependence is perfectly parabolic for both components. This can be explained in the following way. The force is proportional with the dynamic pressure on the surface, this is proportional with the square of the velocity perpendicular to the wedge surface. This again must be proportional with the inlet velocity. This leads to the conclusion that the transversal velocity amplitude averaged in some sense increases proportionally with the inlet velocity.

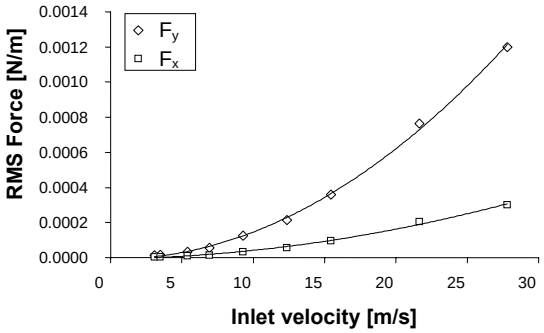

Figure 17. Force per unit length on the upper wedge surface as a function of inlet velocity. h/δ = 10

3.3. Phase velocity of the disturbance along the jet

It is crucial in the understanding of the exact mechanism of the edge tone oscillation to determine the phase velocity of the disturbance along the jet. In the literature values between 0.4 and 0.5 times the exit velocity are given [6, 10]. The phase velocity was determined with a correlation technique; a piece of the signal was taken and the phase of maximum correlation with a reference signal was determined at various spatial locations on a line parallel with the axis. The signal used here was the transversal velocity.

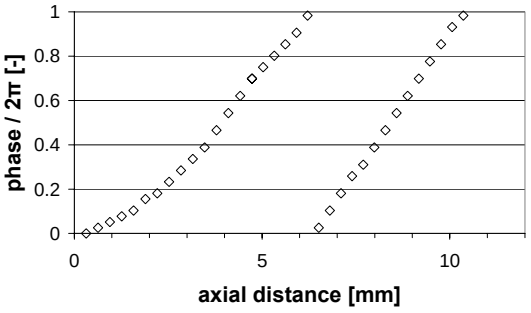

Figure 18. Relative phase of the transversal velocity signal along the jet axis; h/δ = 5, Re = 350, Stage I.

In Figures 18 and 19 the relative phases can be seen for Re = 350 and for two different h/δ. It can be seen that in the 5 *mm* case there is only one "wavelength" along the jet exit – wedge tip distance whereas in the 15 *mm* case where only the second stage exists two "wavelengths". It can also be seen

that in the first half of the first "wavelength", the phase velocity is larger, and later it slows down. The phase velocity along second wavelength is constant with a very good approximation. This finding is physically perfectly reasonable; near the jet exit where the jet is compact, the disturbances can grow easily, whereas further downstream, where the jet is more expanded, and where the mean velocity is also lower, the velocity decreases. Quantitatively, in the beginning, the phase velocity starts from as high values as 0.8*u* but soon settles to a lower value which is with very good approximation 0.4*u*. This trend is found for all Reynolds numbers and all cases and the value 0.4 agrees well with the theoretical expectations.

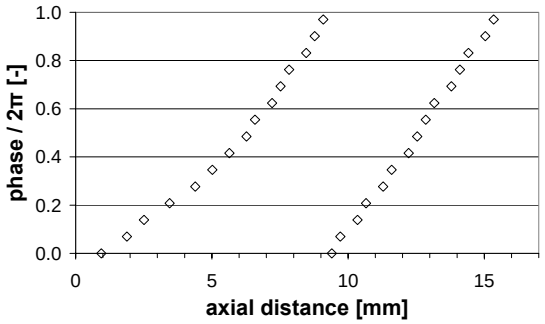

Figure 19. Relative phase of the transversal velocity signal along the jet axis; h/δ = 15, *Re* = 350, Stage II.

4. SUMMARY

Detailed high precision numerical flow simulations have been performed on the edge tone. The existence of the first three stages has been shown. The Reynolds number dependence of the frequencies corresponds to the expectations, whereas the dependence on the jet exit-wedge tip distance was proved to have an exponent of -1 instead of a long-accepted -3/2. This has been already indicated in [8]. The lower stages do not disappear at higher Reynolds numbers within the investigated Reynolds number range. The qualitative shape of the pressure distribution along the wedge has proved to be similar to that in [4] but due to the better resolution and accuracy it has been shown that the point of force action is significantly further behind the wedge tip than stated in [4]. This location, however, is more or less independent of both the Reynolds number and the nozzle exit-wedge distance. The mean force on the wedge surface increases quadratically with the exit velocity. Phase velocities of the disturbance propagating along the wedge have been determined. In the initial part the phase velocity was high, 0.75-0.8 times the exit velocity, later the velocity slowed down to values of 0.4 times the exit velocity.

ACKNOWLEDGEMENTS

This work has been supported by the Hungarian National Fund for Science and Research under contract Nr. OTKA T46304. I. Vaik was supported by the System International Foundation.

REFERENCES

[1] Powell, A., 1961, "On the edge tone", *J. Acoust. Soc. Am.*, Vol. 33, pp. 395-409.

[2] Holger, D., Wilson, T. and Beavers G., 1977, "Fluid mechanics of the edgetone", *J. Acoust. Soc. Am.*, Vol. 62, pp. 1116-1128.

[3] Crighton D., 1992, "The edgetone feedback cycle. Linear theory for the operating stages", *J. Fluid Mech.*, Vol. 234, pp. 361-391.

[4] Kaykayoglu, R. and Rockwell, D., 1986, "Unstable jet-edge interaction. Part 1. Instantaneous pressure fields at a single frequency", *J. Fluid Mech.*, Vol. 169, pp. 125-149.

[5] Kaykayoglu, R. and Rockwell, D., 1986, "Unstable jet-edge interaction Part 2. Multiple frequency pressure fields" *J. Fluid Mech.*, Vol. 169, pp. 151-172.

[6] Ségoufin, C., Fabre, B. and de Lacombe, L., 2004, "Experimental investigation of the flue channel geometry influence on edge tone oscillations", *Acta Acustica united with Acusica*, Vol. 90, pp. 966-975

[7] Ohring, S., 1986, "Calculations of self-excited impinging jet flow", *J. Fluid Mech.*, Vol. 163, pp 69-88.

[8] Bamberger, A., Baensch, E., Siebert, K., 2004, "Experimental and numerical investigation of edge tones", *Z. Angew. Math.* 84. Nr. 6, pp. 1-15

[9] Vaik, I., Paál, G., 2005, "Numerical simulations of the edge tone", *Proceedings of Forum Acusticum 2005,* Budapest, 29 Aug. – 2 Sept. 2005

[10] Mattingly, G. E., and Criminale, W. O., 1971, "Disturbance characteristics in a plane jet", *Phys. Fluids*, Vol. 14(11), pp. 2258-2264

Flow and Acoustics

Conference on Modelling Fluid Flow (CMFF'06)
The 13th International Conference on Fluid Flow Technologies
Budapest, Hungary, September 6-9, 2006

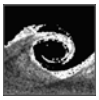

COUPLED FLOW AND ACOUSTIC SIMULATIONS IN THE CASE OF AN EDGE TONE CONFIGURATION AND A SQUARE CYLINDER

Irfan ALI[2], István VAIK[3], Max ESCOBAR[4], Manfred KALTENBACHER[5], György PAÁL[1], Stefan BECKER[6]

[1] Corresponding Author. Department of Hydrodynamic Systems, Budapest University of Technology and Economics, P.O. Box 91, 1521 Budapest, HUNGARY, Tel.: +36 1 463 2991, Fax: +36 1 463 3091, E-mail: paal@vizgep.bme.hu
[2] Institute of Fluid Mechanics, University of Erlangen-Nuremberg, E-mail: irfan@lstm.uni-erlangen.de
[3] Department of Hydrodynamic Systems, Budapest University of Technology and Economics, E-mail: vaik@vizgep.bme.hu
[4] Department of Sensor Technology, University of Erlangen-Nuremberg, E-mail: max.escobar@lse.eei.uni-erlangen.de
[5] Department of Sensor Technology, University of Erlangen-Nuremberg, E-mail: manfred.kaltenbacher@lse.eei.uni-erlangen.de
[6] Institute of Fluid Mechanics, University of Erlangen-Nuremberg, E-mail: stefan.becker@lstm.uni-erlangen.de

ABSTRACT

A large proportion of the total noise in our daily life is generated by flows (e.g. aeroplanes, cars, air conditioning systems, etc.). The physics behind the generation process is quite complicated and still not fully understood. The use of numerical simulation tools is one important way to analyse the generation of flow-induced sound.

We present a recently developed calculation scheme for Computational Aero-Acoustics (CAA). Therewith, we solve the flow field by finite volume method (ANSYS-CFX) and the generation and the propagation of the sound field by Lighthill's analogy and the finite element method, respectively. The developed scheme allows a direct coupling in time domain and provides acoustic field not only in far field but also in the flow region. Furthermore, we can directly investigate the acoustic source terms in the flow region. Furthermore the scheme is well suited for complex geometries and fluid-structure interaction problems.

In the present paper we investigate the problems caused by the length scale disparities between flow and acoustic fields on simple configurations (the edge tone and a square cylinder). In the calculations a mesh-based coupled prediction of flow induced noise was applied. The coupled regions have different mesh element size on both parts of the computation and interpolation of the data is performed in the time domain using a commercial library 'Mesh-based parallel Code Coupling Interface' (MpCCI). Different spatial and time discretisation schemes are tested in order to evaluate their influence on the numerical contamination of the solution. The large size of the acoustic domain in comparison to the flow domain and the inherently different discretisations of the coupled regions present further problems.

Finally the paper shows the sound propagation for the representative basic cases of an edge tone and a three dimensional square cylinder.

Keywords: computational aeroacoustics (CAA), edge tone, Lighthill's analogy, square cylinder, LES

NOMENCLATURE

C_S	[-]	Smagorinsky constant
Re	[-]	Reynolds number
H	[mm]	size of the square cylinder
δ	[mm]	width of the slit of the nozzle
h	[mm]	nozzle - wedge distance
v	[m/s]	inlet velocity

1. INTRODUCTION

Every moment of our urbanized life is accompanied by some kind of noise. Noise reduction became one of the principle goals of environmental protection; it is now generally acknowledged that the noise level in our environment is a significant factor influencing the quality of our life. Out of the many possible kinds of noise sources one of the most challenging one to handle is the flow-induced noise source.

The main difficulty consists in the fact that the orders of magnitude of acoustical and fluid mechanical pressure fluctuations are widely different. To resolve this difficulty, several strategies have been applied in practice out of which we adopted the classical Lighthill's analogy.

Many decades have passed since the pioneering work of Lighthill [1, 2] but it is still the most simple and elegant way of treating the problem of flow noise. Since early nineties there has been only a

slow development in the field of CAA but by now the computer power available at affordable prices has reached such a level that it can be expected to produce answers of realistic situations within reasonable time limits.

Lighthill's original theory has undergone many modifications, improvements, such as the Ffowcs-Williams-Hawkings equation [6], taking into account moving solid bodies or Powell's reformulation of the theory in terms of vortex sound sources [7].

1.1. Hybrid aeroacoustic flow simulation

Figure 1 displays the general situation for the numerical simulation, we are concerned with, when performing CAA. Therein Ω_1 denotes the computational domain, where we have to solve for the flow field and the generation of sound, and Ω_2 the domain where the flow is zero, and where we are interested in the radiated sound. The surface Γ_S defines the interaction between structural mechanics and flow and Γ_1 the boundary of the total computational domain. Now, the computation of the flow induced noise exhibits a lot of difficulties, where the most significant ones can be summarized as follows:

(1) The scale discrepancy between flow pressure and acoustic pressure reaches values of 10^7.
(2) The acoustic domain is in most cases large compared to the fluid flow domain.
(3) The spatial discretization for the flow computation is much finer as compared to the discretization of the acoustic domain.
(4) In many applications, the interface between flow and solid/elastic bodies leads to vibrations, which not only effect the flow, but also emits acoustic sound (vibrational acoustics).

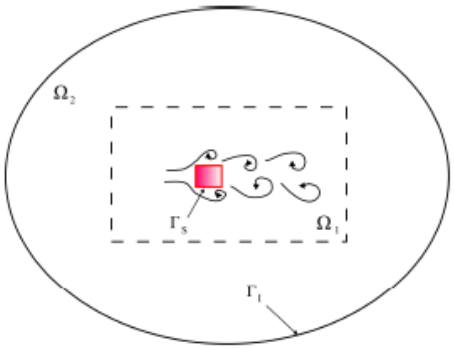

Figure 1. General setup of aeroacoustics

Due to 1-3, a direct numerical simulation (DNS) of Navier Stokes equations, which are capable to describe both the flow as well as acoustic field, is restricted to very few practical cases (see e.g. [3, 4]). Therefore, most approaches, published in the last 20 years, use hybrid methods, e.g. [6]. Since we concentrate on a computational scheme, which allows the computation of the flow generated sound simultaneously with any flow induced vibrational sound (due to solid-fluid interactions), we base our scheme on Lighthill's analogy [1, 2]. This formulation will provide a direct coupling between flow and acoustic sound computation in the time domain and in addition will offer for both physical fields different discretization. At this point, we want to notice, that a similar approach can be found in [5], which however has just been investigated in the time-harmonic case.

1.2. General scheme

In this paper a coupled fluid mechanics-acoustics scheme (so-called hybrid scheme) is applied which is presented in Figure 1.

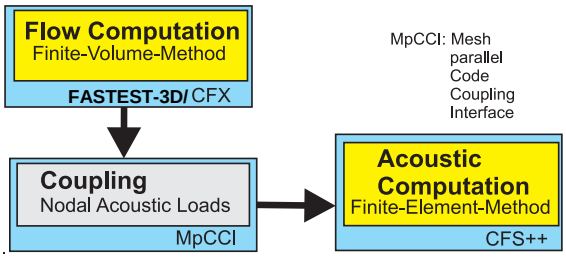

Figure 2. Schematic representation of the computational scheme

The flow field is calculated using two different software packages, ANSYS-CFX and an in-house CFD code FASTEST-3D [8], and from the results the acoustic source terms are calculated on the grid of the flow computation. These are then interpolated in each time step onto the much coarser acoustic mesh in a conservative way using the MpCCI interpolation interface [9]. The interpolation is performed in a large part of the flow domain but this is significantly smaller than the acoustic domain. Using the acoustic source terms, the inhomogeneous wave equation is solved using the CFS++ [10] our in-house code. This software uses a finite element formulation of the Lighthill analogy and works in the time domain. Working in the time domain increases the accuracy in comparison to the frequency domain since there is no need for Fourier transformation during the solution procedure.

The equations and the solution algorithm is described in detail in [11], it will be only shortly summarized in the next section. For the finite element solver a weak formulation of the Lighthill equation is used. The time discretisation is performed by a second order implicit scheme. In the acoustic solver a non-linear multigrid algorithm was built in.

2. PROBLEM DEFINITION AND FLUID MECHANICAL SIMULATION

2.1. Edge tone

The edge tone is an unsteady oscillating flow generated by a jet-wedge interaction. A jet impinges on a wedge shaped object (also called edge) which results in a periodic flow. This periodic flow then may create a dipole-type sound source by exerting a periodic (but opposite phase) force on both sides of the wedge.

The main parameters of the configuration are: the width of the slit (δ), the nozzle-wedge distance (h) and the mean velocity of the jet at the nozzle exit (v) (See Figure 1 in [12]: a related paper at the same conference focussing on the fluid mechanics of the edge tone.) There are some secondary parameters which influence the flow such as the exit velocity profile, the shape of the nozzle and the shape of the wedge. As the Reynolds number or h is varied then the oscillating jet takes different modes, also called "stages". See [13] for more details and boundary conditions.

In this paper the width of the slit was δ = 1 *mm*, the nozzle-wedge distance was h = 10 *mm*. The Reynolds number (based on δ and v) was 225 and 600 since these are fundamentally different cases [13]. When Re = 225 the oscillating jet is in the first stage, and when Re = 600 the first and the second stages are superposed on each other.

ANSYS ICEM 5.1 was used to create the geometry and the mesh and ANSYS-CFX 5.7.1 was used to compute the flow field.

Since the geometry is very simple a structured hexahedral mesh was used and since this was a 2D flow and ANSYS-CFX is a 3D solver the mesh was only one cell thick in the third dimension (Figure 3)

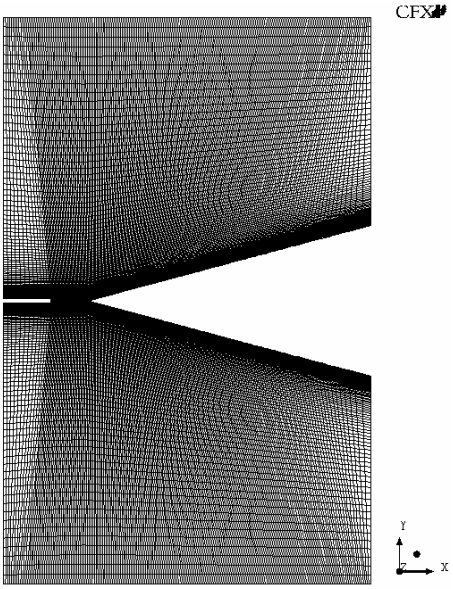

Figure 3. Flow simulation mesh

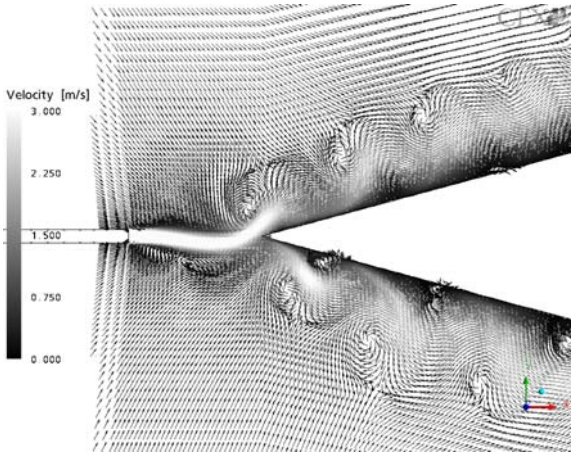

Figure 4. Stage I. Edge tone velocity vector plot

A detailed parameter study was made to find out the optimal parameters for the simulation which can be found in [12] and [13] (See Table 2).

2.2. Square cylinder

Flow around a square cylinder is a typical tonal aeroacoustic flow phenomena. The fluid flow simulation is carried out by FASTEST-3D and then validated with published experimental work. For the computation of the acoustic sound generation and propagation we use CFS++ in the coupled scheme as illustrated in Figure 2.

Large-Eddy-Simulations (LES) based on Smagorinsky model were carried out to compute the flow field. The numerical domain is given in Figure 5 and the boundary conditions are listed in Table 1. For the case where the inlet velocity was 10 *m/s*, H = 20 *mm* and fluid air at 25°*C* a Reynolds number of around 13000 is achieved. Second order spatial discretisation was used with Crank-Nicholson time stepping scheme. Smagorinsky constant C_s = 0.065 was used for the simulation.

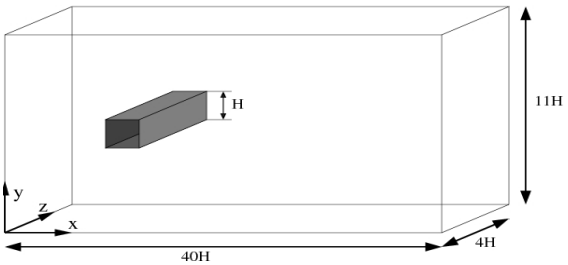

Figure 5. The computational domain

Table 1: Boundary Conditions

Position	*Boundary Condition*
x = 0	block inlet profile
x = 40H	convective exit boundary
y = 0, y = 11H	symmetry boundary condition
z = 0, z = 4H	periodic boundary condition
cylinder	no slip boundary condition
x=20H, y=5.5H	centre of cylinder

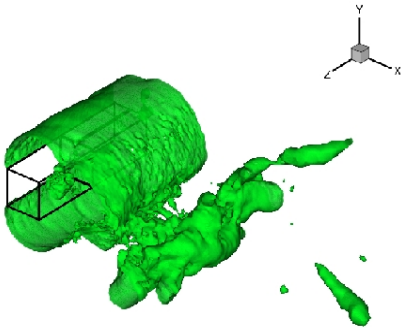

Figure 6. Pressure isosurface

For lower Reynolds numbers, the flow around the cylinder is two-dimensional but as the Reynolds number is increased more complex flow structures are produced. Figure 6 shows the iso-surface plot, highlighting the 3D structures in the flow around the square cylinder.

The numerical fluid simulations were validated by comparing with published experimental work from Durão et al. [14] and also with in-house experiments [15] carried out in the aeroacoustic channel at the University of Erlangen-Nuremberg. A good agreement was found with experimental results. The comparisons were performed at the centreline distribution of axial velocity components (see Figure 7).

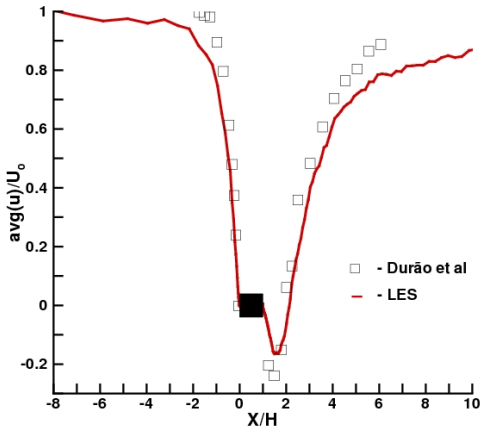

Figure 7. Axial velocity

The turbulent kinetic energy characteristics, as displayed in Figure 8, were similar to the ones measured with experiments.

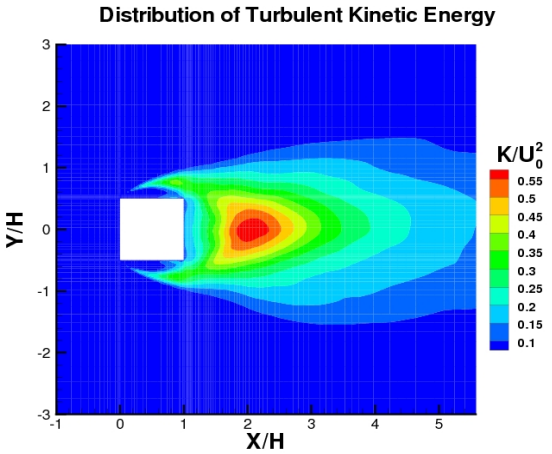

Figure 8. Turbulent kinetic energy

Some discrepancies are seen in the results and can be attributed to the following factors. In the experimental investigation by Durão the cylinder was mounted inside a channel whereas in the numerical work the cylinder cannot be confined in between walls as it would hinder the acoustic measurements. Further, a wall function was used in the LES-computation to resolve the boundary layer in order to avoid doing a DNS at the wall and to keep the computational effort at an acceptable level.

3. RESULTS OF THE ACOUSTIC SIMULATIONS

3.1. Coupling the acoustic and the flow solver

As mentioned above a 3D flow solver was used to calculate a 2D flow field. On the other hand the acoustic solver is able to calculate the acoustic field in 2D and 3D as well. The 2D part was used because this way less computational resources were needed. Thus a 3D flow solver and a 2D acoustic solver had to be coupled. One of the covering planes with symmetry boundary conditions of the 3D flow domain was chosen in every time step, the velocity values were exported from this plane, renumbered and the acoustical loads were calculated from these values. This was done with a self-written FORTRAN code. Afterwards the acoustical loads were interpolated onto the 2D acoustical mesh using MpCCI.

3.2. Edge tone

The acoustic domain is a circle around the tip of the wedge with a radius of 6 *m*. The flow domain

of the ANSYS-CFX simulation is a rectangle with dimensions 97.5 *mm* and 151 *mm*. For the coupling region the whole ANSYS-CFX fluid domain was used. This means that the acoustic sources were calculated and interpolated onto the acoustic mesh in the whole fluid mechanical mesh.

To analyse the results monitoring points were defined on concentric circles around the tip of the wedge with radii of 0.5 *m*, 1 *m*, 2 *m* and 4 *m*, 36 points on each circle with uniform angular distribution. The acoustic pressure was read out from these points. A directivity map was prepared on each circle and the spectrum was calculated with FFT.

3.2.1. Re = 225, First stage oscillation

At this Reynolds number the oscillation takes place purely in the first mode.

For this simulation 216 timesteps were coupled, and the timestep on the acoustic side was twice the timestep on the flow side since only every second timestep was transferred from the flow simulation. Hence the length of the simulation was 0.0675 *s*. The first few *ms* of the acoustic pressure signals do not carry any information because of the finite sound speed so that part was cut off. Having done this the frequency resolution of the acoustic pressure spectrum became 15 *Hz* while the resolution of the of the pressure spectrum in the flow simulation was 2 *Hz*.

Table 2. Parameters of the coupled simulation (*Re* = 225)

	Flow simulation	Acoustic simulation	
		Coupling region	Whole acoustic field
Num. of nodes	73710	6090	103544
Number of cells	36300	1950	34422
Element type	3D, hexa.	2D quadratic quad	
Timestep [ms]	0.15625	0.3125	

The first two diagrams in Figure 9 show the spectrum of the pressure signal on a surface point of the wedge and the spectrum of the y direction of the force acting on the wedge. These are calculated from the flow simulation. The third diagram shows the spectrum of the acoustic pressure signal 0.5 *m* away from the tip of the edge. These spectra are in good agreement; however the first overtone, well visible in the "flow spectrum" disappears in the "acoustic spectrum" because it dissipates over the distance of 0.5 *m*.

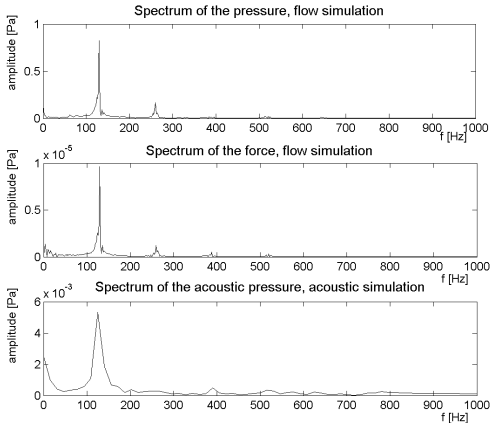

Figure 9. Spectrum of surface pressure, force and acoustic pressure, *Re* = 225

Figure 10 the directivity map of the acoustic pressure calculated from the acoustic result of the acoustic simulation. The results confirm the existence of a dipole sound source [16].

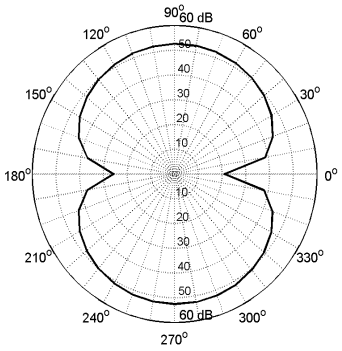

Figure 10. Directivity map of the acoustic pressure, *Re* = 225, at 0.5 *m* from the wedge

It has to be noted, however, that the numerical values of the predicted sound pressure levels have a different meaning compared to usual sound pressure levels. In 2D the unit of the pressure is Pa/m instead of Pa and thus the reference pressure is chosen arbitrarily as $2*10^{-5}$ Pa/m. In 3D the SPL would depend on the thickness of the wedge.

3.2.2. Re = 600, mixed oscillation

At *Re* = 600 the edge tone flow field displays a very interesting phenomenon [13]. Two different stages coexist and are superposed on each other.

For this simulation the timestep of the flow simulation was 0.008 *ms* and every sixth timestep was transferred. So the timestep of the acoustic simulation was 0.048 *ms*. 1043 timesteps were coupled. The same mesh was used in the flow simulation as in 3.2.1., but a finer mesh was used for the acoustic simulation. This mesh had 481328 nodes and 160350 cells.

For this Reynolds number the outlet boundary condition did not seem perfectly absorbing so that some reflections appeared. The finishing part of the signals became uncertain because of the reflections, so that not only the first part of the signals but also the finishing part had to be cut too. This made the frequency resolution of the acoustic pressure spectrum 32 *Hz* while the frequency resolution of the pressure spectrum in the flow simulation was 8 *Hz*.

From the flow simulation the frequency of the lower mode in the pressure signal was 305 *Hz* with a sharp peak in the spectrum, but the higher mode was blurred between 850-935 *Hz*. The force spectrum has the nearly same frequencies. The higher frequency peak became a bit sharper: 885-910 *Hz*. The acoustic spectrum with the much worse frequency resolution yields peaks between 285-317 *Hz* and 888 *Hz* which can be regarded as a good agreement. (See Figure 11) It is however remarkable that the amplitude of the lower mode is higher in the flow simulation and this turns the other way round in the acoustic simulation. We have at present no explanation for this phenomenon.

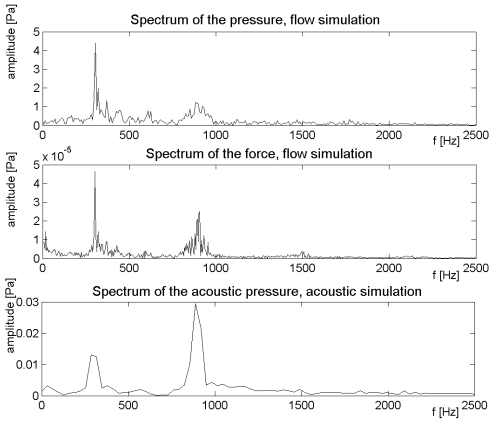

Figure 11. Spectrum of surface pressure, force and acoustic pressure, *Re* = 600

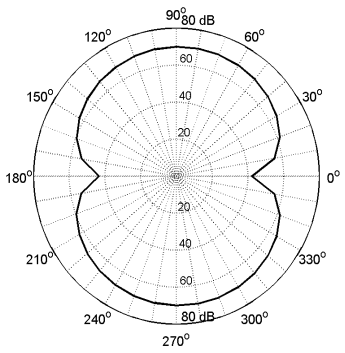

Figure 12. Directivity map of the acoustic pressure, *Re* = 600, at 0.5 *m* from the wedge

The directivity maps again showed a perfect dipole sound source just as in 3.1.2. (Figure 12).

3.3. Square cylinder

Numerical acoustic investigations are performed with the above results. The acoustic propagation is considered in a cutting plane. The fluid simulations are carried out in three dimensions from which a two-dimensional slice is extracted. This 2D slice of the hybrid domain is as depicted in Figure 13 the square cylinder is located in the centre of the circular acoustical domain. Fluid region denotes the area where the coupling quantities (either the scalar nodal sources or the velocity vector) are interpolated from the fluid simulation.

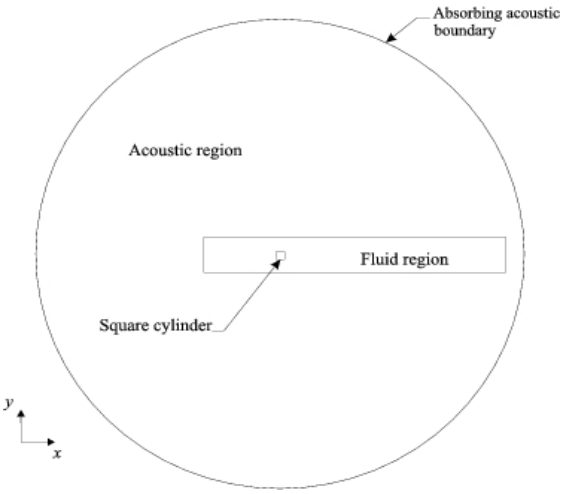

Figure 13. Acoustic domain for the square cylinder simulation

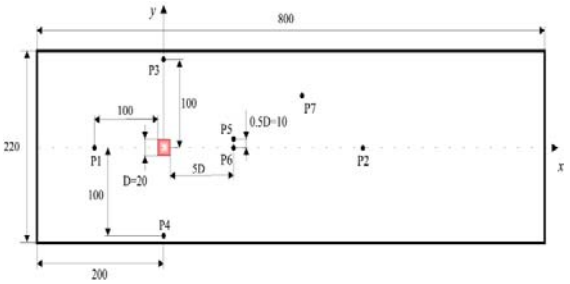

Figure 14. Monitoring points for the square cylinder simulation

The numerical integration of the acoustical source terms has been performed by means of the Finite Element method directly on the fluid domain (explained in detail in [11]) before performing the interpolation of the quantities, since due to the fine mesh on the fluid computation, a higher accuracy is obtained.

Several characteristic points within the turbulent region have been used to investigate the properties of the acoustic sources. The locations of these points are depicted in Figure 14. Herewith, analysis is carried out at two different characteristic points, p5 = (x, y) = (0.1 *m*, 0.01 *m*) and p6 = (x, y) = (0.1 *m*, 0.0 *m*), located at 5*H* (*H* denoting the side length of the square cylinder) in the downstream direction along the fringe of the cylinder and along the x-axis, respectively. Figures 15 and 16 present the results for these two points. Their characteristics confirm the measurements in a turbulent flow around a square cylinder [15]. For the point located along the fringe, among other frequency modes, we find the 65 *Hz* component, which is the actual main component for this tonal problem. On the other hand, for the point located exactly along the x-axis we find, as main frequency component, a value which is twice as high as the main frequency of 65 *Hz*. This fact is due to the combination of the upper and lower main vortices at the centre line, each having a frequency of 65 *Hz*.

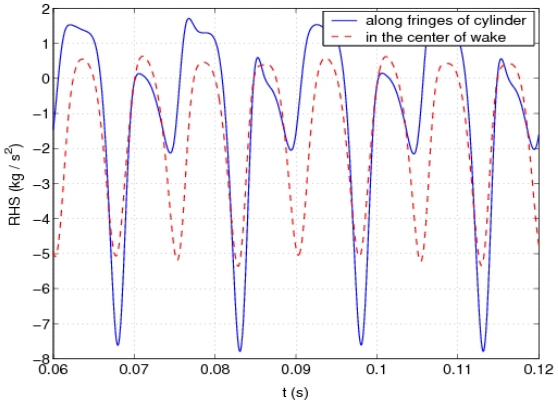

Figure 15. Temporal signal of acoustic source term in the two predefined points

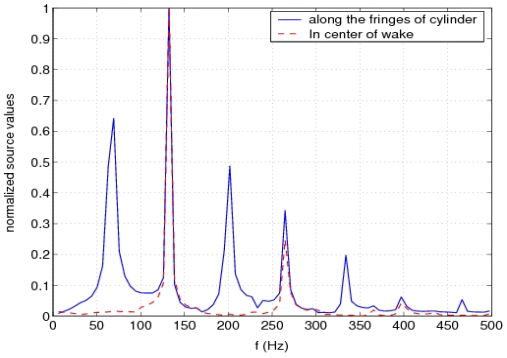

Figure 16. Spectra of the acoustic source term in the two predefined points

Figure 17 presents the acoustic far field using the spatial and temporal parameters producing results with the best quality. It displays results of the acoustic far-field pressure computed using the nodal acoustic sources evaluated on the fluid grid. In Figure 18 the corresponding directivity pattern demonstrates the dipole characteristic of this problem.

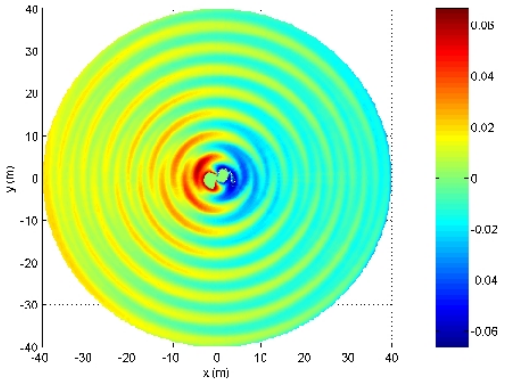

Figure 17. Acoustic far field for the square cylinder

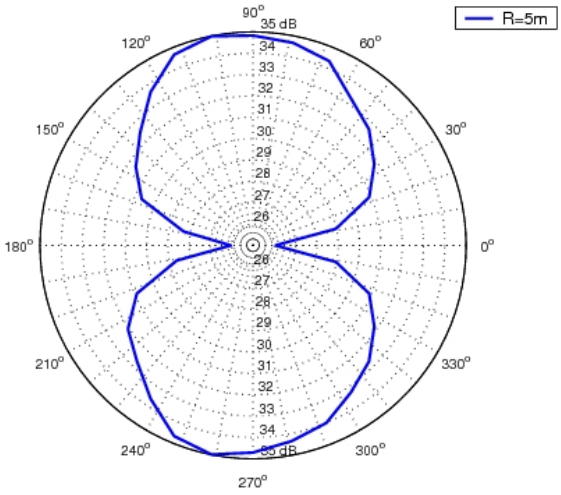

Figure 18. Directivity map for the square cylinder

CONCLUSIONS

The coupling of a fluid mechanics and an acoustic software using Lighthill's analogy has been successfully demonstrated with two different fluid mechanics softwares (ANSYS-CFX and FASTEST-3D) and two different test cases (edge tone and square cylinder). The former was a laminar flow, therefore no turbulence model has been used, while the latter was a turbulent flow and LES was used for the turbulence modelling. In both cases the coupling procedure was the same: the source terms were calculated in the whole fluid domain and a much larger acoustic domain was considered. The acoustic pattern in both cases corresponded to the expectations; a classical dipole pattern has been predicted. The coupling procedure has proved to work well and more complex problems can be handled in the near future.

ACKNOWLEDGEMENTS

The work of the Hungarian authors (3, 6) has been supported by the Hungarian National Fund for Science and Research under contract Nr. OTKA T 46304. The work of the German authors has been supported by BFS (Bayerische Forschungsstiftung). The cooperation of the two research groups has been supported by the DAAD-MÖB joint funding.

REFERENCES

[1] Lighthill, M. J. 1952, "On sound generated aerodynamically I. General theory", *Proc. Roy. Soc. Lond.*, A 211, pp. 564-587.

[2] Lighthill, M. J. 1952, "On sound generated aerodynamically II. Turbulence as a source of sound", *Proc. Roy. Soc. Lond.*, A 222, pp. 1-22.

[3] Tam, C. K. W., Computational Aeroacoustics, *AIAA Journal* 33 (1995) 1788-1796

[4] Tam, C. K. W. Supersonic Jet Noise, Annual *Review of Fluid Mechanics* 27, (1995) 17-43

[5] Oberai; A. , Roknaldin, F., and Hughes, T. J. R., Computational procedures for determining structural-acoustic response due to hydrodynamic sources, *Comp. Methods in applied mechanics and engineering* 190 (2000) 345-361

[6] Ffowcs-Williams, J. E. & Hawkings, D. L. 1969 "Sound radiation from turbulence and surfaces in arbitrary motion", *Phil. Trans. Roy. Soc. A*, 264 pp. 321-342

[7] Powell, A., 1964 "Theory of vortex sound", *J. Acoust. Soc. Am*, 36(1), pp. 177-195

[8] Durst, F., and Schäfer, M., "A Parallel Block-Structured Multigrid method for Prediction of Incompressible Flows". J. Num. Methods Fluids, vol. 22, (1996), 549--565.

[9] http://www.mpcci.org, 2005

[10] Kaltenbacher M., Hauck A., Hofer M., Mohr M. and Zhelezina E., "CFS++: Coupled Field Simulation", LSE, University of Erlangen (2005)

[11] Kaltenbacher, M., Escobar, M., Ali, I., Becker, S. 2005 "Finite element formulation of Lighthill's analogy", *Proceedings of Euromech Colloquium 467, Marseille, 18-20 July 2005*

[12] Vaik, I., and Paál, G., 2006 "Unsteady flow phenomena in the edge tone", *Proceedings of CMFF'06, Budapest, September 6-9 2006*

[13] Vaik, I., and Paál, G., 2005 "Numerical simulations of the edge tone", *Proceedings of Forum Acusticum 2005, Budapest, 29 Aug – 2 Sept 2005*

[14] Durão D. F. G., Heitor M. V. and Pereira J. C. F., "A Laser Anemometry study of Separated flow around a Square Obstacle", LADOAN-IST, Lisbon, Portugal, (R. J. et al. Adrian, ed.), 1986, pp. 227—243.

[15] Ali I., Escobar M., Hahn C., Kaltenbacher M., Becker S., "Numerical and Experimental Investigations of Flow Induced Noise around a Square Cylinder", *10th AIAA/CEAS Aeroacoustics Conference*, Manchester, UK.

[16] Morse, P. M., Ingard, K. U., 1986 *Theoretical Acoustics* Princeton University Press

Conference on Modelling Fluid Flow (CMFF'06)
The 13th International Conference on Fluid Flow Technologies
Budapest, Hungary, September 6-9, 2006

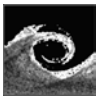

SIMULATION OF THE ACOUSTICS BEHIND A BARRIER GENERATED BY PERIODICALLY PASSING VEHICLES

Magnus ÅBERG[1], Robert-Zoltan SZASZ[2], Laszlo FUCHS [3]

[1] Corresponding Author. Division of Fluid Mechanics, departmendt of Energy Sciences, Lund Institute of Technology, Lund 22100, Sweden. Tel.: +46 2229276, E-mail: Magnus.Aberg@vok.lth.se
[2] Division of Fluid Mechanics, departmendt of Energy Sciences, Lund Institute of Technology, Lund 22100, Sweden
[3] Division of Fluid Mechanics, departmendt of Energy Sciences, Lund Institute of Technology, Lund 22100, Sweden

ABSTRACT

Noise generated by vehicles is a major environmental problem at inhabited areas along high-ways. A way of reducing such noise is by introducing a sound barrier (wall) on the sides of the road. The efficiency of this measure is studied in this paper. We consider a moving object, representing a vehicle, which is subject to a low Mach number air stream. The acoustic field is simulated using a hybrid method where a Mach number expansion of the compressible Navier-Stokes equations results in the incompressible Navier-Stokes equations for the near-field flow field and an inhomogeneous wave-equation describing the propagation of acoustic waves in the far-field. The acoustic sources are determined from the instantaneous near-field flow field. The effects of the barrier are considered in terms of sound pressure levels and the frequency content. The spectral content of the acoustics is directly related to the flow generated sound. Increasing the frequency of the vehicle passing rate leads to increase in the intensity of the main acoustic modes. The effect on the frequency content itself is less pronounced.

CAA, CFD, barrier attenuation, traffic noise.

NOMENCLATURE

D	[-]	vehicle characteristic length scale
p	$[Pa]$	pressure
$\underline{u}$	$[m/s]$	velocity vector
ρ	$[kg/m^3]$	density

Subscripts and Superscripts

´	fluctuating variables
0	incompressible flowsolution

1. INTRODUCTION

Due to the development and increase of road traffic, noise pollution is an important factor for the nearby community. Federal restrictions and public interest have led to the development of several noise control devices, acoustic barriers being a common solution.

Traffic noise and attenuating effects of barriers have been modelled using empirical expressions for acoustic power emission and then analytical or empirical formula for expressing the diffraction [1-3] over a screen or barrier.

In the current approach, a more systematic approach is proposed. This approach is based on computing the flow induced acoustical sources and than computing the acoustic wave propagation. The time-dependent flow field is handled by Large Eddy Simulations (LES) to account for the turbulence of the flow. As compared to a Reynold Average Navier-Stokes (RANS) closure, all of the energy bearing eddies are resolved in space and time. Since the acoustic sources are due to the spatial fluctuations of the flow field, this implies that the acoustic source spectrum is also well resolved. The contribution of the unresolved flow components (i.e. the so-called Sub-Grid-Scale, SGS, fluctuations) can be accounted for by modelling. However, these contributions can be made as small as one wish by increasing resolution. In the present calculations the SGS contribution has been neglected altogether, because of the LES grid resolution. Once the acoustical sources are found, the wave propagation can be handled on a different, less resolved grid, since the wave numbers associated with the acoustics are much smaller than those associated with the turbulent flow. Using the combined approach, one still has to use rather substantial computational effort. Thus, the main drawback of the approach is the computational cost. However, in the present hybrid approach which takes advantage of the separation of turbulent and acoustic scales is characterized by its numerical efficiency while maintaining good accuracy. The approach has been used by Mihaescu and Moroianu

[4] to evaluate the acoustic emission and propagation around a wind turbine and for assessing the acoustics due to running jet engines [5].

The goal of this study is to analyse and estimate the dependence of traffic load on the acoustic field in the vicinity of the road. It is assumed that the vehicles are placed in a row at given intervals. The source of noise is generated by the flow around these vehicles and the acoustic waves propagate and diffracts over a barrier parallel to the road (i.e. the vehicle movement direction). The meteorological effects on the acoustic propagation are neglected.

2. METHOD

In the hybrid approach used, the flow and acoustics are decoupled by assuming that the acoustic pressure fluctuations are much smaller than the pressure fluctuations in the flow field. Thus, the flow field generates the noise sources and the wave-equation is used to propagate the acoustic waves. There is no need for feed-back of these waves into the hydrodynamic flow since compressibility and nonlinear effects are assumed to be small for the low Mach number flows that are considered here.

2.1 Governing equations

The flow solver is based on Eqs. (1) to (2) which describe the isothermal and low Mach number conditions in non-dimensional form.

$$\nabla \cdot \underline{u} = 0 \tag{1}$$

$$\frac{\partial \underline{u}}{\partial t} + \underline{u} \cdot \nabla \underline{u} = -\nabla p + \frac{1}{Re_D} \nabla^2 \underline{u} \tag{2}$$

In the momentum equation, Eq. (2), Re is the Reynolds number based on the object characteristic length, D, free-stream velocity U and the kinematic viscosity of air.

The equations above can be directly solved, together with relevant boundary conditions, if the resolution in the numerics was sufficiently refined using Direct Numerical Simulation, (DNS). But the enormous computational cost would not be justified by the gain in terms of accuracy and resolution. In turbulent flows there is a wide range of spatial and time scales which give rise to the high computational demand when all of the scales are resolved. Since the current flow is clearly turbulent and we intend to solve the equations using a more efficient and economic method as compared to DNS, some treatment must be made to model the effect of the unresolved hydrodynamic scales. One way is to use a time averaged model, RANS, to obtain mean fluctuations. These mean fluctuations usually give an underestimation of the acoustic source and do not account for the flow dynamics. A major issue of the RANS approach is for flows where there are coherent structures that are not separated from the universal range of the turbulent spectrum. Under this condition one cannot have a hope for the existence of a turbulence model, since the coherent structures do interact with the turbulent eddies. On the other hand, the coherent structures are problem dependent and thereby the whole turbulence modelling becomes problem dependent. If on the other hand one resolved completely the coherent structures (and also smaller scales that interact with it), the remaining part of turbulent interactions (i.e. the so-called SGS terms) do not contain problem dependent parts. Thus, in principle one could expect that under such conditions, one has a hope for finding universal models for the SGS terms. These ideas, in essence constitute the motivation for and foundation of the Large Eddy Simulations (LES) that we conduct. Another necessary condition for universal behaviour of the SGS is that the spatial resolution includes a (smaller) part of the inertial sub-range of the turbulent spectrum. Of course, the spatial resolution has to satisfy both criteria mentioned above.

The role of the SGS model is to account for the effects of the unresolved eddies on the resolved scale. There are two major roles for the small scales. One is to drain energy from the large scale and thereby enabling the dissipation of the fluctuations that is normally handled by the molecular viscosity. The second role of the unresolved eddies is to interact with the larger eddies not only by draining energy from them but intermittently supplying energy to them. This process (often termed as “back-scatter”) is taking place by vortex pairing by which smaller eddies become larger. On the average the energy transfer balance, on thermodynamical grounds, is always one directional, namely that energy is transferred from large scales to smaller ones and that this energy is dissipated ultimately to heat on the smallest scales. The two major roles of the unresolved eddies has to be accounted for by the SGS terms [6]. These terms cannot be expressed in terms of the large scales explicitly. Thus, one has to introduce a model, based on the resolved scales, for accounting for the SGS terms. There are several approaches for such modelling. The oldest one is based on the analogy of the SGS role with molecular viscosity. The Smagorisnky model [7] uses a “grid viscosity” instead, that is proportional to the square of the resolved length scale (based on dimensional arguments). This approach accounts naturally for the dissipative character of the small scales. More sophisticated approaches rely on the observation that small scales do have scale similarity behaviour. Under the assumption that the smallest resolved scales are similar to the largest unresolved ones, one may derive the scale similarity and the more general dynamical SGS models. These approaches can account for back-scatter. It should be stressed that it has never been shown that the physical back-scatter do have a scale similar

behaviour or that that for example the dynamic model [8] do account for a physical back-scatter. As to the dissipative character of the SGS models, one may also argue that it is not physical since it is in general proportional to the square of the grid size. However, if the resolution is adequate and the unresolved scales are well within the inertial subrange of the turbulent spectrum, one may argue that in the equilibrium range the amount of energy transferred is not dependent on the rate of energy dissipation and hence the total dissipation is controlled by the resolved parts of the inertial subrange. Furthermore, one may continue to argue that under such conditions, the energy dissipation can be accounted for by any explicit of implicit mechanism. One such implicit approach (used also in conjunction of the scale similarity model) is using dissipative numerical scheme of adequate order so that the effect of the resolved scales is small. Under such conditions (i.e. high resolution and small scale dissipation) the role of an explicit SGS term is marginal and its size is diminishing with the square of the grid size. Thus, for adequately resolved LES and appropriate numerical scheme one can refrain from using an explicit SGS model [9]. This approach is adopted in this paper.

In order to analyse the acoustic emission that is generated by the turbulence induced by the vehicles, a simplified set of equations describing the physical phenomenon is derived by introducing the following decomposition in a system of equations that describe isentropic compressible fluid flow i.e. conservation of mass, momentum and using the isentropic coupling, Eq. (4) betweeen pressure and density in non-dimensional form

$$\begin{aligned} \rho &= \rho_0 + \rho' \\ p &= p_0 + p' \\ \underline{u} &= \underline{u}_0 + \underline{u}' \end{aligned} \tag{3}$$

$$\frac{Dp}{D\rho} = Ma^{-2} \tag{4}$$

The index 0 refers to the vanishingly small Mach number state (i.e. the solution to the incompressible system of equations Eqs.(1) to (2)). The primed variables are referring to perturbations around the solution of the incompressible flow state. In Eq. (3) it is assumed that the thermodynamic and hydrodynamic density field is non varying, ρ_0=*Constant*.

The terms are then recast in the form of an inhomogeneous wave equation describing the acoustic propagation in terms of ρ'.

$$\frac{\partial^2 \rho'}{\partial t^2} - \frac{1}{Ma} \nabla^2 \cdot \rho' = \nabla \cdot \left(\underline{u} \cdot \nabla \underline{u} \right) \tag{5}$$

where higher order terms of $\rho'$and $\underline{u}'$ has been neglected, assuming that the acoustics perturbations are small. It has been shown in [10] that this kind of decomposition has gooda accuracy at low Mach number, Ma.

The term on the right hand side of Eq. (5) represents the source term for the acoustic emissions, generated by the flow field. It is fully determined from the flow field variables that are governed by Eqs. (1) to (2), and are of course a function of time. The source, which is quadrupole, is generated in areas with large gradients such as shear layers and in areas with high intensity of turbulence.

The different sized fluctuations (eddies) are very important for the development and decay of turbulence but the small ones are not major contributors to the noise source, due to their small amplitude. Thus, LES resolution is more than adequate for determining the size of the flow induced acoustical sources.

The boundary conditions for the system of Eqs. (1) to (2) and (5) are rather different in essence, due to the different characters of the two systems. The incompressible system (1)-(2) has a steady-state part which is elliptic and the full system is partially parabolic. One has to specify (three) boundary conditions on each boundary point at all times (in addition to initial condition at all points of the domain). Thus, no slip condition are applied on solid surfaces, one also often specifies the inlet velocity profiles and sets the outflow conditions to so called convective ones. For the hyperbolic Eq. (5) the number of boundary conditions on each boundary point depend entirely on the characteristic directions locally. The number of boundary conditions at each point equals to the number of ingoing characteristic into the domain of interest through that particular boundary point. On solid boundaries totally reflecting conditions are applied, while at the far field non-reflecting ("transmitting") conditions are applied. The latter conditions are expressed as

$$\frac{\partial \rho'}{\partial t} - \frac{1}{Ma} \nabla \cdot \underline{n} \rho' = 0 \tag{6}$$

In this relation, the waves are assumed to approach the boundary with the same direction as the boundary normal, $\underline{n}$.

2.2 Numerical method

The system of equations and their corresponding boundary conditions are discretised on uniform Cartesian grids using finite differences. The flow equations are discretised on a staggered grid with third- and fourth-order spatial schemes, for the convective and viscous terms, respectively. For time marching, an implicit scheme is used. A multigrid method is used in the implicit solver in each time-step, using a defect correction mode for attaining higher-order accuracy [11]. The Cartesian

grid can accommodate local refined regions so as to enhance computational efficiency. The pressure-velocity coupling is implemented as a distributed method where the velocity and pressure is updated simultaneously [12]. A fourth order interpolation scheme is used to calculate the volumetric source term in Eq. (6).

For the acoustic solver a second order discretization of Lax-Wendroff type is used [13]. This system of equations is solved using the Thomas algorithm in a line-wise manner.

A parallel implementation of the computer code is used in order to increase the computational efficiency. This is done easily for the acoustic solver in accordance with the used hybrid method. The solver algorithm contains two major steps. First the LES equations are solved in each time-step. The flow field solution is advanced in time and the instantaneous acoustic sources are calculated. These sources are then linearly interpolated to the acoustic grid which is defined independently of the LES grid. Since the acoustic length scales are larger than the turbulent length scales and the smallest hydrodynamic scales do not contribute much to the main sound intensity, this grid can be coarser with maintained accuracy. The inhomogeneous wave equation (5) is discretised on the acoustical grid, using an implicit scheme. The wave-equation is also advanced in time as the LES solver, though both may be using independently defined intermediate time steps. In this way, we maintain computational stability together with high numerical accuracy.

3. PROBLEM DEFINITION

The computational domains for the flow and acoustics are schematicly shown in Figure 1. The vehicle comprises of two bricks of width D. The distance from the ground (xz-plane) is 0.25D. The bulk of the vehicle (the bottom brick) has a height of 0.5D and the total vehicle height from the ground is D. The length, in z-direction, is 2D for the bulk and 1D for the top brick. The height of the barrier is 1D and the vehicle is located at 0.5D from the barrier.

In order to simulate a row of vehicles periodic conditions are set between the inlet and outlet boundaries. A no-slip condition is imposed on the vehicle surface, on the ground and on the barrier. Slip condition is used on the remaining walls.

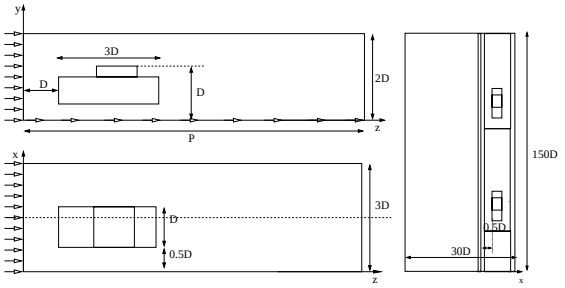

Figure 1. The computational domain for the flow and acoustic solvers. To the left, the flow field where the acoustic sources are calculated can be seen. The right figure shows the acoustic domain including the flow field from where the sources are interpolated

In the acoustic solver, the barrier, ground and vehicle surface have reflecting boundary conditions. All other boundaries are assumed to be non-reflecting.

The flow and acoustics are resolved using approximately 10 and 8 million cells, respecively. The local refinement is located around the vehicle and has a cell size of 0.015D. The acoustic solver has a spatial size of 0.1D. Four periodic distances are considered 20D, 30D, 40D and 50D corresponding to the traffic Strouhal numbers, St_t, 0.025, 0.0167, 0.0125 and 0.01 The Re_D in Eq. (2) is 60000 for all the cases and the Ma in Eq. (5) is 0.1.

4. RESULTS

The flowfield is visualised for in Figures 2 to 3. In Fig. 2 the instantaneous velocity magnitude of the flow field in the zy-plane can be seen. It is clear that large-scale turbulence is developed in the wake of the vehicle. The source calculated from the flowfield is shown in Figure 2 to 3. A high magnitude of the source is, not surprisingly, located in the vicinity of the wake where velocity gradients are largest.

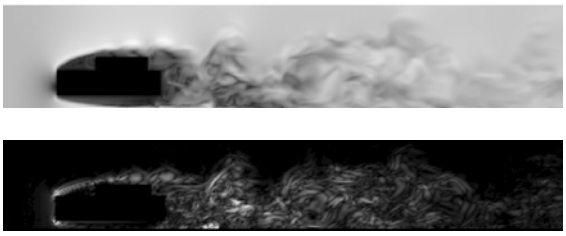

Figure 2. Instantaneous non-dimensional velocity magnitude in a zy-plane placed at the vehicle centre (a). Instantaneous magnitude of non-dimensional acoustic source in the same plane through the vehicle centre (b).

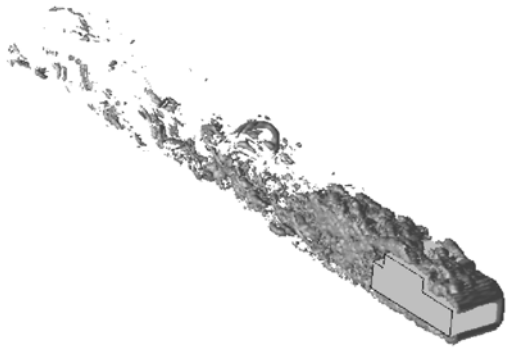

Figure 3. Visualisation of instantaneous iso-contours of the non-dimensional acoustic source.

In order to evaluate whether the spatial resolution is refined enough for LES, monitoring points have been placed at height 1D at the centerplane of the vehicle in the flowsolver. Since the shear-layer around the vehicle in Fig. 2 is the source of turbulence, the total turbulent intensity is assumed to be largest at the highest value of St_t. Therefore this flow case is used when validating the grid resolution. In Figure 4 the turbulent kinetic energy spectra is plotted from monitoring points with increasing downstream distance from the vehicle. The kolmogorov decay of -5/3 is captured and the turbulent kinetic energy dissipates at the large wave-numbers. Point a) is located at the largest distance downstream from the turbulence producing area but is due to periodicity located at z distance 0.5D. Points b) and c) are located at z distance 4D and 5D respectively. These points are in the shear layer and there is a dominating frequencies at St=0.2 due to the large scale periodic structures that can be seen in Fig. 2. This frequency and the harmonic St=0.4 is also present at the point d) z=10D.

In Figure 5 the spectral content of the acoustic source term in Eq. (5) is plotted from the same sample points as the turbulent kinetic energy in Fig. 4. It can be seen that the most energy carrying frequencies are located at point b) and c). Most of the energy is contained at St less than 10. The acoustic spectral content of the four St_t is plotted in Figure 6. The frequency distribution does not have significant differences which indicates that the large wave-numbers induced by traffic load does not influence the small ones. There is neglegible energy in the mid-frequencies under St 1. Acoustic interferens amplifies the higher frequencies as seen when plotted in a linear scale Figure 7, it can also be seen that the acoustic signal for all of the St_t contains harmonics of St 0.2. These signals are harmonics of the periodic shear instability and the spectral content is smeared by the doppler effect and dispersion of the numerical scheme. The interpolation of the sources from the flow solver to the acoustics solver acts like a filter of the size of the acoustic grid size, however most of the energy carrying frequencies in Fig. 5 b) are resolved on the acoustic grid.

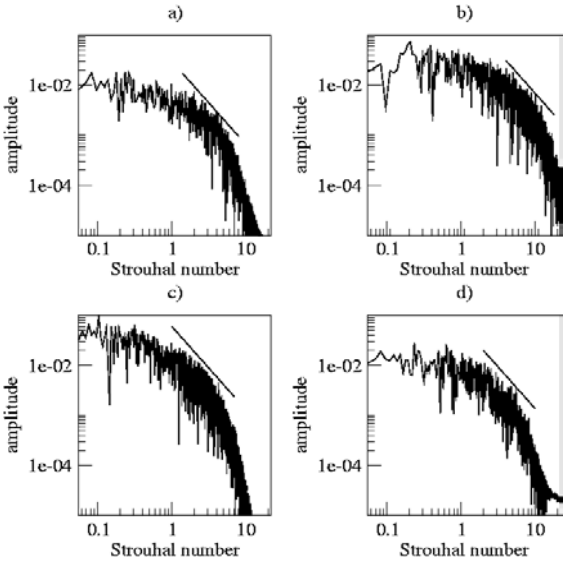

Figure 4. The turbulent kinetic energy spectra is plotted at four points on the center zy plane 1D over the ground. Located at z-distance a) 0.5D, b) 4D, c) 5D and d) 10D.

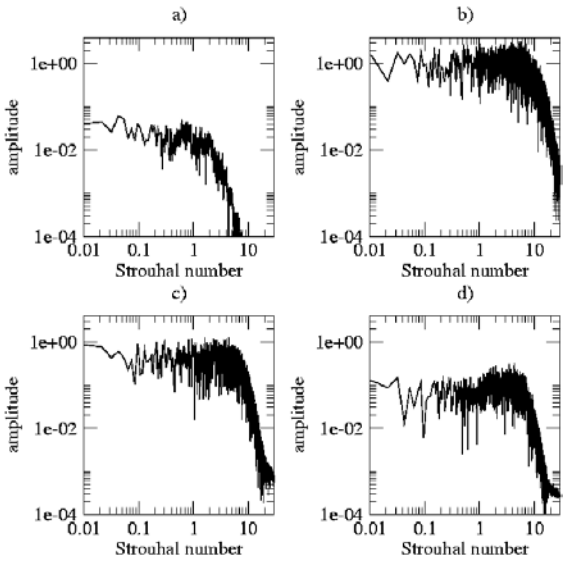

Figure 5. The acoustic source term spectra is is plotted at four differnt points on the center zy plane 1D over the ground. Located at z-distance a) 0.5D, b) 4D, c) 5D and d) 10D.

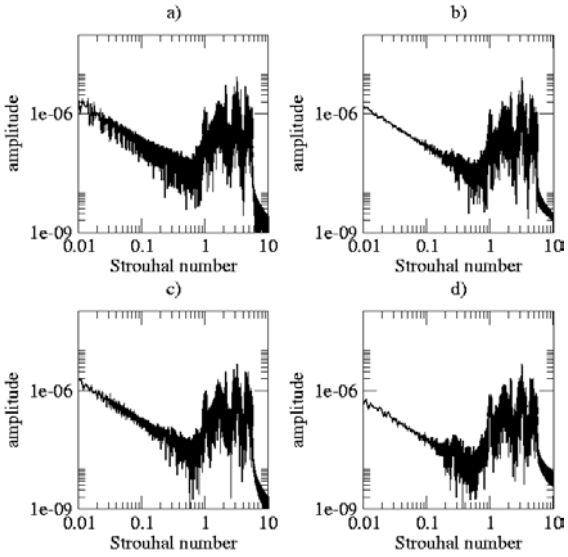

Figure 6. The acoustic spectra is plotted for the four traffic frequencies at one point located in (x,z)=(3D,75D) in the acoustic domain. St_t, numbers are a) 0.025, b) 0.0167, c) 0.0125 and d) 0.01

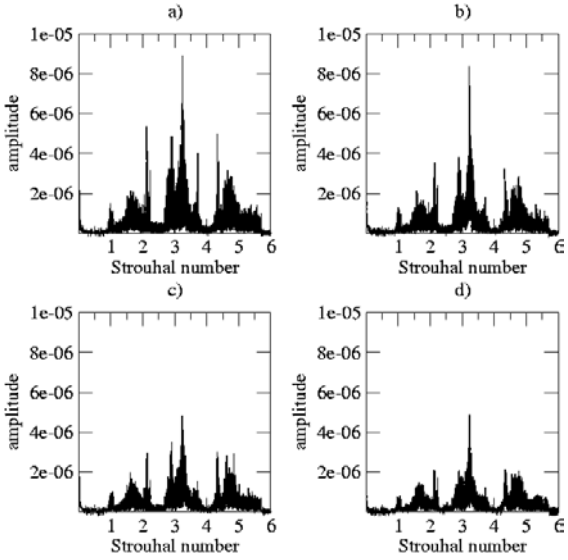

Figure 7 The acoustic spectra is plotted for the four traffic frequencies at one point located in (x,z)=(3D,75D) in the acoustic domain. St_t, numbers are a) 0.025, b) 0.0167, c) 0.0125 and d) 0.01

Figure 8 depicts time averaged Sound Pressure Level (SPL) isocontours in an xy-plane of the acoustic domain. These results are, close to the wall, similar to those obtained by [3] In Fig. 8 SPL is plotted along lines at y 2.5D, 1.5D and 0.5D over the ground. It can be seen that the barrier (at x=27D) has an attenuating effect on the noise propagation. In [14] measurements of attenuation of A-weighted SPL are in the same order of magnitude at locations 10D and 20D from the barrier. The correct assumptotic decrease of SPL can be seen some distance from the near-field.

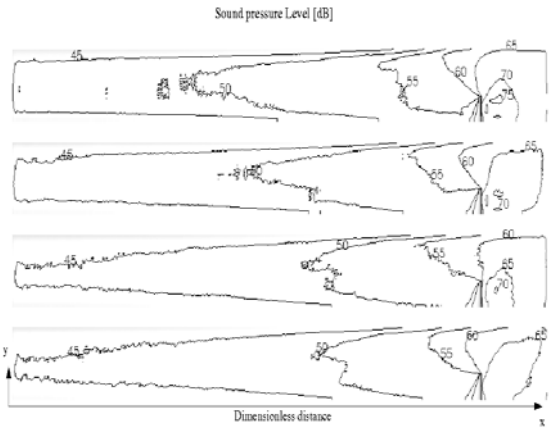

Figure 8. Sound Pressure Level isolines in a xy cut in the center of the acoustic domain. The traffic frequency is increasing downwards.

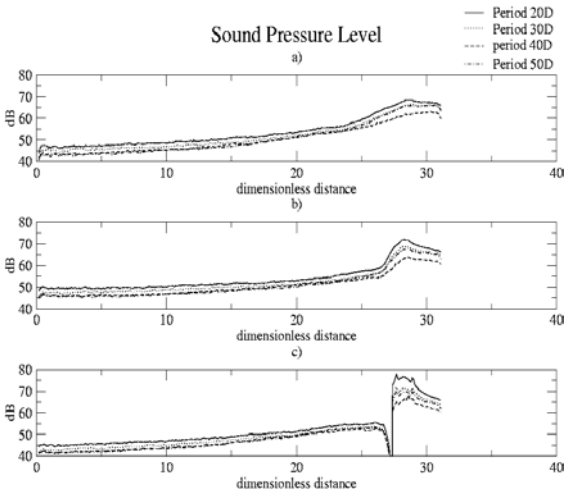

Figure 9. Sound Pressure Level along lines at y-coordinate a) 2.5D, b) 1.5D and c) 0.5D in the xy center plane.

5. CONCLUSIONS

A hybrid approach is used in order to investigate the influence of periodicity on the flow and acoustic field. In this method the problem is solved in two steps firstly, the flow field around a line of moving vehicles parallel to a barrier is modelled with LES and the induced acoustic sources are evaluated. Secondly, the acoustics is evaluated by using an acoustic analogy in form of an inhomogeneous wave equation. Most of the energy carrying frequencies are resolved and it is seen that periodicity is not influencing the spectral content of the signal which is dominated by harmonics of the dimensionless frequency of about 0.2. This

frequency is related to the instability of the shear-layer close to and in the wake of the vehicles. The distribution of SPL, in the far-field, exhibits a correct asymptotic behaviour.

REFERENCES

[1] Maekawa, Z., 1968, "Noise reduction by screens", *Applied acoustics.*

[2] ISO 9613-2,1996, "Attenuation of sound during propagation outdoors general method of calculation".

[3] Dae S. Cho, Jin H. Kim, Tae M. Choi, Byung H. Kim, Douglas Manvell, 2004, "Highway traffic noise prediction using method fully compliant with ISO 9613: comparison with measurement", *Applied Acoustics 65, pp 883-892*.

[4] Moroianu, D. Mihaescu, M. Fuchs, L., , 2003, "Numerical computation of the acoustical field around wind-turbines", *tenth international congress on sound and vibration*.

[5] Mihaescu, M., Gutmark, E., Szasz, R., Fuchs, L. Flow and Acoustics of a Coaxial Nozzle: a Sensitivity Study to the Inlet Boundary Conditions. AIAA paper, AIAA-2006-619, 2006

[6] Stephen B. Pope, 2000, *Turbulent flows*, Cambridge, university press

[7] Smagorinsky J 1963 Mon. Weather Rev. 91 99

[8] Germano M, Piomelli U, Moin P and Cabot W H 1991 Phys. Fluids A 3 1760

[9] Szasz, R., Revstedt, J., Fuchs, L., 2004, "Comparison of some SGS models for turbulent fluxes of momentum and a passive scalar in swirling co-annular jets", *Proceedings of the 5th IUTAM symposium on direct and large eddy simulation, D-LES-5, Kluwer academic publishers*.

[10] Scot A. Slimon, Marios C. Soteriuo, Donald W. Davis, 1999,"Development of computational aeroacoustics equations for subsonic flows using a Mach number expansion approach", *journal of computational physics,* 159, pp 377-406.

[11] Fuchs, L., 1984, "Defect correction and higher numerical accuracy", *Efficient solutions of elliptic systems, proceedings of a GAMM-seminar.*

[12] Fuchs, L., 1984, "Solution of three-dimensional viscous incompressible flows by a multi-grid method", *international journal for numerical methods in fluids, vol.4.*

[13] Tannehill, J. C., Anderson, D. A., Pletcher , R. H. , 1997, "Computational fluid mechanics and heat transfer", *second edition, Taylor & Francis*.

[14] G. R. Watts, 1996, "Acoustic performance of parallel traffic noise barriers",*Applied acoustics*, vol 47, pp 95-119.

Conference on Modelling Fluid Flow (CMFF'06)
The 13th International Conference on Fluid Flow Technologies
Budapest, Hungary, September 6-9, 2006

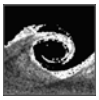

ON SUBSONIC FLOW OVER CAVITIES WITH AERO ACOUSTIC APPLICATIONS

Helge NØRSTRUD[1], Ivar ØYE[2]

[1] Corresponding Author. Department of Energy and Process Engineering, Norwegian University of Science and Technology (NTNU). Kolbjørn Heies vei 2, NO-7491 Trondheim, Norway. Tel.: +47 73 593707, Fax: +47 73 593491, E-mail: helge.norstrud@ntnu.no
[2] CFD norway, Marinteknisk Senter. E-mail: ivar.oye@cfdnorway.no

ABSTRACT

Two-dimensional (2-D) flow over rectangular cavities has been widely analyzed. Rossiter proposed in 1964 an empirical equation which relates the periodic shedding of vortices over the cavity to acoustic radiation from the cavity. This feedback loop system was in the Rossiter equation described as stages (or modes) of frequency resonance. There remain, however, a lack of data for low Mach numbers (M) and the present paper proposes a modified Rossiter equation for the range $0 \leq M < 0.45$. It also provides frequency simulations of helical corrugated gas pipes (carcasses) when the cavity length is replaced by the corrugation pitch. In addition, the onset velocity for resonance has also been estimated.

.

Keywords: aero-acoustic, flow over cavity, gas pipe application, modified Rossiter formula

NOMENCLATURE

C_p	[-]	static pressure coefficient
K	[-]	convection velocity factor
L	[m]	cavity length
M	[-]	Mach number
N	[-]	integer
St	[-]	Strouhal number
U	[m/s]	flow velocity
V_{ref}	[m/s]	reference velocity
c	[m/s]	speed of sound
d	[m]	carcass diameter
f	[Hz]	frequency
h	[m]	vortex sheet height
k	[-]	integer
m	[-]	Rossiter mode number
n	[-]	Sarohia mode number
p	[m]	carcass pitch length
x	[m]	axial length coordinate
γ	[-]	phase factor
δ	[m]	boundary layer thickness
λ_a	[m]	acoustic wave length
λ_v	[m]	vortex sheet wave length

1. INTRODUCTION

Early investigation of flows over cavities were initiated in connection with the sound generation and fluid-structure interaction e.g. from airplane bomb bays or gaps in the vehicle surface. The wind tunnel experiments of Rossiter [1] over single, rectangular cavities found that the measured frequencies f for the periodic pressure fluctuations (read also acoustic radiation) over the 2-D cavity could be represented by the empirical equation

$$f = (U / L)\,(m - \gamma) / (1/K + M) \quad m = 1, 2, 3, \qquad (1)$$

where U and L represents respectively the tunnel velocity and the cavity length. The two cavity configuration constants $\gamma < 1$ and $K < 1$ are related to the frequency f of the vortex shedding over the cavity, i.e.

$$f = KU / \lambda_v \qquad (2)$$

where the product KU represents the convection velocity of the vortex sheet, see Figure 1.

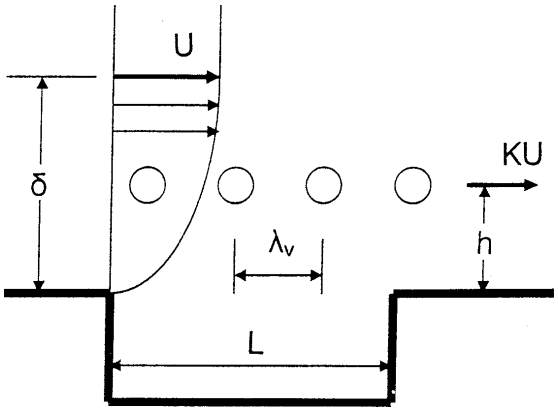

Figure 1. Schematic illustration of 2-D flow over a rectangular cavity

The distance $\gamma\ \lambda_v$ designates the position of a vortex filament [2] behind the cavity trailing edge in terms of the vortex shedding wavelength λ_v at the time when another filament leaves the leading edge. Furthermore, $M = U / c$ is the tunnel Mach number based on the speed of sound c in the wind tunnel. The importance of Eq. (1) is that it describes the frequency ranges between jumps as stages corresponding to the integer modes m. Introducing the dimensionless Strouhal number St_L [-] as

$$St_L = f L / U \tag{3}$$

in Eq. (1) the Rossiter formula is transformed to

$$St_{L,M} = (\mathrm{m} - \gamma) / (1/\mathrm{K} + M) \quad \mathrm{m} = 1, 2, 3, \tag{4}$$

The Mach number dependence in Eq. (4) is indicated by the additional subscript M in the Strouhal number. It should be noted that a modified Rossiter formula for high Mach numbers has been presented by Heller et al [3] and compared with the original Rossiter formula. Both relations gives identical and finite results for $St_{L,M=0}$, but indicates an unrealistic influence of the compressibility as the Mach number increases from zero. That is, the gradient of Eq. (4) with respect to M has a non-zero value at $M = 0$ and for this reason a modified Rossiter formula for low Mach numbers will be presented in the next section.

2. MODIFIED ROSSITER EQUATION FOR LOW MACH NUMBERS

Since Eq. (4) is deduced from experiments performed at $M > 0.4$, we will introduce a modified Rossiter formula for low Mach numbers by applying the Prandtl-Glauert similarity rule for two-dimensional, subsonic flows. This will relate a compressible flow solution (read Strouhal number) at Mach number $M < 1$ to the incompressible solution at $M = 0$ through the corresponding pressure coefficient C_p, i.e.

$$C_{p,M} = (1 - M^2)^{-1/2}\ C_{p,M=0} \tag{5}$$

The pressure coefficient, however, can be written in its linearized form as

$$C_p \approx -\ 2(U - V_{\mathrm{ref}}) / V_{\mathrm{ref}} \tag{6}$$

were V_{ref} is the common reference velocity for the compressible and incompressible flow field. Eq. (6) inserted in Eq. (5) gives

$$U_M = (1 - M^2)^{-1/2}\ U_{M=0} \tag{7}$$

and we can observe that compressibility (i.e. the Mach number influence) will increase the perturbation velocity $(U - V_{\mathrm{ref}})$ or the flow velocity U at the same point in the flow field for $M < 1$. Furthermore, with the introduction of the Strouhal number from Eq. (3), Eq. (7) suggest the relation

$$St_{L,M=0} = (1 - M^2)^{-1/2}\ St_{L,M} \tag{8}$$

Eq. (8) says that a given Strouhal number in a compressible flow ($St_{L,M}$) will define a corresponding incompressible value for $St_{L,M=0}$. Also note that Eq. (3) yields an infinite value for the Strouhal number at $U = 0$. This result in combination with the Rossiter relation will yield the modified Rossiter formula for $0 \le M < 1$. After a differentiation of Eqs. (3) and (8) and setting the results equal, one obtains the condition for a unified gradient for the two equations, i.e.

$$\mathrm{K}\ M\ (1 - M^2) = 1 / (M + 1/\mathrm{K})^2$$

For K = 0.57 (taken from the original Rossiter paper) the above equation is satisfied for $M = 0.453$ and Eq. (8) can now be rewritten to yield

$$\begin{aligned} St_{L,M=0.453} &= (1 - 0.453^2)^{1/2}\ St_{L,M=0} \\ &= 0.453\ (\mathrm{m} - \gamma) \qquad \mathrm{m} = 1, 2, 3, \end{aligned} \tag{9}$$

were the Rossiter Eq. (3) has been adopted to define $St_{L,M=0.453}$. Furthermore, Eq. (9) yields the relation

$$St_{L,M=0} = 0.508\ (\mathrm{m} - \gamma) \qquad \mathrm{m} = 1, 2, 3, \tag{10}$$

and Eq. (10) inserted in Eq. (8) formulates (see Figure 2) the present modified Rossiter formula for low Mach numbers, i.e.

$$St_{L,M \le 0.453} = 0.508\ (1 - M^2)^{1/2}\ (\mathrm{m} - \gamma) \quad \mathrm{m} = 1, 2, 3, \tag{11}$$

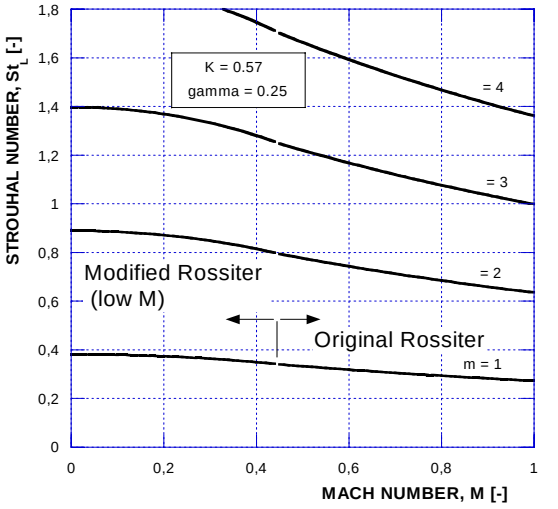

Figure 2. Modified Rossiter formula for low Mach numbers

Table 1 below summarizes the Strouhal numbers for $M = 0$, 0.2 and 0.453 as function of the Rossiter mode number m.

Table 1. Strouhal numbers for the modified and the original Rossiter equation

	$St_{L,M=0}$ Modified (Rossiter)	$St_{L,M=0.2}$ Modified (Rossiter)	$St_{L,M=0.453}$ Modified and Rossiter
m = 1	**0.3812** (0.4275)	0.3733 (0.3838)	0.3398
= 2	**0.8893** (0.9975)	0.8710 (0.8954)	0.7928
= 3	**1.3974** (1.5675)	1.3688 (1.4071)	1.2458
= 4	**1.9055** (2.1375)	1.8665 (1.9188)	1.6988

In comparing the results for the modified formula it is found that the original Rossiter formula (represented in Table 1 in parenthesis) gives about 12% higher values for the Strouhal number at M=0. Further comparisons with experimental data [4] are shown in Figure 3 and comparison with numerical data are found in [5].

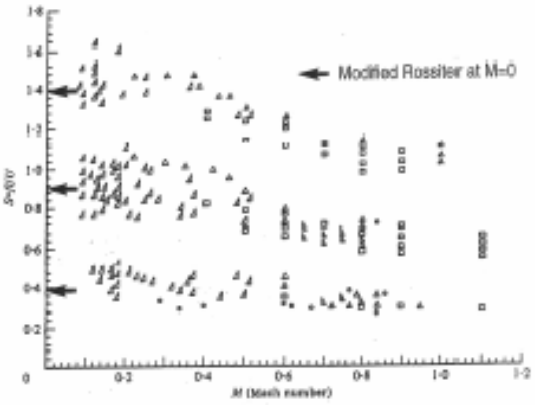

Figure 3. First three modified Rossiter modes compared with various experimental results [4]

2.1. Related Developments

It is interesting to note that Sarohia [6] found, from experimental investigations over axisymmetric bodies at low subsonic speeds ($M < 0.01$), that the wavelength λ_v of the propagating disturbance (vortex filament) was related to the cavity length L through the expression

$$\lambda_v = L / (n + ½) \quad n = 0, 1, 2, 3, \qquad (12)$$

where the integer n indicates the mode of cavity oscillation. Since it was found that the relative phase speed of the vortex sheet was a constant, Eq. (12) can be combined with Eq. (2) to read

$$f = (KU / L) (n + ½) \quad n = 0, 1, 2, 3,$$

or rewritten with Eq. (3) in a non-dimensional form as

$$St_L = K (n + ½) \qquad n = 0, 1, 2, 3, \qquad (13)$$

Inserting the value K = 0.57 from the Rossiter experiment in Eq. (13) we will obtain the results given in Table 2 below.

Table 2. Strouhal number of vortex shedding as deduced from [6]

n =	0	1	2	3
St_L =	**0.285**	**0.855**	**1.425**	**1.995**

As can be observed, the values for the Strouhal number St_L bears a close resemblance with the modified Rossiter values for m = n+1 at $M = 0$, see Table 1. Or in other words, the results of Sarohia [6] supports the modified Rossiter formula at $M = 0$. Eq. (12) is for clarity plotted in Figure 4 where the e.g. the pressure fluctuations over the cavity and its associated transversal wave pattern is visualized as a sine-wave along the cavity length.

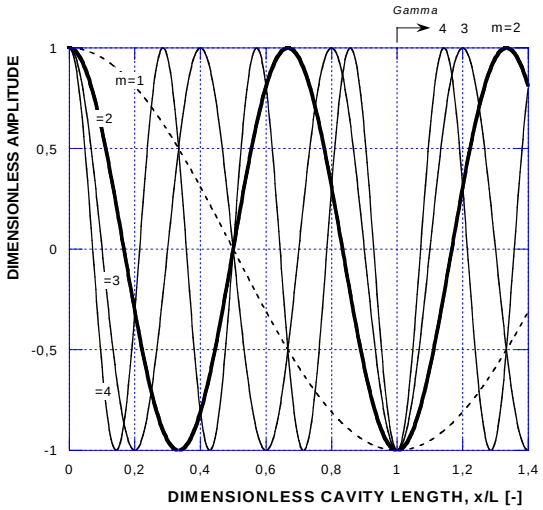

Figure 4. Illustration of the shear layer wave pattern over a cavity and beyond (m = n + 1)

A further confirmation is found in the comprehensive work by Ahuja and Mendoza [7]. Here the resonance frequencies were computed using a modal duct analysis and were these frequencies matched with the Rossiter equation high amplitude tones could be expected. This coupling is also indicated in Figure 5 as full circles. It should be noted that the three low Mach number data ($M = 0.26$) from [7] are found for m = 2 as the middle full circle (value 0.92) and for m = 3 as two overlapping full circles (value 1.42) in Fig. 5. Hence, a very good correspondence with the modified Rossiter values at $M = 0$ can be observed.

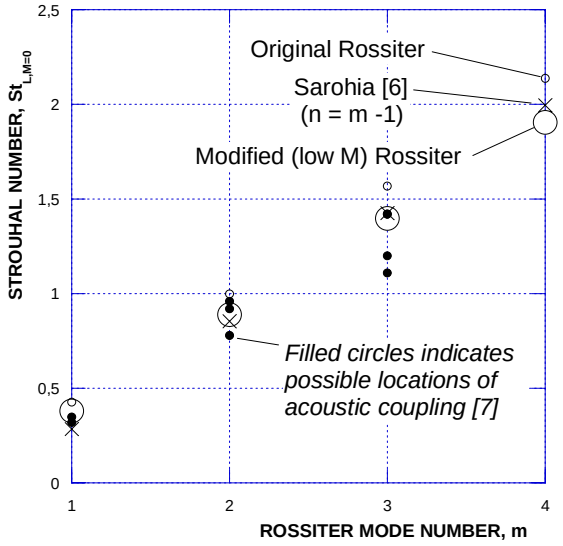

Figure 5. Strouhal number comparison at M ≈ 0

Returning to Eq. (12) and inserting the relation n = m – 1 we obtain

$$\lambda_v / L = (m - ½)^{-1} \quad m = 1, 2, 3, \qquad (14)$$

which in tabulated form yields Table 3 below.

Table 3. Evaluated vortex wavelengths and number of vortex filaments

m =	1	2	3	4
λ_v / L =	**2.000**	**0.667**	**0.400**	**0.286**
N =	1	2	3	4

The integer N in Table 3 is evaluated from the relation

$$N = 1 + \text{integer}\ (L / \lambda_v)$$

and it represents the maximum number of vortex filaments which spans the cavity length for a given Rossiter mode number. Hence, it can be deduced that N = m and this observation has also been pointed out by Koch [8]. A further conclusion can be to realize that an increase of the mode number is related to a higher rate of vortex filament release.

Since the factor γ in the Rossiter formula Eq. (1) indicates the fraction of a wave length λ_v for which a vortex filament is behind the trailing edge, it is instructive to adopt Eq. (14) to evaluate this length as indicated in Fig. 4 and tabulated in Table 4 as $\gamma = ½ (\lambda_v / L) = (2m - 1)^{-1}$.

Table 4. The phase shift factor γ

m =	1	2	3	4
γ =	1/1 =**1.000**	1/3= **0.333**	1/5= **0.200**	1/7= **0.143**

Two observations can be extracted from the results given in Table 4, i.e.

i) We have used in our calculation the common adopted value of $\gamma = 0.25$, which Rossiter dermined as an average over the speed range tested. This value lies in Table 4 between the mode numbers 2 and 3 and can be regarded as a reasonable choice.

ii) For mode number m = 1 we see that γ equals 1 and this value inserted in Eq. (4) will yield $St_{L,M=0} = 0$. However, Sarohia [6] states that his formula Eq. (12) can not be regarded as an exact relation, but more as an approximate integral relation. This means that for γ slightly less than 1, the frequency response would be very low and, as a consequence, not easily detectable. This can also be deduced from Sarohia's own conclusion that the mode n = 0 (or m = 1) was not easily observed.

Before leaving the work of Sarohia [6] we would like to relate his findings to the modified Rossiter formula for low Mach numbers. Firstly, we adopt the Falkner–Skan laminar boundary layer to represent the separation profile at the cavity leading edge. In addition, we place the vortex shear layer at the middle of the boundary layer, i.e. at $h = ½ \delta$, where the streamwise velocity is 0.56 U, see [9]. This value is in close correspondence with the Rossiter constant K = 0.57.

Secondly, we adopt the ratio of $2h / \lambda_v = 0.281$ for the von Kármán vortex street where 2h designates the vertical distance between the two shear layers forming the vortex street [10]. This might appear a little speculative, but with reference to the analysis of Abernathy and Kronauer [11] which showed that vortex streets could be obtained by periodic perturbation of two vortex sheets, rather than by not incorporating bodies. Figure 6, which is reproduced from Figs. 11 and 12 in [11], illustrates two calculation results (of different initial conditions) from a linearized analysis of the growth of the disturbances in two, infinite and initially parallell vortex rows in an inviscid, incompressible fluid. The figure shows six development stages of of the non-linear interaction of the sheets subjected to small amplitude disturbances of wavelength a as indicated. It should be remarked that the upper sheet consists of vortex filaments of clockwise rotation, wereas the lower sheet has elements (filaments) with a counterclockwise rotation.

It should also be pointed out that the obtained convection velocity (designated as U_bar / U in Fig. 6) is in the order of 0.55 and, hence, compares again with the Rossiter factor of K = 0.57.

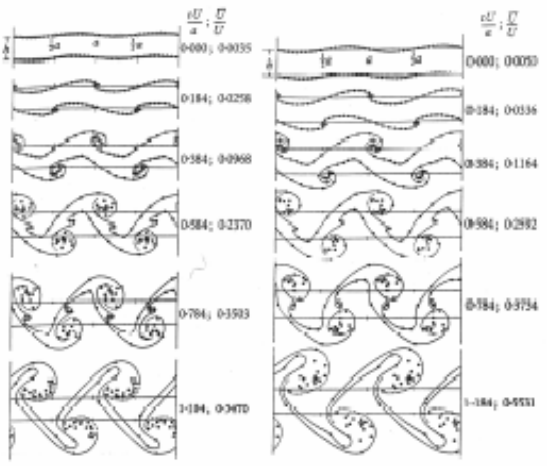

Figure 6. Two modes of vortex street formation [11] at the von Kármán spacing ratio 0.281

Combining the two aforementioned expressions involving the height h will yield $\delta / \lambda_v = 0.281$ and this value inserted in Eq. (14) gives finally

$$\delta / L = 0.281 \, (m - ½)^{-1} \qquad m = 1, 2, 3, \qquad (15)$$

Eq. (15) is tabulated in Table 5 together with the corresponding remarks by Sarohia [6].

Table 5. The dimensionless boundary layer thickness δ / L

m =	**1**	**2**	**3**	**4**
δ / L =	0.5720	0.1907	0.1144	0.0817
L / δ =	**1.7483**	**5.2448**	**8.7413**	**12.2378**
	No cavity oscillation below L / δ = 5.25 [6]		Mode shift above L / δ =8.15 [6]	

As can be observed, the simple analysis leading to Eq. (15) supports the finding expressed in [6] and can be summarized as follows

iii) The Rossiter mode m = 1 can from experimental results [6] be excluded when the boundary layer thickness δ is greater than 19 % of the cavity length L. Higher mode numbers are found to be present for lower values of the ratio δ / L. This means that for a fixed cavity length L a thickening of the boundary layer thickness δ will reduce or eliminate cavity oscillations (sound). Similar statement can be found in the work of Ahuja and Mendoza [7], page 172.

3. APPLICATION TO HELICAL CORRUGATED PIPES

The phenomena of "singing wires" or the Aeolian tone is well known for sound generation when cylindrical bodies are placed in a cross flow. The von Kármán vortex street is fundamental in describing this aero-acoustic interaction. Similar sound generation effects are observed in gas pipe lines and the subject modified Rossiter formula will now be adopted to simulate the aero acoustic response at $M = 0$ over a helical corrugated pipe, i.e. a carcass as shown below.

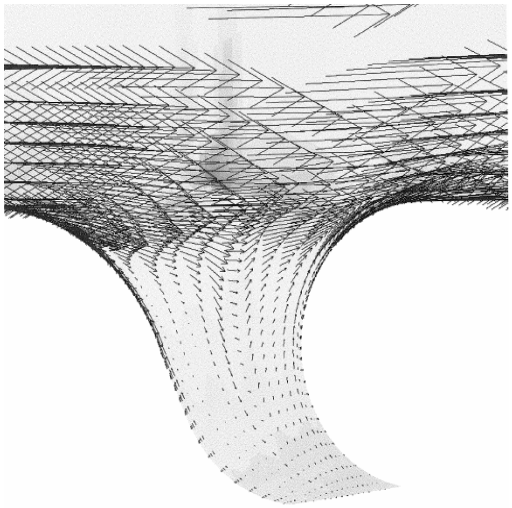

Figure 7. Sample numerical solution of subsonic flow over a carcass depth element

The cavity length L is replaced by the pitch length p of the carcass which is defined as the axial distance between two adjacent depth elements (or the width of Figure 7). The frequency response can according to Eq. (3) be written as

$$f = (U / p) \, St_{p,M=0} \qquad (16)$$

where U < 10 m/s (i.e. $M \approx 0$) is again the gas velocity. The Strouhal number in Eq. (16) is obtained from Eq. (11) as

$$St_{p,M=0} = 0.508 \, (m - \gamma) \qquad m = 1, 2, 3, \qquad (17)$$

Three carcass cases have been simulated, i.e.

1. Case A (p = 0.01397 m) (d = 0.1524 m)
2. Case B (p = 0.0234 m) (d = 0.3556 m)
3. Case C (p = 0.02366 m) (d = 0.381 m)

and the results for the frequency response is compared with operational data (See Figures 13-15 respectively for a preliminary view).

3.1. Estimation of the Cut-On/Off and the Resonance Frequencies

The test cases listed above are gas pipes with a helical continuous cavity (carcass) and a hypothesis of the subject frequencies can be formulated on the basis of the following reasoning (see Figure 8).

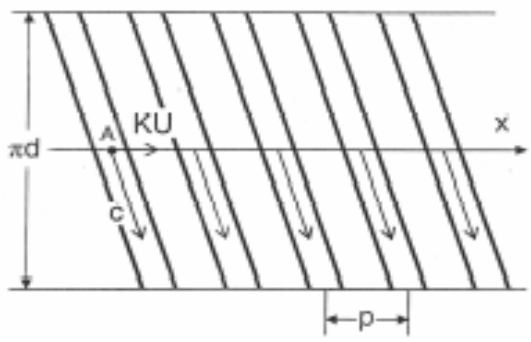

Figure 8. Illustration of an unfolded carcass

The shedding frequency f of the vortex filaments Eq. (2) is identical to the frequency of an acoustic wave traveling inside the helical cavity, i.e

$$f = c / \lambda_a \qquad (18)$$

Here the acoustic wave length λ_a is aproximated as a function of the geometric relationship

$$\lambda_a = \mathrm{k}\,\pi\,d \qquad (19)$$

where d represents the inner diameter of the carcass and the integer k determines the number of repeated turns of the cavity (Note that the pitch is neglected in writing Eq. (19) since p is small compared to the circumferential distance π d), see Table 6 below.

Table 6. Acoustic frequency as function of wavelength and sound speed

f [Hz] = λ_a *[m]* =	k = 4	= 2	= 1
Case A *c [m/s]* = 420	**219.3** 1.915	**438.6** 0.958	**877.2** 0.479
Case B = 400	**89.5** 4.469	**179.0** 2.234	**358.1** 1.117
Case C = 400	**83.5** 4.788	**167.1** 2.394	**334.2** 1.197

A combination of Eqs. (16) to (19) will yield the aero-acoustic coupling as

$$U = 1.969\, p\, c\, /\, \{(\mathrm{m} - \gamma)(\mathrm{k}\,\pi\,d)\} \quad \mathrm{m} = 1, 2, 3, \quad (20)$$

where Eq. (20) is tabulated in Table 7. The reference sound speed c in the carcass is optained from operational gas data such as gas pressure, density and ratio of specific heats.

Table 7. Reference velocities for m = 1 and 2

U [m/s] =	k = 4 Cut-on	= 2 Resonance	= 1 Cut-off
Case A m = 1	8.04	16.08	32.16
= 2	**3.45**	**6.89**	**13.78**
Case B m = 1	5.50	11.00	21.99
= 2	**2.36**	**4.71**	**9.43**
Case C m = 1	5.19	10.38	20.75
= 2	**2.22**	**4.45**	**8.89**

A discussion of the results depicted in Table 7 will now be given with special attention to Figs. 4 and 9.

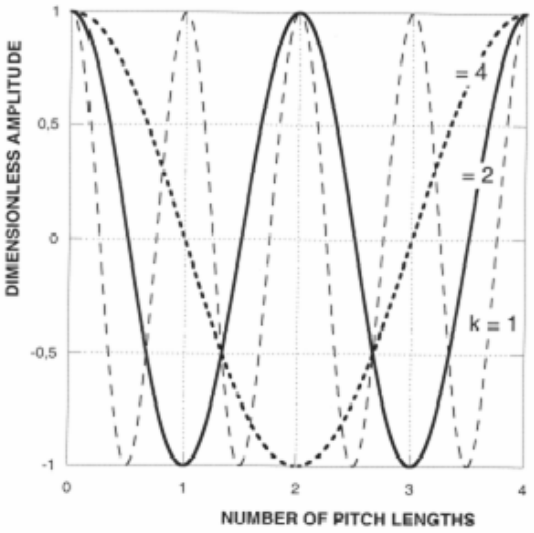

Figure 9. Amplitude of carcass sound wave as function of the acoustic wave length (k = 1, 2. 4)

When a pressure wave generated by the vortex shedding leaves with, e.g. a maximum positive sign from the point A in Fig. 8, it will reach the next axial cavity (after one pitch length) with an opposite sign for all Rossiter modes m, see Fig. 4. After another pitch length the pressure wave will again have a positive sign. Numerical simulation have shown that this alternating pressure pattern to be the case, Figure 10 (Since the figure is a reproduction from a colour picture the quality is bad).

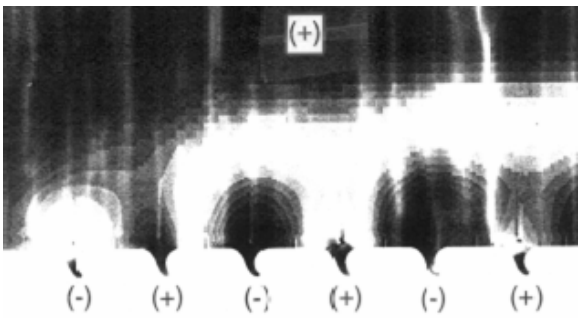

Figure 10. Numerical simulation of the static pressure (+ is compression, - is rarefaction) along an unfolded (2-D) carcass

Comparing this wave pattern with the acoustic wave along the helical carcass we see that for k = 2 an identical pressure development occurs. This means that pressure amplification (positive and negative valued) will occur and, hence, a resonance between the vortex shedding frequency and the frequency of the sound wave is obtained, see Figure 11.

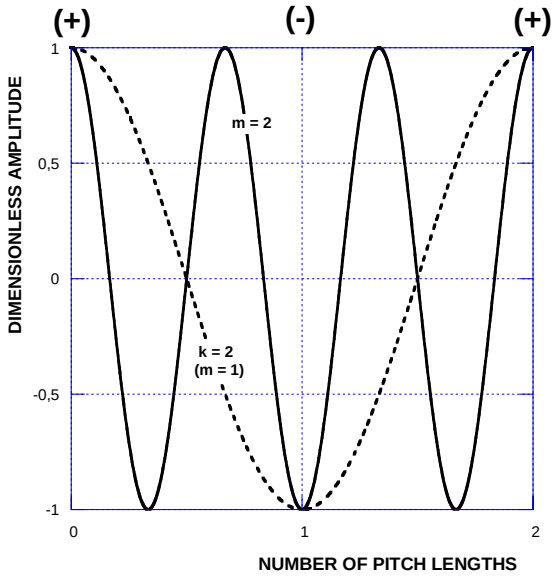

Figure 11. Wave pattern for m=2 and k=2 (m=1)

Similar wave comparisons can be analyzed for k = 4 (which is connected to the lowest frequency in Table 6 and denoted in Table 7 as cut-on or onset) and we can observe that for every fourth pitch length pressure amplification occurs. Between these two antinodes, see Figure 12, a pressure cancellation will be the result since the two wave systems are assumed to be of equal magnitude or strength.

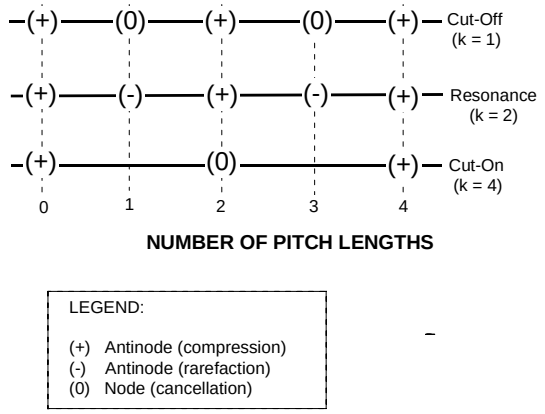

Figure 12. Interaction between the two wave systems at consecutive pitch lengths for all Rossiter modes

For k = 1 (which we assume is related to the socalled cut-off frequency) the positive pressure pulses at every second cavity length shows amplification, but otherwise cancellation at nodes. The results from the described wave interaction as expressed in Table 7 is also indicated in Figs. 13 – 15 as vertical lines crossing the k-lines for the Rossiter modes 1 and 2. As can be seen, the prediction of resonance for k = 2 fits well into the operational results.

It can be further stated that for the Case A carcass resonance (read singing) is from operational data confirmed to be in the range $2.9 < U < 10.0$ m/s and for the Case C carcass no singing is reported for $U < 3.5$ m/s.

The rational behind the analysis given above is based on the interaction of an acoustic wave which in the real carcass configuration is helical and three-dimensional, but is for simplicity compared in the one-dimensional or axial direction x with the flow shedding wave system. Furthermore, the predicted resonance should more accuratly be termed the mean resonance point because resonance (or pressure communication) is in reality confined to a finite axial pipe length defined by the opening of the carcass depth element, see again Figs. 7 and 8. This view can be also be extracted from the operational data shown in Figs. 13-15.

A final question now arises: Will singing of the riser (carcass) always occur within the predicted limits of the cut-on/off frequencies? The simplicity of the present aero-acoustic analysis ignores the structural response of the carcass and, hence, it can not reveal the influence of the construction of the real gas conduit. However, the analysis gives guidelines for estimating the possible occurance of resonance based on gas data and carcass dimensions.

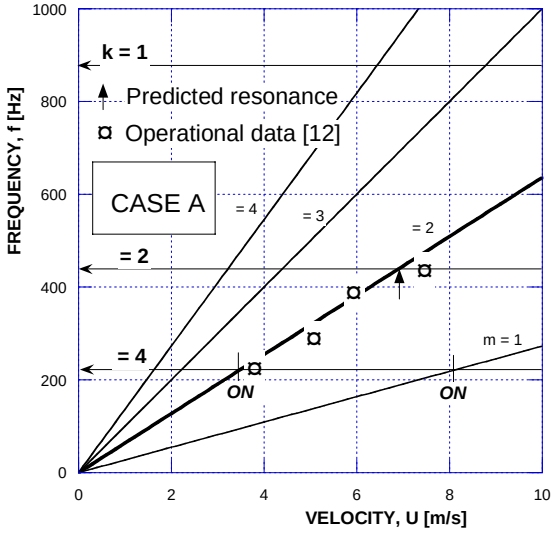

Figure 13. Frequency response for Case A

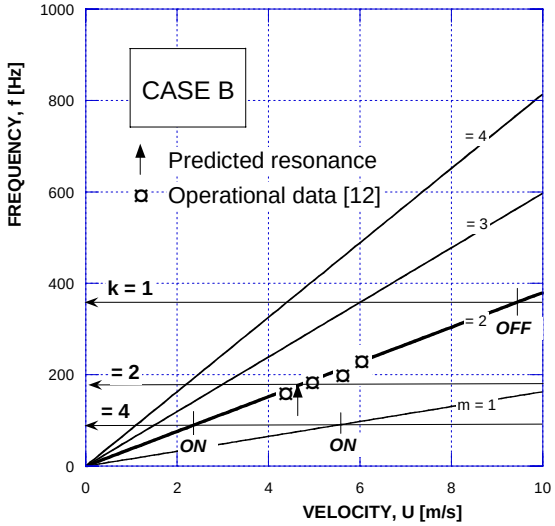

Figure 14. Frequency response for Case B

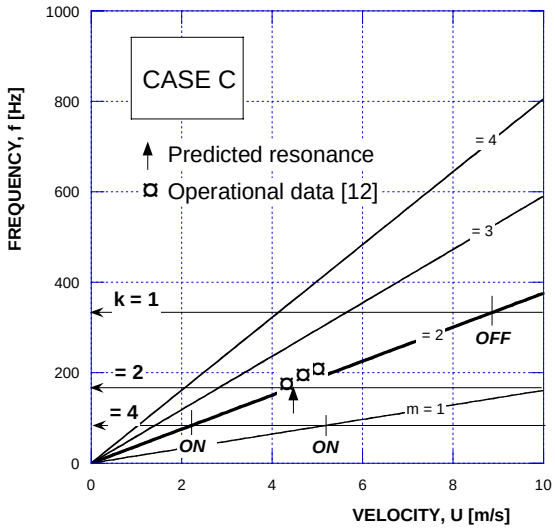

Figure 15. Frequency response for Case C

4. CONCLUDING REMARKS

A modified Rossiter formula for low Mach number cavity flows has been formulated and evaluated in view of related publications with the conclusion that the prediction of the aero-acoustic coupling is also well suited for Mach number zero. Furthermore, application of the modified formula to helical corrugated gas pipes (carcass) shows very good agreement with operational data, especially in explaining the dominant Rossiter mode m = 2.

An estimation of the cut-on/off frequencies which encompasses the resonance frequency for three carcass test cases have also been presented and compared to operational data.

ACKNOWLEDGEMENTS

Thanks goes to the Norwegian ongoing project organization "Singing Riser" who has financial supported a literature study on the subject of flow over cavities.

REFERENCES

[1] Rossiter, J.E., "Wind-Tunnel Experiments on the Flow over Rectangular Cavities at Subsonic and Transonic Speeds", *RAE Tech. Report No.* 64037, 1964.

[2] Saffman, P.G., *Vortex Dynamics*, Cambridge University Press, 1995, p.10.

[3] Heller, H.H. et al, "Flow-induced oscillations in shallow cavities", *Journal of Sound and Vibration*, 18(4), 1971, pp. 545-553.

[4] Tam, C.K.W. and Block, P.J.W., "on the tones and pressure oscillations induced by flow over rectangular cavities", *Journal of Fluid Mechanics*, Vol. 89, part 2, 1978, pp. 373-379.

[5] Colonius, T. et al, "Numerical investigation of the flow past a cavity", *AIAA Paper* 99-1912, May 1999.

[6] Sarohia, V., "Experimental Investigation of Oscillations in Flows Over Shallow Cavities", *AIAA Journal*, Vol.15, No. 7, July 1977, pp. 984-991.

[7] Ahuja, K.K. and Mendoza; J., "Effects of Cavity Dimensions, Boundary Layer, and Temperature on Cavity Noise With Emphasis on Benchmark Data To Validate Computational Aeroacoustic Codes", *NASA Contractor Report* 4653, April 1995.

[8] Koch, W., "Acoustic Resonances in Rectangular Open Cavities", *AIAA Journal*, Vol. 43, No. 11, November 2005, pp. 2342-2349.

[9] Bertin, J.J. and Smith, M.L., *Aerodynamics for Engineers*, Prentice-Hall, Englewood Cliffs, 1989, p. 127.

[10] Kaufmann, W., *Technische Hydro- und Aeromechanik*, Springer-Verlag, Berlin/Göttingen/Heidelberg, 1954, p. 189.

[11] Abernaty, F.H. and Kronauer, R.E., "The formation of vortex streets", *Journal of Fluid Mechanics*, Vol. 13, Part 1, May 1962, pp. 1-20.

[12] *Confidential Report*, August, 2005.

Conference on Modelling Fluid Flow (CMFF'06)
The 13th International Conference on Fluid Flow Technologies
Budapest, Hungary, September 6-9, 2006

COMPUTATION OF THE ACOUSTIC FIELD IN AN ANNULAR GAS TURBINE COMBUSTION CHAMBER

Róbert-Zoltán SZÁSZ[1], Christophe DUWIG[2], László FUCHS[3]

[1] Corresponding Author. Department of Energy Sciences, LTH, Lund University. PO.Box 118, SE-22100, Lund, Sweden
Tel.: +46 46 222 3624, Fax: +46 46 222 4717, E-mail: robert-zoltan.szasz@vok.lth.se
[2] Department of Energy Sciences, LTH, Lund University. E-mail: christophe.duwig@vok.lth.se
[3] Department of Energy Sciences, LTH, Lund University. E-mail: laszlo.fuchs@vok.lth.se

ABSTRACT

The acoustic field in an annular gas turbine combustion chamber is determined using a hybrid approach. The flow solver is based on Large Eddy Simulations to account for turbulence and on a flamelet-based method to model combustion. The acoustic part solves an inhomogeneous wave equation, the acoustic sources being given by the flow solver. The flow computations focus on a single nozzle. To model the entire combustion chamber, the acoustic sources are manifold and imposed in thirty instances. Several perturbing parameters were studied. The computations revealed that time shift in the acoustic sources of consecutive nozzles has a major influence on the resulting acoustic field, space shift of the sources or counter rotation has reduced effect.

Keywords: acoustics, CFD, gas turbine, hybrid approach, LES

NOMENCLATURE

D	[m^2/s]	diffusivity
L	[m]	length scale
M	[-]	Mach number
R	[J/kg K]	gas constant
S_L	[m/s]	laminar flame speed
St	[-]	Strouhal number
T	[K]	temperature
U	[m/s]	velocity scale
Z	[-]	mixture fraction
c	[-]	progress variable
f	[1/s]	frequency
p	[Pa]	pressure
t	[s]	time
u_i	[m/s]	velocity component in direction i
Δ	[m]	filter size
Ξ	[-]	wrinkling factor
ρ	[kg/m^3]	density
ρ'	[kg/m^3]	acoustic density fluctuation

Subscripts and Superscripts

b	burned
u	unburned
~	density-weighted filtered
−	filtered

1. INTRODUCTION

Thermo-acoustic instabilities are a major concern in the development of gas turbine combustion chambers. The amplification of pressure oscillations may lead to the malfunctioning of the device, or, in the worst case, to its failure [1].

There is an intensive research focused on the active control of combustion instabilities (see e.g. Dowling and Morgans [2]), however, it is needed that the combustion instabilities are predicted as early as possible, in the best case already in the design phase. Caraeni et al. [3] developed a fast method, based on the Arnoldi algorithm to determine the resonance frequencies of a combustion chamber. More recently, Bethke et al. [4] determined the resonant frequencies using finite-element based methods.

The acoustic field can be determined by solving the compressible Navier-Stokes equations using Direct Numerical Simulations (DNS) or Large Eddy Simulations (LES) [5]. This method, however, is highly inefficient for low-Mach number flows.

An alternative approach is to use hybrid methods. For low Mach numbers one can assume that the acoustic fluctuations are small, compared to the fluid dynamic fluctuations, and the variables can be split in an incompressible part and a correction, which accounts for the compressibility effects. In this way, the compressible Navier Stokes equations are split in a set of incompressible Navier Stokes equations and a set of acoustic equations. Olbricht et al. [6] used a hybrid approach based on LES and acoustic perturbation equations for studying the noise generated by the isothermal flow in a model

gas turbine combustor. A similar approach has been used by Bui et al. [7] for the evaluation of noise emitted by a non-premixed jet flame. Using first-order approximations, the acoustic equations may be reorganized into an inhomogeneous wave equation. This hybrid approach has higher computational efficiency compared to direct methods, since the time step in the flow solver is not limited by the sound speed, but by the flow velocity. Furthermore, the solution methods for incompressible flows are more robust. Another advantage is that different grids (allowing different grid resolutions) may be used in the flow and acoustic computations. The major disadvantages of the hybrid methods is the increased complexity of maintaining two separate solvers and that they are limited to low Mach number flows.

Here, such a hybrid approach is used. The method was implemented by Mihaescu et al. [8] and successfully applied for the computation of jet noise. Recently, the method was further developed by Duwig et al. [9] to predict thermo-acoustic instabilities in a model gas turbine combustion chamber. Szasz et al. [10] applied the hybrid approach to determine the acoustic field generated by turbulence in a model annular gas turbine combustion chamber.

In this paper, the acoustic field in an annular gas turbine combustion chamber having thirty Lean Premixed Prevaporized (LPP) burners is determined. First, the flow field is determined in a region of the combustion chamber corresponding to a single burner. The flow computations are based on LES to account for turbulence and on a flamelet-based approach to model combustion [11]. Second, the acoustic field is determined for the whole combustion chamber by solving an inhomogeneous wave equation, similar to Lighthill's analogy. The source terms needed for the acoustic computations are provided by the flow solver and interpolated onto the acoustic grid in thirty instances to account for each burner. In the base case the acoustic sources are copied identically to the nozzles. This case is compared to cases where the sources are imposed in a counter-rotating manner, or where phase shifts (in space or time) are imposed for successive nozzles. The resulting acoustic field is evaluated in terms of rms acoustic density fluctuations and its frequency spectra.

2. NUMERICAL METHODS

The computations have been carried out in two steps. First, the unsteady flow field was computed for a model combustion chamber having a single nozzle. The flow solver provided the acoustic source terms needed by the acoustic solver. In the second step the acoustic sources were loaded into the acoustic solver and copied in thirty instances to simulate the presence of all nozzles.

2.1. Flow solver

The semi-compressible Navier-Stokes equations are discretized on a Cartesian staggered grid. By semi-compressibility is meant that the density is depending only on the temperature, but not on the pressure. Flame propagation is described using a progress variable, c, equation [12]:

$$\frac{\partial \overline{\rho}\widetilde{c}}{\partial t} + \nabla \cdot \left(\overline{\rho}\widetilde{u}\widetilde{c}\right) = \frac{\rho_u S_L(\widetilde{Z})\Xi\Delta}{a}\nabla^2\widetilde{c} + \rho_u S_L(\widetilde{Z})\Xi\frac{1}{\Delta}\Pi_c(\widetilde{c},a) + \frac{2}{\widetilde{Z}}\frac{\rho_u S_L(\widetilde{Z})\Xi\Delta}{a}\nabla\widetilde{c}\cdot\nabla\widetilde{Z} \qquad (1)$$

where the production term Π_c is read from a pre-computed library [11].

The mixing is obtained via the filtered mixture fraction equation:

$$\frac{\partial \overline{\rho}\widetilde{Z}}{\partial t} + \nabla \cdot \left(\overline{\rho}\widetilde{u}\widetilde{Z}\right) = \nabla\overline{\rho}D\nabla\widetilde{Z} \qquad (2)$$

The filtered density is computed from the temperature using the ideal gas law. The temperature is computed using the progress variable. That is,

$$\overline{\rho} \approx \frac{P_0}{R\widetilde{T}} \text{ with } \widetilde{T} \approx T_u(\widetilde{Z}) + (T_b(\widetilde{Z}) - T_u(\widetilde{Z}))\cdot\widetilde{c} \qquad (3)$$

The governing equations are discretized using finite differences. Third order discretization is used for the convective part and fourth order for the diffusive part. The high-order accuracy is achieved using a defect correction approach. Large Eddy Simulation (LES) is used to account for turbulent fluctuations. No explicit sub-grid scale (SGS) model is used. It is assumed that the third order upwind scheme accounts for the dissipative effect of the SGS terms. This approach has been successfully used in a wide range of applications [13-15]. The grid can be locally refined to reduce the computational requirement. 1.8 million cells were used in the flow computations, having 60 cells per premixing tube diameter.

2.2. Acoustic solver

In the acoustic solver an inhomogeneous wave equation is solved:

$$\frac{\partial^2\rho'}{\partial t^2} - \frac{1}{M^2}\frac{\partial^2\rho'}{\partial x_i \partial x_i} = \frac{\partial^2 T_{ij}}{\partial x_i \partial x_j} + \alpha\frac{\partial\omega}{\partial t} \qquad (4)$$

where the first term on the right hand side stands for the acoustic sources due to velocity variations and entropy effects:

$$T_{ij} = \rho u_i u_j + \delta_{ij}(p - 1/M^2\rho) \qquad (5)$$

The second term on the right hand side of Eq. 4 represents the sound sources generated by the unsteady heat release and is given by [9]:

$$\omega \approx Cp\left(T_b(\tilde{Z}) - T_u(\tilde{Z})\right)\rho_u S_L(\tilde{Z})\Xi\frac{1}{\Delta}\Pi_c(\tilde{c},a) \qquad (6)$$

Eq. 4 is discretized on a uniform cartesian grid (without local refinements) using finite differences. Second order central differences are used for the space derivatives. In time an explicit Lax-Wendroff type discretization is applied. The acoustic sources (Eqs. 5 and 6) are computed by the flow solver and stored in files. The sources are read in by the acoustic solver and filtered onto the acoustic grid by a Gaussian filter having the filter width of two cell sizes. Since the time step needed by the acoustic solver is shorter then the period with which the acoustic sources have been saved, the acoustic sources are obtained by linear interpolation between two successive source data sets. The acoustic sources being pre-computed, the sources imposed at different nozzles may differ, or may be differently arranged. In this way phase shifts between consecutive nozzles may be easily imposed both in space and time. A low-pass digital filter is used to avoid spurious oscillations [9]. The shape of the combustion chamber is imposed by blocking the inactive cells.

3. PROBLEM SET-UP

The geometry used in the flow computations is sketched in Figure 1. In the flow computations only a section of the annular combustion chamber corresponding to a single nozzle was considered. The geometry is composed of a premixing tube, a combustion chamber and a contraction region. The premixing tube has a conical and a cylindrical part. Since experimental measurements are available only in the cylindrical part, the cone is neglected in the flow computations (but it is accounted for in the acoustic solver). In the followings, all dimensions are normalized with the diameter of the premixing tube and x is the streamwise direction. The premixing pipe has a length of 2.7. The combustion chamber has a rectangular cross-section of 3.8×3.8 and a total length (including the converging outlet) of 8. A preheated (~700 K) methane-air mixture is burned. The overall equivalence ratio is 0.42 but a non-constant equivalence ratio profile is enforced at the inlet. The Reynolds number is 100000 and the inlet swirl number 0.52. The inlet Mach number is ~0.1. The CFL number for the flow computations was 0.2. For the flow solver zero gradient outlet conditions are imposed with flux correction. The walls are non-slip and adiabatic, no wall functions are used. At the inlet a constant velocity profile is set above which fluctuations due to the acoustic velocity fluctuations are imposed.

A 3D view of the acoustic domain is shown in Figure 2. Thirty nozzles are placed equidistantly in azimuthal direction on a circle with a radius of 12.1. The height of the combustion chamber is 3.8 while its length is 10.7. Figure 3 shows a sketch of the transversal cross section of the acoustic domain. L1...L6 denote the location of the axial lines along which data is saved for post-processing. In the followings, by "first burner" we denote the one which has the symmetry axis marked L1. In the acoustic solver reflecting boundary conditions are used everywhere, except the outlet, where non-reflecting conditions were imposed.

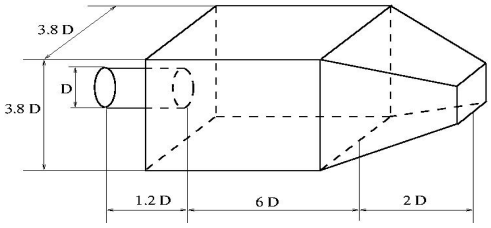

Figure 1 The geometry of the combustor

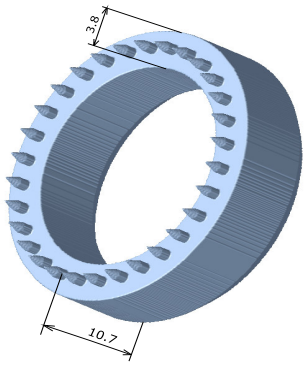

Figure 2 3D view of the acoustic domain

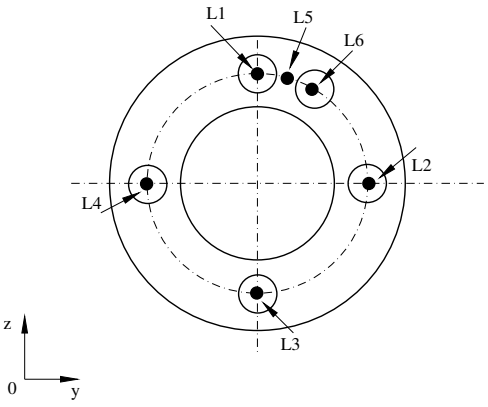

Figure 3 Sketch of the cross section of the acoustic domain. L1...6 mark the axial lines along which data is saved for post processing

4. RESULTS

The computations have been carried out in two steps. First the acoustic sources have been determined using the flow solver described in section 2.1. A qualitative picture of the acoustic source terms can be seen in the instantaneous snapshot shown in Figure 4. The source terms have been normalized with the maximum value. One can observe that the dominant acoustic sources are found in the flame region. The spectrum of the acoustic sources revealed that the lowest dominant frequency is at *St*~0.6. The Strouhal number is defined as:

$$St = \frac{f}{UL} \tag{7}$$

where f is the frequency, U the velocity scale and L the lengthscale. Here, U is the inlet velocity magnitude and L is the diameter of the premixing tube. The sources have been saved for a period covering four periods of this frequency. This data set is imposed periodically in the acoustic solver. For further details about the flow field the user is referred to Duwig et al. [9].

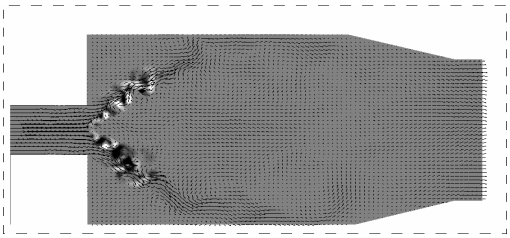

Figure 4 Instantaneous snapshot of the acoustic source terms and velocity vectors.

In the second step, the acoustic sources have been read into the acoustic solver. Altogether eight cases have been run with the acoustic solver, a summary of the cases being presented in Table 1. The grid sensitivity was evaluated by solving the acoustic field using three different grid resolutions, totally having 4.6, 15.3 and 36 million cells, respectively. To simulate counter rotating nozzles, in the fourth case, the sources have been imposed mirrored for every second nozzle. In real annular combustion chambers the flow field is not identical for each nozzle. To simulate the nonuniformity of the flowfield, perturbations have been imposed. In cases 5 and 6 the sources of consecutive nozzles were imposed with a time shift of 0.025 and 0.05, respectively. Similarly, in cases 7 and 8, the sources had an azimuthal phase shift between consecutive nozzles of 6 and 90 degrees, respectively.

In the followings the grid sensitivity study will be presented shortly, followed by a detailed description of the acoustic field for the base case (case 2). Next, the influence of the above-mentioned perturbations will be presented and discussed.

Table 1. Summary of cases

Nr.	Nr. cells [*mill.*]	Counter rot.	Time shift [*/noz.*]	Phase shift [*deg/noz.*]
1	4.6	No	0	0
2	15.3	No	0	0
3	36.0	No	0	0
4	15.3	Yes	0	0
5	15.3	No	0.025	0
6	15.3	No	0.050	0
7	15.3	No	0	6
8	15.3	No	0	90

4.1. Grid sensitivity

Three different cases have been evaluated, having totally 4.6, 15.3 and 36 million cells. The size of the cells was 0.125, 0.0917 and 0.0625 corresponding to 8, 12 and 16 cells per premixing tube diameter, respectively. Figure 5 shows the spectrum of the acoustic density fluctuation for the three considered cases at a point located on the symmetry axis of the first nozzle, immediately downstream of the premixing tube. One can observe that the low frequency fluctuations (*St*=0.15, 0.45, 0.6) are captured in all three cases, thus the lowest resolution would be enough to capture the dominant frequencies in the combustion chamber. However, high grid resolutions are desired to capture accurately the frequencies in the premixing tube. As it regards the computational cost, cases 2 and 3 require a computational time increased with 63% and 173%, respectively. Since case 3 needed almost 2 Gb memory to run, while for case 2 it was enough one Gb, case 2 was chosen as base case for further computations.

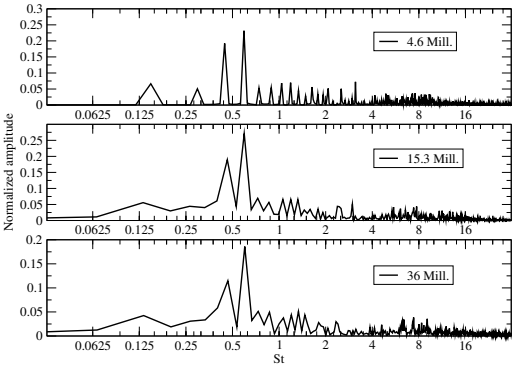

Figure 5 Acoustic pressure fluctuation spectra for three grid resolutions, at a point on line L1, *x*=3

4.2. Base case

Figure 6 presents the rms of the acoustic density fluctuation in a longitudinal cross section. The maximum acoustic sources are located in the flame region. This is where the largest acoustic fluctuations are generated. The waves are propagating downstream and reflected from the combustion chamber walls. One can observe as well that acoustic fluctuations are propagated as well upstream into the premixing tube. These fluctuations are important since they may influence the mixing process and by this may induce thermo-acoustic instabilities.

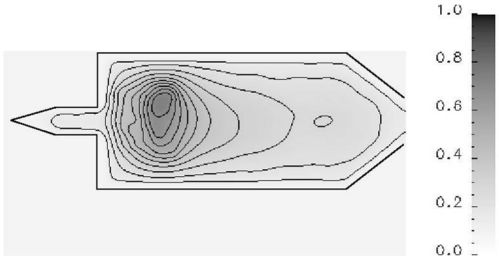

Figure 6 Normalized rms of the acoustic density fluctuation in a longitudinal cross section. The thick line denotes the contour of the combustion chamber

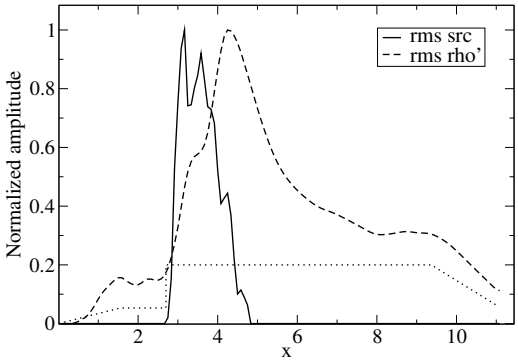

Figure 7 RMS of the acoustic source term (continuous line) and acoustic density fluctuation (dashed line) along line L1. The dotted line marks the contour of the combustion chamber.

Figure 7 shows the evolution of the rms of the acoustic source terms (continuous line) and acoustic density fluctuation (dashed line) along the symmetry axis of the first nozzle (line L1 in Figure 3). The contour of the combustion chamber is also marked with a dotted line. The amplitudes of the fluctuations were normalized with the maximum values. One can observe that the highest acoustic density fluctuations are not located exactly at the place of the largest fluctuations of the acoustic sources, but shifted approximately one length unit downstream. This shift is probably due to the proximity of the premixing tube and the back-wall.

The frequency spectra of the acoustic source term and acoustic density fluctuation at a point located on line L1 at an axial position of three diameters is displayed in Figure 8.

One can observe a peak in both the acoustic source and acoustic density fluctuation spectra at St=0.15 which corresponds to the period where the acoustic sources have been saved. Further peaks can be seen in both spectra at St=0.46, 0.6, and 1.2. A major difference is that while in the acoustic source spectra St=1.2 is dominant, in the acoustic density fluctuation spectra St=0.6 has the largest amplitude. POD analysis of the acoustic density fluctuations revealed that St=0.6 is an axial mode.

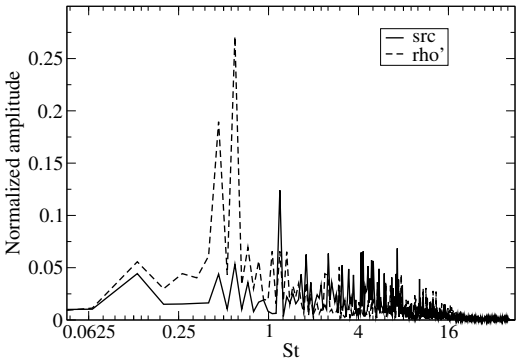

Figure 8 Frequency spectra of the acoustic source term (continuous line) and acoustic density fluctuation (dashed line) at a point on line L1, x=3D

A comparison of the acoustic density fluctuation spectra at three different axial positions is shown in Figure 9. The first point (upper graph) is located in the premixing tube; the second (middle graph) in the source region while the third one towards the outlet of the combustion chamber. In the premixing tube high-frequency (St~9) oscillations dominate. This is due to the fact that the lower frequency waves cannot enter in resonance with the premixing tube due to its reduced diameter compared to the height of the combustion chamber. Towards the outlet of the combustion chamber (lower graph) the dominant frequencies are higher than in the source region because of the interference of the reflected waves.

Figure 10 shows the isocontours of the acoustic density fluctuation in a transversal cut, located at nine diameters downstream. The field is uniform in azimuthal direction indicating the lack of low-frequency azimuthal modes. This conclusion is confirmed by Figure 11 which presents the variation of the rms acoustic density fluctuation along the lines marked L1-L6 in Figure 3. One can observe that the plots along the symmetry axes of the nozzles are practically identical, while the line located between two nozzles (L5) exhibits lower rms values in the flame region.

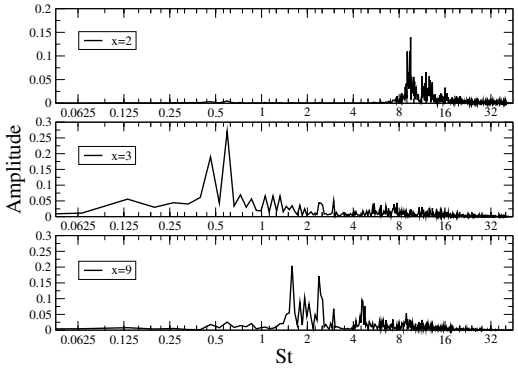

Figure 9 Frequency spectra of the acoustic density fluctuation at points on line L1, *x*=2 (up), *x*=3 (centre), *x*=9 (down)

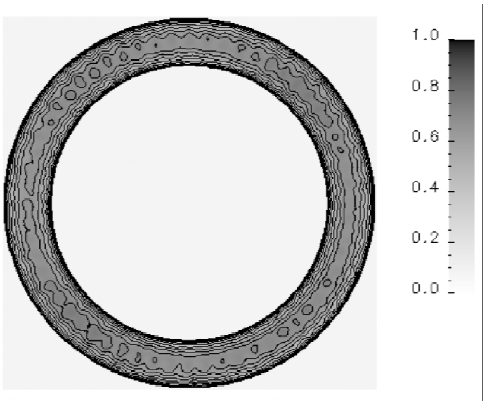

Figure 10 Normalized rms of the acoustic density fluctuation in a transversal cross section (*x*=9)

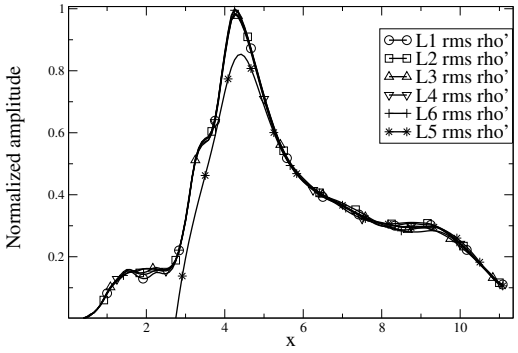

Figure 11 RMS of the acoustic density fluctuation along lines L1-L6.

4.3. Influence of counter-rotation

Counter rotating nozzles were simulated by imposing the acoustic sources in a mirrored way for every second nozzle. Of course, in the real case the flow field generated by counter rotating jets differs from the one produced by corotating jets (see e.g. [16]). Nevertheless, the approach presented here is a "low-cost" approximation.

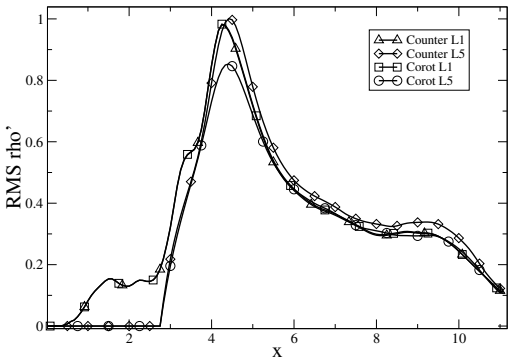

Figure 12 RMS of the acoustic density fluctuation along lines L1 and L2 for the counter- and co-rotating cases

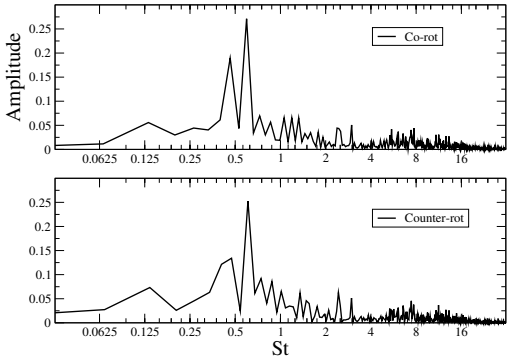

Figure 13 Acoustic density fluctuation spectra for co- (upper graph) and counter-rotating (lower graph) configurations. Monitoring point located on line L1, *x*=3.

The variation of the rms acoustic density fluctuation along two axial lines is presented in Figure 12, for the co- and counter-rotating cases. No difference can be observed along the symmetry axis of the first burner (line L1). Conversely, significant influence can be seen along the axial line located between two nozzles (L5). In the counter-rotating case higher rms values are observed than in the co-rotating case. This observation is in agreement with [10] where isothermal computations in a model annular gas turbine combustion chamber are presented. In [10] counter-rotation was accounted for already in the flow computations, thus the elevated levels of acoustic density fluctuation are not necessarily due to differences in the flow fields of the counter- and co-rotating cases.

The frequency spectra of the acoustic density fluctuation (Figure 13) at point located three diameters downstream reveal minor influences due to the counter-rotating configuration. The frequency with *St=0.46* is slightly damped. At monitoring points located further downstream (not shown) no significant differences compared to the co-rotating case.

4.4. Influence of time shift

To simulate phase shifts between nozzles two cases have been run. The acoustic sources have been shifted in time for successive nozzles with 0.25 and 0.5, respectively. Figure 14 displays the iso-contours of the rms acoustic density fluctuation in a transversal cut at *x*=9, for the case with a time shift of 0.25. It can be clearly seen that the shift causes nonuniformity in azimuthal direction. The same conclusion can be drawn looking at the axial variation of the acoustic pressure fluctuation rms, shown in Figure 15.

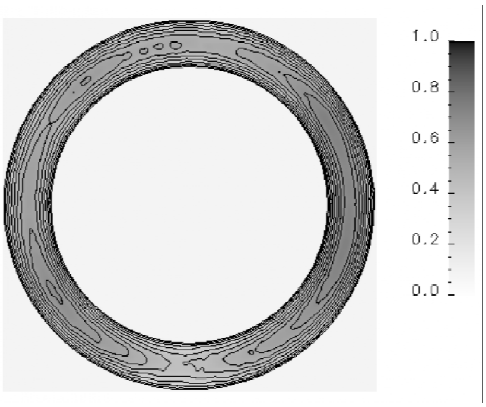

Figure 14 Normalized rms of the acoustic density fluctuation, transversal cross section, *x*=6.

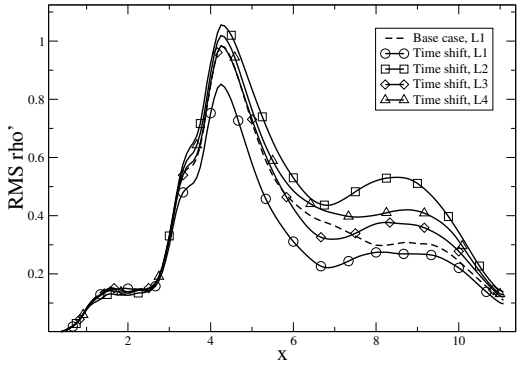

Figure 15 RMS of the acoustic density fluctuation along axial lines for the case with a time shift of 0.025/nozzle (continuous lines) and the base case (dashed line)

Figure 16 shows a comparison of the spectra of the acoustic density fluctuation at a point located on line L1 at *x*=9 for the base case (upper graph), the case with a time shift of 0.025 (centre graph) and the one with 0.5 (lower graph). One can observe that as long as the base case is dominated by frequencies of St ~ 1.6 and St ~ 2.4, the cases with time shift have the highest amplitude at St ~ 1.9. Furthermore, in these cases the *St*~4.6 component is damped as well. Closer to the inlet (not shown) the time shift has no significant influence on the frequency spectra.

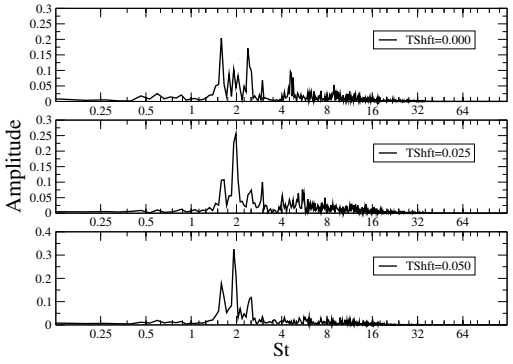

Figure 16 Frequency spectra of the acoustic density fluctuation for three cases at points situated on line L1, *x*=9

4.5. Influence of phase shift

During cases 7 and 8 the acoustic sources of successive nozzles were rotated around the symmetry axes of the burners with 6 and 90 degrees, respectively. These cases were meant to model spatial nonuniformities.

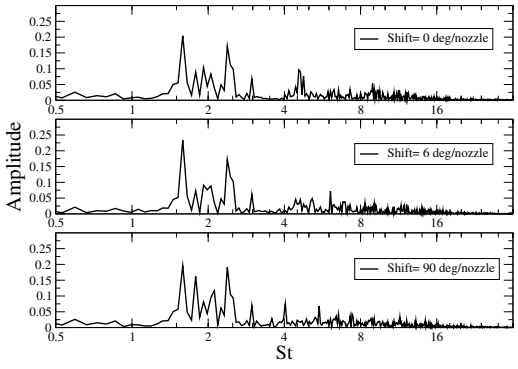

Figure 17 Frequency spectra of the acoustic density fluctuation for three cases at points situated on line L1, *x*=9

Iso-contours of the acoustic density fluctuations as well as axial plots of the acoustic density

fluctuation (not shown) revealed negligible influence of the imposed phase perturbations on the resulting acoustic fields. Neither in the frequency spectra in the source region could be seen differences. Further downstream (see Figure 17) it was found, that the perturbations did not change the low frequency part (St<4) of the spectra, but the mode with St~4.6 is damped. Furthermore, in case 8, a new dominant frequency at St~4 is generated.

5. CONCLUSIONS

The acoustic field in an annular gas turbine combustion chamber has been computed using a hybrid approach. The acoustic field was determined by solving an inhomogeneous wave equation. The acoustic sources have been computed separately in a region of the combustion chamber corresponding to a single nozzle.

The computations revealed that there are low-frequency oscillations present in the combustion chamber. Imposing the acoustic sources in a counter-rotating manner and prescribing a phase shift of successive nozzles was found to have minor effect on the resulting acoustic field. In contrast, when the acoustic sources of consecutive nozzles were shifted in time the acoustic field has been strongly influenced.

Further work is needed to identify the observed low frequency oscillations. Furthermore, the method has to be extended to allow for back-coupling of the acoustic oscillations to the flow field.

ACKNOWLEDGEMENTS

The authors would like to acknowledge the financial support of the Swedish research Council (VR). The computational time offered at the Center for Scientific and technical Computing at Lund University (LUNARC) and within the allocation program SNAC is highly appreciated.

REFERENCES

[1] Lieuwen, T., and Yang, V., 2006, "Combustion instabilities in Gas Turbine Engines: Operational Experience, Fundamental Mechanisms and Modeling", *Progress in Aeronautics and Astronautics*, Nr. 210, AIAA.

[2] Dowling, A., and Morgans, A., 2005, "Feedback control of combustion oscillations", *Annu. Rev. Fluid Mech.*, Vol. 37, pp. 151-182.

[3] Caraeni, M., Caraeni, D., Fuchs, L., 2003, "Fast algorithm to compute resonance frequencies of a combustion chamber", *AIAA paper*, 2003-3235.

[4] Bethke, S., Wever, U., Krebs, W., 2005, "Stability analysis of gas-turbine combustion chamber", *AIAA paper,* 2005-2831.

[5] Menon, S., Stone, C., Sankaran, V., Sekar, B., 2000, "Large-Eddy Simulation of Combustion in Gas Turbine Combustors", *AIAA paper*, 2000-0960.

[6] Olbricht, C., et al., 2005, "A Study of Noise Generation by Turbulent Flow Instabilities in a Gas Turbine Model Combustor", *ASME paper,* GT2005-69029.

[7] Bui, T.P., et al., 2005, "A Hybrid Method for Combustion Noise Based on LES and APE", *AIAA paper,* AIAA 2005-3014.

[8] Mihaescu, M., Szasz, R., Fuchs, L., Gutmark, E., 2005, "Numerical investigations of the acoustics of a coaxial nozzle", *AIAA paper,* 2005-0420.

[9] Duwig, C., Gherman, B., Mihaescu, M., Salewski, M., Fuchs, L., 2005, "Numerical study of thermo-acoustic waves generation by a swirling flame using a new approach based on Large Eddy Simulation", *ASME paper*, GT2005-68136.

[10] Szasz, R. Z., Mihaescu, M., Fuchs, L., 2006, "Computation of the acoustic field in an annular gas turbine combustion chamber using a hybrid approach", *ASME paper*, GT2006-90024.

[11] Duwig, C., and Fuchs, L., 2005, "Study of flame stabilization in a swirling combustor using a new flamelet formulation", *Combust. Sci. Technol.*, Vol. 177, Nr. 8, pp. 1485-1510.

[12] Duwig, C., and Fuchs, L., 2004, "Study of a gas turbine combustion chamber: influence of the mixing on the flame dynamics", *ASME paper,* GT2004-53276.

[13] Fureby, C. and Grinstein, F.F., 2002, "Large Eddy Simulation of High Reynolds-Number Free and Wall-Bounded Flows", *J. Comput. Phys.,* Vol. 181, pp. 68-97.

[14] Garnier, P. et al., 1999, "On the use of shock-capturing schemes for Large Eddy Simulations", *J. Comput. Phys.,* Vol. 153, pp. 273-311.

[15] Mary, I., 2003, "Large Eddy Simulation of vortex breakdown behind a delta wing", *Int. J. Heat and Fluid Flow,* Vol. 24, pp. 596-605.

[16] Szasz, R. Z., and Fuchs, L., 2003, "Numerical modeling of flow and mixing of single and interacting swirling coannular jets", Proc. *of Third International Symposium on Turbulence and Shear Flow Phenomena*, Kasagi, N., Eaton, J., Friedrich, R., Humphrey, J., Leschziner, M., and Miyauchi, T., (eds.), Vol.2, pp.663-668.

Conference on Modelling Fluid Flow (CMFF'06)
The 13th International Conference on Fluid Flow Technologies
Budapest, Hungary, September 6-9, 2006

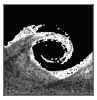

A MODULAR APPROACH FOR TIME DOMAIN MODELLING OF COMPLEX (THERMO-) ACOUSTIC SYSTEMS

Mirko R. BOTHIEN[1], Jonas P. MOECK[2], Christian Oliver PASCHEREIT[3]

Institut für Strömungsmechanik und Technische Akustik (Hermann-Föttinger-Institut), Technical University Berlin.
Müller-Breslau-Straße 8, 10623 Berlin, Germany.
[1] Corresponding Author. Tel.: +49 30 314 23111, Fax: +49 30 314 21101, E-mail: mirko.bothien@tu-berlin.de
[2] Email: jonas.moeck@pi.tu-berlin.de
[3] Email: oliver.paschereit@tu-berlin.de

ABSTRACT

A methodology allowing for a modular setup of complex acoustic systems is developed, where the transfer behaviour of the individual subsystems is formulated in time domain. Subsystem descriptions can be obtained by analytical considerations, numerical methods, or experimental data. Once the complex subsystems have been characterised experimentally, changes in system geometry can be implemented easily. To validate the modelling approach, experiments are conducted in an acoustic test rig with a combustor-type geometry. Results are compared to predictions from the model, demonstrating accuracy in frequency and time domain. Application to thermoacoustic instabilities arising in lean premixed combustion is given. Thereby, an additional advantage of the state-space approach becomes clear: stability of a thermoacoustic system can be determined by simply solving a matrix eigenvalue problem. This is in strong contrast to the traditional approach, where the complete model is formulated in frequency domain with infinite-dimensional transfer functions.

Keywords: stability analysis, state-space system, thermoacoustic instabilities, time domain

NOMENCLATURE

A, B, C, D	[-]	state-space matrices
M	[-]	Mach number
R	[-]	reflection coefficient
S	[-]	scattering matrix
T	[-]	transfer matrix
T	[K]	temperature
U	[V]	loudspeaker voltage
Z	[-]	specific impedance
c	[m/s]	speed of sound
f	[m/s]	downstream travelling wave
f	[Hz]	frequency
g	[m/s]	upstream travelling wave
k	[1/m]	wave number
p	[m/s]	acoustic pressure scaled with ρc
r	[m]	radius
s	[-]	eigenvalue
t	[s]	time
u_0	[m/s]	mean flow velocity
u	[m/s]	acoustic velocity
x	[m]	spatial coordinate
x	[-]	state vector
α	[-]	area ratio
ρ	[kg/m^3]	density
σ	[s]	time-delay variance
τ	[s]	mean time-delay
ω	[1/s]	circular frequency
ζ	[-]	loss coefficient

Subscripts and Superscripts

c	cold
d	downstream
eff	effective
h	hot
u	upstream
+	pseudo-inverse
˙	derivative with respect to time

1. INTRODUCTION

As emission levels of modern gas turbines become more and more restrictive, the combustion process stays abreast of changes by application of lean-premixed combustion. The leaner a combustion system operates the more it is prone to suddenly occurring large pressure oscillations. These thermoacoustic instabilities arise from the interaction of unsteady heat release and the acoustic field in the engine. If the two mechanisms constructively interfere with each other, high amplitude pressure pulsations occur, which have a detrimental effect on the combustion process. Emissions of pollutants (NO_x and CO) rise, system performance of the gas turbine decreases and the

high pressure fluctuations can even cause structural failure [1-3].

To prevent unreliable and unsafe operation, it is necessary to describe the system's acoustic behaviour. A model of the acoustic properties supplemented by information on the flame response allows for predicting and control of combustion instabilities. Due to the high complexity of geometry and interaction mechanisms in full-scale technical systems, a comprehensive description of their acoustic field is very cumbersome [2]. Therefore, the total system is subdivided into different subsystems. Linking together these subsystems results in a representation of the acoustic properties of the total system.

2. STATE-SPACE REPRESENTATION OF ACOUSTIC SUBSYSTEMS

As in the frequency domain transfer matrix approach [4], it is assumed that only plane waves propagate between two subsystems. This assumption is valid for elements that are coupled via ducts for which the frequencies considered are below the cut-on frequency for the first non-planar mode. Neglecting entropy waves, this gives two degrees of freedom for all coupling planes. The variables accounting for that can be either acoustic pressure p and velocity u or the Riemann invariants of the plane wave field, denoted here with f and g for downstream and upstream travelling waves, respectively. The primitive variables are related to the Riemann invariants by $p = f + g$ and $u = f - g$. Here (as in the following), the acoustic pressure has been scaled with the characteristic impedance ρc.

Subsequently, acoustic systems are characterised using the scattering form, i.e. the f-wave upstream and the g-wave downstream are treated as inputs and, accordingly, the f-wave downstream and the g-wave upstream are obtained as outputs. The generic acoustic element in state-space form can then be written as

$$\begin{aligned} \dot{x} &= Ax + B\begin{bmatrix} f_\mathrm{u} \\ g_\mathrm{d} \end{bmatrix}, \\ \begin{bmatrix} f_\mathrm{d} \\ g_\mathrm{u} \end{bmatrix} &= Cx + D\begin{bmatrix} f_\mathrm{u} \\ g_\mathrm{d} \end{bmatrix}, \end{aligned} \qquad (1)$$

where subscripts u and d denote upstream and downstream positions. A, B, C and D are time-invariant $N\times N$, $N\times 2$, $2\times N$ and 2×2 matrices, respectively, and x is the N-dimensional state vector. The dimension of the state depends on the acoustic subsystem to be characterised and has to be chosen sufficiently large so that the system's frequency response is represented with acceptable accuracy in the frequency range considered.

An inlet or exit boundary condition can be written similar to Eq. (1) as a single input single output (SISO) system.

3. SUBSYSTEM CHARACTERISATION

The modular setup allows for different ways of describing the subsystems, i.e. by analytical considerations, experimental data or numerical methods (e.g. using the Finite Element Method [5]). The subsystems' transfer functions relate the incoming and outgoing acoustic waves.

Figure 1. Acoustic subsystem relating up- and downstream travelling plane waves

In the frequency domain the relation of the Riemann invariants (Fig. 1) is given by the scattering matrix S:

$$\begin{bmatrix} f_\mathrm{d} \\ g_\mathrm{u} \end{bmatrix} = \begin{bmatrix} S_{11} & S_{12} \\ S_{21} & S_{22} \end{bmatrix} \begin{bmatrix} f_\mathrm{u} \\ g_\mathrm{d} \end{bmatrix} \qquad (2)$$

3.1. Analytical description

The description of elements with simple geometries (e.g. ducts) is straightforward. Neglecting sound absorption at the walls and in the fluid, a duct only represents a time-delay ($e^{-i\omega\tau}$) in the system. That is, an acoustic wave is transmitted with a delay time, depending on the elements length and the speed of sound.

Unlike systems, which do not contain time-delays, it is not possible to exactly describe a system with time-delay with a rational transfer function. Therefore, it has to be approximated, e.g. with a Padé approximation of the exponential function. The order of the Padé approximation, which is necessary for a sufficient accuracy, depends on the desired frequency range (100 Hz – 1000 Hz) and the delay time. A duct with a length of 0.5 m at ambient conditions requires an order of 8 in the frequency band mentioned above.

3.2. Experimental description

Transfer functions of more complex subsystems can be determined empirically. For this purpose, the element is regarded as a black box for which the four unknown elements of the scattering matrix (cf. to Eq.(2)) have to be determined. This procedure has been applied previously [3, 6, 7] and thus only a short description is presented her.

The system of Eq. (2) consists of two equations. Thus, two linearly independent states are necessary to solve for the four unknowns S_{ij}. The test states

are created by successive excitation on both sides of the element.

To obtain the Riemann invariants from sound pressure measurements at least two microphones at two different axial locations in a duct are necessary. In the presence of measurement uncertainty, better results are obtained by acquiring the pressure at more (n) positions. Having data of more than two microphones, the problem is over-determined. This approach is called the Multi-Microphone Method (MMM) [6]. The up- and downstream travelling waves are fitted to the measured quantities by means of the least squares method:

$$\begin{bmatrix} f \\ g \end{bmatrix} = Z^{+} \begin{bmatrix} p_1 \\ \vdots \\ p_n \end{bmatrix}, \tag{3}$$

where Z is given by

$$Z = \begin{bmatrix} e^{-i\omega \frac{x_1}{c+u_0}} & e^{i\omega \frac{x_1}{c-u_0}} \\ \vdots & \vdots \\ e^{-i\omega \frac{x_n}{c+u_0}} & e^{i\omega \frac{x_n}{c-u_0}} \end{bmatrix}. \tag{4}$$

Here, x_i is the distance of the microphone i to the location where f and g are determined. Z^{+} denotes the pseudo inverse of Z:

$$Z^{+} = (Z^{T} Z)^{-1} Z^{T} \tag{5}$$

4. EXPERIMENTAL VALIDATION OF THE STATE-SPACE APPROACH

4.1. Experimental set-up

The network approach based on state-space models described in the preceding chapter was validated at an acoustic test rig in an anechoic chamber. Figure 2 shows a schematic overview of the experimental facility.

The model for the test rig is split up into subsystems, whose scattering matrices were determined experimentally (burner, up- and downstream end) and analytically (ducts). By interconnecting the subsystems, the acoustic field of the test rig can be predicted.

The up- and downstream ends are equipped with circumferentially mounted loudspeakers, which allow for acoustic excitation of the rig. With these loudspeakers, it is possible to adjust the linearly independent test states that are necessary to experimentally obtain a system's scattering matrix. For determination of the acoustic field, the test rig's duct sections are instrumented with ¼" Brüel & Kjær condenser microphones. There are three microphones upstream of the burner element and four downstream of it, thus, allowing for the application of the MMM.

4.2. Set-up of the simulation model

4.2.1. Loudspeaker elements

The speaker elements' transfer functions were determined experimentally. The elements have two inputs and one output. In the case of the upstream element, the g-wave and the loudspeaker voltage U_1 are the inputs while the f-wave represents the output. This can be written as

$$f = Rg + GU_1, \tag{6}$$

where R is the reflection coefficient and G is the transfer function of the loudspeaker's controlling input voltage to the outgoing f-wave. Eq. (6) implies the assumption that the contribution of the reflection coefficient and the loudspeaker transfer function can be linearly superimposed. Results shown in Section 4.2.4. confirm the validity of this assumption.

Similar to the approach described previously, two excitation states have to be generated. This is achieved using loudspeaker excitation at each side separately. Downstream excitation (index A) yields

$$f_A = Rg_A \tag{7}$$

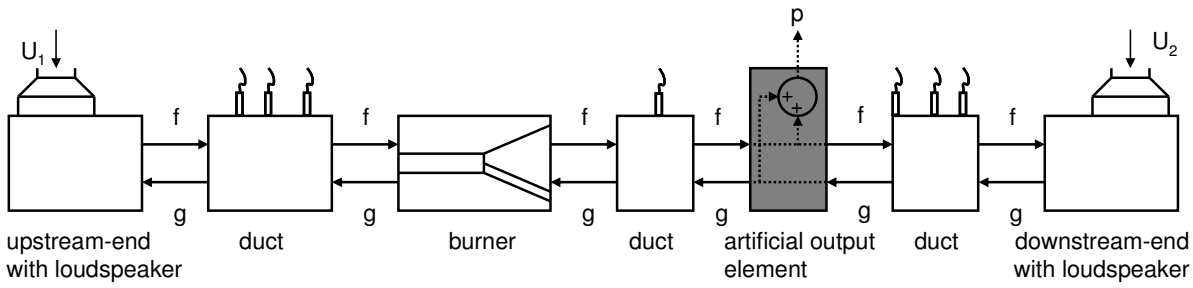

Figure 2. Schematic overview of the acoustic test rig splitted up into its subsystems

from Eq. (6) as U_1 is zero. This allows for direct calculation of the reflection coefficient R. Excitation with the upstream loudspeaker (index B) and solving for G gives

$$G = \frac{f_B - R g_B}{U_1}, \tag{8}$$

where R is calculated from Eq. (7).

With complex values for R and G calculated at discrete frequencies, frequency domain system identification algorithms [8,9] were used to obtain state-space models. Figures 3 and 4 depict gain and phase of R and G. They show results for measured data as well as for models identified with 30 states and 15 states.

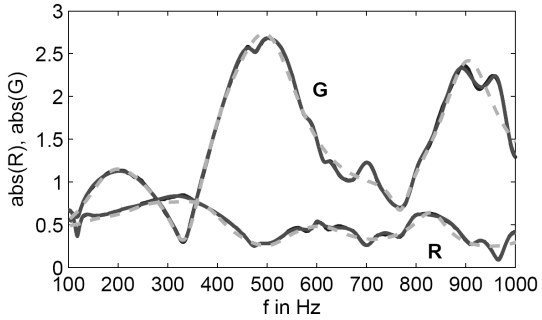

Figure 3. Absolute value of G and R for measured values (black), model with 30 states (grey) and model with 15 states (dashed)

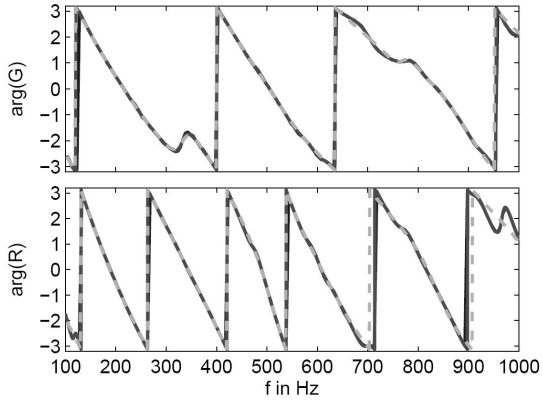

Figure 4. Phase of G (top) and R (bottom) for measured values (black), model with 30 states (grey) and model with 15 states (dashed)

As can be seen in Figs. 3 and 4 measured and modelled curves for gain and phase of the reflection coefficient R modelled with 30 states match almost perfectly. In the frequency regime above 700 Hz, the model obtained with 15 states shows minor deviations. In the case of the loudspeaker's transfer function G, excellent results are obtained with 30 states. With 15 states, the results are fair except for some frequency bands, in which G has several local extremal values. Regarding the phase, both models agree very well to the measured values. The larger slope of R, i.e. the larger time delay, is due to the position of the loudspeaker. The incident wave travels to the upstream element's end and back to the reference plane whereas the emitted wave of the loudspeaker has to travel a much shorter distance.

Up to this point, only two SISO state-space systems exist. These have to be concatenated to a double input single output (DISO) state-space system of the upstream end:

$$\begin{aligned} \dot{x} &= \begin{bmatrix} A_\mathrm{R} & 0 \\ 0 & A_\mathrm{G} \end{bmatrix} x + \begin{bmatrix} B_\mathrm{R} & 0 \\ 0 & B_\mathrm{G} \end{bmatrix} \begin{bmatrix} g \\ U_1 \end{bmatrix}, \\ f &= \begin{bmatrix} C_\mathrm{R} & C_\mathrm{G} \end{bmatrix} x + \begin{bmatrix} D_\mathrm{R} & D_\mathrm{G} \end{bmatrix} \begin{bmatrix} g \\ U_1 \end{bmatrix}, \end{aligned} \tag{9}$$

where indices R and G denote the matrices of the reflection coefficient's and the loudspeaker's state-space systems, respectively.

4.2.3. Artificial output element

The grey highlighted element in Fig. 2, is not part of the real system but only an artificial part of the model system. Through this, it is possible to read out the signal of any microphone by placing the artificial output element at the position of the desired microphone. The element is modelled in state-space as a static gain without additional dynamics:

$$\begin{bmatrix} f_\mathrm{d} \\ g_\mathrm{u} \\ p \end{bmatrix} = \begin{bmatrix} 1 & 0 \\ 0 & 1 \\ 1 & 1 \end{bmatrix} \begin{bmatrix} f_\mathrm{u} \\ g_\mathrm{d} \end{bmatrix} \tag{10}$$

Besides the D matrix, all other matrices of the state-space system (A, B, C) are empty. The output element has a physical length of zero. The up- and downstream travelling waves are neither delayed nor changed in amplitude and therefore, the output element does not influence the acoustic behaviour of the total system.

4.2.4. Interconnected complete system

The outputs of each subsystem have to be connected with the inputs of its adjacent subsystems. Linking together the subsystems' state-space representations, results in one single state-space description of the complete system. Interconnection of the several state-space systems can be done with MATLAB routines.

From the subsystems' interconnection a system order of 200 arose. To reduce the order of the complete system, model reduction techniques were used, allowing the elimination of all states with

negligible influence on the input-output behaviour. Through this, the model's order was reduced to 60 states exhibiting only a slight difference in frequency response compared to the initial system.

Figures 5 and 6 depict the transfer function of the input voltage of the upstream loudspeaker U_1 to the second microphone downstream of the burner for the reduced order system. This is the position where the artificial output element is located in the simulation model.

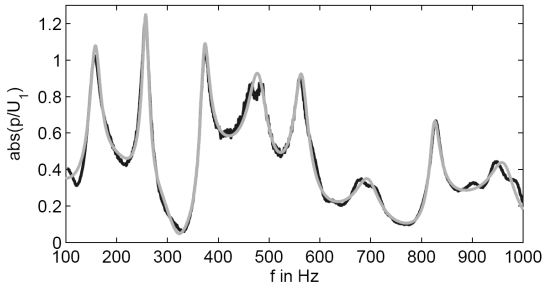

Figure 5. Absolute value of transfer function of input voltage U_1 (upstream loudspeaker) to sound pressure at position of output element; measured (black), interconnected model (grey)

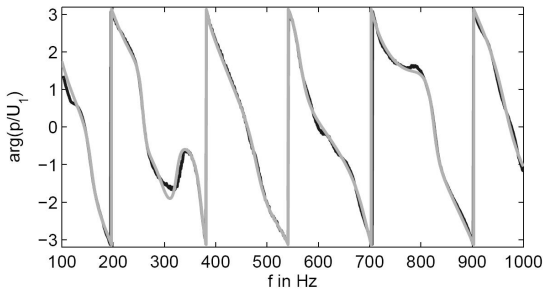

Figure 6. Phase of transfer function of input voltage U_1 (upstream loudspeaker) to sound pressure at position of output element; measured (black), interconnected model (grey)

Note that the grey curves in Figs. 5 and 6 show gain and phase of the transfer function obtained from the interconnection of the subsystems' state-space representations. That is, the individual state-space formulations of the 7 subsystems (up- and downstream end, burner element, ducts and output element) were linked to one state-space system.

Only for frequencies below 150 Hz, around 470 Hz and above 900 Hz, a slight deviation in magnitude is observed. Regarding the phase, results are even better, only showing an observable deviation at 300 Hz.

It is important to note here, that the modelled frequency response shown in Figs. 5 and 6 was not simply identified from the experimental data but was predicted based on the individual subsystem models.

4.3. Results of time domain simulation

The interconnected state-space model of the complete system – reduced to 60 states – was used to simulate the pressure fluctuations at the defined microphone position. For this purpose, the upstream loudspeaker was driven with a signal, which consisted of three sines all the same in amplitude with arbitrary frequencies set to 203 Hz, 440 Hz and 580 Hz. White noise, band-pass filtered between 100 Hz and 600 Hz, superimposed these sines.

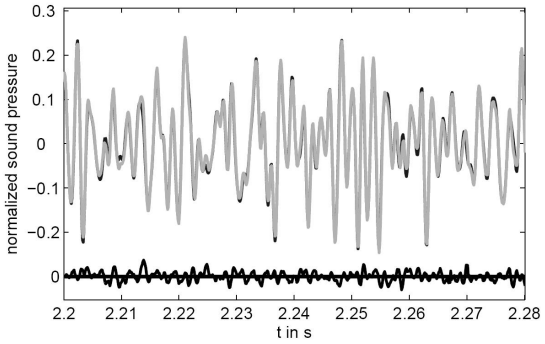

Figure 7. Normalised sound pressure amplitude for measured (black) and predicted (grey) data and their deviation

Time responses of measured and predicted pressure fluctuations are shown in Fig. 7. Both signals show nearly perfect correspondence in phase and in amplitude. For clarity, their difference is also plotted (on the same scale).

A comparison of measured and predicted data obtained with downstream excitation or excitation on both sides exhibited comparably good results.

5. APPLICATION TO THERMO-ACOUSTIC STABILITY ANALYSIS

5.1. Stability of thermoacoustic systems

To assess the linear stability of a thermoacoustic system, the procedure most commonly used is the following [10,11]:

1. the system is divided into different elements (duct, burner, etc.)
2. transfer matrices for the individual elements are set up in frequency domain
3. all transfer matrices are assembled in a system matrix accounting for proper matching conditions
4. the system's dispersion relation det(system matrix) = 0 is solved to obtain the system eigenvalues
5. eigenvalues with negative imaginary parts indicate instability (time dependence $\sim e^{i\omega t}$), the corresponding real parts frequency of the growing oscillation.

Concerning this procedure, some remarks should be made. In 2, the transfer matrices are in general of a non-rational form, since the acoustic wave propagation is governed by a partial differential equation. Also, solving det(system matrix) = 0 will be only possible, if all transfer matrices are available in analytical form. Except for academic examples this will not be the case. At least some elements will have to be determined from CFD or FEM computations or experimentally. However, even if closed-form expressions would be available for all transfer matrices involved, solving for the system's eigenvalues can be quite cumbersome, since the dispersion relation is in general a complex transcendental equation, rapidly increasing in length with network size.

The stability analysis based on a state-space description follows a procedure similar to the one given above for the traditional frequency domain approach. Connecting all subsystems results in a state-space system that represents the dynamics of the complete system. To assess stability, the temporal evolution of free oscillations has to be considered so that no inputs or outputs are present. Therefore, only the dynamics matrix A remains for the total system. Similar to the roots of the transcendental dispersion relation in the traditional approach, the eigenvalues of the A matrix, s (say), govern the stability of the system. $\mathrm{Re}(s) > 0$ indicates an unstable mode with frequency $|\mathrm{Im}(s)|/2\pi$. From a numerical point of view, determining system stability from the state-space approach is straightforward, since calculating the eigenvalues from a given A matrix can be performed with standard linear algebra routines. In contrast to that, solving the transcendental dispersion relations resulting from frequency domain representations of thermoacoustic systems is usually not a trivial task even for networks of medium complexity. These dispersion relations generally have an infinite number of solutions with only those in the low-frequency regime being of physical relevance. Evidently, the state-space approach can only provide a finite number of eigenvalues equal to the dimension of A. This is due to the fact that the infinite-dimensional system has been reduced to a finite-dimensional state-space. In practice, however, the analysis will be limited to the low frequency regime. One reason for that is that thermoacoustic instabilities usually appear in the form of low frequency oscillations. In addition to that, the network approach based on plane wave matching is only valid for frequencies below the cut-on frequency for the first non-planar mode.

5.2. A thermoacoustic model system

To assess feasibility of the state-space approach with regard to linear stability analysis, the stability of a thermoacoustic model system is investigated. In order to consider the accuracy of the state-space approach the results have to be compared to a corresponding frequency domain calculation and therefore, only elements with fully analytic description are chosen.

The model system is shown in Fig. 8 and comprises the following subsystems:

1. constant inlet impedance
2. uniform duct
3. L-ζ model for burner and area expansion
4. distributed time-lag model for the flame with variable mean time-delay and variable variance
5. uniform duct
6. Levine-Schwinger outlet impedance

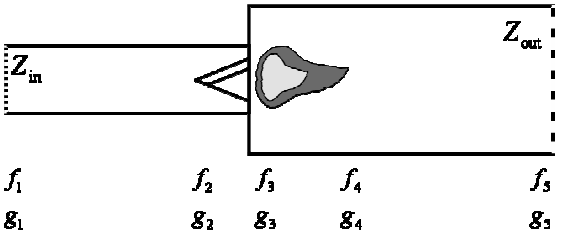

Figure 8. Model system for stability analysis

For the inlet impedance a value of $Z_{in} = 9$ is chosen corresponding to a partially reflecting boundary with a reflection coefficient of 0.8. The duct connecting the inlet and the burner has a length of $L_c = 0.95$ m, a temperature of $T_c = 523$ K and carries a mean flow with velocity $u_0 = 10$ m/s. The burner is represented by the L-ζ model (cf. to [3]) for a compact element with transfer matrix

$$T = \begin{bmatrix} 1 & -\mathrm{i}kL_{\mathrm{eff}} - \zeta M \\ 0 & \alpha \end{bmatrix}. \qquad (11)$$

L_{eff} is the effective length of burner and area expansion and has a value of 0.13 m. ζ is the loss coefficient with a value of 5 and k denotes the wave number of the plane wave field. The change in cross-sectional area is given by $\alpha = 0.3025$. It can be noted here, that the upper right transfer function is improper and therefore cannot be given in state-space form. However, the scattering form of the L-ζ model has a fully proper representation.

For the flame a time-lag model with a Gaussian distribution of time-delays [12] was chosen. In this case, the transfer function coupling the velocities across the flame is written as

$$T_{22} = 1 + \left(\frac{T_h}{T_c} - 1 \right) \mathrm{e}^{-\mathrm{i}\omega\tau} \mathrm{e}^{-\frac{1}{2}\sigma^2\omega^2}, \qquad (12)$$

where τ and σ denote mean and variance of the time-delay distribution.

The duct coupling the flame with the outlet boundary condition is assigned a length of $L_h = 1.3$ m and a temperature of $T_h = 1573$ K. The outlet is modelled as a long wave Levine-Schwinger exit condition [13] where the (specific) impedance is given by

$$Z_{out} = \tfrac{1}{4}(kr)^2 + \mathrm{i}0.6133kr, \qquad (13)$$

where $r = 0.1$ m is the outlet duct radius. The reflection coefficient is related to the impedance through the bilinear transform $R = (Z\text{-}1)/(Z\text{+}1)$. Thus, the condition relating f and g at the boundary is a proper transfer function and can be converted to a state-space realisation.

The ducts are assumed to support undamped acoustic wave propagation. As in Sec. 3.1, a state-space model of the ducts is obtained using Padé approximations.

To obtain stability characteristics, the procedure outlined in Section 5.2. is followed. The roots of the dispersion relation are determined with an iterative solver working on a uniformly distributed random field of initial guesses in the complex ω-plane. The search was restricted to a rectangular domain with $|\mathrm{Re}(\omega)|/2\pi < 1000$ 1/s and $|\mathrm{Im}(\omega)| < 450$ 1/s. As mentioned before, practical relevance justifies the restriction to the low frequency regime. Also, highly damped modes (those with large $\mathrm{Im}(\omega)$) are not of interest and highly unstable ones are usually considered unphysical.

Figure 9 shows the complex eigenfrequencies of the model system in the specified interval for two sets of flame model parameters (σ variable, τ = 7 ms) computed from frequency domain and state-space approach (see Figure caption). The solid lines indicate the domain boundaries in frequency. It can be clearly seen that the frequency domain and the state-space calculations give identical results for both parameter combinations.

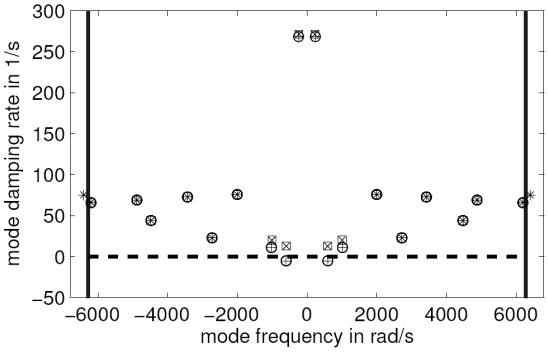

Figure 9. Eigenvalues from frequency domain and state-space computation;
○, □: freq. domain $\sigma_{○}$= 2 ms, $\sigma_{□}$= 2.5 ms
+, ×: state-space σ_{+}= 2 ms, $\sigma_{×}$= 2.5 ms

In Fig. 9 it can further be observed how a slight increase in the variance of the time-delay distribution can lead to a stabilisation of the system. For $\sigma = 2$ ms a low frequency mode of about 100 Hz has a negative damping rate and is therefore linearly unstable. For a 25 % higher variance, the unstable mode and the least stable mode are shifted to higher damping rates resulting in a stable system. Note also, how only the lowest frequency modes are affected by a change in the time-delay variance.

Having shown that the stability analysis based on the state-space model accurately reproduces the results from the traditional frequency domain approach, this method can be used to investigate the influence of the flame model parameters in more detail.

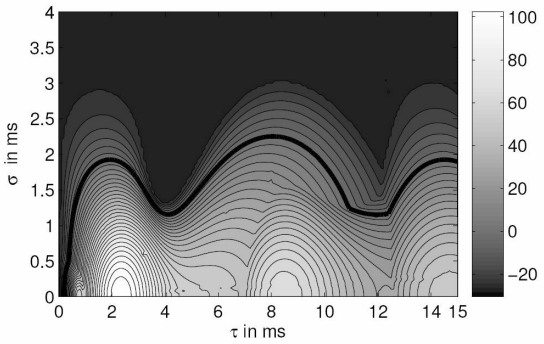

Figure 10. Growth rate in 1/s of the least stable mode as a function of time-delay mean τ and variance σ (see Eq. (12))

Figure 10 illustrates the dependence of system stability on the flame model parameters as obtained from state-space description. The greyscale coding indicates the growth rate of the least stable mode. The solid black line in the plot denotes the stability border. The highest growth rate can be found for a fully concentrated ($\sigma = 0$) time-delay of about 2.5 ms. For this case, two more local maxima in growth rate can be identified at $\tau = 8.5$ ms and $\tau = 14.5$ ms. An increase in time-delay variance has a purely stabilising effect. For a fixed mean time-delay, the growth rate of the most unstable mode decreases monotonically with variance. In fact, for $\sigma > 2.25$ ms all modes are stable. The stabilizing effect of the time-delay variance was already noted by Polifke et. al. [14]

Figure 11 shows a contour plot of the frequency of the least stable mode as a function of time-delay mean and variance. The stability border is added again as a thick black solid line.

In the unstable region, low frequency modes in the range of 75 - 175 Hz are dominant. For certain values of τ and σ isocontours of the dominant mode's frequency meet, indicating that there are at least two unstable eigenvalues. Note that lines of constant mode frequency have an essentially vertical trend. This corresponds to the fact that the

frequency of the least stable mode does not change considerably with time-delay variance [14].

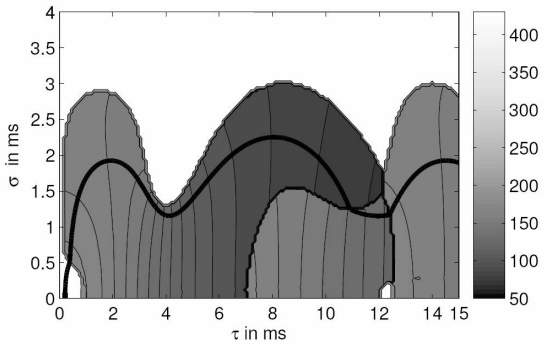

Figure 11. Frequency in Hz of the least stable mode as a function of time-delay mean τ and variance σ (see Eq. (12))

With respect to computing time, the stability analysis based on state-space models was recognized to be clearly more efficient than the frequency domain approach. Additionally, using the latter for parametric studies is not straightforward, since for all sets of parameters all roots of the dispersion relation in the domain considered must be located. This can be only ensured if a high number of initial guesses for the iterative solver is chosen. This, however, results in a considerably higher computing time.

6. SUMMARY

The acoustic properties of a complex (thermo-) acoustic system were described by splitting it up into several subsystems and generating a network model out of these. Based on this approach, the acoustic field of a test rig was simulated by setting up a state-space model of the total system.

The test rig's acoustic field, which resulted from loudspeaker excitation, was compared to the time response of the model charged with the same input signal. An excellent agreement was attained.

Additionally, application to stability analysis of thermoacoustic systems was examined. Results were compared to a standard frequency domain analysis of the same system, which is comparatively much more complex and time-consuming. Exactly the same results were obtained with a fraction of computational effort compared to that of the standard procedure.

REFERENCES

[1] Lieuwen, T. C., Yang, V., (eds.), 2005, *Combustion Instabilities in Gas Turbine Engines*, AIAA, Inc.

[2] Schuermans, B., Bellucci, V., Paschereit, C. O., 2003, "Thermoacoustic Modeling and Control of Multi Burner Combustion Systems", *ASME* paper 2003-GT-38688

[3] Schuermans, B. B. H., Polifke, W. Paschereit, C. O., 1999, "Modeling Transfer Matrices of Premixed Flames and Comparison with Experimental Results", *ASME* paper 1999-GT-0132

[4] Munjal, M. L., 1976, *Acoustics of Ducts and Mufflers*, Wiley & Sons, Inc.

[5] Peat, K. S., 1982, "Evaluation of Four-Pole Parameters for Ducts with Flow by the Finite Element Method", *J. Sound and Vibration*, **84**(3), pp. 389-395

[6] Paschereit, C. O., Schuermans, B., Polifke, W., Mattson, O., 2002, "Measurement of Transfer Matrices and Source Terms of Premixed Flames", *ASME J. Eng. Gas Turbines and Power*, **124**, pp. 239-247

[7] Åbom, M., 1992, "A Note on the Experimental Determination of Acoustical Two-Port Matrices", *J. Sound and Vibration*, **155**(1), pp. 185-188

[8] Gustavsen, B., Semlyen, A., 1999, "Rational Approximation of Frequency Domain Responses by Vector Fitting", *IEEE Transactions on Power Delivery,* **14**(3), pp. 1052-1061

[9] Kollár, I., Pintelon, R., Schoukens, J., 1997, „Frequency Domain System Identification Toolbox for Matlab: Improvements and New Possibilities", Proc. *of the XI. IFAC/IFORS International Symposium on System Identification and Parameter Estimation*, Fukuoka, pp. 991-994

[10] Sattelmayer, T., Polifke, W., 2003, "Assessment of Methods for the Computation of the Linear Stability of Combustors", *Combustion Science and Technology*, **175**, pp. 453-476

[11] Sattelmayer, T., Polifke, W., 2003, "A Novel Method for the Computation of the Linear Stability of Combustors", *Combustion Science and Technology*, **175**, pp. 477-497

[12] Schuermans, B., Bellucci, V., Guethe, F., Meili, F., Flohr, P., Paschereit, C. O., 2004, "A Detailed Analysis of Thermoacoustic Interaction Mechanisms in a Turbulent Premixed Flame", *ASME* paper 2003-GT-53831

[13] Levine, H., Schwinger, J., 1948, "On the Radiation of Sound from an Unflanged Circular Pipe", *Physical Review*, **73**(4), pp. 383-406

[14] Polifke, W., Kopitz, J. Serbanovic, A.., 2001, "Impact of the Fuel Time Lag Distribution in Elliptical Premix Nozzles on Combustion Stability", AIAA paper 2001-2104

Fluid Power

Conference on Modelling Fluid Flow (CMFF'06)
The 13th International Conference on Fluid Flow Technologies
Budapest, Hungary, September 6-9, 2006

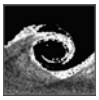

DOWNSIZED ENGINE TORQUE LAG COMPENSATION BY PNEUMATIC HYBRIDIZATION

Iulian VASILE[1], Pascal HIGELIN[1], Alain CHARLET[1], Yann CHAMAILLARD[1]

[1] Ecole Polytechnique de l'Université d'Orléans, Laboratoire de Mécanique et d'Energétique,
8, rue Léonard de Vinci, 45072 Orléans cedex 2
E-mails: iulian.vasile@univ-orleans.fr, pascal.higelin@univ-orleans.fr, alain.charlet@univ-orleans.fr, yann.chamaillard@univ-orleans.fr

ABSTRACT

One of the most promising ways to improve the global efficiency of SI engines is the concept of "downsizing". The principle of the downsizing concept consists in the reducing the size of the engine running on the highest efficiency to maximize global efficiency (minimize consumption) while keeping the maximum torque constant. To maintain the level of torque, the engine is supercharged with a turbocharger, which usually causes an unacceptable lag during torque transients.

A new pneumatic hybridization concept which uses air from a high pressure tank to supercharge a conventional internal combustion engine is proposed. This concept allows to completely compensating the torque lag during transient phases.

The advantages of pneumatic hybridization are notable: The mechanical work provided by a 2 liter engine at full load can be ensured at any time by a smaller engine (around 1.2 liters) functioning in pneumatic supercharged mode. When operated in pneumatic supercharged mode, the engine displays no lag at all, where the same supercharged engine without hybridization displays almost 1 second of lag during transients.

Keywords: downsizing, hybrid turbocharged engine, pneumatic hybrid engine, pneumatically supercharged, turbocharger speed lag, torque lag

NOMENCLATURE

C_d	[-]	dynamic coefficient
I	[$Kg.m^2$]	inertia
P	[W]	power
Q	[J]	heat
S	[m^2]	section
T	[$K°$]	torque, temperature
U	[J]	internal energy
V	[m^3]	volume
W	[J]	work
c_p	[$J/Kg/K$]	specific heat at constant pressure
c_v	[$J/Kg/K$]	specific heat at constant volume
h	[J/Kg]	enthalpy
m	[Kg]	mass
p	[Pa]	pressure
r	[$J/Kg/K$]	gas constant
t	[s]	time
γ	[-]	specific heat ratio
ε	[-]	heat fraction
η	[-]	efficiency
ω	[rad/s]	rotational speed

Subscripts and Superscripts

C	compressor
M	maximum
LHV	lower heating value
T	turbine
atm	atmospheric
d	dynamic
e	exhaust
f	friction
i	intake
m	minimum, manifold
t	tank

Acronyms

BDC:	Bottom Dead Center
IMEP:	Indicated Mean Effective Pressure
TDC:	Top Dead Center

INTRODUCTION

To be able to meet future challenges for internal combustion engines in terms of pollutant emissions and greenhouse effect gases emissions, the global efficiency over a real-world driving cycle needs to be improved.

Today, the internal combustion engines display high overall maximum global efficiencies but this great potential cannot be fully exploited:

o The first problem is that the peak efficiencies cannot be reached at low load. In real-life operation, e.g. in city traffic, the situation is even worse: full load is never reached and the engine is mainly

idling or operating at a very low load, and thus at very low efficiency.

o The second problem with internal combustion engines is that the thermodynamic cycle cannot be reversed: i.e. air and fuel cannot be produced from combustion products by providing reverse torque to the crankshaft. As a result, the kinetic energy of a vehicle cannot be recovered into chemical energy in negative torque, i.e. braking situations: the kinetic energy must be dissipated into heat through the braking system.

One solution to this problem is to use a hybrid power train combining a conventional combustion engine for easy energy storage in fuels and high overall conversion efficiency, and a reversible energy converter and storage subsystem. A new hybrid engine concept, which combines an internal combustion engine with a pneumatic energy converter and storage subsystem has been proposed recently combining a conventional internal combustion engine with a pneumatic motor/pump and storage tank. To lower the cost and weight and to stay with a well-known technology, the internal combustion engine itself has been used as a pneumatic pump or motor when there is no combustion.

Another way to increase the global efficiency of internal combustion engines is to reduce engine displacement while keeping the characteristic performances by strong supercharging. With this concept, the low efficiency operating point at lower load can be completely avoided, but to reach the nominal power, the engine has to be supercharged, typically using a turbocharger. The main drawback of low displacement supercharged engines is the large torque lag during transients. Consequently, a conventional supercharged engine has worse performances than its atmospheric counterpart because of the time necessary to spool the turbocharger.

The present study compares a *conventional engine* with a low displacement *turbocharged engine* and a *hybrid turbocharged engine* in terms of lag during strong torque transients. It could be demonstrated that a downsized engine combined with pneumatic hybridization can provide any level of torque with no lag, while keeping the downsized engine concept benefit in terms of fuel economy.

PNEUMATIC HYBRID ENGINE CONCEPT

The new hybrid concept is based on a conventional internal combustion engine on which one additional valve, named charging valve, connects the combustion chamber of each cylinder to an air tank, "Figure 1". The timing of the opening and closing of this valve can be controlled by an additional camshaft or by an electrical actuator.

The benefit of this concept is that the engine can be optimized to cover 80 to 90 % of the low load situations, without supercharging at high global efficiency. The remaining 10 to 20% are covered by supercharging the engine with compressed air.

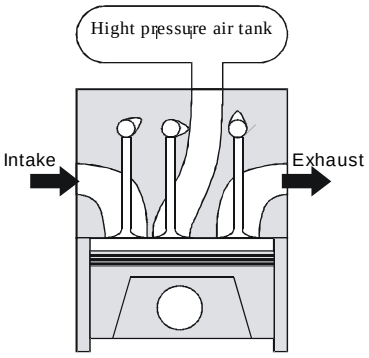

Figure11. Combustion chamber connected to high-pressure air tank through an additional valve and pipe

The operation of the hybrid engine resembles that of a conventional engine except that after intake valve closing the charging valve is opened to admit the supplement of air mass into the combustion chamber which is used to compensate the torque during transient phases.

SUPERCHARGED ENGINE OPERATION

The compressed air of the tank can be used to supercharge the internal combustion engine. The supercharging pressure can be very high: it is limited only by the tank pressure. The pneumatically supercharged cycle consists of several steps: intake, compression 1, supercharging, compression 2, combustion, expansion and exhaust. "Figure 2" displays the idealized P-V diagram:

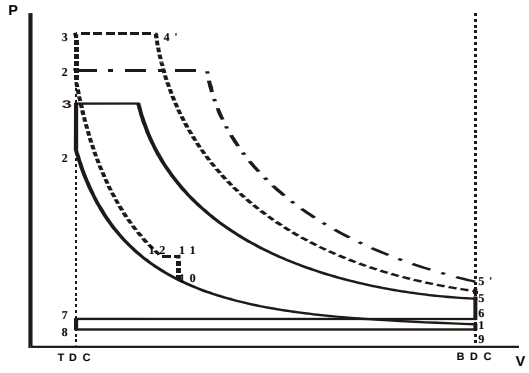

Figure 2: Idealized P-V diagram of engine supercharging with air from high-pressure tank

Exhaust and intake: The pneumatic supercharged cycle is identical to a conventional four-stroke engine cycle during the exhaust ("Figure 2", points 5-6-7) and intake process ("Figure 2", points 8-9-1) process.

Combustion and expansion: The combustion and expansion phases of the supercharged cycle ("Figure 2", points 2'-3'-4'-5') display the same shape as the non-supercharged cycle ("Figure 2", points 2-3-4-5). The higher level of air mass inside the cylinder during the supercharged combustion and expansion phase ("Figure 2", dashed line) comparatively to the atmospheric cycle ("Figure 2", solid line) provides, as expected, a higher IMEP, but also a higher level of maximum cylinder pressure. This higher pressure can be overcome by retarded combustion timing, at the expense of the global cycle efficiency ("Figure 2", dash-dotted line).

Compression: The main difference between a conventional internal combustion engine cycle and the pneumatically supercharged cycle resides in the compression stroke. This compression stroke is composed of three phases ("Figure 2"):

- After the closing of the intake valve, a conventional compression phase starts bringing the air of cylinder to a pressure below the tank pressure (points 1-10).
- Then, the charging valve opens, allowing additional air to flow from the high-pressure tank into the combustion chamber (points 10-11-12).
- At the closing of the charging valve, a second compression stroke is performed (points 12-2').

This strategy offers three main differences compared to a conventional supercharged cycle:

- By using the conventional intake and exhaust stroke, the tank only has to provide an amount of air in excess of the cylinder charge at atmospheric pressure. Consequently, the lifetime of the high pressure tank air charge can be greatly enhanced (2 to 4 times).
- Unlike a conventional supercharged cycle, where the complete air mass is in the cylinder when the intake valve closes, the pneumatically supercharged cycle can provide a higher high-pressure cycle IMEP due to the dual stage compression stroke.
- On the downside, as the exhaust pressure of the hybrid engines is higher than the intake pressure, the IMEP of the low-pressure loop of the cycle is negative. A conventionally supercharged engine can benefit from a positive low-pressure cycle.

THE HYBRID DOWNSIZING CONCEPT

The current tendency of the automotive manufacturers is to make increasingly small engines to operate the engine on higher efficiency operating points. To keep a constant maximum power output in spite of downsizing, the engine needs to be strongly turbocharged. This concept enables a decrease global pollutant emissions and consumption from 30 to 50%. The main drawback of the downsized engines is the high torque lag during strong transients. Consequently, at the same level of power output, a downsized engine perform worse than its naturally aspirated counterpart because of time necessary to spool the turbocharger.

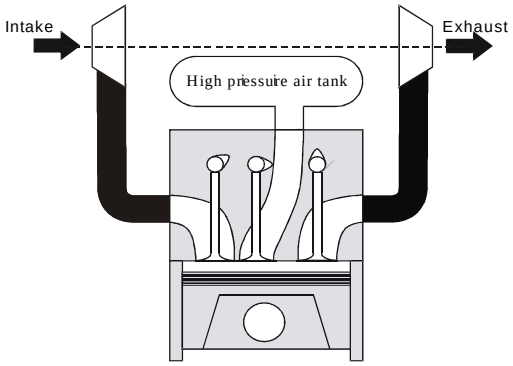

Figure 3. The hybrid engine with turbocharger

The new concept of hybrid engine is able to compensate the main drawback of the downsized engine and its turbocharger lag by pneumatic supercharging (Figure 3). The pneumatic supercharging of the engine is performed in complement of turbocharger supercharging until the latter provides the air needed by the engine. The high pressure air tank is refilled during regenerative braking phases or during charging phases.

Additionally, during the transition phases to supercharged, the intake air mass of the supercharged hybrid engine is higher than the air mass of the supercharged engine and so, the exhaust flow of the hybrid engine is higher than the exhaust flow of the supercharged engine. Therefore, the kinetic energy of the gases provided to the turbine by the hybrid engine is higher than that of a conventional engine, which leads to a faster increase in turbocharger rotational speed and also intake manifold pressure.

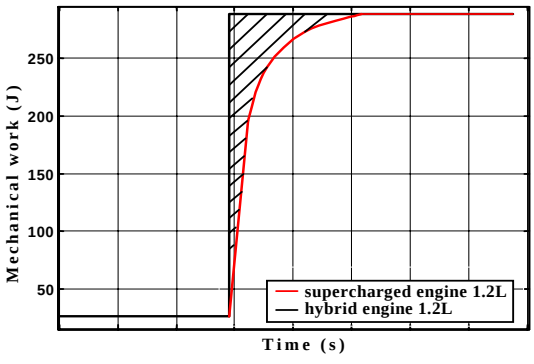

Figure 4. Required mechanical work

The hybrid engine supercharged, thanks to the air injection from the tank, develops an additional mechanical work ("Figure 4", hatched surface) which satisfies the instantaneous mechanical work in the transient acceleration phases.

ENGINE MODEL

To simulate the conventional and hybrid operating engine, a physical, 0D model has been designed. This model is composed of:

- Turbocharger model
- Throttle model
- Manifold and tank model
- Engine model

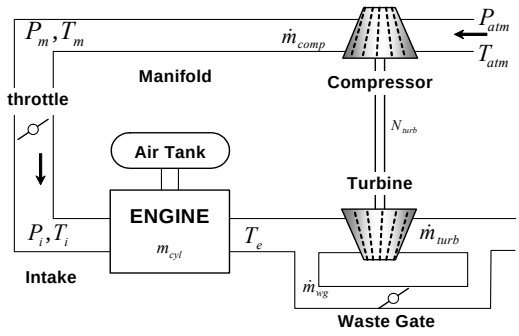

Figure 5. Supercharged hybrid engine

"Figure 5" shows the engine model topology. The compressor is connected to the throttle via a pipe called manifold (subscript m). The throttle is connected to the engine via a pipe called intake (subscript i). The air tank and the pipe that connects it to the engine are considered as one element. The engine is connected to the turbine via a pipe called exhaust (subscript e). The turbine can be bypassed by the waste gate. The inlet of the compressor and the outlet of the turbine are at ambient conditions.

Turbocharger model

The turbocharger model is based on the dynamic equation applied to the revolving machines, where, I is the inertia of the rotational parts and ω the turbocharger rotational speed.

$$P_T - P_C - P_f = I \cdot \omega \cdot \frac{d\omega}{dt} \qquad (1)$$

The power absorbed by the compressor is calculated by following equation:

$$P_C = \frac{dm_C \cdot c_{p_i} \cdot T_i}{\eta_C} \cdot \left(\xi^{\frac{\gamma_i - 1}{\gamma_i}} - 1 \right) \qquad (2)$$

where $\xi = p_i / p_{atm}$. The power provided by the turbine is given:

$$P_T = dm_T \cdot c_{p_e} \cdot T_e \cdot \eta_T \cdot \left(1 - \zeta^{\frac{\gamma_e - 1}{\gamma_e}} \right) \qquad (3)$$

where $\zeta = p_{atm} / p_e$. The power dissipated by friction is a function of rotational speed of the turbocharger. T_f is the friction torque.

$$P_f = T_f \cdot \omega \qquad (4)$$

The turbine and compressor flows and efficiencies are given by experimental data mapped into matrixes.

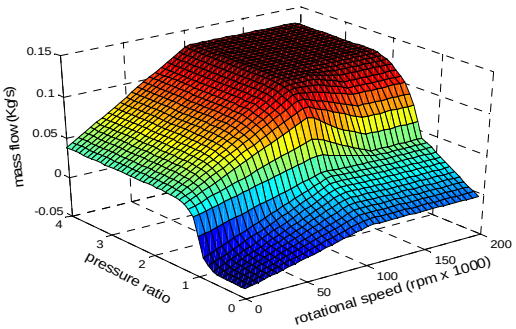

Figure 6. Turbine flow

"Figure 6" and "Figure 7", show the mass flows as a function of pressure ratio and rotational speed of, respectively, turbine and compressor.

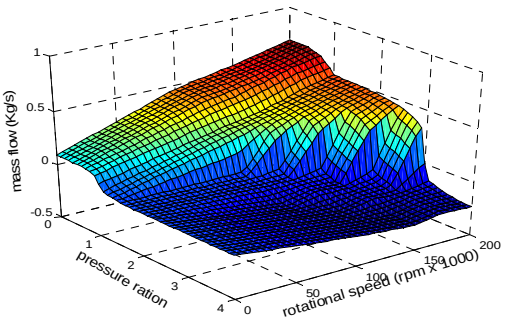

Figure 7. Compressor flow

Throttle model

The throttle pressure losses are computed with the "Barré de Saint Venant" law. If:

$$\frac{p_m}{p_i} \le \left(\frac{2}{\gamma + 1} \right)^{\frac{\gamma}{\gamma - 1}} \qquad (5)$$

then, the mass flow is written:

$$\frac{dm}{dt} = \frac{C_d \cdot S \cdot p_i}{\sqrt{\gamma \cdot r \cdot T_m}} \cdot \gamma^{\frac{1}{2}} \cdot \left(\frac{2}{\gamma + 1} \right)^{\frac{\gamma + 1}{2 \cdot (\gamma - 1)}} \qquad (6)$$

If not, the flow is written:

$$\frac{dm}{dt} = \frac{C_d \cdot S \cdot p_m}{\sqrt{\gamma \cdot r \cdot T_m}} \cdot \gamma \cdot \left(\frac{p_i}{p_m} \right)^{\frac{1}{\gamma}} \cdot \cdot \left\{ \frac{2 \cdot \gamma}{\gamma - 1} \left[1 - \left(\frac{p_i}{p_m} \right)^{\frac{\gamma - 1}{\gamma}} \right] \right\}^{\frac{1}{2}} \quad (7)$$

Manifold and tank model

The manifold, the intake and the exhaust pipes as well as the air tank are modeled as constant volumes, feeded by one or more ducts.

To computes the state of each volume (mass, pressure and temperature), the mass and energy balance is use. The mass balance determines the air mass of the system (Subscript j indicates the ducts that fill the volume):

$$m = \int \sum_j dm_j \quad (8)$$

The volume is considered adiabatic. The energy balance, that is used to determine the temperature of the system, can be written as follows:

$$dU = \sum_j h_j \cdot dm_j \quad (9)$$

$$dU = m \cdot C_v \cdot dT + C_v \cdot T \cdot dm \quad (10)$$

$$dT = \frac{\sum_j h_j \cdot dm_j - C_V \cdot T \cdot dm}{m \cdot C_v} \quad (11)$$

Knowing the mass and the temperature of the system and supposing that the inlet gas is ideal, the pressure of the intake manifold can be compute using the ideal gas law:

$$P = \frac{m \cdot r \cdot T}{V} \quad (12)$$

Supercharging model

The engine is modeled using a theoretical thermodynamic cycle.

The compression from 1 to 10 is considered polytropic without heat exchange (Figure 2):

$$T_{10} = T_1 \cdot \left(\frac{V_M}{V_{10}} \right)^{k_{110}-1} \quad (13)$$

where "k" is the polytropic coefficient computed with the "polytropic transformation model".

$$p_{10} = p_1 \cdot \left(\frac{V_M}{V_{10}} \right)^{k_{110}} \quad (14)$$

$$W_{110} = \frac{p_{10} \cdot V_{10} - p_1 \cdot V_1}{k_{110} - 1} \quad (15)$$

The flow through the charging valve is modelized by a constant volume transformation from 10 to 11 followed by a constant pressure transformation from 11 to 12 (Figure 2):

$$T_{11} = \frac{p_t}{\frac{p_t - p_{10}}{\gamma \cdot T_t} + \frac{p_{10}}{T_{10}}} \quad (16)$$

$$m_{11} - m_1 = \frac{V_{10}}{r} \cdot \left(\frac{p_t}{T_{11}} - \frac{p_{10}}{T_{10}} \right) \quad (17)$$

$$m_{12} = \frac{p_t \cdot V_{12}}{r \cdot T_t} - m_{11} \cdot \left(\frac{T_{11}}{\gamma \cdot T_t} - 1 \right) - \frac{p_t \cdot V_{10}}{c_p \cdot T_t} \quad (18)$$

$$T_{12} = \frac{p_t \cdot V_{12}}{m_{12} \cdot r} \quad (19)$$

$$W_{1112} = -p_t \cdot (V_{12} - V_{10}) \quad (20)$$

Again, the second stage of the compression process is considered polytropic without heat exchange (Figure 2), it comes:

$$T_{2'} = T_{12} \cdot \left(\frac{V_{12}}{V_m} \right)^{k_{122'}-1} \quad (21)$$

$$p_{2'} = p_t \cdot \left(\frac{V_{12}}{V_m} \right)^{k_{122'}} \quad (22)$$

$$W_{122'} = \frac{p_{2'} \cdot V_{2'} - p_{12} \cdot V_{12}}{k_{122'} - 1} \quad (23)$$

The combustion process is modeled by heat transferred to the working gas:

$$Q = \eta_c \cdot m_f \cdot Q_{LHV} \quad (24)$$

The first part (from 2' to 3', "Figure 2") of the combustion process is modeled by a constant volume process; the second part (3' to 4', "Figure 2") is modeled by a constant pressure transformation ("Figure 2"). It is considered that 50 % of the fuel is burned during the isochoric phase (from 2 to 3, "Figure 2") and 50 % during the isobar phase (from 3 to 4, "Figure 2").

$$Q_v = \varepsilon_v \cdot Q \quad (25)$$

$$Q_p = \varepsilon_p \cdot Q = (1 - \varepsilon_v) \cdot Q \quad (26)$$

$$T_{3'} = T_{2'} + \frac{Q_v}{m_{12} \cdot c_v} \ , \ p_{3'} = \frac{m_{12} \cdot r \cdot T_{3'}}{V_m} \quad (27)$$

$$T_{4'} = T_{3'} + \frac{Q_p}{m_{12} \cdot c_p} \ , \ V_{4'} = \frac{m_{12} \cdot r \cdot T_{4'}}{p_{3'}} \quad (28)$$

$$W_{3'4'} = -p_{3'} \cdot (V_{4'} - V_m) \quad (29)$$

The expansion process from 4' to 5' is considered polytropic:

$$T_{5'} = T_{4'} \cdot \left(\frac{V_{4'}}{V_M} \right)^{\gamma - 1} \quad (30)$$

$$W_{4'5'} = \frac{p_{5'} \cdot V_{5'} - p_{4'} \cdot V_{4'}}{k_{4'5'} - 1} \quad (31)$$

The pumping work of the low pressure cycle can be expressed as:

$$W_p = (p_e - p_i) \cdot (V_M - V_m) \quad (32)$$

The supercharged hybrid pneumatic engine efficiency can be written as the quotient of work produced (15, 20, 23, 29, 31 and 32) and thermal energy provided by the combustion (24):

$$\eta_s = \frac{\begin{pmatrix} W_{110} + W_{1112} + W_{122'} + \\ + W_{3'4'} + W_{4'5'} + W_p \end{pmatrix}}{\eta_c \cdot m_f \cdot Q_{LHV}} \quad (33)$$

EXPERIMENTAL CONDITIONS

The performances of the following engines have been compared using the model:

- *Naturally aspirated engine* – is considered as the reference engine
- *Supercharged engine* – is a downsized engine with a turbocharger
- *Hybrid engine* - is a downsized engine with a turbocharger and a pneumatic supercharging system.

The configurations of the studied engines are presented in "Table 1".

Table 1. Different engine configurations

Atmospheric engine	2000 [cm^3]
Supercharged engine	1200 [cm^3]
Hybrid engine	1200 [cm^3]

The turbocharger makes possible that an engine of 1200 cm^3 delivers the same mechanical work as a 2000 cm^3 engine. The simulations are performed under the same operating conditions for the three engines. The "Table 2" recapitulates these conditions.

Table 2. Summary of tests conditions

Atmospheric temperature	300 K
Atmospheric pressure	1 bar
Engine speed	3000 rpm
Tank temperature	300 K
Tank pressure	10 bars
Tank volume	20 liters
Exhaust manifold volume	1.1 liters
Intake manifold volume	20.1 liters
Turbocharger inertia	2.10^6 kg.m

In this study, the mechanical work considered as a low load is 25 Joules. The tests of turbocharger spooling consists in a stabilization phase at low load followed by a full load. The full load conditions are those of the atmospheric engine. The mechanical work is 290 Joules.

RESULTS

The simulations start with a low load phase, where the mechanical work required is 25 Joules ("Figure 8").

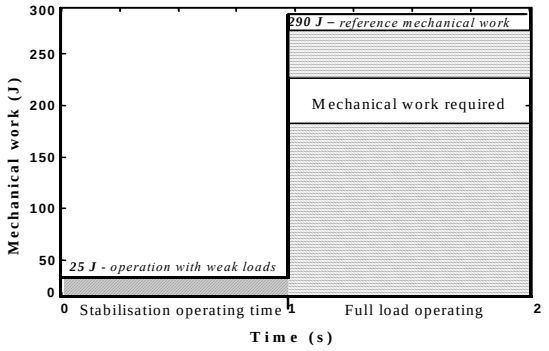

Figure 8. Required mechanical work

After stabilization of mechanical work ("Figure 8", from 0 to 1), the engine is required to deliver instantaneously ("Figure 8", point 1) a mechanical work of 290 Joules ("Figure 8", from 1 to 2) which corresponds to the mechanical reference work, developed by a cylinder of the naturally aspirated two liters engine at full load. These conditions are used for all three engine types.

The work of the 2 liters naturally aspirated engine running at full load can be delivered by a supercharged engine or hybrid engine of 1.2 liters, thanks to the increase of intake pressure. The full opening of throttle and the high flow of air, produced by the turbocharger, brings an increase of the intake pressure and the cylinder pressure compensating the lower displacement.

The selected naturally aspirated reference engine provides mechanical work quicker than the corresponding supercharged engine. The torque lag of the supercharged engine is due to the turbocharger inertia and the volume of the intake pipe which must be filled during the transient phases of acceleration ("Figure 9").

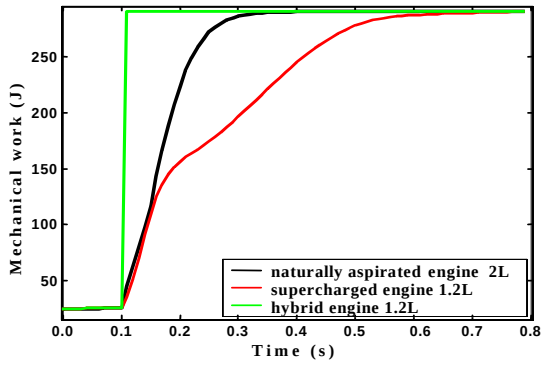

Figure 9. Delivered mechanical work

It can be seen that the supercharged engine torque follows closely that of the reference engine until the supercharged engine reaches an atmospheric pressure level at the intake. Then the torque rise is limited by the turbocharger spooling. For the simulations carried out, the delay is around 0.7 seconds and it varies according to engine displacement, turbocharger and intake system.

On "Figure 9", it can be seen that the new pneumatic hybrid concept, is able to provide immediately the mechanical work requested by supercharging the engine with compressed air on a cycle to cycle basis. Thus the drawback of the turbocharged engine is compensated.

Why does the hybrid engine have such a good behavior during transient operation? Recalling us the concept presented to the beginning of the article, where the operation of the hybrid engine resembles that of a conventional engine except that after the closing of the inlet valve, the charging valve is opened to admit the complement of air mass into the combustion chamber. This additional mass of compressed air from the high pressure tank (10-20 bars) makes it possible to generate a higher indicated work on a cycle to cycle basis.

During transient operation, as long as the turbocharger cannot provide the required air flow necessary to obtain the mechanical work, the pneumatic supercharged mode provides the complement. As soon as the turbocharger is spooled up and provides enough air flow, the pneumatic supercharging mode is disabled ("Figure 9").

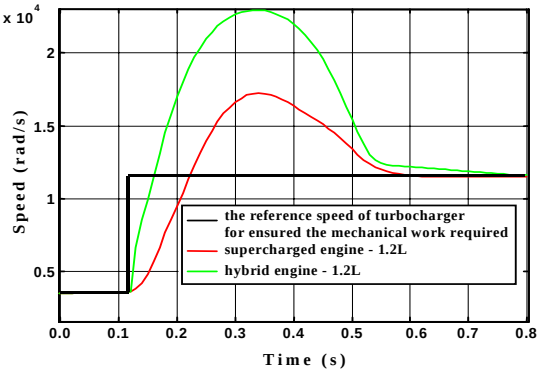

Figure 10. Turbocharger speed

The intake flow of the supercharged engines depends on turbocharger speed. The turbocharger speed which ensures the air flow necessary to provide the mechanical work required, is reached quicker in hybrid running than in supercharged operation. The speed of 12000 rad/s ("Figure 10", black curve) which ensures a expected operating point of the engine at full load is reached 100ms quicker by the hybrid engine than the supercharged engine ("Figure 10"). Indeed, thanks to injection of compressed air into the combustion chamber, the exhaust mass and enthalpy flow is higher with the hybrid engine than with the conventionally turbocharged engine, providing a higher torque to the turbocharger exhaust turbine. Thus, the turbocharger speed of hybrid engine increases quicker than that of the supercharged engine.

The curves of mechanical work of "Figure 9" from 0 to 0.1 seconds characterize the engines operating at partial load. At the time of complete opening of the throttle (0.1 seconds), the intake pipe starts to fill and the intake pressure increases. The exhaust pressure and the low-pressure created in the manifold, just after the throttle opening, from 0.1 to 0.18 seconds leads to a strong increase in turbocharger speed in this first phase of throttle opening ("Figure 10"). The low pressure inside the intake manifold before the throttle is resulting from the displacement of the air mass towards the intake valve, due to fast throttle opening.

The turbocharger speed starts to decrease from t=0.35 to t=0.6 seconds when the intake manifold pressure is stabilized. This decrease, remembering

that the turbine and compressor torques are equal $C_C = C_T$, is the consequence of the increase of the intake pressure ("Figure 11"). As the exhaust flow exerts a driving force onto the turbine and the intake flow exerts a resistant force onto the compressor, the torque balance on the turbocharger shaft produces a reduction in the turbocharger speed which leads to the reduction in the intake flow and thus to the reduction in the exhaust flow.

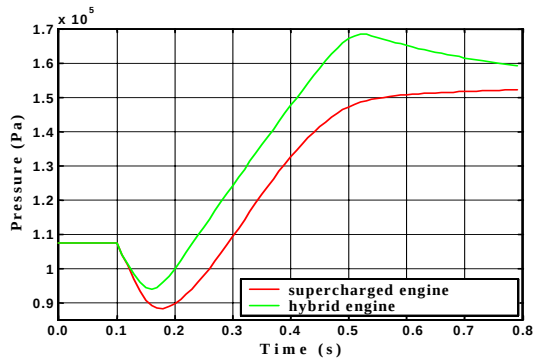

Figure 11. Pressure between compressor and throttle – supercharged and hybrid engine

At t=0.18 seconds, the intake pressure reaches the minimum ("Figure 11"); after this point the pressure increases at same time as the compressor flow, the difference between manifold pressure and intake pressure being lower than at the beginning of the throttle opening. In these conditions the flow ensured by the compressor is higher than the flow which passes through the throttle. The intake pressure between throttle and engine is always lower or equal to the intake pressure between compressor and throttle.

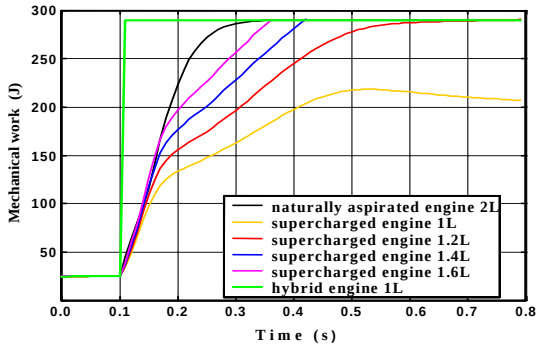

Figure12. Mechanical work

Mechanical work also evolves according to the size of engine. This evolution can be observed by changing the engine displacement and keeping all the other parameters constant. In "Figure 12", the six curves highlight the major advantage of the hybrid engine. The simulations were made for a naturally aspirated 2 liters engine, a hybrid 1 liter engine and several supercharged engines from 1 to 1.6 liters. As expected, it can be seen on "Figure 12" that the torque lag increases as the engine displacement is reduced. This lag can be compensated thanks to the new thermal pneumatic hybrid engine design, the engine torque being provided immediately ("Figure 12", green curve).

CONCLUSION

To improve the global efficiency of SI engines, the engine downsizing is a promising concept. Unfortunately, strong downsizing is plagued with severe torque lag during transients. This lag is due to the slow turbocharger spooling.

A new hybrid pneumatic-combustion engine concept should be able to completely solve the aforementioned problem. Additional air can be admitted into the combustion chamber on a cycle to cycle basis, to complement the conventional supercharging. Simulations showed that:

- The mechanical work provided by a 2 liter engine at full load can be also ensured by a smaller supercharged engine (as small as 1.2 liter) but with considerable torque lag during transients.
- Torque lag is strongly dependent on engine displacement: low displacement engine display more lag than higher displacement engines (0.7 seconds for 1.2 liter engine, 0.25 seconds for 1.6 liter engine).
- The torque lag can be completely compensated with the new hybrid concept, even for low displacement engines. Additional air directly admitted into the combustion chamber, can provide strong *cycle by cycle torque* transitions without being constrained by intake dynamics.

With the hybrid concept, the turbocharger speed lag is lowered compared to a conventionally turbocharged engine (0.6 seconds less). This effect is attributed to the higher level of enthalpy provided to the turbine during transients due to the additional air mass from the high pressure air tank.

REFERENCES

[1] Higelin, P., Charlet, A., Chamaillard, Y., march 2002, “Thermodynamic Simulation of a Hybrid Pneumatic-Combustion Engine Concept”, International Journal of Applied Thermodynamics, Volume 5 N°1 pp 1-11.

[2] Higelin, P., Charlet, A., 2001, “Thermodynamic Cycles for a New Hybrid Pneumatic-Combustion Engine Concept”, 5th International Conference on Internal Combustion Engines.

[3] Heywood, J.B., 1988, "Internal Combustion Engine Fundamentals", Automotive Technology Series, McGraw-Hill International Edition.

[4] Lallemand, A., and Lallemand, M., 1982, "Cours de Thermodynamique", INSA Lyon, Genie Energétique.

Conference on Modelling Fluid Flow (CMFF'06)
The 13th International Conference on Fluid Flow Technologies
Budapest, Hungary, September 6-9, 2006

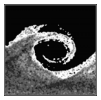

ADVANCED CFD SIMULATION OF A COMPRESSED AIR INJECTION MODULE

Huba NÉMETH[1], Gergely KRISTÓF[2], Viktor SZENTE[3], László PALKOVICS[4]

[1] Corresponding Author. Knorr-Bremse R&D Center Budapest, H-1119 Budapest, Major u. 69., Hungary. Tel.: +36 1 3829-828, Fax: +36 1 3829-810, E-mail: huba.nemeth@knorr-bremse.com
[2] Department of Fluid Mechanics, Budapest University of Technology and Economics. E-mail: kristof@ara.bme.hu
[3] Department of Fluid Mechanics, Budapest University of Technology and Economics. E-mail: szente@ara.bme.hu
[4] Knorr-Bremse R&D Center Budapest. E-mail: laszlo.palkovics@knorr-bremse.com

ABSTRACT

Turbocharged engines exhibit the so called turbo lag phenomenon causing a disadvantageous response comparing to atmospheric or mechanically supercharged engines. There are many solutions developed to reduce the lag effect although each of them has some disadvantages.

This paper investigates a booster module that injects compressed air to increase the response of turbocharged compression ignition engines of commercial vehicles.

The investigations applied 3D computational fluid dynamic (CFD) simulations in stationary and transient manner as well. The transient simulations were applied as standalone and coupled calculations to a 1D engine simulation code to capture more accurate boundary conditions (BC). The drawbacks and problems of this new and advanced approach are emphasized in the paper.

Due to the deformation of the flow field boundary surface during the dynamic process a deforming mesh method has been applied here. Instant shape of flow field boundary has been obtained by solving the equation of motion of the actuator rotor.

By applying the above methods it was possible to validate the booster module design variants and to identify the main characteristics of the complete system including the engine.

Keywords: CFD, compressed air, compression ignition engine, coupled simulation, moving mesh, turbo lag

NOMENCLATURE

I	[A]	current
L	[H]	inductance
F	[N]	force
M	[Nm]	torque
R	[Ohm]	electric resistance
T_c	[Nm/A]	torque constant
U	[V]	voltage
c	[Nm/rad]	spring coefficient
k	[Nms/rad]	damping coefficient
q	[kg/s]	mass flow rate
p	[Pa]	absolute pressure
ϕ	[rad]	angular position
ω	[rad/s]	angular velocity
Θ	[kg/m^2]	inertia

Subscripts and Superscripts

inlet	at the inlet of the test section
outlet	at the outlet of the test section
thr	throttle valve
sup	supply valve
p	caused by pressure

1. INTRODUCTION

Downsizing of a compression-ignition engine is an effective means for commercial vehicles for reducing fuel consumption but it requires supercharging to restore the full load torque. A compact and cost effective solution is with an exhaust turbocharger, which however has the drawback of a slow response to fast load demands by the driver. When the engine is increasing in speed, a delay occurs between advancing the accelerator pedal (which lets more fuel into the engine) and the time the exhaust pressure reaches a steady rate sufficient for the turbine. This delay is known as turbo lag.

To reduce the turbo lag there are several methods such as application of downsized turbines with waste gate valves [1, 2], variable geometry turbo chargers [3] and recently the usage of turbo compounding by using an electric motor [4]. An attractive alternative here is using the external compressed air to boost the turbo charger dynamics since this medium is available on each commercial vehicle [5].

The compressed air injection must occur in a short period to increase the charge in the cylinders of the engine making an increased fuel injection and thus an increased engine torque possible. Meanwhile the turbo charger is accelerated by a high margin by separating the turbo compressor output from the engine input for this short interval.

This paper focuses on the CFD simulation of the characteristics of an air injection module for boosting the turbocharger dynamics. The first part is devoted to identify the static behaviour of the module and the second part investigates the complex transient dynamics of switching from the turbo compressor supply to the air injection and back again after reaching the desired response of the engine.

The transient CFD simulation has been carried out using a 3D dynamic moving mesh governed by the actuator dynamics where the actuator dynamics has been coupled by separate ordinary differential equations. The transient simulation required special treatment of the boundary conditions to achieve a realistic behaviour of the module as being coupled to the compression ignition engine. For this purpose a 1D CFD engine simulation code of GT-Power [6] has been coupled to the 3D CFD code of FLUENT [7]. The 1D-3D coupling method is a new approach so there are just some few examples on its application [8].

The presented methods made it possible to validate the booster module design and identify the most important characteristics of the system.

2. SYSTEM DESCRIPTION

The compressed air injection module is located in the high pressure intake part of the engine between the intercooler and the intake manifold (see Figure 1). The charger air coming from the intercooler is connected by the piping (2) to the air injection module (1) through the port (11), which conducts the air to the intake manifold by the piping (3) through the port (21). The external compressed air injection is provided by the compressed air system through the piping (5) on the port (12). The air injection module includes an electric controller which is supplied by the electric line (4).

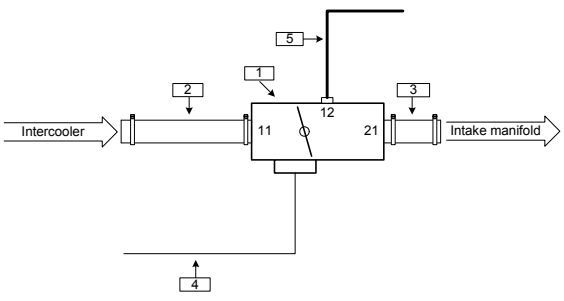

Figure 1. System layout

Additionally the air injection module has a throttle valve that can separate the port (11) form the ports (12) and (21).

The operation of the system is as follows. Under normal conditions when the turbocharger runs at high speed the air is compressed by the compressor of the turbocharger that is cooled down by the intercooler. In this case the throttle valve of the air injection module is fully open and the air coming from the intercooler is conducted to the intake manifold.

In case of low engine speeds when the turbocharger is unable to build up a significant charger pressure the engine is supplied by external compressed air injection from the compressed air system of the vehicle by a supply valve on port (12), meanwhile the throttle valve is fully closed to avoid a back-stream towards the turbo compressor.

After reaching the desired charger pressure the supply valve is closed so the air injection is shut down and with a correct synchronization the throttle valve is opened and the normal air supply from the turbo compressor is restored and the engine can accelerate further with maximal boost.

Switching from the turbocharger to external compressed air injection and back again during a highly transient acceleration raises a complex fluid dynamic process inside the air injection module that has to be strongly considered during the design.

In order that the controller of the system is able to monitor these processes two pressure sensors are installed on the two sides of the throttle valve of the air injection module.

Actuators operating the two alternative air inlets of the module have a significance that can strongly influence the performance of the module.

Since the switching between the two air sources of the engine has to be executed in a short time to have a smooth operation both actuators should have high potentials.

For this purpose the supply valve is designed as a diaphragm construction that is able to open and close big cross sections and can be operated in very short time due to low inertias. The control chamber pressure of the diaphragm is operated by a solenoid magnet valve.

For the electric throttle valve operation a directly driven alternative has been selected, where the actuator is a so called DC torque motor. This is developed specially for throttle valves. The DC torque motor has no brushes so its angular operation range is limited. Since there is no transmission between the throttle valve axis and the torque motor the inertia of the whole actuator is very low and this allows a high response. For safety reasons the throttle valve is equipped with a return spring that can provide a well defined position even if the electric control of the system is lost.

3. STATIONARY OPERATION

As discussed before the system has two distinct and important stationary operation modes. The one is the passive operation mode (throttle valve is open) when the engine is supplied by the turbo compressor with compressed air and the other is the active operation mode (throttle valve is closed) when the engine is supplied from the compressed air system of the vehicle by the air injection.

These two operation modes well characterize the system and many important operation properties can be captured from the stationary results.

The most important questions to be answered by stationary CFD simulations are as follows for the passive mode:

- What is the effect of the open throttle valve to the charge of the particular cylinders of the engine?
- What is the pressure loss caused by the throttle valve?
- What about the velocity map and streamlines around the throttle valve?
- Is the throttle valve stable in its open position if the return spring is broken?

For the active operation mode the following questions are raised for the static investigations:

- What is the throughput of the diaphragm supply valve?
- Where should be the best location for pressure sensors to measure the static pressure on both sides of the throttle valve?
- What is the maximal air speed during the air injection, where is it located?
- How uneven can be the charging process of the particular cylinders of the engine due to the air injection?

3.1 Geometric Versions

During the early development phase there were two main geometric versions of the module. The first one had a direct connection to the intake manifold of the engine by a flange interface (see Figure 2). The second version had circular interfaces on both high cross section ends fitted to rubber pipes (see Figure 3).

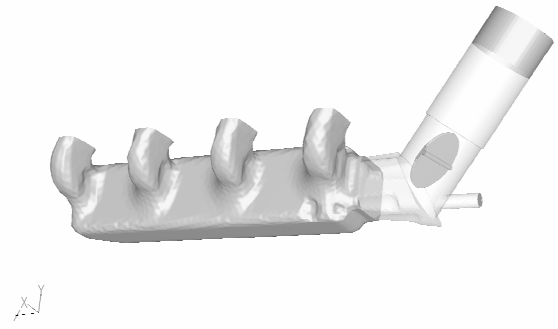

Figure 2. Flange geometry version for passive mode

The air injection module is represented by the transparent bodies in the figures. Since there is no external air injection in the passive mode the complex geometry of the compressed air supply valve head was removed and the air injection tube has only been retained on the geometry.

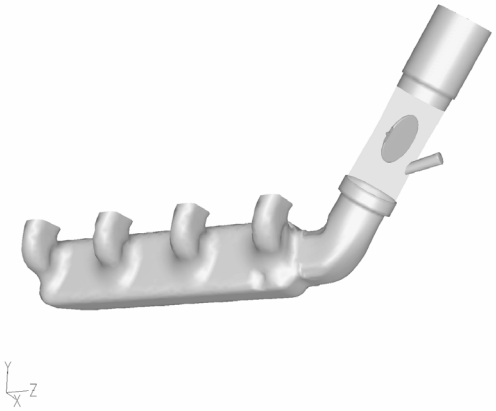

Figure 3. Piping interface version for passive mode

For the simulations of the active operation mode the geometry is basically the same with the exception that the input pipe is cut at the closed throttle valve and the compressed air supply valve head geometry is retained (see Figure 4).

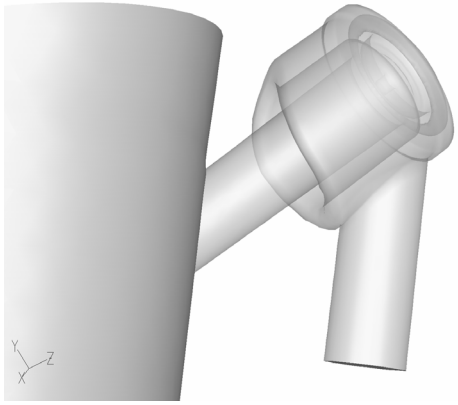

Figure 4. Supply valve head for active operation mode

For all stationary simulations the intake manifold has always been included into the model geometry.

3.2 Numeric mesh

Stationary simulations for passive mode have been prepared using the mesh represented in Figure 5. It can be seen that the mesh has a much finer structure in the vicinity of the throttle valve, with a total cell count of approx. 150 000. The linear cell size at and near the throttle valve is 2 *mm*.

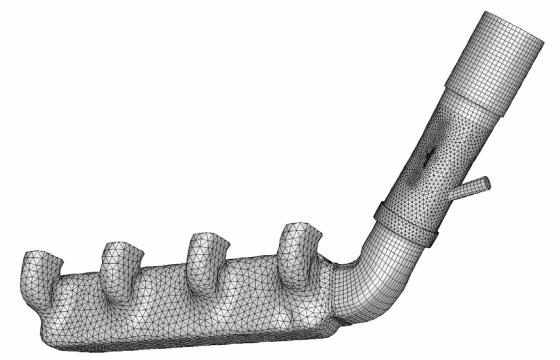

Figure 5. Numeric mesh for passive mode

In case of active mode in Figure 6, the mesh of the supply valve had to be refined similarly, again with a size of 2 *mm*, although on the diaphragm and in the opening the cell sizes had been reduced to 1 *mm*.

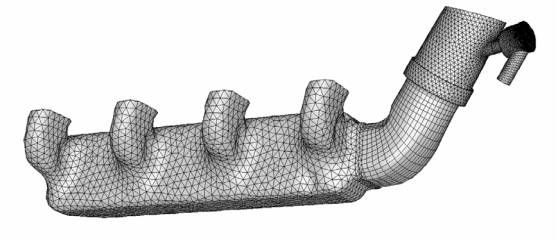

Figure 6. Numeric mesh for active mode

3.3 Physics and Boundary Conditions

Stationary simulations with open throttle valve have been prepared with a constant-density gas model as the value of the Mach number had been quite low. The exact value of 3,187 kg/m^3 gas density had been calculated from the 3 *bar* inlet pressure and 55 °*C* inlet temperature.

Stationary simulations with closed throttle valve have been prepared with an ideal-gas model. This calculates the density from the state equation of ideal gases.

The calculations of the turbulent transport values had been carried out using the Renormalisation Group (RNG) k-ε turbulence model. The boundary conditions of the turbulence models had been set using the hydraulic equivalent diameter of the inlet and outlet pipe sections, assuming 10% turbulence intensity. These values are not expected to affect the simulation results significantly.

The boundary conditions for the two stationary cases are shown in Table 1.

Table 1. Stationary boundary conditions

Case	Outlet	Compr. inlet	Inlet
Passive	0.25 *kg/s*	closed	3 *bar*
Active	3 *bar*	7.5 *bar*	closed

3.4 Results

Some typical results of the stationary models are seen in Figures 7 to 10 for both operation cases.

The pressure drop along the analysed flow field can be calculated from the results of open throttle valve. The value of the pressure drop had been 7772 *Pa*.

In case of closed throttle valve the boundary conditions had been set up differently, therefore from those results the mass flow can be calculated, which is 0.181 *kg/s*.

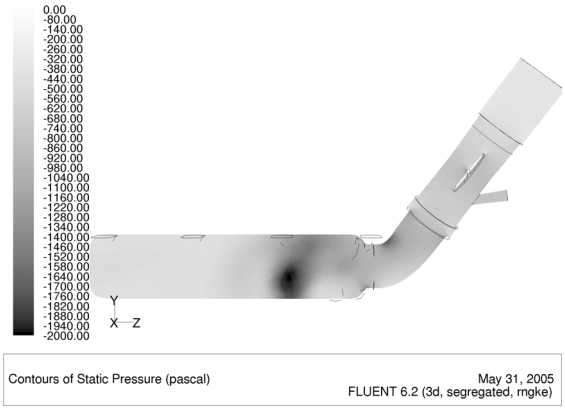

Figure 7. Pressure in passive mode

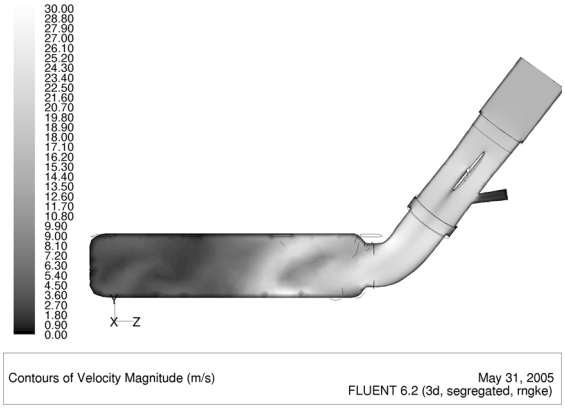

Figure 8. Velocity in passive mode

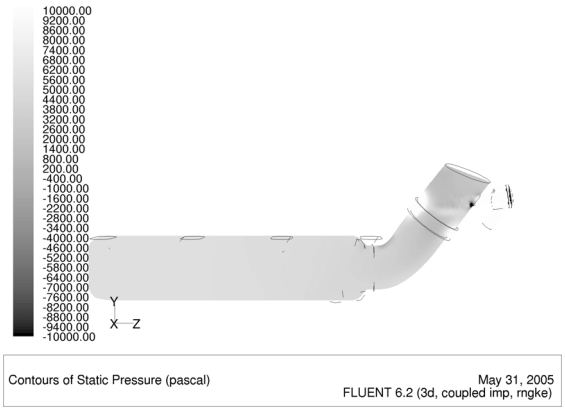

Figure 9. Pressure in active mode

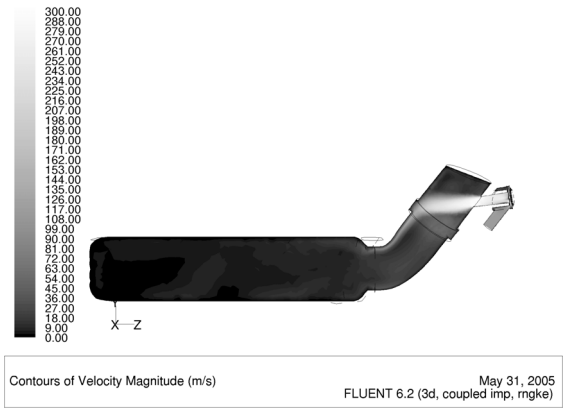

Figure 10. Velocity in active mode

In passive operation mode the open throttle valve has caused almost no perceptible disturbance on the main stream. The maximal velocities are in a low range below 30 *m/s* even at full engine load and nominal speed. The throttle valve can stay stable in its open position even with broken return spring.

At active operation the maximal air speed reaches the sonic speed limit. The charge process of the particular cylinders are less disturbed in case the air injection is directed to the opposite pipe wall than addressed directly into the intake manifold.

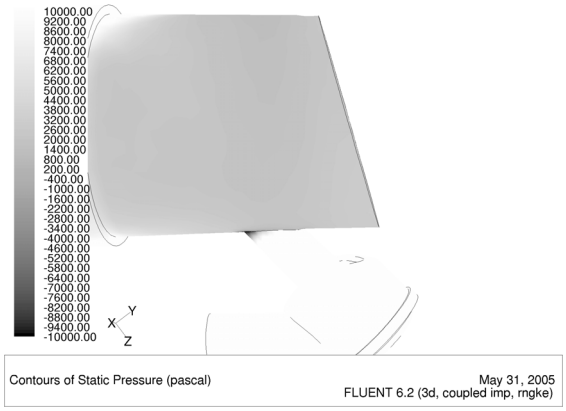

Figure 11. Surface pressure in active mode

The static surface pressure distribution (see Figure 11) shows an even pressure on a big surface providing a free pressure sensor positioning.

4. STANDALONE TRANSIENT OPERATION

The transient simulations address to investigate the time domain effects of the system. According to the preliminary investigations by using lumped parameter models on the two actuators of the system one could conclude that the supply valve diaphragm axle has a very fast dynamics itself although the complete air injection actuation dynamics is mainly influenced by the response of the actuating magnet valve. If the magnet valve has switched to the other state then the movement of the diaphragm is done in a very short time of about 1 *ms*. So the diaphragm dynamics was considered as a binary on/off valve with a predefined actuation delay caused by the magnet valve of 10 *ms*.

In case of the throttle valve actuation the situation is different it has a slower dynamics compared to the supply valve, moreover the air stream and pressure conditions have a bigger influence on its operations. The throttle valve axis has an offset in order that the air stream can open it in case of emergency when the return spring is broken. Due to the above reasons the throttle valve with its actuator is considered to be included in the calculations.

4.1 Handling of deforming mesh

Fluid mechanical simulation using deforming meshes is a new and innovative option which has been provided by the new FLUENT 6.x version. Currently some compromises had been necessary though. It is particularly tough to deal with small gaps, especially when there is a significant shear in the mesh deformation. Therefore the original geometry had been fitted with a spherical-shell-shaped ring as it can be seen in Figure 12. This ring had been filled with cells of very high porosity. Therefore the cells can deform freely allowing the deforming mesh function to work appropriately, while at the same time the flow is heavily constrained in this region. For a fully closed throttle valve it means that only 2.6% of the base flow (stationary flow with open throttle valve) had been able to escape through this porous region. Tetrahedral elements have been applied in the dynamically meshed zone. Local mesh reconstruction was triggered by exceeding values of equiangular skew. For the transient operations the intake manifold is not more included into the geometry domain.

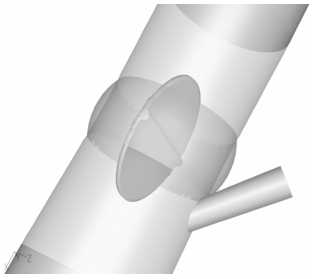

Figure 12. Porous zone for the deforming mesh

The time step size of 0.0001 *s* for the deforming-mesh simulation had been optimised using preliminary test runs for the whole time domain. Mesh independency of the simulation results could not be analysed due to limited timeframe of the project. The standalone simulations applied the constant-density gas model.

4.2 Boundary conditions for unsteady flow model

For standalone simulations the boundary conditions had been modelled as time-independent characteristic curves. Since the objective of these calculations had been the simulation of the closing and the opening transient, which is a quite small time domain, the boundary conditions can be described using static characteristics. These characteristics describe the inlet total and outlet static pressure as a function of the mass flow as it can be seen in Figures 13 and 14. The resulted constant pressure distributions have been applied to the inlet and outlet sections of the booster module.

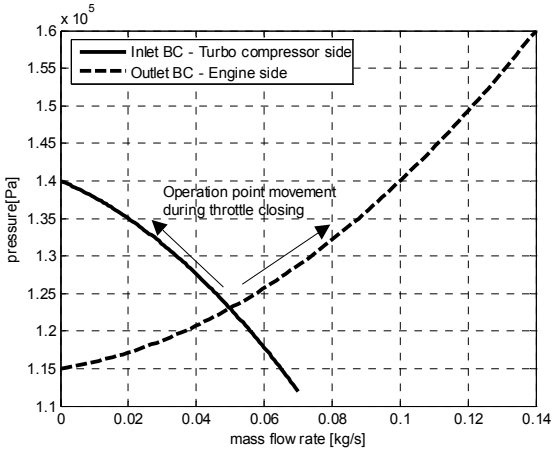

Figure 13. Time-independent boundary conditions for throttle closing

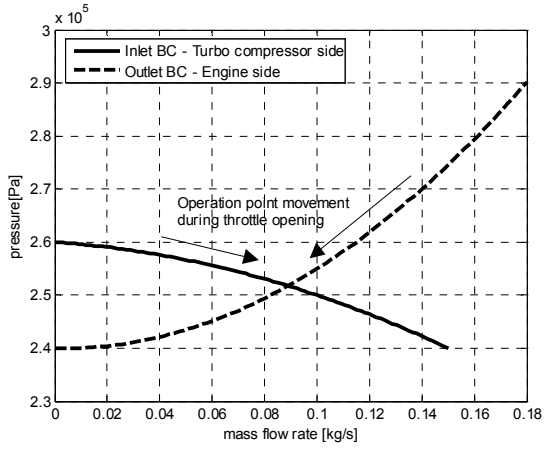

Figure 14. Time-independent boundary conditions for throttle opening

4.3 Dynamic model of the throttle valve

Based on electrical and mechanical state balances the throttle valve dynamics has been calculated using the ordinary differential equations based on first engineering principles for conservation of magnetic linkage and mechanic impulse.

$$\frac{dI}{dt} = \frac{U}{L} - \frac{R}{L} I - \frac{T_c}{L} \omega , \tag{1}$$

$$\frac{d\omega}{dt} = \frac{M_p + T_c I - k\omega - M_f \operatorname{sgn}(\omega) - c\phi}{\Theta} \tag{2}$$

$$\frac{d\phi}{dt} = \omega . \tag{3}$$

The torque M_p caused by the static pressure distribution on the throttle plate is fed back from the surface torque integral from the CFD domain. On the other hand the throttle plate position defines the geometric domain that is given by the angular position from Eq. (3). Eq. (1) to (3) have been integrated by second order Runge-Kutta scheme implemented in C-language under Fluent.

4.4 Results

The throttle dynamics obtained from the simulation is depicted in Figure 15.

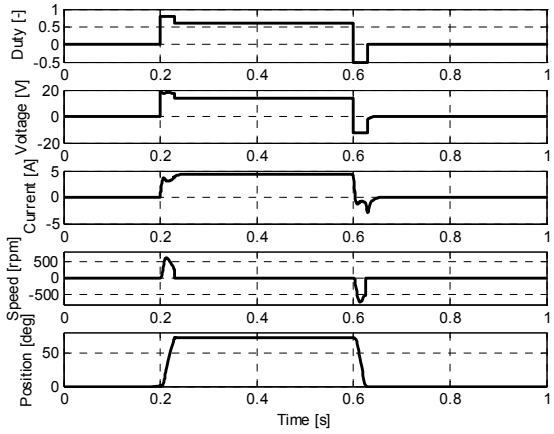

Figure 15. Throttle valve dynamics

The velocity maps as function of the resulted throttle valve positions for open, 30 *degrees*, 60 *degrees* and closed states are given in Figures 16 to 19.

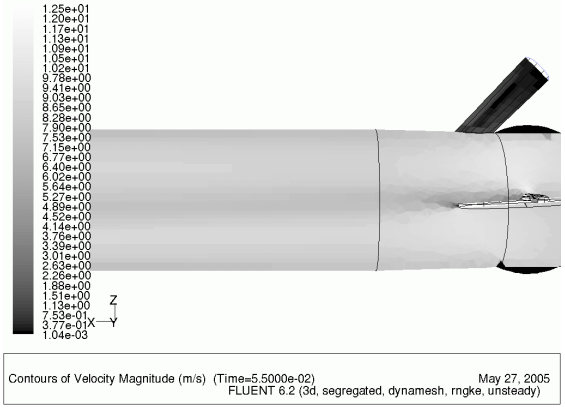

Figure 16. Velocity for open throttle valve

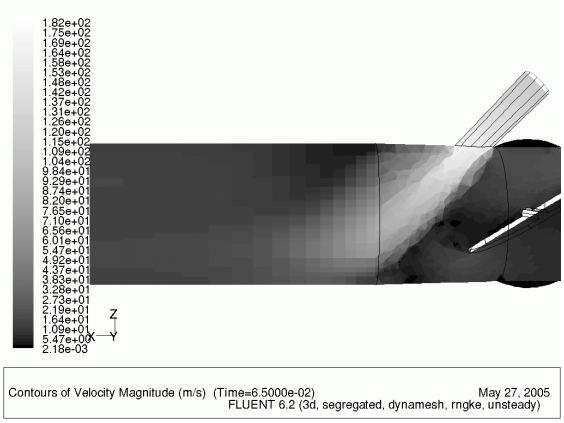

Figure 17. Velocity for 30 *degrees* position

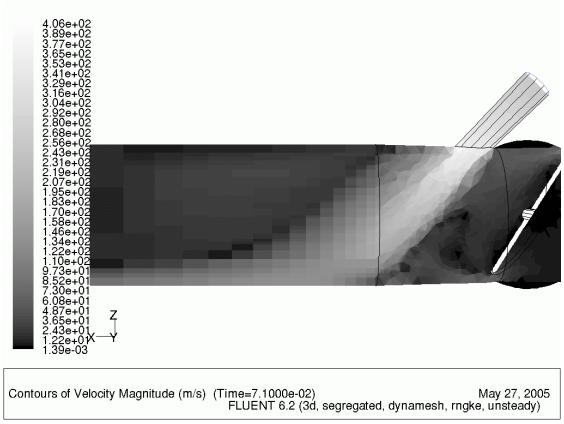

Figure 18. Velocity for 60 *degrees* position

The results have shown that the throttle valve dynamics is only slightly influenced by the pressure distribution on the throttle plate under typical operation conditions.

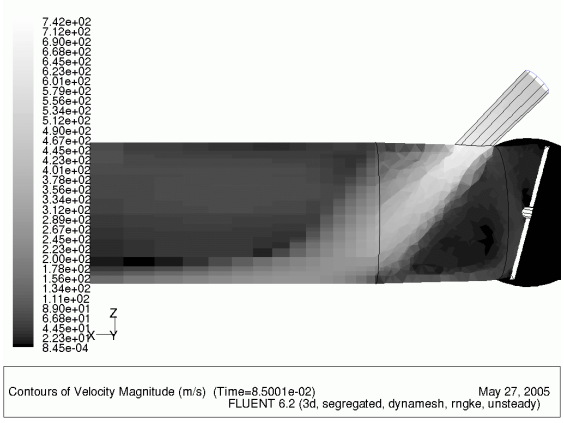

Figure 19. Velocity for closed throttle valve

5. COUPLED TRANSIENT OPERATION

In coupled simulations everything but the gas density and the boundary conditions had been the same as in standalone cases. As the coupling proved to work correctly only with compressible gases, therefore the ideal-gas model must have been used.

5.1 Engine model

The boundary conditions had been provided by GT-Power in such a way that while Fluent's inputs are the mass flow rates at both boundaries, GT-Power receives pressures as inputs on the connecting interfaces. The high pressure intake portion of the GT-Power engine model is shown in Figure 20. On left side the 3D Fluent domain called 'module' with its CFD interfaces, on the right side the intake manifold with the cylinders are seen.

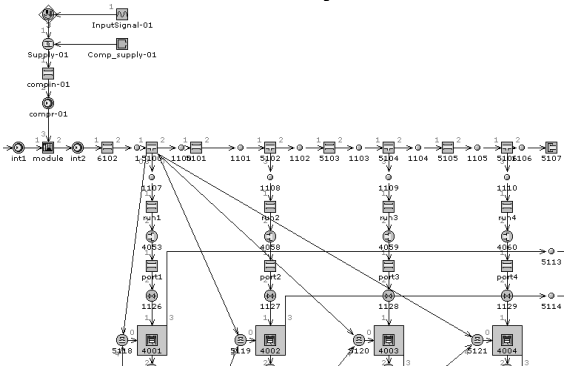

Figure 20. Portion of GT-Power model with coupled 3D domain

In order to have realistic operation conditions the GT-Power engine model has been coupled to a GT-Drive dynamic vehicle model. As test case for the simulations a step response situation has been used by emulating a kick down acceleration on an uphill slope in 4th gear (of a 6 gear gearbox) with an initial engine speed of 1200 *rpm*.

In contrast to conventional GT-Power models with turbocharger it had a big importance of modelling the turbo compressor appropriately since it operates in the surge region during the air injection actuation for some engine cycles. However it has a crucial importance on the resulted boundary condition of the module inlet. For this purpose a mean value compressor surge characteristics has been used based on preliminary dynamometer measurements.

5.2 Results

The coupled iteration time steps are driven by GT-Power that is followed by Fluent however at a particular time step there is no coupled iteration between the two codes in order that the solution could converge at each time step. Due to this reason the coupled convergence is not guaranteed even under highly relaxed conditions. In conclusion the coupled simulations required extensive trials to reach certain convergence properties.

The compressor map with the operation points is shown in Figure 21 with normal and boosted acceleration cases. One can see that the compressor operates for some engine cycles in the surge area if the compressed air injection has been applied. However the mean mass flow rate did not reduce to

zero during this phase. Since the mean power consumption decreases strongly during the boost actuation the charger speed increases very fast.

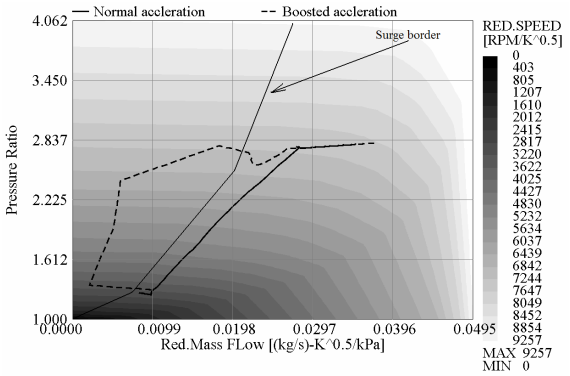

Figure 21. Compressor map and operation trajectory

The engine related inlet and outlet pressures of the module are shown in Figure 22. The accelerator pedal has been kicked down at 1 *s*. The duration of the applied air injection was 0.4 *s* long after kick down.

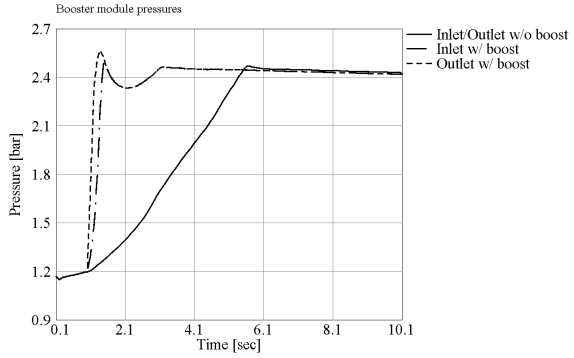

Figure 22. Inlet and outlet pressures

In the normal acceleration case without boost the pressure build up time results in 4.5 *s* due to the low initial engine speed and the stiff characteristics of the load torque working in high gear and uphill.

In the boosted acceleration case the booster outlet (intake manifold) pressure raises fast due to the applied air injection and the pressure build up time results in 0.2 *s*. In the meantime the booster inlet (intercooler) pressure approaches the outlet pressure. This boosting effect has been successfully tested and verified at extensive dynamometer and vehicle test as well.

The coupled transient calculations have confirmed that the air stream is able to open the closed throttle valve if the return spring is broken.

6. SUMMARY

The paper describes a 3D CFD investigation of an air injection module used to improve the dynamics of turbocharged compression ignition engines. The simulations have covered stationary and transient cases that made it possible to capture the most important properties of the system. The transient simulations applied dynamic moving mesh techniques to involve the relevant actuator dynamics that were described by ordinary differential equations. In a second step the transient simulations have been coupled to a 1D engine simulation code to provide more accurate boundary conditions.

By applying the above methods it was possible to validate the booster module design variants and to identify the main characteristics of the complete system including the engine.

REFERENCES

[1] F. M. Schittler,V. Rubi, G. Fraenkle., 1993, “Mercedes-Benz Commercial Vehicle Engines For Euro II And EPA 94 Emission Limits”, *SAE 931636*, pp. 1-16.

[2] B. Ubanwa, M. Kowalczyk., 1993, “Optimization Procedure for Matching Exhaust Waste-Gate Turbocharger to Automotive Diesel Engine”, *SAE931102*, pp. 257-275

[3] Y. Chi, J. Cheong, C. Kim and K. Choi, 2002, “Effects of VGT and Injection Parameters on Performance of HSDI Diesel Engine with Common Rail FIE System”, *SAE 2002-01-0504*, pp. 1-7

[4] U. Hopmann and M. C. Algrain, 2003, “Diesel Engine Electric Turbo Compound Technology”, *SAE 2003-01-2294*, pp. 1-7.

[5] H. Németh and E. Gerum, 2005, “Einrichtung zur Frischluftversorgung einer turbo-aufgeladenen Kolbenbrennkraftmachine und Verfahren zum Betrieb derselben”, *Deutsche Patentanmeldung Nr. 102005051687.4* (patent pending)

[6] Gamma Technologies, 2004, “GT-Power User’s Manual”, *v6.1*, pp. 1-286.

[7] Fluent Inc., 2005, “Fluent User’s Manual”, *v6.2*, pp. 1-473.

[8] U. G. Riegler and M. Bargende, 2002, “Direct Coupled 1D/3D-CFD-Computation (GT-Power/Star-CD) of the Flow in the Switch-Over Intake System of an 8-Cylinder SI Engine with External Exhaust Gas Recirculation”, *SAE 2002-01-0901*, pp. 1-12.

Conference on Modelling Fluid Flow (CMFF'06)
The 13th International Conference on Fluid Flow Technologies
Budapest, Hungary, September 6-9, 2006

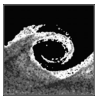

NUMERICAL CHARACTERIZATION THROUGH A CFD APPROACH OF A PRESSURE-RELIEF VALVE FOR AUTOMOTIVE APPLICATIONS

Michele PINELLI[1]

ENDIF, Engineering Deparment in Ferrara, University of Ferrara, Via Saragat, 1 - 44100 Ferrara, Italy

ABSTRACT

This paper describes the numerical characterization through a three-dimensional computational fluid dynamic model of a particular pressure-relief valve used in a steering circuit for automotive applications. A first model of the valve is studied numerically in order to obtain as much information as possible on the valve behaviour. The numerical results are compared to some available experimental data to validate the methodology. The results of the numerical simulations are analysed in details both qualitatively, in terms of fluid dynamic features, and quantitatively, in terms of main macroscopic parameters, such as discharge coefficient and valve characteristic curves. Three different designs of the valve are then taken into consideration and compared in order to optimise the valve performances. Finally, some attention is dedicated as to detect and to obtain information with respect to cavitation by only using single-phase fluid dynamic models.

Keywords. Pressure-relief valve, CFD, fluid dynamic optimization, cavitation

NOMENCLATURE

c_e	[-]	efflux coefficient
C	[-]	model constants
d	[mm]	diameter
f	[-]	dumping function
k	[m/s^2]	turbulent kinetic energy
K_v	[-]	capacity factor
N	[-]	grid points
p	[*Pa*]	pressure
Q	[l/min]	volume flow rate
U	[m/s]	velocity
y	[mm]	elevation
ε	[m/s^3]	dissipation rate of turbulent kinetic energy
ρ	[kg/m^3]	density
μ	[Pa s]	viscosity

Subscripts and Superscripts

h	referred to the hole
inlet	at the inlet of the test section
gap	referred to the gap
max	maximum
out	outlet
t	turbulent

1. INTRODUCTION

Pressure-relief valves have several applications in the field of hydraulic circuits [1]. To optimise the performances of these kind of hydraulic valves, knowledge of their characteristic parameters and understanding of their fluid dynamic behaviour are essential. However, a complete experimental characterization of these devices is time-consuming, difficult or even not feasible. In fact, these components are usually very small and their operating conditions are severe. Hence, the parameters to be obtained for their characterization, such as for instance the spool elevation, are difficult to be measured and the accuracy of these measurements is often not very high.

Numerical modelling and analysis can be a powerful tool to investigate small-scale valve behaviour. The approaches that can be followed can essentially based on: (i) zero-dimensional models, such as Lumped Parameter (LP) models, (ii) one-dimensional models, based on momentum conservation law or (iii) two- or three-dimensional models, such as Computational Fluid Dynamic (CFD) approaches.

In literature, LP models are widely used to investigate pressure valves. These models are characterized by high versatility and very low simulation time. Hence, they allow the fast evaluation of different solutions in terms of the most important parameters and they can easily take into account dynamic effects. Interesting development of an LP model for a pressure-relief valve can be found in Berta et al. [2]. However, the LP models applied to valves suffer of some drawbacks. One of the main one is that they need the determination of the flow coefficients of the orifices and passage area within the valve. This task could be difficult to be performed and it often relies on pressure drop coefficient handbooks (such as [3]) or on *ad hoc* performed experimental tests (see for instance [4]).

Moreover, LM models can not give any indication on the three-dimensional flow field, which can be an essential part of the design process. In fact, when modification of the original geometry aimed at the optimization of its functioning in terms of pressure drops, cavitation resistance, fluid dynamic behaviour are of concern, the knowledge of the fluid dynamics is necessary.

For these reasons, two- or three-dimensional numerical simulations can be the right approach to take into consideration all the issue involved. A numerical characterization based on CFD approaches can represent a great opportunity to thoroughly study the valve behaviour and to obtain all the information required for their optimized design. Mokhtarzadeh-Dehghan et al. [5] used a two-dimensional finite-element technique based on a standard k-ε turbulence model to simulate a hydraulic pressure-relief valve. They analysed the fluid dynamic features of the valve for a number of spool elevations. They found some discrepancies with experimental results, but at the same time they were able to obtain improved understanding of the valve and to optimise its geometry. Naser and Gosman [6] still used a k-ε model but with a two-layer model for the near wall resolution. They obtained significant improvement with respect to standard k-ε models. More recently, Amirante et al. [7] used a CFD approach to explain experimental data on an open center directional control valve by means of a RNG k-ε model.

In this paper, a pressure-relief valve used in a steering circuit for automotive applications is studied numerically by means of a fully three-dimensional steady state model. The aim of the work was the study of the valve in terms of: (i) main macroscopic parameters, such as the discharge coefficient, as a function of the valve actual working condition; (ii) fluid dynamic features; in fact, the reduction of flow oddness (which can generates pressure and force instabilities and, thus, vibration and noise) can be very useful for component optimisation in order to predict and reduce the undesired phenomena. (iii) cavitation-related phenomena, such as aeration and/or foaming. In fact, even if the simulation is single phase (i.e., it does not take into account liquid/vapour change of phase), critical analyses of the results, and, in particular, of the pressure field, can give qualitative but useful information on this phenomena. Then, three different designs of the valve are taken into consideration and compared in order to optimise the valve performances.

2. STATEMENT OF THE PROBLEM

The relief-pressure valve under investigation (denominated Check Pressure Valve, CPV, throughout the paper) is inserted in the hydraulic circuit shown in Fig. 1. The entire circuit is controlled by an Electronic Control Unit (ECU) board which operates by acquiring as inputs the signal from the tachometer, from the steering and from the engine. The ECU is able to determine the rotational speed of the electric motor starting from the vehicle speed and from the magnitude and rate of the steering. A schematic view of the CPV is shown in Fig. 2.

The main elements that can be recognized are:

- a *valve casing* (1), which separates the high pressure hydraulic circuit from the tank, which instead is open at the atmosphere and, thus, is always at ambient pressure. This component has eight passing holes. They can be closed or opened by a *control disk* (2). Throughout this numerical characterization, the holes will be considered in the closed position;
- a *spring* (3), which is fixed between a *gear* (4) and a *plug* (5). The plug can be regulated to change the pre-load of the spring to the desired value;
- a *spool* (7) with its *deflector* (6). The particularity of this valve is the design of the deflector. It has the task of deviating the flow before it enters the tank and to enhance the load on the spool by means of hydrodynamic forces.

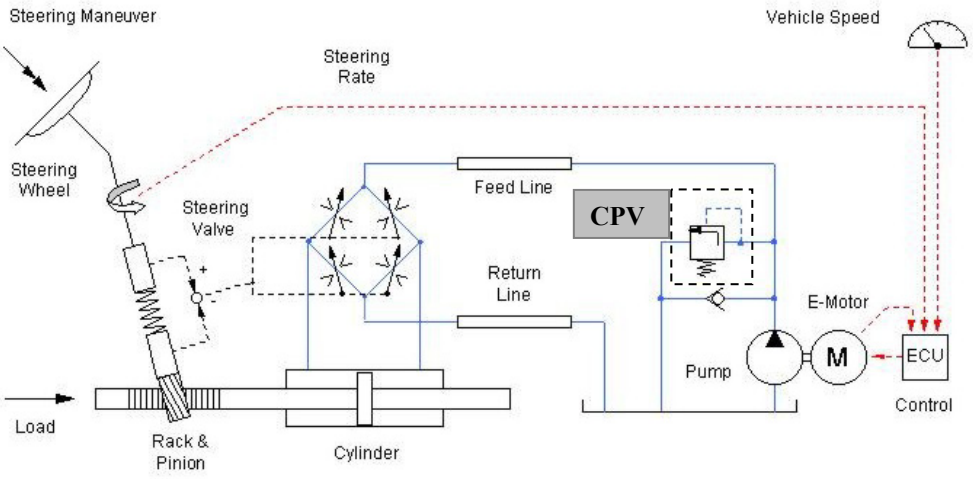

Figure 1. Steering hydraulic circuit with the CPV valve

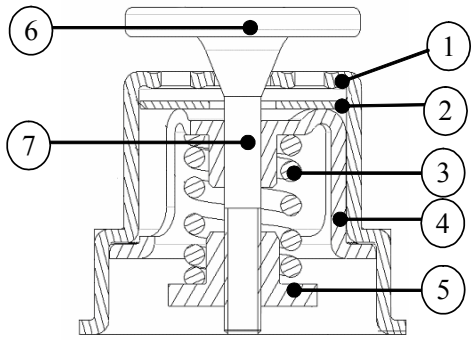

Figure 2. Valve geometry

When the pre-load of the spring is achieved, i.e. the relief pressure reach the design level, the spool begin to rise. The fluid escapes through the *gap* which is formed between the conical part of the spool and the conical part of the hole. The minimum geometrical flow area is located at the conjunction between the end of the cylindrical part and the beginning of the conical part of the hole. When the spool moves from its closed position, the location of minimum flow area remains the same but its value is augmented as a function of the elevation *y* of the spool. Within the gap, the fluid is strongly accelerated and exits towards the deflector where it is deviated and decelerated by the deflector itself. Then, the fluid is evacuated to the tank through the free area between the deflector and the valve casing.

This design of the valve provides two main benefits; first, the deflector provides extra force due to fluid impact under the deflector itself and allows a faster opening of the valve; second, it represents a shield between the still highly energetic fluid exiting the resonator and the tank.

However, some functioning problems arose during the first tests. The essentially were:

- hiss noise, which was present during the normal functioning of the valve;
- foaming. Some experimental visual analysis were performed by applying a glass on top of a test tank. During these tests, it was possible to see that inside the tank a white-coloured foaming mixture of oil and bubbles was originated.

These two phenomena are very critical and highly undesirable, either because the valve does not work in an efficient way and could fail due to the stresses induced by vibrations or because hiss noise and foam have to be avoided when the device has to be commercialized.

2.2 Valve models

In order to study the behaviour of the valve, a "numerical test rig" has been modelled. In Figure 3, the three-dimensional model of the numerical test rig as implemented in SolidWorks is shown. It is formed by three elements:

- a first volume, called *resonator*, which represent a plenum upstream the valve in which oil at the working pressure of the circuit is present;

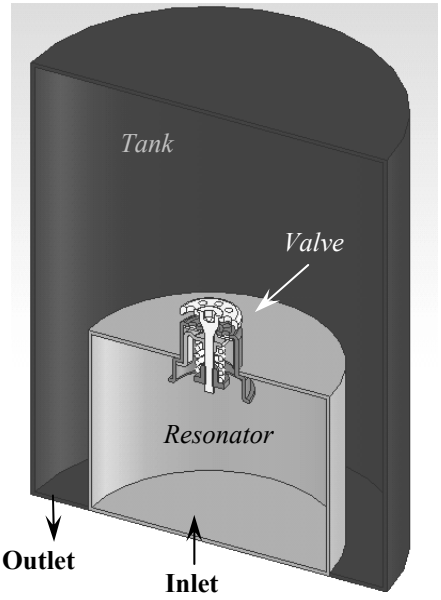

Figure 3. Solid model of the entire geometry: resonator, valve and tank.

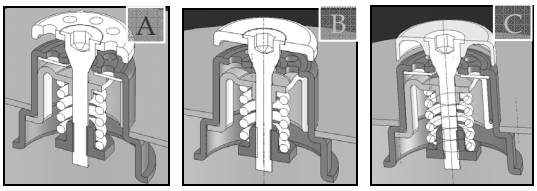

(a) (b) (c)

Figure 4. Valve A (a), Valve B (b),Valve C (c)

- the valve, already described and schematically presented in Fig. 2;
- a second volume, called *tank*. It represents a plenum downstream the valve and simulate the presence of the real tank inside the hydraulic circuit, where oil at atmospheric pressure is present.

This geometry is a simplified one with respect to the real; nevertheless, this model resembles in a consistent way the actual geometry in which the valve is located and it allows the static characterisation of the valve. In this manner, by means of the numerical CFD analysis, the valve has been analyzed in order to detect the possible reasons of the appearance of the undesired phenomena described above. Moreover, in order to improve the valve performances, three different designs of the deflector were analyzed while keeping constant other geometrical parameter such as the hole geometry and the gear displacement, in order to perform a sensitivity analysis on this particular element of the valve. In Figure 4, the three spools analysed with the different mounted deflectors are presented.

3. Grid and numerical models

The numerical code used in this paper is COSMOS FlowWorks (FW) [8]. The code if fully embedded in the three-dimensional solid modeller SolidWorks, which has been used to generate the geometries.

3.1 Type of grid

A rectangular mesh automatically distinguishing the fluid and solid domains in the computational domain is generated. The algorithm to generate the mesh is based on the geometrical discontinuity or "gap size" and it increases the number of cells in proximity of narrow channels, corners gaps, etc. Mesh cell sides are orthogonal to the specified cartesian co-ordinate system axes and are not fitted to the solid/fluid interface. Hence, a partial cell approach is used, in which the solid/fluid interface cuts the near-wall mesh cells and the mass and heat fluxes are treated properly with a special algorithm.

3.2 Numerical models

The FW code solves the Navier-Stokes equations through a Reynolds averaged approach and uses a Finite Volume method for the equation discretisation. A second-order upwind approximation is used for the advection terms. Following the SIMPLE approach, an elliptic type discrete pressure equation is derived by algebraic transformations of the originally derived discrete equations for mass and momentum. A multigrid method is then used to accelerate the solution convergence.

For turbulence modelling, the low Reynolds number k-ε model as in the Lam-Bremhorst formulation is used. In this model, the turbulent eddy viscosity is given by

$$\mu_t = \rho C_\mu f_\mu k^2 / \varepsilon \tag{1}$$

and, while the equation for the turbulent kinetic energy k is in the usual form, the equation for its dissipation ε is modified as follows.

$$\frac{D\varepsilon}{Dt} = \frac{\partial}{\partial x_j}\left[\left(\mu + \frac{\mu_t}{\sigma_\varepsilon}\right)\frac{\partial \varepsilon}{\partial x_j}\right] + \frac{\varepsilon}{k} C_1 f_1 \left(\frac{\partial U_i}{\partial x_j} + \frac{\partial U_j}{\partial x_i}\right)\frac{\partial U_i}{\partial x_j} - \rho \frac{\varepsilon^2}{k} C_2 f_2 \tag{2}$$

Following Lam and Bremhorst [9], the parameters f_1, f_2 and f_μ for near-wall resolution are defined as

$$f_1 = 1 + \left(\frac{0.05}{f_\mu}\right)^3 \text{ and } f_2 = 1 - e^{-R_t^2} \tag{3}$$

$$f_\mu = \left(1 - e^{-0.0165 R_k}\right)^2 \left(1 + \frac{20.5}{R_t}\right) \tag{4}$$

where and $R_t = \rho k^2 / (\mu \varepsilon)$ and $R_k = \rho k^{0.5} y / \mu$ are turbulence Reynolds numbers.

3.3 Boundary and working conditions

The fluid used for the simulations is a commercial oil (Pentosin CHF). Since the usual working condition of the steering circuit is at about T = 55 °C, the properties of the fluid were evaluated at this temperature. In particular the following value were adopted: dynamic viscosity μ = 0.0132 Pa·s and density ρ = 837.3 kg/m^3.

The inlet is located at the bottom surface of the resonator (Fig. 3). At this location, a static pressure boundary condition was set. The value of the pressure was different depending on the simulation performed. The outlet was located on the circular ring surface at the bottom of the tank (Fig. 3). The static standard atmospheric pressure (p_{out} = 1.013 bar) was set as boundary condition and remained constant for all the simulations. As a consequence, the flow rate Q (which was calculated by means of a mass-average of the numerical results at the resonator inlet) was obtained as a result of the simulation. All the solid walls was considered adiabatic and with a no-slip condition.

4. Numerical results

4.1 Grid sensitivity

A grid sensitivity analysis has been carried out on one of the valves analyzed, the Valve A. The results can be extended to the other spool geometries. The domain under consideration presents a wide range of spatial length scales. In fact the gap characteristic dimension has an order of magnitude of 10^{-4} m, while the characteristic dimension of the tank is about 10^{-2} m. Hence, the grids have been separately generated and controlled for each part of the domain.

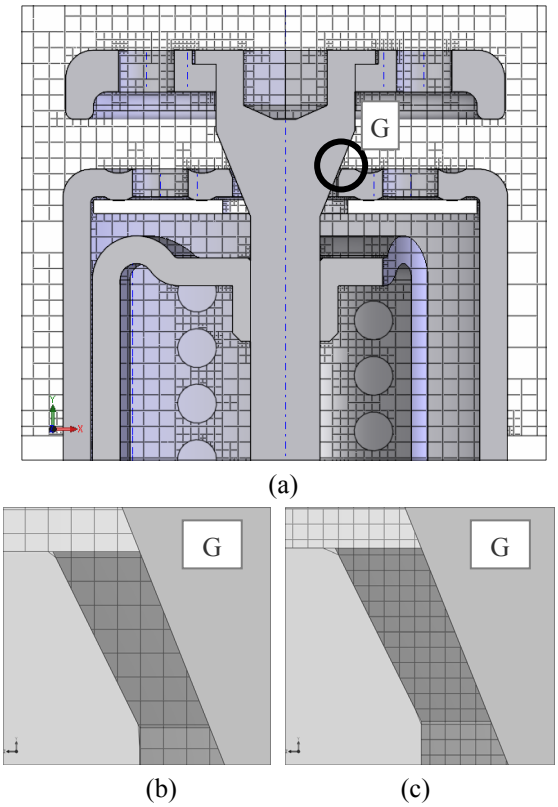

Figure 5. Grid in the valve region (a) and particular inside the gap (G): grid 1 and 2 (b) grid 3 and 4 (c)

Table 1. Grid sensitivity

	N	ΔN [%]	N_{gap}	Q [l/min]	ΔQ [%]
1	603 519	40.5	4	8.514	2.74
2	786 148	22.5	4	8.472	3.23
3	874 958	13.7	6	8.735	0.23
4	1 014 090	-	6	8.755	-

In Figure 5a, an example of a generated grid in the region in proximity of the valve is shown. It can be noticed that the grid distribution is not constant, being finer near the solid walls. Particular attention has been devoted to the generation of the grid within the gap between spool and hole. A particular of this region is shown in Figure 5b and Figure 5c. The two particulars refer to a coarser grid (a) and to a finer grid (b). It can be noticed that in the former there are four grid points across the gap, while in the latter the grid points are at least six. In Table 1, the result of the sensitivity analysis is reported. The monitored parameter was the volumetric flow rate Q, calculated at the inlet of the resonator. It can be noticed that, even if switching from grid 2 to grid 3 the total number of grid points is only slightly different ($\Delta N_{2\text{-}3}$ = 10 %), a step-change in the flow rate value can be noticed ($\Delta Q_{3\text{-}4}$ = 3.00 %).

At the contrary, with almost the same difference of grid points ($\Delta N_{3\text{-}4}$ = 13 %), the value of Q calculated with grid 3 is almost equal to the value calculated with grid 4 ($\Delta Q_{3\text{-}4}$ = 0.22 %). It can be noticed also that the step change occur when the number of grid points across the gap N_{gap} is increased from 4 to 6 grid points. This means that N_{gap} is a key parameter to achieve a good accuracy of the solution. Hence, for all the simulation performed, N_{gap} was checked and kept at least equal to 6.

4.2 Static valve characteristic curves

The static (Q, Δp) characteristic curve of the valve was obtained. This curve was obtained in the following way. Five different solid models of the valve were generated, each of them only differing for the spool elevation. The values of the elevation, chosen within its working condition range, were y = 0.05 mm, 0.10 mm, 0.15 mm, 0.20 mm and 0.30 mm. Then, for each value of the elevation y, three different static pressures were set as inlet boundary condition, i.e. p = 105 bar, 110 bar and 118 bar, while the outlet boundary condition remained constant for all the simulations.

The numerical results, reported in Figure 6, represent the valve working points (Q, p, y). This plot can be conveniently used to determine two out of three among the main parameters. For instance, if pressure and flow rate are known, the spool elevation can be estimated.

Another interesting results is the determination of the efflux coefficients. Among the various definitions, two of them are widely used.

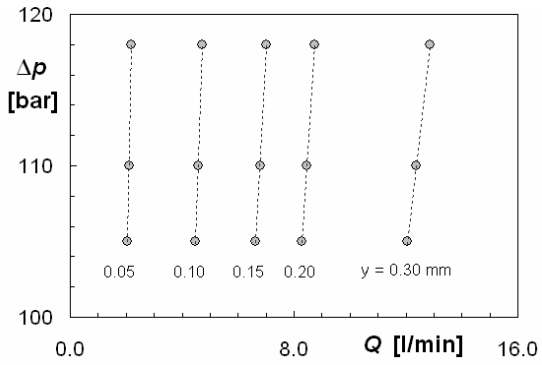

Figure 6. Static characteristic of Valve A.

The *capacity factor* K_v define the global behaviour of the valve and is defined as

$$K_v = \frac{Q}{\sqrt{\Delta p}} \tag{5}$$

in which Δp represent the pressure difference acting on the valve and Q is the flow rate through the valve. The calculated values of K_v as a function of Q are reported in Figure 7. In the same figure, some available experimental data for the Valve A are reported. It can be noticed that the numerical results are in good agreement with the experimental data. This was considered a good validation of the code and of the methodology followed.

In Figure 8, the characteristic curves for Valve A, Valve B and Valve C are shown. The characteristic curves are obtained by plotting the capacity factor K_v, normalised by means of its maximum value K_{vmax}, against the spool elevation y, normalised with the hole diameter d_h. All the valves analyzed show a very similar behaviour and present an almost linear characteristic. By looking more in detail, a slight tendency to follow a quick-opening behaviour, which in these applications is a favourable characteristic, can be recognized. A quick-opening characteristic means that the ratio between the normalized capacity factor and the normalized elevation follows an exponential law $K_v/K_{vmax} = (y/y_{max})^{1/\alpha}$. In these cases, the values of α have been estimated to lay in the vicinity of 1.1. Among the three valves, the model C presents the lower value of α, suggesting that this valve could be less prompt to open quickly.

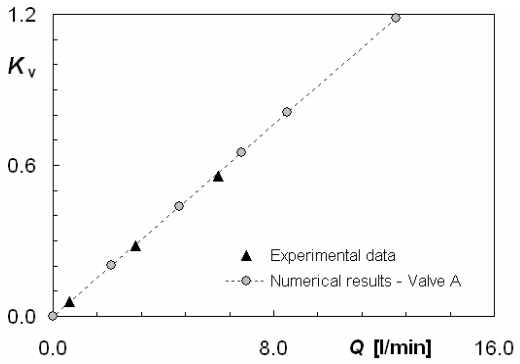

Figure 7. Numerical and experimental capacity factor K_v for Valve A

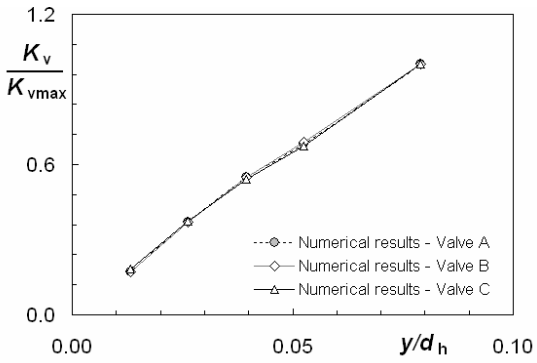

Figure 8. Normalised capacity factor K_v/K_{vmax} for Valve A, Valve B and Valve C.

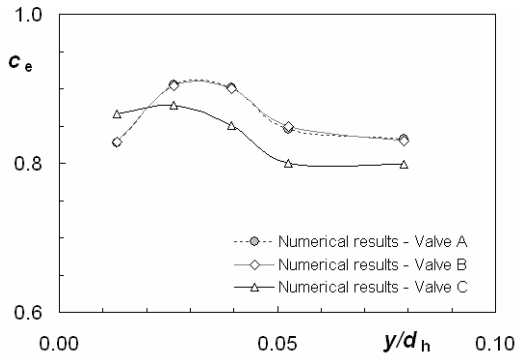

Figure 9. Numerical efflux coefficient c_e for Valve A, Valve B and Valve C.

Another important characteristic that can be evaluated for a valve is the *efflux* or *discharge coefficient* c_e. The efflux coefficient is referred to a particular efflux area, that is

$$Q = c_e A_e \sqrt{\frac{2\Delta p}{\rho}} \tag{6}$$

where A_e is the efflux area. Usually, rather than the fluid dynamic *vena contracta* area, a geometrical reference area is chosen. In the case considered, the area taken into consideration is the minimum free area along the flow path. This area is located between the spool and the upper part of the hole. The area can be calculated as a function of the elevation y by means of geometrical consideration. In this paper, the area is calculated by means of an automatic calculation tool of SolidWorks. The numerical determination of the coefficient c_e has been performed by applying Eq. (6) in which Δp is the imposed pressure difference and Q is the calculated volumetric flow rate for each imposed elevation y.

In Figure 9, the numerical c_e is plotted against the normalized elevation y/d_h. The typical behavior of this coefficient ([1], [3]) is well resolved and the three characteristic zones can be recognized: a first segment in which the coefficient rapidly grows in an almost linearly way (laminar zone), an instability zone which present a maximum (transitional zone) and a stabilized segment (turbulent zone) in which the coefficient tends an asymptotic value. The information that can be extracted from this curve is very important, since the determination of c_e is one of the most problematic issue in valve design. Regarding the three valves analyzed, it can be noticed that Valve C shows a more stable characteristic but at the same time it shows lower values of c_e, resulting in less flow rate evacuated for a given pressure difference.

4.3 Fluid dynamics of the valve

The use of a CFD approach can provide a great insight into the flow regime and pressure distribution within the valve flow passages. Some of the most important information that can be extracted from the fluid dynamic analysis are: (i) the efflux condition, in terms of the magnitude and location of the blockages, i.e fluid dynamic restricted sections with respect to geometrical sections; (ii) pressure distribution along the flow path, to establish the most critical regions in terms of pressure drops and, as will be discussed in a dedicated paragraph, of cavitation behaviour; (iii) flow oddness, which can generates pressure and force instabilities and, thus, vibration and noise.

Very interesting results were found analysing the pressure and velocity distribution under the deflector. In Figure 10 and 11, the velocity distribution and the velocity vector plot referred to Valve A are presented. The figures refer to the simulation in which y = 0.20 mm and Δp = 118 bar. This condition was chosen since it has been considered a representative working condition of the valve.

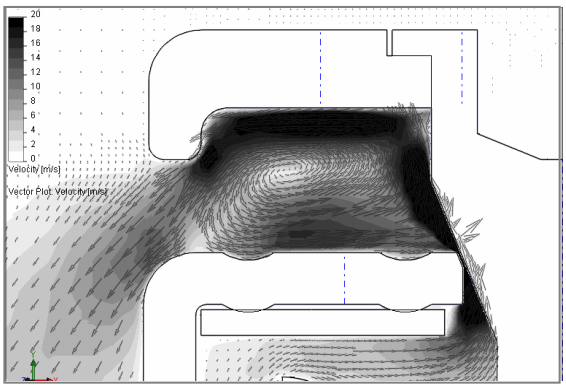

Figure 10. Velocity distribution for Valve A (Δp = 118 bar, y = 0.20 mm) in region WH

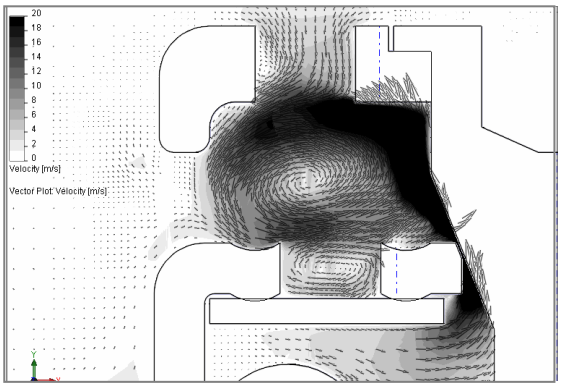

Figure 9. Velocity distribution for Valve A (Δp = 118 bar, y = 0.20 mm) in region H

In Fig. 10, a region under the deflector without the presence of holes (WH) is shown. In Fig 11, a region with a hole (H) is reported. Some interesting phenomena can be recognized:

- in region WH, the main stream of the flow remains attached to the spool and to the deflector. Then, it exits to the tank with a low velocity (6÷8 m/s). As can be seen, a wide recirculation zone is formed and limits the effective flow area, in particular since the fluid velocity is not perpendicular to the exit area;
- in region H, the flow is completely blocked. As can be seen, the recirculation zone occupies all the under-deflector region and does not allow the flowing of the fluid towards the tank. A recirculation is present also within the holes of the valve casing. Regarding Valve B and C, even if their deflectors do not have holes, the same qualitative behavior was observed: in particular, the presence of either region partially blocked or totally blocked were recognized.

In Figure 12, the pressure distribution under the deflector is presented for three different value of the elevation, i.e. y = 0.05 mm, 0.20 mm and 0.30 mm. The pressures has been plotted with a scale ranging from p_{abs} = 0.5 bar to p_{abs} = 1 bar in order to highlight under-atmospheric pressures. It is clearly noticeable that, when the elevation y is increased from 0.05 mm to 0.30 mm, the region in which a below atmospheric pressure acts is widened and occupy most of the deflector area. These under-pressure regions are due to the great recirculation zone already discussed (Figs. 10 and 11). This phenomena can cause instabilities, vibration and, as a consequence, noise. In fact, the deflector is subjected to two conflicting forces. The first acts in the same direction of the opening of the spool and it is due to the pressure difference between the tank and the resonator and to the flow forces. The second, instead, acts against the spool opening and is due to the difference between the upper surface of the deflector, where the atmospheric pressure is sensed, and the lower surface of the deflector, where the under-atmospheric pressure is sensed, as outlined by the analysis of Fig. 12.

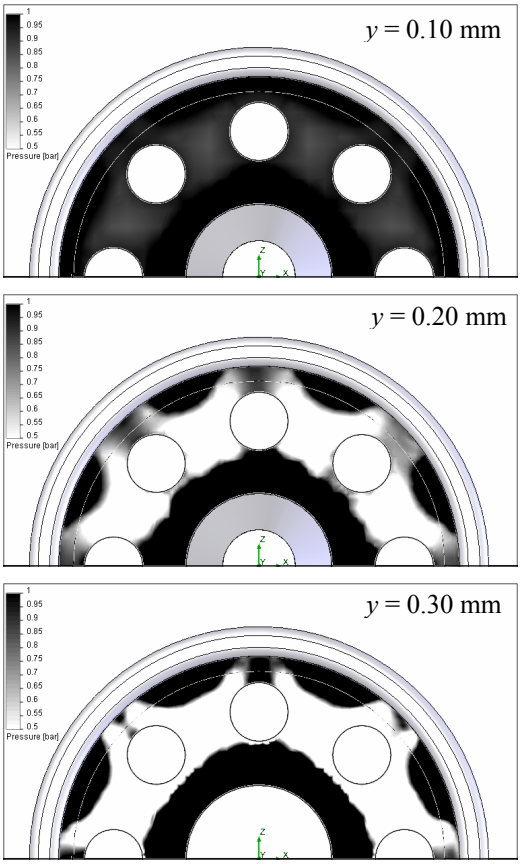

Figure 10. Pressure distribution under the deflector for Valve A (Δp = 118 bar)

4.4 Cavitation issues

In three-dimensional CFD calculations, the simulation of cavitation is numerically very challenging since it requires a two phase model and a good knowledge of the chemical and thermophysical characteristics of the fluids. Hence, at this time, this kind of simulation are quite difficult to be performed and to make them converge. However, some interesting considerations can be drawn if negative pressure is introduced as a concept. In fact, in an incompressible liquid, negative pressure are *dynamically* possible [10]. However, negative pressure are not *thermodynamically* possible. This means that liquids tend to release this negative pressure by forming cavities which expand inside the liquid itself. This phenomenon origins either the cavitation or the aeration, the former being the growth of liquid vapor bubbles and the latter the release of gas trapped inside the liquid.

When a single phase simulation is performed by means of a fluid dynamic solver, negative pressure are calculated whenever are dynamically possible. Hence, by analysing the region where this happens, it is possible to obtain information, even if very qualitatively, on possible cavitation phenomena which can lead, in turn, to foaming and aeration.

In the case considered, negative pressure were calculated within the gap. In fact, due to the high pressure difference (always greater than 100 bar) and the low transversal dimension of the gap which, in the range of elevation considered (Δy = 0.05÷0.30 mm), ranges from about 20 μm to about 110 μm, the velocity are very high (up to 200 m/s). Hence, the conditions for very low, and even negative, pressure takes place. The pressure fields within the gap are shown in Figure 13 for three different values of the elevation, namely y = 0.10 mm, 0.20 mm and 0.30 mm.

The simulation refers to a Δp = 118 bar. It can be noticed that the majority of the pressure loss occurs between the upstream side of the hole and the gap inlet. Downstream the gap inlet, the fluid continue to accelerate.

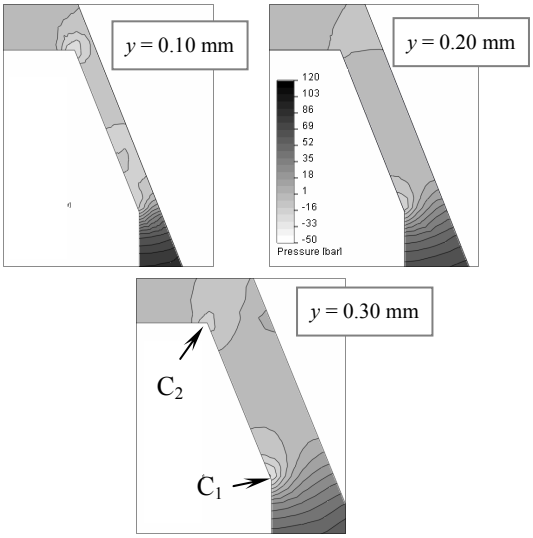

Figure 11. Pressure distribution within the gap

These results showed that the oddness due to the rapid curvatures caused by the hole, the sudden contraction in C_1 and the sudden expansion in C_2 are the main responsible of the pressure drops.

Regarding negative pressure, two critical regions can be recognised, namely C_1 and C_2 in Fig. 13, both of them located at the sharp connections where the fluid is forced to promptly change its direction. It can be noticed also that, for the fluid, the hole acts as a Venturi tube with the throat area just located at the conjunction between the cylindrical part and the conical part of the hole, i.e. at C_1. In fact, as can be noticed, from the gap inlet up to C_1 is convergent, while from C_1 to C_2 the passage diverges since it moves towards higher diameters. This Venturi-effect of the narrow passage enhances the depression in C_1. For these reasons, cavitation is supposed to arise just downstream C_1. Hence, the growth of a vapour/air/liquid foam inside the fluid could start at this point and then is convected downstream to the tank. The appearance of this bubbles is accompanied by characteristic hissing noise.

5. SUMMARY

In this paper, a pressure-relief valve used in a steering circuit for automotive applications has been studied numerically by means of a three-dimensional fluid dynamic code. A number of information, which usually are difficult to be obtained experimentally, were extracted from the simulation. Among these information, the efflux coefficients as a function of the flow rate was one of the most important one. The application of the numerical model provided greater insight into the flow regime and pressure distribution within the valve. Significant recirculation zones were noticed under the deflector. This caused severe blockage and instabilities on the spool due to hydrodynamically-induced depressions. Finally, some attention was dedicated as to detect and obtain information with respect to cavitation by only using single-phase fluid dynamic models.

The result of this analysis was the definition of an improved design of the valve, which can not be reported due to confidentiality. A completely new definition of the deflector geometry was made. Moreover, some changes to the hole and to the narrow passage geometry was performed to reduce the cavitation. As a final result, significant reduction of the foam production and a strong abatement of the hissing noise was noticed when the new valve was tested experimentally.

ACKNOWLEDGEMENTS

This work has been supported by TRW Automotive (Ostellato, Italy) under a Research Contract in the framework of Regione Emilia Romagna PRRIITT Projects.

REFERENCES

[1] Merrit, H.E., 1967, *Hydraulic Control System*, John Wiley & Sons, Inc.

[2] Berta, G.L., Casoli, P., Vacca, A., Franzoni, G., 2004, "Modello di simulazione di una speciale valvola limitatrice di pressione", Proc. *59th Congresso nazionale ATI*, Genova [in Italian].

[3] Casoli, P., Franzoni, G.,Vacca, A., 2003, "A numerical model for the simulation of a load sensing spool valves", Proc. *18th International Conference on Hydraulics and Pneumatics,* Prague.

[4] Idel'cik, E., 1986, *Memento del Pertes de Charge, Coefficients de Pertes de Charge Singulières et de Pertes de Charge par Frottement*, Edition Eyrolles.

[5] Mokhtarzadeh-Dehghan, M.R., Ladommatos, N., Brennan, T.J., 1997, "Finite Element Analysis of Flow in Hydraulic Pressure Valve", *Appl. Math. Modelling,* Vol. 21, pp. 437-445

[6] Naser, J.A. and Gosman, A.D., 1995, "Flow prediction in an axisymmetric inlet valve /port assembly using variants of k-ε", Proc. *Inst. Mech. Eng.,* Vol. 209, pp. 57-69

[7] Amirante, R., Del Vescovo G, Lippolis A., 2006, "Flow forces analysis of an open center hydraulic directional control valve sliding spool", *En. Conv. Manag*, Vol. 47, pp. 114–131.

[8] COSMOS FlowWorks, 2005, *User Manual*, Structural Research and Analysis Corp.

[9] Lam, C.K.G., Bremhorst, K. A., 1981, "A modified form of the k-e model for predicting wall turbulence", *J Fluids Eng*, Vol. 103, pp. 456-460

[10] Batchelor, 1966, *An introduction to fluid dynamics*, Cambridge.

Conference on Modelling Fluid Flow (CMFF'06)
The 13th International Conference on Fluid Flow Technologies
Budapest, Hungary, September 6-9, 2006

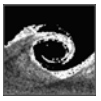

NUMERICAL ANALASYS OF THE VORTEX FLOW IN THE HYDRAULIC POPPET VALVE

Sandor BERNAD[1], Romeo SUSAN-RESIGA[2], Liviu E. ANTON[3]

[1] Corresponding Author. Centre of Advanced Research in Engineering Sciences, Romanian Academy – Timisoara Branch. Bd. Mihai Viteazul no. 24, RO-300223, Timisoara, Romania. Tel.: +40 256 40 3692, Fax: +40 256 40 3700, E-mail: sbernad@mh.mec.utt.ro
[2] Department of Hydraulic Machinery, "Politehnica" University of Timisoara. E-mail: resiga@mh.mec.utt.ro
[3] Department of Hydraulic Machinery, "Politehnica" University of Timisoara. E-mail: Secretariat@casaautotm.ro

ABSTRACT

The paper presents a numerical simulation and analysis of the flow inside a hydraulic poppet valve. Inside the poppet chamber, the annular jet issued through poppet and seat generates several toroidal vortices, witch may generate vortex cavitation with the associated flow instabilities and oscilations. The paper presents an analysis of the main vortex inside at the chamber of a conical poppet valve, as function of the poppet displacement. In a meridional plan the main vortex structure is analysed using an original method developed by the authors. A piecewise linear least square method is employed to compute the radial distribution of vorticity, velocity and pressure within the vortex, using the numerical solution of the hydrodynamic field. It is shown that numerical date can be analytically represented using the Burger's vortex model. This model introduces two vortex parameters: a characteristic radius and a characteristic angular velocity. The main conclusion of the paper is that, we are able to give a concise description of the vortex flow, thus making possible a parametric study with the aim of optimizing the geometry.

Keywords: vortex structure, turbulent flow, CFD, poppet valve

NOMENCLATURE

Ei_1	[-]	exponential integral of degree 1
h	[m]	poppet displacement
p(r)	[Pa]	pressure inside the vortex
p_0	[Pa]	pressure at the vortex center
p	[Pa]	operating pressure
$\overline{p}$	[-]	dimensionless pressure
$\overline{r}$	[-]	dimensionless radius
r	[m]	vortex radius
r_v	[m]	characteristic vortex radius
$v(r)$	[m/s]	tangential velocity
$\overline{v}$	[-]	dimensionless tangential velocity
$\overline{\Omega}$	[-]	dimensionless angular velocity
$\Omega(r)$	[1/s]	angular velocity
Ω_0	[1/s]	characteristic vortex angular velocity
ρ	[kg/m^3]	fluid density
ω	[1/s]	vorticity
Γ	[-]	circulation
ν	[m^2/s]	kinematical viscosity

1. INTRODUCTION

The hydraulic power equipment like poppet valve, in many processes, is the critical elements affecting directly the variability of the process output. In these cases, an improved dynamic and static valve behaviour would have a major impact on the process output. To minimize this major potential of variability, many users have to specify parameters such as response time, hysteresis, and dead band, representing additional requirements to the usual ones given, for example by: flow capacity, shutoff capability, etc. [1, 2, 3].

As the installed valve characteristic varies according to the changing operating conditions, the system must be capable of adapting itself to these new conditions, without intervention of the plant personnel. The flow through the hydraulic poppet is controlled by the displacements of the poppet.

The poppet geometry dictates the flow direction inside the valve. The computational fluid dynamics analysis predicts the flow direction as well as the flow intensity inside the valve. Also, CFD analysis is used to find the fluid pressure and velocity distribution in the valve chamber [4, 5].

Poppet flow is not easily suited to classical mathematical analysis. In order to perform a quantitative analysis of the complicated streamline

pattern inside the poppet valve chamber, an original theoretical model has been proposed [6] thus allowing a parametric study of the poppet valve flow evolution in the whole range of poppet displacement [7].

Under normal operating conditions, the differential pressure across the valve varies due to the dynamics pressure losses in the flow. For an installed valve, the shape of the installed flow characteristic curve is a function of the process pipeline and the inherent flow characteristic of the valve. The gain of an installed valve is defined as the change in relative flow rate divided by the change in relative travel, i.e. the slope of the installed flow characteristic curve. Thus, to obtain an optimum performance it is necessary to obtain a linear installed flow characteristic [8, 9].

Separating interior flows are of the utmost importance for the performance of wide variety of tehchnical applications. Many industrial designs today have to be compromises between the hydrodinamical function and other competing functions e.g. size or mechanical function. In such compromised designs undesired separation is more likely to occur, this drastically decrease the performance of the design. In such cases, active or passive devices which increase ther near wall momentum can be used to remove or reduce the separation [10].

Technological considerations lead to sharp corners, which in conjunction with very narrow passages produce regions of extremely high gradients in the flow field. As pointed in [7, 8], the Cavitation is one of the major problems that hinders the hydraulic machinery performances. Once the flow velocity and blade loading are increased there are regions where the pressure drops well below the vaporization pressure of the liquid and cavitation is developed. The associated noise and vibrations, as well as cavitation erosion, have motivated a great number of theoretical and experimental research [7, 11].

2. THE VORTEX MODEL

The relative simple geometry, Figure 1, produces a very complicated viscous flow field, which can be realistically investigated only by using Computational Fluid Mechanics.

Our previous work on poppet valve hydrodynamics has been mainly focused on two issues: the vortex structu re within the poppet valve chamber [6], vortices size and position evaluation for the whole range of poppet valve.

So far we have investigated only 2D axi-symmetric flows, although the real geometry does not have this symmetry in the outflow region.

This paper continues these investigations and develop an original model for describing the vortex flow inside the hydraulic valve chamber.

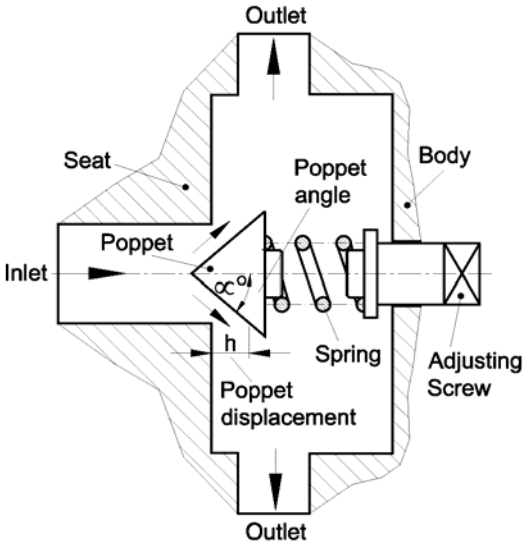

Figure 1. Cross-sectional view of a typical poppet valve.

2.1. Numerical results

Numerical simulations are performed for the 2D axi-symmetric domains (Figure 2).

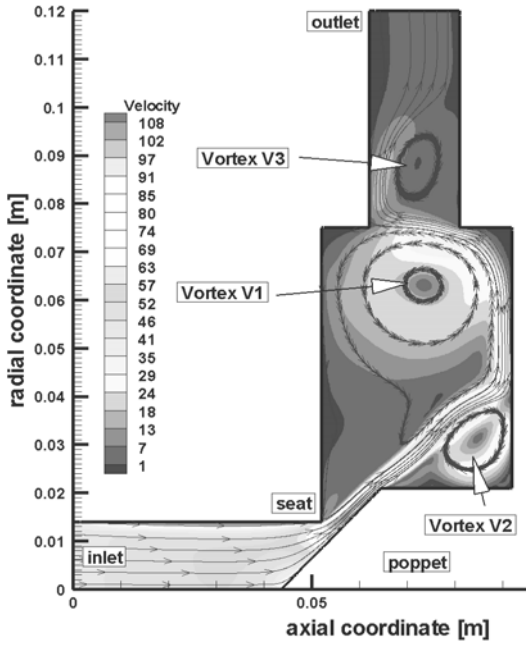

Figure 2. Streamline pattern and velocity field in the meridian half-plane of the poppet valve.

Figure 2 shows the streamlines and velocity field in the poppet valve chamber. A large recirculation region is presented in the valve chamber, and the annular jet issued through poppet-seat slit remains attached to the cylindrical part of the poppet. There is no recirculation in the outlet

section, and the constant pressure seems to be appropriate at outlet.

A typical streamline pattern for the liquid flow through the poppet valve is presented in Figure 3. Three main vortices are developed in the poppet valve chamber. The first two vortices, V1 and V2 are rotating counterclockwise and clockwise, respectively, and are generated on the left-hand side and right-hand side, respectively, of the liquid jet issued from the poppet-seat opening. The third vortex, V3, is generated beyond the valve chamber, in the outflow channel. Such a qualitative analysis of the flow field has been performed also by Dietze [7], who used flow visualization to validate the numerical results, i.e. the streamline pattern. However, Dietze does not provide a quantitative description of the velocity and pressure fields details.

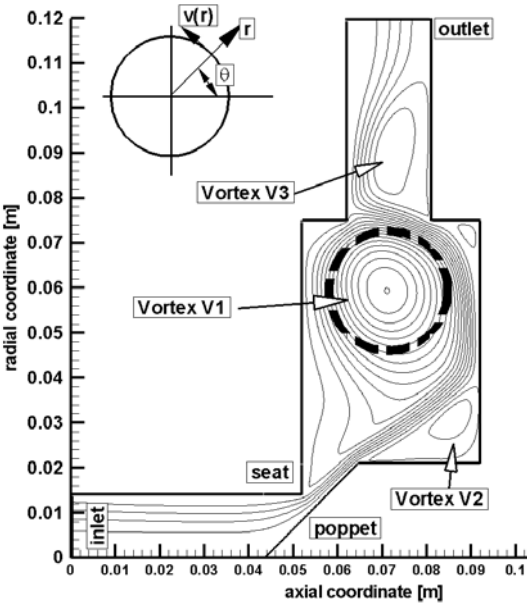

Figure 3. Streamline pattern in meridian half-plane for a conical poppet valve.

Despite the complicated flow pattern, a relatively simple model can be developed to describe the velocity and pressure distribution inside the vortex.

This model, is inspired from the unsteady line vortex diffusion model [12], and has been validated with numerical data for poppet valve flows. Our model uses three parameters to describe the radial distribution of the angular velocity $\Omega(r)$ (half the curl of velocity), tangential velocity *v(r)* and pressure *p(r)* inside the vortex, namely the characteristic vortex angular velocity Ω_0, the characteristic vortex radius r_v, and the pressure at the vortex center (in meridional half plane) p_0.

Inside the vortex we consider a flow with circular streamlines [12, p.201] corresponding to Figures 2 and 3. With r the radius measured from the vortex center (Figure 3) and no θ dependence, our model should establish the vorticity $\omega(r)$, tangential velocity v(r) and pressure p(r) functions.

Let us consider now a two dimensional unsteady flow, initially having zero vorticity everywhere except at the axis $r = 0$ where there is a line vortex of strength Γ. This is the so-called free vortex, with the same circulation Γ round all circles centered on the axis, and $v = \Gamma/(2\pi r)$. If at t=0 the flow stops at the axis, for a viscous fluid with kinematical viscosity ν the vorticity will be diffused radially away [12, p.201],

$$\varpi(r,t) = \frac{\Gamma}{4\pi\nu t}\exp\left(-\frac{r^2}{4\nu t}\right), \qquad (1)$$

and the corresponding velocity radial distribution is

$$v(r,t) = \frac{1}{r}\int_0^r \omega r dr = \frac{\Gamma}{2\pi r}\left[1-\exp\left(-\frac{r^2}{4\nu t}\right)\right] \qquad (2)$$

Starting with this unsteady line vortex diffusion model, we develop a model for the steady vortex flow in the poppet valve chamber. A series expansion of (2) with respect to r gives

$$v(r,t) = \frac{1}{8}\frac{\Gamma}{\pi\nu t}r + O(r^3), \qquad (3)$$

showing a rigid-body rotation for small r. If Ω_0 is the angular velocity for this motion, then

$$\Omega_0 = \frac{1}{8}\frac{\Gamma}{\pi\nu t} \quad [1/s]. \qquad (4)$$

On the other hand, the quantity $4\nu t$ has the dimension of length squared, therefore it can be replaced with a characteristic vortex radius, squared, i.e.

$$r_V = \sqrt{4\nu t} \quad [m]. \qquad (5)$$

Using the two parameters, Ω_0 and r_v, we can rewrite the equations (1) and (2) for a steady vortex flow:

$$\Omega(r) = \Omega_0\exp\left(-\frac{r^2}{r_V^2}\right), \qquad (6)$$

$$v(r) = \Omega_0 \frac{r_v^2}{r}\left[1 - \exp\left(-\frac{r^2}{r_V^2}\right)\right]. \quad (7)$$

The radial pressure distribution is obtained after integrating the radial component of the momentum equation,

$$\frac{v^2}{r} = \frac{1}{\rho}\frac{\partial p}{\partial r}, \quad (8)$$

with ρ the fluid density and $p_0 = p(r=0)$ the pressure at the vortex axis. It results,

$$\frac{p(r) - p_0}{\rho} = \int_0^r \frac{v^2(r)}{r}dr = \frac{\Omega_0^2 r_v^2}{r^2} \times \left[-\frac{r_v^2}{2} + r_v^2 \exp\left(-\frac{r^2}{r_v^2}\right) - r^2 Ei_1\left(\frac{r^2}{r_v^2}\right)\right] - \left[\frac{r_v^2}{2}\exp\left(-2\frac{r^2}{r_v^2}\right) + r^2 Ei_1\left(2\frac{r^2}{r_v^2}\right) + r^2 \ln \right. \quad (9)$$

where Ei_1 denotes the exponential integral of degree 1,

$$Ei_1(x) = \int_1^\infty \frac{\exp(-xt)}{t}dt. \quad (10)$$

The power series representation of (6), (7) and (9) near the vortex axis is:

$$\Omega(r) = \Omega_0 + O(r^2) \quad (11)$$

$$v(r) = \Omega_0 r + O(r^3) \quad (12)$$

$$\frac{p(r) - p_0}{\rho} = \frac{\Omega_0^2 r^2}{2} + O(r^4) \quad (13)$$

which suggests the following dimensionless form for the angular velocity $\overline{\Omega}$, tangential velocity $\overline{v}$ and pressure $\overline{p}$:

$$\overline{\Omega} = \Omega(r)/\Omega_0 \quad (14)$$

$$\overline{v} = v(r)/(\Omega_0 r_v) \quad (15)$$

$$\overline{p} = \frac{p(r) - p_0}{\frac{1}{2}\rho\Omega_0^2 r_v^2} \quad (16)$$

and the dimensionless radius $\overline{r} = r/r_v$. The equations (6), (7) and (9) can be written now in dimensionless form as:

$$\overline{\Omega} = \exp(-\overline{r}^2) \quad (17)$$

$$\overline{v} = \left[1 - \exp(-\overline{r}^2)\right]/\overline{r} \quad (6) \quad (18)$$

$$\overline{p} = \frac{\left[-1 + 2\exp(-\overline{r}^2) - 2\overline{r}^2 Ei_1(\overline{r}^2)\right]}{\overline{r}^2} - \frac{\left[\exp(-2\overline{r}^2) + 2\overline{r}^2 Ei_1(2\overline{r}^2) + 2\overline{r}^2 \ln(2)\right]}{\overline{r}^2} \quad (19)$$

(8)

(15)

A simplified vortex model can also be built by considering a pure rigid body (forced vortex) motion for $0 \le r \le r_v$, followed by a free vortex motion for $r > r_v$. This model is described in Table 1.

Table 1. Simplified vortex model

	$\overline{r} \le 1$	$\overline{r} > 1$
$\overline{\Omega}$	1	0
$\overline{v}$	$\overline{r}$	$1/\overline{r}$
$\overline{p}$	$\overline{r}^2$	$2 - 1/\overline{r}^2$

Figures 4, 5 and 6 show the comparison between the vortex model described by (17), (18) and (19), and the simplified model given in Table 1.

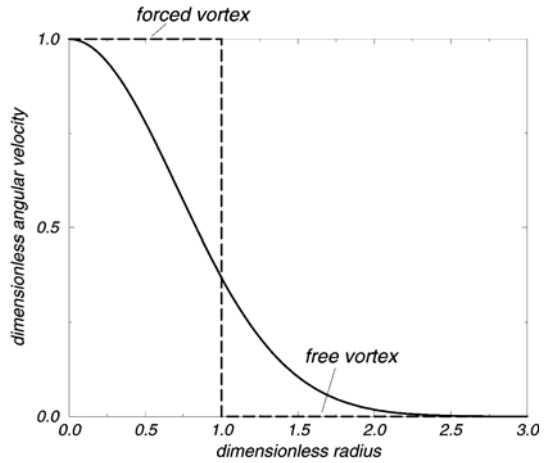

Figure 4. Radial distribution for the angular velocity, according to equation 17 (solid line), and the simplified model (dashed line), respectively.

It can bee seen that the crude approximation for $\overline{\Omega}$ and $\overline{v}$ (dashed curves) can reproduce the correct asymptotic behaviors for $r \to 0$ and $r \to \infty$. On the other hand, the asymptotic value for the dimensionless pressure $\overline{p}$ as $r \to \infty$ gives a value of $2\ln(2)$ from equation (19), while the simplified model gives a larger value of 2. However, the simplified model gives an useful interpretation for the characteristic vortex radius r_v, which according to Figure 5 can be considered as a

fictious boundary between the inner forced vortex and the outer free vortex.

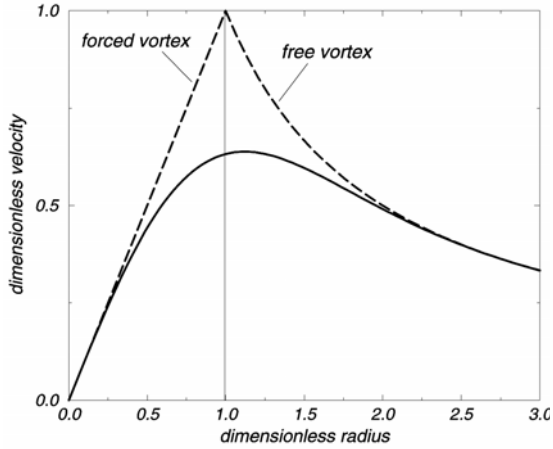

Figure 5. Radial distribution for the tangential velocity, according to equation 18, (solid line), and the simplified model (dashed line), respectively.

In conclusion, the vortex model introduced in this paper uses three parameters Ω_0, r_v and p_0 for describing the radial variation of the angular velocity, tangential velocity and pressure.

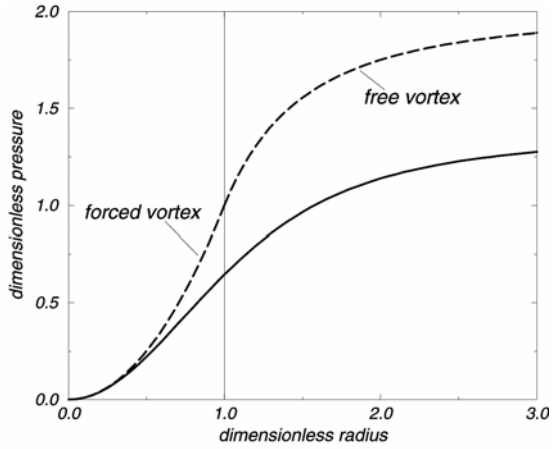

Figure 6. Radial distribution for the pressure, according to equation 19, (solid line), and the simplified model (dashed line), respectively.

If we add the vortex center position in the meridian half plane, we obtain a complete and concise picture of the flow in the poppet valve chamber. The main advantage of this model shows up when conducting a parametric study of the flow in the poppet valve. Instead of getting only qualitative conclusions from the streamline pattern, or using only global quantities, our model allows an engineering analysis of the flow field details.

3. VORTEX MODEL VALIDATION

In order to validate the vortex model described by Equations (6), (7), (9) we consider the numerical results for the main vortex for the operating pressure drop $\Delta p = 6\,bar$ (Figure 7).

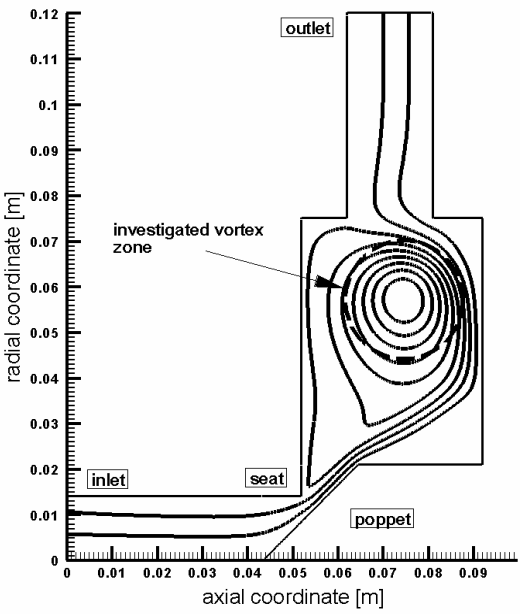

Figure 7. Streamline pattern in the meridian half-plane for a poppet valve with operating pressure drop $\Delta p = 6\,bar$.

Circumferencial average values for the angular velocity Ω, tangential velocity v, and pressure p, are obtained by averaging numerical results and are presented as points in Figures 8, 9 and 10, respectively.

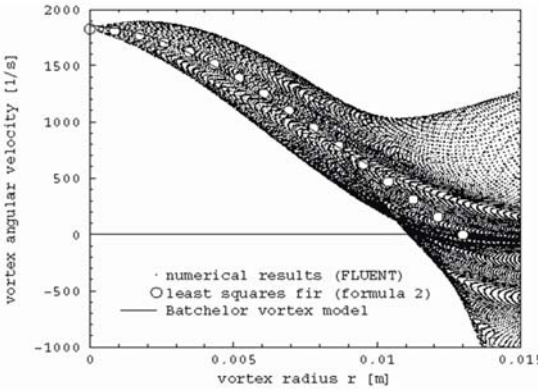

Figure 8. Radial distribution for the angular velocity inside the main vortex from the figure 4. $\Delta p = 6\,bar$.

The three model parameters, Ω_0, r_v and p_0 are obtained as follows. The numerical data for velocity, Figure 10, are approximated with equation

(3) using the least squares method. The fit parameters are Ω_0 and r_v.

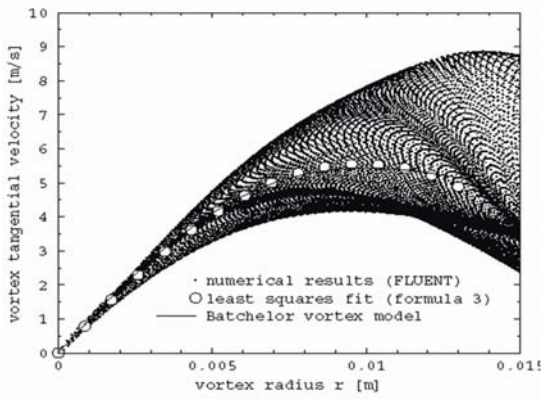

Figure 9. Radial distribution for the tangential velocity inside the main vortex from figure 5. $\Delta p = 6\ bar$**.**

The particular example considered in the paper corresponds to a poppet valve with 22 mm inlet diameter, 45^0 poppet angle and h=2 mm poppet displacement. For a operating pressure drop $\Delta p = 6\ bar$, the main vortex center (in the meridian half plane, Figure 7) is located at X=0.0745 m, R=0.0573 m. After fitting Eq. (7) through numerical data from Figure 9, we get $\Omega_0 = 953{,}7\ s^{-1}$ and $r_v = 0.00892\ m$. With these values, Eq. (9) obviously correctly describes the numerical angular velocity data from Figure 8. The minimum vortex pressure, p_0, is simply determined as the value at the vortex center. With this value, Eq. (9) accurately describe the radial pressure distribution, as shown in Figure 10.

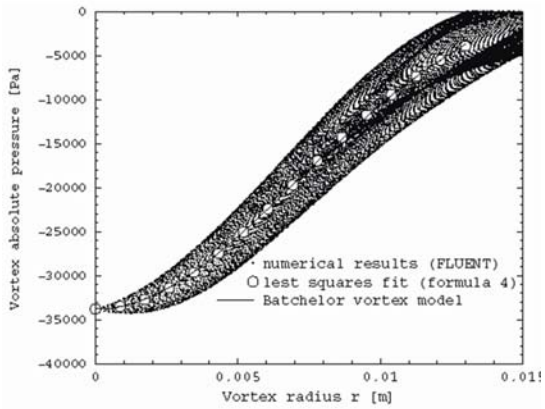

Figure 10. Radial distribution of the absolute pressure inside the main vortex from figure 6. $\Delta p = 6\ bar$**.**

The simplified model, which considers a rigid-body rotation for $r < r_v$, can be considered acceptable only in the neighborhood of the vortex center. On the other hand, it has been observed that the circular streamline approximation is generally valid up to $r = r_v$. Thus, we can introduce a simplified vortex representation as a circle of radius r_v and study of vortex position and radial extension as function of poppet displacement [6].

Table 2 show numerical results for angular velocity Ω_0 and tangential velocity r_v. The first approximation correspond to the velocity field average and the second value corresponde to the pressure field average. Analysisng both numerical value for angular and tangential velocity conclude that the results is same for both approximations.

Table 2. Vortex V1 characteristic parameters

Δp [bar]	Ω_0 [1/s]	r_v [mm]	p_0 [Pa]	x [mm]	R [mm]
6	953.7 923.3	8.92 9.29	-33804	74.5	57.3

4. CONCLUSIONS

A numerical investigation has been performed for a typical axi-symmetrical poppet valve geometry. Although the geometry is axi-symmetric, the computations have been done by assuming the flow to be axi-symmetric as well (2D), or by assuming a full 3D flow.

The paper presents a numerical investigation of the flow inside a poppet valve. For typical poppet valve geometry, an axisymmetric computational domain is assumed, with pressure inlet/outlet boundary conditions, and a steady flow solution is computed.

An original model, developed by the authors, is presented for describing the vortex flow inside the poppet chamber. Our model can provide a concise quantitative description of the radial distribution for the angular velocity, tangential velocity and pressure inside the vortex. A simplified model is also introduced to provide a physical interpretation of the vortex characteristic radius. The vortex model is validated using numerical data obtained with the commercial code FLUENT [13]. When atmospheric pressure is prescribed on the outlet section, large regions inside the poppet valve chamber have negative absolute pressure. This is the result of using the Navier-Stokes equation for the incompressible viscous flow, where the pressure is defined up to an additive constant. From physical viewpoint, when the pressure drops below the vaporization pressure cavitation occurs.

In conclusion, we are able to give a concise description of the vortex flow, thus making possible a parametric study with the aim of optimizing the geometry.

ACKNOWLEDGEMENTS

The authors acknowledge the support from the National University Research Council grants (CNCSIS A 730/2005). All numerical computations have been performed at the Numerical Simulation and Parallel Computing Laboratory of the "Politehnica" University of Timişoara, National Center for Engineering of Systems with Complex Fluids.

REFERENCES

[1] Bulloungh W.A., Chin S.B., 1996, "A numerical study of the effects of poppet valve geometry on its flow characteristics", Proc. of *The Ninth International Symposium on Transport Phenomena in Thermal-Fluids Engineering*, Singapore, pp: 579-584.

[2] Davis J.A., Stewart M., 2002, "Predicting globe Control Valve performance – part I: CFD modeling", *Journal of Fluid Engineering*, Vol. 124, pp: 772-777.

[3] Davis J.A., Stewart M., 2002, "Predicting globe Control Valve performance – part II: Experimental Verification", *Journal of Fluid Engineering*, Vol. 124, pp: 778-783.

[4] Maier A., Sherldrake T.H., Wilcoch D., 2000, "Geometric parameters influencing flow in a axisymmetric IC engine inlet port assembly – part I: valve flow characteristics", *Journal of Fluid Engineering*, Vol. 122, pp: 650-657.

[5] Maier A., Sherldrake T.H., Wilcoch D., 2000, "Geometric parameters influencing flow in a axisymmetric IC engine inlet port assembly – part II: parametric variation of valve geometry", *Journal of Fluid Engineering,* Vol. 122, pp: 658-665.

[6] Bernad S., Susan-Resiga R., Anton I., Ancuşa V., 2001, "Vortex Flow Modeling Inside The Poppet Valve Chamber - Part 2", *Bath Workshop on Power Transmission & Motion Control,* Bath, UK, pp: 161-175.

[7] Dietze M, 1996, "Messung und Berechnung der Innenströmung in hydraulischen Sitzventilen", *Ph.D. Thesis, Düsseldorf.*

[8] Lausch H., Feuser A., Helduser S., 2000, "Development and Optimization of Industrial Proportional Pressure-Relief Valves", *Proc. 48th National Conference on Fluid Power,* Paper I00-13.4, USA.

[9] Roy G., Vo-Ngoc D., Nguyen D.N., Florent P., 2003, "Behavior of Radial Incompressible Flow in Pneumatic Dimensional Control Systems", Journal of Fluid Engineering, Vol. 125, pp: 843-850.

[10] Johnston D.N., Edge K.A., Vaughan N.D., 1991, "Experimentalinvestigation of flow and force characteristics of hydraulic poppet and disc valves", *Proc Instn. Mech. Engrs.* Vol. 205, pp: 161-171.

[11] Martin C. Samuel, Medlarz H., Wiggert D.C., Brennem C., 1981, "Cavitation inception in Spool Valves", *Journal of Fluids Engineering*, Vol. 103, pp: 564-576.

[12] Batchelor G.K., 1967, *An Introduction to Fluid Dynamics*, Cambridge at the University Press, Cambridge.

[13] FLUENT 6.012. User's Guide (2002).

Internal Flows

Conference on Modelling Fluid Flow (CMFF'06)
The 13th International Conference on Fluid Flow Technologies
Budapest, Hungary, September 6-9, 2006

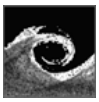

APPLICATION OF NEW TIME-DEPENDENT FRICTION MODELS FOR MODELLING AND SIMULATION OF UNSTEADY FLOWS IN LONG PIPES

Ryszard ROHATYŃSKI[1], Zbigniew ZARZYCKI[2]

[1] Ryszard Rohatyński, Department of Management, University of Zielona Góra. ul. Podgórna 50, 65-246 Zielona Góra, Poland Tel.: +48 68 3282 546, Fax: +48 68 3282 554, E-mail: r.rohatynski@wz.uz.zgora.pl
[2] Zbigniew Zarzycki, Department of Mechanical Engineering, Szczecin University of Technology, E-mail: zbigniew.zarzycki@ps.pl

ABSTRACT

The new method of calculation of transient flows in the hydraulic long pipes is presented in the paper. The method bases on more accurate equations for modeling non-stationary friction of fluid in closed pipes. The changes in time of fluid velocities in radial direction are introduced to the new 2D equations of motion. Owing to that the dissipation of fluid mechanical energy can be better calculated. The variability of wall shear stress has been expressed as a convolution integral of fluid acceleration and a weighting function. The weighting function of this convolution integral depends on previous changes of fluid average velocity in pipe cross-section. Additionally, the function depends also on Reynolds number in case of turbulent flow. These new relationships have been applied for mathematical modeling of harmonic pulsating flow as well as for water hammer. The results of numeric calculations have been compared to experimental results. It has been shown that calculations allowing for variation of friction resistance yield better approximation of the results of real experiment than those obtained for the constant friction resistance.

Keywords: hydraulic long pipe, unsteady flow, friction losses, transient flow equations

NOMENCLATURE

c_o	$[ms^{-1}]$	acoustic wave speed
$p=p(z,t)$	$[kg\ m^{-1}\ s^2]$	average pressure in the pipe cross-section
t	$[s]$	time
$\hat{t} = \nu t / R^2$	[-]	dimensionless time
v_z	$[ms^{-1}]$	axial velocity
$v = v(z,t)$	$[ms^{-1}]$	average flow velocity in the pipe cross-section
w	[-]	weighting function
z	$[m]$	distance along pipe axis
L	[-]	pipe length
Q	$[m^3/s^{-1}]$	discharge
R	$[m]$	radius of pipe
R_e	[-]	Reynolds number
μ	$[kgm^{-1}s^{-1}]$	dynamic viscosity
ν	$[m^2s^{-1}]$	kinematic viscosity
λ	[-]	Darcy–Weisbach friction factor
ρ_0	$[kg\ m^{-3}]$	fluid density (constant)
τ_w	$[kgm^{-1}s^{-2}]$	wall shear stress
τ_{wq}	$[k\ m^{-1}\ s^{-2}]$	wall shear stress for quasi – steady flow
τ_{wu}	$[k\ m^{-1}\ s^{-2}]$	unsteady wall shear stress
ω	$[s^{-1}]$	angular velocity
$\Omega = \omega R^2/\nu$	[-]	dimensionless frequency

1. INTRODUCTION

The domain of research in fluid transient flow in pipes is extremely wide and comprises, among variety of others, such phenomena like dissipation of fluid mechanical energy, cavitation (including problem of column separation), and the pipe wall deformation (so-called fluid-structure interaction). The present paper deals with mathematical models of flow resistance in pipes and is aimed at their applications in calculation and simulation of dynamical phenomena occurring in systems with long hydraulic pipeline.

The commonly used quasi-steady, one-dimensional (1D) model of losses, where the wall shear stress is approximated using Darcy-Weisbach formula is valid only for relatively slow velocity changes in pipe cross-sections, i.e. for small accelerations, or low frequencies of pulsating flow, or in case of considerations of first wave cycle of water-hammer phenomenon. The dissipation of fluid mechanical energy caused by time – variable gradient of radial velocity is not taken into account in 1D model.

There are two classes of models where unsteady friction losses are taken into account. The models belonging to the first class suppose that wall shear stress associated with unsteady friction term is proportional to instantaneous local acceleration (Daily et al. [1], Carrtens and Roller [2], Sawfat and Polder [3]). The popular model of

Brunone at al. [4] also belongs to that class of models. The unsteady friction term of the Brunone's model is expressed as the sum of two components: the first is proportional to instantaneous local acceleration, the second one is proportional to instantaneous convective acceleration.

The more contemporary models, which belong to the second class, assume that unsteady wall shear stress term depends on past flow accelerations, thus they are better theoretically based. Those models use the 2D equation of motion, which makes that time-variable distribution of velocity field in pipe cross-section is not neglected. Zielke [5] was the first, who proposed such an advanced model for laminar flows. The wall shear stress in Zielke's model depends on instantaneous pipe flow accelerations and a function weighting the past changes of velocity. In case of transient turbulent flow the models of friction losses are usually based on distribution of eddy viscosity in pipe cross – section, but this distribution is assumed to be the same as for steady flow. The two-layer model of Vardy and Brown [6] and four-layer model of Zarzycki [7,8] just fit to idea presented above. Recently Vardy and Brown [9] proposed the new model for turbulent viscosity (so-called idealized viscosity distribution model) describing flow through the rough pipe.

The application of non-stationary models of friction to simulation of transient phenomena in pipelines poses a difficult task. The large memory of the computer is required for implementation of traditional Zielke's method [5] and calculations are extremely time-consuming. That is why Trikha [10], and then Suzuki [11], and finally Schohl [12] tried to improve the Zielke's method to make it more efficient. For non-stationary turbulent flow Rahl and Barlamond [13], and then team Ghidaoui - Mansour [14] have applied the model of Vardy to simulation of water-hammer phenomenon. Nevertheless, despite of some improvements, the accuracy and efficiency of calculations are not satisfying till now.

The method described in current paper presents a contribution to the second class of models because it deals with unsteady friction losses. The basic differential equations for unsteady flow are formulated in Section 2. It is shown, that one has to assume the suitable form of weighting function in order to solve the equations system mentioned above. Problems associated with weighting function are considered in Section 3. The two mathematical models for calculation purposes are described in Section 4. These models can be applied to the two basic forms of non-stationary flows, i.e. (i) to that associated with water-hammer phenomenon, and (ii) to that describing harmonically changing flow. The new form of weighting function has been introduced to both models. The calculation results obtained by means of those new formulae are gathered in Section 5. It is showed in Section 5 that these calculation results are more accurate comparing them to results yielded for constant value of the hydraulic friction coefficient.

2. BASIC EQUATIONS

Unsteady flow of fluid in pipes can be represented by two hyperbolic partial differential equations of the momentum and continuity [7,15]:

$$\rho_o \frac{\partial v}{\partial t} + \frac{\partial p}{\partial z} + \frac{2}{R}\tau_w = 0 \tag{1}$$

$$\frac{\partial p}{\partial t} + \rho_o c_o^2 \frac{\partial v}{\partial z} = 0 \tag{2}$$

For unsteady flow in pipe, the shear stress on the wall τ_w is assumed to be the sum of two components: the quasi – steady state component τ_{wq} and an unsteady state component τ_{wu}. For turbulent and for laminar unsteady flows the total shear stress τ_w at the pipe wall may be defined as follows [10,11,16]

$$\tau_w = \frac{1}{8}\rho_o \lambda \cdot v \cdot |v| + \frac{2\mu}{R}\int_0^t w(t-u)\frac{\partial v}{\partial t}(u)du \tag{3}$$

where u is time used in convolution integral.

Eq. (3) relates the wall shear stress to the instantaneous average velocity and to the weighted past velocity changes. The first component in the equation presents the quasi – steady component of wall shear stress while the second one is the contribution due to the flow unsteadiness.

Eqs. (1) to (3) constitute a closed system of nonlinear hyperbolic integro-partial differential equations with Volterra kernel. The nonlinearity is caused also by the Darcy – Weisbach friction factor λ, which depends on unknown instantaneous velocity v. The friction factor λ depends on Reynolds number according to the known Prandtl formulae:

$$\frac{1}{\sqrt{\lambda}} = 0.869 \ln\left(\mathrm{Re}\sqrt{\lambda}\right) - 0.8 \tag{4}$$

or, alternatively, for laminar flow:

$$\lambda = \frac{64}{\mathrm{Re}} \tag{5}$$

To solve Eqs. (1) to (3) one should put the respective form of weighting function to Eq. (3). The next Section deals with this problem.

3. THE WEIGHTING FUNCTION MODEL

The accuracy and duration time of calculation process depend on form of the weighting function. For example, the weighting function in Schol's model [12] for **laminar** flows has got the following form:

$$w(\hat{t}) = \sum_{i=1}^{5} m_i e^{-n_i \cdot \hat{t}} \tag{6}$$

where: $\hat{t}$ - dimensionless time, $m_1 = 1.051$, $m_2 = 2.358$, $m_3 = 9.021$, $m_4 = 29.47$, $m_5 = 79.55$, $n_1 = 26.65$, $n_2 = 100$, $n_3 = 669.6$, $n_4 = 6497$, $n_5 = 57990$.

The other form of weighting function has been proposed by Zarzycki[18,17]:

$$w(\hat{t}) = C_1 \hat{t}^{-0.5} + C_2 e^{-m \cdot \hat{t}} \tag{7}$$

where: $C_1 = 0.2812$; $C_2 = -1.5821$; $m = 8.8553$.

For **turbulent** flows the following Vardy formula [6] has been proposed:

$$w(\hat{t}) = \frac{1}{2 \cdot \sqrt{\pi \cdot \hat{t}}} \cdot e^{-\frac{\hat{t}}{C^*}} \tag{8}$$

where:

$C^* = 12.86/\ \mathrm{Re}^{\kappa}$; $\kappa = \log_{10}(15.29/\ \mathrm{Re}^{0,0567})$.

The formula of Zarzycki [7,8] for turbulent flow has got the simplest form:

$$w(\hat{t}) = C\,\mathrm{Re}^{n} \frac{1}{\sqrt{\hat{t}}} \tag{9}$$

where: $C = 0.299635$, $n = -0.005535$.

The formulae (8) and (9) are rather inconvenient for numeric calculations and for computer simulation [10,12]. Furthermore, they lose usefulness for t=0 (divider is equal to 0!). To overcome these inconveniences Zarzycki and Kudźma [16] have proposed the so-called effective model of shear stress:

$$w_N(\hat{t}) = \left(c_1\,\mathrm{Re}^{c_2} + c_3\right) \cdot \sum_{i=1}^{6} A_i \cdot e^{-b_i} \tag{10}$$

where: $A_1 = 152.3936$, $A_2 = 414.8145$, $A_3 = 328.2$, $A_4 = 640.2165$, $A_5 = 58.51351$, $A_6 = 17.10735$, $b_1 = 207569.7$, $b_2 = 6316096$, $b_3 = 1464649$, $b_4 = 15512625$, $b_5 = 17790.69$, $b_6 = 477.887$, $c_1 = -1,5125$, $c_2 = 0.003264$, $c_3 = 2.55888$.

The next Section deals with application of expression (10) to calculation of non-stationary flows

4. THE INTRODUCTION OF NEW MODEL OF FRICTION LOSSES TO EQUATIONS FOR NON-STATIONARY FLOW

The following two models of non-stationary flows are presented in current Section: the first one holds for water–hammer phenomenon and the second is associated with harmonically pulsating flow.

4.1. The case of water-hammer phenomenon.

It is known, that hyperbolic Eqs.(1), (2) can be solved using the method of characteristics [14]. It yields the system of ordinary differential equations:

$$\pm dp \pm \rho_o c_o\, dV + \frac{2\tau_w c_o}{R} dt = 0 \tag{11}$$

$$dz = \pm c_o dt \tag{12}$$

The grid of characteristics is shown in **Figure 1.**

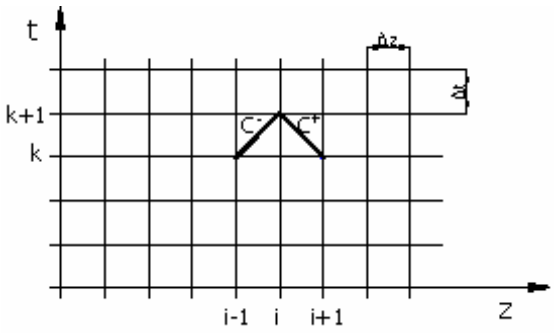

Figure1. The grid of characteristics

Simplifying the above equation system by introduction of finite differences one obtains the following recurrence formulae:

$$p_{k+1,i} = 0{,}5\left[\left(p_{k,i-1} + p_{k,i+1}\right) + \rho_o a\left(V_{k,i-1} - V_{k,i+1}\right)\right] + \\ + 0{,}5\left[\frac{2 \cdot \Delta z}{R}\left(\tau_{w(k,i+1)} - \tau_{w(k,i-1)}\right)\right] \tag{13}$$

$$V_{k+1,i} = V_{k,i-1} - \frac{1}{\rho_o a}\left[\left(p_{k+1,i} - p_{k,i-1}\right) + \frac{2 \cdot \Delta z}{R}\tau_{w(k,i-1)}\right] \tag{14}$$

where: $i = 2, 3, \ldots h$, $k = 1, 2, \ldots n$, m – number of time steps, h – number representing the assumed amount of pipeline sections .

$$\tau_{w(k,i)} = \tau_{wq(k,i)} + \tau_{wn(k,i)} \tag{15}$$

$$\tau_{wq(k,i)} = \frac{1}{8}\rho_o \lambda(\mathrm{Re}_{k,i}) \cdot V_{k,i} \cdot \left|V_{k,i}\right| \tag{16}$$

$$\tau_{wn(k,j)} = \frac{2\mu}{R}[(V_{k,j} - V_{k-1,i})W_{1,i} + (V_{k-1,i} - V_{k-2,j})W_{2,i} + \\ + (V_{k-2,i} - V_{k-3,i})W_{3,i} + \ldots + (V_{2,i} - V_{1,i})W_{k-1,i}] \quad (17)$$

According to Ohmi at al. [19] the critical Reynolds number for unsteady flow is equal to:

$$\mathrm{Re}_c = 800\sqrt{\Omega} \quad (18)$$

Let us note, that weighting coefficients (10) are put into Eq.(17).

4.2. The harmonically pulsating flow.

The mathematical model of this kind of flow is more complicated. The simplified scheme of the system with long pipe-line is shown in Figure 2. The hydraulic long line **H** is connected with flow generator **G** by means of an intermediate element **A** and with load **O** (for example it can be a hydraulic engine**)** by means of an element **B.**

Figure2. The scheme of drive system with hydraulic long line

Thus, the considered hydraulic system can be treated as a complex one-port element composed of two-port elements represented by transmittance matrixes **A,H** and **B** respectively. The load **O** is represented by impedance $\mathbf{Z}_k$ (see Figure 3).

Figure3. The complex one - port drive system with hydraulic long line

The matrix transmittance of the system can be written in the form:

$$\begin{bmatrix} p_I \\ q_I \end{bmatrix} = \mathbf{\Pi} \cdot \begin{bmatrix} p_{II} \\ q_{II} \end{bmatrix} \quad (19)$$

$$\mathbf{\Pi} = \mathbf{A} \cdot \mathbf{B} \cdot \mathbf{H} \quad (19a)$$

The matrix **H** for harmonic excitations can be expressed in the form [7,8]:

$$\mathbf{H} = \begin{bmatrix} \cosh(\chi \cdot \psi) & \left(-j\frac{\rho_0 \cdot c_0 \cdot \psi}{\Omega \cdot \pi \cdot R^2}\right) \cdot \sinh(\chi \cdot \psi) \\ \left(j\frac{\Omega \cdot \pi \cdot R^2}{\rho_0 \cdot c_0 \cdot \psi}\right) \cdot \sinh(\chi \cdot \psi) & \cosh(\chi \cdot \psi) \end{bmatrix} \quad (20)$$

Where

$$\chi = \frac{\nu \cdot l}{R^2 \cdot c_0} \quad (20a)$$

$$\psi = \varepsilon + j\delta \quad (20b)$$

$$\varepsilon = \sqrt{\frac{-(\Omega^2 + 2 \cdot b_2 \cdot \Omega) + \sqrt{(\Omega^2 + 2 \cdot b_2 \cdot \Omega)^2 + (2 \cdot b_1 \cdot \Omega)^2}}{2}} \quad (20c)$$

$$\delta = \sqrt{\frac{(\Omega^2 + 2 \cdot b_2 \cdot \Omega) + \sqrt{(\Omega^2 + 2 \cdot b_2 \cdot \Omega)^2 + (2 \cdot b_1 \cdot \Omega)^2}}{2}} \quad (20d)$$

$$b_1 = re\left(\frac{1}{2}R_o \cdot \frac{\pi \cdot R^4}{\mu} + 2 \cdot j\Omega \cdot L[w(\hat{t})]\right) \quad (20e)$$

$$b_2 = im\left(\frac{1}{2}R_o \cdot \frac{\pi \cdot R^4}{\mu} + 2 \cdot j\Omega \cdot L[w(\hat{t})]\right) \quad (20f)$$

The operator L appearing in the above formulae denotes the Laplace's transform and R_0 – is the constant resistance. If weighting function is known, then coefficients b_1 and b_2 can be determined uniquely. Consequently, elements of transmittances of transfer function of hydraulic long line **H** can be determined as well.

Using (6) for **laminar** flow one obtains:

$$b_1 = re\left(4 + 2 \cdot j\Omega \cdot \sum_{i=1}^{5} \frac{m_i}{j\Omega + n_i}\right) \quad (21a)$$

$$b_2 = im\left(4 + 2 \cdot j\Omega \cdot \sum_{i=1}^{5} \frac{m_i}{j\Omega + n_i}\right) \quad (21b)$$

Using (10) for **turbulent** flow one obtains:

$$b_1 = re\left(\frac{1}{16} \cdot \mathrm{Re} \cdot \lambda + 2 \cdot j\Omega \cdot \left(c_1 \mathrm{Re}^{c_2} + c_3\right) \cdot \sum_{i=1}^{8} \frac{A_i}{j\Omega + b_i}\right) \quad (22a)$$

$$b_2 = im\left(\frac{1}{16} \cdot \mathrm{Re} \cdot \lambda + 2 \cdot j\Omega \cdot \left(c_1 \mathrm{Re}^{c_2} + c_3\right) \cdot \sum_{i=1}^{8} \frac{A_i}{j\Omega + b_i}\right) \quad (22b)$$

The results of computer simulations basing on the above dependencies are presented in the following Section 5.

5. THE EXAMPLARY RESULTS OF COMPUTER SIMULATIONS

5.1. The case of water-hammer phenomenon.

The simulation has been carried out for parameters taken from [19]. The reason of such

choice is very pragmatic, because in this paper the exact results of physical experiments are presented.

The simulation have been carried out for the following parameters of system:

- the length of hydraulic long line L =33160 m
- the internal pipe diameter d= 0,152 m
- the velocity of sound propagation in fluid c_o= =1260 m/s
- the initial velocity of fluid flow v= 0.332 m/s
- fluid density: 860 kg/m3
- the fluid kinematic viscosity: $7.42 \cdot 10^{-6}$ m^2/s
- the value of Reynolds number (under initial conditions) $Re_{om}=2Rv_o/\nu = 6792$
- the critical value of Reynolds number Re_c = 5460

The results of numeric calculations for various models and experimental results are shown in **Figure 4.**

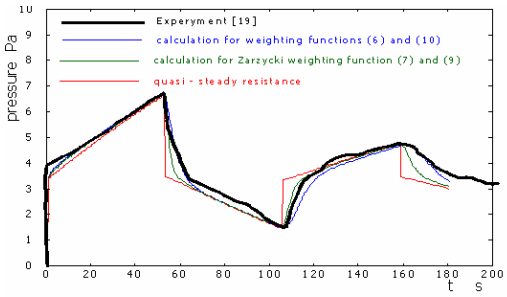

Figure 4. The comparison of measured and calculated values of pressure changes in case of water-hammer

5.2. The simulation of characteristics in frequency domain.

The respective calculations with use of models for variable hydraulic resistances have been done in order to check accuracy of evaluation of frequency characteristics. The exemplary calculations of frequency characteristics of pressure have been done for simple hydraulic system described in [20]. The system was comprised a long copper pipe. Its parameters are as follows: internal diameter d=0,008m, length L=15m, the wall thickness g=0,001m, the average value of flow discharge Q = 8dcm^3/min, the average pressure at the pipe end i.e. directly before the downstream valve - p_2 = 4,6 Mpa. The fluid was hydraulic oil of kinematic viscosity v=23cSt, density ρ_o = 850 kg/m^3, bulk modulus of oil elasticity was β = 1400Mpa. The hydraulic resistance of the downstream was constant. Excitations in form of sine waves were generated by means of an electro-hydraulic amplifier. The calculations were carried out for Z_k =2, where Z_k is dimensionless, linearized impedance of the valve. If one assumes small deviations of pressure angular frequency in relation to its average value then above simplifying assumption yields sufficient accuracy of calculations. Determination of the frequency characteristic p_2/p_1 at input cross-section of the long pipeline was the objective of calculations.

The frequency characteristics calculated for constant and variable hydraulic frictions are shown in **Figure 5**. It can be seen that calculation results obtained for non-stationary models of fluid friction are more close to experimental results than those yielded for constant friction coefficient.

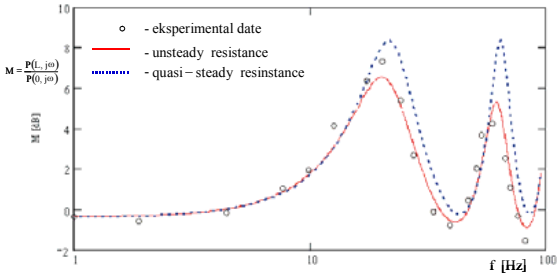

Figure 5 The comparison of frequency characteristics of system with long pipeline obtained from experiments to those obtained by calculations

6. CONCLUSIONS

The new method for calculating transients in hydraulic long pipelines has been proposed. The novelty of presented method consists in substitution of quasi-steady loses of friction in pipelines by a new mathematical formulae for non-stationary friction. The comparison of results of numerical simulation of water hammer phenomenon to experimental results shows clearly that the non-stationary model is better in terms of accuracy. The similar conclusion can be formulated in case of pulsating flow calculations. Hence, it can be claimed that proposed method is satisfactory accurate for calculations of friction losses in non-stationary flows. The better accuracy of results is, however, gained at the expence of calculation amount.

It should be noticed, that besides of good approximation of amplitudes and frequencies of pressure changes due to application of non-stationary friction model one obtains still possibility of almost exact mapping of pressure wave forms. This feature is especially important for investigation of attenuation of pressure waves.

Currently the authors still look for more and more effective methods for calculations of friction losses in non-stationary flows. The latest results are going to be presented at CMFF'06 Conference.

REFERENCES

[1] Dailey J. W. Hankey W. L., Olive R. W., Jordan J. M.,1956, "Resistance coefficient for accelerated and decelerated flows through smooth tubes and orifices", *J. Basic Eng., 78,* pp.1071-1077.

[2] Carstens M.R., Roller J.E., 1959 "Boundary-Shear Stress in Unsteady Turbulent Pipe Flow", *Journ. of Hydraulics Division, Proceedings of the American Society of Civil Engineers,* February, pp. 67-81.

[3] Safwat H.H., Polder J.,1973, "Friction–frequency dependence for oscillatory flows in circular pipe", *Journal of the Hydraulics Division*, ASCE, Vol. 99, HY 11, pp.1933–1945

[4] Brunone, B., Golia, U.M., Greco, M.,1995, "Effects of two – dimensionality on pipe transients modeling", *Journal of Hydraulic Engineering*, ASCE, Vol. 121, pp. 906–912.

[5] Zielke W.,1968,"Frequency - Dependent Friction in Transient Pipe Flow", *Journ. of Basic Eng., Trans.* ASME, pp. 109-115.

[6] Vardy A. E., Brown J., 1996, "On Turbulent, Unsteady, Smooth-Pipe Friction", *Proc. of 7th International Conference on Pressure Surges*, BHRA, Fluid Eng., pp. 289-311, Harrogate, UK,16-18 April,pp.289–311.

[7] Zarzycki Z., 1994, *Hydraulic Resistance in Unsteady Fluid Flow in Pipes* (in Polish), Scientific Papers of Technical University of Szczecin , No 516, Szczecin 1994.

[8] Zarzycki Z., 2000, "On weighting function for wall shear stress during unsteady turbulent pipe flow", Proc.*8th International Conference on Pressure Surges*, BHR Group, The Hague,pp.529–543.

[9] Vardy A. E. and Brown J. M. B., 2004, "Transient turbulent friction in fully rough pipe flows", J*ournal of Sound and Vibration*, 270,pp.233–257.

[10] Trikha A. K.,1975, "An Efficient Method for Simulating Frequency - Dependent Friction in Transient Liquid Flow", *Journ.of Fluids Eng., Trans. ASME , March*,pp.97-105.

[11] Suzuki K., Taketomi T., Sato S., 1991, "Improving Zielke's Method of Simulating Frequency – Dependent Friction in Laminar Liquid Pipe Flow", *Journal of Fluids Engineering, Trans. ASME*, Vol. 113, December,pp. 569–573.

[12] Schohl G.A., 1993, "Improved Approximate Method for Simulating Frequency – Dependent Friction in Transient Laminar Flow", J*ourn.of Fluids Eng., Trans. ASME*, Vol. 115, pp. 420–424.

[13] Rahl F. M. Barlamont J., 1966, "Unsteady pipe flow simulations using unsteady friction flow formulae", Proc.*7th International Conference on Pressure Surges and Transients in Pipeline and Open Channels, pp. 313–322,* BHR Group, Harrogate, UK, pp. 313–322.

[14] Ghidaoui M. S., Mansour S., 2002, "Efficient treatment of the Vardy – Brown unsteady shear in pipe transients", *Journal of Hydraulic Engineering, ASCE,* January, pp.102–112.

[15] Wylie, E. B., Streeter, V. L., 1993, *Fluid Transient in Systems*, Prentice Hall, Englewood Cliffs, NY.

[16] Zarzycki Z., Kudźma S., 2004, "Simulations of transient turbulent flow in liquid lines using time – dependent frictional losses", *Proc. 9th International Conference on Pressure Surges* ,BHR Group, Chester, UK,24–26 March, pp.439–455.

[17] Rohatyński R., Zarzycki Z.,2003, "New formulas for friction loss evaluation in unsteady pipe flow",Proc. *12th International Conference on, Fluid Flow Technologies*, Budapest, Hungary, September 3 - 6, pp. 2003.

[18] Zarzycki Z.,1995, "Weighting functions for simulation of frequency – dependent friction in fluids lines", Proc. *Second International Symposium on Methods and Models in Automation and Robotics*, Międzyzdroje, Poland, 30 August – 2 September, pp.409-412.

[19] Ohmi M., Kyonen S., Usui T.,1985, "Numerical Analysis of Transient Turbulent Flow in a Liquid Line", *Bulletin of JSME*, 28, May, pp.799-806.

[20] Serwach A., 1969, " Dynamical properties of the hydraulic long line", *Archiwum Budowy Maszyn*, 16, 1,pp. 57-80.

Conference on Modelling Fluid Flow (CMFF'06)
The 13th International Conference on Fluid Flow Technologies
Budapest, Hungary, September 6-9, 2006

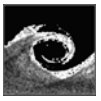

CONTRIBUTION TO EXPERIMENTAL AND NUMERICAL ANALYSIS OF CONFINED SWIRLING FLOW

Žarko STEVANOVIĆ[1], Miroslav BENIŠEK[2], Miroslav SIJERČIĆ[3], Srđan BELOŠEVIĆ[3], Maja ĐUROVIĆ-PETROVIĆ[4]

[1] Corresponding Author. [2] Institute of Nuclear Sciences – Vinca, PO Box 522, 11001, Belgrade, Serbia and Montenego, Tel.: +381 11 2458 222 Ext. 310, E-mail: zare@vin.bg.ac.yu
[2] Institute of Nuclear Sciences – Vinca, PO Box 522, 11001, Belgrade, Serbia and Montenego,
[3] Faculty of Mechanical Engineering, University of Belgrade, Kraljice Marije 16, 11120, Belgrade, Serbia and Montenegro
[4] Republic of Serbia Government, Ministry of Science and Environmental Protection, Nemanjina 24, Belgrade, Serbia and Montenego

ABSTRACT

Swirling turbulent flow in a long straight circular pipe was investigated both experimentally and numerically. The experimental investigations have been performed on special build up test facility. The transport equations for the Reynolds stresses are closed by the second-moment turbulence model. The special attention was paid to the model of pressure-strain-rate correlation as the most dominant transport term, regarding the swirling flow with appreciable streamline curvature. Referring to our previous calculation with the k-ε turbulence model, the downstream constrains up to $z/R\approx25$, predicting a steady recovery, normally expected in "super-critical" conditions. In contrast, the presented second-moment closure for Reynolds stress turbulence model returns a steady decay in good accord with experiment. A comparison of the radial profiles of axial and circumferential velocity correctly mimics the depression of mixing, maintaining the sub-critical nature of the flow. A comparison of predicted Reynolds stresses to the experiment, not included because the experiments were not performed this type of measuring. It was found that the effects of complex strain fields are more correctly predicted using quasi-isotropic model of turbulence part of pressure-strain-rate, even in its linear, but invariance form, than tuning the model constants of degenerative isotropisation-of-production model form of redistributive term.

Keywords: swirling flow, turbulence modelling

NOMENCLATURE

C_i	[-]	turbulence model coefficients
P	[Pa]	averaged pressure
k	[m^2/s^2]	turbulence kinetic energy
p	[Pa]	pressure fluctuation
R	[m]	tube radius
r	[m]	radial coordinate
Q	[m^3/s]	flow rate
U_i	[m/s]	averaged velocity components
u_i	[m/s]	velocity fluctuation components
U	[m/s]	axial velocity
W	[m/s]	circumferential velocity
z	[m]	axial coordinate
ν	[m^2/s]	kinematics viscosity
μ	[$Pa\cdot s$]	dynamic viscosity
Γ	[m^2/s]	circulation
ε	[m^2/s^3]	dissipation rate of turbulence kinetic energy
ρ	[kg/m^3]	air density

Subscripts and Superscripts

i,j,k	space indices
$\bar{}$	time averaged

1. INTRODUCTION

One of the main characteristics of round swirling flow is the streamlines curve in helical paths. The effects on the turbulence structure are no less interesting and influential than those of longitudinal curvature, although they appear to have received less attention from modelers and experimenters alike. Referring to our previous calculation with the k-ε turbulence model, the downstream constrains up to $z/R\approx25$, predicting a steady recovery, normally expected in "super-critical" conditions. In contrast, the presented second-moment closure for Reynolds stress turbulence model returns a steady decay in good accord with experiment. We have referred to Launder and Morse [6] work. The authors recognize that "major changes are needed in modeling the mean-strain contribution to the pressure-strain correlation", but they did not produce any general proposals. Gibson and Younis [3] showed that significant improvement could be obtained from the

Isotropisation-of-Production model (IPM) of pressure-strain term when the model constants have to be adjusted to give relatively less weight to the mean-strain component, and more to the turbulence component. However, this proposal can not be treated as a general improvement of IPM pressure-strain correlation model, so it should better to follow more complex second-moment turbulence model, namely Quasi-Isotropic Model (QIM) that is used in the study.

2. EXPERIMENTAL INVESTIGATION

The experimental investigations have been performed on special build up test facility in Laboratory for hydraulic machinery on Faculty for Mechanical Engineering, University of Belgrade (Fig. 1).

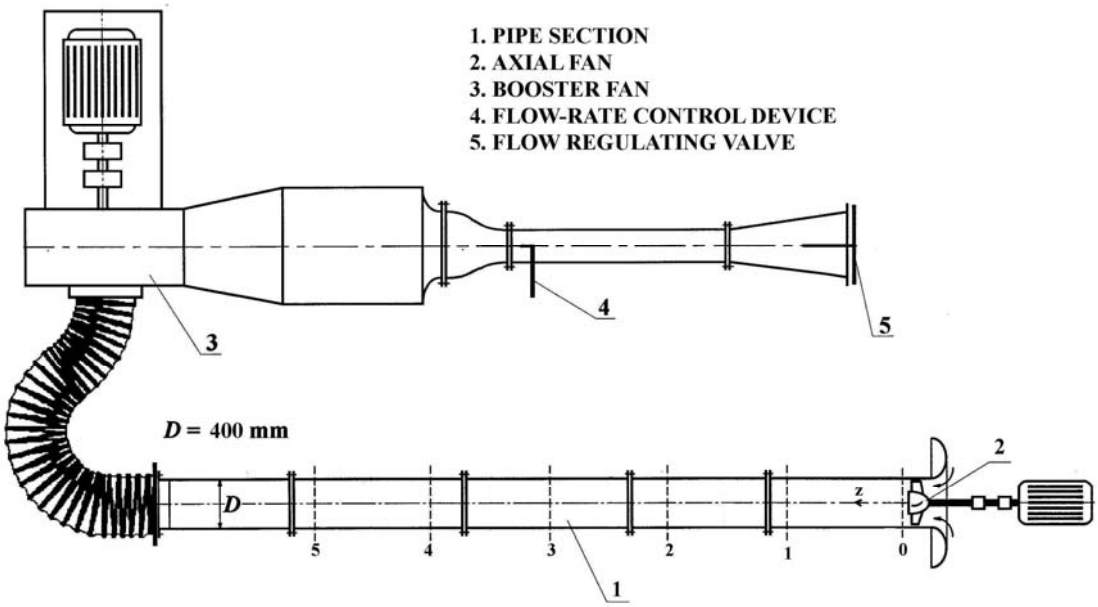

Figure 1. Experimental test facility.

The mean parts of the test facility are: straight pipe section of 21.6 [m] length and 21.6 [mm] inner diameter (1); tube axial flow fan with adjustable impeller blades (2); radial booster fan (3), measuring flow rate device (4) and flow regulating valve (5). The swirl flow is produced by axial fan. Cross sections, designated with numbers 0 to 5 on Fig. 1, show the places were the measurement pf velocities and pressures are performed. For measurement inside the pipe, Conrad 3D probe is used. The measurements for the Reynolds number, $\mathrm{Re} = 4.9 \cdot 10^5$, and swirling flow parameter, $\Omega_0 = 0.748$ are performed. The Re and Ω_0 are experimentally obtained [2], using formulas: $\mathrm{Re} = U_m D / \nu$ and $\Omega_0 = Q / R\Gamma_m$, where $D = 2R$ is the pipe diameter, ν -kinematics viscosity, U_m- mean velocity, Q- flow rate and Γ_m - averaged circulation. These parameters are calculated by:

$$Q = 2\pi \cdot \int_0^R rU \cdot dr \tag{1}$$

$$U_m = Q / \pi R^2 \tag{2}$$

$$\Gamma_m = \frac{4\pi^2}{Q} \int r^2 WU \cdot dr \tag{3}$$

where U and W are axial and circumferential velocities, respectively.

3. MATHEMATICAL MODEL

The averaged transport equations of mass and momentum conservation could be written by usual manner as follows:

$$\partial_0 \rho + \partial_{,j}(\rho U_j) = 0 \tag{4}$$

$$\partial_0(\rho U_i) + U_j \partial_{,j}(\rho U_i) = -\partial_{,i} P + \partial_{,j}[\mu(\partial_{,j} U_i + \partial_{,i} U_j - \rho \overline{u_i u_j})] \tag{5}$$

It is well known that as a result of the time averaging, additional unknown terms have been introduced in the momentum Eq. (5) declared as the Reynolds stress tensor ($-\rho \overline{u_i u_j}$). In order to close the system of averaged Eqs. (4)-(5) it is necessary to deduce the Reynolds stress tensor. The exact kinematics variant of Reynolds stresses transport equations can be written as [5]:

$$D\overline{u_i u_j}/Dt = \overbrace{\partial_0 \overline{u_i u_j}}^{L_{ij}} + \overbrace{U_k \partial_{,k} \overline{u_i u_j}}^{C_{ij}} =$$
$$\overbrace{\partial_{,k}\left(\underbrace{-\overline{u_i u_j u_k}}_{D_{ij}^t} + \underbrace{\nu\,\partial_k \overline{u_i u_j}}_{D_{ij}^\nu} - (1/\rho)\underbrace{\overline{p(u_i \delta_{jk} + u_j \delta_{ik})}}_{D_{ij}^p}\right)}^{D_{ij}} \quad (6)$$
$$+ (1/\rho)\underbrace{\overline{p(\partial_{,j} u_i + \partial_{,i} u_j)}}_{\Phi_{ij}} - \underbrace{(\overline{u_i u_k}\partial_{,k} U_j + \overline{u_j u_k}\partial_{,k} U_i)}_{P_{ij}}$$
$$- \underbrace{2\nu\,\overline{\partial_{,k} u_i\, \partial_{,k} u_j}}_{\varepsilon_{Ij}}$$

where: L_{ij} - local rate of change, C_{ij} - convective transport, $D_{ij} = D_{ij}^t + D_{ij}^\nu + D_{ij}^p$ - diffusive transport by turbulent convection, molecular viscosity and fluctuating pressure, respectively, Φ_{ij} - pressure-strain rate, P_{ij} - stress production rate and ε_{ij} - dissipation rate. In order to resolve the closure problem, the terms D_{ij}^t, D_{ij}^p, Φ_{ij} and ε_{ij} have to be modeled.

The methodology for D_{ij}^t, D_{ij}^p and ε_{ij} modelling can be found in reference [5] therefore it has not been subject of our considerations. However, the principal difficulty in closing the Reynolds stress equations is in modeling the velocity-pressure-gradient correlation. It has a dominated influence to the swirl flow, therefore it was the mean issue of the our study.

From the Eq. (6), it is customary to separate pressure transport by writing,

$$\overline{u_i \partial_{,j} p} + \overline{u_j \partial_{,i} p} = \partial_{,k}(\delta_{ik}\overline{pu_j} + \delta_{jk}\overline{pu_i}) - \overline{p(\partial_{,j} u_i + \partial_{,i} u_j)} \quad (7)$$

where the last term, the pressure-strain correlation, has zero trace and is responsible for inter-component energy transfer. The exact expression for the pressure-strain correlation at some point $\underline{\underline{x}}_0$ may be written as [5]:

$$\overline{(p/\rho)(\partial_{,j} u_i)} = \frac{1}{4\pi}\int_V [\overline{(\partial^2_{,lm} u_l u_m)'(\partial_{,j} u_i)}] + 2\overline{(\partial_{,m} U_l)'(\partial_{,i} u_m)'(\partial_{,j} u_i)}]\,\frac{dV}{\underline{\underline{x}}} \quad (8)$$
$$+ S_{ij} = \Phi_{ij,1} + \Phi_{ij,2} + \Phi_{ij,w}$$

In the above expression terms without superscript are evaluated at point with position vector $\underline{\underline{x}}_0$, while those with a prime superscript are evaluated at the point with the position vector ($\underline{\underline{x}}_0 + \underline{\underline{x}}$). Term S_{ij} is a surface integral which can be negligible away from the vicinity of a solid boundary. This result suggests that the redistributive part of the pressure terms in (8) should also consist of turbulence ($\Phi_{ij,1}$) and rapid ($\Phi_{ij,2}$) components that can be modeled separately. Nearly every worker who has made closure approximations for Reynolds stress turbulence model has adopted Rotta's proposal for $\Phi_{ij,1}$:

$$\Phi_{ij,1} = (\Phi_{ij} + \Phi_{ji})_1 = -C_1(\varepsilon/k)(\overline{u_i u_j} - \tfrac{2}{3}\delta_{ij} k) \quad (9)$$

where $C_1 = 1.5$ and, $k = \frac{1}{2}\overline{u_i u_i}$ and ε are the turbulence kinetic energy and its dissipation rate, respectively. According to (9), the sign of $\Phi_{ij,1}$ is always such as to promote a change towards turbulence isotropy, its magnitude being proportional to the local level of anisotropy. Considering the second part of the pressure-strain term $\Phi_{ij,2}$, it is noted that if the turbulence were homogeneous, the term $\Phi_{ij,2}$ could be expressed following the Launder-Reece-Rodi [5] proposal, as:

$$\Phi_{ij,2} = (\Phi_{ij} + \Phi_{ji})_2 = -\tfrac{1}{11}(C_2 + 8)(P_{ij} - \tfrac{2}{3}P\delta_{ij}) - \tfrac{1}{55}(30C_2 - 2)(\partial_{,j} U_i + \partial_{,i} U_j)k - \tfrac{1}{11}(8C_2 - 2)(D_{ij} - \tfrac{2}{3}P\delta_{ij}) \quad (10)$$

where:

$C_2 = 0.4$,
$P_{ij} = -(\overline{u_i u_k}\partial_{,k} U_j + \overline{u_j u_k}\partial_{,k} U_i)$,
$D_{ij} = -(\overline{u_i u_k}\partial_j U_k + \overline{u_j u_k}\partial_i U_k)$, and
$P = -\overline{u_i u_j}\partial_j U_i$.

Term (10) is refereed as Quasi-Isotropic Model (QIM).

Since each of the three groups of terms on the right side of Eq. (10) vanishes under contraction of indices, one may discard either one or two of the groups without removing the essential property that the term as a whole should be redistributive in character, but without satisfying the symmetry constrain. This implies that Eq. (10) has not invariance form, and will be sensitive to the coordinate system. The first group on the right-side of Eq. (10) turns out to be the dominant one [5]:

$$\Phi_{ij,2} = -\gamma(P_{ij} - \tfrac{2}{3}P\delta_{ij}) \quad (11)$$

where $\gamma = 0.6$. Term (11) is the counterpart of Rotta's proposal for $\Phi_{ij,1}$: as Rotta's term acts to diminish the anisotropy of the stress field so,

according to (11), ($\Phi_{ij,2} + \Phi_{ji,2}$) tends to isotropize the turbulence production tensor. It is the reason that this model is refereed as Isotropisation-of-Production Model (IPM).

The wall-reflection term $\Phi_{ij,w}$ could be accepted for both models by [4]:

$$\Phi_{\mathrm{ij,w}} = (\Phi_{ij} + \Phi_{ji})_w = \\ [0{,}125\frac{\varepsilon}{k}(\overline{u_i u_j} - \frac{2}{3}\delta_{ij}k) + 0{,}015(P_{ij} - D_{ij}]\frac{k^{3/2}}{\varepsilon x_2} \qquad (12)$$

where x_2 is distance to the wall.

Finally, the second-moment turbulence model can be summarized as following [5]:

$$D/Dt(\overline{u_i u_j}) - \\ \partial_k\left[C_s\frac{k}{\varepsilon}(\overline{u_i u_l}\partial_l\overline{u_j u_k} + \overline{u_j u_l}\partial_l\overline{u_i u_k} + \overline{u_k u_l}\partial_l\overline{u_i u_j})\right] \qquad (13) \\ = P_{ij} - \tfrac{2}{3}\delta_{ij}\varepsilon + (\Phi_{ij} + \Phi_{ji})_1 + (\Phi_{ij} + \Phi_{ji})_2 + \Phi_{ij,w}$$

The second order closure problem is closed by transport equation for turbulence dissipation rate [5]:

$$D/Dt(\varepsilon) - \partial_{,k}\left[C_\varepsilon(k/\varepsilon)\overline{u_k u_l}\partial_l\varepsilon\right] = \\ (\varepsilon/k)(C_{\varepsilon 1}P - C_{\varepsilon 2}\varepsilon) \qquad (14)$$

where:

$C_s = 0.22$, $C_\varepsilon = 0.15$, $C_{\varepsilon 1} = 1.45$, $C_{\varepsilon 1} = 1.9$

and $D/Dt = \partial_0 + U_i\partial_k$ is the substantial derivative.

4. COMPUTATIONAL DETAILS

It is instructive to note that swirl flow is highly unusual, for swirl decay very slowly, with circumferential velocity - *W* (Fig.3) profiles indicating a tendency towards solid-body-type rotation, while the axial centerline velocity - *U* (Fig.2) diminishes continuously rather than recovers, with a trend towards reversal far downstream. In such conditions, curvature is expected to severely attenuate turbulence and to inhibit radial diffusion. This type of flow has been termed "sub-critical". Referring to our previous calculation with the *k*-ε turbulence model [1], it can be noted that the *k*-ε model "resists", or more accurately tends to "ignore", the downstream constrains up to *z/R*≈*25*, predicting a steady recovery, normally expected in "super-critical" conditions. In contrast, the QIM second-moment closure for Reynolds stress turbulence model returns a steady decay in good accord with experiment. A comparison of the radial profiles of axial and circumferential velocity in Fig. 2 and Fig. 3., respectively, clearly shows correctly mimics the depression of mixing, maintaining the sub-critical nature of the flow. A comparison of predicted Reynolds stresses profiles (Fig. 4) to the experiment, not included because the experiments were not performed this type of measuring. Comparing to the experimental data given by Hogg and Leschziner [4] for the similar swirl flow, the predicted Reynolds stresses show the same behavior, with the adequate redistribution level.

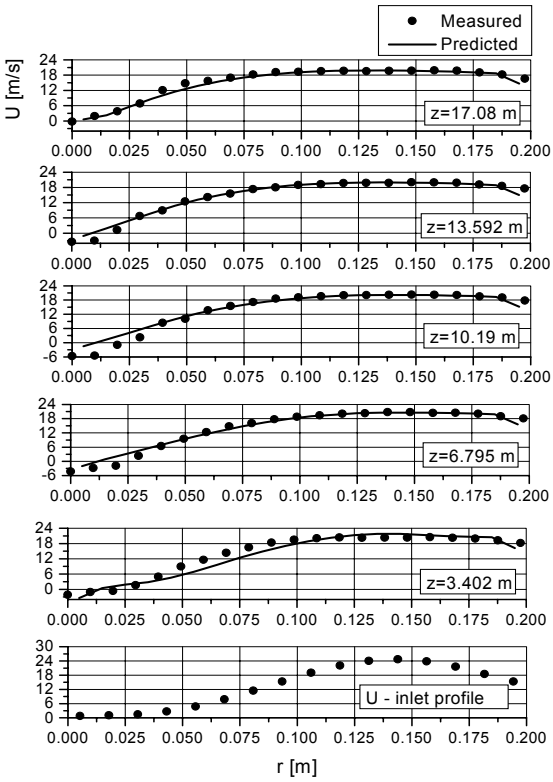

Figure 2. Axial velocity profiles.

5. CONCLUDING REMARKS

Defects in the IPM representation of turbulence stress transport have led us to use exclusively full QIM of Reynolds stress rather than IPM one. Significance of pressure-strain-rate correlation model is pointed in the swirling flows with appreciable streamline curvature. It was found that the effects of complex strain fields are more correctly predicted using QIM of turbulence part of pressure-strain-rate, even in its linear, but invariance form, than tuning the model constants of degenerative IPM form of redistributive term [3]. There are indications that benefits arise here too when viscous transport contributes decisively to the overall balance in the presence of appreciable streamline curvature.

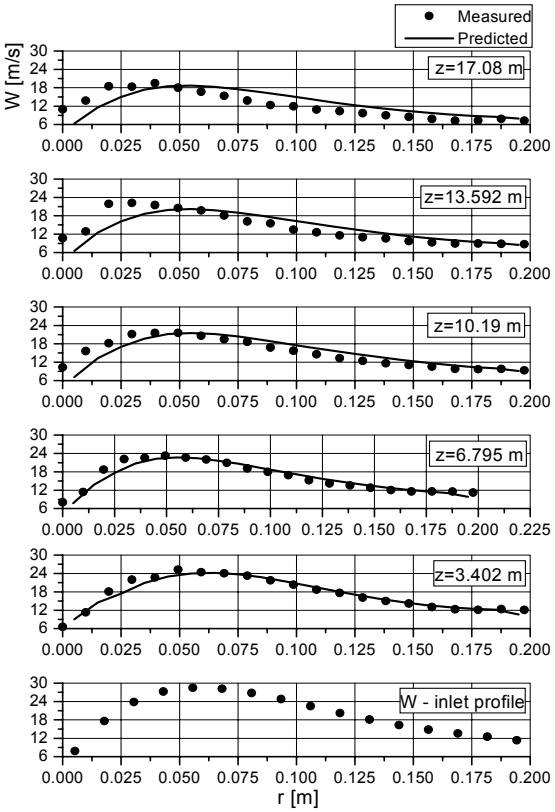

Figure 3. Circumferential velocity profiles.

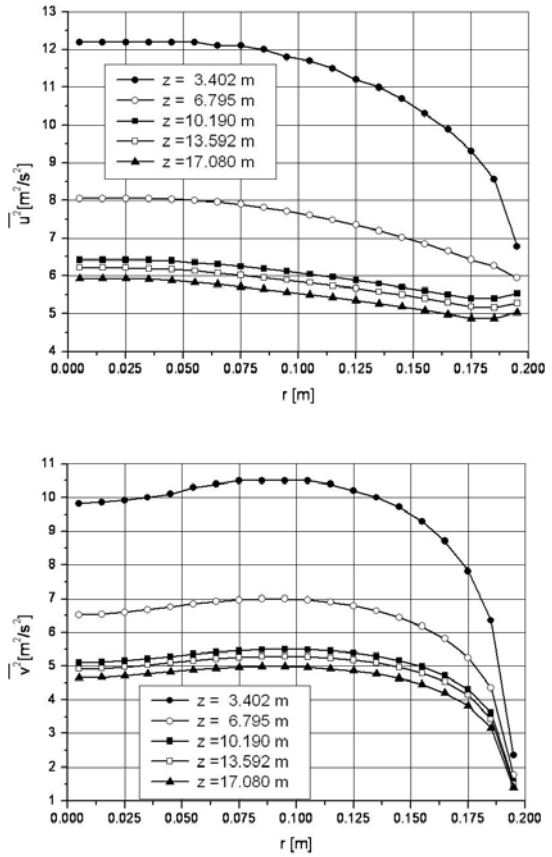

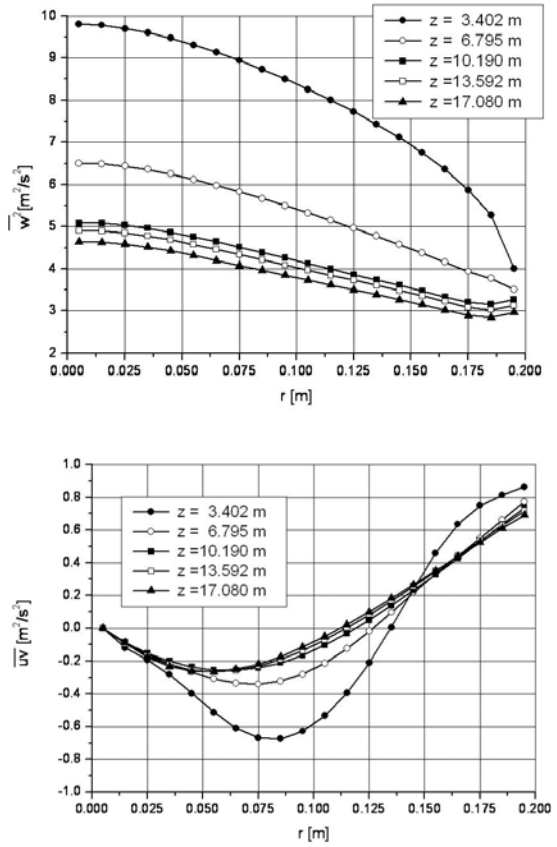

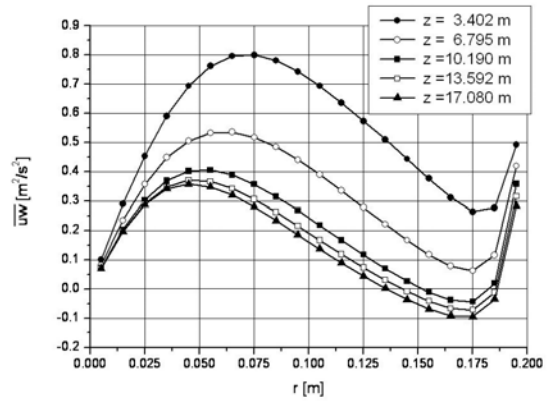

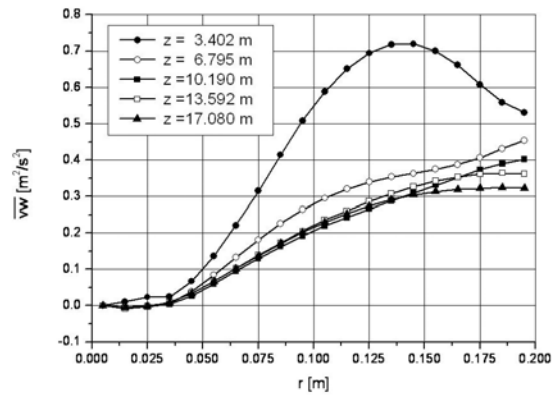

Figure 4. Reynolds stress components profiles.

REFERENCES

[1] Belosevic, V.S., Stevanovic, M.Z. and Benisek H.M., 1998, "A Contribution of the Investigation of Swirling Flow Turbulence Kinetic Energy and its Dissipation in Long Straight Circular Pipe', *CHISA'98, ISBN 80-86059-26-X0879*.

[2] Benisek M, 1979, "Swirling Flow Research in Long-Lined Circular Pipes", *PhD theses,* Faculty of Mechanical Engineering, University of Belgrade.

[3] Gibson, M.M. and Youns, B.A., 1986, "Calculation of swirling jets with a Reynolds stress closure", *The Physics of Fluids,* Vol. 29, p38.

[4] Hogg, W.P. and Leschziner, M.A., 1989, "Second-moment closure calculation of strong swirling confined flow with large density gradients", *Int. J. Heat and Fluid Flow,* Vol. 10, p16.

[5] Launder, B.E., Reece, G.J. and Rodi W., 1979, "Progress in the development of a Reynolds-stress turbulence closure", *J. Fluid Mechanics,* Vol. 68, p537.

[6] Launder, B.E. and Morse, A.P., 1979, *Turbulent Shear Flows,* Springer-Berlin, Vol. 1., p.279.

[7] Stevanovic Z, Sijercic M, Belosevic S and Ilic G, 2004, "Turbulence Modeling of Swirling Flow in a Long Straight Circular Pipe", *Proceedings of The ASME – ZSIS International Thermal Science Seminar II,* Bled, Slovenia, pp.901-906.

Conference on Modelling Fluid Flow (CMFF'06)
The 13th International Conference on Fluid Flow Technologies
Budapest, Hungary, September 6-9, 2006

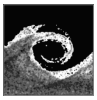

ON THE USE OF ANALYTICAL MODELLING FOR DESIGN IMPROVEMENT OF RIFLED TUBES

Cees van der Geld[1]

[1] Corresponding Author. Department of Mechanical Engineering, Technische Universiteit Eindhoven. W-Hoog 2.135, P.O. Box 513, 5600 MB Eindhoven, The Netherlands. Tel.: +31 40 2472923, Fax: +31 40 2475399, E-mail: c.w..m.v.d.geld@tue.nl.

ABSTRACT

Usually design recommendations for evaporators are based on experiments. However, the value of the added mass coefficients of objects in vorticity flows is the same as those in inviscid flow. This gives the possibility to apply analytical modelling to the hydrodynamics of bubbles in evaporator tubes, and to draw conclusions with regard to tube design. It is shown that a swirl should be created in vertical tubes with up-flow, since hydrodynamic lift forces drive bubbles, once detached from the wall, back towards the wall. So-called rifled tubes create this swirl, and the geometry of rifled tubes is therefore studied in some detail. A combination of CFD modelling and analytical modelling is applied, the latter using a Lagrangian approach. The full added mass tensor for both growing, truncated spheres on a plane wall and for deforming, detached spheres in the vicinity of such a wall is presented as a function of the governing geometrical parameter. Explicit expressions for the hydrodynamic forces are given, in particular for the contributions to the inertia lift force normal to the wall. This force hampers bubble migration. Design recommendations for rifled tubes are given.

Keywords: bubble detachment, rifled tube, tube design, added mass, hydrodynamic forces, potential flow

NOMENCLATURE

A	$[m^2]$	area
b	$[N]$	body force normal to the wall
F	$[N]$	force
C	[-]	force coefficient
g	$[m/s^2]$	acceleration due to gravity
h	$[m]$	distance of centre to the wall
p	$[Pa]$	pressure
T	$[J]$	kinetic energy
r	$[m]$	radius (of bubble foot)
R	$[m]$	radius (of truncated sphere)
t	$[s]$	time
U	$[m/s]$	velocity normal to the wall
U_2	$[m/s]$	velocity parallel to the wall
$\underline{v}$	$[m/s]$	velocity vector
V	$[m^3]$	volume
$\underline{x}$	$[m]$	position vector
α	[-]	added mass coefficient to U^2
α_2	[-]	added mass coefficient to U_2^2
β	[-]	added mass coefficient
θ	[-]	contact angle
ρ	$[kg/m^3]$	mass density
σ	$[N/m]$	surface tension coefficient
ψ	[-]	added mass coefficient
ω	$[s^{-1}]$	vorticity

Subscripts and Superscripts

L, b, w	liquid, bubble, wall
CM	centre of mass
foot	bubble foot
ω	vorticity-related

1. INTRODUCTION

When the escape of volumes of a lighter phase from a heated wall is the most important phenomenon for safe or optimal operation of a steam generator, the performance of a heat exchanger tube is largely determined by such quantities as the bubble size at detachment. Other parameters are given below. In sub-critical conditions, high heat fluxes correspond to boiling, whereas in supercritical flows high heat fluxes create turbulent patches that contain a relatively hot, lighter phase. Since conventionally fired electric power plants in part-load usually operate at sub-critical conditions, the present study focuses at boiling. This study is about prediction tools that may assist in improving the design of rifled tubes (Figure 1).

The advantage of a rifled evaporator tube is the presence of mechanisms that move bubbles, formed at the inner wall, towards the centre. An additional body force, induced by the swirling motion created by fluid flowing along helically shaped ribs (Fig. 1),

and the Coriolis force are created to this effect. However, existing correlations for bubble detachment do not take these forces into account. In addition, the swirling motion induces a non-axial velocity component parallel to the wall, effectively increasing shear at places near the ribs. Would this velocity component promote bubble detachment and would it promote bubble escape from the wall after detachment? So the question arises how to account for the effect of swirl on bubble detachment and migration in simulations of two-phase flow in the complex 3D-geometry of a rifled tube. The present paper addresses this question (section 2).

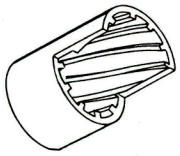

Figure 1 Piece of a rifled tube

The main parameter that makes the difference between boiling in rifled and straight tubes with identical heating conditions (exchange area, heat flux, mass flow rate coolant) is expected to be the bubble detachment diameter, because other parameters, such as

- nucleation site density
- bubble growth time for given detachment size
- waiting time between consecutive bubbles at a nucleation site,

are merely dependent on the velocity profile via the heating conditions [1,2]. In order to predict the bubble detachment diameter, the forces exerted on the bubble should be known at all times during its growth. Previous modelling attempts usually suffered from a lack of knowledge of hydrodynamic lift and inertia forces, which gave rise to fit parameters that had a large experimental uncertainty [3-6]. At present, analytical solutions exist that pave the way towards analytical prediction of detachment radii [7-9]. This analysis is based on Lagrangian modelling of the forces on the bubble. Main features are presented in section 2, where the effect that the bubble approach velocity component parallel to the wall has on both detachment and escape from the wall is highlighted. Also the effects of drag and of vorticity in the flow will be discussed.

Even with a homogeneous heating at the outside, the single-phase heat flux at the inside of a rifled evaporator tube is inhomogeneous. The rifles act as fins that promote heat transfer and cause inhomogeneous wall temperatures. Thus, the occurrence of helically shaped rifles has two main consequences, apart from the increase in heat exchanging area for given outside diameter [10]:

- swirl in the two-phase mixture is created that affects redistribution of heat in the flow, and
- the heat transfer coefficient from the wall to the mixture is locally augmented.

Since these mechanisms obviously affect boiling, optimisation of the geometry of a rifled evaporator tube is only possible if the helical structures are fully modelled. In view of the complexity of the geometry this necessitates the application of CFD. Vice-versa, local heating conditions are affected by boiling, which in principle would necessitate the accounting for a two-way coupling between the dispersed phase (vapour) and the fluid. It has been investigated what nowadays the possibilities are with straightforward extensions of commercially available CFD packages [11]. Results of this are reported in section 3, where design recommendations for the geometry of rifled tubes will be given taking full advantage of the modelling results of section 2.

2. PREDICTION OF BUBBLE DETACHMENT AND MIGRATION

2.1. Vorticity considerations

Two effects of rotational flow in a pipe, swirl, on single bubble detachment are:

- An additional pressure gradient perpendicular to the tube wall is induced, and
- A nonzero azimuthal mean flow component parallel to the wall is introduced.

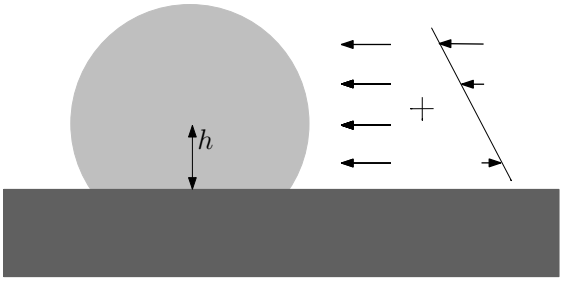

Figure 2. Schematic of the way the flow that approaches a bubble in the shape of a truncated sphere is split up in a uniform part plus a simple shear part.

The result of the first effect is a buoyancy-like force normal to the wall that can easily be accounted for in the conventional way of dealing with gravity and buoyancy, see section 2.2. The second effect might lead to an increased lift force by an increase in vorticity and mean bubble approaching flow, as will now be explained. Any flow field that is approaching a bubble, footed at a wall or not, can in first approximation be thought of as being composed of a uniform flow component plus a simple shear component, in a way depicted in Figure 2. The simple shear component leads to a vorticity-induced lift

force that must be estimated from an expression for isolated bubbles like:

$$F_\omega = V_b \rho_L C_\omega \underline{\nabla} \times \underline{v}_L \times \underline{v}_L \qquad (1)$$

Here C_ω is a Reynolds-dependent coefficient with a value that for bubbles in the vicinity of a wall is expected to be close to 0.5 [4]. Bubble volume is V_b and ρ denotes mass density. Both the approach velocity, $\underline{v}_L$, and the curl of $\underline{v}_L$, the vorticity $\underline{\omega}$ that occurs in the above expression, are in the present study estimated from single phase computations performed with CFD packages. The action of the vorticity lift force is negative in the sense that it drives a fully detached, spherical bubble towards the wall in upward, vertical flow. However, another important force component is the inertia lift force due to the homogeneous flow component that approaches a bubble that is growing at a wall (Fig. 2). This contribution is modelled in section 2.2, and must be added to the force of Eq. (1), as will be discussed shortly.

The vorticity fluctuations introduced by turbulence are an order of magnitude less than the above simple shear component, and can be shown to have a negligible force contribution in boiling applications.

Existing correlations for the drag force coefficient are for flow situations when a fully developed wake downstream of the bubble is present. A typical boiling bubble, on the contrary, grows in 3 ms from a radius of zero to one of 0.5 mm. The wake is practically non-existent in this case and the vorticity generated at the bubble boundary is confined to a thin layer at the surface. Bubble growth is rapid, and known to be controlled by heat transfer from the thermal boundary layer and by inertia forces [1,2]. Surely in low-viscous fluids such as water, drag plays no role of importance [7]. Homogeneous flow over a bubble that is growing by boiling at a solid boundary is therefore a typical example of inviscid flow. It is modelled in section 2.2 as a potential flow with the aid of an Euler-Lagrange-Kirchhoff approach. The inertia forces to be considered are due to deformation of the bubble, due to motion of its centre-point and due to the uniform approaching flow component. The bubble size in high-pressure boiling is relatively small, so deformation is merely isotropic expansion. The bubble shape is therefore assumed to be that of a truncated sphere with radius R and distance h of the centre to the wall.

Much work was expended in the decoupling of the basic force terms governing the motion of the centre point of a bubble. Howe [12] showed that when a body with a constant volume moves in a viscous, rotational flow at rest at infinity, the added mass force can be separated from the force due to vorticity. The added mass coefficients of bubbles computed for inviscid flow retain their value in flows with vorticity. This is an important result for which much other evidence exists, both numerical and analytical [14]. It would be beyond the scope of the present paper to discuss derivations in detail. The main conclusion, however, is that the added (or virtual) mass coefficients computed in section 2.2 are generally applicable, and that the resulting inertia forces retain their values in viscous, rotational flows. The results of section 2.2 are therefore directly applicable to boiling in rifled tubes, and such an application will be performed in section 3.

2.2. Analytical modelling of forces

Ideally, bubble creation in boiling is fast, not hampered much by the slow mechanism of diffusion of heat, and bubbles are rapidly transported away from the evaporator tube wall towards the tube centre. In order to make this happen, hydrodynamic forces on bubbles have to be controlled or even invoked. A first and necessary step in the optimization of rifled tubes is therefore a precise knowledge of the hydrodynamic forces involved and of way to adjust them.

The added mass of a bubble is a function of the shape of the bubble and of its distance to a wall. For example, the usual added mass α corresponding to velocity U can be defined from kinetic energy T with $T/(\rho_L V_b) = \frac{1}{2} \alpha U^2$. There are other added mass coefficients that account for expansion, or more complex deformation, and the connection of deformation to the motion of the centre-point. The resulting added mass tensor depends on distance to the wall and parameters describing the shape of the bubble, as will be shown below. If this dependency is known, the hydrodynamic inertia forces can all be computed, which is done in the present section. Vorticity in the approaching flow leads to a lift force that can be added to the inertia forces (section 2.1). Also drag can be added, but is usually negligible (section 2.1).

Consider a bubble footed at a plane wall with rotational symmetry around the axis perpendicular to the wall through the centre of the bubble. Let A_{bL} denote the area of the interface between liquid and bubble content, A_{bw} the area between the wall and the bubble, r_{foot} the radius of the foot of the bubble, $\underline{x}_{CM}$ the location of the centre of mass of the bubble in a coordinate system with its origin in the centre of the bubble foot. The pressure inside the bubble, p_b, is taken to be homogeneous, constant in time and corresponding to the saturation temperature at the bubble interface. The shape of the bubble is now assumed to be that of a truncated sphere footed on a plane wall, see section 2.1. Two generalized parameters describe the interface: R and h. The time rate of change of R is $\dot{R}$ and that of h is U. Let F_3 be the hydrodynamic force component on the bubble, normal to the wall and positive if pushing it away from the wall. We intend to evaluate the

Lagrangian equation of motion corresponding to parameter h:

$$\frac{d}{dt}\frac{\partial T}{\partial U}-\frac{\partial T}{\partial h}=-F_3 \qquad (2)$$

Force F_3 is minus the force on the liquid and is the sum of all generalized forces acting on the bubble, including the body forces. They have to be identified before the kinetic energy in the liquid, T, is assessed.

In the case of the dynamics of bodies moving in a fluid and/or partly on a wall there is a straightforward and unambiguous way to identify the generalized forces. It starts with the computation of the time rate of change of the kinetic energy in the liquid with the so-called mechanical energy balance. The volume integral over the contribution from body forces like gravity g in the mechanical energy balance is with the lemma of Gauss converted into surface integrals. Let now b denote the body force component that is active normal to the surface. It gets special attention here since it accounts for a body force that is invoked by swirl created by helical structures in a rifled tube. The surface integral over the bubble-liquid interface, A_{bL}, of the contribution of b yields the following two terms:

$$-\rho_L V_b \; \underline{b}\cdot \underline{v}_{CM} - \rho_L \underline{b}\cdot \underline{x}_{CM}\, dV_b/dt. \qquad (3)$$

The first term on the LHS of Eq. (3) is the well-known buoyancy force that in vertical tubes only has a component parallel to the wall. It yields a contribution to the generalized forces if boiling occurs on horizontal surfaces, because the position of the centre of mass depends on distance h. Similar manipulations of terms in the mechanical energy balance that comprise pressure lead to the generalized forces on the RHS of the following equation [7,8]:

$$\begin{aligned} -F_3 \;=\; & p_b \frac{\partial V_b}{\partial h} - \sigma\frac{\partial A_{bL}}{\partial h} - \Delta\sigma\frac{\partial A_{bw}}{\partial h} - \\ & \{p_w - \rho_L\, b\, x_{CM,z}\}\frac{\partial V_b}{\partial h} + \\ & + V_b\,\rho_L\, b\,\frac{\partial x_{CM,z}}{\partial h} - F_{drag}. \end{aligned} \qquad (4)$$

Here $\Delta\sigma$ denotes $\sigma_{bw}-\sigma_{wL}$, $x_{CM,z}$ is the distance to the wall of the centre of mass (unequal to h, generally) and F_{drag} is the drag force that needs no further consideration because of the low viscosity (section 2.1). The surface tension between liquid and bubble, σ, and the hydrostatic pressure at the wall, p_w, do not appear in Eq. (4) in a familiar way. However, since $\frac{\partial V_b}{\partial h}$ is equal to πr^2_{foot} it is easy to see that the sum of the terms containing this derivative in Eq. (4) gives rise to the force that is usually denoted with 'pressure correction force', or such [4]:

$$\pi r^2_{foot}\;\{p_b - p_w\}. \qquad (5)$$

Similarly, the sum of the surface tension terms can be shown to be equal to the usual expression for the component of the surface tension force that attracts the bubble to the wall [4].

$$2\pi\, r_{foot}\;\sigma\,\sin(\theta), \qquad (6)$$

where θ denotes the contact angle.

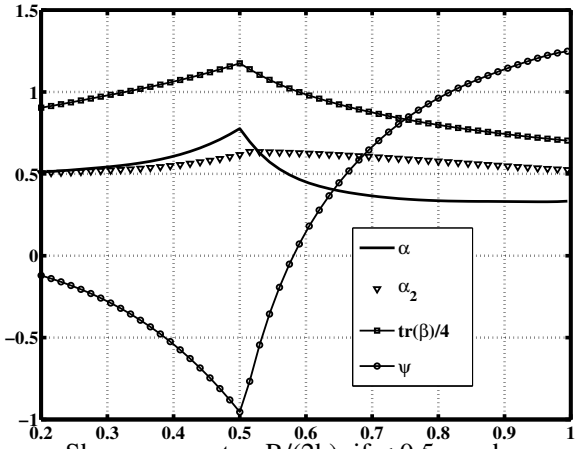

Figure 3. Added mass coefficients for spheres and truncated spheres

Now all generalized forces have been identified, application of the Lagrangrian equation (2) requires the evaluation of the kinetic energy. For this, a velocity potential is required. In the literature solutions for this potential were often found by matching series expansions, implying some arbitrariness in defining the type of expansion. There is a straightforward alternative [7] that sets off with a suitable expansion in elementary functions. The boundary condition, in terms of the generalized velocities that are supposedly not all zero, is written as a matrix equation such that a Hilbert-Schmidt operator can be identified. An inverse exists because of the Fredholm alternative. The solution for the velocity potential is subsequently obtained by application of this inverse to a combination of generalized velocities, as prescribed by the velocity boundary condition at the interface of the bubble, see ref. [7]. A suitable expansion in elementary functions can for the case of a truncated sphere be obtained in various ways, one based on Legendre polynomials of the first order. These have been applied to obtain the added mass coefficients α, α_2, tr(β), and ψ in the following expression for the kinetic energy:

$$T\,/(\rho_L\,V_o) \;=\; \tfrac{1}{2}\,\alpha\,U^2 \;+\; \tfrac{1}{2}\,tr(\beta)\,\dot{R}^{\,2} \;+\; \tfrac{1}{2}\,\psi\;\dot{R}\;U + \tfrac{1}{2}\,\alpha_2\,U_2^{\,2}, \qquad (7)$$

Here V_o denotes $4\pi R^3/3$, and U_2 is the uniform approach velocity component parallel to the wall, see Fig. 2. The added mass coefficients and the volume of the truncated sphere are only dependent on the geometrical parameter $\lambda \equiv R/(2h)$. The dependencies of the added mass coefficients are shown in Figure 3. Equations (2, 7) yield

$$F_3/(\rho_L V_o) = -\,\alpha\,\acute{U} - \tfrac{1}{2}\,\psi\;\ddot{R} + F, \qquad (8)$$

with

$$F = -\,U\,\dot{R}\,\{\frac{\partial\alpha}{\partial R} + \alpha\,4\pi R^2/V_o\} - \tfrac{1}{2}U^2\,\frac{\partial\alpha}{\partial h} - \tfrac{1}{2}\,\dot{R}^{\,2}\{\frac{\partial\psi}{\partial R} - \frac{\partial\,\mathrm{tr}(\beta)}{\partial h} + \psi\,4\pi R^2/V_o\} + + \tfrac{1}{2}U_2^{\,2}\,\frac{\partial\alpha_2}{\partial h}\,. \qquad (9)$$

Here $\acute{U}$ is the time rate of change of velocity U, and F is a hydrodynamic lift force, divided by $\rho_L V_o$, that would be difficult to be captured in analytical form with an approach other than the Lagrangian approach. The derivatives occurring in Eq. (9) can all be expressed as derivatives with respect to λ, since the added mass coefficients only depend on λ.

Figure 3 shows that the derivatives that occur in Eq. (9) change sign when the bubble shape changes from a truncated to a full sphere, *i.e.* when $\lambda = \frac{1}{2}$. It can be shown that because of this change of sign in most practical cases force F changes drastically [14]. It turns out in practice that F can be promoting detachment of a bubble shaped as a truncated sphere, if U_2 is large enough, but that F is driving a spherical bubble back towards the wall once detached.

The actual bubble dynamics before detachment is determined by the combination of equation (4) and (8), and depends on the coupling of volume with pressure of the bubble content. Because bubble growth in boiling is a nearly isothermal process, the interplay of surface energies induces oscillations at relatively low frequency [8, 14]. These oscillations are only possible if the bubble foot is on the wall and if motion of the contact line is not hampered.

2.3 Conclusions for the design of evaporator tubes

The main conclusion to be drawn from the above computations is that high-pressure boiling bubbles after detachment in upflow of water in a vertical tube stick close to the wall. All vorticity-related and inertial hydrodynamic forces near the wall act towards the wall. If downflow of liquid is not an option, migration towards the centre of the tube must be caused by

- Interaction with other bubbles and turbulence
- Deformation after coalescence
- Body forces induced by swirl.

Optimal control is only achieved with the last option. The first design recommendation is therefore to induce swirl. This can either be done with special inserts or by helical structures on the inner tube wall, as shown in Fig. 1. This recommendation explains the focussing on rifled tubes of this study. However, the above analysis also makes clear that hydrodynamic forces not only have a negative effect on boiling heat transfer: before detachment bubble growth can be positively influenced. Bubble growth time is then reduced by hydrodynamic forces that promote detachment irrespective of the direction of the flow parallel to the wall. At places on a structured inner wall of a tube where this velocity component is relatively high bubbles must be expected to leave the position with a relatively small diameter. This leaving place can imply actual detachment or being swept away further downstream, the so-called sliding of bubbles.

The above findings will now be used in a design study of the geometry of a rifled tube.

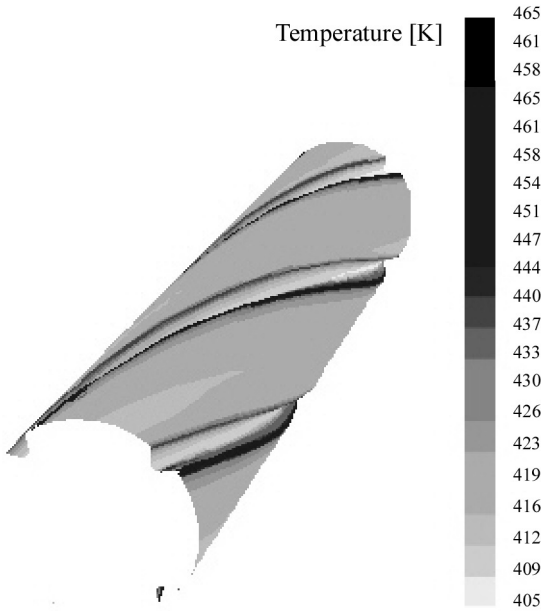

Figure 4. Temperature field at the wall of a tube with rounded inner rifles. Flow is out of the paper. Highest temperatures are just downstream of the rifles and lowest temperatures are on top of the rifles that act as fins. Constant heat flux at the wall; Fluent™.

3. APPLICATION TO DESIGN IMPROVEMENT OF RIFLED TUBES

It has been attempted by our group to implement a mechanistic model for the prediction of bubble detachment and heat transfer that was available in the literature, work of Basu *et al.* [13], in the commercially available CFD package Fluent™ [11]. Correlations used account for the sliding of bubbles, for example, but are essentially 1D in the sense that heat transfer between *the bulk* of the fluid and the wall is predicted. A locally applicable, equivalent 3D version of these correlations had to be found. The main conclusion that must be drawn from this attempt is that with the existing mechanistic models such an implementation is awkward. Apparently, the prediction of two-phase flow with heat transfer in rifled tubes with commercial CFD codes, with special extensions to account for boiling, is all but straightforward with the present state of knowledge.

However, single phase flow with heat transfer is readily modelled with such packages [10, 11], see for example Figure 4. It is therefore possible to apply the conclusions of section 2.3 with the assumption of a one-way coupling in the following way. Single-phase flow in rifled tubes of various geometries is modelled with the aid of commercially available packages, *i.c.* CFX™ and Fluent™. Conclusions are drawn with respect to local conditions (velocity field, temperatures) that are important for bubble detachment. Lastly, resulting bubble escape and migration conditions are estimated. Such a one-way coupling is of course valid in case the bubble density is low, but conclusions are expected to pertain to void fractions as high as 30 % since surprisingly enough many two-phase flow phenomena at void fraction up to 30 % can be interpreted with the aid of single bubble behaviour [1, 2].

The velocity field in the vicinity of the wall is nowhere uniform, of course. There exist, however, locations where boundary layers thickness is negligible as compared to bubble size at detachment. These are the places upstream of a rifle where the flow field resembles stagnation flow, see Figure 5. Heat transfer rates are high there, resulting in relatively low wall temperatures (Fig. 4) and most likely a lower rate of bubble production. Even though fewer bubbles are created there, they still need to be removed efficiently. However, the lift forces due to inertia and vorticity are in up-flow both pushing a detached bubble towards the wall (section 2). Bubble detachment diameter is relatively small (section 2.3) which causes body forces to be relatively small because they are proportional to the volume of the bubble (section 2.2). The axial flow rotation around the tube axis, the swirl, must therefore be significant near the helixes, the rifles, in order to drive bubbles towards the centre. Stagnation flow is more pronounced with rectangular helixes (Figure 5) than with rounded edges (Figure 6) while swirl can be comparable. A rifle with a rounded upstream edge is therefore recommended.

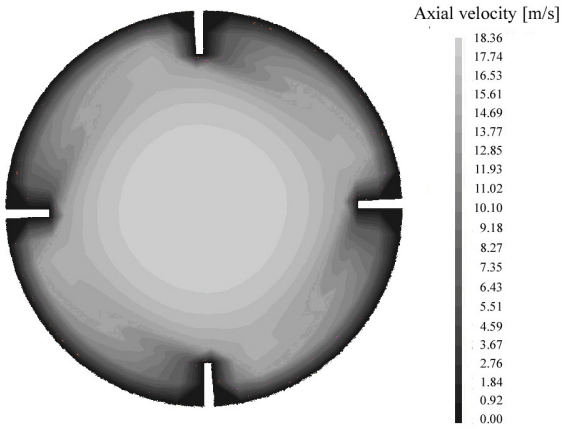

Figure 5. Axial velocity field in a rifled tube with 4 rectangular rifles; CFX™. Notice the lower velocity regions both upstream and downstream of the helical, intruding structures.

The swirl developed follows the sweep of the helix structure and increases with increasing height of the helix structure. However, this is at the cost of an increase in pressure drop. The critical heat flux of relatively short tubes with relatively high helixes is expected to be highest. The swirl should be small in the centre of the tube, which with four or more structures at the wall is readily achieved.

In the wake areas relatively high temperatures and relatively low velocities occur (Fig. 4). Bubble detachment sizes are relatively large (section 2.3) which is beneficial for bubble migration to the core (section 2.2). These are not the wakes that appear behind bluff bodies in a stream of liquid, when bubbles are known to coagulate and even coalesce. The difference is a presence of a strong axial velocity component since the sweep of the helix structure is followed. Nevertheless, the high temperatures are likely to enhance boiling and bubble transport rates are less hampered by the above mentioned lift forces since velocity and vorticity are smaller. If excess heating of the tube wall is not an issue, it is therefore advantageous to have a large wake area. This can be promoted by increasing the pitch or increasing the rib height.

Suppose that a rifled tube has been found working satisfactorily at a certain range of mass flow rates, and that another design must be specified for higher mass flow rates. Based on the above findings, the pitch and rib height of the new design are recommended to be increased in order to foster the additional body force that stimulates migration to the centre. At lower mass flow rates the restraining hydrodynamic forces have lesser

influence, as discussed above, and the compensating body force can be less.

A summary of the above findings is provided in section 4.

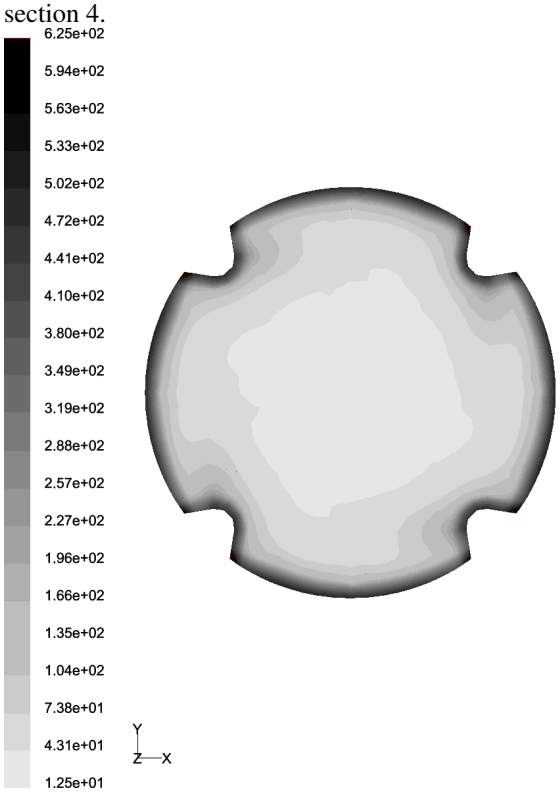

Figure 6. Vorticity field in s^{-1} in a rifled tube with 4 rounded rifles; FLUENT™. Notice the differences with Fig. 5 upstream of the rifles in particular.

4. CONCLUSIONS

The inertia forces induced by expansion of a bubble in a homogeneous flow near or at a wall depend on derivatives of the added mass tensor. It has been shown that these derivatives all change sign at the time the bubble detaches from the wall. As a result, the sum of the inertia forces on a growing truncated sphere at a plane wall is rather different from that on a growing sphere that has escaped from the wall. The lift force due to vorticity, see Eq. (1), can be added to these inertia forces, and drives in upflow an escaped bubble back towards the wall. As a consequence, bubble migration from the wall to the centre of a vertical tube can in upflow *only* be promoted by creating a swirl in the tube. This study has not only shown that swirl is the only mechanism to this effect. It has also demonstrated that bubble detachment is fostered by the homogeneous flow component parallel to the wall, irrespective of the direction of this flow. The mass flow rate in an evaporator tube cannot be unlimitedly reduced without affecting bubble detachment diameter and boiling heat transfer. Reducing the mass flow rate promotes migration of vapour to the centre, but reduces wall heat transfer.

These findings appeal to common sense and are in accordance with existing correlations. They are nevertheless useful for optimization of the design of rifled tubes since it has been found difficult to let commercial 3D CFD codes accomodate for the essentially 1D correlations. In addition, experiments to provide design recommendations for evaporator tubes are elaborate, costly and seldom provide the detailed information necessary to assess local characteristics. Such design experiments are a proper final step in the design process, but should preferably be based on insights and recommendations like the ones provided in the present paper.

Based on one-way coupling of flow with bubble production and bubble motion, and taking full advantage of the above analytical predictions, the following geometry of a rifled tube is recommended. Four or more helix structures with rounded upstream edges with a pitch and with rib heights that in principle should be selected dependent on the prevailing bulk mass flow rates of liquid. An increase in prevailing mass flow rates should be accompanied with an increase in rib heights and pitch. These recommendations are purely based on an assessment of hydrodynamic effects of helical structures on motion of bubbles, and not on such effects as extended fin area of the helical structures, since the hydrodynamic effects are expected to be most important for safe operation and for a high critical heat flux.

ACKNOWLEDGEMENTS

This work has been supported by the EC; project AD-700-2. The author is grateful to A. Zeijsink (Kema) and other members of the Boiling Group for useful discussions, to F. van Mierlo and D. Costello for their contributions with CFD, to J. Kuerten for carefully commenting the manuscript and to B. van Esch for his help with the CFD figures.

REFERENCES

[1] S.van Stralen, R. Cole, 1979, *Boiling Phenomena*, Hemisphere Publishing Corporation, Washington.

[2] J.G. Collier, J.R. Thome, 1994, *Convective boiling and condensation,* Clarendon Press, Oxford.

[3] Helden W.G.J. van, Geld C.W.M. van der, Boot P.G., 1995, "On the effect of the temperature boundary condition on single bubble detachment in flow boiling", *Convective flow boiling,* ed. J.C. Chen, Taylor & Francis, Washington, pp. 149-154.

[4] Helden W.G.J. van, Geld C.W.M. van der, Boot P.G.M.T., 1995, "Forces on bubbles growing

and detaching in flow along a vertical wall, *Int. J. of Heat and Mass Transfer*, 38 (11), pp. 2075-2088.

[5] Duhar G., Colin C., 2004, "A predictive model for the detachment of bubbles injected in a viscous shear flow with small inertial effects", *Physics of fluids,* Vol. 16, pp.31-34.

[6] Qiu D., Geld C.W.M. van der, 1999, "Bubble shapes and forces at detachment". *Convective flow and pool boiling*, ed. F. Mayinger, M. Lehner, Taylor & Francis, Philadelphia, pp. 271-278.

[7] Geld C.W.M. van der, 2002, "On the motion of a spherical bubble deforming near a plane wall", *J. of Eng. Mathematics*, Vol. 42, pp. 91 – 118.

[8] Geld C.W.M. van der, 2004, "Prediction of dynamic contact angle histories of a bubble growing at a wall", *Int. J. of Heat and Fluid Flow*, Vol. 25, pp. 74-80.

[9] Geld, C.W.M. van der, 2005, "Bubble motion induced by strong deformation near a plane wall", Proc. *3th Int. Berlin Workshop on Transport Phenomena with Moving Boundaries*, ISBN 3-00-017322-6, pp. 101-111.

[10] Costello, D.J., 2005, "CFX modelled rifled tube", *Report nr. WPC-2004.03*, Technische Universiteit Eindhoven.

[11] Mierlo, F.P.M. van, 2005, "Towards optimization of the design of a rifled tube for sub-critical heat transfer", *Report nr. PTC-2005.03*, Technische Universiteit Eindhoven.

[12] Howe, M.S. 1995, "On the force and moment on a body in an incompressible fluid, with application to rigid bodies and bubbles at high and low Reynolds numbers", *Q.J. Mech. and Appl. Math.*, 48 (3): pp. 401-426.

[13] Basu, N.., Warrier, G.R. and Dhir, V.K., 2003, "Prediction of flow boiling heat transfer – a mechanistic approach", Proc. *of Int. Conf. on Boiling Heat Transfer*, Jamaica 2003, Keynote Lecture VI,, pp. 1-50.

[14] Geld C.W.M. van der, 2006, "The dynamics of a boiling bubble before and after detachment", Proc. *of Int. Conf. on Boiling Heat Transfer*, Keynote Lecture, manuscript in preparation, pp. 1-24.

Conference on Modelling Fluid Flow (CMFF'06)
The 13th International Conference on Fluid Flow Technologies
Budapest, Hungary, September 6-9, 2006

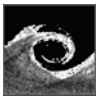

EXPERIMENTAL AND MODELLING VORTEX TUBE PERFORMANCE

Mohamed KALAL[1], Richard MATAS[2], Jiří LINHART[3]

[1] Corresponding Author. Department of Power System Engineering, Faculty of Mechanical Engineering, University of West Bohemia. Univerzitni 8, Plzen 306 14. Czech Republic. Tel.: +420 377 63 8132, Fax: +420 377 63 8102, E-mail: kalal@kke.zuc.cz
[2] New Technologies Research Centre, University of West Bohemia. E-mail: mata@ntc.zcu.cz
[3]Department of Power System Engineering; Faculty of Mechanical Engineering, University of West Bohemia; E-mail: linhart@kke.zcu.cz

ABSTRACT

Vortex tube is a simple mechanical device operating as a refrigerating and heating machine with no moving parts**.** An experimental study of the vortex tube, using compressed air as the working medium, has been carried out to investigate the effect of thermo-physical parameters, which have been designated and studied. An experimental rig was specially built for this project. Experimental results of the temperature of the hot and cold air outlet of the vortex tube, with the cold air mass ratio (CAMR) and the pressure of the inlet air as parameters are presented. It is also shown that the inlet pressure and the CAMR are important factors affecting the performance of the vortex tube.

In this paper a computational fluid dynamics (CFD) package is used to investigate the performance and flow phenomena within a counter-flow vortex tube. A three-dimensional CFD model has been developed that successfully exhibits all of the general behavior expected from a vortex tube. Temperature and velocity profiles in vortex tube from the CFD model are presented. It was found which of the turbulent models are suitable for vortex tube. The CFD results were compared with data obtained from our experiments. They are in reasonable agreement.

Keywords: Cold temperature, Hot temperature, Experiment, CFD, Turbulent model

NOMENCLATURE

m_c	$[kg/s]$	mass flow rate of the cold air
m_i	$[kg/s]$	mass flow rate of the inlet air
T	$[^oC]$	temperature
y	[-]	cold air mass ratio (CAMR)
ΔT_c	$[^oC]$	temperature differences between cold outlet air and inlet air
ΔT_h	$[^oC]$	temperature differences between hot outlet air and inlet air

Subscripts

i	inlet
c	cold
h	hot

1. INTRODUCTION

The vortex tube creates a helical vortex from compressed air and separates it into two air streams, one hot and one cold. Compressed air enters a cylindrical generator, which is proportionately of larger diameter than the long tube, where it causes the air to rotate. Then, the rotating air is forced to flow down along the inner wall of the tube at speeds reaching a sonic value. At the end of the hot tube, a small or big portion of this air exits through a needle valve (control valve) as the hot air exhaust. The remaining air is forced to flow back through the centre of the incoming air stream at a slower speed. The heat from the slower moving air is transferred to the faster moving incoming air, though here is a higher temperature. This cooled air flows through the centre of the generator and exits through the cold air exhaust port, as shown schematically in figure 1. The vortex tube can be used as a refrigeration device or as a heating device.

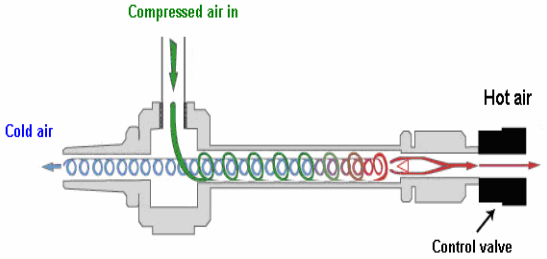

Figure 1. Schematic diagram of a vortex tube

Ranque [1] was the earliest one who investigated compressed air flowing tangentially into a tube and found that air streaming near the

wall had a higher temperature than that one near the axis. He tried to use this effect for refrigeration. Hilsch [2] as the first published systematically experimental results by varying the inlet pressure and the geometrical parameters of the tube. A recent review of the existing literature is given in [3]. In spite of the present uses and the various studies, no adequate physical explanation is available for the actual transport mechanism. Indeed, in the existing literature, there have been several, often contradictory, qualitative theories. Lindstrom-Lang [4] assumed turbulent transfer of thermal energy in an incompressible flow. Kurosaka [5] invoked an acoustic streaming process. Ahlborn, et al. [6] identified the temperature splitting phenomenon of a Ranque–Hilsch vortex tube in which a stream of gas divides itself into a hot and a cold flow as a natural heat pump mechanism, which is enabled by a secondary circulation. Ahlborn, et al. [7] considered the vortex tube as a refrigeration device which could be analyzed as a classical thermodynamic cycle, replete with significant temperature splitting, refrigerant, and coolant loops, expansion and compression branches, and natural heat exchangers.

The effect of various parameters, such as nozzle area, cold orifice area, hot end area and L/D ratio of the tube length to the tube diameter, on the performance of the vortex tube was investigated in [8]. There were experimentally tested variations of the cold air temperature T_c with respect to the change of the hot end area for L/D = 45, 50, 55. They showed the cold air temperature T_c at all the tested ratios L/D decreased if the hot end was opened. Also the effects of length and diameter on the principal vortex tube are considered in [9]. They showed variation of efficiency versus different L/D of vortex tube. An experimental investigation of the energy separation process in the vortex tube was conducted in [10]. There were measured temperature profiles at different positions along the vortex tube axis with conclusion the vortex tube length has an important influence on the transport mechanism inside. In [11] there are presented experimental results of the energy separation in the vortex tube under different operating conditions showing the temperature changes of the cold and hot streams as a function of the inlet pressure. In this study there was found that the hot stream temperature increased with the inlet pressure raising, and that the cold stream temperature decreased with the inlet pressure. The paper [12] resulted in several formulas for determining the performance and efficiency of the vortex tubes under a variety of operating conditions, which induced the optimum ratios of the vortex tube dimensions corresponding to the highest efficiency.

So far there are very plenty of available researches to validate the reliability of CFD analyses for investigating the flow and temperature within the vortex tube. The numerical calculations qualitatively predicted the experimental results presented by [12]. Papers [13, 14] show the dependence of vortex tube performance on the normalized pressure drop by using a numerical model. [15] Presents a numerical analysis in which the fluid dynamic equations are decoupled from the energy equation. The flow pattern was determined using the vorticity stream function formulation of the radial and axial Navier-Stokes equation and a standard k-ε turbulence model. CFD can also be used as a minimal adequate tool for design of engineering components. [16] Presents a detailed analysis of various parameters of the vortex tube through CFD techniques to simulate the phenomenon of flow pattern, thermal separation, pressure gradient etc. And also it's utility as a tool for optimal design of vortex tube towards the optimization of number of nozzles, nozzle profiles, cold end diameter, length to diameter ratio, cold and hot gas fractions and comparison of the experimental results with corresponding CFD analysis. [8] showed successfully utilized a CFD model of the vortex tube to understand the fundamental processes that drive the power separation phenomena. CFD and experimental studies conducted towards the optimization of the Ranque– Hilsch vortex tubes are presented in [17]. They showed the swirl, axial and radial velocity components of the flow, the flow pattern was obtained through CFD. The optimum cold end diameter, the ratios of the vortex tube length to diameter and optimum parameters for obtaining the maximum hot gas temperature and minimum cold gas temperature are obtained through CFD analysis and validated through experiments

2. EXPERIMENTAL SETUP

The arrangement of experimental apparatus and measuring devices which is used for the determination of the performance of the counter flow vortex tube is shown in figure 2. We have chosen model No. 106-8-H of the producer ITW Vortec. This model is one of the smallest, its air consumption is 0.00378 [*kg/s*], which corresponds to the maximum capacity of our compressor 0.005 [*kg/s*], with output pressure between 0.5 and 1.0 [*M Pa*]. The experimentation was started when the air was compressed by the air compressor (1). The high pressure air passes through the pressure tank (2) to suppress impacts and through the valve (3), where its mass rate is regulated. Inlet pressure is read by the pressure gage (4), and then goes through the dust filter (5) and cooler (6) with cyclone separator. The mass flow rate of the inlet air is measured using an orifice (7). Then the compressed air is introduced tangentially into the vortex tube (9), where it expands and separates into the hot and cold air streams. The cold air in the central region leaves the vortex tube near the

entrance, while the hot air goes out to the surrounding at the far end of the vortex tube. The needle valve (10) controls the flow rate of the hot air. Just after the pipe, the mass flow rate of the hot air is measured using the orifice (12). Thermocouples numbered 8, 11 and 13 measure the inlet and outlet temperatures. All temperatures and pressures data were recorded with a data logger (14) on a PC (15). A program was written in Lab VIEW 7.2 to control the data logging parameters and to display the obtained results.

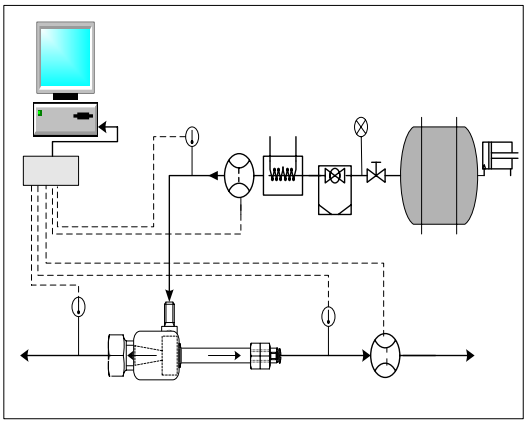

Figure 2. Schematic diagram of the experimental setup

3. EXPERIMENTAL RESULT

During the experimental test, the inlet pressure and the inlet temperature of the compressed air as well as the cold air mass ratio y were varied systemically. The CAMR is defined as follows: $y = m_c/m_i$, where m_c represents the mass flow rate of the cold stream released, while m_i represents the inlet or total mass flow rate of the pressurized inlet working fluid. Therefore, the y changes in the range $0 \leq y \geq 1$.

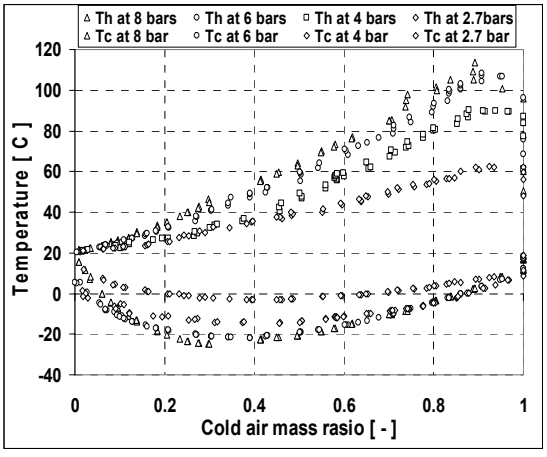

Figure 3. Hot and cold temperature as a function of cold mass ratio

Tests have been conducted at inlet pressure of 2.7, 4, 6 and 8 bars, at constant inlet temperature 20^oC . The experimental temperature of the hot and cold outlet air is shown above in Figure 3 as a function of the cold air mass ratio and as a function of the inlet pressure of the compressed air.

All tests were run at first by holding a constant inlet temperature. Obviously, it can be seen that the temperature of the hot exit air increases with raising CAMR from null up to nearly 0.9. With further increase of the cold air mass ratio higher than 0.85 the hot exit air temperature achieves a maximum value and then decreases to its minimum one. The range of the CAMR, at which the hot outlet air becomes a maximum, is from 0.85 to 0.90. At the cold air mass ratio from 0.9 up to 1 a sharp temperature drop is measured for the hot air exit temperature. Figure 3 gives also the temperature of the hot outlet air as a function of the inlet pressure as a parameter.

It is evident that the diagram 3 can be divided into three parts according the parameter CAMR: 0-0.4, 0.4-0.9, and 0.9 -1.

In the main central region of the diagram act three mechanisms determining state and development of the flow in the tube. In the vicinity of the wall prevail molecular friction caused by the high velocity decrement at the wall and in the boundary between the hot flow and the back cold flow. This is source of heating of the main flow streaming along the wall to the hot exit. Besides here acts further mechanism, probably the most important, namely separation of rapid (hot) and slow (cold) molecules. The molecules of high velocity are centrifuged to the margin layer of the tube cross section and strongly contribute to the higher temperature of the hot flow. The slow molecules are attracted to the tube centre because there is a lower pressure induced by the swirl flow in the tube. This molecular diffusion orientated from outside to the centre contributes to the low temperature in the central cold flow.

The mentioned mechanism stops acting in the CAMR region from 0 to 0.4. The reason is small mass flow rate of the cold flow at which the regular flow pattern is violated and diffusion including centrifuging process interrupted. At this situation exist in vicinity of the cold outlet orifice two flows, one going out and the other in the tube. In the result it causes suppression of the separation mechanism.

For the third CAMR region is characteristic the inside flow not achieving the hot end of the tube and the separation model of molecules is dislocated again.

At all CAMR the temperature of the hot air is proportional to the inlet pressure of air. In all the measured cases the temperature of the exit hot air is higher than that of the inlet air, $T_h > 20^oC$. At CAMR lower than 0.85 more air flows into the hot outlet pipe.

15

8

7

6

T_{in}

14

The temperature differences between the hot outlet air and the inlet air, $\Delta T_h = T_h - T_i$, and between the cold outlet air and the inlet air, $\Delta T_c = T_c - T_i$, as functions of the CAMR, with the pressure of the inlet air as a parameter are presented in figure 4. With the outflow of the hot air coming near zero, y = 1, the temperature of the vortex tube at the hot air outlet is higher than that of the inlet air. Similarly without the outflow of the cold air, y = 0, the temperature measured at the outlet of the cold air, is lower than the temperature of the inlet air. Also Figure 4 demonstrates that for CAMR in a range of 0.1 to 0.4, there is distinctively a potential of higher rate of temperature reduction in the cold outlet but lower rate of temperature reduction for the range around 0.4. For the CAMR in a range between 0.3 and 0.4, there is the lowest temperature reduction in the cold outlet for all inlet pressures supplied. When inlet pressures are at 2.7, 4, 6 and 8 bars, the corresponding highest temperature drops in the cold outlet are 22^oC, 33^oC, 42^oC and 46^oC respectively. The higher is the inlet pressure the more decreasing temperature is obtained for each CAMR used.

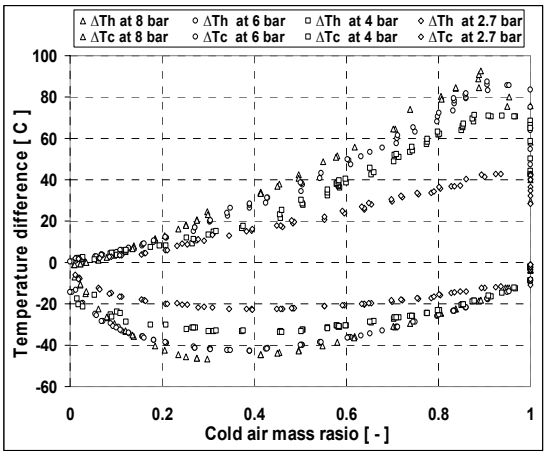

Figure 4. Hot and cold temperature differences as a function of cold mass ratio

The influence of the inlet pressure on the temperature of the hot and cold outlet air is clearly distinctive as shown in Figure 5. It can be seen that the temperature of the hot outlet increases with inlet pressure increasing, and that the cold outlet temperature decreases with inlet pressure. The compressed air begins its vortex flow as soon as it is introduced into the vortex tube. Because of the centrifugal characteristics of the forced vortex flow, the tangential velocity of the air near the vortex tube wall would be larger than that in the central region. This would naturally cause the temperature near the tube wall to be higher than that in the central region. Also, the higher frictional force among fluid particles as well as among the fluid particles and the vortex tube wall near the wall region is responsible for part of this phenomenon. The higher the inlet pressure is, the greater the centrifugal force acts there. Then the difference between the tangential velocity in the near wall region and that in the central region would be larger, and hence the difference between the temperatures of the two outlets.

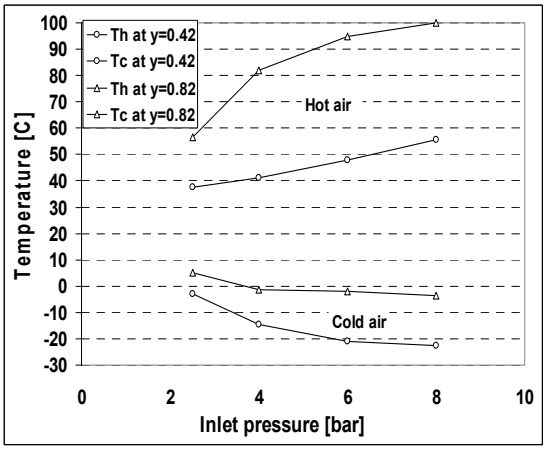

Figure 5. Hot and cold outlet temperature as a function of inlet pressure at 2 CAMR: 0.42, 0.82

4. CFD MODEL

The CFD system FLUENT in version 6.1 was used for the vortex tube numerical simulations. The numerical model was based on experiences with previous solved axisymetric models [18]. Geometry of the vortex tube simulated by a 3D CFD model is depicted in figure 6. It has shown simple vortex tube with six tangential inlet nozzles and vortex tube in sector provided with refinement in mesh. The length is 92mm and inside diameter 5.2*mm*. The geometry comes from the simultaneously measured vortex tube and is simplified. Its periodical segment (angle 60°) was used for the simpler solving; the hot outlet valve wasn't simulated completely and the control valve was replaced by the pressure outlet with variable area.

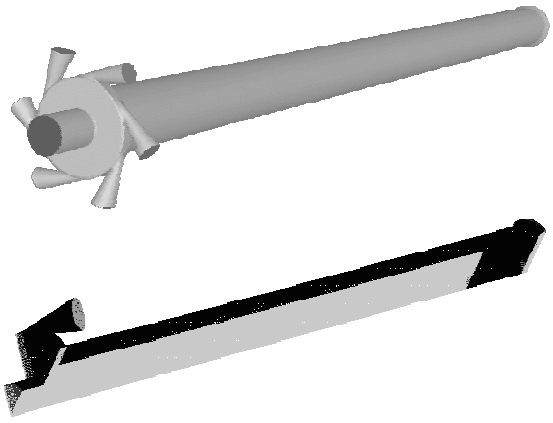

Figure 6. 3D CFD model of vortex tube with six tangential inlet nozzles and vortex tube in sector

5. CFD COMPUTATION

Computational mesh of the periodical segment has about 70 000 mixed cells. The parameters of the model were set up following: inlet mass flow rate $6x10^{-4}$ *kg/s* (one inlet nozzle), inlet total temperature 20 ^{o}C, outlet pressure 95 600 *Pa*, the walls were regarded as adiabatic. It is necessary to initialise the computation suitably in order to obtain converging solution. The computations converged relatively slowly; the number of iterations leading to a converged solution was more than 10 000.

Air was considered as a compressible fluid with ideal gas law for governing density-pressure-temperature relationship. Three dimensional continuity equations, momentum, and energy ones were solved for compressible flow. The standard k-ε model was used, the relation between turbulent and laminar viscosity was reduced to 500 to obtain more realistic velocity profiles, see [18]. The inlet turbulent intensity in described model was set to 3 %. The turbulent Prandtl number in the turbulent model was substantially increased because the performed simulations have given the best results for $Pr_t = 9$, as in the work [16].

Computed results were satisfactory. The computed inlet total pressure for the given mass flow rate was $7x10^5$ *Pa*. This value is smaller than $8x10^5$ *Pa* measured in experiment. Figure 7 shows radial – axial velocity field in the vortex tube for the CAMR 0.5183. It is possible to see the basic character of the flow field, which corresponds to the flow field described by other authors.

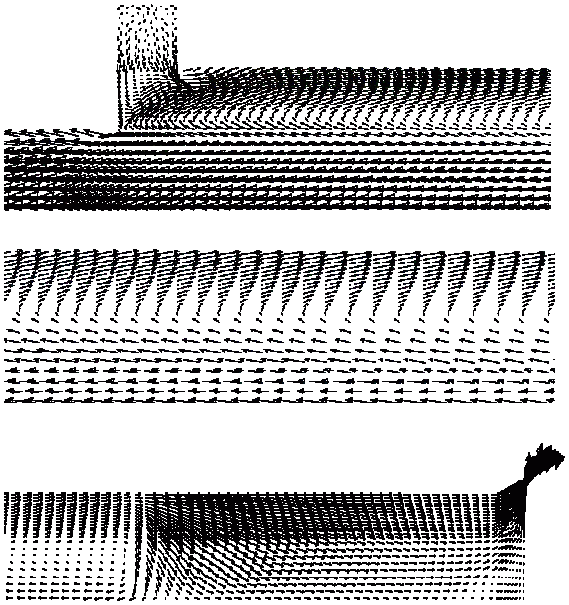

Figure 7. Velocity vectors without tangential component in various locations of the vortex tube for the cold fraction 0.5183

In Figure 8 there is depicted the radial tangential velocity field in the plane of the inlet nozzles and shows the basic vortex. The performance of swirl generator can be characterised by two factors, namely by the magnitude of swirl velocity and radial symmetry of flow.

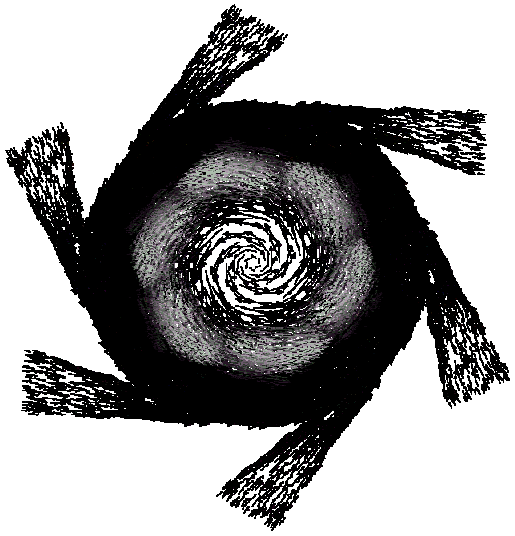

Figure 8. Velocity vectors without axial component in the plane of the inlet nozzles for the cold fraction 0.5183

Figure 9 shows the tangential velocity profiles in the slice 0.0, 44 and 88 *mm* (x/D=0.44, 0.90) from the plane of the inlet nozzles. There is evident decrease of the tangential velocity from the inlet and cold outlet to the hot outlet.

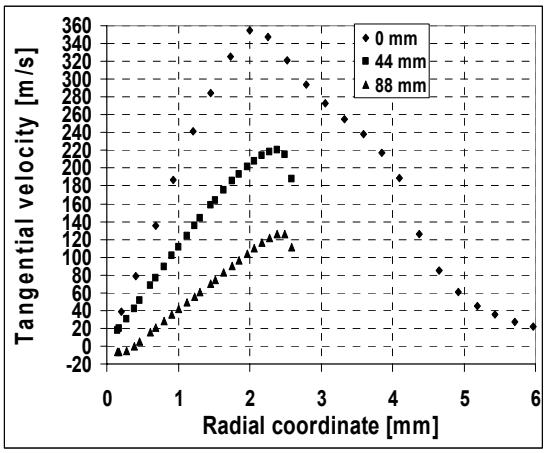

Figure 9. Tangential velocity profiles in the slice 0, 44 and 88 mm from the plane of the inlet nozzles for the cold fraction 0.5183

The total temperature distribution shows figure 10. It is noticeable that the increase of the total temperature from inlet to the hot outlet is relatively constant in the diameter 3.5 *mm* and the own increase of the temperature occurs in the relatively thin layer adjacent to the wall of the vortex tube.

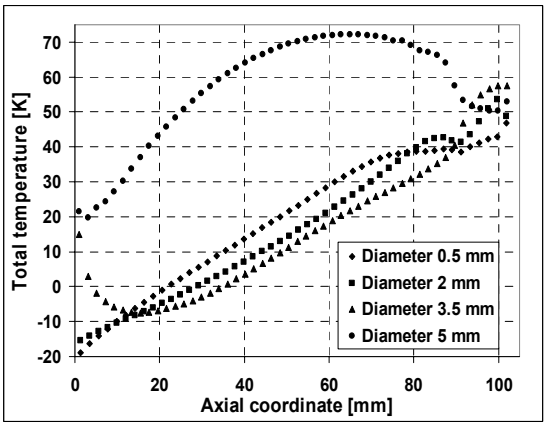

Figure 10. Total temperature profiles on the diameters 0.5, 2, 3.5 and 5 mm for the cold fraction 0.5183

In figure 11 you can see the distribution of the total temperature in the tube for various CAMR. The behaviour of the tube is changed in the range 0.63 to 0.79 of the CAMR, where the temperature distribution has a different order.

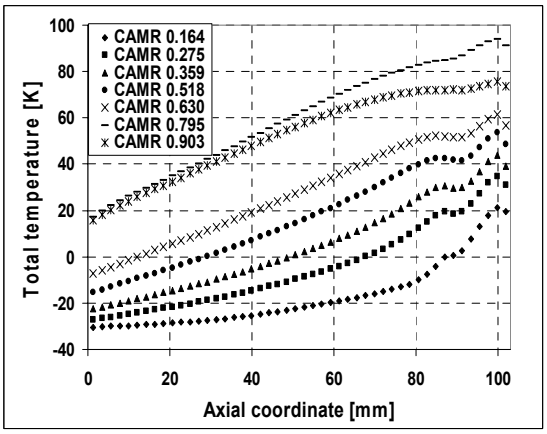

(a)

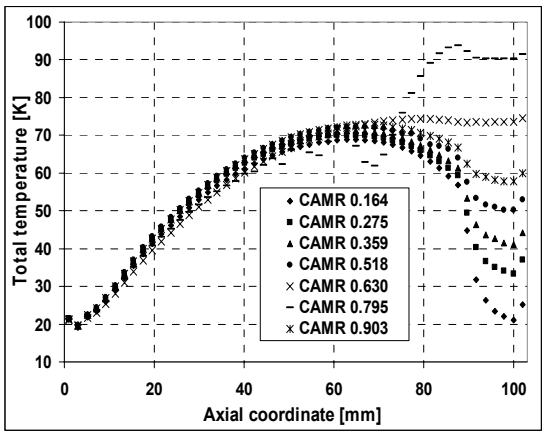

(b)

Figure 11. Total temperature profiles for the various cold fractions: (a) for the diameter 2 *mm* , (b) 5 *mm*

Figures 12 and 13 represent the total and static pressure in the slices 0.0, 44 and 88 *mm* from the plane of the inlet nozzles. We see the minimum pressure in centre of the vortex tube that is caused by the rotation movement of the air. At the wall, the pressure sinks in direction of the hot exit and in the centre has an opposite gradient. Both the pressure courses are closely linked with correct function of the tube.

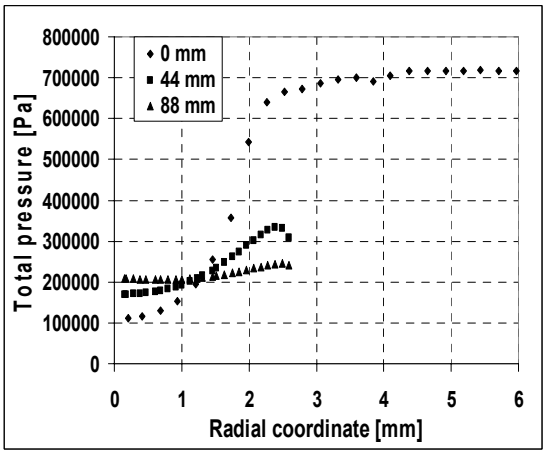

Figure 12. Total pressure profiles in the slice 0, 44 and 88 mm from the plane of the inlet nozzles for the cold fraction 0.5183

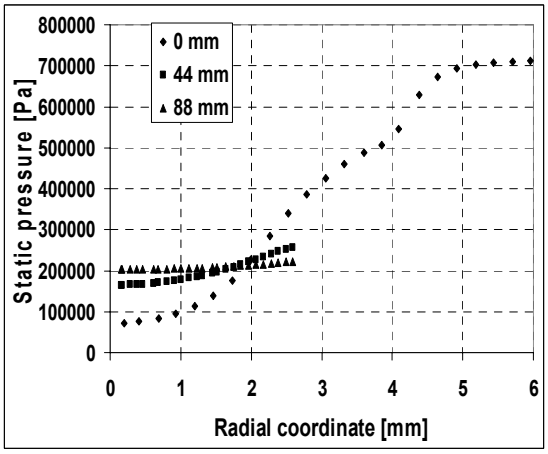

Figure 13. Static pressure profiles in the slice 0, 44 and 88 *mm* from the plane of the inlet nozzles for the cold fraction 0.5183

6. COMPARISON OF EXPERIMENT AND CFD SIMULATION

The inlet temperature and inlet mass flow rate in the CFD model were specified as a constant $20^{o}C$ and 0.0036 *kg/s* respectively, which is consistent with the measured total temperature at the inlet to the vortex tube. The results of the experimental model were compared with three-dimensional, axisymetric CFD models that were developed using

the commercial CFD code FLUENT. Figure 14 shows the experimental and CFD analysis of the hot and cold temperature of air as a function of the parameter CAMR. It can be seen that maximum hot outlet temperature of $90.8^{o}C$ (at 0.8 of CAMR) is obtained from CFD analysis and about 113 ^{o}C (at 0.89 of CAMR) is obtained from experiments. And a minimum cold outlet temperature of -22.6 ^{o}C (at 0.36 of CAMR) is obtained from CFD analysis and about -24.8 ^{o}C (at 0.30 of CAMR) is obtained from experiments. Thus CFD analysis is in acceptable agreement with experimental results if we realize the number of approximations that are necessary in simulation to do.

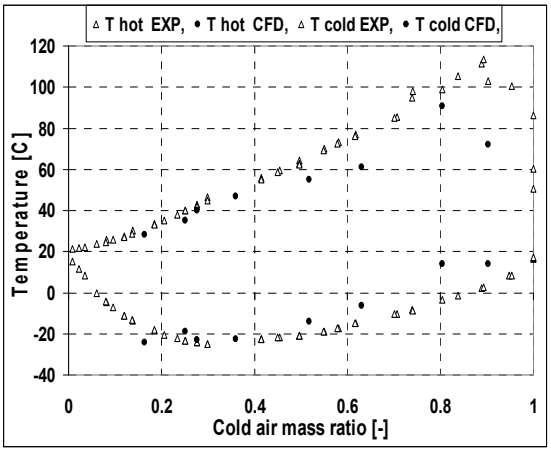

Figure 14. The experiment and CFD analysis of the hot and cold air temperature as a function of CAMR

7. CONCLUSIONS

Experimental results of the hot and cold air outlet temperatures of the vortex tube, with the dimensionless cold air flow rate CAMR and the inlet air pressure as parameters are presented. It is clear from our experiments that the higher inlet pressure causes the greater temperature difference of the two outlet air streams. It is also shown that the CAMR is an important factor affecting the vortex tube performance.

The CFD study has shown that numerical computation of the vortex tube is possible if a convenient model is chosen and special computing parameters set up (turbulent Prandtl number). The computation offers inside flow values - velocity, static and total temperature, static and total pressure profiles that cannot be obtained by simple measurement.

The results of experiment and CFD indicate that maximum hot air temperature is obtained for the lower mass flow rate at the hot end and similarly lowest cold air temperature is obtained at the lower mass flow rate at the cold end (higher mass flow rate at hot end).

REFERENCES

[1] Ranque GJ, 1933, "Experiences sure la detente giratoire avec productions simultaneesd'un echappement d'air chand et d'un echappement d'air froid", *J Phys Radium*, Vol. 4, pp. 112–4.

[2] Hilsch R, 1947, "The use of the expansion of gases in a centrifugal field as a cooling process", *Rev Sci Instrum*, Vol. 8, pp.108–13.

[3] Coccerill T, 1998, "Thermodynamics and Fluid Mechanics of a Ranque–Hilsch Vortex Tube", Ph. D. Thesis, University of Cambridge.

[4] Lindstrom-Lang CU, 1964, "Gas Separation in the Ranque–Hilsch Vortex Tube", *Int J Heat Mass Transfer*, Vol.7, pp. 1195–206.

[5] Kurosaka M, 1982, "Acoustic Streaming in Swirling Flow and the Ranque Hilsch Vortex Tube Effect", *J Fluid Mech*, Vol.124, pp.139–72.

[6] Ahlborn B, Keller JU, Rebhan E, 1998, "The Heat Pump in a Vortex Tube" *J Non- Equilib Thermodyn*, Vol. 23(2), pp. 159–65.

[7] Ahlborn BK, Gordon JM, 2000, "The Vortex Tube as a Classical Thermodynamic Refrigeration Cycle", J Appl Phys, Vol.88 (6), pp.3645–53.

[8] N.F. Aljuwayhel, G.F. Nellis, S.A. Klein, 2005, "Parametric and Internal Study of the Vortex Tube using a CFD model", *Int J Refrigeration* Vol. 28 (3), pp. 442–450.

[9] Saidi M H and Valipour M S, 20003, "Experimental modelling of vortex tube refrigerator". A*pplied thermal engineering*. Vol. 23, No. 15 pp 1971-1980.

[10] Stephan K, Lin S, Durst M, Hunag F and Seher D, 1983, "An investigation of Energy Separation in a Vortex Tube", *International Journal of Heat and Mass Transfer*, Vol. 26, No.3, pp 341-388.

[11] Ting-Quan MA, Qing-Guo, Jian YU, Fang YE, and Chong-Fang, 2002, "Experimental investigation on energy separation by vortex tubes". *12th international Heat Transfer Conference,* 10, Paris.

[12] H. Takahama, and H. Yokosawa, 1981, "Energy Separation in Vortex Tubes with a Divergent Chamber", ASME Journal of Heat Transfer, Vol. 103, pp. 196-203.

[13] H.H. Bruun, 1969, "Experimental Investigation of the Energy Separation in Vortex Tubes*", J Mech Eng Sci,* Vol. 11 (6), pp. 567–582.

[14] B. Ahlborn, J.U. Keller, R. Staudt, G. Treitz, R. Rebhan, 1994, "Limits of Temperature

Separation in a Vortex Tube", *J Phys D: Appl Phys* 27, pp. 480–488.

[15]B.Ahlborn, J. Camire, J.U. Keller, 1996, "Low-Pressure Vortex Tubes", *J Phys D: Appl Phys,* Vol. 29, pp.1469–1472.

[16] W. Frohlingsdorf, H. Unger, 1999, "Numerical Investigations of the Compressible Flow and the Energy Separation in Ranque–Hilsch Vortex Tube", Int. J. Heat Mass Transfer, Vol. 42, pp. 415–422.

[17] Upendra Behera, P.J. Paul, S. Kasthurirengan, R. Karunanithi, S.N. Ram, K. Dinesh and S. Jacob, 2005, "CFD analysis and experimental investigations towards optimizing the parameters of Ranque–Hilsch vortex tube", Int. J. Heat and Mass Transfer, Vol. 48, Issue 10, 2005. pp. 1961-1973

[18] Jiří Linhart, Mohamed Kalal, Richard Matas, 2005, "Numerical study of vortex tube properties", *16th international symposium on transport phenomena*, Prague, Czech Rep.

Conference on Modelling Fluid Flow (CMFF'06)
The 13th International Conference on Fluid Flow Technologies
Budapest, Hungary, September 6-9, 2006

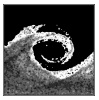

PULSATING TURBULENT FLOW IN DIVERGENT TUBES

Masaru SUMIDA[1]

[1] Corresponding Author. School of Engineering, Kinki University. 1 Takaya Umenobe, Higashi–Hiroshima, 739–2116 Japan.
Tel.: +81 82 434 7000, Fax: +81 82 434 7011, E-mail: sumida@hiro.kindai.ac.jp

ABSTRACT

An experimental investigation was conducted of the pulsating turbulent flow in conically divergent tubes with divergence angles of 12, 16 and 24°. The experiments were carried out under the conditions of Womersley numbers of $\alpha = 10 \sim 40$, mean Reynolds numbers of $Re_{ta} = 15000 \sim 30000$ and oscillatory Reynolds number of $Re_{os} = 10000$ (the flow rate ratios of $\eta = 0.33 \sim 0.67$). Time-dependent wall static pressure and axial velocity were measured at several longitudinal stations and the distributions were illustrated for representative phases within one cycle. The experimental results of the rise between the pressure at the inlet and the exit of the divergent tube almost agree with the approximate results that were derived under the assumption of a quasi-steady flow. The profiles of the phase-averaged velocity and the turbulence intensity in the cross section are very different from those for steady flow. Also, they show complex changes along the tube axis in both the accelerative and decelerative phases.

Keywords: divergent tube, pressure distribution, pulsating flow, quasi-steady flow, turbulent flow, velocity distribution

1. INTRODUCTION

Divergent tubes are an important pipeline component that are widely used as diffusers to convert kinetic energy into pressure one and as devices to connect two tubes of different diameters in pipework systems and fluid machinery. Therefore, there have been a number of studies, e.g., Singh and Azad [1, 2], Gan and Riffat [3], and Xu et al. [4], devoted to the flow in divergent tubes to date. However, all these studies are concerned with steady flow.

On the other hand, unsteady flow has become important in connection with problems concerning the starting and stopping or undesirable accidents of pumps and blowers, because fluid machines are becoming better and fluid transport is becoming diversified and speeded up. Nevertheless, the unsteady flow in divergent tubes has never been treated, to the author's knowledge.

The purpose of the present study is to treat the problem of pulsating turbulent flow through conical divergent tubes. First, the distribution of wall static pressure depending on the various governing parameters is measured and analyzed under the assumption of a quasi-steady flow. Subsequently, periodical changes of profiles, such as the phase-averaged velocity and turbulent intensity, are examined. Furthermore, knowledge of their characteristics is obtained through comparison with the case of steady flow.

2. EXPERIMENTAL APPARATUS AND MEASUREMENT METHOD

2.1. Experimental Apparatus

A schematic diagram of the experimental apparatus is shown in Figure 1. The system, with air as the working fluid, consists of a pulsating-flow generator, a test tube and measuring devices. Moreover, the pulsating-flow generator is composed of a steady flow and an oscillating flow. The steady flow, i.e., time-mean flow was supplied, through a surge tank, by a suction blower. On the other hand, the volume-cycled oscillating flow was introduced by a piston controlled by a personal computer.

Three divergent tubes were employed in the present study. The test tubes had total divergence angles 2θ of 12, 16 and 24° and an area ratio m of 6.25, in which m was $(d_2/d_1)^2$ with $d_1 (= 2a_1 = 80\ mm)$ and $d_2 (= 200\ mm)$ being the diameters at the inlet and the exit, respectively, of the divergent tubes. These dimensions are shown in Figure 2, together with the coordinate system. The divergent tubes were constructed from 3 to 5 transparent acrylic blocks connected via a slip ring. The ring, furthermore, had static pressure holes, 0.8 *mm* in diameter and spaced 90° apart, and a small hole to insert a hot-wire probe. Straight transparent glass

tubes with lengths of 3700 *mm* (= 46.3d_1) and 4200 *mm* (= 21d_2) were connected to the inlet and the exit of the divergent tubes, respectively.

2.2. Measurement Procedures and Data Acquisition

The wall static pressure was measured using a diffusive-type semiconductor pressure transducer (Toyoda MFG, DD102-0.1F). The measurements were executed at 9 ~ 11 stations between $z = -22.1d_1$ in the upstream straight tube and $z = 21.9d_1$ in the downstream one, where z is the length measured along the tube axis from the inlet of the divergent tube. For the divergent tube I with $2\theta = 12°$, velocity measurements were performed with a hot-wire anemometer and the velocity w in the axial direction was obtained at 8 stations including sections of $z/d_1 = -2$ and 9.6.

The voltage output from the pressure transducer and from the anemometer was sampled, with the personal computer, synchronously with a time-marker signal that indicates the position of the piston. The data was processed as follows. For a periodically unsteady turbulent flow, any instantaneous quantity, e.g., the axial velocity w in the pulsation cycle, can be written as

$$w = W + w_t . \qquad (1)$$

Here, W is the phase-averaged velocity and w_t is the fluctuating one. The data at each measuring point was collected for 200 to 500 pulsation cycles. The turbulence intensity w' was obtained as the square root of the ensemble phase-average of w_t^2. It was confirmed beforehand that averaging over 200 cycles has no influence on the values of the quantities. Moreover, the scatter in the results was less than 4 and 6% for the phase-averaged values and the turbulence intensity, respectively. In the hot-wire measurement, it is difficult to gain a correct direction of the flow at the position and time when the ratio of the radial component of the velocity to the axial one is rather large. For such a case, errors of a limited extent are avoidable.

Additionally, in order to have insight into the pulsating flow features, visualization experiment using water was executed for a divergent tube with $2\theta = 12°$ and $d_1 = 22$mm.

3. RESULTS AND DISCUSSION

3.1. Experimental Conditions

Pulsating flow in divergent tubes is governed by five nondimensional parameters: the total divergence angle 2θ, the area ratio m, the Womersley number α, the mean Reynolds number Re_{ta} and the oscillatory Reynolds number Re_{os} (or the flow rate ratio η). Here, the former two and the remainder are related to the geometry of the

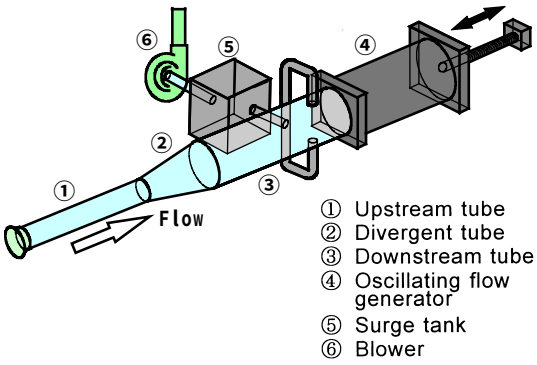

Figure 1. Schematic diagram of experimental apparatus

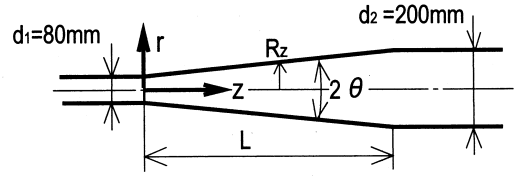

Tube	Divergence angle 2θ °	Length L mm (L/d₁)
I	12	568 (7.1)
II	16	427 (5.34)
III	24	282 (3.53)

Figure 2. Coordinate system and dimensions of test tubes

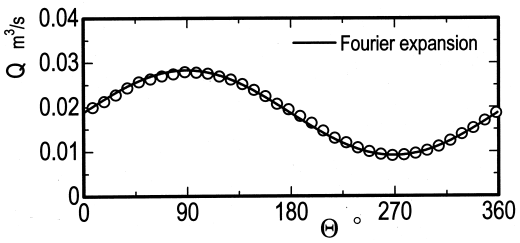

Figure 3. Example of flow rate variation ($\alpha = 20$, $Re_{ta} = 20000$, $\eta = 0.5$)

divergent tubes and the fluid motion, respectively. The Womersley number is defined as $\alpha = a_1(\omega/\nu)^{1/2}$, with ω being the angular frequency of pulsation and ν the kinematic viscosity of the fluid. The mean Reynolds number is expressed as $Re_{ta} = d_1 W_{a1,ta}/\nu$ and the oscillatory Reynolds number as $Re_{os} = d_1 W_{a1,os}/\nu$, where W_{a1} is the cross-sectional average velocity in the upstream tube and the subscripts ta and os indicate the time-mean and amplitude values, respectively. Finally, the flow rate ratio is given by $\eta = W_{a1,os}/W_{a1,ta}$ (= Re_{os}/Re_{ta}). The experiments were performed systematically under the conditions of α

= 10 ~ 40, Re_{ta} = 15000 ~ 30000 and Re_{os} = 10000 (η = 0.33 ~ 0.67).

In order to check the flow coming into the divergent tube, preliminary measurements were conducted for the axial velocity at $z/d_1 = -2$ in the upstream tube. Integrating the measured velocities over the cross section, a time-dependent flow rate Q was calculated. The result is shown in Figure 3. In the figure, the solid line denotes the first fundamental component developed by the Fourier series. This confirms that the prescribed flow is realized, and also yields that a sinusoidal flow rate is accomplished in the form

$$Q = Q_{ta} + Q_{os} \sin\Theta , \qquad (2)$$

Θ (= ωt) being the phase angle and t the time.

3.2. Wall Static Pressure

3.2.1. Distribution of Wall Static Pressure and Its Variation with Time

The wall static pressure P is shown in Figure 4 for Tube I with 2θ = 12°. The pressure P is expressed in the form of the pressure coefficient C_p, which is defined as $C_p = (P - P_{ref}) / (\rho W_{a1,ta}^2 / 2)$, P_{ref} being the pressure at the station of $z/d_1 = -2$ in the upstream tube and ρ the density of the fluid. In the upstream tube, C_p changes in the phase leads of about 80° with flow rate variation. The time-averaged value of C_p is slightly larger than that for the steady flow at Re = 2000. On the other hand, the pressure in the divergent tube rises with an increase of z/d_1, except for a part of the period ($\Theta \approx 300°$) when it shows a gentle favorable gradient.

We examine the pressure rise ΔP_L in the length L, i.e., between the inlet and the exit of the divergent tube. The representative result is shown in Figure 5, in which ΔP_L is nondimensionalized by the dynamic pressure based on $W_{a1,ta}$ in the upstream tube. In the figure, the waveform of ΔP_L is developed with the Fourier series denoted by the solid line. The broken line denotes the result that is theoretically obtained using Bernoulli's theorem for a quasi-steady flow. It is expressed as

$$\Delta P_L = (1 + \eta \sin\Theta)^2 \, (1 - m^{-2}) . \qquad (3)$$

Moreover, the symbol of ← indicates the pressure rise $\Delta P_{L,s}$ for the steady flow, at Re = 20000, with the same cross-sectional average velocity as $W_{a1,ta}$. The pressure rise ΔP_L in the pulsating flow changes almost sinusoidaly. However, it lags behind the variation of the flow rate. The phase difference $\Phi_{\Delta P}$ between the fundamental waveform of ΔP_L and Q becomes large with an increase of the Womersley number. Incidentally, $\Phi_{\Delta P}$ changes from –5° to –60° when α increases from 10 to 40, as shown later in Figure 8. On the other hand, ΔP_L has a value lower than the theoretical one for quasi-steady flow. Furthermore, ΔP_L takes approximately zero values for the phase of 230 ~ 340° with the small flow rate.

As has been stated above, for pulsating flow in divergent tubes, the pressure at the exit of the divergent tube rises when the cross-sectional average velocity is large and is in a decelerative phase. That is, ΔP_L becomes large from the latter half of the accelerative phase to the middle of the decelerative phase ($\Theta \approx 50 \sim 180°$), as seen in Fig. 5. By contrast, C_p exhibits a small change in the axial direction from the ending of the decelerative phase to the first half of the accelerative phase ($\Theta \approx 230 \sim 330°$). This is because the kinetic energy to be converted to the pressure one is small and because, to accelerate the fluid in the axial direction, the downstream pressure requires lowering. Therefore, it can be understood that the pressure distribution at the beginning of the accelerative phase shows the favorable larger gradient for higher Womersley

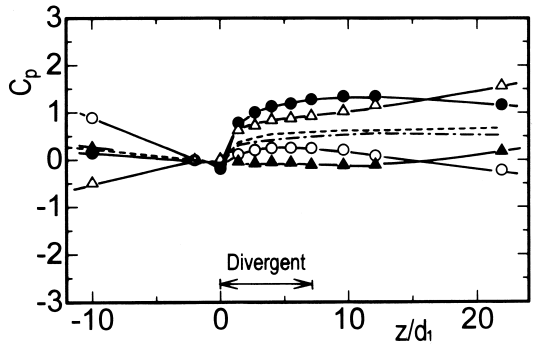

Figure 4. Longitudinal distribution of wall static pressure (2θ=12°, α=20, Re_{ta}=20000, η = 0.5, ○: Θ = 0°, ●: Θ = 90°, △: Θ = 180°, ▲: Θ = 270°, — - — : time-averaged, — — — : steady flow at Re =20000)

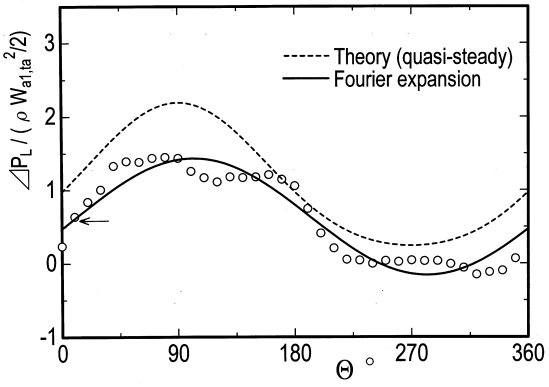

Figure 5. Difference between pressure at the inlet and exit of a divergent tube (2θ = 12°, α = 20, Re_{ta} = 20000, η = 0.5. ← : steady flow at Re = 20000)

number where the fluid is strongly accelerated in the streamwise direction.

3.2.2. Approximate Expression for ΔP_L

Considering practical use, it is desirable to establish a convenient expression for the pressure rise ΔP_L in pulsating flow. Therefore, we introduce an approximate analysis by assuming the quasi-steady state and taking an unsteady inertia force into account. In the analysis, we use the one-dimensional equation of unsteady motion. The detailed description of the analysis procedure is omitted owing to the limited space.

Approximate results were obtained as follows:

$$\Delta P_L = \Delta P_{L,s}\{f_0 + f_1 \sin(\Theta + \Phi_1) + f_2 \sin(2\Theta + \Phi_2)\}, \tag{4}$$

where

$$\left.\begin{aligned} f_0 &= 1+\eta^2/2 \\ f_1 &= 2\eta\left[1+\left\{\frac{2(1-m^{-1/2})\alpha^2}{(1-m^{-2}-\varsigma)\,\mathrm{Re}\,ta\tan\theta}\right\}^2\right]^{1/2} \\ f_2 &= -\eta^2/2 \\ \Phi_1 &= \tan^{-1}\left\{\frac{-2(1-m^{-1/2})\alpha^2}{(1-m^{-2}-\varsigma)\,\mathrm{Re}\,ta\tan\theta}\right\} \\ \Phi_2 &= \pi/2 \end{aligned}\right\} \tag{5}$$

In the above equation, ζ and $\Delta P_{L,s}$ represent the pressure loss coefficient and the pressure rise, respectively, in the case of steady flow with the same flow rate as the mean value, Re_{ta}, of the pulsating flow.

First, we discuss the time-averaged pressure rise, $\Delta P_{L,ta}$, of β [$= \Delta P_{L,ta} / (\rho W_{a1,ta}{}^2/2)$]. From the result of the approximate analysis, β can be written using β_s for steady flow, as

$$\beta = f_0 \beta_s . \tag{6}$$

Figure 6 shows the experimental results for $\eta = 0.5$ (Re_{ta} = 20000). They are close to the approximate results indicated by the solid line. Consequently, β takes a large value f_0 times as high as that of steady flow, being independent of the Womersley number α.

Secondly, we deal with the varying components of ΔP_L. Nevertheless, as easily seen from Fig. 5 and the approximate expressions of Eqs. (4) and (5), the second- or higher order components are small enough, $\eta/4$ at the most, as compared with the first one. Therefore, we examine the amplitude $\Delta P_{L,os}$ and phase difference $\Phi_{\Delta p}$ of the first component.

For $\Delta P_{L,os}$, we define the coefficient as

$$\kappa = \Delta P_{L,os} / (\rho W_{a1,ta}{}^2/2), \tag{7}$$

In the approximate analysis, κ is expressed as

$$\kappa = \left(1 - m^{-2} - \varsigma\right) f_1 / \eta^2 . \tag{8}$$

Figure 7 shows the results. They are plotted with the characteristic number of α^2/Re_{ta} on the abscissa

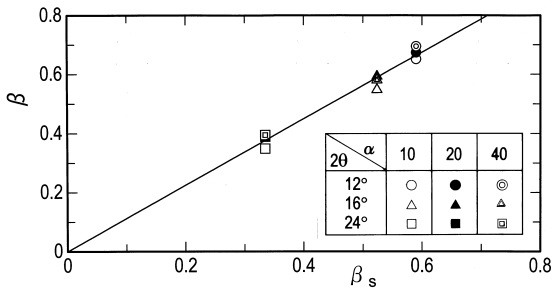

Figure 6. Relationship between β and β_s (η = 0.5, Re_{ta} = 20000). ——: Eq. (6)

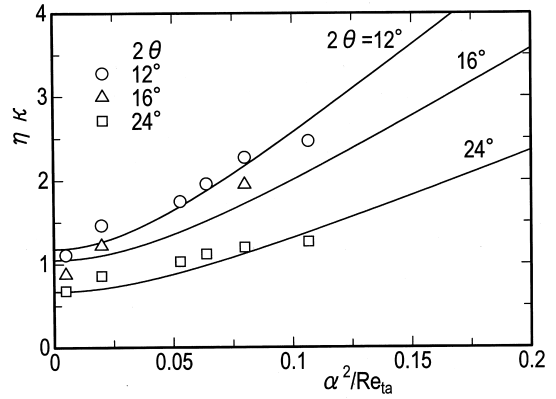

Figure 7. Relationship between $\eta\kappa$ and α^2/Re_{ta}. ——: Eq. (8).

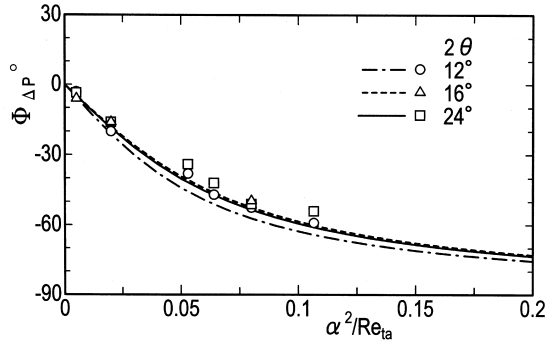

Figure 8. Relationship between $\Phi_{\Delta P}$ and α^2/Re_{ta}. Lines denote the results of Eq. (5).

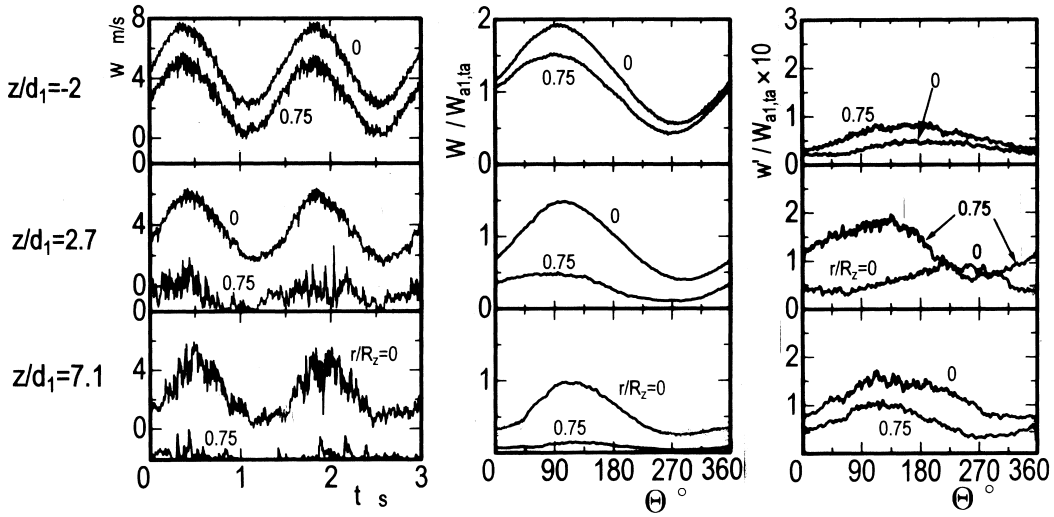

(a) Instantaneous velocity w (b) Phase-averaged velocity W (c) Turbulence intensity w'

Figure 9. Velocity waveforms ($2\theta = 12°$, $\alpha = 20$, $Re_{ta} = 20000$, $\eta = 0.5$)

against $\eta\kappa$ on the ordinate, which is taken from the viewpoint that κ varies inversely to η. The solid lines indicate the approximate results for Re_{ta} = 20000, where the measured values in the steady flow are used for ζ. The measurement data clearly shows the dependence on the flow parameters that was indicated by the approximate analysis. That is, $\eta\kappa$ increases almost in proportion to α^2/Re_{ta} since the unsteady inertia force is intensified with an increase in α. Furthermore, $\Delta P_{L,os}$ required for the de- and acceleration of the flow becomes large proportionately with L, since the fluid mass involved in the divergent section is greater with smaller 2θ and longer L.

Next we consider the phase difference $\Phi_{\Delta P}$ between $\Delta P_{L,os}$ and the flow rate variation. The experimental results are given in Figure 8. Each line in the figure denotes the approximate expression (5) for Re_{ta} = 20000. According to the approximate results, $\Phi_{\Delta P}$ at 2θ = 12° is slightly more negative than those at any other angle. Nevertheless, the experimental results show that the divergence angle 2θ has little effect on $\Phi_{\Delta P}$. Consequently, the phase lag becomes large with an increase of α^2/Re_{ta}, and it changes in close correspondence to Eq. (5).

3.3. Axial Velocity

In this section, we discuss the axial velocities. We deal with the flow case of α = 20, Re_{ta} = 20000 and η = 0.5 measured for 2θ = 12° as a representative condition.

3.3.1. Changes of Centerline Velocity with Time and along the Tube Axis

To start, we will elucidate the outline of the flow features by focusing on the axial velocity on the tube axis. Figure 9 shows waveforms of instantaneous axial velocity w, together with its

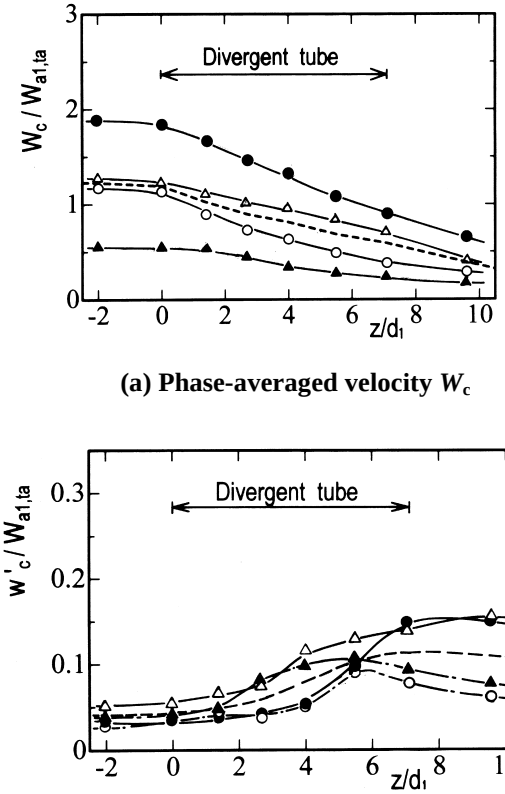

(a) Phase-averaged velocity W_c

(b) Turbulence intensity w'_c

Figure 10. Change of W_c and w'_c along the tube axis ($2\theta = 12°$, $\alpha = 20$, $Re_{ta} = 20000$, $\eta = 0.5$), — — —: time-averaged.

phase-averaged one W and its turbulence intensity w'. For comparison with those on the tube axis, the results measured at the radial position r/R_z = 0.75 near the tube wall are also shown in Fig. 9. Moreover, the changes of W_c and w_c' along the tube axis are illustrated in Figure 10. The subscript c

indicates the quantities on the tube axis and the broken lines indicate the time-averaged values.

The phase-averaged velocity W exhibits an almost sinusoidal change in time, as displayed in Fig. 9(b). However, since the flow extends with increasing z/d_1 in both the divergent tube and the downstream straight tube, W_c in these sections is reduced (see Fig. 10(a)). In particular, the degree of reduction in the divergent section becomes smaller and larger for the middle, i.e., Θ = 180 and 0°, of the decelerative and the accelerative phase, respectively. Thus, the phase angle at which W_c shows the peak is discernibly delayed compared with the flow rate variation as z/d_1 increases. This lag is equivalent to the time at which the fluid flowing into the divergent tube at the maximum flow rate (Θ = 90°) reaches each section. As a result, the time lag at the divergence exit (z/d_1 = 7.1) amounts to approximately one-tenth of one cycle. On the other hand, W near the wall (r/R_z = 0.75) in the divergent tube changes almost in synchronous phase with the flow rate. That is, W takes a maximum value at about Θ = 90°. In the case of steady flow, W_c/W_{a1} at the Reynolds numbers of 10000 and 30000, corresponding to the minimum and maximum flow rates in pulsating flow, respectively, attenuates axially in the same manner as the flow at Re = 20000. Hence the Reynolds number has little effect on W_c/W_{a1} (the illustration is omitted here). It can be drawn from the above that the differences in the change of W_c along the tube axis in phase are attributed to an unsteady effect.

The turbulence intensity w'_c becomes large, at any phase, with an increase of z/d_1 in the first half of the divergent tube. It shows the peak magnitude in the second half of the deccelerative phase, as seen in Figs. 9(c) and 10(b). Furthermore, w'_c near the divergence exit in the first half of the decelerative phase is about 2.6 times the value at the divergence inlet. Consequently, the variation of w'_c over one cycle becomes larger.

On the other hand, w' near the wall (r/R_z = 0.75) in the upstream tube is twice as large as w'_c, but the phase difference between w' and W_a is small. In the section immediately behind the divergence inlet, the turbulence intensity is high in the phase with the high flow rate. However, the change of w' gradually becomes similar to that of waveform w'_c with an increase of z/d_1.

3.3.2. Distributions of Phase-averaged Velocity and Turbulence Intensity

Figure 11 shows distributions of W and w' at four representative phases. The broken lines in the figure denote results for a steady flow at the Reynolds number of Re_{ta}. Moreover, sketches of the stream are displayed in Figure 12, which is drawn, with a moderate exaggaration, from the observation of the water flow. The painted parts enclosed by the broken lines show the main current of the flow.

In pulsating flow, the phase difference among fluid motions in the divergent tube becomes larger as z/d_1 increases. Consequently, the difference between the flow states of the accelerative and the decelerative phases becomes considerable. Therefore, the phase-averaged velocity and turbulence intensity exhibit complicated distributions.

In the upstream tube (Fig.11; z/d_1= –2), the periodic change of the axial velocity leads slightly near the tube wall, whereas it is delayed in the central part of the cross section. Nevertheless, on the whole, the velocity at each phase shows a profile similar to the steady one with a simple 1/7-th-power law. In the divergent tube, the pressure rise in the first half of the accelerative phase is

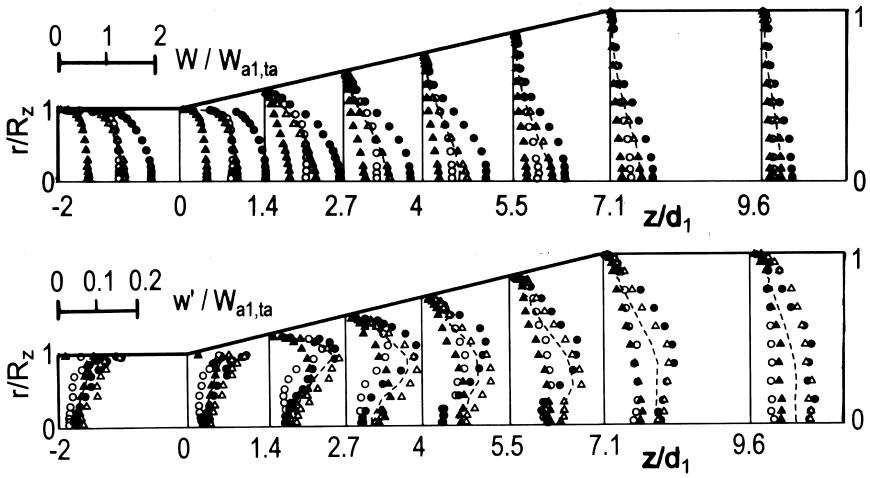

Figure 11. Distributions of W and w' in upper and lower figures, respectively (2θ = 12°, α = 20, Reta = 20000, η = 0.5). ○: Θ = 0°, ●: Θ = 90°, △: Θ = 180°, ▲: Θ = 270°, — — — : steady flow at Re = 20000.

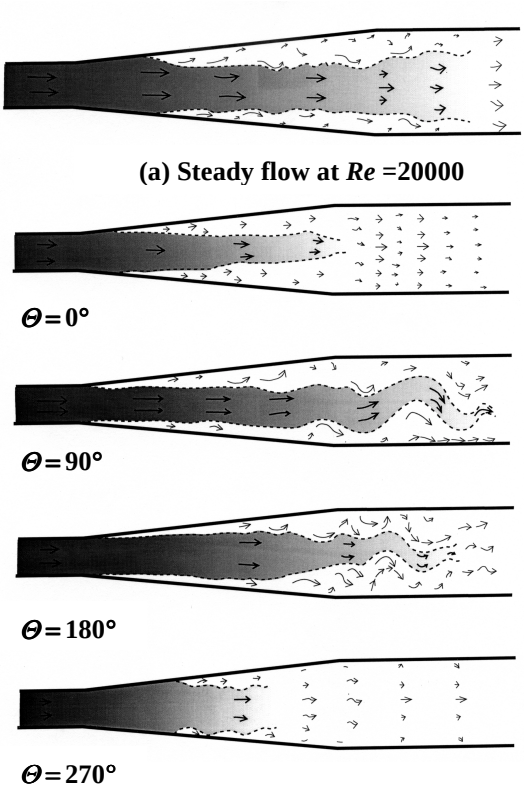

(a) Steady flow at Re =20000

(b) Pulsating flow (α=20, Re_{ta}=20000, η= 0.5)

Figure 12. Sketches of flow pattern obtained by visualization experiment (2θ=12°).

smaller than the theoretical one derived for a quasi-steady flow, as shown in Fig. 5. Moreover, there is little pressure difference in the divergent tube. As a result, the main current in the central part of the cross section reaches the exit plane without extending too much towards the tube wall (Fig. 12(b); $\Theta \approx 0°$). Meanwhile, near the inlet, a local pressure drop occurs, as seen in Fig. 4. This accelerates the fluid in the neighborhood of the wall, where the variation of the velocity is more advanced ($z/d_1 = 1.4$). When the flow rate increases and becomes maximum, eddies generated in the shear layer surrounding the main current grow rapidly, accompanying the acceleration of the flow, to become massive vortices. These vortices strongly interact with each other near the divergence exit. Following this, the main stream suddenly begins to meander in the central part of the cross section, resulting in a rapid increase of w' (Θ = 90°; Fig. 12(b)). By the middle of the decelerative phase (Θ= 180°), the pressure at the divergence exit is, as before, about twice as high as in the case of steady flow at the same flow rate, because the pressure there makes the fluid flow decelerate (Figs. 4 and 5). Thus the stream becomes unstable. As a result, the massive vortices in the section downstream of the divergence exit collapse and start to decay. In addition, the main current is mixed. At the end of the decelerative phase (Θ = 270°), the turbulence intensity in the section downstream of the divergence exit is considerably attenuated and part of the main current retreats to the first half of the divergent tube (Fig. 12(b)). The fluid particle in the vicinity of the wall is carried, locally and momentarily, upstream along the wall. Nevertheless, flow separation and backward flow are not seen clearly, and the fluid almost always flows downstream.

From the view described above, in the phase at which the flow rate increases, the degree of acceleration is high in the central part of the cross section. This results in W near the divergence exit (z/d_1 = 5.5) at the maximum flow rate (Θ = 90°) showing a profile with convexity near the tube axis, as seen in Fig. 11. In the decelerative phase, on the other hand, the velocity is reduced almost uniformly in the cross section because of the stronger action of turbulent mixing in the section further downstream.

The distribution of the turbulence intensity differs appreciably from that in a steady flow, as seen in Fig. 11. That is, the turbulence intensity is high in the phase from the end of the increase to the first half of the decrease of the flow rate. This is because during this phase, the shearing layer between the main current and the tube wall rolls up and becomes the massive vortices. On the other hand, w' is low in the first half of the accelerative phase when these vortices are almost decayed. To put it concretely, when the flow rate is large, the turbulence intensity immediately behind the divergence inlet (z/d_1 = 0 ~1.4) takes large values near the wall. Downstream, the region with high w' extends radially, accompanied by the formation of a shearing layer. Furthermore, the maximum $w'/W_{a1,ta}$ distribution in this section occurs in the first half of decelerative phase and becomes about 18% at z/d_1= 2.7 from the 14% in the upstream straight tube. Downstream, in the middle section of the divergent tube, at z/d_1 = 2.7 ~ 5.5, w' takes a maximum value in the vicinity of the inflection point of the W distribution when a fluid flowing at high speed is passed through the section. Subsequently, the location of the maximum w' shifts toward the tube axis. In this phase ($\Theta \approx 180°$), w' is about 20 percent higher than that of steady flow with Re_{ta}. The maximum value corresponds to 20% of $W_{a1,ta}$. In the section downstream of the divergence exit, the distribution of the turbulence intensity is uniformalized in the cross section (z/d_1 = 9.6).

4. CONCLUSION

The experimental investigations were performed for pulsating turbulent flow in divergent tubes and the flow field was examined. The principal findings of this study are summarized as follows.

(1) The approximate expressions derived for the pressure rise ΔP_L are in good agreement with the experimental results and are very useful in practice.

(2) The time-mean pressure rise $\Delta P_{L,ta}$ is larger than that in the steady flow with the same Re as Re_{ta} and increases proportionately to η. The amplitude $\Delta P_{L,os}$ is larger for the smaller divergence angle. In addition, its value and the phase lag behind the flow rate depend on and increase with the characteristic number α^2/Re_{ta}.

(3) The axial distributions of the pressure coefficient C_p are high in the phase from the latter half of acceleration to the middle of deceleration. By contrast, they are low in other phases.

(4) The phase-averaged velocity W shows profile swelling in the central part of the cross section when the flow rate increases. The phase at which the maximum value is taken in each plane is delayed from $\Theta = 90°$ at the maximum flow rate with an increase of z/d_1. However, as the flow rate decreases, the W profile becomes flat downstream of the divergent tube.

(5) The turbulence intensity w' for a high flow rate takes a maximum value at the position on the radius near the inflection point of the W profile. As the phase proceeds, the region with a large w' extends toward the wall and the tube axis, and the w' profile becomes level at the plane of the divergence exit.

ACKNOWLEDGEMENTS

The author would like to thank Mr. J. Morita of Tokuyama Corporation for his assistance.

REFERENCES

[1] Singh, R. K. and Azad, R. S., 1995, "Measurement of Instantaneous Flow Reversals and Velocity Field in a Conical Diffuser", *Experimental Thermal and Fluid Science*, Vol. 10, pp. 397-413.

[2] Singh, R. K. and Azad, R. S., 1995, "Behavior of Mean and Fluctuating Skin Friction in a Conical Diffuser with Instantaneous Flow Reversals", *Experimental Thermal and Fluid Science*, Vol. 11, pp. 190-203.

[3] Gan, G. and Riffat, S. B., 1996, "Measurement and Fluid Dynamics Prediction of Diffuser Pressure-loss Coefficient", *Applied Energy*, Vol. 54-2, pp. 181-195.

[4] Xu, D., Leschziner, M. A., Khoo, B. C. and Shu, C., 1997, "Numerical Prediction of Separation and Reattachment of Turbulent Flow in Aximmetric Diffuser", *Computers Fluids*, Vol. 26-4, pp. 417-423.

Conference on Modelling Fluid Flow (CMFF06)
The 12th International Conference on Fluid Flow Technologies
Budapest, Hungary, September 6–9, 2006

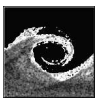

Numerical Modelling of turbulent flow over three dimensional backward facing step

Karel KOZEL[1], Petr LOUDA[2], Jaromír PŘÍHODA[3]

[1] Dept. of Technical Mathematics, Fac. Mech. Eng., Czech Technical University, Karlovo nám. 13, CZ-121 35 Praha 2
[2] Corresponding author: Dept. of Technical Mathematics, Fac. Mech. Eng., Czech Technical University, Karlovo nám. 13, CZ-121 35 Praha 2, Tel. +420 2 2435 7564, Fax: +420 2 2492 0677, E-mail: louda@marian.fsik.cvut.cz
[3] Institute of Thermomechanics AS CR, Dolejškova 5, CZ-182 00 Praha 8

ABSTRACT

The work deals with numerical modelling of 3D steady turbulent flow over backward facing step in a channel of rectangular cross-section. Two geometries with different boundary conditions and Reynolds numbers are computed. The mathematical model is based on Reynolds averaged Navier-Stokes equations for incompressible fluid. The turbulence models are eddy viscosity (SST) and explicit algebraic Reynolds stress model (EARSM). The Navier-Stokes equations are solved by an implicit artificial compressibility method with higher order upwind dicretization for convective term.

The influence of constitutive relation for Reynolds stress is observed. The differences caused by turbulence modeling are apparent already in the inlet straight channel in the form of corner secondary vortices captured only by EARSM model. The vortical structures downstream of the step were observed as well. The results are compared with measurements.

Key words: backward facing step flow, EARSM, SST model

1. INTRODUCTION

In this work, we investigate the 3D turbulent flow over backward facing step. In the previous work [3] the authors presented 2D backward facing step flow simulations. It was shown that the performance of eddy viscosity approach is satisfactory when using the SST-like eddy viscosity limiter. However it shows that for complex 3D flow a more fundamental approach to turbulence modelling is necessary. Using sufficiently accurate implicit finite volume method, in this work we compare the performance of an explicit algebraic Reynolds stress (EARSM) model with the SST extended eddy viscosity model. The two turbulence models considered use very similar systems of k-ω equations for turbulent time scale prediction, including so called cross-diffusion term. This fact enables to observe influence of constitutive relation. The results are considered from the point of view of consistency with 2D simulation and of agreement with experimental data.

2. MATHEMATICAL MODEL

The mean turbulent flow of incompressible Newtonian fluid is governed by Reynolds-averaged Navier-Stokes equations (RANS) in the form

$$\frac{\partial u_j}{\partial x_j}=0,$$
$$\frac{\partial u_i}{\partial t}+\frac{\partial (u_i u_j+\delta_{ij}p)}{\partial x_j}=\frac{\partial (2\nu S_{ij}-\tau_{ij})}{\partial x_j}, \qquad (1)$$

where x_i is Cartesian coordinate, u_i mean velocity vector, t time, p mean static pressure divided by constant density of fluid, δ_{ij} Kronecker delta, ν kinematic viscosity, $S_{ij}=\left(\partial u_i/\partial x_j+\partial u_j/\partial x_i\right)/2$ mean strain rate tensor, and τ_{ij} is Reynolds stress tensor.

We apply two closures for τ_{ij}, the extended eddy viscosity of SST (shear stress transport) turbulence model by Menter [4] and explicit algebraic Reynolds stress model (EARSM) due to Wallin, Hellsten [7, 2]. The Reynolds stress in SST model is given formally by eddy viscosity hypothesis

$$\tau_{ij}=-\nu_T 2S_{ij}+\frac{2}{3}k\delta_{ij},$$
$$\nu_T=\frac{a_1 k}{\max(a_1\omega,\Omega F_2)}, \quad a_1=0.31, \qquad (2)$$

where ν_T is eddy viscosity, k is turbulent kinetic energy, ω is specific dissipation rate, and F_2 is a switch-

ing function given in [4]. The model switches between Bradshaw hypothesis stating that principal Reynolds shear stress equals approx. $0.3k$, and eddy viscosity hypothesis. For this purpose, as a scalar measure of strain rate Menter selected magnitude of vorticity Ω

$$\Omega = \sqrt{2\Omega_{ij}\Omega_{ij}}, \quad \Omega_{ij}=\frac{1}{2}\left(\frac{\partial u_i}{\partial x_j} - \frac{\partial u_j}{\partial x_i}\right), \qquad (3)$$

where Ω_{ij} is rotation rate tensor.

The EARSM constitutive relation can be expressed in terms of dimensionless anisotropy tensor a_{ij}

$$\begin{aligned}
\tau_{ij}=&a_{ij}k + \frac{2}{3}k\delta_{ij}, \qquad (4)\\
a_{ij}=&\beta_1\tau S_{ij}\\
&+\beta_3\tau^2(\Omega_{ik}\Omega_{kj} - II_\Omega\delta_{ij}/3)\\
&+\beta_4\tau^2(S_{ik}\Omega_{kj} - \Omega_{ik}S_{kj})\\
&+\beta_6\tau^3(S_{ik}\Omega_{kl}\Omega_{lj} + \Omega_{ik}\Omega_{kl}S_{lj} - 2IV\delta_{ij}/3)\\
&+\beta_9\tau^4(\Omega_{ik}S_{kl}\Omega_{lm}\Omega_{mj} - \Omega_{ik}\Omega_{kl}S_{lm}\Omega_{mj}),
\end{aligned}$$

where τ is turbulent time scale and II_Ω, IV are invariants formed from S_{ij}, Ω_{ij} given by Hellsten [2] as well as the coefficients β. The original version of model by Wallin [7, 8] has slightly different coefficients β. Due to the use in the viscous sublayer, the turbulent time scale has to be limited from below by Kolmogorov time scale $\sim\sqrt{\nu/\epsilon}$, where ϵ is dissipation rate. In the present model

$$\tau = \max\left(\frac{k}{\epsilon}, 6\sqrt{\frac{\nu}{\epsilon}}\right). \qquad (5)$$

Both turbulence models use k-ω system of equations to estimate k and τ:

$$\begin{aligned}
\frac{Dk}{Dt}=&P - \beta^* k\omega + \frac{\partial}{\partial x_j}\left[(\nu + \sigma_k\nu_T)\frac{\partial k}{\partial x_j}\right],\\
\frac{D\omega}{Dt}=&\gamma\frac{\omega}{k}P - \beta\omega^2 + + \frac{\partial}{\partial x_j}\left[(\nu + \sigma_\omega\nu_T)\frac{\partial \omega}{\partial x_j}\right]\\
&+\frac{\sigma_d}{\omega}\frac{\partial k}{\partial x_j}\frac{\partial \omega}{\partial x_j},\\
P=&-\tau_{ij}\frac{\partial u_i}{\partial x_j}, \qquad (6)
\end{aligned}$$

where the derivative $D\cdot/Dt \equiv \partial\cdot/\partial t + \partial(u_j\cdot)/\partial x_j$. Using specific dissipation rate ω, the dissipation rate e.g. in Eq. 5 is given by

$$\epsilon = 0.09k\omega. \qquad (7)$$

For the coefficients β^*, σ_k, γ, β, σ_ω, σ_d in SST or EARSM model see [4] and [2] respectively. In EARSM model, the eddy viscosity is defined as

$$\nu_T = C_\mu k\tau, \; C_\mu = -\frac{1}{2}(\beta_1 + II_\Omega\beta_6). \qquad (8)$$

3. NUMERICAL METHOD

The system of RANS and turbulence model equations is solved by an artificial compressibility method, which consists of adding a pressure time derivative into the continuity equation

$$\frac{1}{a^2}\frac{\partial p}{\partial t} + \frac{\partial u_i}{\partial x_i} = 0, \qquad (9)$$

where a is selectable parameter. The steady solution of the original system is obtained for $t \to \infty$. The parameter a should be chosen to achieve fast convergence. In this work it is equal to the maximum velocity in the solution domain.

To discretize the equations in space, the cell-centered finite volume method is used. The unknowns are understood as cell averages and are collocated. The grid consists of hexahedral cells forming a structured multi-block grid with matching grid lines at interfaces. The grid has been either orthogonal or with cells expanding from step edge to the almost regular grid in the outlet.

The convective terms are discretized using van Leer interpolation method. The cell face value of momentum, k, ω are interpolated in the direction of grid lines using e.g.

$$u_{i+1/2} = \begin{cases} u_i \quad +\frac{1}{4}(1+\kappa)(u_{i+1} - u_i) & \\ \qquad +\frac{1}{4}(1-\kappa)(u_i - u_{i-1}), & \overline{u} > 0,\\ u_{i+1} - \frac{1}{4}(1+\kappa)(u_{i+1} - u_i) & \\ \qquad -\frac{1}{4}(1-\kappa)(u_{i+2} - u_{i+1}), & \overline{u} < 0. \end{cases} \qquad (10)$$

in the i-direction, where $\overline{u}$ is normall velocity at cell face computed centrally. Two upwind schemes were tested, the third order accurate with $\kappa = 1/3$, and second order accurate Fromm scheme, $\kappa = 0$. We do not use limiter for differences in Eq. 10. Although the schemes for convection are not positive, there were no problems in solving k-ω model equations.

The viscous terms are approximated using 2nd order central scheme. The cell face derivatives are computed using Gauss theorem on a dual octahedral volume constructed by means of face vertices and centres of two adjacent primary hexahedrons. The time integration uses the backward Euler (implicit) scheme. The Newton linearized implicit operator contains both diffusive and convective terms, however has the 1st order upwind stencil. In EARSM, linear part of turbulent diffusion corresponding to eddy viscosity (8) is discretized implicitly, the remaining part explicitly. Only the negative part of source terms in the

turbulence model is discretized implicitly. The resulting block 7-diagonal system of algebraic equations is solved using block relaxation method with direct tridiagonal solver for selected family of grid lines.

To prevent pressure-velocity decoupling, pressure stabilization in the form of pressure Laplacian is added to the continuity equation. Magnitude of stabilization is governed by local grid density, diffusion and reference velocity [5]. It should be noted that this dissipation is isotropic, nevertheless there were no problems with oscillations when applying anisotropic normal Reynolds stresses of EARSM.

4. DISCUSSION OF RESULTS

We consider two cases of the flow over backward facing step in a confined channel. The experimental data considered differ by cross section size of channel and magnitude as well as distribution of inlet velocity:

- wide channel according to Armaly et al. [1]: in experiment very large aspect ratio to model 2D flow in mid-plane, in computation truncated from computational reasons to $6H$: $2.064H$ (width:height) behind the step, and $6H$: $1.064H$ in front of the step, where H is step height. The inflow condition is developed channel flow. Reynolds number using maximum inlet velocity U_{ref} and step height H is $10,000$.
- narrow channel according to Zubík, Šulc [9] : channel aspect ratio $5H$: $5H$ behind the step and $5H$: $4H$ in front of the step. The inflow stream short after honeycomb. Reynolds number $98,000$. The actual height was $H = 40\,\mathrm{mm}$, the fluid water. Measurement technique was PIV and LDA.

4.1. Wide channel

The case of Armaly has been computed on the grid of approx. $290,000$ finite volumes, with the minimum finite volume thickness has been $2 \cdot 10^{-3}H$, $4 \cdot 10^{-3}H$ and 10^{-2} in vertical, span-wise and longitudinal direction respectively. The grid has 50 finite volumes in span-wise direction. The resolution was based on 2D tests, where the domain was longer at $20H$. The length is not critical unlike the resolution of recirculation zone. The length of the domain in 3D is $16H$ downstream of the and $0.2H$ upstream.

The inlet developed straight channel flow has been computed separately on same grid. Since the vorticity in streamwise direction is generated only by anisotropic stresses, one can expect differences between the two different turbulence models, especially in the secondary flow. The Fig. 1 shows the results. The velocity profiles in vertical mid-plane are equal for both turbulence models, and it has been confirmed are same as for 2D developed channel flow. On the other hand, in the horizontal mid-plane, the diference is large. The EARSM model gives larger bulk velocity than SST one. This is caused by the EARSM's better ability to capture secondary flow shown on the upper part of Fig. 1. The profiles nevertheless coincide in the middle portion of channel for $-1 < z/H < 1$, which seems to confirm that channel width is sufficient to make comparisons of vertical mid-plane with 2D simulation.

This comparison in terms of longitudinal velocity is given in Fig. 2. For 3D case, velocity profiles in the mid-plane are shown. We see that results of EARSM simulations differ slightly in the main stream after reatachment only, whereas for SST, the recirculation zone is also differnt. Measuring length of the recirculation zone in mid-plane, the EARSM gives values $8.22H$ and $8.52H$ for 3D and 2D simulation respectively. The SST gives $6.20H$ and $8.40H$. Armaly et al. indicate the value of approx. $8H$.

The SST model agrees well with measurement in 2D case only, the 3D result is unacceptable. The separation under-estimation with SST model is apparent as well in the Fig. 3, where the lines of zero friction on two walls are shown. The image is quite different than from the one of EARSM model shown in upper part of Fig. 4.

On the other hand the EARSM model gives consistent and acceptable results in both cases. This leads us to a conclusion that only model capable of capturing at least qualitatively the secondary flows can be reliable for simulation 3D backward facing step.

4.2. Narrow channel

The computational grid for narrow channel simulation at higher Reynolds number had approx. 320,000 finite volumes, the grid spacing in normal direction along the walls has been $7 \cdot 10^{-4}H$. The span-wise resolution was 50 finite volumes. The downstream length of the domain downstream of the step was again $16H$, upstream $3H$. For computation, the inlet velocity was approximated with artificial nearly top-hat profile. It was confirmed that the shape of inlet velocity profile has very small influence of the flow in recirculation zone.

The convective terms become more important at higher Reynolds number. The convergence history using the third order scheme and the Fromm scheme (10) are shown in Fig. 5. The time step for first scheme has been approx. $0.105H/U_{ref}$. The Fromm scheme has better dispersive characteristics and higher dissipation than third order scheme.

Thus the steady level of residual is lower. Surprisingly the time step had to be decreased to approx. $0.088H/U_{ref}$. The computational time per iteration is the same for both schemes.

The Fig. 6 shows longitudinal component of velocity in the mid-plane compared with measurements [9]. The computational results for both interpolation schemes are practically equal. It can be seen that the computed maximum of negative velocity is smaller than measured. The computed recirculation length is $6.51H$, whereas measured one can be estimated $(5.5-5.7)H$. The under-prediction of velocity after reattachment in Fig. 6 can be explained by delayed reattachment. Velocity vectors in the mid-plane are shown in the Figure 7. Nevertheless, the EARSM model here gives at least qualitatively correct result, since the image of the zero friction lines given in Fig. 4 is similar to the one for wide channel, where the separation length was correct.

The vertical corner vortices can be recognized from the velocity vector field in the horizontal plane given in Fig. 8. The qualitative agreement of results with experiment is acceptable, however the accuracy of separation length is worse than in the previous case. This can be explained by larger relative importance of turbulence model at higher Reynolds number, which made the accuracy limits of EARSM obvious.

5. CONCLUSIONS

Two cases of 3D turbulent flow over backward facing step were computed. The choice of methods was chosen so as to isolate the influence of Reynolds stress constitutive relation as much as possible. The SST eddy viscosity model does not give satisfactory results for 3D BFS flow. While the prediction of 2D flow is well acceptable, the results are inconsistent going to third dimension. On the other hand the EARSM model gives comparable recirculation length for 2D case as well as for large aspect ratio 3D case. Under more dynamic conditions, in narrower channel at higher Reynolds number, the EARSM model overpredicts the recirculation length, however the result is most likely still qualitatively correct. The capturing of large vortical structures in comparison with experiment is also acceptable.

6. ACKNOWLEDGMENT

This work was partially supported by grants No.201/05/005 of GA CR, and Research Plan of MSMT No. 6840770010.

REFERENCES

[1] Armaly, B.F. et al., 1983, "Experimental and Theoretical Investigation of Backward-facing Step Flow", *J. Fluid Mech.*, vol. 127, pp. 473–496.

[2] Hellsten, A., 2004, "New advanced k-ω turbulence model for high-lift aerodynamics", In *42nd AIAA Aerospace Sciences Meeting*. Reno, Nevada.

[3] Kozel, K., Louda, P., Příhoda J., 2003, "Numerical solution of turbulent backward facing step and impinging jet flows", In: *Conference on modelling fluid flow*(Eds. T. Lajos and J. Vad), Budapest, pp. 694–701.

[4] Menter F. R., 1994, "Two-Equations Eddy-Viscosity Turbulence Models for Engineering Applications", *AIAA Journal*, Vol.32, No.8, pp. 1598-1605.

[5] Vierendeels J., Riemslagh K., Dick E., 1998, "A Multigrid Semi-Implicit Line-Method for Viscous Incompressible Flows", *Proceedings of Conference "Euler and Navier-Stokes Equations"* (Eds. Kozel K., Příhoda J., Feistauer M.), Prague, pp. 89-92.

[6] van Leer, B., 1985, "Upwind-difference methods for aerodynamics problems governed by the Euler equations", *Lectures in Appl. Math*, Vol. 22, pp. 327–336.

[7] Wallin, S., 2000, "Engineering turbulence modeling for CFD with a focus on explicit algebraic Reynolds stress models", *PhD thesis*, Royal Institute of Technology, Stockholm.

[8] Wallin, S., Johansson, A. V., 2000, "An explicit algebraic Reynolds stress model for incompressible and compressible turbulent flows ", *J. Fluid Mech.*, Vol. 43, pp. 89–132.

[9] Zubík P., Šulc J., 2005, "Analysis of the internal structure of flow in a channel with negative step", In: *Proc. Conference Engineering Mechanics 2005*, Svratka, CD-ROM, 11 p. (in Czech).

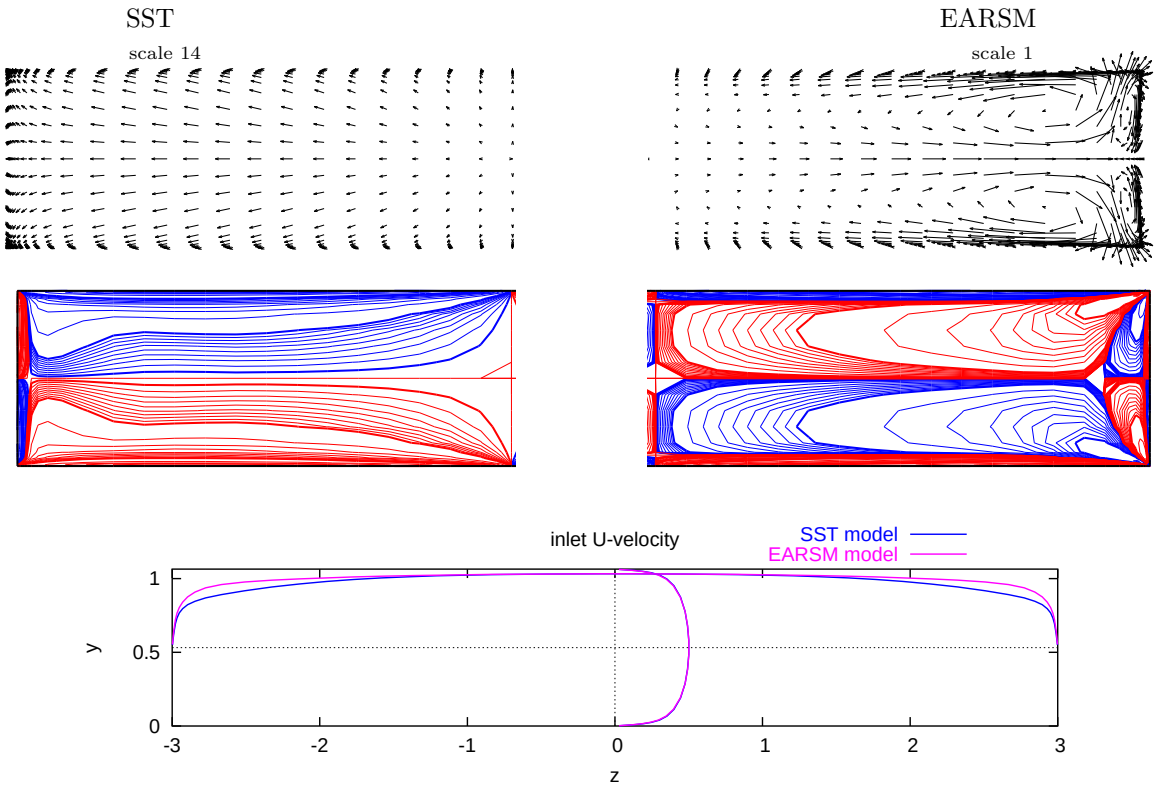

Figure 1. Developed channel flow. From above: velocity vectors of secondary flow, isolines of streamwise component of vorticity, and velocity profiles in horizontal and vertical mid-plane

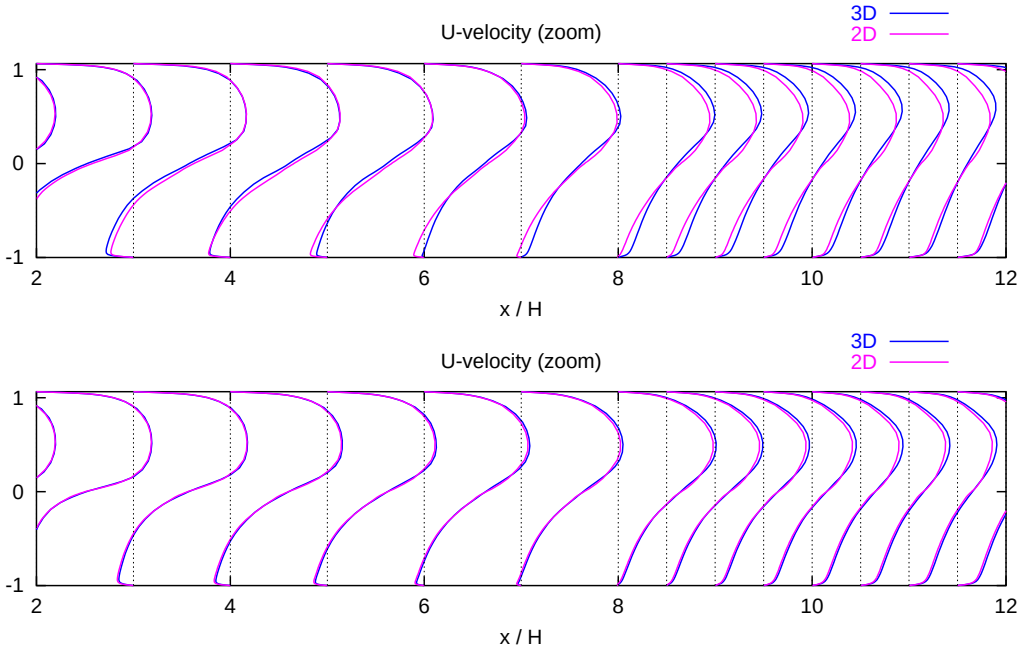

Figure 2. Influence of 3D effects on velocity profiles. SST model (left) and EARS model (right). In 3D, centre-plane shown

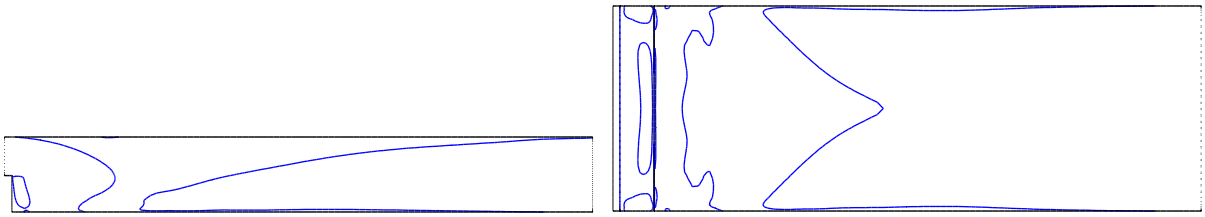

Figure 3. Lines of zero friction on side wall (left) and bottom wall (right) for SST model

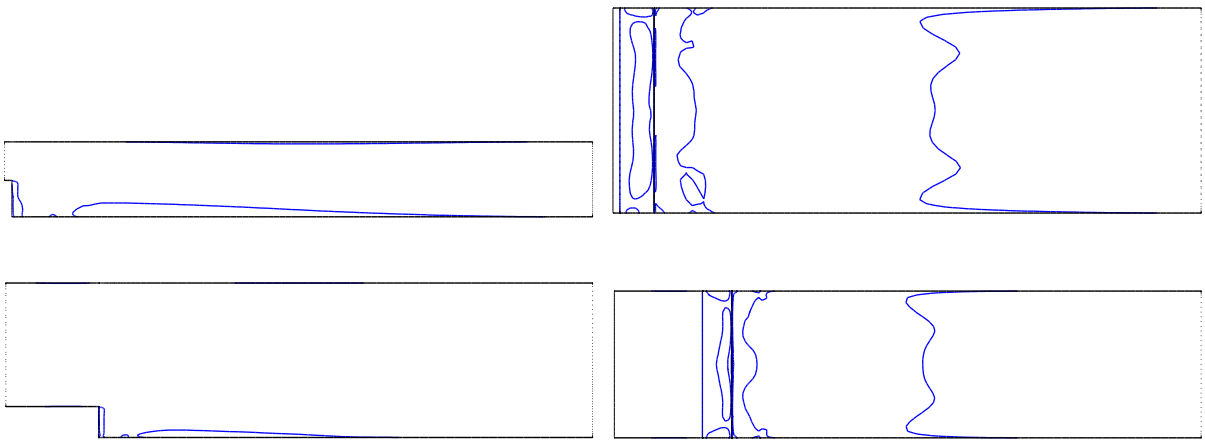

Figure 4. Lines of zero friction on side wall (left) and bottom wall (right) for EARSM model. Wide channel above, narrow channel below.

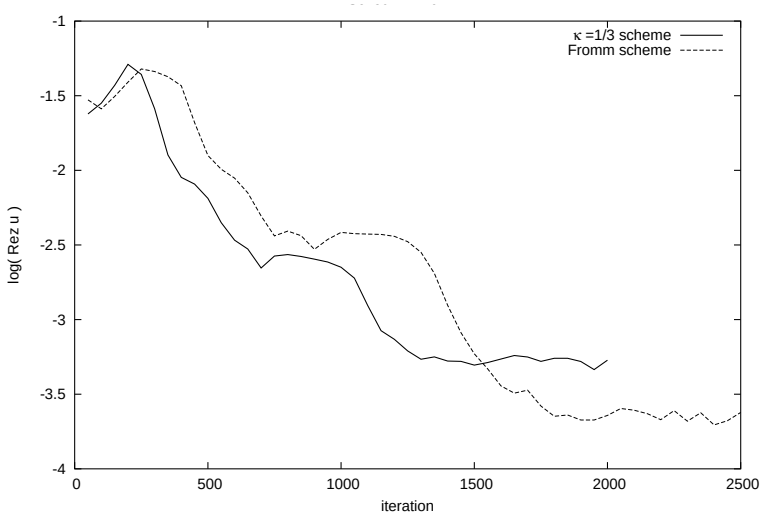

Figure 5. Convergence history for different convective term discretizations

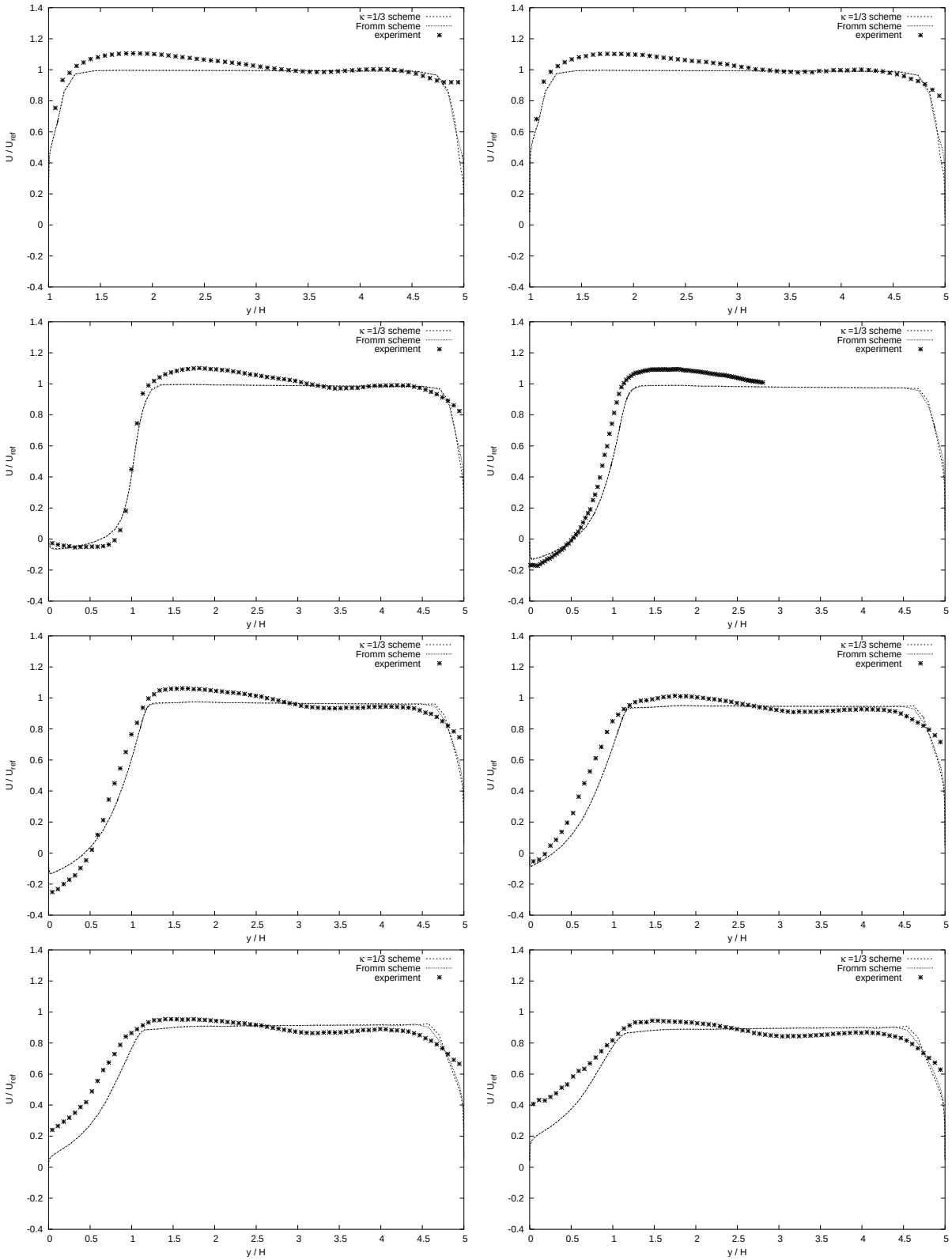

Figure 6. Velocity profiles in the mid-plane for narrow channel, ERASM model. Distance x/H downstream from the step, from above left to below right: $-0.305,\ -0.033,\ 1.193,\ 2.51,\ 3.78,\ 5.00,\ 7.05,\ 8.54$

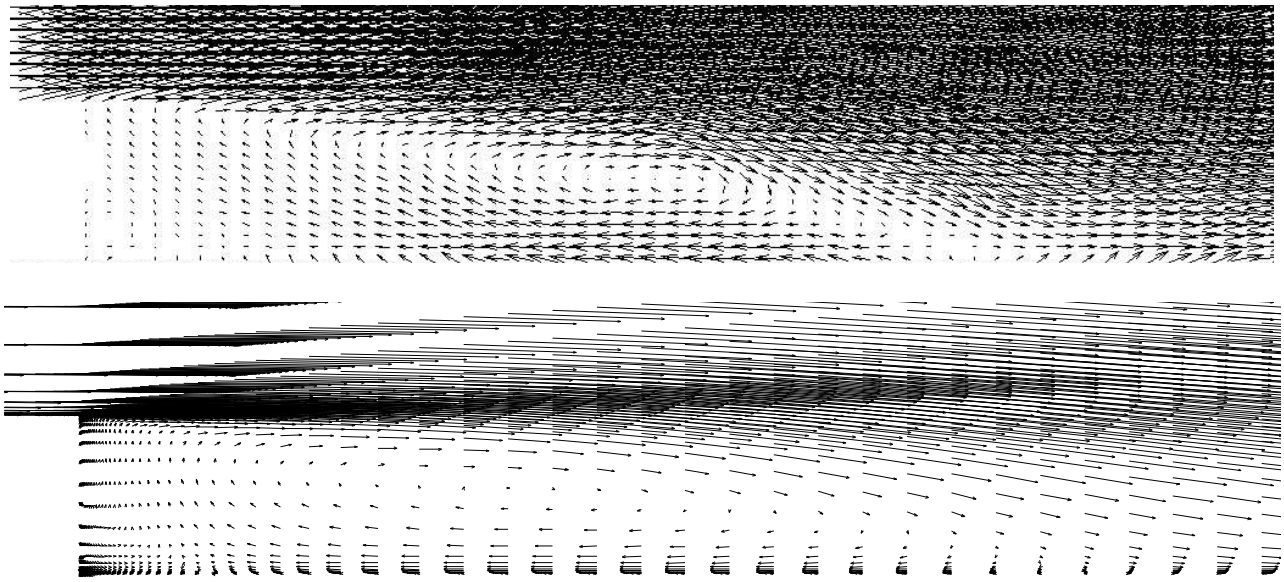

Figure 7. Velocity vectors in the mid-plane. Above: experiment, below: EARSM model

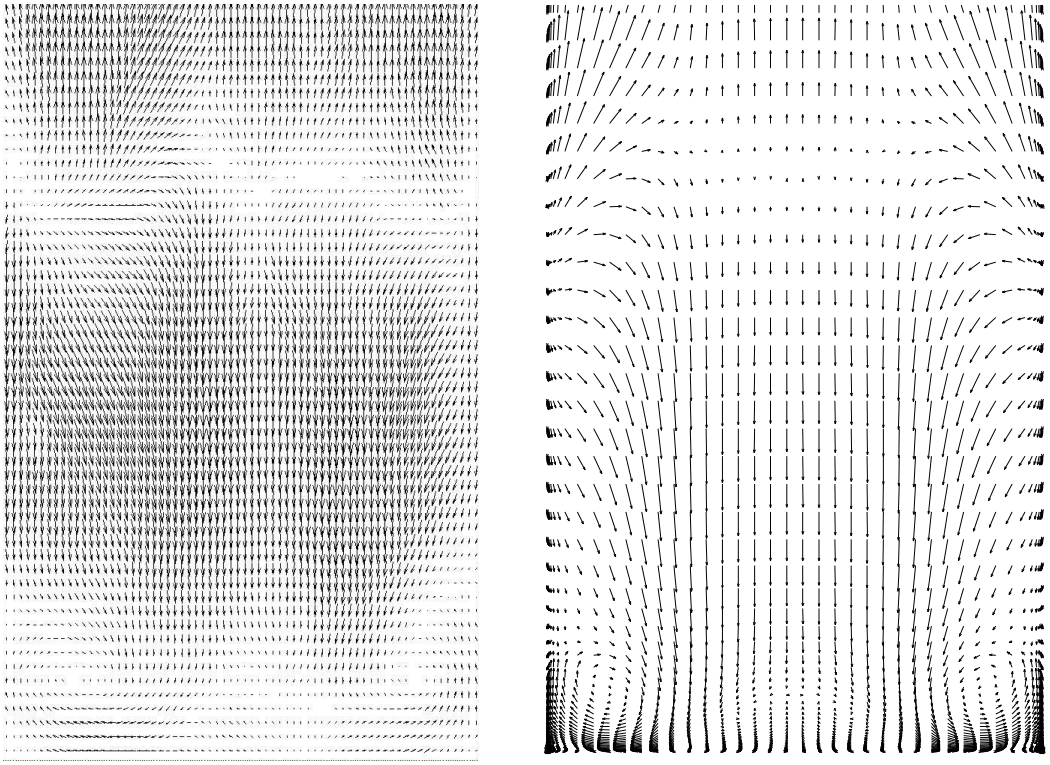

Figure 8. Velocity vectors in horizontal plane, $0.125H$ above bottom wall. Left: experiment, right: EARSM model

Conference on Modelling Fluid Flow (CMFF'06)
The 13th International Conference on Fluid Flow Technologies
Budapest, Hungary, September 6-9, 2006

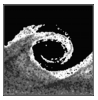

FULLY-DEVELOPED ISOTHERMAL AND INCOMPRESSIBLE TURBULENT FLOWS IN PASSAGES

Tibor CZIBERE[1], László KALMÁR[2], Gábor JANIGA[3]

[1] Department of Fluid and Heat Engineering, University of Miskolc. H-3515 Miskolc-Egyetemváros, Hungary.
[2] Corresponding Author. Department of Fluid and Heat Engineering, University of Miskolc. H-3515 Miskolc-Egyetemváros, Hungary. Tel.: +36 46 565-131, Fax: +36 46 565-453, E-mail: aramka@uni-miskolc.hu
[3] Lab. of Fluid Dynamics and Technical Flows, University of Magdeburg "Otto-von-Guericke"

ABSTRACT

This paper deals with the numerical solution of fully developed turbulent flows in channels. The numerical investigations were carried out at three Reynolds numbers Re_*, 180, 395, and 590, calculated by the half width of the channel h and the friction velocity v_*. The two-equation version of the stochastic turbulent model (2E-STM) proposed by Czibere predicts very well the distributions of the turbulent velocity profiles and the shear stress distribution in channel flows comparing with Direct Numerical Simulation (DNS) data. The distributions of the mean velocity u in the direction of the main flow and the elements of the Reynolds stress tensor are compared with the distributions of data given by DNS. The calculated results by applying 2E-STM show good agreement with the data obtained by DNS for the two higher Reynolds numbers. In the case of the lowest Reynolds number the difference between the two calculated shear stress distributions are greater, because in this case the flow in the channel can not be considered as a fully developed turbulent flow.

Keywords: fully developed turbulent channel flow, stochastic turbulent model, velocity and shear stress distributions

NOMENCLATURE

$\underline{\underline{F}}_R$	[Pa]	Reynolds stress tensor
h	[m]	half width of the channel
k	[m^2/s^2]	specific kinetic energy
p	[Pa]	pressure
u	[m/s]	mean velocity in x-direction
u'	[m/s]	instantaneous value of velocity fluctuations in x-direction
$\underline{v}$	[m/s]	mean velocity vector
v	[m/s]	mean velocity in y-direction
v',w'	[m/s]	instantaneous value of the velocity fluctuations normal to main flow in directions y and z, respectively
v_*	[m/s]	friction velocity
x	[m]	longitudinal co-ordinate in the direction of the main flow
y	[m]	lateral co-ordinate, $y=h$ corresponds to the channel wall
y^+	[-]	dimensionless wall distance
z	[m]	vertical co-ordinate
Re_*	[-]	Reynolds number based on the half width and the friction velocity
$\alpha,\beta,\gamma,\mu,\vartheta$	[-]	elements of the similarity tensor $\underline{\underline{H}}$
ρ	[kg/m^3]	density
Θ	[Pa]	dominant turbulent shear stress
ε	[m^2s^{-3}]	turbulent dissipation
Ω	[s^{-1}]	magnitude of the vorticity vector
υ	[m^2s^{-1}]	kinematic viscosity
η	[Nsm^{-2}]	absolute (dynamic) viscosity

Subscripts and Superscripts

1,2,3	components of the velocity vectors in directions of the co-ordinate axes, respectively
x, y	components of vectors in directions of the co-ordinate axes x and y

1. INTRODUCTION

Most turbulent flows are bounded by one or more solid surfaces. The flow through pipes and ducts are the simplest application for internal flows. These simple flows are of practical importance and play a prominent role in the development of the numerical study of turbulent flows. In this paper plane channel flow are investigated and fully developed turbulent flow is assumed.

In the following a solution method is presented for turbulent channel flows, for which relatively a simple numerical procedure is required for the computation of velocity profiles and turbulence quantities. The proposed new two-equation turbulent model (2E-STM) makes it possible to calculate also the Reynolds shear stress distribution.

The stochastic turbulent model is under continuous development [3,4]. However the algebraic version of the model fails to predict correctly the Reynolds-stresses and the turbulent kinetic energy in the whole flow-domain. That's why in calculating the characteristics of the turbulent flow by 2E-STM the continuity and Reynolds averaged momentum equations were extended by two differential and two scalar transport equations in order to predict the turbulent quantities more accurately. After presenting the governing equations and the details of the model, the numerical issues of the solution method are discussed. Despite the large amount of experimental data available for these relatively simple flows, there is poor agreement among the reported measurements [1]. In this paper, the widely accepted direct numerical simulation (DNS) data were used for comparison with the computed results for channel flow. Three different Reynolds numbers were chosen for the comparison.

2.GOVERNING EQUATIONS

The basic equations in this section are formed in the case of three-dimensional flows. The continuity equation for incompressible flow can be written as:

$$\nabla \cdot \underline{v} = 0 \,. \tag{1}$$

The Reynolds averaged momentum equation for the turbulent flow is given as:

$$(\underline{v}\cdot\nabla)\underline{v} = -\nabla \Pi + \upsilon \Delta \underline{v} + \frac{1}{\rho}\mathrm{Div}\,\underline{\underline{F}}_R \,, \tag{2}$$

where the total potential by using the potential of the conservative body force $U(\underline{r})$ can be defined as:

$$\Pi = U + \frac{p}{\rho} + \frac{2}{3}k \,. \tag{3}$$

The turbulent stress tensor $\underline{\underline{F}}_R$, which is modelled by Czibere can be written in the following form by using the so called "natural coordinate system" [3]:

$$\underline{\underline{F}}_R(\underline{r},t) = \Theta\,(\underline{r},t)\;\underline{\underline{H}}^* - \\ -\rho\;\tfrac{2}{3}k(\underline{r},t)\;\underline{\underline{I}} \quad . \tag{4}$$

In Eq. (4) Θ is the dominant turbulent shear stress

$$\Theta = \rho\,(\kappa\, l\Omega)^2 \,, \tag{5}$$

where κ is the von Kármán constant, l is the length-scale of turbulence and Ω is the vorticity magnitude.

The $\underline{\underline{H}}^*$ is the deviatoric part of the so called similarity tensor $\underline{\underline{H}}$ of the stochastic turbulence model [3]:

$$\underline{\underline{H}} = \begin{pmatrix} \alpha & 1 & \mu \\ 1 & \beta & \vartheta \\ \mu & \vartheta & \gamma \end{pmatrix} \,, \tag{6}$$

where the elements of the tensor $\underline{\underline{H}}$ are the constants of the stochastic turbulence model.

The numerical computations are performed in the so called "computational coordinate system", therefore the turbulent stress tensor $\underline{\underline{F}}_R$ has to be transformed into this coordinate system from the "natural coordinate system":

$$\underline{\underline{F}}_R(\underline{r},t) = \Theta\,(\underline{r},t)\;\underline{\underline{G}}^* - \\ -\rho\;\tfrac{2}{3}k(\underline{r},t)\;\underline{\underline{I}} \quad ,$$

where $\underline{\underline{G}}^*$ is the transformation of the similarity tensor (6).

The specific turbulent dissipation can be determined as:

$$\varepsilon\,(\underline{r},t) = \frac{\eta}{\rho}\,\overline{(\underline{v}'\circ\nabla):(\underline{v}'\circ\nabla+\nabla\circ\underline{v}')} \,,$$

which can be expressed in the following form by using the stochastic turbulent model:

$$\varepsilon\,(\underline{r},t) = -\kappa^2\upsilon\,\Big\{\big(2\alpha+\beta+\gamma\big)A^2+\big(\alpha+2\beta+ \\ +\big(\alpha+\beta+2\gamma\big)C^2+2\big(AB+\mu\,AC+\vartheta\,BC\big)\Big\}. \tag{7}$$

The unknown coefficients A, B and C in this expression can be calculated as:

$$A = E_{11}\frac{\partial\,(l\Omega)}{\partial\,\mathrm{x}} + E_{12}\frac{\partial\,(l\Omega)}{\partial\,\mathrm{y}} + E_{13}\frac{\partial\,(l\Omega)}{\partial\,\mathrm{z}} \,,$$

$$B = E_{21}\frac{\partial\,(l\Omega)}{\partial\,\mathrm{x}} + E_{22}\frac{\partial\,(l\Omega)}{\partial\,\mathrm{y}} + E_{23}\frac{\partial\,(l\Omega)}{\partial\,\mathrm{z}} \,,$$

$$C = E_{31}\frac{\partial\,(l\Omega)}{\partial\,\mathrm{x}} + E_{32}\frac{\partial\,(l\Omega)}{\partial\,\mathrm{y}} + E_{33}\frac{\partial\,(l\Omega)}{\partial\,\mathrm{z}} \,,$$

where E_{ij} (i=1,2,3 and j=1,2,3) are the elements of the coordinate transformation tensor $\underline{\underline{E}}$. The elements of $\underline{\underline{E}}$ are given later in the case of two-dimensional flow.

The Eqs. (1) and (2) can be completed with the equation for the turbulent kinetic energy:

$$\frac{dk}{dt} = \frac{1}{\rho}\Theta\;\underline{\underline{G}}^* : (\nabla\circ\mathbf{v}) - \varepsilon \; - \\ \nabla\cdot\left\{\frac{(l\Omega)^3}{2}\underline{t}^* - \left(\frac{5\upsilon}{3}+\frac{\kappa\,a}{C_k}l^2\Omega\right)\nabla k + \right. \\ \left. +\frac{\upsilon}{\rho}\,\mathrm{Div}(\Theta\;\underline{\underline{G}}^*)\right\}. \tag{8}$$

For the numerical solution of the flow problem it is also necessary to connect the algebraic Eq. (5) with the following equation, which was developed by applying the method of dimensional analysis:

$$\varepsilon = C_E\upsilon^N(l\Omega)^{2(1-N)}\Omega^{N+1} \,. \tag{9}$$

The eight scalar Eqs. (1), (2), (5), (7), (8) and (9) contain 8 unknown variables (v_1, v_2, v_3, Π, Θ, k, ε and $l\Omega$), so the system of equation mentioned above forms a closed system.

2.1. Two-dimensional steady flow between two parallel plates

In this paper constant property fully-developed flow is assumed. In this case properties no longer vary with distance along the channel (*x*-direction).

The velocity vector has only one non-zero component as: $\underline{v} = u(y)\,\underline{i}$, where *y* varies along the channel width 2*h*.

The coordinate-transformation tensor:

$$\underline{\underline{E}} = \begin{pmatrix} 1 & 0 & 0 \\ 0 & \mathrm{sign}(du/dy) & 0 \\ 0 & 0 & \mathrm{sign}(du/dy) \end{pmatrix}. \qquad (10)$$

The transformation of the similarity tensor (6) $\underline{\underline{G}}^*$ can be expressed as:

$$\underline{\underline{G}}^* = \begin{pmatrix} \alpha_* & \mathrm{sign}(du/dy) & 0 \\ \mathrm{sign}(du/dy) & \beta_* & 0 \\ 0 & 0 & \gamma_* \end{pmatrix}. \qquad (11)$$

The elements of the vector $\mathrm{Div}(\Theta\underline{\underline{G}}^*)$ are given by:

$$\mathrm{Div}(\Theta\,\underline{\underline{G}}^*)_x = \mathrm{sign}\left(\frac{du}{dy}\right)\frac{d\Theta}{dy}, \qquad \mathrm{Div}(\Theta\,\underline{\underline{G}}^*)_y = \frac{d}{dy}(\beta_*\Theta). \qquad (12)$$

The two scalar components of the momentum equation can be written as:

$$0 = -\rho\,\frac{\partial \Pi}{\partial x} + \eta\,\frac{d^2u}{dy^2} + \mathrm{sign}\left(\frac{du}{dy}\right)\frac{d\Theta}{dy}, \qquad (13)$$

$$0 = -\rho\,\frac{\partial \Pi}{\partial y} + \beta_*\frac{d\Theta}{dy}. \qquad (14)$$

The two additional differential equations can be derived by using Eqs. (7), (8) and (9), respectively:

$$0 = \mathrm{sign}\left(\frac{du}{dy}\right)\frac{\Theta}{\rho}\frac{du}{dy} - \varepsilon - \frac{d}{dy}\left[\mathrm{sign}\left(\frac{du}{dy}\right)(l\Omega)^3\frac{\hat{t}_2}{2}\right] + \frac{d}{dy}\left[\left(\frac{5\upsilon}{3} + \frac{\kappa\, a}{C_k}l^2\Omega\right)\frac{dk}{dy} + \frac{\upsilon}{\rho}\beta_*\frac{d\Theta}{dy}\right], \qquad (15)$$

$$-\kappa^2(\alpha + 2\beta + \gamma)\left(\frac{d(l\Omega)}{dy}\right)^2 = C_E\upsilon^{N-1}(l\Omega)^{2(1-N)}\Omega^{N+1}, \qquad (16)$$

where $\hat{t}_2$ and C_k are also the parameters of stochastic turbulent model.

The six scalar Eqs. (5), (9), (13), (14), (15) and (16) for two-dimensional flows in this case contain 6 unknown variables (u, Π, Θ, k, ε and $l\Omega$). This system of equation also forms a closed system, the unknown variables mentioned above can be determined using numerical integration as described in the next section.

3. NUMERICAL SOLUTION

The dimensionless coordinate ξ can be introduced as $\xi = y/h$ due to the symmetrical configuration the interval of $0 \le \xi \le 1$ is considered in the numerical investigation.

By integrating the Eq. (13) with respect to *y* and substituting the algebraic Eq. (5) into that, after rearranging the following common differential equation can be written for determination of the dimensionless mean velocity distribution:

$$\frac{d}{d\xi}\left(\frac{u}{v_*}\right) = \mathrm{Re}_*\left[\kappa^2\left(\frac{l\Omega}{v_*}\right)^2 - \xi\right], \qquad (17)$$

where Re_* is the Reynolds number based on the half channel width and the friction velocity.

The Eq. (16) is available to determine the distribution of the unknown variable $l\Omega$ which is also necessary to solve Eq. (17) numerically. By introducing the notation $a_* = \sqrt{-\alpha - 2\beta - \gamma}$, the Eq. (16) can be written as:

$$\kappa^2 a_*^2\left[\frac{d}{d\xi}\left(\frac{l\Omega}{v_*}\right)\right]^2 = C_E\,\mathrm{Re}_*^2\left(\frac{l\Omega}{v_*}\right)^{2(1-N)}\left|\frac{\Theta}{\rho\, v_*^2} - \xi\right|^{N+1}.$$

This equation above by substituting Eq. (5) is suitable to determine the derivative of the unknown variable $\frac{l\Omega}{v_*}$ with respect to ξ :

$$\frac{d}{d\xi}\left(\frac{l\Omega}{v_*}\right) = \frac{\mathrm{Re}_*\sqrt{C_E}}{a_*\kappa}\left(\frac{l\Omega}{v_*}\right)^{1-N}\left|\kappa^2\left(\frac{l\Omega}{v_*}\right)^2 - \xi\right|^{\frac{N+1}{2}}. \qquad (18)$$

In Eqs. (17) and (18) the following values and approximate expression were used in our numerical investigations for the parameters of stochastic turbulent model:

$$\alpha = -3.227 \quad \beta = -1.622 \quad \gamma = -2.612$$
$$\vartheta = \mu = 0 \quad N = 7/4 \quad \kappa = 0.407$$
$$C_E = C_o(1-\xi)^3 \quad C_o = \frac{1206\,\mathrm{Re}_* + 69444}{\mathrm{Re}_* + 7500}. \qquad (19)$$

The numerical solution of the Eqs. (17) and (18) were performed here using Runge-Kutta numerical method implemented in an in-house code written in Fortran program language to calculate the

distributions of $\frac{l\Omega}{v_*}(\xi)$ and dimensionless velocity $\frac{u}{v_*}(\xi)$.

Eq. (15) by using distributions $\frac{l\Omega}{v_*}(\xi)=Y(\xi)$ and $\frac{u}{v_*}(\xi)=V(\xi)$ obtained by solutions of Eqs. (17) and (18) is directly available to calculate the distribution of the specific kinetic energy $K(\xi)=\frac{k}{v_*^2}(\xi)$ as:

$$\frac{1}{\mathrm{Re}_*}\left\{\frac{5}{3}+\frac{\kappa\, a}{C_k}\frac{Y^2}{\left|\kappa^2Y^2-\xi\right|}\right\}\frac{dK}{d\xi}- -2\frac{\beta_*\kappa^2}{\mathrm{Re}_*}Y\frac{dY}{d\xi}+\frac{\hat{t}_2}{2}Y^3- -\int_0^\xi\left\{\kappa^2Y^2\frac{dV}{d\xi'}\right\}d\xi'- -\int_0^\xi\left\{C_E\,\mathrm{Re}_*\,Y^{2(1-N)}\left|\kappa^2Y^2-\xi\right|^{N+1}\right\}d\xi'=0. \quad (20)$$

In the numerical solution of Eq. (20) the following values - as the parameters of the calculation method - were chosen to be $\hat{t}_2=-0.75$ and $C_k=0.75$. The unknown terms of a and β_* in Eq. (20) can be calculated by substituting the parameters of the stochastic turbulent model given in (19) into the following expressions:

$$a=\sqrt{-(\alpha+\beta+\gamma)/2}\,, \quad (21)$$

$$\beta_*=\frac{2\beta-\alpha-\gamma}{3}\,. \quad (22)$$

The numerical solution of the Eq. (20) was also performed using a Runge-Kutta method implemented in the same computer code.

By determining the distributions $Y(\xi)$, $V(\xi)$ and $K(\xi)$ of the turbulent flow finally the elements of Reynolds turbulent stress tensor can be calculated as:

$$\frac{\overline{u'u'}}{v_*^2}=\frac{2}{15}K_0+\frac{2}{3}K(\xi)-\alpha_*\kappa^2Y^2(\xi)\,, \quad (23)$$

$$\frac{\overline{v'v'}}{v_*^2}=-\frac{1}{15}K_0+\frac{2}{3}K(\xi)-\beta_*\kappa^2Y^2(\xi)\,, \quad (24)$$

$$\frac{\overline{w'w'}}{v_*^2}=-\frac{1}{15}K_0+\frac{2}{3}K(\xi)-\gamma_*\kappa^2Y^2(\xi)\,, \quad (25)$$

$$\frac{\overline{u'v'}}{v_*^2}=\frac{\Theta}{\rho v_*}=\kappa^2Y^2(\xi)\,, \quad (26)$$

where K_0 is an constant of the integration, which can be determined using the parameters of the turbulent model as:

$$K_0=k_0/v_*^2=-\kappa^2(\alpha+\beta+\gamma)/2\,. \quad (27)$$

The Eqs. (23), (24) and (25) are available to determine the stresses in main diagonal of Reynolds stress tensor. The Eq. (26) is used to calculate the dominant shear stress of the turbulent flow.

The number of grid points were 5 000 equally spaced in our numerical investigations along the interval of $0\le\xi\le1$. The numerical solution can be achieved less than 20 seconds with a 600 MHz/256 MB-RAM PC. Similar investigations were also carried out to demonstrate the grid-independency with 2500, 10 000 and 20 000 grid points. The results were compared applying the dimensionless least-square method and the obtained discrepancies were found smaller than 0.1 % in all cases.

4. COMPUTATIONAL RESULTS

Figures 1-6 represent the computed dimensionless distributions of the velocity u/v_* in two-dimensional plane channel flow. The velocity distribution data for comparison are obtained from the DNS of Moser et. al. [2] for Re_* = 180, 395 and 590. The computed results show very good agreement with DNS data.

In addition to the velocity distribution, another important characteristic of turbulent channel flows is the shear stress distribution $\Theta/\rho v_*(\xi)$. Figures 7-9 represent the computed dimensionless shear stress distribution in the half-channel. The higher Reynolds number flows show an excellent agreement compared with the DNS data.

Figures 10-12 compare the results of the specific turbulent kinetic energy $k/v_*^2(\xi)$ with the direct numerical simulation. Increasing the Reynolds number the results show a better agreement.

The first component of the Reynolds shear stress tensor $\overline{u'u'}/v_*^2(\xi)$ can be seen in Figures 13-15. The present model predicts well the maximum values, although some discrepancies can be observed in the figures.

The second component in the diagonal of the Reynolds shear stress tensor $\overline{v'v'}/v_*^2(\xi)$ are shown in Figure 16-18. These results show probably the highest difference between the present model and the DNS simulation.

The last component in the diagonal of the Reynolds shear stress tensor $\overline{w'w'}/v_*^2(\xi)$ can be seen in Figures 19-21. These results show a very good agreement, especially for the higher Reynolds number flows.

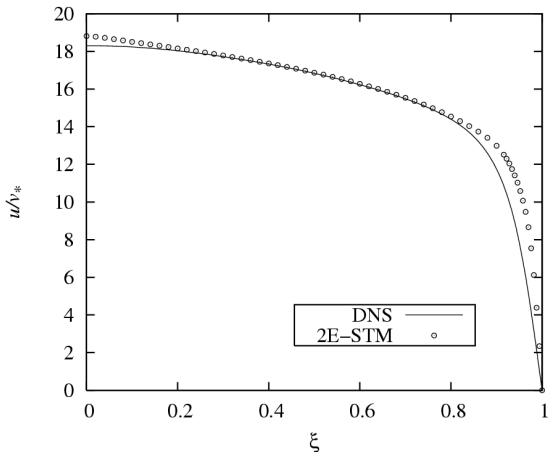

Figure 1. Velocity distribution $\mathrm{Re}_* = 180$

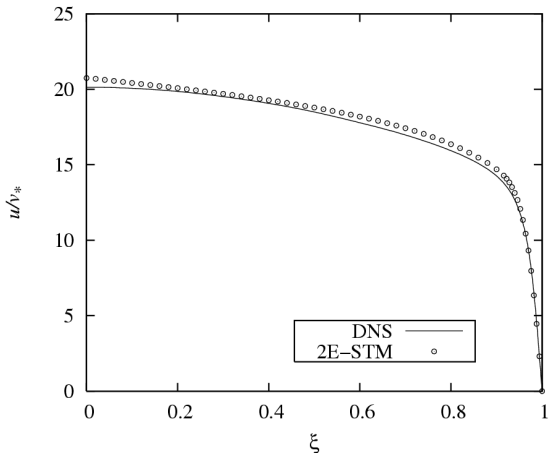

Figure 2. Velocity distribution $\mathrm{Re}_* = 395$

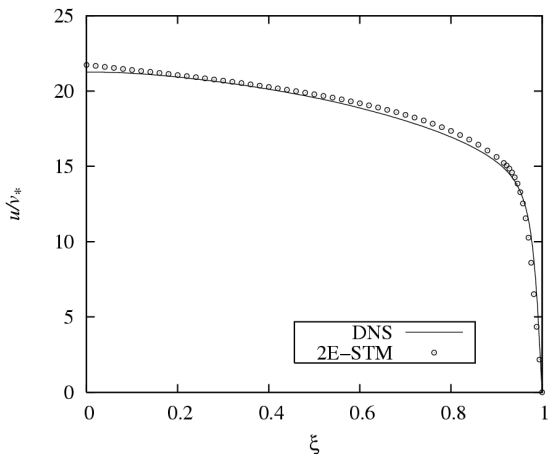

Figure 3. Velocity distribution $\mathrm{Re}_* = 590$

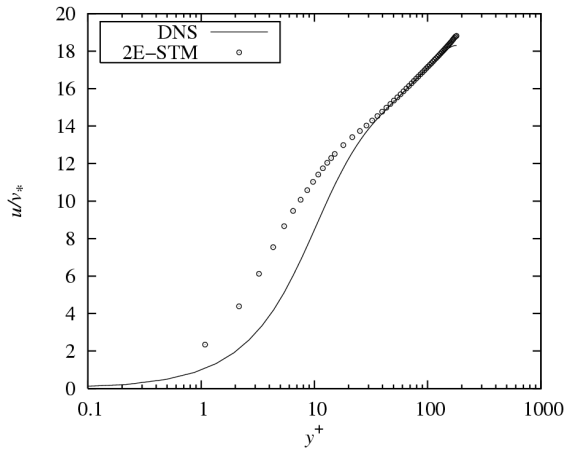

Figure 4. Logarithmic velocity distribution $\mathrm{Re}_* = 180$

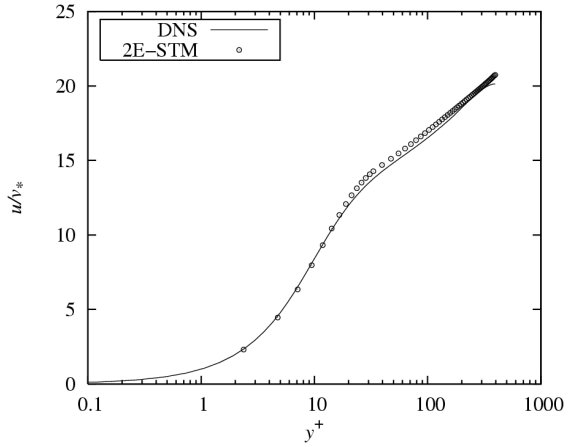

Figure 5. Logarithmic velocity distribution $\mathrm{Re}_* = 395$

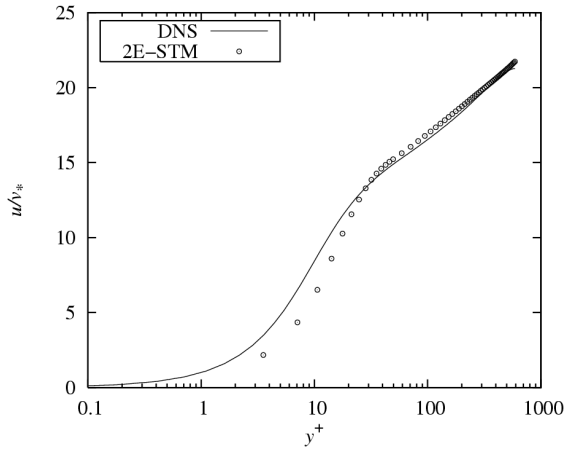

Figure 6. Logarithmic velocity distribution $\mathrm{Re}_* = 590$

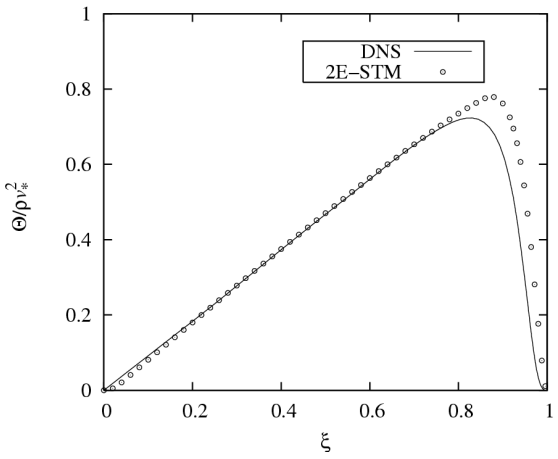

Figure 7. Shear stress distribution $\mathrm{Re}_* = 180$

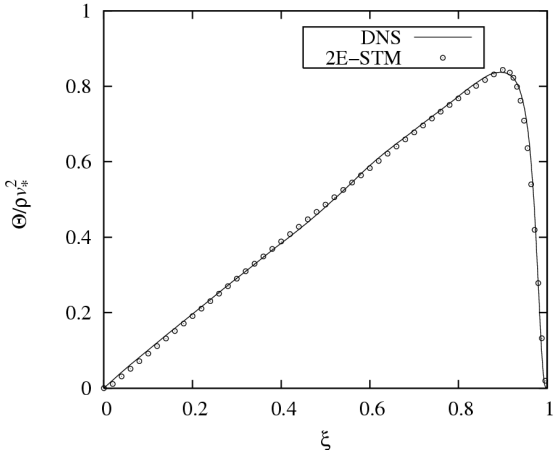

Figure 8. Shear stress distribution $\mathrm{Re}_* = 395$

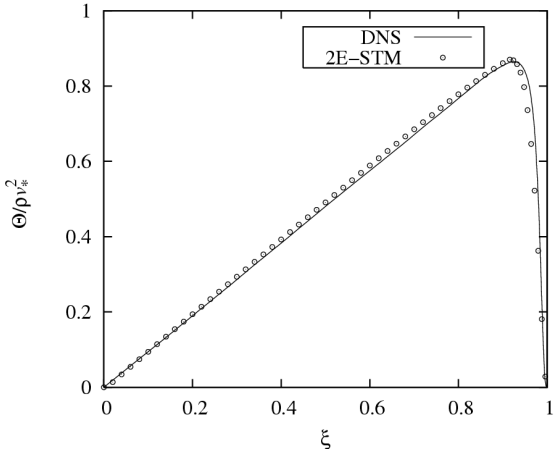

Figure 9. Shear stress distribution $\mathrm{Re}_* = 590$

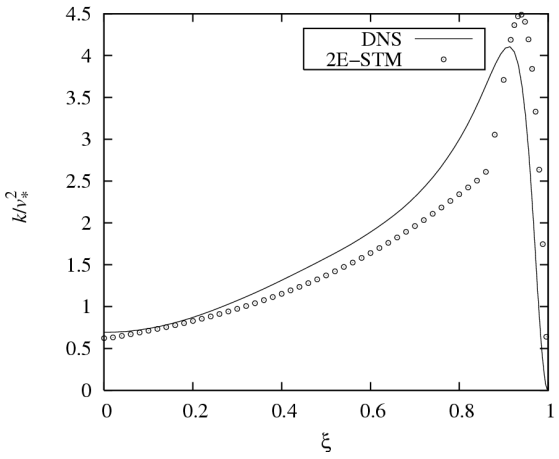

Figure 10. Turbulent kinetic energy $\mathrm{Re}_* = 180$

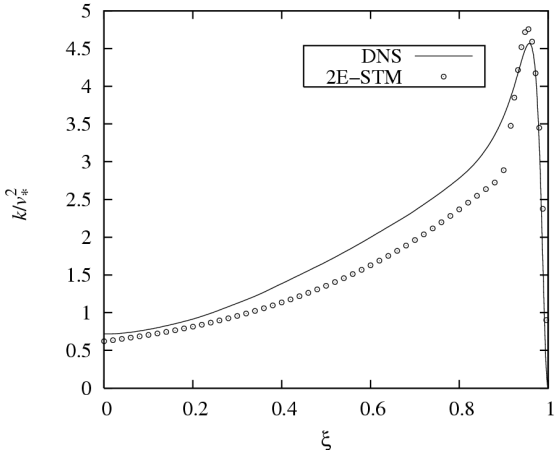

Figure 11. Turbulent kinetic energy $\mathrm{Re}_* = 395$

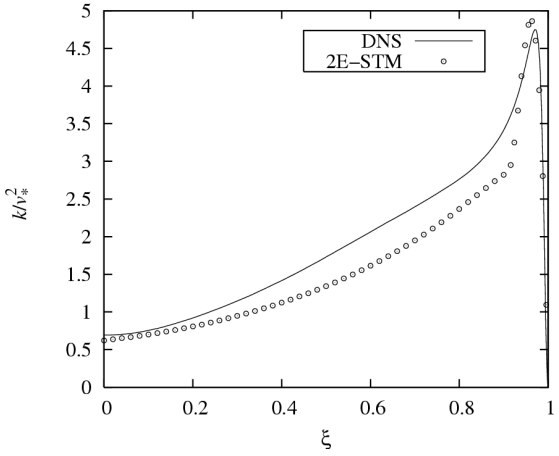

Figure 12. Turbulent kinetic energy $\mathrm{Re}_* = 590$

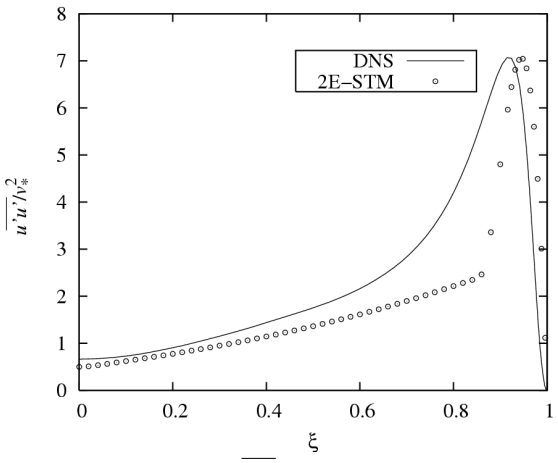

Figure 13. Element $\frac{\overline{u'u'}}{v_*^2}$ of the Reynolds tensor $\mathrm{Re}_* = 180$

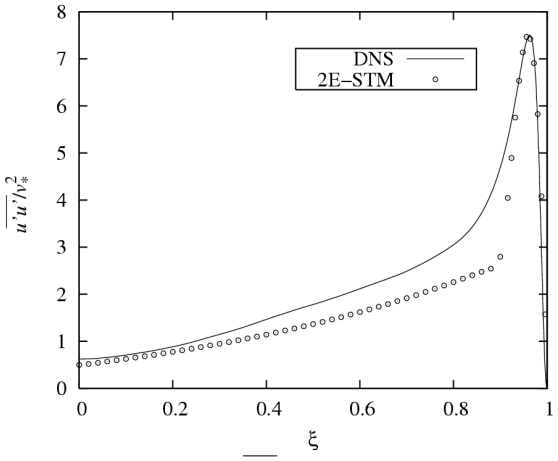

Figure 14. Element $\frac{\overline{u'u'}}{v_*^2}$ of the Reynolds tensor $\mathrm{Re}_* = 395$

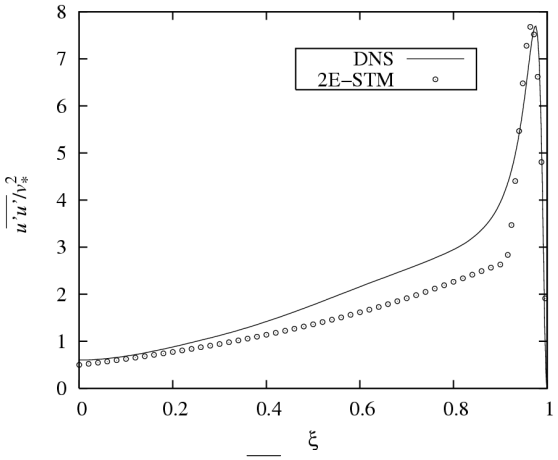

Figure 15. Element $\frac{\overline{u'u'}}{v_*^2}$ of the Reynolds tensor $\mathrm{Re}_* = 590$

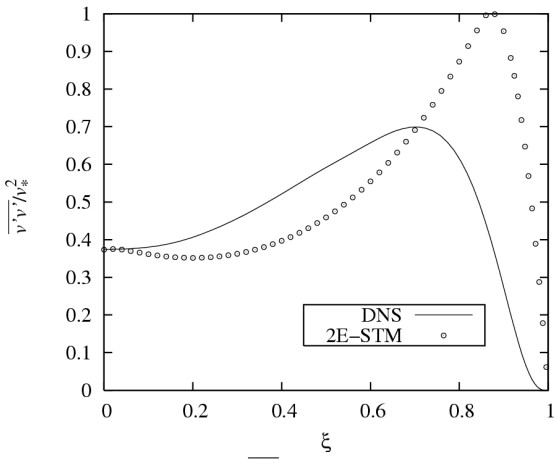

Figure 16. Element $\frac{\overline{v'v'}}{v_*^2}$ of the Reynolds tensor $\mathrm{Re}_* = 180$

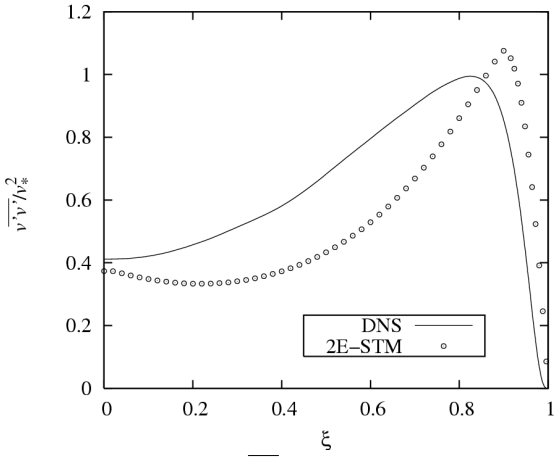

Figure 17. Element $\frac{\overline{v'v'}}{v_*^2}$ of the Reynolds tensor $\mathrm{Re}_* = 395$

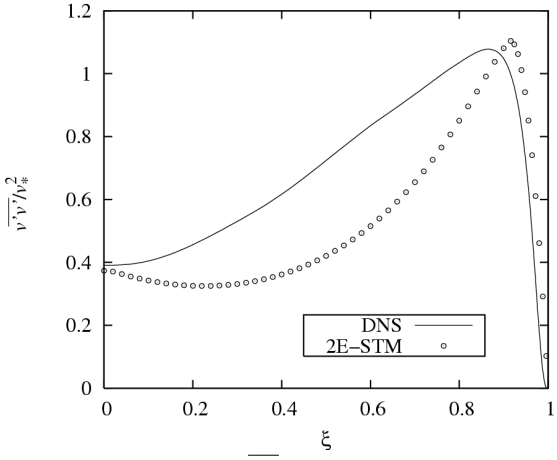

Figure 18. Element $\frac{\overline{v'v'}}{v_*^2}$ of the Reynolds tensor $\mathrm{Re}_* = 590$

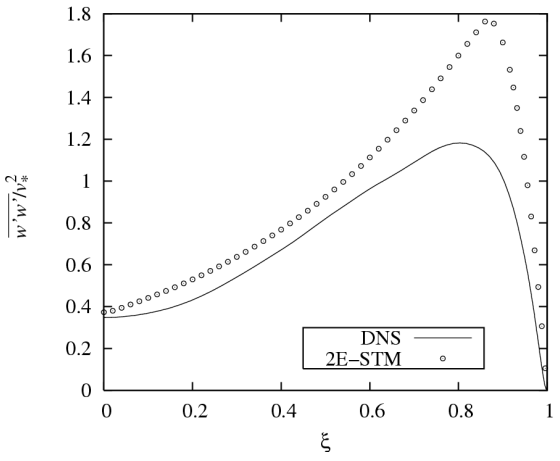

Figure 19. Element $\frac{\overline{w'w'}}{v_*^2}$ of the Reynolds tensor $\mathrm{Re}_* = 180$

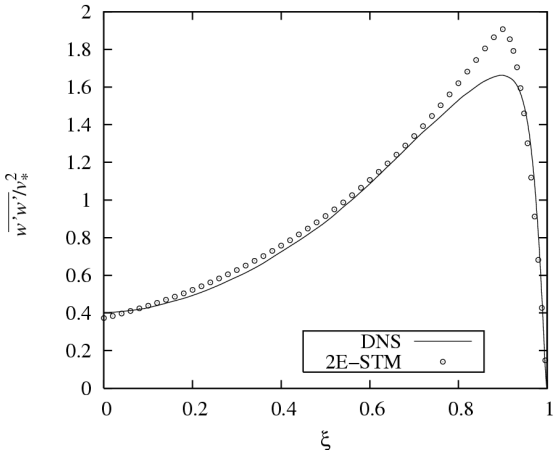

Figure 20. Element $\frac{\overline{w'w'}}{v_*^2}$ of the Reynolds tensor $\mathrm{Re}_* = 395$

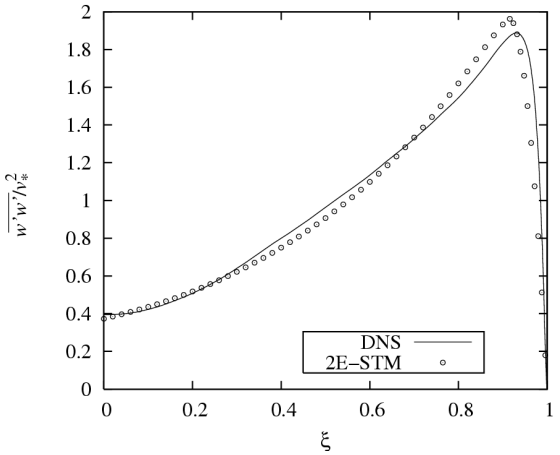

Figure 21. Element $\frac{\overline{w'w'}}{v_*^2}$ of the Reynolds tensor $\mathrm{Re}_* = 590$

5. SUMMARY

The present results show that the presented solution method provides a fast and simple method for the computation of fully-developed turbulent channel flows. Computational results of most of the turbulent quantities show a good agreement compared with DNS data. The second component in the diagonal of the Reynolds shear stress tensor may need some consideration. The smallest Reynolds number flow provide a less accurate result, but this flow is not a fully developed turbulent flow [2].

The presented stochastic turbulent model (2E-STM) predicts well the different characteristics of the turbulent flow far from the walls. The effect of the wall should be taken into account to improve the model capabilities by applying for example so called damping functions [5].

Comparison with higher Reynolds number flows are planned to validate the 2 equation version of the stochastic turbulence model, because the present results show a very good especially for the higher Reynolds number cases.

ACKNOWLEDGEMENTS

This work has been partly supported by DAAD-MÖB in the framework of exchange scientist project 2005-2006/34.

REFERENCES

[1] Kim, J., Moin, P., and Moser, R., 1987, "Turbulence statistics in fully developed channel flow at low Reynolds number", *J. Fluid Mech.* Vol. 177, pp. 133-166.

[2] Moser, R. D., Kim, J., and Mansour, N. N., 1999, "DNS of Turbulent Channel Flow up to $Re_\tau = 590$", *Phys. Fluids*, Vol. 11, pp. 943-945.

[3] Czibere, T., 2001, "Three dimensional stochastic model of turbulence", *Journal of Computational and Applied Mechanics*, Vol 2, No. 1, pp.7-20.

[4] Czibere, T., and Janiga, G., 2003, "Computation of laminar-turbulent transitional flows in plane channels and pipes", *CMFF'03 Conference Proceedings,* Edited by T. Lajos and J. Vad, Vol. I, pp. 632-637.

[5] Wilcox, D. C., 2000, *Turbulence Modeling for CFD*, DCW Industries, Inc.

Conference on Modelling Fluid Flow (CMFF'06)
The 13th International Conference on Fluid Flow Technologies
Budapest, Hungary, September 6-9, 2006

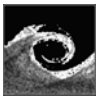

NUMERICAL ANALYSIS OF THE THREE-DIMENSIONAL UNSTEADY FREE CONVECTION AND RADIATION IN AN ELECTRICAL HEATING ELEMENT

Sandor BERNAD[1], Angelo IRRERA[2], Romeo SUSAN-RESIGA[3], Liviu Eugen ANTON[4]

[1] Corresponding Author. Hydrodynamics and Cavitation Laboratory, Romanian Academy – Timisoara Branch. Bvd. Mihai Viteazu No. 24, RO-300223, Timisoara, Romania. Tel.: +40-256-403692, Fax: +40-256-3700, E-mail: sbernad@mh.mec.upt.ro
[2] Engineering Department, Zoppas Industries – IRCA Spa., Italy. E-mail: angelo.irrera@zoppas.com
[3] Department of Hydraulic Machinery, "Politehnica" University of Timisoara, Romania. E-mail: resiga@mh.mec.upt.ro
[3] Department of Hydraulic Machinery, "Politehnica" University of Timisoara, Romania. E-mail: Secretariat@casaautotm.ro

ABSTRACT

The paper presents a complex numerical analysis of unsteady heat transfer with radiation and natural convection in an industrial electrical heating element. Although the normal operating regimes are designed for a pressure-driven air flow, there are abnormal situations when the fan is not working. As a result, the electrical wires are heating up quickly, and only the thermostat protection avoids the wire melting. The classical trial and error approach to adjust the thermostat position and setting is nowadays replaced by a rigorous numerical analysis of the air flow with heat transfer, thus reducing the development costs and allowing a more effective optimization. This paper presents such an analysis for an industrial case. The numerical results are in excellent agreement with the experimental investigations on the prototype, and provide valuable information with respect to both flow and temperature fields.

Keywords: electrical heating element, natural convection, radiation, unsteady flow.

NOMENCLATURE

$\delta[m]$	thickness
$\lambda[W/m\cdot K]$	heat conduction coefficient
$\rho\left[kg/m^3\right]$	density
$c_p\left[J/kg\cdot K\right]$	specific heat
$Vol\left[m^3\right]$	volume

1. INTRODUCTION

Electrical heating devices are found in a variety of home appliances. Although apparently simple from the design point of view, their operation often proves to be a rather complex combination of physical phenomena [1]. Starting with the electrical heat generation in wires, the heat transfer to the operating fluid (air, water or oil) is in general a combination of convection and radiation [2,3,4]. Although the radiative heat transfer is not present when operating with liquids, in air the heating wires reach high enough temperatures to make radiation a main heat transfer mechanism. The high temperature wires radiate heat to the bounding walls and then the heat is transferred to the flowing air through convection. Of course, part of the wire heat flux is also directly convected to the flowing air. This combined heat transfer mechanism is difficult, if not impossible, to be accurately evaluated quantitatively without a full numerical simulation of the flow with heat convection and radiation.

In general, the air flow is generated by a pressure gradient provided by a fan. However, there are abnormal operating regimes, or phases within an operating cycle, when the fan is stopped and the pressure difference that drives the flow vanishes. In such cases, the convection is provided by buoyancy driven flow, thanks to the air density gradients in gravitational field. Such a complex case is examined in the present paper.

First, we present the three-dimensional computational domain for the electrical heating device. In order to simplify the grid generation process, the actual wire geometry is slightly simplified. Second, we briefly review the models for buoyancy driven flow with convection and radiation available in the commercial code FLUENT. Third, we present the main results and the relevant engineering conclusions for an unsteady flow simulation of the so-called abnormal regime when the fan is not operating. The temperature measurements for the thermostat disc are compared with the computed results. The paper conclusions are summarized in the last section.

2. THREE-DIMENSIONAL COMPUTATIONAL DOMAIN AND PROBLEM DEFINITION

Figure 1 shows the 3D computational domain considered for the present study. Symmetry considerations led to a minimal domain that retains all relevant features of the flow with heat transfer.

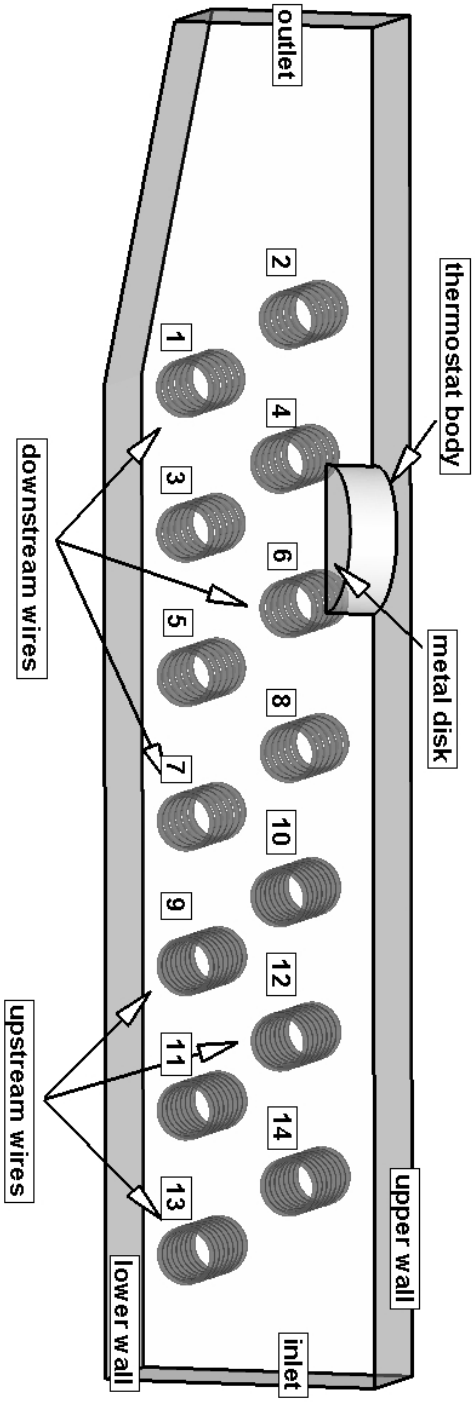

Figure 1. Three-dimensional computational domain for an electrical heating element.

The flow channel is bounded by two walls and two side symmetry planes. The bottom inlet section is larger than the upper outlet section. On the straight wall there is a thermostat with a sensitive disk that triggers an electrical switch at a given temperature. There are two sets of wires: 6 upstream wires with a smaller pitch and 8 downstream wires with larger pitch, such that each set of wires generates 100 W heating power (for the truncated domain width considered in Fig.1).

In order to simplify the mesh generation we have considered the wires as a collection of tori that replaces the actual helical shape, as shown in Figure 2. Each torus surface is discretized with quadrilateral elements, and a boundary layer mesh is built near the wire surface to correctly capture the steep velocity and temperature gradients. The same approach is used for the thermostat cap, where the correct representation of the flow and temperature boundary layers is essential to the accuracy of the results. The final mesh is a combination of tetrahedra and hexahedra, with approximately 10^6 cells. It was found through numerical experiments on previous simplified similar studies that this is the level of grid refinement that insures the accuracy of the results.

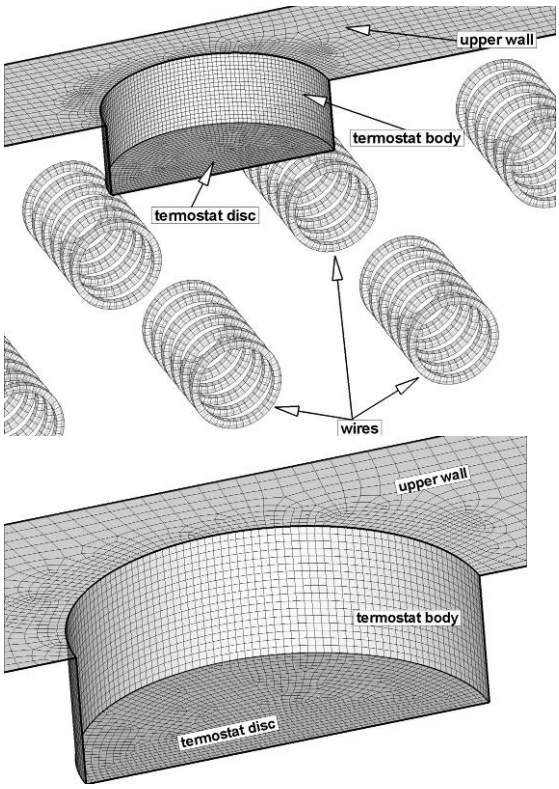

Figure 2. Details of the surface mesh for wires and thermostat neighbourhood. The volume mesh is a mixture of 1.4E6 tetrahedra and hexahedra.

The actual thermostat is shown in Figure 3. However, only the relevant features are retained for

the numerical simulation, as shown in Fig. 3 bottom. There is an air gap between the thermostat cap and metal disk. As it will be further shown, it is essential to correctly account for this air pocket since it produces a significant temperature drop in unsteady operating regimes. For the full 3D computational domain the metal cap – air pocket – metal disc sandwich is represented by a homogeneous wall with equivalent physical properties:

$$\frac{\delta}{\overline{\lambda}} = \frac{\delta_{steel}}{\lambda_{steel}} + \frac{\delta_{air}}{\lambda_{air}},$$

resulting in $\overline{\lambda} = 0.0396\ W/m \cdot K$,

$$\overline{\rho}(Vol_{steel} + Vol_{air}) = \rho_{steel} Vol_{steel} + \rho_{air} Vol_{air}$$

resulting in $\overline{\rho} = 2677\ kg/m^3$,

$$\overline{\rho}(Vol_{steel} + Vol_{air})\overline{c}_p = \rho_{steel} Vol_{steel} c_{p\ steel} + \rho_{air} Vol_{air} c_{p\ air}$$

resulting in $\overline{c}_p = 502.6\ J/kg \cdot K$.

Practically, the heat conduction is dictated by the air pocket, while the specific heat is dictated by the steel.

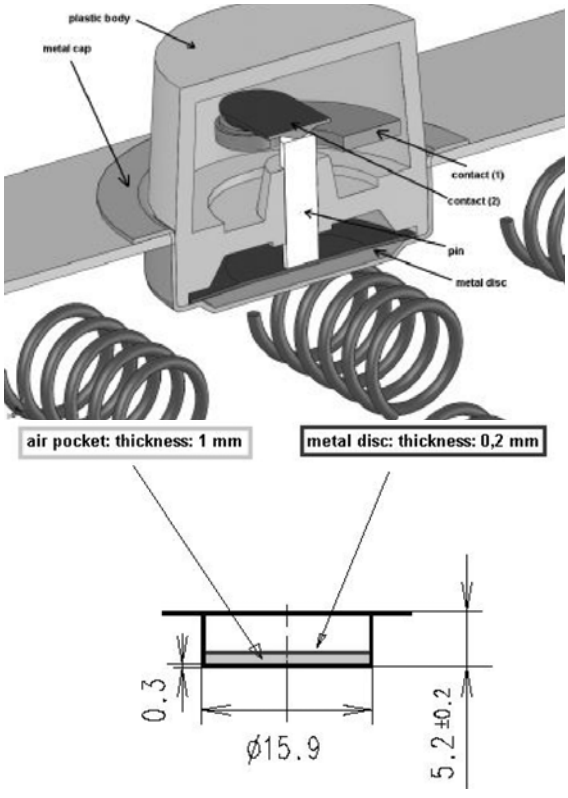

Figure 3. Cross section of the actual thermostat and the simplified model to be used in numerical simulations.

The boundary conditions are simple. There is a volumetric heat source in the wires, uniformly distributed, with a total heat power of $200W$. The walls are made of mica, with corresponding specific heat and density, and have a specified thickness. The heat conduction through walls and wires is accounted for. The actual material properties or exact geometrical dimensions cannot be completely disclosed in this paper.

3. FLUENT MODELLING OF BUOYANCY DRIVEN FLOWS WITH HEAT CONVECTION AND RADIATION

In this section we briefly summarize the models employed in the commercial code FLUENT, relevant to the problem investigated in this paper. More details can be found in [5], and references therein.

When the air is heated, since the air density decreases with temperature at constant pressure, a flow is induced due to the force of gravity acting on the density variations. For many natural convection flows, the Boussinesq model is the most robust and quite accurate. This model treats the fluid density as a constant in all equations, except for the buoyancy term in the momentum equation. The time dependent buoyancy driven flow solving strategy follows the procedure from [6].

For the radiation heat transfer the most suitable model for our problem is the Discrete Ordinates (DO) model. The DO radiation model solves the radiative transfer equation for a finite number of discrete solid angles, each associated with a vector direction fixed in the global Cartesian system. The FLUENT implementation uses a conservative variant of the discrete ordinate model called the finite-volume scheme [7,8], and its extension to unstructured meshes [9]. The main advantage of the DO model is that spans the entire range of optical thicknesses.

Discretization with Finite Volume Method of the system of partial differential equations for flow with heat transfer has been proved to be both robust and accurate [10].

4. NUMERICAL RESULTS AND ANALYSIS

Numerical results presented in this section provide a deep understanding of the complex flow and heat transfer phenomena in the electrical heating device.

Figure 4 presents the temperature variation on the thermostat cap as well as on three adjacent wires. One can see that the wire heating rate is decreasing in time, while the heating rate of the thermostat cap is increasing in time. Eventually, after 20 seconds the heating flow rates becomes approximately equal once the radiation transfer is stabilized.

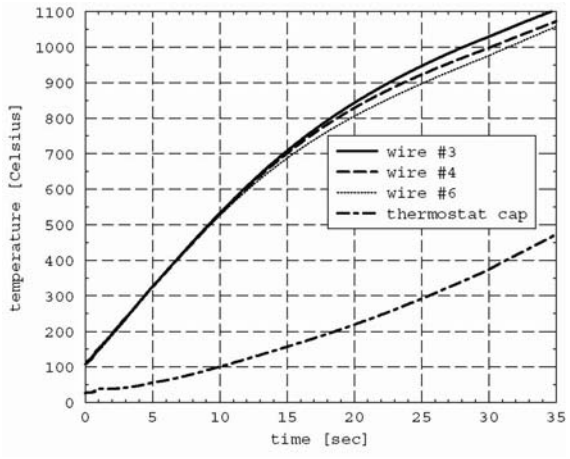

Figure 4. Time variation of several wire temperatures and thermostat cap temperature.

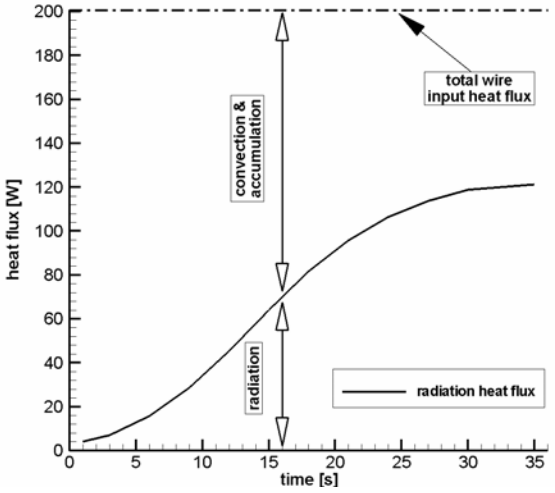

Figure 5. Heat flux balance for the wires.

Figure 5 further details on the wires heat flux balance. In the early stages the wire temperature is relatively low, such is the air velocity, and most of the heat is accumulated in the wires leading to a rapid increase in temperature. As the wire temperature increases, a significant fraction (going up to half and more) of the heat flux is transferred through radiation, while the rest is the sum of a small convective heat flux and heat accumulation in wires. However, the accumulated heat decreases, therefore explaining why the temperature time rate decreases as well for the wires.

Figure 6 presents a similar heat flux balance for the inlet/outlet sections. Practically this is the heat evacuated from the computational domain through both convection and radiation. One can see that as the buoyancy driven flow is building up, the heat flux convected out of the domain increases in time. The radiation accounts roughly for one quarter of the total heat flux, in later stages of evolution.

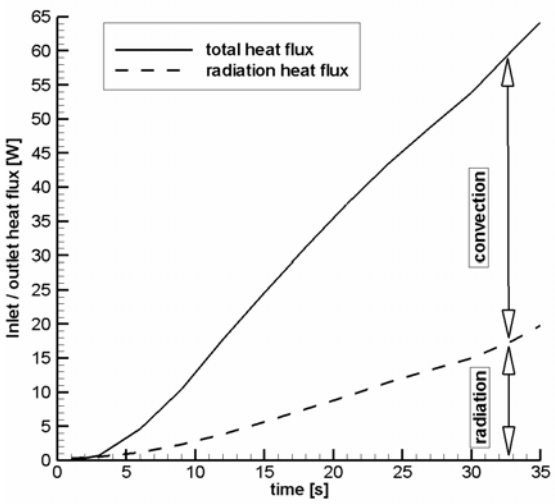

Figure 6. Heat flux balance for the inlet/outlet sections.

Both Figs. 5 and 6 emphasize the importance of the radiative heat transfer in electrical heating devices operating in air. Moreover, it is clear that even in buoyancy driven flow, the natural convection is essential and the flow field needs to be accurately computed with a turbulence model.

A key ingredient of the methodology used in the present investigation is the post-processing of the unsteady temperature field in the thermostat sandwich. First, a four degree polynomial is used for a least-squares fit of the thermostat cap temperature variation in time, corresponding to the dash-dot line in Fig. 4. This temperature-time dependence is imposed as unsteady boundary condition for a simple 2D unsteady heat conduction in a domain like the one shown in Fig. 7. This is done through the User Defined Function (UDF) capability of the FLUENT code. The actual source code is reproduced below.

```
/*********************************
      UDF for time-dependent
temperature boundary condition
*********************************/
#include "udf.h"

DEFINE_PROFILE(variabletemperature,t,i
)
{
face_t f;
real flow_time = CURRENT_TIME;
begin_f_loop(f,t)
      {
            F_PROFILE(f,t,i) =
273.15+34.0121+((0.000421735*flow_time
-.0302159)*flow_time+0.903902)
*flow_time*flow_time;
      }
end_f_loop(f,t)
}
```

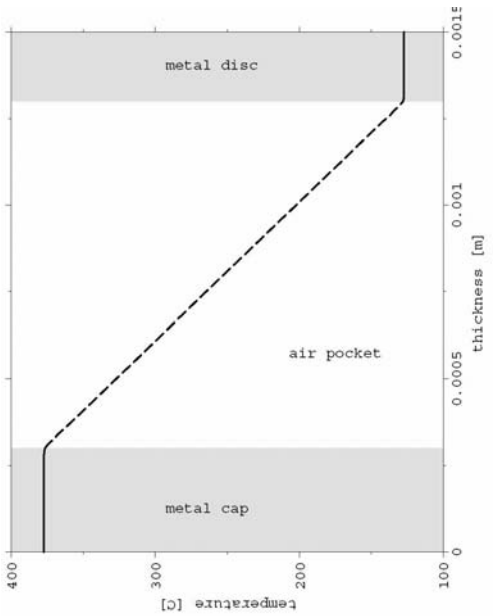

Figure 7. Temperature variation in the metal cap – air pocket – metal disc simplified model for the thermostat at time 30 s.

Figure 7 shows the temperature distribution in the thermostat sandwich after 30 seconds. Obviously the temperature drop in the air gap is significant, the metal disc being significantly colder than the metal cap. This phenomenon is not important for steady operating regimes, when both metal cap and disc practically reach the same temperature.

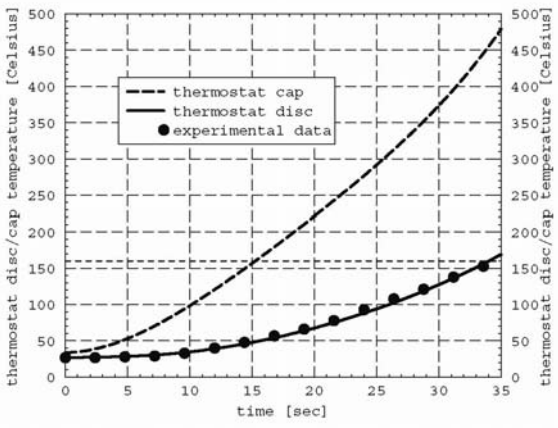

Figure 8. Comparison of measured and computed temperature variation in time for the thermostat disc.

The most important result of this paper is presented in Figure 8. After employing the above post-processing procedure, the thermostat disc temperature (which is actually the temperature that triggers the thermostat electrical switch) is obtained according to the solid line. The trigger temperature of $160\,^{\circ}C$ is reached practically in half a minute. The measured temperature values on the thermostat disc, shown in filled circles, are in excellent agreement with the numerical data. This is a full confirmation that the two-step numerical methodology is accurate and can predict not only the switch-off time, but also the wires and air temperature.

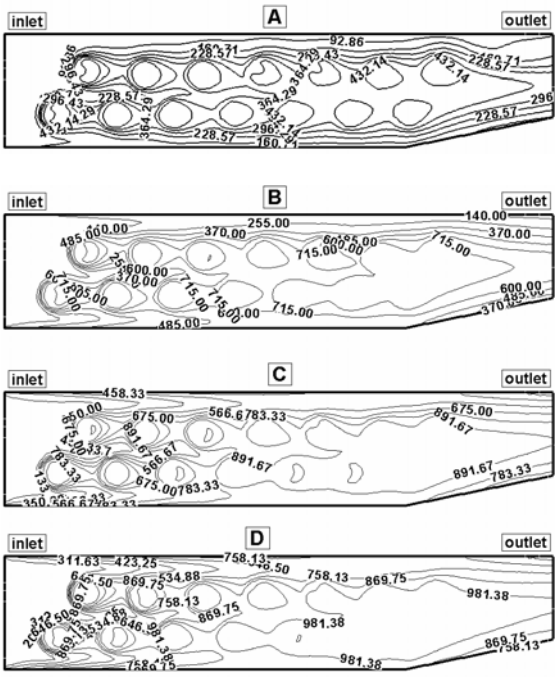

Figure 9. Temperature field on the symmetry plane at successive moments in time: A – 10 s, B – 20 s, C- 30 s, D - 35 s.

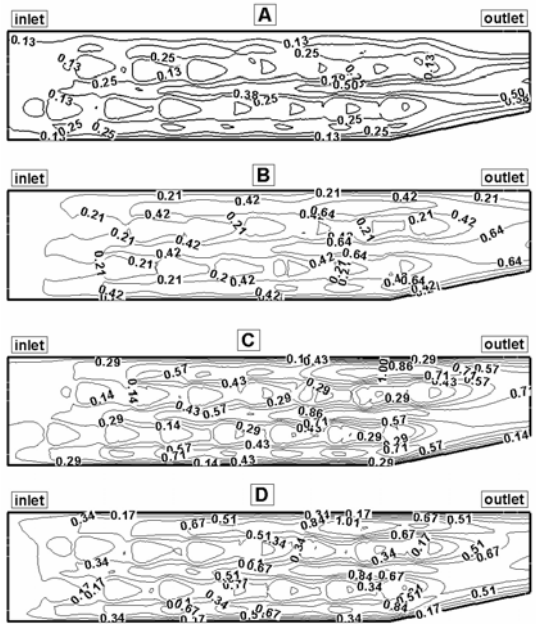

Figure 10. Velocity magnitude field on the symmetry plane at successive moments in time: A – 10 s, B – 20 s, C- 30 s, D - 35 s.

Figures 9 and 10 show the temperature and velocity fields, respectively, at four instants in time. The highest temperature level reaches $1000^{\circ}C$, and the maximum velocity magnitude reaches $1m/s$. At this velocity the convection plays an important role, in addition to radiation, and must be accounted accurately. The chimney effect of the setup shown in Fig. 1 is quite important, and the vertical position of the heating device is essential for natural convection. The velocity magnitude contours shown in Fig. 10 show the flow acceleration (from inlet to the outlet) specific to a buoyancy-driven flow. In addition, the flow is accelerated at the exit thanks to the reduction in the channel cross-section. This particular flow features are refferred to as „chimney effect" in the present paper.

5. CONCLUSIONS

The paper presents a complete methodology for numerical simulation of unsteady buoyancy driven flow with heat convection and radiation in electrical heating devices. A distinct feature of our methodology is a two-step procedure for the thermostat temperature field.

First, the full 3D computational domain is built, using an equivalent wall for the thermostat cap – air gap – disc sandwich. After the numerical simulation the temperature cap variation in time is obtained. Second, the time variation of the temperature cap is used as unsteady boundary condition in an auxiliary problem which provides the correct thermostat disc temperature, in excellent agreement with the experimental data. As a result, the switch-off time can be accurately predicted, together with the all wires temperature at that moment. This is essential for practical applications when the thermostat must be set such that the wire temperature is limited below a given value.

ACKNOWLEDGEMENTS

The authors would like to acknowledge the support from ZOPPAS Industries – IRCA Spa., Italy, in conducting this research-development project in association with the National Center for Engineering of Systems with Complex Fluids from the "Politehnica" University of Timisoara, Romania.

REFERENCES

[1] Shi J.-M., Gerlach D., Breuer M., Biswas G., Durst F., 2004, "Heating effect on steady and unsteady horizontal laminar flow of air past a circular cylinder" Physics of Fluids, vol. 16, no: 12, pp: 4331-4345.

[2] Maynes B.D.J., Kee R.J., Tindall C.E., Kenny R.G., 2003, "Simulation of airflow and heat transfer in small alternators using CFD", *IEE Proc.-Electr. Power Appl.*, Vol. 150, No. 2., pp: 146-152.

[3] Pickering S.J., Lampard D., Hay N., Roylance T.F., 1998, "Heat transfer in a through-ventilated induction motor", *IEE Proc.-Electr. Power Appl.*, Vol. 145, No. 5, pp: 429 -433.

[4] Dessouky Y.G., Williams B.W., Fletcher J.E., 1998, "Cooling enhancement of electric motors", *IEE Proc.-Electr. Power Appl.*, Vol. 145, No. 1, pp: 57-60.

[5] Fluent Inc., 2002, FLUENT 6.0 User's Guide.

[6] Henkes, R.A.W.M., van der Flugt, F.F., and Hoogendoorn, C.J., 1991, "Natural Convection Flow in a Square Cavity Calculated with Low Reynolds Number Turbulence Models", *Int. J. Heat Mass Transfer*, Vol. 34, pp. 1543-1557.

[7] Chui E.H., Raithby G.D., 1993, "Computation of Radiant Heat Transfer on a Non-Orthogonal Mesh Using the Finite-Volume Method", *Numerical Heat Transfer, Part B,* 23, pp: 269-288.

[8] Raithby G.D., Chui E.H., 1990, "A Finite-Volume Method for Predicting a Radiant Heat Transfer in Enclosures with Participating Media" *J. Heat Transfer*, Vol. 112, pp: 415-423.

[9] Murthy J.Y., Mathur S.R., 1998, "A Finite Volume Method For Radiative Heat Transfer Using Unstructured Meshes", *AIAA-98-0860*.

[10] Cadafalch J., Perez-Segarra C.D., Consul C., Oliva A, 2002, "Verification of Finite Volume Computations on Steady State Fluid Flow and Heat Transfer" *Journal of Fluids Engineering*, vol. 124, pp: 11-21.

Conference on Modelling Fluid Flow (CMFF'06)
The 13th International Conference on Fluid Flow Technologies
Budapest, Hungary, September 6-9, 2006

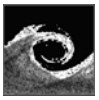

THE EFFECT OF CORNER RADIUS ON THE ENERGY LOSS IN 90° T-JUNCTION TURBULENT FLOWS

György PAÁL[1], Fernando PINHO[2], Rodrigo MAIA[3]

[1] Corresponding author, Department of Hydrodynamic Systems, Budapest University of Technology and Economics, P.O. Box 91, 1521 Budapest, HUNGARY, Tel.: +36 1 463 2991, Fax: +36 1 463 3091, E-mail: paal@vizgep.bme.hu
[2] Transport Phenomena Research Center, Faculty of Engineering, University of Porto and University of Minho E-mail: fpinho@fe.up.pt
[3] Department of Civil Engineering, Faculty of Engineering, University of Porto, E-mail: rmaia@fe.up.pt

ABSTRACT

An extensive numerical parametric investigation of the turbulent flow in 90° T-junctions with sharp and rounded corners is under way aimed at quantifying the energy losses and the size and strength of the recirculating region in the branch pipe. The parameter that is being investigated is the radius of curvature of the corner of the junction and so far simulations have been carried out for an inlet pipe Reynolds numbers of 32,000, to be later extended to the range between 5,000 and 40,000, for flow rate ratios of 0%, 20%, 40%, 50%, 60%, 80% and 100% (ratio between the flow rates in the branch and inlet pipes).

The previous work of Paál et al. [8] on this flow for a sharp corner was aimed at validation by comparing the results of simulations done with various turbulence models with the detailed experimental data of Maia et al. (1998).

Following [8], it was decided to perform the present calculations using a modified version of Menter's [9] model, the shear-stress transport (SST) model, which performed equally well as or even better than the full Reynolds stress model at a considerably lower cost. All the calculations were carried out with the commercial code ANSYS CFX 10.0.

The results show that increasing the radius of curvature of the corner reduces the total energy loss especially because of the reduction in the branch flow loss related to flow separation.

Keywords: T-junction, turbulent flow simulation, rounded edge

NOMENCLATURE

a	[-]	turbulence model parameter
f	[-]	pipe loss coefficient
k	[m^2/s^2]	turbulent kinetic energy
p	[Pa]	pressure
Δp	[Pa]	pressure difference
t	[s]	time
u_i	[m/s]	velocity (fluct. ith comp.)
x	[m]	length coordinate
y	[m]	coordinate normal to the wall
A_i	[-]	turbulence model parameters
C	[-]	turbulence model parameters
F_i	[-]	blending functions
K_{ij}	[-]	loss coefficient due to tee
U	[m/s]	velocity (mean x-component)
V	[m/s]	velocity (mean y-component)
$<U>$	[m/s]	bulk velocity
α_i	[-]	turbulence model parameters
β_i	[-]	turbulence model parameters
δ_{ij}	[-]	Kronecker symbol
φ_i	[-]	turbulence parameters (SST)
μ	[kg/ms]	dynamic viscosity
ν	[m^2/s]	kinematic viscosity
ρ	[kg/m^3]	density
σ	[-]	turbulence model parameters
ω	[$1/s$]	turbulence frequency

Subscripts and Superscript

i, j	ith, jth coordinate, pipe identifier
k, μ, ⌉	turbulence parameter indicator
T	turbulent

1. INTRODUCTION

In pipe networks flow divergence is a major source of energy loss especially when in combination with sudden changes in flow direction leading to severe flow separations. The proper design of pipe networks requires accurate predictions of these complex flows, which is still far from being a trivial matter. In this work, we predict the loss coefficient of Newtonian fluids in 90° T-

junctions with sharp and rounded corners as a function of the flow rate ratio in the two outgoing branches, after a grid convergence study to select the adequate grid characteristics.

Early experimental work on the diverging T-junction flow took place in Munich with Vogel [1, 2] and was continued by Gardel [3]. Among other contributions to the field, reviewed in detail by Maia [4], the most well-known is the comprehensive work of Miller [5] on the resistance coefficients for various pipe accessories. Numerical predictions of this complex flow have been less common: Sierra-Espinoza et al. [6, 7] used various turbulence models and concluded that the standard and renormalization group (RNG) k-ε models could not predict the flow satisfactorily. Their predictions with the Reynolds stress model (RSM) also over-predicted significantly the extent of the recirculation region. Paál et al. [8] compared the performance of the standard RSM and Menter's [9] shear-stress transport (SST) k-ω model, and showed the superiority of the latter in spite of the fact that it is a two-equation model. This did not come totally as a surprise since the SST model was supposed to combine the advantages of the k-ε and the k-ω models, performing better in separated flows under adverse pressure gradients because of the inclusion of transport effects into the formulation of the eddy-viscosity. For details of the used models the numerical approach and the comparison see [8].

The present work is the natural continuation of Paál et al [8]: using the SST k-ω model we performed extensive calculations of the flow in the 90° T-junction to investigate the effect of rounding off the sharp edge of the corner of the junction for flow rate ratios of 0%, 20%, 40%, 50%, 60%, 80% and 100% (ratio between the flow rates in the branch and inlet pipes) at inlet pipe Reynolds number 32,000. The influence of a block-structured mesh as opposed to an unstructured mesh is also discussed. The commercial code used in this work was ANSYS CFX 10.0.

The paper is organized as follows: the governing equations and turbulence model used are briefly presented first, followed by a grid convergence study and validation by comparison with the experimental data of Costa et al. [10]. Then, the results of the parametric investigation are presented and discussed prior to the closure of the paper.

2. GOVERNING EQUATIONS

The equations to be solved for this incompressible flow are the conservation of mass Eq. (1) and momentum Eq. (2)

$$\frac{\partial U_i}{\partial x_i} = 0 \tag{1}$$

$$\frac{\partial \rho U_i}{\partial t} + \frac{\partial \rho U_j U_i}{\partial x_j} = -\frac{\partial \overline{p}}{\partial x_i} + \frac{\partial}{\partial x_j}\left[\mu\left(\frac{\partial U_i}{\partial x_j} + \frac{\partial U_j}{\partial x_i}\right) - \rho\overline{u_i u_j}\right] \tag{2}$$

where a capital letter or an overbar designate time-averaged quantities and a small letter refers to fluctuating quantities. The Reynolds stress tensor must be given by an appropriate equation or model to ensure closure of the set of equations. Here, on the basis of Paál et al. (2003) and also on the basis of further numerical experiments with the standard k-ε model only one turbulence model was used: the shear-stress transport (SST) k-ω model developed by Menter [10]. This model was found to provide the best results at a relatively modest computational cost.

In this model, the Reynolds stress is calculated by

$$-\overline{u_i u_j} = \nu_T\left(\frac{\partial U_i}{\partial x_j} + \frac{\partial U_j}{\partial x_i}\right) - \frac{2}{3}k\delta_{ij} \tag{3}$$

where the turbulent viscosity is related to single velocity and length scales of the turbulent flow, but is limited to avoid overprediction of recirculating regions. It is given by

$$\nu_T = \frac{ak}{\max\left[a\omega, SF_2\right]} \tag{4}$$

The transport equations of k and ω are

$$\frac{\partial \rho k}{\partial t} + \frac{\partial \rho U_j k}{\partial x_j} = -\rho\overline{u_i u_j}\frac{\partial U_i}{\partial x_j} + \frac{\partial}{\partial x_j}\left[\left(\mu + \frac{\rho\nu_T}{\sigma_{k3}}\right)\frac{\partial k}{\partial x_j}\right] - C_\mu \rho k\omega \tag{5}$$

$$\frac{\partial \rho\omega}{\partial t} + \frac{\partial \rho U_j \omega}{\partial x_j} = -\rho\alpha_3\frac{\omega}{k}\overline{u_i u_j}\frac{\partial U_i}{\partial x_j} - \beta_3\rho\omega^2 + \frac{\partial}{\partial x_j}\left[\left(\mu + \frac{\rho\nu_T}{\sigma_{\omega 3}}\right)\frac{\partial \omega}{\partial x_j}\right] + \frac{(1-F_1)2\rho\sigma_{\omega 2}}{\omega}\frac{\partial k}{\partial x_j}\frac{\partial \omega}{\partial x_j} \tag{6}$$

and the blending functions appearing in Eqs. (4) - (6) are

$$F_1 = \tanh(A_1^4) \quad \text{and} \quad F_2 = \tanh(A_2^2) \tag{7}$$

with

$$A_1 = \min\left[\max\left(\frac{\sqrt{k}}{C_\mu \omega y}, \frac{500\nu}{y^2\omega}\right), \frac{4\rho k \sigma_{\omega 2}}{y^2 C_{k\omega}}\right] \quad (8)$$

$$A_2 = \max\left(\frac{2\sqrt{k}}{C_\mu \omega y}, \frac{500\nu}{y^2\omega}\right) \quad (9)$$

and

$$C_{k\omega} = \max\left(\frac{2\rho\sigma_{\omega 2}}{\omega}\frac{\partial k}{\partial x_j}\frac{\partial \omega}{\partial x_j}, 1.0\times10^{-10}\right) \quad (10)$$

The parameters α_i, β_i, σ_{ki}, and σ_ω with i=3 result from a linear combination of the corresponding coefficients having i= 1 and 2 with the blending function F_1, as given by Eq. (11)

$$\phi_3 = F_1\phi_1 + (1 - F_1)\phi_2 \quad (11)$$

The remaining parameters are listed in Table 1.

3. FLOW PARAMETERS

3.1. Flow geometry

The central part of the T-piece with the coordinate system and the notation is presented in Figure 1. A 20 diameter long entrance pipe was attached to the inlet section and a 30 diameter long pipe was attached to each of the two outlet sections. The pipe diameter was everywhere 30 mm.

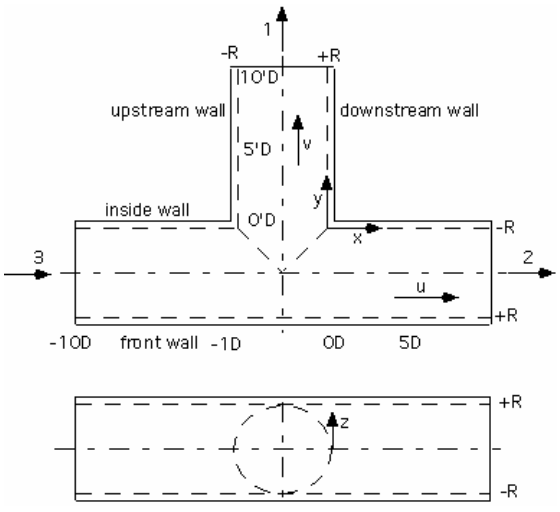

Figure 1. Schematic representation of the T-junction and the central part of the computational domain

The rounded T- piece looks very similar, except that the sharp edges are replaced with a rounded corner with a radius of 3 mm in the central plane.

Table 1. Numerical values of some parameters of the SST model

i	α_i	β_i	σ_{ki}	$\sigma_{\omega i}$
1	5/9	3/40	2	2
2	0.44	0.0828	1	0.856

3.2. Simulation parameters

The fluid used in the simulations was water with a constant density of 997 kg/m^3 and dynamic viscosity of 8.899*10^{-4} kg/ms. Incompressible flow was assumed. The inlet boundary condition was fixed at 0 Pa total pressure (as it is standard practice in incompressible fluids since only the pressure variations matter) and at the two outlets the mass flow rates were specified based on the Reynolds number and the given flow rate ratio between the two branches. Since the inlet boundary condition is located very far from the region of interest (20D = 600 mm) the actual values of the turbulent inlet boundary conditions are irrelevant because the flow is allowed to develop. At all the walls no-slip boundary conditions were assumed.

3.3. Mesh convergence studies

In the case of the sharp edge both an unstructured and a block-structured mesh have been tried with systematic mesh refinement. In both cases a similar, somewhat surprising result, to be discussed next, was obtained.

Table 2. Mesh parameters for the convergence study

Mesh	Number of elements
Coarse	61468
Fine	1004981
Fine mesh with adaptation	2287626
Fine + coarse (final mesh)	454604

First, following Paál et al. (2003), unstructured tetrahedral mesh with 5 layers of prismatic boundary layer cells was used. A systematic mesh refinement study was performed in order to determine the optimum mesh size. Due to the lack of space it is not possible here to go into all the details – they will be presented in a later publication. Altogether 3+1 meshes were used: the last one was created on the basis of the conclusions drawn from the first three. The meshes are listed in Table 2.

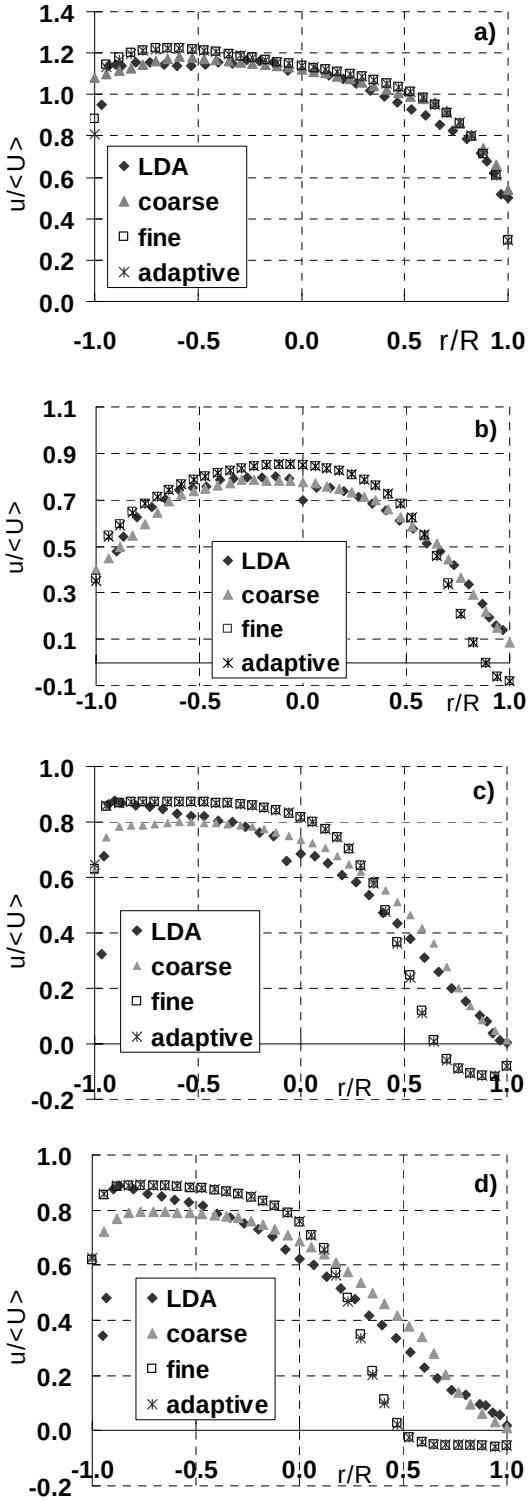

Figure 2. Longitudinal velocity profiles in the main pipe with different meshes compared with LDA data; a) -1D; b) 0D; c) 0.5D; d) 1D (sharp edge)

In Figure 2. some results can be seen with the first three meshes, compared with the LDA-data in the approach flow, inside the tee junction and in the downstream main pipe. It can be observed in the figures that in a paradoxical way the results are

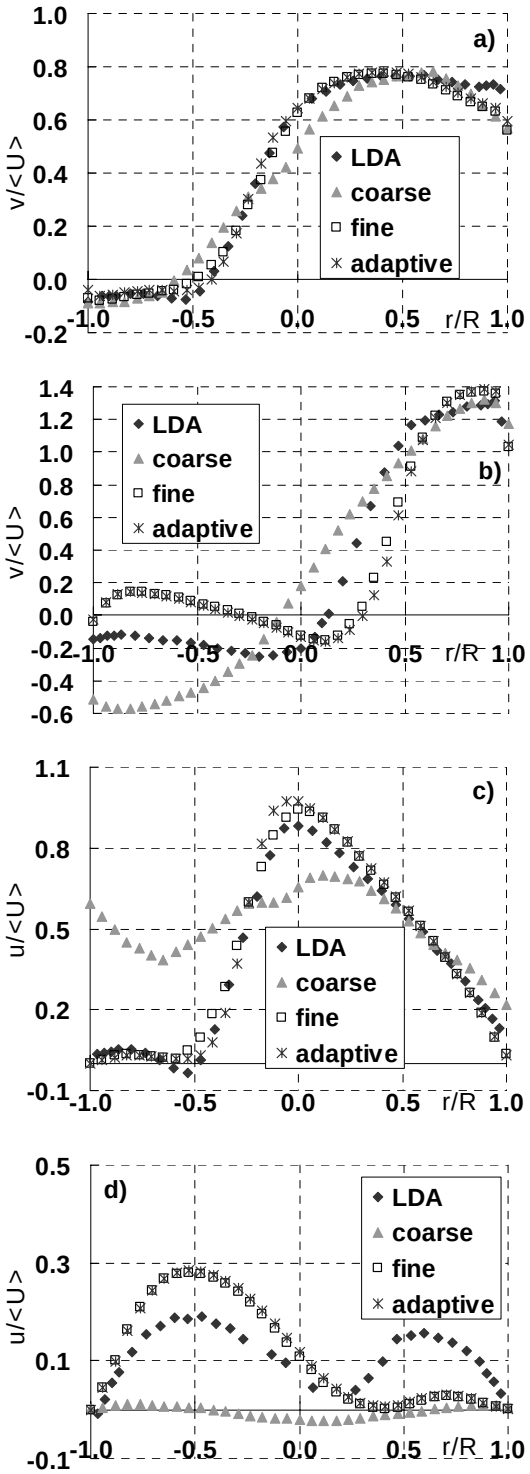

Figure 3. Velocity profiles in the branch pipe with different meshes compared with LDA data; a) longitudinal 0.1'D; b) longitudinal 1.1'D; c) transversal 0.1'D; d) transversal 1.1'D (sharp edge)

everywhere better for the coarse mesh than for the fine mesh or the fine mesh with adaptation. This

happens in the junction region and downstream in the outlet straight pipe.

One possible speculative explanation for this strange phenomenon is that the higher numerical dissipation of the coarse mesh compensates the shortcomings of the turbulence model which usually overpredicts the momentum transfer between wall and bulk flow. In the branch pipe the opposite, usual trend is observed: the fine mesh produces better results (see Figure 3.).

Although the difference is small, the fine mesh performs consistently better than the fine mesh with adaptation and much better than the coarse mesh.

Therefore the final unstructured mesh used in the simulations is a combination of the two meshes: coarse in the main pipe and fine in the branch pipe. The mesh can be seen in Figure. 4.

Due to the rather surprising result obtained with the unstructured mesh an attempt was made with a block-structured mesh with the hope that a systematic refinement of a hexagonal mesh would lead to a systematic improvement of the agreement with measurements. The coarsest mesh can be seen in Figure 5. Three finer meshes were prepared with the same block-structure and the result was the same as before: the results agreed better with the measurements with the coarse mesh in the main pipe and with the fine mesh in the branch pipe. The results are not presented here because of the lack of space, but reinforce the idea put forward above of turbulence model deficiencies being compensated by the excessive numerical diffusion with the coarse mesh.

Due to the above findings it was decided that for the further calculations the unstructured mesh is used because of its greater flexibility since the hexagonal mesh did not bring any tangible advantages.

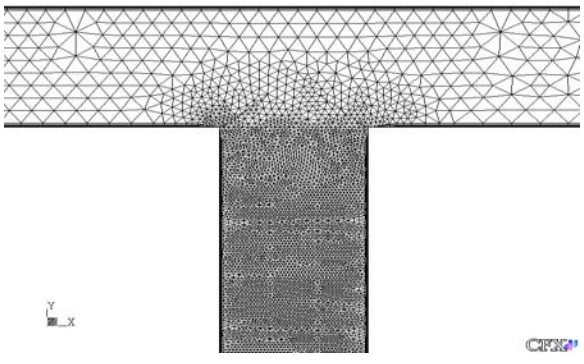

Figure 4. The final unstructured mesh used in the simulations

4. RESULTS AND DISCUSSION

The results are presented in the following way: first some mean velocity profiles of both the sharp-cornered and the rounded-cornered geometry are shown to indicate the well predicted and problematic regions. Then the pressure loss coefficients of both geometries as a function of the flow rate ratio are presented and discussed. The pressure loss coefficients of both branches are defined so that the "excess" pressure loss over the pressure loss of the straight pipe is considered. This is expressed in equations (12) and (13) where i = 1 and 2 stand for the branch and straight outlet pipes, respectively. The velocities in the brackets mean spatially averaged velocities over the cross-section.

$$K_{3i} = \frac{\Delta p_{3i}}{\frac{1}{2}\rho\langle U_3\rangle^2} \tag{12}$$

$$p_3 + \frac{1}{2}\rho\langle U_3\rangle^2 = p_i + \frac{1}{2}\rho\langle U_i\rangle^2 + \\ + f_3\frac{L_3}{D_3}\rho\langle U_3\rangle^2 + f_i\frac{L_i}{D_i}\rho\langle U_i\rangle^2 + \Delta p_{3i} \tag{13}$$

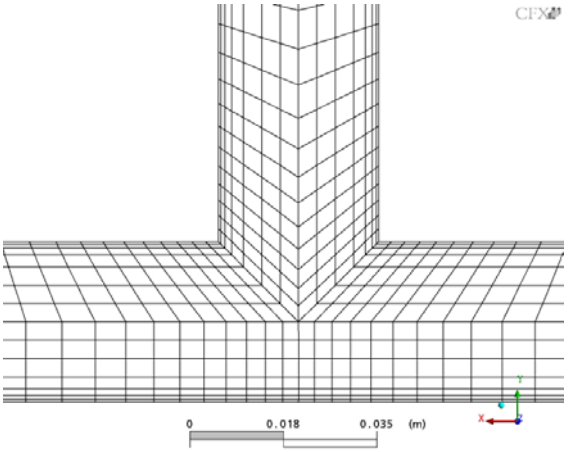

Figure 5. Block-structured mesh in the symmetry plane of the T-piece

4.1. Velocity profiles

Similarly to [8] first comparisons of LDA measurements with simulation results are presented in individual cross sections, everywhere in the symmetry plane. Due to the lack of space only a few typical profiles for the rounded edge are presented; there are also some typical figures for the sharp edge in Figures 2. and 3. Also only longitudinal mean velocity profiles are presented here, i. e. u for the main pipe and v for the branch pipe. Both the sharp edge and rounded edge geometries were measured with a flow rate ratio of 50-50% and with a Reynolds number of 32000.

Figure 6. shows the mean longitudinal velocities in the main pipe. It can be seen that in a remarkable way the agreement is very good just at the beginning of the T-junction and becomes somewhat worse further downstream. Here the velocity is constistently overpredicted near the front wall and underpredicted near the inside wall. The trends are nevertheless well captured and the

quantitative differences remain small with the exception of a few places.

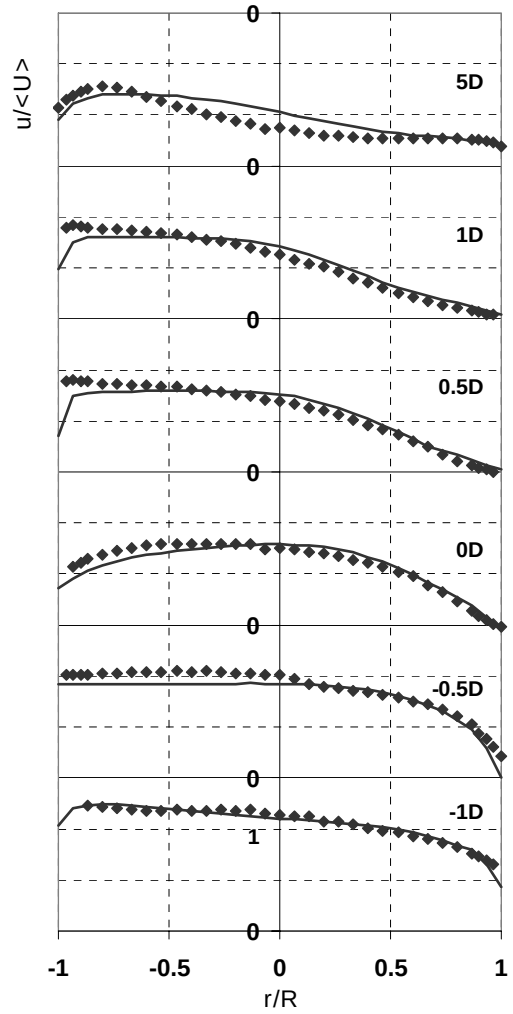

Figure 6. Comparison of the simulation and the LDA measurements for the rounded edge T-piece in the main pipe in various cross sections. Continuous line: simulation; black squares: measurements

The situation is similar in Figure 7. where the branch pipe results are presented. The quality of approximation deteriorates when getting further from the T-piece but the trends are captured everywhere well. Usually the velocity is slightly overpredicted at the downstream wall and sometimes over- sometimes underpredicted in the rest of the pipe. As a general rule we can state that the predictions in the case of the sharp-edged T-piece are slightly better than in the round T. This can be attributed partly due to the increased uncertainty of the measurements due to the complicated geometry and partly to the computational difficulties of treating a boundary layer separating from a round surface.

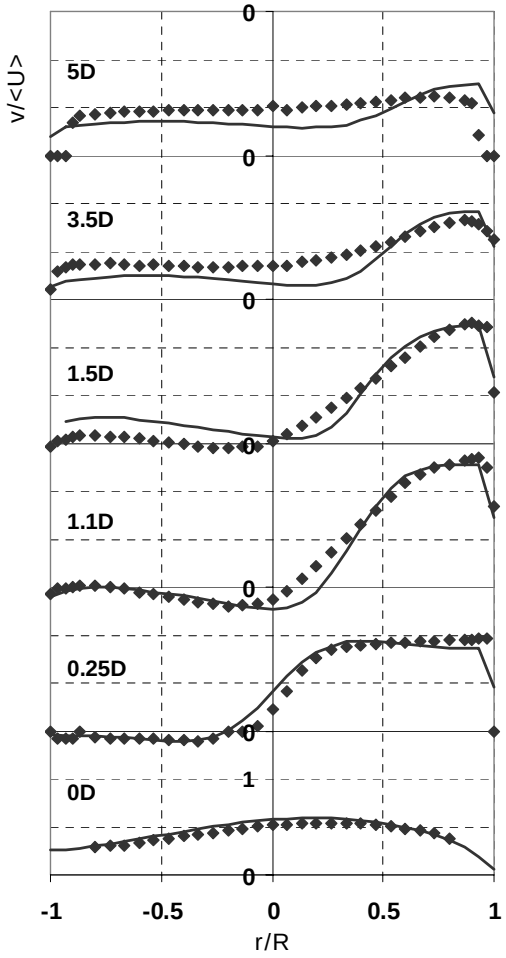

Figure 7. Comparison of the simulation and the LDA measurements for the rounded edge T-piece in the branch pipe in various cross sections. Continuous line: simulation; black squares: measurements

4.2. Loss coefficients

What is most interesting from an engineering point of view is the pressure loss caused by the presence of a T-piece. This is expressed by the nondimensional coefficients defined in Equations (12) and (13).

Although the Reynolds number differed slightly between the two cases we can assume with good reason that in this range the coefficients are almost independent of Reynolds number. Thus the two cases presented in Figs. 8 and 9 are directly comparable with each other. In the sharp-edged case the simulation reproduced the results excellently in the cases of both coefficients. There is a slight discrepancy only at high values of Q_1/Q_3.

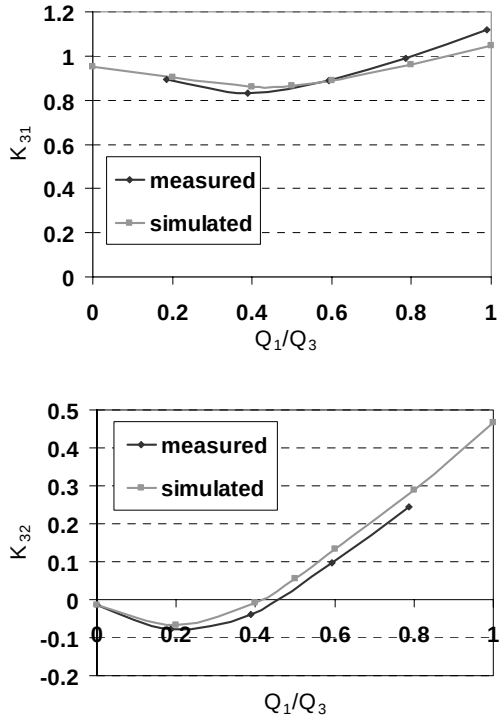

Figure 8. Loss coefficients in the sharp-edged configuration; above: K_{31}; below: K_{32}. Re = 36000.

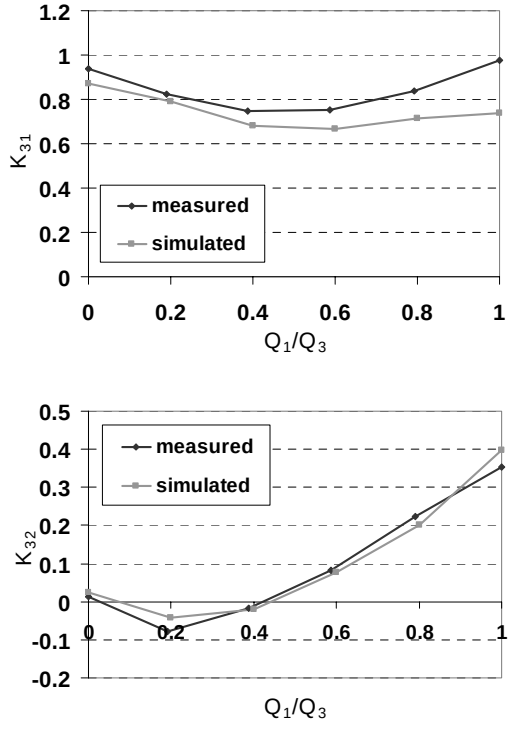

Figure 9. Loss coefficients in the round-edged configuration; above: K_{31}; below: K_{32}. *Re* = 40000

Both curves display a minimum; K_{31} between 0.4 and 0.6 K_{32} at around 0.2. The values of K_{31} are high: they lie between about 0.85 and 1.1 whereas the values of K_{32} are more moderate, between -0.08 and 0.47. However, that the values of K_{32} cover a much wider range, meaning that its dependence on the flow rate ratio is much stronger than that of K_{31}. The fact that K_{32} takes negative values might seem surprising but in reality it is not. It simply expresses the fact that under those conditions the loss caused by the T-piece in the main flow direction is slightly less than the loss would be from a fully-developed flow in a straight pipe. This is probably caused by decreases in the shear rates at the wall, and hence shear stresses, within the junction region due to the flow deviation into the branch.

If we look at Fig. 9 we can see that the agreement for the round-edge configuration, between measurement and simulation is still very good for K_{32}, but less satisfactory for K_{31}. This could be already expected from the less satisfactory agreement of the individual velocity profiles. Nevertheless the trends are again reproduced well. The places of minimum and maximum are at the same place. There is not much change between the two cases for K_{32} but there is a significant decrease in the loss coefficient for the branch pipe. This corresponds to the expectations since rounding the edge should influence mostly the loss in the branch pipe by making the point of separation less well defined.

Looking at the loss coefficients from the measurements [10] we can establish that the Reynolds number dependence in this range is really small.

4.3. Fixed point in the velocity profile?

In the sharp-edged case an interesting phenomenon was observed. Plotting the velocity profiles in the symmetry plane in one diagram for different flow rate ratios at one cross section in the branch pipe it is obvious that all the velocity profiles intersect each other more or less at the same point (Figure 10.).

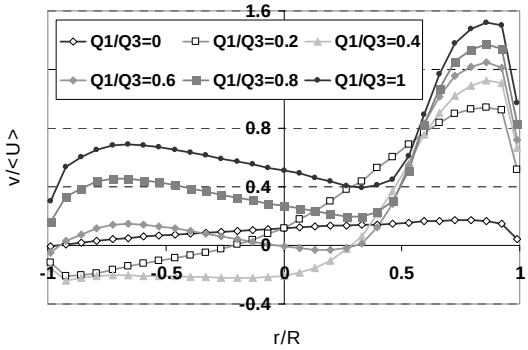

Figure 10. Velocity profiles for different flow rates intersect in one point

Repeating the same procedure for several cross sections the set of intersection points can be plotted (Figure 11.). Along this line on the symmetry plane the velocity is always the same, independently of

the flow rate ratio. On the upstream side of this line the velocity decreases, on the downstream side it increases with increasing flow rate ratio in the branch pipe. Interestingly, no similar phenomenon has been observed in the case of the round-edged T-piece, because the point of separation changes with flow rate ratio.

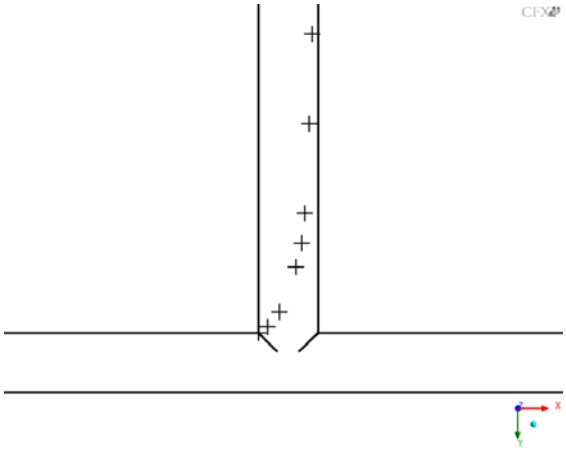

Figure 11. Set of "fixed points" in the symmetry plane of the sharp-edged configuration

5 SUMMARY

Detailed LDA-measurements and flow simulations have been carried out on a sharp-edged and round-edged T-piece configuration. Based on a previous publication the SST k-ω turbulence model was chosen for the simulations. It has been found that the best agreement with the data is obtained if the computational mesh is fine in the branch pipe but coarse in the main pipe. There is no conclusive explanation for this phenomenon. Generally, the simulations reproduced the measurements well but the agreement was better in the case of sharp-edged tee. The same statement can be made for the loss coefficients although the authors think that the uncertainty in the round edged case is also larger in the experiments not only in the computations. The intuitively expected influence of rounding the edge has been confirmed both by the simulations and the experiments: the branch pipe loss coefficient significantly decreased. This means that the overall energy loss also decreased since the overall energy loss is dominated by the branch pipe energy loss.

It has been found that for the sharp-edged configuration a "fixed velocity" line exists. No similar phenomenon was found in the case of the round-edged configuration.

The work can be continued in the direction of examining different cross-section ratios and different angles between main pipe and branch pipe as well as changing systematically .the radius of curvature.

ACKNOWLEDGEMENTS

The cooperation between the partners has been supported by TéT (Nr. P-25/03) on the Hungarian side and by projects GRICES 4.1.1 OMFB and FCT PBIC/C/CEG/2440/95 and POCI/EQU/56243/2004 on the Portuguese side. The help of Messrs. Katsambas and Ugron with the simulations is gratefully acknowledged.

REFERENCES

[1, 2] Vogel, G., 1926 and 1928. "Investigation of the loss in right-angled pipe branches", Mitt. Hydraulischen Instituts der Tech. Hoschul. München, Nr. 1, 75-90 (1926), n. 2, 61-64 (1928) (Translation by Voetsch, C. Technical Memorandum n. 299, US Bureau of Reclamation, 1932)

[3] Gardel, A., 1957. "Les pertes de charge dansles écoulements au travers de branchements en Té", Bulletin Technique de la Suisse Romande, Nr. 9 & 10

[4] Maia, R. J., 1992, "Numerical and experimental investigations of the effect of local losses in piping systems. Methods and Techniques for its systematic investigation. The specific case of the flow in a 90° Tee junction" PhD thesis, University of Porto, Portugal (in Portuguese)

[5] Miller D. S., 1978, „Internal flow systems", BHRA Fluid Engineering,

[6] Sierra-Espinosa, F. Z., Bates, C. J., O'Doherty, J., 2000, „Turbulent flow in a 90º pipe junction. Part 1.: Decay of fluctuation upstream of the flow bifurcation", *Computers and Fluids* Vol. 29, pp. 197-213

[7] Sierra-Espinosa, F. Z., Bates, C. J., O'Doherty, J., 2000, „Turbulent flow in a 90º pipe junction. Part 2.: Reverse flow at the branch exit", *Computers and Fluids* Vol. 29, pp. 215-233

[8] Paál, G., Maia, R. and Pinho, F. T., 2003. Numerical predictions of turbulent flow in a 90 tee junction. *Proceedings of 12th International Conference on Modelling Fluid Flow* , Budapest, Hungary, 3rd to 6th September, paper IF0-31, pp. 573-580

[9] Menter, F., 1994. "Two equation eddy-viscosity turbulence models for engineering", *AIAA J*, 32, pp. 1598-1605.

[10] Costa, N. P. Maia, R., Pinho, F. T., & Proença, M. F. 2006 „Edge effects on the flow characteristics in a 90° T-Junction", Submitted to *ASME Journal of Fluids Engineering*.

Conference on Modelling Fluid Flow (CMFF'06)
The 13th International Conference on Fluid Flow Technologies
Budapest, Hungary, September 6-9, 2006

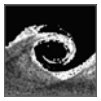

MODELLING OF THE CLOGGING-UP PROCESS IN THE WATER UTILISATION SYSTEM

Mihail LUCA[1], Josef BARTHA[2]

[1] Department of Hydrotechnical Structures and Sanitary Engineering, Technical University "Gh. Asachi" of Iasi, Romania, Bd. D. Mangeron, no. 63-65, Iasi, 6600, Romania. Tel.: +40 232 271959, Fax: +40 232 271959, E-mail mluca2004@yahoo.com
[2]Department of Land Reclamation Hydrotechnical Technical University "Gh. Asachi" of Iasi, Romania, Bd. D. Mangeron, no. 63-65, Iasi, 6600, Romania. Tel.: +40 232 271959, Fax: +40 232 242109, E-mail: E-mail: bartha@hidro.tuiasi.ro

ABSTRACT

The alluviation phenomena in the canals and the pipes of the water utilization systems rises important and difficult technical problems. In order to reduce the alluviation quantity in water supply systems and to keep it under control, continuum self-striping filtration equipment has been designed and manufactured at the Technical University of Iassy, Romania. The equipment is based on a modular system designed according to the alluvium characteristics and it is able to carry out both the separation and filtration functions of the water taken by the pumping station and by the water supply network. The exploitation process of the equipment is full automatized.

In order to analyse the functioning process of the ensemble hydrotechnic construction – filtering installation, an adequate mathematical model was conceived. At the same time, a software for the calculus of filtering parameters in different given circumstances was set - up. Two results for two typical situations in the location of the sieving – filtering installation: at the inlet of the pumping stations and in the nodes of the derivations to the net of pipes are presented.

Keywords: alluviation phenomena, canals, filtering equipment, mathematical model, pumping stations, water system.

NOMENCLATURE

Examples:

A	$[m^2]$	area of filtering
L_f	$[m]$	thickness of filtering layer
N_p	[-]	numbers of pores per area unit
R	$[N]$	specific resistance
r	$[m]$	radius of pores in the filtering layer
h, H	$[m]$	height
Q	$[m^3/s]$	discharge
M_P,	$[s^2/m^5]$	equivalent resistance modulus of the pumps
M_f	$[s^2/m^5]$	equivalent resistance modulus of the network
V	$[m^3]$	volume
p_t	$[Pa]$	total pressure
Δp_t	$[Pa]$	pressure difference
Δz	$[m]$	level difference
t, t_0	$[s]$	moment in time
ε	[%]	porosity of the precipitate
η	[kg/s m]	dynamic viscosity of the filtering layer
g	$[m/s^2]$	gravidity acceleration
θ_0, θ_f	$[kg/m^3]$	turbidity of the suspension and of filtrate respectively
ρ	$[kg/m^3]$	density
ρ_s	$[kg/m^3]$	density of the solid phase,
μ	[]	discharge coefficient
$\underline{w}$	$[m/s]$	absolute velocity vector

Subscripts and Superscripts

f	filtering
p	precipitate
s, u	exponents of power depending on the compressibility of the precipitate and the filtering layer
x, y, s	axial coordinate

1. INTRODUCTION

The water and land resources are two of Romania's main natural attributes, which, if used rationally, contribute to national economic and social development. Romania has 15 million hectares of agricultural land out of which 15 % can, theoretically, be irrigated. However, economic reasons limit this area to less.

Romania's exploited water resources are estimated at about 60×10^9 m^3 per year. This comes mainly from the inland rivers (45 %), the Danube (45%) and the underground water bed (10%). The most important source of water for irrigation is the Danube and its tributaries: Olt, Siret, Prut. A

shortcoming of the water resources is the variable amount of silt in suspension. In comparison to the Danube, which has a low average silt charge – turbidity (e. g. 0.3 kg/m^3 in the area of Braila, Romania), inland rivers have rather high turbidity, from 1.16 kg/m^3 up to 47.2 kg/m^3 [6].

The presence of suspension silt in the water sampled by the hydrotechnic system has a negative influence on the operational factors and leads to an important diminution of the quality of the services rendered to the beneficiaries. The problem becomes increasingly concerning when the needs of the consumers serviced by the same system differ in respect to water quality.

2. THE FILTERING INSTALLATION WITH CONTINUOUS FLOW FOR NEW REQUIREMENT FOR WATER QUALITY

In the process of retechnology of the water systems, an important place is held by the improvement of the quality of water taken from surface resources. One important aspect is the reduction of the concentration of suspended silt and the differentiation in the quality of the distributed water. This will lead to an increase in the number of water consumers, not necessarily those who use water in irrigation purposes only.

Researches were carried out which showed that there are certain functional sections in the system's net where improvements in water quality are called. These sections belong mainly to nodes water is distributed to beneficiaries. In the considered section, a modulated installation for sieving – filtering water is located. These installations have a continuous functional process of filtering and self – cleaning of water. At the same time, the places where these installations were located were chosen according to certain criteria. The conclusions obtained are [4, 5, 6]:

1. For hydrotechnic systems with networks of pipes serving consumers with different requirements, the following locations of the filtering installations have resulted:

A – **Single position**, where the installation is located in the section of water access to the main pumping station.

B – **Multiple positions**. The location of the installation can be: **b1** - in the inlet section of the water into the system, with the purpose of complete protection; **b2** - in the breaching of sections towards beneficiaries who require water purer that the water usually carried by the system.

2. For hydrotechnic system with mixed network more water treatment sections are needed. In these, differentiated sieving installations, modulated in accordance to the physical water parameters are located. The locations are:

A – At **the entrance in the intake reservoir** of the pressure pumping stations, with the purpose of removing certain granulometric fractions from the pumped water.

B – In **the hydrotechnic derivation nodes** on branches delivering water to beneficiaries who require purer water.

In order to improve and modernize the water supply system and especially the irrigation systems, a group of researchers suggest a new constructive and functional solution for the sieving – filtering installations located in the derivate nodes (Figure 1).

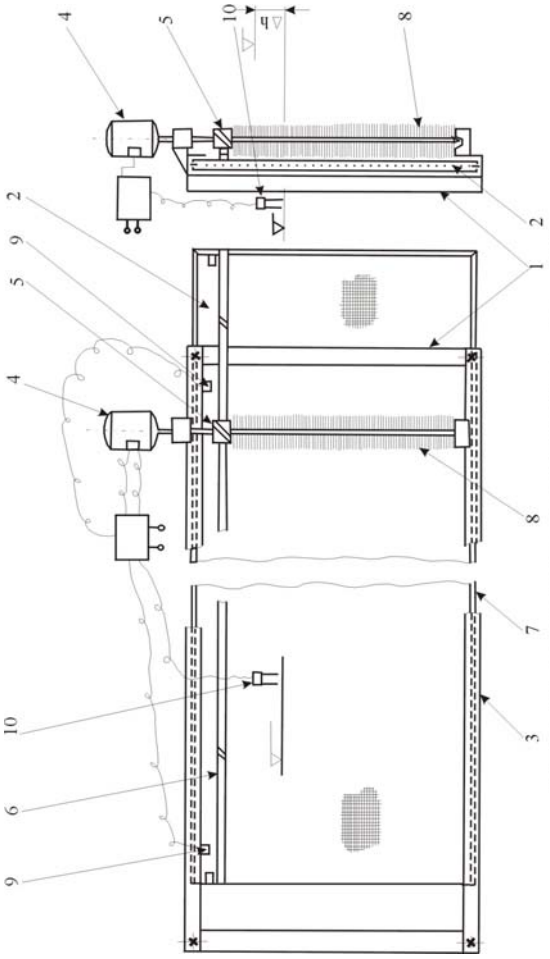

Figure 1. Scheme of the filtering installation.

The installation provides water of the required quality to every beneficiary; it has a compact structure, completely prefabricated that can be easily and quickly located in any functional section of the hydrotechnic system. The main functions of the installation are: the sieving of water in a differentiated way in order to meet the requirements of the beneficiary by reducing turbidity to an acceptable limit; the maintenance of a continuous sieving – filtering process and the automation of the process of cleaning the silt.

The main component parts of the installation are: the assembling frame (1), the mobile sieving – filtering modulus (2), devices for dislodging the sediment and cleaning the sieve (3, 4), the survey instrument – the safety device (5) (figure 1) [6]. The assembling frame is set on the canal slope, where the water that goes onto the intake basin of the pumping station or the sluice comes from. Motioning the filtering modulus is done by a level difference sensor (6). The filtering sieving installation was executed at prototype level on a scale of 1:1 [3, 6].

3 THE CALCULUS MODEL

3.1 The Differential Generalized Equation of Filtration

The transportation of silt and the flow of water in a net of pipes and canals at the water systems are interdependent processes. They cannot be dissociated and analysed separately even in the most severe hypothesis acceptable in physics. Due to the fact that the behaviour of the liquid phase is neither uniform nor permanent, this trait results in the elaboration of a mathematical model to simulate the interaction between the liquid – solid phases and the filtering system perceived in time [2, 7].

The analysis of the filtering process consists in determining the volume of precipitate V_P, as well as the following hydraulic parameters: filtrate discharge Q, volume of filtrate V, filtering speed w and the filtering pressure difference Δp, these values generally vary with time. In order to solve these problems an adequate mathematical model was drawn up at the same time with a calculated programme for computers [1, 2, 9].

The mathematical model for the process of filtration consists of a set of differential and transcendental equations. The differential equations of filtration give the dependency between the discharge Q, the volume V and the difference in pressure Δp. The generalized differential equations of filtration consider simultaneously the following complex aspects of the phenomenon: 1–the compressibility of the filtering layer; 2–the formation of sediment, generally compressible; 3–the means by which pores of the filtering layer are obstructed; 4–the presence of the solid phase in the filtrate too [2, 7].

In the given hypothesis, respectively that the pores are uniformly and gradually blocked, the generalized differential equation results [9]:

$$\frac{dV}{dt}=\frac{\frac{A}{\eta}\Delta p}{R^1_{f0}\frac{(\Delta p)^{\mu}_0}{K_{f1}(\Delta p)^{\mu-1}-K_{f3}V}+K_p R^1_p(\Delta p)^s V}. \quad (1)$$

The K_{f3} and K_P indexes are estimated with the equations:

$$K_p=\frac{1-x_v}{A}K_{f1},\ K_{f1}=\frac{\theta_s-\theta_f}{g(1-\varepsilon)\rho_s-\theta_s}$$
$$K_{f3}=\frac{x_v}{\pi r_0^2 N_p A l_f}K_{f1}. \quad (2)$$

where: R^1_{f0} is the specific resistance of the filtering layer for $(\Delta p)_1 = 1\text{N}\cdot\text{m}^{-2}$ at t_0, R^1_{p1} is the specific resistance of the precipitate for l_P=1m and $(\Delta p)_1$=1N·m^{-2}, r_0 is the radius of pores in the filtering layer at t_0, x_v is the fractions of the precipitate deposited on the walls of the filtering layer's pores, ε is the porosity of the precipitate.

Relations define the discharge Q, speed w and volume V_p:

$$Q = dV/dt,\ w = Q/A, V_p = K_{f1}V \quad (3)$$

When an additional relation, with the general form:

$$G(V, Q, \Delta p, t) \text{ is known for } t \geq t_0, \quad (4)$$

system (1), (2) and (3) generates: one transcendental implicit equation,

$$H(V, \Delta p, t) \text{ is known for } t \geq t_0, \quad (5)$$

and one differential equation of the first order, linear:

$$\frac{dV}{dt}=F(V,t) \text{ is known for } t \geq t_0. \quad (6)$$

Equation (6) is integrated with the initial conditions:

$$t = t_0,\ V = V_0, \quad (7)$$

resulting in the variation law for the volume of filtrate:

$$V = V(t) \text{ is known for } t \geq t_0. \quad (8)$$

The final moment t_f (admissible) for the process of filtration is deduced from additional conditions of the form:

$$\Delta p\left(t_f\right) \le \left(\Delta p\right)_{max} \text{ or } w\left(t_f\right) \ge w_{min} \text{ or } V_p\left(t_f\right) \le \left(V_p\right)_{max} \quad (9)$$

where the values for the $(\Delta p)_{max}$ and the w_{min} and the $(V_P)_{max}$, are required by technical and economic reasons.

Accepting certain hypothesis regarding the evolution of the filtering process specific forms for eq. (5) and (6) is obtained.

3.2 Solutions for the Cases of Pumping Stations and Dams in the Distribution Node

A first analysed case was for pumping stations equipped with filtering installations located at the entrance into the suction basin. Considering the variation of static height H_{st} in the process of filtration and characteristic relations from the equivalent load of the pipe network,

$$H_{st}=H_{st}^{0}+\frac{\Delta p-\left(\Delta p\right)_0}{\rho g},$$

$$H = H_{st} + M_r Q^2 , \; H = H_p - M_p Q^2$$

results from the eq. (4) of the form [9]:

$$\frac{dV}{dt} = \sqrt{\frac{\rho g\left(H_p - H_{st}^{0}\right) + \left(\Delta p\right)_0 - \Delta p}{\rho g\left(M_r + M_p\right)}} \quad (10)$$

where: H_p is the fictive pumping height, at zero discharge; H_{st}^{0} is the static height of the net at t_0.

For the transcendental eq. (5), for $t \ge t_0$, the form is obtained:

$$\frac{\frac{\Delta p}{\eta}}{\frac{R_{f0}}{\left(1-K_{f3}V\right)^2 + K_p R_{p1}^{1}\left(\Delta p\right)^5 V}} - \sqrt{\frac{\rho g\left(H_p - H_{st}^{0}\right) + \left(\Delta p\right)_0 - \Delta p}{\rho g\left(M_r + M_p\right)}} = 0 \quad (11)$$

The dams in the distribution node of canals may have water-filtering installations. In this case, by applying the effects superposition principle and considering the equation for discharge through large openings, for eq. (4) the analytical expression results:

$$Q = \mu A_s \sqrt{2\left(g\Delta z - \frac{\Delta p}{\rho}\right)} \quad , \quad (12)$$

where A_S is the area of the active section of the dam ($A_S \le A$), μ is the discharge coefficient respective to the active area A_s, Δz is the fall induced by the dam and the filtration installation (level difference).

There lore, the transcendental eq. (5) for $t \ge t_0$ becomes:

$$\frac{\frac{\Delta p}{\eta}}{\frac{R_{f0}}{\left(1-K_{f3}V\right)^2 + K_p R_{p1}^{1}\left(\Delta p\right)^s V}} - \mu A_s \sqrt{2\left(g\Delta z - \frac{\Delta p}{\rho}\right)} = 0 \quad (13)$$

In calculus, two cases of evaluating the fall Δz were considered:

- by specifying the law of variation, $\Delta z = \Delta z(t)$ for $t \ge t_0$; is accepted:

$$\Delta z = \left(\Delta z\right)_0 + a_{\Delta z} t \quad (14)$$

- by imposing the condition $Q = Q_0 = constant$, which results:

$$\Delta z = \left(\Delta z\right)_0 + \frac{\Delta p - \left(\Delta p\right)_0}{g\rho} . \quad (15)$$

where $(\Delta z)_0$ represents the value for the Δz for at the t_0 moment in time.

4. NUMERIC APPLICATION - SOFTWARE FILTR.01.BAS.

The programme FILTR.01.BAS is based on the mathematical model and the solving algorithm shown at point 3.1 to 3.2 [9]. The **entry data** consists of 3 subgroups:

E.1. General constants, specific to the programme and the application.

E.2. The functional and constructive parameters of the filtering layer, the suspension, the filtrate and the precipitate.

E.3. The functional and constructive parameters of the hydraulic system equipped with a sieving – filtering installation.

The **output data** consists of 2 subgroups:

O.1. The numeric solution (8) of the differential

equation (1) with the initial conditions (7).

O.2. The laws of variation in time for the parameters Δp, Q, w and V_P.

Using the FILTR.01.BAS for Kod P $\in \{3, 4\}$ the numerical solutions for **Applications PS.1** and **D.1** were obtained. Both applications have the same numerical values for the following entry data E.1 and E.2.

E.1: g = 9.81 ms^{-2}, $\varepsilon_K = 10^{-10}$, $\varepsilon_{TL} = 10^{-8}$, $\varepsilon_{fTL} = 10^{-15}$, $I_{max} = 50$, $n = 1$, $n_{Tmx} = 2$, $n_{Lmx} = 4$, $N_{pas} = 3600$, $n_{SecAf} = 30$, $t_o = 0$, $V_0 = 0$.

E.2: $\theta_s = 5.8$ Nm^{-3}, $\theta_F = 1.6$ Nm^{-3}, $\rho = 998.16$ Kgm^{-3}, $\rho_s = 2200$ Kgm^{-3}, $\eta = 10^{-3}$ $Kgm^{-1}s^{-1}$, $r_0 = 1.5 \cdot 10^{-4}$ m, $l_f = 8 \cdot 10^{-4}$ m, $x_v = 0.1$, $N_p = 2.4 \cdot 10^7$, $R^1_{p1} = 2 \cdot 10^8 N^{-s}m^{-2(1-s)}$, $R^1_{f0} = 4.23 \cdot 10^8$ $N^{-u}m^{2u-1}$, $\varepsilon = 0{,}25$.

Application PS.1. In the case were analysis refers to a pumping station. At the entrance into the canal a sieving – filtering installation was located.

The numeric data **E. 3** are: $A = 50$ m^2, h=3s, $(\Delta p)_{max} = 7500$ Nm^{-2}, $w_{min} = 0.002$ ms^{-1}, $M_r = 222$ $m^{-5}s$, $M_p = 455$ $m^{-5}s$, $H^0_{st} = 19$ m. Two calculus hypotheses are admissible concerning the behaviour of the filtering medium under pressure: a - incompressible filtering medium ($u = s = 0$); b - compressible filtering layer and precipitate ($u = 0.05$; $s = 0.1$).
For the t_i moments within the time interval $[t_o, t_a]$, with $t_a = 9000$ $s \le t_P = 10800$ s and

$$t_i = t_0 + \frac{t_F - t_0}{n_{SecAf}} \cdot i, \quad i = 0,1,2,\ldots \quad (1^o)$$

find the variation laws for Δp, Q, V and V_P.

The numeric results for Δp, Q, V and V_P obtained, are centralized in table 1 and 2.

Table 1. Ap. PS.1, hypotheses u = *s* = 0

t [s]	V [m^3]	Δp [Nm^{-2}]	w [mms^{-1}]
0	0.00	423.0	1.005
2	2.982	424.9	1.09
4	6.003	426.9	1.011
6	9.038	428.9	1.014
8	12.07	430.9	1.018
10	15.13	433.0	1.024
12	18.21	435.1	1.029
14	21.32	437.2	1.033
16	24.43	439.3	1.038
18	27.54	441.5	1.044
20	30.69	443.7	1.049
22	33.84	445.9	1.054
24	37.01	448.1	1.059
26	40.18	450.3	1.064
28	43.40	452.6	1.070
30	46.62	454.9	1.075
32	49.84	457.3	1.081
34	53.09	459.7	1.086
36	56.35	56.35	1.092
38	59.64	59.64	1.098
40	62.93	467.05	1.104
42	66.26	469.5	1.110
44	69.59	472.1	1.115
46	73.03	474.6	1.122
48	76.32	477.3	1.128
50	79.78	479.9	1.134
52	83.14	482.6	1.140
54	86.58	485.2	1.147

Table 2. Variation parameters of the Ap. PS.1, (hypotheses $(\Delta p)_0 = 500$ N/m^2)

t [s]	- $c^* 10^8$	$d^* 10^9$	V [m^3]
2	4.241	1.50	3.515
4	4.251	3.00	7.060
6	4.264	4.50	10.60
8	4.276	6.00	14.15
10	4.287	7.50	17.69
12	4.298	9.00	21.24
14	4.310	10.50	24.78
16	4.321	12.00	28.32
18	4.333	13.50	31.87
20	4.345	15.00	35.41
22	4.356	16.50	38.96
24	4.368	18.00	42.50
26	4.379	19.50	46.05
28	4.390	21.00	49.59
30	4.402	22.50	53.14
32	4,414	24.00	56.68
34	4.425	25.50	60.23
36	4.436	27.00	63.77
38	4.448	28.50	70.32
40	4.459	30.00	70.86
42	4.470	31.50	74.41
44	4.482	33.00	77.94
46	4.494	35.50	81.49
48	4.505	36.00	85.03
50	4.517	37.50	88.58
52	4.528	39.00	92,12
54	4.539	40.50	95,67
56	4.551	42.00	102,7
a* = 0.7148; b * = - 934.446			

The analysis of the results indicates greater values for Δp in (b). The discharge of the filtering agent does not differ much from one calculus hypothesis to another and decreases more little in time. However, it is necessary to analyse the situation when the decrease of the suction height with the value Δp does not lead to the presence of the process of cavitation.

Application D.1. The case under analysis refers to a dam located in the water distribution node of the system equipped with a filtering installation. The following data is known: t = 1s, $A = 30$ m^2,

Δp_{max}= 10000 Nm $^{-2}$, w_{min}= $2 \cdot 10^{-3}$ ms^{-1}, A_s = 0.2 m^2, Δz_0= 0.50 m, μ = 0.5. The following hypothesis of the functioning of the dam and the behaviour of the filtering medium were taken into account: 1^o– functioning with a constant fall $\Delta z = \Delta z_0 = 0.50$ m; 2^o– functioning with a constant discharge, $Q = Q_0$; a - incompressible filtering medium $u = s = 0$; b - compressible filtering layer and precipitate u = 0.05 and s = 0.1. For the t_i moments of time within the time interval $[t_0, t_a]$, with t_a = 360 s ≤ t_P = 3600s and equation 1^o, are obtained: a - the laws of variation for Δp, Q, V and V_P (in the hypothesis 1^o); b - the discharge of the filtrate Q and the laws of variation for Δz, Δp, V and V_p (in the hypothesis 2^o).

The numeric results for Δp, Q, V and V_P obtained are centralized in the Table 3.

Table 3.Variation parameters of the Ap. D.1.

t [s]	Δz [m]	Δp [N/m^2]	10^{-3} Q [m^3/s]	10^{3} V_p [m^3]	w [mm/s]
2	0.211	2074	12.26	3.68	4.90
4	0.223	2192	12.95	7.61	5.18
6	0.236	2310	13.65	11.75	5.45
8	0.248	2427	14.34	16.11	5.73
10	0.260	2545	15.03	20.68	6.01
12	0.272	2662	15.73	25.47	6.29
14	0.284	2780	16.42	30.48	6.56
16	0.296	2897	17.11	35.70	6.84
18	0.308	3015	17.80	41,14	7.12
20	0.320	3132	18.50	46,79	7.39
22	0.332	3250	19.19	52.66	7.67
24	0.344	3367	19.88	58.75	7.95
26	0.356	3485	20.57	65.05	8.22
28	0.368	3602	21.26	71.56	8.50
30	0.380	3720	21.95	78.29	8.78
32	0.392	3837	22.65	85.24	9.05
34	0.404	3955	23.34	92.40	9.33
36	0.416	4072	24.03	99.78	9.61
38	0.428	4190	24.72	107.4	9.88
40	0.440	4307	25.41	115.2	10.16
42	0.452	474,62	26.10	132.1	10.43
44	0.464	506,35	26.79	131.4	10.71
46	0.475	538,91	27.47	139.9	10.99
48	0.487	572,29	28.16	148.5	11.26
50	0.499	4895	28.85	157.4	11.54
54	0.523	5041	30.88	178.6	12.12

5 CONCLUSIONS

The water filtering- sieving installation suggested in this paper satisfies the requirements of retechnology and profitableness of the existing irrigation systems. It allows for the servicing of new beneficiaries with higher requirements in respect to water quality.

The prototype of the sieving–filtering installation was tested in laboratory conditions (Irrigation and Drainage Laboratory of the Technical University Iasi, Romania), and functional correlation was found. Also, the installation was set up in a water system (Irrigation System Braila, Romania) that services beneficiaries with water at different levels of purity (silt suspensions).

In order to analyse the functioning process of the ensemble hydrotechnic construction–filtering installation, an adequate mathematical model was conceived. At the same time, a software for the calculus of filtering parameters in different given circumstances was set - up. Two results for two typical situations in the location of the sieving – filtering installation: at the inlet of the pumping stations and in the nodes of the derivations to the net of pipes are presented.

REFERENCES

[1] Cretu I., 1980, "Numeric models for fluid motion in porous media", *Technical Publishing House, Bucharest, Romania*.

[2] Jujikov V. A., 1962 "Filtration. Theory and the practice of suspension separation", *Technical Publishing House, Bucharest, Romania*.

[3] Ghelase, I., Nitescu, E., Popescu, St., Luca, M., 2000, "Researches of the filtering solution in the irrigation systems" *Ovidius University Annals of Constructions, Vol. 1, no. 2, p. 95-98*.

[4] Luca M., Nitescu E., Ghelase I., 1997, "Improvement of the water filtering systems in pumping stations", *Proc. of the Simp. on Constructions Installations*, ed. Light, Iassy, Romania, pp.76-82.

[5] Luca, M., Nitescu, E., Popescu, St., Ghelase, I., 1998, "Rehabilitation of the water filtering systems in surface water intake", *Proc. of the Simp. on Constructions Installations*, ed. Light, Iassy, Romania, pp.20-26.

[6] Nitescu, E., Luca, M., Popescu, St., Ghelase, I., 1998, "Imbunatatirea calitatii apei din sistemele de irigatie prin sitare in flux continuu", *Rev. Hidrotehnica, vol. 43. no. 5, Bucuresti, Romania.* .

[7] Oroveanu, T., 1963, "The flow of liquids through porous, heterogeneous media", *Romanian Academy Publishing House, Bucharest*.

[8] Rusu, G., Rojanschi, V., 1980, "Filtration in the technique of cleaning and treating water" *Technical Publishing House, Bucharest, Romania*.

[9] Popescu, St., Luca, M., Nitescu, E., 2000, "*Mathematical model for the clogging-up process in the water utilization system*" *Bulet. Iaşi Techn. University, tom XLVI (L) Supl.*

Conference on Modelling Fluid Flow (CMFF'06)
The 13th International Conference on Fluid Flow Technologies
Budapest, Hungary, September 6-9, 2006

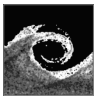

EXPERIMENTAL AND NUMERICAL INVESTIGATION OF AN AIR CAVITY IMMERSED IN A WATER DUCT FLOW

Assen VASSILEV[1], Hamda BEN HADID[2], Mahmoud EL HAJEM[2], Valéry BOTTON[2]

[1] Corresponding Author. Laboratoire de Mécanique des Fluides et d'Acoustique, UMR CNRS 5509, INSA-Lyon/UCBL/ECL, INSA-Lyon, LMFA, Bât. J. Jacquard, 20 av. A. EINSTEIN, 69621 Villeurbanne CEDEX, France. Tel.: +33 4 72 43 70 19, Fax: +33 4 72 43 87 18, E-mail: assen.vassilev@insa-lyon.fr
[2] LMFA, UMR CNRS 5509, INSA-Lyon/UCBL/ECL, E-mail: hamda.benhadid@univ-lyon1.fr, mahmoud.elhajem@insa-lyon.fr, valery.botton@insa-lyon.fr

ABSTRACT

The investigation of horizontal elongated air bubbles (air cavities) immersed in liquid flows has a particular interest because of its importance in various industrial domains. Though, the reconstruction of interfaces between two immiscible fluids is still relatively complex. In this work, a numerical calculation based on the Volume-of-Fluid method is carried out and compared to the experimental study. For this purpose, an air bubble of large aspect ratio is confined in a main liquid duct flow. The characteristic zones of the air-water interface are identified experimentally and discussed in function of the Reynolds number up to 26000. Two-dimensional unsteady numerical calculations are carried out in order to study the behaviour of the air cavity under the same conditions as in the experiment. The results show that the modelled shape of the air cavity and its front are quite well reconstructed. Furthermore, the wavy behaviour of its interface could be explained by the vortices that take place in the air cavity.

Keywords: Air cavity shape, air-water interface, VOF, slug/plug flow

NOMENCLATURE

D_h	[m]	hydraulic diameter
h	[m]	height of the water column under the air cavity (in the test section)
h_{ac}, L_{ac}, w_{ac},	[m]	height, length and width of the air cavity
$h_{ac,0}$, $L_{ac,0}$	[m]	initial height and initial length of the air cavity (at $Re = 0$)
h_{obst}, l_{obst}, w_{obst}	[m]	height, length and width of the obstacle
l_c	[m]	capillary length
U	[m/s]	mean velocity in the x-direction (defined as the ratio between the flow rate and the cross section area)
x, y, z	[m]	coordinates on the test section

Greek symbols

σ	[N/m]	surface tension (air/water interface)
ν	[$m^2 \cdot s^{-1}$]	kinematic viscosity of water
ρ	[$kg \cdot m^{-3}$]	density

Subscripts and superscripts

ac	air cavity
0	index associated to an initial parameter
eq	equivalent
*	non dimensional variable

1. INTRODUCTION

The investigation of large gas bubbles or cavities immersed in liquid flows is relevant to many industrial domains: e.g. the development of pipelines and multiphase pumps used in the chemical and petroleum industry (Falcimaigne *et al.* [7], Henriot *et al.* [10]), the air injection in turbomachines in order to diminish the effect of cavitation near the walls (Arndt *et al.* [2]) or the design of drainage systems (Aimable *et al.* [1], Minato & Nakajima [11]). This type of two-phase flows is also encountered in environmental application (Benjamin [3]). This last author furnished a significant work about the general form of gas bubbles of large aspect ratio. First, he presented an analytical study relative to the 2D steady gravity currents. Then, he investigated this configuration through an analogy with the case of

an air-filled cavity advancing on the upper side of a confined liquid flow.

Ha-Ngoc [9] has determined analytically and numerically the flow characteristics and the shape of 2D gas bubbles immersed in a stagnant or flowing liquid. This study considered the case when the viscosity does not influence the bubble motion accounting for the surface tension effect. The analysis of the propagation of the air cavity in a stagnant fluid was found to be in good agreement with the analytical solution of Benjamin [3] at Bond Number growing up to infinity. Similarly, the comparison with the numerical study of Couët & Strumolo [6] at small Froude Number (0.2 – 0.5) exhibited a good agreement.

Renardy et al. [12] have implemented the moving contact lines in a Volume-of-Fluid (VOF) scheme where the interface is modelled applying the piecewise linear construction (PLIC). Two methods of the contact line implementation are studied. In the first one, the VOF function is extrapolated beyond the flow domain, under condition that its gradient is normal to the interface. At the wall, the normal to the interface is determined by the contact angle. In the second one, the problem is treated as a three-phase configuration using the argument of Young. As this method produces an artificial localized flow, the extrapolated method is considered as a better one. The slip length condition is introduced at the discrete level and found to play an essential role in the spreading of contact lines.

VOF based direct numerical simulations (DNS) of two types of gas-liquid flow in confined geometries are performed by Wörner et al. [13]. Both flows are modelled in a vertical square mini-channel. This analysis reveals that the interfacial term is the only source of turbulent kinetic energy.

The accurate reconstruction of the interface remains a problem for the VOF method, when the surface tension effects play an important role and the density ratio of both phases is high. Under these conditions, an artificial velocity field (called "parasitic currents") could appear at the interface and provoke a significant destabilization of the interface. For this reason, the very recent study of Gerlach et al. [8] compares three existing VOF methods on fixed grids and assesses their capability for the calculation of surface tension-dominant two-phase flows. They are distinguished by the manner how the surface tension force is computed. The first method uses a kernel function for smoothing the interfacial discontinuity. The second one combines two approaches: the VOF and the Level-Set method. The third method includes a parabolic reconstruction of surface tension. A common property of all the analyzed methods is that the interface is represented by piecewise-linear interface segments. This investigation reveals that the third method is more advanced than the other two approaches. The resulting interface is accurately reconstructed and the instabilities due to the parasitic currents are reduced.

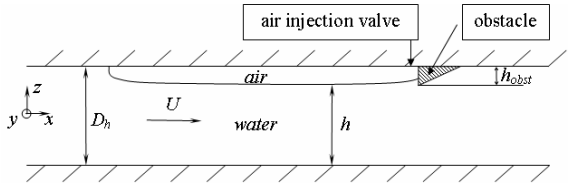

Figure 1. Sketch of the studied air cavity

In the present work, an air bubble of large aspect ratio is studied experimentally and numerically. It is introduced in a water duct of square cross-section ($0.08\ m \times 0.08\ m$). Due to the buoyancy, it occupies the upper part of the test section. In order to analyze the behaviour and structure of this isolated air cavity in a water flow, it is immobilized upstream an obstacle (Figure 1). Thus, the present study differs from the previous ones since the air cavity is kept stationary with respect to the test section frame and is not influenced by the presence of other air bubbles or cavities (slug/plug flow). In particular, the geometry of the air-cavity and the shape of its interface are investigated here over a wide range of flow rates corresponding to Reynolds number, $Re = UD_h/\nu$, from 0 to 26000. Here, U and ν denote respectively the mean velocity and the kinematic viscosity of the liquid phase. A comparison is made between the experimental and numerical results.

This paper is organized as follows: The experimental part of the work is presented in *Section 2*. *Section 3* is dedicated to the numerical study. The comparison between both studies is carried out *in Section 4*. Finally, *Section 5* resumes the results of the actual work.

2. EXPERIMENTAL APPROACH

2.1. Experimental facility

The experimental setup is presented in Figure 2. This facility is designed in order to produce a gravity driven liquid flow that circulates between

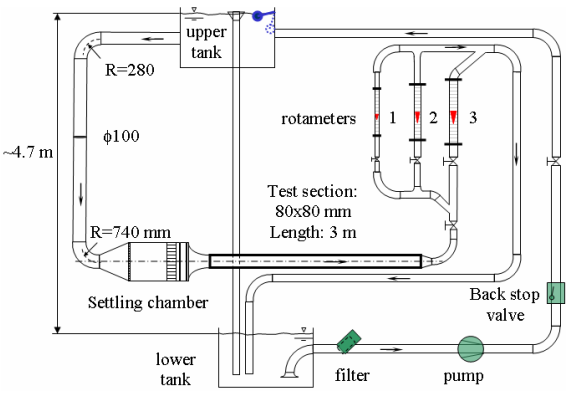

Figure 2. View of the experimental facility

two constant level tanks. The circulating liquid is tap water. The experimental duct has a square section and is entirely made of Plexiglas. The test section length is 3 *m*. An air injection valve is placed in the middle of the test section just upstream from an obstacle fixed at 2.5 *m* from the entry of the test section (Figure 1). The obstacle is also made of Plexiglas and its height, length and width are respectively $h_{obst} = 10$ *mm*, $l_{obst} = 15$ *mm* and $w_{obst} = 80$ *mm*. It has a prismatic profile and occupies the whole width and 1/8 of the duct height. Its function is to prevent the air cavity from being carried away by the water flow. A special attention is paid to the external factors acting on the test section: minimization of dilatation and gravity effects by a rigid support, suspension on girths of the test section and the settling chamber connected to the rest of the facility by flexible conducts, isolation from external vibrations by anti-vibration pads and modules.

The initial length, $L_{ac,0}$, of the air cavity is measured after the injection when the flow rate is zero. In the following, $L_{ac,0}$ is normalized (Eq. 1) using the hydraulic diameter, D_h, as a reference length scale:

$$L_0^* = L_{ac,0} / D_h . \quad (1)$$

Three different L_0^* are selected for the experimental study: 8, 14 and 18. They correspond respectively to volumes of 420, 720 and 1020 *ml* at atmospheric pressure. They are considered much larger than the air water interface capillary length ($l_c \approx 3$ *mm*). Note that this assumption is also made for the spanwise dimension of the air cavity (80 *mm*); the numerical approach could be thus reduced to a 2D model. Besides, the horizontal part of the air water interface is long enough to enable the development of undulations.

2.2. Measurement of the air cavity length

The air and water temperatures (T_{air}, T_{water}) and the atmospheric pressure (P_{atm}) are systematically measured and found to be practically constant during each experiment. Before starting the measurements, the water is circulated in order to let its temperature homogenize. As already mentioned, the air is injected at zero Reynolds number upstream from the obstacle using a medical syringe (Fig. 1). Its volume at atmospheric pressure and temperature are known. The initial length, $L_{ac,0}$ is measured under no-flow conditions (at $Re = 0$) from the front of the air cavity to the obstacle. The front forms triple air-water-Plexiglas contact lines simultaneously with the lateral and upper Plexiglas walls. The air cavity remains upstream from the obstacle and no macroscopic air entrainment is noticed by using optical techniques until the Reynolds number reaches approximately 26000. Then the mean flow carries it away bypassing the obstacle. Note that the critical value (Re_{crit}) can vary depending on the initial length, L_0^*, and the way how the flow rate is increased (smoothly or abruptly). During all the measurements, the variation of *Re* is smooth.

2.3. Morphology of the interface

2.3.1 Air cavity front

The photographs in Figure 3 show top views of the air cavity front for Reynolds number varying from 0 to 25000.

The water flows from the top to the bottom of the image. As *Re* grows, the air cavity contracts, i.e. its length diminishes, whereas its height increases very slightly. Thus, the front is displaced in the streamwise direction. At low $Re < 15000$, the contact line in the *xy* plane is symmetric and parabolic (Figures 3a, 3b). For $Re \geq 15000$, the front of the air cavity becomes almost flat. Thus, in order to measure the air cavity length L_{ac} for $Re \leq 10000$, the front is approximated by a parabolic profile. For $Re \geq 15000$, the mean value is calculated. At these values of *Re*, the front forms a round and thicker profile as shown in the side-views of Figures 4d and 4e. Small ripples can be distinguished on the backside of the air cavity front (Figure 3e and 3f).

2.3.2 Air cavity shape

Generally, the behaviour of the studied air cavities is very similar for all initial lengths ($L_{ac,0}$). Qualitatively, the length L_{ac} diminishes as *Re* grows as illustrated in Figure 4.

According to Clift *et al.* [5], an air cavity (or air bubble of large length/height ratio) forms under static conditions ($Re = 0$) the so called *Sessile bubble* (Fig. 4a). In this case the profile is symmetric in *yz plane*. When *Re* grows, the symmetry is broken. In low Reynolds number regimes (till $Re \sim 3000$) the interface remains uniform and no particular zone is distinguished. It is characterized by the presence of *travelling waves* of relatively small amplitude. Beyond this value of *Re*, a spanwise line arises separating two regions. Its appearance could be explained by the inertia-surface tension ratio, i.e. by Weber number (*We*) defined as $We=\rho U^2 D_h/\sigma$. The increasing *Re* from 0 to higher regimes suggests also the growth of *We*. Thus, it becomes 1 as $Re = 2828$. The formed *separation line* is present for all higher studied *We* and *Re*, i.e. for $We > 1$ and $Re > 2828$. By further increasing *Re* ($Re \geq 16000$), undulations arise in the zone upstream from the *separation line* (Figure 5). These waves are almost straight. It should be emphasized that they are "frozen" and not standing waves since their highs and lows are fixed in time and space (in the test section frame).

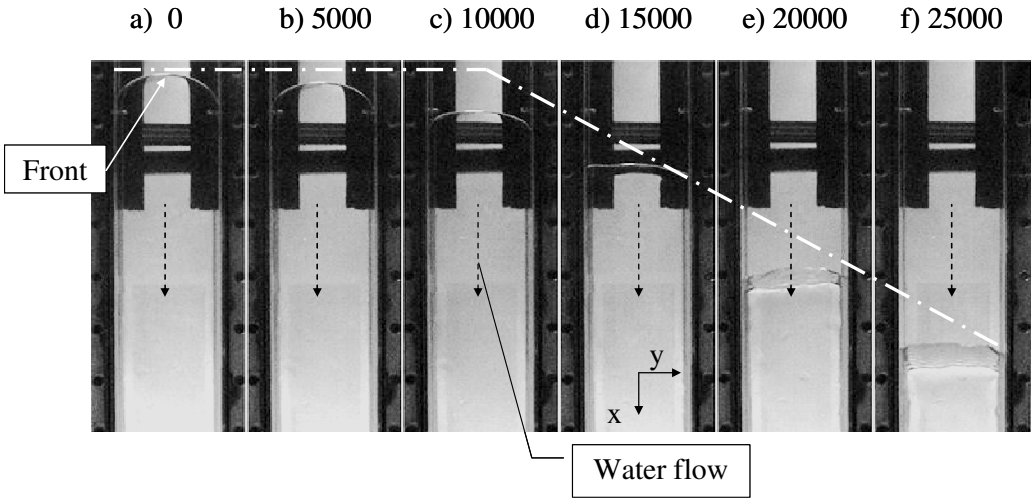

Figure 3. Evolution of the front of the air cavity as a function of *Re* (top view)

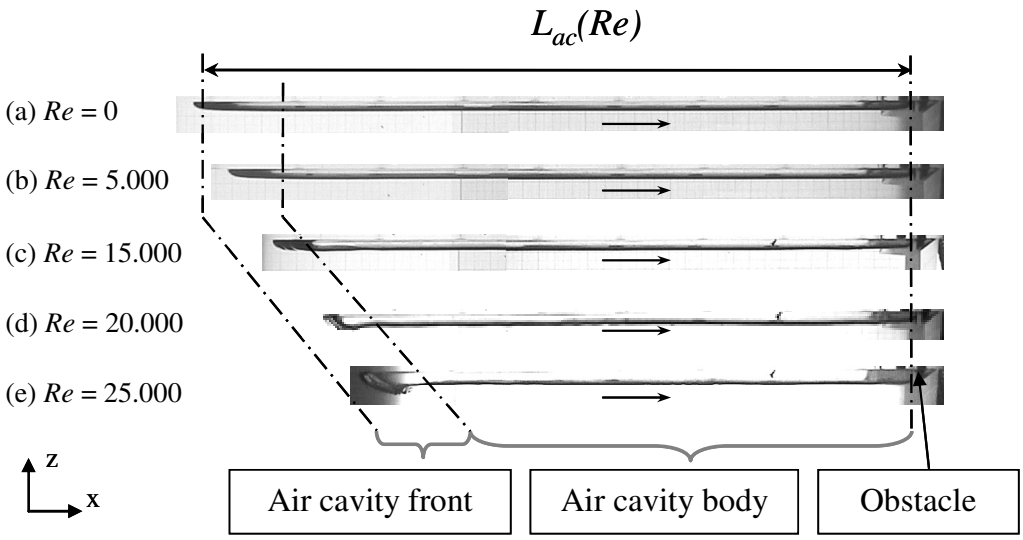

Figure 4. Evolution of the air cavity length ($L_0^* = 8$) as a function of *Re* (side view)

Their amplitude grows with *Re*, whereas their wavelength diminishes. This part of the interface where they arise will be referred to as *Zone 2*. In the same time, the *travelling waves* continue to occupy the whole *air cavity body* and are superposed to the "frozen" waves of *Zone 2*.

The interfacial region, situated between the *air cavity front* and *Zone 2*, will be named *Zone 1*, whereas the part contained between the obstacle and the separation line will represent *Zone 3*. The frontier between *Zone 1* and *Zone 2* is difficult to distinguish because of the decreasing amplitude of the waves in *Zone 2* in the upstream direction from the separation line. Though *Zone 2* looks very similar to a hydraulic jump, in this study, the Froude number, *Fr*, based on the mean velocity, *U*, and the water depth in the duct, *h*, is inferior to 1 in *both* sides of the separation line.

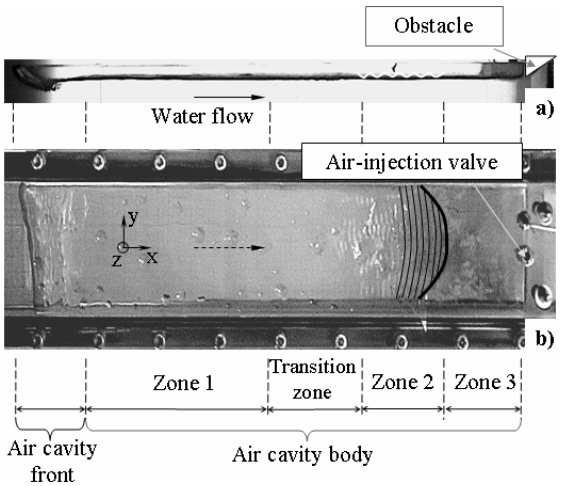

Figure 5. Global view on the air cavity at $Re = 25000$ ($L_0^* = 8$): a) side view, b) top view

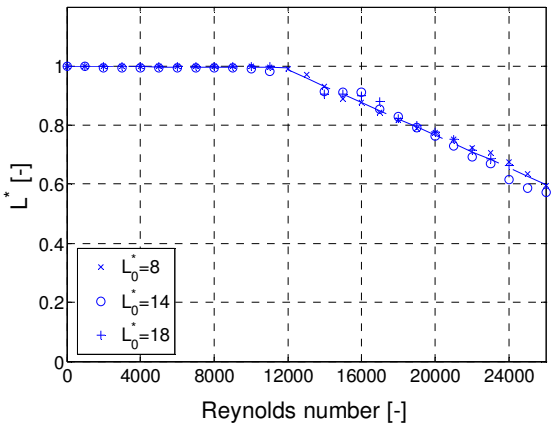

Figure 6: Evolution of the air cavity length as a function of *Re*

Figure 6 gives the evolution of the normalized cavity length $L^* = L_{ac}/L_{ac,0}$ as a function of *Re*. The general behaviour is almost independent of the initial length L_0^*. With increasing *Re* until 11000, L^* remains nearly constant. When *Re* is further increased from 11000 to 26000, L^* diminishes linearly and reaches 0.56–0.60.

3. NUMERICAL APPROACH

The goal of the numerical part is to analyse how precisely could be reproduced the air cavity form and the gas-liquid interface using a commercial code (FLUENT). Because of the similar experimental results obtained for the three air cavities, only $L_0^* = 8$ is studied numerically. The chosen numerical model is the Volume-of-Fluid (VOF) method.

3.1 Description of the numerical model

The selected VOF method is 2D and unsteady. Air and water are considered as two immiscible fluids with constant density and viscosity separated by a phase interface. The physical properties of the gas and liquid phases are summarized in Table 1.

Phase	T $[K]$	P $[bar]$	ρ $[kg/m^3]$	μ $[Pa \cdot s]$	σ $[N/m]$
Water	288.15	1.47	998.2	1.0×10^{-3}	0.1
Air	288.15	1.47	1.8	1.8×10^{-5}	

Table 1. Physical properties of water and air

Numerically the particular fluid is defined by the *void fraction* α_q in each control region. Its value is zero, when the gas phase ($q = 2$) occupies the cell, whereas it becomes 1, when the liquid phase ($q = 1$) is present. The interface cells contain both phases and are characterized by values of α_q between 0 and 1. Based on the void fraction α_q, the solution contains a single set of conservation equations of mass and momentum for the entire computational domain:

$$\frac{\partial \alpha_q}{\partial t} + \nabla\left(\alpha_q \underline{v}\right) = 0 \tag{2}$$

$$\frac{\partial}{\partial t}(\rho \underline{v}) + \nabla \cdot (\rho \underline{v}\underline{v}) = -\nabla p + \nabla \cdot \left[\mu\left(\nabla \underline{v} + \nabla \underline{v}^T\right)\right] + \rho \underline{g} + \underline{F_\sigma} \tag{3}$$

Here $\underline{v} = (u, v)$ is the velocity vector, t is the time, p is the pressure, $\underline{g} = (0, -g)$ is the gravitational acceleration, $\underline{F_\sigma}$ is the surface tension force, ρ and μ are averaged parameters of the density and viscosity that are defined respectively by:

$$\rho = \sum \alpha_q \rho_q = \alpha_2 \rho_2 + (1 - \alpha_2)\rho_1 \tag{4}$$

$$\mu = \sum \alpha_q \mu_q = \alpha_2 \mu_2 + (1 - \alpha_2)\mu_1 \tag{5}$$

The interface is reconstructed using a piecewise linear scheme (PLIC). This algorithm supposes a linear slope of the phase interface within each cell and takes it into account by the calculation of the advection of fluid through the cell faces. More details about this scheme could be found in the work of Youngs [14].

The chosen turbulence model is the RNG k-ε model (*Renormalization Group* k-ε) with enhanced wall treatment function. It is appropriate in regions where the *Re* is small (near wall regions) and is economic in time and computational resources.

The segregated, implicit method of resolution of the equations is used. It linearizes each discrete equation. The result is a scalar system of linear equations with only one equation for each cell of the flow field. The solver "point implicit" (Gauss-Seidel) is applied for the resolution of the linear equations in conjunction with the method AMG (*Algebraic Multigrid Method*) to solve the scalar system.

The jump of the normal stress at the interface is balanced by surface tension, σ, constant during this study. The model of surface tension is a continuum surface force model (CSF) suggested by Brackbill et al. [4]. With this model, the addition of surface tension to the VOF calculations results in a source term in the momentum equation. The force acting at the interface is the volume force $\underline{F_\sigma}$. In a two-phase system, it can be expressed as:

$$\underline{F_\sigma} = \sigma_{12} \frac{\rho \kappa_1 \nabla \alpha_1}{0.5(\rho_1 + \rho_2)}, \tag{6}$$

where κ is the curvature of the interface. Its calculation produces better results when the VOF gradients at the nodes are used rather than the ones

computed at the cell centres. Note that the surface tension force is proportional to the average density in the cell.
An estimation of the importance of the surface tension force could be obtained from the non-dimensional analysis. Based on the mean velocity U for $Re = 25000$, the maximum values of Weber number are $We \approx 78$. Thus, the influence of the surface tension could not be neglected. Besides, the wall adhesion is added to the surface tension force, both compatible with the VOF model. This conjunction is taken from the work of Brackbill et al. [4]. The contact angle θ_w is constant during this study and its value is 90°.

3.2 Geometry and grid mesh

As already mentioned, in the median vertical plane of the test section, the air-water interface is far enough from the side walls. Thus, it is not affected by boundary effects.
The numerical study applies a structured grid with quadrilateral elements. A coarser grid (*G1*) and a finer grid (*G2*) are used in order to adapt the mesh to the studied flow regimes (Table 2).

Grid type	Mesh faces	Re [-]	Δt [*ms*]	Time steps
G1 (coarser)	6.64×10^4	5000, 10000	1.0	20000
G2 (finer)	1.98×10^5	15000, 20000, 25000	0.5	40000

Table 2. Computational parameters applied in the numerical simulation

The computational domain representing the main interest is the air cavity situated upstream the obstacle. Thus, the grid here is refined and the vertical mesh size is 1/40 and 1/100 for *G1* and *G2* respectively. In contrast, the mesh size is relatively coarser in the other regions. The mesh size for *G2* is everywhere finer than in the case of *G1*. Comparing the number of mesh faces in Table 2, the factor of refinement is close to 3. Besides, *G2* is optimized to the dimensions of the air cavity in order to reduce the computational time.

The initial pressure is 1.47 bar which is measured inside of the duct. The initial turbulent parameters (at the entry of the duct) k and ε as well as the velocity profiles for $Re = 5000$ and 10000 result from numerically obtained values in absence of air cavity at the exit of the duct where the flow is established. In these regimes, it is already established at the position occupied by the air cavity. In contrast, for higher Re, the water velocity profile is chosen uniform at the entry of the duct, since it is not established in vicinity of the air cavity. This situation corresponds to the experimental conditions.

4. COMPARISON BETWEEN THE EXPERIMENTAL AND THE NUMERICAL APPROACH

The comparison is based on an air cavity $L_0^* = 8$. The shape of the air cavity front is presented in Figure 7 for five studied flow regimes. The numerical results are shown for the time $t = 20$s. Generally, when grid G2 is applied for flow regimes corresponding to $Re < 15000$, the calculated air-water interface is characterized by undulations with amplitudes larger than that observed experimentally.
The numerical and experimental results show small modifications in the shape of the air cavity for $Re \leq 15000$. In contrast, for larger Reynolds number, $Re = 20000$, the numerical result predicts a front that is less influenced by the inertia effects. However, at $Re = 25000$, the shape can be reproduced numerically quite well. The thickening of the front is clearly identifiable and the straight slope downstream the minimum interface level is well reconstructed. The fact that the numerically obtained shape is more compact is probably due to the chosen contact angle, i.e. 90°. Note that $Re = 25000$ is very close to the flow regime at which the carrying away phenomenon could appear experimentally. The numerical result shows a partial escapement of air due to the mean flow after which the air cavity length is stabilized. In spite of the air lost, the obtained front shape is comparable to the experimental one.
The recirculation in the air phase presented in Figure 8 gives a further insight into the behaviour not only of the air cavity but also of the air-water interface. Here, the air is in contact with the liquid phase and entrained by it in the downstream direction. The air deficit in the air cavity front is compensated by a flow propagating along the upper wall from the obstacle in the upstream direction (Fig. 8a). The two opposite air currents produce an important shear stress within the air cavity. The result is the generation of local secondary vortices oriented in the same sense (Fig. 8b). Their positions are associated with the lower positions of the interface, whereas at the higher positions the gas flow is accelerated. The characteristic length of the vortices is of the same magnitude as the undulation wavelengths. This is also the case at the air cavity front. Here, at higher regimes ($Re = 25000$), the thickening is accompanied with an increase of the characteristic length of the frontal vortex.
In contrast to the experiment, homogenous undulations from the air cavity front to the obstacle appear on the interface (Fig. 9). Thus, no morphological difference is noted.

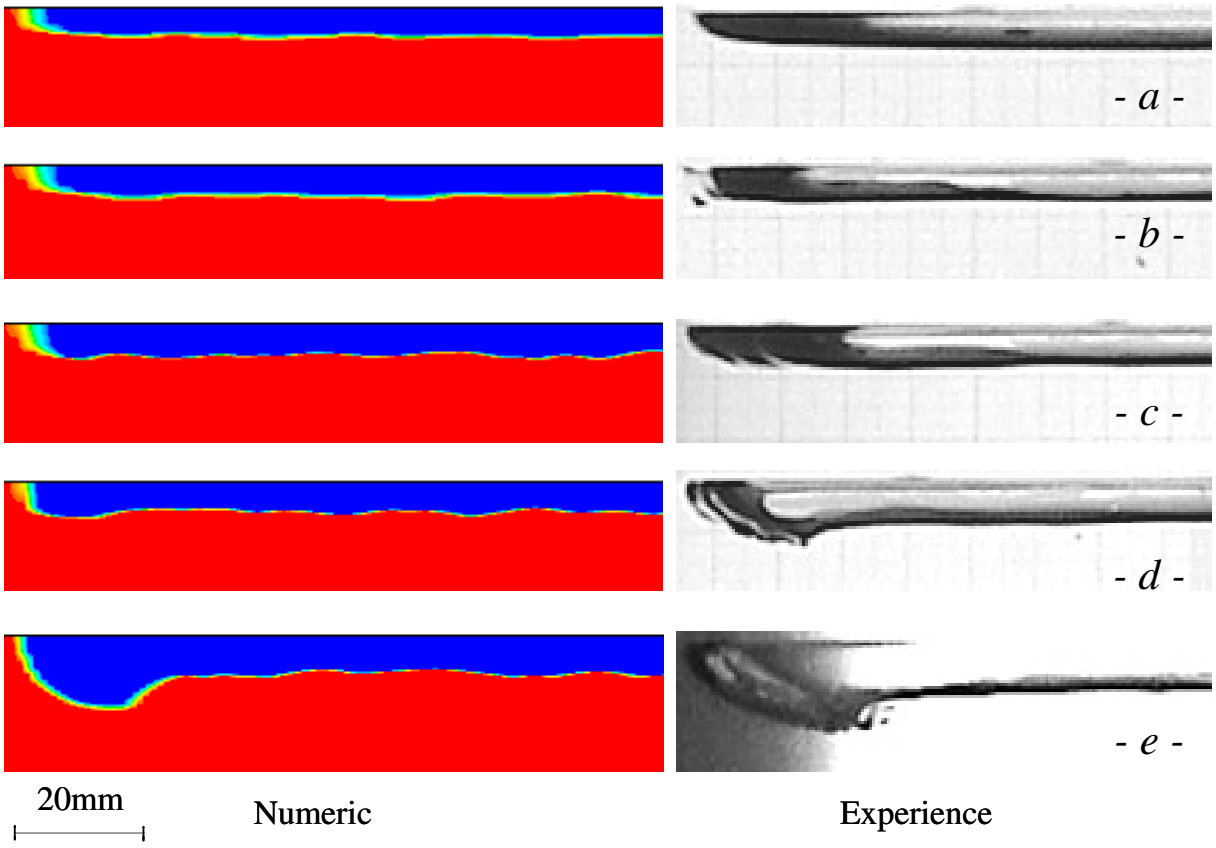

Figure 7. Comparison between the numerical study (on the left) and experimental study (on the right): (a) *Re* = 5000, (b) *Re* = 10000, (c) *Re* = 15000, (d) *Re* = 20000, (e) *Re* = 25000

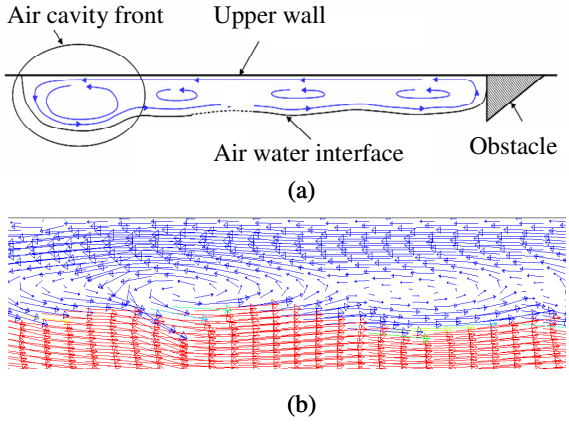

Figure 8. Recirculation and vortices in the air cavity, secondary vortex in the air cavity at *Re* = 25000 (a) global view (b) computation

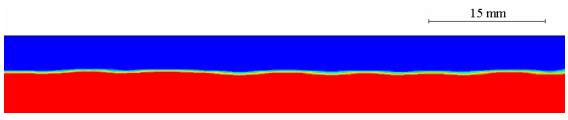

Figure 9. Undulations at the air-water interface

5. CONCLUSIONS

The presented experimental data show that the length of air cavity remains unchanged up to *Re* = 11000. When *Re* is further increased, the length of the air cavity starts to shrink following a linear law and reaches 56–60% of its initial length for *Re* = 26000.

We also performed numerical calculations using the Volume-of-Fluid method and analyzed the shape and the interfacial behaviour of an air cavity immersed and fixed in a confined geometry. Good agreement with the experiment is obtained concerning the shape of the front of the air cavity. Its thickening at *Re* = 25000 is well reproduced numerically. Further details are also acquired about the recirculation and secondary vortices within the air cavity. It was also shown that the characteristic length of these vortices have the same magnitude as the interfacial wavelengths.

REFERENCES

[1] Aimable, R., Zech, Y., 2003. "Résultats Expérimentaux sur la Formation de Poches

d'Air Isolées dans un Collecteur de Drainage Urbain", *La Tribune de l'eau*, Vol. 56 (624), pp. 60-69.

[2] Arndt, R. E. A., Ellis, C. R., Paul, S., 1995, "Preliminary Investigation of the Use of Air Injection to Mitigate Cavitation Erosion", *J of Fluids Engineering*, Vol. 117(3), pp. 498-504.

[3] Benjamin, B., 1968, "Gravity Currents and Related Phenomena", *J of Fluid Mech*, Vol. 31, pp. 209–248.

[4] Brackbill J. U., Kothe D. B., Zemach, C., 1992, "A Continuum Method for Modeling Surface Tension", *J. Comput. Phys.*, Vol. 100, pp. 335-354.

[5] Clift, R., Grace, J. R., Weber, M.E., 1978, Bubbles, Drops and Particles, Academic Press, New York.

[6] Couët, B., Strumulo, G. S., 1987, "The Effects of Surface Tension and Tube Inclination on a Two-dimensional Rising Bubble", *J Fluids Mech*, Vol. 184, pp. 1-14.

[7] Falcimaigne, J., Brac, J., Charron, Y., Pagnier, P., Vilagines, R., 2002, "Multiphase Pumping: Achievements and Perspectives", *Oil & Gas Science and Technology*, Rev. IFP Vol. 57(1), pp. 99-107.

[8] Gerlach, D., Tomar, G., Biswas, G., Durst, F., 2006, "Comparison of Volume-of-Fluid Methods for Surface Tension-Dominant Two-Phase Flows", *Int J of Heat and Mass Transfer*, Vol. 49, pp. 740-754.

[9] Ha-Ngoc, H., 2003, "Etude Théorique et Numérique du Mouvement de Poches de Gaz en Canal et en Tube", *PhD thesis*, Institut National Polytechnique de Toulouse, France.

[10] Henriot, V., Duret, E., Heintzé, E., Courbot, A., 2002, "Multiphase Production Control: Application to Slug Flow", *Oil & Gas Science and Technology*, Rev. IFP Vol. 57(1), pp. 87-98.

[11] Minato, A., Nakajima, N., 2004, "Simulation of Two-Phase Flow in Pumping Stations", *Congress of advances in the modelling methodologies of two-phase flows*, Lyon, France.

[12] Renardy, M., Renardy, Y., Li, J., 2001, "Numerical Simulation of Moving Contact Line Problems Using a Volume-of-Fluid Method", *J of Comp Physics*, Vol. 171, pp. 243-263.

[13] Wörner, M, Ghidersa, B. E., Ilić, M., Cacuci, D. G., 2004, "Volume-of-Fluid Method Based Numerical Simulations of Gas-Liquid Two-Phase Flow in Confined Geometries", *Congress of advances in the modelling methodologies of two-phase flows*, Lyon, France, paper Nr. 4.

[14] Youngs, D. L., 1982, "Time-Dependent Multi-Material Flow with Large Fluid Distortion", In K. W. Morton and M. J. Baines, editors, *Numerical Methods for Fluid Dynamics*, Academic Press.

Conference on Modelling Fluid Flow (CMFF'06)
The 13th International Conference on Fluid Flow Technologies
Budapest, Hungary, September 6-9, 2006

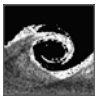

STUDY ON TURBULENT CHANNEL FLOW WITH SUCTION THROUGH A SLIT

Kaoru FUKASAWA[1], Masatoshi SANO[2]

[1] Corresponding Author. Department of Mechanical Engineering, Chiba Institute of Technology, 2-17-1 Tsudanuma, Narashino-shi, 275-0016 Japan. Tel.: +81 47 478 0266, Fax: +81 47 478 0299, E-mail: g0371501FE@it-chiba.ac.jp
[2] Department of Mechanical Engineering, Chiba Institute of Technology, 2-17-1 Tsudanuma, Narashino-shi, 275-0016 Japan. Tel.: +81 47 478 0266, Fax: +81 47 478 0299, E-mail: sano.masatoshi@it-chiba.ac.jp

ABSTRACT

Experiments have been performed on turbulent channel flow with suction through a slit. The inclined angle of the suction is varied at 30°, 60°and 90° at the mainstream velocity of 10*m/s*. The dimensionless suction ratio is varied at nine steps in the range of 0.067～0.500. In order to investigate the relationship between fluid flow and heat transfer characteristics, local heat transfer coefficient, wall static pressure, wall shear stress, velocity profile and turbulence intensity are measured. In addition, the velocity profiles of the suction region are measured by the particle image velocimetry (PIV). Differences due to the inclined angle are not observed in the results for wall pressure and heat transfer coefficient. The heat transfer coefficient decreases as the suction ratio increases. The recovery mechanism of turbulence varies greatly between the lower side and upper side of the channel.

Keywords: Channel Flow, Suction, Heat Transfer, Pressure Drop, PIV, Wall Shear Stress

NOMENCLATURE

C_p	[-]	static pressure coefficient
de	[m]	hydraulic diameter
H	[mm]	height of the channel (30mm)
L	[mm]	width of the slit (10mm)
Nu	[-]	Nusselt number
Nu_0	[-]	Nusselt number without suction
Q	[-]	suction ratio
T	[K]	temperature
U	[m/s]	streamwise mean velocity
U_{in}	[m/s]	bulk velocity in the inlet of the test section
U_m	[m/s]	bulk velocity in the downstream of the slit
V	[m/s]	wall-normal mean velocity
V_s	[m/s]	suction velocity
u_{rms}	[m/s]	streamwise turbulence intensity
u_τ	[m/s]	friction velocity
h	[W/m^2K]	local heat transfer coefficient
p	[Pa]	pressure
p_{atm}	[Pa]	pressure at atmosphere
q	[W/m^2]	heat flux
x	[mm]	streamwise coordinate
y	[mm]	wall-normal coordinate
α	[°]	inclined angle of the slit
κ	[W/mK]	thermal conductivity
ρ	[kg/m^3]	density of air
ζ	[-]	pressure loss coefficient

1. INTRODUCTION

Suction and injection of fluid from a wall are highly effective techniques for controlling wall bounded turbulent flows. In particular, the suction makes it possible to prevent flow separation by removing low momentum fluid near the wall, and to delay boundary layer transition. Furthermore, it is known that re-laminarization occurs due to a decrease of turbulence near-wall region, when the suction is performed on a turbulent boundary layer [1]. Methods for performing suction from a wall are typically divided into two categories: a uniform suction at a porous wall surface, and a localized suction at a round hole or slit. A number of studies have been performed theoretically and experimentally for a fluid flow with uniform suction at a wall [2,3]. On the other hand, Sano *et al*. [4] performed research concerning the localized suction of the flow characteristics at turbulent boundary layer with suction through a slit, and investigated the process of recovery to an equilibrium state from a non-equilibrium state. Antonia *et al*. [1] and Oyewola *et al*. [5] reported the effect of suction through a porous wall strip on a flat plate turbulent boundary layer. Komori *et al*. [6] investigated the fluid flow and heat transfer characteristics in a laminar boundary layer with localized suction and showed that the heat transfer coefficient increases just downstream the suction region. These studies were carried out for the boundary layer. As an

example of research on internal flow with suction, Sofialidis *et al*. [7] carried out the numerical calculation for the fully developed turbulent pipe flow and examined the accuracy of various turbulent models from comparison with the experimental result. However, there are very few reports of experimental studies including heat transfer characteristics on turbulent channel flow with suction. In this paper, the influence of suction through a slit in a fully developed turbulent channel flow is made clear. The heat transfer coefficient, wall static pressure, wall shear stress, velocity profile and turbulence intensity are measured by altering the inclined angles and suction ratios. Based on these results, the relationship between fluid flow characteristics and heat transfer is investigated.

2. EXPERIMENTAL APPARATUS AND PROCEDURE

Figure 1 shows a schematic diagram of the experimental apparatus. The coordinate system and the definition of symbols used in this paper are shown in figure 2. The test section, made of plexiglass, is 250*mm* wide and 30*mm* high. The slit width L is 10*mm*. Two blowers are used in the experiment. One is used for main flow; the other is used for the suction. The suction ratio is measured by an orifice flow meter. The upstream edge of the slit is 1500*mm* downstream of the channel entrance. A tripping wire with a diameter of 1.5*mm* is installed perpendicular to the main flow on the lower and upper walls to provide fully developed turbulent channel flow. In order to obtain a uniform suction velocity over the whole spanwise, the porous plate made of sintered metal fibres is installed in the chamber of the suction tunnel after the slit. The origin of the x, y coordinates is located at a position on the trailing edge of the slit (as shown in figure 2). The mean and fluctuating velocity components in the x and y directions are U, u and V, v, respectively. The inclined angle α is changed to 30°, 60° and 90°, and the velocity at the inlet of channel U_{in} is set at 10*m/s*. The dimensionless suction ratio Q is varied nine steps in the range of 0.067～0.500. Q is defined as follows:

$$Q = \frac{V_s L}{U_{in} H} \tag{1}$$

where, V_s is the suction velocity. Additionally, the experiments at Q=0 is performed in the condition when there is no slit. In the experiment to analyze the fluid flow characteristics, all measurements are performed under an unheated conditions. To measure the wall static pressure, a number of pressure taps, 0.5*mm* in diameter, are installed in the test section along the centerline of the flow direction. The wall static pressure coefficient Cp and pressure loss coefficient ζ are defined as follows:

$$Cp = \frac{p - p_{atm}}{\frac{1}{2}\rho U_{in}^{\ 2}} \tag{2}$$

$$\zeta = \frac{\Delta p_{loss}}{\frac{1}{2}\rho U_{in}^{\ 2}} = \left\{ 1 - \left(\frac{U_m}{U_{in}} \right)^2 \right\} - \Delta Cp \tag{3}$$

where, ΔP_{loss} is the pressure drop and ΔCp is pressure recovery (=Cp_2-Cp_1) illustrated in figure 3, it is the result of the upper wall at α=90°, Q=0.500. The friction velocity u_τ is measured using a micro flow sensor. The micro flow sensor is a thermal sensor which is integrated in the heater, and the temperature sensors are on a silicone chip. It is

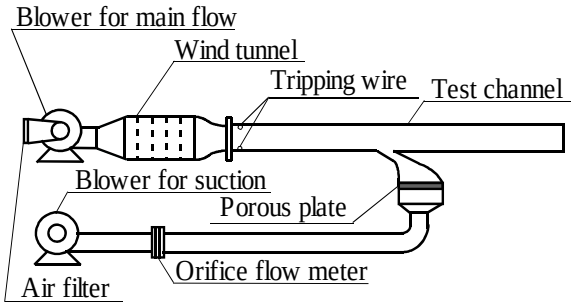

Figure 1. Experimental apparatus

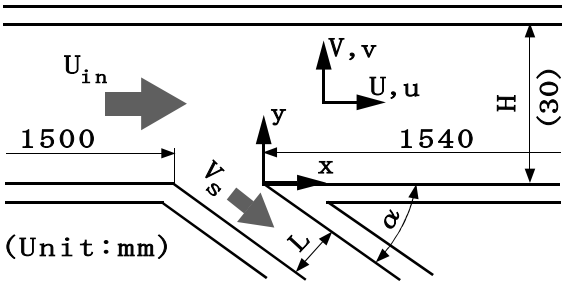

Figure 2. Coordinate system and definition of symbols

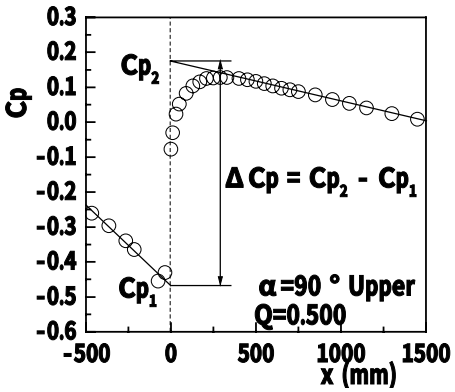

Figure 3. Evaluation method of loss factor

possible to measure the wall shear stress and the flow direction [9]. The mean velocity and turbulence intensity are measured by a constant-temperature-type hot-wire anemometer with an I-type probe. The wire is made of tungsten and is $5\mu m$ in diameter and $1mm$ in length. In addition, the velocity profiles of the suction region are measured by the particle image velocimetry (PIV). For the heat transfer experiment, the bottom plate located downstream of the slit is replaced by the test plate having $1540mm$ long and $250mm$ wide heated section. Metal (stainless steel) foil $30\mu m$ in thickness is glued to the surface of the plate made of bakelite. The foil is heated with a uniform heat flux by an alternating electric current. The experiments are carried out for the heating condition of a constant heat flux of about $400W/m^2$. For measuring the wall surface temperature, T-type thermocouples $0.1mm$ in diameter are attached to the back surface of a metal foil glued along the centerline of the flat plate. The local heat transfer coefficient h and local Nusselt number Nu is defined as follows:

$$h = \frac{q}{T_w - T_m} \tag{4}$$

$$Nu = \frac{h \cdot de}{\kappa} \tag{5}$$

Here, q is the wall heat flux compensated for a thermal loss. T_w and T_m are the wall and bulk temperature, respectively. κ is denoted as the thermal conductivity at the bulk temperature.

3. EXPERIMENTAL RESULT AND DISCUSSION

3.1. Influence of the inclined angle

Figure 4 shows the streamwise distributions of the local Nusselt number Nu measured for the cases of α=30°, 60° and 90° at Q=0.200 and 0.400. In all cases, Nu is increases near the slit and decreases toward downstream. At downstream with values over x=800mm, Nu almost becomes a constant value. The difference due to the inclined angles is not observed at each Q. This tendency is similar at the other suction ratios. Figure 5 shows the streamwise distributions of the wall static pressure coefficient Cp measured on the lower side of the test section. Like the result of Nu, Cp is almost same distribution at all inclined angles. The pressure loss ζ at the lower wall is plotted against the suction ratio in figure 6. In the case of all angles, a negative value is observed at the range of Q=0.067~0.267. This result means that the pressure loss near the slit decreases by the effect of the suction. However, when Q is greater than 0.200, ζ increases with increasing suction ratio. Such trends are also observed at the pressure loss of a main flow on a T-branch pipe [8]. From these results of Nu, Cp and ζ, it is found that the influence of the inclined angles is very small. Therefore, in the investigated following results of the influence of the suction ratio, the results at α=90º are shown as the representative case.

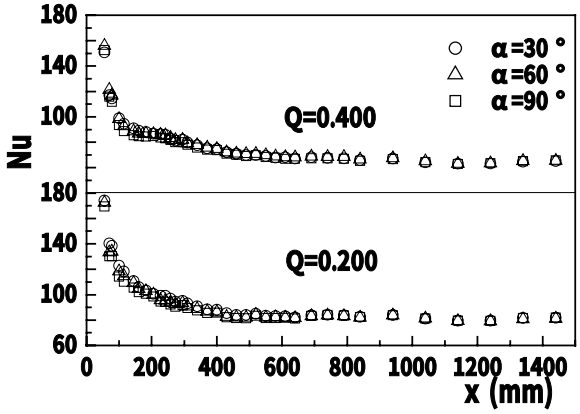

Figure 4. Distributions of local Nusselt number

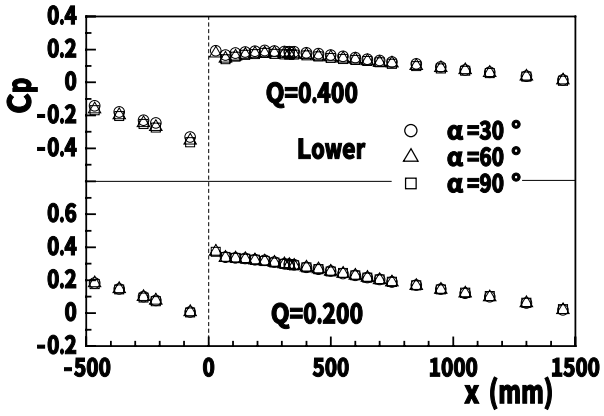

Figure 5. Distributions of wall static pressure coefficient

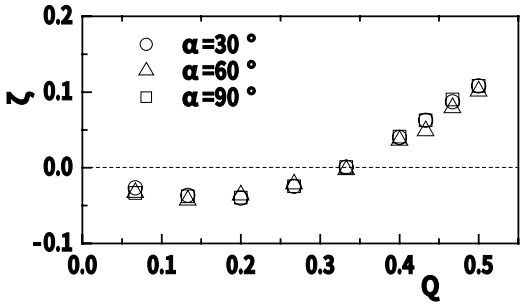

Figure 6. Pressure loss against suction ratio

3.2. Influence of the suction ratio

3.2.1. Distribution of the Nusselt Number

Figure 7(a) shows the streamwise distributions of the local Nusselt number *Nu* measured for the cases of α=90°, and Nu/Nu_0 (Nu_0 is the measurement result without suction at no slit) are shown in figure 7(b). It is seen from figure 7(a) that a leading-edge effect (such as increasing *Nu* on the heated starting point) is observed near the slit in both conditions, suction and no suction. In the case of suction, *Nu* of all the suction conditions decreases as compared to condition without suction. However, these are not constant decreases. As *Q* increases, the decrease in the range from *x*=100 to 250*mm* is weakened, and in the suction above *Q*=0.333, there is a region where the value of *Nu* barely changes in the streamwise direction. Downstream of this region, *Nu* decreases slowly and becomes a constant value. In figure 7(b), in the distribution of Nu/Nu_0 at all *Q*, although the minimum value is observed in the range of about *x*=100*mm*, then Nu/Nu_0 increases toward downstream, and the second peak appears near *x*=200*mm*. These results indicate that fluid flow characteristics downstream of the slit changes by the suction. Komori *et al*. [6] investigated laminar boundary layer with suction and showed that the heat transfer coefficient increases remarkably near the suction region. However, such a phenomenon does not occur in a turbulent channel flow. This is considered to be a cause of that the mean flow rate reduced by the suction is not supplemented at a turbulent channel flow; it differs with the case of the boundary layer.

3.2.2. Distribution of the wall static pressure coefficient

Figure 8(a) shows *Cp* measured for the lower wall of the channel, and the results of the upper wall are shown in figure 8(b). With increasing *Q*, it is observed that *Cp* decreases at both the upstream and the downstream of the slit. Here, as *Q* increases, the pressure gradient of the distribution in the downstream of the slit becomes small, because the bulk velocity U_m in the downstream reduced as the

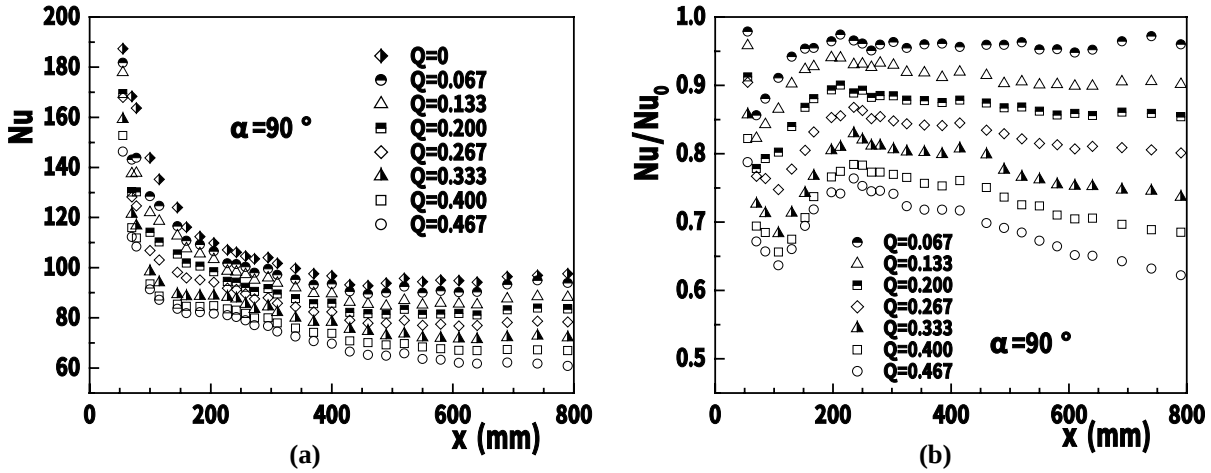

Figure 7. Distributions of local Nusselt number

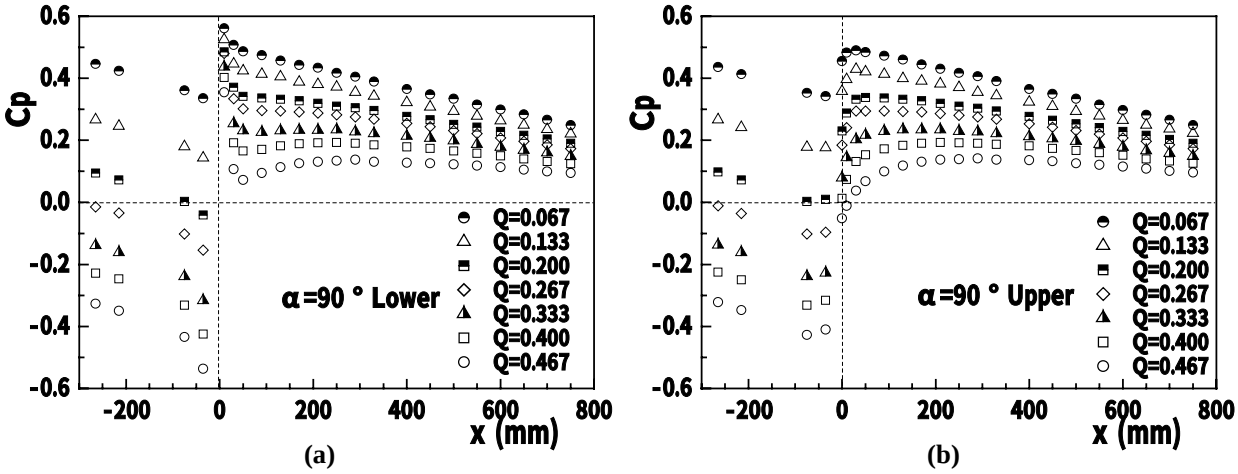

Figure 8. Distributions of wall static pressure coefficient

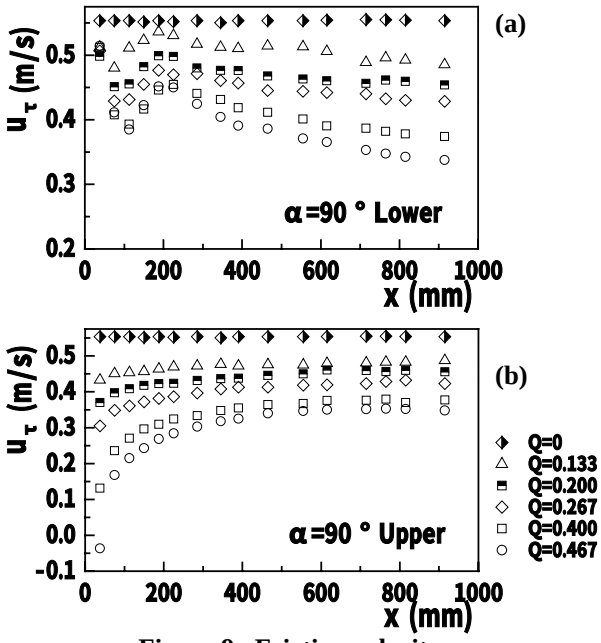

Figure 9. Friction velocity

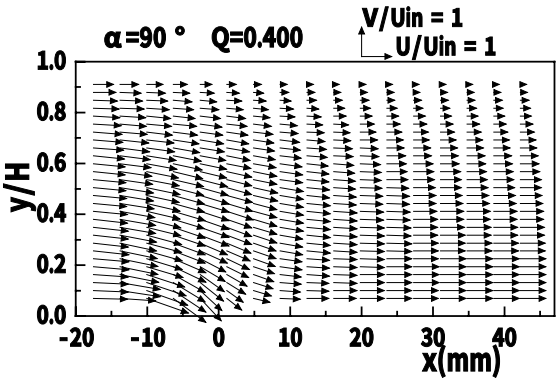

Figure 10. Velocity vector (Q=0.400)

suction flow rate increases. The minimum value appears near the slit upstream, and the pressure recovery occurs rapidly just after the slit. This result is similar to the tendency of the *Cp* distribution of a turbulent channel flow with a sudden expansion [10]. The maximum value appears downstream of the slit in all *Q*, and after that, the *Cp* shifts to a linear distribution immediately, when *Q* is small. On the other hand, in cases when *Q* is large, *Cp* decreases close to x=50*mm* from a point of the maximum value, and the second minimum value appears. As this tendency is particularly so remarkable in cases when *Q* is large, it is considered that acceleration of a flow occurs behind a slit. In addition, *Cp* increases again downstream and the second maximum value appears. In the upper wall shown in figure 8(b), a second minimum value like the result of the lower wall is not observed. At Q=0.467 only, *Cp* has a negative value just after the slit. This result suggests that the flow separation occurred on the region, due to the adverse pressure gradient and the expansion of the low-speed flow area in the streamwise direction.

3.2.3. Distribution of the friction velocity

The friction velocity u_τ investigated on conditions of various *Q* is shown in figure 9(a) and (b). Where, figure 9(a) and 9(b) show the results of the lower wall and the upper wall, respectively. In both figures, u_τ decreases with increasing *Q* because the mass flow rate in the downstream of the slit is reduced by the suction. In the distribution of the lower wall (Fig. 9(a)), in all suction cases, the minimum value appears to range of x=70 ~ 100*mm*, and u_τ increases after that, the peak value is

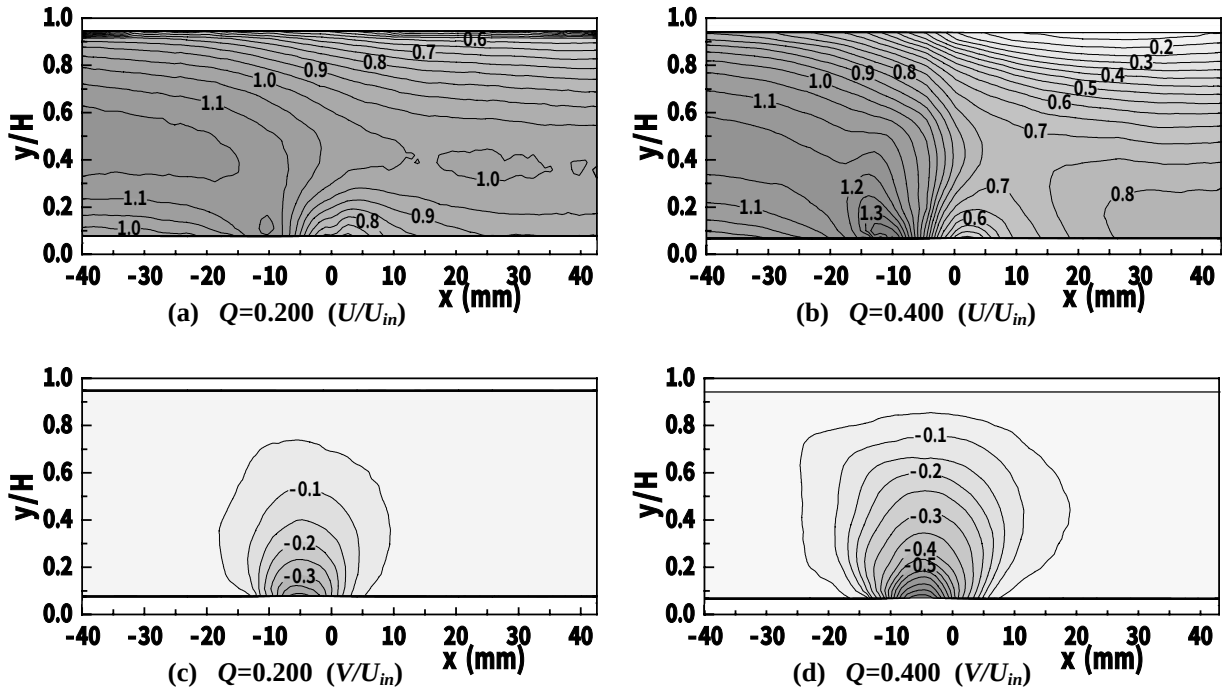

Figure 11. Contours of mean velocity

obtained. Then, friction velocity decreases slowly in the downstream of that region. These tendencies agree with the streamwise distribution of Nu/Nu_0 shown in figure 7(b). It is seen that the behavior of the friction velocity is closely related to the increase and decrease of the heat transfer coefficient. For the result of the upper wall(Fig. 9(b)), the maximum and minimum values do not appear at all conditions, and u_τ increases gradually toward downstream. Moreover, u_τ on the upper wall becomes a constant value relatively quickly when compared with that of the lower wall. Therefore, this result indicates that the fluid flow of the upper side achieves recover to an equilibrium state, more quickly than the lower side. In addition, the value of u_τ of the upper wall becomes negative (u_τ≒-0.04) just downstream of the slit at Q=0.467, so the a slight backflow is caused, and the flow separation suggested in the measurement of the wall static pressure coefficient is confirmed from the result of wall shear stress measurement.

3.2.4. Mean velocity profile

Figure 10 shows the mean velocity vector around the slit measured by PIV, Q=0.400 as an example of representation. The streamwise velocity U and wall-normal velocity V are normalized by U_{in}. Here, U_{in} is the bulk velocity at the inlet of the test section, and the slit area is located in the range of x=-10~0mm. The strong downward flow is observed around the slit. Downstream of the slit, the downward flow quickly becomes almost parallel to the wall, and further downstream than x=30mm, the wall-normal velocity is very small. The contours of U and V around the slit measured by PIV, Q=0.200 and 0.400 as an example, are shown in figure 11(a) ~ (d). For the streamwise velocity shown in Fig. 11(a) and (b), the region of the high velocity appears from the area of the channel center in the upstream to the slit. Although low velocity region is recognized near the lower wall just downstream of the slit, the flow accelerates again further downstream than that. At Q=0.400, the low velocity region exists on considerably large area of the upper side downstream of the slit, because the fluid is strongly drawn to the lower side by the suction. For the wall-normal velocity shown in Fig. 11(c) and (d), the isograms are distributed in the fan shape and almost symmetrically about the slit. Moreover, near x=20mm in the case of Q=0.400, the value of V/U_{in} already becomes less than 0.05. This result shows that the wall-normal velocity component generated by the suction is only large around the slit and rapidly decreases in the region far from the slit. Therefore, in order to observe the flow characteristics near-wall region in detail, a constant-temperature-type hot-wire anemometer with an I-type probe is used for the measurement of the velocity profiles and the turbulence intensity in downstream of x=40mm.

Figure 12 shows the streamwise mean velocity profiles measured at Q=0.400, and the solid line in the figure is the measurement result without suction (Q=0). Due to the mass flow rate decreasing with the suction, a large deceleration occurs in the channel. This deceleration is more remarkable in the upper side. The peak of the velocity appears near y/H=0.1 in the lower side. This peak continues to x=150mm. As the flow advances downstream, it decelerates gradually in response to the recovery of the velocity in the upper side. The result of the mean velocity U normalized by the bulk velocity U_m (in the downstream of the slit at each Q) is shown in figure 13. In the upper side, as Q increases, U/U_m near the slit decreases and the distribution

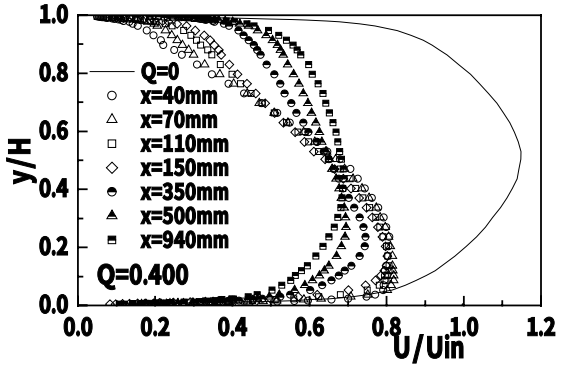

Figure 12. Velocity profiles (U/U_{in})

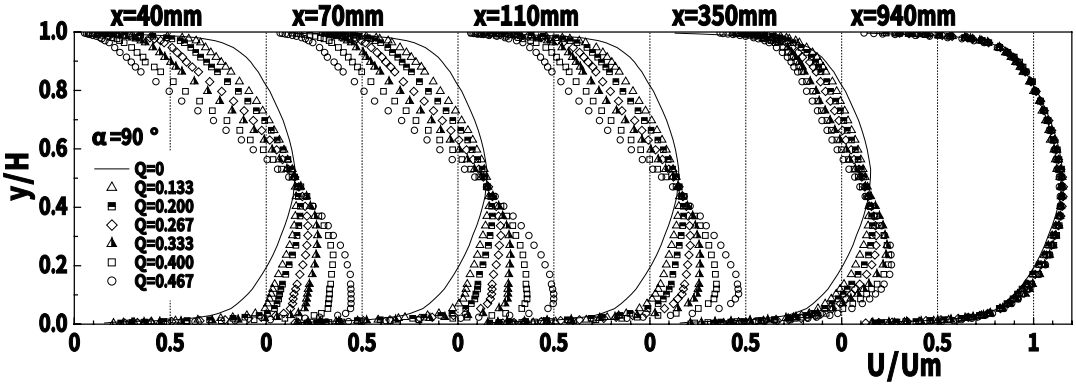

Figure 13. Velocity profiles (U/U_m)

becomes rectilinear. On the other hand, in the lower side, the velocity increases locally as Q increases and thus the peak appears near y/H=0.1. Moreover, the velocity gradient of the region in which the maximum value appears is very small. It is observed that the degree of asymmetry is more enhanced as the suction flow rate increases. As the flow advances toward downstream, though the velocity profiles returns to the symmetry profile, the recovery is slow in all Q. The influence of the suction remains slightly at x=940mm also, and there is asymmetry.

3.2.4. Turbulence intensity profile

Figure 14 shows the streamwise turbulence intensity u_{rms} measured at Q=0.400. u_{rms} is normalized by U_{in}. In response to the peak of the velocity near y/H=0.1 shown in Fig. 12, the value of u_{rms}/U_{in} becomes very small at the same location. Though the distribution recovers gradually with symmetry as the flow advances downstream, this minimum value which appears near y/H=0.1 barely changes to x=150mm as well as the result of the mean velocity distribution. For the region near the wall, the turbulence intensity near the slit decreases on the upper side, and the peak near the wall which is usually observed as a fully developed turbulent channel flow, disappears. On the other hand, on the lower side, the peak near the wall is remarkable and becomes the value of approximately 90% of the turbulence obtained at Q=0. The streamwise turbulence intensity normalized by U_m is shown in figure 15. Due to the suction, u_{rms}/U_m in the upper side increases markedly compared with Q=0. Moreover, as Q increases, the region in which the turbulence increases also enlarges. It is found that the ratio of the turbulence intensity to the bulk velocity increases by the suction. In addition, the change of this large turbulence is slow, and the increased turbulence remains at a comparatively large value to x=350mm. In the lower side at x=40mm, u_{rms}/U_m near y/H=0.1 in all cases of the suction is almost the same value. Moreover, the peak which appeared near the wall enlarges compared with Q=0. Figure16 shows the peak value, which is $u_{rms\ p}/U_m$, of the turbulence intensity near the wall on the lower and upper side at Q=0.200 and

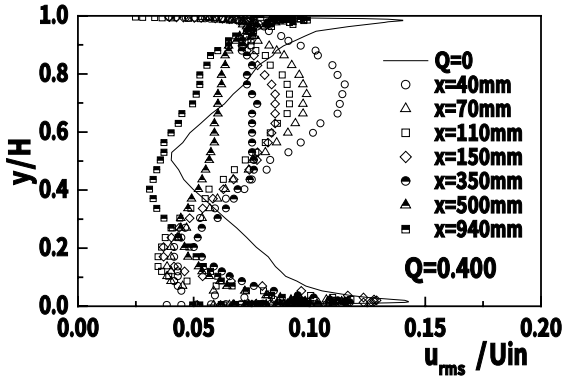

Figure 14. Turbulence intensity (u_{rms}/U_{in})

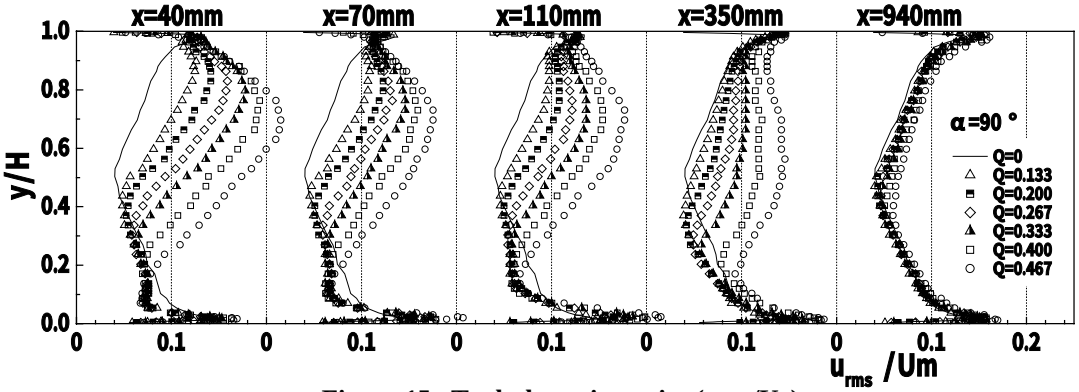

Figure 15. Turbulence intensity (u_{rms}/U_m)

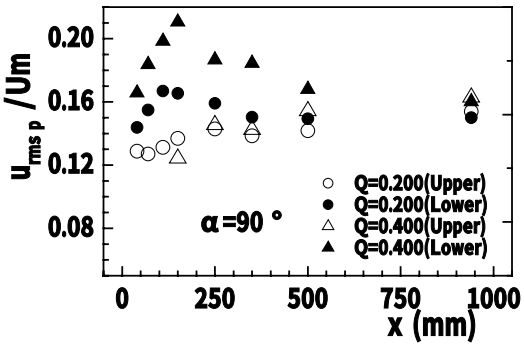

Figure 16. Peak values of turbulence intensity near the wall

0.400. The peak value of the lower side increases toward downstream at both Q. In particular, the value becomes very large at Q=0.400, $u_{rms\ p}/U_m$ over 0.2. The location of a large $u_{rms\ p}/U_m$ corresponds with the region in which the decrease of Nu weakens, as shown in figure 7. Therefore, it is confirmed that this local increase of the turbulence near the wall controls the decrease of the heat transfer coefficient in this region. Since $u_{rms\ p}/U_m$ shows constant increase in the upper side, it is considered that the recovery of the turbulence intensity in the lower side greatly differs from the upper side. Asai *et al.* [11] investigated a turbulent boundary layer with suction at a porous wall surface and reported as following: A low-speed streak and a longitudinal vortex, which exists near-wall region, disappears and then the peak value of the turbulence decreases also. However, after the flow has passed through a suction area, the turbulence near the wall rapidly begins to recover. The present result on the lower side is corresponds with the tendencies in the research by Asai *et al.*

4. CONCLUSIONS

The main results obtained in this study are summarized as follows:

(1) The effect of the difference of the suction angle on the wall static pressure distribution and the heat transfer coefficient is very small.

(2) The local Nusselt number of all the suction condition decreases as compared to conditions without suction. However, in the case of large suction ratio, a region appears in which a value barely changes toward streamwise direction. This region matches that of the turbulence intensity near the wall increasing and of the maximum value of the friction velocity.

(3) The wall-normal velocity component generated by the suction is large only around the slit and rapidly decreases in the region far from the slit.

(4) The deceleration becomes marked in the upper side of the channel with increasing suction ratio. Moreover, the peak of the velocity appears near y/H=0.1 in the lower side. This asymmetry of the distribution is enhanced with increasing suction ratio, and the recovery toward downstream is slow.

(5) The ratio of the turbulence intensity to the bulk velocity downstream of the slit increases with the suction. The recovery process of the turbulence in the lower side greatly differs from the upper side.

REFERENCES

[1] Antonia, R. A., Zhu, Y. and Sokolov, M., 1995, *Physics of Fluids*, Vol.7, pp. 2465-2474.

[2] Antonia, R. A. and Fulachier, L., 1989, *Journal of the Fluid Mechanics*, Vol.198, pp. 429-451.

[3] M., Sano and N., Hirayama, 1984, *Transactions of the Japan Society of Mechanical Engineers*, Series B, Vol.50, No.450, pp. 520-529.

[4] M., Sano and N., Hirayama, 1984, *Transactions of the Japan Society of Mechanical Engineers*, Series B, Vol.50, No.457, pp. 2041-2049.

[5] Oyewola, O., Djenidi, L. and Antonia, R. A., 2004, *Experiments in Fluids*, Vol.37, pp. 187-193.

[6] Komori, K. and Inagaki, T., 1990, *Kagaku Kogaku Ronbunshu(in Japanese)*, Vol.16, No.2, pp. 275-279.

[7] Sofialidis, D. and prinos, P., 1996, *Transaction of the ASME, Journal of Fluid Engineering*, Vol.118, pp. 33 - 39.

[8] The Japan Society of Mechanical Engineers ed., 1979, *JSME Date book : Hydraulic Losses in Pipe and Ducts*, pp. 86-95, The Japan Society of Mechanical Engineers.

[9] Nagata, N. et al., 1999, *3rd ASME/JSME Fluids Engineering Conference*, FEDSM 99-7356, pp. 1-8.

[10] Vogel, J. V. and Eaton, J. K., 1985, *Transaction of the ASME, Journal of Heat Transfer*, Vol.107, pp. 922-929.

[11] Asai, M., Hoshi, T. and Tabei, K., 2002, *Transactions of the Japan Society of Mechanical Engineers*, Series B, Vol.68, No.668, pp. 1016 -1021.

Conference on Modelling Fluid Flow (CMFF'06)
The 13th International Conference on Fluid Flow Technologies
Budapest, Hungary, September 6-9, 2006

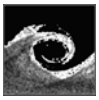

A NUMERICAL STUDY ON THE FREE-SURFACE CHANNEL FLOW OVER A BOTTOM OBSTACLE

Csaba HŐS[1], László KULLMANN[2]

[1] Corresponding Author. Department of Hydrodynamic Systems, Budapest University of Technology and Economics. Műegyetem rkp. 3, H-1111 Budapest, Hungary. Tel.: +36 1 463 2216, Fax: +36 1 463 3091, E-mail: csaba.hos@hds.bme.hu
[2] Department of Hydrodynamic Systems, Budapest University of Technology and Economics. E-mail: kullmann@hds.bme.hu

ABSTRACT

This paper presents the results of a numerical study on a two-dimensional free-surface channel flow over a bottom obstacle. Of main interest is the capability of commercial CFD codes to solve such problems. ANSYS CFX 10.0 was used with its built-in two-phase flow model. While keeping the upstream water level in the channel constant, the downstream water level was systematically decreased, which results in increasing flow rate, supercritical flow and weak hydraulic jump. The surface shapes of subcritical and supercritical CFD computations are compared to the results of the classic 1D theory. Two-dimensional features of the flow field are presented and the deviations from the classic 1D theory are explained.

Keywords: free-surface flow, hydraulic jump, CFD, undular hydraulic jump

NOMENCLATURE

B	$[m]$	width of the channel
C	$[m^{1/2}/s]$	Chézy constant
Fr	[-]	Froude number
Q	$[m^3/s]$	flow rate
R_h	$[m]$	hydraulic radius
g	$[m^2/s]$	gravitational acceleration
q	$[m^2/s]$	flow rate per unit width
v	$[m/s]$	mean velocity across the depth
h'	$[m]$	head loss
i	[-]	bottom inclination
y	$[m]$	water surface height
z	$[m]$	channel bottom height

Subscripts and Superscripts

1 upstream location of a hydraulic jump
2 downstream location of a hydraulic jump
u upstream location of the computational domain (inlet)
d downstream location of the computational domain (outlet)
wc location at the first wave crest of an undular hydraulic jump
wt location at the height trough between the first and second wave crest

1. INTRODUCTION

Free-surface flows and hydraulic jumps are important for environmental engineering (river flows, sediment distribution), ship engineering, water turbine engineering etc. The actual problem motivating this paper was the need for open-surface channel modelling for the steady-state calculation of an urban water supply network. Classic theory gives only limited description of the flow but cannot handle e.g. transcritical cases. Also, there are parameters (notably the friction coefficient), which are hard to estimate. Finally, two-dimensional (and three-dimensional) effects are interesting as understanding these issues might help to improve the simple 1D models.

Most models on free-surface flows are based on the shallow water equations [1,2], neglecting the deviation from the hydrostatic pressure distribution (vertical accelerations). These simple models are suitable only for subsonic flows, i.e. in the case of flow velocities below the wave propagation speed. More sophisticated models are needed for capturing transcritical flows or hydraulic jumps, which are analogous to the shock waves in gas dynamics. The hydraulic jump is a spectacular phenomenon, with a lot of turbulence, waves, unsteadiness and air entrainment, hence seems to be an appropriate test case for advanced numerical techniques of fluid mechanics.

The corresponding literature mainly concerns with measurements, see e.g. [3] or [4]. Less work was found on the application of Computational Fluid Dynamics (CFD) techniques on free-surface flows, see e.g. [5] or [6]. The aim of the present paper is to test the capabilities of a commercial CFD code (ANSYS CFX 10.0) in terms of free-

surface flows on a test case with subcritical and weakly supercritical flows.

This paper is organized as follows. First, the classic theory is briefly summarized. Then, the modelling equations in ANSYS CFX are given and the CFD set-up (grid, turbulence model, boundary conditions, etc.) is presented. The results are split into two groups; subcritical and supercritical cases. The results of subcritical cases are compared to the classic 1D theory. The supercritical cases are studied with the help of dimensionless pressure and velocity profiles highlighting the two-dimensional features of the flow.

2. THEORY

Consider the free-surface flow of an incompressible fluid in a prismatic channel of uniform width. In the case of steady-state behaviour, the losses in the flow (friction head loss) are compensated by the bottom slope. The flow is governed by the Bernoulli (energy) equation

$$\frac{d}{dx}\left(y + z + \frac{v^2}{2g} + h' \right) = 0, \qquad (1)$$

where y denotes the water height, z represents the bottom contour and h' is the head loss. The continuity equation can be written as

$$Q = Byv = const, \qquad (2)$$

with channel width B, water height y and average flow velocity v. Note that Eq. (1) assumes uniform velocity distribution (straight streamlines) and hydrostatic pressure distribution along the depth. For most open-channel flows, the friction factor is independent of the Reynolds number and is only a function of the wall roughness. Its actual value is usually calculated by means of the Chézy rule:

$$\frac{dh'}{dx} = \frac{v^2}{C^2 R_h}, \text{ where } C = \frac{R_h^{1/6}}{n}. \qquad (3)$$

Here R_h is the hydraulic diameter ($R_h=A/P$, i.e. wetted area over wetted perimeter) and n is a roughness coefficient having different values for different types of boundary roughness.

Our study neglects 3D effects, thus only a segment of the flow with width B is considered, without side walls. Thus, $A=By$, $P=B$, $R_h=y$ and $q=yv$ [m^2/s]. Inserting Eq. (2) and (3) into (1) we arrive at the ordinary differential equation for the water surface $y(x)$

$$\left(1 - \frac{q^2}{gy^3}\right)\frac{dy}{dx} = i - q^2 n^2 y^{-\frac{10}{3}}, \qquad (4)$$

where the new notation $i=-dz/dx$ was introduced. Note that if the term on the right-hand side vanishes, the water height will not change. This flow rate is called the normal flow rate and is given by

$$q_n = \frac{\sqrt{iy^{10/3}}}{n}. \qquad (5)$$

On the other hand, if the term on the left-hand side vanishes, the slope of the surface becomes infinite. Let us rewrite this term as

$$1 - \frac{q^2}{gy^3} = 1 - \left(\frac{v}{\sqrt{gy}}\right)^2 = 1 - Fr^2. \qquad (6)$$

The Froude number Fr is the ratio of the fluid velocity to the wave velocity and is analogous to the Mach number in gas dynamics. As $Fr \to 1$, $dy/dx \to \infty$, which is not possible. Indeed, with strongly curved water surface, the assumptions of straight streamlines and hydrostatic pressure variations are no longer valid. If $Fr < 1$, the flow is called subcritical while if $Fr > 1$, the flow is called supercritical.

The transition from subcritical to supercritical flow (or vice versa) cannot be computed by means of Eq. (4). Instead, let us apply the frictionless momentum equation:

$$\frac{v_1^2}{g} y_1 + \frac{y_1^2}{2} = \frac{v_2^2}{g} y_2 + \frac{y_2^2}{2}. \qquad (7)$$

By making use of the continuity equation and supposing hydrostatic pressure variation at sections 1 and 2, it is easy to show that

$$\frac{y_2}{y_1} = \frac{1}{2}\left(\sqrt{1 + 8Fr_1^2} - 1\right). \qquad (8)$$

Eq. (6) gives the connection between the upstream and downstream velocities and surfaces across a hydraulic jump.

3. CFD SETUP

The commercial computational fluid dynamics code ANSYS CFX 10.0 was used for steady-state numerical simulation. The set of equations solved by CFX 10.0 are the unsteady Reynolds-averaged Navier-Stokes equations in their conservation form. The volume conservation equation consists of two parts: the phasic continuity equation

$$\sum_{\alpha=1}^{N_\alpha} r_\alpha = 1, \qquad (9)$$

where r_α is the volume fraction of the αth component, and the continuity equation

$$\sum_{\alpha} \frac{1}{\rho_\alpha}\left(\frac{\partial \rho_\alpha}{\partial t} + \nabla \bullet \left(r_\alpha \rho_\alpha \overrightarrow{U_\alpha}\right)\right) = 0, \qquad (10)$$

where ρ_α is the density of phase α, and $\vec{U}_\alpha$ denotes its velocity. The momentum equation

$$\begin{aligned} &\frac{\partial}{\partial t}\left(r_\alpha \rho_\alpha \overrightarrow{U_\alpha}\right) + \nabla \bullet \left(r_\alpha \left(\rho_\alpha \overrightarrow{U_\alpha} \otimes \overrightarrow{U_\alpha}\right)\right) = \\ &= -r_\alpha \nabla p_\alpha + \nabla \bullet \left(r_\alpha \mu_\alpha \left(\nabla \overrightarrow{U_\alpha} + \left(\nabla \overrightarrow{U_\alpha}\right)^T\right)\right) \\ &+ \sum_{\beta=1}^{N_\alpha}\left(\Gamma^+_{\alpha\beta}\overrightarrow{U_\alpha} - \Gamma^+_{\beta\alpha}\overrightarrow{U_\alpha}\right) + \overrightarrow{S_{M\alpha}} + \overrightarrow{M_\alpha} \end{aligned} \qquad (11)$$

consists of the following terms. The left-hand side and the first two terms on the right-hand side are the standard terms in the Navier-Stokes equations. The third term represents the momentum transfer between phases α and β induced by interphase mass transfer. $\overrightarrow{S_{M\alpha}}$ describes the momentum source due to external body forces (and user-defined momentum sources) while $\overrightarrow{M_\alpha}$ represents the interfacial forces.

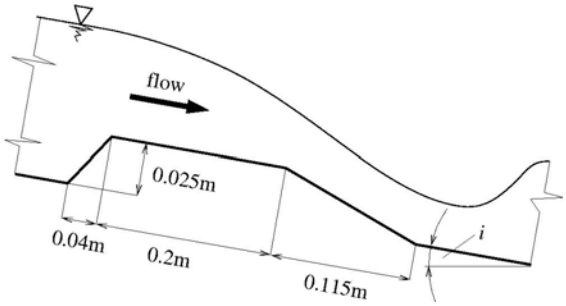

Figure 1. Geometry of the bottom obstacle.

The inclination of the bottom was set to $i = 3 \times 10^{-4}$, which was taken into account by defining the appropriate components of the gravity force g_x and g_y. The total length of the bottom obstacle was L=0.355m (see Fig.1.) and the computational domain stretched 3L length before and 10L after the obstacle. The height of the domain was 0.5m. Two-dimensional structured mesh was created, with a thickness of 0.01m in the z direction. Due to the simple geometry, the mesh quality easily meets the standard requirements (skewness, aspect ratio, etc.). The blow-up of the mesh close to the obstacle is shown in Fig.2, after mesh adaption. The total number of cells was approx. 25k.

Water level boundary conditions were set on the upstream and downstream side, which was prescribed through appropriate hydrostatic pressure profile. Rough wall with 1mm roughness was set for the channel bottom and opening boundary condition with uniform static pressure of 1bar was set for the upper boundary. High resolution spatial difference scheme was applied and relatively small, 0.01s physical time step was prescribed. Note that as the wave velocity was typically $a = \sqrt{gy} = 1.33\,{}^{m}/_{s}$ (y_u=0.18m) and the overall length of the computational domain was 4.97m, the characteristic time was 3.73s. Yet, numerical experiments showed that a maximal time step of 0.01s was needed for stable simulation. This small time step resulted in a large number of iterations, typically between 5000 and 10000. The convergence was judged by means of mass flow rate balance at the inlet and outlet because it was found that, the usual convergence criteria for the residuals (typically, 10^{-5}) does not guarantee a mass balance error smaller than 0.01%.

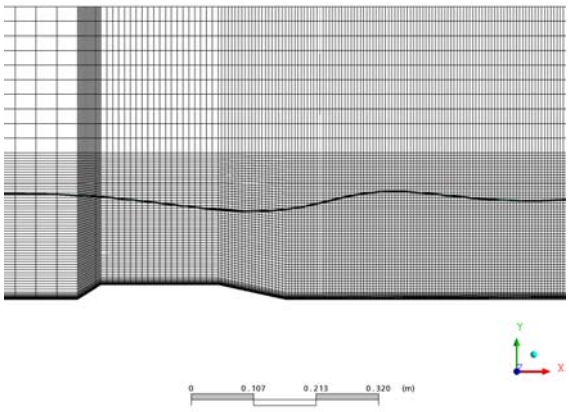

Figure 2. Computational mesh close to the obstacle and an example of fluid surface.

4. RESULTS

Table 1 gives a general overview of the simulations. The upstream water height was kept constant at y_u=0.18m while the downstream water height was decreased systematically, from y_d=0.18m to y_d=0.11m. The water surface is defined as an isosurface with 50% volume fraction of water. The water surface shapes are depicted in Fig. 3.

The very first simulation with the same upstream and downstream water level allows us to calculate the normal flow rate and thus to identify the wall roughness parameter n defined in Eq. (5),

which was found to be $n=0.0149$. As the downstream water level was decreased, the flow rate increased. Calculating the maximal Froude number along the channel shows that the subcritical/supercritical transition occurs at approx. y_d=0.16m. Indeed, this calculation was unstable and only approximate values of flow rate and Froude number were obtained. (By "unstable" a periodic oscillation with an amplitude of about 10% of the flow rate is meant. During the oscillation, the RMS value of the residuals was continuously below 10^{-5}.)

Table 1. Summary of the CFD runs.

h_d [m]	Qx10^3 [m^3/s]	Fr_{max} [-]	Comment
0.180	0.667	0.334	subcritical
0.175	1.104	0.630	subcritical
0.170	1.256	0.791	subcritical
0.160	~1.410	~0.958	unstable
0.155	1.402	1.076	undular jump
0.150	1.422	1.236	undular jump
0.145	1.429	1.415	undular jump
0.140	1.432	1.411	undular jump
0.130	1.463	1.402	supercritical
0.120	1.487	1.395	supercritical
0.110	1.529	1.349	supercritical

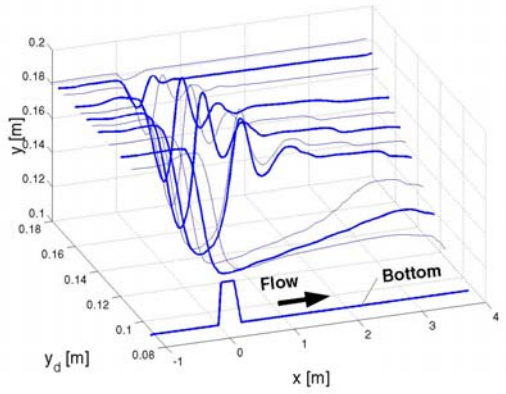

Figure 3. Fluid surface curves for several downstream water heights (see Table 1 for the actual values).

Further decreasing the downstream water height below 0.16m, the flow became supercritical. As it is known from the literature [3], for small Froude numbers of 1<Fr<1.7, undular jumps are formed. Such hydraulic jumps were indeed observed in the simulations but in our case their presence could not be predicted merely by the Froude number. In the last three simulations, the Froude number was between 1.4 and 1.35 yet no undular jumps were observed. Although the authors do not have an ultimate answer for this phenomenon, there are several possible explanations. First, the 1.7 limit was determined for channels with constant bottom slope, without an obstacle. Second, the computational domain might not be large enough in the downstream dimensions for the last three cases. This issue needs further study and the analysis of these results is not addressed in this paper. Yet, for the sake of completeness, the main parameters of these runs and the corresponding surface shapes are given.

4.1. Subcritical flow, comparison with theory

In the case of subcritical flow (first three simulations in Table 1), the CFD results are compared to the surface predicted by the 1D model. The ordinary differential equation Eq. (4) together with the upstream and downstream water heights defines a boundary value problem with two boundary conditions and one free parameter, the flow rate. The problem was solved with Matlab's boundary value solver "bvp4c". The roughness parameter n was kept constant (0.0149) during the calculations. The 1D model predicts the subcritical/supercritical transition to y_d~0.172m, thus the solution obtained with y_d=0.173m was plotted vs. the CFD result with 0.17m. Note that the boundary value problem was solved on the same domain as the CFD calculations (total length of 14 times the obstacle length) but for better visibility, only the region close to the obstacle is presented in Figure 4.

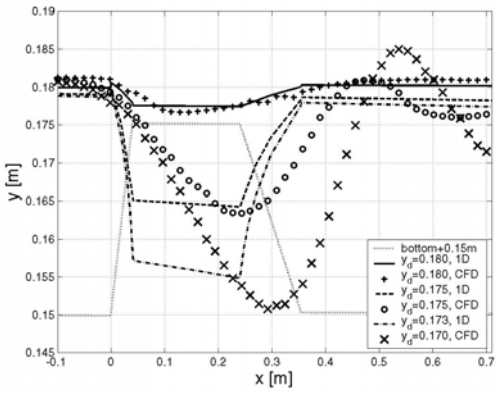

Figure 4. Subcritical computations, comparison of 1D model and CFD results. Note that for better visibility, the bottom obstacle was shifted with 0.15*m* in the *y* direction.

As the flow rate increases (y_d decreases), an increasing difference between the 1D model and the CFD results is observed. The reason for this increasing deviation is the increasing curvature of the streamlines and the loss of validity of the 1D assumptions (uniform flow profile, hydrostatic pressure distribution). Thus we conclude that although Eq. (4) remains physically meaningful up to Fr=1, it provides acceptable results only for a

much narrower range of the Froude number, i.e. for flows with slightly curved surface.

4.2. Supercritical flow, undular jump

For slightly supercritical flows (1<Fr<1.7), it is known that undular jump is formed, as sketched in Figure 5.

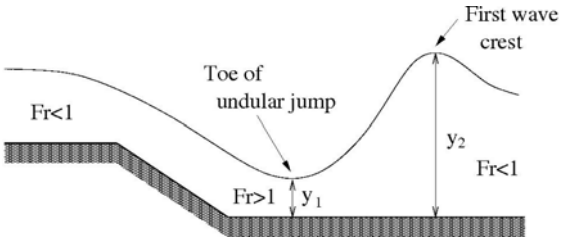

Figure 5. Undular hydraulic jump.

The most important parameters are the Froude number and the water height at the toe of the jump and at the first wave crest. According to the classic 1D theory, these values are connected through Eq. (8). Table 2 presents the comparison between the CFD results and Eq. (8).

Table 2. Undular jump parameters.

y_d [m]	y_1 [m]	Fr_1 [-]	Fr_2 [-]	y_2 [m] CFD	y_2 [m] Eq.(8)
0.155	0.1192	1.179	0.617	0.184	0.147
0.150	0.1091	1.310	0.631	0.184	0.154
0.145	0.1010	1.460	0.678	0.173	0.164
0.140	0.0970	1.457	0.684	0.173	0.164

As it can be seen in Table 2, the water heights at the first wave crest predicted by theory and given by the CFD computations differ significantly. The reason of this discrepancy is that (again) the two basic assumptions of the theory are not valid. First, the velocity distribution is not uniform across the depth and the pressure distribution is not hydrostatic. There are corrections to the classic theory that take into account these issues, see e.g. [3]. However, the analysis of these improvements is not in the scope of this study.

Next, the pressure distributions are studied. Figures 6 and 7 depict the dimensionless pressure distributions across the depth at the toe of the jump and at the crest. The reference pressure was set to $p_{ref} = \rho g y_j$ (j=1,2) i.e. the hydrostatic pressure according to the water height. There is a significant deviation at the toe of the jump in the case of y_d=0.155m and y_d=0.15m. The reason is probably that the location of the toe (x coordinate) changes and for larger y_d values, it is located close to the end of the obstacle and the slope change of the bottom influences the flow. On the other hand, the dimensionless pressure profiles beneath the first wave crest agree well but differ from the hydrostatic profile with a factor up to 15%, due to the acceleration of the fluid discussed later.

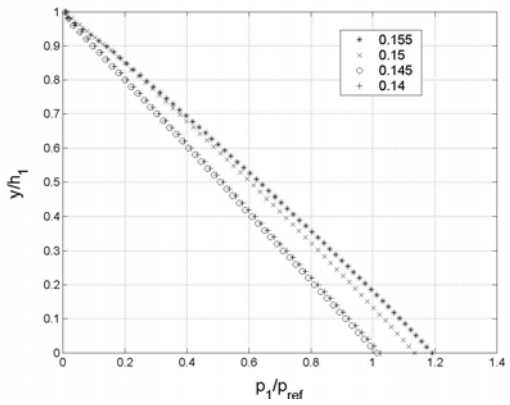

Figure 6. Dimensionless pressure distribution vs. dimensionless depth at the toe of the undular jump.

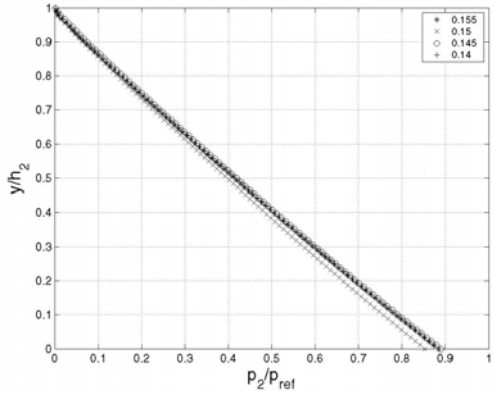

Figure 7. Dimensionless pressure distribution vs. dimensionless depth at the crest of the first wave.

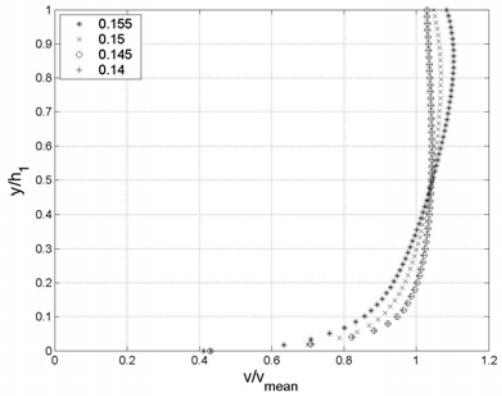

Figure 8. Dimensionless velocity distribution vs. dimensionless depth at the toe of the hydraulic jump.

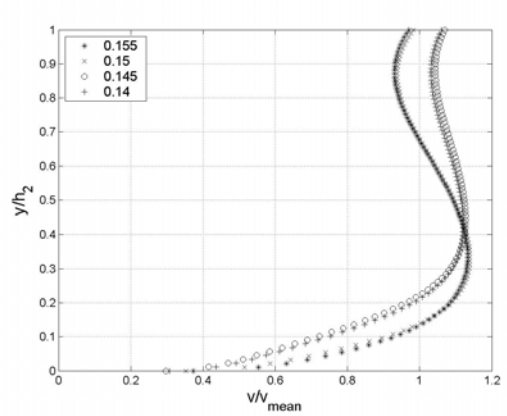

Figure 9. Dimensionless velocity distribution vs. dimensionless depth at the crest of the first wave.

Figures 8 and 9 depict the dimensionless velocity distribution at the toe of the jump and at the first wave crest. The absolute value of the velocity vector was used and the mean velocity was computed from the flow rate and the water depth. At the toe of the jump - apart from the simulation with y_d=0.155*m* - the other three profiles agree well. The velocity distributions beneath the first wave crest differ significantly. Moreover, the acceleration close to the water level (y/h_2 ~1) seems to be unexpected as at the free surface level, the shear stress vanishes and thus the profile should have zero gradient at the surface.

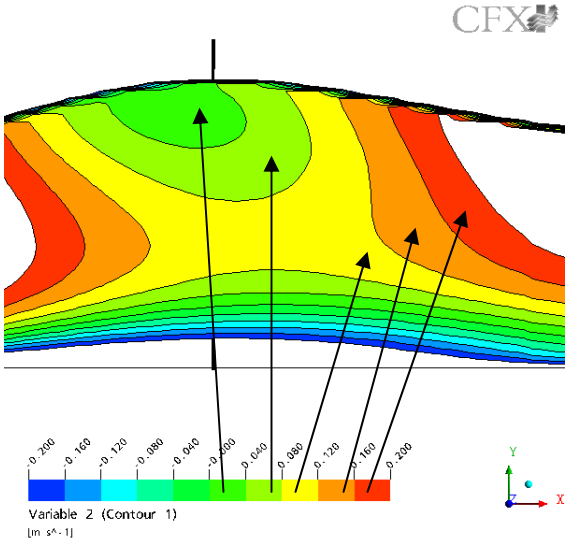

Figure 10. Contour plot of the velocity deviation from the mean value around the first wave crest.

Figure 10 depicts the deviation from the mean velocity around the first wave crest. To be specific, the mean velocity was defined at cross section beneath the highest point of the wave crest (y_2), v_{mean}=q/y_2 and this value was subtracted from the *x* component of the velocity vector. As it can be seen, there is an asymmetric low-velocity regime close to the top of the wave. Its presence can be explained energetically; if the potential energy of the fluid increases, kinetic energy should decrease. The asymmetric feature of the low-velocity region probably originates from the fact that the flow itself before and after the wave is also asymmetric. However, this issue is not fully understood yet and needs further study.

4.3. Comparison with experiments

The experiments of Ohtsu et al. [8] are used as reference for validating the above computations. The authors in [8] give the following conditions for the classification of undular jumps (UJ).

$$1.0 < F_1 < F_{1\mathrm{lim}it} \quad \text{breaking UJ and}$$
$$F_{1\mathrm{limit}} < F_1 < F_{1u} \quad \text{nonbreaking UJ,}$$

where

$$F_{1\mathrm{limit}} = 1.78 - 0.03\left(10 - \frac{B}{y_1}\right)^{1.35}, \qquad (12)$$

$$F_{1u} = 2.1 - 0.03\left(12 - \frac{B}{y_1}\right)^{1.35}, \qquad (13)$$

with $2 \le B/y_1 \le 10$ and $2 \le B/y_1 \le 12$ for (12) and (13), respectively. Here *B* is the channel width. As 2D simulations were only performed in this study, we use the largest value of the B/y_1 values, giving F_{1limit}=1.78 and F_{1u}=2.1. Indeed, the largest Froude number in the simulation was 1.457 where undular jumps were observed in the computations.

Let y_{wc} denote the height of the first wave crest and y_{wt} stand for the height trough between the first and second wave crest. Than, according to [8], we have

$$\frac{y_{wc}}{y_1} = -0.76\left(F_1 - 1\right)^2 + 2.3\left(F_1 - 1\right) + 1 \qquad (14)$$

and

$$\frac{y_{wt}}{y_1} = 0.90\left(F_1 - 1\right)^{2.5} + 2.0\left(F_1 - 1\right) + 1 \qquad (15)$$

The comparison between the results of the above formulae and the CFD runs are summarized in Table 3.

Table 3. Undular jump details.

$y_d\,[m]$	0.1550	0.150	0.145	0.140
$y_1\,[m]$	0.1192	1.1091	0.1010	0.0970
$Fr_1\,[-]$	1.1790	1.310	1.460	1.457
$y_{wc}/y_1\,[-]$ eq. (14)	1.3873	1.6400	1.8972	1.8924
$y_{wt}/y_1\,[-]$ eq. (15)	1.0480	1.1102	1.2212	1.2185
$y_{wc}\,[m]$ eq. (14)	0.1654	0.1789	0.1916	0.1836
$y_{wt}\,[m]$ eq. (15)	0.1249	0.1211	0.1233	0.1182
$y_{wc}\,[m]$ CFD	0.1888	0.1875	0.1798	0.1785
$y_{wt}\,[m]$ CFD	0.1525	0.1485	0.1433	0.1430

The most striking discrepancy between the experimentally found formulae (14) and (15) and the CFD runs is that y_{wc} increases with increasing Froude number while decreases in the numerical computations. Also, the value of y_{wt} is highly overpredicted in the CFD runs. The most trivial reason can be that CFD runs were not fully converged. However, it is not trivial to judge whether during the iterations, the water surface is still varying or not as typically, even if the residuals are continuously below 1e-4, integral quantities such as flow rate or force may vary significantly. Another reason can be that the analytical formulae were extracted from 3D experiments and it is not clear in what extent do 3D effects influence the surface shape in the middle of the channel.

4. SUMMARY

It was shown that commercial CFD codes offer the possibility of analyzing free-surface flows without differentiating between or separately modelling subcritical, transcritical and supercritical cases. The price is the computation time; typically, one steady-state run for the presented problem would require 10-15 hours of computation on a 2.4GHz PC with ~1GB RAM. On the other hand, valuable information can be gained on the two-dimensional features of the flow. For example, it was found that the main limitation of 1D models is that the velocity distribution is not uniform and the pressure distribution is not hydrostatic even in the case of moderate Froude numbers (~0.5). Limited accordance was found between 2D numerical simulations and experimental data.

REFERENCES

[1] Fox, R.W. and McDonald, A.T., 1994, *Introduction to Fluid Mechanics*, John Wiley & Sons, ISBN: 0-471-59274-9

[2] Halász, G., Kristóf, G., Kullmann, L. 2002, *Flow in Pipe Systems*, Műegyetem Kiadó, ISBN: 963-420-708-1 (in Hungarian)

[3] Svendsen, IB.A., Veeramony, J., Bakunin, J. and Kirby, J.T., 2000, "The flow in weak turbulent hydraulic jumps", *Journal of Fluid Mechanics,* Vol. 418, pp.25-57.

[4] Chanoson, H., „Boundary shear stress measurements in undular flows: Application to standing wave bed forms", 2000, *Water Resources Research,* Vol.36, No. 10, pp.3063-3076

[5] Metcalf, B., Longo, J., Ghosh, S. and Stern, F. 2006 „Unsteady free-surface wave-induced boundary-layer separation for surface-piercing NACA-0024 foil: Towing tank experiments" *Journal of Fluids and Structures,* Vol.22, pp.77-98.

[6] Rhee, S.H., Stern, F., 2002 „RANS model for spilling breaking waves", *Journal of Fluids Engineering,* Vol.124, pp.424-432.

[7] ANSYS CFX 10 User's Manual, 2005

[8] Ohtsu, I., Yasuda, Y., Gotoh, H. 2003 „Flow conditions of undular hydraulic jumps in horizontal rectangular channels" , *Journal of Hydraulic Engineering,* Vol.129, pp.948-955.

Conference on Modelling Fluid Flow (CMFF'06)
The 13th International Conference on Fluid Flow Technologies
Budapest, Hungary, September 6-9, 2006

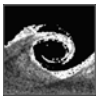

CONTROL OF A CHANNEL-FLOW BEHIND A BACKWARD-FACING STEP BY SUCTION / BLOWING

Václav URUBA[1], Pavel JONÁŠ, Oton MAZUR

Department of Fluid Dynamics, Institute of Thermomechanics, Academy of Sciences of the Czech Republic, Dolejškova 5, 182 00 Praha 8, Czech Republic.
[1] Corresponding Author. Tel.: +420 / 286 588 547, Fax: +420 / 286 584 695, E-mail: uruba@it.cas.cz

ABSTRACT

Results of the experimental investigation on control of narrow channel flow behind a backward-facing step by blowing / suction near the step foot are presented. The slots differ in both the orifice shape (rectangle or serrated) and area ($50-375\cdot10^{-6}$ m^2) of its cross-section. The intensity of flow control is characterized by the suction / blowing flow coefficient (mass flow through the slot over mass flow above the step, suction: negative values) that varies from -0.035 up to 0.035 at Reynolds number 5.10^4 (defined on the basis of the hydraulic diameter and volume velocity). Preliminary results indicate that both blowing and suction are able to reduce the length of the separation zone down to one third of its value without control. Control effectiveness is given by absolute value of the flow coefficient. The other parameters (slot area and shape) is important only for blowing, in this case small cross-section with serrated edge is the most effective. The existing three-dimensional vortex structures near the step (resulting from interaction of boundary layers near the step-edge) are influenced by suction more then by blowing. The experiments are still in progress.

Keywords: channel flow, backward-facing step, reattachment control, blowing, suction.

NOMENCLATURE

a	$[m]$	effective slot gap
d_h	$[m]$	hydraulic diameter
ei	$[V]$	voltage difference
f	$[Hz]$	frequency
h	$[m]$	step height
p	$[Pa]$	pressure
p_0	$[Pa]$	static pressure
w	$[m]$	channel width
x_d	$[m]$	position of maximum pressure derivative
x_e	$[m]$	position of maximum pressure
x_r	$[m]$	reattachment position
C_p	[-]	static pressure coefficient
C_Q	[-]	suction / blowing flow coefficient
F	$[m^2]$	cross section
H	$[m]$	channel height
P_c	$[m]$	contact perimeter
Re	[-]	Reynolds number
T	$[s]$	total observation period
T_f	$[s]$	additive time of forward flow
U_e	$[m/s]$	mean velocity in the inlet
γ_p	[-]	forward-flow-fraction coefficient
ρ	$[kg/m^3]$	fluid (air) density

Subscripts

e	at the inlet of the test section
s	at the suction / blowing slot

1. INTRODUCTION

Active flow control concepts have become an increasingly attractive topic in fluid mechanics in the last few years. Separated flows result in negative effects such as drag increase, lift reduction and noise generation. The most common objective in the control of separated flows is the control of the size of the separation region. Thus the reattachment length x_r can be defined as a control variable, the control goal is in reducing this parameter.

Prandtl already in 1904 showed the modern way of flow control. In his famous paper he described several experiments in which the boundary layer was controlled. Prandtl used suction to delay boundary-layer separation from the surface of a cylinder.

The backward-facing step flow has been established as a benchmark configuration for separated flow studies in fluid mechanics first. The presented paper deals with possibilities of three-dimensional backward-facing step flow control at high Reynolds numbers (*Re* order of 5.10^4 based on

hydraulic diameter d_h of the inlet channel and the bulk velocity U_e just upstream the step edge). A backward-facing step configuration of a channel occurs in many engineering applications ranging from various fluidic elements, cooling of turbine blades, air-conditioning pipelines to many other devices.

Flow separation on the step edge is a source of pressure loss, vibrations, and noise and affects heat transfer (reattachment region corresponds to maximum heat transfer however low heat transfer appears in separation region). Many papers have been published on this subject up to now as a result of its practical importance as well as relevance to basic research of complex shear flows, see e.g. Biswas et al [1], Lee et al. [2] and Sakuraba et al. [3].

The presented paper summarizes a recent stage of the work on the above mentioned subject in the Institute of Thermomechanics AS CR, some older achievements on this subject could be found in e.g. [4, 5].

The channel arrangement could be characterized by dimensions of the channel with rectangular cross section, width w and height H upstream the step and step height h.

It has been shown, that the flow-field is well symmetrical with the plane of symmetry (identical with geometric). However, a three-dimensional vortex system could be observed in the flow behind the step. The mechanism of the vortices formation has not been fully explained yet, nonetheless their existence was confirmed also by mathematical modelling, e.g. Příhoda and Sedlář [6]. Initially, a couple of nearly stable contra-rotating corner vortices in input channel near sidewalls are passing towards the plane of symmetry, they are pushed downwards in the same time. Finally, they form a kidney-shaped common footprint on the bottom wall behind the step (see wall visualisation Figure 3).

The aim of the presented investigation is to prove conclusions of the preliminary study of Jaňour and Jonáš [7] on control strategy using more sophisticated experiments and examining the blowing / suction slot shape effect on the flow control effectiveness.

2. EXPERIMENTAL APPARATUS

The existing blow-down test rig was modified for experiments with the separated flow in a channel with a backward-facing step. The tunnel has rectangular cross-section with filled corners (to suppress corner vortices), honeycomb and a system of damping screens followed by contraction with contraction ratio 16.5. The area of the test section input is 0.25 m in height and 0.1 m in width. The time mean velocity departures from homogeneity in planes perpendicular to the tunnel axis are of order tenth of percent with the exception of corners, where corner vortex starters could be detected. The natural turbulence level is about 0.1 % in the working section input. The channel with the backward-facing step is 1.4 m in length, the ratio of the step height h to the input channel height H is 0.1 ($H = 0.25\ m$, $h = 0.025\ m$). A detailed description of the experimental arrangement could be found in [8]. The interchangeable step face allows varying slot for suction / blowing in the step foot. This allows modelling different area and / or shape of the slot cross section. The layout is schematically shown in Figure 1.

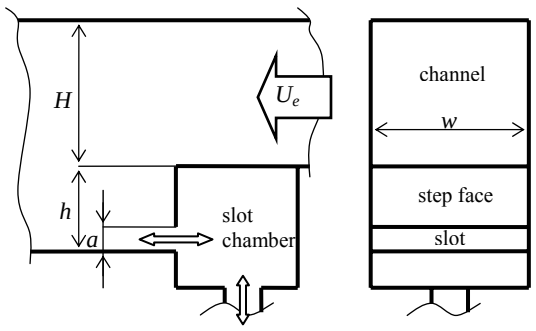

Figure 1. Experimental setup

Various slots with rectangular and serrated cross section shape were tested. The sketches of slots with fundamental dimensions and definitions are shown in Figure 2, a is the effective width of the slot.

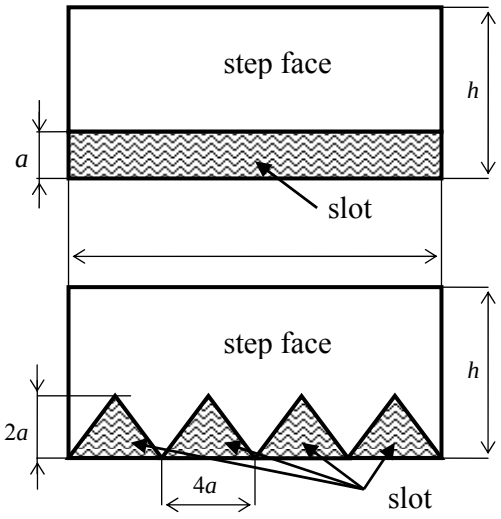

Figure 2. Slots

The reason for various shapes of the slot is to study influence of the slot perimeter which forms the jet-like flow from the slot with different contact area with the controlled flow behind the step, if blowing from the slot is applied.

List of examined slots is given in Table 1 including some important characteristics: F_s is slot cross-section, d_s is slot hydraulic diameter and P_c is contact perimeter.

Table 1. Slots parameters

No.	type	a $[10^{-3}m]$	F_s $[10^{-6}m^2]$	d_s $[10^{-3}m]$	P_c $[10^{-3}m]$
1	rect.	0.95	95	1.88	100.0
2	rect.	2.25	225	4.40	100.0
3	rect.	3.75	375	7.23	100.0
4	serr.	1.00	50	0.83	141.4
5	serr.	2.00	100	1.66	141.4
6	serr.	4.00	200	3.31	141.4

The special exhauster / air pump serves for suction / blowing through the slot. It is connected with a metering nozzle and via a tube (inner diameter = 24.5 *mm*) with the slot chamber.

3. EXPERIMENTAL METHODS

The investigated flow-field is of very complex three-dimensional and non-stationary nature. Unfortunately, the study was limited by the methods available.

Short description of measurement techniques used in the presented study is to be given. Description covers used instrumentation, measuring and evaluation methods.

3.1. Reference quantities

The main flow parameters were measured by means of a Pitot-static tube (Prandtl type, dia 4 *mm*) and a RTD thermometer Pt100 inserted upstream the step. The bulk velocity U_e upstream the step was calculated from measured data. The mass flow through the slot was calculated from pressure differences measured on the metering nozzle (output section: dia = 13.7 *mm*, the contraction ratio is about 20) and temperature measured upstream from the inlet of metering nozzle. The velocity in the slot output was calculated with the respect to the static pressure value in the chamber upstream the slot.

The following differential pressure transducers were used at the mentioned measurements: two OMEGA PX653-05D5V 5, range 1,25 *kPa*, error < ±0.2 % FS (OMEGA Technologies Ltd., England) and BHV 5355, range 10 *kPa*, error < ±0.1 % FS and range 100 *kPa*, error < ±0.1 % FS (BHV Sensors, Czech Republic). The pressure transducers were calibrated using the Betz type micromanometer (AVA Göttingen, Germany, range 4 *kPa*, direct reading 0.1 *mm* H_2O).

3.2. Wall pressure

Static pressure distribution on the bottom wall downstream from the step was measured with 0.4 *mm* diameter orifices (near the bottom wall centreline, spacing 0.01 *m*) successively connected to the sixteen-channel pressure transducer (Intelligent Pressure Scanner model 9010, Pressure Systems Int., range 2.5 *kPa*, accuracy ±0.1 % FS).

The pressure distribution was originally analysed according to Chandrasuda and Bradshaw [9]. The length of the separated region x_r is evaluated from the position x_e of the maximum value of the pressure coefficient

$$C_P(x) = \frac{P(x) - P_0}{0.5\rho U_0^2}, \quad \max C_P = C_P(x_e). \tag{1}$$

Later on Příhoda [10] found out (from the wall friction measurement) that the maximum C_P appears farther downstream from the reattachment x_r and proposed the empirical formula derived from measurements of numerous authors

$$\frac{x_r}{h} \cong \frac{x_e}{h} - 0.238 \exp\left(0.25 \frac{x_e}{h}\right). \tag{2}$$

Jaňour and Jonáš [7] and Jonáš et al. [4] noticed that the time mean position of reattachment lies between the locations x_e and x_d indicating positions of $\max C_P$ and $\max dC_P/dx$. In the paper [5] a different empirical formula for the evaluation was derived

$$\frac{x_r}{h} \cong 0.49\left(\frac{x_d}{h} + \frac{x_e}{h}\right)(1 \pm 0.04), \qquad \max C_P = C_P(x_e), \quad \max \frac{dC_p}{dx} = \left[\frac{dC_p}{dx}\right]_{x=x_d}. \tag{3}$$

The accuracy of presented formulae is comparable and quite satisfactory. More details see the paper [5].

3.3. Wall visualisations

The spreading over method is an old one (see e.g. [11], [12]), but this technique still gives a lot of information about the organisation of a complex flow near the wall. For this work a coating of magnesia (MgO) particles in a suspension in kerosene (70 *g/l*) is chosen. The coating is spread on the wall before starting the blower. When the fluid impinges the wall, the coating spreads over the surface showing the directions of the flow. After the coating has dried the wall is photographed and analysed.

The method works well for the suction control, for the blowing case there is a wall-jet along the wall behind the step with no back-flow near the wall. So the method fails to indicate the reattachment region is this case.

An example of the wall visualisation result is shown in Figure 3 for the case without control, flow is coming from the right-hand side to the left. The forward- and back-flow regions as well as the reattachment could be easily identified.

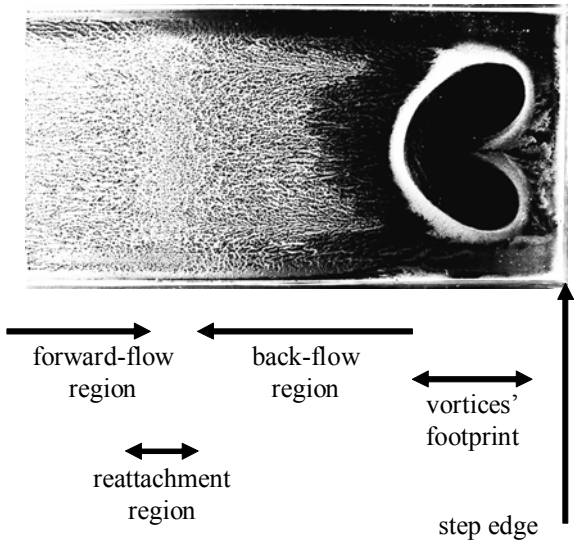

Figure 3. Wall visualisation

The reattachment positions evaluated from the wall pressure distribution have been checked by visualisations.

3.4. Back-flow indication

The third approach to detection of the flow reattachment is based on measurement of the flow direction by means of a thermo-anemometer using a split-film probe. In a preliminary study of recirculation flow in separation region Uruba et al. [13] applied a two-sensor split-film probe, which could detect direction of the velocity vector in plane perpendicular to the sensors' axis. The probe (DANTEC t. 55R58; both sensors heated to 200°*C*, DANTEC StreamLine anemometer) was moving downstream from the step in the *x* direction with the sensor's axis perpendicular to the channel axis and parallel to the surface in the distance approximately 1 *mm* – see Figure 4.

The probe calibration has been performed in a channel just on the exit of the contraction, air-flow velocity has been varied from -33 to 33 *m/s*, the sensor was located outside the boundary layer. To suppress influence of different voltage output levels the still air values were subtracted. The voltage differences with respect to still-air case were used for following analysis.

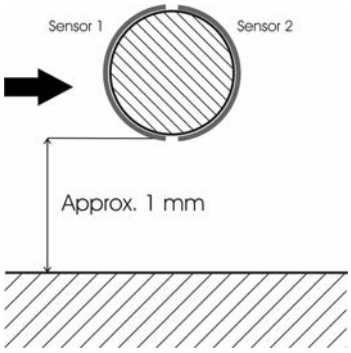

Figure 4. The probe sensors

In Figure 5 the voltage differences *ei* (*i* = 1, 2) acquired from the split-film probe respective sensors are shown. From the graph it is clear that the windward sensor gives always higher output voltage difference then the downwind one.

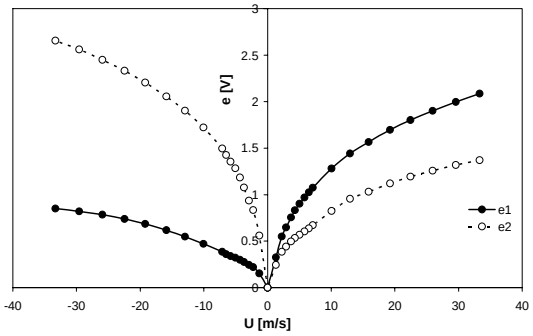

Figure 5. Output voltage differences of the sensors

The dynamical process of intermittent nature could be characterized by distribution of the local forward-flow-fraction coefficient γ_p, which is defined as follows:

$$\gamma_p = T_f / T , \tag{4}$$

where T_f is an additive time of forward flow and T is total time of observation.

The forward-flow-fraction coefficient distribution $\gamma_p(x)$ was calculated from the anemometer output voltages ($\gamma_p = 0$ corresponds to the backward-flow – direction oriented to the step root; while $\gamma_p = 1$ corresponds to the same local flow direction as the outer stream). The "reattachment point" position x_r is defined as the point where the probabilities of the occurrence of the backward- and forward-flows are equal, that is $\gamma_p(x_r) = 0.5$. In the reattachment region, the γ_p lays in open interval $(0,1)$.

The 20 *s* records of voltage signals were acquired in 7 *kHz* acquisition frequency has been analyzed point-by-point.

4. RESULTS

The intensity of blowing / suction is characterized by the flow coefficient C_Q defined as the ratio of mass-flux through the slot over the amount of the incoming air-flow through the area of the step-head

$$C_Q = \frac{\rho_s U_s F_s}{\rho_e U_e F_e}, \qquad (5)$$
$$F_s = w \cdot a, \quad F_e = w \cdot H.$$

The coefficient is positive for blowing from the slot and negative for suction.

A systematic study of the wall pressure distributions has been carried out. An example of the blowing / suction effect on pressure coefficient (defined by (1)) is shown in Figure 6 and 7 for the configuration with a canonical slot No.2 (rectangular cross section). The typical shape with pressure drop just behind the step followed by steep pressure increase could be seen in both graphs. The pressure drop is more pronounced for suction, as expected, however even for blowing significant negative values were obtained. The pressure maxima are rather flat.

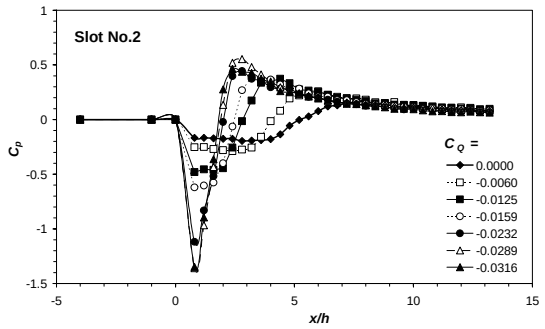

Figure 6. Pressure distribution for suction

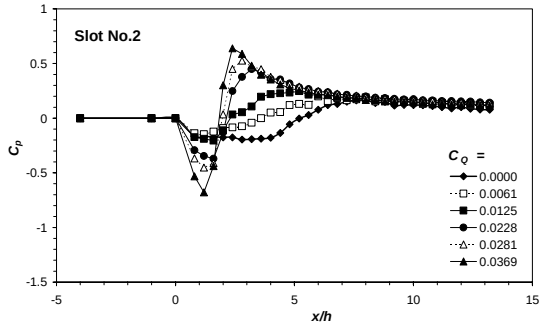

Figure 7. Pressure distribution for blowing

The pressure distributions were examined for all defined combinations of slots and flow coefficients. The separated region length x_r has been evaluated using the formula (2), which is considered to give reliable results. The formula (3) has been tested as well, but no important difference in results was detected.

The effect of blowing / suction in reducing the separated zone length is shown in Figure 8.

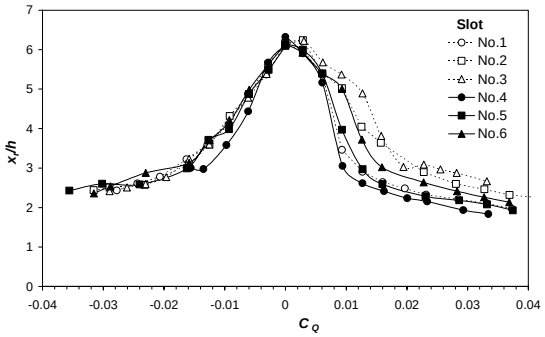

Figure 8. Reattachment length from pressure distribution

From Figure 8 it is clear that both suction (negative C_Q) and blowing (positive C_Q) is effective in shortening the recirculation zone. While suction effectiveness is relatively insensitive to the slot profile, that of blowing strongly depends on the slot geometrical parameters. Reduction of the recirculation zone length is more effective for smaller slot cross-section keeping the same C_Q value. Shape of the slot orifice is not very important, serrated shape gives slightly shorter recirculation zone then rectangular one for the same blowing rate and orifice cross-section. The most effective is the slot No.4 producing the fastest jet flow for a given flow rate, while the longest recirculation zone produces slot No.3 with the biggest cross-section.

Unfortunately, reattachment is highly non-stationary dynamical process, so we could rather speak about "zone of reattachment" instead of "line" or "point of reattachment". Detailed study of dynamical behaviour of the reattachment process has been carried out for suction control. The back-flow indication method described in section 3.4. has been applied. In Figure 9 distributions of forward-flow-fraction coefficient for the slot No.1 and various suction coefficients are shown. A typical S-shape of the curves is apparent.

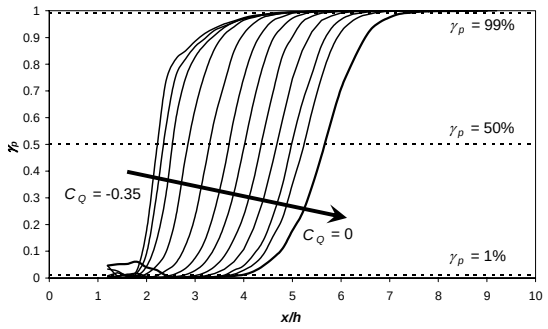

Figure 9. Back-flow-fraction coefficient for suction control

Position of the conventional "reattachment point" x_r could be defined by the γ_p value equal to 50 % (0.5), the reattachment zone could be delimited by γ_p values 1 % (0.01) and 99 % (0.99). For low absolute values of blowing coefficient the γ_p distributions are nearly symmetrical with conventional reattachment point nearly in the middle of the reattachment region. For greater negative values the characteristics is steeper with more pronounced upper curved part resulting in non-symmetrical configuration – see Figure 9. The positions of crossing points indicating the reattachment region and conventional reattachment point are shown in Figure 10.

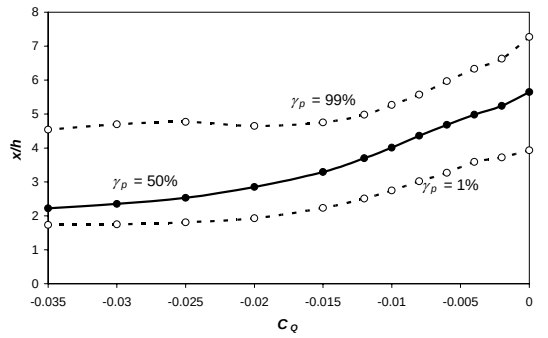

Figure 10. Reattachment region and point for suction control

The process dynamics should be examined in time and/or frequency domain. Frequency characteristics of the reattachment process were studied by means of the time periods length analysis of staying the flow direction unchanged in a given point of space. Typical distribution of the mean length of forward- and backward-flow time intervals within the reattachment region in semi-logarithmic coordinate system for $C_Q = 0$ is shown in Figure 11.

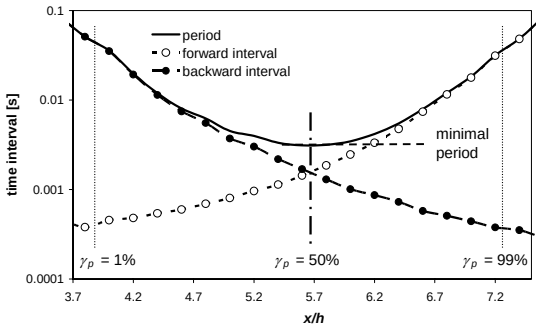

Figure 11. Time intervals without control

The mean length of forward and backward time intervals could characterize the mean period of changes of flow direction, which is given by sum of the two intervals. The minimal period corresponds to γ_p equal to 0.5 and indicates typical frequency of reattachment point fluctuation f. In Figure 12 this frequency is shown against the suction coefficient.

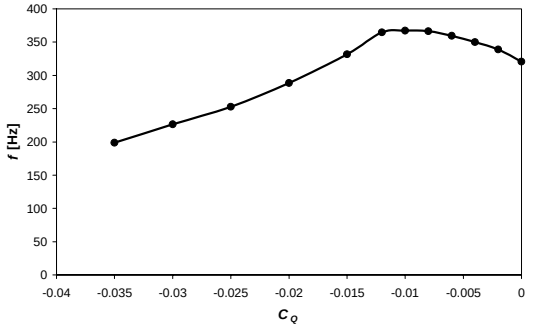

Figure 12. Mean frequency of reattachment point fluctuations

The reattachment point fluctuation is nearly constant for low suction rates up to $C_Q = -0.012$, when the corresponding frequency is about 350 *Hz*. For more intensive suction the frequency f falls linearly with C_Q absolute value, for $C_Q = -0.035$ its value reaches 200 *Hz*.

The reattachment point fluctuations seem to be damped by suction. This conclusion is supported by steeper back-flow-fraction coefficient characteristics (see Figure 9) showing smaller amplitude of typical fluctuations.

Of course, the mean recirculation zone length could be evaluated on the basis of reattachment point dynamical measurements as well. The results for rectangular No.1 and serrated No.5 slots evaluated from pressure distribution measurements and dynamical moving hot-film probe data are compared in Figure 13.

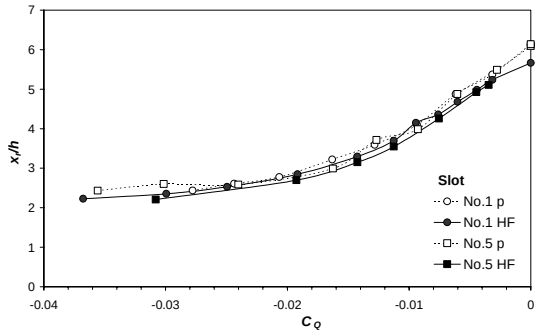

Figure 13. Comparison of pressure (p) and hot-film (HF) measurements

Very good agreement of both methods is evident. However the hot-film probe method gives more precise results, this is indicated by nicely smooth curves. Further, this is a direct method of the flow direction indication, no additional assumptions are needed, unlike the method based on pressure distribution.

Unfortunately, for the blowing control the method could not be applied, so only indirect pressure distribution evaluation method of the recirculation region length is available.

5. CONCLUSIONS

The suggested control method based on suction or blowing in the step foot seems to be effective in shortening the recirculation zone length. Shortening of the separation zone was evaluated using direct measurement only for suction, blowing relies on indirect evaluation method using wall pressure distribution.

The suction control mechanism is based on removing of low-velocity fluid from the recirculation zone. The slot works as a sink, only its capacity is important and not the orifice geometrical parameters, nor the suction velocity.

Blowing control, unlike suction, is influenced by the slot geometry. Higher velocity (that is smaller slot area) gives more intensive static pressure drop, which promotes the control mechanism. Also entrainment process in the wall-jet boundary plays an important role in the control process. This hypothesis is supported by effect of interface area on control effectiveness. (Compare results in blow-control for rectangular and serrated slot orifice).

However energetic considerations of the flow-control process are to be done to estimate its energetic effectiveness. The continuous suction / blowing is rather demanding from energetic point of view, pulsating flow seems to be good alternative for future experiments. Hot candidate is synthetic jet actuator, review of this type of actuators used for flow control could be found e.g. in Uruba [14] study.

In the future we intend using the time resolved PIV method for studying the non-stationary structures within the recirculation region. This seems to be necessary for checking the blowing control case results.

ACKNOWLEDGEMENTS

This work has been supported by the Grant Agency AS CR, project No. A2076403 and the Grand Agency of the Czech Republic, project No. 101/03/0018.

REFERENCES

[1] Biswas, G., Breuer, M., Durst, F., 2004, “Backward-facing Step flows for various expansion rations at low and moderate Reynolds numbers”, Transactions of the ASME, J. Fluids Engineering, Vol. 126, pp.362-374.

[2] Lee, I., Ahn, S.K., Sung, H.J., 2004, “Three-dimensional coherent structure in a separated and reattaching flow over a backward-facing step”, Experiments in Fluids, Springer-Verlag, 15 p.

[3] [3] Sakuraba, K., Fukazawa, K., Sano, M., 2004, “Control of turbulent channel flow over a backward-facing step by suction or injection”, Heat Transfer – Asian Research, 33 (8), pp.490-504.

[4] Jonáš, P., Mazur, O., Uruba, V., 2005, “The effect of the backward facing step height on flow in a channel with rectangular cross section”, PAMM Vol.5, Issue1, pp.549-550.

[5] Jonáš, P., Mazur, O., Uruba, V., 2006, “Comment on the analysis of measurements downstream a step expansion in a channel with rectangular cross section”, accepted for the conference: Topical Problem of Fluid Mechanics 2006, IT AS CR, Prague.

[6] Příhoda, J., Sedlář, M., 2006, “Flow separation and relaxation of the shear layer behind a backward facing step”, accepted for the conference: Aplikácia experimentálnych a numerických metód v mechanike tekutín, April 2006, Žilina – Strečno, Slovakia.

[7] Jaňour, Z., Jonáš, P., 2004, “Some methods of the control of the separation region behind a backward-facing step”, PAMM Vol.4, Issue1, pp.438-439.

[8] Jonáš, P., Mazur, O., Uruba, V., 2004, “Experimental apparatus for flow separation modelling at a step expansion of a channel”, (in Czech). In: Vodohospodářská konference 2004, Práce a studie Ústavu vodních staveb FAST VUT v Brně. Brno, Akademické nakladatelství CERM, s.r.o., 2004, pp.205-212.

[9] Chandrasuda, C., Bradshaw, P., 1981, "Turbulence structure of a reattaching mixing layer", J.Fluid Mech., 110, 1981, pp.171-194.

[10] Příhoda, J., 1991, "Effect of the outer stream turbulence on two dimensional backward facing flow" (in Czech). Strojnický časopis 42, 4, 1991, pp.289-304.

[11] Rosenhead, L., 1963 "Laminar boundary layers", Clarendon Press, Oxford.

[12] Jaňour, Z. sen., 1972, "Boundary layer on a wing in highly turbulent flow" (in Czech). Aeronautical Research and Test Institute, Prague – Letňany, Rep. No. V-1151/72.

[13] Uruba, V., Mazur, O., Jonáš, P., 2005, "Study on reversing flow in reattachment region", In: Proceedings Colloquium Fluid Dynamics 2005. (Ed.: Jonáš, P., Uruba, V.), Prague, IT AS CR, pp.171-174.

[14] Uruba, V., 2005, "Flow control using synthetic jet actuators". Engineering Mechanics, vol. 12, No. 1, pp.41-62.

Conference on Modelling Fluid Flow (CMFF'06)
The 13th International Conference on Fluid Flow Technologies
Budapest, Hungary, September 6-9, 2006

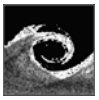

FLOW IN SIMPLIFIED AND REAL MODELS OF INTRACRANIAL ANEURYSMS

Ádám UGRON[2], Ferenc NASZTANOVICS[3], István SZIKORA[4], Imre BOJTÁR[5], György PAÁL[1]

[1] Corresponding author, Department of Hydrodynamic Systems, Budapest University of Technology and Economics, P.O. Box 91, 1521 Budapest, HUNGARY, Tel.: +36 1 463 2991, Fax: +36 1 463 3091, E-mail: paal@vizgep.bme.hu
[2] Student, Department of Hydrodynamic Systems, Budapest University of Technology and Economics, E-mail:ua488@hszk.bme.hu
[3] Student, Department of Structural Mechanics, Budapest University of Technology and Economics, E-mail: naszta@naszta.hu
[4] National Institute of Neurosurgery, Hungary, E-mail: h13424szi@ella.hu
[5] Department of Structural Mechanics, Budapest University of Technology and Economics, E-mail: ibojtar@mail.bme.hu

ABSTRACT

Intracranial aneurysms are bulges growing out of the brain artery walls. When these bulges burst it is called a subarachnoid hemorrhage, (a special type of stroke), leading to death or paralysis. Factors influencing the risk of rupture for a particular aneurysm are quite unclear. In a joint research effort with medical doctors and solid mechanics experts the fluid mechanical conditions leading to growth and damage of aneurysms are investigated. To this end numerical flow simulations are performed using a commercial software assuming unsteady, laminar flow, rigid walls and newtonian fluid. As a first step, simplified models of aneurysms are generated, typical flow patterns are identified and their dependence on various geometrical parameters studied. Interesting qualitative differences can be observed in the flow patterns when the neck length is varied. Next, real artery models including aneurysms obtained from rotational angiography are transformed, meshed and the flow within them is simulated. With the help of the wall pressure and shear stress data obtained from the flow simulations one-way coupled elasticity simulations are performed using complex wall elasticity material models. The blood flow and wall deformation simulation in and around aneurysms prove to be a useful diagnostic tool for medical doctors in identifying wall regions with unusual stress distribution.

Keywords: Aneurysm, hemodynamics, blood flow

NOMENCLATURE

a	[*mm*]	diameter of the pipe
b	[*mm*]	neck width
d	[*mm*]	distance between cavity centre and centre line of the pipe

1. INTRODUCTION

1.1. Background

Intracranial aneurysms are defined as thin walled bulges of the arterial walls located on the basal surface of the brain. These lesions are found in approximately 5% of the population [1]. Rupture of such aneurysms is the most frequent reason of subarachnoid hemorrhage, a special type of stroke, that affects 0,1-0,15% of the population each year and results in death or permanent disability in 35-40% of its victims [2]. The ethiology of intracranial aneurysms is not yet fully understood. Most aneurysms are thought to develop due to a combination of structural and hemodynamic factors. Similarly, little is known about the reasons of aneurysm rupture. Comparing the frequency of aneurysms (5%) with the yearly rate of subarachnoid hemorrhage (0,1-0,15%/year) it becomes evident, that less than 1/3 of all aneurysms will ever rupture. Considering that preventive treatment of these lesions requires high risk surgical intervention, it would be mandatory that only those lesions are treated that have a high likelihood of rupture and bleeding.

1.2. Purpose

Hemodynamic stress at certain points of the arterial tree might be an important factor in both triggering aneurysm growth and leading to rupture of an existing aneurysm. Medical imaging techniques, such as digital subtraction angiography (DSA), computer tomographic angiography (CTA), or magnetic resonance angiography (MRA) are now

capable of providing accurate three-dimensional information on intracranial vessel geometry. Current knowledge on the risk of bleeding from a known aneurysm (and subsequent decision on invasive treatment) is derived exclusively from such morphological information. As these techniques are not yet capable of delineating flow conditions within the visualized vascular segments, hemodynamic factors are not considered in the therapeutic decision making process.

The purpose of this study is to develop a technique that is able to simulate arterial flow in an around intracranial aneurysms in order to study the effect of local hemodynamics on aneurysm growth and risk of aneurysm rupture. This information may lead to better indication of high risk surgical procedures.

There have been several research efforts to investigate the problem using numerical simulations. There are basically two approaches: using artificial models which are supposed to include the important geometrical and flow characteristics of the aneurysm [3, 4, 5] and working on real models derived from medical imaging techniques [6, 7]. Both approaches will be followed here.

2. NUMERICAL METHOD

2.1. The softwares

The ANSYS ICEM CFD was applied to generate the geometries of the artificial models and their computational meshes. The setup of the physical problem, the solution and the presentation and post-processing of the results was performed by various modules of ANSYS CFX 5.7.1. The meshes of the real artery geometries were created with a self-written code.

2.2. Geometries and meshes

Initially several simplified two-dimensional (2D) and three-dimensional (3D) geometries were made to study basic flow phenomena. Afterwards real artery geometries were exported from rotational angiography images.

2.2.1. Artificial geometries

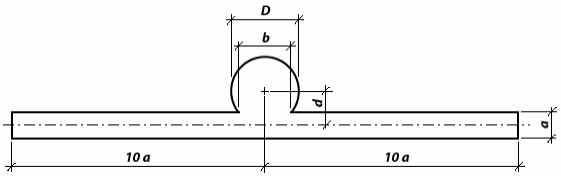

Figure 1. The geometry of a simplified aneurysm containing the two main parts, the bulge and the pipe

The simplified geometries were made, based on a traditional medical view of the aneurysm shape (Figure 1.).

Four two dimensional (2D) geometries were made with varying neck widths (b). The 2D geometry was a thin slice bordered by two planar surfaces. In the third direction the thickness was one computational cell. Also four three dimensional (3D) geometries were created for studying the influence of the neck width on the flow pattern. In a next step, based on careful observation of the real geometries, several further geometrical elements were built in the models. Partly the zero neck length, visible in Fig. 1., was extended to yield a finite length and partly various types of bend were added before the aneurysm (Fig. 2.).

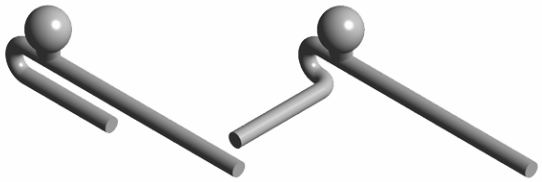

Figure 2. Three-dimensional simplified geometries containing pipe bends

The numerical meshes were topologically always identical: a block-structured hexagonal mesh was used in the pipe and in the aneurysm bulge (Figure 3.). This had an advantage over the unstructured mesh of a better computational accuracy, especially near the wall, in spite of the more cumbersome preparation of the mesh.

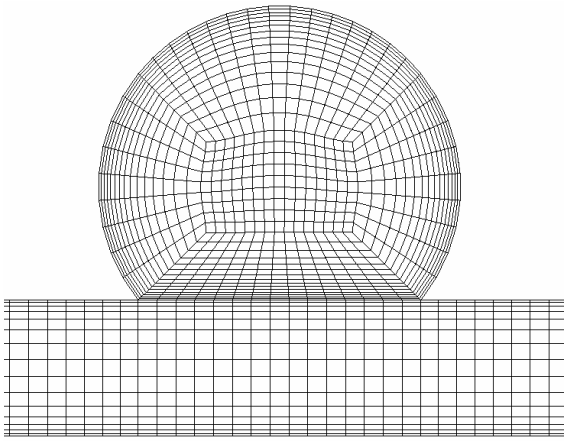

Figure 3. Mesh topology used for the simplified geometries

2.2.2. Real geometries

The geometries of the real aneurysms were obtained from rotational angiography (Fig. 4.). A contrast material is introduced in the blood and the

angiography detects the presence or absence of contrast material by labelling voxels (volumetric pixels) in an appropriate way.

The artery geometry is thus obtained in a relatively coarse cubic structure. A custom-made software smoothes this structure and fits a tetrahedral unstructured mesh onto it (Fig. 5.). The only disadvantage of using an unstructured mesh is the worse treatment of the near-wall region, but the error made is relatively insignificant compared with the gains in flexibility.

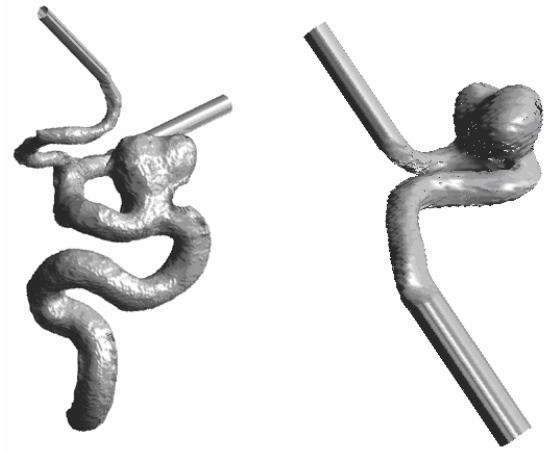

Figure 4. Models of real arteries containing aneurysms

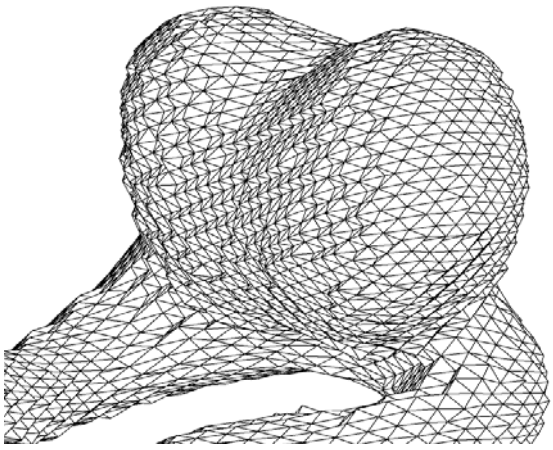

Figure 5. Surface mesh of an artery with aneurysm

2.3. The applied settings

2.3.1. The fluid and the flow

The applied fluid was assumed to be newtonian, incompressible, with a density of 1050 kg/m^3, and a viscosity of 0.003 kg/ms. The flow was laminar, steady or unsteady.

2.3.2. Boundary conditions

The walls of the geometries were assumed to be rigid and no-slip. In a later stage of the research coupled wall deformation-fluid flow simulations are planned but in this paper, due to the short length of the studied artery section neglecting the wall elasticity does not seem to have a significant effect. In the 2D simulations symmetry boundary conditions were applied on the two planar faces. Both steady and unsteady cases were studied. In the stationary simulations a static inlet velocity with a parabolic profile, and a constant static pressure outlet were prescribed. In the unsteady simulations a time- dependent inlet velocity function was given (also with parabolic distribution in space). This is a synthetic function reproducing a typical shape of the cardiac cycle. The outlet boundary condition remained constant pressure modelling the fact that on the capillary level the pressure is really nearly constant (peripheral resistance). In principle the resistance of the whole arterial system between the studied arteries and the capillary level ought to be modelled, however, this resistance is only an additive constant in the pressure level which has no importance in an incompressible flow.

Both the spatial and temporal discretisation was second order. The residual level for convergence was 10^{-5}.

2.4. Preliminary studies

Before moving to the main simulations several preliminary studies were made to decide certain further parameters. These include a mesh convergence study and the effect of the unstructured mesh.

2.4.1. Selecting the meshes

In both 2D and 3D a good quality base mesh was made. In 2D the number of elements was around 8600, in 3D approximately 30500. Four further meshes with increasing density were created in both cases. Stationary simulations were made with all of the meshes and relative errors between some representative results in subsequent meshes were compared. Fig. 6. shows the relative error field in velocity between results of the simulations made with the doubled and tripled meshes in 2D.

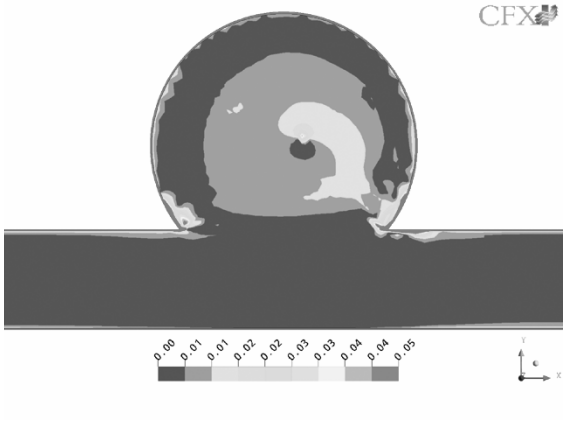

Figure 6. The relative error between velocities obtained from the simulations made with the doubled and tripled meshes

It can be seen in Figure 6. that the error remains everywhere under 5% which is considered acceptable. With this method the finally used 2D mesh had 30500 elements and the 3D mesh 652000 elements.

2.4.2. Effects of the unstructured mesh

The numerical meshes of the real geometries were unstructured and without prismatic layers near the walls. A study was carried out to check to what extent such a mesh distorts the results compared to the more accurate block-structured mesh. On the basis of a stationary simulation in a 3D geometry it was found that the results agreed well in most of the aneurysm with the exception of the near wall region where the error remained under 15%.

3. RESULTS

3.1. Parameter studies in 2D

The goal was to see how the variation of the neck width influences the flow in the aneurysm. Four 2D models were made with different neck widths, the parameter *d*, the distance between the aneurysm centre and the centreline of the pipe was set to 3, 4, 4.45, 5 mm, respectively, making the neck width to change along. The dominant movement in the cavity was a rotation (Fig. 7.).

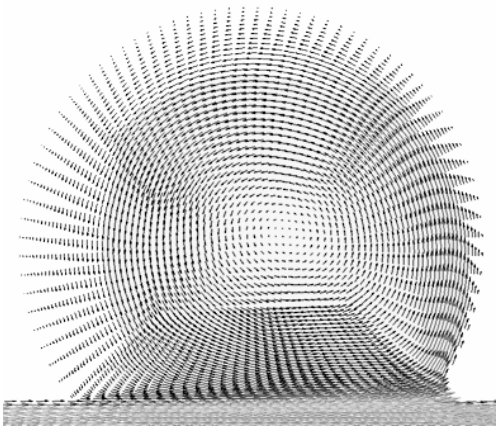

Figure 7. Vector diagram of the vortex in the 2D aneurysm

It can be observed that the dominant inflow takes place at the downstream end of the aneurysm and the velocity is also highest here. To characterise the rotational motion quantitatively in the cavity, the surface integral and the average of the z component of the curl vector was chosen (Eq. (1)).

$$curl(v)_z = \frac{\partial v_y}{\partial x} - \frac{\partial v_x}{\partial y} \qquad (1)$$

Fig. 8. shows the relationship between the neck width and the averaged rotation.

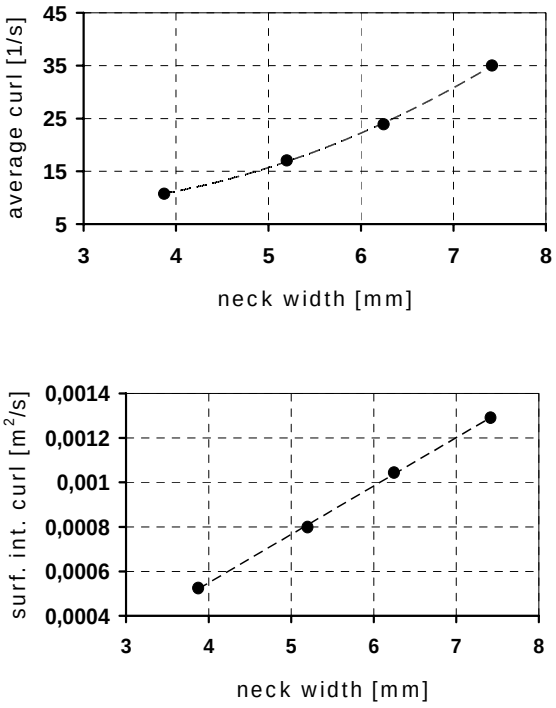

Figure 8. Dependence of the surface average (above) and surface integral (below) of the curl in the aneurysm on the neck width in 2D

3.2. Unsteady simulations in 2D

Three cardiac cycles were simulated lasting altogether 2.4 seconds. In the first cycle the flow developed from standstill. In the last two periods the flow was considered to be developed and the flow parameters were studied during this time.

In the velocity distribution there was no qualitative change in comparison to the steady simulations, only the magnitude of the velocity changed in time according to the input boundary condition.

The highest value of the wall shear appeared in each case on the pipe wall near the downstream end of the cavity. This is because the highest values of the velocities can be found here in the aneurysm so the highest velocity gradient can evolve here. The maximum shear shows a linear relationship with the neck width.

3.3. Parameter studies in 3D (steady flow)

In the central plane the appearance of the velocity distribution was similar to that in 2D.

In the case of 3D models the rotational movement was characterized with the volume average, and volume integral of the z component of the curl vector (perpendicular to the symmetry plane) (Fig. 9). Here the independent variable was the neck surface.

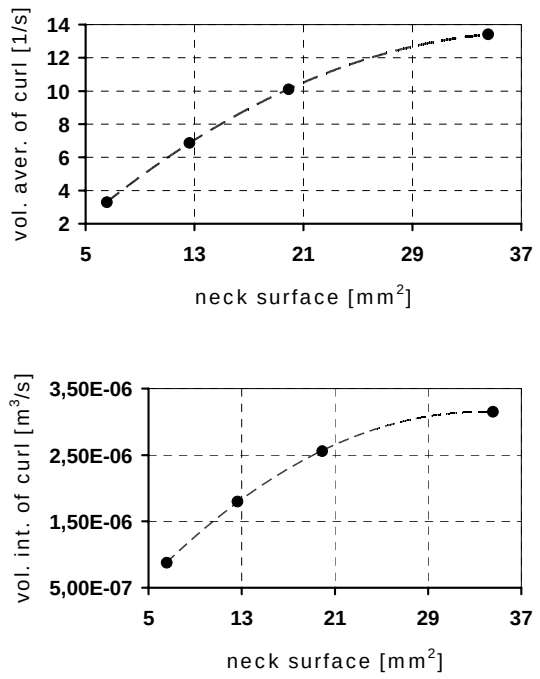

Figure 9. Dependence of the volumetric average (above) and volumetric integral (below) of the curl in the aneurysm on the neck surface size in 3D

The linear relationship is replaced with a parabolic dependence, but the rising trend remained.

3.4. Unsteady simulations in 3D

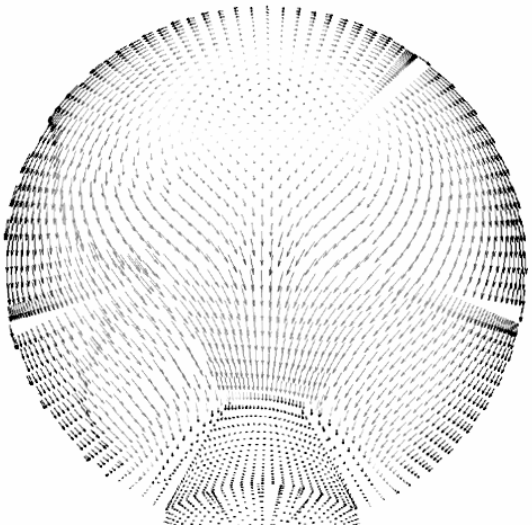

Figure 10. Symmetrical velocity distribution in the plane perpendicular to the main flow direction in the 3D simulations

The time-dependent inlet boundary condition was also applied to the 3D geometries. Again the flow pattern of the 3D flow in the symmetry plane was quantitatively the same as in 2D. Observing the flow in the third dimension it turns out that the flow is symmetrical (Fig.10.).

The maximum of the wall shear appeared again at the downstream end of the bulge on the wall of the pipe (Fig. 11.). At the medium neck surface size the maximum shear was 11.1 Pa. The dependence of the maximum wall shear on the neck surface size was linear.

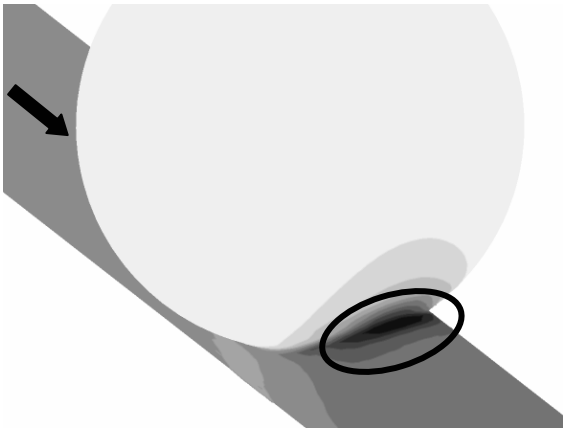

Figure 11. Shear stress distribution near the aneurysm (the maximum is indicated with the ellipse)

3.5. Effect of bends before the cavity

Two further artificial models were created. Secondary flow and centrifugal force appeared in both geometries, with the consequence that the velocity of the inflow into the aneurysm increased compared with the symmetrical geometry. In addition, the separated regions reduce the effective cross-section of the pipe thereby further raising the local velocity (Fig.12).

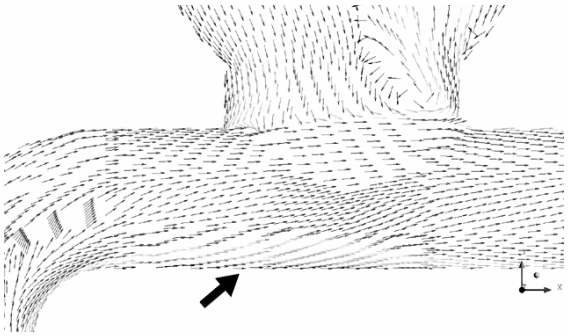

Figure 12. Accelerating fluid regions near the aneurysm due to the bend

The velocity of the inflow was lower in the geometry with two bends than in the previous case because of the increased losses.

The effect of the accelerated fluid regions appeared in the values of the wall shear. While in the straight pipe case the maximum wall shear was between 10 and 12 Pa in the case of bends the maximum wall shear rises to 30-35 Pa depending on the number of bends. The location of the maximum remains the same.

These simulations demonstrate that the details of the geometry before and after the aneurysm are highly important both regarding the maximum shear stress and the details of the flow. Fig. 13 shows the changed velocity pattern in the symmetry plane of the one-bend geometry.

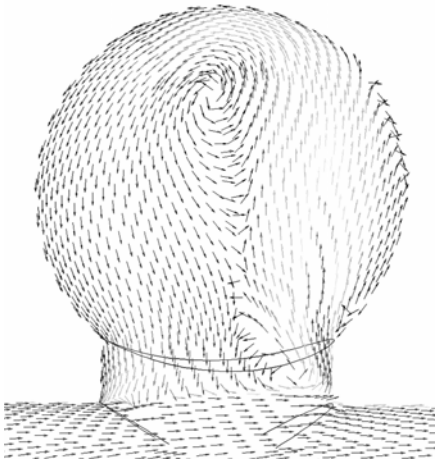

Figure 13. Changed velocity pattern inside the aneurysm because of the bend

It can be seen that the presence of the neck makes the velocity pattern qualitatively change: instead of one vortex centre there are two and in addition there is a back flow on the right hand side near the wall. Adding the bends leaves the pattern qualitatively unchanged; only the magnitude of the velocity and the position of the vortices change. The same applies to the relative length of the neck.

3.6. Simulations with real geometries

Three geometries were chosen for the purposes of this study one of which is presented here due to the lack of space. The location of these arteries in the brain is about the same. The double bends appear in all tree geometries. Despite of the similarity in the location and some similarity in the topologies many individual features can be detected in the geometries. The complicated geometries lead to complex flows in them.

3.6.1. First real geometry

The flow in the first geometry (left hand side in Fig. 4.) is shaped by the two bends before the aneurysm and the cavity itself sitting on the second bend. The secondary flow appears right after the first bend and the second bend modifies this to a rotational movement filling the whole cross-section of the pipe (Fig. 14.).

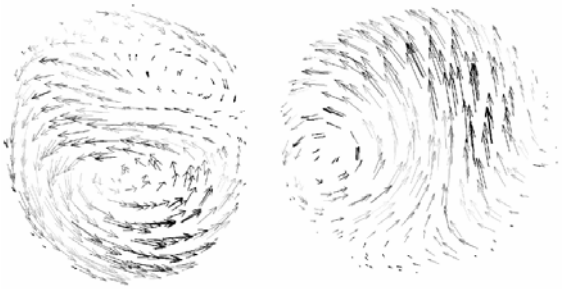

Figure 14. Secondary flow in the pipe after the first bend (left) and the rotational movement superposed on the main flow after the second bend (right) in the first real geometry

The complex flow in the geometry can be well studied with the help of streamlines.

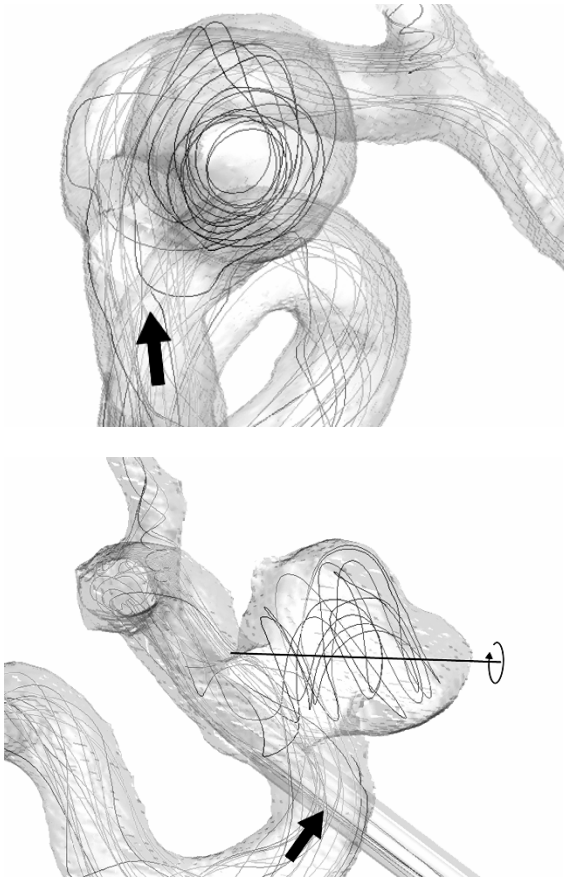

Figure 15. Visualized streamlines in one timestep of the flow in the first real geometry

On the top of Fig. 15. the rotating movement can be observed and the axis of the rotation can be marked easily (Fig. 15. lower part). It is also noticeable that the fluid flows directly into the aneurysm, totally contrary to the generally accepted and expected picture which was also obtained in the artificial geometries (for example Fig. 7.). This leads to much higher velocities in the aneurysm than in the artificial geometries. By visualizing the velocity vectors in a plane perpendicular to the supposed axis of the circulation, the rotational movement can be well detected (Fig. 16.).

It has to be noted, however, that the streamline diagrams have to be treated with care. In an unsteady flow an instantaneous picture of the streamline is not necessarily representative; a fluid particle probably moves on a completely different path. In a later publication this question will be analyzed further.

The wall shear was not thoroughly studied because of the questionable reliability of the results near the wall. The distribution of the wall shear represented the velocity field well, the values were around 10-20 Pa.

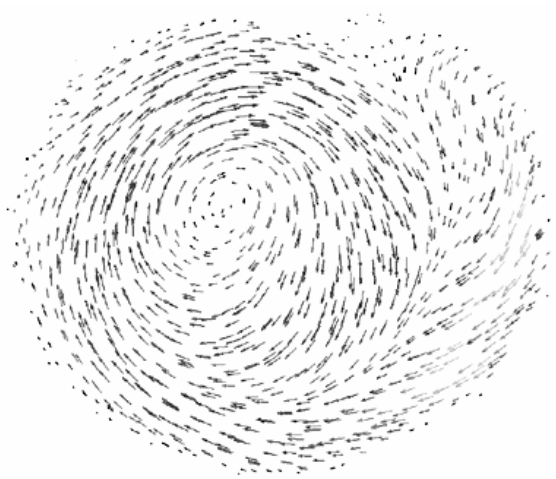

Figure 16. Rotational movement in the bulge of the first real geometry visualized with the velocity vectors

4. SUMMARY

In the first phase of the research several idealised models were studied which are based on the traditional medical view of aneurysms. A number of typical flow phenomena have been identified in the idealized models but the simulations also showed that the geometry preceding the aneurysm largely influences the details of the flow in the aneurysm. This can also lead to counterintuitive motions. It has been established the increase the neck surface makes the maximum wall shear increase. Bends can increase or decrease the wall shear depending on their orientation. Studying the real models it turned out that there are some similarities with the artificial models. The rotation appears in the aneurism, and the bends have the same effect. On the other hand the complexity of the geometries causes a much more complex flow pattern inside these geometries.

In the near future a number of real models will be studied and it will be attempted to find categories of geometries associated with categories of flow pattern. These again will be correlated with medical findings. Another direction of research will be the coupling of flow and elasticity simulations and the assessment of the importance of artery wall deformation on the flow phenomena and their clinical relevance.

ACKNOWLEDGEMENTS

This work has been supported by the Hungarian National Fund for Science and Research under contract Nr. OTKA T047150 OPR. Ádám Ugron wishes to thank for the support of his participation at this conference by the SZEFH Foundation.

REFERENCES

[1] The International Study of Unruptured Intracranial Aneurysm Investigators, 1999, “Unruptured intracranial aneurysms – risk of rupture and risk of surgical intervention”, *The New England Journal of Medicine*, Vol. 339. pp. 1725-1733

[2] Longstreth, W. T., Koepsell, T. D., Yerby, M. S., 1985, “Risk factors for subarachnoid hemorrhage”, *Stroke*, Vol. 16., pp. 377-385

[3] Paál, G., Bojtár, I., Szikora I., 2004, “Simulation of unsteady flow in brain aneurysms”, *First Hungarian Conference on Biomechanics*, Budapest, 11-12 June

[4] Egelhoff, C. J., Budwig R. S., Elger D. F., Khraishi, T. A., Johansen, K. H., 1999, “Model studies of the flow in abdominal aortic aneurysms during resting and exercise conditions” *Journal of Biomechanics* Vol. 32 pp. 1319-1329

[5] Gonzalez, G., Cho, Y. I., Ortega, H. V., Moret J., 1992, “Intracranial aneurysms: flow analysis of their origin and progression”, *AJNR Vol. 13 pp.* 181-188

[6] Oshima, M., 2004, “A new approach to cerebral hemodynamics – patient-specific modelling and numerical simulation of blood flow and arterial wall interaction” *IACM Expressions 16/04*

[7] Steinman, D. A., Milner, J. S., Norley C. J., Lownie, S. P., Holdsworth, D. W., 2000, “Image-based computational simulation of flow dynamics in a giant intracranial aneurysm”, *AJNR Am. J. Neuroradiol*. Vol. 24, pp 559-566

Conference on Modelling Fluid Flow (CMFF'06)
The 13th International Conference on Fluid Flow Technologies
Budapest, Hungary, September 6-9, 2006

Simulation of nasal flow by Lattice Boltzmann methods

Markus FINCK [1], Dieter HÄNEL [2]

[1]Corresponding author. Institute of Combustion and Gasdynamics, University of Duisburg-Essen. Lotharstr. 1, D-47048 Duisburg, Germany, E-mail: markus@ivg.uni-duisburg.de
[2]Institute of Combustion and Gasdynamics, University of Duisburg-Essen. E-mail: haenel@ivg.uni-duisburg.de

ABSTRACT

The present study is concerned with the numerical simulation of the viscous and incompressible fluid flow through a human nose using a variant of the lattice Boltzmann method. The knowledge of the characteristics of nasal breathing is a significant contribution to the new concept of CAS (computer aided surgery). To increase the success of nose surgery, the prediction of nasal functions like climatization and filtering is desirable. This requires a fast and reliable method for flow prediction in complex geometries.

Our current studies document that the lattice Boltzmann method matches this postulate. The results show good agreement with a conventional finite-volume method. Essential advantages are seen in the fast grid generation (Cartesian grids with Octree refinement) even in complex physiological geometries, the high granularity for parallelization and the second order accuracy in space and time. Besides the pure flow prediction we also investigate the nose's climatization functionality using a finite difference scheme to simulate the transport of heat and water vapor in the air. Moreover we use a Lagrangian method to model particle and aerosol transport through the nose which is an indicator for the filtering functionality.

Keywords: Lattice Boltzmann, nasal flow, vapor transport, particle transport

NOMENCLATURE

f	$[kg/m^3]$	Molecular distribution function
F	$[kg/m^3]$	Equilibrium distribution
$\vec{\xi}$	$[m/s]$	Molecular velocity vector
t	$[s]$	Time
$\vec{x}$	$[m]$	Spatial coordinate
ω	$[1/s]$	Molecular collision frequency
δx	$[m]$	Space step
δt	$[s]$	Time step
i	$[-]$	Discrete molecular direction
α	$[-]$	Cartesian direction
$\vec{\xi_i}$	$[m/s]$	Discrete molecular velocity
ξ_s	$[m/s]$	Scalar molecular velocity
c_s	$[m/s]$	Isothermal speed of sound
p	$[-]$	Square modulus
Ω	$[-]$	Dimensionless collision frequency
$\tilde{f}_i$	$[kg/m^3]$	Post-collision distribution
P	$[Pa]$	Hydrodynamic pressure
u_α	$[m/s]$	Macroscopic velocity
U_{ref}	$[m/s]$	Flow in velocity
ρ_0	$[kg/m^3]$	Density
ν	$[m^2/s]$	Kinematic viscosity
m_p	$[kg]$	Particle mass
v_p	$[m/s]$	Particle velocity
d_p	$[m]$	Particle diameter
A_p	$[m^2]$	Particle cross section
$\vec{F}_f$	$[kg\,m/s^2]$	Fluid force
$\vec{F}_g$	$[kg\,m/s^2]$	Gravity force
$c_{W,p}$	$[-]$	Drag coefficient
Re_p	$[-]$	Particle Reynolds number
$n_{p,d}$	$[-]$	Number of deposited particles
$n_{p,in}$	$[-]$	Number of particles at the inlet
η_d	$[-]$	Particle deposition efficiency
Φ	$[-]$	Transport property
D	$[-]$	Numerical diffusion coefficient
T	$[K]$	Temperature
λ	$[W/m\,K]$	Thermal conductivity

c_p	$[J/kg\,K]$	Heat capacity
ψ	$[-]$	Mass fraction
D_{AB}	$[m^2/s]$	Diffusion coefficient of a binary mixture

1 INTRODUCTION

The present study is concerned with the numerical simulation of fluid flow and particle deposition in a human nose. The knowledge of deposition mechanisms and the transporting fluid's characteristics in general are valuable to understand physiological phenomena in the context of ENT medicine and the new field of computer-aided surgery (CAS, [1]). This new approach is supposed to improve the success of nasal surgery. In particular the nose's functionality as a filter must be preserved; therefore, it is necessary to develop technics that make reasonable predictions for the state after a medical intervention. Currently, a surgeon can only rely on his or her experiences.

Fluid flow through a human nose [1] is neither laminar nor turbulent, it is in the transitional regime. It is very difficult to model this class of flows. Particle transport and deposition is another problem that has to be addressed in this scope. Thus a fast and reliable method for fluid and particle transport prediction is required in complex physiological geometries [2].

Our current studies document that the lattice Boltzmann method is a promising candidate for these needs. The results for the pure fluid flow show good agreement with a conventional finite-volume method [2] and corresponding experimental data [3]. Essential advantages are seen in the fast grid generation (Cartesian grids with Octree refinement) even in the complex nasal cavity, the high granularity for parallelization and the second order accuracy in space and time.

Special attention is given to the nose's filtering functionality. Several studies (e.g. [4]) show that the range from about $1 - 10\,\mu m$ in diameter is of particular interest since many inartificial particles and aerosols fall in this category. For this reason a Lagrangian approach was chosen that treats every particle individually and is taken from [5]. Here a particle is modeled as a sphere that is affected by fluid forces, gravity and its own inertia.

Besides the filtering functionality heating and moistening are important tasks fulfilled by the human nose. Clinical investigations show that incoming air is warmed close to blood heat and saturated with water vapor before it arrives in the lungs [6]. This process is simulated using a conventional finite difference scheme for the governing transport equations.

Details of the present lattice Boltzmann method of solution, the choice of flow cases and the results for inspiration with the discussed transport phenomena are reported in the subsequent sections.

2 THE LATTICE-BGK METHOD

2.1 Basics

The viscous, incompressible fluid flow through the nasal cavity is computed using the Lattice-BGK (LBGK) method which is a variant of the Lattice Boltzmann methods. Its original form was published in the Nineties by Qian et al.[7] and Chen et al. [8]. It is inspired by the kinetic gas theory and proved well as a fast prediction method for fluid flows. Several improvements were published, e.g. second-order accurate boundary conditions and local grid refinement in [9, 10]. Additional transport equations (temperature, species) can be solved with coupled finite-difference schemes [11].

The LBGK method is a discrete solution method of the Bhatnagar-, Gross-, Krook-(BGK-) model of the Boltzmann equation. The BGK model describes the temporal evolution of a molecular velocity distribution f in a phase space towards the equilibrium state F:

$$\frac{\partial f}{\partial t} + \vec{\xi}\,\frac{\partial f}{\partial \vec{x}} = \omega\,(F - f) \qquad (1)$$

The LBGK model introduces a discrete distribution f_i. The discrete phase space is represented by Cartesian-like lattices in two or three dimensions as sketched in Figure 1.

An amount of molecules f_i moves from node to node along each lattice link i with a discrete molecular speed $\vec{\xi_i}$ of constant Cartesian velocity components ξ_s. This velocity is chosen such that a Mach number $Ma = \frac{u_\infty}{\xi_s} \ll 1$ is maintained.

[1] More accurate: the human nasal cavity

[2] This geometry may be obtained in a computer tomography

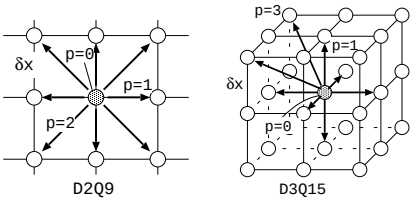

Figure 1. Discrete phase space (lattices) in two (D2Q9) and three (D3Q15) dimensions

Additionally a "zero-direction" with a corresponding speed $\vec{\xi_0} = \vec{0}$ is assumed such that there are 9 molecular speeds $\vec{\xi_i}$ in 2-D (D2Q9) and 15 in 3-D (D3Q15). The spatial steps $\vec{\delta x}$ and the time step δt is related to ξ_s by

$$\delta x_\alpha = \xi_s \, \delta t, \qquad p = \frac{\vec{\xi}^2}{\xi_s}, \qquad c_s^2 = \frac{1}{3}\,\xi_s^2$$

with the definitions of the isothermal speed of sound c_s and the square modulus p. Thus the LBGK equation for the discrete distribution function $f_i(t, \vec{r})$ in direction of the discrete molecular speed $\vec{\xi_i}$ reads

$$f_i(t+\delta t, \vec{r}+\vec{\xi_i}\,\delta t) = f_i(t, \vec{r}) + \Omega\,[F_i(t, \vec{r}) - f_i(t, \vec{r})] \tag{2}$$

where the last term represents the BGK collision approach. The relaxation factor Ω is a function of the kinematic viscosity ν:

$$\Omega = \omega\,\delta t = \frac{c_s^2}{\nu/\delta t + \frac{1}{2}\,c_s^2} \tag{3}$$

Equation (2) can be split into a collision- and a transport step which read as follows:

$$\tilde{f}_i(t, \vec{r}) = (1-\Omega)\, f_i(t, \vec{r}) + \Omega\, F_i(t, \vec{r}) \tag{4}$$

and

$$f_i(t+\delta t, \vec{r}+\vec{\xi_i}\,\delta t) = \tilde{f}_i(t, \vec{r}) \tag{5}$$

introducing the post-collision distribution $\tilde{f}_i$.

The LBGK scheme is stable for Ω in the range $0 < \Omega < 2$. The equilibrium distribution function F_i in (2) is derived from the Maxwell distribution that reads for small Mach numbers:

$$F_i = t_p\,[\frac{P}{c_s^2} + \frac{\rho_0\, u_\alpha\, \xi_{i\alpha}}{c_s^2} + \frac{\rho_0\, u_\alpha\, u_\beta}{2\, c_s^2}(\frac{\xi_{i\alpha}\,\xi_{i\beta}}{c_s^2} - \delta_{\alpha\beta})] \tag{6}$$

where ρ_0 is the constant density of the fluid, $P = P(t, \vec{r})$ is the hydrodynamic pressure and $u_\alpha = u_\alpha(t, \vec{r})$ is a macroscopic fluid velocity component in a Cartesian direction $\alpha = x, y, z$. The Kronecker symbol $\delta_{\alpha\beta}$ denotes the unit tensor. The weighting factor t_p is a function of the square modulus p (Table 1).

Table 1. Weighting factor t_p

D2Q9	$p = 0, 1, 2$	$t_p = 4/9,\ 1/9,\ 1/36$
D3Q15	$p = 0, 1, 3$	$t_p = 2/9,\ 1/9,\ 1/72$

The macroscopic moments pressure P and velocity u_α are defined as

$$P = c_s^2 \sum_i f_i \tag{7}$$

$$u_\alpha = \frac{1}{\rho_0} \sum_i \xi_{i\alpha}\, f_i. \tag{8}$$

It can be proved (e.g. in [12]) that the present LBGK approach satisfies the Navier-Stokes equations for a viscous fluid with constant density $\rho_0 = const.$ in Cartesian coordinates $\alpha, \beta = x, y, z$ with a formal accuracy of second order in space and time. The resulting system of equations reads:

$$\partial_\alpha u_\alpha = 0$$

$$\partial_t u_\alpha + \partial_\beta\, u_\beta u_\alpha + \partial_\alpha P/\rho_0 = \partial_\beta\, \nu\, [\partial_\beta u_\alpha + \partial_\alpha u_\beta]$$

There exist a number of investigations where the accuracy and efficiency of this approach is documented (e.g. [9, 10]).

2.2 Grid concept and methodical extensions

In recent time a number of extensions have been developed to improve the basic LBGK scheme, e.g. local grid refinement [9], boundary fitting on walls [13], a non-reflecting pressure boundary condition and parallelization. Since the LBGK algorithm is limited to Cartesian grids the implemented local refinement concept causes extra complexity.

A useful structure for organizing this refinement concept in 3-D are Octree grids. Here a cubic grid element can have up to 8 subelements that locally increase the resolution as

shown in Figure 2. In highly complex computational domains like the nasal cavity unstructured addressing is required. A rescaling procedure performed in the transport step (5) is outlined in [10] in the intersection zones between two refinement levels.

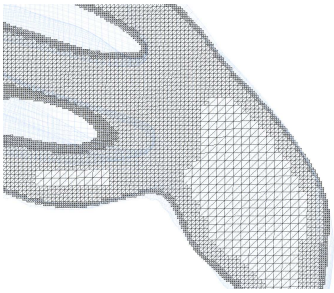

Figure 2. Cut through an Octree grid

For boundary treatment we use a boundary fitting approach for the distribution function f. This concept is described in [10] and is extendable to more complex boundary models. In our case a non-slip condition on the mucosa is assumed.

We chose steady conditions for in- and outflow of the nasal cavity since the breathing frequency (or the Strouhal number) is sufficiently small. The inflow boundary is prescribed by a constant volume flux with the pressure extrapolated from the interior.

The outflow boundary is implemented using a non-reflecting boundary condition that suppresses the reflection of pressure disturbances. In flows with low viscosity these pressure waves travel nearly undamped with the speed of sound c_s slowing down the convergence rate or even cause a breakdown of the solution. Based on experiences with usual finite-volume schemes for conservation laws, a well known non-reflecting boundary condition for the pressure, [14], was modified for the use in LBGK computations. The pressure $P_b(t)$ at the exit boundary $\vec{x}_b$ is assumed to be relaxed to its final, prescribed value P_{out} in the following form:

$$\frac{\partial}{\partial t}\left(P_b - \rho_0\, c_s\, u_n\right) + \alpha\left(P_b - P_{out}\right) = 0 \qquad (9)$$

with the isothermal speed of sound c_s, the flow velocity u_n normal to the boundary and a constant parameter $\alpha \approx 0.125$, tuned by numerical experiments. A significant gain of stability has been observed with this approach.

For parallelization a spectral bisection method has been used for grid partitioning [15]. The communication between the individual parts is performed using the message-passing technics MPI.

3 LAGRANGIAN PARTICLE MODEL

In the Lagrangian approach each floating particle is treated as a sphere that is affected by gravity and the surrounding fluid as shown in Figure 3. It is assumed that individual particles do not interact with each other. This model is adopted from [5] and proved its eligibility in many practical applications.

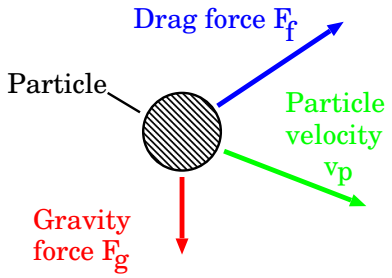

Figure 3. Floating spherical particles

The motion of a single particle can be described by the equation

$$m_p \frac{d}{dt}\vec{v}_p = \vec{F}_f + \vec{F}_g \qquad (10)$$

where $\vec{F}_f$ is a drag force applied by the fluid, $\vec{F}_g$ is due to gravity, $\vec{v}_p$ is the particle velocity and m_p the particle's mass.

In the diameter range from $1 - 10\,\mu m$ the influence of diffusion is marginal and neglected here. Thus the fluid force $\vec{F}_f$ depends on the particle diameter and the difference velocity:

$$\vec{F}_f = \frac{1}{2}\, c_{W,p}\, \rho_0\, A_p\, (\vec{u} - \vec{v}_p) \cdot |\vec{u} - \vec{v}_p| \qquad (11)$$

With the fluid density ρ_0, the particle cross section A_p and the local fluid velocity $\vec{u}$. The drag coefficient $c_{W,p}$ is taken from Stokes' solution for creeping flows and reads

$$c_{W,p} = \frac{24}{Re_p} \quad \text{for} \quad Re_p < 0.01,$$

$$c_{W,p} = \frac{24}{Re_p}\left(1 + 0.15 \cdot {Re_p}^{0.687}\right)$$

for

$$0.01 \le Re_p < 1000$$

and

$$c_{W,p} = 0.44 \quad \text{for} \qquad Re_p \geq 1000.$$

The particle Reynolds number Re_p is defined by

$$Re_p = \frac{d_p \, |\vec{u} - \vec{v}_p|}{\nu}$$

using the particle diameter d_p and the fluid viscosity ν. Equation (10) is solved by a Heun integration which yields the trajectory and is of $O(\Delta t^2)$ in time.

With this approach a particle can move through the whole computational domain. This requires a knowledge of neighborhood relations between the grid elements as well as a mechanism that handles the particle transfer from one cluster node to the other in parallel computing. This extra effort was necessary to cover realistic flow configurations that require high grid resolutions.

Since a particle's velocity normally does not agree with the velocity of the surrounding fluid it is possible that a particle collides with the domain boundary. If the outlet is hit the particle is deleted and plays no role in the further computation. In case of a collision with the wall (mucosa) the particle is deposited and filtered out.

4 NASAL FLOW SIMULATION

In the scope of this study we adopted the nasal geometry model which has already been used in [2, 16] and is validated with satisfactory accuracy. The nasal septum is used as a symmetry plane. The geometry is shown in Figure 4 both from the front- as from the back side.

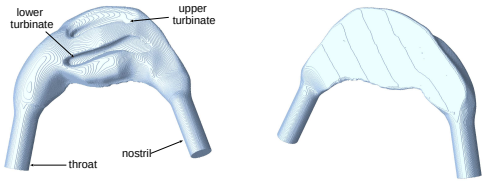

Figure 4. Nasal geometry model

In [16] the incompressible flow through the nasal cavity has been simulated until steady state for inspiration as well as for expiration. In the present study we adopted the inspiration configuration only. Here a Reynolds number $Re = 1000$ was chosen with reference quantities defined on the throat side of the geometry. The diameter here is considered as $12mm$ with the viscosity of air as $\nu = 1.5 \cdot 10^{-5} m^2/s$ resulting in a volume flux of $\dot{V} = 8.48 \, l \, min^{-1}$ per side. A parabolic velocity profile is prescribed at the inlet. Computation has been performed with about 4.7 mill. grid points distributed over 20 cluster nodes. Figure 5 shows the streamlines of the resulting fluid field.

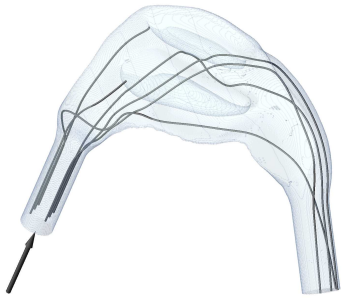

Figure 5. Streamlines at inspiration

The results are presented in [16] and show good agreement with [2]; i.a. we compared the pressure loss coefficient ζ which is related to the total pressure loss P_t as

$$\Delta P_t = P_{t,entrance} - P_{t,exit} = \zeta \, \frac{\rho_0}{2} U_{ref}^2$$

with

$$P_t = P + \frac{\rho_0}{2} \, u_\alpha^2, \qquad \alpha = 1, 2, 3.$$

The resulting pressure loss coefficients ζ from the present calculations (LBGK) and from the finite-volume method (FVM) are listed in Table 2.

Table 2. Comparison of relative pressure loss ζ for LBGK and finite volume method

ζ	LBGK	FVM	difference
inspiration	2.99270	3.0059	0.4423%
expiration	5.34597	5.4796	2.4361 %

5 NASAL FLOW WITH PARTICLE TRANSPORT

In the particle transport simulation the different particle size classes were simulated independently of each other. The corresponding particles were distributed over the inflow cross section with their initial velocity identical to the

readily computed fluid field. Computation was performed until a physical time of $t = 1.2s$ has been elapsed or all particles have either been deposited or left the computational domain. Using the number of $n_{p,d}$ deposited particles the deposition efficiency

$$\eta_d = \frac{n_{p,d}}{n_{p,in}}$$

with the number of particles $n_{p,in}$ at the inlet could be determined. A typical quantity for $n_{p,in}$ is about 10000 particles in our computations.

The deposition efficiency is highly dependent on the particle diameter. For particles in a size class of $1 - 10\,\mu m$ the dominating mechanisms for deposition are mass inertia and sedimentation whereas diffusion can be neglected.

Since these effects are dependent on the particle volume ($m_p \sim {d_p}^3$) their influence vanishes if the particle size is decreased. Particles with lower diameter are filtered with less efficiency since the fluid force $\vec{F}_f \sim {d_p}^2$ becomes the dominating effect which constrains the particles to follow the streamlines. More detailed analytical estimations for this dependency are available only in special geometrical configurations; anyway, the computational results show a reasonable agreement to other filter devices [17].

The particle deposition efficiency with respect to the diameter is shown in Figure 6. Figure 7 shows the temporal formation of the incoming particle cloud and locations of deposited particles.

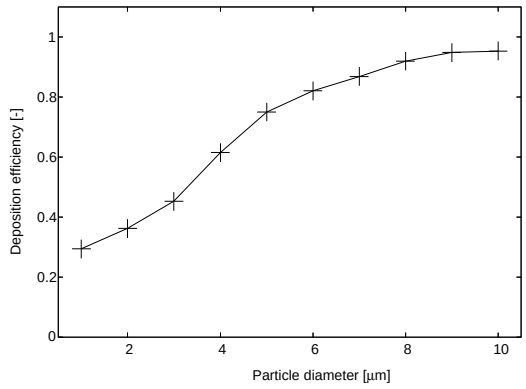

Figure 6. Particle deposition efficiency η_d as a function of particle diameter

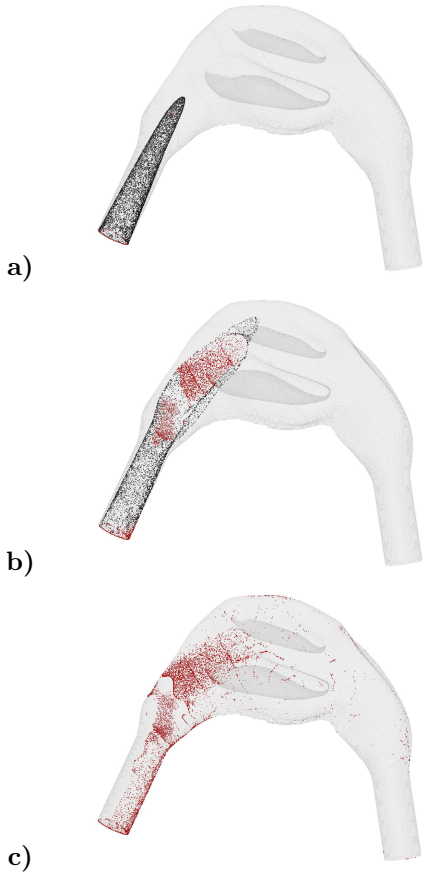

Figure 7. Particle inflow and deposition with $d_p = 10\mu m$. Deposited particles are light colored.

6 HEAT AND WATER VAPOR TRANSPORT

The transport processes of heat and water vapor in the nasal cavity are responsible for the heating and moistening functionalities of the human nose. The governing equations are of type convection-diffusion equation which is of the following general form:

$$\frac{\partial \Phi}{\partial t} + u_\alpha \frac{\partial \Phi}{\partial x_\alpha} = D \frac{\partial}{\partial x_\alpha}\left(\frac{\partial \Phi}{\partial x_\alpha}\right) \qquad (12)$$

where Φ is the transported property and D is the coefficient of diffusion. This equation can be discretised with standard methods; we applied a 3-steps Runge-Kutta time integration in conjunction with central differences for the spatial derivatives.

The temperature transport equation can be derived from the energy equation of a transported fluid whereas the simulation of water va-

por transport is described by the diffusion equation of a binary mixture. So Φ and D are set according to the transport equation as

- Temperature transport: $\Phi \equiv T$, $D \equiv \frac{\lambda}{\rho_0 \, c_p}$
- Vapor transport: $\Phi \equiv \psi$, $D \equiv D_{AB}$

where T is the fluid temperature, λ the thermal conductivity of the mixture, c_p the heat capacity of the mixture, ψ the mass fraction of air respective water vapor and D_{AB} the diffusion coefficient of binary mixture air/water vapor.

With the simplified assumption of saturated air with $T = 37°C$ at the mucosa and an inflow temperature of $T = 25°C$ it was found that the air is almost saturated and warmed to blood heat at the outlet (Figures 8 to 9). A qualitative comparison with [6] shows an acceptable agreement though an experimental validation has been omitted.

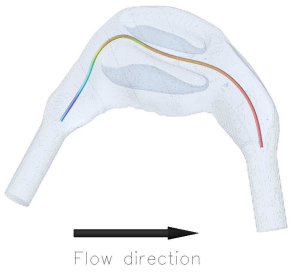

Figure 8. Measurement path through the nasal cavity

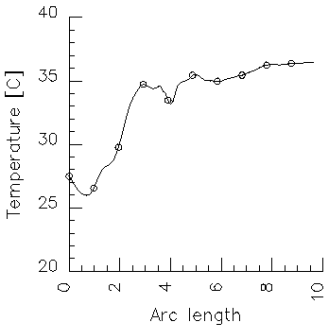

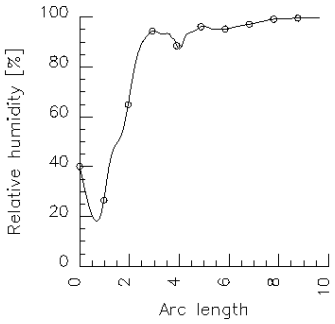

Figure 9. Measured quantities Temperature and Relative Humidity along the path

7 CONCLUSIONS

In the present study we discussed the mechanisms that govern the functionality of the human nasal cavity as a heating- and filtering device. The process has been simulated using the LBGK method for the transporting fluid and a Lagrangian approach for the particle transport. Heat and vapor transport has been included using a conventional finite difference approach.

The transitional flow regime in conjunction with the complex nasal geometry turned out to be the major challenges. In accordance to literature [4] we found that particles in a size class of $1\,\mu m \leq d_p \leq 10\,\mu m$ are filtered with highest efficiency.

We conclude that the LBGK method in conjunction with Lagrangian particle transport are well suited technics that enable us to predict many interesting fluid mechanical problems in the frame of computer aided surgery in detail.

References

[1] Bockholt U., Mlynski G., Muller W., and Voss G., 2000, "Rhinosurgical therapy planning via endonasal airflow simulation", *Computer Aided Surgery 5:* 175-179.

[2] Hörschler I., Meinke M., and Schröder W., 2003, "Numerical simulation of the flow field in a model of the nasal cavity", *Computers & Fluids*, 32: 39-45.

[3] Opitz R., and Limberg W., 1998, "Druckverlustmessungen an einem Nasenmodell bei unterschiedlichen Volumenströmen", *Abhandlungen aus dem Aeorodynamischen Institut 33*: 119-125.

[4] Cheng Y. S.,Yeh H. C., and Swift D L., 1991, "Aerosol deposition in human nasal airway for particles $1nm$ to $20\mu m$: A model study", *Nuclear Technology Publishing* Vol. 38 No. 1/3 pp. 41-47.

[5] Hänel D., and Lantermann U., 2006, "Lattice-Boltzmann and Particle Monte-Carlo Methods for Particle Transport and Deposition", *Submitted to Computers & Fluids*.

[6] Keck T. et al., 2000, "Humidity and temperature profile in the nasal cavity" *Rhynology 38*: 167-171.

[7] Qian Y. H., d'Humieres D., and Lallemand P., 1992, "Lattice BGK models for Navier-Stokes equation", *Europhys. Lett.* 17(6).

[8] Chen S., Wang Z., Shan X., and Doolen G. D., 1992, "Lattice BGK models for Navier-Stokes equation", *J. Stat. Phys. 68*: 379.

[9] Filippova O., and Hänel D., 1998, "Boundary Fitting and Local Grid Refinement for Lattice-BGK Models", *Int. Journal of Modern Physics C 9*: N 8.

[10] Filippova O., and Hänel D., 1998, "Grid Refinement for Lattice-BGK Models", *J. Comp. Physics 147*: 219-228.

[11] Filippova O., Succi S., Mazzocco F., Arrighetti C., Bella G, and Hänel D., 2001, "Multiscale Lattice Boltzmann Schemes with Turbulence Modeling", *J. Comp. Physics 170*: 812.

[12] Filippova O., and Hänel D., 2000, "A Novel Lattice BGK Approach for Low Mach Number Combustion", *J. Comp. Physics 158*: 136-160.

[13] Filippova O., and Hänel D., 2000, "Acceleration of Lattice-BGK Schemes with Grid Refinement", *J. Comp. Physics 165*: 407-427.

[14] Rudy, and Strikwerda, 1981, "Supersonic Navier-Stokes Calculations", *Computers & Fluids*.

[15] Karypis G., and Kumar V., 1998, "A Fast and High Quality Multilevel Scheme for Partitioning Irregular Graphs", *SIAM Journal on Scientific Computing*.

[16] Hänel D., and Finck M., 2005, "Simulation of Nasal Flow by Lattice Boltzmann Methods", *Submitted to Computers in Biology and Medicine*.

[17] Friedlander S. K., 2000, "Smoke, Dust and Haze", *Oxford University press*.

Conference on Modelling Fluid Flow (CMFF'06)
The 13th International Conference on Fluid Flow Technologies
Budapest, Hungary, September 6-9, 2006

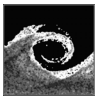

NUMERICAL AND EXPERIMENTAL INVESTIGATION OF CYLINDER CAVITY FLOWS

Leonid BAZYMA[1], Victor KULESHOV[2]

[1] Corresponding Author. Department of Spacecraft Power Unites, National Aerospace University „Kharkov Aviation Institute". Chkalov St. 17, 61070 Kharkov, Ukraine. Fax: +380 57 707 4869, E-mail: bazyma@rambler.ru bazima@htsc.kipt.kharkov.ua
[2] Aerodynamic Laboratory, National Aerospace University „Kharkov Aviation Institute". E-mail: kuleshov_v@mail.ru

ABSTRACT

It is well-known that supersonic flow around bodies with cavities located on the nose is accompanied by pulsation. A forward-facing cavity may be regarded as a resonance tube. The flow in forward-facing cavities have been the subject many experimental and numerical investigations. However, the majority models used in their experiments were blunt, hemispherical nose pieces with an axial cylindrical cavity of variable depth. In general, the cavity resonated at the primary-mode frequency, and the bow shock oscillated in a stable, symmetric manner about the nose. However, for intermediate cavity lengths, $0.4 \leq L/D \leq 0.7$, the pressure signal switched randomly between two modes of oscillation. The numerical and the experimental research of a supersonic flow past the cylinder with a cavity is carried out in the given work. Relative depth of a cavity (L/D, D – cylinder diameter) varied in a range from 0,3 up to 1,6. Experiments for Mach number M=3, Reynolds number $Re>10^6$ and 2D, 3D numerical modeling were carried out. Shock wave be-modal pulsations have been experimentally found for depth of a cavity L/D=0.4. Comparison of the experimental and numerical data has shown their good conformity.

Keywords: cavity, pulsations, bow shock, supersonic flow

NOMENCLATURE

a	$[m/s]$	sound velocity
D	$[m]$	cylinder diameter
E	$[J/kg]$	total energy per unit mass
L	$[m]$	depth of the cavity
M	[-]	Mach number
q	$[m/s]$	velocity vector
p	$[Pa]$	total pressure
Re	[-]	Reynolds number
t	$[s]$	time
u, υ, w	$[m/s]$	velocity vector (q) components on the axes x, y and z
γ	[-]	ratio of specific heats
Δ	$[m]$	bow shock wave average standoff distance from the rim of the cup
δ	$[m]$	cup wall thickness
ρ	$[m]$	density

Subscripts and Superscripts

∞	freesteam flow conditions

1. INTRODUCTION

It is well-known that supersonic flow around bodies with cavities located on the nose is accompanied by pulsation [1-3]. A forward-facing cavity may be regarded as a resonance tube. One of the characteristics of a hollow-nosed missile at supersonic Mach number is an oscillating bow shock that can significantly influence missile drag, heat transfer and optical signal propagation through the cavity [4]. Several methods of the bow shock stabilization have been considered. For example, the cavity can be gas pressurized in order to maintain a stable pressure and reduce the amplitude of shock oscillations in front of the cavity produced by movement of the bow shock [5].

Flow stabilization by jet injection from the cavity bottom is discussed in previous work[3]. Control and manipulation of the pulsation process by energy deposition due to the influence of a pulse laser is considered as well [6-9]. Cavity geometry influence on a cavity pulsation was also investigated [10-11].

The experimental investigations of cylinder with cavity at Mach number 2.9 have been performed in [1] but there is no information for two-mode oscillation regime and for intermediate cavity lengths $0.4 \leq L/D \leq 0.7$. The numerical simulation and experimental investigation of cylinder with cavity past flow for $0.3 \leq L/D \leq 1.6$ are performed in present work.

2. BACKGROUND

A forward-facing cavity may be regarded as a resonance tube. Experimental and numerical investigations have consistently found that the forward-facing cavity resonates and that the oscillations have a dominant frequency. This fundamental or primary mode frequency is approximated from resonant tube theory as

$$\omega = 2\pi f = \pi a_0 / 2L^* \qquad (1)$$

Here a_0 is the speed of sound in the cavity, based on stagnation temperature; L^* is the axial distance from the cavity base to the mean shock position, $L + \delta$. In Equation (1), it is assumed that the flow velocity in the tube, or cavity, is small, so that the stagnation temperature can be used to estimate the average speed of sound.

The flow in forward-facing cavities have been the subject many experimental and numerical investigations [2]. However, the majority models used in their experiments were blunt, hemispherical nose pieces with an axial cylindrical cavity of variable depth. In general, the cavity resonated at the primary-mode frequency, and the bow shock oscillated in a stable, symmetric manner about the nose. However, for intermediate cavity lengths, $0.4 \leq L/D \leq 0.7$, the pressure signal switched randomly between two modes of oscillation.

Antonov and Shalaev [1] investigated the flow around cylinder with a cavity in the Mach 2.9 wind tunnel, but for intermediate cavity lengths, $0.4 \leq L/D \leq 0.7$, two modes of oscillation did not observe. The present investigations corroborate and explain the measurements reported by Antonov and Shalaev [1].

3. EXPERIMENTAL APPARATUS

The tests of a 85 mm diameter cylinder with cavity were conducted in the National Aerospace University (KhAI) Mach 3 supersonic wind tunnel (T-6). Figure 1 is a schematic of this supersonic wind tunnel facility, and Table 1 lists the operating parameters for this facility.

Table 1. Operating Parameters for the KhAI Mach 3 Supersonic Wind Tunnel (T-6)

Mach Number	3
Stagnation Pressure	392.3 kPa
Typical Stagnation Temperature	300 K
Total Run Time	4.0 minutes
Reynolds number	2.81×10^6
Test Area Cross Section	60 cm × 60 cm
Test Area Length	160 cm

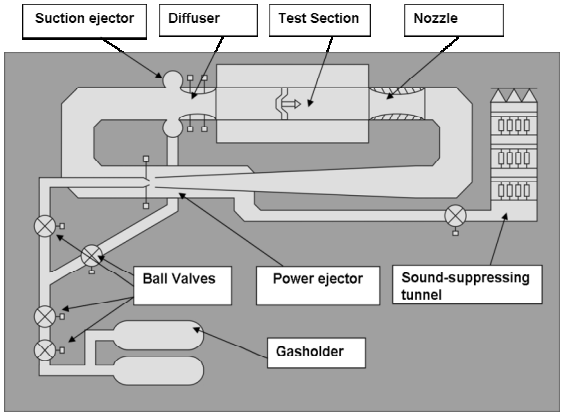

Figure 1. Schematic of National Aerospace University (KhAI) Mach 3 supersonic 60 cm by 60 cm wind tunnel (T-6) field

Adjusting the tunnel for a given Mach number is effectuated by adjusting nozzle size, the test section height and top bottom and wall inclination. The adaptive wall of the test section ensures minimisation of the boundary layer effect on the parameters under test, increase of the Re numbers.

Figure 2 show the experimental setup. The model used in this study consisted of 85 mm diameter cylinder with a flat tip. A 81.6 mm diameter hole along the axis of the cylinder served as a forward-facing cavity. The cavity length was varied by changing the position of the insert. Pressure ports were placed on the cavity base.

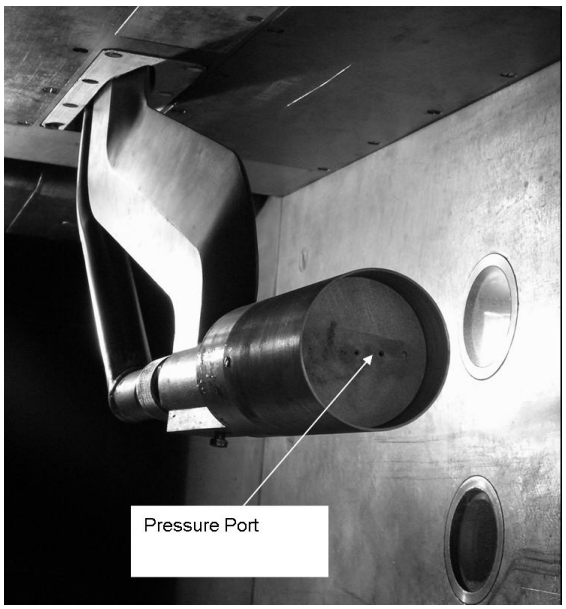

Figure 2. A 85 mm diameter cylinder with cavity model mounted in the 60 cm by 60 cm test section of the Mach 3 National Aerospace University (KhAI) wind tunnel (T-6)

Shadowgraph device IAB-451 was used for optical researches. Mercury lamp DRSh-250 was a

light source. Images were registered by superfast SFR-1 camera [12]. This camera can be used as the photoregistrar giving continuous development of researched process or as the high-speed camera giving a number of consecutive photos of investigated process with rate up to $2.5 \cdot 10^6$ frames per second. In the given work the shock shape, standoff distance, and oscillation amplitudes were recorded at rates up to 40000 frames per second. Photographing was carried out on a motionless film by means of a rotating mirror. The SFR-1 camera has system of automatic electronic management. Accuracy of adjustment and measurement of mirror rotation speed is within 0.1 %. The photographic film "Kodak Professional ProFoto 400 bw" has been used. The film image was scanned with the resolution of 3200 pixels to inch. Then computer processing of the image was carried out.

4. NUMERICAL MODEL

Consider the problem of constant flow around a cup cylindrical cavity ($l/D = 0.3-1.6$; $\delta/D = 0.04$); with a uniform, ideal supersonic gas flow. The forward-facing cavity scheme is depicted in Figure 3.

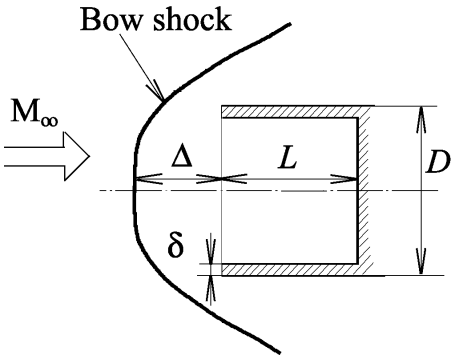

Figure 3. Schematic of forward-facing cavity

The unsteady 3D Euler equations for an arbitrary volume Ω may be written in integral form as

$$\frac{\partial}{\partial t}\int_{\Omega} F d\Omega + \int_{\sigma} \overline{A}\overline{n} d\sigma = 0, \qquad (2)$$

where

$$F = \begin{bmatrix} \rho \\ \rho u \\ \rho \upsilon \\ \rho w \\ \rho E \end{bmatrix}, \quad \overline{A} = \begin{bmatrix} \rho\overline{q} \\ \rho u\overline{q} + p\overline{i}_x \\ \rho \upsilon \overline{q} + p\overline{i}_y \\ \rho w\overline{q} + p\overline{i}_z \\ \rho E\overline{q} + p\overline{q} \end{bmatrix}. \qquad (3)$$

Here $\overline{i}_x$, $\overline{i}_y$, $\overline{i}_z$ are the unit vectors of the Cartesian coordinate system; F are conservative vector variables; $\overline{A}$ are conservative flow vector variables; σ is the limiting surface of a certain volumetric element Ω, which has an external normal $\overline{n}$; $\overline{q} = u\overline{i}_x + \upsilon\overline{i}_y + w\overline{i}_z$ is the velocity vector of gas flow; u, υ and w are the velocity vector components along the x, y and z axes; p is the pressure; ρ is the density; E is the total energy per unit mass of the gas; and t is the time.

The above system of equations is closed by the equation of state of the ideal gas

$$\rho E = p/(\gamma - 1) + \rho q^2/2. \qquad (4)$$

In order to use dimensionless values, we make use of the following equalities:

$$\begin{aligned} &x = \overline{x}D/2, \quad y = \overline{y}D/2, \quad t = \overline{t}D/(2a_\infty), \\ &a = \overline{a}a_\infty, \quad u = \overline{u}a_\infty, \quad \upsilon = \overline{\upsilon}a_\infty, \\ &w = \overline{w}a_\infty, \quad \rho = \overline{\rho}\rho_\infty, \quad p = \overline{p}\rho_\infty a_\infty^2, \end{aligned} \qquad (5)$$

where a_∞ is the incident flow sound velocity. In the following text, we have omitted bars above the dimensionless values x, y, t, a, u, υ, ρ, p.

On the body surface solid-wall inviscid boundary conditions were applied. Along the external inflow boundary, undisturbed freesteam conditions were utilized. On the downstream outflow boundary, extrapolation of the flow quantities from the adjacent internal boundary was performed.

The initial data in calculations without injection corresponded to the dimensionless parameters of the incident stream:

$$\begin{aligned} &p = p_\infty = 1/\gamma, \quad \rho = \rho_\infty = 1, \\ &u = u_\infty = \mathrm{M}_\infty, \quad \upsilon = 0, \quad w = 0. \end{aligned} \qquad (6)$$

Equation system (2) solution was conducted by Godunov´s method [13] on a 110×60×32 grid mesh, which was designed by densening the mesh point all around the body region, with the exception that in the cavity, the mesh points distribution were set to be uniform. The calculations were performed using the same finite-difference scheme as that employed in [3, 13].

The some computational results in this investigation are generated using the numerical method with modified finite-difference Godunov´s scheme based on a mobile grid [14-16]. The system equations for the two-dimensional flow can be presented in the vector form (1), and F, $\overline{A}$ vectors may be written as

$$F = \begin{bmatrix} \rho \\ \rho u \\ \rho v \\ \rho E \end{bmatrix}, \quad \overline{A} = \begin{bmatrix} \rho\left(\overline{q} - \overline{\lambda}\right) \\ \rho u\left(\overline{q} - \overline{\lambda}\right) + p\overline{i}_x \\ \rho v\left(\overline{q} - \overline{\lambda}\right) + p\overline{i}_y \\ \rho E\left(\overline{q} - \overline{\lambda}\right) + p\overline{q} \end{bmatrix} \qquad (7)$$

Here σ is the limiting surface of a certain volumetric element Ω (see equation system (2)), which has an external normal $\overline{n}$ and moving at velocity $\overline{\lambda}$.

The difference between the present formulation and the regular one is that the cell velocity $\overline{\lambda}$ is included into the main equation (5) and each volume element depends on time. Results of [14,16] has demonstrated that the use of a mobile grid in the calculations with a relative cavity depth $L/D < 1.6$ has permitted to better determine the pulse amplitude of the shock wave (it is difficult to realize this on the immobile grid, since the pulse amplitude was commensurable to the grid dimension of a cell).

5. EXPERIMENTAL AND CALCULATION RESULTS

The relative depth of a cavity (L/D, D – cylinder diameter) varied in a range from 0.3 up to 1.6, and all of the experiments and calculations were conducted with the model at zero-degree angle of attack.

Measurement of the bow shock oscillations were performed in a wind tunnel. For each of the runs performed during the test, the bow shock oscillated. The oscillation frequency was found to be inversely proportional to cavity depth and corresponds to the fundamental acoustic frequency of the cavity, with a wavelength that was four times the distance from the cavity base to the mean shock position (for L/D >0.4).

Instantaneous images of the shock wave provide the wave shapes during the unstable mode of oscillations occurring at a particular cavity depth case of L/D =0.4.

Figure 4 shows the shadowgraph images of the shock in front of the model with cavity sizes L/D =0.4. In figure 4b shock wave appears quite axisymmetric. Figures 4a, 4c depicts a shock wave shapes with a bulge on either the lower or upper part resulting from the unsteady mode encountered at this cavity depth range. Thus this cavity exhibit a random character resulting in highly unstable oscillations and nonaxisymmetric shock wave shapes at random instances and durations.

For L/D =0.8 shock shape is quite axisymmetric.

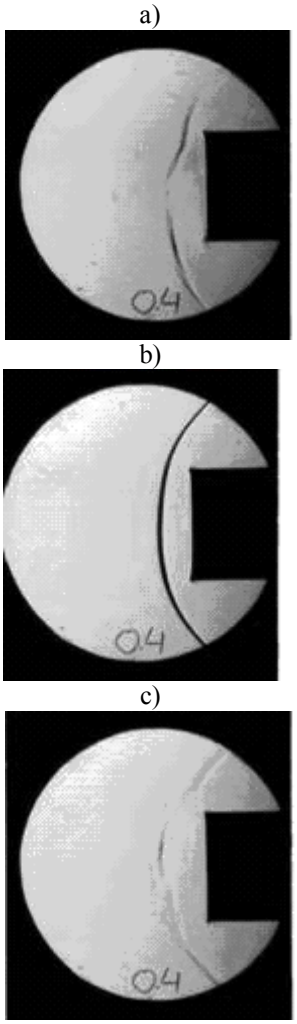

Figure 4. Shock shapes for *L/D* = 0.4 at Mach 3, (a) with a bulge at the lower part, (b) shock wave appears quite axisymmetric, (c) with a bulge at the upper part cavity

With a relative cavity depth $L/D < 1.6$ the use of a mobile grid in the calculations permitted to determine the pulse amplitude of the shock wave.

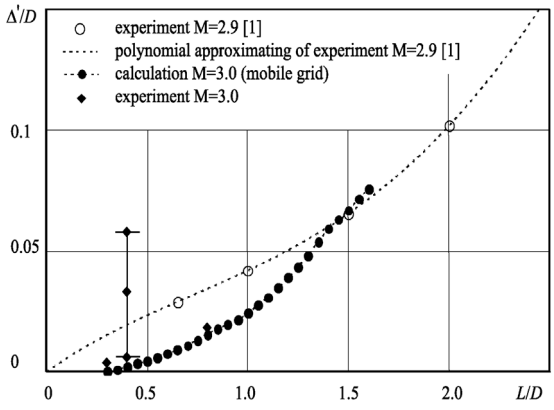

Figure 5. The bow-shock amplitudes

A representative comparison of the calculation (on mobile grid) and experimental results is shown in figure 5. With a relative cavity depth $L/D < 1.6$ the use of a mobile grid in the calculations permitted to determine the pulse amplitude of the shock wave. However bi-modal and randomly unstable oscillations in 2D and 3D calculations for L/D =0.4 have not been found out. Deepenings on the cavity base (for accommodation of pressure transducer ports) can generate small flow disturbances in a cavity. Figure 6 shows the numerical result for model L/D =0.4 with deepening on the cavity base.

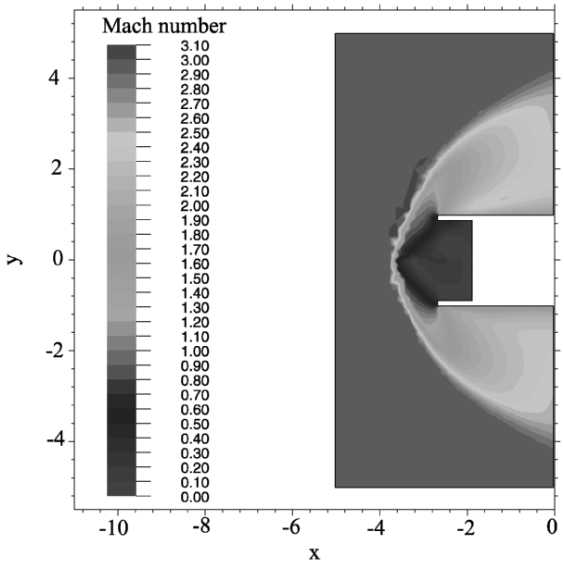

Figure 6. Mach number isolines; L/D = 0.4

5. SUMMARY

A discussion of the bow-shock behavior associated with a cylinder cavity with flat circular base at Mach 3 is presented.

The following have been defined after the conducted measurements:

1. The bow shock oscillations were observed in all wind tunnel experiments.
2. The oscillation frequency was proportional to the cavity depth and was in agreement with fundamental acoustic frequency for this cavity with wavelength equal to quadruple distance from cavity bottom to the average bow shock standoff (for L/D >0.4).
3. The non steady regime for bow shock oscillation was observed as well that occurring if the relative cavity depth was L/D =0.4. In cause of L/D =0.4 the bimodal, non-steady oscillations were generated and they have random character. The bow shock shape was non-axisymmetric with bulges from one and/or another side.
4. The shape of bow shock was axisymmetric if L/D > 0.8.

The numerical cavity past flow simulation for depths $L/D < 1.6$ with use of mobile grid showed the good agreement with experimental data. Nevertheless for the bow shock bimodal non-steady oscillation phenomena were not observed after the mobile grid implementation in simulations (in 2D approximation). During the conducting of 3D cavity flow simulation for L/D = 0.4 and non-axisymmetric deposition of small recesses within cavity base the non-symmetric oscillations of bow shock were observed that are quality cognate with ones observed in experiment.

REFERENCES

[1] Antonov, A. N., and Shalaev, S. P., 1979, "Experimental investigation of unsteady flow in recesses in a supersonic flow", *Izvestya Academii Nauk USSR, Mekhanika Zhidkosti i Gaza*, No5, pp. 180-183.

[2] Ladoon, D. W., Shneider S. P., and Schmisseur, J.D., 1998, "Physics of Resonance in a Supersonic Forward-Facing Cavity", *Journal of Spacecraft and Rockets*, Vol.35, No.5, pp. 626-632.

[3] Bazyma, L. A., 1995, "Interaction between axial and annular jets leaving a cylindrical cavity and an incoming supersonic gas flow", *Journal of Applied Mechanics and Technical Physics*, Vol. 36, No. 3, pp. 381 - 384. (Translated from *Pricladnaya Mekhanika i Tekhnicheskaya Phyzica*, Vol. 36, No. 3, 1995, pp. 69 – 73).

[4] Huebner, L. D., and Utreja, L. R., 1993, "Mach 10 Bow-Shock Behavior of a Forward-Facing Nose Cavity," *Journal of Spacecraft and Rockets*, Vol. 30, No. 3, pp. 291–297.

[5] Utreja, L. R. and Gurley, W.H. 1989, "Aircraft hollow nose cone", U.S. Patent 4,850,275 BDM International, Huntsville, AL, July.

[6] Tret'yakov, P. K., Grachev, G. N., Ivanchenko, A. I., Krainev, V. L., Ponomarenko, A. G. and Tishenko, V. N., 1994, "Optical breakdown stabilization in the supersonic argon flow", *Physics-Doclady*, Vol. 39. No. 6, pp. 415 – 416. (Translated from *Doklady Akademii Nauk*, Vol. 336, No. 4, 1994, pp. 446 – 447).

[7] Tret'yakov, P. K., Garanin, A. F, Grachev, G. N., Krainev, V. L., Ponomarenko, A. G., Tishenko, V. N. and Yakovlev, V. I., 1996, "Control of supersonic flow around bodies by means of high-power recurrent optical breakdown", *Physics-Doclady*, Vol. 41, No. 11, pp. 566 – 567).

[8] Guvernyuk, S. V., and Samoilov, A. B., 1997, "Control of supersonic flow around bodies by means of a pulsed heat source", Technical *Physics Letters*, Vol. 23, No. 5, pp. 333 – 336. (Translated from *Pis'ma v Zhurnal Tekhnicheskoi Fiziki*, Vol. 23, No.9, pp.1 - 8, 1997).

[9] Bazyma, L. A., and Rashkovan, V. M., 2005, „Stabilization of Blunt Nose Cavity Flows Using Energy Deposition", *Journal of Spacecraft and Rockets*, Vol.42, No.5, pp. 790-794.

[10] Sambamurthi, J. K., Huernbner, L. P., and Utreja, L. R., 1987, "Hypersonic flow over a cone with a nose cavity", AIAA Paper, No 87-1193, New York.

[11] Bochachevsky, I. D., and Kostoff, R. N., 1972, "Supersonic flow over convex and concave shapes with radiation and ablation effects", *AIAA Journal*, Vol. 10, No. 8, pp. 1024–1031.

[12] Dubovic, S.A., 1964, *Photographic registration of quickly proceeding processes*, Nauka, Moscow, (in Russian).

[13] Godunov, S. K. (ed), 1976, *Numerical Solution of Multidimensional Problems in Gas Dynamics*, Nauka, Moscow, (in Russian).

[14] Bazyma, L. A., and Holyavko, V. I., 1996, ''Modification of Godunov's Finite Difference Scheme on a Mobile Grid,'' *Computational Mathematics and Mathematical Physics*, Vol. 36, No. 4, pp. 525–532. (Translated from *Zhurnal Vychislitelnoy Mathemetiki I Mathematicheskoy Fiziki*, Vol.36, No.4, 1996, pp. 124-133).

[15] Bazyma L. A., and Rashkovan V. M., 2005, "Numerical Simulation of a Plasma Plume Exhaust from an Electrothermal Plasma Thruster", *Journal of Propulsion and Power*, Vol. 21, No. 2, pp.378–381.

[16] Bazyma L. A., and Rashkovan V. M., 2001, "On numerical simulation of supersonic flow using bow-shock-fitting technique", Proceedings of ICFDP7: *Seventh International Congress on Fluid Dynamics and Propulsion*, Sharm el-Sheikh, Sinai, Egypt, DC, pp.1-7.

Conference on Modelling Fluid Flow (CMFF'06)
The 13th International Conference on Fluid Flow Technologies
Budapest, Hungary, September 6-9, 2006

A THREE-HOLE PRESSURE PROBE EXPOSED TO WALL PROXIMITY EFFECTS: EXPERIMENTAL, NUMERICAL AND ANALYTICAL INVESTIGATION

Reinhard WILLINGER

Institute for Thermodynamis and Energy Conversion, Vienna University of Technology. Getreidemarkt 9/302, A-1060 Vienna, Austria.
Tel.: +43 1 58801 31312, Fax: +43 1 58801 30299, E-mail: reinhard.willinger@tuwien.ac.at

ABSTRACT

This paper presents results of the calibration of a three-hole pressure probe (cobra probe). The conventional calibration coefficients for a probe Reynolds number of about 7400 are obtained in a free jet wind tunnel at subsonic conditions. Furthermore, the probe is exposed to wall proximity effects using a flat plate boundary layer with neglecting thickness. The experimental calibration is extended by computational as well as analytical results. The calibration coefficients are predicted by the streamline projection method, at least qualitatively. The method can also be used to take into account the wall proximity effect. This fact is supported by unsteady computational fluid dynamics (CFD) calculations as well as by the measurements.

Keywords: CFD, experimental calibration, hot-wire anemometry, pressure probe, wall proximity effect

NOMENCLATURE

A_3	[-]	wall distance function
Ma	[-]	Mach number
Re	[-]	Reynolds number
Sr	[-]	Strouhal number
d	$[m]$	probe width
f	$[1/s]$	frequency
k_i	[-]	hole coefficient
k_β	[-]	direction coefficient
k_s	[-]	static pressure coefficient
k_t	[-]	total pressure coefficient
p	$[Pa]$	static pressure
p_t	$[Pa]$	total pressure
w	$[m/s]$	velocity
y	$[m]$	wall distance
Δt	$[s]$	time increment
$\Delta\beta$	[°]	yaw angle
δ	[°]	probe wedge angle
$\Delta\varepsilon$	[°]	flow angle error
ν	$[m^2/s]$	kinematic viscosity
ρ	$[kg/m^3]$	density

Subscripts and Superscripts

d	related to probe width
i= 1, 2, 3	related to hole number

1. INTRODUCTION

Three-hole pressure probes are robust and reliable tools for flow measurements in turbomachinery components. They yield the total as well as the static pressure and the direction of a two-dimensional flow field. An extension to the three-hole probe is the five-hole probe, which can be used for three-dimensional flow measurements. Due to space restrictions in turbomachinery applications, both probe types are used in the non-nulling mode and a calibration procedure prior to the measurement is necessary. A free jet wind tunnel can be used for this purpose. According to Dominy and Hodson [1], the main factors influencing the calibration of five-hole pressure probes are probe geometry, Reynolds number, Mach number and turbulence intensity. Compared with the calibration conditions (free jet), the flow field in a turbomachinery component is influenced by solid walls (hub wall, casing wall, blades). When a pressure probe is placed in the vicinity of a solid wall, two sources of systematic errors occur: (1) the velocity gradient effect due to the wall boundary layer, (2) the potential effect due to the interaction of the probe and the solid wall. The influence of velocity gradients on the behaviour of a three-hole probe has been investigated in a previous paper [2]. Therefore, the present paper focuses on the influence of the potential effect which is also known as wall proximity effect.

Treaster and Yocum [3] calibrated a prismatic five-hole probe (3.175 *mm* diameter) at different yaw angles near a solid wall. The orientation of the shaft axis was normal to the wall. Therefore, the constant pitch angle was zero throughout the investigation. Since the boundary layer was very thin, the potential effect dominates the interaction of the probe and the wall. The main result is that the static pressure coefficient is altered if the probe to wall spacing is lower than about two to four probe diameters.

Heikal [4] investigated the near wall behaviour of a spherical five-hole probe (3 *mm* diameter) as well as a three-hole probe (1.3 *mm* width) in a duct wind tunnel with rectangular cross section. The three-hole probe is of special design to allow three-dimensional flow measurements. The paper gives no information on the thickness of the wall boundary layer. Therefore, it is difficult to differentiate between gradient effects and potential flow effects. Nevertheless, the results indicate that there appears a systematic error of the total as well as of the static pressure when the probe is placed near the solid wall. Furthermore, an error is induced to the measured flow angle due to the interaction of the probe head and the wall.

Sitaram et al. [5] investigated the behaviour of a hemispherical five-hole probe near a solid wall. The orientation of the shaft axis was parallel to the wall. The authors stated that whenever a probe is located near a solid wall, the flow acceleration in that region introduces an additional error of the measured velocity. This error is negligible when the distance between the probe and the wall is more than two probe diameters.

An experimental investigation of two five-hole probes (hemispherical, pyramid) as well as a four-hole wedge probe near a solid wall has been performed by Bubeck [6]. Since the wall boundary layer was rather thin, velocity gradient effects have been eliminated. Detailed results are presented for the five-hole pyramid probe. When the probe head approaches the wall, the pressure sensed by the side hole near the wall increases. On the other hand, the pressure sensed by the opposite hole decreases. As a result, a systematic flow angle error appears if the distance between the probe and the wall is lower than about three probe diameters.

Smout and Ivey [7] performed an experimental investigation on the wall proximity effects of a three-hole wedge probe. The shaft axis of the probe was normal to a wall and the work was focused on the influence of the wall on the static pressure measurement as well as the yaw angle sensitivity. In a companion paper [8], Smout and Ivey performed CFD calculations to explain the mechanisms which are responsible for the wall proximity effect. Key flow structures in the probe wake were identified that control the pressures indicated by the probe in a given environment. Finally, the authors derived a simple analytical model from the CFD simulations that is able to capture the dominant flow features in good agreement with the experiments.

Recently, Borges and Vaz [9] investigated the influence of wall proximity effects on the behaviour of a conical five-hole probe (12 *mm* diameter). To eliminate velocity gradient effects, the experimental study was performed using an image method. Therefore, a replica of the probe was positioned parallel to the original probe. The experimental results have been extended by a numerical simulation using a commercial CFD code with the *k/ε* turbulence model. The authors stated that the wall proximity effect influences the measured flow angle as well as the measured velocity if the distance between the probe and the wall is lower than about three probe diameters.

The present paper summarizes an investigation on the wall proximity effect of a three-hole pressure probe. Results from the experimental calibrations will be correlated using a simple analytical approach. A CFD simulation will be performed to explain the potential interaction effect between the probe head and the wall.

2. PROBE GEOMETRY, HOLE AND CALIBRATION COEFFICIENTS

The three-hole probe used for the present investigation is a cobra probe with a characteristic dimension $d = 3 \times 0.8 = 2.4$ *mm* and a wedge angle $\delta = 30°$. The pressure holes are forward faced with a diameter of 0.5 *mm* and are numbered "1", "2" and "3". Figure 1 shows the geometry, the numbering of the holes as well as the definition of the yaw angle $\Delta\beta$. This is the angle between the velocity vector w and the probe axis. The pressure p_i, sensed by the hole "i" differs from the free stream static pressure p. Since the experiments are conducted at Mach numbers $Ma < 0.2$, the conditions are essentially incompressible and a hole coefficient can be defined according to

$$k_i = \frac{p_i - p}{(\rho/2)w^2}. \qquad (1)$$

The hole coefficient k_i can be interpreted as a nondimensional pressure sensed by the hole "i".

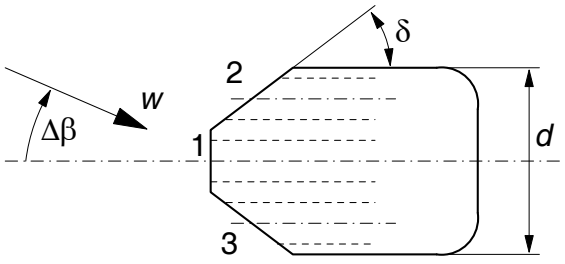

Figure 1. Hole numbering and definition of the yaw angle $\Delta\beta$

The three-hole probe can be used to measure the direction of the flow as well as the total and the static pressure. The relationship between these quantities and the yaw angle $\Delta\beta$ is given by the nondimensional calibration coefficients. Various definitions of these calibration coefficients can be found in the literature. The present work uses the common definition of Treaster and Yocum [3] for the direction coefficient k_β, the total pressure coefficient k_t and the static pressure coefficient k_s, reduced to the conditions for a three-hole probe:

$$k_\beta = \frac{p_2 - p_3}{p_1 - \bar{p}} = \frac{k_2 - k_3}{k_1 - \bar{k}}, \tag{2}$$

$$k_t = \frac{p_1 - p_t}{p_1 - \bar{p}} = \frac{k_1 - 1}{k_1 - \bar{k}}, \tag{3}$$

$$k_s = \frac{\bar{p} - p}{p_1 - \bar{p}} = \frac{\bar{k}}{k_1 - \bar{k}}. \tag{4}$$

The quantities

$$\bar{p} = \frac{p_2 + p_3}{2} \quad \text{and} \quad \bar{k} = \frac{k_2 + k_3}{2} \tag{5}$$

represent the mean pressure and the mean hole coefficient, respectively. As can be seen from Eqs. (2) to (5), the calibration coefficients are related directly to the three hole coefficients.

3. STREAMLINE PROJECTION METHOD

The streamline projection method is a simple analytical approach which is used in addition to the experimental as well as the computational investigations. This method is based on the assumption that the free stream velocity is projected on each of the three sensing holes [2]. The velocity component normal to the probe surface results in a "dynamic pressure" which is added to the free stream static pressure. Under the assumption of constant velocity magnitude w, the three hole coefficients are

$$k_1 = \cos^2 \Delta\beta, \tag{6}$$

$$k_2 = \sin^2(\delta + \Delta\beta) \quad \text{and} \tag{7}$$

$$k_3 = \sin^2(\delta - \Delta\beta). \tag{8}$$

The corresponding calibration coefficients follow from Eqs. (2) to (5). For small yaw angles $\Delta\beta$, a Taylor series expansion of Eq. (2) gives

$$k_\beta = \Delta\beta \frac{\pi}{45°} \tan\delta. \tag{9}$$

The streamline projection method can be used for an approximation of the influence of a wall on the flow angle error of the three-hole probe. Figure 2 shows the three-hole probe arranged at a distance y away from the wall. It is assumed that the flow direction is parallel to the wall. Therefore, the stagnation streamline approaching the centre hole "1" is parallel to the wall. Furthermore, it is assumed that the centre hole "1" and the side hole "2" away from the wall see the undisturbed freestream velocity: $w_1 = w_2 = w$.

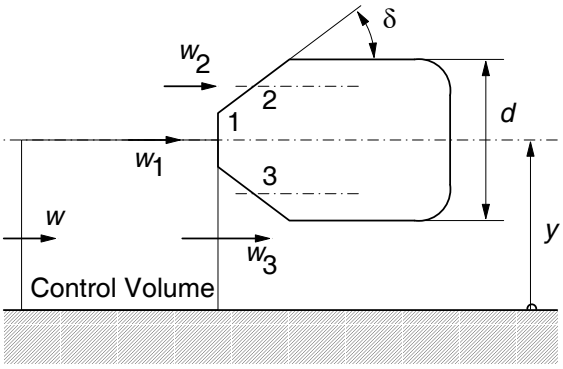

Figure 2. Three-hole probe near the wall (wall distance *y*)

Due to a gap nozzle effect between the probe and the wall, the hole "3" sees a velocity higher than the freestream velocity. If a mass balance is applied to the control volume, the increased velocity approaching at hole "3" can be estimated to

$$w_3 = w \frac{6y/d}{6y/d - 1} = wA_3. \tag{10}$$

Due to the higher velocity, the hole "3" near the wall senses a higher pressure compared with hole "2". The pressure difference between these holes is interpreted by the probe as an artificial flow angle which is called the flow angle error $\Delta\varepsilon$. Following the concept of the streamline projection method, the difference of the side hole coefficients is

$$k_2 - k_3 = \left[1 - \left(\frac{6y/d}{6y/d - 1}\right)^2\right] \sin^2\delta. \tag{11}$$

Furthermore, the denominator of the directional coefficient in Eq. (2) is

$$k_1 - \bar{k} = 1 - \frac{1}{2}\left[1 + \left(\frac{6y/d}{6y/d - 1}\right)^2\right] \sin^2\delta. \tag{12}$$

Finally, the combination of Eqs. (2), (9), (11) and (12) gives an approximation of the flow angle error induced by the wall proximity effect:

$$\Delta\varepsilon = \frac{45°}{\pi} \frac{\left(1 - A_3^2\right)}{\tan\delta\left[\frac{1}{\sin^2\delta} - \frac{1}{2}\left(1 + A_3^2\right)\right]}. \tag{13}$$

As can be seen from Eq. (13), the streamline projection method gives a nonlinear relationship between the flow angle error $\Delta\varepsilon$ and the nondimensional distance y/d from the wall to the probe axis. The sensitivity of the flow angle error depends on the probe wedge angle δ.

4. EXPERIMENTAL CALIBRATION

4.1 Free Jet Wind Tunnel

A free jet wind tunnel is used for the probe calibration at constant speed but various yaw angles. The probe is mounted in a support device to

adjust yaw angles in the range ±30° in steps of 2.5°. The throat diameter of the convergent nozzle is 120 *mm* and the probe head is located 190 *mm* downstream of the nozzle exit plane. Air is supplied by a radial blower with variable rotational speed. The free stream velocity is adjusted to set the probe Reynolds number

$$\mathrm{Re}_d = \frac{wd}{\nu} \approx 7400. \qquad (14)$$

Since the throat Mach number Ma<0.2, the conditions are essentially incompressible. The streamwise turbulence intensity is about 1%. At a fixed yaw angle, the following measurement data are taken: a) the pressures sensed by the probe holes, b) the total pressure and the total temperature (Pt-100 resistor thermometer) and c) the ambient pressure. The ambient pressure is used as the free stream static pressure for the subsequent calculation of the hole as well as calibration coefficients. All pressures are sensed by piezoresistive transducers (HONEYWELL). The HP 3852A data acquisition system is controlled by a PC using LabVIEW (NATIONAL INSTRUMENTS).

4.2 Duct Wind Tunnel

The duct section of a low speed linear cascade wind tunnel is used for the experimental investigation of the wall proximity effects. The rectangular working section (150 *mm* by 400 *mm*) is located 29 *mm* upstream of the duct exit. The three-hole probe is traversed by a DANTEC traversing system normal to a thin flat plate which is positioned at the working section. Therefore, the probe is exposed to various wall proximity effects depending on its distance y from the flat plate. Air is supplied to the test section by an axial blower with constant rotational speed but variable inlet guide vanes. Prior to the investigation of the three-hole probe, the velocity distribution near the flat plate is measured with a DANTEC 55P15 hot-wire probe. The probe is calibrated in a DANTEC 90H02 flow unit according to King's law. The minimum distance from the wall is y=0.5 *mm* and a total of 200 points of spacing 0.25 *mm* are measured. At each point 50000 samples at a sampling rate of 50 *kHz* are taken. This results in a sampling time of 1000 *ms* per point. A low pass filter is set to 10 *kHz* for signal conditioning. Figure 3 shows the velocity distribution versus the wall distance y. The velocity distribution is quite constant with a boundary layer thickness of about 2 *mm*. Since the diameter of the probe stem is 6 *mm*, the minimum wall distance that can be established is y=3 *mm*. Therefore, the probe head experiences no velocity gradient and the velocity distribution can be used to investigate the wall proximity effect. The streamwise turbulence intensity is about 2% in the freestream region and it increases if the wall is approached.

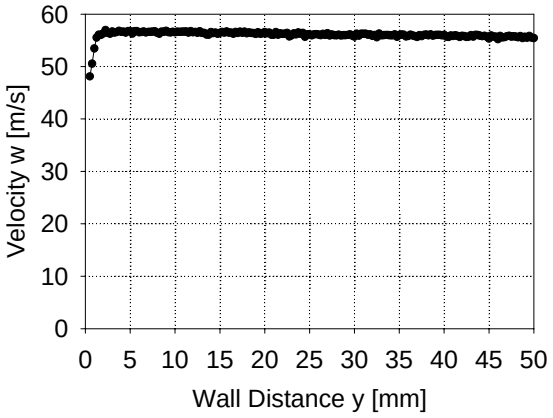

Figure 3. Velocity distribution near the flat plate

5. NUMERICAL INVESTIGATION

5.1 Numerical Method and Finite-Element Mesh

The numerical method is based on the governing equations for two-dimensional, incompressible, unsteady flow. The probe Reynolds number during the wind tunnel calibration is Re_d≈7400. The same Reynolds number is used for the numerical investigation and, therefore, the flow is treated as laminar. The finite-element based CFD code FIDAP8.7.0 [10] is performed to solve the governing equations. A nondimensional time step

$$\Delta t \frac{w}{d} = 0.1 \qquad (15)$$

is used for the 2nd order implicit time integration. A single vortex shedding period is resolved by about 70 time steps. Periodic flow is established after about 500 time steps at Strouhal numbers

$$Sr = \frac{fd}{w} \approx 0.136. \qquad (16)$$

This value can be compared with Sr≈0.134 for the flow around a square cross-section cylinder [11]. Figure 5 and Figure 6 show the probe head and the computational domain for the freestream flow and for the investigation of the wall proximity effect, respectively. The computational domain comprises a rectangle 25d by 38.5d. The inlet plane is positioned 15d upstream of the probe. The finite-element mesh in the vicinity of the probe is plotted in Figure 7. The total number of nodes of the structured mesh is about 24000. As can be seen from Fig. 7, the probe is modelled with smooth surfaces. This means that the geometry of the centre as well as the side holes is not modelled in detail.

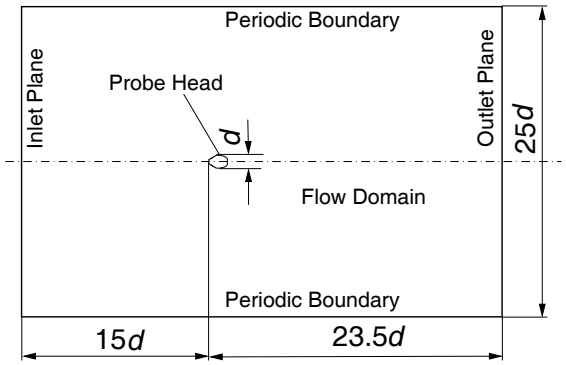

Figure 5. Computational domain with boundaries (freestream flow)

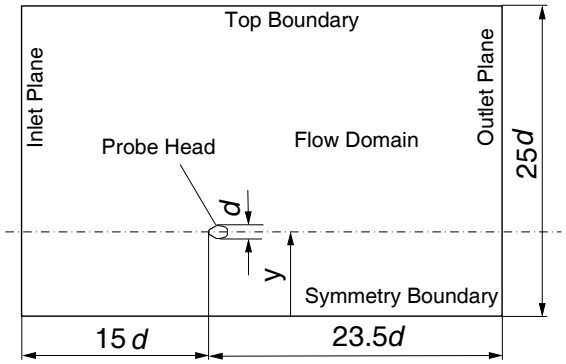

Figure 6. Computational domain with boundaries (wall proximity effect)

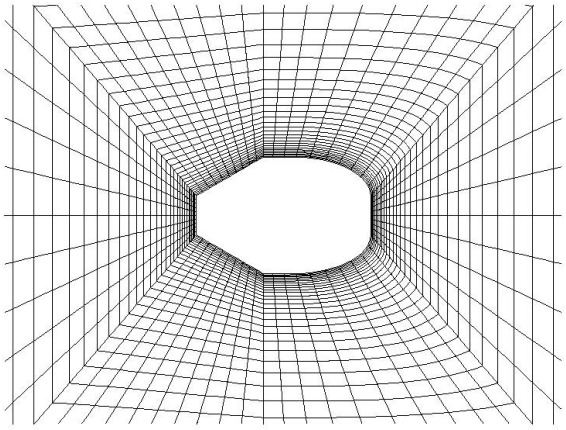

Figure 7. Finite-element mesh in the vicinity of the probe head

5.2 Boundary Conditions

The boundary conditions can be explained according to Fig. 5 and Fig. 6, respectively. At the inlet plane the constant velocity components are set according to the desired yaw angle $\Delta\beta$. Furthermore, no slip boundary conditions are applied to the surface of the probe head. At the outlet plane, the applied "traction-free" condition is equivalent to a constant static pressure distribution. For the investigation of the probe behaviour at different yaw angles, periodic boundary conditions are applied to the bottom and the top boundary (Fig. 5). The investigation concerning the wall proximity effect is performed with a symmetry boundary condition at the bottom boundary and a "traction-free" condition at the top boundary, respectively (Fig. 6).

6. RESULTS AND DISCUSSION

The hole coefficients k_1, k_2 and k_3 versus the yaw angle $\Delta\beta$ are plotted in Figure 8, Figure 9 and Figure 10, respectively. The agreement between the measured hole coefficient k_1 and the results gained from the streamline projection is acceptable. The measured distribution shows asymmetries for positive and negative yaw angles. These asymmetries are caused by a small deviation of the front face of the probe with respect to the plane normal to the probe axis. The CFD simulation gives lower values for k_1 at large yaw angles compared with the measurement as well as the streamline projection method. This difference is caused by the centre hole "1" which is not modelled by the CFD simulation. Due to this centre hole, the stagnation point is "fixed" at the front of the probe head and the decrease of the hole coefficient k_1 is less pronounced in the measured distribution. Great discrepancies between measurement, streamline projection method and CFD simulation are in part observed for the hole coefficients k_2 and k_3. These are the nondimensional pressures, sensed by the side holes. The general agreement is acceptable for the "pressure side" hole coefficients. These are k_2 for $\Delta\beta > 0$ and k_3 for $\Delta\beta < 0$, respectively. Great discrepancies occur for the "suction side" hole coefficients. These are k_3 for $\Delta\beta > 0$ and k_2 for $\Delta\beta < 0$, respectively. The computed hole coefficients are considerably too low. The flow separates at the sharp corner and a large laminar separation is established. It is expected that the real flow undergoes a separated flow transition and reattaches as a turbulent boundary layer. The streamline projection method does not take into account any separation and, therefore, the hole coefficients k_2 and k_3 are positive throughout the entire yaw angle range.

The direction coefficient k_β, the total pressure coefficient k_t and the static pressure coefficient k_s versus the yaw angle $\Delta\beta$ are plotted in Figure 11, Figure 12 and Figure 13, respectively. These coefficients are of practical interest for the application of the probe to measure a flow field. Good agreement between measurement, streamline projection and CFD simulation is achieved for the direction coefficient k_β as well as for the total pressure coefficient k_t. However, the yaw angle sensitivity of the direction coefficient is somewhat underpredicted by the streamline projection method. The slight asymmetry of the probe head with respect to the probe axis is reflected by the measured distribution of the total pressure

coefficient k_t. Great discrepancies between measurement, computation and streamline projection method are observed for the static pressure coefficient k_s. According to Eq. (4), these discrepancies are caused by the "suction side" hole coefficients k_2 and k_3, respectively.

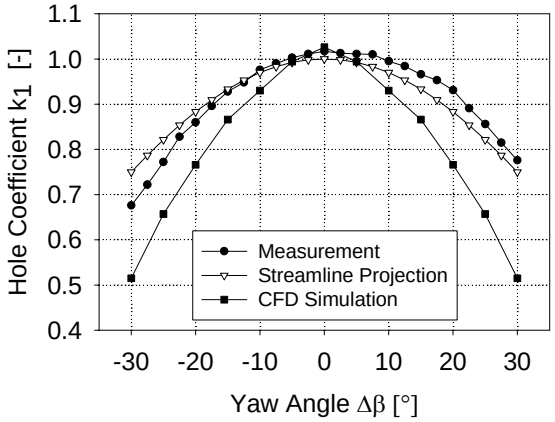

Figure 8. Hole coefficient k_1

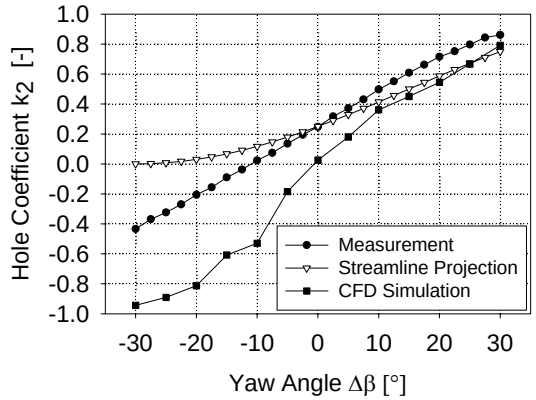

Figure 9. Hole coefficient k_2

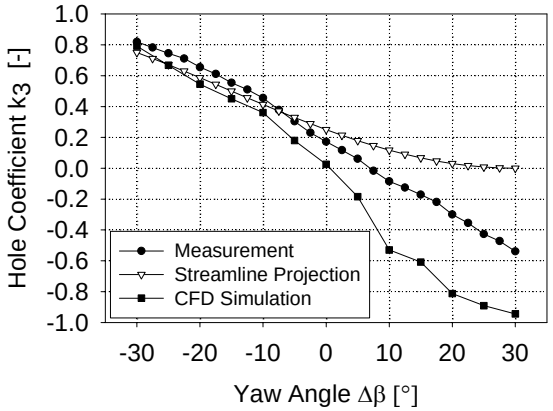

Figure 10. Hole coefficient k_3

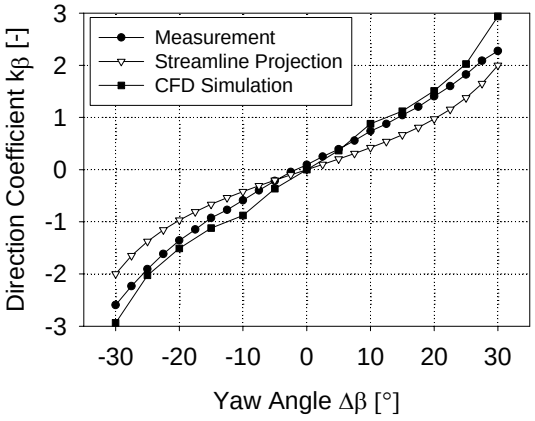

Figure 11. Direction coefficient k_β

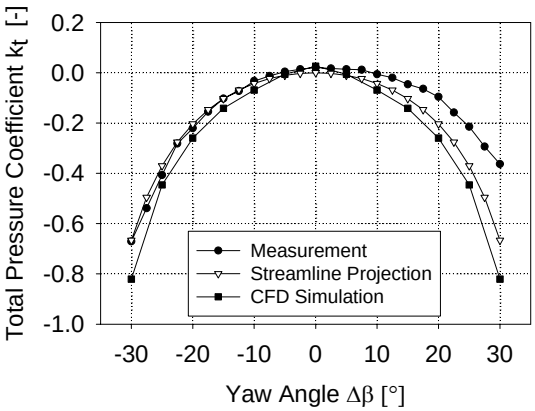

Figure 12. Total pressure coefficient k_t

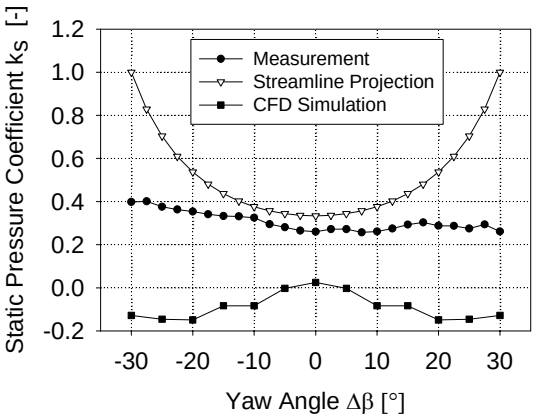

Figure 13. Static pressure coefficient k_s

The flow angle error $\Delta\varepsilon$ versus the nondimensional wall distance y/d is plotted in Figure 14. According to the definition of the positive yaw angle $\Delta\beta$, a negative flow angle error $\Delta\varepsilon$ indicates a flow direction away from the wall (Figs. 1 and 2). The measured flow angle error diminishes far away from the wall and it increases if the probe approaches the wall. The flow angle error

obtained from the streamline projection method (Eq. (13)) is plotted in Fig. 14, too. The streamline projection method over predicts the flow angle error. The discrepancy increases if the probe approaches the wall. Finally, the flow angle error obtained from the CFD simulation is given in Fig. 14. For $y/d > 4$, the agreement with the measurement results is acceptable. If the probe approaches the wall, the flow angle error is over predicted by the CFD simulation as well. It can be expected that the difference between the calculated and the measured flow angle errors for low values of y/d are due to three-dimensional effects. These effects are not taken into account by the streamline projection method nor by the CFD simulation.

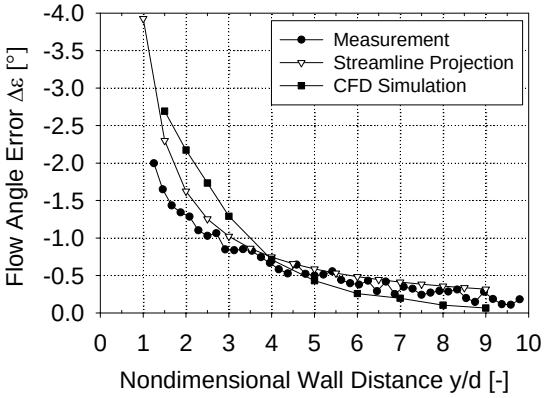

Figure 14. Flow angle error $\Delta\varepsilon$ due to the wall proximity effect

To support the assumptions of the streamline projection method, the measured hole coefficients k_1, k_2 and k_3 versus the nondimensional wall distance y/d are plotted in Figure 15. Far away from the wall, the hole coefficients can be compared with their respective values for zero yaw angle (Figs. 8 to 10). As can be seen k_2 and k_3 are not equal. This is due to a manufacturing inaccuracy of the probe head. If the probe approaches the wall the centre hole coefficient k_1 decreases slightly. Furthermore, the side hole coefficient k_2 away from the wall decreases slightly. Based on the distribution of k_1 and k_2 it can be expected that the stagnation point at the probe head is shifted toward the wall and the probe experiences a small negative yaw angle. Finally, the side hole coefficient k_3 increases if the probe approaches the wall. The streamline projection method assumes that the flow acceleration in the nozzle between the probe head and the wall is responsible for this behaviour. On the other hand, the reason for the increase of k_3 can be the negative yaw angle due to the shift of the stagnation point.

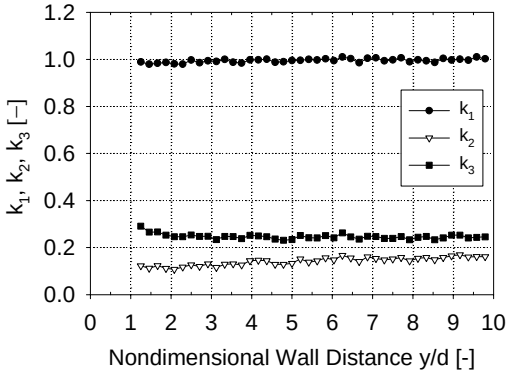

Figure 15. Measured hole coefficients k_1, k_2, k_3

Figure 16 presents a comparison of the measured flow angle error with results from the open literature. If the data are compared, it should be taken into account that the probes differ according to their head geometries. The geometry of the pyramid five-hole probe investigated by Bubeck [6] is not documented in detail, whereas for the five-hole cone probe of Borges and Vaz [9] a wedge angle $\delta = 45°$ is given. According to Eq. (13), the wedge angle influences the flow angle error sensitivity due to wall proximity effects. The data from Borges and Vaz [9] show a similar trend for the flow angle error induced by the wall proximity effect. It should be noted however that the results seem to decay asymptotically to an angle above zero, suggesting a small experimental error due to a shaft misalignment. The data from Bubeck [6] indicate that the flow angle error is positive for $y/d > 2.5$. It can be expected that this behaviour is also a result of a slight misalignment of the probe axis with respect to the wall. Nevertheless, the results from [6] and [9] show a steep increase of the flow angle error due to the wall proximity effect if the probe approaches the wall.

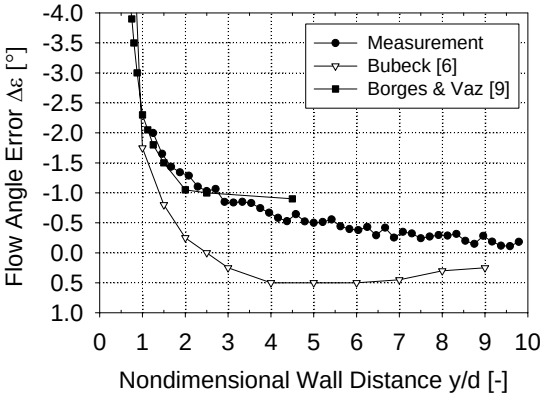

Figure 16. Comparison of measured flow angle error $\Delta\varepsilon$ with literature results

7. SUMMARY

A three-hole cobra probe has been calibrated in a free jet wind tunnel at different yaw angles in the range ±30°. The experimental results for the hole coefficients as well as the calibration coefficients are compared with data obtained from a simple streamline projection method. Furthermore, an unsteady CFD simulation has been performed to predict the flow field as well as the hole and calibration coefficients.

In contrast to external flow fields, internal flow fields in turbomachinery components are bounded by solid walls. Beside the velocity gradient due to wall boundary layers, a potential effect influences the flow around the probe head near the wall. The influence of this so-called wall proximity effect on the measured yaw angle has been investigated. Using a flat plate, a nearly constant velocity distribution with a very thin boundary layer has been established in a duct wind tunnel. When the probe head approaches the wall, the probe indicates an artificial flow angle induced by the wall proximity effect. The corresponding systematic flow angle error increases with decreasing distance between the probe head and the wall. If the flow angle error is limited to about 1°, the probe head should be placed more than about three head diameters away from the wall. This figure corresponds to the experimental findings from other investigations documented in the literature. Finally, it is shown that the streamline projection method as well as the CFD simulation can be used to estimate the flow angle error due to the wall proximity effect, at least qualitatively.

REFERENCES

[1] Dominy, R.G., and Hodson, H.P., 1993, "An Investigation of Factors Influencing the Calibration of Five-Hole Pressure Probes for Three-Dimensional Flow Measurements", *ASME J Turbomachinery*, Vol. 115, pp. 513-519.

[2] Willinger, R., and Haselbacher, H., 2003, "A Three-Hole Pressure Probe Exposed to Velocity Gradient Effects – Experimental Calibration and Numerical Investigation", Proc. *Conference on Modelling Fluid Flow (CMFF'03)*, September 3 – 6, Budapest, Hungary, pp. 413 – 420.

[3] Treaster, A.L., and Yocum, A.M., 1979, "The Calibration and Application of Five-Hole Probes", *ISA Transactions*, Vol. 18, No. 3, pp. 23 - 34.

[4] Heikal, H., 1980, „Dreidimensionale Vermessung aerodynamischer Strömungen mit Hakensonden. Teil 2: Ermittlung der Korrekturfaktoren", *Technisches Messen tm*, 47, Heft 12, pp. 449 – 453.

[5] Sitaram, N., Lakshminarayana, B., and Ravindranath, A., 1981, "Conventional Probes for the Relative Flow Measurement in Turbomachinery Rotor Blade Passages", *ASME J Engineering for Power*, Vol. 103, pp. 406 – 414.

[6] Bubeck, H., 1987, "Entwicklung einer Keilsonde zur dreidimensionalen instationären Strömungsmessung und deren Anwendung in einem Axialverdichter", *Dissertation Univ. Stuttgart, Institut für Thermische Strömungsmaschinen und Maschinenlaboratorium*.

[7] Smout, P.D., and Ivey, P.C., 1997, "Investigation of Wedge Probe Wall Proximity Effects: Part 1 – Experimental Study", *ASME J Engineering for Gas Turbines and Power*, Vol. 119, pp. 598 – 604.

[8] Smout, P.D., and Ivey, P.C., 1997, "Investigation of Wedge Probe Wall Proximity Effects: Part 2 – Numerical and Analytical Modeling", *ASME J Engineering for Gas Turbines and Power*, Vol. 119, pp. 605 – 611.

[9] Borges, A.R.J., and Vaz, D., 2003, "Simulations of a Conical Yaw Probe", Proc. *Conference on Modelling Fluid Flow (CMFF'03)*, September 3 – 6, Budapest, Hungary, pp. 407 – 412.

[10] FLUENT, 1998, "FIDAP8 Users Manual", FLUENT Inc.

[11] Sakamoto, H., Haniu, H., and Kobayashi, Y., 1989, "Fluctuating Force Acting on Rectangular Cylinders in Uniform Flow (on Rectangular Cylinders with Fully Separated Flow)", *Transactions of the Japan Society of Mechanical Engineers*, Series B 55, No. 516, pp. 2310 – 2317.

Conference on Modelling Fluid Flow (CMFF'06)
The 13th International Conference on Fluid Flow Technologies
Budapest, Hungary, September 6-9, 2006

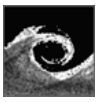

PHASE CHANGE PROCESS WITH FREE CONVECTION IN AN ANNULUS ENCLOSURE: NUMERICAL SIMULATIONS

Esam M. Alawadhi [1]

[1] Corresponding Author. Department of Mechanical Engineering, Kuwait University. POBox # 5969 Safat, KUWAIT. Tel.: +965 4985805, Fax: +965 4847131, E-mail: esam@kuc01.kuniv.edu.kw

ABSTRACT

Finite element technique is utilized to solve the solidification process of water in a horizontal annulus enclosure. The governing equations are Navier-Stokes and heat diffusion equations, and phase change simulation is based on apparent capacity method formulation. Water is initially still in the annulus at a temperature higher than the solidification temperature. Suddenly, the annulus inner cylinder temperature is dropped to a temperature lower than the solidification temperature. Ice is formed at the inner cylinder while natural convection flow is induced in the liquid portion. The goal of this paper is to evaluate the effect of natural convection flow of water on the solidification process. The results are presented in the form of a parametric study of effect of Rayleigh number on the significance of natural convection flow. Water density peak near solidification temperature creates a unique flow structure. High resolution capturing of solid/liquid moving boundary and the details of flow structure and temperature contour are presented. Accuracy of the simulations is evaluated by comparing the numerical results with available experimental data for natural convection flow in an annulus.

Keywords: water, solidification process, natural convection, phase change, annulus enclosure.

NOMENCLATURE

C_p	[*kJ/kg K*]	specific heat
$\overline{C}_p$	[*kJ/kg K*]	apparent heat capacity
h	[*kJ/kg*]	enthalpy
k	[*kW/m K*]	thermal conductivity
ΔL	*[kJ/kg*]	Latent heat
Nu	[-]	Nusselt number
n	[-]	normal to the surface
P	[kN/m^2]	pressure
PCM	[-]	Phase Change Materials
Pr	[-]	Prandtl number
Q	[kJ/m^2]	heat flux
Ra	[-]	Rayleigh number
r, R	[*m*]	dimensional and dimensionless *radii*
T	[*K*]	temperature
t	[*s*]	time
St	[-]	Stefan number
u, v	[*m/s*]	x-and y-direction velocity
C_p	[-]	static pressure coefficient

Greeks

α	[m^2/s]	thermal diffusivity
β	[*1/K*]	thermal expansion
θ	[-]	dimensionless temperature
μ	[*Pa s*]	viscosity
τ	[-]	dimensionless time
ρ	[kg/m^3]	density
Φ	[-]	general field variable
ν	[m^2/s]	kinematics viscosity

Subscripts and Superscripts

i	inner
ini	initial
o	outer
p	peak
s	solidification
n	iteration number
*	dimensionless quantity

1. INTRODUCTION

Phase change heat transfer has been extensively studied experimentally and theoretically in literature during past decade. Phase change has a wide range of application in science and engineering, for example, in solar energy storage units, industrial refrigeration, crystal growth, welding and casting. During melting, the specific heat of a substance increases by more than 100 times to store large amount of energy. On the other hand, during

solidification, the specific heat decreases to release the stored energy. The substance used to store or to release thermal energy by utilizing specific heat variation with the phase is called Phase Change Material (PCM), such as water, wax, and salt. Salt substrates are rarely used because they are highly corrosive.

PCMs are extensively employed in electronic devices as a method of thermal management [1, 2]. In electronic cooling, PCMs are used to absorb heat from high thermal dissipating components during operating times, and then, to release the stored energy during OFF times. In the thermal storage systems, especially in solar storage units, water PCM is commonly used to store energy during low-energy demand periods [3]. Typically, the PCM is placed in a rigid container close to a source of energy. Understanding phase change heat transfer mechanism in an enclosure is, therefore, essential to predict the thermal performance of a PCM thermal unit.

Modeling melting and solidification within a fixed enclosure have been of special interest in literature. Modeling phase change involves conduction mode of heat transfer in the solid portion, and conduction plus convection in the liquid portion. Two numerical techniques were developed for phase change simulations: transformation grids [4] and fixed grids [5]. Lacroix and Vollar [6] evaluated the accuracy of both techniques by comparing numerical results with experimental results. PCM melting in a rectangular enclosure by heating the bottom side was accomplished by Gong and Mujumdar [7]. The obtained complex flow pattern was consistent with published experimental results. Phase change heat transfer of a pure metal in a rectangular enclosure was studies by Mbaye and Bilgen [8]. Their results indicate that the Nusselt number passed through maximum when the enclosure aspect ratio is one. A rectangular composite cell filled with PCM and water was investigated by Ho and Chu [9], and The effect of ON/OFF pulsing boundary heat load was examined by Pal and Joshi [10].

In order to enhance the PCM melting or solidification rates, a high thermal conductivity metal matrix is commonly inserted into the PCM. Costa et al. [11] used a metal matrix to enhance PCM melting rate. A high porosity metal matrix was examined by Xing et al. [12] to increase the rate of PCM melting or solidification in a rectangular enclosure. Their results indicated that an order of magnitude of heat transfer enhancement over case where no metal matrix was used. When the PCM in the system is relatively small, or the PCM is placed in a metal matrix, natural convection flow in liquid portion is neglected, because conduction mode dominates heat transfer in the domain. This approximation is widely used in phase change simulations [13,14,15], but it could produce a significant computational error.

In this research, solidification process of pure water in a horizontal annulus enclosure is investigated. The annulus enclosure is chosen because it represents a practical geometry for thermal storage pipes [16,17]. Water is commonly used in thermal storage units, because of its availability, non-toxicity, non-flammability, and chemically stable. In addition, its latent heat of fusion is relatively high between the PCMs. Initially, water temperature is higher than solidification temperature. At a certain instant, the temperature at the inner cylinder is decreased to temperature lower than the solidification temperature. Ice is formed at the inner surface, and density gradient in liquid portion induces natural convection flow. The main objective of this paper is to evaluate the significance of natural convection flow on the solidification time. This is accomplished by comparing the thermal characteristics of conduction mode with conduction plus convection modes of heat transfer during water solidification, for wide range of Rayleigh numbers. The accuracy of the computations, including mesh refinement and solvers, is evaluated by comparing the numerical with available experimental data for natural convection flow.

2. Physical problem

A schematic diagram of the model that was used for numerical simulations is presented in Figure 1, as shown, a two-dimensional annulus enclosure of outer radius (r_o) and inner radius (r_i), with $r_o=2\times r_i$. The enclosure is initially at a temperature (T_{ini}) higher than water solidification temperature (T_s). At a certain instant (t = 0), the annulus inner cylinder temperature is dropped to (T_i), lower than the water solidification temperature. Solidification process of water begins at the inner cylinder, and simultaneously, natural convection flow is induced in the liquid portion until the water is completely solidified.

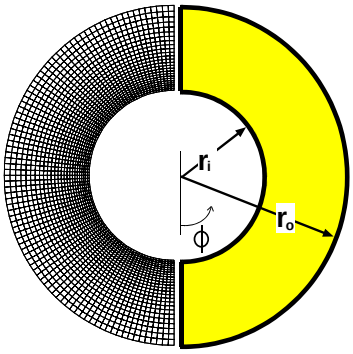

Figure 1. Schematics ad element mesh of phase change problem in an annulus enclosure.

2.1. Mathematical Model

The ensuing transient phase change heat transfer process inside an annulus enclosure is modeled with the following assumptions:

a. Buoyancy-induced convention in the liquid portion is laminar.
b. The effect of the thermal expansion of solid and liquid is not considered.
c. Viscous dissipation is neglected
d. Radiation effect is not considered.

Phase change simulations are done by using apparent capacity method, which is the sum of the sensible and latent heats, as follows

$$\overline{C}_p = C_p + \frac{\partial L}{\partial T} \tag{1}$$

C_p is the specific heat, and $\partial L/\partial T$ is the released latent heat. The apparent capacity can be approximated if the phase change transient temperature is finite, as follows:

$$\overline{C}_p = C_p + \frac{\Delta L}{\Delta T} \tag{2}$$

For numerical simulation, the apparent capacity is approximated as:

$$\overline{C}_p = \begin{cases} C_p & T \le T_s \\ C_p + \dfrac{\Delta L}{\Delta T} & T_s < T < T_s + \Delta T \\ C_p & T \ge T_s + \Delta T \end{cases} \tag{3}$$

The used dimensionless variables to make the governing equations are Rayleigh number (Ra), Prandtl number (Pr), Stefan number (St), and Fourier number (τ), and they are defined as, respectively:

$$Ra = \frac{g\beta \Delta T r_o^{\,3}}{\nu\alpha} \tag{4a}$$

$$\Pr = \frac{\nu}{\alpha} \tag{4b}$$

$$Ste = \frac{C_p \Delta T}{L} \tag{4c}$$

$$\tau = \frac{t}{r_o^{\,2}/\alpha} \tag{4d}$$

Based on the assumptions listed, the non-dimensional form of the governing equations are obtained as follows:

Continuity equation

$$\frac{\partial u^*}{\partial x^*} + \frac{\partial v^*}{\partial y^*} = 0 \tag{5}$$

x^*-momentum equation

$$\frac{\partial u^*}{\partial \tau} + u^* \frac{\partial u^*}{\partial x^*} + v^* \frac{\partial u^*}{\partial y^*} = -\frac{\partial P^*}{\partial x^*} + \Pr(\theta)\left[\frac{\partial^2 u^*}{\partial x^{*2}} + \frac{\partial^2 u^*}{\partial y^{*2}}\right] \tag{6}$$

y^*-momentum equation

$$\frac{\partial v^*}{\partial \tau} + u^* \frac{\partial v^*}{\partial x^*} + v^* \frac{\partial v^*}{\partial y^*} = \tag{7}$$

$$-\frac{\partial P^*}{\partial y^*} + \Pr(\theta)\left[\frac{\partial^2 v^*}{\partial x^{*2}} + \frac{\partial^2 v^*}{\partial y^{*2}}\right] + Ra\,\Pr(\theta)\theta$$

Energy equation

$$\Phi(Ste,\theta)\frac{\partial \theta}{\partial \tau} + u^* \frac{\partial \theta}{\partial x^*} + v^* \frac{\partial \theta}{\partial y^*} = \frac{\partial^2 \theta}{\partial x^{*2}} + \frac{\partial^2 \theta}{\partial y^{*2}} \tag{8}$$

where

$$\Phi(St,\theta) = \begin{cases} 1 & \theta \le \theta_s \\ 1/St & \theta_s < \theta < \theta_s + \Delta\theta \\ 1 & \theta \ge \theta_s + \Delta\theta \end{cases} \tag{9}$$

The dimensionless variables used to make the governing equations are defined as:

$$x^* = \frac{x}{r_o} \tag{10a}$$

$$y^* = \frac{y}{r_o} \tag{10b}$$

$$u^* = \frac{u}{\alpha/r_o} \tag{10c}$$

$$v^* = \frac{v}{\alpha/r_o} \tag{10d}$$

$$P^* = \frac{P}{\rho\alpha^2/r_o^2} \tag{10e}$$

$$\theta = \frac{T - T_i}{|T_s - T_i|} \tag{10f}$$

The dimensionless initial and boundary conditions are as follows:

$\tau = 0$: $u^* = v^* = 0$, and $\theta = \theta_{ini}$

$\tau > 0$:

At the annulus inner cylinder, $u^* = v^* = 0$, and $\theta = \theta_i$,

At the annulus outer cylinder, $u^* = v^* = 0$, and $\dfrac{\partial \theta}{\partial n} = 0$

At the top and bottom symmetries, $u^* = 0$, and $\dfrac{\partial \theta}{\partial n} = 0$

The local heat flux at the inner cylinder is extensively used to illustrate heat flow into the annulus, and it is defined as

$$q^* = \frac{\partial \theta}{\partial n} \tag{11}$$

2.2. Finite element model

Finite element model is used to solve the governing equations of viscous fluid flow and energy equations. The governing equations are coupled and solved simultaneously in the computational domain. The velocity components are obtained from the conservation of momentum

principle, and the pressure is from the conservation of mass principle, while temperature is from the energy equations. A four nodes quadrilateral element is used to discretize the computational domain, as shown in Figure 1. The finite element model consists of 2250 elements and 2366 nodes. Notice that the computational domain is reduced by half after taking the advantage of symmetry in the problem. Mesh independent solution is obtained by comparing the results of the shown model with models with higher number of elements. When increasing number of elements in the domain has an insignificant effect on the solution, the solution is called mesh independent solution. To ensure that the results are mesh independent, number of elements in the model is increased by 5%, 10%, and 25%. The difference between the 2250 elements model with other models was under 1.5%, and therefore, the 2250 elements model is adopted for the numerical simulations. Preconditioned Generalized Minimum Residual (PGMR) solver is employed to solve a set of discretized equations of energy and pressure, while Tri-Diagonal Matrix Algorithm (TDMA) solver is utilized to solve the velocity fields. The advection term in momentum and energy equations is formulated by using Streamline Upwind/Petrov-Galerkin (SUPG) approach [18]. All field variables are converged, and the following condition was used to declare convergence:

$$Max\left[\left|\frac{\Phi_{i,j}^{n+1}-\Phi_{i,j}^{n}}{\Phi_{i,j}^{n+1}}\right|\right]\le 1\times 10^{-6} \qquad (12)$$

Φ is any degree of freedom (DOF) of general field variable. The convergence monitor represents the sum of changes of a variable calculated from the result between the current $(n+1)^{th}$ iteration and previous $(n)^{th}$ iteration divided by the sum of the current values. In addition, the conservation of energy is examined, and the difference between the heat flow in and stored energy through latent and sensible heats was less than 1%.

2.3. Numerical validation

Kuhen and Goldstein [19] conducted an experimental study of natural convection without phase change in a cylindrical annulus. The code was validated by simulating natural convection in an annulus for the conditions presented by Kuhen and Goldstein. The inner and outer radii of the annulus, respectively, are 0.0463m and 0.0178 m. the working fluid is air, and its properties are assumed temperature independent, except the density. The inner and outer cylinder walls are set to a temperature of 373K and 327K, respectively. No slip velocity boundary condition is imposed on the walls. Based on the air properties, temperature boundary conditions and geometry, the Rayleigh number is 4.95×10^4. The temperature profiles long the top and bottom symmetry lines of numerical results and the experimental data are shown in Figure 2a and Figure 2b, respectively. As shown, the agreement between the numerical and experimental results is excellent.

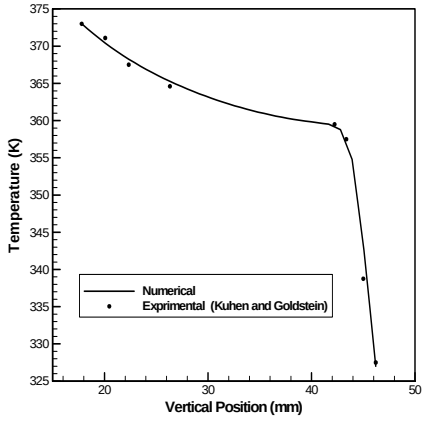

(a)

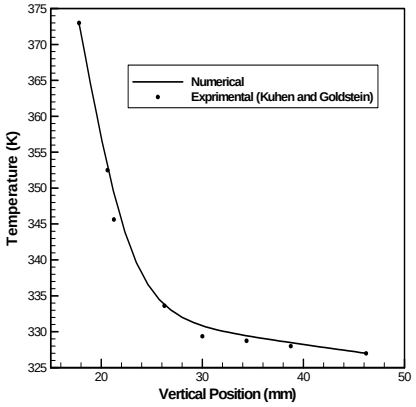

(b)

Figure 2. Comparison of temperature along symmetry line at a) top and b) bottom for natural convection flow in an annulus enclosure.

3. Results

3.1. Phase Change Simulations

Water is used as a PCM, water is selected because it is commonly used in thermal storage pipes, and its thermo physical properties are listed in Table 1 [20]. Water exhibits a negative volume expansion coefficient below 4^oC and positive volume expansion above 4^oC. This phenomenon creates a unique flow structure during water solidification. The effect of free convection flow in liquid portion during the solidification process is examined in the following.

Table 1. Thermo-physical properties of water

Specific heat (C_p)	4.202 kJ/kg K
Thermal conductivity (k)	0.56 W/m K (liquid) 2.26 W/m K (solid)
Viscosity (μ)	1.53×10^{-3} Pa s
Latent heat (L)	335 kJ/kg K
Density (ρ)	$999.840281 + 0.067326\ T - 0.008944\ T^2 + 8.78 \times 10^{-5}\ T^3 - 6.62 \times 10^{-7}\ T^4$

Figure 3 shows the flow field evaluation and temperature contour at four time steps, τ = 0.05, 0.1, 0.15, 0.25, for Ra = 1×10^7. Each curve in the plot on the right hand side represents a streamline, while each curve on the left hand side represents isotherm. Initially, water temperature is in liquid phase (θ_{ini}). At $\tau > 0$, the inner wall temperature (θ_i=0) is dropped to temperature lower than water freezing temperature (θ_s=1). Ice starts to form at the inner wall, and at the same time, contour clockwise (with respect to the right half of the annulus) natural convection flow is induced in the liquid portion.

Figure 3a shows one recirculating cell is formed and the temperature of water is higher than its peak density temperature (θ_p = 3). In addition, there is a wide temperature gradient at the upper region near the inner wall. Cold water adjacent to the inner cylinder is continually replaced by warm water coming from the outer cylinder. Water stream is cooled as it flows naturally close to the inner cylinder to leave the inner to outer cylinder. Therefore, the temperature differences the inner cylinder and the water is maximum at the upper region, and minimum at the lower region. The variations of the temperature difference explain the observed wide temperature gradient at the upper region of the annulus. Up to this time (τ = 0.05), one recirculating cell is formed. As time progresses, two additional recirculating cells are formed, as shown in Figure 3b, one at the top and the other at the bottom of the original recirculating cell. The original cell is counter clockwise direction, while the other two are clockwise direction. Water temperature decreases as it flows close to the inner cylinder, and reaches the density peak temperature. When water temperature becomes less than (θ_p), water density decreases to create a clockwise flow cell, and therefore, the direction of flow is reversed from contour clockwise to clockwise direction to create a small cell below the original cell. The direction of original cell is still contour clockwise, because the temperature of the cell is higher than the density peak temperature. The formation of the top recirculating cell is due to thermal instability.

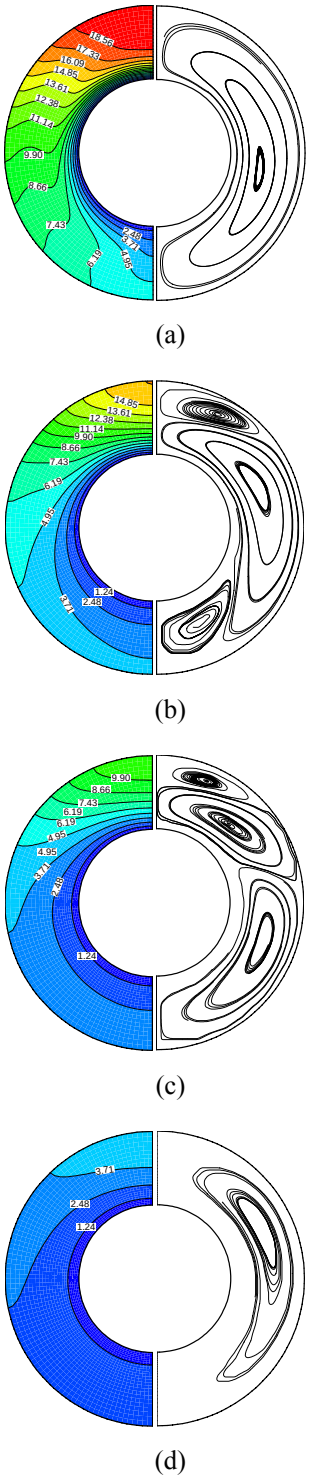

Figure 3. Flow field evaluation and temperature contour of the solidification process for Ra = 1 × 10^7 at (a) τ = 0.05, (b) τ = 0.1, (c) τ = 0.15, (d) τ = 0.25.

This phenomenon is not explained in this research because it is extensively illustrated in literature [21,22]. At τ = 0.15 (Figure 3c), liquid water is further cooled and the temperature of the lower half of the annulus becomes less than θ_p. The bottom cell is expanded to occupy most of the annulus

space. At τ = 0.25 (Figure 3d), The temperature contours indicates that the entire water temperature is decreased to temperature less than θ_p. Hence, water density decreases with temperature, and one clockwise recirculating cell dominates the liquid water portion.

3.2. Heat flux at the inner cylinder

Figure 4 shows the local heat flux at the inner cylinder for Ra=1×10^7 at different time instants. This figure indicates that heat flux at the top region is higher than the bottom region. At the beginning of the solidification process, warm water stream coming from the outer cylinder firstly contacts the upper section of the inner cylinder. The temperature difference between the water and inner cylinder is maximum at the upper section of the inner cylinder, and therefore, the local heat flux is maximum. As time progresses (τ > 0.4), the local heat flux decreases and the difference between the top and bottom section is reduced, showing effect of natural convection becomes insignificant, and heat transfer mode in the annulus is dominated by conduction. At $\tau = \infty$, the heat flux approaches zero, indicating all water becomes ice.

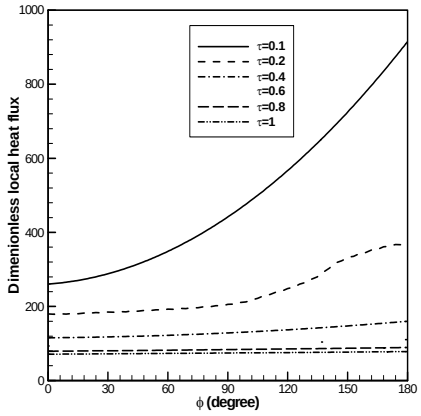

Figure 4. Variation of local heat flux at the inner cylinder with time, for Ra = 1×10^7

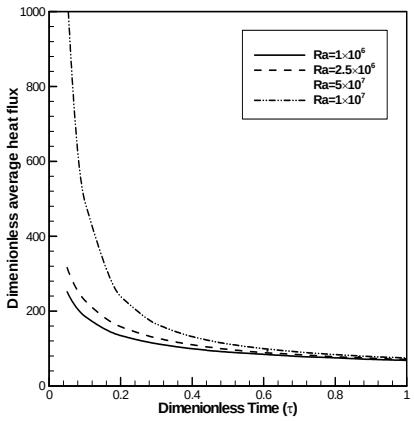

Figure 5. Variation of average heat flux at the inner cylinder with time.

The variation of average dimensionless heat flux at the inner cylinder with time is presented in Figure 5, for Ra = 1×10^6 to 1×10^7. For all Ra, the heat flux at the beginning of the solidification process is high due to high temperature difference between the inner cylinder and water. As time progresses, the average heat flux decrease to eventually reaches zero. At any instant of time, the average heat flux increases as the Ra increases. This observation is expected because high Ra means high initial temperature difference between the inner cylinder and water.

3.3. Effect of natural convection flow

In order to evaluate the effect of natural convection flow on the phase change process, the solidification process in the annulus is solved without natural convetion flow by solving only the energy equation. Figure 6 shows the solidification time for conduction and conduction plus convection modes of heat transfer with Ra = 0.25×10^6 to 1×10^7. For 1.25×10^6<Ra<1.25×10^6, the solidification time for conduction and conduction plus convection is almost the same, showing a negligible effect of the convection as a mode of heat transfer. Hence, eliminating the natural convection flow during phase change simulation is an acceptable approximation. For Ra $\geq$ 1.25×10^6, Figure 6 indicates that the effect of natural convection becomes significant. High speed of the recirculating flow decreases the thermal resistance at the moving solid/liquid interface by transporting warm water from the outer cylinder boundary to the interface.

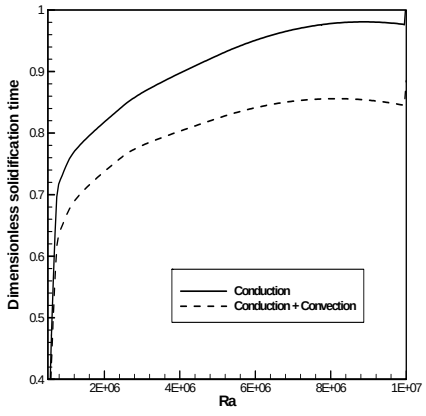

Figure 6. Effect of Rayleigh number on the water solidification time, for conduction and conduction plus convection modes of heat transfer, for Ra = 1×10^7.

As the Ra increases, the strength of the natural convection flow increases which reduces the thermal resistance in the domain and accelerates the solidification time. With Ra=1×10^7, the natural convection decreases the solidification time by 13.3

%. Figure 7a and 7b show the average heat flux at the inner cylinder for conduction and conduction plus convection, for Ra = 1×10^6 and 1×10^7, respectively. For Ra = 1×10^6, Figure 7a indicates that the heat flux differences between the conduction and conduction plus convection is negligible. The strength of the natural flow is weak that does not decrease the thermal resistance in the annulus. When the Ra is increase to 1×10^7, Figure 7b indicates that the effect of natural convection is initially insignificant (τ <0.15), because the difference between the two cases is negligible. During the period 0.15 <τ < 0.6, the natural flow increases the heat flow into the annulus by decreasing the thermal resistance in the annulus. Natural convention flow improves heat flow in the annulus by transporting warm water from the outer boundary to the freezing interface. For τ > 0.6, the heat flux of the two cases is close, indicating that the natural flow is speeding down and flow temperature becomes close to freezing temperature.

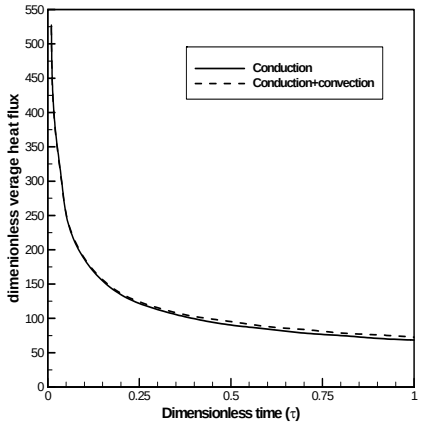

(a)

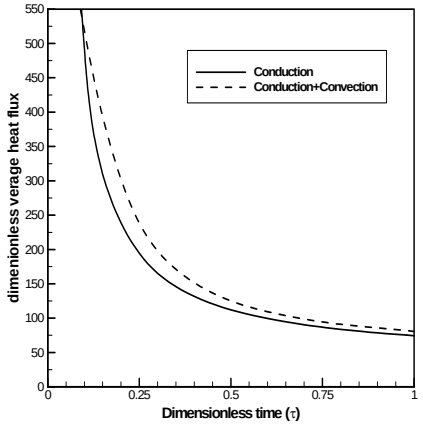

(b)

Figure 7. Variation of average heat flux at the inner cylinder with time, for (a) Ra = 1×10^6, (b) Ra = 1×10^7

4. SUMMARY

Numerical simulations of water solidification in a horizontal annulus enclosure are accomplished by utilizing finite element method. The main objective of this paper was to evaluate the effect of natural convection flow during water solidification. Natural convection is commonly neglected in phase change simulations, even if the Rayleigh number is high. The results indicate that the effect of natural convention flow is significant for wide range of Rayleigh numbers, and this significance is increased as the Rayleigh number is increased. If the Rayleigh number is less than 1.25×10^6, the convection mode of heat transfer becomes insignificant factor on the solidification rate. Therefore, eliminating the convection effect in the simulation is a valid approximation. This approximation will highly simplify the computations. For Rayleigh number higher than 1.25×10^6, natural convection flow plays an important rule in reducing thermal resistance in the domain, which accelerates the solidification rate. Therefore, neglecting natural convection flow produces a significant numerical error.

REFERENCES

[1] Alawadhi, E. and Amon, 2002, C., "PCM for Time-Dependent Thermal Management for Electronic Devices," *Proceedings of 34th National Heat Transfer Conference*, Proceeding CD.

[2] Estes, R. C., "The Effect of Thermal Capacitance and Phase Change on Outside Plant Electronic Enclosure," 1992, *IEEE Transactions on Components, Hybrids, and Manufacturing Technology*, Vol. 5, pp. 843-849.

[3] Velraj, R., Seeniraj, R. V., Hafner, B., Faber, C., Schwarzer, K., 1999, "Heat Transfer Enhancement in a Latent Heat Storage System," *Solar Energy*, Vol. 65, pp. 171-180.

[4] Voller, V., Cross, M., 1981, "Accurate Solution of Moving Boundary Problem Using the Enthalpy Method," *Int. J. Heat Mass Transfer*, Vol. 24, pp. 545-556.

[5] Voller, V. R., Swaminathan, C. R., 1990, "Fixed Grid Techniques For Phase Change Problems: A Review," *International Journal for Numerical Methods in Engineering*, Vol. 30, pp. 875-898.

[6] Lacroix, M. and Voller, V. R., 1990, "Finite Difference Solution of Solidification Phase Change Problem: Transformed Versus Fixed Grids," *Num. Heat Transfer Part B*, Vol. 17, pp. 25-41.

[7] Gong, Z. Mujumdar, A., 1998, "A Finite Element method for Convection-Dominated Melting and Solidification Problem," *Int. J. num. Meth. Heat Fluid Flow*, Vol. 8, no. 4, pp. 393-408.

[8] Mbaye, M., and Bilgen, E., 2001, "Phase change process by natural convection-diffusion in rectangular enclosures," *Heat and Mass Transfer,* Vol. 37, pp. 35-42.

[9] Ho, C. and Chu, C. , 1999, "On Cooling Behavior of Vertical Plane in a Phase Change/Water Composite Enclosure Under Pulsing Heat Load," *Heat Mass Transfer*, Vol. 34, pp. 509-514.

[10] Pal, D., and Joshi, Y., 1998, "Thermal management of an avionics model using solid-liquid phase change materials," *J. of Thermophysics and Heat Transfer* , Vol. 256, pp. 12-17.

[11] Costa, M., Buddhi, D., and Oliva, A., 1998, "Numerical simulation of a latent heat thermal energy storage system with enhanced heat conduction," *Energy Conver.s Mgmt*., Vol. 9, pp. 319-325.

[12] Xing, T., Khan, J., Amin, R., 1996, "Enhancement of heat transfer by inserting a metal matrix into a phase change material," *Num. Heat Transfer: Part A*, Vol. 30, pp. 125-131.

[13] Li, H., Hsieh K., Goswami, D. Y., 1996, "Conjugate Heat Transfer Analysis of Fluid Flow in a Phase-Change Energy Storage Unit," *Int. J. Num. Meth. Heat Fluid Flow*, Vol. 6, pp. 77-90.

[14] Ismail, K., Goncalves M. , 1999, "Thermal Performance of a PCM Storage Unit," *Energy Conv. Manag*. , Vol. 40, pp. 115-138.

[15] Lu, T., 2000, "Thermal Management of High Power Electronics with Phase Change cooling," *Int. J. Heat Mass Trans*., Vol. 43, pp. 2245-2256.

[16] Cao, Y., Faghri, A., 1991, "Performance Characteristics of a Thermal Energy Storage Module: a Transient PCM/Forced Convection Conjugate Analysis," *Int. J. Heat Mass Transfer*, Vol. 34, pp. 93-101.

[17] Lacroix, M., 1993, "Study of the Heat Transfer Behavior of a latent Heat Thermal Energy Storage Unit with a Finned Tube," *Int. J. Heat Mass Transfer*, Vol. 36, no. 8, pp. 2083-2092.

[18] Brooks A.,. Hughes, T., 1982, "Streamline Upwind/Petrov-Galerkin formulation for convection dominated flow with particular emphasis on the incompressible Navier-Stokes equations," *comp. Meth. Appl. Mech. Eng*., Vol. 32, pp. 199-259.

[19] Kuehn T., Goldstein, R., 1978, "An Experimental Study of natural Convection Heat Transfer in Concentric and Eccentric Horizontal Cylindrical Annuli," *J. Heat Transfer*, Vol. 100, pp. 635-640.

[20] Giangi, M., Stella, F., Kowalewski, T., 1999, "Phase change problem with free convection: fixed grid numerical simulation," *Comput Visual Sci*., Vol. 2, pp. 123-128.

[21] Yoo, Joo-Sik, 1998, "Natural Convection in a Narrow Horizontal Cylinder Annulus: Pr ≤ 0.3," *Int. J. Heat Mass Transfer*, Vol. 41, pp. 30553-3073.

[22] Mizushima, J., Hayashi, S., Adachi, T., 2000, "Transitions of Natural Convection in a Horizontal Annulus," *Int. J. Heat Mass Transfer*, Vol. 44, pp. 1249-1257.

Conference on Modeling Fluid Flow (CMFF'06)
The 13th International Conference on Fluid Flow Technologies
Budapest, Hungary, September 6-9, 2006

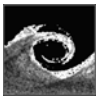

NUMERICAL SIMULATION OF INFLUENCE OF CHANGES OF FLOW PARAMETERS AT NOZZLE OUTLET ON DISTRIBUTION OF MASS AND ENERGY TRANSPORT IN CYLINDRICAL CHAMBER

Jarosław BARTOSZEWICZ[1], Leon BOGUSŁAWSKI[2]

[1] Corresponding Author. Poznan University of Technology, Chair of Thermal Engineering, Piotrowo 3, PL-60965 Poznan, Poland
Tel.: +48 61 6652209, Fax: +48 61 6652281, E-mail: jaroslaw.bartoszewicz@put.poznan.pl
[2] Poznan University of Technology, Chair of Thermal Engineering. E-mail: leon.boguslawski@put.poznan.pl

ABSTRACT

The results of numerical analysis of a turbulent flow in a cylindrical chamber will be presented in this paper. Results of calculations for different velocity at a nozzle outlet will be analyzed. The model of calculation assumed that the time of averaging is long in comparison with the time scale of the turbulent vortex. For the simulation of the turbulent flow the standard high-Reynolds-number form of the k-ε model was used, as proposed by Launder and Spalding, with inclusion of allowance for buoyancy effects. Results of the numerical analysis are presented in the pictures for average velocity, pressure, kinetic energy of turbulence and rate of dissipation of kinetic energy of turbulence on the walls of a cylindrical chamber. The results of calculations of velocity field for many variants of entrance velocity will be presented. This paper is a first part of analysis of the influence of boundary conditions on the change of the flow in a cylindrical vessel.

Keywords: reverse chamber, cylindrical vessel, turbulent flow, turbulent model, round jet

NOMENCLATURE

C	[-]	empirical constant
D	$[m]$	diameter
g	$[m/s^2]$	gravitational vector
k	$[m^2/s^2]$	kinetic energy of turbulence
p	$[Pa]$	pressure
Pr	[-]	Prandtl number
t	$[s]$	time
U	$[m/s]$	axial component of velocity
V	$[m/s]$	radial component of velocity
x	[m]	axial coordinate along chamber
y	[m]	radial coordinate across chamber
z	[m]	distance from the outlet
ε	$[m^2/s^3]$	dissipation rate of turbulence
φ	[-]	dependent variable
ν	$[m^2/s]$	kinematic viscosity
ρ	$[kg/m^3]$	density
τ	$[Pa]$	shear stresses

Subscripts and Superscripts

t	turbulent
max	maximum

1. INTRODUCTION

Applications of round jets in different configurations are widely used in technique. Usually, published applications concern axisymmetrical round jets leaving the nozzles with or without combustion, axisymmetrical round jets impinging the wall with or without combustion, jets of fluid generated by multi-hole nozzles systems, laminar or turbulent jets flows around a body and other configurations. The return flow in two coaxial pipes can be treated as a flow similar to round impinging jet in a special configuration. This kind of flow geometry can be found in many technical applications. There is no literature information concerning such a geometry. Because of it a numerical simulation of the distribution of velocity, temperature, pressure and turbulence in a jet flowing through a cylindrical vessel was performed and analyzed. The authors compared first results of numerical analysis with experimental investigations for a jet impinging a flat wall [1,2]. The results of comparisons are discontenting, because the differences between values are quantitative and qualitative, as well. The experimental data for an impinging jet can be compared with the numerical results only in the first part of a round jet, when the distance between the outlet of the nozzle and the impinging wall is very small. The first numerical solution gives new information about the structure of the fluid flow in the cylindrical vessel and distribution of time-average value as well as about turbulence parameters on the walls. Most of the previous experiments and numerical computations

on solar heat energy storage tanks were performed to analyze and measure the heat transfer with the negligence or the limitation in the turbulence analysis for a liquid flow [2,5,8].

For the numerical simulation of a turbulent flow in a cylindrical vessel the Phoenics program developed by CAM Ltd. [5] was used. For turbulent flows, Phoenics can solve equations that are time-averaged. It is presumed that the time over which the averaging is made is long compared with the time scale of the turbulent motion. In non-stationary flows it must also be small compared with the time scale of the mean flow. The k-ε turbulence model proposed by Harlow and Nakayama is by far the most widely used two-equation eddy-viscosity turbulence model, mainly because the ε does not require extra terms near walls. This model is widely used because its effectiveness is well documented in the literature. PHOENICS code provides the standard high-Reynolds-number form of the k-ε model, as presented by Launder and Spalding [3,4], with the inclusion of allowance for buoyancy effects for low Reynolds number flows.

The results of the flow analysis are presented in the pictures for: pressure, an average velocity, kinetic energy of the turbulence and shear stresses. The geometry of the analyzed cylindrical chamber is shown in Figure 1. A numerical calculation was carried out for the diameter of the nozzle D = 10 mm, where this diameter is used as a characteristic dimension of the vessel. The distance between the nozzle and the impinging wall was $10{\cdot}D$ and the radius of the cylindrical vessel was $5{\cdot}D$. Because of many combinations of the dimensions only such a numerical simulation using numerical code validated experimentally for a few dimensions gives a possibility to predict the flow and local shear stresses distributions.

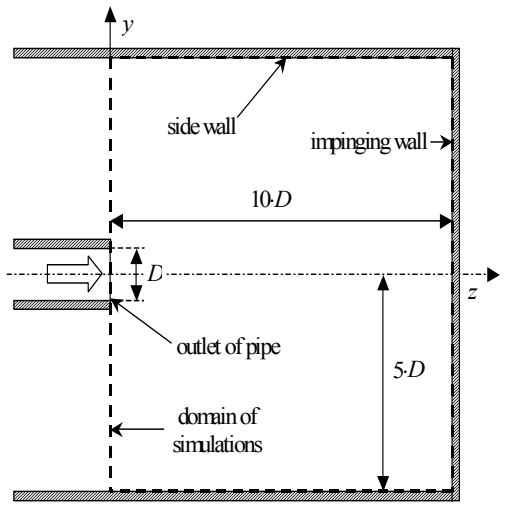

Figure 1. The scheme of numerical domain

2. NUMERICAL ANALYSIS

Phoenics provides solutions of discretized versions of sets of differential equations having the general form as follow:

$$\frac{d(\rho\cdot\varphi)}{dt} + div\left[\rho\cdot\vec{u}\cdot\varphi - G\cdot grad(\varphi)\right] = S \qquad (1)$$

where ρ is density, φ stands for any conserved property, such as enthalpy, momentum per unit mass, mass fraction of a chemical species, turbulence energy, etc., $\vec{u}$ stands for the velocity vector component, G represents the exchange coefficient of the entity φ and S stands for the source rate of φ. When time-averaged correlations of various quantities are not described precisely, as it happens commonly when turbulent flows are to be simulated, special expressions have to be introduced for G and S, accounting for the correlations between the velocity, density, φ, and other properties of the flow and of the fluid. Auxiliary variables are distinguished from dependent variables by being derived from algebraic equations rather than from differential ones. The examples of auxiliary variables are: molecular properties of the media such as laminar viscosity, diffusivity, Prandtl number etc., thermodynamic properties such as density, saturation enthalpy, temperature (if not a dependent variable), etc., quantities characterizing the state of the turbulence such as the length scale, the turbulent kinematic viscosity, the generation rate, etc. and inter-phase-transport parameters such as the rates of evaporation and condensation, the coefficient of inter-phase friction and heat transfer, etc.

For high turbulent Reynolds numbers, the standard form of the k-ε model of turbulence may be summarized as follows:

$$\frac{\mathrm{d}(\rho k)}{\mathrm{d}t} + \frac{\mathrm{d}}{\mathrm{d}x}\left[\rho U k - \frac{\rho\nu_t}{Pr(k)}\frac{\mathrm{d}k}{\mathrm{d}x}\right] = \rho(P_k + G_b - \varepsilon), \qquad (2)$$

$$\frac{\mathrm{d}(\rho\varepsilon)}{\mathrm{d}t} + \frac{\mathrm{d}}{\mathrm{d}x}\left[\rho U \varepsilon - \frac{\rho\nu_t}{Pr(\varepsilon)}\frac{\mathrm{d}\varepsilon}{\mathrm{d}x}\right] = \rho\frac{\varepsilon}{k}(C_1 P_k + C_3 G_b - C_2\varepsilon), \qquad (3)$$

$$\nu_t = C\frac{k^2}{\varepsilon}. \qquad (4)$$

P_k is the volumetric production rate of k by shear forces. It can be calculated from the equation:

$$P_k = \nu_t\left(\frac{\mathrm{d}U}{\mathrm{d}y} - \frac{\mathrm{d}V}{\mathrm{d}x}\right)\frac{\mathrm{d}U}{\mathrm{d}y} \qquad (5)$$

G_b is the volumetric production rate of k by gravitational forces interacting with density gradients. It is calculated from the following relation:

$$G_b = -v_t \cdot g \cdot \frac{\frac{\mathrm{d}\rho}{\mathrm{d}x}}{\rho \cdot Pr(h)} \tag{6}$$

where $P_r(h)$ is the turbulent Prandtl number. Using the Boussinesq approximation in which the variations of density are expressed by means of variation of enthalpy, G_b can be reduced to the following expression:

$$G_b = -v_t \cdot \beta \cdot g \frac{\frac{\mathrm{d}h}{\mathrm{d}x}}{c_p \cdot Pr(h)} \tag{7}$$

where h is the enthalpy, c_p is the specific heat at constant pressure, and β is the volumetric coefficient of expansion. The following constants are normally used: $Pr(k) = 1.0$, $Pr(\varepsilon) = 1.314$, $C = 0.09$, $C_1 = 1.44$, $C_2 = 1.92$, $C_3 = 1.0$.

3. BOUDARY CONDITIONS

In the paper the results of numerical calculations of the flow of a round jet in a cylindrical chamber are shown in Figure 1. The diameter of the nozzle D is 0.01 m, the distance between the nozzle and the impinging wall is 0.1 m and the radius is 0.05 m. The chamber is an axisymmetrical vessel, where one can observe 180 degree change of the fluid flow direction. The numerical calculation was performed for many variants velocity at the outlet section of the nozzle. The velocity was changing from 2 to 50 m/s and the turbulence intensity was 4%. The results of numerical analysis are presented as normalized by maximum value in the domain of simulations on an axis and on the impinging wall and a side wall, because these distributions are the effect of the reactions between the round jet and the walls. In first part of the flow has a structure of a free jet, next it has a structure of an impinging jet and modified impinging jet and in the last one it flows out of the chamber.

4. RESULTS

The results of numerical calculations were presented in the pictures, which are divided into four parts: axis distribution of dependent variables, distribution on the impinging and the side wall. The radial distribution of axial and radial components of the velocity and kinetic energy of turbulence were shown in the last part. In Figure 2 axial distribution of the components of velocity, pressure and kinetic energy of turbulence are presented. In Figures 3 and 4 the radial distribution of pressure, the component of velocity, kinetic energy of turbulence and shear stresses on the impinging surface and the side wall are illustrated. In Figures from 5 to 7 the radial distribution of the component of velocity, kinetic energy of the turbulence inside a reverse chamber are presented.

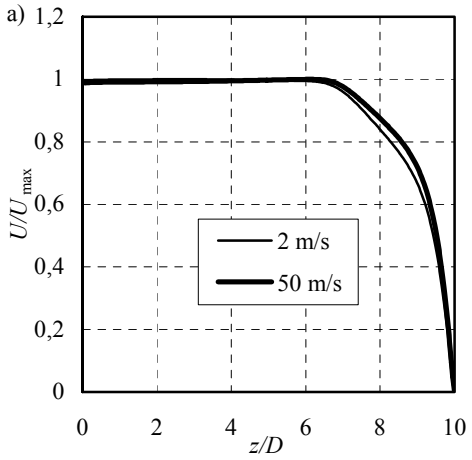

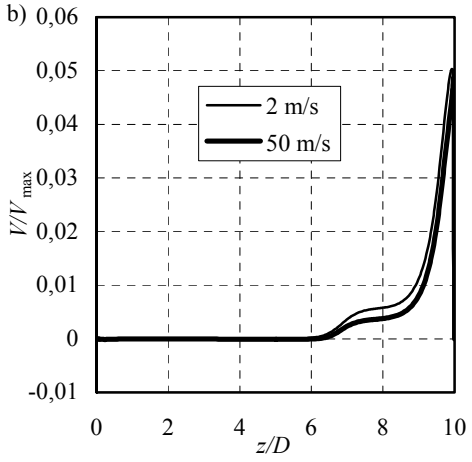

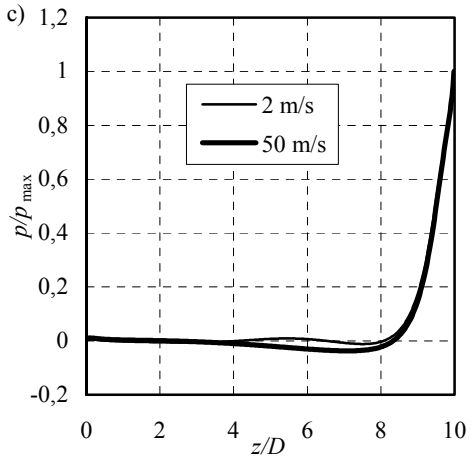

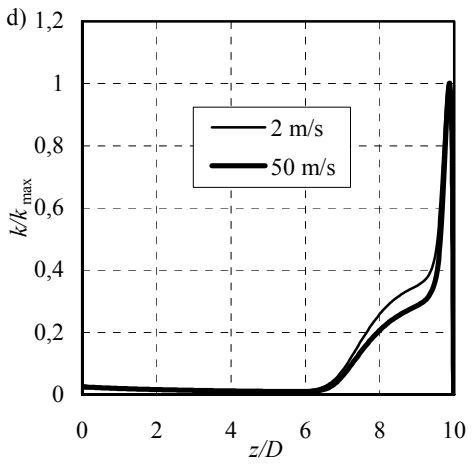

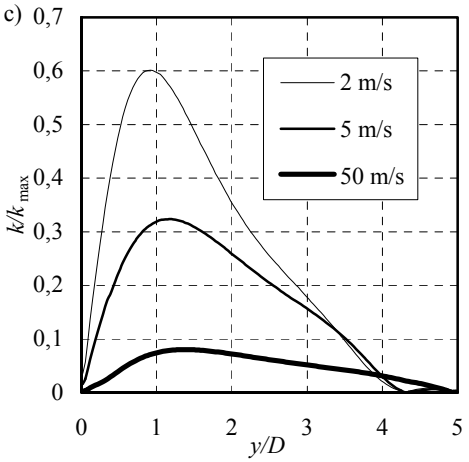

Figure 2. The distributions of dependent values in jet axis: a – axial component of velocity, b – radial component of velocity, c – pressure, d – kinetic energy of turbulence

In all the pictures characteristic lines for the velocity from 2 to 50 m/s at the outlet of the nozzle, or only characteristic profiles, are shown.

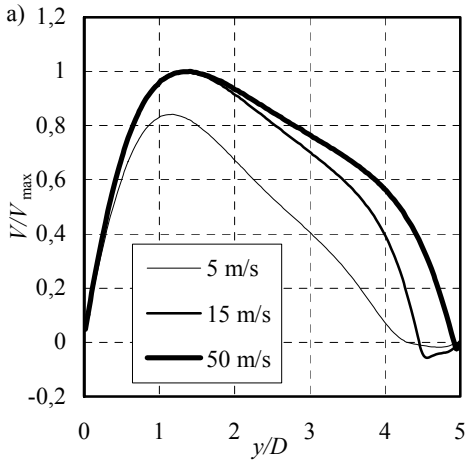

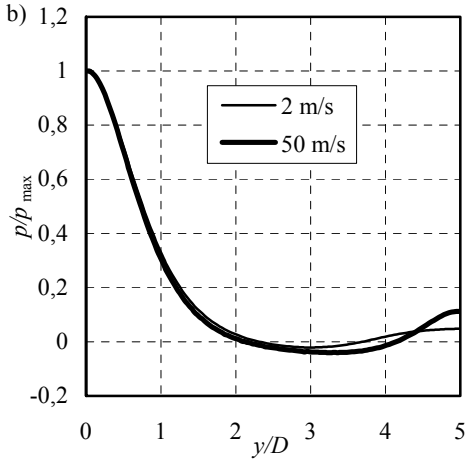

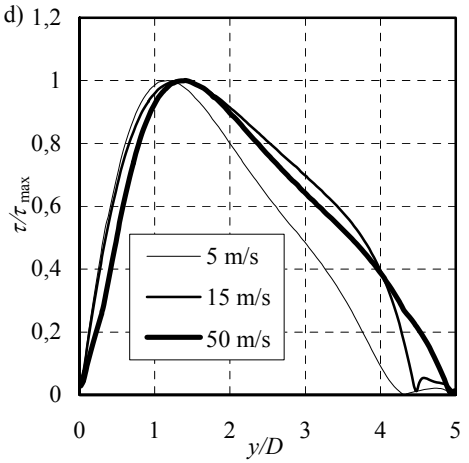

Figure 3. Distributions of dependent values on the impinging wall: a – radial component of velocity, b – pressure, c – kinetic energy of turbulence, d – shear stresses

All the dependent variables are presented as values normalized by maximum value in a reverse chamber for all pictures. In Figure 2a it is clearly visible that above the stagnation point in the distance of about $3 \cdot D$, the flow velocity in axial direction drops rapidly to zero at the stagnation point. The kinetic energy of the flow is converted to pressure as it is shown in Figure 2c, where pressure increases, as the velocity decreases, and reaches its maximum value at the stagnation point.

High pressure region at the stagnation point generates the flow in a radial direction as shown in Figure 3a. The radial distribution of velocity and pressure near the stagnation point corresponds well with each other. The differences in distributions for both velocities 2 and 50 m/s can be neglected. The velocity drop generates the increase of the kinetic energy of the turbulence as it can be observed in Figure 2d and 3c. Only at the surface a vicinity dumping effect of viscosity near the surface causes that k drops rapidly to zero.

All numerically simulated distributions in the axis directions, shown in Figure 2, are physically acceptable and the obtained solutions are very low dependent on the entrance velocity. The radial wall jet is generated on the impinged surface and the obtained radial distributions, shown in Figure 3, indicate a small dispersion for different entrance velocities.

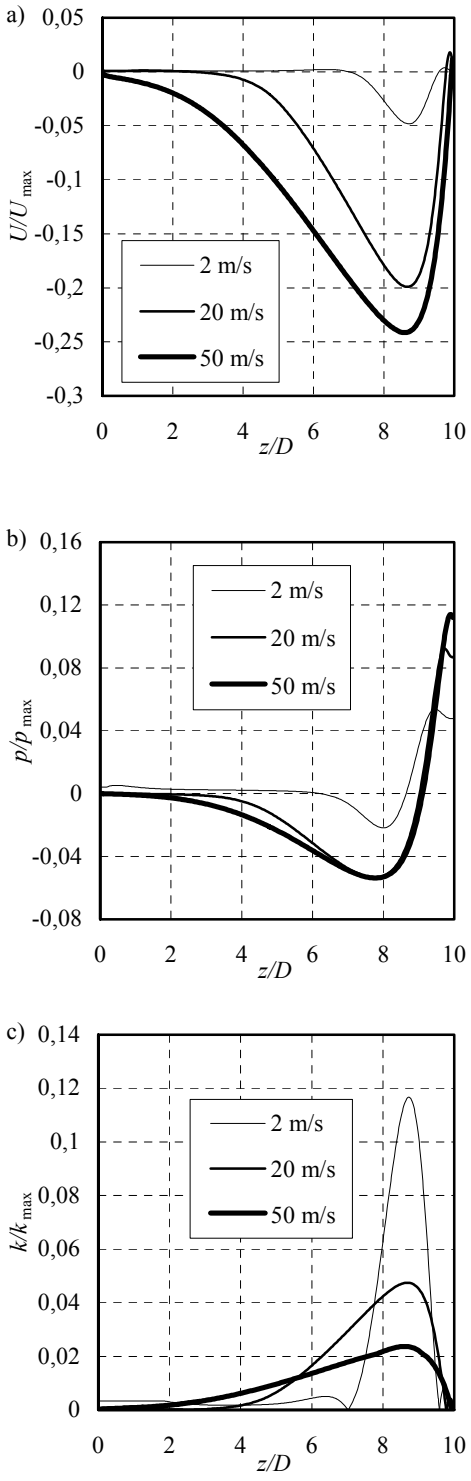

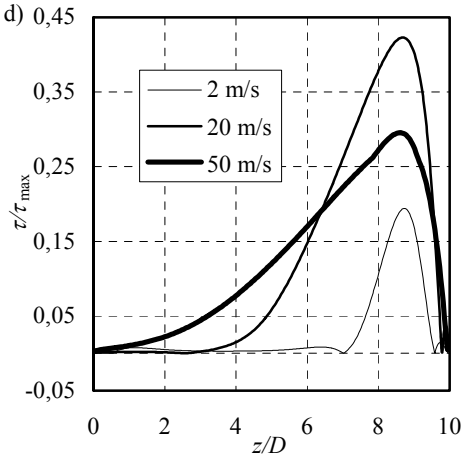

Figure 4. Distribution of dependent values on the side wall: a – axial component of velocity, b – pressure, c – kinetic energy of turbulence, d – shear stresses

Generally, a radial velocity near the impinging wall, Figure 3a, reaches the maximum value where radial pressure gradient decreases to zero. The distributions of radial velocity are very similar to the calculated shear stress distributions, Figure 3a and 3d. The increase of velocity has a similar tendency to increase the kinetic energy of the turbulence.

A much more complicated situation can be observed on the side wall as it is shown in Figure 4. The return flow established along the side wall indicates differences dependent on the entrance velocity. Despite this character the obtained plots look similar. The most interesting region is the area of *z/D* about 9 where all calculated values reach maximal values. This is due to the drop of pressure which reaches its minimum.

A much more complicated situation can be observed on the side wall as it is shown in Figure 4. The return flow established along the side wall indicates differences dependent on the entrance velocity. Despite this character the obtained plots look similar. The most interesting region is the area of *z/D* about 9 where all calculated values reach maximal values. This is due to the drop of pressure which reaches its minimum.

The field of flow in the analyzed chamber is presented in Figures 5 and 6. In Figures 5 and 6 the radial distribution of components of velocity are shown for three distances from the outlet of nozzle: z/D = 1, z/D = 5 and z/D = 9. In small distances from the nozzle the jet has almost a perpendicular profile. The return flow in a round channel is very balanced. Far away from the jet outlet the velocity at the jet axis goes down whereas the volume of the jet increases.

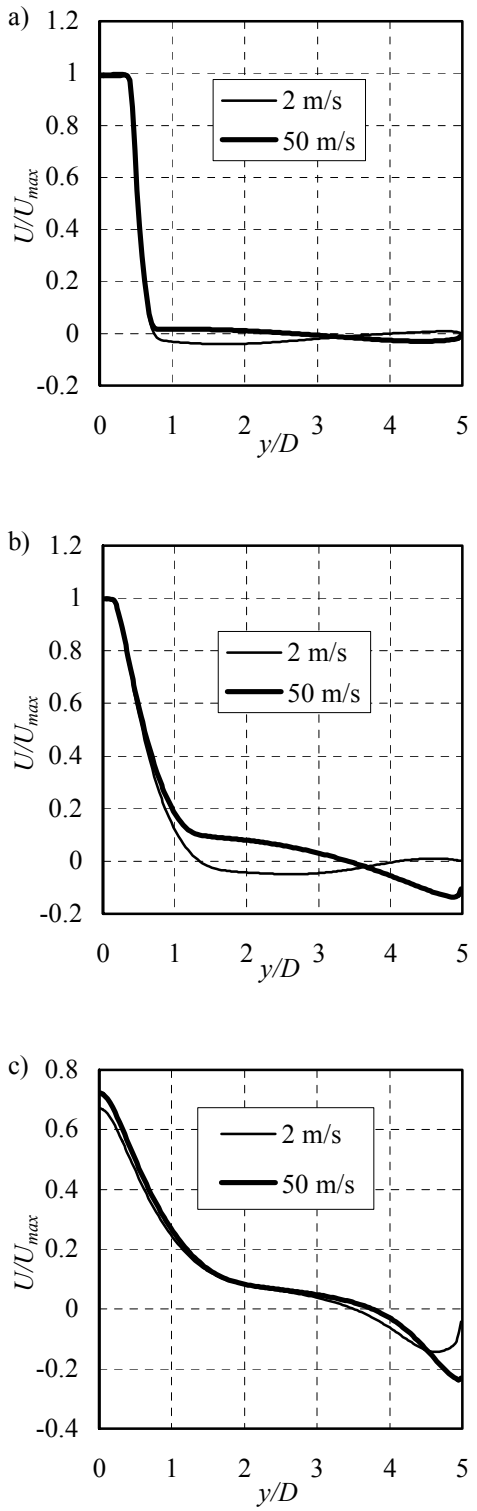

Figure 5. The radial distribution of the axis component of velocity for distances from the outlet of the nozzle: a - 1·*D*, b - 5·*D*, c - 9·*D*

Because of this the return flow velocity obtains a higher value but it is concentrated near the side wall. Relative velocity distributions look similar for both analyzed velocities. In Figure 6 radial distributions of the radial component of the velocity in the spreading jet are shown. In all presented figures positive values of the radial velocity component can be seen in the mixing region because the resultant value of the axial component must be positive due to gradual expansion of the jet in this direction.

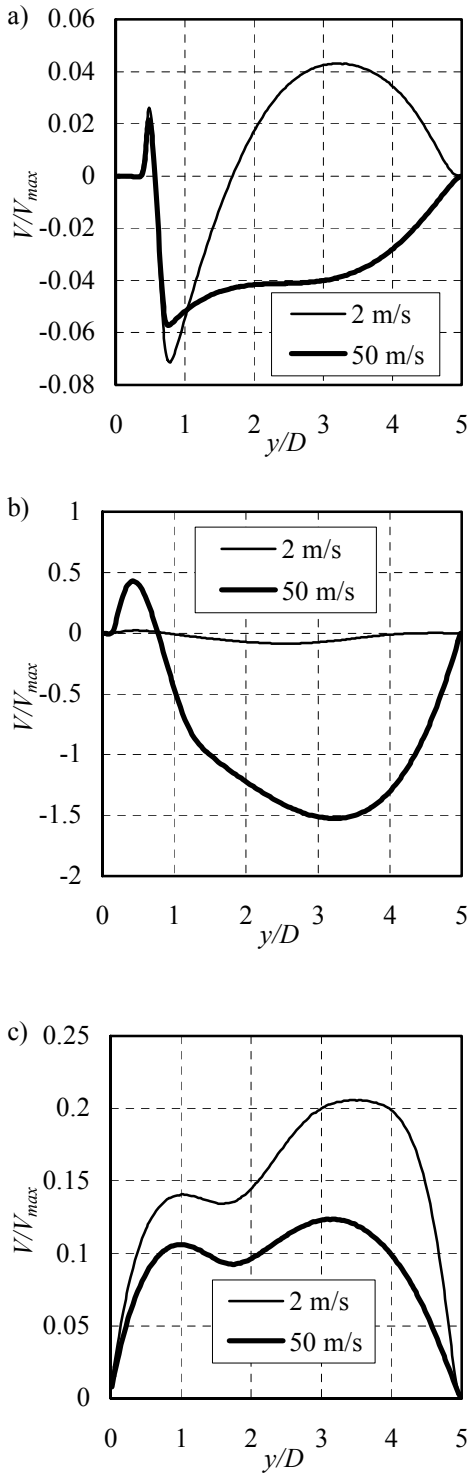

Figure 6. The radial distribution of a radial component of velocity for the distance from the outlet of the nozzle: a - 1·*D*, b - 5·*D*, c - 9·*D*

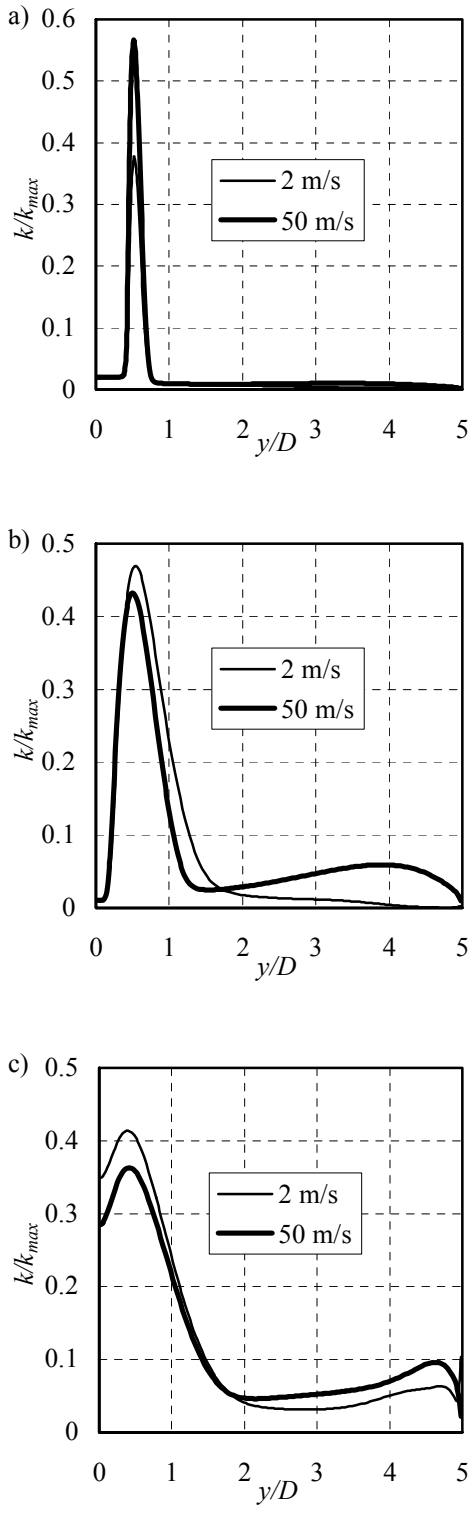

Figure 7. The radial distribution of kinetic energy of the turbulence for the distance from the outlet of the nozzle: a - 1·*D*, b - 5·*D*, c - 9·*D*

The expansion of the jet is realized by the entrainment of the fluid from the area surrounding the out-flowing jet. This phenomenon is illustrated by negative values of the radial component of the velocity in Figures 6a and 6b. In the impinging region this relationship does not exist. The jet flows along the wall which is shown by radial profiles in Figure 6c. With the growth of the jet outflow velocity the region of the change of the main flow direction begins in another distance from the impinged wall.

The distribution of the kinetic energy of the turbulence in an axisymmetric chamber is shown in Figure 7. It is visible that maximum value of k is reached in the region where the gradient of the jet velocity profile obtains its local maximum. In the external jet region the value of k is rather small. This indicates that the gradient of the jet velocity is the main source of the turbulence in the analyzed flow. A small effect of the convection of turbulence is also visible when *k* increases in jet axis, for long distances from the jet outlet. Again, the simulation for both jet entrance velocities looks very similar. In figures from 5 to 7 only characteristic profiles of axial and radial component of velocity and kinetic energy of turbulence normalized by maximum values in domain of simulation is shown.

5. SUMMARY

The results of numerical calculations present a very complicated structure of the flow inside a cylindrical vessel. The influence of changes of the velocity at the nozzle outlet on the distribution of mass and energy transport in a cylindrical chamber is strong in the whole space of simulation. The velocity at the outlet of the nozzle changes the distribution of mean parameters of the flow (pressure and components of velocity) and the parameters of turbulence (kinetic energy of turbulence and shear stresses) on the impinging and side wall. The changes in axis, as well as on the walls, do not change the distribution of the first stagnation point region and the structure of the flow near the impinging and side wall.

REFERENCES

[1] Bartoszewicz, J., and Bogusławski, L., 2005, "*The optimization of numerical grid for flow of round jet in cylindrical vessel*", Heat-SET 2005 Conference, Grenoble, France, pp. 102-103.

[2] Bartoszewicz, J., and Bogusławski, L., 2005, "*Influence of numerical grid on results of flow analysis of round jet in cylindrical chamber*", Turbomachinery, Nr 128, Vo. I, pp. 53-60.

[3] Cabelli, A., 1977, "*Storage Tanks-A Numerical Experiment"*, Solar Energy Journal, Vol.19, pp. 45-57.

[4] Knudsen, S., Furbo, S., and Shah, L.J., 2001, "*Design of the Inlet to the Mantle in a Vertical Mantle Storage Tank"*, Proc. of ISES 2001 Solar World Congress, Adelaide, South Australia.

[5] Launder, B. E., and Spalding, D.B., 1972, "*Mathematical models of turbulence*", Academic Press.

[6] Launder, B. E., and Spalding, D.B., 1974, "*The numerical computation of turbulent flows*", Comp. Meth. in Appl. Mech. & Eng., Vol. 3, pp. 269.

[7] Rosten, H. I., Spalding, D. B., 1985, "*The PHOENICS beginners guides. CHAM report. No TR100*", CHAM Limited, Wimbledon, England.

[8] Shah, L. J., and Furbo, S., 2003, "*Entrance Effects in Solar Storage Tanks"*, Solar Energy, Vol. 75, pp. 337–348.

Conference on Modelling Fluid Flow (CMFF'06)
The 13th International Conference on Fluid Flow Technologies
Budapest, Hungary, September 6-9, 2006

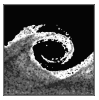

A NUMERICAL STUDY OF AXISYMMETRIC LAMINAR COMPRESSIBLE FLOW IN NOZZLE UNDER VARIABLE WALL THERMAL CONDITIONS

Said ABBOUDI[1], Jing DENG[2], Michel IMBERT[3]

[1] Corresponding Author, FEMTO-ST, UMR 6174 CNRS, Dpt CREST, UFC – UTBM, Site de Sévenans, 90010, Belfort Cedex, France, E-mail : said.abboudi@utbm.fr
[2] FEMTO-ST, UMR 6174 CNRS, Dpt CREST, UFC – UTBM, Site de Sévenans, 90010, Belfort Cedex, France, E-mail : jing.deng@utbm.fr
[3] FEMTO-ST, UMR 6174 CNRS, Dpt CREST, UFC – UTBM, Site de Sévenans, 90010, Belfort Cedex, France, E-mail : michel.imbert@utbm.fr

ABSTRACT

The present work concerns a numerical study of an axisymmetric laminar flow of a compressible gas in a small size convergent-divergent nozzle. The geometry and the reservoir conditions are like that they make important dissipative effects. The numerical study is performed with Mac-Cormack explicit scheme and the splitting of the operator in the two spatial directions is adopted. Comparisons between different thermal wall conditions (adiabatic, cooling and heating) are realized and show the influence of these conditions on the structure of the flow, in particular in predominant viscous effects region.

Keywords : compressible, Mac-Cormack scheme, nozzle, numerical study, viscous flow wall thermal conditions

NOMENCLATURE

e	$[m^2/s^2]$	internal energy per mass unit
E	$[m^2/s^2]$	total energy per mass unit
k	$[W/(m.K)]$	thermal conductivity
M	[]	Mach number
P	$[Pa]$	pressure
T	$[K]$	temperature
u	$[m/s]$	axial velocity
v	$[m/s]$	radial velocity
r	$[m]$	radial coordinate
x	$[m]$	axial coordinate
η	[]	non dimensional radial coordinate
ξ	[]	non dimensional axial coordinate
ρ	$[kg/m^3]$	density
μ	$[kg/(m.s)]$	dynamatic viscocity

Subscripts and Superscripts

1. INTRODUCTION

Although the most obvious applications of compressible gas flow are in aerospace, the knowledge of the effects of compressibility in a flow is absolutely necessary for many others engineering applications: gas turbines, combustion chambers for examples.

Compressible gas flows at moderate Reynolds number in channels of constant or variable cross section are also frequently met in several branches of contemporary techniques as for examples: micro-channels, chemical and gasodynamic lasers.

The calculation of viscous nozzle flows can be accomplished by either solving the inviscid core and viscous boundary layer equations separately or by solving the complete Navier-Stokes equations for the entire flow field. In this study, the very small size convergent-divergent nozzle and the reservoir conditions lead to a Reynolds number on the order of 10^3 based on the throat radius. In these conditions the thickness of the boundary layer cannot be regarded as thin when compared to the nozzle diameter and the splitting of the flow in two parts is a questionable assumption.

The conservative form of the complete Navier-Stokes equations for axisymmetric, compressible, viscous time dependent flow of a perfect gas is solved. The numerical study is performed with Mac-Cormack explicit finite difference scheme and the splitting of the two-dimensional operator in two one-dimensional operators is adopted [1-6].

The obtained numerical results are shown in figures for the cases (a) of an adiabatic wall, (b) of cooling of the wall, and (c) of heating of the wall.

Comparisons between these different wall thermal conditions are realized and show their influence on the structure of the flow, in particular

in the region where the viscous effects are predominant.

2. GOUVERNING EQUATIONS

The governing equations for a compressible, viscous fluid in the absence of body forces consist of the unsteady Navier-Stokes equations. In the cylindrical coordinates (r, θ, x), these equations for axisymmetric flows can be written in conservative form as follows :

$$\frac{\partial \widetilde{U}}{\partial t} + \frac{\partial \widetilde{F}}{\partial x} + \frac{\partial \widetilde{G}}{\partial r} + \frac{1}{r}\widetilde{H} = 0 \qquad (1)$$

where $\widetilde{U}, \widetilde{F}, \widetilde{G}, \widetilde{H}$ are 4-component vectors defined as :

$$\widetilde{U} = [\rho, \rho u, \rho v, \rho E]^t$$

$$\widetilde{F} = [\rho u, \rho u^2 + P - \tau_{xx}, \rho uv - \tau_{xr}, (\rho E + P)u - u\tau_{xx} - v\tau_{xr} - q_x]^t$$

$$\widetilde{G} = [\rho v, \rho uv - \tau_{xr}, \rho v^2 + P - \tau_{rr}, (\rho E + P)v - u\tau_{xr} - v\tau_{rr} - q_r]^t$$

$$\widetilde{H} = [\rho v, \rho uv - \tau_{xr}, \rho v^2 - (\tau_{rr} - \tau_{\theta\theta}), (\rho E + P)v - u\tau_{xr} - v\tau_{rr} - q_r]^t$$

The stress and heat transfer components are given as:

$$\tau_{xx} = (\lambda + 2\mu)\frac{\partial u}{\partial x} + \lambda \frac{1}{r}\frac{\partial}{\partial r}(rv)$$

$$\tau_{rr} = (\lambda + 2\mu)\frac{\partial v}{\partial r} + \lambda\left(\frac{\partial u}{\partial x} + \frac{v}{r}\right)$$

$$\tau_{xr} = \mu\left(\frac{\partial u}{\partial r} + \frac{\partial v}{\partial x}\right)$$

$$\tau_{\theta\theta} = (\lambda + 2\mu)\frac{v}{r} + \lambda\left(\frac{\partial u}{\partial x} + \frac{\partial v}{\partial r}\right)$$

$$q_x = k\frac{\partial T}{\partial x}, \quad q_r = k\frac{\partial T}{\partial r}$$

The total energy is given as:

$$E = e + \frac{1}{2}\left(u^2 + v^2\right)$$

The state equation of perfect gas is used to close the system (1):

$$P = \rho \Re T$$

The coefficient of viscosity is assumed to vary according to the temperature and the second coefficient of viscosity is assumed to follow Stokes' hypothesis: $3\lambda + 2\mu = 0$.

As it is usual in nozzle flow calculations, the physical domain D (x, r) is transformed into a rectangular one by means of the transformation T:

$$D(x, r) \xrightarrow{T} D(\xi, \eta)$$

with:

$$\xi(x) = \frac{x}{r_p^*} \quad \text{and} \quad \eta(x, r) = 1 - \frac{r}{r_p(x)}$$

where r_p^* and $r_p(x)$ are respectively the radius of the throat and the wall.

This transformation applied to equation (1) leads to the following weakly conservative form:

$$\frac{\partial U}{\partial t} + \frac{\partial F}{\partial \xi} + \frac{\partial G}{\partial \eta} + H = 0 \qquad (2)$$

with :

$$U = \frac{\widetilde{U}}{J}, \qquad F = \frac{\widetilde{F}}{J}\frac{\partial \xi}{\partial x},$$

$$G = \frac{1}{J}\left(\widetilde{F}\frac{\partial \eta}{\partial x} + \widetilde{G}\frac{\partial \eta}{\partial r}\right), \quad H = \frac{\widetilde{H}}{rJ}$$

where $J = \dfrac{\partial(\xi, \eta)}{\partial(x, r)}$ is the Jacobian of the transformation.

2.1. Computational domain

The domain of integration is limited by the wall at $\eta = 0$, the nozzle axis at $\eta = 1$ and the two boundaries, upstream $\xi = 0$ and downstream $\xi = \xi_{max}$ normal to the axis. The line ($\eta = 0$) gives the position of the wall, while the symmetry axis of the nozzle is situated midway between the two last lines of the grid. In the longitudinal direction ξ, the step is chosen constant. In the transverse direction η, in order to take into account the viscous effects, the step is taken to be variable from the wall to η_f, and then it is constant up to the nozzle axis.

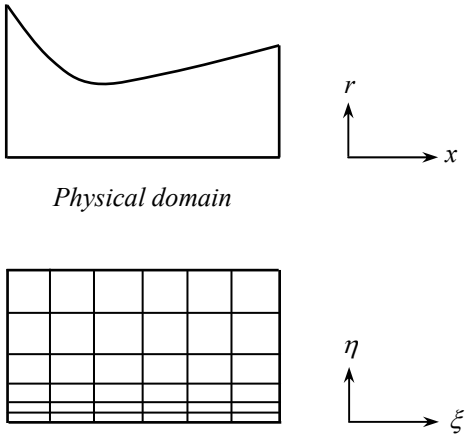

Figure 1. Definition of the domain of integration

2.2. Boundary conditions

The values on the symmetry axis (η = 1) are taken to be $\partial\varphi / \partial\eta = 0$ for $\varphi = u, T, P$ and $v = 0$.

At the nozzle exit the flow values are obtained by a linear extrapolation.

At the wall (η = 0) the no-slip condition gives $u = v = 0$.

The pressure P is obtained from the second momentum equation.

The wall of the nozzle is submitted to an adiabatic or variable temperature conditions.

At the inlet boundary, the value of the velocity is obtained by an extrapolation from the adjacent interior grid points. The temperature is deduced by using the conservation of the total enthalpy between the reservoir and the inlet grid boundary.

An isentropic evolution between the reservoir and the inlet is adopted to obtain the pressure.

3. NUMERICAL METHOD

The Navier-Stokes equations system is solved by an explicit predictor-corrector scheme as given by Mac-Cormack [3]. The accuracy of this numerical method is second order in space and time. The solution at the time (n + 1) Δt is calculated from knowledge of the solution at $n\ \Delta t$ by:

$$U_{i,j}^{n+1} = L(\Delta t)\, U_{i,j}^{n} \qquad (3)$$

The two dimensional operator $L(\Delta t)$ is split into two one-dimensional operators $L_\xi(\Delta t_\xi)$ and $L_\eta(\Delta t_\eta)$.

The operators L_ξ and L_η are respectively applied to the following one-dimensional system of equations:

$$\frac{\partial U}{\partial t} + \frac{\partial F}{\partial \xi} = 0$$

$$\frac{\partial U}{\partial t} + \frac{\partial G}{\partial \eta} + H = 0$$

L_ξ being defined as predictor under the form:

$$\overline{U}_{i,j}^{**} = U_{i,j}^{*} - \frac{\Delta t_\xi}{\Delta \xi}\left(F_{i+1,j}^{*} - F_{i,j}^{*}\right)$$

and as corrector:

$$U_{i,j}^{**} = \frac{1}{2}\left[U_{i,j}^{*} + \overline{U}_{i,j}^{**} - \frac{\Delta t_\xi}{\Delta \xi}\left(\overline{F}_{i,j}^{**} - \overline{F}_{i-1,j}^{**}\right)\right]$$

L_η is defined as predictor:

$$\overline{U}_{i,j}^{**} = U_{i,j}^{*} - \frac{\Delta t_\eta}{\Delta \eta}\left(G_{i,j+1}^{*} - G_{i,j}^{*}\right) - \Delta t_\eta\ H_{i,j}^{*}$$

and as corrector:

$$U_{i,j}^{**} = \frac{1}{2}\Big[\, U_{i,j}^{*} + \overline{U}_{i,j}^{**} - \frac{\Delta t_\eta}{\Delta \eta}\left(\overline{G}_{i,j}^{**} - \overline{G}_{i,j-1}^{**}\right) - \Delta t_\eta\, \overline{H}_{i,j}^{**}\Big]$$

The properties relating to the stability, the consistency and the accuracy require the use of the following sequence [3]:

$$U_{i,j}^{n+1} = L_\eta\left(\frac{\Delta t}{2}\right) L_\xi(\Delta t)\, L_\eta\left(\frac{\Delta t}{2}\right) U_{i,j}^{n} \qquad (4)$$

with Δt = 0.9 min (Δt_ξ, $2\Delta t_\eta$).

Notice that the spatial derivates of F and G are discretized with opposite one-sided finite differences in the predictor and corrector stages.

The details of this numerical scheme are given in the references [3].

4. NUMERICAL RESULTS AND DISCUSSION

The numerical results are obtained in the following conditions:

- The half angle of the conical convergent is *45°*
- The half angle of the conical divergent is *10°*
- The convergent and the divergent are connected by an arc of circle,
- The radius of the throat is R_{col} = *0.03 cm*,
- The reservoir conditions are: P_0 = *1.2 10*^{5} Pa and T_0 = *1500 K*.

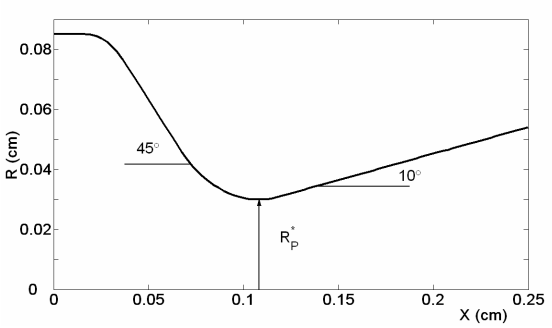

Figure 2. Geometry of the nozzle.

The results are presented for three different wall thermal conditions:

- Case a: Insulated (or adiabatic) wall

- Case b: Variable temperature profile, cooling wall
$T_w(x) = Ax^2 + B\,x + C$ for $0 < x < 0.25$
with $A = 7.2\ 10^{-3}$, $B = -0.12$ and $C = 1$.
The minimum of T_w is equal to 0.5 T_0 at $x = 0.25$ *cm*.

- Case c: Variable temperature profile, heating wall
$T_w(x) = Ax^2 + B\,x + C$ for $0 < x < 0.25$
with $A = -7.2\ 10^{-3}$, $B = 0.12$ and $C = 1$.
The maximum of T_w is equal to 1.5 T_0 at $x = 0.25$ *cm*.

In the computational field, we have used 90 grid points in the ξ direction and 32 grid points in the η direction. The time step is chosen according to the stability criterion of the numerical scheme "Eq (4)", [2, 3].

In these conditions, the isotherms curves in the physical plane are presented in the figures 3 a, b, c for the three studied cases.

The figure 3 a shows that the dissipative effects are significants on about a third of the exit radius. With regard to the cases (b) and (c), the cooling of the wall involves a decrease of the thickness of the thermal boundary layer and an increase in the heating case. In this last case, this thickness reaches 40% of the exit radius, figure 3 c and figure 4 for *x=0.25 cm*.

On the inviscid core of the flow, the effects of the parietal thermal conditions are obviously less important but nevertheless visible as it can be seen on figure 4 for *x=0.18 cm* and *x=0.25 cm*.

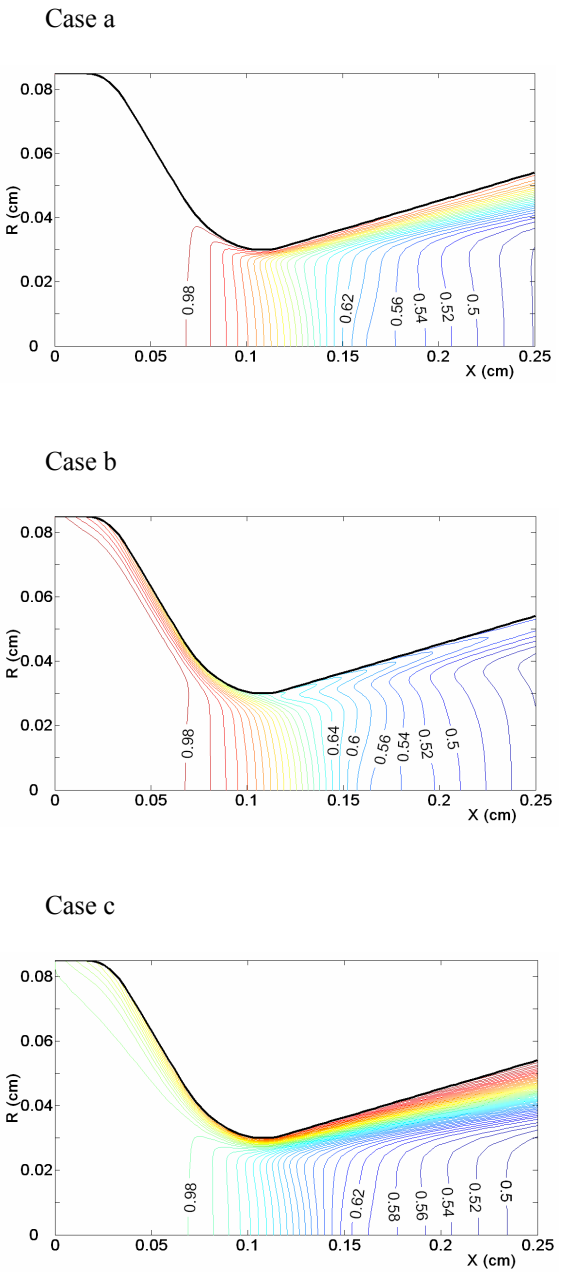

Figures 3 a, b, c. Contours of constant dimensionless temperature in the physical plane ($\Delta T = 0.02$) for the three cases.

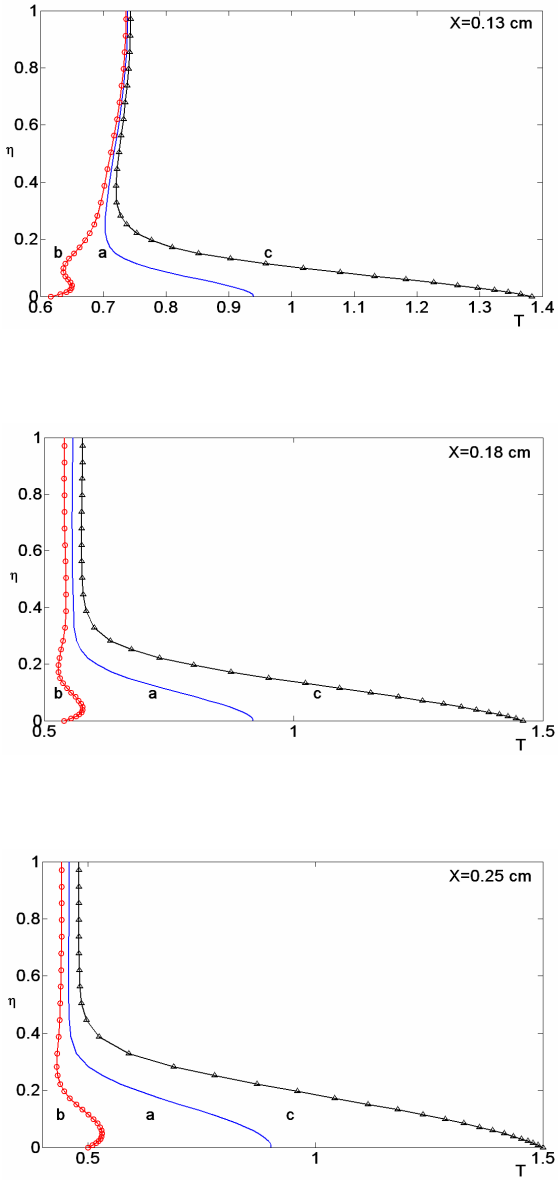

Figure 4. Non-dimensional temperature profiles in different cross sections for the three cases.

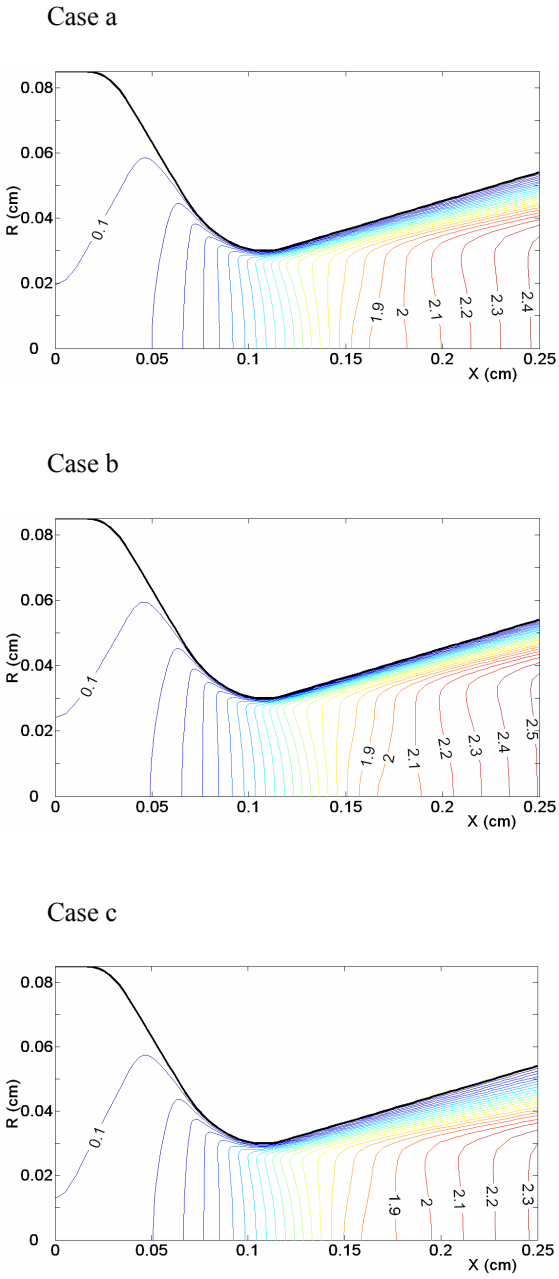

Figures 5 a, b, c. Isomachs in the physical plane ($\Delta M = 0.05$).

In the supersonic expansion, the dynamic effects play a prominent role compared to the parietal heating effects. The thicknesses of the dynamic boundary layer are almost of the same order for the three cases, figures 5 and 6.

However, a certain number of expected results are found. In the divergent of the nozzle, the supersonic velocities, for the adiabatic case, are lower than that corresponding to the cooling case and higher than that corresponding to the heating case, figure 6, for *x=0.18 cm*, *x=0.25 cm*.

These results can also be seen on the isomach curves, figures 5 a, b c where the values of the exit mach numers are respectivelly *M=2.5* for the case (b), *M=2.4* for the case (a) and *M=2.3* for the case (c).

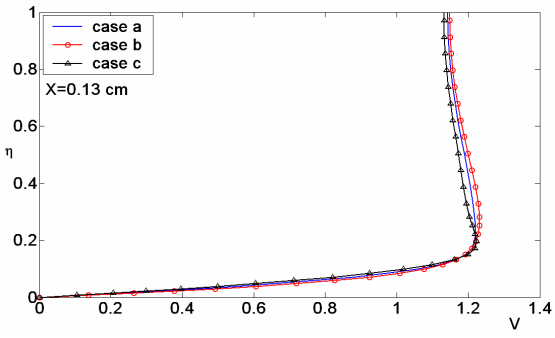

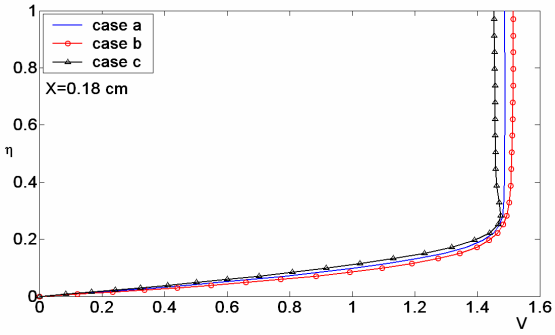

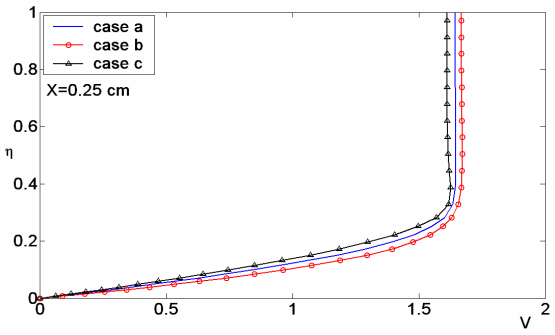

Figure 6. Non-dimensional velocity profiles in different cross section for the three cases.

The same remarks can be made on the isobar curves, plotted in the physical plane, figures 7 a, b, c. The strongest expansion of the gas flow corresponds to the cooling case and the weakest expansion corresponds to the heating case, figures 7a, b c and figures 8 for *x=0.13, 0.18* and *0.25 cm*.

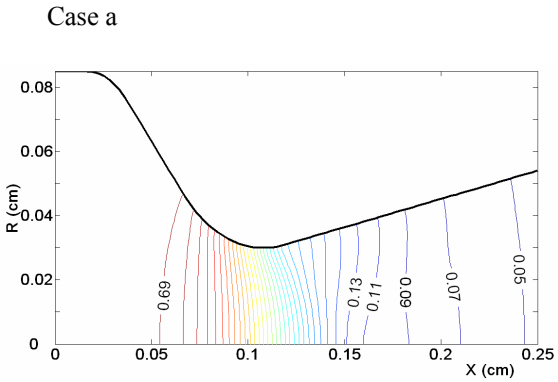

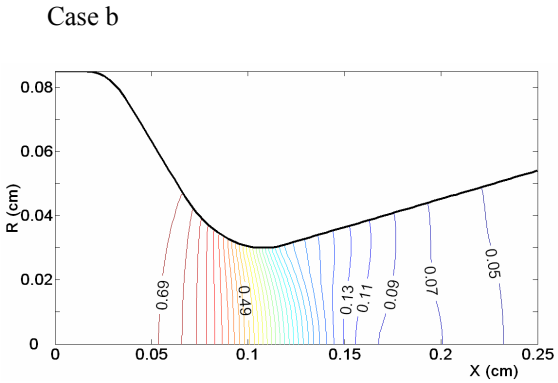

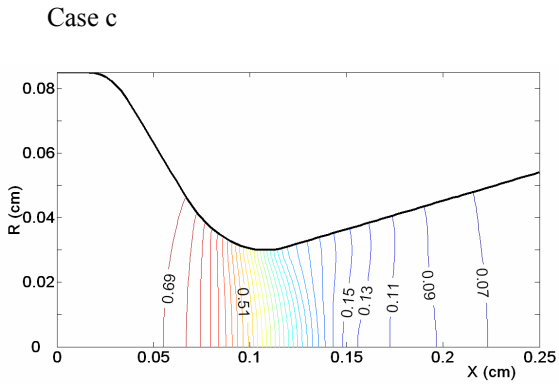

Figures 7 a, b, c. Contours of constant dimensionless pressure in the physical plane ($\Delta P = 0.02$) for the three cases.

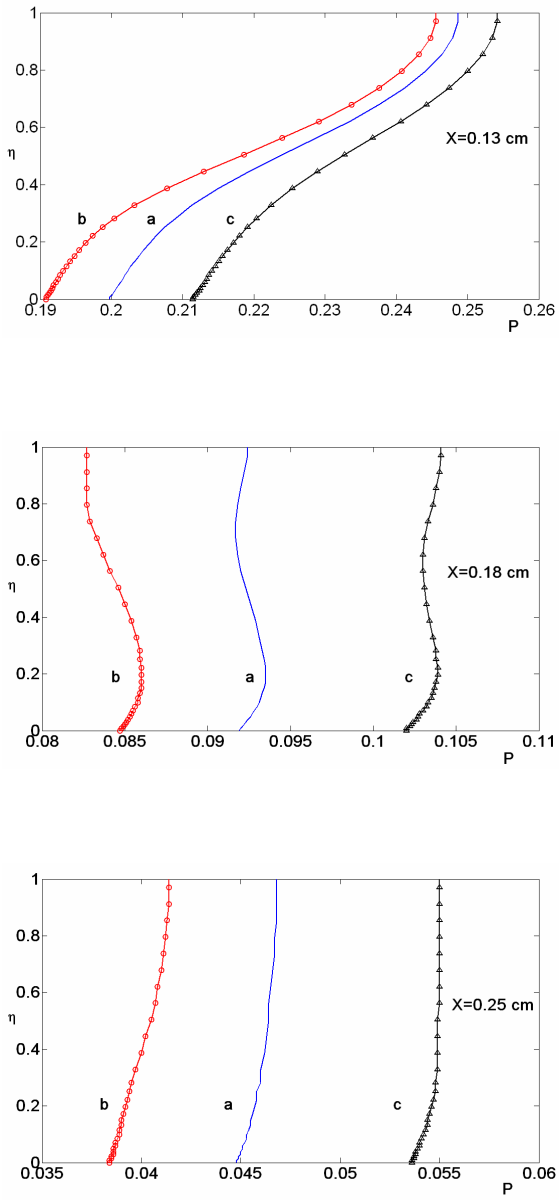

Figure 8. Non-dimensional pressure profiles in different cross sections for the three cases.

CONCLUSION

Solutions for an axisymmetric nozzle flow were obtained numerically using the full Naviers Stokes equations. The numerical study were performed with Mac Cormack finite difference scheme splitting of the operator in the two spatial directions. Three wall thermal conditions were analyzed (adiabatic, cooling and heating). The results show that the dissipative effects are more significants for the heating case while of course, the expansion in the supersonic divergent is more important in the cooling case.

REFERENCES

[1] D. A. Anderson, J. C. Tannehill, R. H. Pletcher, 1984. "Computational Fluid Mechanics and Heat Transfer." *Hemisphere Publishing, Corporation*.

[2] M. Imbert et D. Zeitoun, 1982. "Etude numérique d'un écoulement à nombre de Reynolds modéré dans une tuyère." *Journal de Mécanique Théorique et Appliquée,* Vol.1, N°4, pp. 595 à 609.

[3] R. W. Mac Cormack and B. S. Baldwin, 1975. "A Numerical method for solving the Navier-Stokes equations with application to shock-boundary layer interactions." AIAA *13th Aerospace Sciences Meeting,* Pasadena, Calif. January 20-22.

[4] J. L. Steger and R.F. Warming, 1981. "Flux vector splitting of the inviscid gasdynamic equations with application to Finite-Difference methods." *Journal of Computational Physics,* Vol.40, pp. 263-293.

[5] Y. M. Yang, 1996. "Modélisation mathématique d'un système de projection thermique à la flame de type H.V.O.F.: application à l'élaboration de revêtements protecteurs." *Thesis, Institut Polytechnique de Sévenans*.

[6] A. Perrin, H. H. Hu, 2006. "An explicit finite-difference scheme for simulation of moving particles." *J. of Computational Physics* Vol.212, pp. 166-187.

Conference on Modelling Fluid Flow (CMFF'06)
The 13th International Conference on Fluid Flow Technologies
Budapest, Hungary, September 6-9, 2006

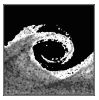

TURBULENT BOUNDARY LAYER WITH A STEP CHANGE IN SURFACE ROUGHNESS

Per-Åge Krogstad[1], Tim Nickels[2]

[1] Corresponding Author. Department of Energy and Process Engineering, The Norwegian University of Science and Technology, N-7491 Trondheim, Norway. Tel.: +47 73 59 10, E-mail: per.a.krogstad@ntnu.no
[2] Department of Engineering, University of Cambridge, Trumpington St., Cambridge, CB2 1PZ, UK. E-mail: tbn22@hermes.cam.ac.uk

ABSTRACT

The flow transition from a fully developed smooth wall boundary layer to that of a fully developed layer over a rough wall has been studied experimentally using PIV. It is found that the wall friction almost immediately increases to the value for a fully developed rough surface. This causes a strong increase in the Reynolds stresses in the near wall region and therefore a strong wall normal diffusion. After only about 0.5 initial boundary layer thicknesses downstream of the step a new rough wall logarithmic layer can be identified underneath the smooth wall log-region. This internal layer is found to grow as $\delta_i \sim x^{0.7}$. After about 20 initial boundary layer thicknesses the internal layer has grown across the entire boundary layer and the new fully developed rough wall profiles have been formed. Data is reported for the streamwise development of mean velocity, Reynolds stresses and vorticity.

Keywords: PIV, boundary layer, surface roughness, turbulence

NOMENCLATURE

C_f	[-]	friction coefficient $= 2\tau_w / \rho U_e^2$
k	[m]	roughness length scale
U	[m/s]	mean streamwise velocity
u_τ	[m/s]	friction velocity $= \sqrt{\tau_w / \rho}$
x	[m]	streamwise coordinate
y	[m]	wall normal coordinate
δ	[m]	boundary layer thickness
κ	[-]	von Karman constant
ν	[m^2/s]	Kinematic viscosity
θ	[m]	momentum thickness
τ	[Pa]	shear stress

Subscripts and Superscripts

+	normalization with u_τ and ν
e	external
s	sand
w	wall

1. INTRODUCTION

The flow over rough surfaces has considerable engineering interest due to its ability to increase turbulent mixing and therefore increase surface drag and heat transfer. Classical theories rely on the assumption that there is a layer of the order of a few roughness heights which is directly affected by the roughness. Further out the flow variables, properly scaled, are assumed to be the same as for a smooth surface. Traditionally flows over rough surfaces have therefore been computed using simple analogies with sand roughness. Recent studies (e.g. Krogstad and Antonia [1], Lee et al. [2]) have suggested that in boundary layers the response to the surface roughness may depend on the actual geometric properties of the roughness elements rendering the sand roughness analogy questionable.

One such roughness geometry where significant differences between the smooth and rough wall outer layer flows have been reported is the flow over rod type roughness (see e.g. Krogstad and Antonia [1]). Unlike traditional surface roughnesses, such as sand grain type roughness, which is highly irregular and three-dimensional, rod type roughness consists of spanwise rods or cavities in the surface, forming a regular, two-dimensional pattern. This is likely to behave differently from a random three-dimensional roughness in the near wall region. It is generally agreed that a roughness layer extending from the surface up to about 5-6 times the roughness layer exists where the local flow characteristics are determined by the roughness geometry. However, there is more uncertainty as to how the roughness affects the flow further out. For sand type roughness there is strong evidence both from channel flows, pipes and boundary layers that the region further out is not affected.

For two-dimensional rod type roughness the picture seems to be less clear. Krogstad et al. [3]

performed a combined experimental and numerical (DNS) investigation for a channel flow where both surfaces were covered by rod roughness consisting of square rods with a rod- to channel height ratio of 3.4% and a rod pitch of 8. They concluded that very little effect of the surface geometry could be detected above y ≈ 5k. However in the DNS of Leonardi et al. [4], where only one wall was fitted with roughness elements a significant effect was evident also in the outer layer. $\langle u^2 \rangle^+$ was strongly reduced in the roughness layer as found by Krogstad et al., but a significant increase was also observed for y > 5k.

This effect is similar to the effects reported by Krogstad and Antonia [1] for boundary layers, who performed a comparative study using a three-dimensional mesh type surface roughness and a two-dimensional roughness geometry consisting of circular spanwise rods. They concluded that the outer layer effect caused by the surface roughness depends on the roughness geometry. The rod roughened surface was found to produce considerable outer layer effects, while the stresses in the outer layer for the mesh surface were much less affected. This led Krogstad and Antonia to conclude that the interaction between the inner and outer layers may be dependent on the surface geometry. This was explained for the boundary layer by the conjecture that for two-dimensional roughness geometries considerable spanwise correlation of the bursting events are likely, in particular if the roughness height is significant compared to the layer thickness. The differences in DNS results from Krogstad et al. [3] and Leonardi et al. [4] for similar roughness geometries but with symmetric and asymmetric boundary conditions also suggest that roughness effects may be case dependent.

Based on these observations the investigation reported below was initiated in order to study the inner – outer interaction due to surface roughness. This was done by subjecting the boundary layer over a smooth surface to a two-dimensional surface roughness geometry and studying how the footprints from the roughness are diffused into the outer layer as the flow develops downstream. Eventually when the flow has adapted fully to the new boundary condition the asymptotic rough surface profile should be obtained.

2. EXPERIMENTAL DETAILS

The experiment was performed in the water channel of the Department of Engineering at University of Cambridge, UK. The channel has a test section which is 8 *m* long and 0.9 *m* wide. The first 5 *m* of the test section had a smooth test surface made up of 10 *mm* acrylic plates. Further downstream a 3 *m* section of machined acrylic plates were inserted where 20 *mm* wide and k = 3 *mm* deep cavities were machined with a spacing of p = 23 *mm*. Hence a rod type recessed surface was produced with respect to the upstream plate with a pitch to roughness height ratio of 7.7 (see Figure 1). According to the DNS of Leonardi [4] this is close to the ratio that produces the largest shift in the logarithmic law and hence the maximum surface roughness effects on the flow. The experiments were done at a water depth of 40 *cm* under slightly favourable pressure gradient conditions. Measurements were done using PIV with a few LDA traverses taken to verify the PIV measurements.

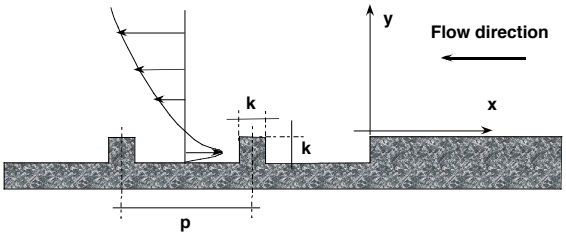

Figure 1. Flow geometry

The flow was seeded with 10 μm silver coated almost neutrally buoyant glass spheres and the flow was recorded using a 4Mpixel Kodak camera. Typically the field of view was adjusted to cover a square region extending out to about 1.5 times the boundary layer thicknesss. The time between the recordings was adjusted to give a displacement in the free stream of about 12 pixels.

3. RESULTS

The experiment was set up so that a well developed, smooth wall boundary layer with a layer thickness of about 120 *mm* was exposed to a step change in boundary condition. At the step the layer Reynolds number was $Re_\theta = \theta U_e/\nu = 5700$ (where θ is the momentum thickness, U_e the free stream velocity and ν the kinematic viscosity of water) and the friction coefficient was $C_f = 0.0029$.

As the flow enters the rough wall section an internal layer develops which affects the mean velocity by reducing the velocity in the inner layer. This is demonstrated in Figure 2 where the mean velocities above a selected number of cavities are compared with the upstream reference profile. All data is scaled with the smooth wall friction velocity to demonstrate which part of the profile is affected by the roughness. Initially the near wall region is seen to drop while the outer part of the log layer and the wake region is maintained. As the flow is convected downstream the internal layer grows and a new logarithmic layer at a different slope is seen to form. This change in slope represents the increase in wall friction over the rough wall. At the most downstream station the process is seen to be completed in the sense that a comprehensive

logarithmic layer is formed which blends smoothly into a wake region.

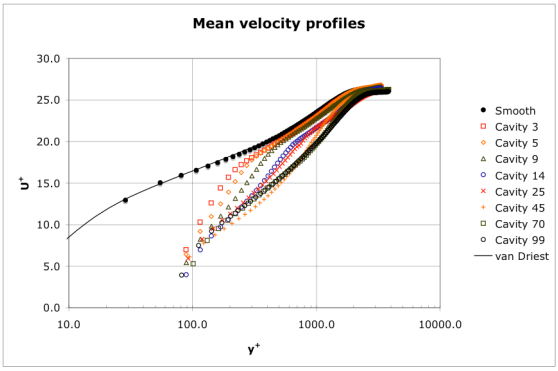

Figure 2. Mean velocity profiles normalized with the smooth wall friction velocity.

The roughness effects are also very pronounced in the Reynolds stresses shown in Figures 3 to 5. Just downstream of the step a dramatic increase in the near wall region is observed in all the Reynolds stresses as the interaction with the transverse bars causes a rapid reorganization of the flow. The bars causes a strong vertical movement in front of its upstream face accompanied by considerable vortex stretching and increase in the wall normal vorticity. At the downstream side of the rods a strong shear layer is formed over the separated region which generates a strong increase in turbulent kinetic energy.

Above the centre of the third cavity, i.e. between bar 2 and 3, the interaction with just the two upstream rods has caused a roughly fourfold increase in the peak levels of all Reynolds stresses. This position corresponds to a streamwise distance of slightly less than x=0.5δ and the interaction extends roughly out to y=0.1δ. This represents a diffusion angle of about 11.5 degrees which is not very different from the angle reported for smooth wall boundary layers .

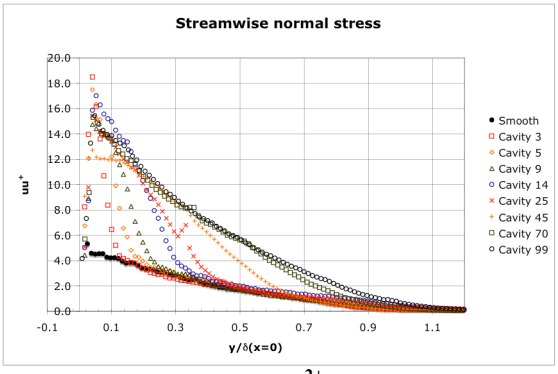

Figure 3. Reynolds stress u^{2+} normalized with the smooth wall friction velocity.

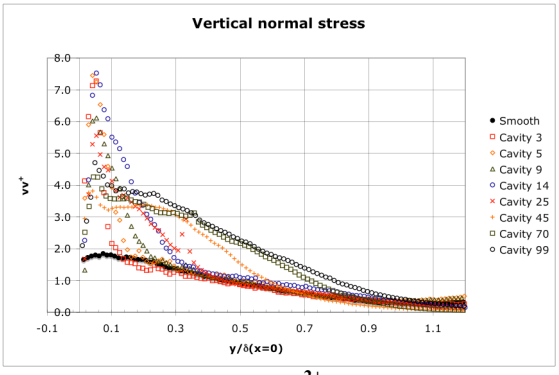

Figure 4. Reynolds stress v^{2+} normalized with the smooth wall friction velocity.

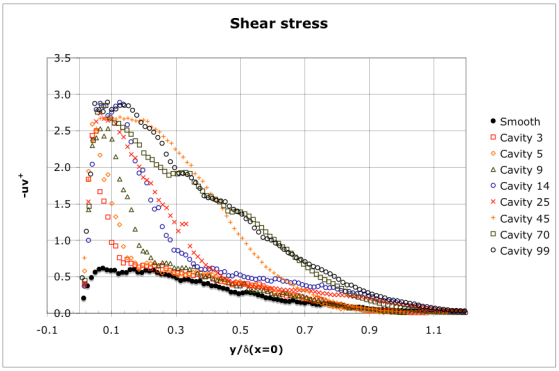

Figure 5. Reynolds shear stress -uv normalised with the smooth wall friction velocity.

It is evident from the stress profiles shown that at a given streamwise position there is a distinct separation between the inner layer that has been affected by the surface roughness and the outer layer that still carries the characteristics of the incoming smooth wall layer. The growth of the internal layer was mapped by fitting the outer part of the roughness layer and the inner part of the outer layer with two straight lines. The limit of the inner layer was taken as the position where the two lines intersect. The results from this analysis (applied to about 60 profiles) is shown in Figure 6. A fit to the data gave a growth rate proportional to $\sim x^{0.7}$. This is not too different from the growth rate of $\delta_i \sim x^{0.72}$ found by Antonia and Luxton [5] for a similar surface geometry based on the effects of the surface roughness on the mean profile. Cheng and Castro [6] looked at the response of a boundary layer going from a surface consisting of small fences to a surface roughened by square rods with a pitch ratio of 9. Using a number of different definitions for the internal layer they found that the exponent ranged from about 0.37 to 0.46. Although the roughness geometry is very similar to the one used in this experiment, the present exponent is very different and therefore supports their statement that "the height of the internal layer is strongly dependent on the way it is defined". The figure shows that it takes about 20 initial boundary layer

thicknesses for the entire layer to adapt to the new wall condition.

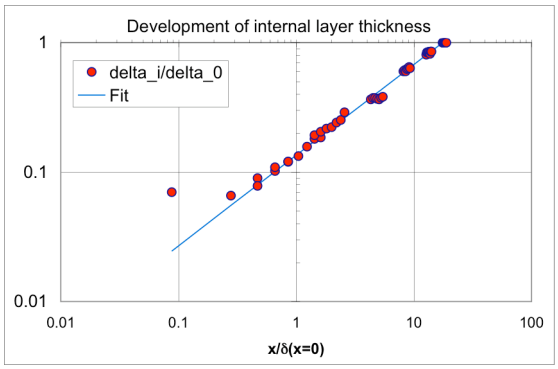

Figure 6. Growth of internal layer.

One of the major problems when analyzing rough wall boundary layer experiments is to determine the friction velocity. This contains both the effects of the pressure drag on the roughness elements and the viscous shear stress at the wall. Beyond transitional roughness the viscous contribution can be neglected, but the pressure drag is difficult to determine experimentally. In the smooth wall case the wall shear may be determined in a number of reliable ways which are not so easily adapted to rough walls, such as oil films, measurement of the linear inner layer etc.

A number of methods have been proposed in the literature for rough surfaces where a profile description based on the log law is fitted to the measured mean velocity profile (e.g. Krogstad et al. [7]). These methods use the friction velocity as an adjustable variable and the value that gives the best fit is taken as the proper scaling variable. However, these methods are difficult to use since the level of the logarithmic region is in principle unknown and depends on the friction velocity through the non-dimensional roughness length scale k^+. The methods seem to give acceptable results where an extensive logarithmic region is found, but will not work in the present case where the logarithmic region is considerably perturbed.

The friction velocity for the incoming smooth wall boundary layer was determined by fitting the mean velocity profile to the smooth wall logarithmic law

$$U^+ = \frac{1}{\kappa}\ln y^+ + B \qquad (1)$$

with κ=0.41 and B=5.2. For the developing rough wall boundary layer the friction velocity was determined by extrapolating the measured turbulent shear stress to the wall. Figure 7 shows the friction coefficient derived in this way, normalized with the smooth wall value.

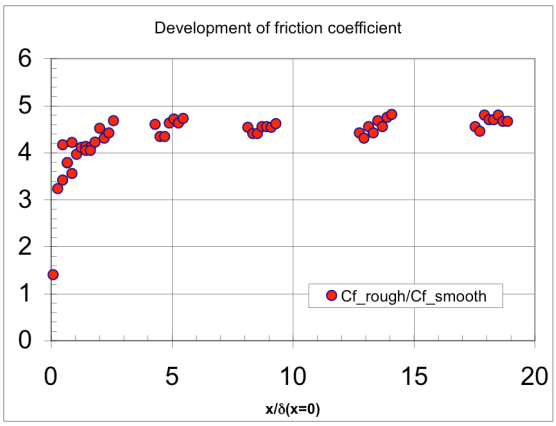

Figure 7. Ratio between the rough and smooth wall friction coefficients, C_f/C_f(x=0).

The figure shows that the skin friction almost instantly jumps to a new level which is about 4.5 times the smooth value. This gives a friction coefficient for this type of surface of about C_f=0.013. This is somewhat higher than the value of C_f=0.008 that was found by Antonia and Luxton [5] for a pitch ratio of p/k=4 by a direct measurement of the pressure drag on a tapped rod. It has been demonstrated many times that the drag for this type of surfaces depends strongly on the density of the rods (see e.g. Leonardi [4]) with a maximum drag around p/k=8. He found C_f to be 0.0129 for p/k=8 and 0.0091 at p/k=4, hence confirming our findings. Our skin friction coefficient also agrees well with the value that can be extracted from the data of Cheng and Castro [6] by extrapolating the shear stress profiles to the wall at their downstream stations. This gives $C_f \approx$ 0.012 for p/k=9 which also agrees well with Leonardi [4].

Figure 7 shows that C_f stays virtually constant at this level while the inner layer grows, confirming that the flow is in the fully rough regime. In the experiment of Antonia and Luxton [5] a slight overshoot in C_f was found for the first couple of boundary layer thicknesses. This was not captured in this experiment and is not evident in the experiment of Cheng and Castro [6] either.

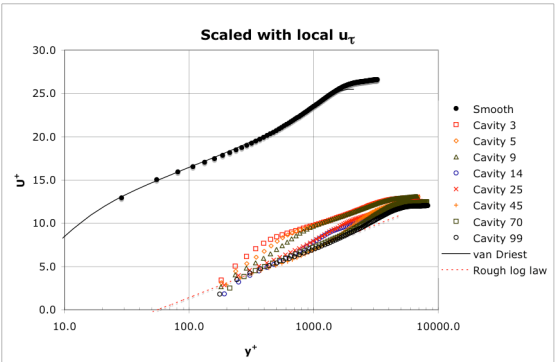

Figure 8. Development of new logarithmic layer.

Figure 8 shows the mean velocity profiles scaled using the local friction velocities. The

asymptotic shift in the logarithmic layer was found to be close to $\Delta U^+=15$. The ratio between the physical roughness scale and the equivalent sand roughness can be estimated from the expression

$$\frac{k_s}{k} = \frac{\exp\left[\kappa\left(\Delta U^+ - A + C\right)\right]}{k^+} \qquad (2)$$

(see e.g. [1]). The asymptotic value for k^+ was about 125 which indicates that k_s^+ is of the order of 1800, confirming that this geometry has a very strong roughness effect on the flow, even though the physical scale is only about δ/40.

One of the benefits of PIV compared to other measurement techniques is its ability to measure vorticity. Figure 9 shows how the mean vorticity, $\Omega_z = \partial V/\partial x - \partial U/\partial y$, is increased as the the boundary layer leaves the smooth surface and starts to interact with the roughness elements. Ω_z is increased near the top of the bars due to the mean flow acceleration here. Also a high level of vorticity is seen in the shear layer formed over the separated flow in the cavities. This effect is most dramatic for the first few cavities due to the remnants of the high velocity gradients near the wall from the smooth wall boundary layer. As the inner layer is retarded over the rough wall and grows in the wall normal direction, the mean vorticity is reduced. After about 10 roughness elements (or a streamwise distance corresponding to about 2 initial boundary layer thicknesses), the mean flow vorticity pattern around the bars appears to be independent of streamwise position.

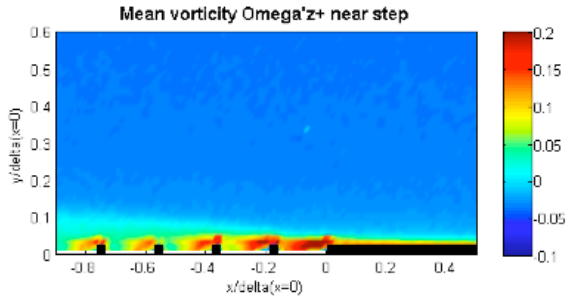

Figure 9. Development of mean vorticity near the step. Inner scaling.

As shown in figure 8, the mean velocity inner layer appears to develop a new logarithmic layer very quickly. Ignoring the streamwise gradient, $\partial V/\partial x$, in expression for the vorticity, we therefore expect Ω_z to scale as

$$\Omega_z^+ = \Omega_z \nu/u_\tau^2 = \partial V^+/\partial x^+ - \partial U^+/\partial y^+ \approx -1/\kappa y^+ \qquad (3)$$

Figure 10 shows the vorticity scaled with the estimated local friction velocity. The figure shows that this relation is closely satisfied for most of the profiles within experimental scatter.

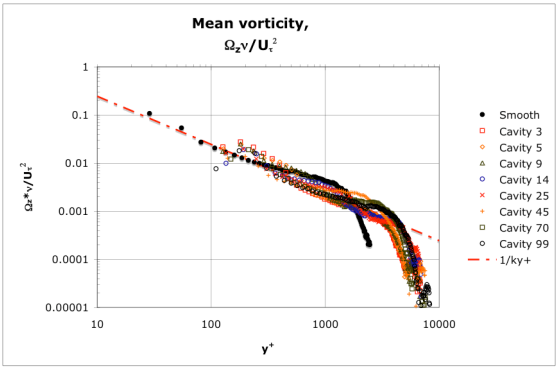

Figure 10. Mean vorticity profiles

In figure 11 the rms vorticity, $\omega_z^+ = \omega_z \nu/u_\tau^2$, is shown for the same initial region as in figure 9. The rapid growh rate of the inner layer after the step is quite evident here. Above the separated region inside the cavities a distinct shear layer is seen, causing a band of increased vorticity.

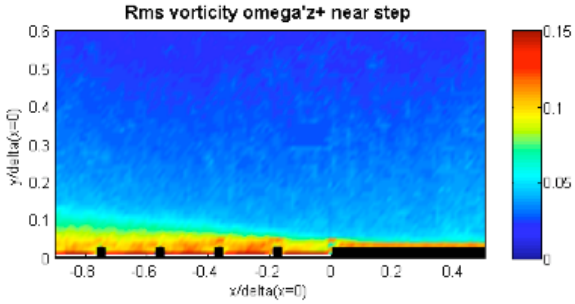

Figure 11. Development of rms vorticity near the step. Inner scaling.

To be able to cover the development over a range of bars a large measurement area was needed. Therefore the spatial resolution had to be sacrified, giving a resolution of $\Delta x/\delta = \Delta y/\delta \approx 0.012$. This corresponds to about 2 vectors across the face of the roughness elements. It is obvious that this is too coarse to accurately represent the turbulent vorticity near the wall, but should provide a good indication of the large scale turbulent vorticity further out.

It is seen (Figure 12) that the rough wall data collapse onto a single line for y/δ > 0.25 at all stations. From the findings from the mean velocity vorticity it would be expected that also the turbulent vorticity should scale on u_τ. This appears not to be the case as all the rough wall profiles fall well below the data from the smooth wall. As shown in figure 7, u_τ is virtually constant along the rough

wall and about a factor 2.1 higher than for the rough surface. Scaling the data with outer variables, U_e and δ, instead causes a very good collapse (Figure 13). The reason for the lack of collapse in figure 12 is not known.

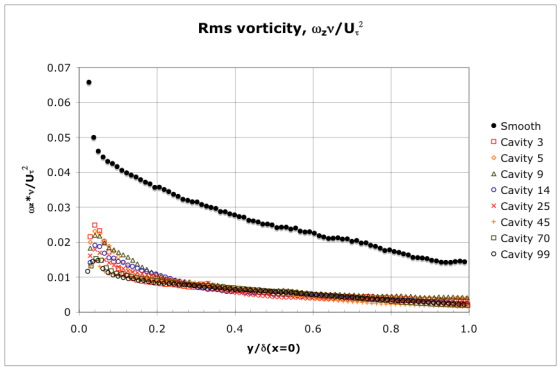

Figure 12. Turbulent vorticity profiles. Inner scaling.

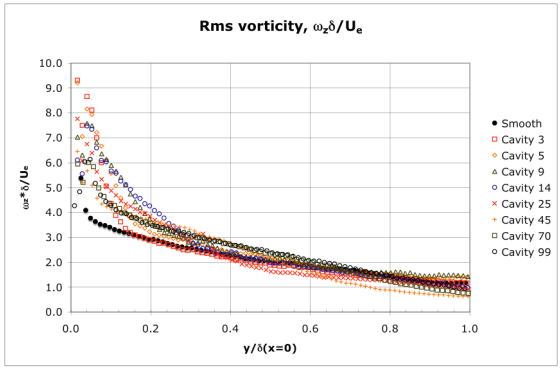

Figure 13. Turbulent vorticity profiles. Outer scaling.

5. CONCLUSIONS

The flow over a surface with step change in roughness represents an interesting flow case because the flow changes from one equilibrium condition to a new one. The way the information about the new boundary condition is diffused across the layer can provide important information about turbulent mixing processes. In the present study spanwise cavities are used to perturb a fully developed smooth wall boundary layer and the development was studied using PIV. Profiles of mean and turbulent quantities averaged in the streamwise direction over one cavity length have been presented.

The flow immediately responds by a step change in friction velocity which remains virtually constant over the length it takes for the flow to reach its new equilibrium condition. The formation of a new logarithmic region close to the wall is evident after only a few cavities downstream of the step.

A corresponding substantial increase in the Reynolds stresses is found near the wall. Initially the wall normal stress gradients are very large, causing a strong vertical diffusion and rapid growth. The growth rate gradually decreases as the wall information diffuses outwards. The internal layer is found to grow at a rate of about $\delta_i \sim x^{0.7}$. After about 20 smooth wall boundary layer thicknesses the rough wall profiles have been fully developed, both in the mean velocity and Reynolds stresses.

ACKNOWLEDGEMENTS

The support by the Engineering & Physical Sciences Research Council under contract EP/C002202/1 is gratefully acknowledged.

REFERENCES

[1] Krogstad, P.-Å. and Antonia, R.A., 1999, "Surface roughness effects in turbulent boundary layers", *Exp. Fluids*, **27**, pp. 450-460

[2] Lee, S., Sung, H.J. and Krogstad, P.-Å., 2004, "Direct numerical simulation of a turbulent boundary layer over a rough wall", in Andersson and Krogstad (eds.) *Advances in Turbulence X*, pp. 297-300.

[3] Krogstad, P.-Å., Andersson, H.I., Bakken, O.M. and Ashrafian, A., 2005, "An experimental and numerical study of channel flow with rough walls", *J. Fluid Mech.*, **530**, pp. 327-352.

[4] Leonardi, S., 2002, "Turbulent channel flow with roughness: Direct Numerical Simulations", Ph.D. Thesis, University of Rome "La Sapienza".

[5] Antonia, R.A. and Luxton, R.E., 1971, "The response of a turbulent boundary layer to a step change in surface roughness. Part 1. Smooth to rough" *J. Fluid Mech.*, **48**, pp. 721-761.

[6] Cheng, H. and Castro, I.P., 1998, "Near-wall flow development after a step change in surface roughness", *Boundary-Layer Meteorology*, **105**, pp. 411-432.

[7] Krogstad, P.-Å., Antonia, R.A. and Browne, L.W.B., 1992, "Comparison between rough- and smooth-wall turbulent boundary layers", *J. Fluid Mech.*, **245**, pp. 599-617

Conference on Modelling Fluid Flow (CMFF'06)
The 13th International Conference on Fluid Flow Technologies
Budapest, Hungary, September 6-9, 2006

EFFECTS OF SEPARATION IN ISOTHERMAL MULTICOMPONENT GAS SYSTEMS WHERE INSTABILITY OF MECHANICAL EQUILIBRIUM OF MIXTURE HAS PLACE

Vladimir KOSOV[1], Natalia ANKUSHEVA[2], Alexander LYSENKO[3], Dusembek KUL'ZHANOV[4]

[1] Corresponding Author. Kazakh National Pedagogical University named after Abai, Dostyk street, 13, 480100 Almaty, Kazakhstan. Tel.: +8 10 3272 91 83 82, E-mail: Kosov@abai.uni.sci.kz,
[2] Kazakh National Pedagogical University named after Abai.E-mail: Natalie_@inbox.ru;
[3] Kazakh National Pedagogical University named after Abai.
[4] Atyrau Institute of Petroleum and Gas. E-mail: aing-atr@nursat.kz

ABSTRACT

Experimental research of conditions of the onset of convection at isothermal diffusion in ternary gas mixtures in system of two vessels connected by a vertical capillary has shown, that mechanical equilibrium can be broken not only on condition when more dense mixture is in the top vessel, but also at opposite ratio of mass densities [1-4]. For this anomalous case experimental researches have allowed to find out effect of separation of components of a mixture (enrichment by the heaviest component) with some its maximal value at the certain pressure [5, 6]. The size of separation is influenced by such conditions as geometry of the diffusive channel [7, 8], pressure [9, 10], temperature [11, 12], viscosity [13].

In this work experimental results regarding anomalous concentration separation in multicomponent gas mixtures at various conditions are brought. Using the theory of stability, areas of existence of multicomponent diffusion and of convective effects of separation can be determined in terms of Rayleigh numbers. The reasons of the effect transpired and its theoretical interpretation is brought. Comparison of the experimental and theoretical data shows the good satisfactory.

Anomalous separation of components, diffusion, gas mixtures, instability of the mechanical equilibrium, linear theory of stability, plane of Rayleigh numbers

NOMENCLATURE

$a \times b$	[m^2]	cross section of the diffusive channel
d	[m]	diameter of the diffusive channel
n	[m^{-3}]	numeric concentration
t	[s]	time
$\underline{u}$	[m/s]	velocity
z	[m]	vertical coordinate
C	[-]	concentration
D	[m^2/s]	factor of diffusion
L	[m]	length of the diffusive channel
P	[Pa]	pressure
Q	[kg/s]	amount of the hydrodynamical stream
T	[K]	temperature
V	[m^3]	volume
α	[-]	dimensionless parameter, showing stability or instability of a mechanical equilibrium in a gas mixture

Subscripts and Superscripts

i, j	numeration of components in multicomponent gas mixture
I, II	characteristics, relating to top and bottom vessels, accordingly
r, l	characteristics, relating to left and right parts of channel, accordingly
exp	experimental value of physical quantity
theor	theoretical value of physical quantity

1. INTRODUCTION

The experimental researches described in works [5-13] have shown that under certain conditions (pressure, temperature, geometrical parameters of diffusive channel) in the regime of developed convection the transfer occurs not as a uniform mass, and with a prevalence of a heaviest component. At the studying of dependence of amount of the transferred components on time at fixed initial composition of mixture it has been marked, that if factors of diffusion are comparable with each other, under such conditions of experiment convective instability is absent and the

natural diffusion is observed. Completely other picture arises in diffusely unstable systems, for example $H_2 + Ar - N_2$, or $H_2 + N_2 - CH_4$. For them factors of diffusion of components considerably differ from each other. If the heaviest component has small partial charge in regime of steady diffusion, that in regime of convection it should be observed as $Q_2/Q_1 = C_{2I}/C_{1I}$.

2. EXPERIMENTAL RESULTS

Measurements were carried out on the device realizing a method of two vessels [1, 3-6, 8, 10, 11, 13]. Geometrical parameters of the diffusive apparatus were: volumes of the top and bottom vessels $V_I = 214{,}6 \cdot 10^{-6} m^3$ и $V_{II} = 226{,}8 \cdot 10^{-6} m^3$ accordingly; length and diameter of the diffusive channel $L = 0{,}165\ m$, $d = 6{,}1 \cdot 10^{-3} m$. The technique of carrying out of experiment was standard [1, 3-6, 8, 10, 11, 13]. The diffusive transfer of a binary gas mixture to a pure component was studied. The structure of a binary mixture at the fixed pressure and temperature was selected so that its density was less than density of the unicomponent gas, which was situated in the bottom part of the device. At the fixed initial composition and conditions of experiment the dependence of amount of transferred components on time was determined. Each experiment was carried out numerous amounts of times under the given conditions and final values were determined as arithmetic average of results.

On Figure 1 the dependence of parameter α_i (which is equal to the relation of experimentally measured concentration of i^{th} component to the calculated in the assumption of diffusion $\alpha_i = C_{\exp}/C_{\text{theor}}$) on time of experiment for systems $0{,}5673H_2(1) + 0{,}4327Ar(2) - N_2(3)$; $0{,}6179H_2(1) + 0{,}3821N_2(2) - CH_4(3)$ (numbering of components is specified in brackets at chemical symbols) is shown. At the first hours abnormal concentration separation of components of a binary mixture consisted in the increased percentage of the heaviest component in the bottom vessel is observed. Eventually the effect decreased, but distinction in the divided concentration is kept for a long time.

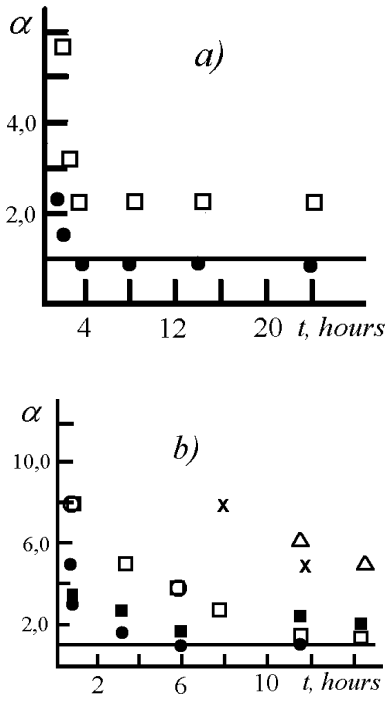

Figure 1. Parameter α_i for unsteady systems: a) $0{,}5673H_2(1) + 0{,}4327Ar(2) - N_2(3)$, P=3,04 *MPa*, points ●, □ – experimental data for H_2 and N_2, accordingly, b) $0{,}6179H_2(1) + 0{,}3821N_2(2) - CH_4(3)$, P=2,54 *MPa*, points O, △, □, ●, x, ■ – experimental data for H_2, N_2 and CH_4 at T=293,0 *K* and T=353 *K*, accordingly. Solid line – value of parameter α_i at diffusion.

3. THE THEORETICAL EXPLANATION OF EFFECT

Enrichment of a mixture by a heaviest component can be explained by the distinction in factors of mutual diffusion of gases D_{ij} and the presence of counter convective streams in the channel (experimentally found out in [3, 5]) at the diffusive instability. Modeling the observable streams, we shall consider in the flat vertical channel (Figure 2) counter movement of the binary gas mixture, entering into an input of the left half of the channel with concentration C_{2I}, and the unicomponent gas current upwards on its right half. We also suppose that speed of gas is homogeneous on section of each half of channel and equal u .

Counter streams differ on composition and consequently will exchange molecules, and during movement of a binary mixture on the length L it is impoverished by the lightest component as due to diffusion it will faster penetrate into a counter stream.

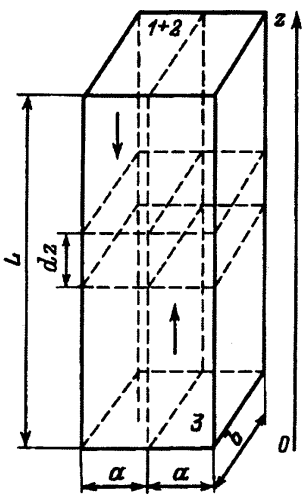

Figure 2. The diffusive channel. Geometry of a task

To calculate effect of separation in the described situation, we shall consider the equation of balance of number of particles of 1st component in the element with thickness dz in the right part of channel (Fig. 2)

$$\frac{dC_1^r}{dt} = \frac{J}{n \cdot a}, \tag{1}$$

where n – numerical concentration, C_1^r, C_1^l – concentration of molecules of 1st component in the right and left parts of the channel, J – density of diffusive stream.

Considering, that

$$dt = \frac{dz}{u},$$
$$u = \frac{Q}{a \cdot b \cdot n},$$
$$J = nD_{13}\frac{C_1^l - C_1^r}{a},$$

the Eq. (1) becomes

$$\frac{dc_1^r}{dz} = \frac{b}{Q} nD_{13}\frac{C_1^l - C_1^r}{a}, \tag{2}$$

where Q – amount of the hydrodynamical stream.

The similar ratio takes place and for molecules of 1st component in other half of channel

$$\frac{dC_1^r}{dz} = \frac{b}{Q} nD_{13}\frac{C_1^l - C_1^r}{a}. \tag{3}$$

At the Eq. (3) it is necessary to take into account, that in the left and right parts of the channel the directions of the stream are opposite. Eqs. (2) to (3) in view of boundary conditions $z = 0$, $c_3^r = 1$; $z = L$, $C_1^l = C_1^l(L)$, $C_2^l = C_2^l(L)$ and assumption, that the transfer is carried out in the channel with identical square sections of its parts ($b = a$), look like

$$C_1^l = \frac{nD_{13}z \cdot C_1^l(L)}{Q + nD_{13}L},$$
$$C_1^r = \frac{(Q + nD_{13}z) \cdot C_1^l(L)}{Q + nD_{13}L}, \tag{4}$$

where L – length of the diffusive channel.

Approach, which is similar to Eqs. (1) to (3), gives expression for a heavy component 2

$$C_2^l = \frac{nD_{23}z \cdot C_2^l(L)}{Q + nD_{23}L},$$
$$C_2^r = \frac{(Q + nD_{23}z) \cdot C_2^l(L)}{Q + nD_{23}L} \tag{5}$$

Carrying out the transition from Eqs. (4) to (5) to expressions for partial charges of components, it is necessary to take into account presence of gases 1 and 2 in both parts of the channel, and also a directions of each of Q_i. For system of coordinates on Fig. 2 and according to a condition of the analysis of components 1 and 2 ($z = 0$) finally received

$$\frac{Q_2}{Q_1} = \frac{C_2^l(L)}{C_1^l(L)}\left(\frac{Q + nD_{13}L}{Q + nD_{23}L}\right). \tag{6}$$

The maximal value of Eq. (6) will be determined by a condition $Q << nD_{ij}L$, i.e.

$$\frac{Q_2}{Q_1} = \frac{C_2^l(L)}{C_1^l(L)}\frac{D_{13}}{D_{23}}.$$

For experimentally investigated systems this relation is 2,8 and 6,1 accordingly. Comparison of the measured data (Fig. 1) shows that at the first hours of convective mixing such ratio if rightly and determines the maximal amount of separation of components of a mixture. Further quantitative measurements are necessary to carry out in the assumption that $Q > 0$, that requires its correct definition.

5. SUMMARY

Comparison of the experimental and theoretical data shows the satisfactory consent in definition of areas where take place instability and convective modes. It allows to suppose that the proposed theoretical description is correct.

ACKNOWLEDGEMENTS

The separate stages of work were supported by:

1. Fund of Science of the Ministry of the Science of Republic of Kazakhstan (project: № 0103RK00617);

2. Russian Fund of Basic Researches (the project 98-01-00879);

3. Ministry of Education and Sciences of Republic of Kazakhstan (the project № 387-2001 applied researches)

REFERENCES

[1] Zhavrin Yu.I., Kosov V.N., Seleznev V.D., 2000, "Anomalous gravitational instability of mechanical equilibrium during diffusion mixing in isothermal three-component gas mixtures", *Fluid Dynamics*, Vol. 35, No. 3, pp. 464-470.

[2] Zhavrin Yu. I., Kosov V. N., Kul'zhanov D. U., and Karataeva K. K., 2002, "Experimental Determination of the Boundary of Monotonic Disturbances upon Instability of the Mechanical Equilibrium in Three-Component Gas Mixtures", *Journal of Engineering Physics and Thermophysics (JEPTER)*, Vol. 75, No 4, pp. 868-872.

[3] Kosov V.N., Seleznev V.D., 2003, *"Anomalous onset of natural gravitational convection in isothermal ternary gas mixtures",* Ekaterinburg, 140 p.

[4] Kosov V.N., Zhavrin Yu.I., Kul'zhanov D.U., Ankusheva N.B., Poyarkov I.V, 2003, "Instability Of A Mechanical Equilibrium Of Isothermal Gas Mixtures At Multicomponent Diffusion", Proc. *Conference on Modelling Fluid Flow*, Budapest, Hungary, pp. I.268 - I.274.

[5] Kosov V.N., Seleznev V.D., Zhavrin Yu.I., 1997, "Separation of components during isothermal mixing of ternary gas systems under free-convection conditions", *Journal of Technical Physics*, Vol. 42, No. 10, pp. 1236-1237.

[6] Zhavrin Yu.I., Kosov V.N., Kulzhanov D.U., Poyarkov I.V., Ankusheva N.B., 2003, "Effect of cell rotation speed upon mutual diffusion in a three-component gas mixture", *Technical Physics Letters,* Vol. 29, No. 2, pp. 108-110.

[7] Zhavrin Yu.I., Kosov V.N., 1993, "Formation of structures and concentration convection at isothermal diffusion in ternary gas mixtures in the devices with various numbers of channels of the same cross section", *Technical Physics Letters,* Vol. 19, No. 10, pp. 18-21. (in russian)

[8] Kulzhanov D.U., "Experimental research of the border of transition "diffusion – gravitational concentration convection" at various radiuses of diffusive channel at multicomponent gas mixtures with unsteady stratification of density", *Vestnik of KazSU, part phys.,* No 2. pp. 119-121. (in russian)

[9] Zhavrin Yu.I., Kosov V.N., Kulzhanov D.U., Karataeva K.K., 2000, "Effect of the pressure on the type of mixing in a three-componeny gas mixture containing a component possessing the properties of a real gas", *Technical Physics Letters,* Vol. 26, No. 12, pp. 1108-1109.

[10] Kosov V.N., Kulzhanov D.U., Ankusheva N.B., Zhavrin Yu.I., 2002, "Instability of mechanical equilibrium in isothermal ternary gas mixtures at various pressures", *Izvestia of NAN RK, part phys.-math.,* No 2, pp. 81-87. (in russian)

[11] Zhavrin Yu.I., Kosov V.N., 1988, "Effect of temperature on the process of diffusion instability", *Journal of Engineering Physics and Thermophysics (JEPTER)*, Vol. 55, No 1, pp. 92-97. (in russian)

[12] Zhavrin Yu.I., Kosov V.N., Krasikov S.A., 1996, "Some pecularities of convective heat mass transfer in multicomponent gas mixtures", *Journal of Engineering Physics and Thermophysics (JEPTER)*, Vol. 69, No 6, pp. 977-981.

[13] Zhavrin Yu.I., Aytkozhaev A.Z., Kosov V.N., Krasikov S.A., 1995, "Effect of viscosity on stability of diffusion mass transfer in isothermal ternary gas mixtures", *Technical Physics Letters,* Vol. 21, No. 6, pp. 7-12.

Conference on Modelling Fluid Flow (CMFF'06)
The 13th International Conference on Fluid Flow Technologies
Budapest, Hungary, September 6-9, 2006

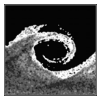

DESCRIPTION OF 3D FLOW FIELD INSIDE WHEELHOUSES OF CARS

Tamás RÉGERT[1], Tamás LAJOS[2]

[1] Corresponding Author. Department of Fluid Mechanics, Budapest University of Technology and Economics. Bertalan Lajos u. 4 – 6, H-1111 Budapest, Hungary. Tel.: +36 1 463 1560, Fax: +36 1 463 3464, E-mail: regert@ara.bme.hu
[2] Department of Fluid Mechanics, Budapest University of Technology and Economics. E-mail: lajos@ara.bme.hu

ABSTRACT

Numerical simulations of flow past simplified vehicle bodies with wheelhouses and rotating wheels have been carried out in order to understand the flow phenomena through detailed analyses of flow in the wheelhouses. The vortex skeleton method was used to characterize the flow structure. The second scalar invariant of the velocity gradient tensor (Q) and iso-surfaces of total pressure have been applied for detecting dynamic structures. It was found that the flow field in the wheelhouse can be characterized by 8 vortices out of which 7 were found to be unaffected by the body shape. Aerodynamic forces acting on the body, wheelhouse and wheel were determined separately for different configurations. Based on the results of investigations, general conclusions can be drawn concerning the aerodynamics of wheelhouses.

Keywords (Style "Keywords"): aerodynamics, car, wheelhouse, wheel, flow field, Computational Fluid Dynamics

NOMENCLATURE

A, B, C, D, E, H, S, L, R vortex indentifiers

B, D	$[m]$	width and diameter of wheelhouse
b, d	$[m]$	width and diameter of the wheel
C_D	[-]	drag coefficient
C_L	[-]	lift coefficient
p	$[Pa]$	local static pressure
p_∞	$[Pa]$	ambient static pressure
Re	[-]	Reynolds number
V_∞	$[m/s]$	free stream velocity
ρ	$[kg/m^3]$	density of the air
F	$[m^2]$	projected area
L	$[N]$	lift force
D	$[N]$	drag force
Q	$[1/s^2]$	second scalar invariant of velocity gradient tensor
k	$[m^2/s^2]$	turbulent kinetic energy
ε	$[m^2/s^3]$	dissipation rate of k
ω	$[1/s]$	specific dissipation rate

Subscripts and Superscripts
L, D lift, drag

1. INTRODUCTION

Road vehicle aerodynamics seems to reach its limits in terms of body shape optimization. Basic low-drag body shapes were developed during the last few decades (Hucho [11]). The effect of rotating wheels exposed to a free stream, or being partially covered by the car wheelhouse, leads to a dramatic increase in drag coefficient through mechanisms that are still not fully understood. Also wheels influence mud deposition on the vehicle body [22] and are important elements of the under-body flows [23]. The contribution of the wheels and wheelhouses to the total aerodynamic drag and lift of a modern car is around 30% and 40%, respectively [1], [2]. Road vehicles, especially their wheels and wheelhouses are bluff bodies, characterized by large regions of flow field influenced by boundary layer separation. The resultant flow field is an extremely complex, unsteady, 3D flow field that cannot be simplified to a 2D problem. The Reynolds number is in the order of $8 \cdot 10^5$, so the flow is far into the turbulent regime. The fluid can be regarded as incompressible and isothermal.

2. VALIDATION OF COMPUTATIONS

For the numerical simulation of flow field in wheelhouses of cars, the commercial code Fluent 6 was used. First the level of independency on the grid resolution and iteration was checked. The mathematical error of the computations were obtained within 1% concerning to the lift and drag coefficients of the investigated bodies.

Validation of the simulation model applied was carried out on an isolated wheel of varying profile shape and aspect ratio, rolling on a moving road. Computations were carried out using a combination of different near-wall treatment approaches, turbulence models and mesh structures to analyze

the structure of the flow field. The typical validation references were: integral quantities (lift and drag coefficients, defined in Eqs. (2) and (3)) and pressure coefficient (Eq. (1)) distribution in the central plane of the wheel, which were measured by Fackrell [6], Skea et al. [5] and Mears et al. [13].

$$C_p = \frac{p - p_\infty}{\frac{\rho}{2} V_\infty^2} \tag{1}$$

$$C_L = \frac{L}{\frac{\rho}{2} V_\infty^2 \cdot F} \tag{2}$$

$$C_D = \frac{D}{\frac{\rho}{2} V_\infty^2 \cdot F} \tag{3}$$

The computation results are compared to those of the experiments in Figure 1.

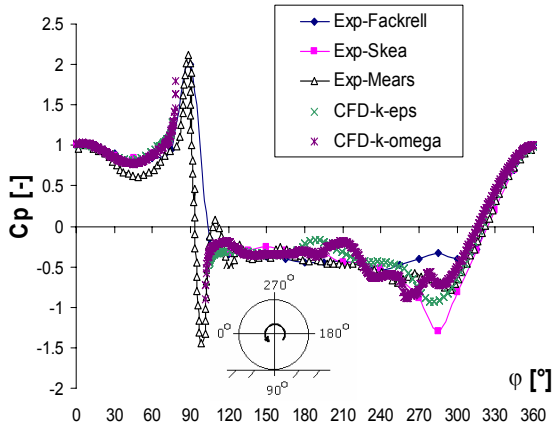

Figure 1. Pressure coefficient distribution over the periphery of an isolated rotating wheel (aspect ratio = 0.5)

The agreement is quite good for almost all parts of the wheel periphery except for the top region between 250-310 degrees. Here the experimental results are also in disagreement. This discrepancy is assigned to a boundary layer separation that occurs in Fackrell's case but does not occur in Skea's case. The agreement in the wake region of the wheel is remarkably good, so the problematic point is - similarly to the experiments - the prediction of the location of boundary layer separation. The CFD results indicate the presence of a depression maximum in good agreement with the corresponding literature of Skea [5] and Mears [13].

The pressure distribution on the whole surface of the wheel is validated also via its integral leading to drag and lift coefficients. For the stationary wheel, the measured drag and lift coefficients were in the range C_D=0.76±15% and C_L=0.77±15% (Fackrell [6], Skea [5], Mears [13], Axon [7]), respectively, where the extent of the range of coefficients indicates the difference between the measurement results of the previously mentioned publications. For the rotating wheel, the same properties were typically C_D=0.58±15% and C_L=0.44±15% (Fackrell [6], Skea [5], Mears [13], Axon [7]). For the stationary wheel, numerical simulation resulted in a prediction of lift and drag coefficient within 10-15% and ±10% range around the measured mean values, respectively. In the case of the rotating wheel, the drag and lift coefficients were estimated within 8%-10% and 15-20% of the mean of the measured drag and lift values, respectively. In addition, a qualitative comparison of the flow structures was made based on the experiments of Schiefer [10] and good agreement was found between measured and calculated flow structures [15].

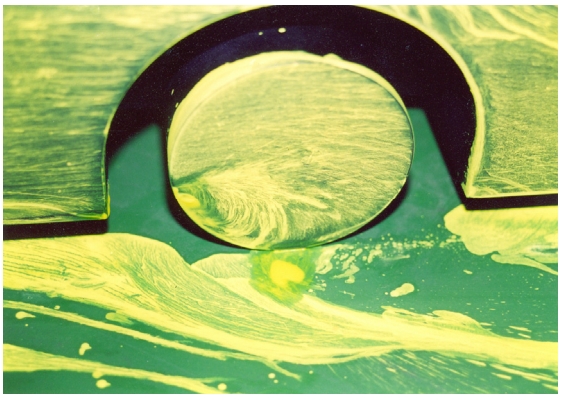

a)

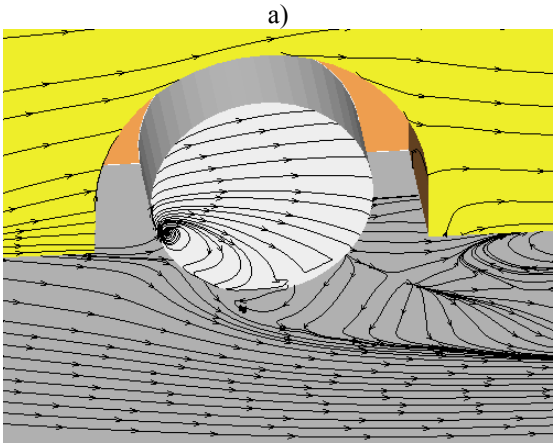

b)

Figure 2. Flow at a stationary wheel and ground: a) oil-film visualization in wind tunnel; b) numerical simulation (curves of wall shear stresses) [17]

Flow past a simplified vehicle model with wheelhouse and stationary wheel and ground was investigated by the first author [17] in a wind tunnel with flow visualization by using the oil-film method. Flow past the same arrangement (geometry, Reynolds number, boundary conditions)

was also calculated. The results of flow visualization and simulation are compared in Figure 2. The qualitative agreement of the observed oil-film pattern and wall shear stress lines (the tangents of these lines are the wall shear stresses) is quite good, reinforcing the reliability of the CFD simulation used.

Flow past the wheel in a wheelhouse was simulated also for validation purposes. Two validation tests based on the measurements of Axon et al. [8] and Fabijanic [3] were carried out. Axon et al. [8] and Fabijanic [3] used a moving belt to simulate the moving ground, and the aerodynamic forces acting on the body and the wheels were measured separately by both authors. The Reynolds numbers based on the diameters of the wheels and the free stream velocity were $1.57 \cdot 10^5$ and $8.5 \cdot 10^5$ for Fabijanic [3] and Axon et al. [8], respectively. Since no information was published about the structure of the flow field, the validation was made with comparison of integral quantities like aerodynamic drag and lift.

The difference between the measured ([8] and [3]) drag and lift coefficients were in an agreement of 10% and 65%, respectively. The differences between measured and computed lift and drag coefficients were small, i.e. 0.01-0.07 in absolute value. Since the exact details of the experimental set-up are not available, and the uncertainty of lift measurements on moving ground is high, the relatively large difference in lift force (65%) might be accepted level of accuracy.

The size of computational domain was also set in regard to its effect on the results. For the validation reported above and in the parameter studies described below the 'realizable' k-ε model was used since this turbulence model proved to be most accurate in calculation of aerodynamic forces (Rodi [21]), however best agreement with the structure of flow field can be achieved using Shear Stress Transport k-ω model (Reynolds Stress Model did not give convergent solution in any of the investigated cases). The logarithmic wall function with modifications to take pressure gradient into account (Launder and Spalding correction) was used near the walls. Boundary conditions were: total pressure at the inlet surface, static pressure at the outlet face, and no-slip boundary condition on the walls. These boundary conditions were applied in all the cases investigated in this paper.

In order to verify the numerical modelling used, grid independence was checked by using local refinements for each geometry. To see the dependence on the applied turbulence model, several eddy viscosity turbulence models were tested.

Numerical parameter studies were carried out by changing the main parameters influencing the flow: the depth (B) and diameter (D) of the wheelhouse related to the width (b) and diameter (d) of the wheel, respectively [16]. In parameter studies the simplified car model shown in Figure 3-a) was used. The basic topological features of the bodies used for the CFD investigations were similar to those used in the experiments: there was only one pair of wheels and the surface of the under-body was smooth.

The simulation results were compared to the experimental results of Fabijanic [3] (also in good agreement with Cogotti [4]). The geometries of the vehicle bodies, the change of aerodynamic force coefficients of which are shown in Fig. 4, are different from each other (see Figure 3-a) and 3-b)) but the flow characteristics are similar: attached flow on the surface of the vehicle upstream from the wheel.

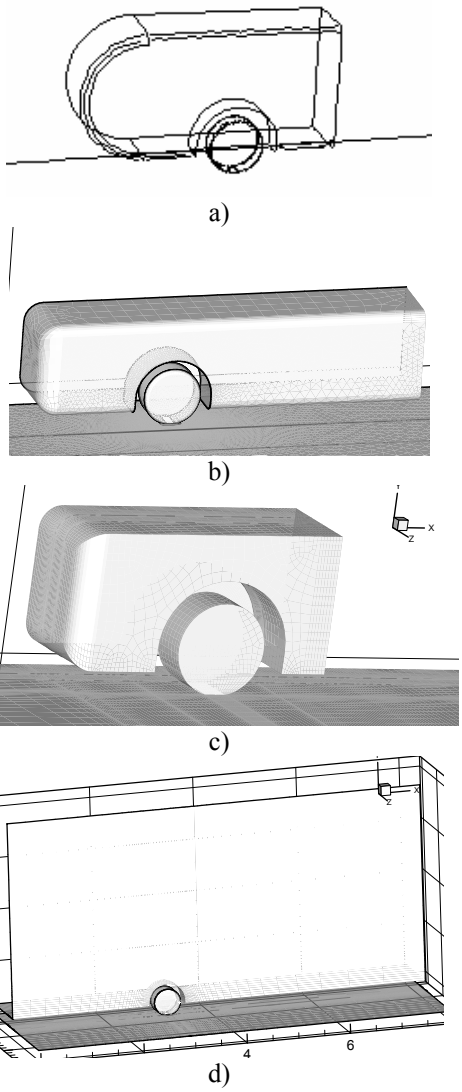

Figure 3. Body geometries for investigation of flow in wheelhouses

Here, in Figure 4, changes in the drag and lift coefficients are plotted against the relative diameter

(D/d) and width (B/b) of the wheelhouses. ΔC values indicate differences of the coefficients belonging to vehicle-model configurations with wheel and wheelhouse to those belonging to configurations with no wheel and no wheelhouse. The agreement is good in both the tendency and the quantitative values. A linear trend-line was fitted to the CFD data. Deviation of the CFD values from this line is very close to that of the experimental values.

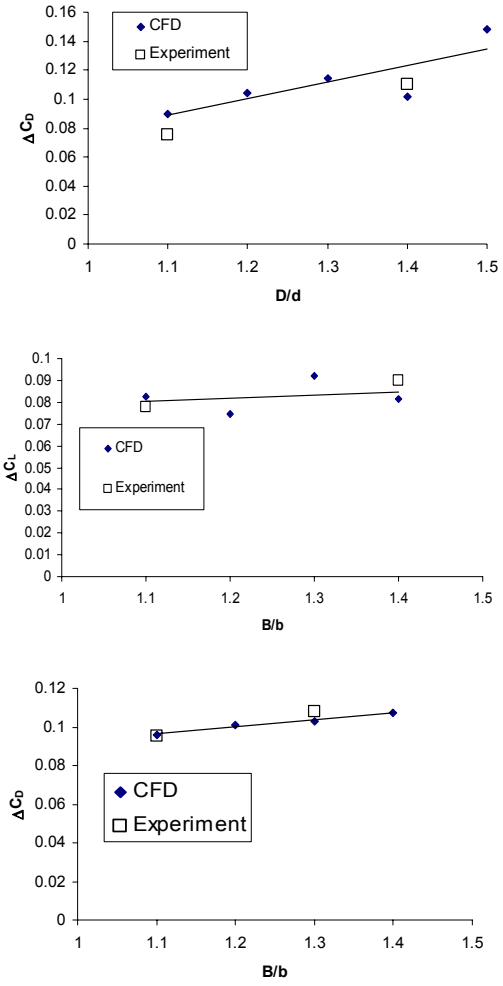

Figure 4. Comparison of numerical parameter studies with experimental ones (Experiment by [3])

On the basis of comparing the results of numerical simulations and experiments as well as regarding the results of various verifications of the models used – in accordance with the general practice reported in the literature – it can be concluded that numerical modelling of the flow used describes the real flow processes with an acceptable accuracy and reliability, so the CFD results can be used for analyses of the characteristics of flow field, for investigation of influence of various parameters and for establishing technical proposals for improvement of the aerodynamics of vehicle bodies.

3. VEHICLE MODELS USED FOR THE INVESTIGATIONS

In the frame of this investigation four different simplified body geometries were studied. The geometries investigated are shown in Figure 3. The diameter of the wheels for the cases given in Figure 3.-a), c) and d) was 0.5m, while for b) it was 0.105m according to the experiments of Fabijanic [3]. All investigations were made in a reference frame fixed to the vehicle body. The Reynolds number based on the free stream velocity and the diameter of the wheel varied in the range of $1.57 \cdot 10^5 – 8.5 \cdot 10^5$.

Figure 3-a) shows a fore-body different from that of the other two cases. This body geometry was defined to determine the effect of the shape of the fore-body on flow in the wheelhouse. The models shown in Figure 3-b) and c) have a similar fore-body shape but the distance between the wheel and the front of the vehicle is smaller in the case of Figure 3-c) than in the case of Figure 3-b) (Fabijanic [3] model). In the case of the model in Figure 3-d) the body in front of the wheel is infinite long.

It is a well known phenomenon (Wiedemann [18], Fabijanic [3] and Hucho [11]) that the distance between the front face and the wheel axis considerably influences the yaw angle of the wheel approaching flow in the vicinity of the underbody: the closer the wheel axis is situated to the front face of the vehicle, the bigger is the yaw angle. It has been concluded from the results of computations that the characteristics of the flow field are substantially controlled by the yaw angle. A comparison of the results belonging to different fore-body lengths indicates the effect of changing yaw angle on the flow field in the wheelhouse.

4. CHARACTERISTICS OF FLOW FIELD IN THE WHEELHOUSE

4.1 A model for description of flow in vehicle wheelhouses

A 3D, complex flow field develops in the wheelhouse. To understand this flow field and to identify the effect of, for example, geometrical changes on it, a qualitative structure model has been applied. In flows dominated by boundary layer separation vortices essentially determine the flow field, so the vortex skeleton [20] method was used, where the flow field is characterized, described by position, size and shape of vortices.

A number of numerical simulations were carried out at different Reynolds numbers, various geometrical and simulation parameters in order to

investigate the flow structure and its dependence from these parameters.

The vortex skeleton model of the wheelhouse flow field consisting of vortex filaments (tubes) identified by capital letters is shown in Figure 5.

The direction of flow in these vortices is indicated by lines with arrows. The cross-section of the filaments characterizes the size of the vortices and their change.

The vortex filaments were defined by using several methods. The traditional representation of the flow field: plotting of streamlines (or path lines) gives valuable information about the position, size of recirculation zones, the velocity direction and the origin of fluid particles flowing through the flow structure under consideration (see Figure 6-a).

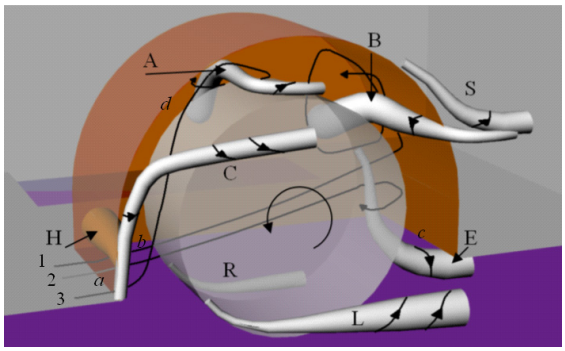

Figure 5. Vortex skeleton model of the wheelhouse flow field

The strength of the vortices determining their influence on the overall flow field was determined by analysis of other quantities. Vortices can be detected by analysis of the distribution of Q [19], the second scalar invariant of the velocity gradient tensor expressing the domination of "swirling" as opposed to the deformation (Figure 6-c). Flow structures characterized by tube-shaped iso-Q surfaces indicate vortices of large dynamical effect. A further characteristic of vortices is the low total pressure (head) inside them, so tube-shaped iso-total pressure surfaces of small values indicate the presence of vortices (Figure 6-d). Since the change of total pressure (head) correlates with the line integral of the rotation a given low total pressure (head) value in contrast to high Q value does not always indicate dynamic structures [14]. The method of critical points (Perry and Chong [12]) was also used to identify vortex filaments (Figure 6-b).

The analysis of wall shear stresses can also help in detecting vortices. Figure 6-b shows lines the tangents of which are the wall shear stresses (envelope of wall shear stresses). The base points of vortices, separation and reattachment lines of boundary layer can be recognized in Figure 6-b and also in Figure 2.

The vortex filaments and tubes shown in Figure 5 were determined by simultaneous application of the methods listed above. By analyzing three different simplified vehicle bodies, 8 flow structures (vortices) were detected in the wheelhouses the position as well as the size and strength of which depends on the wheelhouse geometry.

4.2 Characteristics of the flow inside wheelhouses

The lower part of the wheel, not covered by the wheelhouse, is exposed to the flow in the under-body gap. When comparing the flow past the lower part of the wheel in the wheelhouse with that of an isolated wheel, it was concluded that they resemble each other very closely. This observation is in accordance with the experiences of Morelli [9]. Outside the wheelhouse, near the ground, attached to the lower part of the wheel two permanently existing longitudinal vortices can be observed marked with L and R (see Figure 5).

The reason for the development of these vortices is separation of the boundary layer of the lateral outflow from the narrowing gap between the rolling wheel and the ground over the edges of the wheel running surface, close to the ground where the angle between these edges and the direction of flow velocity in the under-body gap is small. The separation bubbles attached to these edges are stretched by the under-body flow, so the separation bubbles become vortices extending into the under-body gap and wake of the vehicle model. The existence of these vortices is practically independent of the vehicle geometry, and their size and position depends on the profile of the wheel and the yaw angle of the wheel approaching flow.

Air enters the wheelhouse below and around three sections of the leading edge, "*a*" in Figure 5, and, because of the slanted wheel approaching flow, also below and around the longitudinal edge, "*b*". Air entering the wheelhouse below section *1* (close to the inner wall of the wheelhouse) flows slightly upwards and will be deflected upwards by the downstream part of the wheel arch, then gives rise to vortex (recirculation zone) B (see Figure 5). The base point of this vortex is shown to the right of Figure 6-b. The sense of rotation of vortex B corresponds to that of the wheel.

Air entering the wheelhouse below section *2* of edge "*a*" flows close to the inner side of the wheel and will be deflected by the downstream part of the wheel arch in a horizontal plane towards the side of the model. The boundary layer separates on the downstream inner edge of the running surface of the wheel. This separation bubble reaches the underbody flow that stretches it towards the under-body and the wake, giving rise to vortex E (see Figures 5 and 6)).

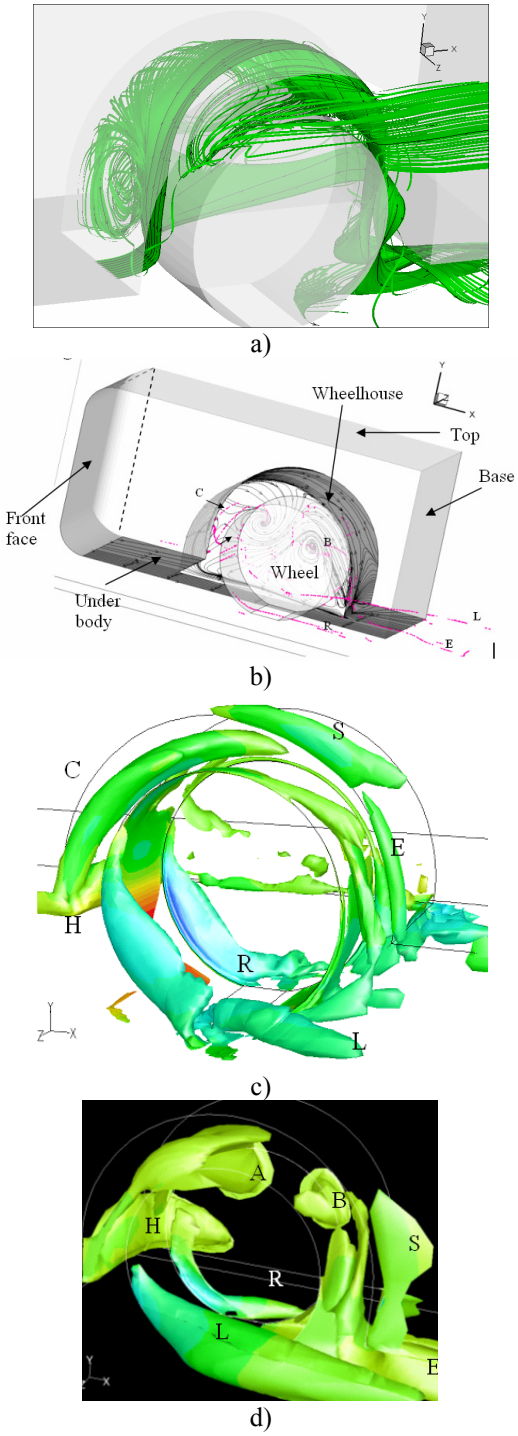

Figure 6. Flow field investigation methods: a) cricical points ([12]) and surface flow pattern; b) path lines; c) iso-*Q* surfaces; d) iso-head (total pressure) surfaces

Path lines started below section *3* of the wheelhouse leading edge "*a*", i.e. in front of the lower part of the wheel exposed to the wind are deflected upwards by the wheel. The same pattern of inflow was observed and published by several researchers [2, 3, 5, 10, 14, 21] but no explanation or model was given on the flow structure. The interaction of up-flow and the running surface of the wheel moving in the opposite direction to the flow cause boundary layer separation over the upper part of the running surface of the wheel. The separation bubble elongates towards the inner part of the wheelhouse and reaches the inner wall (base point of vortex A, see Figure 6-b). In the outer part of the separation bubble (vortex A) air flows towards the middle of the vehicle model. After reaching the inner wall air seems to flow in the middle of the vortex in the opposite direction towards the side of the model. When vortex A reaches the flow beside the side of the model, it will be deflected in the direction of the outside flow and elongated. Vortex A, in which the sense of rotation is opposite to that of the wheel, is shown in Figures 5, 6-a and 6-d.

Inside the wheelhouse behind the leading edge "*a*" (see Figure 5) boundary layer separation causes vortex H, the sense of rotation of which corresponds to that of the wheel (Figures 6-a, 6-c and 6-d)). In the case of larger yaw angle of the wheel approaching flow, vortex H will be complemented by the vortex (Fig. 6-a) caused by boundary layer separation along edge "*b*" in Figure 5. For the same reason vortex C develops over the upstream edge of wheel arch "*d*" in Figure 5. At a higher point of the wheel arch edge "*d*" vortex C separates and as a consequence of the interaction with the outside flow it turns beside the upper part of the wheel in the direction of flow beside the model and elongates towards the outside flow. It is an interesting characteristic of vortex C that it causes no inflow into the wheelhouse.

In the interior of wheelhouse the flow is characterized mainly by vortices A, B, H, and E. The size of vortex A depends on the quantity of air entering the wheelhouse below section *3* of the leading edge and turned upwards by the rotating wheel. If the yaw angle of the wheel approaching flow is small, i.e. the fore-body length is big the flow rate entering vortex A is big, so this vortex dominates the flow field in the wheelhouse. In this case vortex B does not emerge, the air entering the wheel arch under section *1* of edge " *a* " will follow the same path as the flow entering under section *2*, strengthening vortex E. With increasing yaw angle the flow rate of air entering the wheel arch under section *3* of edge " *a* " decreases, so the upstream part of the wheelhouse is filled by the air entering the wheelhouse under section *1* and forming vortex B.

A large part of the air entering the wheelhouse flows out through vortex A: in the outer part of it air flows inside the wheelhouse and in the internal part of the vortex air flows out. If vortex B exists (for shorter fore-body, larger yaw angle) considerable outflow also occurs in this vortex. Air leaving the wheelhouse through vortex E gets in the underbody flow and – if the rear wheel is considered – it influences the flow field of the wake.

It should be noted that vortex tubes A, B, C, E elongate when entering the high-velocity flow beside the side wall and in the underbody gap, consequently they will be dissipated and disappear quickly. This process is clearly demonstrated by the streamlines of the calculated flow field. Vortices A and C can be seen at the front wheelhouses of vehicles in rainy weather when water drops dispersed by the wheels make the flow field visible.

At the downstream part of the wheel arch outflow occurs in the gap between the wheel and the wheel arch, which is in agreement with the observation of Fabijanic [3]. As a consequence of boundary layer separation over the downstream edge of the wheel arch vortex S forms. If vortex B is present, it can influence the size of vortex S.

4.3 Determination of aerodynamic forces

For the investigations, the vehicle model shown in Figure 3-c was used. The surface of the basic body (no wheel and no wheelhouse) and simplified car body (wheel and wheelhouse, see Figure 3-c) was divided into parts and on the basis of flow fields calculated with the validated CFD model aerodynamic forces acting on these parts were determined by integrating the pressure and shear stress distribution over them. So the contribution of different body elements, wheel and wheelhouse to overall aerodynamic force coefficients was determined. The results reported here belong to Reynolds number $Re=8.5\cdot10^5$ calculated with wheel diameter and undisturbed flow velocity. Where wheels were present, they were rotating and the ground was moving.

The front face of the bodies includes the vertical wall and the surrounding rounded-up leading edges. It was concluded that the wheels and wheelhouses increase pressure on the front face, causing 37% increase in fore-body drag and decrease the pressure over the base that results in 6% increase in base drag. This change can be explained by the effect of the lower part of the wheels that reduce the velocity of under-body flow and increase in this way the pressure on the lower side of the fore-body. The minor change of the base drag indicates the interaction of the wake of the wheels (mainly vortex E [15]) and that of the body. The overall increase of drag acting on the simplified car model as a consequence of the wheels and wheelhouses is 62% with respect to that of the basic model. Out of this, 17.2% is the increase of drag acting on the body (predominantly the increase of the sum of fore-body and base drag). In addition to this the drag acting on the wheels and wheelhouses causes individually 35.6% and 9.1%, respectively and 44.7% increase in overall drag. It can be concluded that ¼ and ¾ of the significant increase in drag can be assigned to an increase of drag on the body and on the wheel and wheelhouse, respectively. The majority 57.4% of increase is due to the drag acting on the wheel.

The exact values presented above correspond to the vehicle model represented in Figure 3-c, but the proportions, tendencies and the basic mechanism can be concluded to be general.

CONCLUSIONS

This work reports the results of extensive investigations of the flow fields past wheels in wheelhouses of passenger cars by using numerical simulation. The validation of the numerical models was carried out by comparing the results of simulations (pressure distributions, aerodynamic forces) to those of experiments published in literature. Good agreement was achieved.

Based on the simultaneous application of three alternative vortex detection methods a procedure was developed using the concept of vortex skeleton method and applied to detect dynamic structures, vortices in the flow field in wheelhouses. The complex analyses of flow field resulted in the definition of 8 vortices in the wheelhouse, out of which the existence of 7 vortices are found to be independent on the change of geometry of the vehicle body.

From the viewpoint of flow in wheelhouses, i.e. the extent and strength of characteristic vortices, the main effect of the car body is the deflection of under-body flow towards the sides of the car, resulting in a yaw angle of attack when approaching the wheel. The wheelhouse flow has very little correlation with the flow along the sides of the vehicle.

During the investigations it was found that the rotation of wheel has relatively small effect on the structure of the flow field if the gap between the wheel and the wheelhouse cavity is larger than the thickness of the boundary layers.

It was found that the substantial increase of drag force is due mainly to the drag acting on the wheel and to the change of fore-body and base drag caused mainly by the wheel influencing the under-body flow. Increase of lift force, on the other hand, is purely due to the flow field modification of the wheel and has no connection with the forces acting on the wheel and wheelhouse.

Further investigation of the results of computations showed that the flow field, and thus the aerodynamic forces in wheelhouse are mainly influenced by the under-body flow through the lower opening of the wheelhouse and is slightly sensitive to the side gap coverage.

Based on the results of numerical investigations, general conclusions can be drawn and development measures can be determined concerning the characteristics and control of aerodynamics of wheelhouses.

ACKNOWLEDGEMENT

Authors wish to thank for OTKA T 043493, T 037651, T 037730, K 63704 and SZEFH Foundation for the financial support.

REFERENCES

[1] Wickern G., Zwicker, K., 1995, "Zum Einfluß von Rädern und Reifen auf den aerodynamischen Widerstand von Fahrzeugen" *Tagung "Aerodynamik des Kraftfahrzeugs", Haus der Technik e. V.*, Essen.

[2] Eloffson, P., Bannister, M., 2002, "Drag reduction mechanisms due to moving ground and wheel rotation in passenger cars" *Society for Automotive Engineers*, paper, 2002-01-0531. p. 185-198

[3] Fabijanic, J., 1996, "An experimental investigation on wheel-well flows" *Society for Automotive Engineers*, paper, 960901. p. 161-172

[4] Cogotti, A., 1983, "Aerodynamic characteristics of car wheel. Impact of Aerodynamics on Vehicle Design" *Int. Journal of Vehicle Design*, SP3, pp. 173-196

[5] Skea, A.F., Bullen, P.R., Qiao, J., 1998, "The use of CFD to predict air flow around a rotating wheel", *31st. Int. Symposium on Automotive Technology and Automation*, Düsseldorf, pp. 187-196

[6] Fackrell, J. E., Harvey, J. K., 1973, "The flow field and pressure distribution of an isolated road wheel", *Advances in Road Vehicle Aerodynamics*, pp. 155-164

[7] Axon, L., Garry, K., Howell, J., 1998, "An Evaluation of CFD for Modelling the Flow Around Stationary and Rotating Isolated Wheels" *Society for Automotive Engineers*, Paper 980032, Detroit, pp. 205-215

[8] Axon, L., Garry, K., Howell, J., 1999, "The Influence of Ground Condition on the Flow Around a Wheel Located Within a Wheelhouse Cavity", *Society of Automotive Engineers*, Inc. 1999-01-0806, pp. 149-158

[9] Morelli, A., 1969, "Aerodynamic actions on an automobile wheel", *Symposium on Road Vehicle Aerodynamics*, City University, London

[10] Schiefer, U., 1993, "Zur Simulation des freistehenden Fahrzeugrades im Windkanal", *Dissertation am IVK*, Universität Stuttgart

[11] Hucho, W.H., 1998, "Aerodynamics of Road Vehicles", *Butterworth and Co. Publishing*, Boston

[12] Perry, A.E., Chong, M.E., Cantwell, B.J., 1990, "A general classification of three-dimensional flow fields", *Physics of Fluids* A 2 (5), May, pp. 765-777

[13] Mears, A.P., Dominy, R.G., Sims-Williams, D.B., 2002, "The air flow about an exposed racing wheel", *Society for Automotive Engineers*, paper, 2002-01-3290. p. 37-43

[14] Lajos, T., 2004, "Az áramlástan alapjai", *Műegyetemi könyvkiadó*

[15] Régert, T., Lajos, T., 2003, "Investigation of flow field past rotating wheels of cars", *Proceedings of Conference on Modelling Fluid Flow (CMFF)*, pp. 387-394

[16] Régert, T., 2001, "Investigation of flow field about wheels of road vehicles", *Diploma thesis*, Budapest University of Technology and Economics (BME)

[17] Régert, T., 2003, "Visualization studies in TU Dresden NWK", *Technical report*, Dresden

[18] Wiedemann, J., 1996, "The influence of ground simulation and wheel rotation on aerodynamic drag optimization – Potential for reducing fuel consumption", *Society for Automotive Engineers*, paper 960672

[19] Jeong, J., Hussain, F., 1995, "On the identification of a vortex", *J. Fluid Mechanics*, vol. 285, p. 69-94

[20] Perry A.E., Hornung H.: "Some Aspects of Three-Dimensional Separation, Part II: Vortex Skeletons", Zeitschrift für Flugwissenschaften und Weltraumforschung, 8, Heft 3, 1984.

[21] Rodi W., 1997, "Comparison of LES and RANS calculations of the flow around bluff bodies", *Journal of Wind Engineering and Industrial Aerodynamics* 69-71, pp. 55-75

[22] Lajos T., Preszler L., Finta L., 1984, "A Wind-Tunnel Investigation of Mud Deposits on the Body of a Bus", *International Journal of Vehicle Design*, 5 (6), pp. 693-703

[23] Lajos, T, Preszler, L, Finta, L., 1988, "Styling and Aerodynamics of Buses" *International Journal of Vehicle Design*, 9 (1), pp. 1-15

Conference on Modelling Fluid Flow (CMFF'06)
The 13th International Conference on Fluid Flow Technologies
Budapest, Hungary, September 6-9, 2006

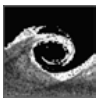

PIV SYSTEM FOR FLUID FLOW MEASUREMENT IN FUEL ASSEMBLY OF NUCLEAR REACTOR

Dániel TAR, Gábor BARANYAI, György ÉZSÖL, Iván TÓTH

Hungarian Academy of Sciences KFKI Atomic Energy Research Institute, Thermohydraulics Department, Budapest, P.O. Box 49. 1525 Hungary Tel.: +36 1 392 2222/1307, Fax: +36 1 395 9293, E-mail: tar@sunserv.kfki.hu

ABSTRACT

There are several fluid dynamics calculations modelling the coolant water flow in the core of nuclear power plants. The main purpose of our experiments was to investigate flow conditions in the fuel assemblies of VVER type nuclear reactors and provide experimental results for validation of simulations. A well-specified particle image velocimetry (PIV) system was installed. The experimental models were made of plexiglas, in order to be transparent for the visible laser beam. The plexiglas vessels were filled with deionised water and with seeding material, and connected to a closed water circulation loop. Experiments were made with two small models, with a square vessel, and with a segment of a fuel assembly. Two dimensional velocity vector fields have been obtained. The capability of PIV method has been tested for detection the more than one order of magnitude velocity difference in the cross flow and mainstream. The experiments have shown that PIV method is an adequate procedure to give appropriate vector fields in the fuel assembly geometry determined flow conditions, and it is a suitable method for the verification of the calculations.

Keywords: fuel assembly, nuclear reactor, PIV, subchannel

NOMENCLATURE

t_0	[s]	time of the first light pulse generating the first particle image
Δt	[s]	time between the two light pulses generating the particle image pair
v	[m/s]	absolute velocity magnitude

1. INTRODUCTION

The particle image velocimetry (PIV) is a state-of-the-art, whole-flow-field velocity measurement technique, and provides also an outstanding possibility for comparing the computational results with experimental data. [1]

PIV is a novel measurement technique that can be applied to the investigation the flow in the subchannels of the fuel assemblies of VVER type nuclear reactor. The main purpose of our experiments was to investigate the flow conditions and mixing processes in the subchannels of fuel assemblies, by determining two dimensional velocity distributions. Preliminary measurements realized with simplified models of a whole fuel rod bundle are discussed in this study.

The experiments detailed below can prove the suitability of the installed PIV system to get appropriate velocity vector maps in the required condition. This can be the basis to use PIV as an experimental verification of CFD calculations.

The main advantage to use PIV for this purpose is that it is a non-intrusive measurement technique. The seeding particles follow the flow completely without influencing it.

2. EXPERIMENTAL EQUIPMENT

2.1. Description of the PIV equipment

The main parts of the PIV equipment are a Nd YAG laser system, a CCD camera, a system hub, and a software package.

The laser system comprises two Nd YAG lasers, with optical flash lamps and quality switch, mounted in the same unit for the generation of the light impulses at t_0 and $t_0+\Delta t$ separately. The alignment of the overlap of the two laser beams has to be set with mirrors. The frequency is doubled by

a second harmonic generator crystal; from the originally infrared light with the wavelength of 1064 nm visible green light with the wavelength of 532 nm is produced. There is also an optical attenuator applied, allowing a very fine adjustment of the laser energy. From the beam with circle cross-section a light sheet suitable to illuminate the investigated flow is produced with an optical lens system. The repetition frequency can be adjusted up to 15 Hz. The diameter of the cross section of the laser beam (and so the thickness of the light sheet) is an important parameter for our experiments, as for measurement of the flow in the subchannels of the fuel assemblies a light-sheet with the width of about 1 *mm* required. The minimum light-sheet thickness proved to be about 700 μm.

The CCD camera has 2 million pixel resolution, the pixel clock frequency is 40 *MHz*, the maximum number of *frame/s* is 30. A Nikon lens is used with 60 *mm* f2.8, and with a 532 *nm* filter. Some distance rings are also applied as in many cases of the measurements recordings made at about 100 *mm* distance are necessary.

The system hub is also a very important part of the equipment. It can be considered as a central unit, connecting the laser, camera, and the PC together and responsible for their communication.

The software package is running in a PC, and makes possible the acquisition and the analysis. The dimension of the interrogation area (the region on the particle image, producing one velocity vector) is user-selectable by altering the number of pixels in the side of the interrogation area. The particle images are recorded and stored. For producing velocity vector maps, the software offers advanced cross correlation methods. The numeric data underlying vector maps can be exported as ASCII values to a text file and can thus be used as input to other programs. One such application would be when comparing measured data with data calculated from a flow simulation program. [2] When recording a sequence of particle image pairs, there are more options to get an average result velocity vector map based on the determination of the average correlation function, the average velocity vectors, or the average particle image pair. [3]

For seeding material polyamide particles with the diameter of 20 μm and density of 1.016 g/cm^3 were used. The particles were dispersed into the circuit.

2.2. Description of the plexiglas models

Two models were made of plexiglas. The vessels were filled with deionised water and with the seeding particles, and connected into a closed hydraulic loop, including the circulation pump, operated at room temperature and atmospheric pressure.

As PIV means a new measurement technique for measuring the flow inside a fuel assembly, first a simple model was built in order to control the components of the installed PIV system and the whole measurement process. This model is a square shaped vessel providing convenient access for the laser and camera. (A schematic drawing can be seen on Figure 4.) As the inner dimensions are 250 × 160 × 35 *mm*, it is designed thin enough in the third dimension, so the flow can be considered practically two dimensional.

Based on the experiments of the simple model, another closed circulation loop was made, the so called fuel channel model. This serves as preparation for the measurements with a whole bundle of fuel elements arranged in a hexagonal lattice. The fuel channel model has two main types of parts. The middle unit includes the five half-rods following the hexagonal geometry, its length is 300 *mm*; see Figures 1, 2, 3 and 9. The units with the inlet and outlet contain no half-rods, as it can bee seen on Figures 3, 6 and 9.

Figure 1. Cross section of the fuel channel model

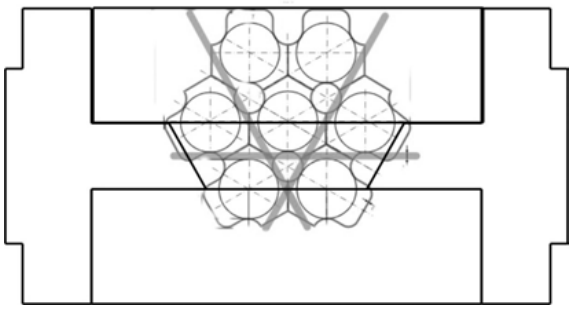

Figure 2. Explanation of the positions of the half-rods and the spacer grid in the fuel channel model, and the possible laser pathways

With the fuel channel model a fragment of the total fuel rod bundle can be examined, where the flow is limited to a channel with a trapezoid cross section (see Figs.1 and 2). Two types of the middle unit of the fuel channel were investigated: without the spacer grid, and including it at the middle, according to Figs. 2 and 9.

3. MEASUREMENTS, RESULTS

The main parameters of the measurements were set to the same value almost in all cases, as it is listed below. If there was a difference at a certain measurement, it will be indicated. Generally, the dimension of the interrogation areas was chosen 32×32 pixels and 64×64 pixels respectively. The laser energy was set to 20% of the maximum, Δt was chosen for 100 μs, and 10 s was sampled with 1 Hz frequency. Thus, 10 image pairs (velocity vector maps) were produced, than an average was calculated; the results presented below are showing velocity profiles of the flow, averaged for 10 s. Although, in some cases other parameters were also tried, e.g. higher sampling frequency, lower Δt, etc., but the optimal performance for the simple experiments (where the capabilities of the system were not completely utilized) proved to be at the parameters listed above. Higher sampling frequency would be necessary for example, when information about large-scale turbulent features is required. [4]

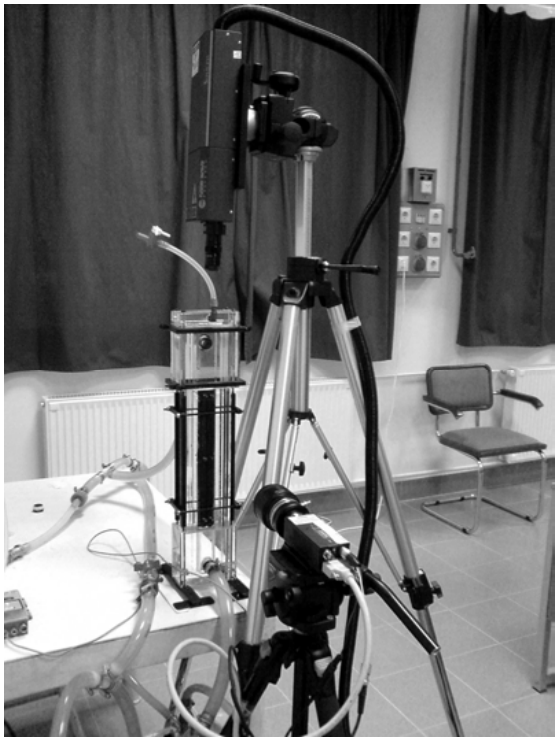

Figure 3. The arrangement of the equipments with the fuel channel model

Appropriate scaling is very important in order to get the absolute velocity magnitudes. This has to be determined for every single setup. The uncertainties will be discussed later.

On Fig. 4 the setup of the measurement with the square vessel can be seen. The schematic drawings are showing the illuminated plane of the thin laser light sheet. A typical velocity vector map of this experiment produced in this plane can be seen on Figure 5. The range of v was between about 0.01 and 0.5 *m/s*.

On Figs. 3, 6 and 9 the setups of the main measurements with the fuel channel model are illustrated by the schematic drawings. They show the realized laser pathways. As a consequence of the hexagonal geometry there is a wall at 60° causing the refraction of the laser lights, it had to be taken into account. Two typical velocity vector maps obtained by measuring the outlet part can be seen on Figures 7 and 8.

In the case shown on Fig. 7 no spacer was inserted, while Fig. 8 is showing a result with the spacer grid.

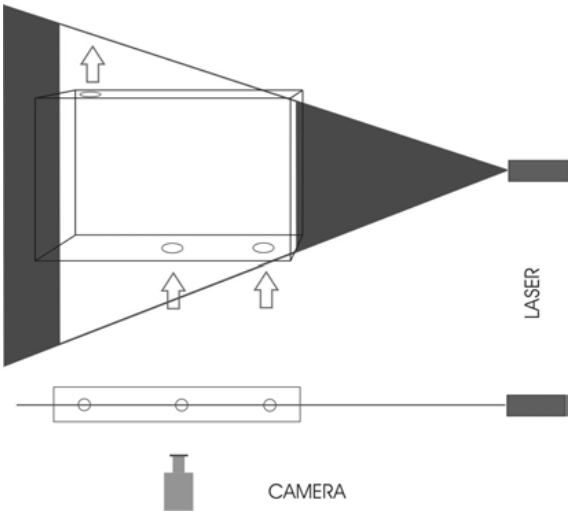

Figure 4. Setup of the measurement with the square vessel

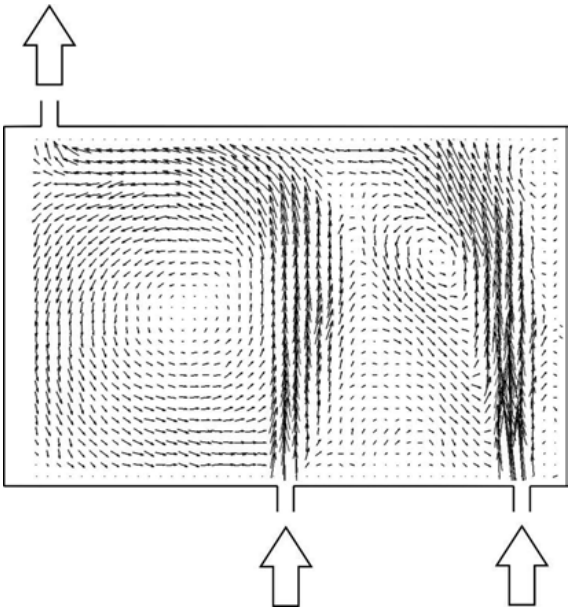

Figure 5. Velocity vector map obtained in the square vessel. *v* is about 0.01 to 0.5 *m/s*.

In both cases the range of *v* was between about 0.1 and 3.5 *m/s*, so there was more than one order of magnitude difference between the velocity maximum and minimum.

Although there are no half-rods in the outlet part, their effect can be still discovered on both vector maps as plumes of higher velocities.

In both cases an asymmetry of the flow can be observed resulting in a spiral-shaped flow at the outlet. This is caused by a little asymmetry of the plexiglas model, and gives a good opportunity to study irregular flow conditions in the fuel channel geometry. In the case without a spacer there is a little vortex, included little velocity magnitudes. On the other hand the result obtained with the spacer shows more symmetry, this can be assigned to a better mixing between the fuel rods. The velocity magnitudes in the vortex are about the minimum (~0.1 *m/s*), and just right beside it the maximum velocities (~3.5 *m/s*) appear in the two plumes. This result means that the installed PIV system is suitable for the detection and visualization of the more than one order of magnitude velocity difference in the cross flow and mainstream.

Above, the mixing effect of the spacer was demonstrated by the results of the PIV measurements in the outlet part, which is about at 150 *mm* distance from the spacer. The velocity vector map recorded just above the spacer is shown on Fig. 9. This was the most difficult experiment as the laser sheet had to be positioned exactly into the space between the half-rods. From the possible laser pathways indicated on Fig. 2 the horizontal option was realized. The arrangement of the PIV equipment at this measurement can be seen on Figs. 3 and 9 – this time the laser sheet was positioned from the top, since the spacer is not transparent.

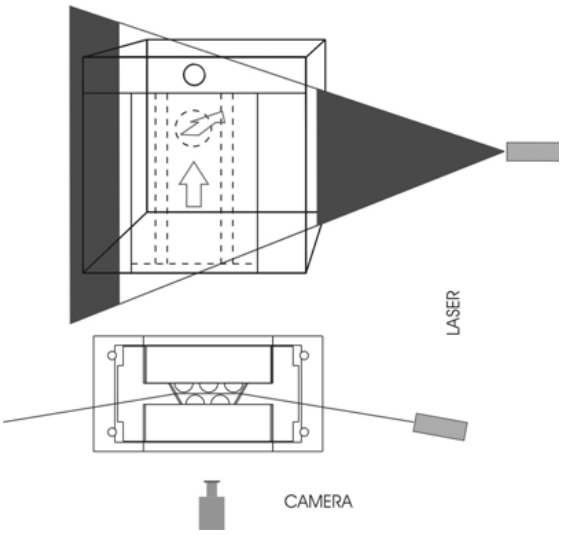

Figure 6. Setup of the measurement with the fuel channel model

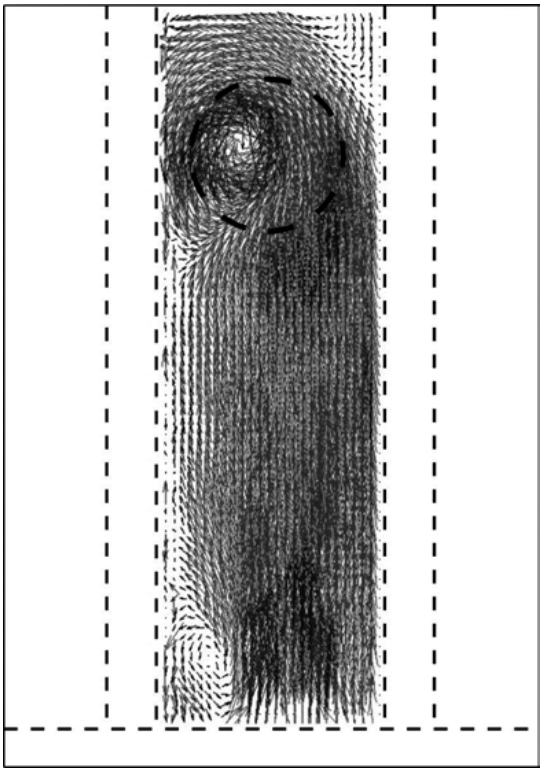

Figure 7. Velocity vector map obtained in the outlet part of the fuel channel model, without spacer included in the middle part. *v* is about 0.1 to 3.5 *m/s*.

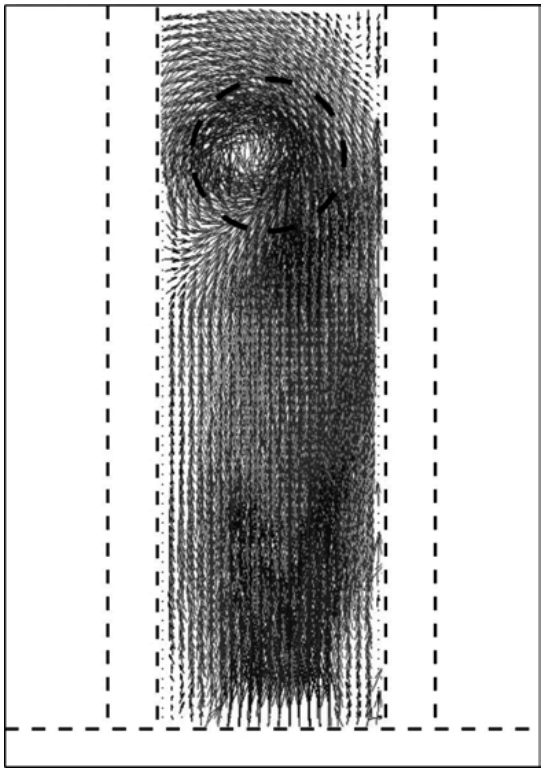

Figure 8. Velocity vector map obtained in the outlet part of the fuel channel model, when there was a spacer included in the middle part. *v* is about 0.1 to 3.5 *m/s*.

Because of the longer distance, the laser energy was doubled to 40%. On the vector map (Fig. 9.) the mixing effect of the spacer can be observed; along a few *mm* distance after the spacer the velocity vectors are jumbled.

As in this study the results are qualitatively interpreted and visualized no overall uncertainty analysis was made. However, the error range of the velocity magnitudes can be well approximated by measuring the flow rate at a well known cross section of the loop – practically it was mounted into a transparent plastic tube which could be illuminated by the laser sheet. This way the averages of the measured velocities could be compared. The relative uncertainty maximum proved to be about 5 %. This can be assigned to the limitations of measuring the two dimensional projection of the particle velocities in the flow field.

4. SUMMARY

Preliminary measurements have been introduced to investigate the flow conditions and mixing processes in the subchannels of fuel assemblies of VVER type nuclear reactor. A PIV system was used to obtain two dimensional velocity vector fields; this is a novel measurement technique in this field of research. The purpose of the preliminary measurements was to prove the suitability of the installed PIV system to get appropriate velocity distributions in the hexagonal fuel assembly geometry. Very important also to prove PIV as an experimental verification tool of CFD calculations.

The experiments were realized with the use of simple models made of plexiglas connected to a closed water circulation loop. After installation of the equipments, some test measurements were done with a simple plexiglas model to prove the reliability of the system. A simplified model of the fuel assembly was than examined.

Based on the qualitatively interpreted results of experiments it was shown, that with the installed PIV system it is possible to determine the velocity distribution in the subchannels of the fuel element bundles, and to detect the mixing effect of the spacer grid. Also the parameters and capability of the PIV system are applicable for measurements of far bigger models and for higher velocities determined by a whole fuel rod bundle.

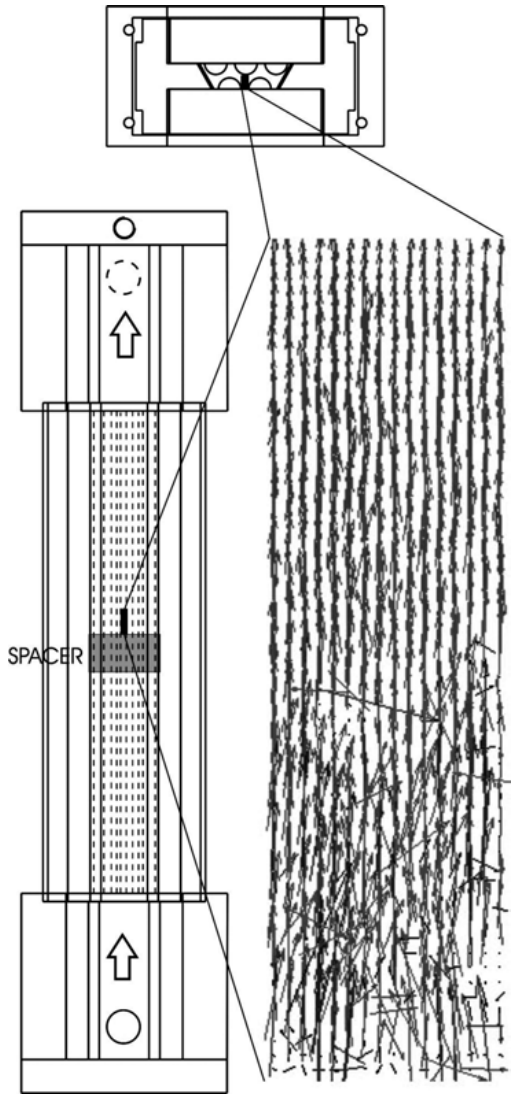

Figure 9. Velocity vector map obtained between the half-rods in the fuel channel model just above the spacer. *v* is about 2.5 to 4 *m/s*. The dimensions of the recorded area (velocity vector map) are 4 ×15 *mm*.

REFERENCES

[1] M. Raffel, C. Willert, J. Kompenhans, 1996, *Particle Image Velocimetry*, Springer

[2] Dantec Measurement Technology, 2000, *FlowMap® Particle Image Velocimetry Instrumentation*

[3] K. Okamoto, S. Nishio, T. Saga, T. Kobayashi, 2000, *Standard images for particle-image velocimetry,* Meas. Sci. Technol. Vol. 11 pp. 685–691.

[4] R.B. Bird, W.E. Stewart, E.N. Lightfoot, 1960, *Transport Phenomena*, John Wiley & Sons

Conference on Modelling Fluid Flow (CMFF'06)
The 13th International Conference on Fluid Flow Technologies
Budapest, Hungary, September 6-9, 2006

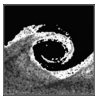

DEVELOPMENT OF A SIMULATION METHOD TO PREDICT UV DISINFECTION REACTOR PERFORMANCE AND COMPARISON TO BIODOSIMETRIC MEASUREMENTS

Christoph REICHL[1], Christoph BUCHNER[2], Georg HIRSCHMANN[3], Regina SOMMER[4], Alexander CABAJ[5]

[1] Corresponding Author. arsenal research – Austrian Research Centers. Giefinggasse 2, 1210 Vienna, Austria. Tel.: +43 50550 6605, Fax: +43 50550 6439, E-mail: Christoph.Reichl@arsenal.ac.at
[2] Technical University of Vienna, arsenal research. E-mail: christoph_buchner@gmx.at
[3] arsenal research. E-mail: Georg.Hirschmann@arsenal.ac.at
[4] Division of Hygiene and Medical Microbiology, Medical University of Vienna. E-mail: regina.sommer@meduniwien.ac.at
[5] Institute of Medical Physics and Biostatistics, University of Veterinary Medicine Vienna. E-mail: alexander.cabaj@vu-wien.ac.at

ABSTRACT

Nowadays, water disinfection with ultraviolet (UV) radiation becomes increasingly important. This work presents a simulation method to predict the disinfection efficacy of an UV disinfection reactor and compares the results to biodosimetric measurements.

CFD calculations have been performed for a set of operation parameters. A discrete phase model was used to generate particle tracks. The fluence rate field inside the reactor has been simulated using several radiation models. Particle tracks and radiation models have been combined to calculate the reduction equivalent fluence (*REF*), an important quantity in biodosimetry. The obtained simulation results are compared to experimental data to assess the achieved accuracy.

The simulated pressure loss of the reactor agreed very well with the experiments. In contrast to the biodosimetric measurements, only a limited amount of data for the flow field and fluence rate distribution is provided by Austrian standard certification procedures. Considering this, good predictions of the *REF* were obtained by the presented simulation method. Average error values varied between 7 and 25%, depending on the chosen radiation model. The potential use of this method for designing and improving UVD reactors has been demonstrated.

Keywords: biodosimetry, CFD, particle tracking, radiation models, REF, UV disinfection

NOMENCLATURE

E'	$[W/m^2]$	fluence rate
H'	$[J/m^2]$	fluence
REF	$[J/m^2]$	reduction equivalent fluence
T	[-]	optical transmittance for 10mm of medium at λ=253.7nm
d	$[m]$	optical path length
dA	$[m^2]$	infinitesimal area
g	$[m]$	length of a cone generatrix
n	[-]	refractive index
r	$[m]$	radial distance
x	$[m]$	axial distance
λ	$[m]$	wavelength
θ	[-]	angle of incidence

Subscripts

1, 2, 3	air, quartz and water, respectively
W, WO	with and without considering refraction, respectively

1. INTRODUCTION

Disinfection of potable and wastewater using additives like chlorine or ozone has a long tradition [1]. However, these treatments can result in the formation of disinfection by-products which are harmful to humans. Additionally, certain microorganisms are particularly resistant to chemical disinfection. Treatment with UV radiation offers a way out, since it is a purely physical process, producing very few by-products compared to chemical methods, and does not alter taste or chemical composition. For this reason, water treatment with UV radiation becomes increasingly important.

Disinfection facilities exist in various sizes, ranging from conventional single-lamp reactors to up to 8000 lamp wastewater installations. Commonly, quasi-monochromatic as well as polychromatic ultraviolet lamps are employed whose radiation permeates the water flow.

Pathogenic microorganisms, which are present in the fluid, are deactivated by the incident photons and lose their danger of infection for humans.

The efficacy of UV disinfection (UVD) reactors strongly depends on several design and operation parameters, namely fluence rate distribution in the reactor chamber, water mass flow and UV transmittance, as well as geometric and hydrodynamic properties of the reactor. This is why great care has to be exercised when adjusting these parameters to achieve optimal operation.

In a normal design process, the last stage is the certification of the reactor for a certain set of operational parameters. In Austria, this certification uses biodosimetric tests (frequently called "bioassay") according to ÖNORM M 5873-1 [2]. If this certification fails, part of the design process has to be repeated. The certification procedure and necessary construction of a prototype is costly and time-consuming. The increasingly powerful numerical simulation techniques available enable the designer to predict reactor performance under certain operating conditions without incurring the high cost of prototype construction and certification. This also makes it possible to examine many different parameter configurations with respect to their performance. In the traditional design process, different operating points need to be certified to determine the disinfection efficacy.

UV disinfection and the associated processes have been investigated by several researchers. The main areas of research are radiation modelling and measurement [3-8], analysis and simulation of the performance of UV disinfection reactors [9-12], bacterial inactivation and repair processes [13-18] and others [19-22]. The guidance manual of the U.S. Environmental Protection Agency [23] provides extensive information on many aspects of the implementation of UV disinfection systems.

The aim of this work is to combine the different aspects of UVD into an overall simulation of a small UVD reactor. This simulation includes Computational Fluid Dynamics (CFD) simulation of the water flow, particle tracking of microorganisms in the water and radiation modelling of the radiation emitted by the UV lamp. As a result, the calculated disinfection efficacy of the UVD reactor is compared to results from three different certification reports [24].

2. METHODS

2.1 Ultraviolet Disinfection

UV light for disinfection applications is produced in mercury vapour arc lamps. In the reactor examined in this work, a low-pressure (LP) lamp was used. This lamp uses mercury vapour with a pressure of <1.3 kPa. This causes one sharp emission line at $\lambda = 253.7\ nm$.

UVD disinfects water by deactivating the contained microorganisms. This happens when high-energy photons of the so-called germicidal band (with a wavelength between 200 and 300nm) cause a transformation of a microorganism's DNA, inhibiting its ability to replicate [19].

2.2 Biodosimetry

The last step in the UVD reactor design process is to check if the reactor reaches the necessary disinfection efficacy under specified operating parameters. This validation is realized with the biodosimetry or bioassay method:

A surrogate (challenge) microorganism is injected into the water flowing through the UVD system. The reduction (i.e. the fraction of surviving microorganisms) is measured for a set of desired operating parameters (mainly flow rate, water UV transmittivity and lamp power) by cultivating and counting water samples from before and after the reactor. Since the delivered UV fluence (see section 2.6 for a definition) cannot be measured directly, the received fluence has to be related to the surrogate microorganism's reduction in a separate test. This relation, the survival curve, is normally generated with a collimated beam experiment beforehand. This curve is used to determine the reduction equivalent fluence (*REF*) from the reduction values (see section 2.6).

The Austrian standard for UV disinfection with LP UVD reactors, ÖNORM M 5873-1 [2], requires a minimum *REF* of 400 J/m^2 and *Bacillus subtilis* spores as a challenge microorganism. The spores are roughly cylindrical with approximately 1μm in length and 0.5μm in diameter. A detailed description of certification processes can be found in [23].

Recently, the actual fluence distribution of a reactor has been measured using fluorescent microspheres. This technique could improve confidence in the use of mathematical models for UVD and complement biodosimetry testing [3].

2.3 The UVD reactor

The modelled reactor is a single low-pressure lamp, closed-channel, axial flow reactor designed for flow rates ranging from 0.7 to 6m^3/h, with a lamp power rating from 60 to 130W.

As can be seen in Figure 1, the model of the reactor comprised not only the reactor chamber itself, but also an inlet region before the inlet pressure sensor, an elbow connected to the reactor vessel and an outlet pipe. It was important to include these segments into the actual simulation, because they mimicked the situation at validation as closely as possible, and they had a great influence on the velocity distribution of the flow when entering the reactor. The reactor vessel had an inner diameter of 100mm and a length along the main axis of 1048mm. The quartz sleeve protecting the UV

lamp was located along the main axis of the reactor and had an outer diameter of 30*mm*, running along the entire length of the reactor. The inlet and outlet pipes had several different diameters ranging from 37 to 43*mm*, creating several forward and backward facing steps in those regions. Shortly above the reactor vessel inlet, an annular plate with 8 evenly spaced circular holes was welded into the reactor.

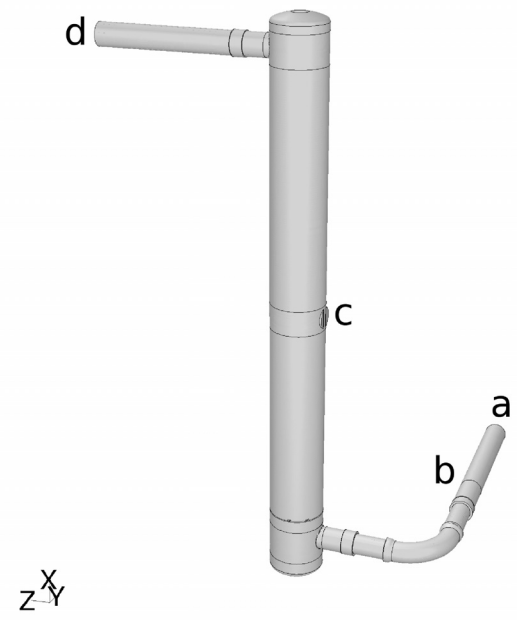

Figure 1. 3D model of the UVD reactor. *a:* water inlet, *b:* pressure sensor, *c:* UV sensor window, *d:* water outlet

2.4 Computational Fluid Dynamics

The mesh of the reactor consisted of approximately 3 million cells, with the smallest cells 1.2*mm* in size. Additionally, a mesh adaptation was made to improve resolution where necessary.

From the validation reports, data for 23 different sets of operational parameters ("cases") were available. For these cases, steady-state calculations have been carried out with the CFD package Fluent, using the realizable-k-ε turbulence model. Additionally, for one case, the elbow has been transformed into a straight pipe to judge the influence of the elbow on the disinfection performance. Thus, the disinfection simulation could be performed for 24 different cases encompassing the whole operational spectrum of the UVD reactor.

It is possible that significant fluctuations occur in the water flow, which influence disinfection results, but cannot be reproduced by steady-state calculations. Unfortunately, at the time being, unsteady calculations were computationally too expensive to perform, especially in light of potential future industry applications of UV disinfection simulation.

2.5 Particles

Particle tracking was performed for simulated *Bacillus subtilis* spores having the density of the surrounding water.

The particle tracking was performed with a ready-made discrete phase model: Particle tracks are calculated by solving the force balance equation for the particle in question. A formulation for non-spherical particles was used in the drag term to account for the cylindrical form of the particles [25].

Particles were injected at every cell location of the inlet face, which resulted in 1666 particles. This number was too small for reliable calculations. Thus, a stochastic tracking approach using a random-walk model was included. In this approach, the interaction of a particle with a succession of discrete stylized fluid phase turbulent eddies is simulated. Each eddy is characterized by a Gaussian distributed random velocity fluctuation and a time scale. The magnitude of the velocity fluctuation is calculated with the turbulent kinetic energy and a random number. Using this model, multiple non-identical particle paths ("tries") can be computed for a single cell on the inlet face. Thus, the number of particles can be increased, only limited by the memory capacity of the calculating workstation. It has been found that 16 tries, resulting in approximately 26600 particle paths, were a good compromise between accuracy and computational demand.

The spores are small enough and in such low concentrations that an interaction with the fluid phase could be ruled out.

2.6 Radiation

The main relevant radiation quantities in UVD are:

• *Fluence rate (E'):* the radiant power passing from all directions through an infinitesimally small sphere of cross-sectional area *dA*, divided by *dA*. Fluence rate and irradiance are similar, but conceptually quite different terms. Since a microorganism can receive UV radiation from any direction (especially with multiple lamps involved), fluence rate is the appropriate term to use in a UV reactor *[8]*.

• *Fluence or UV Dose (H'):* defined as the total radiant energy from all directions passing through an infinitesimally small sphere of cross-sectional area *dA*, divided by *dA*. The fluence is the fluence rate times the irradiation time in seconds *[8]*.

• *Reduction equivalent fluence (REF):* To be able to compare different reactor designs, which may have been evaluated with different challenge microorganisms, the reduction is unsuitable. To obtain a more comparable quantity, the fluence distribution has to be weighted with the survival curve, yielding the *REF*. This quantity can easily be calculated by forming the inverse function of the

survival curve, and inserting the calculated total reduction [2, 16].

2.6.1 Optics

In UVD reactors, UV radiation from the lamp has to travel through a layer of air surrounding the lamp and pass the quartz sleeve encasing the lamp before it reaches the water to be disinfected. This causes the radiation to be attenuated by the reflection and absorption processes as it travels along the optical path. A depiction of these different factors and a typical optical path for the examined UVD reactor is shown in Figure 2. Furthermore, values for the relevant optical parameters used in this work are given in Table 1.

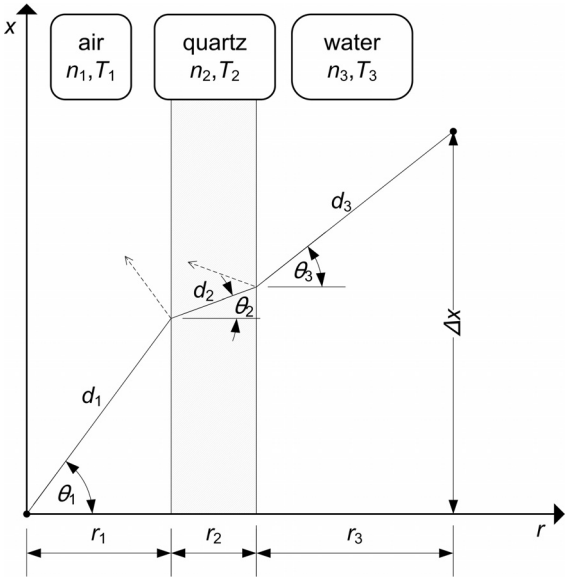

Figure 2. Optical path in the UVD reactor: Light is travelling from the source on the x-axis to the destination coordinate

Table 1. Optical parameters of the examined reactor at $\lambda = 254nm$. Transmittance values are for 10mm of material

	Air	Quartz	Water
Refractive index	n_1 1	n_2 1.506	n_3 1.376
Transmittance	T_1 1	T_2 0.8208	T_3 differs
Layer thickness	r_1 13mm	r_2 2mm	$r_{3,\max}$ 35mm

It has been found [8] that for drinking water applications (with a water transmittance of $T_3 >$ 0.7), the effects of refraction and reflection at media interfaces have to be included to permit an accurate calculation.

2.6.2 Focus effect

Another component of refraction is the focus effect [9]. Considering no refraction, the radiation power emitted from a point source within a finite difference angle $2\Delta\theta_1$ (see Figure 3) and travelling for a distance of $d_1+d_2+d_3$, would cover a circle with a diameter of g_{WO}. When exploiting the cylindrical symmetry of the lamp, this cross-section becomes a frustum or truncated cone of area A_{WO} with an aperture angle of $2\theta_1$, the lamp axis as frustum axis and the generatrix g_{WO}.

Now, when including refraction at the media interfaces, while keeping the optical path length $d_1+d_2+d_3$ constant, this frustum has the area A_W, the aperture angle $2\Delta\theta_3$ and the generatrix g_W.

Liu [9] introduced the so-called focus factor, which describes the extent by which the focus effect concentrates the light, thus changing the fluence rate at any given point. This focus factor is the ratio of the two aforementioned frustum areas A_{WO} and A_W. It has been calculated to:

$$Focus = \frac{(d_1 + d_2 + d_3)^2}{(r_1 + r_2 + r_3)\cos\theta_3 n_1} \cdot \left(\frac{r_1}{n_1 \cos^3\theta_1} + \frac{r_2}{n_2 \cos^3\theta_2} + \frac{r_3}{n_3 \cos^3\theta_3} \right) \quad (1)$$

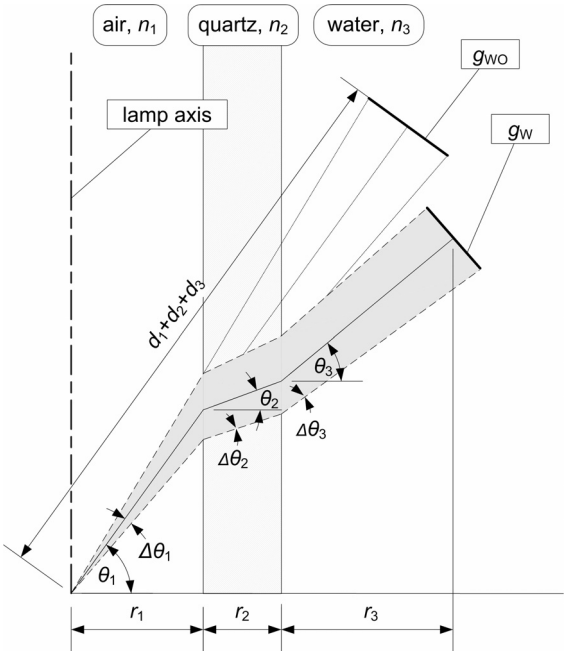

Figure 3. The focus effect: The optical path with and without refraction and the resulting generatrices g_W and g_{WO} for the focus effect calculation are shown

2.6.3 Radiation modelling

For all radiation models treated in this section, the fluence rate has been calculated with self-developed routines for a cylindrical grid which filled the reactor chamber.

A refinement study has been performed to obtain the necessary grid resolution. The fluence rate along several straight paths was evaluated for increasingly coarse grids. The deviation of said values from the values for the smallest computationally possible cell size was computed. The size of the grid cells at the outer quartz sleeve surface was determined by deciding that neither the maximum deviation nor the mean + 3 standard deviations for any given path should exceed 1%. It was found that a cell size of 2*mm* was sufficient for this criterion.

To successfully calculate the fluence rate, the calculation of the refraction angles θ is necessary. The relevant relation, Eq. (2), can be found by using Snell's law and trigonometry. To ease calculation, all angles have been related to θ_1.

$$r_1 \tan\theta_1 + n_1 \sin\theta_1 \frac{r_2}{\sqrt{n_2^2 - n_1^2 \sin^2\theta_1}} + \\ + n_1 \sin\theta_1 \frac{r_3}{\sqrt{n_3^2 - n_1^2 \sin^2\theta_1}} = \Delta x \qquad (2)$$

Unfortunately, this equation can only be solved numerically. This was accomplished with Brent's method, a root finding algorithm described in [26]. After finding θ_1, all other optical quantities can easily be calculated.

Several radiation models have been implemented:

The Multiple Point Source Summation with focus effect (**MPSS-F**) represents the UV lamp as a number of point sources. The fluence rate at a certain point in the reactor is calculated by summing up the fluence rate values of all point sources. The focus effect has been included in this model.

In the Multiple Segment Source Summation (**MSSS**) model, the point sources are replaced by cylindrical segment sources, resulting in an additional cos θ_1 term. This model has also been included with the focus effect (**MSSS-F**). MSSS-F models the physical processes most closely of all presented models.

The Line Source Integration (LSI) model is the continuous or integral version of the MPSS model. These models are mathematically identical as the number of point sources approaches ∞ [9]. However, a computationally fast closed-form solution only exists in absence of absorption, reflection and refraction. To correct for this shortcoming, Liu [9] developed the attenuation factor approach, where the LSI model is multiplied with a correcting attenuation factor. In this work, an attenuation factor which used the MSSS-F model was used (**LSI-F**).

Bolton and Liu developed a modified form of the LSI model to correct inaccuracies when approaching the quartz sleeve [9]. This model, called **RADLSI**, was implemented with a MPSS attenuation factor.

A more extensive description of the different models can be found in [9].

2.6.4 Refinement

Again, a refinement study has been done to find the number of necessary sources for the different radiation models.

For the MPSS and MSSS models, the fluence rate at 4 points in the reactor volume was calculated using a MSSS-F model with an increasing number of sources ranging from 10 to 10000. Afterwards, it was decided that to be sufficiently accurate, the calculated fluence rate at any point should not deviate by more than 1% from the value for 10000 sources. This was deemed to sufficiently represent the fluence rate in the limit of an infinite number of sources. It was found that 2000 sources were sufficient to fulfil this criterion. Thus, 2000 sources were used for the MPSS/MSSS models.

An important advantage of LSI models over MPSS/MSSS is the greatly reduced computational cost. Thus, choosing 2000 sources, while being very accurate, is impracticable because it would neutralize this advantage. When plotting fluence rate values of axial paths, it turns out that an insufficient number of sources leads to unnatural oscillations in the fluence rate distribution. Since these oscillations are worst at small distances to the lamp, a path adjacent to the quartz sleeve was evaluated. It was found that 100 sources were enough to eliminate the unphysical oscillations when using LSI models.

2.6.5 UV reference sensor

An important part of the radiation calculation is the determination of the irradiance of the UV reference sensor in the reactor vessel: This value was the only available radiation measurement with which to check the radiation model. Unfortunately, the conversion efficiency from electrical power to light at 253.7*nm* is not measured during certification processes, and only the electrical power rating was given in [24]. Furthermore, some validation cases use reduced lamp power to simulate an aged lamp near the end of its designated lifetime.

For these reasons, a sensor simulation was developed, including the known sensor assembly geometry and parameters into a MSSS-F model. With this sensor model, the radiation models were calibrated. The MSSS-F model was deemed most appropriate for this task since it matches the

occurring physical processes best of all treated radiation models. The UV conversion efficiency was adjusted such that the simulated sensor reading equalled the experimental reading from the validation reports.

2.6.6 Disinfection calculation

When particle tracks and fluence distribution are known, a fluence value is calculated for each particle. This fluence value is combined with the survival curve to determine the reactor's reduction. From the reduction, the *REF* is easily calculated.

3. RESULTS

3.1 CFD

To compare the CFD results against the experiments, pressure loss data were available from the validation reports. A quadratic fit (R^2=0.9981) has been calculated, and the CFD pressure loss information has been compared to these two data sets. The mean of the absolute values of the error (in %) has been calculated. Compared to the experiment and fit, mean values of 5.4 and 3.2%, respectively, have been obtained.

Replacing the elbow with a straight pipe reduced the pressure loss by 6.6%. It has been found that the inlet pipe is responsible for about 50% and the reactor chamber for about 40% of the pressure loss.

3.2 Radiation models

The fluence rate distribution has been evaluated along several axial and radial paths in the reactor. Reactor validation according to ÖNORM M 5873-1 [2] does not demand a laborious measurement of the radiation distribution in the reactor. Thus, only the reference sensor data were available. This data already being needed for the UV efficiency calibration, the different radiation models could only be compared among themselves.

It has been found that there is an excellent agreement between the MSSS-F and LSI-F models. This is consistent with findings in [9].

Calculating a fluence rate field for the reactor with the MSSS-F model takes approximately 17 times as long as with a LSI-F model. Therefore, using the LSI-F model seems to be highly tempting. However, one should keep in mind that the fluence rate calculation takes a rather small part of the computation time compared to particle track generation and particle fluence calculation, especially for a high number of particle tracks.

When comparing the MSSS, MSSS-F and MPSS-F results, it can be concluded that the influence of the focus effect (i.e. the difference between MSSS and MSSS-F) is far smaller than the influence of the segment source representation (i.e. the difference between MPSS-F and MSSS-F). Thus, it was concluded that implementing segment sources is definitely necessary. Fortunately, this does not measurably increase computation time, and thus has no drawbacks.

3.3 Disinfection

Disinfection simulations have been performed for 24 cases. Figure 4 shows the *REF* values obtained with the UVD simulation. Black crosses are the experimental results with error bars from [24]. The different results have been connected with lines only to guide the eye and facilitate analysis.

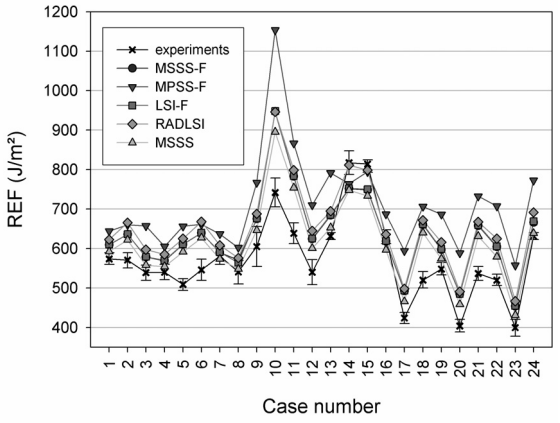

Figure 4. Disinfection simulation results: *REF*. The simulated *REF* values for the different cases and experimental results with error bars are shown. Connecting lines have been added to ease analysis

As expected from the fluence rate distributions, the MPSS-F model generally produces the highest *REF* values. All other plots typically are very close together. Also, MSSS-F and LSI-F produce nearly identical results - the MSSS-F plot is not visible because it lies behind the LSI-F plot. This further confirms that the LSI-F model is a good approximation of the MSSS-F model.

Figure 5 shows a plot of the relative errors of the different radiation models. An analysis of the error value distribution has been done. Mean value and standard deviation of the errors have been calculated for all radiation models and cases, excluding the case with the straightened elbow (case 24) because it has a different geometry. The results can be found in Table 2.

Table 2. Error statistics. Mean value and standard deviation of *REF* simulation errors (in %) are given for different radiation models

	MSSS-F	MPSS-F	LSI-F	RADLSI	MSSS
mean	11.58	24.65	11.71	14.64	7.54
σ	9.90	15.37	9.97	9.06	8.93

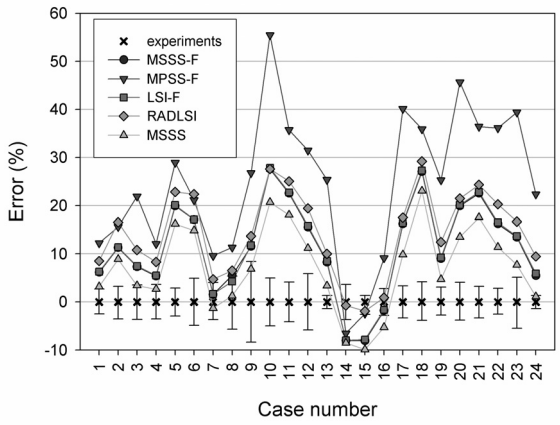

Figure 5. Disinfection simulation results: relative error. The relative error is plotted for the different cases. Connecting lines have been added to ease analysis

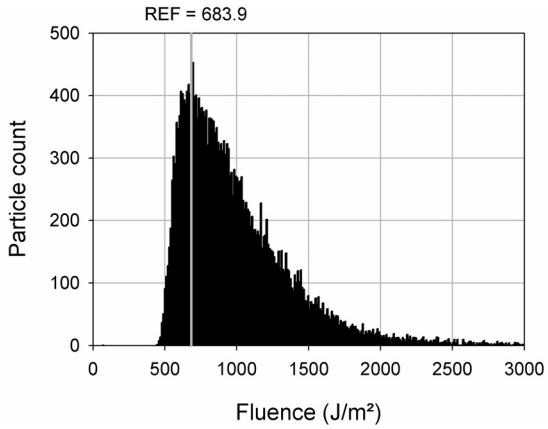

Figure 6. Calculated fluence histogram for case 13 using the MSSS-F model. The resultant *REF* of the fluence distribution is indicated

The MSSS model produces the smallest mean error, and also the smallest standard deviation. MSSS-F and LSI-F rank next, producing virtually identical results. RADLSI comes next, and MPSS-F produces the least accurate results. However, one has to keep in mind that the UV efficiency was used to calibrate the radiation models such that the experimental reference sensor reading is matched by the MSSS-F model. A different UV efficiency value would shift all *REF* results up or down, thus changing the error values and the ranking of the different radiation models.

The consistently positive mean values show that all radiation models generally over-predict the *REF* values. This over-prediction may be corrected by shifting the resultant *REF* values by a certain value. However, the amount of this shift may be influenced by e.g. geometry, and thus cannot be assumed to be generally valid.

3.3.1 Straight inlet pipe

The *REF* values for the different radiation models for case 24 show an average drop in *REF* of 2% compared to the same case with an elbow (case 13). This does not seem to be significant as such a fluctuation is very small.

3.3.2 Fluence histograms

Using the data from the UVD simulation, fluence histograms can easily be calculated. Figure 6 displays a typical histogram, showing the fluence distribution for case 13 using the MSSS-F model. The resultant *REF* of the fluence distribution is additionally shown. The x-axis scale has been limited to 3000 J/m^2 to improve display of the relevant portion of the fluence histogram. Actual fluence values reach up to 5200 J/m^2, but the particle counts are negligibly small above the chosen limit.

4. CONCLUSIONS

A simulation method to predict UV reactor disinfection performance has been presented. Calculations have been performed for several radiation models and have been compared to biodosimetric measurements. Considering the limited amount of available experimental data for the flow field and fluence rate distribution, good predictions of the *REF* were obtained. The potential use of this method for designing and improving UVD reactors has been demonstrated.

Future work will encompass unsteady CFD calculations, which will yield unsteady particle tracks. Furthermore, different reactor geometries can be examined. Ray-tracing can additionally be employed to include reflection at the reactor walls.

REFERENCES

[1] Gelzhäuser, P., Bewig, F., Holm, K., Kryschi, R., Reich, G., and Steuer, W., 1985, *Desinfektion von Trinkwasser durch UVBestrahlung*, vol. 182 of *Kontakt & Studium*, Technische Akademie Esslingen and expert verlag.

[2] Österreichisches Normungsinstitut, 1021 Wien, 2001, *ÖNORM M 5873-1: Anlagen zur Desinfektion von Wasser mittels Ultraviolett-Strahlen - Anforderungen und Prüfung - Teil 1: Anlagen mit Quecksilberdampf-Niederdruckstrahlern*.

[3] Bohrerova, Z., Bohrer, G., Mohanraj, S. M., Ducoste, J., and Linden, K. G., 2005, "Experimental Measurements of Fluence Distribution in a UV Reactor Using Fluorescent Microspheres", *Environ. Sci. & Technol.*, vol. 39, pp. 8925-8930, accepted August 29, 2005.

[4] Ducoste, J. J., Liu, D., and Linden, K., 2005, "Alternative Approaches to Modeling Fluence Distribution and Microbial Inactivation in

Ultraviolet Reactors: Lagrangian versus Eulerian", *Journal of Environmental Engineering*, vol. 131, pp. 1393-1403.

[5] Ducoste, J. and Linden, K., 2005, "Determination of ultraviolet sensor location for sensor set-point monitoring using computational fluid dynamics", *J. Environ. Eng. Sci.*, vol. 4, pp. 33-43.

[6] Jin, S., Linden, K. G., Ducoste, J., and Liu, D., 2005, "Impact of lamp shadowing and reflection on the fluence rate distribution in a multiple low-pressure UV lamp array", *Water Research*, vol. 39, pp. 2711-2721.

[7] Bolton, J. R., Wright, H., and Rokjer, D., 2005, "Using a mathematical fluence rate model to estimate the sensor readings in a multi-lamp ultraviolet reactor", *J. Environ. Eng. Sci.*, vol. 4, pp. 27-31.

[8] Bolton, J. R., 2000, "Calculation of ultraviolet fluence rate distribution in an annular reactor: Significance of refraction and reflection", *Wat. Res.*, vol. 34, pp. 3315-3324.

[9] Liu, D., 2004, "Numerical Simulation of UV disinfection reactors: Impact of fluence rate distribution and turbulence modeling", Ph.D. thesis, North Carolina State University.

[10] Chiu, K., Lyn, D., Savoye, P., and III, E. B., 1999, "Integrated UV Disinfection Model Based in Particle Tracking", *Journal of Environmental Engineering*, vol. 125, pp. 7-16.

[11] Downey, D., Giles, D., and Delwiche, M., 1998, "Finite element analysis of particle and liquid flow through an ultraviolet reactor", *Computers and Electronics in Agriculture*, vol. 21, pp. 81-105.

[12] Buffle, M.-O., Chiu, K.-P., and Taghipour, F., 2000, "UV reactor conceptualization and performance optimization with computational modeling", *Proceedings WEF Specialty Conference on Disinfection*, New Orleans, LA.

[13] Kowalski, W., Bahnfleth, W., Witham, D., Severin, B., and Whittam, T., 2000, "Mathematical Modeling of Ultraviolet Germicidal Irradiation for Air Disinfection", *Quantitative Microbiology*, vol. 2, pp. 249-270.

[14] Zimmer, J. and Slawson, R., 2002, "Potential Repair of *Escherichia coli* DNA following Exposure to UV Radiation from Both Medium- and Low-Pressure UV Sources Used in Drinking Water Treatment", *Applied and Environmental Microbiology*, vol. 68, pp. 3293-3299.

[15] Cabaj, A., Sommer, R., Pribil, W., and Haider, T., 2002, "The spectral UV sensitivity of microorganisms used in biodosimetry", *Water Science and Technology: Water Supply*, vol. 2, pp. 175-181.

[16] Cabaj, A. and Sommer, R., 1999, "Measurement of UV-Radiation with Microorganisms (Biodosimetry)", R. Matthes and D. Sliney (editors), *Measurements of Optical Radiation Hazards, A Reference Book*, ICNIRP, CIE.

[17] Cabaj, A., Sommer, R., and Schoenen, D., 1996, "Biodosimetry: Model calculations for UV water disinfection devices with regard to dose distributions", *Water Research*, vol. 30, pp. 1003-1009.

[18] Mamane-Gravetz, H., Linden, K. G., Cabaj, A., and Sommer, R., 2005, "Spectral Sensitivity of *Bacillus subtilis* Spores and *MS2 Coliphage* for Validation Testing of Ultraviolet Reactors for Water Disinfection", *Environmental Science and Technology*, vol. 39, pp. 7845-7852.

[19] Das, T. K., 2001, "Ultraviolet disinfection application to a wastewater treatment plant", *Clean Products and Processes*, vol. 3, pp. 69-80.

[20] Das, T. K., 2002, "Evaluating the life cycle environmental performance of chlorine disinfection and ultraviolet technologies", *Clean Technologies and Environmental Policy*, vol. 4, pp. 32-43.

[21] U.S. Environmental Protection Agency, 1999, "Ultraviolet Disinfection", *Wastewater Technology Fact Sheet*.

[22] Jeyanayagam, S. and Bryck, J., 2002, "Practical Considerations in the Use of UV light for Drinking Water Disinfection", presented at the International Conference on Environmental Engineering in Niagara Falls, Ontario, Canada.

[23] U.S. Environmental Protection Agency, 2003, *Ultraviolet Disinfection Guidance Manual, Draft,* Washington, DC.

[24] Hirschmann, G., Cabaj, A., Sommer, R., Mann, M., Pascoli, G., Windischbauer, G., and Rotter, M., 2004 and 2005, "Biodosimetrische und strahlungsmesstechnische Untersuchung einer UV-Desinfektionsanlage für Trinkwasser mit Niederdruck Quecksilberdampfstrahler, ", 3 te*chnological reports*, ÖFPZ Arsenal Ges.m.b.H., Veterinärmedizinische Universität Wien, Medizinische Universität Wien.

[25] Fluent Inc., Lebanon, NH, USA, 2005, *FLUENT 6.2 User's Guide*.

[26] Press, W. H., Teukolsky, S. A., Vetterling, W. T., and Flannery, B. P., 1992, *Numerical Recipes in C, The Art of Scientific Computing*, Press Syndicate of the University of Cambridge, 2nd edition.

Conference on Modelling Fluid Flow (CMFF'06)
The 13th International Conference on Fluid Flow Technologies
Budapest, Hungary, September 6-9, 2006

MATHEMATICAL MODELLING AND SIMULATION OF NATURAL CONVECTION OF OIL INSIDE DISTRIBUTION TRANSFORMERS

Jon GASTELURRUTIA[1], Juan Carlos RAMOS[2], Alejandro RIVAS[3], Josu IZAGIRRE[4], Luis DEL RÍO[5]

[1] Corresponding Author. Research engineer. Fluid Flow and Thermal Engineering Chair - Department of Mechanical Engineering. TECNUN (University of Navarra). Paseo Manuel Lardizábal 13, 20018 San Sebastián, Spain. Tel.: (+34) 943219877, Fax: (+34) 943311442, E-mail: jgastelurrutia@tecnun.es
[2] Professor. Fluid Flow and Thermal Engineering Chair - Department of Mechanical Engineering. TECNUN (University of Navarra). E-mail: jcramos@tecnun.es
[3] Professor. Fluid Flow and Thermal Engineering Chair - Department of Mechanical Engineering. TECNUN (University of Navarra). E-mail: arivas@tecnun.es
[4] Patents & projects manager. Ormazabal Corporate Technology. E-mail: jiz@ormazabal.com
[5] Research engineer. Ormazabal Corporate Technology. E-mail: lre@ormazabal.com

ABSTRACT

Oil flow and heat dissipation by natural turbulent convection inside a distribution transformer have been modelled using Computational Fluid Dynamics (*CFD*) techniques. Three mathematical models of the transformer have been developed. The first one is a complete three-dimensional model of the entire transformer. The other two are 3D simplified models consisting of perpendicular "slices" of the transformer contained inside planes equally spaced between two fins. The results of one of the slice models are in agreement with the results of the complete one. This allows the use of the simplified model to perform the analysis and optimisation of the cooling phenomena in the transformer in order to reduce the "hot-spot" and the top oil temperatures. The temperature distribution of the oil, the oil flow pattern and the temperature distributions on the external and internal surfaces can be obtained from simulations. The influence on the results of two different turbulence models with two near wall approaches has been analysed. Some discrepancies have been found with experimental values. Calibration of the external convective boundary conditions is needed in order to obtain better adjustment.

Keywords: *CFD*, distribution transformers, heat transfer, "hot-spot" temperature, natural convection, turbulence models

NOMENCLATURE

Pr_T	[-]	turbulent Prandtl number
T	[K]	temperature
c_p	[$J/kg{\cdot}K$]	specific heat
k	[m^2/s^2]	turbulent kinetic energy
p	[Pa]	total pressure
u_i	[m/s]	velocity magnitude components
x_i	[m]	Cartesian coordinates
d_{ij}	[-]	Kronecker delta
e	[m^2/s^3]	dissipation rate of k
l	[$W/m{\cdot}K$]	thermal conductivity
l_T	[$W/m{\cdot}K$]	turbulent thermal conductivity
m	[$kg/m{\cdot}s$]	dynamic viscosity
m_T	[$kg/m{\cdot}s$]	turbulent viscosity
r	[kg/m^3]	density
t_{ij}	[N/m^2]	stress tensor
Δt	[s]	time step

1. INTRODUCTION

A distribution transformer is one of the most common elements of an electrical power delivery network. They are usually confined inside prefabricated concrete enclosures called "substations" to ensure security and protection, but this normally makes difficult the optimal refrigeration of the transformers. Moreover, validation tests on transformers are normally carried out under open air operation, and it is often difficult to extrapolate the results when they are operating inside the substations.

The main purpose of the experimental tests is to determine the top oil and the "hot-spot" temperatures of the transformer in a normal operating state. Both temperatures are critical factors in transformer loading and they are directly related to the ageing of the transformers [1]. The direct determination of these temperatures is an extremely complicated and expensive task. It is desirable to generate a mathematical model that can predict the values and analyse the improvements of

the refrigeration of transformers with low economical costs.

Different works have studied the performance of the transformers by means of simplified equivalent thermal circuits [2-4]. These models are based on characteristical temperatures inside the transformer and they can be used to determine load capability and ageing of transformers. Their main limitations are that the models must be adjusted for each transformer and the analysis of the refrigeration is restricted. The equivalent thermal circuit model idea has been applied to entire transformer substation enclosures in other works [5], but with similar limitations.

Knowledge of the actuating real physical phenomena is required to improve transformer refrigeration. The oil flow inside the transformer enclosure must be studied, different coil channel configurations must be compared and the influence of hollow fins must be measured. In order to make that possible, simplified thermal circuit models are not useful and other mathematical models must be developed and studied. Several works have also been carried out in that direction [6-8]. In these works the authors developed models of the interior of different transformers and solved them using the Finite Volume Method (*FVM*). Ramos et al. developed a *FVM* based model for both a transformer and an entire transformer substation [9].

In the present work, the oil flow and the heat dissipation by natural turbulent convection inside a distribution transformer have been modelled using the *FVM* in order to obtain a model that represents a real transformer with sufficient accuracy. With this model it is possible to analyse the influence of different variables (turbulence models, precise boundary conditions, etc.) affecting its performance and to identify the fundamental parameters governing the heat exchange process. Lastly, with all this information, it would be possible to develop a simplified model and to implement it in an application tool in order to be used by transformer designers to analyse and optimise the refrigeration.

The developed models will be used to study the internal oil flow pattern and the influence of different constructive elements on it. Other interesting results will be the oil temperature and its thermal stratification, and the temperatures and heat fluxes on the surfaces of the transformer.

In conclusion, the model presented here aims at providing transformer manufacturers with a valid simplified tool to estimate the internal and external highest temperatures of a transformer, and to analyse means of reducing them properly at minimum cost.

2. MODELLING OF THE DISTRIBUTION TRANSFORMER

2.1. Description of the system

In Figure 1, the distribution transformer modelled in the present work inside its respective substation is represented.

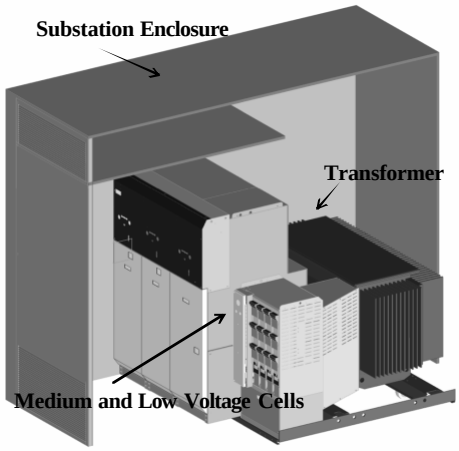

Figure 1. General view of the distribution transformer inside the substation

The specific modelled substation transformer has an input voltage of 25 kV and a power of 630 kVA. Its height is around 1 m and the area of the lid is approximately 0.65 m^2. It has two main sources of internal heat generation due to power losses. The first one is the conductive losses in the coils, and the second one the magnetic losses in the core. The coils have a particular channel configuration in order to ensure dielectric insulation and good refrigeration. The coils are made of copper with special oil saturated insulating paper and the core is made of laminated steel.

The transformer is filled with oil with suitable dielectric and heat conductive properties. Three of the lateral walls of the casing have a distribution of hollow fins to increment the effective dissipation area. In the remaining lateral wall there are no fins because there is a connection backpack. Using superimposed extra hollow fins on the extremes makes up this net loss of dissipation area. It is known that hollow fins are much more effective than solid ones at dissipating heat [9].

The heat is dissipated from the outer surface of the transformer by natural convection with the air and by radiation exchanges with the walls of the substation enclosure. Experimentation has been made in order to have a better knowledge of the thermal conditions inside the enclosure. The thermal handicap introduced by different types of enclosures is indicated in some other works [10].

2.2. Description of the mathematical model

The oil flow inside the transformer is described by the suitable differential equations and boundary conditions applied to the three developed flow domains.

2.2.1. Governing equations

The oil properties inside the transformer are all temperature dependent. Density is assumed to be linear with temperature in order to generate buoyancy driven flow. It has been noticed that flow becomes turbulent when it gets out of the coil channels and at the upper part of the transformer. The Reynolds Average Navier-Stokes (*RANS*) equations are used to include turbulence effects in the mean flow variables:

$$\frac{\partial}{\partial x_i}\left(r \cdot u_i\right) = 0 \tag{1}$$

$$\frac{\partial}{\partial x_j}\left(r \cdot u_i \cdot u_j\right) = -\frac{\partial p}{\partial x_i} + \frac{\partial}{\partial x_j}\left[\left(m + m_T\right) \cdot \frac{\partial u_i}{\partial x_j}\right] \tag{2}$$

$$\frac{\partial}{\partial x_i}\left(r \cdot u_i \cdot c_p \cdot T\right) = \frac{\partial}{\partial x_i}\left[\left(l + l_T\right) \cdot \frac{\partial T}{\partial x_i}\right] + \frac{\partial\left(u_i \cdot t_{ij}\right)}{\partial x_j} \tag{3}$$

where

$$l_T = \frac{c_p \cdot m_T}{Pr_T} \tag{4}$$

$$t_{ij} = \left(m + m_T\right) \cdot \left(\frac{\partial u_i}{\partial x_j} + \frac{\partial u_j}{\partial x_i}\right) - \frac{2}{3} \cdot r \cdot k \cdot d_{ij} \tag{5}$$

In an initial simulation, the S*tandard k-e* turbulence model with standard wall functions was used in order to compare the three developed models of the transformer.

Later, the *RNG k-e* model with standard wall functions (*WF*) and a two layer model for enhanced wall treatment (*EWT*), has been used to analyse its influence on the results of one of the slice mo dels.

Both turbulence models, the *Standard* one and the model based on *Renormalization Group* theory, add two transport equations for the turbulent quantities (*k* and *e*) and particular definitions for the turbulent viscosity [11, 12].

2.2.2. Flow domain

Three different models of the same transformer have been developed: a Complete one and two Slice models. Slice models consist of perpendicular cuts of the transformer contained inside two planes equally spaced between two fins. Slice 1 model cuts a central part of the transformer between two *ZY* planes, and Slice 2 is the perpendicular cut between two *ZX* planes.

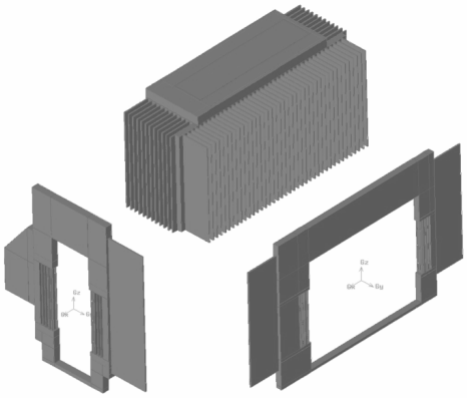

Figure 2. Developed flow domains

In the Slice models, coil channels are geometrically modelled. In the Complete model, the channels zone is modelled using an equivalent porous media zone. The flow regime in the porous media is laminar as in the real channels and its porosity and viscous resistance represent the real ones in a simplified way. Obviously, the Complete model is computationally more expensive than the Slice models because it includes a bigger domain. The number of cells is approximately $3.5 \cdot 10^6$ in the Complete model and $1.4 \cdot 10^6$ in the Slice models. In all the models, a finer mesh has been used in the oil zones close to the different walls and a coarser one far from them. This has been done by means of a non-conformal grid that also provides modularity. A high quality hexahedral mesh has been used.

2.2.3. Boundary conditions

To resolve the fundamental equations governing the oil flow inside the transformer, adequate boundary conditions must be specified.

A non-slide condition is imposed on fluid velocity at all solid walls. The transformer power losses are modelled imposing adequate uniform heat fluxes on coil and core surfaces. Outer casing and fin surfaces are modelled as solid walls with one-dimensional heat conduction and convective boundary conditions. Radiation heat exchanges with the walls of the substation enclosure are not negligible at some of these outer walls, especially on the lid of the casing.

The normal velocity component and the normal gradients of all the other variables are set to zero at the planes of symmetry of the Slice models.

The temperatures of the air and the walls of the substation are obtained from experimentation. In an initial stage, bibliographical correlations are used to establish the heat transfer coefficients on the different casing and fin surfaces [13]. Since the real geometrical and flow conditions are different from the bibliographical ones, the values of the different

convective heat transfer coefficients will have to be adjusted in order to calibrate the models.

2.2.4. Discretization and resolution

The Finite Volume Method is used to discretize the governing differential equations. Both, steady and transient states have been considered in the simulations and a segregated implicit solver has been used. Equations are linearized and then sequentially solved using Gauss-Seidel algorithm accelerated by an Algebraic Multigrid method. Pressure-Velocity coupling is achieved through the use of SIMPLE algorithm. Diffusive and convective terms of the equations are discretized using second order upwind accurate schemes. The Body Force Weighted scheme is chosen in the discretization of pressure to deal with this buoyancy driven flow. This entire numerical procedure is implemented in the unstructured *CFD* code Fluent V. 6.2.16 [14].

2.2.5. Convergence criteria

It is often difficult to establish the complete convergence of the iterative procedure in problems involving enclosures and natural turbulent convection [15].

In the present problem, three main convergence criteria have been considered. The first one is the balance of energy of the transformer power losses dissipation. The second one is to reach perdurable stationary values for selected superficial temperatures. And the last one is to obtain values of scaled residual below certain magnitudes (10^{-3} for mass and momentum equations and 10^{-6} for energy equation).

Under-relaxation techniques must be used to handle the non-linearity of the equations, taking special care with the discretized energy equation.

In the simulations in steady state, the first two convergence criteria were achieved but the scaled residuals did not drop sufficiently. It was necessary to perform some transitory iterations with an adequate time step to achieve values of residuals below established criteria [15, 16]. In the transient simulations the scaled residuals convergence criterion was fulfilled but there was a small energy imbalance because the temperature of the base was continuously decreasing.

3. RESULTS AND DISCUSSION

The three developed models for the transformer are compared using the *Standard k-e* turbulence model with standard wall functions at near wall regions. Later, the effect of using theoretically more adequate low Reynolds number turbulence models and an enhanced wall treatment is studied. Finally, an experimental validation is carried out to see how precisely the model can predict real temperatures on the transformer external surfaces.

3.1. Results of the different models

Some temperatures and heat fluxes of the different models are compared in Table 1. The external temperatures are obtained at the same locations as the measured ones during the experimental test.

T_2 is the temperature measured by a probe situated in the centre of the lid. T_6, T_4, T_9 and T_7 are temperatures of thermocouples situated on the external surface of a central hollow fin (contained in the Slice 2 model). T_6 and T_4 are situated on the upper zone of the fin, at the base and at the tip, respectively. Similarly, T_9 and T_7 are also situated at the base and at the tip of the fin but on the lower part. T_{22}, T_{24}, T_{25} and T_{27} are temperatures of thermocouples analogously situated in another central hollow fin of the transformer (contained in the Slice 1 model). $T_{Hot\text{-}spot}$ is the maximum temperature, obtained on the upper zone of the low voltage coil channels in the three models, coinciding with other works [17]. The averaged value of the base temperature and total wall heat fluxes in different areas are also used as comparative values.

Table 1. Comparison between models

Values	Complete	Slice 1	Slice 2
T_2 (K)	**359.0**	370.8	**360.3**
T_6 (K)	**360.5**	-	**361.7**
T_4 (K)	**355.8**	-	**359.0**
T_9 (K)	**358.4**	-	**358.8**
T_7 (K)	**354.8**	-	**357.8**
T_{22} (K)	360.6	372.6	-
T_{24} (K)	355.8	369.2	-
T_{25} (K)	358.4	370.0	-
T_{27} (K)	354.8	367.7	-
$T_{Hot\text{-}spot}$ (K)	**379.4**	413.1	**379.9**
$\overline{T}_{Base}$ (K)	**347.9**	354.9	**349.8**
$\overline{q''}_{Lid}(W/m^2)$	**601.1**	835.6	**633.4**
$\overline{q''}_{Fins}(W/m^2)$	**233.4**	305.6	**232.0**
$\overline{q''}_{Base}(W/m^2)$	**465.1**	549.6	**488.0**

As can be seen in Table 1, the Complete and the Slice 2 models give similar results, both for the temperatures and the heat fluxes. On the contrary, the results of the Slice 1 model are very far from the results of the Complete model.

This difference is due to the special geometry of the transformer, as shown in Figures 1 and 2. The transformer has a lateral wall without fins and with a connection backpack. The Slice 1 model represents a cut of the transformer containing the corresponding part of that connection backpack and

the opposite fin. On the other hand, the Slice 2 model represents a normal cut including two opposite fins. As the fins play the major role in the transformer heat dissipation (about 75%), the latter simplified model resembles the Complete model more than the former one does.

The asymmetrical distribution of the fins on the lateral walls of this transformer is such that the behaviour of the oil flow and the heat dissipation of the Complete model can be well represented by means of the Slice 2 model, but not by the Slice 1 model. For this reason the Slice 1 model has been discarded.

Relating the quantitative comparison of the Complete and the Slice 2 models, it can be seen that both models give similar results for the temperatures. The bigger discrepancy between both models is found in the temperatures at the tip of the fin (T_4 and T_7), where the maximum absolute difference is of 3.2 *K* corresponding to a relative difference of 5%. The relative difference is calculated using as reference the ambient temperature outside the transformer substation ($T_{Reference}$ = 293.5 *K*) with the following expression:

$$Dif_{rel} = \frac{\left|T_{Complete} - T_{Slide2}\right|}{T_{Complete} - T_{Reference}} \cdot 100\,\% \qquad (6)$$

It is believed that this difference is due to the fact that the fins of the Complete model do not have enough cells to simulate the oil flow inside them, creating a false horizontal temperature gradient. This is confirmed by the results of the experimental test presented later. Unfortunately, the grid of the Complete model is at the limit of our present computational facilities and it has not been possible to increase its number of cells.

Regarding the average heat fluxes, the similarity of the results of both models is quite acceptable: in the fins the difference is negligible, in the lid it is 5.5% and in the base it is less than 5%. Since the fins dissipate most of the transformer power losses (75%), the heat fluxes of the Slice 2 model are acceptable.

Some common characteristics of the oil flow regime between both models can be pointed out. At the bottom of the transformer the temperatures are very low and the oil movement is inappreciable. The movement is focused on the upper hot zone of the transformer. In general, movement appears close to the walls while in the central zones oil is more static, especially in the lower zone. Oil movement in the upper part of the hollow fins is very active and decreases when the oil moves down. Oil flow inside the hollow fins is clearly influenced by their relative position to the coils. The main oil flow enters in the hollow fins from the highest zone of the transformer. When it arrives to the first coil influenced zone, flux is divided into two parts. A fraction is redirected to the outlets of the coil channels and exists the hollow fins. The other fraction moves down and exits at the height of the bottom inlets of the coil channels. This flow pattern is shown in Figure 3. This special movement will affect the vertical and horizontal thermal gradients of the external fin surfaces, and subsequently, the heat flux distribution.

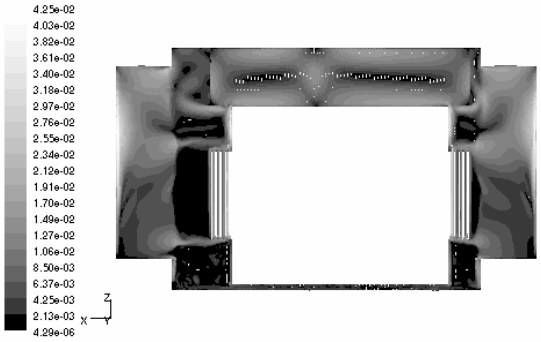

Figure 3. Oil flow pattern in the central section of the Slice 2 model (velocity magnitude in *m*/*s*)

Turbulence is focused on the upper zone of the transformer and at the outlets of the coil channels. The flow regime in the rest of the domain, including hollow fins, seems to be la minar.

A considerable temperature difference exists in the vertical direction of the transformer, especially on the fins (≈ 14 *K*). The vertical thermal variation is focused on the lower part of the fins, and temperature on the upper zone is more uniform as can be seen in Figure 4.

Figure 4. Superficial wall temperatures on the hollow fins (*K*)

In conclusion, results of the Complete and Slice 2 model are consistent, allowing the use of the computationally less expensive, and simplified, Slice 2 model.

3.2. Comparison of turbulence models

The *Standard k-e* model with *WF* treatment at near wall regions is one of the most widely used and validated turbulence models for general industrial flows. Previously obtained values in the Slice 2 model (small velocities, turbulent Reynolds number < 200 in the first ten cells close to the walls,

$y^+ \approx 1$ in the first cells) have made feasible the use of a specific low Reynolds number turbulence model with a two-layer model for the treatment of the turbulence near the walls.

The combinations of two different turbulence models with two different treatments of the turbulence at near wall regions have been analysed: *Standard k-e* with *WF*, *Standard k-e* with *EWT*, *RNG k-e* with *WF* and *RNG k-e* with *EWT*.

As mentioned above, some transitory iterations are needed in order to obtain low values of scaled residuals. The time step used must be small enough to take into account transient phenomena [15, 16].

But these transitory simulations have a peculiar effect in all the models: the average temperature of the base starts to decrease, although the rest of the temperatures (lid, fins and coils) stay almost invariable.

In Table 2, the results of these simulations are shown with the following code: M1 (*Standard k-e* with *WF* steady); M2 (*Standard k-e* with *WF* transitory); M3 (*Standard k-e* with *EWT* transitory); M4 (*RNG k-e* with *WF* transitory); M5 (*RNG k-e* with *EWT* transitory).

Table 2. Comparison between different turbulence models

Values	M1	M2	M3	M4	M5
T_2 (*K*)	360.3	360.3	359.8	360.2	358.3
T_6 (*K*)	361.7	361.7	362.3	361.8	362.3
T_4 (*K*)	359.0	359.0	357.4	357.0	357.5
T_9 (*K*)	358.8	358.8	358.2	357.8	358.4
T_7 (*K*)	357.8	357.8	354.7	353.9	355.1
$\overline{T}_{Base}$ (*K*)	349.8	343.3	329.9	333.2	330.4
$\overline{q''}_{Lid}$ (W/m^2)	633.4	633.5	633.2	624.6	632.0
$\overline{q''}_{Fins}$ (W/m^2)	232.0	232.1	230.5	229.2	230.9
$\overline{q''}_{Base}$ (W/m^2)	488.0	410.8	263.5	298.9	268.5

The differences in temperatures T_2, T_6, T_4 and T_9 between the five combinations of models and simulations are small: less than 2 *K* and 3% of relative difference. The same can be said about the average heat fluxes on the lid and the fins. In T_7 the differences are higher but acceptable.

Higher differences arise when comparing the magnitudes in the base of the transformer: the average temperature and heat flux decrease when performing a transient simulation independently of the turbulence model and the near wall treatment employed. The reason for the difference in the values of base temperature between the different transitory models is that the same number of time steps have not been simulated. Models with low temperatures on the base have been run much more time than the others. In any case, no stationary solution has been reached since the base temperature decreases in all the simulations.

It seems clear that it is necessary to perform transitory simulations to detect the transient phenomena appearing at the bottom part of the transformer. In this zone the oil flow is almost negligible and the speeds are so low that the model can not reach a steady solution.

In any case, the transitory effects of the bottom part do not affect the main flow at the top part and inside the fins. The temperatures predicted by the stationary simulations agree with the temperatures obtained by the transitory simulations in those zones.

As the base temperature is lower, the range of the oil temperature variation is wider than before using transitory simulation (≈ 30 *K*).

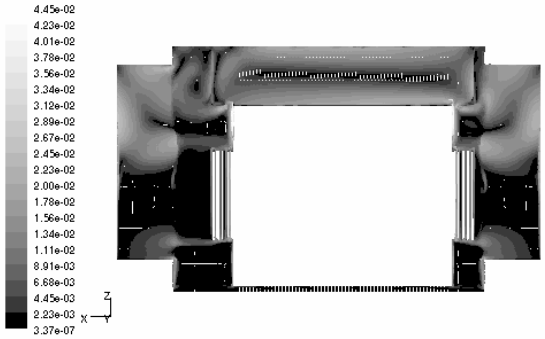

Figure 5. Oil flow pattern in Slice 2 under M5 simulation conditions (velocity magnitude in *m/s*)

The oil flow patterns in steady and transitory simulations are quite similar, as can be seen in Figures 3 and 5. The maximum velocity has been found near the core, where the oil gets out of the coil channels and has the same value in both simulations (≈ 43 *mm/s*). Some small changes can be noticed in the flow inside the hollow fins and at the upper zone of the transformer. Inside the hollow fins, the simulation M5 doesn't obtain such high velocities near the lateral edge and, at the upper zone, the oil flow isn't divided into two parts.

Figure 6. Superficial wall temperatures on the hollow fins under M5 simulation conditions (*K*)

The same effect of temperature decrease takes place at the bottom part of the fins. Comparing Figures 4 and 6 it can be deduced that the transitory simulation gives a sharper vertical temperature variation on the surface of the fins that is concentrated at the lower zone. At the upper zone the temperature is more uniform and the values of both simulations, M1 and M5, are similar.

This sudden variation of the bottom part predicted by simulation M5 agrees with the experimental results, as will be shown in the next section.

3.3. Experimental validation

An experimental validation is needed to see how precisely the Slice 2 model under conditions M5 can represent the refrigeration of the real transformer inside the substation. It is technically complicated and quite expensive to perform experimental measurements of internal oil and surface temperatures; so, only external temperatures have been experimentally checked. Unfortunately, no temperatures have been measured at the base.

In Table 3 a comparison of measured and simulated values of reference temperatures is presented.

Table 3. Experimental validation

Values	M5	Experimental
T_2 (*K*)	358.3	348.1
T_6 (*K*)	362.3	352.1
T_4 (*K*)	357.5	347.4
T_9 (*K*)	358.4	341.4
T_7 (*K*)	355.1	343.2

The values obtained in the Slice 2 model are higher than the experimental ones, especially at the lower part of the transformer. There is a maximum difference of 17 *K*. At the upper zone the difference is restricted to 10 *K*. However, the qualitative form of the temperature variations on the hollow fins is well represented. This is shown in Figure 7 where simulated and experimental vertical temperature variations are compared. The experimental values have been obtained by thermography (only the shape is comparable because thermographies are obtained under different operating conditions).

The main reason to explain this difference between the model and the experimental temperatures is the uncertainty in the external boundary conditions. During the test, measurement errors of superficial temperatures can be considered negligible.

Concerning the air temperature, during the test the thermocouples employed to measure it close to the transformer casing were not protected against radiation. It is thought that the measured values of air temperature are affected by this radiation heat coming from the transformer and are higher than the real ones.

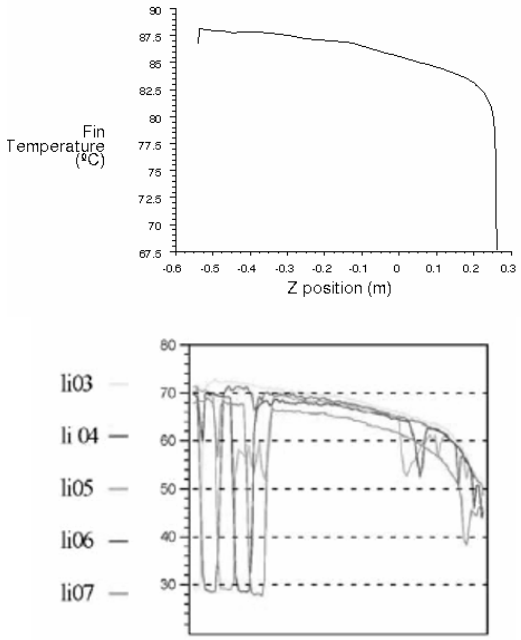

Figure 7. Vertical distributions of temperature on the external surfaces of the fins: simulation (above) and experimental (below) values in *ºC*

Another source of discrepancy is the heat transfer coefficients used. They have been obtained from bibliographical correlations deduced for geometrical and flow conditions that are not exactly the same as the actual ones of the substation. Since the real geometrical and flow conditions are different from the bibliographical ones, the mean values of the different convective heat transfer coefficients will have to be adjusted in order to calibrate the model. Moreover, a vertical variation of different convective values has to be considered in order to obtain better results, especially at the lower zone of the transformer.

Sensibility analysis of the external boundary conditions (bulk air temperatures, heat transfer coefficients and temperatures for the radiative heat exchange) of the model, in conjunction with more exhaustive experimental measurements, are needed to obtain more precise information and results.

It has been pointed out that 75% of the heat is dissipated by the hollow fins, so it is obvious that an extremely suitable choice of convective parameters is needed for this critical zone of the transformer.

4. CONCLUSIONS

Three different models of a distribution transformer have been developed using *CFD* techniques. The results of the so-called Slice 2 model are in good agreement with the results of the Complete model of the transformer, which allows the use of that computationally less expensive and simplified model to analyse the temperatures and the cooling of the transformer.

A transitory simulation is needed in order to ensure the complete convergence of the iterative process. Under these conditions, the superficial temperature on the base of the transformer decreases, but the temperatures on the lid and on the fins are equal to that obtained in the steady state run. A non-stationary effect located at the bottom zone of the transformer, where the oil flow is almost at rest, affects the temperatures, and transient simulations are needed to perceive it.

Two turbulence models with two treatments of the turbulence at near wall regions have been analysed and no remarkable differences in the results have been obtained.

The superficial temperatures predicted by the model are higher than the experimental values, but the qualitative form of the temperature variations on the fins are quite acceptable. The convective boundary conditions must be adjusted in order to obtain a better fit between experimental and simulated results.

The developed simplified Slice 2 model can be used to investigate improvements in the cooling of distribution transformers and in the reduction of the top oil and "hot-spot" temperatures.

ACKNOWLEDGEMENTS

The authors wish to acknowledge the Antonio Aranzabal Foundation and Ormazabal Corporate Technology for their economic support and collaboration.

REFERENCES

[1] IEC, 1991, "Loading Guide for Oil-Immersed Power Transformers", *2nd edition, IEC Standard*, Publ. 354.

[2] Z. Radakovic, Dj. Kalic, 1997, "Results of a Novel Algorithm for the Calculation of the Characteristic Temperatures in Power Oil Transformers, *Electrical Engineering*, Vol. 80, No. 3, pp. 205-214.

[3] G. Swift, T. S. Molinski, W. Lehn, 2001, "A Fundamental Approach to Transformer Thermal Modeling - Part I: Theory and Equivalent Circuit - Part II: Field Verification, Circuit", *IEEE Transactions on Power Delivery*, Vol. 16 (2), pp. 171-180.

[4] G. Pudlo, S. Tenbohlen, M. Linders, G. Krost, 2002, "Integration of Power Transformer Monitoring and Overload Calculation into the Power System Control Surface", *IEEE/PES Transmission and Distribution Conference 2002*, Yokohama, Vol. 1, pp. 470-474.

[5] Radakovic, Z., Maksimovic, S., 2002, "Non-Stationary Thermal Model of Indoor Transformer Stations", *Electrical Engineering*, Vol. 84, pp. 109-117.

[6] Mufuta, J.-M., Van den Bulck, E., 2000, "Modelling of the Mixed Convection in the Windings of a Disc-Type Power Transformer", *Applied Thermal Engineering*, Vol. 20, pp. 417-437.

[7] Oh, K.-J., Ha, S.-S., 1999, "Numerical Calculation of Turbulent Natural Convection in a Cylindrical Transformer Enclosure", *Heat Transfer – Asian Research*, Vol. 28, pp. 429-441.

[8] Smolka, J., Nowak, A. J., Wrobel, L. C., 2004, "Numerical Modelling of Thermal Processes in an Electrical Transformer Dipped into Polymerised Resin by Using Commercial CFD Package *Fluent*", *Computer & Fluids*, Vol. 33, pp. 859-868.

[9] J. C. Ramos, A Rivas, J. M. Morcillo, 2005, "Numerical Thermal Modelling of the Natural Ventilation of a Half-Buried Transformer Substation using CFD Techniques", *4th International Conference on Computational Heat and Mass Transfer*.

[10] IEC, 1976, "Power Transformers. Part 2: Temperature Rise", *IEC Standard*, Publ. 76-2.

[11] B. E. Launder, D. B. Spalding, 1972, "Lectures in Mathematical Models of Turbulence", *Academic Press, London, England*.

[12] D. Choudhury, 1993, "Introduction to the Renormalization Group Method and Turbulence Modeling", *Fluent Inc. Technical Memorandum*, TM-107.

[13] Incropera, F. P., De Witt, D. P., 2002, "Fundamentals of Heat and Mass Transfer", *5th edition, John Wiley & Sons*, New York.

[14] Fluent Inc., 2005, "Fluent 6.2 User's Guide", *Cavendish Court, Lebanon*, NH 03766.

[15] Henkes, R. A. W. M., and Hoogendoorn, C. J., 1994, "Scaling of the Turbulent Natural Convection Flow in a Heated Square Cavity", *Trans. Of the ASME*, 116, pp. 400-408.

[16] M. J. Cook, K. J. Lomas, 1997, "Guidance On The Use Of Computational Fluid Dynamics For Modelling Buoyancy Driven Flows", *Proceedings of Building Simulation '97*, Prague, Vol. 3, pp. 57-72.

[17] M. K. Pradhan, T. S. Ramu, 2003, "Prediction of Hottest Spot Temperature (HST) in Power and Station Transformers", *IEEE Trans. Power Delivery*, Vol. 18, pp. 1275-1283.

Conference on Modelling Fluid Flow (CMFF'06)
The 13th International Conference on Fluid Flow Technologies
Budapest, Hungary, September 6-9, 2006

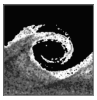

GENERATOR COOLING USING HEAT PIPES

Bert de LEEUW[1], Harry HAGENS[2], Steven BRAND[3], Mart GROOTEN[4], Frank GANZEVLES[5], Cees van der GELD[6], Erik van KEMENADE[7]

[1] VDL Klima b.v. Eindhoven, the Netherlands. E-mail: b.d.leeuw@klima.com
[2] VDL Klima b.v. Eindhoven, the Netherlands. E-mail: h.hagens@klima.com
[3] VDL Klima b.v. Eindhoven, the Netherlands. E-mail: s.brand@klima.com
[4] Department of Mechanical Engineering, Technische Universiteit Eindhoven. E-mail: m.h.m.grooten@student.tue.nl
[5] Department of Mechanical Engineering, Technische Universiteit Eindhoven. E-mail: f.l.a.ganzevles@tue.nl
[6] Corresponding Author. Department of Mechanical Engineering, Technische Universiteit Eindhoven. Postbus 513, 5600 MB Eindhoven, The Netherlands. Tel.: +31 40 2472923, Fax: +31 40 2475399, E-mail: c.w.m.v.d.geld@tue.nl
[7] Department of Mechanical Engineering, Technische Universiteit Eindhoven. E-mail: h.p.v.kemenade@tue.nl

ABSTRACT

This paper presents the study of a heat pipe-equipped heat exchanger with two filling ratios of R134a 19% and 59%, respectively. The airflow rate varies from 0.4 to 2.0 *kg/*s. The temperatures at the evaporator side of the heat pipe vary from 40 to 70°*C* and at the condenser part from 20 to 50°*C*. The performance of the heat exchanger has been compared with two pool boiling models, Cooper and Gorenflo, and two filmwise condensation models, Nusselt and Butterworth. A fairly good agreement is found for measurements and the model of Cooper at low airflow Reynolds number at the evaporator side of the heat exchanger. The result of this study is that a heat pipe equipped heat exchanger can replace a water-cooled heat exchanger without loss of performance. The tested process conditions are typical for warmer countries.

Keywords : finned tube, heat exchanger, heat pipe, R-134a, thermosyphon

NOMENCLATURE

A	$[m^2]$	surface area
D	$[m]$	diameter
D_h	$[m]$	hydraulic diameter
F	$[N]$	force
F_e	[-]	filling degree
H	$[m]$	fin distance
L	$[m]$	length
M	$[kg/kmol]$	molecular weight
Nu	[-]	Nusselt number
Pr	[-]	Prandtl number
Q	$[W]$	heat flow rate
R	$[K/W]$	heat resistance
Re	[-]	Reynolds number
T	[℃]	temperature
W	$[m]$	distance between pipes
c_p	$[J/kgK]$	heat capacity at constant pressure
d_i	$[m]$	inner pipe diameter
g	$[m/s^2]$	acceleration due to gravity
Δh_{fg}	$[J/kg]$	enthalpy of evaporation
$\dot{m}$	$[kg/s]$	mass flow rate
p	$[Pa]$	pressure
p_r	[-]	reduced pressure
q	$[W/m^2]$	heat flux
r	$[m]$	radius
α	$[W/m^2K]$	heat transfer coefficient
λ	$[W/mK]$	thermal conductivity
δ	$[m]$	thickness
η_{fin}	[-]	fin efficiency
μ	$[Pas]$	dynamic viscosity
ρ	$[kg/m^3]$	mass density
χ	[-]	geometric correction factor

Subscripts and Superscripts

cond	condenser
evap	evaporator
f	fluid
i	inner
lm	logarithmic mean
max	maximum
min	minimum
o	outer
tot	total
v	vapour
w	wall
x, y	Cartesian coordinates

1. INTRODUCTION

Stand-alone electricity power generators are usually cooled with ambient air. Standard practice is air to air heat transfer or using a tube in plate heat

exchanger with water as an intermediate medium. In some situations water is not available or ambient temperatures are too high to use ambient air. In those cases heat pipes may provide an alternative for cooling powers in excess of 100 *kW*. Multiple heat pipes then connect two plate heat exchangers.

The heat transfer in the system is based on the continuous cycle of the vaporization and condensation process. The thermosyphon, or heat pipe if equipped with a wick inside, is heated at the evaporator, which causes evaporation of a part of the fluid. The vapour flows to the condenser, where the fluid condenses while giving off its latent heat, caused by cooling from the outside. The condensate flows back to the heated section along the wall by gravitation, which closes the cycle.

Thermosyphons can be used to transfer heat between two gas streams. The advantages are the high heat recovery effectiveness, compactness, no moving parts, light weight, relative economy, no external power requirements, pressure tightness, no cross-contamination between streams and reliability [1, 2].

The heat transfer being based on evaporation and condensation, the latent heat of the fluid is an important parameter. The higher the latent heat of a fluid is the higher the transfer of heat at a lower pressure. The working principles of the thermosyphon imply that the fluid should evaporate and condense within the temperature range. Taking the possible application of cooling an electricity generator with ambient air into account, the working fluid R-134a is an option, considering the expected temperature ranges in practice. The hot air will be in a range of 40 – 80 ℃, the ambient air will be in a range of -20 – 50 ℃. R-134a sublimates at -40 ℃ and 51 *kPa*, so phase change from liquid to gas only occurs above this temperature [3]. The critical temperature of R-134a is 101.06 ℃ [4], which defines the extremes of the temperature range of R-134a, with a critical pressure of 4.06 *MPa*.

Other possible working fluids are ammonia, pentane or water [1]. All these fluids have the advantage over R-134a that they have a higher latent heat, which enables higher heat transfer.

Unfortunately, the maximum practical temperature limit of ammonia is 50 ℃ [5], which is too low for the situation at hand. Water has a risk of freezing at the lower temperature range. Pentane could be a useful alternative for R-134a, considering its temperature range from -20 – 120 ℃, the higher latent heat and the higher surface tension [1, 6, 7]. A higher surface tension has the benefit of lowering the risk of entrainment, which is the most likely occurring limit in the application of the thermosyphon [8]. Possibly, other hydrocarbon refrigerants mentioned by Lee et al.[9] are possible working fluids as well. The type of filling fluid, and the operational limits will be subject of later research.

This paper presents experimental data of air-heat pipe-air heat exchangers with two filling ratios. The results are compared with those of a model that is based on existing correlations of the literature. Results of this study show which conditions foster application of this novel type of heat exchanger.

2. EXPERIMENTAL SET-UP AND METHOD OF ANALYZING

2.1. Test setup

A laboratory scale test rig was designed and built to compare the performances of conventional plate-type exchangers (with water as intermediate medium) and heat pipe equipped plate heat exchangers. A range of mass flow rates of ambient air of 0.2–2.5 *kg/s* is possible. Temperature differences between hot and cold sides of the heat pipe of 60°*C* are possible. Two filling degrees, F_e see Eq. (1), of the heat pipe have been examined.

$$F_e = \frac{liquid\_fill\_volume}{evaporator\_volume} \quad (1)$$

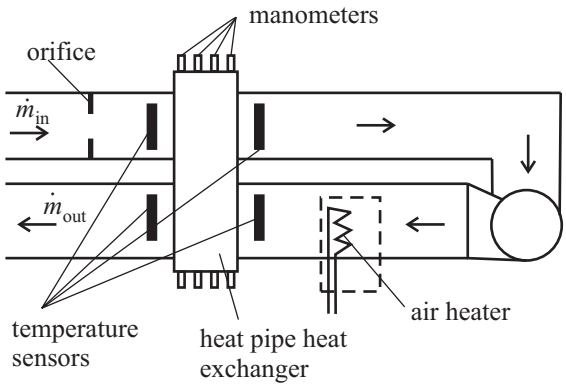

Figure 1. Schematic of the test rig

In this study, the overall heat transfer and temperature distribution are assessed under mass flow rates of ambient air varying from 0.4 *kg/s* to 2.0 *kg/s*. The ambient air temperature varies from 20 – 50 ℃, whereas the hot air flow has temperatures in the range from 40 – 70 ℃. The heat pipe is filled with R-134a at ratios of 19% and 59%. A schematic overview of the setup is shown in Figure 1. The upper side is the cold side, where ambient air enters. Up- and downstream of the heat exchanger temperatures are measured with 16 Pt100's (IC Istec ME 1009), with an accuracy of 0.1°*C*. The temperatures of four sensors are averaged and they are denoted as T_1, T_2, T_3 and T_4 (see Figure 2) respectively. The sensors are mounted at ¼ and ¾ of the length of the diagonal cross cut of the 645 × 520 mm^2 rectangular duct. The air stream velocity profile was measured and found to have a homogeneous profile. Downstream

the hot section, ten Pt-100 temperature sensors are mounted to investigate the temperature variation in the height of the pipe at the evaporator section. They are mounted vertically at 50 *mm* apart and 117 *mm* of the sidewall. The Pt-100 sensors are all calibrated with accuracy better than 0.1 °C for the temperature range of 0 – 100 °C. The measurement section is thermally insulated minimize errors in the heat fluxes deduced.

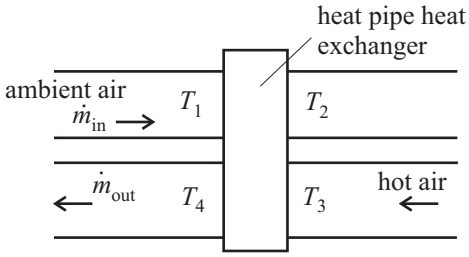

Figure 2. Definition of temperatures in air streams

At the entry, the dynamic pressure measurement with an orifice results in the air mass flow rate, at an accuracy of 2%. The uncertainties of all measured and calculated parameters are estimated according to [10].

The air heater is a water-air heat exchanger, with 3 *mm* spaced vertical fins, which allows a uniform velocity profile upstream the evaporator. This neutralizes the induced swirl in the airflow caused by the radial fan.

The heat exchanger consists of 4 rows of alternating 14 and 13 copper pipes. The pipes have an outer diameter of 16 *mm* and a wall thickness of 0.8 *mm*. The total length of a pipe is 1.5 *m*, with 0.64 *m* in the condenser section and the evaporator section each. The adiabatic length is 0.22 *m*. This is the distance between the two sections of the airflow in the wind tunnel. The inner surface of each pipe has small spiral grooves, to enhance the heat transfer in evaporation and condensation. The grooves are 0.2 *mm* wide and 0.2 *mm* deep each, separated 1 *mm*, under an angle of 25° with the vertical. The distance between the pipes in a row is 36.5 *mm*. Each row is filled with R-134a separately. The rows are 27.5 *mm* apart and the total depth of the aluminium fins including the 4 rows is 114.5 *mm*. At the top of each row, the pressure is measured with a WIKA type RB manometer, at a frequency of 100 *Hz*, with an accuracy of 1% after calibration. The range of the manometers is 0 – 10 *MPa*. The saturation temperature of R134a is given by the Antoine relation (2) obtained from data from NIST [4] with temperatures in degrees Celsius and pressure in *kPa*

$$T = \frac{B}{A - \ln\left(100\, p_v\right)} - C \tag{2}$$

with A = 10.52, B = 2484, C = 263.1

2.2. Heat transfer performance

To analyze the performance of the heat pipe equipped heat exchanger, the heat flow rate is given by Eq. (3)

$$Q = \dot{m} c_p \Delta T \tag{3}$$

with the temperature differences of the air flows up- and downstream the 4 rows of the heat pipe heat exchanger.

The effectiveness of the heat transfer at both the hot and cold side of the heat pipe heat exchanger is expressed in the overall heat transfer coefficient α_{tot} and it is defined by Eq. (4) [11]:

$$\alpha_{tot} = \frac{Q}{A \chi \Delta T_{lm}} \tag{4}$$

with the corresponding Q from Eq. (3), A the heat transferring area of whether the hot or the cold side, χ a geometrical correction factor, here 0.99 [11], if each side is seen as a cross flow heat exchanger with 4 passes and

$$\Delta T_{lm} = \frac{\Delta T_{max} - \Delta T_{min}}{\ln\left(\frac{\Delta T_{max}}{\Delta T_{min}}\right)} \tag{5}$$

with ΔT_{max} and ΔT_{min} the maximum and minimum temperature differences between the airflow and heat pipes of the first and last row.

The heat transfer from the air stream to the fins and from the fins to the tube is described with a fin efficiency according to [12]. The Nusselt number for the airflow between the fins is given by Hewitt [13]

$$\begin{aligned} Nu &= 0.19\left(\frac{a}{b}\right)^{0.2}\left(\frac{S}{d}\right)^{0.18}\left(\frac{h}{d}\right)^{-0.14} Re^{0.65} Pr^{0.33} \\ &= 0.1124 Re^{0.65} \end{aligned} \tag{6}$$

with a the tube distance in a row, b the distance between the tube in two successive rows, S the fin distance, d the tube diameter and h the fin length in gas flow direction.

The heat resistance of the heat pipe is given by

$$R_w = \frac{\ln\left(r_o / r_i\right)}{2\pi \lambda_w L_{cond}} = \frac{1}{\alpha_w A_w} \tag{7}$$

with r_o and r_i the outer and inner radius of the pipe, λ_w the thermal conductivity of the copper pipe

and L_{cond} the length of the evaporator or the condenser section respectively.

The heat transfer from the air stream to the fins and from the fins to the tube can be described with a fin efficiency according to [12]

$$\eta_{fin} = \frac{\tanh\left(m l_{fin}\right)}{m l_{fin}} \tag{8}$$

with

$$m = \left[2\alpha_{fin} \left(1 + \frac{\delta_{fin}}{l_{fin}} \right) \Big/ \left(\lambda_{fin} \delta_{fin} \right) \right]^{1/4} \tag{9}$$

with l_{fin} the length from fin tip to tube wall, α_{fin} the heat transfer coefficient to the fin, δ_{fin} the fin thickness, here 0.2 *mm*, λ_{fin} the thermal conductivity of the fin material, here aluminium, 236 *W/mK*. Every tube in the tube bank is observed as having its own segment of fins. This leads to a local fin length l_{fin} of half the distance between two tubes. The heat transfer coefficient α_{fin} is determined with the Nusselt relation (6). The total heat transferring area equals the heat transferring area of the fins, so from this assumption follows [12]:

$$R_{fin} = \frac{1}{\eta_{fin} \alpha_{fin} A_{fin}} \tag{10}$$

2.3 Phase change heat transfer

The heat resistance of the condensate in the thermosyphon is defined as:

$$R_f = \frac{\delta_f(y)}{\lambda A_f} = \frac{1}{\alpha_f A_f} \tag{11}$$

with δ_f the thickness of the condensate layer and λ_f the thermal conductivity of the fluid.

The local thickness of the condensate is [4], assuming laminar flow following Nusselt theory:

$$\delta_x = \left(\frac{4\mu_f \lambda_f \Delta T y}{\rho_f^2 g \Delta h_{fg}} \right)^{1/4} \tag{12}$$

with ρ_f the fluid mass density, g the gravitational constant, δ_x the thickness of the condensate film layer, μ_f the dynamic viscosity of the condensate, ΔT the temperature difference between saturation temperature of the vapour and wall temperature and Δh_{fg} the latent heat of the fluid.

By draining heat at the condenser from the vapour, a film of condensate forms, which becomes thicker in the direction of the evaporator. The film flows down to the evaporator conserving the film thickness in the part between the two measuring sections of the wind tunnel. At the evaporator, the film starts thinning under influence of the added heat. Under stationary operating conditions of the thermosyphon, the overall film thickness over the condenser can be described by Eq. (13)

$$\delta_L = \left(\frac{4\mu_f \lambda_f \Delta T_{cond} L_{cond}}{\rho_f^2 g \Delta h_{fg}} \right)^{1/4} \tag{13}$$

with L_{cond} the location at the condenser. The Reynolds number of the film is given by [12]:

$$\mathrm{Re}_f = \frac{4\dot{m}_{cond}}{\mu_f} \tag{14}$$

with $\dot{m}_{cond}$ the mass flow rate of liquid per unit of periphery. The condensate mass flow rate is equal to Eq. (15), see also [5], with the heat flow rate obtained from Eq. (3).

$$\dot{m}_{cond} = \frac{Q}{\Delta h_{fg}} \tag{15}$$

Assuming laminar flow, similar to the condenser section, the Nusselt theory can be applied again, now for overall film thickness of downward flowing evaporating films:

$$\delta_f = \left(\frac{3\mu_f \dot{m}_{cond}}{\rho_f^2 g} \right)^{1/3} = \left(\frac{3\mu_f^2}{4\rho_f^2 g} \right)^{1/3} \mathrm{Re}_f^{1/3} \tag{16}$$

The heat transfer coefficient for a vertical tube is given by:

$$\alpha = \frac{\lambda_f}{\delta_f} = \left(\frac{4\rho_f^2 g \lambda_f^3}{3\mu_f^2} \right)^{1/3} \mathrm{Re}_f^{-1/3} \tag{17}$$

and all fluid properties evaluated at the average film temperature, see Eq. (18), at the inlet:

$$T_{film} = \frac{T_{gas,in} - T_{fin,average}}{2} \tag{18}$$

Another model for filmwise condensation is obtained from Butterworth [15]:

$$\alpha = \frac{\mathrm{Re}_f}{1.08\,\mathrm{Re}_f^{1.22} - 5.2} \lambda_f \Big/ \left(\mu_f^2 \left(\rho_f - \rho_v \right) g \right)^{1/3} \tag{19}$$

with ρ_v the mass density of the vapour.

In the evaporator the condensed film evaporates due to pool boiling. The models of Cooper, see Eq.

(20), and Gorenflo, see Eq. (21) describes this phenomena [15].

$$\alpha = 55 p_r^{0.12-0.4343\ln(R_p)} \times \left(-0.4343\ln(p_r)\right)^{-0.55} M^{-0.5} q^{0.67} \quad (20)$$

with p_r the reduced pressure, R_p surface roughness in μm, M molecular weight of the condensate in *kg/kmol* and q the heat flux.

$$\alpha = 4500 F_{PF} \left(q/20000\right)^{0.9-0.3 p_r^{0.3}} \times \left(R_p/0.4\right)^{0.133} \quad (21)$$

with

$$F_{PF} = 1.2 p_r^{0.27} + 2.5 p_r + p_r/(1-p_r) \quad (22)$$

The total heat transfer coefficient, see Eqn. (23) and (24), is found from the summation of the partial heat resistances, which are given by Eqn. (7), (10) and the desired heat transfer coefficient of condensation or pool boiling.

$$\alpha_{tot} = \frac{1}{R_{tot} A_{fin}} \quad (23)$$

$$R_{tot} = \frac{1}{\alpha A_w} + \frac{1}{\alpha_w A_w} + \frac{1}{\alpha_{fin} A_{fin}} \quad (24)$$

3. RESULTS

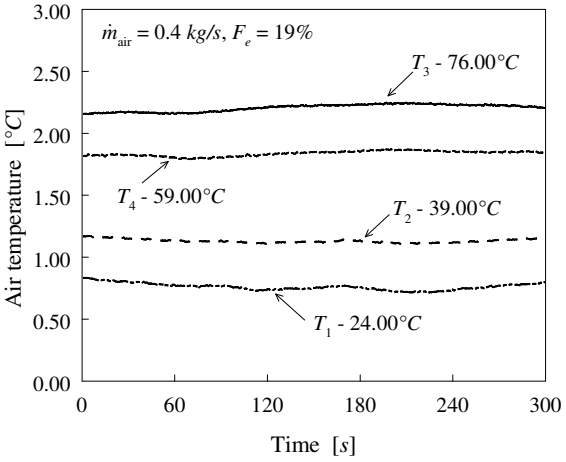

Figure 3. Typical histories of air temperatures, see also Fig. 2, up- and downstream of the heat exchanger: T_3=78.21 ± 0.03°C, T_4=60.84 ± 0.02°C, T_1=24.76 ± 0.03°C and T_2=40.13 ± 0.02°C

The measurements are performed at steady state and each condition lasts 5 minutes. Figure 3 shows a typical example of the airflow temperature histories during a measurement. This figure shows that the variation is less than 0.1°C.

The heat flow rate is measured from the temperature difference over the heat exchanger at the evaporator and condenser part of the heat pipe. At steady state both heat flow rates should be equal. Figure 4 shows the comparison of the heat flow rates at the evaporator side and condenser part of the experiments. This figure shows that the heat flow rate of evaporator is about 4% larger than the heat flow rate of the condenser, for which we have no explanation.

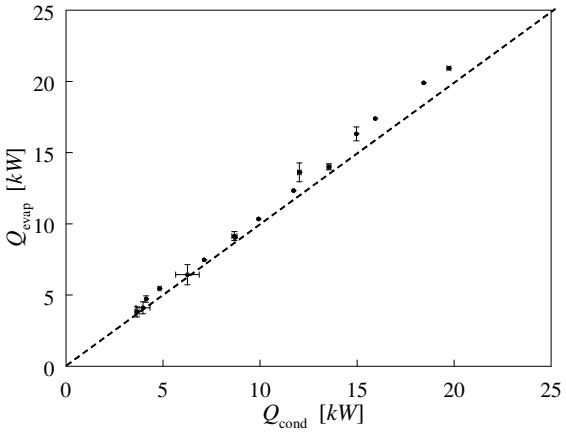

Figure 4. Comparison of measured heat flow rates at evaporator and condenser side of the heat pipe

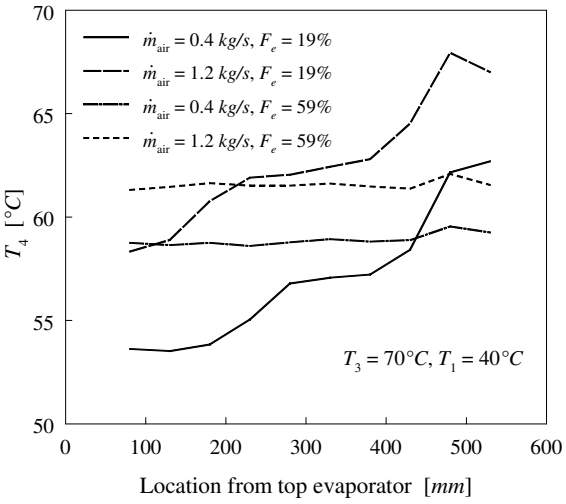

Figure 5. The effect of filling degree and of mass flow rate on temperature distribution downstream of the evaporator

In some cases the heat flow rate is that high that the heat pipe can dry out. Ten Pt100's were mounted downstream the evaporator to measure the temperature distribution along the evaporator. Figure 5 shows four distributions at two process conditions for two filling degrees of the heat pipe. A local, nongradual increase in temperature along

the evaporator indicates a dry out. The inner wall if the thermosyphon is in this situation not fully covered with liquid. This occurs at low filling degree and high heat flow rate (Fig. 5). If dry-out occurs, the measurement is skipped from the analysis.

Figures 6 and 7 show the performance of the heat pipe at the evaporator side for various Reynolds numbers and filling degrees. In Fig. 6 the total heat transfer coefficient at F_e of 19% is shown, whereas Fig. 7 shows results at the higher filling degree. The figures show that the performance increase with increasing heat flow rate. An increase of the Reynolds number of the airflow leads also to a better performance. Some process conditions have been repeated with a higher filling degree. The results are given in Fig. 7. A higher filling degree gives a higher overall heat transfer coefficient at otherwise identical process conditions.

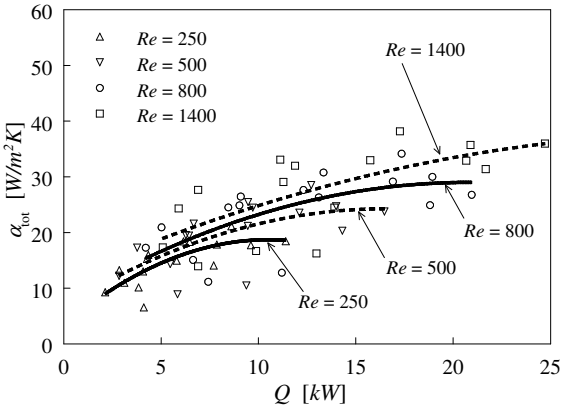

Figure 6. Measured heat transfer coefficient evaporator side for various Reynolds numbers at F_e=19%

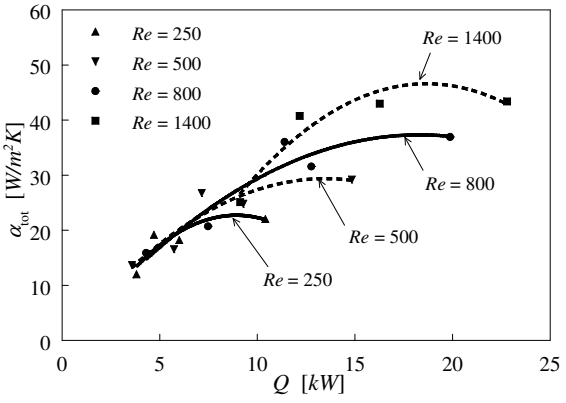

Figure 7. Measured heat transfer coefficient evaporator side for various Reynolds numbers at F_e=59%

Figures 8 and 9 show the performance of the heat pipe at the condenser side for various Reynolds numbers and filling degrees. Fig. 8 presents the total heat transfer coefficient at F_e of 19% and that of the filling degree of 59% is shown in Fig. 9. The figures show that the performance improves with increasing heat flow rate. An increase of the Reynolds number of the airflow leads also to a better performance. Some process conditions have been repeated with a higher filling degree. The results are given in Fig. 9. A higher filling degree gives a higher overall heat transfer coefficient at some process conditions. The Figs. 6-9 show that the performance of the condenser is better than that of the evaporator at the same heat flow rate, if performance is measured in terms of net heat transfer coefficient.

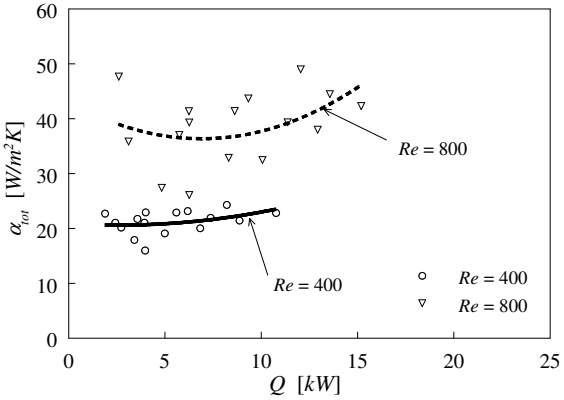

Figure 8. Measured heat transfer coefficient condenser side for various Reynolds numbers at F_e=19%

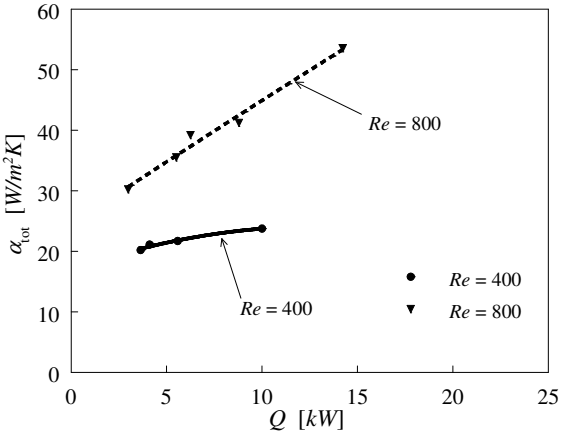

Figure 9. Measured heat transfer coefficient condenser side for various Reynolds numbers at F_e=59%

4. ANALYSIS

Figures 10 and 11 show a comparison of the measured total heat transfer coefficient and predictions based on models of pool boiling of Gorenflo and Cooper [15]. Fig. 10 shows the comparison at airflow Reynolds number of 250 whereas Fig. 11 presents the comparison at *Re* = 800. In both cases the Gorenflo correlation predicts a higher transfer coefficient than Cooper. Both

correlations have the same trend with respect to dependency on heat flux as the corresponding measurements. The difference between the two models and the measured ones could be caused by an overestimate of the Nusselt number for the airflow to the fins. Here it is assumed that the fins have a constant temperature due to high thermal conductivity of the fins. If the temperature is not homogenously distributed the Nusselt number is lower. The heat transfer from the air to the fins has a large influence to the heat transfer, so any uncertainty in it is directly reflected in discrepancies in comparisons like those of Figs. 10-11.

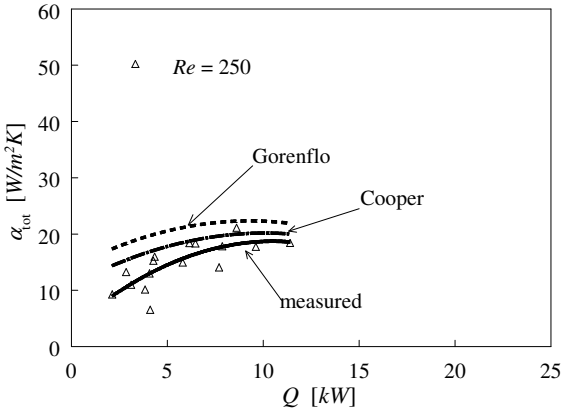

Figure 10. Comparison of measured and predicted total heat transfer coefficient of the evaporator at airflow Reynolds number of 250

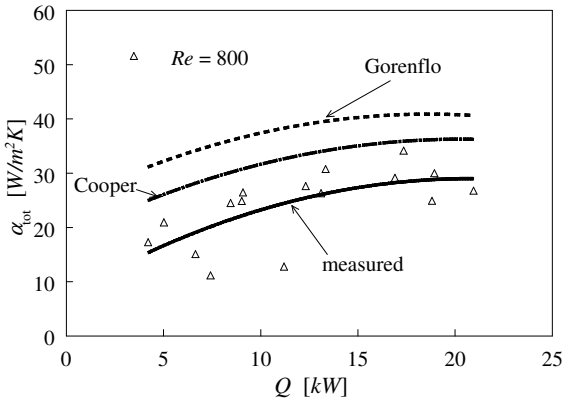

Figure 11. Comparison of measured and predicted total heat transfer coefficient of the evaporator at airflow Reynolds number of 800

Figures 12 and 13 show a comparison of the measured total heat transfer coefficient and predictions based on models of filmwise condensation of Butterworth and Nusselt [15]. The film Reynolds number has been taken into account (laminar gas and laminar liquid and condensate layer with waves). Fig. 12 shows the comparison at airflow Reynolds number of 400 whereas Fig. 13 presents the comparison at *Re* = 800. Fig. 12 shows a fairly good agreement between the predictions and the measurements. At higher airflow Reynolds number the difference between prediction and measured heat transfer coefficient becomes large (Fig. 13) and in this case the models underpredict the heat transfer. In both cases Butterworth predicts a higher result than Nusselt. However, in both cases (Figs. 11-12) the predicted heat flux decreases with increasing heat flow rate, which is a different trend than the one measured.

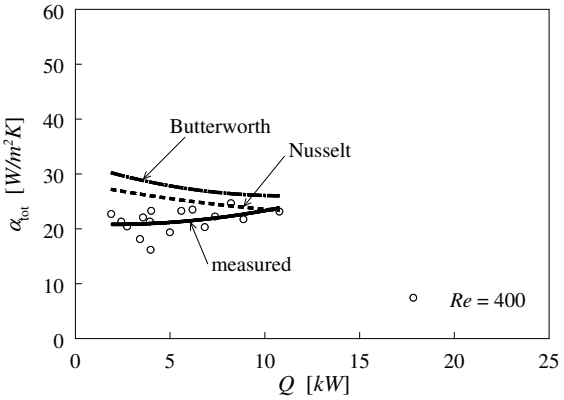

Figure 12. Comparison of measured and predicted total heat transfer coefficient of the condenser at airflow Reynolds number of 400

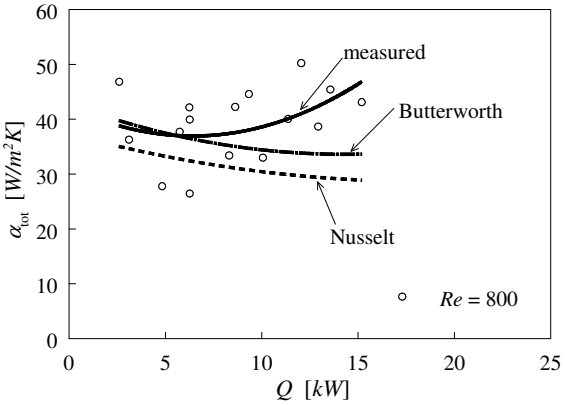

Figure 13. Comparison of measured and predicted total heat transfer coefficient of the condenser at airflow Reynolds number of 800

For the predictions in Figs. 10-14 the Nusselt relation (6) for airflow has been used. Apparently the best predictions are obtained with correlations for boiling in the heat pipe (Gorenflo or –even better– Cooper) and for convective heat transfer on the gas side (Nusselt-relation (6)), if the last one is corrected slightly. The reason why this correction is necessary is not fully clear, but might have to do with some loss of contact between fins and tubes.

5. CONCLUSIONS

The performance of a heat pipe equipped heat exchanger on a laboratory test rig has been measured and analyzed at the most common process

conditions: various mass flow rates of ambient air, various temperature differences between hot and cold sides of the heat pipe and various filling degrees of the heat pipe. The overall heat transfer of the heat exchanger has been assessed. At the evaporator side 10 to 40 W/m^2K has been measured and at the condenser side of the heat pipe 20 to 50 W/m^2K. The temperature distribution over the evaporator has been found to be indicative of proper filling degree.

The results are rewarding, although more research has to be carried out to find the most suitable working fluid, the optimal heat pipe geometry, operating limits and filling degree.

A model to predict the heat transfer and to calculate the performance of the heat pipe equipped heat exchanger has been set up. This model is a first step towards a full predictive model to optimize the heat pipe equipped heat exchanger.

The result of this study is that a heat pipe equipped heat exchanger can replace a water-cooled heat exchanger without loss of performance. The tested process conditions are typical for warmer countries like Bahrain. This study therefore demonstrates that it is possible to apply heat-pipe-based cooling equipment in practical conditions of warmer countries.

REFERENCES

[1] Dunn, P.D and Reay, D.A., 1994, *Heat Pipes,* fourth edition, Pergamon

[2] Wadowski, T., Akbarzadeh, A. and Johnson, P., 1991, "Characteristics of a gravity assisted heat pipe based heat exchanger", *Heat Recovery Systems* CHP, Vol. 11, pp. 69-77.

[3] Morgan M.J. and Shapiro, H.N., 1992 *Fundamentals of Engineering Thermo-dynamics*, 2nd ed., John Wiley & Sons, Inc.

[4] NIST Standard Reference Database 69, June 2005 Release: *NIST Chemistry WebBook.*

[5] Unk J., 1988, "Ein Beitrag zur Theorie des geschlossenen Zweiphasen-Thermosiphons", *Dissertation Technische Universität* Berlin.

[6] Fröba, A.P., Penedo Pellegrino, L. and Leipertz, A., 2004, "Viscosity and Surface Tension of Saturated n-Pentane", *Int J Thermophysics*, Vol. 25, pp. 1323-1337.

[7] Fröba, A. P., Will, S. and Leipertz, A., 2000, "Saturated liquid viscosity and surface tension of alternative refrigerants", *14th Symposium on Thermophysical Properties*, Boulder, Colorado, U.S.A.

[8] Reay, D.A., 1984, *Heat exchanger selection part 4: Heat pipe heat exchangers*, Int. Research & Development Co. Ltd.

[9] Lee, H.S., Yoon J.I., Kim, J.D. and Pradeep Bansal, 2005, "Evaporating heat transfer and pressure drop of hydrocarbon refrigerants in 9.52 and 12.70 mm smooth tube", *Int J Heat Mass Transfer*, Vol. 48, pp. 2351-2359.

[10] Kline, S.J., McKlintock, F.A., 1953, "Describing uncertainties in single-sample experiments", *Mech. Eng*, Vol. 75, pp. 3-8.

[11] VDI-Wärmeatlas, 1991,: *Berechnungsblaetter fuer den Waermeuebergang,* 6. erw. Auflage, VDI Verlag GmbH.

[12] Rohsenow, W. M., Hartnett, J. P.and Cho, Y. I., 1998, *Handbook of Heat Transfer*, 3rd ed., McGraw-Hill.

[13] Hewitt, G.F., 1998, *Heat Exchanger Design Handbook*, Begell House.

[14] Baehr, H.D. and Stephan, K., 1998, *Heat and Mass Transfer*, Springer.

[15] Collier. J.G. and Thome, J.R., 1994, *Convective boiling and condensation*, Clarendon Press.

Conference on Modelling Fluid Flow (CMFF'06)
The 13th International Conference on Fluid Flow Technologies
Budapest, Hungary, September 6-9, 2006

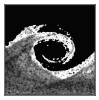

A REVIEW OF WATER AND HEAT MANAGEMENT FOR PEM FUEL CELLS

Elena Carcadea[1], Ioan Stefanescu[2], Horia Ene[3], Derek B Ingham[4], Roxana Elena Lazar[5]

[1] National R&D Institute for Cryogenics and Isotopic Technologies – ICIT, Uzinei Street, No. 4, PO Box 10, 240050, Rm. Valcea, Romania Tel. +40.250.733890, Fax +40.250.732746, E-mail: lili@icsi.ro
[2] National R&D Institute for Cryogenics and Isotopic Technologies – ICIT, Rm. Valcea, Romania, istef@icsi.ro
[3] Romanian Academy of Sciences, Mathematical Institute, Bucharest, Romania, Horia.Ene@imar.ro
[4] Department of Applied Mathematics, University of Leeds, Leeds, UK, amt6dbi@amsta.leeds.ac.uk
[5] National R&D Institute for Cryogenics and Isotopic Technologies – ICIT, Rm. Valcea, Romania, roxana@icsi.ro

ABSTRACT

PEM fuel cell technology has emerged as viable energy conversion devices for terrestrial applications (stationary and mobile). They offer huge economical and environmental potentials in the next generation of power systems, but they are still more expensive than most conventional power conversion devices. Therefore, there is a need to optimize these technologies from the performance and cost points of view. Mathematical modeling proved to be the most important tool for PEM fuel cell optimization, providing the best solution for design, operating condition, experimentation and exploitation.

Water and Thermal Management is one of the key technical issues that influence the fuel cell performance. Most of the previous studies deal with the cell performance or water and thermal issues separately, even though they are closely related and the water and thermal management significantly influences cell performance. Elaborating a comprehensive and detailed mathematical model for studying electrochemical, thermodynamical and fluid dynamical relations that occur in a PEM fuel cell, and solving numerically this model using a CFD software will result in a powerful modeling tool that can be viewed as an important alternative for fuel cell optimization processes and for reduction of exploitation/experimentation costs.

Keywords: CFD, fuel cell, heat management, water management

NOMENCLATURE

D	$[m^2/s]$	species diffusivity
I	$[A/m^2]$	current density
R	$[J/molK]$	gas constant
S	[ ]	source terms in transport equations
T	$[°K]$	temperature
V	$[V]$	cell potential
Y	[-]	species mass fraction
a	[ ]	water vapor activity
c	[ ]	molar concentration
j	$[A/m^3]$	current density
j_0	[ ]	exchange current density
p	$[atm]$	pressure
$\underline{v}$	$[m/s]$	velocity vector
ε	[-]	porosity
η	$[V]$	overpotential
ϕ	$[V]$	phase potential
ρ	$[kg/m^3]$	density
μ	$[kgm/s]$	viscosity
σ	$[S/m]$	membrane conductivity
λ	[-]	water content of the membrane

Subscripts and Superscripts

a	anode
c	cathode
i	species
mem	membrane
sol	solid phase
ref	reference value
sat	saturation value

1. INTRODUCTION

Hydrogen and electricity together represent one of the most promising ways to realize sustainable energy, whilst fuel cells provide the most efficient conversion device for converting hydrogen, and possibly other fuels, into electricity. Hydrogen and fuel cells open the way to integrated *open energy systems* that simultaneously address all of the major

energy and environmental challenges, and have the flexibility to adapt to the diverse and intermittent renewable energy sources that will be available in Europe.

The demands regarding the pollution decreasing, the needs to find clean power generation and conversion systems both for mobile and stationary applications have led, in the last decade, to new researches into PEM fuel cells. The PEM fuel cells offer huge economical and environmental potentials, but they are still more expensive than most conventional power conversion devices. Therefore, there is a need to optimize these technologies from the performance and cost points of view. Mathematical modeling has proved to be the most important tool for PEM fuel cell optimization, providing the best solution for design, operating conditions, experimentation and exploitation.

Despite many limitations and uncertainties, fuel cells remain a very interesting option which is worthy of further R&D efforts. Water and Thermal Management is one of the key technical issues that have to be well understood in the process of fuel cell system development.

Under usual fuel cell operating conditions, liquid water is known to be generated, but the exact location where condensation occurs is unknown. If water condenses on or near the catalyst layer (where the product H_2O enters the cathode), then pockets of water may collect which could potentially narrow the channels through which oxygen gas is supplied to the catalyst. In turn, these pockets of water could restrict or interrupt the supply of oxygen to the catalyst and thereby degrade fuel cell performance. As a result, management of liquid water is of prime importance in fuel cells.

2. OPERATION PRINCIPLES OF FUEL CELLS

Figure 1 illustrates the geometry of the fuel cell that is simulated in this work. It consists of two serpentine flow channels (anode and cathode), two diffusion layers (anode and cathode), two catalyst layers (anode and cathode) and a membrane. There are three serpentine passes in the flow path, which is approximately fifteen centimeters long in the flow direction. The cross-section flow areas of the geometrie are 0.2 cm x 0.15 cm and each diffusion layer has dimensions of 0.037 (height) x 2.20 (width) x 2.20 (length) cm. The catalyst layer has the dimensions 0.012 (height) x 2.20 (width) x 2.20 (length) cm.

The rest of this geometry are graphite current collectors and a 0.007cm thick membrane.

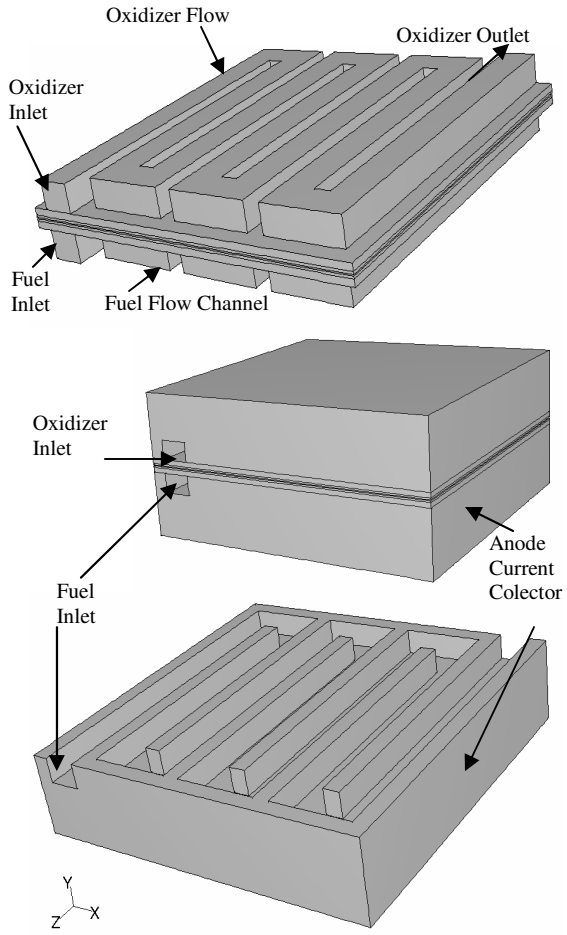

Figure 1. PEM Fuel Cell

The PEM fuel cell operation was described in the previous paper of the authors [1]. Brefly, the operation principle is characterized as gas mixture transport and electro-chemical transformation of hydrogen and oxygen species to form electricity and water.

The overall reaction can be written as follows:

$$2H_2 + O_2 \Rightarrow 2H_2O + electricity + heat \qquad (1)$$

This equation reveals the impact of two important issues that occur inside the PEM fuel cell; namely, the thermal and water management and mass transport limitations. Water management ensures that the membrane remains fully hydrated to maintain good protonic conductivity and performance. An imbalance between production and removal of water can occur and both of the results (dehydration or flooding) have a very detrimental effect on the performance. Thermal management is very important in removing the excessive heat produced by the electrochemical reaction because we wish to prevent the drying out

of the membrane and the excessive thermal stresses which can cause damage to the membrane.

3. WATER TRANSPORT PROCESSES

Water management is a key to high performance and longevity of PEM fuel cells. This is because currently available membranes, such as Nafion, require water in order to exhibit good proton conductivity. In other parts of the cell, the amount of liquid water should be kept to the minimum. Liquid water must be prevented from accumulating on the electrode surfaces, in the pores of the gas diffusion layers, and in the gas channels. Liquid water in these regions obstruct the transport of reactants to the active catalyst sites, thus reducing the performance [2]. The objective of effective water management is to regulate the transport of water in such a way that a sufficient amount of water is retained in the proton conductive phases, but excess liquid water is removed from the cell at the same rate as it is produced, with minimum obstruction of the gas transport paths.

Figure 2 illustrates the flows of water in a PEMFC. Water is produced on the cathode, and additional water may be supplied to the cell along the inlet gas streams if the product water is not sufficient to maintain the proton conductive phases humidified. The amount of water fed into the cell by humidified reactant gases depends on the gas temperature, pressure and flow rate, whereas water production on the cathode depends only on the current density, to which it is directly proportional.

When current is drawn from the cell, protons migrate through the membrane from the anode to the cathode and carry water molecules with them. The process is called electro-osmotic drag and the average number of water molecules carried over by one proton is called the electro-osmotic drag coefficient. The formation of a water concentration gradient inside the membrane gives rise to diffusion, which usually counters the electro-osmotic drag and is, therefore, often referred to as "backdiffusion". Furthermore, if there is a pressure difference across the membrane, hydraulic permeation contributes to the water transport. The net water transport through the membrane is the resultant of these processes [3].

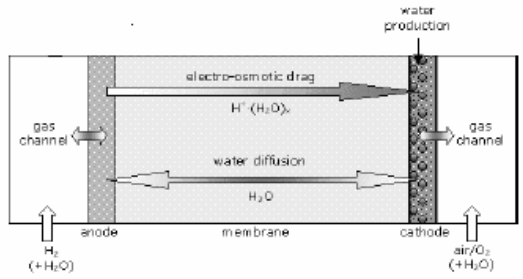

Figure 2. Water transport processes

The electro-osmotic drag, together with the production of water by the cathode reaction, results in accumulation of water at the cathode. From the cathode, water is either transported to the flow channel through the gas diffusion backing or diffused through the membrane towards the anode due to the water concentration gradient.

Water is removed from a PEM fuel cell by the reactant streams. Liquid water drops are pushed along the channels, and undersaturated reactant gases pick up water vapor.

The rate of water removal and the ratio of liquid and gaseous water depend both on the operating conditions and cell design. Temperature and operating pressure have a substantial effect on water evaporation and vapor pressure, and thus to the water vapor content of the reactant gases. Therefore, the efficiency of water removal strongly depends on the operating temperature. The ratio of liquid and gaseous water is dictated by the operating temperature and the humidity of input reactant gases. Reactant pressure and flow rates change the mass transfer conditions in the gas diffusion backings and the flow channels.

It must be noted that water management conditions change along the flow channel.

4. MODEL DEVELOPMENT

A three-dimensional computational fluid dynamics model of a Polymer Electrolyte Membrane (PEM) fuel cell with serpentine gas flow channels is presented in this paper. This comprehensive model accounts for important transport phenomena in a fuel cell, such as heat transfer, mass transfer, electrode kinetics, and potential fields. Results obtained from this model reveal the detailed transport phenomena occurring inside the fuel cell such as reactant gas distributions, temperature distribution, potential distribution, and local current density distribution. The focus in this paper in on water distribution and heat management.

4.1 Model equations

The paper reports a numerical model that includes a full three-dimensional solution to the Navier-Stokes equations for the PEM fuel cell layers. A fundamental fuel cell model consists of five principles of conservation: mass, momentum, species, charge and thermal energy. These transport equations are coupled with electrochemical processes through source terms. Such convection – diffusion – source equations can be summarized in the following general form:

$$\nabla(\rho \underline{v}\phi) = \nabla(\Gamma \nabla \phi) + S \qquad (2)$$

where ϕ is a general variable to be solved, ρ the density, $\underline{v}$ is the velocity vector, and Γ the diffusion

coeficient. The source S on the right hand side of Eq. (2) is the mass added to the continuous phase, for example, a source of the chemical species added to the system, or a change in the mass due to condensation/vaporization of a second phase, such as the water [4].

The main assumptions invoked in the model are: (1) the cell operates under isothermal conditions at 80° C, and (2) incompressible and laminar gas flow due to small pressure gradients and Reynolds numbers.

The mass conservation equation (Eq. (3)) is modified to include the electrochemical aspects of a fuel cell, by using the source term S_m, and is given as follows:

$$\nabla(\varepsilon\rho\underline{v}) = S_m \tag{3}$$

The source term corespond to the consumption of hydrogen and water vapour in the anode and the consumption of oxygen and production of water vapor in the cathode, as we can see from Eq. (4).

$$S_m = \begin{cases} S_{H_2} + S_{H_2O} \; in\ anode\ \ catalyst\ \ layer \\ S_{O_2} + S_{H_2O} \; in\ cathode\ catalyst\ layer \end{cases} \tag{4}$$

The momentum equation (Eq. (5)) for the fluid flow through the porous matrix of the fuel cell electrodes reduces to the Darcy law as follows:

$$\nabla\cdot(\varepsilon\rho\underline{v}\underline{v}) = -\varepsilon\nabla p + \nabla\cdot(\varepsilon\mu\nabla\underline{v}) + S_v \tag{5}$$

$$S_v = -\frac{\mu}{k}\varepsilon v \tag{6}$$

The species transport equations are solved for the mass flow rates of the hydrogen, water and oxygen species based on the mixture velocities ($\underline{v}$) and the diffusion mass fluxes. There is one inert component on each side and the mass fraction of this component was determined by subtracting from unity the sum of the other species that appear in the anode and cathode, separately, namely

$$\nabla\cdot(\varepsilon\underline{v}Y_i) = \nabla(D_i\nabla Y_i) + S_i \tag{7}$$

where Y_i is the mass fraction of the i^{th} species, D_i is the mass diffusivity of species and S_i is the volumetric source term for the species implied by the reactions.

$$S_{H_2} = -\frac{M_{H_2}}{2F}\cdot j_a \tag{8}$$

$$S_{O_2} = -\frac{M_{O_2}}{4F}\cdot j_c \tag{9}$$

$$S_{H_2O} = \begin{cases} -M_{H_2O}\cdot\alpha & in\ \ anode\ \ \ catalyst\ \ \ layer \\ M_{H_2O}\cdot\alpha + \frac{M_{H_2O}}{2F}\cdot j_c & in\ cathode\ \ catalyst\ \ layer \end{cases} \tag{10}$$

where M_{H_2}, M_{O_2} and M_{H_2O} are the molecular weight of hydrogen, oxygen and water, respectively, and α is the molar flux of water.

The transfer current densities in the above source terms are given by the Butler - Volmer equation (Eqs. (11-12)):

$$j_a = j_{0,a}^{ref}\left(\frac{c_{H_2}}{c_{H_2}^{ref}}\right)^{\gamma_a}\cdot\left[e^{\left(\frac{\alpha_a F}{RT}\eta_a\right)} - e^{\left(-\frac{\alpha_c F}{RT}\eta_a\right)}\right] \tag{11}$$

$$j_c = j_{0,c}^{ref}\left(\frac{c_{O_2}}{c_{O_2}^{ref}}\right)^{\gamma_c}\cdot\left[e^{\left(\frac{\alpha_a F}{RT}\eta_c\right)} - e^{\left(-\frac{\alpha_c F}{RT}\eta_c\right)}\right] \tag{12}$$

where c_i denotes the i^{th} reactant concentration, α_a and α_c are the transfer coefficients, η_a and η_c are the activation over-potential from the anode and the cathode, and $j_{0,a}^{ref}$ and $j_{0,c}^{ref}$ are the reference exchange current density from the anode and cathode.

The molar flux of water, α, is based on the electro-osmotic drag coefficient, n_d, water content, λ, and water activity, a. These parameters are given by the following expressions:

$$a = \frac{X_{H_2O}\,p}{p^{sat}} \tag{13}$$

$$\lambda = \begin{cases} 0.043 + 17.18a - 39.85a^2 + 36a^3, & a < 1 \\ 14 + 1.4(a-1) & a > 1 \end{cases} \tag{14}$$

$$\alpha = 2.5\frac{\lambda}{22} \tag{15}$$

$$\log_{10} P^{sat} = -2.1794 + 0.02953(T - 273.17) - 9.1837\cdot10^{-5}(T-237.17)^2 + 1.4454\cdot10^{-7}(T-237.17)^3 \tag{16}$$

The overpotential is the difference between the phase potential of the solid and the phase potential of the electrolyte/membrane and represents the driving force for an electrochemical reaction. The gain in electrical potential from crossing from the anode to the cathode side can be taken into account by subtracting the open-circuit voltage V_{oc} on the cathode side. The V_{oc} is an input into the Fluent PEM model.

$$\eta_a = \phi_{sol} - \phi_{mem} \tag{17}$$

$$\eta_c = \phi_{sol} - \phi_{mem} - V_{OC} \tag{18}$$

Therefore, two potential equations are solved in the Fluent PEM model: one potential equation accounts for the electron transport e^- through the

solid conductive materials (the current collectors and the solid grids of the porous media); the other potential equation represents the protonic transport of H^+. These potential equations are given by:

$$-\nabla\cdot(\sigma_{sol}\nabla\varphi_{sol})=S_{sol} \quad (19)$$

$$-\nabla\cdot(\sigma_{mem}\nabla\varphi_{mem})=S_{mem} \quad (20)$$

where σ is the electrical conductivity (1/ohm-m), ϕ is the electric potential (V), S is the volumetric transfer current (A/m^3).

$$S_{sol}=\begin{cases}-j_a & on\ the\ anode\ side\\ j_c & on\ the\ cathode\ side\end{cases} \quad (21)$$

$$S_{mem}=\begin{cases}j_a & on\ the\ anode\ side\\ -j_c & on\ the\ cathode\ side\end{cases} \quad (22)$$

The heat generated in a fuel cell may come from a number of mechanisms. Most of the heat comes from the exothermal chemical reactions, which combine the hydrogen with oxygen to form water, and the eletrochemical activation (kinetic) losses that split molecules into ions and electrons in the catalyst layer. In addition, the ohmic losses in the electronic conducting elements also produce a significant amount of heat, particularly when the cell is operating at a high current density. All these heat generation mechanisms are linked to the current density of the fuel cell in the operation. The overall heat generation due to the chemical reactions may be estimated by the change in the entropy ΔS, of the system and the current density [5].

The energy equation, which expresses all the above mentioned heat generation mechanisms, can be expressed as:

$$\nabla\cdot(\rho c_p \underline{v} T)=\nabla(k\nabla T)+S_T \quad (23)$$

where k is the conductivity, and S_T is the source term. The volumetric sources from the energy equation implemented in the Fluent PEM model include ohmic heating, heat of formation of water, electric work and latent heat of water, as follows:

$$S_T=S_{ohm}+S_{reaction}+S_{act} \quad (24)$$

$$S_{ohm}=\frac{i^2}{\sigma} \quad (25)$$

$$S_{reaction}=j\left(\sum\frac{T(-\Delta S)}{n_e F}\right) \quad (26)$$

$$S_{act}=j\eta \quad (27)$$

Most general CFD software packages have these equations and many numerical techniques (such as the control volume method or the finite element method) built in. For this paper, we have selected the Fluent software, that recently has developed a new tool for fuel cell analysis to include the electrochemistry. The Fuel Cell model from Fluent Inc. is directly coupled with the solutions for mass, momentum and energy, and account for the three primary loss mechanisms in fuel cell: ohmic overpotential, concentration overpotential, and electro-chemical overpotential.

4.2 Boundary conditions

All the numerical calculations are performed under the appropriately specified boundary conditions of the fuel cell under investigation so that the solution to the governing partial differential equations is uniquely determined.

Typical boundary conditions include flow rates of the fuel and oxidant (air/oxygen), operational pressure, current density or voltage of the fuel cell, plus the necessary thermal – physical properties of the materials of the cell.

At the inlet of both anode and cathode flow channels the boundary values are prescribed for mass flow rate, temperature and mass fraction.

Regarding the boundary conditions for outlets, since the reactant gas flow channels are separate and generally have different pressures, pressure boundary conditions are used.

The interface between the gas channels and current collectors is defined as a wall. This is implemented by creating a shadow of the wall cell layer, the walls being thermally coupled. The interface between the other layers are interior walls, so no boundary conditions are prescribed.

Dirichlet bounadary conditions with constant values are set for the solid phase potential on the lateral sides of the fuel cell and zero flux conditions are applied to the inlet and outlet front.

5. TEST CASE GEOMETRY AND PARAMETERS

The geometry of the fuel cell simulated in this work has two current collectors with serpentine channels for fluid flow separated by a membrane electrode assembly. The dimensions of the fuel cell are given in the table 1. A uniform grid was used in the computations, the mesh having 464,000 cells.

Table 1 Physical dimensions for the fuel cell

Parameter	Value	Unit
Cell width	11.05	*mm*
Channel length	15	*mm*
Channel height	1.5	*mm*
Channel width	2	*mm*
GDL thickness	0.37	*mm*
CL thickness	0.12	*mm*
Membrane thickness	0.07	*mm*

Table 2 provides the basic operating conditions used for the simulations and the inlet mass fractions.

Table 2 Operational parameters

Parameter	Value	Unit
Inlet temperature, anode/ cathode	353	*°K*
Pressure	1.5	*atm*
Anode mass flow inlet	10^{-7}	*kg/s*
Cathode mass flow inlet	10^{-6}	*kg/s*
H_2 mass fraction, anode	0.9	-
H_2O mass fraction, anode	0.1	-
O_2 mass fraction, cathode	0.25	-
H_2O mass fraction, cathode	0.22	-
N_2 mass fraction, cathode	0.53	-

6. RESULTS AND DISCUSSIONS

The focus of the numerical simulations performed in this paper is mainly on water management and its effect on fuel cell performance.

6.1 Velocity Profile

The velocity profile in the serpentine channel turn has a few distinctive characteristics. Far away from the turning region, the velocity exhibits a laminar fully developed profile where the highest velocity is located at the center of the channel. However, as the flow approaches the turning region, separation occurs and the symmetric velocity profile becomes asymmetric with the highest velocity closer to the inner wall. Further downstream from the turning region, the symmetric velocity profile becomes fully developed again and this profile is maintained until the next turning region of the channel.

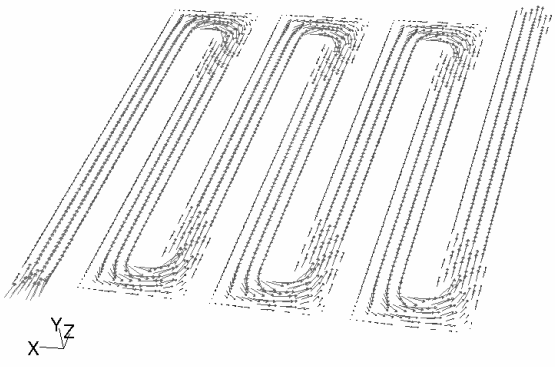

Figure 3. Vectorial velocity profile in the anode flow channel

6.2 Hydrogen Distribution

The hydrogen mass fraction distribution in the anode gas channel is shown in the figure 4. In general, the hydrogen concentration decreases from the inlet (mass fraction at inlet is 0.9) to outlet (mass fraction at outlet is 0.6) as it is consumed by the reaction that takes place inside the fuel cell.

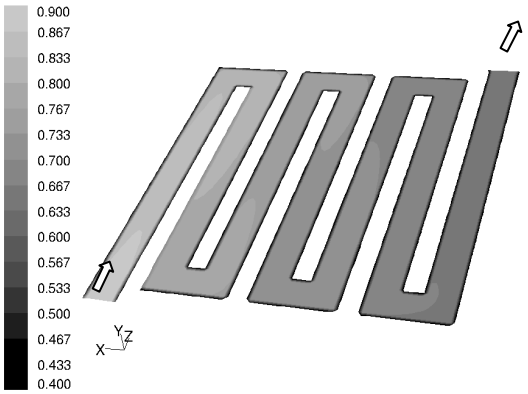

Figure 4. Hydrogen profile in the anode gas channel

6.3 Oxygen distribution

The transport limitation of oxygen has a large effect on the performance of PEM fuel cell. Therefore, it is important to understand the behaviour of oxygen transport in the cathode channel, see figure 5, which shows that the oxygen concentration decreasing gradually from inlet (0.25) to outlet (almost zero) due to the consumption of oxygen at the catalyst layer.

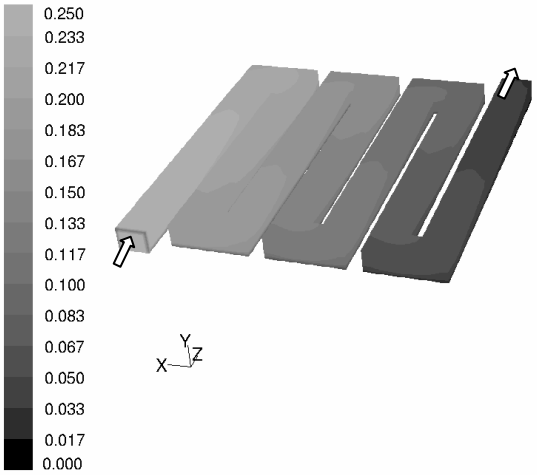

Figure 5. Oxygen distribution in the cathode gas channel

6.4 Water Distribution

The water mass fraction distribution in the anode and cathode gas channel is shown in Figure 6. In general, the water concentration increases from inlet to outlet, in the anode side the mass fraction of water increses from 0.1 to 0.3421, and in the cathode side from 0.22 to 0.477.

Figure 7 shows that the water distribution in the membrane has the same trend mention above, i.e. it increases from the inlet to the outlet.

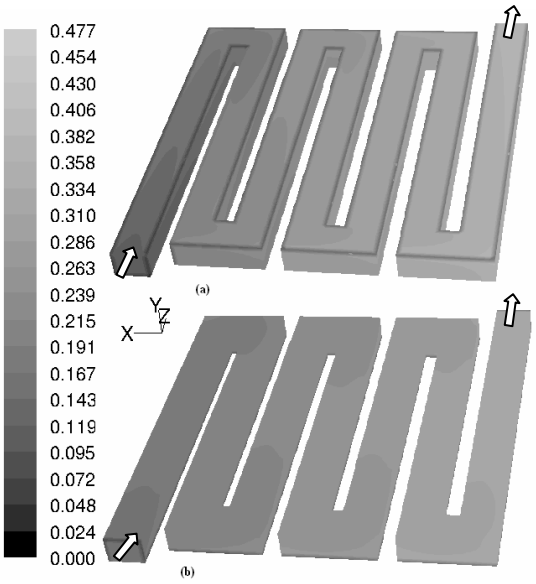

Figure 6. Water mass fraction distribution in (a) the anode gas channel and (b) the cathode gas channels

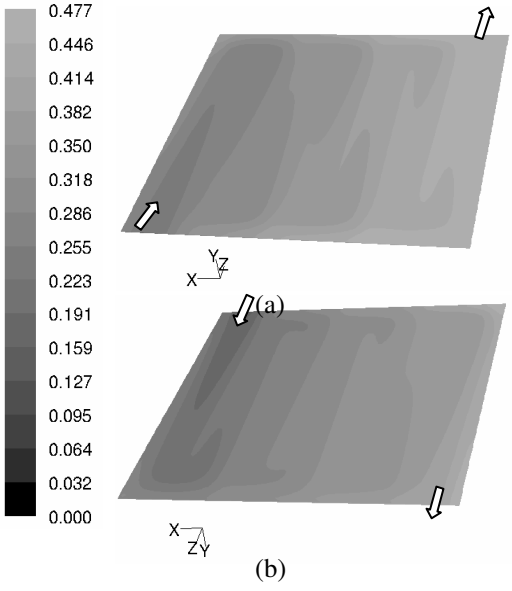

Figure 7. Water distribution in the membrane: (a) on the anode side, and (b) on the cathode side

The water content (λ) profile on the cathode side of the membrane for the base case choosen is shown in Figure 8. It is observed that from the inlet the water profile is established across the membrane and, from the simulation, we obtained a value for the water content at the anode side lower than that from the cathode. This is due to the electroosmotic drag of water, from the anode to the cathode, and insufficient backdiffusion from the cathode side (where water is produced) to the anode side.

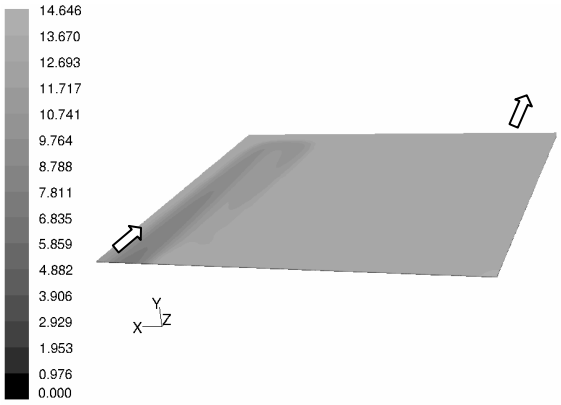

Figure 8. Water content profile in the membrane

6.5 Voltage distribution

The cell voltage value of 0.5 was chosen as a typical PEM fuel cell operation voltage and figure 9 shows the increase of voltage in the solid phase both for the current collector and the diffusion layer from the cathode side. The increase in the cell voltage is about 1%.

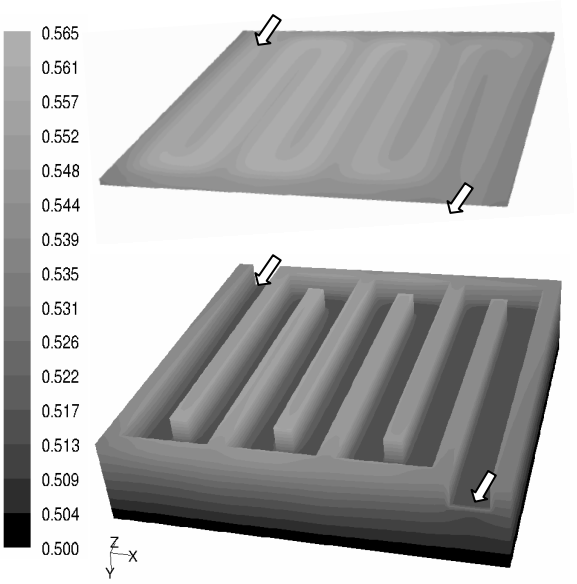

Figure 9. Voltage contours in the cathode diffusion layer (upper plan) and the cathode current collector (bottom geometry)

6.6 Temperature distribution

In order to calculate a temperature field in the fuel cell, a constant temperature (353°K) boundary

condition was imposed at both lateral walls of the anode and cathode current collectors. The computed distribution of temperature in the membrane, shown in figure 10, ilustrates an increase of almost 3°K from the inlet side to the outlet side of the membrane, which will only affect cell performance slightly. However, the temperature variation depends strongly on the thermal conductivities of the diffussion layer and current collector, as well as thermal boundary conditions.

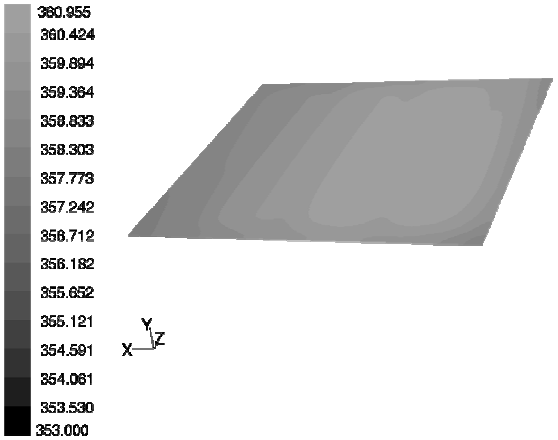

Figure 10. Temperature distribution in the membrane

7. CONCLUSIONS

The complexity of fuel cells requiers many interacting physico-chemical models in order for computational fluid dynamic models to be successful. Therefore, a fundamental understanding of the electrochemical and transport processes in fuel cells continues to be necessary.

A three-dimensional computational fluid dynamics model of a PEM fuel cell with serpentine flow channels was developed in this work. This model provides valuable information about the transport phenomena inside the fuel cell, especially for water transport, gas concentration distribution, temperature distribution and voltage distribution in the current collector and gas diffusion layer.

It is appreciated that the CFD modelling of fuel cell in general is still facing significant challenges due to the limited understanding of the complex physical and chemical processes existing within the fuel cell. However, with the further development of the modelling capabilities, the modelling of fuel cells using CFD techniques can be an important alternative to costly experiment measurements in providing information that is critical to the fuel cell design and optimization.

REFERENCES

[1] Carcadea, E., Ene, H., Ingham, D.B., Lazar, R., Ma. L., Pourkashanian, M., Stefanescu, I., „Numerical simulation of mass and charge transfer for a PEM fuel cell", International Communications in Heat and Mass Transfer 32 (2005), pp 1273-1280

[2] Fuller, T.F., Newman, J., „Water and thermal management in solid-polymer-electrolytefuel cells", Journal Electrochemical Society 140 (1993), pp.1218 –1225

[3] Nguyen, P.T., Berning, T., Djilali, N., „Computational model of a PEM fuel cell with serpentine gas flow channels, Journal of Power Sources 2004

[4] Bernadi, D.M., and Verbrugge, M.W., „ A mathematical model of the solid polymer electrolyte fuel cell", J Electrochemical Society 139(9), 1992

[5] Djilali, N., Lu, D., „Influence of heat transfer on gas and water transport in fuel cells", International Journal of Thermal Sciences, 41 (2002), pp. 29-40

Conference on Modelling Fluid Flow (CMFF'06)
The 13th International Conference on Fluid Flow Technologies
Budapest, Hungary, September 6-9, 2006

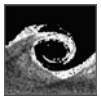

NUMERICAL STUDY OF THE AIR-FLOW IN AN OSCILLATING WATER COLUMN WAVE ENERGY CONVERTER

J. M. PAIXÃO CONDE[1], L. M. C. GATO[2]

[1] Corresponding Author. Department of Mechanical and Industrial Engineering, Faculdade de Ciências e Tecnologia, Universidade Nova de Lisboa. Monte de Caparica, 2829-516 Caparica, Portugal. Tel.: +351 212948300, Fax: +351 212948531, E-mail: jpc@fct.unl.pt
[2] Department of Mechanical Engineering, Instituto Superior Técnico, Technical University of Lisbon, Portugal, E-mail: lgato@mail.ist.utl.pt

ABSTRACT

The paper presents a numerical study of the air-flow in a typical pneumatic chamber geometry of an oscillating water column (OWC) type wave energy converter, equipped with a vertical-axis air turbine, asymmetrically placed on the top of the chamber. Outwards and inwards air-flow calculations were performed to investigate the flow distribution at the turbine inlet section, as well as the properties of the air jet impinging on the water free-surface. The numerical study was performed using the FLUENT code. Steady flow conditions were assumed in the calculations. Dependence studies were made for the grid, the interpolation scheme and the turbulence model, assuming the outwards flow conditions.

The original design of the OWC is likely to be harmful for the operation of the turbines due to the possible air-jet-produced water-spray at the water free-surface subsequently ingested by the turbine. A geometry modification of the air chamber was proposed and proved to be very effective in reducing the risk of water-spray production from the inwards flow. The flow distribution at the turbine inlet section for the outwards flow was found to be fairly uniform for both geometries, providing good inlet flow conditions for the turbines.

Keywords: CFD analysis, oscillating water column, wave energy

NOMENCLATURE

U, V	$[m\,s^{-1}]$	horizontal components of velocity (x and y axis)
W	$[m\,s^{-1}]$	vertical component of velocity
k	$[m^2 s^{-2}]$	turbulence kinetic energy
x, y	$[m]$	horizontal coordinates
y^+	[-]	dimensionless wall distance
z	$[m]$	vertical coordinate
ε	$[m^2 s^{-3}]$	dissipation rate
μ	$[kg\,m^{-1}s^{-1}]$	viscosity
ρ	$[kg\,m^{-3}]$	density

Subscripts and Superscripts

a	at the turbine duct axis
in	at the inlet section

1. INTRODUCTION

The potential for ocean wave energy utilization is capable of covering a large part of the European consumption of electricity if extensive use is made of the resource. Based on various energy-extracting methods, a wide variety of systems has been proposed but only a few full-sized prototypes have been built and deployed in open coastal waters and connected to the grid.

The oscillating water column (OWC) wave energy converter (WEC) comprises a partly submerged structure, open below the water surface, inside which air is trapped above the water free surface [1]. The oscillating motion of the internal free surface produced by the incident waves causes the air to flow through a turbine that drives an electric generator, Fig.1. Several shoreline OWC type WECs are now in operation [2]. Floating versions of the OWC WEC are to be installed offshore in arrays [3]. The energy conversion chain in an OWC includes: the wave-to-pneumatic conversion in the OWC chamber; the pneumatic-to-shaft conversion in the turbine; the electrical energy conversion [4, 5]. The air turbine is the most critical element of the energy conversion chain of an OWC. It is subject to much more demanding conditions than the turbines in any other application (the flow is random and highly variable over several time-scales).

A typical problem for the OWC system is the design of the air-chamber and the duct, between the water column free-surface (large cross-sectional area and low velocity) and the turbine entrance (small cross-sectional area and high velocity), which requires a sense of balance between safety and efficiency. The air passage should be designed to be as smooth and short as possible, avoiding

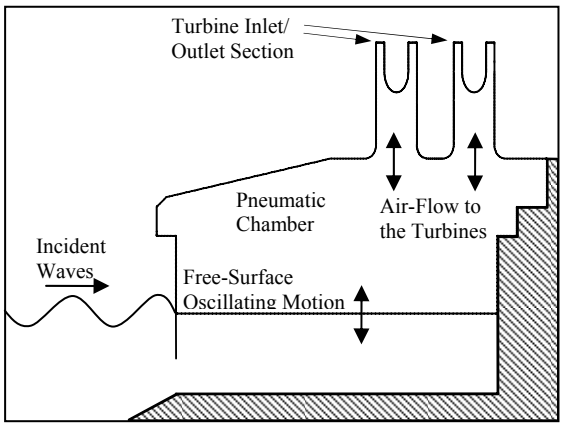

Figure 1. Operation of an OWC WEC equipped with two vertical-axis air turbines

sudden changes in the flow direction, to prevent poor distribution of the flow at the turbine inlet section, which would seriously reduce the turbine efficiency [6]. A straight connection between the air chamber and the turbine may also raise problems, due to the interaction of the inwards air jet with the water free-surface, which may produce water-spray that is swallowed by the turbine [7].

Numerical results obtained for a simplified two-dimensional geometry equipped with two vertical-axis air turbines show that the flow distributions at the turbines inlet sections are more uniform for periodical oscillating flow than for steady flow [8]. The flow rate unbalance between the two turbine-ducts in the simplified two-dimensional geometry is also smaller for oscillating flow than for steady flow. This suggests that steady state simulations instead of unsteady simulations can be performed for a generic three-dimensional geometry, aiming to investigate the flow distribution at the turbines inlet sections, as well as the properties of the inwards air jet impinging on the water free-surface.

The paper presents a numerical study of the air-flow in a typical OWC pneumatic chamber geometry equipped with two vertical-axis air turbines asymmetrically placed on the top of the chamber. Outwards and inwards air-flow calculations were performed to investigate the flow distribution at the turbine inlet section, as well as the properties of the air jet impinging on the water free-surface. The numerical study was made using the FLUENT code. Dependence studies were made for the grid, the interpolation scheme and the turbulence model. Steady flow conditions were assumed in the calculations.

2. THE ANALYZED DOMAIN

2.1. Geometry

The computational domain is presented in Figure 2. The OWC pneumatic chamber spans from: 2 *m* to 10 *m* in the *z*-direction; -1 *m* to 19.1 *m* in the *x*-direction; and -2.45 *m* to 9.2 *m* in the *y*-direction.

Two turbine ducts are asymmetrically located on the top of the chamber. The dimensions of these ducts are shown in Fig. 2d. The inlet sections of the two turbines coincide with the exit sections of these ducts, at coordinate $z = 15.985$ *m*. The axes of the turbines are at coordinates $y = -0.45$ *m*; $x = 11.35$ *m* (turbine 1) and $x = 15.35$ *m* (turbine 2).

2.2. Mesh

The grid generation was performed with the GAMBIT 2.2.30 code, a pre-processor for the FLUENT code. A bottom-up procedure (vertexes → edges → faces → volumes) was automated using the GAMBIT journal file [9].

Four levels of mesh refinement were considered (meshes: I, II, III and IV). Figures 2a and 2b represent the coarser grid (mesh I) for the external surface of the computational domain. The grid for the OWC chamber is divided in two regions: the lower part, from $z = 2$ *m* to 4 *m*, composed of regular, structured grid of hexahedral mesh elements, and the upper part, from $z = 4$ *m* to 10.9 *m*, composed of unstructured tetrahedral mesh elements.

The edges of the domain surfaces from $z = 2$ *m* to 10 *m* are divided into 0.3 *m*-long segments for the surface discretization of mesh I. The corresponding segments for mesh II are 0.2 *m* long. For meshes III and IV the edges division are equal to that of mesh II from $z = 2$ *m* to 6 *m*, and are equal to 0.17 *m* for mesh III, and 0.15 *m* for mesh IV, from $z = 6$ *m* to 10 *m*.

The external edges of the ducts are discretized with 40 segments evenly distributed angularly for mesh I, 60 for mesh II, 68 for mesh III and 80 for mesh IV. In the annular exit section ($z = 15.985$ *m*) the radial segment division is 8 for mesh I, 10 for mesh II, 12 for mesh III and 15 for mesh IV.

A boundary layer type mesh was applied to improve the quality of the solution. Figure 2c represents a detail of the mesh in the upper part of a duct where three layers of volumes can be seen in the external side and two layers in the internal side. The thickness of the first layer is equal to 0.04 *m* for mesh I, 0.03 *m* for mesh II, 0.025 *m* for mesh III and 0.02 *m* for mesh IV.

The total number of control volumes in these meshes is 301910 for mesh I, 919378 for mesh II, 1071622 for mesh III, and 1324910 for mesh IV.

3. CFD CODE DETAILS

The computations of the flow field were made using the FLUENT 6.2.16 code assuming steady flow conditions. This code applies a cell centred based finite volume technique to solve the governing equations. The linearized form of the discretized system of equations is solved using a point implicit Gauss-Seidel linear equation solver in conjunction with an algebraic multigrid method [10].

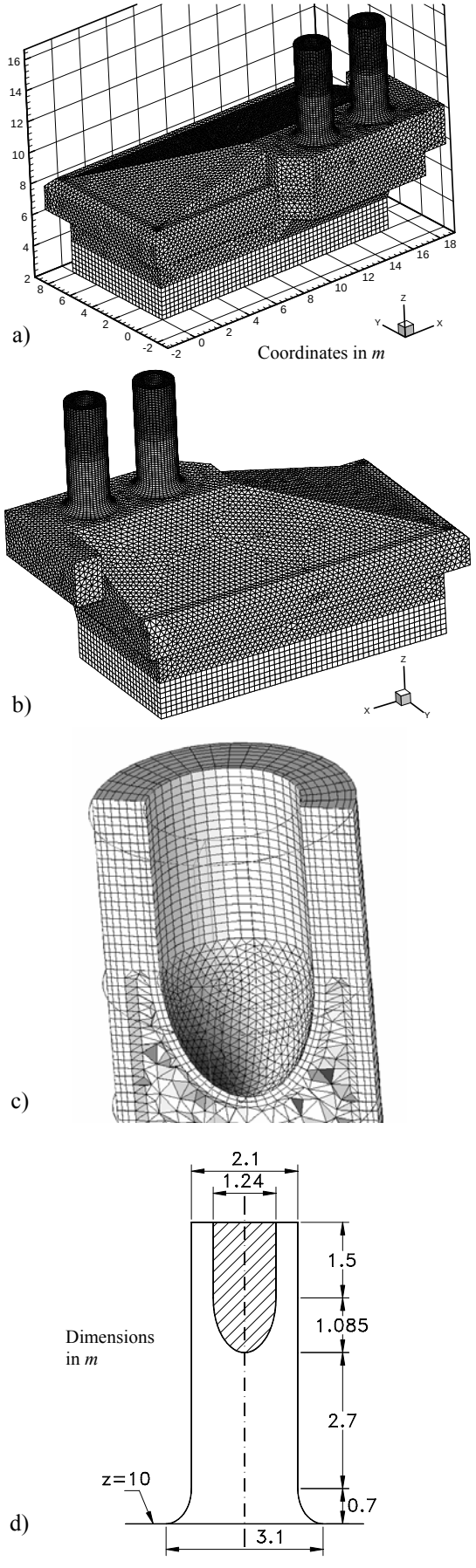

Figure 2. Geometry and discretization grid

The governing equations are the continuity and the Reynolds Averaged Navier-Stokes (RANS) equations. The turbulent stresses are modelled by the two-equation k-ε turbulence model. The solutions obtained with the Standard, the RNG and the Realizable k-ε turbulence models [10] were compared.

The diffusive terms of the governing equations are discretized by the 2nd order central difference scheme (CDS). For the convective terms the face values can be interpolated by the: 1st order upwind differencing scheme (UDS); 1st order power-law differencing scheme (PLDS); 2nd order or linear upwind differencing scheme (LUDS); 2nd order MUSCL differencing scheme; and 3rd order QUICK scheme. For the pressure-velocity coupling the SIMPLE algorithm was selected. The default under-relaxation factors were selected to stabilise the solution: 0.7 for momentum, 0.3 for pressure and 0.8 for k and ε.

The three-dimensional, single precision, implicit, segregated steady solver was selected. The solutions have been considered to be converged when all scaled residuals were less then 10^{-4}. The fluid was assumed to be air with constant properties: $\rho = 1.225\ kg\ m^{-3}$, $\mu = 1.789\ kg\ m^{-1}s^{-1}$.

3.1. Boundary conditions

Taking as reference numerical results for a $16\ m \times 9\ m$ (internal cross-section at free-surface level) breakwater-integrated OWC plant [11], the flow rate in each turbine duct was assumed to be $120\ m^3s^{-1}$, which gives a turbine flow rate coefficient $U^* = 2W_{in}/(\omega D) = 0.275$, for a $D = 2.1\ m$ outer diameter Wells turbine, rotating at $\omega = 1700$ r.p.m. (see [4-6]). The study was made considering two main directions for the flow: inwards and outwards.

The inlet section for the outwards flow simulation is the surface boundary $z = 2\ m$, which corresponds to the mean water free-surface. A velocity-inlet boundary condition with uniform distribution is imposed on this surface: $U_{in} = V_{in} = 0$; $W_{in} = 1.77\ m\,s^{-1}$; turbulence intensity equal to 5 % ($k_{in} = 0.012\ m^2s^{-2}$); and hydraulic diameter equal to $1\ m$ ($\varepsilon_{in} = 0.003\ m^2s^{-3}$). The outlet boundaries for the outwards flow simulation are the annular surfaces at $z = 15.985\ m$. The outflow boundary type conditions were imposed at both exits. These boundary conditions assume zero normal gradient for all flow variables except pressure. All remaining boundaries are treated as solid impermeable stationary walls, where the wall-law is applied.

The inlet sections for the inwards flow simulations are the annular surfaces at $z = 15.985\ m$. A velocity-inlet boundary condition with uniform distributions is imposed on these surfaces: $U_{in} = V_{in} = 0$; $W_{in} = -53.19\ m\,s^{-1}$; turbulence intensity equal to 5 % ($k_{in} = 10.61\ m^2s^{-2}$); and hydraulic

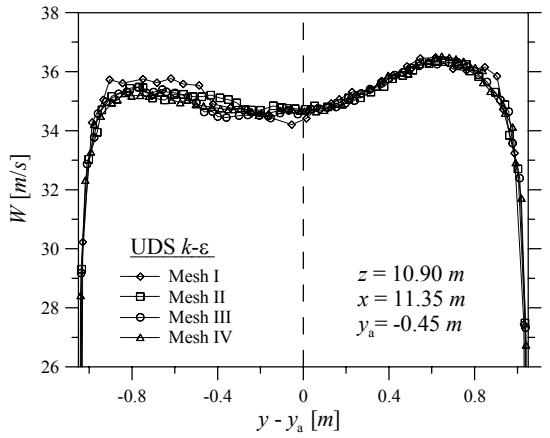

Figure 3. Grid dependence

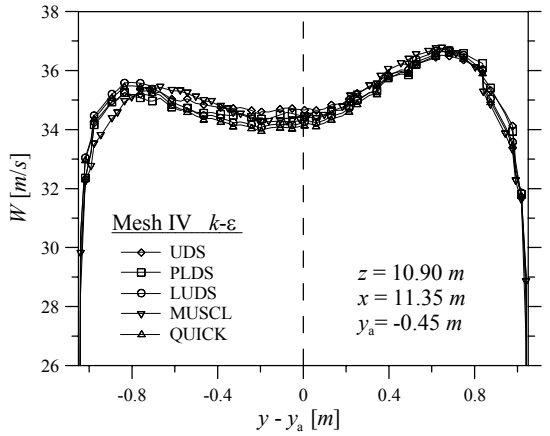

Figure 4. Interpolation scheme dependence

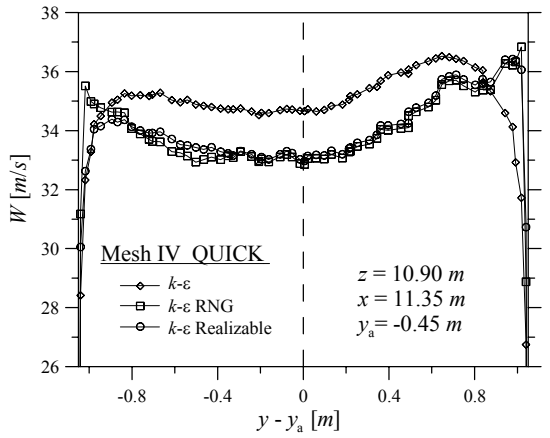

Figure 5. Turbulence model dependence

diameter equal to 0.86 *m* ($\varepsilon_{in} = 94.33\ m^2s^{-3}$). The outlet boundaries (outflow boundary type) are the two rectangular surfaces spanning from $z = 2\ m$ to $z = 4\ m$, one with $x = 0$ and the other with $y = 8\ m$.

All remaining boundaries are treated as solid impermeable stationary walls. This flow simulation was performed to evaluate the flow characteristics of the inwards air jet interaction with the water free-surface.

4. SOLUTION DEPENDENCE

A comparison of velocity distributions was made for the outwards flow simulation to assess how the solution depends on the mesh refinement, the interpolation scheme used and the turbulence model selected.

The *W* velocity component was selected and represented in the duct of turbine 1, at $z = 10.9\ m$ and $x = 11.35\ m$. At this cross-section there are 426 elements in mesh I, 868 elements in mesh II, 1090 elements in mesh III, and 1426 elements in mesh IV.

The results of the grid dependence study are presented in Figure 3. It can be seen that the quality levels of the solutions obtained with meshes II, III and IV are very similar, and that the solution obtained with mesh I is poorer.

The values of y^+ for these velocity distributions are: 1.9×10^3 for mesh I; 1.5×10^3 for mesh II; 1.3×10^3 for mesh III; and 10^3 for mesh IV. These values are larger than the upper bound of the interval of validity for the wall-law ($30 < y^+ < 300$). However, due to memory and computation time constraints it was not practical to limit the range of y^+ to the referred interval for the entire simulation domain.

The results from the interpolation scheme dependence study are presented in Figure 4. This study was made for five interpolation schemes using the more refined mesh and the standard k-ε turbulence model. The solutions obtained are very similar. The QUICK and LUDS schemes present a solution with less diffusion than the lower order schemes (UDS and PLDS), as would be expected. The MUSCL scheme presents a solution that is slightly apart from the others. This behaviour might be originated by the non-limited implementation of this scheme in the FLUENT code [10].

The results of the turbulence model dependence study are presented in Figure 5. The solutions obtained with the RNG and Realizable k-ε turbulence models are very similar and present about 5 % difference with respect to the Standard model. The residual of the RNG model solution was greater than that of the Realizable model. This may be due to the higher velocity gradient predicted near the wall with the RNG model. A more detailed comparison between the Standard and the Realizable models is presented in the next section.

5. RESULTS

5.1. Original geometry

Figures 6, 7 and 8 present a more detailed representation of the results of the outwards flow simulation described in section 3.1, comparing the solutions obtained with the Standard and the Realisable k-ε turbulence models, using the more refined mesh (mesh IV) and the QUICK interpolation scheme.

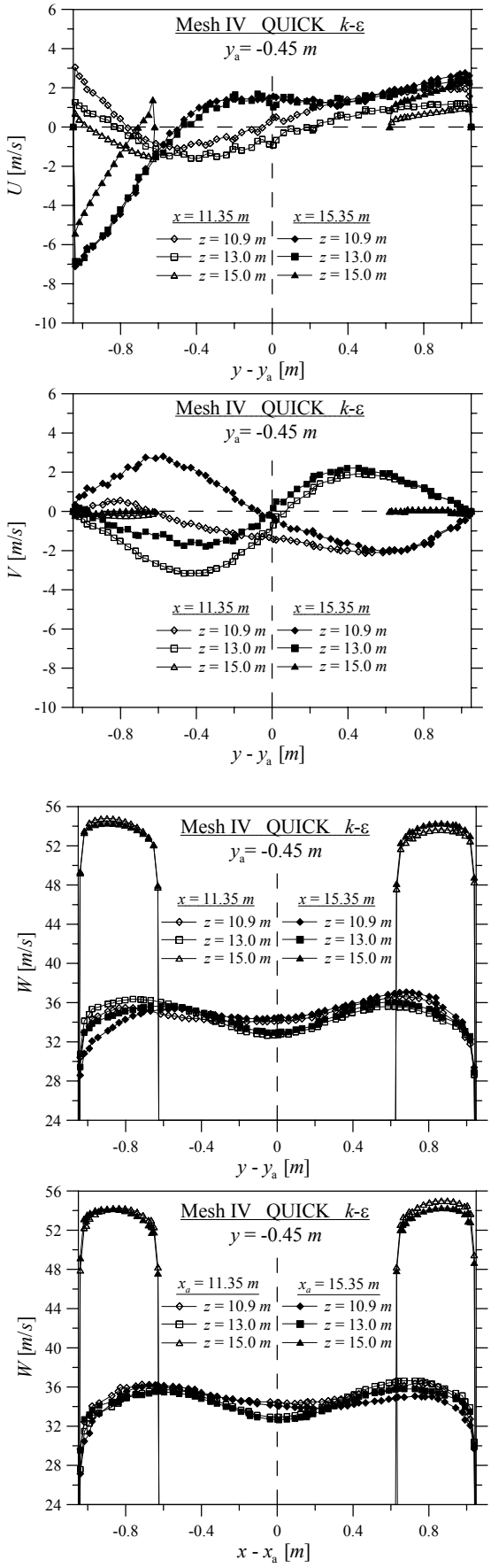

Figure 6. Velocity distribution in the turbine ducts

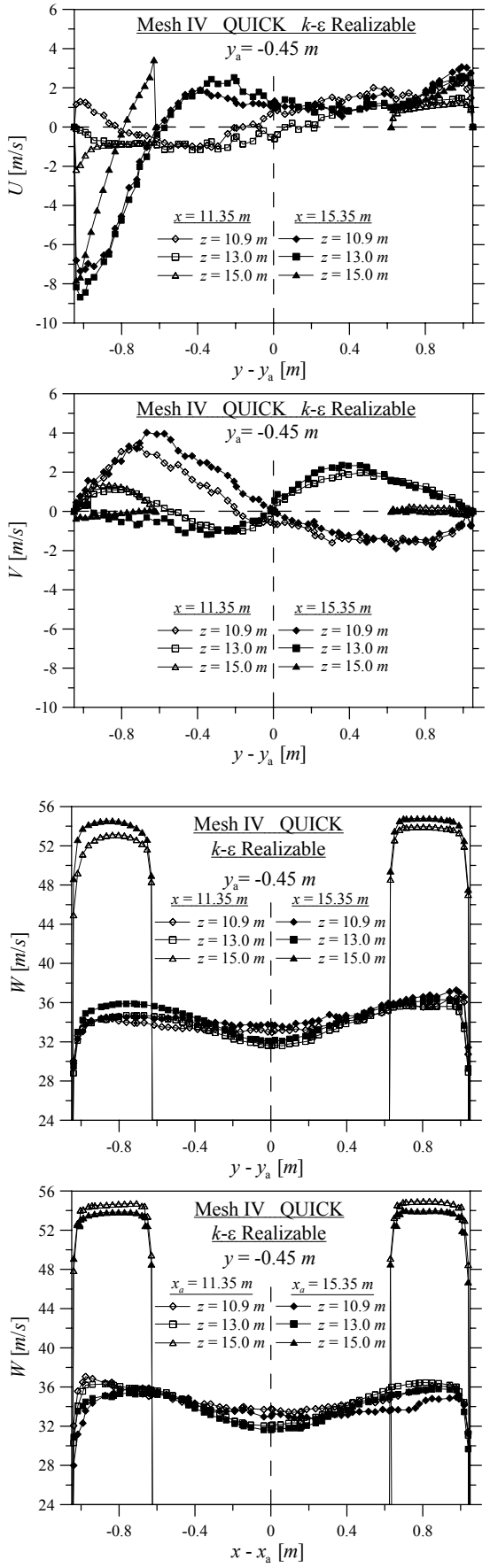

Figure 6. Cont.

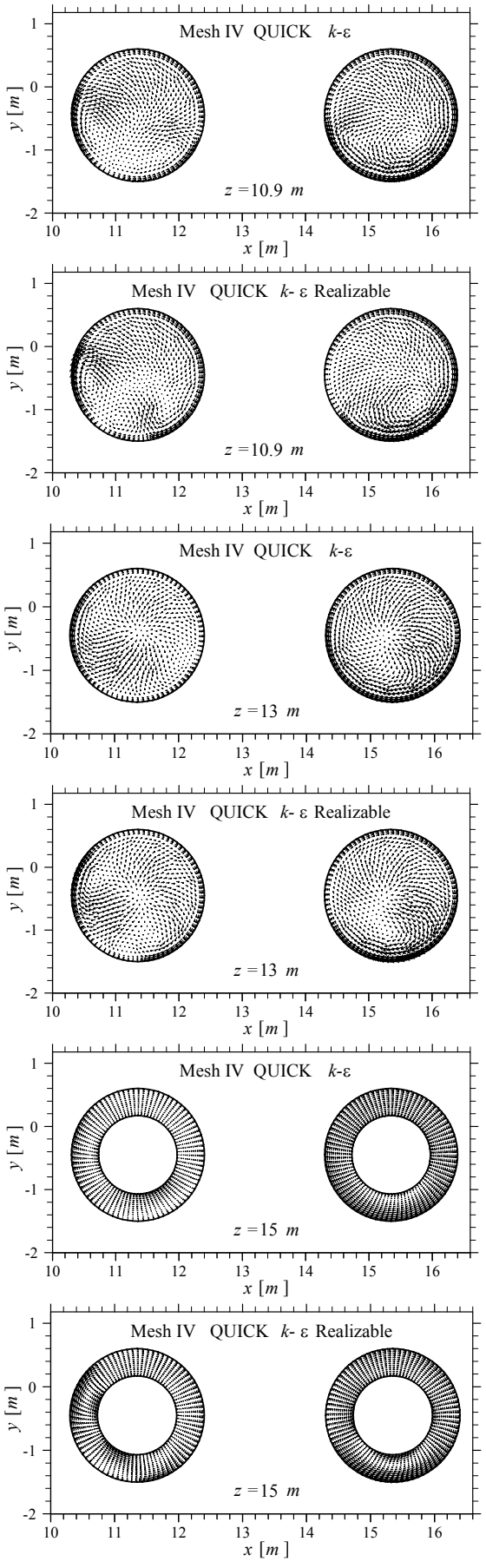

Figure 7. Flow field in the turbine ducts

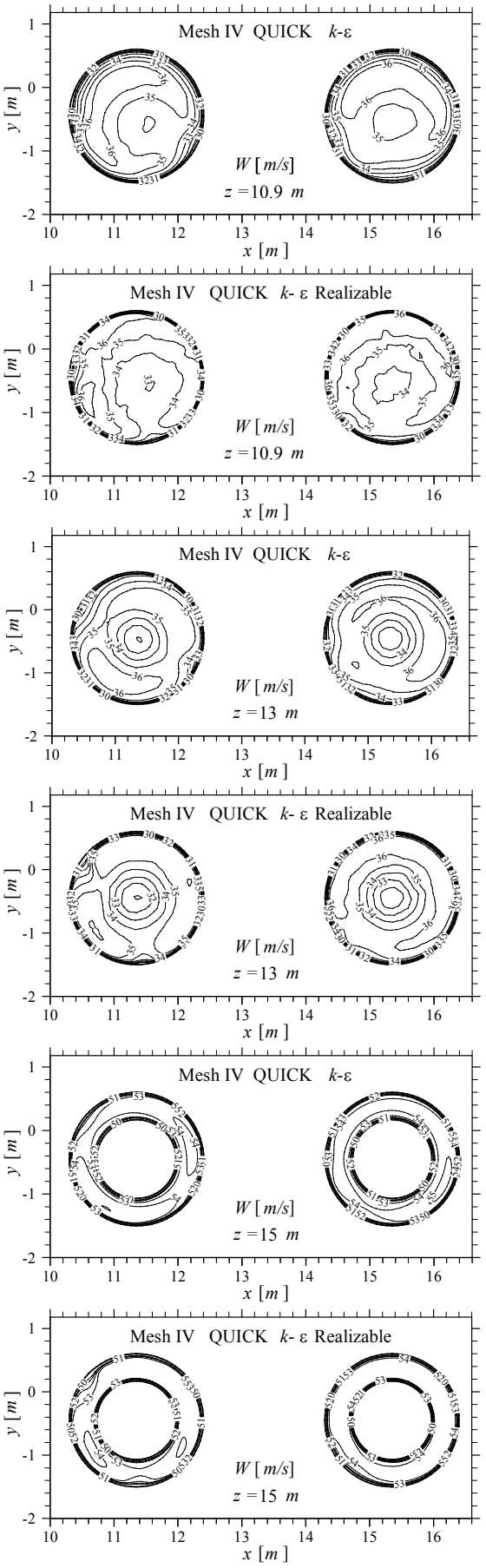

Figure 8. Iso-contours of *W* in the turbine ducts

The overall solutions from the two tested turbulence models are very similar although the Standard model presents lower gradients than the Realizable model near the walls.

The swirl of the flow in turbine 2 duct ($x_a = 15.35\ m$) is greater than the one in turbine 1 duct ($x_a = 11.35\ m$). This is due to turbine 2 duct being closer to the corner walls of the pneumatic chamber. The comparison of the U and V distributions with the W distribution allows us to conclude that the U and V values are, at the most, around 20 % of W, being in average about 5 %.

The W distributions are almost uniform in the three sections for which results are presented. The non-uniformity is around 6 % at the sections $z = 10.9\ m$ and $z = 13\ m$ and around 4 % for the section $z = 15\ m$.

These results indicate that the outwards flow is sufficiently uniform at $z = 15\ m$, providing good inlet flow conditions to the turbine.

Figure 9 presents the iso-contours of U in y-z planes for the inwards flow simulation described in section 3.1. For the prescribed flow conditions, it can be seen that the tangential velocities above the water free-surface can reach about $10\ m\,s^{-1}$. These high values of velocity may produce water-spray that will be swallowed by the turbine in the outwards flow part of the cycle. For this reason, the present configuration of the OWC chamber might be harmful for the turbine operation.

5.2. Modified geometry

A horizontal baffle-plate was introduced in the OWC chamber to prevent the water-spray production, as shown in Figure 10, in white, and in Figure 11, in black. This solid impermeable wall is a $2.1 \times 4\ m^2$ rectangle, with two semi-circular ends. The diameter of these semi-circles is equal to the turbine-duct diameter ($2.1\ m$). The baffle-plate is placed at $z = 7.5\ m$ with the semi-circle centres coincident with the turbine axes. The plate thickness was ignored in the simulations. Three layers of boundary layer type mesh were used on each side of the plate.

Results plotted in Fig. 10 for U at y-z planes show that the modified geometry is very effective for the inwards flow. The low velocities occurring at around $z = 2\ m$ are expected to inhibit the production of water-spray at the water free-surface.

However, a recirculation bubble is produced by the outwards flow on the top of the baffle-plate which may induce poor distribution of the flow in the turbine ducts. Results plotted in Fig. 11 for the iso-contours of W in x-y planes show that there is some disturbance to the uniformity of the flow in the lower part of the ducts. This flow disturbance is absent in the upper part of the ducts. This indicates that the adopted geometry solution is quite effective in reducing the water-spray production without otherwise affecting the operation of the turbines.

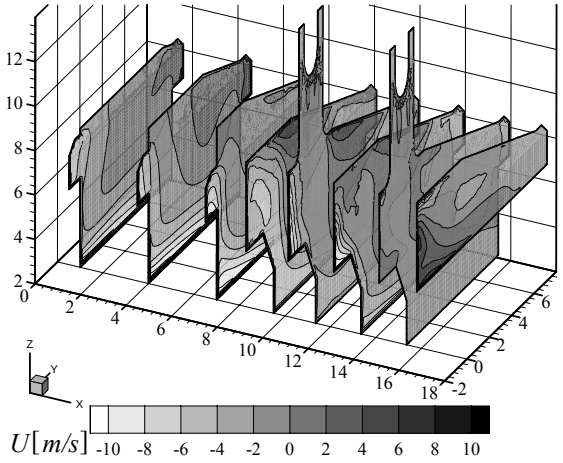

Figure 9. Inwards flow simulation for the original geometry: iso-contours of U in y-z planes

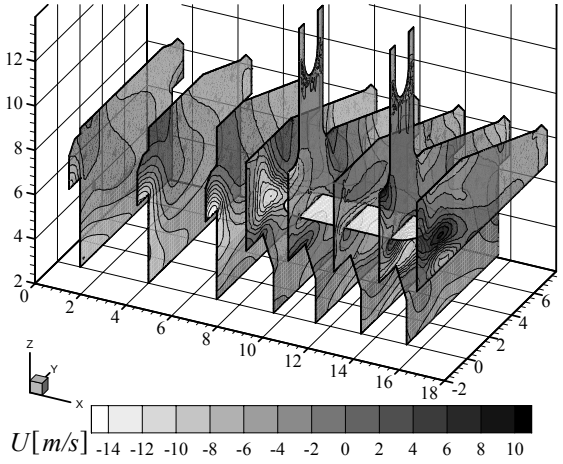

Figure 10. Inwards flow simulation for the modified geometry: iso-contours of U in y-z planes

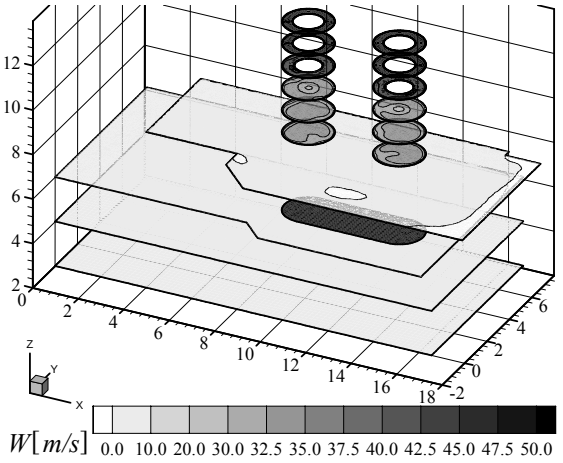

Figure 11. Outwards flow simulation for the modified geometry: iso-contours of W in x-y planes

6. CONCLUSIONS

A numerical study of the air-flow in the pneumatic chamber of an OWC WEC was made for the outwards and the inwards flow directions. Dependence studies were made for the grid, the interpolation scheme and the turbulence model, considering the outwards flow simulation conditions. Grid, turbulence model and interpolation scheme independent solutions could be obtained with relatively coarse grids. It was verified that the outwards flow distribution is sufficiently uniform at the turbine inlet section to provide good operational conditions for the turbines.

Results from the inwards flow simulation showed that high tangential velocities are likely to occur at the water free-surface level, which may originate the production of water-spray. For this reason the original OWC chamber configuration is expected to be harmful for the turbines operation.

The application of a horizontal baffle-plate underneath the turbine ducts proved to be very effective in reducing the water-spray formation by the inwards flow, at the water free-surface level. This new configuration does not disturb significantly the outwards flow in the turbines ducts, as shown by the predicted flow distribution at the inlet sections of turbines.

ACKNOWLEDGEMENTS

This work has been partially supported by Innovation Agency (AdI) and Portuguese Foundation for Science and Technology, with support from the European Regional Fund under POCTI Programme (Projects POCTI-IDEA 130203 FDR-01293 and POCTI/EME/59024/2004).

REFERENCES

[1] Falnes, J., 2002, *Ocean Waves and Oscillating Systems. Linear Interactions Including Wave-Energy Extraction*, Cambridge University Press.

[2] Clément, A., McCullen, P., Falcão, A. F. de O., Fiorentino, A., Gardner, F., Hammarlund, K., Lemonis, G., Lewis, T., Nielsen, K., Petroncini, S., Pontes, M. T., Schild, P., Sjöström, B- O., Sorensen, H. C., Thorpe, T., 2002, "Wave Energy in Europe: Current Statues and Perspectives", *Renewable and Sustainable Energy Reviews*, Vol. 6, pp. 405-431.

[3] Lewis, A.W., Gilbaud, T., and Holmes, B., 2003, "Modelling the Backward Bent Duct Device – B2D2 A Comparison between Physical and Numerical Models", Proc. *5th European Wave Energy Conference*, Cork, Ireland, pp. 54-58.

[4] Falcão, A. F. de O., Rodrigues, R. J. A., 2002, "Stochastic Modelling of OWC Wave Power Plant Performance", *Applied Ocean Research*, Vol. 24, pp. 59-71.

[5] Brito-Melo, A., Gato, L. M. C., and Sarmento, A. J. N. A., 2002, "Analysis of Wells Turbine Design Parameters by Numerical Simulation of the OWC Performance", *Ocean Engineering*, Vol. 29/12, pp. 1463-1477.

[6] Folley, M., Curran, R., and Whittaker, T., 2006, "Comparison of LIMPET Contra-Rotating Wells Turbine with Theoretical and Model Test Predictions", *Ocean Engineering*, Vol. 33, pp. 1056-1069.

[7] Martins, E., Ramos, F. S., Carrilho, L., Justino, P. A. P., Gato, L. M. C., Trigo, L., and Neumann, F., 2005, "CEODOURO Project: Overall Design of an OWC in the New Oporto Breakwater", Proc. *6th European Wave and Tidal Energy Conference*, Glasgow, U.K..

[8] Conde, J. M. P., Didier, E., Gato, L. M. C., 2006, "Numerical Simulation of Periodic Flows: Pneumatic Chamber of an OWC Wave Energy Converter", in Portuguese, Proc. *Conferência Nacional de Métodos Numéricos em Mecânica dos Fluidos e Termodinâmica*, FCT-UNL, Monte da Caparica, Portugal.

[9] Fluent Incorporated, 2004, *GAMBIT 2.2 Modelling Guide*.

[10]Fluent Incorporated, 2005, *FLUENT 6.2 User's Guide*.

[11] Gato, L. M. C., Justino, P. A. P. Falcão, A. F. de O., 2005, "Optimization of Power Take-off Equipment for an Oscillating Water Column Wave Energy Plant", Proc. *6th European Wave and Tidal Energy Conference*, Glasgow, U.K..

Conference on Modelling Fluid Flow (CMFF'06)
The 13th International Conference on Fluid Flow Technologies
Budapest, Hungary, September 6-9, 2006

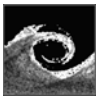

CFD ANALYSIS OF MIXING PROCESS IN SEWAGE SLUDGE REACTOR TANKS

Gergely KRISTÓF[1], Ákos CSÉCS[2]

[1] Department of Fluid Mechanics, Budapest University of Technology and Economics. Bertalan Lajos u. 4 – 6, H-1111 Budapest, Hungary. Tel.: +36 1 463 4073, Fax: +36 1 463 3464, E-mail: kristof@ara.bme.hu
[2] Corresponding Author. Department of Fluid Mechanics, Budapest University of Technology and Economics. E-mail: csecs@ara.bme.hu

ABSTRACT

Mixing process in wastewater sludge reactors have been analyzed with the application of CFD simulation technique. As a first step of the investigation, flow field induced by the mixing agitators was determined by using sliding mesh approach and URANS simulation. From the resulting flow field, long term mixing and sludge quality fluctuation caused by periodic operation of the reactor feeder, have been computed. It was necessary to develop a simplified model of the biochemical reaction and two-phase flow for obtaining proper definition of mixing quality. Fluid viscosity was determined by on-site measurements. In view of computed flow field and mixing process data proposals could be developed for the structural modifications of the reactors and agitator systems for both improving reactor efficiency and elimination operation problems.

Keywords: CFD, stirred vessel, URANS, wastewater sludge reactor

NOMENCLATURE

ρ	$[kg/m^3]$	density of the sludge
τ	$[s]$	time constant
t	$[s]$	residence time
c	[-]	concentration of secondary phase
N	$[1/s]$	rotational velocity of the impellers
μ	$[kg/ms]$	viscosity of the sludge
S	$[kg/m^3s]$	source term of the secondary phase
y^+	[-]	wall boundary layer distance
D/T	[-]	ratio of impeller and vessel diam.
h/H	[-]	ratio of impeller and vessel height
N_p	[-]	Power number
N_Q	[-]	Flow number
D_m	$[m^2/s]$	Molecular diffusivity
σ_t	[-]	Turbulent Schmidt number
μ_t	$[kg/ms]$	Turbulent viscosity
TKE	$[m^2/s^2]$	turbulent kinetic energy
TDR	$[m^2/s^3]$	turbulent dissipation rate
SM		sliding mesh
RANS		Reynolds-averaged Navier-Stokes modelling approach
URANS		unsteady RANS
CFD		computational fluid dynamics
LES		large eddy simulation

1. INTRODUCTION

The aim of the investigation was to ensure reliable long-term operation of the new thermofil reactors of the Capital Canalization Plant in South-Budapest. The mixing reactor was emptied for service work after 6 months of operation, so further information about the operation experiences and the geometry of the impeller could be collected which is not possible during normal operation. In order to suggest modifications of operation and structure of the reactor CFD results had to be produced at a short date. In order to reach the goal, following points were defined:

1. Determination of the flow field of the reactors by numerical simulation.
2. Characterization of the effectiveness of the mixing.
3. Suggestion of improvements based on results.

2. GEOMETRY AND NUMERICAL MODEL

The thermofil vessel is cylindrical and has a conical shaped bottom (see Fig. 1). Its diameter is D=12.5 m and the liquid level is at H=19.2 m. The volume is 2000 m^3. It has three narrow-foiled impellers, attached on one common top-entry shaft. The upper impeller has two blades, the lower two have three blades, with diameters from 2.25 m to 2.9 m. The D/T ratios and the h/H ratios from the bottom are shown in Table 1.

Three different CFD models were applied. The first was a sliding mesh (SM) approach with realistic modelling of the impellers, in the two other cases the impellers were substituted by a pressure jump (fan) boundary condition. In the second case a steady flow field had been calculated (steady RANS). In the third case an unsteady flow field has been calculated (unsteady RANS) in the simplified model.

Table 1. Geometry of the impellers

	D/T ratios	*h/H* ratios
Upper impeller	0.176	0.958
Central impeller	0.232	0.688
Lower impeller	0.232	0.344

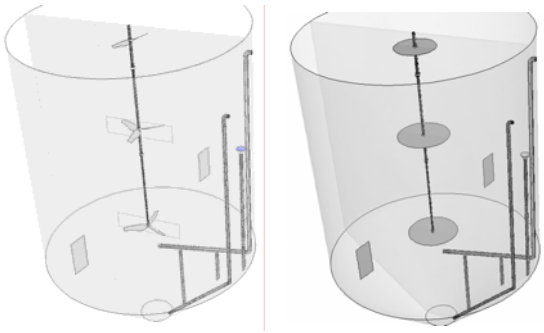

Figure 1. Geometry of the SM and simplified model

The first modelling challenge was the identification of impeller geometry since it was not made available by the manufacturer (see Figure 2). Digital camera pictures taken during the construction of the vessel had to be used instead of the exact geometrical model. After the recognition of some important features such as the blade profile being cylindrical and the leading-edge tangents being perpendicular to the rotational axis direction it was possible reduce the problem to manageable number of unknown parameters.

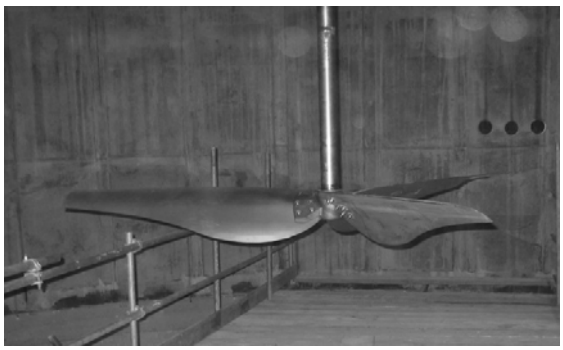

Figure 2. Photo of the lower narrow foiled impeller

Two baffle plates (height 2m, width: 1m) are attached at the height of the lowest impeller. The mixed inlet of the fresh and the recirculated (heated) mud is below the lowest impeller, given by a horizontal oriented pipe. The main outlet is at the bottom of the cone. The outlet for the recirculation is appr. at the height of the central impeller.

During operation the heater recirculation circuit works continuously. Its flow rate (33 *l/s* at a head of 6.3 *m*) was determined based on the hydraulics of the recirculation system and the characteristic curve of the pump, see Fig. 3. The fresh sludge is mixed into the pipeline of recirculation system. The mixed inlet and the main outlet are switched on and off simultaneously at cycles of eight hours.

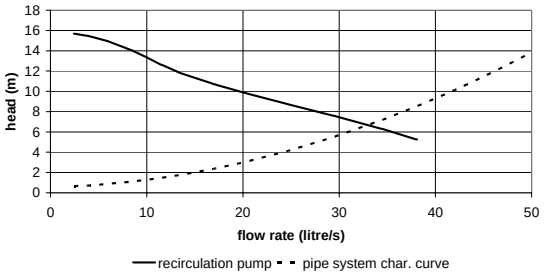

Figure 3. Characteristic curve of the recirculation pump

In order to have a reasonable resolution and computation time for a long-term model time of 10 days, application of pressure jump boundary condition with additional rotational and radial velocity parameters for the impellers were considered. To receive these parameters, a short 8 minute simulation with fully modelled impeller blades with sliding mesh approach was applied. The amount of cells (tetrahedral) in case of fully modelled impeller was 820000, in the simplified model 680000, see Fig. 4. Cell skewness, aspect ratio and expansion ratio were overall reasonable low due to mesh size functions around critical regions. A mesh was used with a resolution at least that of examples found in literature mentioned later. At least 50% more nodes are recommended in each direction for a step in a Richardson extrapolation [1]. This results in 3.4-times more cells and 2/3 of the time step, meaning 5 times of the calculation time, which was not available. The Courant number was below 1 in almost the entire domain. The speed of rotation of the impeller was 0.23 *1/s*.

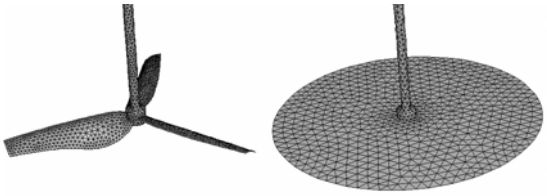

Figure 4. Mesh quality of the impellers

The density of the mud was almost equal to water. Viscosity was measured on-site by a purpose developed capillary measurement device. Sludge viscosity has been found to be changing depending on the altitude of decant level. Simply giving a constant viscosity value does not represent an adequate model for the mud. Although the flocs represent only 3-4 mass percent in the water, they are continuously in contact and have a special phase-separation process. Differences in viscosity were observed at the three decant levels in the thermofil reactor indicating an undesired separation of the phases, see Table 2.

Table 2. Viscosity differences at different heights

Tapping point height *h/H*	Viscosity (*kg/ms*)
0.378	$5.7 \cdot 10^{-3}$
0.69	$4.5 \cdot 10^{-3}$
0.969	$4.8 \cdot 10^{-3}$

Since there was no possibility for measurement to have a more detailed distribution of viscosity values, for simplification the average value was set to $5 \cdot 10^{-3}$ kg/ms.

Further investigation is necessary to introduce a model of wastewater mud of different quality for practical use. In [2] the laminar flow in a pipe was based on a Bingham-plastic fluid. The head loss and velocity profiles are in good agreement with analytical results and measurement data, but for stirring purposes no validation was found. In engineering practice local shear-rate or velocity-gradient dependent viscosity can be observed – further viscosity measurement will be conducted to give proof. In [3] a pseudoplastic solution was already applied, defining and average apparent viscosity calculated through the Metzner-Otto method, where the shear rate's influence is based indirectly by the rpm of the impeller.

The Reynolds-number of the two lower impellers was:

$$\mathrm{Re} = \frac{\rho N D^2}{\mu} = 133400 \qquad (1)$$

The operational flow parameters of the impellers lied between: $N_p = 0.15 - 0.31$, $N_q = 0.48 - 0.54$.

For turbulence modelling the realizable k-ε approach of the commercial application FLUENT 6.2 was applied for each case. The under-relaxation parameters were set for pressure 0.3, momentum 0.7, TKE 0.8 and TDR 0.8. The realizable k-ε constants were $C_{2\varepsilon}$ =1.9, TKE Prandtl number 1, TDR Prandtl number 1.2 and turbulent Schmidt number 0.7. Secondary upwind schemes were used.

The URANS k-ε approaches usually underestimate the turbulence values and deficient tangential velocity profiles can develop, observed e.g. in [4] for a Rushton turbine for a SM standard k-ε. Although the axial velocity profiles had a good agreement with measurements results. In [5] a pitched blade turbine was investigated having similar experiences and having a good agreement of the flow number between measurements and simulation with SM approach with k-ε modelling and higher upwinding. Zonal modelling was applied with partially good validation results by [6] for different propellers and pitched blade turbines.

Similar shaped narrow foiled impeller like the recent impeller was validated by [7] in a SM approach. Exactly the same shape was not investigated, but the axial and radial velocity had a qualitative agreement with measurement results. The tangential velocity and TKE profiles had the same order of magnitude, giving adequate average values for the cross section.

The first simulation for defining the flow characteristics of the impellers took 9 cpu-weeks with a time step of 0.02 *s* and with three 2.2 *GHz* Athlon64 cpu's with >90% parallelization efficiency. The time step was defined by the mesh size and velocity at the interface of the SM. This resulted in an 8 *min* modelling time. The simplified model needed 4 days for the steady flow field and 2 weeks for the URANS simulation with 2 *s* time steps resulting in 2 hours modelling time. This model was applied for verification of the stability of the flow pattern of the steady model.

A LES approach had been taken into consideration for the first model, but URANS approach requires less computation capacity and lower mesh resolution. Realistic results were expected since the length scale and time scale of the macroscopic unsteady phenomena were orders of magnitudes longer than the turbulence in the free jets and wall boundary layers. In the future a LES approach will be considered for the estimation of a more realistic flow field estimation for the first part of the modelling in order to get better results for TKE and TDR. [8] had very good validation agreement of velocity and turbulence values for a Rushton turbine, [9] modelled mixing behaviour in a similar stirred vessel, where mixing time was in good correlation with measurement data. In [10] macro-instabilities were predicted successfully in a vessel with a pitch-bladed turbine.

The steady flow field and the unsteady simulation of the thermofil reactor were used to prove the hydraulic mixing ability. A species model was used to model a solved material with same properties as the primary phase and no own momentum equation. A source term in the conservation equation (2) of convection-diffusion ensured linear increase of the concentration depending on time, where τ time constant is related to the average residence time in the vessel, see eq. (3). An Euler approach to residence time could be displayed taking the inverse of the time-integrated equation of the concentration source term, see eq. (4). This approach is similar to the case in [11].

$$\frac{\partial}{\partial t}(\rho c)+\nabla\cdot(\rho \underline{v} c)+\nabla\cdot\left[-\left(\rho D_m+\frac{\mu_t}{\sigma_t}\right)\nabla c\right]=S \qquad (2)$$

$$\text{where: } S=\rho\frac{1}{\tau} \qquad (3)$$

$$c=\frac{t}{\tau} \quad \rightarrow \quad t=c\,\tau \qquad (4)$$

Since chemical/biochemical reactions are extremely complicated and depend on the actual input composition, they can be implemented based on empirical correlations observed in test-reactor experiments.

3. RESULTS

The 8 min simulation time was enough to develop the final structure of the flow around the lower two impellers and to mix the entire reactor half-way through. In the practice ca. 15-20 minutes were necessary for starting of the circulation in the whole vessel.

The fully modelled impellers of the thermofil reactor resulted in the expected cylinder-shaped free-jets, which is characteristic to this type of narrow-foiled impellers of the manufacturer.

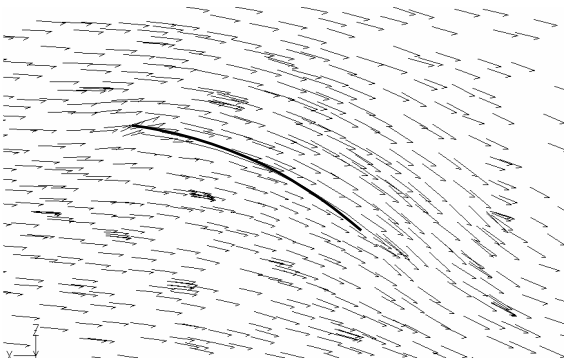

Figure 5. Relative velocity vector distribution at the impeller

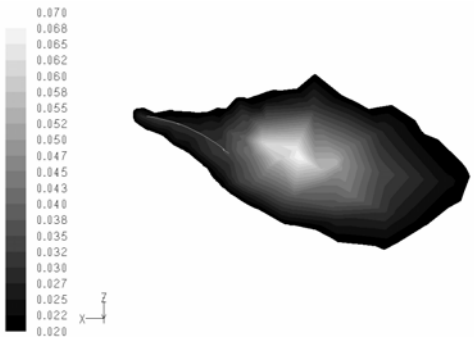

Figure 6. Turbulent kinetic energy at the impeller [m^2/s^2]

The relative flow velocity vectors of the lower impeller are displayed at the impeller radius of 1.3 *m* in Figure 5. It shows a smooth near-laminar flow around the blade. The average y^+ values were between 60 and 140. Figure 6 shows the TKE, which is one of the sources of mixing. Similar flow fields were observed at inner radiuses.

The starting procedure of the mixer from resting of the whole fluid zone until upper free-jets reaching the lower impeller represents a complete flow curve at given rpm. The pumping cross-section was defined directly below the impellers to calculate the flow rate. The axial force on the impeller was projected to this surface to get the pressure value. The lower two impellers gave similar results for the flow curve despite of different operating conditions. The lower impeller was at the end already reaching its asymptotic operation state: it was blown through by the central impeller and it developed the quasi-steady flow field in the cone. The total flow rate produced by three consequential impellers was within 10% error bound to the nominal value calculated by the manufacturer (7.715 m^3/sec).

The upper impeller could give only approximated parameters; this was mainly caused by unfavourable inflow.

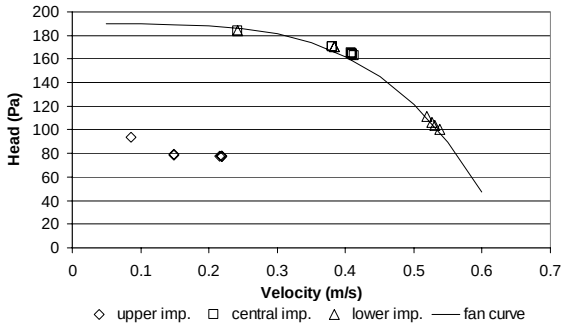

Figure 7. Estimated flow curve of the lower and central impeller

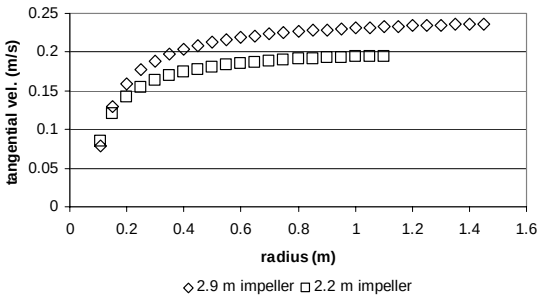

Figure 8. Average tangential velocity of the impellers

These flow curves and the extracted tangential velocity profiles below the impellers were applied for the simplified model boundary condition. This approximation resulted in some percentages

decrease in the total flow rate produced by the mixer. In the simplified case definitely the upper impeller caused the lower flow rate (see Table 4).

Table 4. Flow rate of the impellers

Impellers	Sliding mesh model (m^3/sec)	Simplified model (m^3/sec)
Upper	0.85	0.66
Central	2.7	2.6
Lower	3.5	3.4
Total	7.05	6.66

Despite of good average results the detailed comparison showed significant differences leaving headroom for further development.

On one hand TKE due to shear layers produced by the impeller blades was not represented in the simplified model. Furthermore in the stationary model the mixing effect of large eddies and pulsating flow induced by individual impeller blades were not represented. On the other hand the fan boundary conditions produced TKE due to high tangential velocity gradients, especially at the edge of the cross-section. This effect can be seen on Fig. 9 – the asymmetry is due to the influence of the asymmetric inflow from the upper impeller.

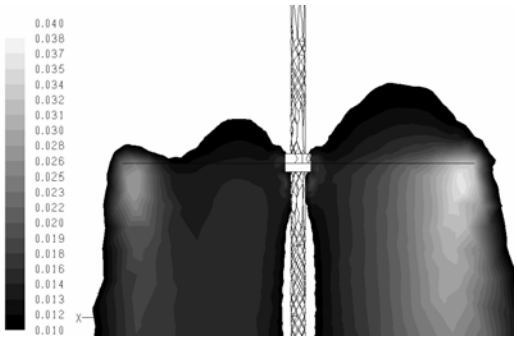

Figure 9. Distribution of TKE in the axial plane of the central impeller of the simplified model

Fig. 10. and Fig. 11. shows the average TKE on the 2.9 *m* diameter areas below the impeller. The SM impeller produced significantly lower values, despite of the upper impeller free jet already reached the central impeller and the inflow TKE was for the SM model 0.0045 m^2/s^2 and for simplified 0.0063 m^2/s^2. The effect of the improved operation – which will be described later – was that much higher initial TKE reached the central impeller.

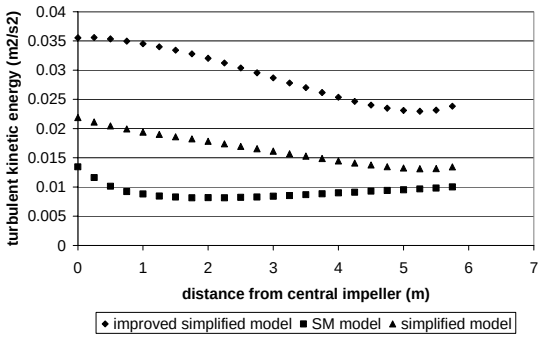

Figure 10. Average TKE on the area of the cross-section of the impeller

The tendencies of TDR were similar in all three cases. The SM and the simplified model were almost the same; only near to the SM impeller a high TDR was observed.

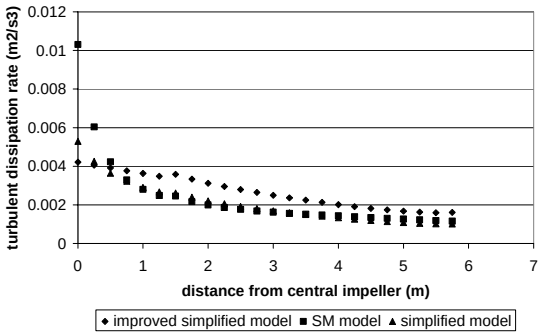

Figure 11. Average TDR on the area of the cross-section of the impeller

The flow field and pressure distribution of the three different modelling approaches of the thermofil reactor around the impellers and in the lower half of the domain were very similar to each other. These allowed assuming an adequate modelling of the flow field by the simplified model in the steady case and in the unsteady case; see Fig. 12-15 for the SM and the steady RANS approaches. The y^+ average value on the walls were 250 ranging mainly from 30 to 750 in the SM case, and in the simplified case the average was around 200 with a range from 30 to 600.

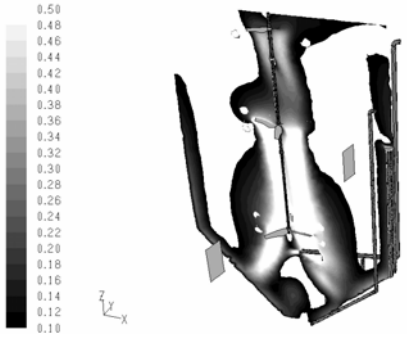

Figure 12. Absolute velocity distribution in the SM model [*m/s*]

Figure 13. Absolute velocity distribution in the simplified steady model [*m/s*]

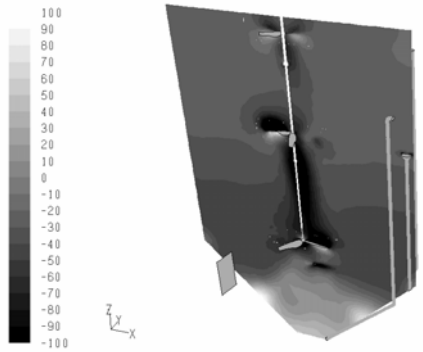

Figure 14. Static pressure distribution in the SM model [*Pa*]

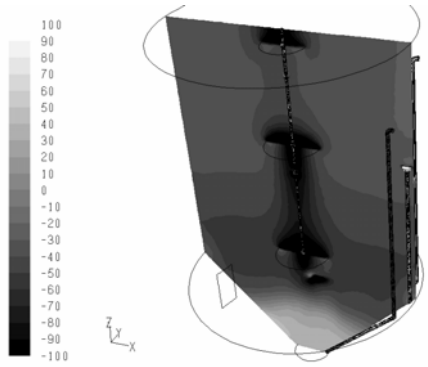

Figure 15. Static pressure distribution in the simplified steady model [*Pa*]

Detailed analyse of the flow field showed that the thermofil mixer was not able to generate intense flow in the bottom of a conical vessel. In design guidelines it is usually not allowed to put the impellers too close to the bottom due to danger of radial overload of the shaft. Therefore other operational parameters had to be changed to solve the problem.

The upward flow along the upper half of the cone walls and the lower third of the cylindrical wall had a value of at least 0.3 *m/s*, satisfying the design requirements for upward moving of settling flocs.

Both the steady and the unsteady simulation in the simplified model showed an unfavourable flow pattern in the upper third of the vessel. The circulation was done mainly through the central and the lower impeller. The upper impeller caused a swirling flow with mainly horizontal path lines (see Fig. 16).

As a consequence the geometry had to be modified. Two additional baffles were introduced at the height of the upper impeller. The upper impeller was replaced by one with higher flow rate. Furthermore it was positioned lower to have a better inflow. As a conclusion the flow field changed dramatically, showing a total circulation of the fluid domain (see Fig. 17).

Figure 16. Path lines in the simplified stationary model

Figure 17. Path lines in the improved simplified stationary model

The flow rates of the impellers increased respectively to 2.34, 3 and 3.2 m^3/s from top to bottom, altogether 8.54 m^3/s. A slight rotation on the top remained which is necessary to avoid developing of agglomerated foam. Otherwise in the engineering practice on long term a carpet was built blocking the ascending biogas.

The efficiency of the reactor can be defined in this case for example by calculating the ratio of theoretical methane production and effective methane production. The theoretical production is achieved by maximum possible biodegradation of organic material to methane, for example in a tubular reactor or in a batch reactor. According to the experience of full-scale running the reactor produced only about 2/3 of the expected efficiency.

Interestingly, the result of the hydraulic mixing calculations in the stationary and URANS case was that related to the defined average residence time of 10 days the mixing was completely done even in the unfavourable flow field. The residence time was homogenous in the whole fluid domain.

The conclusion was that the upper swirling zone had presumably been less participating in the biodegradation process. Evidence of this indirect conclusion will be given after further operation of the modified reactor.

Originally the final outlet of the sludge was at the bottom of the cone and the inlet of the fresh sludge directly below the lower impeller (horizontal pipe on Fig. 1.). It was a suspected that this caused a short circuit, reducing the efficiency of the reactor.

Due to pre-mixing in the inlet pipe and adequate mixing in the free-jet of the impeller maximal 1% percent of the fresh mud quits directly through the outlet, so the effect of hydraulic short-circuit was negligible.

Another issue was the clogging of the outlet at the bottom of the cone due to the dead zone and periodic operation. The logical consequence was that the heating recirculation should evacuate settling material from the bottom and pump it back onto the top. So it was recommended to operate the bottom outlet of the thermofil reactor as the heating recirculation outlet.

4. CONCLUSION

Following statements can be done based on the investigation of the reactors:

1. The geometry of the narrow foiled impeller has been reproduced based on photographic digitalization successful regarding the total flow rate achieved in the simulation results. It was within 10% error bound to the nominal value calculated by the manufacturer.
2. Design of the parameters of the stirring of wastewater sludge must be done in each case careful. Even small changes to the shape of the vessel can have significant effect on the overall flow field.
3. It is hard to avoid the settling by the intensification of primary mixing. An outer circulation pipeline delivering sludge to bottom up direction seems to be safer and less energy consuming way of avoiding sedimentation.
4. Due to special physical properties of the sludge and the size of the vessel validation of the simulation result is only possible by comparing certain operational results like efficiency and settling effects. Reliability of the simulation flow field results can be based on stirring vessel investigation found in literature for constant viscosity one-phase fluids.

ACKNOWLEDGMENTS

This work was part of a R+D project initiated by Budapest Sewage Works aimed at fluid mechanical review of sewage sludge vessels. The authors wish to thank for strenuous cooperation of the employees and for the permission of publication of information related to their thermofil reactor.

The corresponding author wishes to thank for the SZEFH Foundation for supporting the participation at the CMFF'06.

REFERENCES

[1] Ferziger, J.H., Peric, M., 2002, "Computational Methods for Fluid Dynamics", Springer-Verlag Berlin Heidelberg NewYork, 3. rev., pp. 334.

[2] Bechtel, T. B., 2003, "Laminar Pipeline Flow of Wastewater Sludge: Computational Fluid Dynamics Approach", *Journal of Hydraulical Engineering*, Vol. 129, pp. 153 – 158.

[3] Montante, G., Moštěk, M., Jahoda, M., Magelli, F., 2005, "CFD simulations and experimental validation of homogenisation curves and mixing time in stirred Newtonian and pseudoplastic liquids", *Chemical Engineering Science,* Vol. 60, 2427 – 2437.

[4] Harris, C.K., Roekaerts, D., Rosendal, F.J.J., "Computational Fluid Dynamics for Chemical Reactor Engineering", 1996, *Chemical Engineering Science*, Vol. 51, No. 10, pp. 1569-1594.

[5] Aubin, J., Fletcher, D.F., Xuereb, C., 2004, "Modeling turbulent flow in stirred tanks with CFD: the influence of the modeling approach, turbulence model and numerical scheme", *Experimental Thermal and Fluid Science*, Vol. 28, pp. 431–445.

[6] Sahu, A.K., Kumar, P., Patwardhan, A.W., Joshi, J.B., 1999, "CFD modelling and mixing in stirred tanks", *Chemical Engineering Science*, Vol. 54, 2285-2293.

[7] Kumaresan, T., Joshi, Jyeshtharaj B., 2006, "Effect of impeller design on the flow pattern and mixing in stirred tanks", *Chemical Engineering Journal*, Vol. 115, pp. 173–193.

[8] Alcamo, R., Micale, G., Grisafi, F., Brucato, A., Ciofalo, M., 2005, "Large-eddy simulation of turbulent flow in an unbaffled stirred tank

driven by a Rushton turbine", *Chemical Engineering Science*, Vol. 60, pp. 2303 – 2316.

[9] Yeoh, S.L., Papadakis, G., Yianneskis, M., 2005, "Determination of mixing time and degree of homogeneity in stirred vessels with large eddy simulation", *Chemical Engineering Science*, Vol. 60, pp. 2293 – 2302.

[10] Roussinova, V., Krestab, S. M., Weetman, R., 2003, "Low frequency macroinstabilities in a stirred tank: scale-up and prediction based on large eddy simulations", *Chemical Engineering Science*, Vol. 58, pp. 2297 – 2311.

[11] Salter, HE, Williams, SC, 2000, „Three-dimensional computational fluid dynamic modelling of a facultative lagoon", *Water Science and Technology*, Vol. 42 (10-11), pp. 335-342.

Conference on Modelling Fluid Flow (CMFF'06)
The 13th International Conference on Fluid Flow Technologies
Budapest, Hungary, September 6-9, 2006

FLUID VELOCITY MEASUREMENTS AROUND A STATIC MIXER USING LASER-DOPPLER ANEMOMETRY AND PARTICLE IMAGE VELOCIMETRY

Stefan LESCHKA[2], Dominique THÉVENIN[3], Katharina ZÄHRINGER[1]

Lehrstuhl für Strömungsmechanik und Strömungstechnik, Institut für Strömungstechnik & Thermodynamik, Otto-von-Guericke-Universität Magdeburg, Universitätsplatz 2, 39106 Magdeburg, Germany.
[1] Corresponding Author. Tel.: +49 391 6712097, Fax: +49 391 6712848, E-Mail: katharina.zaehringer@vst.uni-magdeburg.de
[2] E-Mail: stefan.leschka@vst.uni-magdeburg.de
[3] E-Mail: dominique.thevenin@vst.uni-magdeburg.de

ABSTRACT

Liquid phase hydrodynamics around a static mixer have been investigated using Laser-Doppler Anemometry (LDA) and Particle Image Velocimetry (PIV). A standard industrial mixer has been chosen as a first configuration. Water is used as flow medium with a very low mean velocity of 6.2 mm/s in the inflow section, which results in a mass flow of 184.8 l/h and a Reynolds number of 562. Three-dimensional velocity fields are measured in two vertical sections in the laminar inflow duct and in two sections in the disturbed laminar outflow. The experimental uncertainty has been investigated in detail. The PIV data has been used to characterize velocity profiles for different inflow conditions. The inflow mainly consists of an axial laminar duct flow without transversal components. The mixer leads to vortex structures in the outflow. Behind the mixer, the structure of the velocity field mimics the mixer geometry in all three directions.

Keywords: static mixer, LDA, PIV

NOMENCLATURE

Q	[l/h]	flow rate
Re	[-]	Reynolds number
V	[l]	volume
d	[µm]	tracer diameter
g	[m/s²]	acceleration due to gravity
$\underline{u}$	[m/s]	absolute velocity vector

Subscripts and Superscripts

10	10 % sum fraction
50	50 % sum fraction
90	90 % sum fraction
f	fluid
p	particle (relative to the fluid)
s	stopping
x, y, z	streamwise (along the channel axis), transversal, vertical (coordinate)
$\bar{}$	temporal mean

1. INTRODUCTION

Laser-Doppler Anemometry (LDA) and Particle Image Velocimetry (PIV) are widely used methods to determine flow characteristics. Here, they have been used to investigate the fluid behaviour around a static mixer in order to determine the flow conditions for the study of the mixing behaviour. The measurements are also used in a second step of the project to validate numerical calculations using LES and adaptive grid methods. Therefore, the boundary and starting conditions have to be determined exactly in the measurements. The LDA results serve here for the validation of the PIV results, which will later on be compared with numerical results. Especially the temporal resolution of the PIV measurements has been validated in that way, since the flow velocity is very small.

Static mixers have been investigated in several previous studies by optical measurement techniques. Some recent works are presented in the following. Kling *et al.* [1, 2] used reacting tracer dyes, in order to determine the macro- and micromixing by laser-induced fluorescence. Fourcade *et al.* [3, 4] used optical measurements of velocity and concentrations for comparison with numerical simulations. Gas mixing by lobed static injectors has been examined by the group of Karagozian [5-7] for the mixing of hot and cold combustion gases in burners.

The aim of this project is the validation of computational models in order to calculate static mixers for industrial applications. A first step is the complete determination of the flow field induced by

the mixer, which will be presented here. A test track has been designed, which allows the set-up of suitable experiments in order to measure the flow and mixing conditions of static mixers. The mixer section can be easily changed and different mixers can thus be examined.

2. EXPERIMENTAL SETUP

A schematic view of the test apparatus is given in figure 1.

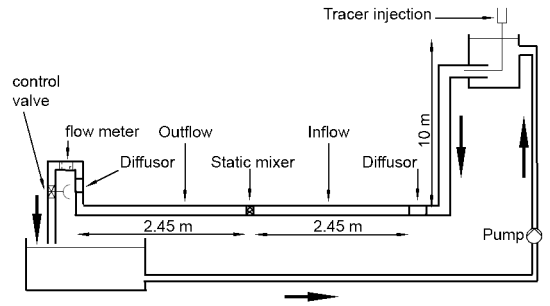

Figure 1. Schematic view of experimental set-up

A pump delivers the fluid from a lower basin to an upper basin, which water level lies 10 m above the channel axis. After the downpipe follows a diffuser, which changes the cross section from circular to quadratic. This shape has been chosen for the measurement sections in order to simplify the optical access for LDA and PIV. After that, the 2.45 m long inflow section leads the fluid to a static mixer, shown in Figure 2.

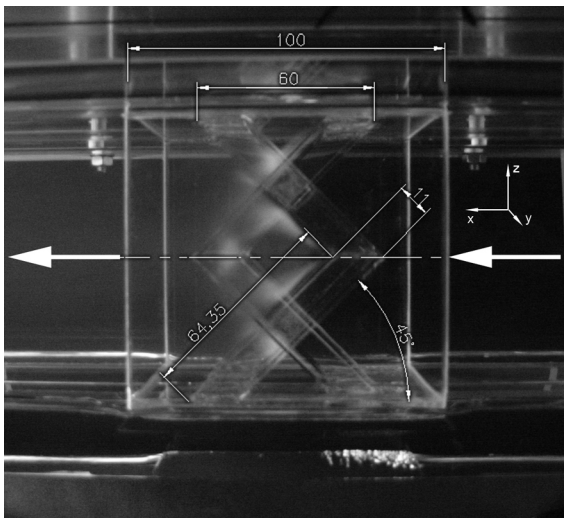

Figure 2. Geometry of the static mixer

As also illustrated in Figure 3, the mixer consists of seven rectangular lamellas with a width of 13 mm. Four lamellas (1-4) are turned in direction of the flow; between them, three (lamellas 5-7) are turned against the flow.

The outflow section has a length of 2.45 m, too. Inflow, outflow and mixer consist of acrylic glass and have a cross section of 91 x 91 mm. A flow meter is installed at the end of the test section, which provides a precision of 0.15 %.

The required flow rates have been adjusted using a control valve. From there, the water goes down to the lower basin.

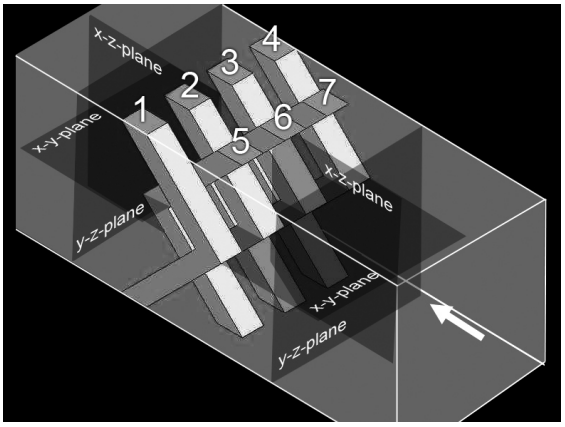

Figure 3. Mixer lamellas and measurement planes

Water with a temperature of 15 °C is used as flow medium. The static over-pressure in the test track is 1 bar.

For the LDA measurements, an argon laser with a wavelength of 514.5 nm and a laser power of 100 mW has been installed. The measurement volume has a width of 0.65 mm and a diameter of 0.08 mm. The resulting number of stripes is 35. At every measuring point between 40 and 1000 values have been acquired with an acquisition time of 60 s, which resulted in an acquisition frequency between 0.67 and 16.67 Hz.

For the PIV measurements, a Nd:YAG laser doubled to a wavelength of 532 nm with an energy of 200 mJ has been used. Under the governing optical conditions, a laser power of 80 mJ has been applied in order to be sure not to destroy the acrylic glass walls. The CCD camera provides a resolution of 1600 x 1186 pixels. It is combined with a Nikon AF Micro Nikkor 60mm/2.8D objective and a laser line filter of 532 nm.

For the measurements, spherical hollow glass balls 110 P8 CP00 with a mean diameter of d_{50} = 10.2 µm (d_{10} = 2.9 µm, d_{90} = 21.6 µm), a mean density of 1.1 g/cm³ and a bulk volume between 2220 and 2850 ml/kg have been used. In function of the fluid velocities, the concentration has been chosen to be 15 to 20 particles in a 16 x 16 pixel area of the PIV camera. This results in a volume fraction of $V_p/V_f = 6.86 \cdot 10^{-5}$.

Referring to the coordinate system in fig. 2, the streamwise velocity u_x, the transversal velocity u_y and the vertical velocity u_z have been measured with LDA in *y*-*z*-planes at x = -112 mm and x = -60.5 mm (before the mixer) and x = 60.5 mm and x = 112 mm behind the mixer with the coordinate system having its origin in the centre of the mixer. Before the mixer, the distance between two measurement points is 4 mm, behind the mixer 2 mm.

For PIV, the velocities in the *x*-*z*-planes with a distance of 6.5 mm in the *y* direction, which is half the thickness of a mixer lamella, have been investigated, as well as in the *x*-*y*-planes with a distance of 22.75 mm. These planes are shown in Fig 3. These PIV planes intersect the *y*-*z*-planes of the LDA measurements and the corresponding velocity values can be compared.

The Reynolds numbers with the corresponding flow rates Q and mean velocities $\overline{u}_x$ are given in Table 1.

Table 1. Reynolds numbers, flow rates and mean velocities

Case	Re [-]	Q [l/h]	$\overline{u}_x$ [m/s]
1	562	184.8	0.0062
2	1000	328.9	0.0110

PIV data has been evaluated using a cross correlation over an interrogation area of 64 x 64 pixels with 50 % overlapping and a Gaussian low-pass filter has been applied. In the area, values lying in the range of 1.2 times the second highest value have been accepted. For Case 1, velocity vectors smaller than -30 and larger than 30 mm/s have been declared erroneous. For Case 2 the corresponding range is between -60 and 60 mm/s. No averaging has been performed during data analysis of the single double-images.

One has to bear in mind, that the velocities measured with LDA and PIV are not the velocities of the fluid but the velocities of the tracer particles floating in the water. Following [8], the final velocity of a particle relative to the fluid is $u_p = 2.2 \cdot 10^{-2}$ mm/s with a relaxation time of $\tau = 2.4 \cdot 10^{-5}$ s. This is faster than the residence time of the fluid in the test section. By means of the dynamic behaviour of the tracer particles in the flow they suit very well to the investigated flow conditions.

3. RESULTS

3.1. Case 1 (Re = 562)

For the flow rate Q = 184.8 l/h LDA and PIV measurements have been performed. During the measurements the flow meter has shown flow rates between 184.0 and 185.3 l/h. The resulting mean velocities for these flow rates are 6.17 and 6.21 mm/s. By reference to the desired mean velocity, this is a variation of 1.05 %, including the imprecision of the flow meter.

LDA measurements

The LDA results at x = -60.5 mm (before the mixer) are shown in figure 4. The streamwise velocities, presented in Fig. 4a, lie between 0 and 10.9 mm/s. The highest values occur in the lower left corner. The flow does not seem to be completely symmetrical around the duct axis. Near the lateral boundary layer velocity variations of about 4 mm/s can be observed. The upper part of the profile presents a homogeneous laminar shape. Concerning fluctuation (RMS) values, the variation of the measured values lies between 0.07 and 2.4 mm/s.

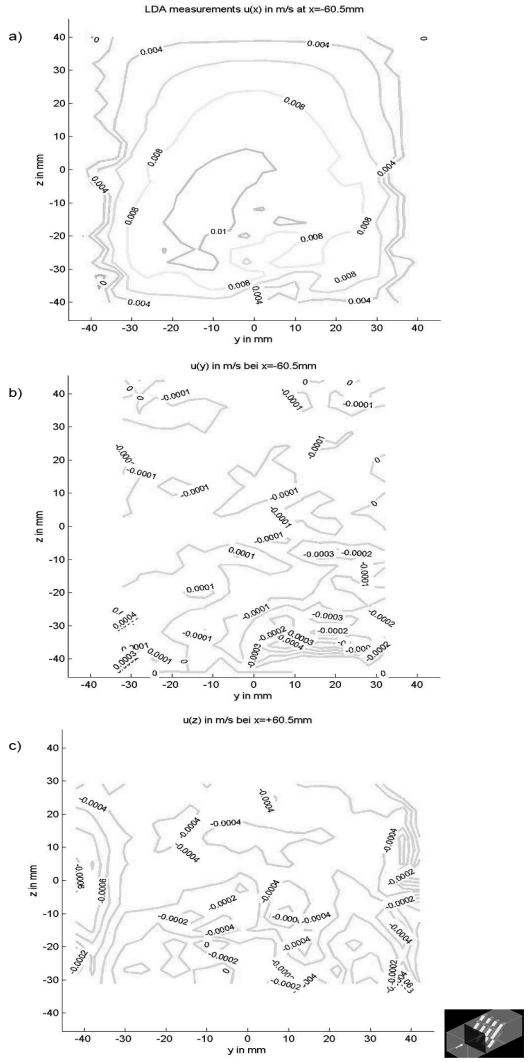

Figure 4. Case 1: LDA measurements in the *y*-*z*-plane 60.5 mm before the mixer: a) streamwise, b) transversal, c) vertical velocity

The range of the transversal velocity components presented in Fig. 4b spans from –0.4 to 0.4 mm/s. The RMS values lie between 0.08 and 0.4 mm/s.

For the vertical velocity profile (Fig. 4c) it can be seen, that the measured values in the centre cross section lie between -0.2 and 0.4 mm/s. In the near of the lateral boundary layer values around -0.7 mm/s are found. Outside of the boundary layer the RMS values lay typically around 0.1 mm/s. In the near of the lateral boundary layer values between 0.2 and 0.4 mm/s can be found.

The occurrence of homogeneously distributed regions with larger RMS values suggests periodic uncertainties in the test section or the measurement system. Reviewing the acquisition data, the larger RMS values (typically around 0.4 mm/s) occur at times, where the pump delivers water in the upper tank, which apparently causes slight vibrations, transferred through the floor to the measurement system. These vibrations had to be taken into account for measurements of total velocities at levels below 0.5 mm/s. The values for the vertical and transversal velocities lay under the measurement uncertainty and this means that, practically, only a streamwise velocity component exists in the inflow section.

Behind the mixer, the three velocity components are represented in Figure 5.

The predominantly straight flow in front of the mixer has been changed to a flow dominated by vortices, as expected. In Fig. 5a four symmetrically-ordered locations around the duct axis with higher streamwise velocities between 16 and 17.3 mm/s can be observed. In Fig. 5b four locations with transversal velocities between 6 and 6.3 mm/s are found. In comparison to the spots in Fig. 5a they are located nearer to the duct axis. In Fig. 5c four spots can be noticed as well. There, vertical velocities between 3 and 6 mm/s have been determined, but the highest velocities of 10.1 mm/s are located just above and below the channel axis.

Considering these small flow velocities and fluctuations, the high acquisition frequency of LDA measurements is not necessary to resolve the flow conditions temporally. In fact, for our flow standard PIV acquisition frequencies of 8 Hz become „time resolved" PIV.

PIV measurements

The PIV measurements have been applied before and behind the static mixer in *x*-*z*-planes all 6.5 mm. In Figure 6 the measured raw velocity vectors, calculated from a single double-image in the *x*-*z*-plane before and behind the mixer at the coordinates y = 0, -6.5 and -13 mm are presented. The images cover areas between 109.7 x 81.3 and 111.3 x 82.5 mm, caused by the different refraction indices of water and air.

In front of the mixer laminar flow has been observed in all investigated cases. The highest streamwise velocity is 12.2 mm/s at y = 0 mm in the middle of the mixer cross section. In Fig. 6 one can see, that at the entrance of the mixer the fluid is forced to change its direction along the lamellas on the upper and lower boundaries of the channel. In Fig. 6b the fluid reaches the mixer at vertical boundaries of the mixer lamellas 3 and 6, whereas in Fig. 6c the fluid has to change its direction, when it reaches the tip of lamella 7 in the middle of the test section.

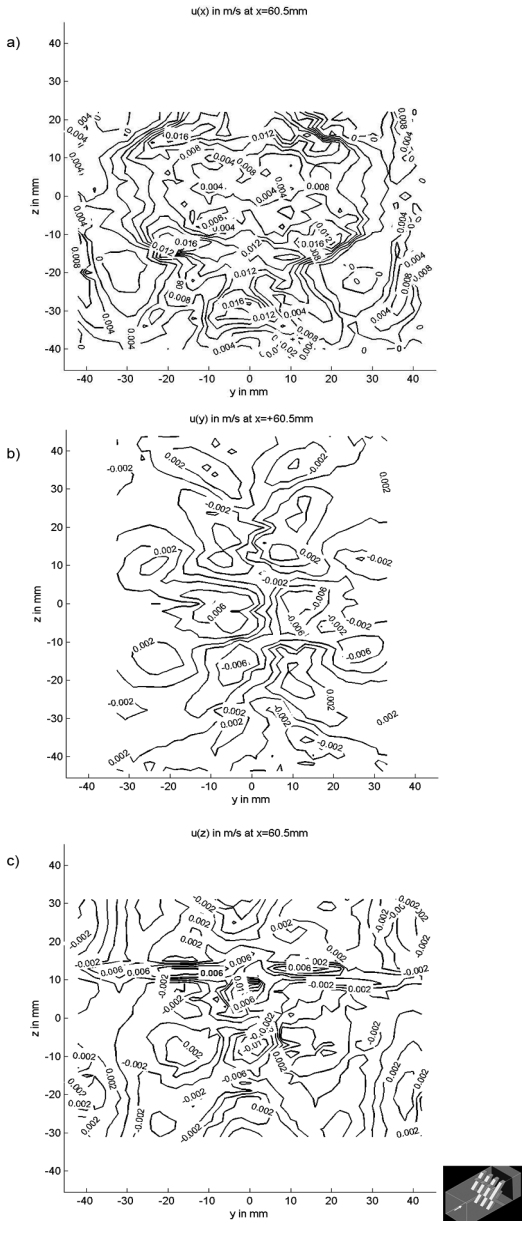

Figure 5. Case 1: Velocity components measured with LDA 60.5 mm behind the mixer: a) streamwise, b) transversal, c) vertical velocity

Behind the mixer, the fluid follows an almost parallel path along the nearest lamella. The highest velocity is 23.8 mm/s and has been measured at y = 0 mm in the very neighbourhood of the upper end of a lamella. In Fig. 6d lamella 6 points in the flow direction; in Fig. 6f lamella 7 points against the flow direction. In Fig. 6e where the investigated shape lies at the boundary of lamellas 6 and 3, the fluid does follow mainly the lamella borders, which are orientated to the channel boundary. When the fluid moves away from the mixer, small vortices can be observed at all investigated locations. The standard deviation value of this variation is about 10 % of the measured velocities.

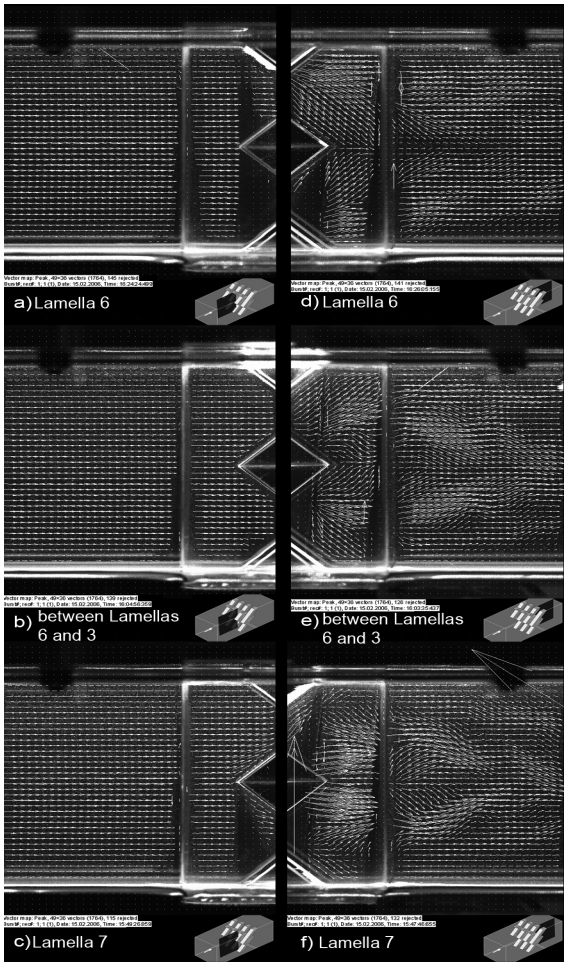

Figure 6. Case 1: Raw PIV vectors in the *x*-*z*-plane before the mixer at a) y = 0, b) y = -6.5, c) y = -13 mm and behind the mixer at d) y = 0, e) y = -6.5 and f) y = -13 mm

In Figure 7 the raw data of the velocity vectors in the *x*-*y*-plane in front and behind the mixer at the coordinates z = -22.75, 0 and 22.75 mm are presented.

In front of the mixer, the flow field is clearly laminar. The highest velocity of 20.37 mm/s is measured at z = 0 mm at the entrance of the mixer between the forward-orientated lamellas 2 and 3. At the position where the *x*-*y*-plane crosses the *x*-*z*-plane at the axis (y, z) = (0 mm, 0 mm), during the two measurements velocities of 12.5 mm/s and 12.1 mm/s have been measured respectively. This means that the variations found with PIV are of the same order as for the LDA measurements.

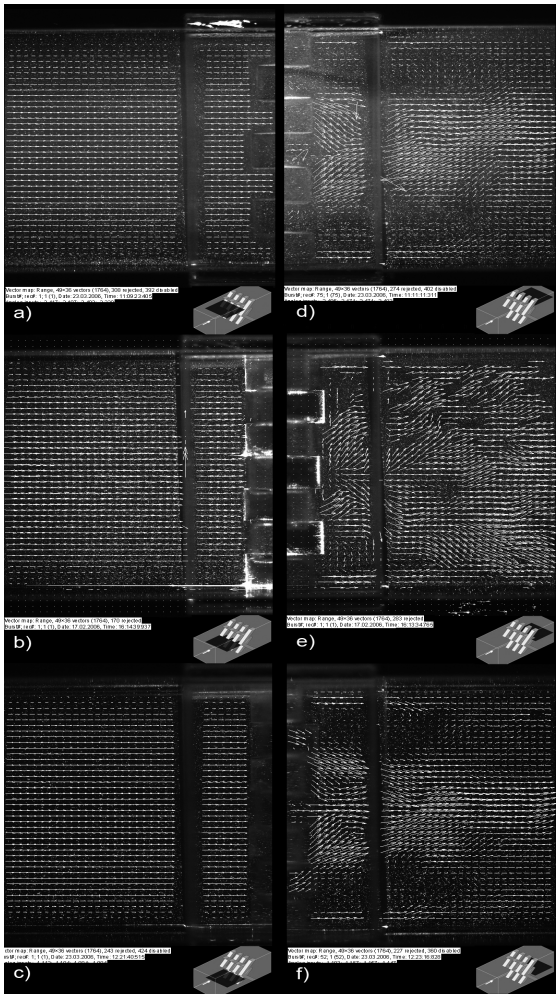

Figure 7. Case 1: Raw PIV vectors in the *x*-*y*-plane in front of the mixer at a) z = 22.75, b) z = 0, c) z = -22.75 mm and behind the mixer at d) z = 22.75, e) z = 0 and f) z = -22.75 mm

Behind the mixer at the outlet in Figs. 7d and 7f the flow is orientated towards the axis of the channel, whereas in Fig. 7e the vectors point mainly towards the boundaries of the channel. The highest velocity of 21.19 mm/s is measured in the z = 0 mm plane between the backward-orientated lamellas 6 and 7.

In the upper parts of the images during the measurements in the *x*-*y*-plane a number of erroneous vectors have been dropped out during the data analysis procedure. For all PIV measurements, the standard deviation lies in the range of 10 %.

Comparison of LDA and PIV

The measured data of LDA and PIV have been compared at the measurement points of LDA by interpolation of the PIV data. The PIV data itself has been averaged over 100 double-images, taken within 60 s, which has been the acquisition time of LDA. Figure 8 presents the velocity isolevels of this comparison 60.5 mm before the mixer.

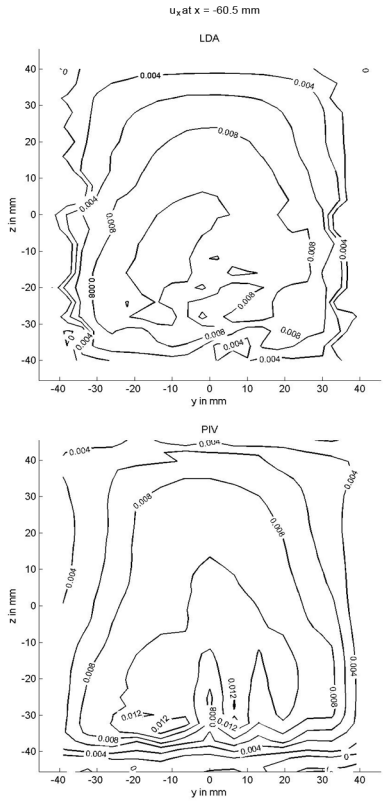

Figure 8. Case 1: Streamwise velocity isolevels of LDA and PIV measurements at x = -60.5 mm

In both contour plots the streamwise velocity components have the highest value in the lower left part of the cross section. The maximum velocities of PIV are roughly 2 mm/s higher than the ones of LDA, which means a variation of 16.7 %. The calculation of the mean velocities results in 5.8 mm/s for LDA and 5.6 mm/s for PIV, a variation of 3.5 %.

In the upper parts homogeneous laminar velocity profiles have been determined. In the lower part higher velocities than in the upper part have been measured with both methods. In the lower right corner, the PIV data suggests velocity variations of 2 mm/s, as the LDA data.

Figure 9 shows the isolevels of the streamwise velocity component 60.5 mm behind the mixer.

In both measurements the regions of high and low velocities correspond to each other. The highest velocities of 12 mm/s are found 30 mm above and below the channel axis, in the centre velocities of 4 mm/s can be found. Furthermore, there exist four spots with lower velocities at (y,z) = (-30 mm, 20 mm), (30 mm, 20 mm), (-30 mm, -20 mm) and (20 mm, -20 mm). For LDA, these velocities have been determined as 0 mm/s, for PIV as 3 mm/s.

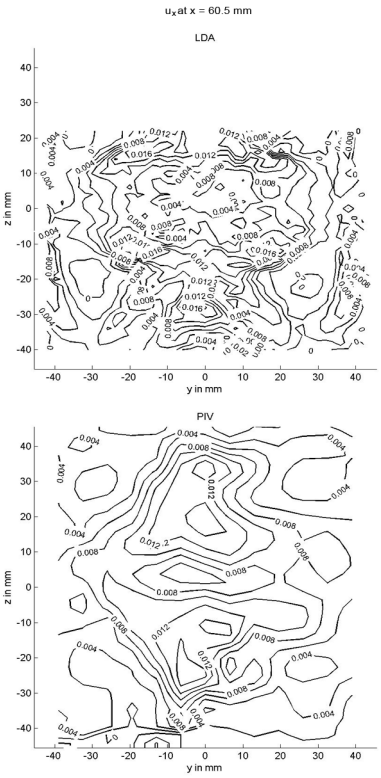

Figure 9. Case 1: Streamwise velocity isolevels of LDA and PIV measured at x = 60.5 mm

The vertical velocities 60.5 mm behind the mixer are shown in Figure 10. Corresponding to the streamwise velocities, 10 mm above and below the channel axis the highest velocities occur, with LDA 10 mm/s have been measured, with PIV 5 mm/s. As for the streamwise velocities, four zones with transversal distances of 20 mm and vertical distances of 30 mm from the channel axis can be observed, where the velocities are higher than in their neighbourhood. There, LDA determined vertical velocities between 4 and 6 mm/s, PIV showed vertical velocities of 4 mm/s.

The images of the transversal velocity components correspond to these images of the flow field in terms of velocity values and differences between PIV and LDA. Vibrations of the pump, which caused a wider RMS range of measured velocities of LDA, could be suppressed for PIV due to a modification of the water supply system. This is a part of an explication for the slightly different values.

*3.2 Case 2 (*Re = *1000)*

For this flow condition the flow rate of Q = 328.9 l/h is used. During the measurements the flow meter has shown flow rates between 328.4 and 330.7 l/h. The resulting mean velocities for these flow rates are 11.01 to 11.09 mm/s. In reference to the required mean velocity, this is a variation of 0.85 % including the imprecision of the flow meter.

The measurements have been performed in the same planes as for Case 1.

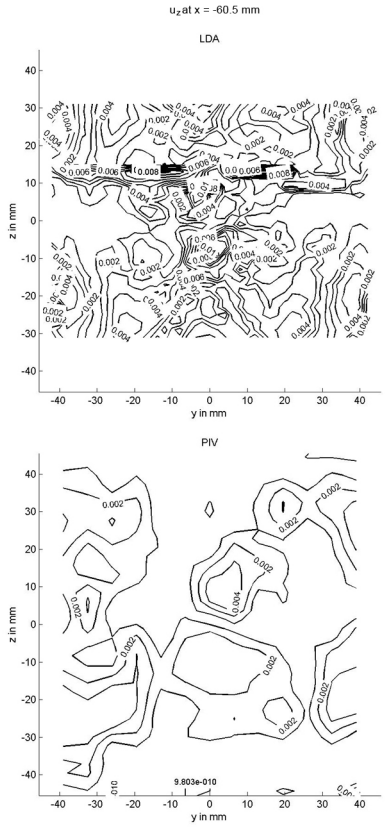

Figure 10. Case 1: Vertical velocity isolevels of LDA and PIV measured at x = 60.5 mm

In Figure 11 the measured raw velocity vectors in the x-z-plane before and behind the mixer at the coordinates y = 0, -6.5 and -13 mm are shown. As for Case 1, laminar flow has been observed in front of the mixer in all investigations. In Figs. 11a and 11b, the fluid goes directly in the mixer. In Fig. 11c it is forced to change its direction, when it reaches the backward orientated lamella 7. The highest velocity is 32.85 mm/s at y = -6.5 mm at the entrance of the mixer between lamellas 6 and 7.

Behind the mixer, the fluid follows a parallel path along the nearest lamella but, in contrast to Case 1, this is only observed very near the lamella. This effect is shown in Figs. 11d and 11f. In Fig. 11d the plane hits the centre of the forward orientated lamella 6, in Fig. 11f the backward orientated lamella 7. At the outlet of the mixer, the fluid more closely follows the border of the central lamella, which is orientated to the middle of the channel. Moving away from the mixer, vortices can be observed. Even if they can already be seen clearly for Re = 562, they become even clearer for Case 2. The highest velocities of 38.99 mm/s are found in the y = -6.5 mm plane at the upper side of the mixer. The standard deviation value is in the range of 10 % of the measured velocities.

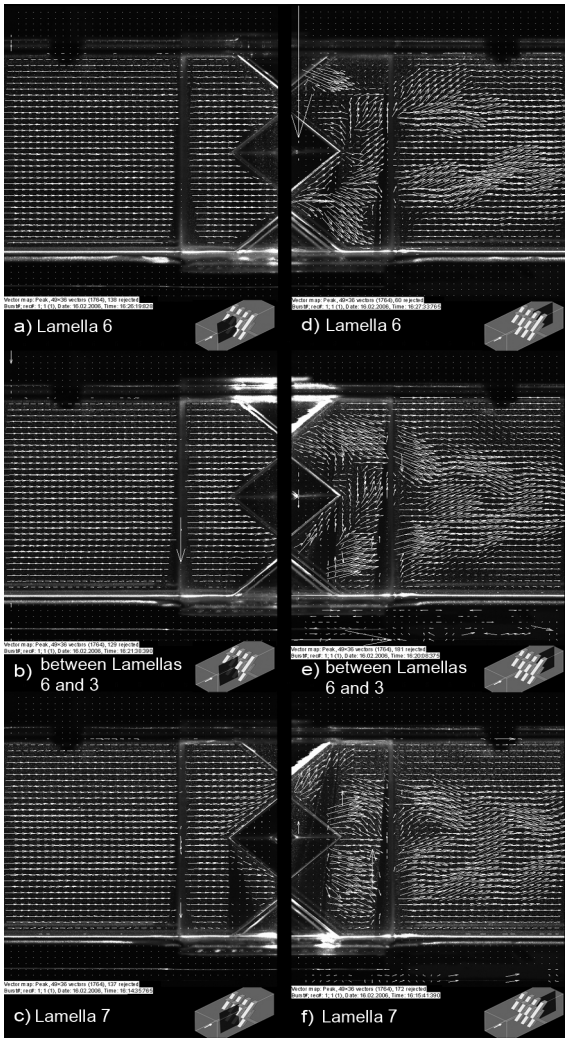

Figure 11. Case 2: Raw PIV vectors in the x-z-plane before the mixer at a) y = 0, b) y = -6.5, c) y = -13 mm and behind the mixer at d) y = 0, e) y = -6.5 and f) y = -13 mm

In Figure 12 the velocity vectors in the x-y-plane at z = -22.75, 0 and 22.75 mm are presented.

In front of the mixer laminar flow is always found. The highest velocity of 19.68 mm/s has been measured between lamellas 2 and 3, at the same location as for Case 1.

At the outlet of the mixer the transversal component of the velocities rises particularly at the

forward orientated lamella 6 in the z = 0 mm plane. There, the highest velocity of 43.09 mm/s has been determined. Vortices can be noticed in the flow further away from the mixer.

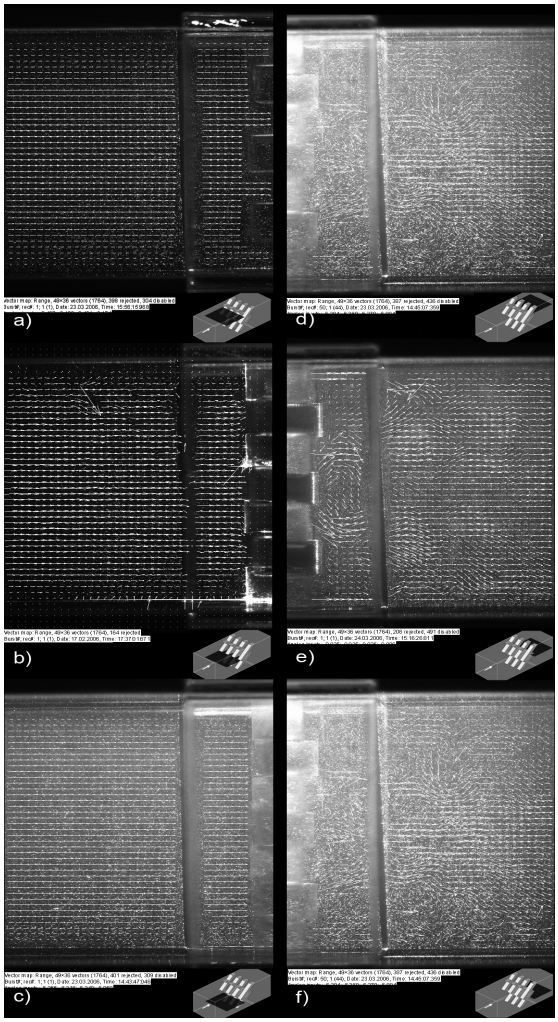

Figure 12. Case 2: Raw PIV vectors in the *x-y*-plane before the mixer at a) z = 22.75, b) z = 0, c) z = -22.75 mm and behind the mixer at d) z = 22.75, e) z = 0 and f) z = -22.75 mm

5. SUMMARY

The flow field around a static mixer has been determined by LDA and PIV measurements for laminar flow conditions. These measurements are used to determine the mixing characteristics of the mixer and to validate numerical simulations, which are used to calculate such mixers.

The measured data shows the flow structure induced by the mixer, starting from a one-dimensional laminar flow field at the inflow. There, the acquired PIV and LDA data agree very well. In the mixing region differences for the highest velocities between both measurements have been observed. These are in the range of the measurement errors and fluctuation range of the inflow velocities.

Further measurements for higher Re-numbers are in work and will allow a complete characterisation of the flow field. Next step for the mixing characteristics will also be measurements of the mixing quality by introducing fluorescent tracers and follow their mixing by laser-induced-fluorescence.

ACKNOWLEDGEMENTS

The authors would like to acknowledge the financial support of the DFG "SPP Strömungsmischer" program.

REFERENCES

[1] Kling, K. and Mewes, D., 2003, "Visualization of micro- and macro-mixing with the aid of two fluorescent chemically reacting dyes," Chemie Ingenieur Technik, Vol. 75 No. 12, pp. 1844-1847.

[2] Kling, K. and Mewes, D., 2004, "Two-colour laser induced fluorescence for the quantification of micro- and macromixing in stirred vessels," Chemical Engineering Science, Vol. 59 No. 7, pp. 1523-1528.

[3] Fourcade, E., Hoefsloot, H., van Vliet, G., Bunge, S., Mutsers, S. and Iedema, P., 2001, "The influence of micromixing on molecular weight distribution during controlled Polypropylene degradation in a static mixer reactor," Chemical Engineering Science, Vol. 56 No. 23, pp. 6589-6603.

[4] Fourcade, E., Wadley, R., Hoefsloot, H., Green, A. and Iedema, P., 2001, "CFD calculations fo laminar striation thinning in static mixer reactors," Chemical Engineering Science, Vol. 56 No., pp. 6729-6741.

[5] Majamaki, A. J., Smith, O. I. and Karagozian, A. R., 2003, "Passive mixing control via lobed injectors in high-speed flow," AIAA Journal, Vol. 41 No. 4, pp. 623-632.

[6] Mitchell, M. G., Smith, O. I. and Karagozian, A. R., 2004, "Passive fuel-air mixing and emissions control via lobed injectors," AIAA Journal, Vol. 42 No. 1, pp. 61-69.

[7] Smith, L. L., Majamaki, A. J., Lam, I. T., Delabroy, O., Karagozian, A. R., Marble, F. E. and Smith, O. I., 1997, "Mixing enhancement in a lobed injector," Physics of Fluids, Vol. 9 No. 3, pp. 667-678.

[8] Ruck, B., 1990, “Einfluss das Teilchengröße auf die Signalinformation in der Laser-Doppler-Anemometrie”, Technisches Messen, Vol. 57 7/8, pp. 284-295.

Conference on Modelling Fluid Flow (CMFF'06)
The 13th International Conference on Fluid Flow Technologies
Budapest, Hungary, September 6-9, 2006

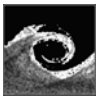

NUMERICAL STUDY TO FIND OPTIMAL GEOMETRICAL ARRANGEMENT OF A FLOW DISTRIBUTOR TO IMPROVE TEMPERATURE STRATIFICATION IN STORAGE TANKS

András ZACHÁR

Institute of Informatics, College of Dunaújváros, Táncsics Mihály u 1/a, Dunaújváros, H-2400, and Department of Informatics, Szent István University, Páter K. u. 1., Gödöllő, H-2103, Hungary, +36-28-522051, zachar.andras@gek.szie.hu.

ABSTRACT

Geometrical parameters of a flow distributor have been studied to improve the temperature stratification in cylindrical enclosures. Numerical investigations have been carried out to describe the velocity and temperature fields inside a storage tank in the case of upper inflow configuration. The aim of the study was to enhance the temperature stratification in a sensible heat store when a colder inflow enters at the top of the tank. Vertical position of the top slot of the cylindrical flow distributor has significant impact on the temperature stratification because lower the top slot higher the temperature stratification inside the storage tank. Finite volume formulation was applied to solve the governing transport equations. Vertical position of the top slot significantly increases or decreases the temperature stratification in the case of hotter inflow also. Higher the top slot, better the stratification in side the storage tank. Optimal position can be found to keep the stratification level as high as possible. The developed code was validated by comparison of measurements carried out for a simple flat plate diffuser. The numerical calculation predicts with reasonable accuracy the experimental results in the case of plate diffuser.

Keywords: temperature stratification, sensible heat store

NOMENCLATURE

c_p	[J kg^{-1} K^{-1}]	specific heat of the water
d_{in}, d_{out}	[m]	diameter of the inlet and outlet pipe
d_t	[m]	diameter of the tank
E_t	[J]	energy content of a cylindrical section of the tank
mix	[-]	mix-number
m_{str}	[Jm]	first moment of energy in a perfectly stratified storage tank
m_{mix}	[Jm]	first moment of energy in a perfectly mixed storage tank
m_{calc}	[Jm]	first moment of energy of the calculated temperature field
Q_{in}	[m^{3}s^{-1}]	volumetric flow rate of the inflow
Q_{slot}	[m^{3}s^{-1}]	volumetric flow rate through the top slot
Q_{sum}	[m^{3}s^{-1}]	volumetric flow rate under the edge of the top slot
r	[m]	radial coordinate
t	[s]	time
T	[^{o}C]	temperature function of the tank
T_{ini}	[^{o}C]	initial temperature of the tank
T_{in}	[^{o}C]	inlet temperature
T_{iniup}	[^{o}C]	initial temperature of the upper layer in the tank
$T_{inidown}$	[^{o}C]	initial temperature of the lower layer in the tank
ΔT_{max}, ΔT_{min}	[^{o}C]	maximum and minimum temperature difference between the measured and calculated data
ΔT_{avg}	[^{o}C]	average temperature difference between the measured and calculated data
U	[m s^{-1}]	radial velocity component
y	[m]	vertical coordinate
V	[m s^{-1}]	vertical velocity component
$V_{hotstart}$	[dm^3]	initial amount of hot water inside the flow distributor
V_{hotend}	[dm^3]	amount of preserved hot water inside the flow distributor
V_{in}, V_{out}	[m s^{-1}]	inlet and outlet velocity

Greek symbols

β	[K^{-1}]	volumetric thermal expansion of the water
η	[N s m^{-2}]	laminar dinamic viscosity of the water
λ	[W m^{-1} K^{-1}]	laminar thermal conductivity of the water

ν	[$m^2\ s^{-1}$]	laminar kinematic viscosity of the water
ρ	[kg m^{-3}]	density of the water
ρ_0	[kg m^{-3}]	reference density of the water

1. INTRODUCTION

Temperature stratification is an important factor of hot water storage tanks especially in solar systems. System performance can be significantly improved with good temperature stratification in comparison to a system with a fully mixed tank. Temperature stratification in storage tanks depends mainly on the flow rates of the fluid streams entering the tank, the size and location of the inlets and outlets and the volume of the tank. The main destratification factor in a thermal storage tank is mixing introduced by the inlet flows of the fluid Kleinbach *et al*. [1]. Different stratification manifolds were studied experimentally by Davidson *et al*. [2]. The measurements were carried out using three different inlet designs, a conventional drop-tube inlet, a rigid porous manifold and a flexible fabric manifold. Detailed description of the temperature stratification in storage tanks can be found in Duffie and Beckman[3]. An evaluation of the effect of storage tank geometry on store performance was studied by Eames and Norton [4]. A comprehensive description of the numerical treatment of the problem can be found in Patankar [5], and Versteeg *et al*. [6]. Measurements and numerical calculations show that the natural convection driven by heat from the vertical wall of a closed enclosure can develop a stratified temperature distribution Aszódi *el al.* [7]. The aim of this study is to develop specially constructed flow distributors to make the temperature field of the water as highly stratified as possible in different inflow cases. Axisymmetrical inlet and outlet flow conditions are supposed because this arrangement makes it possible to use a two dimensional approach to model the fluid motion inside the tank.

The studied flow distributors are cylindrical enclosures closed with a plate at the upper side. This study presents the impact of this flow distributor for the temperature field inside a hot water storage tank. Two different inflow situations are studied. In the first case a hotter inlet flow is examined at the top of the storage tank and in the second case a colder inflow configuration is studied with similar arrangement. The water enters the tank at the top with velocity V_{in} through an inlet pipe d_{in}. The inlet jet collides with the upper side of the flow distributor and the inflow water is forced toward the vertical wall. The main purpose of the application of the flow distributor is to slow down the inflow water. The water leaves the tank at the bottom with velocity V_{out} through an outlet pipe d_{out}. An outlet pipe is formed in the calculation domain because it makes it possible to specify a better outlet boundary condition where the flow field is fully developed and the gradient of the flow variables is zero along the down-stream direction. The following geometrical sizes are specified for the equipment: L=0.8 m, d_t=0.4 m, d_{in}=0.02 m; d_{out}=0.02 m. The volume of the tank is approximately 100 litres (V=100.48 litres) because the experimental setup is built with the above mentioned parameters. The different slot positions from the top of the flow distributor are specified in the fourth section where the result of the simulation for the studied configurations can be seen.

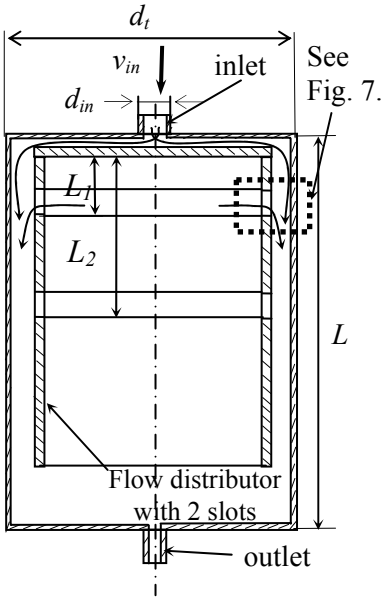

Figure 1. Schematic figure of the tank and the studied flow distributors

2 MATHEMATICAL FORMULATION

This section provides the basic equations that must be solved to describe the velocity field and the temperature distribution inside the storage tank. The physical problem is an unsteady, two dimensional flow, in axisymmetric, cylindrical geometry. Two spatial dimensions are used in the mathematical model to calculate the velocity and temperature field. The momentum equation of the fluid is based on the two dimensional Navier-Stokes equations. The SIMPLE method is applied to solve the momentum and continuity equations. According to the geometrical symmetry of the problem the calculation is carried out between the centerline of the tank and the physical boundary. The dependent variables that describe the present flow situation are the temperature, T, the velocity component in the radial direction, U, and the velocity component in the vertical direction, V.

2.1. Conservation equations

The following set of partial differential equations for U, V and T as functions of r, y and t

describes the flow and temperature field in the storage tank.

2.1.1. Continuity equation

The continuity equation is formulated in the following manner in cylindrical coordinate system.

$$\frac{1}{r}\frac{\partial}{\partial r}(\rho\, r\, U)+\frac{\partial}{\partial y}(\rho\, V)=0 \qquad (1)$$

2.1.2. Momentum equations

The following equation system is the representation of the momentum equations in cylindrical co-ordinate system where r means the radial and y means the vertical directions,

$$\frac{\partial}{\partial t}(\rho U)+\frac{1}{r}\frac{\partial}{\partial r}\left(\rho\, r\, U^2\right)+\frac{\partial}{\partial y}(\rho VU)=$$
$$-\frac{\partial P}{\partial r}+\frac{1}{r}\frac{\partial}{\partial r}\left(r\eta\frac{\partial U}{\partial r}\right)-\eta\frac{U}{r^2}+\frac{\partial}{\partial y}\left(\eta\frac{\partial U}{\partial y}\right) \qquad (2)$$

$$\frac{\partial}{\partial t}(\rho V)+\frac{1}{r}\frac{\partial}{\partial r}(\rho\, r\, U\, V)+\frac{\partial}{\partial y}\left(\rho V^2\right)=$$
$$-\frac{\partial P}{\partial y}+\frac{1}{r}\frac{\partial}{\partial r}\left(r\,\eta\frac{\partial V}{\partial r}\right)+\frac{\partial}{\partial y}\left(\eta\frac{\partial V}{\partial y}\right) \qquad (3)$$

and η is the laminar dinamic viscosity.

2.1.3. . Heat transport equation

The two-dimensional energy equation is solved to calculate the temperature field

$$\frac{\partial}{\partial t}\left(\rho c_p T\right)+\frac{1}{r}\frac{\partial}{\partial r}\left(\rho c_p\, r\, UT\right)+\frac{\partial}{\partial y}\left(\rho c_p VT\right)$$
$$=\frac{1}{r}\frac{\partial}{\partial r}\left(r\lambda\frac{\partial T}{\partial r}\right)+\frac{\partial}{\partial y}\left(\lambda\frac{\partial T}{\partial y}\right) \qquad (4)$$

where λ is the laminar thermal conductivity of the fluid and c_p is the specific heat of water at constant pressure. The transport equations have been formulated in a conservative form according to Patankar [5]. The Boussinesq approximation $\rho(T) = \beta\ \rho_0(T - T_{ref})$ is applied to express the buoyancy term where β is the coefficient of the volumetric thermal expansion and g is the acceleration of gravity.

2.2. Domain of discretization

More than ten different geometrical arrangements of the flow distributor and the tank have been studied on different grids. A schematic diagram of the tank and the flow distributor indicating one of the applied grids for the computational domain is shown in Fig. 2. A careful check for the grid-independence of the numerical solution has been made to ensure the accuracy and validity of the numerical scheme. The grid-independence study has been carried out on several geometrical arrangements. For example when the top slot size is 1.25 mm the following two different grids spacing have been applied. In the first case a 132 × 290 and in the second case a 136 × 296 grid have been tested. The slot region has been divided into 4 × 6 cells in the case of coarser grid and 8 × 12 cells in the case of finer grid. The applied grid can be seen in Fig. 3. is non-uniform near the slots. Comparison of the results of the calculation on the different grids is shown in Table 1.

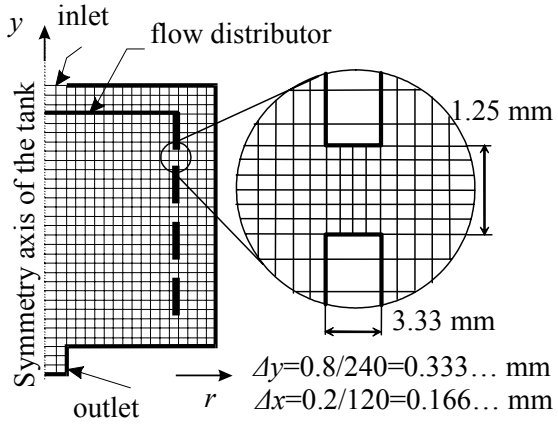

Figure 2. Grid applied for the calculations

Table 1. Relative error of the induced flow rates and the error of the continuity at the top slot with the studied grid

induced flow rates	t=1 s	t=40s
132 × 290, Q_slot_c [dm^3/min]	4.64	6.78
136 × 296, Q_slot_f [dm^3/min]	4.70	6.69
Relative error of the induced flow rates		
$100\left\lvert\frac{Q_{slot\ c}-Q_{slot\ f}}{Q_{slot\ f}}\right\rvert$ [%]	1.32 %	1.43 %
Relative error of continuity		
$Q\_s = Q\_in + Q\_slot$ [dm^3/min]	1.296	12.69
Q_sum [dm^3/min]	1.296	12.69
$100\left\lvert\frac{Q_s-Q_{sum}}{Q_s}\right\rvert$ [%]	8.649 10^{-5} %	1.09 10^{-4} %

The induced flow rate has been used to test the grid independency of the numerical model. The calculated results show that the difference between the induced flow rates through the top slot on the finer and coarser grids are approximately 1.5 %. Continuity of the flow field has also been checked with comparison of the sum of the slot flow Q_{slot}

and the inflow Q_{in} with the flow Q_{sum}. The following formulas have been used to calculate the different volumetric flow rates,

$$Q_{slot} = 2r_i \pi \sum_j \Delta y_j U_{j,i}$$

$$Q_{sum} = \pi \sum_i ((r_i + \Delta r_i)^2 - r_i^2) V_{j,i}$$, where Δr_i and Δy_j are the grid spacing in the radial and vertical directions.

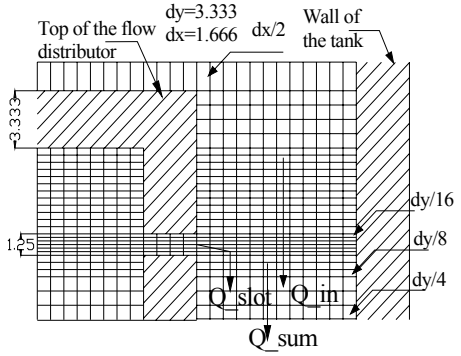

Figure 3. Grid near the top slot

2.3. Initial conditions

The initial velocity field is zero everywhere in the calculation domain. The velocity and the temperature of the inflow are specified from the first calculated time step. In the first case the initial state of the temperature field to be considered is constant everywhere inside the tank, in the second case a two-layer configuration is used and the thermocline is placed halfway between the top and bottom of the tank.

2.4. Boundary conditions

A uniform, constant velocity profile is assumed at the inlet position of the tank. The gradient of the velocity profile and of the temperature field is assumed to be zero at the end of the outlet pipe. Adiabatic condition is specified for the outer wall of the tank because the heat loss is negligible in the studied time scale. The heat flow across the wall of the flow distributor is also neglected because it is insignificant compared to the heat flow transported by convection.

2.5. Numerical solution of the transport equations

Finite volume code has been developed in C programming environment to solve the transport equations with the specified boundary conditions. The "Up-Wind" method [5] is used to discretize the convection term in the transport equations. The resulting large linear set of equations is solved with two different linear solvers. The discretized transport equations of *U*, *V*, *T* functions are solved by the TDMA method. A preconditioned conjugate gradient solver (CGSTAB) is applied to solve the pressure correction equation. Stone's incomplete LU decomposition is used to produce the preconditioning matrix for the conjugate gradient solver [8]. Results of the velocity and temperature field are presented with the Matlab built-in functions.

3. EXPERIMENTAL SET-UP AND MODEL VALIDATION

Comparisons have been made between the measurements and the result of the calculations and the experimental set-up is described in this paragraph. The experimental set-up is only applicable to investigate direct inflow configuration and inflow configurations with different diffuser plates. The experimental set-up is built at the Department of Buildings and Energy, Danish Technical University, Copenhagen, Denmark. The tank wall is made of transparent material, making it possible to see the stratification when dye is injected into the water. Water temperatures in the tank are measured with T-type thermocouples (± 0.5 ^{o}C) mounted in a thermocouple tree. Twenty thermocouples are employed to measure temperature distribution of the water along a vertical line situated half way between the symmetry axis and the vertical wall. The temperature values are measured every 10 s. The measured temperature information is recorded with a data acquisition unit connected to a personal computer. A picture and the schematic figure of the experimental set-up can be seen in Figure 4 and Figure 5.

Figure 4. Picture of the experimental setup

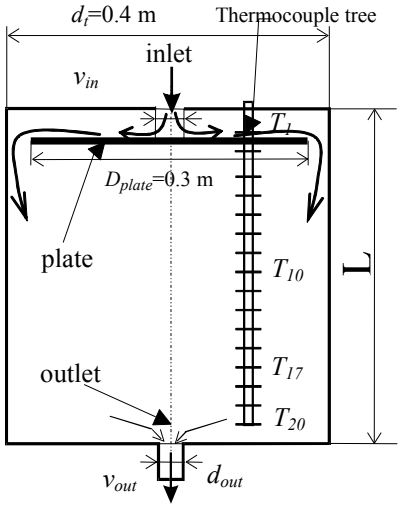

Figure 5. Schematic figure of the experimental setup

Several inflow configurations have been tested experimentally in the case of flat plate diffuser. Hotter and colder inflow tests are carried out with different volumetric flow rates. The measured results are used to validate the developed numerical model. Table 2 shows the studied inflow configurations used to validate the numerical calculations.

Table 2. Test configurations

test		T_{ini}	T_{in}	Q_{in}
I.	Hotter inflow	23 ^{0}C	44.5 ^{0}C	6.3 litres/min
II.	Hotter inflow	21 ^{0}C	41 ^{0}C	1.8 litres/min
III.	Colder inflow	43 ^{0}C	20 ^{0}C	2 litres/min

Table 3 shows a quantitative comparison of the measured and calculated results with simple statistical measures.

Table 3. Comparison of the measured and the calculated data

	experimental test I	experimental test III
maximum difference	1.8667 ^{o}C	1.9808 ^{o}C
minimum difference	0.05 ^{o}C	0.0359 ^{o}C
average difference	0.3759 ^{o}C	0.7034 ^{o}C
mix-number based on measurements	0.1455	–
mix-number based on calculations	0.1397	–

Figure 6a contains the measured data and the numerically calculated results of the upper inflow configuration with flow rates Q=*6.3* litres/min. The continuous lines show the calculated results and the different symbols show the measured data. Fig. 6a shows the vertical temperature distribution inside the storage tank at the end of the simulation period half-way between the symmetry axis and the vertical wall of the tank. The results clearly show that the water inside the storage tank is in a well stratified state. The calculation result and the measurement also show that the application of plate is significantly increase the temperature stratification in storage tanks even in the case of much larger flow rates than the conventional low flow systems. It is important to note that the applied flow rate is very large for a 100 litres storage tank, but the studied plate size is large enough to maintain a well stratified water in the tank. This statement can be concluded from Fig. 6a where the vertical temperature profile of the water is close to one in the upper part of the tank and the curve close to zero in the lower part. A transition zone can be seen in the middle of the tank where the thermocline should be situated in an ideally stratified case.

Comparison between the measured and the calculated results is also presented for the colder inflow configuration in Fig. 6b. Vertical temperature distributions can be seen at fixed time moments in Fig. 6b. The results show that the incoming cold water completely mixes-up the entire water volume inside the tank.

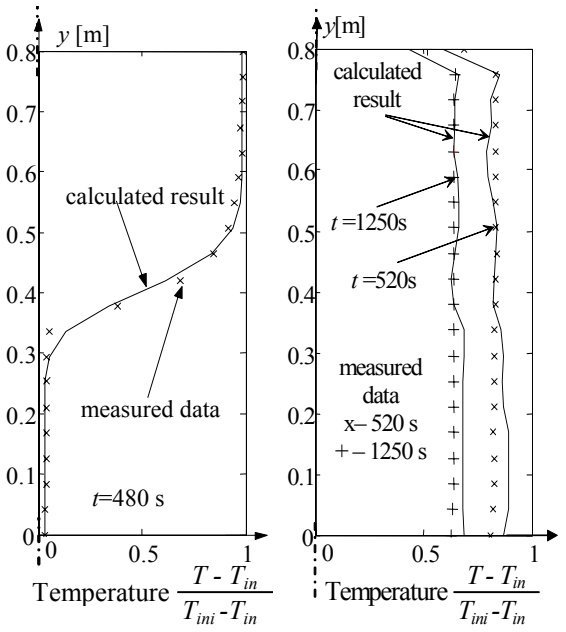

a. **b.**

Figure 6. Comparison of the results of the calculations with measured data in different inflow configurations

4. RESULTS

Several geometrical and physical parameters of the studied flow distributor and the inflow water could be influenced the temperature stratification inside a cylindrical storage tank. These parameters are the inflow rate (Q_{in}), the temperature difference between the inflow water and the upper temperature layer of the tank (T_{iniup}–T_{in}), the height and diameter of the tank (H, D), the number of the slots on the flow distributor, vertical size (total area) of the top slot, and the vertical position of the top slot. Most of the above mentioned parameters of the flow distributor have been studied by A. Zachár and A. Aszódi [9]. The basic purpose of this study is to find optimal vertical position for the top slot where most of the flow occurs.

Because of comparison purposes a quantitative measure of the mixing is needed. Davidson and Adams [2] suggest a quantitative measure of mixing in a storage tank is based on the stored energy multiplied by the vertical location measured from the bottom of the tank. The mix number is, $mix = \frac{M_{str} - M_{calc}}{M_{str} - M_{mix}}$ where M is the first moment of energy given by the following formula $M = \int_0^L y\, dE \cong \sum_{i=1}^{n} y_i E_i$.

L is the height of the tank, with n isothermal nodes. E_i is the energy content of a cylindrical section of the storage tank. M_{str} is the theoretical moment of energy of the tank in which no mixing occurs. The losses to the surroundings and the conduction through the thermocline are not included in this idealized case. M_{mix} is the moment of energy of an ideally mixed storage tank and M_{calc} is the moment of energy of the numerically calculated temperature field. It is important to note the smaller the mix-number larger the stratification level of the storage tank.

Two basically different inflow configurations are studied in this section. Both hotter and colder inflow configurations are examined to study the developing temperature field inside the storage tank and to analyse the effect of different slot positions for the temperature stratification.

4.1. Colder inflow from the top

Four different vertical positions of the top slot have been tested numerically. These slot positions are (5, 50, 100, 200 mm) from the top of the flow distributor. The size of the top slot is 1.25 mm and the size of the second slot located midway between the top and bottom of the tank is chosen to 5 mm. A two-layer initial temperature distribution is used to study the impact of the slot positions for the temperature stratification in the numerical calculations. Temperature of the water (T_{iniup}) in the upper layer of the storage tank is 40 °C and the temperature of the lower layer ($T_{inidown}$) is 20 °C. Temperature of the inlet water is chosen to 30 °C and the volumetric flow rate of the inflow is Q=6 litres/min. Numerical calculation is carried out over 500 s period. This time interval with the applied flow rate is approximately enough to replace the total amount of cold water ($T_{inidown}$=20 °C) by the hotter inflow (T_{in}=30 °C) theoretically, allowing the main features of the stratification process and impact of the flow distributor on the temperature stratification to be studied more easily. Flow field near the top slot can be seen in Figure 7 where the colder inflow moves downward between the wall of the tank and the outer side of the flow distributor.

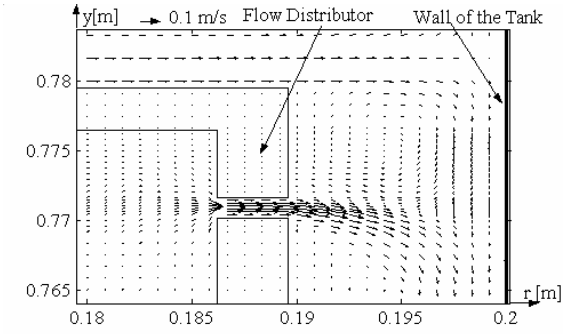

Figure 7. Flow field near the top slot in the case of colder inflow configuration

Besides the mix-number the ratios of the preserved hot water V_{hot_end}/V_{hot_ini} [%] has also been used to measure quantitatively the temperature stratification inside the storage tank. V_{hot_end} and V_{hot_ini} contain hot water with temperature drop smaller than 1 °C from the initial temperature of the hottest layer. For example the temperature of the upper layer of the storage tank (T_{iniup}) is 40 °C and the V_{hot_end} contains water inside the flow distributor hotter than 39 °C. Mix-numbers and the ratios of the preserved hot water can be seen in Table 4.

Table 4. Mix-numbers and the relative amount of the preserved hot water

Vertical position of the top slot	mix-number	Preserved hot water $V_{hot\_end}/V_{hot\_start}$ [%]
5 mm	0.7114	3.82
50 mm	0.6512	15.06
100 mm	0.5279	24.25
200 mm	0.2183	52.64

4.2. Hotter inflow from the top

Five different vertical positions of the top slot have been tested numerically in the case of hotter inflow. These slot positions are (100, 150, 200, 400, 600 mm) from the top of the flow distributor. The initial temperature of the water (T_{ini}) in the the

storage tank is 20 °C. Temperature of the inlet water is chosen to 40 °C and the volumetric flow rate of the inflow is Q=6 litres/min. Numerical calculation is carried out over 500 s period.

Flow field near the top slot can be seen in Figure 8. The hotter inflow moves downward between the wall of the tank and the outer side of the flow distributor to the top slot. Most part of the hot water goes through the top slot. Inside the flow distributor the water moves upward and continuously mixing with the colder water (entrainment effect).

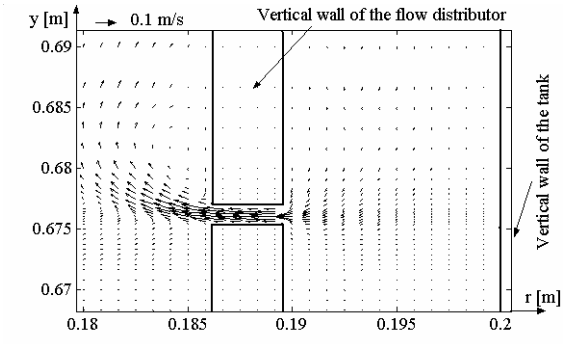

Figure 8. Flow field near the top slot in the case of hotter inflow configuration

Besides the mix-number the ratios of the charged hot water V_{hot_end}/V_{hot_in} [%] has also been used to measure quantitatively the temperature stratification inside the storage tank. V_{hot_end} and V_{hot_in} contain hot water with temperature difference smaller than 2 °C from the temperature of the inlet water. For example the temperature of the inlet (T_{in}) is 40 °C and the V_{hot_end} contains water inside the flow distributor hotter than 38 °C. V_{hot_in} is the total amount of the charged hot water loaded at the inlet with temperature (T_{in} = 40 °C). Mix-numbers and the ratios of the charged hot water can be seen in Table 5

Table 5. Mix-numbers and the relative amount of the charged hot water

Vertical position of the top slot	mix-number	charged hot water V_{hot_end}/V_{hot_in} [%]
100 mm	0.3792	69.75
150 mm	0.4530	33.01
200 mm	0.4912	19.85
400 mm	0.6618	0
600 mm	0.7812	0

5. CONCLUSIONS

An important geometrical parameter of a cylindrical flow distributor is examined from thermal stratification point of view. Both hotter and colder inflow configuration at the top are studied to analyse the impact of the vertical position of the top slot for the resulting temperature distribution. Vertical position of the top slot has significant effect for the temperature stratification in the case of colder inflow at the top because most of the flow through the slots occurs at the top slot. It can be concluded that the optimal position of the top slot from the top of the tank is located 15%–20% of the vertical size of the tank. This statement is valid for storage tanks with vertical size interval [0.6 –1] m. To investigate further this statement larger and smaller tanks should be examined. Possibly in case of tanks with larger vertical sizes the optimal position is located closer the top of the tank than the currently studied case because of the entrainment process.

ACKNOWLEDGEMENTS

The author thanks the suggestions of G. Stoyan in the topic of the numerical techniques of the computational fluid dynamic. I also would like to thank to A. Aszódi for the useful references and discussions in the topic of the applied heat and mass transfer problems and making possible to use the CFX code to validate my developed code. The author also would like to thank to J. Tóth the reading and surveying the manuscript from mathematical point of view. Present work has partially been supported by MÖB (Eötvös Grant).

REFERENCES

[1] E. M. Kleinbach, W. A. Beckman, S. A. Klein, Performance study of one-dimensional models for stratified thermal storage tanks. *Solar Energy*, 1993, **50**, 155-166.

[2] J. H. Davidson, D. A. Adams, Fabric stratification manifolds for solar water heating, Transactions of the ASME, *Journal of Solar Energy Egineering*, 1994, **116** (August), 130-136.

[3] J. A. Duffie, W. A. Beckman, *Solar engineering of thermal processes*, Wiley, New York, 1980.

[4] Eames P.C. and Norton B, The effect of tank geometry on thermally stratified sensible heat storage subject to low Reynolds number flows, *International Journal of Heat and Mass Transfer*, 1998, **41** (**14**), 2131-2142.

[5] S. V. Patankar, *Numerical heat transfer and fluid flow*, Taylor & Francis, New York, 1980.

[6] H. K. Versteeg, W. Malalasekera, *An introduction to computational fluid dynamics, The finite volume method,* Addison Wesley Longman Limited, Essex, 1995.

[7] A. Aszódi, E. Krepper, H-M Prasser, Experimental and numerical investigation of one and two phase natural convection in storage

tanks. *Research Journal of Heat and Mass Transfer*, Springer, 2000, **36**, 497-504.

[8] G. D. Smith, *Numerical Solution of Partial Differential Equations: Finite Difference methods,* Clarendon Press, Oxford, 1978.

[9] A. Zachár, A. Aszódi, Numerical analysis of different flow distributors to improve the temperature stratification in a storage tank. Resubmitted to the *Numerical Heat Transfer Part A.*

Conference on Modelling Fluid Flow (CMFF'06)
The 13th International Conference on Fluid Flow Technologies
Budapest, Hungary, September 6-9, 2006

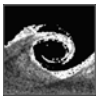

NUMERICAL STUDY ON THE EFFECT OF LONGITUDINAL VENTILATION VELOCITY ON THE BURNING RATE IN TUNNEL FIRES

Jae Seong ROH[1], Hong Sun RYOU[2], Seong Hyuk LEE[3], Seung Woo KO[4], Woo Sung JUNG[5], Dong Hyun KIM[6]

[1]. School of Mechanical Engineering, Chung-Ang University, Seoul 156-756, Korea. E-mail: forcfild@hanmail.net
[2] Corresponding Author. School of Mechanical Engineering, Chung-Ang University, Seoul 156-756, Korea. Tel.: +82 2 820 5280, Fax: +82 2 813 3669, E-mail: cfdmec@cau.ac.kr
[3]. School of Mechanical Engineering, Chung-Ang University, Seoul 156-756, Korea. E-mail: shlee89@cau.ac.kr
[4]. School of Mechanical Engineering, Chung-Ang University, Seoul 156-756, Korea. E-mail: eurotwin@hotmail.com
[5] Korea Railway Research Institute, Gyeonggi 437-757, Korea. E-mail: wsjung@krri.re.kr
[6] Korea Railway Research Institute, Gyeonggi 437-757, Korea. E-mail: dhkim@krri.re.kr

ABSTRACT

Since the prediction of 'critical velocity' is important to control the smoke in tunnel fires, many researches have been carried out to predict critical velocity with various fire sizes, tunnel shape, tunnel slope, and so forth. But few researches have been conducted to estimate critical ventilation velocity for varied burning rate by longitudinal ventilation, although burning rate of fuel is influenced by ventilation conditions. Therefore, there is a need to investigate the difference of upstream smoke layer (e.g. backlayering) between naturally ventilated heat release rate and varied heat release rate by longitudinal ventilation. In the present study, three dimensional simulations of smoke flow in the tunnel fire with the measured burning rates have been carried out using FDS (Fire Dynamics Simulator; Ver. 406) code, which is developed by National Institute of Standards and Technology (NIST). The results are presented and their implications are discussed. Since ventilation velocity had a greater enhancing effect on the burning rate of fuel due to oxygen supply effect, the critical ventilation velocity should be calculated on the basis of varied HRR by ventilation velocity.

Keywords : backlayering, burning rate, critical velocity, heat release rate, tunnel fire

NOMENCLATURE

A	$[m^2]$	area
B	$[m]$	tunnel width
C_p	$[J/kg \cdot K]$	specific heat capacity
D	$[m]$	pool diameter
Fr	[-]	Froude number
g	$[m/s^2]$	gravitational force
H	$[m]$	tunnel height
$\bar{H}$	$[m]$	mean hydraulic tunnel height
ΔH_c	$[kj/kg]$	heat of combustion
$\dot{m}''$	$[kg/m^2 s]$	burning rate
Q	$[W]$	heat release rate
Q''	[-]	dimensionless heat release rate based on hydraulic tunnel height
R_i	[-]	Richardson number
T	[ ]	temperature
V	$[m/s]$	flow velocity
V''	[-]	dimensionless critical velocity based on hydraulic tunnel height
ρ	$[kg/m^3]$	density
$\Delta\rho$	$[kg/m^3]$	density rise above ambient

Subscripts and Superscripts

c	critical value
f	fuel
o	ambient/standard conditions

1. INTRODUCTION

Due to the confining geometry of the tunnel, tunnel fire represents a major risk in the event of fire in tunnel. When a fire occurs in a tunnel, the most hazardous factor is not flame and high temperature but toxic smoke. These large quantities of smoke are likely to spread rapidly along the ceiling of tunnel due to confinement of the tunnel wall and will reduce visibility. Then, they become an obstacle to fire extinction and can cause deaths by asphyxiation.

In many tunnel fires one of the most important issues in fire safety is smoke control/extraction. To

maintain an evacuation path that is free of smoke and hot gases, mechanical ventilation systems such as longitudinal, transverse and semi-transverse ventilation system was commonly installed. The longitudinal ventilation systems operated by blowing smoke towards a tunnel exit are commonly designed to prevent upstream smoke flow and make an offer safe evacuation path. The 'critical velocity' is defined as the minimum longitudinal ventilation velocity needed to avoid the upstream smoke flow (also called backlayering, i.e. the smoke moving in the opposite direction of the ventilation system). Therefore, it is paramount important to predict the value of critical ventilation velocity at any fire size represented by heat release rate (HRR) in longitudinal ventilation system.

There have been many theoretical and experimental studies of critical ventilation velocity in tunnel fires. The methods for prediction of the values of the critical ventilation velocity for various fire sizes were mainly based on empirical relationships obtained from Froude number preservation using some experimental data.

The Froude number is defined as the ratio between the buoyancy forces generated by the fire and the inertia forces due to the ventilation air flow.

$$Fr = \frac{V^2}{gD} = \frac{inertia\ \ forces}{gravity\ \ forces} \tag{1}$$

For theoretical studies, Thomas [1] was one of the earliest who used theory based on Froude number preservation in fire situations, and suggested that Richardson number is close to unit at critical condition. Richardson number defined as:

$$R_i = \frac{gD}{V^2} \cdot \frac{\Delta\rho}{\rho} = \frac{1}{Fr} \cdot \frac{\Delta\rho}{\rho} \tag{2}$$

The critical ventilation velocity is;

$$V_c = \sqrt{\frac{\Delta\rho}{\rho} \cdot g \cdot H} \tag{3}$$

Then, he also expressed critical ventilation as a function of the HRR by:

$$V_c \approx \left(\frac{gHQ}{\rho_0 T_0 C_p A} \right)^{1/3} \tag{4}$$

Based on Thomas's theory, Hinkley [2] drived a formula for calculation the smoke velocity moving along the roof of a shopping mall.

Heselden[3] derived another formula based on Hinkleys theory for calculating the critical ventilation velocity as;

$$V_c = CK \left(\frac{gQT}{C_p \rho_0 T_0^2 B} \right)^{1/3} \tag{5}$$

Both C and K are constant obtained from experiments in a disused rail tunnel. These results were the most widely used correlations to predict critical ventilation velocity. Danziger and Kennedy [4] were devised a simple relationship to calculate the critical ventilation velocity and installed in the US Department of Transport Subway Environment Simulation Program [5].

For experimental studies based on dimensionless analysis, Oka and Atkinson [6] carried out small scale experiments with a fuel burner for a wide range of dimensionless HRR. The one-third power law is found under a certain value of the HRR. Beyond this value, critical ventilation velocity is supposed to become independent of the HRR. It is also confirmed that application of the theory based on Froude number preservation is very limited and should not be used for the prediction of critical ventilation velocity at high HRR. But the formulae proposed by Oka and Atkinson cannot correlate the experimental results from various cross-sectional tunnel shapes into a single form on the ground that tunnel height is used as the characteristic length in the analysis. Therefore, Oka and Atkinson's formulae should not be used for tunnel with different cross-section. Wu and Bakar [7] carried out a series of experimental tests in five model tunnels with same height but different cross-sections to investigate the effect of tunnel geometry on the critical velocity. Based on their results, they proposed to use ‘hydraulic tunnel height’ to replace the tunnel height as the characteristic length on the dimensional analysis. The formulae proposed by Wu and Bakar confirmed one-third power law by Oka and Atkinson and all the experimental results could be correlated into a single form. Therefore, it was possible to derive a universal correlation for predicting the critical ventilation velocity for tunnels with various cross-sectional shapes. They proposed the experimental correlation with dimensionless variables, Q^* and V^*, by Froude scaling.

$$V^* = 0.4(0.2)^{-1/3}(Q^*)^{1/3} \quad for \quad Q^* < 0.2$$
$$V^* = 0.4 \quad for \quad Q^* > 0.2 \tag{6}$$

where,
$$Q^* = \frac{Q}{\rho_0 C_p T_0 g^{1/2} \bar{H}^{5/2}}$$
$$V^* = \frac{V}{\sqrt{g\bar{H}}} \tag{7}$$

Furthermore, Lee[8] et al. investigated the effect of aspect ratio of a tunnel cross-section on the critical ventilation velocity in pool fire experiments

and suggested a new correlation model to dimensionless critical ventilation velocity and HRR.

The most of tunnel fire experiments used gas burner as fire sources, which are not same as fire source for pool fire influenced by ventilation and tunnel wall, so that it produced fires with fixed HRR by control of fuel mass flow rate. It was expected that ventilation velocity has no influence on the HRR because fuel mass rate was not changed during experiment. In real fire situation in tunnel, however, it was expected that the HRR of a fire in a tunnel will vary significantly with ventilation velocity because the HRR is dependent on fuel composition, area involved with fire, availability of oxygen, ambient temperature and so forth. For example, longitudinal ventilation may blow through the fire load. And it causes the fire to spread and grow fire intensity in different manner rather than natural ventilation.

Even though many studies have been carried out to predict critical ventilation velocity in tunnel fire, the influence of ventilation velocity on fire spread and its development in the near field of a fire source had rarely been taken into account. Carvel[9] *et al* focused their interest mainly on the issue of the influence of ventilation velocity on fire spread and its development using Bayesian methodology with past fire test data and opinions of experts in the field of fire safety. They found that ventilation velocity had a great enhancing effect on the HRR of heavy good vehicle fires, but had little effect on the HRR of car fires.

For liquid fuel pool fire, ventilation velocity mainly affects burning rate of fuel and combustion efficiency. Ventilation in pool fire may not make fire to spread due to confinement of pool area, but grow or reduce fire intensity by varied burning rate of fuel. Carvel [10] investigated the behavior of three different sizes of pool fires with a range of forced ventilation velocities. It has been found that for some fires the ventilation would be expected to reduce the HRR and for some fires to increase it. The variation of burning rate by ventilation velocity was studied experimentally by Yang and Roh[11] in their reduced scale tunnel fire. They suggested that ventilation velocity had a greater enhancing effect on the burning rate of n-heptane fuel on the ground that oxygen supply effect became more significant than the cooling effect of fresh air. They emphasized that the ventilation system designed with the constant HRR based on the empirical relationship could make the fire grow further so that it might give rise to conflagration in tunnel. Nevertheless, their reduced scale fire experiments give no insight into the phenomena involving ventilation velocity and burning rate of fuel in pool fire. Therefore, there is a need to look into the mechanism and especially relationship between the backlayering and varied HRR by longitudinal ventilation. The present study attempts to show the difference in back-layer distance between naturally ventilated HRR and varied HRR by longitudinal ventilation under critical ventilation velocity using CFD technique.

Three-dimensional simulations of smoke flow in the tunnel fire with the measured burning rates were carried out using FDS (Fire Dynamics Simulator; Ver. 406) code, developed by National Institute of Standards and Technology[12,13] .

2. NUMERICAL SIMULATION

2.1. Configurations

The numerical simulations were of a reduced scale tunnel fire experiment carried out by Yang and Roh [11], who performed sixteen experiments with the pool size and velocity of the ventilation flow varied. The model tunnel has an arched ceiling, 9 *m* long, 0.4 *m* wide and 0.4 *m* high. The fire source was located at 4.3 *m* from the entrance. A square heptane pool fire with lengths of 4.5 *cm* and 8.5 *cm* was used in numerical simulation. Only fire area from 3 *m* to 7 *m* is simulated so that the length of computation domain is 4 *m*. The configuration and dimension of the model tunnel are shown in Fig. 1. More detailed information on the model tunnel and experimental methods used in the present work are shown in ref erence[11].

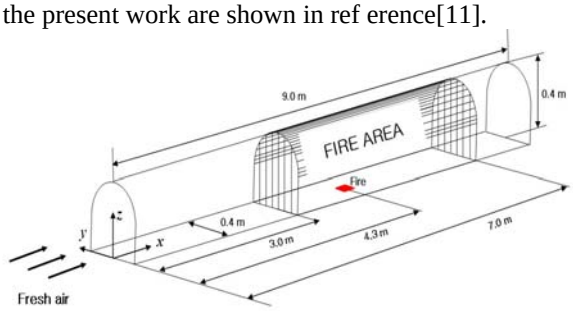

Figure 1. The configuration and dimension of the tunnel

2.2. Grid System

Figure 2 shows the longitudinal grid distribution near fire source and cross-sectional grids for the tunnel used in the present study.

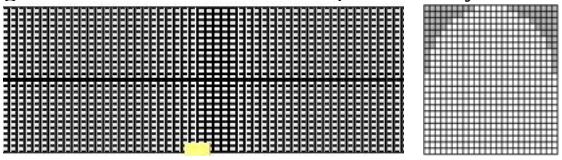

Figure 2. Grids distribution

The curved cross-section of tunnel was represented by stepwise grid approximation because the FDS program adopted basically the rectangular grid system. In fact, these constructions of stepwise grid change the smoke flow pattern near the curved

surface. To lessen this impact on the smoke flow near the curved surface, the parameter SAWTOOTH was prescribed. Because grid size in LES code is directly concerned with filter width, grid spacing is very important to simulate fire driven flow. In order to get proper numerical grid spacing, grid independent tests at 15 *kW* HRR and V=0.6 *m/s* were carried out for different grid spacing.

For mesh sizes ranging from case A and case D cells were used in the present simulations. Table 1 shows the grid sensitive test conditions.

Table 1. Grid sensitive test conditions

Case	Number of grid	Total number of grid	Back-layer distance
Case A	90 16 16	23,040	-0.325
Case B	120 20 20	48,000	-0.15
Case C	180 24 24	103,680	0.05
Case D	240 32 32	245,760	0.06

Based on the results of grid sensitive test, the optimal mesh of 103,680 cells was used.

2.3. Boundary Conditions

Initially, atmospheric boundary conditions were applied at both ends of the tunnel. Fresh air with 20 enters uniformly from entrance of tunnel after a specific time when the developed fire is detected. In the present works, that time is assumed 60 *s*.

The wall near fire source 3 *m* to 6 *m* is assumed thermally thick (sheet metal). A one-dimensional heat conduction equation for the material temperature is applied. The remaining wall downstream of fire is assumed thermally thin (PMMA).

2.4. Heat Release Rate of Fire

The rate at which energy is released, generally known as the heat release rate(HRR) is the most important variable which characteristics the behavior of a fire. It is defined as follows:

$$Q = \dot{m}'' \cdot \Delta H_c \cdot A_f \qquad (8)$$

where $\dot{m}''$ is the burning rate per unit area and per unit time($kg/m^2 \cdot s$), ΔH_c is the heat of combustion (kJ/kg) and A_f is the fuel surface area (m^2). The heat of combustion of heptane is 44,300 kJ/kg. The fire sources indicated as HRR are based on the mass loss rates measured in reduced scale tunnel fire experiment. Figure 3 shows the variations of fuel weight with time for different cases. The curve was obtained by curve fitting to overcome measurement error of load cell with ±3*g* accuracy installation.

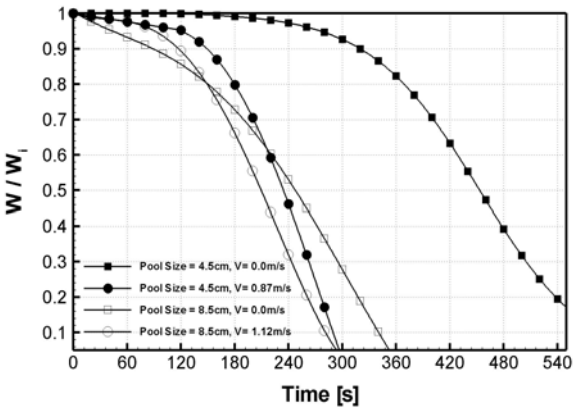

Figure 3. Time history of fuel weight

Based on transient mass loss of the fuel, it can be seen that the fuel in the longitudinally ventilated case at the critical ventilation velocity was consumed in approximately 1/2 and 5/6 of the time taken for the fuel in the naturally ventilated case to be consumed for both 4.5 *cm* and 8.5 *cm* pool size, respectively. It allows us to estimate that the HRR at critical ventilation velocity was about 50% and 20% higher than the naturally ventilated HRR.

2.5. Simulations

In order to examine the difference in back-layer distance between naturally ventilated HRR and varied HRR by longitudinal ventilation under critical ventilation velocity, three-dimensional simulations of smoke flow in the tunnel fire with the measured burning rates were carried out using FDS(Fire Dynamics Simulator; Ver. 406) code, developed by National Institute of Standards and Technology (NIST).

The FDS program describes fire-driven flows using LES turbulence model, the mixture fraction combustion model, finite volume method of radiation transport for a non-scattering gray gas, and conjugate heat transfer between wall and smoke flow. The governing equations for this code can be found in reference [12,13]. From experimental measurements, the critical ventilation velocities were 0.87 *m/s* and 1.12 *m/s* for the square heptane pool fire with a length of 4.5 *cm* and 8.5 *cm*, respectively. Also, HRR was obtained by measurement of mass loss rate of fuel for each case.

To show the effect of ventilation velocity on backlayering between naturally ventilated HRR and varied HRR by longitudinal ventilation under critical ventilation velocity, four runs were performed. The conditions specified for each of the simulation are shown in Table 2.

Table 2. Runs for numerical simulations

Run No	Pool Size (cm)	HRR(kW)	Ventilation Velocity (m/s)
RUN 1	4.5 4.5	HRR under Critical Ventilation	0.87
RUN 2	4.5 4.5	HRR under Natural Ventilation	0.87
RUN 3	8.5 8.5	HRR under Critical Ventilation	1.12
RUN 4	8.5 8.5	HRR under Natural Ventilation	1.12

3. RESULTS AND DISCUSSION

Three-dimensional simulations of smoke flow in the tunnel fire were carried out with the measured burning rates as input data in FDS code. This simulations show the difference of backlayering distance between naturally ventilated HRR and longitudinally ventilated HRR under critical ventilation velocity. All the flow field figures were processed by time averaging during quasi-steady state for each case.

Figure 4 shows the predicted temperature distributions at the symmetry plane at 4.5 *cm* pool size and critical ventilation conditions, *Vc*= 0.87 *m/s.*

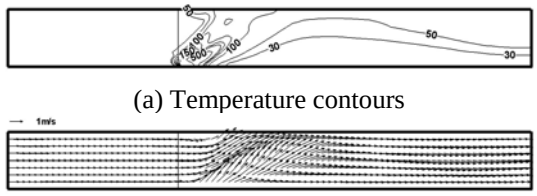

(a) Temperature contours

(b) Velocity vectors

Figure 4. The temperature contours and velocity vectors on the centreline for RUN 1 (Pool size of 4.5 *cm*, *Vc* =0.87 *m/s* and *Q* curve under critical ventilation velocity)

As can be seen from Fig.4, numerical simulation captured the features of the backlayering, fire plume and downstream smoke flow. As expected from experimental measurements, the predicted back-layer distance(-0.04 *m*) and the measured back-layer distance(0 *m*) are much the same because input parameters used in numerical simulation are the values obtained under critical conditions (ventilation velocity, HRR curve under critical ventilation velocity). According to Wu and bakar's tunnel fire plume theory[7], since the height of the intermittent flame between 250 and 500 was much smaller than the tunnel height, only the buoyant smoke flow reached the tunnel ceiling, in all fire sizes used in the present simulaton, longitudinally ventilated HRR under critical condtions was coverd in the one-third power region as dimensionless ventilation velocity. The predicted tilt angle of fire plume from vertical direction is about 53°.

The temperature contours and velocity vectors at the symmetry plane for RUN 2 are shown in Fig.5. Because HRR curve measured under naturally ventilation was used as input, about less 50% than that under critical ventilation, back-layer distance had negative value of -0.4 *m*, about 10 times than RUN 1 . The decrease in HRR was coupled with severe decrease in the back-layer distance. The predicted tilt angle of fire plume from vertical is about 60°.

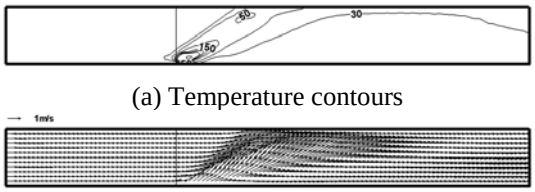

(a) Temperature contours

(b) Velocity vectors

Figure 5. The temperature contours and velocity vectors on the centreline for RUN 2 (Pool size of 4.5 *cm*, *V*=0.87 *m/s*, *Q* curve under naturally ventilation)

The temperature contours and velocity vectors at the symmetry plane for RUN 3 are shown in Fig.6. The predicted back-layer distance (+0.11 *m*) is similar to that measured back-layer distance. From Fig. 4 and 6, we can see a good degree of agreement between the predicted back-layer distance and measured back-layer distance because input parameters used in numerical simulation are the values obtained under critical conditions. And the predicted flame tilt angle is about 65°.

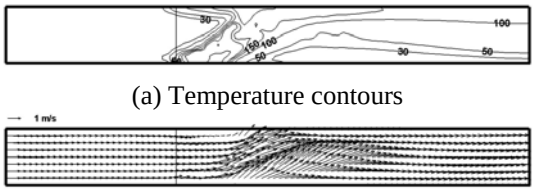

(a) Temperature contours

(b) Velocity vectors

Figure 6. The temperature contours and velocity vectors on the centreline for RUN 3 (Pool size of 8.5 *cm*, *V*=1.12 *m/s*, *Q* curve under critical ventilation velocity)

The temperature contours and velocity vectors at the symmetry plane for RUN 4 are shown in Fig.7.

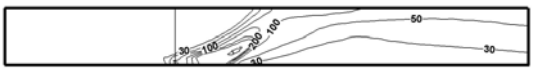

(a) Temperature contours

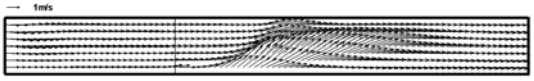

(b) Velocity vectors

Figure 7. The temperature contours and velocity vectors on the centreline for RUN 4 (Pool size of 8.5 *cm*, *V*=1.12 *m/s*, *Q* curve under naturally ventilation)

The predicted back-layer distance is -0.6 *m* and the predicted flame tilt angle is about 72 ° . As mensioned in the results of RUN 2, the decrease in HRR has been coupled with an severe decrease in the back-layer distance.

4. CONCLUSIONS

The conclusions are as follows.

1. The predicted back-layer distance is about the same as that of experimental results under critical conditions.

2. The difference in back-layering calculated by naturally ventilated HRR and varied HRR by longitudinal ventilation under critical ventilation velocity is a remarkable contrast, and is larger severely as fire size increases.

3. The critical ventilation velocity should be calculated on the basis of varied HRR by longitudinal ventilation velocity.

ACKNOWLEDGEMENTS

The authors gratefully acknowledge the financial and other support received for this project from “Development of the Fire Safety Evaluation and Prevention Technology for Railway System (T305C1000005-05C0100-00512)”.

REFERENCES

[1] Thomas PH., 1968, “The movement of smoke in horizontal passages against an air flow,” *Fire Research Station Note No. 723, Fire Research Station*, UK.

[2] Hinkley PL, 1970, “The flow of hot gases along an enclosed shopping mall.” *A tentative theory. Fire Research Note No. 807.*

[3] Heselden AJM, 1976, “Studies of fire and smoke behaviour relevant to tunnels.” *Proceedings of the Second International Symposium of Aerodynamics and Ventilation of Vehicle Tunnels*, Paper J1

[4] Danziger NH, Kennedy WD., 1982, “Longitudinal ventilation analysis for the Glenwood canyon tunnels”. *Proceedings of the Fourth International Symposium Aerodynamics and Ventilation of Vehicle Tunnels*, p. 169-86.

[5] Parsons Brinkerhoff Quade & Douglas, Inc., 1980, “Subway environmental design handbook, vol. II, Subway Environment Simulation (SES) Computer Program Version 3, Part I: User's manual”

[6] Oka Y, Atkinson GT., 1995, “Control of smoke flow in tunnel fires”. *Fire Safety J*. 25, 305-22.

[7] Y. Wu, M.Z.A. Bakar, 2000, “Control of smoke flow in tunnel fires using longitudinal ventilation systems - a study of the critical velocity”, *Fire Safety Journal*, 35, 363–390.

[8] Lee S.R, Ryou H.S., 2004, “An Experimental Study of the Effect of the Aspect Ratio on the Critical Velocity in Longitudinal Ventilation Tunnel Fires,” *Journal of Fire Sciences*, 23, 119-138.

[9] Carvel, R.O., Beard, A.N., Jowitt, P.W., Drysdale, D.D., 2001, “Variation of heat release rate with forced longitudinal ventilation for vehicle fire in tunnels.” *Fire Safety Journal* 36 (6), 569–596.

[10] Carvel RO, Beard AN, Jowitt PW., 2001, “A Bayesian estimation of the effect of forced ventilation on a pool fire in a tunnel.” *Civil Engng Environ Systems* , 18(4).

[11] Seung Shin Yang, Jae Seong Roh, Hong Sun Ryou, Myong O Yoon, Youn Tae Jung, 2006, “An Experimental Study on the effect of Ventilation Velocity on Burning Rate in Tunnel Fires – Heptane pool fire case”, *Building and Environment(Submit)*

[12] Kevin McGrattan, Glenn Forney, 2004, “Fire Dynamics Simulator(version 4) User's Guide”, *National Institute of Standards and Technology*, NIST Special Publication 1019

[13] Kevin McGrattan, 2004, “Fire Dynamics Simulator (version 4) Technical Reference Guide,” *National Institute of Standards and Technology*, NIST Special Publication 1018

Conference on Modelling Fluid Flow (CMFF'06)
The 13th International Conference on Fluid Flow Technologies
Budapest, Hungary, September 6-9, 2006

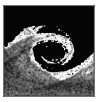

NUMERICAL SIMULATION OF TURBULENT STRATIFIED 3D FLOW IN TUNNEL FIRE WITH A FOUR-EQUATION TURBULENCE MODEL

Loïc AUDREN[1], Gabriel GIOVANNELLI[2], Gildas AUGUIN[1],
Bernard FORESTIER[1], Eric CASALÉ[3],

[1]Laboratoire MSNM-GP, UMR CNRS 6181, IMT La Jetée, Technopôle de Château-Gombert,
38 Rue Frédéric Joliot-Curie 13451 MARSEILLE Cedex 20. Email : audren@L3M.univ-mrs.fr
[2]AGEFLUID SARL, Les Pennes Mirabeau. Email : giovan@L3M.univ-mrs.fr
[3]FLUIDARAVIS, Chavanod. Email : fluidaravis@wanadoo.fr

ABSTRACT

An advanced turbulence model for driven flow in tunnel fire is tested. The turbulence modelling is based on the four-equation model with algebraic models for Reynolds stresses and turbulent heat fluxes. A high Reynolds number formulation is proposed, with new .boundary conditions for $\widetilde{\theta^2}$ and ε_θ . Radiation transfer is solved by the Discrete Ordinate Method. The wall temperatures are determined by solving the one-dimensional equation of conduction including convective and radiative heat transfers. Implemented in the CFD code PHOENICS, the validity of the model is examined through the full scale tests of Toulon tunnel. Results indicate the turbulent diffusion of heat through the interface to the cold layer. Thermal radiation plays an important role in the ceiling heat transfer and in the destratification by the means of the heat diffusion through the interface.

Keywords: buoyancy forces, heat transfer, radiation, turbulence

NOMENCLATURE

Latine notations

C_P	$[J\,kg^{-1}K^{-1}]$	specific heat coefficient
e_w	[-]	wall emissivity
g_i	$[m\,s^{-2}]$	gravitational acceleration
H	$[J\,kg^{-1}]$	enthalpy
I_i	$[W\,m^{-2}sr^{-1}]$	radiant intensity in the i-direction
h_c	$[W\,K^{-1}m^{-2}]$	heat exchange coefficient
k	$[m^2s^{-2}]$	turbulent kinetic energy
K_a, K_s	$[m^{-1}]$	absorption, scattering coefficients
P	$[Pa]$	pressure
Pr	[-]	Prandtl number
q	$[Wm^{-2}]$	thermal flux density
T	$[K]$	mean temperature
U_i	$[ms^{-1}]$	mean velocity in the i-direction

Greek notations

α	[°]	tunnel slope
β	$[K^{-1}]$	thermal expansion coefficient
ε	$[m^2s^{-3}]$	dissipation rate of turbulent kinetic energy
ε_θ	$[K^2\,s^{-1}]$	dissipation rate of temperature variance
ν	$[m^2s^{-1}]$	kinematic viscosity
κ	$[m^2s^{-1}]$	thermal diffusivity
λ	$[W\,m^{-1}K^{-1}]$	thermal conductivity
μ	$[kg\,m^{-1}s^{-1}]$	dynamic viscosity
θ	$[K]$	temperature fluctuation
ρ	$[kg\,m^{-3}]$	density
σ	[-]	turbulent Prandtl number
σ^B	$[W\,m^{-2}K^{-4}]$	Stefan-Boltzman constant
τ_w	$[kg\,m^{-1}s^{-2}]$	wall shear stress

Subscripts

p	near wall
t	turbulent
w	wall

Superscripts

h	thermal
rad	radiative
$conv$	natural convection
cf	forced convection
$\overline{}$	Reynolds average
$\widetilde{}$	Favre average

1. INTRODUCTION

During a tunnel fire, the strategy of the aerolic reaction is to obtain smoke stratification, favourable to the evacuation of the users in their maintaining air fresh.

The importance is thus related to the stratification of the smoke which will be the resultant of several physical dynamics: impact of the hot air jet, stratified flow of the hot fume due to buyancy, shear between the hot and cold layers, swirls influenced by the walls and the radiation.

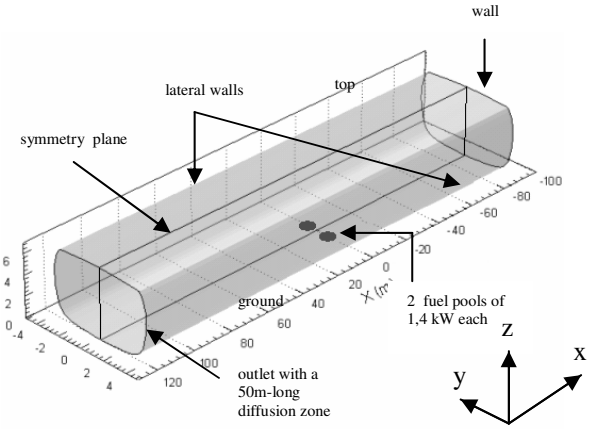

Figure 1: Geometry of the Toulon tunnel

In gravitational direction the transfer of turbulence is largely suppressed by the damping effect due to buoyancy.

At the same time, the turbulent and radiative vertical diffusion act to transfer, downward through the interface, the turbulent quantities as well as the mean temperatures.

For numerical-experimental comparisons in real tunnel fire, this paper proposes to test the turbulence modelling of Hanjalic *et al*. [1] where the Davidson model of Reynolds stresses [2] is introduced, coupled with radiative model using the Discrete Ordinate Method (DOM) [3] [4].

2. MATHEMATICAL MODEL

The governing equations consist of the Favre average equations together with the radiative heat transfer equation based on DOM [3].

$$\frac{\partial(\bar{\rho})}{\partial t} + \frac{\partial\left(\bar{\rho}\tilde{U}_j\right)}{\partial x_j} = 0 \tag{1}$$

$$\frac{\partial\left(\bar{\rho}\tilde{U}_i\right)}{\partial t} + \frac{\partial\left(\bar{\rho}\tilde{U}_j\tilde{U}_i\right)}{\partial x_j} = -\frac{\partial\bar{p}}{\partial x_i} + \frac{\partial}{\partial x_j}\left(\bar{f}_{ij} - \overline{\rho u_i u_j}\right) + \bar{\rho} g_i \tag{2}$$

$$\frac{\partial\left(\bar{\rho}\tilde{H}\right)}{\partial t} + \frac{\partial\left(\bar{\rho}\tilde{U}_j\tilde{H}\right)}{\partial x_j} = \frac{\partial\bar{p}}{\partial t} + \frac{\partial}{\partial x_j}\left(\frac{\mu}{Pr}\frac{\partial\tilde{H}}{\partial x_j} - \overline{\rho u_i h}\right) - \frac{\partial q_j^R}{\partial x_j} \tag{3}$$

with

$$\bar{f}_{ij} = \mu\left(\frac{\partial\tilde{U}_i}{\partial x_j} + \frac{\partial\tilde{U}_j}{\partial x_i}\right) - \frac{2}{3}\frac{\partial\tilde{U}_k}{\partial x_k}\delta_{ij} \tag{4}$$

$$-\overline{\rho u_i u_j} = -\bar{\rho}\widetilde{u_i u_j} \tag{5}$$

$$-\overline{\rho u_i \theta} = -\bar{\rho}\widetilde{u_i\theta} \tag{6}$$

$$-\frac{\partial q_j^R}{\partial x_j} = K_a\left(\sum_{j=1}^{2M}\omega_j I_j - 4I_b\right) \tag{7}$$

The density is evaluated through the ideal gas law.

2.1. Turbulence modelling

The model is based on the Hanjalic equations [1] for the turbulent quantities $k-\varepsilon-\widetilde{\theta^2}-\varepsilon_{\theta^2}$ modified in high Reynolds form:

$$\frac{D(\bar{\rho}k)}{Dt} = D_k + \bar{\rho}(P+G-\varepsilon) \tag{8}$$

$$\frac{D(\bar{\rho}\varepsilon)}{Dt} = D_\varepsilon + \frac{\varepsilon}{k}\bar{\rho}\left(C_{1\varepsilon}P + C_{3\varepsilon}G - C_{2\varepsilon}\varepsilon\right) \tag{9}$$

$$\frac{D\left(\bar{\rho}\theta^2\right)}{Dt} = D_{\theta^2} + 2\bar{\rho}\left(P_\theta - \varepsilon_\theta\right) \tag{10}$$

$$\frac{D(\bar{\rho}\varepsilon_\theta)}{Dt} = D_{\varepsilon_\theta} + \frac{\varepsilon_\theta}{k}\bar{\rho}\left(C_{1\varepsilon}^\theta P - C_{4\varepsilon}^\theta\varepsilon\right) + \frac{\varepsilon_\theta}{\overline{\theta^2}}\bar{\rho}\left(C_{3\varepsilon}^\theta P_\theta - C_{2\varepsilon}^\theta\varepsilon_\theta\right) \tag{11}$$

with

$$D_\varphi = \frac{\partial}{\partial x_j}\left(C_\varphi\frac{k}{\varepsilon}\overline{\rho u_j u_k}\frac{\partial\varphi}{\partial x_k}\right) \tag{12}$$

$$P = -\widetilde{u_i u_j}\frac{\partial\tilde{U}_i}{\partial x_j} \tag{13}$$

$$G = -\beta g_i\widetilde{u_i\theta} \tag{14}$$

$$P_\theta = -\widetilde{u_i\theta}\frac{\partial\tilde{T}}{\partial x_j} \tag{15}$$

The Davidson modelling [2] for Reynolds stresses which accounts for the anisotropic turbulence due to buoyancy is written as:

$$-\widetilde{u_i u_j} = \nu_t\left(\frac{\partial\tilde{U}_i}{\partial x_j} + \frac{\partial\tilde{U}_j}{\partial x_i}\right) - \frac{2}{3}k\delta_{ij} - \frac{k}{\varepsilon}C\left(G_{ij} - \frac{2}{3}\delta_{ij}G\right) \tag{16}$$

$$G_{ij} = -\beta\left(g_i\widetilde{u_j\theta} + g_j\widetilde{u_j\theta}\right) \tag{17}$$

The algebraic heat flux model is given by the following Hanjalic and Vasic formulation [5] for buoyancy driven flow:

$$-\widetilde{u_i\theta} = C_\theta\frac{k}{\varepsilon}\left[\widetilde{u_i u_j}\frac{\partial\tilde{T}}{\partial x_j} + \xi\widetilde{u_j\theta}\frac{\partial\tilde{U}_i}{\partial x_j} + \eta g_i\beta\widetilde{\theta^2}\right] \tag{18}$$

The excessive production of k near the stagnation point is tempered by the modification of

Kato and Launder [6] for the production term by shear:

$$P = C_\mu \varepsilon S \Omega \tag{19}$$

And if the buoyancy is to increase the turbulence when the vertical turbulent heat flux is greater than zero, the contribution from the vertical heat flux should bear the same weight on the modifications to the shear stress as the horizontal one. So we modify the shear stress generation rate owing to buoyancy in the vertical plane (Liu and Wen [7]):

$$G_{i3} = \beta g \widetilde{u_i \theta} \frac{1}{2}\left(1 + \max\left(\widetilde{w\theta}, \left|\widetilde{u_i \theta}\right|\right) / \left|\widetilde{u_i \theta}\right|\right) \tag{20}$$

It will tend to narrow the vertical plume and to widen a little the hot layer.

2.2. Radiation

The radiative transport equation for the intensity for an absorbing and emitting medium is:

$$\frac{\partial I}{\partial \xi} = -K_a I + K_a I_b \tag{21}$$

where ξ is the line-of-sight distance in the direction of propagation of the radiant intensity I, κ is the absorption coefficient of the medium, and I_b is the local blackbody intensity. The development of the discretized form using the DOM is initiated by subdividing the solutions domain into a number of control volumes or quadrant. Application of Eq. (23) to discrete direction i yields in 3D [3]:

$$\mu_i \frac{\partial I_i}{\partial x} + \eta_i \frac{\partial I_i}{\partial y} + \zeta_i \frac{\partial I_i}{\partial z} = -K_a I_i + K_a I_b \tag{22}$$

where $I_i = I(x,y,z;\mu_i,\eta_i,\zeta_i)$ and i=1 to 4M, M denoting the number of discrete angles within a quadrant. Here we have M=6 for a S6 approximation.

The finite-difference form of Eq.(22) is derived by applying this expression to the control volume, where is integrated over the six faces. The leaving intensities at these faces being approximated by:

$$I_i^e = \frac{1}{\psi}\left[I_i^P - (1-\psi) I_i^w\right] \tag{23a}$$

$$I_i^n = \frac{1}{\psi}\left[I_i^P - (1-\psi) I_i^s\right] \tag{23b}$$

$$I_i^t = \frac{1}{\psi}\left[I_i^P - (1-\psi) I_i^b\right] \tag{23c}$$

where I^e_i, I^n_i, I^t_i are radiant intensities leaving the control volume by the east, north and top face respectively, and ψ is the finite-difference weighting factor, Eq. (22) yields:

$$I_i^P = \frac{|\mu_i| A_X I_i^w + |\eta_i| A_Y I_i^s + |\zeta_i| A_Z I_i^b + \psi K_a I_b^P \Delta V}{|\mu_i| A_X + |\eta_i| A_Y + |\zeta_i| A_Z + \psi K_a \Delta V} \tag{24}$$

Here ψ=1 for a "step" schema.

2.3. Wall boundary conditions

The radiative conditions at the walls are stated as follows (Sanchez *et al* [3] and Morvan *et al* [8]):

$$I_i^{wall} = \frac{e_w I_{bw}}{\pi} + \frac{1-e_w}{\pi} \sum_{\substack{j=1 \\ \vec{n}.\vec{s}<0}}^{2M} \omega_j I_j \left|\vec{n}.\vec{s}_i\right| \tag{25a}$$

$$q_w^{rad.} = \frac{e_w}{2-e_w}\left(\sigma^B T_W^4 - \sum_{\substack{j=1 \\ \vec{n}.\vec{s}<0}}^{2M} \omega_j I_j \left|\vec{n}.\vec{s}_i\right|\right) \tag{25b}$$

The wall temperature is determined by:

$$\frac{\partial T}{\partial n} = \frac{q_w^h / \overline{\rho}\, C_P}{\kappa_\theta \left(\tau_w / \overline{\rho}\right)^{1/2} y} \tag{26}$$

where the wall total heat flux is determined from the radiative heat flux, the natural and forced convective heat fluxes via the adiabatic condition:

$$0 = q_w^h + 2\, q_w^{rad} + q_w^{conv} + q_w^{cf} \tag{27}$$

$$q_w^{conv.} = h_c\left(T_W - T_\infty\right) \tag{28}$$

$$h_c = 0.16\lambda\left(g\beta(T_W - T_\infty)\frac{Pr}{\nu^2}\right)^{1/3} \qquad \lambda = \rho C_P \kappa \tag{29}$$

$$q_w^{cf.} = h_c^{cf}\left(T_W - T_\infty\right) \tag{30}$$

$$h_c^{cf} = C_p\, \tau_W \,/ U_\infty \tag{31}$$

The classical wall functions are used for the streamwise velocity, the turbulent kinetic energy and its dissipation rate:

$$\tau_w = \frac{\overline{\rho} C_\mu^{1/4} k_P^{1/2} U_P}{U^+} \tag{32}$$

$$\rho P = \tau_W \frac{U_P}{y_P} \tag{33}$$

$$\overline{\rho}\varepsilon = \overline{\rho}\; C_\mu^{3/4}\; k_P^{3/2}\; U^+ / y_P \tag{34}$$

$$\varepsilon_P = C_\mu^{3/4} k_P^{3/2} / \kappa y_P \tag{35}$$

New boundary conditions for the temperature variance and its dissipation rate are employed. In $\widetilde{\theta'^2}$-equation where the diffusion to the wall is assumed to be zero, the generation and dissipation terms are modified to take account of the wall heat flux:

$$\rho P_\theta = \frac{q_w^h}{C_p}\frac{\partial T}{\partial n} \tag{36}$$

$$\overline{\rho}\varepsilon_\theta = \rho \widetilde{\theta_P^2} \frac{U_P}{y_P} \tag{37}$$

The dissipation rate ε_θ is prescribed instead of obtaining from its equation:

$$\varepsilon_{\theta P} = \frac{C_\mu^{1/4} k_P^{1/2} \widetilde{\theta_P^2}}{\kappa_\theta y_P} \qquad (38)$$

Constant values for these equations are presented in the following table:

Table 1: constant values

C_p	Pr_θ	μ	C_μ	$C_{\theta 2}$	ξ	η	C
1005	0.9	1.82e-5	0.09	0.18	0.6	0.6	0.22
C_k	C_ε	C_θ	e_w	κ	κ_θ	Ka	Ks
0.22	0.16	0.28	0.9	0.41	0.45	0.1	0.01
$C_{1\varepsilon}$	$C_{2\varepsilon}$	$C_{3\varepsilon}$	$C_{1\varepsilon}^\theta$	$C_{2\varepsilon}^\theta$	$C_{3\varepsilon}^\theta$	$C_{4\varepsilon}^\theta$	
1.44	1.92	1	0.72	2.2	1.3	0.8	

2.4. Numerical methods

This modelling is implemented into the commercially available code PHOENICS. The numerical approach is based on the finite-volume method calculated on a cartesian staggered grid of 194x59x66 cells. A symmetry plane is used in the z-direction. The first near wall nodes are located in the turbulent region. The SIMPLEST algorithm [10] is adopted for pressure calculations. The convective terms are approximated by means of upwind scheme, at second-order for the velocity and at first order for the scalars.

The fire is represented as a volume heat source with a specific heat flux per unit volume

3. RESULTS

The full scale fire tests [11] have been performed in the road tunnel of Toulon. The rectangular section is 6,7 m high, 220m long and 10 m wide. The positive tunnel slope is 1%.

A fire load of 2,8 MW was reproduced by two fuel pools 1m² area and placed at 1685 m from the entry.

The five transversal sections were installed between –12m and +75m from the fuel pool location. They were provided with K or T type thermocouples and with Mc Caffrey velocity probes linked to differential pressure sensors. The contribution of turbulent structures smaller than 1 m is not taken in account, due to temporal filtering (one acquisition every 3 seconds). Variances of temperature and velocity have been roughly estimated from extrapolation of spectral densities.

Experimental results show a sheared thermally stratified layer thickening with the abscissa and a diffusive thermal layer penetrating the return flow.

An internal hydraulic jump is observed in the near field of the fire and a stable discharge configuration is obtained.

Profiles of mean temperature and velocity are in good agreement with experimental data. Three models are proposed in order to compare: the present model (a), the actual four-equation model with a six-flux radiation model (b) (Spalding [12]), and a standard k-ε model with DOM radiation (c) (Figures 2 and 3).

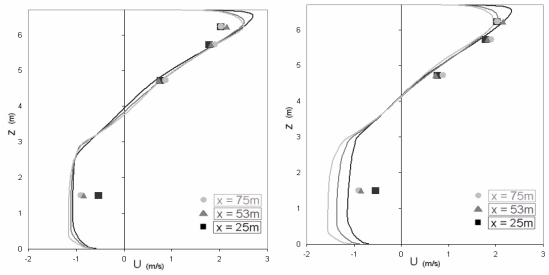

(a) (b)

Figure 2: Mean longitudinal velocity: computed (lines) and measured (points) at 25, 53 and 75 m from fire.

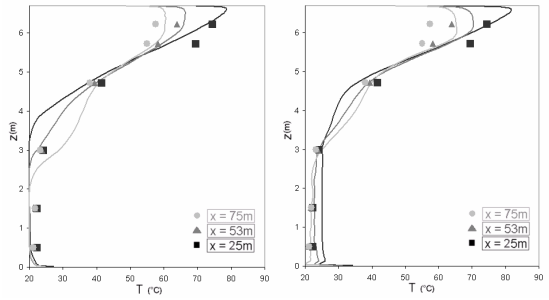

(a) (b)

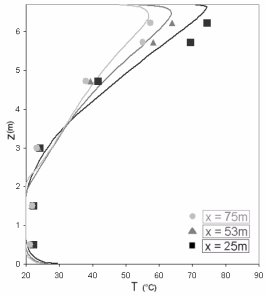

(c)

Figure 3: Mean temperature: computed (lines) and measured (points) at 25, 53 and 75 m from fire.

As observed, the k-ε model is more dissipative and isotropic, and so tends to destratify, than the four-equation model, thanks to $C_\theta \frac{k}{\varepsilon} \eta g_i \widetilde{\beta\theta^2}$ for its contribution on stratification, opposite at

$C_\theta \frac{k}{\varepsilon} \widetilde{ww} \frac{\partial \tilde{T}}{\partial z}$ in Eq. (18). The six-flux model for radiation, due to its equation, creates a false-diffusion for temperature into the cold layer and so affect the stratification. The DOM model can warm the ground without directly disturbing this cold layer by the middle-high section.

The velocity and temperature variances decrease with the abscissa in the hot upper layer due to buoyancy effects that affect the turbulence (Figures 4 and 5). But in the cold layer the experimental data show that the closer to the fire source they are, the smaller they are.

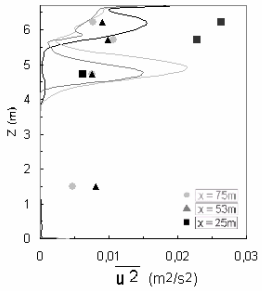

Figure 4: Variances of longitudinal velocity fluctuations computed (lines) and measured (points) at 25, 53 and 75 m from fire.

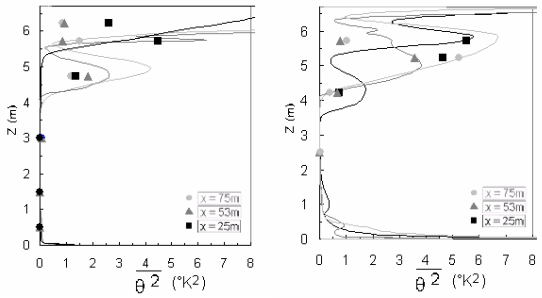

Figure 5: Temperature variances computed (lines) and measured (points) at 25, 53 and 75 m from fire, in the longitudinal median plane (a) and in the plane close to the lateral wall (b)

We can observe in Fig.4 the presence of two maxima in the profile of longitudinal variance fluctuations, one in the upper layer and the other in the cold layer (out boundary layers), and of a relaminarization zone between the two layers.

For the variance of the temperature, the fluctuations increase with abscissa in the diffusion zone, involving destratification. The Fig.5 (b) shows the dynamical and thermal effects close to the lateral wall, and the correct behaviour of the simulation.

The destratification of the flow with the abscissa is the result of a vertical diffusive exchange from the hot layer to the cold one (Fig.6):

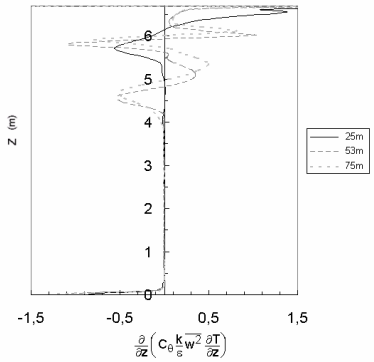

Figure 6: Vertical diffusion term for temperature $\frac{\partial}{\partial z}\left(C_\theta \frac{k}{\varepsilon} \overline{w^2} \frac{\partial T}{\partial z} \right)$

4. CONCLUSION

The simulations with the four-equation turbulence model of Hanjalic coupled with a radiation modelling (DOM) are compared to a full scale fire test.

The main contribution was in modifying the boundary conditions for a high Reynolds number formulation for the temperature variance equation and its dissipation rate.

The model provides an acceptably accurate method for simulation of stratified flow. The turbulence diffusion (anisotropy due to buoyancy) is well described as show the variance profiles.

This modelling has been tested for a stably stratified flow (without ventilation), and it would be interesting to evaluate it in ventilated tunnel with strong three-dimensional effects (destratification mechanisms).

REFERENCES

[1] Hanjalic K., Kenjeres S., Durst F., 1996. "Natural convection in partitioned two-dimensional enclosures at higher Rayleigh number". *International Journal of Heat Mass Transfer*, vol.39, n°7, p.1407-1427

[2] Davidson L., 1990. "Second order corrections of the k-ε model to account for non-isotropic effects due to buoyancy". *International Journal of Heat Mass Transfer*, vol.33, n°12, p.2599-2608

[3] Sanchez A., Smith T.F., 1992. "Surface radiation exchange for two-dimensionnal rectangular enclosures using the discrete ordinates method". *Journal of Heat Transfer*, Vol.114, p.465-472

[4] Fiveland W.A., 1988. "Three-dimensionnal radiative heat-transfer solutions by the discrete-ordinates method". *Journal of Thermophysics*, Vol.2 No. 4, p.309-316

[5] Hanjalic K., Vasic S., 1993. “Computation of turbulent natural convection in rectangular enclosures with an algebraic flux model”. *International Journal of Heat Mass Transfer*, vol.36, n°14, p.3603-3624

[6] Kato S., Launder B., 1993. “The modelling of turbulent flow around stationary and vibrating square cylinders”. *9th Symposium Turbulent Shear Flows. Actes de colloque*, vol.10, n°4

[7] Liu F., Wen J.X., 1999. “Development and validation of an advanced turbulence model for buoyancy driven flows in enclosures”. *International Journal of Heat Mass Transfer*, vol.42, p.3967-3981

[8] Morvan D., Porterie B., Larini M., Loraud J.C., 1998. “Numerical simulation of turbulent diffusion flame in cross flow”. *Combustion Sciences and technology*, vol.140, p.93-122

[9] Porterie B., Loraud J.C., 2001. “The prediction of some compartment fires. Part 1: Mathematical model and numerical method”, *Numerical Heat Transfer*, Part A, Vol.39, p.139-153

[10] Patankar S.V., Spalding B., 1972. “A calculation procedure for heat, mass and momentum transfer in three-dimensional parabolic flows”. *International Journal of Heat and Mass Transfer*, vol.15, p.1787-1806

[11] Giovannelli G., Auguin G., Forestier B., 2000. “Simulation d’incendie dans la traversée souterraine de Toulon”. *Rapport d’essai pour la DDE83*, AGEFLUID.

[12] Spalding D., 1980. “Mathematical Modelling of Fluid Flow, Heat Transfer and Chemical Reaction Processes”. *A Lecture Course*. Londres, Imperial College of Science and Technology.

Conference on Modelling Fluid Flow (CMFF'06)
The 13th International Conference on Fluid Flow Technologies
Budapest, Hungary, September 6-9, 2006

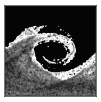

ADJUSTMENT OF VENTILATION WINDOWS OF WORKSHOPS BY USING MATHEMATICAL OPTIMIZATION

László GYULAI[1], Szilárd SZABÓ[2]

[1] Corresponding author: Department of Combustion Technology, University of Miskolc. H-3515 Miskolc-Egyetemváros.
Tel.: +36 46 565 108, Fax: +36 46 431 820, E-mail: aramgyl@uni-miskolc.hu
[2] Department of Fluid and Heat Engineering, University of Miskolc. E-mail: aram2xsz@uni-miskolc.hu

ABSTRACT

Adjustable windows serve to regulate the natural ventilation of large workshops. The efficiency of the ventilation can be characterised by the number of air changes. For technological and health protection purposes there is a required "number of air changes per hour" which should be ensured for any weather conditions. For a fixed adequate number of air changes per hour the appropriate angles of window slats can be determined by using the numerical CFD simulation coupled with mathematical optimisation. The present paper introduces an application of this method for a smelter potroom. The FLUENT commercial software package was used for the numerical simulations and the DYNAMIC–Q optimisation algorithm for the mathematical optimisation. This paper represents an approximate solution for the automatic mesh generation needed for the three-dimensional optimisation, and an example of its optimisation.

Keywords: CFD simulation, smelter pot room, air change number, natural ventilation, optimization

1. INTRODUCTION

The degree of natural ventilation in a large workshop is strongly dependant on the prevailing weather conditions. Ventilation depends especially on the wind speed and velocity profile of the wind [4]. In the case of natural ventilation, the only way to regulate the ventilation is to adjust the window slats. The relation between the angle at which the window slats are opened and the effectiveness of ventilation can be analysed by numerical simulation, assisted by wind tunnel measurements on scaled models [5]. The numerical simulation focuses on both the interior of the workshop and its nearby surroundings. In the first phase of the numerical simulation a two-dimensional model was used consisting of a characteristic cross-section of the workshop [6]. Simulations made by this simple (2D) model are relatively easy to perform, but have two main drawbacks. First of all, the side windows at both sides of the real workshop do not cover the wall continuously, because there are gaps (walls and columns) among them. The width of the side windows is approximately equal to the width of the wall between windows. Second, there are corridors among the smelter pots parallel with the characteristic cross-section that can not be modelled in two dimensions, therefore the flow pattern inside the workshop can never be realistically represented by this model. Therefore a three-dimensional model of the workshop has been developed [5]. Instead of modelling the complete workshop (440 m long) just one segment (approx. 9 m, having 4 smelter pots) has been considered for the 3D simulations. This model was validated by on-site measurements [7]. Both numerical simulations (based on the 2D and 3D models) were carried out using the FLUENT commercial software package [1].

An algorithm has been developed in which CFD simulations are coupled with a mathematical optimisation method, ensuring an appropriate degree of ventilation by finding the optimal opening angles of window slats for different weather conditions. The method was tested on the 2D model as its CPU time is short [8]. The name of the applied optimisation algorithm is DYNAMIC-Q [2,3]. This method is especially applicable for optimising complex and time-consuming CFD simulations, because it can find the target value within a few optimisation cycles. After success in 2D optimisation, an extended 3D model was developed. Some simplification of the 3D model was needed and automatic grid generation was required to deal with the adjustable windows. This modification is detailed below.

2. COMPARISON OF 2D AND 3D SIMULATIONS

The structure of the smelter potroom can be seen in its plexiglass model. Figure 1 shows the location of electrolytic smelter pots in 4 rows (176 altogether in the actual potroom) and the adjustable side windows.

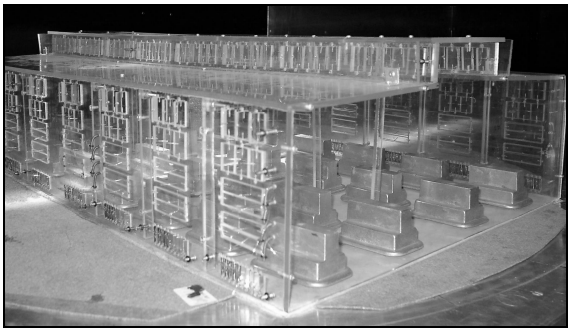

Fig 1. The plexi-glass model of the workshop for wind-tunnel measurements

The 2D model investigates a typical cross-section which intersects the smelter pots (illustrated in Figure 2). The adjustable middle side windows can be seen, as well as the bottom and roof windows which are fixed fully open.

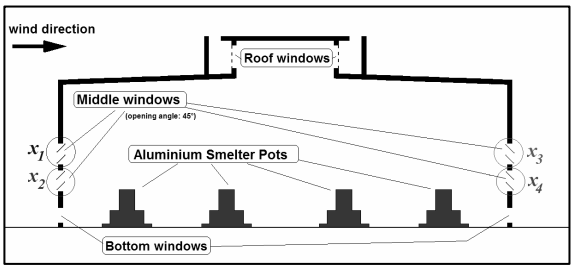

Figure 2. The cross-section of the workshop for 2D simulation

The 3D simulation contains a segment of the workshop including one pot of each row. Figure 3 shows that neither the middle windows nor the pots extend across the whole segment, and that is why the flow field is different from the 2D flow field. A typical setting of window slats was used for comparison between the 2D and 3D simulations. A typical example illustrates the differences between them. The wind has a parabolic wind-profile (at the height of $z_0 = 1.5m$ the reference velocity is $v_0 = 1.05m/s$) perpendicular to the longitudinal axis of the workshop. The ambient temperature was set to $T_0 = 300K$. The opening angles of the middle windows are: $x_1 = 30^\circ$, $x_2 = 30^\circ$, $x_3 = 75^\circ$, $x_4 = 75^\circ$ (see Fig. 2. for determination of variables x_1 to x_4).

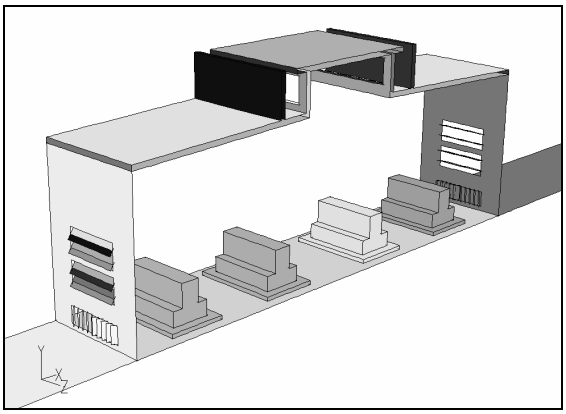

Figure 3. One segment of the workshop for the 3D simulations

Simulations made for the 2D and 3D models under the same boundary conditions gave the following results: the number of air changes per hour were $L_{2D} = 47.4/h$ and $L_{3D} = 28.3/h$, respectively. The number of air changes per hour L is defined by the following form:

$$L\left[\frac{1}{h}\right] = \frac{q_m\left[\frac{kg}{s}\right]\cdot 3600\left[\frac{s}{h}\right]}{\rho\left[\frac{kg}{m^3}\right]\cdot V\left[m^3\right]} \qquad (1)$$

where:

V volume of the pot room,

ρ the mean density of air in the pot room,

q_m the net flow rate of fresh air enters through the windows.

The required number of air changes per hour is $L_0 = 30/h$.

The difference between the two models originates from the problems of the 2D model. The fact that $L_{3D} < L_{2D}$ is caused by the assumption of windows of infinite length (i.e. with no wall between) in the 2D model. In the 3D model there are walls at both sides of a window, and their size ratio is 1 to 1. This means that even having the same geometry for 2D and 3D, the area through which air can flow is substantially less in the 3D model than in the 2D. In the 2D model there are no neighbouring walls for middle window, so the air flows through the windows without any blockage; just the direction of the flow is influenced by the angle of the window slats. A substantial part of the incoming fresh air crosses the workshop quickly as a cross-draft. Air exits the workshop also through the leeward side windows, instead of just through the roof windows as was expected because of heat convection. Figure 4 shows this phenomenon by path lines. However, the situation is totally different in the 3D model. Here, the effect of the draft is minimal. The incoming fresh air mixes with the hot polluted air

and the majority of it exits through the roof windows (as expected). These effects are seen in Figure 5. If the correct way of exit of the exhausted gases leads through the roof windows, then the number of air change per hour of the roof windows L' should be considered. Its computed value for the 2D model is $L'_{2D} = 17.6/h$ ($L_{2D} = 47.4/h$), and for 3D $L'_{3D} = 23.7/h$ ($L_{3D} = 28.3/h$). Although L_{2D} seems to be extremely high for a 2D model, only just over one-third of the exited air exits through the roof windows. In the 3D model the situation is reversed. In this case L_{3D} is less than L_{2D}, but most of the exhausted air mass exits through the roof windows (L'_{3D}).

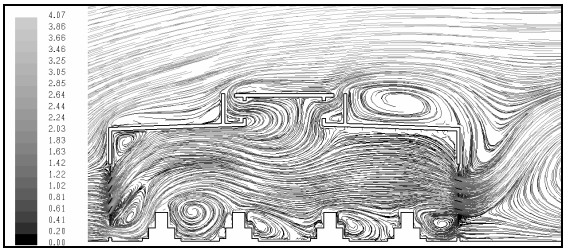

Figure 4. Path lines coloured by velocity magnitude [m/s] of the 2D model ($v_0 = 1.05 m/s$, $T_0 = 300K$)

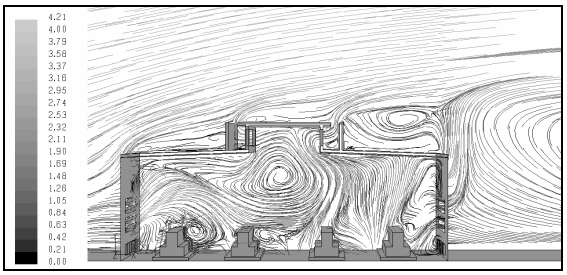

Figure 5. Path lines coloured by velocity magnitude [m/s] in the main cross-section of the 3D model ($v_0 = 1.05 m/s$, $T_0 = 300K$)

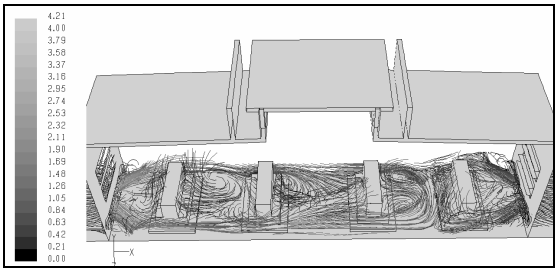

Figure 6. Path lines coloured by velocity magnitude [m/s] at the height of ($z = 1.5m$) by the 3D model ($v_0 = 1.05 m/s$, $T_0 = 300K$)

The present investigation has proved the empirical fact that the higher the reference velocity, the stronger the developed draft. This phenomenon appears also with the 3D model but only when the reference velocity is higher than $v_0 > 3m/s$. The phenomenon also depends on the opening angles of the window slats. Figure 6 shows the flow around the smelter pots in the 3D model. Naturally, a 2D simulation cannot display this. With the more realistic 3D model it was possible to perform a detailed analysis of the effect of ambient weather conditions on the ventilation of the potroom [5].

3. OPTIMIZING THE 2D MODEL

Although the results of the 2D model are not sufficient for making conclusions and suggestions when handling real problems, they may help in identifying tendencies of the effects of weather changes. 2D simulations are also applicable for testing of combined CFD modelling and mathematical optimisation, as shown in [9]. The objective function for the CFD optimisation is:

$$f(x) = |L(x) - L_0| \,, \qquad (2)$$

where L is defined by Eq. (1).

The design variables, adjusted in the optimisation, are the respective window angles x_1, x_2, x_3, x_4 (see Fig. 2). The optimisation procedure searches for the minimum value of the objective function (see Eq. (2)), which corresponds to the best possible match between the actual and adequate number of air changes per hour. The optimisation is carried out for different prevailing wind velocities, corresponding to different weather conditions.

However the optimization process in 2D was done for the number of air change per hour of the roof windows L' instead of L. In this case the entering fresh air mixes with the inner air (which is warm and polluted), and exits through the roof windows. Exit through the side windows is to be avoided.

4. 3D CFD MODEL FOR OPTIMIZATION

When carrying out a 3D optimization, the vital point is to ensure automatic grid generation. The geometry should be changed with each optimisation cycle, as the opening angle of the middle windows is the design variable, and thus a new mesh is required. The volume elements should not be distorted during meshing. Mesh quality can be characterised by its "equi-angle-skew" factor. This is scaled from 0 to 1, with zero being good and 1 poor quality, and for reliable results it should be under 0.8. The mesh quality affects the numerical simulation, and a smooth mesh is recommended. But in some special cases it is not so easy to do so. The case is even worth, when mesh should be generated automatically, without any human control. In the present model the geometry should

have been modified a little, in order to avoid such problems. In the present case, mesh quality problems may occur, especially with automatic meshing, if the windows are nearly closed. The window slats and the neighbouring walls intersect (see Fig. 7) at a critical angle ($0^\circ < x < 5^\circ$). Our solution was to deform the neighbouring sections of wall coupled with the window slats. Figure 8 shows the modified geometry, where the window slats are dark-grey and its neighbouring walls are light-grey. In this way the angle x is always equal to 0°. The effect of this modification on the geometry can be neglected.

Figure 7. The critical side (middle) windows

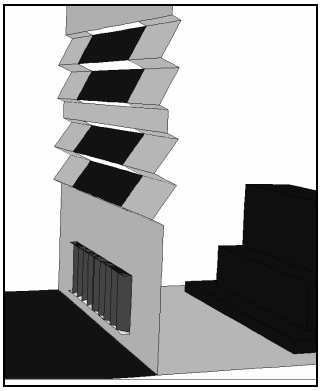

Figure 8. The modified wall geometry

Figure 9 shows a set of variations of different opening angles of window slats (*cf* Fig. 3 for original geometry). In the right upper corner of the figure a closed window is shown, and therefore the angle of the neighbouring walls does not require adjustment.

We analysed the effect of the geometry modification on the flow field and on ventilation. For comparative investigation, a typical weather condition and relatively widely opened middle windows were chosen. These conditions were used in Section 2 for the comparison of 2D and 3D optimization. No significant differences in the global parameters of ventilation were found as a result of the modification. The ventilation number changed from $L'_{3D} = 23.7/h$ to $L'_{3D,m} = 23.3/h$.

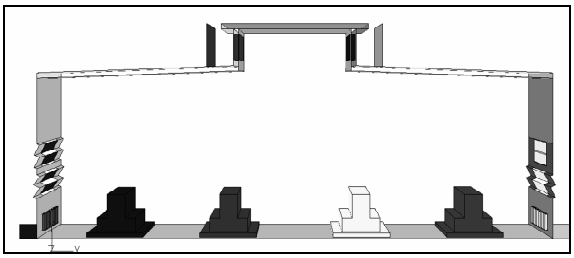

Figure 9. 3D model illustrating windows at different angles

In the structure of flow and in the temperature field there is only a minimal difference. The effect of the modification was found to be negligible compared to the neglect of other factors from previous simplifications (internal columns, supporting pillars, exhaust pipelines, etc. were ignored). The effect of wall shape can be seen by comparing Fig. 5 (flat, unmodified wall) and Fig. 10 (modified, wavy wall).

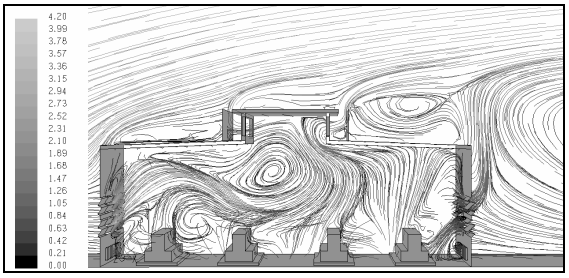

Figure 10. Path lines coloured by velocity magnitude [m/s] in the main cross-section of the workshop for the modified 3D model ($v_0 = 1.05 m/s$, $T_0 = 300K$)

The conclusion of the investigation is that the modified geometrical model is also suitable for modelling the ventilation of a workshop and for coupling with an optimisation procedure. Naturally, further possibilities will be investigated in order to find alternative methods for automatic meshing with less compromise.

5. THE 3D OPTIMIZATION

The modified 3D model used for optimisation was built into the DYNAMIC-Q optimization method. The objective function remains the same as defined in Eq. (2), as in 2D, but L' was used instead of L. The design variables of the optimisation were the middle window opening angles x_1, x_2, x_3, x_4. The optimisation procedure was used

under different weather conditions. Here we present a case when the weather conditions were as used above, i.e. the reference velocity was $v_0 = 1.05 m/s$, perpendicular to the length axis of the workshop, and the ambient temperature was $T_0 = 300K$. Based on the results of the optimisation, we can find how to adjust the ventilation windows in different weather conditions in order to approach (or reach) the required number of air changes per hour $L_0' = 30/h$.

Figure 11 and Table 1 show the changes of the $f(x) = |L'(x) - L_0'|$ objective function in the main optimisation.

Table 1. The results of optimisation cycles

No. of cycles	$f(x)$	$L'[1/h]$	$x_1[^\circ]$	$x_2[^\circ]$	$x_3[^\circ]$	$x_4[^\circ]$
0	6.04	23.96	30.00	30.00	30.00	30.00
1	5.05	24.95	20.00	20.00	20.00	40.00
2	4.94	25.06	14.08	26.68	10.00	30.37
3	5.08	24.92	24.08	36.68	0.00	20.37
4	4.83	25.17	14.48	29.19	0.00	29.86
5	4.77	25.23	17.71	39.19	1.75	32.97
6	4.63	25.37	13.23	34.38	0.00	37.61
7	4.78	25.22	21.36	33.79	0.00	36.69
8	4.73	25.27	11.36	43.79	10.00	46.69
9	5.27	24.73	20.08	46.07	0.00	45.78
10	4.45	25.55	10.08	36.97	0.00	55.78
11	4.31	25.69	16.63	39.48	0.00	54.90
12	5.83	24.17	26.63	49.48	10.00	44.90
13	4.31	25.69	16.63	39.48	0.00	54.90

Optimisation is complete in the 13th cycle as it has found the same minimum of the objective function as in the 11th optimisation cycle. Its value is:

$$f(\boldsymbol{x}_{opt}) = |L'(\boldsymbol{x}_{opt}) - L_0'| = 4.31\frac{1}{h}. \qquad (3)$$

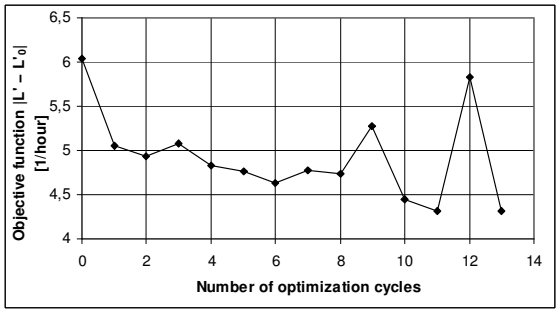

Figure 11. The changing of the objective function according to the number of optimisation cycles

Analysis of the results should be begun with the original problem, namely the number of air changes per hour of the workshop. Figure 12 illustrates the changes of the number of air changes per hour according to the number of optimisation cycles. This figure includes the data system of the main- and sub-cycles of optimisation too. The DYNAMIC-Q algorithm uses a gradient based successive approximation of sub-problems, and therefore it is necessary to have sub-cycles, when just one design variable is changed. With four design variables, the number of sub-cycles in one main optimisation cycle is also four.

Based on the results of the sub-cycles, the optimiser calculates the direction and degree of change for the design variables in the next main cycle.

Figure 12 shows that in this case there was no sub-cycle that would give a better result than:

$$L'(x_{opt})^{(11.0)} = 25.69\frac{1}{h}, \qquad (4)$$

which is the optimum.

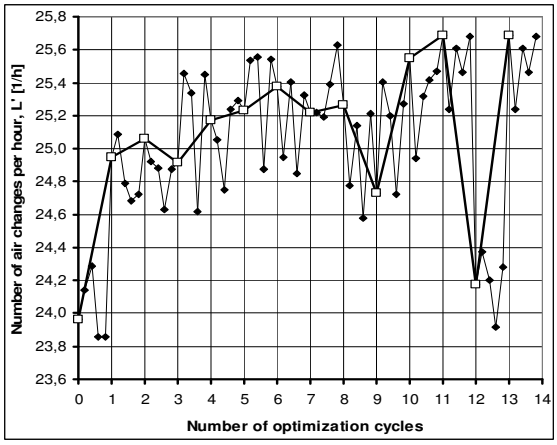

Figure 12. Number of air changes per hour versus optimisation cycle

It is very interesting that the value of the number of air changes per hour $L'^{(3.1)} = 25.46\frac{1}{h}$ is very close to the optimum even as soon as in sub-cycle 3.1. The difference is only 0.9%. This proves that the optimiser searched for the optimum in the proper direction and has almost found it within just a few cycles. The precise value of the final optimum has mathematical importance, but the improvement in ventilation is not significant. In order to choose among window settings giving similar results, other aspects can be taken into consideration, such as the temperature distribution in the workshop or the extent of the draft. The initial (cycle 0.0) opening angles of middle windows were: $x_1^{(0.0)} = x_2^{(0.0)} = x_3^{(0.0)} = x_4^{(0.0)} = 30^\circ$. Figure 13 shows the variation in the middle window opening angles according to the main and sub-cycles, and Fig. 14 illustrates them just in the main cycles.

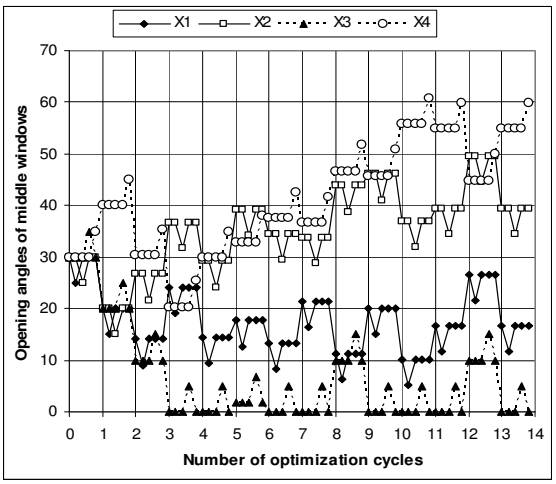

Figure 13. Variation of the opening angles of middle windows for main and sub-cycles

As was mentioned above, just one of the angles was modified in each sub-cycle shown in Fig. 13. In the optimisation algorithm the rate of change of the design variable, i.e. the step size, was set to 5° in the present investigation.

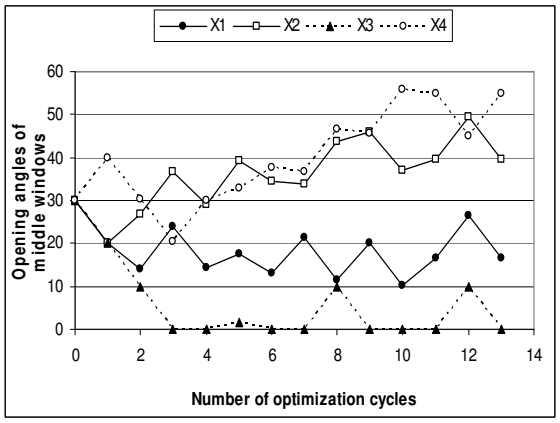

Figure 14. Variation of the opening angles of middle windows for main cycles

Figure 14 shows that after the fourth main cycle the upper middle windows are closed or almost closed, having $x_1^{(4.0\div4.4)} = 10^\circ \div 20^\circ$, $x_3^{(4.0)} = 0^\circ$, and this state seems to be stabilized. The lower middle windows tend to open to a larger extent, and moving from $x_2^{(4.0)} \approx x_4^{(4.0)} \approx 30^\circ$ (at the 4th cycle) to $x_2^{(11.0)} = 39.5^\circ$, $x_4^{(11.0)} = 54.9^\circ$ in the 11th cycle. In the meanwhile the number of air changes per hour increases just a little, from $L'^{(4.0)} = 25.17\frac{1}{h}$ to the value $25.69\frac{1}{h}$, as shown in Eq. (4). Even the optimal number of air change per hour is substantially (14%) lower than that required ($30\frac{1}{h}$).

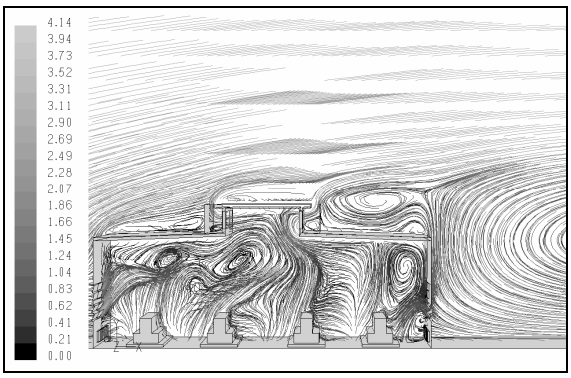

Figure 15. Path lines coloured by velocity magnitude [m/s] in the main cross-section of the 3D model at cycle 4.0 ($v_0 = 1.05 m/s$, $T_0 = 300K$)

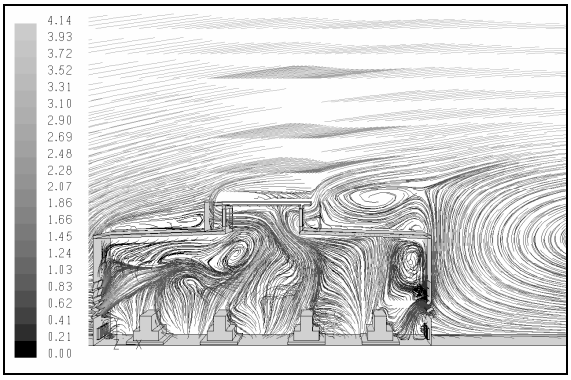

Figure 16. Path lines coloured by velocity magnitude [m/s] in the main cross-section of the workshop, 3D optimisation in cycle 11.0
($v_0 = 1.05 m/s$, $T_0 = 300K$)

Investigating the detailed structure of ventilation in different optimisation cycles, we can conclude that:

- Comparing the velocity field of optimisation cycle 4.0 (see Fig. 15) with cycle 11.0 (see Fig. 16), we find no significant difference between them.
- Ventilation in the optimal case (see Fig. 16) is much more pleasant than that shown in Fig. 10. There is no crossdraft through the middle windows on the leeward side and no more eddies among the smelter pots, but there is an effective upstream.
- The same conclusion can be drawn after analysing the temperature fields (see Figs. 17 and 18).
- The temperature fields at the operators' level (at $1.5m$ height) in different optimisation cycles do not change significantly, and Fig. 19 shows the temperature field for the optimum.

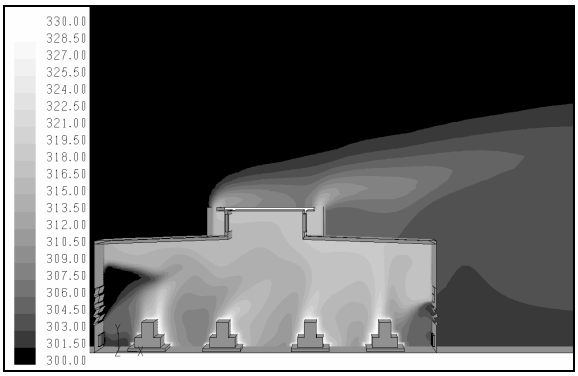

Figure 17. Temperature field [K] in the mean cross-section of the workshop, modified 3D model in cycle 4.0 ($v_0 = 1.05 m/s$, $T_0 = 300 K$)

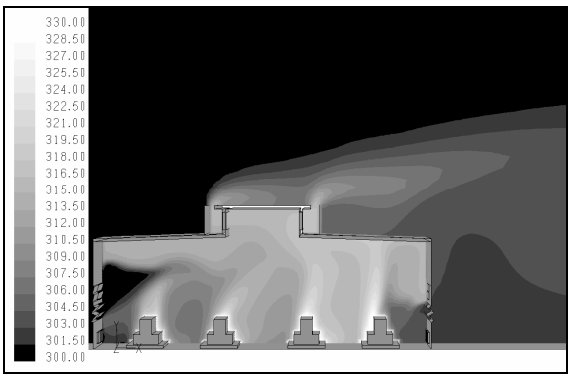

Figure 18. Temperature field [K] in the mean cross-section of the workshop, modified 3D model in cycle 11.0 ($v_0 = 1.05 m/s$, $T_0 = 300 K$)

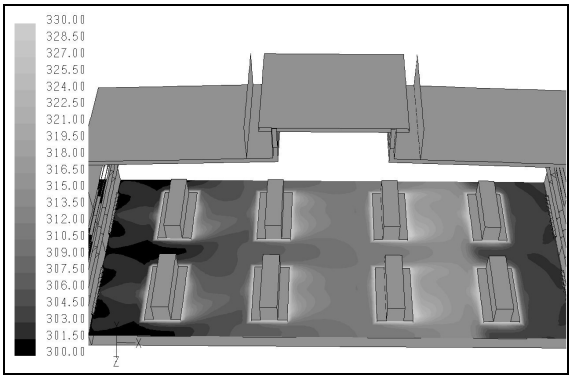

Figure 19. Temperature field [K] in the operating level at height of $z = 1.5 m$ in cycle 11.0 of the 3D optimisation ($v_0 = 1.05 m/s$, $T_0 = 300 K$)

6. CONCLUSIONS AND FUTURE PLANS

To summarise the findings of this investigation, we can state that the combination of CFD simulation and mathematical optimisation can be used successfully to determine optimal settings for the natural ventilation of a large workshop under different weather conditions. This can be further developed by using inequality constraints. These can ensure the avoidance of drafts by monitoring air movement in the cross-sections of the leeward side windows.

The DYNAMIC-Q algorithm contains the following inequality constraints [9]:

$$g_j(\boldsymbol{x}) \le 0, \qquad j = 1,2,...,m . \tag{5}$$

The penalty function is defined by

$$p(\boldsymbol{x}) = f(\boldsymbol{x}) + \sum_{j=1}^{m} \alpha_j g_j^2(\boldsymbol{x}) , \tag{6}$$

where

$$\alpha_j = \begin{cases} 0 \text{ if } g_j(\boldsymbol{x}) \le 0 \\ \rho_j = a\ large\ positive\ number \\ \quad for\ all\ j \text{ if } g_j(\boldsymbol{x}) > 0 \end{cases} . \tag{7}$$

For simplicity the penalty parameters $\rho_j, j = 1,2,\ldots,m$ take on the same positive value, $\rho_j = \mu$. It can be shown that, as μ tends to infinity, the unconstrained minimum of $p(\boldsymbol{x})$ tends to the constrained minimum of the original problem. In the application of the dynamic trajectory method used here, and with the objective and gradient functions appropriately scaled, the penalty parameter μ is introduced at a certain specified value, here $\mu = 10^2$, and then increased to $\mu = 10^4$ when the intersection of active constraints is found.

In case of using the inequality constraints it is possible to prevent the exit of air from the workshop through the leeward side windows. If the outflow is directed to the positive x direction, and the x-velocity of each cell (n) of the middle windows is known, then it is possible to determine the direction of the flow, whether there is outflow, inflow or both. The maximum value of $v_{x,i}$ should be found:

$$v_{x,maz} = max(v_{x,i}) , \quad i = 1 \div n \tag{8}$$

From this value, the inequality function can be determined as follows:

$$g(\boldsymbol{x}) = v_{x,max}(\boldsymbol{x}) \le 0 . \tag{9}$$

This means that if $v_{x,max}$ is negative then all of the other velocity values are also negative, meaning that there is just incoming air. Application of this inequality constraint may increase the number of optimisation cycles and so lengthen the computational time. Another option is to make the bottom

windows fully adjustable (at present they have vertical axes and are open at a fixed angle of 45°). This would mean two further design variables. This solution makes the optimisation more complicated, but it can ensure better control over the flow field and ventilation of the workshop.

ACKNOWLEDGEMENTS

This work has been supported by the Hungarian National Fund for Science and Research under contract OTKA T 042781, and by the Hungarian-South African Intergovernmental S&T co-operation program DAK 7/2002.

REFERENCES

[1] Fluent Inc. 2001, "Fluent Version 6 Manuals", Centerra Resource Park, 10 Cavendish Court, Lebanon, New Hampshire, USA

[2] Snyman, J.A., 1982, "A new dynamic method for unconstrained minimization", *Applied Mathematical Modelling*, 6, pp. 449-462.

[3] Snyman, J.A., 1992, "An improved version of the original leap-frog dynamic method for unconstrained minimization LFOP1(b)", *Applied Mathematical Modelling*, 7, pp. 216-218.

[4] Snyman, J.A., 2005, *Practical mathematical optimization – An introduction to basic optimization theory and classical and new gradient-based algorithms*, Springer, Cambridge, MA.

[5] Gyulai, L., Szabó, Sz., 2005, "Környezeti viszonyok hatása üzemcsarnok természetes szellőzésére", (*title in English*: "*Effects of environment on the natural ventilation of workshops*"), *Miskolci Egyetem Közleménye, Mechatronika, Anyagtudomány*, 1(2), pp. 83-91.

[6] Szabó, Sz., Schifter, F., Gyulai, L., Lukács, T., Szabó, Á., 2003, "Modelling the Natural Ventilation of Smelter Potrooms". Proc. *Conf. on Modelling Fluid Flow*, Budapest; pp. 660-667.

[7] Gyulai, L., 2002, "Computational Simulation of the natural ventilation of the Aluminium Factory Hall in Inota in Hungary", *MSc Thesis, University of Miskolc.*

[8] Szabó, Sz., Gyulai, L., Tolvaj, B., 2005, "Üzemcsarnok szellőzés számításának és mérésének összehasonlítása", (*title in English*: *"Comparison of Measured and Computed Ventilation of a Workshop"*), *Gép,* 8, pp. 49-54.

[9] Gyulai, L., Szabó, Sz., De Kock, D.J., Snyman, J. A., 2006, "Optimal adjustment of the number of air changes of a smelter pot room by using mathematical optimization", *Journal for Structural and Multidisciplinary Optimization* (to appear)

Conference on Modelling Fluid Flow (CMFF'06)
The 13th International Conference on Fluid Flow Technologies
Budapest, Hungary, September 6-9, 2006

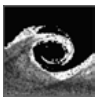

AERODYNAMIC SEALING BY AN AIR CURTAIN IN A PARTICLE-POLLUTED OUTDOOR ENVIRONMENT – NUMERICAL PREDICTIONS

Luis A. OLIVEIRA[1,2], José J. COSTA[2] and Luis C. OLIVEIRA[3]

[1] Corresponding Author. Department of Mechanical Engineering, University of Coimbra – Pólo II, 3030-201 Coimbra, Portugal
Tel. : +351 239 790732; Fax: +351 23 790771, E-mail: luis.adriano@dem.uc.pt
[2] Department of Mechanical Engineering, University of Coimbra – Pólo II, 3030-201 Coimbra, Portugal
Tel. : +351 239 790732; Fax: +351 23 790771, E-mail: jose.costa@dem.uc.pt
[3] Pneumologic Center, University of Coimbra – HUC, Praceta Prof. Mota Pinto, 3000-075 Coimbra, Portugal
Tel. : +351 239 836262; Fax: +351 239 836262, E-mail: lcoliv@mail.telepac.pt

ABSTRACT

A criterion to evaluate the particle sealing performance of an air curtain device (ACD) in two-phase flow conditions is proposed, standing on the definition of an assessment parameter, the particle sealing *efficiency*. A numerical procedure to calculate that parameter is reported (including a Lagrangian tracking for the particulate phase and an Eulerian, control-volume type approach for the carrier fluid flow), and then applied to the two-phase, ACD sealing of a working room with a particle-polluted outdoor environment. Pollution is represented by silica particles within the respirable size range, $1\ \mu m \le d^{p} \le 10\ \mu m$, that may be either instantaneously or continuously released in the polluted outdoor domain.

Keywords: aerodynamic sealing, air curtain, CFD, Lagrangian-Eulerian, multiphase flow, particle dispersion.

NOMENCLATURE

ACD		air curtain device
b	[m]	jet slot width
Cp	[mg/m^3]	average particle mass concentration
$(C\mathrm{p_i})_0$	[mg/m^3]	reference average particle concentration within the inner room
C_μ	[-]	constant of the turbulence model (=0.09)
g_i	[m/s^2]	gravity acceleration in direction i
H	[m]	room height (Figure 1)
H_d	[m]	height of the doorway (Fig. 1)
J	[-]	total number of trajectories that cross an Eulerian control volume
k	[m^2/s^2]	turbulence kinetic energy
L	[m]	cumulative length of the two rooms (Fig. 1)
m^p	[kg]	mass of a single particle
m_j^p	[kg]	particulate mass associated with trajectory j
$\dot{m}_j^\mathrm{p}$	[kg/s]	particulate mass rate associated with trajectory j
$\langle m^\mathrm{p} \rangle_\mathrm{cell}$	[kg]	particulate mass that occupies one Eulerian control volume at an instant $t=t_1$
N_j	[-]	number of particles in trajectory j
$\dot{N}_j$	[s^{-1}]	number flow rate in trajectory j
p	[Pa]	fluid pressure
Re	[-]	Reynolds number
S_ϕ		source term in Eq. (1)
t	[s]	time
t_0	[s]	initial instant of Lagrangian tracking
t_1	[s]	subsequent instant in Lagrangian tracking ($t_1>t_0$)
T	[$^\circ C$]	temperature
u_i	[m/s]	velocity coordinate in direction i (Eqs. (2) to (4))
V_j	[m/s]	jet velocity
$\underline{V}^\mathrm{rel}$	[m/s]	particle-fluid relative velocity
W	[m]	domain width (=1, in 2-D)
x, y	[m]	space coordinates (Fig. 1)
x_i	[m]	space coordinate in direction i (Eqs. (2) to (4))
2-D		two-dimensional type analysis

Subscripts

i	inner
o	outer
0	initial ($t=t_0$)
j	trajectory j

Superscripts

p	particulate phase	

Greek symbols

Δt	[s]	Lagrangian time interval
Δt_j	[s]	time of residence of trajectory j in an Eulerian control volume
ε	[m^2/s^3]	dissipation rate of k
ϕ	generic variable in Eq. (2): $\phi \equiv 1, u_i, T, k, \varepsilon$	
Γ_ϕ	generic diffusion coefficient (Eq. (2))	
μ	[$kg/m/s$]	fluid dynamic viscosity
ν_t	[m^2/s]	turbulent kinematic viscosity
ρ	[kg/m^3]	fluid density
ρ^p	[kg/m^3]	particle density
η_s	[-]	particle sealing efficiency
ψ	[m^2/s]	stream function (2-D)
Ψ	[-]	dimensionless stream function

1. INTRODUCTION

The principle of aerodynamic sealing through the use of air curtain systems is commonly used to confine environments with specific conditions. The basic idea is to reduce the airflow through adjoining spaces, while preserving an easy access between them. Through the use of an air curtain system, it is thus possible to divide a whole domain into two or more sub-domains with controlled atmospheres, where the ambient parameters (temperature, humidity, air quality, among others) are kept within acceptable, pre-defined levels dictated by economic, comfort or health impacts. Aerodynamic sealing devices can be used either in single phase or multiphase flows. In the latter case, most of the present technological devices employed in the control of particle pollution were conceived and developed − and are operated − on an empirical basis. However, the relevant physics can be better understood and predicted through the use of techniques for numerical calculation and experimental measurement that have been recently made available and progressively became indispensable engineering design and assessment tools.

Several studies on aerodynamic sealing with air curtains are reported in the available literature (see *e.g.* [1-10]). In the last decades, numerical predictions have been conducted by the present team on single phase aerodynamic sealing between two adjoining spaces [11-15]. Namely, in a recent paper [16], a numerical study, dedicated to the influence of dynamic and geometrical parameters on the sealing efficiency of a downward-blowing air curtain device (ACD), is reported. The ACD is installed between two contiguous rooms with distinct ambient temperatures. Two-dimensional numerical predictions are performed by using an Eulerian, control-volume type approach to solve the differential equations governing the fluid flow. A global, yet detailed characterization of the airflow pattern is made and guidelines are provided for the appropriate operation of such devices.

On the multiphase side, numerical prediction of particle dispersion in fluid flow has been addressed in a great number of relevant, recent researches [17-19] (see *e.g.* [20], for a review on the subject). As a contribution in this direction, a two-dimensional calculation procedure was recently developed and validated by Oliveira et al. [21] for the transport of particles in the laminar or turbulent flow of a carrier fluid. A Lagrangian type approach was used in the model to calculate both particle velocities and trajectories.

In this work, the above mentioned Eulerian fluid flow and Lagrangian particle-tracking procedures are briefly recalled and then applied to the two-phase, aerodynamic sealing of a working room with a particle-polluted outdoor environment, which is simulated here by a similar adjacent compartment. Dilute conditions are assumed to hold for the present solid, dispersed phase. The ratio of the density of the carrier fluid (air) to that of the dispersed phase (respirable silica particles) is thus sufficiently low for aerodynamic drag, gravity and fluid pressure gradient to be the only significant forces responsible for particle inertia. The effect of airflow turbulence upon particle dispersion is taken into consideration through a stochastic generation of fluctuating fluid velocity. Results for the dispersed phase, obtained from the space distribution of particle velocity and position, include the pattern of particle trajectories and the evaluation of particle mass transfer between the two adjoining rooms. A definition for particle sealing efficiency is proposed and then used in two distinct situations, to illustrate a performance evaluation of the ACD.

2. STUDIED CONFIGURATION

The configurations under analysis correspond to typical situations where the thermal and particle leakage between a room and its outdoor environment can be significantly reduced by means of an ACD installed on top of a permanently open doorway. A single phase laboratory study by the present team [22] was formerly addressed to a configuration of that type, which is thus adopted as a reference case for the numerical predictions of this paper. A commercial ACD is mounted above a 2 m high, 1.12 m wide doorway that connects two equal, contiguous $6 \times 6 \times 3.27\, m^3$ sized rooms. Prior to the measurements, the laboratory ambient air was uniformly conditioned to 25 ^oC in the "inner" room (with the ACD installed) and to 35 ^oC in the "outer room" (a warm outdoor environment, *e.g.*, in summertime), while the doorway was kept sealed by a plastic sheet, witch was then removed. A transient tracer gas technique and a concentration decay method were used to assess the convective

heat/mass transfer across the doorway, with the ACD switched on and off.

3. NUMERICAL MODELLING

The geometry of the calculation domain corresponds to the vertical plane of symmetry at half-width of the rooms, as represented in Figure 1, together with the relevant boundary conditions and dimensions.

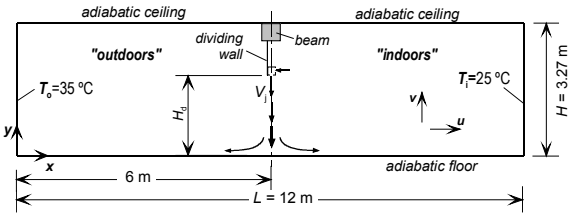

Figure 1. Geometrical configuration and dimensions of the calculation domain (*b*=4.5 cm).

It is assumed that the ACD is mounted on the dividing wall at the height of the doorway, H_d=2 *m*, and that the jet slot width is *b*=4.5 *cm*. Ceiling, floor, concrete beam and separating wall are all assumed to be adiabatic. On the other hand, the extreme (nominal) temperature levels of the rooms are specified by imposing those values in the wall-adjacent control volumes. The hypothesis of two-dimensionality (2-D) means that any gradient normal to the plane of the calculation domain is neglected. In practice, this assumption corresponds to a configuration where both the air curtain and the doorway would size the whole width of the rooms ($W = 6\ m$). Accordingly, in the present two-dimensional analysis, the quantities estimated after the numerical simulation results (*e.g.* heat and mass transfer rates) should be understood as meaning *per unit width* of the calculation domain and, therefore, of the air curtain.

3.1. Eulerian representation of the continuous phase

The confined, turbulent flow of the carrier fluid (air) is considered to be two-dimensional, incompressible, steady-state in average and the Boussinesq approximation is assumed to hold for the air physical properties. The numerical method is based on the solution of the Reynolds-averaged equations for the conservation of mass, momentum and thermal energy. In analogy with laminar flow, the turbulent stresses and the heat fluxes that arise in these equations are related to the mean velocity and temperature gradients through the Boussinesq concept of eddy viscosity, ν_t. In the k-ε model, here employed in a high-Reynolds-number version together with two-layer wall functions, ν_t is obtained from the usually called Prandtl-Kolmogorov relation:

$$\nu_t = C_\mu k^2 / \varepsilon \tag{1}$$

thus implying the solution of two further transport equations for the turbulent kinetic energy, k, and its dissipation rate, ε. The set of equations to be solved can be cast into a general conservation equation:

$$\frac{\partial}{\partial x_i}\left(u_i \phi\right) = \frac{\partial}{\partial x_i}\left(\Gamma_\phi \frac{\partial \phi}{\partial x_i} \right) + S_\phi \tag{2}$$

where $\phi \equiv 1, u_i, T, k, \varepsilon$ is a general dependent variable, to which are associated specific values or expressions for the corresponding effective diffusion coefficient, Γ_ϕ, and source term, S_ϕ. Equation (2) represents mass, momentum or energy conservation if the general variable ϕ is specified as unity, velocity component u_i, or temperature T, respectively.

The partial differential equations are here discretized using the finite volume method described in [23] and the convective fluxes at each control volume face are approximated with the hybrid central/upwind difference scheme. Velocities and pressures are calculated by the SIMPLEC algorithm and the discretized equations are solved by a tri-diagonal matrix algorithm. Following a grid dependence analysis, a 80×80 staggered grid is used for the present calculations: uniformly distributed along *Oy* and gradually compressed from the lateral walls towards the central plane. Uniform profiles are specified at the jet slot section to all variables. In order to ensure steady-state distinct thermal conditions in both rooms, temperature is specified at the (vertical) lateral room walls: T_i=25 *ºC* at the right side wall (room with "indoor" controlled ambient); T_o=35 *ºC* in the left side wall that limits the "outdoor" environment (cf. Fig. 1). All iterative calculations are started from initial uniform fields in the interior flow domain, namely zero mean velocity and T=T_o (left side half), T=T_i (right side half). Further details are available in reference [16].

3.2. Lagrangian tracking procedure for the particle phase

The solid phase is assumed to be composed of hard, spherical, non-rotating, smooth, elastic particles of uniform diameter d^p, mass m^p and mass density ρ^p, where the superscript "p" is used to identify the particulate phase. In the problems considered here, the only significant forces acting on each particle are the drag, gravitation and local pressure gradient forces. The equation of motion for a single particle of unit mass is thus reduced to the following form (cf. [24]):

$$\frac{du_i^{\mathrm{p}}}{dt} = \frac{3}{4}\frac{\mu}{\rho^{\mathrm{p}}(d^{\mathrm{p}})^2} C_D Re^{\mathrm{p}} \left(u_i - u_i^{\mathrm{p}}\right) + g_i\left(1 - \frac{\rho}{\rho^{\mathrm{p}}}\right) - \frac{1}{\rho^{\mathrm{p}}}\frac{\partial p}{\partial x_i} \qquad (3)$$

where the three terms of the right-hand side represent, in the same order, the forces that were mentioned above and are responsible for the particle acceleration (left-hand side). In Eq. (3), the particle Reynolds number Re^{p} is based upon the relative velocity $\left|\underline{V}^{\mathrm{rel}}\right| = \sqrt{(u_i - u_i^{\mathrm{p}})^2}$. Particle location, x_i^{p}, is related to the instantaneous particle velocity, u_i^{p}, by the following equation:

$$\frac{dx_i^{\mathrm{p}}}{dt} = u_i^{\mathrm{p}} \qquad (4)$$

The integration of Eqs. 3 and 4 is performed numerically through a fourth-order Runge-Kutta procedure. The particle position and velocity are thus calculated for a time level $t+\Delta t$ as functions of the corresponding values that are available for the previous time level, t. The effect of fluid flow turbulence upon particle dispersion is based on the concept of particle-eddy encounters: the instantaneous fluid velocity components to be used in Eq. (3) are estimated by superimposing, on the corresponding mean values, fluctuating components that are obtained through stochastic generation (see [25] for further details). The presence of solid boundaries is modelled through elastic collisions with introduction of a restitution coefficient. The trajectory calculation is terminated if the particle is captured in the ACD (particle filtering) or when the (preset) running time expires.

In the problem addressed here, particle concentration ($\leq 10\ mg/m^3$) is low enough for the influence of the particulate phase upon the carrier fluid (two-way coupling effect) to be neglected. In other words, fluid flow calculations are first performed without taking into account the presence of particles. In order to simulate an outdoor, uniformly polluted environment, a number of particle injection points are evenly distributed in the left side room. Once the flow field is obtained from the Eulerian calculation procedure, particles are then injected through those injection points and their trajectories are tracked by the Lagrangian procedure.

4. RESULTS AND DISCUSSION

4.1. The carrier fluid flow

The airflow streamline pattern is represented in Figure 2. Three main distinct flow regimes can be identified within the studied range of values of the air curtain jet velocity ($0 \leq V_{\mathrm{j}} \leq 9\ m/s$), as follows.

i) In the *natural convection* regime (zero or rather low jet velocities, cf. Fig. 2*a*), the flow is mainly dominated by buoyancy forces and characterized by a single recirculating cell that covers the whole volume of both rooms and totally deflects the jet (if any). In the limiting case of no jet at all ($V_{\mathrm{j}} = 0$), taken here as a reference for later estimation of η_{s}, the heat transfer rate between both rooms is maximal.

ii) For the highest values of V_{j}, a *forced convection* regime prevails: the jet inertial forces are dominant, the air curtain is continuous and stable all the way down to the floor, and the airflow pattern is practically Reynolds number independent. Two main recirculation cells of opposite signs are visible, one in each room (cf. Fig. 2*c*). The recirculation in the inner room is more intense, as it is reinforced by both the ACD jet and intake.

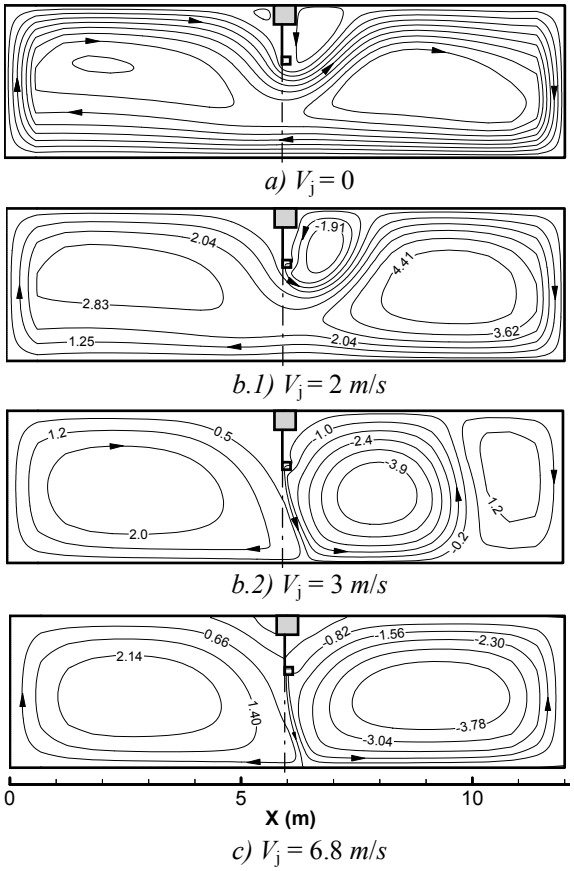

Figure 2. Streamline patterns illustrating the three flow regimes: *a*) *natural* convection; *b.1*) and *b.2*) *mixed* convection and *c*) *forced* convection. [$\Psi = \psi/(V_{\mathrm{j}} b)$; $\Psi = 1$ means a volumetric flow rate equal to that of the air curtain.]

iii) For intermediate jet velocities (cf. Figs. 2*b*.1 and 2*b*.2), a mixed convection regime occurs, where the jet initial momentum is the same order of magnitude as the transversal, buoyancy-generated

forces that tend to deflect it prematurely and/or destabilize it, if it ever reaches the floor. Two main recirculating cells are now present in the inner room, while a single one persists in the outer room. In the light of this global analysis, the ACD should work near the lower limit of the forced convection regime.

4.2. The two-phase flow

According to the one-way coupling hypothesis accepted here, all the above mentioned (steady-state) configurations of the carrier fluid are thus kept unchanged during the whole (transient) procedure of particle tracking. Actually, the evaluation procedure presented below indicates that when the air curtain jet does reach the floor in stable conditions, particle sealing is virtually perfect (only turbulent diffusion may be responsible for leakage), and thus the sealing efficiency is nearly unity for all particle diameters. In order to test the evaluation procedure for the particle sealing performance of the ACD, it is thus preferable to make it work in such conditions where its performance is only partial and considerably sensitive to both fluid flow and particle characteristics. This is the reason why the following evaluation of the ACD performance is established by comparison of particle transport infiltration into the inner room for the flow conditions of Fig. 2*b*.1 (partial sealing) with those of Fig. 2*a* (no sealing at all, reference condition).

The proposed evaluation procedure for the ACD sealing capability is now illustrated in two distinct, alternative scenarios: *i*) instantaneous particle release; *ii*) permanent particle release. In both cases, particles are released in the domain with zero initial velocity and then entrained by the fluid flow itself. An approximately uniform space distribution of pollutant concentration in the outdoor environment, $C\mathrm{p_o}$, is generated here by a number of 64 injection points, evenly distributed throughout the whole volume of the left side room. For the particulate phase, solid silica particles are considered (ρ^{p}=2.65×10^3 *kg*/*m*^{3}), the corresponding diameter, d^{p}, ranging within typical respirable particle sizes (1 $\mu m \le d^{\mathrm{p}} \le 10\ \mu m$).

***i*) Instantaneous particle release**. The number of particles, N_j, simultaneously injected at each injection point *j* is adjusted as a function of particle size, in order to ensure that the initial (instant of injection, $t=t_0$) concentration of pollutant is the same for all particle sizes and equal to 10 *mg*/*m*^{3}, a realistic value for practical applications. Once all the particles are simultaneously released in the outdoor environment (leading to $C\mathrm{p_o}$= 10 *mg*/*m*^{3} at $t=t_0$), the main goal is to analyse how the global particle concentration in the inner room, $C\mathrm{p_o}$, evolves with time, $t>t_0$ ($C\mathrm{p_i}=0$ at $t=t_0$). Along its own trajectory *j*, a particle with mass m^{p} is representative of a number N_j of analogous particles, introduced in the domain through the same injection point, at the same injection instant (as if each injection point were actually a localized "injection cloud"). Each trajectory *j* is thus associated with a particulate mass given by $m_j^{\mathrm{p}} = N_j\, m^{\mathrm{p}}$. The numerical process of particle tracking makes it possible to localize any particle at any instant, t_1, thus meaning that the mean particle concentration within the inner room, $C\mathrm{p_i}$, may be easily determined at that same instant. Being zero at $t=t_0$, the average concentration $C\mathrm{p_i}$ actually quantifies the mass of particulate phase that crossed the doorway, from left to right, during the time interval $t_0 \le t \le t_1$. This particle *mass leakage*, $C\mathrm{p_i}$, is then used to evaluate the particle sealing performance of the ACD. For that purpose, the sealing efficiency, η_{s}, is defined as a dimensionless parameter that quantifies the ratio between actual and ideal sealing effect, with reference to the open-door situation (jet velocity V_{j}=0, $C\mathrm{p_i} = (C\mathrm{p_i})_0$ − ACD absent or not in function − hereafter considered as the *reference* or *open door situation*). The parameter η_{s} is estimated by dividing the actual reduction of particle mass leakage, $[(C\mathrm{p_i})_0 - C\mathrm{p_i}]$, by the maximum possible reduction, $(Cp_i)_0$, leading to: $\eta_{\mathrm{s}} = 1 - C\mathrm{p_i}/(C\mathrm{p_i})_0$. According to this definition, $\eta_{\mathrm{s}} = 0$ means no sealing at all, while $\eta_{\mathrm{s}} = 1$ would mean no leakage at all, *i.e.*, $C\mathrm{p_i} = 0$.

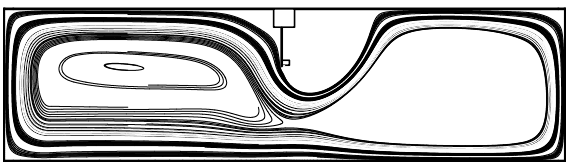

Figure 3. Pattern of $d^{\mathrm{p}} = 1\,\mu m$ particle trajectories for $t_0 \le t \le 300\,s$. Fluid phase as in Fig. 2*b.1*.

For the case where the ACD is active, with the jet velocity equal to $V_{\mathrm{j}} = 2\ m/s$, the trajectories described by silica particles with diameter $d^{\mathrm{p}} = 1\,\mu m$, between the instants $t=t_0$ and $t=t_0+300\,s$, are represented in Figure 3. For the sake of clarity, only a limited number of trajectories are actually shown. Particles injected in the central region of the left side room are trapped within the fluid main recirculation; in contrast, those injected in the periphery of the same room are entrained in the outer fluid recirculation (see Fig. 2*b*.1), and thus successively visit both the inner room and its external environment. As a consequence, the mean

particle mass concentration in the inner room, $C\mathrm{p_i}$, changes from zero (at $t=t_0$) to a very pronounced first oscillation (corresponding to the first passage of particle cloud) and then to a progressively more damped oscillating behaviour about a nearly constant time mean. This is shown in Figure 4, where the same time evolution for $V_\mathrm{j}=0$ (ACD shut down) is also included for comparison.

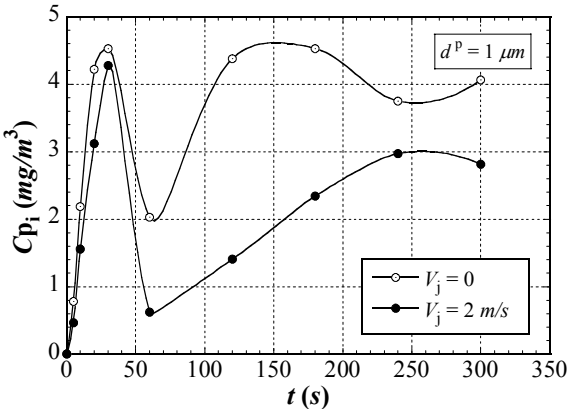

Figure 4. Instantaneous particle injection: influence of the ACD on the $C\mathrm{p_i}$ initial time evolution.

According to this latter figure and as a first approach, a running period of 5 minutes (300 *s*, the running time used for Fig. 3) seems sufficient for nearly regular particle patterns to have been established in time.

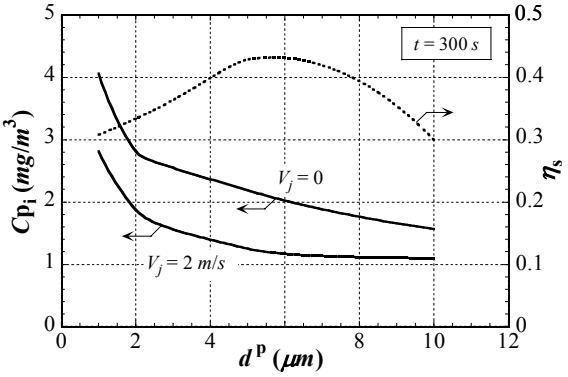

Figure 5. Instantaneous particle injection: influence of the ACD on $C\mathrm{p_i}$, at instant $t=300\ s$, and resulting sealing efficiency, η_s, for different particle diameters.

A comparison is thus performed in Figure 5, for $t=300\,s$ and different particle sizes, between the mean particle concentration within the inner room (which means particle leakage from left to right, through the central plane), when the ACD is switched on ($V_\mathrm{j}=2\,m/s$) and off ($V_\mathrm{j}=0$). The evaluation of the particle sealing efficiency, η_s, is a direct result of that comparison, and is also represented in the figure. Although general and simple, the calculation procedure adopted in this example to determine the particle concentration $C\mathrm{p_i}$ is only valid for *instantaneous* particle injection. It is thus not applicable when particles are *continuously* injected throughout time, as in the following case.

***ii*) Permanent particle release**. In this second scenario, each particle trajectory *j* is associated with a particle mass *rate*, $\dot{m}_j^\mathrm{p}=\dot{N}_j\,m^\mathrm{p}$, where the number flow rate, $\dot{N}_j$, is the number of particles *per second* that travel along that same trajectory. Each control volume of the Eulerian mesh may be crossed by one or more particle trajectories. The follow up Lagrangian procedure allows one to calculate the time of residence of each trajectory *j* within every cell of the Eulerian mesh. Denoting this residence time of trajectory *j*, within a specified control value, by Δt_j, the particulate mass that occupies that cell at any instant $t_1>t_0$ is given by:

$$\left\langle m^\mathrm{p}\right\rangle_\mathrm{cell}=\rho^\mathrm{p}\,\frac{\pi}{6}\left(d^\mathrm{p}\right)^3\sum_{j=1}^{J}\dot{N}_j\,\Delta t_j \qquad (5)$$

where J is the number of particle trajectories (if any) crossing the cell at that instant, t_1. Summing up the $\left\langle m^\mathrm{p}\right\rangle_\mathrm{cell}$ contributions for all Eulerian cells within the whole or part of the flow domain yields the total particulate mass contained in that flow domain, at that same instant. The mean particulate concentration $C\mathrm{p_i}$ results from applying that sum to all Eulerian cells within the inner room, and then dividing the result by the inner room volume.

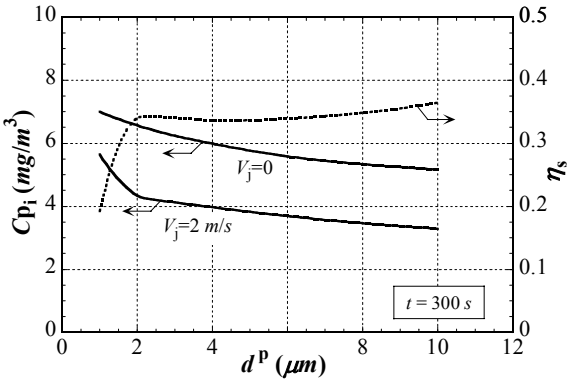

Figure 6. Permanent particle injection: influence of the ACD on $C\mathrm{p_i}$, at instant $t=300\ s$, and resulting sealing efficiency, η_s, for different particle diameters.

In the example represented in Figure 6, the total (*total* meaning the whole set of injection points) mass flux of particle injection is 0.5 *mg*/*s* for all considered particle diameters, so that, for instance,

the calculation of $d^{p}=5\,\mu m$ mean particle concentration in the inner room yields $Cp_i = 5.77$ mg/m^3 for $t_1 = 300\,s$, when the ACD is shut down ($V_j = 0$). The meaning of the curves in this figure is analogous to the ones in Fig. 5.

It is interesting to note that in both examples of instantaneous and permanent particle release, the sealing efficiency is relatively poor for the smallest particles. This is probably due to the very low inertia inherent in that particle size, thus meaning that the local action of the ACD jet hardly succeeds in interfering with the trend of those particles to simply follow the main flow. On the other side, the inner room particle concentration tends to decrease with increasing particle size. Actually, the trajectories of the biggest particles are clearly influenced by their own weight: for $d^{p}>15\,\mu m$ (not shown), the trend for gravity deposition is quite apparent.

Owing to the continuous injection of particles in the present case, the mean particle concentration is permanently increasing in both rooms, as illustrated in Figure 7. Accordingly, the ACD sealing efficiency could also have been based on the increasing rate of Cp_i, $\dot{C}p_i$, rather than in Cp_i itself. This would not be a problem, since Eq. (5) allows the determination of Cp_i at any time.

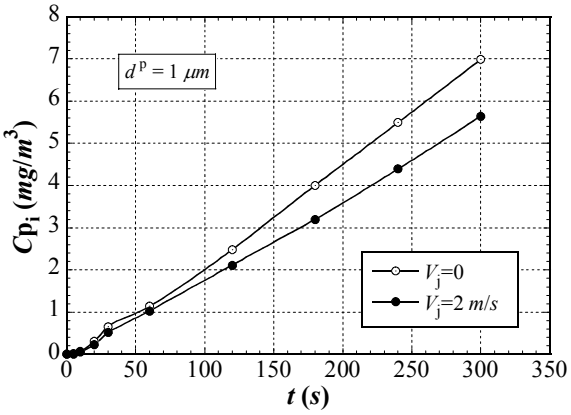

Figure 7. Permanent particle injection: influence of the ACD on the Cp_i initial time evolution.

Obviously, the two-phase flow conditions addressed above are far from exhaustive. However, the definitions of sealing performance and the corresponding evaluation procedures are reliable, simple to implement and can be easily applied in a fairly large range of practical applications.

5. CONCLUSIONS

A simple yet general numerical procedure to assess the particle sealing performance of an air curtain device (ACD) was proposed and successfully implemented in two illustrative examples of two-phase, non isothermal, highly recirculating turbulent flows. The performance evaluation stands on the definition of an assessment parameter, the *particle sealing efficiency*. It is based on the numerical prediction of particulate concentration within the domain region that the ACD is meant to protect against pollution. In both cases studied here, pollution is represented by solid, silica respirable particles ($1\,\mu m \le d^{p} \le 10\,\mu m$), that are either instantaneously or permanently injected in the polluted outdoor domain. These two distinct situations require two qualitatively different calculation procedures for the particulate phase concentration within the calculation domain. The two-phase flow conditions addressed in this work are two-dimensional in nature. However, the extension of the proposed assessment procedure to three-dimensions is quite straightforward and will be published in a near future.

ACKNOWLEDGEMENTS

This work was conducted under a research project -n.º POCTI/CBO/39284/2001- sponsored by "Fundação para a Ciência e a Tecnologia" (FCT, Portugal).

REFERENCES

[1] Hetsroni, G., 1963, "Heat transfer through an air curtain", *PhD thesis, Michigan State University, East Lansing, USA*.

[2] Hetsroni, G., Hall, C.W., Dhanak, A.M., 1963, "Heat transfer properties of an air curtain", *Trans. ASAE*, pp. 328-334.

[3] Hayes, F., 1968, "Heat transfer characteristics of the air curtain: a plane jet subjected to transverse pressure and temperature gradients", *PhD thesis, University of Illinois, USA*.

[4] Hayes, F.C., Stoecker, W.F., 1969, "Heat transfer characteristics of the air curtain", *ASHRAE Trans.*, Vol. 75, Nº. 2, pp. 153-167.

[5] Hayes, F.C., Stoecker, W.F., 1969, "Design data for air curtains", *ASHRAE Trans.*, Vol. 75, pp. 168-180.

[6] Van, N.Q., Howell, R.H., 1976, "Influence of initial turbulence intensity on the development of plane air-curtain jets", *ASHRAE Trans.*, Vol. 82, pp. 208-228.

[7] Howell, R.H., Shibata, M., 1980, "Optimum heat transfer through turbulent recirculated plane air curtains", *ASHRAE Trans.,* Nº 2567, pp. 188-200.

[8] Lam, J.K.-W., Ruddick, K.G., Whittle, G.E., 1990, "Air curtains for infiltration control – a computational fluid dynamics analysis", Proc. *11th AIVC Conference*, Paper 16, pp. 301-324, Belgirate, Italy.

[9] Stribling, D., Tassou, S. A., Marriott, D., 1997, "A Two Dimensional CFD Model of a Refrigerated Display Case", *ASHRAE Transactions: Research*, Vol. 103, Nº 1, pp. 88-95.

[10] Shen, Y.N., Wang, Z., Zhang, F.C., Wang, H.M., 1998, "The characteristic research into the air conditioning umbrella with an air curtain", Proc. *Int. Conference on Cryogenics & Refrigeration, ICCR'98*, Hangzhou, China, pp. 286-290.

[11] Oliveira, L.A., Costa, J.J., Carvalho, M.G., 1989, "Numerical prediction of aerodynamic sealing by jet flow", Proc. *8th Colloquium on Industrial Aerodynamics*, Aachen, Germany.

[12] Oliveira, L.A., Costa, J.J., Carvalho, M.G., Gerhardt, H.J., Kramer, C., 1991, "On aerodynamic sealing for industrial applications", *J. Wind Engineering and Industrial Aerodynamics*, Vol. 37, pp. 255-268.

[13] Oliveira, L.A., Penot, F., Costa, J.J., 1996, "Aerodynamic sealing through a double jet curtain: a parametric numerical study", Proc. *ROOMVENT'96–Fifth Int. Conference on Air Distribution in Rooms*, Vol. 1, pp. 437-444, Yokohama, Japan.

[14] Oliveira, L.A., Penot, F., Costa, J.J., Mousset, S., 1997, "Étude Numérique 2D de l'Isolation Dynamique par Double Rideau d'Air, incluant les Effets Thermiques et un Modèle de Turbulence", Poster, *13ème Congrès Français de Mécanique*, Futuroscope, Poitiers, France.

[15] Costa, J.J., Oliveira, L.A., 2002, "Vedação aerodinâmica: parametrização numérica do isolamento de duas divisões" (in portuguese), *V Congresso de Métodos Numéricos em Engenharia*, Madrid, Spain, 3-6 June, (CD-ROM: "Métodos Numéricos en Ingeniería V", J. M. Goicolea, C. Mota Soares, M. Pastor, G. Bugeda (Eds.), © SEMNI, Spain 2002).

[16] Costa, J. J., Oliveira, L. A., Silva, M. G., 2006, "Energy Savings by Aerodynamic Sealing with a Downward-Blowing Air Curtain – A Numerical Approach", accepted for publication in *Energy and Buildings*.

[17] Crowe, C.T., Sommerfeld, M. Tsuji, Y., 1998, *Multiphase Flows with Droplets and Particles*, CRC Press LLC.

[18] Fan, L.-S. Zhu, C., 1998, *Principles of Gas-Solid Flows*, Cambridge Univ. Press, UK.

[19] Loth, E., 2000, "Numerical approaches for motion of dispersed particles, droplets and bubbles", *Progr. Energy and Combustion Science*, Vol. 26, pp. 161-223.

[20] Baliga B.R., 1997, "Control-volume finite element methods for fluid flow and heat transfer". *Advances in Numerical Heat Transfer*, Vol 1, Chap. 3.

[21] Oliveira, L.A., Costa, V.F. Baliga, B.R., 2002, "A Lagrangian-Eulerian model of particle dispersion in a turbulent plane mixing layer", *Int. J. Numer. Meth. Fluids*, Vol. 40, pp. 639-653.

[22] Neto, L. C., Silva, M. G., Costa, J.J., 2006, "On the use of infrared thermography in studies with air curtain devices", accepted for publication in *Energy and Buildings*.

[23] Patankar, S.V., 1980, *Numerical Heat Transfer and Fluid Flow*, Hemisphere Publishing Corporation, Washington, DC.

[24] Maxey, M.R. Riley, J.J., 1983, "Equation of motion of a small rigid sphere in a nonuniform flow", *Physic of Fluids*, Vol. 26, pp. 883-889.

[25] Gosman, A.D. Ionnides, E., 1981, "Aspects of computer simulation of liquid fuelled combustors", *AIAA Paper, No 81-0323*.

Multiple Fluid Phases and Components

Conference on Modelling Fluid Flow (CMFF'06)
The 13th International Conference on Fluid Flow Technologies
Budapest, Hungary, September 6-9, 2006

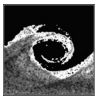

DROPS EJECTION FROM A CAPILLARY NOZZLE BY DROP-ON-DEMAND TECHNOLOGY

Sanda-Carmen GEORGESCU[1], Édouard CANOT[2], Jean-Luc ACHARD[3], Arthur SOUCEMARIANADIN[4]

[1] Corresponding Author. Hydraulics Department, University "Politehnica" of Bucharest. 313 Spl. Independentei, S6, RO-060042, Bucharest, Romania. Tel.: +40 723624418, Fax: +40 214029865, E-mail: carmen@hydrop.pub.ro
[2] Institut de Recherche en Informatique et Systèmes Aléatoires, INRIA, Rennes, France. E-mail: Edouard.Canot@irisa.fr
[3] Laboratoire des Écoulements Géophysiques et Industriels (LEGI), Grenoble, France. E-mail: Jean-Luc.Achard@hmg.inpg.fr
[4] Laboratoire des Écoulements Géophysiques et Industriels (LEGI), Grenoble, France. E-mail: Arthur.Soucemarianadin@ujf-grenoble.fr

ABSTRACT

Drop-on-Demand (DOD) technology enables to control the ejection of drops, from a vertically capillary nozzle, by piezoelectric stimulation. DOD applies in microfluidics, from the ink-jet printers to Bio-MEMS. This study emphasizes on the numerical simulation of the drop evolution during its formation and ejection by DOD technology. The highly distorted interface evolution represents an axisymmetric transient free-boundary problem, which is modelled here through a Boundary Element Method. An irrotational flow model can reproduce most observed experimental data on drop size, velocity, frequency, and conditions for non-satellite formation. Viscous effects are included to some extent, as it is allowed for potential flows of fluids with constant viscosity, the normal viscous stress at the interface being expressed in terms of the velocity potential. The time progression is made with a 4th order Runge-Kutta explicit numerical scheme. The time step is varied upon a stability criterion. The interface evolution is determined through a Lagrangian description of a variable number of nodes, unevenly redistributed on the boundary at each time step. The numerical code accuracy is evaluated through the global mechanical energy balance, expressed only in surface integrals terms. Our computed results fit well the available DOD data for ejected drops with volume of picolitres order.

Keywords: Boundary Element Method, drop formation, Drop-on-Demand, ink-jet fluid microdispensing, interface distortion

NOMENCLATURE

Fr	[-]	Froude number
H	[$1/m$]	total curvature
M		observation point
P		singularity point
R	[m]	orifice radius; length scale
R_1, R_2	[m]	local principal radii of curvature
Re	[-]	Reynolds number
We	[-]	Weber number
dA	[m^2]	axisymmetric surface element
g	[m/s^2]	gravity
n	[m]	normal co-ordinate
r	[m]	radial co-ordinate
s	[m]	curvilinear abscissa
t	[s]	time
v	[m/s]	velocity
z	[m]	axial co-ordinate
Δs	[m]	arc length
Δt	[s]	time step
Ω		domain in a meridian plane
Σ		surface; interface
β	[rad]	azimuthal angle
ϕ	[m^2/s]	velocity potential
μ	[$Pa \cdot s$]	dynamic viscosity of the liquid
ρ	[kg/m^3]	density of the liquid
σ	[N/m]	surface tension

Subscripts and Superscripts

D	domain
L	liquid
P	related to the singularity point
W	solid wall
n	normal direction
z	axial direction
*	dimensionless variable

1. INTRODUCTION

There are two main approaches in ink-jet printing technology [1].

Within the "Continuous, Charge and Deflect" ink-jet printing technology, also called CIJ for Continuous Ink-Jet, the fluid under pressure issues from an orifice and breaks up into uniform drops by

the amplification of capillary waves induced onto the jet, usually by an electromechanical device. The ejected drops are electrically charged and deflected to their desired location. This approach is suitable for high-speed coverage of relatively large areas. The "Continuous, Charge and Deflect" ink-jet printing technology has been studied for the past 30 years: the characteristics of the ejected drops, as well as the conditions for satellite droplets formation are well known and analysed in [2-5].

Within the now more widely used "Drop-on-Demand" (DOD) ink-jet printing technology, smaller drops can be ejected from the device orifice, by applying a stimulation method (piezoelectric, or thermal). A DOD device produces drops of 20-100 microns in diameter, which are approximately equal to the diameter of the drop generator orifice. The DOD technology enables to control the size, velocity and frequency of the ejected drops. The piezoelectric DOD ink-jet method is commonly used, and the present paper will focus on it, i.e. on the drop ejected at a capillary nozzle tip, when a voltage pulse is applied to the nozzle-transducer, which is placed up-stream of the nozzle on the capillary. Piezoelectric ink-jet print heads have dominated the DOD industrial and commercial market for last two decades, because they offer high jetting frequency, long life expectancy, and the ability to jet a wide range of fluids under harsh working conditions [6]. The piezoelectrically driven DOD ink-jet printing technology has been studied experimentally [7-9] and/or numerically [10-12], in order to depict the ejected drops characteristics, and the conditions for non-satellite formation. The drop behaviour depends on the velocity profile at the orifice level, thus on the nozzle-transducer [6, 9, and 13]. The characteristics of the ejected drops are also influenced by the fluid properties [14, 15].

The DOD study is sustained by its many applications in microfluidics, ranging from the classical ink-jet printers, to various microdispensers and nanolitre dispensers [16-18] in chemical and pharmaceutical engineering, to jet printing for large area electronics [19, 20], as well as to DNA chips (the deposition of polymeric fluids on microchips for DNA in-situ synthesis) [21].

The present paper points on the numerical simulation of drop evolution during its formation at a vertical capillary tip, and its ejection by piezoelectrically driven DOD technology. The phenomenon involves strong nonlinear and coupled effects. The rapidity of the phenomenon, of microseconds order, and the space scales, of microns order, induce difficulties in experimental investigations. The advantage of numerical computations consists in analysing a large spectrum of droplet sizes, velocities, frequencies, and conditions for non-satellite formation. The modelling is achieved through an axisymmetric Boundary Element Method (BEM), assuming an irrotational flow of a viscous fluid [22], by using a personal numerical code built in Fortran. The numerical code has been validated in ultra-high speed interface hydrodynamics, especially to simulate the collapsing interface evolution for bursting bubbles at a free surface, finalised by microjet breaking and droplets ejection [23, 24].

Initial conditions, boundary conditions, and governing motion equations for the physical model are depicted in the second section of the present paper. The numerical procedure is outlined in the 3rd section. Results and comments are presented in the 4th section.

2. PROBLEM STATEMENT

An axisymmetric liquid domain Ω_L is considered in a meridian plane rOz (Figure 1). Inside the capillary nozzle, the domain is bounded by the liquid surface Σ_L in a radial direction. Laterally, it is bounded by the vertical solid wall Σ_W of the cylindrical nozzle, and at its bottom by the gas-liquid interface (drop surface) Σ, which is attached at the nozzle orifice edge. The orifice level is set at $z = 0$.

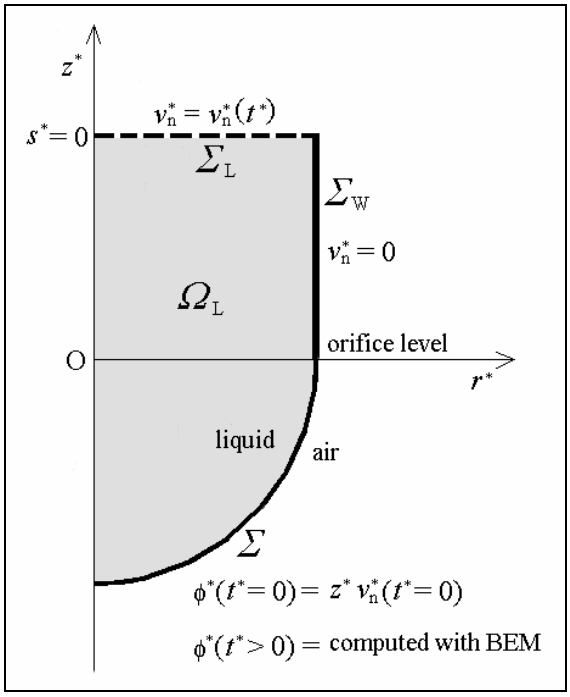

Figure 1. Geometrical configuration and boundary conditions

An outward normal unit vector is considered on the domain boundary. On the Oz axis, at the liquid surface Σ_L level, the curvilinear abscissa s is set to zero; its value increases when moving to the right along Σ_L, then downward along the wall Σ_W, then along the drop surface Σ, and reaches its maximum at the drop apex, on the Oz axis. Between the

tangential unit vector at any point on the boundary, and the radial unit vector, the azimuthal angle is denoted as β.

The orifice radius R is adopted as length scale, σ/R as pressure scale, $\sqrt{\sigma/(R\rho)}$ as velocity scale, where σ is the surface tension and ρ is the liquid density. The ratio between the length and velocity scale gives the time scale. Accordingly, the Weber number equals the unity, $We=1$, the Froude number is $Fr=\sigma/\left(\rho g R^2\right)$, and the Reynolds number is $Re=\sqrt{\rho\sigma R}/\mu$, where μ is the dynamic viscosity of the liquid. Dimensionless variables will be denoted with an asterisk. At the free drop surface, the adjacent gas pressure is assumed to be constant, since the gas inertia is neglected.

A potential liquid flow assumption is appropriate because of the impulsive character of the phenomenon. The dimensionless equations governing the potential liquid flow are classically the Laplace equation $\nabla^2\phi^*=0$ for the velocity potential ϕ^*, and the Euler's equation. The velocity v is defined by its normal component $\partial\phi^*/\partial n^*$, and tangential component $\partial\phi^*/\partial s^*$. In this type of model, viscous effects can be partially considered through a boundary condition, namely the normal momentum balance at any point of the interface Σ, which includes the normal viscous stress at the interface: $2\mu\left(\partial v_{\mathrm{n}}/\partial n\right)$, where v_{n} is the normal component of the velocity.

Combining the Laplace equation and the Euler's equation in order to reduce the pressure terms, yields the dimensionless Bernoulli's equation, i.e. the local time derivative of the velocity potential:

$$\frac{\partial\phi^*}{\partial t^*}=-\frac{\left(v^*\right)^2}{2}-\frac{H^*}{We}-\frac{z^*}{Fr}-\frac{2}{Re}\frac{\partial^2\phi^*}{\partial n^{*2}}. \qquad (1)$$

The dimensionless total curvature is written $H^*=\left(1/R_1^*+1/R_2^*\right)$, where R_1^* and R_2^* are the corresponding dimensionless local principal radii of curvature. There are distinct forms of Eq. (1) on the axis of symmetry Oz, and outside. The singularities at $r^*=0$ are removed by taking into account that on the Oz axis, the axisymmetric curvature, $1/R_2^*=\left(\sin\beta\right)/r^*$, equals the planar curvature, $1/R_1^*=\partial\beta/\partial s^*$. The expressions of the normal second derivative of the velocity potential $\partial^2\phi^*/\partial n^{*2}$ outside of the symmetry axis Oz, and on that axis, are defined in [23, 25].

Initial and boundary conditions are functions of the stimulation process, i.e. they depend on the excitation waves that are converted into velocity variations at the capillary nozzle tip. The hydrodynamics of the viscous liquid inside the capillary nozzle has been obtained by solving the Navier-Stokes equation [9, 26]: the imposed periodical wall deformation produces perturbations of the pressure field inside the capillary, and subsequently perturbations of the velocity field. So, the velocity reaches a peak during the voltage pulse, and relaxes after. For example [9], over a period of 0.1 *ms*, and voltage pulse duration of 20 μ*s*, the maximum axial velocity inside the capillary nozzle varies between about 3.2 *m/s* (at a voltage of 50 *V*) and 6.5 *m/s* (at 100 *V*).

Firstly, the resulting time dependent axial velocity profile inside the capillary nozzle (parabolic Poiseuille profile), has been averaged to obtain the mean axial velocity profile [26], for a voltage of 80 *V*. Secondly, its averaged form has been approximated for the BEM computations. The dimensionless time dependent normal velocity profiles $v_{\mathrm{n}}^*=v_{\mathrm{n}}^*\left(t^*\right)$ from Figure 2 are considered for BEM computations within this paper. The upper frame of Fig.2 corresponds to distilled water: at the initial moment, and over the first 8.5% of each period between two consecutive voltage pulses, the normal velocity value is set to $v_{\mathrm{n}}^*\left(t^*\right)=2$. The lower frame of Fig.2 corresponds to ink: at $t^*=0$, and over the first 9.9% of each period (of 3.42 dimensionless duration) between two consecutive voltage pulses, the normal velocity is $v_{\mathrm{n}}^*\left(t^*\right)=2.5$. In both frames, drop ejection instants are marked (by triangles). Ink drop ejection requests a higher maximum v_{n}^* value inside the capillary (so, a higher voltage), and a shorter period (ink being 8.7 times more viscous than water).

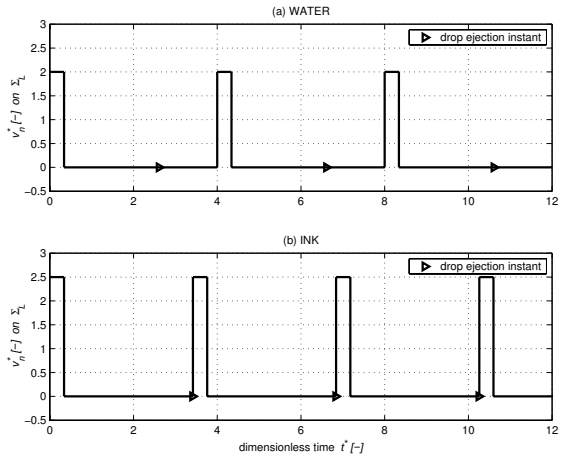

Figure 2. Dimensionless profile of the time dependent normal velocity inside the capillary nozzle, for water (a) and ink (b), used in BEM

For the BEM computations, the normal velocity profile $v_{\mathrm{n}}^*=v_{\mathrm{n}}^*\left(t^*\right)$ inside the capillary nozzle (Fig. 2) is inserted as a Neumann type boundary condition on the liquid surface Σ_{L} (Fig. 1). A

Neumann type boundary condition also corresponds to the solid wall Σ_W, where the normal velocity is zero. At the initial moment, the boundary conditions of Dirichlet type on the interface Σ are: $\phi^*(t^*=0)=z^* v_n^*(t^*=0)$. For further moments, the velocity potential $\phi^*(t^*>0)$ on Σ is obtained within the BEM (Fig. 1).

In the absence of non-linear analytical tests, the evaluation of numerical code accuracy is checked through the global mechanical energy balance, expressed only in surface integrals terms [23]:

$$\frac{d}{dt^*}\left(\frac{1}{2}\int_{\Sigma_D}\phi^*\frac{\partial\phi^*}{\partial n^*}dA^*+\frac{1}{We}\int_{\Sigma}dA^*\right)+$$
$$+\frac{d}{dt^*}\left(\frac{1}{2Fr}\int_{\Sigma}(z^*)^2 dA^*\right)= \qquad (2)$$
$$=-\frac{2}{Re}\int_{\Sigma_D}\frac{\partial\phi^*}{\partial n^*}\frac{\partial^2\phi^*}{\partial n^{*2}}dA^*,$$

where $\Sigma_D=\Sigma_L\cup\Sigma_W\cup\Sigma$ is the liquid domain boundary; dA^* is the dimensionless axisymmetric surface element. The dissipation of the mechanical energy due to shear viscosity depends only on the normal component of the velocity, and on the normal second derivative of the velocity potential, $\partial^2\phi^*/\partial n^{*2}$. Upon azimuthal integration, the mechanical energy balance deals with line integrals of the terms computed through the BEM, thus being easy to implement in the computational procedure.

3. NUMERICAL METHOD

The Boundary Element Method has been used in modelling the drop formation of the continuous jet [3], or the jet atomization [29], but under simpler assumptions, like the pure potential fluid flow, and even the absence of the gravity in [29]. Within the present study, the DOD modelling is achieved through a BEM, by assuming a potential flow of a viscous fluid [22]; it is a new approach for this type of process, and first results are presented in [26].

The drop surface Σ, highly distorted during its formation, represents a transient free-boundary problem that involves two types of calculations. We have indeed to cope with the task of calculating the potentials at a sequence of instants $t^*\in\{\Delta t^*,2\Delta t^*,\ldots,(k-1)\Delta t^*,\ldots\}$. The small time step Δt^* is selected according to rules further defined. Firstly, a time-stepping scheme applied to Eq. (1) allows to link known values of the position of fluid particles on the interface, and of the velocity potential values on the same interface, evaluated at $t^*=(k-1)\Delta t^*$, to the corresponding values of these quantities at the following instant $t^*=k\,\Delta t^*$. Then, the potential values being known from this first type of calculation on the interface Σ, and the normal velocity components being also known on $\Sigma_L\cup\Sigma_W$ at $t^*=k\,\Delta t^*$, the Laplace equation can be solved with the BEM, to obtain the velocity potential values at the same instant $t^*=k\,\Delta t^*$ in the whole liquid domain. The time stepping technique requiring the normal component $\partial\phi^*/\partial n^*$, and tangential component $\partial\phi^*/\partial s^*$ of the velocity [27] on the interface Σ, can then be used again to connect the instants $t^*=k\,\Delta t^*$ and $t^*=(k+1)\Delta t^*$.

Within the second type of calculation, the Boundary Element Method allows replacing the Laplace's equation extended in the whole liquid domain Ω_L, by a second kind Fredholm integral equation extended only on the domain boundary Σ_D. For this direct BEM computation, the velocity field is generated by source and normal doublet type singularities spread over Σ_D. The integral equation on Σ_D is written:

$$-\int_{\Sigma_D}\phi^*(P)\frac{\partial\left(1/|MP|^*\right)}{\partial n_P^*}dA_P^*+$$
$$+\int_{\Sigma_D}\left(1/|MP|^*\right)\frac{\partial\phi^*(P)}{\partial n_P^*}dA_P^*=2\pi\,\phi^*(M), \qquad (3)$$

where $|MP|^*$ is the dimensionless distance between the observation point $M\in\Sigma_D$ and the singularity point P. The kinetic conditions of Neumann type on the surfaces Σ_L and Σ_W, where the normal velocity is known, as well as of Dirichlet type on the interface Σ, where the velocity potential is known, have been already depicted in the previous section (Fig.1).

The temporal interface evolution, which is based on Eq. (1), allows a Lagrangian description of a variable number of nodes $M(r^*(t^*),z^*(t^*))$, representing the position of fluid particles, unevenly redistributed on the boundary $\Sigma_D(t^*)$ at each instant, with respect to some criteria like the adaptation at the surface gradients [23]. This leads to a concentration of nodes at places where the interface's curvature is important, or where two portions of the interface approach one another. Thus, the simulation of the interface evolution is performed during the whole process, without applying any smoothing techniques that can affect the physics of the phenomenon.

The time step Δt^* is varied in accordance with a stability criterion, linked to the gravity-capillary dispersion equation [28]:

$$\Delta t^*\le 2\left(\frac{\pi^3}{We\left(\Delta s_{min}^*\right)^3}+\frac{\pi}{Fr\,\Delta s_{min}^*}\right)^{-0.5}, \qquad (4)$$

where $\Delta s^*_{\min}$ is the minimum value of the arc length measured between two consecutive points of the boundary $\Sigma_D(t^*)$.

The time progression is made with an explicit numerical scheme of 4th order Runge-Kutta type. Within this scheme, the material derivative of the velocity potential is defined by:

$$\frac{D\phi^*}{Dt^*} = \left(v^*\right)^2 + \left.\frac{\partial \phi^*}{\partial t^*}\right|_{\text{Eq.(1)}} . \tag{5}$$

The derivatives of the polar co-ordinates are:

$$\begin{aligned} \frac{Dr^*}{Dt^*} &= -\frac{\partial \phi^*}{\partial n^*}\sin\beta + \frac{\partial \phi^*}{\partial s^*}\cos\beta , \\ \frac{Dz^*}{Dt^*} &= \frac{\partial \phi^*}{\partial n^*}\cos\beta + \frac{\partial \phi^*}{\partial s^*}\sin\beta . \end{aligned} \tag{6}$$

4. RESULTS AND COMMENTS

The numerical modelling of drop evolution during its formation at a vertical capillary tip, and its ejection by piezoelectrically driven DOD technology has been systematically performed for distilled water and ink (at $20^{\circ}C$), for different orifice sizes, $R \in [13;100]\mu m$, in order to compare numerical and experimental data. Ink's physical properties [9, 26] are: $\rho = 1019\ kg/m^3$, $\mu = 8.7 \cdot 10^{-3}\ Pa \cdot s$, and $\sigma = 0.034\ N/m$. According to the investigated orifice sizes, the Froude and Reynolds numbers vary between the limits $Fr \in [743;43954]$, $Re \in [30.6;85]$ for distilled water, and $Fr \in [340;20125]$, $Re \in [2.44;6.76]$ for ink. The Weber number equals always the unity, $We = 1$, because of the scale choice. We note that for small orifices, the Froude number has greater values, so the gravity becomes negligible in this case. On the other hand, the Reynolds number has small values, especially for ink, so the viscous effects may be important. In this paper the model includes partially viscous effects, namely those characteristic to irrotational flows. These effects show themselves via the normal viscous stress at the interface. Irrotational flow is usually a good approximation for low viscosity fluids, set in motion from rest.

We present in Figures 3 and 4 the interface temporal evolution during the DOD process, for a water drop, and an ink drop, issuing into air. For water, the orifice radius is $R = 35\,\mu m$, and the characteristic numbers are: $Fr = 6064$, $We = 1$ and $Re = 50.3$. For ink, the orifice radius is $R = 13\,\mu m$, and the characteristic numbers are: $Fr = 20125$, $We = 1$ and $Re = 2.44$.

The dimensional volume of the ejected water drop is of $77\ pl$. The equivalent radius of that drop (the radius of a sphere with the same volume) is of $26.4\,\mu m$. The dimensional volume of the ejected ink drop is of $5.58\ pl$, and its equivalent radius is of $11\,\mu m$. Thus the ejected drop size is respectively about 75%, and 85% of the orifice size, for water, and ink case, which is consistent with available DOD data.

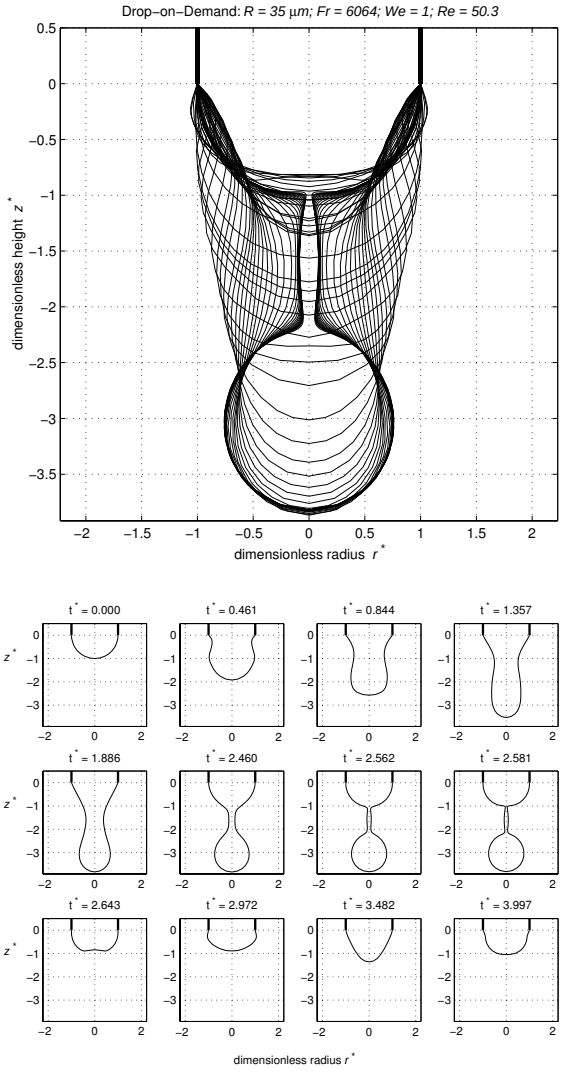

Figure 3. Superposed profiles (upper image), and some characteristic profiles at specified time t^* in separate frames (lower images), of the interface evolution, for a water drop formed by piezoelectrically driven DOD technology at an orifice of radius $R = 35\,\mu m$

The temporal variation of the velocity of the interface apex (i.e. the normal velocity of the node placed on the interface, on the Oz axis), during the interface evolution, is presented in Figure 5, for the water case (upper frame), and ink case (lower frame). The instant corresponding to drop ejection is marked on the figure, for both cases. The ejection time is $t^* = 2.61$ for the water drop, and $t^* = 3.416$ for the ink drop. For water, the interface apex

oscillates during the first 20% of the time period, and also after the drop ejection instant, and recovers its initial shape at the end of the time period. Due to the viscosity, which damps inertial effects, the interface apex for ink is more stable, and after the drop ejection instant, the interface recovers quickly its initial shape, so the DOD process can continue after a shorter time period. This should help working at a higher frequency with ink.

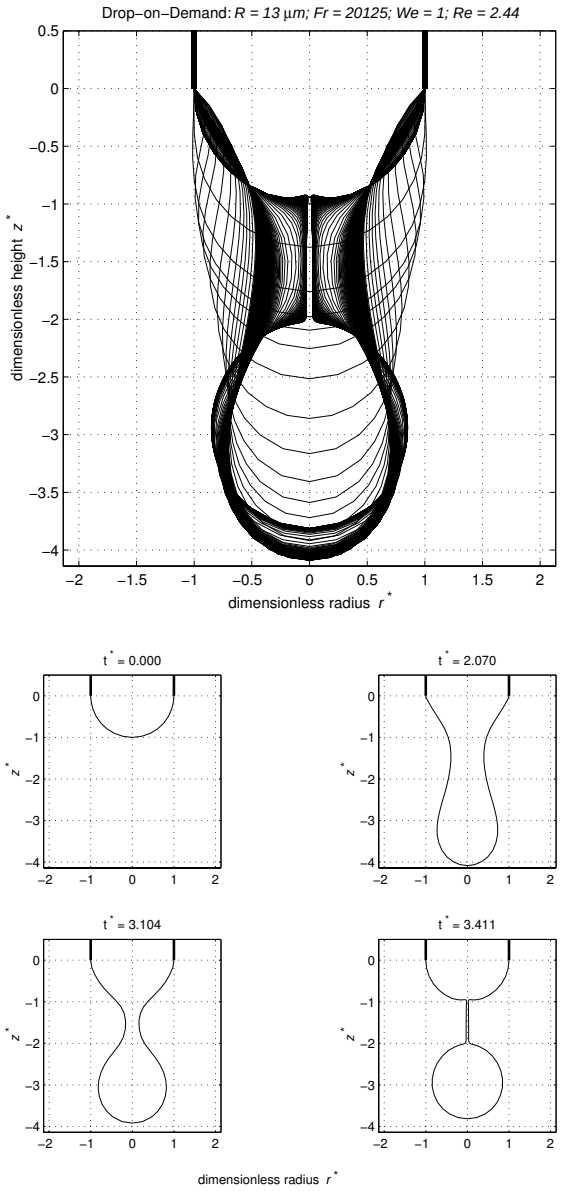

Figure 4. Superposed profiles (upper image), and some characteristic profiles at specified time t^* in separate frames (lower images), of the interface evolution, for an ink drop formed by piezoelectrically driven DOD technology at an orifice of radius $R = 13\,\mu m$

The conditions for obtaining different drop shapes immediately after ejection have been examined. We did recover the observed columnar liquid bridge joining the nascent drop to its parent body. This stage precedes necking and drop separation. In Figs 3 and 4 it is not clear whether the effective necking occurs at the upper or lower part of the column. The break-up occurs at the upper part of the column, at $z^* = -0.872$ for water, and $z^* = -0.966$ for ink case. The ejected drop shape is like the one plotted at $t^* = 2.581$ in Fig. 3 (just before the water drop detachment at $t^* = 2.61$), or like the one plotted at $t^* = 3.411$ in Fig. 4 (just before the ink drop detachment at $t^* = 3.416$).

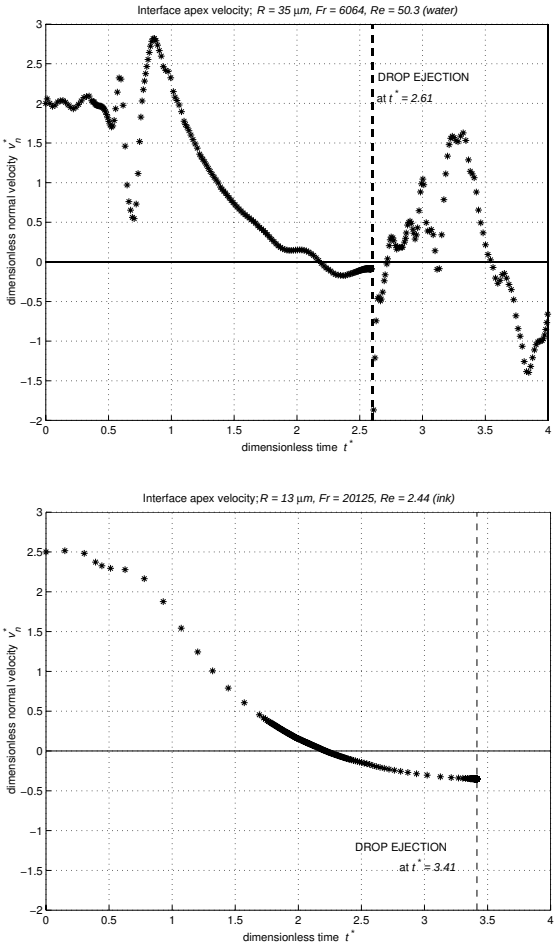

Figure 5. Temporal variation of the interface apex velocity during the DOD evolution, for the water case (upper frame), and ink (lower frame)

At the necking instant, unbalanced surface tension rapidly accelerates liquid in both liquid bodies [30]: this is the recoil stage. Waves due to separation then propagate along the column that has become a drop tail and may generate one or several satellites. This stage is difficult to be captured numerically in all the details. However some attempts have been made to describe the unique satellite formation. As the ejected ink drop from Fig.4 has a thin neck, it can be assumed that there will be a second pinching at the connection between

the long neck and the parent drop. That will lead to a satellite, which size can be estimated from the neck volume (a quasi-cylindrical shape, of 0.974 height and 0.026 mean dimensionless radius); the corresponding dimensional volume of the satellite is of $0.0045\ pl$, and equivalent radius of about $1\,\mu m$. This represents a ratio of 0.09 between the satellite radius and its parent drop radius.

With respect to industrial applications, there are desirable configurations as those leading to a simple neck pinching and drop detachment, but also undesirable configurations that must be avoided (e.g. with a wide neck). For too small values of the velocity inside the capillary nozzle, drops may not be successfully ejected (e.g. for the same *Fr* and *Re* values as in Figs. 3 and 4, for a maximum value of $v_n^* = 0.6$ for water, and $v_n^* = 2$ for ink, there is no drop ejection). In those cases, the interface grows at the beginning because of the velocity pulse, but the liquid has not sufficient inertia, and capillary effects pull back the interface to the orifice, then the drop hangs up and oscillates slowly.

Our computed results fit well the available numerical and experimental DOD data [8-12] for drops with volume of picolitres order. Encouraging agreement is obtained, but the numerical model will require added sophistication, like the evaluation of the whole viscosity effects, which would result in the introduction of the rotational part of the flow, before detailed agreement can be expected, especially for ink drops, which are much viscous than water. Moreover surfactants tend to migrate to interface when area is created during growth in order to restore the interfacial equilibrium conditions. As this process has a long time scale compared to hydrodynamic scales, they may affect the end of drop formation.

5. SUMMARY AND PERSPECTIVES

The Drop-on-Demand numerical simulation was made through a Boundary Element Method, by taking into account the capillary effects and only partially the viscous effects. In order to prevent numerical instabilities, the progression time step was obtained from a gravity-capillary waves stability criterion. The precision of the numerical code was checked through the global mechanical energy balance.

Our computed results fit well the available numerical and experimental data, for water and ink drops, with volume of picolitres order.

The present modelling can be refined in the future, by introducing the Helmoltz decomposition [31] in order to incorporate the rotational part of the velocity field, thus to evaluate the whole viscosity effects. We have to address the vorticity – stream function formulation of axisymmetric unsteady incompressible flows in conjunction with moving boundaries. The BEM leads in these cases to domain integrals that detract from the boundary only features. There are several techniques to preserve advantages of the BEM and to extend its theoretical foundations and numerical implementation to tackle this broader class of equations. One technique that we will use is based on the Greengard and Strain algorithm [32].

ACKNOWLEDGEMENTS

This work has been supported by the Programme ECO-NET from the French Ministry of Foreign Affairs, under the project “Stimulation et formation de goutte à la demande: étude expérimentale et numérique des effets non-linéaires” (2004-2005), led by professor A. Soucemarianadin from LEGI Grenoble, and by the Romanian National University Research Council (CNCSIS), under the project “DOD numerical simulation, applied in microfluidics” (2004-2005), Grant A-1405, led by S.-C. Georgescu.

REFERENCES

[1] Le, H. P., 1999, “Progress and Trends in Ink-Jet Printing Technology”, In: *Recent Progress in Ink Jet Technologies II*, ed. E. Hanson, IS&T, Springfield, pp. 1-14.

[2] Pimbley, W. T., and Lee, H. C., 1977, “Satellite Droplet Formation in a Liquid Jet”, *IBM J. Res. Develop.*, Vol. 21 (1), pp. 21-30.

[3] Hilbing, J., and Heister, S., 1996, “Droplet size control in liquid jet breakup”, *Phys. Fluids*, Vol. 8 (6), pp. 1574-1581.

[4] Lopez, B., Soucemarianadin, A., and Attané, P., 1999, “Break-up of Continuous Liquid Jets: Effect of Nozzle Geometry”, *J. Imaging Sci. Techn.*, Vol. 43 (2), pp. 145-152.

[5] Soucemarianadin, A., Pierron, P., Normandin, M., Clermont, J.R., and Attané, P., 1999, “Modeling of Liquid Jet Break-up and Drop Formation”, In: *Recent Progress in Ink Jet Technologies II*, Springfield, pp. 218-222.

[6] Chen, T., 2005, “Recent Advances in Piezoelectric Inkjet Print Head Technology”, Proc. *IS&T’s NIP21*, Baltimore, pp. 268-268.

[7] Bogy, D. B., and Talke, F. E., 1984, “Experimental and Theoretical Study of Wave Propagation Phenomena in Drop-on-Demand Ink Jet Devices”, *IBM J. Res. Develop.*, Vol. 28 (3), pp. 314-321.

[8] Blumberg, A., and Semiat, R., 2002, “Velocity Measurements of Ink Drops Ejected from a Piezoelectric DOD Print Head. I Technique Presentation, II Parameters of Ejecting Signal”, *J. Imaging Sci. Techn.*, Vol.46 (2), pp. 171-189.

[9] Cittadino, J. M., Mendes, E., Soucemarianadin, A., 2005, "A Tool for Monitoring Piezoelectric Micro-Pumps", Proc. *IS&T's NIP21*, Baltimore, pp. 278-282.

[10]Fromm, J. E., 1984, "Numerical Calculation of the Fluid Dynamics of Drop-on-Demand Jets", *IBM J. Res. Develop*., Vol. 28 (3), pp. 322-333.

[11]Shield, T. W., Bogy, D. B., and Talke, F. E., 1987, "Drop Formation by DOD Ink-Jet Nozzles: A Comparison of Experiment and Numerical Simulation", *IBM J. Res. Develop.*, Vol. 31 (1), pp. 96-110.

[12]Feng, J., 2002, "A General Fluid Dynamic Analysis of Drop Ejection in Drop-on-Demand Ink Jet Devices", *J. Imaging Science and Technology*, Vol. 46 (5), pp. 398-408.

[13]Bugdayci, N., Bogy, D. B., and Talke, F. E., 1983, "Axisymmetric Motion of Radially Polarized Piezoelectric Cylinders Used in Ink Jet Printing", *IBM Journal of Research and Development*, Vol. 27 (2), pp. 171-180.

[14]Bruce, C. A., 1976, "Dependence of Ink Jet Dynamics on Fluid Characteristics", *IBM J. Res. Develop*., Vol. 20 (3), pp. 258-270.

[15]Magdassi, S., Ben-Moshe, M., Berenstein, L., and Zaban, A., 2003, "Microemulsion Based Ink-Jet Ink: Properties and Performance", *J. Imaging Sci. Techn.*, Vol. 47 (4), pp. 357-360.

[16]Koltay, P., Birkle, G., Steger, R., Kuhn, H., Mayer, M., Sandmaier, H., and Zengerle, R., 2001, "Highly Parallel and Accurate Nanoliter Dispenser for High-Throughput-Synthesis of Chemical Compounds", Proc. *IMEMS Workshop*, Singapore, pp. 1-10.

[17]Wallace, D., and Hayes, D., 2002, "Solder Jet™ - Optics Jet™ - AromaJet™ - Reagent Jet - Tooth Jet and Other Applications of Ink-Jet Printing Technology", Proc. *IS&T's NIP18*, San Diego, USA, pp. 228-235.

[18]Chen, C.-T., Chiu, C.-L., and Chen, S.-S., 2004, "Simulation and Experiment of Micro-Lens Fabrication Using Droplet Deposition Method", Proc. *IS&T's NIP20*, Salt Lake City, USA, pp. 265-268.

[19]McDonald, M., Heun, S., and Tallant, N., 2002, "Advances in Piezoelectric Deposition of Organic Electronic Materials", Proc. *IS&T's NIP18*, San Diego, pp. 433-436.

[20]Shah, V., and Hayes, D., 2002, "Trimming and Printing of Embedded Resistors Using Demand-Mode Ink-Jet Technology and Conductive Polymer", Proc. *IPC Printed Circuits Expo*, Long Beach, USA, pp. 1-5.

[21]Kuroiwa, T., Ishikawa, N., Obara, D., Vinet, F., Ang, E. S., Guelbi, A., and Soucemarianadin, A., 2003, "Dispensing of Polymeric Fluids for BIO-MEMS Applications", Proc. *IS&T's NIP19*, New Orleans, USA, pp. 884-890.

[22]Joseph, D. D., Liao, T. Y., and Hu, H. H., 1993, "Drag and moment in viscous potential flow", *Eur. J. Mech. B-Fluids*, Vol. 12 (1), pp. 97-106.

[23]Georgescu, S.-C., Achard, J.-L., and Canot, É., 2002, "Jet drops ejection in bursting gas bubble processes", *Eur. J. Mech. B-Fluids*, Vol. 21, pp. 265-280.

[24]Canot, É., Georgescu, S.-C., and Vincent, S., 2005, "Test-case No 21: Gas bubble bursting at a free surface, with jet formation (PN-PE)", In: *Validation of Advanced Computational Methods for Multiphase Flows*, eds. H. Lemonnier, D. Jamet, O. Lebaigue, Begell House Inc., New York, Chapter 19, pp.135-142.

[25]Georgescu, S.-C., 1999, "Evolution d'une bulle: Formation à partir d'un orifice et éclatement à la traversée d'une surface libre", *PhD Thesis, Institut National Polytechnique de Grenoble*.

[26]Georgescu, S.-C., Canot, É., Broboană, D., and Soucemarianadin, A., 2005, "Numerical Simulation of Drop-on-Demand Jetting Applications in Microfluidics", *EUROMECH Colloquium 472 «Microfluidics and Transfer»*, Grenoble, France, pp. 139-140.

[27]Machane, R., and Canot, É., 1997, "High-order schemes in Boundary Element Methods for transient non-linear free surface problems", *Int. J. Numer. Methods Fluids*, 24, pp. 1049-1072.

[28]Canot, É., 1999, "Stability Criteria for Capillary/Gravity Free-Surface Waves in BEM Simulations of Viscous Potential Flows", Proc. *Int. Conf. Boundary Element Techniques*, ed. M. H. Aliabadi, London, U.K., pp. 321-330.

[29]Spangler, C., Hilbing, J., and Heister, S., 1995, "Nonlinear modeling of jet atomization in the wind-induced regime", *Phys. Fluids*, Vol. 7 (5), pp. 964-971.

[30]Peregrine, D. H, Shoker, G., and Symon, A., 1990, "The bifurcation of liquid bridges", *J. Fluid. Mech.*, Vol. 212, pp. 25-39.

[31]Machane, R., Achard, J.-L., and Canot, É., 2000, "A new velocity-vorticity Boundary Integral Formulation for Navier-Stokes equations", *Int. J. Numer. Methods Fluids*, Vol. 34, pp. 47-63.

[32]Greengard, L., and Strain, J., 1990, "A fast algorithm for the evaluation of heat potentials", In: *Communications on Pure and Applied Mathematics*, XLIII, John Wiley & Sons, pp. 949-963.

Conference on Modelling Fluid Flow (CMFF'06)
The 13th International Conference on Fluid Flow Technologies
Budapest, Hungary, September 6-9, 2006

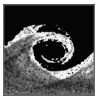

BASICS OF THE NUMERICAL SIMULATION OF OIL DROPLET FORMATION IN THE CRANKCASE OF AN IC ENGINE

Wilfried EDELBAUER[1], Heinrich KRATOCHWILL[1],
Günter BRENN[2], Reinhard TATSCHL[3]

[1] Corresponding Author. Austrian Center of Competence for Tribology, AC²T research GmbH. Viktor Kaplan-Straße 2, A-2700 Wr.Neustadt, Austria. Tel.: +43 316 787 1902, Fax: +43 316 787 777, E-mail: edelbauer@ac2t.at / kratochwill@ac2t.at
[2] Institute of Fluid Mechanics and Heat Transfer, Graz University of Technology, Austria. E-mail: brenn@fluidmech.tu-graz.ac.at
[3] Advanced Simulation Technologies, AVL List GmbH, Graz, Austria. E-mail: reinhard.tatschl@avl.com

ABSTRACT

Due to the increasing demand for high efficiency of Internal Combustion (IC) engines, engineers are compelled to pay attention to the complex two-phase flow of oil and air in the crankcase. Reduction of the ventilation losses and limitation of the oil consumption due to oil droplets leaving the crankcase are the targets of optimisation.

The aim of this work is to provide a better understanding of the flow phenomena in the crankcase and to model formation and transport processes of the two-phase flow. Oil disintegration at the crank drive and oil atomisation due to blow-by effects at the piston rings are the major sources for the oil droplets. Droplet formation due to condensation of evaporated oil components is not considered due to negligible contribution in simulations of a few engine cycles.

Model correlations have been implemented into a multi-phase CFD code. Separate simulations of the blow-by gas flow and the oil disintegration at the crankweb have been performed on simplified crankcase geometries. Besides the oil droplet propagation, the simulations show that blow-by generates small droplets with diameters of a few microns, while large droplets are generated by the oil disintegration at the crankweb.

Keywords: blow-by, CFD, crankcase, multi-phase, rotary atomisation

NOMENCLATURE

A	$[m^2]$	area
C, K	[-]	model constants
K_F	[-]	fluid number
$\underline{M}$	$[N/m^3]$	momentum transfer rate
R	$[J/kgK]$	gas constant
V	$[m^3]$	volume
We	[-]	Weber number
Y	[-]	total mass fraction
Z	[-]	Ohnesorge number squared
d	$[m]$	diameter
g	$[m/s^2]$	gravitational acceleration
m	$[kg]$	mass
p	$[N/m^2]$	pressure
t	$[s]$	time
$\underline{u}$	$[m/s]$	absolute velocity vector
α	[-]	volume fraction
γ	[-]	model constant
Γ	$[kg/m^3s]$	mass transfer rate
κ	[-]	adiabatic exponent
μ	$[Ns/m^2]$	dynamic viscosity
ν	$[m^2/s]$	kinematic viscosity
ρ	$[kg/m^3]$	density
σ	$[N/m]$	surface tension
ω	$[rad/s]$	angular velocity

Subscripts and Superscripts

32	Sauter mean value
cir	circumferential
crn	crankcase
cyl	cylinder
disc	disc/crankshaft
drop	droplet
g	gaseous phase
i	chamber
j,k	phase indices
l	liquid (here oil)
n	number of phases
rad	radial
t	turbulent

1. INTRODUCTION

Due to the motion of the crank drive, an airflow is created in the crankcase which carries lubricating

oil droplets. For the droplet formation processes, one can distinguish between processes producing small droplets with diameters less than 10 μm, the oil mist, and processes producing large droplets and splash oil [1]. It is believed that the liquid disintegration of oil on the moving crank drive, especially at the rotating crankwebs, and the splash oil from the piston cooling jets are the major sources for large droplets. Condensation of evaporated oil and unburnt fuel components, as well as droplet formation due to blow-by at the piston rings, are most certainly the sources for oil mist. On the one hand, the airflow which carries the oil droplets is required to wet the cylinder wall and to guarantee sufficient lubrication between piston and cylinder. On the other hand, oil droplets leaving the crankcase through the ventilation system would cause high oil consumption, if they were not separated by the oil mist separator. The propagation of the oil droplet flow is therefore a matter of particular interest in the crankcase.

The present study treats the oil detachment from the crankwebs and the atomisation due to blow-by as the most relevant processes of droplet formation. It is done in separate models which yield the base for multi-phase CFD simulations [2]. Condensation is neglected because it is slow and its contribution in simulations of a few engine revolutions is small. Piston cooling jets are only used in engines with high thermal load, and hence they are not yet treated in the current investigations, which are the first step in CFD simulations of the crankcase flow.

The models of droplet formation are implemented into the commercial multi-phase CFD code AVL FIRE. Simplified geometries are used for the CFD simulations to show the influence of the models in separate calculations. Oil and gas are treated as separate, interpenetrating phases. The inter-phase exchange terms take into account the interactions between the phases and introduce the specific physics of the problem. The analogy to rotary atomisation is used to describe the liquid oil disintegration on the rotating crankwebs, which are modelled, in a first step, as cylindrical discs. To determine the blow-by gas flow at the piston rings, a zero-dimensional chamber model is used. A further semi-empirical model describes the generation of the atomised oil droplets due to the blow-by gas flow. Finally, these models act as boundary conditions for the oil and gas phases of the CFD simulations which describe the transport of the oil droplets in the crankcase.

Section 2 of the present paper describes the applied multi-phase conservation equations, the analogy to rotary atomisation for the oil disintegration at the crankweb and the blow-by model. Section 3 shows the results of the CFD simulations. At the current stage, separate simulations for rotary atomisation and blow-by are presented to show the effects of the models. In future work these models will be combined.

2. THEORY

2.1 Multi-phase Conservation Equations

The flow simulations are based on the Eulerian multi-phase approach, where the conservation equations are solved for an arbitrary number of interpenetrating phases [3]. Each phase is characterised by its volume fraction α, and all volume fractions sum up to unity. Eqs. (1) and (2) below describe the conservation of mass and momentum for phase k. The terms Γ and $\underline{M}$ on the right hand sides of Eqs. (1) and (2) account for the interaction between the phases. Γ represents the rate of mass transfer, e.g. by condensation and evaporation, and $\underline{M}$ represents the forces between the phases, such as drag, which act between the gaseous and the liquid phases. In addition, the conservation equations for enthalpy, turbulence kinetic energy and turbulence dissipation rate are solved (not shown here).

$$\frac{\partial \alpha_k \rho_k}{\partial t} + \nabla \cdot \alpha_k \rho_k \underline{u}_k = \sum_{j=1, j\neq k}^{n} \Gamma_{kj} \tag{1}$$

$$\frac{\partial \alpha_k \rho_k \underline{u}_k}{\partial t} + \nabla \cdot \alpha_k \rho_k \underline{u}_k \underline{u}_k = -\alpha_k \nabla p + \alpha_k \rho_k \underline{g} + \nabla \cdot \alpha_k \underline{\underline{\tau}}_k^t + \sum_{j=1, j\neq k}^{n} \underline{M}_{kj} + \underline{u}_k \sum_{j=1, j\neq k}^{n} \Gamma_{kj} \tag{2}$$

Two phases are used for the simulation of the crankcase flow – air as the continuous phase and liquid oil as the dispersed phase. A droplet diameter must be specified for the oil phase to take into account the dynamic interaction with the air by drag forces. Condensation and evaporation of oil droplets is not considered in this study. Therefore the term Γ in Eq. (1) is zero. The basis for the simulations is the CFD software package AVL FIRE. The models for liquid disintegration on the crankweb and the blow-by gas flow used in the multi-phase simulations are described in the subsequent sections.

2.2 Rotary Atomisation on Crankwebs

Due to the motion of the crank drive, the lubricating oil is separated from the moving parts, especially from the rotating crankwebs. The liquid disintegration on rotary atomisers is a very similar physical process, and hence it is reasonable to use this process as an analogy. Depending on the fluid properties, disc diameter, oil volume flow rate and rotational velocity, the oil forms a liquid rim along the disc edge [6] and disintegrates according to different disintegration regimes. There are drop-

wise, ligament and sheet disintegration [5]. Very high rotational velocity may result in atomisation into small droplets without rim formation along the edge.

Figure 1 shows the oil volume flow rate over one side of the crankweb depending on the engine speed. This curve results from one-dimensional simulations of the oil flow in the lubricating oil circuit. It is assumed that approximately half of the oil passing the bearing disintegrates at the edge of the rotating crankweb. In Figure 2, the correlations describing the different disintegration regimes reported by different authors, [4] in Fig. 2 top and [5] in Fig. 2 bottom, are compared. The volume flow rate curve of Fig. 1 is applied on three different disc diameters of 50, 100 and 200 *mm*. The dimensionless parameters from Eqs. (3) to (6) are combined to determine the coordinate axes of the disintegration regime map as defined from Eqs. (7) to (10). One can see that the angular velocity ω is the dominating parameter of the ordinates. There is a good agreement between the disintegration regime correlations from [4] and [5], because in both maps the volume flow rate curves pass the regimes of drop-wise, ligament and sheet disintegration in a similar way.

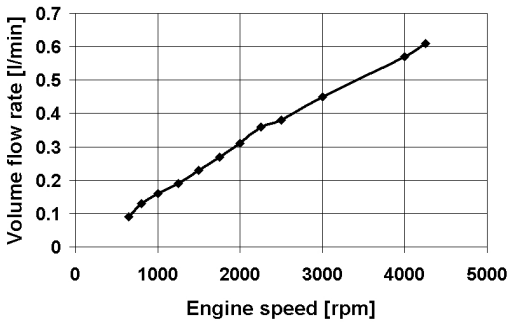

Figure 1. Oil volume flow rate over the crankweb in [l/min]

$$We = \frac{\omega^2 d_{\text{disc}}^3 \rho_\text{l}}{\sigma} \tag{3}$$

$$Z = \frac{\mu_\text{l}^2}{\rho_\text{l} d_{\text{disc}} \sigma} \tag{4}$$

$$K_\text{F} = \frac{\rho_\text{l} \sigma^3}{g \mu_\text{l}^4} \tag{5}$$

$$\dot{V}^* = \frac{\dot{V}^2 \rho_\text{l}}{d_{\text{disc}}^3 \sigma} \tag{6}$$

For the flow simulation it is necessary to estimate the droplet diameter, which depends on the disintegration regime, the fluid properties, the volume flow rate and the rotational speed. Eqs. (11) and (12) show the droplet diameter correlations for drop-wise and ligament disintegration, respectively, as presented in [6]. Eq. (13) represents the droplet diameter correlation for sheet disintegration, which is taken from [7] and adapted for the present application.

$$x_{1,\text{I}} = Z^{0.5} \tag{7}$$

$$x_{2,\text{I}} = We^{0.5} Z^{0.138} \dot{V}^{*0.833} \tag{8}$$

$$x_{1,\text{II}} = \dot{V}^{*0.5} Z^{-0.47} K_F^{-0.295} \tag{9}$$

$$x_{2,\text{II}} = We^{0.5} Z^{0.922} K_F^{0.491} \tag{10}$$

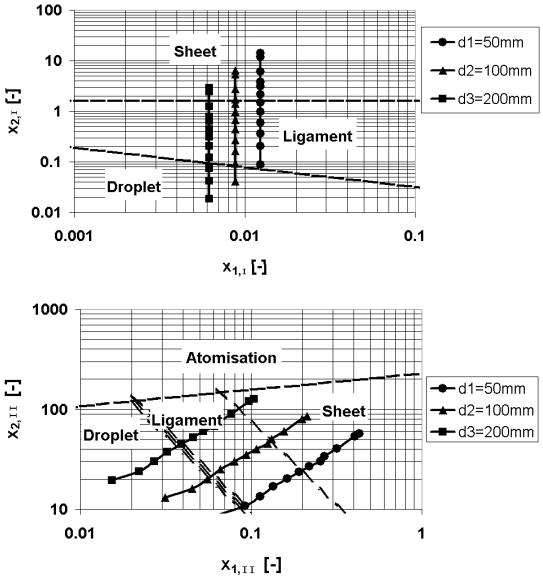

Figure 2. Comparison of the different disintegration regime correlations according to [4] (top) and [5] (bottom) for the oil volume flow rate curve at three disc diameters

$$d_{\text{drop}} = \text{C}_1 \sqrt{\frac{4\sigma}{d_{\text{disc}} \omega^2 \rho_\text{l}}} \tag{11}$$

$$d_{\text{drop}} \approx \sqrt{\frac{2\sigma}{d_{\text{disc}} \omega^2 \rho_\text{l}}} \nu_\text{l}^{-\frac{1}{12}} \tag{12}$$

$$d_{\text{drop}} = \frac{1.175 \text{C}_2}{d_{\text{disc}} \omega} \left(\frac{\rho_\text{l}}{\rho_\text{g}} \right)^{\frac{1}{6}} \left(\frac{\sigma \dot{V}}{\rho_\text{l}} \right)^{\frac{1}{3}} \tag{13}$$

The estimated droplet diameter depending on the engine speed is shown in Figure 3 for the three disc diameters. The disintegration regimes have been distinguished according to the correlations shown in Fig. 2 bottom. It is evident that the droplet diameter is reduced with increasing engine speed. A slight discontinuity in the graphs is due to the transition from ligament to sheet disintegration. The radial component of the droplet velocity at the edge of the disc is derived from a mass balance for ligament disintegration [6]. The circumferential

velocity of the disc edge determines the tangential velocity component.

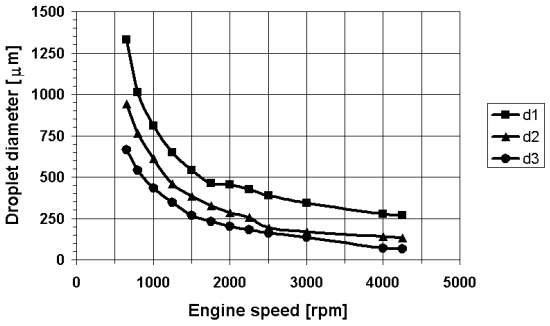

Figure 3. Diameters of detached droplets

2.3 Atomisation Due to Blow-by

The atomisation of oil due to blow-by gas is a major source for the small oil droplets in the crankcase. Blow-by is the leakage of gas from the combustion chamber into the crankcase. The gas leaks down between the piston rings and the liner, as well as through the piston ring gaps. Due to the high velocity of the blow-by gas jet, small droplets are stripped from the wall oil film, which represent a fraction of the oil mist in the crankcase. For the flow simulation in the crankcase, the introduced gas and oil mass flow rates, and the estimated oil droplet diameters are boundary conditions of interest. The mass flow rate of the blow-by gas is calculated using a zero-dimensional chamber model [8, 9], as shown in Figure 4. The captured volumes between the piston rings represent the chambers. The number of chambers is defined by the number of compression rings and the oil control ring. Three piston rings, two compression rings and one oil control ring, e.g., result in two chambers of the model.

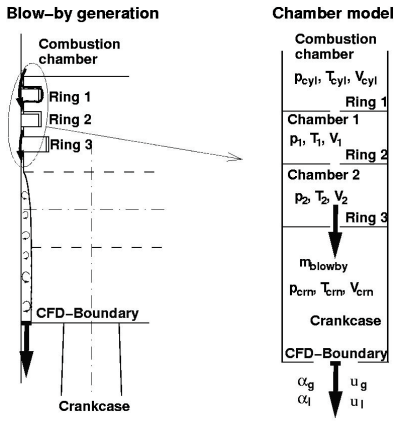

Figure 4. The Chamber model describes the blow-by generation in the combustion engine.

The time dependent pressure and temperature in the combustion chamber and in the crankcase are boundary conditions for the chamber model. The change of state is calculated by Eqs. (14) and (15) below. The gas mass flow rate from one chamber into the other is calculated by Eq. (16) and depends on the pressure difference between the chambers. In the case of supercritical pressure ratio, choked flow occurs, and the speed of sound is the upper limit of the gas velocity. Combining Eqs. (14) and (16) and applying them to every chamber leads to a system of ordinary differential equations of first order, which is solved with a Runge-Kutta scheme. The results are the time dependent pressure variation inside the chambers and the gas mass flow rate over the piston rings, as shown in Figure 6. The mass flow rate across the oil control ring acts as a boundary condition of the CFD simulation and represents the mass entering the crankcase.

$$\frac{dp_i}{dt} = \left(\dot{m}_{i-1,i} - \dot{m}_{i,i+1}\right)\frac{R \cdot T_i}{V_i} + \frac{m_i \cdot R}{V_i} \cdot \frac{dT_i}{dt} \tag{14}$$

$$T_i \approx const. \rightarrow \frac{dT_i}{dt} = 0 \tag{15}$$

$$\dot{m}_{i-1,i} = \begin{cases} \dfrac{K A_i}{\sqrt{R T_{i-1}}}\, p_{i-1} \sqrt{\dfrac{\kappa}{\kappa-1}\left[\left(\dfrac{p_i}{p_{i-1}}\right)^{\frac{2}{\kappa}} - \left(\dfrac{p_i}{p_{i-1}}\right)^{\frac{\kappa+1}{\kappa}}\right]} & \text{subcr.} \\ \dfrac{K A_i}{\sqrt{R \cdot T_{i-1}}}\, p_{i-1} \left(\dfrac{2}{\kappa+1}\right)^{\frac{1}{\kappa-1}} \sqrt{\dfrac{\kappa}{\kappa-1}} & \text{supercritical} \end{cases} \tag{16}$$

It is assumed that a certain fraction of the oil, which is contained in the chambers between the piston rings, is atomised by the high-speed blow-by gas jet [1]. Figure 5 illustrates the oil atomisation process at the oil control ring. The amount of this oil fraction corresponds to a fictitious oil film thickness, which is stripped during the engine cycle and has to be estimated for the simulation. The Sauter mean diameter of the atomised droplets is calculated with Eq. (17). This semi-empirical correlation is derived from the atomisation of a liquid jet by a surrounding gas jet [10].

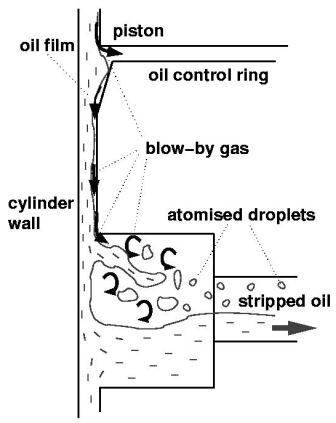

Figure 5. Oil atomisation due to blow-by

$$d_{32,\mathrm{drop}} = \frac{0.68\gamma^{\frac{1}{2}}\left(\rho_l \nu_g\right)^{\frac{1}{4}}\sigma^{\frac{1}{2}}}{\rho_g^{\frac{3}{4}}\left[u_g\left(1+\left(\frac{\rho_g}{\rho_l}\right)^{\frac{1}{2}}\right)-u_l\right]u_g^{\frac{1}{4}}} \qquad (17)$$

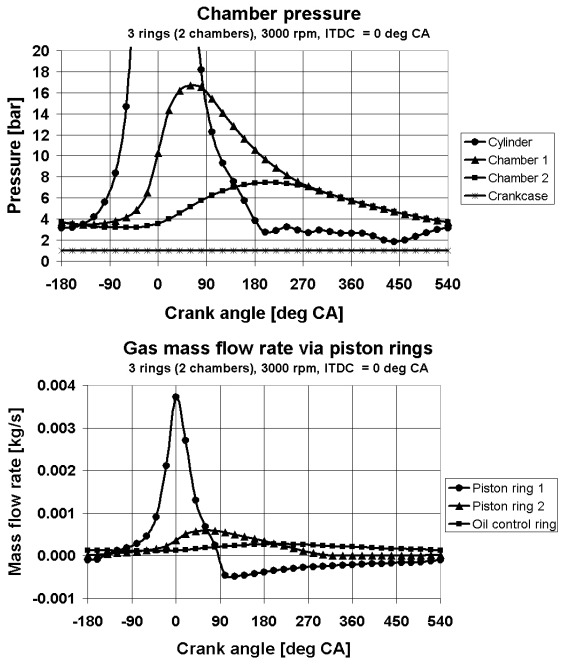

Figure 6. Calculated pressure and gas mass flow rate due to blow-by from the chamber model

Referring to Fig. 6 it is important to mention that the ignition top dead center (ITDC) is placed at 0 *deg CA*. In the graph of the chamber pressure it is interesting to see that the pressure in the combustion chamber decreases below the pressure of chamber 1 at approximately 80 *deg CA*. After this time, gas flows back from chamber 1 into the combustion chamber. From the pressure peak in chamber 2 at about 200 *deg CA* it is evident that there is a time delay for the mass flow rate from the combustion chamber to the crankcase. This time delay increases with engine speed. For the CFD simulation the mass flow rate from chamber 2 passing the oil control ring into the crankcase is the relevant blow-by boundary condition. The average gas mass flow rate is about 0.19 *mg/s* resulting in 6 *m/s* inlet velocity. The maximum blow-by mass flow rate occurs at 200 *deg CA*.

3. CFD SIMULATIONS

In section 2 the theoretical background of the oil droplet formation was shown. The air and oil flow is represented by a multi-phase approach. The models of rotary droplet atomisation and blow-by gas mass flow provide the boundary conditions for the simulation of the oil droplet formation and propagation. The introduced oil is defined by its volume fraction and the inlet velocity. This study shows the rotary atomisation and the blow-by in separate simulations. In the future these two models will be combined into one simulation.

3.1 Simulation of Droplet Detachment from Crankwebs

A simplified crankshaft is used to investigate the oil droplet detachment from a rotating geometry. The computational grid is shown in Figure 7. The simplified crankshaft consists of two cylindrical discs. The rotating part of the mesh rotates together with the crankshaft. The fixed part of the mesh is stationary and is connected to the rotating part by a sliding interface. Inlet boundaries are defined at the edges of the discs. The oil flow from the bearings along the wall of the crankwebs is not modelled. The engine speed is 4000 *rpm*, and one revolution of the crankshaft is simulated.

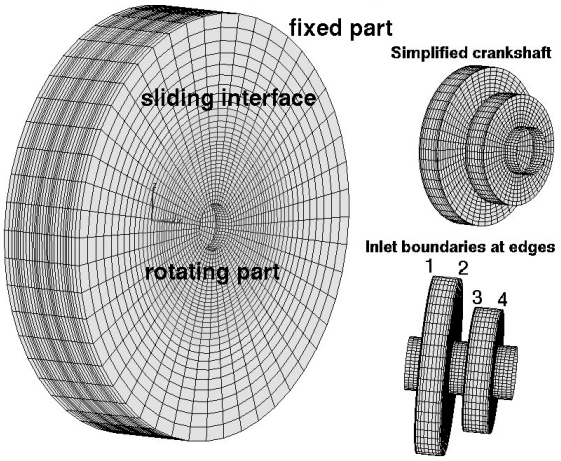

Figure 7. Computational grid with simplified crankshaft for droplet detachment

The inlet velocity at the disc edge is a composition of radial and circumferential components. The volume fraction of the oil phase is defined by the amount of oil leaving the bearings and moving to the edge of the disc. Table 1 contains four selected oil volume flow rates and the calculated components of the detachment velocities. The volume flow rate of inlet 1 is taken from Fig. 1, and the others are used to show the influence of variations.

Table 1. Boundary conditions at inlets

Inlet	d_{disc} [*mm*]	V_{oil} [*l/min*]	u_{cir} [*m/s*]	u_{rad} [*m/s*]
1	100	0.57	20.9	2.15
2	100	0.3	20.9	1.13
3	70	0.7	14.7	3.15
4	70	0.2	14.7	0.9

From this data the disintegration regimes from Fig. 2 and the oil droplet diameters are calculated for the inlets. For the momentum exchange between the droplets and the gaseous phase, one representative oil droplet diameter has to be determined. Therefore the average value of the four inlets of 139.8 μm was calculated. This value confirms the assumption that rotary atomisation is a source for large droplets in the crankcase.

Figure 8 shows the oil volume fraction in a cut through inlet 1 and a cut along the crankshaft axis. The higher the density of the iso-lines, the higher the amount of oil mass. The smaller disc has a smaller circumferential velocity at the edge, and hence the oil detaches with a lower velocity. Nevertheless, there is a strong oil flow from inlet 3, which has the highest volume flow rate.

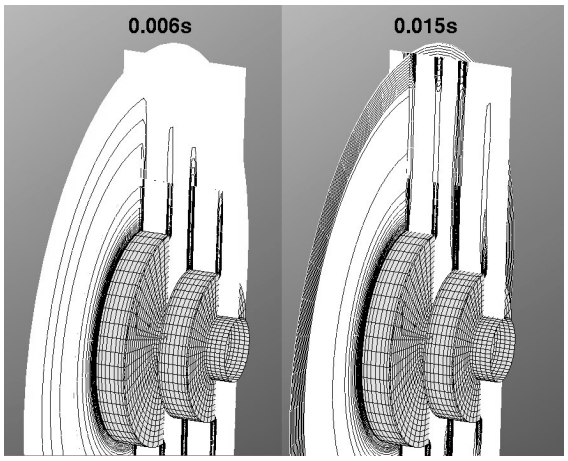

Figure 8. Oil volume fractions at 6 and 15 *ms*

After one revolution, i.e. 15 *ms*, the oil has reached the outer wall and accumulates there. Only the oil of inlet 4, which has the smallest volume flow rate and the smallest circumferential velocity, does not reach the wall within the simulation time.

The velocity distribution of the oil phase in cuts through inlets 1 and 4 is presented in Figure 9. After entering the flow field, the droplets slow down and move to the outer wall on nearly straight trajectories. For an observer rotating with the disc, the droplets move away on an involute [6]. Besides the aerodynamic drag, the gravitational force acts on the droplets, creating a slight difference to an axially symmetric result.

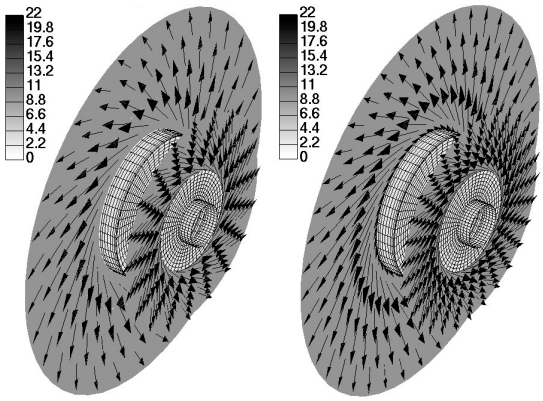

Figure 9. Velocity vectors of the liquid oil phase at 6 *ms* (left) and 15 *ms* (right) (absolute values in *m/s*)

3.2 Blow-by Flow Simulation

The flow simulation with blow-by boundary conditions was done on a simplified crankcase with two 90-degrees cylinder sectors. The crankshaft and the connecting rod are not modelled and the bottom of the piston is assumed to be flat. The computational grid is shown in Figure 10. The zoomed window shows the blow-by inlet at the position of the piston skirt, where the piston diameter is usually slightly reduced. The boundary conditions, as velocities and mass flow rates of air and oil, are calculated using the equations of section 2.3. The engine speed is 3000 *rpm* and five engine cycles are simulated. Initial conditions used in the crankcase are 1 *bar* for pressure and 373 *K* for temperature. The simulation starts from rest with cylinder 1 in the top dead center and cylinder 2 in the bottom dead center (BDC). The calculated diameter of the atomised droplets is about 4.6 μm. This value confirms the assumption that blow-by atomisation is a source of small droplets in the crankcase.

Figure 11 shows the gas velocities and the oil mass fraction in the symmetry plane through the cylinder axes at 180 *deg CA*. The dark regions of the oil mass fraction indicate an increased concentration of oil droplets. The blow-by gas jet along the liner wall can be seen, which produces a remarkable oil droplet cloud there. In addition, the three-dimensional flow transports some oil radial inwards under the flat piston.

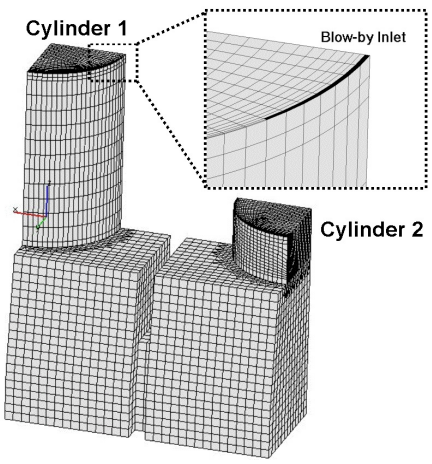

Figure 10. Computational grid with blow-by inlet

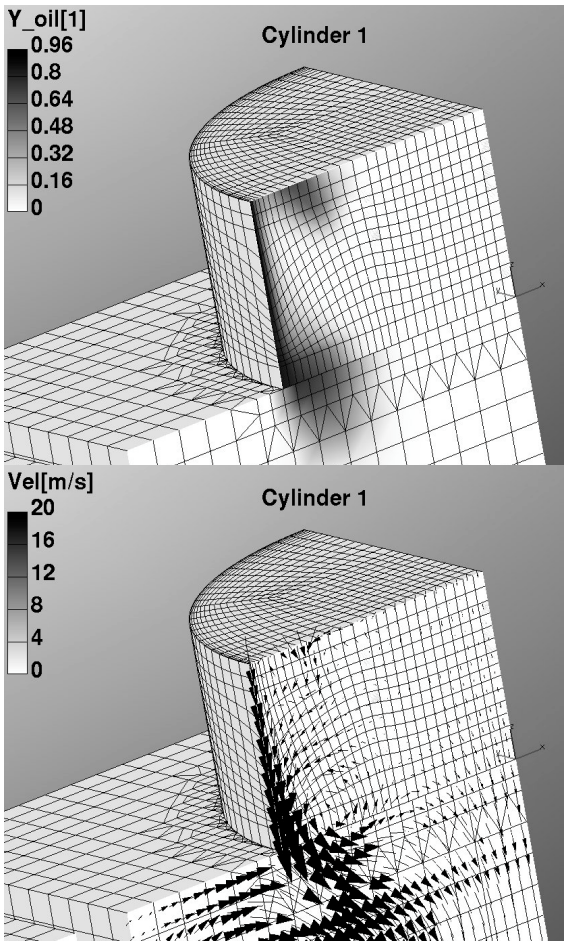

Figure 11. Oil mass fraction and velocity vectors at 180 *deg CA* close to the blow-by inlet region

Figure 12 shows the gas velocities and the oil mass fraction in the symmetry plane through the cylinder axes at 270 and 1800 *deg CA*. For this plot the velocities were interpolated onto a coarser grid to get a smooth velocity vector distribution for showing the overall flow field. Due to starting from rest, the velocity field is not yet fully developed during the first engine cycle. It is evident that, at 270 *deg CA*, the piston velocity is dominant. As a consequence of the coarser resolution of the velocity plot, the blow-by jet of cylinder 2 is not visible at BDC for 1800 *deg CA*. Although the induced recirculation can be observed.

The oil mass fraction at 270 *deg CA* is different in the two cylinders, as the cylinders start at different positions. Piston 1 starts at TDC, producing a gas and oil jet pushed forward by the piston motion. Thereafter this oil cloud is partially sucked back into cylinder 1, following the upward motion of the piston. Piston 2 starts at BDC, depositing some oil along the liner, as the blow-by inlet velocity is of the order of the mean piston velocity of about 8 *m/s*. During the downward motion, the deposited oil is accumulated and transferred in a radial direction towards the cylinder axis.

At 1800 *deg CA*, the oil is already distributed in the whole crankcase. In the cylinders, the maximum oil concentration is located close to the liner. Also, in the region near the cylinder axes, an increased oil concentration is visible. In the case presented, the overall oil concentration in the flow field increases continuously, as a crankcase ventilation system is not modelled.

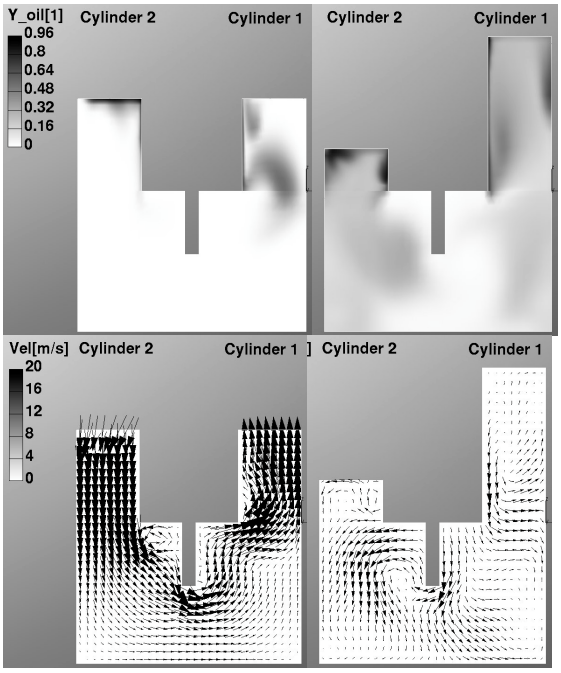

Figure 12. Oil mass fraction (top) and velocity vectors (bottom) at 270 *deg CA* (left) and 1800 *deg CA* (right)

4. SUMMARY

The aim of this work was to develop basic tools for the simulation of air and oil two-phase flows to improve the understanding of the complex flow phenomena in the crankcase of IC engines. The oil atomisation was investigated separately for the rotating crankshaft and for the blow-by at the piston rings. Simplified physical models are used on simple crankcase geometries. Extended modelling, improved boundary conditions and the combination of the presented models in one single simulation will be the next steps.

ACKNOWLEDGEMENTS

This work has been supported by the Austrian Kplus-program and has been performed at the Austrian Competence Center for Tribology (AC²T research GmbH) in co-operation with Advanced Simulation Technologies at AVL List GmbH.

REFERENCES

[1] Meinig, U., Pietschner, S., and May, T., 2004, "Kurbelgehäuse-Entlüftung aktueller und zukünftiger Fahrzeugmotoren – Teil 1: Aktuelle Entlüftungssysteme", *MTZ 10/2004 Jahrgang 65*, pp. 768-777.

[2] Edelbauer, W., Kratochwill, H., and Suffa, M., 2005, "Numerische Simulation der Schmierölzerstäubung im Kurbelgehäuse eines Verbrennungsmotors", Proc. *Symposium der Österreichischen Tribologischen Gesellschaft*, Graz, Austria, pp. 13-24.

[3] Drew, D. A., and Passman, S. L., 1998, *Theory of Multicomponent Fluids*, Springer, New York.

[4] Mehrhardt, E., 1978, "Zerstäubung von Flüssigkeiten mit rotierenden Scheiben. Flüssigkeitsauflösung, Tropfengrößen und Tropfengrößenverteilungen*", Dissertation Technische Universität Berlin, Fachbereich 10 – Verfahrenstechnik*.

[5] Brauer, H., 1971, *Grundlagen der Einphasen- und Mehrphasenströmungen*, Sauerländer Verlag, Frankfurt am Main, Germany.

[6] Hege, H., 1964, "Flüssigkeitsauflösung durch Schleuderscheiben", *Chem.-Ing.-Tech. 36*, pp. 52-59.

[7] Walzel, P., 1982, "Auslegung von Einstoff-Druckdüsen", *Chem.-Ing.-Tech. 54*, pp. 313-328.

[8] Chang, H., Zhang, Y., and Chen, L., 2003, "Gray Forecast of Diesel Engine Performance Based on Wear", *Applied Thermal Engineering 23*, pp. 2285-2292.

[9] Miyachika, M., Hirota, T., and Kashiyama, K., 1984, "A Consideration on Piston Second Land Pressure and Oil Consumption of Internal Combustion Engine", *SAE 840099*.

[10] Varga, C. M., Lasheras, J. C., and Hopfinger, E. J., 2003, "Atomization of Small-Diameter Liquid Jet by a High-Speed Gas Stream", Proc. *9th International Conference on Liquid Atomisation and Spray Systems*, paper 03-05.

Conference on Modelling Fluid Flow (CMFF'06)
The 13th International Conference on Fluid Flow Technologies
Budapest, Hungary, September 6-9, 2006

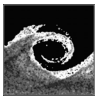

ANALYSIS OF LIQUID-GAS FLOW NEAR A FAN-SPRAY NOZZLE OUTLET

Alejandro Rivas[1], Mireia Altimira[2], Gorka Sánchez[3], Juan Carlos Ramos[4],

[1] Professor. Corresponding Author. Department of Mechanical Engineering – Fluid Flow and Thermal Engineering Chair Technological Campus of the University of Navarra (TECNUN) – Engineering School. Paseo Manuel Lardizábal 13, 20018 San Sebastian, Spain. Tel.: (+34) 943219877, Fax: (+34) 943311442, E-mail: arivas@tecnun.es
[2] Research engineer. Department of Mechanical Engineering – Fluid Flow and Thermal Engineering Chair, Technological Campus of the University of Navarra (TECNUN) – Engineering School E-mail: maltimira@tecnun.es
[3] Research engineer. Department of Mechanical Engineering – Fluid Flow and Thermal Engineering Chair, Technological Campus of the University of Navarra (TECNUN) – Engineering School E-mail: gsanchez@tecnun.es
[4] Professor. Department of Mechanical Engineering – Fluid Flow and Thermal Engineering Chair, Technological Campus of the University of Navarra (TECNUN) – Engineering School E-mail: jcramos@tecnun.es

ABSTRACT

This paper reports the results of mathematical modelling and simulation of two-phase flow near the outlet of six different industrial fan-spray atomizers under different operating conditions.

The Finite Volume Method, implemented in the commercial code, Fluent V.6.2, has been used to solve the mathematical model numerically, whilst the Volume of Fluid (VOF) approach has been employed to track the interface between liquid and gas. Surface tension effects have been included using the Continuum Surface Force method (*CSF*).

Results from simulation have been validated with experimental data and compared with those from previous works. Interesting conclusions about sheet thickness, velocity and vorticity of the flow have been obtained; some of them differ from hypotheses assumed in previous works. These conclusions may reflect the way in which break-up models are used to obtain drop size and break-up length.

Keywords: CFD, Fan-spray atomizer, Liquid sheet, Two-phase flow.

NOMENCLATURE

A	$[m^2]$	cross-sectional area
C, C'	[-]	constants
K	$[m^2]$	sheet thickness factor
Q	$[m^3/s]$	flow rate
L	$[m]$	break-up length
U	$[m/s]$	sheet velocity
d_D	$[m]$	drop diameter
r	$[m]$	radial coordinate
α	[-]	volume fraction
δ	$[m]$	sheet thickness
φ	$[rad]$	angular coordinate
μ	$[N{\cdot}s/m^2]$	fluid viscosity
ρ	$[Kg/m^3\}$	fluid density
σ	$[N/m\}$	surface tension
θ	$[rad]$	sheet angle

Subscripts

0	outlet
S	sheet
R	rim
T	total
1	primary phase, air
2	secondary phase, water

1. INTRODUCTION

Liquid atomization and spray processes take place in a multitude of technical applications, from combustion of liquid fuels to agriculture. For this reason these processes are the object of active research and the number of theoretical and experimental works devoted to analysing the basic mechanisms of instability and atomization of liquid streams is considerable. An understanding of the mechanisms governing these processes improves the possibility of optimising atomizer design, whereby spray characteristics can be adapted to their respective applications.

The field of atomization has yielded many theoretical works based on the linear and non-linear mathematical stability analysis of jets and liquid sheets [1]. These works, from the earliest of Rayleigh [2], Taylor [3], Squire [4], Hagerty and Shear [5] or Dombrowski [6] up to those of the present day, have provided a lot of important information about atomization mechanisms. However, they have been limited to the analysis of

very simple flow configurations. Consequently, several important effects remain to be adequately considered, such as certain more complex nozzle configurations, turbulence, non-linear effects and a complete description of the interaction between liquid and gaseous phase.

Numerical techniques of Computational Fluid Dynamics have been used to study atomization and spray processes. Complex mathematical models have been employed in the analysis, capable of including the effects mentioned previously. Works that have used more complex mathematical models can be separated into two groups. On the one hand, there are those studies whose models focus on the direct simulation of the instability mechanisms which lead to the disintegration of the liquid stream: [7], [8], [9], [10] and [11]. Even though they reproduce more of the physics of the process, they are not usually used to study real atomizer configurations due to limited computational resources. On the other hand, there are those works which don't attempt to simulate the instability and break-up processes, thereby reducing computational requirements. They analyse real atomizer geometries and obtain useful information about the flow very near the outlet of the atomizer, upstream of the break-up point. This information can be used as input in break-up models to obtain spray characteristics.

Currently, the thrust is towards the development of mathematical models and simulation techniques which are capable of analysing real atomization systems and which take greater account of the physics of the atomization process [12],[13].

Several works which belong to the second group use the Volume of Fluid (VOF) approach to model and simulate the two-phase flow inside and outside Simplex atomizers. This type of atomizer is widely used in combustion applications, and has been analysed in a multitude of works [14], [15], [16] and [17].

In contrast, Fan-Spray atomizers, which are widely used in agricultural and painting applications, although studied by Dombrowski et al. [6], have not been deeply analysed using Computational Fluid Dynamics Techniques. In fan-spray atomizers the spray is produced by disintegration of a liquid sheet formed as the liquid leaves the outlet (Figure 1). The liquid flow at the sheet (as well as its interaction with the surrounding gaseous phase) has several special features that make it complex. For example, due to surface tension, the boundaries of the liquid sheet contract, forming a curved rim as the sheet extends from the outlet of the atomizer.

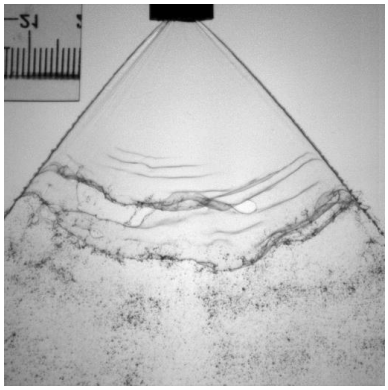

Figure 1: Break-up and disintegration of fan-spray liquid sheet

Certain characteristic design parameters of these atomizers refer to sheet thickness and liquid velocity in the sheet. Several studies assume the magnitude of the liquid velocity in the sheet to be constant and its direction radial. Consequently sheet thickness varies with the radial coordinate, r, measured from the atomizer outlet according to the following expression [6], [18]:

$$\delta = \frac{K}{r} \tag{1}$$

where K is the sheet thickness factor. Its value depends on the fluid atomised, the operating conditions and the design of the atomizer.
These hypotheses have been partially proven experimentally [6], [19].

In this paper the results of mathematical modelling and simulation of two-phase flow near the outlet of different industrial fan-spray atomizers are presented. Hypotheses mentioned previously concerning the outflow of fan-spray atomizers are checked by means of simulation using CFD techniques. Moreover, valuable information which may be used as input in break-up models to calculate the spray drop-size and break-up length [20], [21] has been obtained. For example, the break-up model proposed by Dombrowski and Hooper [18] established that the drop-size and break-up length of fan sheets depended on the sheet thickness factor and the air-liquid relative velocity. The expressions derived from this model for long wave disturbances are the following:

$$L = C \cdot \left[\frac{\sigma \cdot K}{2 \cdot \rho_2 \cdot (\rho_1/\rho_2)^2 \cdot U_S^2} \right]^{1/3} \tag{2}$$

$$d_D = C' \cdot \left[\frac{\sigma \cdot K}{U_S^2} \right]^{1/3} \cdot \left(\frac{\rho_1}{\rho_2} \right)^{-1/6} \tag{3}$$

2. PROBLEM DESCRIPTION

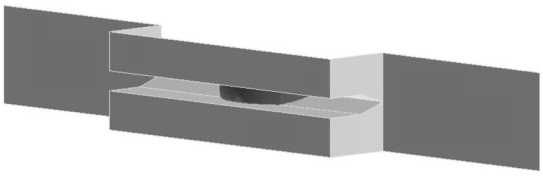

Figure 2: Exterior geometry of an analysed design

2.1. Description of the atomizers

Six different commercial designs of fan atomizer have been analysed. A description of their interior geometry can be found in reference [22]. The geometry of the outlet orifice of one of the analysed designs is presented in Figure 2.

2.2. Description of mathematical model

A mathematical model has been developed to study the two-phase flow that takes place near the outlet of the atomizer.

2.2.1. Governing equations

The fluids employed are water, which is assumed to be incompressible and whose properties are considered constant (ρ_2=998.2 kg/m^3, μ_2=1.003·10^{-3} Pa·s) and air, whose properties are also considered constant (ρ_1=1.225 kg/m^3, μ_1=1.789·10^{-5} Pa·s). Previous simulations [22] have shown that the flow at the atomizer outlet is turbulent, and in all cases the Reynolds Average Navier-Stokes (*RANS*) approach is used to model the turbulence effects. The standard k-ε turbulence model is used to calculate the effective viscosity.

2.2.2. Flow domain

The external geometry of each design has been accurately modelled in order to observe the corresponding effect on flow.

The geometry of the nozzles, permits the domain to be simplified using two planes of symmetry (Figure 3). Thus only a quarter of each design has been modelled. As simulating the appearance and growth of dynamic disturbances, which lead to the atomization of the liquid sheet, is not considered, this assumption has been perfectly accepted.

Fixing the limits of the domain requires care. It might seem that simply enlarging the domain should provide better results. However, it is also necessary to consider that the liquid sheet narrows very rapidly, such that its thickness downstream determines a limit superior to the extension of the domain if a good balance between space resolution in the sheet and number or cells of the model is desired. As mentioned previously, the mathematical model used is not capable of reproducing the destabilisation and break-up of the sheet. Consequently, the simulation of an extensive domain doesn't necessarily fit its real behaviour because it breaks up at a certain distance from the nozzle.

In spite of this shortcoming, a simulation with a larger domain has been carried out to confirm the above. The results show a series of phenomenon that, due to the previous sheet break-up, don't appear in real flat sheets.

The break-up length of the flat sheet and its angle have been experimentally measured for all the nozzles under different operating pressures. These results, together with the height of the boundary layer created on the interface, have been used to establish the minimum dimensions for the domain. The values of these dimensions (x_{max}, y_{max}, z_{max}), nondimensionalized with a characteristic length, i.e. the maximum height of the atomizer's outlet, can be seen in Figure 3.

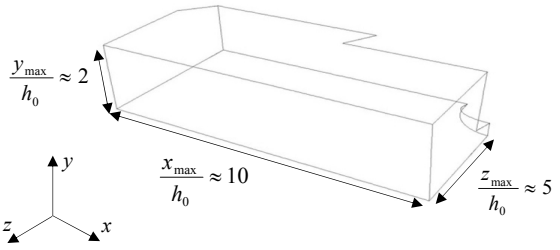

Figure 3: Dimensions of the flow domain

2.2.3. Boundary conditions

Previous simulations of the interior flow of these atomizers under different operating pressures [22] provided profiles of velocity (U_i), turbulent kinetic energy (k) and dissipation ratio of k (ε). These profiles have been imposed at the outlet of the nozzle as boundary conditions.

At the atmosphere boundaries a uniform zero value of gauge static pressure has been prescribed.

At the solid walls a no-slip condition has been imposed on fluid velocity.

Finally, at both symmetry planes the normal velocity component and the normal gradients of all other variables have been set to zero.

2.2.4. Discretization and resolution

The mathematical model is solved numerically by first discretizing the flow domain into a grid and then discretizing the governing equations.

The flow domain has been discretized using high quality cells, most of which are hexahedral in shape. The number of cells is about 10^6. The maximum height of the atomizer's outlet contains

30 grid points. At the end of the domain there are at least 10 nodes within the width of the sheet, which ensures an acceptable resolution.

The CFD code, Fluent V.6.2, is used to solve the mathematical model numerically. It employs the Finite Volume Method to discretize the flow-governing equations.

The Volume of Fluid (VOF) approach [23] is considered the most appropriate as it is designed for two or more immiscible fluids where the position of the interface is of interest.

Its formulation is based on the fact that two or more phases do not interpenetrate, so in each cell the sum of volume fractions of all phases must be unity.

A single momentum equation is solved for the entire domain, and the resulting velocity field is shared by both phases.

$$\frac{\partial}{\partial t}(\rho U_i)+\frac{\partial}{\partial x_j}(\rho U_i U_j)= \\ =-\frac{\partial p}{\partial x_i}+\frac{\partial}{\partial x_j}\left[(\mu+\mu_T)\cdot\left(\frac{\partial U_i}{\partial x_j}\right)\right]+S_i \tag{4}$$

With regard to turbulence quantities, a single set of transport equations is solved and, as for the momentum equations, the resulting variables are shared by the phases throughout the field.

The tracking of the interface is carried out by solving a continuity equation for the volume fraction of water (secondary phase):

$$\frac{\partial}{\partial t}(\alpha_2\rho_2)+\frac{\partial}{\partial x_i}(\alpha_2\rho_2 U_i)=S_{\alpha_2} \tag{5}$$

The volume fraction equation is not solved for the primary phase (surrounding air), but computed from the following constraint:

$$\alpha_1+\alpha_2=1 \tag{6}$$

Depending on the local value of α_i, the values of properties and variables, namely density, viscosity, etc., are evaluated with the following expression

$$\phi=\alpha_2\phi_2+(1-\alpha_2)\phi_1 \tag{7}$$

and assigned to each cell within the domain.

Finite volume formulation demands the convective and diffusive fluxes through the control volume faces to be computed and balanced with source terms within the cell itself. The VOF model implemented in Fluent has four schemes for the calculation of face fluxes, depending on the type of interface reconstruction method used: Geometric Reconstruction, Donor-Acceptor, Euler explicit, and Euler implicit.

The last one can be used for both time-dependent and steady-state calculations, whereas the other approaches are valid only for time-dependent calculations. In order to obtain the face fluxes, the implicit scheme applies the same interpolation treatment to the cells lying near the interface as to those that are completely filled with one of both phases.

This scheme has been considered to be the most suitable for the present purpose, as transient flow behaviour is not of interest, the steady-state solution is not affected by the initial conditions and each phase has an independent inflow boundary.

Surface tension effects along the interface have been included in the model. The surface tension model in Fluent is the continuum surface force (CSF) model developed by Brackbill et al. [23]. With this model, the surface tension effects become a source term in the momentum equation.

The governing equations are linearized and solved using the pressure-correction algorithm SIMPLE for pressure-velocity coupling.

Second-order schemes are employed to discretize the governing equations. An upwind scheme is used for convective terms, whereas a centred scheme is adopted for diffusive terms. Pressure interpolation to cell faces is performed using coefficients of the momentum equations to avoid pressure checker-boarding

2.2.5. Convergence criteria

In order to check the convergence of the iterative procedure all the scaled residuals of the variables are diminished under 10^{-5}.

3. RESULTS AND DISCUSSION

3. 1. Results

The air-liquid interface has been obtained from the values of flow variables provided by simulations. It has been considered as interface that iso-surface having a constant value of liquid volumetric fraction equal to 0.5.

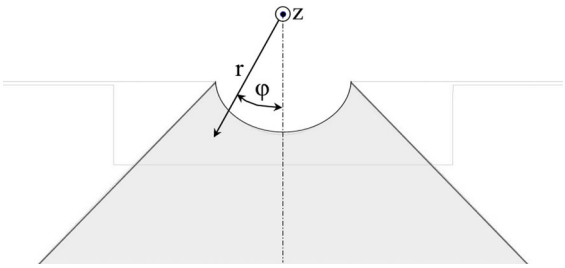

Figure 4: Coordinates System

To present the results of the study, cylindrical coordinates (r,φ) have been adopted, as shown in Figure 4. The reference frame origin is fixed at the

pressure centre, i.e. at a point inside the atomizer determined by the sheet angle at the outlet [8].

Values of the thickness factor, calculated with Eq. (1), have been obtained at different radial distances. In Figure 5, the results for two different circumferential surfaces are presented.

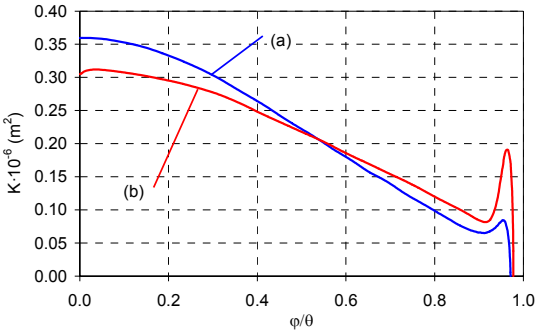

Figure 5: Variation of the sheet thickness factor with the angular coordinate (a) Near the outlet (b) Further downstream of the outlet

Once the sheet surface and its thickness are defined as a function of radial and angular coordinates, $\delta(r,\varphi)$, information about the shape and volumetric flow of the sheet and its rim are obtained.

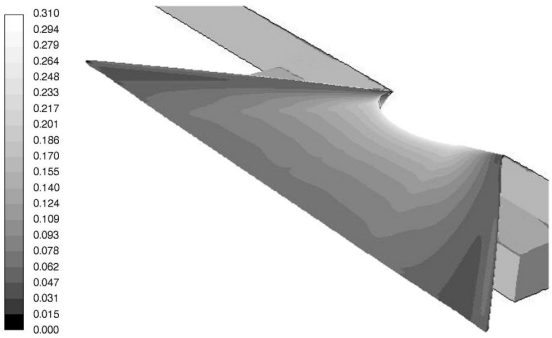

Figure 6: Sheet thickness variation with radial coordinate (mm)

Values of cross-sectional area (A_S), flow-rate (Q_S) and mean velocity (U_S) of the sheet have been adimensionalized with their corresponding values at the outlet. These magnitudes have been defined neglecting the rim as:

$$A_S(r) = \int_{-\varphi_R}^{\varphi_R} \delta \cdot r \cdot d\varphi \tag{8}$$

$$Q_S(r) = \int_{-\varphi_R}^{\varphi_R} \int_{-\delta/2}^{\delta/2} \underline{U} \cdot \underline{e}_r \cdot r \cdot d\varphi \cdot dy \tag{9}$$

$$U_S(r) = \frac{Q_S}{A_S} \tag{10}$$

where φ_R is the angle at which the rim starts.

These parameters, calculated for one of the analysed designs under an operating pressure of 3 bar, are shown in Table 1. Similar magnitudes have been obtained for the rim of the sheet, as shown in Table 2.

Table 1. Sheet nondimensional quantities

$(r-r_O)/h_O$	A_S/A_O	Q_S/Q_T	U_S/U_O
0	100.0%	100.0%	1.00
0.425	60.7%	99.0%	1.57
0.85	59.5%	98.8%	1.59
1.275	59.0%	98.5%	1.59
1.7	58.6%	98.1%	1.59
2.125	58.2%	97.8%	1.59
2.55	58.0%	97.5%	1.59
2.975	57.7%	97.2%	1.58
3.4	57.5%	96.9%	1.58
3.825	57.3%	96.6%	1.58
4.25	57.0%	96.3%	1.57

Table 2. Rim nondimensional quantities

$(r-r_O)/h_O$	$A_R/(A_R+A_S)$	Q_R/Q_T	U_R/U_O
0.425	1.4%	1.0%	1.7
0.85	1.8%	1.2%	1.07
1.275	2.2%	1.5%	1.09
1.7	2.6%	1.9%	1.13
2.125	3.0%	2.2%	1.15
2.55	3.4%	2.5%	1.17
2.975	3.7%	2.8%	1.19
3.4	4.1%	3.1%	1.2
3.825	4.4%	3.4%	1.21
4.25	4.7%	3.7%	1.2

These quantities have also been calculated for the rest of the designs, obtaining very similar values.

Other interesting results are the radial and tangential velocities of the sheet and the vorticity distribution throughout the flow domain, as can be seen in Figures 7, 8 and 9.

Figure 7: Radial Velocity (m/s) at the nozzle outlet and a radial plane

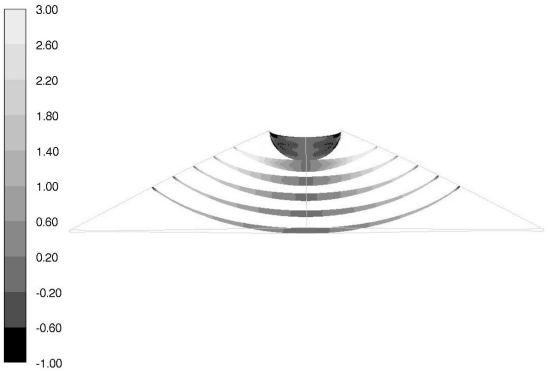

Figure 8: Tangential Velocity (m/s) at different circumferential surfaces

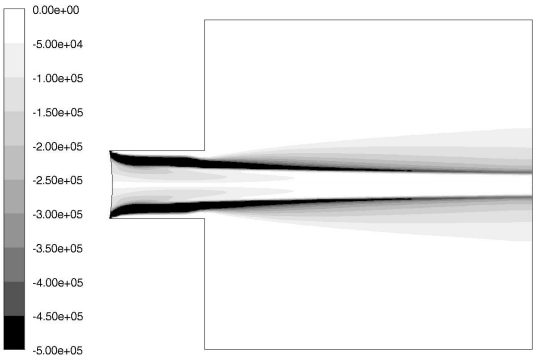

Figure 9: X Vorticity (s^{-1}) at the symmetry plane YZ

3.2. Experimental validation

To validate the results obtained by means of numerical simulation it would be necessary to measure experimentally both sheet thickness and velocity. However, it has been very difficult to carry out experimental measurements, due to the dimensions of both the nozzles and the sheet.

An interferometric technique, proposed by Dombrowski [6], [25] has been used to measure the sheet thickness experimentally. Basically, this technique consists of illuminating the sheet with a light beam of a specific wavelength. Due to changes in the sheet thickness, intervals of constructive and destructive interference appear, as shown in Figure 10. Measuring the distance between two bright intervals, q and t, the thickness factor of the sheet can be calculated using the following expression:

$$K = \frac{\lambda}{2n \cdot \cos\beta} \cdot \frac{q - t}{\frac{1}{r_t} - \frac{1}{r_q}} \qquad (11)$$

where λ is the wavelength of the light beam.
n is the refractive index.
β is the angle of refraction of the light in the sheet.
r_q and r_t are the radial coordinates corresponding to the q^{th} and the t^{th} intervals.

With this technique, values of K have been measured for all the designs under different operating pressures.

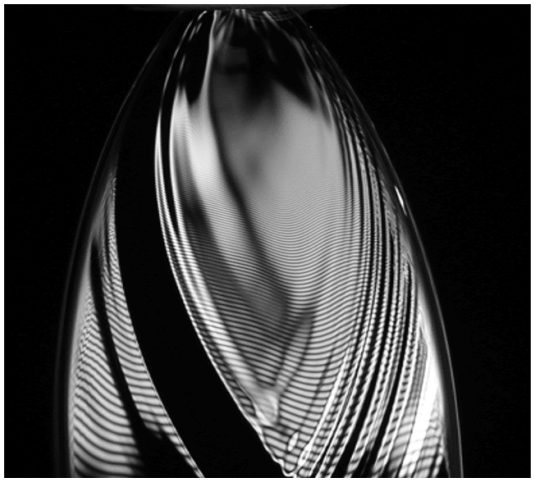

Figure 10: Image taken with the interferometric technique

As the pressure is increased, all the nozzles exhibit the same behaviour, as noticed previously by Fraser et al. [20]: at low pressures the sheet is completely flat and fringes are perfectly visible. At higher pressures disturbances appear, making the identification of fringes difficult. Finally, when a certain pressure is reached, the sheet becomes turbulent and, due to random disturbances, no fringes can be observed. This critical pressure varies depending on the design.

These experimental values have been compared with data from simulations. In only one of the six analysed designs has it been possible to see fringes clearly. For this atomizer, the values of the thickness factor obtained from interferometry differ by 15% from those obtained using simulation.

Velocity distributions obtained with simulations are in agreement with those observed by Stetler et al. [26], who measured the velocity in liquid sheets from fan-spray atomizers similar to those analysed in this work with an LDA system.

4. CONCLUSIONS

The main conclusions of the present work concern changes of sheet thickness with the radial coordinate, the velocity of the fluid within the sheet and the flow vorticity.

Regarding sheet thickness, the analysis undertaken shows that, from a certain distance downstream of the outlet, sheet thickness follows Eq. 1. Moreover, the thickness factor cannot be considered constant; rather, it is dependent on the angular coordinate (Figure 5). The shape of the

outlet in its immediate vicinity has a strong influence in the sheet thickness.

In agreement with several previous works, the simulations show that, from a certain distance downstream of the nozzle, the velocity of the sheet is constant and mainly radial with a slight tangential component. However, in the region near the outlet, the liquid in the sheet has an appreciable tangential component. The radial velocity of the fluid in this region also suffers an increase from the value at the outlet, reaching a maximum and then decreasing to a value that remains constant as the liquid goes downstream of the sheet. A further conclusion related to those presented above is the difference observed between the mean velocity at the atomizer outlet and that reached in the sheet. Simulations have shown the latter to be 55% higher than the former. This fact, observed previously by Stetler et al. [26], would invalidate the assumption made in several works, which considers both velocities equal [6], [21].

In fact, the velocity of the liquid in the rim is more similar to the velocity at the outlet.

Regarding the vorticity, the highest values are located near the surface of the sheet, those in the rest of the flow domain being negligible. Even the vorticity conveyed from inside the atomizer is diffused downstream of the outlet. This result confirms the fact used in several works [10], [27], that the sheet surfaces are vortex sheets at the inviscid limit.

Finally, mention can be made of the fact that several conclusions reached in this study can affect the way in which break-up models are used. For example, some of these models [6], use the sheet velocity and the thickness factor as inputs to predict the mean drop size and break-up length. Estimations of these inputs can be the velocity at the outlet, obtained from the discharge coefficient and the operating pressure, and a mean value of the thickness factor calculated with the following expression [28]:

$$K = \frac{Q_T}{U_O \cdot 2\theta} \tag{12}$$

where Q_T is the flow rate, U_O is the mean velocity and θ is the sheet angle, at the atomizer outlet.

The velocity and the thickness factor obtained with latter estimations are significantly different to those obtained from simulations, as are the results obtained when they are used as inputs in break-up models.

ACKNOWLEDGEMENTS

This research project is partially supported by the Basque Government through grant UE-2004-14. The authors are grateful to the Antonio Aranzabal Foundation for its economic support.

REFERENCES

[1] W. A. Sirignano, C. Mehring, 2000, "Review of theory of distortion and disintegration of liquid streams", *Progress in energy and combustion science*, Vol. 26, pp. 609-655.

[2] F. R. S. Rayleigh, 1879, "On the stability of jets", *Proc. Lond. Math. Soc.,* 10, pp.4-13.

[3] H. B. Squire, 1953, "Investigation of the instability of a moving liquid film", *British Journal of applied physics*, vol. 4, pp. 167-169.

[4] W. W. Hagerty, J. F. Shear, 1955, "A study of the stability of plane fluid sheets", *Journal of applied mechanics*, vol. 22, pp. 509-514.

[5] G. I. Taylor, 1959, "The dynamics of thin sheets of fluid II. Waves on fluid sheets", *Proc. Roy. Soc.,* pp. 253-289.

[6] N. Dombrowski, D. Hasson and D. E. Ward, "Some aspects of liquid flow through fan spray nozzles", *Chemical Engineering Science*, vol. 12, pp. 35-50, 1960.

[7] A. Leboissetier and S. Zaleski, 2001, "Direct numerical simulation of the atomization of a liquid jet", *ILASS-Europe Metting 2001.*

[8] M. Kutzbach, P. Berthoumieu, J. L. Estibalezes and G. Lavegne, 2001, "Numerical simulation of a planar liquid sheet in a co-flowing air stream", *ILASS-Europe Metting 2001.*

[9] E. López-Pagués, C. Dopazo and N. Fueyo, 2004, "Very-near-field dynamics in the injection of two-dimensional gas jets and thin liquid sheets between two parallel high-speed gas streams", *Journal of fluid mechanics,* vol. 515, pp. 1-31.

[10] A. Lozano, A. García-Olivares, C. Dopazo, 1998, "The instability grouth leading to a liquid sheet break-up", *Physics of fluids*, vol. 10, 9, pp. 2188-2197.

[11] A. Sou, H. Hasegawa, T. Nakahima, 2000, "Numerical Simulation of the instability and the break-up of a viscous liquid jet", *ICLASS 2000.*

[12] M. Herrmann, 2003, "Modelling primary break-up: a three-dimensional eulerian level set slash vortex sheet method for two-phase interface dynamics", *Center for turbulent research. Annual Research Briefs*, pp. 185-196.

[13] M. Buonfiglioli, F. Mendongça, 2005, "LES-VOF simulation of primary diesel spray break-up with synthetic inlet perturbations", *ILASS America 2005.*

[14] U. Maatje, E. Von Lavante, F. O. Albina and M. Peric, 2001, "Experimental and numerical study of simplex nozzles", *ILASS- Europe 2001*.

[15] C. L. Yeh, 2004, "Numerical investigation of liquid jet emanating from plane orifice atomizer with chamfered or rounded orifice inlets", *JSME International journal Series B*, vol. 47, 1, pp. 37-47

[16] J. Xue, M. A. Jog, S. M. Jeng, E. Stainthorsson and M. A. Benjamin, 2004, "Effects of geometric parameters on simplex atomizer performance", *AIAA journal,* vol. 42, 12, pp. 2408-2415.

[17] C. L. Yeh, 2005, "Turbulent flow investigation inside and outside plane orifice atomizers with rounded orifice inlets", *Heat Mass transfer*, vol. 41, pp. 810-823.

[18] N. Dombrowski, P. C. Hooper, 1962, "The effect of ambient density on drop formation in sprays", *Chemical engineering science*, vol. 17, pp. 291-305.

[19] J. W. M. Bush and A. E. Hasha, 2004, "The collision of laminar jets: fluid chains and fishbones", *Journal of fluid mechanics,* vol. 511, pp. 285-310.

[20] R. P. Fraser, P. Eisenklam, N. Dombrowski and D. Hasson, 1962, "Drop formation from rapidly moving Liquid sheets", *A.I.Ch.E. Journal*, vol. 8, pp.672-680.

[21] P. K. Senecal, D. P. Schmidt, I. Nouar, C. J. Rutlan, R. D. Reitz, M. L. Corradini, 1999, "Modelling high-speed viscous liquid sheet atomization", *International journal of multiphase flow,* vol. 25, pp. 1073-1097.

[22] A. Rivas, G. Sánchez, A. Estévez, J.C. Ramos, 2005, "Improving the design of fan spray atomizers through Computational Fluid Dynamics Techniques", *20th ILASS – Europe Meeting.*

[23] C. W. Hirt, A. A. Amsden and J. L. Cook, 1997, "An arbitrary lagrangian-eulerian computing method for all flow speeds", *Journal of computational physics,* vol. 135, pp. 203-216.

[24] J. U. Brackbill, D. B. Kothe, and C. Zemach, 1992, "A Continuum Method for Modeling Surface Tension", *J. Comput. Phys*., vol. 100, pp.335-354.

[25] Y. J. Choo, B. S. Kang, 2001, "Parametric study on impinging-jet liquid sheet thickness distribution using an interferometric method", *Experiments in fluids,*vol. 31, pp. 56-62.

[26] M. Stetler, G. Brenn and F. Durst, 2002, "The influence of viscoelastic fluid on spray formation from flat-fan and pressure-swirl atomizers", *Atomization and Sprays*, vol. 12, pp. 299-327.

[27] R. H. Rangel and W. A. Sirignano, 1991, "The linear and non-linear shear stability of a fluid sheet". *Physic of Fluids A*, 3(10), 2392-4000.

[28] Q. Zhou, P. C. H. Miller, P. J. Walklate and N. H: Thomas, 1996, "Prediction of Spray Angle from Flat Fan Nozzles", *Journal of Agricultural Engineering Resources*, 64, 139-148.

Conference on Modelling Fluid Flow (CMFF'06)
The 13th International Conference on Fluid Flow Technologies
Budapest, Hungary, September 6-9, 2006

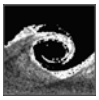

MODELLING OF DIESEL INJECTION PROCESS USING A PRIMARY BREAKUP APPROACH

András KADOCSA[1], Reinhard TATSCHL[2], Gergely KRISTÓF[3]

[1] Corresponding Author. Department of Fluid Mechanics, Budapest University of Technology and Economics. Bertalan Lajos u. 4–6, H-1111 Budapest, Hungary. Tel.: +36 1 463 2464, Fax: +36 1 463 3464, E-mail: kadocsa@ara.bme.hu
[2] AVL List GmbH, reinhard.tatschl@avl.com
[3] Department of Fluid Mechanics, Budapest University of Technology and Economics. E-mail: kristof@ara.bme.hu

ABSTRACT

Numerical simulation plays an established role in diesel engine development. New injection systems and increased expectations regarding prediction of emissions however have induced the introduction of new approaches in mixture formation simulation. The implementation of separate models for simulation of primary fuel breakup leads to more detailed and more accurate simulation results. The aim of this paper is to introduce some special aspects of using a commercially available combination of spray submodels. The results are compared to measurement data concerning spray penetration, micro and macro spray cone angel, and Sauter Mean Diameter, and are comprehensively assessed in terms of droplet size class distribution.

Keywords: diesel injection, CFD, primary breakup

NOMENCLATURE

C_i	[-]	breakup model constants
C_μ	[-]	turbulence model constant
D	[m]	droplet diameter
SMD	[m]	Sauter Mean Diameter
We	[-]	Weber number
a	[m]	stable droplet radius
k	[m^2/s^2]	turbulent kinetic energy
n	[-]	number of droplets
r	[m]	actual droplet radius
t	[s]	time
u	[m/s]	relative velocity
ε	[m^2/s^3]	turbulent dissipation rate
τ	[s]	characteristic breakup time
Λ	[m]	wavelength of fastest growing surface wave
Ω	[1/s]	growth rate of fastest growing surface wave
ρ_g	[kg/m^3]	density at ambient pressure
σ	[N/m]	surface tension

1. INTRODUCTION

Diesel engines experienced a great development in the past decade in performance as well as concerning the decreasing level of emissions. However, this development is continued to be driven by new emission legislation and market forces aiming at more economical powertrains. These requirements lead to more sophisticated mixture preparation philosophies and more advanced fuel atomization devices.

Computational Fluid Dynamics (CFD) has been commonly used for over two decades in the automobile industry, and also specifically in internal combustion engine development. For accurate, time resolved, 3 dimensional simulation of a whole engine cycle mixture preparation has to be modelled by means of a number of submodels and implementation of time step subcycles.

Numerical simulation of spray breakup has experienced a great development in the last decade, and the methods suitable to capture the breakup regimes typical in diesel engines have also improved in accuracy. However, new mixture preparation and combustion strategies such as HCCI (Homogenous Charge Compression Ignition) or application of multiple injection have shown the limits of capabilities of the generally available models.

Based on these new needs, new approaches as well as new submodels have been recently developed and implemented into the specialized commercial code FIRE. The aim of this paper is to introduce a representative configuration of an up to date diesel spray calculation, based on using a primary breakup model in Lagrangian approach.

2. BREAKUP OF FLUIDS

Fluid columns break up into ligaments or droplets, and these latter break up into further droplets according to different, simultaneously

acting mechanisms, depending on a number of physical characteristics.

The most important quantity summarizing the influential factors concerning the intensity and type of breakup is the Weber number, calculated with droplet (or nozzle orifice) diameter, but with ambient gas density according to Eq. (1).

$$We = \frac{u^2 \rho_g D}{\sigma} \quad (1)$$

In general it can be stated that the higher the Weber number, the more intensive the breakup is, thus ranging from Rayleigh type of breakup through first and second wind-induced breakup to atomization. In case of our investigations the general Weber number far exceeds the highest limit of regime switch, therefore the breakup process is characterised by properties of the regime "atomization".

The subsequent breakup of ligaments and droplets can also be classified according to Weber number. It ranges from bag breakup through bag and stamen type of breakup to boundary layer stripping and catastrophic breakup, with increasing Weber number. For diesel conditions boundary layer stripping, capillary wave detachment (Kelvin-Helmholtz instability) and catastrophic breakup by Rayleigh-Taylor waves are typical.

3. BACKGROUND OF CALCULATION

3.1. Applied CFD software

The software applied for the calculations is the 8.4 version of FIRE, a commercial CFD code specialised on internal engine related simulations. The code features a number of submodels for modelling the phenomena related to spray formation, as described in section 3.3.

3.2. General framework of the Lagrangian spray modelling approach

3.2.1. Discrete Droplet Model

In the generally used approach the droplets are tracked in a Lagrangian way in a gas flow field, which latter is treated by conservation equations for mass, momentum and energy as well as turbulence in an Eulerian frame of reference.

The typical number of droplets arising during a high pressure diesel injection is in the order of magnitude of 10^6-10^8. Therefore the registration and tracking of each and every individual droplet is not practical and not even necessary.

Therefore, in the Discrete Droplet Model (DDM) a high number of droplet types is represented by so called parcels, and in each parcel the number of droplets contained is determined. Within one parcel, the droplets have uniform properties (diameter, velocity, temperature etc.), so in this sense a parcel behaves like one drop with the additional information on the number of identical droplets represented.

Hence, the calculation is not necessary to be performed for every single droplet, however, the diversity of droplets is still well represented.

3.2.2. Subcycling and rate approach

The calculation of the parcel movement is done with a subcycling procedure between the gas phase time steps taking into account the forces exerted on parcels by the gas phase as well as the related heat and mass transfer. In an analogous way the gas phase receives the forces resulted from spray movement as source terms in the next gas time step.

A commonly used approach for mathematically expressing breakup is the rate approach. It grabs the phenomenon through the velocity of loss of droplet radius, as expressed in Eq. (2).

$$\frac{dr}{dt} = -\frac{r-a}{\tau} \quad (2)$$

The submodels for breakup used in most of CFD codes all aim at determining the value of stable radius a and characteristic breakup time τ determining the breakup rate.

3.3. Submodels in a spray calculation

For each important phenomenon (e.g. breakup or evaporation) related to the properties of a spray we are seeking, there are a number of alternative submodels we can choose from.

Since research of spray simulation started to become intense in the early 80s, it became clear that the crucial point in accurate estimation of important spray characteristics is the extent of appropriateness in modelling of breakup. Although the efforts spent on understanding and modelling of other important mechanism such as evaporation or droplet collision have been also considerable, the most interest was captured by breakup models.

The early attempts (for detailed descriptions see [1]) were focusing on finding one particular analogy by which the breakup – characteristic for one specific breakup regime – can as accurate as possible be accounted for. Despite different underlying mechanisms the results gained from these models were in many cases similar, and after careful calibration they were applicable to a certain range of operating conditions.

However, with the continuous and intense increase of injection pressures characteristic to new diesel engines, it became clear that this approach to uniformly handle the whole breakup process delivers in certain cases unsatisfactory results.

To overcome these difficulties there have been efforts [2, 3] to combine different analogies in one

single breakup model. These models usually used physical properties of the spray, such as Weber number to determine which of the equations of the model should be applied for a certain parcel.

Through these attempts the earlier stages of breakup could be better captured, and the applicability of the simulation could be successfully extended to higher injection pressure cases.

In commercial application of CFD software the use of one of these single breakup models for modelling the entire breakup process is still usual, thanks to its easy use and satisfactory results in a considerable part of applications. However, for more sophisticated calculation these methods can no longer considered to be satisfactory.

Therefore, in up to date calculation methods these models are used only for predicting the breakup once the initial liquid column had been disintegrated into ligaments or droplets, and they are – in this relation – called secondary breakup models. The breakup phenomena occurring before that are handled by separate models, called primary breakup models [4, 5].

The models used in present study are discussed in the following paragraphs.

3.3.1. Secondary Breakup Model: Wave

The Wave breakup model implemented in FIRE is based on the work of Reitz [6], and can be considered to be the most commonly used (secondary) breakup model.

The basic idea of this model is that breakup of liquid drops occur due to initial surface perturbations, amplified by the flow passing by the droplet. According to the rate approach, the stable diameter of the droplet and the characteristic timescale of breakup under the prevailing circumstances are sought.

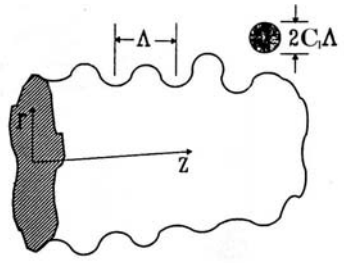

Figure 1. The stable diameter of a droplet resulted from breakup according to Reitz [6]

As shown in Figure 1, the stable diameter of a droplet, resulting from a breakup is proportional to the wave length of the fastest growing surface wave (a=$C_1\Lambda$) while the breakup time is calculated with a number of factors as follows:

$$\tau = C_2 \frac{3.726r}{\Lambda\Omega} \qquad (3)$$

When exposed to certain conditions, the droplets of a parcel start "loosing" diameter as prescribed by the Eq. (2) In basic case, the mass shed from these droplets throughout subsequent breakup subcycles is accumulated, and when the breakup effectively happens, all drops in the parcel receive the diameter calculated based on this shed mass loss (the shed mass is also split up to drops with identical diameter). Hence, the mass in a parcel is always conserved (not considering evaporation, or child droplet production as described later), only the number of droplets contained is changing according to droplet diameter.

As this model was formerly used for simulating the entire breakup process of a spray, there have been observations that the model – due to this working principle – does not deliver enough small droplets near the nozzle. Therefore, a child production mechanism was inserted into Wave, which is available also in the currently used version.

When the child production mechanism is switched on, a certain amount of the mass shed is used to create a new parcel. These – so called child – droplets immediately have the diameter of a stable droplet, which is in most cases much lower than the value reached by the parent droplets during the available time, on their way towards the stable diameter. Hence, an adjustable proportion of small droplets is available in the vicinity of the injection nozzle.

3.3.2. Primary Breakup Model: Diesel Breakup

The Diesel Breakup model implemented in FIRE is also based on the rate approach, and represents a combination of the aerodynamic mechanisms already know from Wave and another approach based on [7] taking into account effects of turbulence contained in the droplets "historically", i.e. based on the preceding nozzle flow conditions.

In order to account for these breakup forces arising from turbulence, a time resolved information concerning nozzle flow conditions is necessary. In our case it is available from a nozzle file, which is a result of previous calculations aiming to deliver time and space resolved information about the fluid exiting the nozzle hole. [8] In beginning of each time step, the spray model reads the necessary data from the nozzle file, and applies the appropriate values for each droplet.

In each spray subcycle time step breakup velocity is calculated for both breakup mechanisms, and the faster breakup will be applied for the considered droplet. The stable diameter and the characteristic time scale for breakup are in both cases adjustable through parameters, hence the dominance of one or the other model can artificially be influenced.

The equations for aerodynamic breakup are identical with those of Wave model. The stable diameter and the characteristic time scale for turbulent breakup contain the properties of nozzle flow turbulence, as described in Eqs. (4) and (5):

$$a = C_3 C_\mu^{0.75} \frac{k^{1.5}}{\varepsilon} \tag{4}$$

$$\tau = C_4 C_\mu \frac{k}{\varepsilon} \tag{5}$$

Once a droplet reaches the conditions described in the code, e.g. critical transition Weber number, it is handed over to the secondary breakup model.

3.3.3. Evaporation Model: Dukowicz

Evaporation models account for the mass and heat transfer from the droplets to surrounding gas. Since the calculation with Lagrangian method uses only one phase (the gas phase), the vapour resulted in this process is contained and transported in the gas as separate species.

The evaporation model is responsible for determination of the mass transfer and the change in droplet temperature through energy transfer. In equilibrium the heat flow between droplet and gas is only to supply the energy necessary for evaporation, otherwise a change in droplet temperature also occurs.

The model elaborated by Dukowicz [9] is one of the common evaporation model in diesel simulations. It utilizes the analogy between heat and mass transfer, and determines the proportion of these two rates.

3.3.4. Other spray models: collision, turbulent dispersion, droplet drag

Besides the three most influential models discussed in the past sections, there are also other models which have an impact on spray formation. However, in the current investigation they play a minor role.

After a number of test runs in the framework of earlier investigations the collision model based on Schmidt's model was found to represent a reasonable compromise between accuracy and calculation time.

The interaction of drops with the individual turbulent eddies can not be resolved by the flow field, therefore a turbulent dispersion model is used. The instantaneous gas velocity within a turbulent eddy is estimated from the mean gas field velocity and turbulence kinetic energy.

For estimation of drag coefficient drops are pretended to have spherical form, however a correction due to oscillation of droplets is taken into consideration.

4. CALCULATION SETUP

A diesel direct injection into a non deforming calculation domain with cold ambient gas was examined. Only one hole of the multi-hole injection nozzle was simulated.

4.1. Characteristics of Calculation

The most important characteristics of the calculation can be summarized in Table 1.

Table 1. Characteristics of calculation

Injection time	2 ms
Total simulated time	8 ms
Length of time step	1e-5 s
Maximum number of iterations per time step	100
Injection pressure	87.5 MPa
Total volume injected	1.01316e-8 m^3
Gas pressure	2.1e+6 Pa
Gas temperature	293 K

4.2 Computational Domain

A fully structured domain was used with only hexagonal cells. The total number of cells is 45144.

5. RESULTS BACKGROUND

5.1. Qualification of Results

The most common basis of judgment concerning the quality of a spray simulation is the temporal development of spray tip penetration. When measurements are available, this property is investigated in almost all cases.

Another important field of investigation concerns the size of droplets. This is an important quantity regarding the evaporation capability of the spray, which is determinative for the subsequent combustion processes. Because of this aspect, the most commonly used mean quantity for sprays regarding diameter is Sauter Mean Diameter, defined in Eq. (6).

$$SMD = \frac{\sum D^3 \Delta n}{\sum D^2 \Delta n} \tag{6}$$

Depending on the measurement available, the SMD is either determined as global SMD (whole spray), or SMD for a certain part of the spray (spray axis, a fixed cut or a point in the spray). The measurement of SMD requires increased investment into the measurement procedure, therefore it is not available in many cases. Hence, some of the currently used models were also calibrated without information regarding this important quantity. [10, 2]

A further aspect of examination is the shape of the spray, which – besides the optical, quantitative

comparison – can qualitatively also be captured. For this purpose the micro and the macro spray angle is to be measured and compared. According to a commonly used definition, micro spray angle refers to the cone angle of the first 1 mm of the spray, while macro spray angle means the cone angle for a larger portion of the spray.

5.2. Measurement Data

The conditions of the simulation have been chosen according to a set of measurements, which have been provided in a research cooperation of Toyota Central Research and Development Laboratory (TCRDL) and Dosisha University. [11]

Spray tip penetration was determined for the whole injection process, and 0.3 ms thereafter.

SMD was measured in a 1 mm radius vicinity of a fixed location, time averaged between 3 to 8 ms after start of injection. The measurement location is positioned ahead of the maximum spray tip penetration at the end of injection. The time window is chosen in a way that the tip of spray is already passed through the measurement point when measurement starts. Hence, a more realistic measurement data, relevant for the whole spray is believed to be received.

Micro spray angle is measured with the first 1 mm of the spray cone, while macro spray angle is defined as the cone angle of the first 70 % of the whole spray.

5.3 Simulation Output Data

The code FIRE delivers time and spatial resolved data about the spray and about the whole domain. The frequency and the content of these outputs are determined by the user.

Global SMD and penetration data is available from the standard outputs of FIRE. For determination of SMD in the measurement volume used in the measurements, a user function was implemented, too. However, as it turned out from the results, there was another way – based on another approach – to gain more appropriate comparison data. This involves measurement of all droplets passing through an entire cut at the same distance to the nozzle, as the measurement volume. The reason for using this simulation data instead of the smaller measurement volume for the purposes of comparison is to avoid misrepresentation of droplet diameters characteristic for the entire spray, because of an effect described in section 6.4.

6. RESULTS

In this paper, a sample set of results is presented. All chosen results show a very good agreement with measurement concerning penetration.

However, depending on some slight changes in settings, they exhibit significantly different SMD values (of ±30%) and SMD distributions.

6.1. Settings of Presented Cases

6.1.1. General Settings

In current investigation, in order to maintain comparability, and to see the effect of single changes, most of the breakup parameters are kept to be constants for all cases.

The parameter influencing characteristic breakup time (c2) for secondary breakup is set to 40, while the parameter of stable diameter is remained at the value recommended by most of literature sources (c1=0.61). The parameters determining child droplet production are set to realize a perceptible, but rather low proportion of child droplets, except the cases where they were set to 0 in order to cease child production in secondary breakup.

In case of primary breakup, there are two mechanisms available and competing with each other to determine breakup. The parameters of these mechanisms were set so that breakup under control of turbulent breakup is explicitly favoured. Parameters concerning stable diameter remained the same in both cases (c1=0.61 and c3=5), just as the characteristic breakup time parameter of aerodynamic breakup remains constant (c2=80), while that of turbulent breakup is varied according to the goal of the investigation.

Hence, it is set either to c4=1 to guarantee fast diameter decrease of drops, or c4=7 to sustain larger – parent – diameters for longer droplet lifetime.

The rest of primary breakup parameters are set to have recommended values, except the parameter influencing spray angle, which has been 20 % increased to better match experimental data.

6.1.2. Case Specific Settings

The two basic variations are represented by the two different values for characteristic breakup time of primary turbulent breakup mechanism. The other dimension of changes is represented by the use or release of child droplet mechanism for one or both of the breakup regimes (primary and secondary).

These settings are summarized in Table 2.

Table 2. Calculation variations

Child production	**Fast breakup** (c4=1)	**Slow breakup** (c4=7)
Both	Case_1A	Case_1B
Only primary	Case_2A	Case_2B
None	Case_3A	Case_3B

6.2. Penetration Curves

As shown in Figure 2 the penetration curves of all variations give a good agreement with measurement data.

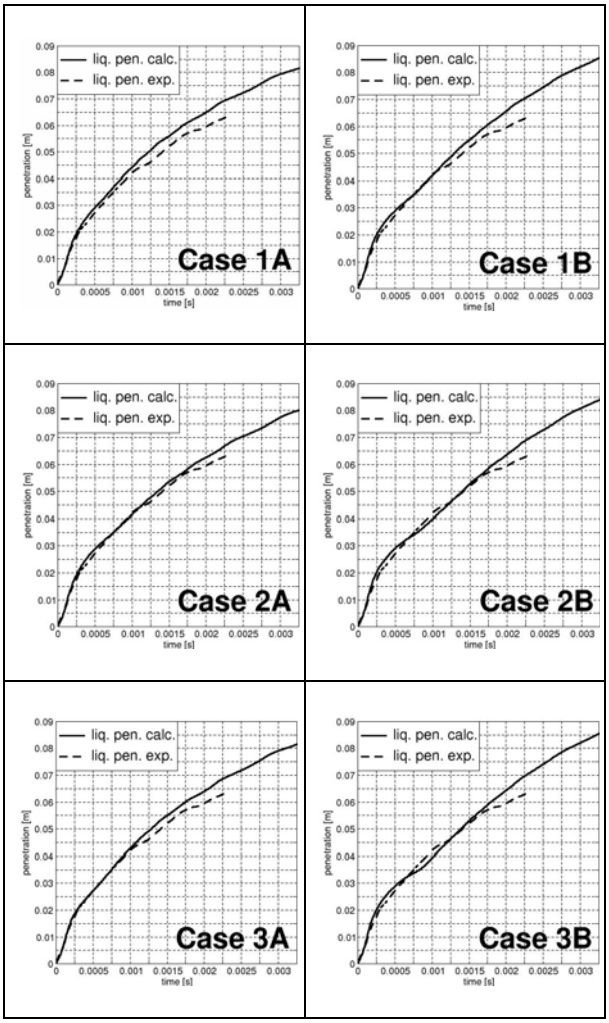

Figure 2. Penetration curves of all cases

6.3. Spray Angle Values

After prior adjustment of the main parameter influencing spray angle (c11 of Diesel Breakup), all micro and macro spray cone angle results were in less than 10 % proximity of measured values, and showed little change from calculation to calculation. Hence, these parameters did not prove to be critical concerning the prediction capability of calculations.

6.4. SMD Values

As discussed earlier, the measurement was carried out in 1 mm vicinity of a fixed point ahead the spray tip penetration by the time of end of injection. In case of simulation, besides the user function created to provide the same type of data, two other methods were also used to determine size characteristics of spray. In Table 3 the results for all these three methods are presented.

As clearly visible from the displayed values, the three different methods did not always deliver similar values. This of course also might be due to real physical differences (since we measure different extent of the spray), but it is interesting to focus our attention on the evolution of these differences in case of different settings.

It is obvious that the cases in the first column of results show much smaller difference between the SMD values according to different computational determination methods, while those in the second column show considerable differences except the last case.

Table 3. SMD values for all cases according to different methods

[in μm]	**Case_1A**	**Case_1B**
measurement	23.2	
user function	16.5	19.1
cut average	17.0	22.9
global value	17.3	25.1
	Case_2A	**Case_2B**
measurement	23.2	
user function	16.5	24.6
cut average	17.4	27.8
global value	17.9	29.5
	Case_3A	**Case_3B**
measurement	23.2	
user function	16.7	30.9
cut average	16.4	31.4
global value	16.4	31.2

The reason for this phenomenon is to be sought in the differences of breakup time. All the cases in the first column undergo fast breakup (low characteristic breakup time parameter). It means that the droplets, behave potentially as parent drops lose their diameter rapidly, and hence lose on velocity also faster. As a result of this, they are not able to produce so many – and so small – child droplet (the higher the velocity difference, the smaller child droplets are being produced).

In the cases in the second column, the characteristic breakup time parameter is set to be higher, therefore the droplets retain their diameter – and thus velocity – longer. Because of that, they are able to produce a large number of – very small – child droplets.

An exception from this is represented by Case_3B, where child production is switched off. As we can see in Table 3, the SMD results are in this case just as close to each other, as in cases with lower characteristic breakup time parameter (and therefore smaller child droplet production).

This phenomenon is supposed to be due to the effect that smaller droplets possess a significantly lower momentum to "resist" the flow of surrounding gas. Hence, they rapidly lose their outward directed radial velocity component, and

tend to travel with inward directed entrained gas towards the axis of the spray.

It means that the cases with relatively large proportion of child droplets articulate an effect that exist independently concerning very small droplets, and hence, mislead the computational determination focusing only on the 1 mm surrounding of a point located on the axis of spray. Better interpreted, the user function correctly measures the droplets passing through its measurement volume, but these droplet do not represent the entirety of the spray.

The question might arise that a similar effect can cause similar phenomenon in reality. However, the problem in case of calculation is the unevenness of size distribution, i.e. the presence of disproportionately large amount of very small droplets (which are extremely sensitive to this phenomenon).

In this term, the symptom experienced in case of these size determination discrepancies highlight a conceptual weakness of the idea of child production. It is that a reasonable SMD value is targeted with a number of larger than average parent droplets (accounting for most of the injected mass), and a high number of very small child droplets.

To confirm this theory it is reasonable to investigate the size distributions of each case.

6.5. SMD Distributions

In order to obtain information about the portion of different size classes of the entire spray, a user function was implemented to collect information about all the droplets passing through planes perpendicular to spray axis, at different – user defined – distances from nozzle position.

From aspect of the phenomenon discussed in previous section, it is reasonable to choose the same cut as for the collection of SMD values, and the time frame 3 to 8 ms after injection start.

The droplets passing through this cut are averaged with number, surface and mass, and are displayed in 1 micron size classes. The curves represent a cover curve of all bar charts of a quantity (curves are used instead of bar charts for better visibility).

As it can be seen in the diagrams of Figure 3, the size distributions of these cases are significantly different. In the first four cases, where child production is allowed at least in one of the breakup regimes, there is a higher number of smaller droplets. However, in cases of fast breakup (1A and 2A) the injected mass is evenly distributed among the size classes, and the surface weighted size distribution (which relates to SMD) peaks at one single size class, with a more or less even triangulate shape around it.

Contrary to this, in cases where a slower breakup is allowed (1B and 2B), the number of very small droplets resulted in child breakup process is extremely high, but the mass remains predominantly in the parent droplets. As a result of this phenomenon, the surface weighted distribution shows in both cases an unfavourable bimodality. It means that the average SMD is produced in these cases from a bimodal spectrum of a large number of much smaller, and a large mass of larger droplets.

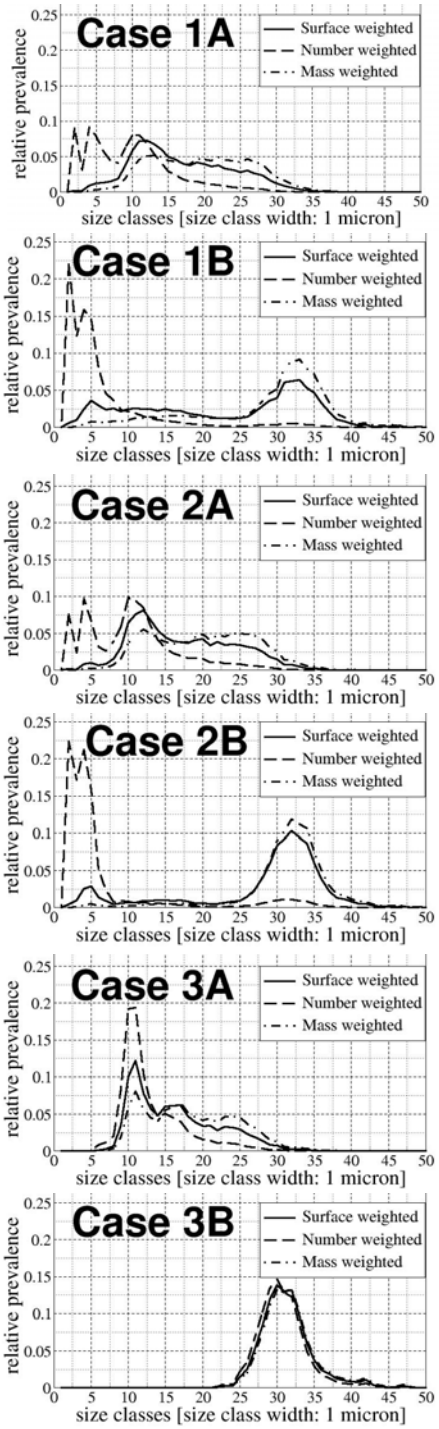

Figure 3. Size distribution of all cases

In Cases 3A and 3B no child production was allowed, hence the three distributions are almost the same. In case of fast breakup the mass is still evenly

distributed among size classes, while in case of slow breakup it has a clear peak at around 30 micron.

Based on these finding we can state that investigating only one single SMD value created with any of the methods might be misleading if the composition of the droplet size spectrum has an importance (for example in cases of detailed emission simulations). However, for usual diesel combustion calculations the evaporation velocity of the entire spray is well represented by one single SMD, calculated in a way that avoids the improper sampling resulted as a side effect of size spectrum bimodality.

5. SUMMARY

A high pressure diesel injection process was simulated with the specialized commercial code FIRE, with 6 different parameter settings. All calculation showed good agreement with measurement data concerning spray penetration, micro and macro spray cone angle data. However, regarding SMD, there were significant differences between the cases, and also between the results gained with different sampling methods.

Based on the analysis of SMD size class distributions, it was shown that the models with child production can result in bimodal droplet size spectrum. The extent of this effect however, is strongly dependent on the promptness of breakup, determined through other model parameters.

There is an ongoing research of the authors aiming a more realistic modelling of child droplet size distribution.

ACKNOWLEDGEMENTS

The authors would like to express their gratitude towards Dr. Sakata of TOYOTA Motor Corporation, Professor Senda of Doshisha University and Dr. Nagaoka of TCRDL for providing the experimental data for this paper.

This work has been supported by the Hungarian National Fund for Science and Research under contract No. OTKA T 037651.

The corresponding author wishes to thank for the SZEFH Foundation for supporting the participation at the CMFF'06.

REFERENCES

[1] Bower, G., Chang, S. K., Corradini, M. L., El-Beshbeeshy, M., Martin, J. K., Krueger, J., 1988, "Physical mechanisms for atomization of a jet spray: a comparison of models and experiments", *SAE Technical Papers*, 881318

[2] Habchi, C., Verhoeven, D., Huynh huu, C., Lambert, L., Vanhemelryck, J. L., Baritaud, T., 1997, "Modeling atomization and break up in high-pressure diesel sprays", *SAE Technical Papers*; 970881

[3] Su, T. F., Patterson, M. A., Reitz, R.D., Farell, P. V., 1996, "Experimental and numerical studies of high pressure multiple injection sprays", *SAE Technical Papers*; 960861

[4] Tatschl, R., v. Künsberg Sarre, C., v. Berg, E., 2002, "IC-engine modelling – status and outlook", *Proceedings of the International Multidimensional Engine Modeling User's Group Meeting at the SAE Congress 2002*

[5] v. Berg, E., Alajbegovic, A., Greif, D., Poredos, A., Tatschl, R., Ganippa, L., 2002, "Primary break-up model for diesel jets based on locally resolved flow field in injection hole", *Proceedings of ILASS-Europe Conference*, Zaragoza, Spain, 9-11 September

[6] Reitz, R. D., 1987, "Modeling atomization processes in high-pressure vaporizing sprays", *Atomization and Spray Technology*, vol. 3. pp. 309-337

[7] Huh, K. Y., Gosman, A. D. (1991) Phenomenological model of Diesel spray atomization; *Proceedings of International Conference on Multiphase Flows*, Tsukuba, Japan, 24-27 September

[8] v. Berg, E., Edelbauer, W., A., Tatschl, R., Alajbegovic, A., Volmajer, M., Kegl, B., Ganippa, L. (2003) Validation of a CFD model for coupled simulation of nozzle flow, primary fuel jet break-up and spray formation; *Proceedings of ICES03*, Spring Technical Conference of the ASME Internal Combustion Engine Division, Salzburg, 11-14 May

[9] Dukowicz, J. K., 1979, "Quasi-Steady droplet phase change in the presence of convection", *Internal Report*, Los Alamos Scientific Laboratory, University of California

[10] Rotondi, R., Bella, G., Grimaldi, C., Postrioti, L. (2001) Atomization of high-pressure diesel spray: experimental validation of a new break-up model; *SAE Technical Papers*, 2001-01-1070

[11] Personal communication with Dr. M. Nagaoka,, TCRDL, Nagakute, Japan

Conference on Modelling Fluid Flow (CMFF'06)
The 13th International Conference on Fluid Flow Technologies
Budapest, Hungary, September 6-9, 2006

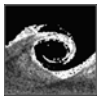

EULER/EULERIAN MODELLING OF PARTICLE DIFFUSION AND WALL INTERACTION IN TURBULENT GAS/SOLID FLOWS

Rodion GROLL

Corresponding Author. Center of Applied Space Technology and Microgravity, University of Bremen. Am Fallturm, D-28359 Bremen, Germany ,Tel.: +49 6151 281739, Fax: +49 6151 4921135, E-mail: rodion.groll@gmx.de

ABSTRACT

Volume-fraction weighted and Reynolds averaged momentum transport equations are solved in an Euler/Euler approach to numerically simulate the turbulent, dispersed two-phase flow in a two-dimensional channel. Particular attention is given to the modeling of turbulent diffusion, assuming local equilibrium but introducing individual terms for particle/fluid drag interaction, particle collisions and trajectory crossings.

These influences have been quantified in terms of partial viscosities, a restitution power and a turbulence structure parameter. Boussinesq approximations have been used for each phase and their interaction. The results show improvements over conventional Euler/Euler modeling schemes and advantages and disadvantages over Euler/Lagrange schemes are discussed.

Keywords: particle diffusion, particle/particle collision, particle/turbulence interaction, particle/wall collision, two-phase flows

NOMENCLATURE

C_α	[-]	turbulence structure parameter
C_1	[-]	ε-production coefficient
C_2	[-]	ε-dissipation coefficient
C_3	[-]	ε-drag coefficient
E	[-]	log-wall law coefficient
Z	[-]	mass loading
g	[ms^{-2}]	gravity constant
k	[m^2s^{-2}]	turbulent kinetic energy
p	[Pa]	static pressure
q	[m^2s^{-2}]	phase velocity covariance
u	[ms^{-1}]	velocity
u_t	[ms^{-1}]	turbulent velocity
u_+	[-]	characteristic velocity
x	[m]	distance
y_+	[-]	characteristic wall distance
Π_w	[$Pams^{-2}$]	wall turbulence production
α	[-]	volumetric fraction
ε_α	[m^2s^{-3}]	effective power loss
ε_β	[m^2s^{-3}]	ε_α viscous component
ε_d	[m^2s^{-3}]	ε_α crossing trajectory component
ε_c	[m^2s^{-3}]	ε_α collision component
ε_p	[m^2s^{-3}]	ε_α drag component
ε_t	[m^2s^{-3}]	tubulence dissipation
κ	[-]	Prandtl constant
μ	[$kgm^{-1}s^{-1}$]	dynamic viscosity
ν_α	[m^2s^{-1}]	effective diffusion coefficient
ν_t	[m^2s^{-1}]	turbulent diffusion coefficient
π_α	[m^2s^{-3}]	effective restitution power
π_β	[m^2s^{-3}]	π_α viscous component
π_d	[m^2s^{-3}]	π_α crossing trajectory component
π_c	[m^2s^{-3}]	π_α collision component
π_p	[m^2s^{-3}]	π_α drag component
ϱ	[kgm^{-3}]	density
σ_k	[-]	Schmidt constant for k
σ_ε	[-]	Schmidt constant for ε
τ_α	[s]	effective diffusion time scale
τ_p	[s]	drag relaxation time scale
τ_w	[Pa]	wall shear stress

Subscripts and Superscripts

C	continuous phase
D	dispersed phase
c	collision component
d	crossing trajectory component
p	drag component
β	viscous component
–	temporal mean
<>	volume fraction weighted averaged mean
{}	deviation of <>-averaged values

1. INTRODUCTION

The momentum transport equation includes a turbulent diffusion term, which characterizes motion not resolved by the convective term. This turbulent diffusion depends on the turbulent kinetic energy and the characteristic turbulent time scale. Based on *"Csanady's Approximation"* (*Csanady*, 1963), the time scale of the dispersed phase is coupled with the turbulent time scale of the continuous phase. This time scale quantifies the diffusion intensity and is influenced by the drag interaction of the particles with the viscous gas phase and inter-particle collisions.

2. MATERIALS AND METHODS

Modeling the diffusion character of particle flows transported in a viscous carrier phase the diffusion is not dominated by the eddy dissipation as it is in turbulent shear flows in a continuous gas phase. This dispersed phase diffusion is characterized by unsteady drag influences and crossing trajectory characteristics defined by the correlation of the velocities of the continuous phase and the dispersed phase itself.

2.1. Transport Equations

The Reynolds averaged, volume-fraction weighted momentum transport equations for the continuous and the dispersed phase read:

$$\begin{aligned}&\frac{\partial}{\partial t}\left(\rho^k\bar{\alpha}^k<u_i^k>^k\right)+\frac{\partial}{\partial x_j}\left(\rho^k\bar{\alpha}^k<u_i^k>^k<u_j^k>^k\right)\\&=-\bar{\alpha}^k\frac{\partial p^C}{\partial x_i}+\bar{\alpha}^k\frac{\partial\tau_{ij}^k}{\partial x_i}+\rho^k\frac{\bar{\alpha}^k}{\tau_p^k}\left(<u_i^{\bar{k}}>^k-<u_i^k>^k\right)\\&\quad+\rho^k\bar{\alpha}^k g_i-\frac{\partial}{\partial x_j}\left(\rho^k\bar{\alpha}^k<\{u_i^k\}^k\{u_j^k\}^k>^k\right)\end{aligned}\qquad(1)$$

where *k* stands for *C* (continuous phase) and *D* (dispersed phase). A negation notation is used here, i.e. $\overline{C}=D$, $\overline{D}=C$ The drag force relaxation time scale τ_p^k depends on the particle Reynolds number, based on the velocity difference between the continuous and the dispersed phase (*Schiller et al.*, 1933), see e.g. *Crowe et al.* (1998). The equation terms are described with the help of an averaging operator $<.>^k$ (see, e.g. *Politis*, 1989).

$$<u_i^k>^l=\frac{\overline{\alpha^l u_i^k}}{\overline{\alpha^l}}\ ;\ u_i^k=<u_i^k>^l+\left\{u_i^k\right\}^l$$

The fluctuation of the filter variable is written:

$$\{\varphi\}^k=\varphi-<\varphi>^k$$

Collision and crossing trajectory terms were approximated by *Grad* (1949) and *Csanady* (1963). The sum of pressure gradient of the continuous phase and gravity forces the particle motion as the lift force in case of a hydrostatic motion. τ_{ij}^k defines the viscous stresses inside the phase k. Because of the character of the dispersed phase τ_{ij}^D is zero.

The underlying turbulence model for both phases is based on the Boussinesq analogy, employing eddy viscosity as the model quantity, whose formulation was provided in the framework of the standard *k*-ε modeling concept. k^C defines the turbulent kinetic energy of the continuous phase. The corresponding variable of the dispersed phase k^D describes the particle velocity variance at a point.

$$\begin{aligned}&\frac{\partial}{\partial t}\left(\rho^k\bar{\alpha}^k k^k\right)+\frac{\partial}{\partial x_j}\left(\rho^k\bar{\alpha}^k k^k<u_j^k>^k\right)\\&=\frac{\partial}{\partial x_j}\left(\left(\mu^k+\rho^k\frac{\nu_t^k}{\sigma_k^k}\right)\bar{\alpha}^k\frac{\partial k^k}{\partial x_j}\right)-\rho^k\bar{\alpha}^k\varepsilon_\alpha^k\\&\quad-\rho^k\bar{\alpha}^k<\{u_i^k\}^k\{u_j^k\}^k>^k\frac{\partial<u_i^k>^k}{\partial x_j}\end{aligned}\qquad(2)$$

$$\sigma_k^C=1.0\quad,\quad\sigma_k^D=2.5$$

The transport equations for the turbulent kinetic energy k^k and its dissipation rate ε_t^k differ from those for a single-phase flow by several additional production terms and the modified dissipation. This total turbulent kinetic energy loss ε_α^k in the present model arises from relative drag and particle collision processes.

$$\begin{aligned}&\frac{\partial}{\partial t}\left(\rho^k\bar{\alpha}^k\varepsilon^k\right)+\frac{\partial}{\partial x_j}\left(\rho^k\bar{\alpha}^k\varepsilon^k<u_j^k>^k\right)\\&=\frac{\partial}{\partial x_j}\left(\left(\mu^k+\rho^k\frac{\nu_t^k}{\sigma_\varepsilon^k}\right)\bar{\alpha}^k\frac{\partial k^k}{\partial x_j}\right)-C_2\rho^k\bar{\alpha}^k\frac{\varepsilon_t^k\varepsilon_\alpha^k}{k^k}\\&\quad-C_1\frac{\varepsilon_t^k}{k^k}\rho^k\bar{\alpha}^k<\{u_i^k\}^k\{u_j^k\}^k>^k\frac{\partial<u_i^k>^k}{\partial x_j}\\&\quad+C_3\frac{\varepsilon_t^k}{k^k}\rho^k\frac{\bar{\alpha}^k}{\tau_p^k}\left(q^k-2k^k\right)\end{aligned}\qquad(3)$$

$$\sigma_\varepsilon^C=1.3\quad,\quad C_1=1.44\quad,\quad C_2=1.92\quad,\quad C_3=1.20$$

Because of the different phase velocities inside the drag relation term a general formulation is needed for the complimentary index of k. For this notation a little circle used (C°=D, D°=C). The velocity covariance $q^k=<\{u_i\}^k\{u_i^{k^\circ}\}^{k^\circ}>^k$ of *He and Simonin* (1993) represents the trace of the velocity vector correlation tensor of both phases:

$$
\begin{aligned}
&\frac{\partial}{\partial t}\left(\rho^k\bar{\alpha}^k q^k\right)+\frac{\partial}{\partial x_j}\left(\rho^k\bar{\alpha}^k q^k < u_j^k >^k\right)\\
&=\frac{\partial}{\partial x_j}\left(\rho^k\bar{\alpha}^k\nu_\alpha^k\frac{\partial q^k}{\partial x_j}\right)+\rho^k\frac{\bar{\alpha}^k}{\tau_p^k}\left(2Z^k k^k+2k^{\bar{k}}-\left(1+Z^k\right)q^k\right)\\
&\quad-\rho^k\bar{\alpha}^k < \{u_i^{\bar{k}}\}^{\bar{k}}\{u_j^k\}^k >^k\frac{\partial < u_i^k >^k}{\partial x_j}\\
&\quad-\rho^k\bar{\alpha}^k < \{u_i^k\}^k\{u_j^{\bar{k}}\}^{\bar{k}} >^k\frac{\partial < u_i^{\bar{k}} >^{\bar{k}}}{\partial x_j}-\rho^k\bar{\alpha}^k\frac{q}{\tau_\alpha^k}\\
&\quad with\ \ Z^k=\frac{\rho^k\bar{\alpha}^k}{\rho^{\bar{k}}\bar{\alpha}^{\bar{k}}}
\end{aligned}
\tag{4}
$$

which completes the present three-equation model for each of both phases. Velocity correlations, representing the turbulent momentum diffusion are modeled by the following *Boussinesq approximations*:

$$
\begin{aligned}
&-< \{u_i^k\}^k\{u_j^k\}^k >^k=-\frac{2}{3}k^k\delta_{ij}\\
&\quad+\nu_t^k\left(\frac{\partial < u_i^k >^k}{\partial x_j}+\frac{\partial < u_j^k >^k}{\partial x_i}-\frac{2}{3}\frac{\partial < u_l^k >^k}{\partial x_l}\delta_{ij}\right)\\
&-< \{u_i^k\}^k\{u_j^{\bar{k}}\}^{\bar{k}} >^k=-\frac{1}{3}q^k\delta_{ij}\\
&\quad+\nu_\alpha^k\left(\frac{\partial < u_i^k >^k}{\partial x_j}+\frac{\partial < u_j^k >^k}{\partial x_i}-\frac{2}{3}\frac{\partial < u_l^k >^k}{\partial x_l}\delta_{ij}\right)
\end{aligned}
\tag{5}
$$

The diffusivity coefficients of momentum and turbulent transport equations are given by the characteristic diffusion time scale $\tau_\alpha{}^k$.

$$
\nu_t^k=-\frac{2}{3}\tau_\alpha^k k^k\quad,\quad\nu_\alpha^k=-\frac{1}{3}\tau_\alpha^k q^k \tag{6}
$$

To close the present formulation of particle and carrier gas phase motion this time scale has to be modeled.

2.2. Diffusion Modelling

Based on this model of momentum diffusion, which depends on the velocity gradients of the diffusing phase, the characteristic diffusion time scales have to be defined by the velocity correlation and its associated loss rate $\varepsilon_\alpha{}^k$. Local equilibrium describes the equivalence of production and loss of turbulent kinetic energy. Assuming $\partial/\partial x_1\approx 0$ yields an expression (i=1, j=2) for the non-diagonal element of the Reynolds stress tensor.

$$
\begin{aligned}
&\varepsilon_\alpha^k=-< \{u_1^k\}^k\{u_2^k\}^k >^k\frac{\partial < u_1^k >^k}{\partial x_2}\\
&\Rightarrow\ -< \{u_1^k\}^k\{u_2^k\}^k >^k=\frac{\left(< \{u_1^k\}^k\{u_2^k\}^k >^k\right)^2}{\varepsilon_\alpha^k}\frac{\partial < u_1^k >^k}{\partial x_2}
\end{aligned}
\tag{7}
$$

With the definition of the turbulence structure parameter $C_\alpha{}^k$ of the phase k

$$
\begin{aligned}
&C_\alpha^k=-\frac{< \{u_1^k\}^k\{u_2^k\}^k >^k}{\frac{2}{3}k^k}\\
&\Rightarrow\ -< \{u_1^k\}^k\{u_2^k\}^k >^k=\frac{\frac{2}{3}C_\alpha^k k^k}{\varepsilon_\alpha^k}=\nu_t^k\frac{\partial < u_1^k >^k}{\partial x_2}
\end{aligned}
\tag{8}
$$

the turbulent viscosity is calculated using the turbulent kinetic energy k^k, its loss rate and the turbulence structure parameter. Based on the diffusivity definition (Eqn. 8) the turbulent time scale is also defined by these values:

$$
\nu_t^k=-\frac{2}{3}\tau_\alpha^k k^k\ \Rightarrow\ \tau_\alpha^k=\frac{\nu_t^k}{\frac{2}{3}k^k}=\frac{2}{3}\left(C_\alpha^k\right)^2\frac{k^k}{\varepsilon_\alpha^k} \tag{9}
$$

With the definition of the restitution power $\pi_\alpha{}^k$, the turbulent viscosity is determined by the turbulent kinetic energy and the restitution power.

$$
\pi_\alpha^k=\frac{2}{3}\frac{k^k}{\tau_\alpha^k}=\frac{\varepsilon_\alpha^k}{\left(C_\alpha^k\right)^2}\Rightarrow\ -< \{u_1^k\}^k\{u_2^k\}^k >^k=\frac{\left(\frac{2}{3}k^k\right)^2}{\pi_\alpha^k} \tag{10}
$$

The power $\pi_\alpha{}^k$ describes the restitution of turbulent shear forces based on the dissipation and structure of turbulence and reduces the turbulent diffusion.

2.3. Restitution Power

This restitution power consists of the partial powers defined by four different effects (see table 1), which are described in the following subsections with the indices β, p, c and d. The total turbulence loss rate $\varepsilon_\alpha{}^k$ is given by the sum of individual loss rates ($\varepsilon_\gamma{}^k$, see table 1):

$$
\varepsilon_\alpha^k=\varepsilon_\beta^k+\varepsilon_d^k+\varepsilon_p^k+\varepsilon_c^k \tag{11}
$$

The different diffusion rates and turbulence loss rates are induced by the viscous turbulent shear stress ($\pi_\beta{}^k$,$\varepsilon_\beta{}^k$: *Jones et al.*, 1972), crossing trajectory effects ($\pi_d{}^k$,$\varepsilon_d{}^k$: *Csanady*, 1963), drag forces ($\pi_p{}^k$,$\varepsilon_p{}^k$: *Schiller et al.*, 1933) and collision terms ($\pi_c{}^k$,$\varepsilon_c{}^k$: *Jenkins et al.*, 1985). Adding together these influences, the new restitution power term of the turbulent diffusion is modeled.

$$
\pi_\alpha^k=\pi_\beta^k+\pi_d^k+\pi_p^k+\pi_c^k \tag{12}
$$

Simulating the general restitution power $\pi_\alpha{}^k$ and energy loss $\varepsilon_\alpha{}^k$ the resulting turbulence structure parameter $C_\alpha{}^k$ is computed in the following way:

$$\pi_\alpha^k = \frac{2}{3}\frac{k^k}{\tau_\alpha^k} = \frac{\varepsilon_\alpha^k}{\left(C_\alpha^k\right)^2} \Rightarrow C_\alpha^k = \sqrt{\frac{\varepsilon_\alpha^k}{\pi_\alpha^k}} \tag{13}$$

The turbulent time scale τ_α^k depends on the sum of all diffusion rates:

$$\tau_\alpha^k = \frac{2/3\,k^k}{\pi_\beta^k + \pi_d^k + \pi_p^k + \pi_c^k} \tag{14}$$

This way of calculation yields a deterministic method to compute the turbulent time scale, which is needed for the calculation of the general turbulent viscosity of both phases (Eqn. 7).

γ	model	π_γ^C	ε_γ^C	π_γ^D	ε_γ^D
β	Jones et al.	$\frac{2}{3}\beta\varepsilon_\beta^C$	ε_t^C	0.	0.
d	Csanady	0.	0.	$\frac{2}{3}\frac{k^D}{\tau_\alpha^C}\bullet(1+C_\beta^C\xi_r^{C2})^{\frac{1}{2}}$	0.
p	Schiller et al.	$\frac{2/3}{\tau_p^C}\cdot(2k^C - q^C)$	$\frac{1}{\tau_p^C}\cdot(2k^C - q^C)$	$\frac{2/3}{\tau_p^D}\cdot(2k^D - q^D)$	$\frac{1}{\tau_p^D}\cdot(2k^D - q^D)$
c	Jenkins et al.	0.	0.	$\frac{\sigma_c^D}{\tau_p^D}\frac{2}{3}k^D$	$\frac{k^D}{\tau_c^D}\cdot\left(1-\left(e_c^D\right)^2\right)$

Table 1: Diffusion rates and turbulence loss components

2.4. Boundary Conditions

The wall shear stress of the particle phase is defined analog to the carrier phase with the modified turbulence structure parameter C_α^k:

$$\tau_w^k = \rho^k\alpha^k\left(u_t^k\right)^2;\ u_t^k = \sqrt{C_\alpha^k\cdot\frac{2}{3}k^k} \tag{15}$$

The stress coefficient is calculated by the void velocity scale u_+^k based on the "Logarithmic-Wall Law" (κ=0.41 ; E=8.431) and the turbulent time scale u_t^k .

$$\tau_w^k = \rho^k\alpha^k\left(\frac{u_t^k}{u_+^k}\right)^2 \text{ with } \frac{<u^k>^k}{u_t^k} = u_+^k = \frac{1}{\kappa}\ln\left(Ey_+^k\right)$$
$$;\ y_+^k = y\frac{u_t^k}{\nu^C}\sqrt{C_\alpha^k\cdot\frac{2}{3}k^k} \tag{16}$$

Resulting from this modeling the wall shear stress of the momentum equation

$$\tau_w^k = \rho^k\alpha^k\kappa\sqrt{C_\alpha^k\cdot\frac{2}{3}k^k}\,/\ln\left(Ey_+^k\right) \tag{17}$$

and the turbulence production at the wall

$$\Pi_w^k = \tau_w^k <u_1^k>^k \frac{\partial <u_1^k>^k}{\partial x_2} = \rho^k\alpha^k <u_1^k>^k \frac{\partial <u_1^k>^k}{\partial x_2}\kappa\sqrt{C_\alpha^k\cdot\frac{2}{3}k^k}\,/\ln\left(Ey_+^k\right) \tag{18}$$

are determined in this modified way corresponding to the standard wall law.

Analog to the turbulence generation of the continuous phase the particle velocity variance is increasing near the wall. The turbulence structure parameter of the continuous phase $C_\alpha^C=\sqrt{(\varepsilon_\alpha^C/\pi_\alpha^C)}$ mainly depends on the viscous character of the continuous phase itself. The turbulence structure parameter of the dispersed phase $C_\alpha^D=\sqrt{(\varepsilon_\alpha^D/\pi_\alpha^D)}$ is predicted by collision and crossing trajectories effects.

3. RESULTS

This model was validated using experimental data of *70μm* copper particles in a fully-developed channel flow [Exp.: *Kulick et al.*, 1994]. The results using the present model (Eul./Eul. [2]) were also compared with the results obtained by an Euler/Lagrange scheme [*Huber et al.* 1994, Sim.: *Kohnen* 1997 (Eul./Lag.)] and a well-known Euler/Eulerian diffusion approach [*He et. al.* 1993, Sim.: *Groll et al.* 2002 (Eul./Eul. [1])]. Gravity acts in the positive *x*-axis direction. The channel flow Reynolds number, based on channel height ($2h$=40*mm*) and single phase channel centerline velocity (U_0^C=*10.5m/s*) is Re_{2h}=27600. The flow is regarded as fully developed after 125 channel heights and at this position it is assumed that the particle velocity and particle turbulence has reached an asymptotic state. The copper particles have a density of ρ^D=*8800kg/m3* and a diameter of D_p=*70μm*. The inlet mass loading of particles is Z_0^D=*10%* and the parameter of elasticity is e_c^D=*0.90*. The results obtained using the present method were also compared with the computational results obtained by an Euler/Lagrange scheme (*Kohnen*, 1997).

Fig. 1 shows the normalized particle stream-wise mean velocity U^D/U_0^C, its normalized standard deviation values u^D/U_0^C and the normalized standard deviation of the particle velocity magnitude $u^D{}_{mag}/U_0^C$.

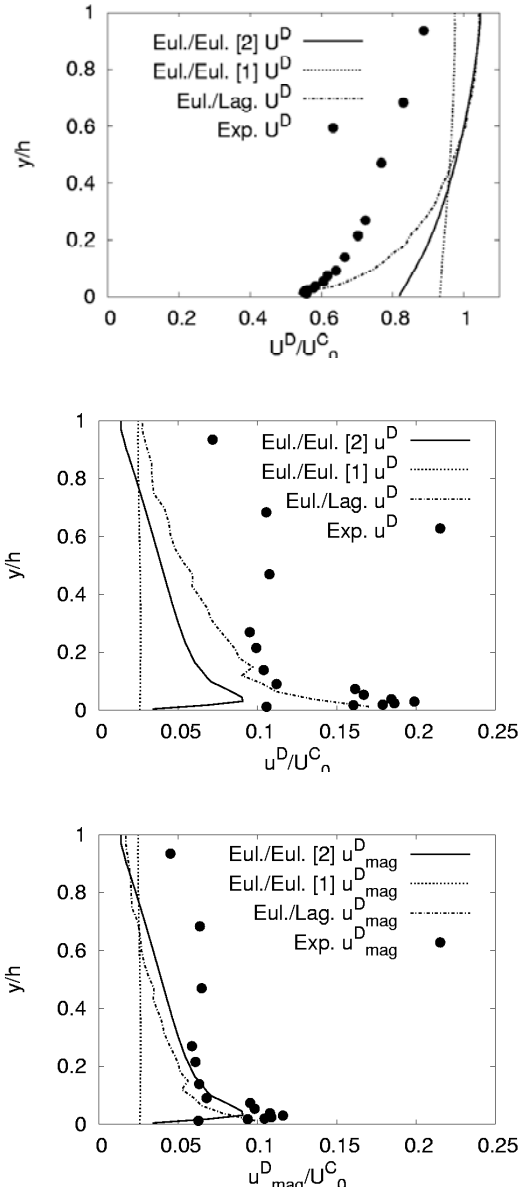

FIGURE 1: Normalized stream-wise particle mean velocity U^D, normalized stream-wise standard deviation u^D and normalized standard deviation u^D_{mag} of the particle velocity magnitude in the fully developed, particle-laden channel flow

Comparing the present model (Eul./Eul. [2]) with a standard particle diffusion model (Eul./Eul. [1]), the velocity and the standard deviation of the velocity magnitude of the present model agree better with the Euler/Lagrangian results.

Because of the assumed isotropy of the present model, the standard deviation of the stream-wise particle velocity does not agree as well with the predicted standard deviation of the particle velocity magnitude.

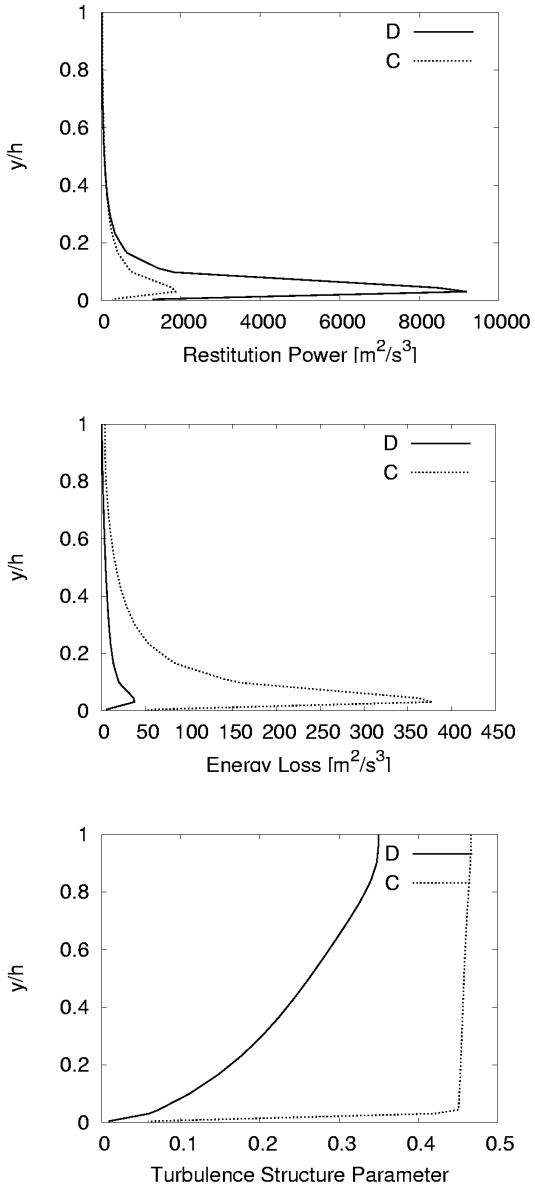

FIGURE 2: Turbulent kinetic energy loss rate ε_α^k, turbulence restitution power π_α^k and the turbulence structure parameter C_α^k of the dispersed phase (D) and the continuous phase (C)

The characteristic model values describing diffusion: the energy loss rate of the turbulent kinetic energy ε_α^k, the restitution power π_α^k and the turbulence structure parameter C_α^k are shown in Fig. 2. The dissipation loss of the continuous phase and the restitution power of the dispersed phase dominate over the respective values of the other phase.

As expected the turbulence structure parameter of the dispersed phase C_α^D decreases near the wall, because of the decreasing ratio $\sqrt{(\varepsilon_\alpha^D/\pi_\alpha^D)}$ against the nearly constant turbulence structure parameter of the continuous phase C_α^C. Comparing the

positions of these restitution maxima of the momentum diffusion with local minima of the turbulence structure parameter C_α^D (Fig. 2, right) near the wall the difference between the different kinds of diffusion, with and without viscous turbulence dissipation, in dispersed and continuous phase are shown.

4. SUMMARY

Using this kind of diffusion blending, simulations are able to give better results for turbulent wall layers of the dispersed phase, including their turbulence production. The prediction of turbulent particle diffusion is limited by the quality of modeling of the momentum diffusion and the turbulence production of the dispersed phase.

Compared to classical equilibrium models, which solve an additional differential equation for the energy loss, coming up to the dissipation rate in viscous systems, the energy loss of the dispersed phase is given by algebraic equations. The turbulence structure parameter remains nearly constant in the dissipative systems examined here. So the ratio of restitution and dissipation power of the involved submodels keeps also nearly constant.

For the not viscous, dispersed phase the turbulence structure parameter decreases corresponding to the high restitution and the locally low momentum diffusion inside the wall layer. This characteristic behavior is based on the additional restitution power without the corresponding loss rate induced by crossing trajectories effects.

Basically the added modeling of the turbulence structure parameter influences the production of particle velocity variance near the wall in that kind, that the gradients of the stream-wise particle velocity agree much better with the measurement data.

REFERENCES

[1] Crowe, C.T., M. Sommerfeld, and Y. Tsuji. 1998. *Multiphase flows with droplets and particles.* CRC Press LLC, Florida

[2] Csanady, G.T. 1963. Turbulent diffusion of heavy particles in the atmosphere. *J. Atm. Sc.* 20, 201

[3] Grad H. 1949. On the kinetic theory on rarefied gases. *Communications on Pure and Applied Mathematics* 2(4), 331-407

[4] Groll, R., S. Jakirlic, and C. Tropea. 2002. Numerical modeling of particle-laden flows with a four-equation model. *5th International Symposium on Engineering Turbulence Modeling and Measurements*, Elsevier Science Ltd., 939-948

[5] He, J., and O. Simonin. 1993. Non-equilibrium prediction of the particle-phase stress tensor in vertical pneumatic conveying. *ASME-FED : Gas-Solid Flows* 166, 253

[6] Huber, N., and M. Sommerfeld. 1994. Characterization of the cross-particle concentration distribution in pneumatic conveying systems. *Powder Techn.* 79, 191

[7] Jenkins, J. T., and M. W. Richman. 1985. Grad's 13-moment-system for a dense gas of inelastic spheres. *Arch. Ration. Mech. Anal.* 87, 355

[8] Jones, W. P., and B. E. Launder. 1972. The prediction of laminarization with a two-equation model of turbulence. *Int. J. Heat and Mass Transf.* 15, 301

[9] Kohnen, G. 1997. Über den Einfluss der Phasenwelchselwirkungen bei turbulenten Zweiphasenströmungen und deren numerische Erfassung in der Euler/Lagrange Betrachtungsweise (tranl. On the influence of phase interactions of turbulent two-phase flows and their numerical description in the Euler/Lagrangian approach), Shaker Verlag, Aachen, Germany

[10] Kulick, J. D., J. R. Fessler, and J. K. Eaton. 1994. Particle response and turbulence modification in fully developed channel flow. *J. Fluid Mech.* 277, 109

[11] Schiller, L., and A. Naumann. 1933. Über die grundlegenden Berechnungen bei der Schwerkraftaufbereitung (transl.: *On the basic calculations in gravity conditioning*), *VDI-Journal* 77, 318

[12] Politis S. 1989. Prediction of two-phase solid-liquid turbulent flow in stirred vessels, PhD Thesis, Imperial College London

Conference on Modelling Fluid Flow (CMFF'06)
The 13th International Conference on Fluid Flow Technologies
Budapest, Hungary, September 6-9, 2006

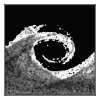

THE EFFECT OF TURBULENCE ON THE EFFICIENCY OF THE ROTATIONAL PHASE SEPARATOR

J.G.M. Kuerten[1], B.P.M. van Esch[2], H.P. van Kemenade[3], J.J.H. Brouwers[4]

[1] Corresponding Author. Department of Mechanical Engineering, Technische Universiteit Eindhoven. Postbus 513, 5600 MB Eindhoven, The Netherlands. Tel.: +31 40 2472362, Fax: +31 40 2475399, E-mail: j.g.m.kuerten@tue.nl
[2] Department of Mechanical Engineering, Technische Universiteit Eindhoven. E-mail: b.p.m.v.esch@tue.nl
[3] Department of Mechanical Engineering, Technische Universiteit Eindhoven. E-mail: h.p.v.kemenade@tue.nl
[4] Department of Mechanical Engineering, Technische Universiteit Eindhoven. E-mail: j.j.h.brouwers@tue.nl

ABSTRACT

The Rotational Phase Separator (RPS) is a device to separate liquid or solid particles from a lighter or heavier fluid by centrifugation in a bundle of channels which rotate around a common axis. Originally, the RPS was designed in such a way that the flow through the channels is laminar in order to avoid eddies in which the particles keep circulating and do not reach the walls. However, in some applications the required volume flow of fluid is so large, that turbulent flow can no longer be avoided. Direct numerical simulation (DNS) of the flow in a rotating pipe and particle tracking in this flow are applied to study the influence of turbulence on the collection efficiency of the RPS. The results show that especially the collection efficiency for larger particles decreases due to the turbulence. For high rotational speeds the efficiency decreases further as the particles are trapped in a counter-rotating vortex.

Keywords: Phase separation, Turbulence, DNS

NOMENCLATURE

D	[m]	pipe diameter
L	[m]	pipe length
R	[m]	distance between pipe and rotation axis
Re	[-]	Reynolds number
U	[m/s]	velocity
d	[m]	particle diameter
f	[N]	force
m	[kg]	mass
r	[m]	radial coordinate
t	[s]	time
u	[m/s]	fluid velocity
v	[m/s]	particle velocity
x	[m]	position
P	[Pa]	total pressure
Ω	[rad/s]	angular velocity
ρ	[kg/m^3]	mass density
μ	[$Pa\ s$]	dynamic viscosity
ν	[m^2/s]	kinematic viscosity
τ	[s]	relaxation time
φ	[rad]	tangential coordinate
ω	[$1/s$]	fluid vorticity

Subscripts and Superscripts

ax	axial
p	particle
r	radial
τ	friction
φ	tangential
Ω	rotation

1. INTRODUCTION

The Rotational Phase Separator is a separation technology built around a rotating filter element comprising a multitude of small parallel channels. The filter element can be used in addition to a conventional tangential or axial cyclone to enhance the collection efficiency by one order of magnitude in terms of particle diameter [1-4]. Usually, the flow in the channels of the filter element is kept in the laminar regime to prevent capture of particles or droplets in turbulent eddies or swirls. In case of the tangential design (Figure 1), mainly used to separate droplets or particles from a gas flow, it is normally not a problem to design within this limit as the throughput is low compared to the flow area of the cyclone and filter element. In typical applications, the main design criterion is the pressure drop over the separator, while the dimensions are of less concern.

The opposite holds for the axial version (Figure 2) which is mainly used for in-line (offshore) separation of condensed or de-sublimated droplets from another liquid or gas flow. In those applications 100% collection of particles is not necessary and the laminar flow condition may impose a too severe restriction on the design.

However, in many cases the Reynolds number is low enough for the flow and particle behaviour to be studied in detail by means of direct numerical simulation of the fluid flow and Lagrangian particle tracking. In this study, the consequences of allowing low turbulent conditions in the channels of the filter element are investigated by comparing the results of an analytical model for the laminar regime with turbulent DNS results.

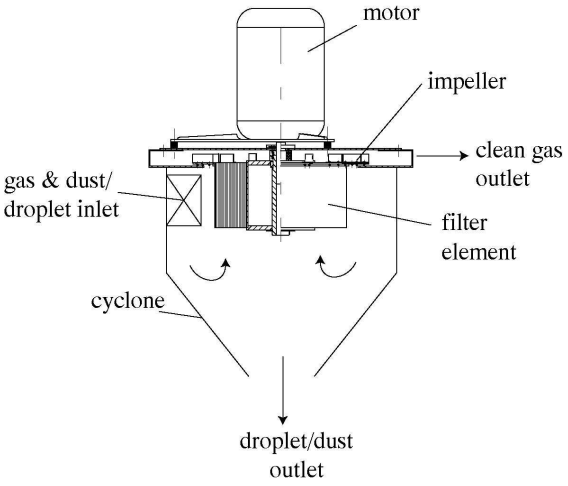

Figure 1. RPS mounted in a cyclone in the tangential version

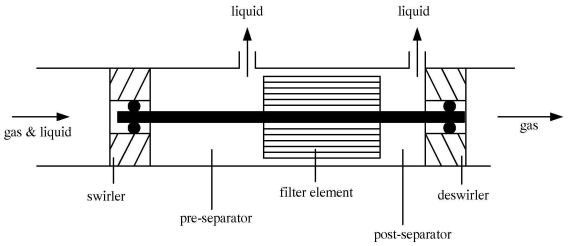

Figure 2. Axial version of RPS in an inline configuration, separating liquid droplets from a gas

In section 2 of this paper the analytical model for the calculation of particle collection efficiency will be presented. Section 3 provides the governing equations and numerical method for the DNS of particle-laden flow in a rotating pipe and in section 4 results are presented. Finally, in section 5 the conclusions of the paper and an outlook to future work are given.

2. ANALYTICAL MODEL

Brouwers [5] derived the elementary particle collection efficiency of the Rotational Phase Separator for channels with circular, triangular and sinusoidal shape in case the flow in the channels is laminar. At entry of the filter element, or soon after, the fluid co-rotates with the filter element. As we are concerned with particles (or droplets) in the micrometer range, inertial forces are neglected [6]. Whether a particle reaches the outer wall depends on the distance to be travelled by the particle, the centrifugal force, the axial velocity profile and the length of the channel. The centrifugal force depends on the angular velocity of rotation, the difference in mass density between particle and fluid, the viscosity of the fluid and the distance between particle and axis of rotation. The velocity at which the particles move radially can be calculated using Stokes' law. Assuming a constant axial fluid speed u_{ax} and a uniform distribtion of the particles over the cross-sectional area, an expression can be derived for the smallest particle which is collected with 100% probability in a channel at a radial location R [5]:

$$d_{p,100\%} = \left(\frac{18 \mu u_{ax} D}{\rho_p \Omega^2 R L} \right) \tag{1}$$

Here μ denotes the dynamic viscosity of the fluid, D the pipe diameter, ρ_p the mass density of the particle, Ω the angular velocity and L the length of the pipe.

Moving with the gas through the channel, all particles of a certain diameter will move with the same velocity in the radial direction. If a collection wall were absent, at the exit of the separation channel two cross sectional areas could be distinguished (see Figure 3): the cross sectional area of the channel itself and the cross sectional area formed by the particles. The ratio of particles that do not reach the wall to the total number of particles is equal to the ratio of the shaded area to the total cross section of the pipe.

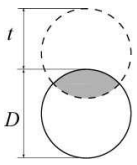

Figure 3. Centrifugally induced particle displacement in a circular channel

To derive an expression for the particle collection efficiency in the presence of a Hagen-Poiseuille velocity profile, the circular cross section is divided into a system of parallel planes within which the movement of particles takes place. Equation (1) can be used for the local conditions and integration gives after some algebraic manipulation the particle collection efficiency η in circular channels subject to Hagen-Poiseuille flow

$$\eta = \frac{4}{\pi} x^2 a - \frac{4}{3\pi} \left(1 - a^2\right)^{1/2} a \left(\frac{5}{2} - a^2 \right) - \frac{2}{\pi} \left(\arcsin a - \frac{\pi}{2} \right), \tag{2}$$

if $x \leq (4/3)^{1/2}$ and $\eta=1$ if $x \geq (4/3)^{1/2}$. Here the dimensionless particle diameter $x = d_p/d_{p,100\%}$ and $a = [1-(3x^2/4)^{2/3}]^{1/2}$. Using the same procedure also expressions for channels with a sinusoidal and with a triangular shape are derived. The results are given in Figure 4.

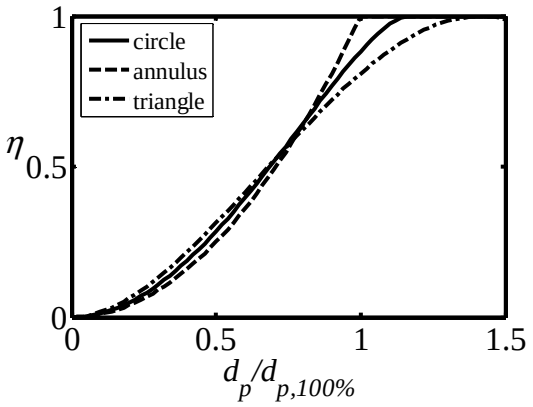

Figure 4. Collection efficiency of one channel of an RPS in laminar conditions for various channel shapes

Although current production methods produce sinusoidal or rectangular channel geometries, the case of a circular geometry is adopted for this study as there are more reference cases available [7,8] and a DNS is more easily feasible.

3. NUMERICAL METHOD

In the DNS the three-dimensional Navier-Stokes equation for incompressible flow is solved in a cylindrical geometry in the vorticity formulation. The equation is solved in a rotating frame of reference and reads:

$$\frac{\partial \mathbf{u}}{\partial t} + \boldsymbol{\omega} \times \mathbf{u} + \Omega \times (\Omega \times \mathbf{r}) + 2\Omega \times \mathbf{u} = -\frac{1}{\rho} \nabla P + \nu \Delta \mathbf{u}. \quad (3)$$

Here, P denotes the total pressure, $P=p+\frac{1}{2}\rho\mathbf{u}^2$, $\mathbf{u}$ the fluid velocity, $\boldsymbol{\omega}$ the fluid vorticity, ρ the fluid density, ν the kinematic viscosity and $\mathbf{r}$ the distance to the rotation axis. Compared to the Navier-Stokes equation in a stationary frame of reference, two additional terms appear. The centrifugal force, $\Omega \times (\Omega \times \mathbf{r})$, can be incorporated in the pressure [1]. The Coriolis force, $2\Omega \times \mathbf{u}$, does not depend on the distance to the rotation axis. Hence, the fluid velocity does not depend on this distance, which implies that in one DNS calculation the flow in all pipes in the bundle can be simulated. Note however, that the pressure field does depend on this distance; only the sum of the pressure and centrifugal pressure is independent of the distance to the rotation axis.

In the DNS a pipe of a finite length equal to five times its diameter is taken with periodic boundary conditions in the axial direction. Since the tangential direction is periodic by definition, a spectral method with a Fourier-Galerkin approach in the two periodic directions is a natural choice. In the radial direction a Chebyshev-collocation method is applied, but, in order to avoid a large number of collocation points near the axis of the pipe, the radial direction is divided into five elements with a Chebyshev grid in each element [9]. The coupling between the elements is continuously differentiable. The choice for five elements is a compromise between collocation point distribution and accuracy. More elements can lead to a better distribution of collocation points, but, since the continuity conditions are imposed at the element boundaries instead of the Navier-Stokes equation, this results in a decrease in accuracy.

For integration in time a second-order accurate time-splitting method is chosen. In the first step the nonlinear terms, including the Coriolis force, are treated in an explicit way. The nonlinear terms are calculated pseudo-spectrally by fast Fourier transform, where the 3/2-rule is applied to prevent aliasing errors. In the second step the pressure is calculated in such a way that the velocity field at the new time level is approximately divergence free. Finally, in the last step the viscous terms are treated implicitly. Since the Fourier modes can be completely decoupled, only a one-dimensional system of equations needs to be solved for each Fourier mode. The wall of the pipe acts as a no-slip wall. The wall boundary condition for the pressure follows from the wall-normal component of the Navier-Stokes equation, whereas the correct boundary conditions at the pipe axis follow from the property that the Cartesian velocity components and pressure are single-valued and continuously differentiable there.

The mean axial pressure gradient is chosen in such a way that the volume flow, and hence the Reynolds number based on the bulk velocity, remains constant. The simulations are started from an arbitrary initial solution. After a large number of time steps a state of statistically stationary turbulent flow is reached. In [9] it is shown that for turbulent flow in a non-rotating pipe the DNS results for mean flow, velocity fluctuations and terms in the kinetic energy balance agree well with results of other DNS codes [10-12] and experimental results [13].

Particle-laden flows can be described in two different ways. In Lagrangian methods an equation of motion for each particle is solved, whereas in Eulerian methods the particles are described as a second phase for which conservation equations are solved. Lagrangian methods [14] are useful if the number of particles is not too large. Forces exerted by the fluid on the particles can easily be

incorporated and for low particle mass loadings the effect of the particles on the fluid and the effect of interactions between particles are negligible. Eulerian methods [15] are necessary if the number of particles is large.

We have chosen for a Lagrangian approach for two reasons. First, the number of particles is limited and the particle mass loading small, so that a Lagrangian method with one-way coupling is possible. Second, the length of an actual channel of an RPS is much larger than the length of the pipe used in the DNS. In Eulerian approaches a particle concentration field for the whole channel length and for each particle diameter would be needed, which leads to huge memory and computational resources. Hence, particles are tracked by solving an equation of motion for each particle. If **x** is particle position and $\mathbf{v}=d\mathbf{x}/dt$ its velocity, the equation of motion reads in general [16]:

$$m\frac{d\mathbf{v}}{dt} = \sum \mathbf{f}. \tag{4}$$

Here, m denotes the mass of the particle and the right-hand side contains all forces acting on the particle. In the simulations considered here, we restrict to cases where particles are small and have a large mass density compared to the fluid mass density. As a result the only forces which cannot be neglected are the drag force and centrifugal force. This leads to an equation of motion of the form:

$$\frac{d\mathbf{v}}{dt} = \frac{(\mathbf{u}(\mathbf{x}(t),t)-\mathbf{v})}{\tau_{\mathrm{p}}}\left(1+0.15\,\mathrm{Re}_{\mathrm{p}}\right)^{0.687} + \Omega^2(R+\mathbf{r}), \tag{5}$$

where τ_{p} is the particle relaxation time and **r** the position vector of the particle in the two-dimensional plane perpendicular to the pipe axis. The standard drag correlation for particle Reynolds number, Re_{p}, between 0 and 1000 is used [16]. Note that in contrast to the fluid velocity, the particle equation of motion depends on the distance between the pipe axis and axis of rotation through the centrifugal force. Since the particle relaxation times of the particles considered are very small, the inertia term in Eq. (5) could be neglected. However, since the equation is nonlinear in the particle velocity, it is easier to solve it in this way. A partially implicit two-step Runge-Kutta method is used to this end. Finally, the fluid velocity at the particle position, which appears in Eq. (5) is found from fourth-order accurate interpolation from its values at grid points.

The particle simulations start from a fully-developed turbulent velocity field with a homogeneous distribution of particles over the entire pipe. The initial particle velocity is chosen in such a way that its initial acceleration equals zero. In a real RPS the length of a channel is much larger than the length of the computational domain. Therefore, if a particle reaches the end of the computational domain in the axial direction, it is re-inserted at the corresponding position at the pipe entrance until it has traveled an axial distance equal to the length of the real pipe. If a particle reaches the wall of the pipe before it travels the whole length it is considered as being collected.

In an actual experiment where the particles are homogeneously distributed over the total flow domain, the number of particles that enter a channel of the RPS at a certain radial position, is proportional to the axial velocity at that position. Therefore, in the calculation of the collection efficience, each particle has a weight proportional to its initial axial velocity.

The computer program has been implemented on a linux cluster of PC's, where it is parallelized with the use of MPI. A full simulation of fluid and 400,000 particles takes two weeks on 8 processors.

4. RESULTS

In this section results will be presented. We will consider only one test case. Results of other simulations will be presented elsewhere. The fluid flow is determined by two non-dimensional parameters, the bulk Reynolds number $Re=U_{\mathrm{b}}D/\nu$, and the rotation Reynolds number $Re_{\Omega}=\Omega D^2/(4\nu)$, where U_{b} is the bulk velocity and D the diameter of the pipe. In the test case considered Re=5300 and Re_{Ω}=980. The ratio of the rotation Reynolds number and the bulk Reynolds number is related to the rotation number used by Orlandi and Fatica [18]. The rotation number in our simulations equals 0.37. The DNS is performed with 106 collocation points in the wall-normal direction and 128 Fourier modes in both the axial and tangential direction.

In the following, results of the fluid calculations will be presented and analysed first, and then the results of the particle simulations will be discussed.

4.1. Fluid Properties

In flow in a non-rotating pipe, time-averaged quantities depend on the radial coordinate only and the mean radial and tangential velocity components are equal to zero. This follows from the axial symmetry of the problem and the continuity equation. For rotating pipe flow, this symmetry is partly broken. Time-averaged quantities still depend on the radial coordinate only and from the continuity equation it still follows that the mean radial velocity component equals zero, but the mean tangential velocity is no longer equal to zero.

A second difference between flow in a non-rotating and in a rotating pipe is the region where the laminar Poiseuille flow becomes unstable. It is well known that linear stability theory predicts that

Poiseuille flow in a non-rotating pipe is stable at all Reynolds numbers. Transition to turbulence occurs through the nonlinear interaction of perturbations of finite amplitude. However, it has been shown that already a small rotation rate leads to linear instability [19-21]. The flow case we consider in this paper is at a bulk Reynolds number for which the flow without rotating wall is also turbulent. In Figure 5 the mean tangential velocity component in wall units is plotted as a function of the radial coordinate. In this figure also the result for the same bulk Reynolds number and Re_Ω=490 is included. It can be seen that the mean tangential velocity is almost exactly linearly dependent on Re_Ω when scaled with the friction velocity,

$$u_\tau = \sqrt{\nu \left. \frac{du_{ax}}{dr} \right|_{r=D/2}} \qquad (6)$$

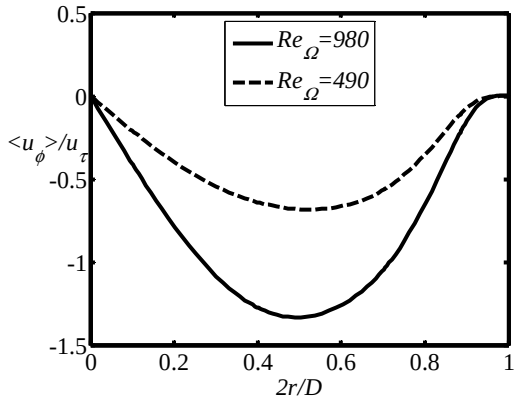

Figure 5. Mean tangential velocity component in wall units

The non-zero mean tangential velocity can be understood from the equation for the radial-tangential component of the Reynolds stress tensor, which reads after disregard of the very small viscous terms:

$$\begin{aligned} &\bar{u}_\varphi\left(2\overline{u'^2_\varphi} - \overline{u'^2_r}\right) - r\overline{u'^2_r}\frac{d\bar{u}_\varphi}{dr} = \\ &-2\Omega r\left(\overline{u'^2_\varphi} - \overline{u'^2_r}\right) + \frac{1}{r}\frac{d}{dr}\left(r^2\overline{u'^2_r u'_\varphi}\right) - \\ &\overline{u'^3_\varphi} + \frac{1}{\rho}\left(r\overline{u'_\varphi\frac{\partial p'}{\partial r}} + \overline{u'_r\frac{\partial p'}{\partial \varphi}}\right). \end{aligned} \qquad (7)$$

In this expression primes denote the fluctuating part of a quantity, subscripts r and φ refer to the radial and tangential component and bars denote mean quantities. The third order moments appearing in Eq. (7) turn out to be very small throughout the pipe, whereas the last term on the right-hand side, which involves moments of pressure gradient and velocity component, is only significant close to the wall of the pipe. Furthermore, due to the behaviour of the tangential velocity component near the pipe axis $r\frac{d\bar{u}_\varphi}{dr} \cong \bar{u}_\varphi$ there. Therefore, Eq. (7) simplifies to $\bar{u}_\varphi \cong -\Omega r$ close to the axis of the pipe. The results presented in Fig. 5 indeed agree with this behaviour close to the axis of the pipe.

A further fluid property which is important for the understanding of particle behaviour is the fluctuating part of the fluid velocity in the plane perpendicular to the pipe axis. In Figure 6 the root-mean-square of the tangential velocity component is plotted as a function of the radial coordinate in wall units. Included are results at Re_Ω=490 and in a non-rotating pipe. It can be seen that the rotation slightly increases the velocity fluctuations and this holds for all three velocity components. Moreover, it appears that the magnitude of the velocity fluctuations is almost equal to the maximum of the mean tangential velocity component in case Re_Ω=980.

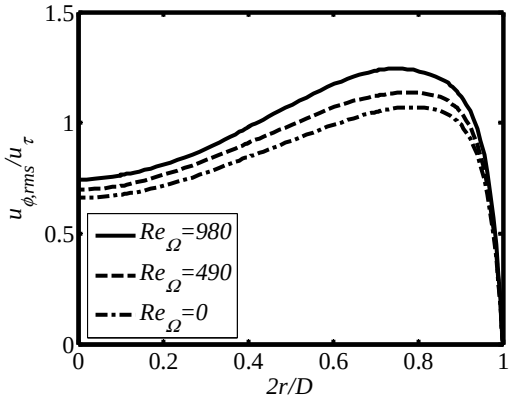

Figure 6. Root-mean-square of tangential velocity component in wall units

4.2. Particle Behaviour

Particle behaviour in turbulent rotating pipe flow can be understood from a simplified equation of motion in the plane perpendicular to the pipe axis. To this end all forces on the particle are disregarded except the linearized drag force and the centrifugal force. If r and φ are the radial and tangential coordinate of a particle, the equations of motion are:

$$\begin{aligned} \frac{dr}{dt} &= u'_r + \tau_p\Omega^2(r + R\cos\varphi) \\ r\frac{d\varphi}{dt} &= \bar{u}_\varphi + u'_\varphi - \tau_p\Omega^2 R\sin\varphi \end{aligned} \qquad (8)$$

The equations of motion contain three different terms: the mean tangential fluid velocity, which has Ωr as order of magnitude, the fluctuating velocity with the friction velocity u_τ as order of magnitude and the last terms on the right-hand side of Eq. (8), which represent the centrifugal velocity. For particles which are just separated in uniform laminar flow, the order of magnitude of the centrifugal velocity equals $U_{ax}D/L$ with L the length of the pipe. For situations relevant in practice, the centrifugal velocity is always smaller than the fluctuating velocity. In our example calculation the mean tangential velocity is only slightly smaller than the fluctuating velocity.

Before turning to the simulation results, we first consider a calculation of a hypothetical velocity field in which the mean tangential velocity is present, but the velocity fluctuations equal zero. Note that this is not a laminar solution of the Navier-Stokes equation; it only serves to understand the nature of the different contributions to Eq. (8). In Figure 7 the collection efficiency for this hypothetical flow is compared with the collection efficiency for laminar Hagen-Poiseuille flow. The particle diameter is non-dimensionalized with the smallest diameter which is collected with 100% probability for uniform laminar flow. Fig. 7 shows that the collection efficiency is reduced dramatically by the presence of the axial vortex. Particles are trapped in this vortex and follow a path which differs only slightly from the path they would follow without centrifugal force. Only those particles which are initially close to the wall are collected. This situation is similar to the one obtained for laminar flow in a slightly tilted rotating pipe, which was studied by Brouwers [8]. Also in that case particles are trapped in the secondary flow perpendicular to the pipe axis, which results in a reduced collection efficiency.

Next, we turn to particle behaviour in turbulent rotating pipe flow. In the simulation particles with diameters ranging between $0.1d_{p,100\%}$ and $1.6d_{p,100\%}$ are inserted in the flow, where $d_{p,100\%}$ is the smallest particle collected with 100% probability in a uniform laminar flow. For each diameter 25,000 particles are initially uniformly distributed over the pipe and their motion is subsequently tracked by solving their equation of motion until they either reach the wall of the pipe or travel over an axial distance larger than the length of the pipe, which equals 133.5D. The mass density of the particles equals 22.5 times the mass density of the fluid and only one pipe is considered with its axis at a distance of 26.7D from the rotation axis.

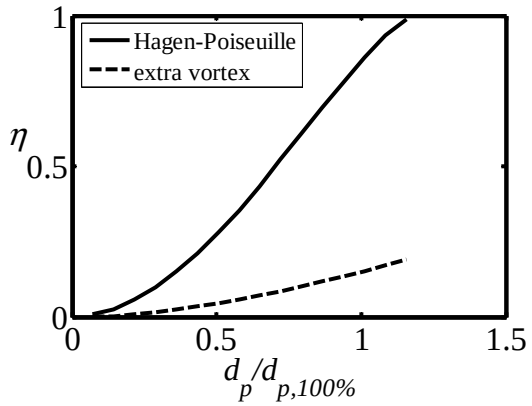

Figure 7. Collection efficiency for laminar flow with and without extra tangential velocity

In Figure 8 the collection efficiency calculated in this simulation is compared with the result for a laminar Hagen-Poiseuille fluid velocity profile. Although the collection efficiency for a turbulent RPS is lower than for a laminar RPS, the reduction obtained is not as dramatic as for the hypothetical flow without turbulent velocity fluctuations shown in Fig. 7. Fig. 8 shows that the collection efficiency of the smallest particles is hardly affected by turbulence, whereas the reduction in efficiency for particles near $d_{p,100\%}$ is almost 30%.

This result can be explained in the following way. Particles with diameter equal to $d_{p,100\%}$ will reach the collecting wall exactly at the end of the channel if they are located just opposite of the collecting wall at the beginning of the channel. In turbulent flow conditions the path of a particle becomes more irregular due to turbulent velocity fluctuations. The turbulent dispersion of particles at the end of the pipe depends on the magnitude of the velocity fluctuations and the time of travel and is for particles with diameter equal to $d_{p,100\%}$ on the order of the diameter of the pipe. Hence, due to turbulent velocity fluctuations some of these particles will reach the collection wall at a more upstream axial position and will still be collected in turbulent flow, whereas other particles would reach the collection wall at a more downstream position and will not be collected in turbulent flow. Hence, the collection efficiency of particles with diameter close to $d_{p,100\%}$ will decrease in turbulent flow.

On the other hand, some of the particles with a diameter much smaller than $d_{p,100\%}$ that are collected in laminar flow conditions, will not be collected in turbulent flow, whereas some of these small particles that are not collected in laminar flow, will be collected due to turbulent velocity fluctuations in turbulent flow. The effects of both phenomena on the total collection efficiency approximately cancel, so that the collection efficiency for small particles is approximately the same in laminar and turbulent flow.

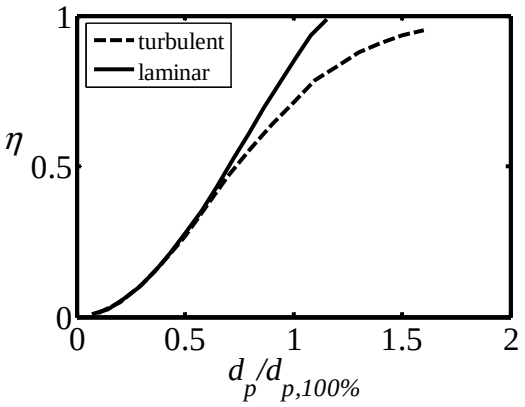

Figure 8. Collection efficiency for laminar and turbulent flow

Another conclusion that can be drawn from the simulation results is that $d_{p,100\%}$ cannot be defined for turbulent flow conditions. Even for large particle diameters, some particles will be trapped in flow structures and will not reach the collecting wall before the end of the pipe.

The results shown in Figs. 7 and 8 imply that the presence of turbulent velocity fluctuations counteracts the trapping of particles in the axial vortex. This is due to the fact that the tangential velocity fluctuations are as large as or larger than the mean tangential velocity. Two extra simulations have been performed to verify this. In the first the Coriolis force in the Navier-Stokes equation has been switched off, but the centrifugal force in the particle equation of motion has been kept. Hence, in this simulation the mean tangential fluid velocity in Eq. (8) equals zero, but the velocity fluctuations are almost the same. The resulting collection efficiency is only slightly higher than the turbulent result in Fig. 8. On the other hand, a simulation with an artificially increased mean tangential velocity by a factor of 3 resulted in a substantial reduction in collection efficiency. The collection efficiency obtained from these two simulations are compared with the results of the ordinary simulation in Figure 9.

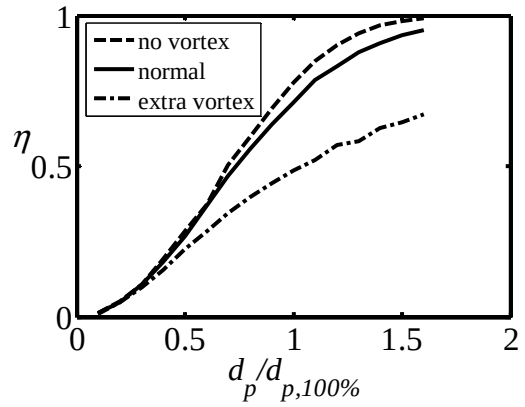

Figure 9. Collection efficiency for turbulent flow, turbulent flow without vortex and turbulent flow with increased vortex strength

5. CONCLUSIONS AND FUTURE WORK

In this paper we studied the effect of turbulent flow in the circular channels of a Rotational Phase Separator on the collection efficiency. To that end direct numerical simulation of the flow and Lagrangian particle tracking were performed. The results of the fluid flow show that an axial vortex is present in the flow, caused by the rotation, but, in contrast to the secondary flow in laminar flow in a slightly tilted pipe, this vortex hardly influences the collection efficiency for the parameter setting of the simulated test case. However, turbulent velocity fluctuations have a negative influence on the collection efficiency, especially for larger particles. One of the consequences is that $d_{p,100\%}$, the diameter of the smallest particles which is collected with 100% probability, can no longer be defined for turbulent flow conditions. In order to meet design criteria in practice, the length of the RPS should be chosen about 20% larger than laminar design criteria prescribe to obtain the same collection efficiency.

In the near future also other test cases will be performed. For other conditions, where particles and particle relaxation times are larger, inertial terms in the particle equation of motion will play a larger role. This implies that the results are also affected by turbophoresis [22, 23], which drives particles towards the walls of a channel. Moreover, the effect of turbulent flow in slightly tilted channels will be studied.

ACKNOWLEDGEMENTS

This work was sponsored by the National Computing Facilities Foundation, NCF for the use of supercomputer facilities, with financial support from the Netherlands Organization for Scientific Research, NWO.

REFERENCES

[1] Brouwers, J. J. H., 2002, ”Phase separation in centrifugal fields with emphasis on the Rotational Particle Separator”, *Exp. Thermal and Fluid Science*, Vol. 26, pp. 325-334.

[2] Van Kemenade, H. P., Mondt, E., Hendriks, A. J. A. M., and Verbeek, P. H. J., 2003, ”Liquid phase separation with the Rotational Particle Separator”, *Chem. Eng. Technol.*, Vol. 26, pp. 1176-1183.

[3] Kuerten, J. G. M., Van Kemenade, H. P., and Brouwers, J. J. H., 2005, ”Numerical study of

the Rotational Particle Separator sealing", *Powder Technol.*, Vol. 154, pp. 73-82.

[4] Brouwers, J. J. H., 1996, "Rotational Particle Separator: a new technology for separating fine particles and mists from gases", *Chem. Eng. Technol.*, Vol. 19, pp. 1-10.

[5] Brouwers, J. J. H., 1997, "Particle collection efficiency of the Rotational Particle Separator", *Powder Technol.*, Vol. 92, pp. 89-99.

[6] Hinds, W. C., 1982, *Aerosol Technology*, John Wiley.

[7] Schlichting, H., 1979, *Boundary Layer Theory*, McGraw-Hill.

[8] Brouwers, J. J. H., 1995, "Secondary flows and particle centrifugation in slightly tilted rotating pipes", *Appl. Scientific Research.*, Vol. 55, pp. 95-105.

[9] Walpot, R. J. E., Kuerten, J. G. M., and Van der Geld, C. W. M., 2006, " Experimental determination of Lagrangian velocity statistics in turbulent pipe flow", *Flow, Turbulence and Combustion*, Vol. 76, to be published.

[10] Veenman, M. P. B., 2004, *Statistical analysis of turbulent pipe flow: a numerical approach*, Ph.D. Thesis, Technische Universiteit Eindhoven.

[11] Loulou, P., 1996, *Direct numerical simulation of incompressible pipe flow using a B-spline spectral method*, Ph.D. Thesis, Stanford University, Department of Aeronautics and Astronautics.

[12] Wagner, C., Hüttl, T. J., and Friedrich, R., 2001, "Low-Reynolds number effects derived from direct numerical simulations of turbulent pipe flow", *Comp. & Fluids*, Vol. 30, pp. 581-590.

[13] Westerweel, J., Draad, A. A., van der Hoeven, J. G. Th., and van Oord, J., 1996, "Measurement of fully-developed turbulent pipe flow with digital particle image velocimetry", *Exp. Fluids*, Vol. 20, pp. 165-177.

[14] Yeung, P. K., and Pope, S. B., 1988, "An algorithm for tracking fluid particles in numerical simulation of homogeneous turbulence", *J. Comp. Phys.*, Vol. 79, pp. 373-416.

[15] Markatos, N. C., 1986, "Modelling of two-phase ftransient flow and combuston of granular propellants", *Int. J. Multiphase Flow*, Vol. 12, pp. 913-933.

[16] Maxey, M. R., and Riley, J. J., 1983, "Equation of motion for a small rigid sphere in a nonuniform flow", *Phys. Fluids*, Vol. 26, pp. 883-889.

[17] Clift, R., Grace, J. R., and Weber, M. E., 1978, *"Bubbles, drops and particles"*, Academic Press.

[18] Orlandi, P, and Fatica, M., 1997, "Direct simulations of turbulent flow in a pipe rotating about its axis", *J. Fluid Mech.*, Vol. 343, pp. 43-72.

[19] Mackrodt, P.-A., 1976, "Stability of Hagen-Poiseuille flow with superimposed rigid rotation", *J. Fluid Mech.*, Vol. 73, pp. 153-164.

[20] Fernandez-Feria, R., and del Pino, C., 2002, "The onset of absolute instability of rotating Hagen-Poiseuille flow: a spatial stability analysis", *Phys. Fluids*, Vol. 14, pp. 3087-3097.

[21] Sanmiguel-Rojas, E., and Fernandez-Feria, R., 2005, "Nonlinear waves in the pressure driven flow in a finite rotating pipe", *Phys. Fluids*, Vol. 17, 014104.

[22] Kuerten, J. G. M., and Vreman, A. W., 2005, "Can turbophoresis be predicted by large-eddy simulation", *Phys. Fluids*, Vol. 17, 011701.

[23] Reeks, M.W., 1983, "The transport of discrete particles in inhomogeneous turbulence," *J. Aerosol Sci.*, Vol. 14, pp. 729-739.

Conference on Modelling Fluid Flow (CMFF'06)
The 13th International Conference on Fluid Flow Technologies
Budapest, Hungary, September 6-9, 2006

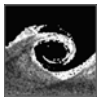

LDV SIGNALS PROVIDE MORE INFORMATION THAN USED BEFORE

Bernd WUNDERLICH [1], Thomas HAGEMEIER[2],
Dominique THÉVENIN[3], Róbert BORDÁS[4]

[1] Corresponding Author. Department of Fluid Dynamics and Thermodynamics, Otto-von-Guericke-University Magdeburg
Universitätsplatz 2, D-39106 Magdeburg, Germany. Tel.: +49 391 67 12443, Fax: +49 391 67 12840,
E-mail: Bernd.Wunderlich@vst.uni-magdeburg.de
[2] Department of Fluid Dynamics and Thermodynamics, Otto-von-Guericke-University Magdeburg.
E-mail: Thomas.Hagemeier@student.uni-magdeburg.de
[3] Department of Fluid Dynamics and Thermodynamics, Otto-von-Guericke-University Magdeburg.
E-mail: Dominique.Thevenin@vst.uni-magdeburg.de
[4] Department of Fluid Dynamics and Thermodynamics, Otto-von-Guericke-University Magdeburg.
E-mail: Robert.Bordas@student.uni-magdeburg.de

ABSTRACT

Laser Doppler Velocimetry (LDV) is a widely used measuring technique to examine the local velocity of the continuous and of the disperse phase in two phase flows of air and water. Now it is possible to obtain also the diameter information of the disperse phase. A commercial LDV system has been used with backscattering, and a Bragg cell for a 40 *MHz* shift. The received burst signals can be split into the high frequency Doppler and the pedestal part. The Doppler signals are used to determine the velocity of the passing particles. The pedestal signals are used to identify particles and parts of them that is neccessary to calculate their diameter. After downmixing the signals with the 40 *MHz* frequency of the Bragg cell, the signals are leaded by an USB-supported A/D-converter PicoScope to the PC. This can be triggered by a certain amplitude value of the rawsignal to ensure that only droplet or bubble signals are recognized. With the same trigger the CCD-camera of the shadowgraphy system has been released. This system has been used for both the diameter confirmation and with the help of a semipermeable mirror to reinforce the theoretical signal structure.

Keywords: Air bubbles, Diameter measurement, LDV, Water drops

NOMENCLATURE

d	[m]	diameter
f	[Hz]	frequency
v	[m/s]	velocity
δ	[m]	fringe distance
λ	[m]	wavelength
θ	[m]	included angle of the laser beams.

Subscripts and Superscripts

cann	cannula
drop	water drop
drop_d	water drop with detergent

1. INTRODUCTION

Laser Doppler Velocimetry (LDV) is usually applied to obtain information about local velocities. Tracer particles are used to seed the flow. It is known that the phase border between bubbles and fluid-phase or droplets and surrounding air generate Laser-bursts with a higher pedestal than by tracer particles.

Signals of bubbles contain still more information that can be obtained with few expenditure. The presented basic research is executed with rising bubbles in steady water and with falling droplets in steady air [1,3]. The front and backward phase transition generate a Laser-burst with well-separable parts. This way the beginning and end parts of bubble signals can be recognized and their diameters can be determined.

An analog/digital (A/D) box transfers the signals via universal serial bus (USB) to a computer. After filtering, the signals are evaluated by Fast Fourier Transformation (FFT) to get the velocity information. Similar to a former used hardware solution where the pedestal amplitude was used to trigger a circuit to separate signals from bubbles and tracers, software is used now to exploit the pedestal for separation purposes.

Shadowgraphy has been applied to verify the results. The microscope camera can be triggered with the mentioned signal amplitude to realize pictures of the bubble or droplet during their travel through the measurement volume of the LDV.

Series of experiments have been carried out to examine the minimum measurable diameter of bubbles and droplets and the influence to the signal behavior if the bubbles and droplets do not pass the center of the measuring volume. Comparisons between LDV diameter measurements and results of shadowgraphy show a good agreement, also the agreement with theoretical velocity as function of diameter is very good.

2. THEORETICAL OVERVIEW

It is a remarkably important process in fluid mechanics to determine velocity. There are many kinds of procedures to measure flow velocity, which are based on the connection between fluid flow and other physical quantities. Optical measuring techniques are able to bring information about flow velocities without disturbing the flow, thus the results can be closer to the real conditions.

2.1. Laser Doppler Velocimetry

Laser Doppler Velocimetry is a widely accepted optical device, which gives information about flow velocity in gases and liquids. It is a well-established procedure that has been used for several years. The most important characteristic of this device is that it is non-intrusive, so it is very suitable to measure in such flows, where conventional sensors cannot be applied: chemical reacting or high-temperature media, rotating machines, reversing flows, or any case where it is important not to disturb the flow. But tracer particles are indispensable, to have information about the flow-velocity.

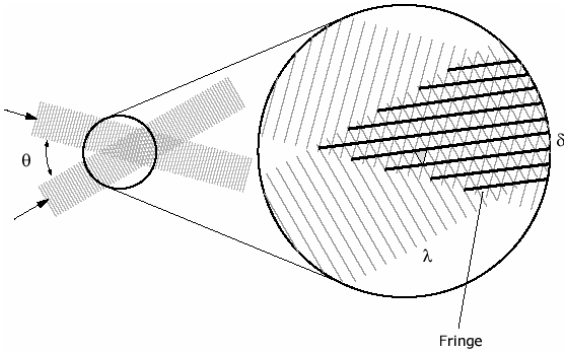

Figure 1. Fringe pattern

In the followings LDV is briefly introduced. The source, where a beam is generated is a single laser. To create a fringe pattern (shown in Figure 1), where measurements can be carried out, the laser beam is needed to be split with a beam splitter. The two parallel and equal intensity beams are forced to change direction with the help of the sending lens, causing them to cross at the measuring or probe volume.

The fringes are parallel to the bisector of the two beams and the distance between two fringes is

$$\delta = \frac{\lambda}{2\sin\left(\frac{\theta}{2}\right)} \qquad (1)$$

During the measurement we use seeding, i. e. we place microscopic light scattering particles into the flow, which have to be small enough to follow accurately the movement of the flow. As they pass through these fringes, the amount of light received by the particles fluctuates with the fringes. Therefore the light scattered by the particles also fluctuates. The frequency of this fluctuation is proportional to the velocity of the flow, normal to the fringes.

To detect the frequency generated by the passing particles, the scattering light is collected by the receiving lens and focused onto the photomultiplier, which converts the light intensity into voltage signal.

With the fringe spacing the relationship can be determined between the velocity of the particle and the generated frequency.

$$f = \frac{v}{\delta} = \frac{2v\sin\left(\frac{\theta}{2}\right)}{\lambda} \qquad (2)$$

The electronic signal coming from the photodiode can be seen in Figure 2, where the overall shape can be explained by the Gaussian intensity distribution of the laser beams. As the particle passes through the edges, where the fringes are weakly illuminated, the fluctuation is also weak, and as it passes through the measurement volume center, the signal fluctuation becomes larger and then decays again. This burst signal can be split into two parts: the low frequency pedestal (Figure 3) and the high frequency Doppler signal (Figure 4). Using Fast Fourier Transformation we can get the velocity of the particles passing through the probe volume.

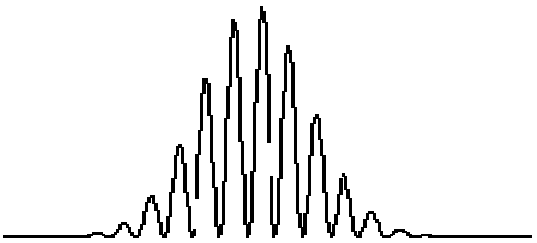

Figure 2. Burst signal

Figure 3. Pedestal signal

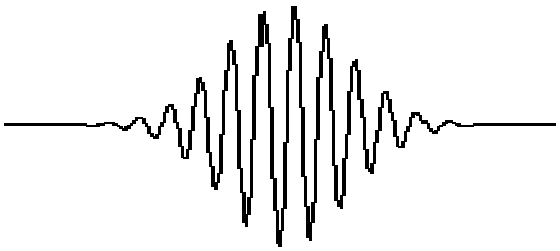

Figure 4. Doppler signal

3. MEASUREMENTS

LDV measurements with rising bubbles have shown that the burst signals contain not only the velocity but also the diameter information of the particles. [1,3]

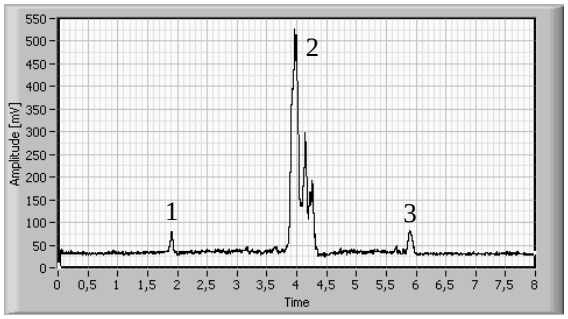

Figure 5. Pedestal signal of a single droplet with its three parts

To confirm the general validity of this perception, examinations should have been carried out on single water drops falling in steady air.

The structure of typical pedestal signals of water drops (Figure 5) is composed of three different parts. The first and third parts are generated by the phase-transition according to the inlet and outlet surface of the droplet. The central part of the signals is created by the reflected laser beams. This phenomenon can be the explanation for the higher pedestal in this region, because these signals are caused by reflection, not by scattering and the pedestal amplitude is proportional to the light intensity received by the photomultiplier. [2,4]

3.1. Measuring setup

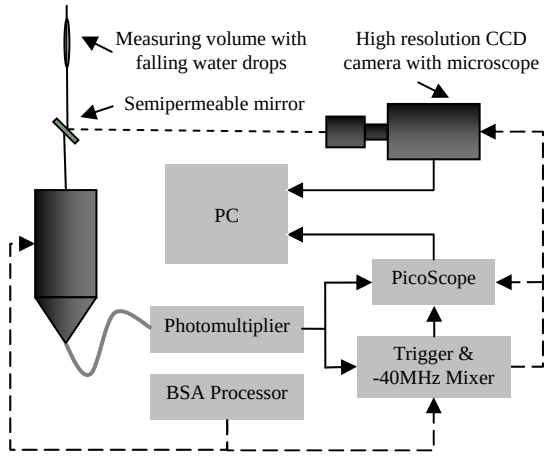

Figure 6. Measuring setup

To verify the above supposition, the existing measuring setup has been expanded with the help of a semipermeable mirror (Figure 6). For this time the shadowgraphy system has not only been applied for diameter measurements but also for examination of the reflections on the surface of the water droplets.

As a particle passes through the measuring volume, a burst signal is generated by the LDV. This signal can be easily filtered and the amplitude is also high enough to be used for triggering. To be able to synchronise the measuring system this pedestal signal is transformed to a TTL signal, as it is required for the shadowgraphy system. This trigger signal can also be used to trigger the A/D converter. A PicoScope general purpose oscillator has been used as an A/D converter. It can be connected to a normal PC or notebook through USB. Two BNC inputs are available. One input is used for the LDV signals that have been previously downmixed by the 40 *MHz* of the Bragg cell. This channel is used to examine the high frequency part of the signals to estimate the velocity. The other input is used to acquire the raw LDV signals to get the pedestal signals using a low pass filter. The

trigger signal assures that both the picture and signal of a passing particle is acquired in the same time.

3.2. Confirmation by shadowgraphy

Appling the previously mentioned mirror and the shadowgraphy system by LaVision [5], the view of the photo sensor can be analysed in the images taken by the CCD camera (Figure 7). The system is triggered at the moment when the reflection occurs on the surface of the droplets. Therefore in the shadowgraphy image this reflection should be seen. With these images it is confirmed that the parts of the signals with higher pedestal are caused by the reflection on the surface of the water drops.

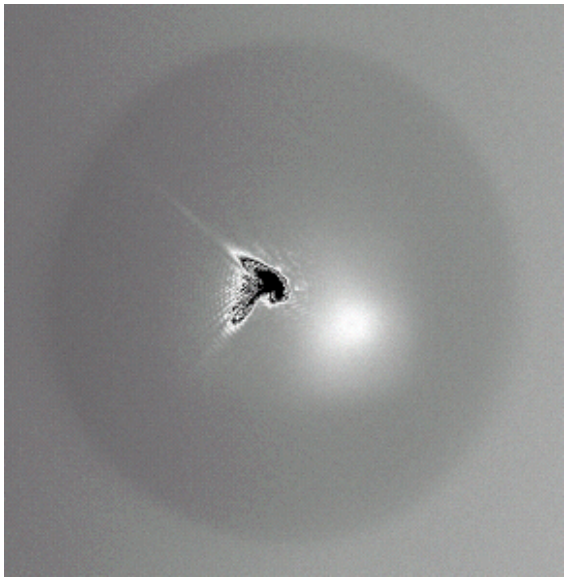

Figure 7. Shadowgraphy image of a droplet with reflection on its surface

3.3. Verification measurements

To make the most of possibilities and to recognize relations between properties of the passing particles and the generated signal, experimental measurements have been made approaching the ideal case. These measurements have been conducted with the help of a rotating disk, on which wires with different diameters can be fixed (Figure 8).

The configuration is positioned so, that the wire crosses the measuring volume at each and every revolution of the disk. The disk is moved very finely along the length of the measuring volume and in quite a few measuring points signals are collected. With the help of this setup, we can simulate signals of particles with a well defined diameter and position in the measuring volume.

This measurement is also suitable to check how precise the determination of the velocity is.

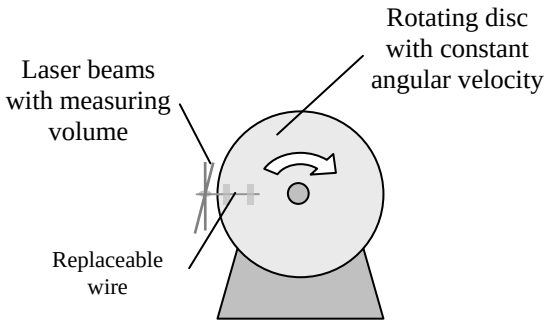

Figure 8. Rotating disk with a fixed wire

For the first time three wires with different diameters are applied: 0.1, 0.3 and 0.5 *mm*. The measuring volume is scanned in several positions from one end to the other.

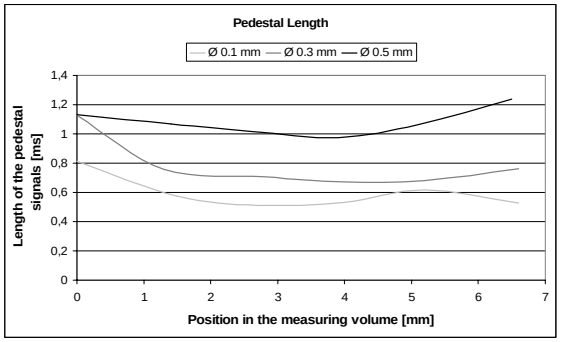

Figure 9. Signal length calculated from the pedestal signals

Figure 9 shows that in the measuring volume the measured signal length are comparatively uniform and the signal lengths also increases with the wire diameters

There is an interesting occurrence that can be discovered if we are outside the measuring volume. Namely that two separate pedestal signals belong to one passing particle which can be explained by the two discrete laser beams. From this experience it can be understood that if the particles are outside of the measuring volume, the reflection from the surface generates two separate pedestal peaks according to the laser beams.

3.4. Size Control

To control the size of the drops and bubbles hypodermic needles have been used with different diameters. In case of bubbles the diameter could be controlled by both the diameter of the cannulas and the regulation of the pressure valve in the air pipe.

The diameter of water drops can be influenced by different cannula diameters as well as by additives reducing the surface tension. Reducing the water surface tension not only the drop size can be reduced, but also the larger water drops can be forced to remain spherical. The list of average droplet diameters can be found in Table 1 according to the different needles.

Table 1. Average diameter of the droplets

d_{cann} [mm]	d_{drop} [mm]	d_{drop_d} [mm]
0.4	2.16	1.74
0.5	2.4	1.92
0.8	2.86	2.34
0.9	2.99	2.45
1.2	3.3	2.73

3.5. Signal formation

Monodisperse water drops have been created with the help of a medical drip infusion. These drops can be simultaneously measured by LDV as well as by shadowgraphy. To make measurements possible with LDV and even shadowgraphy from the same direction a semipermeable mirror has been used in the measuring equipment. The obtained shadowgraphy images have been used to validate the LDV results. This way information is obtainable about special signal characteristic.

The pedestal signal of a single droplet has always the structure that is represented in Figure 5. The three well-separable peaks emerge in different moments as the droplet passes trough the measuring volume. The first peak is generated by the bottom surface of the drop. When the boundary between air and water phases crosses the measuring volume the laser beam is scattered like in case of normal tracer particles. Thereafter the water drop surrounds the measuring volume completely so no recognisable peak follows up to the middle of the signals.

In the middle of the pedestal signals are the higher peaks, which are generated by the reflection of the laser beams from the front side of the drops. Normally two peaks should be visible close to each other according to both laser beams (see Figure 10).

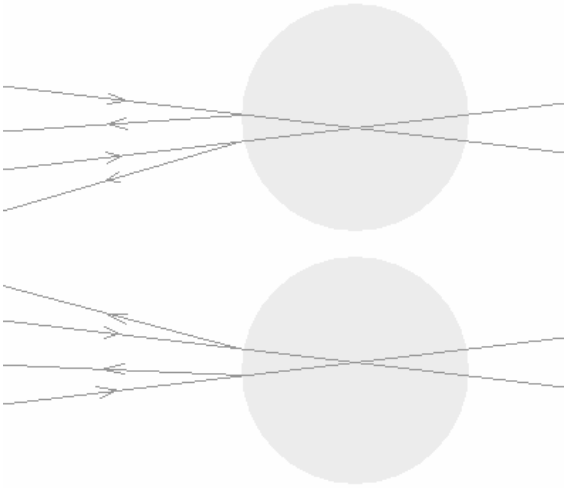

Figure 10. Laser beam reflections on the surface of an air bubble or a water drop

Since the light intensity of the reflection is higher than scattering, the signals are mostly overdriven. That is why only one, but something wider peak can be detected. The third peak identifies the passage of the upper phase boundary of the droplet through the measuring volume. Now the measuring volume is no more enclosed by the water drop. The time from the first to the last peak corresponds to the time that the droplet needs to cross the measuring volume. This time can be measured in the pedestal signal. With the knowledge about the signal structure it is possible to determine the diameter of the water drops.

3.6. Measurement results

The diameter of the drops can be calculated with the measured time and the velocity information. The verification measurements by shadowgraphy have been evaluated by the software DaVis 7.1 [6] and resulted the associated diameter d_{drop}=2.16 *mm* for the cannula with d_{cann}=0.4 *mm*. During the evaluation of the LDV signals the diameter of the droplets are determined by a signal processing software written in LabView. These results together with the validation results and a tolerance range are shown in Figure 11.

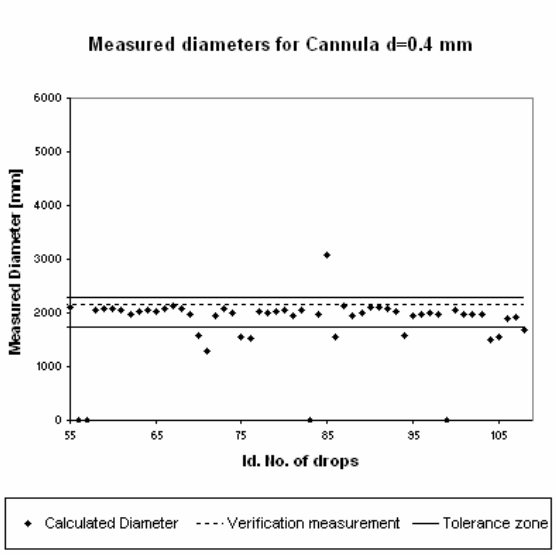

Figure 11. Diagram of the measured diameters of water drops

Usually the first part of the signals cannot be sensed, only the first or the second half of the signals can be seen (Figure 12). In such cases the distance between the area of reflection and the phase transition can be measured, from which the diameter of the droplet or bubble can be calculated.

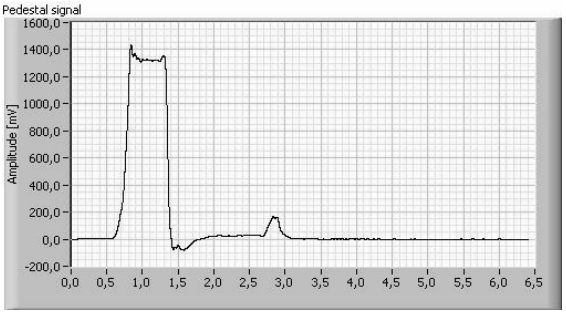

Figure 12. Pedestal signal of an air bubble in water

CONCLUSIONS

During the further measurements it has been cleared up that the signal structures of air bubbles in continuous water phase and water drops surrounded with air are very similar. The mostly overdriven part of the pedestal is generated by the laser beam reflections from the surface of the particles. If the pedestal signal contains in addition at least one further peak that is generated by the phase transitions between air and water, the diameter of the crossing particles can be calculated besides their velocity.

The smallest measurable diameter with this method is influenced by the length of the measuring volume. As the reflections are developed on the surface of the bubbles or drops, this surface should be crossed by the two independent laser beams.

The experimental measurements have been carried out with single water drops for ten different diameters between 1.7 and 3.3 *mm*. This diameter range corresponds approximately to the standard size of raindrops. Further measurements should be carried out for smaller diameter and also in higher particle concentration.

REFERENCES

[1] Bordás, R., 2005, "Separate LDA velocity measurement of simultaneously existing tracer particles and air bubbles in a water flow", *Final Project Budapest University of Technology and Economics*, pp. 13-57.

[2] Dantec Dynamics: "Laser Doppler Anemometry Introduction to principles and applications", *Educational Slideshow*, pp. 5-38.

[3] Bordás, R., Wunderlich, B., Thévenin, D., 2005, "Separate LDV measurements of simultaneously existing tracer particles and air bubbles in a water flow", *Joint FZR & ANSYS Multiphase Flow Workshop,* 1-3 June, 2005. Dresden, Germany.

[4] Albrecht, H.-E., Borys, M., Damaschke, N., Tropea, C., 2003, "Laser Doppler and Phase Doppler Measurement Techniques" *Springer-Verlag,* Berlin Heidelberg.

[5] LaVisison Ltd., "Particle Characterisation with size analysis – Shadowgraphy", http://www.lavision.de/application/T /particleanalysis/index.html

[6] LaVision Ltd., "DaVis (Data Acquisition and Visualization Software) ", http://www.lavision.de/products/ /software/index.htm

Conference on Modelling Fluid Flow (CMFF'06)
The 13th International Conference on Fluid Flow Technologies
Budapest, Hungary, September 6-9, 2006

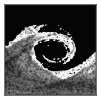

MODELLING OF TURBULENT BUBBLE-LADEN FLOW IN A PARALLEL PLATE ELECTROCHEMICAL REACTOR

Thomas NIERHAUS[1], David VANDEN ABEELE[2], Herman DECONINCK[3], Philippe PLANQUART[4]

[1] Corresponding Author. Von Karman Institute for Fluid Dynamics, Aeronautics and Aerospace Department, Waterloose Steenweg 72, B-1640 St-Genesius-Rode, Belgium. Tel.: +32 2 359 96 00, Fax: +32 2 359 96 11, E-mail: nierhaus@vki.ac.be
[2] Von Karman Institute for Fluid Dynamics, Aeronautics and Aerospace Department. E-mail: david.vanden.abeele@vki.ac.be
[3] Von Karman Institute for Fluid Dynamics, Aeronautics and Aerospace Department. E-mail: deconinck@vki.ac.be
[4] Von Karman Institute for Fluid Dynamics, Environmental & Applied Fluid Dynamics Department. E-mail: planq@vki.ac.be

ABSTRACT

We perform Direct Numerical Simulation (DNS) of turbulent bubble-laden flow to analyze mass transfer in a parallel plate electrochemical reactor. We set aside the electrochemical part of the problem and focus on the simulation of a turbulent channel flow of a liquid electrolyte with gas bubbles evolving from an electrode located at the bottom wall. We use an Eulerian-Lagrangian representation to simulate the dispersed two-phase flow. Two-way momentum coupling between the bubbles and the electrolyte is taken into account. Three-dimensional simulations are obtained using a distributed memory parallel computer architecture. Investigations on bubble dispersion and interaction of bubbles with turbulent flow structures are made.

Keywords: Bubble-laden Flow, Direct Numerical Simulation, Electrochemical Reactor, Eulerian-Lagrangian Modelling, Turbulent Flow

NOMENCLATURE

C_D	[-]	drag coefficient
C_L	[-]	lift coefficient
R	[-]	residual
Re	[-]	Reynolds number
V_b	$[m^3]$	bubble volume
V_i	$[m^3]$	cell volume
d	$[m]$	bubble diameter
$\mathbf{f}$	$[N/m^3]$	volume specific force
$\mathbf{g}$	$[m/s^2]$	gravitational acceleration
h	$[m]$	channel half-height
n	[-]	time step
p	$[N/m^2]$	pressure
t	$[s]$	time
u_{adv}	$[m/s]$	advection velocity
u_r	$[m/s]$	rise velocity
u_τ	$[m/s]$	shear velocity
$\mathbf{u}$	$[m/s]$	fluid velocity vector
$\mathbf{v}$	$[m/s]$	bubble velocity vector
$\mathbf{x}$	$[m]$	bubble position vector
α_d	[-]	dispersed phase volume fraction
γ	[-]	advection over rise velocity ratio
ν	$[m^2/s]$	kinematic viscosity
ρ_c	$[kg/m^3]$	continuous phase density
ρ_d	$[kg/m^3]$	dispersed phase density
τ_b	$[s]$	bubble response time
τ_w	$[N/m^2]$	wall shear stress
Ω	[-]	flow domain
$\boldsymbol{\omega}$	$[1/s]$	fluid vorticity

1. INTRODUCTION

Turbulent bubble-laden flows occur in a variety of industrially relevant processes, such as electro-chemical graining. In this technique, a peak and valley structure is etched into the surface of a metallic electrode by an acidic electrolyte. Due to chemical reactions between the metal and the electrolyte, small bubbles of diameters in the micrometer regime are generated at the electrode surface and detach into the flow.

We perform DNS of turbulent bubble-laden flow to analyze mass transfer in a parallel plate reactor, which is a simplified electrochemical experimental device approximating existing industrial set-ups (see sketch in figure 1). Basically, the reactor features turbulent flow of an electrolyte in a channel with a cathode at the bottom and an anode at the top. An externally applied potential difference causes ion migration in the electrolyte and electrochemical reactions at the electrodes. Due to those reactions, microbubbles can appear and detach from the cathode into the flow.

Microbubbles do not deform and therefore remain spherical. Their dynamics is independent of their surface tension. Moreover, microbubbles do not break up as fast as large bubbles and therefore interact with the carrier flow for a significant time,

influencing both its local and its macroscopic behaviour. In the present study, we therefore assume spherical and non-deforming bubbles.

From the theory of turbulent flows, it is known that the energy transfer in the flow covers the range between the system scale and the Kolmogorov scale, where the smallest scale eddies are dissipated into heat. The physics of microbubbles encounters kinematic phenomena that lie significantly below the smallest turbulence length scales. This allows us to use simple models to take into account the presence of bubbles.

In terms of modelling the physics of two-phase flows, one can distinguish between cases where the momentum transfer from the bubbles to the carrier fluid is neglected (*one-way coupling*) or taken into account (*two-way coupling*). For very dilute flows, a one-way coupling approach is suitable. In this case, only the momentum transfer from the carrier flow to the bubbles is regarded. Back-coupling effects should be taken into account when sufficiently high concentrations of bubbles are present. In turbulent flows, it is known that the presence of bubbles can significantly influence the turbulent flow structures. For very dense flows, one has to additionally take into account interactions between bubbles, such as hydrodynamic effects and collisions. The modelling of those effects is referred to as *four-way coupling*.

Recent work in the frame of dispersed two-phase flow focused on collective effects of particles, droplets and bubbles, such as dispersion and evolution of local concentrations [1]. One-way coupled bubble dispersion has been analyzed numerically in [2,3,17]. Two-way coupling effects have been mainly analyzed for particulate flow in a variety of numerical test cases such as isotropic turbulence [4,5] and particle-laden channel flow [6,7]. For bubbly flow, the effect of two-way coupling has been studied using the two fluid formulation [8,9] as well as the Eulerian-Lagrangian formulation [10,11,18].

In this contribution, we set aside the electrochemical part of the problem described above and model a parallel plate reactor as a turbulent channel flow of a liquid electrolyte with gas bubbles evolving from a wall electrode.

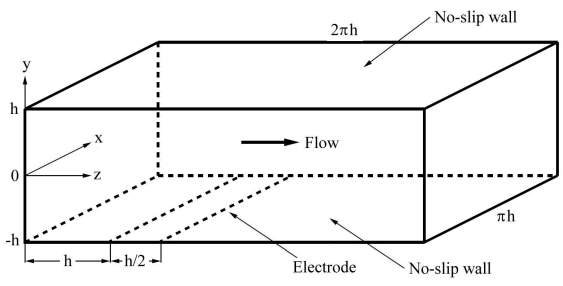

Figure 1: Channel flow test case geometry

A simple sketch of the test case geometry is shown in figure 1. The channel is bounded by no-slip walls on its top and bottom, where the half-height of the channel is denoted by h. The electrode from which the gas bubbles evolve is located at the bottom of the channel and covers the entire width in the transverse direction. The periodic length of the channel in the streamwise direction is $2\pi h$ and the periodic width in the spanwise direction is πh, which corresponds to half of the dimensions in [19].

We select an Eulerian-Lagrangian model to simulate the flow in the channel. Two-way momentum coupling between the bubbles and the electrolyte is taken into account. The flow is regarded to be dilute, i.e. the dispersed phase volume fraction is below the order of $\alpha_d = O(10^{-3})$. In this way, hydrodynamic effects and bubble collisions do not play an important role and four-way coupling can be neglected.

Interactions of bubbles with solid walls are simulated in terms of elastic rebounds. We apply a simple model for bounces of spherical bubbles at ideally smooth walls.

Fully three dimensional simulations of turbulent bubbly flow in a simplified model of a parallel plate electrochemical reactor are achieved by coupling a Lagrangian tracking solver with a Navier-Stokes solver for DNS. Both codes are designed to work on parallel computer architectures.

2. MATHEMATICAL DESCRIPTION

The modelling of the physical phenomena of bubble-laden flow is achieved by using an Eulerian-Lagrangian formulation. This approach describes the continuous phase by the incompressible Navier-Stokes equations, while the trajectories of the gas bubbles are tracked sequentially, each one represented by an equation of motion following Newton's second law. The phases are coupled in terms of a two-way coupling approach, where Newton's principle of reciprocal actions is realized by appropriate momentum source terms in the equations of both phases.

2.1. Turbulent channel flow

The primary flow inside the parallel plate reactor is modelled as a turbulent channel flow between two no-slip walls, as discussed in §1. The fluid velocity field $\mathbf{u}$ is obtained by DNS of the incompressible Navier-Stokes equations:

$$\nabla \cdot \mathbf{u} = 0\,, \tag{1}$$

$$\frac{\partial \mathbf{u}}{\partial t} + (\mathbf{u}\cdot\nabla)\mathbf{u} + \frac{1}{\rho_c}\nabla p - \nu\nabla^2\mathbf{u} = \frac{1}{\rho_c}\mathbf{f}\,. \tag{2}$$

Here, ρ_c is the density of the continuous fluid phase, ν is the kinematic viscosity of the fluid, p is the pressure and the vector $\mathbf{f}$ contains the forces acting on the flow. It can be decomposed into a large scale forcing term $\mathbf{f_f}$ and a force $\mathbf{f_d}$ due to momentum transfer from the dispersed phase (see §2.3 for a closer description). No-slip boundary conditions are applied at the channel top and bottom walls, while periodic boundary conditions are used in the streamwise and spanwise directions. We use the shear velocity u_τ and the length scale ν/u_τ as characteristic scales to describe the turbulent flow of the continuous phase. The shear velocity is defined by

$$u_\tau = \sqrt{\frac{\tau_w}{\rho_c}}, \tag{3}$$

where τ_w is the average wall shear stress. The shear Reynolds number is defined to be

$$\mathrm{Re}_\tau = \frac{h \cdot u_\tau}{\nu}. \tag{4}$$

The numerical framework used for the channel flow simulations is a spectral/finite element code, as described in [12]. The Navier-Stokes equations are discretized in x-y-planes using P1 linear finite elements, while the transverse z-direction of the flow field is represented by means of a truncated Fourier series, assuming periodicity in this direction. In this procedure, equations (1) and (2) are discretized in time in a second order accurate manner:

$$\mathrm{R_C}^{n+1} = \nabla \cdot (\mathbf{u}^{n+1}) = 0, \tag{5}$$

$$\begin{aligned} \mathbf{R_M}^{n+1} &= \frac{1}{\Delta t}(\mathbf{u}^{n+1} - \mathbf{u}^n) + \frac{3}{2}((\mathbf{u}\cdot\nabla)\mathbf{u})^n \\ &- \frac{1}{2}((\mathbf{u}\cdot\nabla)\mathbf{u})^{n-1} + \frac{1}{\rho_c}\nabla p^{n+\frac{1}{2}} \\ &- \nu\nabla^2(\mathbf{u}^{n+1} + \mathbf{u}^n) - \frac{1}{\rho_c}\mathbf{f}^n = 0. \end{aligned} \tag{6}$$

The Crank-Nicholson scheme is used to integrate the pressure and viscous terms in time while the Adams-Bashforth method is used for the convective terms. For the finite element discretization of the continuity equation, the well-known Pressure-Stabilized Petrov-Galerkin (PSPG) dissipation is used to avoid spurious pressure oscillations that are encountered when using equal order elements for pressure and velocity. To eliminate convective instabilities, a fourth order Laplacian dissipation term similar to the one used in [14] is used to stabilize the momentum equation. To eliminate the remaining z-derivatives occurring after the finite element discretization, a truncated Fourier series is used. The 3D problem in physical space is thus transformed into a system of $N/2$ loosely coupled 2D problems in Fourier space by means of an FFT. For reasons of computational efficiency, the convective terms are computed in physical space and then transformed to Fourier space. The 2D linear problems are solved sequentially on a distributed memory parallel computer. Inter-process communication is realized through MPI [13].

2.2. Lagrangian tracking of bubbles

The motion of a bubble in a turbulent carrier fluid is determined by the body and surface forces acting on it. In case of spherical microbubbles, this corresponds to the forces of a flow around a rigid sphere. We define the bubble Reynolds number as

$$Re_b = \frac{|\mathbf{u} - \mathbf{v}| \cdot d}{\nu}, \tag{7}$$

where d is the diameter of the bubble, $\mathbf{v}$ is its velocity and $\mathbf{u}$ is the fluid velocity at the bubble center. At small values of Re_b, viscous effects are dominant and the relative motion of the bubble in the fluid is in the Stokes regime, where the bubble response time is defined by $\tau_b = d^2/36\nu$. In the present work, we will restrict ourselves to bubble motion of $Re_b = O(1)$ so that turbulent wakes, which occur behind the bubbles at higher bubble Reynolds number, can be neglected [15]. We state Newton's second law as a Lagrangian equation of motion for each bubble, as it is denoted in [16]:

$$\begin{aligned} \frac{\partial \mathbf{v}}{\partial t} &= \frac{3}{4}\frac{C_D}{d}\frac{\rho_c}{\rho_d}|\mathbf{u} - \mathbf{v}|(\mathbf{u} - \mathbf{v}) \\ &+ 9\frac{\sqrt{\pi\nu}}{d}\frac{\rho_c}{\rho_d}\int_{t_0}^{t}\frac{d(\mathbf{u} - \mathbf{v})}{dt}\frac{d\tau}{\sqrt{t-\tau}} \\ &+ \frac{1}{2}\frac{\rho_c}{\rho_d}\left(\frac{D\mathbf{u}}{Dt} - \frac{d\mathbf{v}}{dt}\right) + \frac{\rho_c}{\rho_d}\frac{D\mathbf{u}}{Dt} \\ &+ C_L\frac{\rho_c}{\rho_d}(\mathbf{u} - \mathbf{v}) \times \boldsymbol{\omega} + \left(1 - \frac{\rho_c}{\rho_d}\right)\mathbf{g}. \end{aligned} \tag{8}$$

Here, ρ_d is the density of the dispersed phase and C_D and C_L are the drag and list coefficients respectively. The first three terms on the right hand side of the above equation are, in order of appearance, the Stokes drag force, the Basset history force and the virtual mass force. These forces are due to the unsteady Stokes flow of the fluid relative to the particle. The other forces in equation (8) are the force due to the fluid pressure gradient and viscous stresses, the slip-shear lift force and the forces due to gravity and buoyancy. In the lift force term, $\boldsymbol{\omega} = \nabla \times \mathbf{u}$ denotes the vorticity of

the fluid. The derivative d/dt is following the moving bubbles with respect to time, while D/Dt is the total acceleration of the fluid as seen by the bubble, evaluated at the bubble position. The vector **g** denotes the gravitational acceleration.

Following the empirical correlations for a fluid sphere, the drag coeffcient for a spherical bubble can be evaluated as $C_D=16/Re_b$ for small bubble Reynolds numbers [10]. The lift coefficient is chosen to be $C_L=0.5$ throughout our investigations. We neglect the influence of the Basset history force, which takes into account the time lag of the velocity profile around the bubble occurring in case of viscosity-driven acceleration, because we assume that velocity differences are balanced rapidly for bubbles of small Reynolds numbers.

The Lagrangian equation of motion (8) is integrated in time using the Crank-Nicholson scheme. Together with the relation $\mathbf{v}=\delta\mathbf{x}/\delta t$ between the bubble velocity and its position, a system of six ordinary differential equations in three space dimensions is formed, which has to be solved for each bubble. Sequential tracking of all bubbles in the system is performed at each time step n of the Navier-Stokes solver. All bubble velocities **v** and positions **x** are updated and the source terms for the back-coupling to the Navier-Stokes solver (as explained in §2.3) are computed. The Lagrangian solver adapts the mesh partitioning strategy of the Navier-Stokes solver, to which it is coupled via standardized data interfaces. This allows to distribute the tracking of the bubbles to the parallel partitions according to the mesh partitioning. The parallel architecture of the Lagrangian solver is realized through MPI.

Two-way coupling between the continuous and the dispersed phase is taken into account through a procedure originating from the Particle-in-Cell (PIC) method described in [5], where a contribution of the forces of all bubbles inside a control volume V_i around a grid node i is added to the fluid momentum equation (2) in this node:

$$\mathbf{f_{d,i}} = \frac{\sum_{j=1}^{N_i} V_{b,j} \cdot \mathbf{f_{b,j}}}{V_i}. \qquad (9)$$

Here, N_i is the number of bubbles in the volume unit and $V_{b,j}$ is the volume of a single bubble, which is modeled as a point source inside the continuous carrier flow field. Note that the forces **f** and $\mathbf{f_b}$ are per unit volume in order to agree with the formulation stated in equation (2).

We assume the volume fraction of the gaseous phase to be small ($\alpha_d<10^{-3}$). Thus we neglect mass coupling between the phases, i.e. there is no mass source term appearing in the fluid continuity equation (1) and the flow variables in the Navier-Stokes equations are not averaged by the volume fraction as it is done in [18], where higher values for the volume fraction were investigated.

In two-way coupling, no interactions between bubbles are taken into account. In this way, the bubble trajectories are independent and in no way coupled to each other. This way of modelling turbulent dispersed two-phase flows gives statistically reliable results for sufficiently low volume fractions of the dispersed phase.

3. NUMERICAL RESULTS

The behaviour of microbubbles injected from an electrode located at the bottom of a channel into a fully developed turbulent flow (see figure 1) was investigated numerically. From a macroscopic point of view, we observed that the bubbles detach from the electrode and are advected in streamwise direction, while they experience a rise due to buoyancy (see figure 2). Irregular bubble dispersion and clustering effects due to turbulent fluctuations of the carrier flow are clearly visible. Those phenomena will be discussed in the following.

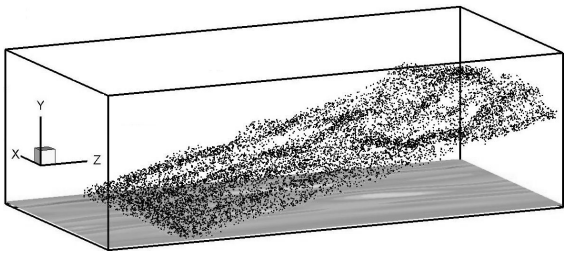

Figure 2: Macroscopic bubble distribution in the channel and iso-surfaces of skin friction

We introduce a dimensionless factor $\gamma=u_{adv}/u_r$, which gives the ratio between the advection velocity of the primary phase and the rise velocity of a bubble. These characteristic velocities are defined by

$$u_{adv} = \frac{1}{2h}\int_0^{2h} \langle u \rangle dy\,, \qquad (10)$$

$$u_r = \frac{g \cdot d^2}{12\nu}\,, \qquad (11)$$

where g is the gravitational constant. In our simulations, we choose the parameters d and g in a way that the bubble Reynolds number according to equation (7) is kept at a constant value of $Re_b=1$ and the factor γ gives reasonable values in comparison with the geometry of an existing experimental reactor. This reference device has half-height of $h_{ref}=0.005m$, it is operating at a reference velocity $u_{ref}=0.4m/s$ and includes bubbles of a reference diameter $d_{ref}=2\cdot10^{-4}m$. This configuration leads to a value of $\gamma_{ref}=12.6$.

We performed simulations of a fully turbulent carrier flow with a bulk Reynolds number of $Re_{bulk}=u_{adv}\cdot h/\nu=2000$, which corresponds to a shear Reynolds number of $Re_\tau=131{,}25$ in our simulations. The channel height was chosen to be of unity ($h=1m$). The carrier fluid was considered as water with a density of $\rho_c=1000\,kg/m^3$ and a kinematic viscosity of $\nu=1.025\cdot10^{-6}m^2/s$, while the bubbles were considered as air with a density of $\rho_d=1{,}2kg/m^3$.

All DNS simulations were obtained on 8 Pentium 4 machines (3.4GHz, 2GB of memory) of a Linux cluster with a network connectivity of 1GBs. The calculations were performed on a grid consisting of 80x128x64 points in the spanwise, transverse and streamwise direction respectively. The flow is going in the z-direction, i.e. the direction of the Fourier decomposition of the computational domain.

3.1. Bubble dispersion in a channel

We analyzed dispersive effects in a two-way momentum coupled flow. The periodic boundary on the downstream side of the channel served as outlet for the gaseous phase, i.e. the bubbles were not transferred back to the corresponding upstream inlet together with the carrier flow. The flow itself, however, was subjected to a periodic boundary condition in this direction. Three computational runs (denoted as A, B and C) were performed. The input parameters for the different test cases are shown in Table 1.

Table 1: Configurations of the bubble-laden channel flow test cases A, B and C

	Case A	Case B	Case C
d	0.002	0.004	0.006
g	$1.58\cdot10^{-3}$	$1.97\cdot10^{-4}$	$5.83\cdot10^{-5}$
γ	3.9	7.8	11.7
τ_b	0.11	0.43	0.98

Three different bubble diameters were chosen while the bubble Reynolds number was kept at a constant value of $Re_b=1$ as described above. In all three cases the chosen diameters were below the Kolmogorov length scale of the turbulent flow. The bubbles were placed at random positions a radius away from the electrode. Their lift-off velocity was set to be equal to the rise velocity u_r. The production rate of bubbles detaching from the bottom wall electrode was chosen to be $5Hz$. The bubbles are advected in the streamwise direction due to the drag force and experience a rise due to buoyancy (see figure 2). This macroscopic motion was found to depend on the parameter γ.

We analyzed the relation between the spanwise average bubble y-position (i.e. the average height h to which the bubble has risen) and the z-position in the streamwise direction. The spanwise averaging has been performed according to

$$y_{avg}=\frac{1}{2\pi}\int_0^{2\pi}\langle y\rangle dx\,. \tag{12}$$

From figure 3 we can see that there is an almost linear behaviour between the advection and rise velocities of a bubble. For an increasing value of γ, the influence of the advection is stronger and the angle $\beta=\arctan(y/z)$, under which the bubble rises in the streamwise direction, gets smaller.

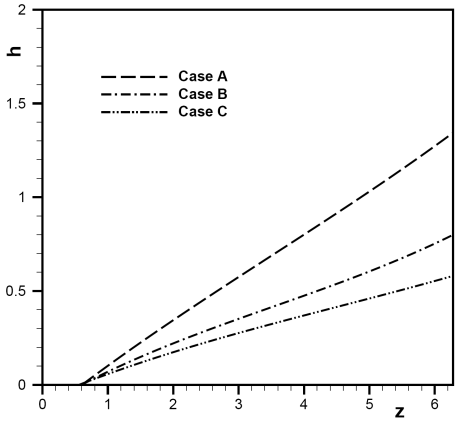

Figure 3: Average bubble y-positions as a function of z

We computed the statistically averaged gas volume fraction at the outlet of the channel ($z=2\pi$) for all three computations. The average of the volume fraction was computed as

$$\alpha_{avg}=\frac{1}{2\pi T}\int_0^T\int_0^{2\pi}\langle\alpha_d\rangle dxdt\,, \tag{13}$$

where T is the time interval of averaging. The peak volume fractions obtained were $\alpha_{avg}=7\cdot10^{-6}$, $\alpha_{avg}=5\cdot10^{-5}$ and $\alpha_{avg}=2\cdot10^{-4}$ in cases A, B and C respectively. This indicates that the assumption of a dilute flow was valid. If we define the bubble spacing as

$$\frac{L}{d}=\left(\frac{\pi}{6\alpha_d}\right)^{1/3}, \tag{14}$$

where L is the average distance between two bubbles, its peak value of $L/d\approx15$ for test case C stresses this statement. However, the volume fraction in the region above the electrode, on which the bubbles are generated, reaches a peak value of $\alpha_d=1.6\cdot10^{-3}$ in case C, which corresponds to $L/d\approx7$. These values are on the brink of the dilute flow regime, for higher volume fractions four-way coupling effects should be taken into account.

From the theory of bubble interaction with turbulent flow structures it is known that bubbles tend to concentrate in regions of high vorticity [11]. In the present study of wall-bounded turbulent channel flow, bubbles detaching from the lower wall into the flow are found to concentrate in streamwise vortex filaments, which are created in a turbulent boundary layer. Figure 4 shows a horizontal crosscut of the channel at y^+=32, indicating iso-surfaces of the z-component of the vorticity and the positions of the bubbles inside an interval of Δy^+=5 for case C. The streamwise vortex filaments are indicated by high relative values of z-vorticity. The alignment of the bubbles with the coherent structures is clearly visible. It was observed that the bubbles tend to cluster along the coherent structures. This effect was regarded to be most distinct in case C, where the bubble diameter, the response time and the value for γ were larger than in cases A and B. This can be related to the fact that for a higher value of γ the effect of the gravitational rise of a bubble becomes weaker compared to the advection and it takes more time for the bubbles to vertically pass the boundary layer vortices. Thus, the bubbles have more time to align with the coherent structures than they have for low values of γ.

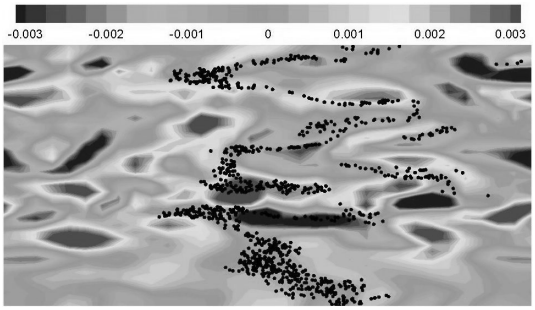

Figure 4: Instantaneous bubble distribution and contours of ω_z in the y^+=32 plane (case C)

Figures 5 and 6 show vertical crosscuts of the channel at z=3.4 and indicate only the lower half-height ($0<h<0.5$) of the channel. In figure 5, the tangent velocity vectors of the primary phase flow field in the plane are shown, while figure 6 indicates the distribution of the gas bubbles in an interval of Δz=0.1.

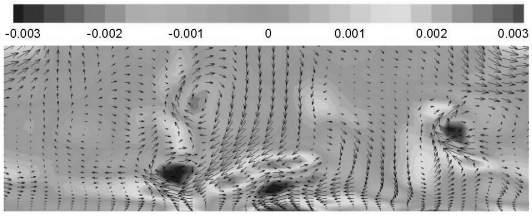

Figure 5: Tangent velocity vectors and contours of ω_z in the z=3.4 plane (case C)

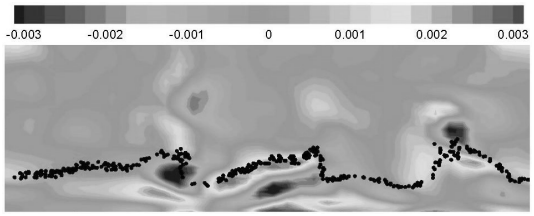

Figure 6: Instantaneous bubble distribution and contours of ω_z in the z=3.4 plane (case C)

We see from figure 6 that the bubbles are not exactly located inside the coherent vortical structures, although their motion in the spanwise and transverse directions seems to be highly influenced by these vortices. The bubbles are dragged towards the low-pressure regions inside the vortices by a centripetal force. This is due to the high density ratio (ρ_c/ρ_d>1) between the fluid and the bubbles. However, this motion is superimposed by the buoyancy force. The bubbles rise vertically through the coherent vortical structures and are not captured inside them.

Figure 7 shows a horizontal crosscut of the channel at y^+=32 together with iso-surfaces of the streamwise velocity component and the bubble distribution in an interval of Δy^+=5 for case B. The characteristic streamwise low-speed and high-speed streak regions of the turbulent boundary layer can be identified and the bubbles are found to align with these velocity streaks. The bubbles in the low-speed regions are advected less than those located in the high-speed regions. This effect can be related to the drag force, which acts very rapidly in case of low bubble Reynolds numbers. For a higher value of γ, this effect is even more distinct (see figure 4).

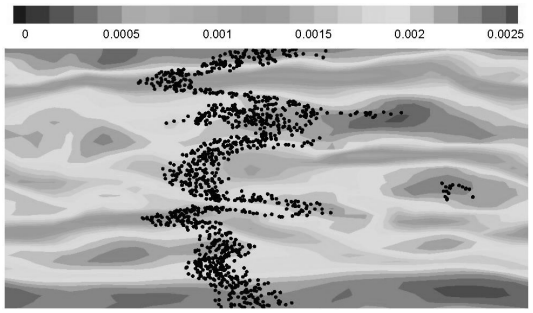

Figure 7: Instantaneous bubble distribution and contours of w in the y^+=32 plane (case B)

From figures 4, 6 and 7 we can conclude that the motion of gas bubbles lifting off from a wall electrode into a turbulent boundary layer of a channel flow involves quite complex kinematic phenomena, since gravitational rise, advective transport, motion due to pressure differences and the usteady behaviour of the coherent structures are superimposed. According to our investigations, the drag force and the buoyancy can be considered to

be driving phenomena for dispersive effects of bubbly flow in an electrochemical channel reactor, where the parameter γ determines their relative importance.

3.2. Effect of the lift force

According to the definition stated in equation (8), the slip-shear lift force depends on the instantaneous velocity difference **u**-**v** and the fluid vorticity $\boldsymbol{\omega}$. Since we have relatively short bubble response times and low bubble Reynolds numbers in the present study, the difference in velocity between the flow and the dispersed bubbles is overcome quite rapidly. This indicates that the effect of the lift force does not play a significant role in the present case.

The effect of the lift force on the bubbles was investigated in regions of high vorticity. Therefore, the computations of test case C were repeated with a lift coefficient of C_L=0, i.e. no lift force present. Figure 8 shows a comparison between included and excluded lift force in terms of the instantaneous bubble positions in a small vertical section of the channel at z=3.0 and an interval of Δz=0.1. The bubbles experiencing the lift force are represented by black spheres, while white spheres represent the bubbles without lift force. The displacements are found to be of a small order of magnitude, as it was expected due to the small bubble response time.

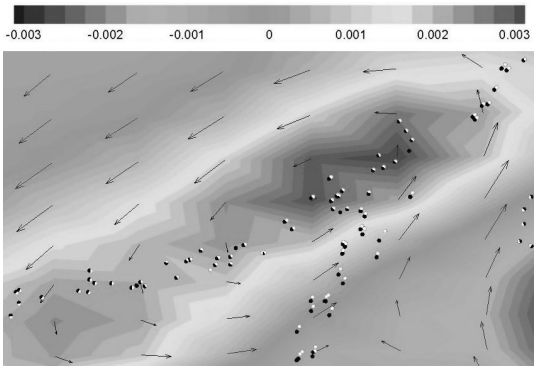

Figure 7: Instantaneous bubble distributions and contours of ω_z in the z=3.0 plane (case C)

It is known that in the case of lift force acting on bubbles inside a vortical structure, those bubbles tends to move to the downwash side of the vortex [11]. This behaviour can be verified in our investigations. The lift force moves the bubbles in the direction of the downwash side of the vortex, although its effect is small compared to advection and buoyancy effects.

3.3. Effect of two-way coupling

We investigated the effect of momentum back-coupling of the gas bubbles on the flow (see §2.3). This study indicated that the back-coupling terms $\mathbf{f_d}$ do not seem to have a major influence on the flow patterns of the primary phase in case of a dilute bubbly flow, since in all flow configurations we tested throughout this study, the differences of the results between one-way ($\mathbf{f_d}$=0) and two-way coupled flows were marginal. This leads to the conclusion that in flows at low bubble Reynolds numbers, the advective transport from the primary to the secondary phase is highly dominant. If we regard the ratio of momentum between the dispersed phase and the continuous carrier phase inside a control volume V and assume the velocity difference **u**-**v** to be small, we end up with

$$\frac{m_d \mathbf{u}}{m_c \mathbf{v}} = \frac{\rho_d V_d}{\rho_c (V - V_d)} = \frac{\alpha_d}{1-\alpha_d}\frac{\rho_d}{\rho_c}. \qquad (15)$$

This value tends to zero for dilute bubbly flow, where the volume fraction of the dispersed phase α_d and the density ratio ρ_d/ρ_c are small compared to unity. This indicates neglible back-transfer of momentum from the dispersed entities to the flow, as it was observed in the present study.

4. CONCLUSIONS

DNS simulations of bubble-laden turbulent channel flow were obtained using a spectral/finite element based Navier-Stokes solver coupled with a Lagrangian tracking solver. Microbubbles of diameters below the Kolmogorov length scale were injected to the flow from a bottom wall electrode. All computations were performed on a distributed memory parallel computer. Two-way momentum coupling was used to simulate the interaction of the gas bubbles and the turbulent carrier flow.

It was found that the motion of the bubbles is influenced by the coherent vortical structures of a turbulent boundary layer, i.e. the quasi-streamwise vortex filaments which are ocurring in turbulent boundary layers. The bubbles are pulled towards the vortex centers by a centripetal force when passing these structures. Due to buoyancy, they overcome this influence and do not stay inside the vortices.

Drag force and gravitational effects were found to be the driving phenomena for bubbly flow in an advection-dominated channel, whereas the effect of the lift force was found to be small. Furthermore, the effect of momentum back-coupling from the bubbles to the flow was found to be negligible for dilute bubbly flow.

We conclude that the motion of gas bubbles inside a turbulent channel flow involves complex kinematic phenomena, since gravitational rise, advection and the usteady motion of the coherent structures are superimposed. This will be subject to further numerical investigations. On top of this, we will compare our results with experiments (PIV measurements) in a real electrochemical parallel plate reactor in a further study.

ACKNOWLEDGEMENTS

We acknowledge the support from the Instituut voor de aanmoediging van innovatie door Wetenschap & Technologie in Vlaanderen (IWT) for the MuTEch project (contract nr. SBO 040092).

REFERENCES

[1] Crowe, C. T., Troutt, T., and Chung, J. N., 1996, „Numerical models for two-phase turbulent flows", *Ann. Rev. Fluid. Mech.*, Vol. 28, pp. 11-43.

[2] Wang, L. P., and Maxey, L. R., 1993, "The motion of microbubbles in a forced isotropic and homogenous turbulence", *Appl. Sci. Res.*, Vol. 51, pp. 291-296.

[3] Maxey, M. R., Chang, E. J., and Wang, L. P., 1994, "Simulation of interactions between microbubbles and turbulent flows", *Appl. Mech Rev.*, Vol. 46, pp. 70-74.

[4] Elghobashi, S., and Truesdell, G. C., 1993, "On the two-way interaction between homogenous turbulence and dispersed solid particles. I: Turbulence modification", *Phys. Fluids A*, Vol. 5, pp. 1790-1801.

[5] Boivin, M., Simonin, O., and Squires, K. D., 1998, "Direct numerical simulation of turbulence modulation by particles in isotropic turbulence", *J. Fluid. Mech.*, Vol. 375, pp. 235-263.

[6] Pan, Y., and Banerjee, S., 1996, "Numerical simulation of particle interactions with turbulence", *Phys. Fluids*, Vol. 8, pp. 2733-2755.

[7] Soldati, A., 2005, "Particles turbulence interactions in boundary layers", *J. Appl. Math. and Mech.*, Vol. 85, pp. 683-699.

[8] Druzhinin, O. A., and Elghobashi, S., 1998, "Direct numerical simulations of bubble-laden turbulent flows using the two-fluid formulation", *Phys. Fluids*, Vol. 10, pp. 685-697.

[9] Druzhinin, O. A., and Elghobashi, S., 2001, "Direct numerical simulation of a three-dimensional spatially developping bubble-laden mixing layer with two-way coupling", *J. Fluid Mech.*, Vol. 429, pp. 23-61.

[10] Lain, S., Bröder, D., Sommerfeld, M., and Göz, M. F., 2002, "Modelling hydrodynamics and turbulence in a bubble column using the Euler-Lagrange procedure", *Int. J. Multiphase Flow*, Vol. 28, pp. 1381-1407.

[11] Mazzitelli, I. M., Lohse, D., and Toschi, F., 2003, "The effect of microbubbles on developed turbulence", *Phys. Fluids*, Vol. 15, pp. L5-L8.

[12] Snyder, D. O., and Degrez, G., 2003, "Large eddy simulation with complex 2D geometries under a parallel finite-element/spectral algorithm", *Int. J. Numer. Meth. Fluids*, Vol. 41, pp. 1119-1135.

[13] Vanden Abeele, D., Degrez, G., and Snyder, D. O., 2004, "Parallel turbulent flow computations using a hybrid spectral/finite element method on Beowulf clusters", *Third International Conference on Computational Fluid Dynamics*, Toronto.

[14] Jameson, A., Schmidt, W., and Turkel, E., 1981, "Numerical solutions of the Euler equations by finite volume methods using Runge-Kutta time stepping schemes", *AIAA 14th Fluid and Plasma Dynamic Conference*, paper 81-1259.

[15] de Vries, A. W. G., Biesheuvel, A., and van Wijngaarden, L., 2002, "Notes on the path and wake of a gas bubble rising in pure water", *Int. J. Multiphase Flow*, Vol. 28, pp. 1823-1835.

[16] Maxey, M. R., and Riley, J. J., 1983, "Equation of motion for a small rigid sphere in a nonuniform flow", *Phys. Fluids*, Vol. 26, pp. 883-889.

[17] Giusti, A., Lucci, F., and Soldati, A., 2005, "Influence of the lift force in direct numerical simulation of upward/downward turbulent channel flow laden with surfactant contaminated microbubbles", *Chem. Eng. Sci.*, Vol. 60, pp. 6176-6187.

[18] Ferrante, A., and Elghobashi, S., 2004, "On the physical mechanisms of drag reduction in a spatially developing turbulent boudary layer laden with microbubbles", *J. Fluid Mech.*, Vol. 503, pp. 345-355.

[19] Kim, J., Moin, P., and Moser, R., 1987, "Turbulence statistics in fully developed channel flow at low Reynolds number", *J. Fluid Mech.*, Vol. 177, pp. 133-166.

Conference on Modelling Fluid Flow (CMFF'06)
The 13th International Conference on Fluid Flow Technologies
Budapest, Hungary, September 6-9, 2006

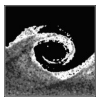

A SIMULATION STUDY ON THE GAS PHASE EXPANSION IN VERTICAL SLUG FLOW

T. Sotto Mayor[3], A.M.F.R. Pinto[2] and J.B.L.M. Campos[1]

[1] Corresponding Author. Centro de Estudos de Fenómenos de Transporte, Departamento de Engenharia Química, Faculdade de Engenharia da Universidade do Porto, Rua Dr. Roberto Frias 4200-465 Porto, Portugal, Fax: +351 225081449, E-mail: jmc@fe.up.pt
[2] Departamento de Engenharia Química, Faculdade de Engenharia da Universidade do Porto. E-mail: apinto@fe.up.pt
[3] Departamento de Engenharia Química , Faculdade de Engenharia da Universidade do Porto. E-mail: tsmayor@gmx.net

ABSTRACT

A study on the gas phase expansion occurring in free bubbling vertical slug flow is reported. A recently developed slug flow simulator supported by air-water experimental data was used for this purpose. The study was accomplished by implementing in the simulator the gas phase expansion along the column (considering effects over bubble lengths and bubble velocities). The flow in a 6.5 *m* long column with internal diameter of 0.032 *m* was simulated. Expansion of gas phase along the column is shown to decrease the bubble coalescence occurrence. Liquid free-surface oscillations (due to bubble burst events and continuous liquid and gas input in the column) were found to affect considerably the expansion of the gas phase, especially for high gas flow rates. According to the findings, the use of a large cross sectional area tank, placed at the outlet of the column, does not assure a permanent expansion rate of the gas phase.

Keywords: bubble velocity; gas phase expansion; slug flow simulation

NOMENCLATURE

C	*[-]*	empirical coefficient
D	*[m]*	column internal diameter
$H_{hyd,\,i}$	*[m]*	hydrostatic liquid height above bubble i
P_{atm}	*[Pa]*	ambient pressure
$P_{hyd,\,i}$	*[Pa]*	hydrostatic pressure on buble i
R	$[JK^{-1}mol^{-1}]$	universal gas constant
S_b (S_c)	$[m^2]$	bubble (column) cross section area
T	*[K]*	temperature
U_B (U_∞)	$[ms^{-1}]$	upward bubble velocity (drift velocity)
U_G (U_L)	$[ms^{-1}]$	superficial gas (liquid) velocity
U_i	$[ms^{-1}]$	bubble i upward velocity
V_{film}	$[m^3]$	volume of liquid in the film
g	$[ms^{-2}]$	gravity acceleration
h_b (h_s)	*[m]*	length of bubble (slug)
n	*[#]*	number of bubbles
n_i	*[mol]*	number of moles of air of bubble i
t_j, t_{j+1}	*[s]*	consecutive time instants
z (z_T)	*[m]*	vertical coordinate of the column (tank base)
$z_{liq.}$	*[m]*	liquid free-surface coordinate
z_{nose} (z_{rear})	*[m]*	vertical coordinate of bubble nose (rear)

Greek Symbols

a_i (e_i)	*[-]*	fraction of bubble (slug) length above tank base
Dh_i	*[m]*	expansion of bubble i
r	$[kgm^{-3}]$	density of liquid

1. INTRODUCTION

Much of the primary modelling of slug flow was based on the early works of Dumitrescu [1], Davies and Taylor [2] and Nicklin et al. [3]. They set the bases for the initial understanding of two-phase slug flow pattern. Several works followed focussing different aspects of such flow pattern (e.g.[4-6]). The numerical simulation of two-phase vertical slug flow pattern has been attempted by several researchers (e.g. [7-9]). It serves as a tool

for the study of the influence of several phenomena over the development of the flow, as well as an outcome predictor for any process/application in which this flow occurs. The usual approach requires the input of bubble-to-bubble interaction correlations relating the trailing bubble velocity to the length of the liquid slug ahead of the bubble. Different interaction correlations are proposed (e.g. [8-10]) depending, for instance, on experimental conditions, fluid properties, flow regimes, etc.. The simulation of slug flow pattern is often achieved, however, without accurate implementation of the gas phase expansion along the column (in terms of effect over bubble length and over bubble velocity). A usual simplification is to correct gas related parameters for the pressure at the middle of the column (considering an average gas hold-up). Such assumptions may jeopardize the accurateness of the resulting simulation data, in particular regarding bubble length and bubble velocity parameters. The suitability of such simplifications decreases, for instance, with increasing length of the column to be simulated or, ultimately, with parameters that augment the pressure gradient along the column.

The main goal of this work is to provide information on the influence of the gas phase expansion over the development of the slug flow pattern. For that purpose, an algorithm for implementation of gas phase expansion along the column is proposed. Effects over coalescence, bubble length and bubble velocity are discussed.

2. SLUG FLOW SIMULATOR

A slug flow simulator supported by air-water co-current slug flow experiments ([10]) has been used in the present study. The reported bubble-to-bubble interaction correlation, obtained for turbulent regime in the liquid and in the bubble wake, has been used to implement the movement of bubbles along the column.

$$U_i / U_B^{\exp} = 1 + 2.4 e^{-0.8\left(h_{s,i-1}/D\right)^{0.9}} \quad (1)$$

where D is the column internal diameter (ID) and U_i refers to the velocity of the trailing bubble i, flowing behind a liquid slug of length $h_{s,\,i-1}$. The experimental upward bubble velocity in undisturbed conditions, $U_B^{\exp}$, was shown ([10]) to follow the theoretical predictions of Nicklin [3] :

$$U_B = U_\infty + C(U_L + U_G) \quad (2)$$

with U_∞, the drift velocity, equal to 0.196 *m/s* (inertial controlled regime in a 0.032 *m* ID column) and C, the ratio between the maximum and average liquid velocity, equal to 1.2 (for turbulent regime in the liquid). The symbols U_L and U_G are the superficial liquid and gas velocities, respectively.

The displacement of the bubbles along the column is implemented as the incremental movement of their boundaries (bubble nose and rear). The position of the bubble rear, at instant t_{j+1}, $z_{rear,i}^{t_{j+1}}$, is computed by updating its position at t_j, $z_{rear,i}^{t_j}$, according to its velocity (U_i).

$$z_{rear,i}^{t_{j+1}} = z_{rear,i}^{t_j} + U_i\,(t_{j+1} - t_j) \quad (3)$$

The velocity of the bubble i (U_i) has two contributions: one related to the length of the liquid slug ahead of it (Eq. (1)), and another related to the expansion of the gas bubbles flowing upwards (below) the bubble. This latter contribution will be described in detail in the following section. The position of the bubble nose is updated according to:

$$z_{nose,i}^{t_{j+1}} = z_{rear,i}^{t_{j+1}} + h_{b,i}^{t_{j+1}} \quad (4)$$

Taking the boundaries of two consecutive bubbles, the length of the liquid slug flowing between them is given by:

$$h_{s,i}^{t_{j+1}} = z_{rear,i}^{t_{j+1}} - z_{nose,i+1}^{t_{j+1}} \quad (5)$$

This strategy extends to all the bubbles flowing in the column.

2.1. Expansion of the gas phase along the column

The upward movement of the gas bubbles along a vertical column reduces the hydrostatic pressure acting on each bubble. Discarding pressure drops in the liquid phase, one can estimate the volume (or length) of a bubble at a given column vertical coordinate by inputting the corresponding hydrostatic pressure in the *ideal gas law*. However, that computation requires a priori knowledge of the mass of air of each bubble. This parameter can be assessed, for instance, at the base of the column (inlet position) where hydrostatic pressure can easily be computed.

2.1.1. Evaluation of the amount of air in a bubble

As bubbles enter the simulation domain (where expansion phenomena are acknowledged), different hydrostatic pressures act on each bubble depending on the gas hold-up in the column. Figure 1 illustrates this instant.

The hydrostatic liquid height above a bubble entering the column can be calculated by:

$$H_{hyd,i} = z_{liq.} - z_T + \sum_{k=t-1}^{i-1} \left(h_{s,k}(1-e_k) \right) + \\ + \left(1 - S_b/S_c\right) \sum_{k=t-1}^{i-1} \left(h_{b,k}(1-a_k) \right) \quad (6)$$

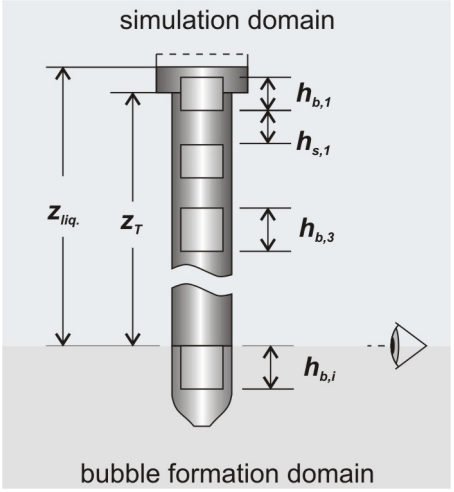

Figure 1 - Representation of the upward movement of a Taylor bubble at column inlet

where $z_{T.}$ is the vertical coordinate of the base of the tank (if present), t is the index of the first bubble flowing under the base of the tank. Notice that the index of the sums in the previous equation ($k = t$-1) is, at least, equal to 1. The symbols a_k and e_k are the fractions of the length of bubble k and liquid slug k above z_T, respectively. The parameter a_k is 0 for bubbles flowing inside the column (or if no tank is present), 1 for bubbles flowing inside the tank, and in the range 0-1 for bubbles crossing the vertical coordinate z_T. The value in this range can be computed by:

$$a_k = (z_{nose,k} - z_T) / h_{b,k} \quad (7)$$

As for a_k, e_k is 0 for slugs flowing inside the column (or if no tank is present), 1 for slugs flowing inside the tank, and in the range 0-1 for slugs crossing the vertical coordinate z_T. The value in this range can be computed by:

$$e_k = (z_{rear,k} - z_T) / h_{s,k} \quad (8)$$

Notice that although the pressure along the liquid film (between bubble and pipe wall) for bubbles flowing inside the column, is approximately constant, there is a pressure recovery at the rear of the bubbles (where film expands) proportional to the volume of liquid in the film around each bubble. Therefore, the hydrostatic liquid height equivalent to the pressure recovery at the rear of a bubble i can be computed as the ratio between the volume of liquid in the film and the column cross sectional area:

$$V_{film,i}/S_c = \left(1 - S_b/S_c\right) h_{b,i} \quad (9)$$

The last parcel of the right hand side of Eq. (6) computes, thus, the pressure recovery contribution at the rear of the bubbles. Notice that (1-a_k) is required to assure that, for bubbles crossing the base of the tank, only the percentage of the bubble length inside the column (under z_T) is considered in the computation of the pressure recovery at the bubble rear.

The percentage of the bubble length or slug length already inside the tank ($a_k\, h_{b,k}$ or $e_k\, h_{s,k}$, respectively) is discarded in the computation of hydrostatic pressure since the hydrostatic height at the base of the tank is assumed equal to the height of liquid inside it (regardless of the presence or absence of bubbles or slugs crossing its base).

Considering Figure 1 the following general exprvvession can be established:

$$z_T = \sum_{k=t-1}^{i-1} \left(h_{s,k}(1-e_k) \right) + \sum_{k=t-1}^{i-1} \left(h_{b,k}(1-a_k) \right) \quad (10)$$

with t = 2 (for the particular situation illustrated in Figure 1). By substituting the previous equation in Eq. (6) and rearranging, one obtains a simplified expression for the calculation of the hydrostatic liquid height above bubble i, at the instant it enters the column:

$$H_{hyd,i} = z_{liq.} - S_b/S_c \sum_{k=t-1}^{i-1} \left(h_{b,k}(1-a_k) \right) \quad (11)$$

As already mentioned, the index of the sum ($k = t$-1) is, at least, equal to 1. The hydrostatic pressure acting on bubble i at the inlet coordinate can now be computed as:

$$P_{hyd,i} = r\, g H_{hyd,i} \quad (12)$$

where r is the density of the liquid and g gravitational acceleration. An algebraic transformation of the *ideal gas law* with further substitution of the pressure according to Equation (12) gives origin to an expression that computes the amount of air in a bubble i, at the inlet coordinate:

$$n_i = h_{b,i}\, S_b \left[P_{atm} + r\, g H_{hyd,i} \right] / RT \quad (13)$$

where P_{atm} stands for ambient pressure, T refers to the temperature, R is the *ideal gas* constant and n_i is the number of moles of air in bubble i. This strategy extends to all the bubbles entering the column. The

computation of n_i is a requirement for the implementation of the bubble expansion along the column.

2.1.2. Effect over the length of the bubble

Figure 2 illustrates an instant in the upward movement of bubbles inside the simulation domain. The hydrostatic pressure acting on bubble *i* is given by an expression similar to Eq. (11), with a correction to account for the positioning of the bubble ($z_{nose,i}$).

$$H_{hyd,i} = z_{liq.} - z_{nose,i} - S_b/S_c \sum_{k=t-1}^{i-1} \left(h_{b,k}(1-a_k) \right) \quad (14)$$

If Eq. (13) is transformed to isolate $h_{b,i}$ and $H_{hyd,i}$ is further substituted according to the aforesaid, one obtains:

$$h_{b,i} = n_i RT \Big/ S_b \left[P_{atm} + r\, g\, H_{hyd,i} \right] \quad (15)$$

Eqs. (14) and (15) compute the length of a bubble *i*, as a function of its position in the column (through the hydrostatic pressure acting on it).

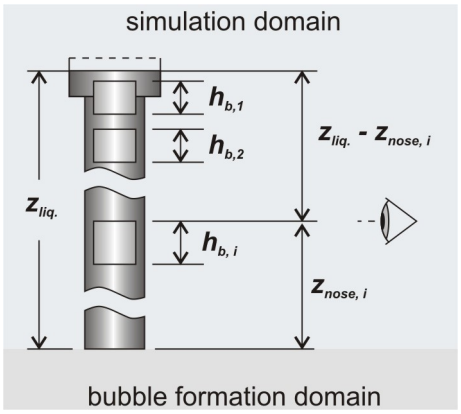

Figure 2 - Representation of the upward movement of a Taylor bubble inside the column

The expansion of bubbles along the column is implemented iteratively since their lengths are a function of the vertical coordinate of their noses (see Eq. (15)) whose computation, in turn, requires an estimate of the length of the bubbles (see Eq. (4)).

2.1.3. Effect over the velocity of the bubble

The bubble expansion is seen as a rise of the bubble nose region (reference frame attached to the bubble). Therefore, bubble expansion results in the upward displacement of everything ahead of the bubble (liquid and gas) by an amount proportional to the expansion of the bubble. Consider Figure 3, representing the position of several bubbles, flowing upwards in a column, at instant t_j. Consider that, at instant t_{j+1} all bubbles had their positions updated according to their upward velocity (see Eq. (3)). The hydrostatic height above each bubble decreased from instant t_j to t_{j+1}, therefore, all the bubbles expanded accordingly (as described in the previous section).

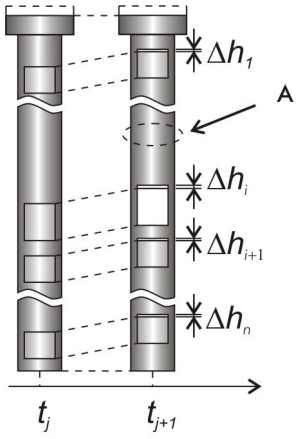

Figure 3 - Two consecutive moments in the upward movement of bubbles

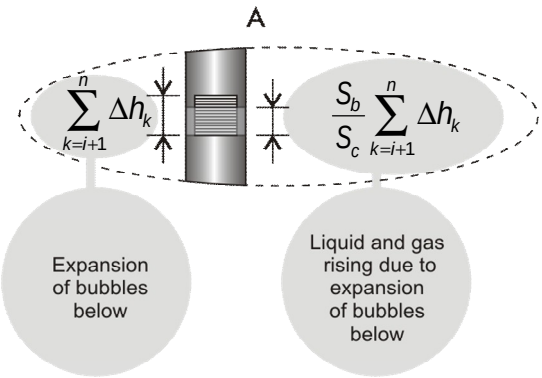

Figure 4 - Liquid and gas rise ahead bubble *i* due to the expansion of bubbles below it (zone A in Figure 3)

Consider bubble *i*, in white in Figure 3, and the liquid flowing ahead of it (zone A). The expansion of the bubbles under bubble *i* induces a raise in the liquid and gas ahead of them, proportional to the sum of the individual expansions undergone by each bubble (Δh_1, ..., Δh_n), and given by:

$$\Delta z_{\text{expans.}}^{\text{ahead } i} = S_b/S_c \sum_{k=i+1}^{n} \Delta h_k \quad (16)$$

This "extra" upward displacement of liquid and gas can be seen as an increase in the liquid and gas superficial velocities. This increase can be calculated dividing $\Delta z_{\text{expans.}}^{\text{ahead } i}$ by the time increment between the two consecutive instants under focus ($t_{j+1} - t_j$), as in the following equation:

$$\Delta U_{\text{expans.}}^{\text{ahead } i} = \frac{\Delta z_{\text{expans.}}^{\text{ahead } i}}{t_{j+1} - t_j} = \frac{S_b}{(t_{j+1} - t_j) S_c} \sum_{k=i+1}^{n} \Delta h_k \qquad (17)$$

where $\Delta U_{\text{expans.}}^{\text{ahead } i}$ is the increase in the flow velocity ahead of bubble *i*, due to the expansion of all bubbles flowing below it.

The upward velocity of gas bubbles flowing in a co-current liquid flow depends on the velocity profile of the liquid phase ahead. This dependence is usually introduced by parameter *C* (equal to the ratio between the maximum and average liquid velocity), whose value depends on the flow regime (or velocity profile) in the liquid. Thus, the overall velocity of a bubble flowing in co-current flow is the result of two contributions: one related to the length of the liquid slug ahead of it (Eq. (1)), and another related to the "extra" upward displacement of the liquid and gas due to the gas phase expansion (Equation (17)). The following equation allows the computation of the overall velocity of a bubble, *i*, in a train of bubbles flowing upwards:

$$U_i = U_B^{\exp} \left[1 + 2.4 e^{-0.8 \left(\frac{h_{s,i-1}}{D} \right)^{0.9}} \right] + \frac{C S_b}{(t_{j+1} - t_j) S_c} \sum_{k=i+1}^{n} \Delta h_k \qquad (18)$$

where the experimental average upward bubble velocity is computed by a transformed version of Nicklin's equation:

$$U_B^{\exp} = U_\infty + C(U_L + U_G^{inlet}) \qquad (19)$$

where U_G^{inlet}, the superficial gas velocity at the inlet coordinate, is used instead of U_G in order to estimate the undisturbed upward bubble velocity discarding the effect of the gas phase expansion along the column. Recall that this effect is computed by the last parcel of the right hand side of equation (18). Theoretical values of U_∞ and *C* (0.196 *m/s* and 1.2, respectively) were used in the simulations (experimentally validated by Sotto Mayor et al. [10]). The overall bubble velocity, given by Eq. (18), is used in Eq. (3) to update the positioning of bubble boundaries, and thus, to implement the bubble displacement.

3. RESULTS

3.1. Effect of gas expansion over bubble coalescence

A special simulation was done in order to isolate the effect of the gas phase expansion over the flow development along the column. Non-distributed liquid slug lengths were considered at the inlet of the column (corresponding distribution featuring null standard deviation), and the bubble-to-bubble interaction was discarded. The former constrain assures that every liquid slug (and gas bubble) enter the column featuring equal length. Additionally, the fact that no bubble-to-bubble interaction is implemented in the upward movement of the bubbles guarantees that any evolution of the flow characteristics can be ascribed to the gas phase expansion. In Figure 5, the length of bubbles (h_b) and liquid slugs (h_s) and the velocity of bubbles (*U*) are plotted against the column vertical coordinate, for a given instant after the start-up of a simulation.

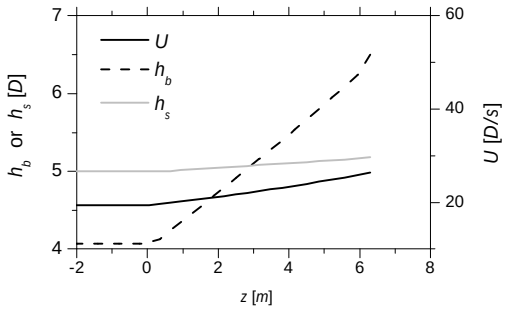

Figure 5 - Bubble length, slug length and bubble velocity along the vertical coordinate of the column, for a given instant (simulation discarding bubble-to-bubble interaction and constant lengths of bubbles, slugs and bubble velocity at the inlet)

The origin of the vertical coordinate (horizontal axis) is positioned at the base of the column. The expansion of the gas phase is computed only above the inlet position. Above the column inlet, and due to the computation of the gas expansion, the bubble and slug lengths and the bubble velocity increase along the column.

Although the increase in the length of the bubbles (above column inlet) can be directly related to the expansion of the gas phase, a deep analysis of all the effects influencing the flow pattern is required to fully interpret the variation of the liquid slug length along the column (increasing slightly). According to Eq. (18), the velocity of a bubble *i*, flowing in the column has a contribution related to the expansion of the bubbles flowing under that bubble (last parcel of the right hand side of the equation). This means that the first bubble (from top to bottom), of a train of bubbles flowing in the column, has its velocity affected by the expansion of more bubbles than does, for instance, the 2nd bubble (flowing after the 1st). Consequently, this "extra" velocity, due to expansion, is higher for the 1st bubble than for the 2nd one, which is, in turn, higher than for the 3rd bubble, and so on. These ordered relations ($U_1 > U_2 > U_3$, …, clearly

perceivable in Figure 5) lead to the increase in the length of the liquid slugs as the train of bubbles flow upwards (see previous figure). This shows, therefore, that the gas expansion phenomenon "opposes" to the merging of consecutive bubbles (coalescence) as it induces the increase (though smooth) in the length of the slugs.

3.2. Effect of the outlet configuration over the gas expansion

The expansion of gas bubbles along the column is a function of the hydrostatic pressure acting on the bubbles, which is, in turn, dependent on the coordinate of the liquid free-surface, among other parameters (see Eqs. (14) and (15)). Considering that the outlet configuration of the column (with or without a large cross sectional area tank at its top) influences the coordinate of the liquid free-surface (dampening effect), it is interesting to assess the extent of the influence of the outlet configuration over the gas expansion in the column. The following sections describe this issue.

3.2.1. Column without a tank at the top (outlet)

The flow in a 6.5 *m* long column with internal diameter of 0.032 *m* was simulated considering superficial liquid and gas velocities (U_L and U_G) equal to 0.25 *m/s* and 0.36 *m/s*, respectively. Gas superficial velocity is given at ambient pressure. This pressure reference is used for all U_G data used in this document. Gas expansion and bubble-to-bubble interaction is considered in the simulation. Focus is put on the evolution of the velocity of the first bubble along time. Notice that the so-called first bubble in the column changes every time a bubble reaches the liquid free-surface (2nd bubble becomes the new 1st bubble). The velocity of the first bubble (comprising and discarding gas expansion) is plotted against time in Figure 6.

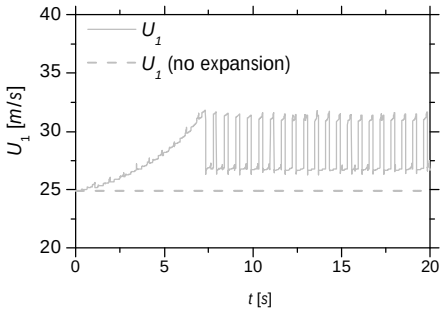

Figure 6 – Values of the velocity of the first bubble along time for a simulation with $U_L \approx$ 0.25 *m/s* and $U_G \approx$ 0.36 *m/s*; without a tank at the column outlet

As expected, the velocity of the first bubble discarding the gas expansion contribution is constant and equal to the undisturbed upward bubble velocity as computed in Eq. (19). However, if the gas expansion contribution is considered, the evolution of the velocity of the first bubble is rather interesting. There is a continuous increase in U_1 in the first seconds of the simulation, followed by an oscillatory behaviour. The initial escalation of U_1 is related to the fact that the simulation starts with the column full of liquid (no bubbles inside the column). As bubbles enter the column (increasing gas hold-up) the first bubble of the train is affected by the expansion of an increasing number of bubbles. Therefore, there is a continuous escalation of U_1 due to the increase in the last parcel of the right hand side of Eq. (18). This increase continues until the first bubble reaches the liquid free-surface. From that moment onward, an oscillatory behaviour is observed. In order to fully understand the causes of this behaviour special attention must be put in the evolution along time of other parameters as bubbles reach the liquid free-surface. Those parameters are the vertical coordinates of the liquid free-surface and of the nose of the first bubble, as well as the hydrostatic liquid height above the first bubble. These parameters are plotted against time in Figure 7 (in the range 9-11 *s*)

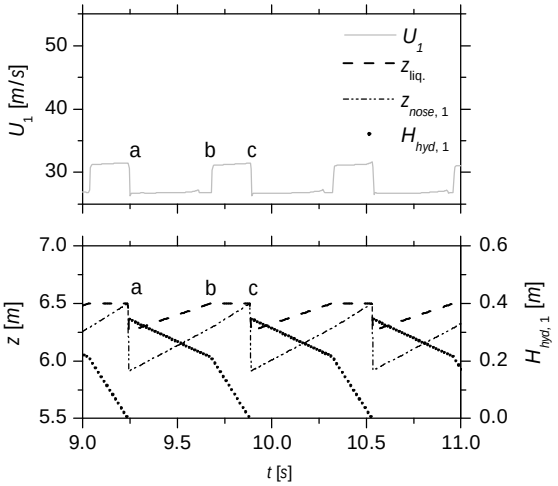

Figure 7 – Plot of velocity and nose coordinate of the first bubble (U_1 and $z_{nose,\,1}$), hydrostatic liquid height above first bubble ($H_{hyd,\,1}$) and vertical coordinate of the liquid free-surface ($z_{liq.}$) along time, in the range 9-11 *s*; simulation with $U_L \approx$ 0.25 *m/s* and $U_G \approx$ 0.36 *m/s*; without a tank at the column outlet; without a tank at the column outlet

Consider an instant *a* at which the first bubble of a train of bubbles reaches the liquid free-surface. At that instant, this interface, previously at 6.5 *m* (outlet coordinate) from the base of the column, drops instantly by an amount proportional to the height of the bubble exiting the column. Moreover, there is a sudden drop in the coordinate of the nose

of the first bubble, since the new first bubble (previously second bubble) is flowing somewhere below in the column. From that moment onward, the liquid free-surface will rise steadily due to the continuous entrance of gas and liquid in the column. This rise will continue until the liquid reaches again the outlet system (at 6.5 *m* from the base of the column; instant *b*). Additionally, the new first bubble will rise in the column until it reaches the liquid free surface (at instant *c*). Considering that the hydrostatic liquid height above the first bubble is calculated as the difference between the liquid free-surface coordinate (z_{liq}) and the bubble nose coordinate ($z_{nose,\,1}$), it is obvious that this parameter has different variation rates in time intervals *a*-*b* and *b*-*c*. The movement of the liquid free-surface, in the time interval *a*-*b*, accounts for this difference. As a direct consequence of the different variation rate of the pressure gradient acting on the bubbles in these time intervals, different expansion rates occur. Indeed, the expansion of all bubbles flowing in the column between instants *a* and *b* is considerably smaller than between instants *b* and *c*. As a consequence, the expansion contribution for the velocity of the first bubble (but also for the remaining bubbles), in the former time interval is smaller than in the latter time interval. The aforementioned oscillatory behaviour of U_1 is, therefore, the result of the dynamic evolution of the of the liquid free-surface coordinate.

3.2.2. Column with a large cross sectional tank at the top (outlet)

A large (square) cross sectional tank is often used at the top of the columns to assure proper separation of gas and liquid phases. Moreover, besides phase separation, such a tank has the advantage of strongly decreasing the oscillation of the liquid free-surface. Considering that liquid free-surface oscillation originates considerable variations in the velocity of the bubbles inside the column (as described in the previous section), it is interesting to investigate if the dampening effect of a large cross sectional tank affects also the evolution of the bubble velocity inside the column. For this purpose, the operating conditions used in the previous section were simulated again considering the existence of a large (square) cross sectional tank at the top of the column. As before, both gas expansion and bubble-to-bubble interaction were included in simulation. The velocity of the first bubble (with and without gas expansion) is plotted against time in Figure 8.

As for the case with no tank at the column top, a constant value is obtained when the gas expansion contribution is withdrawn from U_1. However, despite the strongly dampened oscillations of the liquid free-surface (practically nonexistent) very strong oscillation of U_1 is observed. Indeed, the overall variation of this variable is very similar to the one observed when no tank is present.

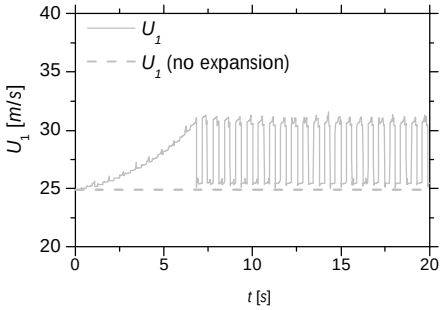

Figure 8 – Values of the velocity of the first bubble along time for a simulation with $U_L \approx$ 0.25 *m/s* and $U_G \approx$ 0.36 *m/s*; with a large tank at the column outlet (0.5 *m* height)

In order to clarify the reasons for this behaviour, a closer analysis of the variation of several parameters must be done. Attention must be focused on the variation of the vertical coordinates of the nose and rear of the first bubble, in particular in the vicinity of the base of the tank (vertical coordinate $z_T = 6$ *m*). Additionally, the hydrostatic liquid height above the second bubble, $H_{hyd,\,2}$, is monitored. The variation of these parameters is plotted against time (in the range 9-11 *s*) in Figure 9.

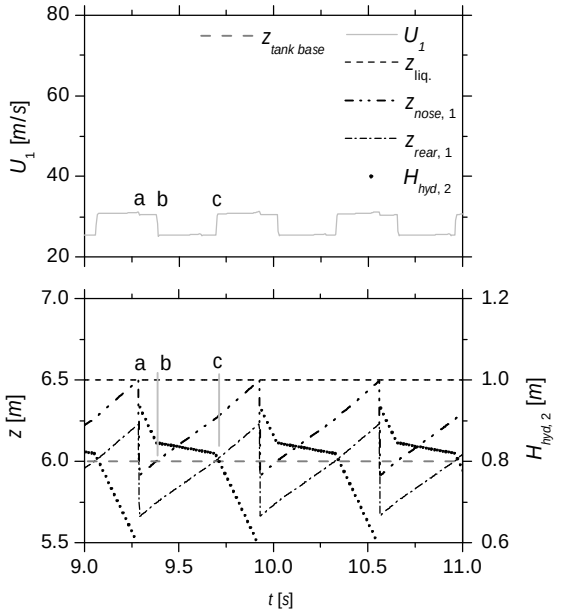

Figure 9 – Plot of nose and rear coordinates and velocity of the first bubble ($z_{nose,\,1}$, $z_{rear,\,1}$, U_1), hydrostatic liquid height above second bubble ($H_{hyd,\,2}$) and vertical coordinate of the liquid free-surface ($z_{liq.}$) along time, in the range 9-11 *s*; simulation with $U_L \approx$ 0.25 *m/s* and $U_G \approx$ 0.36 *m/s*; with a large tank at the column outlet (0.5 *m* height)

Three different time instants are relevant for the understanding of the oscillations of U_1: instant *a* refers to the moment at which a first bubble reaches the liquid free-surface (z = 6.5); instants *b* and *c* refer to the moments at which the nose and rear of a first bubble, respectively, reach the base of the tank (z = 6.0). Notice that instant *a* is prior to instants *b* and *c* because, after the burst of a first bubble at instant *a*, the previously second bubble, flowing somewhere below, becomes the new first bubble. Unlike the simulation with no tank at the top of the column, no major change in the velocity of the first bubble is observed when a bubble reaches the liquid free-surface (instant *a*, in Figure 9). The large cross sectional tank at the top of the column assures that the coordinate of the liquid free-surface remains practically unchanged at that event. Therefore, the evolution of the hydrostatic pressure acting on the "old" second bubble is fairly steady during the burst of the first bubble ($P_{hyd,\,2}$ prior to the burst event is practically similar to $P_{hyd,\,1}$ after the burst event; despite the change in indexes these parameters refer to the same bubble). Attention must be focused now on the evolution, of the hydrostatic liquid height above the second bubble ($H_{hyd,\,2}$), along time. The variation rate of this parameter between instants *a* and *b* is fairly constant (negative but almost constant slope). However, at instant *b* there is a sudden change in the variation rate (slope) of $H_{hyd,\,2}$. Between instants *b* and *c* the first bubble is crossing the base of the tank and, as a consequence, the last parcel of the right hand side of Eq. (14) is smaller than before instant *b* ($a_1 = 0$ before instant *b*, and increasing from 0 to 1 between instants b and c). As a result, the evolution of $H_{hyd,\,2}$ in that time interval is less pronounced and, consequently, the corresponding bubble expansion is smoother. The original variation rate of $H_{hyd,\,2}$ is observed again as soon as the rear of the first bubble is above the tank base (after instant *c*, and until the next burst event; $a_1 = 1$ in that time interval). Notice that this analysis has been focused on the hydrostatic liquid height above the second bubble for the sake of simplicity. Similar effects occur for all the bubbles in the column, although with different extent. Thus, because all bubbles in the column undergo smaller expansion rate when the first bubble of the train of bubbles is crossing the base of the tank, strong oscillation on the velocity of bubbles are observed.

A large cross sectional tank mounted at the top of a slug flow column assures an almost constant aerated liquid level, but it does not guarantee a steady expansion rate of the gas phase inside the column. It does not even attenuate the oscillations of this parameter.

4. CONCLUSIONS

A simulation study on the gas phase expansion in co-current slug flow is reported. The expansion of the gas phase along the column decreases (slightly) the coalescence of bubbles. The movement of the liquid free-surface (at bubble burst events) affects strongly the expansion rate of the gas phase and, consequently, the velocity of the bubbles. Although a large cross sectional tank at the top of the column assures an almost steady liquid free-surface, it does not guarantee a steady expansion rate of the gas phase. It does not prevent, therefore, the oscillation of the velocity of bubbles.

ACKNOWLEDGMENTS

The authors gratefully acknowledge the financial support of Fundação para Ciência e Tecnologia through project POCTI / EQU / 33761 / 1999 and scholarship SFRH / BD / 11105 / 2002. POCTI (FEDER) also support this work via CEFT.

REFERENCES

[1] Dumitrescu, D.T., *Stromung an Einer Luftblase im Senkrechten Rohr*. Z. Angeus. Math. Mec., 1943. 23: p. 139-149.

[2] Davies, R.M. and Taylor, G.I., *The mechanics of large Bubbles rising through extended liquids and through liquids in tubes.* Proc. R. Soc. Lond., 1950. A 200: p. 375-392.

[3] Nicklin, D.J., Wilkes, J.O., and Davidson, J.F., *Two-phase flow in vertical tubes.* Trans. Inst. Chem. Engrs., 1962. 40: p. 61-68.

[4] Collins, R., De Moraes, F.F., Davidson, J.F., and Harrison, D., *The Motion of Large Gas Bubble Rising Through Liquid Flowing in a Tube.* J. Fluid Mech., 1978. 28: p. 97-112.

[5] Fabre, J. and Liné, A., *Modeling of two-phase slug flow.* Ann. Rev. Fluid Mech., 1992. 24: p. 21-46.

[6] White, E.T. and Beardmore, R.H., *The Velocity of Single Cylindrical Air Bubbles Through Liquids Contained in Vertical Tubes.* Chem. Engng Sci., 1962. 17: p. 351-361.

[7] Barnea, D. and Taitel, Y., *A model for slug length distribution in gas-liquid slug flow.* International Journal of Multiphase Flow, 1993. 19(5): p. 829-838.

[8] Hasanein, H.A., Tudose, G.T., Wong, S., Malik, M., Esaki, S., and Kawaji, M., *Slug flow experiments and computer simulation of slug length distribution in vertical pipes.* AIChE Symposium Series, 1996. 92(310): p. 211-219.

[9] Van Hout, R., Barnea, D., and Shemer, L., *Evolution of statistical parameters of gas-liquid slug flow along vertical pipes.* International Journal of Multiphase Flow, 2001. 27(9): p. 1579-1602.

[10] Sotto Mayor, T., Ferreira, V., Pinto, A.M.F.R., and Campos, J.B.L.M., *Hydrodynamics of gas-liquid slug flow along vertical pipes in turbulent regime. Part I - experimental data.* Submitted to Chemical Engineering Science, 2005a.

Conference on Modelling Fluid Flow (CMFF'06)
The 13th International Conference on Fluid Flow Technologies
Budapest, Hungary, September 6-9, 2006

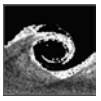

INFLUENCES OF MATERIAL PROPERTIES, EXPOSURE TIME AND COATING ON EROSION PROCESS PRODUCED BY SUBMERGED CAVITATING JET ACTION

Ezddin Ali Farag HUTLI[2], Miloš NEDELJKOVIĆ[1]

[1] Corresponding Author. University of Belgrade, Faculty of Mechanical Engineering, Department for Hydraulic Machinery. Kraljice Marije 16, SCG-11120 Beolgrade 35, Serbia. Tel.: +381 11 337 0428, Fax: +381 11 337 0364, E-mail: mnedeljkovic@mas.bg.ac.yu
[2] University of Belgrade, Faculty of Mechanical Engineering, Ph.D. student

ABSTRACT

Erosion is the most prominent effect of cavitation action. That is why a lot of studies have been dedicated to this process. In general the cavitation erosion is a very complex process, which involves a multitude of geometric, hydraulic, chemical factors, and thermodynamic parameters as well as material properties. A number of these parameters are extremely difficult to quantify.

The main reason of using cavitating jet in this work was to test the resistance of the materials to the cavitation erosion. Additional reasons rely on wide applications of cavitating jet in a life, such as in the drilling, cutting, cleaning etc.

The experimental setup with submerged cavitating jet has been used for the study of influences of material and exposure time on the erosion process. These influencing parameters are experimentally proved to be very significant for the cavitation erosion process. Each of the parameters has been varied separately, and the results of erosion are analysed in detail. Additionally, a comparison of experiments with coated and non-coated material has been made in order to study the enhancement of erosion resistance achieved by the coating.

Keywords: cavitation, coating, corrosion, erosion, submerged jet.

NOMENCLATURE

A	$[m^2]$	nozzle outlet cross-section area
D_{in}	$[mm]$	inlet nozzle diameter
D_{out}	$[mm]$	outlet nozzle diameter
L	$[mm]$	stand-off distance
T	$[^0C]$	temperature
ΔW	$[mg]$	weight loss
p_{ref}	$[bar]$	reference pressure
p_v	$[bar]$	saturation (vapour) pressure
u_{ref}	$[m/s]$	reference velocity = Q / A
Vj	$[m/s]$	jet velocity = Q / A
P_1	$[bar]$	upstream pressure
P_2	$[bar]$	downstream pressure
Δt	$[h, s]$	exposure time
ρ	$[kg/m^3]$	density of the liquid
σ	[-]	cavitation number – defined as

$$\sigma = \frac{p_{ref.} - p_v}{\frac{1}{2}\rho u_{ref}^2}$$

1. INTRODUCTION

Erosion is the most prominent effect of cavitation action. That is why a lot of studies have been dedicated to this process. In general the cavitation erosion is a very complex process, which involves a multitude of geometric, hydraulic, chemical factors, and thermodynamic parameters as well as material properties, that an exact solution by either analytical or experimental methods is out of reach for a long time. A number of these parameters are extremely difficult to quantify [1-3, 5-8, 10, 13, 18-22]. Consequently, the results of erosion tests are and will remain as subject to a large scatter. A statistical approach, based on realistic but simplified physical model, is there to improve confidence in the damage prediction [9,11,13,18,20,25,30]. The main reason of using cavitating jet in this work was to test the resistance of the materials to the cavitation erosion. Additional reasons rely on wide applications of cavitating jet in a life, such as in the drilling, cutting, cleaning etc.

The jet method has many advantages over the other methods used for the erosion testing. The apparatus is small, the testing times can readily be adjusted by choosing a suitable upstream pressure, the results can then be scaled up or down provided the cavitation number is kept constant. However,

the greatest advantage is the fact that the flow parameters can be controlled independently.

The behaviour of severely erosive cavitation clouds depends on pressure gradient in the jet nozzle, jet geometry, and material of the subject. [12,14,17-19,27,30]. As the cavitation bubbles collapse on the surface of a specimen, the surface will be increasingly eroded. This erosion can be quantified by measuring the weight loss in a given time.

2. EXPERIMENTAL SETUP AND MEASUREMENT PROCEDURE

The experimental setup for jet performance investigation is a closed hydraulic loop shown on Fig.1. High-speed submerged cavitating jet is produced in the test chamber by adjustment of appropriate hydrodynamic conditions and by final outflow to the test chamber through the nozzle.

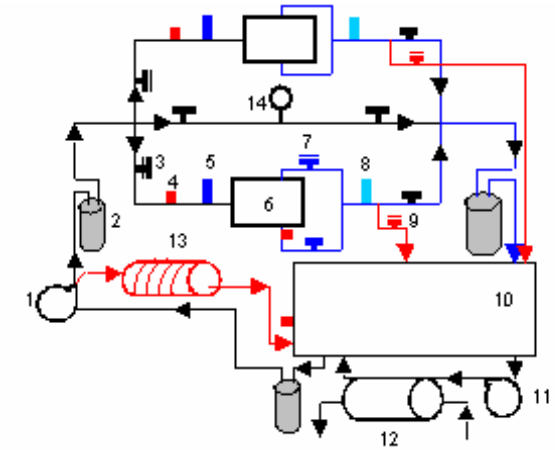

Figure 1. Schematic diagram of Cavitating jet machine (1. Plunger pump; 2. Filter; 3. Regulation valve; 4 Temperature sensor; 5. High-pressure transducer; 6. Test chamber; 7. Pass valve; 8. Low-pressure transducer; 9. Safety valve; 10. Tank; 11. Circulation pump; 12. Heat exchanger; 13. Distracter energy; 14. Pressure gauge)

Test chamber geometry is shown in Figure 2. The specimens are mounted in the chamber co-axially with the nozzle, the chamber is filled up with water, and then the water is pressurized by a plunger pump. Only one chamber is functional, the other is for reserve. Shortcut line with pressure gauge has the function of regulation of the pressure in the system and maintaining of the water temperature within maximum 3^0C of variation during the erosion tests is fulfilled by cooling circuit with the heat exchanger.

Jet impacts the sample S located L =25.67 mm away from the nozzle (on the opposite side of the chamber – Fig.2). A rotating holder is used to attach up to 6 specimens (samples).

Hydrodynamic conditions were varied within the following limits: test chamber was 0.87 liters in volume and nozzles used were with diameters of 0.4, 0.45, 0.55 and 0.6 mm. The top speed of the jet is more than 200 m/s for upstream pressure set to 450 bar. The downstream pressure could be adjusted from atmospheric pressure up to 4 bar.

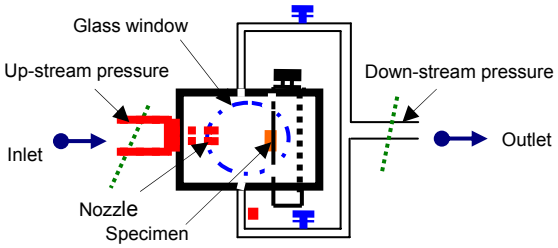

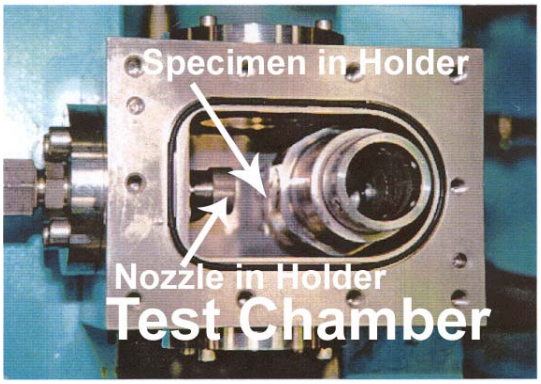

Figure 2. Side-view (sketch) and upper-view (photo) of the rectangular test chamber in a Cavitating jet machine

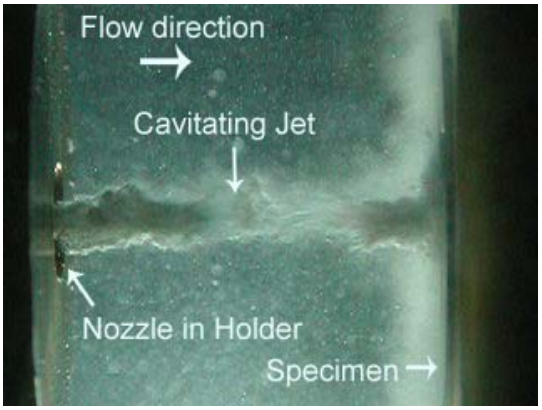

Figure 3. Side-view of the test chamber with cavitating jet impacting on a specimen. The flow is from left to right

The specimen is first weighted and then mounted in the holder. The test chamber is filled with tap water from the tank in the facility. Pressurized water is pumped from the tank using the plunger pump via the nozzle into the test chamber. Hydrodynamic conditions are settled on to produce cavitating jet. The cavitating jet is then impinging the specimen at 90 degrees to its diameter. After certain exposure time the facility is turned off, the chamber is evacuated and then the

specimen removed. Specimens are dried and weighted and the procedure is then repeated with other specimens. The intensity of cavitating jet is controlled via the upstream pressure and downstream pressure, which are measured precisely by transducers and controlled using the needle valves (regulation valves). The filters are used to purify impurities from the circulating water. The temperature regulator and temperature sensors are used to control the water temperature. The nozzle may be mounted in holder in two ways in respect to the inlet and outlet diameters: divergent and/or convergent conicity.

2.1. Instruments and calibration

In order to get the results with high accuracy, the calibration of all apparatus in facility was done. The pressure transducers used to measure the upstream and downstream pressure were calibrated precisely with a reference pressure transducer HUBER of high precision (maximum pressure is 25 bar), then the flow rate for different nozzle diameters and different directions of flow were measured precisely in order to get the constant K in different cases for calculating the exit jet velocity. The temperature sensors in the test rig were calibrated perfectly by the use of NORMA (Digital Thermometer) as the reference in the calibration process. Validity of the cooling system was proved by examined validity of the heat exchanger and the temperature regulator.

2.2. Cavitation erosion parameters and erosion quantification

Cavitation number σ is the most important parameter for a cavitating jet. It represents a measure of the resistance of flow to the incidence of cavitation, since the lower it is the cavitation is more intensive. The value of this parameter has been established by measurements of upstream and downstream pressure, and by calculation of the reference velocity from the measured flow-rate.

Between the start of the test on a specimen and the beginning of a visible damage some time elapses. This time period is called **the incubation time**, and it is increased as the ratio of cavitation intensity to cavitation resistance decreases. However, there are no quantative data on this relationship. [2,8,17,20-23]

At regular intervals, the specimen was carefully removed from the chamber and dried sufficiently. Then the mass (weight) loss was measured by a high precision balance (METTLER AE 100), with accuracy and sensitivity of 0.1 mg.

3. TESTED MATERIALS

The erosion, produced by impingement of a cavitating jet, was investigated experimentally using three basic kinds of tested materials: aluminum alloy (Al-alloy), stainless steel (St.St.316) and copper (Cu), with water as a working fluid. In order to precisely understand the erosion results, it is important to know the exact composition of the materials tested.

X-ray fluorescence spectroscopy has been used to establish the exact composition of each material. Results signify that St.St.316 (Fe+Cr+Ni), and Cu are pure, but Al-alloy is the mixture of Al, Mn, Fe Cu and Zn. So, it is to be expected that this mixture will have higher erosion resistance than Cu, and that is the reason why the most number of short-time experiments has been conducted with specimanes out of Cu.

Experiments with coating have been done on another material which is designated with X in this paper. The composition of this material, as well as of the coating, was not allowed to be published.

4. EXPERIMENTAL RESULTS AND CONSIDERATIONS

All the tests were performed under the same hydrodynamic conditions as described in Table 1.

Table 1. Hydrodynamic operating conditions in investigation of influence of material

P_1 [*bar*]	P_2 [*bar*]	Vj [*m/s*]	σ	T [^0C]
195 ±1	2.19 ±0.1	170 ±0.5	0.013 ±0.001	21 ±1

4.1. The influence of material on the erosion rate

Series of tests were carried out involving repeated exposure of the specimens of Al-alloy, St.St.316 and Cu to the action of cavitating jet for periods of 0.5 up to 5 hours. The exposure times were chosen so that the level of damage on each specimen could be readily evaluated. The weight loss was calculated from weighings of the specimen before and after the erosion test.

Some quantitative test results are shown in Fig.5. Also, some photos are shown in Fig.4 in order to realize that the erosion occurred as an annular ring on the disc specimen, with regions inside and outside the ring which essentially look like unaffected.

Figure 4. Erosion pattern in different kinds of tested materials (Al - left, Cu – middle, St.St. – right). Conditions P_1=145±1 *bar*, P_2=2.1±0.1 *bar*, Vj=147±0.5 *m/s*, σ= 0.0193 ±0.001, T=20°*C*, exposure time = 0.5 h, x/d=57, (convergent nozzle)

We can note that in case of St.St. there is no significant difference in weight before and after the time of exposure to cavitation, but the changes happened only in the colour of the exposed area. It looks like a gray ring on the disc specimen, and it means for St.St. that we are still in the period of incubation time.

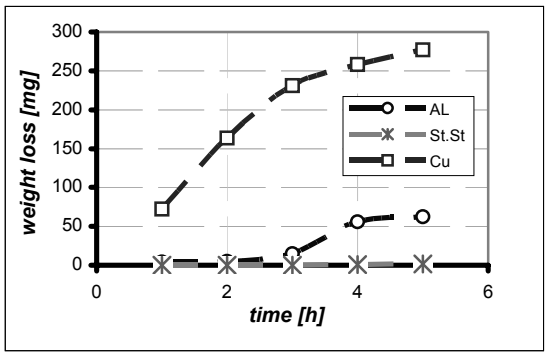

Figure 5. Dependency of weight loss on exposure time. Conditions: Vj=170m/s, ϙ=0.013, T=23°C, x/d=57.5, (convergent nozzle).

But for the cases of Al-alloy and Cu we passed that period (incubation time), so there are significant differences between the weight before and after cavitation exposure. The differences in these cases are interpreted as a consequences of the differences in mechanical properties of tested materials (hardness, toughness, etc.).

4.2. SEM for tested materials

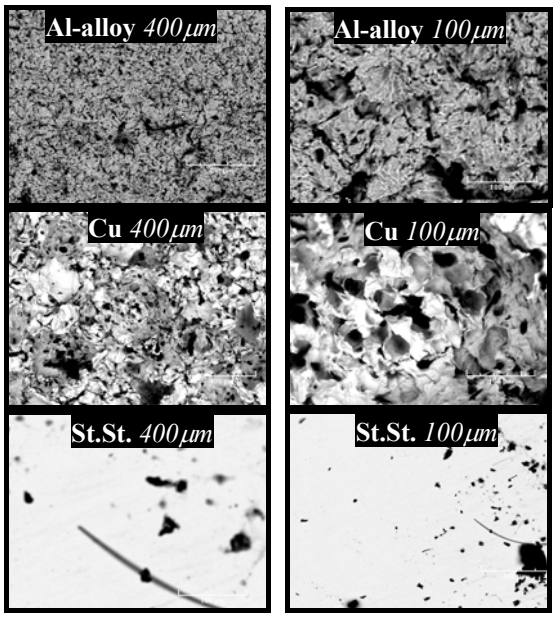

Figure 6. The group of images of severely eroded surfaces established by SEM FEIQANTA 200. *Conditions:* P_1=145 bar, P_2=2.1 bar, Vj=147 *m/s*, ϙ= 0.0193, T=20°C, exposure time =0.5 *h*, x/d=57, (convergent nozzle).

In order to observe and compare eroded surfaces, scanning electron microscope (SEM) technique has been used. Comparison has been done for the three kinds of material (Al-alloy, Cu and St.St.316), which were exposed to the cavitating jet for 30 minutes of exposure time, under the same hydrodynamic conditions. The SEM which was used is FEIQANTA 200.

The observed images reveal that in the first four images (Fig.6) the surface is principally characterized by a huge number of very fine, deep cylindrical holes developed within the Al-alloy and Cu. Also, the surface is characterized by a typical fracture features in both of specimens (Al-alloy and Cu). Comparing the pictures of Al-alloy and pictures of Cu, the differences in fracture features may be noticed, and also in the number and the depth of the holes (in Cu specimens more fatigue features are noticed, with more holes which are deeper).

In the case of St.St.316, other two images reveal that there are no holes on the surface. Black features that may be noticed on the surface appear from sample preparation of specimen and will not be discussed.

4.3. The influence of coating on the cavitation erosion rate

Specimens of material X were tested, one non-coated and the other coated. Coating was introduced to improve the resistance of material X to cavitation erosion, so that the increase of incubation time for the coated material is expected as a result. Material X is normally used in the manufacturing of drilling hammer casings.

First, preliminary long term test have been carried out for exposure times of 0.5 to 4 hours. Then, the short-term test has been run for further investigation.

4.3.1. Long term test

Two specimens (one non-coated and another coated) were exposed to cavitation created by the cavitating jet machine. The exposure times were 0.5, 1, 2, 3 and 4 h, under operating conditions given in Table 2.

Table 2. Hydrodynamic operating conditions at the long term test

P_1 [bar]	P_2 [bar]	Vj [m/s]	σ	T [^{0}C]
166 ±1	2.2 ±0.1	157 ±0.5	0.017 ±0.001	21 ±1

After each exposure time the specimen was weighted again, and the weights of the specimen before and after the exposure to cavitation were compared - Table 3.

The curves of results obtained by the long term test (Figure 7) show that for exposure time less than

2 hours, the coated material was more resistent to cavitation erosion, but after 2 hours the trend was opposite - the damage on the coated material was larger.

Table 3. Weights of specimens during the long-term test

Exposure time Δt [h]	0	1	2	3	4
Weight of coated specimen [g]	7.1691	7.1653	7.1584	7.1390	7.1200
Weight of non-coated specimen [g]	7.1464	7.1408	7.1317	7.1191	7.1034

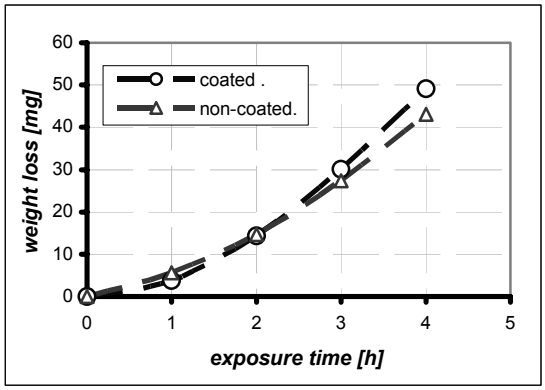

Figure 7. Weight loss dependency on exposure time (coated and non-coated material), (convergent nozzle)

This is most probably because after 2 hours the layer(s) of the coating was removed by cavitation and the craters and pits which were made trapped the liquid and some dissolved gas, so that subsequent collapse of the next cavity occurred in the same or nearby position of the previous one. Such a mechanism produces waves which propagate in and inbetween the layers, so the coating layer(s) wiil be removed until the original specimen surface appears. Then the erosion will take place in the original surface and there will be another incubation time (although the intensity of the cavitation remains constant, its effectiveness will be increased after the incubation time). Also, in addition, the corrosion will take place on the surface, thus contributing to removing of the coating from the surface.

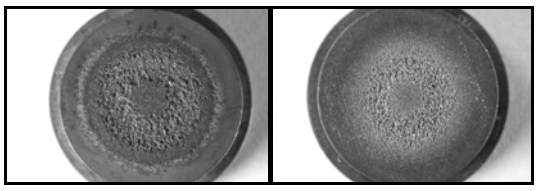

Figure 8. Top view of the specimens, left is coated and right is non-coated specimen, exposure time is 4 hours

Visual investigation of images (Figure 8) of two specimens (coated and non-coated) reveals that a corrosion has also contributed to the weight loss. This clearly indicates that the weight loss is not only a result of cavitation. Not distinguishing the effects acting in this problem may lead to a mistake in the cavitation erosion rate calculation, where the cavitation damage accelerates the corrosion and vice versa. In order to distinguish between erosion and corrosion, some steps were done in this paper to investigate the resistence of the material to corrosion before going on with cavitation experiments.

4.3.2. Corrosion existence test

In the first phase, two samples, one of coated and the other of non-coated material, were put in water for a period of 24 hours. The corrosion products were then removed (Figure 9) and weighted. This proved the existence of corrosion in both specimens as well as the weight loss due to corrosion (1.6mg non-coated, 0.7mg coated).

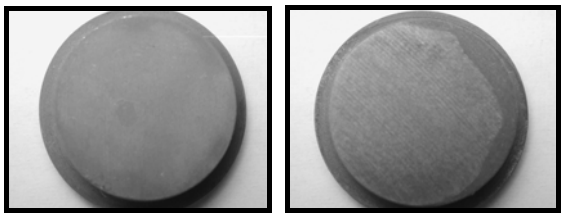

Figure 9. Corrosion existence test - 24h in water - corrosion products removed. Left is coated and right is non-coated specimen (top view)

In the second phase, the same two samples were put in the water for additional 48 hours, in order to see more clearly the effect of corrosion in the weight loss. The result shows that the weight loss of the non-coated material is increased by +2.7mg, and of the coated material by +1.8mg above the weight losses for a period of 24h (before this test of 48h). It is concluded that the non-coated specimen has considerably higher tendency to corrosion than the coated specimen.

The results show that the weight loss due to corrosion is considerably small, but for the case of existing cavitation erosion, the corrosion process will be much faster, as will be the cavitation erosion itself. Thus the existing of corrosion contributed in the weight loss established in previous investigation, confirming that it is not easy to distinguish them separately. It may be concluded that in corrosive media, like in our case water, the weight loss is not a fully confident indicator for just a cavitation erosion measure.

That is why the short term tests were carried out, thus trying to avoid the influence of corrosion. The attempt was focused to find the incubation time as a valid parameter of cavitation erosion resistence.

This parameter is valuable, since in order to increase the resistence of the materials to cavitation erosion, the incubation time must be increased, and after it the effectiveness of cavitation will significantly increase.

4.3.3. Short term test

The exposure time was set very short (15 seconds) in order to avoid the effect of corrosion and to attempt to find the incubation time. Another reason for this short time exposure was to try to eliminate the difference between the intensity of cavitation phenomenon in our test rig and the one in a real case.

P_1 [bar]	P_2 [bar]	Vj [m/s]	σ
115	2.21	130	0.026

Table 4. Hydrodynamic operating conditions at the short term test.

After 15 seconds, the specimens were dried and investigated using a microscope. It was found that there are many pits on the top surfaces of the two specimens. By comparison of the two specimens, it is found that the non-coated specimen has no folds pits much more than that in coated specimen (figure 10).

Figure 10. Short-term cavitation test - specimens after 15 s exposure to cavitating jet. Left is coated and right is non-coated specimen. (top view)

4.3.4. Scanning electron microscope (SEM)

Scanning electron microscope (SEM) technique was used after the exposure of the coated and non-coated specimens to the cavitating jet for 0.5 h for each one with the condition as shown in Table 5 (not a short-term test). The aim was to see the cavitation holes in both specimens and to see the aspects of surfaces deformations in both specimens.

For the coated specimen the result of this investigation reveals the homogeneity and composition of the surface (coating):

- Inside the hole the composition is C (carbon), O_2 (oxigen), Fe (iron) and Si (Silicon).
- At medial depth of the pit the composition is C, O_2 and Si.
- At the edges it is Si and Fe.

For the surface without cavitation composition is C, O_2, and Si (with Si percentage less than in other points).

So, from these data the unknown material composition of the coating can be partly deducted.

Photos are given in Figures 11-13. For the group of images in Figure 11 SEM FEIQANTA 200 digital microscope was used, but for the group of images in Figures 12 and 13 older technique with SEM analogue microscope and classic polaroid camera was used.

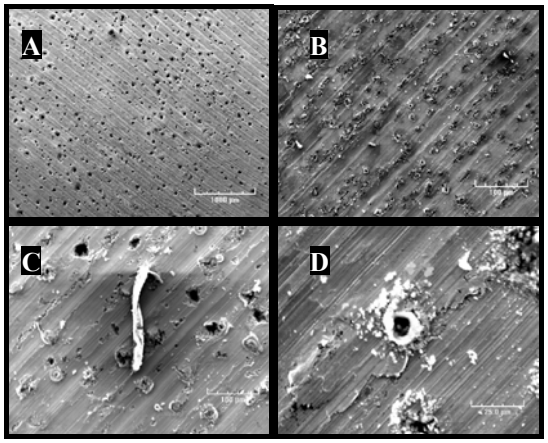

Figure 11. Images of severely eroded surfaces established by SEM FEIQANTA 200 for coated and non coated materials.

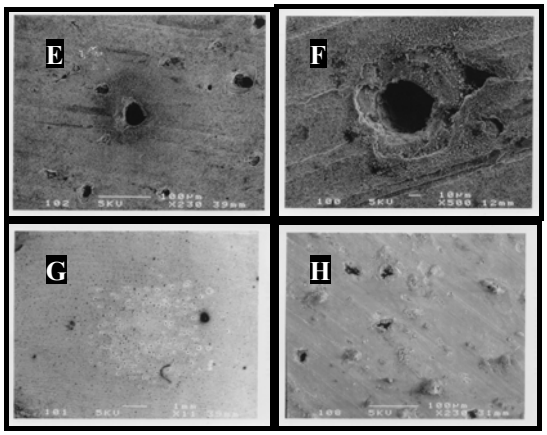

Figure 12. Images of severely eroded surfaces for coated and non-coated materials.

In Fig.11 in the first image A (coated specimen), with 1000μm as a reference scale, many holes in the cavitated surface may be seen as also in the image B (non-coated specimen), with 100μm as a reference scale. However, in the image B many holes are surrounded by white rings so the surface looks like exploded. The impression is that the look of the surface (non-coated) is such as it is exposed to corrosive media.

In the image C (coated), with 100 μm scale, the holes are much bigger as compared to the holes in

image B (non-coated), 100 μm scale. The long white shape in the image is just a dust or dirt and it is not a result of cavitation attack.

In the image D (non-coated), 25μm scale, the hole is surrounded by wider white ring and in some places with white parts, which are the result of cavitation. The interpretation of this phenomenon is that the upper part in the surface is removed by cavitation.

In Fig.12 in the image E (coated),100 μm scale, the big black ring around the pit (hole) can be noticed. This is just the change of colour since no changes in surface structure exist.

In the image F (coated), 10 μm scale, the coating is removed around the pit and thus the sharp edges around the hole are produced. Many layers of coating one over another can be seen. This is a result of the imperfection in coating performance on the specimen surface.

In the image G (coated), 1mm scale, the erosion ring pattern can be distinguished in which every pit is surrounded by a white ring (curved black line is not a part in the specimen, and the big black points are dust or dirt or something else reacted with the surface).

In the image H (non-coated), 100μm scale, the surface was more severely attacked by cavitation and it contains more pronounced holes (pits) and hills (uplands).

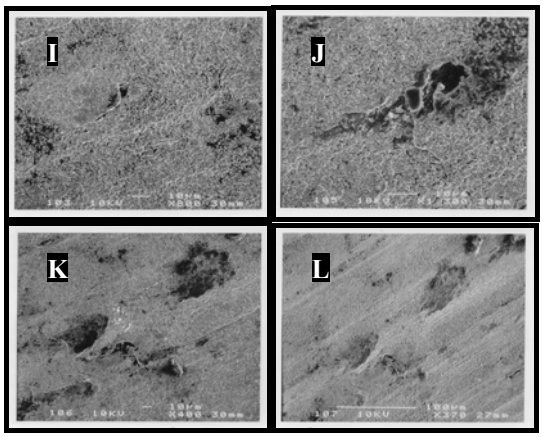

Figure 13. Pictures show the defects in the coated surface (no cavitation).

In Fig.13 there are some holes and cracks in the surface - in pictures I and J 10 and 100μm scale respectively the hole may be seen. Pictures K and L were taken with different angles in order to be sure that the surface has that defects (K at Θ=90° & L at 45° between the specimen surface and the SEM lens).

5. CONCLUSIONS

From the test method for erosion of solid materials by a cavitating liquid jet we can say that, this test method covers a test that can be used to compare the cavitation erosion resistance of solid materials; this test method can also be used to compare the cavitation erosion capability of various liquids and at different conditions easily.

The cavitation erosion in a certain material is increased gradually as exposure time increases until it arrives to the steady state at a certain time; then it decreases gradually (no more erosion [2,8,18,22]).

The incubation time is dependent on the kind of material, where for the case of St.St. the incubation time has not been passed, but for Al (alloy) and Cu – it was. After this time, although the intensity of the cavitation remains constant, effectiveness of erosion process increases.

The degree of cavitation erosion and its pattern are very strongly dependent on the kind of material, i.e. on the material mechanical properties. The degree of the surface roughness produced by cavitation erosion is the direct consequence of the cavitation erosion manner.

The erosion pattern looks like a group of many rings (ring manner) with different degrees in roughness. These rings are not symmetric, which means that the intensity of bubbles is varied along the jet diameter. So, it may be concluded that the cavitation intensity varies from non-damaging values outside the eroded area to the strongest attack at the location of maximum depth of material.

The coating used to cover the exposed surface to cavitation may increase the resistance of the surface material to cavitation erosion by increasing the incubation time. Off course the degree of this benefit it will depends on the kind of coating, the perfection degree of coated surface, and the kind of working fluid.

The existence of corrosion phenomena during the investigation on cavitation erosion may require avoidance of erosion rate as a confident indicator for cavitation erosion in order to prevent the error in weight loss calculation.

REFERENCES

[1] Zhang, Yi., Wang, Z., and Cui, Y., 2000, "The Cavitation Behavior of a Metastable Cr–Mn–Ni Steel," Wear, 240(May), pp. 231-234.

[2] Krella, A., 2005, "Influence of Cavitation Intensity on X6crniti18-10 Stainless Steel Performance in the Incubation Period," Wear, (January).

[3] Dular, M., Bachert, B., Stoffel, B, and Sirok, B., 2004, "Relationship between Cavitation Structures and Cavitation Damage," Wear, 257(December), pp. 1176-1184.

[4] Iwai, Y., and Li, S., 2003, "Cavitation Erosion in Waters Having Different Surface Tensions," Wear, 254(January), pp. 1-9.

[5] Mann, B.S., and Arya, V., 2002, "An Experimental Study to Correlate Water Jet Impingement Erosion Resistance and Properties of Metallic Materials and Coatings," Wear, 253(September), pp. 650-661.

[6] Okada, T., Iwai, Y., Hattori, S. and Tanimura, N., 1995, "Relation between Impact Load and the Damage Produced by Cavitation Bubble Collapse," Wear, 184(May), pp. 231-239.

[7] Coleman, S.L., Scott, V.D., McEnaney, B., Angell, B, and Stokes, R.K., 1995, "Comparison of Tunnel and Jet Methods for Cavitation Erosion Testing," Wear, 184(April), pp. 73-81.

[8] Ahmed, S.M., Hokkirigawa, K, Ito, Y., and Oba, R., 1991, "Scanning Electron Microscopy Observation on the Incubation Period of Vibratory Cavitation Erosion," Wear, 142(March), pp. 303-314.

[9] Richman, R.H., and McNaughton, W.P., 1990, "Correlation of Cavitation Erosion Behavior with Mechanical Properties of Metals," Wear, 140(October), pp. 63-82.

[10] Karimi, A., Avellan, F., 1986, "Comparison of Erosion Mechanisms in Different Types of Cavitation," Wear, 113(December), pp. 305-322.

[11] Oba, R., 1994, "The Severe Cavitation Erosion," 2nd international symposium on cavitation, (April), Tokyo, Japan

[12] Soyama, H., and Asahara, M., 1999, " Improvement of the Corrosion Resistance of a Carbon Steel Surface by a Cavitating Jet," Journal of Material Science Letters 18, pp 1953-1955.

[13] Lecoffre , Y. ,and Archer,A., 1998, "A method to evaluate cavitation erosion in valves," 3rd international symposium on cavitation, (April), Grenoble, France.

[14] Berchiche, N., Franc,J.P., and J.M. Michel, 2002, "A Cavitation Erosion Model for Ductile Materials," Journal of Fluid Mechanics, Volume 124, (September), pp.601-606.

[15] Yamaguchi, A., and Shimizu S., 1987, "Erosion Due to Impingement of Cavitating Jet," Transaction of the ASME, Volume 109,(December),pp 442-447.

[16] Guelich, J. F. , Colther,A., and Martens,H.J., 1993, "Cavitation Noise and Erosion in Jet Cavitation Test Devices and Pumps ," FED-Volume 154, Pumping Machinery ASME .

[17] Karimi, A., and Martin, J. L. , 1986, "Cavitation erosion of materials," International Metals Reviews, Volume 31 no. 1, p p.1-26.

[18] Simoneau, R., 1994, "Cavitation Erosion of Hydraulic Turbines," Proc. A CEA Cavitation Workshop Montréal Vancouver, IMHEF/EPFL (March).

[19] Kato, H., and Shimomura, Y., 2001 "Erosive Intensity Measurements of Cavitating Jet with Various Configuration, " CAV(2001), session A4.002.

[20] Zhou Y.K., Hammitt F.G., 1983, "Cavitation Erosion Incubation Period," *Wear,* Volume 86, (April), pp. 299-313

[21] Syama, H., Kumano, H., and Saka M., 2001, "A New Parameter to Predict Cavitation Erosion," CAV(2001), session A3.002.

[22] Krella, A. , and Zielinski, A. , 2001, "Characteristics of the Incubation Period of the Cavitation Erosion of Aluminium-Magnesium Alloy PA2," Advences in Materials sciences, volume 1, No.1, (November), pp. 62-73.

[23] Lecoffre, Y. , 1995, "Cavitation Erosion, Hydrodynamic Scaling Laws, Practical Method of Long Term Damage Prediction," CAV95, Deauville, France.

[24] Hattori, S., Mori, H., and Okada, T., 1998, "Quantitative Evaluation of Cavitation Erosion," Journal of Fluids Engineering, volume 120, (March), pp.179 -185.

[25] Williams, P.R., Williams,P.M., and Brown S.W.J., 1997, "A Technique for Studying Liquid Jets by Cavitation Bubble Collapse under Shockwaves Near a Free Serface," Journal of Non-Newtonian Fluid Mechanics, Volume 72, pp.101-110.

[26] Fujikawa, S., Takasugi, N., and Peng, G., 1998, "Cavitation Characteristics of Submerged Water Jet," 3rd international symposium on cavitation, (April), Grenoble, France.

[27] Karimi, A., 1987, "Cavitation Erosion of a Duplex Stainless Steel," Materials science and engineering, volume 86, p p. 191-203.

[28] Tanibayashi, H., Ogura,K., and Kanehiro, K., 1994, "Factors Affecting Cavitation in Vibratory Testing Device," 2nd international symposium on cavitation, (April), Tokyo, Japan.

[29] Bistafa, S. R. , 1989, "noise generated by cavitation in orifice plates," Journal of Fluids Engineering, volume 111, (September) Transactions ASME, pp.278 -288.

[30] Knapp, R. T., Daily, J. W., and Hammitt, F. G. 1970, "Cavitation", McGraw-Hill Inc., pp.349-351

Conference on Modelling Fluid Flow (CMFF'06)
The 13th International Conference on Fluid Flow Technologies
Budapest, Hungary, September 6-9, 2006

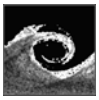

NUMERICAL SIMULATIONS OF TRANSIENT CAVITATING TURBULENT FLOW USING TIME DEPENDENT FRICTIONAL LOSSES

Kamil Urbanowicz[1], Zbigniew Zarzycki[2], Sylwester Kudźma[3]

[1] Corresponding Author. Department of Mechanical Engineering, Szczecin University of Technology, Al. Piastów 19, 70-310 Szczecin, Poland. Tel.: +48 091 449 42 57, Fax: +48 091 449 45 64, E-mail: kurbanowicz@ps.pl
[2] Department of Mechanical Engineering, Szczecin University of Technology. E-mail: zbigniew.zarzycki@ps.pl
[3] Department of Mechanical Engineering, Szczecin University of Technology. E-mail: sylwester.kudzma@ps.pl

Abstract

The paper presents two crucial mathematical models of transient cavitating pipe flow, i.e. column separation model (CSM) and bubbly cavitation model (BCM). The transient state models of friction between liquid and pipe wall have been associated with those models. The equations describing the CSM and BCM models have been solved basing on method of characteristics and finite differences method afterwards. The results of numeric simulations have been compared to results of experiments. Putting the dependences representing the non-stationary resistances of friction between liquid and pipe walls to considered models one can observe, that simulation results are quite similar to referring experimental results.

Keywords: bubbly flow, cavitation, column separation, numerical simulation, transient turbulent flow, unsteady friction.

Nomenclature

c	$[m/s]$	acoustic wave speed
g	$[m/s^2]$	acceleration due to gravity
p	$[N/m^2]$	pressure
p_v	$[N/m^2]$	vapour pressure
t	$[s]$	time
$\hat{t} = \nu t / R^2$	[-]	dimensionless time
v	$[m/s]$	instantaneous mean flow velocity
w	[-]	weighting function
x	$[m]$	distance along pipe axis
A	$[m^2]$	pipe cross-sectional area
L	$[m]$	pipe length
R	$[m]$	radius of pipe
$Re = 2Rv/\nu$	[-]	Reynolds number
α	[-]	volumetric fraction of liquid
γ	$[^\circ]$	pipe slope angle
λ	[-]	Darcy – Weisbach friction factor
μ	$[kg/ms]$	dynamic viscosity
ν	$[m^2/s]$	kinematic viscosity
ρ_l	$[kg/m^3]$	liquid density (constant)
ρ_m	$[kg/m^3]$	density of homogenous mixture of liquid and vapour
ρ_v	$[kg/m^3]$	vapour density (constant)
τ_w	$[N/m^2]$	wall shear stress
τ_{wq}	$[N/m^2]$	wall shear stress for quasi - steady flow
τ_{wn}	$[N/m^2]$	unsteady wall shear stress
$\Omega = \omega R^2/\nu$	[-]	dimensionless frequency

1. INTRODUCTION

During the water hammer phenomena, which can be caused, for example, by flow shut off or emergency switching off the electric motor driving the hydraulic pump, the cavitation process in hydraulic pipelines of hydraulic system can appear. There are two kinds of possible cavitation phenomena: liquid-vaporous and gas ones. The liquid –vaporous cavitation comes into existence , if pressure drops to the value which is lower than pressure of liquid vaporization for existing temperature. If pressure becomes lower than pressure necessary for keeping the dissolved gases "inside" of saturated solution, than gases in liquid (like dissolved air) are released and described phenomenon is called gas cavitation. From mathematical point of view one can select two basic models. The first one refers to discrete cavitation. This type of cavitation causes column separation of liquid stream. The column separation model (CSM) describes the discrete cavitation. The second model, i.e.. bubbly cavitation model (BCM) ,is associated with phenomenon of bubbly cavitation distributed along of pipe axis. The wave nature of changes of pressure accompanying the water hammer phenomena makes, that cavitation can appear and

disappear periodically. Taking into account the technical needs one should be able to predict the maximal amplitudes of that pulsating pressure.

The present paper deals with prediction of pressure changes during transient states of fluid flow. The cavitation phenomena are taken into account. The computer software programs dedicated for simulation of fluid transients under the presence of cavitation usually use quite simple calculation algorithms. The basing on models of quasi-steady hydraulic resistances can be treated as essential matter of simplifications. For example, we can specify the Streeter's model of CSM type [1] or Chaundhry 's at al. model [2] of BCM type, where quasi-steady headlosses are assumed. Fuji at all. in [3] neglect the hydraulic resistances. The introduction of time-variable hydraulic resistances to both considered models can be treated as novelty of present paper. The time-variable hydraulic resistances are included to models for laminar flow as well as turbulent one.

The variable hydraulic resistances are represented by convolution integral. The integrand is expressed by fluid acceleration and certain weighing function for wall shear stress. The presented results of computer simulations show changes of pressure during water hammer phenomena. The cavitation has been taken into account during simulations. For comparison purposes, simulations have been carried out for variable and quasi-steady hydraulic resistances. The obtained simulation results have been compared to credible experimental results published by Bergant and Simpson [4-6]. The above comparison shows, that models with variable hydraulic resistances are more accurate comparing them to models with quasi-steady resistances, because results generated by means of those models are 'close' to referring experimental results.

2. BASIC EQUATIONS

The two models of cavitation are taken into consideration:

- modified column separation model (CSM) [6-10]:

$$\frac{\partial p}{\partial t} + \rho_l \cdot c^2 \frac{\partial v}{\partial x} = 0 \tag{1}$$

$$\frac{\partial p}{\partial x} + \rho_l \cdot \frac{\partial v}{\partial t} + \rho_l \cdot g \cdot \sin\gamma + \frac{2}{R} \cdot \tau_w = 0 \tag{2}$$

- modified bubbly cavitation model (BCM) [10]:

$$\frac{1}{c^2} \cdot \frac{\partial p}{\partial t} + (\rho_l - \rho_v) \cdot \frac{\partial \alpha}{\partial t} + \rho_m \cdot \frac{\partial}{\partial x} \cdot \left(\frac{v}{\alpha}\right) = 0 \tag{3}$$

$$\rho_m \cdot \frac{\partial}{\partial t} \cdot \left(\frac{v}{\alpha}\right) + \frac{\partial p}{\partial x} + \frac{2}{R} \cdot \tau_w \left(\frac{v}{\alpha}, \alpha\right) + \rho_m \cdot g \cdot \sin\gamma = 0 \tag{4}$$

where:

$$\rho_m = \alpha \cdot \rho_l + (1-\alpha) \cdot \rho_v \tag{5}$$

3. MODELS OF FRICTION

The calculations of transient states taking into account cavitation are based on the usually used quasi-steady model of friction losses, which is directly associated with friction between fluid and pipe walls. This type of friction models has been applied both to CSM model as well as BCM one:

- in CSM:

$$\tau_w = \tau_{wq} = \frac{1}{8} \rho_l \cdot \lambda \cdot v \cdot |v| \tag{6.1}$$

- in BCM:

$$\tau_w = \tau_{wq} = \frac{\left(\frac{1}{8} \rho_m \cdot \lambda \cdot v \cdot |v|\right)}{\alpha^2} \tag{6.2}$$

The shear stress at pipe wall in case of unsteady flow may be presented as the sum of two components, namely: quasi-steady state shear component τ_{wq} and unsteady state shear component τ_{wn} [11]:

$$\tau_w = \tau_{wq} + \frac{2\mu}{R} \int_0^t w(t-u) \frac{\partial v}{\partial t}(u) du \tag{6.3}$$

where w(t) is weighting function. The following forms of weighting functions have been selected for application in current work:

- for laminar flow:

a) model of Zarzycki [11,12]:

$$w(\hat{t}) = C_1 \hat{t}^{-0.5} + C_2 e^{-m\hat{t}} \tag{7}$$

where: $C_1 = 0.2812$, $C_2 = -1.5821$, $m = 8.8553$.

b) model of Schohl [13]:

$$w(\hat{t}) = \sum_{i=1}^{5} m_i e^{-n_i \hat{t}} \tag{8}$$

where: $m_1 = 1.051$, $m_2 = 2.358$, $m_3 = 9.021$, $m_4 = 29.47$, $m_5 = 79.55$;
$n_1 = 26.65$, $n_2 = 100$, $n_3 = 669.6$, $n_4 = 6497$, $n_5 = 57990$.

- for turbulent flow, model of Zarzycki–Kudźma [11,14]:

$$w(\hat{t}) = \left(c_1 Re^{c_2} + c_3\right) \cdot \sum_{i=1}^{8} A_i \cdot e^{-b_i \cdot \hat{t}} \tag{9}$$

c_1 = -13.27813, c_2 = 0.000391, c_3 = 14.27658;
A_1 =1.568, A_2 =60.73, A_3 =10.76, A_4 =33.26, A_5 =2.799, A_6 =5.527, A_7 =0.2137, A_8 =18.99;
b_1 = 8.44, b_2 =96940, b_3 = 2162, b_4 = 29250, b_5 = 88.02, b_6 = 480.5, b_7 = 0.09834, b_8 = 8425.

4. CALCULATION PROCEDURE

Equations (1), (2) and (3), (4) can be transformed to pair of differential equations by application of method of characteristics (MOC). For CSM model is:

$$\pm dp + \rho_l \cdot c \cdot dv + \frac{2 \cdot \tau_w \cdot c}{R} \cdot dt + \rho_l \cdot c \cdot g \cdot dt \cdot \sin\gamma = 0 \quad (10)$$

if $$dx = \pm c \cdot dt \quad (11)$$

For bubbly cavitation is:

$$\frac{d}{dt}\left(\frac{v}{\alpha}\right) \pm \frac{1}{\rho_l \cdot c} \cdot \frac{d}{dt}(p - p_v) \pm c \cdot \frac{\partial}{\partial t}\left(ln\frac{\rho_m}{\rho_l}\right) + g \cdot \sin\gamma + \frac{2 \cdot \tau_w}{R \cdot \rho_m} = 0 \quad (12)$$

if $$dx = \pm c \cdot dt \quad (13)$$

In case of Zarzycki's model (7) the shear stress τ_w was computed according to traditional Zielke method [15], where integral convolution was replaced by finite sum.

$$\tau_{w(k,i)} = \tau_{wq(k,i)} + \tau_{wn(k,i)} \quad (14)$$

The component $\tau_{wq(k,i)}$ is calculated from (6.1) for CSM model and from (6.2) for BCM model respectively.

$$\tau_{wn(k,i)} = \frac{2\mu}{R}\left[(v_{k,i} - v_{k-1,i})W_{1,i} + (v_{k-1,i} - v_{k-2,i})W_{2,i} + \ldots + (v_{2,i} - v_{1,i})W_{k-1,i}\right] \quad (15)$$

The stress τ_{wn} for Schohl's model (8) has been calculated as it follows:

$$\tau_{wn} = \frac{2 \cdot \mu}{R} \cdot \sum_{i=1}^{5} y_i \quad (16)$$

where:

$$y_i(t + \Delta t) = y_i(t) \cdot e^{-n_i\left(\frac{\nu}{R^2}\right)\Delta t} + m_i \cdot e^{-n_i\left(\frac{\nu}{R^2}\right)\frac{\Delta t}{2}} \cdot [v(t + \Delta t) - v(t)] \quad (16.1)$$

It is model which was created on the base of effective Trikha model [16].

For effective model of Zarzycki-Kudźma (9) [14]:

$$\tau_{wn}(t + \Delta t) = \frac{2 \cdot \mu}{R} \cdot \sum_{i=1}^{8} y_i(t) \cdot A_i \cdot e^{-b_i \cdot \frac{\nu}{R^2} \cdot \Delta t} + \left(c_1 Re^{c_2} + c_3\right) \cdot \frac{A_i \cdot R^2}{\Delta t \cdot b_i \cdot \nu} \cdot \left[1 - e^{-b_i \cdot \frac{\nu}{R^2} \cdot \Delta t}\right] \cdot [v(t + \Delta t) - v(t)] \quad (17)$$

The solution of equation system (1),(2) describing fluid column separation is well known. However, it should be mentioned about important assumption, that simulated model allowed to create the discontinuity area only inside of one among set calculation cross-sections [7,9,17]. That only one, distinguished cross-section is located directly in neighborhood of cut-off valve. The above attitude is applied in order to eliminate the possibility of generating of "virtual numeric peaks of pressure", which are results of distribution of discontinuity areas to several calculation cross-sections. According to considered procedure, for those calculation cross-sections (except the next to cutting valve) where estimated pressure is $p \le p_v$ one has to calculate the average flow velocities, i.e. $v = 0.5 \cdot (v^+ + v^-)$. The values of v^+ (downstream velocity of the vapour cavity section) and v^- (upstream velocity of the vapour cavity section) are calculated from equations of characteristics C^+ and C^- under assumption that $p_D = p_v$. The volume of cavitation zone inside of pipelines with constant diameter is calculated using continuity equation in the form:

$$V_c = A \cdot \int_{t_o}^{t} (v^+ - v^-) \cdot dt \quad (18)$$

where:
t_o – time of appearing of cavitation (defined by moment when value of p becomes less than p_v),
v^+ and v^- - fluid flow velocities , respectively for downstream and upstream of the vapour cavity section.

Initially, the value of volume V_c grows, which is an evidence of progress of cavitation process, and next V_c decreases, when cavitation disappears. If V_c becomes to value $V_c = 0$, then process of cavitation is finished and returns the state of continuous flow of fluid. The above (18) mentioned equation of continuity can be formulated as it follows:

$$V_{C_{k+1}} = V_{C_k} + 0.5 \cdot A \cdot (v^+_{k+1} + v^+_k - v^-_{k+1} - v^-_k) \cdot \Delta t \quad (19)$$

For bubbly cavitation model BCM:

Using method of characteristics and rewriting - later on - in finite difference form equations (3),(4) for BCM model we obtain [10]:

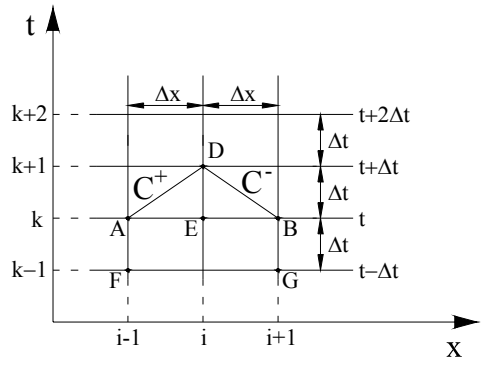

Fig. 1. Rectangular grid of characteristics.

$$C^{+}: \frac{v_D}{\alpha_D} + \frac{1}{\rho_l \cdot c} \cdot (p_D - p_v) + \frac{c}{2} \cdot ln \frac{\rho_{mD}}{\rho_l} = C_A \quad (20)$$

$$C^{-}: \frac{v_D}{\alpha_D} - \frac{1}{\rho_l \cdot c} \cdot (p_D - p_v) - \frac{c}{2} \cdot ln \frac{\rho_{mD}}{\rho_l} = C_B \quad (21)$$

where:

$$C_A = \frac{v_A}{\alpha_A} + \frac{1}{\rho_l \cdot c} \cdot (p_A - p_v) + \frac{c}{2} \cdot ln \frac{\rho_{mE} \cdot \rho_{mF}}{\rho_l \cdot \rho_{mA}} - \frac{2 \cdot \Delta t}{R \cdot \rho_{mA}} \cdot \tau_{wA} - \Delta t \cdot g \cdot \sin\gamma \quad (22)$$

$$C_B = \frac{v_B}{\alpha_B} - \frac{1}{\rho_l \cdot c} \cdot (p_B - p_v) - \frac{c}{2} \cdot ln \frac{\rho_{mE} \cdot \rho_{mG}}{\rho_l \cdot \rho_{mB}} - \frac{2 \cdot \Delta t}{R \cdot \rho_{mB}} \cdot \tau_{wB} - \Delta t \cdot g \cdot \sin\gamma \quad (23)$$

the value of C_A and C_B are known from previous time steps.

- It's no cavitation when $C_A \geq C_B$, than $\alpha_D = 1$

and:

$$p_D = \frac{\rho_l \cdot c}{2} \cdot (C_A - C_B) + p_v \quad (24)$$

- Cavitation occurs when: $C_A < C_B$, than:

$$p_D = p_v$$

Transforming equation (5) one obtains:

$$\alpha_D = (\rho_{mD} - \rho_v) / (\rho_l - \rho_v) \quad (25)$$

From equations (20),(21),(22),(23) for p_D=p_v one can determine ρ_{mD}. Putting it to formula (25) we obtain:

$$\alpha_D = \frac{\rho_l \cdot exp\left(\frac{C_A - C_B}{c}\right) - \rho_v}{\rho_l - \rho_v} \quad (26)$$

- For both considered cases we use the following formula in order to calculate the velocity:

$$v_D = \frac{\alpha_D}{2} \cdot (C_A + C_B) \quad (27)$$

5. RESULTS OF SIMULATION

To verify results of simulation of presented models they have been compared to experimental results [4-6]. The experiments have been carried out using apparatus shown in Fig. 2. The experimental apparatus comprises a 37.2 [*m*] long sloping copper pipe of 22 [*mm*] internal diameter and 1.63 [*mm*] wall thickness connecting the two pressurized tanks.

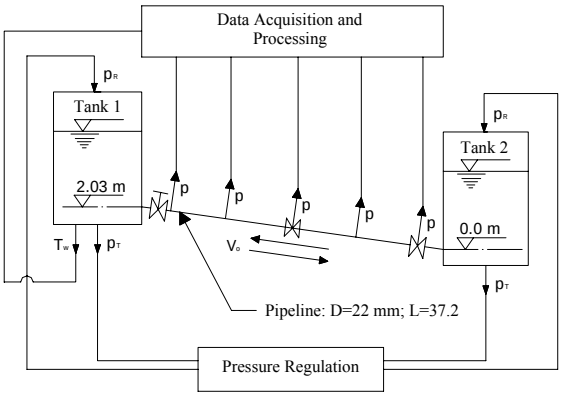

Fig. 2. Experimental apparatus.

The following parameters where kept constant for purpose of all further considerations: time of operation of quick shut- off ball valve T_f =*0,009* [*s*]; velocity of propagation of pressure wave *c=1319* [*m/s*]; water temperature T_w = *15,5* [^oC]. The water density and viscosity have been determined from characteristics for known temperature. The graphical representations of chosen transient states are presented below.

A) The steady state velocity v_o=*0.3* [*m/s*]; pressure near tank p_{zb}=*0,2158* [*MPa*]; model of non-stationary friction losses for laminar flow – effective model of Schohl.

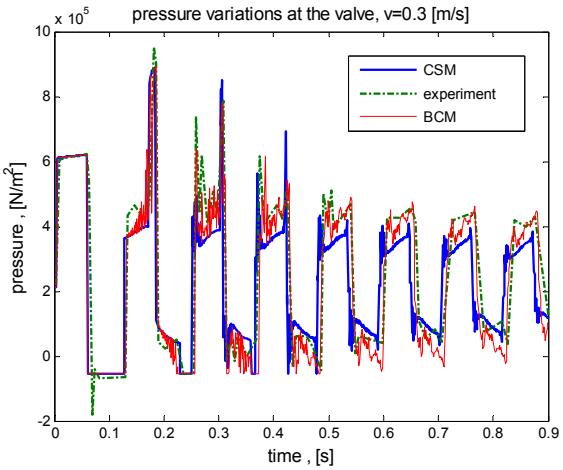

Fig. 3. Pressure variation at the valve (v_o=0.30 m/s, p_{zb}=0.2158 MPa).

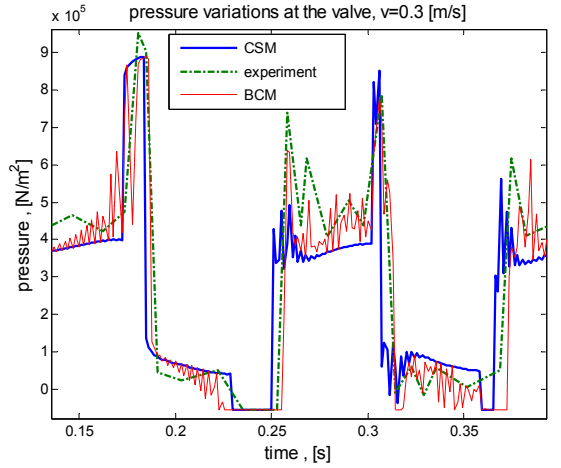

Fig. 4. Pressure variation at the valve - zoom (v_o=0.30 m/s, p_{zb}=0.2158 MPa).

Looking at Fig. 3 we can observe, that behind the fourth peak of curve representing pressure near valve model of BCM type is better comparing it to model CSM. Simulation of CSM model yields to low amplitudes of pressure peaks. Furthermore, simulation results for BCM model allow for better fit of periods to those reference ones.

B) The steady state velocity v_o=1,5 [m/s]; pressure near tank p_{zb}=0,3139 [MPa]; model of friction losses - quasi-linear.

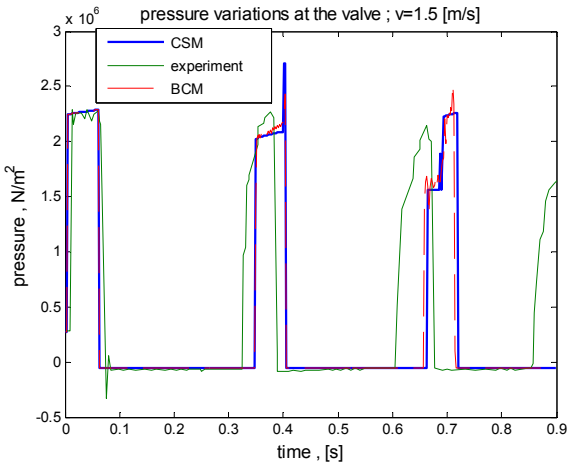

Fig. 5. Pressure variation at the valve (v_o=1.50 m/s, p_{zb}=0.3139 MPa).

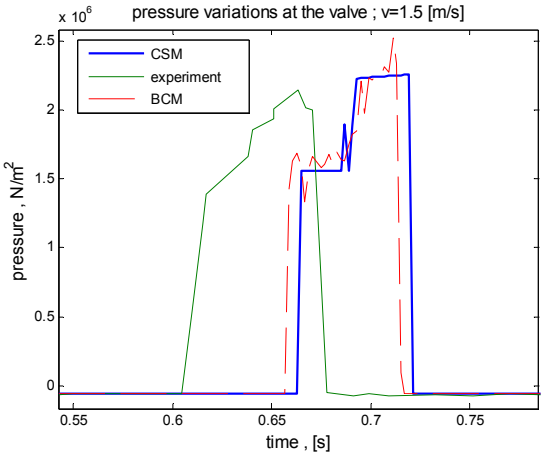

Fig. 6. Pressure variation on the valve - zoom (v_o=1.50 m/s, p_{zb}=0.3139 MPa).

We can observe (see Fig. 5) the differences between simulation results obtained for simple, commonly used quasi-stationary friction representation and experimental results. The same curve is shown in Fig. 7. However, the additional curve, that representing results yielded by CSM model where non-stationary friction was calculated, is attached as well. We can observe the positive influence caused by application of models of non-stationary friction.

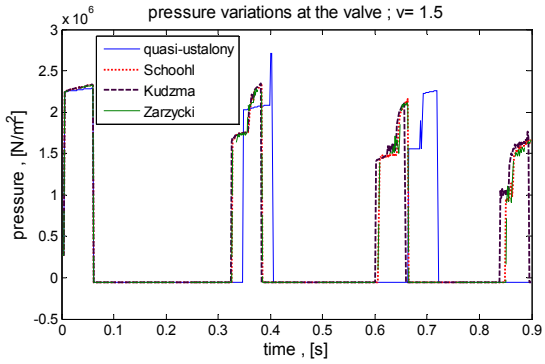

Fig. 7. Pressure variation on the valve - unsteady friction (v_o=1.50 m/s, p_{zb}=0.3139 MPa).

C) The steady state velocity v_o=1,5 [m/s]; pressure near tank p_{zb}=0,2158 [MPa]; model of friction losses for turbulent flow – effective model given by Zarzycki-Kudźma.

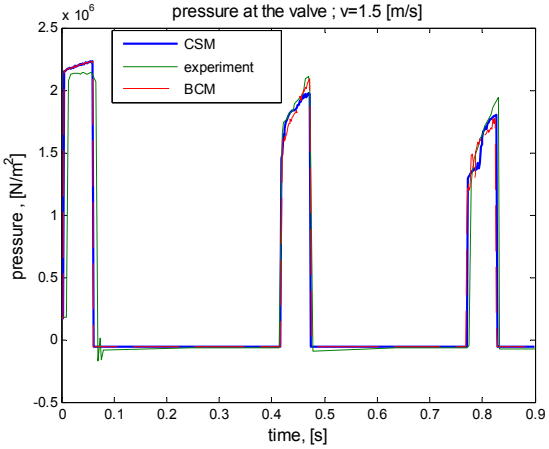

Fig. 8. Pressure variation on the valve (v_o=1.50 m/s, p_{zb}=0.2158 MPa).

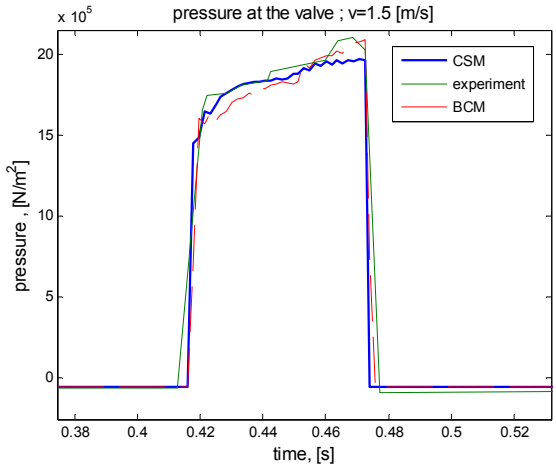

Fig. 9. Pressure variation on the valve - zoom (v_o=1.50 m/s, p_{zb}=0.2158 MPa).

The comparison of results in Fig.8 proves, that for initial steady state velocity v_o of range 1,5 [m/s] we can not observe the differences between accuracies of BCM and CSM models. However, for more precise evaluation we should observe process over the bigger range of time. The observation time range equal to 0.9 [s] does not allow to answer the question, how the correlation between experimental results and simulation results looks like, if the fourth, fifth and subsequent peaks of pressure are considered, till the end of the cavitation process and its transformation into oscillations of pressure without cavitation effects.

D) The steady state velocity v_o=0,28 [m/s]; pressure near tank p_{zb}=0,1962 [MPa]; model of friction losses for laminar flow – traditional one given by Zarzycki.

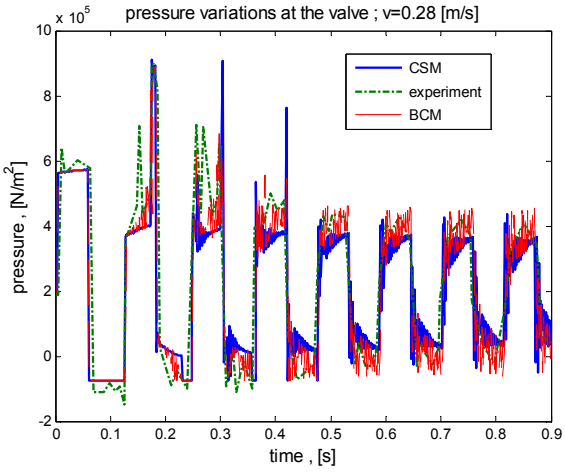

Fig. 10. Pressure variation on the valve (v_o=0.28 m/s, p_{zb}=0.1962 MPa).

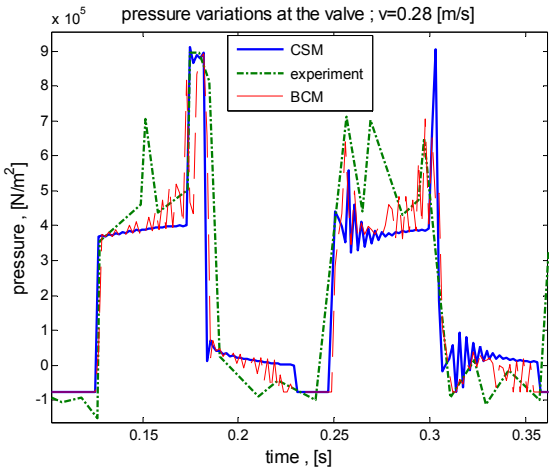

Fig. 11. Pressure variation on the valve - zoom (v_o=0.28 m/s, p_{zb}=0.1962 MPa).

Observing results gathered in Fig. 10 we can conclude, that BCM model is better than CSM one. Note, that CSM model yields "virtual" third and fourth peaks of pressure, which are not confirmed by experimental results. The amplitudes of these virtual peaks are quite different than reference ones, i.e. those obtained by measurements. Let us note, that both models perfectly simulate the period of oscillations.

The comparison of quality of numeric simulations for various models of fluid friction is presented in Fig. 7, where model of liquid column separation is "visualized". For laminar flow model given by Schohl and model proposed by Zarzycki yield almost identical results. The above conclusion confirms the high accuracy of effective model of Schoohl. The calculations with use of Zarzycki's model have been carried out with use of traditional method. The Zarzycki-Kudźma's non-stationary model of fluid friction has been obtained on the base of model of Zarzycki for turbulent flow. The accuracy of this model is considered in [11,14]. The effectiveness of presented model of Zarzycki-Kudźma has been widely described in [14].

6. SUMMARY

The two models of transient cavitation are presented in the paper. The first is column separation model CSM. This traditional model is commonly used by those dealing with practical tasks. The second model which is the new one is called bubbly cavitation model (BCM). The experiments carried out by Bergant and Simson incline to conclusion, that for small Reynolds numbers the courses of pressure reveal substantially more oscillations (see Fig. 3,4,10,11). Probably, it is caused by cavitation in form of bubbles. Also for those cases the numerical simulation basing on models of bubble cavitation (BCM) is a little bit more accurate than simulation based on column separation model (CSM). For flows characterized by large Reynolds number, where liquid column separation columns probably took place, we can observe (see Figs. 5,6,8,9), that experimental courses of pressure do not contain the additional oscillations. It can be treated as result of conserving of discontinuity area for relatively long time. It is difficult to chose the better model of cavitation for Reynolds numbers belonging to range considered above.

Many comparisons incline to unique conclusion, that application of models of non-stationary fluid friction substantially improves the accuracy of simulations decreasing the differences between simulation results and experimental ones. The simulations based on quasi-stationary models of friction yield inaccuracies in evaluation of period of oscillations as well as subsequent amplitudes of pressure peaks.

The other visible differences between values of simulated courses of pressure and referring real (experimental) values and observable slips (very small differences between simulated and real periods) are probably caused by:

- neglecting of gas cavitation,
- simplifying assumption about one-dimensional movement of fluid,
- neglecting of convection derivatives,
- numerical errors of computer simulations.

The choice of type of non-stationary model of friction depends on type of flow (laminar or turbulent). For all presented calculations the critical number $Re_c = 2320$ was the only agent determining that choice. For transient flows with existence of cavitation (like water hammer phenomena) there are no transparent criteria determining the type of flow. We can find only one formula, i.e. that presented by Ohmi [18]. However, it has been shown in [19], that application area of Ohmi formula is rather narrow. Furthermore, it does not consider possibility of appearing of cavitation.

Authors of present paper think, that further works should be concentrated on more accurate experimental researches for wide range of Reynolds numbers and additional investigations aimed at determination of criteria enabling prediction of conditions for turbulent flow.

REFERENCES

[1] Streeter, V. L. 1969, "Water hammer analysis", *ASCE, Journal of Hydraulic Division*, 95(6), pp. 1959-1972.

[2] Chaudhry, M. H., Bhallamudi S. M., Martin C. S., and Naghash M., 1990, "Analysis of transient pressure in bubbly, homogeneous, gas-liquid mixtures", *Journal of Fluids Engineering, June* , Vol. 112, pp. 225-231.

[3] Fujii T., and Akagawa K., 1986, "Analysis of water hammering in bubbly flows", *JSME*, vol. 29, no. 265, pp. 1746-1751.

[4] Bergant A., and Simpson A. R., 1996, "Interesting lessons from column separation experiments", *Proceedings of the 7th International Conference on Pressure Surges and Fluid Transients in Pipelines and Open Channels*, Publication 19, BHR Group, pp. 83-97.

[5] Bergant A., and Simpson A. R., 1994, "Estimating unsteady friction in transient cavitating pipe flow", *Proceedings of the 2nd International Conference on Water Pipline Systems, BHRA Group Conf. Series Publ.,* No. 110, UK, 24-26 May, Edinburgh, pp. 3-16.

[6] Bergant A., and Simpson A. R., 1999, "Pipline column separation flow regimes", *Journal of*

Hydraulic Engineering, August 1999, pp. 835-848.

[7] Simpson A. R., and Bergant A., 1994, "Numerical comparison of pipe-column-separation models", *Journal of Hydraulic Engineering*, vol. 120, no. 3, march, pp. 361-377.

[8] Wylie E.B., and Streeter L.V., 1978, *"Fluid Transients"*, McGraw-Hill, New York.

[9] Safwat H. H., and Polder Jaap van Den, 1973, "Experimental and analytic data correlation study of water column separation", *Journal of Fluids Engineering*, march 1973, pp. 91-97.

[10] Shu J. J., 2003, "Modelling vaporous cavitation on fluid transients", *Intern. Journal of Pressure Vessels and Piping*, Vol. 80, pp. 187-195.

[11] Zarzycki Z., and Kudźma S., 2004, "Simulations of transient turbulent flow in liquid lines using time – dependent frictional losses", *Proceedings of the 9th International Conference on Pressure Surges, BHR Group,* Chester, UK, 24–26 March, pp. 439–455.

[12] Zarzycki Z., 2000, "On Weighting Function for Wall Shear Stress During Unsteady Turbulent Flow", *Proc. of 8th International Conference on Pressure Sergues, BHR Group Conference Series*, No 39, 12-14 April, The Hague, The Netherlands, pp. 529-534.

[13] Schohl G. A., 1993, "Improved Approximate Method for Simulating Frequency – Dependent Friction in Transient Laminar Flow", *Journ.of Fluids Eng., Trans. ASME*, Vol. 115, September 1993, pp. 420–424.

[14] Kudźma S., 2005, "Modeling and simulation dynamical runs in closed conduits of hydraulics systems using unsteady friction model", *PhD work at Szczecin University of Technology*, February, In Polish.

[15] Zielke W., 1968, "Frequency-Dependent Friction in Transient Pipe Flow", *Journ. of ASME*, 90, March 1968, pp. 109-115.

[16] Trikha A. K., 1975, "An Efficient Method for Simulating Frequency-Dependent Friction in Transient Liquid Flow", *Journ. of Fluids Eng., Trans. ASME*, March 1975, pp. 97-105.

[17] Adamkowski A., 1996, "*Theoretical and experimental investigation of waterhammer attenuation by cut-off and bypass valves in pipeline systems of hydraulic turbomachines"* In Polish. WIMP PAN, Gdańsk.

[18] Ohmi M., Kyomen S., and Usui T., 1985 "Numerical Analysis of Transient Flow in a Liquid line", *Bulletin of JSME*, Vol. 28. No 239, May 1985, pp. 799–806.

[19] Carpinlioglu M. O., and Gundogdu M. Y., 2001, "A critical review on pulsatile pipe flow studies directing towards future research topics", *Flow Measurement and Instrumentation 12,* pp. 163-174.

Conference on Modelling Fluid Flow (CMFF'06)
The 13th International Conference on Fluid Flow Technologies
Budapest, Hungary, September 6-9, 2006

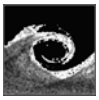

NUMERICAL SIMULATION AND MEASUREMENT OF CAVITATION AROUND A SQUARE OBSTACLE

Tamás TÁBI[1], Zoltán PANDULA[2], Csaba HŐS[3]

[1]Department of Hydrodynamic Systems, Budapest University of Technology and Economics. Stoczek u. 2/b, H-1111, Budapest, Hungary. Tel.: + 36 1 463 2216, Fax: +36 1 463 3091, E-mail: tabitamas@freemail.hu
[2]Department of Hydrodynamic Systems, Budapest University of Technology and Economics. E-mail: pandula@hds.bme.hu
[3]Corresponding author. Department of Hydrodynamic Systems, Budapest University of Technology and Economics. E-mail: hos@hds.bme.hu

ABSTRACT

The aim of the presented study was to test the capabilities of the built-in cavitation models of a commercial Computational Fluid Dynamics (CFD) code in the case of cavitating flow around a square obstacle. First, several measurements were performed in a test rig and the characteristic quantities (acceleration levels and geometric dimensions of the cavitating regime) were recorded, for various flow velocities (i.e. cavitation numbers). Secondly, two-dimensional steady and unsteady CFD calculations were performed for the same flow velocities and the influence of the turbulence model was studied. It was found that the applied turbulence model affects the results essentially; typically isotrop turbulence models (e.g. k – ε) fail to describe the unsteadiness of the cavitating flow.

Keywords: cavitation, cavitation coefficient, CFD, noise measurement

NOMENCLATURE

R_B	$[mm]$	bubble diameter
S_E	$[kg/ms^3]$	energy source
$\vec{S}_M$	$[kg/m^2s^2]$	momentum source
T	$[°C]$	temperature
$\vec{U}$	$[m/s]$	velocity vector
a	$[m/s^2]$	acceleration
f	$[\%]$	volume fraction
g	$[m/s^2]$	gravitational acceleration
h_{tot}	$[m/s^2]$	specific total enthalpy
n_g	$[dB]$	noise acceleration (level)
p	$[Pa]$	pressure
t	$[s]$	time
v	$[m/s]$	velocity magnitude
$\underline{\delta}$	[-]	identity matrix
λ	$[kgm/s^3°C]$	thermal conductivity
μ	$[kg/ms]$	dynamic viscosity
ρ	$[kg/m^3]$	density
σ	[-]	cavitation coefficient
σ_T	[-]	surface tension coefficient between the liquid and vapour

Subscripts and Superscripts

M	mixture
V	vapour
∞	undisturbed flow
L	liquid
ref	reference

1. INTRODUCTION

Presence of cavitation in hydraulic machines - notably pumps - leads to several problems like erosion, pressure pulsation, decreased flow rate, or reduced machine life expectancy. Under cavitating operation not only the hydraulic parameters of the pump decrease, but due to the damage of steam bubble implosion, a strong erosion effect appears. This leads to heavy damage of the bladed wheel and may result in the malfunction of the whole machine.

For engineering purposes, two kinds of cavitation are usually distinguished; physical and technical cavitation. Physical cavitation is the phase when only single bubbles appear and technical cavitation is the case when the bubbles form a "continuous" cavity cloud. Obviously, when a hydraulic system moves to cavitating operation from a non-cavitating one, physical cavitation occurs first and technical cavitation develops only later. The latter one is relatively easy to detect because there is a characteristic change in the hydraulic parameters (head, flow rate). Contrary, although physical cavitation causes significant erosion, no easy-to-verify practical criteria can be given for its presence.

Computational fluid dynamic technique is a suitable tool for predicting the onset of cavitation. However, it is not clear whether the built-in models

of commercial CFD codes are reliable and robust enough for every-day practical purposes. The aim of this study is to test the capabilities of a commercial CFD code (ANSYS CFX 10.0) in terms of cavitating flow simulation. Although "in house" codes are more flexible and there are more possibilities to test new ideas and models, they are often specialized for some narrow range of applications and are lack of user-friendly graphical interfaces.

Cavitating flows are challenging not only from the viewpoint of measurements (due to their two-phase nature) but also their mathematical modelling is highly nontrivial. Some examples of such investigations can be found in e.g. [1-2], [7-8]. Usually, the cavitation models are based on the linear part of the Rayleigh-Plesset equations (see [1]). The main problem with this model is that it includes some quantities that are hard or impossible to determine, for example bubble number density or initial bubble diameter. Although the authors are aware of other advanced models (see e.g. [2]), the Rayleigh-Plesset model was employed in this study as this is the cavitation model implemented in CFX 10.0.

2. CAVITATION TUNNEL TESTS

Experiments were set up in the laboratory of Hydrodynamic Systems, Budapest University of Technology and Economics. The sketch of the test rig is given in Figure 1. The system is closed in order to allow the control of the system pressure (hence the cavitation number). A square obstacle of 20*mm* was inserted into the test section of the cavitation tunnel (denoted by "D" in Figure 1). The width, height and length of the test section is 48*mm*, 200*mm*, and 300*mm*, respectively. For further details on the test rig, see [3-4].

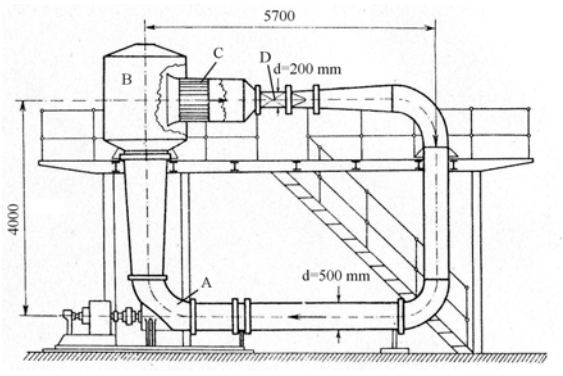

Figure 1. Cavitation tunnel.

The flow velocity (in the test section) was varied from 3*m/s* to 12*m/s* and the system pressure from 1.04*bar* to 0.68*bar*, resulting in a cavitation number between 17.67 and 0.96. The wall of the test section was made of Plexiglas to allow visual access (Fig.2.).

In each measurement point, images were captured with a fast CCD camera (50 fps), the pressure difference on the confusor in-, and outlet and the absolute pressure before the obstacle was measured with U tubes and the noise level was also recorded by the HB PULSE vibration measurement system in a the range of 0 to 25 kHz. The confusor pressure difference allows the calculation of fluid velocity and absolute pressure close to the obstacle gives the pressure level. These values were used later as boundary conditions in the numerical simulations.

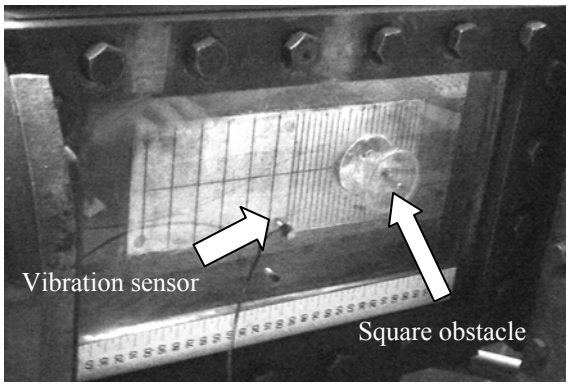

Figure 2. Test section arrangement. (Note that the round body next to the obstacle is only the fixing in the wall - made also of Plexiglas - thus it does not influence the flow.)

3. CAVITATIONAL TUNNEL TEST RESULTS

The cavitation number is defined as the ratio of the system pressure (p_∞) above the vapour pressure $p_V(T_\infty)$ (at system temperature) and the dynamic pressure, i.e.

$$\sigma = \frac{p_\infty - p_V(T_\infty)}{\rho \cdot v^2 / 2}. \qquad (1)$$

Another quantity often used for cavitation detection is the vibration level (noise level), defined as

$$n_g = 20 \cdot \lg \frac{a}{g}, \qquad (2)$$

where *a* represents the averaged acceleration over the frequency range.

Plotting the vibration spectra vs. the cavitation number (see Fig.3.), we experience an increasing vibration level as the cavitation number drops. This corresponds to the increasing bubble activity and the presence of periodic detachment of cavitation

clouds (similar to the von Kármán swirling flow). However, below a critical cavitation number (approx. 1.1) the amplitude of the spectra drops again to almost the same level as that one in the case of non-cavitating flow. This phenomenon is related to the appearance of supercavitation, i.e. a large steady separation cloud after the obstacle. The origin of the decreased noise level is that before supercavitation, there is a large number of 'individual' bubbles, which act as 'individual' noise sources. However, with the appearance of supercavitation, there is only one noise source, which is the large cavitation cloud after the body.

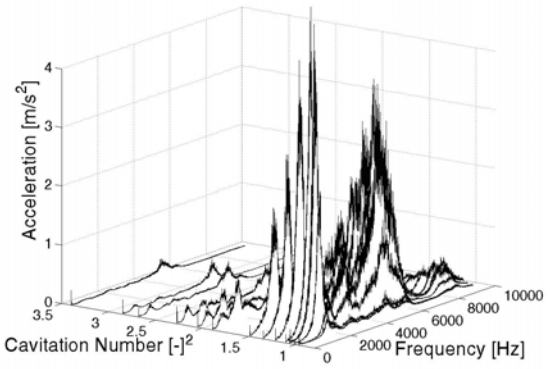

Figure 3. Spectra of the acceleration signal as a function of the cavitation number.

Although the vibration signals were registered up to 25 kHz, there was no significant information above 10 kHz, so that range was not presented in the Fig.3. Two frequency peaks are to be noticed on the noise level spectrum: approx. 1500 Hz and 5000 Hz. These peaks were identified – with a Dirac-delta excitation – as eigenfrequencies of the test tunnel. This observation is consistent with the white noise-nature of cavitation, i.e. it excites the system at all frequencies – hence resonance occurs with the system eigenfrequencies.

The same phenomenon is to be noted in Fig. 4. Here, the average acceleration level is plotted vs. the cavitation number (see Eq.(2)). It is clearly seen that as supercavitation forms, there is a sudden drop in the noise level.

Figure series 5 depicts the pictures captured by the CCD camera. The flow is from the right to the left. Until the supercavitation limit ($\sigma \approx 1.1$) the obviously unsteady nature of the cavity cloud is clearly seen. We experience a periodic cloud separation, which is formed by the alternating re-entrant jet on the upper and lower side of the cavitation cloud.

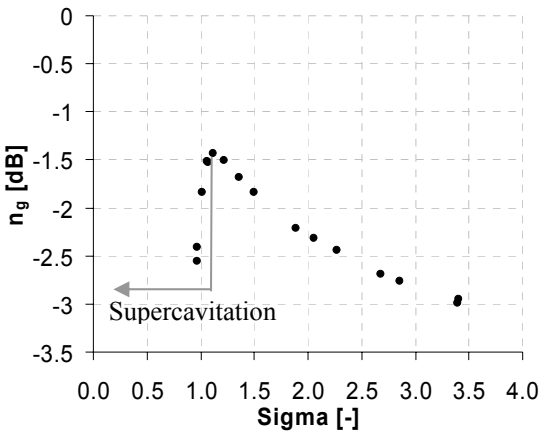

Figure 4. Noise level vs. cavitation number.

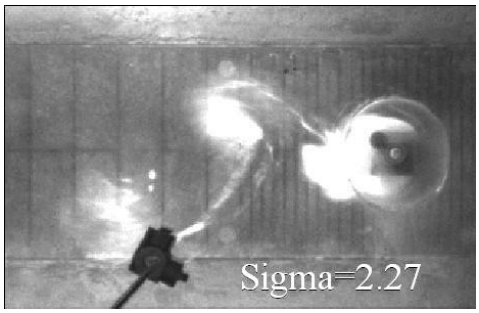

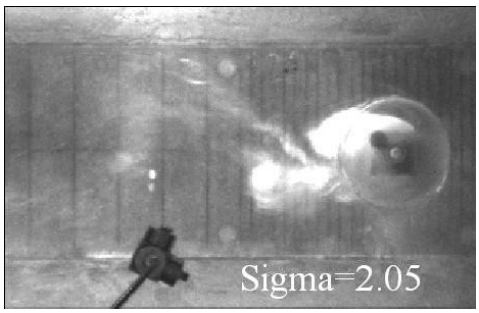

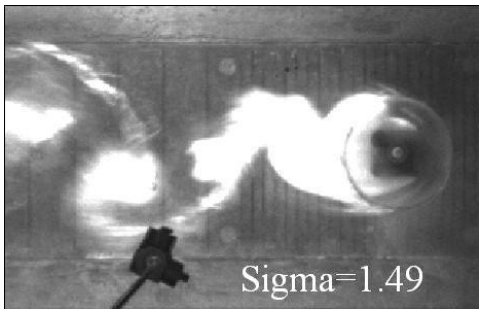

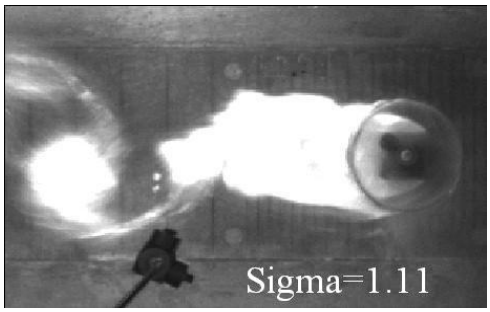

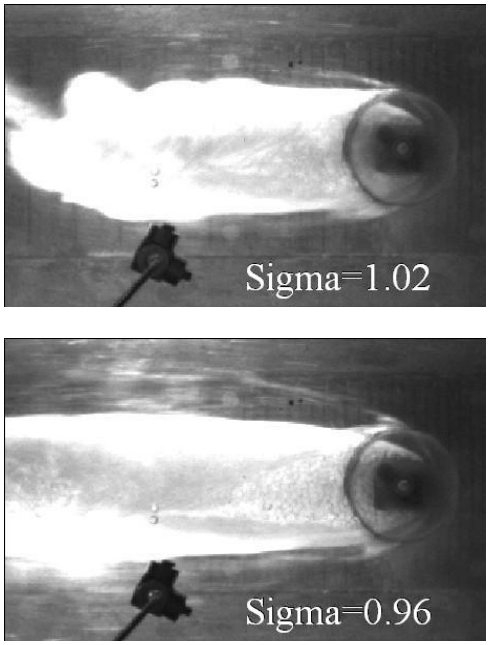

Figure 5. Cavitation cloud separation for several cavitation numbers.

4. CFD SIMULATIONS

The software ANSYS CFX 10.0 was used for 2D numerical simulations. The computational domain followed the real geometry until well-defined boundary conditions could be prescribed (see Fig. 6). The flow is from the right to the left.

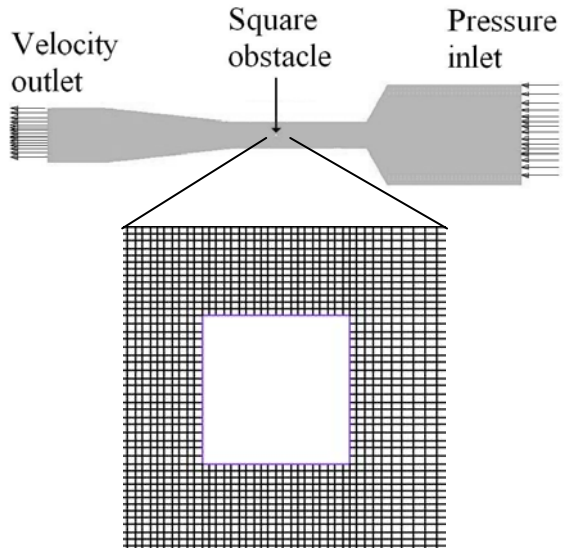

Figure 6. Upper panel: the entire computational domain. Lower panel: the roughest computational grid close to the obstacle.

Fine mesh was built around the square and in the wake while about 25 times courser mesh was used in the outer regions. Three meshes were generated with increasing density. The total number of the cells was approx. 102k, 305k and 515k. Pressure inlet and velocity outlet boundary conditions were used (the actual values were calculated from the measurements). Standard wall functions were applied, hence the value y^+ lies between 30 and 80. Several turbulence models were tested e.g. k - ε, SST (Shear Stress Transport) and SSG Reynolds Stress (see [6] for details).

The set of equations solved by CFX 10.0 are the unsteady Reynolds-averaged Navier-Stokes equations in their conservation form. The instantaneous equations of mass Eq. (3), momentum Eq. (4) and transport equation for the vapour Eq. (5) can be written as follows in a stationary frame [6], [7]:

$$\frac{\partial \rho_M}{\partial t} + \nabla \bullet \left(\rho_M \vec{U}\right) = 0 \tag{3}$$

$$\begin{aligned} &\frac{\partial \rho_M \vec{U}}{\partial t} + \nabla \bullet \left(\rho_M \vec{U} \otimes \vec{U}\right) = \\ &= \nabla \bullet \left(- p\underline{\delta} + \mu\left(\nabla \vec{U} + \left(\nabla \vec{U}\right)^T\right)\right) + \vec{S}_M \end{aligned} \tag{4}$$

$$\frac{\partial \rho_M f_V}{\partial t} + \nabla \bullet \left(\rho_M \vec{U}\ f_V\right) = R_e - R_c \tag{5}$$

Single-fluid (mixture phase) approach was used for multiphase modelling. The mixture density-vapour mass fraction relationship for the multiphase model is:

$$\frac{1}{\rho_M} = \frac{f_V}{\rho_V} + \frac{1 - f_V}{\rho_L}. \tag{6}$$

The Rayleigh-Plesset equation provides the basis for the rate equation controlling vapour generation (liquid evaporation) and condensation, terms R_e and R_c, respectively. Neglecting higher orders terms, the source terms are given by (the derivation can be found in [5])

$$R_e = C_e \frac{\sqrt{k}}{\sigma_T} \rho_L \rho_V \sqrt{\frac{2}{3} \frac{p_V - p}{\rho_L}} \left(1 - f_V\right), \tag{7}$$

if $p < p_V$ and

$$R_c = C_c \frac{\sqrt{k}}{\sigma_T} \rho_L \rho_L \sqrt{\frac{2}{3} \frac{p - p_V}{\rho_L}} f_V, \tag{8}$$

when $p > p_V$. C_e and C_c are empirical constants (their values were set to 0.02 and 0.01, respectively, see [7]) and k is the local kinetic energy.

Steady and unsteady simulations were performed in two steps. First, a cavitation-free flow

was calculated with two-phase model but the volume fraction of vapour was artificially set to zero. Then, a proper simulation was initiated from the results of the previous cavitation-free run.

5. STEADY-STATE CFD RESULTS

Although the authors are aware of the essentially unsteady nature of cavitation, steady-state computations were performed first. Our expectation was that the simulation would not converge indicating the impropriate assumption of steady flow. However, stable steady-state runs were experienced with k – ε and SST turbulence models while the computations would fail to converge with the SSG turbulence model.

A symmetric cloud was formed if the k – ε or SST turbulence models were used, whose evolution while decreasing the cavitation number is presented in Figure series 7. As reported by Dulat et al. in [7], the problem seems to be the overprediction of turbulent viscosity in the region of cavity closure and thus not allowing the formation of the re-entrant jet, which is the main cause of cloud separation. The authors are aware that there are improvements of the (RNG) k – ε turbulence model for overcoming this problem, see e.g. [7]. However, our primary aim was to study the built-in capabilities of CFX thus such modifications of the code are beyond the scope of this work.

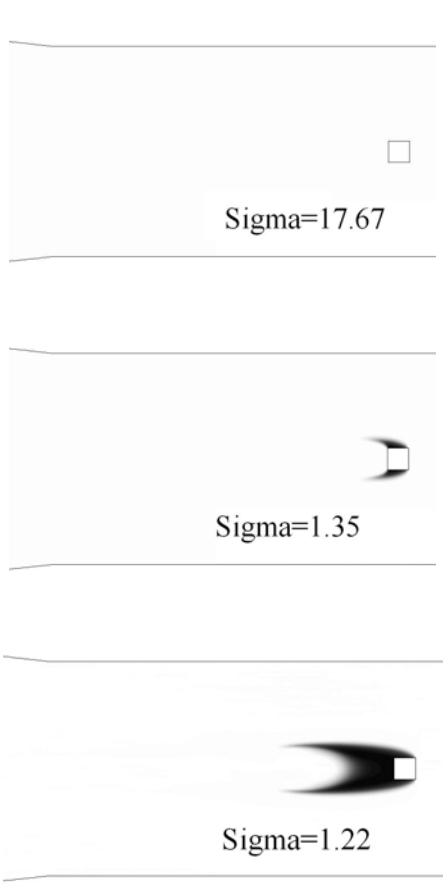

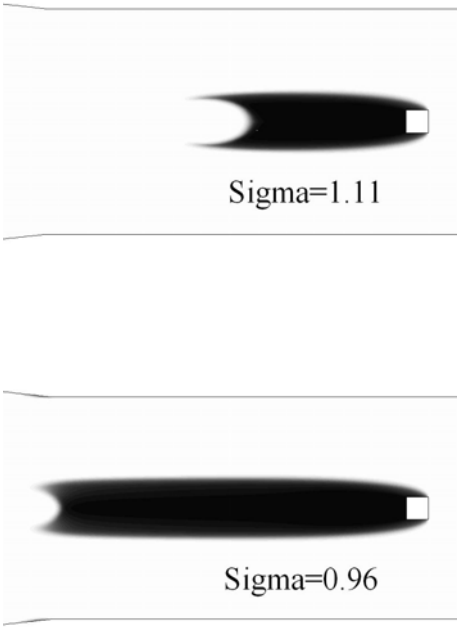

Figure 7. Results of the steady-state CFD runs with k – ε turbulence model. Water volume fraction contour plots are depicted, the dark regimes correspond to low water volume fraction.

With the help of the images recorded by the CCD camera an average (~ 50 frames) length of the cavitation zone was calculated and compared to the steady-state CFD results of k – ε and SST. It was concluded that no clear tendency could be found; both turbulence models over predict the length at small cavitation numbers and under predict at large ones. It is concluded that these models – in their current form – are unsuitable for such purposes.

Table 1. The comparison of the average length of measured and calculated cavitational zones.

Cavitation number, σ [-]	Lengths of the cavitational zone [mm]		
	Measured value	Calculated value	
		k - ε	SST
17.67	0	0	0
1.35	80	45	63
1.22	130	122	129
1.11	150	210	259
1.06	200	240	330
0.96	>250	335	457

6. UNSTEADY CFD RESULTS

Time-dependent but "quasi-single phase" CFD computations were initiated from the steady-state results. "Quasi-single phase" means that the multiphase model was switched on but the vapour volume fraction was artificially set to zero. This results in a time-dependent flow field, from which the proper multiphase calculation could be initiated. An example of such initial flow field is shown in Fig. 8. The time step was $10^{-3}s$ and the target residual was 10^{-5} (RMS) with a maximum number of iteration steps of 20. Typically, after 10-15 iteration steps all residuals would fall beneath the prescribed value except the transport equation for the vapour, which would be between 10^{-4} and 10^{-5} after the 20th iteration.

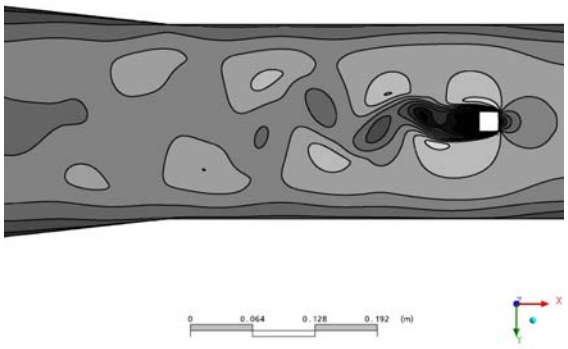

Figure 8. An example of the initial velocity field for unsteady cavitation computations. Black regions represent low-velocity, while white regions represent higher velocities.

When using the k – ε and SST turbulence models, although the initial flow field was time-dependent, the calculation led to a quasi steady behaviour and the results would be similar to those ones of the steady-state runs.

However, the SSG Reynolds stress model resulted in a periodic cavity separation as expected. Figure series 9-12 depict instantaneous contour and superficial velocity (velocity times volume fraction) vector plot of the water volume fraction at σ*=2.0, 1.5, 1.0, 0.88*, respectively. The unsteady nature of cavitation separation is clearly captured and also the growing cloud when decreasing the cavitation number. However, the re-entrant jet causing the periodic separation was not clearly captured and it is not sure whether this was due to the shortage in turbulence modelling, the grid quality should be improved or other effects detain its formation.

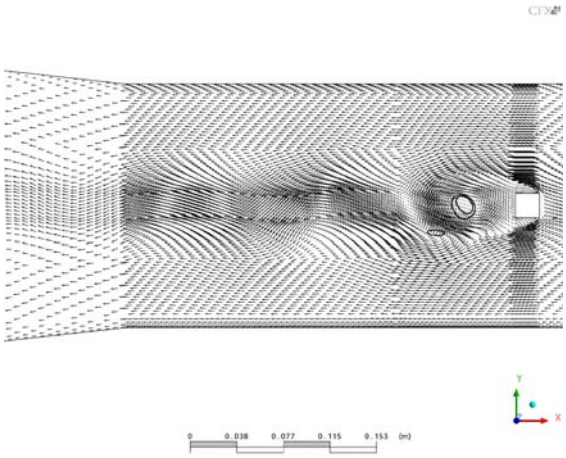

Figure 9. σ=2.0. Instantaneous water vapour volume fraction contour plot and water superficial velocity vector plot.

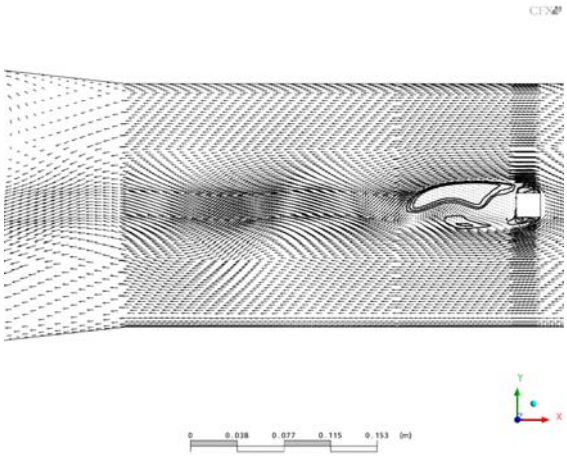

Figure 10. σ=1.5. Instantaneous water vapour volume fraction contour plot and water superficial velocity vector plot.

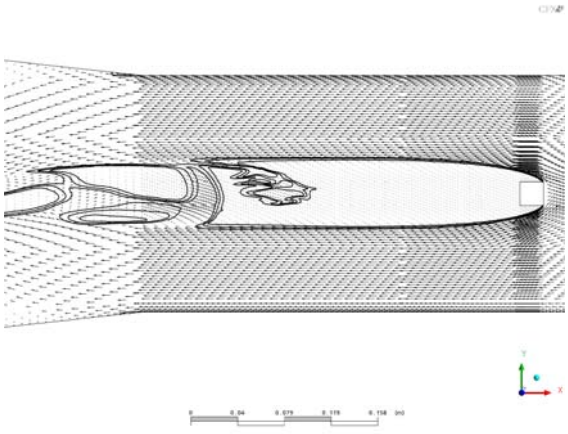

Figure 11. σ=1.0. Instantaneous water vapour volume fraction contour plot and water superficial velocity vector plot.

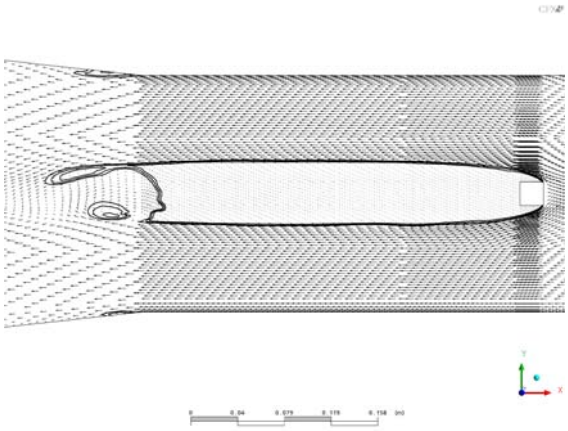

Figure 12. σ=0.8. Instantaneous water vapour volume fraction contour plot and water superficial velocity vector plot.

7. SUMMARY

Experimental and numerical investigations of cavitating flow around a square obstacle have been performed. Vibration levels and visual results were obtained from the experiment. The commercial code CFX 10.0 was used for numerical computations. As one of the main issues was to test the capabilities of such commercial codes, the standard settings (parameters) were not changed in CFX (cavitation and turbulence models). It was found that isotropic turbulence models lead to steady behaviour even in those cases, where the experimentally observed flow was highly unsteady. However, these models might be appropriate for (a) detecting the onset of cavitation and (b) for supercavitation cases.

The non-isotropic turbulence model SST Reynolds stress was found suitable for describing the unsteady nature of the cavitation. The basic features of the unsteady cavitation cloud was captured and – based on visual judgment - the size of the cavities agree with the measurements within an acceptable tolerance. Detailed investigations (e.g. shedding frequency, pressure history comparison) are planned in the future.

REFERENCES

[1] Singhal A.K., Li, H., Atahavale, M.M., Jiang, Y., 2002, "Mathematical basis and validation of the full cavitation model", *Journal of Fluids Engineering,* Vol. 124, pp. 617-624.

[2] Delannoy Y., Kueny, J.L., 1990, "Two phase flow approach in unsteady cavitation modelling"*, in Cavitation and Multiphase Flow Forum,* ASME-FED, Vol. 98, pp. 153-158.

[3] Sebestyén, Gy., Rizk, M., Al-Asaimi Awad, S.A., Szabó, Á., 1995, "Velocity Scale-Number of Cavitation Noise"*,Proceedings of the Tenth Conference on Fluid Machinery,* Budapest, Hungary, pp. 438-447.

[4] Fáy, Cs., 1958, "The cavitation channel of Dept. of Watermachines", *Technical Report for the Hungarian Academy of Sciences.,* Vol. 22. (in Hungarian)

[5] S. C. Li, 2000, "Cavitation of Hydraulic Machinery", *Imperial College Press,* Series on Hydraulic Machinery, Vol. 1, pp. 47-61

[6] CFX 5.7.1 User's Manual, ANSYS Inc.

[7] Dular, M., Bachert, R., Stoffel, B., Ŝirok, B., 2005, "Experimental Evaluation of Numerical Simulation of Cavitating Flow Around Hydrofoil", *European Journal of Mechanics B/Fluids,* Vol.24, pp 522-538.

[8] Frobenius, M., Schilling, R., 2004, "Cavitation Prediction in Hydraulic Machinery", *Proc. of the 22nd IAHR Symposium on Hydraulic Machinery and Systems*, Stockholm, Sweden

Conference on Modelling Fluid Flow (CMFF'06)
The 13th International Conference on Fluid Flow Technologies
Budapest, Hungary, September 6-9, 2006

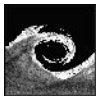

EXPERIMENTAL AND NUMERICAL WORK ON THE TWO-PHASE FLOWS THROUGH EXPANSION VALVE

Yasuhiko FUJII[1], Shigeo KIMURA[2], Takahiro KIWATA[2], Atsushi OKAJIMA[3], Kazuhiko MATSUMURA[1]

[1] Corresponding Author. Pacific Industrial Co., LTD. Godo-Cho, Anpachi, Gifu, 503-2397, Japan. Tel.: +81 584 28, Fax: +81 584 28 0130, E-mail: ysfujii@pacific-ind.co.jp
[2] Graduate School of Natural Science and Technology, the University of Kanazawa. Kakuma-machi, Kanazawa, Ishikawa, 920-1192, Japan. E-mail: skimura@t.kanazawa-u.ac.jp
[3] Kanazawa-Gakuin Tanki University, 10 Sue-Machi, Kanazawa, 920-1392, Ishikawa, Japan, E-mail: a-okaji@kanazawa-gu.ac.jp

ABSTRACT

Expansion valves used for air-conditioning systems are an important component, and they sometimes become a source of significant noise generation of the system. In order to identify the cause of the noise generation, it is necessary to look into the flow regime when the refrigerant passes through the valve. The present work is concerned about two-phase flows through the expansion valves. In general the upstream side of the valve has a higher pressure enough to keep the refrigerant in a liquid phase. Passing through the valve, however, the pressure will suddenly decrease to become a two-phase flow. A special experimental set up simulating the flow through expansion valve is manufactured by polycarbonate for flow visualization purpose. Both the temperatures and pressures along the refrigerant expansion process are also measured and recorded during the experiment. The data will be used to locate the thermodynamic state of the refrigerant when it undergoes phase change. Numerical simulation is also conducted in order to understand the mechanism of detailed two-phase flows, particularly when bubbly flows are realized in the entire region of the valve.

Keywords: Air-Conditioning, Expansion Valve, Noise, Numerical simulation, Two-Phase Flow, Visualization,

1. INTRODUCTION

Recently, a demand for noise reduction in room air conditioner is spotlighted together with energy saving. The acoustic noise by refrigerant fluid passing through the expansion valve, has become an important issue. An air-conditioning system generally consists of the exterior unit and the interior unit. The acoustic noise mainly comes from the ventilation fan, and the piping system such as valves, through which refrigerant runs. By the improvement in a technical level, the noise generated by ventilation fan, and by various parts in the piping system has been reduced significantly.

Due to the much reduction of noise achieved by the ventilation system, the parallel improvement for the refrigerant flow-noise in the piping is in demand. Especially, the elusidation of noise generation mechanism in the expansion valve and its reduction have been a central issue in a last decade. The present research is particularly concerned with this problems. [1-4]

In order to carry out the acoustic noise reduction of the expansion valve, the investigation of the two-phase flow phenomena in the expansion valve becomes indispensable. However, the work focused on the throttling mechanism of the flow in the expansion valve using an actual expansion valve, is hardly found.

Therefore, the present work aims at the elucidation of the cause of noise resulting from refrigerant flow, and a possible re-design of throttle shape in the expansion valve, which is used for the exterior unit of air-conditioning systems. The visualization of refrigerant flow in the throttle, measurements of fluid pressure and temperature, the rate of void fraction, and the acoustic noise are carried out. Numerical simulation of the two-phase refrigerant flow in the valve is also provided for investigating the qualitative nature of the flow.

2. EXPERIMENTAL DEVICE AND EXPERIMENTAL METHOD

2.1. Experimental Device

The experimental device was based on the air-conditioning systems of 2.8 *kW* in the market, which uses the R410a refrigerant, and a part of

piping into and from the valve was modified. A valve for visualization purpose and one for other measurements were made separately. The valve throttle for visualization was made precisely after a real product, and it has to satisfy other conditions, i.e. the resistance against refrigerant, refrigerating machine oil, temperature changes, structure strength for the pressure of over 4.5 *MPa*, and sufficient transparency for visualization. A photograph of experimental set-up for flow visualization is shown in Figure 1.

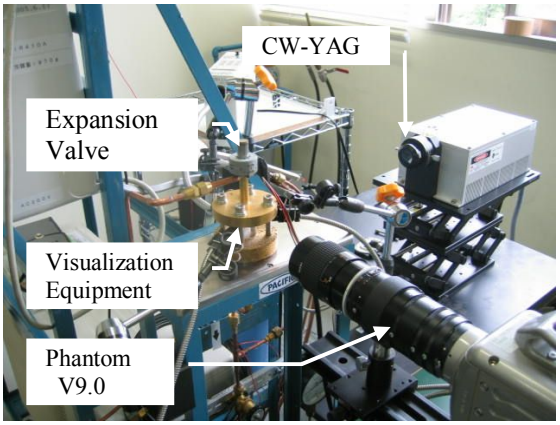

Figure 1. A photograph of experimental set-up for visualization

Two pressure sensors are positioned in the upstream of the throttle in the valve, and three are in the downstream of the throttle, which enables us to determine the pressure variation when the refrigerant passes through the throttle. In a similar fashion two temperature sensors are in the upstream, and three in the downstream. Some of them are at the same positions as the pressure sensors, so that we can determine the change of both pressure and temperature of the refrigerant in the flowing direction. The photograph of those sensors and the valve is shown in Figure 2, and the cross-sectional drawing is shown in Figure 3.

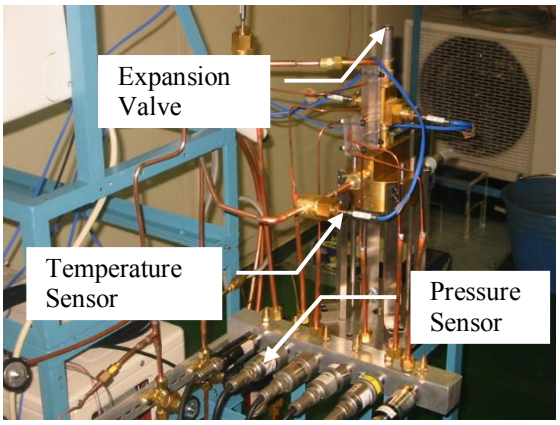

Figure 2. A photograph of expansion valve and the pressure and temperature sensors

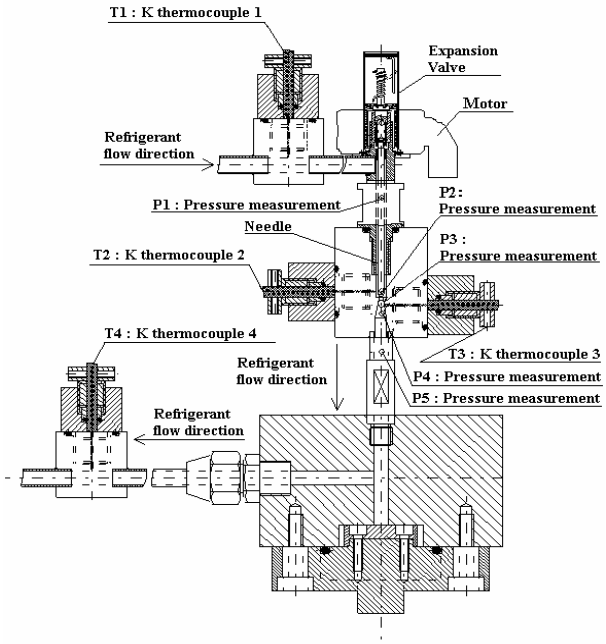

Figure 3. The cross-sectional drawing of experimental set-up

The microphone is set up in 3 *mm* distance from the surface of the throttle in the expansion valve, and the acoustic noise in different conditions was measured. The noise measurement set-up is shown in Figure 4. In addition, the two valves, one for visualization purpose and the other for pressure and temperature measurement, are used for the noise measurement.

By a partial conversion of commercially available air conditioning system, the flow rate of the experimental system was controlled by varying the revolutions per minute of the compressor.

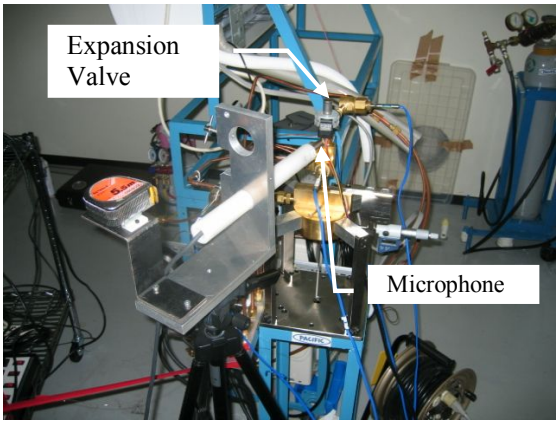

Figure 4. Acoustic noise measurement

2.2. Experimental Method

Four different flow conditions, 0.73×10^{-2} *kg/s* (26.3 *kg/h*), 1.11×10^{-2} *kg/s* (40.0 *kg/h*), 1.67×10^{-2}

kg/s (60.0 *kg/h*), 2.01×10^{-2} *kg/s* (72.5 *kg/h*), and four different opening conditions in the expansion valve, 16 *%*, 22 *%*, 29 *%*, 40 *%*, were set during the present experiments, for considering the actual operation.

Laser light (CW-YAG: Shizuoka University) was employed for visualization, and photographs were taken with the high-speed video camera (Phantom V9.0: Shizuoka University). [5,6]

3. EXPERIMENTAL RESULTS AND DISCUSSIONS

3.1. Visualization result

(a) 0.73×10^{-2} *kg/s* (26.3 *kg/h*), Valve opening 16 *%*

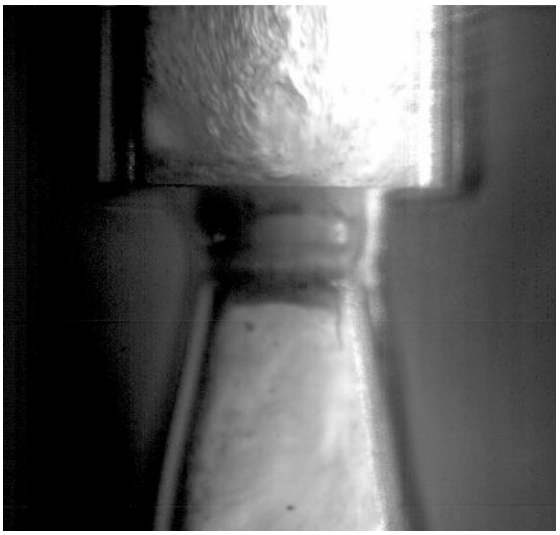

(b) 2.01×10^{-2} *kg/s* (72.5 *kg/h*), Valve opening 40 *%*

Figure 5. Flow-visualization of upstream of throttle

As a representative example of upstream visualization of the throttle for the rate 0.73×10^{-2} *kg/s* (26.3 *kg/h*) and the valve opening 16 *%*, a photograph taken with a shutter speed 49 *μs*, is shown in Figure 5 (a).

The two-phase flow is notably observed there and is showing the characteristics of a slug flow, where the size of large bubble is estimated about 2.5 *mm*.

As shown in Figure 5 (b), with an increased flow rate and valve opening, 2.01×10^{-2} *kg/s* (72.5 *kg/h*) and 40 *%*, it becomes bubbly flow, and the size of bubbles is about 0.15 *mm*. On the other hand, a photograph of the refrigerant flow in the downstream of the throttle is taken with a shutter

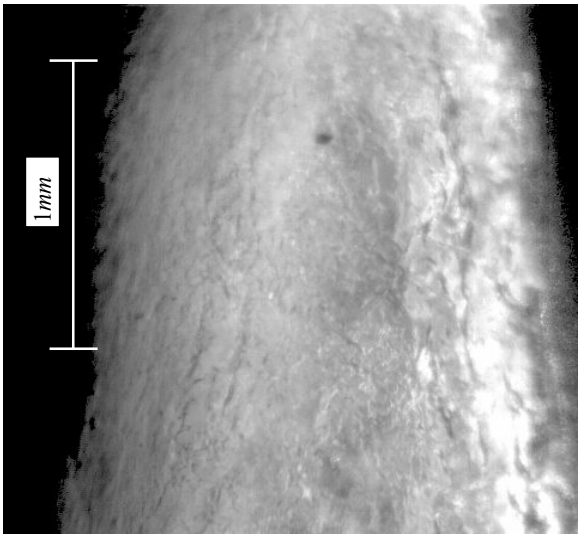

(a) 0.73×10^{-2} *kg/s* (26.3 *kg/h*), Valve opening 16 *%*

(b) 2.01×10^{-2} *kg/s* (72.5 *kg/h*), Valve opening 40 *%*

Figure 6. Flow-visualization of downstream of throttle

speed 159 μs, and is shown in Figure 6 (a). The size of bubble seems to be dozens of micrometers for the flow rate 0.73×10^{-2} *kg/s* (26.3 *kg/h*) and the valve opening 16 *%*. As it is shown in Figure 6 (b), the larger flow rate and valve opening condition with 2.01×10^{-2} *kg/s* (72.5 *kg/h*) and 40 *%* still produces a similar flow characteristic to that for 0.73×10^{-2} *kg/s* (26.3 *kg/h*) and 16 *%* in the downstream.

It seems that the down stream flow characteristic is insensitive to the flow rate and the valve opening.

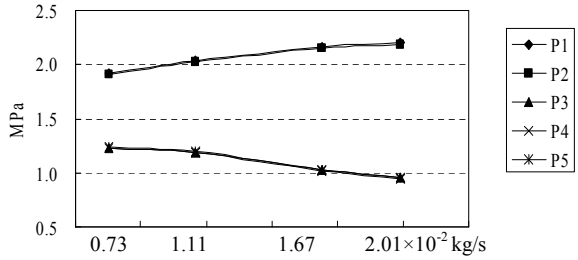

(a) Valve opening 16 *%*

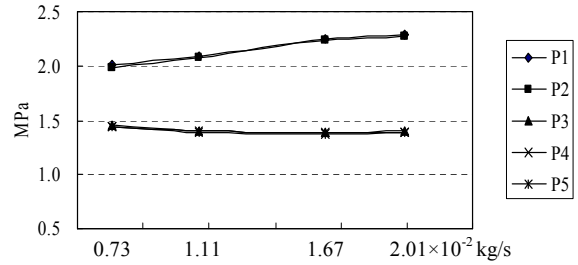

(b) Valve opening 40 *%*

Figure 7. Pressure differences across the throttle with various refrigerant flows

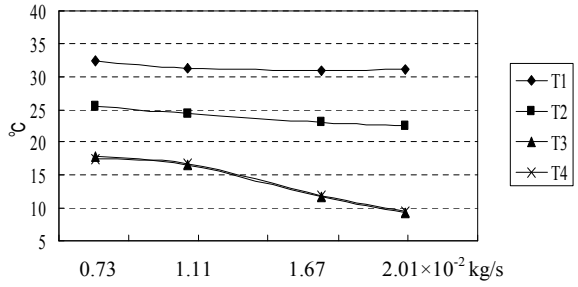

(a) Valve opening 16 *%*

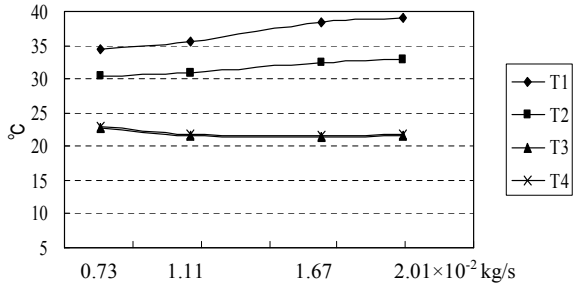

(b) Valve opening 40 *%*

Figure 8. Temperature differences across the throttle with various refrigerant flows

3.2. Refrigerant pressure and temperature measurement

As examples, the pressure measurements with the valve opening 16 *%* (Figure 7 (a)) and the 40 *%* (Figure 7 (b)) for four different flow rates are shown in Figure 7.

There were no differences in two positions of the pressure P1 and P2 in the upstream of the throttle, and similarly no differences were found among three pressures P3, P4, and P5, in the downstream. But the remarkable difference in pressure between the upstream and the downstream was observed.

Next, the measurement results of the refrigerant temperatures for the same conditions as those for pressure are shown in Figure 8(a) and 8(b). The temperatures at T1 and T2 in the upstream show differences about 5 to 8 *°C*. The temperature at T3 and T4 show the same value and they are lower by 8 to 12 *°C* than T2.

3.3. Void fractions in the downstream

The void fractions in the downstream were calculated using the pressure-enthalpy diagram of refrigerant R410a, using the refrigerant pressures

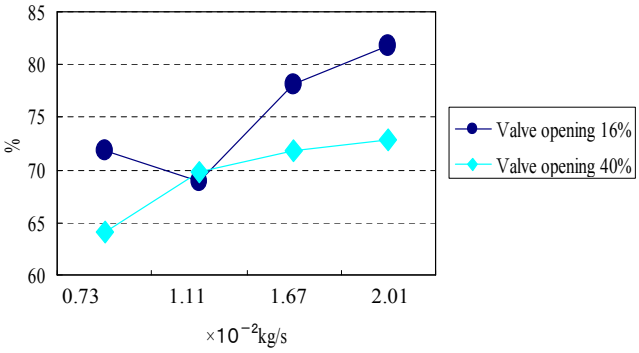

Figure 9. Void fractions in the downstream

and temperatures obtained in section 3.2.

The quality of vapour and liquid mixture was read from the diagram, and with that information the void fraction can be computed based on the concepts of mass conservation. The results were between 70 *%* and 82 *%* for the valve opening 16 *%* and between 64 *%* and 73 *%* for the valve opening 40 *%*, as shown in Figure 9.

3.4. Noise analysis

FFT analysis of the actual noise measurement for the flow rate 0.73×10^{-2} *kg/s* (26.3 *kg/h*) and the valve opening 16 *%* is shown in Figure 10 (a). Similarly for the higher flow rate 2.01×10^{-2} *kg/s* (72.5 *kg/h*) and the higher valve opening 40 *%*, the FFT of the noise measurement is shown in Figure 10(b).

When Figure 10(a) is compared with Figure 10(b), the difference of a spectral power is observed notably. In a frequency range from 10 *Hz* to 200 *Hz*,a difference in spectral power is visible, and Figure 10(a) is larger by a 9 *dB*. In other frequency ranges from 800 *Hz* to 1050 *Hz*, 2 *kHz* to 3 *kHz*, and 7*kHz* to 8 *kHz*, differences in the power are similarly observed, and Figure 10(a) is larger by a 10 *dB*.

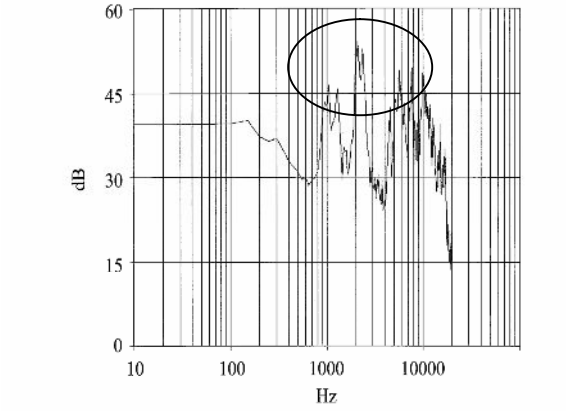

(a) 0.73×10^{-2} *kg/s* (26.3 *kg/h*), Valve opening 16 *%*

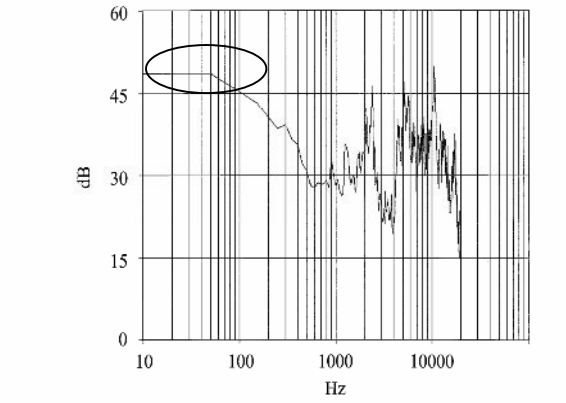

(b) 2.01×10^{-2} *kg/s* (72.5 *kg/h*), Valve opening 40 *%*

Figure 10. FFT analysis of noise data

When we actually hear the generated noise for the flow rate 0.73×10^{-2} *kg/s* (26.3 *kg/h*) and the valve opening 16 *%*, it is an unpleasant sound, which certainly poses a problem in actual operations. The noise is a jarring one and the strong spectral power at about 2000 *Hz*, is clearly seen.

A jarring noise is not heard for the higher flow rate 2.01×10^{-2} *kg/s* (72.5 *kg/h*) and the larger valve opening 40 *%*. It is thought that the sound is generated when the refrigerant passes through the throttle, and that it will be sensitive to the shape of the throttle.

3.5. Relation between noise and flowing condition

The noise analysis and the flow visualization obtained in section 3.1 are compared. In the upstream of the throttle, two-phase flows are observed in general. It is a slug flow, and bubbles are as large as 2.5 *mm* for 0.73×10^{-2} *kg/s* (26.3 *kg/h*) and the valve opening 16 *%*.

On the other hand, bubbles have much finer scales for the increased flow rate and valve opening, and they are 0.15 *mm* or smaller. Therefore the flow condition in the upstream seems to have a great influence on the noise generation.

On the contrary, in the downstream of the throttle in the expansion valve, it always consists of fine bubbles for the flow rates and the valve openings. Therefore, the noise is primarily dependent of the upstream flow condition.

3.6. Acoustic noise and the void fraction in the dowmstream

Relation between the void fraction in the downstream of the throttle and the noise generation is examined. However, any notable difference in void fraction between the two different valve openings is not found. It seems that there is no particular relation between the void fraction in the downstream and the magnitude of the acoustic noise.

3.7. Numerical simulation

Numerical simulations are also conducted in order to understand the mechanism of detailed flow structures. Although the actual flows involve cavitation phenomena and the gas-liquid two-phase is common, it will be possible to obtain some insight to the flow structures through the throttle, by carrying out a simpler single phase model. A

commercial software FLUENT is used to generate the numerical flow fields.

The governing equations for the mass and momentum conservation, and the boundary conditions are described as follows;

$$\frac{\partial \rho}{\partial t} + \nabla \cdot \left(\rho \vec{\mathrm{v}} \right) = 0 , \qquad (1)$$

$$\frac{\partial}{\partial t}\left(\rho \vec{\mathrm{v}} \right) + \nabla \cdot \left(\rho \vec{\mathrm{v}} \vec{\mathrm{v}} \right) = -\nabla p + \nabla \cdot \bar{\tau} + \rho \vec{g} , \qquad (2)$$

where p is the pressure, $\bar{\tau}$ is the deviatoric stress tensor, $\rho \vec{g}$ is the gravitational body force.

The stress tensor is defined by

$$\bar{\tau} = \mu \left[\left(\nabla \vec{\mathrm{v}} + \nabla \vec{\mathrm{v}}^{T} \right) - \frac{2}{3} \nabla \cdot \vec{\mathrm{v}} I \right] , \qquad (3)$$

where μ is the fluid viscosity, I is the unit tensor, and the last term denotes the rate of expansion. The corresponding boundary conditions are the inlet fluid velocity 0.3 [*m/s*] and the exit fluid pressure of 1013 [*hPa*]. Non-slip boundary condition is used on the solid surface. The discretization is made using a finite volume method. The pressure term is obtained by the SIMPLE algorithm. The convection terms are approximated by the second order upwind, and the other terms are by the second order central difference. The standard $k-\varepsilon$ model is employed for computing the eddy viscosity.

The velocity vectors of refrigerant in the present design throttle is shown in Figure 11. Based

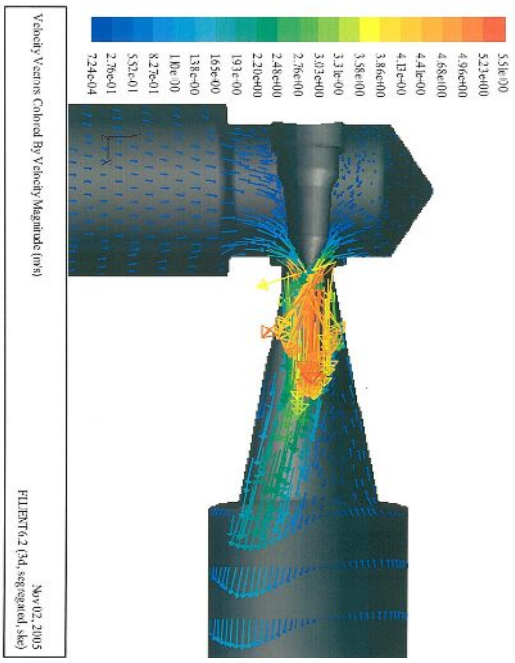

Figure 11. Numerical simulation of refrigerant flow in the present design of throttle

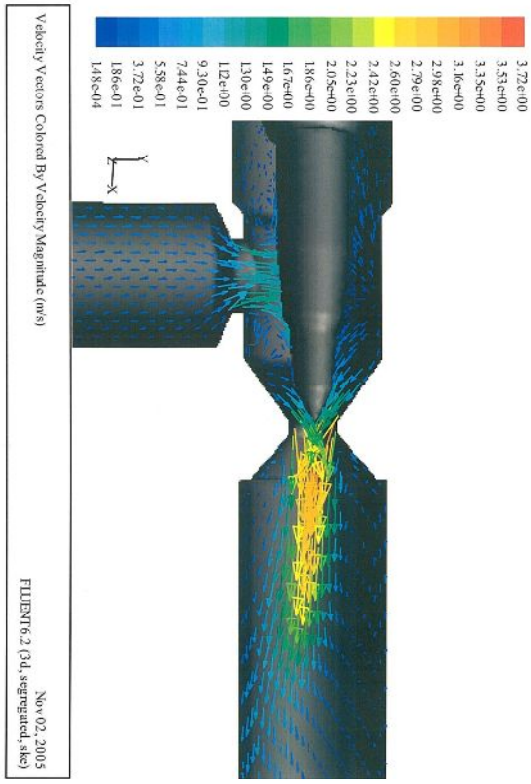

Figure 12. Numerical simulation of refrigerant flow in the newly-designed throttle

on the simulated flow visualization, a new design of the throttle has been proposed.

The numerical simulation of flow pattern in the proposed throttle is shown in Figure 12. According to the numerical result the flow of the refrigerant through the throttle in the valve is more symmetic and in fact become much smoother.

We are preparing the experiment to examine the noise level of the newly-designed valve.

4. CONCLUSIONS

In this study, the relation between the two-phase flow phenomena and the noise generation at the throttle in the expansion valve was investigated by visualization tecnique of refrigerant flow, measurements of fluid pressure and temperature, the void fractions, the acoustic noise and the numerical simulations. As a result the following conclusions are drawn.

(1) Visualization of the flow in the upstream and the downstream of the throttle in the expansion valve was performed by developing a transparent throttle made by polycarbonate.

(2) It was found that the upstream of the throttle in the expansion valve was occupied by a slug flow or a bubbly flow with fine bubbles and that the

downstream was always occupied by the bubbly flow containing equally fine bubbles.
(3) When the noise measurement at the flow rate 0.73×10^{-2} *kg/s* (26.3 *kg/h*) and the valve opening 16 *%* is compared with that at the flow rate 2.01×10^{-2} *kg/s* (72.5 *kg/h*) and the valve opening 40 *%*, a notable difference in the magnitude of spectral peak powers and their locations in the frequency is observed. In frequency ranges from 800 *Hz* to 1050 *Hz*, 2 *kHz* to 3 *kHz*, and 7 *kHz* to 8 *kHz*, the differences in spectral peak powers are particularly noticeable, and in those frequency ranges the former condition has larger by 10 *dB* difference. The acoustic sound at the former condition raises unpleasant feeling. The jarring noise contains strong spectral powers in high frequencies.
(4) From visualization of the refrigerant flow and the measurement of acoustic noise, it becomes clear that the flow in the upstream of the throttle determines the quality of the acoustic sound.
(5) The redesign of the throttle, which possibly reduces the noise generation, has been proposed from the result of numerical simulation of the refrigerant flow through the throttle in the expansion valve.

REFERENCES

[1] Kannon, T., Tomimasu, K., and Sato, K., 1991, "Prediction and Reduction of R22 Two-Phase Flow Noise in Pipe of Air Conditioner", *Mitsubishi Heavy Industries Review*, Vol. 28, No. 2, 135.

[2] Kannon, T., 1997, "Study on Noise Caused by Slug Flow through a Capillary Tube", *Transactions of the Japan Society of Mechanical Engineers, Series B*, Vol. 63, No. 611.

[3] Umeda, T., Nakamura, S., Oguni, K., Fukushima, T., Shimode, S., Nagai, M., and Kunugi, Y., 1993, "Reduction of Noise Caused by Gas-Liquid Two-Phase' Refrigerant Flow through an Expansion Valve", *Transactions of the Japan Society of Mechanical Engineers, Series B*, Vol. 59, No. 557.

[4] Umeda, T., Fukushima, T., Nakamura, S., Sato, R., Fukano, T., and Itoh, M., 1994, "Noise Caused by Gas-Liquid Two-Phase Flow with Singe Large Gas Bubble through an Orifice", *Transactions of the Japan Society of Mechanical Engineers, Series B*, Vol.60, No. 574.

[5] Miyamoto, Y., and Saito, T., 2005, "Relationship between Interface Motion of an Isolated Bubble and its Zigzagging Motion of the Center of Gravity", *Transactions of the Japan Society of Mechanical Engineers, Series B*, Vol. 71, No.5.

[6] Saito, T., Tsuchiya, K., and Kajishima, T., 2005, "Local and global scale structure of bubbly flows in glad (gas lift advance dissolution) system", *Experimental Thermal and Fluid Science,* Vol. 29, Issue 3, pp. 305-313.

Conference on Modelling Fluid Flow (CMFF'06)
The 13th International Conference on Fluid Flow Technologies
Budapest, Hungary, September 6-9, 2006

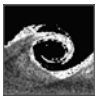

NUMERICAL SIMULATION OF THE UNSTEADY 3D FREE-SURFACE VISCOUS FLOW AROUND BLUNT PIERCING BODIES

Adrian LUNGU[1]

[1] Corresponding Author. Department of Ship Hydrodynamics, "Dunarea de Jos" University of Galati. 47 Domneasca Street, 800008 Galati, Romania. Tel.: +40 722 362604, Fax: +40 236 495400, E-mail: adrian.lungu@ugal.ro

ABSTRACT

Moving a blunt piercing body through the free surface often results in a bow wave that breaks either in a plunging or in a spilling manner. Studying the breaking bow wave has relevance for naval architects involved in the design of hull forms since as much as 15% of the wave resistance of a full-form ship hull is associated with its breaking bow wave. The subject is difficult since most solution techniques for waves modeling are valid only when the waves have sufficiently small slopes, their speeds are considerably smaller than the phase speed, and the particle accelerations are not large compared to the acceleration due to gravity.

The investigation is aimed at comprehending the transition from the sub-breaking regime to the fully breaking one, and to introduce a numerical implementation that enables detailed computational investigations of the transition. Several flow cases are considered in this numerical simulation which is based on a finite-difference solution of the 3D incompressible Reynolds Averaged Navier-Stokes (RANS hereafter) equations written on a body and boundary-fitted co-ordinate system. The turbulent nature of the breaking wave is described by the k-ε model.

Keywords: CFD, RANSE, unsteady free-surface flow, turbulence

NOMENCLATURE

C_p	non-dimensional pressure coefficient normalized by the wetted surface
Fr	Froude number; $Fr=U_0/(g.L)^{1/2}$
k	von Karman constant
K	turbulent kinetic energy per unit mass
L	hydrofoil chord length
P_{atm}	atmospheric pressure
Re	Reynolds number $Re=U_oL/\nu$
R_x,R_y,R_z	Reynolds stress components
U, V, W	mean velocity components
U_o	free-stream velocity
h	wave height
$\underline{n}_j$	unit outward normal vector to the free surface
$\underline{n}_x,\underline{n}_y,\underline{n}_z$	the (x, y, z) components of the unit outward normal vector to the free surface
n^+	the nondimensional distance from the wall
p	non-dimensional pressure
t, T	non-dimensional time
$\underline{t}_i$	unit tangential vector to the free surface
u,v,w	non-dimensional fluctuating velocity components in the (x,y,z) direction of the Cartesian coordinates system
$\overline{v}_t$	mean velocity parallel to the wall
w_d	non-dimensional disturbing velocity
x,y,z	non-dimensional Cartesian coordinates
ε	rate of dissipation of the turbulent kinetic energy
Φ	modified pressure
ν_t	non-dimensional turbulent eddy viscosity
Ψ	turbulence generation term
σ_{ij}	fluid stress tensor
ξ,η,ζ	curvilinear coordinates in the transformed domain (girthwise, normal-to the foil and vertical direction).

1. INTRODUCTION

Traditionally, breakers are classified into two categories. The first one is the spilling type, characterized by white water spilling down and in contact with the front face, and the second is the plunging type characterized by a prominent and coherent jet falling in an overturning trajectory from crest to base. However, the path to breaking under either of these types crosses an intermediate stage in which a sort of free-surface turbulent flow with intense surface fluctuations is exhibited [1]. Experiments have shown that when the velocity is less than a critical value, wave crests appear rounded and no symptoms of breaking are present. If, however, the velocity increases slightly, without otherwise alter-

ing the flow, a steady breaker develops suddenly. Even though the difference between velocities of the two regimes is rather small, the wave profiles differ substantially. Duncan [2] also observed that the transition from a non-breaking wave to a breaking one occurs over a narrow range of submergence depths within which it was possible to induce steady breaking by disturbing the non-breaking wave train.

The criteria of the appearance of breakers were formulated by Mori and Shin [3, 4], by mean of the critical condition based on the instability analysis. The validity of the model has been confirmed through experimental investigation. Steady breakers have also been studied numerically by making use of the boundary element and/or finite difference methods. Turbulence treatments such as 0-equation or K-ε models were introduced in the numerical simulation since the experiments have proved that breaking is a kind of free-surface turbulent flow. However, it may cast a doubt whether such treatments are proper since the free-surface turbulence seems to be rather different from that developed close to the solid body.

Within the boundary layer developing along a solid surface, the velocity profile exhibits a significant defect. Such a defect works as a trigger for the transition to turbulence and may even be presumed to be a sustaining source for the turbulent state in such flows. In order to numerically simulate a similar behavior on the free surface in the absence of such triggering mechanism, the author proposed the introduction of a high frequency disturbance on the free surface over a prescribed region around the wave crest, [5]. To accommodate the triggering source, the free-surface kinematic boundary condition was modified accordingly. Under such circumstances steady breakers were induced by disturbing the otherwise non-breaking train, thus giving rise to wave profiles that differ drastically from those obtained in corresponding non-breaking computations.

An important issue of any free-surface flow under the breaking assumption is the separation provoked by the wave-induced effects. When an oncoming free-surface flow encounters a piercing body, the flow may separate as a result of a sort of blocking effect. The separated flow forms several vortices around the body, which are topologically rather similar to the horseshoe vortices generated around a juncture. The flow is completely three-dimensional and becomes more complicated as the vortices interact with the water wave and the boundary layer developed on the body surface. This convoluted three-dimensional flow can be found in many places where a piercing body intersects the water surface, such as the flow around appendages mounted on submarine fuselages, etc.

The heterogeneous character of the flow is due to the number of vortices originating upstream of the piercing body. These vortices result from the wave-induced separation due to the adverse pressure gradient in front of the body. Apart of the three dimensional separation that eventually takes place, complex free-surface deformations occur as a result of the breaking inception, contributing to the vorticity production in the immediate vicinity of the breaking wave-crest. Complex interactions that produce there unveil topological flow structures that resemble, up to some extent, to those generated by the contingence between a separated flow around a juncture and the corresponding boundary layer.

In the following, the present study aimed at clarifying the transition from the sub-breaking regime to the fully breaking regime introduces a numerical implementation that will enable further detailed computational investigations. The two-equation model of K-ε describes the turbulent nature of the breaking wave. Special numerical formulations are proposed for the accurate boundary treatment. Different transient and turbulent regimes are considered by varying the Reynolds number within a wide range, and wave properties are checked at various Froude numbers. The numerical solutions are shown to be in good agreement with the available experimental data in terms of free surface profiles, hydrodynamic forces, and turbulence quantities.

2. GOVERNING EQUATIONS

The RANS and continuity equations are solved for the primitive variables to describe the unsteady flow around a 3D piercing blunt hydrofoil in which all the other variables are non-dimensionalized based on the uniform oncoming flow velocity, density of water, and the chord length respectively.

Closure of the RANS equations is attained through the use of the K-ε model modified for free-surface effects by Harlow and Nakayama, [6]. The Boussinesq eddy viscosity concept that assumes Reynolds stresses as being proportional to the rate of deformation of the mean flow is employed. The closure assumptions of the K-ε model are only valid for high-intensity and nearly isotropic turbulence. Free surface flows however, are characterized by zones where the turbulence is intense and zones where the flow is almost laminar. Transition from one zone to the other is often abrupt and intermittent. For a better description of the transition, a reduction of the effective eddy viscosity for low-intensity turbulence is considered by replacing υ_t by a coefficient computed as in [6].

The values for the turbulent number is set at $\sigma_K=1.0$ whereas the Prandtl-Schmidt is $\sigma_\varepsilon=1.3$. Apart of that, the other constants are $\sigma_U=\sigma_V=\sigma_W=1.0$, $C_\mu=0.09$, $C_{1\varepsilon}=1.44$, and $C_{2\varepsilon}$=1.92 The transport equation for the kinetic energy and its dissipation rate are coupled with the momentum and continuity equations. A body and boundary fitted coordinate system over which a coordinate trans-

formation changes the physical domain $(x_i,t) \equiv (x,y,z,t)$ into a rectangular one in the computational space $(\xi_i,\tau) \equiv (\xi,\eta,\zeta,\tau)$. Partial derivatives with respect to Cartesian co-ordinates are related to ones with respect to curvilinear co-ordinates by the chain rule.

The calculation proceeds through a sequence of loops, each advancing the entire flow configuration through sufficiently small finite increments of time. The output of each loop is taken as an initial condition for the next one and the computation is performed until T_{max}. An explicit time-stepping scheme is employed for the time marching procedure. All spatial derivatives are expressed by second-order accurate central differences while third-order upwind schemes are employed for the convective terms. The pressure field is computed by an iterative relaxation solution of a Poisson equation within the limitations imposed by the boundary conditions. An Euler technique is employed to calculate the location of the free surface. The still state condition is used as an initial condition. For numerical stability, the flow is progressively accelerated from the rest condition to the uniform inlet velocity. The duration of the acceleration stage is chosen according to the flow condition to avoid having the solution break down as a result of an eventual overturning of numerically-induced waves.

2.1 Boundary Conditions

Free Surface According to Jeong et al. [7], the viscous boundary condition requires the equilibrium of stresses on the free surface. The formulation of such a condition can be written as follows:

$$\sigma_{ij}\underline{n}_j\underline{n}_i = P_{atm}, \quad \sigma_{ij}\underline{n}_j\underline{t}_i = 0 \tag{1}$$

where $\underline{n}_j, \underline{t}_i$, are the unit outward normal and unit tangential vectors to the free surface, respectively. In the equations above summation over *i* and *j* is understood by virtue of the repeated suffix. The first condition leads to the imposition of the exact pressure condition on the free surface because the uppermost grid line always coincides with the water surface. By applying this scheme, further interpolations are avoided. The second condition leads to the following set of equations

$$\begin{cases} 2U_x\underline{n}_x + (U_y + V_x)\underline{n}_y + (U_z + W_x)\underline{n}_z = 0 \\ (U_y + V_x)\underline{n}_x + 2V_y\underline{n}_y + (V_z + W_y)\underline{n}_z = 0 \\ (W_x + U_z)\underline{n}_x + (W_y + V_z)\underline{n}_y + 2W_z\underline{n}_z = 0 \end{cases} \tag{2}$$

which is solved for the velocity components on the free surface. A kinematic condition requiring fluid particles to always remain on the free surface is used in the following form

$$h_t + Uh_x + Vh_y - W = 0 \tag{3}$$

in order to compute the free surface location. A finite-difference scheme for the calculation of the wave elevation is proposed where the third derivative term of the wave elevation is additionally introduced in the Eulerian expression of the free-surface condition. Its inclusion contributes only to the periodic propagation either in the time domain or in the progressive direction. It was shown in [5] that when such a scheme is used, the accuracy of the solution is not affected by the coarseness of the grid. Turbulent flows are always dissipative. Viscous tangential stresses perform deformation work that increases the internal energy of the fluid at the expense of the kinetic energy of the turbulence. The turbulence needs a supply of energy to make up for these viscous losses. Therefore, a high frequency disturbance is introduced at the uppermost grid into the vertical component of the velocity, right ahead of the first wave crest and only at a prescribed time step. The expression used to generate the fluctuation on the free surface appears as follows:

$$w_d = A\sin k_t t \sum_{i=1}^{3} (\sin k_i x + \sin k_i y) \tag{4}$$

A in the equation above is the amplitude expressed as a part of the initial value of *w*. k_t and k_i are constants chosen so that the periods of the disturbance are slightly larger than the grid size and time increment, respectively. As soon as the transition is triggered, the disturbance is removed.

Open Boundaries The limited computing domain has a different physical meaning than the unbounded viscous flows without waves. The perturbed velocity exists even at the far downstream and propagates through the wavy motion of the free surface much farther downstream than for the unbounded viscous flows. Consequently, added dissipation zones are used at the open boundaries. Waves are numerically damped by artificially suppressing the vertical component of the velocity within a certain range inside the dissipation zone in order to avoid potential numerical instabilities generated by the eventual wave reflections.

Body The no-slip boundary condition for the velocity and an exact formulation of the Neumann-type condition for the pressure are imposed on the solid boundary. If the no-slip condition is applied on the hydrofoil, the following set of equations gives the modified pressure gradients on the body

$$\begin{cases} \xi_x\Phi_\xi + \eta_x\Phi_\eta + \zeta_x\Phi_\zeta = \dfrac{1}{Re}\nabla^2 U + R_x \\ \xi_y\Phi_\xi + \eta_y\Phi_\eta + \zeta_y\Phi_\zeta = \dfrac{1}{Re}\nabla^2 V + R_y \\ \xi_z\Phi_\xi + \eta_z\Phi_\eta + \zeta_z\Phi_\zeta = \dfrac{1}{Re}\nabla^2 W + R_z \end{cases} \tag{5}$$

Other boundaries The oncoming uniform flow condition and static pressure are fixed for the inlet while a full symmetric implementation is used for the symmetry plane. The bottom of the domain is placed far enough from the free surface such that zero-gradient extrapolation is used for all variables there. Boundary conditions are needed for the turbulence modeling as well. If the computational boundary is far from solid walls, the following conditions proposed by Ferziger and Peric [8] are used if the surrounding flow is turbulent:

$$U\frac{\partial K}{\partial x} = -\varepsilon; \quad U\frac{\partial \varepsilon}{\partial x} = C_{2\varepsilon}\frac{\varepsilon^2}{K} \tag{6}$$

Similar conditions are derived for the other directions. K, ε and ν_t are set to zero in a free stream. At the inlet $K=0$ and ε is chosen so that the length scale be approximately one-tenth of the width of the shear layer or the domain size are used. Whenever solid boundaries are involved, wall functions, which rely on the existence of a logarithmic region in the velocity profile, are used under the following form:

$$\tau_w = \rho C_\mu^{1/4}\sqrt{K}\,\frac{\overline{v_t}}{\kappa \ln(n^+ E)} \tag{7}$$

where $\overline{v_t}$ is the mean velocity parallel to the wall, κ is the von Karman constant, and $E = e^{\kappa B}$ where $B=5.2$ is an empirical constant related to the thickness of the viscous sublayer developed on a flat plate. n^+ is the nondimensional distance from the wall. Apart from that, the zero-gradient on the normal direction to the wall is used for K while the dissipation boundary condition is derived by assuming the balance of production and dissipation in the near wall region. To represent the turbulence in the free surface is so complicated that any prescription of boundary condition is still highly speculative. In the present work, the derivation of simple free-surface condition is based on the assumptions proposed by Lemos [9]: (a)- The air influence is negligible; (b)- Turbulence does not diffuse across the free surface; and (c)- Cross-stream convection is neglected at the free surface. Under these premises the homogeneous Neumann boundary conditions are prescribed for K and ε on the free surface.

3. GRID GENERATION

A **C-H** type grid topology is geometrically generated to accommodate the finite difference expressions written in a boundary-fitted coordinate system. Quality requirements such as smoothness, clustering near the body and water surface, orthogonality and minimum spacing are satisfied through an iterative adjustment of node positions. Four different grids used in the present study have the minimum spacing in each direction chosen so that the grid convergence tests and the order-of-accuracy studies could be performed. Let these grids be denoted by 1 to 4 as tabulated in Table 1.

Table 1. Resolutions for the computational grids

	Grid 1	Grid 2	Grid 3	Grid 4
No. of nodes				
ξ-direction	128	128	110	90
η- direction	60	50	50	45
ζ-direction	40	30	25	20
Resolutions				
$\Delta\xi_{min}$	10^{-3}	10^{-3}	$2.7\cdot10^{-3}$	$5\cdot10^{-3}$
$\Delta\eta_{min}$	$2\cdot10^{-4}$	$5\cdot10^{-4}$	$5\cdot10^{-4}$	$6.8\cdot10^{-4}$
$\Delta\zeta_{min}$	$2\cdot10^{-4}$	$5\cdot10^{-3}$	10^{-3}	10^{-3}

The arrangement of the finest computational grid consisting of *128x60x40* nodes in the ξ,η,ζ directions, respectively, and the orientation of the Cartesian system of coordinates are presented in Figure 1. The minimum mesh spacing that corresponds to Grid 1 are $10^{-3}\times2\cdot10^{-4}\times2\cdot10^{-4}$ in the ξ,η,ζ directions respectively, for which the normal distance to the hydrofoil results at a value of n^+=1.6.

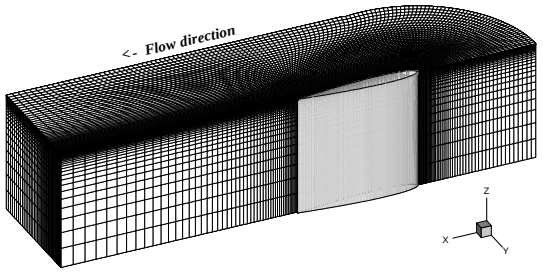

Figure 1. Grid topology

Several simulations are carried out for flow at Reynolds numbers ranging from $5\cdot10^4$ to $2\cdot10^6$ and Froude numbers of *0.22*, *0.25*, *0.3*, and *0.4*. Lower Froude numbers describe the non-breaking regimes. Grids 2 and 3 host the computations at the lowest Re number that correspond to the investigations carried out for validation purposes. Grid 4 serves only for performing the grid convergence test, as shown in Figure 2, which presents the bow wave elevations computed on the four grids tabulated in Table 1. Time increments for the solutions reported herein have been chosen so that the Reynolds mesh number be less than the limit value established according to the stability criteria imposed for a convergent solution.

4 RESULTS AND DISCUSSIONS

Since the grid size, boundary treatment, and turbulence modeling in general affect the numerical solutions, validation against experimental results is indispensable. Consequently, a set of computations is performed for the sake of validating the code

through comparisons of the numerical solutions computed by using the proposed method with the experimental data [10]. The experiment was carried out at the cavitation tunnel of the ICEPRONAV, on a piercing hydrofoil with a chord length of 150 mm and a span of 800 mm which was mounted through a six-component dynamometer on the free-surface measuring section. Figure 3 shows a comparison between the predicted and measured wave profiles on the body surface. Free-surface elevations computed for $Re=5\cdot10^4$ and $Fr=0.25$ generally agree with the experiment, except for the trailing edge of the foil where a small departure is observed. The difference is seemingly due to the fairly poor grid clustering for the Froude number considered.

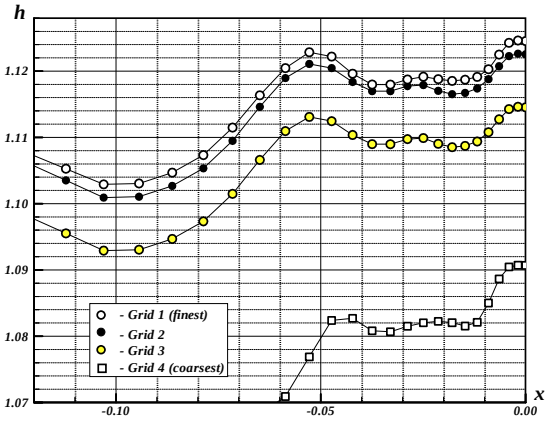

Figure 2. Grid convergence test

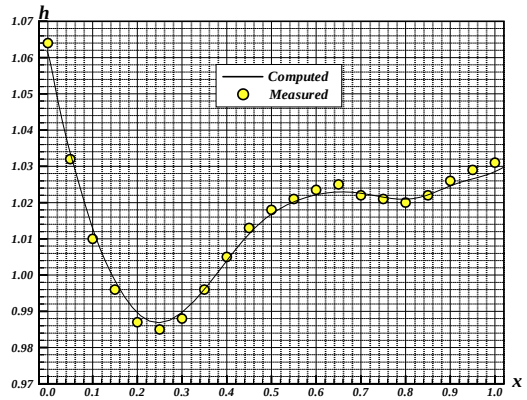

Figure 3. Comparison between wave profiles computed and measured. $Re=5\cdot10^4$, $Fr=0.25$

The comparison shown in Figure 4 presents the distribution of the pressure coefficient on the hydrofoil computed and measured at four different depths. Again, the computed values agree rather well with the measured ones although some differences are apparent for the deeper cases. The discrepancies are attributable to the blocking effect of the tunnel.

The primary purpose of the present work is to demonstrate and quantify the influence of the bow waves under the incipient breaking assumption on the boundary-layer configuration. Extensive works done independently by Patel et al. [11], and Stern [12] have proved that the boundary layer development upon a body intersecting the free surface can be greatly influenced by the presence of the wave system generated by the bow.

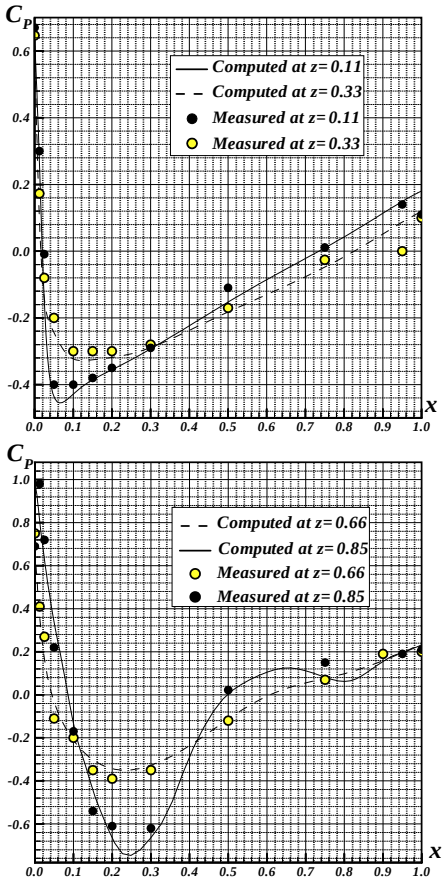

Figure 4. Comparison between C_p computed and measured on the body. $Re=5\cdot10^4$, $Fr=0.25$

Waves of significant sharpness as depicted in Figure 5 originate in front of the leading edge to induce near the free surface a region of flow separation that may otherwise be absent. Experimental observations reported in [1] shown that while accelerating the flow in the tunnel, the elevation of the bow wave increases progressively until it reaches a stationary height. However, if the velocity exceeds a critical value, the free surface becomes unstable, showing clear signs of breaking. Waves of a shorter length form in front of the body, thus resulting in a major change of the initial shape of the free surface. This modification which reveals a prominent turbulent behavior brings forth oscillations in the pressure distributions on the body, and as a result, fluctuations in the hydrodynamic forces. Because of the difficulty of measurements, as well as of the uncertainty of the experimental data, the computational results used for validating the method only address the non-breaking wave developed under a progressive acceleration of the water flow.

The progressive acceleration not only prevents overturning, but also allows the bow wave to reach almost steady amplitudes as Figure 6 shows. If the velocity increases from a value that corresponds to a Froude number of *0.22* to *0.3* or *0.4*, the incipient breaking is induced. Increasing the Reynolds number from $Re=5\cdot10^4$ to $Re=2\cdot10^6$ results in higher elevations at the bow because of the lower viscous dissipation, a fact which is confirmed by theory.

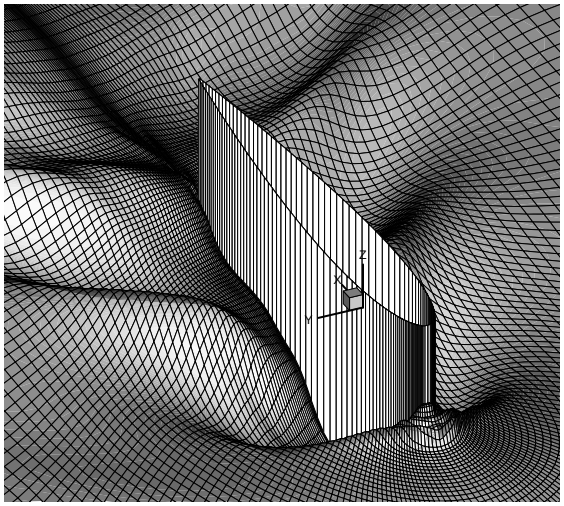

Figure 5. Free surface profile

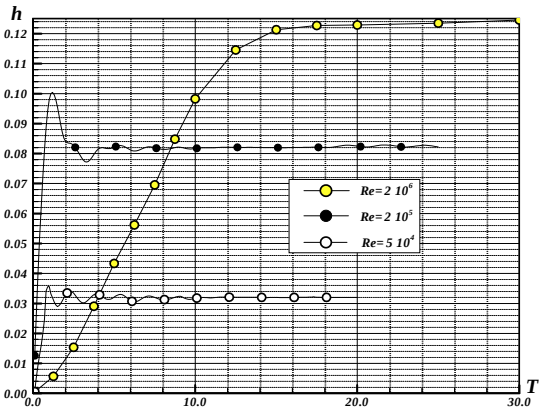

Figure 6. Time history of the bow wave height

A close-up view of the streamtraces computed in the highest Reynolds number case ($Re=2\cdot10^6$, *Fr=0.3*), and plotted on the free surface at *T=20* unveils the strong activity in front of the bow, inside the region that corresponds to the first crest as depicted in Figure 7. The author believes that the interaction between the boundary layers developed around the body and just beneath the water surface is responsible for such a flow pattern.

The flow topology, which is shown in Figure 8(a) consists of a pair of nodal points; N_2 on the body and N_1 in front of it, a saddle point S_1, and a half-saddle point S'. Apart of them two corresponding pairs of coalescent and divergence lines denoted by l_{C1}, l_{C2}, l_{D1}, and l_{D2} respectively, are seen. The incoming flow in the free surface, instead of separating in the traditional manner, generates pairs of stagnation or saddle points in the symmetry plane, from where it goes around the body along the coalescent lines l_{C1} and l_{C2}. Two diverging lines denoted by l_{C1} and l_{C2} stem from the nodal points N_2 and N_1. A detail of the streamtraces along the body reveals the formation of a nodal point N_3 and two half-saddle points denoted by S' in Fig. 8(b).

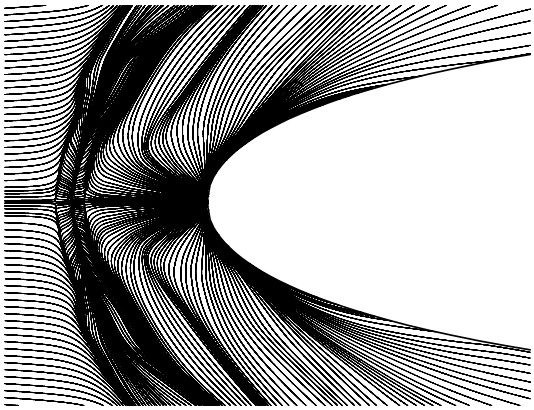

Figure 7. Particle streamtraces on the free surface. T=20

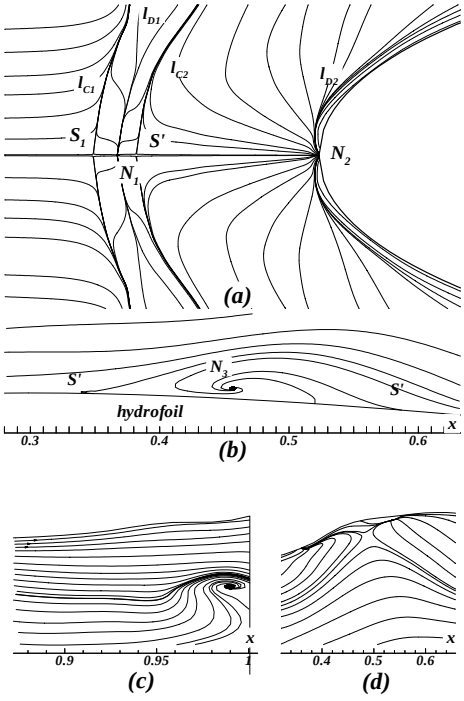

Figure 8. Flow topology on the free surface and closely beneath of it. T=20

The figure shows the flow topology in the (*x*-*y*) plane at the halfway of the foil, in the correspondence of the reversed flow region developed there. A cross flow streamtraces representation presented in Fig. 8(d) shows the flow topology in the (*x*-*z*) plane drawn through N_3. At

the trailing edge of the hydrofoil a nodal point and a half-saddle point are observed on the symmetry plane. Besides, a pair of saddle points is placed on each side of the body as shown in Fig. 8(c) to satisfy the topological rule proposed by Zhang et al. [13] or that proposed by Hunt et al. [14]:

$$\left(\sum_N + \frac{1}{2}\sum_{N'}\right) - \left(\sum_S + \frac{1}{2}\sum_{S'}\right) = -1 \qquad (8)$$

where $\sum_N, \sum_{N'}, \sum_S$ and $\sum_{S'}$ represent the numbers of nodes (N), half-nodes (N'), saddles (S), and half-saddles (S') respectively.

The author proved in [5] that the early-stage breakers are turbulent-like flows accompanied by important free-surface fluctuations. Such high frequency modifications of the free surface configuration are responsible for the periodic change of the separation process. The oscillations of the physical parameters of the flow propagate downward determining significant modifications of the streamtraces beneath the water surface. On the other hand, it has been found that vorticity diffusing from the crest of the bow wave is restricted to a very thin layer below the water surface. The intensity of this activity decreases downwards as the vorticity and the fluctuating components of velocity or the turbulent quantities decrease in this direction. This is clearly seen in Figure 9 that depicts the streamtraces computed at *0.02L* beneath the free surface for the same flow conditions as above.

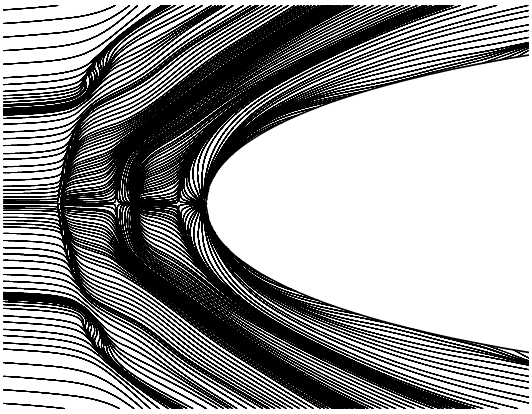

Figure 9. Particle streamtraces at 0.02L beneath the free surface. T=20

As the computation proceeds, the flow around the bow evolves to a configuration which modifies to the structure shown in Figure 10 that presents the particle streamtraces on the free surface computed at *T=25*. A sort of contamination takes place so that the diverging line l_{D1} emerging from the nodal point N_1 becomes shorter and eventually split and joins the coalescent lines denoted by l_{C1}, l_{C2} in Figure 11 (a). The figure shows the flow topology on the free surface and closely beneath of it computed at *T=25*. Figs. 11(b) to 11(d) are similar to Figs. 8(b) to 8(d), respectively. Topologically, based on the criterion that a saddle-to-saddle connection is unstable, a streamline originating from a saddle point of separation, will ultimately connect to a spiral focus of separation or to a nodal point.

As a result, the separation surface will spiral into a swirling vortex, whose kernel is detectable at *0.02L* below the free surface as Figure 12 shows. Aside of the symmetry plane at about 4% of the chord length, a region of swirling flow can be seen which is the footprint of an arch-like vortex. Inside that region, the flow is fully three-dimensional; therefore, significant vertical particle movement is found within a certain depth.

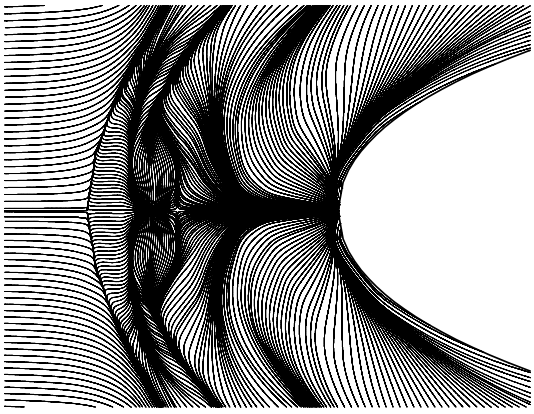

Figure 10. Particle streamtraces on the free surface. T=25

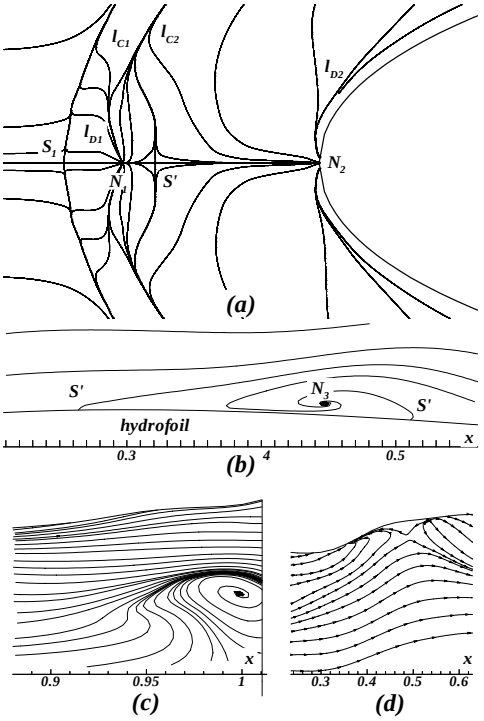

Figure 11. Flow topology on the free surface, and in the (*x*-*z*) plane. T=25

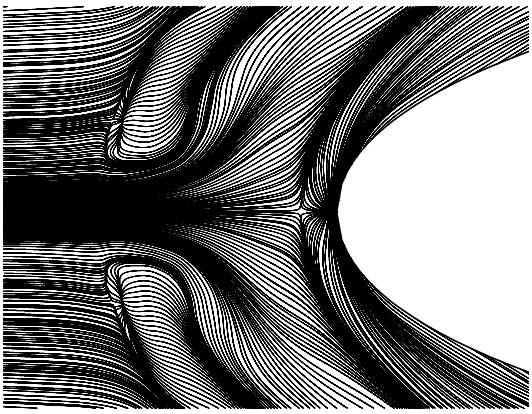

Figure 12. Particle streamtraces at 0.02L beneath the free surface. T=25

During trial computations it has been found that such topologies are emblematic only for the flow under the incipient breaking assumption, therefore only for Froude numbers larger than 0.25. At lower Fr numbers the flow is not completely mature, therefore the energetic condition for breaking appearance is not yet fulfilled, the particle streamtraces in the free surface look similar to those that develop in a laminar flow around a juncture.

5. CONCLUDING REMARKS

Some characteristics of the unsteady free surface prior to wave breaking have been theoretically investigated. Numerical evidence consistent with experimental data was used to provide additional insight into the physics of the incipient breaking phenomenon. The main findings of the present work are as follows:

- When the velocity reaches a critical value, the production of turbulence may dissipate the accumulated energy around the crest to maintain the rounded wave without overturning;
- In front of the bow, vorticity is generated to satisfy the shear-free condition on the free surface. As a result, a necklace vortex is induced around the bow. Its strength is larger when the vorticity is larger;
- Free surface waves and separation patterns are strongly dependent on the Froude number. Both wave magnitude and separation area increase as the Fr number increases;
- The presented method which includes turbulence provides acceptable values for the physical parameters that describe the flow for a range of Reynolds and Froude numbers at which the wave breaking is expected to occur.

REFERENCES

[1] Mori, K., 1984, "Necklace Vortex and Bow Wave around Blunt Bodies," Proc. *15th Symposium on Naval Hydrodynamics*, Hamburg, Germany, pp.63-71.

[2] Duncan, J.H., 1983, "The Breaking and Non-Breaking WaFerziger, J. H., Peric, M., 1996, "*Computational Methods for Fluid Dynamics*", Springer Verlag, Berlin Heidelberg.

[3] Mori, K., Shin, M. S., 1988, "Sub-Breaking Wave: Its Characteristics, Appearing Condition and Numerical Simulation", Proc. *16th Symposium on Naval Hydrodynamics*, pp. 499-511.

[4] Shin, M. S., Mori, K., 1989, "On Turbulent Characteristics and Numerical Simulation Of 2-Dimensional Sub-Breaking Waves", *Journal of The Society of Naval Architects of Japan*, Vol.165, pp.1-7.

[5] Lungu, A., 1994, "Numerical Analysis of the Free-Surface Flow around a Submerged Hydrofoil," *Ph.D. Thesis, Hiroshima University, Japan.*

[6] Harlow, F. H., Nakayama, P. I., 1968, "Transport of Turbulence energy Decay Rate", *Los Alamos Scientific Laboratory, Report LA-3854.*

[7] Jeong, U-C., Doi, Y, 1995, "Numerical Study of Vortical Flows beneath the Free Surface around Struts," *Journal of The Society of Naval Architects of Japan*, Vol. 178, pp. 23-31.

[8] Ferziger, J. H., Peric, M., 1996, "*Computational Methods for Fluid Dynamics*", Springer Verlag, Berlin Heidelberg.

[9] Lemos, C. M., 1992, *"Wave Breaking - A Numerical Study"*, Springer Verlag, Berlin Heidelberg.

[10] Lungu, A., 1996, "Researches on the Free-Surface Flow around Submerged and Piercing Bodies", *Report No. AC2893, ICEPRONAV Galati, Romania.*

[11] Patel, V. C., Sarda O. P., Shahshanan, A., 1983, "Calculation of Ship Boundary Layers", Proc. *4th Symposium on Turbulent Shear Flow*, Karlsruhe, Germany, p. 3.1.

[12] Stern, F., 1986, "Effects of Waves on the Boundary Layer of a Surface-Piercing Body", *Journal of Ship Research*, Vol. 30, No. 4, pp. 256-274.

[13] Zhang, Z. J., Stern, F., 1996, "Free-Surface Wave-Induced Separation", *Journal of Fluids Engineering*, Vol.118, pp. 546-554.

[14] Hunt, J. C. R., Abell, C., J., Peterka, J. A., Woo, H., 1986, "Kinematical Studies of the Flows around Free or Surface-Mounted Obstacles; Applying Topology to Flow Visualization", *Journal of Fluid Mechanics*, Vol. 86, Pt. 1, pp. 179-200.

Conference on Modelling Fluid Flow (CMFF'06)
The 13th International Conference on Fluid Flow Technologies
Budapest, Hungary, September 6-9, 2006

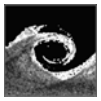

A RANKINE SOURCE METHOD CALCULATION OF THE WAVE RESISTANCE FOR A PANAMAX BULK-CARRIER HULL

Florin PACURARU[1], Dan OBREJA [2], Gabriel POPESCU[3]

[1] Corresponding Author. Naval Architecture Faculty, "Dunarea de Jos" University of Galati, E-mail: florin.pacuraru@ugal.ro
[2] Naval Architecture Faculty, "Dunarea de Jos" University of Galati, , E-mail: dan.obreja@ugal.ro
[3] Naval Architecture Faculty, "Dunarea de Jos" University of Galati, , E-mail: gabriel.popescu@ugal.ro

ABSTRACT

The present work describes a boundary element method (BEM hereafter) based numerical simulation where non-linear Rankine source extension of the Dawson method [1] for defining the flow around a bulk-carrier hull is employed. The total velocity potential is firstly divided into two parts, i.e., the double-model lifting flow potential and the free-surface flow potential. The double-model lifting-flow potential is expressed by the sources and doublets distributed on the body and wake surfaces, and determined by the method of Maskew. The free-surface-flow potential is expressed by a simple Rankine-type source distribution of the undisturbed free surface while sources and doublets are placed on the body and wake surfaces. The linearized free-surface boundary condition is used to determine the potential. Introducing the first and the second derivative of the potential not only in the flow equation, but also in the combined boundary condition on the free surface, they become linear equations in source strengths (or in source strengths computed in the collocation points in the second approach). The algebraic equations set is solved either directly, or by Gaussian elimination, or iteratively. It should be remarked that at the free-surface block level, the diagonal dominance is lost. Having the system solved for the source strengths, the velocity components may be later obtained from the derivatives. Pressure is computed with the Bernoulli equation. To obtain the hydrodynamic forces on the hull, the pressure is integrated over it.

An experimental investigation of the influence of two different hull forms is performed to check the overall accuracy of the solver. Experimental resistance tests on the PANAMAX bulk carrier models have been carried out in the Towing Tank of Galati University, at the full loading condition. The interference of the wave pattern and the associated vortical phenomena were observed and analysed during the model tests. The total ship resistance for both forms approaches the computed solution within a margin of 4-5% error.

Keywords: boundary, potential flow, sources, resistance, towing tank

NOMENCLATURE

perpendiculars

F_n	[-]	Froude number
L	[m]	reference length
M_T	[Nm]	trim moment by stern
R_w	[kN]	wave resistance
R_{Ts}	[kN]	total ship resistance
S	[m^2]	wetted hull surface area
T	[N]	sinkage force
U_∞	[m/s]	velocity of advancing ship in still water
c_A	[-]	correlation coefficient
c_p	[-]	pressure coefficient
$\underline{n}$	[-]	outward normal vector to the ship hull
n_x	[-]	x component of the outward normal vector to the hull
n_y	[-]	y component of the outward normal vector to the hull
p	[N/m^2]	pressure
x_0	[m]	the coordinate of the centre of gravity
v_s	[m/s]	ship speed
λ	[m]	wave lenght
ϕ	[-]	total velocity potential
ϕ_0	[-]	velocity potential of double model flow
ϕ_w	[-]	perturbation velocity potential
ζ	[m]	wave height

1. INTRODUCTION

Evaluation of the ship hull hydrodynamic performance is commonly achieved by using three approaches:

- Towing tank experimental investigation;
- Systematic series of data or statistic regression;
- Computational fluid dynamic.

The quantity and quality of the information produced by the Computational Fluid Dynamics (CFD hereafter) methods and the affordable cost have imposed the numerical technique as a very powerful tool not only for research purposes, but also for the initial design process of a ship.

Basically the CFD methods opperates with two different approaches; one is the potential flow and the other is viscous flow, depending on the initial hypotheses accepted. In this work the potential fluid supposition it used to simulate the free-surface flow around a ship hull. The attractiveness of any potential-based solver resides in the efficiency in terms of the CPU time consumption, in spite of lower level of accuracy that may, sometimes, be harmful for the final solution. Since the Reynolds number is well above the critical value for auto-modelling, i.e. the viscosity influence is negligible, it is expected that the use of the ideal fluid hypothesis does not ultimately contaminate the accuracy of the prognosis.

Supposing the fluid as inviscid, irrotational and incompressible, the characteristic equations are integrated following a standard Hess and Smith BEM technique. The Rankine source method based on sources distribution is employed to find out the position of the water free-surface. The no-slip kinematic boundary condition is imposed on the hull. The same condition must be satisfied on the free surface where the water particle must always stay on the free surface. Dynamic boundary condition on free surface requires the balance between the pressure on free surface and the atmospheric one.

The radiation condition i.e. waves generated by the ship hull may develop downstream the ship only, is also employed to completely describe the flow spectrum. Free surface conditions are non-linear and they are imposed on the surface that has an unknown in terms of their shape and position. A non-linear approach is used to find out the unknowns of the problem. Although versatile, proposed method does not allow the prognosis of the strongly non-linear phenomenon such as the spray or the wave braking. The wave resistance is finally obtained by integration the pressure over the wetted ship hull surface.

Experimental investigations were carried out in the towing tank of Galati University not only to check the accuracy of the theoretical approach, but also to clarify the details of the flow around the PANAMAX ship hull.

2. MATHEMATICAL MODEL

Basically, the algorithm follows the model previously proposed by Lungu and Raad [2]. Assuming that the ship hull advances in the undisturbed water with a constant velocity U_∞. The potential flow assumption of inviscid and irrotational flow is made for the steady flow around the hull. The ship is specified in a coordinate system having its x-axis parallel to the longitudinal direction, the y-axis to the direction of starboard and the z-axis pointing upwards. The total velocity potential ϕ, which can be expressed as follows:

$$\phi = \phi_0 + \phi_w \tag{1}$$

where ϕ_0 is the double model flow velocity potential, whereas ϕ_w is the perturbation potential due to the free-surface presence, satisfies the Laplace equation:

$$\nabla^2 \phi = 0 \tag{2}$$

2.1 Boundary conditions

The potential is subject to the several conditions on the hull and free-surface boundaries. Thus, the assumption of no flow across the body surface with normal direction $\underline{n}$ is imposed on the hull

$$\underline{n}\nabla\phi = 0\,. \tag{3}$$

The radiation condition provides for the unicity of the solution and its conformity to the physical reality.

$$\nabla\phi = (U,0,0) \tag{3}$$

is introduced at the upstream $(x \to -\infty)$ to enforce the waves to develop and remain behind the body.

The dynamic boundary condition on the free surface, which requires the pressure to be constant there, reads as follows:

$$\phi_x\zeta_y + \phi_y\zeta_y - \phi_z = 0 \text{ on } z = \zeta\,. \tag{4}$$

where g is the acceleration of gravity while ζ is the wave height. On the free surface, the kinematic condition is imposed under the following form:

$$g\zeta + 0.5(\phi_x^2 + \phi_x^2 + \phi_x^2 - U_\infty) = 0 \text{ on } z = \zeta \tag{5}$$

The free-surface problem described above is a non-linear one since the boundary conditions (5) and (6) are non-linear and must be satisfied on the initially unknown wavy surface. A solution method for the problem described here is to linearize the conditions around a known solution and solve the problem in an iterative manner. The linearization consists in replacing (5) and (6) by the following double-hull boundary condition:

$$\phi_{0l}^2\phi_{wll} + 2\phi_{0l}\phi_{0ll}\phi_{wll} + g\phi_{wz} = -\phi_{0l}\phi_{0ll} \quad \text{on } z = 0 \tag{6}$$

where l is the streamline direction. A four-point Dawson's finite-difference operator is employed to satisfy (4). The Laplace equation (2) is solved by imposing simultaneously the conditions (3) and (7). Once the velocity potential is determined, the free-surface elevation is computed by solving equation (5). Either the classical pressure integration or the procedure proposed by Hwangbo et al. in [3], which applies the Lagally theorem, is used to compute the wave resistance.

2.2 Wave height, forces and moment

Once the total velocity field is determined, the free-surface elevation ζ is computed by using the boundary condition, then the pressure is defined as follows:

$$p = \frac{1}{2}\rho(U - |q|^2) - \rho g \delta H \tag{7}$$

Finally, based on typical pressure integration, the wave resistance, R_w , sinkage force, T and the trim moment by stern MT are given as follows:

$$R_w = -\iint_{S_H} pn_x dS \tag{8}$$

$$T = \iint_{S_H} pn_z dS \tag{9}$$

$$M_T = \iint_{S_H} pn_z (x - x_0) dS \tag{10}$$

where x_0 is the x-co-ordinate of the center of gravity, $\underline{n}_x$, $\underline{n}_y$ are the x- and y-components of the outward normal on the hull. The above hydrodynamic forces will define new trim and sinkage conditions and computations may be iterated successively until the solution converges.

Although the wave making resistance is still widely calculated by means of pressure integration over the body, it sometimes brings significant errors due to the complicate geometry or to the sharp change of pressure. Adopting a very small panel size, with the disadvantage of large storage requirements or increased computational time can reduce the demerit of the pressure integration. Alternatively, the use of a wave resistance expression derived in terms of the Lagally theorem may represent a better choice.

3. RESULTS AND DISCUSSIONS

A series of five numerical simulation were performed not only to check the hydrodynamic performances of the PANAMAX bulk carrier hull (see Figures 1 and 2), but also to study the possibility of increasing the speed of the ship. The ship hull is characterised by a large block coeficient and a very blunt waterline.

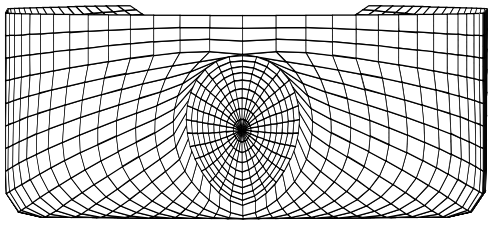

Figure1. Bow view of the initial hull

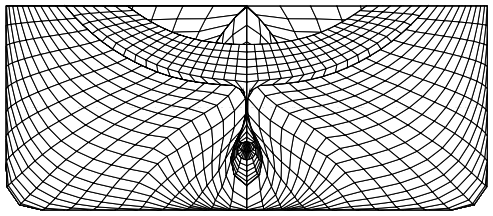

Figure 2. Stern view of the initial hull

The computational domain extends from a quarter ship length at the upstream, to two ship lengths downstream of the hull, whereas in the lateral direction a ship length is considered as being sufficient. The hull is discretized at first by using panels of constant source strength up to a horizontal plane above the free surface. At this plane, and at the centre plane of the ship, using mirror images of same source strength reflects the panels. Part of the water surface around the body is discretized by collocation points where the linearized free-surface condition is imposed. Discrete Rankine sources are placed as a layer of a constant height. Single sources are replaced by four-point sources in order to compute the influence on collocation points in the near vicinity.

When the wave resistance is obtained by integrating the pressure over the body surface, a constant distribution over each flat panel is assumed for the pressure. A more accurate integration for higher order panels where the pressure is assumed to vary either linearly or parabolically is also proposed. The sinkage and trim are taken into account in the computations presented here.

Figure 3 shows the wave cut profiles drawn for the ship speeds of 7.073 m/s and 8.525 m/s. As

prooved in the figure above-mentioned, the wave magnitude increases as the ship speed increases, a fact which is confirmed by the wave theory. The height of the bow crest rises from 2.06 to 3.24 m. Its magnitude is obviously due to the bluntness of the waterline and it is responsible for the total resistance raise. Moreover, a large bow wave may eventually lead to the imminence of the wave braking. Fig. 3 also proves that that the computed wave length completely agree with the theory in terms of the wave lenght:

$$\lambda = 2\pi \cdot L \cdot F_n^2 \qquad (11)$$

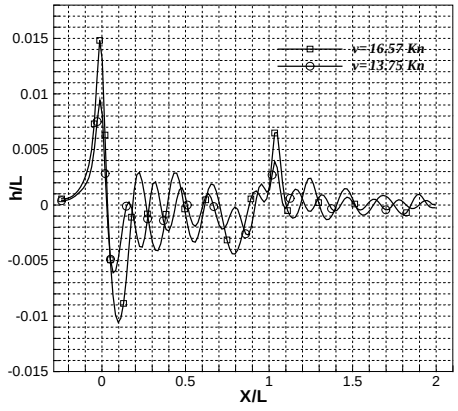

Figure 3. The wave cut profiles drawn for 7.073 m/s and 8.525 m/s.

Same conclusion may be drawn from Figure 4, which depicts the developement of the wave pattern for the same two speeds. The number of the waves crests decreases with the speed increase, according to the wave length computed by using (11).

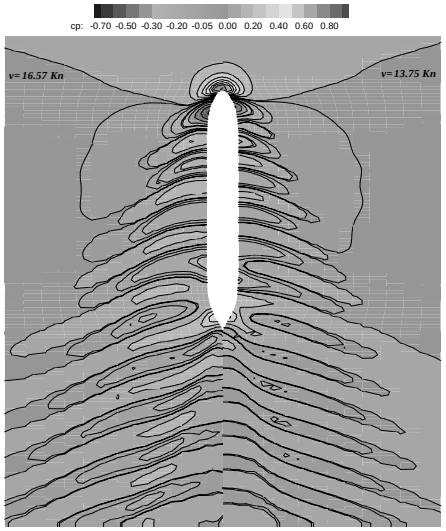

Figure 4 Comparison between the free surface topologies computed for 7.073 and 8.525 m/s.

The pressure fields computed at the same two considered speeds and plotted on the ship bow are comparatively shown in Figures 5 and 6. Analysing the drawings, one may notice the lower pressure area below stern becomes more intense once the speed increases.

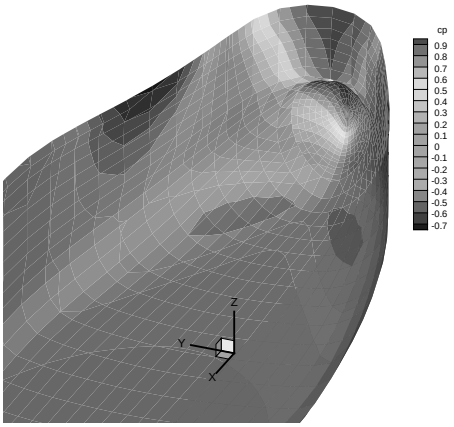

Figure 5. Pressure distribution on the ship bow at 7.073 m/s

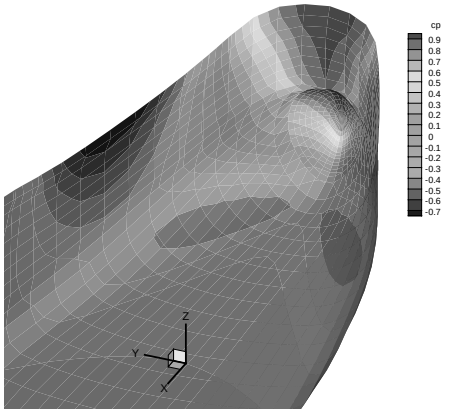

Figure 6. Pressure distribution on the ship bow at 8.45 m/s.

4. EXPERIMENTAL TESTS FOR THE "PANAMAX" BULK CARRIER MODEL

An experimental procedure has been employed to study the flow around the model at full loading condition and to determine the ship resistance for the Panamax bulk carrier. The resistance tests were performed in the Towing Tank of the Faculty of Naval Architecture at University "Dunarea de Jos" of Galati, with the main dimensions of 43x4x3 meters (Fig.7). The towing tank is equipped with a digital computer data acquisition and analysis system. The transposition of the still water test data to the ship scale is done authomatically by using an in-house software. Measurements are performed for the force required to pull the model in the still water at a constant speed. Resistance and speed are

measured and the own wave train is recorded and visually analysed.

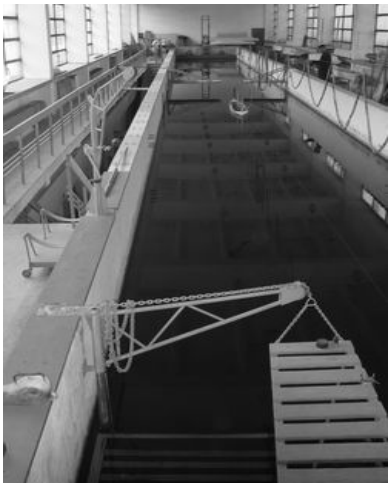

Figure 7. Towing Tank of Galati University

The resistance force is measured by means of electronics dynamometers with an accuracy factor of about 0.2% and the velocity transducer is based on an impulse generating sensor with the accuracy factor of 1%. The turbulence stimulation is obtained with a strip-wire of about 1 mm in diameter, which is attached to the model around the 19th station. The experimental model shown in Figure 8 was manufactured on a scale of 1:80, considered good enough to avoid the blocking effect, that usually occur if the model size is not correlated to the dimension of the towing tank.

The model tests results are extrapolated to the full-scale ship by using Froude ship-model correlation line (ITTC 1957 [4]). The prognosis of the ship resistance can be performed with an overall accuracy of ±3% . The characteristics of the ship and of the experimental model are presented in Table 1 and the tests results for the model at full load condition are given in Table 2 [5].

Figure 8. PANAMAX bulk carrier model

Table 1. Full scale ship and ship model main characteristics

Main characteristics	Full scale	Model
Length at the waterline [*m*]	220.915	2.761
Length between perpendiculars [*m*]	217.30	2.716
Moulded breadth [*m*]	32.20	0.403
Mean draught [*m*]	13.830	0.173
Volumetric displacement [m^3]	82626.0	0.161
Wetted surface area [m^2]	11762.4	1.838
Block coefficient	0.837	0.837
Mid shipsection coefficient	0.995	0.995
Waterline coefficient	0.923	0.923

Table 2. Resistance measured on the ship model working at full load condition

F_n	R_{Tm} [*N*]	c_{Fm}	c_R
0.088	1.619	0.0048080	0.0035272
0.097	1.736	0.0047083	0.0026754
0.106	1.864	0.0046181	0.0020111
0.114	2.019	0.0045509	0.0017133
0.120	2.172	0.0044985	0.0015465
0.130	2.376	0.0044277	0.0012662
0.139	2.644	0.0043643	0.0011589
0.146	2.882	0.0043200	0.0011415
0.152	3.149	0 .0042825	0.0012043
0.157	3.439	0.0042524	0.0013457
0.165	3.798	0.0042087	0.0013848
0.174	4.098	0.0041668	0.0013065
0.183	4.413	0.0041213	0.0011716

The full scale extrapolation is given in Table 3. The correlation coefficient is c_A=0.0001

Table 3. Full scale extrapolation

F_n	v_s [*m/s*]	c_T	R_T [*kN*]
0.088	4.115	0.0052100	531.7
0.097	4.527	0.0043393	536.2
0.106	4.949	0.0036576	540.4
0.114	5.298	0.0033467	566.8
0.120	5.597	0.0031696	598.4
0.130	6.029	0.0028754	630.5
0.139	6.461	0.0027553	693.1
0.146	6.785	0.0027291	756.8
0.152	7.073	0.0027842	839.7
0.157	7.320	0.0029195	942.6
0.165	7.695	0.0029497	1052.6
0.174	8.076	0.0028627	1126.2
0.183	8.525	0.0027184	1190.9

The model resistance diagram is given in Fig.9 and the ship resistance diagram is presented in

Figure 10. The wave pattern at full load condition for different speeds is presented in Figures 11-15.

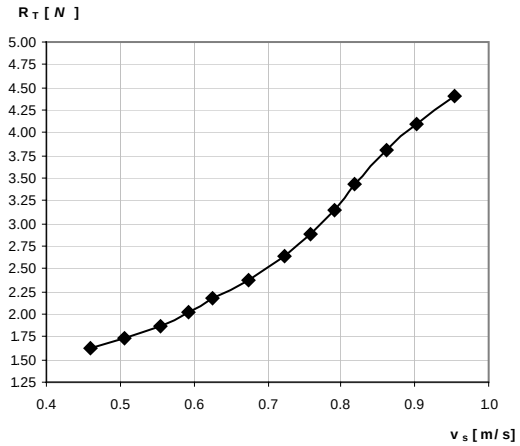

Figure 9. Model resistance diagram

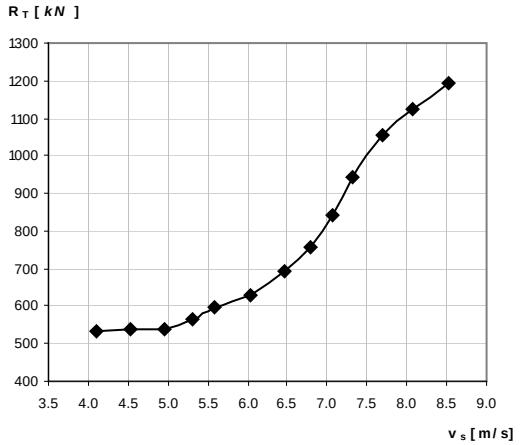

Figure 10. Ship resistance diagram

Figure 11. Bow wave geometry, v_s=7.073 m/s

Figure12. Bow wave geometry, v_s=7.32 m/s

Figure 13. Bow wave geometry, v_s=7.695 m/s

Figure 14. Bow wave geometry, v_s=8.076 m/s

Figure 15. Bow wave geometry, v_s=8.525 m/s

For flow around the at Froude numbers greater than a critical value, wave braking may occur and involve further complicated phenomena such as vortex and turbulence generation. When velocity is less the critical value, the wave crest look roundes and no symptoms of breaking are present. All the same, if the velocity increases a little the steady breaker suddenly takes place. Even though the differece between the velocitiess of the two regimes is rather small, the wave profiles differ substantially. The wave amplitude under the sub-braking becomes smaller while the wave length shorter as if Froude number were smaller. If the flow is further accelerated this intermediate stage is overcome and the breakers such as spilling or overturning should eventually take place [6]. The structure of the wake reflects the flow phenomena around the hull. A typical horse-shoe vortex is developed around the bow, which is generated by the high angle of waterplane entrance. Whenever the vertical velocity component increases around the bow, magnitude of the steep waves increases as well. The waves may break and eventually modify

the front slope there. The breaking waves were revealed in the bow area of the flow at higher speeds. The interference of the wave pattern, the breaking waves and the vortical phenomena were clearly visualized during the model tests. These phenomena are of primary importance for improvement of the hull design, because as much as 15% of the resistance of a full-form ship is associated with its breaking bow wave as proved by Baba in [7].

5. COMPARISON OF NUMERICAL AND EXPERIMENTAL RESULTS

A comparative, experimental and numerical view of the wave pattern profiles is shown in Fig.16 7.073 m/s.

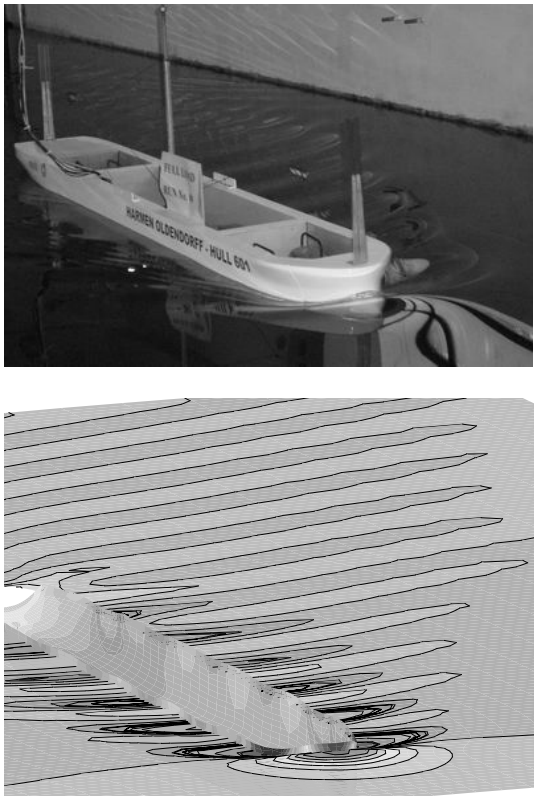

Figure 16. Wave profile comparison betweeen numerical simulation and experimental test at 7.073 m/s.

Figure 17 depicts the numerical and experimental ship resistance results for initial lines forms and the Figure 18 for modifyed lines forms. A good agreement throughout the considered Froude numbers range was obtained. In order to increase the ship resistance performance at full load condition, a numerical and experimental procedure has been employed to determine a new bulb solution.

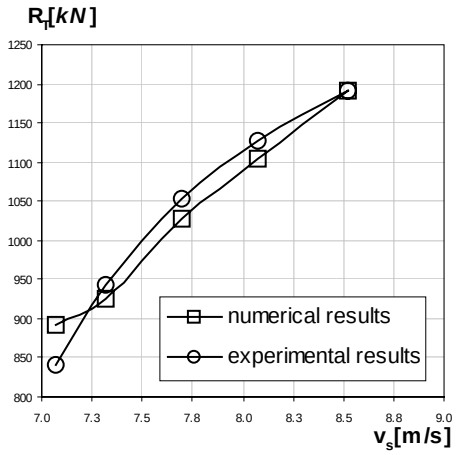

Figure 17. Numerical and experimental, ship resistance results. Initial version

The mesh of the optimum modified solution is drawn in Figure 18 and the bow part of the experimental modified model is presented in Figure 19 [8]. The comparative numerical and experimental ship resistance diagrams on the modified bulb are presented in Figure 20. The comparative experimental ship resistance diagrams between the initial and modified solutions are given in Figure 21. The total ship resistance for the modified solution is about 4-5% less then initial shape.

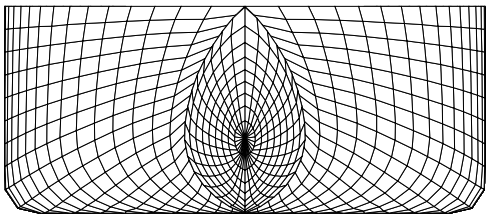

Figure 18 . Bow view. Modified model

Figure 19 Bow part of the modified model

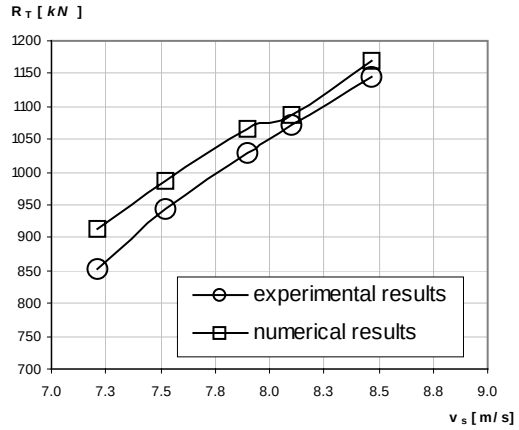

Figure 20. Numerical and experimental results. Modified version.

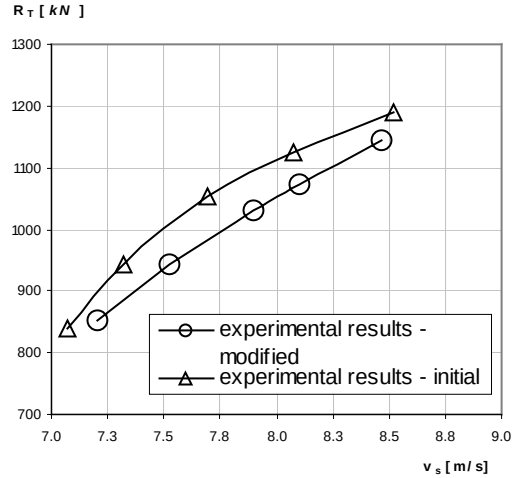

Figure 21. Comparative experimental results. Initial and modified versions

5. CONCLUSIONS

Results of a numerical and experimental investigation on the resistance of a PANAMAX bulk carrier have been presented. The fore body lines plan with a high angle of water plane entrance and the dissatisfactory bulb profile are the main causes of ship resistance increasing. The breaking waves and the vortices were put in the evidence at the bow domain of the flow, with negative influence over the ship resistance.

Comparison of numerical computation with experiment model results has shown a good agreement throughout the considered Froude number range. In order to decrease the ship resistance, an analysis for several bulb solutions was performed. At full load condition the optimised bulb solution decrease the ship resistance with about 4-5%.

The present numerical method can be integrated in optimisation procedures, in order to reduce ship the resistance in the preliminary design stage.

ACKNOWLEDGEMENTS

This work has been supported partly by the Oldendorff Carriers GmbH & Co. KG, Germany and partly by The National University Research Council under research contract, for which they all are acknowledge.

REFERENCES

[1] Dawson, C.W., "A Practical Computer Method for Solving Ship-Wave Problems", Proceedings of The Second International Conference on Numerical Ship Hydrodynamics, University of California, Berkeley, pp. 30-38, 1977.

[2] Lungu, A., Raad, P., Non-linear Potential Free-Surface Flow Around the Series-60 Ship Hull, 1998 ASME Fluids Engineering Division Summer Meeting, June 21 - 25, 1998 Washington DC

[3] Hwangbo, S. M., Mori, K., Doi, Y., 1995, "Numerical Investigation on Wave Reduction by Wings Attached to Hull", *Journal of Society of Naval Architects of Japan*, Vol.177, pp. 41-48.

[4] Bertram, V., „*Practical Ship Hydrodynamics*", Butterworth-Heinemann, Oxford, 2000.

[5] Obreja, D., Popescu, G., Domnisoru, L., Pacuraru, F., (2005), *Hull E601. Experimental Test Report for Bow Bulb Optimisation*. Research Project No. 388/2005, "Dunarea de Jos" University of Galati.

[6] Lungu, A., Numerical Analysis of the Free-Surface Flow Around a 2D Submerged Hydrofoil, PhD Thesis, pp. 167-168, 1994

[7] Baba, E., "A New Component of Viscous Resistance", Journal of The Society of Naval Architects of Japan, col.125, pp.23-30, 1969

[8] Obreja, D., Popescu, G., Domnisoru, L., Pacuraru, F., (2005), Resistance Test Report for PANAMAX Bulk Carrier Model (E601). Research Project No. 377/2005, "Dunarea de Jos" University of Galati.

Conference on Modelling Fluid Flow (CMFF'06)
The 13th International Conference on Fluid Flow Technologies
Budapest, Hungary, September 6-9, 2006

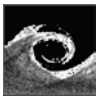

NUMERICAL INVESTIGATION ON THE KELVIN-HELMHOLTZ INSTABILITY IN THE CASE OF IMMISCIBLE FLUIDS

Yann Bartosiewicz[1], Jean-Marie Seynhaeve

[1] Corresponding Author.
Université Catholique de Louvain (UCL), Faculty of Applied Sciences, Mechanical Department, TERM division, Place du levant 2, 1348 Louvain la Neuve, Belgium. Tel. +3210472206, Fax +3210452692, E-mail : yann.bartosiewicz@term.ucl.ac.be

ABSTRACT

This paper presents the set up of a benchmark for the NEPTUNE code. This latter consists in modelling the Thorpe's experiment to provide numerical for code to code validation. Computational results are in good agreement with experimental data. In addition, results show that surface tension is an important parameter for the temporal growing dynamics of the waves.

Keywords: CFD, Kelvin-Helmoltz instability, Thorpe's experiment, Two phase flow

NOMENCLATURE

F_s	[N]	Interface force
H	[m]	Channel height
L	[m]	Channel length
g	[$m.s^{-2}$]	Gravity acceleration
k	[m^{-1}]	Wave-number
l	[m]	Channel width
t	[s]	Time
u	[$m.s^{-1}$]	Longitudinal velocity
x	[m]	Longitudinal direction
y	[m]	Transverse direction
α	[-]	Volume fraction
λ	[m]	Wavelength
μ	[$kg.m^{-1}.s^{-1}$]	Dynamic viscosity
ρ	[$kg.m^{-3}$]	Density
σ	[$N.m^{-1}$]	Surface tension
ΔU		

Subscripts and Superscripts

0	Initial time
1	Phase 1
2	Phase 2
c	Critical
i,j, q	Direction indexes

1. INTRODUCTION

The European project NURESIM (Nuclear Reactor SIMulation) aims at developing and validating a numerical platform to model complex multiphase flows, relevant to nuclear reactor thermal hydraulics. In this way, the NEPTUNE code has been developed within the framework of the EDF-CEA co-development project.

One of the issues of this project is to set up relevant benchmarks in order to assess the code potentials for a variety of situations encountered in nuclear reactors. Among these situations, safety related flows are those that are more complex and of a great interest. One of the possible scenarios is cold water Emergency Core Cooling (ECC) into the cold leg during a Lost of Coolant Accident (LOCA). A relevant problems occurring in this situation is the development of wavy stratified flows which may be single-phase or two-phase depending on the leak size, location, and operating conditions. These instabilities may give rise to Kelvin-Helmholtz structures which may induce a slug situation [1, 2]. In two phase flows situation, the Kelvin-Helmholtz roll-up may capture bubbles that may further condense and give water hammers [3].

The proposed benchmark aims at tackling this kind of flows but in the case of immiscible fluids. This simplification allows to deal with two-phase related aspects such as surface tension, density differences, free surface, and to compare both with a simple inviscid analysis [4, 5] and experimental results. However, the linear inviscid theory is valid for the case of two fluids of similar density [6]. This problem has been tackled by Meignin et al. [7] with the nonlinear analysis or by Staquet [8, 9] with numerical simulations of a single phase flow. A review of experiments of Kelvin-Helmholtz instability with large density differences can be found in Funada and Joseph [10]. Concerning the

case of two-phase flows with heat and mass transfer, many studies can be found in literature and they are mostly devoted to the modelling or measurement of interfacial transfers [11-13]. Moreover, due to the additional difficulty related to the nature of the flow (liquid water-water steam) and the associated modelling issues, this kind of studies cannot be used as an objective benchmark to assess the code potential.

A possible benchmark could be that of Hou et al. [14] who analysed two inviscid fluids of equal density in zero gravity conditions. However, this case is not realistic, and an experimental background is missing. Therefore the proposed benchmark in this paper is the same that is planned in Tiselj et al. [15] and relies on the work of Thorpe [6]. Indeed, this work is very convenient for the targeted benchmark, because experimental data and matching theoretical results are available for comparison to CFD ("Computational Fluid Dynamics") simulations.

2. DESCRIPTION OF THE THORPE'S EXPERIMENT

The Thorpe's experiment (figure 1) consists in a glass channel containing two immiscible fluids of different but similar densities. The fluids were water (fluid 2) and a mixture of tetrachloride and commercial paraffin (fluid 1) with the following properties:

$$\begin{aligned} \rho_1 &= 780 \text{ kg/m}^3,\ \mu_1 = 0.0015 \text{ Pa.s} \\ \rho_2 &= 1000 \text{ kg/m}^3,\ \mu_2 = 0.001 \text{ Pa.s} \end{aligned} \quad (1)$$

Concerning the geometry parameters, the following dimensions have been used in the experiment:

$$L = 1.83 \text{ m},\ H = 0.03 \text{ m},\ l = 0.1 \text{ m} \quad (2)$$

Initially, the tube was completely filled with the fluids. Both fluid layers have the same initial height $h_1 = h_2 = 1.5$ cm. The surface tension was estimated to $\sigma = 0.04$ N/m by measurements with 10% accuracy; however Thorpe [6] claimed that errors due to this uncertainty are small in calculations. After allowing the fluids to settle, the channel was sharply tilted such as $\sin\alpha = 0.072$. The resulting motion is a wavy flow giving rise to Kelvin-Helmholtz instabilities. The motion of the interface is recorded from the side and the flow is also filmed from above by means of a mirror. From the theoretical and computational point of view, the tube width is large compared to the thickness of the shear layer, justifying a two dimensional approach.

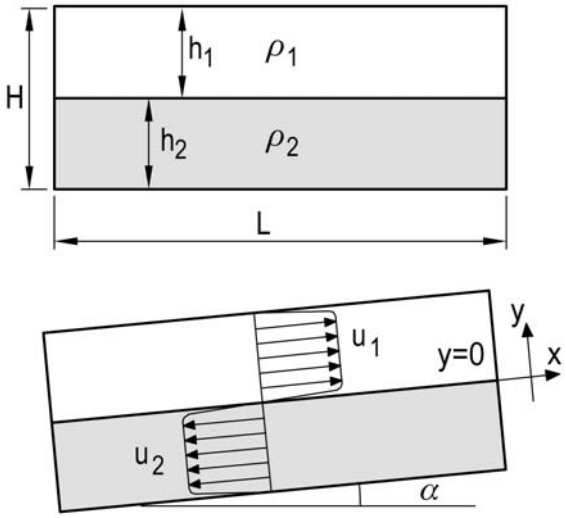

Figure 1. Description of the Thorpe's experiment

3. EXPERIMENTAL RESULTS AND INVISCID LINEAR ANALYSIS

3.1. Experimental results

For the operating conditions mentioned above, Thorpe [6] took ten pictures (Ex. Figure 2) of the interface, separated by 0.059 seconds. The first picture is taken at a time of onset of the instability has been observed. This time is 1.88 ± 0.07 seconds and includes half the time taken to tilt the channel (about 0.25 seconds). In his paper, Thorpe claims that this uncertainty might be even larger.

Figure 2. Example of a picture taken in experiments [6]

The most unstable wave-number is estimated with the distance between two wave crests (Figure 3). The measured value is $\lambda_c = 2.5 - 4.5$ cm, the uncertainty comes from the different critical wavelengths observed under the same operating conditions [6]. After the onset on the instability

Thorpe observed the growth of the waves for approximately 0.52 seconds. Beyond this time, this growth was almost stopped and the roll-up of these waves started. At this time the estimated amplitude of the waves was about $2a = 6-8$ mm (Fig. 3). The downward wave speed was also measured to 2.6 cm. As far as possible, all these experimental data will be compared to numerical simulations.

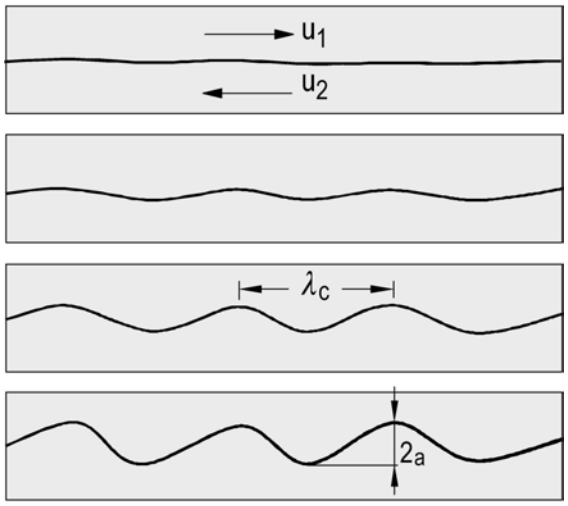

Figure 3. Wavy flow topology and parameters

3.2. Linear inviscid analysis

In this section, we recall some important results of linear-hydrodynamics instability theory, which are of interest to determine criteria for the occurrence of instabilities, and the associated parameters. For a more complete presentation, the reader is referred to Drazin and Reid [5]. Consider an inviscid fluid such as

$$\begin{aligned} -h_2 < y < 0 &\begin{cases} \rho = \rho_2 \\ u_2 = -\Delta U/2 \end{cases} \\ 0 < y < h_1 &\begin{cases} \rho = \rho_1 \\ u_1 = \Delta U/2 \end{cases} \end{aligned} \qquad (3)$$

with $h_1 = h_2$. This parallel flow is assumed to be a solution of Euler equations upon which is superposed a small perturbation proportional to $\exp i(kx + \omega t)$. In this latter equation, k is real, and it is the longitudinal wave number of the perturbation; ω is complex where the real part ω_r is the phase speed and the complex part ω_c is the temporal growth rate of the perturbation. Once the 2D Euler equations are linearized, the following dispersion relation can be obtained for ω [4]:

$$\omega = k\frac{\Delta U(\rho_2 - \rho_1)}{2(\rho_2 + \rho_1)} \pm \sqrt{\frac{\sigma k^3 + gk(\rho_2 - \rho_1)}{\rho_2 + \rho_1}\tanh(kh) - \frac{k^2(\Delta U)^2 \rho_1 \rho_2}{(\rho_2 + \rho_1)^2}} \qquad (4)$$

The system is unstable when $\omega_c \neq 0$, providing a condition for the minimum (critical) velocity difference:

$$(\Delta U)^2 > \frac{\rho_1 + \rho_2}{\rho_1 \rho_2}\left(\sigma k + (\rho_2 - \rho_1)\right)\tanh(kh) \triangleq F \qquad (5)$$

Therefore, the minimum of the function F gives the most unstable wave-number k_c. In the case matching geometrical and operating boundary conditions realized in Thorpe's experiment [6], this critical wave-number is $k_c = 229$ m^{-1} (Figure 3): this gives a critical wave-length $\lambda_c = 2.7$ cm and a critical velocity difference $\Delta U_c \approx 0.2$ m/s. In his paper [6], Thorpe claims that the critical velocity and therefore the time of onset of instability predicted by the theory may be underestimated by as much as 10% because an abrupt transition in velocity is assumed at the interface. However, the minimum of the function F is relatively flat (Fig. 3), explaining the reason of several possible critical wave-numbers. Furthermore, Fig. 3 also depicts the influence of the surface tension σ on the critical velocity difference and wave-numbers.

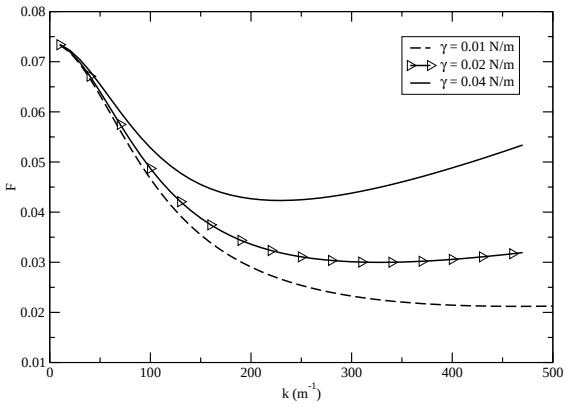

Figure 3. Values of F as a function of k

As surface tension is decreased, the minimum velocity required to get instability is also decreased which means that the time for onset of these instabilities should be shorter as well. In addition, the minimum of F becomes less and less sharp as σ is decreased, giving several possibility of critical

wave-numbers, and these critical wave-numbers are increasing: this means that the distance separating two waves decreases when surface tension at interface decreases.

The time dependent solution may be easily derived if closed-end effects are neglected [6], and gives the following velocity field:

$$U=\begin{cases} u_1=\dfrac{(\rho_2-\rho_1)h_2 g\sin\alpha}{\rho_1 h_2+\rho_2 h_1}t,\ 0<y<h_1 \\ u_2=-\dfrac{(\rho_2-\rho_1)h_1 g\sin\alpha}{\rho_1 h_2+\rho_2 h_1}t,\ -h_2<y<0 \end{cases} \quad (6)$$

From this equation, it is possible to estimate for a given $U=\Delta U_c/2$, the time of onset of the instability t_0. The critical velocity may be obtained as a function of the surface tension σ keeping all others parameters constant and matching those of the Thorpe experiment. Figure 4 illustrates the time t_0 and the matching critical velocity as a function of the surface tension. The benchmark conditions are stressed on the graph: for these conditions, the time of onset of the instability is about $t_0=1.2$ s for a critical velocity slightly higher than 0.2 m/s. Thorpe found that this results have to be corrected of about 10% to take into account corrections due to viscosity and accelerated flow. For instance, Thorpe evaluate the theoretical time $t_0=1.5\text{ s}-1.7\text{ s}$ including half the time to tilt the channel.

In addtion, Fig. 4 clearly shows that increasing the surface tension involves an increase of t_0 and ΔU_c. Therefore, computational tests with different surface tension than in the benchmark should be realized at lower σ to avoid an increasing CPU time.

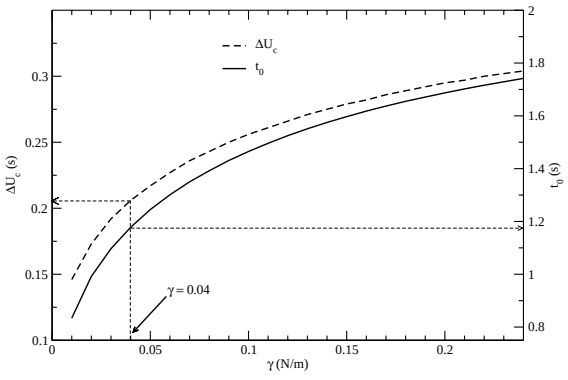

Figure 4. Critical velocity and time of onset of the instability

4. MODELLING APPROACH

The modelling work was performed with the use of the commercial CFD package FLUENT 6.2.16 which solves governing equation with a finite volume approach.

4.1. Governing equations

The conservation equations governing the fluid flow in the channel are of the incompressible, unsteady, and two-dimensional form. Furthermore, as the point of interest is the formation of Kelvin-Helmholtz instabilities up to their roll-up, and the maximum matching Reynolds Number is about 183 [6], only the laminar form of these equations is solved in the present work. The channel is assumed adiabatic and no thermal energy is exchanged between flows, so the energy equation is not solved. As far as two immiscible fluids are concerned, the Euler-Euler VOF technique is suited to track the interface.

The governing equation can therefore be written in their vector form

$$\frac{\partial\alpha_2}{\partial t}+\underline{u}.\underline{\nabla\alpha_q}=0 \quad (7)$$

$$\alpha_1+\alpha_2=1 \quad (8)$$

$$\frac{\partial(\rho\underline{u})}{\partial t}+\underline{\nabla}.(\rho\underline{u}\underline{u})=-\underline{\nabla P}+\underline{\nabla}.\left[\mu\left(\overline{\overline{\nabla\underline{u}+\nabla\underline{u}^T}}\right)\right]+\rho\underline{g}+\underline{F_s} \quad (9)$$

In Eq. (9) the source term F_s accounts for the surface tension effects at the interface between both fluids. This term is modelled following the continuum surface force proposed by Brackbill et al. [16], and can be cast in a volume force as follows:

$$\underline{F_s}=\sigma_{ij}\frac{\rho\kappa_i}{\frac{1}{2}(\rho_i+\rho_j)}\underline{\nabla\alpha_i} \quad (10)$$

where

$$\underline{n_i}=\underline{\nabla\alpha_i}$$
$$\underline{\hat{n}_i}=\frac{\underline{n_i}}{|\underline{n_i}|} \quad (11)$$
$$\kappa_i=\underline{\nabla}.\underline{\hat{n}_i}$$

The volume averaged properties such as the density and viscosity are evaluated by a volume-fraction-averaged:

$$\rho = \sum \alpha_i \rho_I$$
$$\mu = \sum \alpha_i \mu_i \quad (12)$$

4.2. Numerical aspects

The interface treatment is accomplished via a geometric reconstruction scheme. If a given cell is completely filled with one or another phase, no special treatment is performed. However, if the interface is included within a cell, it is represented by linear slope by using piecewise-linear interpolation. The first step in this reconstruction is computing the position of the linear interface in the cell, based on the volume fraction and their derivatives. The second step is calculating convective fluxes trough each face of the cell using the computed interface and velocities (normal and tangential) on the face. The final step is to update volume fractions based on the balance of fluxes calculated during the previous step.

The pressure-velocity coupling is realized by using the PISO (Pressure-Implicit with Splitting of Operators) algorithm [17] which ensures that the corrected velocities satisfy both the continuity and momentum equations after one or more additional loops. This algorithm takes more CPU time per solver iteration than SIMPLER or SIMPLEC, but it can dramatically decrease the number of iterations required for convergence in transient problems. Spatial discretization is achieved by a QUICK scheme with a staggering technique for the pressure term in the momentum equation. The time discretization uses a first order implicit scheme for flow equations, while an explicit time marching technique is used for the volume fraction equation (Equ. (7)). The global time step is adapted in order to ensure a maximum CFL = 2.

The resulting system is then solved using a point implicit Gauss-Seidel solver in conjunction with an algebraic multigrid method.

4.3. Domain, boundary conditions, initial conditions

The computational domain is two-dimensional and dimensions matches with those of Thorpe's experiment [6]. The channel is taken horizontal, but the gravity vector is inclined to model real experimental conditions (Figure 5). For this geometry, three different orthogonal meshes have been tested in order to check grid convergence:

- Mesh 1: 1830*30
- Mesh 2: 2588*42
- Mesh 3: 3660*60

All boundary conditions are walls with no-slip condition for the mixture. At $t = 0$, each fluid fills half the height of the channel, so the interface is initially located along the middle line of the domain. Initially all velocities equal zero and the pressure field is uniform and equal to the reference pressure (atmospheric pressure): this pressure field does not match with operating conditions since the channel is already tilted in simulations. To ensure a good initial pressure field, a small time ($t = 1.10^{-5}$ s) step is performed in order to make the pressure converge toward its hydrodynamics distribution. At this time, the computation can be started with the adaptive time procedure.

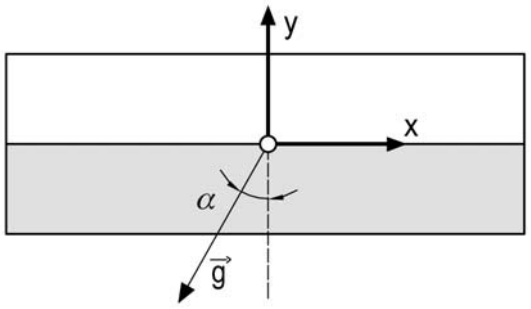

Figure 5. Computational domain and axis origin

5. RESULTS AND DISCUSSION

5.1. Comparison with Thorpe's experiment

In order to assess grid convergence, the three different meshes have been tried out. Figure 6a illustrates the results in terms of radial profiles of longitudinal velocity component at $t = 2$ s for the three tested meshes.At this time, the instability is well established, the velocity difference $\Delta U \approx 0.35$ m/s is largely higher than the theoretical velocity $\Delta U_c \approx 0.21$ m/s. The three tested meshes do not exhibit significant differences, while the CPU time is multiplied by 4 between MESH 1 and MESH 3. For the thinner mesh the capture of the velocity gradient trough the shear layer is slightly improved (Fig. 6a). Figure 6b depicts the Fourier analysis of the interface ($\alpha = 0.5$) for MESH 1 and MESH3: overall results showed that MESH 1 contains the essential spectral information and can be sufficient for this study.

Figures 7a and 7b show the Fourier analysis of the interface between $t = 1.5$ s and $t = 2.4$ s. Fourier transforms have been obtained with a FFT algorithm and a running average upon 5 values has been performed. The dash-dot curve represents an additional running average for each FFT. Fig. 7a illustrates that the time of onset of the instability is $1.6 \text{ s} < t_0 < 1.7$ s because the growing rate seems to become significant between this value. This is in accordance with Thorpe observation $t = 1.88$ s including half the time to tilt the channel ($t_0 = 1.63 \pm 0.07$ s).

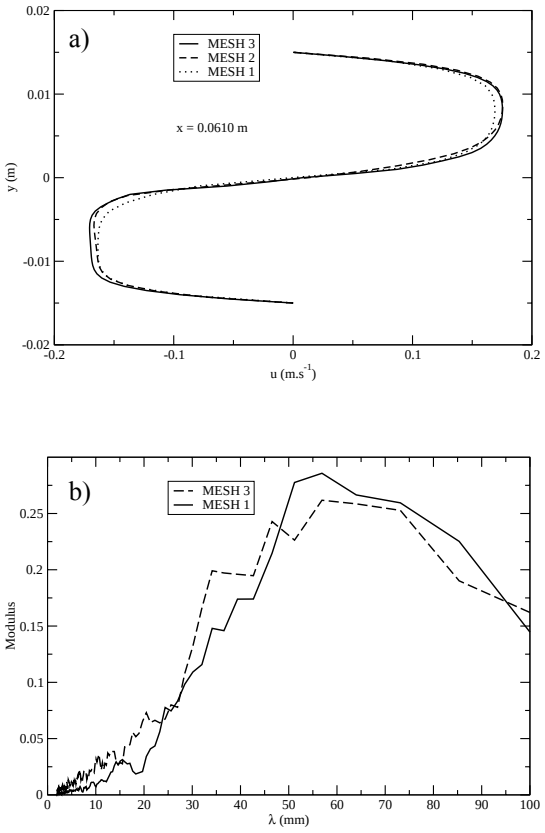

Figure 6. Grid convergence: velocity profiles

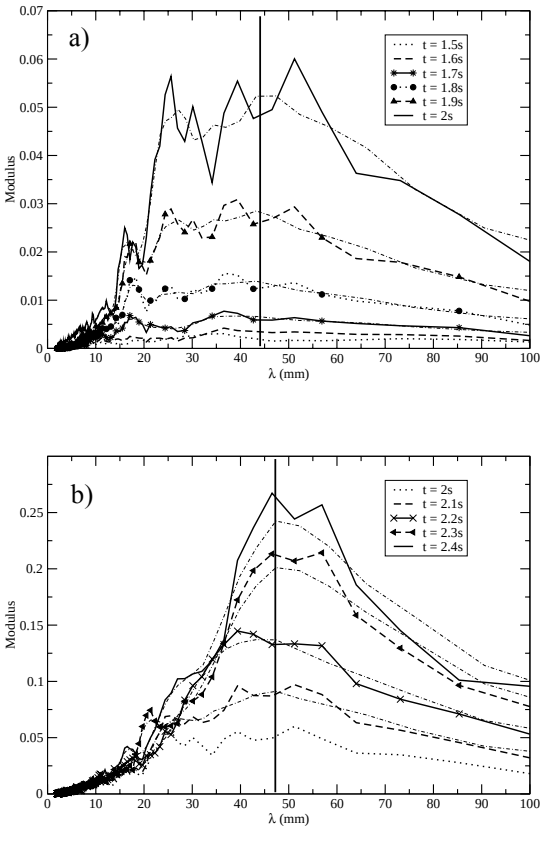

Figure 7. Fourier analysis of the interface

Moreover the critical wavelength matching to the most unstable wave-number can be evaluated at $\lambda_c \approx 44$ mm ($k_c = 142.8$ m^{-1}) compared to the Thorpe value $\lambda_c = 25 - 45$ mm ($k_c = 197 \pm 58$ m^{-1}). The computed values agree well with Thorpe observations, because the range of possible critical waves is quite wide (Fig. 7) ($\lambda_c = 25 - 50$ mm) in accordance with results found Fig. 3. In addition, it is also observed that this critical wavelength does not much change significantly with time as observed by Thorpe [6].

Figure 8 exhibits the location of the physical interface between $t = 1.7$ s and $t = 1.9$ s. The crest to crest distance allows to determine the velocity of the wave moving downward. The computed distance for this 0.2 s time period is evaluated to 0.5cm, which gives a velocity of $u \approx 2.5$ cm.s^{-1}: Thorpe evaluated this velocity at $u \approx 2.6$ cm.s^{-1}.

In order to evaluate more precisely the time of onset of the instability and to asses the growing rate of waves, the integral of each FFT has been computed. The returned value may be seen as a relative image of the waves amplitude. Figure 9 depicts the curve obtained by calculating each integral for each time. The curve shows too breakpoints:

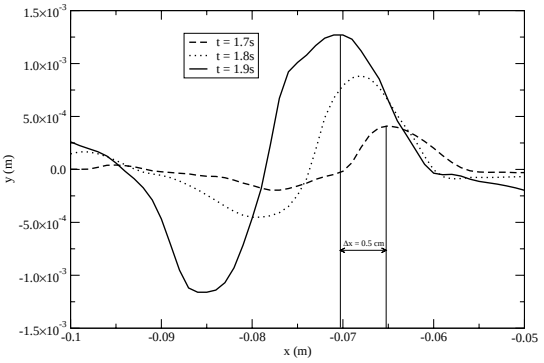

Figure 8. Physical location of the interface

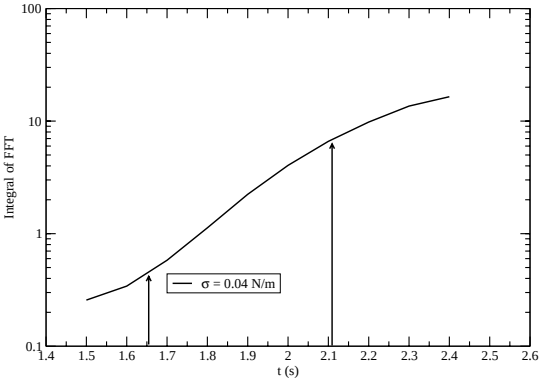

Figure 9. Waves growing rate

the first one matches with the time of the onset of a significant growing rate and may be evaluated to $t_0 = 1.66$ s ; the second breakpoints matches with a time where growing is stopping, giving rise to waves roll-up.

5.2. Surface tension effects

In order to assess the effect of surface tension on the development of instabilities, two additional surface tensions have been tried out: $\sigma = 0.02$ N.m^{-1} and $\sigma = 0$ N.m^{-1}. From the linear invisvid theory, the most unstable wavelength should decrease as surface tension is decreased (Fig. 3). In addition the minimum of function F (Fig. 3) becomes more and more flat, which means that the number of possible critical wavelengths increases; for zero surface tension infinity wave-numbers are possible. Figure 10 shows the spectral analysis of the interface for $\sigma = 0$ N.m^{-1}. For this case, the results revealed a growing wavy flow very early in the computation with a much smaller wavelength than the previous case ($\sigma = 0.04$ N.m^{-1}). Indeed, at the beginning, the critical wavelength is $\lambda_c \approx 13$ mm (Fig. 10a).

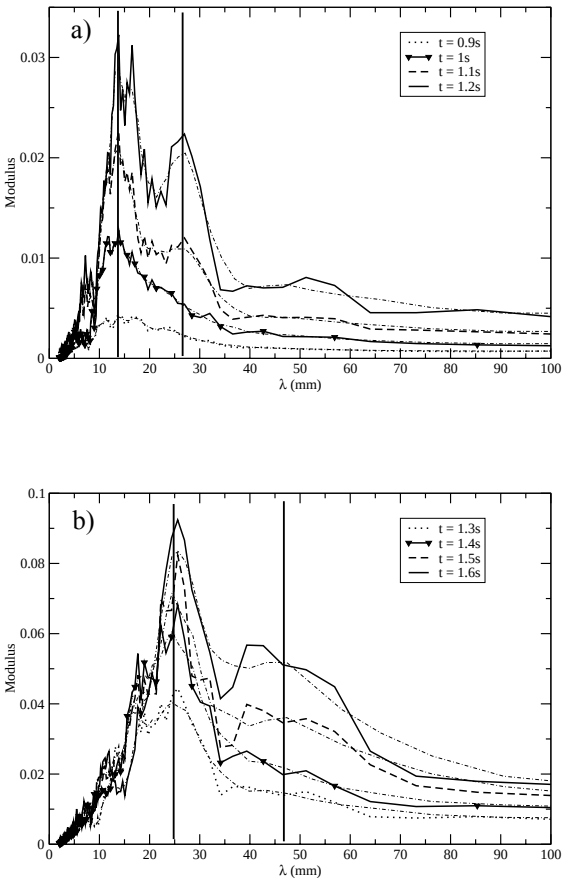

Figure 10. Fourier analysis of the interface for $\sigma = 0$ N.m^{-1}

However, at later times, a second wave rises for $\lambda_c \approx 27$ mm . Beyond $t = 1.2$ s-1.3 s (Fig. 10b), the two initial wavelengths are shifted to higher wavelengths $\lambda_c \approx 25$ mm and $\lambda_c \approx 47$ mm . A possible explanation would be that a pairing of similar structures occurred, giving rise to new structures with a higher wavelength.

Figure 11 confirms that the wavy dynamics starts earlier as the surface tension is decreased. For $\sigma = 0$ N.m^{-1} and $\sigma = 0.02$ N.m^{-1} the growing rate is decreased at two times (two breakpoints, Fig. 11) compared to that with $\sigma = 0.04$ N.m^{-1} (one breakpoint). However, it seems that the initial growing phase for each case is similar in terms of growing rate since curves are almost parallel. But for lower surface tensions, there is more than one growing phase. Figure 12 illustrates a volume fraction field for each surface tension at $t = 3$ s . It is clearly shown again that the overall dynamics is inhibited as the surface tension is increased. Nevertheless, the laminar model is questionable beyond the waves roll-up.

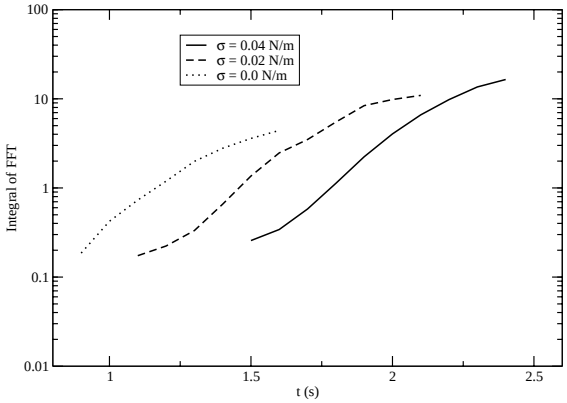

Figure 11. Growing rates for different surface tensions

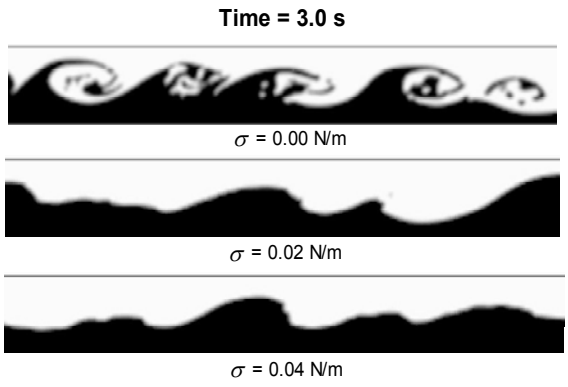

Figure 12. Volume fraction fields

6. CONCLUSIONS

In this paper, a benchmark to validate NEPTUNE, a new european code for modelling two phase flows relevant to nuclear safety is set up, and results are presented. This benchmark consists in the modeling of a wavy flow of two immiscible fluids, and relies on the Thorpe's experiment [6]. The numerical data to compare with NEPTUNE are obtained with FLUENT. In this case, FLUENT provides rather good results compared to Thorpe's observations. In addtion, the effect of the surface tension could be also studied. Results showed this parameter is of primary importance for the temporal growing dynamics of the waves (onset of instability, growing, pairing, etc.).

Future works will be devoted to the study of other parameters such as viscosity or density ratios between the two phases. Also, computations with matching conditions will be achieved with NEPTUNE.

ACKNOWLEDGEMENTS

The NURESIM project is supported by the European commision in the framework of the sixth R&D programm. Authors wish also to acknowledge François Vercheval from the TERM division for the different drawings of this paper.

REFERENCES

[1] Wallis, G. B., and Dobson, J. E., 1973, "The onset of Slugging in Horizontal Stratified Air Water Flow", Int. J. Multiphase Flow, vol. 1, pp. 173-193.

[2] Tailtel, Y., and Ducker, A. E., 1976, "Model for Predicting Flow Regime Transitions in Horizontal and Near Horizontal Gas Liquid Flow", AICHE J., vol. 22, pp. 47-55.

[3] Ansari, M. R., 1998, "Numerical Analysis for Slugging of Steam-Water Stratified Two-Phase Flow in Horizontal Duct", Fluid Dynamics Research, vol. 22, pp. 329-344.

[4] Chandrasekhar, S., 1961, "Hydrodynamics and hydromagnetic stability", Oxford University Press.

[5] Drazin, P. G., and Reid, W. H., 1982, "Hydrodynamics stability", Cambridge University Press.

[6] Thorpe, S. A., 1969, "Experiments on the instability of stratified shear flows: immiscible fluids", J. Fluid Mech., vol. 39, pp. 25-48.

[7] Meignin, L., Gondret, P., Ruyer-Quil, C., and Rabaud, M., 2003, "Subcritical Kelvin-Helmholtz instability in a Hele-Shaw cell", Physical Review Letters, vol. 90, no. 23, 234502-1-234502-4.

[8] Staquet, C., 1995, "Two-dimensional secondary instabilities in a strongly stratified shear layer", J. Fluid Mech., vol. 296, pp. 73-126.

[9] Staquet, C., 2000, "Mixing in a stably stratified shear layer: two- and three-dimensional numerical experiments, Fluid Dynamics Research, vol. 27, pp. 367-404.

[10] Funada, T., and Joseph D. D., 2001, "Viscous potential flow analysis of Kelvin-Helmholtz instability in a channel". J. Fluid Mech., vol. 445, pp. 263-283.

[11] Lioumbas, J. S., Paras, S. V., and Karabelas, A. J., 2005, "Co-current stratified gas-liquid flow field on interfacial structure, Int. J. of Multiphase Flow, vol. 31, pp. 869-896.

[12] Kim, H. J., Lee, S. C., and bankoff, S. G., 1985, "Heat transfer and interfacial drag in countercurrent steam-water stratified flow", Int. J. of Multiphase Flow, vol. 11, pp. 593-606.

[13] Biberg, D., and Halvorsen, G., 2000, "Wall and interfacial shear stress in pressure driven two-phase laminar stratified pipe flow", Int. J. of Multiphase Flow, vol. 26, pp. 1645-1673.

[14] Hou, T. Y., Lowengrub, J. S., and Shelley, M. J., 2001, "Boundary integral methods for multicomponent fluids and multiphase materials. J. Comp. Physics, vol. 169, pp. 302-362.

[15] Tiselj, I. Strubelj, L., and Bajsic, I., 2004, "Test-case No 36: Kelvin-Helmholtz instability", Multiphase Science and technology, vol. 16, no. 1-3, pp. 273-280.

[16] Brackbill, J. U., Kothe, D. B., and Zemach, C., 1992, "A continuum method for modelling surface tension", J. Comp. Phys., vol. 100, pp. 335-354.

[17] Issa, R. I., 1986, "Solution of implicitly discretized fluid flow equations by operator splitting", J. Comp. Physics, vol. 62, pp. 40-65.

Conference on Modelling Fluid Flow (CMFF'06)
The 13th International Conference on Fluid Flow Technologies
Budapest, Hungary, September 6-9, 2006

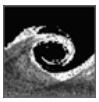

INVESTIGATION OF VORTICES EXISTENCE AT THE INTERFACE BETWEEN IMMISCIBLE FLUIDS

Diana BROBOANA, Andreea CALIN, Corneliu BALAN[1]

Department of Hydraulics and Fluid Machineries, REOROM Laboratory, Politehnica University of Bucharest, Splaiul Independentei 313, 060042 Bucharest, Romania. Tel.: +40 21 402 9705, Fax: +40 21 402 9865.
[1]Corresponding Author, Email: balan@hydrop.pub.ro, www.hydrop.pub.ro/reorom.html

ABSTRACT

The paper is dedicated to the study of vortices and existence of internal flows at the interface between two immiscible Newtonian fluids. One goal of the present work is to establish a proper kinematical criteria to detect more precisely the space location of a moving interface. The experimental investigations are performed in a specially designed Hele-Shaw cell, a pseudo-planar flow where the two fluids (water and oil, respectively) are put in motion by a controlled flow rate syringe pump. The evolution of interface and the onset of vortical structures are visualized and compared with the corresponding numerical simulations performed with FLUENT code through the VOF method. The vorticity number in the flow domain is computed and its distribution is related to the geometries of vortices and interface. A necessary condition for the presence of internal flows outside the wall is considered the existence of close areas surrounded by iso-vorticity number greater than one.

Keywords: vortices, interface, immiscible fluids, vorticity number, Hele-Shaw flow, VOF method

NOMENCLATURE

Re	[-]	Reynolds number
Sh	[-]	Strouhal number
Wo	[-]	vorticity number
Ca	[-]	capillary number
t	[s]	time
p	[Pa]	pressure
$\underline{v}$	[m/s]	velocity vector
$\underline{b}$	[m/s^2]	specific mass force
ρ	[kg/m^3]	mass density
η	[Pas]	viscosity
σ	[Pam]	interfacial surface tension
θ	[^{o}]	wetting angle at the wall

Superscripts

^	non-dimensional quantity

1. INTRODUCTION

The investigation and modeling of internal flows developed in multiphase liquid systems is of great importance for many applied scientific domains: chemical engineering, hydrodynamics, transport and mixing of fluids, polymer technology, biofluid mechanics, see [3], [6], [7], for examples.

The present paper reports the numerical and experimental investigations on the flow of a two-fluid system (water and oil), separated by a freely moving interface, within a Hele-Shaw cell. The evolution of an interface between two immiscible incompressible Newtonian liquids is studied, in relation to the formation of vortices and flow separated regions outside the walls.

The aim of the work is to establish a necessary condition for the existence of internal flows in a two-fluid immiscible system. The dynamic process is considered planar (2D approximation of the Hele-Shaw motion), with well established boundary conditions: (i) adherence of fluids at solid walls and interface; (ii) entrance velocity and outer pressure imposed. The Hele-Shaw cell is initially filled with liquid-B and, at moment t = 0, the liquid-A enters the domain, displacing liquid-B. Within the cell, the boundary between fluids is evolving, as well as the internal flows domains (if they exist); therefore the motion is not stationary, even though the boundary conditions are maintained constant. Flow topologies with multiple interface boundaries, i.e. one fluid surrounded completely by the other one, are not considered in this paper.

In this study, the internal flow area is defined as a region where kinematics of the motion is characterized by the existence of a closed vortex outside the solid boundary; hence, at one moment, there exists a pattern of pathlines within the flow domain which is isolated by the presence of an outer flow.

It is the authors' interest to investigate the relation between internal flows and the interface evolution between immiscible fluids, in order to

define more accurately the interface geometry through a kinematical criterion.

The existence of a criterion for the vortex presence in a flow, and the relation between vortex and vorticity field, is a major subject of study not only in hydrodynamics ([10], [12], [14]), but also in non-Newtonian fluid mechanics, see [1], [21] and [22].

Establishing a relation between vorticity and vortex is not straight-forward. Both terms have the meaning of rotation, but from different "perspectives": (i) **vorticity** is defined as the angular (rotational) velocity of a fluid element located at the space point:

$$\underline{\omega} = 1/2 \operatorname{curl} \underline{v} \tag{1}$$

while (ii) the **vortex** is a large-scale concept associated to "a rotating motion of a multitude of material particles around a common center", see [14].

Obviously, vorticity is a field in a continuum and the vortex is a structure (called sometimes "vortical structure" or "spiraling pathlines") generated by a particular velocity distribution in the flow field. The conditions for a vortex existence were discussed in detail by Broboana et al. in [4].

The present work extends some results from [4], one of the vortex existence criteria, i.e. $Wo > 1$, being used to define more properly the internal flow boundary in vicinity of the evolving interface between immiscible fluids.

The paper has an exploratory character and the first experimental and numerical results are mainly qualitative. Even though, the investigations are consistent with the assumption that it is possible to define a proper kinematical constrain (criteria) to establish more precisely the location in the flow domain of a moving interface between immiscible fluids.

2. THEORETICAL CONSIDERATIONS

Starting from the paper of Truesdell in early fifties of last century, [18], the concept of vorticity number – *Wo* was a permanent topic of study for scientists working in fluid mechanics and rheology. Traditionally, vorticity is directly related to the vortex and vortical flows, [14], and to some extend to the boundary layer theory, [16].

Vorticity $\underline{\omega}$, defined in (1), represents also the axial vector of the spin tensor $\underline{\underline{\Omega}}$, where $\underline{\underline{\Omega}}$ is the skew part of the velocity gradient $\underline{\underline{L}} = \operatorname{grad} \underline{v}$, i.e.

$$\underline{\underline{L}} = \underline{\underline{D}} + \underline{\underline{\Omega}} \tag{2}$$

with $\underline{\underline{D}}$ the symmetric strain rate tensor (stretching), [21]. It is well known that $\underline{\underline{D}}$ represents the local deformation and $\underline{\underline{\Omega}}$ is giving the local rotation in the flow field. It is also important to remark that $\underline{\underline{D}}$ is always objective and $\underline{\underline{\Omega}}$ is only in very particular kinematical processes objective, respectively $\underline{\underline{\Omega}}$ is generally not invariant under change of the reference frame, [1, 21].

The balance between rotation and deformation in a fluid is given by the ratio between the magnitude of $\underline{\underline{\Omega}}$ and the magnitude of $\underline{\underline{D}}$, i.e.

$$Wo := \frac{\left|\underline{\underline{\Omega}}\right|}{\left|\underline{\underline{D}}\right|} = \left(1 + \frac{2Q}{\left|\underline{\underline{D}}\right|^2}\right)^{1/2} \tag{3}$$

where

$$Q = \frac{1}{2}\left(\left|\underline{\underline{\Omega}}\right|^2 - \left|\underline{\underline{D}}\right|^2\right) = -\frac{1}{2} tr\left(\underline{\underline{D}}^2 + \underline{\underline{\Omega}}^2\right) \tag{4}$$

is the second invariant of $\underline{\underline{L}}$, see for details [12], [19] and [20]. In (3) the magnitude of a tensor $\underline{\underline{A}}$ is defined as

$$\left|\underline{\underline{A}}\right| = \sqrt{\operatorname{tr}\left(\underline{\underline{A}}\,\underline{\underline{A}}^{\mathrm{T}}\right)} \tag{5}$$

Finally, the vorticity number is present in the dimensionless Cauchy equation of momentum:

$$Re\left[Sh\frac{\partial \hat{\underline{v}}}{\partial \hat{t}} + \left(\underline{\underline{\hat{D}}} + Wo\,\underline{\underline{\hat{\Omega}}}\right)\hat{\underline{v}} - \hat{\underline{b}} + \operatorname{grad}\hat{p}\right] = \operatorname{div}\underline{\underline{\hat{T}}} \tag{6}$$

where *Wo* plays a major role in the balance of the inertia components, for details see [21] (here $\underline{\underline{T}}$ is the extra-stress tensor, p is pressure and $\underline{b}$ is the specific mass force).

A vortex region is a region with complex eigenvalues of $\underline{\underline{L}}$ where $Q > 0$, i.e. $Wo > 1$ in (3), and a local pressure minimum determined by a negative second eigenvalue of the symmetric tensor $\underline{\underline{D}}^2 + \underline{\underline{\Omega}}^2$, i.e. $\lambda_2 < 0$, [12]. These two conditions (so called Q - criteria, respectively λ_2 - criteria) seem to be necessary, but not sufficient for proving the existence of a vortex.

Since the phenomenological definition of the vortex given by Lugt in [14] is valid only in a reference frame that does not move with respect to the center of the vortex and the vorticity number is not objective (due to non-objectivity of $\underline{\underline{\Omega}}$, see [1]), one can conclude that a general definition of the vortex existence has to be objective. Such definition is introduced by Haller in [10] and states that "the vortex is a set of fluid trajectories along which the strain acceleration tensor is *indefinite* over

directions of zero strain". The vortices are identified here as material tubes in which material elements do not align with directions suggested by the strain eigenvalues. This criteria is also consistent with the assertion that the presence of a vortex is determined by the existence of a spiral or center critical points in the trajectory phase representation of the flow, see also [14] and for some numerical representations [4].

In conclusion, there is considered that vortices are present in areas where the vorticity number is maximum and the Q – criteria is locally fulfilled. At the same time, the existence of spiral or center singular points in the trajectory field is a strong indication that a vortex exists.

In this paper, the only first criteria for a vortex presence, i.e. $Wo > 1$, is taken into consideration. The distribution of local vorticity number has also a major significance in relation to the definition of internal flows topology in vicinity of the interface. Therefore, partial boundaries of close regions where $Wo > 1$ might accurately define the interface evolution between immiscible fluids.

Finally, the aim is to obtain a geometrical description of the interface, as precisely as possible, based exclusively on kinematical criteria. Dynamic constraints due to particular stress distributions at the interface are not investigated in the present paper (for details see [11] and [13]).

3. EXPERIMENTAL

The experiments have been performed in the REOROM Laboratory from P.U. Bucharest. The Hele-Shaw cell of 150x180 mm, with a 2 mm gap has been built of transparent plates with a thickness of 7 mm. The cell is provided with 6 capillaries of diameter d = 0.8 mm, which can be used as entrances or exits, according to the desired flow configuration. One single inlet, respectively one outlet (at normal pressure), located symmetrically with respect to the cell wall, were used for experiments, see Figure 1. During the tests, the cell has a perfect horizontal position, so gravity plays no role in the motion. The displacing liquid is introduced into the cell through a controlled flow rate syringe pump; the tested inlet velocities within the capillary, $V \in [10^{-4}, 0.1]$ m/s, were maintained at constant value during each experiment. The cell is initially filled with fluid B and through the syringe fluid A is pumped (fluid B being simultaneously evacuated from the cell). The set-up is presented in Figure 2.

The sample fluids are water (η = 0.001 Pas, ρ = 1000 kg/m^3) and two different oils of viscosity η = 0.05 Pas (mineral oil, ρ = 940 kg/m^3), respectively η = 0.95 Pas (silicon oil, ρ = 880 kg/m^3), at temperature of 22^o C. The viscosities of the samples have been measured with a Physica MC1 rheometer, double and simple Couette geometries. The value of the surface tension between the water and oils was determined through the pendant drop method at the Interface Laboratory from T.U. Darmstadt. For determining the interfacial tension, drops of the heavier liquid (water) were formed in the lighter fluid (oils), using a DSA device, see Figure 3. The value of the interfacial tension is then calculated from the profile of the drop, using the so-called Laplace – Young relation; the obtained values are: σ = 0.034 Pam for the mineral oil, respectively σ = 0.046 Pam for the silicon oil.

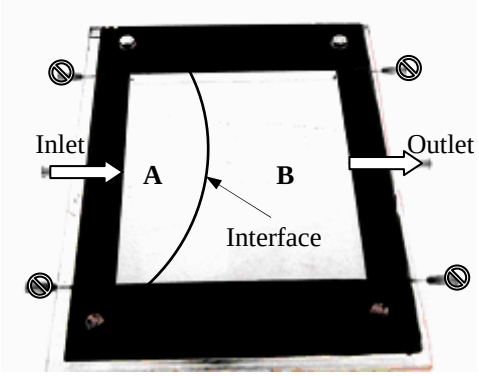

Figure 1. Hele-Shaw cell.

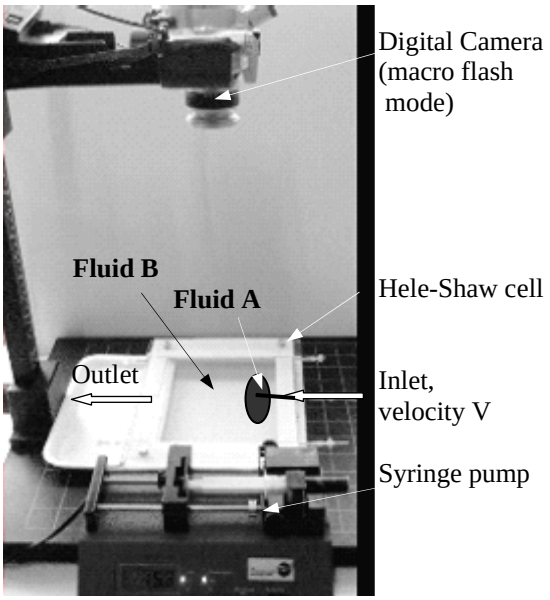

Figure 2. Experimental set-up for interface visualization within the Hele-Shaw cell.

Visualization of the interface (Figs. 1 and 2) between water colored with ink (fluid A) and mineral oil (fluid B) is shown in Figure 4; here the Reynolds number and the capillarity number are defined as: $Re = \rho V d / \eta_A$ and $Ca = \eta_A V / \sigma$.

Similar experimental pictures with Fig. 4 have been obtained for water in oils at different velocity values. Unfortunately, the interface can not be kept

symmetric for long time at higher Reynolds numbers, the flow being subject to specific hydrodynamic instabilities as Kelvin-Helmholtz, [10], [14], or Saffman-Taylor, [3] (the destabilization factor which acts against a symmetric developing of interface is the change of the wetting angle along the solid surfaces, due to impurities stuck on the walls of the cell).

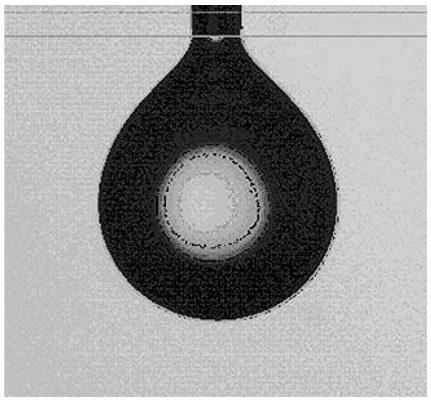

Figure 3. Static drop shape (water in oil); DSA device, needle diameter 0.2 mm.

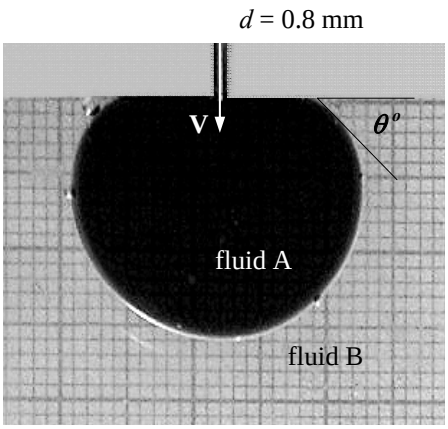

Figure 4. Water - mineral oil interface at V=0.025 m/s (*Re* = 0.04, *Ca* ≅ 10^{-4}, η_B/η_A =50). The interface is here slightly non-symmetric against the position of the inlet. The wall wetting angle θ^o is also represented.

From our own experience, see also [3], [15] and [17], to increase stability of interface (in the absence of surfactants) it is indicated to work at very low capillarity and Reynolds numbers, $Ca << 1$, $Re < 1$, and viscosity ratio η_B/η_A between fluids not far from one. Under these conditions, the developing in time of the interface and internal vortices structures can be well observed, see Figure 5.

Same vortical structures as in Fig. 5 have been experimentally observed also for the samples under investigation, but at higher velocity than in Fig. 4, respectively V = 0.1 m/s, but in that case the symmetry of interface was not achieved .

The results from this paper are mainly qualitative, but they put in evidence the presence of vortical structures at the interface, for particular defined flow conditions and material properties.

The experiments are in progress in REOROM Laboratory. The investigations are currently focused on: (i) increasing the stability of interface evolution (by developing a special cleaning procedure of the cell walls) and (ii) improving the quality of visualization of vortices onset in vicinity of interface, using a microscopic device.

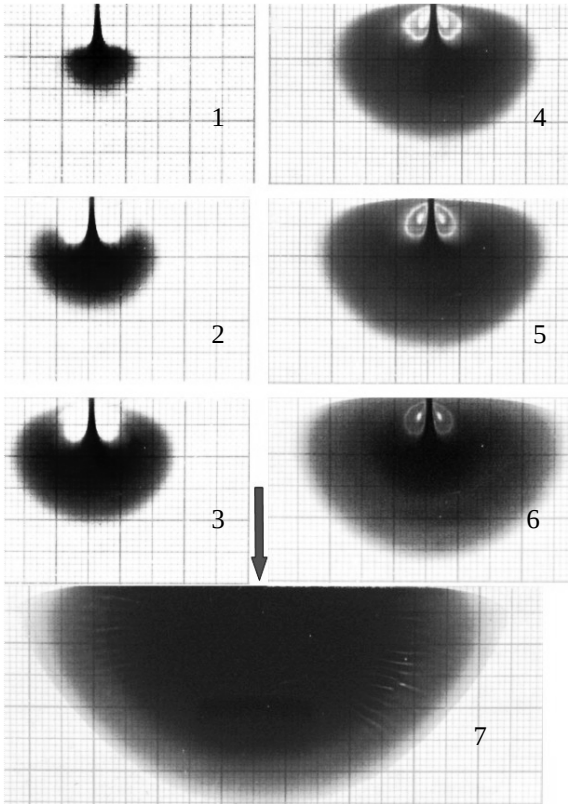

Figure 5. Evolution of vortices at the entrance of a dilute polymer solution colored with ink (fluid A) in water (fluid B), at different time steps (1 – 7); V = 0.0075 m/s, *Re* ≅ 0.01, η_B/η_A ≅ 3. Due to presence of water in the polymer solution the diffusivity effect is observed at the interface.

4. NUMERICAL SIMULATIONS

At this stage of the work, the numerical simulations play an important role in analyzing the vortical structures distribution and the location of vortices against the interface. There are numerous techniques and procedures to compute the flow field in the presence of an interface, in particular to reconstruct the time dependence geometry of the interface between two immiscible fluids, see for example [8] and [17].

The present simulations are performed with the FLUENT 6.0 code. The code can model multiphase

flows (two or more immiscible fluids) through the volume-of-fluid (VOF) model, see for details [9].

The VOF formulation is based on the assumption that the fluids are not interpenetrating. Each additional phase introduces a new variable, the volume fraction in the computational cell. In the VOF model, the fluids share a single set of momentum equations and the volume fraction of each of the fluids in each computational cell is tracked throughout the domain. In each control volume, the volume fractions of all phases sum to unity. The fields for all variables and properties are shared by the phases and represent volume-averaged values, as long as the volume fraction of each of the phases is known. Through this method, an Eulerian transport equation for fluid fractions is solved in a fixed mesh domain. The interface is then reconstructed from these fractions, and in the next time step the fluxes are calculated.

One example of 2D test computation by VOF is shown in Figure 6. Two immiscible viscous Newtonian fluids, silicon oil - A and water - B, enter in a symmetric geometry with same velocities, $V_{A,B}$ = 0.1 m/s, initially the domain being filled with fluid B.

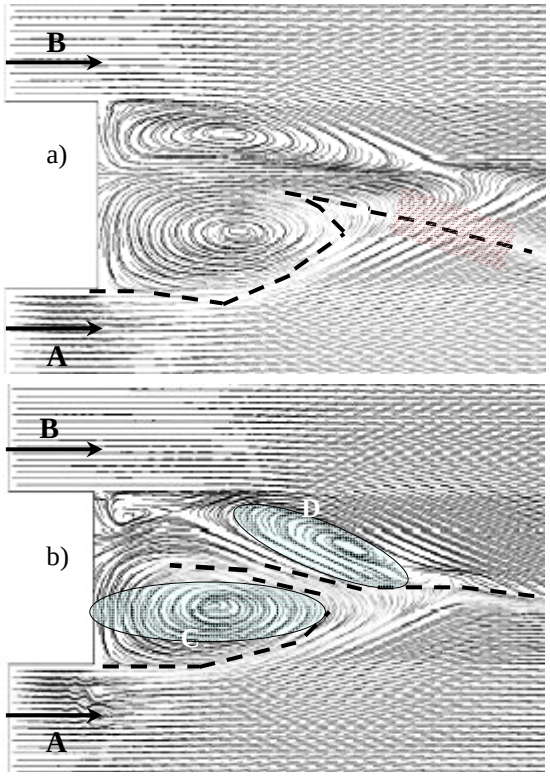

Figure 6. Similar evolution with Kelvin-Helmholtz instability at the interface between immiscible fluids, $t_a < t_b$. The interface (dash line) is actually a "medium line" through the "band", see region marked in a), which separates the two liquids. Vortical structures D and C define more precisely some parts of the interface.

The vortices are developed only in the less viscous fluid and the evolution in time of interface discloses a pattern similar to a Kelvin-Helmholtz instable interface, see [14] and [15]. Of course, applying this reconstruction technique, the VOF procedure by FLUENT 6.0 discloses a diffusive interface (an interface band) between the two immiscible fluids, see Fig. 6.a, and a continuous distribution of pathlines and stream lines in the whole flow domain.

As can be observed in Fig. 6, vortical structures are present in vicinity of "numerical interface band" and their boundaries contributes to a better space definition of the separation between the two fluids. We have to remark here that, accordingly to the definition from §1 and numerical results from Fig. 6.b, only the vortex D defines an internal flow, the vortex C being closed partially by the solid boundary.

Numerical simulations of the experimental tested flows from §3 (similar geometry as in Fig. 4) started with the Navier-Stokes non-stationary solution, see Figure 7 (an almost identical solution is obtained using VOF procedure for one single fluid).

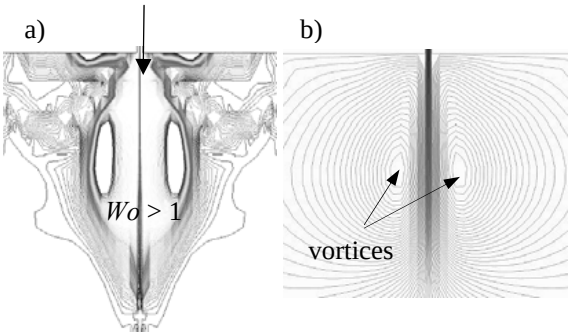

Figure 7. Navier-Stokes 2D solution; distribution of vorticity number *Wo* (a) and stream lines (b), in vicinity of the entrance (water, V = 0.1 m/s).

The VOF implicit solutions are obtained, for a 2D mesh with almost 15.000 nodes, at a convergence criterion of 10^{-5} for each time step (adaptive time step option, with the medium step size of 0.005 s). In Figure 8 and Figure 9, VOF instantaneous solutions are shown after around 7 s of iteration time.

In Fig. 8.b one can observe the presence of internal flows in fluid A, phenomena which is less observable in Fig. 9.b. This difference in the flow structure between the two simulations is given by the value of the contact angle. Distribution of vorticity number corresponding to each separate fluid properly defines the interface in Fig. 8. Also, the domains of $Wo > 1$ put in evidence the vortices, both in Figs. 7 and 9.

Figure 10 presents a VOF solution for fluids with very similar properties and zero wetting angle

(here the domains defined by $Wo = 1$ are located at the wall).

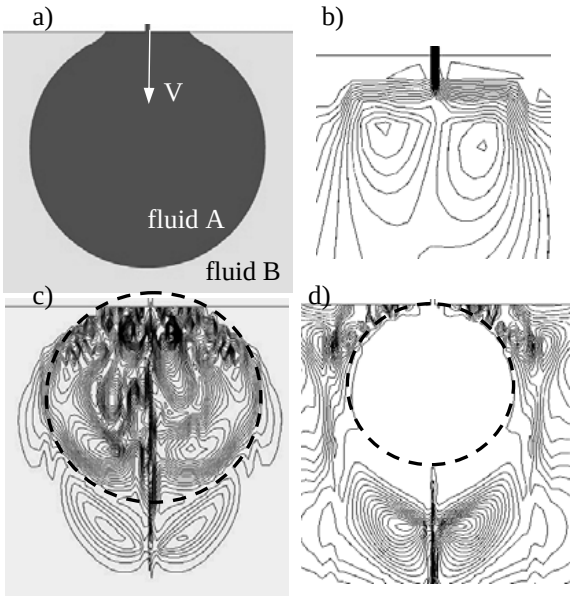

Figure 8. VOF solution at V = 0.05 m/s; fluid A – water, fluid B – silicon oil ($\theta = 179^o$): a) averaged interface, b) stream lines distribution, c) iso-vorticity number distribution in fluid A, d) iso-vorticity number distribution in fluid B.

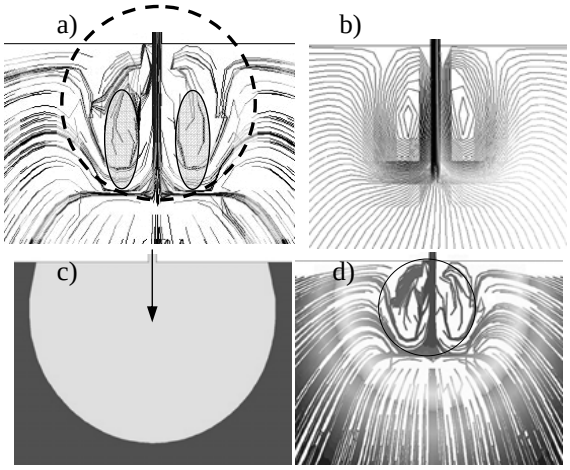

Figure 9. VOF solution at V = 0.1 m/s; same conditions as in Fig. 8, but $\theta = 90^o$: a) pathline distribution (areas with $Wo > 1$ are marked), b) distribution of stream lines, c) averaged interface, d) numerical diffusion of interface.

Two main conclusions are obtained from the analysis of numerical simulations: (i) the interface produced by VOF is not sharp, actually it is a band in space which separates the immiscible fluids, (ii) distribution of vorticity number, especially the detection of areas where $Wo > 1$, is directly related to the interface geometry and it can remarkable improve the quality of location within the flow domain of the interface.

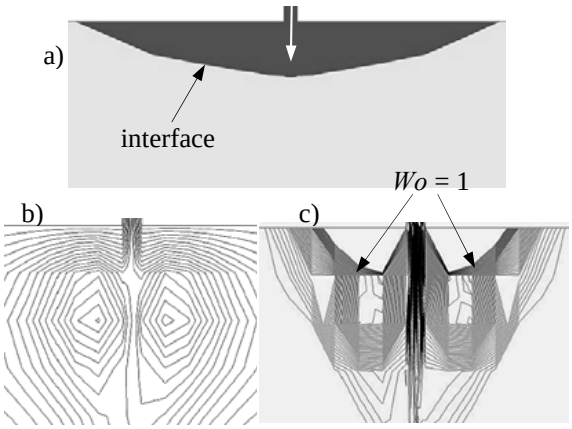

Figure 10. VOF solution with V = 0.1 m/s; similar fluids ($\rho_A = \rho_B = 1000$ kg/m^3, $\eta_A = 2$ mPas, $\eta_B = 1$ mPas, $\sigma = 0.02$ Pam, $\theta = 0^o$); a) interface geometry, b) stream lines, c) iso-vorticity number distribution (in the very vicinity of the entrance).

5. FINAL REMARKS. CONCLUSIONS

The starting point of the work was the assumption that vorticity number plays a major role in the proper establishing of the interface between two immiscible fluids.

The experimental investigations in a Hele-Shaw flow configuration and the numerical 2D simulations put in evidence the interface evolution and the vortical structures generated in the vicinity of the interface.

Numerical simulations by FLUENT with VOF method disclose the interdependence between vortices and a particular distribution of the vorticity number within the flow. If we extract from the domain the areas with $Wo > 1$, one can observe that the boundaries defined by $Wo = 1$ delimit more precisely some parts of the interface, see Figure 11.

Following the unity iso-vorticity lines, we can also determine the structure and evolution of vortices in the neighborhood of the interface, see Figure 12.

Same procedure can be applied to establish areas with possible internal flows. In Fig. 11.a internal flows are developed in fluid B, but in Fig. 11.b disclose internal flows in both fluids. In Fig. 12, for example, the internal flows are not present, since the stream lines and the iso-vorticity lines at $Wo > 1$ are closed by solid boundary (in that case the wall of the capillary).

Therefore, the authors conclude that the existence of close domains in the flow of immiscible fluids by the value $Wo = 1$ ($Wo > 1$ inside the domain) better puts into evidence some parts of the interface and also the presence of internal flows within one liquid phase.

This kinematical restriction can be considered a necessary condition for the existence of internal

flows, but we cannot state that $Wo > 1$ is also sufficient for proving the developing of isolated vortical structures within the flow field, far from the wall.

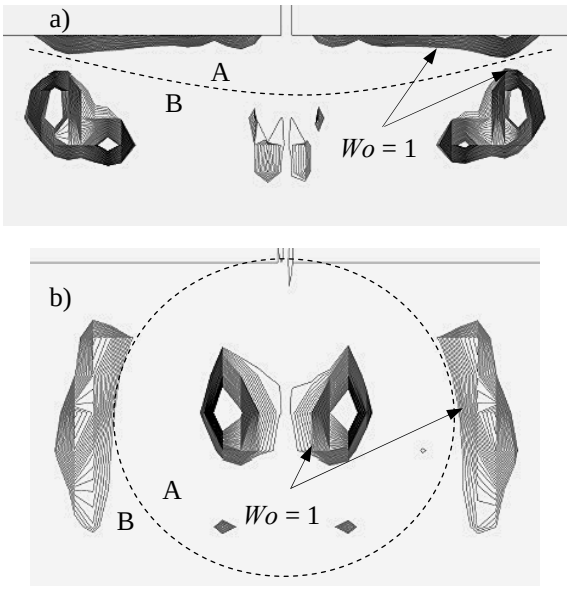

Figure 11. Areas with $Wo \geq 1$ contribute to a better location in space of the interface between fluids A and B (dash line is medium interface); a) simulations from Fig. 10, b) simulations from Fig. 8.

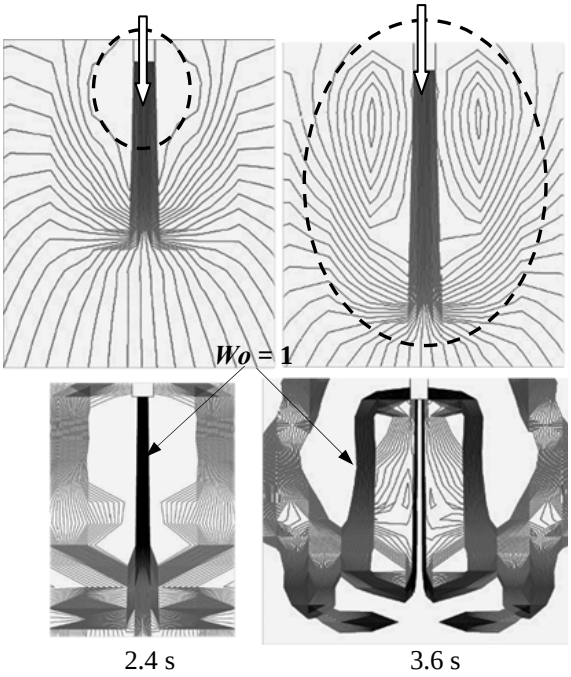

Figure 12. Evolution in time of the averaged interface (dash line), stream lines and vorticity number ($Wo > 1$) (entrance of water in silicon oil through a capillary of 0.8 mm, located far from the wall; V = 0.1 m/s).

This study only presents partial results, since a procedure to generate an interface profile starting with the distribution of the vorticity number is not yet established.

Further investigations of the work are focused in the near future to the following areas:

1. Implementation of all conditions for the vortices existence in a flow domain, see [4], and developing a reconstruction technique of the interface, accordingly to the numerical computations of the flow with VOF method;
2. Improving the experimental set-up and visualization procedure of vortical structures within the Hele-Shaw cell, in order to obtain a precise flow configuration and interface geometry, for controlled material properties and boundary conditions.

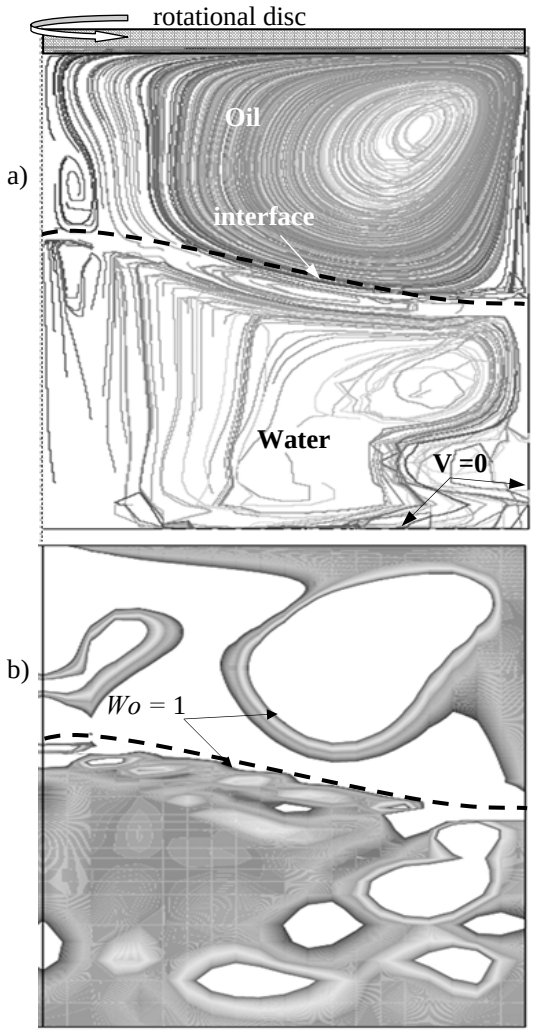

Figure 13. Interface (dash line) between two immiscible fluids in rotational motion (upper disc generates the motion in a vessel); a) pathline pattern and the interface, b) iso-vorticity. The interface is tangent to the vorticity lines $Wo = 1$ (numerical simulations by Ph.D. student Catalin Marculescu).

Before extending the present work to complex applications, it is compulsory to prove experimentally the numerical results for other simple flow configurations and to establish more accurately the location of the evolving interface during dynamic processes. For example, one new case under study in our laboratory is the interface evolution between two immiscible fluids (water and oil), due to rotation of a disc in a vessel with zero velocity on the walls, see Figure 13 (the volumes of the two fluids are constant in the domain).

We also intend to study in more detail the dynamic conditions at the interface and the stress dependence on vorticity at boundaries, see [2], [5] and [22], especially in relation to the modeling of viscoelastic interfaces. Developing the work in the area of non-Newtonian fluid mechanics and creating models for particular flows in the presence of viscoelastic interfaces are the main targets for REOROM activity in the next years.

ACKNOWLEDGEMENTS

The present work has been supported by the Romanian National Research Council – CNCSIS: grant no. 33 (Consortium) and grants directed by the authors in the period 2004-2005. PhD student Andreea Calin acknowledges the scientific support of Professor Manfred Hampe and Professor Manfred Wilhelm from T.U. Darmstadt and Max Planck Institute for Polymer Research in Mainz, Germany, as well as the financial support of EU through the Marie-Curie MEST-CT-2004-513924 contract.

REFERENCES

[1] Astarita, G., 1979, "Objective and generally applicable criteria for flow classification", J. Non-Newtonian Fluid Mech., Vol. 6, pp. 69-76.

[2] Berker, R., 1951, "Sur certaines propriétés de l'effort qui s'exerce sur une paroi en contact avec un fluide visqueux", *C. R. Acad. Sci. Paris*, Vol. 232, pp. 148-149.

[3] Briscoe, B.J., Lawrence C.J., and Mietus W.G.P., 1999, "A review of immiscible fluids mixing", *Adv. Colloid Inter. Sci.*, Vol. 81, pp. 1-17.

[4] Broboana, D., Calin, A., Muntean, T., Balan, M.C., and Balan C., 2005, "Is the vorticity number a possible quantification of a vortex?", *Sci. Bull. Politehnica Univ. Timisoara – Tran. Mechanics*, Vol. 50(64), pp. 155-160.

[5] Caswell, B., 1967, "Kinematics and stress on a surface of rest", *Arch. Rational Mech. Anal.*, Vol. 26, pp 385-399.

[6] Delbende, I., Gomez, T., Josserand, C., Nore, C., and Rossi M., 2004, "Varius aspects of fluid vortices", *C. R. Mecanique*, Vol. 332, pp. 767-781.

[7] Doorly, D. J., Sherwin, S. J., and Franke, P. T., 2002, "Vortical flow structure identification and flow transport in arteries", *Comp. Method. Biomech. and Biomech. Eng.*, Vol. 5, pp. 261-275.

[8] Dufour, S., Pelletier, D., "An adaptive finite element method for incompressible flows with interface", *Technical Report* AIAA-98-2669.

[9] Fluent, Inc., 2001, *FLUENT 6. User's Guide*, Fluent Inc.

[10] Haller, G., 2005, "An objective definition of a vortex", *J. Fluid Mech.*, Vol. 525, pp. 1-26.

[11] Hutter, K., 1995, *Fluid – und Thermodynamik*, Springer Verlag.

[12] Jeong, J., and Hussain, F., 1995, "On the identification of a vortex", *J. Fluid Mech.*, Vol. 285, pp. 69-94.

[13] Lhuillier, D., 2003, "Stress at the interface of immiscible fluids", *C. R. Mecanique*, Vol. 331, pp. 113-118.

[14] Lugt, H. J., 1996, *Introduction to vortex theory*, Vortex Flow Press Inc.

[15] Riaz, A., and Meiburg, E., 2004, "Vorticity interaction mechanism in variable-viscosity heterogeneous miscible displacements with and without density contrast", *J. Fluid Mech.*, Vol. 517, pp. 1-25.

[16] Schlichting, H., 1968, *Boundary layer theory*, Mc-Graw Hill.

[17] Tang, H., and Wrobel, L. C., 2005, "Modelling the interfacial flow of two immiscible liquids – mixing process", *Int. J. Eng. Sci.*, Vol. 43, pp. 1234-1256.

[18] Truesdell, C., 1953, "Two measures of vorticity", *J. Rational Mech. Anal.*, Vol. 2, pp. 173-217. (in this article the author acknowledges the contribution on the subject of the Romanian scientists Pompei and Carstoiu)

[19] Truedell, C., 1970, "De pressionibus negativis in sinu et periete regionis fluido viscose moventi impletae schedula" (in Latin), *Ann. Matematica Pura ed Appl.*, Vol. 84, pp. 213-224.

[20] Truesdell, C., 1988, "On the vorticity numbers of monotonous motions", Arch. Rational Mech. Anal., Vol. 104, pp. 105-109.

[21] Truesdell, C., 1977, *A fist course in rational continuum mechanics – vol. 1*, Academic Press.

[22] Wedgewood, L. E., 1999, "An objective rotation tensor applied to non-Newtonian fluid mechanics", *Rheol. Acta*, Vol. 38, pp. 91-99.

Turbulence Modelling, Numerical Methods

Conference on Modelling Fluid Flow (CMFF'06)
The 13th International Conference on Fluid Flow Technologies
Budapest, Hungary, September 6-9, 2006

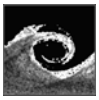

PERSPECTIVES OF FIC STABILIZATION METHOD: NUMERICAL MODELLING OF TURBULENCE

Aleix VALLS[1], Eugenio OÑATE[2], Julio GARCÍA[3]

[1] Corresponding Author. International Center for Numerical Methods in Engineering CIMNE, Universidad Politécnica de Cataluña. Gran Capitán s/n, 08034 Barcelona, Spain. Tel.: +34 93 4017403, E-mail: aleix@cimne.upc.edu
[2] International Center for Numerical Methods in Engineering CIMNE. E-mail:onate@cimne.upc.edu
[3] International Center for Numerical Methods in Engineering CIMNE. E-mail: julio@cimne.upc.edu

ABSTRACT

We present a general formulation for incompressible fluid flow analysis using the finite element method (FEM). The necessary stabilization for dealing with convective effects and the incompressibility condition are introduced via the Finite Calculus (FIC) method using a matrix form of the stabilization parameters. This allows to model a wide range of fluid flow problems for low and high Reynolds numbers flows without introducing a turbulence model. Examples of application to the analysis of incompressible flows with moderate and large Reynolds numbers are presented.

Keywords: Finite calculus, finite element method, high Reynolds numbers, incompressible fluid, stabilized formulation, turbulence model.

NOMENCLATURE

N	[-]	shape functions
Re	[-]	Reynolds Number
p	[Pa]	absolute pressure
q	[Pa]	pressure test fucntion
u	[m/s]	velocity vector
t	[s]	time
x	[m]	space coordinate
n	[-]	space dimensions
n_d	[-]	normal boundary vector
b	[N]	vector body forces
Ω	[-]	analysis domain
Γ	[-]	domain boundary
σ	[N/m^2]	total stress tensor
$\vec{\xi}$	[-]	local element axes
δ_{ij}	[-]	delta Kronecker
μ	[m^2/s]	dynamic viscosity
ν	[m^2/s]	kinematic viscosity
τ	[s]	intrinsic time
δu	[m/s]	virtual velocity vector

Subscripts and Superscripts

i,j,k	i-th global axis
d	respect to mass balance
m	respect to momentum equation
free	at free stream
-	nodal variables
a,b	node indexes
p	prescribed
0	intial

1. INTRODUCTION

Much effort has been spent in developing the so called stabilized numerical methods overcoming the two main sources of instability in incompressible flow analysis, namely those originated by the high values of the convective terms and those induced by the difficulty in satisfying the incompressibility condition.

In this contribution a stabilized FEM for incompressible flows is derived via a finite calculus (FIC) approach [4],[5]. The FIC method is based in invoking the balance of fluxes in a fluid domain of finite size. This introduces naturally additional terms in the classical differential equations of momentum and mass balance of infinitesimal fluid mechanics which are a function of characteristic length dimensions related to the element size in the discretized problem. The FIC terms in the modified governing equations provide the necessary stabilization to the discrete equations obtained via the standard Galerkin FEM. The FIC/FEM formulation allows to use low order finite elements (such as linear triangles and tetrahedra) with equal order approximations for the velocity and pressure variables.

The FIC/FEM formulation has proven to be very effective for the solution of a wide class of problems, such as convection-diffusion [1][2][3] and convection-diffusion-reaction [2][3] involving arbitrary high gradients, incompressible flow

problems accounting for free surface effects and fluid-structure interaction situations [1-5].

The FIC equations for incompressible flow derived in previous works of the authors assumed that the dimensions of the domain where the momentum conservations law was enforced remain the same independently of the direction along which balance of momentum is imposed. As a consequence, each of the resulting FIC momentum equations contain *the same* characteristic dimensions which can be grouped in a *characteristic distance vector*. In this contribution, a refined FIC momentum equations are derived by accepting that *the dimensions of the momentum balance domain are different for each of the momentum equations*. This introduces a *matrix form* of the characteristic distances and of the corresponding FIC terms which have better intrinsic stabilization properties.

Stabilized FEM have been successfully used in the past to solve a wide range of fluid mechanics problems. The intrinsic dissipative properties of the stabilization terms (which can interpreted as an additional viscosity) typically suffices to yield good results for low and moderate values of the Reynolds number. For high values of Re most stabilized FEM fail to provide physically meaningful results and the numerical solution is often unstable or inaccurate. The introduction of a turbulence model is mandatory in order to obtain meaningful results in these cases.

The relationship between the additional dissipation introduced by the turbulence model and the intrinsic dissipative properties of stabilized FEM is an open topic which is attracting increasing attention in the CFD community. It is clear that both remedies (the turbulence model and the stabilization terms) play a similar role in the numerical solution, i.e. that of ensuring a solution which is ``physically sound" and as accurate as possible.

It is our belief that the matrix stabilization terms introduced by the FIC/FEM formulation here presented allow to model accurately high Re number flows without the need of introducing any turbulence model. The background of this belief originates in the positive experiences in the application of a very similar formulation for solving advection-diffusion and advection-diffusion-reaction problems with arbitrary sharp gradients without introducing any transverse dissipation terms. The extension of these ideas to the Navier-Stokes equations described here provides a straightforward procedure for solving a wide class of flow problems from low to high Reynolds numbers, as demonstrated by the good results presented in the paper.

The layout of the paper is the following. In the next section the FIC equations for incompressible flows with matrix stabilization terms are presented. The finite element discretization is introduced and the resulting matrix equations are detailed. A fractional step scheme for the transient solution is detailed. Examples of applications to the 2D analysis of flows passing a backward facing step and a cylinder at different Reynolds numbers are presented.

2. GENERAL FIC EQUATIONS FOR VISCOUS INCOMPRESSIBLE FLOW

The FIC governing equations for a viscous incompressible fluid can be written in an Eulerian frame of reference as

Momentum

$$r_{m_i} - \frac{1}{2} h_{ij} \frac{\partial r_{m_i}}{\partial x_j} = 0 \qquad in\ \Omega \tag{1}$$

Mass Balance

$$r_d - \frac{1}{2} h_j \frac{\partial r_d}{\partial x_j} = 0 \qquad in\ \Omega \tag{2}$$

Where

$$\begin{aligned} r_{m_i} &= \rho\left(\frac{\partial u_i}{\partial t} + u_j \frac{\partial u_i}{\partial x_j} \right) + \frac{\partial p}{\partial x_i} - \frac{\partial s_{ij}}{\partial x_j} - b_i \\ r_d &= \frac{\partial u_i}{\partial x_j} \qquad i, j = 1 \div n_d \\ s_{ij} &= 2\mu\left(\varepsilon_{ij} - \frac{1}{3} \frac{\partial u_k}{\partial x_k} \delta_{ij} \right) \qquad \varepsilon_{ij} = \frac{1}{2}\left(\frac{\partial u_i}{\partial x_j} + \frac{\partial u_j}{\partial x_i} \right) \end{aligned} \tag{3}$$

The FIC initial and boundary conditions are

$$\begin{aligned} & n_j \sigma_{ij} - t_i + \frac{1}{2} h_{ij} n_j r_{m_i} = 0 \quad on \quad \Gamma_t \\ & u_j = u_j^p \quad on \quad \Gamma_u \\ & u_j = u_j^0 \quad for \quad t = t_0 \end{aligned} \tag{4}$$

Summation convention for repeated indices in products and derivatives is used unless otherwise specified.

In Eq. (4) t_i and u_j^p are surface tractions and prescribed displacements on the boundaries Γ_t and Γ_u, respectively and σ_{ij} are total stress given by $\sigma_{ij} = s_{ij} - p\delta_{ij}$.

The h_{ij} and h_j are characteristic distances of the domain where balance of momentum and mass is enforced.

Eqs. (1) to (4) are the starting point for deriving stabilized FEM for solving the incompressible Navier-Stokes equations. An interesting feature of the FIC formulation is that it

allows to use equal order interpolation for the velocity and pressure variables [3,4].

3. STABILIZED INTEGRAL FORMS

From the momentum equations it can be obtained [4,5]

$$\frac{\partial r_d}{\partial x_i} \simeq \frac{h_{ii}}{2a_i}\frac{\partial r_{m_i}}{\partial x_j} \qquad \text{no sum in } i$$
$$a_i = \frac{2\mu}{3} + \frac{u_i h_i}{2} \qquad \text{no sum in } i \tag{5}$$

Substituting Eq.(5) into Eq.(2) and retaining the terms involving the derivatives of r_{m_i} with respect to x_i only, leads to the following alternative expression for the stabilized mass balance equation

$$r_d - \sum_{i=1}^{n_d} \tau_i \frac{\partial r_{m_i}}{\partial x_i} = 0\,;\ \tau_i = \left(\frac{8\mu}{3h_{ii}h_i} + \frac{2\rho u_i}{h_{ii}} \right)^{-1} \tag{6}$$

The τ_i's in Eq.(6) when multiplied by the density are equivalent to the *intrinsic time parameters*, seen extensively in the stabilization literature. The interest of Eq.(5) is that it introduces the first space derivatives of the momentum equations into the mass balance equation. These terms have intrinsic good stability properties as explained next.

The weighted residual form of the momentum and mass balance equations (Eqs.(1) and (5)) is written as

$$\int_\Omega \delta u_i \left[r_{m_i} - \frac{1}{2} h_j \frac{\partial r_{m_i}}{\partial x_j} \right] d\Omega + \int_{\Gamma_t} \delta u_i \left(n_j \sigma_{ij} - t_i + \frac{1}{2} h_j n_j r_{m_i} \right) d\Gamma = \int_\Omega q \left[r_d - \sum_{i=1}^{N} \tau_i \frac{\partial r_{m_i}}{\partial x_i} \right] d\Omega = 0 \tag{7}$$

Integrating by parts the r_{m_i} terms in Eq.(7) leads to

$$\int_\Omega \delta u_i r_{m_i} d\Omega + \int_{\Gamma_t} \delta u_i \left(n_j \sigma_{ij} - t_i \right) d\Gamma + \int_\Omega \frac{1}{2} h_j \frac{\partial \delta u_i}{\partial x_j} r_{m_i} d\Omega = 0$$
$$\int_\Omega q r_d d\Omega + \int_\Omega \left[\sum_{i=1}^{n_d} \tau_i \frac{\partial q}{\partial x_i} r_{m_i} \right] d\Omega - \int_\Gamma \left[\sum_{i=1}^{n_d} q \tau_i n_i r_{m_i} \right] d\Gamma = 0 \tag{8}$$

We will neglect hereonwards the third integral in Eq.(8) by assuming that r_{m_i} is negligible on the boundaries. The deviatoric stresses and the pressure terms in the first integral of Eq. (8) are integrated by parts in the usual manner. The resulting momentum and mass balance equations are

$$\int_\Omega \delta u_i \left(\frac{\partial u_i}{\partial t} + u_j \frac{\partial u_i}{\partial x_j} \right) + \frac{\partial \delta u_i}{\partial x_j} \left(\mu \frac{\partial u_i}{\partial x_j} - \delta_{ij} p \right) d\Omega - \int_\Omega \delta u_i f_i d\Omega$$
$$- \int_{\Gamma_t} \delta u_i t_i d\Gamma + \int_\Omega \frac{h_j}{2} \frac{\partial \delta u_i}{\partial x_j} r_{m_i} d\Omega = 0 \tag{9}$$

And

$$\int_\Omega q \frac{\partial u_i}{\partial x_i} d\Omega + \int_\Omega \left[\sum_{i=1}^{n_d} \tau_i \frac{\partial q}{\partial x_i} r_{m_i} \right] d\Omega = 0 \tag{10}$$

In the derivation of the viscous term in Eq.(9) we have used the following identity holding for incompressible fluids (prior to the integration by parts)

$$\frac{\partial s_{ij}}{\partial x_j} = 2\mu \frac{\partial \varepsilon_{ij}}{\partial x_j} = \mu \frac{\partial^2 u_i}{\partial x_j \partial x_j} \tag{11}$$

3.1. Convective and pressure gradient projections

The computation of the residual terms are simplified if we introduce the convective and pressure gradient projections c_i and π_i, respectively defined as

$$c_i = r_{m_i} - u_j \frac{\partial u_i}{\partial x_j}\ ; \quad \pi_i = r_{m_i} - \frac{\partial p}{\partial x_i} \tag{12}$$

We can express r_{m_i} in Eqs.(9) and (10) in terms of c_i and π_i, respectively which then become additional variables. The system of integral equations is now augmented in the necessary number (12)of equations by imposing that the residual r_{m_i} vanishes (in average sense) for both forms given by Eq. (12). This gives the final system of governing equation as:

$$\int_\Omega \delta u_i \rho \left(\partial_t u_i + u_j \frac{\partial u_i}{\partial x_j} \right) + \frac{\partial \delta u_i}{\partial x_j} \left(\mu \frac{\partial u_i}{\partial x_j} - \delta_{ij} p \right) d\Omega -$$
$$- \int_\Omega \delta u_i f_i d\Omega - \int_{\Gamma_t} \delta u_i t_i d\Gamma + \int_\Omega \frac{h_{ik}}{2} \frac{\partial \delta u_i}{\partial x_k} \left(u_j \frac{\partial u_i}{\partial x_j} + c_i \right) d\Omega = 0 \tag{13}$$

$$\int_\Omega q \frac{\partial u_i}{\partial x_i} d\Omega + \int_\Omega \left[\sum_{i=1}^{n_d} \tau_i \frac{\partial q}{\partial x_i} \left(\frac{\partial p}{\partial x_i} + \pi_i \right) \right] d\Omega = 0 \tag{14}$$

$$\int_\Omega \delta c_i \rho \left(\rho u_j \frac{\partial u_i}{\partial x_j} + c_i \right) d\Omega = 0 \quad \text{no sum in } i \tag{15}$$

$$\int_\Omega \delta \pi_i \tau_i \left(\frac{\partial p}{\partial x_i} + \pi_i \right) d\Omega = 0 \quad \text{no sum in } i \tag{16}$$

In Eqs.(15) and (16) δc_i and $\delta\pi_i$ are appropriate weighting functions and the ρ and τ_i weights are introduced for convenience.

4. FINITE ELEMENT DISCRETIZATION

We choose C^0 continuous linear interpolations of the velocities, the pressure, the convection projections c_i and the pressure gradient projections π_i over 3-noded triangles (2D) and 4-noded tetrahedra (3D). The linear interpolations are written as

$$\begin{aligned} u_i &= N^k \bar{u}_i^k \quad , \quad p = N^k \bar{p}^k \\ c_i &= N^k \bar{c}_i^k \quad , \quad \pi_i = N^k \bar{\pi}_i^k \end{aligned} \tag{17}$$

Where the sum goes over the number of nodes of each element *n* (*n*=3/4 for triangles/tetrahedra).

Substituting the approximations (17) into Eqs.(13) to (16) and choosing the Galerkin form with $\delta u_i = q = \delta c_i = \delta\pi_i = N^i$ leads to following system of discretized equations

$$\begin{aligned} &\mathbf{M}\dot{\bar{\mathbf{u}}} + \mathbf{H}\bar{\mathbf{u}} - \mathbf{G}\bar{\mathbf{p}} + \mathbf{C}\bar{\mathbf{c}} = \mathbf{f} \\ &\mathbf{G}^{\mathbf{T}}\bar{\mathbf{u}} + \hat{\mathbf{L}}\bar{\mathbf{p}} + \mathbf{Q}\bar{\boldsymbol{\pi}} = \mathbf{0} \\ &\mathbf{C}\bar{\mathbf{u}} + \mathbf{M}\bar{\mathbf{c}} = \mathbf{0} \\ &\mathbf{Q}^{\mathbf{T}}\bar{\mathbf{p}} + \hat{\mathbf{M}}\bar{\boldsymbol{\pi}} = \mathbf{0} \end{aligned} \tag{18}$$

Where

$$\mathbf{H} = \mathbf{A} + \mathbf{K} + \hat{\mathbf{K}} \tag{19}$$

The element contributions to the components of the arrays involved in these equations are (*i*,*j*=1,3 for 3D problems)

$$\begin{aligned} &M_{ij}^{ab} = \left(\int_{\Omega_e} \rho N^a N^b d\Omega \right) \delta_{ij} \, , \, A_{ij}^{ab} = \left(\int_{\Omega_e} \rho N^a \left(\mathbf{u}^{\mathbf{T}} \nabla N^b \right) d\Omega \right) \delta_{ij} \\ &K_{ij}^{ab} = \left(\int_{\Omega_e} \mu \boldsymbol{\nabla}^T N^a \boldsymbol{\nabla} N^b d\Omega \right) \delta_{ij} \, , \boldsymbol{\nabla} = \left[\frac{\partial}{\partial x_1}, \frac{\partial}{\partial x_2}, \frac{\partial}{\partial x_3} \right]^T \\ &C_i^{ab} = \int_{\Omega_e} h_{ij} \frac{\partial N^a}{\partial x_j} N^b d\Omega, \; \mathbf{C} = \left[C_1, C_2, C_3 \right]^T \end{aligned} \tag{20}$$

$$\begin{aligned} &\hat{L}_{ij}^{ab} = \int_{\Omega_e} \left(\boldsymbol{\nabla}^{\mathbf{T}} N^a \right) [\tau] \boldsymbol{\nabla} N^b d\Omega \, , \; [\tau] = \begin{bmatrix} \tau_1 & 0 & 0 \\ 0 & \tau_2 & 0 \\ 0 & 0 & \tau_3 \end{bmatrix} \\ &\mathbf{Q} = \left[Q_1, Q_2, Q_3 \right], \; Q_i^{ab} = \int_{\Omega_e} \tau_i \frac{\partial N^a}{\partial x_i} N^b d\Omega \quad \text{no sum in } i \\ &\hat{\mathbf{C}} = \left[\hat{C}_1, \hat{C}_2, \hat{C}_3 \right], \; \hat{C}_i^{ab} = \int_{\Omega_e} \rho^2 N^a \left(\mathbf{u}^{\mathbf{T}} \boldsymbol{\nabla} N^b \right) d\Omega \end{aligned} \tag{21}$$

$$\hat{M}_{ij}^{ab} = \frac{\tau_i}{\rho} M_{ij}^{ab} \, , \quad f_i^a = \int_{\Omega_e} N^a f_i d\Omega + \int_{\Gamma_e} N^a t_i d\Gamma$$

It is understood that all the arrays are matrices (except **f** which is a vector) whose components are obtained by grouping together the left indices in the previous expressions (*a* and possibly *i*) and the right indices (*b* and possibly *j*).

Note that the stabilization matrix $\hat{\mathbf{K}}$ in Eq.(21) adds additional orthotropic diffusivity terms of value $\rho h_{ij} u_i / 2$.

The overall stabilization terms introduced by the FIC formulation above presented have the intrinsic capacity to ensure physically sound numerical solutions for a wide spectrum of Reynolds numbers without the need of introducing additional turbulence modelling terms. This interesting property is validated in the solution of the examples presented in a next section.

4.1. Transient solution scheme

The solution in time of the system of Eq. (18) can be written in general form as

$$\begin{aligned} &\mathbf{M}\frac{1}{\Delta t}\left(\bar{\mathbf{u}}^{n+1} - \bar{\mathbf{u}}^{n} \right) + \mathbf{H}^{n+\theta}\bar{\mathbf{u}}^{n+\theta} - \mathbf{G}\bar{\mathbf{p}}^{n+\theta} + \mathbf{C}^{n+\theta}\bar{\mathbf{c}}^{n+\theta} = \mathbf{f}^{n+\theta} \\ &\mathbf{G}^{\mathbf{T}}\bar{\mathbf{u}}^{n+\theta} + \hat{\mathbf{L}}^{n+\theta}\bar{\mathbf{p}}^{n+\theta} + \mathbf{Q}\bar{\boldsymbol{\pi}}^{n+\theta} = \mathbf{0} \\ &\mathbf{C}\bar{\mathbf{u}}^{n+\theta} + \mathbf{M}\bar{\mathbf{c}}^{n+\theta} = \mathbf{0} \\ &\mathbf{Q}^{\mathbf{T}}\bar{\mathbf{p}}^{n+\theta} + \hat{\mathbf{M}}^{n+\theta}\bar{\boldsymbol{\pi}}^{n+\theta} = \mathbf{0} \end{aligned} \tag{22}$$

Where $\mathbf{H}^{n+\theta} = \mathbf{H}^{n+\theta}\left(\mathbf{u}^{n+\theta} \right)$, etc and the parameter $\theta \in [0,1]$. The direct monolithic solution of Eqs.(22) is possible using an adequate iterative scheme [5]. However, in our work we have used the fractional step method described in [5].

5. COMPUTATION OF THE CHARACTERISTIC DISTANCES

The computation of the stabilization parameters is a crucial issue as they affect both the stability and accuracy of the numerical solution. The different procedures to compute the stabilization parameters are typically based on the study of simplified forms of the stabilized equations. Contributions to this topic are reported in [3,4,5]. Despite the relevance of the problem there still lacks a general method to compute the stabilization parameters for all the range of flow situations.

Recent work of the authors in the application of the FIC/FEM formulation to convection-diffusion problems with sharp arbitrary gradients [4,5] has shown that the stabilizing FIC terms take the form of a simple orthotropic diffusion if the balance equation is written in the principal curvature

directions of the solution. Excellent results were reported in [4,5] by computing first the characteristic length distances along the principal curvature directions, followed by a standard transformation of the distances to global axes. The resulting stabilized finite element equations capture the high gradient zones in the vicinity of the domain edges (boundary layers) as well as the sharp gradients appearing randomly in the interior of the domain [3]. The FIC/FEM thus reproduces the best features of both the so called transverse (cross-wind) dissipation or shock capturing methods [2,3].

The numerical computations are simplified without apparent loss of accuracy if the main principal curvature direction of the solution at each element point is approximated by the direction of the gradient vector at the element center. The second principal direction (for 2D problems) is taken in the orthogonal direction to the gradient. For linear triangles and quadrilaterals these directions are assumed to be constant within the element [5].

Above simple scheme has been extended in this work for the computation of the characteristic distances h_{ij} for the momentum equations. As for the length parameters h_i in the mass conservation equation, the simplest assumption $h_i = h_{ii}$ has been taken. Details of the algorithm for computing h_{ij} are given next (the method is explained for 2D problems although it is readily extendible to 3D problems).

For the *i*-th momentum balance equation and every step of the method described in Section 4:

1. A coordinate system $\vec{\xi}_1^i, \vec{\xi}_2^i$ is defined at each element point such that $\vec{\xi}_1^i$ is aligned with the gradient of u_i ($\vec{\xi}_1^i = \nabla u_i$) and $\vec{\xi}_2^i$ is orthogonal to $\vec{\xi}_1^i$ in anticlockwise sense (Figure 1). The angle that $\vec{\xi}_1^i$ forms with the global x_1 is defined as α_i. Recall that upper and lower index *i* denotes the *i*-th momentum equation.
2. The element characteristic distances l_{i1} and l_{i2} are defined as the maximum projections of the element sides along the $\vec{\xi}_1^i$ and $\vec{\xi}_2^i$ axes, respectively (Figure 2).
3. The characteristic distances h_{i1} and h_{i2} are computed as

$$\begin{Bmatrix} h_{i1} \\ h_{i2} \end{Bmatrix} = \begin{bmatrix} c_i & -s_i \\ s_i & c_i \end{bmatrix} \begin{Bmatrix} \bar{h}_{i1} \\ \bar{h}_{i2} \end{Bmatrix} \quad , i = 1,2 \qquad (23)$$

with $c_i = \cos\alpha_i, s_i = \sin\alpha_i$ and the local distances $\bar{h}_{i1}$ and $\bar{h}_{i2}$ are

$$\bar{h}_{ij} = \left(\coth\bar{\gamma}_{ij} - \frac{1}{\bar{\gamma}_{ij}} \right) l_{ij} \ , \ \bar{\gamma}_{ij} = \frac{\bar{u}_j l_{ij}}{2\mu} \quad , j = 1,2 \qquad (24)$$

where $\bar{u}_1$ and $\bar{u}_2$ are the components of the velocity vector along the local axes $\vec{\xi}_1^i$ and $\vec{\xi}_2^i$, respectively (Figure 1).

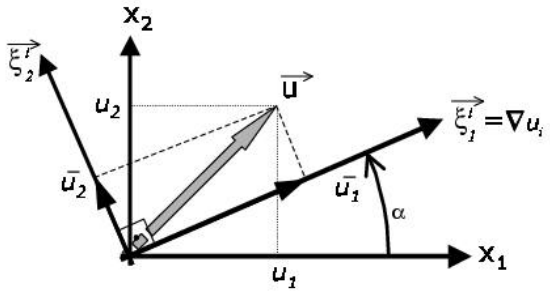

Figure 1. Definition of the principal curvature direction $\vec{\xi}_1^i$ along the gradient of u_i

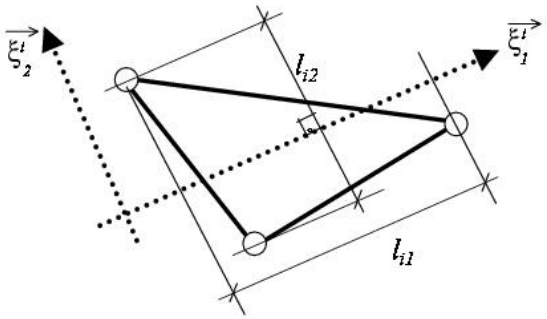

Figure 2. Definition of the element characteristic distances l_{i1} and l_{i2} corresponding to the *i*-th momentum equation.

6. EXAMPLES

The examples were solved with the Tdyn code where the formulation here presented has been implemented.

6.1 Backward facing step at high Reynolds number

Figure 3 shows the geometry of the standard backwards facing step problem. The boundary conditions were the following: $u_1 = 1$ and $u_2 = 0$ were taken at the entry while $p = 0$ was assumed at the exit. Slipping conditions were assumed at the rest of the vertical and horizontal walls. A value of

the kinematic viscosity $\nu = 2.1\times10^{-5}$ was taken giving a Reynolds number of $\mathrm{Re} = \frac{u_{free}H}{\nu} = 47619$ for H=1 and $u_{free} = 1$.

Figure 3 also shows the relatively coarse mesh chosen of 30850 three-node triangular elements and 15426 nodes. The contours of the horizontal and vertical velocities and details of the velocity vectors are shown in Figures 4, respectively. Figure 5 shows the distribution of the horizontal velocity along the bottom line starting from the vertical wall of the step. The point where the horizontal velocity changes sign indicates the end of the recirculation area.

The length of the circulation area computed from Figure 5 is 6.79. This value compares very well (3.2%) with the experimental value reported at. [6] (see Table 1). The FIC/FEM results are remarkably accurate in comparison with other results reported in the literature obtained using $k-\varepsilon$ and $k-\tau$ turbulence models [6,7,8]. We note again that the FIC/FEM formulation does not include any additional turbulence terms.

Table 1. Backward facing step. Length of the recirculation distance *D* for Re=47619. Comparison of the FIC/FEM result with experimental data and with numerical results obtained using different turbulence models.

Model	Length	Error
Exp. [6]	7.0	
K-E [6]	5.2	26%
K-E[7]	5.88	16%
K-E [8]	6.2	11.4%
K-Tau [8]	6.82	2.5%
Present work	**6.707**	**4.2%**

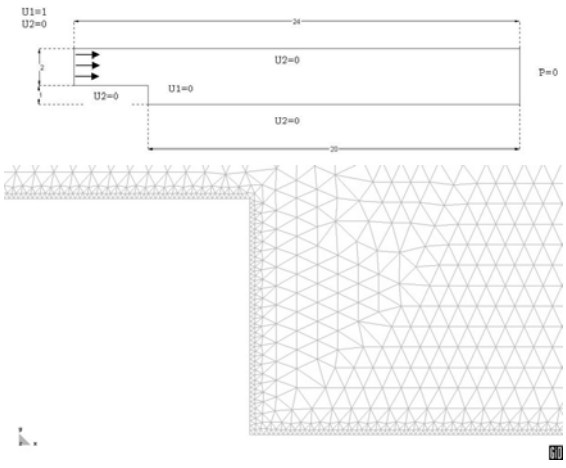

Figure 3. Backward facing step. Geometry and finite element mesh of 30850 three-node triangles. Mesh detail at the vicinity of the step.

Figure 4. Backwards facing step. Contours of horizontal (above) and vertical velocities.

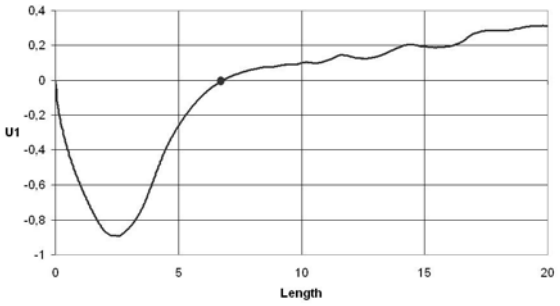

Figure 5. Distribution of the horizontal velocity along the bottom line starting from the vertical wall of the step. The circle shows the end of the recirculation region.

6.2 Flow past a cylinder. Computation of the Strouhal instability

Figure 6 shows the geometry for the analysis of the flow past a cylinder of unit diameter *D*. A unit horizontal velocity is prescribed at the inlet boundary and at the two horizontal walls. Zero pressure is prescribed at the outlet boundary. The dimensions of the analysis domain are 36x27 units. The origin of the coordinate system has been sampled at the center of the cylinder located at a distance of 13.1 units from the entry wall. Zero velocity is prescribed at the cylinder wall. The kinematic viscosity is $\nu = 0.01$. Figure 7 shows the mesh of 91316 three-node elements used for the computation. A detail of the mesh in the vicinity of the cylinder is also shown in Figure 7.

The problem has been analyzed first for a value of the horizontal velocity at the entry of $u_1 = 1$ giving a Reynolds number of Re =100. Figures 8 and 9 respectively show the velocity modulus contours and the velocity vectors for t=100 secs.

Figure 10 shows the oscillations of the horizontal velocity at the point A with coordinates (6.7, -1.02). The Strouhal number computed from the shedding frequency *n* as $S = {}^{nD}\!/\!_{|\mathbf{u}|}$ is *S*=0.1702.

This number compares very well with the experimental result available in the literature.

The same problem was analyzed for a value of the kinematic viscosity $\nu = 0.001$ giving Re =1000. The same mesh of 91316 linear triangles of Figure 7 was used. Figures 11 and 12 show respectively the velocity modulus contours, the velocity vectors in the vicinity of the cylinder for t=100 secs. Figure 13 finally shows the oscillations of the horizontal velocity at point A. The computed value of the Strouhal number in this case was S=0.2103. This value again coincides well with the reported experimental data.

It is a well known fact that for $Re > 300 the flow past a cylinder exhibits 3D features. In [9] results from 2D and 3D computation were compared for Re=300 and 800. While 3D features were observed even at Re =300 and more so at Re =800, there were no large discrepancies between the global flow parameters (such as drag, lift and Strouhal number) obtained from 2D and 3D computations. These conclusions justify the results of the 2D computations presented in the paper.

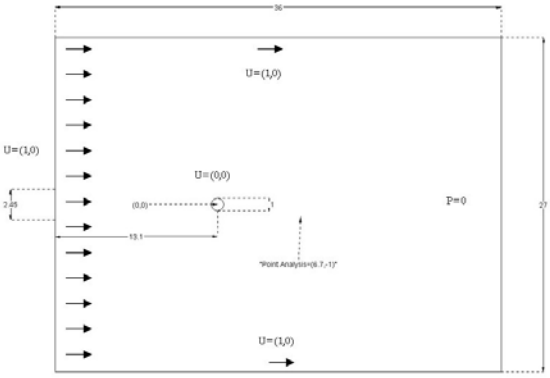

Figure 6. Analysis domain and boundary conditions.

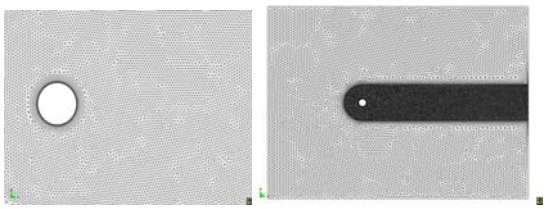

Figure 7. Mesh of 91316 three-node triangles used for the computations

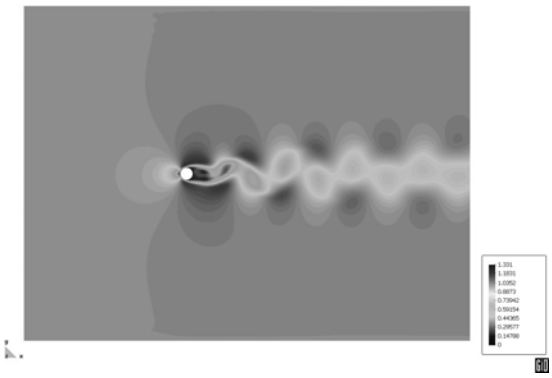

Figure 8. Re=100. Contour of the velocity vector modulus for t=100 secs.

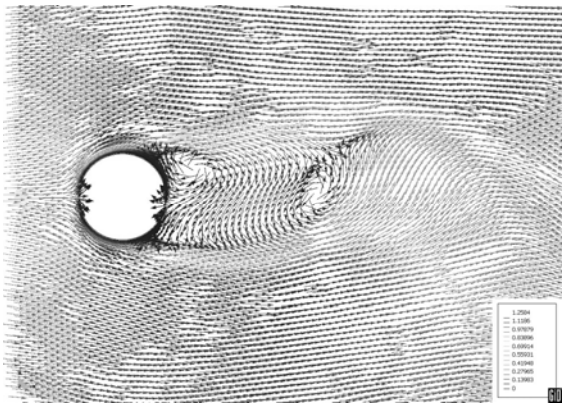

Figure 9. Re =100. Velocity vectors for t=100 secs

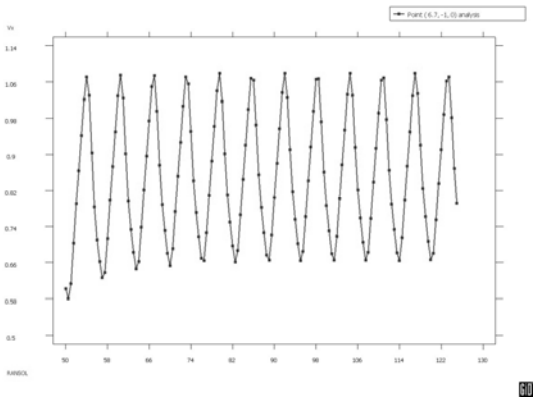

Figure 10. Re =100. Oscillations with time of the horizontal velocity at the point with coordinates A (6.7,-1.02).

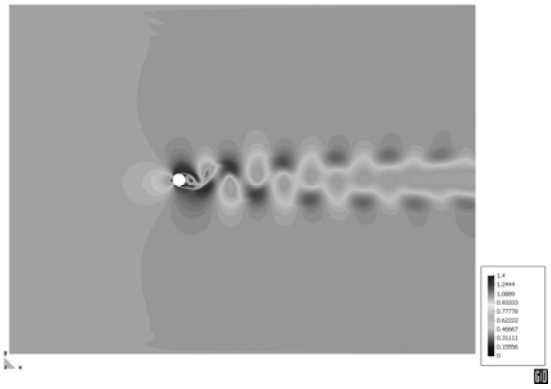

Figure 11. Re=1000. Contour of the velocity vector modulus for t=100 secs.

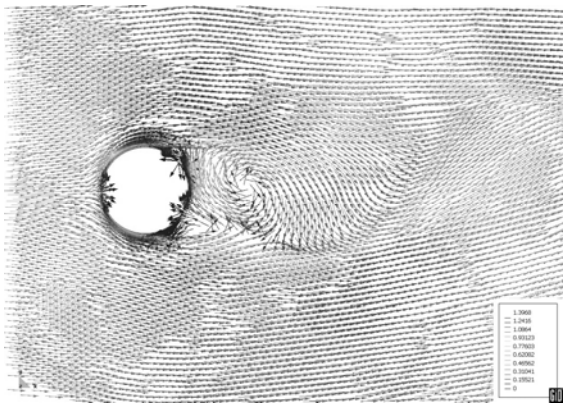

Figure 12. Re =1000. Velocity vectors for t=100 secs

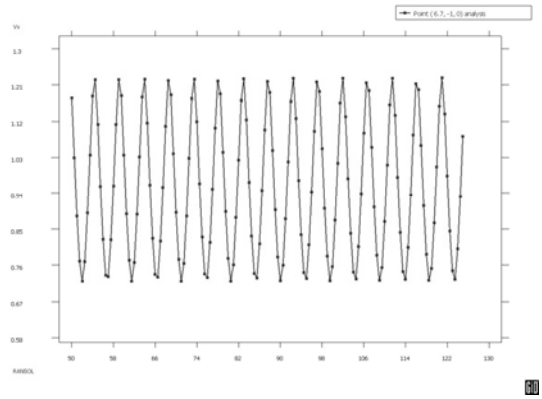

Figure 13. Re =1000. Oscillations with time of the horizontal velocity at the point with coordinates A (6.7,-1.02).

7. CONCLUSIONS

The finite calculus (FIC) form of the fluid mechanics equations is a good starting point for deriving stabilized FEM for solving a variety of incompressible fluid flow problems. The matrix stabilization terms introduced by the FIC formulation here presented allow to obtain physically sound solutions in the presence of sharp gradients occuring for high Reynolds numbers without the need of introducing a turbulence model. Good numerical solutions have been obtained in the 2D examples solved with relatively coarse meshes for moderate and high values of the Reynolds number. These preliminary results reinforce our idea that the stabilization terms introduced by the FIC formulation suffice to provide good results for problems for which turbulence models are required using alternative numerical methods. These results also confirm the close link between the stabilized methods and turbulence models, which surely will be the object of much research in the near future.

REFERENCES

[1] T.J.R. Hughes, G. Hauke and K. Jansen, ``Stabilized finite element methods in fluids: Inspirations, origins, status and recent developments", in *Recent Developments in Finite Element Analysis*. T.J.R. Hughes, E. Oñate and O.C. Zienkiewicz (Eds.), (CIMNE, Barcelona, Spain, pp. 272--292, 1994.

[2] T.J.R. Hughes, L.P. Franca and G.M. Hulbert, ``A new finite element formulation for computational fluid dynamics: VIII. The Galerkin/least-squares method for advective-diffusive equations", *Comput. Methods Appl. Mech. Engrg*, 73, pp. 173--189, 1989.

[3] R. Codina and J. Blasco, ``Stabilized finite element method for the transient Navier-Stokes equations based on a pressure gradient operator", *Comput. Methods in Appl. Mech. Engrg.*}, bf 182, 277--301, 2000.

[4] E. Oñate, ``Derivation of stabilized equations for advective-diffusive transport and fluid flow problems", *Comput. Meth. Appl. Mech. Engng.*, Vol. 151, pp. 233--267, (1998).

[5] E. Oñate and J. García, ``A finite element method for fluid-structure interaction with surface waves using a finite calculus formulation", *Comput. Methods Appl. Mech. Engrg.*, 191, 635--660, (2001).

[6] N.N. Mansour and T. Morel, *In AFOSR-HTTM Stanford Conference on Complex Turbulent Flows III*, Stanford University, CA, pp. 1418--1423, 1981.

[7] A. Pollard, *In AFOSR-HTTM Stanford Conference on Complex Turbulent Flows III*, Stanford University, CA, pp. 1486--1490, 1981.

[8] F. Illinca, J.-F. Hetu and D. Pelletier, ``A Unified Finite Element algorithm for two-equations models of turbulence". *Computers and Fluids*, Vol. f 27, No. 3, 291--310, 1998.

[9] V. Kalro and T. Tezduyar, ``Parallel 3D computation of unsteady flows around circular cylinders", *Parallel Computing*, 23, 1235--1248, 1997.

Conference on Modelling Fluid Flow (CMFF'06)
The 13th International Conference on Fluid Flow Technologies
Budapest, Hungary, September 6-9, 2006

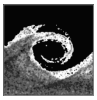

TURBULENCE MODELLING FOR A 2D SYNTHETIC JET

Oliver R. HEYNES[1], Mark A. COTTON[2], Tim J. CRAFT[3]

[1] Corresponding Author. School of Mechanical, Aerospace and Civil Engineering (MACE), The University of Manchester, Manchester M60 1QD, UK. e-mail: o.r.heynes@postgrad.manchester.ac.uk
[2] MACE, The University of Manchester. e-mail: mark.cotton@manchester.ac.uk
[3] MACE, The University of Manchester. e-mail: tim.craft@manchester.ac.uk

ABSTRACT

The near-field of a 2D plane unsteady jet is computed using various turbulence models and the results compared with experimental data. The strain field generated by the 'synthetic' (reciprocating) jet under consideration contains regions of strong normal and shear straining, while vortex pairs formed by the issuing jet are highly rotational. Turbulence closures at the eddy viscosity (standard k-ε and two-timescale models) and stress-transport levels are examined. It is found that the extreme nature of the strain environment presents a severe challenge to the models tested; in particular, fundamental weaknesses in the constitutive equation of linear eddy viscosity models are revealed. An additional term in the dissipation rate equation of the two-timescale model is found to hinder the development of clearly defined vortex pairs. In contrast to the eddy viscosity schemes, the second moment model is able to render turbulence quantities with some degree of accuracy, a feature that is due to its inclusion of transport equations for the individual Reynolds stresses. The vortex pairs generated in the near-field are shown to play a critical role in determining the downstream pattern of jet development.

Keywords: Flow Control, MEMS, Synthetic Jets, Two-Timescale Models, URANS

NOMENCLATURE

P	$[Pa]$	pressure
Re	[-]	Reynolds number, $U_{c,rms}h/\nu$
St	[-]	Strouhal number, $\omega h/U_{c,rms}$
T	$[s]$	period of cycle
U	$[m/s]$	phase-averaged axial velocity
V	$[m/s]$	phase-averaged lateral velocity
f	$[Hz]$	frequency, $1/T$
h	$[m]$	orifice width
k	$[m^2/s^2]$	turbulent kinetic energy
t	$[s]$	time
u	$[m/s]$	fluctuating axial velocity
v	$[m/s]$	fluctuating lateral velocity
x, y	$[m]$	axial, lateral coordinate
Π	[-]	pi-parameter
δ_{ij}	[-]	Kronecker delta
$\in_{ijk}$	[-]	alternating tensor
ε	$[m^2/s^3]$	rate of dissipation of k
ν	$[m^2/s]$	molecular viscosity
ν_t	$[m^2/s]$	eddy viscosity
ρ	$[kg/m^3]$	density
ω	$[rad/s]$	circular frequency, $2\pi f$

Subscripts

P	production region
T	transfer region
c	centreline
max	maximum value
rms	root mean square value

$\langle\,\rangle$	phase-average
$\bar{}$	(overbar) long-time-average

1. INTRODUCTION

Synthetic, or 'massless', jets belong to a family of novel devices known as Micro-Electro-Mechanical-Systems (MEMS) used in flow manipulation and other applications [1]. Air is alternately ejected and ingested from a small cavity through an orifice by the pulsating motion of a diaphragm, usually driven at resonance (Figure 1). The resulting flow field is dominated by the presence of vortex pairs (for a plane jet) or rings (for a round jet) arising from the separation and roll-up of the shear layer generated as the jet exits the orifice. If certain conditions are satisfied [2], these vortex pairs will advect downstream and undergo a transition to turbulence, eventually losing their coherence and coalescing to form a quasi-steady jet in the far-field [3, 4]. The starting impulse imparted to the jet means that, while there is no net mass flow into the external domain from the

synthetic jet, a flux of momentum does enter the surrounding field.

The synthetic jet has a number of potential applications, including mixing enhancement [5], thrust vectoring [6], and turbulent boundary layer separation control [7]. It is an attractive choice of flow control device because it does not require any external piping, has low parasitic drag and is relatively robust. The present study seeks to undertake a rigorous assessment of various Unsteady Reynolds-Averaged Navier-Stokes (URANS) turbulence models in application to a plane synthetic jet issuing into a quiescent environment, and forms part of a wider work programme investigating the application of the devices to turbulent boundary layer control.

A number of experimental studies and Direct Numerical Simulations (DNS) of synthetic jets have been carried out, both in quiescent conditions [3, 8-10] and cross-flow [4, 11]. An important contribution to the experimental database was made available recently as part of a NASA Langley Research Center Workshop [12]. Particle Image Velocimetry (PIV) measurements were presented in [12], and the Workshop sought to make comparisons between the experimental data and turbulence model simulations undertaken at a number of centres internationally. Significant differences emerged and, in part, these findings have provided the motivation for the present work which seeks to undertake a detailed analysis of some aspects of turbulence model response to the straining associated with 2D plane synthetic jets.

Table 1 gives the parameters of the NASA Langley test case. Although the Reynolds number based on r.m.s. centreline velocity is low, it is typical of many practical synthetic jet flows. Despite the moderate Reynolds number, turbulence effects cannot be neglected in this flow, and significant differences in turbulence model performance are shown below.

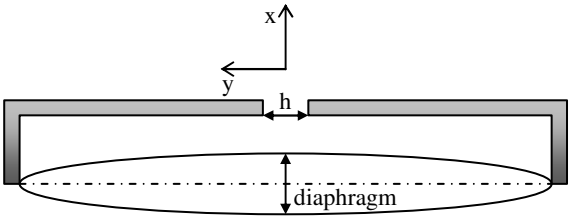

Figure 1. Schematic diagram of the synthetic jet.

Table 1. Synthetic jet parameters.

f	h	$U_{c,max}$	St	Re
444.7	0.00127	28.3	0.19	1600

2. TURBULENCE MODELS

All equations are written for phase-averaged quantities. For clarity, Reynolds stresses are denoted by caret brackets.

2.1 Linear Eddy-Viscosity Modelling

Models of the linear eddy viscosity class relate the Reynolds stress tensor to the mean rate-of-strain via a turbulent, or eddy, viscosity, ν_t:

$$\left\langle u_i u_j \right\rangle = -\nu_t \left(\frac{\partial U_i}{\partial x_j} + \frac{\partial U_j}{\partial x_i} \right) + \frac{2}{3}\delta_{ij} k \qquad (1)$$

2.1.1 Standard k-ε Model

In the standard high-Reynolds-number k-ε model [13] the constitutive equation is complemented by equations for the transport of the turbulent kinetic energy, k, and its rate of viscous dissipation, ε:

$$\nu_t = C_\mu \frac{k^2}{\varepsilon} \qquad (2)$$

$$\frac{Dk}{Dt} = P_k + \frac{\partial}{\partial x_j}\left(\frac{\nu_t}{\sigma_k} \frac{\partial k}{\partial x_j} \right) - \varepsilon \qquad (3)$$

$$\frac{D\varepsilon}{Dt} = C_{\varepsilon 1} \frac{\varepsilon}{k} P_k + \frac{\partial}{\partial x_j}\left(\frac{\nu_t}{\sigma_\varepsilon} \frac{\partial \varepsilon}{\partial x_j} \right) - C_{\varepsilon 2} \frac{\varepsilon^2}{k} \qquad (4)$$

where

$$P_k = -\left\langle u_i u_j \right\rangle \frac{\partial U_i}{\partial x_j} \qquad (5)$$

and model constants are given in Table 2.

A low Reynolds number k-ε model was also tested, however, the results showed very little difference and therefore the standard scheme above was adopted.

Table 2. Standard k-ε model coefficients.

C_μ	$C_{\varepsilon 1}$	$C_{\varepsilon 2}$	σ_k	σ_ε
0.09	1.44	1.92	1.0	1.3

2.1.2 Two-Timescale Eddy-Viscosity Model

The two-timescale, or split-spectrum, approach of Hanjalić, Launder and Schiestel [14] (hereafter the 'HLS' model) separates the turbulence energy spectrum into a 'production' range, a 'transfer range', and a 'dissipation' range. Turbulent kinetic energy in the low-wavenumber production range, k_P, is generated by the action of mean straining. Energy is drained from this range to the intermediate-scale transfer range at a rate ε_P. The turbulent kinetic energy associated with the transfer range is denoted k_T, and the rate of loss from this range to the highest wavenumber dissipation range, ε_T, is equal to ε, the true rate of viscous dissipation.

(It is assumed that the dissipation range itself contains no energy and that therefore $k = k_P + k_T$.)

The HLS model has a modified constitutive equation, Eq. (6), and k_P, k_T, ε_P and ε_T are the subjects of transport equations:

$$\nu_t = C_\mu \frac{k k_P}{\varepsilon_P} \tag{6}$$

$$\frac{Dk_P}{Dt} = P_k + \frac{\partial}{\partial x_j}\left(\nu_t \frac{\partial k_P}{\partial x_j}\right) - \varepsilon_P \tag{7}$$

$$\frac{Dk_T}{Dt} = \varepsilon_P + \frac{\partial}{\partial x_j}\left(\nu_t \frac{\partial k_T}{\partial x_j}\right) - \varepsilon_T \tag{8}$$

$$\frac{D\varepsilon_P}{Dt} = C_{P1}\frac{\varepsilon_P}{k_P}P_k + C_{P1}^{'}k_P \frac{\partial U_l}{\partial x_m}\frac{\partial U_i}{\partial x_j}\in_{lmk}\in_{ijk} + \frac{\partial}{\partial x_j}\left(\nu_t \frac{\partial \varepsilon_P}{\partial x_j}\right) - C_{P2}\frac{\varepsilon_P^2}{k_P} \tag{9}$$

$$\frac{D\varepsilon_T}{Dt} = C_{T1}\frac{\varepsilon_P \varepsilon_T}{k_T} + \frac{\partial}{\partial x_j}\left(\nu_t \frac{\partial \varepsilon_T}{\partial x_j}\right) - C_{T2}\frac{\varepsilon_T^2}{k_T} \tag{10}$$

where P_k is given by Eq. (5), and model coefficients given in Table 3.

The ε_P-equation resembles the ε-equation of the k-ε model, apart from a new source term involving the mean vorticity which is added so that energy is transferred across the spectrum preferentially by irrotational straining [15]. The HLS model was included in the present study due to encouraging results from studies of 'fully-pulsed' (on/off) uni-directional jets [16, 17].

Table 3. HLS model coefficients.

C_μ	C_{P1}	$C_{P1}^{'}$	C_{P2}
0.09	2.2	-0.11	$1.8\text{-}0.3\frac{k_P/k_T - 1}{k_P/k_T + 1}$
C_{T1}	C_{T2}		
$1.08\,\varepsilon_P/\varepsilon_T$	1.15		

2.2 Reynolds Stress Transport Model

The Gibson-Launder stress-transport model [18] (hereafter the 'GL' model) was also tested in the present study. The model, sometimes referred to as the 'basic' form, possesses the essentials of modelling at the second moment level, namely the inclusion of the convective terms in the individual stress-transport equations and the exact representation of stress production in those equations. These features make it suitable for a first examination of second moment modelling in application to synthetic jets, and it comes naturally before any subsequent evaluation of more recent models that feature various refinements to the basic scheme. The model is unchanged from its published form; however, details of the model are omitted here for the sake of brevity.

3. NUMERICAL TREATMENT

3.1 Solver

Computations have been performed using the in-house elliptic code STREAM [19], a finite volume based solver employing the UMIST numerical discretization scheme for the convective terms. Data were stored using a collocated grid system, and the SIMPLE pressure correction algorithm was used with the Rhie & Chow [20] scheme employed to avoid chequerboarding. Time-stepping was fully implicit.

3.2 Domain Size

Computational studies of the synthetic jet differ in that some represent both the cavity and the external field, while others model only the flow field external to the cavity, see [12] for example. While truer to the experimental arrangement, inclusion of the cavity may itself introduce uncertainties to a simulation, these being related to the requirement to represent the detailed motion of the diaphragm and to resolve the complex flow field within the cavity. Here we adopt the second route, imposing boundary conditions at the orifice exit plane.

Due to the symmetry of the problem, only half the jet was computed. A non-uniform expanding grid was employed, extending from the symmetry axis to a lateral distance of 4-6h, and from the orifice exit to a distance 20h downstream. The grid consisted of 240 cells in the axial direction and 60 in the cross-stream direction. The origin of the coordinate system was located on the axis of symmetry at the exit plane.

The cycle was divided into 500 time steps for each pulse. Tests confirmed the grid and time step independence of the solutions.

4. BOUNDARY CONDITIONS

The experimental data closest to the orifice were obtained at a distance of 0.12 *mm* downstream of the orifice exit. In order to allow valid comparison between the modelled solutions and the experimental data, these conditions were closely matched, as detailed below.

4.1 Orifice Axial Velocity Profile

The phase-averaged variations of the experimentally measured axial velocity profile at the centreline (y = 0) and y = 0.45h are shown in Figure 2.

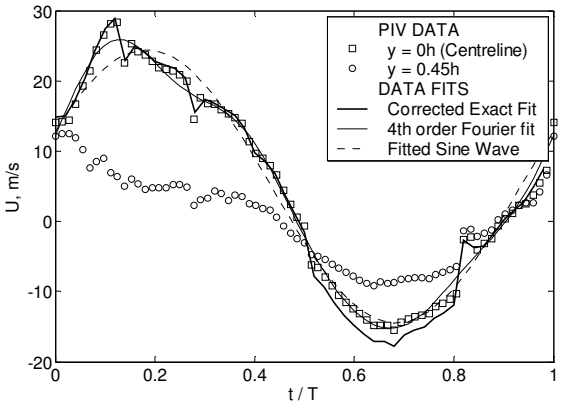

Figure 2. Experimental axial velocity profiles and data fits at x = 0.12 *mm*.

It is clear that at both lateral positions (y = 0 and 0.45h) the phase displacement from peak to trough differs from 180°. If this feature is to be accounted for, a pure harmonic ('Fitted Sine Wave' on Fig. 2) is inadequate. Instead, a higher-order fit (shown) or an exact match to the data would be required. A second feature that can be observed is the slight phase shift in the velocity variation between the two lateral locations. DNS studies of synthetic jets show this to be typical of the velocity profile in the lateral direction [9].

To account for these variations, it was deemed necessary to match exactly the experimental velocity profiles at the orifice, via an interpolation from the experimental to the computational grid. As the experimental 'boundary' was at x = 0.12 *mm*, a small correction was applied after determining the extent to which the velocity changed over this region. The centreline velocity inlet condition adopted ('Corrected Exact Fit') is shown in the figure.

One shortcoming of the above approach is that the zero net mass flow rate condition at the orifice is not necessarily rigorously enforced. Indeed, the 'Corrected Exact Fit' will, in fact, result in a positive orifice net mass flow rate. However, recent simulations that have enforced the zero net mass inflow condition have shown this not to be a critical defect of the present simulations.

4.2 Other Variables at the Orifice

During the ejection phase of the cycle (where the local axial velocity is positive), the process outlined in the previous section was followed for all variables except ε and P, for which no experimental data were given.

Two formulations were compared for ε, namely one derived from a prescribed turbulence length-scale and another based on local equilibrium ($\varepsilon = P_k$). The simulations showed very little difference, and it was decided to adopt the second approach.

Pressure was given a zero-gradient condition at the orifice at all phases of the cycle. Furthermore, all variables (except axial velocity) were prescribed a zero-gradient condition when the local axial velocity was negative i.e. during the ingestion phase of the cycle.

5. RESULTS

5.1 Standard k-ε Model

Figure 3 shows a comparison of the centreline velocity variation at four phases of the cycle. At the orifice $(x/h = 0)$, the axial velocity follows the inlet condition detailed in the previous section. The pulse can clearly be seen travelling downstream at $t/T = 0.25$, however, the k-ε model under-predicts the maximum velocity. It is interesting to observe that, unusually for jet flows, the value of the maximum velocity is greater than the peak ejection velocity. Previous simulations have identified this feature in the near-field of the synthetic jet, the cause lying in the action of a detached vortex pair limiting the lateral spread of fluid exiting the orifice at later times. This 'channelling effect' of the vortex pair also causes the centreline velocity decay rate of the synthetic jet to be far lower than that of the equivalent steady jet.

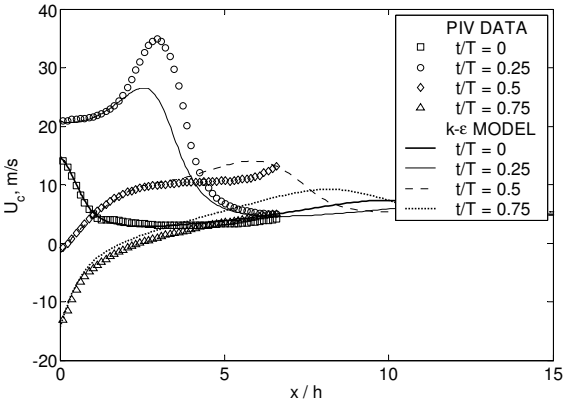

Figure 3. Centreline velocity comparison at various phase locations.

The pulse travels downstream at a velocity greater than that predicted by the k-ε model, so that at $t/T = 0.5$ the computed centreline velocity maximum lags the experimental value by approximately one orifice width.

Despite the high negative streamwise velocities close to the orifice during the ingestion phase, the surrounding fluid appears only to be drawn into the orifice from a region extending up to around 3h from the jet exit. The two distinct flow regimes can be seen in Figure 4.

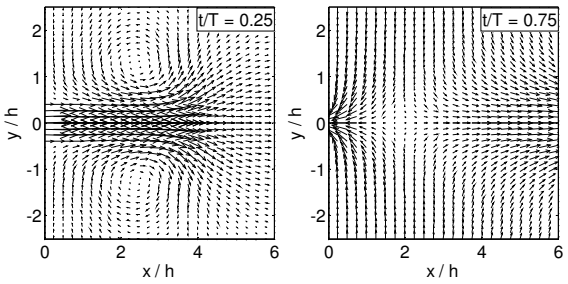

Figure 4. Velocity vectors during the ejection (left) and ingestion (right) phases.

From the above comments it is clear that the centreline flow is affected significantly by off-axis features, in particular the vortex pair. Following Hunt [21] a parameter, Π, was defined in order to characterize the complex nature of the strain field (due to space constraints, the definition of Π is not given here, but $\Pi = -1$ in pure rotation motion, $\Pi = 0$ in pure shear, and $\Pi = +1$ in pure normal strain). It should be noted that the parameter contains information only about the type of straining motion, and not the magnitude.

Figure 5 shows contours of Π at $t/T = 0.25$. The highly rotational vortex pair is clearly visible (dark region), as is the narrowing shear layer generated by the fluid ejected from the orifice after the vortex pair has detached (mid-grey region). The ingestion phase (not shown) is dominated by strong normal straining in the vicinity of the orifice exit.

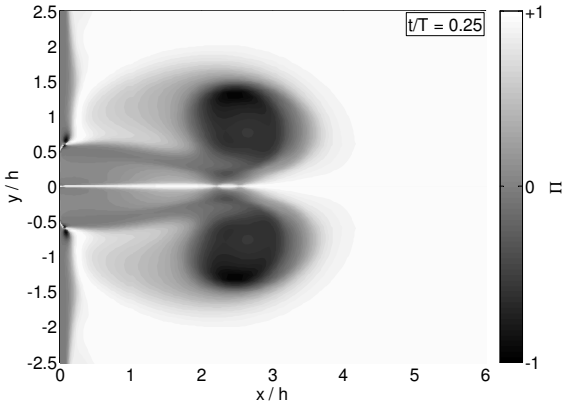

Figure 5. Π-parameter contour plot at $t/T = 0.25$.

The level of agreement between the k-ε model predictions and the experimental data that was shown for the velocity field is not replicated for the turbulent kinetic energy (Figure 6). The experimental data show low levels of k at the centreline throughout the cycle due to the low Reynolds number of the jet; however, the k-ε model predicts a very large build-up of k at the orifice during the ingestion phase, which is then transported downstream as fluid is ejected.

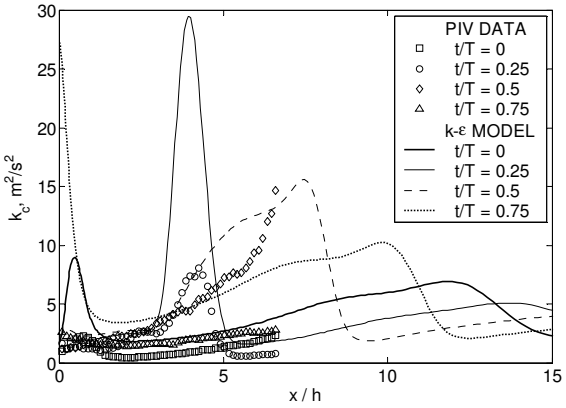

Figure 6. Centreline turbulent kinetic energy comparison at various time locations.

The unduly high levels of k seen in Fig. 6 may be attributed to the intense normal straining occurring near the orifice during the ingestion phase. To illustrate this point consider the exact expression for turbulent kinetic energy production in 2D normal straining:

$$P_k = -\left(\left\langle u^2 \right\rangle - \left\langle v^2 \right\rangle\right)\frac{\partial U}{\partial x} \qquad (11)$$

Eqn. (11) shows that P_k depends upon the difference between the streamwise and lateral normal stresses. By contrast, the constitutive equation of a linear eddy viscosity model indicates erroneously that the stress components are mutually reinforcing, resulting in a generation term of the form:

$$P_k = 4\nu_t\left(\frac{\partial U}{\partial x}\right)^2 \qquad (12)$$

In this particular application the above weakness does not appear to have a significant adverse effect on the mean velocity prediction. This may be partly due to the low Reynolds number of the flow, but also to the fact that in the near-field examined, the high levels of k generated on the centreline have not been diffused out to the jet mixing layers, where they would be expected to significantly affect the mean velocity. A greater effect on mean flow development might be expected to result from more complex configurations, such as interactions between multiple jets or between jets and a cross-flowing boundary layer.

5.2 Two-Timescale Model

Figure 7 shows PIV data for the long-time-averaged centreline velocity together with results of the standard k-ε model and the two-timescale HLS model. While a fair level of agreement is found for

the k-ε model, the HLS model significantly over-predicts the rate of centreline velocity decay.

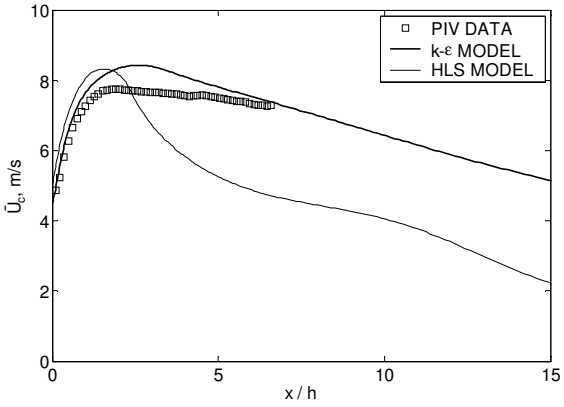

Figure 7. k-ε and HLS model variation of time-averaged centreline velocities.

Further investigation showed that the centreline velocity decay as computed using the HLS scheme was qualitatively similar to that calculated previously using the same scheme for fully-pulsed jets (Bremhorst et al. [16]). The fully-pulsed jets are largely unaffected by the presence of vortex rings, as the roll-up timescale [22] is significantly shorter than the pulsation period. Particle tracings confirmed that the HLS model did not predict the formation of a vortex pair, and consequently left the jet free to spread and decay at a much higher rate than in the k-ε simulation. These findings indicate that the clear formation of a vortex pair in a simulation is a pre-requisite for the accurate prediction of centreline statistics of the synthetic jet.

As the HLS scheme is of the linear eddy viscosity class, it is subject to the same weaknesses associated with normal straining on the suction phase as the standard k-ε model. However, it is the highly rotational straining of the initial ejection phase that highlights a further weakness in the HLS model. Section 2.1.2 described the two predominant features of the model, namely the split spectrum approach and the inclusion of a new source term in the ε_P-equation that sensitizes energy transfer across the spectrum to irrotational straining. It is instructive to consider the ε_P-production as the sum of two terms, $P_{\varepsilon P1}$ and $P_{\varepsilon P2}$:

$$P_{\varepsilon P1} = C_{P1}\frac{\varepsilon_P}{k_P}P_k \qquad (13)$$

$$P_{\varepsilon P2} = C'_{P1}k_P\frac{\partial U_l}{\partial x_m}\frac{\partial U_i}{\partial x_j}\in_{lmk}\in_{ijk} \qquad (14)$$

The coefficient C_{P1} is given a value greater than the equivalent term in the standard k-ε model (C_{P1} = 2.2, cf. $C_{\varepsilon 1}$ = 1.44). However, C'_{P1} is negative (Table 3) ensuring that, in simple shear, the net source of ε_P is similar in magnitude to the ε-source in the standard model. In irrotational straining, on the other hand, $P_{\varepsilon P2}$ is zero and the net ε_P-source is thus considerably larger than the corresponding term in the standard model. This formulation of the HLS model has been shown to offer significant advantages in application to the fully-pulsed jet where normal straining on the axis is a principal flow feature [16].

However, the near-field of the synthetic jet contains regions of almost pure *rotational* straining, and in this case $P_{\varepsilon P2}$ dominates $P_{\varepsilon P1}$ to such an extent that the total production of ε_P can become negative. Because ε_P represents the transfer of turbulent kinetic energy away from the production range, the effect in highly rotational regions is to halt this transfer, despite the continued generation of k_P. The resulting high levels of turbulent viscosity cause the flow to be highly diffusive, generally tending to smooth out distinct flow features, and in particular hindering the roll-up of the shear layer that produces the vortex pair.

5.3 Reynolds Stress Transport Model

The long-time-averaged centreline velocity computed using the standard k-ε model and the GL stress-transport scheme is shown in Figure 8. The initial centreline velocity decay is qualitatively similar to that of the standard k-ε model and the experimental data, a feature that is attributed to the correct generation of a vortex pair. However, the peak value is apparently over-predicted to a greater extent than with the k-ε model. It is possible that this over-prediction derives, at least partly, from some experimental uncertainty in the exact conditions at the orifice, a feature of the data highlighted by the review paper [12]. Significant differences were found between data measured using hotwire and PIV techniques when comparing the centreline axial velocity at $x = 0.4\ mm$, suggesting that the peak velocity value may not be as indicative of the turbulence models' performance as first appears. As with many jet flows, velocity decay rate can more confidently be thought of as representing the modelling accuracy and here the GL model better mirrors the behaviour of the experimental data, especially beyond $6h$ downstream.

Better agreement with the data is found for turbulence quantities using the GL model. Figure 9 shows phase-averaged centreline turbulent kinetic energy at $t/T = 0.125$. Here, the GL model predictions are considerably closer to the PIV data than those of the k-ε scheme, although large discrepancies still exist. Analysis of the experimental data shows that most of the turbulent kinetic energy generated in the initial shear layer becomes contained within the vortex pair after the 'roll-up' process. However, the GL model predicts a

significant diffusion of turbulent kinetic energy from the vortex pair towards the centreline, forming a 'front' of k that is convected downstream with the pulse. This leads to the over-predicted centreline peak seen in Figure 9.

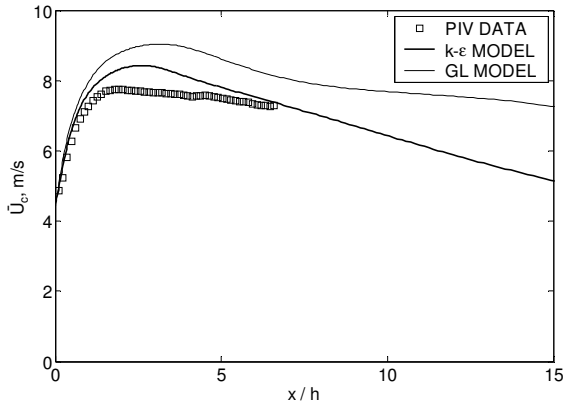

Figure 8. k-ε and GL model comparison of time-averaged centreline velocities.

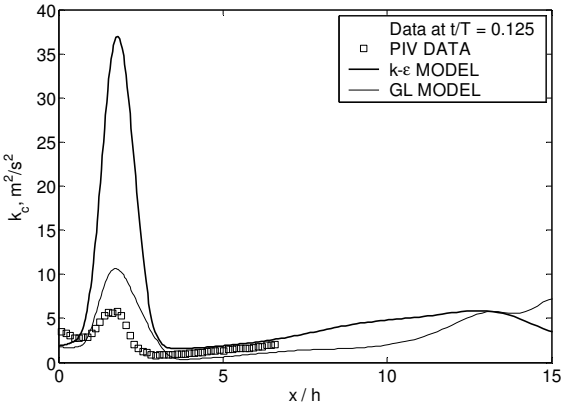

Figure 9. Centreline turbulent kinetic energy at t/T = 0.125.

It is often questioned whether synthetic jet flows such as the one considered here are mostly pressure driven, and therefore whether it is necessary to use a turbulence model within an URANS technique. While it is undoubtedly true that in some regions of the flow the pressure gradient term dominates the right-hand-side of the momentum equation, the present calculations show that in most regions the Reynolds stress term is significant, especially, for example, in the initial shear layer or the jet wake. Figure 10 shows terms from the streamwise momentum budget at $x = 5h$ and $t/T = 0.5$, just after the main pulse of the jet has passed through. It can clearly be seen that at this point the Reynolds stress terms do indeed play a significant role in the jet wake. This general budget shape remains throughout much of the cycle at this point, as the pulse passes through much more quickly than the ensuing wake decays.

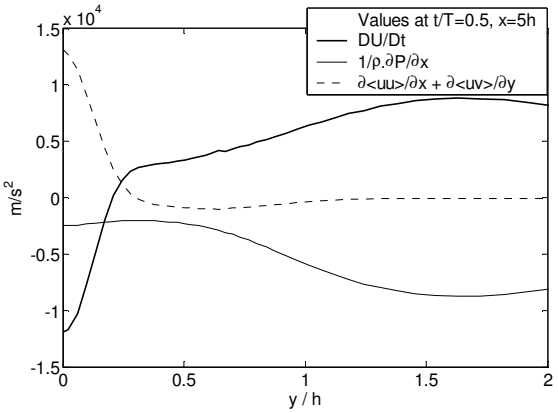

Figure 10. Streamwise momentum budget at t/T = 0.5 and x = 5h, viscous terms omitted.

6. CONCLUSIONS

The near-field of a synthetic jet is characterized by a complex strain field consisting of regions that experience high levels of normal and shear strain, while the vortex pairs formed in the roll-up of the shear layer created at the orifice exit are strongly rotational. The complexity of the flow field presents a severe test of turbulence model capabilities. In relation to the k-ε model, normal straining during the ingestion phase of the cycle reveals a fundamental weakness in the constitutive equation that is common to all linear eddy viscosity schemes.

The highly rotational flow associated with the creation and subsequent development of a vortex pair has proved to cause particular difficulties for the two-timescale eddy viscosity model. The problem can be traced to an additional term in the ε_P-equation of the scheme; under highly rotational conditions the term can become dominant and hinder the transfer of energy across the spectrum, causing a build up of turbulence kinetic energy in the production region.

A Reynolds stress transport scheme did not display either of the above weaknesses. Fair agreement was found with the data, showing that this type of scheme has a greater potential in modelling this particular flow than the tested eddy-viscosity approaches. However, it may be necessary to use a more advanced stress-transport model than that adopted here, and some more certainty regarding some of the experimental conditions would allow more definitive conclusions to be drawn.

Work is currently in progress to extend the present study to 3D synthetic jets in cross-flow [23].

ACKNOWLEDGEMENTS

The authors are pleased to acknowledge the generous support for this work provided by the Douglas Prestwich Charitable Trust.

REFERENCES

[1] Ho, C.-M., and Tai, Y.-C., 1998, "Micro-Electro-Mechanical-Systems (MEMS) and Fluid Flows", *Annual Review of Fluid Mechanics*, Vol. 30, pp. 579-612.

[2] Utturkar, Y., Holman, R., Mittal, R., Carroll, B., Sheplak, M., and Cattafesta, L., 2003, "A Jet Formation Criterion for Synthetic Jet Actuators", *41st Aerospace Sciences Meeting and Exhibit*, AIAA 2003-0636.

[3] Smith, B. L., and Glezer, A., 1998, "The Formation and Evolution of Synthetic Jets", *Physics of Fluids*, Vol. 10, No. 9, pp. 2281-2297.

[4] Glezer, A., and Amitay, M., 2002, "Synthetic Jets", *Annual Review of Fluid Mechanics*, Vol. 34, pp. 503-529.

[5] Wang, H., and Menon, S., 2001, "Fuel-Air Mixing Enhancement by Synthetic Microjets", *AIAA Journal*, Vol. 13, No. 12, pp. 2308-2319.

[6] Smith, B. L., and Glezer, A., 2002, "Jet Vectoring using Synthetic Jets", *Journal of Fluid Mechanics*, Vol. 458, pp. 1-34.

[7] Crook, A., 2002, "The Control of Turbulent Flows using Synthetic Jets*", Ph.D. Thesis, The University of Manchester*.

[8] Mallison, S. G., Reizes, J. A., Hong, G., and Westbury, P.S., 2004, "Analysis of Hot-wire Anemometry Data obtained in a Synthetic Jet Flow", *Experimental and Thermal Fluid Science*, Vol. 28, pp. 265-272.

[9] Rizetta, D. P., Visbal, M. R., and Stanek, M. J., 1998, "Numerical Investigation of Synthetic Jet Flowfields", *29th AIAA Fluid Dynamics Conference*, AIAA 98-2910.

[10] Kotapati, R. B., and Mittal, R., 2005, "Time-Accurate Three-Dimensional Simulations of Synthetic Jets in Quiescent Air", *43rd Aerospace Sciences Meeting and Exhibit*, AIAA 2005-0103.

[11] Schaeffler, N. W., 2003, "The Interaction of a Synthetic Jet and a Turbulent Boundary Layer", *41st Aerospace Sciences Meeting and Exhibit*, AIAA 2003-0643.

[12] Rumsey, C. L., Gatski, T. B., Sellers, W. L., Vatsa, V. N., Viken, S. A., 2004, "Summary of the 2004 CFD Validation Worksop on Synthetic Jet and Turbulent Separation Control", *2nd AIAA Flow Control Conference*, AIAA 2004-2217.

[13] Launder, B. E., and Spalding, D. B., 1974, "The Numerical Computation of Turbulent Flows", *Computer Methods in Applied Mechanics and Engineering*, Vol. 3, pp. 269-289.

[14] Hanjalić, K., Launder, B. E., and Schiestel, R., 1979, "Multiple-Time-Scale Concepts in Turbulent Transport Modelling", *Turbulent Shear Flows 2*, pp. 37-39.

[15] Hanjalić, K., and Launder, B. E., 1980, "Sensitizing the Dissipation Equation to Irrotational Strains", *Journal of Fluids Engineering*, Vol. 102, pp. 34-40.

[16] Bremhorst, K., Craft, T. J., and Launder, B. E., 2003, "Two-Time-Scale Modelling Turbulence Modelling of a Fully Pulsed Axisymmetric Air Jet", *Proc. 3rd International Symposium on Turbulence and Shear Flow Phenomena, Sendai, Japan*.

[17] Kim, K. R., 2006, "A Turbulence Modelling Study of Fully-Pulsed Round Jets", *PhD Thesis in preparation for submission to The University of Manchester*.

[18] Gibson, M. M., and Launder, B. E., 1978, "Ground Effects on Pressure Fluctuations in the Atmospheric Boundary Layer," *Journal of Fluid Mechanics*, Vol. 86, pp. 491–511.

[19] Lien, F. S., and Leschziner, M. A., 1994, "A General Non-Orthogonal Collocated Finite Volume Algorithm for Turbulent Flow and All Speeds incorporating Second-Moment Turbulence-Transport Closure", *Computer Methods in Applied Mechanics and Engineering*, Vol. 114, pp. 123-148.

[20] Rhie, C. M., and Chow, W. L., 1983, "Numerical study of the turbulent flow past an aerofoil with trailing edge separation", *AIAA Journal*, Vol. 21, pp. 1525-1532.

[21] Hunt, J. C. R., 1992, "Developments in Computational Modelling of Turbulent Flows", *in Numerical Simulation of Unsteady Flows and Transition to Turbulence (Eds. O. Pironneau et al.)*, pp. 2-76.

[22] Gharib, M., Rambod, E., and Shariff, K., 1998, "A Universal Time Scale for Vortex Ring Formation", *Journal of Fluid Mechanics*, Vol. 360, pp. 121-140.

[23] Heynes, O. R., 2006, "Eddy-viscosity and Stress Transport Modelling of Synthetic Jets with and without Cross-Flow", *Ph.D. Thesis in preparation for submission to The University of Manchester.*

Conference on Modelling Fluid Flow (CMFF'06)
The 13th International Conference on Fluid Flow Technologies
Budapest, Hungary, September 6-9, 2006

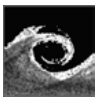

PARAMETRIC METHOD IN UNSTEADY MHD BOUNDARY LAYER THEORY OF FLUID WITH VARIABLE ELECTROCONDUCTIVITY

Dragisa Nikodijevic[1], Zoran Boricic[2], Dragica Milenkovic[3], Zivojin Stamenkovic[4]

[1] Corresponding Author Department of Fluid Mechanics, Faculty of Mechanical Engineering Nis, Aleksandra Medvedeva 14, 18000 Nis, Serbia and Montenegro, E-mail: dragisan@masfak.ni.ac.yu
[2] Department of Fluid Mechanics, Faculty of Mechanical Engineering Nis, Serbia and Montenegro, E-mail: dragica@masfak.ni.ac.yu
[3] Department of Fluid Mechanics, Faculty of Mechanical Engineering Nis, Serbia and Montenegro. E-mail: zboricic@masfak.ni.ac.yu
[4] Department of Fluid Mechanics, Faculty of Mechanical Engineering Nis, Serbia and Montenegro. E-mail: zikas@masfak.ni.ac.yu

ABSTRACT

In this paper is considered unsteady plane MHD boundary layer. Present external magnetic field is uniform and perpendicular to the body, which the fluid flows around. Fluid, which forms the boundary layer, is incompressible and its electroconductivity varies according to Rosow assumption. Parametric method with three infinite sets of parameters is used for obtaining universal equations of observed problem. Impulse and energy equations of problem in consideration are also used for derivation of universal equations.

Keywords: boundary layer, MHD, parametric method, electroconductive fluid

NOMENCLATURE

B	$[T]$	magnetic field induction
F	[-]	dimensionless parameter
H	[-]	dimensionless parameter
H_1	[-]	dimensionless parameter
K	$[m]$	
N	$[1/s]$	magnetic number
R	[-]	dimensionless parameter
U	$[m/s]$	velocity at the edge of boundary layer
a_0	[-]	constant
b_0	[-]	constant
$f_{k,n}$	[-]	dimensionless parameter
$g_{k,n}$	[-]	dimensionless parameter
p	[-]	dimensionless parameter
t	$[s]$	time
u	$[m/s]$	streamwise velocity in boundary layer
x	$[m]$	longitudinal coordinate
y	$[m]$	transversal coordinate
z	$[s]$	ratio δ^{**2}/ν
δ^{**}	$[m]$	thickness of impulse loss
μ	$[Ns/m^2]$	coefficient of dynamic viscosity
ν	$[m^2/s]$	coefficient of the kinematics viscosity of fluid
$\lambda_{k,n}$	[-]	dimensionless parameter
σ_0	$[A^2s^3/kgm^2]$	electroconductivity on the body.
ρ	$[kg/m^3]$	density of fluid
ζ	[-]	dimensionless parameter
Φ	[-]	dimensionless parameter
Ψ	$[m^2/s]$	stream function

Subscripts and Superscripts

0	values for $x=x_0$
1	values for $t=t_1$

1. INTRODUCTION

There are different problems of magneto-hydrodynamic boundary layer in technical practice, and not only steady but also unsteady cases. The problems with constant electroconductivity have been considered [1] and also the problems with variable electroconductivity [2,3]. For solving of this problem, in recent time, the method of "universality" of boundary layer equations have been used very often and in very different versions [4,5,6]. This method have been created for steady boundary layer, problems, and later has been extended to the different unsteady boundary layer problems [7,8,9,10]. The universal results obtained by this method enable us to bring more general conclusions about the boundary layer development and these results can be used for calculations of particular problems. The general conclusions are independent of the velocity distribution at the edge of boundary layer, and if it is MHD boundary layer, they are independent of external magnetic field.

In order to extend this theory, in this paper is investigated the unsteady plane MHD boundary

layer on the body. The existing external magnetic field is homogenous and perpendicular to the body which the fluid flows around, and it is stationary with respect to the body (Figure 1).

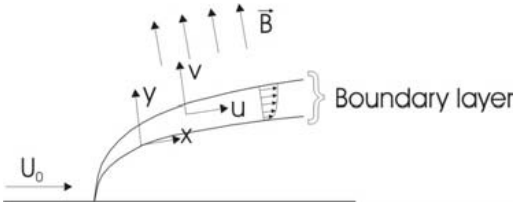

Figure 1. Considered flow problem

The fluid is incompressible and its electroconductivity varies according to the Rosow assumption:

$$\sigma=\sigma_0\left(1-\frac{u}{U}\right). \tag{1}$$

2. MATHEMATICAL MODEL

The mathematical model of the described flow (Figure 1.) is presented by the following equations:

$$\frac{\partial^2\Psi}{\partial t\partial y}+\frac{\partial\Psi}{\partial y}\frac{\partial^2\Psi}{\partial x\partial y}-\frac{\partial\Psi}{\partial x}\frac{\partial^2\Psi}{\partial y^2}= =\frac{\partial U}{\partial t}+\nu\frac{\partial^3\Psi}{\partial y^3}-N\frac{\partial\Psi}{\partial y}\left(1-\frac{1}{U}\frac{\partial\Psi}{\partial y}\right); \tag{2}$$

with the boundary and initial conditions:

$$\begin{aligned}&\frac{\partial\Psi}{\partial y}=0,\Psi=0 \text{ for } y=0;\\ &\frac{\partial\Psi}{\partial y}\to U(x,t) \text{ for } y\to\infty.\\ &\frac{\partial\Psi}{\partial y}=u_1(x,y) \text{ for } t=t_1;\\ &\frac{\partial\Psi}{\partial y}=u_0(t,y) \text{ for } x=x_0.\end{aligned} \tag{3}$$

In the equation (2) and in the boundary and initial conditions (3) the following notations have been used: $N=\sigma_0B^2/\rho$, where is B - magnetic induction, $u_1(x,y)$ - velocity distribution in boundary layer at the moment $t=t_1$; $u_0(t,y)$ - velocity distribution at the distance $x=x_0$.

3. UNIVERSAL EQUATIONS

Following the method of "universality" the following variables are introduced:

$$x=x,\ t=t,\ \eta=\frac{y}{K(x,t)},$$

$$\Phi(x,\eta,t)=\frac{\Psi(x,y,t)}{U(x,t)K(x,t)}, \tag{4}$$

where is:

$$K(x,t)=\left(a_0\nu U^{-b_0}\int_0^x U^{b_0-1}dx\right)^{\frac{1}{2}};$$

and the constants a_0 and b_0 have got the values $a_0=0.44$ and $b_0=5.35$. In that case the derivation operation at the old variables is substituted by the new ones:

$$\begin{aligned}&\frac{\partial}{\partial x}=\left(\frac{\partial}{\partial x}\right)+\frac{\partial}{\partial\eta}\frac{\partial\eta}{\partial x}=\left(\frac{\partial}{\partial x}\right)-\frac{\eta}{K}\frac{\partial K}{\partial x}\frac{\partial}{\partial\eta};\\ &\frac{\partial}{\partial t}=\left(\frac{\partial}{\partial t}\right)+\frac{\partial}{\partial\eta}\frac{\partial\eta}{\partial t}=\left(\frac{\partial}{\partial t}\right)-\frac{\eta}{K}\frac{\partial K}{\partial t}\frac{\partial}{\partial\eta};\\ &\frac{\partial}{\partial y}=\frac{1}{K}\frac{\partial}{\partial\eta};\\ &\frac{\partial^2}{\partial y^2}=\frac{1}{K^2}\frac{\partial^2}{\partial\eta^2};\\ &\frac{\partial^3}{\partial y^3}=\frac{1}{K^3}\frac{\partial^3}{\partial\eta^3}.\end{aligned} \tag{5}$$

Further, introducing in consideration the momentum thickness:

$$\delta^{**}(x,t)=\int_0^\infty\frac{u}{U}\left(1-\frac{u}{U}\right)dy=K(x,t)R(x,t); \tag{6}$$

where is

$$R(x,t)=\int_0^\infty\frac{\partial\Phi}{\partial\eta}\left(1-\frac{\partial\Phi}{\partial\eta}\right)d\eta; \tag{7}$$

and the value

$$z=\frac{\delta^{**2}}{\nu}=\frac{K^2R^2}{\nu}; \tag{8}$$

the equation (2) is transformed to the equation

$$\begin{aligned}&\frac{\partial^3\Phi}{\partial\eta^3}+\frac{a_0}{2}\Phi\frac{\partial^2\Phi}{\partial\eta^2}+\frac{K^2}{\nu U}\left(1-\frac{\partial\Phi}{\partial\eta}\right)+\\ &\frac{K^2}{\nu}\frac{\partial U}{\partial x}\left[1-\left(\frac{\partial\Phi}{\partial\eta}\right)^2+\left(1-\frac{b_0}{2}\right)\Phi\frac{\partial^2\Phi}{\partial\eta^2}\right]-\\ &-N\frac{K^2}{\nu}\frac{\partial\Phi}{\partial\eta}\left(1-\frac{\partial\Phi}{\partial\eta}\right)+\frac{\eta}{2R^2}p\frac{\partial^2\Phi}{\partial\eta^2}=\\ &=\frac{K^2}{\nu}\frac{\partial^2\Phi}{\partial t\partial\eta}+\eta\frac{z}{R^3}\frac{\partial R}{\partial t}\frac{\partial^2\Phi}{\partial\eta^2}+U\frac{K^2}{\nu}X(\eta;x);\end{aligned} \tag{9}$$

in which the denotes used, are

$$p=\frac{\partial z}{\partial t}\ ;$$
$$X(x_1;x_2)=\frac{\partial \Phi}{\partial x_1}\frac{\partial^2 \Phi}{\partial \eta \partial x_2}-\frac{\partial \Phi}{\partial x_2}\frac{\partial^2 \Phi}{\partial x_1 \partial \eta}\ . \tag{10}$$

The boundary and initial conditions, have the form:

$$\begin{aligned}
&\frac{\partial \Phi}{\partial \eta}=0, \Phi=0 \ \text{ for } \eta=0\ ;\\
&\frac{\partial \Phi}{\partial \eta}\to 1 \text{ for } \eta\to\infty\ ;\\
&\frac{\partial \Phi}{\partial \eta}=\frac{u_1}{U} \ \text{ for } t=t_0\ ;\\
&\frac{\partial \Phi}{\partial \eta}=\frac{u_0}{U} \text{ for } x=x_0\ ;
\end{aligned} \tag{11}$$

but the conditions, written in the second row of conditions, are used for the calculation of particular problems and they do not have significance at the derivation of universal equation. Assuming that $U(x,t)$ and $N(x,t)$ are the differential functions, the following group of parameters are introduced:

$$\begin{aligned}
f_{k,n}&=U^{k-1}\frac{\partial^{k+n}U}{\partial x^k \partial t^n}z^{k+n}\\
&\quad (k,n=0,1,2,...k\vee n\neq 0);\\
g_{k,n}&=U^{k-1}z^{k+n}\frac{\partial^{k-1+n}N}{\partial x^{k-1}\partial t^n}\\
&\quad (k,n=0,1,2,...;k\neq 0);
\end{aligned} \tag{12}$$

where can be noticed that the first parameters have the form:

$$\begin{aligned}
&f_{1,0}=z\frac{\partial U}{\partial x}=\frac{R^2K^2}{\nu}\frac{\partial U}{\partial x}\ ;\\
&f_{0,1}=\frac{z}{U}\frac{\partial U}{\partial t}=\frac{R^2K^2}{\nu U}\frac{\partial U}{\partial t}\ ;\\
&g_{1,0}=Nz=\frac{R^2K^2}{\nu}N\ .
\end{aligned} \tag{13}$$

In this way chosen parameters, which substitute streamwise coordinate x and time t, express the influence on the characteristics of MHD boundary layer, on the velocity at the edge of boundary layer and on the magnetic field, and on the flow prehistory. These parameters are mutual independent and in the next paragraphs we hold them for independent variables.

For further transformations of the equation (9) the following operators are used.

$$\begin{aligned}
&\frac{\partial}{\partial x}=\sum_{\substack{k,n=0\\ k\vee n\neq 0}}^{\infty}\frac{\partial f_{k,n}}{\partial x}\frac{\partial}{\partial f_{k,n}}+\sum_{\substack{k=1\\ n=0}}^{\infty}\frac{\partial g_{k,n}}{\partial x}\frac{\partial}{\partial g_{k,n}}\ ;\\
&\frac{\partial}{\partial t}=\sum_{\substack{k,n=0\\ k\vee n\neq 0}}^{\infty}\frac{\partial f_{k,n}}{\partial t}\frac{\partial}{\partial f_{k,n}}+\sum_{\substack{k=1\\ n=0}}^{\infty}\frac{\partial g_{k,n}}{\partial t}\frac{\partial}{\partial g_{k,n}}\ ;
\end{aligned} \tag{14}$$

where the derivations of parameters with respect to x and t are determined by immediate differentiation of the expression (12) and they have the forms:

$$\begin{aligned}
&\frac{\partial f_{k,n}}{\partial x}=\frac{A_{k,n}}{Uz}=\\
&=\frac{1}{Uz}\left\{\left[(k-1)f_{1,0}+(k+n)F\right]f_{k,n}+f_{k+1,n}\right\};\\
&F=U\frac{\partial z}{\partial x}\ ;\\
&\frac{\partial g_{k,n}}{\partial x}=\frac{Q_{k,n}}{Uz}=\\
&=\frac{1}{Uz}\left\{\left[(k-1)f_{1,0}+(k+n)F\right]g_{k,n}+g_{k+1,n}\right\};\\
&\frac{\partial f_{k,n}}{\partial t}=\frac{C_{k,n}}{z}=\\
&=\frac{1}{z}\left\{\left[(k-1)f_{1,0}+(k+n)p\right]f_{k,n}+f_{k+1,n}\right\};\\
&\frac{\partial g_{k,n}}{\partial t}=\frac{D_{k,n}}{z}=\\
&\frac{1}{z}\left\{\left[(k-1)f_{1,0}+(k+n)p\right]g_{k,n}+g_{k+1,n}\right\}.
\end{aligned} \tag{15}$$

By using the operators (14) and the derivations (15), the equation (9) is transformed to the equation

$$\begin{aligned}
&\frac{\partial^3 \Phi}{\partial \eta^3}+\frac{1}{2R^2}\left[a_0R^2+(2-b_0)\right]\Phi\frac{\partial^2 \Phi}{\partial \eta^2}+\\
&\frac{f_{1,0}}{R^2}\left[1-\left(\frac{\partial \Phi}{\partial \eta}\right)^2\right]+\frac{f_{0,1}}{R^2}\left(1-\frac{\partial \Phi}{\partial \eta}\right)-\\
&-\frac{g_{1,0}}{R^2}\frac{\partial \Phi}{\partial \eta}\left(1-\frac{\partial \Phi}{\partial \eta}\right)+\frac{1}{2}\eta\frac{p}{R^2}\frac{\partial^2 \Phi}{\partial \eta^2}=\\
&\eta\frac{1}{R^3}\left(\sum_{\substack{k,n=0\\ k\vee n\neq 0}}^{\infty}C_{k,n}\frac{\partial R}{\partial f_{k,n}}+\sum_{\substack{k=1\\ n=0}}^{\infty}D_{k,n}\frac{\partial R}{\partial g_{k,n}}\right)+\\
&+\frac{1}{R^2}\sum_{\substack{k,n=0\\ k\vee n\neq 0}}^{\infty}\left[C_{k,n}\frac{\partial^2 \Phi}{\partial f_{k,n}\partial \eta}+A_{k,n}X(\eta;f_{k,n})\right]+\\
&+\frac{1}{R^2}\sum_{\substack{k=1\\ n=0}}^{\infty}\left[D_{k,n}\frac{\partial^2 \Phi}{\partial g_{k,n}\partial \eta}+Q_{k,n}X(\eta;g_{k,n})\right].
\end{aligned} \tag{16}$$

From the equation (16) can be seen, that for the chosen particular electroconductivity variation, the characteristics of external flow dominate by the means of functions F and p. In order the equation (16) to be independent of the outer flow characteristics i.e. to be universal, it is necessary to show the existence of the equality:

$$F = F\left[\left(f_{k,n}\right),\left(g_{k,n}\right)\right];\ p = p\left[\left(f_{k,n}\right),\left(g_{k,n}\right)\right]. \qquad (17)$$

So as to show the existence of such equalities, we start from the momentum equation:

$$\frac{\partial}{\partial t}\left(U\delta^{*}\right)+\frac{\partial}{\partial x}\left(U^{2}\delta^{**}\right)+U\delta^{*}\frac{\partial U}{\partial x}+ +NU\widetilde{\delta}^{*}-\frac{\tau_w}{\rho}=0; \qquad (18)$$

and energy equation:

$$\frac{\partial}{\partial t}\left(U^{2}\delta^{**}\right)+U^{3}\frac{\partial \delta_1^{**}}{\partial x} +U^{2}\left(\frac{\partial \delta^{*}}{\partial t}+3\delta_1^{**}\frac{\partial U}{\partial x}+2N\widetilde{\delta}^{**}-2ve\right)=0 \qquad (19)$$

of the problem considered where the following denotes have been used:

$$\delta^{*}(x,t)=\int_0^{\infty}\left(1-\frac{u}{U}\right)dy=K\int_0^{\infty}\left(1-\frac{\partial \Phi}{\partial \eta}\right)d\eta;$$

$$\widetilde{\delta}^{*}(x,t)=\int_0^{\infty}-\frac{u}{U}\left(1-\frac{u}{U}\right)dy=$$

$$=-K\int_0^{\infty}\frac{\partial \Phi}{\partial \eta}\left(1-\frac{\partial \Phi}{\partial \eta}\right)d\eta;$$

$$\tau_w(x,t)=\mu\left.\frac{\partial u}{\partial y}\right|_{y=0}=\mu\frac{U}{K}\left.\frac{\partial^{2}\Phi}{\partial \eta^{2}}\right|_{\eta=0};$$

$$\delta_1^{**}(x,t)=\int_0^{\infty}\frac{u}{U}\left(1-\frac{u^{2}}{U^{2}}\right)dy=$$

$$=K\int_0^{\infty}\frac{\partial \Phi}{\partial \eta}\left(1-\left(\frac{\partial \Phi}{\partial \eta}\right)^{2}\right)d\eta; \qquad (20)$$

$$\widetilde{\delta}^{**}(x,t)=\int_0^{\infty}-\frac{u^{2}}{U^{2}}\left(1-\frac{u}{U}\right)dy=$$

$$=-K\int_0^{\infty}\left(\frac{\partial \Phi}{\partial \eta}\right)^{2}\left(1-\frac{\partial \Phi}{\partial \eta}\right)d\eta;$$

$$e(x,t)=\int_0^{\infty}\left[\frac{\partial\left(\frac{u}{U}\right)}{\partial y}\right]^{2}dy=\frac{1}{K}\int_0^{\infty}\left(\frac{\partial^{2}\Phi}{\partial \eta^{2}}\right)d\eta;$$

μ - coefficient of dynamic viscosity.

First, we write the derivations with respect to x and t in equation (18) in the developed form and we substitute τ_w with the expression (20), and afterwards we introduce the values:

$$H=\frac{\delta^{*}}{\delta^{**}}=\frac{1}{R}\int_0^{\infty}\left(1-\frac{\partial \Phi}{\partial \eta}\right)d\eta;$$

$$\widetilde{H}=\frac{\widetilde{\delta}^{*}}{\delta^{**}}=-\frac{1}{R}\int_0^{\infty}\frac{\partial \Phi}{\partial \eta}\left(1-\frac{\partial \Phi}{\partial \eta}\right)d\eta;$$

$$\zeta=\frac{\tau_w\delta^{**}}{\mu U}=R\left.\frac{\partial^{2}\Phi}{\partial \eta^{2}}\right|_{\eta=0}; \qquad (21)$$

and in this way we obtain the equation from which it is obtained the following expression

$$F=2\left[\zeta-2f_{1,0}-H\left(f_{1,0}+f_{0,1}+\frac{1}{2}p\right)\right] -2\left[\widetilde{H}g_{1,0}+z\frac{\partial H}{\partial t}\right]. \qquad (22)$$

From the expression (21) it can be seen, that the value H is the function only of the parameter (12), so that its derivation with respect to t determines by mediate derivation the value H with respect to the parameters, and afterwards the parameters with respect to t. After this determination of derivation of the value H with respect to t, the expression (21) obtains the form:

$$F=2\left[\zeta-2f_{1,0}-H\left(f_{1,0}+f_{0,1}+\frac{1}{2}p\right)+\widetilde{H}g_{1,0}\right] -2\left[\sum_{\substack{k,n=0\\ k\vee n\neq 0}}^{\infty}C_{k,n}\frac{\partial H}{\partial f_{k,n}}+\sum_{\substack{k=1\\ n=0}}^{\infty}D_{k,n}\frac{\partial H}{\partial g_{k,n}}\right] \qquad (23)$$

As the values ζ, H, $\widetilde{H}$ depend only on parameter (12), than the function F, given by the expression (23), depends only on the same parameters and on the value p, which appears in it explicitly and implicitly by the means of values $C_{k,n}$ and $D_{k,n}$. So for the evidence of the existence of the first equality (17), it is needed and sufficient to prove also the existence of the second equality

(17). For the evidence of the second equality existence (17) let's write first in developed form the derivations with respect to x and t in the energy equation (19) and let's introduce the values:

$$H_1=\frac{\delta_1^{**}}{\delta^{**}}=\frac{1}{R}\int_0^{\infty}\frac{\partial\Phi}{\partial\eta}\left(1-\left(\frac{\partial\Phi}{\partial\eta}\right)^2\right)d\eta;$$
$$e\delta^{**}=R\int_0^{\infty}\left(\frac{\partial^2\Phi}{\partial\eta^2}\right)d\eta=\alpha\left[\left(f_{k,n}\right);\left(g_{k,n}\right)\right]; \quad (24)$$

than the energy equation obtains the form:

$$z\frac{\partial H}{\partial t}+\frac{1}{2}(H+1)p+2f_{0,1}+Uz\frac{\partial H_1}{\partial x}+$$
$$+\left(\frac{1}{2}p+3f_{1,0}\right)H_1+2\tilde{H}_1g_{1,0}-2\alpha=0; \quad (25)$$

going to, in the last equation, to the new variables - parameters, substituting function F by the expression (23) and solving in such way obtained equation with respect to p, it is obtained that is:

$$p=\{2(2M+H_1)[\zeta-2f_{1,0}-H(f_{1,0}+f_{0,1})-$$
$$-\tilde{H}g_{1,0}-M_1^*]+2(M1+M_1^*+2f_{0,1})+6H_1f_{1,0}$$
$$+4\tilde{H}_1g_{1,0}-4\alpha\}/[(H+2M^*)(2M+H_1-1)-1] \quad (26)$$

where the denotes are introduced:

$$M=\sum_{\substack{k,n=0\\k\vee n\neq 0}}^{\infty}(k+n)f_{k,n}\frac{\partial H_1}{\partial f_{k,n}}+$$
$$+\sum_{\substack{k=1\\n=0}}^{\infty}(k+n)g_{k,n}\frac{\partial H_1}{\partial g_{k,n}};$$
$$M_1=\sum_{\substack{k,n=0\\k\vee n\neq 0}}^{\infty}\theta_{k,n}\frac{\partial H_1}{\partial f_{k,n}}+\sum_{\substack{k=1\\n=0}}^{\infty}\theta_{k,n}^*\frac{\partial H_1}{\partial g_{k,n}};$$
$$\theta_{k,n}=(k-1)f_{1,0}f_{k,n}+f_{k+1,n};$$
$$\theta_{k,n}^*=(k-1)f_{1,0}g_{k,n}+g_{k+1,n}; \quad (27)$$
$$M^*=\sum_{\substack{k,n=0\\k\vee n\neq 0}}^{\infty}(k+n)f_{k,n}\frac{\partial H}{\partial f_{k,n}}+$$
$$+\sum_{\substack{k=1\\n=0}}^{\infty}(k+n)g_{k,n}\frac{\partial H}{\partial g_{k,n}};$$
$$M_1^*=\sum_{\substack{k,n=0\\k\vee n\neq 0}}^{\infty}\lambda_{k,n}\frac{\partial H_1}{\partial f_{k,n}}+\sum_{\substack{k=1\\n=0}}^{\infty}\lambda_{k,n}^*\frac{\partial H_1}{\partial g_{k,n}};$$
$$\lambda_{k,n}=(k-1)f_{0,1}f_{k,n}+f_{k,n+1};$$
$$\lambda_{k,n}^*=(k-1)f_{0,1}g_{k,n}+g_{k,n+1}.$$

As the values $M,H_1,\zeta,H,\tilde{H},M_1^*,$ $M_1,\tilde{H}_1,\alpha,M^*$ which exists in the expression (26) depends only on parameters $f_{k,n}$ and $g_{k,n}$, so the same expression is also the expression (26), and in that way the existence of the second equality (17) has been confirmed, and much more, it explicit form has been determined. As it has been shown till now, the value of T depends only on parameters, and than on the basis of the expression (23) it is shown that also the value F is only the function of parameters.

Now we conclude that the equation (16), for the chosen electroconductivity variation, do not depend explicitly on characteristics of outer flow and outer magnetic field, and in that sense we can consider it as universal equation of the problem investigated. The boundary conditions, also universal that correspond to the equation (16) have the form:

$$\frac{\partial\Phi}{\partial\eta}=0,\ \Phi=0,\ \text{for}\ \ \eta=0;$$
$$\frac{\partial\Phi}{\partial\eta}\to 1,\ \text{for}\ \ \eta\to\infty;$$
$$\Phi=\Phi_0(\eta),\ for \quad (28)$$
$$\begin{cases}f_{k,n}=0\ \ k,n=0,1,2,...;k\vee n\neq 0;\\ g_{k,n}=0\ \ k,n=0,1,2,...,k\neq 0\end{cases}$$

where is $\Phi_0(\eta)$ the Blausius solution for steady boundary layer on the flat plate. The independence of the equation (16) and boundary conditions (28) of particular velocity distribution at the edge of boundary layer and of outer magnetic field enable the integration of this equation, for the chosen electroconductivity variation of the form (1), once for all. In the procedure of integration we determine the velocity dimensionless profiles in cross-stream sections of boundary layer Φ, friction coefficient ζ, and also the characteristic functions $H_1,H,\tilde{H},$ α,F,p and in the dependence of parameters $f_{k,n}$ and $g_{k,n}$.

That obtained so called universal solutions should, in appropriate manner, be kept and be used not only for drawing the general conclusions about the unsteady MHD boundary layer development, but also for the calculation of the particular problems. Surely, the equation (16) can be used only in the some corresponding approximation, which assumes the finite number of terms on the right-hand side of that equation.

4. SUMMARY

In this paper is considered unsteady plane MHD boundary layer. Present external magnetic field is uniform and perpendicular to the body, which the fluid flows around. Fluid, which forms the boundary layer, is incompressible and its electroconductivity varies according to Rosow assumption. Parametric method with three infinite sets of parameters is used for obtaining universal equations of observed Obtained universal differential equation (16) is independent from values that characterized particular problems. Universal equation with boundary conditions can be numerically integrated once for all by computer using and during that only snipping of equations has been considered. Obtained results can be on convenient way saved and then used for general conclusion conveyance about fluid flow and for calculations of particular problems.

REFERENCES

[1] Юферев В., 1967, "Ободном приближенном расчета ламинарного пограничного слоя в магнитној гидродинамике", *Механика жидкости и газа,* Vol 1., pp 124-127.

[2] Rossow V. J., 1958, "On flow of electrically conducting fluids over a flat plate in the presence of a transverse magnetic field", *NACA Report*., No 1358.

[3] Boricic Z., Nikodijevic D., Milenkovic D., Stamenkovic Z., 2005, "A form of MHD universal equations of unsteady incompressible fluid flow with variable electroconductivity on heated moving plate", *Theoretical and applied mechanics*, Vol 32. pp. 65-79.

[4] Loicianskij, L. G., 1967, Universal equations and parametric approximations in the theory of laminar boundary layer, *PMM – Appl. Math. Mech.,* Vol. 29, No. 1, pp. 70–87, (in Russian).

[5] Bushmarin, O. N., Basin B., 1972, A parametrical method of calculation for a laminar instationary boundary layer, *Journal Engng. Phys*., Vol. 22, pp.282-292, (in Russian).

[6] Saljnikov V. N., 1978, "A contribution to universal solutions of the boundary layer theory", *Theoretical and applied mechanics*, Vol. 4, pp. 139-163.

[7] Obrovic B., Savic S., 2003, "Dissociated gas flow in the boundary layer in the case of a porous contour of the body within fluid", *Facta Universitatis Series Mechanics, Automatic Control and Robotics,* Vol.3, No 15, pp.989-1000.

[8] Ivanovic D., 2005, "On injection-ejection fluid influence through different accelerating porous surfaces on unsteady 2D incompressible boundary layer characteristics", *Theoretical and applied mechanics*, Vol. 32-1, pp. 147-165.

[9] Saljnikov V., Boričić Z., Nikodijević D., 1996, "Generalized similar solutions in the theory of unsteady MHD boundary layer", *International Symposium - Contemrorary Problems of Fluid Mechanics*, Yugoslav Society of Mechanics, University of Belgrade, Belgrade, Proceedings II pp.169-172.

[10] Saljnikov V., Boričić Z., Nikodijević D., 2000, "General similarity method for unsteady mhd free convection problems on the vertical wall", *Facta univesitatis- Series Mechanics, Automatic Control and Robotics,* Vol 2. No10, pp.1233-1241.

Conference on Modelling Fluid Flow (CMFF'06)
The 13th International Conference on Fluid Flow Technologies
Budapest, Hungary, September 6-9, 2006

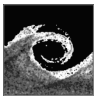

SCRUTINIZING HYBRID LES/RANS APPROACHES IN SEPARATING FLOWS WITH HEAT TRANSFER

Björn KNIESNER[1], Suad JAKIRLIĆ[1,2], Kemal HANJALIĆ[3]

[1] Chair of Fluid Mechanics and Aerodynamics, Department of Mechanical Engineering, Darmstadt University of Technology, Petersenstr. 30, D-64287 Darmstadt, Germany. E-mail: b.kniesner@sla.tu-darmstadt.de
[2] Corresponding Author: Tel.: +49 6151 163554, Fax: +43 6151 164754, E-mail: s.jakirlic@sla.tu-darmstadt.de
[3]Thermal and Fluid Sciences Section, Department of Multi-Scale Physics, Delft University of Technology, Lorentzweg 1, CJ Delft, The Netherlands. E-mail: hanjalic@ws.tn.tudelft.nl

ABSTRACT

We report some results of testing of the coupling of a low-Reynolds-number k-ε RANS (Reynolds-Averaged Navier-Stokes) model with large-eddy simulations (LES) in a two-layer Hybrid (HLR) scheme. The RANS model covers the near-wall region and the LES model the remainder of the flow domain. Two different subgrid-scale (SGS) models in LES were considered, the Smagorinsky and the one-equation model (for the residual kinetic energy, Yoshizawa and Horiuti, 1985), combined with two versions of the RANS ε equation, one using the "isotropic" $\tilde{\varepsilon}$ (Chien, 1982) and the other the "homogeneous" ε^h (Jakirlic and Hanjalic, 2002). Both fixed and self-adjusting interface locations were considered. The exchange of the variables across the interface was adjusted by smoothing the turbulence viscosity either by adjusting the RANS model parameters, such as C_μ; Temmerman et al. (2005), or by applying an additional forcing at the interface using a method of digital-filter-based generation of inflow data for spatially developing DNS and LES due to Klein et al., 2003). The method was tested against the available DNS, fine- and coarse grid LES and experiments in turbulent flow and heat transfer over a backward-facing step at a low (Yoshioka et al., 2001) and a high Re number (Vogel and Eaton, 1985), periodic flow over a series of 2-D hills (Fröhlich et al., 2005), and in a fully-developed channel flow at a moderate Re number $Re_m \approx 24000$ (Abe et al., 2004).

Keywords: Hybrid LES/RANS, flow and heat transfer with separation.

1. INTRODUCTION

A large majority of technical flows, especially those including separation, involve large-scale unsteadiness (e..g. flow around vehicles and other bluff bodies, combustors, turbomachinery). The flow in the shear layer that separates the main stream from the recirculation is dominated by the organized, large-scale coherent structures, influencing to a large extent the overall flow behaviour. Its correct capturing is beyond the reach of the conventional time-averaged RANS methods, which are most widely used in engineering practice. These methods capture well the general character of the flow but due to the statistical nature of the method, unsteady effects are only captured partially or not at all. The LES method, by which the large eddies are resolved directly and the contribution of the small ones is modelled, is regarded as the most suitable tool for capturing the repeatable, but also the non-regular unsteadiness in an oscillatory separation region. However, a well-resolved LES requires high spatial and temporal resolution of the flow field, and thus adequately large computer resources. As computer power increases exponentially, the LES method becomes increasingly the tool of the choice for numerical flow simulations. However, the price one has to pay compared to conventional RANS methods remains still high especially when considering wall-bounded flows at high Re numbers because of formidable resolution requirements imposed by the need of resolving well the near wall region. Here, the hybrid LES/RANS method comes into play. Its aim is to combine the advantages of both methods in order to provide a numerical procedure that is able to capture the large-scale eddy structure and the bulk flow unsteadiness, but at affordable costs. Following this basic idea, a number of proposals for combining a RANS and LES approach have been reported[1], e.g., Hanjalic et al. (2003), Hamba

[1]The present work deals with a zonal hybrid LES/RANS scheme. An example of a non-zonal (seamless) scheme is certainly the DES (Detached Eddy Simulation) method, Spalart et al. (1997).

(2003), Piomelli et al. (2003), Temmerman et al. (2005) and Davidson and Dahlström (2005). The main problem reported in just about all publications is the buffer layer between LES and RANS. The lack of proper resolution of the near-wall streaky structure, which cannot be fully compensated by modelling, leads to unphysical effects. The modelled turbulence, provided by the RANS and LES SGS on the two sides of the interface differ significantly, whereas the resolved contribution should be the same or close to each other. This leads to an unphysical bump at the mean velocity and mean temperature profiles. This is especially visible in computations of wall-attached flows where there is no dominating forcing. Several earlier investigations have shown that one can diminish or even eliminate this bump by adding some additional correlated or even uncorrelated forcing in form of variable fluctuations in the interface region e.g., by appropriate adjusting and using the instantaneous, instead of locally averaged coefficient C_μ in RANS models, a stochastic backscatter, a priori obtained set of DNS fluctuations, etc.

The work here reported aims at developing a hybrid LES/RANS model for turbulent flows and heat transfer by accounting for the near-wall effects with a RANS model and capturing the large-scale structures and bulk unsteadiness in the rest of the flow using a coarse LES. The goal is to achieve the accuracy comparable to that of a conventional LES, but at much lower computational costs.

2. COMPUTATIONAL METHOD

The three-dimensional, incompressible unsteady equations governing the velocity and temperature fields read:

$$\frac{\partial \overline{U}_i}{\partial t}+\frac{\partial\left(\overline{U}_i \overline{U}_j\right)}{\partial x_j}=-\frac{1}{\rho}\frac{\partial \overline{p}^*}{\partial x_i}+\frac{\partial}{\partial x_j}\left[(\nu+\nu_m)\left(\frac{\partial \overline{U}_i}{\partial x_j}\right)+\nu_m\frac{\partial \overline{U}_j}{\partial x_i}\right] \quad (1)$$

$$\frac{\partial \overline{T}}{\partial t}+\frac{\partial\left(\overline{U}_j \overline{T}\right)}{\partial x_j}=\frac{\dot{q}}{c_p}+\frac{\partial}{\partial x_j}\left[\left(\frac{\nu}{\mathrm{Pr}}+\frac{\nu_m}{\mathrm{Pr}_t}\right)\frac{\partial \overline{T}}{\partial x_j}\right] \quad (2)$$

The eddy-viscosity ν_m originates from the model formulation either for the subgrid-stress tensor τ_{ij} or for the Reynolds-stress tensor $\overline{u_i u_j}$. The latter tensors are expressed in terms of the mean strain tensor $\overline{S}_{ij}$ via the Boussinesq relationship (see next subsection). These equations operate as the Reynolds-averaged Navier-Stokes equations in the near-wall layer ($\overline{U}_i$ represents the ensemble-averaged velocity field) or as the filtered Navier-Stokes equations in the outer layer ($\overline{U}_i$ represents the spatially filtered velocity field)[2].

[2] Note that the overbar for averaging is not explicitely used everywhere throughout the paper.

The mathematical model of turbulence will be outlined in the following subsection. In order to illustrate some important issues with respect to coupling the LES and RANS regions the results of the channel flow simulations are interactively shown. More details about the channel flow configuration considered and the simulations performed are given in subsection 3.1.

2.1. Model Description

Two different low-Reynolds number k-ε models are applied in the near-wall RANS region. The first model is that of Chien (1982) employing the "isotropic" $\tilde{\varepsilon}$ ($\tilde{\varepsilon}=\varepsilon-2\nu(\partial k^{1/2}/\partial x_n)^2$) of the total viscous dissipation rate ε as the scale-providing variable. The second one is based on the homogeneous-dissipation concept (Jakirlic and Hanjalic, 2002), which solves the equation for the "homogeneous" ε^h ($\varepsilon^h=\varepsilon-0.5\,\partial(\nu\,\partial k/\partial x_j)/\partial x_j$) while the inhomogeneous part follows exactly by adding one half of the molecular diffusion of the turbulent kinetic energy D_k^ν. The latter concept offers certain advantages with respect to the asymptotic behaviour of turbulence quantities when approaching a solid wall. The model equations, with ε representing either $\tilde{\varepsilon}$ or ε^h[3], read

$$\frac{\partial k}{\partial t}+U_j\frac{\partial k}{\partial x_j}=\frac{\partial}{\partial x_j}\left[\left(\nu+\frac{\nu_t}{\sigma_k}\right)\frac{\partial k}{\partial x_j}\right]+P_k-\varepsilon \quad (3)$$

$$\frac{\partial \varepsilon}{\partial t}+U_j\frac{\partial \varepsilon}{\partial x_j}=\frac{\partial}{\partial x_j}\left[\left(\nu+\frac{\nu_t}{\sigma_\varepsilon}\right)\frac{\partial \varepsilon}{\partial x_j}\right]+C_{\varepsilon 1}P_k\frac{\varepsilon}{k}-f_2C_{\varepsilon 2}\frac{\varepsilon^2}{k}-P_{\varepsilon,3} \quad (4)$$

Within the LES region, the well-known Smagorinsky subgrid-scale model (both in the conventional and dynamic version) and the one-equation model of Yoshizawa and Horiuti (1985) for the kinetic energy of the subgrid-scales were used:

$$\frac{\partial k_{SGS}}{\partial t}+U_j\frac{\partial k_{SGS}}{\partial x_j}=\frac{\partial}{\partial x_j}\left[(\nu+\nu_{SGS})\frac{\partial k_{SGS}}{\partial x_j}\right]+P_{k_{SGS}}-\varepsilon_{SGS} \quad (5)$$

Independently of the models used, a major issue in a zonal hybrid LES/RANS strategy is the coupling of the instantaneous LES field and the ensemble-averaged RANS field at the interface. In the present method the coupling is realised via the turbulent viscosity, which makes it possible to obtain

[3] The equations for ε^h and ε are related by $D\varepsilon^h/Dt=D\varepsilon/Dt-0.5\,\partial(\nu\,\partial\varepsilon/\partial x_j)/\partial x_j$. Both equations contain near-wall and viscous damping functions f_2, f_μ and the production term $P_{\varepsilon,3}$ (Eqs. 4 and 6), which are modelled in line with the proposal of Launder and Sharma (LSH, 1974).

solutions using one system of equations. This means practically that Eqs. (1) and (2) are solved in the entire solution domain irrespective of the flow sub-region (LES or RANS). Depending on the flow zone, the hybrid model implies the determination of the turbulent viscosity ν_m either from the RANS:

$$\nu_m = \nu_t = C_\mu f_\mu \frac{k^2}{\varepsilon} \tag{6}$$

or from the LES formulation:

$$\begin{aligned} \nu_m &= \nu_{SGS} = (C_S \Delta)^2 \left|\overline{S}\right|, \quad Smagorinsky \\ \nu_m &= \nu_{SGS} = C_k \Delta k_{SGS}^{1/2}, \quad Yoshizawa \end{aligned} \tag{7}$$

The Smagorinsky constant C_S takes the value of 0.1; $C_k = 0.07$. $\Delta = (\Delta x \times \Delta y \times \Delta z)^{1/3}$ represents the filter width and $\left|\overline{S}\right| = \left(\overline{S}_{ij}\overline{S}_{ij}\right)^{1/2}$ the strain rate modulus.

Because ε (and also k in the case of the Smagorinsky model) is not provided within the LES sub-domain, it is either possible to solve the model equation for ε (and k) in the whole solution domain (without using their values in the LES sub-region) or to estimate their SGS values at the interface (to be used as the boundary conditions for the RANS sub-domain) using the proposal of Mason and Callen (1986) (see also Sagaut, 2005):

$$\begin{aligned} k_{SGS} &= \frac{(C_S \Delta)^2 \left|\overline{S}\right|^2}{0.3} \\ \varepsilon_{SGS} &= (C_S \Delta)^2 \left|\overline{S}\right|^3 \quad \text{or} \quad \varepsilon_{SGS} = C_\varepsilon \frac{k_{SGS}^{3/2}}{\Delta} \end{aligned} \tag{8}$$

Both procedures have been investigated. The latter was finally adopted in the present work, but using the total (resolved + sgs) k and ε as the boundary (interface) condition leads to their too high values in the RANS sub-domain in the region of interface. Because the unsteady RANS field excited by the unsteadiness in the LES sub-domain leads to a too high turbulence level, the approach based on providing the boundary conditions for the RANS sub-domain using equations (8) has several major advantages. First, the discretization coefficients corresponding to the grid cells in the LES domain do not have to be computed. This significantly reduces the computational time. Furthermore, the memory already allocated for k and ε arising from the RANS model equations can be used to store the subgrid-scale kinetic energy and dissipation, which is anyhow of interest in the framework of the hybrid LES/RANS computations, where LES is performed on a relatively coarse grid. Finally a smooth transition of the turbulent viscosity is ensured in accordance to the Eqs. (6), (7) and (8) (f_μ is generally very close to unity at the interface location).

In order to additionally smoothen the turbulent viscosity profile, a condition originating from the equality of the (modelled) turbulence viscosities on both sides of the interface (*ifce*)

$$\nu_{t,ifce}\,|_{RANS-side} = \nu_{SGS,ifce}\,|_{LES-side} \tag{9}$$

can be applied, Temmerman et al. (2005). Eq. (9) is the condition, which the structure parameter C_μ in the RANS formulation for ν_t (Eq. 6) has to satisfy at the interface. From (6) and (7) we obtain:

$$C_{\mu,ifce} = \frac{\nu_{SGS,ifce}\,\varepsilon_{ifce}}{f_{\mu,ifce}\,k_{ifce}^2} \tag{10}$$

By applying an appropriate form of blending function ($C_\mu = 0.09 + (C_{\mu,ifce} - 0.09)\, y^+ / y^+_{ifce}$) the standard C_μ value of *0.09* will continuously reduce to the interface value. Such a procedure leads to an appropriate damping of turbulence in this region causing finally the reduction of the specific bump at the mean velocity (Fig. 1) and temperature profile in the region around interface (not shown here). On the other hand, such a blending leads to a certain discrepancy of the profiles in the region corresponding to the inner part of the log-law region and consequently in the buffer layer. ν_t exhibits too low level in this region departing substantially from the DNS and k-ε model results, Fig. 1. A lower level of modelled turbulence would allow higher turbulence level in the resolved motion. However, using coarser grids as aimed in a hybrid LES/RANS approach, it cannot provide a sufficient turbulence level. This motivated the proposition of another treatment at the interface in the present work.

From the physical point of view the velocity mismatch is caused by the fact that due to the relatively high turbulent viscosity in the RANS region, the fluctuations are strongly damped and do not recover until some distance behind the interface. Within this so-called buffer region, the flow is neither RANS nor LES, and the corresponding ν_t is not exactly adjusted to the flow. The idea of the forcing method, which was introduced by Piomelli et al. (2003) and followed by Davidson and Dahlström (2005), is to generate fluctuations at or around the interface in order to accelerate their recovery. Hereby, the important issues are the type and intensity of these fluctuations. Preliminary computations showed that only stochastic fluctuations are not sufficient. A method originating from a digital-filter-based generation of inflow data for spatially developing DNS and LES due to Klein et al. (2003) was adopted in the present work. Its use increases the computational costs to some

extent. However, it should be emphasized that the fluctuations are computed only at the interface. The steps to be performed are summarized as follows:

1. creation of random fluctuations,
2. filtering of fluctuations in space and time,
3. adjustment to local Reynolds stresses and
4. introduction into momentum equations through a source term

The strength of the forcing depends on the interface position. The closer the interface is to the wall, the less forcing is needed. Two important observations emerged. First, it seems sufficient to introduce forcing only into the equations governing the velocity field, which also reduces the bump in the mean temperature profile. Second, the forcing is needed only in the direction normal to the interface.

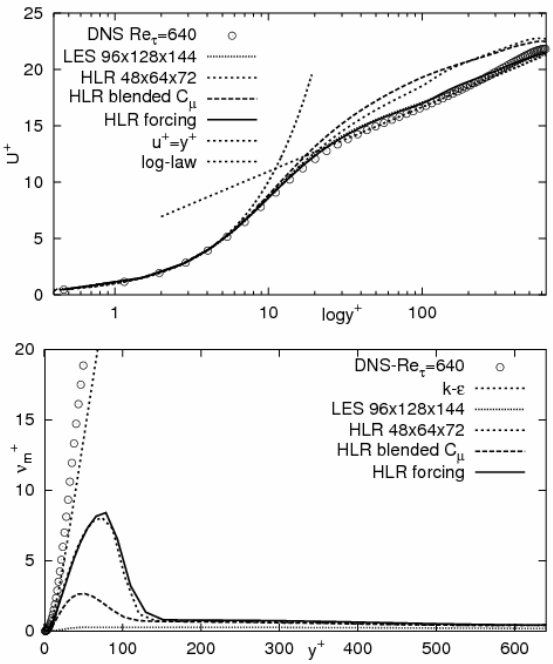

Figure 1 Effects of different variable exchange techniques at the LES/RANS interface on mean velocity and turbulent viscosity in a channel flow (no C_μ adjustment or forcing)

One of the advantages of a zonal approach is the possibility to predefine the LES-RANS interface. However, in unknown flow configurations, this could be a difficult issue. Therefore, a certain criteria expressed in terms of a control parameter should be introduced. Presently, a following control parameter

$$k^* = \left\langle \frac{k_{\mathrm{mod}}}{k_{\mathrm{mod}} + k_{res}} \right\rangle \qquad (11)$$

is adopted, representing the ratio of the modelled (SGS) to the total turbulent kinetic energy in the LES region, averaged over all grid cells in homogeneous direction at the interface on the LES side. As soon as this value exceeds about 20 %, the interface is moved farther from the wall and in opposite direction when the values go below 20%. This additionally ensures that in the limit of a very fine grid (very low level of the residual turbulence) LES is performed in the most of the solution domain. Contrary, in the case of a coarse grid, RANS prevails. As the interface separates the near wall region from the reminder of the flow, it would be suitable to choose a wall-defined parameter for denoting the interface location. In the present study, the dimensionless wall distance y^+ was adopted. Despite possible difficulties in respect to the definition of y^+ in the flow domains where the wall shear stress approaches zero, as e.g. in separation and reattachment regions, no problems in the course of the computations have arisen[4]. It is noted, that the interface y^+ is not active in the computational procedure. It only denotes the computational nodes, at which the prescribed value of k^* was obtained. Fig. 2 top displays the time evolution of the interface position in the high-Re number backstep flow, averaged over all cells at the interface. Fig. 2 bottom shows the snapshot of the instantaneous velocity field with the corresponding evolution of the averaged interface value $y^+_{ifce} = 230$ along the upper wall and the lower (step) wall.

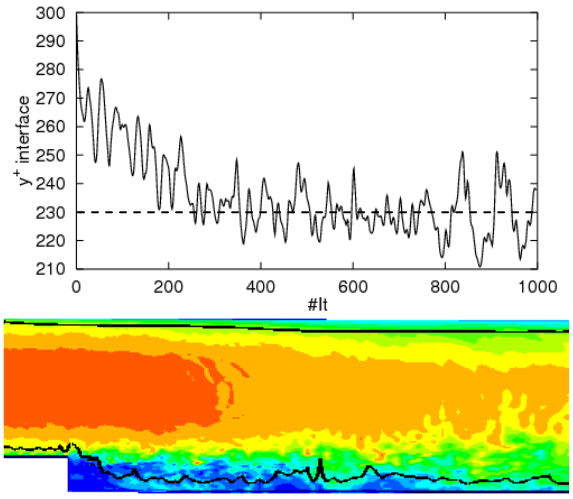

Figure 2: Time evolution of the averaged y^+_{ifce} in a high-Re number back step flow (upper) and instantaneous velocity field and the corresponding evolution of the interface value $y^+_{ifce} = 230$ along the upper and bottom walls.

The use of another control parameter in terms of the (wall-distance free) Reynolds number of turbulence ($\mathrm{Re_t}$) is currently under investigation. As the interface does not necessarily have to be a grid line, nor to be at a fixed position during the computation,

[4] The same non-dimensional wall distance y^+ is regularly used in the Van Driest's wall-damping of ν_t also in separating and reattaching flows.

the boundary (interface) values for the model RANS equations governing k and ε have to be provided in the entire flow domain. This is also realized by using the estimation given by Eq. (8).

The turbulent heat flux $\overline{u_i\theta}$ in the equation governing the temperature field were modelled by using the simple gradient diffusion hypothesis.

$$\rho c_p \overline{u_i\theta} = -\rho c_p a_t \frac{\partial \bar{\theta}}{\partial x_i} = -\lambda_t \frac{\partial \bar{\theta}}{\partial x_i}, \quad \lambda_t = \frac{\mu_t c_p}{\mathrm{Pr}_t} \qquad (12)$$

where λ_t is the turbulent heat conductivity. Pr_t is the turbulent Prandtl number: $Pr_t = \nu_t/a$, here assumed to be unity.

2.2. Numerical Method

All computations were performed with an in-house computer code FASTEST based on a finite volume numerical method for solving both three-dimensional filtered and Reynolds-averaged Navier–Stokes equations on block structured, body fitted, non-orthogonal meshes. Block interfaces are treated in a conservative manner, consistent with the treatment of inner cell faces. A cell centered, collocated variable arrangement and Cartesian vector and tensor components are used. The well-known SIMPLE algorithm was applied for coupling the velocity and pressure fields. The convective terms in all equations were discretized by a second-order central differencing scheme, whose stability was enhanced through the so-called deferred correction approach (see e.g., Khosla and Rubin, 1974). The time discretization was accomplished by applying the second order (implicit) Crank–Nicolson method.

3. RESULTS AND DISCUSSION

As the main target was to model flows involving separation, the highly-resolved LES of the periodic flow over a smoothly-contoured 2-D hill by Fröhlich et al., 2005, and experiments of turbulent flow over a backward-facing step at a low (Re_H=*3700*, Exp.: Yoshioka et al., 2001) and a high Reynolds-number (Re_H=*28000*, Exp.: Vogel and Eaton, 1985) were chosen as the reference. The latter case includes also heat transfer due to the imposed heat flux at the step wall. The flow and heat transfer in a fully-developed channel flow at a moderate Re number $Re_m \approx$ *24000* (Abe et al., 2004) were also considered. The LES (Smagorinsky SGS model with van Driest damping) of all afore-mentioned flows were also performed for comparison. In addition, the results obtained were compared with the reference LES, performed in the present study or available in the literature.

3.1. Fully developed channel flow

The reference DNS of a channel flow used in the present work is that of Abe et al., 2004, at Re number based on friction velocity about $Re_\tau \approx$*640*. The dimensions of the computational domain were $(L_x, L_y, L_z) = (2\pi h, 2h, \pi h)$. Periodic boundary conditions were used in both homogeneous directions, x and z. The computations with the hybrid model have been performed on several grids. Results shown in Figs. 1 and 3 were obtained at the grid $(N_x, N_y, N_z) = (48,64,72)$ leading to $\Delta x^+ = 100$, $\Delta y^+ = 0.5 - 40$ and $\Delta z^+ = 24$. It is coarsened by the factor of eight compared to the fine LES ($96x128x144$); $(\Delta x^+, \Delta y^+, \Delta z^+) = (50, 0.2 - 24, 12)$. Fig. 3 depicts also the results obtained by the pure LES using the same (coarse) grid as HLR. The HLR results shown in Figs. 1, 3-4 are all obtained by using the Chien model in the RANS layer and the Smagorinsky model in the LES region. Other model combinations resulted in similar results (not shown here). Fig. 3 displays the mean temperature and the scalar flux profiles obtained using the forcing at the interface.

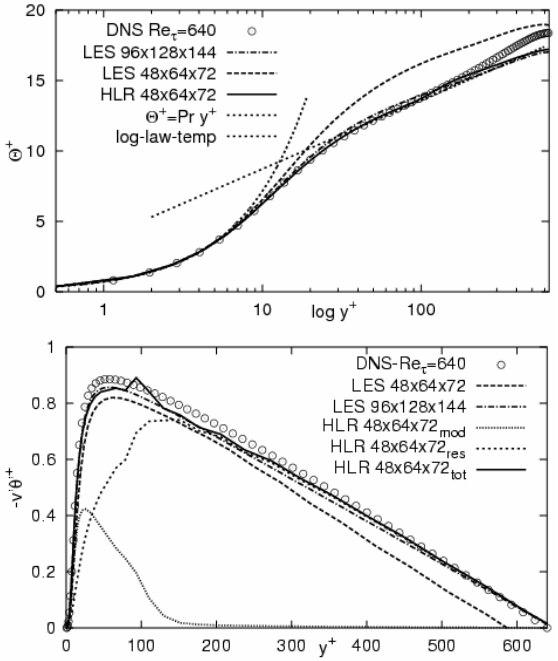

Figure 3: Mean temperature and scalar flux profiles obtained by LES and HLR

It is clearly visible that the HLR method with forcing performs better than the corresponding coarse LES. The results obtained are even very close to the fine LES. The computational costs of HLR exceeds that of the coarse LES by about 30% due to the solving of additional equations for k and ε. Fig. 3 lower shows the profile of the total $\overline{v\theta}$ (tot), which is obtained by summing up the resolved (res) and modelled (mod) parts. The modelled part is determined by the model used and the resolved part resulted from the averaging of the instantaneous velocity and temperature fields over a certain time period. Due to unsteady treatment of the RANS layer and the RANS field excitation by

the adjacent instantaneous LES field through the interface, one can observe a resolved part also in this region. The modelled part clearly diminishes when crossing the interface at about $y^+=100$. One can note a certain kink at the $\overline{v\theta}$, which originates by largest extent from the resolved part. However, this fact does not influence the computational procedure.

3.2. Backward-facing step flows

The boundary layer at the step-wall separates at the step edge (fixed separation point) and reattaches at the bottom wall building the recirculation zone immediately behind the step. Two configurations were considered. Here, only the results of the high Reynolds number backward-facing step flow ($Re_H=28000$; Exp., Vogel and Eaton, 1985) will be shown. Heat transfer realised by imposing a constant heat flux at the lower wall (SOQ) is also accounted for, Fig. 4. The computational domain was discretized by 112x100x64 grid points (without inlet channel), which is about three times coarser than the gird used in LES of Akselvoll and Moin (1995).

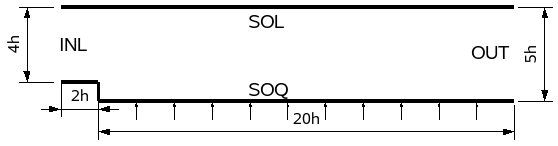

Figure 4: Computational domain adopted for the high-Reynolds number flow simulations

The instantaneous inflow corresponding to a boundary layer developing at the step wall was generated by using the method proposed by Klein et al., 2003 (the same procedure was adopted for the forcing technique, section 2.1). The mean flow quantities necessary for the inflow generation were provided from the separate boundary-layer computations performed by using a near-wall second-moment closure model. Both near-wall RANS models coupled with standard Smagorinsky model, applied using the forcing technique at the interface, led to similar results, Figs. 5 and 6. Admittedly, the application of other coupling methods described in section 2.1 resulted in almost identical flow field (not shown here). Additional large-eddy simulation was performed using the same grid. The variable interface method (Eq. 11) was applied (see Fig. 1 and appropriate discussion for more details).

The results of the reattachment length obtained by several computational methods and experiment are summarized in Table 1. The HLR results are very close to the experimental finding and to the results obtained by dynamic Smagorinsky model (Akselvoll and Moin, 1995). Remarkable are the deviations of the LES results obtained on the same, relatively coarse grid and especially of the Chien k–ε model results. It is interesting to note, that just these two models are constitutive parts of the present HLR method.

Fig. 6 displays the evolution of the friction coefficient along the lower wall. Both HLR models show results which closely follow the experimental ones. Somewhat overpredicted C_f in the recovery region obtained by HLR (LSH/SM) pointed out the necessity to adjust the model coefficient with respect to the employment of a new scale-determining variable – homogeneous dissipation rate. This activity is in progress.

Table 1. Comparison of reattachment lengths of different models

	reattachment length (h=step height)	Grid points [10^6]
Experiment	**6.7 h**	-
LES (Dyn., Akselvoll)	**6.74 h**	**2.25**
LES coarse (Smag.)	**6.3 h**	**0.76**
Hybrid LES/RANS	**6.78 h**	**0.76**
low-Re k-ε (Chien)	**5.87 h**	**0.012**

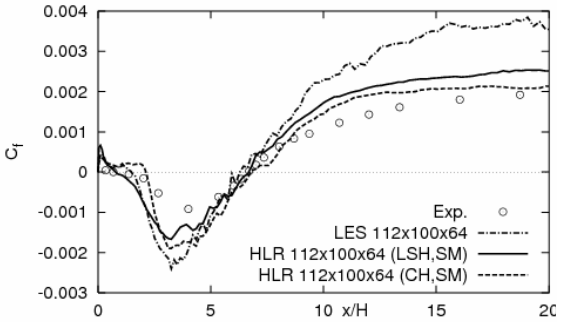

Figure 5: Friction coefficient $C_f=2\tau_w/(\rho U_c^2)$ along the lower wall

Fig. 6 shows the evolution of the mean axial and mean temperature profiles as well as the streamwise turbulence intensity profiles at selected location. Some differences in the computed temperature field are noticeable only immediately behind the step (locations x/H=0.33 and 1.67). Also, the HLR (CH/SM) model returned somewhat higher back-flow intensity. Other results exhibit very good mutual agreement as well as agreement with available experimental data.

3.3. Periodic flow over a 2-D hill

Unlike the flow over a backward-facing step, the periodic flow over a smoothly contoured hill mounted on the bottom wall in a plane channel (Fig. 7) is characterized by a separation from a curved, smooth surface. The highly-resolved LES performed at a grid comprising about 4.6 Mio. cells (Fröhlich et al., 2005) was taken as reference. This case has been intensively used as a benchmark for RANS models validation, e.g. Jakirlic et al. (2002). Three different HLR model schemes, combining the Yoshizawa's one-equation SGS model and the Smagorinsky's SGS model with two different near-wall, k-ε models (see Section 2.1 for details) and

using the forcing technique at the interface, were applied. The computational grid (Fig. 7) comprises only 250.000 (80*x*100*x*32) computational cells, which is about eighteen times coarser than the grid used for the reference LES.

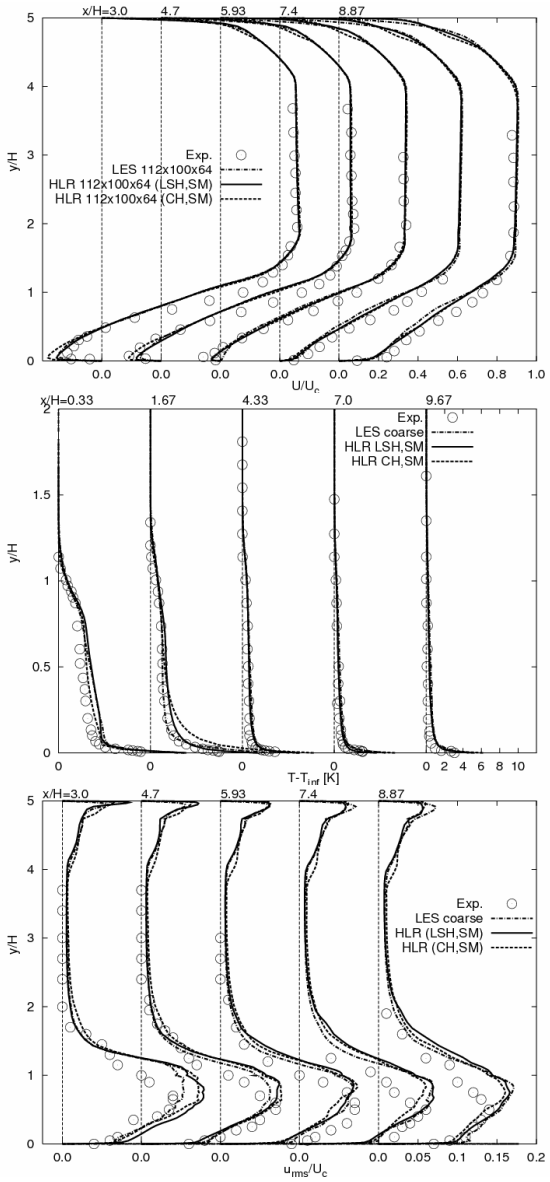

Figure 6: Mean axial velocity, temperature and streamwise turbulence intensity profiles at selected locations in the high-Reynolds number backward-facing step flow

Table 2 summarizes the reattachment lengths obtained. It is encouraging to see, that the HLR results, especially the scheme employing the RANS model based on the homogeneous dissipation concept, agree well with the reference data. As expected, the pure RANS computation using this model resulted in a too short reattachment length. Unlike in the flow separating at a sharp edge, the reattachment length depends here strongly on the separation position.

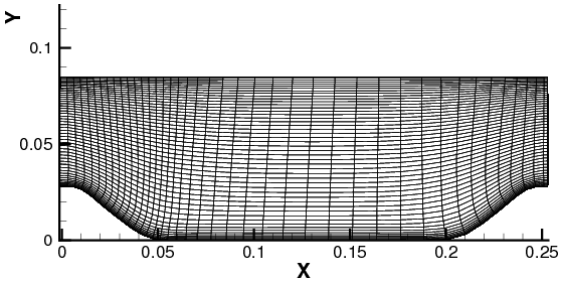

Figure 7: Computational grid of the periodic flow over a 2-D hill (only every second grid line shown)

Table 2. Separation and reattachment locations obtained with different models (h=hill height)

	Separation point	Reattach-ment point	Grid points [Mio.]
LES (Fröhlich et al.)	**0,22 h**	**4,72 h**	**4.6**
LES coarse	**0,19 h**	**4,90 h**	**0.25**
HLR Smag./Chien	**0.16 h**	**4.85 h**	**0.25**
HLR Yosh./Chien.	**0.18 h**	**4.29 h**	**0.25**
HLR Smag./Hom.	**0.24 h**	**4.62 h**	**0.25**
RANS Hom.	**0.47 h**	**3.23 h**	**0.024**

Closest agreement with the reference LES with respect to the wall shear stress evolution displayed in Fig. 8, especially within the recirculation zone itself exhibiting certain back-flow acceleration and deceleration, was obtained with the HLR scheme including the Yoshizawa's one-equation SGS model. Two HLR model schemes detected also a small separation bubble at *x/H=7*, denoted by negative τ_w values.

The evolution of the mean axial velocity and turbulent kinetic energy profiles (Fig. 9) follows closely the reference LES results. Only the combination Yoshizawa-SGS/Chien-RANS returns a somewhat premature reattachment associated with enhanced turbulence level in the separated shear layer bordering the recirculation zone.

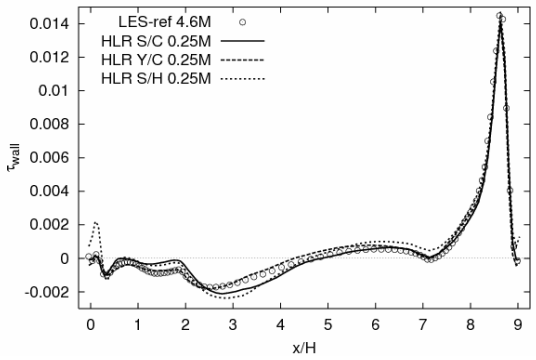

Figure 8: Wall shear stress evolution at the lower wall in a flow over a symmetric, 2-D hill

5. CONCLUSIONS

Potential of a newly proposed hybrid LES/RANS model scheme employing low-Reynolds number, eddy-viscosity-based RANS models in the near-wall layer and the Smagorinsky and Yoshizawa/Horiuti SGS models in the core

flow was demonstrated by computing several flow configurations featured by separation and heat transfer. A variable interface between RANS and LES regions was applied, whose position was controlled by a parameter corresponding to an in-advance prescribed fraction of kinetic energy of turbulence. Forcing technique implying the superposition of the fluctuations at the interface in order to adjust the SGS turbulence to the RANS turbulence was introduced into the equations governing the velocity field. This procedure reduces to a large extent the velocity mismatch typically encountered in the region of interface. The results obtained with respect to the reattachment length, wall shear stress evolution, mean flow and turbulence fields follow closely the reference (fine) LES results and are superior to the LES data obtained on the same grid, substantially coarser than that of the fine LES.

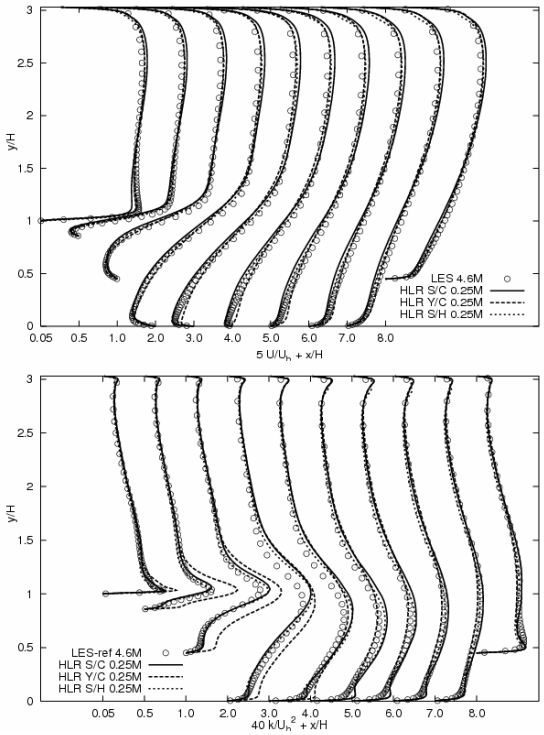

Figure 9: Mean axial velocity and turbulent kinetic energy profiles obtained using three different HLR models

ACKNOWLEDGEMENTS

The financial support of the Deutsche Forschungsgemeinschaft (DFG) through the grant SFB568, TPC3 for B. Kniesner and the award of guest professorship from the German scientific exchange service (DAAD) for K. Hanjalic are gratefully acknowledged.

REFERENCES

[1] Abe, H., Kawamura, H., and Matsuo, Y. (2004): Surface heat-flux fluctuations in a turbulent channel flow up to Re_τ=1020 with *Pr=0.025* and *0.71*. *Int. J. Heat and Fluid Flow*, Vol. 25, pp. 404-419

[2] Akselvoll, and Moin, P. (1995): Large eddy simulation of turbulent confined coannular jets and turbulent flow over a backward-facing step. Technical Report TF-63, Dept. of Mechanical Engineering, Stanford University

[3] Chien, K.-Y. (1982): Predictions of Channel and Boundary-Layer Flows with a Low-Reynolds-Number Turbulence Model. *AIAA Journal*, Vol. 20(1), pp. 33-38

[4] Davidson, L. and Dahlström, S. (2005): Hybrid LES/RANS: computation of the flow around a three-dimensional hill. *6th Int. Symp. on Eng. Turbulence Modelling and Measurements*, Sardinia, Italy, Mai 23-25

[5] Fröhlich, J., Mellen, C.P., Rodi, W., Temmerman, L., and Leschziner, M.A. (2005): Highly resolved large-eddy simulation of separated flow in a channel with streamwise periodic constrictions. *J. Fluid Mech.*, Vol. 526, pp. 19-66

[6] Hamba, F. (2003): A hybrid RANS/LES simulation of turbulent channel flow. *Theoret. Comp. Fluid Dynamics*, Vol. 16, pp. 387-403

[7] Hanjalic, K., Hadziabdic, M., Temmerman, L., and Leschziner, M. (2003): Merging LES and RANS Strategies: Zonal or Seamless Coupling? *5th Workshop on Direct and Large-Eddy Simulations – DLES5*, Munich

[8] Jakirlic, S., Jester-Zürker, R., and Tropea, C. (2002): Report on 9th ERCOFTAC/IAHR/ COST Workshop on Refined Turbulence Modelling. October, 9-10, 2001, Darmstadt University of Technology, *ERCOFTAC Bulletin*, No. 55, pp. 36-43

[9] Jakirlic, S., and Hanjalic, K. (2002): A new approach to modelling near-wall turbulence energy and stress dissipation. *J. Fluid Mech.*, Vol. 539, pp. 139-166

[10] Khosla, P.K., and Rubin, S.G. (1974): A diagonally dominant second-order accurate implicit scheme. *Computers and Fluids*, Vol. 2, pp. 207-209

[11] Klein, M., Sadiki, A., and Janicka, J. (2003): A digital filter based generation of inflow data for spatially developing direct numerical or large-eddy simulations. *J. Comp. Physics*, Vol. 186, pp. 652-665

[12] Launder, B.E., and Sharma, B.I. (1974): Application of the Energy-Dissipation Model of Turbulence to the Calculation of Flow Near a Spinning Disc. *Letters in Heat and Mass Transfer*, Vol. 1, pp. 131-138

[13] Mason, P.J., and Callen, N.S. (1986): On the magnitude of the subgrid-scale eddy coefficient in large-eddy simulation of turbulent channel flow. *J. Fluid Mech.*, Vol. 162, pp. 439-462

[14] Piomelli, U., Balaras, E., Pasinato, H, Squires, K.D., and Spalart, P.R. (2003): The inner-outer layer interface in large-eddy simulations with wall-layer models. *Int. J. Heat and Fluid Flow*, Vol. 24, No. 4, pp. 538-550

[15] Sagaut, P. (2005): LES for Incompressible Flows, Springer

[16] Spalart, P.R., Jou, W.-H., Strelets, M., and Allmaras, S. (1997): Comments on the feasibility of LES for wings and on hybrid RANS/LES approach. *1st AFOSR Int. Conf. on DNS and LES*

[17] Temmerman, L., Hadziabdic, M., Leschziner, M.A., and Hanjalic, K. (2005): A hybrid two-layer URANS-LES approach for large eddy simulation at high Reynolds numbers. *Int. J. Heat and Fluid Flow*, Vol. 26, p. 173-190

[18] Vogel, J.C., and Eaton, J.K. (1985): Combined heat transfer and fluid dynamics measurements downstream of a backward-facing step. *ASME Journal of Heat Transfer*, Vol. 107, pp. 922-929

[19] Yoshioka, S., Obi, S., and Masuda, S. (2001): Turbulence statistics of periodically perturbed separated flow over backward-facing step. *Int. J. Heat and Fluid Flow*, Vol. 22, pp. 393-401

[20] Yoshizawa, A., and Horiuti, K. (1985): A statistically-derived subgridscale kinetic energy model for the large-eddy simulation of turbulent flows. *J. Phys. Soc. Jpn.*, Vol. 54, pp. 2834-2839

Conference on Modelling Fluid Flow (CMFF'06)
The 13th International Conference on Fluid Flow Technologies
Budapest, Hungary, September 6-9, 2006

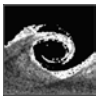

INLET CONDITION FOR LARGE-EDDY SIMULATION APPLIED TO A COMBUSTION CHAMBER

Balázs PRITZ[1], Franco MAGAGNATO[2], Martin GABI[3]

[1] Corresponding Author. Department of Fluid Machinery, University of Karlsruhe. Kaiserstr. 12, D-76131 Karlsruhe, Germany. Tel.: +49 721 608 3624, Fax: +49 721 608 3529, E-mail: balazs.pritz@ism.uka.de
[2] Department of Fluid Machinery, University of Karlsruhe. E-mail: franco.magagnato@ism.uka.de
[3] Department of Fluid Machinery, University of Karlsruhe. E-mail: martin.gabi@ism.uka.de

ABSTRACT

The formation of combustion-driven instabilities in modern low-NOx combustors is still a problem. In order to investigate the resonant characteristics of a combustor, numerical investigations by means of compressible large eddy simulation (LES) are carried out. The investigations of the foregoing work were focused on the combustion chamber. The results gave a good prediction of the resonant characteristics [1].

The purpose of the present investigation is to determine the resonant characteristics of the coupled system consisting of a burner and a chamber. Since the inflow turbulence can influence the resonant characteristics, an appropriate inflow condition has to be applied. In order to prescribe the turbulent flow at the inlet for the LES, a precursor simulation type boundary condition is chosen. The present paper describes the first implementation of the method for compressible subsonic flows. As a test case the turbulent channel flow of Reynolds number Re_τ=395 is simulated. The results show good agreement with data from direct numerical simulation (DNS). The ongoing work is to extend this inlet condition to produce pulsating mass flow rate as required for the investigation of the burning system.

Keywords: compressible large eddy simulation, inlet condition, oscillating flow, combustion instabilities

NOMENCLATURE

C_S	[-]	Smagorinsky model coefficient
L_y	[m]	span of the channel
Ma	[-]	Mach number
Q	[kg/s]	mass flow rate
Re_τ	[-]	Reynolds number based on h and u_τ
S_{ij}	[s^{-1}]	strain-rate tensor
a	[m/s^2]	acceleration
f	[Hz]	frequency
g	[m/s^2]	forcing term
h	[m]	channel half width
u^+	[-]	normalized streamwise velocity component
u_τ	[m/s]	friction velocity
x, y, z	[m]	streamwise, wall normal and spanwise coordinates
y^+	[-]	normalized wall normal coordinate
Δ	[m]	filter size
Δt	[s]	time step
$\Delta x^+, \Delta y^+, \Delta z^+$	[-]	normalized cell size
δ_{ij}	[-]	Kronecker delta
ρ	[kg/m^3]	density
τ_{ij}	[N/m^2]	subgrid scale Reynolds stress

Subscripts and Superscripts

excit	excitation
ref	reference
^	amplitude
< >	spatial average
~	resolved component

1. INTRODUCTION

Self-excited (thermo-acoustic) oscillations often occur in combustion systems due to the combustion instabilities. The high pressure oscillations can lead to higher emissions and structural damage of the chamber. There is an extensive research to develop a reduced physical model, which allows – without time-consuming measurements – to calculate the resonance characteristics of a Helmholtz-resonator-type combustion chamber. For the formulation of this model numerical investigations by means of compressible large eddy simulation (LES) are carried out [1]. In these investigations the flow in the combustion chamber is isothermal, non-reacting

and excited with a sinusoidal mass flow rate. The target of the foregoing investigations was the chamber and the exhaust gas pipe. The results gave a good prediction of the resonant characteristics and enabled the identification of the mean damping mechanism. The comparison with experiments shed light on the significant role of the surface roughness in the exhaust gas pipe.

The target of the current work is to determine the resonant characteristics of the coupled system consisting of burner and chamber. In the case of the simple chamber the configuration allowed the use of a simplified inlet boundary condition for the LES [1]. In the case of the new configuration this simplification is no longer justified. Former experiments show that the inflow into the burner is highly turbulent. It is very important to investigate the effect of the turbulence intensity of the inflow on the resonant characteristics of the coupled system. Therefore, an appropriate inflow condition has to be applied. In order to prescribe the turbulent flow at the inlet for the LES, a precursor simulation type boundary condition is chosen. The flow in the precursor domain is driven by a controlled body force to obtain the required mass flow rate. The body force is necessary to reproduce the fast changes of the flow conditions in the case of pulsating mass flow rate, which is not possible with the use of a pressure gradient. As a test case the turbulent channel flow of Reynolds number Re_τ=395 is simulated. The results compared well with data from DNS. In the next stage of the work this inlet condition is to be extended to describe pulsating mass flow rate for the investigation of the combustion chamber.

2. INLET CONDITIONS FOR LES

For the investigation of the chamber a simplified condition was used at the inlet [1]. A nozzle was located downstream of the inlet boundary before the fluid enters the chamber. Since the turbulence level decreases strongly in the nozzle downstream, the fluctuations at the inlet could be neglected and a turbulent mean velocity profile was simply applied with a boundary layer thickness that was known from experiment.

In the configuration of the burner and chamber there is no possibility to use a simplified inlet boundary condition. It is known from experiment that the inflow into the burner is highly turbulent. In order to investigate the influence of the inflow turbulence, an appropriate inlet condition has to be employed. Since a pulsating mass flow rate has to be produced for the investigation of the resonant characteristics of the burning system, the use of a complex inlet condition is required.

It is widely accepted that the specification of realistic inlet boundary conditions plays a major role in the accuracy of a numerical simulation [2-4].

In the case of a Reynolds averaged Navier-Stokes (RANS) simulation it is relatively simple to define proper data at the inlet. The profile of the mean velocity and the turbulence variables have to be prescribed simply.

For LES and DNS a time dependent series of data for all the velocity components and in the case of a subsonic compressible flow for a further thermodynamic variable (e.g. temperature) are required. In order to produce time dependent turbulent inflow for LES and DNS there are some methods in the literature.

The simplest procedure for specifying turbulent inflow conditions is to superpose random fluctuations on a desired mean velocity profile. The shortcoming of this boundary condition is that the turbulence spectrum of the incoming flow is not recovered. Since these fluctuations are not coherent and have no correlations in space and time, they do not reflect real turbulent fluctuations. Turbulent coherent large-scale structures initiate the cascade of turbulent kinetic energy from large to small scales. The inflow fluctuations are inserted with the frequency of the time step hence they do not contain the whole energy spectrum of turbulence. As a result, the fluctuations have more energy in the high wave numbers and dissipate very fast without sustaining or initiating real turbulence.

The most accurate method that retains a degree of generality consists of obtaining inflow data from a precursor simulation [2, 4-6]. Here an auxiliary simulation of wall bounded flow produces fully developed turbulent flow data with periodic conditions in the streamwise direction. Spatially developing turbulent boundary layer data by means of a rescaling method [2, 5, 6] is also possible.

In the first stage the method to produce fully developed turbulent flow was implemented in the in-house developed flow solver SPARC [7] and it was extended for subsonic compressible flow. In the future work the method has to be extended to describe a pulsating mass flow rate up to about f_{excit}=200 Hz.

2.2. Precursor simulation

In the precursor region the desired mass flow rate can be obtained with a prescribed pressure gradient or with a forcing term. The use of a body force has two advantages. Unlike the use of a pressure gradient, a better homogeneity of the flow can be obtained, and the adjustment of the mass flow rate is fairly faster.

The body force is added to the streamwise momentum and energy equations in order to compensate the wall-friction forces and to obtain the required mass flow rate.

Lenormand et al. [8] described a method for the calculation of the body force for a compressible channel flow. The method is constructed to maintain a constant mass flow rate which should be

previously obtained by the initialization. Furthermore the initialized velocity profile is of great importance since the wall shear stress is used to predict the driving term.

In the general case it is very laborious to construct proper initialization values for each computation therefore a generally working method is needed. On the other hand in SPARC a full multigrid method is implemented, which is very useful in the case of complex geometries, where a proper initialization is almost impossible. If the precursor simulation is coupled to the main domain, the flow in the precursor region develops parallel to the main domain from the initialization in each multigrid level. In the case of the combustion chamber the method described in [8] is difficult to realise because of the required pulsation of the mass flow rate. In order to solve these problems a controller based on the instantaneous mass flow rate difference is constructed. The controller has to handle the flow in the precursor region as a dynamical system consisting of a mass, spring (compressibility) and weak nonlinear damping with hard definable parameters. To prevent overshootings of the mass flow rate the forcing term is maximized with $g_{\max}$. The streamwise component of the forcing term at the time step n+1 is read:

$$g_1^{n+1} = g_1^n + g_{\max} \cdot MIN\left(1, \left|\frac{\Delta Q}{Q_{ref}}\right|\right) \cdot SIGN(\Delta Q) - a^n \quad (1)$$

with

$$\Delta Q = Q^n - Q^{n-1} , \quad (2)$$

$$a^n = \frac{1}{\langle\rho\rangle 2hL_y}\frac{\Delta Q}{\Delta t} \quad (3)$$

The maximum value of the forcing term can be approximated by the amplitude and the frequency of the excitation mass flow rate:

$$g_{\max} \approx 2\pi \cdot \frac{1}{\langle\rho\rangle 2hL_y}\hat{Q} \cdot f_{excit} \quad (4)$$

In the case of the initialization, the exaggerated oscillations can be avoided by means of an exponential type driving function, and the prescribed mass flow rate can be reached much faster. This is demonstrated with a steady test case of laminar flow, where a constant mass flow rate is to realise (Figure 1 and 2).

In the compressible channel flow the shear stresses produce heat which results in decreasing of the density along the channel. In terms of the mass conservation with decreasing density the velocity has to increase. In this manner, unlike an incompressible channel flow, the state of the fluid has to be described more accurately if periodicity is used in streamwise direction. For the simulation the total temperature is held constant in the channel centreline at the inlet boundary. This can be applied, if the total temperature fluctuation is negligible as discussed in [9].

In order to test the precursor simulation the turbulent channel flow of Reynolds number Re_τ=395 is simulated. The mass flow rate is constant in this test case.

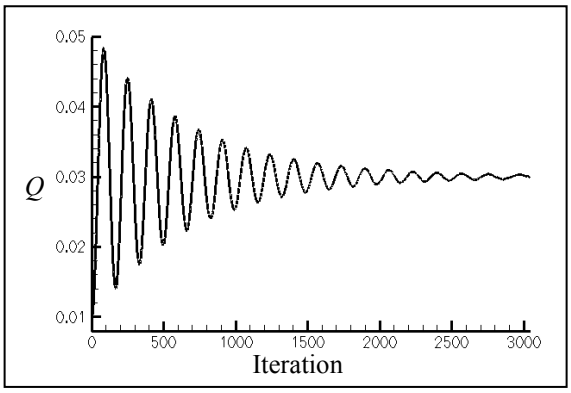

Figure 1. Control of the mass flow rate based on the instantaneous mass flow rate difference

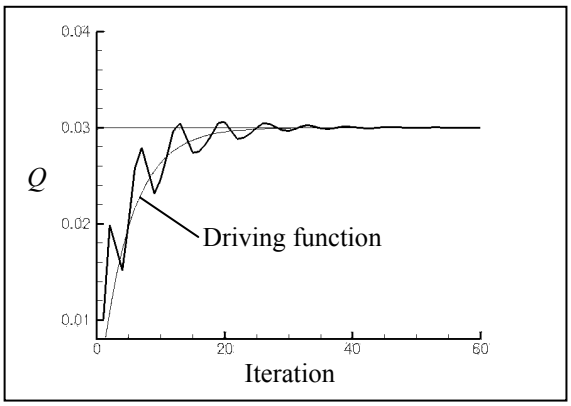

Figure 2. Control of the mass flow rate completed with a driving function

3. TURBULENT CHANNEL FLOW SIMULATION

3.1. Numerical setup

For the numerical investigation the in-house developed flow solver SPARC [7] is used to solve the compressible Navier-Stokes equations. The solver is block-structured and parallelized by the message passing interface (MPI).

For the discretisation in space a second order accurate central difference scheme was used. In time a second order dual time stepping scheme was applied. The time step was set to Δt=1·10^{-5} s. A full multigrid method is used to accelerate the

convergence in the inner iterations. The use of the full multigrid method allows also the investigation of the effect of grid refinement.

The computations were performed using the Smagorinsky-Lilly subgrid scale model:

$$\tau_{ij} - \frac{1}{3}\delta_{ij}\tau_{kk} = -2\rho(C_S\Delta)^2\left|\widetilde{S}\right|\widetilde{S}_{ij} \qquad (5)$$

where C_S is the Smagorinsky model coefficient, $\widetilde{S}_{ij}$ is the resolved strain-rate tensor:

$$\widetilde{S}_{ij} = \frac{1}{2}\left(\frac{\partial\widetilde{u}_i}{\partial x_j} + \frac{\partial\widetilde{u}_j}{\partial x_i}\right), \qquad (6)$$

$\left|\widetilde{S}\right| = \sqrt{2\widetilde{S}_{ij}\widetilde{S}_{ij}}$ is the modulus of the resolved strain-rate tensor and Δ is the filter size. This model allows only forward energy transfer from the resolved scales to the subgrid scales, and is used in many applications. In the simulations implicit filtering was used and near the wall van Driest damping was applied. The Smagorinsky coefficient was set to C_S=0.13. A computation with C_S=0.1 gave approximately the same results for the turbulent channel flow.

The Reynolds number is Re_τ=395, the Mach number based on the bulk velocity and sound speed at the walls is Ma=0.3. The mass flow rate is held at a constant value.

The computational domain of the precursor simulation is ($2\pi h$, $2h$, πh) in (x, y, z), where x is the streamwise direction, y the wall normal direction, and z the spanwise direction. The grid resolution is (64, 160, 64) in (x, y, z). The grid size is in the streamwise direction Δx^+=25, in the spanwise direction Δz^+=12 and in the wall normal direction Δy^+=0.4 at the wall and stretched up to Δy^+=2 at the centreline of the channel. A body force g as discussed above is applied in this domain to obtain the prescribed mass flow rate (Figure 3).

Periodic boundary conditions are applied in the spanwise direction, while no-slip conditions are applied at the adiabatic walls.

Boundary conditions comprise always approximations furthermore a standard static pressure outlet is very stiff against oncoming waves like e.g. the turbulent vortices and produces reflections. Therefore an outlet condition at the end of the precursor domain is not applicable. Downstream of the precursor simulation a domain with the same geometry is coupled. This domain substitutes now also the main domain of interest. At the outlet boundary the static pressure condition is used. In order to avoid reflections the grid is stretched towards the outlet boundary and a non-reflecting layer is used as described in [10].

As soon as the statistical stationary state was obtained the statistics were sampled till the mean value of the spanwise velocity component was less then 1 % of the mean streamwise velocity. Additionally to time averaging, the statistics were averaged also over the z direction (homogeneous direction).

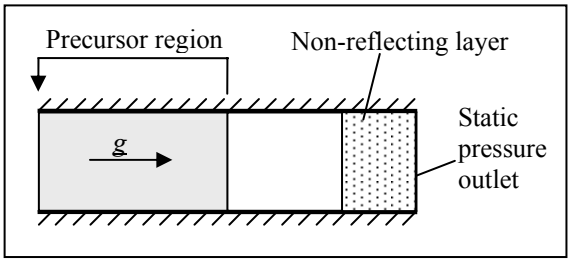

Figure 3. The sketch of the computational domain

3.3. Results

The results of the simulation are compared to the DNS data by Iwamoto and Iwamoto et al. [11, 12] for the mean velocity and for the velocity fluctuations.

Figure 4 shows the mean profile of the streamwise velocity component. For the sake of the perspicuity only each fourth of the DNS data are plotted.

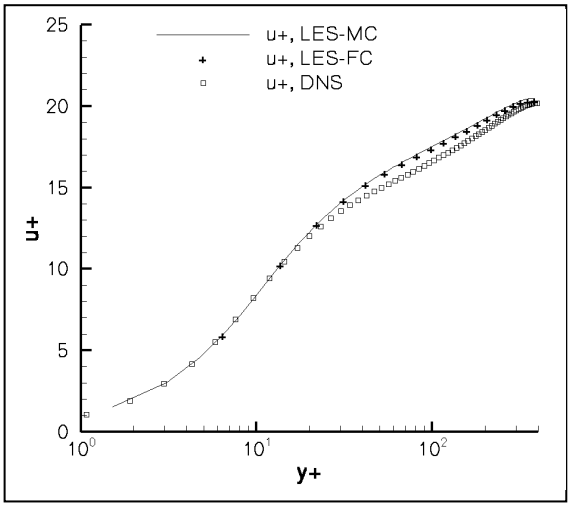

Figure 4. The mean velocity profile in wall units (only each fourth data are plotted in the case of DNS and LES-FC)

The LES results compare well with the DNS data although the LES overpredicts somewhat the mean velocity profile in the buffer layer and in the log-law region. Since the same result is obtained in the domain downstream of the precursor region, this seems not to be an effect of the precursor simulation. The overprediction can arise from the grid resolution, from the filtering or from the

discretisation scheme etc. It is not the aim of this work to investigate the source of this discrepancy.

The difference between pressure gradient driven flow and body force driven flow is negligible small, as discussed by Huang et al. [13], and can not produce such a deviation in the velocity profile.

In order to check the propriety of the precursor simulation, another investigation was more relevant. For the control of the forcing term the mass flow rate in each time step is needed. The instantaneous mass flow rate can be calculated in one cross section of the precursor region, e.g. at the inlet plane. In this case, if the flow becomes turbulent, the mass flow rate starts to oscillate, and therefore the forcing term oscillates strongly, too. For the reduction of this oscillation the mass flow rate in the precursor domain was averaged in the streamwise direction. This reduced the amplitudes but the oscillation remained. Therefore one computation was performed with a constant forcing term to investigate the effect of this oscillation.

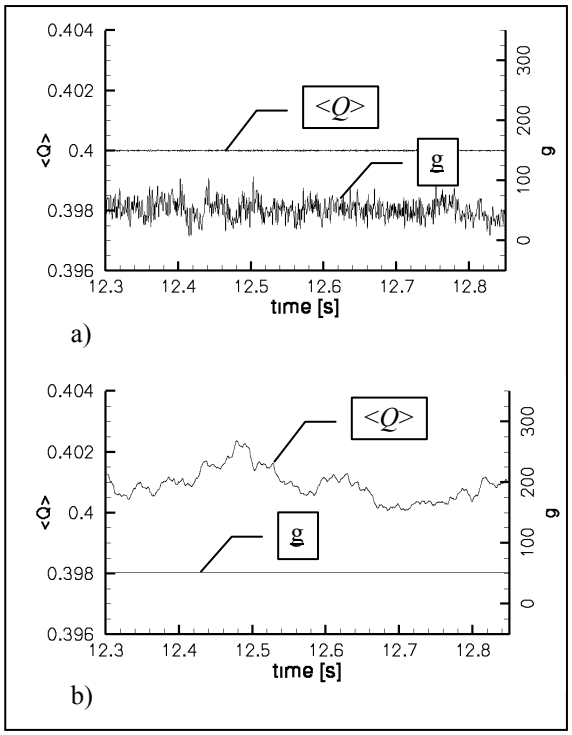

Figure 5. Temporal evolution of the averaged mass flow rate and forcing term; a) LES-MC, b) LES-FC

Figure 4 shows that the results of the calculation with controlled force (LES-MC) do not deviate substantially from the calculation with constant forcing term (LES-FC). For the sake of the perspicuity only each fourth of the LES-FC data are plotted.

In the case of controlled forcing term (LES-MC) the maximal relative error of the mass flow rate is within 0.01%. The constant value for the forcing term was approximated with the integral of the oscillating forcing term on a certain time interval. Although the exact value was not caught the mass flow rate deviates from the desired Q_{ref}=0.4 kg/s within 0.5%. The temporal evolution of the averaged mass flow rate and the forcing term are plotted in Figure 5.

Figure 6 and 7 show the filtered RMS-fluctuations and the Reynolds shear stress. The LES results compare satisfactorily with the DNS data. The results from LES-FC are not plotted in Fig. 6 and 7 because of the negligible deviation from the LES-MC.

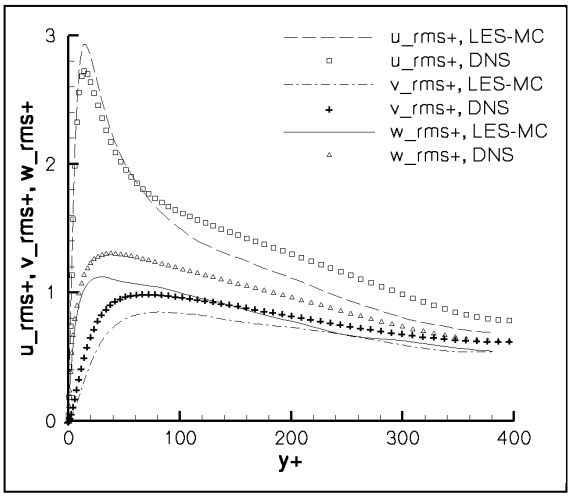

Figure 6. Filtered RMS velocity profiles in wall coordinates (only each fourth DNS data are plotted)

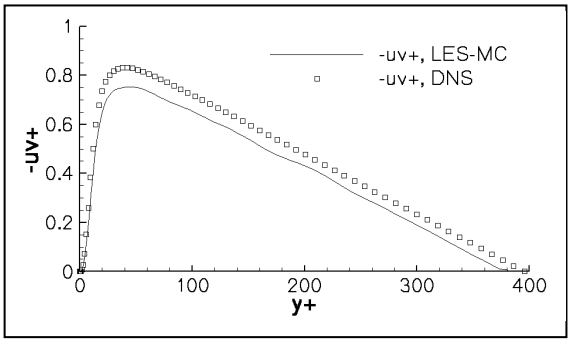

Figure 7. Filtered Reynolds shear stress profile (only each fourth DNS data are plotted)

4. CONCLUSIONS

For the investigation of the resonant characteristics of a Helmholtz-Resonator-type combustion chamber a pulsating mass flow rate inlet boundary condition is required. Since the turbulence intensity at the inlet can take effect on the resonant characteristics of the coupled system consisting of a burner and a combustion chamber a proper inlet condition is required. The precursor simulation is chosen to generate data at the inlet of the compressible LES. In the precursor simulation

the mass flow rate is obtained with a controlled forcing term. In order to test the implementation, the fully turbulent channel flow of Reynolds number Re_τ=395 was computed. The results compared to DNS data satisfactorily. An investigation showed that the oscillation of the forcing term resulting from the oscillating mass flow rate does not take notable effect on the solution.

The current work is to extend the precursor method for a pulsating mass flow rate for the investigation of the combustion system.

ACKNOWLEDGEMENTS

The present work is a part of the subproject A7 of the Collaborative Research Centre (CRC) 606 – "Unsteady Combustion: Transportphenomena, Chemical Reactions, Technical Systems" at the University of Karlsruhe. The project is supported by the German Research Foundation.

REFERENCES

[1] Magagnato, F., Pritz, B., Büchner, H., Gabi, H., 2005, "Prediction of the Resonance Characteristics of Combustion Chambers on the Basis of Large-Eddy Simulation", *7th ISAIF, International Symposium on Experimental and Computational Aerothermodynamics of Internal Flows*, Tokyo, Japan, 2005.

[2] Lund, T., Wu, X., Squires, D., 1998, "Generation of Turbulent Inflow Data for Spatially-Developing Boundary Layer Simulations", *Journal of Computational Physics*, Vol. 140, pp. 233-258.

[3] M. Klein, A. Sadiki, J, Janicka, 2003, „A Digital Filter Based Generation of Inflow Data for Spatially Developing Direct Numerical or Large Eddy Simulation", *Journal of Computational Physics*, Vol. 186, pp. 652-665.

[4] Kaltenbach, H.J., Fatica, M., Mittal, R., Lund, T.S., Moin, P., 1999, "Study of Flow in a Planar Asymmetric Diffuser Using Large-Eddy Simulation", *Journal of Fluid Mechanics*, Vol. 390, pp. 151-185.

[5] El-Askary, W.A., Ewert, R., Schröder, W., 2002, "On Large Eddy Simulation as a Tool to Predict Acoustical Fields", in T. Hüttl, C. Wagner, J.W. Delfs edit., Proceedings 7-8 Oct. 2002, *LES for Aeroacoustics*, DGLR-Report 2002-03, German Aerospace Center, DLR, Göttingen, Germany.

[6] Sagaut P., Garnier E., Tromeur E., Larchevêque L., Labourasse E., 2004, „Turbulent Inflow Conditions for Large-Eddy Simulation of Compressible Wall-Bounded Flows", *AIAA Journal*, Vol. 42, No. 3, pp. 469-477.

[7] Magagnato, F., 1998, "KAPPA – Karlsruhe Parallel Program for Aerodynamics", *TASK Quarterly*, Vol. 2, pp. 215-270.

[8] Lenormand, E., Sagaut, P., Phuoc, L.T.,Comte, P., 2000, "Subgrid-scale models for Large-Eddy Simulations of Compressible Wall Bounded Flows", *AIAA Journal*, Vol. 38, pp. 1340-1350

[9] Bradshaw, P., 1977, "Compressible Turbulent Shear Layers", *Ann. Rev. Fluid Mech.*, Vol. 9, pp. 33-54.

[10] Magagnato, F., Pritz B., Gabi, M., 2006, "Calculation of a Turbine Blade at High Reynolds Numbers by Large-Eddy Simulation", *The 11th International Symposium on Transport Phenomena and Dynamics of Rotating Machinery*, Honolulu, Hawaii, February 26 - March 2, 2006.

[11] Iwamoto, K., 2002, "Database of Fully Developed Channel Flow", *THTLAB Internal Report*, No. ILR-0201., THTLAB, Dept. of Mech. Eng., The Univ. of Tokyo.

[12] Iwamoto, K., Suzuki, Y., and Kasagi, N., 2002, "Reynolds Number Effect on Wall Turbulence: Toward Effective Feedback Control", *Int. J. Heat and Fluid Flow*, Vol. 23, pp. 678-689.

[13] Huang, P.G., Coleman, G.N., Bradshaw, P., 1995, "Compressible Turbulent Channel Flows: DNS Results and Modelling", *J. Fluid Mech.*, Vol. 305, pp. 185-218.

Conference on Modelling Fluid Flow (CMFF'06)
The 13th International Conference on Fluid Flow Technologies
Budapest, Hungary, September 6-9, 2006

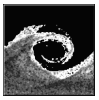

ON THE POSSIBILITY OF REVERSIBLE SIMULATION OF HARD SPHERE FLUIDS

Juraj Kumičák[1]

[1] Corresponding Author. Department of Power Engineering, Technical University of Košice. Vysokoškolská 4, 042 00 Košice, Slovakia. Tel.: +421-55-602 4363, Fax: +421-55-602 2452, E-mail: juraj.kumicak@tuke.sk

ABSTRACT

The paper describes a 2D simulation of the motion of a system of regular polygons within the unit square. The polygons, having $4p$ sides, are not allowed to rotate and their interactions are of the hard body type. The requirement of reversibility necessitates to use rational values for the positions and velocities. The latter then enable to introduce the notion of absolute age which gives a novel look at the irreversibility. It is observed that with growing p the dynamics approaches the hard sphere one with the Maxwell-Boltzmann distribution of velocities. The simulation enables to demonstrate the gradual appearance of hydrodynamic behavior with growing p, retaining at the same time the reversibility of the dynamics.

Keywords: absolute age, collisions of polygons, computer algebra methods, hard sphere fluid, reversible simulation

1. INTRODUCTION

The evolution of many particle systems can be solved only with the help of numerical simulation, the method usually called molecular dynamics. Already in the beginnings of the latter a question arose about the possibility to preserve the reversibility induced by the dynamics. For example, N. Margolus [1] gave a description of universal reversible cellular automata thus outlining the essentials of reversible computation. However, it is only after the appearance of the Levesque-Verlet bit reversible algorithm [2], which represents apparently the most efficient method used to obtain reversible trajectories, that the reversible computer simulation of dynamical systems has become an important field of computational physics [3].

Several authors have compared the behavior of exactly reversible simulations with standard molecular dynamics, demonstrating that even a negligibly small deliberate noise can cause the loss of reversibility [4]. Nevertheless, not too much attention is being paid to possible interrelations existing between numerical ir/reversibility and corresponding system's dynamics.

Recently the Generalized Baker Map (GBM) model, treated as a system displaying the combination of microscopic reversibility with macroscopic irreversibility, has been studied by the author of the present paper. The goal of the study was to analyze the interrelation between both these aspects of evolution and to arrive — with the help of the analysis – at an understanding of the origin of irreversibility in reversible systems.

It seemed plausible that many of the results concerning GBM, described in the paper [5], and some properties observed in the author's animation[1] of GBM, should apply also to models mimicking more realistic systems. To corroborate this view, the simulation of 2D hard sphere fluid has been undertaken which would be reversible to essentially *unlimited* precision. The most serious obstacle on this way is the collisional dynamics of spheres, the simulation of which necessarily involves the use of goniometric functions. The latter return irrational values and in such a way prevent attaining the "numerical reversibility". To avoid this drawback, the "particles" have been approximated by regular polygons and the dynamics of collisions has been adjusted appropriately. Moreover, all the calculations have been performed with rational numbers, i.e. with fractions of integers.

Very interesting aspect of the GBM model is its „absolute age" τ, which can be assigned to any point in an unambiguous way and with reasonable precision [5]. It increases in equal steps from the present to the future (and decreases from the present to the past) — except the small neighbourhood of the „present" state where its behavior is less predictable. This age is *absolute* in the sense that it does depend only on the distance from the present, i. e., on the number of iteration steps. This is due to the fact that coordinates of points contain „traces" of their evolution, which enable us — at least in principle — to recover the iteration index k from the

[1] See BakAnima.html at the author's web site: http://www.geocities.com/kumicak/.

coordinates of an arbitrary point. Since this notion is intimately connected to the origin of irreversibility, it was interesting to find out whether it would be possible to introduce it into the hard polygon model.

2. THE MODEL

In all simulations described here the particles move within the unit square and are being reflected by its boundaries. They are supposed to be regular polygons with $4p$ sides, $p \geq 1$, four of which are parallel to the sides of the unit square.

The particles interact via elastic collisions and they are not allowed to rotate (their motion is restricted to translations). It is supposed that during collisions they exchange components of velocities perpendicular to the sides which are in contact, irrespective of positions of their centers. Hence the dynamics — which can be viewed alternatively as simulating the flow of granular materials — can be treated as a sequence of two-body elastic collisions.

The system starts with all particles having the same speed but with pseudorandom uniform distribution of directions over the interval $[0; 2\pi)$. The particles are initially placed on a regular square lattice covering the whole unit square — or just a quarter of it. Such conditions were chosen to readily recognize the return of the system to initial state after velocity reversal.

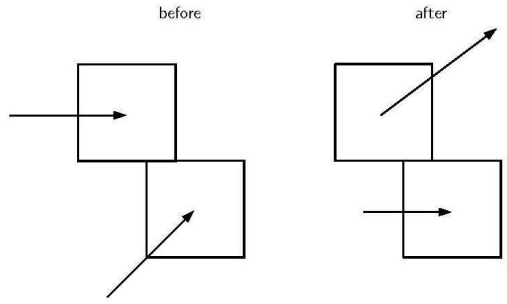

Figure 1: Collisional dynamics of squares. The squares collide in vertical direction so that vertical components of velocities are exchanged and horizontal ones are preserved.

The inner diameter of the polygons is chosen to be either 1/25 or 1/50 of the unit square side, so that the number of particles, corresponding to the maximum density (to avoid ternary collisions), is bounded from above by 400 and 900, respectively. The lower bound is four particles which corresponds to the minimum density.

Due to the hard disk potential, the calculations evidently reduce to consideration of all pairs of particles i and j and finding the minimum of times t_{ij} for their next collision. One then moves all particles forward in time until the collision occurs and calculates the postcollisional velocities of the colliding pair.

Evidently, in the case of non-rotating *squares* one can in this way compute the dynamics with *absolute* precision, provided all the initial values are rational. The collisional time t_{ij} is, namely, a linear combination of rational values in such a case, and velocity components are just exchanged. With the growing p the situation is less simple but can be handled in a way to be explained later.

In order to compare the model with real fluid, we suppose that the chosen diameter of particles corresponds to about 1 nm in reality, so that to simulate the gas at normal pressure and temperature we should have about four particles in the box — the lowest number used in the simulations. Choosing the initial speed of particles so as to correspond to about 500 m/s we then obtain mean free paths comparable to those of real gases.

The simulation was programmed in the Java programming language that enables the program to be run as an application as well as an applet that can be embedded into an HTML page (good for demonstration purposes on the web). However, when used as an applet, the program was very slow for $p > 1$, and therefore it was necessary to make it faster without losing reversibility. Simulations, using rational (double precision) numbers for both positions and velocities, confirmed that the contributions of positions to irreversibility are negligible for small p so that one can obtain reasonable approximation to reversible dynamics using rational values for velocities and letting positions as floats. Such are the simulations given at the authors web site[2] (denoted there as "animations"), representing a compromise between the number of particles and the speed of the system's evolution. These animations can serve consequently only demonstrative purposes, but the full program is free of such limitations.

3. SIMULATION WITH SQUARES

The simulation has started with $p = 1$, i. e. with hard squares, see Fig. 1. Such system lacks one of the essential problems of numerical simulation: the appearance of irrational numbers which would be introduced by goniometric functions in calculations of projections. The squares namely collide only in the x and y directions so that they exchange only horizontal or vertical components of their velocities, but do not change their values. Under such conditions, components of velocities are just interchanged between particles, so that the speeds quickly attain a distribution determined by the initial one which will not change thereafter. This means that there is no universal distribution function — namely, that the Maxwell-Boltzmann distribution of speeds, expressed for a 2D system of N particles with mean velocity v_0

[2] www.geocities.com/kumicak/HSqGas.html

$$f(v)\,dv = \frac{2v}{v_0^2}\exp(-v^2/v_0^2)\,dv \qquad (1)$$

cannot be reached if the system has started in a different one, see the example of a "singular" initial distribution in Fig. 2. Sufficiently random and homogeneous set of initial velocities will approach the distribution shown in Fig. 3. This will be, with sufficient precision, the limit of all "non-singular" initial distributions.

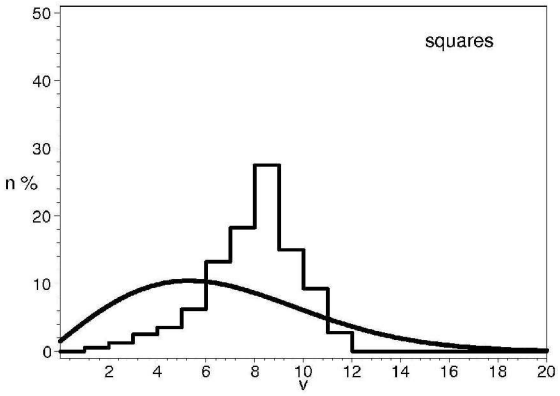

Figure 2: The histogram of velocities of 400 squares, having originally the same length, after 5000 collisions. The velocities are divided into 20 intervals and *n* denotes the percentage of particles with corresponding values. The figure demonstrates that the Maxwell-Boltzmann distribution (represented by the continuous line) is not being approached.

The damped oscillatory motion of the center of mass is the first sign of macroscopic "hydrodynamic" behavior. The exclusive use of rational numbers in all computations, however, slows down the calculations even under these favorable conditions. Fortunately, this does not prevent to demonstrate reversibility for moderate number of particles — the reversibility was confirmed for 500,000 collisions with 400 particles.

The system of hard squares is evidently ergodic and mixing with respect to positions. It is even chaotic but these properties are not shared by velocities which are essentially preserved due to the above mentioned reasons.

One *cannot* assign absolute age τ to the states of hard squares system, since if we start with rational positions and velocities, the positions will be linear functions of time (number of iteration steps), and velocities will belong to a finite set of combinations of starting values. There is no way how to extract information about time elapsed from such data.

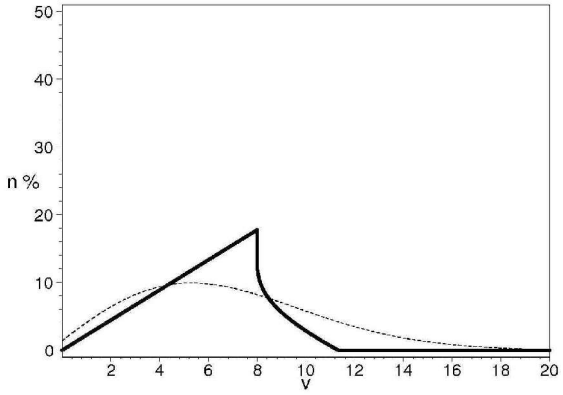

Figure 3: Theoretical distribution of velocities of squares as compared to the Maxwell-Boltzmann distribution (dashed line).

4. SIMULATION WITH OCTAGONS

The reversible behavior of simulation using polygons is necessarily only approximate but it is expected to retain — at least in certain respects — the most essential properties of reversible systems with macroscopic irreversible behavior. Some of such features can be readily observed already in the next approximation to the 2D hard sphere gas — the gas composed of regular octagons.

The octagons are again not allowed to rotate so that they can collide in four different directions only, two of which are identical with those of the squares and the two new ones are inclined with respect to vertical and horizontal directions by the angle of $\varphi = \pi/4$, see Fig. 4. To calculate the projections of velocities onto the two new directions, requires to multiply corresponding values by the *irrational* factor of $\cos(\pi/4) = \sqrt{2}/2 = 1/\sqrt{2}$. To prevent the latter from causing irreversibility, we can think of $\cos(\pi/4)$ as $\sqrt{2}/2$ in the forward evolution and as $1/\sqrt{2}$ in the backward one. This has the effect that factors $\sqrt{2}$, accumulated during the forward evolution, are being cancelled out in reversed evolution so that the velocities are perfectly recovered.

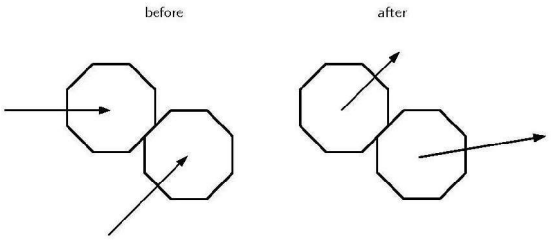

Figure 4: Collisional dynamics of octagons. The octagons collide in the direction perpendicular to the line of contact so that components of velocities in this direction are exchanged and components parallel to it are being preserved.

In numerical calculations we must, of course, approximate $\sqrt{2}$ by a rational number. Such approximation evidently introduces an error into positions so that the longer the time required for the reversible evolution, the more places are to be kept in decimal approximation of the number. However, any finite time of reversible evolution can be achieved by appropriate choice of the approximation. Practical tests show that 1.4142 represents sufficient rational approximation of $\sqrt{2}$ to obtain reversibility for reasonable number (at least thousands) of collisions.

We therefore see that the described simulation of octagons cannot be absolutely reversible for an *unlimited* time. But since the deviation from reversibility can be made arbitrarily small, and the time of reversible evolution consequently arbitrarily long, the simulation retains the most salient property of reversible systems with macroscopic irreversible behavior — irreversibility is practically not observable during *any finite* run. We can say that such evolution is *practically reversible*.

One would evidently expect that the collisional dynamics of 4*p*-gons will approach with growing *p* the dynamics of hard spheres. This can be seen already when one compares squares with octagons, see Fig. 5.

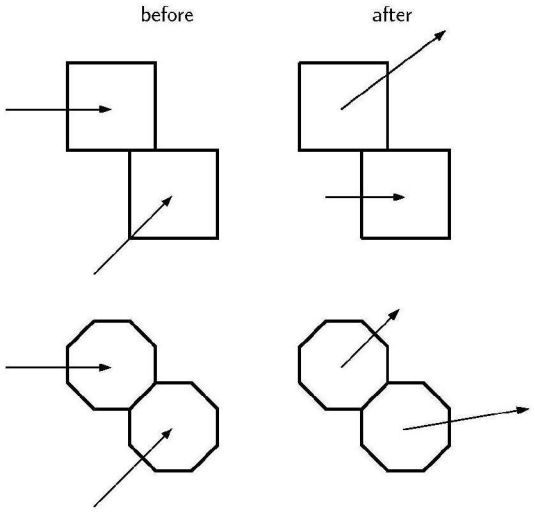

Figure 5: Comparison of collisional dynamics of squares with that of octagons. One can prove that the dynamics of 4*p*-gons approaches that of spheres with growing *p*. The figure suggests this result.

It should be moreover noted that the behavior of positions is further influenced by the specific character of polygon scattering. Since the effective cross section is in this case discrete, the dependence of positions on initial conditions is "sensitive" only at a discrete set of angles (corresponding to the vertices of the polygons). One could call such sensitivity "singular" as it is defined on the set with zero measure. With growing *p* the set becomes larger so that the sensitivity is the more pronounced the greater the *p*. The simulation with octagons demonstrated that the irreversibility of positions is in this specific case still practically negligible.

The absolute age τ [5] cannot again be brought into relation with *positions* due to their linear dependence on time (equivalent to the number of iterations). However, the *velocities* of particles are multiplied, after each collision occurring in the direction not parallel to *x* or *y* axes, by (rational approximation to) $\cos(\pi/4)$ so that a possibility arises that their rational expressions will consist of fractions of growing natural numbers. Actually, the simulation confirms that such a situation is typical. Therefore, it is possible to construct an explicit expression for the absolute age based on rational components of velocities of all *N* particles which will be growing both in the future and in the past — one can make τ even approximately linear function of the iteration index *k*, $\tau = const\ |k|$. Denoting numerators and denominators in rational expressions of numbers by superscripts *A* and *B*, respectively, one of possible choices is represented by the formula

$$\tau = \sigma\, c \sum_{l=1}^{N} (\log |v_{lx}^{A}| + \log |v_{ly}^{A}|) \qquad (2)$$

where v_{lx} and v_{ly} denote *x* and *y* components of the velocity of the *l*-th particle and *c* is the scaling factor which adapts the age to be approximately equal to the iteration index *k* (we keep meanwhile $\sigma = 1$). This may seem to be a bit artificial and unphysical but, nevertheless, such definition of τ turns out to be very reliable.

Such age will grow as positive both in the future and in the past. To make it negative in the past one should calculate σ as follows. If the sum

$$\begin{aligned} s = &(|v_{xi}^{A}| - |v_{xi}^{B}|) + (|v_{xj}^{A}| - |v_{xj}^{B}|) + \\ &+ (|v_{yi}^{A}| - |v_{yi}^{B}|) + (|v_{yj}^{A}| - |v_{yj}^{B}|) \end{aligned} \qquad (3)$$

of differences of absolute values of numerators and denominators of particles *i* and *j* is greater after the collision than before it, then $\sigma = +1$, if it is smaller, then $\sigma = -1$; otherwise it does not change. This rather artificial way to keep the sign of the age monotonous has, however, the drawback that the age is then not the function of the state of the system — which is our primary goal — but depends on two consecutive states.

Since the change of velocities is now limited by less constraints, there do not seem to exist reasons for the Maxwell-Boltzmann distribution to be unattainable. The observations actually confirm that the latter is readily approached by this system, see Fig. 6. In this sense, the octagons represent quali-

tatively sufficient approximation to hard spheres fluid.

It is evident that the same behavior will be seen with all other regular 4*p*-gons with $p > 2$. The only difference expected will be the speed of approach to the equilibrium distribution of positions and velocities.

There is a distant resemblance of the age to the entropy in that both depend on the distance of the current state of the system from the initial (non equilibrium) state. However, the age is monotonously growing with time whereas entropy approaches a limit value. Entropy is the measure of equilibrium, the age is roughly proportional to the number of collisions. This difference is best seen in the fact that the age is growing even if the system starts in equilibrium.

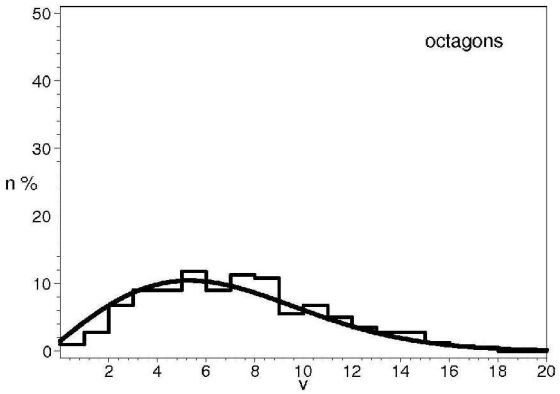

Figure 6: The histogram of velocities after 1200 collisions of 400 octagons demonstrates that the Maxwell-Boltzmann distribution (represented by the continuous line) is being approached quickly.

5. CONCLUSIONS

Numerical molecular dynamics simulation of fluids is of great theoretical and practical importance. It enables to replace real experiments with computational ones and allows to calculate relevant parameters of flows — such as, e. g., transport coefficients — departing from theoretical assumptions.

But the reversible *microscopic* basis of fluid behavior is not taken into account in the usual case of simulations which are based on double precision calculations. The inherent rounding errors themselves, namely, generate irreversibility of the models, and this irreversibility is just a numerical artefact having no physical counterpart. This makes such simulations microscopically irreversible and therefore hides one of the important aspects of the problem: the observed macroscopic irreversibility should ensue from underlying reversible dynamics and under no condition should it be the result of calculation errors.

The fully *reversible* simulation, on the contrary, enables to observe irreversibility in a model with granted microscopic reversibility which would be otherwise impossible to obtain in real experiments. That is why only such simulation can serve the basis for the exact explanation of origin of ubiquitous macroscopic irreversibility of microscopically reversible dynamics.

The reversible simulation of many-particle systems was undertaken by several authors who arrived at many interesting results, concerning mostly the approach to equilibrium [1, 2] and influence of noise on reversibility [4]. The stress of this work was more on the influence of system's dynamics on the properties of reversible evolution. That is why particles were simulated by polygons with 4*p* sides with an effort to see how the growing *p*, entailing the approach of polygons to disks, will influence the behavior of the systems. The case of low *p* shows rapid appearance of thermodynamic behavior, the case of high *p* will be the subject of a separate work.

In the extreme case of $p = 1$, the system is less sensitive to changes of positions than to those of velocities, since small changes of impact parameter (i. e. changes smaller than the particle diameter) do not influence the direction of particles after collision. This restricts the variability of speeds to the extent that the attainment of the Maxwell-Boltzmann distribution is being excluded. In the next step, $p = 2$, the discrete set of collisional angles is less restricted, and the octagons model described in the paper demonstrated that the reversible dynamics of octagons has already most macroscopic properties expected of gases with hard particle potential. As a result, no assumptions about irreversibility on microscopic level are needed in order to obtain macroscopic irreversibility.

The simulation using rational numbers for coordinates and velocities enabled to introduce the notion of absolute age τ which proved to be rather fruitful for understanding the origin of irreversibility. The possibility to define τ is enabled by the fact that velocities of particles contain "traces" of their evolution, which allow us, at least in principle, to recover the iteration index *k* from arbitrary state. Then the question, why we are not able to prepare states which would evolve contrary to the second law of thermodynamics, can be answered trivially by stating that we can prepare states with "simple" particle velocities (corresponding to "present" states) more easily then those with "complex" ones (corresponding to the future states which upon velocity reversal become the past ones). From this point of view, the irreversibility is related to substantially different requirements for preparation of the present and past states and this seems to be the full explanation.

It should be noted that the most salient property of the described simulation is its ability to regain the positions *and velocities* of the hard disks in the

reversed trajectory. This makes our method comparable to that of the Levesque-Verlet bit reversible algorithm [2] in which only positions are exact and energy is not being preserved.

ACKNOWLEDGEMENTS

The author is thankful to William G. Hoover for his many suggestions. This work was partly supported by the Scientific Grant Agency (VEGA) of the Slovak Academy of Science and Ministry of Education of the Slovak Republic under the Grant No. 1/2198/05. The support is herewith greatly acknowledged.

REFERENCES

[1] Margolus, N., 1984, "Physics-like models of computation", *Physica D* 10, 81-95.

[2] Levesque, D. and L. Verlet, L., 1993, "Molecular Dynamics and Time Reversibility", *J. Stat. Phys*. 72, 519-537.

[3] Hoover, W. G., 1999, *Time Reversibility, Computer Simulation, and Chaos*. World Scientific, Singapore.

[4] Nobuyoshi Komatsu and Takashi Abe, 2004, "Numerical irreversibility in time-reversible molecular dynamics simulation", *Physica D* 195, 391-397.

[5] Kumičák, J., 2005, „Irreversibility in a simple reversible model", *Phys. Rev. E*, 71, (1-2), 016115, 1–15.

Conference on Modelling Fluid Flow (CMFF'06)
The 13th International Conference on Fluid Flow Technologies
Budapest, Hungary, September 6-9, 2006

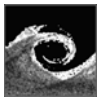

NUMERICAL SOLUTION OF INCOMPRESSIBLE LAMINAR FLOWS

R. Keslerová[1], K. Kozel[2]

[1] Corresponding. Author: Department of Technical Mathematics, Czech Technical University in Prague, Karlovo nám. 13, 121 35 Praha 2, Czech Republic. Tel.: +420-22435-7413, E-mail: keslerov@marian.fsik.cvut.cz
[2] Department of Technical Mathematics, Czech Technical University in Prague. E-mail: Karel.Kozel@fs.cvut.cz

ABSTRACT

This paper deals with a numerical solution of two and three dimensional (2D/3D) flows through a branching channel, where viscous incompressible laminar fluid flow is considered. The mathematical model in this case can be described by a system of the incompressible Navier-Stokes equations and the continuity equation. In order to obtain the steady state solution the artificial compressibility method is applied. The finite volume method is used for spatial discretization. The arising system of ordinary differential equations is solved by multistage Runge-Kutta method. The numerical results for 2D and 3D case are presented.

Keywords: finite volume method, Navier-Stokes equations, Newtonian and non Newtonian fluids, steady incompressible laminar flow

NOMENCLATURE

D_{ij}		the basic cell
$\underline{F}$		flux in x-direction
$\underline{G}$		flux in y-direction
MN		number of grid cells
O	[m]	circumference of the entrance
$\underline{R}$, $\underline{S}$		flux in x and y direction for non Newtonian fluid
S_1	[m^2]	volume of the entrance
Re	[-]	Reynolds number
$\underline{W}$		vector of primitive variables
l	[-]	the height of the entrance (reference length)
p	[-]	kinetic pressure in dimensionless form
$\hat{p}$	[Pa]	physical static pressure
q_∞	[m/s]	reference velocity value
$(u, v)^T$	[-]	velocity vector in dimensionless form
$\hat{u}, \hat{v}$	[m/s]	physical velocities
α_i		Runge-Kutta coefficients
ν	[m^2/s]	the kinematic viscosity
μ	[Pa . s]	dynamic viscosity
μ_{ij}	[-]	volume of the basic cell
ρ	[kg/m^3]	density
τ	[Pa]	the shear stress exerted by the fluid
Δt	[-]	time step
Δx_k	[-]	the length of k-th edge of the basic cell in x direction
Δy_k	[-]	the length of k-th edge of the basic cell in y direction

Subscripts and Superscripts

n	time discretization
t	time derivative
x, y	space derivatives

1. INTRODUCTION

The motivation for numerical solution of the fluid flow in branching channels arises in many applications, e.g. in a biomedicine, a solution of blood flow in cardiovascular system. The study of blood flow in large and medium arteries is a very complex task because of a heterogeneous nature of the problem and a extreme complexity of blood and arterial wall dynamics. In this paper there are presented the first results for non-Newtonian fluids in two dimensional case and for Newtonian fluids there are the corresponding results for non-Newtonian fluids for 2D. The last part of numerical results deals with results for Newtonian fluids in three dimensional case.

2. MATHEMATICAL MODEL

2.1. Newtonian fluids

Firstly, Newtonian fluids are considered. A Newtonian fluid is a fluid that flows like water - its shear stress is linearly proportional to the velocity gradient in the direction perpendicular to the plane of shear. The constant of proportionality is known as the viscosity.

A simple equation to describe Newtonian fluid behaviour is

$$\tau = \mu \frac{\partial u}{\partial x}, \tag{1}$$

$\frac{\partial u}{\partial x}$ is the velocity gradient perpendicular to the direction of shear.

In common terms, this means the fluid continues to flow, regardless of the forces acting on it. For example, water is Newtonian, because it continues to exemplify fluid properties no matter how fast it is stirred or mixed. Contrast this with a non-Newtonian fluid, in which stirring can leave a "hole" behind (that gradually fills up over time), or cause the fluid to become thinner, the drop in viscosity causing it to flow more (this is seen in non-drip paints).

For a Newtonian fluid, the viscosity, by definition, depends only on temperature and pressure (and also the chemical composition of the fluid if the fluid is not a pure substance), not on the forces acting upon it.

If the fluid is incompressible and viscosity is constant across the fluid, the equation governing the shear stress, in the Cartesian coordinate system, is

$$\tau_{ij} = \mu\left(\frac{\partial u_i}{\partial x_j} + \frac{\partial u_j}{\partial x_i}\right). \tag{2}$$

If a fluid does not obey this relation, it is termed a non-Newtonian fluid, of which there are several types.

The Navier-Stokes equations, named after Claude-Louis Navier and George Gabriel Stokes, are a set of equations that describe the motion of fluid substances like liquids and gases. These equations establish that changes in momentum (acceleration) of the particles of a fluid are simply the product of changes in pressure and dissipative viscous forces acting inside the fluid. These viscous forces originate in molecular interactions and dictate how viscous a fluid is. Thus, the Navier-Stokes equations are a dynamical statement of the balance of forces acting at any given region of the fluid.

The Navier-Stokes equations are the fundamental partial differential equations that describe the flow of incompressible fluids. The system of two dimensional Navier-Stokes equations for Newtonian fluids in conservative form has the form

$$\begin{aligned} &\underline{\underline{\widetilde{R}}}\,\underline{W}_t + \underline{F}_x + \underline{G}_y = \frac{\underline{\underline{\widetilde{R}}}}{\mathrm{Re}}\Delta\underline{W}, \\ &\underline{\underline{\widetilde{R}}} = \mathrm{diag}\,(0,1,1)^T, \end{aligned} \tag{3}$$

where Reynolds number for 2D is given by $\mathrm{Re} = \frac{q_\infty l}{\nu}$ and for 3D is given by $\mathrm{Re} = \frac{q_\infty 4S_1}{\nu O}$ and

$$\begin{aligned} &\underline{W} = (p,u,v)^T, \\ &\underline{F} = \left(u, u^2 + p, uv\right)^T, \\ &\underline{G} = \left(v, uv, v^2 + p\right)^T, \end{aligned} \tag{4}$$

where definition of kinetic pressure and definition of velocity vector in dimensionless form are given by $p = \frac{\hat{p}}{\rho q_\infty^2}$, $(u,v)^T = \left(\frac{\hat{u}}{q_\infty}, \frac{\hat{v}}{q_\infty}\right)^T$, $\hat{p}, \hat{u}, \hat{v}, q_\infty$ are dimensional values.

2.2. Non-Newtonian fluids

A non-Newtonian fluid is a fluid in which the viscosity changes with the applied shear force. As a result, non-Newtonian fluids may not have a well-defined viscosity.

Although the concept of viscosity is commonly used to characterize a material, it can be inadequate to describe the mechanical behavior of a substance, particularly non-Newtonian fluids.

For the non-Newtonian fluids the system of 2D Navier-Stokes equations and the continuity equation written in conservative form reads

$$\underline{\underline{\widetilde{R}}}\,\underline{W}_t + \underline{F}_x + \underline{G}_y = \frac{\underline{\underline{\widetilde{R}}}}{\mathrm{Re}}\left(\underline{R}_x + \underline{S}_y\right), \tag{5}$$

where the definitions of the vector $\underline{W}$ as the vector of primitive variables and of the fluxes $\underline{F}$, $\underline{G}$ are the same as for Newtonian fluids mentioned above.

The expression of the different part of Navier-Stokes equations is

$$\underline{R} = (0, g_{11}, g_{21})^T, \ \underline{S} = (0, g_{12}, g_{22})^T, \tag{6}$$

$$g_{ij} = 2|e|^r e_{ij}, \quad e_{ij} = \frac{1}{2}\left(\frac{\partial u_i}{\partial x_j} + \frac{\partial u_j}{\partial x_i}\right), \tag{7}$$

then the main part of the right hand side of the Eq. (5) will be

$$\begin{aligned} &(g_{11})_x + (g_{12})_y = \\ &\quad 2|e|_x^r u_x + |e|_y^r (u_y + v_x) + |e|^r \Delta u, \\ &(g_{21})_x + (g_{22})_y = \\ &\quad |e|_x^r (u_y + v_x) + 2|e|_y^r v_y + |e|^r \Delta v. \end{aligned} \tag{8}$$

2.3. Boundary conditions

At the inlet the Dirichlet boundary condition for velocity vector $(u, v)^T$ is prescribed and the other variable are computed by extrapolation from a domain. At the outlet a pressure value is given and velocity components are computed by extrapolation from values inside of the domain. On the wall the zero Dirichlet boundary conditions for the components of velocity are used. Pressure at solid boundaries is not possible to prescribe in advance.Authors used extrapolation from computed domain to boundary where normal derivative of pressure is zero,Prandtls boundary layer relation.

3. NUMERICAL SOLUTION BY FINITE VOLUME METHOD

In what follows a steady state solution is considered. In such a case the artificial compressibility method can be applied for the solution of the system (3), i.e.

$$\underline{W}_t + \underline{\widetilde{F}}_x + \underline{\widetilde{G}}_y = \underline{0}, \tag{9}$$

where

$$\underline{\widetilde{F}} = \underline{F} - \frac{1}{\mathrm{Re}}\underline{F}^v, \quad \underline{\widetilde{G}} = \underline{G} - \frac{1}{\mathrm{Re}}\underline{G}^v \tag{10}$$

and $\underline{F}$, $\underline{G}$ are inviscid fluxes defined by Eq. (4), $\underline{F}^v$, $\underline{G}^v$ are viscous fluxes,

$$\underline{F}^v = (0, u_x, v_x)^T, \quad \underline{G}^v = (0, u_y, v_y)^T. \tag{11}$$

The Eq. (7) is integrated over D_{ij}

$$\iint_{D_{ij}} \underline{W}_t \, dx\, dy = -\iint_{D_{ij}} \left(\underline{\widetilde{F}}_x + \underline{\widetilde{G}}_y\right) dx\, dy. \tag{12}$$

The mean value theorem is applied to the left-hand side of Eq. (12), and Green's theorem on the right-hand side of Eq. (12), so that

$$\underline{W}_t\big|_{ij} = -\frac{1}{\mu_{ij}} \oint_{\partial D_{ij}} \underline{\widetilde{F}}\, dy - \underline{\widetilde{G}}\, dx. \tag{13}$$

Next the integrals on the right hand side of (13) are numerically approximated by

$$\underline{W}_t\big|_{ij} = -\frac{1}{\mu_{ij}} \sum_{k=1}^{4} \underline{\widetilde{F}}_{ij,k} \Delta y_k - \underline{\widetilde{G}}_{ij,k} \Delta x_k, \tag{14}$$

where viscous fluxes in $\underline{\widetilde{F}}$, $\underline{\widetilde{G}}$ are computed using dual volumes. For computation of these viscous fluxes the dual volumes for each edge of each cell inside the domain are used. The shapes of the basic cell and dual cell are shown in the Figure 1 and Fig. 2. Quadrilateral basic cells are used and therefore dual cells are also quadrilaterals. It results that the maximal value of k used in, e.g., Eq. (14) is $k = 4$.

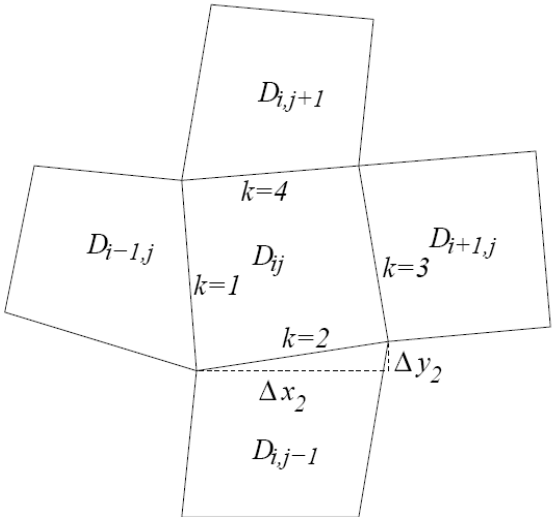

Figure 1. Finite volume cell D_{ij}

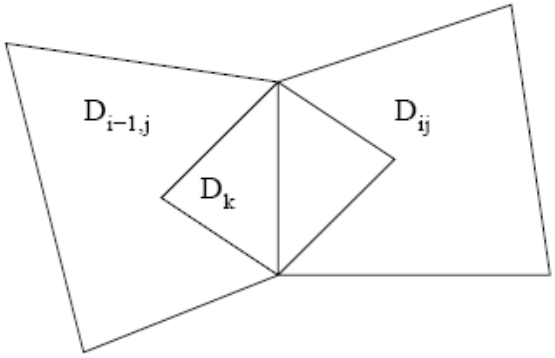

Figure 2. Dual volume cell D_k

The ODE system Eq. (14) is time discretized with the aid of multistage Runge-Kutta method

$$\begin{aligned} \underline{W}_{ij}^{n} &= \underline{W}_{ij}^{(0)} \\ \underline{W}_{ij}^{(r)} &= \underline{W}_{ij}^{(0)} - \alpha_r \Delta t \overline{R}\underline{W}_{ij}^{(r-1)} \\ \underline{W}_{ij}^{n+1} &= \underline{W}_{ij}^{(m)} \qquad r = 1, \ldots, m, \end{aligned} \tag{15}$$

where $m = 3$, $\alpha_1 = \alpha_2 = 0.5$, $\alpha_3 = 1$, $\overline{R}\underline{W}_{ij}^{n} = R\underline{W}_{ij}^{n} - D\underline{W}_{ij}^{n}$, and the steady residual $R\underline{W}_{ij}$ is defined by

$$\begin{aligned} R\underline{W}_{ij} = \frac{1}{\mu_{ij}} \sum_{k=1}^{4} \Bigg[&\left(\underline{F}_k - \frac{1}{\mathrm{Re}}\underline{F}_k^v\right)\Delta y_k \\ &- \left(\underline{G}_k - \frac{1}{\mathrm{Re}}\underline{G}_k^v\right)\Delta x_k \Bigg]. \end{aligned} \tag{16}$$

The term $D\underline{W}_{ij}$ presents the artificial viscosity of Jameson's type (for details see, e.g., [3]).

In order to satisfy the stability condition the time step is chosen as (for details see, [1]):

$$\Delta t = \min_{i,j,k} \frac{\mu_{ij}}{\rho_A + \rho_B + \frac{2}{\mathrm{Re}} \frac{\Delta x_k^{\,2} + \Delta y_k^{\,2}}{\mu_{ij}}}, \qquad (17)$$

where

$$\rho_A = \left(|\hat{u}| + \sqrt{\hat{u}^2 + 1}\right)\Delta y_k, \quad \rho_B = \left(|\hat{v}| + \sqrt{\hat{v}^2 + 1}\right)\Delta x_k \qquad (18)$$

and $|\hat{u}|$, $|\hat{v}|$ are the maximal values of the components of velocity vector inside the computational domain. The definitions of Δx_k, Δy_k are shown in Fig. 1.

The computation is performed until the value of the L^2-norm of residual satisfies $\mathrm{Rez}\ \underline{W}_{ij}^{n} \le \varepsilon_{\mathrm{ERR}}$ with $\varepsilon_{\mathrm{ERR}}$ small enough, where

$$\mathrm{Rez}\ \underline{W}_{ij}^{n} = \sqrt{\frac{1}{MN}\sum_{ij}\left(\frac{\underline{W}_{ij}^{n+1} - \underline{W}_{ij}^{n}}{\Delta t}\right)^2}. \qquad (19)$$

3. NUMERICAL RESULTS

In this paper the numerical results for channels with one entrance and two exit parts are presented. Results for two dimensional case and for three dimensional case are shown. The reference length l is equal to 1.

The domain topology of the first 2D simulation is shown in Fig. 3. The structured quadrilateral mesh used consists of 24 000 cells.

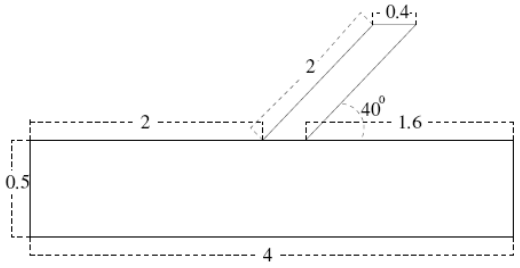

Figure 3. Domain topology of 2D branching channel

For the second type of the considered channel the domain topology is presented in the Fig. 4. The structured quadrilateral mesh used consists of 40 000 cells.

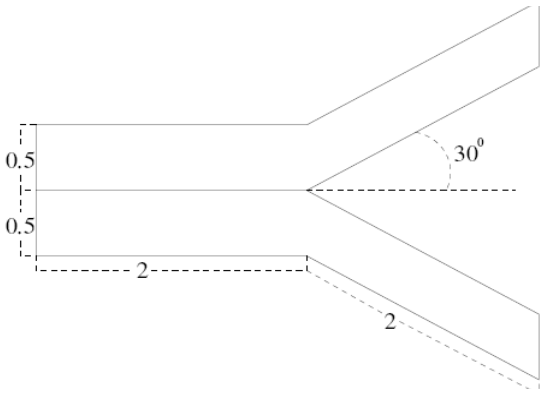

Figure 4. Domain topology of the branching channel

Figures Fig. 5 and 9 show the fluid velocity distribution for Reynolds number 1500 for the non-Newtonian fluids. In Fig. 6 and 10 reader can follow convergence history of p, u, v using steady rezidual behavior in L2 norm and convergence to steady state is very good. We also investigated convergence behavior using different grids with satisfactory results at finer grid. By the symbol q the velocity magnitude is denoted, i.e. $q = \sqrt{u^2 + v^2}$.

In Fig. 7 and 11 numerical results for the two dimensional and Newtonian fluids case are shown. Convergences of residuals of the vector $\underline{W} = (p, u, v)^{\mathrm{T}}$ for both cases of various shape of the channels are presented in Fig. 8 and 12.

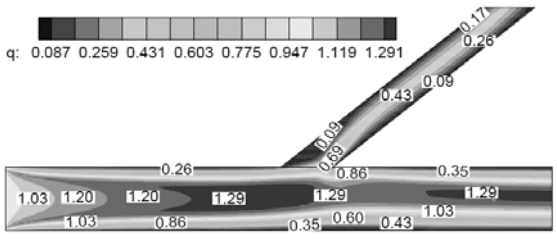

Figure 5. Velocity magnitude distribution in two dimensional channel for non-Newtonian fluids (Reynolds number Re = 1500)

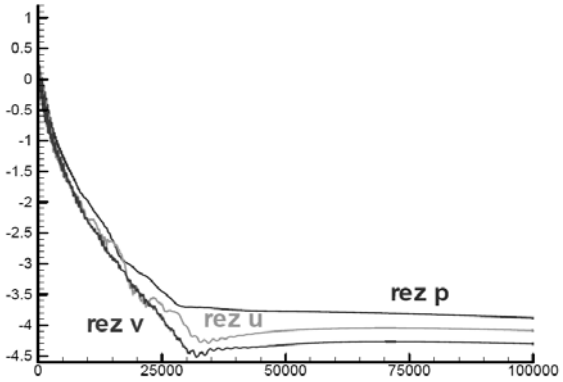

Figure 6. History convergence for two dimensional channel in Fig. 5

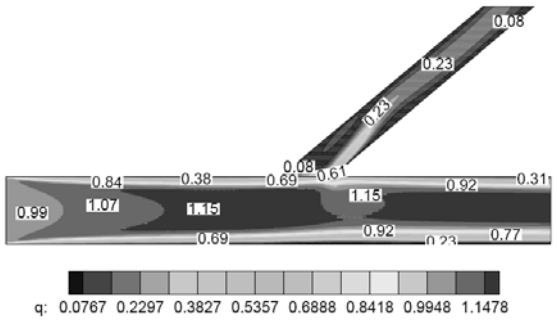

Figure 7. Velocity magnitude distribution in two dimensional channel for Newtonian fluids (Reynolds number Re = 1500)

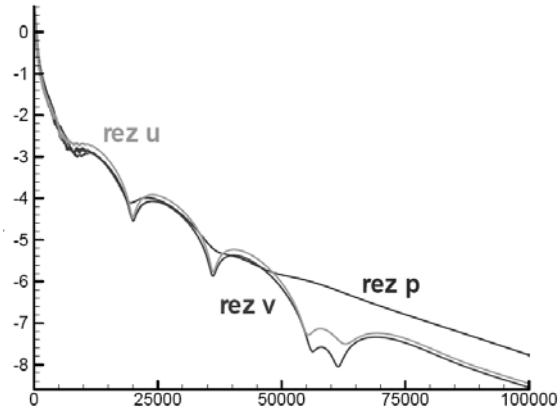

Figure 8. Convergence history for two dimensional channel in Fig. 7

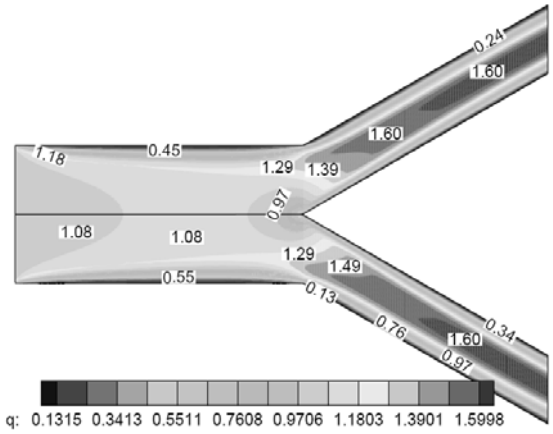

Figure 9. Velocity magnitude distribution in two dimensional channel for non-Newtonian fluids (Reynolds number Re = 1500)

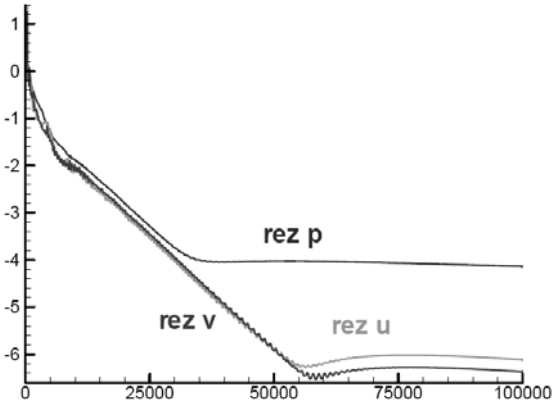

Figure 10. History of convergence for two dimensional channel from Fig. 9

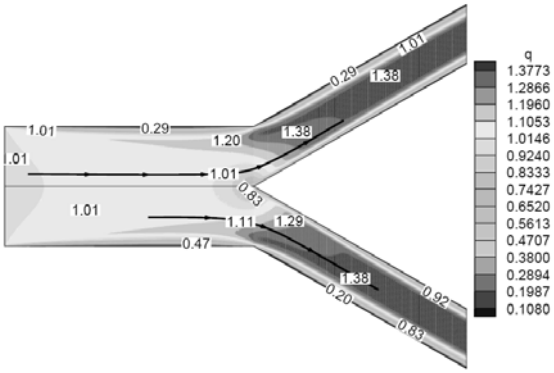

Figure 11. Velocity magnitude distribution in two dimensional channel for Newtonian fluids (Reynolds number Re = 1500)

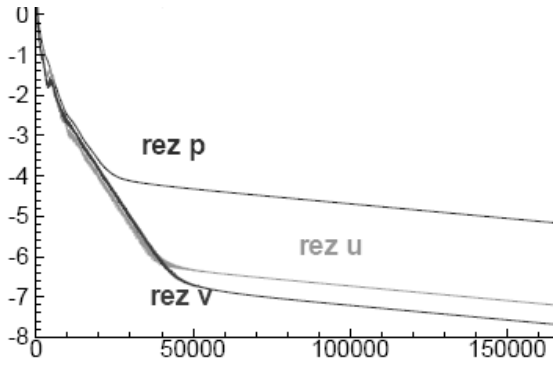

Figure 12. Convergence of residual for two dimensional channel from Fig. 11

Next, the computation for fully three dimensional fluid flows in two distinct cases was performed.

The domain topology for the first 3D branching channel is shown in the Fig. 13. The structured mesh used consists of 196 000 hexahedrons cells.

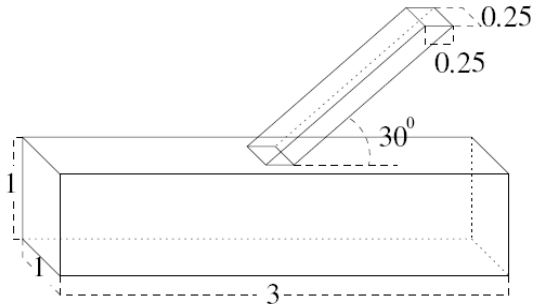

Figure 13. Domain topology of 3D branching channel

The domain topology for the second 3D branching channel is shown in the Fig. 14. The structured mesh used consists of 187500 hexahedrons cells.

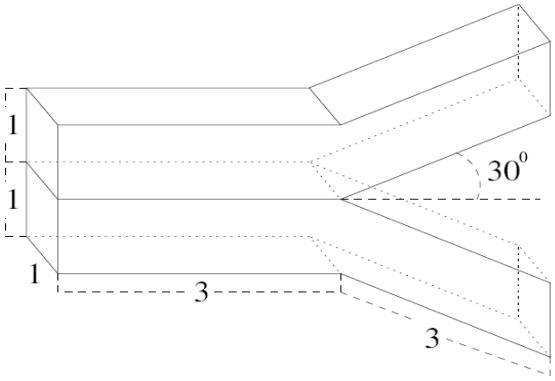

Figure 14. Domain topology of 3D branching channel

Fig. 15 shows velocity isolines in the cross-section of *x-y* plane of branching channel for Reynolds number 300. By the symbol *q* the velocity magnitude is denoted, i.e. $q = \sqrt{u^2 + v^2 + w^2}$.

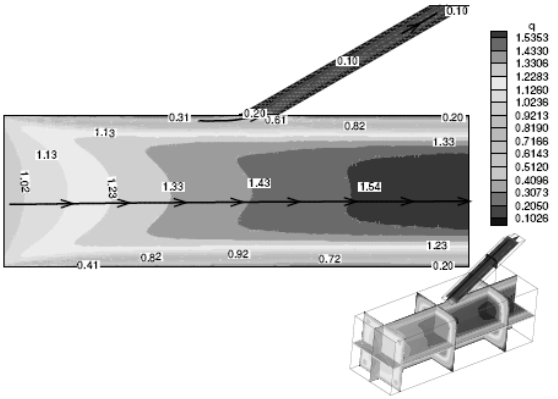

Figure 15. Velocity magnitude distribution in the central cut of the three dimensional channel (Reynolds number Re = 300)

Fig. 16 shows velocity isolines in the cross-section of the main part of the channel (see Fig. 15) and the cross-section of the small branch of the channel.

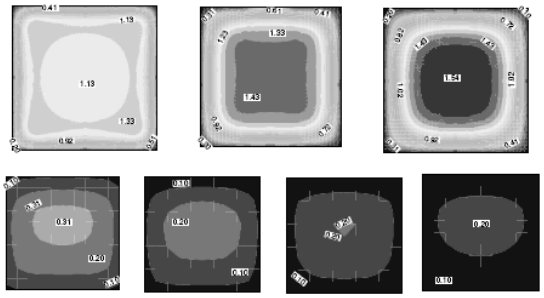

Figure 16. Velocity magnitude distribution in the cuts of the 3D channel from Fig. 15

Fig. 17 shows the velocity isolines in the cross-section of *x-y* plane of symmetric branching channel for Reynolds number 300. In this figure the convergence of the residuals of the vector $\underline{W} = (p, u, v, w)^T$ is shown.

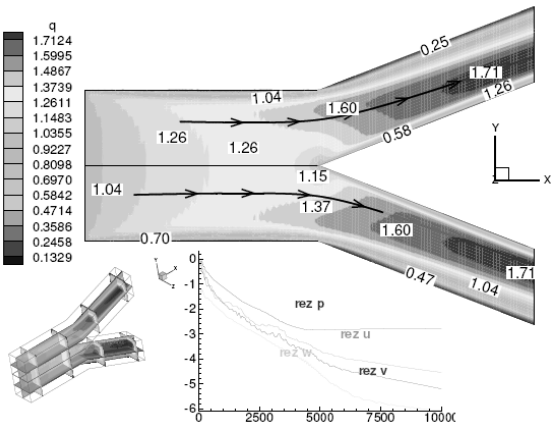

Figure 17. Velocity magnitude distribution in the central cut of the three dimensional channel (Reynolds number Re = 300)

Fig. 18, 19 and 20 show velocity isolines for cross-section of both parts of the branching channel from Fig. 17. Due to a symmetry of the channel can be observed the symmetry of the flow in both branches.

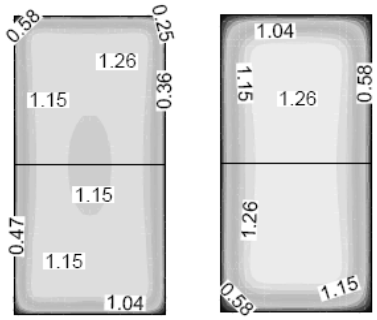

Figure 18. Velocity magnitude distribution in the cuts of the 3D channel from Fig. 17 (both branches near to entrance)

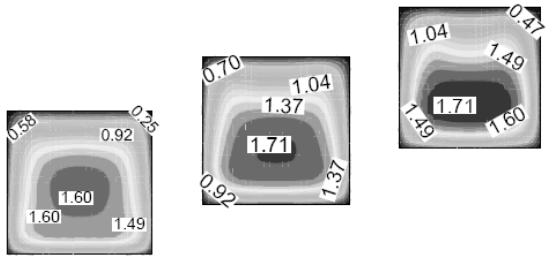

Figure 19. Velocity magnitude distribution in the cuts of the 3D channel from Fig. 17 (upper branch)

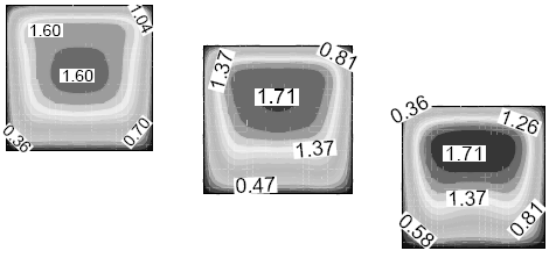

Figure 20. Velocity magnitude distribution in the cuts of the 3D channel from Fig. 17 (lower branch)

4. CONCLUSIONS

Numerical model for simulation of fluid flow in a branching channel for two dimensional and three dimensional cases was developed. However, the method was applied for several different types of channel configurations. The presented results should be useful as a blood flow approximation, the fact that several significant simplifications were made in the model should be mentioned. In this work the simple model of non-Newtonian flows was mentioned and the first results of these flows are presented in comparison with Newtonian fluids.

ACKNOWLEDGEMENTS

This work has been partly supported by the grant No. 201/05/0005 and Research Plan MSM 68 40770003.

REFERENCES

[1] R. Dvořák, K. Kozel, 1996, *Mathematical Modelling in Aerodynamics*. (in Czech), CTU Prague.

[2] K. Kozel, R. Keslerová, V. Prokop, 2002, "Numerical Solution of Icompressible Laminar Flows through a Branching Channel", Proc. *International Conference of Applied Mathematics and Informatics at Universities*, Trnava, Slovak Republic

[3] R. C. Swanson, E. Turkel, 1997, "Multistage Schemes with Multigrid for Euler and Navier-Stokes Equations", *NASA Technical Paper 3631*

[4] P. Louda, K. Kozel, J. Příhoda, 2004, "Numerical Solution of Flow through a Curved Difusser", Proc. *Colloquium Fluid Dynamics* pp. 107-110, Prague, Czech Republic

[5] K. Kozel, P. Louda, P. Sváček, J. Příhoda, 2004, "Finite Volume and Finite Element Methods Applied to Backward Facing Step Flows", Proc. *1st International Conference "From Scientific Computing to Computational Engineering"* Athens, Greek

Conference on Modelling Fluid Flow (CMFF'06)
The 13th International Conference on Fluid Flow Technologies
Budapest, Hungary, September 6-9, 2006

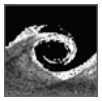

UFS SOFTWARE AND ITS APPLICATIONS FOR MODELLING OF GAS FLOWS

V. V. Aristov[1], A. A. Frolova[2], S. A. Zabelok[3], V. I. Kolobov[4], R. R. Arslanbekov[5]

[1] Corresponding Author. Dorodnicyn Computing Centre of Russian Academy of Sciences, ul. Vavilova, 40, Moscow GSP-1, 119991, Russian Federation. Tel.: +7 495 135 2087, Fax: +7 495 135 6159, E-mail: aristov@ccas.ru
[2] Dorodnicyn Computing Centre of Russian Academy of Sciences. E-mail: afrol@ccas.ru
[3] Dorodnicyn Computing Centre of Russian Academy of Sciences. E-mail: serge@ccas.ru
[4] Computational Fluid Dynamics Research Corporation, Huntsville, AL, USA. E-mail: vik@cfddrc.com
[5] Computational Fluid Dynamics Research Corporation, Huntsville, AL, USA. E-mail: rra@cfddrc.com

ABSTRACT

The aim of the paper is to outline a new approach which can be applied to simulate a wide class of supersonic and subsonic gas flows. This approach constructs a hybrid rarefied/transient/continuum flow solver suggested in [1] and is now developed in the framework of a software product "Unified Flow Solver" (UFS). The UFS can separate non-equilibrium and near-equilibrium domains using breakdown criteria and automatically select continuum and kinetic solvers. The solver in the kinetic domains is based on the direct numerical solution (DNS) of the Boltzmann equation. The so-called continuum kinetic schemes approximating the Euler or Navier-Stokes equations are used in the near-equilibrium domains. Cartesian mesh generation and refinement around arbitrary-shape solid bodies is implemented. Parallel capabilities with dynamic load balancing are realized for the UFS. Solutions of some external and internal problems are presented. The UFS demonstrates robustness and flexible properties in simulation of different 2D and 3D flows around bodies of different shapes and in description of flows in 2D and 3D micronozzles. Slow flows through a slit, an orifice and in channels are also solved keeping in mind possible applications for descriptions of flows in microdevices.

Keywords: the Boltzmann equation, external aerodynamic problems, hybrid schemes, internal flows, the Unified Flow Solver (UFS)

1. INTRODUCTION

Many external and internal problems are characterized by the presence of rarefied and continuum domains. Accurate simulation of rarefied domains requires particle level models, continuum domains are naturally described by the traditional Computational Fluid Dynamics (CFD) models. The development of hybrid solvers combining particle and continuum models has been an important area of research over the last decade [1-3]. In this paper, we describe a recently developed Unified Flow Solver (UFS) and demonstrate the current UFS capabilities for different applications.

The direct Boltzmann solver for simulations of rarefied flow domains is used. Traditionally, Direct Simulation Monte Carlo (DSMC) has been used for simulations of rarefied gas flows [4]. Recently, Direct Numerical Solution (DNS) of the Boltzmann equation emerged as a viable alternative to DSMC [5, 6]. The DNS is preferable to DSMC for coupling kinetic and continuum solvers because similar numerical techniques are used for solving both the Boltzmann and continuum equations. For the slow subsonic flows DNS has also some advantages. For this reasons, DNS was selected for the UFS implementation described in this paper.

Another component of the UFS is a continuum flow solver. Since the continuum solver should be correspondent to the Boltzmann solver in the UFS framework, it is preferable to implement such a solver using numerical algorithms similar to the Boltzmann solver. From this point of view, recently introduced kinetic schemes of gas dynamics are very attractive because they use kinetic equation is a starting point for the development of computational algorithms [7, 8]. The remaining components of the UFS include criteria for domain decomposition into kinetic and continuum parts and coupling algorithms.

The open source code GERRIS Flow Solver (GFS) [9] was selected as a framework for the UFS. The original GFS contained a tree-based incompressible flow solver with dynamically adaptive Cartesian grid and support of complex solid boundaries [10]. Using the GFS framework, we have added all the UFS components including a

deterministic Boltzmann solver for a one-component mono-atomic gas, compressible Euler and NS solvers based on kinetic schemes, and developed practical criteria for domain decomposition and coupling kinetic and continuum solvers. The UFS can automatically generate Cartesian mesh around embedded solid boundaries defined through standard files, perform dynamic adaptation of the mesh to the solution and geometry, detect kinetic and continuum domains and select appropriate solvers based on continuum breakdown criteria.

2. MAIN FEATURES OF THE UNIFIED FLOW SOLVER (UFS)

Key components of the UFS are shown in Figure 1. Numerical schemes for DNS are referred in our papers. Kinetic schemes differ from the traditional CFD schemes by using the Boltzmann equation for building the computational CFD algorithms. These schemes are described in the literature (see [5, 7, 8]). We have implemented kinetic schemes for both Euler and NS type equations in the UFS framework. Domain decomposition according to some (kinetic and continuum) criteria is constructed. The coupling algorithm is developed. Parallelization in the framework of the GERRIS is proposed and effective schemes for the UFS are suggested.

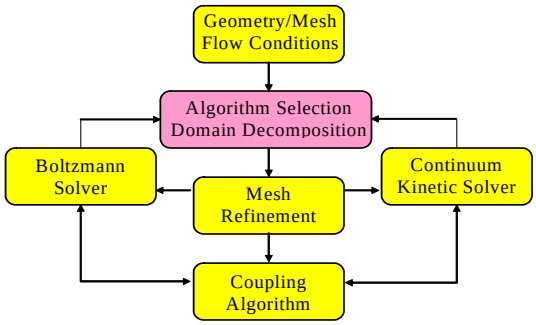

Figure 1. Key UFS components

The main problem of hybrid methods is correct separation of kinetic and continuum domains. Selection of adequate switching criteria is crucial because wrong domain decomposition could lead to non-positive distribution function for the kinetic NS solution and failure of the Boltzmann solver. We have tested and used the following switching criteria:

$$S_p = \sqrt{p_{xx}^2 + p_{yy}^2 + p_{zz}^2} \Big/ p,$$

$$S_{Kn\_local} = Kn \frac{1}{\rho} \frac{\partial \rho}{\partial x},$$

$$S_{NS} = Kn \sqrt{\left(\frac{\nabla \rho}{\rho}\right)^2 + \frac{\left(\frac{\partial u}{\partial x}\right)^2 + \left(\frac{\partial v}{\partial x}\right)^2 + \left(\frac{\partial w}{\partial x}\right)^2}{T}},$$

$$S_{NS} = \tau \sqrt{\left(\frac{\nabla p}{p}\right)^2 + \frac{\left(\frac{\partial u}{\partial x}\right)^2 + \left(\frac{\partial v}{\partial x}\right)^2 + \left(\frac{\partial w}{\partial x}\right)^2}{u^2 + v^2 + w^2}}$$

where p_{xx}, p_{yy}, p_{zz} are appropriate components of the non-equilibrium stress tensor, p is the pressure, ρ is density, T is temperature, u, v, w are appropriate component of velocity (all values are given in dimensionless form), Kn is the Knudsen number of the problem under consideration (e.g., for a flow around a cylinder $Kn = \lambda / R$ where λ is the reference mean free path and R is the radius of a cylinder). If S is greater then a threshold value, then the kinetic solver must be used. The applicability of different criteria and the best ways of choosing the threshold value is currently being studied. It was found experimentally that the S_{Kn_local} criterion allows correctly separate the non-equilibrium domains near the shock wave and behind the body at moderate Knudsen numbers, but at small Knudsen numbers (Kn<<0.1) the non-equilibrium domain behind the body appears to be too small. We found experimentally that criterion S_{NS} (it is not shown here due to a long formula) gives correct kinetic regions and allows one to successfully couple the NS and Boltzmann solvers.

The possibility of dynamic domain decomposition into sub-domains of arbitrary shape has been implemented in the UFS. To achieve dynamic load balancing (DLB) between multiple processors during a parallel run, the computational domain is partitioned into sub-domains using a space filling curves (SFC) algorithm [11]. It is natural to use SFC for the tree-based mesh generation and refinement engine, since the cell traversing routines work exactly as Morton N-ordering SFC algorithm. Figures 2 and 9a) show examples of DLB between 8 processors for the problems of flow around cylinder and flow in a channel respectively. Different colors represent sub-domain solved by different processors. It is seen that grid adaptation results in redistribution of the load between the processors. The SFC algorithm allowed us to obtain a good parallel efficiency for the problems that have been computed so far. However, in the SFC algorithm, the edge-cut weights are not taken into account, so for some problems this algorithm might not provide good partitioning. In the future it is planned to use METIS library for optimal domain partitioning for the UFS.

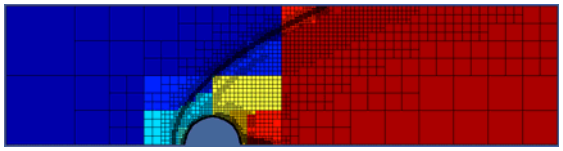

Figure 2. Dynamic load balancing between 8 processors for gas flow around a cylinder. Each processor is shown by a different color

3. VERIFICATION AND VALIDATION OF THE METHOD

The Boltzmann direct schemes have been verified by numerous computing experience (see [5]). The Boltzmann solver in the framework of the UFS have been tested, e.g. by the comparison of two schemes in [1]. The UFS Boltzmann solver have been tested by the comparison with available experimental data as well. (1D problem with shock wave structure in the density profile in Argon for Mach number M=3.8 according to the experiment by [12] and the temperature profile in Helium for M=1.59 is given according to the experiment [13]; 2D problem of a flow around a circular cylinder [14]). The comparison with available experiment has been made as well. The continuum solvers have been tested for the well-known problem on an internal gas flow in a channel with a forward-facing step, for the SOD problem and for flows in channel with different shapes.

We performed testing of the Boltzmann and NS kinetic solvers for 2D problem of heat transfer between two parallel plates with nonuniform temperature along the plate surfaces. The problem of gas flow and heat transfer in rarefied gas confined between non-uniformly heated boundaries have been studied in a number of publications starting from works by Sone (see [15]). As described by Sone, traditional NS equations (with the no-slip boundary conditions) in this case give zero flow velocity and symmetric distribution of gas temperature. We considered a rarefied gas contained between two parallel plates with temperatures T=1 at y=0.5 and T=1-0.5sin(πx) at y=-0.5. The computational domain was a unit box with symmetry (specular) boundary conditions at x=-0.5 and x=0.5. Diffuse reflection at the top and bottom boundaries (y=0.5 and y=-0.5) was assumed. We solved this problem for different Kn numbers using the Boltzmann solver (with BGK collision operator and the HS model to compare directly with results by Sone et al.) and using the NS kinetic solver with the kinetic boundary conditions. The results of calculations using the kinetic NS solver are presented in Figure 3. One can see that there is a well-formed vortex in the middle of the simulation domain. This vortex is temperature-driven. The simulation with the kinetic NS solver (with the kinetic boundary conditions) reproduced well results of the Boltzmann solver and permitted to obtain the same vortex structure.

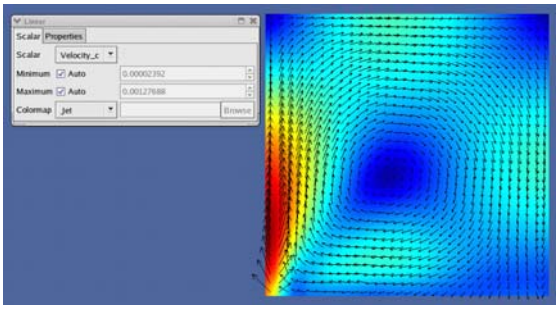

Figure 3. Temperature (color) and mean flow velocity for Kn=0.03.

4. PROBLEMS OF EXTERNAL AERODYNAMICS

We describe some supersonic external problems. The flow around a cylinder at M=3 was studied in a wide range of Kn numbers (0.001-10) with different criteria of domain decomposition. The boundary condition on the surface of the cylinder corresponds to diffusion reflection with the temperature of the wall T=4. Figure 4 shows the results of computations with Boltzmann solver and Euler solver.

Important quantities of the gas flow interaction with solid bodies are the vector of forces (F_x, F_y, F_z), the normal force F_n (pressure) and the shear force or shear stress F_t and the heat flux H. Both integral and local quantities can be calculated by the UFS code. We have tested this implementation for the problem of gas flow around a cylinder for different Mach, Knudsen numbers and different temperatures of the cylinder surface. In Figure 5 the convergence of the computations with respect to a breakdown parameter is illustrated for the case of M=3, Kn=0.25. It is seen that the normal force on the cylinder surface calculated at 5 breakdown parameters S = 0.025, 0.05, 0.1, 0.2, and 0.4 converge at small S numbers when the Boltzmann region grows. At the same time, by decreasing the S number, the computation time increases. Therefore, for quick results one can use larger S numbers if precision of the order of 10% is satisfactory.

Figure 6 shows the UFS results the Orbital Reentry Experiment (OREX) for M=10 and Kn=0.1. The density distribution is shown in color on the vertical plane with a maximum plotted value of 6 for clarity (maximum of density is 24). The horizontal plane displays kinetic (red) and continuum cells. Figure 7 shows simulations of the Space Shuttle Orbiter at an angle of attack of 45 degrees and Mach number of 5. The surface of the Shuttle was defined using a standard stl file [16]. One can see the grid refinement and color indicates the Mach number.

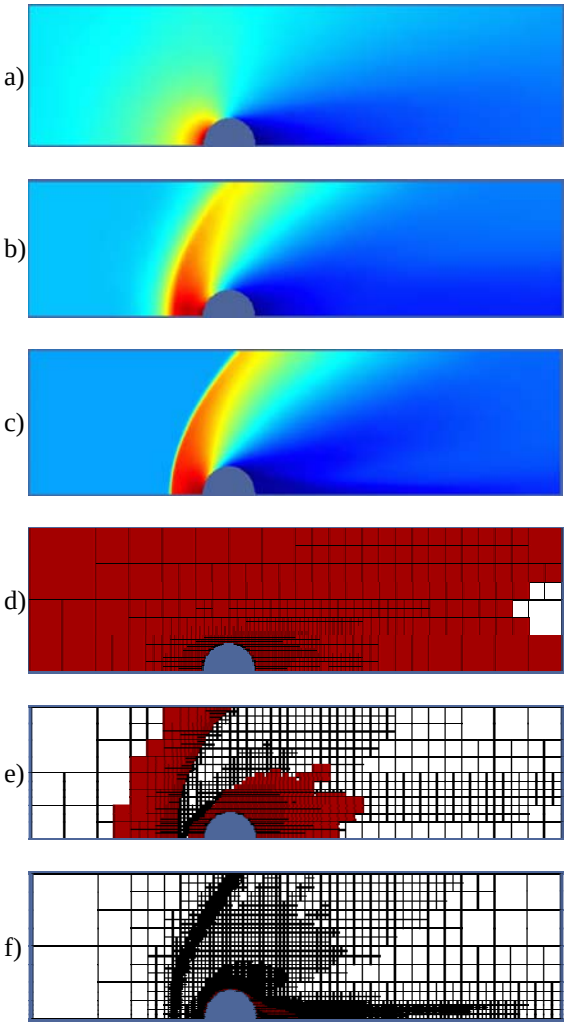

Figure 4. Gas flow around a cylinder at M=3 for different Kn numbers ($Kn = \lambda / R = 5$ (a, d), 0.5 (d, e), 0.005 (c, f)). On the top plots (a, b, c) are the density profiles, on the bottom plots (d, e, f) are the computational grid with kinetic (red) and continuum (white) domains.

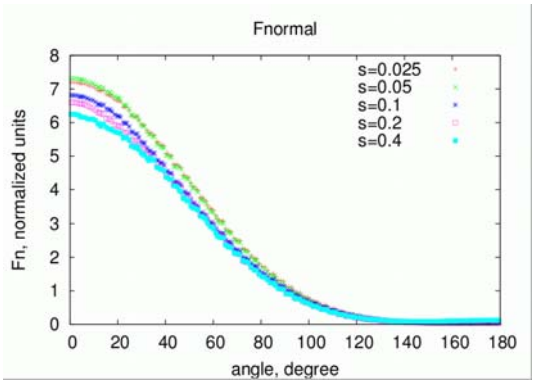

Figure 5. Distribution of normal force over the cylinder surface for different values of the continuum breakdown parameter S.

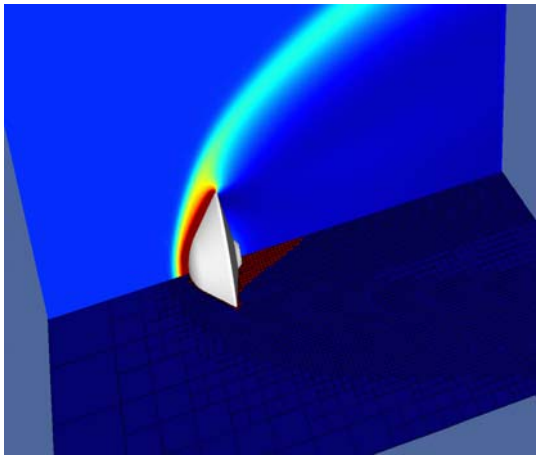

Figure 6. Simulation of OREX reentry, using the UFS solver at M=10 and Kn =0.1

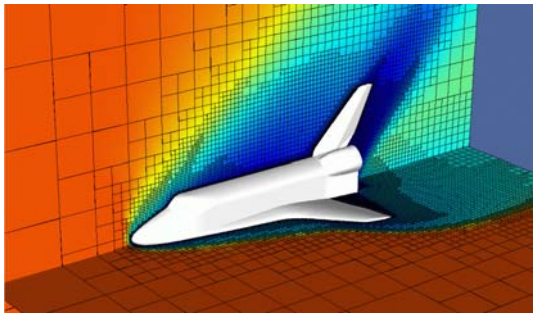

Figure 7. Simulation of a flow around a the Space Shuttle Orbiter. The color map shows distribution of Mach number in two planes.

4. INTERNAL PROBLEMS

Accurate simulation of micro flow problems is important for a number of modern practical applications. Kinetic treatment can be crucial for studies of gas flows in micro-electro-mechanical systems (MEMS) that can operate in a transitional regime ($0.1<Kn<10$) where the rarefied gas effects can be significant. The Navier-Stokes solver with a velocity slip boundary conditions can be inadequate for the transitional regime. Direct methods for solving the Boltzmann equation possess attractive features intrinsic for low speed flows. We simulate gas flows through an orifice for a wide range of pressure ratios including small values 0.9, 0.95, 0.99 using either the Boltzmann solver or the UFS. We can also analyze several low speed flow problems such as external flows around a planar plate, internal flows between two plates maintained at non-uniform temperature, flows through a slit both for isothermal and non-isothermal regimes and different pressure ratios. We also study flows in short and relatively long channels. We demonstrate the UFS technology for gas flows in micronozzles.

We have simulated flows through a slit and a channel for various values of the pressure ratio. We have performed verification of the Boltzmann

solver at first for the isothermal flow through a slit. Two different equilibrium functions (0 denotes the inlet, 1 denotes the outlet) are maintained at the free boundaries of two chambers. The diffuse reflection was assumed at the wall with the wall temperature equal to the initial gas temperature. We have performed 2D simulations for Kn=0.5 and different pressure ratios in the chambers P_1/P_0=0.99, 0.95, 0.9, 0.5, 0.1. The gas temperatures in both chambers were kept the same $T_1=T_0=1$. Figure 8 shows results of our simulations for the density contours in the case of the pressure ratio P_1/P_0=0.95.

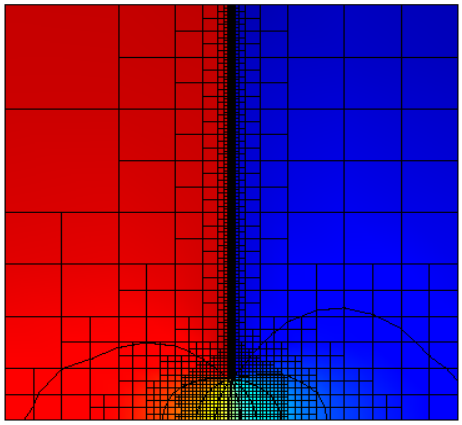

Figure 8. Mesh and density contours for the isothermal flow through a slit (P_1/P_0=0.95) We performed a series of calculations for a relatively long channel (L/d=21) with isothermal conditions (the pressure ratio P_0/P_1=2.) for different Knudsen numbers Kn=1, 0.2, 0.02. In Figure 9 the stream-wise velocity distribution (for the Lennard-Jones molecular model) in a channel is shown. One can see the increase of the velocity from the inlet boundary to the outlet boundary and a non uniform distribution of the velocity in cross-sections. The Knudsen number Kn=0.5. In Figure 10 the mass flow rate in dependence of the Knudsen number is shown, one can see Knudsen's minimum in the vicinity of Kn~1.

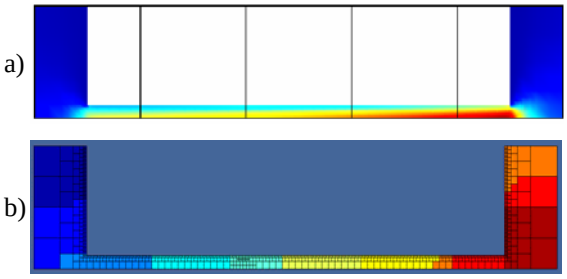

Figure 9. Flow in a relatively long channel: a) distribution of the streamwise velocity; b) dynamic load balancing between 8 processors, each processor is shown by a different color;

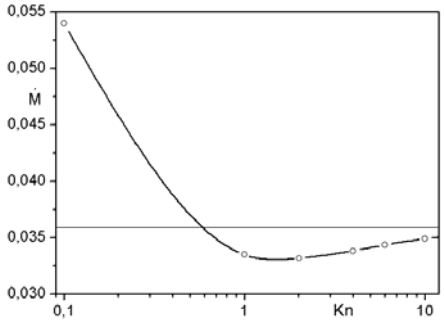

Figure 10. The Knudsen effect (non-monotonous character of mass flow rate) for a relatively long channel

Figure 11 shows results of UFS simulations of a nozzle. The boundary conditions for the first case were accepted as follows: in the inlet of the nozzle n_{in}=1, T_{in}=1.2, the Mach number M=0.2 for the outlet of the nozzle n_{out}=0.05, T_{out}=0.2. The velocity is determined from the conservation of the enthalpy along the symmetry line. Figure 12 demonstrates similar results for 3D micronozzle simulation.

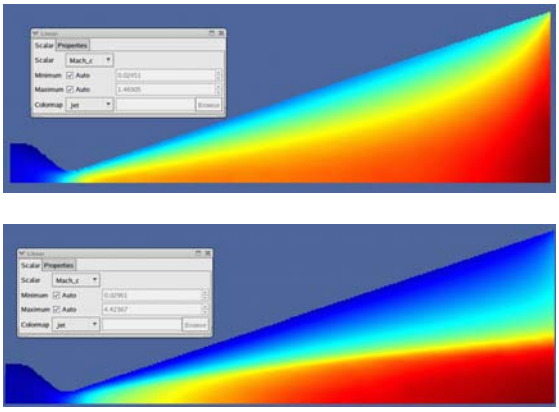

Figure 11. UFS for a nozzle for two Knudsen numbers Kn=0.01 (top), Kn=0.001 (bottom) Mach number distributions (0.03<M<1.47 for the top plot, 0.03<M<4.42 for the bottom plot).

6. CONCLUSION

We have developed a Unified Flow Solver with adaptive mesh and algorithm refinement based on direct numerical solution of the Boltzmann equation coupled to kinetic schemes of gas dynamics. This strategy allows easy coupling of continuum and Boltzmann solvers. The work has confirmed that UFS methodology results in significant savings of computational resources by limiting expensive kinetic solutions only to the regions where they are needed. We have demonstrated that the Unified Flow Solver can automatically introduce or remove kinetic patches to maximize accuracy and efficiency

of simulations. Current work is focused on extension to multi-component reactive gas mixtures for simulation of practical problems of polyatomic gas mixtures of different degrees of rarefaction.

ACKNOWLEDGMENTS

This work is supported by the Russian Foundation for Basic Research, Grant N 04-01-00347 and also by the US Air Force SBIR Project F33615-03-M-3326.

a)

b)

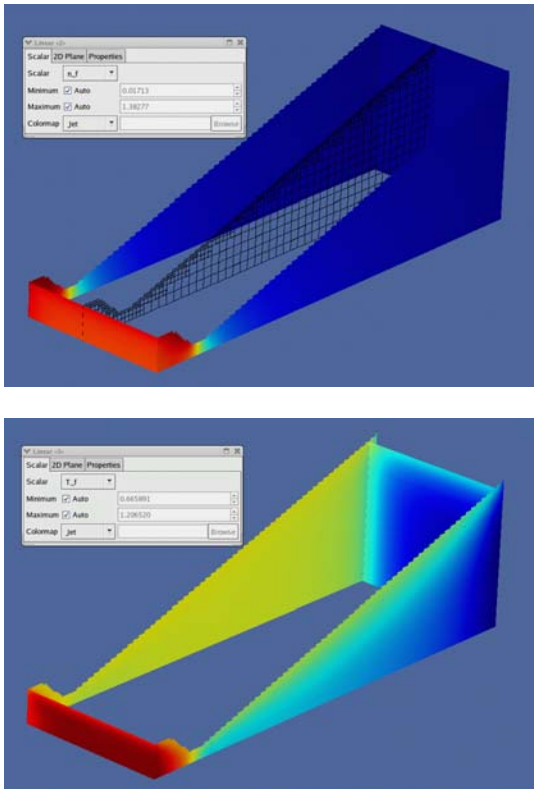

Figure 12. 3D micronozzle simulation: a) density; b) temperature

REFERENCES

[1] V.I.Kolobov, S.A.Bayyuk, R.R.Arslanbekov, V.V.Aristov, A.A.Frolova, and S.A.Zabelok, Construction of a Unified Continuum/Kinetic Solver for Aerodynamic Problems, *AIAA Journal of Spacecraft and Rockets* 42, 598 (2005)..

[2] V.V.Aristov, A.A.Frolova, and S.A.Zabelok V.I.Kolobov, S.A.Bayyuk, R.R.Arslanbekov, in RAREFIED GAS DYNAMICS: *24th International Symposium on Rarefied Gas Dynamics, AIP Conference Proceedings* ***762****, Monopoli, Bari,* Italy, 10-16 July 2004, p. 96.

[3] V.Kolobov, R.R.Arslanbekov, V.V.Aristov, A.A.Frolova, and S.A.Zabelok, Unified Solver for Rarefied and Continuum Flows with Adaptive Mesh and Algorithm Refinement, submitted to *J. Comp. Phys.*, Dec. 2005.

[4] G. Bird, *Molecular Gas Dynamics and the Direct Simulation of Gas Flows*, Claredon Press, Oxford, 1994

[5] V.V.Aristov, *Direct Methods for Solving the Boltzmann Equation and Study of Non-Equilibrium Flows*, Kluwer Academic Publishers, 2001.

[6] F.G.Tcheremissine, Direct Numerical Solution of the Boltzmann Equation, in RAREFIED GAS DYNAMICS: *24th International Symposium on Rarefied Gas Dynamics, AIP Conference Proceedings* ***762****, Monopoli, Bari,* Italy, July 2004, p. 677

[7] K.Xu, A gas-kinetic BGK scheme for the Navier-Stokes equations and its connection with artificial dissipation and Godunov method, *Journal of Computational Physics*. Vol. 171, (2001), pp. 289–335.

[8] T.Ohwada and S.Fukata, Simple derivation of high-resolution schemes for compressible flows by kinetic approach, *J.Comp. Phys*. 211, 424 (2006)

[9] http://gfs.sourceforge.net

[10] S.Popinet, *J. Comp Physics* 190, 572 (2003)

[11] M.J. Aftosmis, M.J. Berger, S.M. Murman, Application of Space-Filling Curves to Cartesian Methods in CFD, *AIAA 2004-1232*

[12] H.Alsmeyer, Density profiles in argon and nitrogen shock waves measured by the absorption of an electron beam, *J. Fluid. Mech.* 74, 497 (1976)]

[13] E.P.Muntz and L.N.Harnett, *Phys. Fluids*, 12, 2027 (1969)];

[14] G.J.Maslach and S.A.Schaaf, Cylinder drag in the transition from continuum to free-molecule flow. *Phys Fluids* 6(3), 315 (1963)

[15] Sone, Y., *Kinetic Theory and Fluid Dynamic. Birkhauser*. Boston. 2002

[16] K.A.Boyles, G.J.LeBeau, F.E.Lumpkin III, and R.C.Blanchard, The use of virtual sub-cells in DSMC analysis of Orbiter aerodynamics at high altitudes, *AIAA 2003-1030*.

Conference on Modelling Fluid Flow (CMFF'06)
The 13th International Conference on Fluid Flow Technologies
Budapest, Hungary, September 6-9, 2006

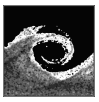

APPLICATION OF LOCAL DEFECT CORRECTION TO A TIME DEPENDENT PROBLEM

J. de Hoogh[1], J.G.M. Kuerten[2]

[1] Corresponding Author. Department of Mechanical Engineering, Technische Universiteit Eindhoven, P.O box 513, 5600 MB Eindhoven, the Netherlands . E-mail: j.d.hoogh@tue.nl
[2] Department of Mechanical Engineering, Technische Universiteit Eindhoven

ABSTRACT

To investigate the behavior of the concentration of a passive scalar in a turbulent flow with realistic high Schmidt numbers, one needs a very fine grid to capture all length-scales that are present in the concentration. An efficient method to increase the spatial resolution without a drastic raise of the computational costs is to apply a Local Defect Correction method. To compute the turbulent velocity field, a Direct Numerical Simulation is used that consists of a pseudo-spectral method in two periodic directions and a Chebyshev expansion in the wall-normal direction. The concentration equation for the passive scalar is solved using a finite volume method. The main concern with an LDC method in a hyperbolic time-dependent problem is the interpolation of the concentration when the refinement area is moved. The interpolated solution has to be smooth and continuous to ensure numerical stability. Results show that with Local Defect Correction it is possible to accurately compute the development of the concentration of a passive scalar in turbulent flow.

Keywords: Local Defect Correction, Turbulence, Passive Scalar

NOMENCLATURE

A,a	$[m^2]$	surface area
C,c	$[mol\ m^3]$	concentration
Cc	$[mol\ m^3]$	corrected concentration
Cb	$[mol\ m^3]$	best approximation
$Cfit$	$[mol\ m^3]$	fitted concentration
D	$[m^2\ s^{-1}]$	diffusivity
Dc	$[mol\ m^3]$	defect
Dq	$[mol\ s^{-1}]$	defect of flux
H	$[m]$	height
L	$[m]$	length
P	$[Pa]$	pressure
Q,q	$[mol\ s^{-1}]$	flux of concentration
Re	[-]	Reynolds number
Sc	[-]	Schmidt number
U_b	$[m\ s^{-1}]$	bulk velocity
V,v	$[m^3]$	volume
T,t	$[s]$	time
$\underline{n}$	[-]	unit normal vector
$\underline{u}$	$[m\ s^{-1}]$	velocity vector
u_τ	$[m\ s^{-1}]$	friction velocity
x,y,z	$[m]$	position
$\Delta X, \Delta x$	$[m]$	discrete spatial step
$\Delta T, \Delta t$	$[s]$	discrete time step
α,β,γ	[-]	fit parameters
η	[-]	threshold
ν	$[m^2\ s^{-1}]$	kinematic viscosity
ρ	$[kg\ m^3]$	density
σ	[-]	standard deviation
τ	$[m]$	position offset
$\underline{\omega}$	$[s^{-1}]$	vorticity vector

Subscripts and Superscripts

i	surface index
j,k,l	discrete position
n	discrete time level

1. INTRODUCTION

In many applications in industry and the environment particles are transported in a turbulent flow. There are various ways to model such a particle-laden flow. In so-called Lagrangian simulation methods the time-dependent velocity field of the carrier fluid is calculated by means of direct numerical simulation (DNS) or large-eddy simulation (LES) and for each particle an equation of motion is solved to track its position in time. In this way it is possible to take all forces that are exerted by the fluid on the particle into account, but

in view of computational requirements the method is restricted to relatively small numbers of particles, say on the order of one million.

Eulerian simulation methods, on the other hand, do not consider individual particles but particle concentration. In the simplest case, where the particles are so small that they move as passive particles with the fluid, the governing equation for particle concentration is a convection-diffusion equation. The convection velocity equals the local fluid velocity and the diffusion coefficient depends on the properties of particles and fluid molecules. In many applications involving small particles in water or air, the diffusivity is orders of magnitudes smaller than the kinematic fluid viscosity. This implies that structures in the particle concentration are much smaller than the structures in the fluid velocity and a very fine grid is needed to accurately capture all scales. If the particles are distributed over the total computational domain this goes beyond presently available computer capacities.

However, if the particles are mostly located in a confined region, a very fine local grid could be superposed on a global coarse grid to capture all relevant structures. This situation resembles that of a stationary fine-scaled flame in a coarser stationary fluid flow, which has been studied by Anthonissen [1,2,3]. His work was based on previous work by Ferket [4] and uses local defect correction (LDC) [5]. In LDC first a global coarse grid solution is calculated, which is used as a boundary condition for a local fine grid solution in the region where the small structures are located. The difference between the fine and coarse grid solutions on the fine grid region is a measure for the error on the coarse grid. Subsequently the coarse grid solution is improved by a defect term in the governing equation based on this error.

The present problem differs from the original setting in which LDC was applied, since the present problem is governed a time-dependent hyperbolic equation and is three dimensional. In a time-dependent problem the local fine grid region should move with the fluid flow. Minero [6,7,8,9] already applied LDC to a two-dimensional convection-diffusion equation. The main problem in extension to three spatial dimensions is that the number of grid points needed to maintain stability is too large in three dimensions. In this paper it will be investigated how the LDC method can be applied to a three-dimensional convection-diffusion equation, describing the concentration of a passive particle in turbulent channel flow. In section 2 the governing equations for fluid and particles and their discretization will be presented. Section 3 describes the basic principles of the LDC method. In section 4 the motion of the refinement region is discussed, in section 5 results are presented together with some preliminary conclusions.

2. GOVERNING EQUATIONS AND NUMERICAL METHOD

In the DNS the three-dimensional Navier-Stokes equation for incompressible flow is solved in the vorticity formulation. The equation reads:

$$\frac{\partial \underline{u}}{\partial t} + \underline{\omega} \times \underline{u} + \frac{1}{\rho} \nabla p = \nu \Delta \underline{u} \tag{1}$$

Here, P denotes the total pressure, $P=p+\frac{1}{2}\rho\underline{u}^2$, $\underline{u}$ the fluid velocity, $\underline{\omega}$ the fluid vorticity, ρ the fluid density and ν the kinematic viscosity.

In the DNS the computational domain consists of a channel of a finite length equal to $4\pi H$ and finite width equal to $2\pi H$, where H is half the height of the channel. In both directions periodic boundary conditions are applied. This makes a spectral method with a Fourier-Galerkin approach in the two periodic directions the natural choice. In the wall-normal direction a Chebyshev-collocation method is applied.

For integration in time a second-order accurate method is chosen, which is a combination of the explicit Adams-Bashforth method for the nonlinear terms and the implicit Crank-Nicolson method for the linear terms. In the first step the nonlinear terms are calculated pseudo-spectrally by fast Fourier transform, where the 3/2-rule is applied to prevent aliasing errors. In the second step the pressure is calculated and in the last step the viscous terms are treated implicitly. Since the Fourier modes are completely decoupled, only a one-dimensional system of equations needs to be solved for each Fourier mode. The walls of the channel act as no-slip walls. In order to satisfy the continuity equation the velocity field is made divergence free within machine accuracy following the approach proposed by Kleiser and Schumann [10] applied to the collocation approximation [11].

The mean axial pressure gradient is chosen in such a way that the volume flow, and hence the Reynolds number based on the bulk velocity, remains constant. The simulations are started from an arbitrary initial solution. After a large number of time steps a state of statistically stationary turbulent flow is reached. All results shown have been calculated at a Reynolds number based on the bulk velocity, $Re=U_bH/\nu=2800$, where U_b is the bulk velocity. This corresponds to a Reynolds number based on the friction velocity u_τ of 180,

$$u_\tau = \sqrt{\nu \left| \frac{d\overline{u_x}}{dz} \right|_{z=\pm H}} \tag{2}$$

where *x*, *y*, and *z*, denote the stream wise, span wise and wall normal coordinate. At this Reynolds number results can be compared with DNS results by Moin *et* al. [12]. As an example the fluctuations of the three velocity components are compared in figure 1. It can be seen that the agreement is good. The same conclusion can be drawn for other quantities, such as the terms in the balance equation for the turbulent kinetic energy.

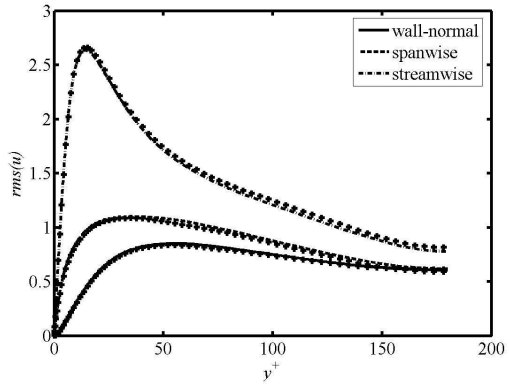

Figure 1. Velocity fluctuations as functions of the wall-normal coordinate wall units. Lines: present results, symbols: Moin *et al* [12].

2.1 Concentration equation for a passive scalar

The DNS code is extended with a convection-diffusion equation for the concentration of a passive scalar. The governing equation reads,

$$\frac{\partial c}{\partial t} + \underline{u} \cdot \nabla c = D \Delta c \tag{3}$$

where *D* is the diffusivity. The equations of fluid and particle concentration are non-dimensionalized with half the channel height and the friction velocity. When these scaling quantities are applied to Eq. (3), this results in,

$$\frac{\partial c}{\partial t} + \underline{u} \cdot \nabla c = \frac{1}{\mathrm{Re}\, Sc} \Delta c \tag{4}$$

With *Re* the Reynolds number and *Sc* the Schmidt number that is defined as the ratio of the kinematic viscosity ν and the diffusivity *D*.

The numerical method that is used for the fluid velocity, is not well suited for the concentration. The velocity has many points located near the wall, but less point in the centre of the channel. The concentration will be released in the centre of the channel and therefore has no need for many points in the wall region. Secondly, a spectral method is not suited for grid refinement techniques, because the solution inside the refinement area is not periodic.

For the computation of the particle concentration a finite volume method is implemented on a Cartesian mesh. The convection-diffusion equation is integrated over small control volumes that are formed by connecting the midpoints of the grid cells closest to a grid point. Since the Cartesian mesh for the concentration is different from the grid of the fluid velocity. The latter has to be converted towards the Cartesian mesh on every time step. This is done using a fourth-order cubic Lagrange interpolation method [13].

To allow the use of the finite volume method, Eq. (4) is rewritten, using Gauss's theorem, into

$$\iiint_V \frac{\partial c}{\partial t} dV + \iint_A \underline{u} \cdot \underline{n} c dA = \frac{1}{\mathrm{Re}\, Sc} \iint_A \frac{\partial c}{\partial n} dA \tag{5}$$

where *V* is the volume and *A* the surface of the control-volume. $\underline{n}$ is the outward unit-normal on the surface. In discrete form at time level *n* Eq. (5) is written as

$$\frac{(c^n_{j,k,l} - c^{n-1}_{j,k,l}) V_{j,k,l}}{\Delta t} = \sum_{i=1}^{6} \left(\frac{1}{\mathrm{Re}\, Sc} Qd_{j,k,l} - Qc_{j,k,l} \right) \tag{6}$$

with $Qd^n_{j,k,l}$ and $Qc^n_{j,k,l}$ the fluxes for the convection and diffusion terms resp. with the indices *j*, *k* and *l* denote the stream wise, wall-normal and span wise point indices of the control volumes. The total flux that leaves or enters a control volume is computed through summation over *i* of the partial flux through each surface of that control volume. On a Cartesian grid, the surface area is, in each direction, independent of the position and can be taken as a constant.

The fluxes are computed using a second order central discretisation method. The benefit of a central method over upwind methods is that it does not contain numerical diffusion, which is especially important at high Schmidt numbers. Higher than second order methods have the disadvantage that

the discretisation consists of more grid points. That makes the coupling of the fine and coarse grids more complex. In the remaining part of the paper only the stream wise direction of the flow are treated and the indices *k* and *l* are dropped to improve readability. In discrete form both flux terms from Eq. (6) become,

$$Qc_j = -\frac{A}{2}\left(u_{j+1}c_{j+1} - u_{j-1}c_{j-1}\right) \tag{7}$$

$$Qd_j = A\left(\frac{c_{j+1} - 2c_j + c_{j-1}}{\Delta x}\right) \tag{8}$$

where Δx is the grid size in stream wise direction.

For time integration both an explicit and an implicit method are applied. A first order explicit method can be used to compute the solution on the fine grid. On the coarse grid an implicit Crank-Nicolson method is needed because of LDC. An implicit method allows the local information to be applied to the whole coarse domain. With an explicit method that would not be possible. The disadvantage of an implicit method in a 3D problem is that the matrices become very large and are therefore computationally expensive to solve. Due to LDC, fewer points are needed on the coarse grid, without losing accuracy, so that an implicit method can still be applied. The following section will go into details that are behind LDC.

3. GENERAL PRINCIPLE OF LDC

The principle of LDC [5] is based on the assumption that a solution computed on a fine grid is more accurate than a solution of the same equation approximated on a coarser grid. The solution on the fine grid is used to correct the less accurate coarse solution. This correction is performed by computing a defect term from the difference between both approximations and feeding this difference, as a source term, into the equation for the coarse grid solution. The corrected coarse concentration is used to generate improved boundary conditions for the refinement area. This is an iterative process that can be repeated until convergence [14]. In a time dependent problem, the correction process has to be repeated every time step [8]. A point wise description of the steps needed to perform one LDC time step is given below. In the following part all upper-case symbols denote quantities on the coarse grid. Lower-case symbols refer towards to the same quantities on the fine grid.

1) Compute the coarse grid approximation using the implicit Crank-Nicolson scheme,

$$\frac{C_j^n - C_j^{n-1}}{\Delta T} + \frac{Q_j^n}{2V_j} + \frac{Q_j^{n-1}}{2V_j} = 0 \tag{9}$$

where Q_j^n contains both the convective and the diffusive flux terms from Eq. (6).

2) Compute the fine grid approximation using Euler forward time integration.

$$\frac{c_j^n - c_j^{n-1}}{\Delta t} + \frac{q_j^{n-1}}{v_j} = 0 \tag{10}$$

Because of the difference in grid size, the time step applied to the coarse is larger than the time step of the fine grid. To be able to compute the best possible solution that is needed in step 3 and the defect term from step 5, both the coarse and fine approximations need to be at the same position in time. On the fine grid multiple steps have to be taken to reach the next coarse time level. For each time step on the fine grid, the boundary conditions need to be interpolated in time using linear interpolation. Note that the time interpolation also needs to be applied to the fluid velocity to evaluate the flux terms on the corresponding time level.

3) Assemble the best possible coarse approximation for the concentration and the flux by combining the coarse and the fine grid approximations. The best possible concentration can be obtained by taking,

$$Cb_j^n = \begin{cases} C_j^n & \text{Outside the refinement area} \\ c_k^n & \text{Inside the refinement area} \end{cases} \tag{11}$$

where *k* denotes those points where the fine and coarse grid coincide. The best flux approximation Qb_j^n can be computed by inserting the new best solution for the concentration into Eq. (7) and Eq. (8). Figure 2 shows a schematic overview of a refinement area with the corresponding coarse grid.

4) Determine the defect terms by taking the difference between the coarse approximation and the best possible solution for both the concentration and the flux. This results in the defect terms to become

$$Dc_j^n = \left((C_j^n - Cb_j^n) - (C_j^{n-1} - Cb_j^{n-1})\right) \tag{12}$$

$$Dq_j^n = (Q_j^n - Qb_j^n) \tag{13}$$

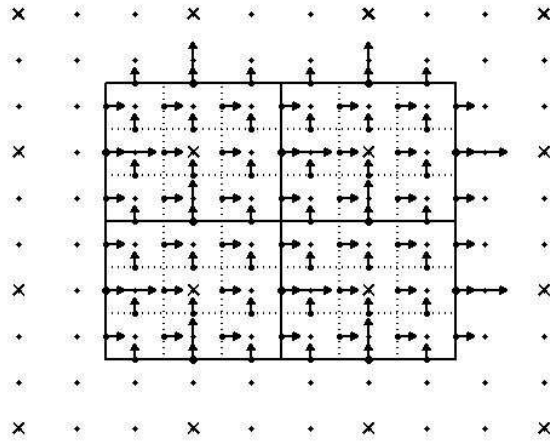

Figure 2. Schematic overview of a refinement area with the corresponding coarse grid. The coarse grid points are denoted with an (x), the fine grid points using a (.). The fluxes through the surfaces of the control volumes are visualised using different sized arrows.

5) Correct the global approximation by applying the defect, as a source term, to Eq. (9),

$$\frac{(Cc_j^n - C_j^{n-1}) - Dc_j^n}{\Delta T} + \frac{(Q_j^n - Dq_j^n)}{2V_j} + \frac{(Q_j^{n-1} - Dq_j^{n-1})}{2V_j} \tag{14}$$

and solve the updated equation to obtain the corrected coarse solution Cc_j^n.

6) Update the boundary conditions of the refinement area and re compute the local solution.

7) Iterate from point 3 until convergence has been reached and move towards the next time level when convergence is reached.

In a time-dependent problem, the total number of iteration steps that are needed to reach convergence is small. This is due to the fact that the solution at the previous time step already is a good initial condition for the iteration process. Experiments have shown that one or two LDC-iterations are sufficient to reach convergence. If many iterations are needed, this would severely reduce the overall efficiency of LDC in a time dependent problem.

Another feature of LDC is that multiple levels of refinement can be stacked. That allows for a very fine local region, without increasing the total number of points. Furthermore, it keeps the difference in grid size between two subsequent levels of refinement small. The latter is important for a proper estimate of the updated boundary conditions and the interpolation of the concentration that is needed, when the refinement area is moved. Figure 3 shows a schematic drawing for one LDC time step containing 3 levels of refinement, using one LDC iteration. After each correction the underlying fine grid has to be recomputed using the new boundary conditions from the corrected coarse concentration. These last steps are straightforward and have been left out of figure 3, to maintain readability.

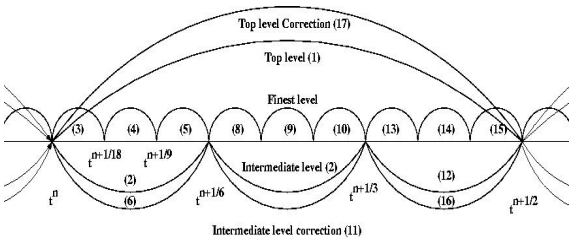

Figure 3. A schematic representation of a part of an LDC time step.

A side note towards time integration, when using multiple levels of refinement, is that only on the finest level an explicit time integration scheme can be applied. On every other grid, an implicit scheme is necessary to be able to apply the defect correction.

4. MOVEMENT OF THE REFINEMENT AREA

Due to the time-dependent behavior of the problem, the initial condition for the concentration will move along with the flow, with the refinement area moving accordingly. To detect the position of the refinement area, a weighted and averaged function of the magnitude of the concentration gradient is evaluated [1]. If the normalized weight function exceeds a certain threshold η_{upper} the control volume is marked for refinement. While the concentration moves along with the flow, new control volumes become marked for refinement and the area needs to be adjusted. A marked control volume can only be reset if the weight function drops below a second, lower threshold η_{lower}. The lower threshold was added to the detection method to prevent the refinement area from continuously changing back and forth, when the weight function

has a value close to η_{upper}. With this approach a moving, rectangular, area is created and due to the small movement per unit of time, the box will remain in the same position for several time steps.

A critical and non-trivial point in the movement of the refinement area is the definition of the concentration on the new grid points that are added through resizing. The only way to obtain information on those points is through interpolation between the already known concentration on the coarse grid and the known fine grid values from the previous grid. A requirement to the interpolation method is that the solution must remain smooth and positive after interpolation to prevent numerical instabilities.

The current approach is to fit a one-dimensional exponential function through the last points on the fine grid in the direction in which the grid is moving. The exponential fit function is given by,

$$Cfit = \alpha e^{(\beta x_j - \tau)} + \gamma \tag{15}$$

where α, β and γ are the fit parameters and x_j the coordinate and τ the coordinate offset equal to the last known point on the fine grid. After the fitting, the result is scaled to match both the coarse point at the refinement boundary and a point from the fine grid. A 1D-example of the interpolation is shown in figure 4. Here the coarse grid and both the interpolated and the previous fine grid points are shown. Note that the scaling point from the fine grid is not the boundary point of the refinement area. This is due to the fact that there are several dummy points around the refinement area. Those points ensure a smooth transition between the refinement levels.

In the two remaining directions, the fit parameters from the nearest coarse point are used to evaluate Eq. (15) and the resulting concentration curve is scaled to its corresponding fine grid point. In some cases, e.g. when the coarse grid solution is not monotonic, exponential fitting is not meaningful and a linear interpolation is applied instead.

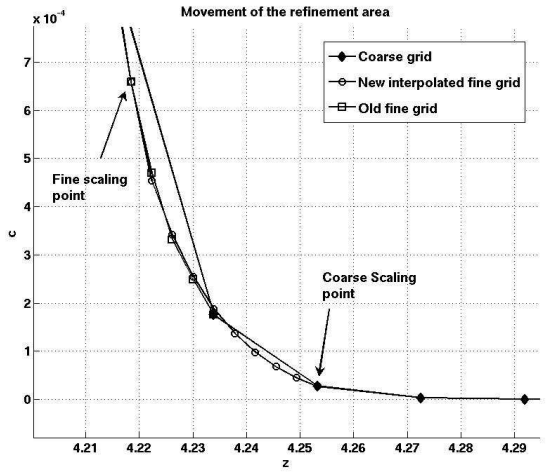

Figure 4. 1D example of the interpolation of fine grid point needed for the movement of the refinement area.

5. RESULTS

To investigate the results of the LDC-method, some numerical experiments were done. The tests were run on standard i686 dual Xeon machine with 2Gigabytes running on Linux. In a fully developed turbulent velocity field, the initial concentration field is chosen to be a Gaussian shaped sphere, which is given by,

$$C^0_{j,k,l} = \frac{1}{\sigma\sqrt{2\pi}} e^{\left((x_j - x_0)^2 + (y_k - y_0)^2 + (z_l - z_0)^2\right)} \tag{16}$$

where $\sigma = 5 \cdot 10^{-2}$ is the standard deviation, and x_0,y_0 and z_0 are chosen in such a way that the initial concentration is almost equal to zero at the boundaries of the concentration domain. Note that the initial concentration has to be applied to all levels of refinement. During the computations the Schmidt number is set to unity and the time step of the coarsest grid is equal to $\Delta t = 8.5 \cdot 10^{-5} H/u_\tau$. Due to time limitations and computational resources, a Schmidt number larger than unity was not feasible. However, to demonstrate the principle of LDC, applied to a complex time dependent problem, the height of the Schmidt number is not important. When the Schmidt number is increased further, only a finer grid is needed to maintain a stable and accurate solution. In this simulation a total of four stacked levels of refinement are used to reach a final grid size of approximately $2.5 \cdot 10^{-3} H$ in wall-normal and span wise direction and $1.25 \cdot 10^{-3} H$ in stream wise direction. The time step on each level decreases accordingly and matches the grid size. Figure 5 shows a contour plot of the initial condition for the two top levels of refinement. The two-dimensional cross section through the center of the sphere is made in the stream wise and wall

normal direction. The boundaries of the two grids are marked to be able to clearly identify the different levels of refinement.

Figure 6 shows the same contour plots of concentration, but now after 450 time steps on the coarsest grid. At this point in time it can be seen that the initial sphere of concentration has mainly been transported by the fluid. Some early influences of turbulence can already be identified by looking at the distortion from the initial round shape. The fact that the solution is still both smooth and positive means that the movement of the refinement area is working correctly. From these preliminary results, it is possible to conclude that LDC is working for a complex time dependent problem and it provides an efficient method to compute the concentration of a passive scalar in a turbulent flow.

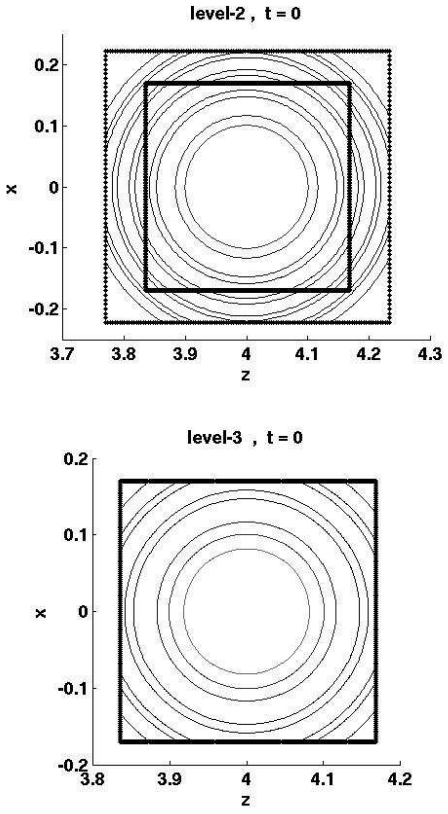

Figure 5. Contour plot of the initial concentration for the two topmost levels of refinement. The lower figure shows the 2D-contour plot of the finest level. The top figure shows a contour plot at the same position, but on one on coarser levels of refinement.

Further research is focusing on improving the overall efficiency of the method and the extension of LDC towards time dependent combustion problems.

ACKNOWLEDGEMENT

This work was sponsored by the National Computing Facilities Foundation, NCF for the use of supercomputer facilities, with financial support from the Netherlands Organization for Scientific Research, NOW. The author would like to thank the Netherlands Organization of Scientific Research (NWO) for funding this research, Computational Science grant 635.000.002.

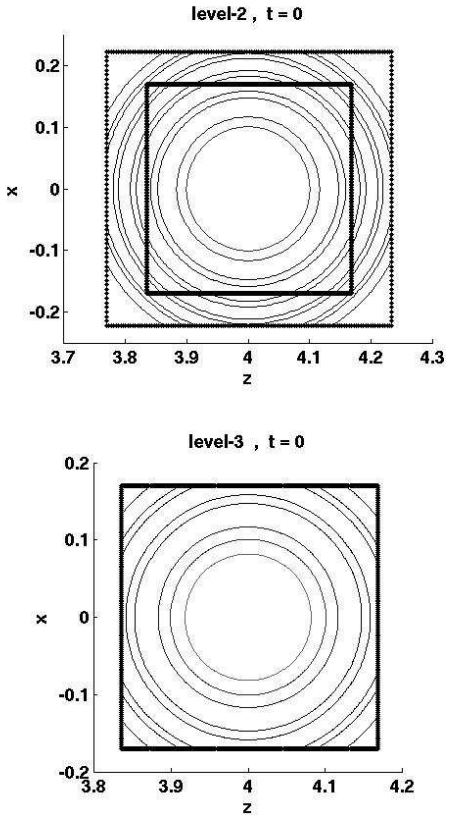

Figure 6. Contour plot of the development of the initial sphere in a turbulent flow after 450 time steps. The lower figure shows the 2D-contour plot of the finest level. The top figure shows a contour plot at the same position, but on one on coarser levels of refinement.

REFERENCES

[1] Anthonissen, M.J.H., *Local defect correction techniques: analysis and application to combustion,* Ph.D. Thesis, Eindhoven University of Technology, 2001.

[2] M.J.H. Anthonissen, B. van 't Hof, A. A. Reuskens. A finte volume scheme for solving

elliptic boundary value problems on composite grids. *Computing*, 61:285-305, 1998.

[3] M.J.H. Anthonissen, B. van 't Hof, A. A. Reuskens. An iterative finite volume discretisation method for solving elliptic boundary value problems on locally refined grids. *Nieuw Archief voor Wiskunde*, **17**:111-123 1999

[4] Ferket, P.J.J., *Solving boundary value problems on composite grids with an application to combustion*, PhD Thesis, Eindhoven University of Technology, 1996

[5] W. Hackbush. Local defect correction and domain decomposition techniques. In K. Bohmer and H.J. Stetter, editors, *Defect Correction Methods. Theory and Applications, Computing, Suppl.5*, 83-113, Wien, New York, 1984. Springer.

[6] Minero, R., Anthonissen, M.J.H., Mattheij, R.M.M, *Solving parabolic problems using local defect correction in combination with the finite volume method*, Eindhoven University of Technology, 2005.

[7] R. Minero, M.J.H. Anthonissen, R.M.M. Mattheij. Solving parabolic problems using local defect correction in combination with the finite volume method. *Numerical Methods for Partial Differential Equations*, 2006, In press.

[8] R.Minero, M.J.H. Anthonissen, R.M.M. Mattheij. A local defect correction technique for time-dependent problems. *Numerical Methods for Partial Differential Equations*, **22**:128-144, 2006.

[9] R.Minero, M.J.H. Anthonissen, R.M.M. Mattheij. Local defect correction for time-dependent partial differential equations. In *Proceedings of the 16th International Conderence on Domain Decomposition Methods*, 2005. Available online at http://cims.nyu.edu /dd16/proceedings.html.

[10] Kleiser L. and Schumann U., "Treatment of incompressibility and boundary conditions in 3-D numerical spectral simulations of plane channel flows," in *Proceeding of the Third GAMM-Conference on Numerical Methods in Fluid Mechanics*, edited by Hirschel E.H. Vieweg-Verlag, Braunschweig, 1980, pp. 165-173.

[11] Canuto C., Hussaini M.Y., Quarteroni A. and Zang T.A., *Spectral methods in fluid dynamics* Springer-Verlag, Berlin, 1988.

[12] P. Moin and J. Kim: Numerical investigation of turbulent channel flow, *J. Fluid Mech*., **118**, p 341-377, 1982.

[13] Veenman, M.P.B., *Statistical Analysis of turbulent pipe flow: a numerical approach*, Ph.D Thesis, Eindhoven University of Technology, 2004.

[14] R. Minero, H.G. ter Morsche, M.J.H. Anthonissen. Convergence properties of the local defect correction method for parabolic problems. Technical Report CASA 05-40, Eindhoven University of Technology, Eindhoven, November 2005. Submitted for publication.

Conference on Modelling Fluid Flow (CMFF'06)
The 13th International Conference on Fluid Flow Technologies
Budapest, Hungary, September 6-9, 2006

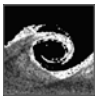

TRIDIMENSIONAL GEOMETRIC GRID GENERATION FOR THE FREE-SURFACE FLOW MODELLING

Ana-Maria TOCU[1], Adrian LUNGU[2]

[1] Department of Ship Hydrodynamics, "Dunarea de Jos" University of Galati. E-mail: ana.tocu@ugal.ro
[2] Corresponding Author. Department of Ship Hydrodynamics, "Dunarea de Jos" University of Galati. 47 Domneasca Street, 800008 Galati, Romania. Tel.: +40 722 362604, Fax: +40 236 495400, E-mail: adrian.lungu@ugal.ro

ABSTRACT

An implicit geometrical generation is described in the present work. According to it, the equations for iterative change of locations are regarded as those for grid point movement. Implicit time-differencing operators are used and converged grids are obtained under a suitable balance of orthogonality, smoothing, clustering toward the solid boundaries and minimum spacing. The requirements are combined with suitable weightings to generate converged grids so that each criterion is stable if used alone and interfere as little as possible with other criteria. Orthogonality is iteratively achieved through a series of loops within which, grid points are successively moved to minimize the cell skew. Smoothing in every node is realized by taking the average of the Cartesian coordinates of the neighbouring points with weighting factors inversely proportional to the average distance in each direction. Clustering is imposed along each grid line with the specified minimum spacing.

Keywords: CFD, grid generation, geometric method, orthogonality, smoothness, clustering

1. INTRODUCTION

The final goal for those who are involved in the field of marine CFD is to simulate numerically the free-surface flow around the ship hull by solving the full Reynolds Averaged Navier-Stokes equations (RANSE hereafter). Any numerical simulation always requires three different steps: grid generation, discretization and solution. All of them pose particular difficulties that are, to some extent, intertwined. A grid represents an organised set of points chosen not randomly rather so that they can be indexed according to the dimensionality of the problem and where the solution is prospected. As derivatives are approximated by formula which involve values expressed at points, the locations of these points must satisfy some requirements to yield accurate difference quotients. Defects concerning the grid spacing, orthogonality, clustering or smoothness that easily occur may sometimes have undesirable influences on the final solution. Moreover, an improper choice of the grid point locations can lead to an apparent instability or lack of convergence. These requirements are not always easily met especially when the domain of interest has a complicated geometry. That is why the grid generation stage represents an unavoidable prerequisite for the numerical simulation. There are several grid generation techniques but none of them can cover bodies with shapes of a wide variety in a black-box manner.

Basically the procedures for generation of curvilinear coordinate systems are of three types: (a) algebraic methods, (b) techniques based on the numerical solutions of partial differential equations and (c) geometrical methods. Among them the algebraic generation is the fastest and allows an explicit control of the grid point distribution. Grids referred in the present paper are generated by following a geometric method in a succession of two stages. At first the coordinates for the inner (i.e., body surface) and outer boundaries are set. The grid numbers in the axis directions are set as well. The clustering is the only criterion considered at this stage. This is an important requirement to satisfy in the vicinity of the body, around edges and just below the free surface. The grid ordinates are established by making use of the unidirectional polynomial interpolation [1]. The least-squares method is used to find the coefficients for the approximating polynomial. The accomplishment of the aforementioned requirements on each stage is realised easily since the grid lines joining the points have neither smoothing nor orthogonality near the body.

The following stage corresponds to the grid modification when the orthogonality and smoothness are realised. Coordinate systems that are orthogonal or at least nearly orthogonal in the vicinity

of the solid body make the boundary condition formulation more straightforward. Although a full orthogonality is not always necessary [2] and conditions involving expressions that combine one-sided differences along the lines emerging from the body with central differences along the body make the scheme more robust and computationally efficient, the accuracy deteriorates if the departure from orthogonality is too large.

An implicit geometrical generation for both **C** and **O** grid topologies is described in the present work. According to it, the equations for iterative change of locations are regarded as those for grid point movement. Implicit time-differencing operators are used and converged grids are obtained under a suitable balance of orthogonality, smoothing, clustering toward the solid boundaries and minimum spacing. The requirements are combined with suitable weightings to generate converged grids so that each criterion is stable if used alone and interfere as little as possible with other criteria. Orthogonality is iteratively achieved through a series of loops within which, grid points are successively moved to minimize the cell skew. Smoothing in every node is realized by taking the average of the Cartesian coordinates of the neighbouring points with weighting factors inversely proportional to the average distance in each direction. Clustering is imposed along each grid line with the specified minimum spacing following the work of Kodama [3]. During the grid modification all the mesh points are moved to satisfy the abovementioned requirements. However, it would often be better for the grid points laying on the boundary to be fixed or remain on the frontier plane for an easier boundary condition implementation, i.e., in the same manner as for the inner points. They are projected to the boundary plane after each iteration so that smooth grids may also be obtained near the frontier. During the modification procedure, the displacements of grid points due to each requirement are computed based on the grids obtained from the previous iteration. The total displacements are obtained by summing each displacement multiplied by a weighting factor and the grids are finally updated by using them. The weightings for each requirement are determined depending on the grid topology and mesh spacing. Usually, the weightings are chosen smaller than unity so that they limit the points movements within an iteration and enable the grid modify gradually. Smaller weighting factors are generally used to avoid undesirable overlapping. Finally, the paper will present several grids to emphasize the performances of the proposed method.

2. GEOMETRIC METHOD FOR 2D GRID GENERATION

A rather complex but still feasible method for generating grids is the geometric one. As said above, the generation process consists in two different steps. The first one establishes the position for all the points located on the frontiers whatever type they are, i.e., inner, outer or re-entry boundaries. Afterwards, the initial grid is iteratively modified to satisfy the quality criteria before mentioned.

2.1. Initial Grid Generation

Since the iteration number required for the generation and ultimately the convergence speed depend on the initial grid, it is advisable that this grid has a reasonably topology (nodes defined in a sense in which a coordinate is increasing, thus avoiding lines overlapping). Generation the initial grid is accomplished in two steps: (a)-definitions of points on the boundaries; (b)-grid generation inside the domain. Although the points on the boundaries may be left free to move along them, usually those on the solid boundaries are kept fixed to assure the minimum spacing requirement. Those on the outer frontiers may be redistributed to force the clustering inside the areas where the flow solution has significant gradients. At this stage, the clustering is achieved by employing hyperbolic functions. Once the location on the boundaries is established, the grid inside the domain is generated through the transfinite interpolation following the formulation of Gordon and Hall [4], which is based on a interpolation-transforming function of the coordinates of the Cartesian system (x, y, z) into a computational one (ξ, η, ζ) defined on the domain:

$$\xi_1 \le \xi \le \xi_L,\ \eta_1 \le \eta \le \eta_M,\ \zeta_1 \le \zeta \le \zeta_N \qquad (1)$$

The interpolation-transforming function

$$F(\xi,\eta,\zeta) = [x(\xi,\eta,\zeta),\ y(\xi,\eta,\zeta),\ z(\xi,\eta,\zeta)]$$

is known on the outer boundaries only and is defined in each plan by the following set of equations:

$$\begin{aligned} a_I(\eta,\zeta) &= F(\xi_I,\eta,\zeta), \quad I = 1, 2, ..., L \\ b_J(\xi,\zeta) &= F(\xi,\eta_J,\zeta), \quad J = 1, 2, ..., M \\ c_K(\xi,\eta) &= F(\xi,\eta,\zeta_K), \quad K = 1, 2, ..., N \end{aligned} \qquad (2)$$

Interpolating the points between the boundaries, a set of functions $\alpha_I(\xi), \beta_J(\eta), \chi_K(\zeta)$ that has to satisfy the conditions:

$$\alpha_K(\xi_l) = \delta_{kl}\ ;\ \beta_K(\eta_l) = \delta_{kl}\ ;\ \chi_K(\zeta_l) = \delta_{kl} \qquad (3)$$

is defined. δ_{kl} stands for the Kronecker symbol.

$$\delta_{kl} = 1 \text{ if } l = k \quad \text{and} \quad \delta_{kl} = 0 \text{ if } l \ne k \qquad (4)$$

The transfinite interpolation procedure permits to obtain the interpolation-transforming function in the following succession of steps:

$$
\begin{aligned}
&F_1(\xi,\eta,\zeta) = \sum_{l=1}^{L} \alpha_l(\xi) a_l(\eta,\zeta) \\
&F_2(\xi,\eta,\zeta) = F_1(\xi,\eta,\zeta) + \\
&+ \sum_{J=1}^{M} \beta_J(\eta)\left[b_J(\xi,\zeta) - F_1(\xi,\eta_J,\zeta)\right] \\
&F(\xi,\eta,\zeta) = F_2(\xi,\eta,\zeta) + \\
&+ \sum_{K=1}^{N} \gamma_K(\zeta)\left[c_K(\xi,\eta) - F_2(\xi,\eta,\zeta_K)\right]
\end{aligned}
\qquad (5)
$$

An example of a **C**-type mesh generated in the initial stage is shown in Figure 1, which depicts a two-dimensional grid around a NACA 0012 hydrofoil. As it may be seen, except for the grid points distribution on the body, no other quality requirement is fulfilled.

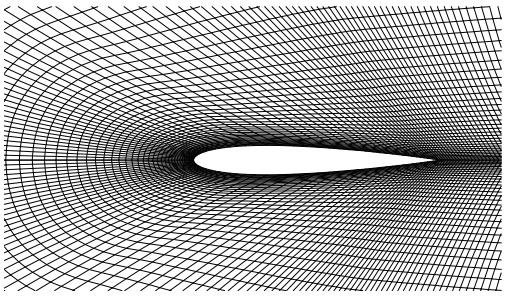

Figure 1. Initial around a NACA 0012 hydrofoil

2.2. Grid Modification

An implicit geometrical modification in which, the equations for iterative change of locations are regarded as those for grid point movement is further proposed. Implicit time-differencing operators are used and converged grids are obtained under a suitable balance of orthogonality, smoothing, clustering toward the body and minimum spacing. The requirements are combined with suitable weightings to generate converged grids so that each criterion is stable if used alone and interfere as little as possible with other criteria.

2.2.1. Orthogonality

Let two parallel lines be intersected by a secant as shown in Figures 2 (a) to (c). The orthogonality of the intersecting lines can be achieved by moving either one of the points (the upper or the lower) or both $P_{i,k}$ and $P_{i,k+1}$. There are infinite combinations of the displacement vectors $\underline{\Delta p}_{i,k}$ and $\underline{\Delta p}_{i,k+1}$ that are able to make the lines orthogonal. Their contribution to the orthogonality is specified by making use of a distribution parameter s that defines the ratio of the displacement vectors between the k^{th} and $(k+1)^{th}$ grid lines. When s=1.0 only the upper point $P_{i,k+1}$ moves to fulfil the orthogonality condition whereas the lower $P_{i,k}$ moves when s=0. The intermediate value of s=0.5 makes both $P_{i,k}$ and $P_{i,k+1}$ move in opposite directions. The distribution parameter is specified on the boundaries and the corresponding values for the inner grids are found through the interpolation. Either s=0 or s=1.0 are generally used to obtain an orthogonal mesh at the body boundary.

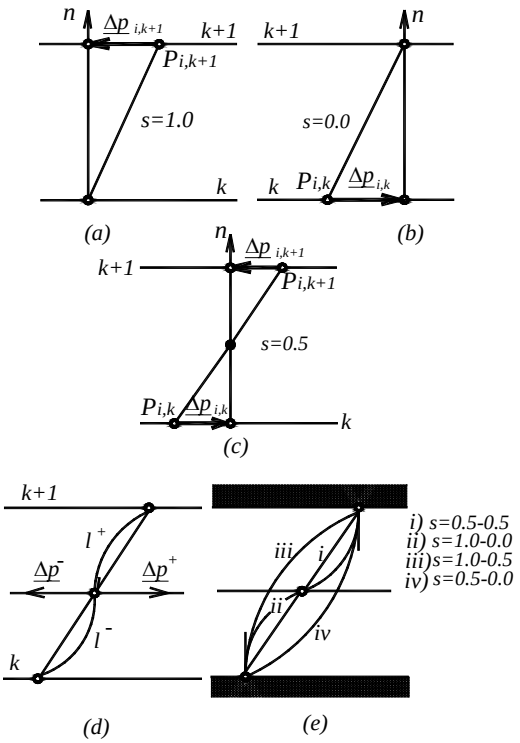

Figure 2. Orthogonality fulfilment

Nevertheless, when the boundary is rather complicate or concave the grids may become stiffer close to the boundary and eventually overlap. Such a situation may be avoided by distributing the displacement, i.e., s=0.5, although the orthogonality might be compromised to some extent. The displacement vector $\underline{\Delta p}_{i,k+1}$ is calculated by taking a vector product of the normal vector $\underline{n}$ at $P_{i,k}$ and the vector $\underline{p_{i,k+1} - p_{i,k}}$, where $\underline{n}$ is defined as an average of $\underline{n}_k$ and $\underline{n}_{k+1}$ which are the vectors normal to the ζ line at $P_{i,k}$ and $P_{i,k+1}$ respectively as shown in Fig. 2(d). Since $\underline{\Delta p}_{i,k}$ is found by imposing the orthogonality condition at the upper and lower lines, the actual displacement vector is calculated as an average of the upper $\underline{\Delta p^+}$ and lower $\underline{\Delta p^-}$ contributions weighted inversely proportional to the distances l^+ and l^-:

$$
\underline{\Delta p}_{i,k} = \frac{1}{l^+ + l^-}\left[l^+ \underline{\Delta p}^- s_k + l^- \underline{\Delta p}^+ (1 - s_{k+1})\right] \qquad (6)
$$

as depicted in Fig. 2(d). s_k and s_{k+1} in the equation above stand for the distribution parameters at $P_{i,k}$ and $P_{i,k+1}$. It is possible to obtain grid lines showing

various orthogonality behaviours by giving different distributions to s between the inner and outer boundaries as shown in Fig. 2(e). The end points are both assumed to be fixed and the displacement is simply neglected there.

2.2.2. Smoothing

The smoothness offers an elliptic nature to the grid. The simplest way to get smoothness is to average coordinates of two adjacent points as shown in Figure 3(a). The displacement of the inner point P_i corresponds to a second differencing scheme, which is given by:

$$\Delta P_i = \frac{P_{i-1} + P_{i+1}}{2} - P_i = \frac{P_{i-1} - 2P_i + P_{i+1}}{2} \qquad (7)$$

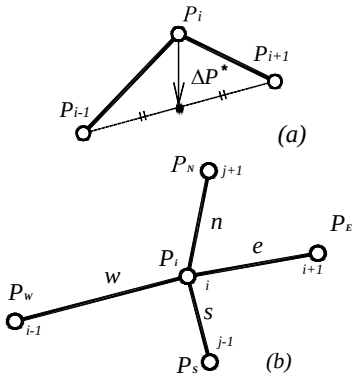

Figure 3. Sketch of averaging. (a)- with two points; (b)- with four points

However, the simple averaging often generates unreasonable grids especially near the body. This is due to either a high aspect ratio (determined, for instance, by a high *Rn* computation request) or to certain singularities, e.g., kinks. To reduce this drawback the smoothness is realised by averaging the coordinates of the four neighbouring points with weightings inversely proportional to the average distance in each of the two directions, ξ and ζ. The displacement shown in Fig. 3(b) is in this case as follows:

$$\Delta P_i = w_\xi \Delta P_{i-1}^{(\xi)} + w_\zeta \Delta P_i^{(\zeta)} \qquad (8)$$

where:

$$w_\xi = \left(\frac{1}{e+w} + \frac{1}{n+s}\right)^{-1} \cdot \frac{1}{e+w}$$
$$w_\zeta = \left(\frac{1}{e+w} + \frac{1}{n+s}\right)^{-1} \cdot \frac{1}{n+s} \qquad (9)$$
$$\Delta P_i^{(\xi)} = \frac{\underline{E} + \underline{W}}{2}\,;\ \Delta P_{i-1}^{(\zeta)} = \frac{\underline{N} + \underline{S}}{2}$$

Abbreviations *e*, *w*, *s*, and *n* appearing in Fig. 3(b) stand for segment lengths on the east, west, south and north direction respectively, whereas $\underline{E}$, $\underline{W}$, $\underline{S}$, and $\underline{N}$ in the equation above are the corresponding vectors on those directions. The difference between the initial grid and the modified one in terms of the orthogonality is shown in Figure 4, which depicts in the upper half the initial grid while in the lower one, is shown the modified one generated in ten iterations. Over 50 iterations are required for a modification to achieve satisfactory orthogonality and smoothness. An example of the grid around the same hydrofoil modified to fulfil the orthogonality and smoothing requirements is shown in Figure 5. The weighting factors are set at 0.5 and 0.4 respectively. The distribution parameters *s* are 1.0 on the body, on the re-entry boundary while on the outer and downstream frontiers *s*=0.5. Since the clustering has not initially been taken into account (weighting factor equal to zero) the grid lines parallel to the body are rather far from each other. To cluster them close to the body, a non-zero weighting for clustering has to be set, e.g. w_c=0.5 and the resulted grid is plotted in Fig. 5.

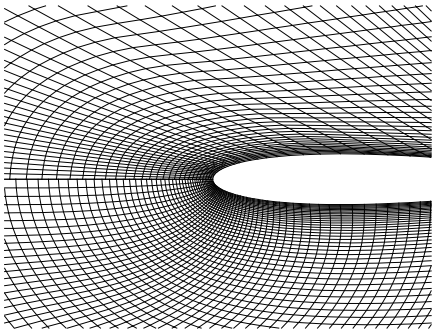

Figure 4. Comparison between the initial and the modified grid (imposed orthogonality)

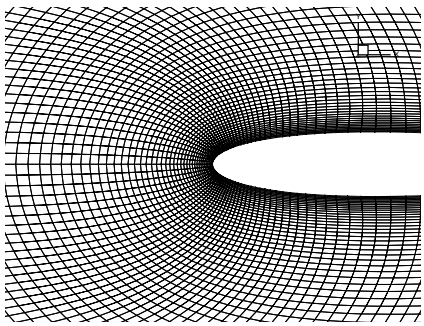

Figure 5. Grid modified to fulfil the orthogonality requirement

2.2.3. Clustering

Clustering is done along each grid line with the specified minimum spacing Δ_{min}. At first, the grid coordinates are expressed by a spline function of a variable representing the distance from the body calculated by the sum of each segment along the grid line. Assuming the lower boundary as a solid surface as shown in Figure 6, the nodes laying on the η direction are forced to distribute progressively

starting with a minimum distance Δ_{min}. Let s be the coordinate along the η=ct line and δ_s the difference between the s coordinates corresponding to the location of the point denoted by P_C, the old position P_C^{old} and the new one P_C^{new}, after clustering.

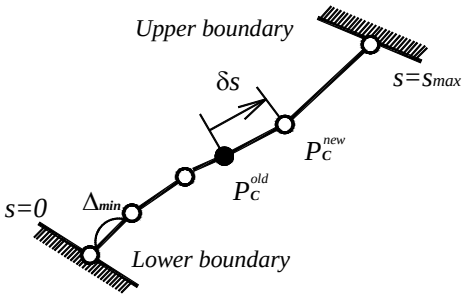

Figure 6. Sketch of clustering in geometric progression

Making an analogy between the movement of the grid nodes and the water particle movement, one may observe that for determining the displacement of a node, a convective term may be introduced in the equation that describes the point movement. Since in the previous discussions we analysed the point movement along a certain direction, the displacement is expressed by a first order upwind scheme, which is one of the simplest and the more stable schemes. The scheme is given by:

$$\begin{aligned}\Delta P_C &= \delta_S \frac{(P_N - P_C)}{|P_N - P_C|} \quad (\text{if } \delta_S > 0) \\ &= \delta_S \frac{(P_S - P_C)}{|P_S - P_C|} \quad (\text{if } \delta_S < 0)\end{aligned} \tag{10}$$

and the sketch of the displacement is shown in Figure 7.

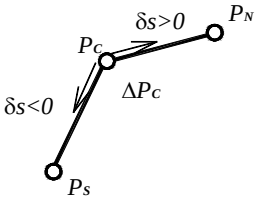

Figure 7. Node displacement (1st order upwind scheme)

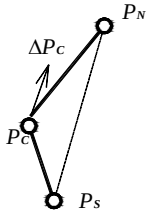

Figure 8. Node displacement (2nd order scheme)

If a three-point central difference operator is used, the following equation is obtained:

$$\Delta P_C = \delta_S \frac{\delta_S}{|P_N - P_S|}(P_N - P_S) \tag{11}$$

In this case P_C moves parallel to P_N-P_S, as depicted in Figure 8. Equation (11) is neutrally stable and cannot be used alone. Although numerical experiments have proven that either the use of first order schemes or of those written in three points leads to the same results, the upwind scheme is better to use since it has a better numerical stability. An example of how the clustering is achieved without applying the smoothing criterion is shown in Figure 9.

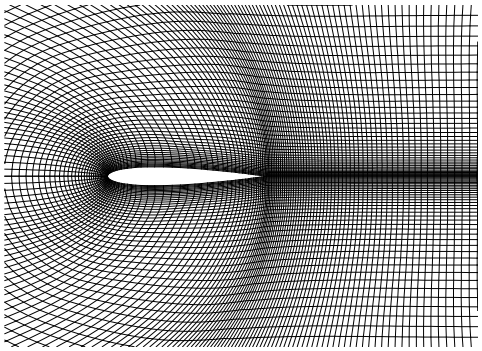

Figure 9. C-type grid modified to fulfil the orthogonality and clustering requirements

2.2.4. Minimum Spacing

Once the orthogonality, smoothing and clustering requirements were fulfilled, a final check is performed to verify if the minimum spacing is kept or not. This check is necessary to avoid the grid lines overlapping during the iteration. The displacement of a grid point denoted by δ_ξ in the ξ direction to keep the minimum spacing relatively to the neighbouring points is given by the equation:

$$\Delta p_{i,k} = \frac{\gamma_E}{|P_{i+1,k} - P_{i,k}|}(P_{i+1,k} - P_{i,k}) + \frac{\gamma_W}{|P_{i-1,k} - P_{i,k}|}(P_{i-1,k} - P_{i,k}) \tag{12}$$

If the grid spacings e and w are defined as in Fig. 3(b), γ_E and γ_W in the above equation are chosen as follows:

	$e < \delta_\xi$	$\delta_\xi \le e$
$w < \delta_\xi$	if $e > w$ $\gamma_E = \frac{e-w}{2}$; $\gamma_W = 0$ else $\gamma_E = 0$; $\gamma_W = \frac{w-e}{2}$	if $e + w > 2\delta_\xi$ $\gamma_E = \delta_\xi - w$ else $\gamma_E = \frac{e+w}{2}$; $\gamma_W = 0$
$\delta_\xi \le w$	$\gamma_E = 0$ if $e + w > 2\delta_\xi$ $\gamma_W = \delta_\xi - e$ else $\gamma_W = \frac{w-e}{2}$	$\gamma_E = 0$ $\gamma_W = 0$

From the above table it may be seen that if either *e* or *w* is smaller than δ_ξ, the space is enlarged to δ_ξ. On the other hand, if the other spacing is not enough and the enlargement makes its value smaller than δ_ξ, the enlargement is modified so that the spacings are taken equal. An important feature of the described grid generation method is that it allows also the generation of **O**-type meshes. Although the restrictions imposed by the orthogonality requirement are a little weaker for these meshes, compared to those of the C-type, all the other quality criteria are fulfilled in the same manner, i.e. with the same computational expenses. Figures 10 and 11 depict **O**-type grids drawn around two different bodies of revolution to prove the ability of the method to deal with such geometries.

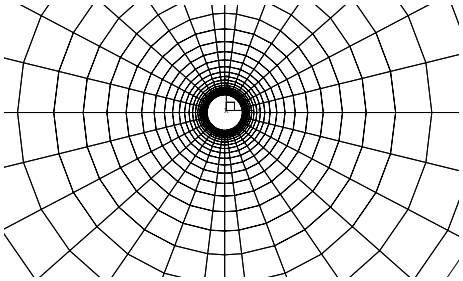

Figure 10. O-type grid around a circular cylinder

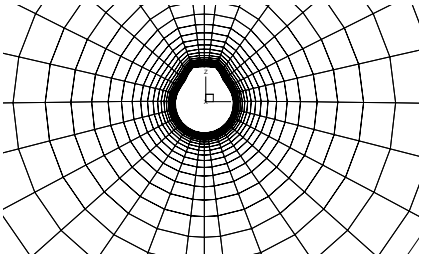

Figure 11. O-type grid around a body of revolution

3. THE 3D GRID GENERATION

The 3D grid around a ship hull generated by using the present geometric method is further presented. The grid topology is of an **H**-**O** type. Figure 12 shows the ground around a container vessel hull viewed isometrically the forepeak towards the after peak. Grids on the hull surface, on the symmetry plane as well as on the body are plotted. The surface grid has been obtained by using the 2D geometric method and projecting normally on the hull surface that is defined by means of bi-cubic splines. The plotting shows good orthogonality, clustering and smoothness properties. Critical areas such as the bow or stern are well mapped as borne out in the figure abovementioned. The sectional grids near the midship and downstream of it, viewed from the downstream are also depicted. Satisfactory smoothness and orthogonality are shown in all the figures. To grasp a better understanding of how the mesh looks like, every fifth grid line is drawn.

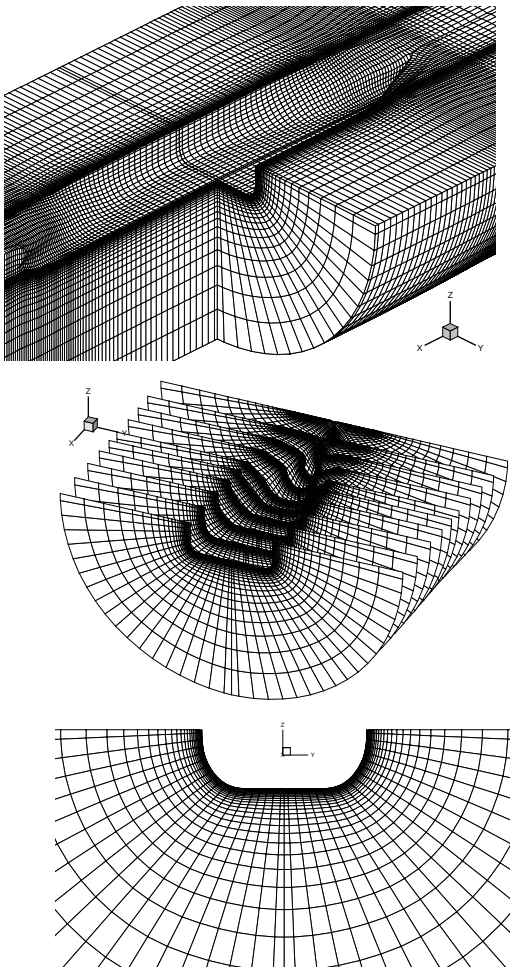

Figure 12. Three-dimensional grid topology generated around a container vessel

Another example of a three-dimensional grid generated geometrically is shown in Figure 13 where the domain surrounding a submerged body of revolution is covered by an **O**-type mesh.

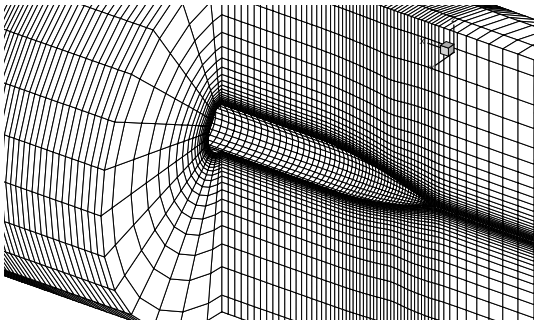

Figure 13. Three-dimensional grid topology generated around a submerged body of evolution

Several sets of computations have been carried out for a Wigley ship hull at a range of Froude numbers between 0.16 and 0.36. The lower Froude number calculations are the most problematic because the grid size must be very small to fulfil the requirement of at least 30 grid points per dominant wavelength for simulating properly the development. The solutions computed for Fn=0.16 and 0.20 shown in Figure 14, which depicts the free-surface profile prove that in spite of the small wavelength, the free-surface overall configuration is appropriately simulated. Wave patterns are accurately reproduced not only in terms of the locations of the fore and aft crests, but also in terms of the magnitudes.

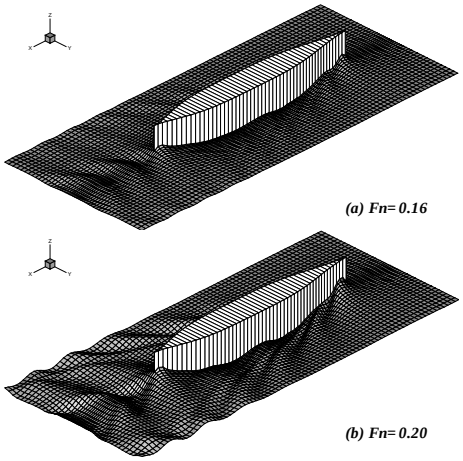

Figure 14. Free-surface profiles around a Wigley hull

A comparison between the free-surface contours computed for five different Froude numbers of 0.16, 0.2, 0.24, 0.28 and 0.316 respectively, is shown in Figure 15. All the reported solutions are computed by solving the unsteady RANS equations employing the FDM method. The distance between two consecutive curves is 0.002. The contingency between the Fn number value and the wavelength is obvious. Higher ship speed determines significant decreases of the transverse distance between the divergent wave fronts, as expected. There is no significant wave propagating towards the upstream boundary, which means that the free-surface boundary condition works properly. The other boundary conditions seem well formulated since there is no evidence of wave reflection laterally or downstream of the domain.

For two reasons an important issue of the numerics is the grid resolution. The first one is related to the overall accuracy of the computation while the second is related to the efficiency of the simulation. Obviously, a larger number of grid points may help the achievement of a convergent solution within a reasonable margin of errors. Besides, a finer discretization requires a larger amount of CPU for arriving to the final result.

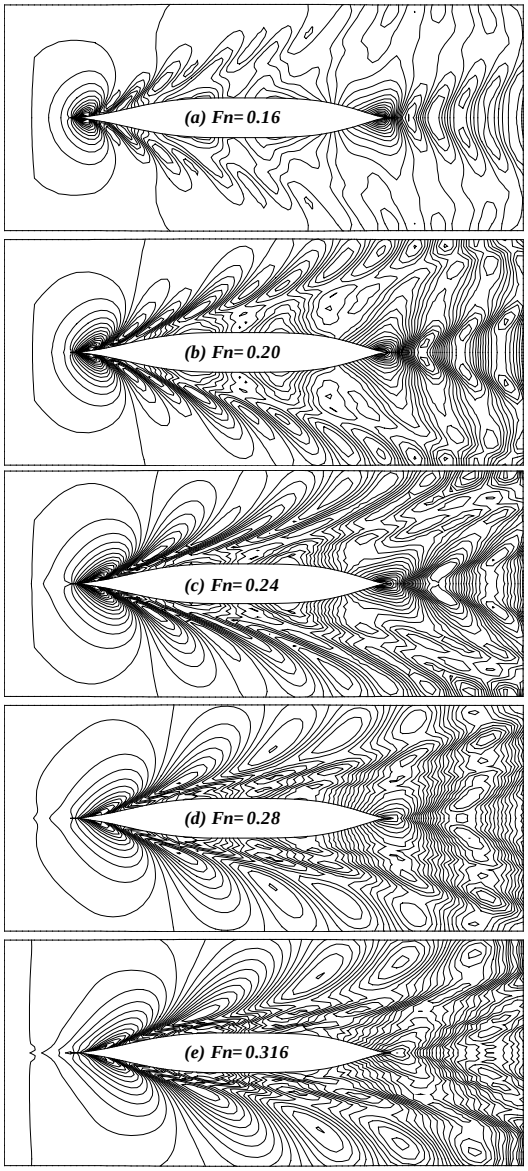

Figure 15. Free-surface profiles around a Wigley ship hull

Since the grid generation is mostly a trade-off process, it is important to clarify how the minimum grid size should be chosen. Usually references suggest at least 30 nodes per wavelength. For a ship hull model whose length is L=2 and Fn=0.316, the wavelength is λ=1.254 to which a minimum cell size of 0.0418 corresponds. Trial computations however, proved that the above minimum requirement should be two times more restrictive to ensure a satisfactory accuracy for an unconditionally stable solution. A comparison is proposed in Figure 16 for validation purposes. The wave resistance coefficients are computed by using two methods. The first one is based on the integration over the wetted hull surface of the pressure field computed as a finite difference solution of the RANS equations. The equatons were discretized on a grid generated by following the geometric method proposed in the present paper. The second one

represents the solution of the potential flow computed by using a boundary element method, where wave coefficient is determined by employing the Lagally theorem. The computed wave coefficients for the six Froude numbers ranging between 0.16 and 0.36 are compared with those experimentally measured in the towing tank and reported in [8] and [9]. Experimental data are drawn by squares, while lines plot the computational results.

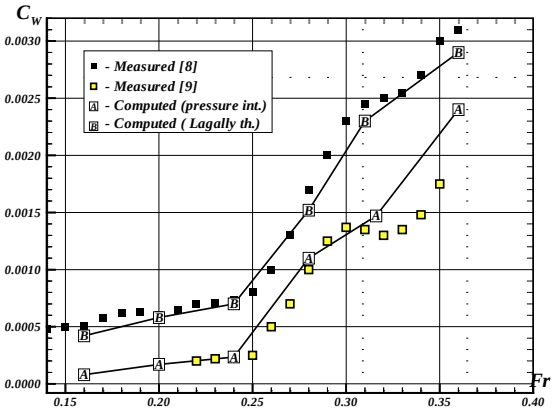

Figure 16. Comparisons between the measured and computed wave resistance coefficients

The similarity is good, except for Fn higher than 0.31 at which a significant difference between the C_W computed and measured in [9] occurs. In author's opinion, the reason for such a departure is the difference between the wave profiles around the fore part of the body that manifests at higher Fn. On the other hand, wave coefficients computed by using pressure integration seem to be fairly underestimated comparing to those computed by using the Lagally theorem. The disagreement is due to the geometry of the hull around the edges where the pressure changes sharply, as anticipated.

4. CONCLUDING REMARKS

The paper main purpose is to develop a reliable method for grid generation. Since the grid quality greatly influences the performances of any Navier-Stokes solver based on the finite difference method, the generation represents one of the most important and, sometimes, difficult problem to accomplish. The bird's-eye view of the basic problems given in the preceding sections and involved in solving the theme sets the stage for a brief outline of the present paper. An algebraic method based on using the transfinite interpolation is used at first for the initial generation then a geometric procedure is employed to modify the initial grid. The findings throughout the present work are as follows:

- The H-type grid is the most suitable one for a free-surface flow problem in spite of the difficulties to map accurately the simple-conex domain especially around the body;
- The proposed algebraic method based on using transfinite interpolation allows the reasonable initial nodes distribution;
- A more flexible grid can be obtained by employing a geometric method whose better results are proved either on 2D or 3D cases.

ACKNOWLEDGEMENTS

The present work has completely supported by the Romanian National Council of Research in Higher Education, under the framework of the Grant No.33, for which it is greatly acknowledged.

REFERENCES

[1] Thompson, J.F., Warsi, Z.V.A., Mastin, C.W., 1985, *"Numerical Grid Generation, Foundations and Applications"*, North-Holland, Amsterdam

[2] Kodama, Y., 1988, "Three Dimensional Grid Generation around a Ship Hull Using the Geometrical Method", *Journal of The Society of Naval Architects of Japan,* vol.164, pp. 1-8

[3] Kodama, Y., 1991, "Grid Generation around a Practical Ship Hull Form Using the Implicit Geometrical Method", *Journal of The Society of Naval Architects of Japan,* vol.169, pp.1-17

[4] Gordon, W.J., Hall, C.A., 1973, "Construction of Curvilinear Coordinate Systems and Applications of Mesh Generation", *International Journal of Numerical Methods in Engineering,* vol.7

[5] Ikehata M., Tahara, Y., 1987, "Influence of Boundary Layer and Wake on Free Surface Flow around a Ship Model", *Journal of Society of Naval Architects of Japan,* Vol.161, pp. 49-57

[6] Ni, S. Y., 1987, "Higher Order Panel Methods for Potential Flows with Linear or Nonlinear Free Surface Boundary Conditions", Ph.D. Thesis, Chalmers University of Technology, Göteborg

[7] Jensen, G., Bertram, V., Söding, H., 1989, "Ship Wave-Resistance Computations", Proceedings of the 5th International Conference on Numerical Ship Hydrodynamics, Hiroshima, Japan, Vol. 2, pp. 424-436

[8] Toda, Y., Stern, F., Longo, J., 1991, "Mean-Flow Measurements in the Boundary Layer and Wake and Wave Field of a Series 60 C_B=0.6 Ship Model for Froude Numbers .16 and .316", IIHR Report No. 352

[9] Kim, Y.H, Jenkins, D., 1981, "Trim and Sinkage Effects on Wave Resistance with Series 60, C_B=0.60", DTNSRDC Report No. SPD-1013-01 Bethesda

Conference on Modelling Fluid Flow (CMFF'06)
The 13th International Conference on Fluid Flow Technologies
Budapest, Hungary, September 6-9, 2006

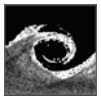

MATHEMATICAL MODELS AND NUMERICAL METHODS FOR TURBULENT REACTIVE FLOWS

Antonio ATTILI[1], Bernardo FAVINI[2]

[1] Corresponding Author: Ph. D. Student, Dipartimento di Meccanica e Aeronautica, Università di Roma "La Sapienza". Address: Dipartimento di Meccanica e Aeronautica, via Eudossiana 18 00184 Roma Italy. Tel: +39 06 44585214. Fax: +39 06 484854. E-mail: antonio.attili@libero.it
[2] Professor Dipartimento di Meccanica e Aeronautica, Università di Roma "La Sapienza"

ABSTRACT

One-dimensional model of compressible fluid flow with forcing term is proposed as an analog for reacting turbulent flow. The forcing terms consist of randomly generated momentum and energy that can simulate the effect of both turbulence and heat release due to chemical reactions. Different integration techniques are applied to the numerical solution of the system of equations: a centered scheme, a centered scheme with non-linear filter, a Godunov-type scheme and WENO scheme. The solutions are computed for different discretization and, in particular, also for very low grid resolution. The comparison of the numerical simulations in term of spectral feature, numerical dissipation and spurious oscillations is performed and as a result it can be shown that WENO scheme allows to reach a very high level of resolution also with coarsest grids. The application of the same numerical schemes to some typical combustion poblems as deflagration and detonation confirm the same conclusion.

Keywords : Reactive flows, WENO Schemes

NOMENCLATURE

A_f	$[Kg/m^2\ s^2]$	amplitude of forcing term
C_{p_s}	$[J/Kg\ K]$	specific heat at constant pressure
C_v	$[J/Kg\ K]$	specific heat at constant volume
E	$[J/kg]$	total internal energy
$\hat{E}(k)$	$[J]$	energy spectrum
H	$[J/Kg]$	total enthalpy
H_s	$[J/kg]$	sensible enthalpy
H_s^0	$[J/Kg]$	formation enthalpy
N_s	$[-]$	number of species
R	$[J/Kg\ K]$	mixture constant
$\Re$	$[J/mol\ K]$	universal gas constant
Y_s	$[-]$	mass fraction of species s
e	$[J/Kg]$	internal energy
f	$[Kg/m^2\ s^2]$	forcing term for momentum equation
k	$[W/m\ K]$	conductibility
p	$[Pa]$	pressure
q	$[Kg/m\ s]$	forcing term for energy equation
t	$[s]$	time
u	$[m/s]$	velocity
x	$[m]$	spatial coordinate
ϕ_f ϕ_q	$[-]$	phases for forcing terms
μ	$[Kg/m\ s]$	viscosity
ρ	$[Kg/m^3]$	density
$\dot{\omega}_s$	$[Kg/m^3\ s]$	source term of specie equations

1. INTRODUCTION

Compressible flows are characterized by zones where variables gradients are very sharp and this circumstance is particular severe if chemical reactions occur, because in addition to shock and contact discontinuities, interfaces with different species concentration exist. Therefore robust numerical methods must be used to obtain high quality solutions, also if the simulation is performed with a low level of grid resolution, which is a major constrain in order to reduce computational time. While central finite difference schemes produce spurious non physical oscillation near sharp gradient; shock capturing schemes (i.e. Godunov

method) introduce numerical dissipation to avoid oscillations formation. So it's important to study characteristics of schemes with regard to capability to avoid spurious oscillations but with low numerical dissipation. These characteristics can be studied with spectral analysis. Some significant tests case have been developed for that purpose, based on the simulation of forced statistically stationary flows. Schemes characteristics have been studied both on fine and coarse grids. The schemes has also be applied to some combustion problem, like deflagrations and detonations.

Studies reported in the paper are part of the thesis by Attili Antonio: Modelli fisico matematici e metodi di integrazione numerica a controllo delle oscillazioni per flussi reagenti turbolenti.

2. MATHEMATICAL MODELS

In the present section mathematical models used to perform simulations described in the paper are shortly presented.

2.1. System for one dimensional, viscous, reactive flow

To model reactive flows has been introduced the following system of eqution:

$$\frac{\partial \rho}{\partial t} + \frac{\partial \rho u}{\partial x} = 0 \tag{1}$$

$$\frac{\partial \rho u}{\partial t} + \frac{\partial (\rho u^2 + p)}{\partial x} = \frac{\partial}{\partial x}\left(\mu \frac{\partial u}{\partial x}\right) + f \tag{2}$$

$$\frac{\partial \rho E}{\partial t} + \frac{\partial \rho u H}{\partial x} = \frac{\partial}{\partial x}\left(u\mu \frac{\partial u}{\partial x}\right) + \frac{\partial q}{\partial x} + uf + q \tag{3}$$

$$\frac{\partial \rho Y_s}{\partial t} + \frac{\partial \rho u Y_s}{\partial x} = -\frac{\partial \rho Y_s V_s}{\partial x} + \dot{\omega}_s \tag{4}$$

$$E = e + \frac{1}{2}u^2 \quad H = E + \frac{p}{\rho} \tag{5}$$

where:

$$q = k\frac{\partial T}{\partial x} + \rho \sum_{s=1}^{N_s} H_s Y_s V_s \tag{6}$$

$$V_s = -D\frac{1}{Y_s}\frac{\partial Y_s}{\partial x} \tag{7}$$

$$H_s = H_s^0 + c_{ps}(T - T_0) \tag{8}$$

$$e = c_v T - c_p T_0 + \sum_{s=1}^{N_s} Y_s H_s^0 \tag{9}$$

$$e = \sum_{s=1}^{N_s} Y_s H_s - \frac{p}{\rho} \tag{10}$$

$$c_p = \sum_{s=1}^{N_s} Y_s c_{ps} \tag{11}$$

$$p = \rho R T \tag{12}$$

$$R = \frac{\Re}{\overline{W}} \quad \overline{W} = \left[\sum_{s=1}^{N_s}\left(\frac{Y_s}{W_s}\right)\right]^{-1} \tag{13}$$

$$c_v = c_p - R \tag{14}$$

The mass production term $\dot{\omega}$ is specified with an Arrhenius relation.

The subsystem constituted by eq. (1), (2), (3), without chemical reaction, has been introduced to test performances of some numerical schemes; forcing terms for momentum and energy equations can simulate effects of turbulence and chemical reactions.

Forcing term are expressed by the following relations:

$$f(x) = \sum_{k=k_{f,\min}}^{k_{f,\max}} A_f(k)\cos(2\pi k x + \phi_{f,k})$$
$$q(x) = \sum_{k=k_{q,\min}}^{k_{q,\max}} A_q(k)\cos(2\pi k x + \phi_{q,k}) \tag{15}$$

Amplitude $A(k)$ and phase $\phi_{\ldots,k}$ are randomly generated.

3. NUMERICAL METHODS

The following methods has been tested:

- A second order Godunov method, a shock capturing scheme based on an exact Riemann solver. Second order accuracy is obtained by a linear reconstruction; TVD (total variation diminishing) property by the minmod flux limiter (ENO scheme) [1-2].
- A second order central finite difference methods (Rubin Burstein scheme) [3].
- The Rubin Burstein scheme, coupled with a nonlinear filter; central schemes create spurious oscillation near zones where gradient are sharp. The non-linear filter has been applied to eliminate, or, at least, to control this circumstance; every time-step the non-

linear filter diminish local maximums and increase local minimums, limiting spurious oscillations [4].

- Two Weighted Essentially Non Oscillatory schemes with third and fifth order of accuracy; these methods are finite difference schemes based on a weighted fluxes reconstruction; convective flux are evaluated by a linear combination of polynomials based on different stencils that contain the point where fluxes must be calculated. Weights of linear combination depend from the degree of regularity of corresponding polynomial (WENO schemes) [5-6].

4. SCHEMES TESTING

All the schemes are tested performing simulations of a periodic forced one dimensional problem. Spectral features and numerical dissipation characteristics are examined, especially with regard to capability to avoid spurious oscillations in zones where solutions are sharp. Simulations are carried out for different level of grid refinement, to analyse schemes characteristics also on grids with very few points.

Performance of all schemes are analysed studying energy spectra. Both kinetic and internal energy spectra have been considered; for internal energy the spectrum has to be considered as the distribution of the modulus of Fourier coefficient of the field, for kinetic energy the spectrum is:

$$\hat{E}(k) = \frac{1}{2}\overline{\sqrt{\rho}u(k)} * \overline{\sqrt{\rho}u(k)}^{*} \qquad (16)$$

Where $\overline{\sqrt{\rho}u(k)}$ is the k[th] Fourier coefficient of $\sqrt{\rho(x)}u(x)$. Following Kida and Orszag [7], this definition has been used because the sum of all term of the spectrum is equal to the integral of kinetic energy over the periodic domain (Parseval identity):

$$\sum E_k = \frac{1}{2}\int_{\Lambda} \rho u^2 \qquad (17)$$

4.1. Reference Solution

First of all a reference solution has been developed; for that purpose the Godunov scheme has been used, because it has strong reliability and hits characteristics are well understood. Fig. 1. contains kinetic and internal energy spectra for that solution; both kinetic then internal energy spectrum present the typical behaviour of Kolmogov spectrum, with an inertial range and a dissipative range. The slope of inertial range, in logarithmic scale, is -2 for kinetic energy spectrum and -1.2 for internal energy spectrum. Dissipative ranges are related to numerical dissipation introduced by the scheme to control spurious oscillations. A simulation on a very fine grid has been also performed; Fig.2 . shows a comparison between solutions on different grids; the figure underlines that the particular shape of the dissipative range is due to the dissipative characteristics of the scheme, because, for different grid resolutions, the behaviour remain the same, but is distributed on different wave number.

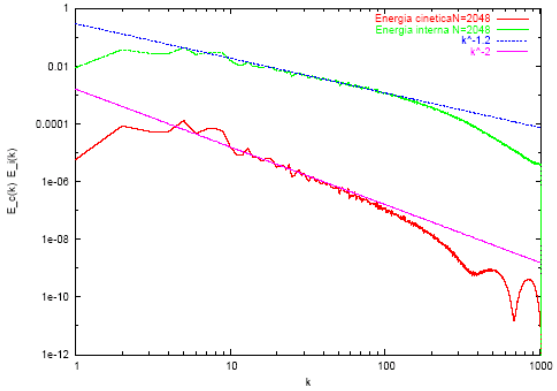

Figure 1. Reference solution, obtained with Godunov method (N=2048): kinetics energy spectrum (bottom curve) and internal energy spectrum (upper curve). Lines with inertial range slope are also shown.

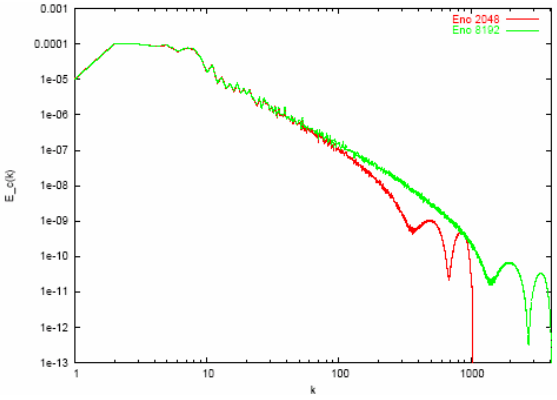

Figure 2. Reference solution: solutions obtained with different grid spacing are shown (N=2048, N=8192).

4.2. Solutions on Fine Grids with Different Numerical Schemes

In this section are presented results obtained with all the schemes presented in section 3.

Figs. 3. and 4. shows the solution obtained with Rubin Burstein's scheme; it can be observed in the velocity field that this scheme produces spurious

oscillation near zones with sharp gradients. This fact is underlined by energy spectrum: there is an excess amount of energy's contain in the inertial range.

If the nonlinear filter is coupled with the Rubin Burstein scheme the excess amount of energy present in the inertial range is sensitively reduced (Fig. 5.). In the figure are reported solutions obtained with ENO schemes on grids with different cells number (N=2048 and N=8192), with the Rubin Burstein scheme and two solutions obtained respectively with an explicit and an implicit version of the nonlinear filter.

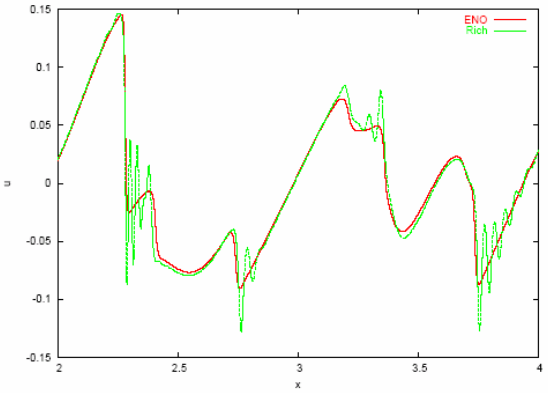

Figure 3. Solution with the Rubin Burstein scheme (N=2048) compared with the reference solution: velocity field

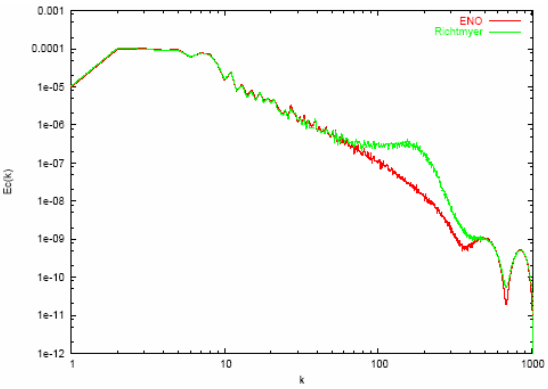

Figure 4. Solution with the Rubin Burstein scheme (N=2048) compared with the reference solution: kinetics energy spectra

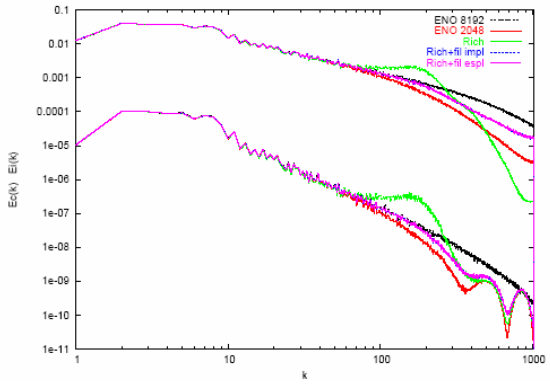

Figure 5. Solutions obtained with Rubin Burstein scheme coupled with nonlinear filter. Upper curves are internal energy spectra, bottom curves kinetics energy spectra.

The last tested are WENO schemes; it has been observed that these schemes have the best performance in term of non physical oscillation control coupled with a very small numerical dissipation. Fig. 6. shows their behaviour; nearest curves to the reference solution are calculated with an high order WENO scheme. These spectra present no oscillation in the inertial range but have small numerical dissipation if are compared with reference solution obtained on a grid with so many cells.

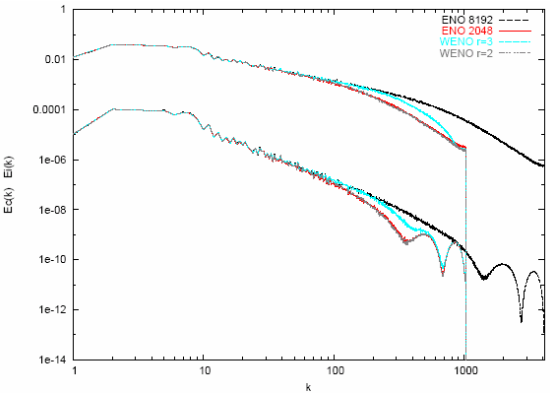

Figure 6. Solutions obtained with WENO schemes, compared with reference solution; upper curves are internal energy spectra, bottom curves kinetics energy spectra.

4.3. Solutions on Grids with Very Few Point (N=128) with Different Numerical Schemes

Schemes' characteristics are very important if simulations are carried on grid with few points, because this is the case for flows' simulations of industrial interest. In this section schemes' behaviour on coarse mesh are analyzed (N=128).

The central difference scheme (Rubin Burstein) produce a solution completely different from the reference one (Fig.7.).

Fig. 8. shows that the application of the non linear filter improve the quality of solution, but errors are still sensible. Fig. 9. explain this fact: the solution obtained with the filter is different respect to the reference also at low wave numbers.

WENO schemes, especially at high order, produce very good solution, also on the coarse grid. It can be observed on Fig. 10. that solution on coarse grid with high order WENO scheme is very near to reference solution (calculated on a very fine grid with a high order WENO scheme). Fig. 10. also shows a comparison between low order WENO scheme and the Godunov method (ENO scheme); these two schemes have the same order (second) on very sharp zones, like shocks and contact discontinuities, but WENO scheme's order is increased to third order in smooth zones. For this reason the solution with WENO scheme is better than Godunov method one. This circumstance is underlined also by Fig. 11., that contains energy spectra; low order WENO scheme is less dissipative than Godunov method.

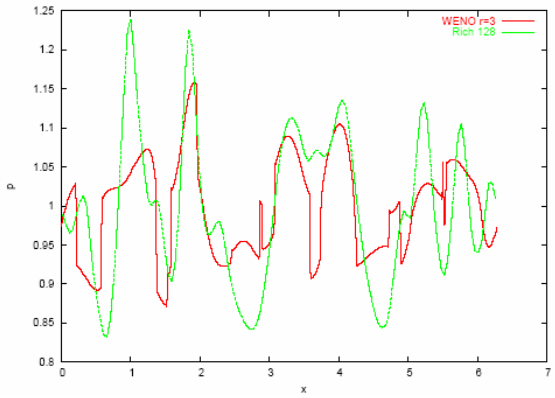

Figure 7. Solution obtained with Rubin Burstein scheme on a coarse grid, compared with WENO solution on a fine grid: pressure field. The results is very far from reference.

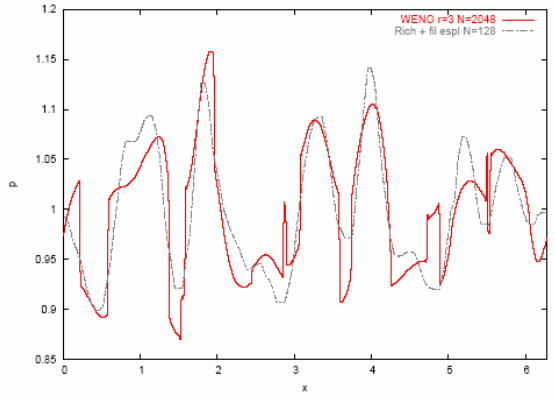

Figure 8. Pressure field obtained with Rubin Burstein scheme coupled with non linear filter.

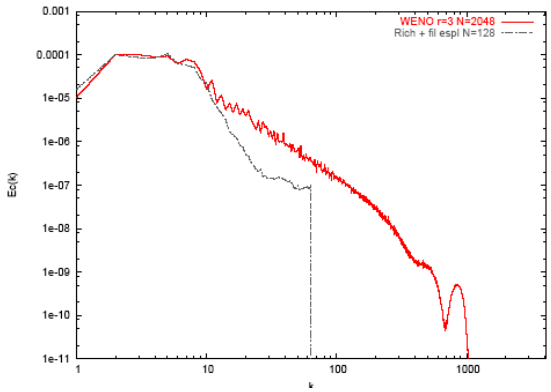

Figure 9. Energy spectrum obtained with Rubin Burstein scheme coupled with non linear filter.

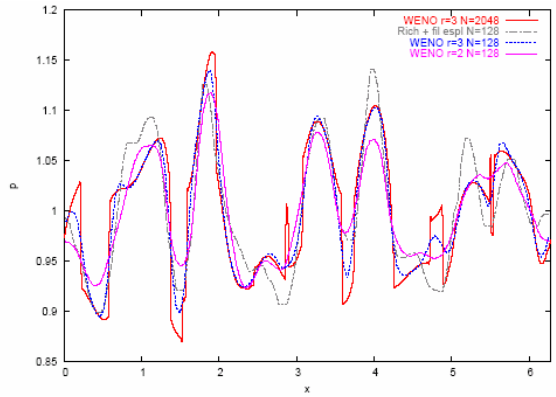

Figure 10. Pressure field with the two WENO schemes and the ENO scheme on coarse grid. The reference solution is obtained with high order WENO scheme on fine grid (the best solution obtained)

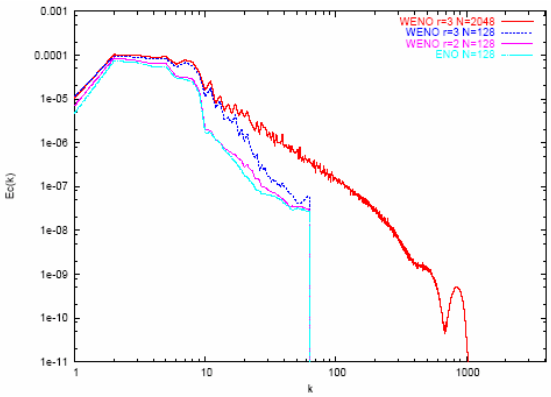

Figure 11. Kinetic energy spectra for solutions with ENO and WENO scheme. Reference solution obtained with high order WENO scheme on fine grid.

5. REACTING FLOWS

WENO schemes, methods with best performances, has been applied to some classical problem of one dimensional combustion, like deflagration and detonation waves, ascertaining their capability to reach high quality solutions.

A stoichiometric mixture of Hydrogen in Air has been considered both for deflagration and detonation; air has been modelled as a mixture of oxygen and nitrogen ($X_{N_2} = 3.773 X_{O_2}$). The chemical kinetic is based on the Marinov model [8] and [9]

5.1. Simulation of Deflagration Waves

Initial condition are uniform for pressure and velocity ($p = 1\,atm \quad u = 0\,m/s$) ; for temperature there's a little zone in the centre of the domain with a value of $1800\,k$; in the rest of domain the temperature is $300\,k$. This condition is sufficient to activate the reaction of Hydrogen and Oxygen in Water.

Fig. 12. and 13. shows temperature and H_2 concentration field and Fig. 15. the flame front velocity; product temperature is about $2400\,k$ and the flame front velocity $2\,m/s$; both results are in good agreement with experimental data and analytical formulas.

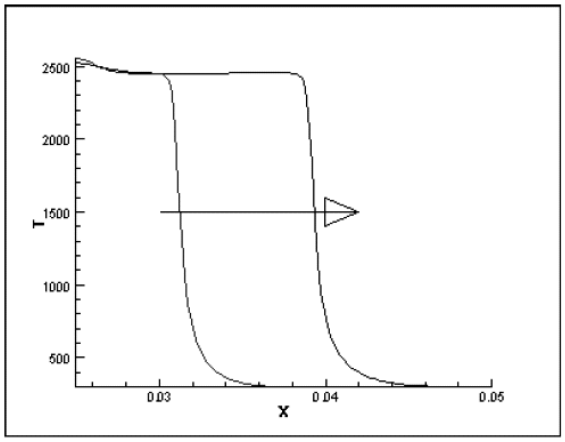

Figure 12. Deflagration: temperature field for two different instant

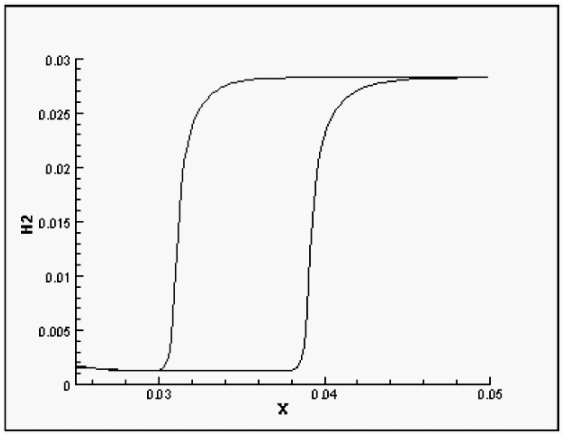

Figure 13. Deflagration: H_2 concentration field for two different instant

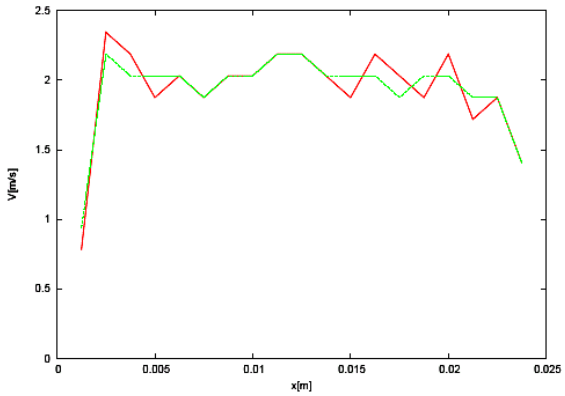

Figure 14. Deflagration: flame front velocity

5.2. Simulation of Detonation Waves

Initial concentration for this simulation consist of stoichiometric mixture of air and hydrogen; a strong shock provide the necessary high temperature to ignite the mixture. Fig. 15. contains temperature field for some different instant; it can be observed the formation of the detonation and the reaching of a definitive structure. Fig. 16. and 17. contain enlargements of the formed detonation. It can be observed the structure described by theory of Zeldovich, Von Neumann, Doring: a shock followed by a reaction layer where temperature increase and pressure decrease. Fig. 18. shows Hydrogen, Oxigen, Water concentration field.

Simulation for the detonation wave has been also performed with Rubin Burstein scheme, both with and without the filter; for these case the results are not shown because numerical simulations blow up in a finite time.

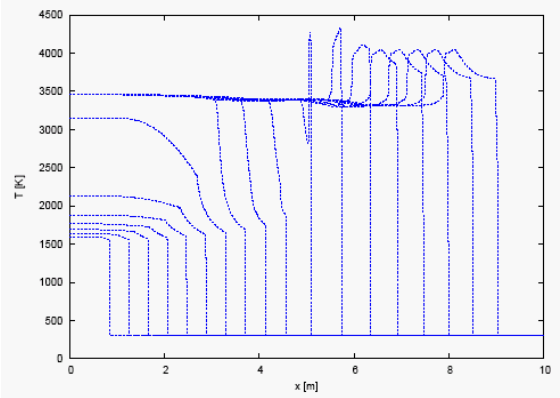

Figure 15. Temperature field for detonation at different time instant

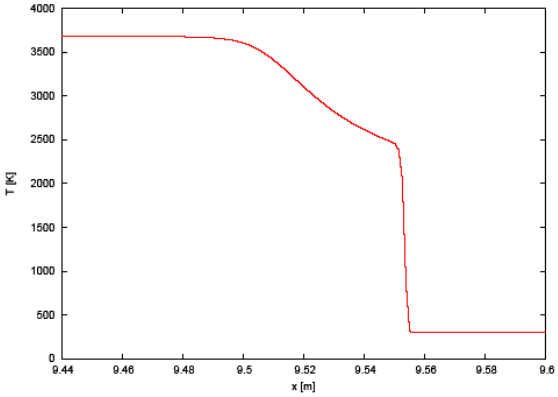

Figure 16. Enlargement of temperature field for detonation

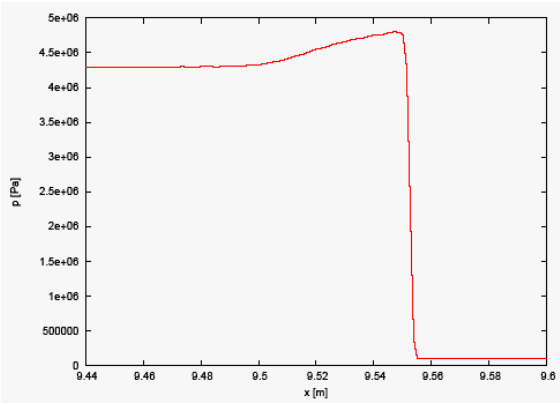

Figure 17. Enlargement of pressure field for detonation

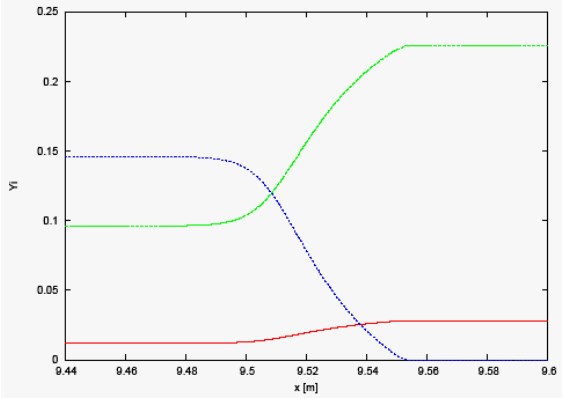

Figure 18. Enlargement of Hydrogen, Oxigen, Water concentration field for detonation

5.3. Turbulence Flame Interaction

A simulation of an interaction between a stationary deflagration and a temporal random disturbance, introduced from the boundary, has been carried out. The deflagration has been stopped in a divergent duct (a quasi-one dimensional model has been introduced to model it); the disturbance introduced from the contour interact with the stationary deflagration; Fig. 19. shows the temporal behaviour of the introduced disturb before and after the interaction with the flame; its structure is different in the two point, there's transfer between different wave numbers as shown by Fig.20, that contains temporal kinetic energy spectra calculated before and after the flame. Also for that case, only with WENO scheme acceptable solutions have been carried out.

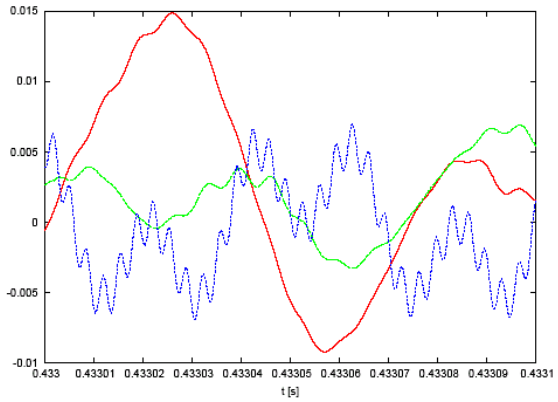

Figure 19. Turbulence deflagration interation: time history of $\sqrt{\rho}u$ disturbance introduced from the boundary (red); the same variable near before the flame (green) and after (blue).

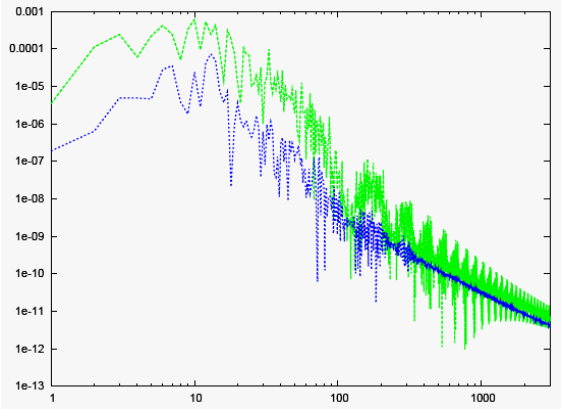

Figure 20. Temporal kinetic energy spectra near before the flame (green) and after (blue).

7. CONCLUSIONS

Some schemes have been tested in the point of view of simulating compressible reactive flows; WENO schemes have been resulted the most powerful technique, spectral features and numerical dissipation characteristics have been examined, especially with regard to capability to avoid spurious oscillations in zones where solutions are sharp.

Tests developed to analyse schemes can be considered significant for studying their spectral features and capability to avoid spurious oscillations.

The scheme with best performance (WENO) has been applied to some classical reactive flow like deflagration and detonation waves. Results obtained are in very good agreement with experimental data and analytical formulas.

REFERENCES

[1] A. Harten, B. Engquist, S. Oscher and S. R. Chakravarthy, "Uniformly High Order Accurate ENO Schemes, III", *J of Comp. Physics*, 71, 1987, 231-303.

[2] C. Shu and S. Oscher, "Efficient Implementation of ENO Shock-Capturing Schemes", *J of Comp. Physics*, 77, 1988, 439-471.

[3] P. J. Roache "Foundamentals of Computational Fluid Dynamics", 1988, Hermosa Publishers, PO BOX 9110, Albuquerque, New Mexico, USA.

[4] B. Engquist, P. Lotstedt and B. Sjogreen, "Non Linear Filter for Efficient Shock Computation", *Mathematics of Computation*, Vol. 52, No 186, 1989, 509-537.

[5] X. D. Liu, S. Oscher and T. Chan, "Weighted Essentially Non-Oscillatory Schemes", *J of Comp. Physics*, 115, 1994, pag. 115-200.

[6] G. S. Jiang, C. W. Shu, "Efficient Implementation of Weighted ENO Schemes".

[7] S. Kida and S. A. Orszag, "Energy and Spectral Dynamics in Forced Compressible Turbulence", *J of Scientific Computing* , Vol. 5, No 2, 1990, pag 85 seg.

[8] Irvin Glassman, "Combustion (3rd edition)", *Academic Press* , 1996

[9] K. K. Kuo, "Principles of Combustion", *Jonh Wiley & Sons* , 1986

Conference on Modelling Fluid Flow (CMFF'06)
The 13th International Conference on Fluid Flow Technologies
Budapest, Hungary, September 6-9, 2006

STRUCTURED MULTI-BLOCK BODY- FITTED GRIDS SOLUTION OF 2D/ AXISYMMETRIC TRANSIENT INVERSE HEAT CONDUCTION PROBLEMS

Aziz AZIMI[1], Siamak KAZEMZADEH HANNANI[2], Bijan FARHANIEH[3]

[1] Corresponding Author. School of Mechanical Engineering, Sharif University of Technology. Azadi Ave., P.O. Box 11365-9567, Tehran, Iran. Tel.: +98-21-6600-5716, Fax: +98-21-6600 0021, E-mail: aazimi@mech.sharif.edu
[2] School of Mechanical Engineering, Sharif University of Technology. E-mail: hannani@sharif.edu
[3] School of Mechanical Engineering, Sharif University of Technology. E-mail: bifa@sharif.edu

ABSTRACT

In this work, iterative regularization algorithms based on parameter estimation technique are developed to solve two-dimensional/axisymmetric transient inverse heat conduction problems in curvilinear coordinates system. The block-structured body-fitted grids with interface patched-overlapped points are used to solve numerically the partial differential equations needed for inverse analysis. The computational code developed for numerical solution of these equations considers a central finite difference version of an alternating-direction implicit technique. In inverse analysis, the Levenberg-Marquardt and the conjugate gradient methods are applied to search for the minimum of the functional. The temperature histories are delivered by noisy/non-noisy sensors located on the lower boundary of the domain. Two cases are considered to show the performance of the developed code: an estimation of two quadratic time-varying heat sources and an estimation of linear time-space varying boundary condition. The results of the present study are compared to those of exact heat sources and boundary condition, and good agreement is achieved.

Keywords: Central Differencing, Curvilinear Coordinates System, Finite Difference Method, Multi-Block Method, Inverse Heat Conduction

NOMENCLATURE

a, b	boundaries in x direction
$C_j(t)$	time dependent trial coefficients of a polynomial for function $g(t)$
c, d	boundaries in y direction
$D_j(x,t)$	time-space dependent trial coefficients of a polynomial for function $F(x,t)$
$\underline{d}^n$	direction of descent
$F(x,y,t)$	dimensionless time-space varying surface temperature
$g(t)$	dimensionless time-varying strength of heat source
$\underline{P}$	vector of unknown parameters
I	total number of time measurements at each sensor location
$\underline{\underline{J}}$	sensitivity coefficients matrix
k	thermal conductivity
L	length scale
M	total number of sensors
N	total number of unknown coefficients of a polynomial function
$S(\underline{P})$	objective function
T	temperature
T_1, T_2, T_3	arbitrary temperature values
t	time
x, y	Cartesian coordinates
α	dimensional thermal diffusivity
β	search step size
δ	Dirac delta function
ε_1	tolerance for convergence of the iterative inverse method
$\underline{\underline{\varepsilon}}$	the error due to measuring instrument
γ_i^k	conjugate coefficient
$\xi_x, \eta_x, \ldots$	Metrics
ω	a random number between -2.576 and 2.576
σ	a coefficient used to calculate the errors in measured data
$\nabla S(\underline{P})$	the gradient direction of $S(\underline{P})$

Subscripts and Superscripts

b	representing boundary condition
i	representing each unknown function
ref	representing reference variable
s	representing the heat source

c	representing computed value from direct problem
m	representing measured value (sensor value)
n	current iteration number
T	the transpose

1. INTRODUCTION

Inverse problems belong to the class of challenging problems, because of their ill-posed nature. In all ill-posed problems, only a reasonable approximation to the solution can be found. Therefore, special geometrical and computational tools are needed to solve an Inverse Heat Conduction Problem (IHCP) for obtaining reasonable solution.

Hadamard [1] is among the first who identified well and ill-posed problems. He stated that if the solution of a problem is not stable and any small perturbation in the data results in significant changes in the solution, this problem is ill-posed.

One of the main characteristics of inverse problems is that the solutions are very sensitive to perturbations in input data and these problems are ill-posed. As a result, special mathematical tools may be required to obtain an inverse solution. Iterative regularization is one of the most efficient and universal approaches for solution of IHCPs [2]. Recently, many researchers have worked on solution of IHCPs to estimate heat sources and boundary conditions in different practically simple geometries. Also, most of these researchers have used finite element and boundary element methods as the numerical schemes to solve Partial Differential Equations (PDEs) of the inverse problem [3-4]. However, numerical solution of PDEs with Finite Difference Methods (FDMs) has also proven to be efficient and accurate. These methods require a structured grid. However, single structured grids are not sufficient in many realistic applications, i.e. composites with complex geometry. In addition, the single structured grid system may carry over high grid density to the region where high accuracy is not necessary and waste computational time. Therefore, to solve efficiently these PDEs in complex geometries, the multi block method can be employed with structured body-fitted grids. This method is based on domain decomposition techniques, with the computational domain being divided into a number of subdomains (blocks). Within each subdomain, the PDEs can be resolved in an independent manner, with the global nature of the inverse analysis. This procedure is accounted by the periodic exchange of boundary information between neighboring subdomains.

Several investigations have been reported in the literature for the solution of steady/transient IHCPs in two- dimensional and axisymmetric geometries in Cartesian or cylindrical coordinates systems proposed by Silva Neto and Ozisik [5], Le Niliot and Lefèvre [6], Abou Khachfe and Jarny [7] and Su and Silva Neto [8]. However, only few works have studied the solution of inverse problems in curvilinear grids such as shape design problems proposed by Lan et. al [9], Cheng and Cheng [10] and Cai et. al [11].

This study is concerned with the application of an approach combining finite difference method and iterative regularization algorithms based on parameter estimation techniques to solve two-dimensional/axisymmetric transient inverse heat conduction problems. The block-structured body-fitted grids with interface patched-overlapped points are used, to solve numerically those of the PDEs needed for inverse analysis. A structured discretization of the computational domain of each block is done using a simple algebraic grid generation method [12]. The computational code developed for numerical solution of the PDEs considers a central FDM. An Alternating-Direction Implicit (ADI) technique [13] is used for temporal and spatial discretizations. The inverse analysis techniques employed are the Levenberg-Marquardt and the conjugate gradient methods [14]. The temperature histories needed for inverse analysis are delivered by noisy/non-noisy sensors located on the lower boundary of the domain. Two sample problems are considered to demonstrate the ability of the developed code, a simultaneous estimation of two linear/quadratic time-varying heat sources and an estimation of linear time-space varying boundary condition. The results of the present study are compared to those of exact heat sources and boundary condition.

2. MATHEMATICAL FORMULATION OF DIRECT PROBLEM

2.1. The Heat Conduction Equation in the Cartesian Coordinates System

The unsteady two-dimensional/axisymmetric heat conduction equation together with heat source in Cartesian coordinates system and dimensionless form is given as follows:

$$\frac{\partial T}{\partial t} = \frac{\partial^2 T}{\partial x^2} + \frac{\partial^2 T}{\partial y^2} + \frac{\kappa}{y}\frac{\partial T}{\partial y} + G \qquad \begin{array}{l} a \le x \le b\,, \\ c \le y \le d\,, \\ t > 0 \end{array} \tag{1}$$

In equation (1), G is defined as follows:

$$G = g(t)\,\delta(x - x_s)\,\delta(y - y_s) \tag{2}$$

and κ is defined as:

$$\begin{array}{ll} 0 & \text{two dimensional bodies} \\ 1 & \text{axisymmetric bodies} \end{array} \tag{3}$$

The boundary conditions associated with equation (1) are shown in figure 1 and the initial condition is considered as $T = 0$. The following groups of the dimensionless parameters are introduced for normalizing the variables:

$$t \quad \frac{t^*}{/ L_{ref}^2}, \qquad x_i \quad \frac{x_i^*}{L_{ref}}, \; T \quad \frac{T^*}{T_{ref}},$$
$$g(t) \quad \frac{g^*(t)}{k\,T_{ref} / L_{ref}^2}, \qquad F = \frac{F^*}{T_{ref}} \tag{4}$$

It is assumed that k, , L_{ref} and T_{ref} are constant values and are known.

2.2. The Heat Conduction Equation in Curvilinear Coordinates System

By considering the following mapping

$$\tau = t, \qquad \xi = \xi(x,y), \qquad \eta = \eta(x,y) \tag{5}$$

and using metric derivatives, the transformed unsteady heat conduction equation (1) can be rewritten in curvilinear coordinates system as follows:

$$\frac{T}{t} \quad A\frac{^2T}{^2} \quad B\frac{^2T}{} \quad C\frac{^2T}{^2} \quad D\frac{T}{}$$
$$E\frac{T}{} \quad G \tag{6}$$

where

$$A=\xi_x^2+\xi_y^2, \quad C=\eta_x^2+\eta_y^2, \quad B=2(\xi_x\eta_x+\xi_y\eta_y),$$
$$D=\xi_{xx}+\xi_{yy}-\frac{\kappa}{y}\xi_y, \qquad E=\eta_{xx}+\eta_{yy}-\frac{\kappa}{y}\eta_y \tag{7}$$

Now, using a curvilinear grid, the heat conduction equation and the initial and boundary conditions are then discretized and solved in the computation domain (,).

2.3. Numerical Method

The heat equation (6) is a parabolic-elliptic equation with a source term and it is solved using the central differencing method together with the Alternating-Direction Implicit (ADI) method [13]. The ADI method requires tridiagonal matrices to be inverted. The solution of the heat conduction equation by this method is conducted in the following two steps,

Step 1) solution in ξ direction:

$$-\frac{\Delta t}{2}(A-\frac{D}{2})_{j,l}^{n} T_{j-1,l}^{n+1/2}+[1+\Delta t(A+C)]_{j,l}^{n} T_{j,l}^{n+1/2}$$
$$-\frac{\Delta t}{2}(A+\frac{D}{2})_{j,l}^{n} T_{j+1,l}^{n+1/2}=\frac{\Delta t}{2}\Big[\, B\,T_{\xi\eta}+E\,T_{\eta}\,\Big]_{j,l}^{n}$$
$$+\frac{\Delta t}{2}C_{j,l}^{n}(T_{j,l+1}^{n}+T_{j,l-1}^{n})+\frac{\Delta t}{2}G_{j,l}^{n}+T_{j,l}^{n} \tag{8}$$

Step 2) solution in η direction:

$$-\frac{\Delta t}{2}(C-\frac{E}{2})_{j,l}^{n+1/2} T_{j,l-1}^{n+1}+[1+\Delta t(C+A)_{j,l}^{n+1/2}]T_{j,l}^{n+1}$$
$$-\frac{\Delta t}{2}(C+\frac{E}{2})_{j,l}^{n+1/2} T_{j,l+1}^{n+1}=\frac{\Delta t}{2}\Big[\, B\,T_{\xi\eta}+D\,T_{\xi}\,\Big]_{j,l}^{n+1/2}$$
$$+\frac{\Delta t}{2}A_{j,l}^{n+1/2}(T_{j+1,l}^{n+1/2}+T_{j-1,l}^{n+1/2})+\frac{\Delta t}{2}G_{j,l}^{n+1/2}+T_{j,l}^{n+1/2} \tag{9}$$

Using equations (8) and (9), the values of temperature are computed at the time $(n+½)\Delta t$ and $(n+1)\Delta t$, respectively.

3. MATHEMATICAL FORMULATION OF INVERSE PROBLEM

3.1. Inverse Analysis

In inverse analysis, there are one or more unknowns in the mathematical model of the problem which must be determined by employing the measured values of temperature inside the field or on the boundaries [2, 3].

Time-space dependent inverse heat conduction problems frequently require the reconstruction of the unknown parameters using the discrete temperature history at interior locations. Numerical solution of these problems consists of the following sequential steps:

1. Solution of direct problem as noted in section 2,
2. Definition of error and minimizing it,
3. Optimization procedure,
4. Regularization procedure to stabilize the usually ill-conditioned discretized system.

Error in inverse analysis is defined by the difference between measured and computed temperatures:

$$\underline{\underline{e}} = \underline{\underline{T}}^m - \underline{\underline{T}}^c \tag{10}$$

Minimization of this error is the main goal of inverse analysis. The least squares method is one of the minimization schemes

$$S \quad \underline{P} \qquad \underline{\underline{T}}^m \quad \underline{\underline{T}}^c \;^T \underset{M \quad I}{\underline{\underline{T}}^m} \quad \underline{\underline{T}}^c \quad \text{or}$$
$$S(\underline{P}) \qquad\qquad T_{ij}^m \quad T_{ij}^c(\underline{P})^{\,2} \tag{11}$$
$$j \;\; 1 \;\; i \;\; 1$$

It is noted that the measured temperatures are different from the exact temperatures

$$\underline{\underline{T}}^m \quad \underline{\underline{T}}^{exact} \quad = \tag{12}$$

As mentioned in the introduction, IHCPs do not satisfy the well-posed conditions introduced by Hadamard [1] and mathematically, they belong to the ill-posed problems. Therefore, the IHCPs are very sensitive to random errors in the measured temperature data and thus, special techniques are developed to predict unknown quantities.

Inverse analysis methods based on estimation of unknown quantities can be divided basically into two categories, parameter and function estimation approaches. The parameter estimation approaches are, in general, nonlinear and the number of the unknown parameters is strongly limited. For function estimation, if the functional form of the unknown function is available, the inverse problem is reduced to the problem of estimating the unknown parameters [2].

In inverse analysis, sensitivity coefficient is quite instrumental and plays an important role. In fact, the sensitivity coefficient is a measure of the sensitivity of the estimated temperature with respect to changes in the unknown quantities, $\underline{\underline{J}} = \partial \underline{\underline{T}} / \partial \underline{P}$.

It can be easily noticed that the estimation of the parameters is extremely difficult for small value of sensitivity coefficient. In such a case, basically the same value for temperature could be obtained for a wide range of values of parameters and the inverse problem is ill-conditioned. Thus, it is desirable to have linearly-independent sensitivity coefficients with large magnitude, so that the inverse problem is not very sensitive to measurement errors and accurate estimates of the parameters can be obtained. In this research, the sensitivity coefficient is calculated by differentiating the original direct problem with respect to the unknown coefficients [14].

3.2. Optimization Procedure

The method is referred to an optimization problem if a certain algorithm that minimizes the difference between the estimated and the specified condition over the parameter estimation is employed. To optimum and minimize the least squares norm (11), two methods are considered, the Levenberg-Marquardt and the conjugate gradient methods [14].

3.2.1. The Levenberg-Marquardt Method

In this method, it is assumed that unknown time-dependent functions (strength of heat source) or time-space dependent functions (boundary condition) are parameterized in the form of a polynomial function with N coefficients:

$$g(t) \quad \sum_{j\ 1}^{N_s} P_j C_j(t), \quad F(x,y,t) \quad \sum_{j\ 1}^{N_b} P_j D_j(x,y,t) \tag{13}$$

Thus, the problem of the function estimation is converted to the problem of the parameter estimation. In this method, for minimization of equation (11), the gradient of $S(\underline{P})$ with respect to the vector of the unknown parameters must be equated to zero and therefore, we can write [14],

$$\underline{P}^{n+1} = \underline{P}^{n} + \Delta \underline{P}^{n} \tag{14}$$

Thus, for estimation of the unknown parameters, it is needed to calculate the sensitivity Matrix $\underline{J}$ that is determined by differentiating equation (1) with respect to the vector of the unknown coefficients [14]:

$$\frac{\partial \underline{\underline{J}}}{\partial t} = \frac{\partial^2 \underline{\underline{J}}}{\partial x^2} + \frac{\partial^2 \underline{\underline{J}}}{\partial y^2} + \frac{\kappa}{y}\frac{\partial \underline{\underline{J}}}{\partial y} + \delta_{i1}\frac{\partial G}{\partial \underline{P}} \quad \begin{array}{l} a \le x \le b, \\ c \le y \le d, \\ t > 0 \end{array} \tag{15}$$

The initial and boundary conditions are as follows:

$$\begin{array}{lll} \underline{\underline{J}}(a,y,t) & 0 & c \le y \le d,\ t > 0 \\ \underline{\underline{J}}(b,y,t) & 0 & c \le y \le d,\ t > 0 \\ \dfrac{\underline{\underline{J}}(x,c,t)}{y} & 0 & a \le x \le b,\ t > 0 \\ \underline{\underline{J}}(x,d,t) & 0 \text{ or } {}_{i2}\dfrac{F}{\underline{P}} & a \le x \le b,\ t > 0 \\ \underline{\underline{J}}(x,y,t) = 0 & & a \quad x \quad b,\ c \quad y \quad d \end{array} \tag{16}$$

For heat source function, $i = 1$ and boundary condition, $i = 2$, equation (15) together with initial and boundary conditions (equations (16)) must be solved separately using the numerical procedure noted in section 2.3. This method is presented in details in references [14, 15].

3.2.2. The Conjugate Gradient Method

This method is a powerful parameter estimation method for the solution of the linear and nonlinear inverse problems using conjugate gradient method. This method minimizes objective function, equation (11), by applying a suitable search step size [14]

$$\underline{P}_i^{k\ 1} \quad \underline{P}_i^{k} \quad {}_i^{k}\underline{d}_i^{k} \tag{17}$$

along a direction of descent in each step based on the following relation:

$$\underline{\mathrm{d}}_i^{k} = \nabla S(\underline{P}^{k})_i + \gamma_i^{k}\underline{\mathrm{d}}_i^{k-1} \tag{18}$$

In the above equation, the gradient direction is computed by the following expression that is obtained by differentiating equation (11) with respect to the unknown parameters:

$$\nabla S(\underline{P}) = -2\left[\frac{\partial \underline{\underline{T}}^{c}(\underline{P})}{\partial \underline{P}}\right]^{T}\left[\underline{\underline{T}}^{m} - \underline{\underline{T}}^{c}(\underline{P})\right] \tag{19}$$

To evaluate the search step sizes of two functions, the objective function is minimized with respect to β_1^k and β_2^k. Finally, these search step sizes are computed by the following expressions:

$$\beta_1^{k} = \frac{F_1 A_{22} - F_2 A_{12}}{A_{11} A_{22} - A_{12}^2}, \quad \beta_2^{k} = \frac{F_2 A_{11} - F_1 A_{12}}{A_{11} A_{22} - A_{12}^2} \tag{20}$$

where

$$A_{11} = \sum_{j=1}^{M}\sum_{i=1}^{I}\left[\left(\frac{\partial T_{ij}^{c}}{\partial \underline{P}_1^{k}}\right)^{T} \underline{\mathrm{d}}_1^{k}\right]^2$$

$$A_{12} = \sum_{j=1}^{M}\sum_{i=1}^{I}\left[\left(\frac{\partial T_{ij}^{c}}{\partial \underline{P}_1^{k}}\right)^{T} \underline{\mathrm{d}}_1^{k}\right]\left[\left(\frac{\partial T_{ij}^{c}}{\partial \underline{P}_2^{k}}\right)^{T} \underline{\mathrm{d}}_2^{k}\right]$$

$$A_{22} = \sum_{j=1}^{M}\sum_{i=1}^{I}\left[\left(\frac{\partial T_{ij}^{c}}{\partial \underline{P}_2^{k}}\right)^{T} \underline{\mathrm{d}}_2^{k}\right]^2 \qquad (21)$$

$$F_1 = \sum_{j=1}^{M}\sum_{i=1}^{I}\left[\left(\frac{\partial T_{ij}^{c}}{\partial \underline{P}_1^{k}}\right)^{T} \underline{\mathrm{d}}_1^{k}\right]\left[T_{ij}^{c} - T_{ij}^{m}\right]$$

$$F_2 = \sum_{j=1}^{M}\sum_{i=1}^{I}\left[\left(\frac{\partial T_{ij}^{c}}{\partial \underline{P}_2^{k}}\right)^{T} \underline{\mathrm{d}}_2^{k}\right]\left[T_{ij}^{c} - T_{ij}^{m}\right]$$

The above procedure is discussed in details in references [14, 15].

3.3. Regularization Procedure

As can be noted the inverse problems are ill-posed and sensitive to the measurement errors in input data due to location of sensors and frequency of oscillations, therefore, the solution and its stability of these problems has to be obtained in a special way. To stabilize inverse analysis, it is needed to use regularization techniques. The regularization of the optimization procedure is required to avoid the extreme sensitivity of the solution of these problems to the errors in the measured data. One of the most popular and most general regularization techniques is the iterative procedure that is used in this article. In the iterative procedure, the solver iterates within each of the iterations of the optimization technique and the problem to be solved is to determine the number of iterations of the minimization procedure to have optimum solution. In fact, the iterative method employs the least squares method taking into account that the optimum solution does not imply the best solution.

Solution of the inverse problems using the iterative regularization involves some sequential items, solution of the direct problem, solution of the inverse problem, a stopping criterion and finally an iterative process. A criterion based on the Discrepancy Principle to stop the iterative procedure of solution is as follows [14]:

$$S(\mathbf{P}^{k\ 1}) \qquad {}_1 \qquad (22)$$

where ε_1 is a user prescribed tolerance. The solution of inverse problems using iterative algorithm may become well-posed if the Discrepancy Principle [14] is used to stop the iterative procedure.

4. RESULTS

Two sample problems are considered to demonstrate the estimation of unknown quantities in the IHCPs using parameter estimation techniques of the inverse analysis.

The first problem considers the estimation of two heat sources in a two dimensional geometry. The strength of the heat sources are a function of time. The second problem considers the case of a heat source and boundary condition identification in an axisymmetric geometry. In this case, the strength of the heat source is a function of time and one of the boundary conditions is a function of both time and space.

The methods applied for these cases are the Levenberg-Marquardt and the conjugate gradient algorithms for estimation of the unknown parameters. The initial guesses of the parameters are taken equal to zero. To solve the direct problem and other partial differential equations required in inverse analysis, a structured discretization of the computational domain is done. The discretization method is a simple algebraic grid generation method [12] with 45×51 and 35×15 grids for two blocks, respectively. In figure 1, the definition of the inverse problem, the blocks of discretized domain and the boundary conditions of the problem are shown and figure 2 presents the grid system of the computational domain in these cases.

It is customary that the simulated temperature measurement, requiring for testing the solution procedures of inverse problems, is generated by introducing some perturbation to the exact computational temperature field in each sample. In addition, it is presumed to have measurement errors with zero mean value by the following equation:

$$T^{m}(x_m, y_m, t) \quad T^{c}(x_m, y_m, t) \qquad 0.001 \quad T_{\max}^{c} \qquad (23)$$

However, both exact and inexact values of the exact computational temperature field have been used for estimation of the unknown parameters. The time domain in these cases is from $t = 0$ to $t = 7$ with the temporal increment $\Delta t = 0.1$. $T_{\max}^{c}$ is 71 for case 1 and 52 for case 2. The results of the estimation of the unknown parameters from the knowledge of the temperature at measurement points near the lower boundary are examined. These

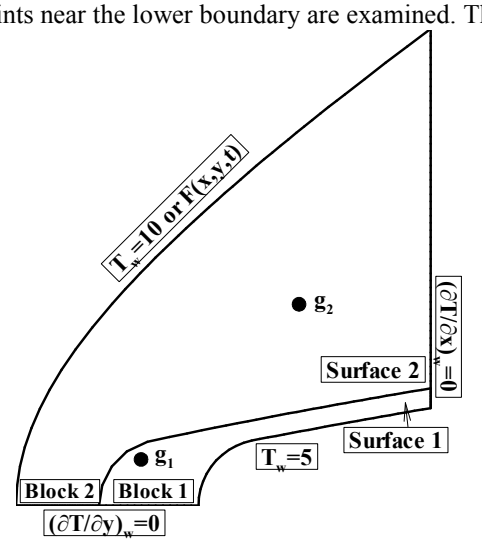

Figure 1. The blocks of discretized domain and the boundary conditions of the problem

Table 1: Sensors' locations for exact/noisy values of computed temperature

Sample Number	Exact/Noisy Values	Estimation Method		Sensor Number									
				1	2	3	4	5	6	7	8	9	10
Sample Problem 1	For the Exact Values	Levenberg-Marquardt	x	0.49	0.50	-	-	0.96	1.04	-	-		
			y	0.12	0.15	-	-	0.36	0.38	-	-		
		Conjugate Gradient	x	-	0.50	0.53	0.58	-	1.04	1.07	1.15		
			y	-	0.15	0.20	0.24	-	0.38	0.38	0.40		
	For the Noisy Values	Both of Two Method	x	0.49	0.50	0.53	0.58	0.96	1.04	1.07	1.15		
			y	0.12	0.15	0.20	0.24	0.36	0.38	0.38	0.40		
Sample Problem 2	For the Exact/ Noisy Values	Levenberg-Marquardt	x	0.49	0.50	0.53	0.58	0.96	1.04	1.07	1.15	1.18	1.26
			y	0.12	0.15	0.20	0.24	0.36	0.38	0.38	0.40	0.41	0.42

sensors' locations are presented in table 1.

4.1. Sample Problem 1

In the first sample, we consider a two-dimensional transient heat conduction problem with the quadratic time-varying functions of two heat-source strengths, $g_1(t)$ and $g_2(t)$:

$$g_1(t)=P_{11}+P_{12}\,t+P_{13}\,t^2=1500+1000\,t+2000\,t^2$$
$$g_2(t)=P_{21}+P_{22}\,t+P_{23}\,t^2=300+100\,t+300\,t^2 \quad (24)$$

These heat sources are located at $x_{s1}=0.19$, y_{s1}=0.25 and $x_{s2}=0.94$, $y_{s2}=0.94$. The value of temperature of the lower boundary is set to 5 for this case. The objective of this case is to estimate the unknown strengths of these heat sources, simultaneously (see figure 1).

The estimated results of these functions are shown in figures 3 and 4 for the Levenberg-Marquardt and the conjugate gradient algorithms and the numerical results are presented in Table 2.

Figure 3 shows the temperature field computed by the direct problem of the IHCP with two quadratic heat sources after estimating the functions, at t 7. In addition, in figure 4, the estimated functions of the quadratic source strengths have been compared with those of exact functions for the noisy measured temperature and they are in accordance with each other.

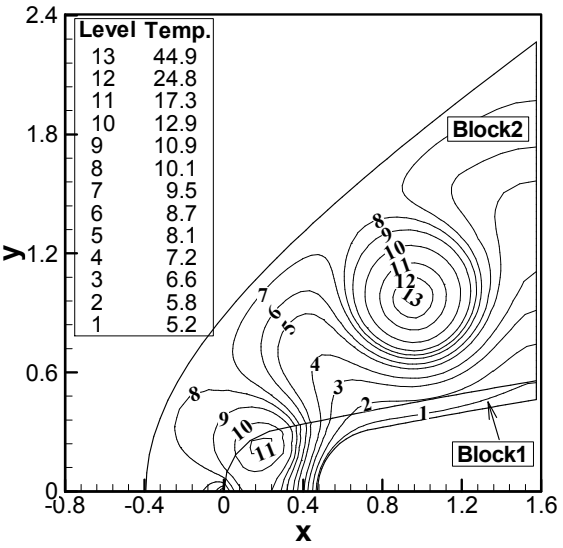

Figure 3. Temperature field of sample problem 1

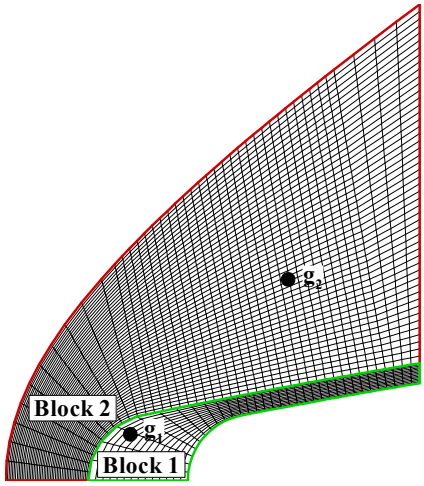

Figure 2. The grid system of the computational domain

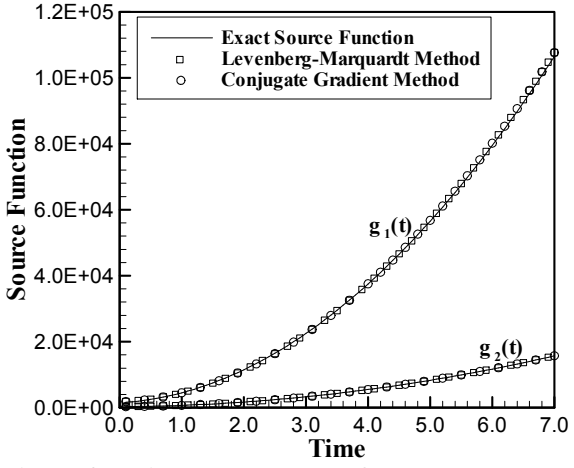

Figure 4. Estimated strengths of the heat sources in sample problem 1

Table 2: Numerical results of estimated functions in sample problem 1

Parameter Estimation Method	Function	Exact Measured Temperatures ($\sigma = 0$)			Noisy Measured Temperatures ($\sigma = 0.001$)			RMS* Error	
		P_1	P_2	P_3	P_1	P_2	P_3	Exact	Inexact
Levenberg-Marquardt	G_1	1500.0	1000.0	2000.0	1740.1	706.25	2060.5	0.004	521.8
	G_2	300.0	1000.0	300.0	327.1	76.44	303.9	0.011	23.98
Conjugate Gradient	G_1	1500.0	1000.0	2000.0	1740.1	706.24	2060.5	0.022	521.8
	G_2	300.0	1000.0	300.0	327.2	76.42	303.9	0.033	24.03

*Root Mean Square

4.2. Sample Problem 2

The second sample problem which can be classified as an axisymmetric transient boundary condition estimation problem, considers the simultaneous prediction of the strength of a linear time-varying heat source, $g_1(t)$, located at x_{s1} 0.19, y_{s1} 0.25 and a linear time-space varying function of the upper boundary condition. We consider these functions with constant parameters as follows:

$$g_1(t) = P_{11} + P_{12}\,t = 2000 + 4000\,t$$
$$F(x,y,t) = P_{21} + P_{22}\,t + P_{23}\,x\,t + P_{24}\,x$$
$$= 3 + 2\,t + x\,t + 2\,x \qquad (25)$$

The value of temperature of the lower boundary is set to zero for this case. The solution of this case is presented in figures 5 to 7 for the Levenberg-Marquardt algorithm and the numerical results are presented in Table 3.

Figure 5 shows the temperature field computed by the direct problem of the IHCP with a linear time-varying heat source and a linear time-space varying upper boundary condition after estimating these functions, at t 7. In addition, in Figures 6 and 7, the estimated functions of the strength of the heat source and upper boundary condition have been compared with those of the exact functions for the noisy measured temperatures and show good agreement.

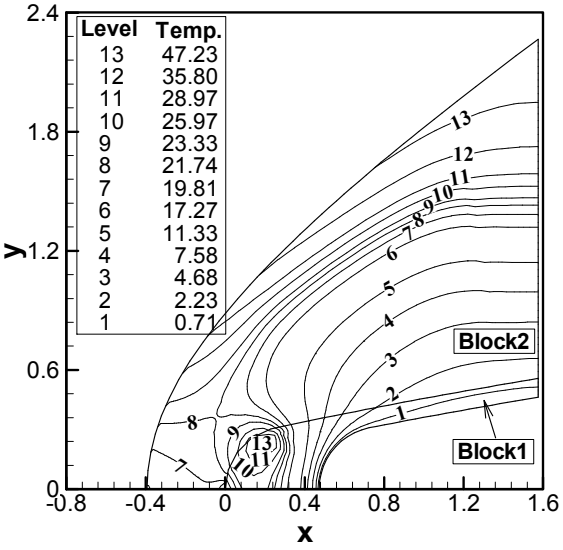

Figure 5. Temperature field of sample problem 2

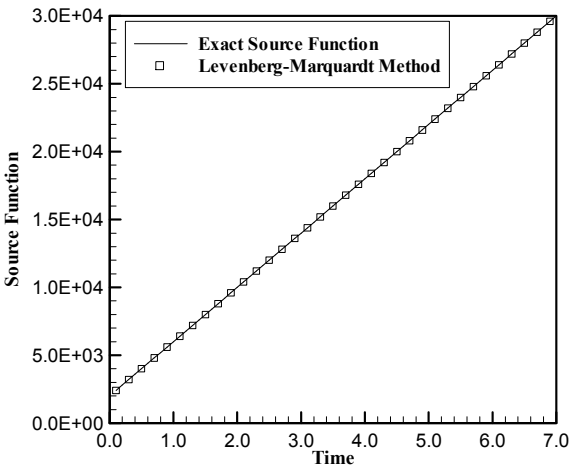

Figure 6. Estimated strength of the heat source in sample problem 2

As can be seen from tables 2 and 3, the estimated results have excellent approximations when measurement errors are not considered, especially for the Levenberg-Marquardt method. When measurement errors are considered, the approximations of the estimated parameters are different with those of exact parameters. In general, the further the measurements are taken from the more sensors, the further the estimated results deviate away from the exact solution. However, the conjugate gradient needs more sensors to estimate unknown parameters. Further work is needed to remedy the difficulties encountered in using the conjugate gradient method for sample problem 2, due to insufficient sensitivity of sensors.

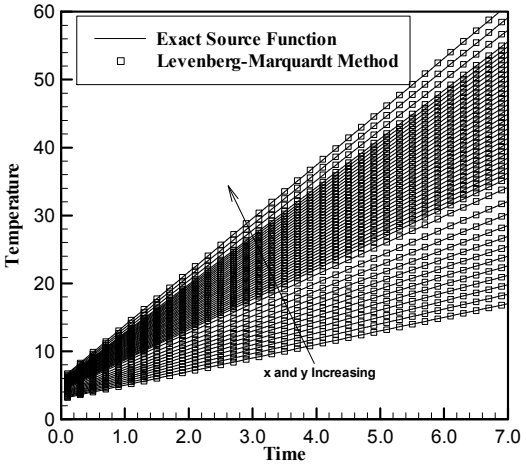

Figure 7. Estimated upper boundary condition in sample problem 2

5. DISCUSSION AND REMARKS

Two 2D/axisymmetric sample problems are solved using the inverse design methodology explained in the preceding sections. The proposed computer code has been developed for solving the 2D/axisymmetric transient IHCPs. A finite difference method is employed to solve the temperature field when the boundary condition is represented as known. These sample problems have been used to show the performance of the Levenberg-Marquardt and the conjugate gradient algorithms for simultaneous estimations of unknown heat sources and unknown boundary condition. From the results for both cases, it is evident that there is nearly no difference in result of the two individual parameter estimation methods when there are no measurement errors. In general, large errors force the estimated results to diverge from the exact solution. However, when measurement errors are considered, more sensors are required in order to increase the congruence of the estimated results to the exact solutions.

REFERENCES

[1] Hadamard, J., 1923, "Lectures on: Cauchy's Problem in Linear Differential Equations," Yale University Press, New Haven, CT.

[2] Beck, J.V. and Arnold K.J., 1977, Parameter Estimation in Engineering and Science, John Wiley & Sons, New York.

[3] Silva Neto, A.J. and Ozisik, M.N., 1993, "Inverse Problem of Simultaneously Estimating the Timewise-Varying Strengths of Two Plane Heat Sources," *J. Appl. Phys.*, Vol. 73, No. 5, pp. 2132–2137.

[4] Le Niliot, C., 1998, "The Boundary Element Method for the Time Varying Strength Estimation of Point Heat Sources: Application to a 2D Diffusion System," *Numer. Heat Transfer B*, Vol. 33, pp. 301–321.

[5] Silva Neto, A.J. and Ozisik, M.N., 1992, "Two-Dimensional Inverse Heat Conduction Problem of Estimating the Time-Varying Strength of a Line Heat Source," *J. Appl. Phys*., Vol. 71, pp. 5357-5362.

[6] Le Niliot, C. and Lefèvre, F., 2001, "Multiple Transient Point Heat Sources Identification in Heat Diffusion: Application to Numerical 2D and 3D Problems," *Numer. Heat Transfer B*, Vol. 39, pp. 277–301.

[7] Abou Khachfe, R. and Jarny, Y., 2001, "Determination of Heat Sources and Heat Transfer Coefficient for 2-D Heat Flow: Numerical and Experimental Study," *Int. J. Heat Mass Transfer*, Vol. 44, No. 7, pp. 1309–1322.

[8] Su, J. and Silva Neto, A.J., 2001, "Two-Dimensional Inverse Heat Conduction Problem of Source Strength Estimation in Cylindrical Rods," *Appl. Math. Modeling*, Vol. 25, pp. 861.

[9] Lan, C.H., Cheng, C.H. and Wu, C.Y., 2001, "Shape Design for Heat Conduction Problems Using Curvilinear Grid Generation, Conjugate Gradient and Redistribution Methods," *Numer. Heat Transfer A*, Vol. 39, No. 5, pp. 487–510.

[10] Cheng, C.H. and Cheng, M.H., 2003, "Shape Identification by Inverse Heat Transfer Method," *J. Heat Transfer*, Vol. 125, pp. 224–231.

[11] Cai, R., Zhu, Y. and Jiang, H., 1986, "A Rapid Method for Solving Laplace Equation in a Doubly Connected Region," *Int. Comm. Heat and Mass Transfer*, Vol. 13, Issue 4, pp. 413–421.

[12] Tannehill, J. C., Anderson, D. A., and Pletcher, R. H., 1997, "Computational Fluid Mechanics and Heat Transfer," 2nd Edition, McGraw Hill Book Company, New York.

[13] Peaceman, D.W. and Rachford H.H., 1955, "The Numerical Solution of Parabolic and Elliptic Differential Equations," *J. Soc. Ind. Appl. Math.*, Vol. 3, pp. 28-41.

[14] Ozisik, M.N. and Orlande Helcio R.B., 2000, "Inverse Heat Transfer: Fundamentals and Applications," Taylor & Francis Inc., New York.

[15] Azimi, A., Kazemzadeh Hannani, S. and Farhanieh, B., 2005, "Application of Multi Block Method for Solution of Two-Dimensional Transient Inverse Heat Conduction Problems," Proc. 5th Int. Conf. on Inverse Problems in Engineering: Theory and Practice, Cambridge, UK, Paper No. A10.

Table 3: Numerical results of estimated functions in sample problem 2

Parameter Estimation Method	Function	Exact Measured Temperatures ($\sigma = 0$)				Noisy Measured Temperatures ($\sigma = 0.001$)				RMS* Error	
		P_1	P_2	P_3	P_4	P_1	P_2	P_3	P_4	Exact	Inexact
Levenberg-Marquardt	G_1	2000.0	4000.0	--	--	2.002	3.999	--	--	0.000	0.046
	B.C.+	3.000	2.00	1.00	2.00	3.008	1.995	0.984	2.010	0.000	2.787

*Root Mean Square

+Boundary Condition

Conference on Modelling Fluid Flow (CMFF'06)
The 13th International Conference on Fluid Flow Technologies
Budapest, Hungary, September 6-9, 2006

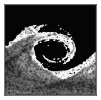

A FAST FULLY-COUPLED SOLUTION ALGORITHM FOR THE UNSTEADY INCOMPRESSIBLE NAVIER-STOKES EQUATIONS

Tamás BÁNYAI[1,2], David Vanden ABEELE[3], Herman DECONINCK[4]

[1] Corresponding Author. Von Karman Institute for Fluid Dynamics, Waterloose steenweg 72, B-1640 St-Genesius-Rode, Belgium
E-mail: banyai@vki.ac.be,
[2] Department of Fluid Mechanics, Budapest University of Technology and Economics. Bertalan Lajos u. 4 – 6, H-1111 Budapest, Hungary,
[3,4] Von Karman Institute for Fluid Dynamics, Waterloose steenweg 72, B-1640 St-Genesius-Rode, Belgium.

ABSTRACT

The direct numerical simulation or large-eddy simulation of incompressible turbulent flows requires to perform a large number of time steps on very fine 3D meshes, which can easily contain 20 million points or more. Besides supercomputing facilities, such simulations rely on performant numerical schemes. Up to now, most of the simulation codes in this field use an explicit treatment for the convective terms, which leads to a family of schemes, which are fast and memory efficient, but due to stringent timestep restrictions require a large number of timesteps to obtain useful results. Segregated implicit schemes (e.g. SIMPLE, PISO, …) allow to use larger time steps; however, this gain is offset by a considerably larger computational cost per time step, due to the need of inner iterations. In this contribution we present an alternative fully coupled approach, which allows to perform time-accurate Navier-Stokes computations without timestep restriction and requiring only a single linear solve per time step. This new approach is illustrated for a standard finite element formulation, stabilized with PSPG/SUPG methods, using unstructured meshes of linear triangular elements. The performance and accuracy analysis of the method has been validated on the Taylor-Green testcase, for which an analytical solution exists.

Keywords: Navier-Stokes, unsteady flow, finite element method, CFD, implicit

NOMENCLATURE

$\underline{x}$	[*m/s*]	position vector
x,y	[*m/s*]	position vector components
h	[*m*]	grid spacing
t	[*s*]	time
Δt	[*s*]	timestep
$\underline{u}$	[*m/s*]	velocity vector
u,v	[*m/s*]	components of the velocity vector
U,V	[*m/s*]	comps. of constant velocity vector
$\underline{a}$	[*m/s*]	stabilized velocity vector
p	[*Pa*]	static pressure
φ		scalar quantity
ρ	[kg/m^3]	density
ν	[m^2/s]	kinematic viscosity
ν_φ		scalar diffusion coefficient
D	[*m*]	vortex diameter
R		residual
$\underline{\phi}$		unknown vector
δ	[-]	kronecker function
Ω	[m^2]	area
$\partial\Omega$	[*m*]	boundary of area
$\underline{n}$	[*m*]	normal vector on boundary of area
N	[-]	basis function
ω	[-]	test function
τ	[*s*]	time scale
ψ		undefined property
$c_0,c_1,\ldots$	[-]	extrapolation factors
O	[-]	order of accuracy

Acronyms

CFD	computational fluid dynamics
PS	pressure stabilized
SU	streamline upwind
PG	Petrov-Galerkin
FE	finite element
GFEM	Galerkin finite element method
SIMPLE	semi-implicit method for pressure-linked equations
PISO	pressure-implicit with splitting operators

Subscripts and Superscripts

$_{m,c,\varphi}$	momentum, continuity, scalar
$^{n,n-1}$, …	time stamp
$_{PS,SU,BULK}$	parameter of PSPG/SUPG/BULK stabilization
$_e$	per element
$_a$	advection
$_s$	swirl

1. INTRODUCTION

For simplicity, we restrict ourselves to two-dimensional situations. The unsteady incompressible Navier-Stokes equations can then be expressed in terms of the velocity components $\underline{u}=[u,v]^T$, pressure p and a scalar φ. The scalar quantity φ with appropriate source terms can for instance represent the turbulent kinetic energy. The momentum equation is written in skew symmetric form due to its better stability and accuracy properties [5] and transport equations for scalar quantities are cast under conservative form.

The most straightforward way of reaching second order accuracy in time, is to use the Crank-Nicholson method. The resulting system of equations can then be written in semi-dicrete form:

$$\begin{aligned}&\frac{\underline{u}^{n+1}-\underline{u}^{n}}{\Delta t}+\\&+\frac{1}{2}\left[(\underline{u}\cdot\nabla)\underline{u}+\frac{\underline{u}\nabla\cdot\underline{u}}{2}+\frac{\nabla p}{\rho}-\nu\nabla^2\underline{u}\right]^{n+1}+\\&+\frac{1}{2}\left[(\underline{u}\cdot\nabla)\underline{u}+\frac{\underline{u}\nabla\cdot\underline{u}}{2}+\frac{\nabla p}{\rho}-\nu\nabla^2\underline{u}\right]^{n}=0\end{aligned} \tag{1}$$

$$\nabla\cdot\underline{u}^{n+1}=0 \tag{2}$$

$$\begin{aligned}&\frac{\varphi^{n+1}-\varphi^{n}}{\Delta t}+\frac{1}{2}\left[\nabla.(\underline{u}\,\varphi)-\nu_\varphi\nabla^2\varphi\right]^{n+1}+\\&+\frac{1}{2}\left[\nabla.(\underline{u}\,\varphi)-\nu_\varphi\nabla^2\varphi\right]^{n}=0.\end{aligned} \tag{3}$$

To solve the equations above both in time and space the finite element method was employed at each time step.

$$\underline{R}\,[\phi(t,\underline{x})]=0, \tag{4}$$

where $\underline{R}$ is the left hand side of the governing Eqs. (1-3) and $\underline{\phi}=[\underline{u},p,\varphi]^T$ is the vector consisting the set of dependent variables:

$$\underline{R}=\begin{bmatrix}\underline{R}_m\\R_c\\R_\varphi\end{bmatrix},\quad \underline{\phi}=\begin{bmatrix}\underline{u}\\p\\\varphi\end{bmatrix}. \tag{5}$$

The discrete solution is represented by means of piecewise linear (P1) elements. These are defined on 2D triangular meshes:

$$\phi(t,\underline{x})=\sum_j \phi_j(t)\,N_j(\underline{x}). \tag{6}$$

Herein, N_j is the P1 basis function (Fig. 1), which is equal to 1 in node j and decreases to zero on the neighbouring nodes in a linear manner:

$$N_j(\underline{x}_i)=\delta_{ij}\,. \tag{7}$$

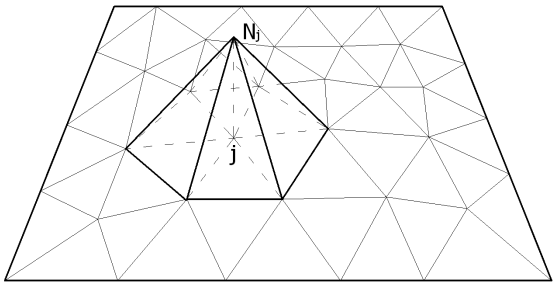

Figure 1. Shape of the basis function

In order to obtain a discrete solution, the equations are multiplied by a set of test functions (ω_i) and integrated over the whole computational domain. The result is set equal to zero in order to minimize the residual. This is called the weighted residual finite element (FE) formulation:

$$\int_\Omega \omega_i(\underline{x})\underline{R}(t,\underline{x})d\Omega=0\,. \tag{8}$$

The most common approach is to set the test functions equal to the basis functions, in this case the so-called Galerkin FE formulation (GFEM) is being applied.

$$\omega_i(\underline{x})=N_i(\underline{x}) \tag{9}$$

For linear elements, the GFEM method is known to be of second order accurate in space. In steady one-dimensional cases, the GFE method can easily be seen to be equivalent to the central finite differencing scheme. It suffers from the same oscillations as central finite difference methods, unless appropriate stabilization terms are added. Pressure wiggles are eliminated by using the well-known Pressure Stabilized Petrov-Galerkin method (PSPG). The idea is to add an extra term based upon the divergence of the momentum equation to the mass conservation law. The pressure Laplacian in this term keeps the pressure field smooth. This approach is known to retain second order accuracy [1]:

$$\int_\Omega N_i\,\nabla\cdot\underline{u}\,d\Omega+\underbrace{\int_\Omega \tau_{PS}\nabla N_i\cdot\underline{R}_m d\Omega}_{PSPG\ stabilization\ term}=0. \tag{10}$$

For convection dominated flows, moreover, the momentum residual needs to be formulated in an upwind manner. This is done by adding the Streamline Upwind Petrov Galerkin stabilization (SUPG) to the Galerkin discretization of the momentum equation. It can be interpreted as a modification of the test functions that increases the

influence of the upstream values to mimic the relative weight of the upstream nodes in the discrete residual. Analogous to the PSPG method, this term is also designed in such a manner that second order accuracy is kept [2]. The same approach is implemented for the scalar transport equation:

$$\int_\Omega \left(N_i + \tau_{SU}\, \underline{u}\cdot\nabla N_i\right)\underline{R}_m d\Omega = \\ = \underbrace{\int_\Omega N_i\, \underline{R}_m d\Omega}_{GFEM} + \underbrace{\int_\Omega \tau_{SU}\, \underline{u}\cdot\nabla N_i\, \underline{R}_m d\Omega}_{SUPG\ stabilization\ term} = 0 \qquad (11)$$

At high Reynolds numbers, the PSPG term induces oscillations in the velocity field which should be damped out by adding an artificial bulk viscosity term to the momentum equation. In the present work the approach presented in [4] was applied, which boils down to adding the following term to the momentum equation:

$$\underbrace{\int_\Omega N_i\, \underline{R}_m d\Omega + \int_\Omega \tau_{BULK} \nabla N_i\, R_c d\Omega}_{BULK\ viscosity\ term} \qquad (12)$$

2. NUMERICAL METHOD

In this section we present the derivation of the numerical method:

- The main idea is to transform the Navier-Stokes equation into a series of Oseen problems, by replacing and extrapolating in time the convective velocity in the advective term, thereby transforming each timestep into a single linear problem.
- Moreover, to ensure a divergence free velocity field that advects other scalars, a consistent stabilized velocity field must be used.

2.1. Applying the extrapolated velocities

To linearize the governing equations, it is necessary to extrapolate the velocity fields in time. This can be done by an appropriate extrapolation, in the current implementation up to 4th order extrapolation is accessible, assuming constant time steps:

$$\phi^{n+1/2} = c_0\phi^n + c_1\phi^{n-1} + c_2\phi^{n-2} + c_3\phi^{n-3} \qquad (13)$$

The coefficients can be obtained by Taylor series expansion and their values are given in Table 1.

Table 1. Extrapolation factors

	C_0	C_1	C_2	C_3
O(h)	1	0	0	0
$O(h^2)$	1.5	-0.5	0	0
$O(h^3)$	1.875	-1.25	0.375	0
$O(h^4)$	2.1875	-2.1875	1.3125	-0.3125

2.2. Resulting system of discrete equations

After the process of linearization, the equations that are needed to be solved and discretized at each time step become:

$$\int_\Omega N_i \frac{\underline{u}^{n+1} - \underline{u}^n}{\Delta t} d\Omega + \\ + \int_\Omega N_i \left(\underline{u}^{n+1/2}\cdot\nabla\right)\left(\frac{\underline{u}^{n+1} + \underline{u}^n}{2}\right) d\Omega + \\ + \int_\Omega N_i \frac{\underline{u}^{n+1/2}}{2}\nabla\cdot\left(\frac{\underline{u}^{n+1} + \underline{u}^n}{2}\right) d\Omega + \\ + \int_\Omega N_i \frac{\nabla\left(p^{n+1} + p^n\right)}{2\rho} d\Omega + \\ + \int_\Omega \nabla N_i \nu \nabla\left(\frac{\underline{u}^{n+1} + \underline{u}^n}{2}\right) d\Omega + \\ + \int_\Omega \tau_{SU}\, \underline{u}_e^{n+1/2}\cdot\nabla N_i \left(\frac{\underline{R}_m^{n+1} + \underline{R}_m^n}{2}\right) d\Omega + \\ + \int_\Omega \tau_{BULK}\nabla N_i \left(\frac{R_c^{n+1} + R_c^n}{2}\right) d\Omega = 0, \qquad (14)$$

$$\int_\Omega N_i \nabla\cdot\underline{u}^{n+1}\, d\Omega + \int_\Omega \tau_{PS}\nabla N_i\cdot\underline{R}_m^{n+1} d\Omega = 0. \qquad (15)$$

$$\int_\Omega N_i \frac{\varphi^{n+1} - \varphi^n}{\Delta t} d\Omega + \\ + \int_\Omega N_i \nabla\left(\underline{u}^{n+1/2}\frac{\varphi^{n+1} + \varphi^n}{2}\right) d\Omega + \\ + \int_\Omega \nabla N_i \nu_\varphi \nabla\left(\frac{\varphi^{n+1} + \varphi^n}{2}\right) d\Omega + \\ + \int_\Omega \tau_{SU}\, \underline{u}^{n+1/2}\cdot\nabla N_i \left(\frac{\underline{R}_\varphi^{n+1} + \underline{R}_\varphi^n}{2}\right) d\Omega = 0, \qquad (16)$$

The viscous terms in Eqs. (14) and (16) can only be expressed using linear elements through integration by parts:

$$\int_\Omega N_i \nu_\phi \nabla^2\phi\, d\Omega = \int_\Omega \nabla(N_i \nu_\phi \nabla\phi)\, d\Omega - \\ - \int_\Omega \nabla N_i \nu_\phi \nabla\phi\, d\Omega \qquad (17)$$

This representation is called the weak formulation of second derivatives. The first term of the right hand side in Eq. (17) can be expressed as a boundary integral (using Gauss' theorem) and is zero, because N_i vanishes on the boundary of its compact support surface.

2.3. Correction of the advection velocity field for the additional scalar transport equation

The continuity equation has been reconsidered with the added PSPG stabilization term:

$$\int_\Omega N_i \, \nabla\cdot\underline{u}\, d\Omega + \int_\Omega \tau_{PS} \, \nabla N_i \cdot \underline{R}_m d\Omega = 0. \qquad (18)$$

Upon integration by parts, this can be written as:

$$\begin{aligned} &-\int_\Omega \nabla N_i \cdot \underline{u}\, d\Omega + \int_\Omega \nabla\left(N_i \underline{u}\right) d\Omega + \\ &+\int_\Omega \tau_{PS} \, \nabla N_i \cdot \underline{R}_m d\Omega = 0. \end{aligned} \qquad (19)$$

Similar to the discretisation of the viscous terms (Eq. (17)) the first term on the left hand side in Eq. (19) vanishes.

$$\int_\Omega \nabla.\left(N_i \underline{u}\right) d\Omega = \int_{\partial\Omega} N_i \underline{u}\cdot\underline{n}\, d\partial\Omega = 0 \qquad (20)$$

The remaining expression directly leads to the definition of the pressure stabilized velocity (<u>a</u>):

$$\int_\Omega \nabla N_i \cdot \underbrace{\left(\underline{u} - \tau_{PS}\underline{R}_m\right)}_{\underline{a}} d\Omega = 0, \qquad (21)$$

where <u>a</u> is the stabilized velocity vector:

$$\frac{\int_{\Omega_e} \left(\underline{u} - \tau_{PS}\underline{R}_m\right) d\Omega_e}{\Omega_e} = \underline{a}_e. \qquad (22)$$

In the sacalar transport equation the extrapolated (presented in 2.1.) stabilized velocity can then be applied:

$$\begin{aligned} &\int_\Omega N_i \frac{\varphi^{n+1}-\varphi^n}{\Delta t} d\Omega + \\ &+\int_\Omega N_i \nabla\left(\underline{a}_e^{n+1/2} \frac{\varphi^{n+1}+\varphi^n}{2}\right) d\Omega + \\ &+\int_\Omega \nabla N_i \nu_\varphi \nabla\left(\frac{\varphi^{n+1}+\varphi^n}{2}\right) d\Omega + \\ &+\int_\Omega \tau_{SU}\, \underline{a}_e^{n+1/2} \cdot \nabla N_i \left(\frac{\underline{R}_\varphi^{n+1}+\underline{R}_\varphi^n}{2}\right) d\Omega = 0, \end{aligned} \qquad (23)$$

2.4. Properties of the method

The method outlined in Eq. (14),(15) and (23) has the following properties:

- Since all approximations made involve errors of second order or higher, the method remains second order accurate.
- Since the Crank-Nicholson time integration is used, the method has absolute stability from a linear stability point of view. In other words a von Neumann stability analysis indicates that there is no time step restriction.
- The method may still be sensitive to nonlinear instabilities and, obviously, the extrapolations made (Eq. (13)) are valid only for sufficiently small time steps. However, this was already the case for the original Crank-Nicholson scheme (Eq. (1-3)).
- Because Eqs. (14),(15) and (23) are linear in the unknowns $\underline{\phi}^{n+1}=[\underline{u}^{n+1},p^{n+1},\varphi^{n+1}]^T$, only a single linear system needs to be solved per time step. This is to be compared with several inner iterations (Newton, SIMPLE, PISO, … or other steps) per time step for the pure Crank-Nicholson scheme. It is therefore expected that the present linearized scheme will be much faster than the original nonlinear Crank-Nicholson method.
- Skew-symmetric convective terms: for a pure GFEM discretization, the skew symmetric form in conjunction with an exact Crank-Nicholson time-integration can be shown to preserve the discrete kinetic energy. It is not only more accurate but also guarantees the numerical stability of the implementation [5]. Although we are using a stabilized FEM, we nevertheless retained the skew-symmetric form because of these desirable properties.

3. COMPUTATIONAL ALGORITHM

The process of calculating the solution at time step $n+1$ requires that the following five steps be performed:

- ***Step 1:*** calculate the pressure stabilized velocity at time step n in each element of the mesh:

$$\frac{\int_{\Omega_e} \left(\underline{u}^n - \tau^n \underline{R}_m^n\right) d\Omega_e}{\Omega_e} = \underline{a}_e^n. \qquad (24)$$

- ***Step 2:*** extrapolate the velocities (and other properties in the case of more complete fluid models) to time step $n+1/2$ by using the factors listed in Table 1 corresponding to the desired order of accuracy:

$$\phi^{n+1/2} = c_0\phi^n + c_1\phi^{n-1} + c_2\phi^{n-2} + c_3\phi^{n-3} \qquad (25)$$

(where for the sake of simplicity, we assume again constant time steps).

- ***Step 3:*** According to the finite element method, this step contains the discetization and the

assembly of the linear system on the computational grid:

$$\underline{\underline{A}}\,\Delta\underline{\phi} = \Delta\underline{b}. \tag{26}$$

- ***Step 4:*** solve the above linear system. In the present work it is done by the linear solver package SAMG [3].
- ***Step 5:*** the final step in the process is to update the solution to prepare for the next cycle.

4. VALIDATION ON THE TAYLOR-GREEN TESTCASE

This test consists of an infinite number of periodic vortices which are decaying in time and for which a non-trivial analytical solution of the complete two-dimensional, laminar, viscous, incompressible unsteady Navier-Stokes equations exists. In the present work an extension of [6] was derived. A scalar transport equation can be obtained by using the vorticity as the scalar :

$$\varphi(x,y,t) = -\frac{\partial u(x,y,t)}{\partial y} + \frac{\partial v(x,y,t)}{\partial x} \tag{27}$$

The analytical solution used can be written in the following form:

$$u(x,y,t) = U_a - V_s \cos\left[\frac{\pi}{D}(x-U_a t)\right] \sin\left[\frac{\pi}{D}(y-V_a t)\right] e^{-2\nu\frac{\pi^2}{D^2}t} \tag{28}$$

$$v(x,y,t) = V_a + V_s \sin\left[\frac{\pi}{D}(x-U_a t)\right] \cos\left[\frac{\pi}{D}(y-V_a t)\right] e^{-2\nu\frac{\pi^2}{D^2}t} \tag{29}$$

$$p(x,y,t) = -\frac{V_s^2}{4}\left\{\cos\left[\frac{2\pi}{D}(x-U_a t)\right] + \cos\left[\frac{2\pi}{D}(y-V_a t)\right]\right\} e^{-4\nu\frac{\pi^2}{D^2}t} \tag{30}$$

$$\varphi(x,y,t) = -\frac{2V_s\pi}{D}\cos\left[\frac{\pi}{D}(x-U_a t)\right] \cos\left[\frac{\pi}{D}(y-V_a t)\right] e^{-2\nu\frac{\pi^2}{D^2}t} \tag{31}$$

The geometry of the testcase is the simplest possible, it is only a square 1m x 1m domain with periodic boundary conditions both in x and y directions. A structured grid consisting of 50x50 square cells which were sub-divided into triangles, was used. The following parameters have been used for the numerical tests:

- U_a, V_a are the advection velocities in the x and y direction. The solution converges in time towards a uniform flow with these prescribed velocity components, which were set to $0.3^{m}/_{s}$ and $0.2^{m}/_{s}$ for the present simulations.
- V_s is the max swirl velocity of the vortices at flow time t=0s: a value of $1^{m}/_{s}$ has been used.
- D is the diameter of the vortices. The smallest possible periodic domain was chosen (D=0.5m).
- ν is the kinematic viscosity which was set to $0.001^{m2}/s$

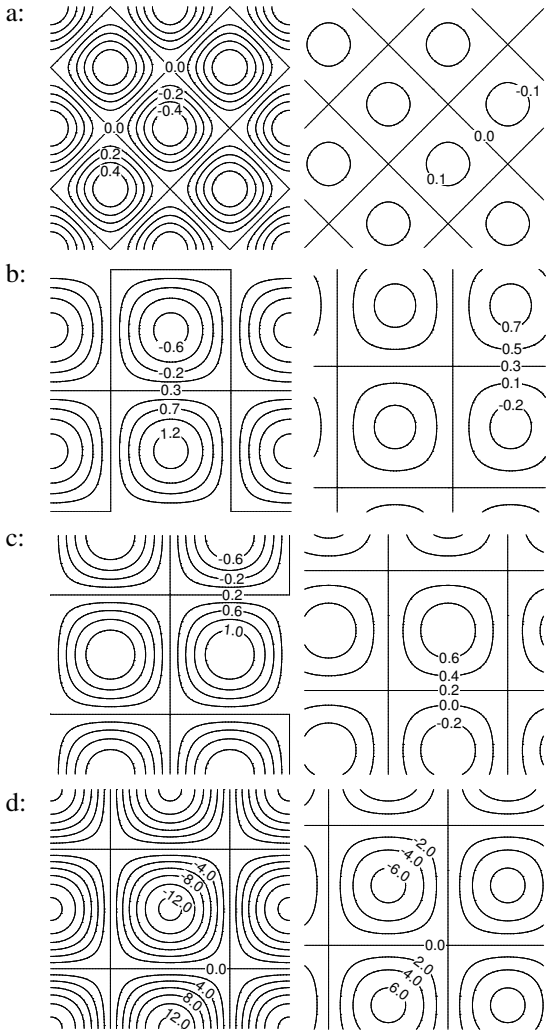

Figure 1. primitive variable contours at t=0s (left) and t=8s (right): pressure(a), x (b) and y (c) velocity component and φ (d)

Comparison has been made between the analytical solution and the computational results at the midpoint of the computational domain both with and without the skew-symmetric part of the convective term added to the momentum equations. Figure 2 shows that both solutions are close to the

exact solution (on the same graph nearly indistinguishable) but in case of the skew symmetric formulation the deviations of the components of velocities were significantly reduced.

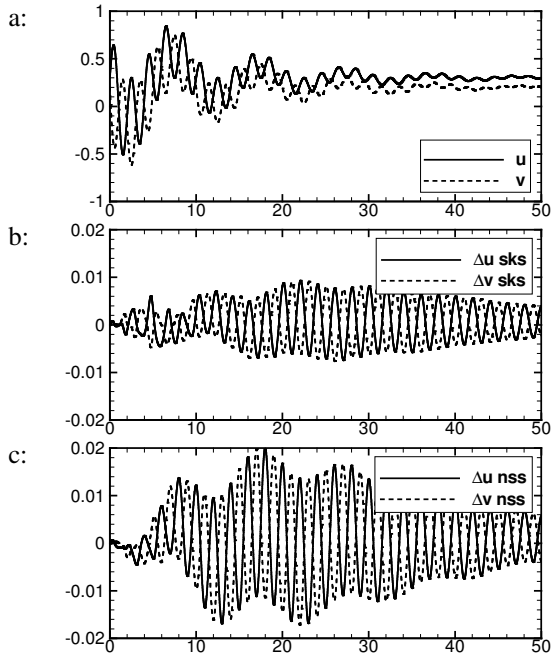

Figure 2. Velocity components (a) and their deviations in case of skew-symmetric (b) and non-skew-symmetric formulation (c) versus time

Another quantity used for comparison is the spatially averaged kinetic energy evolution in time, in order to obtain this quantity which characterizes the behaviour over the whole computational domain:

$$k(t) = \frac{\int_{-D}^{D}\int_{-D}^{D} \frac{u^2(x,y,t)+v^2(x,y,t)}{2} dxdy}{4D^2} = \\ = \frac{U_a^2+V_a^2}{2} + \frac{V_s^2}{4} e^{-4\nu\frac{\pi^2}{D^2}t} \qquad (32)$$

As Figure 3 indicates both formulations were resulting as good approximations of the exact solution (Figure (3/a)). But comparing their deviation against it was observed that the skew symmetric formulation reduces this error by around 20-25%.

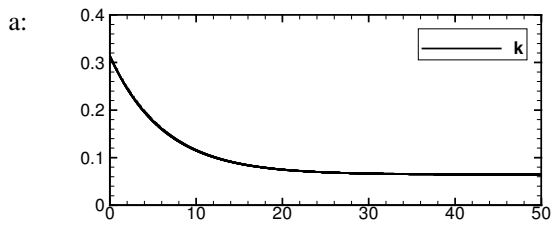

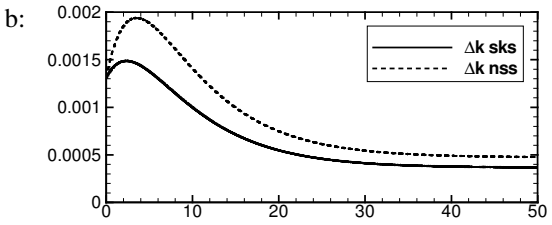

Figure 3. Spatially averaged kinetic energy (a) and its deviation in case of skew-symmetric and non-skew-symmetric formulation (b) versus time

This testcase was also used to verify the method's accuracy. Structured grids converted into triangular meshes with different refinement levels (32x32, 64x64, 96x96, 128x128 and 160x160 grid points on each side) were used. Structured grids Therefore the grid spacing h was h=1/32, 1/64, 1/96, 1/128 and 1/160 respectively. The influence of the extrapolation order on the order of accuracy was also investigated. Except 32x32 grid results and cases where the order of extrapolation was one the infinite error norm ($||\Delta\phi||_\infty$) of the solution was varying quadratically ($||\Delta\phi||_\infty = \varepsilon \cdot h^2$, where ε is a constant) against the grid resolution (Figure 4), meaning that second order accuracy has been obtained when at least second order extrapolation has been applied. The 32x32 grid was not fine enough to mimic the process correctly, therefore the solution broke down and the error increased.

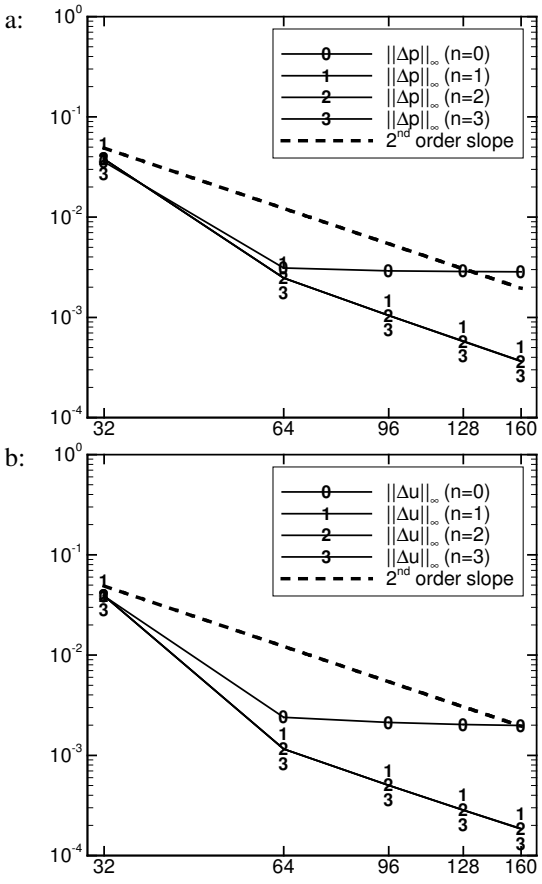

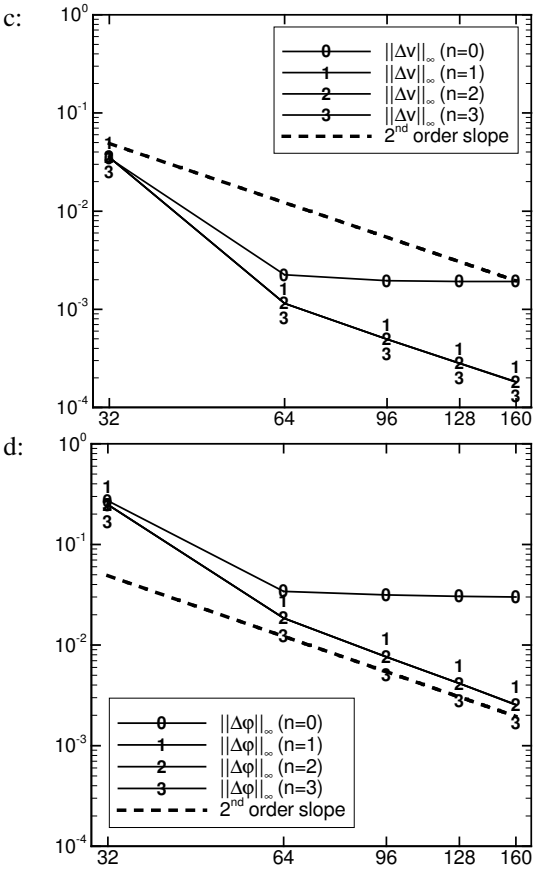

Figure 4. infinite error norms in the center of the domain at time t=0.5s versus the size of the grid for the dependent variables pressure (a), u (b) and v (c) component of velocity and advected scalar (d)

5. SUMMARY

As an alternative to unsteady solvers based upon an explicit or a fully implicit nonlinear treatment of the convective terms, we have proposed a fully implicit scheme in which the convective terms are linearized in time. The resulting method is of second order accuracy in space and time and has absolute linear stability and requires only a single linear solve per time step. To obtain accurate statistics, we found it important to restrict time steps to a value, which is highly dependent on the type of the investigated flow. We hope that our contribution will be helpful to researchers studying turbulent flows using DNS, LES, DES and unsteady RANS simulations.

ACKNOWLEDGEMENTS

The corresponding author wishes to thank for the SZEFH Foundation for supporting the participation at the CMFF'06.

REFERENCES

[1] Hughes, J. R., Franca, L. P., Balestra, M., "A New Finite Element Formulation for Computational Fluid Dynamics: V. Circumventing the Babuska-Brezzi Condition: A Stable Petrov-Galerkin Formulation of the Stokes Problem Accommodating Equal-order Interpolations", *Comp. Meth. App. Mech. and Eng.*, 59 (1986) 85—99

[2] T.J.R. Hughes, L.P. Franca, M.Mallet, A new finite element formulation for computational fluid dynamics: VI. Convergence analysis of the generalized SUPG formulation for linear time-dependent multi-dimensional advective-diffusive systems, *Comput. Meths. Appl. Mech. Engrg.* 63 (1987) 97--112.

[3] T, Clees, AMG strategies for PDE systems with application in industrial semiconductor simulation. Ph.D. thesis, University of Cologne, Germany (2004)

[4] D. O. Snyder, A parallel finite-element/spectral LES algorithm for complex two-dimensional geometries. Ph.D. thesis, Utah State unviersity and von Karman Institute for Fluid Dynamics (2002)

[5] T.A. Zang, On the rotation and skew symmetric forms for incompressible flow simulations. *Applied Numerical Mathematics.*, 7 (1991) 27-40

[6] Randy McDermott. A non-trivial analytical solution to the 2-d incompressible Navier Stokes equations. 2003, *eccentric.mae.cornell.edu/~randy/NS_exact_soln.pdf*

Conference on Modelling Fluid Flow (CMFF'06)
The 13th International Conference on Fluid Flow Technologies
Budapest, Hungary, September 6-9, 2006

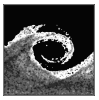

NUMERICAL SOLUTION OF 2D UNSTEADY VISCOUS LOW MACH NUMBER FLOWS IN A CHANNEL

Petra PUNČOCHÁŘOVÁ[1], Karel KOZEL[2], Jiří FÜRST[3], Jaromír HORÁČEK[4]

[1] Corresponding Author. Department of Technical Mathematics, Faculty of Mechanical Engineering, Technical University in Prague. Karlovo nám. 13, 121 35 Prague, Czech Republic. Tel.: +420 224 35 7229, Fax: +420 224 911 406, E-mail: puncocha@marian.fsik.cvut.cz
[2] Institute of Thermomechanics, Centre of energetics, Academy of sciences in Czech Republic, Prague. E-mail: kozelk@fsik.cvut.cz
[3] Department of Technical Mathematics, Faculty of Mechanical Engineering, Technical University in Prague. E-mail: jiri.furst@fs.cvut.cz
[4] Institute of Thermomechanics, Centre of energetics, Academy of sciences in Czech Republic, Prague. E-mail: jaromirh@it.cas.cz

ABSTRACT

The work deals with numerical solution of unsteady flows in a 2D channel where one part of the channel wall is changing as a given function of time.

The flow is described by the system of Navier-Stokes equations for compressible (laminar) flows. The flow has low velocities (low Mach numbers) and is numerically solved by finite volume method. Moved grid of quadrilateral cells is considered in the form of conservation laws using ALE (Arbitrary Lagrangian-Eulerian) method.

Keywords : FVM, ALE method, flow in channel, compressible, laminar, viscous flow, low Mach number, MacCormack finite volume scheme, Jameson artificial dissipation.

NOMENCLATURE

A	[-]	amplitude of oscillation
C		constant
D		computational domain
$\underline{F}$, $\underline{G}$	[-]	vectors of inviscid fluxes
$\tilde{\underline{F}}_k$, $\tilde{\underline{G}}_k$	[-]	numerical inviscid fluxes on edge
H_∞	[m]	inflow width of domain
L	[-]	length of domain
M_∞	[-]	inflow Mach number
Pr	[-]	Prandtl number
Re	[-]	Reynolds number
$\underline{R}$, $\underline{S}$	[-]	vectors of viscous fluxes
$\tilde{\underline{R}}_k$, $\tilde{\underline{S}}_k$	[-]	numerical viscous fluxes on edge
T	[K]	temperature
$\underline{W}$	[-]	vector of conservative variables
c	[m/s]	inflow velocity of sound
e	[-]	total energy per unite volume
f, f_{non}	[Hz],[-]	frequency
k	[-]	coefficient of thermal diffusivity
$\underline{n}$	[-]	normal vector
p	[Pa]	static pressure
$\underline{s}_k$	[-]	vector of velocity of edge motion in cell $D_{i,j}$
t	[s]	time
u	[m/s]	1st component of velocity vector
v	[m/s]	2nd component of velocity vector
w	[-]	channel width
x, y	[-]	coordinates
α_∞	[-]	angle of flow (at inlet)
$\underline{\gamma}$	[-]	vector of pressure gradients
η	[Pa.s]	dynamic viscosity
κ	[-]	adiabatic exponent
$\mu_{i,j}$	[-]	volume of cell $D_{i,j}$
ρ	[kg/m^3]	density

Subscripts and Superscripts

bnd	boundary of domain
i, j	position data in x-direction, y-direction
k	edge position in each cell
max, min	maximum, minimum of magnitude
n	time layer
n, t, x, y	differentiation with respect to $\underline{n}$, x, y, t
0	stagnation variables
1, 2	components of vector or notation of domain
2	outflow variables
∞	inflow variables
T	transposition

1. INTRODUCTION

This work presents unsteady numerical solution of the system of Navier-Stokes equations for compressible laminar flow. Unsteady flow is caused by a moving part of the channel wall as a function of time. Physically the flow can present some very simple model of flow in a human vocal tract (see Fig. 2).

Authors investigated flows in two types of the channel, in an unsymmetrical channel and in a symmetrical channel. The changing part of the wall is between points A, B (see Figs. 1, 2).

Numerical solution was achieved by finite volume version of MacCormack scheme on a grid of quadrilateral cells.

2. MATHEMATICAL MODEL

The 2D system of Navier-Stokes equations (1) was used as mathematical model to describe an unsteady, viscous compressible laminar flow in a channel:

$$\underline{W}_t+\underline{F}_x+\underline{G}_y=\frac{1}{Re}(\underline{R}_x+\underline{S}_y) \qquad (1)$$

$$\underline{W}=[\rho,\rho u,\rho v,e]^T \quad , \qquad (2)$$

$$\underline{F}=[\rho u,\rho u^2+p,\rho uv,(e+p)u]^T \quad , \qquad (3)$$

$$\underline{G}=[\rho v,\rho uv,\rho v^2+p,(e+p)v]^T \quad , \qquad (4)$$

$$\underline{R}=\eta\begin{bmatrix}0\\ \frac{2}{3}(2u_x-v_y)\\ (u_y+v_x)\\ \frac{2}{3}(2u_x-v_y)u+(u_y+v_x)v+kT_x\end{bmatrix} \quad , \qquad (5)$$

$$\underline{S}=\eta\begin{bmatrix}0\\ (u_y+v_x)\\ \frac{2}{3}(-u_x+2v_y)\\ (u_y+v_x)u+\frac{2}{3}(-u_x+2v_y)v+kT_y\end{bmatrix} \quad , \qquad (6)$$

$$k=\frac{\kappa}{Pr(\kappa-1)},\ \kappa=1.4,\qquad Re=\frac{\rho_\infty u_\infty H_\infty}{\eta_\infty},\ \eta=\eta(T)=\left(\frac{T}{T_\infty}\right)^{\frac{3}{4}} \quad . \qquad (7)$$

For ideal gas, static pressure is expressed by the relation:

$$p=(\kappa-1)[e-\tfrac{1}{2}\rho(u^2+v^2)] \quad . \qquad (8)$$

The systems of Navier - Stokes equations (1) is non-linear parabolic systems writen in conservative form. If right hand side of Eq. (1) is zero, 2D system of Euler equations is considered.

2.1. Mathematical formulation

For numerical solution the domain of solution D and boundary conditions have to be defined. Two channels were tested. The first is an unsymmetrical channel and the second is a symmetrical channel which simply corresponds to geometry of a human vocal tract. Boundary conditions were considered in the following form:

a) Upstream conditions: 3 values of $\underline{W}$ are given, pressure is extrapolated.

b) Downstream conditions: pressure is given, other values are extrapolated or $\underline{W}_n=\underline{0}$.

c) On the solid wall $(u,v)_{bnd}=\underline{0}$ non-slip condition is considered for viscous flows or $(u,v)_{bnd}\cdot\underline{n}=0$ is considered for inviscid flows. Temperature condition for viscous flow is $T_n=0$.

Figure 1 shows domain of solution D_1 of the unsymmetrical channel. The upper and lower boundary represents solid wall. The lower wall of the channel has a time changing part between A, B points and this part was changed by the following way as a function of time:

$$w_1(t)=H-A_1\cdot[2+sin(t)]\cdot\{sin[\pi(-2.5+2x)]+1\}\ ,$$
$$x\in\langle 1;2\rangle \quad .$$

The boundary conditions were considered in the following form: At the inlet stagnation state density ρ_0 and pressure p_0 of the fluid and angle of flow $\alpha_\infty=0^o$ are given and at the outlet pressure p_2 is given.

Figure 2 shows domain of solution D_2 of the symmetrical channel. The computational domain is only the lower half of the channel. Lower boundary represents time-changing solid wall between A, B points according to formula:

$$w_2(t)=H-A_2\cdot sin(t\cdot 2\pi f_{non})\cdot\{0.5\cdot sin[x-(L_1+(L_2-L_1)\cdot 0.5)\cdot(\pi\cdot 1/(L_2-L_1))]+0.5\}+H\ ,$$
$$x\in\langle L_1;L_2\rangle \quad .$$

The upper boundary represents the axis of symmetry. Boundary conditions were considered in following form: at the inlet part M_∞, ρ_∞, $\alpha_\infty=0^o$ are given. At the outlet $\underline{W}_n=0$. Domain in Fig. 2 with its boundary conditions represents a very simple case of flow in a human vocal tract.

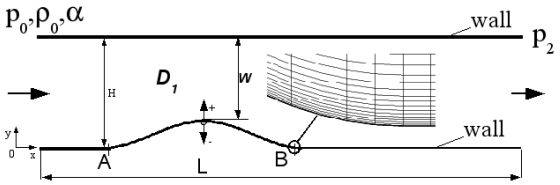

Figure 1. Domain of solution D_1 (Unsymmetrical channel)

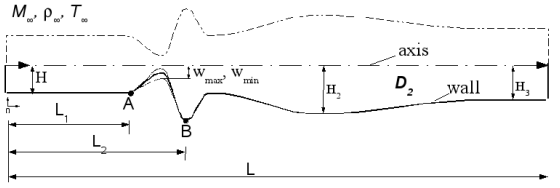

Figure 2. Domain of solution D_2 (Symmetrical channel)

3. NUMERICAL SOLUTION

Numerical solution of 2D problems uses finite volume "cell centered" method (FVM) on a grid of quadrilateral cells.

The computational domain D is divided into subdomains $D_{i,j}$ where $D \equiv \mathrm{U}_{i,j} D_{i,j}$ and $D_{i,j}$ are mutually disjoint. The Eq. (1) is integrated over subdomain $D_{i,j}$ and using Green formula we get the integral form:

$$\iint_{D_{i,j}} \underline{W}_t \, dxdy = \oint_{\partial D_{i,j}} (\underline{F}\, dy - \underline{G}\, dx) - \frac{1}{Re} \oint_{\partial D_{i,j}} (\underline{R}\, dy - \underline{S}\, dx) \quad . \tag{9}$$

Further double integral on the left side is repaired using Mean value theorem as follow:

$$\iint_{D_{i,j}} \underline{W}_t \, dxdy = (\underline{W}_t)_{i,j} \cdot \mu_{i,j} \quad . \tag{10}$$

For quadrilateral cells a basic formula has the form:

$$(\underline{W}_t)_{i,j} = -\frac{1}{\mu_{i,j}} \sum_{k=1}^{4} \left[\left(\tilde{\underline{F}}_k - \tilde{\underline{R}}_k \right) \Delta y_k - \left(\tilde{\underline{G}}_k - \tilde{\underline{S}}_k \right) \Delta x_k \right] \tag{11}$$

3.1. Numerical scheme

For computation of compressible system of Navier–Stokes equations explicit MacCormack (MC) scheme in the form of finite volume method (predictor – corrector) has been used in the form:

$$\underline{W}_{i,j}^{n+1/2} = \underline{W}_{i,j}^{n} - \frac{\Delta t}{\mu_{i,j}} \sum_{k=1}^{4} \left[\left(\tilde{\underline{F}}_k^{\,n} - s_{1k} \underline{W}_k^{\,n} - \tilde{\underline{R}}_k^{\,n} \right) \Delta y_k - \left(\tilde{\underline{G}}_k^{\,n} - s_{2k} \underline{W}_k^{\,n} - \tilde{\underline{S}}_k^{\,n} \right) \Delta x_k \right]$$

$$\widetilde{\underline{W}}_{i,j}^{n+1} = \frac{1}{2} \left(\underline{W}_{i,j}^{n} + \underline{W}_{i,j}^{n+1/2} \right) - \frac{\Delta t}{2} \frac{1}{\mu_{i,j}} \sum_{k=1}^{4} \left[\left(\tilde{\underline{F}}_k^{\,n+1/2} - s_{1k} \underline{W}_k^{\,n+1/2} - \tilde{\underline{R}}_k^{\,n+1/2} \right) \Delta y_k - \left(\tilde{\underline{G}}_k^{\,n+1/2} - s_{2k} \underline{W}_k^{\,n+1/2} - \tilde{\underline{S}}_k^{\,n+1/2} \right) \Delta x_k \right] \tag{12}$$

Next part of MC scheme is artificial dissipation $AD(W_{i,j})^n$ that stabilize the numerical solution. In this case Jameson type of artificial dissipation has been used and last step of scheme has the form:

$$\underline{W}_{i,j}^{n+1} = \widetilde{\underline{W}}_{i,j}^{n+1} + AD(W_{i,j})^n \quad , \tag{13}$$

$$AD(W_{i,j})^n = C_1 \gamma_1 \left(\underline{W}_{i+1,j}^{n} - 2\underline{W}_{i,j}^{n} + \underline{W}_{i-1,j}^{n} \right) + C_2 \gamma_2 \left(\underline{W}_{i,j+1}^{n} - 2\underline{W}_{i,j}^{n} + \underline{W}_{i,j-1}^{n} \right) \tag{14}$$

$$C_1, C_2 \in R$$

$$\gamma_1 = \frac{|p_{i+1,j}^n - 2\mathrm{p}_{i,j}^n + p_{i-1,j}^n|}{|p_{i+1,j}^n| + 2|p_{i,j}^n| + |p_{i-1,j}^n|} \quad . \tag{15}$$

$$\gamma_2 = \frac{|p_{i,j+1}^n - 2\mathrm{p}_{i,j}^n + p_{i,j-1}^n|}{|p_{i,j+1}^n| + 2|p_{i,j}^n| + |p_{i,j-1}^n|}$$

The Equations (12), (13) represent MC scheme for viscous flow in a domain with moving grid of quadrilateral cells (see Figure 3). Moving grid in unsteady solution is described using Arbitrary Lagrangian-Eulerian (ALE) method which defines projection of reference domain D_0 to domain in time D_t [1]. It defines another fluxes $\underline{s}_k \cdot \underline{W}_k$ in MC scheme. Approximation of conservative variable $\underline{W}_k$ on edge $(\partial D_{i,j})_k$ and diffusive components $\underline{R}_k$, $\underline{S}_k$ is central, the second derivatives (of dissipative terms) on edge are approximated using dual volumes [2] as is shown in Figure 4. Inviscid fluxes are approximated e. g.:

$$\begin{aligned} &\tilde{\underline{F}}_1^{\,n} = \underline{F}_{i,j}^{\,n}, \; \tilde{\underline{F}}_1^{\,n+1/2} = \underline{F}_{i+1,j}^{\,n+1/2}, \; \tilde{\underline{F}}_3^{\,n} = \underline{F}_{i-1,j}^{\,n}, \\ &\tilde{\underline{F}}_3^{\,n+1/2} = \underline{F}_{i,j}^{\,n+1/2} \\ &\tilde{\underline{G}}_2^{\,n} = \underline{G}_{i,j}^{\,n}, \; \tilde{\underline{G}}_2^{\,n+1/2} = \underline{G}_{i,j+1}^{\,n+1/2}, \; \tilde{\underline{G}}_4^{\,n} = \underline{G}_{i,j-1}^{\,n}, \\ &\tilde{\underline{G}}_4^{\,n+1/2} = \underline{G}_{i,j}^{\,n+1/2} \end{aligned} \tag{16}$$

The time step is bounded by following stability condition:

$$\Delta t \le \frac{CFL}{\left(\frac{|u_{max}| + c}{\Delta x_{min}} + \frac{|v_{max}| + c}{\Delta y_{min}} + \frac{2}{Re} \left(\frac{1}{\Delta x_{min}^2} + \frac{1}{\Delta y_{min}^2} \right) \right)} \tag{17}$$

where Courant-Fridrichs-Levy (CFL) condition is in computation $CFL \approx 0.5$. For viscous flow the grid near wall-boundary have succesive refinement in y-direction $(\Delta y_{min} \approx \frac{1}{\sqrt{Re}} \approx 8 \cdot 10^{-4}, y_{max} \approx 0.01)$ due to existing boundary layer. Example of grid detail is shown in Fig. 1.

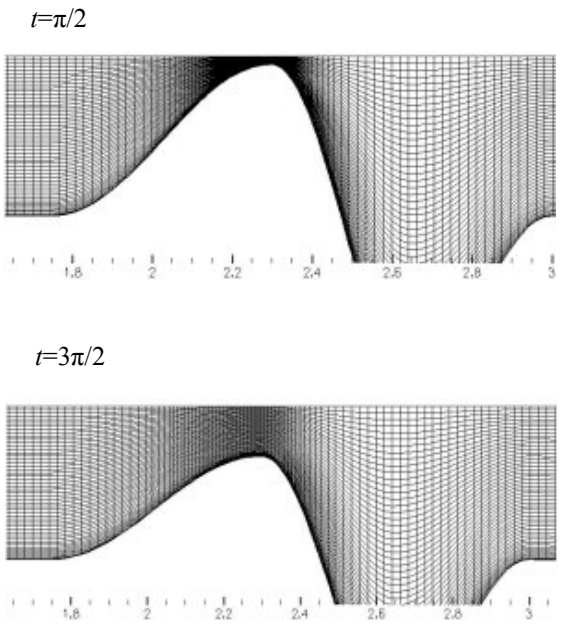

Figure 3. Detail of moving grid in time $t=\pi/2$, $t=3\pi/2$

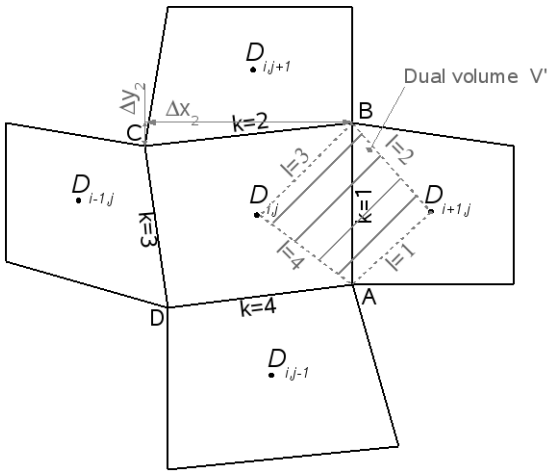

Figure 4. Finite volumes D_{ij}, dual volumes V_k'.

Convergence of solution is observed using L_2 norm of residual of momentum (ρu).

4. NUMERICAL RESULTS

4.1. Numerical results in the domain D_1

In this section numerical solutions of the system of Euler eqs. and of the system of Navier-Stokes (laminar) eqs. in the domain D_1 (see Fig. 1) are shown. Numerical solution of inviscid flow and viscous flow is realised by MC scheme with Jameson artificial viscosity.

Figure 5 shows comparison of steady solutions between inviscid flow and viscous flow in the channel. The flow is mapped by Mach number isolines and also by velocity vectors.

a) Inviscid flow, $p_2=0.9p_\infty$ ($M_\infty=0.254$), $M_{max}=0.664$ (light colour), $M_{min}=0.279$, mesh 200x50 cells ($L=3$, $H=0.5$).

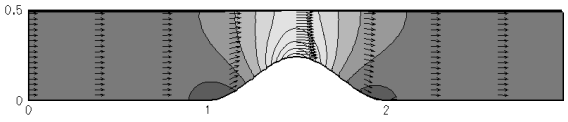

b) Viscous laminar flow, $p_2=0.9p_\infty$ ($M_\infty=0.120$), $M_{max}=0.345$ (light colour), $Re\approx 5\cdot 10^5$, mesh 600x50 cells ($L=12$, $H=0.5$).

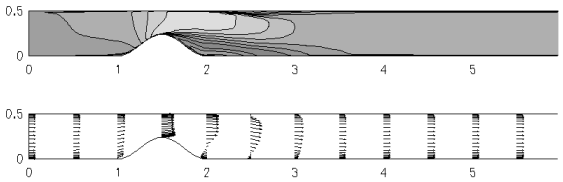

Figure 5. Inviscid flow and viscous laminar flow in a channel (steady solution).

Steady inviscid flows are not able to consider separation but steady solution of viscous flows has a significant flow separation past bump (see Fig. 5b). It means that only viscous model can be used to describe main features of this part of unsteady flows.

Figure 6 shows development of unsteady viscous compressible laminar flows in the channel (see Fig. 1) in several time layers starting by the second period. Parametres considered for computation: $p_2=0.9p_\infty$ and $Re\approx 5\cdot 10^5$. The domain D_1 contains 600x50 cells ($L=12$, $H=0.5$). The steady solution of this case which was used as initial condition for unsteady solution ($t=0$) is shown in Fig. 5b.

a) $t=2\pi$, $M_{max}=0.455$

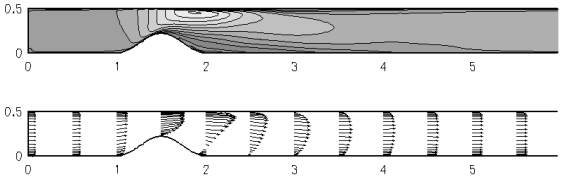

b) $t=2\pi+\pi/2$, $M_{max}=0.338$

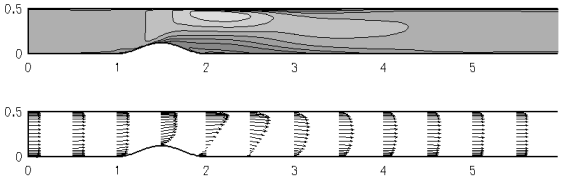

c) $t=3\pi$, $M_{max}=0.374$

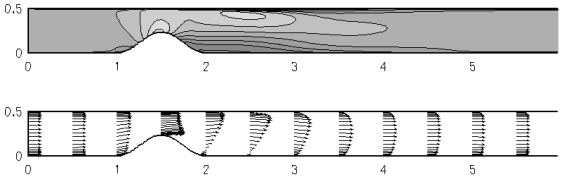

d) $t=2\pi+3\pi/2$, $M_{max}=0.568$

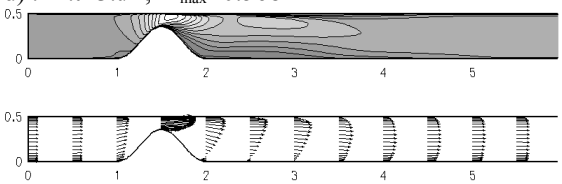

e) $t=4\pi$, $M_{max}=0.464$

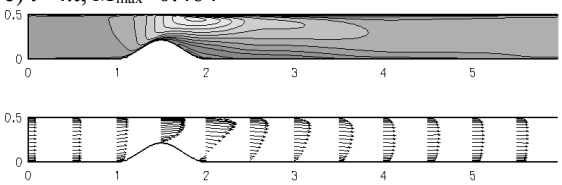

Legend of Mach numbers:

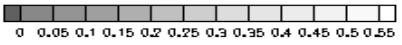

Figure 6. Unsteady viscous laminar flow in the domain D_1, $p_2=0.9p_\infty$ ($M_\infty\approx 0.120$), $Re\approx 5\cdot 10^5$.

4.2. Numerical results in the domain D_2

In this section unsteady numerical results of the system of laminar Navier – Stokes equations (1) in the domain D_2 (see Fig. 2) are considered.

Parameters considered for computation of flow in a channel: Inlet Mach number M_∞=0.02 (6.68 m/s), frequency of solid wall between points A, B (see Fig. 2) is f=20Hz and Reynolds number is $Re \approx 9 \cdot 10^3$. These values approximately correspond to a real flow in a human vocal tract.

The domain D_2 contains 400x50 cells (L=8, H=0.4).

Results of numerical solution are mapped by Mach number isolines and also by vectors of velocity .

a) t=0 (steady solution), M_{max}=0.096

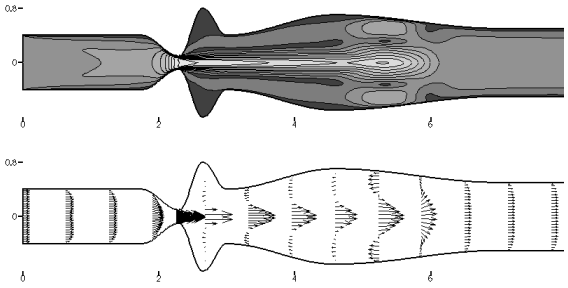

b)

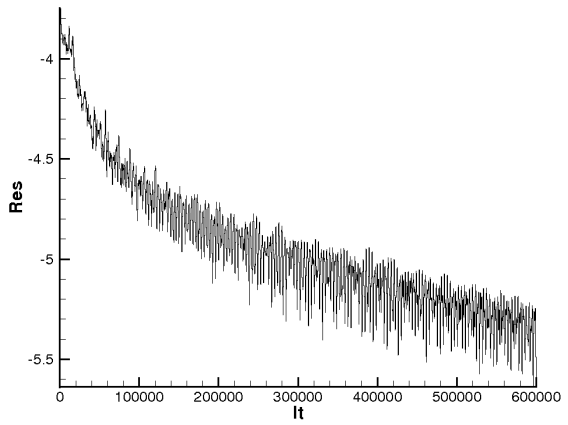

Figure 7. a) Steady solution of viscous laminar flow in the domain D_2 (400x50 cells), M_∞=0.020, Re≈9·10³. b) Convergence to a steady solution.

Firstly the steady solution that is shown in Figure 7a) was computed. The steady solution was used as initial conditions for unsteady solution (see Fig. 8). Figure 7b) shows convergence to a steady solution in L_2 norm of residual of momentum (ρu), that seems to be relatively good for this case with very low Mach number.

a) t=4π, M_{max}=0.094

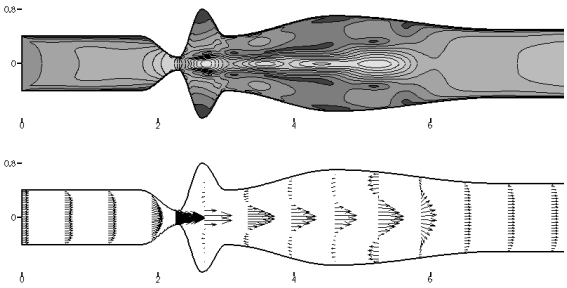

b) t=4π+π/2, M_{max}=0.077

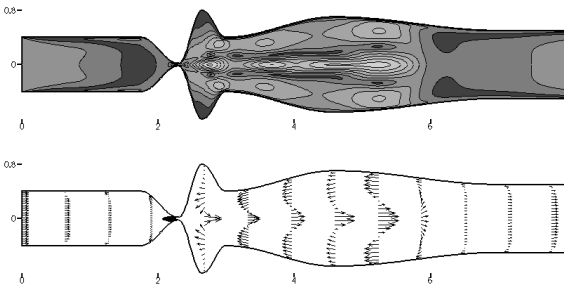

c) t=5π, M_{max}=0.129

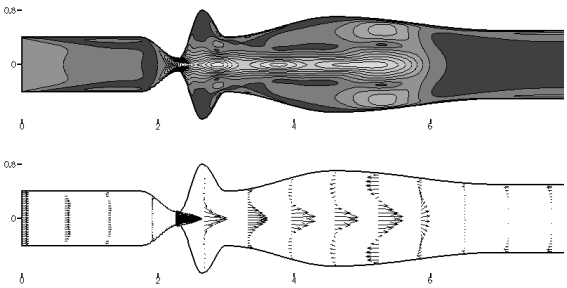

d) t=4π+3π/2, M_{max}=0.145

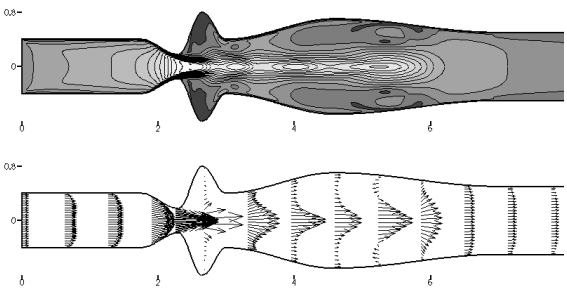

f) $t=6\pi$, $M_{max}=0.102$

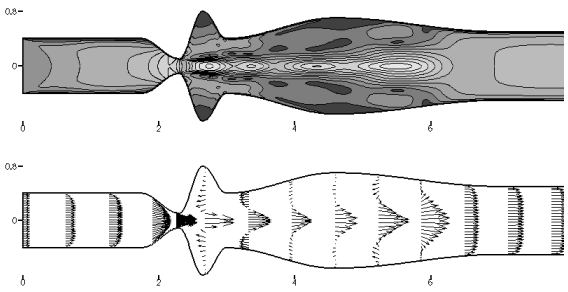

Legend of Mach numbers:

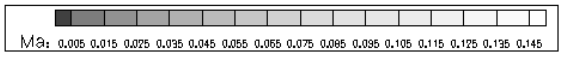

Figure 8. Unsteady solution of viscous laminar flow in the domain D_2, M_∞=0.020, Re≈9·10³, f=20Hz. Mesh 400x50 cells (L=8, H=0.4).

Figure 8 (a, b, c, d, e) shows development of unsteady numerical results in the third period $(t \in \langle 4\pi, 6\pi \rangle)$. One can see typical behavior with choking flows in very narrow part of channel and with time development of flow including separation domains.

Domain D_2 with its boundary conditions represents a simple case of flow in a human vocal tract [3, 4].

5. SUMMARY

A numerical method solving 2D unsteady compressible system of Navier-Stokes equations using finite volume method was developed.

This unsteady method was realized for low Mach number flows in a 2D channel with changing part of solid wall as a given function of time.

Numerical results represent a very simple case of flow in a human vocal tract. To verify our results in the future one has to find some experimental results for comparison or compare our numerical results to other numerical results.

ACKNOWLEDGEMENTS

This work has been partially supported by the grant GAČR No. 201/05/0005 and by the Research Plan MSM No. 6840770010.

REFERENCES

[1] Honzátko, R., Kozel, K., Horáček, J., 2004, "Flow over a profile in a channel with dynamical effects", *Proceedings in Applied Mathematics*, Vol. 4, No. 1, pp. 322-323, ISSN 1617-7061.

[2] Fürst, J., Janda, M., Kozel, K., 2001, „Finite volume solution of 2D and 3D Euler and Navier-Stokes equations", *Mathematical fluid mechanics*, Ed. Neustupa J., Penel P., Berlin, ISBN 3-7643-6593-5.

[3] Punčochářová, P., Kozel, K., Fürst, J., 2005, „Unsteady, subsonic inviscid and viscous flows in a channel", *Fluid Dynamics 2005*, IT CAS CZ, pp.125-128, ISBN 80-85918-94-3.

[4] Horáček, J., Šidlof, P., Švec, G., 2005, "Numerical simulation of self-oscillations of human vocal folds with Hertz model of impact forces", *Journal of fluid and structures 20*, pp. 853-869.

Reactive Flows

Conference on Modelling Fluid Flow (CMFF'06)
The 13th International Conference on Fluid Flow Technologies
Budapest, Hungary, September 6-9, 2006

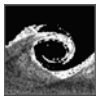

APPLICATION OF REDUCED MECHANISMS FOR NITROGEN CHEMISTRY IN NUMERICAL SIMULATION OF A TURBULENT NON-PREMIXED FLAME

Milan VUJANOVIĆ[1], Mario BABURIĆ[2], Neven DUIĆ[3],
Peter PRIESCHING[4], Reinhard TATSCHL[5]

[1] Corresponding Author. Department of Energy, Power Engineering and Environment, Faculty of Mechanical Engineering and Naval Architecture, University of Zagreb. Ivana Lučića 5, 10 000 Zagreb, Croatia. Tel.: +385 1 6168494, Fax. +385 1 6156940, E-mail: milan.vujanovic@fsb.hr
[2] AVL AST d.o.o., Zagreb. E-mail: mario.baburic@avl.com
[3] Department of Energy, Power Engineering and Environment, Faculty of Mechanical Engineering and Naval Architecture, University of Zagreb. E-mail: neven.duic@fsb.hr
[4] Advanced Simulation Technologies, AVL List GmbH, Graz. E-mail: reinhard.tatschl@avl.com
[5] Advanced Simulation Technologies, AVL List GmbH, Graz. E-mail: peter.priesching@avl.com

ABSTRACT

In this paper, the formation of nitrogen pollutants in computational fluid dynamics (CFD) simulation of turbulent non-premixed flame was modelled by coupling a reduced NO chemical reaction mechanisms with comprehensive combustion model in commercial CFD code FIRE™. The reduced nitrogen scheme is based on thermal NO formed by oxidation of atmospheric nitrogen and prompt NO formed by reactions of atmospheric nitrogen with hydrocarbons radicals in fuel-rich regions of the flame. The effects of the turbulent fluctuations on the NO reaction rates were accounted for by integrating the kinetic rates with respect to fluctuating temperatures over presumed probability density function (PDF). For combustion prediction a steady laminar flamelet model (SLFM) was employed. The NO formation was decoupled from the comprehensive combustion model and considered in post-processor routine using converged solution of a pre-calculated flame structure. The NO predictions are compared with experimental data.

Keywords: FIRE™, NO_x, Sandia flameD, steady laminar flamelet model

NOMENCLATURE

D_t	$[m^2/s]$	molecular diffusivity
E	$[J/mol]$	activation energy
M	$[kg/mol]$	molecular weight
N	[-]	total number
P	[-]	probability density function
S	$[kg/m^3s]$	source
T	$[K]$	temperature
Y	[-]	mass fraction
Z	[-]	mixture fraction
$\widetilde{Z''^2}$	[-]	mixture fraction variance
c	$[mol/m^3]$	concentration
c_p	$[J/kgK]$	mixture specific heat coefficient
c_{pi}	$[J/kgK]$	species specific heat coefficient
$ercf^{-1}$	[-]	inverse compl. error function
f	[-]	correction factor
h_i	$[J/kgK]$	species specific enthalpy
k	$[m^2/s^2]$	turbulent kinetic energy
k	$[m^3/mols]$	reaction rate coefficient
n	[-]	number of carbon atoms
q_R	$[W/m^3]$	radiative volumetric source term
t	$[s]$	time
u_i	$[m/s]$	Cartesian velocity component
x_i	$[m]$	Cartesian co-ordinate
α, β	[-]	arguments in beta function
Γ	[-]	gamma function
ε	$[m^2/s^3]$	turbulent kinetic energy diss. rate
χ	$[1/s]$	scalar dissipation rate
ν	$[m^2/s]$	kinematic viscosity
ρ	$[kg/m^3]$	density
σ_t	[-]	Prandtl number
τ	$[s]$	time
θ	[-]	equivalence ratio
$\dot{\omega}_i$	$[kg/m^3s]$	species reaction rate

Subscripts and Superscripts

1f, 2f, 3f	forward reaction number
1b, 2b, 3b	reverse reaction number
H	hydrogen
HCN	hydrogen cyanide
N	nitrogen
NO	nitric oxide
O	oxgen
OH	hydroxide
spec	species
st	stoichiometric

− Reynolds average
~ Favre average

1. INTRODUCTION

Of the many pollutants emitted by combustion of fossil fuels, the nitrogen oxides (NO_x) are among the most harmful. NO_x directly affect human health and cause environmental problems as photochemical smog, acid rain, greenhouse effect and depletion of atmospheric ozone in the stratosphere. As the awareness of these harmful effects has risen, emissions of NO_x have become world-wide concern and subject to increasingly stringent regulations. In response to these regulations, newer combustion techniques for nitrogen pollutants reduction need to be developed and this requires complete understanding of the NO_x reaction processes in practical combustion systems.

Development and application of comprehensive combustion models, advances in the science of NO_x reactions, and dramatic improvements in computer hardware have made a modelling of the NO_x chemical reaction processes a valuable tool in understanding NO_x emissions from combustion systems. This paper presents a review of modelling work performed at Department of Energy, Power Engineering and Environment regarding the prediction of NO_x formation in combustion of non-premixed methane-air flame. This modelling work has involved approach that couples reduced NO_x reaction mechanisms with a detailed description of the combustion process [1], which are described in the following sections.

A joint solution of detailed CFD equations for turbulent flow, combined with NO_x reduced chemical reaction mechanisms was used for prediction of NO_x formation in numerical simulation of turbulent, non-premixed, piloted methane-air jet diffusion flame. Turbulence was modelled using the k-ε model, with standard wall functions. Combustion modelling was based on the steady laminar flamelet model [2], where stationary flamelet profiles and appropriate probability density function (PDF) tables were created in pre-processor step by using CSC solver [3]. A detailed chemical reaction mechanism GRI Mech 3.0 [4] for methane, which consists of 53 species and 325 elemental reactions and contains nitrogen chemistry, was used for methane oxidation. A conservative form of the discrete transfer radiation method (DTRM) [5, 6] was applied for radiative heat transfer calculation.

2. COMBUSTION MODEL

For combustion prediction a steady laminar flamelet model (SLFM) [2, 7] was employed. In SLFM the instantaneous values of the species mass fractions and temperature are uniquely related to the instantaneous values of mixture fraction as:

$$\rho\frac{\partial Y_i}{\partial \tau}-\rho\frac{\chi}{2}\frac{\partial^2 Y_i}{\partial Z^2}-\dot{\omega}_i=0 \tag{1}$$

$$\rho\frac{\partial T}{\partial \tau}-\rho\frac{\chi}{2}\frac{\partial^2 T}{\partial Z^2}-\rho\frac{\chi}{2c_p}\frac{\partial T}{\partial Z}\frac{\partial c_p}{\partial Z}-\sum_{i=1}^{N_{spec}}\rho\frac{\chi}{2}\frac{c_{pi}}{c_p}\frac{\partial Y_i}{\partial Z}\frac{\partial T}{\partial Z}+\frac{1}{c_p}\sum_{i=1}^{N_{spec}}h_i\dot{\omega}_i-\frac{q_R}{c_p}=0 \tag{2}$$

where t is time, Z is the mixture fraction, T is temperature, Y_i , $\dot{\omega}_i$, and h_i are the mass fraction, chemical reaction rate and specific enthalpy of species i, respectively, c_p is the specific heat coefficient, while q_r is the radiative heat gain/loss.

Mixture fraction is a scalar representing the mass fraction of all the elements that originate from the fuel stream. Various definitions of this scalar can be found in [2]. The scalar dissipation rate $\chi = \chi(Z)$ is an important variable and it is given in a parameterized form as [2]:

$$\chi=\chi(Z)=\chi_{st}\frac{\exp\left\{-2\left[erfc^{-1}(2Z)\right]^2\right\}}{\exp\left\{-2\left[erfc^{-1}(2Z_{st})\right]^2\right\}} \tag{3}$$

For given values of the stoichiometric scalar dissipation rate parameter χ_{st} ($0 < \chi_{st} < \chi_{st,\ ext}$) the flamelet equations (Eqs. (1) and (2)) are solved in the pre-processing step, using the CSC solver [3], until the stationary solutions are obtained.

The combustion/turbulence interaction is accomplished via the presumed beta probability density function (beta PDF) as:

$$\widetilde{Y}_i=\int_0^1 Y_i(Z,\chi_{st})P(Z)dZ \tag{4}$$

$$\widetilde{T}=\int_0^1 T(Z,\chi_{st})P(Z)dZ \tag{5}$$

where $\widetilde{Y}_i$ is a time-mean mass fraction of the species i and $\widetilde{T}$ is time-mean temperature.

The PDF approach requires two additional transport equations for mean mixture fraction and its variance, which are calculated as:

$$\frac{\partial\left(\bar{\rho}\tilde{Z}\right)}{\partial t}+\frac{\partial\left(\bar{\rho}\widetilde{u_i}\tilde{Z}\right)}{\partial x_i}=\frac{\partial}{\partial x_i}\left(\bar{\rho}D_t\frac{\partial\tilde{Z}}{\partial x_i}\right) \tag{6}$$

$$\frac{\partial\left(\bar{\rho}\widetilde{Z''^2}\right)}{\partial t}+\frac{\partial\left(\bar{\rho}\tilde{u}_i\widetilde{Z''^2}\right)}{\partial x_i}= \frac{\partial}{\partial x_i}\left(\bar{\rho}\frac{\nu_t}{\sigma_t}\frac{\partial\widetilde{Z''^2}}{\partial x_i}\right)+2\bar{\rho}\frac{\nu_t}{\sigma_t}\left(\frac{\partial\tilde{Z}}{\partial x_i}\right)^2-\tilde{\chi}\widetilde{Z''^2} \quad (7)$$

By appropriately choosing the stoichiometric scalar dissipation rate χ_{st} parameters and by discretising the mixture fraction moments space, it is possible to calculate the flamelet profiles (Eqs. 1 and 2) and to account for turbulence-chemistry interaction (Eqs. 4 and 5) in advance, and to create, the so-called, PDF look-up tables for further interaction with CFD code [7].

3. THE REDUCED REACTION MECHANISMS FOR NITROGEN CHEMISTRY

Hundreds of elementary reactions are involved in a detailed description of the formation and destruction of oxides of nitrogen in combustion systems. However, it is not currently feasible to use such detailed reaction mechanisms to model a turbulent reacting system in which large reaction kinetics schemes are coupled with the turbulent fluid dynamics [1]. Consequently, present model for nitrogen chemistry based on reduced chemical reaction mechanisms was used in commercial CFD code FIRE^{TM} to describe the NO_x reaction process in combustion of hydrocarbon fuels.

NO_x represents a family of seven compounds: nitric oxide (NO), nitrogen dioxide (NO_2), nitrous oxide (N_2O), dinitrogen dioxide (N_2O_2), dinitrogen trioxide (N_2O_3), dinitrogen tetroxide (N_2O_4) and dinitrogen pentoxide (N_2O_5). As far as air pollution is concerned NO, NO_2 and N_2O are the most important. However, combustion sources emit NO_x mostly in the form of NO, approximately 90-95 % of total NO_x emissions. Thus, in this study the formation of NO determines the total amount of NO_x, while the presence and effects of other nitrogen oxides formed during combustion processes are neglected.

The formation of NO in the combustion processes is characterized by using the following transport equation for the NO mass fraction:

$$\frac{\partial(\bar{\rho}\tilde{Y}_{NO})}{\partial t}+\frac{\partial(\tilde{u}_i\bar{\rho}\tilde{Y}_{NO})}{\partial x_i}= \frac{\partial}{\partial x_i}\left(\bar{\rho}D_t\frac{\partial\tilde{Y}_{NO}}{\partial x_i}\right)+\overline{S}_{NO} \quad (8)$$

where $\tilde{Y}_{NO}$ is the mean mass fraction of NO and $\overline{S}_{NO}$ is the mean turbulent source of nitric oxide.

The prediction of NO_x emissions may be decoupled from the generalized combustion model and executed after the flame structure has been predicted because total amount of nitrogen oxides formed in combustion are generally low and does not affect the flame structure. Moreover, the different time-scales of major species and NO pollutants allow the decoupling of the two processes. NO_x reactions occur at much slower rates than the main heat release, and thus NO_x formation can be analyzed separately.

In this work, CFD solver was used in a "post-processing" step to solve NO transport equation, where a converged combustion flow field solution was first obtained before performing the prediction of NO formation. Consequently, the quality of the prediction of NO formation is highly dependent on the quality of the flame structure prediction.

The NO in methane flames is formed primarily by two separate reaction processes, thermal and prompt, in the gas phase. It follows that the source term, S_{NO} in Eq. (8), which represents the NO production, is calculated from these two predominant chemical mechanisms as:

$$S_{NO}=M_{NO}\left(\frac{dc_{NOthermal}}{dt}+\frac{dc_{NOprompt}}{dt}\right) \quad (9)$$

The thermal NO mechanism arises from the thermal dissociation and subsequent reaction of nitrogen and oxygen molecules in combustion air at relatively high temperatures in fuel-lean environment. The major factors that influence thermal NO formation are temperature, atomic oxygen, concentrations of nitrogen and residence time. This process is described by a set of chemical reactions known as the extended Zeldovich mechanism:

$$N_2+O\overset{k_1}{\leftrightarrow}NO+N \quad (9)$$

$$N+O_2\overset{k_2}{\leftrightarrow}NO+O \quad (10)$$

$$N+OH\overset{k_3}{\leftrightarrow}NO+H \quad (11)$$

Using these three reactions, the net rate of NO formation can be calculated as:

$$\frac{dc_{NO}}{dt}=k_{1f}c_Oc_{N_2}+k_{2f}c_Nc_{O_2}+k_{3f}c_Nc_{OH} -k_{1b}c_{NO}c_N-k_{2b}c_{NO}c_O-k_{3b}c_{NO}c_H \quad (12)$$

where k_1, k_2, k_3 are the rate coefficients for positive reactions, while k_{1b}, k_{2b}, k_{3b} are for negative reactions. The rate constants were measured and reported in many investigations, whose data have been critically evaluated by and Hanson and Salimian [8, 9]. The rate coefficients for reactions

(1-3) used in present model are based on the evaluation of Hanson and Salimian [9].

Using the quasi-steady assumption that the rate of consumption of free nitrogen atoms becomes equal to its formation rate, the expression for the overall rate of thermal NO formation process is given by:

$$\frac{dc_{\mathrm{NO}}}{dt} = 2k_{1f}c_{\mathrm{O}}c_{\mathrm{N_2}} \frac{\left(1-\dfrac{k_{1b}k_{2b}c_{\mathrm{NO}}^2}{k_{1f}c_{\mathrm{N_2}}k_{2f}c_{\mathrm{O_2}}}\right)}{\left(1+\dfrac{k_{1b}c_{\mathrm{NO}}}{k_{2f}c_{\mathrm{O_2}}+k_{3f}c_{\mathrm{OH}}}\right)} \qquad (13)$$

Temperature and remaining unknown species concentrations are obtained from converged combustion code solution.

Prompt NO is formed much earlier in the flame than the thermal NO by chemical reactions between hydrocarbon fragments and atmospheric nitrogen in fuel-rich regions of the flames. The prompt NO formation is significant in most hydrocarbon fuel combustion conditions, such as low temperature and fuel-rich conditions.

The mechanism is initiated by the rapid reactions of hydrocarbon radicals, which arise from fuel fragmentation during combustion, with molecular nitrogen, resulting in the dissociation of the N_2 and in the formation of intermediates such as hydrogen cyanide (HCN):

$$\mathrm{CH_x} + \mathrm{N_2} \leftrightarrow \mathrm{HCN} + \mathrm{N} + \ldots \qquad (14)$$

The model used in the present study to predict prompt NO concentration is calculated from the De Soete [10] global model as:

$$\frac{dc_{\mathrm{NO}}}{dt} = kfc_{\mathrm{O_2}}^{b}c_{\mathrm{N_2}}c_{fuel}\exp\left(-\frac{E}{RT}\right) \qquad (15)$$

where c denotes the concentration, k is rate constant, E is the activation energy and b is the order of reaction for molecular oxygen. Values of k and E are experimental constants [11]. In the above equation f is an empirical function designed to account for the effect of various aliphatic hydrocarbon fuels and air/fuel ratio effects.

In the following relation for correction factor f, n is the number of carbon atoms in the fuel and Φ is the equivalence ratio.

$$f = 4.75 + 0.082n - 23.2\phi + 32\phi^2 - 12.2\phi^3 \qquad (16)$$

The combustion process typically takes place in a turbulent environment, which requires special consideration when predicting NO concentrations. Therefore, incorporating the effects of the turbulent fluctuations on presented NO pollutant reaction process is very important. Time-mean reaction rates of NO cannot be calculated from the time-mean value of temperature because relationship among NO kinetic rates and temperatures are highly nonlinear. The presumed probability density function (PDF) approach was used to account for effects of turbulent fluctuations on the kinetic rates of NO, integrating the kinetic rates with respect to fluctuating temperature:

$$\overline{S}_{\mathrm{NO}} = \int_0^1 P(T)S_{\mathrm{NO}}(T)dT \qquad (17)$$

where $P(T)$ is the probability density function of the normalized temperature T, S_{NO} is the instantaneous NO source. For the PDF of the temperature, a beta function is given by:

$$\begin{aligned} P(T) &= \frac{T^{\alpha-1}(1-T)^{\beta-1}dT}{\int_0^1 T^{\alpha-1}(1-T)^{\beta-1}dT} \\ &= \frac{\Gamma(\alpha+\beta)}{\Gamma(\alpha)\Gamma(\beta)}T^{\alpha-1}(1-T)^{\beta-1} \end{aligned} \qquad (18)$$

where Γ is given by:

$$\Gamma(z) = \int_0^\infty e^{-t}t^{z-1}dT \qquad (19)$$

The parameters α and β depends on the mean value of the temperature from the main combustion calculation and its variance.

$$\alpha = \tilde{T}\left[\frac{\tilde{T}(1-\tilde{T})}{\widetilde{T''^2}} - 1\right] \qquad (20)$$

$$\beta = (1-\tilde{T})\left[\frac{\tilde{T}(1-\tilde{T})}{\widetilde{T''^2}} - 1\right] \qquad (21)$$

The temperature variance is calculated in post-processor step by solving the variance transport equation as:

$$\begin{aligned} &\frac{\partial}{\partial t}\left(\overline{\rho}\widetilde{T''^2}\right) + \frac{\partial}{\partial x_i}\left(\overline{\rho}\tilde{u}_i\widetilde{T''^2}\right) = \\ &\frac{\partial}{\partial x_i}\left(\overline{\rho}\frac{\nu_t}{\sigma_t}\frac{\partial\widetilde{T''^2}}{\partial x_i}\right) + 2\overline{\rho}\frac{\nu_t}{\sigma_t}\left(\frac{\partial\tilde{T}}{\partial x_i}\right)^2 - 2\overline{\rho}\frac{\tilde{\varepsilon}}{\tilde{k}}\widetilde{T''^2} \end{aligned} \qquad (22)$$

4. NUMERICAL SIMULATION

The presented reduced reaction mechanisms for nitrogen chemistry were implemented through user functions in commercial CFD code FIRE^{TM} and numerically tested and investigated for turbulent methane-air jet diffusion flame (Sandia flame D), experimentally investigated by Barlow & Frank [12]. The burner configuration is shown in Figure 1.

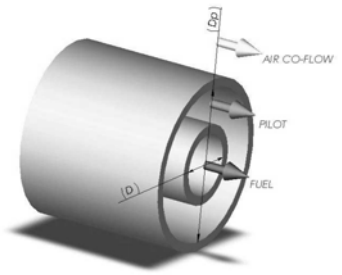

Figure 1. Burner configuration

The burner is placed in a co-flow of air and the flame is stabilized by a pilot jet. A stream of fuel is injected through the inner tube, while a pilot stream is injected through the outer tube surrounding it and the co-flow of air is injected outside of the pilot, as illustrated in Figure 1. The fuel is the mixture of 25% methane and 75% air by volume. The bulk velocity of the fuel jet is 49.6 m/s and the temperature is 294 K. The annular pilot burns a mixture of C_2H_2, H_2, air, CO_2 and N_2 having the same equilibrium state as methane/air mixture at Z=0.27, with temperature 1880 K. The bulk velocity of the pilot is 11.4 m/s. The air co-flow temperature is 291 K, and the velocity is 0.9 m/s.

The 3D steady-state simulations were performed using the AVL's CFD package FIRE^{TM}, which uses conventional numerical methods and a differencing schemes for a completely arbitrary mesh, and can solve a large computational meshes required for simulating practical combustion devices. The simulation was performed using a computational mesh with 338 400 cells, which are refined towards the inlets and axis.

The methane-air reaction mechanism was taken into account via the SLFM model. Stationary flamelet profiles and appropriate probability density function (PDF) tables were created in pre-processor step by using CSC solver. A detailed chemical reaction mechanism GRI Mech 3.0 for methane, which consists of 53 species and 325 elemental reactions and contains nitrogen chemistry, was used for the calculation of flamelet profiles in pre-processor step. Turbulent flows were modelled using the standard k-ε turbulence model, which quantifies turbulence in terms of its intensity k and its rate of dissipation ε. The model constant $C_{\varepsilon 2}$ in turbulent kinetic energy dissipation rate transport equation was adjusted to $C_{\varepsilon 2}$=1.8 instead the standard value in order to obtain a correct spreading rate. The radiative heat transfer was calculated using the discrete transfer method, where the radiative properties are modelled as the weighted sum of grey gases. Reduced reaction mechanisms were used in a post-processing mode, to model nitrogen chemistry, which have little effect on the flow field and the flame structure, as described in the previous section.

5. RESULTS AND DISCUSSION

The numerical predictions of NO obtained by NO reduced mechanisms for the turbulent non-premixed jet diffusion flame are compared with the results obtained by SLFM and with the experimental data. The experimental measurements of Barlow and Frank (1998) are obtained for axial profile and radial profiles at different locations, which are provided in the web site [12].

Figure 2 shows comparison of the temperature and NO mass fraction profiles with experimental data along axis symmetry of the burner for Sandia flame D. The predicted NO mass fraction profile obtained by NO reduced reaction mechanism is in good agreement with the experimental data, while NO mass fraction profile calculated by SLFM is over-predicted.

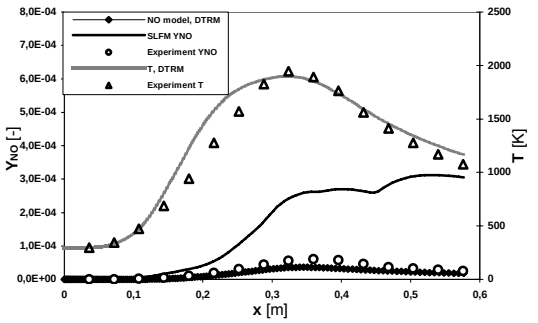

Figure 2. Axial profiles of mean temperature and NO mass fraction

The mean temperature and NO mass fraction profiles along the flame axis obtained with and without radiation modelling are shown in Figure 3. The adiabatic calculation over-predicts the peak temperature values, while non-adiabatic values (with DTRM) are in better agreement with the experimental data, indicating the importance of radiation modelling for the present flame. A similar behaviour is observed with NO mass fraction profile in the case when radiation was not included, while in non-adiabatic case the NO mass fraction profile is slightly under-predicted. The calculated NO mass fraction profiles show similar trends with the calculated temperature profile, where the

temperature maximum corresponds to the peak of the NO concentration.

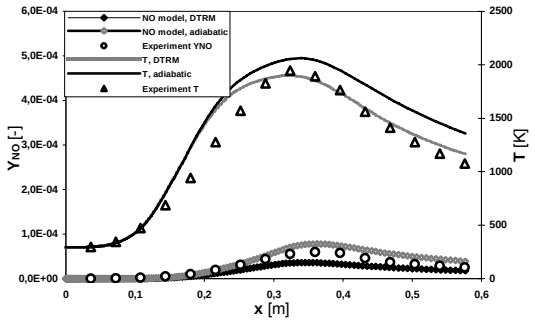

Figure 3. Axial profiles of mean temperature and mean NO mass fraction

The radial profiles of NO mass fraction at axial location x/d=15 are given in Figure 4. The agreement between NO mass fraction profile predicted by reduced NO reaction mechanisms and the measurements is fairly good, while NO concentrations predicted by SLFM are more than several times over-predicted.

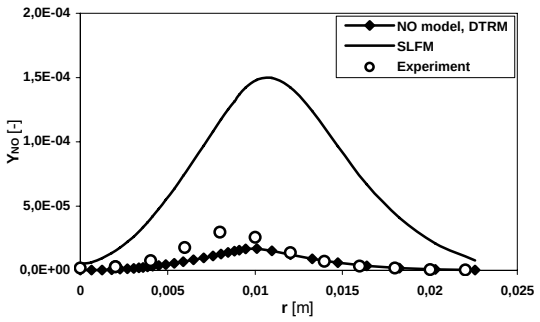

Figure 4. Radial profiles of mean NO mass fraction at axial distance r/d=15

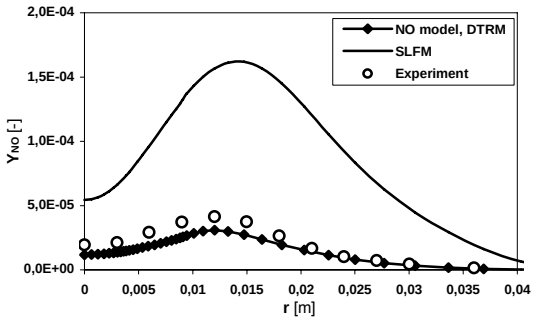

Figure 5. Radial profiles of mean NO mass fraction at axial distance r/d=30

The radial profiles of mean NO mass fraction are shown in Figures 5-8. The predicted NO mass fraction profiles obtained by NO reduced reaction mechanism are again in fairly good agreement with the experimental data, including the magnitude and radial positions corresponding to peak value. The radial profiles of NO mass fraction obtained by SLFM, also as in the case of axial profile, are over-predicted.

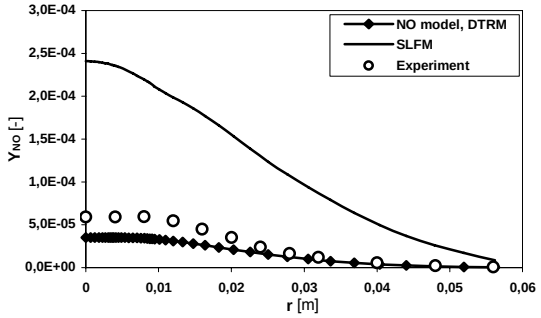

Figure 6. Radial profiles of mean NO mass fraction at axial distance r/d=45

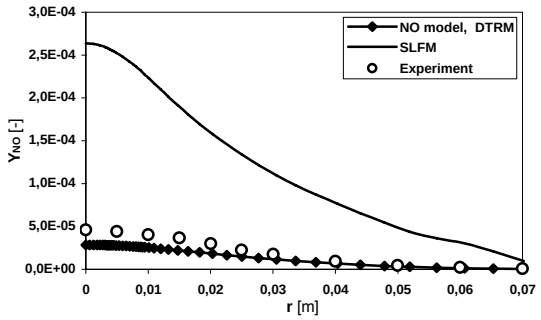

Figure 7. Radial profiles of mean NO mass fraction at axial distance r/d=60

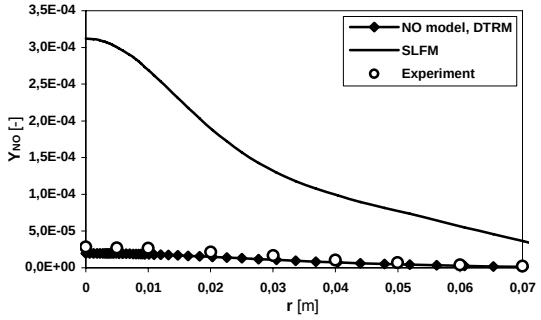

Figure 8. Radial profiles of mean NO mass fraction at axial distance r/d=75

It is noticeable that NO formation calculated by SLFM is a clearly over-predicted, making this model not adequate to predict important aspects of the flame as NO concentrations, while using the reduced chemical mechanisms for nitrogen

chemistry leads to a significant improvements showing good agreement with the measurements.

6. CONCLUSION

In this paper, reduced chemical reaction mechanisms for nitrogen chemistry were applied to Sandia National Laboratories Flame D, turbulent non-premixed methane-air flame. The NO formation was predicted in the post-processing mode using converged solution of pre-calculated flame structure. Two chemical kinetic processes, thermal and prompt NO, were used to predict NO pollutant emissions. The numerical results of NO formation have been presented in detail and compared with the results obtained by SLFM and with experimental data. The overall agreement between predictions of NO formation, obtained by reduced mechanisms for nitrogen chemistry, and measurements are good, while NO formation calculated with SLFM is over-predicted quite severely. It has been shown that the results obtained with reduced mechanisms provide a significant improvement over the SLFM nitric oxide results.

REFERENCES

[1] Hill, S. C., and Smoot, L. D., 2000, "Modeling of nitrogen oxides formation and destruction in combustion systems", *Progress in Energy and Combustion Science*, Vol. 26, pp 417-458.

[2] Peters, N., 2000, "Turbulent Combustion", *Cambridge University Press*, Cambridge.

[3] http://powerlab.fsb.hr/mbaburic/CSC.htm.

[4] http://www.me.berkeley.edu/gri_mech.

[5] Coelho, P. J. and Carvalho, M. G., 1997, "A Conservative Formulation of Discrete Transfer Method", *ASME Journal of Heat Transfer*, Vol. 119, pp. 118-128.

[6] Lockwood, F. C., and Shah, N. G., 1981, "A New Radiation Method For Incorporation In General Combustion Prediction Procedures", Proc. *Eighteenth Symposium (International) on Combustion*, The Combustion Institute, London, pp. 1405-1414.

[7] Baburić, M., Schneider, D. R., Duić, N., Basara, B., Priesching, P., Tatschl, R., 2004, "Steady laminar flamelet concept and hybrid turbulence modelling strategy applied on numerical simulation of a turbulent piloted jet diffusion flame", Proc. *The 2nd International Workshop on trends in numerical and physical modelling of turbulent process in gas turbine combustors (and automotive engines)*, Heidelberg, Germany, pp. 45-51.

[8] Miller, J. A. and Bowman, C. T., 1989, "Mechanism and modeling of nitrogen chemistry in combustion", *Progress in Energy and Combustion Science*, Vol. 15, pp. 287-338.

[9] Hanson, R. K. and Salimian, S., 1984, "Survey of Rate Constants in H/N/O System", *Combustion Chemistry*, W.C. Gardiner, Jr (Ed.), Springer, New York.

[10] De Soete, G. G., 1975, "Overall reaction rates of NO and N_2 formation from fuel nitrogen", Proc. *15th Symposium (International) on Combustion*, The Combustion Institute, Pittsburgh.

[11] Dupont, V., Porkashanian, M., Williams, A., Woolley, R., 1993, "The reduction of NO_x formation in natural gas burner flames", *Fuel*, Vol. 72(4), pp. 497-503.

[12] http://www.ca.sandia.gov/TNF/DataArch/FlameD.html.

Conference on Modelling Fluid Flow (CMFF'06)
The 13th International Conference on Fluid Flow Technologies
Budapest, Hungary, September 6-9, 2006

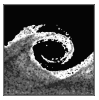

A TURBULENT COMBUSTION MODEL BASED ON AN ASSUMED PDF APPROACH USING A CHEMICAL DATABASE FOR HYDROCARBONS

Daniel GAFFIE[1], Raphaëlle LECOT[2], Pascal BRUEL[3]

[1] Corresponding Author. Fundamental and Applied Energetics Department, ONERA. 29, Avenue de la Division Leclerc. BP 72. 92322 Châtillon, France. Tel.: +33 1 46734332, Fax: +33 1 46734147, E-mail: Daniel.Gaffie@onera.fr
[2] Fundamental and Applied Energetics Department, ONERA. 29, Avenue de la Division Leclerc. BP 72. 92322 Châtillon, France. Tel.: +33 1 46734332, Fax: +33 1 46734147, E-mail: Raphaelle.Lecot@onera.fr
[3] LMA. UMR 5142. CNRS-UPPA. Rue de l'Université. BP 1155. 64013 Pau cedex, France. Tel: +33 5 59407552, Fax : +33 5 59407555, E-mail : Pascal.Bruel@univ-pau.fr

ABSTRACT

This paper presents the main features of a turbulent combustion modelling approach aimed at taking into account the interaction between the turbulent flow and the combustion process. The proposed model is characterized by i) the recourse to a chemical database adapted for the treatment of a complex chemistry and ii) the use of an original multi-dimensional joint presumed Probability Density Function (PDF) method. The PDF is approximated by the product of beta functions determined at any point of the reactive flow as soon as the time averages and the variances of the mixture fraction and mass fractions of all relevant chemical species are known via the resolution of dedicated transport equations. A simple interpolation procedure through the chemical database – in which all the thermo-chemical states are previously stored - allows to determine an approximated values of the mean chemical production rates which are then reintroduced as source terms in the different mass fractions transport equations.

The model has been applied quite successfully in the case of the well known two-dimensional piloted methane/air flame experimentally studied at the National Sandia Laboratories. Further developments of the model are now in progress in order to evaluate its ability to be used in the more realistic and challenging context of the development of jet engines combustion chambers designed to ensure an efficient control of the level of pollutants emissions.

Keywords : assumed PDF approach, CFD, hydrocarbon combustion, turbulent combustion modelling, RANS.

NOMENCLATURE

C_k $[moles/m^3]$	molar concentration of species k
D $[m^2/s]$	diffusion coefficient
P, P^*, P	probability density functions
T $[K]$	static temperature
W_k $[moles/m^3/s]$	chemical source term of species k
Y_k	mass fraction of species k
Z, Z^*	mixture fraction, given value of Z
m_k $[kg/moles]$	molar weight of species k
p $[Pa]$	static pressure
$\upsilon_{ik}^{(1)}, \upsilon_{ik}^{(2)}, \upsilon_{ik}$	stoichiometric coefficients
W_k	chemical source term of species k
ω_i	reaction rate for reaction i
A_k	name of molecule k

Subscripts and Superscripts

$\tilde{}$	density-weighted (Favre) average
$\bar{}$	Reynolds average
i, k	reaction, chemical species
*	used for non dimensional quantity

1. INTRODUCTION

The prediction of most turbulent and reacting flows of practical interest requires an accurate modelling of the combustion process development and of its interaction with the turbulent flow. Unfortunately, the use of detailed reaction mechanisms for the simulation of multidimensional reacting flows of practical importance, is still computationally prohibitive, especially for hydrocarbon combustion. Thus, the development of new methods able to describe accurately the dynamics of the chemical system while using

simplified kinetics models appears to be still highly desirable.

In the framework of RANS approach, it is well-known that the Reynolds averaging applied to the transport equations which govern the behavior of the different chemical gaseous species, introduces two terms which have to be closed, namely the turbulent fluxes of mass and momentum and the mean chemical source terms. In the present paper, primarily devoted to the closure of the mean source terms, a classical gradient assumption is used to close the various turbulent fluxes and proves to yield rather good results in weakly sheared flow regions.

Obtaining a well adapted closure of the chemical source terms is everything but an easy task. Indeed, their strong non linear dependence on the temperature and compositions makes impossible the application of a mathematical formulation deduced from the direct application of the time average operator. The time average of the Reynolds decomposition of the species production rates yields a large number of terms, most of which are new correlations which require the introduction of new closure assumptions. The introduction of a Probability Density Function (PDF) is an attractive solution to solve this problem. Indeed, the knowledge of the PDF, for any time and any position within the turbulent reacting flow, permits the determination of the time average of the chemical source terms. Following a purely statistical point of view, each scalar quantity which fluctuates within the turbulent flow is considered as a random variable. It follows that the PDF evolves in a large dimension space, especially when the combustion process is described via detailed chemistry mechanisms.
The numerical determination of the PDF can be achieved through two different approaches. The first one, which is quite attractive but complex, relies on the resolution of a PDF transport equation. In such a case, classical finite volume techniques are unsuited and Monte Carlo approaches are generally used instead [1–2]. Basically, the implementation of Monte Carlo methods can be achieved via two different strategies, either purely a lagrangian one via the follow-up of fluid particles [3], or purely eulerian by the introduction of eulerian stochastic fields [4–5]. Hybrid approaches associating both techniques are also encountered. Such advanced modelling generally provide excellent numerical results for premixed or non premixed test cases [6–9], but is still computationally expensive, especially when detailed reaction schemes have to be accounted for.

The second theoretical approach, retained in this paper, is based upon the introduction of an assumed PDF shape chosen in order to close the mean chemical source terms. A finite number of moments which allows to completely determine the PDF at any point of the turbulent reacting flow is numerically provided by solving specific transport equations.

The choice of a joint presumed PDF is not easy when a comprehensive description of the chemical phenomena is retained to take into account the combustion-turbulence coupling. Indeed, the dimension of the PDF is directly dependent on the number of chemical species considered to describe the reacting flow. Thus, it is clear that, to maintain a reasonable computational efficiency, such an approach will benefit from the recourse to reduction methods of kinetic systems. During the last two decades, such reduction techniques based on the mathematical representation of behaviour of chemical systems, have been developed [10–11]. More recently, classical reduction techniques based upon sensibility analysis or Quasi-Steady State Approximation have been replaced by more general time scale based methods allowing to reduce the dimension of the composition space in which the chemical system evolves. Among them, the Intrinsic Low-Dimensional Manifolds approach (ILDM) [12] which approximates the time evolution of the chemical system in a low-dimensional space defined by a reduced number of degrees of freedom proves to be able to significantly increase the performances of the computations. By automatically reducing the chemical kinetics, the thermo-chemical states which evolve in such a space of reduced dimension are generally stored under the form of multi-dimensional tabulation, accessed during the reacting flow calculations through via interpolation procedures. Today, this research topic is largely investigated. New theoretical approaches are developed to overcome some limitations of ILDM as the FPI technique describing more efficiently the low temperature regions [13].

The turbulent combustion model described in the present paper, focused on the description of the development of hydrocarbon-air combustion process in the turbulent flow is based on such techniques. It is assumed that the chemical system evolves within a reduced domain defined by the scalar quantities classically chosen in the ILDM approach in order to parameterize these low-dimensional manifolds. These scalar quantities are the mixture fraction, and water vapour and carbon dioxide mass fractions.

Supposing that the evolution of the chemical system can be defined solely with these three degrees of freedom, it is then possible to easily construct a three dimensional domain which includes all thermo-chemical states determined by any more detailed reaction scheme.

2. DESCRIPTION OF THE COMBUSTION PROCESS

2.1. Generalities

The turbulent combustion model presented in this paper will be described in three distinct steps. The first one describes how are taken into account the chemical kinetics mechanisms which control the development of the combustion process. Then, the second step presents in detail the coupling between the turbulence and the combustion process. The various procedures described in these two steps, permits the built-up of a database which contains all the thermo-chemical states that will be accessible during the subsequent reacting flow simulations. The last step is devoted to the description of this predefined table and the interpolation technique used to evaluate the mean chemical source terms required when solving the RANS governing equations describing the turbulent reacting flows to be simulated.

2.2. Description of the combustion process

Usually, any comprehensive reaction mechanism, involving N chemical species, can be written under the following symbolical form:

$$\sum_{k=1}^{N} \nu_{ik}^{(1)} A_k \quad \Leftrightarrow \quad \sum_{k=1}^{N} \nu_{ik}^{(2)} A_k \qquad (1)$$

The chemical source terms are non linear functions of the temperature and the concentrations of the chemical species, namely:

$$W_k = \sum_{i=1}^{n} \left(\nu_{ik}^{(2)} - \nu_{ik}^{(1)}\right) \omega_i \left(T, C_1, ..., C_n\right) \qquad (2)$$

The model described in this paper, which was especially developed to the need of air breathing propulsion, exclusively deals with the combustion of usual hydrocarbons with air and is based on the ILDM theory. Accordingly, it is supposed that the chemical system, whatever the complexity of the reaction mechanism considered, evolves in a reduced three-dimensional space defined by the variation fields of three degrees of freedom; e.g; the mixture fraction and the mass fractions of carbon dioxide and water vapour, respectively. If carbon dioxide and water vapour mass fractions are in all situations (premixed or diffusion flames) among the relevant variables that represent the evolution of the chemical system, it is not the case for the mixture fraction which is a constant in premixed flames of constant stoichiometry. According to that, it follows that the number of dimensions of the phase space corresponding to the accessible thermo-chemical states will be flow dependent, either two or three dimensional.

As it is illustrated in "Figure 1", for a fixed value Z* of the mixture fraction, the thermo-chemical state of the system evolves along a trajectory which belongs to a triangular two-dimensional domain and links the initial state to the equilibrium conditions.

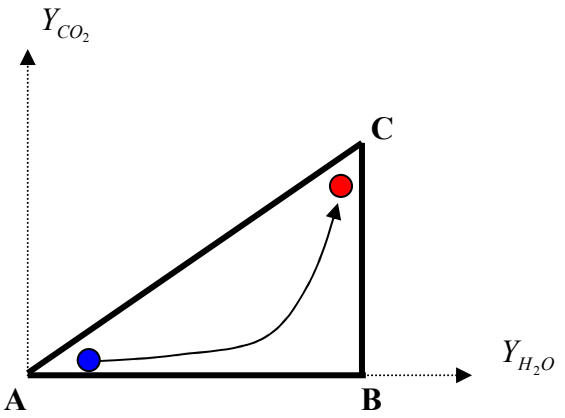

Figure 1. Schematic representation of the triangular domain containing the states of the chemical system physically accessible, for a given value *Z of the mixture fraction.**

The three vertices A, B, C of this triangle which depend on Z* are given by considering the following simple two-step global reaction mechanism [14]:

$$\begin{aligned} &C_n H_m + \left(\frac{n}{2} + \frac{m}{4}\right) O_2 \longrightarrow n\,CO + \frac{m}{2} H_2O \\ &CO + \frac{1}{2} O_2 \Leftrightarrow CO_2 \end{aligned} \qquad (3)$$

Point A corresponds to the mixture of fresh gases, hydrocarbon and air, without combustion. Point B is the virtual point, given by the first step of the reaction scheme. It is associated to a maximum CO formation, by blocking CO_2 oxidation. Point C corresponds to a total oxidation of the CO created at point B.

The interior triangle delimitated by points A, B and C is then discretized. The knowledge of the mass fractions of carbon dioxide and water vapour allows to determine the thermo-chemical conditions prevailing at each node of the mesh.

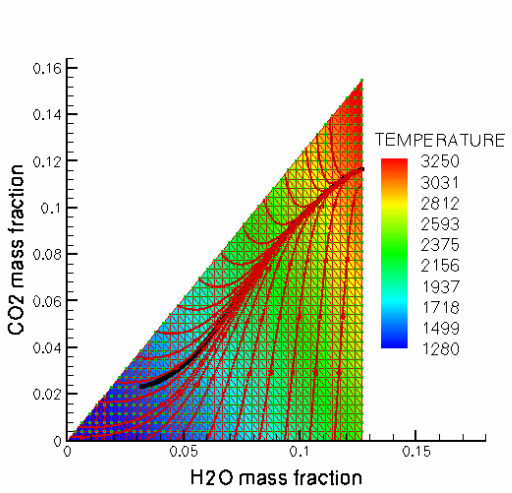

Figure 2. PSR calculations: Trajectories in the composition space associated with the time evolution of the thermo-chemical states from the initial condition to the thermodynamic equilibrium (Initial conditions: T ~ 1500 K, P = 1 bar).

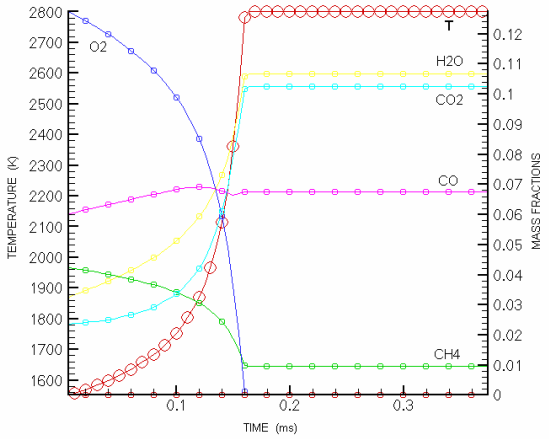

Figure 3. PSR calculations: typical time evolution of the temperature and mass fractions of chemical species from their initial conditions to those of thermodynamic equilibrium.

For a given pressure, for example, the pressure fixed in a Perfectly Stirred Reactor (PSR), and a reaction mechanism perfectly defined by the knowledge of the Arrhenius parameters, it is indeed possible to associate one and only one thermo-chemical state at each node of the grid. In addition to the mass fractions and concentrations which can be stored at each node of the grid, the chemical sources terms (expressed in $kg/m^3/s$) can be also calculated. For laminar reacting test cases, all these results can be saved in a thermo-chemical database. During the course of the numerical simulation, the source terms will be interpolated in the look-up table and then introduced directly wherever required without any other additional calculations.

A remarkable property of the domain thus defined, is that it contains all the time evolution trajectories of the chemical system whatever the complexity of the selected reaction scheme. As it is illustrated in "Figure 2", which presents results obtained from PSR calculations, all the trajectories converge towards the same point corresponding to the equilibrium conditions, regardless of the selected initial conditions chosen. "Figure 3" presents a typical time evolution of the temperature and concentration variation associated to a given trajectory in the compositions space.

For the same reaction mechanism, the accuracy of the results given by the interpolation method previously described has been checked against that obtained with the classical method, e.g. the method based on the direct integration of the chemical source terms. A good agreement has been obtained and the method of interpolation has demonstrated its ability to produce accurate results for a far lower computational cost, provided that the composition space discretisation is properly handled.

2.3. Definition of a local mixture fraction

The case of the diffusion flame can be studied by considering a two-dimensional mixing layer created by the confluence of two parallel flows of air on one side and pure hydrocarbon fuel (or hydrocarbon-air premixed flow) on the other side ("Figure 4").

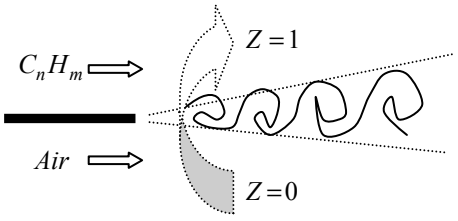

Figure 4. Transverse evolution of the reduced mixture fraction in a turbulent reactive mixing layer.

In the field of the turbulent combustion modelling, the introduction of the mixture fraction which behaves as a passive scalar thanks to the conservation of atoms is the usual way of starting to address the modelling of the interaction between combustion and turbulence [15]. This mixture fraction, which is therefore independent of the combustion process, can be built even in the case where a comprehensive reaction scheme is chosen.

In the simplest case, for which the thermo-chemical state is only controlled by the mechanisms of chemical kinetics, the variation rate of the molar concentrations of the chemical species present in the reaction scheme is given by the following relation:

$$\frac{dC_i}{dt} = W_i \tag{4}$$

It follows that the local element molar concentration is obtained by solving the following system:

$$\begin{aligned} &\frac{dC_q}{dt} = \sum_{i=1}^{n} \lambda_{iq} \frac{dC_i}{dt} \\ &\text{with} : \sum_{i=1}^{n} \lambda_{iq} W_i = 0 \end{aligned} \tag{5}$$

Where subscript q indicates the atomic elements which compose the molecules considered in the reaction mechanism.

Generalization to multi-dimensional flows is immediate assuming that the diffusion coefficients have the same constant value for all species i. In such a case, the following standard expression for the local element molar concentration governing equation is readily obtained:

$$\frac{\partial C_q}{\partial t} + \frac{\partial U_j C_q}{\partial x_j} = \frac{\partial}{\partial x_j}\left(\frac{\rho}{m_i} D \frac{\partial Y_i}{\partial x_j} \right) \tag{6}$$

"Equation 6" shows that the element mass fractions do not depend on the combustion process and therefore can be linearly related to the mixture fraction [15].

3. TIME AVERAGE OF THE CHEMICAL SOURCE TERMS

3.1. Introduction of a PDF methodology

The knowledge of the PDF, completely determined for any time and any position of the turbulent reacting flow, allows to determine the time average of the chemical source terms which can be expressed under the following form:

$$\overline{W_i} = \int_{D_\phi} W_i(\phi)\ P(\phi) d\phi \tag{7}$$

Where ϕ is a vector defined by:

$$\phi = {}^t\left(p, h, Y_1, ..., Y_n; \underline{x}, t\right) \tag{8}$$

When the turbulent reacting flow is not perfectly stirred the shape of the PDF depends upon the mean fields and the variances of the components of vector ϕ.

It is then interesting to introduce new assumptions in order to reduce the dimension of the PDF, as low flow Mach number condition. Assuming that i) the pressure fluctuations related effects can be neglected, ii) the turbulence kinetic energy is negligible compared to the specific enthalpy, iii) the radiative losses also negligible and iv) the Lewis numbers of each chemical species are close to unity, it can then be shown that the specific enthalpy is a linear function of the mixture fraction. Assuming that the external inlet conditions, which control the development of the turbulent reactive mixing layer, are completely defined and similar for the mixture fraction and the specific enthalpy, it is then possible to write that:

$$Z = \frac{h - h_2}{h_1 - h_2} \tag{9}$$

where subscripts 1 and 2 refer to fuel and oxidiser streams, respectively.

Under these assumptions, the thermo-chemical system is entirely defined by the knowledge of the PDF whose associated random variables are the mixture fraction and the species mass fractions, namely:

$$P = P_z(Z) P*\left(Y_1, ..., Y_n\big|_Z\right) \tag{10}$$

3.2. Assumed PDF of mixture fraction

The PDF of mixture fraction, P_z, is assumed to follow a β-distribution. It can be noticed that such a distribution is only defined for a random variable varying between zero and one. Since the minimum and maximum values of Z are known, it is then possible to build a reduced mixture fraction compatible with such a β-distribution. Moreover, for any mean value of the mixture fraction a reduced mixture fraction variance - which varies between zero (micromixing) and one

(macromixing) - is also defined. As an example, "Figure 5" shows the evolution of the PDF field of mixture fraction - obtained for a mean value of the mixture fraction equal to 0.25 – from the micromixing to the macromixing.

When the RANS equations are solved an additional transport equation is required to determine the variance.

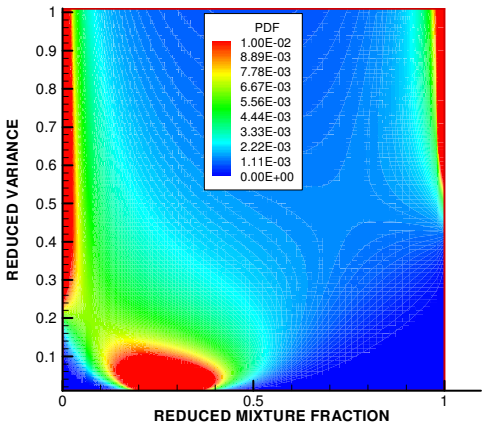

Figure 5. Representation of the PDF versus the mixture fraction and the reduced variance, from the micromixing to the macromixing.

3.3. Assumed PDF of composition

The multi-variable β-distribution is chosen in order to represent the PDF of the conditional composition *P**. The form of *P** which is described in detail in [16-17], is supposed to be given by :

$$P^* = \frac{\prod_{i=1}^{n} \phi_i^{\beta_i - 1}}{\int_{D_\phi} \prod_{i=1}^{n} \phi_i^{\beta_i - 1} \, d\phi_1 \ldots d\phi_n} \qquad (11)$$

Where:

$$\beta_i = \tilde{Y}_i \left[\frac{1}{\sigma_*^2} - 1 \right] \qquad (12)$$

σ_*^2 which varies between zero and one, is the reduced variance, defined by:

$$\sigma_*^2 = \frac{\sum_{m=1}^{n} \sigma_{(m)}^2}{\sum_{m=1}^{n} \tilde{Y}_m \left(1 - \tilde{Y}_m\right)} \qquad (13)$$

With:

$$\sigma_{(m)}^2 = \frac{\overline{\rho \, y_{(m)}^{"2}}}{\bar{\rho}} \qquad (14)$$

An attractive feature of this strategy based upon the introduction of an assumed form of the PDF under a multi-variate function is that it is completely defined at any time and any position within the flow by the knowledge of the mean mass fractions and the sum of the variance Σ :

$$\Sigma = \sum_{m=1}^{n} \sigma_{(m)}^2 \qquad (15)$$

Consequently, this approach only requires the introduction in the numerical code solving the RANS equations of an additional transport equation to determine the sum of the mass fraction variances. This equation, which needs new closure assumptions described in detail in [17], is obtained by summing the equations for each mass fraction variances.

"Figures 6" shows an example of the field of the conditional PDF *P** for a given value of *Z*.

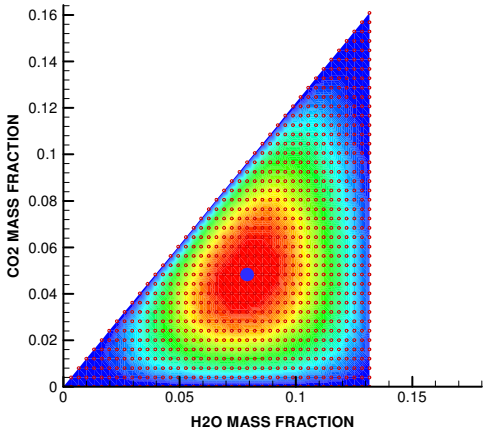

Figure 6. Example of the field of the conditional PDF $P(Y_{H_2O}, Y_{CO_2}\big|_Z)$ for Z^*=0.06.

4. NUMERICAL SIMULATIONS

4.1. Piloted CH4/air Flame

The test case of a piloted methane-air flame stabilized on a burner, experimentally studied at the Sandia National Laboratories, has been simulated using the turbulent combustion model described previously. A very detailed experimental database providing multiscalar measurements, including temperature, mixture fraction and concentration of different chemical species, is available for four piloted flames (labelled C, D, E, F) corresponding to different experimental conditions [18].

The results presented in this paper concern the conditions of the flame D. The burner geometry is supposed to be axisymmetrical. A rich methane / air mixture (equivalence ratio ϕ = 3.17) is injected at the level of the symmetry axis. The pilot flame corresponds to the equilibrium composition of an initial lean methane / air mixture at ϕ = 0.77. The flame is unconfined and burns in a diffusion regime. Burner dimensions and boundary conditions are provided in the pdf document "SandiaPilotDoc20.pdf" available in the Sandia database of the TNF workshop [19]. The geometrical characteristics and boundary conditions useful for the numerical simulation of this test case are listed in "Table 1".

"Figures 7 to 8" present the fields of the averaged mass fractions of the different chemical species considered (CO2, O2, CO and OH). These numerical results have been obtained by using the turbulent combustion model previously described, firstly based upon the preliminary storage of possible thermo-chemical states which takes into account the boundary conditions specified in "Table 1", and then followed by the application of the interpolation procedure allowing to approximate the mean source terms during the equation resolution step.

The experimental database provides the radial evolution of the temperature and species mass fractions chemical at different axial locations. These results are given versus the non dimensional radial direction r* = r/d, where d is the inner diameter of the exit section of the main jet. Some of these measurements have been realized at locations close to the injection port (x* = 1, 2, 3). These results have been considered to define realistic inlet boundary conditions. Measurements are also available for six other positions located further downstream and for which comparisons with the results of the present simulations can be carried out. (e.g. x* = 7.5, 15., 30., 45., 60., 75.).

"Figures 9 to 10" present the temperature and CO mass fraction radial profiles obtained at x* = 30. Until this location, a rather good agreement is obtained between the numerical results and the measurements. Nevertheless, a significant difference between the two profiles can be observed close to the symmetry axis. This difference increases beyond this location.

Table 1. Piloted methane / air flame test case - Burner dimensions and boundary conditions for Sandia flame D.

BURNER DIMENSIONS	
Main jet inner diameter (mm)	7.2
Pilot annulus inner diameter (mm)	7.7
Pilot annulus outer diameter (mm)	18.2
Burner outer wall diameter (mm)	18.9
Wind tunnel exit (cm^2)	30 x 30
MAIN JET	
Velocity (m/s)	49.6
Equivalent ratio (methane / air)	3.17
Temperature (K)	294.
PILOT ZONE	
Velocity (m/s)	11.4
Temperature (K)	1880.
Nitrogen mass fraction	0.734
Oxygen mass fraction	0.056
Water vapour mass fraction	0.092
Carbon dioxide	0.110
OH radical mass fraction	0.0022
Mixture fraction	0.27
COFLOW	
Velocity (m/s)	0.9
Temperature (K)	291.
Oxygen mass fraction	0.21
Nitrogen mass fraction	0.79
Water vapour mass fraction	~ 0

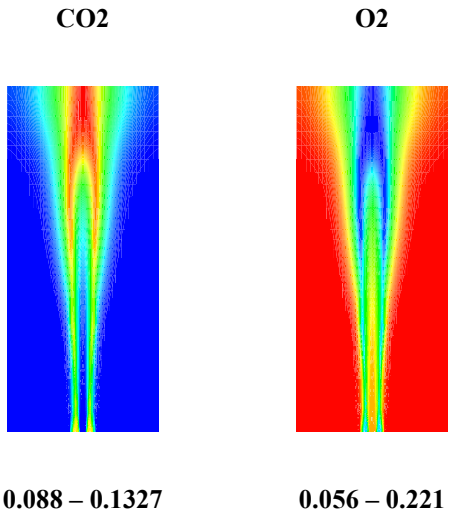

Figure 7. Carbon dioxide and oxygen averaged mass fractions obtained from the simulations of the Sandia flame D.

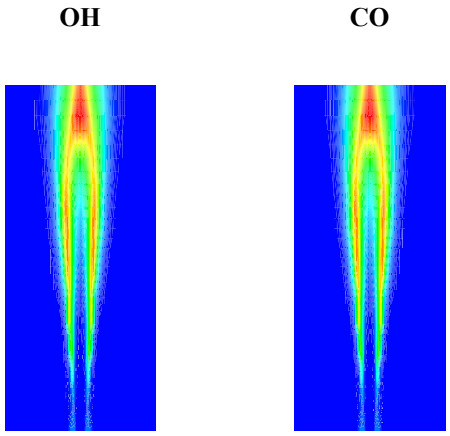

Figure 8. OH radical and carbon monoxide averaged mass fractions obtained from the simulations of the Sandia flame D

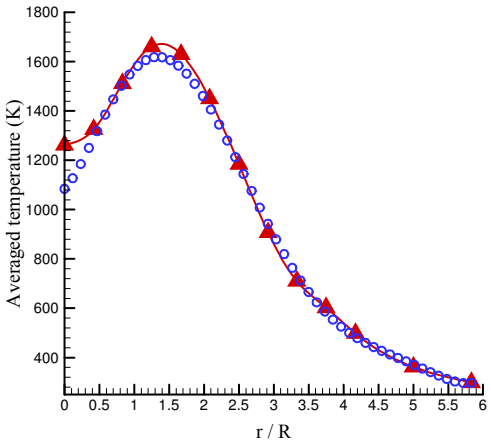

Figure 9. Radial distribution of the averaged temperature at location x* = 30 (Simulations: hollow circles; Experiments: filled triangles).

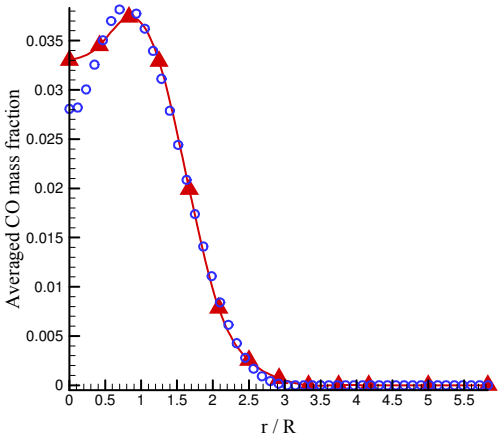

Figure 10. Radial distribution of the OH averaged mass fraction at location x* = 30 (Simulations: hollow circles; Experiments: filled triangles).

5. CONCLUSIONS - FUTURE WORKS

The turbulent combustion model described in this paper has to be considered as an intermediate model located between the simple models - founded on an infinitely fast chemistry assumption - and the advanced Monte Carlo approaches solving a transport equation for the PDF. The great interest of the model is its ability to take into account the chemical kinetics mechanisms of the hydrocarbon-air combustion process using new mathematical representation of the chemical system behaviour. Particularly based on the ILDM assumptions, the model considers that the time evolution of the combustion process can be only described by three degrees of freedom; mixture fraction and carbon dioxide and water vapour mass fractions.

The model has been evaluated with success on a well-known test case of piloted methane/air flame experimentally studied at the Sandia laboratories. A rather good agreement between numerical and available experimental results has been obtained. In the frame of the European research project CFD4C, the model has also been applied to a TURBOMECA combustor showing the capacity of the model to be used in flow configurations of practical interest.

With respect on the fundamental assumptions of the turbulent combustion model which introduce an assumed PDF approach to represent the turbulence-combustion interactions, works are currently carried out with in order to develop an efficient coupling between the model and reduction techniques able to describe in a comprehensive way

the processes of combustion encountered in the aeronautics combustors. The final objective of these works is to have a reliable numerical tool, efficient in the computational field, allowing to evaluate new concepts of combustion chambers designed to ensure a relevant control of the pollutant emissions.

ACKNOWLEDGEMENTS

This work has been supported by the Department For Aircraft Projects of DGA and the European project on Computational Fluid Dynamics for Combustion (CFD4C).

REFERENCES

[1] Pope S.B., 1985, "PDF methods in turbulent reactive flows", Prog. Energy Combust. Sci., vol. 11, pp. 119-192.

[2] Libby P.A., Williams F.A., 1994, "Fundamental aspects and review", Turbulent Reacting Flows", (PA Libby and FA Williams editors), Academic Press.

[3] Pope S.B., 1997, "Mean field equations in PDF particle methods for turbulent reactive flows", Cornell University Report FDA 97-06.

[4] Valiño, L., Dopazo, C., 1998, "A field Monte Carlo formulation for calculating the probability density function of a single scalar in a turbulent flow", Flow Turbulence and Combustion, vol. 60, pp. 157-172.

[5] Sabel'nikov, V., Soulard, O., 2005, "Rapidly decorrelating velocity field model as a tool for solving Fokker-Planck PDF equations of turbulent reactive scalars", Phys. Rev. E72, 016301.

[6] Eswaran, V., Pope, S.B., 1988, "Direct numerical simulations of the turbulent mixing of a passive scalar", Physics of Fluids, vol. 31, pp 506-520.

[7] Anand M.S., Pope, S.B., 1987, "Calculations of premixed turbulent flames by PDF methods", Combustion and Flame, vol. 67, pp. 128-142.

[8] Masri, A.R., Pope, S.B., 1992, "PDF calculations of piloted non-premixed flames of methane", Combustion and flame, vol. 83, pp. 27-42.

[9] Wouters H.A., Nooren P.A., Peters T.W.J., Roekaerts D., "Simulation of a Bluff-Body-Stabilized Diffusion flame Using Second-Moment Closure and Monte Carlo Methods", 1996, *26th International Symposium on Combustion,* The Combustion Institute, pp. 177-185.

[10] Smooke M. D., 1991,"Reduced Kinetic Mechanisms and Asymptotic Approximations for Methane-Air Flames", Lecture Notes in Physics, Vol.384, Springer, Berlin.

[11] Jones W. P., Lindstedt R. P., 1988, "Global Reaction Schemes for Hydrocarbon Combustion" Combustion and Flame, Vol. 73, pp. 233-249.

[12] Mass U., Pope S.B., 1992, "Simplifying Chemical Kinetics: Intrinsic Low-Dimensional Manifolds in Composition Space", Combustion and Flame, Vol. 88, pp. 239-264.

[13] Fiorina B., Carpentier S., Gicquel O., Vervisch L., Darabiha N., 2003, Approximating the chemical structure of diffusion and partially premixed laminar counter-flow using FPI (Flame Propagation of ILDM), 19th ICDERS, Hakone, Japan.

[14] Wesbrook C. K., 1981, "Simplified Reaction Mechanisms for the Oxidation of Hydrocarbon Fuels in Flames", Combustion Science and Technology, Vol. 27, pp. 31-43.

[15] Bray K., 1997, "Turbulent Combustion", AGARD FDP Special Course, von Karman Institute for Fluid Dynamics, Belgium, R-819, pp. 1-74.

[16] Girimaji S.S., 1991, "A Simple Recipe for Modeling Reaction-Rates in Flows with Turbulent Combustion", AIAA Paper 91-1792.

[17] Baurle R.A., Girimaji S.S., 1999, "An Assumed PDF Turbulence-Chemistry Closure with Temperature-Composition Correlations", 37th Aerospace Sciences Meeting & Exhibit, Reno, NV, AIAA 99-0928, pp. 1-18.

[18] Barlow, R.S., Frank J.H., 1998, "Effect of turbulence on Species Mass Fraction in Methane / Air Jet Flames", *27th International Symposium on Combustion*, The Combustion Institute, pp. 1087-1095.

[19] Barlow, R.S., http://www.ca.sandia.gov/TNF, TNS Workshop, Eds Sandia National Laboratories, USA.

Conference on Modelling Fluid Flow (CMFF'06)
The 13th International Conference on Fluid Flow Technologies
Budapest, Hungary, September 6-9, 2006

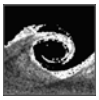

SIMULATION OF GAS EVOLUTION IN ELECTROCHEMICAL REACTIONS USING A COUPLED LAMINAR INCOMPRESSIBLE TWO-FLUID FLOW MODEL AND MULTI-ION TRANSPORT MODEL

Calin DAN[1], Gert NELISSEN[1], David Vanden ABEELE[2], Johan DECONINCK[1], Herman DECONINCK[2]

[1] Corresponding Author. Computational Electrochemical Group, TW/ETEC, Vrije Universiteit Brussel, Pleinlaan 2, Be-1050 Brussel, Belgium. Tel.: +32 2 629 2811, Fax: +32 2 629 3620, E-mail: calindan@vub.ac.be
[2] Aeronautics and Aerospace Department, Von Karman Institute, Belgium. E-mail: david.vanden.abeele@vki.ac.be

ABSTRACT

The formation of gas in electrochemical processes is either the aimed product or an unwanted side product, primarily due to the decomposition of water. The purpose of this work is to take into account the changes brought to an electrolyte by gas evolution at electrodes in a simulation tool based on the multi-ion electrochemical transport model (which considers diffusion, convection, migration and homogeneous reactions inside the electrolyte). The electrolyte conductivity depends on the gas distribution in the electrochemical reactor, which is calculated using an Eulerian-Eulerian two-phase flow model based on a laminar, single-pressure two-fluid description. The gas flux produced at the electrode is calculated using an electrochemical model and it is imposed as a boundary condition to the two-phase flow model. Both the fluid and electrochemical models are discretised with Residual Distribution Schemes and solved using an implicit iterative algorithm. In this paper, the implementation of the two-phase model is discussed. Preliminary results, calculated using the coupled fluid and electrochemical solvers, are presented.

Keywords: coupled solvers, incompressible, laminar, multi-ion transport and reaction model, two-fluid model

NOMENCLATURE

C	[-]	constant value
D_k	$[m^2/s]$	diffusion coefficient
$E_{0,r}$	$[V]$	equilibrium potential
F	$[C/mol]$	Faraday's constant
$\underline{F}$	$[N]$	force
J_r	$[A/m^2]$	reaction current density
$\underline{N}_k$	$[A/m^2]$	flux normal to the electrode
R	$[J/mol\ K]$	ideal gas constant
R_k	$[mol/m^3 s]$	production rate per unit volume
T	$[K]$	temperature
U	$[V]$	electrical potential
V	$[V]$	metal potential
c_k	$[mol/m^3]$	concentration
g	$[m/s^2]$	gravitational acceleration
$k_{ox/red}$	$[A\ m/mol]$	pre-exponential constants in Butler-Volmer formula
n_{el}	[-]	number of electrons
p	$[Pa]$	pressure
r_b	$[m]$	diameter of the bubble
t	$[s]$	time
z_k	$[C]$	electrical charge
u_k	$[m^2\ mol/J\ s]$	ionic mechanical mobility
$\underline{u}_s$	$[m/s]$	phase velocity vector
α_s	[-]	phase volume fraction
$\beta_{ox/red}$	[-]	charge transfer coefficient
ε	$[C^2/N\ m^2]$	dielectric permittivity
ρ_s	$[kg/m^3]$	phase density
η	$[V]$	overpotential
σ	$[1/\Omega]$	electrical conductivity
ν_s	$[m^2/s]$	phase kinematic viscosity

Subscripts and Superscripts

0	next to the electrode
b	bubble
$bulk$	bulk electrolyte
el	electron
g	gas
k	ion
l	liquid
m	mixture
ox	oxidation
red	reduction
r	reaction
s	phase
drag	drag force
VM	virtual mass force

1. INTRODUCTION

Accurate simulations of processes in electrochemical reactors require modelling of many complex phenomena, amongst which the gas evolution due to electrode reactions. The purpose of this work is to develop a simulation tool to estimate the ionic concentration, electrostatic potential distribution and local reaction kinetics when the electrolyte evolves into a two-phase bubbly flow regime. Simulations of gas evolution in (electro)chemical reactors are not extensively reported in literature. This is the consequence of the complexity of both electrochemical and two-phase flow models:

- Ziegler and Evans ([20], 1986) applied the drift-flux model to an electrochemical cell in order to predict the bubble velocity profiles and mass transfer rates. The bubble distribution is determined from a concentration equation and no electrochemical model accounts for the gas production.
- Hur et al. ([6], 2003) aimed to optimize the design of a fluorine production cell by determining hydrogen bubble trajectories using an Eulerian-Lagrangian two-phase model. The concentration distribution of the hydrogen bubbles is expressed by a convection-diffusion equation and the bubble formation on the cathode is determined a priory from data taken from literature.
- Dahlkild ([4], 2001) used the mixture (diffusion) model to resolve the fluid flow profile in an electrochemical reactor with vertical electrode. The local volumetric production rate of gas per unit surface is given by Faraday's law as a function of the local current density, which is determined by the net molar flux density considering diffusion and migration effects (convection and homogeneous reactions are disregarded).

The simulations reported in this contribution are based on more accurate electrochemical and/or two-phase flow models than the models used in the above references. Moreover, the gas evolving electrode models are dedicated to specific geometries, flow regimes or electrochemical conditions, whereas the work presented here is applicable to generic geometries. In section 2, the electrochemical model is introduced; in section 3 the physics of the gas evolving electrodes and the physical effects considered in these simulations are discussed. Section 4 is dedicated to the description of the Eulerian-Eulerian two-phase model used to calculate the liquid phase velocity field and the gas volume fraction profile. The coupling between the electrochemical and fluid-flow solvers and the preliminary results are presented in section 5.

2. ELECTROCHEMICAL SYSTEM

Simulations of electrochemical processes that involve gas evolution are important for both applications where the gas is the desired end product and for applications where it is a (possibly unwanted) side product. For example in the chromium plating process, hydrogen evolution consumes ~80% of the total current in the cell. In order to describe these phenomena properly, the Multi-Ion Transport and Reaction Model (MITReM) [2, 15, 10] is used; this formulation is based on the 'dilute solution model' proposed by Newman [12] and consists of the mass conservation and Potential equations, which are solved in a strongly coupled manner to determine the ionic concentrations c_k and electric potential field U. The mass conservation equations consider diffusion, convection, migration and homogeneous reactions for each ionic species:

$$\frac{\partial c_k}{\partial t} = -\nabla \cdot \underline{N}_k + R_k \,, \tag{1}$$

where $\underline{N}_k$ represents the molar flux of ion k given as:

$$\underline{N}_k = c_k \underline{u}_l - D_k \nabla c_k - z_k u_k F c_k \nabla U \,. \tag{2}$$

Here in, $\underline{u}$ is the mass-averaged velocity of the fluid, D_k represents the diffusion coefficient, z_k is the electrical charge, u_k is the mechanical mobility (which is related to the diffusion coefficient D_k by means of Nenst-Einstein equation) and F stands for the Faraday constant. The production per unit volume term R_k takes into account the homogeneous reactions inside the electrolyte.

The charge density at each point of the solution is the algebraic sum of the charges of all charged particles per unit volume (charges times concentrations). The electric potential U in the electrolyte with dielectric permittivity ε and with a charge density distribution is given by Poisson's equation:

$$\nabla^2 U = \frac{F}{\varepsilon} \sum_k z_k c_k \,. \tag{3}$$

Electrode reactions are introduced in MITReM as non-linear boundary conditions imposed on electrode surfaces [11]. A common description of these boundary conditions is the Butler-Volmer formulation. The net local current density (J_r) of each reaction is given as a function of the local overpotential η and reacting ions concentration:

$$J_r = k_{ox}\, c_{0,ox}\, e^{\frac{\beta_{ox} n_{el} F}{RT}\eta} - k_{red}\, c_{0,red}\, e^{-\frac{\beta_{redx} n_{el} F}{RT}\eta} \tag{4}$$

where R is the ideal gas constant, T the temperature, n_{el} the number of electrons involved in the reaction, $\beta_{ox/red}$ the anodic/cathodic charge transfer coefficient and $k_{ox/red}$ the pre-exponential constant of the anodic/cathodic part. For one-step reactions, one should consider $\beta_{ox} + \beta_{red} = 1$. The pre-exponential constants k_{ox} and k_{red} are chosen in order to obtain zero current at equilibrium, *i.e.* when the

overpotential is zero (η = 0) and the surface concentrations equal their bulk values. The overpotential (η) is given as:

$$V - U = \eta + E_{0,r} \tag{5}$$

where V represents the metal potential on the electrode and $E_{0,r}$ the equilibrium potential for a reaction r (Nernst potential). The first term in the right hand side of formula (4), which represents the anodic current density, is dominant for oxidation reactions, whereas the second one is dominant for reduction reactions (cathodic curent density). The pre-exponential constants $k_{ox/red}$, the charge transfer coefficients $\beta_{ox/red}$ and the equilibrium potential $E_{0,r}$ are controlling the electrons transfer at the electrode and they are determined based on the experimental polarization curves.

3. GAS EVOLVING ELECTRODES

The gas produced in electrochemical reactors is generated by one or several electrode reactions and then freed in the electrolyte. When the current density is very low, the gas dissolved in the electrolyte is removed from the electrode by diffusion and convection and displaced towards the liquid bulk without formation of a real gas phase. Only when the concentration of gas in the electrolyte adjacent to the electrode reaches a certain critical level (supersaturation), bubbles are formed. These gas bubbles develop at nucleation sites on the electrode, grow in size until they reach the break-off diameter and then spread into the liquid [16].

Although it is difficult to estimate the critical diameter of the bubbles, Vogt [16] mentioned the range of 50 μm for aqueous solutions to 1 mm for salt melts. According to Marrucci and Nicodemo [9], bubbles detach from electrodes at a constant size. Detached bubbles can still grow in size if the electrolyte is saturated with the dissolved gas. As mentioned by Vogt [17] and Kheifets and Goldberg [8], for oxygen and hydrogen evolution in the electrolysis of aqueous H_2SO_4 solutions, at current densities between 3 and 10^4 A/m^2, only 20% to 60% of the gas generated at the electrode is immediately desorbed into growing bubbles. According to Beek and Muttzall [1], the bubbles may be regarded as rigid spheres when the size of the bubble is small. Coalescence between bubbles generated in electrochemical reactors may be disregarded, because of the existence of electrical repulsive forces acting between bubbles [10].

The presence of gas in the electrolyte influences the mass transport of ions and the electron transfer at electrodes. The charge exchange mechanisms suffer from a partial coverage of the electrode by gas bubbles: the active surface of the electrode then decreases, which changes the current density distribution. In the electrolyte, the presence of gas changes the conductivity and modifies the liquid velocity field. The relation between the local conductivity and the gas fraction (α_g) has been intensively studied and the empirical relations proposed by different authors are discussed by Vogt [16] and Kreysa and Kuhn [9]. For large void fractions $\alpha_g > 0.1$, the Bruggemann formulation of conductivity dependency was found to fit best the experimental data [3]:

$$\sigma = \sigma_l (1 - \alpha_g)^{3/2} \tag{6}$$

where σ_l represents the conductivity of the liquid. As a consequence of the linear variation of the conductivity σ with the ionic mobility u_k :

$$\sigma = F^2 \sum_k z_k^2 u_k c_k \tag{7}$$

the ionic mobility u_k is scaled according to the Bruggemann relation (6).

4. TWO-PHASE FLOW MODEL

We are mainly interested in the macroscopic liquid velocity and gas distribution in the reactor and their mutual interaction with the electrochemical process. Among the different two-phase models proposed in the literature for bubbly flows (mixture, drift-flux, etc), the two-fluid model has been chosen because it provides a good compromise between accuracy and computational effort.

This two-phase description is obtained by an Eulerian averaging for each phase of the conservation equations formulated in local instantaneous values. Averaging the local instantaneous equations yields unspecified terms which contain the effect of the information lost by averaging. They are defined by local instantaneous variables and represent interfacial interactions, to be modelled by constitutive laws using only the averaged macroscopic unknowns. The interfacial interaction terms considered here are the drag force ($\underline{F}_{drag}$) and virtual mass force ($\underline{F}_{VM}$). The drag force is compulsory for the two-fluid models, whereas the virtual mass force is retained to ensure the well-posedness of the incompressible two-fluid model [14]. As a matter of fact, the drag force is at least one order of magnitude larger than any other interaction force derived from averaging procedure [7].

The two-fluid model implemented in this work is formulated in primitive variables, namely the pressure p, the phase velocity vector $\underline{u}_k$, $k = l, g$ and the liquid/gas fraction α_s. A single-pressure incompressible two-fluid model for laminar flow is considered. This approximate description is justified for the two-phase bubbly flows encountered in electrochemical reactors, because the bubbles generated at the electrodes are of small size and may be regarded as non-colliding rigid spheres (see section 3). Buoyancy

forces are neglected because they need special numerical treatment which is not available at this moment in the two-phase solver such that the incompressible two-fluid model writes:

$$
\begin{aligned}
&\alpha_g \nabla \underline{u}_g + \underline{u}_g \nabla \alpha_g + \alpha_l \nabla \underline{u}_l + \underline{u}_l \nabla \alpha_l = 0 \\
&\frac{\partial \underline{u}_g}{\partial t} + (\underline{u}_g \cdot \nabla)\underline{u}_g + \frac{1}{\rho_g}\nabla p = \\
&\qquad \frac{1}{\rho_g}\nabla \cdot \underline{\underline{\tau}}_g + \frac{1}{\alpha_g \rho_g}\left(\underline{F}_{drag} + \underline{F}_{VM}\right) \\
&\frac{\partial \underline{u}_l}{\partial t} + (\underline{u}_l \cdot \nabla)\underline{u}_l + \frac{1}{\rho_l}\nabla p = \\
&\qquad \frac{1}{\rho_l}\nabla \cdot \underline{\underline{\tau}}_l - \frac{1}{\alpha_l \rho_l}\left(\underline{F}_{drag} + \underline{F}_{VM}\right) \\
&\frac{\partial \alpha_g}{\partial t} + \alpha_g \nabla \underline{u}_g + \underline{u}_g \nabla \alpha_g = 0 \\
&\frac{\partial \alpha_l}{\partial t} + \alpha_l \nabla \underline{u}_l + \underline{u}_l \nabla \alpha_l = 0
\end{aligned}
\qquad (8)
$$

where $\underline{\underline{\tau}}_s$ represents the viscous stress tensor and:

$$F_{drag} = \frac{3 C_D}{8 r_g}\alpha_g (1-\alpha_g)\rho_m \left\|\underline{u}_g - \underline{u}_l\right\|(\underline{u}_g - \underline{u}_l) \qquad (9)$$

$$F_{VM} = C_{VM}\,\alpha_g (1-\alpha_g)\rho_m \left(\frac{D_g \underline{u}_g}{Dt} - \frac{D_l \underline{u}_l}{Dt}\right) \qquad (10)$$

In these equations, ρ_s represent the density of phase $s = l, g$, the mixture density $\rho_m = \alpha_g\rho_g + \alpha_l\rho_l$, r_g is the effective radius of gas bubbles, the drag C_{drag} and virtual mass C_{VM} coefficients are taken constant values and $D_s\underline{u}_s/Dt$ represents the material (substantial) derivatives:

$$\frac{D_s}{Dt} = \frac{\partial}{\partial t} + \underline{u}_s \cdot \nabla \qquad (11)$$

As boundary conditions for this incompressible model, one imposes the phase velocity vectors and the void fraction at the inlet and the pressure at the outlet. No-slip conditions $\underline{u}_s = 0$ are imposed on all solid walls on which no gas is generated.

Imposing proper boundary conditions on a gas evolving electrode is not straight-forward. The velocity of an isolated bubble generated and detached from a gas evolving electrode may be calculated as [15]:

$$u_b = \frac{g\, r_b^2}{3\nu_l}\left(1 - \frac{\rho_g}{\rho_l}\right) \qquad (12)$$

where g represents the gravitational acceleration and ν_l is the kinematic viscosity of the liquid phase. Considering the ideal gas law, one may derive from Faraday's law the local average volumetric production rate [4]:

$$\underline{1}_n \underline{u}_g \cdot \alpha_g = \frac{RT}{n_{el} F\, p}\, J_r \qquad (13)$$

By putting $\underline{1}_n\underline{u}_g = \underline{u}_b$, the value of α_g to be imposed is determined from formula (13).

The steady-state solution of the two-fluid model is obtained using a second-order accurate unstructured solver on two-dimensional triangular meshes. The system of equations (8), (9) and (10) is discretised using the Residual Distribution Method [5, 13, 18] with distribution matrix given by a simplified Lax-Wendroff scheme [19]. The algebraic system obtained after discretisation is solved using Newton's method. Numerical experiments showed instability in the void fraction when the ratio between phase densities was large (e.g. for water and hydrogen $\rho_l / \rho_g = 10000$). A small amount of second-order artificial dissipation is added to the liquid/gas fraction equations to overcome this problem.

5. NUMERICAL RESULTS

The electrochemical and two-phase steady-state solvers are run to convergence in a loosely coupled manner (Figure 1).

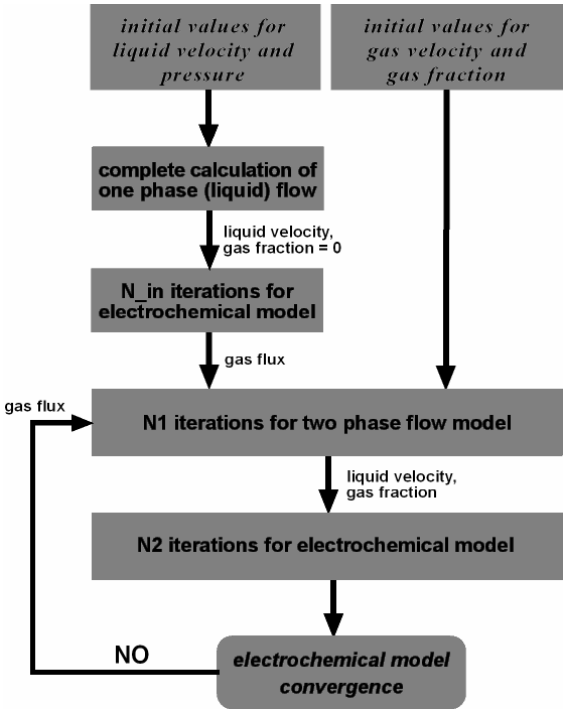

Figure 1. The coupling algorithm of the electrochemical and two-phase flow solvers

The iterative procedure begins with a calculation of the electrochemical system in a reactor without gas dissolved in the electrolyte ($\alpha_g = 0$ in the bulk) and the liquid velocity vector ($\underline{u}_l$) is determined by solving the single-phase incompressible Navier-Stokes equations. Based on the electrochemical solution, the gas flux generated in the electrode reactions is calculated using Eq. (12) and imposed as boundary condition in the two-phase flow model. Further on, the liquid velocity ($\underline{u}_l$) and

gas distribution (α_g) calculated in the two-phase flow model are used to evaluate the convection and migration contributions in MITReM. The loop consisting of electrochemical and two-phase solvers runs until the current densities calculated on the gas-evolving electrodes reach steady-state values.

In order to validate the global coupled system, we consider a parallel plate channel with two electrodes placed respectively on the bottom and top walls. The gas evolution reaction takes place only at the bottom electrode. At the inlet, we assume a mixture with a gas fraction $\alpha_g = 0.05$ and a parabolic velocity profile with equal amplitude for both phases $u_s = 0.01$ *m/s*. The geometry of the channel employed for this test case is given in Figure 2(a), with $h = 0.01$ *m*. The Reynolds number of the liquid phase is 100. The grid used for both electrochemical and two-phase solvers (Figure 2(b)), contains 1337 nodes and 2448 elements with a stretching applied to resolve the boundary layer next to the cathode (bottom side electrode).

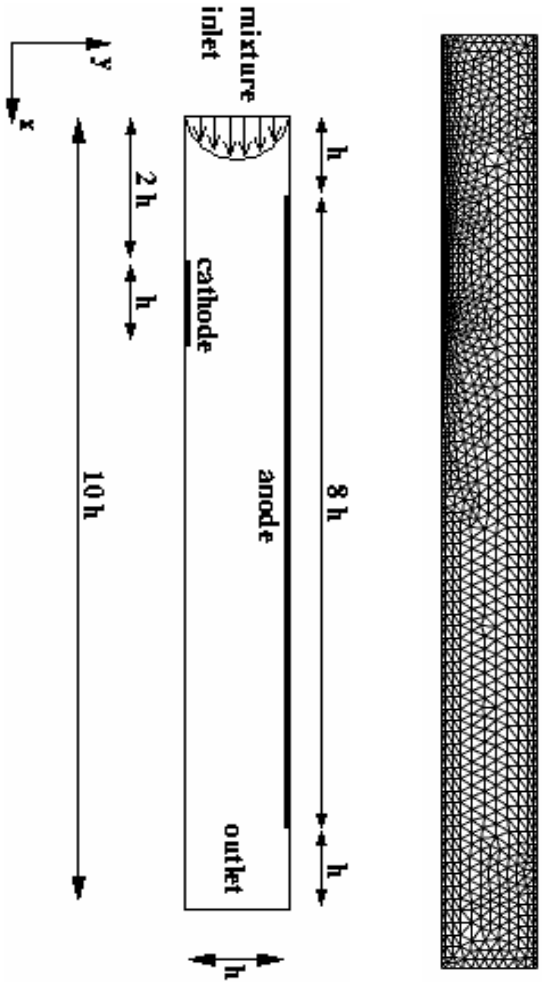

a) b)

Figure 2. The geometry (a) and the grid (b) of the parallel plate channel

Since the purpose of this test case is so far only to evaluate the coupling between the solvers, the electrochemical system is a purely theoretical one, but in some sense it approximates the chromium deposition process.

Table 1. The ion system

Ion	$\mathbf{z_k}$[C]	$\mathbf{D_k}$ [m^2/s]	$\mathbf{c_{bulk}}$ [mol/m^3]
A^+	1	$2\cdot10^{-9}$	800
H_2O	0	10^{-9}	47000
OH^-	-1	$2\cdot10^{-9}$	6
C^-	-1	$1.5\cdot10^{-9}$	3088
D^{2+}	2	$2.2\cdot10^{-9}$	1147

The electrochemical system (Table 1) consists of two parallel reactions on the cathode, namely A^+ deposition:

$$A^+ + e^- \rightarrow A \tag{14}$$

and water decomposition:

$$2H_2O + 2e^- \rightarrow 2OH^- + H_2 \tag{15}$$

and production of ion A^+ reaction on the anode:

$$A \rightarrow A^+ + e^- \tag{16}$$

The water decomposition reaction considered for the hydrogen evolution is preferred to the hydrogen evolution reaction because it guarantees an `infinite` source of H_2 in order to avoid getting to the limiting current regime. The limiting current regime corresponds to zero concentration of the ion consumed at the electrode and therefore, the convergence of the electrochemical solver slows down, which is an unwanted complication for a numerical experiment meant to validate the coupling of the electrochemical and two-phase solver.

Table 2. Electrode reaction coefficients in Butler-Volmer formula

reaction	$\mathbf{k_{red}}$ [A m/ mol]	$\mathbf{k_{ox}}$ [A m/ mol]	$\mathbf{\beta_{red}}$ [-]	$\mathbf{\beta_{ox}}$ [-]	$\mathbf{E_{0,r}}$ [V]
Eq. (14)	10^{-4}	$3\cdot10^{-8}$	0.3	0.7	-0.3
Eq. (15)	$3\cdot10^{-8}$	10^{-10}	0.17	0.01	0
Eq. (16)	$5\cdot10^{-5}$	$8\cdot10^{-3}$	0.7	0.3	0

The ions C^- and D^{2+} represent an excess of supporting electrolyte: they are assumed electrochemically inert, but they are included in the system to ensure a constant conductivity of the electrolyte (when no gas is present in the electrolyte). The reactions are modelled by using the Butler-Volmer formula with coefficients given in Table 2. The gas evolving reaction takes the major part of the total current on the cathode, resulting in a low

efficiency of the ion A^+ deposition reaction. None of the electrode reactions reaches the limiting current.

Because no numerical simulations or experimental data for this test case are available in the literature, the consistency of the results and the feasibility of the coupling are evaluated by comparing the solutions obtained for several potential differences imposed at the reactor electrodes.

In a first calculation the applied potential difference between the electrodes is 2.16V and the coupled solvers converge after 3 loops. In the first step, i.e. there is no gas in the electrolyte, the current density along the cathode (■ symbols in Figures 3(a) and 4(a)) exhibits a small non-symmetry: the local current density values are larger on the right hand side of the cathode because of the non-symmetrical configuration of the electrodes in the reactor (see the anode position in Figure 1(a)).

When the gas is produced in the electrode reactions, the current density along the cathode (▼ symbols in Figure 3(a)) decreases towards the outlet (right hand side of the electrode). Because the void fraction imposed on the cathode is proportional to the current density (Eq. (13)), its local value also decreases towards the outlet due to a gas diffusion layer that is built.

Increasing the potential difference imposed between the electrodes to 2.26 V, the convergence of the coupled solvers is slower (7 iterations), but the change of current density normal to the cathode is similar with the one obtained with 2.16 V: the current density normal to the cathode (● symbols in Figure 4(a)) decreases towards the outlet (right hand side of the electrode). Although the void fraction imposed on the electrode is larger on the upstream side (Figures 3(b) and 4(b)), that is the electrical resistivity increases, the profile current density normal to the electrode decreases towards the outlet.

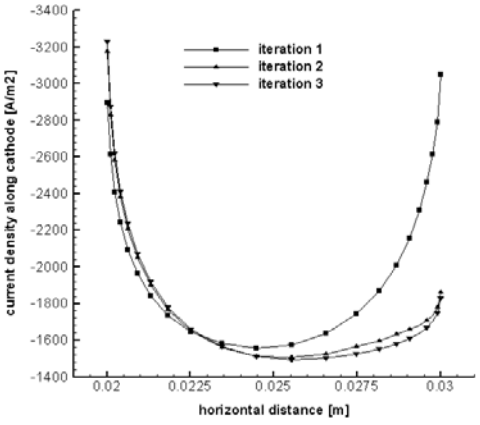

a)

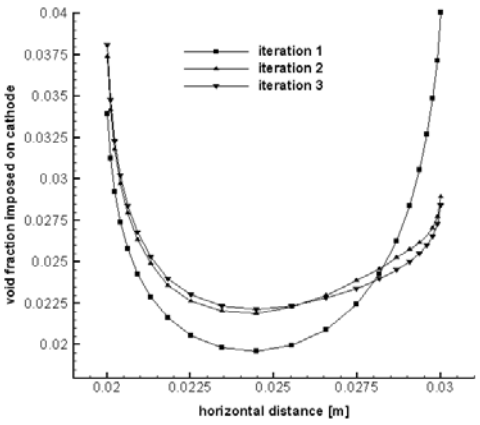

b)

Figure 3. The current density (a) and imposed void fraction (b) along the cathode for potential difference 2.16 V imposed at the reactor electrodes

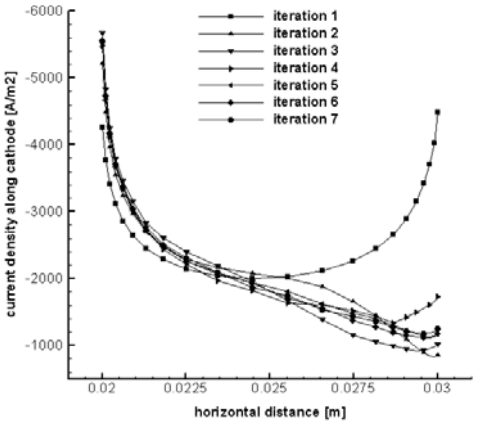

a)

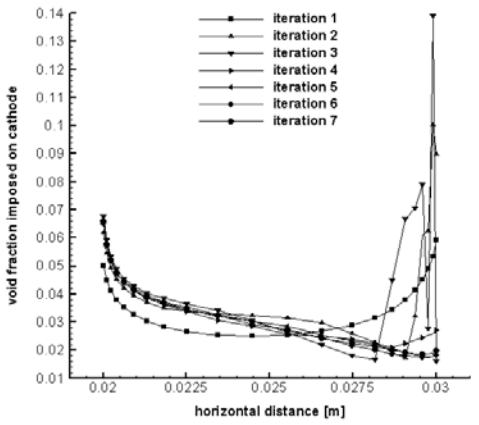

b)

Figure 4. The current density (a) and imposed void fraction (b) along the cathode for potential difference 2.26 V imposed at the reactor electrodes

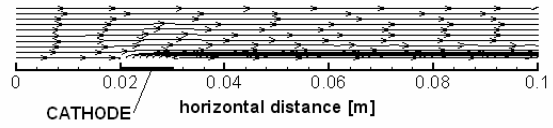

a)

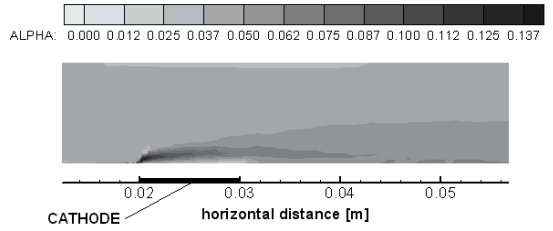

b)

Figure 5. The streamlines (a) and void fraction profile (b) of gas phase for a 2.26 V potential difference imposed between the reactor electrodes

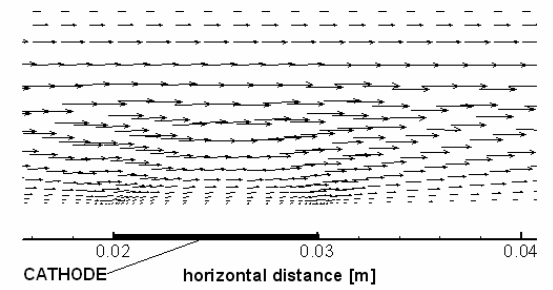

Figure 6. The liquid velocity vectors for a 2.26 V potential difference imposed between the reactor electrodes (zoom over the region next to the electrode between 0.02 and 0.03 m)

In order to understand this effect, one should look at the convection of the flow. When the flux of gas evolving at the cathode is sufficiently large to influence the flow coming from the inlet (Figure 5(a)), a liquid velocity component normal to the cathode is developing next to the cathode. The drag between phases forces the liquid next to the cathode, to follow the gas flow. The electrolyte is pushed away from the cathode (Figure 6) and therefore, the concentration of reacting ions in the region next to the cathode decreases. Nevertheless, on the left hand side of the cathode, the flow coming from the inlet is refreshing the electrolyte whereas on the right hand side of the cathode the amount of fresh electrolyte coming from the inlet is smaller because of the liquid velocity component normal to the electrode which hinders the tangential flow along the cathode. Therefore, the current density on the right hand side of the cathode is smaller than on the left hand side when gas is evolving at the electrode. Because the void fraction imposed on the cathode is proportional to the current density (Eq. (12)), the largest amount of gas is accumulating on the left hand side of the electrode (Figure 5(b)).

The coupling procedure performs well if the amount of gas generated at the electrode is not too large. When the potential difference between the electrodes further increases, it becomes impossible to reach the steady-state. The large flux of gas is blocking the convection of electrolyte at the cathode and the coupling procedure drops into an infinite loop oscillating between two states: the electrochemical solver will determine either a large amount of gas, when no vertical component of liquid velocity is developing in the flow, or the electrode reactions (hence also the gas evolution) are blocked by the large vertical component of liquid velocity. Avoiding this situation will need an improved understanding of the coupling effect and maybe also an improved physical description of the way how to split the gas flux into a velocity and void fraction. Also a time-accurate coupling of the solvers, may improve the convergence.

6. CONCLUSIONS

The objective of this work was the improvement of the quality of simulations in the electrochemical reactors by modelling the evolution of the gas generated at the electrode. The multi-ion transport and reaction model (MITReM), which calculates ionic concentrations and the electrostatic potential distribution in the reactor, is modified to account for the change in electrical conductivity of the electrolyte and the current density distribution due to the presence of gas. The electrolyte convection field and the void fraction are determined using a single-pressure incompressible two-fluid model. A loosely coupled solution algorithm between the electrochemical and fluid flow solvers has been realised based on newly proposed coupling equations. The results obtained using the present coupling procedure seems to be physically consistent but need further physical/numerical elaboration and experimental validation in order to deal with high gas fluxes. Based on the simulations performed with the coupled solvers, one found that the electrolyte flow driven by the gas evolving at the electrode yields major changes in the solution of the electrochemical system. Therefore, only a multi-ion transport model is able to take into account the major effects of gas evolution, whereas the electrochemical models which do not model the convection contribution are incomplete.

ACKNOWLEDGEMENTS

This work has been supported by European Commission project BE-97-4761 (DESINER) and IWT contract SBO2004, no. 040092 (MUTECH).

REFERENCES

[1] Beek, W.J. and Muttzall, K.M.K., 1975, *Transport phenomena*, Wiley, New York.

[2] Bortels, L., Deconinck, J. and van den Bossche, B., 1996, "The Multi-Dimensional

Upwinding Method (MDUM) as a new simulation tool for the analysis of multi-ion electrolytes controlled by diffusion, convection and migration. Part I. Steady-state analysis of a parallel plane flow channel", *Journal of Electroanalytical Chemistry*, Vol. 404, pp. 15.

[3] Bruggemann, D.A.G., 1935, "Berechnung verschiedener physikalischer kon-stanten von heterogenen substanzen", *Ann. Phys.,* Vol. 24, pp. 659.

[4] Dahlkild, A., 2001, "Modelling the two-phase flow and current distribution along a vertical gas-evolving electrode", *Journal of Fluid Mechanics*, Vol. 428, pp. 249-272.

[5] Deconinck, H., Sermeus, K., and Abgrall, R., 2000, "Status of multidimensional upwind residual distribution schemes and applications in aeronautics", In *Fluids,* AIAA-2328.

[6] Hur, J.S., Shin, C.B, Kim, H., and Kwon, Y.S., 2003, "Modeling of the trajectory of the hydrogen bubbles in a fluorine production cell", *Journal of Electrochemical Society*, Vol. 150, pp. D70-D78.

[7] Issa, R.I. and Oliveira, P.J., 1994, "Numerical prediction of phase separation in two-phase flow through T-junction", *Computers Fluids*, Vol. 32, pp. 347.

[8] Kheifets, L.I. and Goldberg, A.B., 1989, "Mathematical modeling of electrochemical reactors", *Elektrokhimiya* - translated, Vol. 25, pp. 3-33.

[9] Kreysa, G. and Kuhn, M., 1985, "Modelling of gas evolving electrolysis cell. I. the gas voidage problem", *Journal of Applied Electrochemistry*, Vol 15, pp. 517-526.

[10] Marrucci, G. and Nicodemo, L., 1967, "Coalescence of gas bubbles in acqueous solution of inorganic electrolytes", *Chem. Engng. Sci.*, Vol. 22, pp. 1257.

[11] Nelissen, G., van Den Bossche, B., Deconinck, J., van Theemsche, A. and Dan, C., 2003 "Laminar and turbulent mass transfer simulations in parallel plate reactor", *Journal of Applied Electrochemistry,* Vol. 33, pp. 863.

[12] Newman, J. S., 1989, *Electrochemical Systems*, 2nd edition, Prentice-Hall, Inc.

[13] Paillere, H., 1995, *Multidimensional upwind residual distribution schemes for the Euler and Navier-Stokes equations on unstructured grids*, PhD thesis, Universite Libre de Bruxelles.

[14] Prosperetti, A. and van Wijngaarden, L., 1976 "On the characteristics of the equations of motion for a bubbly flow and the related problem of critical flow", *Journal of Engineering Mathematics,* Vol. 10, pp. 153.

[15] van den Bossche, B., Bortels, L., Deconinck, J., Vandeputte, S. and Hubin, A., 1996, "Numerical steady-state analysis of current density distributions in axisymmetrical systems for multi-ion electrolytes: application to the rotating disc electrode", *Journal of Electroanalytical Chemistry*, Vol. 411, pp. 129.

[16] Vogt, H., 1983, "Gas evolving electrodes", *Comprehensive treatise of electrochemistry. Plenum. New-York,* pp. 445.

[17] Vogt, H., 1984, "The rate of gas evolution at electrode I. An estimate of the efficiency of gas evolution from the supersaturation of electrolyte adjacent to a gas evolving electrode", *Electrochemical Acta*, Vol. 29, pp. 175-180.

[18] Van Der Weide, E., 1998, *Compressible Flow Simulation on Unstructured Grids using Multi-dimensional Upwind Schemes*, PhD thesis, Technische Universiteit Delft.

[19] Waterson, N., 2003, *Simulation of turbulent flow, heat and mass transfer using Residual-Distribution approach*, PhD thesis, Technische Uni-versiteit Delft.

[20] Ziegler, D., and Evans, J.W., 1986, "Mathematical modeling of electrolyte circulation in cell with planar vertical electrodes", *Journal of Electrochemical Society*, Vol. 103, pp. 567-576.

Conference on Modelling Fluid Flow (CMFF'06)
The 13th International Conference on Fluid Flow Technologies
Budapest, Hungary, September 6-9, 2006

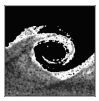

NUMERICAL SIMULATION OF A LAB- SCALE SYNGAS BURNER USING COMPLEX CHEMISTRY

Thomas KRETSCHMER[1], Dr. Harald SCHÜTZ[2], Michael TSURIKOV[3], Dr. Berthold NOLL[3], Prof. Manfred AIGNER[3]

[1] Corresponding Author. DLR - German Aerospace Centre, Institute of Combustion Technology, Linder Höhe, 51147 Cologne, Germany, Tel.: +49 2203 6012052, Fax: +49 2203 64395, E-mail: thomas.kretschmer@dlr.de
[2] German Aerospace Centre, Institute of Combustion Technology, Cologne, E-mail: herald.schuetz@dlr.de
[3] German Aerospace Centre, Institute of Combustion Technology, Pfaffenwaldring 38 – 40, Stuttgart, Germany, Tel:+49 711 6862308, Fax: +49 711 6862349

ABSTRACT

A lab scale burner was investigated at DLR institute of Combustion Technology within the context of a EU project and in cooperation with industrial partners. Experiments were followed by numerical simulations used for CFD code validation. A commercial CFD code is used for solving the transport equations of the flow, while an external combustion code is coupled to the solver, which calculates source terms due to chemical reactions. After each computational time step chemistry sources are returned to the solver and implemented into the energy and species transport equations. The combustion code is an internal DLR development while the coupling is done via user defined interfaces supported by the CFD code. However, with some adaptation work, it can also be used for different CFD codes. The core of the combustion code is a program package which calculates chemical reaction rates of complex chemical systems. In the combustion code turbulence-chemistry interactions are modelled with the Partially Stirred Reactor Concept (PaSR) which is suited for taking detailed chemistry into account. The results are compared with measurements for two different syngas mixtures done for the lab scale burner.

Keywords: CFD, Complex Chemistry, Mixed-Language Programming, Syngas, Turbulence-Chemistry Interactions

1. INTRODUCTION

Natural gas or fuel oil is commonly used for power generation. Because of higher prices for oil and gas and a sustainable development, so-called dirty fuels such as coal or refinery residues as well as biomass become more and more important when they are pretreated in a gasification process that produces low calorific fuels called syngas. The highly efficient combined cycle process opens the use of these fuels applying in advanced gas turbine combustion systems, which are operating at higher temperatures and pressure levels. In order to enable the proper operation and the demanded performance of these applications intensive research is necessary to adapt well proven gas turbine combustion systems to syngas applications. Within an EU project (HEGSA - High Efficient Gas Turbine for Syngas Application) industrial partners and research institutions cooperate in this subject. The results will directly affect future burner design. The project's main targets, such as reduced CO_2 emissions or improved fuel flexibility, are outlined in the project report [1].

2. SYNGAS COMBUSTION

For syngas combustion a specially adapted burner design is needed. A general feature of syngas is its low heating value in comparison to natural gas, while the reactivity is still comparatively high due to the high amount of hydrogen. Under full load conditions the mass flow of syngas is about one order of magnitude higher compared to that of natural gas. Consequently, the effective cross sections of the syngas passages have to be distinctly larger. Moreover, the elevated hydrogen content does not contribute to CO_2 emissions. The particular burning behaviour of hydrogen such as higher flame temperatures and velocities increases the risk of flash back conditions and higher NO_x emissions. To avoid this risk the combustor design should be capable to burn hydrogen-rich fuel by using different dilution options as N_2, CO_2 or steam injection. It is furthermore desirable for the burner to have operational fuel flexibility using different syngas compositions as well as natural gas or fuel oil. New design features as well as adaptations of

existing systems including the possibility to inject syngas through more then one burner passage, are necessary. Blending operation with natural gas is also very important, as is increasing variations on the syngas composition itself. For the burner development a generic lab scale burner was used that fulfils the aforementioned requirements to validate and improve the combustion behaviour of different syngas mixtures. The burner was designed by the Laboratory of Thermal Engineering at the University of Twente in the Netherlands (one of the project partners) and is similar to the design which would be used in a syngas burner of the industrial partners. Adaptations to the burner were done and combustion tests were carried out to provide flame (DLR) and thermoacoustic data (Univ. of Twente). The tests were supported by numerical simulations using a reduced reaction mechanism, which was one target of the project. In the following paper results of the experiments in comparison with the numerical results are presented. The numerical tool, an external combustion code coupled with a CFD solver that uses complex finite rate chemistry with a simple turbulence - chemistry interaction model is described in detail.

3. GENERIC BURNER SETUP

The total setup consists of the burner itself, the pressure housing and the gas delivery system. The housing is rated up to 40 bars and has a relatively large inner diameter (150 mm) with optical access and active pressure control. After some adaptation the assembly to the burner finally resulted in a combustion chamber with dimensions 90x90x180mm. The chamber has fused silica windows on four sides supported by four brass alloys posts; these and other metal parts are water cooled while the windows are cooled with air jets from the outside. Figure 1 shows the cross-sectional of the main burner assembly components and dimensions.

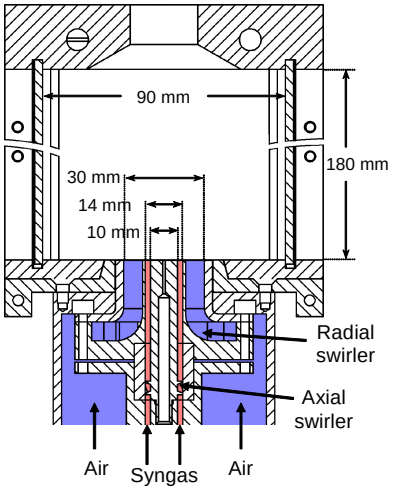

Figure 1. Schematic of the HEGSA burner and the combustion chamber

The design consists of four gas passages. Three are required for the burner design - swirled syngas, air, and an independent methane flow required for ignition. Initial combustion tests were carried out at a power load of 10kW/bar (based on the higher heating value).

Later the load was increased up to 20kW/bar; this required additional technical changes to the configuration, e.g. in cooling air supply. Two different mixtures were investigated in the experimental tests. The first mixture (mixture 6, m6) contained only carbon monoxide and hydrogen as burnable components. The second mixture (mixture 7, m7) was based on m6 but replaced 40% of the thermal load with methane. All experiments were carried out at a global air to fuel ratio λ of 2.0. Inlet air temperatures varied between ambient temperature (293 K) and 423 K. Table 1 gives an overview of operating conditions and fuel composition. Mixture 7 has less nitrogen then mixture 6, clearly indicating its weaker reactivity. Due to the constriction at the pressure housing exit, the ambient pressure was slightly higher than atmospheric pressure. A complete description of the burner design is given in [1, 3].

Table 1. Operating conditions for generic burner tests applied for both mixture

	m6	**m7**	**m6**	**m7**
Load[kW]	10	10	20	20
Pressure	1-1.15 bar			
CO [g/s]	0.581	0.344	1.162	0.687
H_2 *[g/s]*	0.029	0.017	0.058	0.034
CH_4 *[g/s]*	-	0.074	-	0.148
N_2 *[g/s]*	1.256	0.745	2.519	1.490
T_{air}	293K / 423K			
T_{Fuel}	293K			

4. NUMERICAL SIMULATION ENVIRONEMENT

The experimental setup was followed by numerical simulations used for CFD code validation. The commercial CFD code FLUENT [4] is used for solving all the transport equations of the flow including turbulence modelling. An external combustion code coupled to the main solver, calculates only the source terms due to chemical reactions. All properties, such as temperature or species composition needed to calculate reaction rates and thus, changes in species mass fraction and internal energy are provided by the solver. These values are taken from the cell centres and no care has to be taken on cell types or connectivities. After each computational time step, chemistry sources are calculated and returned to the solver where they are implemented into the energy and species transport

equations. Because of the solving procedure for the reaction rates, it is strongly recommended to calculate them for each time step; otherwise, problems of convergence may occur. Kinetic reaction parameters such as activation energy or the preexponential factor for each elementary reaction are read in via an input parameter file that can always be adapted to other reaction mechanism data. The segregated unsteady solver of the CFD code is used, where balance equations are solved sequentially, i.e., segregated from one another. Source term implementation is called by each "Solve" routine for the variable currently under consideration. In some cases the available coupled solver is better fitted to the problem or yields a solution more quickly. The combustion code is an in-house DLR development; while the coupling is done via user defined interfaces supported by the flow solver. However, with some adaptation work, it can also be used for different CFD codes. The coupling between the solver and the combustion code is very simple because of the well working interface, which enables the users to intervene in the transport equations by source term definitions, to define new scalar transport equations, or to include their own computational models. A simple schematic of the coupling process can be seen in Figure 2. While the chemistry code is written in Fortran 90, a Fortran-C coupling has to be applied. Data needed to calculate chemistry sources are transferred via a parameter list to the Fortran 90 part of the program and vice versa. The combustion code provides its own graphical user interface to set parameters for the combustion chemistry calculation even within a running program; it also enables the user to control the computation very comfortably. As combustion does not need information about cell connectivities, the combustion code can be parallelized very easily.

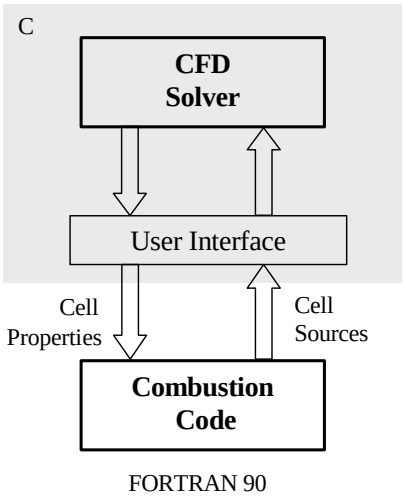

Figure 2. Schematic of Coupling the CFD solver with the external combustion code

5. THE COMBUSTION CODE

Finite Rate Chemistry

The core of the combustion code is a program package, which calculates chemical reaction rates of complex chemical systems no matter how many reactions and species are considered. For a set of elementary reactions changes in species concentrations are solved using the following form,

$$\frac{dc_i}{dt} = \sum_r \frac{dc_i^r}{dt} = \sum_r F_i^r(c_j) \qquad (1)$$

where c_i is the molar concentration of species i and F_i^r is the reaction rate of each elementary reaction r. Using the law of mass action, the reaction rate can be expressed as follows

$$F_i^r(c_j) = (b_{ir} - a_{ir})\left[k_{fr}\prod_j c_j^{a_{jr}} - k_{br}\prod_j c_j^{b_{jr}}\right] \qquad (2)$$

In Eq. (2) k_{fr} and k_{br} are the rate coefficients for the forward and backward reactions defined by using Arrhenius law, and a_{ir} and b_{ir} are the stoichiometric coefficients of indicated species. A fully implicit solution to Eq. (1) can be obtained applying Newton linearization, which is a very expensive procedure because of the strong nonlinearities of the systems due to the different chemical time scales. An alternative way to solve the equations is an explicit approach that is time step depended and thus can lead to negative species concentrations in some cases. The so-called "reference species technique" [5] as a semi-implicit solution method is used to overcome this drawback, enabling a very stable solution. The main idea of this approach is the definition of a reference species for each elementary reaction, in which Eq. (1) is linearized. The reference species is the one that is in greatest danger of being driven negative at the end of the given time step. It is consumed by the reaction and has the lowest concentration. For each reaction it is determined from the following condition

$$c_k^r = \left\{ c_i^r \left| \frac{\frac{dc_i^r}{dt}}{c_i^r} = \min imum \right. \right\} \qquad (3)$$

All reactions are treated sequentially, i.e., segregated from one another. After a reaction rate is calculated for reaction r, species concentrations and internal energy representing temperature are updated and used as input values for reaction $r + 1$ until $r = NR$ is reached, where NR is the total number of all reactions. For sufficient small time steps, this procedure yields to correct results. For

each elementary reaction a characteristic chemistry time τ^{r}_{chem} can be calculated [6]. Doing this a wide range of chemical time scales can be found covering very fast equilibrium reactions, reactions with chemistry times in the order of the turbulent mixing time, which are kinetically controlled up to the slow reactions, such as NO formation reactions. To improve the solution the sequence of the elementary reactions should adapt to the characteristic chemistry time. One can put fast reactions at the beginning and slow reactions at the end of the solution loop using a quick sorting algorithm.

Turbulence Chemistry Interactions

In the combustion code turbulence-chemistry interactions are modelled with the Partially Stirred Reactor Concept (PaSR), which is suited for taking detailed chemistry into account [7]. As a basic assumption in the model, a computational cell is divided into a reactive and a non-reactive part and reactions only occur in the volume fraction κ of the cell. Changes in compositions occur due to mass exchange with the reaction zone, while the reaction zone itself is treated as a perfectly stirred reactor, where species are perfectly mixed and all fluctuations can be neglected to calculate the chemical source term. The mean concentration $\overline{c}_i$ in the cell is then determined by the following relation

$$\overline{c}_i = (1 - \kappa)\, c_i^N + \kappa\, c_i^R \quad ; \quad \kappa \in [0,1] \qquad (4)$$

where *N* denotes the non-reactive and *R* the reactive part of the computational cell, respectively, and c_i is the molar concentration on a sub grid level. The question now is how to split the cell into these two parts and how large is the mass fraction of the mixture taking part in the combustion. A very detailed description can be found in [7]. The transformation process leads to the conclusion that the sub grid fraction is accounted through a filter κ_r, which is included in the calculation of the reaction rate formulation linearized in the reference species. The factor κ_r only depends on an integral mixing time τ_{mix} and the characteristic chemistry time τ^{r}_{chem} for reaction r and is specified as

$$\kappa_r = \frac{\tau^{r}_{chem}}{\tau^{r}_{chem} + \tau_{mix}} \qquad (5)$$

While τ^{r}_{chem} can be clearly defined for each reaction the calculation of the integral mixing time τ_{mix} varies and depends strongly on the turbulence model for the flow. The simplest form to calculate τ_{mix} using the Taylor scale can be written as follows

$$\tau_{mix} = C_{mix} \frac{k}{\varepsilon} \qquad (6)$$

in which C_{mix} is a constant that varies between 0.001 and 0.3 [7]; k is the turbulent kinetic energy and ε is the turbulent dissipation rate. Other formulations to calculate τ_{mix} can be found in literature [8, 9, 10] and are discussed in detail in [6]. Regarding Eq. 4 states that κ_r is limited between 0 and 1. If τ^{r}_{chem} is very large in comparison to the integral mixing time, κ_r tends to be unity and turbulent mixing does not influence the reaction rate. Reactants are already mixed and able to react. On the other hand, if τ^{r}_{chem} is small in comparison to the integral mixing time, κ_r tends to become zero and no reactions occur because reactants are not yet mixed completely. If τ^{r}_{chem} and τ_{mix} are of the same order of magnitude, kinetically controlled reactions are influenced by the mixing process, and interaction is described. Even though the combustion model is easy to implement, but it has to be adapted by the constant C_{mix}, due to the insufficient formulation of τ_{mix} as an integral value. Furthermore there is only one concentration in the cell - the mean concentration - which is the main drawback of all empirical closures for the chemical source term in RANS simulation. Information about the species and temperature distribution are needed to solve the fine scales on a computational grid.

6. COMPUTATIONAL SETUP

For the computation a 3-D mesh representing a 90 degree rotational sector of the burner (including the swirl body and the combustion chamber) was created, with very few cells to accelerate the computation at the beginning. With the first solution on a coarse level of about 16000 hexahedral cells, the refinement tools of the CFD solver allow an improved solution on a refined grid up to 60000 cells. For both setups the overall specific heat release is shown in Figure 3, which of course differs noticeably from 3a) to 3b).

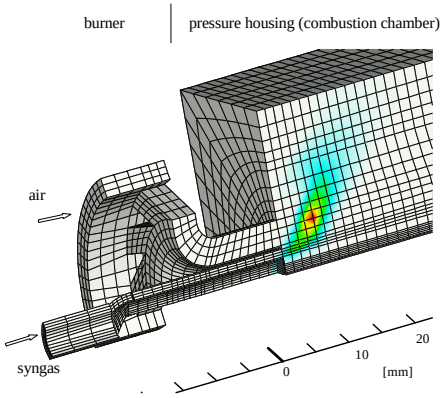

Figure 3a. Solution with a coarse grid

The adaptation of the grid is done dynamically after a number of user-defined time steps, whereas the amount of the reaction rate is used to determine regions for grid refinement or coarsening.

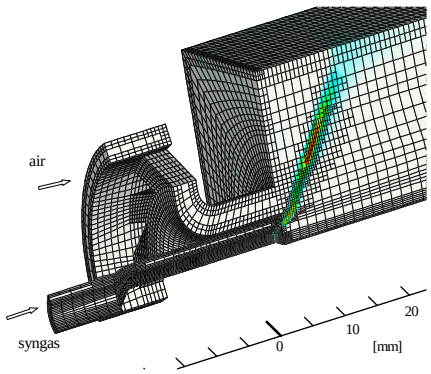

Figure 3b. Solution with after grid adaptation

Reduced Reaction Mechanism

For the numerical calculation two different mixtures (cf. Table 1) were used and compared with the experimental results. Within the project a reduced chemical mechanism (M-I) for a syngas mixture containing methane for defined operating conditions was developed [1, 3]. The mechanism consists of 19 species and 86 elementary reactions and can be applied to m7. The reaction path for methane combustion is not necessary for calculations using m6, because only carbon monoxide and hydrogen are in the fuel. Therefore, a second reaction mechanism (M-II) containing 11 species and 21 reactions is developed, which only can be applied to the pure syngas mixture. Both reduced mechanisms are based on the GRI3.0 methane combustion mechanism. More details about the reduction procedure can be found in [3]. Since M-I also describes path ways for carbon monoxide and hydrogen combustion, it should be applied to m6 as well. Thus, for a better comparison of the computational results it is recommended to use M-I for both mixtures.

7. RESULTS AND DISCUSSION

Flowfield

PIV (Particle Image Velocimetry) measurements of velocity fields were done for a burner load of 10kW/bar for both mixtures. In a longitudinal slice through the combustor, that splits the combustion chamber in the middle at z = 45 mm, measurements and computational results are compared. Axial and radial components of the velocity field are measured starting directly at burner exit up to x = 50 mm into the combustion chamber for the hot burning case. In Figure 4 a contour plot of the axial and radial velocities of the measurements and the numerical simulation for m6 is shown. At position y = 5 to 7 mm syngas enter the combustor, whereas between y = 8 to 15 mm air is injected.

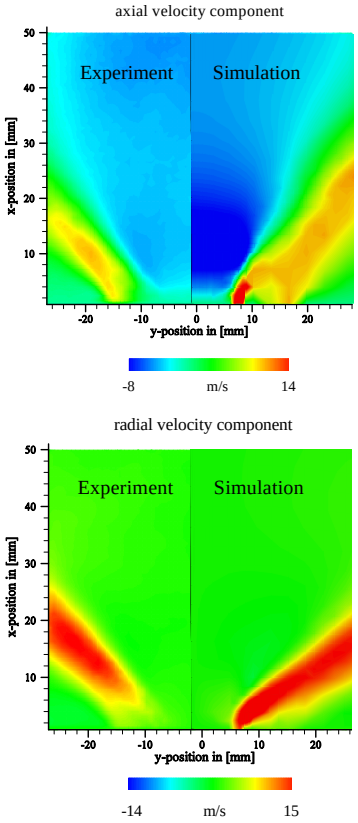

Figure 4. Axial and radial velocities components in a longitudinal slice through the combustion chamber for m6

Only weak velocities right at the burner exit can be seen for both air and syngas in the experiment. The recirculation zones - the mixing that occurs between inner recirculation zone, outer recirculation zone and syngas is strong. PIV measurements at the exit of a swirled burner are biased – the flow is 45 degrees out of plane. Thus, 0.7 of the velocity magnitude could only be measured. The flowfield is characterized by a flame cone that is directed outwards and a large inner recirculation zone is formed around the burner axis, due to the swirled inflow streams, which are responsible for stabilization and the shape of the burning flame. Further out the flow is accelerated due to heat release from combustion and axial velocities increase to up to 13 m/s. For the flames with a thermal load of 20 kW the velocities are expected to be as twice as high as in the 10 kW case. The axial and radial velocity profiles for m7 are shown in Figure 5. Both, the experimental result and the computational flowfield are given and are in good correlation, but the calculated recirculation speeds are overpredicted compared to the measurements. Comparison of m6 and m7 shows that the flow fields differ slightly, and one can conclude from the

velocity distribution, that the combustion behaviour for both mixtures is not equal because of their different inflow compositions. Velocities for m6 are higher compared with those from m7, where the maximum is about 10m/s. The latter uses less hydrogen, carbon monoxide and nitrogen, which reduces the total mass flow for the fuel. In contrast to the lower fuel mass flow in m7 due to methane, more air has to be injected to achieve the desired global air to fuel ratio.

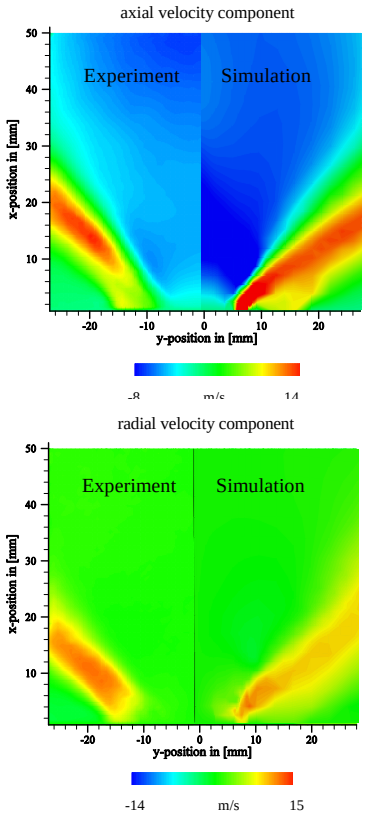

Figure 5. Axial and radial velocities components in a longitudinal slice through the combustion chamber for m7

Reaction Zone

Although the amount of chemical bounded energy in the fuel varies, the burner load is the same for both mixtures. Nevertheless, the reaction behaviour of m6 and m7 are interesting to investigate because of the two heating values caused by their different compositions. The higher heating values of m6 and m7 are 5.4 MJ/kg and 8.4 MJ/kg, respectively. The flame shape and reaction zone structure were identified using PLIF (Planar Laser Induced Fluorescence) measurements of OH concentrations as well as OH chemiluminescence [2] and are compared with the results from the computation. Using the reduced reaction mechanism (M-I) one can get information about species formation and consumption. A typical temperature distribution from the calculation of the generic syngas burner is shown in Figure 6a.

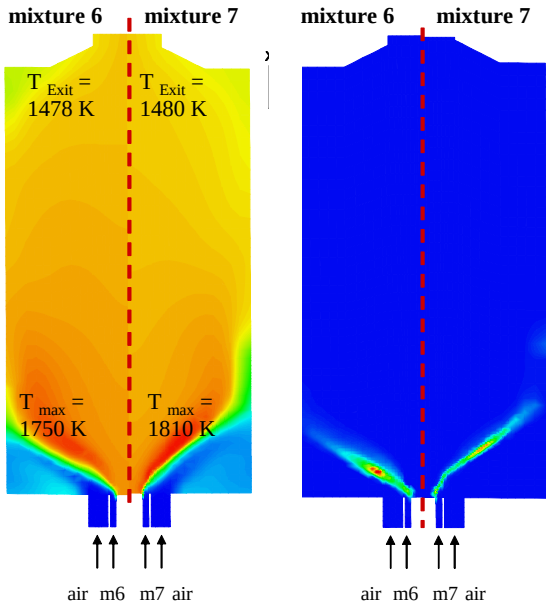

Figure 6a. Calculated temperature distribution (left) and corresponding specific heat release (right) for m6 and m7 at air inlet temperature of 293 K and a burner load of 10kW/bar

In all cases and for both mixtures the averaged temperatures at the combustor exit are almost near the adiabatic temperature for the global mixture (λ = 2), i.e., about 1478 K for m6 and 1480 K for m7 at air inlet temperatures of 293 K, whereas the maximum temperatures within the combustor vary. The walls of the combustion chamber are assumed to be adiabatic in all calculations. The maximum temperature of m6 is about 1750 K within the main reaction zone. Because of the separated inflow stream for air and syngas combustion is characterized by a diffusion flame where the reactants have to be mixed first before they start to react. Regions at nearly stoichiometric conditions exist depending on the mixing process, where a consequent refinement of the computational grid improves the solution. The maximum temperature for m7 is calculated with 1810 K which is slightly higher then for m6. However, a higher maximum temperature at m7 is always calculated for all other cases. The adiabatic flame temperature for m7 at stoichiometric conditions is about 2077 K but only 1991 K for m6. Thus, turbulence reduces maximum temperatures in the flame, which is predicted well with the used turbulence combustion model. The recirculation of the flow transports hot gases near the combustor axis and preheats the reactants. From the contour plot one can recognize that fuel and air do not react immediately when entering the combustor. The main reaction zone is located a few mm behind the nozzle. The specific heat release due to combustion for the same configuration is presented in Figure 6a as well. A more open flame cone for m6 can be observed in comparison to m7.

The pure syngas mixture seems to be more reactive then m7. Fast reactions of hydrogen decomposition take place first, while methane decomposition requires more time to split the molecular bonds. The measured data show that all flames burn with almost the same shape, they do not change significantly from each other, and burn very stably. Regarding images of OH chemiluminesence, the area of the reaction zone can be localized. It was found that preheating of the air temperature has no influence on the flame shape, whereas a change in the composition from m6 to m7 leads to a slight increase of the flame height [2]. The influence is quite small but can also be observed in the computational results, e.g., in Figure 6a. Furthermore, a significant change is seen in the measured data for the chemiluminescence intensity which is higher for m6. The maximum of the calculated specific heat release for m6 is about 1.352e+09 W/m^3, whereas it is calculated with 1.04e+09 W/m^3 for m7 and thus, confirms the measured results as well. The burner load affects also the reaction behavior. The reaction zone moves a little bit downstream when increasing burner load from 10 to 20 kW and its maximum temperature value is higher in the 10 kW case. A better mixing process of air, fuel and burnt gases in the 20 KW case seems to be the reason for the lower temperatures.

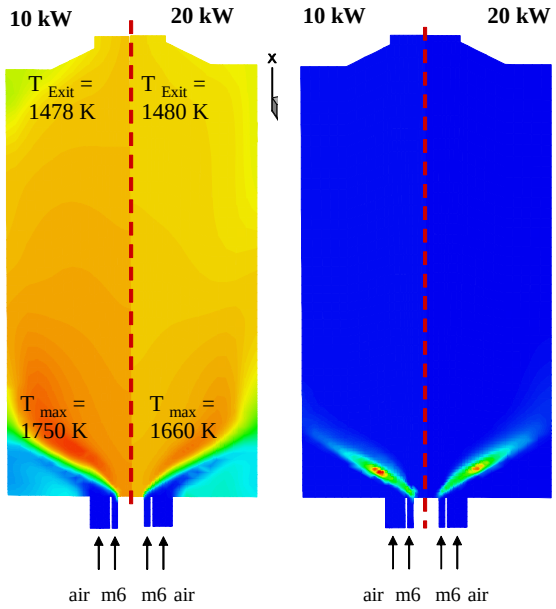

Figure 6b. Calculated temperature distribution (left) and corresponding specific heat release (right) for m6 at air inlet temperature of 293 K and a burner load of 10 kW/bar and 20 kW/bar

Temperature and specific heat release for m6 at different burner load is shown in Figure 6b. The maximum temperature of the 20 kW case decreases to 1660 K. Of course, air preheating leads to higher temperatures. In Table 2 the calculated maximum and combustor exit temperatures are summarized. Computational results for the preheating case and 10 kW are not calculated yet.

Table 2. Calculated maximum and mean exit temperatures for m6 and m7 at different operating conditions

	m 6	**m 7**	**m 6**	**m 7**
Load [kW]	10	10	20	20
T_{air}	293 K			
$T_{adiabatic,(\lambda=2)}$	1476	1478	1476	1478
$T_{calc,exit}$	1474	1476	1482	1478
$T_{adiabatic,(\lambda=1)}$	1991	2082	1991	2082
$T_{calc,max}$	1750	1810	1650	1715
T_{air}	423 K			
$T_{adiabatic,(\lambda=2)}$	1580	1582	1580	1582
$T_{calc,exit}$	1565	1583	1568	1576
$T_{adiabatic,(\lambda=1)}$	2077	2158	2077	2158
$T_{calc,max}$	-	-	1730	1827

The intensity of the OH concentrations of the PLIF measurements leads to the same conclusions that are made for OH chemiluminescence concerning air temperature, load and fuel composition. In Figure 7a and 7b the intensity of measured OH concentrations is given in comparison to the calculated OH concentrations. The values from the simulation are normalized between 0 and 1 to represent the values from the PLIF measurements. It is pointed out in [2], that the highest OH concentrations within a PLIF image probably stem from superequilibrium OH, i.e., “young” OH which had just been formed in a reaction zone. If comparing the results, a strong intensity on OH within the main reaction zone can be found, while there is no OH in the outer recirculation zone outside the flame.

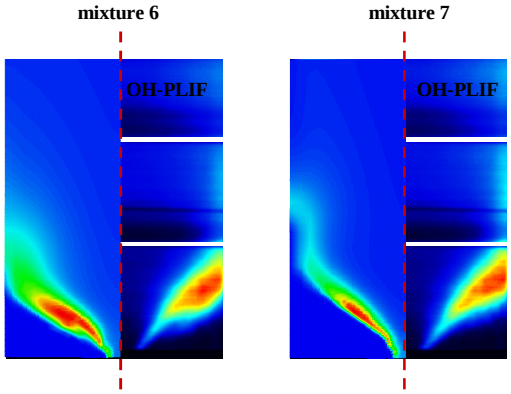

Figure 7a. Calculated normalized OH concentrations and measured OH intensity for m6 and m7 at air inlet temperature of 293K and burner load of 10 kW/bar

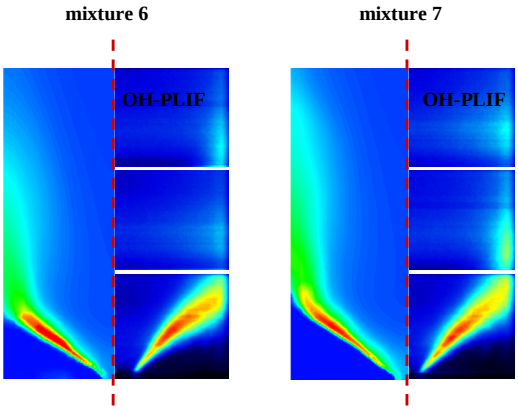

Figure 7b. Calculated normalized OH concentrations and measured OH intensity for m6 and m7 at air inlet temperature of 293K and burner load of 20 kW/bar

Before interpreting the results, a short remark to the colour map of the figures should be made. The black colour in the measured images indicates an intensity of almost zero, where in the calculation it is the blue colour. Nevertheless, OH concentrations can be found in the blue section as well, but they are too low to be illustrated. In the inner recirculation zone a little amount of OH can be seen both in the calculations and in the measurements, which is supposed to be the equilibrium composition. At the exit of the combustion chamber near-equilibrium concentrations are reached and are computed with 7.5e-07 kmole/m^3 for m6 at 10 kW and 293 K air temperature. OH concentrations from equilibrium calculations are always lower for m6 than for m7 and never exceed the maximum values that are calculated from equilibrium at stoichiometric conditions.

8. SUMMARY

A powerful and reliable external tool for the calculation of complex chemistry in combustion processes is coupled to the commercial flow solver FLUENT 6.2 and applied to a generic lab scale burner using two different syngas mixtures. The results are in good agreement with the measured OH-PLIF data and the same observations that are found in the experiments are made from the numerical simulation. Flame shapes do not vary significantly when burning two syngas mixtures using the same burner at different operating conditions. Nevertheless, a slightly higher flame can be observed for m6 and m7 both in experiments and in the simulation. To achieve a better performance the next step will be the parallelization of the combustion code which in principle is simple to manage because of the of the cell based code structure. The module itself is easy to handle and all input parameters are set by the user supporting a graphical user interface.

ACKNOWLEDGMENTS

The author wants to thank Mr. Michael Tsurikov for the excellent cooperation in the project and the detailed review of the manuscript. Furthermore he likes to thank Mrs. Marina Braun-Unkhoff, the person in charge for the project at the DLR for her assistance. The financial support of this work by the EU project HEGSA (NNE5-2001-0644) is gratefully acknowledged by the author.

REFERENCES

[1] FP5 Project NNE5-2001-00644: High Efficient Gas Turbine with Syngas Application (HEGSA), Progress Report, Period Jan-Dec 2004

[2] Tsurikov, M., Meier, W., Geigle, K.P. „Investigations of a Syngas-Fired Gas Turbine Model Combustor by Planar Laser Techniques", ASME Turbo Expo 2006, GT2006-90344, May 8-11, Barcelona, Spain

[3] Slavinskaya, N., Braun-Unkhoff, M., Frank, P. "Reduced Reaction Mechanism for Methane and Syngas Combustion in Gas Turbines, ASME Turbo Expo 2005, Paper Number GT2005-68287, June 6-9, 2005, Reno-Tahoe, Nevada, USA

[4] Fluent, 6.2.16, Documentation: User Guide: 2005-01-04, 2005

[5] Amsden, A.A., O'Rourke, P.J. and Butler, T.D. KIVA-II: A Computer Program for Chemically Reactive Flows with Sprays. LA-11560-MS, May, 1989

[6] Schütz, H., Lückerath, R., Kretschmer T., Noll, B., Aigner, M. "Analysis of Pollutant Formation in the FLOX® Combustion", ASME Turbo Expo 2006, GT2006-91041, May 8-11, Barcelona, Spain

[7] Nordin, P.A.N. "Complex Chemistry Modelling of Diesel Sprays". PhD Thesis, Chalmers University of Technology, Göteborg, 1995

[8] Kjaldman, L., Brink, A., Hupa, M. "Micro Mixing Time in the Eddy Dissipation Concept", Combustion Science and Technology, Vol. 154, pp.207-227, 2000

[9] Byggestøyl, S., Magnusson, B.F. "A Model for Flame Extinction in Turbulent Flow", 4th Symposium on Turbulent Shear Flows, pp. 381-395, 1985.

[10] Karlsson, J.A.J., Chomiak, J. "Physical and Chemical Effects in Diesel Spray Ignition" 21st Congress of CIMAC, Interlaken Switzerland, May 15-18, 1995

Conference on Modelling Fluid Flow (CMFF'06)
The 13th International Conference on Fluid Flow Technologies
Budapest, Hungary, September 6-9, 2006

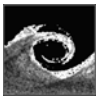

INVESTIGATION OF THE RENEWABLE GASES

Bence SOMOGYI[4], Balázs PETRÓ[3], Ákos BERECZKY[1], Gyula GRÓF[2],

[1] Corresponding Author. Department of Energy Engineering, Budapest University of Technology and Economics, Műegyetem rkp. 3., H-1111 Budapest, Hungary. Tel.: +36 1 463 2464, Fax: +36 1 463 3464, E-mail: bereczky@energia.bme.hu
[2] Department of Energy Engineering, Budapest University of Technology and Economics. E-mail: grof@ energia.bme.hu
[3] Department of Energy Engineering, Budapest University of Technology and Economics. E-mail: petro@ energia.bme.hu
[4] Department of Energy Engineering, Budapest University of Technology and Economics. E-mail: somogyi.bence@freemail.hu

ABSTRACT

The investigateon of the renewable gases, like biogas, wood gas, pyrolysis gas (etc) have great importance in the sustainable development. The development of the validation methods and systems is fundamental in the CFD modelling of combustion such types of gases. In this article we introduce our system and technique used for qualitative validation and investigation of the combustion processes. The system based on the evaluation of the optical non-homogeneities caused by the temperature, by the pressure and/or by the concentration distributions. Later the used system, the picture post processing method and some results are presented. The results are compared with a reference temperature measurement made by micro size thermocouples. The paper gives a review of the errors and the possible causes. After the part dealing with "schlieren" the CFD simulations results are presented. Three models were built with different detailed reaction mechanisms. The results are compared with the same reference measurement already mentioned.

Finally the paper gives a summary of the possible usage of "schlieren" in CFD validation.

Keywords: Schlieren, flame, CFD

NOMENCLATURE

ε	[-]	deviation angle
n	[-]	refraction index
φ	[-]	angle between the grad(n) vector and the curved light ray
R	[m]	radius of the curved light ray
r	[m]	coordinate
T	[K]	temperature
p	[Pa]	pressure
δ	[-]	n-1
ρ	[kg/m^3]	density
ν	[1/m]	refraction gradient *y* component
μ	[1/m]	refraction gradient *r* component

Subscripts and Superscripts

0	undisturbed case
x,y	directions in the Cartesian coordinate system
y,r	directions in the cylindrical coordinate system
λ,*I*	indexes in summation

1. INTRODUCTION

Generally the literature refers to „schlieren" as a kind of optical non-homogeneity. Optical non-homogeneity means those places of the given medium that cause deviation of the light transmitted through on. This change of direction of the light beam can be made visible by the proper optical device. If a transparent object containing „schlieren" is illuminated by the parallel light beam, the light beam deviate at the place of „schlieren". Placing a screen in the path of beams that transmitted through the examined area, the image of the area containing „schlieren" will be displayed with darker shade on the screen, and the value of deviation will be proportional to the intensity displayed on the image.

2. PROCESSING OF CYLINDRICAL SCHLIEREN IMAGES

The „schlieren" photographs typically present qualitative information about the phenomena that cause the change of refraction index inside the object. During the data processing, the deviation angle ε must be determined from the blackening. The variation of the refraction index namely the gradient of the refraction index might be determined from the deviation angle. The following equation can be written for the deviation and the variation of the refraction index $\frac{1}{R} = \frac{gradn}{n}\sin\varphi$. We have been typically analyzing the images of cylindrical

symmetric objects during our measurements. Ignoring the deductions found in bibliography, in this case we can declare that the number of the independent variables decreases to two. [1,4]

In cylindrical symmetric analysis we start from the assumption that the given object, as a concentric medium, is composed of circles with constant refraction indexes.

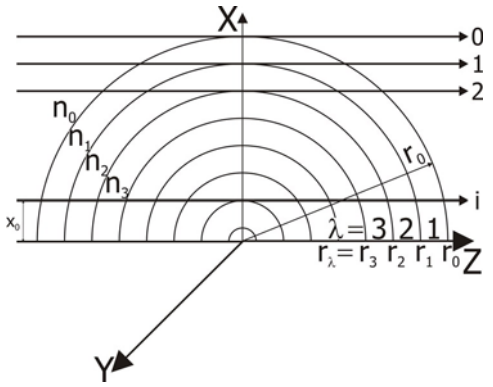

Figure 1. Assumed cylindrical zones with constant refraction index

The concentric circles can be placed in the *x-z* plane and light diffraction can appear only in planes normal to *x* and *y* if the path of light ray is parallel with the *z*-axis. The use of the cylindrical coordinate system is appropriate, as we can see on the "Figure 1". So, the two independent variables are *y* and *r*. Ignoring the deduction again, the equation system written for the deviation angles takes the following form:

$$\left(\varepsilon_x\right)_{x,y_k} = 2\frac{x_i}{n_0}\sum_{\lambda=1}^{\lambda=i}\mu\left(arch\frac{r_\lambda - 1}{x_i} - arch\frac{r\lambda}{x_i}\right) \qquad (1)$$

$$\left(\varepsilon_y\right)_{x,y_k} = 2\frac{x_i}{n_0}\sum_{\lambda=1}^{\lambda=i}\nu_\lambda\left(\sqrt{\frac{r_{\lambda-1}{}^2 - x_i{}^2}{x_i{}^2}} - \sqrt{\frac{r_\lambda{}^2 - x_i{}^2}{x_i{}^2}}\right) \qquad (2)$$

$\mu_\lambda = \frac{\partial n}{\partial r}$ and $\nu_\lambda = \frac{\partial n}{\partial y}$ are constants referring to one zone. [4]

The equations are expressed for the deviation. In reality just the deviation is available, and from this the gradient of the refraction index can be calculated as a function of *r* and *y*. The evaluation might be made advancing inwards starting at radius r_0, and step by step from one radius to the other calculating the refraction indexes.

2.1. Physical variables influencing the refraction index

In order to analyze the images, it is important to know the phenomena that cause the deviation. Generally, the refraction index depends on wavelength, temperature, pressure, material quality and concentration of components in case of mixtures. For given material quality, the refraction index depends exclusively on density ρ. In our flame experiments the mediums are always gaseous. The pressure and temperature of gases determines the density according to the ideal gas equation: $\frac{p}{\rho} = \frac{R}{M}T$. If we apply this equation for a known state on one hand and the unknown state on the other hand, the result will be as follows: $\frac{\rho}{\rho_0} = \frac{p}{p_0}\frac{T}{T_0}$. According to the Gladston-Dale formula, the right side of the equation is also equal to the $\frac{\delta}{\delta_0}$ ratio, and magnitude of δ is 10^{-3}. Since for gases the change of refraction index depends exclusively on change of density, the following differential equation can be formed:

$$d\delta = \frac{\partial\delta}{\partial P}dP + \frac{\partial\delta}{\partial T}dT \qquad (3)$$

In case of free jet flames the pressure might be considered almost equal to the ambient pressure. Since the variation of the pressure can be neglected comparing to the variation of temperature we consider dP=0, therefore the first term disappears from equation "Eq (3)". Since $p=p_0$ and $\delta=n-1$, from the equation $\delta = \delta_0\frac{T}{T_0}$ the following relation can be derived:

$$n_t = 1 + (n_0 - 1)\frac{T}{T_0} \qquad (4)$$

Finally, the change of the refraction index might be expressed as follows

$$\frac{d\delta}{dT} = -\delta_0\frac{T_0}{T^2} \qquad (5)$$

The relation presents the variation of the refraction index as function of the temperature, in other words it shows also the change of sensitivity as a function of the temperature. Increase of temperature means decreasing of the sensitivity.

The refraction index of a mixture containing a certain amount of components can be calculated from the refraction indexes of the individual compound elements, including the molar quantities of the compound elements. The refraction index of a stochiometric mixture of methane-air is n=1.000295 at the ambient temperature and the refraction index of the combustion product is n=1.00029. The deviations of refraction indexes are less than 2%. The values of the refraction indexes in the whole temperature region produced during the combustion are shown on "Figure 2". [2]

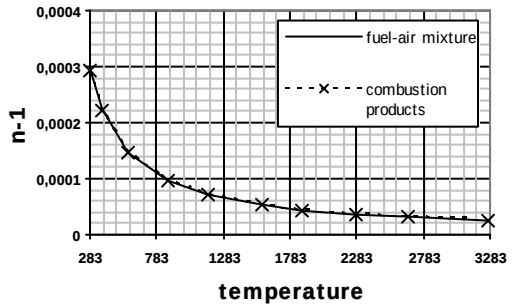

Figure 2. Refraction index as the function of the temperature using CH4 as a fuel

As one can see on the diagram, the change of refraction index is less and less by increasing the temperature. The first derivative of the refraction index with respect to temperature gives the slope of the curve and the gradient of the variation at the same time. The diagram on "Figure 3" represents the gradient of the refraction index as a function of temperature. As one can see on "Fig. 2", during the combustion of methane, the difference between the refraction index of the air-fuel mixture and the refraction index of the combustion products is not significant therefore the gradients can be considered identical and represented with a common curve.

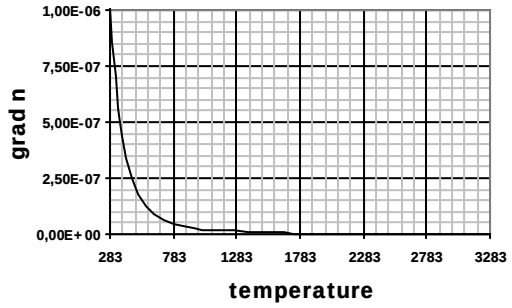

Figure 3. The gradient as a function of the temperature

One can follow on the diagram of "Fig. 3" that the gradient of the refraction index decreases as the temperature increases. The gradient of the refraction index becomes visible on the „schlieren" image. In respect of the flame analysis this means that the curve flattens out exactly inside of this interval (800-2500K), where the combustion takes place. [3]

2.2. Evaluation of Schlieren pictures

In order to make „Schlieren" pictures appropriate for further evaluation, pre-processing and filtering have to be done. We manage the pictures as matrices. Converting the pictures to greyscale one can reduce the number of necessary matrices into one. One element of this matrix related to the picture represents the intensity of one pixel. In the course of pre-processing we need a picture of the empty examining field as a reference. To clean all pictures we make a conversion matrix. This matrix contains the difference between each element and the largest element of the reference. With the summarization of the reference matrix and the conversion matrix we get a smooth vision field. First we clean all the pictures with this matrix summarization method. In order to get a clean result we used a remote controlled camera so that we could avoid the shifting of the edges. If the shifting of edges can't be avoided the usage of some feature detector method is necessary. The random errors still remained in the pictures were filtered with Gaussian smoothing.

In the further processing from the intensity change according to the smooth surroundings we compute the light beams deflection angle. Knowing the deflection angle distribution the refraction coefficient, the density, and the temperature distribution might be determined.

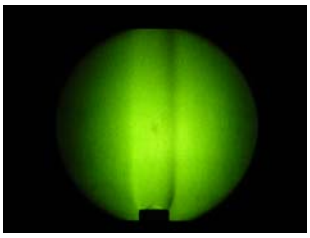

Figure 4a. Original picture

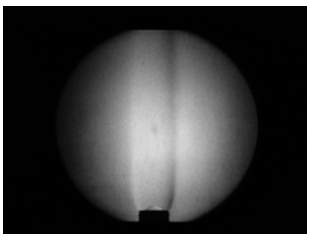

Figure 4b. Original black and white picture

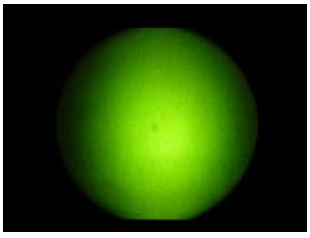

Figure 5. Original reference

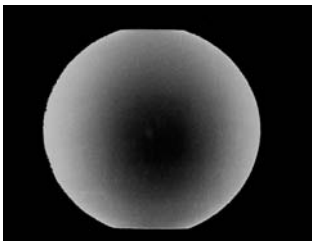

Figure 6. Picture of reference matrix

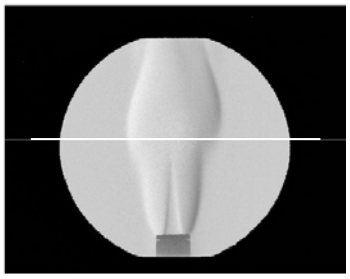

Figure 7a. Cleaned picture

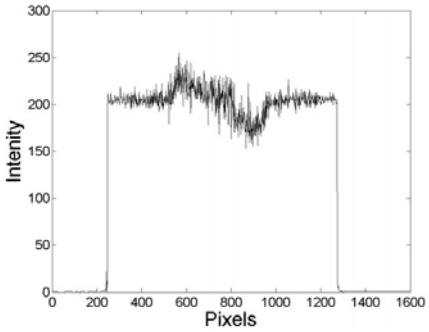

Figure 7b. Intensity distribution along the line specified on "Figure 7a"

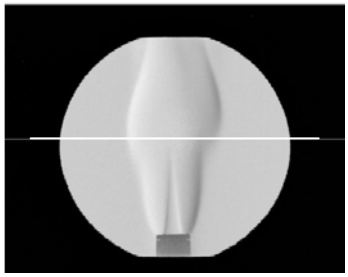

Figure 8a. Gauss filtered picture

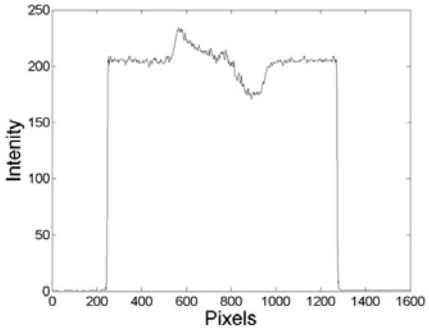

Figure 8b. Intensity distribution along the line specified on "Figure 8a"

3. INVESTIGATION OF DIFFERENT LAMINAR PRE-MIXED FLAMES

To test the „schlieren" system three different fuel gases were investigated. First gas was normal natural gas (CH_4>92%) as a reference, second gas was a typical biogas (CH_4 = 60%, CO_2 = 40%), the third one was a typical producer gas (CH_4 =5%, CO_2 = 5%, CO =20%, H_2 = 20%, N_2 = 50%).

Table 1. Main parameters of investigated gases (* stochiometric conditions)

	Natural gas	Biogas	Producer gas
Heating value [MJ/m^3]	33,435	20,086	6,032
Theoretical air demand,[-]	9,52	5,71	1,43
Laminar* flame velocity, [m/s]	0,3991	0,2561	0,4044
Adiabatic* flame temperature, [K]	2224	2096	1973

The deviation angles of the three different gases are presented on "Figure 9". The volumetric flows of the three flames are equal, and the excess air ratios are stochiometric. The artificial colouration is (colours mean different deviation angles) useful only for comparison of the flames, because the flames are cylindrical symmetric, therefore the relationship of the deviation angle and the refractive index are non obvious.

Comparing the pictures some important statements might be done. The most important differences are in the shape of the outer paths and in the contour of the inner flame cone. The cone angle of the biogas – the highest flame cone – is the narrowest and the cone angle of the producer gas is the widest, inasmuch as the flame velocity is the highest here.

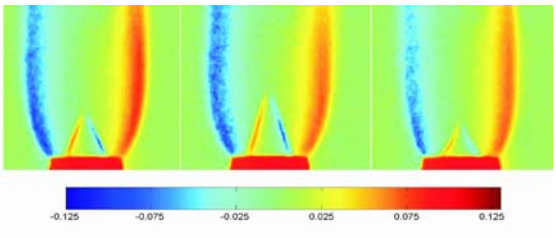

Figure 9. Deflection angle distributions: 1 natural gas; 2 biogas; 3 producer gas

The contour of inner flame cone has the same thickness both in the biogas and natural gas flame, unlike in the producer gas, where the combustion of H_2 and CO is the most representative. The shapes of the flue gas streams are similar in the case of biogas and natural gas, whilst the geometry of the inner flame cones is different. Combusting the biogas the shape of the flue gas stream is determined by the geometry of the inner flame cone (perpendicular outflow), in the case of natural gas the geometry of the stream is determined by the shape of the inner flame cone and the more intensive heat liberation.

3.1 Flame temperature distribution

The temperature distribution holds valuable information for different phenomenon and it has great importance in the combustion research also.

As it was treated in the previous sections, the „schlieren" technique has potentials in determination of the temperature field but one should compromise with the performance as the temperature increases and reaches the most interesting region connected to the combustion. In order to taking into account this unbeneficial character of the method the direct temperature measurement was done by the help of the micro thermocouples. The flame that was investigated by the „schlieren" technique, in parallel, the flame cross sections were scanned by the help of the micro meter spindle in different height. For example the "Figure 10" shows the temperature profile that were measured and determined by the „schlieren" technique at different height in a natural gas flame. Independently of the obvious errors it might be seen as the method performance and applicability becomes more non acceptable as the temperature increases.

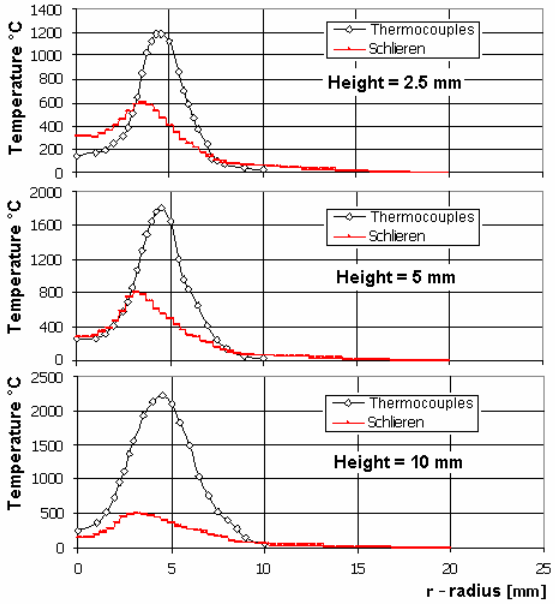

Figure 10. Temperature profiles in different height

It is more than obvious that the temperature profiles provided by „schlieren" method are far away from those that one might accepted. It should be mentioned here that the result temperature profiles provided by the thermocouples were corrected by taking into account the radiation heat losses as well. The corrected profiles are shown in "Figure 10".

4. CFD SIMULATION

Besides applying of the „schlieren" method the CFD simulation was performed, but still only for the natural gas type flames. Different combustion mechanisms were tested for flame calculation:

- Methane – Air 1 step
- Methane – Air 2 step
- DRM-19 Model

The physical data of the modelled burner is shown in "Figure 11" together with the modelled zone with its boundary conditions. It was assumed that the phenomenon is cylindrical.

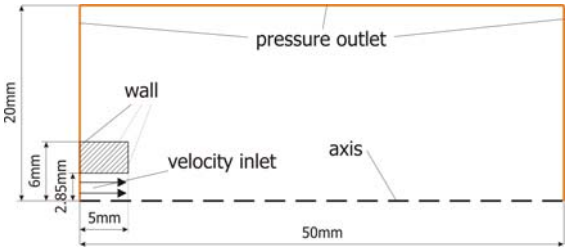

Figure 11. Physical dimension and boundary condition of the modelled zone

The heat transfer interactions between of the burner spout – air methane mixture, burner spout – air flow and burner spout – flame were neglected as well itself the burner spout was skipped. These assumptions mean that we neglect the flame cooling as well the fuel mixture preheating caused by the burner spout. Uniform speed distribution was declared in the burner spout since a ferrule is installed here to uniform the air – methane mixture flow. The homogenisation of the air – methane mixture was performed by the chamber, filled with steel biscuit.

Table 2. Velocity inlet data

Inlet speed	1.25	m/s
Inlet temperature	300	K
O_2 mass percent (23.3 m/m %)	0.2048	kg/kg
N_2 mass percent (76.7 m/m %)	0.6740	kg/kg
CH_4 mass percent	0.1212	kg/kg

Table 3. Pressure outlet data

Pressure (gauge)	0	Pa
Outlet temperature	300	K
O_2 mass percent (23.3 m/m %)	0.2048	kg/kg
N_2 mass percent (76.7 m/m %)	0.6740	kg/kg

As it is clear from the "Table 1" it was assumed that the fuel is 100% CH_4.

In the CFD simulation a structured mesh was applied, based on the "Schlieren" visualization, at the location of the reaction zone the mesh was settled fined. The mesh contains 15690 cells as it is shown on "Figure 12".

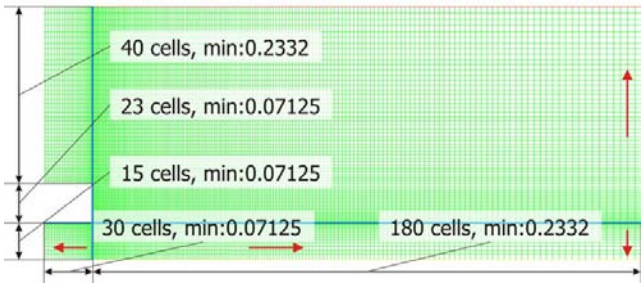

Figure 12. Applied structured mesh

4.1 Modeling of the combustion

Since complex combustion mechanism is not available in the database provided by the FLUENT, a freely downloaded database was applied. This DRM-19 mechanism is the reduced version of the GRI-Mech. 1.2.[//diesel.me.berkeley.edu/~gri_mech/new21]

In the case of the applied excess air-fuel ratio the mechanism results great error, but comparing with the built in 1 step and 2 step model the provided accuracy is the best. The major part of the error might be due to that the GRI Mech 1.2 is optimized for different component ratio that we had. The initial flow field was defined equal with the previously calculated flow field without combustion and in a small zone the high temperature is prescribed as the starting point of the reactions.

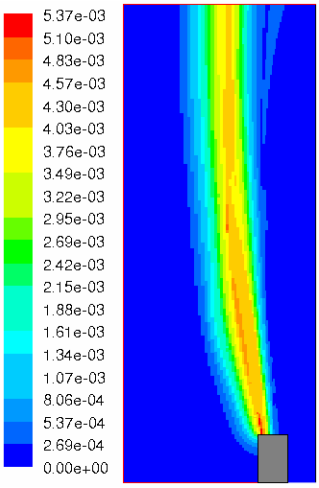

Figure 13. OH distribution by DRM-19 model

Only the multi stage reaction mechanism offers modeling the inter combustion products, like OH ions, (chemical entities). The OH ions concentration has special importance in predicting the outer flame cone shape (See "Figure 13"), as well as the temperature and the inner flame cone shape predicting. Comparing the OH ion concentration and the temperature field with common and "Schlieren" pictures one can see that the computed flame is larger.

However the results calculated with the multi stage reaction mechanism shows a flame larger in height and diameter than the original, the shape of temperature profiles are close to the ones measured with thermocouples. With the axial profiles the difference is in the rate of rising of temperature. The calculated axial profile rises at higher axial positions and at the peak achieves lower temperature.

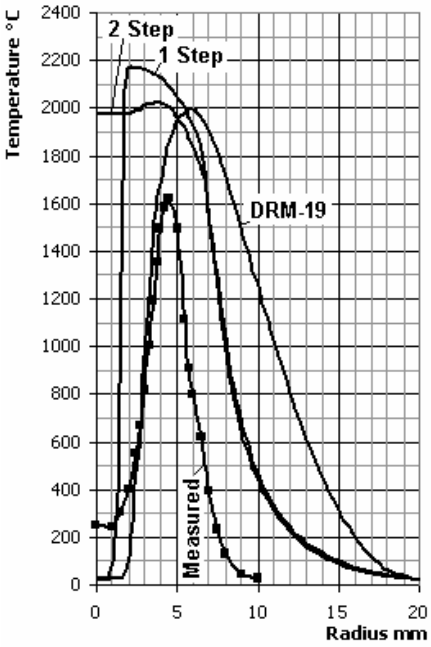

Figure 14. Temperature profile at 5 mm height

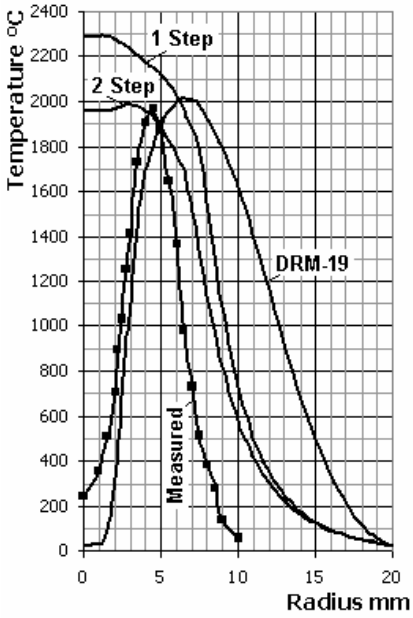

Figure 15. Temperature profile at 10 mm height

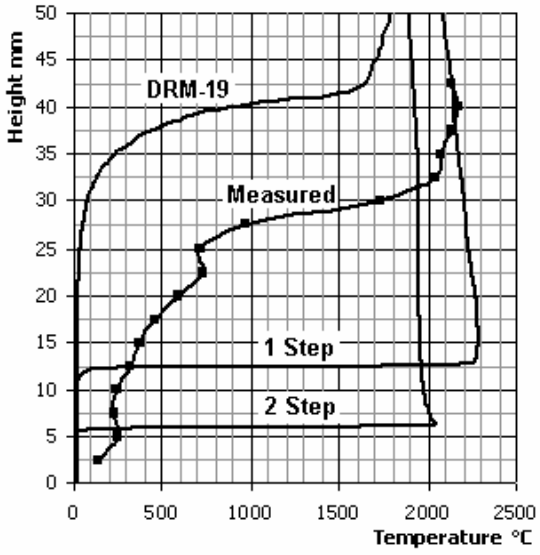

Figure 16. Temperature profiles in height

4.2 Result rating

It is more than obvious from the results that either the "Sclieren" method either the CFD modeling results are greatly different from the measured values. There are some possible causes among the others connected to the image capture, image processing and in the evaluation also. The direct image capture helps prevent the mottled glass caused random failures that difficult taking into account. During the evaluation only the temperature dependence of the refraction index was considered. The effects of different inter combustion products on the refraction index change together with the pressure might be comparable to the temperature in case of high temperature values since here the temperature dependence of the refraction index is weak. The self illumination of the flame also disturbs the intensity distribution.

The simulation of the combustion process, even in the case of simple flames that were investigated, needs sophisticated reaction mechanism. Using the simple methods the results might be far away from the acceptable ones. However the temperature profiles from the "Schlieren" pictures also are disadvantageous, the applicability in the observation of the flame structure (i.e. inner and outer cone) is valuable.

5. SUMMARY

The "Schlieren" method raises many problems. The tight relation between the sensitivity and the detection range could cause loss of information in case of processing the images. The method affords quantitative results also but the real strength of the method manifests in the qualitative analysis. This feature is advantageous in visualizing those effects in different phenomena which are invisible.

Beyond the simple visualization the "Schlieren" method might be applied as a validation tool in different CFD simulation. The process might be twofold. One hand the direct compare of the calculated flow field, temperature distribution, concentration distribution etc. with the visualized phenomenon. The other hand an artificial "Schlieren" picture might be constructed summarizing different effects on the refraction index and comparing this artificial image to the real one. This technique is mentioned in the literature and the authors efforts are going on in applying this way of the "Schlieren" method.

ACKNOWLEDGEMENTS

This research supported by OTKA (Hungarian Scientific Research Fund Programs) project T 046860 entitled "Investigation of Combustion Properties of Biogases" and partly by project D 048678 entitled „Investigation of Combustion Properties of Renewable Energy Sources"

REFERENCES

[1] H. Scahrdin, 1934, "Das toeplersche Schlierenverfahren", VDI Forschunsheft,

[2] R.W. Ladenburg, 1955, "Physical Measurements in Gas Diynamics and Combastion", London

[3] Németh A.-Szalay O.., 1962, "A résoptikai módszer és alkalmazása az égési kutatásban.", Máfki, 258, Veszprém,

[4] F.J. Weinberg, 1963, "Optics of flames", Butterworths,

Conference on Modelling Fluid Flow (CMFF'06)
The 13th International Conference on Fluid Flow Technologies
Budapest, Hungary, September 6-9, 2006

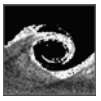

NUMERICAL SIMULATION AND ANALYSIS OF THE DECELERATED SWIRLING FLOWS IN HYDRAULIC TURBINES

Romeo SUSAN-RESIGA[1], Sebastian MUNTEAN[2], Sandor BERNAD[3], Ioan ANTON[4]

[1] Corresponding Author. Department of Hydraulic Machinery, "Politehnica" University of Timisoara. Bd. Mihai Viteazu, No.1, RO-300222, Timisoara, Romania, Tel: +40-256-403692, Fax: +40-256-403700, E-mail: resiga@mh.mec.upt.ro
[2] Hydrodynamics and Cavitation Laboratory, Romanian Academy – Timisoara Branch E-mail: seby@acad-tim.tm.edu.ro
[3] Hydrodynamics and Cavitation Laboratory, Romanian Academy – Timisoara Branch E-mail: sbernad@mh.mec.upt.ro
[4] Department of Hydraulic Machinery, "Politehnica" University of Timisoara. E-mail: anton@acad-tim.tm.edu.ro

ABSTRACT

The paper presents an investigation into swirling flow models relevant to decelerated swirling flows in hydraulic turbines. Only incompressible axi-symmetric flow models are considered. First, we review the inviscid swirling flow models, from Euler equations to the Long-Squire equation. For the second one we present our finite element solver, and we discuss its limitations. Second, we recall the turbulent flow models suitable for non-homogeneous swirling flows.

Two numerical examples are presented. The first one deals with an inviscid decelerated swirling flow that develops a central stagnation zone. The solution is obtained here with an unsteady Euler solver. The second one corresponds to the actual turbulent swirling flow downstream a Francis turbine runner. Experimental data are used to impose inlet conditions, and numerical results are compared with data in a downstream survey section. It is shown that the turbulent flow model captures the vortex breakdown, but in this case the quasi-stagnant region is closed, in contrast with the inviscid case.

Keywords: decelerated axisymmetric swirling flows, Francis turbine draft tube flow, vortex breakdown, turbulence modelling in swirling flows.

NOMENCLATURE

x, r, θ	cylindrical system of coordinates
$V_x, V_r, V_\theta \left[m/s\right]$	axial, radial and circumferential (swirl) velocity components
$V_m \equiv \sqrt{V_x^2 + V_r^2}$	meridional velocity magnitude
$V \equiv \sqrt{V_m^2 + V_\theta^2}$	velocity magnitude
$C \equiv rV_\theta$	swirl function
$p\left[Pa\right]$	static pressure
$\rho\left[kg/m^3\right]$	density
$p_{\text{tot}}\left[Pa\right] \equiv p + \rho V^2/2$	total pressure
$H \equiv p_{\text{tot}}/\rho$	total head
ψ	Stokes streamfunction
χ	circumferential vortex density
$\mu\left[Pa \cdot s\right]$	dynamic viscosity
$k\left[m^2/s^2\right]$	turbulent kinetic energy
$\varepsilon\left[m^2/s^3\right]$	turbulent dissipation rate
$L_\varepsilon\left[m\right]$	turbulence length scale
$c_{\text{PR}}\left[-\right]$	pressure recovery coefficient

1. INTRODUCTION

Swirling flows and their various technical applications benefit from a large body of literature dealing with both the desired result of design or unavoidable, possibly unforeseen side effects [1]. In this paper we will focus on decelerated swirling flows encountered in hydraulic turbines draft tube cone. The draft tube of a hydraulic turbine is the machine component where the flow exiting the runner is decelerated, thereby converting the excess of kinetic energy into static pressure. In the case of machine rehabilitation mostly the runner is modified, leading to a new swirling flow structure at the draft tube inlet. The practical importance of predicting the complex flow downstream the turbine runner motivated the FLINDT research project [2] on Flow Investigation in Draft Tubes. The extensive experimental data base built as a result of this project has been complemented with numerical analyses and numerical simulations [3,4]

aimed at elucidating various aspects of the complex hydrodynamics of the draft tube flows. This paper continues these efforts by investigating axi-symmetric swirling flow models that can be reliably used for turbomachinery analysis, design and hydrodynamic optimization.

In Section 2 we review the mathematical and numerical models for incompressible axi-symmetric swirling flows. Both inviscid and viscous flow models are discussed, and used in subsequent sections of the paper. An inviscid decelerated swirling flow example is presented in Section 3, with the emphasis on the stagnation region developed as an instance of the vortex breakdown. Section 4 presents numerical investigations of the turbulent swirling flow in a Francis turbine draft tube cone. The problem setup, as well as the turbulence model parameters, are discussed and the numerical results are carefully validated with experimental data from the FLINDT project. The main conclusions of the paper are summarized in Section 5.

2. SWIRLING FLOW MODELLING

Although swirling flows are usually associated with axial symmetric geometries, the flow itself may or may not retain the axi-symmetric character. The well-known helical vortex (or vortex rope in hydraulic engineering terminology) is an example when 3D effects are developing from an upstream flow with axial symmetry. However, in this paper we focus only on axi-symmetric flow models, since valuable results can be obtained in many cases with a reduced computational effort. Since our main focus is the turbomachinery hydrodynamics, we will examine only incompressible flows. The mathematical models and some of the associated numerical algorithms are briefly reviewed in this section for both inviscid and viscous flows.

2.1. Inviscid Flows

The equations governing the inviscid, incompressible, axisymmetric flow are the Euler equations written in cylindrical coordinates:

$$\frac{\partial V_x}{\partial x}+\frac{\partial V_r}{\partial r}+\frac{V_r}{r}=0 \tag{1}$$

$$\frac{\partial V_x}{\partial t}+V_x\frac{\partial V_x}{\partial x}+V_r\frac{\partial V_x}{\partial r}=-\frac{1}{\rho}\frac{\partial p}{\partial x} \tag{2a}$$

$$\frac{\partial V_r}{\partial t}+V_x\frac{\partial V_r}{\partial x}+V_r\frac{\partial V_r}{\partial r}-\frac{V_\theta^2}{r}=-\frac{1}{\rho}\frac{\partial p}{\partial r} \tag{2b}$$

$$\frac{\partial V_\theta}{\partial t}+V_x\frac{\partial V_\theta}{\partial x}+V_r\frac{\partial V_\theta}{\partial r}+\frac{V_rV_\theta}{r}=0 \tag{2c}$$

From the radial momentum equation (1c) one may derive a radial equilibrium outflow condition,

$$\frac{\partial p}{\partial r}=\frac{\rho V_\theta^2}{r}, \tag{3}$$

to be used whenever the flow has a significant swirl component at the exit and the streamlines are aligned with the symmetry axis (i.e. vanishing V_r). The continuity equation (1a) can be automatically satisfied by introducing the Stokes streamfunction

$$\left(V_x,V_r\right)=\frac{1}{r}\left(\frac{\partial\psi}{\partial r},-\frac{\partial\psi}{\partial x}\right). \tag{4}$$

Following Szeri and Holmes [5] it is convenient to introduce the swirl function $C\equiv rV_\theta$ and the circumferential vortex density $\chi\equiv\omega_\theta/r$,

$$\begin{aligned}\chi&\equiv\frac{1}{r}\left(\frac{\partial V_r}{\partial z}-\frac{\partial V_z}{\partial r}\right)\\&=-\frac{1}{r^2}\left(\frac{\partial^2\psi}{\partial x^2}+\frac{\partial^2\psi}{\partial r^2}-\frac{1}{r}\frac{\partial\psi}{\partial r}\right)\equiv\mathcal{L}\psi\end{aligned}. \tag{5}$$

The Euler equations (2) can be expressed now as evolution equations for C and χ,

$$\frac{\partial C}{\partial t}+\{\psi,C\}=0,\ \frac{\partial\chi}{\partial t}+\{\psi,\chi\}=\frac{1}{4y^2}\frac{\partial\left(C^2\right)}{\partial x} \tag{6}$$

where $\{f,g\}=\left(\partial f/\partial y\right)\left(\partial g/\partial x\right)-\left(\partial f/\partial x\right)\left(\partial g/\partial y\right)$ is the Poisson bracket or Jacobian, and $y=r^2/2$ is the transformed radial coordinate. The elliptic Eq. (5) and the two evolution Eqs. (6) are a generalization of the 2D plane vorticity-streamfunction formulation for incompressible Euler equations.

While the elliptic operator $\mathcal{L}$ can be optimally discretized with classical continuous finite elements, the convection operators in the left-hand side of Eqs. (6) require special techniques within the finite element framework in order to insure stability. Probably the best approach is to use a combination of continuous and discontinuous Galerkin finite elements, as developed by Liu and Shu [6]. One key feature of this approach is that for the continuous finite element approximation of Eq. (5) the normal velocity component on the element edges is continuous across elements. As a result, there is a natural matching beween the continuous and discontinuous finite element spaces, allowing the correct upwinding gluing in the discontinuous Galerkin framework for Eqs. (6).

If the flow is considered steady, Eqs. (6) reduce to a single non-linear equation,

$$\mathcal{L}\psi=\frac{1}{4y}\frac{\mathrm{d}\left[C^2(\psi)\right]}{\mathrm{d}\psi}-\frac{\mathrm{d}H(\psi)}{\mathrm{d}\psi}, \tag{7}$$

where the total head and the swirl function are constant on a streamtube, i.e. depend only on ψ. This celebrated equation is known in literature as the Long-Squire or Bragg-Hawthorne equation, although Goldshtik and Hussain [7] noted that, in fact, Eq. (7) was derived much earlier by Meissel (in 1873). It was Benjamin [8] who introduced the equivalent variational formulation for boundary value problems corresponding to Eq. (7), where the solution ψ minimizes the functional

$$\mathsf{F}(\psi)=\int_0^L\int_0^{y_w(x)}\left[\begin{array}{l}\dfrac{1}{2}\left(\dfrac{\partial\psi}{\partial y}\right)^2+\dfrac{1}{4y}\left(\dfrac{\partial\psi}{\partial x}\right)^2\\ -\dfrac{C^2(\psi)}{4y}+H(\psi)\end{array}\right]\mathrm{d}y\,\mathrm{d}x. \qquad (8)$$

The functional (8) does not include any boundary integrals since usually homogeneous Neumann conditions are assumed at outlet, while on inlet, axis and wall Dirichlet conditions are prescribed.

The natural choice for solving the boundary value problem in variational formulation is the finite element method. The finite element algorithm we have developed for steady axisymmetric incompressible swirling flows is briefly summarized below. The first step is to approximate the solution as $\psi(x,y)\approx\sum_j\psi_j N_j(x,y)$ where ψ_j are the nodal values of the streamfunction and $N_j(x,y)$ are the shape functions associated with the nodes. After substituting this approximation into the variational formulation (8), the functional F becomes a function of nodal values ψ_j. The conditions for extremum correspond to vanishing partial derivatives with respect to nodal values, leading to the following system of equations:

$$\mathbf{A}\boldsymbol{\psi}+\mathbf{b}(\boldsymbol{\psi})=\mathbf{0}\text{, where}$$
$$A_{ij}=\iint\left(\frac{\partial N_i}{\partial y}\frac{\partial N_j}{\partial y}+\frac{1}{2y}\frac{\partial N_i}{\partial x}\frac{\partial N_j}{\partial x}\right)\mathrm{d}y\,\mathrm{d}x \qquad (9)$$
$$b_i=\iint N_i\left(H'(\psi)-\frac{C(\psi)C'(\psi)}{2y}\right)\mathrm{d}y\,\mathrm{d}x$$

where the prime denotes the differentiation with respect to ψ. The matrix $\mathbf{A}$ does not depend on the solution vector $\boldsymbol{\psi}$, while $\mathbf{b}$ is a vector dependent on the solution. The non-linear system of equations (9) is solved using Newton's iterative method. Let us assume that at iteration m the solution vector is $\boldsymbol{\psi}^m$. Let $\tilde{\boldsymbol{\psi}}^m$ be a small correction to $\boldsymbol{\psi}^m$ such that the solution at the next iteration step will be $\boldsymbol{\psi}^{m+1}=\boldsymbol{\psi}^m+\tilde{\boldsymbol{\psi}}^m$. The nonlinear term $\mathbf{b}(\boldsymbol{\psi})$ can then be linearized about $\boldsymbol{\psi}^m$ as

$$\mathbf{b}\left(\boldsymbol{\psi}^m+\tilde{\boldsymbol{\psi}}^m\right)=\mathbf{b}\left(\boldsymbol{\psi}^m\right)+\frac{\partial\mathbf{b}}{\partial\boldsymbol{\psi}}\tilde{\boldsymbol{\psi}}^m \qquad (10)$$

where the Jacobian matrix $\mathbf{B}=\partial\mathbf{b}/\partial\boldsymbol{\psi}$ is

$$B_{ij}\equiv\left(\frac{\partial\mathbf{b}}{\partial\boldsymbol{\psi}}\right)_{ij}\equiv\frac{\partial b_i}{\partial\psi_j}=$$
$$\iint N_iN_j\left(H''(\psi)-\frac{\left[C'(\psi)\right]^2+K(\psi)C''(\psi)}{2y}\right)\mathrm{d}y\,\mathrm{d}x$$

Obviously, the double prime denotes the second order differentiation with respect to ψ. At each iteration step we have to solve a linear system of equations,

$$\left[\mathbf{A}+\mathbf{B}\left(\boldsymbol{\psi}^m\right)\right]\tilde{\boldsymbol{\psi}}^m=-\left[\mathbf{A}\boldsymbol{\psi}^m+\mathbf{b}\left(\boldsymbol{\psi}^m\right)\right] \qquad (11)$$

in order to obtain the solution correction $\tilde{\boldsymbol{\psi}}^m$. The left-hand side matrix of (11) is the Jacobian of nonlinear system (9), and the right-hand side of (11) is the residual of system (9), with negative sign, both evaluated with the solution approximation $\boldsymbol{\psi}^m$. Since $\tilde{\boldsymbol{\psi}}^m$ satisfies only homogeneous essential and natural conditions, the correction vanishes as the residual goes to zero, provided the symmetric matrix $\left[\mathbf{A}+\mathbf{B}\left(\boldsymbol{\psi}^m\right)\right]$ is non-singular [9]. This is actually the main limitation of the steady axisymmetric Euler model. The original equation (7) may have multiple solutions or the solution may not exist at all, depending on the *generating functions* $C(\psi)$ and $H(\psi)$. There are several interpretations of this behavior in conjunction with the so-called vortex breakdown (VB), although a general consensus over the definition of this phenomenon has not been reached yet.

Keller et al. [10] further developed the theory for steady axisymmetric incompressible and inviscid swirling flows, by extending the Benjamin's variational principle (8). The main idea is to interchange the variables $\psi(x,y)\to y(x,\psi)$, then redefine the functional to be minimized as

$$\mathsf{F}(y)=\int_0^L\int_0^1\left[\begin{array}{l}\dfrac{1}{2y_\psi}+\dfrac{y_x^2}{4yy_\psi}\\ +y_\psi\left(H(\psi)-\dfrac{C^2(\psi)}{4y}\right)\end{array}\right]\mathrm{d}\psi\,\mathrm{d}x \qquad (12)$$

This formulation has the main advantage that the domain of integration is fixed, while the flow may have an internal free boundary enclosing a stagnation region. Such an example is presented and discussed later in this paper, being relevant to decelerated swirling flows downstream turbine runners.

2.2. Viscous Flows

The equations governing the viscous, incompressible, axisymmetric in cylindrical coordinates are:

$$\frac{\partial V_x}{\partial t}+\frac{1}{r}\frac{\partial}{\partial x}\left(rV_xV_x\right)+\frac{1}{r}\frac{\partial}{\partial r}\left(rV_rV_x\right)=-\frac{1}{\rho}\frac{\partial p}{\partial x}$$
$$+\frac{1}{r}\frac{\partial}{\partial x}\left[r\frac{\mu}{\rho}2\frac{\partial V_x}{\partial x}\right]+\frac{1}{r}\frac{\partial}{\partial r}\left[r\frac{\mu}{\rho}\left(\frac{\partial V_x}{\partial r}+\frac{\partial V_r}{\partial x}\right)\right] \quad (13)$$

$$\frac{\partial V_r}{\partial t}+\frac{1}{r}\frac{\partial}{\partial x}\left(rV_xV_r\right)+\frac{1}{r}\frac{\partial}{\partial r}\left(rV_rV_r\right)=-\frac{1}{\rho}\frac{\partial p}{\partial r}$$
$$+\frac{1}{r}\frac{\partial}{\partial x}\left[r\frac{\mu}{\rho}\left(\frac{\partial V_r}{\partial x}+\frac{\partial V_x}{\partial r}\right)\right]+\frac{1}{r}\frac{\partial}{\partial r}\left[r\frac{\mu}{\rho}2\frac{\partial V_r}{\partial r}\right] \quad (14)$$
$$-2\frac{\mu}{\rho}\frac{V_r}{r^2}+\frac{V_\theta^2}{r}$$

$$\frac{\partial V_\theta}{\partial t}+\frac{1}{r}\frac{\partial}{\partial x}\left(rV_xV_\theta\right)+\frac{1}{r}\frac{\partial}{\partial r}\left(rV_rV_\theta\right)=$$
$$\frac{1}{r}\frac{\partial}{\partial x}\left[r\frac{\mu}{\rho}\frac{\partial V_\theta}{\partial x}\right]+\frac{1}{r^2}\frac{\partial}{\partial r}\left[r^3\frac{\mu}{\rho}\frac{\partial}{\partial r}\left(\frac{V_\theta}{r}\right)\right]-\frac{V_rV_\theta}{r} \quad (15)$$

Turbulent flows are commonly modelled using the Reynolds-averaged Navier-Stokes (RANS) equations. The additional terms that appear as a result of the averaging procedure, the so-called Reynolds stresses, represent the effects of turbulence and must be modelled in order to close the flow equations. A common method relies on Boussinesq hypothesis to relate the Reynolds stresses to the mean velocity gradients, e.g. the $k-\varepsilon$ models. However, for highly anisotropic turbulent flow, such as the swirling flows with high swirl number, the Reynolds stress transport models (RSM) produce far better results. With RSM, one solves transport equations for each of the terms in the Reynolds stress tensor [11, §11.2.11]. Since RSM accounts for the effects of streamline curvature, swirl, rotation, and rapid changes in strain rate in a more rigorous manner than one-equation or two-equation models, it has greater potential to give accurate predictions for complex flows.

To complete the discussion, we should note that the vorticity-streamfunction formulation can be applied as well for viscous incompressible axisymmetric swirling flows, by adding the viscous effects in the evolution Eqs. (6), [5]

$$\frac{\partial C}{\partial t}+\{\psi,C\}=-2\nu y\mathbf{L}C, \quad (16a)$$

$$\frac{\partial \chi}{\partial t}+\{\psi,\chi\}=\frac{1}{4y^2}\frac{\partial\left(C^2\right)}{\partial x}-2\nu y\mathbf{L}\chi+4\nu\frac{\partial \chi}{\partial y} \quad (16b)$$

where $\nu=\mu/\rho$ is the kinematic viscosity.

For the numerical investigations presented in this paper we have used the primary variables solver for both inviscid as well as turbulent swirling flow investigations.

3. INVISCID VORTEX BREAKDOWN IN DECELERATED SWIRLING FLOWS

In this section we will analyze an example of decelerated swirling flow taken from Keller et al. [10]. The fluid is incompressible and inviscid, and the flow is axisymmetric with swirl. The diffuser shape is given by

$$\frac{r}{R_{\text{inlet}}}=1+\frac{1}{2}\left[1-\cos\left(\frac{\pi}{6}x\right)\right] \text{ for } 0\le x\le 6,$$

with $R_{\text{inlet}}=\sqrt{2}$ and, obviously, $R_{\text{outlet}}=2R_{\text{inlet}}$. Two cylindrical sections are added upstream and downstream the divergent pipe. The inlet flow is a simple solid-body vortex, i.e. a uniform axial velocity, $V_{x\,\text{inlet}}=1$, a swirl velocity distribution $V_{\theta\,\text{inlet}}=0.5r/R_{\text{inlet}}$, and $V_{r\,\text{inlet}}=0$. This simplified swirling flow is a "surrogate" for the more complex swirl structure downstream Francis turbine runners. The average cone half-angle is 13.3°, larger than the usual values for Francis turbines draft tube cones.

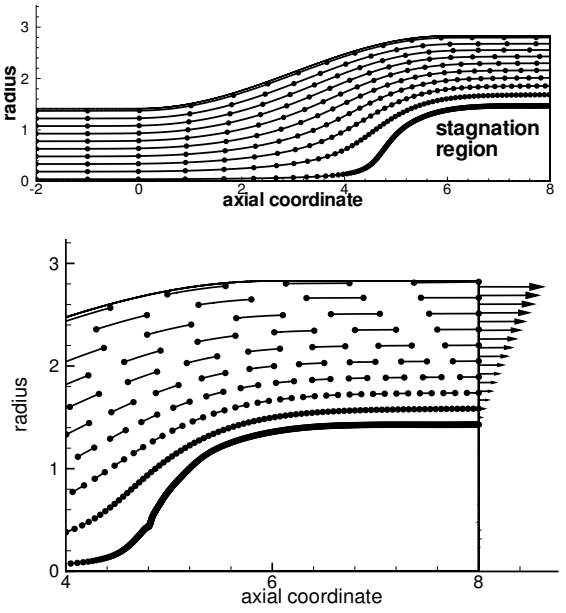

Figure 1. Vortex breakdown in a diffuser with inlet solid-body vortex.

The flow is computed with the axisymmetric inviscid finite volume solver from the FLUENT code [11], using the primary variables formulation. In addition to the velocity components at inlet, the problem setup requires the axis condition, zero normal velocity component on the diffuser wall, and radial equilibrium pressure at outlet. In order to correctly capture the downstream stagnation region, the backflow velocity components have been all set to zero. Moreover, although the final solution is a steady one, the unsteady solver has been used for stability reasons. It has been found by numerical experiments that only an unsteady flow simulation will eventually converge to the final steady flow field, while a steady solver always diverges. This is in agreement with the fact that the unsteady Euler equations always have a solution, while the solution non-uniqueness for the steady Euler model may lead to divergence of the iterative solver.

The streamlines for the diffuser flow are shown in Figure 1. Time markers are shown on each streamline, with a unit time step. This representation offers a quick quantitative assessment of the velocity magnitude variation along the streamlines. For example, for the streamline originating near the axis at inlet, the velocity decreases until stagnation and remains zero on the stagnation region boundary. This is why the time markers are getting clustered on the quasi-stagnation streamline. The flow detail in the outflow neighborhood also shows the meridional velocity variation on the annular flow region with non-zero flow. The streamlines pattern is identical with the one found by Keller et al. [10, Fig.6] by solving the steady axisymmetric Euler equation for $y(x,\psi)$, as mentioned in §2.1. Moreover, the primary variable solution presented here confirms two important features of the flow: first, within the stagnation region the velocity magnitude vanishes and no recirculating regions with closed streamlines are generated; second, the overall swirling flow transition is loss-free, since the flux of the total head has the same value through both inlet and outlet sections. The direct numerical confirmation of the stagnation region supports the conclusion of Goldshtik and Hussain [7], that there is no need for extending the definition of the generating functions beyond the streamfunction domain in the inlet section.

The pressure coefficient, defined as $c_p = \left(p - p_{\text{out axis}}\right)/\left(\rho V_{x\,\text{inlet}}^2/2\right)$ is plotted in Fig. 2 along both axis and wall of the diffuser. The pressure coefficient on the symmetry axis shows a monotonic increase, and becomes constant in the stagnation region. However, on the wall c_p undershoots and overshoots with respect to the upstream and downstream values. As a result, the diffuser shape might be slightly improved in order to have a monotonic increase in pressure on the wall. The adverse pressure gradient encountered by a fluid particle travelling near the wall is not the one computed as the slope of the dashed curve in Fig. 3. This meridional pressure gradient should be multiplied by the cosine of the swirl angle, i.e. the ratio between the meridional velocity component and the velocity magnitude, V_m/V. This is an important mechanism for avoiding flow detachment from the divergent wall by significantly reducing the adverse pressure gradient.

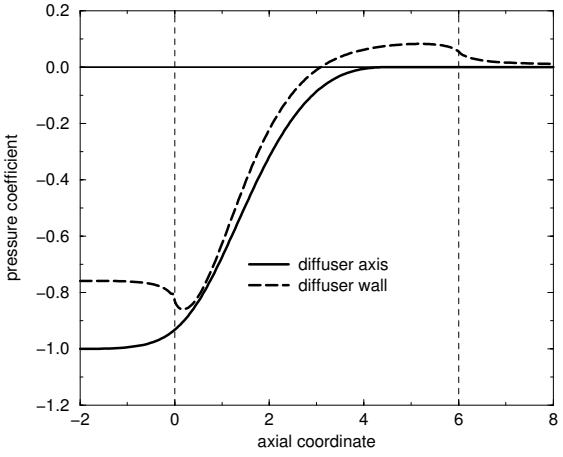

Figure 2. Pressure coefficient on the axis and wall of the diffuser.

Although increasing the swirl is beneficial to avoid viscous detachment at wall, the development of the central stagnation region decreases the actual static pressure recovery coefficient, defined as

$$c_{\text{PR}} = \frac{\dfrac{1}{Q}\left[\displaystyle\int_{S_{\text{out}}} p\mathbf{V}\cdot\mathbf{n}\,\mathrm{d}S - \int_{S_{\text{in}}} p\mathbf{V}\cdot\mathbf{n}\,\mathrm{d}S\right]}{\rho Q^2/2A_{\text{in}}^2} \qquad (17)$$

For the diffuser considered here, with the solid-body inlet swirl the pressure recovery coefficient is $c_{\text{PR}} = 0.882$. If there is no inlet swirl, and the flow is loss free, the ideal pressure recovery coefficient for the diffuser with outlet radius twice the inlet radius would be $c_{\text{PR ideal}} = 1 - 1/16 = 0.9375$, obviously larger than the value obtained for a swirling flow with vortex breakdown.

3. TURBULENT FLOW IN THE DRAFT TUBE CONE OF A FRANCIS TURBINE

Figure 3 shows the simplified geometry of a straight diffuser considered for the present numerical investigations. The dots correspond to the equivalent radius of the actual cross-section variation downstream a real Francis turbine draft tube. The simplified diffuser has a conical part of

8.5° half-angle and twice the inlet diameter in length, followed by a cylindrical section.

Two survey sections are located in the draft tube cone, as shown in Fig. 3. The experimental data for axial and swirl velocity components, as well as for the turbulent kinetic energy, were obtained with a two-component probe Laser Doppler Anemometer (LDA), using back-scattered light and transmission by optical fiber [2,12]. The uncertainties in velocity measurements are below 2% of the measured value.

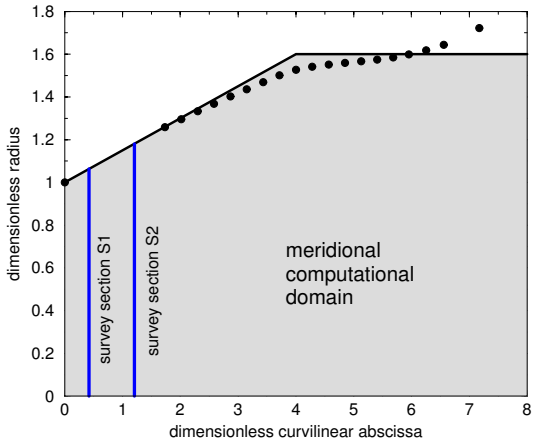

Figure 3. Simplified axisymmetric straight diffuser derived from an actual Francis turbine draft tube.

The first survey section (S1) is considered as inlet section for our computational domain. Axial and swirl velocity profiles are specified on S1, according to experimental data, using an analytical representation we have developed in [4]. The inlet radial velocity is considered linear with respect to the radius, such that the flow tangency at wall is satisfied. The measured turbulent kinetic energy [12] on S1 is imposed simply by a piecewise linear interpolation of data. At outlet, the radial equilibrium condition (3) is used, thus allowing for radial pressure variation according to the swirl.

In addition to the turbulent kinetic energy, most turbulence models available in commercial codes require the turbulent dissipation rate to be specified on inlet. One may approximate the dissipation rate via an eddy-viscosity hypothesis when strain rates and Reynolds stresses are known. However, the stresses were unavailable, and in addition, the eddy viscosity is likely to be highly anisotropic. Hence, the alternative employed was to specify the dissipation rate at the inlet at the inlet through a relation of the form given by Launder and Spalding [13]:

$$\varepsilon = C_\mu^{3/4} \frac{k^{3/2}}{L_\varepsilon} \qquad (18)$$

where $C_\mu = 0.09$ is an empirical constant and L_ε is the turbulence length scale which is selected rather arbitrarily. Indeed, by examining the literature dealing with decelerated swirling flows one can easily observe that L_ε is a parameter chosen such that numerical results be in best agreement with experimental data: $L_\varepsilon = 0.1R_{in}$, [14]; $L_\varepsilon = 0.02R_{in}$, [15]; $L_\varepsilon = 0.01R_{in}$, [16]; $L_\varepsilon = R_c$, [17]; $L_\varepsilon = 0.000657R_{in}$, [3] where R_{in} is the radius of inlet section and R_c radius of the viscous core.

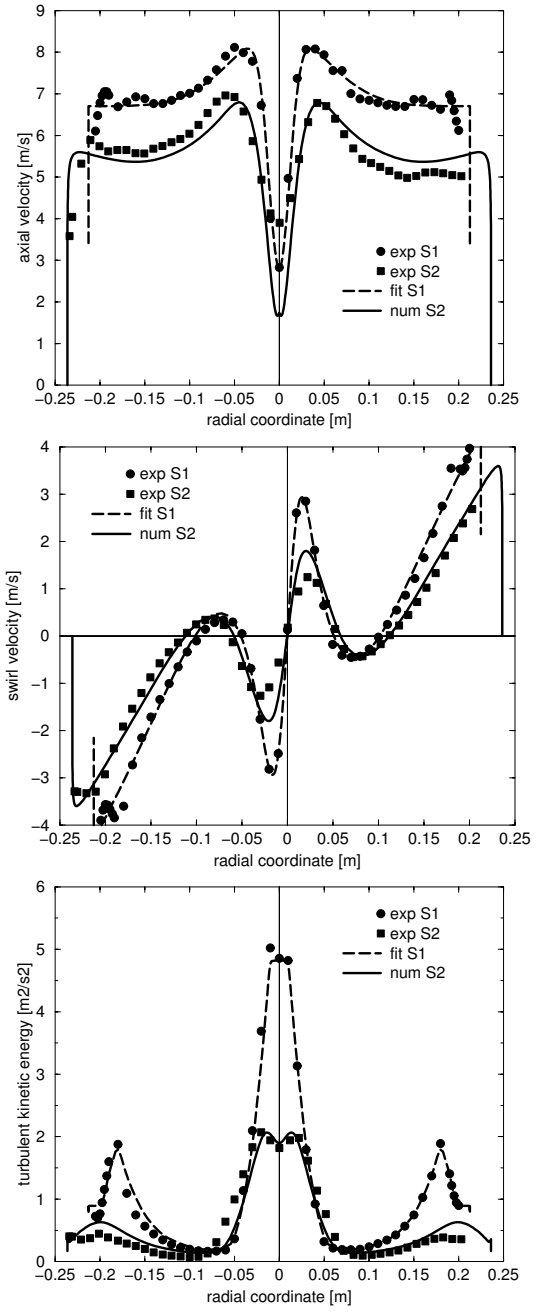

Figure 4. Axial and circumferential velocity profiles, and turbulent kinetic energy at discharge $\varphi = 0.368$.

Numerical experiments carefully validated with experimental data led us to the turbulence length scale in Eq. (18) equal to $L_\varepsilon = 0.02R_{in}$. As shown in Section 1.2, the Reynolds stress transport model (RSM) is best suited for highly non-homogeneous decelerated swirling flows, and it is employed in the present investigations.

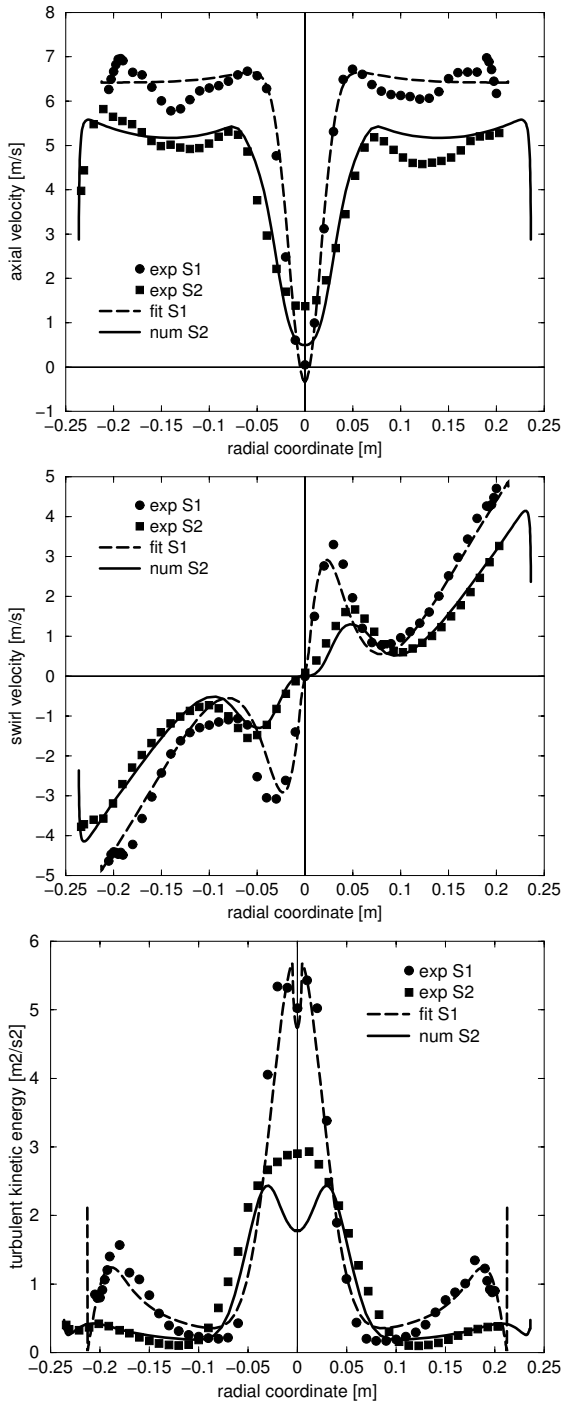

Figure 5. Axial and circumferential velocity profiles, and turbulent kinetic energy at discharge $\varphi = 0.340$.

Figures 4 and 5 show the main results of the turbulent swirling flow simulation in the Francis turbine draft tube cone. Only two operating points are presented in this paper: the first one corresponds to the best efficiency regime with a discharge coefficient $\varphi = 0.368$, while the second one has the same head but lower discharge $\varphi = 0.340$.

Each plot includes experimental data in survey sections S1 (filled circles) and S2 (filled squares), least squares data fits for inlet conditions in S1 (dashed lines) and numerical results for the survey section S2 (solid lines). We have shown in [4] that the inlet swirl structure can be represented as a three-vortex superposition: a solid-body rotation with constant axial velocity, a counter-rotating and co-flowing Bachelor vortex with a vortex core radius $\approx 0.4R_{in}$, and a co-rotating and counter-flowing Bachelor vortex with a vortex core radius $\approx 0.1R_{in}$. The last vortex is directly associated with the runner crown wake, as well as with peak turbulent kinetic energy near the axis. The runner crown wake increases as the turbine discharge decreases.

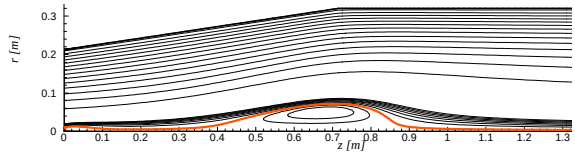

Figure 6. Turbulent vortex breakdown at discharge $\varphi = 0.340$.

Figure 6 reveals that when the turbine discharge decreases a bubble-type vortex breakdown occurs in the conical part of the diffuser. When further lowering the discharge, the quasi-stagnant region grows and moves upstream in the cone, eventually evolving into the spiral vortex breakdown known in the turbomachinery literature as precessing vortex rope. In contrast with the quasi-stagnant region from Fig. 1, predicted with inviscid flow models, turbulent flow simulations predict a closed stagnant region as shown in Fig. 6.

5. CONCLUSIONS

The paper investigates numerical solutions for decelerated swirling flows. First we summarize the mathematical models for both inviscid and viscous incompressible axisymmetric swirling flows. For steady axisymmetric Euler equations the model reduces to the celebrated non-linear Long-Squire equation for the Stokes streamfunction. Our finite element solver for this equation is briefly presented and its main limitation is revealed. This is important since the steady axisymmetric swirling flow model is widely used in quasi-three dimensional (Q3D) turbomachinery design, and the above limitation is

responsible for convergence failure when the draft tube cone is included in the computational domain.

An example of inviscid decelerated swirling flow is presented and discussed. The results obtained with an unsteady axisymmetric Euler solver support the stagnation flow model which postulates that a stagnation central core emerges downstream in the diffuser if the swirl intensity is high enough. However, our numerical experiments show that although a steady flow configuration is obtained it is essential to use an unsteady flow solver since the steady solver does not converge.

The turbulent swirling flow is investigated numerically in a simplified straight diffuser. Comparisons with highly accurate experimental data allowed us calibrate the turbulence length scale for inlet turbulence conditions. The Reynolds stress transport model is found to be most suitable for highly non-homogeneous decelerated swirling flows. The turbulence decay is correctly captured for two successive survey sections, and the velocity profiles are in very good agreement with experimental data.

It is shown that the turbulent axisymmetric flow models correctly capture a closed quasi-stagnant regions corresponding to vortex breakdown, while the inviscid models predict an open central stagnation region.

ACKNOWLEDGEMENTS

The authors take the opportunity to thank Prof. François Avellan and Dr. Gabriel Ciocan from the École Polytechnique Fédérale de Lausanne, as well as their partners in the FLINDT Project Eureka No. 1625 for providing the experimental data. This work has been supported by the Romanian Council for University Research under grant No. CNCSIS 33/2005 "Vortex Hydrodynamics and Applications".

REFERENCES

[1] Escudier, M., 1987, "Confined Vortices in Flow Machinery", *Annu. Rev. Fluid Mech.*, Vol. 19, pp. 27-52.

[2] Avellan, F., 2000, "Flow Investigation in a Francis Draft Tube: the FLINDT Project", Proc. *20th IAHR Symposium*, Charlotte, North Carolina, USA.

[3] Mauri, S., Kueny, J.L., and Avellan, F., 2004, "Werlé-Legendre Separation in a Hydraulic Machine Draft Tube", *J. Fluids Eng.*, Vol. 126, pp. 976-979.

[4] Susan-Resiga, R., Ciocan, G.D., Anton I., and Avellan F., 2006, "Analysis of the Swirling Flow Downstream a Francis Turbine Runner", *J. Fluids Engineering*, Vol. 128, pp. 177-189.

[5] Szeri, A., and Holmes, P., 1988, "Nonlinear Stability of Axisymmetric Swirling Flows", *Phil. Trans. R. Soc. Lond. A*, Vol. 326, pp. 327-354.

[6] Liu, J.-G., and Shu, C.-W., 2000, "A High-Order Discontinuous Galerkin Method for 2D Incomplessible Flows", *J. Comput. Physics*, Vol. 160, pp.577-596.

[7] Goldshtik, M., and Hussain, F., 1998, "Analysis of Inviscid Vortex Breakdown in a Semi-infinite Pipe", *Fluid Dyn. Res.*, Vol. 23, pp. 189-234.

[8] Benjamin, T.J., 1962, "Theory of the Vortex Breakdown Phenomenon", *J. Fluid Mech.*, Vol. 14, pp. 593-629.

[9] Susan-Resiga, R., Avellan, F., Ciocan, G.D., Muntean, S., and Anton, I., 2005, "Mathematical and Numerical Modeling of Swirling Flow in Francis Turbine Draft Tube Cone", *Scientific Bulletin of the Politehnica University of Timisoara, Trans. Mech.* Tom 50(64), pp. 1 - 10.

[10] Keller, J.J., Egli, W., Althaus R., 1988, "Vortex breakdown as a fundamental element of vortex dynamics", *J. Applied Math. and Physics (ZAMP)*, Vol. 39, pp. 404-440.

[11] Fluent Inc.,2005," FLUENT 6.2 User's Guide".

[12] Ciocan, G.D., and Avellan, F., 2004, "Flow Investigations in a Francis Draft Tube: Advanced Experimental Methods", Proc. *3rd Conference of Romanian Hydropower Engineers*, Bucharest, Romania.

[13] Launder, B.E., and Spalding, D.B., 1974, "The Numerical Computation of Turbulent Flows", *Comp. Methods in Appl. Mech. And Eng.*, Vol. 3, pp. 269-289.

[14] Armfield, S.W., and Fletcher, C.A.J., 1989, "Comparison of k-ε and Algebraic Reynolds Stress Models for Swirling Diffuser Flow", *AIAA J.*, Vol. 28(3), pp. 453-460.

[15] Armfield, S.W., Cho, N.-H., and Fletcher, C.A.J., 1990, "Prediction of Turbulence Quantities for Swirling Flow in Conical Diffusers", *AIAA J.*, Vol. 28(3), pp. 453-460.

[16] Benim, A.C., 1990, "Finite Element Analysis of Confined Turbulent Swirling Flows", *Int. J. Numer. Meth. in Fluids*, Vol. 11, pp. 697-717.

[17] Gatski, T.B., and Spall, R.E., 1996, "An Experimental and Numerical Investigation of Turbulent Vortex Breakdown and Aircraft Wakes", *Technical Report* NASA/CR-97-205857.

Conference on Modelling Fluid Flow (CMFF'06)
The 13th International Conference on Fluid Flow Technologies
Budapest, Hungary, September 6-9, 2006

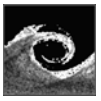

NUMERICAL INVESTIGATION AND ANALYSIS OF SWIRLING FLOW UPSTREAM OF KAPLAN RUNNER FOR VARIABLE DISCHARGE

Sebastian MUNTEAN[1], Romeo RESIGA[2], Daniel BALINT[3], Sandor BERNAD[4], Ioan ANTON[5]

[1] Corresponding Author. Hydrodynamics and Cavitation Laboratory, Romanian Academy – Timisoara Branch. Bv. Mihai Viteazu 24, Ro-300223 Timisoara, Romania. Tel.: +40 256 403 692, Fax: +40 256 403 700, E-mail: seby@acad-tim.tm.edu.ro
[2] Department of Hydraulic Machinery, Politehnica University of Timisoara. E-mail: resiga@mh.mec.upt.ro
[3] Department of Hydraulic Machinery, Politehnica University of Timisoara. E-mail: balint@acad-tim.tm.edu.ro
[4] Hydrodynamics and Cavitation Laboratory, Romanian Academy – Timisoara Branch. E-mail: sbernad@mh.mec.upt.ro
[5] Department of Hydraulic Machinery, Politehnica University of Timisoara. E-mail: anton@acad-tim.tm.edu.ro

ABSTRACT

In order to improve both energetic and cavitational behaviour of the Kaplan turbine, the velocity field upstream to the runner is analysed. The spiral case and distributor generate a suitable swirling flow further ingested by the Kaplan runner. An important step in designing and/or optimizing the runner blades is the determination of both axial and tangential velocity components at runner inlet. The radial distribution of both tangential (c_u) and axial (c_a) velocity coefficients on the annular section upstream the runner blades are presented. Traditionally, the analytical expression considered for c_u corresponds to a free vortex, while c_a is considered constant. However, these design assumptions are quite far from the actual velocity field, particularly as the turbine guide vane opening is decreased. An original analytical representation of the swirling flow in a section just upstream the runner blades is proposed, and it is shown to fit almost perfectly the numerical data. This conclusion is important in the framework of hydraulic turbines refurbishment, as well as for design optimization.

Keywords: analytical representation of swirling flow, Kaplan turbine, 3D numerical investigation

NOMENCLATURE

H	$[m]$	head
Q	$[m^3/s]$	discharge
a_0	$[m]$	guide vane opening

$H_\wedge = \dfrac{H}{H_{BEP}}$ [-] dimensionless head

$Q_\wedge = \dfrac{Q}{Q_{BEP}}$ [-] dimensionless discharge

$a_{0\wedge} = \dfrac{a_0}{a_{0BEP}}$ [-] dimensionless guide vane opening

$c_r = \dfrac{V_r}{U_{BEP}}$ [-] radial velocity coefficient

$c_u = \dfrac{V_u}{U_{BEP}}$ [-] tangential velocity coefficient

$c_z = \dfrac{V_z}{U_{BEP}}$ [-] axial velocity coefficient

$U_{BEP} = \Omega R_S$ $[m/s]$ transport velocity

V	$[m/s]$	velocity
Ω	$[rad/s]$	angular velocity
g	$[m/s^2]$	gravity
R	$[m]$	radius

Subscripts and Superscripts

r	radial direction
u	tangential direction
z	axial direction
c	characteristic
ref	reference section
h,s	hub, shroud
in, out	inlet section, outlet section
BEP	best efficiency point
^	dimensionless

1. INTRODUCTION

The hydrodynamics of Kaplan turbines is a more than a century old subject that benefits from a large body of both theoretical and experimental investigations [1, 2]. Traditionally, the main subject of these studies has been the turbine runner, with the development of powerful and reliable tools for designing the runner blades. Simplified quasi-3D methods are currently used in the runner domain, taking advantage on the quasi-axial meridional flow

in this region. On the other hand, the spiral case, distributor (stay vanes and guide vanes), as well as the draft tube, do not lend themselves to such a simplified analysis due to the intrinsic three-dimensionality of the flow. As a result, a realistic analysis of the spiral case/distributor hydrodynamics must consider a full 3D flow simulation. This is the approach employed by most of recent studies that use numerical simulations [3-5]. On the other hand, the flow upstream the turbine runner can be considered steady. As a result, a 3D steady flow model is employed in the present study.

The main purpose of the spiral case and distributor is to prepare a suitable swirling flow further ingested by the Kaplan runner. An important step in designing and/or optimizing the runner blades is the determination of both axial and tangential velocity components at runner inlet. Traditionally, the analytical expression considered for tangential velocity component c_u corresponds to a free vortex, while axial velocity component c_a is considered constant. However, these design assumptions are quite far from the actual velocity field. As a result, we have introduced a new analytical representation of the velocity components upstream to the Kaplan runner at best efficient point [5].

The energetical and cavitational behaviors of the Kaplan runner at off-design operating points represent a crucial requirement. Consequently, the velocity profile downstream to the distributor at off-design operating conditions is needed. Since we are not interested in modeling the perturbations produced by the stay and guide vane wakes, we are performing in the present paper an inviscid 3D steady flow numerical simulation. The 3D incompressible Euler flow is computed using the commercial expert code FLUENT 6.0.12 [6]. Moreover, according to the IEC 60193 Standard [7], the characteristic Reynolds number of the prototype hydraulic turbine is larger than 10^7, supporting the Euler simulation.

Section 2 presents the computational domain for a real Kaplan spiral case and distributor. The outflow section is conventionally defined as the Kaplan turbine runner reference plane. A 3D structured mesh is generated, with approximately $2*10^6$ finite volume cells [8]. This section also presents the inflow/outflow boundary conditions considered in the present study.

Section 3 is devoted to the flow numerical simulation and analysis of the 3D hydrodynamic field for the 6 operating points considered at constant head and variable guide vane opening reveals the main flow features of the swirling flow upstream the Kaplan runner.

The last section presents the main conclusions of the present study as well as its relevance to the Kaplan turbine design and optimization.

2. COMPUTATIONAL DOMAIN. EQUATIONS AND BOUNDARY CONDITIONS

2.1. Computational domain

Figure 1 presents the cross section through the Kaplan turbine as well as the computational domain considered in the present study. The inlet section of computational domain corresponds to the power plant inlet section. Figure 2 shows the 3D computational domain considered in the present study.

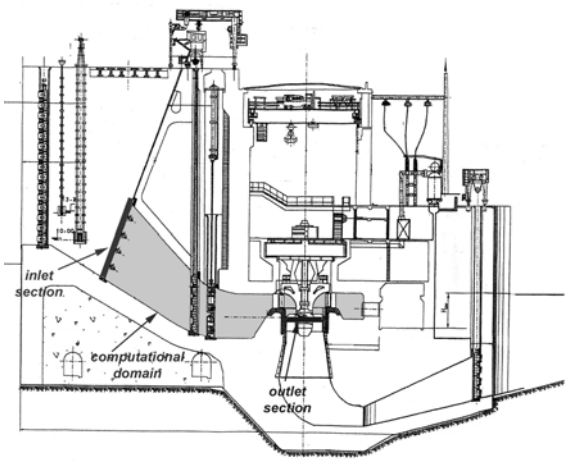

Figure 1. Cross section in Kaplan turbine.

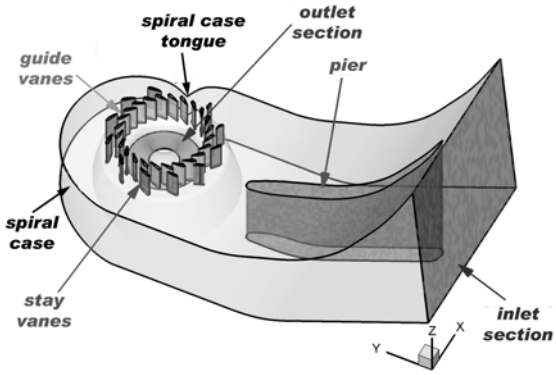

Figure 2. 3D computational domain extends from the power plant inlet to the runner reference plane. The computational domain includes the spiral case and distributor of the turbine.

The stay vanes have different profiles, as shown in Figure 3. The first seven (1 … 7) stay vanes are identical, followed by a different vane 8, two identical vanes 9 and 10, and finally a different stay vane 11 near the spiral case tongue. All 24 guide vanes are identical and have a symmetrical profile, as shown in Fig. 3.

The oulet section is conventionally chosen in the runner reference plane. Normally, one would

consider a computational procedure that couples the steady absolute flow in spiral case/distributor domain with the relative flow in the runner [4, 3]. However, a separate flow simulation can still be performed in the domain from Fig. 2, by choosing a suitable boundary condition on the outlet section.

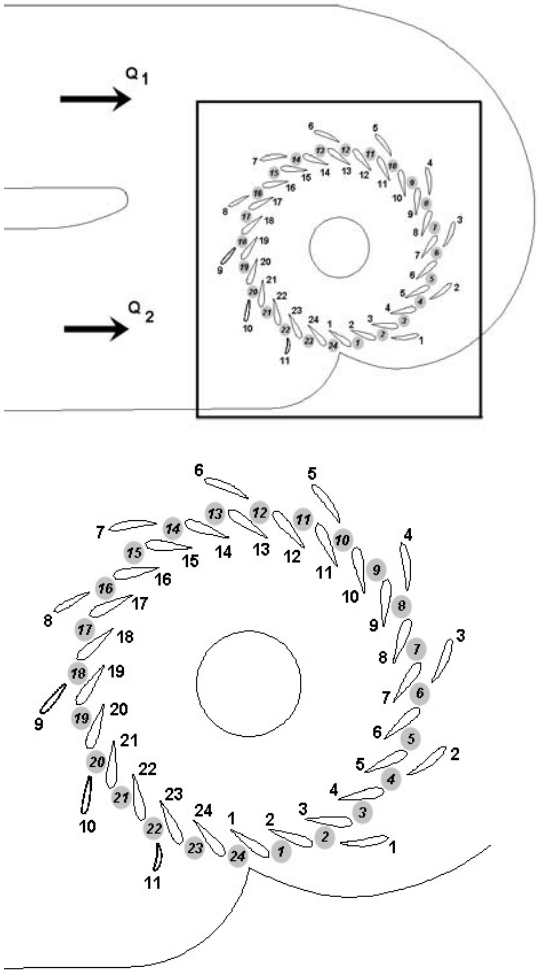

Figure 3. Top view of the spiral case and distributor (above) and a detail view of the stay and guide vanes (below).

2.2. Equations and boundary conditions

A 3D steady, inviscid and incompressible flow is considered, thus we solve the steady Euler equations:

$$\nabla \cdot \underline{V} = 0 \tag{1}$$

$$\rho\left(\underline{V} \cdot \nabla\right)\underline{V} = -\nabla p \tag{2}$$

On the inlet section we prescribe a constant total pressure. The value of the total pressure is adjusted to obtain the operating flow rate for the Kaplan turbine under consideration. On the outlet section, the swirling flow structure is compatible with the so-called pressure radial equilibrium. This condition is derived from the radial component of the Euler equation,

$$V_r \frac{\partial V_r}{\partial r} + \frac{V_u}{r}\frac{\partial V_r}{\partial \theta} + V_z \frac{\partial V_r}{\partial z} - \frac{V_u^2}{r} = -\frac{1}{\rho}\frac{\partial p}{\partial r} \tag{3}$$

If the radial velocity component is negligible, $V_r \approx 0$, one obtains the pressure radial equilibrium condition

$$\frac{1}{\rho}\frac{\partial p}{\partial r} = \frac{V_u^2}{r} \tag{4}$$

This condition has been successfully employed on the draft tube inlet section when computing the runner flow [9], and it has been validated experimentally [9, 10]. A reference pressure is conventionally set to zero at the hub on the outlet section, since condition Eq. (4) defines the pressure only up to an additive constant.

Note that Eq. (4) does not actually takes into account the runner influence on the flow upstream, but we consider it appropriate for evaluating the performance of the spiral case and distributor. The rest of the domain boundary corresponds to solid walls, with zero normal velocity condition.

The computations have been performed at six operating point displaced with constant head and variable discharge, see Figure 4. The hydraulic parameters of the operating points investigated are presented in Table 1.

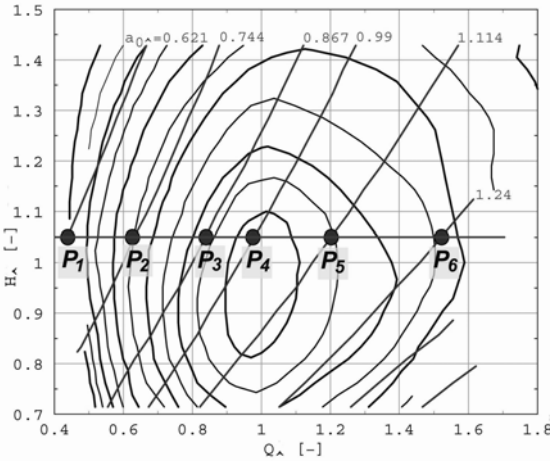

Figure 4. The Kaplan turbine hill chart. The operating points investigated are diplaced at constant head and variable guide vane opening.

In order to significantly reduce the time of the user interactive work an automatic procedure is used, [11]. The particular scripts of text command files are implemented in the *C* programming language and developed on *Korn Shell* of *Linux*

operating system. Using this procedure the computational domain with different guide vane opening is automatically generated as well as its structured mesh. Moreover, the boundary conditions associated for each operating point is imposed then the computation is performed.

Table 1. Hydraulic parameters for the operating points investigated

Operating points	$H^{\wedge}$	$Q^{\wedge}$	$a_{0}{}^{\wedge}$
P_1	1.05	0.4589	0.621
P_2		0.6453	0.744
P_3		0.8442	0.867
P_4		0.9767	0.990
P_5		1.2000	1.114
P_6		1.5139	1.240

3. Analytical Representation of Axial and Tangential Velocity Profiles upstream the Kaplan Runner

As mentioned before, the spiral case and distributor generate a suitable swirling flow further ingested by the Kaplan runner. An important step in designing and/or optimizing the runner blades is the determination of both axial and tangential velocity components upstream the Kaplan runner. Consequently, the hydrodynamic field in a annular section displaced at $0.2R_{ref}$ upstream the reference plane of runner is investigated, see Figure 5. In order to generate a parametric description of both tangential and axial velocity components upstream to the Kaplan runner an original analytical representation of the swirling flow is developed by Resiga et al. [12] and applied to the flow field upstream to the Kaplan runner at best efficiency point, [5].

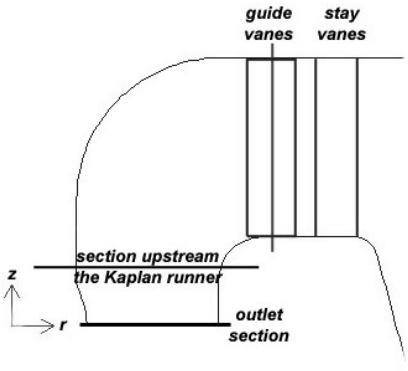

Figure 5. Displacement of the annular section upstream the Kaplan runner.

Several swirling flow models have been developed in the literature to study the vortex flow. The distribution of the tangential velocity in a real swirling flow is mainly due to the method used to generate the swirl. From a mathematical point of view, it is possible to create models to properly approximate the behavior of the flow field. A Rankine vortex represents a simply model for rotating flow (see Figure 6). It displays a solid body rotation core followed by a r^{-1} decay in the radial direction corresponding to a free vortex. In application to a swirling flow, it is worth to note that the model does not take into account the finite thickness of the shear layer region at $r = R_c$ where the curve has a singularity, Fig. 6. The characteristic vortex radius R_c measures the vortex core radial extent (see the grey region marked in Fig. 6).

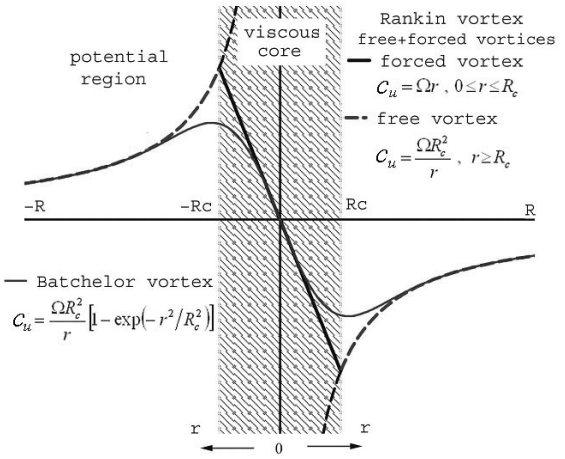

Figure 6. The models of tangential velocity distribution in swriling flow.

These two parameters define the Rankine vortex tangential velocity,

$$c_u(r) = \begin{cases} \Omega r \ , \ 0 \le r \le R_c \\ \dfrac{\Omega R_c}{r} \ , \ r \ge R_c \end{cases} \tag{5}$$

where r is the radial distance from the vortex axis. This simplified model provides a continuous function for $c_u(r)$, but the derivative is discontinuous.

A more suitable model for developed swirling flows is the Batchelor vortex (solid line in Fig. 6). The tangential velocity field is described via a similarity solution applied to wakes in the far field:

$$c_u(r) = \frac{\Omega R_c^2}{r}\left[1 - exp\left(-\frac{r^2}{R_c^2}\right)\right] \tag{6}$$

As a result, we introduce in this paper a new analytical representation of the velocity components as

$$c_u = \Omega_0 r + \Omega_1 \frac{R_1^2}{r}\left[1 - exp\left(-\frac{r^2}{R_1^2}\right)\right] + \frac{\Omega_2}{r} \qquad (7a)$$

$$c_z = V_0 + V_1 exp\left(-\frac{r^2}{R_1^2}\right) + V_2 r \qquad (7b)$$

The last term in Eq. (7b) has been added in agreement with the constant used by Dahlhaug [10] for representing $c_u(r)$. The velocity coefficients are defined as $c = V/U_{ref}$. The same normalization is considered for the characteristic velocities V_0, V_1 and V_2 in Eq. (7b). The characteristic angular velocities Ω_0, Ω_1 and Ω_2 in Eq. (7a) are normalized by ΩR_{ref} , while the radius r and the characteristic radii R_1, R_2 are normalized with the reference radius R_{ref}.

Equations (7) correspond to a superposition of one solid body vortex, one Batchelor vortex [13] and one free vortex, [14]. The particular expression of an elementary vortex,

$$c_u = \Omega \frac{R^2}{r}\left[1 - exp\left(-\frac{r^2}{R^2}\right)\right] \qquad (8a)$$

$$c_z = V exp\left(-\frac{r^2}{R^2}\right) \qquad (8b)$$

has been successfully used later by Faler and Leibovich [15] to describe the swirl structure generated by a radial vane apparatus. Note that if the vortex characteristic radius R_c goes to infinity, the Batchelor vortex Eqs. (8) becomes a pure forced vortex:

$$c_u = \Omega r \qquad (9a)$$

$$c_z = V \qquad (9b)$$

A special least-square procedure has been developed by the authors to fit Eqs. (7) with numerical data. The first forced vortex has a dimensionless angular velocity Ω_0 and an associated constant axial velocity V_0. The second vortex of Batchelor type (denoted with subscript 1), is co-rotating with the first vortex, Ω_1, and has a characteristic radius R_1. The second vortex is counter-flowing with respect to the first one, V_1. The third is a free vortex.

Figures 7 show the radial distribution of the radial (*cr* denoted with circles ○), tangential (*cu* labeled with squares □) and axial (*cz* plotted with triangles Δ) velocity coefficients on the annular section upstream the runner blades for all operating points as well as the curves fitted with Eqs. (7a) and (7b) (solid lines). The velocity coefficients are negative because the axial velocity component is negative in the coordonate system from Fig. 5.

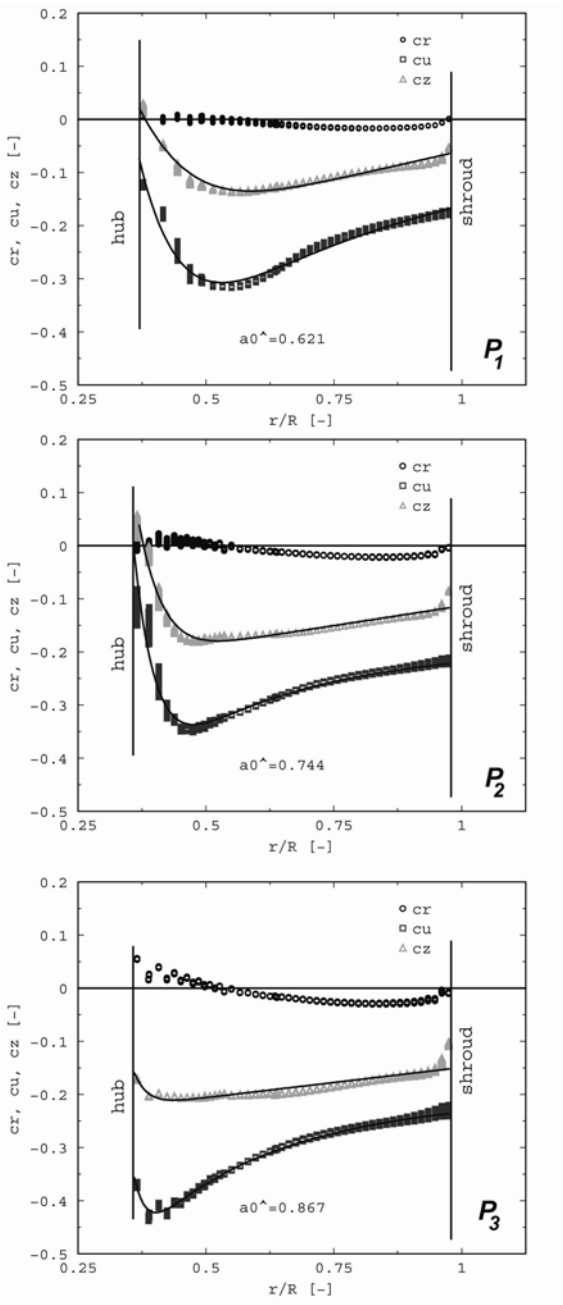

Figure 7a. The velocity coefficients versus dimensionless radius upstream the Kaplan runner for operating points P1 – P3.

The analytical expressions match almost perfectly the numerical data for both tangential and axial velocity components. Swirl parameters found by fitting Eqs. (7) to numerical data for operating points are listed in Table 2 and Table 3, respectively.

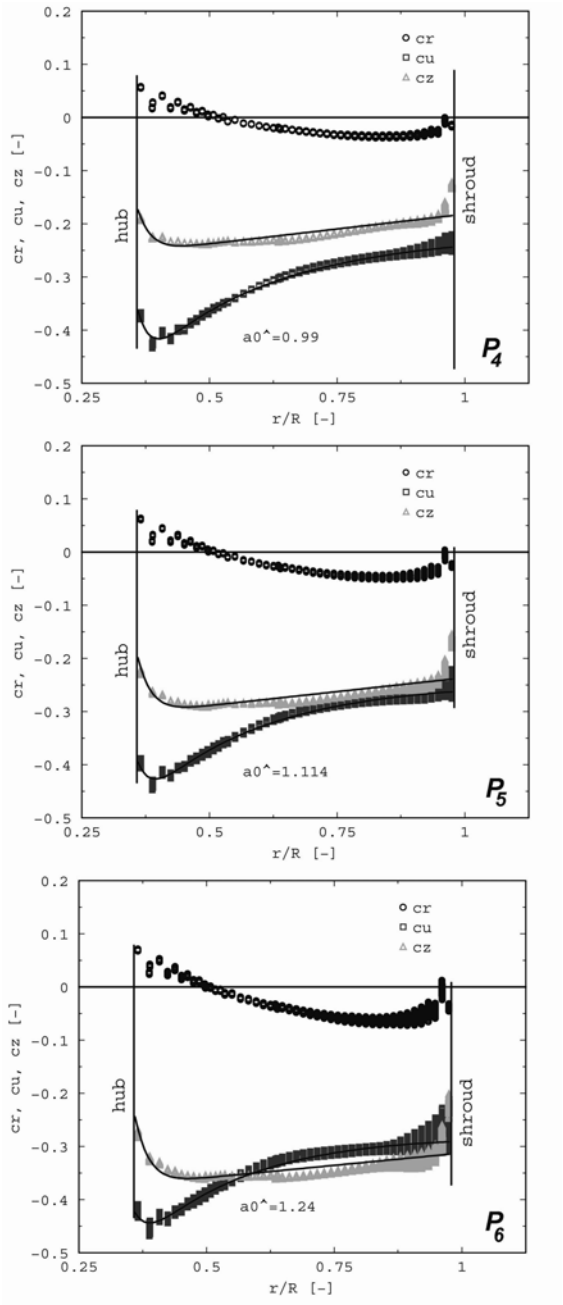

Figure 7b. The velocity coefficients versus dimensionless radius upstream the Kaplan runner for operating points P4 – P6.

Table 2. Fit parameters of the axial velocity component for operating points

OP	V_0	V_1	V_2
P_1	-0.278091	1.2923	0.218939
P_2	-0.262482	11.847	0.149239
P_3	-0.262984	57.7044	0.113895
P_4	-0.292984	63.0590	0.111705
P_5	-0.341409	73.3568	0.105257
P_6	-0.405412	69.5708	0.093206

Table 3. Fit parameters of the tangential velocity component for operating points

OP	Ω_0	R_1	Ω_1	Ω_2
P_1	0.035110	0.2772	-12.759	0.7827
P_2	-0.063804	0.1857	-177.465	6.1080
P_3	-0.065119	0.1378	-2354.01	44.5086
P_4	-0.078983	0.1393	-1723.33	33.2816
P_5	-0.099701	0.1406	-1147.77	22.5286
P_6	-0.128013	0.1434	-689.65	14.0217

One can observe that the radial velocity coefficient at all operating points investigated is negligible relative to other two velocity coefficients.

A significant modification of the tangential and axial velocity coefficients are obtained at operating points P_1 and P_2. Figure 8 presents the axial velocity coeficient versus dimensionless radius for all points investigated. One can observe at operating points P_1 and P_2 the axial velocity is positive near the hub. Consequently, a recirculation region is generated at high intensity of the swirl.

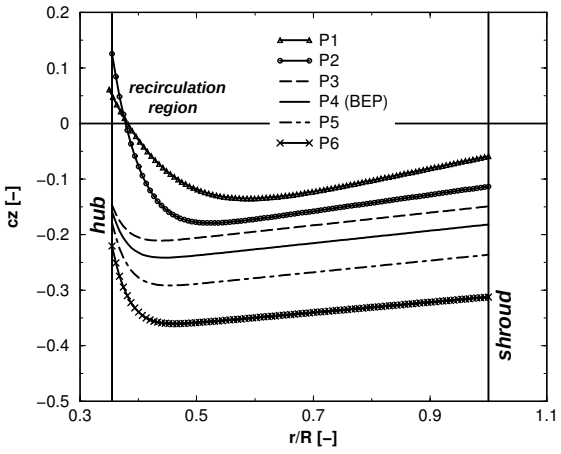

Figure 8. The distribution of the axial velocity coefficient versus dimensionless radius upstream the Kaplan runner for operating points.

Ploting the characteristic velocity V_0 of solid body vortex from Table 2 in terms of the dimensionless guide vane opening it is found the boundary between two domains, see Figure 9. The minimum V_0 is reached at dimensionless guide vane opening 0.777 ($a_{0_\wedge} \approx 0.8$). Accordingly, velocity profiles start to modify when the dimensionless guide vane opening smaller than 0.8 ($a_{0_\wedge} < 0.8$).

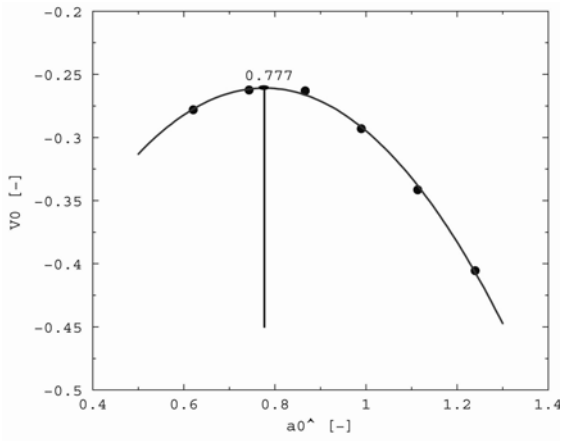

Figure 9. The distribution of the characteristic velocity of solid body vortex versus dimensionless guide vane opening.

Figure 10 shows the tangential velocity coeficient in terms of the dimensionless radius. The same conclusion emerges from tangential profiles like axial profiles when dimensionless guide vane is smaller then $a_{0^\wedge} < 0.8$. Moreover, one can see all tangential velocity profiles present a transition region from solid body vortex to free vortex near the hub. It means that the hub radius is chosen too small. Unfortunately, this situation induces hydrodynamics instabilities when the hydraulic turbine operates at partial loading.

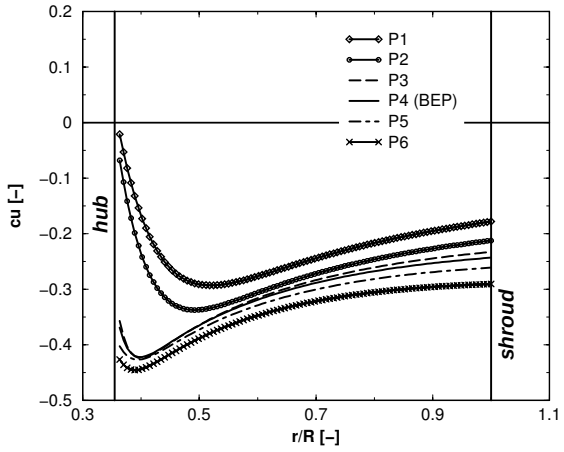

Figure 10. The distribution of the tangential velocity coefficient versus dimensionless radius upstream the Kaplan runner for operating points.

A global quantitative of the incompressible swirling flow is provided by the swirl number *S* as the axial momentum divided by the axial flux of axial momentum.

$$S = \frac{\int_{R_h}^{R_s} r^2 V_z V_u dr}{R \int_{R_h}^{R_s} r V_z^2 dr} \tag{9}$$

The swirl number computed for the swirling flow given by Eq. (9), with parameters from Table 4, is plotted versus the dimensionless guide vane opening, Figure 11. One can see that for the investigated range of the swirl number decreases as the dimensionless guide vane opening increases, but nevertheless the variation is quasi-linear.

Table 4. Swirl number for operating points

OP	$Q_\wedge$	$a_{0\wedge}$	S
P_1	*0.4589*	*0.621*	*1.276*
P_2	*0.6453*	*0.744*	*1.178*
P_3	*0.8442*	*0.867*	*1.016*
P_4	*0.9767*	*0.990*	*0.879*
P_5	*1.2000*	*1.114*	*0.747*
P_6	*1.5139*	*1.240*	*0.636*

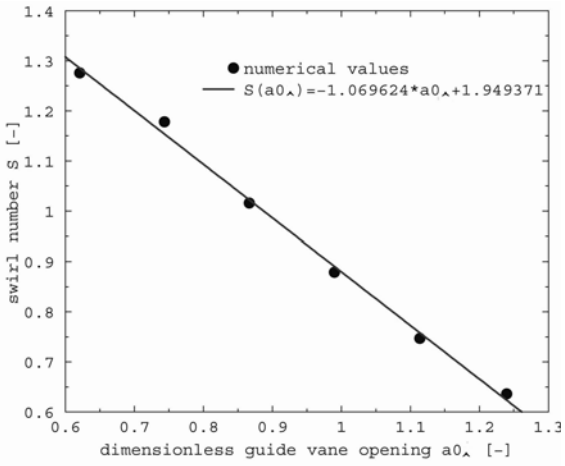

Figure 11. The swirl number versus dimensionless guide vane opening.

4. CONCLUSIONS

The paper presents a methodology for computing the full three-dimensional flow upstream the Kaplan turbine runner. We have developed a methodology for accurately describing the complex 3D geometry, as well as for building a suitable structured 3D mesh. A significant step forward has been made to reduce the time devoted to the problem definition (geometry and mesh), in order to be able to apply the present approach for design improvement and optimization.

The velocity component profiles upstream the runner are presented for six operating points (variable guide vane opening). It is shown that even

at the design point, the tangential velocity profile significantly departs from the simplified one (free vortex distribution, i.e. $c_u \propto 1/r$) usually considered in preliminary design. This departure accentuates as the discharge decreases, while the axial velocity gradually develops a velocity deficit near the hub.

For the velocity field analysis on a section just upstream the runner blades we have developed an original technique to quantitatively describe the radial variation of both axial and tangential mean flow velocity components. An analytical representation of the tangential and axial velocity components is derived using a combination of three elementary vortices (one solid body vortex, Batchelor vortex and free vortex). The analytical expression parameters are computed using a special least-squares method. It is shown that our swirling flow formulae perfectly match the numerical data from the 3D flow simulation. We appreciate that this result is extremely useful for the turbine design, since it reduces the complex flow on an interface between the distributor and runner to a set of eight parameters.

The swirling flow number is shown to vary quasi-linearly with the guide vane opening in the investigated operating range even if the velocity profiles is changed significantly.

ACKNOWLEDGEMENTS

The authors acknowledge the support from the National University Research Council grants (CNCSIS A Consortium 33/2005). All numerical computations have been performed at the Numerical Simulation and Parallel Computing Laboratory of the "Politehnica" University of Timisoara, National Center for Engineering of Systems with Complex Fluids.

REFERENCES

[1] Anton I., 1979, *Hydraulic turbines*, Facla Publishing House, Timisoara, Romania. (in Romanian).

[2] Radha Krishna H.C. (Editor), 1997, *Hydraulic Design of Hydraulic Machinery*, Avebury Publishing House.

[3] Bartholomä, K., 1997, "Experimentelle und Theorethische Verlustanalysein einer Kaplan Vollspiralturbine", *PhD Thesis Technische Universität München,* Munich, Germany.

[4] Nilsson, H., 2002, "A Numerical Investigation of the turbulent Flow in a Kaplan Water Turbine Runner", *PhD Thesis Chalmers University of Technology,* Göteborg, Sweden.

[5] Muntean, S., Balint, D., Resiga, R., Anton, I., and Darzan, C., 2004, "3D Flow Analysis in the Spiral Case and Distributor of a Kaplan Turbine", Proc. *22nd IAHR Symposium,* Stockholm, Sweden, paper A10-2, pp. 1-10.

[6] Fluent Inc., 2001, FLUENT 6. User's Guide, Fluent Incorporated, Lebanon USA.

[7] International Electrotechnical Commision, 1999, "Hydraulic Turbines, Storage, Pumps and Pumps-Turbines-Model Acceptance Tests", International Standards IEC 60193, 2nd ed.

[8] Fluent Inc., 2001, Gambit 2. User's Guide, Fluent Incorporated, Lebanon USA.

[9] Muntean, S., 2002, "Numerical methods for the analysis of the 3D flow in Francis turbine runners", *PhD Thesis Politehnica University of Timisoara,* Timisoara, Romania. (in Romanian)

[10] Dahlhaug, O.G., 1997, "A study of swirling flow in draft tube", *PhD Thesis Norwegian University of Science and Technology,* Trondheim, Norway.

[11] Balint, D., Muntean, S., Resiga, R., and Anton, I., 2005, "Automated Algorithms for Computing the Full 3D Turbulent Flows in Kaplan Turbines", Proc. *South Eastern Europe Fluent Event 2005*, Halkidiki, Greece. (on CD-ROM)

[12] Resiga, R., Ciocan G.D., Anton, I., and Avellan, F., 2006, "Analysis of the Swirling Flow Downstream a Francis Turbine Runner", *J. Fluids Eng.*, Vol. 128(1), pp. 177-189.

[13] Batchelor, G.K., 1964, "Axial flow in trailing line vortices", *J. Fluid Mech.*, Vol. 20, pp. 645-658.

[14] Mattner, T.W., Joubert, P.N., and Chong, M.S., 2002, "Vortical flow. Part 1: Flow through a constant diameter pipe", *J. Fluid Mech.*, Vol. 463, pp. 259-291.

[15] Faler, J.H., and Leibovich, S., 1977, "Disrupted states of vortex break flow and vortex breakdown", *Phys. Fluids*, Vol. 20(9), pp. 1385-1400.

Conference on Modelling Fluid Flow (CMFF'06)
The 13th International Conference on Fluid Flow Technologies
Budapest, Hungary, September 6-9, 2006

DESIGN AND VALIDATION OF A CONICAL-WALLED INLET GUIDE VANE ROW FOR A SMALL HYDRAULIC BULB TURBINE

L.M.C. FERRO[1], J.C.C. HENRIQUES[2], L.M.C. GATO[3], A.F. de O. FALCÃO[3]

[1] Corresponding author. Department of Mechanical Engineering, Escola Superior de Tecnologia, Polytechnic Institute of Setúbal, Portugal, Tel.:+35126579000, Fax.:+351218417398, E-mail:lferro@hidro1.ist.utl.pt
[2] Department Renewable Energies, Instituto Nacional de Engenharia, Tecnologia e Inovação, Portugal, E-mail: joao.campos@ineti.pt
[3] Department of Mechanical Engineering, Instituto Superior Técnico, Technical University of Lisbon, Portugal, E-mail: lgato@mail.ist.utl.pt; falcao@hidro1.ist.utl.pt

ABSTRACT

The paper presents a fast design method for the inlet guide vanes of low-cost small hydraulic bulb turbines. The conical-walled inlet guide vane row is designed using a quasi-three-dimensional calculation method, by prescribing the angular-momentum distribution along the span at the exit of the guide vanes. The meridional through-flow is computed by a streamline curvature method and the blade-to-blade flow by a singularity surface method. The stagger angle and the vane camber are computed to fulfill the required design circulation and zero-incidence flow at the leading edge. The final vane shape is a single-curvature surface with straight leading and trailing edges. To validate the design method, a conical diffuser-model with six fixed vanes was designed, manufactured and tested in an airflow rig. Traversing measurements along the circumferential and radial directions were made with a five-hole probe. The experimental results are compared with the prescribed design conditions and with numerical results from a three-dimensional analysis Euler code. The numerical method uses a second-order in space and a third-order in time Runge-Kutta discontinuous Galerkin method to solve the Euler equations.

Keywords: axial flow turbine, design method, guide vane row, singularity method, Euler code.

NOMENCLATURE

Roman symbols

c	$[m]$	chord
c_{p_0}	[-]	total pressure coefficient
c_p	[-]	pressure coefficient
C_p	$[m^2/(s^2K)]$	specific heat at constant pressure
C_v	$[m^2/(s^2K)]$	specific heat at constant volume
f	$[m]$	camber
H	$[m]$	available head
S_1	$[m^2]$	blade-to-blade surface
S_2	$[m^2]$	meridional surface
N	$[s^{-1}]$	angular speed
Q	$[m^3/s]$	volume flow rate
U	$[m/s]$	rotor tip speed
V	$[m/s]$	velocity
Z	[-]	number of blades
p	[*Pa*]	static pressure
p_0	[*Pa*]	stagnation pressure
r	$[m]$	radius
s	$[m]$	blade thickness
t	$[m]$	circumferential pitch of cascade

Greek symbols

γ	C_p/C_v, specific heat ratio
Δ	variation
λ	stagger angle
ϕ	conical surface angle
Ω	computational domain
ϱ	density

Subscripts and Superscripts

j	element number
r, θ, z	radial, circumferential and axial coordinates
η	relative to nominal condition
ψ	tangential direction on the unfolded conical surface
$^-$	left state
$^+$	right state
*	adimensional value

1. INTRODUCTION

There is still a huge potential for power generation from small-scale hydro installations with outputs ranging between a few kilowatts and a few megawatts. This is mainly due to a coincidence of

two factors: the strategic interest in the use of renewable energy sources and the recent advances in electronics which enables the control of the output of small turbo-generators to follow the demand and meet the (voltage and frequency) standards of the electrical network at low cost. When available, small-scale hydro power systems represent a good technological solution to produce electrical power to disperse communities specially in less developed regions of the world. The development and the installation of locally manufactured hydro plants in those regions are appreciated by the governments and bring further large social impact.

The paper presents a fast design method for the inlet guide vanes of low-cost small hydraulic bulb turbines. The guide vanes are bounded by two coaxial conical surfaces with a common vertex. The vanes have constant thickness with rounded leading edges and sharp trailing edges. The mean lines of the vane sections on the two unfolded conical surfaces are arcs of circumference. The conical-walled inlet guide vane row is defined using a quasi-three-dimensional design method, by prescribing a constant angular-momentum distribution along the span at the exit of the guide vanes. The meridional through-flow is computed by a streamline curvature method and the blade-to-blade flow by a singularity surface method. For the inner and the outer sections, the stagger angle and the vane camber are computed to fulfill the required design circulation and zero-incidence flow at the leading edge. The final shape of the vane is obtained by moving a straight line along the mean line of the two reference sections. This produces a single-curvature surface vane shape with straight leading and trailing edges. To validate the design method, a $0.95\,m$ inlet diameter conical diffuser-model with six fixed vanes was designed, manufactured and tested in an airflow rig. Traversing along the circumferential and radial directions was made with a five-hole probe. Measurements include the radial and circumferential distributions of velocity and pressure at the exit of the guide vanes. The experimental results are compared with the prescribed design conditions and with numerical results from a three-dimensional analysis Euler code.

2. QUASI THREE-DIMENSIONAL DESIGN METHOD

A classical analysis method for the inviscid flow through a turbomachine is presented by Wu [1]. According to Wu the solution of the three-dimensional flow field (for pressure and velocity) is obtained by means of the iterative solution of the two-dimensional flow defined in two families of stream surfaces. Any three-dimensional streamline can then be obtained through the intersection of the two families of stream surfaces. For a closed turbomachine, where the flow is bounded by two surfaces of revolution, one of the families must included these two surfaces, it being expected that the intermediate surfaces can be approximately assumed as surfaces of revolution. The other family includes the surfaces of the vanes and a set of intermediate surfaces with a shape not too different from the mean blade surface. Wu [1] named the first family as S_1 and the second family as S_2. The solution of the flow using the above three-dimensional approach is expensive, difficult to use, and usually produces double curvature blade surfaces. The Wu method can then be simplified, using a quasi-three-dimensional approach called through-flow analysis approach, where the family of S_2 surfaces is reduced to just one surface - the middle surface between the two blades - and the S_1 surfaces are assumed to be surfaces of revolution generated from the streamlines of the flow computed at the middle surfaces S_1. The flow at the S_2 surfaces is assumed to be axisymmetric and the influence of the blade thickness s (measured in the circumferential direction) is taken into account by a blockage factor, $1 - s/p$, where p is the circumferential pitch of the blade cascade.

The through-flow analysis approach allows the solution of the three-dimensional flow by the iterative solution of the two-dimensional flows on the S_1 and the S_2 surfaces. The solution of the meridional flow is only possible if the distribution of angular momentum rV_θ is known on the S_2 surfaces; this distribution is computed by the solution of the flow on the S_1 surfaces. However, the calculation of the blade-to-blade flow (S_1 surfaces) requires the knowledge of the geometry of the streamlines in the meridional plane, as well as the distance between two adjacent streamlines surfaces, which are obtained from the solution of the meridional flow.

The flow on the S_1 and S_2 surfaces can be solved numerically using different methods like the streamline curvature method [2], the finite element method and the singularity method (boundary elements). In the present work the streamline curvature method is used for the solution of the meridional flow and a singularity method is utilized for the blade-to-blade flow.

3. DESIGN OF INLET GUIDE VANES

The through-flow analysis approach described in section 2. is applied to the design of a conical inlet guide vane system of a small hydraulic turbine. The bladed duct has six vanes. The vanes are placed between two coaxial conical wall surfaces with a common vertex, which coincide with the inner and the outer walls of the guide vane system. The cone angles of the inner and the outer walls are $\phi = 15^\circ$ and $\phi = 32^\circ$, respectively. Upstream of the guide vanes is a cylindrical annular duct, and the flow at the inlet

section of the conical zone is assumed to be uniform without swirl ($rV_\theta = 0$).

Three steps need to be considered in the design of any turbine:

a) Specification of the design variables: flow rate Q_η, available head H_η and rotor speed N.

b) Definition of the velocity diagrams upstream and downstream of the blade rows.

c) Calculation of the blade geometry: camber and thickness distributions and cascade chord-to-pitch ratio c/p.

The specification of the design variables H_η, flow rate Q_η and rotor speed N can be done starting from one of these variables (for example the available head H_η) and computing the other two variables from dimensionless values of the tip speed velocity, $k_u = U/(2gH_\eta)^{1/2}$ and the meridional velocity $k_{V_m} = V_m/(2gH_\eta)^{1/2}$, obtained from the experience from different manufacturers of hydraulic turbines [3, 4]. A hub-to-tip ratio $D_H/D = 0.44$ is chosen for the rotor. The radial distribution of the angular momentum rV_θ at the exit of the guide vanes (inlet section of the rotor) can then be calculated from the known values of H_η, Q_η and N.

3.1. Computation of the Meridional Velocity Field Between the Guide Vanes

The meridional flow field through the guide vanes is computed by the streamline curvature method as described in [2]. The following distribution of the angular momentum is prescribed along the median surface of the vanes:

1 - The angular momentum is constant along the span at the trailing and the leading edges.

2 - Between the leading and the trailing edges the angular momentum follows a cosine law distribution

$$rV_\theta = \frac{K}{2}\left[1 - \cos(\pi x')\right], \tag{1}$$

where K is the maximum angular momentum at the trailing edge and x' is a dimensionless distance measured along a straight line containing the common vertex ($x' = 0$ at the leading edge and $x' = 1$ at the trailing edge). It is noted that the x' derivative of the above cosine law distribution is zero for $x' = 0$ and $x' = 1$, thus respecting the zero load condition at the leading and trailing edges of the vanes.

3.2. Computation of the Blade-to-blade Velocity Field Between the Guide Vanes

The method described in [5] for the velocity potential due to a row of vortex and source lines spanning a conical annular duct is used for the computation of the flow field through the conical cascade of guide vanes. The walls are at $\phi = \phi_1, \phi = \phi_2\,(0 < \phi_1 < \phi_2)$. The expressions for the velocity potential induced by these rows of vortex and sources when the angular distance between the conical walls becomes infinitely small are also presented in [5]. The induced velocities at a point $z(x, y)$ due to a vortex or a source located at $z_0(x_0, y_0)$ are obtained from the potential velocity derivative and may be split into two components: the first one due a two-dimensional conical cascade (U_1, V_1) and the other one due the thickness variation of the conical layer (U_{r_2}, V_{ψ_2}) and (U_{r_3}, V_{ψ_3}),

$$U_1 - iV_1 = \frac{q}{2\pi}\left[\frac{1}{z - z_0} + \frac{Z^*}{2z}\frac{(z^*)^{-Z^*} + 1}{1 - (z^*)^{-Z^*}}\right], \tag{2}$$

$$U_{r_2} = \frac{qZ^*}{4\pi}\left[\pm\frac{1}{r}\left(1 - \frac{r_0}{r}\right)\right], \quad V_{\psi_2} = 0, \tag{3}$$

$$U_{r_3} = -\frac{qZ^*}{2\pi r}\sum_{n=1}^{\infty}\cos\left[nZ^*(\psi - \psi_0)\right]\Lambda_1, \tag{4}$$

$$V_{\psi_3} = \frac{qZ^*}{2\pi r}\sum_{n=1}^{\infty}\sin\left[nZ^*(\psi - \psi_0)\right]\Lambda_2, \tag{5}$$

with

$$\Lambda_1 = \left(\pm 1 - \frac{1}{2\alpha_n}\right)(r^*)^{\pm\alpha_n - \frac{1}{2}} \mp (r^*)^{\pm nZ^*}, \tag{6}$$

$$\Lambda_2 = \left(\frac{nZ^*}{\alpha_n}\right)(r^*)^{\alpha_n - \frac{1}{2}} \mp (r^*)^{nZ^*}, \tag{7}$$

where $r^* = r/r_0$, $z^* = z/z_0$, $Z^* = Z/\sin\phi$, r is the radial direction in the spherical co-ordinates system (r, ϕ, θ) and ψ is the tangential direction on the unfolded conical surface. Similar equations can be derived for the velocity induced by the vortex lines. The velocity induced by sources and vortex distributions over the panels are computed by a numerical gaussian integration. The number of terms of the series to be considered in Eqs. (4) and (5) depends on the value of r^* (the number of terms increases when r^* approaches unity). The velocity and the pressure fields over the surface are computed using a panel method [6] with linear elements and constant strength distributions of sources and vortices. The resulting linear system of equations is solved by a Gauss elimination direct method.

3.3. Computation of the Aerodynamics Parameters of the Guide Vanes

For economical reasons, simple shapes are considered in the design of the guide vanes. The mean lines for the hub and shroud profiles are arcs of circumference on the unfolded conical surfaces.

The first step consists in a conformal transformation from a rectilinear straight (cylindrical) cascade to a conical cascade. This transformation allows

the change from the cartesian plan $z(x, y)$ to the unfolded conical plane $\zeta(r, \psi)$,

$$z = \frac{Zp}{2\pi \sin\phi} \ln\zeta \tag{8}$$

where $p = 2\pi R_0/Z$ is the pitch of the cylindrical cascade, with $R_0 = \sqrt{R_1 R_2}$ (here the subscripts 1 and 2 indicate the inlet and the outlet sections of the conical cascade, respectively). For a rectilinear straight cascade with circular-arc profiles the inlet and the outlet velocity conditions are related to the stagger angle λ as follows [7]: $\tau_1 + \tau_2 = 0$, $\tau_2 + \beta_2 = \lambda$ and $\tau_1 = \lambda$, where τ_1 and τ_2 are the angles of the velocity vector relative to the chord of the profile and $\beta_2 = \arctan V_\theta/V_m$. For the hub and the shroud sections, the above conformal transformation is used to define (a) the length of the chord, (b) the shape of the mean line and (c) the camber that will be changed in an ultimate phase of the design.

A constant 1.5% thickness distribution for the vane section is prescribed, except near the leading and trailing edges. The final shape of the profiles is obtained combining the thickness and camber distribution as for the NACA sections [8].

A panel method code based on Eqs. 2 to 5 is used to optimize the pressure distribution over the blade surface by modifying the camber and the stagger angles of the vanes at the hub ($\phi = 15°$) and the shroud ($\phi = 32°$).

The meridional distributions of rV_θ and V_m at the exit section of the guide vane system are computed from the solution of the meridional flow using the streamline curvature method as referred in Section 3.1.. The spanwise distributions of the meridional and the circumferential components of the velocity at the exit section of the guide vanes are used as input for the panel method program. The stagger angle is adjusted so that the prescribed value of rV_θ, i.e. the circulation Γ, around the section is obtained. The section camber is then optimized so that the pressure distribution on the upper surface is smooth without high suction peaks near the leading edge. The boundary of the vane sections is discretized into 200 elements. A constant strength distribution of sources is assumed at each panel, as well as constant intensity vortex distribution is imposed over the section contour.

Assuming the vane sections at the hub and the shroud to be known, the median surface of the vane is generated by connecting with a straight line the leading edges of the two profiles, and moving it along the mean line of each profile up to the trailing edge. Therefore the median section of the vane is a single curvature surface.

The relative position of the vane sections along the circumferential direction is adjusted to minimize the slope of the leading and the trailing edges relative to the radial direction. The angles of the leading and trailing edges relative to the radial direction are equal in magnitude with opposite signs. The shape of the mean lines of intermediate sections are obtained by the intersection of the conical surfaces ($15° < \phi < 32°$) with the straight line that generates the vane mean surface. An isometric perspective of the conical-walled inlet guide vane row is plotted in Fig. 1 and the geometric characteristics of the vane sections are shown in Table 1, for different ϕ angles.

Table 1. Characteristics of the vane sections

$\phi(°)$	c (m)	$f_{\max}/c$	$t_{\max}/c$	$\lambda(°)$
15.00	0.333	0.113	0.0150	33.55
19.25	0.341	0.103	0.0146	28.96
23.50	0.354	0.092	0.0141	24.85
27.75	0.371	0.082	0.0135	20.88
32.00	0.393	0.071	0.0127	17.00

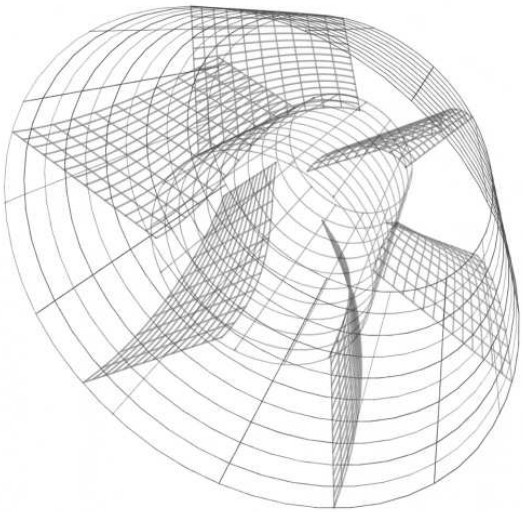

Figure 1. Isometric perspective of the inlet guide vanes system showing the hub and the shroud conical surfaces.

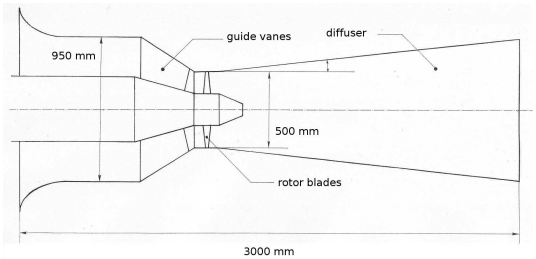

Figure 2. Schematic representation of the turbine model.

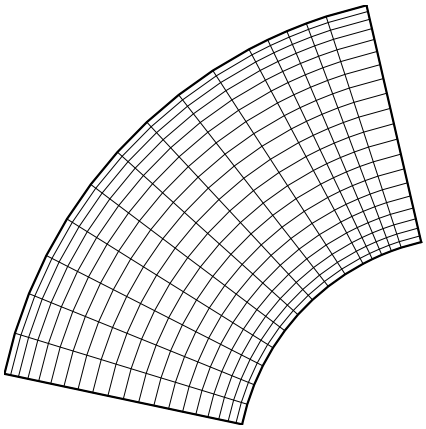

Figure 3. Grid of measuring points.

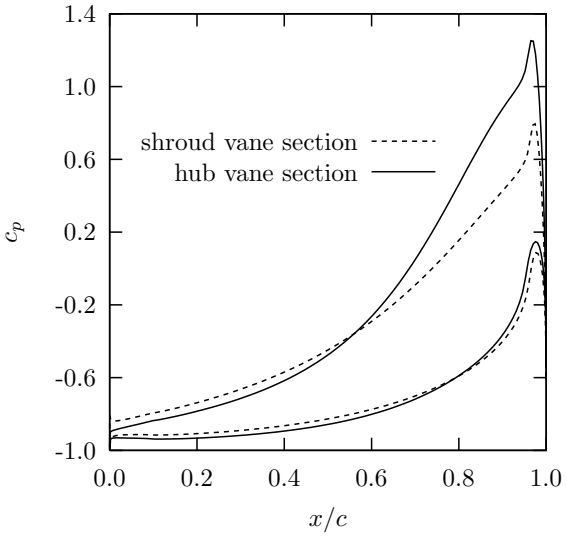

Figure 4. Pressure coefficient distribution around the hub and shroud vane sections.

4. EXPERIMENTAL FACILITY

The experimental facility shown in Fig. 2 was built to validate the whole turbine design. Air is the working fluid. The turbine is composed by an upstream annular duct with $950\,mm$ outer diameter, an inlet conical guide vane system, a 0.5 m tip diameter rotor (not installed in the present tests) and a $2\,m$ long and 7° angle diffuser. There is a plenum chamber between the fan and the turbine diffuser. The flow rate is measured by a calibrated nozzle with an ellipsoidal longitudinal section and a $400\,mm$ diameter throat.

The measurement of the velocity and pressure distributions at the outlet sections of the guide vane system were made with a five-hole probe: one central hole and four equidistant lateral holes (two holes with the centre on a plane normal to the axis of the probe - right and left holes - and other two on the axis of the probe - upper and lower holes). The probe has two degrees of freedom: a linear displacement and a rotation around its axis. The radial and yaw movements of the probe are produced by a mechanical system with a minimum displacement of $0.01\,mm$ and a minimum angle of rotation of 0.1°. The probe axis is placed in a meridional plane with a displacement direction making an angle of 20º relative to the radial direction. The direction of the flow is measured by rotating the probe around its axis till the pressure difference between the left and right holes vanishes. The velocity direction, the total pressure and the dynamic pressure are obtained by linear interpolation from the calibration curves of the probes.

5. EQUATIONS FOR THREE-DIMENSIONAL FLOW

The equations describing three-dimensional adiabatic compressible gas flow can be written in the so-called conservative form [9],

$$\partial_t \underline{U} + \partial_x \underline{F} + \partial_y \underline{G} + \partial_z \underline{H} = \underline{0}, \tag{9}$$

with $\underline{x} \in \Omega$ and $t \in [0, \mathcal{T}]$. The vector of conservative variables, $\underline{U}$, the flux vectors, $\underline{H}$, $\underline{G}$ and $\underline{H}$ are given by

$$\underline{U} = \begin{pmatrix} \varrho \\ \varrho u \\ \varrho v \\ \varrho w \\ \varrho E \end{pmatrix}, \qquad \underline{F} = \begin{pmatrix} \varrho u \\ \varrho u^2 + p \\ \varrho uv \\ \varrho uw \\ \varrho uH \end{pmatrix},$$
$$\underline{G} = \begin{pmatrix} \varrho v \\ \varrho uv \\ \varrho v^2 + p \\ \varrho vw \\ \varrho vH \end{pmatrix}, \underline{H} = \begin{pmatrix} \varrho w \\ \varrho uw \\ \varrho vw \\ \varrho w^2 + p \\ \varrho wH \end{pmatrix}, \tag{10}$$

The system of equations (9) is subject to suitable initial conditions and boundary conditions. The variables of the system are: the density, ϱ; the flow velocity components, $\underline{u} = (u, v, w)$; the pressure, p; the specific total energy, E; and the specific total enthalpy, $H = E + p/\varrho$. The first equation is known as the equation of continuity and states the conservation of mass. The second, third and fourth equations result from the momentum conservation. The fifth equation expresses the conservation of energy. To close the system, we use the equation of state $p = \varrho RT$, where R is the gas constant. This equation introduces an additional variable, the temperature of the fluid, T. Assuming that the specific heat at constant pressure, C_p, is constant, in the range of the pressure and the temperature of the flow, then $E = C_v T + V^2/2$, $H = C_p T + V^2/2$, $V^2 = \underline{u} \cdot \underline{u}$ and $R = C_p - C_v$. The above relationships close the system. Therefore, the pressure can be written as $p = (\gamma - 1)\left(\varrho E - \varrho V^2/2\right)$, where $\gamma = C_p/C_v$.

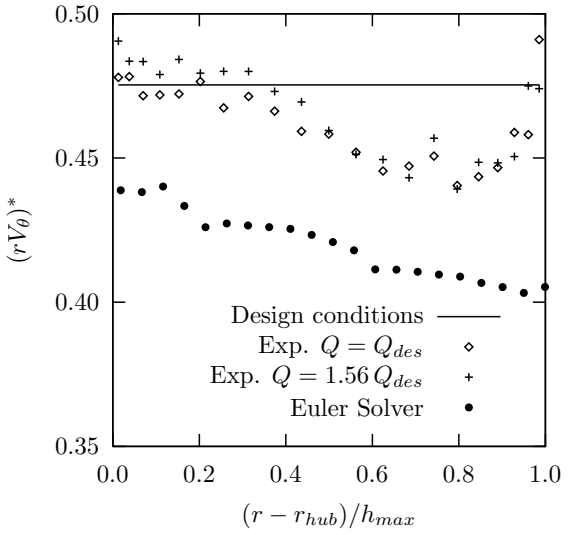

Figure 5. Circumferential averaged angular momentum distribution.

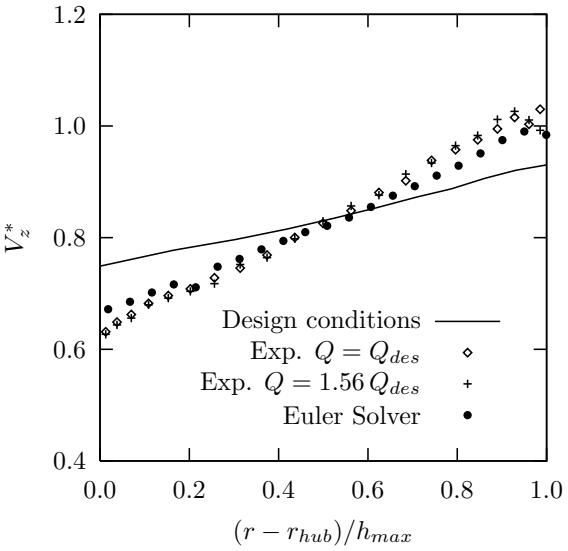

Figure 6. Circumferential averaged axial velocity component distribution.

6. THE RUNGE-KUTTA DISCONTINUOUS GALERKIN METHOD

The computational domain Ω is split into N tetrahedral finite elements, Ω_j, not necessarily with linear shape. To find the approximate solution $\underline{U}_h$, a weak formulation is used as follows. First, each equation of the system (9) is multiplied by an arbitrary smooth function ϕ, and integrated in Ω_j. Integration by parts gives

$$\int_{\Omega_j} \phi_h \partial_t \underline{U}_h d\Omega - \int_{\Omega_j} \nabla\phi_h \cdot \underline{F}\left(\underline{U}_h\right) d\Omega + \int_{\partial\Omega_j} \phi_h \, \underline{F}^* \cdot \underline{n} \, d(\partial\Omega) = \underline{0}, \tag{11}$$

where the functions ϕ were replaced by discrete test functions ϕ_h, the exact solution $\underline{U}$ by the approximate solution $\underline{U}_h$, and the non-linear flux, $\underline{F}$, in $\partial\Omega_j$ by a numerical flux function $\underline{F}^* = \underline{F}^*\left(\underline{U}_h^-, \underline{U}_h^+, \underline{n}\right)$. In the present paper the well-known Lax-Friedrichs flux function is used [10]

$$\underline{F}^* = \frac{1}{2}\left(\underline{F}(\underline{U}_h^-) + \underline{F}(\underline{U}_h^+) + |\lambda_{\max}|(\underline{U}_h^- - \underline{U}_h^+)\right) \tag{12}$$

with $|\lambda_{\max}| = |\underline{u} \cdot \underline{n}| + a$, where $a = (\gamma p/\rho)^{1/2}$ is the speed of sound.

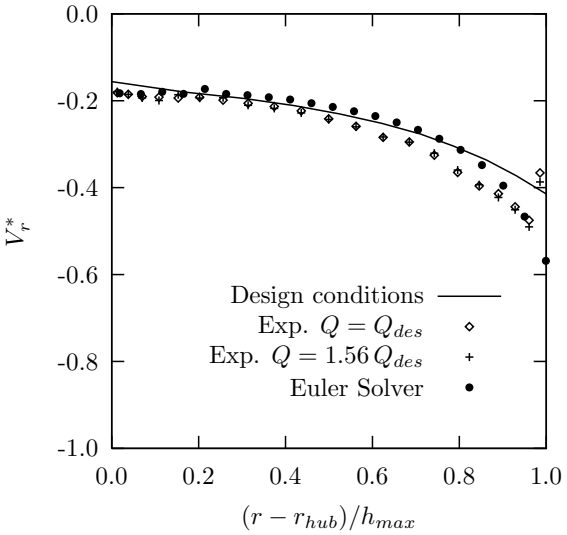

Figure 7. Circumferential averaged radial velocity component distribution.

7. RESULTS

Measurements with the five-hole probe described in Section 4. were made at the outlet section of the guide vanes, at 16 meridional planes with a circumferential amplitude of 65° - larger than the 60° angular amplitude of the pitch of the cascade, Fig. 3. The first reading line is placed at $\varphi = 13°$, where φ is angle measured in a plane normal to the turbine axis, with $\varphi = 0$ when the radial direction coincides with the vertical direction. There are 14 five-degrees-spaced lines from $\varphi = 13°$ to $\varphi = 78°$ with two intermediate lines at $\varphi = 21.5°$ and $\varphi = 25.5°$, Fig. 3. At each reading line, the span of the probe displacement is $137.5\,mm$. A total of N =21 points are considered at each measurement line with a cosine law distribution for the position of the probe,

$$h_i = h_1 + \frac{h_{\max}}{2\,\cos 20°}(\cos\varphi_1 - \cos\varphi_i) \tag{13}$$

where h is the normal distance to the inner wall and $h_{\max} = 137.5\,mm$. The values of ϕ_i are given by

$$\phi_i = \phi_1 + \frac{180° - 2\times 20°}{N-1}(i-1) \tag{14}$$

with $i = 1, \ldots, N-1$.

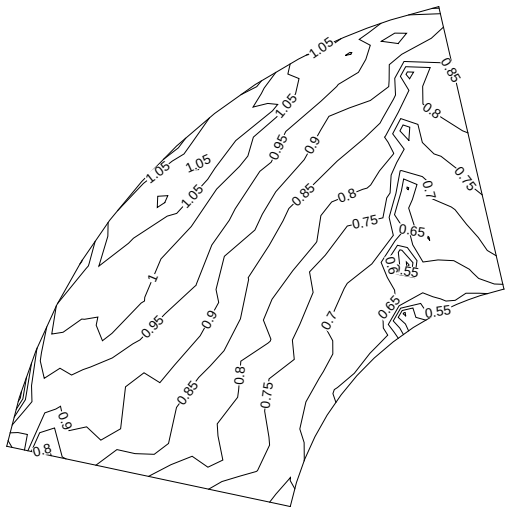

Figure 8. Axial velocity isolines at the measurement section.

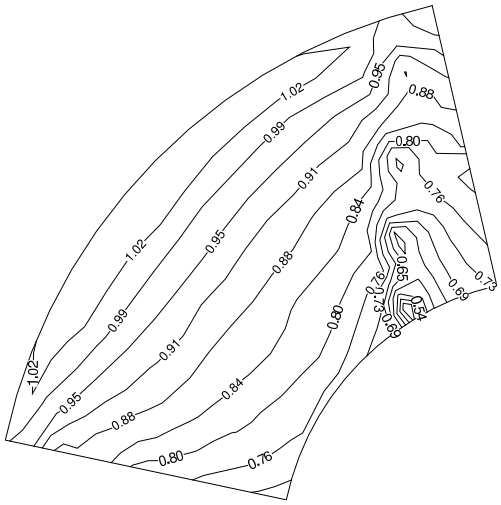

Figure 9. Axial velocity isolines as computed by the Euler solver.

A total of $16 \times 21 = 336$ measuring points were taken for two different flow rates $Q = Q_\eta$ and $Q = 1.56 \times Q_\eta$. The design values are $Q_\eta = 3.36\, m^3/s$ and $(rV_\theta)_\eta = 2.491\, m^2/s$. The velocity is non-dimensionalized by the mean axial-velocity at the rotor inlet section

$$V_{\rm ref} = \frac{4Q}{\pi\,(D^2 - D_{\rm H}^2)} \tag{15}$$

where $D = 0.5\, m$ is the diameter of the rotor tip and $D_{\rm H} = 0.107\, m$ is the diameter of the rotor hub. The angular momentum is made non-dimensional by the velocity $V_{\rm ref}$ and the rotor outer radius.

The design pressure coefficient distributions around the contour of hub and shroud sections are plotted Fig. 4. Except in the vicinity of the leading and trailing edges, these distributions show a monotone flow acceleration that increases the vane pressure load with the axial distance. As a consequence of the prescribed design law Eq. (1), the vanes introduce small deflection in the flow up to about 30% of the vane chord.

The numerical simulation was performed in a unstructured tetrahedral mesh with 40764 quadratic elements to obtain good geometrical approximation in the curved boundaries, as required [11]. The inlet flow Mach number is 0.1. The computed numerical solution used a linear set of basis functions to achieve second-order accuracy. The boundary conditions were imposed using an extension for three-dimensional flow of the formulation presented in [12].

The pressure coefficient distributions around the contour of hub and shroud sections are plotted Fig. 4. Except in the vicinity of the leading and trailing edges, these distributions show a monotone flow acceleration that increases the vane pressure load with the axial distance. As a consequence of the prescribed design law Eq. (1), the vanes introduce small deflection in the flow up to about 30% of the vane chord.

Results shown in Fig. 5 to 7 show the design values given by the solution of the meridional flow and the values obtained by a circumferential mass flow average of the experimental values and the results from the 3D Euler solver. These figures plot the span-wise distributions of the dimensionless axial and radial velocity components, $V_x^* = V_x/V_{\rm ref}$, $V_r^* = V_r/V_{\rm ref}$, and the angular momentum $(rV_\theta)^* = (2rV_\theta)/(DV_{\rm ref})$.

The results plotted in Fig. 5, 6 and 7 show fairly good agreement between the experimental, the design and the Euler code results. It is shown that the design method is able to produce the desired flow deflection distribution with good accuracy. The small differences found in Fig. 5 between the design values and the distribution of the experimental results are attributed to the three-dimensional effects not taken into account by the quasi-three-dimensional design method. This is corroborated by the close agreement found between the trends of the experimental and the Euler result distributions. According to the radial equilibrium equation [13] the slight increase in the r derivative of the axial velocity distribution (Fig. 5) is in close agreement with the small decrease in the r derivative of the angular momentum distribution (Fig. 6). The isolines for the angular momentum and the axial velocity component at the measurement plane are plotted in Fig. 8 and 10. The isolines plotted in Fig.s 8 and 9 for the experimental and the numerical results for the axial velocity show a fairly good agreement. Figure 11 represents the distribution of the values of the total pressure coefficient c_{p_0} at the measurements plane. The values of c_{p_0}

Figure 10. Angular momentum isolines at measurement section.

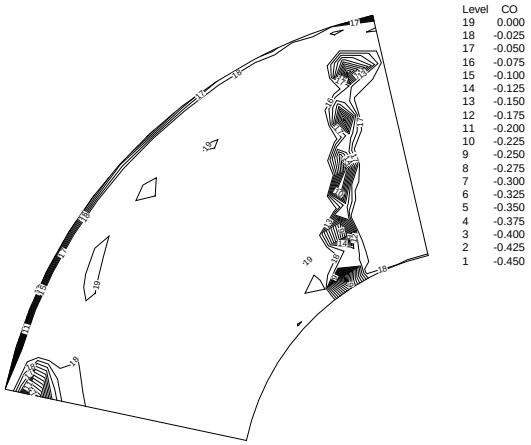

Figure 11. Total pressure coefficients isolines at the measurement section.

are almost constant showing that the pressure losses though the inlet guide vanes are small. A loss of total pressure is observed close to the outer wall due to the presence of the boundary layer, although the dimension of the probe tip and the interaction of the probe with the wall do not allow good precision of the results obtained close to a wall. In fact, the probe was unable to detect the boundary layer at the hub surface. Figure 11 also shows the thin wakes of the blades.

8. CONCLUSIONS

A guide vane system of a small hydraulic turbine was designed using a quasi-three-dimensional method, combining the streamline curvature method for the solution of the meridional flow and the panel method for the blade-to-blade flow. A conical diffuser-model with six fixed vanes was manufactured and tested in an airflow rig. Experimental results for the velocity and pressure distributions obtained with a five-hole probe are compared with the design values and the numerical values obtained using a three-dimensional Euler code. The experimental results show that the final shape of the vanes produces with good approximation the prescribed angular momentum distribution at the exit of the guide vane system, although small deviations between the experimental and the design values appear at the axial and the radial velocity distributions. Results from a three-dimensional Euler code have shown fairly good agreement with the experimental results. This was seen to be an important tool for the analysis of the flow through a guide vane system.

REFERENCES

[1] C. Wu. General through-flow theory of fluid flow with subsonic or supersonic velocity in turbomachinery of arbitrary hub and casing shapes. *NASA TN 2302*, 1951.

[2] J. D. Denton. Throughflow calculations for transonic axial flow turbines. *ASME Journal of Engineering for Power, Vol. 97, pp 549-560*, 1978.

[3] J. Raabe. *Hydro Power*. VDI-Verlag, Düsseldorf, 1985.

[4] N. Nechleba. *Hydraulyc Turbines, their Design and Equipment*. Artie, Prague, 1957.

[5] A. F. de O. Falcão and L. M. C. Ferro. Flow field due to a row of vortex and source line spanning a conical annular duct. *Journal of Engineering Mathematics*, 23:203–208, 1989.

[6] J. L. Hess and A. M. O. Smith. Calculation of potential flow about arbitrary bodies. *Progress in Aeronautical Sciences*, 8:1–138, 1967.

[7] N. Scholz. *Aerodynamics of Cascades*. AGARDograph No. 220, 1977.

[8] I.H. Abbott and A.E. von Doenhoff. *Theory of Wing Sections*. Dover, 1959.

[9] J. C. C. Henriques and L. M. C. Gato. A multidimensional upwind matrix distribution scheme for conservative laws. *Computers & Fluids*, 33(5-6):755–769, 2004.

[10] B. Cockburn. Discontinuous galerkin method. In T. J. Barth and H. Deconinck, editors, *High-Order Methods for Computational Physics*, volume 9 of *Lecture Notes in Computational Science and Engineering*. Springer, 1999.

[11] F. Bassi and S. Rebay. High-order accurate discontinuous finite element solution of the 2d euler equations. *Journal of Computational Physics*, 2(138):251–285, 1997.

[12] L. M. C. Gato and J. C. C. Henriques. Dynamic behaviour of high-pressure natural-gas flow in pipelines. *International Journal of Heat and Fluid Flow*, 26(5):817–825, 2005.

[13] B. Lakshminarayana. *Fluid Dynamics and Heat Transfer of Turbomachinery*. John Wiley & Sons, Inc, 1996.

Conference on Modelling Fluid Flow (CMFF'06)
The 13th International Conference on Fluid Flow Technologies
Budapest, Hungary, September 6-9, 2006

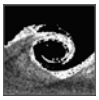

NUMERICAL STUDY OF THE CAVITATION PHENOMENON IN HYDRAULIC TURBINES

Daniel BALINT[1], Romeo RESIGA[2], Sebastian MUNTEAN[3], Ioan ANTON[4]

[1] Corresponding Author. Department of Hydraulic Machinery, University Politehnica of Timisoara, Bul. Mihai Viteazul 1, RO – 300222 Timisoara, Romania. Tel.: +40 -256 -403692, Fax: +40 -256 -403700, E-mail: balint@acad-tim.tm.edu.ro
[2] Department of Hydraulic Machinery, University Politehnica of Timisoara. E-mail: resiga@mh.mec.utt.ro
[3] Romanian Academy – Timisoara Branch. E-mail: seby@mh.mec.utt.ro
[4] Romanian Academy – Timisoara Branch. E-mail: anton@acad-tim.tm.edu.ro

ABSTRACT

This paper presents the numerical investigation of the 3D two-phase flow in the hydraulic turbines, particularly in Kaplan ones. First, the 3D single phase flow in the full turbine is computed (spiral casing, stay and guide vanes, runner and draft tube). Then assuming a stationary flow at the inlet of the runner, the two-phase flow was computed in the runner domain.

The goal is to develop a technique of studying the 3D flow and to compare different designs at same cavitational conditions. For that, the volume of the vapor was computed for each cavitational regime. This helps to define all stages of the turbine: the cavitation inception, the critic cavitation and the industrial limit of accepted cavitation. The modification of the pressure distribution on the runner blades due to the cavitation is analyzed. Further, the distribution of the wall shear stress is investigated to visualize the region of the instability region, cavitation detachment and re-attachment on the runner blades.

The whole study is made on Kaplan hydraulic turbines of Iron Gates I power plant at best efficiency operating point.

Keywords: design comparison, full 3D Kaplan runner, numerical computation and analysis, two-phase fluid flow

NOMENCLATURE

$C_p = \dfrac{p - p_{ref}}{\rho g H}$ [-] pressure coefficient

H	$[m]$	turbine head
g	$[ms^{-2}]$	gravity
p	$[Pa]$	static pressure

$\sigma_{inst} = \dfrac{p_{atm} - p_{vap} \mp H_s}{\rho g H}$ [-] Thoma number [1]

η	[-]	hydraulic turbine efficiency
ρ	$[kg/m^3]$	density

Subscripts and Superscripts

atm	value of the atmosphere
out	outlet section
ref	reference location
s	suction
vapor	secondary phase of the flow

1. INTRODUCTION

The hydraulic turbines became in the last decades the interest of the engineering due to the low price of the energy delivered. In the same idea, the Kaplan turbines of Iron Gates I power plant were refurbished by replacing the runner blades and the auxiliary system of automatization [2]. The old Russian runner blades were suspected to have not-optimal cavitating performances, but also the goal was to improve the net power of the plant [3, 4].

This paper clearly shows the numerical computing analysis of the old blades at best efficiency operating point [5]. In this study, the two-phase flow was employed in the runner of the turbine and the its behavior was analyzed for a wide range of cavitating conditions: from the non-cavitating stage to super-cavitating regime [6]. A detailed analysis will be made for the super-cavitating regime describing the types of the cavitation encountered in the runner domain of the turbine: the leading edge cavitation, the tip cavitation close to the trailing edge and the unsteady cavitation.

The intention of this paper is also to develop a methodology for comparing quantitatively the cavitating flows in the hydraulic turbomachinery. Moreover, very useful for the hydraulic engineers is to compute by numerical simulation the level of the turbine corresponding to the cavitation inception. Therefore, this issue was taken into account in this paper.

2. DOMAIN OF THE COMPUTATION

The present work is made for the Kaplan turbines of Iron Gates I power plant. The interest for these turbines increased in the last decade when a rigurous stage of refurbishment was made for the runner blades and the auxiliary equipment of automatization.

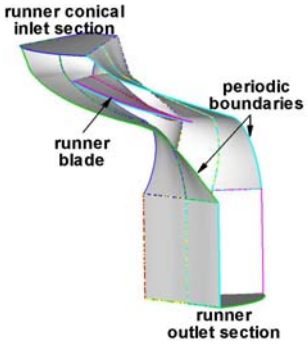

Figure 1. 3D runner interblade channel of the Kaplan turbine

In the above figure, the domain of computation is presented. This is represented by one single interblade channel of the hydraulic runner. It was decomposed from the whole hydraulic channel of the turbine by employing the mixing interface technique for coupling the flow with the one of the distributor.

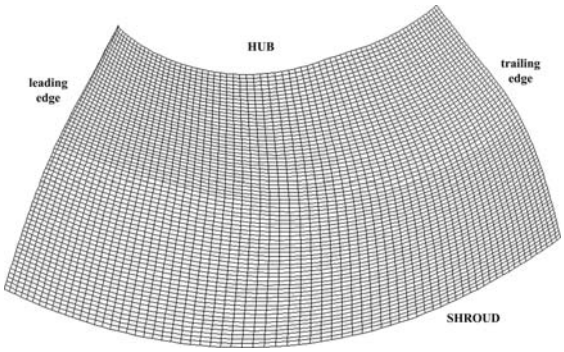

Figure 2. Discretization of the runner blade with quadrilateral cells

The inflow velocity field is considered steady as delivered by the distributor of the turbine. Respectively, at the outlet of the runner, the radial pressure equilibrium boundary condition was used which links the radial pressure variation to the tangential velocity of the flow.

Whole investigation presented in this paper corresponds to best efficiency operating point of the Kaplan turbines. The runner diameter is 9.5 [m] and its speed is 71.429 [min^{-1}]. The discharge is equal to 600 [m^3/s] and the head is 28.9 [m].

The runner blade surface was discretized using quadrilaterals and the domain was meshed with hexahedrals (approx. 550.000 cells) [7, 8].

3. PROBLEM SETUP

The setup of the two-phase flow comprises the turbulence model employed, the cavitation model and the boundary conditions used for the flow. For the investigation, the Fluent commercial software was employed.

3.1. Cavitating flow modeling

The flow motion is governed by the continuity equation and by the momentum equation, together with the transport equations for the turbulent kinetic energy k and its dissipation ε.

The continuity equation for the two-phase model (water and water vapour) is as follows:

$$\frac{\partial \rho_m}{\partial t} + \nabla \cdot \left(\rho \vec{v}_m\right) = \dot{m} \tag{1}$$

where $\vec{v}_m$ is the mass-averaged velocity, ρ_m is the mixture density and $\dot{m}$ is the mass transfer due to cavitation [9].

The momentum equation for the mixture can be obtained by summing the individual momentum equations for all phases as:

$$\begin{aligned} &\frac{\partial\left(\rho_m \vec{v}_m\right)}{\partial t} + \nabla \cdot \left(\rho_m \vec{v}_m \vec{v}_m\right) = -\nabla p + \\ &+ \nabla \cdot \left[\mu_m \left(\nabla \vec{v}_m + \nabla \vec{v}_m^T\right)\right] + \rho_m \vec{g} + \\ &+ \vec{F} + \nabla \cdot \left(\sum_{k=1}^{n} \alpha_k \rho_k \vec{v}_{dr,k} \vec{v}_{dr,k}\right) \end{aligned} \tag{2}$$

where n is the number of phases, F is a body force, μ_m is the viscosity of the mixture and $\vec{v}_{dr,k}$ is the drift velocity for secondary phase k:

$$\vec{v}_{dr,k} = \vec{v}_k - \vec{v}_m \tag{3}$$

The volume of the individual bubbles is a function of space and time as follows:

$$\phi\left(\vec{r}, t\right) = \frac{4}{3}\pi R^3 \tag{4}$$

where R is the bubble radius. The volume fraction of vapor is defined as:

$$\alpha_v = \frac{\phi\eta}{1 + \phi\eta} \tag{5}$$

where η is the population or number of bubbles per unit volume of liquid. The volume fraction equation is derived from the continuity equation of the mixture. By assuming an incompressible liquid l, the following equation is obtained:

$$\frac{\partial(\alpha_p)}{\partial t}+\nabla(\alpha_p\vec{v}_m)=\frac{\rho_l}{\rho_m}\frac{\eta}{(1+\eta\phi)^2}\frac{d\phi}{dt}+ \\ +\frac{\alpha\rho_v}{\rho_m}\frac{d\rho_v}{dt} \quad (6)$$

The Rayleigh-Plesset equation relates the pressure and the bubble volume:

$$R\frac{d^2R}{dt^2}+\frac{3}{2}\left(\frac{dR}{dt}\right)^2=\frac{p_B-p}{\rho_l}-\frac{2\sigma}{\rho_l R}- \\ -4\frac{\mu_l}{\rho_l R}\frac{dR}{dt} \quad (7)$$

where p_B denotes the pressure within the bubble, represented by the sum of a partial pressure p_v of the vapor and a partial pressure of non-condensable gas p, and σ is the surface tension coefficient.

The process of bubble growth is given by:

$$\frac{dR}{dt}=\begin{cases}\sqrt{\frac{2(p_B-p)}{3\rho_l}}, p_v>p \\ -\sqrt{\frac{2(p_B-p)}{3\rho_l}}, p_v<p\end{cases} \quad (8)$$

3.2. Turbulence and wall approaches

The RNG k-ε turbulence model was employed in this computation, turbulence model implemented in commercial software Fluent 6 with a swirl factor equal to 0.07 [10]. For the near-wall treatment, the non-equilibrium wall function was used where the two-layers of the boundary layer is adopted to compute the budget of turbulent kinetic energy in the wall-neighboring cells [11]. The non-equilibrium wall functions are suitable for complex flows involving separation, reattachment, and impingement where the mean flow and turbulence are subjected to severe pressure gradients and change rapidly [12, 13].

3.3. Boundary conditions

The inflow boundary condition of the Kaplan runner is obtained using the mixing interface methodology to couple the flows of the runner and the distributor for the single phase flow modeling case. Therefore, a circumferentialy constant velocity distribution was imposed at inlet together with the turbulence intensity (2.3%) and length scale (4 *mm*).

The outflow boundary condition is given by the radial pressure equilibrium as follows:

$$\frac{\partial p}{\partial r}=\rho\frac{v_u^2}{r} \quad (9)$$

4. CAVITATION INVESTIGATION

The intention of this paragraph is to clearly present the methodology to investigate the cavitating flows in hydraulic machinery, particularly the two-phase numerical computations. The problem is represented by the need to numericaly compare the particular technical solutions by cavitation point of view, but also to compare the same technical solution in different cavitating conditions [14].

Whole this investigation is made for the best efficiency operating point of the Kaplan turbines from Iron Gates I power plant. These blades are the ones before the refurbishment of the plant.

Few cavitation types are encountered in the hydraulic machinery: the leading edge cavitation and the tip clearance cavitation on the suction side of the blade, but also cavitation on the pressure side for particular operating regimes of the turbine [15]. The goal is to analyze the types of the cavitation that mainly influence the hydraulic efficiency drop [16].

Further, the flow modifications due to cavitation occurrence and size are subjects of interest for this investigation.

4.1. Cavitation primary curve

In order to globaly have the information about the flow behavior in cavitating conditions in the Kaplan runner, the primary cavitation curve was computed [17, 18].

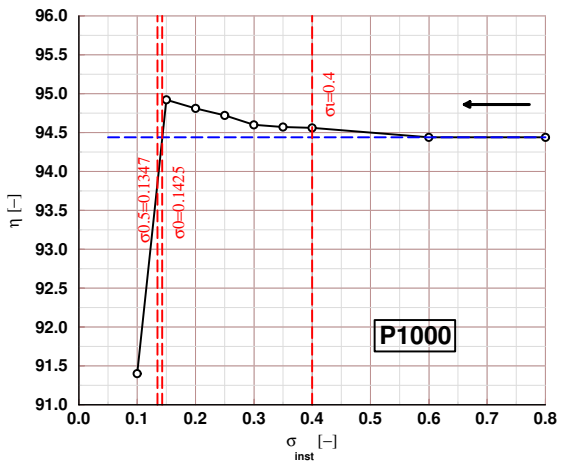

Figure 3. Primary cavitation curve of Kaplan turbine at best efficiency point computed numericaly (experimental curve not available)

This helps to analyze the stage of the cavitation which describes globaly the cavitating behavior. The non-cavitating regime for Thoma number equal to 0.80 was modified by reducing sequentially the pressure at the exit of the runner. So the cavitation inception was found for Thoma number equal to 0.40, the maximum efficiency of the turbine was found for Thoma number equal to 0.143 and the efficiency drop with 0.5% was found for σ_{inst} =

0.135 [19, 20]. These regimes are significant for industrial interpretation and therefore they will be analyzed in the following sections. For all the cavitating regimes, the snapshot of the runner blade was shown, together with the iso-pressure coefficient distribution and the streamlines for the wall shear stress. All of them are presented for the suction side of the runner blade where the cavitation occurred.

4.2. Cavitation occurrence and growth

The regime far from the cavitating conditions is presented first. This corresponds to σ_{inst} = 0.80. The comparison between the single-phase computation and this regime with two-phase flow has shown no notable differences for the pressure distribution. Therefore, the single-phase computation was excluded from this paper.

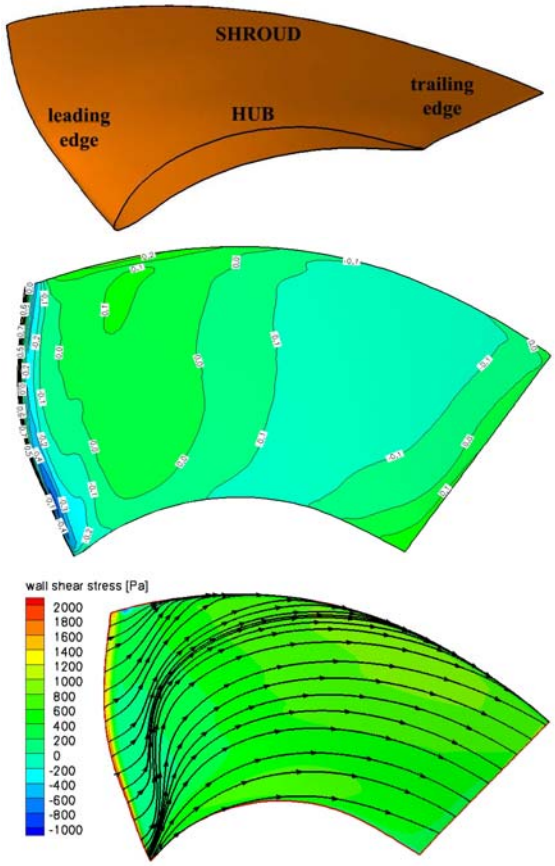

Figure 4. Operating regime corresponding to σ_{inst}=0.80 (runner blade suction side without cavitation [above], pressure coefficient [middle] and streamtraces of wall shear stress [below])

The wall shear stress distribution shows significant 3D motion from the hub to shroud of the suction side of the runner blade. These 3D effects occur as effects of the runner blade loading. The leading edge of the blade is significant loaded in the hub neighborhood, therefore the shear stress on the suction side of the blade presents locally a deviation to the tip of the runner blade. This influences substantially the 3D effects on the runner suction side even for this regime with no cavitation.

The regime of the turbine for which the cavitation was encountered corresponds to σ_{inst} = 0.40. For this regime, the cavitation occurred onto the suction side of the runner blade in the leading edge neighborhood close to the hub as shown in the pictures below.

The iso-pressure coefficient area corresponding to C_p=-0.4 ploted below presents a greater extention comparing to the regime if σ_{inst}=0.80. This particularity of the pressure field gives the hydrodynamic conditions leading to the cavitation inception in the runner domain of the hydraulic turbomachinery.

Even if the cavitation occurred onto the suction side of the runner blade, no visible modifications could be found for the wall shear stress distribution.

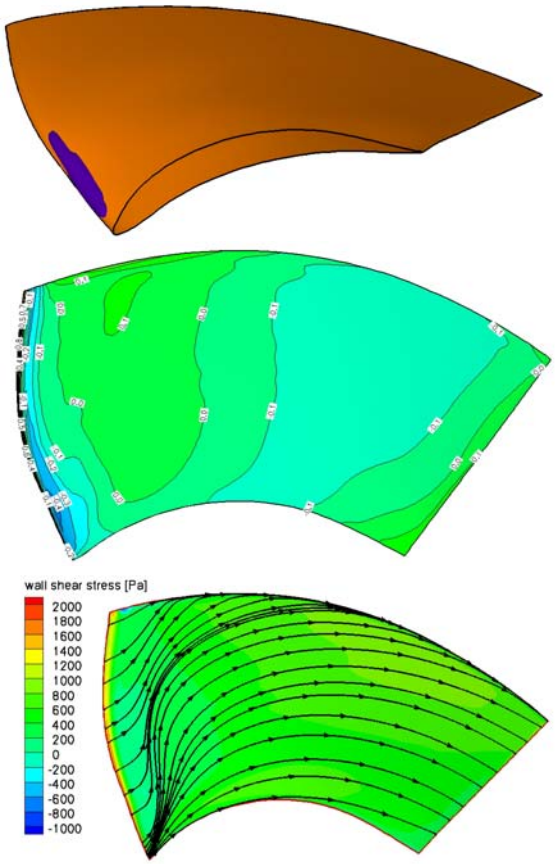

Figure 5. Operating regime corresponding to σ_{inst}=0.40 (runner blade suction side with cavitation [above], pressure coefficient [middle] and streamtraces of wall shear stress [below])

The hydraulic efficiency of the entire turbine was slighty lifted up in this cavitational regime stage (as shown in Figure 3).

This modification of the hydraulic efficiency is given by the increasing of the hydraulic torque of

the runner for constant hydraulic losses in the runner domain.

The next significant cavitational regime of the hydraulic turbine is represented by the σ_{inst}=0.15. For this case of numerical computation, the hydraulic efficiency of the turbine was maximum (approx. 95%). The leading edge of the suction side of the runner blade was found full of cavitation as well as in the shroud neighborhood close to the trailing edge of the runner blade [21]. This is extended in normal direction on blade as shown below.

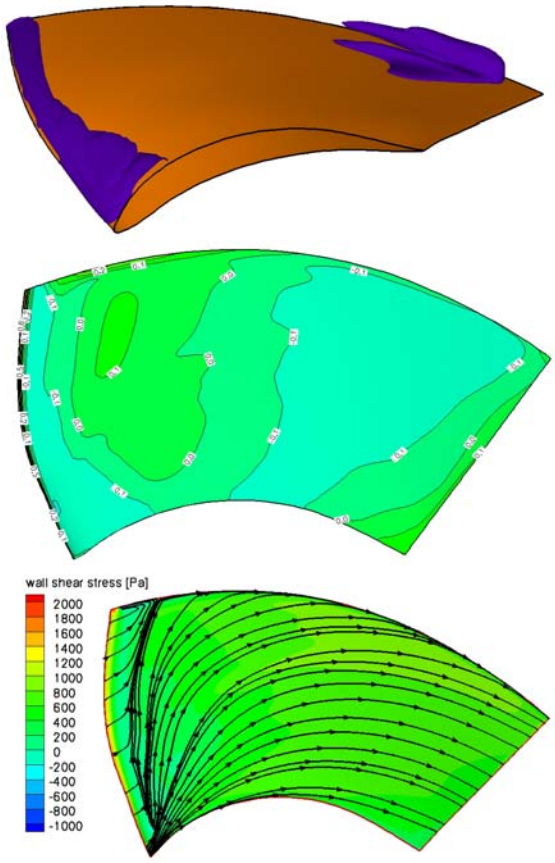

Figure 6. Operating regime corresponding to σ_{inst}=0.15 (runner blade suction side with cavitation [above], pressure coefficient [middle] and streamtraces of wall shear stress [below])

Comparing to the previous regime, this one shows a larger extention of the low pressure close to the trailing edge of the runner blade favouring the cavitation occurrence and growth in this region. Also, the extention of the low pressure on the leading edge of the runner blade was modified correlated with the cavitation location as shown in the above figure [22].

The streamtraces of the wall shear stress field in the leading edge neighborhood are deflected from hub to the shroud of the runner blade at the edge of the cavitation corresponding to the re-entrant flow downstream the cavitation. The direction of the flow is toward the shroud of the runner blade as a consequence of the blade loading at hub.

The final cavitational regime investigated is represented by σ_{inst}=0.10. The hydraulic efficiency of the turbine presents in this case a sharp drop as shown in Fig. 3. The leading edge cavitation on the suction side of the runer blade became double comparing to the previous cavitational regime affecting the pressure distribution for whole the suction side of the runner blade as shown in the figures below.

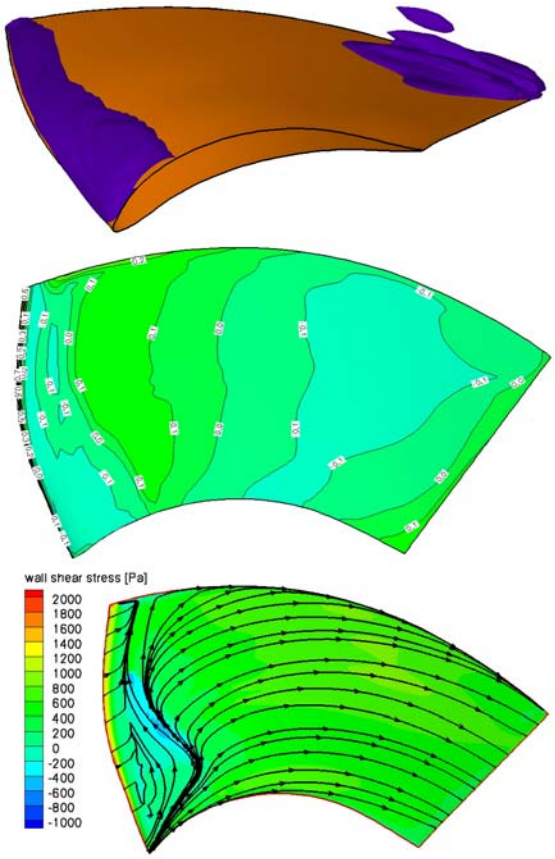

Figure 7. Operating regime corresponding to σ_{inst}=0.10 (runner blade suction side with cavitation [above], pressure coefficient [middle] and streamtraces of wall shear stress [below])

The effects of the cavitation fluctuation can be easily seen by the pressure sharp modification close to the leading edge of the runner blade suction side in the superior half part [23]. The constant region of the pressure coefficient equal to -0.1 found in the previous cavitational regime is now broken by higher pressure of C_p=0.0. Correspondingly, the wall shear stress in this region presents two sharp drops. This leads us to the conclusion that the re-entrant jets below the cavitation lead to flow vorticity that affects the global torque of the runner blade [24].

The details of the cavitation found for this cavitational regime are delivered in Figure 8. That

presents both the leading edge cavitation and the tip one close to the trailing edge of the runner blade suction side. The surface of constant 0.01 volume fraction for the secondary phase (water vapor) was built and presented in Fig. 8 for describing the cavitation extention and formation in the hydraulic runner of the turbine. The cavitation occurs starting right from the leading edge of the blade as the effect of the flow high speeds in this region. This is due to the leading edge high loading given by the blade flow incidence onto the blade.

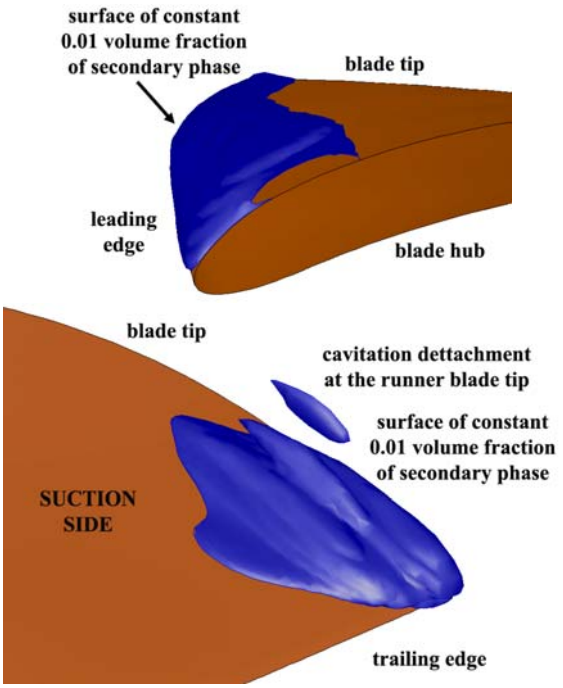

Figure 8. Details of cavitation at σ_{inst}=0.10

Further, the cavitation of this regime moved toward the trailing edge of the blade close to the tip comparing to the previous regime. This affects significantly the outflow angle of the runner blade and correspondingly the torque taken to the shaft of the runner [25].

This is even more clear when the location of the cavitation is taken into account. As shown in figure above, the cavitation covers entirely the corner of the blade which is the most far placed from the blade axle pin. This can be one of the cause that leads to the hydraulic efficiency drop and the unsteady flow pattern [26].

One important cavitation type caught in this regime is the unsteady cavitation given by the dettached cavitation close to the trailing edge of the runner blade as shown in Fig. 8. This was found only for this cavitational regime.

The tip clearance of the blade was neglected in this numerical computations, so in the real geometry (in practice) the unsteady cavitation can arise earlier for greater Thoma numbers.

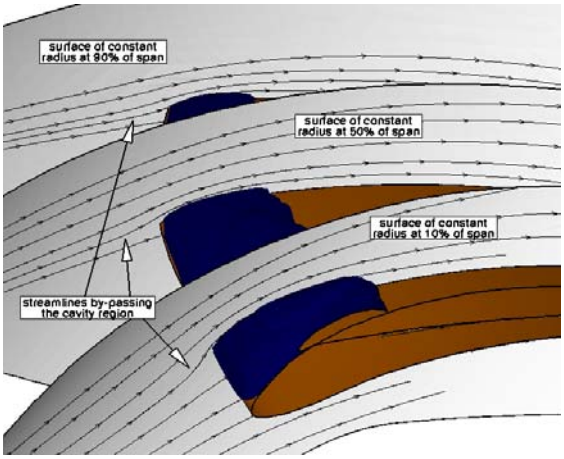

Figure 9. Flow behavior in the leading edge cavitation neighbourhood (σ_{inst}=0.10)

An important effect of the leading edge cavitation is the modification of the flow incidence onto the runner blade. In Figure 9 the streamlines of the flow (for 10-50-90% of the span locations) must by-passing the cavitation which covers the entire leading edge of the blade. This lead to unsteady recirculations at the edges of the cavitation and 3D effects of the flow.

4.3. Secondary phase developping

One goal of this paper was to prepare a method of comparing particular flows in hydraulic turbomachinery in cavitating conditions.

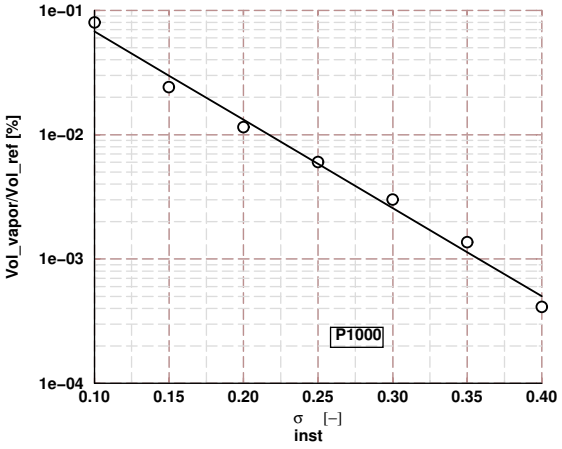

Figure 10. Cavitation growth versus Thoma number at best efficiency operating point

This is given by the prediction of the cavitation inception made possible by stating a threshold of the relative concentration of the cavitation [27].

In Figure 10 the distribution of the cavitation concentration is delivered versus the Thoma number for this best efficiency operating point of the turbine in logarithmic scale for the ordinate as given in Equation (10) where Vol_{ref} is the refe-

rence volume of the runner domain as given by Equation (11). The constants of the line have the following values: A = -1.0587 and B = -16.35.

$$\ln\left(100\frac{Vol_{vapor}}{Vol_{ref}}\right) = A + B\sigma_{inst} \qquad (10)$$

$$Vol_{ref} = \frac{4\pi R_{runner}^3}{3}\left(1-\upsilon^3\right) = 409\left[m^3\right] \qquad (11)$$

where υ=0.448 is the relative diameter of the hub and R_{runner}=4.75 [m] is the runner radius.

If a threshold of 1e-9 is imposed for the percentage concentration of the water vapor, then for the Thoma number is obtained the value of σ_{inst}=1.2 for the cavitation inception. This is very close to the values delivered by prof. Anton in [1].

Moreover, this method can be easily used when two numerical cavitating flows must be compared quantitatively. The coefficients from the Eq. (10) can clearly show the global cavitating performances of a particular two-phase flow.

5. CONCLUSIONS

This paper has shown a robust and efficient methodology of analyzing the two-phase flows in cavitating conditions encountered in hydraulic turbomachinery, particularly of Kaplan hydraulic turbines. Section 3 presented the cavitating flow model used, the turbulence models and the boundary conditions employed.

Section 4 has shown the variation of the hydraulic efficiency of the Kaplan turbine computed numerically. This helped to compute the engineering coefficients as the cavitation inception and industrial tolerance. Moreover, it has presented the patterns of the cavitating flow onto the runner blade suction side for the significant regimes computed. A detailed investigation was made for the regime presenting the steep drop of the hydraulic efficiency σ_{inst}=0.10. Next, the methodology of comparing different cavitating flows by computing the water-vapor concentration was presented.

The further investigation of the cavitating flows will be for off-design operating points where the 3D effects are greater and the cavitation presence is much distructive.

ACKNOWLEDGEMENTS

Numerical computations have been performed at the Numerical Simulation and Parallel Computing Laboratory from the University Politehnica of Timisoara, National Centre for Engineering of Systems with Complex Fluids. The present work was supported from the Romanian National University Research Council Grant CNCSIS-Td No. 80/2006.

REFERENCES

[1] Anton, I.M., 2002, *Energetic and Cavitational Scale-Up Effects in Hydraulic Turbines*, Orizonturi Universitare, Timisoara, Romania

[2] Ion, E., Paunescu, N., and Trambita, I, 2000, „Modernization and Refurbishment of Hydro Power Plant Iron Gates I", Proc. *HydroVision*, North Carolina, USA, pp. 12M

[3] Dean, T., Gerrard, A., Palylyk, L., and Philips, G., 2000, „Nipawin Hydroelectric Station: Modifications to Extend the Life of 84 MW Kaplan Turbines", Proc. *HydroVision*, North Carolina, USA, 2000, pp. 12N

[4] Huser, L., Ravicini, L., Niederer, C., Zahler, M., Annen, H., and Bleier, I., 2000, „A Complete Electromechanical Upgrading Package for the 1200 MW Kaplan Power Plant Portile de Fier I", Proc. *HydroVision*, North Carolina, USA, pp. 12A

[5] Ignatovic, B., Katic, B., Savic, Z., Skvortov, F., and Vasiliu, A., 1994, „Large Hydraulic Kaplan Turbines at HPP Djerdap I – Iron Gate I", Proc. *The 17th IAHR Symposium on Hydraulic Machinery and Systems*, Beijing, China, pp. 1043-1054

[6] Zhang, L., and Fang-Jun, X., 1994, „Studies of Solid-Liquid Two-Phase Flow Field in Kaplan Turbines", Proc. *The 17th IAHR Symposium on Hydraulic Machinery and Systems*, Beijing, China, pp. 151-164

[7] Ahuja, V., Hosangadi, A., and Arunajatesan, S., 2001, „Simulations of Cavitating Flows using Hybrid Unstructured Meshes", *ASME J Fluids Engineering*, Vol. 123, pp. 331-340

[8] Miner, S.M., 2000, „Evaluation of Blade Passage Analysis using Coarse Grids", *ASME J Fluids Engineering*, Vol. 122, pp. 345-348

[9] Singhal, A.K., Athavale, M.M., Li, H., and Jiang, Y., 2002, „Mathematical Basis and Validation of the Full Cavitation Model", *ASME J Fluids Engineering*, Vol. 124, pp. 617-624

[10] Schilling, R., Riedel, N., and Ritzinger, S., 1994, „A Critical Review of Numerical Models Predicting the Flow through Hydraulic Machinery Bladings", Proc. *The 17th IAHR Symposium on Hydraulic Machinery and Systems*, Beijing, China, pp. 15-32

[11] Margolin, L.G., Smolarkiewicz, P.K., and Wyszogrodzki, A.A., 2002, „Implicit Turbulence Modeling for High Reynolds Number Flows", *ASME J Fluids Engineering*, Vol. 124, pp. 862-867

[12]Coutier-Delgosha, O., Fortes-Patella, R., and Reboud, J.L., 2003, „Evaluation of the Turbulence Model Influence on the Numerical Simulations of Unsteady Cavitation", *ASME J Fluids Engineering*, Vol. 125, pp. 38-45

[13]Zhang, Q., Woo Lee, S., and Ligrani, P.M., 2004, „Effects of Surface Roughness and Turbulence Intensity on the Aerodynamic Losses Produced by the Suction Surface of a Simulated Turbine Airfoil", *ASME J Fluids Engineering*, Vol. 126, pp. 257-265

[14]Takahira, H., Horiuchi, T., and Banerjee, S., 2004, „An Improved Three-Dimensional Level Set Method for Gas-Liquid Two-Phase Flows", *ASME J Fluids Engineering*, Vol. 126, pp. 578-585

[15]Medvitz, R.B., Kunz, R.F., Boger, D.A., Lindau, J.W., Yocum, A.M., and Pauley, L.L., 2002, „Performance Analysis of Cavitating Flow in Centrifugal Pumps using Multiphase CFD", *ASME J Fluids Engineering*, Vol. 124, pp. 377-383

[16]Bajic, B., 2002, „Multidimensional Diagnostics of Turbine Cavitation", *ASME J Fluids Engineering*, Vol. 124, pp. 943-950

[17]Cravero, C., and Satta, A., 2003, „Comparison of Semi-Empirical Correlations and a Navier-Stokes Method for the Overall Performance Assessment of Turbine Cascades", *ASME J Fluids Engineering*, Vol. 125, pp. 308-314

[18]Vu, T., and Retieb, S., 2002, „Accuracy Assessment of Current CFD Tools to Predict Hydraulic Turbine Efficiency Hill Chart", Proc. *The 21st IAHR Symposium on Hydraulic Machinery and Systems*, Lausanne, Switzerland, pp. 193-198

[19]Astolfi, J.A., Dorange, P., Billard, J.Y., and Cid Tomas, I., 2000, „An Experimental Investigation of Cavitation Inception and Development on a Two-Dimensional Eppler Hydrofoil", *ASME J Fluids Engineering*, Vol. 122, pp. 164-173

[20]Farrell, K.J., 2003, „Eulerian/Lagrangian Analysis for the Prediction of Cavitation Inception", *ASME J Fluids Engineering*, Vol. 125, pp. 46-52

[21]Grekula, M., and Bark, G., 2002, „Cavitation Observations and Noise Measurements in a 9.3 MW Kaplan Turbine", Proc. *The 21st IAHR Symposium on Hydraulic Machinery and Systems*, Lausanne, Switzerland, pp. 491-498

[22]Watanabi, S., and Brennen, C.E., 2003, „Dynamics of a Cavitating Propeller in a Water Tunnel", *ASME J Fluids Engineering*, Vol. 125, pp. 283-292

[23]Lindau, J.W., Boger, D.A., Medvitz, R.B., and Kunz, R.F., 2005, „Propeller Cavitation Breakdown Analysis", *ASME J Fluids Engineering*, Vol. 127, pp. 995-1002

[24]Kern, I., and Vesko, D., 2000, „Experience with Model and Field Testing of Cavitation of Low Head Kaplan Turbines", Proc. *The 20th Hydraulic Machinery and Systems*, North Carolina, USA, pp. CAV02/1-10

[25]Lindau, J.W., Kunz, R.F., Boger, D.A., Stinebring, D.R., and Gibeling, H.J., 2002, „High Reynolds Number, Unsteady, Multiphase CFD Modeling of Cavitating Flows", *ASME J Fluids Engineering*, Vol. 124, pp. 607-616

[26]Gajic, A., Ignjatovic, B., Predic, Z., and Vuskovic, B., 2002, „Stresses of Kaplan Turbine Runner Blade during Transients", Proc. *The 21st IAHR Symposium on Hydraulic Machinery and Systems*, Lausanne, Switzerland, pp. 887-894

[27]Lipej, A., Jost, D., and Markov, Z., 2002, „Numerical Prediction of Cavitation in Water Turbines", Proc. *The 21st IAHR Symposium on Hydraulic Machinery and Systems*, Lausanne, Switzerland, pp. 425-430

Conference on Modelling Fluid Flow (CMFF'06)
The 13th International Conference on Fluid Flow Technologies
Budapest, Hungary, September 6-9, 2006

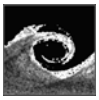

NUMERICAL SIMULATION AND ANALYSIS OF FLOW AROUND MARINE PROPELLER

Mihaela AMORĂRIȚEI

Corresponding Author. Hydrodynamic Department, "Dunarea de Jos" University of Galati, 47 Domnesca Street, Galati, Romania, Tel.: (+40) 236 495400 E-mail: mamor@ugal.ro

ABSTRACT

The paper presents numerical investigations of flow fields around marine propellers. In order to evaluate the propeller hydrodynamic performances the 2D and 3D computations were performed. The problems are solved using the commercial code FLUENT. The propeller geometry is known and the pressure distribution on blade and the open water characteristics of a marine propeller are calculated. To validate the methodology extensive comparisons with available experimental data are performed.

Keywords: CFD, propeller.

NOMENCLATURE

J	[-]	advance ratio
k_T	[-]	thrust coefficient
k_Q	[-]	torque coefficient
T	[kN]	propeller thrust
Q	[kNm]	propeller torque
c_p	[-]	pressure coefficient
D	[m]	propeller diameter
n	[s^{-1}]	rotation speed
v_A	[m/s]	advance velocity

Subscripts and Superscripts

m	measured value
c	computed value

1. INTRODUCTION

The screw propeller is the most common, efficient and cost-effective propulsion device. A marine propeller converts the engine torque into thrust force to propel a ship, accelerating the fluid in which it works. The propeller plays an important role in the interaction between ship and main engine.

Actual trends in shipbuilding regard the increase in speed and size for certain ship types and the strict noise and vibrations requirements on ship board demand not only the increase of propeller efficiency but also the minimizing of undesired phenomena such as cavitation, noise and vibrations. Priority considerations imposed either by the design theme or by the ship destination make sometime impossible the task of fulfilling all the requirements that are related to the performances of a new ship: maximization of the cargo capacity, minimum fuel consumption, maximal speed performances, low noise and vibrations level. These facts oblige to improve continuously the propeller design methods, to develop and use the numerical techniques for the analysis of the hydrodynamic performances of the marine propeller as an intermediate step in improving the performances of the ship-propulsion system.

Computational Fluid Dynamics (CFD) methods have become an indispensable tool in ship propellers design and analysis. In conjunction with experimental tests and analytical methods based on circulation theory and standard series, CFD codes represent a new capability to greatly improve the propeller design and analysis process.

The paper presents a numerical investigation of flow fields around a marine propeller working in steady flow. Using a commercial code FLUENT the flow around propeller was numerically simulated to find out the pressure distribution on the blades and to define the propeller hydrodynamic characteristics K_T (J), K_Q (J). The problems were numerically approached in two ways:

- using a hybrid method which based on the definition of the incoming flow on circulation theory, analyses the flow around the blade profile (2D computation);
- solving the equations that describe the flow around propeller blades using a three dimensional model which includes the fluid domain as well as the solid surfaces of interest (3D computation).

In order to validate the numerical methodology comparisons with available experimental data are performed.

1.1. Propeller design and analysis

A marine propeller must be designed to absorb minimum power and to give maximum efficiency,

with minimum cavitation, noise and vibrations. For the performance of the ship, propeller efficiency is related to speed, cavitation to noise and unsteady forces induced by propeller (pressure pulses and bearing forces) are related to vibrations of the hull structure. The design of screw propeller behind ship is an iterative process; the procedure follows a few steps.

In preliminary design stage, a propeller of optimal efficiency is determined using the design charts based on model tests with series of propellers (such as the Wageningen B-series). The main characteristics of the propeller: diameter, number of blade, rotation rate, etc. are fixed and these are a starting point for the propeller design using the circulation theory: lifting line/lifting surface theory. The propeller geometry is unknown and the required thrust or specified power at given rpm are given. The incoming flow varies in radial sense and the problem is to find the blade geometry for a specified distribution of blade loading over the radius (wake adapted propeller). A straight design method is based on lifting line theory with lifting surface corrections. In lifting line theory, propeller is replaced by a vortex system and the induced velocities in the propeller plane can be calculated without knowing propeller geometry. In a first stage known as hydrodynamic design, the circulation, the induced velocities, the resultant velocity and the hydrodynamic pitch at the various radii are calculated. After the hydrodynamic calculations the optimum blade geometry from point of view of cavitation suppression at the shock free angle of attack and strength criteria is determined. In lifting line theory the induced velocities are evaluated only on a lifting line. Since the propeller blades are lifting surfaces, have finite thickness and operate in viscous flow, the angle of attack and chamber are corrected taking into account the lifting surface, thickness and viscous effects. Once the design is completed, the propeller can be evaluated in several ways: computational analysis, experimental model tests and tests on full scale. The analysis requires the detailed geometry of propeller, the effective wake distribution and the operational conditions of the propeller. The experimental tests in towing tanks and tunnel cavitation are expensive, time consuming and for this reason analytical and numerical methods have been developed and used for the study of the propeller's behaviour in off design conditions. The objectives of this stage are the evaluation of the hydrodynamic performances of propeller in steady and unsteady flow:

- steady analysis:

-calculation of the open water characteristics;
-calculation of the pressure distribution on propeller blades operating in uniform flow or in a radially varied circumferential mean flow;

- unsteady analysis:

-calculation of the pressure distribution on propeller blades in various blade positions and cavitation prediction;
-calculation of the unsteady forces and moments acting on propeller shaft (bearing forces);
-calculation of the hull pressure fluctuations.

It will be clear that unsatisfactory results from these calculations could lead to a new iterative design cycle with changed propeller geometry (Figure1).

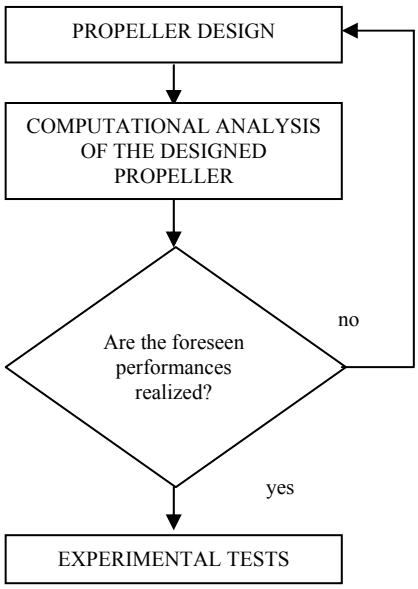

Figure 1. Iterative propeller design procedure

Eventual problems related to the failure in getting the foreseen performance may be found out even in the early stages of the initial design process, thus avoiding the risks of getting with them during the most expensive stage of the experiments. In this way the reduction of the design durations and costs becomes feasible.

The computational analysis can be done using quasi-steady methods, circulation theory and CFD methods. Lifting line theory, RANS (Reynolds Averages Navier-Stokes) and Panel methods can predict the open water performance of a propeller very accurately. The quasi-steady methods are still used for calculation of unsteady hydrodynamic propeller forces (bearing forces). The pressure distributions on propeller blades can be evaluated using the steady and unsteady surface theory and CFD methods. Panel methods are potential flow codes, equation of motion is Laplace's equation and the boundary condition of tangential flow is satisfied at the panels on the surface of blades and hub. Panel codes are useful for problems where pressure distribution on blade surface of propeller operating in steady and unsteady flow is desired. The RANS equations solvers are used for problems where viscous flow is dominant: investigation of interaction between wake field of the ship and the propeller inflow, the tip vortex, hub vortex,

separation along the leading edge, etc. Current applications of analysis of viscosity effects on propulsion devices are: open and ducted propellers, azimuthing thrusters and podded drives [1]. RANS codes require computational grids in the entire fluid region including the body surfaces.

Numerical simulations compliment traditional towing tests, cavitation tests and propeller design process with analytical methods based on circulation theory and standard series. The detailed flow field solutions provided by CFD codes enable the designer to develop or modify design quickly; different main dimensions for the propeller geometry can be investigated in a less time with reduced expenses. CFD codes offer the possibility of flow visualization and a better comprehension of the flow phenomena.

2. GOVERNING EQUATIONS. BOUNDARY CONDITIONS.

All numerical simulation presented in this paper were carried out using the commercial code FLUENT, a computer program which solves the governing equations for incompresible/compresible flows, inviscid/viscous flows, laminar/turbulent flows.

Assuming a viscous and incompressible flow, the governing equations which express the mass and momentum conservation, so-called Navier Stokes equations, are [9]:

$$\frac{\partial v_i}{\partial x_i} = 0 \tag{1}$$

$$\frac{\partial v_i}{\partial t} + v_j \frac{\partial v_i}{\partial x_j} = -\frac{1}{\rho}\frac{\partial p}{\partial x_i} + \nu \nabla^2 v_i \tag{2}$$

where v is the generical symbol for velocity, p is the static pressure and ν the kinematic viscosity. When the equations of motion are solved in a rotating reference frame, the relative velocity is introduced:

$$w = v - \varpi \times r \tag{3}$$

These equations are valid for laminar flow. Turbulent flows are characterized by fluctuating velocity fields which mix the transported quantities and for practical calculations the governing equations can be timed averaged. The velocity components and other scalar quantities Φ (pressure, energy, etc) are decomposed into a mean component (time averaged) $\overline{\Phi}$ and fluctuating components Φ' :

$$\Phi - \overline{\Phi} = \Phi' \ , \ \ \overline{\Phi} = \frac{1}{T}\int_{t_0}^{t_0+T} \Phi dt \tag{4}$$

The governing equations can be written:

$$\frac{\partial \bar{v}_i}{\partial x_i} = 0 \tag{5}$$

$$\rho \frac{\partial \bar{v}_i}{\partial t} + \rho \bar{v}_j \frac{\partial \overline{v_i}}{\partial x_j} = \\ = -\frac{\partial \bar{p}}{\partial x_i} + \frac{\partial}{\partial x_j}\left(\bar{\tau}_{ij} - \rho \overline{v'_i v'_j}\right) \tag{6}$$

These equations called Reynolds Average Navier Stokes equations (RANS) have the same general form as the Navier Stokes equations (1),(2) with the exception of the additional term $-\rho \overline{v'_i v'_j}$ which represent the transfer of momentum due to turbulent fluctuations. Empirical models (turbulence models) are necessary to describe the effects of turbulence and to determine the additional terms.

Different turbulence models are available in FLUENT [5]. The RNG k-ε turbulence model was used for the numerical investigations presented in this paper. The RNG k-ε turbulence model is similar in form to the standard k-ε turbulence model and it was derived using a rigorous statistical technique called renormalization group theory. The standard k-ε turbulence model is the simplest turbulence model with two separate equations for the turbulent kinetic energy k and the dissipation rate ε. The RNG k-ε turbulence model has an additional term in its ε equations and the effect of swirl on turbulence is included.

Taking into account that "a numerical simulation can consider only a part of the real physical domain"[9], boundary conditions must be used to specify the flow variable on the boundaries of the physical models investigated. The velocity inlet boundary conditions, available in FLUENT, were used to define the velocity of the flow at inlet boundaries. The outflow boundary conditions were used to model the flow exits. In FLUENT, the outflow boundary condition assumes a zero diffusion flux in the exit direction for all flow variables and they are used to model the flow exits where the details of the flow velocity and pressure are not known prior to solution of the flow problem [5]. Wall boundary conditions were used for blade surfaces. In a viscous flow, the boundary condition at a wall is the no slip condition.

3. NUMERICAL PROCEDURE. RESULTS

The numerical simulation of flow around marine propeller in steady flow was approached in two ways:

1. using a hybrid method which based on the definition of the incoming flow on circulation

theory, analyses the flow around the blade profile (2D computation);

2. solving the equations that describe the flow around propeller blades using a three dimensional model which includes the fluid domain as well as the solid surfaces of interest (3D computation).

The models are based on the RANS and continuity equation written for the incompressible flow and the computations were performed using the commercial code FLUENT. The flow around propeller was numerically simulated to find out the pressure distribution on the propeller blades operating in uniform flow or in a radially varied circumferential mean flow and to define the propeller hydrodynamic characteristics for various advance ratio K_T (J), K_Q (J).

3.1. 2D flow computation

The incoming flows data resulted from the hydrodynamic design with circulation theory are used as a starting point for a numerical investigation of flow around blade profiles of the propeller. From lifting line method with lifting surface correction the complete geometry of blade sections, the resultant velocity and angle of attack at the various radii are calculated. Using these data, the numerical simulation and analysis of flow around the blade profile give information regarding the pressure distributions on propeller blades operating in a radially varied circumferential mean flow, data which, sometimes, can be taken as an indication of the behaviour of the cavitation on the blades.

The 2D model was tested on two benchmark problems.

First, the computation was made for a 2D laminar flow around a hydrofoil NACA 0018, at an angle of attack of 0 degree and for Re = 2000. The computational domain is presented in Figure 2, and two boundary conditions were used: velocity inlet for three sides of the trapezoidal domain and outflow for the right remaining side.

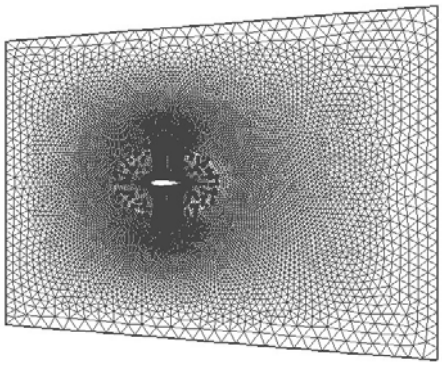

Figure 2. The 2D computational domain

A hybrid mesh with quadrilateral and triangular cells was used. A mesh refinement zone was defined near the profile (Figure 3), minimum grid spacing was given as follow

$$\Delta_{\min} = \frac{0.05}{\sqrt{\mathrm{Re}}} \qquad (7)$$

Figure 4 shows the pressure distribution around NACA 0018 profile and the computed pressure coefficient c_p presented in Figure 5 agrees very well with the experimental data available [2]. In this case the pressure coefficient was defined as $c_p=(v/V)^2$, where v is the local velocity and V the velocity of incident flow.

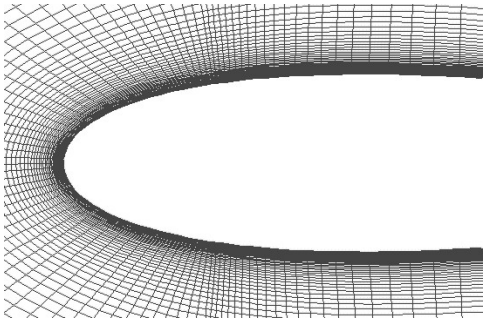

Figure 3. Mesh near profile

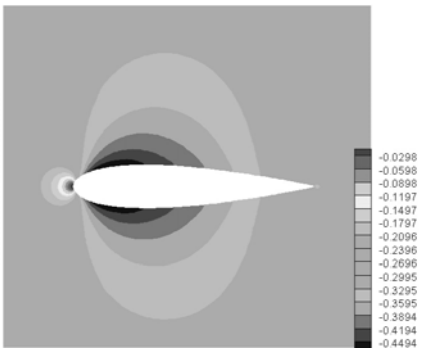

Figure 4. Pressure distribution around NACA 18 profile

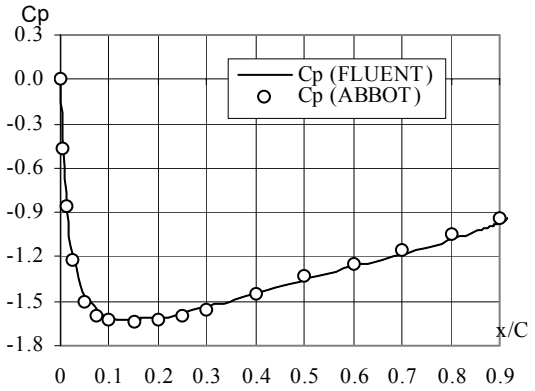

Figure 5. Pressure coefficient around NACA 18 profile

Second, the computation was made for a 2D turbulent flow around a hydrofoil NACA 66 modified, at an angle of attack of 1.5 degree and for a Reynolds number 8.5 x10^5. NACA 66 modified (a = 0.8 mean line – chamber distribution offers a constant lift over about 80 per cent of the chord) is one of the most used types of section for the marine propeller. The propeller blade section geometry, the inflow velocity and angle of attack at the 0.7R radius (R=D/2 - propeller radius) were given by lifting line method with lifting surface correction. The effect of turbulence was modelled by RNG k-ε model. The Reynolds number to the blade sections is defined by:

$$\mathrm{Re} = \frac{V_R \cdot c_{0.7}}{\nu} \tag{8}$$

where $c_{0.7}$ is the expanded chord of the blade section at the 0.7R radius and V_R is the resultant speed at the blade section at the 0.7R radius:

$$V_R = \sqrt{v_A^2 + (0.7\pi \cdot n \cdot D)^2} \tag{9}$$

Figures 6 and 7 present the computed pressure distribution around propeller blade section (NACA 66 profile).

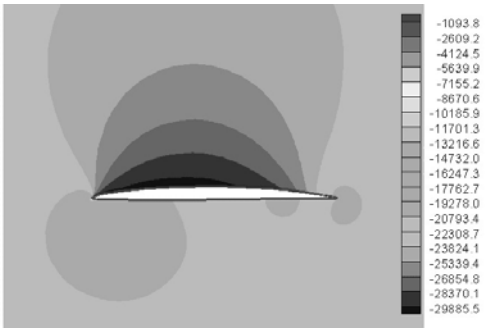

Figure 6. Pressure distribution around propeller blade profile (NACA 66)

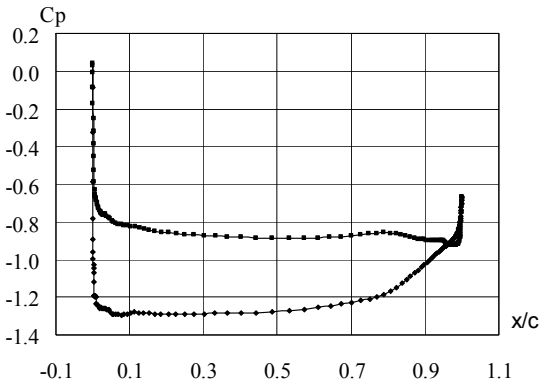

Figure 7. Pressure coefficient around propeller blade profile (NACA 66)

3.2. 3D flow computation

Marine propellers have complex geometry, with variable section profile and pitch and for this reason the 3D model was tested on two benchmark problems. First, a three blade propeller DTMB P4119 was selected for 3D computation. The 4119 propeller has no rake and skew and it was proposed by International Towing Tank Conference (ITTC) Propulsion Committee for comparative steady calculation with RANS and surface panel methods [3]. The propeller diameter is D = 304.8 mm and the design point parameters are: advance ratio J= 0.833, rotation speed n =10 s^{-1}, advance velocity v_A =2.54 m/s. The advance ratio is defined by:

$$J = \frac{v_A}{nD} \tag{10}$$

The numerical simulation of 3D flow around P4119 propeller was performed in two cases:
I. the computational domain is cylindrical and it includes all three blade propeller surfaces (Figure 8)
II. the computational domain includes only one propeller blade and rotational periodic boundary conditions are used to reduce mesh size (Figure 9).

Unstructured tetrahedral cells are used to define the volume control. A mesh refinement zone was defined near the propeller blades, but the size is not enough to boundary layer analysis and tip vortex details. The main characteristics of computational domains are presented in Table 1.

Table 1. Computational domains

	Case I	Case II
Distance between propeller plane-velocity inlet	1.8D	2D
Distance between propeller plane-outflow	4D	4D
Domain's radius	2.6D	2D
Total cells	153255	180691

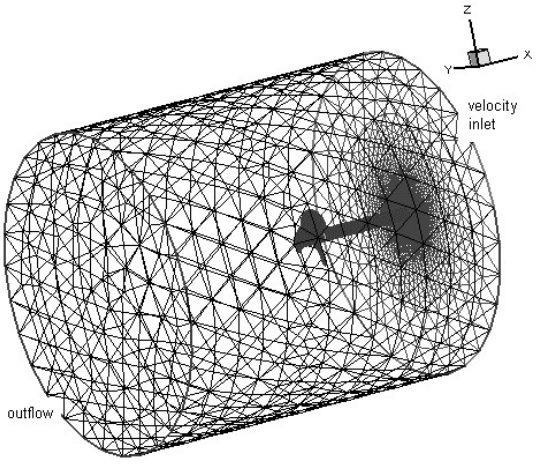

Figure 8. Computational domain around propeller (case I)

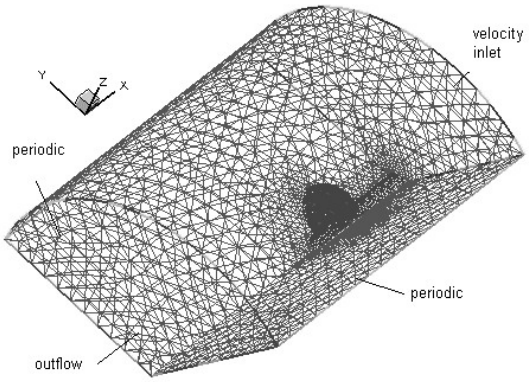

Figure 9. Computational domain around propeller blade (case II)

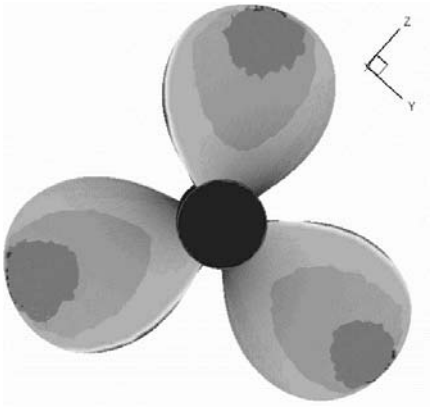

Figure 10. Pressure distribution on propeller blades – back side (case I)

Figure 11. Pressure distribution on propeller blade – back side (case II)

Taking into account that the propeller is in uniform flow and the physical geometry of interest and the expected pattern of the flow solution have a periodically repeating nature, in case II the periodic boundary conditions were used to reduce the computational domain size. The second-order discretization schemes available in FLUENT were chosen to obtain more accurate results. For triangular and tetrahedral grids, since the flow is never aligned with the grid, the first-order convective discretization increases the numerical discretization error (numerical diffusion). The numerical calculations were carried out for a Reynolds number Re = 7.6×10^5 using RNG k-ε model and moving (rotation) reference frame model in FLUENT. Figures 10 to 11 show the pressure distribution on the back side of the propeller at the design point J=0.833.

In FLUENT the forces on a wall zone can be computed by summing the dot product of the pressure and viscous forces on each face with the specified force vector. The moment vector about a specified center can be computed by summing the product of the force vectors for each face with the moment vector--i.e., summing the forces on each face about the moment center. This feature was used to report the thrust force acting parallel to the axis of rotation and the torque absorbed by the propeller. The propeller hydrodynamic characteristics K_T (J), 10 K_Q (J) computed for various advance ratio were compared with available experimental data [3] in Figure 12. Usually for plotting the torque coefficient K_Q is multiplied by 10. The computations for all J values were done using the same grid, the angular velocity was kept constant and velocity inlet was varied. The thrust and torque coefficients are defined by:

$$K_T = \frac{T}{\rho \cdot n^2 D^4} \qquad (11)$$

$$K_Q = \frac{Q}{\rho \cdot n^2 D^5} \qquad (12)$$

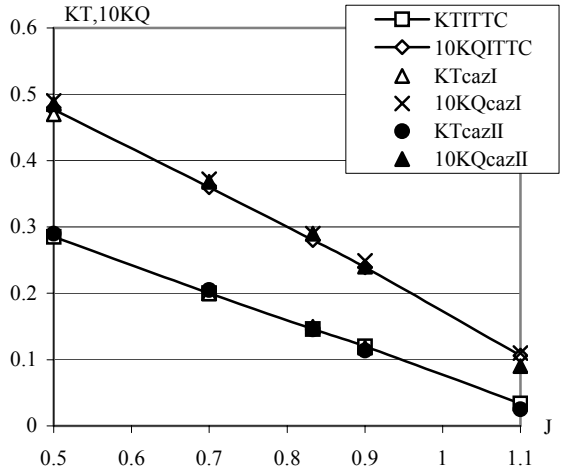

Figure 12. Measured and calculated open water characteristics

Agreement between the computational results and the corresponding experimental data is good; the differences at the design point are presented in Table 2.

Table 2. Comparison between measured and calculated open water characteristics

J	ΔK_T (I)	ΔK_Q (I)	ΔK_T(II)	ΔK_Q(II)
0.833	-2.3%	-3.5%	0.3%	-3.2%

Second, a modern propeller P0209 with variable pitch and skew was selected for 3D numerical calculation. The main characteristics of propeller are: number of blade z=5, diameter D = 0.21 m, blade area ratio A_e/A_0 = 0.718, mean pitch ratio P/D = 1.03, skew = 25 degree. The detailed propeller geometry is known and it is presented in Figure 13. The experimental open water tests of this propeller were carried out at ICEPRONAV Galati.

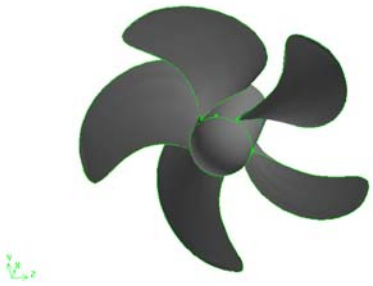

Figure 13. Propeller geometry

Only one blade was modelled (flow is circumferentially periodic) and the rotational periodic boundary was used. The computational domain with 1.5D radius, the inlet displaced at 1D and the outlet at 2D from the propeller plane is shown in Figure 14. Unstructured tetrahedral cells are used to define the volume control with 235718 cells. A size function was used to control the size of mesh elements near the propeller blade.

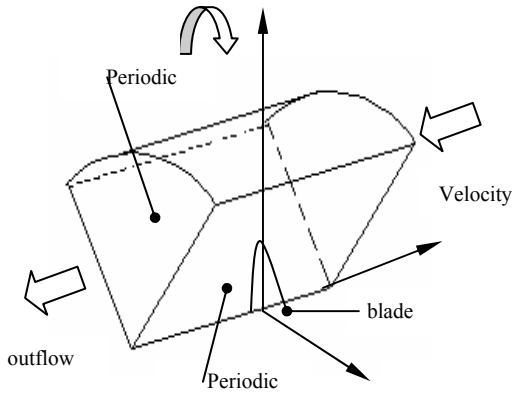

Figure 14. Computational domain around propeller blade

The numerical solutions were computed for a flow regime characterized by a Reynolds number Re = 7.9×10^5 using RNG k-ε model and moving (rotation) reference frame model in FLUENT. Using the numerical methodology developed, the pressure distribution on propeller blade was well reproduced: a high pressure region on the face side (Figure 15) and a low pressure region on the back side (Figure 16).

In figure 17, the computed thrust coefficient K_T and torque coefficient $10K_Q$ for various advance ratio were compared with experimental data carried out at ICEPRONAV Galati. The numerical results are in agreement with experimental data and the differences are presented in Table 3.

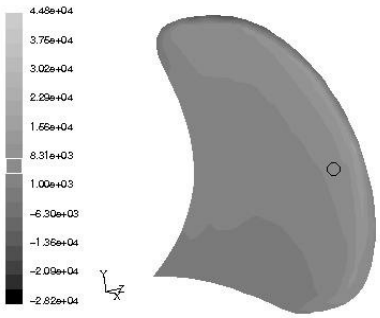

Figure 15. Pressure distribution on propeller face side

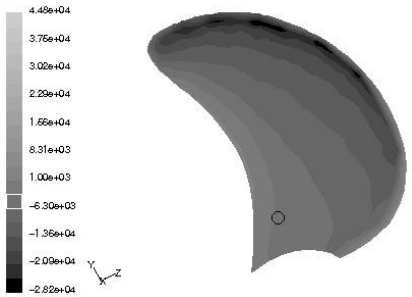

Figure 16. Pressure distribution on propeller back side

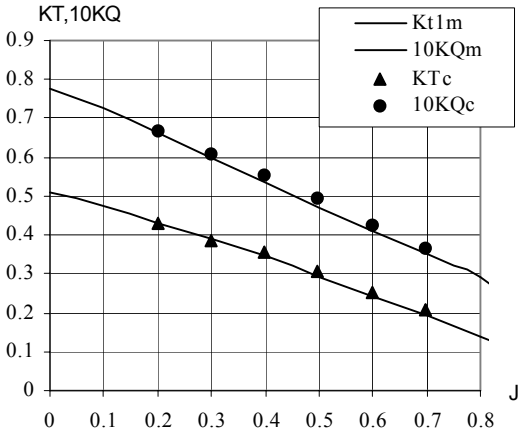

Figure 17. Open water characteristics

Table 3. Comparison between measured and calculated open water characteristics

J	ΔK_T	ΔK_Q
0.3	1.3%	-1.%
0.4	-3.7%	-2.7%
0.5	-5%	-5.3%
0.6	-4.4%	-4.5%

4. CONCLUSIONS

The results of numerical simulations of flow around marine propellers in steady flow were presented. The computations were performed using the commercial code FLUENT.

First, a hybrid method was proposed to simulate the 2D flow around propeller blade starting from the definition of the incoming flow on circulation theory. The pressure distribution around blade section for a propeller operating in a radially varied circumferential mean flow was evaluated.

Second, the RANS equations were used to analyse the 3D flow around propeller blades and to evaluate the hydrodynamic characteristics of propellers working in uniform flow. Two propellers with experimental data available were selected for 3D computation: a propeller with a simple geometry without rake and skew (DTMB P4119) and a skew propeller tested at ICEPRONAV Galati (P0209). The computed thrust and torque coefficients were plotted in comparison with experimental data and the results are considered satisfactory.

Numerical solutions were obtained using unstructured tetrahedral cells for mesh generation. The mesh size was not enough for boundary layer and vortex tip analysis but it offered correct results for prediction of the hydrodynamic propeller performances.

The results presented in this paper are only the beginning of a research program including numerical simulation of flow fields around marine propellers. Taking into account that the quality of the mesh is a key factor to the success of a numerical simulation, the future author's investigations will be focused on mesh generation. A structural mesh or a hybrid mesh allow for fine resolution on region where the pressure and velocity gradients are expected to be significant as boundary layer and vortex tip developed behind propeller. Further studies are necessary to analyse other aspects of flow fields like circumferential velocities distribution upstream and downstream of the operating propeller, detailed resolution on tip vortex development, etc. Besides, different turbulence models will be investigated (k-ε standard, k-ω [4], RSM) and the results will be compared. The choice of the turbulence model can affect the numerical results and it is a matter of experience (validation of calculation) which model is the best.

Also as a future research, a numerical investigation of cavitating flows around propeller blade using the mixture model in FLUENT will be important to reproduce accurately the cavities location, shape and extent and to assess the overall performance alteration due to cavitation presence.

Extensions of numerical modelling of the flow phenomenon around propeller in unsteady flow behind ship is a challenging problem in CFD and an important step in improving the performances of the ship-propulsion system as well as in increasing the efficiency and the quality of the research and design activities.

REFERENCES

[1] ***, 2002, 23rd International Towing Tank Conference, Propulsion Committee, *Proceedings of the 23rd ITTC*, Vol. 1, pp 121.

[2] Abbot, I.,H., Doenhoff, A.,E., 1959, "Theory of Wing Sections", *Dover Publications*, New York, pp. 325.

[3] Jessup, S., 1998, "Experimental Data for RANS Calculation and Comparisons (DTMB P4119)", *22nd ITTC Propulsion Committee Propeller RANS/Panel Methods Workshop*

[4] Fluent Inc. 2003, "Marine Propeller", *Application brief from Fluent,* Ex 212

[5] Fluent Inc. 2001, FLUENT 6. User's Guide, Fluent Incorporated, Lebanon, USA

[6] Fluent Inc. 2001, Gambit 2. User's Guide, Fluent Incorporated, Lebanon, USA

[7] Holtrop, J., 2000, "The Design of Propellers", Wegemt School, Delft

[8] Martinez-Calle, J., Balbona-Calvo, L., Gonzales-Perez, J., Blanco-Marigorta, E., 2002, "An Open Water Numerical Model for a Marine Propeller: a Comparison with Experimental Data", *Proceedings of the ASME FEDSM'02,* Montreal, Canada.

[9] Blazek, J., 2001, "Computational Fluid Dynamics: Principles and Applications", Elsevier

[10] Uto, S., 1998, "RANS Simulation of Turbulent Flow around DTMB4119 Propeller", *22nd ITTC Propulsion Committee Propeller RANS/Panel Methods Workshop,* Grenoble, Franta

[11] Amoraritei, M., 2005, "Contributions to the Hydrodynamics of the Propeller working in Unsteady Conditions. Applications to the Propeller in Oblique Flow and Azimuthing Thrusters",, *Ph.D. Thesis "Dunarea de Jos" University of Galati*

[12] Amoraritei, M., 2005, "Developments in the Design of ship Propeller", *Proceeding of the Workshop on Vortex Dominated Flows Achievements and Open Problems,* Timisoara, Romania, pp.131-138

[13] Amoraritei, M., 2005, "Application of CFD in Analysis of Conventional Propeller and Azimuth Thruster", *Proceeding of the Workshop on Vortex Dominated Flows Achievements and Open Problems,* Timisoara, Romania, pp. 139-142

Conference on Modelling Fluid Flow (CMFF'06)
The 13th International Conference on Fluid Flow Technologies
Budapest, Hungary, September 6-9, 2006

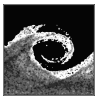

COMPUTING THREE-DIMENSIONAL TURBOMACHINERY FLOWS WITH AN IMPLICIT FLUCTUATION SPLITTING SCHEME

Aldo BONFIGLIOLI[1], M. Sergio CAMPOBASSO[2]

[1] Corresponding Author. Department of Environmental Engineering and Physics, University of Basilicata. Viale dell'Ateneo Lucano 10, 85100 Potenza, Italy. Tel.: +39 0971 205203, Fax: +39 0971 205160, E-mail: bonfiglioli@unibas.it
[2] School of Engineering, Building 83, Cranfield University, Bedfordshire MK43 0AL, United Kingdom. Tel.: +44 1234 750111 ext. 5710 Fax: 44 1234 758203 E-mail: m.s.campobasso@Cranfield.ac.uk

ABSTRACT

Progress on the development and the application of an accurate and efficient flow solver for steady turbomachinery flows is reported. The code uses unstructured tetrahedral grids, its space-discretization is based on a fluctuation splitting scheme and an implicit strategy is used for the time integration. Results include the three-dimensional analysis of the flow field of a compressor stator and thorough comparisons with experimental data and numerical results obtained with other codes.

Keywords: CFD, Fluctuation Splitting, GMRES, Turbomachines

1. INTRODUCTION

In the perpetual quest for improved accuracy of Computational Fluid Dynamics (CFD) solvers, two distinct approaches have emerged over the last decade. One advocates the use of higher order shape functions for data representation while retaining an essentially one-dimensional physical model, typically modelled with the Riemann problem. The other approach makes use of linear shape functions for data representation, but tries to incorporate truly multi-dimensional physical models. Higher order Finite Volume (FV) and Discontinuous Galerkin Finite Element (FE) methods belong to the former class. The numerical method considered in this paper is instead based on Fluctuation Splitting (FS) schemes, which are a typical example of the latter class. Because of algorithmic complexity, both approaches incur a substantial computational overhead when compared to state-of-the-art CFD techniques, such as those based on artificial dissipation or upwind schemes. Therefore they require the implementation of convergence acceleration techniques in order to be competitive with more conventional solvers in terms of CPU cost. Explicit multigrid methods have dominated the CFD arena for a long time, but implicit methods based on Newton's rootfinding algorithm have recently received increasing attention. This is because of their potential to converge in a very small number of iterations. The main objective of this paper is to present the application of EULFS, an implicit FS code [1,2], to complex three-dimensional (3D) turbomachinery flows.

2. GOVERNING EQUATIONS AND NUMERICAL DISCRETIZATION

The turbulent motion of a Newtonian fluid can be modelled using the Reynolds-Favre averaged Navier-Stokes (RANS) equations. The objective here is to determine a steady state solution of this system. When one considers a control volume C_i and denotes by ∂C_i its boundary and by $\underline{n}$ the inward normal of this latter, the integral form of the RANS equations can be symbolically written as:

$$\int_{C_i} \frac{\partial \underline{U}}{\partial t} dV = \oint_{\partial C_i} \underline{n} \cdot (\underline{F} - \underline{G}) dS + \int_{C_i} \underline{S} dV \qquad (1)$$

Eq. (1) holds both for compressible and incompressible flows. In both cases, turbulence closure is achieved by using the 1-equation model of Spalart and Allmaras, whereas Chorin's artificial compressibility is used to model incompressible flows. The terms $\underline{F}$ and $\underline{G}$ represent the inviscid and viscous flux vectors respectively. The only nonzero entry of the volumetric source term $\underline{S}$ is that associated with the turbulence transport equation. In both compressible and incompressible analyses, the last entry of the vector $\underline{U}$ is the turbulent variable. The remaining entries are instead the conservative flow variables in the compressible case, and the primitive variables in incompressible problems. Hence denoting by d the problem dimensionality, the length of the vector of nodal unknowns is $m=d+2$ for incompressible flows and $m=d+3$ for compressible flows.

2.1 Spatial discretization

The RANS equations are discretized in space using *Fluctuation Splitting* or *residual distribution* schemes [3]. Introduced in the early eighties by Roe, these schemes have features of both FE and FV methods. Just as with iso-P1 FE, the dependent variables are stored in the vertices of the computatioanl mesh, made up of triangles in the 2D space, and tetrahedra in 3D domains. The dependent variables are assumed to vary linearly in space. In the 2D case, a control volume (C_i) is constructed around each grid point by joining the centroids of the surrounding triangles to the midpoints of all the edges that connect that grid point with its nearest neighbours. An example of tessellation based of these polygonal shaped control volumes or *median dual cells* is shown in Figure 1, where the dual cells are drawn with a dashed line.

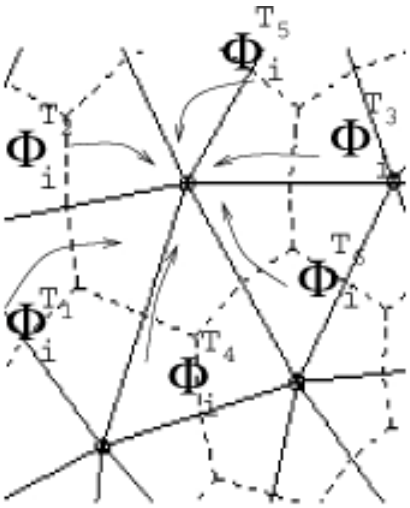

Figure 1. Vertex *i* gathers scattered residuals from all surronding cells

Using a FV-type approach, the conservation laws (1) are discretized over each control volume C_i. Unlike conventional FV schemes which compute the fluxes by numerical quadrature along the boundary ∂C_i of the dual cell, however, here the flux integral is first evaluated over each triangle (or tetrahedron in 3D) and then scattered to its vertices.The grid point *i* will then collect fractions $\underline{\Phi}_i^T$ of the flux balance of all the elements by which it is surrounded, as sketched in Fig. 1.
Using this approach, the space-discretized form of Eq. (1) is:

$$\int_{C_i} \frac{\partial \underline{U}_i}{\partial t} dV = \sum_{T \ni i} \underline{\Phi}_i^T \qquad (2)$$

in which the summation ranges over all cells *T* which share the grid node *i*, and

$$\underline{\Phi}^T = \oint_{\partial T} \underline{n} \cdot (\underline{F} - \underline{G}) dS + \int_T \underline{S} dV \qquad (3)$$

is the cell residual evaluated over cell *T*. Denoting by $\underline{\Phi}_j^T$ the fraction sent to its j^{th} vertex, flux conservation requires that the sum over the vertices of a given cell *T* of the split residuals $\underline{\Phi}_j^T$ equal the total cell residual, *i.e.*: $\sum_{j \in T} \underline{\Phi}_j^T = \underline{\Phi}^T$. The properties of the scheme will depend upon the criteria used to scatter the cell residual. Distributing the convective flux balance along the characteristic directions gives the discretization an upwind flavour, while the distribution of the viscous flux balance can be shown to be equivalent to a standard Galerkin FE discretization. It should also be emphasized that the Riemann problem, typically used in standard FV discretizations, is not needed in the present FS algorithm. This is because the dependent variables are assumed to be continuous across the surface of the elements. As a consequence, this rather unusual approach to a FV-type discretization leads to a set of discrete equations that shows closer resemblance [4] to FE Petrov-Galerkin rather than FV schemes. A thorough description of the spatial discretization can be found in [1,3].

2.2 Time integration

The space-discretization of the governing equations can be viewed as a system of ordinary differential equations of the form:

$$\underline{\underline{V}} \frac{d\underline{U}}{dt} = \underline{R}(\underline{U}) \qquad (4)$$

where $\underline{R}(\underline{U})$ represents the vector of nodal residuals and $\underline{\underline{V}}$ is a diagonal matrix, the entries of which are the volumes of the median dual cells. Note that although the objective here is to calculate steady state solutions, the time-derivative of equation (4) is retained. As explained below, this is done because the integration strategy is partially based on pseudo-time marching. This is achieved by discretizing the time-derivative with a FD and time-marching the solution towards a stationary state. The residual vector $\underline{R}(\underline{U})$ is a block-array of length equal to the product of the number of grid nodes and the number of dependent variables *m*. The *i*-th block of $\underline{R}(\underline{U})$ represents the discretization of the conservation laws at the mesh point *i*, and is given by:

$$\underline{R}_i = \sum_{T \ni i} \underline{\Phi}_i^T = \sum_{j=1}^{N_i} \left(\underline{\underline{C}}_{ij} - \underline{\underline{D}}_{ij} \right) \underline{U}_j \qquad (5)$$

The second summation in Eq. (5) ranges over $\mathcal{V}_i$, the set made up of grid node *i* and all its neighbours. The matrices $\underline{\underline{C}}_{ij}$ and $\underline{\underline{D}}_{ij}$ account for the contribution of the inviscid and viscous terms respectively and their description is given in [1].

If the time-derivative in equation (4) is approximated with a two-point one-sided FD formula, an explicit scheme is obtained by evaluating $\underline{R}(\underline{U})$ at time-level n. An implicit scheme results instead by evaluating $\underline{R}(\underline{U})$ at time-level n+1. In the latter case, linearization of $\underline{R}(\underline{U})$ at time level n yields the implicit scheme:

$$\left(\frac{1}{\Delta t^n}\underline{\underline{V}} - \frac{\partial \underline{R}}{\partial \underline{U}}\right)\left(\underline{U}^{n+1} - \underline{U}^n\right) = \underline{R}(\underline{U}^n). \qquad (6)$$

Equation (6) represents a large nonsymmetric (though structurally symmetric) sparse linear system in the unknown $\underline{\Delta} = \underline{U}^{n+1} - \underline{U}^n$. The matrix $\partial \underline{R} / \partial \underline{U}$ is the Jacobian of the flow equations and it has a block structure, whereby each block is associated with a particular grid node. Due to the compact stencil $\mathcal{N}_i$ of the scheme, the sparsity pattern of the Jacobian corresponds to the graph of the underlying unstructured mesh. This is because the scheme only involves distance-1 neighbours. Typically the number of non-zero blocks per row equals 7 in 2D and 14 in 3D.

At each pseudo-time t^n, system (6) is solved by using a preconditioned restarted GMRES algorithm, as implemented in [5], and the flow state $\underline{U}$ is updated using the newly computed $\underline{\Delta}$.

The analytical evaluation of the Jacobian matrix is rather cumbersome [3]. Therefore two alternative approaches have been adopted in EULFS: one is based on an approximate analytical estimate of the Jacobian, whereas the other uses a numerical approximation of the "true" Jacobian, obtained by means of one-sided finite differencing. In both cases, the elements of the Jacobian matrix are stored in memory.

The approximate or Picard linearization consists of computing a particular Jacobian entry as:

$$\frac{\partial \underline{R}_i}{\partial \underline{U}_j} \approx \underline{\underline{C}}_{ij} - \underline{\underline{D}}_{ij} \qquad (7)$$

that is by neglecting the dependence of the convective and diffusive matrices on $\underline{U}$.

In the FD approximation, the individual entries of the vector of nodal unknowns are perturbed by a small amount, the nodal residual corresponding to the perturbed state is recomputed and the elements of the Jacobian are then approximated using one-sided FD formulae. Although the matrix assembly can be performed using a single loop over all cells [3], its evaluation is computationally expensive because it requires $(d+1)\times m$ residual evaluations. Therefore the use of the FD approximation of the true jacobian pays off only if the number of iterations to obtain a converged solution can be significantly reduced with respect to that of simpler iterative schemes. This condition may be achieved by exploiting the quadratic convergence of Newton's method, which is recovered from Eq. (6) as the time-step approaches infinity. On the other hand, the residual reduction of Newton's method is quadratic only if the initial guess lies in a sufficiently small neighbourhood of the steady state. This condition is certainly not met if the numerical simulation has to be started from "scratch". Therefore a two-step approach is adopted, similarly to what reported in [6]. The first step is used at the early stages of the calculation, and it consists of solving the equations in an iterative loosely coupled fashion: the turbulent viscosity is kept frozen and the other variables are advanced over a single time-step using an approximate Jacobian; then the turbulent variable is advanced over one or more pseudo time steps using a FD jacobian with frozen mean flow variables. This cycle is applied recursively. However, due to this partial decoupling and also to the use of a finite time-step for stability reasons, this procedure would lead to linear convergence, at most. This is precisely the reason for introducing the second step. Once the solution is sufficiently close to the steady state, a true Newton strategy is adopted: the solution of the mean flow and turbulence transport equation is fully coupled, the Jacobian is computed by FD and the time-step is rapidly increased. Following the Switched Evolution Relaxation (SER) strategy proposed in [7], this is accomplished by letting Δt^n in Eq. (6) be a function of the ratio between the L_2 norm of the residuals at the initial and current time-step, that is:

$$\Delta t^n = \Delta t \frac{\| \underline{R}(\underline{U}^0) \|}{\| \underline{R}(\underline{U}^n) \|} \qquad (8)$$

where Δt is the time-step computed using the stability criterion of the explicit scheme.

3. RESULTS

This section presents some results of the flow analysis of two turbomachinery test cases obtained by using EULFS: the compressible flow of a 2D turbine section and the incompressible flow of a 3D compressor stator. The predictive capabilities of EULFS are validated against both measured data and numerical results computed by other CFD codes. The 2D test case mainly serves the purpose of illustrating the computational efficiency of Newton's method. Its performance in the case of complex 3D flows is still being investigated, and for this reason it will not be addressed in the presentation of the 3D test case. The analysis of this latter is instead used to assess the predictive capabilities of EULFS.

3.1 2D Turbine section

The 2D turbine section of the 11th Standard Configuration is the mid-span blade-to-blade section of an annular cascade with 20 blades. Reference [8] documents an exhaustive series of steady and unsteady experimental flow

measurements and it also describes the cascade geometry and test-rig configuration. The subsonic steady flow regime with exit Mach number of 0.68 has been computed with EULFS. Figure 2 shows the residual convergence history of the fully coupled algorithm featuring FD Jacobian calculations. Due to the quadratic convergence rate, all residuals converge to within machine accuracy in about 10 Netwon steps.

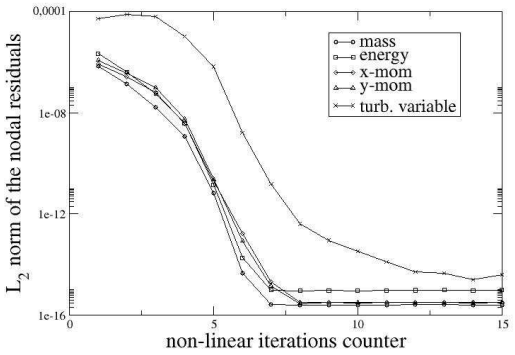

Figure 2. Convergence history for the 2D turbine test case.

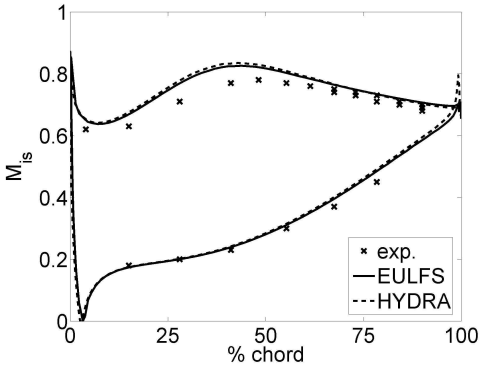

Figure 3. Isoentropic Mach number profile for the 2D turbine test case.

However, it should be noted that the convergence rate of this algorithm is crucially affected by the distance of the initial state from the sought solution. Worse convergence rates may be observed when such a distance is too large. Figure 3 reports the measured profile of isentropic Mach number on the blade surface (crosses) and two numerical estimates of the same variable. The solid line denotes the EULFS result and the dashed profile is computed using HYDRA, an unstructured multigrid code [9]. An excellent agreement between the two numerical results is observed. The differences between the numerical and the measured profiles are also encountered considering the results of other CFD codes [8]. The grids used for the EULFS and HYDRA calculations are substantially different, and they are documented in [10] and [11] respectively. The HYDRA result of Figure 3 is also taken from the latter reference.

3.2 3D Compressor stator

In order to assess the predictive capabilities of EULFS for three-dimensional problems, the flow field of the cantilevered stator of the third stage of a four-stage low-speed research compressor has been analysed. This machine was previously used in an experimental and numerical study aimed at assessing the aerodynamic performance of axial compressors using either shrouded or cantilevered stators. That investigation is reported in reference [12], which also provides a detailed description of the test rig and its operating conditions, and a thorough comparison of experimental data and numerical results. The latter ones were obtained by using the 3D incompressible NS structured code HYDRO [13], which uses a cell-centred FV scheme, Chorin's artificial compressibility and the Baldwin-Lomax turbulence model. In this section we compare the stator flow field computed by EULFS to the experimental data and numerical results computed by HYDRO.

This cantilevered stator has 83 blades, an aspect ratio of 1.349 and a midspan pitch-to-chord ratio of 0.587. The annulus is cylindrical and the radial gap at the hub is 1.5% of the blade height. The considered flow regime is that associated with the design conditions. The Reynolds number is $3.5\ 10^5$ and the flow field is considered incompressible as the peak isentropic Mach number is well below 0.3.

The unstructured grid used by EULFS is made up of 290125 nodes and 1637076 tetrahedra. This grid has been obtained by subdividing the hexahedra of a structured multi-block grid into tetrahedra by using the algorithm reported in [14]. The starting block-structured grid was obtained using the mesh generation capability of PADRAM [15]. Figure 4 shows the blade-to-blade mesh at the casing end wall. The structured single-block grid used for the HYDRO calculation is a quasi-orthogonal H-type mesh and it has 293265 nodes and 278784 hexahedra. The blade-to-blade mesh at the casing end wall is reported in Figure 5. It should be noted that the two grids have comparable number of nodes and node distribution in the blade-to-blade surfaces. On the other hand, the model of the hub clearance used by EULFS and HYDRO is significantly different: the stator tip is modelled exactly by the EULFS grid, as the blade is cut sharply (Figure 6a), whereas the tip is tapered in the HYDRO mesh (Figure 6b).

In order to compare measured and computed results, let us start off by introducing the total pressure coefficient C_{p0}, defined as:

$$C_{p0} = \frac{p_{01,MID} - p_0}{p_{01,MID} - p_{1,MID}} \quad (9)$$

Here p_0 is the local total pressure, and $p_{01,MID}$ and $p_{1,MID}$ are the pitchwise averaged values of inflow total and static pressure at midspan respectively.

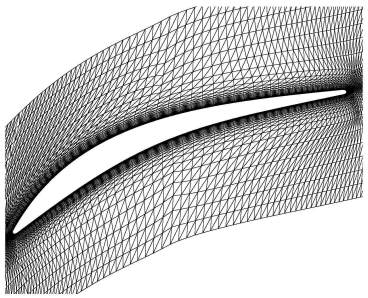

Figure 4. EULFS computational mesh at the casing end wall

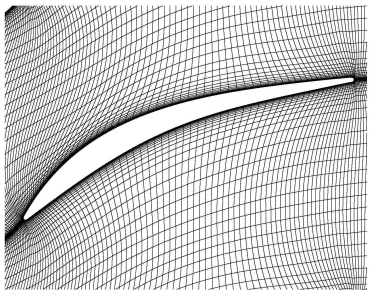

Figure 5. HYDRO computational mesh at the casing end wall

The axial position where averaging of the latter two quantities is made is that of the axial plane before the stator leading edge (LE) and behind the trailing edge (TE) of the preceding rotor, namely the plane where experimental measurements of the flow field were carried out. Note that high values of C_{p0} denote regions of high aerodynamic loss.

The contours of measured C_{p0} in an axial plane between the stator TE and the LE of the following rotor (*reference outlet plane*) are reported in Figure 7. This contour plot clearly shows the footprints of the wakes shed by two adjacent stator blades as well as two areas of higher loss close to the end walls. One is the triangular area close to the casing end wall (upper curvilinear boundary) and the other is the bubble-shaped region close to the hub end wall. The former high loss patch is due to the flow separation associated with the casing corner stall, and the latter patch is due to the loss associated with the leakage flow of the hub clearance.

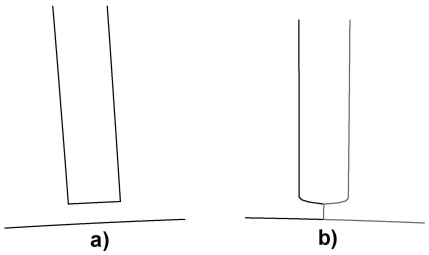

Figure 6. Radial clearance model: a) EULFS and b) HYDRO

The inflow boundary condition of the CFD calculations reported below have been obtained by using the pitchwise averaged radial profiles of measured total pressure and pitch angle, and the value of the hub static pressure at the outflow boundary has been chosen to match the measured mass flow. All calculations are steady single-row analyses: the computational domain consists of the isolated stator, and the flow is assumed to be steady.

Note that the contours of Fig. 7 as well as all other experimental data presented hereafter *do contain* all effects of the inherent unsteadiness of turbomachinery flows. The pressure map of Fig. 7, for example, was obtained by traversing the flow field behind the stator TE with a stationary pressure probe. The flow field at this location, however, is not steady both because of the fluctuations caused by the motion of the upstream rotors, and because of possible unsteady character of the flow field of the stator itself (e.g. unsteady separation bubbles). Both types of unsteadiness are 'averaged' by the stationary probe, which samples the flow field over a certain period of time and it then averages it over the same period. These effects are not considered in the numerical results presented below, because these simulations merely consider the steady flow of the isolated stator.

The EULFS contours of C_{p0} in the reference outlet plane are reported in Figure 8. The contour pattern is similar to that of the experimental data of Fig. 7. However the EULFS solution seems to overestimate the loss associated with the casing corner stall, as pointed by the fact that the computed triangular loss patch adjacent to the casing end wall is significantly wider than the measured one. The high loss predicted by EULFS is in line with the presence of a substantial pocket of flow separation at the corner between the blade suction side (SS) and the casing end wall in this numerical solution. At the hub end wall, the predicted loss due to the leakage flow is again higher than the measured one.

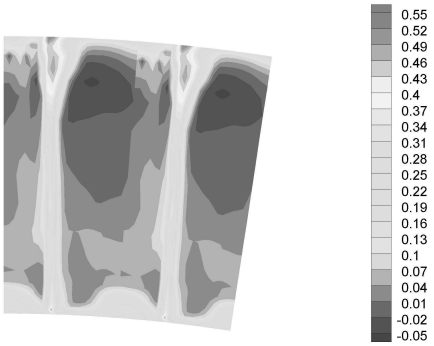

Figure 7. Measured total pressure coefficient C_{p0} in reference outlet plane

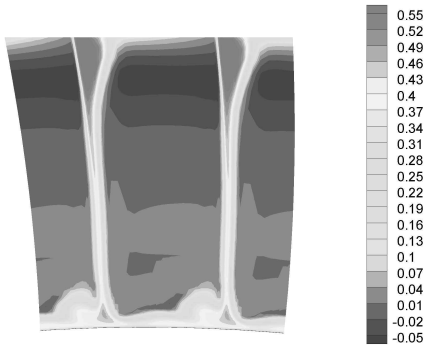

Figure 8. EULFS total pressure coefficient C_{p0} in reference outlet plane

The HYDRO contours of C_{p0} in the reference outlet plane are reported in Figure 9. Comparing this plot with the experimental contours of Fig. 7 and the EULFS result in Fig. 8, one notes a good qualitative resolution of the main flow features. A closer inspection reveals the following peculiarities of the HYDRO solution: 1) the level of the loss due to the casing corner stall is closer to that of the measurements, and 2) the bubble-shaped loss area due to the hub leakage flow is more smeared than that computed by EULFS, which seems to better mimic the experimental contours. The former difference between the two computed results is in line with the observation that the extent of the hub corner separation predicted by HYDRO is negligible with respect to that predicted by EULFS and one possible explanation for this is the use of substantially different turbulence models. The latter difference on the hub side may be due not only to different turbulence closures, but also to the use of a significantly different clearance model.

Figures 10, 11 and 12 compare measured and computed blade static pressure coefficient C_p close to the hub (12.5% blade height), at midspan (50% blade height) and close to the casing (96.25% blade height) respectively. Its definition is:

$$C_p = \frac{p - p_{1,MID}}{p_{01,MID} - p_{1,MID}} \qquad (10)$$

where p is the blade static pressure. The blade loading curves of Fig. 10 show that both the near-hub pressure distribution predicted by EULFS and HYDRO are in good agreement with the experimental data. The pressure side (PS) profile computed by HYDRO is actually slightly closer to the measured pressure than the profile computed by EULFS. This result is quite surprising as the more realistic model of the hub clearance in EULFS would make one expect the opposite trend.

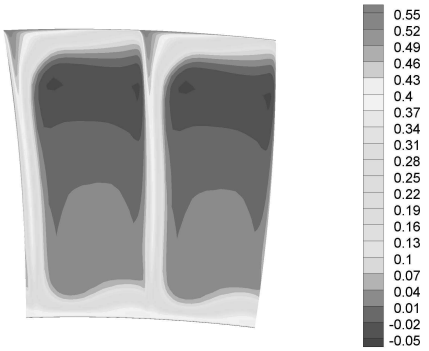

Figure 9. HYDRO total pressure coefficient C_{p0} in reference outlet plane

This discrepancy is being investigated further. Fig. 11 highlights that the differences between the two loading predictions at midspan are instead negligible, and the numerical results are in very good agreement with the measured pressure profile. Computed and measured profiles of blade pressure coefficient on the near-casing airfoil are depicted in Fig. 12. Both computed profiles appear to match reasonably well the measured pressure profile on the PS (the two experimental points apparently out of alignment with the profile may be due to fault of the experimental devices). Both the EULFS and the HYDRO pressure profiles differ from the experimental SS C_p profile in the first 25% of blade chord. More remarkably, the slope of the EULFS profile has a discontinuity at about 50% chord. This is due to the presence of a large separated flow region at the casing/SS corner in the EULFS solution. Such separation is in line with the fact that the loss associated with the casing corner stall predicted by EULFS (Fig. 8) is significantly higher

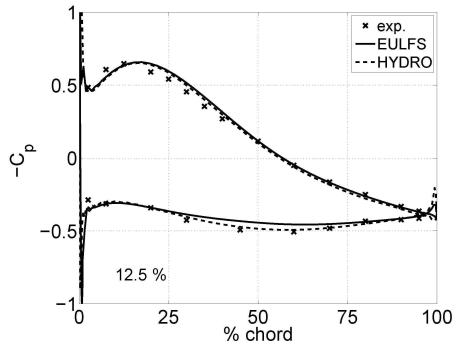

Figure 10. Measured and computed pressure coefficient C_p close to hub end wall

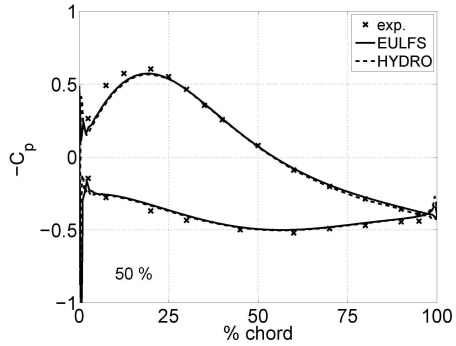

Figure 11. Measured and computed pressure coefficient C_p at midspan

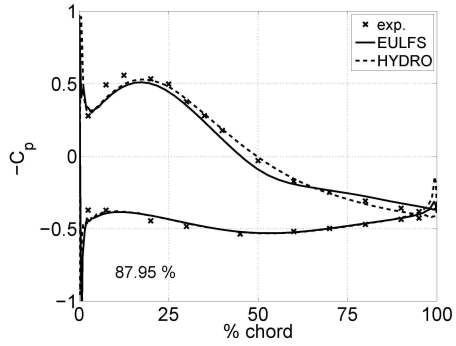

Figure 12. Measured and computed pressure coefficient C_p close to casing end wall

than that computed by HYDRO (Fig. 9). The comparison of the radial profiles of the pitchwise averaged C_{p0} at the inflow and outflow plane is presented in Fig. 13. The measured and computed inflow profiles are nearly superimposable, because the experimental profile has been used as inflow boundary condition. The small discrepancies are due to the fact that the actual inflow plane of the computational domain has been positioned slightly ahead of the plane where the measurements were made.

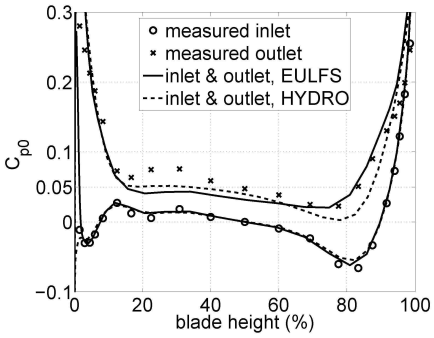

Figure 13. Measured and computed pitchwise averaged total pressure coefficient C_{p0} in reference inlet and outlet planes

The outflow plane is the previously defined reference outlet plane. Here both numerical results are in good agreement with the experimental data in the first 20% of the blade height, which means that the overall loss associated with the hub leakage flow is predicted fairly well. From 20% to about 60% blade height, both calculations underpredict the aerodynamic loss. This is because the computed wakes (Figs. 8 and 9) are thinner than the measured ones (Fig. 7). The loss profile from 60% to the casing end wall is strongly affected by the corner stall flow development. The overall loss predicted by EULFS seems to compare better than the HYDRO result with the experimental data. Close inspection of Figs. 8 and 9, however, points to the fact that this is probably because the underestimated total pressure in the corner stall area largely outweighs the overestimated total pressure in the remaining portions of the casing boundary layer.

The comparison between measured and computed radial profiles of pitchwise averaged pitch angle is presented in Figure 14.

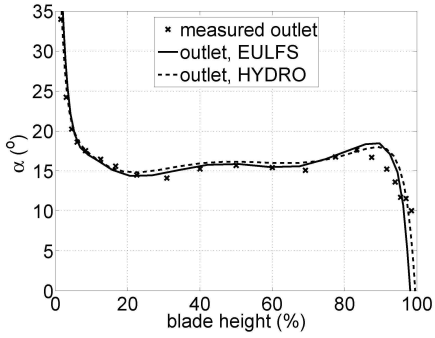

Figure 14. Measured and computed pitchwise averaged pitch angle in reference outlet plane

The agreement between the two CFD results is very good along the whole blade height, and that between the two computed results and the experimental data is also fairly good from the hub end wall to about 80% blade height. In the remaining 20% the agreement is somehow poorer. Note that the two calculations yield comparable results also in this interval despite fundamental differences in the computational models they make use of. Assuming that the experimental profile is correct, this discrepancy may be due to some unsteady effect such as blade-row interaction or unsteady nature of the flow separation associated with the casing corner stall, which neither calculations account for.

4. SUMMARY

The theory behind the implementation of the EULFS code has been summarized. The main features of this solver are a space-discretization based on Fluctuation Splitting schemes and an implicit integration strategy. The former feature is adopted to enhance accuracy and the latter to increase the convergence rate. The predictive capabilities of EULFS for complex 3D turbomachinery flows have been assessed by considering the incompressible flow field of a compressor stator. Ongoing work includes further investigation of some unexpected discrepancies between the EULFS prediction and the results of other numerical simulations and flow measurements for the 3D test case, and validation and improvement of the integration strategy for 3D flow problems.

ACKNOWLEDGEMENTS

We are grateful to Rolls-Royce Deutschland and Mr. U. Wenger for permitting to use the compressor blade geometry for this study. We also greatly acknowledge Rolls-Royce plc., Dr. S. Shahpar and Dr. L. Lapworth for permitting to use the PADRAM-derived mesh for EULFS calculations.

REFERENCES

[1] Bonfiglioli A., 2000, "Fluctuation splitting schemes for the compressible and incompressible Euler and Navier-Stokes equations", *IJCFD* , Vol. 14, pp. 21–39.

[2] Bonfiglioli, A., De Palma, P., Pascazio, G. and Napolitano, M., 2005, "An Implicit Fluctuation Splitting Scheme for Turbomachinery Flows", ASME *J of Turbomachinery*, Vol. 12, No. 2.

[3] van der Weide, E., Deconinck, H., Issman, E. and Degrez, G., 1999, "A parallel, implicit, multi-dimensional upwind, residual distribution method for the Navier-Stokes equations on unstructured grids", *Computational Mechanics* Vol. 23, pp. 199–208.

[4] Carette J.-C., Deconinck H., Paillère H. and Roe P.L., 1995, "Multidimensional upwinding: its relation to finite elements", *International Journal for Numerical Methods in Fluids*, Vol. 20, pp. 935–955.

[5] Balay, S., Buschelman, K., Gropp, W. D., Kaushik, D., Knepley, M.G., Curfman McInnes, L., Smith, B. F. and Zhang H., PETSc home page, http://www.mcs.anl.gov/petsc, 2001.

[6] Nichols, J.C., and Zingg, D.W., 2005, "A Three-Dimensional Multi-Block Newton-Krylov Flow Solver for the Euler Equations", *AIAA Paper 2005-5230.*

[7] Mulder, W. and Van Leer, B., 1985, "Experiments with an Implicit Upwind Method for the Euler Equations", *Journal of Computational Physics*, Vol. 59, pp. 232–246.

[8] Fransson, T.H., Joeker, M., Bolcs, A., Ott, P., 1999, "Viscous and Inviscid Linear/Nonlinear Calculations versus Quasi Three-Dimensional Experimental Cascade Data for a New Aeroelastic Turbine Standard Configuration", *ASME J Turbomachinery*, Vol. 121, pp. 717-725.

[9] Moinier, P., Mueller, J.D., Giles, M.B., 2002, "Edge-based Multigrid and Preconditioning for Hybrid Grids", *AIAA J*, Vol. 40, No. 10.

[10] Bonfiglioli, A., 2004, "On the use of Newton's rootfinding algorithm for solving the RANS equations", Proc. *59th ATI Congress*, Genoa, Italy, pp. II.1409 - II.1419.

[11] Campobasso, M.S., 2004, "Effects of Flow Instabilities on the Linear Harmonic Analysis of Unsteady Flow in Turbomachinery", *PhD Thesis, Oxford University*.

[12] Campobasso, M.S., Mattheiss, A., Wenger. U., Arnone, A., and Boncinelli, P., 1999, "Complementary Use of CFD and Experimental Measurements to Assess the Impact of Shrouded and Cantilevered Stators in Axial Compressors", *ASME paper* 99-GT-208.

[13] Arnone, A., Pacciani, R., 1995, "Three-Dimensional Viscous Analysis of Centrifugal Impellers Using the Incompressible Navier-Stokes Equations", Proc. *1st European Conference on Turbomachinery* Erlangen, pp. 181-195.

[14] Max, N., 2001, "Consistent Subdivision of Convex Polyhedra into Tetrahedra", *Journal of Graphics Tools*, Vol. 6, No. 3, pp. 29-36.

[15] Shahpar, S., Lapworth, L., 2003, "PADRAM: Parametric Design and Rapid Meshing System for Turbomachinery Optimization", *ASME paper* GT 2003-38698.

Conference on Modeling Fluid Flow (CMFF'06)
The 13th International Conference on Fluid Flow Technologies
Budapest, Hungary, September 6-9, 2006

CORE FLOW INSTABILITY IN WIDE VANELESS DIFFUSERS FOR THE PURPOSE OF ROTATING STALL INVESTIGATION

Svetlana LJEVAR[1], Rick DE LANGE[2], Anton VAN STEENHOVEN[3], Patrick DUPONT[4], Guy CAIGNAERT[5], Gerard BOIS[6]

[1] Department of Mechanical Engineering, Eindhoven University of Technology. Den Dolech 2, 5600 MB Eindhoven, the Netherlands. Tel.: +31 (0)40 247 2768, Fax: +31 (0)40 247 5399, E-mail: s.ljevar@tue.nl
[2] Department of Mechanical Engineering, Eindhoven University of Technology. E-mail: h.c.d.lange@tue.nl
[3] Department of Mechanical Engineering, Eindhoven University of Technology. E-mail: a.a.v.steenhoven@tue.nl
[4] Laboratoire de Mecanique de Lille (UMR CNRS 8107), Ecole Centrale de Lille. E-mail: patrick.dupont@ec-lille.fr
[5] Laboratoire de Mecanique de Lille (UMR CNRS 8107), ENSAM. E-mail: guy.caignaert@lille.ensam.fr
[6] Laboratoire de Mecanique de Lille (UMR CNRS 8107), ENSAM. E-mail: gerard.bois@lille.ensam.fr

ABSTRACT

A study of the core flow instability in the radial vaneless diffusers is performed for the purpose of better understanding of the rotating stall mechanism. In this paper the numerical results are compared with the experimental results.

A commercial code with the standard incompressible viscous flow solver is applied, to model the vaneless diffuser core flow in the plane parallel to the diffuser walls. Since the analysis is restricted to the core flow region, the influence of the wall boundary layers is neglected. Therefore, this model is only applicable to the wide vaneless radial diffusers. Using this numerical model a two-dimensional rotating flow instability, similar to rotating stall, is found to exist.

The numerical results are compared with the Particle Image Velocimetry (PIV) measurements performed in the vaneless diffuser behind a radial flow pump impeller. The measurements are performed at low mass flow rates, when the unsteady flow phenomena like rotating stall occur.

In the PIV measurements similar flow structures are observed as obtained by the numerical model. In both cases, clockwise and counter-clockwise rotating vortex structures are observed near the diffuser outlet. Comparison of these flow structures is made and discussed in this paper.

Keywords: centrifugal compressor, core flow, PIV measurements, radial flow pump impeller, rotating stall, vaneless diffuser

NOMENCLATURE

A	[-]	amplitude
c	[*m/s*]	speed of sound
D	[-]	constant for function steepness
Ma	[-]	Mach number
N	[-]	number of impeller blades
Q	[m^3/s]	volume flow rate
V	[*m/s*]	absolute velocity
Y	[-]	defined parameter
h	[*m*]	diffuser width
n_o	[-]	number of order of the PIV image
p	[*Pa*]	pressure
r	[*m*]	radius
t	[*s*]	time
u	[*m/s*]	radial velocity
v	[*m/s*]	tangential velocity
α	[^{o}]	flow angle
Ω	[*rpm*]	radial pump impeller speed
μ	[Pa s]	molecular viscosity
θ	[*rad*]	circumferential position
σ	[-]	constant factor
ω	[*rad/s*]	angular impeller velocity

Subscripts and Superscripts

cr	critical
i	impeller
m	mean
n	design operating condition
p	plane
tip	impeller tip
2	diffuser inlet
3	diffuser outlet

1. INTRODUCTION

Flow instabilities in centrifugal compressors, such as rotating stall, result in lower efficiency operating point and reduced pressure ratios. Rotating stall limits the operating range of compressors and can cause damage and noise nuisance. To improve the operating conditions of compressors, understanding of rotating stall flow dynamics is required.

The most common type of rotating stall in centrifugal compressors is the diffuser rotating stall. This paper deals with the study of the rotating stall mechanism within the vaneless radial diffusers.

In the literature different analytical and experimental approaches have been used to investigate the rotating stall phenomenon, and several theories that explain the vaneless diffuser rotating stall mechanism have been developed. The literature survey on the vaneless diffuser rotating stall indicates that different flow mechanisms are held responsible for the occurrence of rotating stall. Authors in [1-3] found that vaneless diffuser instability is different for narrow and wide diffusers. One mechanism is associated with the two-dimensional core flow instability occurring in the wide vaneless diffusers when the critical flow angle is reached, and the other mechanism is associated with the three-dimensional wall boundary layer instability occurring in the narrow diffusers.

The three-dimensional approach, where the wall boundary layer theory is used to study the rotating stall in vaneless diffusers, was applied by references [4-7]. These authors generally state that the effect of the three-dimensional boundary layers near the walls causes the rotating stall in the vaneless diffuser. On the other hand, Abdelhamid [8] and Tsujimoto et al. [9] used a two-dimensional inviscid and incompressible flow analysis, where the effect of the wall boundary layers is not taken into account, to study the vaneless diffuser rotating stall. These studies suggest the existence of a two-dimensional core flow instability at the onset of rotating stall in vaneless diffusers. Senoo and Kinoshita [5] have, for instance, made a distinction between the narrow and wide diffuser in their model.

However, little is known about the rotating stall mechanism and further research is necessary to reveal its flow dynamics. Before performing the three-dimensional analysis of rotating stall the authors decided to perform a two-dimensional analysis first, to see if there are any two-dimensional instabilities that might contribute to rotating stall in the vaneless diffusers. A two-dimensional analysis of the vaneless diffuser core flow was performed using the Computational Fluid Dynamics (CFD). A two-dimensional incompressible flow model of the vaneless diffuser core flow was developed, where the influence of the wall boundary layers is not taken into account. Therefore, this model applies only to the wide vaneless radial diffusers with parallel diffuser walls, where it can be assumed that mainly two-dimensional core flow in between the diffuser plates is present. Wide vaneless diffusers that compare well with this numerical model all satisfy $h/r_2 > 0.1$, see reference [10]. Therefore, the vaneless diffusers that satisfy this condition will be considered as wide vaneless diffusers.

In this paper the results of the numerical model are compared with the PIV measurements performed in the vaneless diffuser behind the radial flow pump impeller. These measurements, performed at the Laboratoire de Mecanique in Lille (France), are not meant to be compared with this numerical model in the first place. Despite the differences between the experimental setup and the numerical model, similar flow structures are observed, and therefore, this comparison is made.

In the next section, the numerical model is described, and the obtained numerical results are presented. This is followed by the section about the experimental setup and the performed PIV measurements. Then, the results of the numerical model are compared with the PIV measurements, and finally, the paper is ended with a few conclusions.

2. NUMERICAL MODEL

To study the core flow instability in the vaneless radial diffuser, a two-dimensional flow model was made of the plane parallel to the diffuser walls. No diffuser width is modeled, and the influence of the wall boundary layers is not taken into account.

2.1. Methodology

It is assumed that the outlet of the vaneless radial diffuser is connected to the space with constant static pressure. At the diffuser inlet a clockwise rotating jet-wake pattern is specified. The tangential velocity component v, prescribed at the diffuser inlet, is constant around the circumference. In this numerical model, the tangential velocity component is related to the impeller speed as follows:

$$v = \sigma \cdot v_{tip} \tag{1}$$

where v is the tangential velocity component, v_{tip} the impeller tip speed and σ the factor equal to 0.9. The radial velocity component at the diffuser inlet is described by the periodic hyperbolic tangent function:

$$u = u_m + A \cdot \frac{\tanh(D \cdot Y)}{\tanh(D)} \tag{2}$$

where u is the radial velocity component, u_m the mean radial velocity, A the amplitude and D the constant indicating the steepness of the jet-wake function. The circumferential position θ and the angular impeller velocity ω_i, are defined within the parameter Y:

$$Y = \sin\left(N \cdot \theta + \omega_i \cdot t\right) \qquad (3)$$

where t is the time and N the number of jet-wakes around the circumference corresponding to the number of impeller blades.

The reference geometry and the operating conditions of the vaneless diffuser model are obtained by scaling the existing air compressor configuration at the near stall operating conditions. For the details and motive of the scaling, the reader is referred to reference [11]. The reference geometry and operating conditions are: r_3/r_2 = 1.52, N = 17, Ω = 255.2 *rpm* and $v_{tip}/u_m = 9.3$. In the reference situation the jet-to-wake circumferential extent ratio equals 1 and the jet-to-wake radial intensity ratio equals approximately 5.5.

For the numerical analysis, a commercial software package FLUENT was used. The governing integral equations for the conservation of mass and momentum are solved using the finite-volume approach. For discretization of the time-dependent terms the second-order implicit time integration is used, and for convection terms the QUICK scheme, as proposed in reference [12], is used.

Although the studied flow is turbulent, the incompressible viscous flow model, with no eddy viscosity but only molecular viscosity, is applied. Use of the turbulence models is avoided because of the excessive numerical dissipation of the turbulence models. It is assumed that the two-dimensional core flow instabilities have the length scale of the prescribed jet-wake pattern at the diffuser inlet. Since turbulence models capture the diffusion-like character of turbulent mixing, associated with many small eddy structures, they damp out the solutions of large eddy structures like this one.

This numerical model is similar to the analytical analyses in references [8] and [9], because it is two-dimensional, incompressible and can be considered as virtually inviscid since molecular viscosity has a value of $\mu = 10^{-3}$. The major difference between these models is the way of approach to the situation, since different parameters are used as input parameters to obtain the two-dimensional instability.

To mesh this geometry a simple two-dimensional quadrilateral grid consisting of 750 by 62 elements is applied. The performed calculations are unsteady. The convergence criterion of 10^{-3} is applied to the continuity, *x*-velocity and *y*-velocity residual, and is satisfied at each time step.

2.2. Numerical results

Using this numerical model of the vaneless diffuser core flow, a two-dimensional rotating instability similar to rotating stall is found. In figure 1 two solutions are shown, which are colored by the velocity magnitude. The solution on the left represents the steady stable operating flow condition and the solution on the right represents the two-dimensional rotating instability. For this particular diffuser geometry the two-dimensional rotating instability consists of 7 rotating cells. The rotating cell area is the high velocity region, while the flow in between the cells is a low velocity region.

The two-dimensional rotating instability occurs when the mean flow angle α_m becomes smaller than the critical flow angle α_{cr}. The mean flow angle α_m is defined as $\alpha_m = \tan^{-1}\left(u_m/v\right)$. The obtained two-dimensional rotating instability is similar to rotating stall because it consists of a number of rotating cells that propagate with approximately 40 % of the impeller speed. Because of this similarity with rotating stall and good agreement with the measurements found in the literature, see reference [10], the authors believe that this instability might contribute to the vaneless diffuser rotating stall.

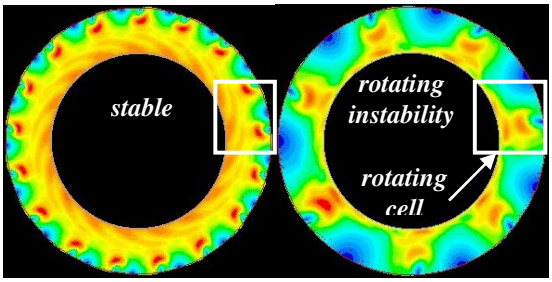

Figure 1. Stable ($\alpha_m \approx 12^o$) and unstable ($\alpha_m \approx 5^o$) operating flow condition obtained by the numerical model

To better study the flow mechanisms that contribute to this rotating instability, the velocity field of fluctuation is analyzed for the steady stable operating flow condition as well as for the two-dimensional rotating instability solution. The fluctuation velocity field was obtained by subtracting the mean velocity, averaged along the circumference at each radius, from the absolute velocity field.

In figure 2, the fluctuation velocity field is shown, for the rectangular area in figure 1 corresponding to the steady stable operating flow condition. Here, the outward and reversed flow areas alternate near the diffuser outlet. The number of these alternating areas exactly corresponds to the number of the prescribed jet-wakes at the diffuser inlet. The prescribed jet-wake pattern at the diffuser

inlet can be distinguished from the alternating clockwise and counter-clockwise rotating areas near the diffuser outlet.

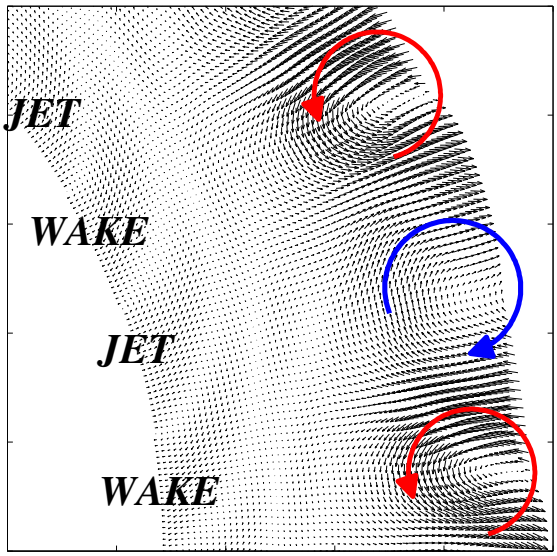

Figure 2. Fluctuation velocity field of the steady stable operating condition

In figure 3, the fluctuation velocity field is shown, for the rectangular area in figure 1 corresponding to the two-dimensional rotating instability. This velocity field clearly shows the counter-clockwise rotation of the flow field within the rotating cell, and the clockwise rotation of the flow field in between the rotating cells. The counter-clockwise rotation of the cells is a consequence of the clockwise rotating jet-wake pattern at the diffuser inlet.

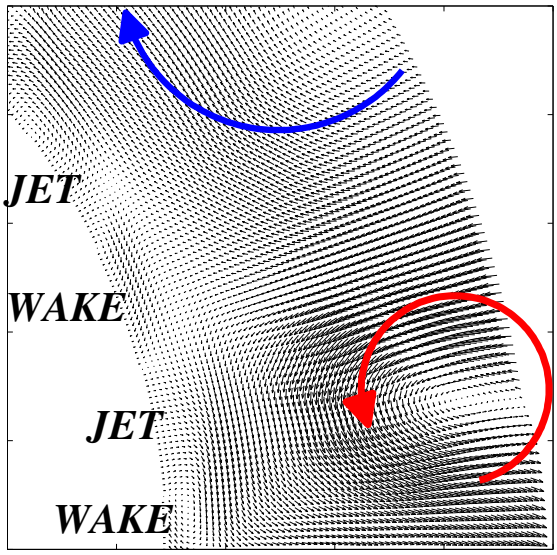

Figure 3. Fluctuation velocity field of the two-dimensional rotating instability

3. PIV MEASUREMENTS

The PIV measurements, performed by Wuibaut et al. [13] on an air test rig of a radial flow pump, are used for comparison with the numerical model. These measurements are performed in a pump configuration with a wide vaneless diffuser and no volute, which makes them interesting for comparison with this numerical model. Here, only the off-design measurements, where the unsteady flow phenomena occur, are used for comparison.

3.1. Experimental setup

The radial pump impeller consists of 7 impeller blades. The outlet part of the impeller is characterized by a two-dimensional design. The main characteristics of the vaneless diffuser are r_3/r_2 = 1.12 and h/r_2 = 0.15. The h/r_2 ratio satisfies the suggested condition for the wide vaneless diffusers. The off design operating conditions, at which the unsteady flow measurements are performed, are: Ω = 1710 *rpm*, Q/Q_n = 0.45 and Q/Q_n = 0.26.

A schematic drawing of the experimental setup is shown in figure 4. The laser sheet is inserted through the diffuser outlet into the stage. The PIV images are made in the outer part of the impeller and in the vaneless diffuser. The YAG pulsed laser has been synchronized to pulse each two complete revolutions of the impeller. Then, the camera makes the images of the flow through the transparent diffuser wall and impeller shroud.

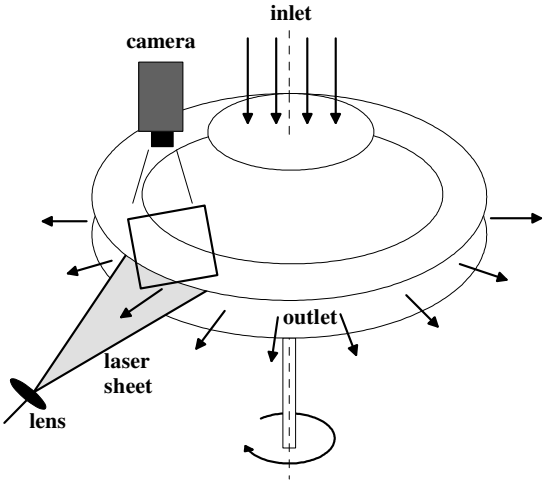

Figure 4. Schematic drawing of the experimental setup

The PIV measurements are performed at low mass flows, when the unsteady flow phenomena occur. The images are made in planes parallel to the diffuser walls. The measurement planes at h_p/h ratios 0.25, 0.5 and 0.74 are used for this comparison, where h is the diffuser width and h_p

the distance of the measurement plane from the diffuser bottom wall.

The instantaneous PIV data are averaged by summing the data of all images and dividing by the total number of images. The fluctuation velocity field is then obtained by subtracting the averaged flow field from the instantaneous velocity field of each image. For further analysis of this velocity field, a MATLAB file is written that computes the circulation strength across the flow field, and then selects the vortex structures based on their strength and magnitude. In this case, the larger and stronger vortex structures, in and around the vaneless diffuser space, are selected.

3.2. Measurement results

The PIV images, shown in this section, are taken just after the impeller blade has left the image. The tip of the impeller blade can be found in the left upper corner, where the arrow indicates the rotation direction of the impeller. The upper line, crossing the image, represents the vaneless diffuser inlet, while the lower line represents the vaneless diffuser outlet. The velocity vectors represent the velocity field of the fluctuations, and the background represents the field of vorticity.

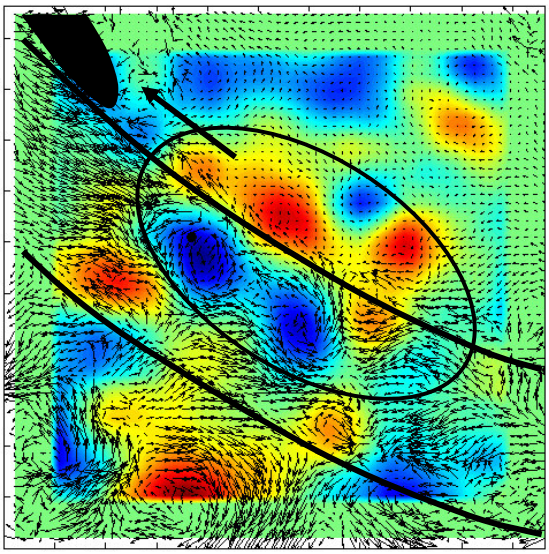

Figure 5. PIV image of the impeller blade wake, $Q/Q_n = 0.26$, $h_p/h = 0.25$, $n_o = 45$

Different flow structures were found in the performed measurements. In figure 5, a PIV image is shown, in which the wake behind the impeller blade is clearly visible. Besides the blade-wake also some other flow structures could be noticed, such as the larger vortex structures just outside the vaneless diffuser space. In figure 6, a few images are shown where the vortex pairs just outside the vaneless diffuser space are clearly visible. These clockwise and counterclockwise structures are only existent at low mass flow rates and are not observed during the stable operating flow condition.

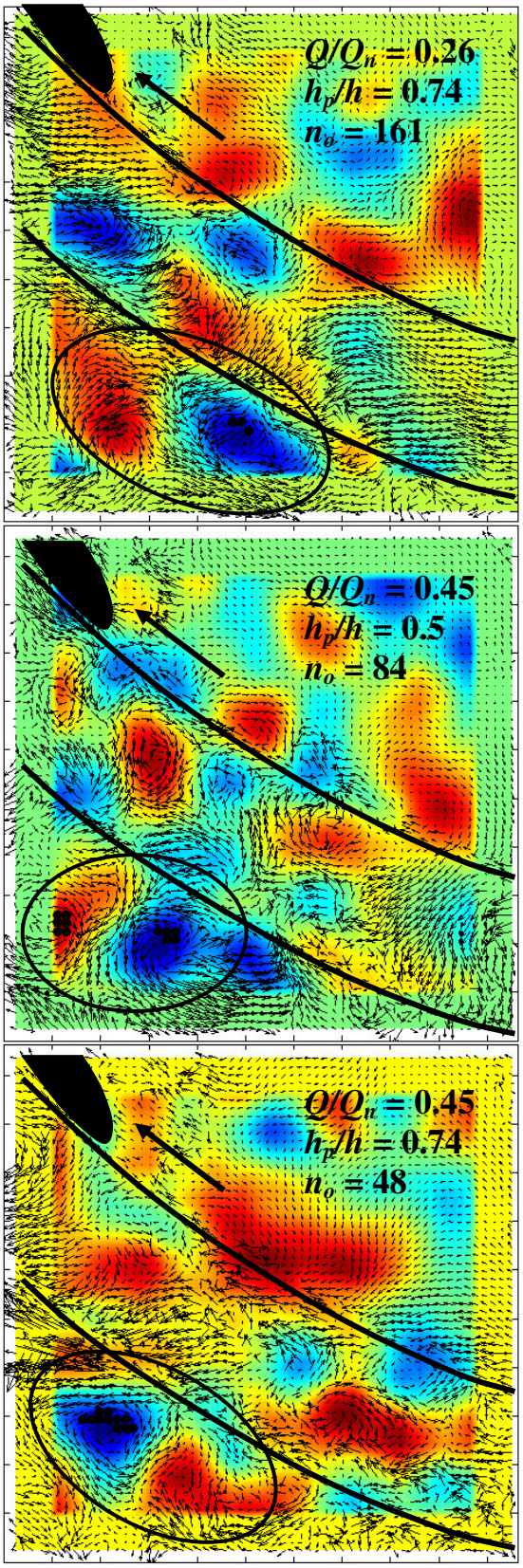

Figure 6. PIV images of the vortex pair near the diffuser outlet

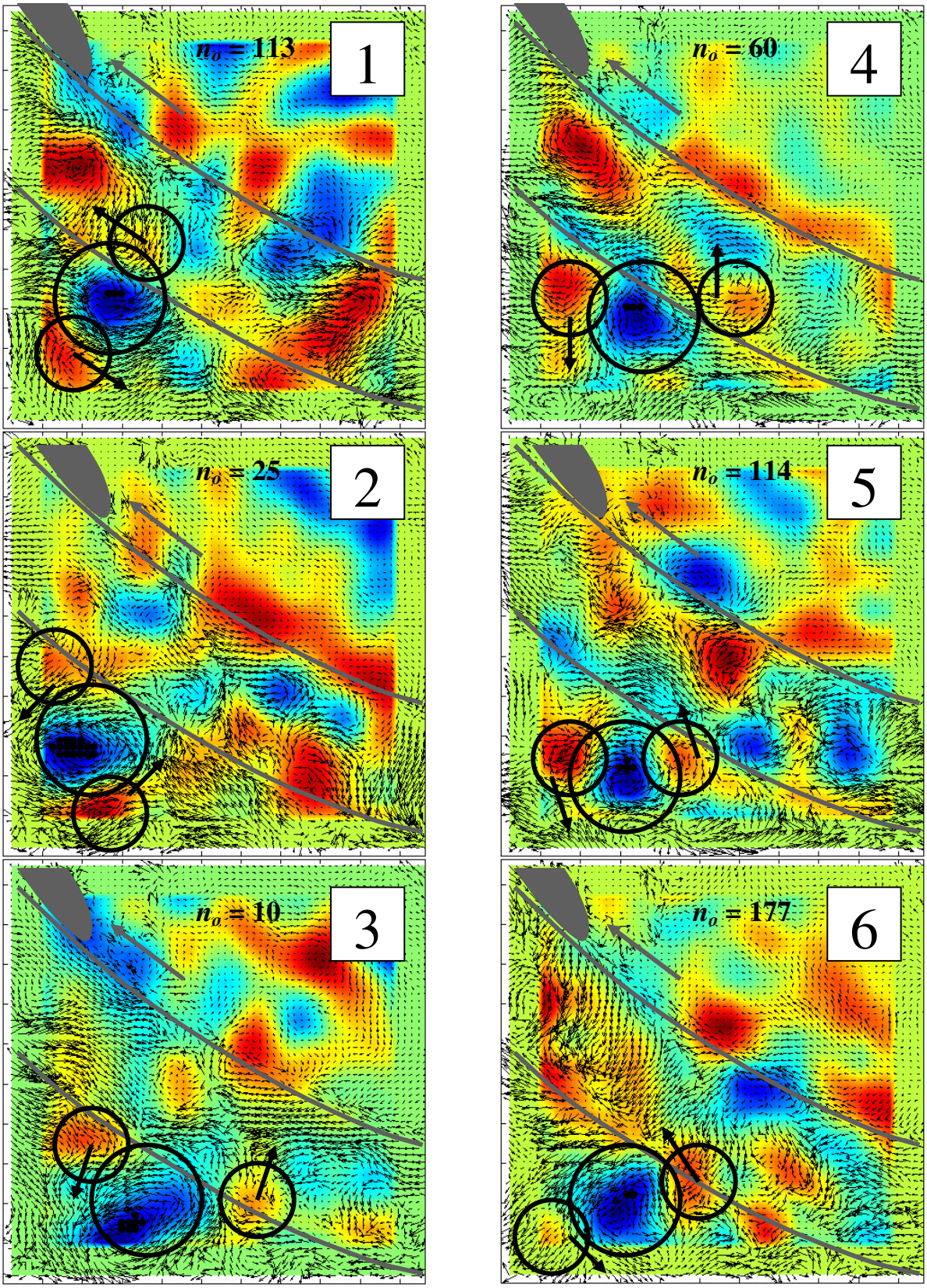

Figure 7. PIV images showing that the flow structures near the diffuser outlet rotate around each other, Q/Q_n = 0.26, h_p/h = 0.5

These vortices, shown in figure 6, remind us on the clockwise and counter-clockwise rotating structures of the two-dimensional rotating instability obtained by the numerical model.

A few differences are observed in the structure and behaviour of the rotating cells, which are probably due to the difference in environments. The clockwise and the counter-clockwise cells observed in the PIV measurements extend along 5º to 20º of the circumference, while the rotating cells in the numerical model extend along 20º to 35º of the circumference. Furthermore, the rotating cells observed in the PIV measurements are able to move around each other, while in the numerical model this movement is suppressed by the outlet boundary condition. In figure 7, a counter-clockwise rotating vortex is observed together with the surrounding clockwise rotating vortices. These PIV images show that the clockwise and counter-clockwise rotating vortices move around each other, because in each PIV image the surrounding vortices are observed at different positions with respect to the central vortex. Concerning figure 7, it must be mentioned that the images in figure 7 are not the successive images of one measurement, but are 6 randomly chosen images out of 230 images, which corresponds to one measurement. The number of order of each PIV image is given by the value of n_o. Subsequently, these images are sorted by the authors keeping in mind the rotation order of the vortices.

Despite of the differences between the experimental setup and the numerical model, similar flow structures are observed in the PIV measurements as obtained by the numerical model, which is a remarkable observation. In the following section, the differences between the experiments and the numerical model are considered and discussed.

4. DISCUSSION

Besides the similarity in the flow structures, found between the numerical model and the PIV measurements, also some differences need to be considered, which are discussed in this section.

The velocity field computed in the numerical model is fully two-dimensional, while the PIV measurements also contain some secondary flows. The major three-dimensional effects in this experimental setup are probably due to the wall boundary layers and the wake-behind the impeller blade. However, the amount of the secondary flows in this experimental setup is not expected to be very high, because the design of this experimental setup contributes to the two-dimensional character of the vaneless diffuser core flow. For instance, the outlet part of the impeller is characterized by a two-dimensional design, and the vaneless diffuser space is wide enough ($h/r_2 > 0.1$) to avoid the near wall regions, where the wall boundary layers are present. The PIV measurements are performed far enough from the vaneless diffuser walls to avoid the wall boundary layers. The secondary flows due to the wake behind the blade can not be avoided, but the two-dimensional design of the impeller exit should minimize these effects.

Another difference between the experiment and the numerical model is the working medium, which is air in the experimental case and water in the numerical model. To obtain exact equality between the experimental setup and the numerical model, their geometry and the working medium should be properly scaled with respect to each other. When scaled properly, the Reynolds number and the Mach number should be equal in both situations. Although, this experiment and the numerical model are not scaled with respect to each other, the similarity check indicates that the Reynolds number is of the same order in both cases, which is in the order of 10^6. It is not possible to satisfy the Mach number similarity as in the numerical model incompressibility is assumed. But in the experimental setup the Mach number, defined as $Ma = v_{tip}/c$, equals 0.14, which is very small. This means that the density changes over the radial pump stage are small enough, to assume that the flow is incompressible in this experimental setup.

On the other hand, a similarity between the numerical model and the experimental setup is found in the diffuser outlet boundary condition. In the experimental setup, there is no volute, and thus the vaneless diffuser outlet is connected to the open space. This situation approaches the boundary condition, p = *constant*, as prescribed in the numerical model. Because this diffuser is a very short diffuser $(r_3/r_2 = 1.12)$ compared to the commonly used vaneless radial diffusers $(1.4 < r_3/r_2 < 2)$, the outlet boundary condition can be improved by increasing the diffuser radius ratio. Increase of the diffuser radius ratio should result in better circumferential distribution of pressure at the diffuser exit. Therefore, longer vaneless diffuser should be used in this experiment for better comparison with the numerical results.

5. CONCLUSIONS

A two-dimensional viscous incompressible flow model was developed to study the core flow instability within the wide vaneless radial diffusers of centrifugal compressors. With this numerical model of the vaneless diffuser core flow, a two-dimensional rotating instability was found.

Similar flow structures, as obtained by the numerical model, are observed in the PIV measurements performed in the air test rig of the radial flow pump. In both cases, clockwise and counter-clockwise rotating structures near the diffuser outlet are observed.

It is not completely fair to compare the numerical model with this experimental setup. Therefore, new PIV measurements will be performed, with larger vaneless diffuser space behind the impeller. In these experiments, the vaneless diffuser space will have a diffuser radius ratio of 1.52, which is the same diffuser radius ratio as used in the numerical simulation. Larger diffuser radius ratio will give the rotating cells more space to develop and grow. They can move further into the diffuser and thus further away from the impeller, and they also have more chance to survive when not immediately reaching the diffuser exit, where they are being blown out of the diffuser space.

ACKNOWLEDGEMENTS

TNO from Delft, CNRS and Region Nord-Pas de Calais from France are thanked for their contribution to this project.

REFERENCES

[1] Abdelhamid, A. N., and Bertrand, J., 1980, "Distinctions between Two Types of Self-Excited Gas Oscillations in Vaneless Radial Diffusers", *ASME Paper* 79-GT-58*, Canadian Aeronautics and Space J*, Vol. 26, pp. 105-117.

[2] Dou, H. -S., 1991, "Investigation of the Prediction of Losses in Radial Vaneless Diffusers", *ASME Paper* 91-GT-323.

[3] Shin, Y. H., Kim, K. H., and Son, B. J., 1998, "An Experimental Study on the Development of a Reverse Flow Zone in a Vaneless Diffuser", *JSME International J*, Vol. 41, series B, pp.546-555.

[4] Jansen, W., 1964, "Rotating Stall in a Radial Vaneless Diffuser", *ASME J of Basic Engineering*, Vol. 86, pp. 750-758.

[5] Senoo, Y., and Kinoshita, Y., 1977, "Influence of Inlet Flow Conditions and Geometries of Centrifugal Vaneless Diffusers on Critical Flow Angle for Reverse Flow", *ASME J of Fluids Engineering*, Vol. 99, pp. 98-103.

[6] Frigne, P., and Van den Braembussche, R., 1985, "A Theoretical Model for Rotating Stall in the Vaneless Diffuser of a Centrifugal Compressor", *ASME J of Engineering for Gas Turbines and Power*, Vol. 107, pp. 507-513.

[7] Dou, H. –S., and Mizuki, S., 1998, "Analysis of the Flow in Vaneless Diffusers with Large Width-to-Radius Ratio", *ASME J of Turbomachinery*, Vol. 120, pp. 193-201.

[8] Abdelhamid, A.N., 1980, "Analysis of Rotating stall in Vaneless Diffusers of Centrifugal Compressors", *ASME Paper* 80-GT-184.

[9] Tsujimoto, Y., Yoshida, Y., and Mori, Y., 1996, "Study of Vaneless Diffuser Rotating Stall Based on Two-Dimensional Inviscid Flow Analaysis", *ASME J of Fluids Engineering*, Vol. 118, pp. 123-127.

[10] Ljevar, S., de Lange, H. C., and van Steenhoven, A. A., 2005, "Rotating Stall Characteristics in a Wide Vaneless Diffuser", Proc. *ASME Turbo Expo 2005*, Reno-Tahoe, Nevada, USA, Vol.6, part B.

[11] Ljevar, S., de Lange, H. C., and van Steenhoven, A. A., 2006, "Two-Dimensional Rotating Stall Analysis in a Wide Vaneless Diffuser", *Int J Rotating Machinery*, Vol. 12, pp. 1-11.

[12] Leonard, B. P., 1979, "A Stable and Accurate Convective Modeling Procedure Based on Quadratic Upstream Interpolation", Comp Meth Appl Mech Eng, Vol. 19, pp. 59-98.

[13] Wuibaut, G., Bois, G., Dupont, P., Caignaert, G., and Stanislas, M., 2002, "PIV Measurements in the Impeller and the Vaneless Diffuser of a Radial Flow Pump in Design and Off-Design Operating Conditions", *ASME Journal of Fluids Engineering*, Vol. 124, pp. 791-797.

Conference on Modelling Fluid Flow (CMFF'06)
The 13th International Conference on Fluid Flow Technologies
Budapest, Hungary, September 6-9, 2006

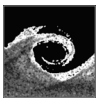

STEADY SIMULATION OF WIND TURBINE ROTORS

Abhishek GUPTA[1], Amr HENNI[2]

[1]Corresponding Author. Graduate Student, Industrial Systems Engineering Department, University of Regina, 3737 Wascana Parkway, Regina Saskatchewan, Canada S4S0A2. Tel.: +1 306 585 6664, Fax: +1 306 585 4855, E-mail: gupta20a@uregina.ca
[2]Associate Professor, Industrial Systems Engineering Department, University of Regina. E-mail: amr.henni @uregina.ca

ABSTRACT

The aerodynamic performance of the NREL (National Renewable Energy Laboratory) Combined Experiment Phase II and III Horizontal axis wind turbine rotors has been studied with 3-D steady Navier-Stokes solver. A range of Turbulence models including Spalart-Allmaras (S-A), Standard k-e, k-e-Realizable and k-w-SST were used and evaluated. The experimental data from IEA Annex XIV database was used to compare the predicted results. The experimental data was reduced to steady state with known deviation in velocity and yaw angle. The results were obtained in the form of rotor power and pressure distribution at various radial locations of the blade. All turbulence models predicted the power well for low wind speeds but under-predicted the power at higher wind speeds for both rotor blades however the stall was captured by k-e and k-w SST turbulence models. The pressure distribution comparison with the experimental data was good except at inboard span locations of the blade for higher wind speeds.

Keywords: Aerodynamics, CFD, Power, Pressure distribution, Wind Turbine

NOMENCLATURE

y+ [-] Sub layer distance from the wall

1. INTRODUCTION

Wind is the most abundant source of renewable energy and therefore it is the fastest growing energy technology in the world. Its chief benefits include cost-effective energy generation, reduction of air pollution, reduction of global warming, zero waste production and agriculture support. Modeling the aerodynamics of wind turbine rotor is a challenging area in wind energy industry.

Various methodologies have been used in this area including Blade Element Momentum theory [1, 2, and 3], Vortex Lattice methods [4] and variants of Navier-Stokes solver [5-9].

Both Blade Element Method and Vortice Lattice methods had showed inadequacies in predicting rotor power at higher wind speeds due to lack of satisfactory stall delay models. The Navier-Stokes methodologies show promise in capturing aerodynamics at blade stall but unsteady flow effects and grid resolution have restricted its accuracy. In order to account for this phenomenon, these methods require large computational resource which is primarily responsible for its restricted use.

The applications of Computational Fluid Dynamics (CFD) for wind turbine can be found in the works of Duque et al. [7, 9] and Xu and Sankar [6, 8]. For low wind speeds, they generally obtained good agreement with the experimental results but for high wind speeds, they were unable to capture the flow phenomena well.

Majority of the work done for calculating aerodynamic characteristics of wind turbine has been done on in-house codes that are not readily available for a common wind turbine designer. Therefore a commercially available CFD software FLUENT has been used in this study.

Experimental data for NREL wind turbine has been obtained from IEA Annex XIV database [10]. This database was made by several European Union research labs and NREL to obtain experimental field data for different wind turbines [11]. However, the data is in unsteady form and has to be reduced to steady state in order to make it possible for benchmamrking purposes.

This paper describes the application of Navier-Stokes methodology through the application of Spalart-Allmaras [12], k-e standard [13], k-e-realizable [14] and k-w-SST [15] turbulence models. This data have been obtained from IEA Annex XIV database and have been reduced to steady wind and certain yaw error. The paper discusses and compares the aerodynamic prediction capabilities of the above mentioned turbulence models for both twisted (Phase III) and untwisted (Phase II) wind turbine rotors .

2. EXPERIMENTAL DATA

The NREL combined experiment Phase II and III wind turbine data was used for comparisons. Both wind turbines are downwind three-bladed HAWTs (Horizontal axis wind turbine) and have blades with a rectangular planform. The S809 airfoil is used throughout the span of the blades. The S809 airfoil is a 21% thick laminar flow airfoil designed specifically for Horizontal Axis Wind Turbine (HAWT) purpose [16]. The S809 airfoil is specified in terms of coordinates.

Both blades have a constant chord of 0.457 *m* and diameter of 10.0 *m*. The phase II rotor blade is untwisted and has a fixed pitch of 12 degrees. The phase III rotor blade is twisted throughout the span and been manually pitched to 3 degrees. The twist distribution of phase III rotor blade is shown in Figure 1. The details of the experiment are given in References [11, 17].

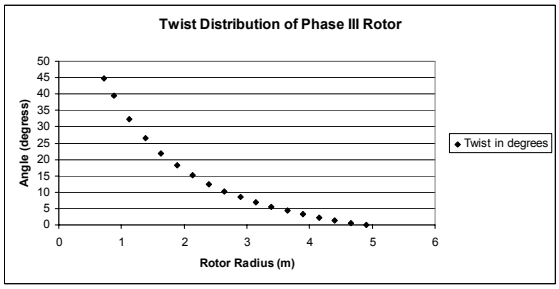

Figure 1. Twist Distribution of Phase III Rotor Blade

The documented experimental data provided by IEA Annex XIV database has large fluctuations in wind speed and nacelle yaw errors. In order to make it suitable for benchmarking, the steady state data was extracted having minimum wind speed variation and yaw errors. The methodology used was similar to as done by Duque et al. [9]. The experimental data is organized in five wind speed bins for phase II and four wind speed bins for phase III. Each bin was reduced to sets of five consecutive revolutions of rotor in which the wind speed deviation is less than 0.45m/s. These sets were further reduced by eliminating those having excessive difference between yaw angles.

Five sets of data were obtained for both rotors. The obtained data points were compared with the reported NREL power curve in the database as shown in Figures 2 and 3. The sorted power data show good agreement with NREL power curve for Phase II rotor. For Phase III rotor, there are certain deviations.

3. METHODOLOGY

The computations were done on commercial general purpose computational fluid dynamics (CFD) software FLUENT. It is a multi-purpose CFD software which solves the Reynolds-Averaged-Navier-Stokes (RANS) equation in finite volume formulation.

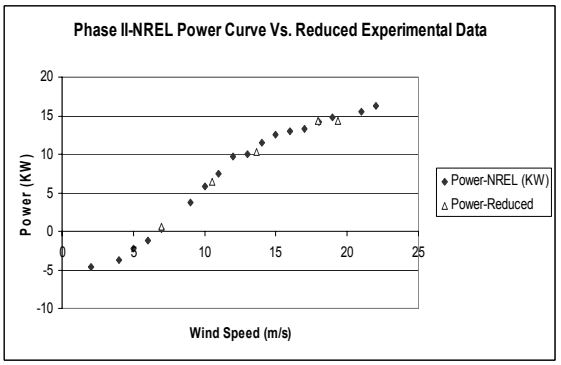

Figure 2. Comparison of NREL Power Curve and Reduced Experimental Data Points of Phase II Rotor.

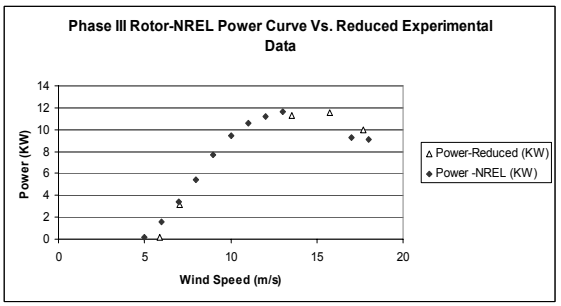

Figure 3. Comparison of NREL Power Curve and Reduced Experimental Data Points of Phase III Rotor

Various turbulence models were studied including, Spalart-Allmaras [12], k-e standard [13], k-e-realizable [14] and k-w-SST [15]

All computations were done only on rotor i.e. the nacelle and the tower were excluded. The unstructured (tetrahedral cell) grid was generated for both rotors. The single blade of both the rotors was modeled and periodic condition was imposed to account for the other two blades. The periodic boundary condition is used when the physical geometry has periodically repeating nature as in the case of wind turbine.

Both blades employ S809 airfoil with varying thicknesses at cross-sections. The coordinates of S809 airfoil were interpolated to form face at various blade spans and a skin surface was generated to connect them. The details regarding the geometry of both NREL Phase II and III rotors can be found in ref [11, 17].

The flow domain was made as a 120 degree azimuthally angled sphere. The domain is extended to eight times radius of the blade. The Gambit pre-processor tool was used for mesh generation. Figures 4 and 5 shows the grid of phase II and III rotor blade respectively. The unstructured blade mesh was generated with Pave scheme. The Phase

II and III blade surface was covered with 23022 and 24162 triangular cells respectively. The unstructured domain grid was created with TGrid meshing scheme. The domain grid of Phase II and Phase III rotor has 433,117 and 435,960 tetrahedral cells respectively. The cell-equiangle-skew and cell-equivolume-skew was below 0.7 in both the grids.

The steady state simulation is done with implicit, segregated, three-dimensional solver using Multiple Reference Frame (MRF) Model [18] of FLUENT. The MRF model is a time-averaged flow model for moving and rotating zones. The standard discretization scheme for pressure is used. The pressure velocity coupling was done with SIMPLE [19] technique. Fully turbulent computations were performed.

FLUENT has several inbuilt turbulence models. Among them, four turbulence models including Spalart-Allmaras [12], k-e standard [13], k-e-realizable [14] and k-w-SST [15] were used and evaluated for rotor aerodynamic predictions. The normal grid spacing from the blade was kept such that the nodes above the surface gave y+ values greater than 30. The results were obtained for residual value of 1e-3.

The velocity inlet and pressure outlet boundary condition of FLUENT was used for inlet and outlet respectively. The no-slip boundary condition was imposed on the blade. The simulation was done at five wind speeds for four turbulence models for NREL phase II and phase III rotor blade.

In order to check the sensitivity of Phase II rotor mesh, two wind speeds; 7m/s and 10.56 m/s were chosen. The new mesh had 200 cells stretched by a factor of 1.05 on periodic face in the X direction. The cells on the blade were doubled. The difference in the power obtained between the previous and this grid were 2.33% and 0.028% for wind speed of 7 m/s and 10.56 m/s respectively. For Phase III rotor mesh, the cells on the blade were doubled and the difference in the power computed was negligible when compared with initial grid computations.

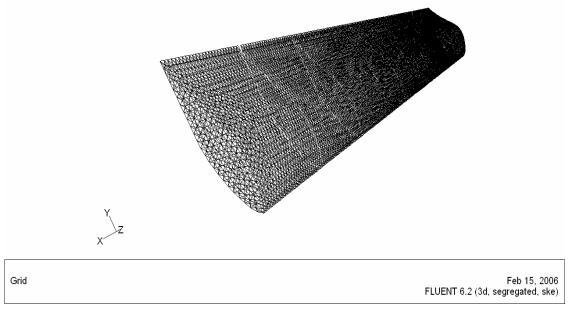

Figure 4. NREL Phase II Rotor Blade

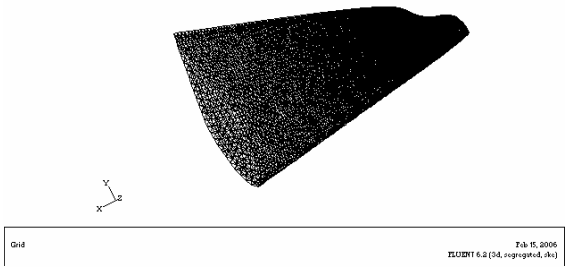

Figure 5. NREL Phase III Rotor Blade

4. RESULTS

The results in the form of power, pressure distribution, stagnation pressure and thrust have been obtained for Phase II and III and were compared with reduced IEA Annex XIV experimental data.

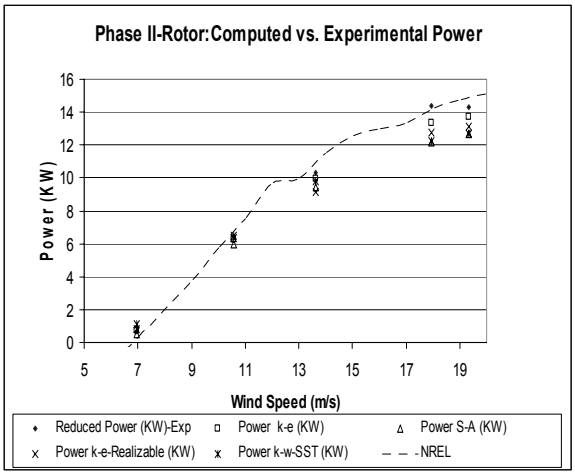

Figure 6. Comparison of Experimental Power with computed Power of Phase II Rotor

Figure 6 show the comparison between the power obtained from reduced experimental data against the computed power for Phase II rotor. All turbulence models show good agreement with experimental data; however the power was under-predicted at higher wind speeds.

The S-A and k-e-Realizable turbulence models did a reasonable job in predicting power at low wind speeds but under-predicted the power at the stall and higher wind speeds. The k-w-SST turbulence model predicted the power well at low wind and medium wind speeds and captured the stall well but under-predicted the power at high wind speeds.

The best job was done by k-e turbulence model which not only captured the stall well but also show minimal deviation of power at higher wind speeds. The performance of k-e turbulence model for NREL Phase VI rotor [20] was studied by Sarun and

Sankar [21] in which the k-e model did a reasonable job in predicting aerodynamic forces on wind turbine rotor.

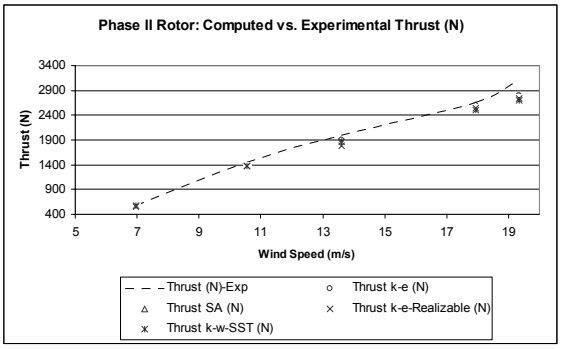

Figure 7. Comparison of Experimental Thrust with computed Thrust of Phase III Rotor

Figure 7 shows the comparison between computed and experimental thrust values. All turbulence models show good agreement with the experimental data except for high speed were the thrust is under-predicted.

Since the pressure distribution predicted by all the turbulence models cannot to shown because of the space limitation, the results computed by k-w-SST turbulence model has been discussed. Similarly, two wind speeds, each representative of low and high wind speed range has been chosen for both rotor blades.

Figure 8 and 9 show pressure distribution at four span locations of Phase II rotor blade for wind speed 7m/s and 18m/s respectively as calculated by k-w-SST turbulence model.

All pressure distributions compares well with the experimental data. However certain difference exists at the inboard span at 18m/s speed. Also there are certain discrepancies in the nose region which can be due to unresolved grid.

The agreement between the experimental and computation value of pressure for wind speed 7 m/s is good for all radial locations as can be seen in Figure 8.

In Figure 8, at 63% and 80% span locations where the flow is fully attached, a bubble shown by the experimental data at suction side was not modeled. This may be a laminar separation bubble. Since the calculations were fully turbulent, this effect was not reflected in the result.

Some error can be seen in the tail of the airfoil section of the blade. This is because the effect of thickening of airfoil boundary layer was not captured.

As can be seen in Figure 9, the computed and experimental pressure difference can be seen from 30% to 63% span with greater difference at the 30% span. This is due to the separation of flow at the suction side which is not captured properly. The inaccurate pressure prediction at the suction side of the blade is responsible for the error. Also this lower pressure prediction is responsible for the under-prediction in power for high wind speeds. At the outer radial sections, the error between computation and experimental value decreases.

The stagnation pressure at leading edge for four radial locations is calculated and compared with experimental data for wind speeds 7m/s and 18m/s as shown in Figure 10. The experimental and computed values of stagnation pressure as in good correlation.

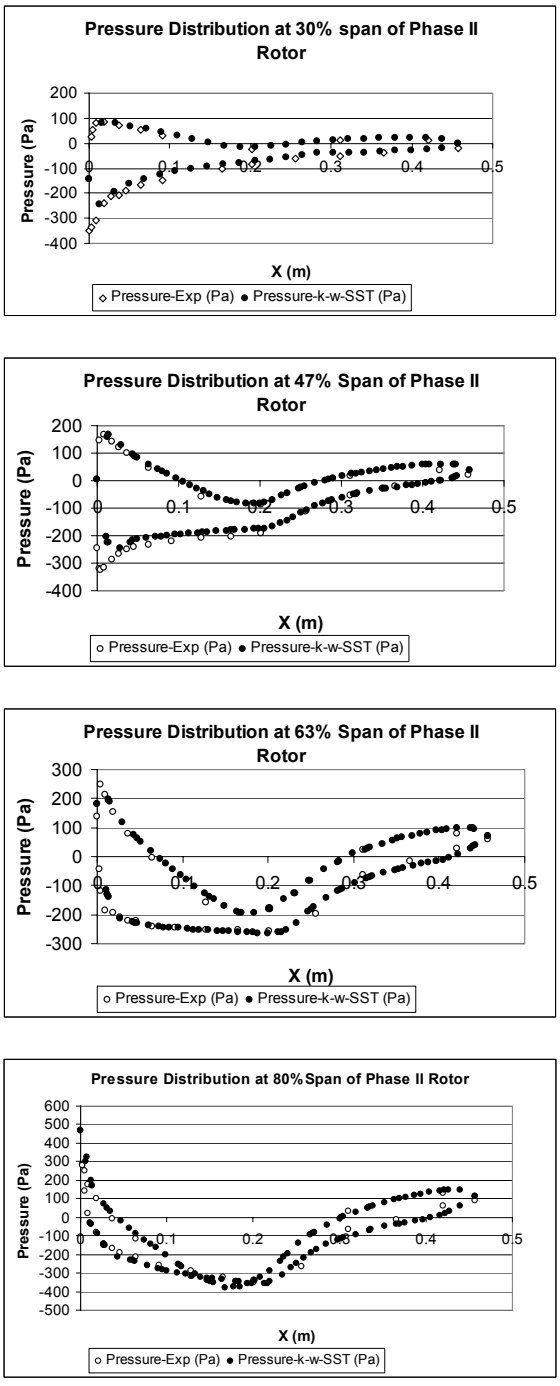

Figure 8. Pressure Distribution comparison between experimental and calculated by k-w-

SST turbulence model at four span locations of Phase II Rotor for wind speed 7m/s.

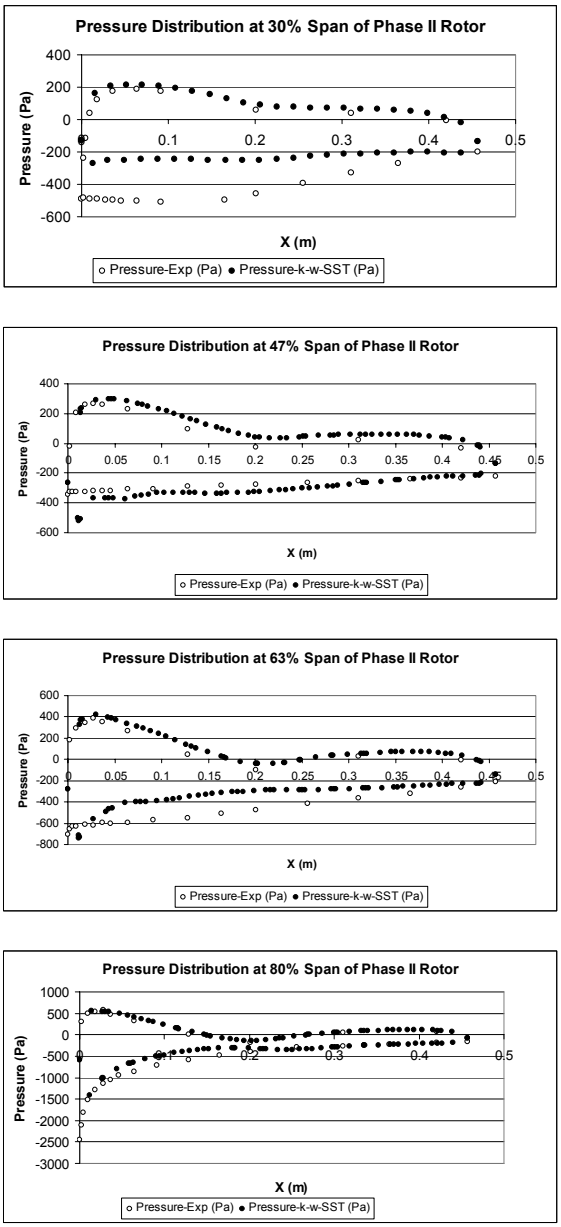

Figure 9. Pressure Distribution comparison between experimental and calculated by k-w-SST turbulence model at four span locations of Phase II Rotor for wind speed 18m/s.

Figure 11 show the comparison between the experimental power obtained from reduced experimental data against the computed power for Phase III rotor

The S-A turbulence model under-predicted the power for the entire range of wind speed. The deviation of computed with the experimental power increases with the wind speed. The k-e-Realizable predicted the power well at lower wind speeds but under-predicted it at higher wind speeds. Both k-e and k-w-SST turbulence models predicted the power well and were better than k-e-Realizable model at low wind speeds but under-predicted at higher wind speeds.

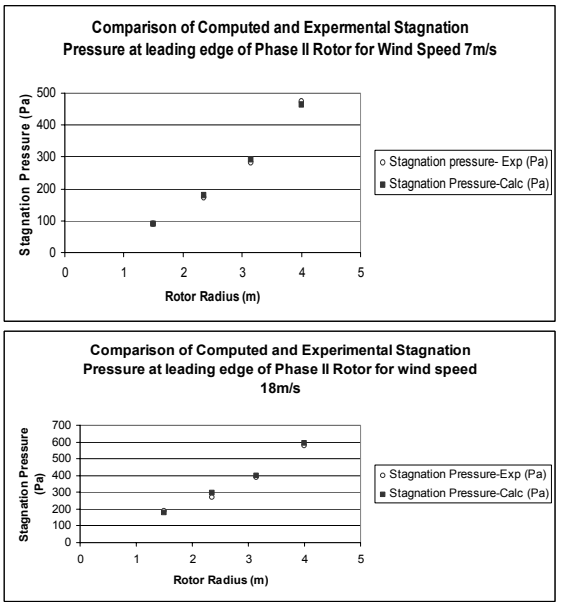

Figure 10. Stagnation pressure computation by k-w-SST turbulence model for Phase II rotor and comparison with experimental data.

The k-w-SST model was able to model the stall because the drop in power after the stall region was predicted well. The k-e model could not model the post-stall region well. This is logical because the k-e model uses wall functions based on law of the wall which does not hold for separated flows [13].

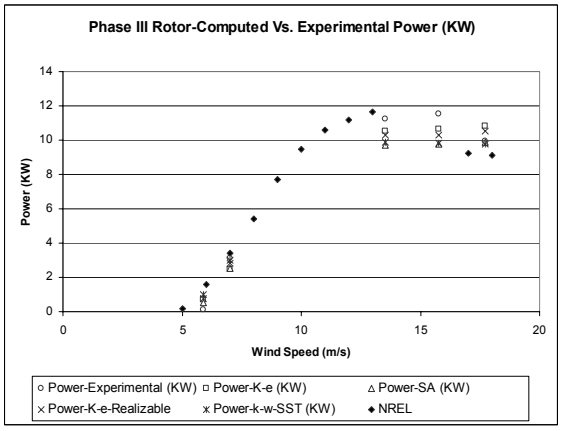

Figure 11. Comparison of Experimental Power with computed Power of Phase III Rotor

Figure 12 shows the comparison between computed and experimental thrust values for Phase III rotor. All turbulence models show good agreements with the experimental data, except for high speed were the thrust is under-predicted but is in acceptable range.

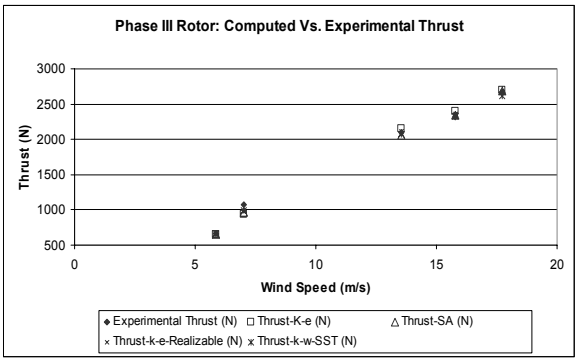

Figure 12. Comparison of Experimental Thrust with computed Thrust of Phase III Rotor

Figures 13 and 14 show pressure distribution at five span locations of Phase III rotor blade for wind speed 7m/s and 16m/s respectively as calculated by k-w-SST turbulence model. The experimental and computed values of pressure compares well for both the wind speeds as shown in Figures 13 and 14. However there is certain incongruity at inboard span of 30% as well as in the nose region which may be attributed to the same reason as discussed for pressure distribution of Phase II rotor blade.

The stagnation pressure at leading edge for five radial locations is calculated and compared with experimental data for wind speeds 7m/s and 16m/s as shown in Figure 15. The values compared well for wind speed 7m/s but for 16 m/s there was some under-prediction at the outer radius of the rotor. There was some error in two stagnation pressure data points in experimental data and are not included as can be seen in Figure 15.

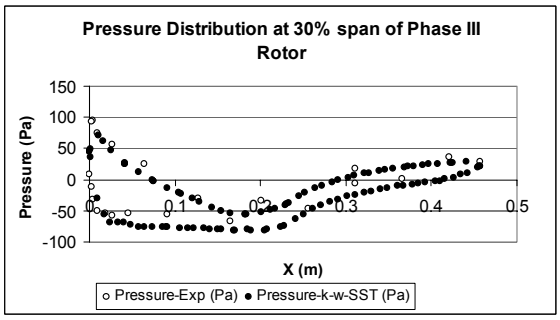

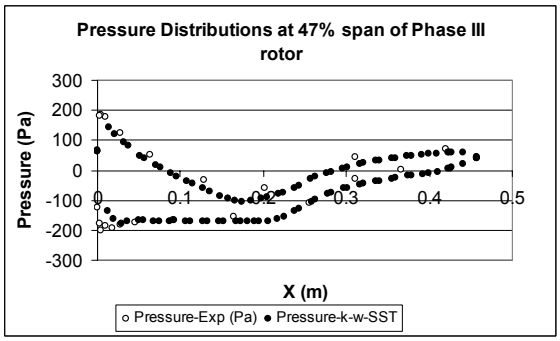

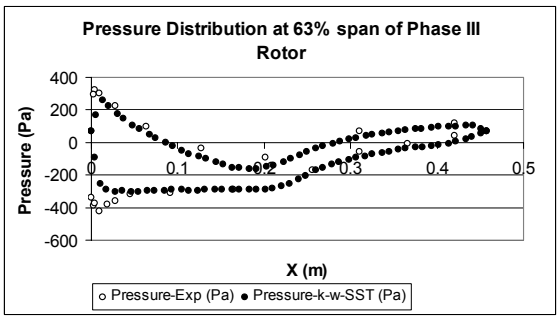

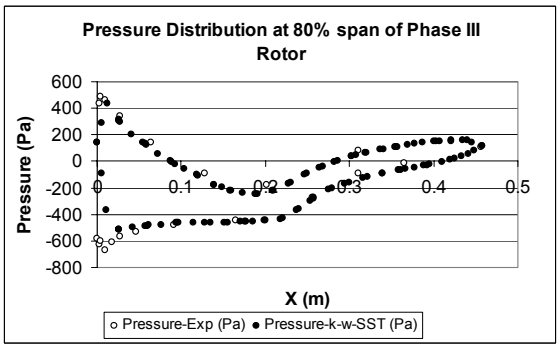

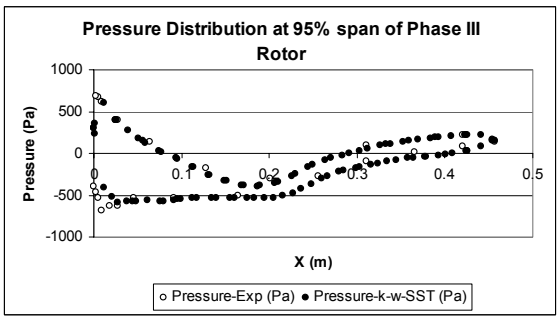

Figure 13. Pressure Distribution comparison between experimental and calculated by k-w-SST turbulence model at four span locations of Phase III Rotor at wind speed 7m/s.

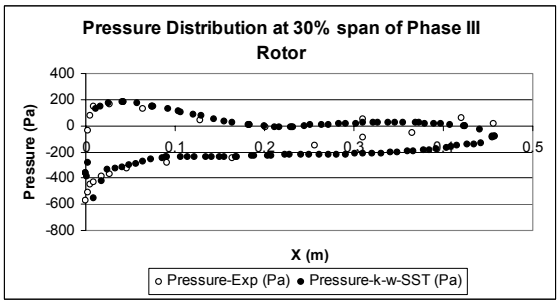

At the inboard sections, the local flow begins to stall. This flow unsteady in nature and since all the computations performed were steady, this feature was not captured as can be seen at the pressure distributions at inner span of the blade in Figures [13] and [14].

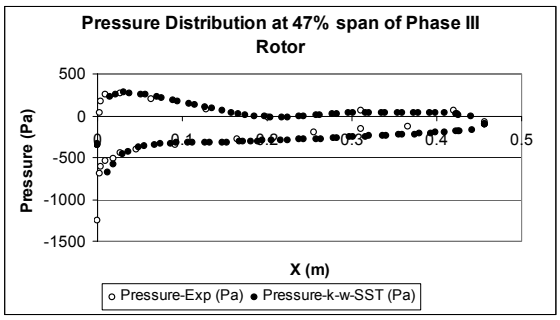

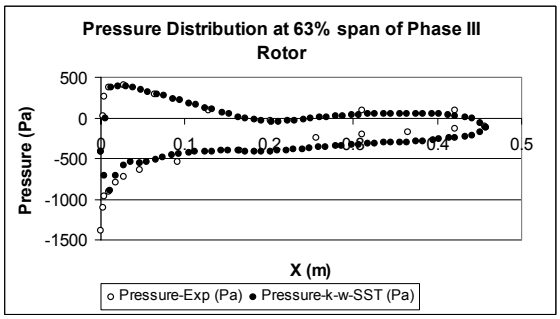

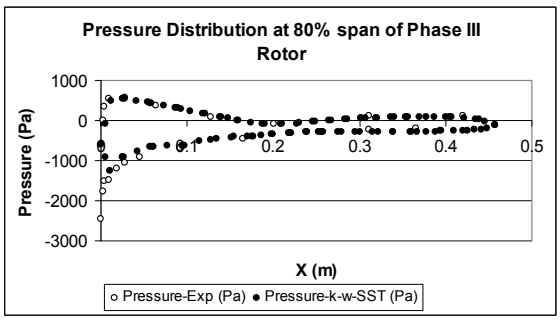

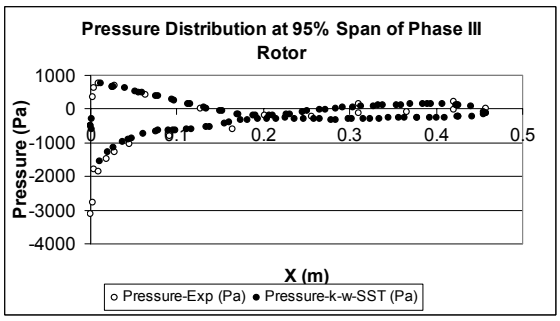

Figure 14. Pressure Distribution comparison between experimental and calculated by k-w-SST turbulence model at four span locations of Phase III Rotor at wind speed 16m/s.

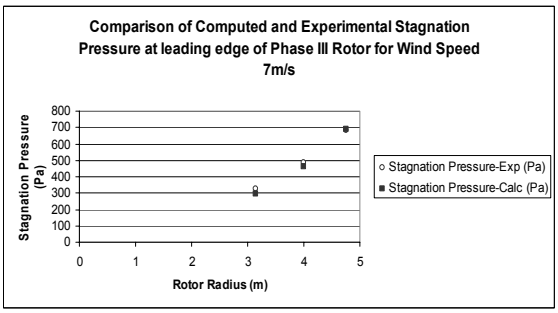

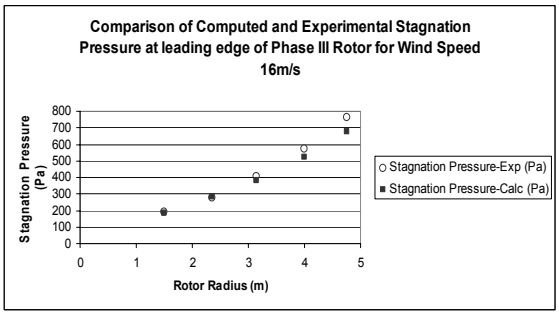

Figure 15. Stagnation pressure computation by k-w-SST turbulence model for Phase III rotor and comparison with experimental data.

5. CONCLUSIONS

This paper gives the study of simulating wind turbine rotors using commercial CFD software to calculate the aerodynamic characteristics and flow phenomena present in a rotating rotor blade.

The performance of four turbulence models was studied to predict the aerodynamics characteristics of two wind turbine rotors over a range of wind speed. All the turbulence models did a good job in predicting power, thrust and pressure distribution over the blade at low wind speeds. But at higher wind speeds where the flow is highly separated, the k-e and k-w-SST gave the best performance.

Also at high speeds, the large portion of rotor blade operates in post stall region. These separated regions are highly dynamic in nature and hence the steady state assumption does not hold. Future studies will be done on unsteady computations.

The laminar separation bubble in Figure 8 was not modeled since the computations were fully turbulent. This requires the need for transition modeling which is not supported in any commercial software and also none of the transition models are universal. The incorporation of both laminar and turbulent flow can be done but this will require the accurate prediction of transition point. If this model is integrated in the software, it will greatly improve the surface pressure prediction especially in transitional Reynolds number

The pressure distribution as seen in Figure 8, show error near the nose region. This requires the need to tighten the grid at the nose region so as to capture the physics well.

The experimental data used in this work was field data and had large fluctuations which made it difficult to be used for benchmarking purposes. Hence the future studies would be done on more reliable wind tunnel test data of wind turbine.

The reduced experimental data for Phase III rotor did not match well with the reported NREL curve. This is due to the large fluctuations inherently present in the data and thus a rigorous statistical method has to be applied in order to reduce it in steady state form.

ACKNOWLEDGEMENTS

The authors would like to thank the technical support group of FLUENT for their assistance in using the FLUENT solver.

REFERENCES

[1] Martínez, J., Bernabini, L., Probst, O., and Rodríguez, C., 2004, "An improved BEM model for the power curve prediction of stall-regulated wind turbines", *Wind Energy Journal*, Vol. 8, pp. 385-402.

[2] Rajagopalan, R.G., and Fanucci, J.B., 1985, "Finite Difference Model for the Vertical Axis Wind Turbines", *Journal of Propulsion and Power*, Vol. 1, pp. 432-436.

[3] Leclerc, C., and Masson, C., 1999, "Predictions of Aerodynamic Performance and Loads of HAWTS Operating in Unsteady Conditions", Proc. *ASME Wind Energy Symposium, 37th AIAA Aerospace Sciences Meeting and Exhibit*, Reno, NV, AIAA-99-0066.

[4] Whale, J., Fisichella, C.J., and Selig, M.S., 1999, "Correcting Inflow Measurements from HAWTS using a Lifting Surface Code", Proc. *ASME Wind Energy Symposium, 37th AIAA Aerospace Sciences Meeting and Exhibit*, Reno, NV, AIAA-99-0040.

[5] Sorenson, N. N., and Hansen, M.O.L, 1998, "Rotor Performance Predictions using a Navier-Stokes Method", Proc. *ASME Wind Energy Symposium, 36th AIAA Aerospace Sciences Meeting and Exhibit,* Reno, NV, AIAA-98-0025.

[6] Guanpeng, Xu, and Sankar, L., 1999, "Computational Study of Horizontal Axis Wind Turbines", Proc. *ASME Wind Energy Symposium, 37th AIAA Aerospace Sciences Meeting and Exhibit*, Reno, NV, AIAA-99-0042.

[7] Duque, E, P. N., and Burkland, M., 2003, "Navier-Stokes and Comprehensive Analysis Performance Predictions of the NREL Phase VI Experiment", Proc. *22nd ASME Wind Energy Symposium,* Reno, NV, AIAA-2003-0355.

[8] Xu, G., and Sankar, L. N., 2002, "Development of engineering aerodynamics models using a viscous flow methodology on the NREL Phase VI rotor" , *Wind Energy Journal*, Vol. 5(2-3), pp. 171-183.

[9] Duque, E. P. N., Wayne, J., vandam, C.P., Cortes, R., Yee, K., 2000, "Numerical Predictions Of Wind Turbine Power and Aerodynamics Load For The Phase II Combined Experiment Rotor", 2000, Proc. *AIAA/ASME Wind Energy Symposium , AIAA 38th Aerospace Sciences Meeting,* Reno, NV, AIAA-2000-38.

[10] http://www.ecn.nl/wind/other/IEA/dbform.html

[11] Schepers, J.G., Brand A. J., Bruining A., Graham J.M.R., Hand M.M., Infield D.G., Madsen H.A., Paynter R.J.H. and Simms D.A., 1997, "*Final report of IEA AnnexXIV : Field Rotor Aerodynamics*" ECN-C-97-027.

[12] Spalart, P., and Allmaras, S., 1992, "A One-Equation Turbulence Model for Aerodynamic Flows", *Technical Report* AIAA-92-0439.

[13] Wilcox, D. C., 1998, "*Turbulence Modeling for CFD"*, DCW Industries, Inc.

[14] Shih, H., Liou, W. W., Shabbir, A. , Yang, Z. , and Zhu, J. , 1995, "A New k-e Eddy-Viscosity Model for High Reynolds Number Turbulent Flows - Model Development and Validation", *Computers and Fluids Journal*, Vol. 24, pp. 227-238.

[15] Menter, F.R., 1993, " Zonal Two Equation k – ω Models for Aerodynamic Flows", *AIAA Journal*, AIAA-93-2906.

[16] Somers, D. M., 1989, "*Design and Experimental Results for the S809 Airfoil*" ,Airfoils, Inc., State College, PA

[17] Simms, D.A., Hand, M.M., Fingersh, L.J., Jager, D.W., 1999, "*Unsteady Aerodynamics Experiment Phases II–IV Test Configurations and Available Data Campaigns*", NREL/TP-500-25950.

[18] FLUENT-6.2 Documentation

[19] Patankar, S. V., 1980, "*Numerical Heat Transfer and Fluid Flow"*, Hemisphere, Washington, D.C.

[20] Hand, M. M., Simms, D. A., Fingersh, L. J., Jager, D. W., Cotrel, J. R., Schreck, S., and Larwood, S. M., 2001, "*Unsteady Aerodynamics Experiment Phase VI: Wind Tunnel Test Configurations and Available Data Campaigns*", NREL/TP-500-29955.

[21] Benjanirat, S., and Sankar, L. N., 2003, "Evaluation of Turbulence Models for the Prediction of Wind Turbine Aerodynamics" *AIAA Journal*, AIAA-2003-0517.

Conference on Modelling Fluid Flow (CMFF'06)
The 13th International Conference on Fluid Flow Technologies
Budapest, Hungary, September 6-9, 2006

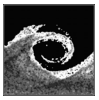

APPLICATION OF A CROSS FLOW FAN AS WIND TURBINE

Toni Klemm[1], Martin Gabi[2], Jean-Nicolas Heraud[3]

[1] Corresponding Author. Department of Fluid Machinery, University of Karlsruhe (TH). Kaiserstraße 12, D-76128 Karlsruhe, Germany. Tel.: +49 721 608-2350, Fax: +49 721 608-3529, E-mail: toni.klemm@ism.uka.de
[2] Department of Fluid Machinery, University of Karlsruhe (TH). E-mail: martin.gabi@ism.uka.de
[3] Department of Fluid Machinery, University of Karlsruhe (TH). E-mail: jean-nicolas.heraud@gadz.org

ABSTRACT

In this paper investigations of the flow structure in a cross flow wind turbine are presented. To determine the flow field CFD simulations and PIV measurements were carried out. These results are the starting point to develop efficient casings for cross flow wind turbines.

Wind Turbine, Wind Power, Performance, CFD, PIV

NOMENCLATURE

c	$[m/s]$	absolute velocity
D	$[m]$	diameter
L	$[m]$	length
M	$[Nm]$	torque
n	$[rpm]$	rotation speed
p	$[Pa]$	pressure
Q	$[m^3/s]$	volume flow rate
R	$[m]$	radius
$\Re$	$[-]$	degree of reaction
S	$[m]$	chord length
t	$[s]$	time
u	$[m/s]$	circumferential velocity
w	$[m/s]$	relative velocity
η	$[-]$	efficiency

Subscripts and Superscripts

n	normalize
u	peripheral direction
st	static
tot	total
1	inner diameter
2	outer diameter

1. INTRODUCTION

Cross Flow Turbines are widely used in small hydroelectric power plants. The design of these turbines is based on Banki-type turbine (Figure 1). The turbine is partial loaded to avoid churning losses. The water supply is realized at the top of impeller with a control device. The water jet leaves the blade channels at the inner rotor diameter and after crossing the space inside the second blade row is passed in outside direction. The rotational speed is limited as the jet should not touch the shaft of the rotor. The advantages of this type are smaller size and costs as well as the performance at operating conditions with low head compared to classical turbines. This is a result of the high power density. To apply these favourable properties on a wind turbine investigations have to be carried out. This is

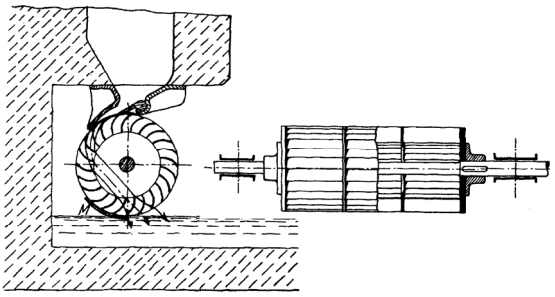

Figure 1. Banki-type turbine [1]

necessary as the modification of fluid results in different flow conditions. In the water turbine the blades are partial loaded with energy transforming fluid contrary to the wind turbine. This leads to a highly complex flow structure inside and outside of the rotor and in the blade channels with inducing flow losses.

Cross flow wind turbines can be established to use wide but flat fluid flows. These flows occur for instance at mountain sides and valleys due to warming or cooling of air films next to the soil. Applications are spanned furthermore onto the use of buoyancy flows at warmed facades on buildings [2] and flows in tunnel systems. The capacity taken from the mechanical energy of the wind can be used for example in combination with a photovoltaic solar power plant to charge the accumulator at days

with poor light and at night. Considerations about reasonable applications in economical and energetic point of view aren't accomplished yet.

2. INVESTIGATION OBJECT

Due to the similarities of flow inside a cross flow fan and a Banki-type turbine casing and rotor design of a typical cross flow fan are used. The data of rotor and casing are shown in Figure 2 and Table 1.

length L	0.3 m
outer blade diameter D_2	0.098 m
ratio D_1/D_2	0.82
blade angles	β_1=88°, β_2=27°
number of blades	36
chord length S	0.01 m
blade profile	circular arc R=0.086m
blade thickness b	0.004 m

Table 1. Rotor Data

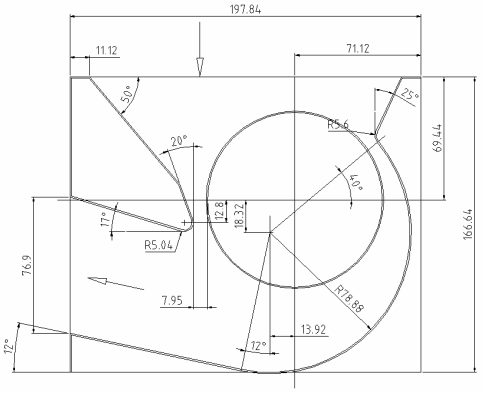

Figure 2. Geometry of the original cross flow fan

Cross flow fans are used in ventilation technology because of their compact design and high specific pressure ratio. A cross flow fan consists of a cylindrical rotor, forward curved blades, and a casing with suction side inflow, rear wall contour, vortex wall and pressure side outlet (Figure 3). The air flows from the suction side into the blade channels radially, passes through in a direction transverse to the rotor axis for discharge in another direction (Fig. 3). The flow traverses the blade row twice. For a theoretical design of fluid machines with cross flow the inflow and outflow blade row can be joined (Figure 4).

The theoretical high deflection of the flow leads to a high energy transfer into the fluid due to the large changing of circumferential component of the absolute velocity (c_u) according to the Euler equation (Eq. (1)).

$$a = \Delta(uc_u) \qquad 1$$

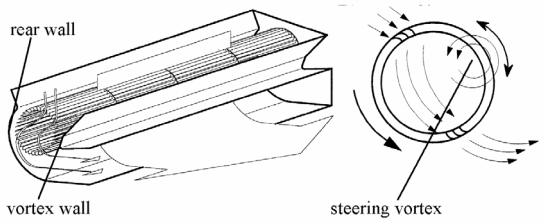

Figure 3. Functionality of a cross flow fan

The flow pattern inside the fan is characterized by steering vortex whose position and size depend on the operating point. The center of the vortex is inside the rotor near the vortex wall. This effects a transient flow in the blade channels and a less efficiency of about $\eta = 0.5$. To realize a wind turbine the flow direction is inverted (Figure 4). In a wind turbine the static pressure before and after the impeller is identical. That means a wind turbine is off type action turbine. With consideration of a cross flow fan it can be seen that the degree of reaction is about zero (Eq. (2)). On that reason an inverse passed cross flow fan is adequate to use as wind turbine.

$$\Re = \frac{\Delta p_{st}}{\Delta p_{tot}} \qquad 2$$

The aim of this study is the investigation of the flow pattern at theoretical operating point with no power delivery at the shaft of the turbine (M=0 Nm).

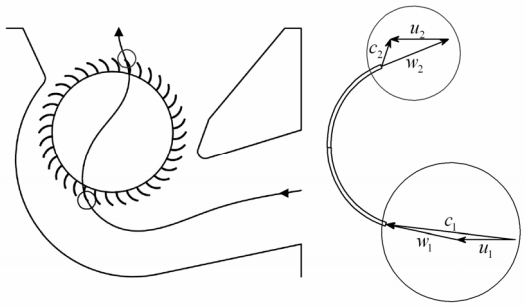

Figure 4. Principle of a cross flow turbine

To visualize the flow numerical and experimental investigations are carried out. The numerical calculations are necessary for visualization of the flow inside the rotor. To validate the flow in the casing PIV-measurements in the casing were carried out.

3. EXPERIMENTAL AND NUMERICAL SETUP

The experimental test rig is a suction side cross flow fan test section with applied PIV-Metrology (Figure 5).

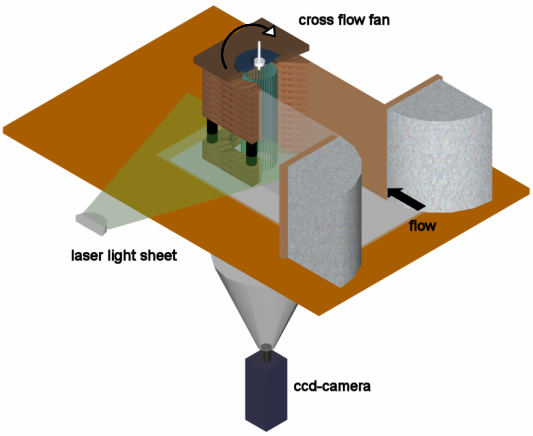

Figure 5. PIV-measurement test section for cross flow fans [3]

Contrary to the cross flow fan the mounting position of the wind turbine is rotated by 90°. To apply laser metrology it is necessary to ensure optical access inside the casing. For this reason the rear wall is formed in a small area with thin acrylic glass. The optical access in the outlet channel is also ensured with acrylic glass. The nozzle at the inlet area should guarantee an inflow into the turbine which is free of separation. The auxiliary fan of the test rig is used to generate the flow. Per definition at the drive shaft shouldn't be any power output. On that reason an electric motor adjust the bearing losses to zero. To realize that in the power train a torque measurement axle is integrated. The rotating speed of the rotor is $n = 1000 rpm$. The PIV-measurements are accomplished in plane to the mean flow direction (Fig. 5). For performance data logging of the fan, a computer aided measurement system is used. The applied PIV-system consists of 2 ND-YAG lasers, a digital CCD-camera, a synchronizer to synchronize laser and camera and a PC to gather and evaluate the measurement data. To measure the velocity of the flow very small particles in the flow are necessary. The used seeding particles are generated by atomizing of olives oil and are supplied into the inlet of the test rig.

For the prediction of the flow through the cross flow turbine the commercial CFD package STAR-CD is used. The advantage of this package is the combination of flow solver, pre- and post processing. The numerical computation is reduced to a 2-dimensional, incompressible description of the flow field due to reduce calculation time. This restriction is possible as the flow in a cross flow turbine is nearly 2-dimensional. For discretization and approximation of the velocity components the MARS-scheme is used [3]. The calculation is performed unsteady, because of the highly transient flow in the blade channels. The time discretization is implicit with a time step of $\Delta t = 10^{-4} s$. The pressure correction is realized with the PISO-algorithm.

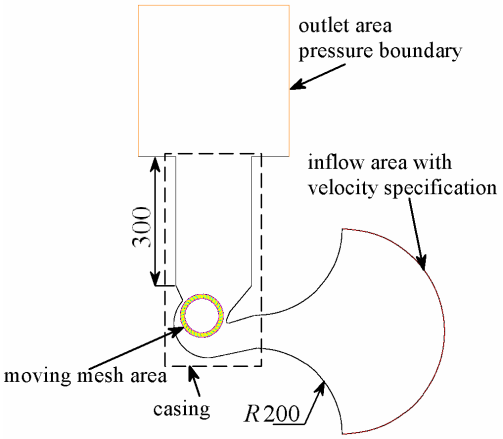

Figure 6. Computational domains

Figure 6 shows the computational domain and the boundary conditions. The computational domain is divided into four sub domains. These are the inflow area, the casing of the cross flow turbine, the outlet area and the moving blade area. The connection between the rotating and static mesh is realized with an "arbitrary sliding mesh method" (ASI), which is implemented in STAR-CD. At the walls, including the blade surfaces, turbulent flow wall boundary conditions are implemented, using a cubic low-Re $k-\varepsilon$ turbulence model. The inlet condition is realized with a constant velocity. The volume flow rate follows from a variation of the inlet velocity that the torque at the blades is equal to zero. At outlet a constant static pressure is presumed. The numerical grid has about 100000 nodes. Variations of the number of nodes at investigations of cross flow fans validate the numerical discretization [4].

4. RESULTS AND DISCUSSION

Due to the type of the investigation the most important criterion for evaluating the simulation results is the required volume flow rate to rotate the rotor with a rotational speed of $n = 1000 rpm$ and M=0 Nm. Table 2 shows the different volume flow rates for the experiment and the simulation.

	simulation	experiment
$Q\ [m^3/s]$	0.1	0.18

Table 2. Comparison of the volume flow rates

It is obvious that the simulation predicts the real volume flow rate only unsatisfactory. To analyse these differences, flow pattern of the numerical results and the PIV-measurements are compared. For comparing the flow patterns with the same contour legend the absolute velocity is normalized respectively with the mean flow velocity in the blade channels (Eq. (3)). The mean flow velocity is estimated with the cross section of the rotor diameter.

$$c_n = \frac{cLD}{Q} \qquad 3$$

Due to the design of the casing and the rotor optical access in all areas couldn't realized. These areas are blanked. The depiction of the velocity distribution inside the turbine shows unfavourable flow behaviour (Figure 7). These primarily result from gap losses between rotor and casing. Another problematic point is the large vortex inside the rotor which reduces the energy transfer from the flow into mechanical power due to obstruction of the blade channels. On that reason two zones with high velocity components and a back flow in the middle of the outlet channel are generated.

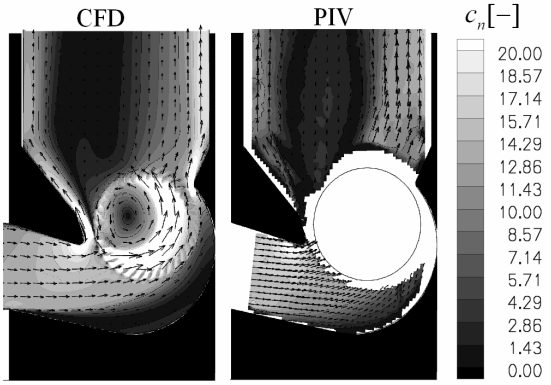

Figure 7. Comparison of the experimental and numerical flow pattern

The back flow in the experiment is more developed. This requires a higher amount of energy to rotate the impeller which results in a higher volume flow rate. Due to enlarged velocity components friction losses rise as well as the required energy. That is why the differences of the volume flow rate between the numerical calculation and the experimental measurement are so high. Another difference between the simulation and the experiment occur at the bottom side in the inflow channel. The separation in the simulation begins obviously earlier than in the experiment. This is an influence due to the 2-d assumption of the flow. The turbulent quantities are thereby much lower than in the experimental conditions where the radial limitation of the side walls of the channel produce more turbulence.

The investigation shows the capability of the numerical method to simulate the flow field in a cross flow turbine qualitative. Thereby it is possible to start a numerical optimization process to design a suitable casing of a cross flow turbine. The casing has to be characterized by an optimal energy transfer from the fluid into mechanical power. To accomplish this primarily gap flow and vortex size have to be reduced. Figure 8 shows a possible arrangement of the casing components around the impeller. If a practicable application is possible further investigations have to be carried out.

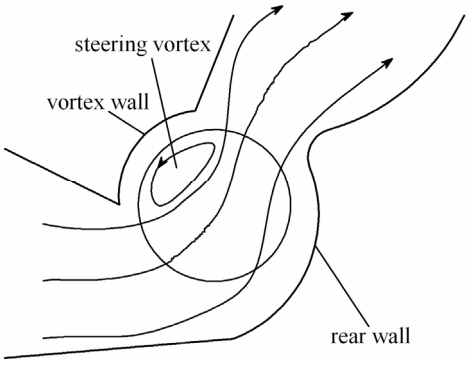

Figure 8. Concept of a cross flow wind turbine with possible improved energy transfer

5. OPTIMIZATION

To realize this concept (Fig. 8) further numerical investigations are carried out. The geometry and the numerical model of an improved cross flow turbine are shown in Figure 9.

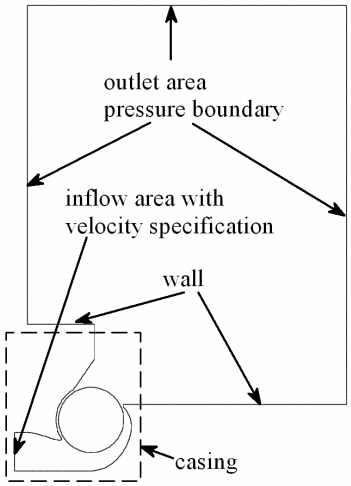

Figure 9. New geometry: Numerical model

The calculation result shows a significant improvement in the volume flow rate required for rotation the impeller with $n = 1000\,rpm$ (Table 3).

	New Geometry
$Q\ [m^3/s]$	0.056

Table 3. New geometry (simulation)

The volume flow rate is reduced almost by half of the value of the cross flow turbine with the casing of a cross flow fan. This is mainly the result of the new vortex wall design. Due to the long small gap at the vortex wall the flow structure inside the gap is very complex (Figure 10).

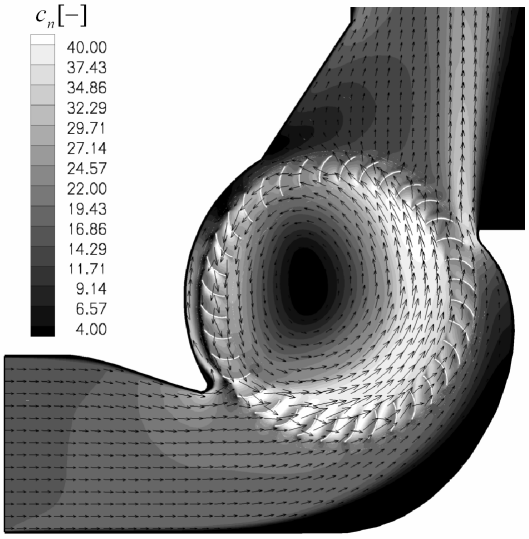

Figure 10. New geometry: Flow pattern

It's a combination of gap flow in mean flow direction and backflow against the mean flow direction. This leads to a high flow resistance with the effect of a reduced gap flow. The energy of the flow dissipates inside the gap. Furthermore due to the large vortex wall the back flow in the outlet channel could be avoided. But the flow structure shows still possibilities for improvements. The new casing design couldn't reduce the steering vortex drastic. Another point is the still high gap flow at the rear wall.

For improvements of the energy transfer from the fluid into mechanical power the flow inside the blade channels have to be considered. For a high efficiency of the wind turbine a blade congruent and a uniform distribution of the energy transfer along the circumference of the rotor is necessary. But due to the working principle this couldn't completely realized. Especially along the vortex wall a transfer of the energy of the fluid into mechanical power isn't possible because the fluid couldn't pass the blade channels. In Figure 11 and 12 a satisfactory energy transfer can be seen only in a small part of the second blade row. Fig. 11 shows the distribution of normalized circumferential values of the absolute velocity. According to Eq. (1) only in the second blade row significant changes of c_{un} can be seen. This is the same for pressure distribution in the blade channels (Fig. 12). Only in the second blade row a developed pressure and suction side of the blades is recognizable. At the first blade row pressure peaks at the first part of the blade could be seen. This results due to the drive of the impeller to guarantee a torque of M=0 Nm at the shaft. The resulting resistance against the rotating direction of the impeller should be avoided. To raise efficiency and energy transfer the relative flow in the blade channels has to be improved. Especially at the first blade row the relative velocity is highly separated and swirled (Figure 13). That means for the further process in developing casings for cross flow turbines the application of guide vanes in front of the first blade row have to be taken into account.

6. CONCLUSION

The accomplished investigations show the possibility of an application of a cross flow fan as wind turbine. However the flow structure and the performance aren't satisfactory. On that reason an optimization process of the casing was started. The presented new geometry of the casing shows a significant improvement of the performance. Potential for further improvements of the casing could be derived from the analysis of the flow structure. To ensure correctness in the numerical developing process CFD results have to be verified with further experimental measurements.

REFERENCES

[1] Sonneck, E.: Durchströmturbine, Springer Verlag, Germany, 1923

[2] Tanino, T., Nakao, S., Uebayashi, G.: Improving Ambient Wind Enviroments of a Cross Flow Wind Turbine near a Structure by Using an Inlet Guide Structure and a Flow Deflector, Proceedings of the 7th International Symposium on Experimental and Computational Aerothermodynamics of Internal Flows, Tokyo, Japan, September 11-15, 2005, pp. 225-230.

[3] CD adapco Group: Methodology, London, England, 2004

[4] Klemm, T.: Numerische und experimentelle Untersuchungen an Ventilatoren hoher Leistungsdichte; Dissertation, University Karlsruhe (TH), Germany, 2005

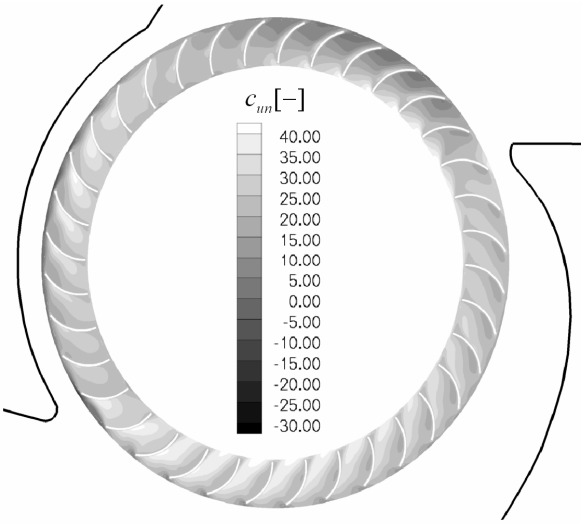

Figure 11. New geometry: Distribution of normalized circumferential component of the absolute velocity c_{un}

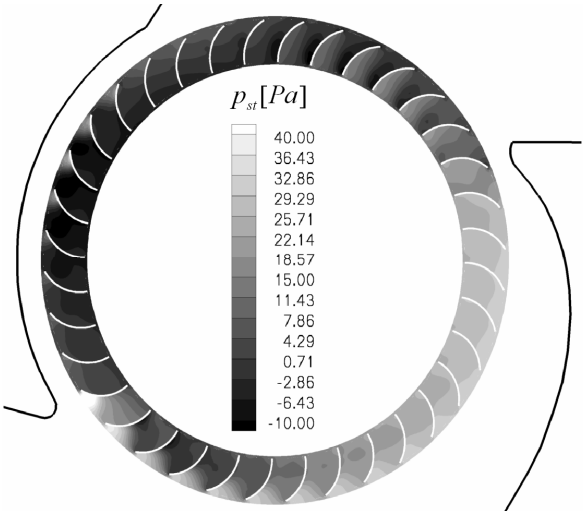

Figure 12. New geometry: Distribution of static pressure p_{st} inside the blade channels

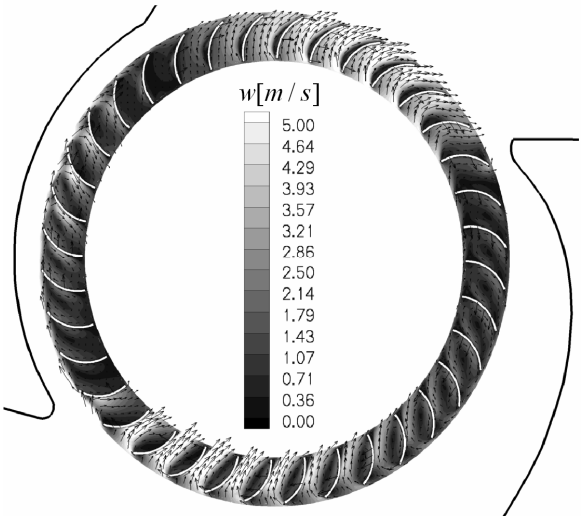

Figure 13. New geometry: Distribution of relative velocity w

Conference on Modelling Fluid Flow (CMFF'06)
The 13th International Conference on Fluid Flow Technologies
Budapest, Hungary, September 6-9, 2006

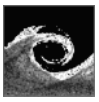

PERFORMANCE MODELLING OF A HYBRID WIND TURBINE / FUEL-CELL POWER GENERATION SYSTEM

Aikaterini PSARRA, Maria KALLIVRETAKI, Nikolaos I. KARAGEORGAKIS, Anestis I. KALFAS[1]

Department of Mechanical Engineering, Aristotle University of Thessaloniki. GR-54124 Thessaloniki, Greece.
[1]Corresponding Author. Tel.:+302310994166, Fax.:+302310996002, Email: akalfas@auth.gr

ABSTRACT

Hybrid systems, which combine various power generating components, including micro gas turbines, fuel cells and wind turbines are becoming increasingly more important for distributed power generation. This paper presents the modelling of experimental data that were obtained from a small-scale fuel cell hybrid power generation system. The modelling provides a set of polynomial equations that describe the performance of the hybrid system and simulate accurately the nature of the fluid flow phenomena.

The derived analytical models are applied to simulate the dynamic performance of a large-scale hybrid system. This system should provide complete and uninterrupted power coverage for an off-grid installation of a transmitter tower. The dynamic model estimates the fuel cell power output response and the fuel cell temperature behaviour when four parameters are varied. Four different test conditions are presented and analysed.

It has been demonstrated that for this realistic scenario, superior performance is attained when the four critical operation parameters are varied gradually, for zero relative fuel to air pressure, without delay relative to each other. The resultant moderate temporal gradients are at the root of the improved performance. The associated potential stresses are limited and the fuel cell is protected against excessive risk of degradation.

Keywords: fuel cell, wind turbine, hybrid system, modelling, dynamic modelling

NOMENCLATURE

$\dot{W}_{out}$	[Watt]	Power Output
$\Delta\dot{W}$	[Watt]	Difference between theoretical and real power output
T	[K]	Fuel cell Temperature
P_{air}	[kPa]	Inlet air overpressure
P_{H_2}	[kPa]	Inlet H_2 overpressure
$\dot{Q}_{H_2}$	[m^3/sec]	Hydrogen volume flow rate
$\dot{Q}_{air}$	[m^3/sec]	Air volume flow rate
$F_i(\dot{Q}_{air})$	[-]	Capacity Polynomial Function
$a_i(t)$	[-]	Temporal Polynomial Function
t	[sec]	time

Abbreviations

FC	Fuel Cell
PEMFC	Polymer Electrolyte Membrane Fuel Cell
SOFC	Solid Oxide Fuel Cell
MCFC	Molten Carbonate Fuel Cell
μGT	micro Gas turbine
WT	Wind Turbine
B	Battery
G	Generator
NiMH	Nickel-Metal Hydride

1. INTRODUCTION

In recent years, there has been a surge of interest in the development of hybrid power generation systems mainly due to the increasing demand for energy and related environmental concerns. Although hybrid power generation systems carry the disadvantage of high initial cost, their high efficient nature and a near-zero emission

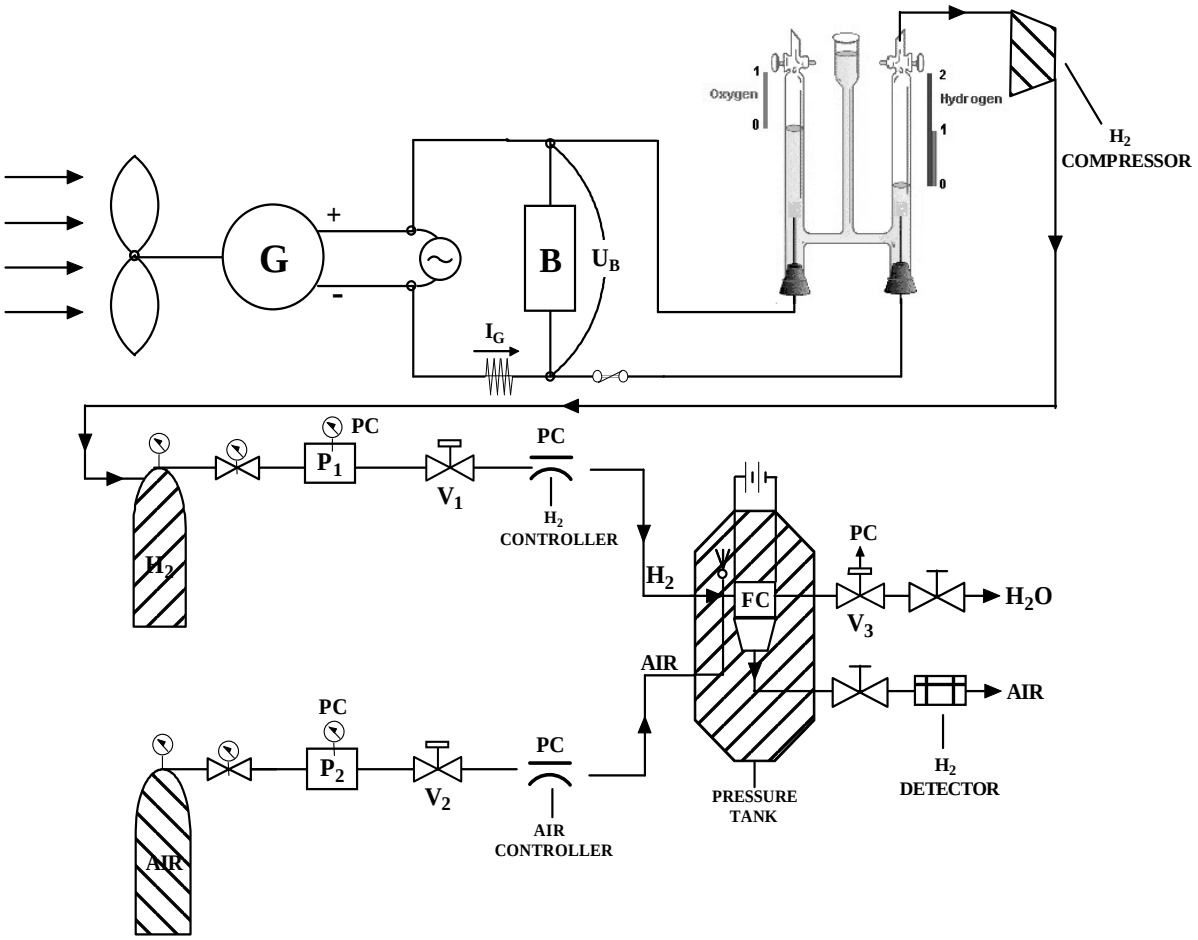

Figure 1. Small-scale fuel cell hybrid power generation system

of primary pollutants makes them highly attractive for electrical power generation applications. Even the more established and mature technologies in power generation use, in some fashion, the principles of a hybrid system. A powerful example is the combined cycle systems used to re-power old power generation plants. The present work aims to demonstrate the performance benefits from hybrid systems.

Hybrid systems have been studied by a number of research groups. The extended research resulted in highlighting some of the features that need to be considered in the design of hybrid systems. In recent publications, hybrid systems have been analysed with regard to design and off-design performance. In 2001, Palsson and Selimovic [1], presented the off-design calculations of a recuperated SOFC/GT system investigating different ambient conditions and part load behaviour of this system. In 2002, Kimijima and Kasagi [2], have investigated the design point and part load performance of a 30 kW μGT-SOFC to find a strategy for highly efficient operation by developed simulation code. In early 2003, Magistri et. al. [3], carried out a design point analysis and an off-design performance of a MW hybrid system based on Rolls-Royce integrated planar SOFC. In order to improve the performance of combined systems, Nisida et. al. [4], proposed the multi-stage type SOFC/GT combined system, and compared the system performance of it with other combined systems using thermal efficiency and exergy evaluation.

The modelling and the dynamic analysis of a hybrid power generation system are very important in the system optimization, to achieve high efficiency at low cost. In this direction, Gemme et. al. [5], developed dynamic models for the basic components of SOFC and MCFC gas turbine hybrids. The results provided understanding of some of operation characteristics of fuel cells and indicated the complexity of the dynamic response of fuel cell hybrid components. In 2004, Hildebrandt et. al. [6], presented steady state and unsteady state hybrid system modelling and calculation results with regard to surge. In 2005, Stiller et. al. [7], investigated the dynamic behaviour of a small SOFC/GT hybrid system on rapid load changes and showed strategies for the dynamic controlling of power by manipulating fuel flow.

In 2005, Karageorgakis et. al. [8], studied a novel hybrid power generation system, including a wind turbine coupled with a fuel cell. The current

paper presents the development of analytical performance model, which is based on the operation data of the novel hybrid power system. Furthermore, a development of a realistic scenario from published data aims to the use of the novel hybrid system in large scale application. The primary goal of the scenario is to provide complete and uninterrupted coverage of the power requirement of a transmitter tower, located in a remote area. The performance of the hybrid power generating unit is dynamically simulated, for the case where the wind turbine suddenly goes out of operation and a major part of the power demand is covered by the fuel cell.

2. SMALL SCALE EXPERIMENT

The modelling presented in this paper is based on experimental data that were obtained from a small-scale fuel cell hybrid power generation system.

The small-scale hybrid system consists of a pressurized 50 W nominal power rating PEM fuel cell, a wind turbine of a nominal power rating of 100 W at 12.5 m/sec wind speed, a battery that stores the electricity produced and a resistance of 12 Ω, which has the role of power consumption.The experimental arrangement of the hybrid system is shown in Figure 1. The air driven from the wind tunnel is used as a source of wind energy to rotate the wind turbine and as a result electricity is produced by the WT. The generator is considered as a unit separate to the wind turbine, so that in cases that wind is not available, electricity could be generated by an externally connected internal combustion engine or an electric motor. The electricity is stored in a NiMH rechargeable battery of nominal voltage 24 V and storage capacity 54 Ah. In large-scale application, this battery may represent a system of water electrolysis, producing the necessary amount of hydrogen. This quantity of H_2 can be stored in storage combination system, including tank and batteries, fly wheels or any other energy storage unit. The hydrogen produced, then, would be channelled to a fuel cell stack to produce electricity depending on consumer demand.

3. QUASI-STEADY MODELLING

The modelling of the experimental data that were obtained from a small-scale is realised using visual programming language and the least squared method.

The experimental arrangement (Fig. 1) provided values of fuel cell temperature and output power values when four critical parameters, airflow, hydrogen flow, inlet air and hydrogen overpressure, are varied independently from each other within certain limits.

Figure 2 shows the experimental results and the simulation curves for various airflows and fuel flows when the inlet air overpressure and inlet fuel overpressure are equal to 25 kPa. The simulation curves are based on an mathematical model. A second order polynomial equation expresses fuel cell temperature as a function of hydrogen flow. The calculated polynomial factors depend on the airflow rate, which is varied between 33% and 100% of the 84.6 10^{-3} m^3/sec and can be developed with respect to the airflow as a second order polynomial. The equation of fuel cell temperature:

$$T = F_{a1}(\dot{Q}_{air}) \cdot \dot{Q}_{H_2}{}^2 + F_{b1}(\dot{Q}_{air}) \cdot \dot{Q}_{H_2} + F_{c1}(\dot{Q}_{air}) + 273 \quad [K] \qquad (1)$$

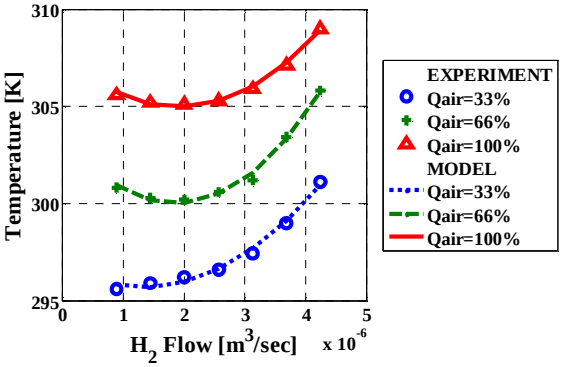

Figure 2. Fuel cell temperature with hydrogen flow for various airflows and 25 kPa inlet air and fuel overpressure

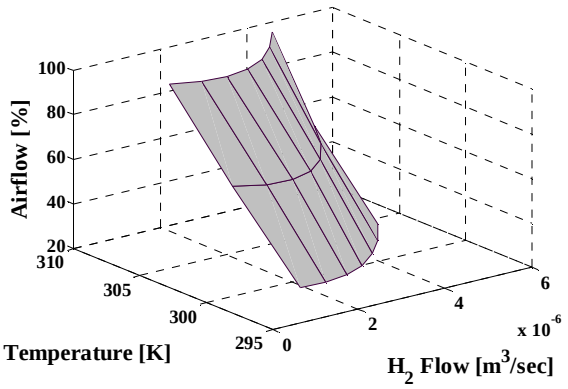

Figure 3. Fuel cell temperature for 25 kPa inlet air and fuel overpressure

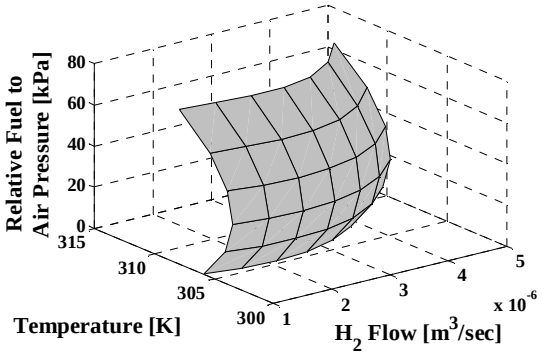

Figure 4. Fuel cell temperature with hydrogen flow and relative fuel to air pressure for airflow equal to $84.6 \cdot 10^{-3}$ m^3 /sec

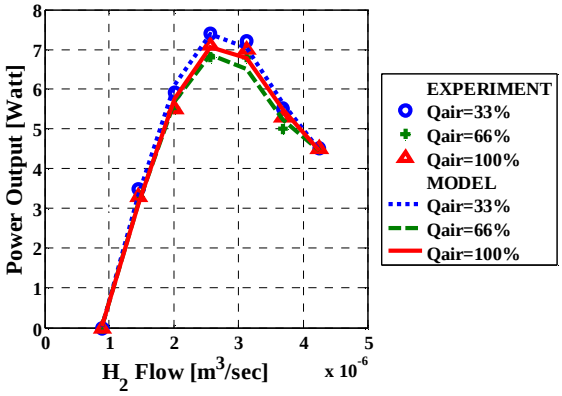

Figure 5. Power produced with increasing hydrogen and air flow for 25 kPa inlet air and inlet hydrogen overpressure

The simulation curves plotted in Figure 3 are developed as 4th order polynomial functions. The polynomial equation simulates accurately the nature of the fluid flow phenomena. The deviation between experimental data and the models are of the order of 1 %.

The fuel cell temperature is of prime interest for the operation of the power plant. Temperature should be as low as possible, because efficiency in the fuel cells reduces linearly with the increase of the temperature. From eq. (1) and Fig. 3 fuel cell temperature can be predicted for airflow and hydrogen flow rates that are not included in the experimental data.

The mathematical model of FC temperature as a function of relative fuel to air pressure and hydrogen flow, when airflow is maximized, is shown in Figure 4. The fuel cell temperature rises sharply when the inlet relative fuel to air pressure is increased more than 40 kPa. Lower relative fuel to air pressure has no significant influence on the temperature.

The experimental data showed that the output power increases sharply with respect to the hydrogen flow until a maximum value and then it reduces rapidly. As a result the experimental data of output power is modelled as a function of hydrogen flow using polynomial functions of 4th order. The analytical model that expresses the dependence of output power on the hydrogen and air flow is a 6th order polynomial. Its equation is:

$$\dot{W}_{out} = F_{a2}(\dot{Q}_{air}) \cdot \dot{Q}_{H_2}{}^4 + F_{b2}(\dot{Q}_{air}) \cdot \dot{Q}_{H_2}{}^3 + F_{c2}(\dot{Q}_{air}) \cdot \dot{Q}_{H_2}{}^2 + F_{d2}(\dot{Q}_{air}) \cdot \dot{Q}_{H_2} + F_{e2}(\dot{Q}_{air}) \quad [Watt] \qquad (2)$$

The comparison between experimental data and calculated power output, in case of 25 kPa inlet air and hydrogen overpressure, is plotted in Figure 5. The maximum error is approximately 1%. Good agreement between model results and operation data is evident.

4. A REALISTIC SCENARIO

The mathematical models from the small-scale experiment have been applied to simulate the operation of a large-scale WT/FC power generation system. The realistic scenario is based on the development of a power generating unit for an off-grid application. The primary goal of the system is to provide complete and uninterrupted coverage of the power requirement of a transmitter tower, located in a remote area. This area has the advantage of high wind force, which gives the opportunity of establishing a hybrid power generation system.

The suggested hybrid system combines the alternative energy source with the technology of fuel cell. Four wind turbines of a nominal power rating of 5 kW each produce electrical power to cover the power requirement of the radio transmitter. A surplus of the produced electrical power starts the procedure of water electrolysis for the production of hydrogen. The hydrogen is stored and can be supplied to the fuel cell in cases that the wind turbines are incapable of covering the power requirement of the transmitter. The technology of PEM fuel cells is suggested for this application. PEMFCs operate at low temperature, which allow them to start quickly and results in less wear on system components, resulting in better durability.

The type of the radio transmitter is an OR 5 K-01/A [9] and its power requirement is 5 kW. The energy efficiency of the PEMFC is nearly 45% while the procedure of water electrolysis has an efficiency of 80%. Because small quantity of hydrogen is produced, the influence of compressor and pressure valves on the system performance is

considered to be small. In order to cover completely the power demand of 5kW, the nominal power of PEMFC stack block should be of the order of 12 kW.

The PEMFC stack block operates at higher fuel and air volume flow than a stack, but the inlet pressure and the temperature have a constant value, unaffected by the nominal power of the PEMFC stack block.

5. DYNAMIC MODELLING

In this part of the paper, the control parameters of the fuel flow, airflow, inlet air and fuel overpressure are changed between specified limits and the performance of the fuel cell is investigated.

The integrated model is implemented using Matlab/Simulink. The dynamic model estimates the fuel cell power response and the fuel cell temperature behaviour.

The output power of the wind turbine decreases sigmoidally with time. In order to cover the power requirement of the radio-transmitter, the fuel cell load should increase sigmoidally during the same length of time. The relation between hydrogen flow and load applied on the fuel cell is linear.

In the present scenario fuel flow, airflow and input pressures variations can be achieved by a control valve. For the dynamic simulation, it is assumed that the above crucial parameters increase sigmoidally with the time between specified limits. The sigmoid function has the form of:

$$f(t) = h \cdot \left[\frac{1}{1 + e^{-a \cdot (t-c)}} + p \right] \quad (3)$$

The time dependant function is formulated through a number of constants namely α, c, h, p. These constants characterise the dynamic behaviour of simulated test conditions. In particular, constant α is the exponential multiplier and obtains values which are limited by the value of the constant c. Smaller values of constant α indicate a slower change in parameters. Constant c is connected with the start delay time and obtains values between 0 and 100 in this scenario. Constant h and p have been introduced in order to rectify the results of the function between the appropriate limits for each parameter.

The analytical model of temperature calculation and output power is expressed as a function of airflow, hydrogen flow and inlet air overpressure for two cases: Case A. Zero relative fuel to air pressure. Case B. 100 kPa inlet fuel overpressure and inlet air overpressure vary between 25 and 75 kPa.

Fig. 5 shows that the output power changes linearly with the increasing hydrogen flow until a point, at which the produced power deviates gradually from the linear increase. The non-linear increase of the power output depends on temperature change which leads to membrane dehydration. The resistance of the membrane is increased due to dehydration, resulting in decreasing power output. The difference between the theoretical (linear) and the real (non-linear) power output is expressed as a function of fuel cell temperature. The equation that simulates the power difference is polynomial:

$$\Delta \dot{W} = a_2(t) \cdot T(t)^2 + a_1(t) \cdot T(t) + a_0(t) \quad [Watt] \quad (4)$$

The overall time span of the simulation is 100 seconds. This choice was dictated by the dynamic performance studies discussed in the following paragraphs. A number of test conditions have been investigated. Among them four selected cases are represented here.

		$\dot{Q}_{H_2}$	$\dot{Q}_{air}$	P_{H_2}	P_{air}
TCI	α	0.5	0.5	0.5	0.5
	c	20	20	80	80
	h	$7.47 \cdot 10^{-4}$	$21.15 \cdot 10^{-3}$	50	50
	p	1.58	1	0.5	0.5
TCII	α	0.2	0.2	0.5	0.5
	c	50	50	50	50
	h	$7.47 \cdot 10^{-4}$	$42.30 \cdot 10^{-3}$	50	50
	p	1.58	0.5	0.5	0.5
TCIII	α	0.5	0.5	const.	0.5
	c	50	20		70
	h	$8.44 \cdot 10^{-4}$	$42.30 \cdot 10^{-3}$		25
	p	1.4	0.5		1
TCIV	α	0.5	constant		
	c	30			
	h	$7.47 \cdot 10^{-4}$			
	p	1.58			

Table 1. Dynamic Simulation Test Cases

Test Case I (TCI) involves fast transition to full load and long start delay of the inlet air overpressure. This test case is set to simulate a rapid change in consumer demand, while the pressurisation system cannot follow in the same rate. Slow transition to full load and the same start delay for each parameter are applied in Test Case II (TCII). This test case simulates a scenario, in which the PEMFC meets gradually the power demand. Test Case III (TCIII) shows the operation of the system when the relative fuel to air pressure is

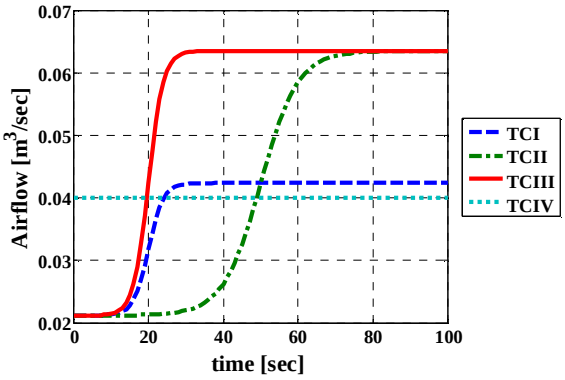

Figure 6. Air volume flow rate

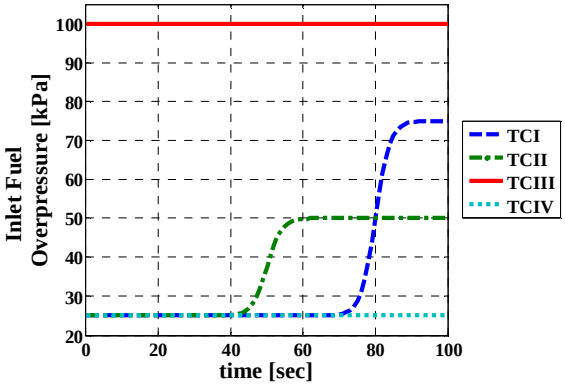

Figure 8. Inlet Fuel Overpressure

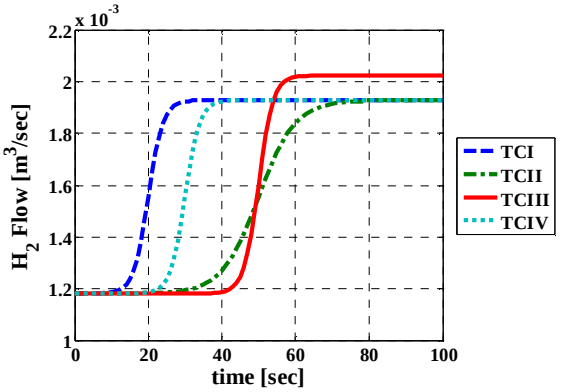

Figure 7. Hydrogen volume flow rate

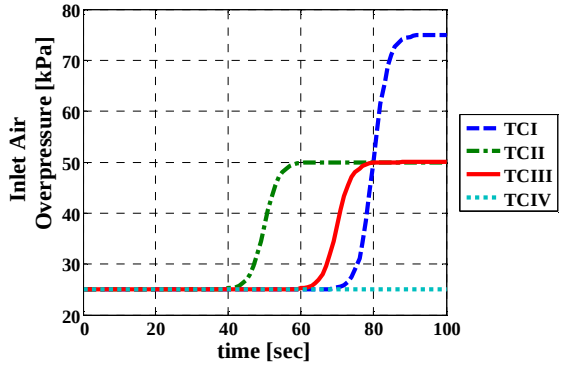

Figure 9. Inlet Air Overpressure

varied. This condition is introduced to show the effect of relative fuel to air pressure on the realistic scenario. The power output cannot cover the demand of the transmitter, so the wind turbines should produce a certain amount of power. In Test Case IV (TCIV) hydrogen flow increases while the other parameters remain constant. This condition is applied to systems, which achieve to cover power requirement by a fuel flow increase. Figures 6, 7, 8 and 9 represent the variation of the air volume flow, the hydrogen volume flow, the inlet air overpressure and inlet hydrogen overpressure respectively. According to the variation of the four parameters, the performance of the PEMFC stack block is shown in Figures 10, 11, 12 and 13. The primary goal of the dynamic simulation is to provide important information about the operation of the hybrid system. The fuel cell should meet as quickly as possible, the power requirement without compromising its high efficiency electricity for production.

The main parameters of interest for the fuel cell are the power output and the temperature. The fuel flow influences power output to a large extent. Thus, the most efficient way to change the power output is by controlling the hydrogen flow rate. A quick increase in hydrogen flow from $1.18 \cdot 10^{-3}$ m^3/sec to $1.93 \cdot 10^{-3}$ m^3/sec as it happens in TCI causes a fast response of PEMFC power output. The FC temperature is not significantly affected while the difference between theoretical and real power output increases sharply. Although a rapid increase in hydrogen flow results in meeting the power requirement in a short time, this operation can cause problems to fuel cell. High gradient of power difference may result in excessively high load, leading to premature deterioration of the PEMFC. Thus, a way to eliminate the degradation of the fuel cell is by controlling the increase in hydrogen flow.

When the hydrogen flow rate changes slightly (TCII), it takes long until the PEMFC power output

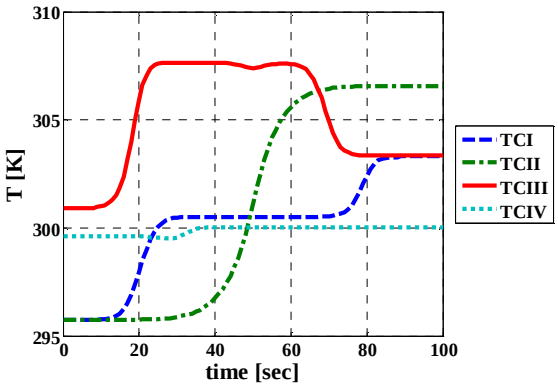

Figure 10. Average PEMFC Temperature

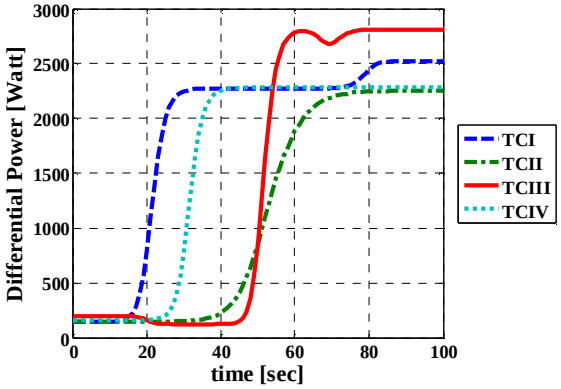

Figure 12. Difference between PEMFC theoretical and real power output

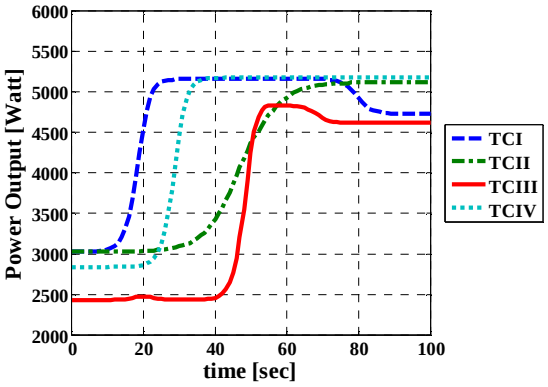

Figure 11. PEMFC Power output

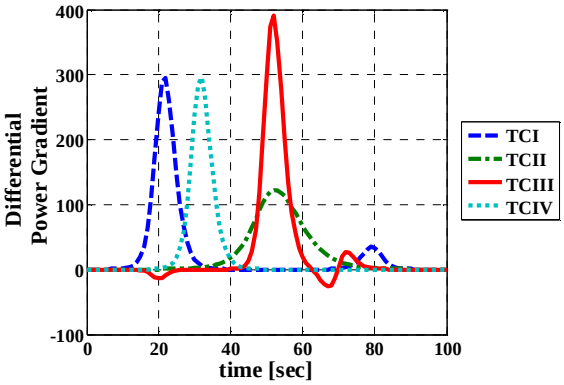

Figure 13. Time derivative of PEMFC power difference

reaches its steady value. Hence, this condition is applied when the electrical power of wind turbines is gradually reduced. Test case II has the advantage of low time derivative of power difference, concluding more efficient operation of the hybrid system.

The variation of the airflow rate (Fig. 6) affects the fuel cell temperature (Fig. 10). With increasing airflow, fuel cell temperature is increased. A rapid airflow variation leads to a sharp rise in temperature. From a view of thermal endurance of fuel cell stack, the fast increase in temperature may provoke dehydration resulting in resistance change and reduction in power output.

In Test Case III (TCIII), the inlet hydrogen overpressure remains constant, while the pressure difference of air increases fast resulting in a reduction in relative fuel to air pressure. This PEMFC operation is incapable of producing the desired power output, even when the fuel flow increases to a higher value (Fig.7). An increase in relative fuel to air pressure leads to a fuel cell temperature drop. Fig. 10 shows the temperature variations. Furthermore, the power difference is highly increased in comparison to the other test cases. This operation represents a danger as it may impose stresses on the fuel cell stack block that could affect the lifetime of the PEMFC.

The last case (TCIV) deals with the investigation of the PEMFC operation when hydrogen flow rate increases sharply and the other parameters remain constant. This case has the advantages that the fuel cell operates at a fairly constant temperature and the PEMFC covers the power demand. However, a high value of time derivative is introduced due to a fast change in hydrogen mass flow.

6. CONCLUSIONS

In this paper, a full performance model for quasi steady-state and dynamic simulation of a hybrid generation system has been developed. Analytical models are verified by operation data of

a small scale experiment. The derived analytical models are applied to evaluate the performance of a large-scale hybrid system application, which is based on a realistic scenario of a transmitter, located in a remote area. From the above study, the following major conclusions are derived:

- The analytical models are based on polynomial equations. The polynomial equations simulate accurately the experimental data. These models can be applied to simulate appropriately the performance of the hybrid system in areas that are not included in the experimental data.
- The analytical models have sufficient capability to evaluate performance of a large-scale WT/FC power generation system. The PEMFC stack block of the large scale hybrid system consists of many bundles of 50 kW. The temperature and power evolution of each bundle is verified by the small scale experiment.
- The power output of the wind turbine decreases sigmoidally with the time. Hence, it is assumed that fuel and air flow increase sigmoidally with time in order to produce the power demand of the transmitter.
- The PEMFC temperature response is more sensitive to the airflow change, compared to the dependency on varied fuel flow.
- The power output response and the difference between theoretical and real power output are affected more from fuel flow variation than airflow variation.
- Excessively high relative fuel to air pressure leads to malfunction of the fuel cell due to fluctuation of the time derivative of the difference between theoretical and real power output.
- A sharp increase in the fuel flow results in steep increase in power output and power difference $\left(\Delta \dot{W}\right)$. A quick variation in power difference can cause the fuel cell degradation.
- The optimal condition is achieved for a gradual change in the four critical parameters. In particular, the best condition is obtained for zero relative fuel to air pressure and when the start of the process is synchronized. This condition produces moderate temporal gradients, which benefit the life of the fuel cell.

ACKNOWLEDGEMENTS

The experimental results on which the present modelling work was based were obtained during Mr Karageorgakis' visit at ETH Zurich in the summer of 2004. The authors would like to thank Prof. Reza S. Abhari of ETH Zurich for his hospitality, co-operation and kind permission to use these experimental resources for the development of the quasi-steady model. Thanks are also due to Mr Cornel Reshef who supported Mr Karageorgakis in obtaining these data.

REFERENCES

[1] Palsson, J., Selimovic, A., 2001, "Design and Off-Design of a combined SOFC and gas turbine system", ASME Paper 2001-GT-0379, Proceedings of the 46th ASME TurboExpo, New Orleans, Lousiana, USA.

[2] Kimijima, S., Kasagi, K., 2002, "Performance Evaluation of Gas Turbine-Fuel Cell Hybrid Micro Genaration System", ASME Paper GT-2002-30111, Proceedings of the 47th ASME Turbo-Expo, Amsterdam, The Netherlands.

[3] Magistri, L., Bozzolo, M., Tarnowski, O., Agnew, G., Massardo, A.F., 2003, "Design and Off-Design Analysis of a MW Hybrid System based on Rolls-Royce Integrated Planar SOFC", ASME Paper GT2003-38220, Proceedings of the 48th ASME TurboExpo, Atlanta, Georgia, USA.

[4] Nisida, K., Takagi, T., Kinoshita, S., Tsuji, T., 2002, "Performance Evaluation of Multi-stage SOFC and Gas Turbine Combined Systems", ASME Paper GT-2002-30109, Proceedings of the 47th ASME Turbo-Expo, Amsterdam, The Netherlands.

[5] Gemme, R.S., Liese, E., Rivera, J.G., Jabbari, F., Brouwer, J., 2000, "Development of Dynamic Modeling Tools for Solid Oxide and Molten Carbonate Hybrid Fuel Cell Gas Turbine Systems", ASME Paper 2000-GT-554, Proceedings of the 45th ASME TurboExpo, Munich, Germany.

[6] Hildebrandt, A., Genrup, M., Assadi, M., 2004, "Steady-State and Transient Compressor Surge Behavior within a SOFC-GT-Hybrid System", ASME Paper GT2004-53892, Proceedings of the 49th ASME TurboExpo, Vienna, Austria.

[7] Stiller, C., Thorud, B., Bolland, O., 2005, "Safe Dynamic Operation of a Simple SOFC/GT Hubrid System", ASME Paper GT2005-68481, Proceedings of the 50th ASME TurboExpo, Reno-Tahoe, Neveda, USA.

[8] Karageorgakis,N.I., Kalfas,.A.I., Abhari, R.S., "Performance Investigation of a Hybrid Wind-Turbine/Fuel-Cell Power Generation System through a Small Scale Experiment", Paper EFC-2005-86258, Proceedings of the First European Fuel Cell Technology and Applications Conference, Rome, Italy.

[9] Communication Transmitter Type OR5K-01/A, http://www.transmitter.be/riz-or5k01a.htm

Conference on Modelling Fluid Flow (CMFF'06)
The 13th International Conference on Fluid Flow Technologies
Budapest, Hungary, September 6-9, 2006

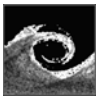

NUMERICAL INVESTIGATION OF STEAM FLOW AND HEAT TRANSFER IN HIGH PRESSURE TURBINE CASINGS

Sándor EICHINGER[1], Péter PANDAZIS[2], Ákos RUMMEL[3], Michael WECHSUNG[4]

[1] Corresponding Author. Siemens Erőműtechnika Kft. Késmárk u. 24-28, H-1158 Budapest, Hungary. Tel.: +36 1 414 4821, Fax: +36 1 414 4754, E-mail: sandor.eichinger@siemens.com
[2] Siemens Erőműtechnika Kft. Késmárk u. 24-28, H-1158 Budapest, Hungary. Tel.: +36 1 414 4794, Fax: +36 1 414 4754, E-mail: peter.pandazis@siemens.com
[3] Siemens Erőműtechnika Kft. Késmárk u. 24-28, H-1158 Budapest, Hungary. Tel.: +36 1 414 4859, Fax: +36 1 414 4754, E-mail: akos.rummel@siemens.com
[4] Siemens AG Power Generation (PG) Rheinstrasse 100, D-45478 Mülheim an der Ruhr, Tel.: +49 208 456 3644, Fax: +49 208 456 2023, E-mail: michael.wechsung@siemens.com

ABSTRACT

This paper presents the numerical investigation of the flow field in high pressure turbines between the inner and outer casing and the inner casing's temperature distribution. The motivation for the numerical investigation was that during operation the temperature distribution in the inner casing should be distributed as evenly as possible in the radial and axial directions. Additionally local undercooling should be avoided. Non-uniform temperature distribution as well as local undercooling may cause excessive material deformation. The numerical simulations were done with the CFD software package CFX – 5. The body fitted mesh was created with ICEM CFD. The heat transfer between the solid and fluid part was calculated by the conjugate heat transfer model. Radiation between the fluid and the solid parts was neglected. Different variations of cooling and different geometries of the inner and outer casing were tested. Swirl of the HP steam from the blading section and distinct numerical boundary condition settings were investigated as well. It was found that the cooling variants can affect significantly the temperature distribution of the inner casing. The investigated swirl affects the flow field and therefore the temperature distribution of the inner casing. The simulations have shown the advantages and disadvantages of each cooling variant and have helped to understand the flow phenomenon.

Keywords: high pressure turbine, inner casing, heat transfer, pressure losses, temperature distribution

NOMENCLATURE

M	[*kg/kmol*]	molar mass
Nu	[-]	Nusselt number
T	[℃]	temperature
Pr	[-]	Prandtl number
R	[-]	spec. gas constant
y+	[-]	dimensionless wall distance
λ	[*W/mK*]	thermal conductivity
α	[W/m^2K]	heat transfer coefficient
$\dot{Q}$	[W/m^2]	heat flux
p	[*Pa*]	pressure
μ	[*kg/ms*]	dynamic viscosity
υ	[m^2/s]	kinetic viscosity
ρ	[kg/m^3]	density

Subscripts and Superscripts

f	along fluid
w	along wall

1. INTRODUCTION

Industrial developments are mainly motivated to find more cost effective solutions. Computational Fluid Dynamics (CFD) could open the door to offer acceptable answers to interesting questions, such as complex 3D internal flow fields with conjugate heat exchange.

Steam turbines have small allowable tolerances during operation. Thus designers would like to know accurate pressure and temperature distributions in order to perform structural analysis to determine elongations, vibrations etc. They make corrections based on these results and the iterative process continues. In case of High Pressure (HP) steam turbines which consist of inner and outer

casing unacceptable deformations can appear. In order to avoid them a typical HP turbine (approximately 30 bar exhaust steam pressure and 350 °C outlet steam temperature) was investigated numerically in this project. Figure 1 shows the geometrical and physical structure of the model.

Although a lot of work has been done in the past the simulation of conjugate heat transfer is still challenging. The determination of the heat transfer properties in annular pipe-like geometries with varying diameters cannot be easily done in an analytical way [1, 3]. The flow has high turbulence intensity and strong time dependence, which has been studied by several authors. Appropriate turbulence models have been developed [2] as well. However in this work a commercial CFD package was used which limits the authors' freedom, on the other hand it offers a wide range of possibilities for general usage.

The scope of this paper was to study the effect of leakage flows on the variable distributions in different operating points. They can be controlled with steam discharge (see Figure 1.), but the path of the "leakage steam" is not known. The temperature must be evenly distributed along the inner casing. The outgoing flow direction from the blades under different operating conditions has a significant effect on the flow field and therefore on the heat exchange.

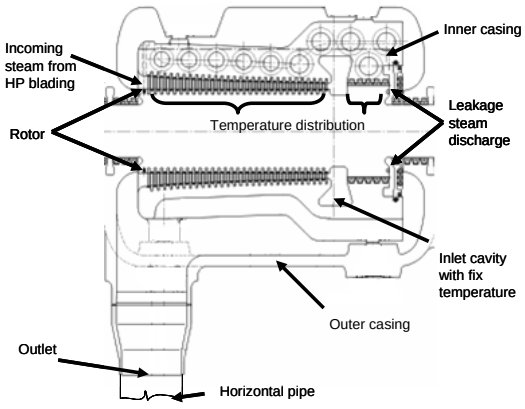

Figure 1. Vertical sketch of the investigated HP turbine and boundary conditions

2. INVESTIGATION METHOD

In the following a brief overview can be found about the governing equations which describe the investigated physical phenomena [3, 9, 10]. The given equations build a closed system, which has an analytical solution only in special cases. Thus with such complicated geometries like the turbine in question numerical simulation has to be done. The numerical procedure is described in the second part of this chapter.

2.1. Analytical description

The investigated problem can be split in two subsystems, namely the main fluid field around the inner casing and the heat flow within the inner and the outer casing. The coupling between the solid and the fluid is realized through the thermal and momentum boundary layer.

The main flow field can be assumed to be a compressible substance. The fluid is an ideal gas therefore the closed system of equations without the continuity equation consists of Eq.(1-3).

$$\frac{\partial v}{\partial t}+(v\nabla)v=-\frac{1}{\rho}\mathrm{grad}p+ \\ +\mu\Delta v+\left(\zeta+\frac{\eta}{3}\right)\mathrm{graddiw} \tag{1}$$

For the thermal energy in the fluid the Fourier-Kirchoff equation was used (Eq. (2)).

$$\frac{\partial T}{\partial t}+(v\nabla)T=-\frac{\lambda}{c\rho}\Delta T \tag{2}$$

Heat transfer between fluid and solid is defined by Eq. (3).

$$-\lambda\left(\frac{\partial T}{\partial n}\right)_w dA=\alpha\left(T_w-T_f\right)=\dot{Q} \tag{3}$$

2.2. Numerical procedure

The numerical simulation procedure can be divided into the following steps. Firstly an acceptable geometrical model has been created. Not every detail of the geometry has a significant effect on the flow field nor on the thermal behaviour of the inner casing. According to the interested physical phenomenon, on the other hand, the generated mesh has to fulfil different requirements. The geometry was simplified and split into two parts. These parts are the fluid field and the solid inner casing. These grids were created separately with point to point connection between them. Meshes were generated by usage of the ICEM CFD software. They are presented in Figure 2. and 3.

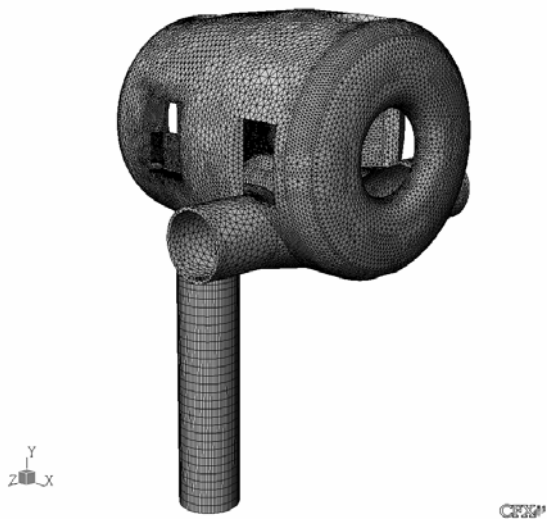

Figure 2. The generated numerical grids (fluid mesh)

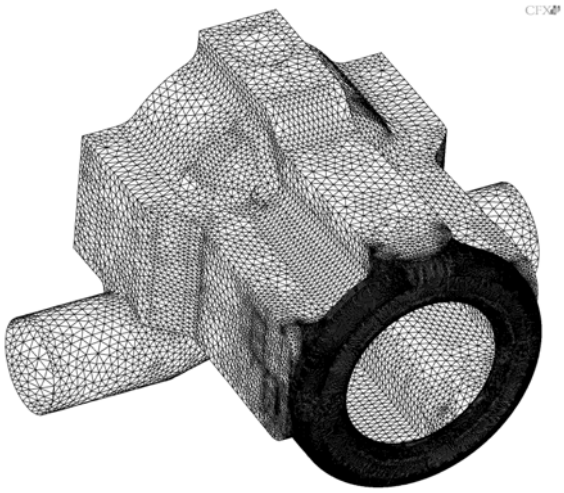

Figure 3. The generated numerical grids (solid mesh)

In the fluid field mesh the included layer of prismatic elements makes it possible to resolve the boundary layer flow and heat transfer through it. The prism layer is split into 10 sub layers. The quality of the generated boundary layer mesh could be judged through the y+ parameter. For the boundary layer mesh the dimensionless distance should lay between 30 and 300 [4]. The viscous sublayer is described by wall functions [7, 8]. If the viscous layer is modelled the y+ has to reach a maximum value of 2 or should be smaller [4].

The numerical model construction took place in the ANSYS CFX Pre software. Depending on the location various types of boundary conditions were used. Within the solid inner casing domain there are walls with constant temperature and also with linear temperature distribution. The values are taken from the steam cycle analysis.

At the fluid domain inlet total temperature, total pressure and average turbulent intensity were specified as physical parameters, while at the outlet the mass flow was given. Next to the inlet a circular surface can be found in the bended diffuser which is defined as the rotational wall. The rest of the boundary walls were set to stationary. The created boundary conditions are presented in Figure 1.

The coupling between solid and fluid is realised with fluid solid interface in which in order to ensure more accurate heat transfer point to point connections were created between the fluid and solid grids.

The material properties of the fluid were considered as ideal gas with constant specific heat and the other steam attributes were taken from the IWAPS steam table [4]. The inner casing solid material was described through the following physical parameters: M, λ and ρ.

After the successful numerical model construction an initial solution has to be defined. In this case the temperature and the pressure was specified in advance, with zero velocity for the whole fluid domain. Subsequently the simulation itself was performed. During the computation different residuals and imbalances were monitored [4]. At final convergence level the calculation should reach 0.1% imbalances and 1.0E-4 residuals.

3. RESULTS

Figure 4. shows the streamlines coming out from the blading section and from the leakage of the steam discharge. The picture corresponds to 2.28% leakage flow (based on outlet mass flow rate and which is fresh steam, therefore it has higher temperature than the normal exhaust substance) and the flow is assumed to be axial. One can observe some typical features of the stream which appear in all investigated cases. Over the top of the inner casing there are two regions located symmetrically along the *x* axis which has high turbulence level with small vortices. On the bottom side two vortex tubes can be seen similarly settled as at the top side. A strong swirling flow pattern exists right after the blading section at the diffuser segment.

As mentioned before smooth temperature distribution would be preferred on the inner casing, thus the spreading of the leakage steam and its mixing is relevant. Figure 5 shows the streamlines which are coming from the leakage so the mixing process can be observed. This plot shows the 2.28% mass flow rated case with basically no swirling.

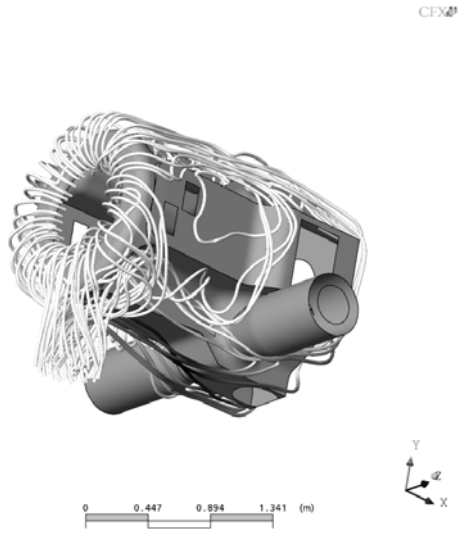

Figure 4. Streamlines around the Inner casing at 2.28% coolant case without swirl

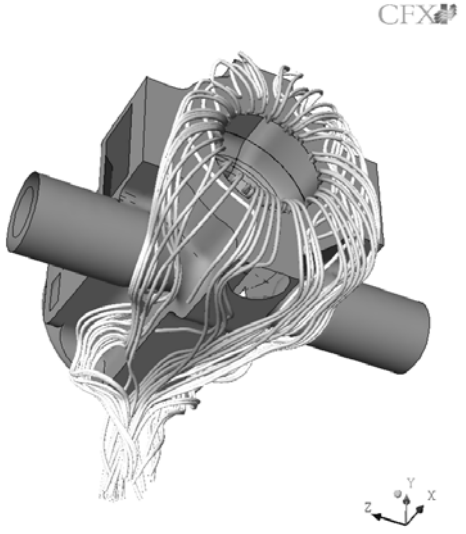

Figure 5. Streamlines starting from leakage at 2.28% coolant without swirl

The leakage stream goes downwards and heats up the bottom side, and especially the back side which is close to the discharge orifice. This part of the casing is always the hottest part.

Table 1. Re and Nu numbers at different operating points

Mass flow rate percentage [%]	0.13	0.94	0.94	0.94	2.28
Swirl angle [degree]	0	-10	0	10	0
Reynolds number at outlet [-]	9.08E+06	9.18E+06	9.21E+06	9.21E+06	9.13E+06
Nusselt number [-]	18394.9	17108.6	17418.8	16404.7	14555.9

The presented Nusselt numbers in Table 1 indicate that the heat exchange is convection dominant. The index is based on an average wall heat flux coefficient value over the whole inner casing. During the simulation the gravitational (Buoyancy) effects are neglected and since the Nusselt number has such high values it is a reasonable assumption. The heat transfer mostly takes place in the near wall regions; therefore the smooth distribution of turbulence structures is an important feature of the aimed requirements.

After the deliberation of one investigated case the authors would like to draw attention to the temperature distributions of the different cases.

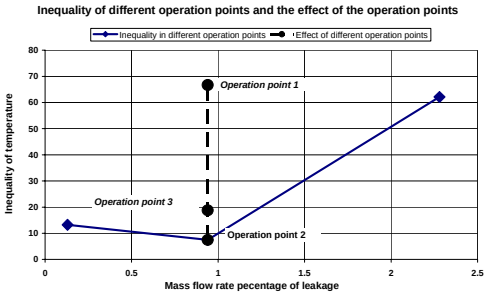

Figure 6. Inequality of the different load cases

The inner casing surface of the turbine was cut into 12 pieces. There were two perpendicular cut planes (XZ and XY) and two cut planes located at the level of the inlet cavity axis and one parallel to the previous plane. The average temperatures weighted by the area of these parts were determined. The differences of the neighbouring temperatures were put into a 12x12 stripped symmetrical matrix and the elements of the lower or upper triangular matrix were summarized. This way an index was created for each simulation so the comparison can be made. The lower this index is the smoother the temperature distribution is. Figure 6 contains the results of this comparison, which shows that the one of the 0.94% cases has the best dispersion. Unfortunately this is the case in which the steam enters axially so it is only theoretical. If the turbine operates with real operating conditions the flow field tends to be more asymmetric like the temperature print. In operation point 3 the rotating disk next to the bended diffuser inlet amplifies the vertical motion of the flow. Thus larger separation will appear than in case operation point 1. Subsequently the reduced cross section accelerates the flow and the temperature gradient on the inner casing surface decreases. The distribution seems more even if the cooling effect is reduced. Contradictory phenomena can be observed for the counter swirl inlet. As a consequence one can say that the above mentioned index itself is modest parameter for the judgement. The absolute temperature values are needed as well.

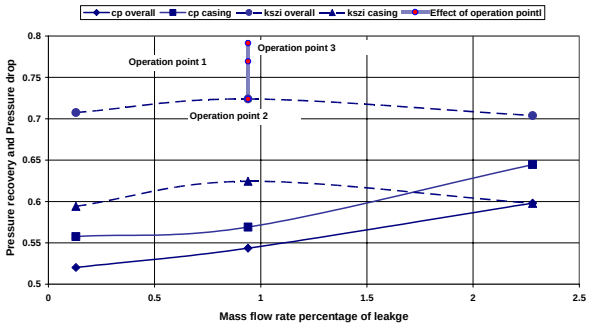

Figure 7. Pressure drop and recovery

Figure 7 includes pressure drop and recovery values for the investigated domain, which is considered as a diffuser. The overall values are defined between the system inlet and the outlet of the corresponding horizontal pipe, while the other does not take the tube into account. The amount of the discharge flow has an optimum at 0.94% from the pressure drop point of view. Operation point 3 has more axial path in the bended diffuser therefore the pressure drop is smaller than in operation point 1. Obviously the least pressure loss belongs to the axial inlet.

4. CONCLUSIONS

The presented numerical simulation shows that it is possible to compute the flow field around such inner casings. However, the authenticity of the quantitative results is questionable since the actual turbulence has high complexity which brings causes inaccuracy and the measurements cannot be done for each investigated problem. The determined tendencies have the important meaning.

According to Schlichting [5] and Peric [6], if the momentum and the thermal boundary layer thickness is comparable (when the Prandtl number is close to unity) the heat conduction within the boundary layer takes place inside the first sublayer. Therefore an accurate boundary layer is needed; however it requires a large amount of grid points. The disadvantage of such a modelling is that the invested numerical efforts are not comparable with the benefits gained by the more accurate resolution of the boundary layer.

On the other hand the flow field around of the inner casing has been understood with its limitations and some modifications have been made based on the presented results. The preformed numerical simulations have shown that the investigated high pressure turbine can operate safely in wide operational regions.

REFERENCE

[1] Mihejev, M. A. 1990, *A hőátadás számításának gyakorlati alapjai,* Tankönykiadó

[2] Abe, K., Kondoh, T., Nagano, Y., 1995, "A new turbulence model for predicting fluid flow and heat transfer in separating and reattaching flows – II. Thermal field calculations." *Int. J. Heat Mass Transfer*, Vol.38, No. 8, pp 1467-1481.

[3] Landau, L.D. and Lifsic, E. M. 1980, *Elméleti fizika VI Hidrodinamkia*, Tankönyvkiadó

[4] ANSYS CFX User's Guide

[5] Schlichting,. 1972, *Boundary Layer Theory*, Springer Verlag

[6] Peric,. 1972, *Boundary Layer Theory*, Springer Verlag

[7] Launder, B.E. and Spalding, D.B. 1972, *Mathematical Model of Turbulence*, Academic Press, Ltd.

[8] Wilcox, C,. 2000, *Turbulence Modeling for CFD,* DCW Industries, Inc.

[9] Bird, R. B. Stewart, W. E. and Lightfoot, E. N., 1960, *Transport Phenomena* ,John Wiley & Sons, Inc.

[10] Traupel, W., 2001, *Thermische Turbomaschinen*, Springer Verlag

Conference on Modelling Fluid Flow (CMFF'06)
The 13th International Conference on Fluid Flow Technologies
Budapest, Hungary, September 6-9, 2006

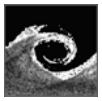

NUMERICAL OPTIMISATION OF A HP STEAM TURBINE BLADE USING A GENETIC ALGORITHM

Wolfgang BEER[1], Reinhard WILLINGER[2]

[1] Corresponding Author. Institute for Thermodynamics and Energy Conversion, Vienna University of Technology. Getreidemarkt 9/302, A-1060 Vienna, Austria. Tel.: +43 1 58801 30201, Fax: +43 1 58801 30299, E-mail: wolfgang.beer@gmx.at
[2] Institute for Thermodynamics and Energy Conversion, Vienna University of Technology. E-mail: reinhard.willinger@tuwien.ac.at

ABSTRACT

The paper presents results of the numerical optimisation of a high-pressure (HP) steam turbine nozzle blade. The starting point of the investigation is a two-dimensional cascade geometry with a flow turning angle of about 90°. The three-dimensional flow field in the linear turbine cascade is computed using the computational fluid dynamics (CFD) code FLUENT with the standard k/ε turbulence model. The blade stacking line is build up by two symmetric parabolic arcs near the end walls and a straight line in the mid section. This restriction results in two independent geometric parameters for the subsequent optimisation which is based on a genetic algorithm approach. The total pressure loss coefficient is performed as the objective function. The optimisation process gives a number of candidates with a potential for a loss reduction of about 1.5% due to the three-dimensional blade shape. Three configurations are discussed in detail using the results of the computed flow fields.

Keywords: axial flow turbine, CFD, compound lean blade, genetic algorithm, optimisation

NOMENCLATURE

AR	[-]	blade aspect ratio
C_p	[-]	static pressure coefficient
C_{pt}	[-]	total pressure coefficient
H	[m]	blade height
Ma	[-]	Mach number
Re	[-]	blade Reynolds number
Tu	[-]	turbulence intensity
b	[m]	axial chord length
c	[m]	chord length
g	[m]	length of straight stacking line
k	[J/kg]	turbulent kinetic energy
t	[m]	blade pitch
p	[Pa]	static pressure
p_t	[Pa]	total pressure
x	[m]	axial coordinate
y	[m]	pitchwise coordinate
y^+	[-]	nondimensional wall distance
z	[m]	spanwise coordinate
α	[°]	lean angle of blade stacking line
β'	[°]	blade angle
γ	[°]	stagger angle
ε	[W/kg]	turbulent dissipation rate
ω	[-]	loss coefficient

Subscripts and Superscripts

1	[-]	inlet
2	[-]	outlet
MS	[-]	midspan
t	[-]	total
$\bar{}$	[-]	pitchwise averaged quantity
$=$	[-]	area averaged quantity

1. INTRODUCTION

One way to improve the thermal efficiency of modern fossil-fuelled steam turbine powerplants is to increase the component efficiency of the turbine. The efficiency of the turbine is a result of the aerodynamic losses in the steam flow path. Since steam turbines for powerplants are of the axial type, the key components of the flow path are the bladings of the stator as well as of the rotor. It is generally accepted [1] that the total loss in an axial turbine blade row is divided into the following three components: profile loss, endwall loss, leakage loss. The relative contribution of the various losses depends mainly on the blade aspect ratio. Due to their rather low aspect ratio, the endwall loss plays an important role in HP steam turbine sections [2]. Endwall loss is also referred to as secondary loss since it arises mainly from the secondary flows generated when the endwall boundary layers pass through a blade row. A comprehensive review on the secondary flow in axial turbine blade rows is given by Sieverding [3] and more recently by Langston [4]. Therefore, the main objective of the

reduction of endwall losses is the reduction of the strength of the secondary flow in the blade row. Traditional turbomachinery design concepts perform two-dimensional profiles which are stacked on a straight line to produce the full blade shape. However, this design concept gives no degree of freedom to influence the secondary flow in the blade channel in a positive manner. Therefore, it is necessary to extend the design concept by replacing the radial straight blade axis by a bowed shape which results in a so-called three-dimensional blade. Due to structural reasons, this approach can be applied mainly to stator blade rows.

One of the earlier works on the effect of a bowed stacking line on the performance of a low aspect ratio turbine cascade is the experimental investigation of Harrison [5]. The author compared three sets of cascades with the same section but different stacking lines: a cylindrical blade, a straight leaned blade inclined at 20° from perpendicular and a circular arc inclined at 30° from perpendicular. The latter is called positive compound lean since there is an acute angle between the endwall and the blade pressure side. The inclination is in the circumferential direction. It turned out that the effect of blade lean on the overall loss is minimal. However, compound lean increased flow turning, reduced downstream mixing losses and substantially reduced spanwise variation of the pitchwise averaged flow angle.

Recently, Lampart [6] did a numerical study on the optimisation of a high-pressure steam turbine stage. The objective function which was used by the optimisation algorithm (simplex method) was the enthalpy loss of the stage. Actual values of the objective function were found from three-dimensional Reynolds-Averaged Navier Stokes computations, performing the Baldwin-Lomax as well as the Menter SST turbulence model. The optimised parameters were the stator and rotor blade numbers and stagger angles, rotor blade twist angle and parameters of stator compound lean at root and tip. Blade profile shapes were not changed. The optimisation resulted in a new three-dimensional stacking line of the blades. The reduction of the total stage loss was about 0.4%, compared with the original design.

It should be mentioned that most of the investigations on compound lean turbine blades deal with so-called positive compound lean. This means that there is an acute angle between the endwall and the blade pressure side. Two exceptions are the papers of Wanjin et al. [7] and Bagshaw et al. [8]. These investigations are on the effects of negative compound lean. This means that there is an obtuse angle between the endwall and the blade pressure side.

The objective of the present work is the optimisation of a HP steam turbine nozzle blade. Since it is the idea to investigate a large solution space without limiting the possible outcome of the optimisation in advance, a genetic algorithm is used. Total pressure loss coefficient will be chosen to be the objective function. Three sets of blades with different characteristic geometries are chosen after the optimisation process and are compared with one another.

2. BLADE AND CASCADE GEOMETRY

The blade chosen to be optimized is scaled from a HP stage steam turbine nozzle with a geometric turning angle of 89.4°. The profile coordinates are documented in a paper by Perdichizzi and Dossena [9]. Figure 1 shows a sketch of the blade profile and Tab. 1 summarizes the main geometric date of the cascade section. The computed results are going to be verified by future experiments in the cascade wind tunnel of the Institute for Thermodynamics and Energy Conversion, Vienna University of Technology. Therefore, the blade height is determined to H = 150 *mm*. Since an aspect ratio which is typical for HP steam turbine nozzle sections is chosen (AR = H/c = 1.5), the chord length c = 100 *mm*. Since the cascade is operated at design incidence, the inlet flow angle corresponds to the blade inlet angle β_1'.

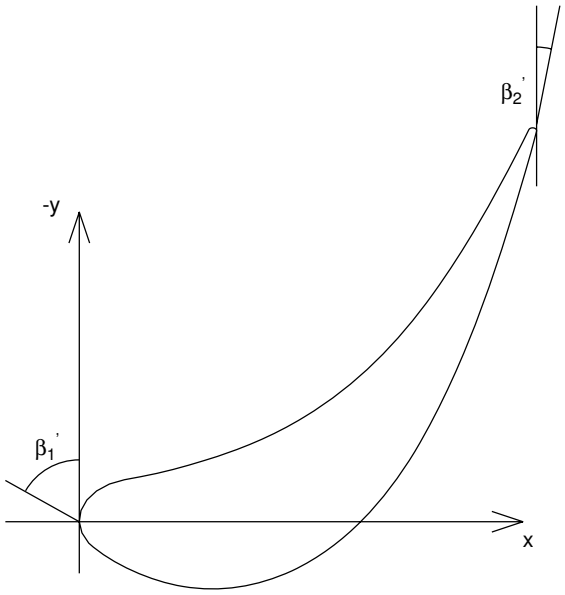

Figure 1. Sketch of blade profile shape

Table 1. Cascade geometric data

chord length	c	100	*mm*
axial chord length	b	61.85	*mm*
aspect ratio	AR	1.5	-
blade inlet angle	β_1'	76.1	°
blade exit angle	β_2'	14.5	°
stagger angle	γ	39.9	°
blade pitch	t	73	*mm*

If a straight stacking line perpendicular to the endwall is chosen, the corresponding blade is cylindrical. Furthermore, the stacking line of the compound lean nozzle is modelled using a parabolic arc at the endwall and a straight line at the mid section. Figure 2 shows the stacking line of an arbitrary compound lean blade with a plane of symmetry at midspan (z/H = 0.5). If the two-dimensional blade section is kept constant, the stacking line of the compound lean blade is determined by two parameters: (1) the angle α between the tangent to the parabolic arc and the spanwise direction at the endwall, and (2) the nondimensional length g/H of the straight section from the apex of the parabolic arc to midspan. These two parameters are varied during the subsequent optimisation process. A positive angle α (acute angle between the endwall and the blade pressure side) gives a so-called positive compound lean blade. On the other hand, a negative angle α (obtuse angle between the endwall and the blade pressure side) gives a so-called negative compound lean blade.

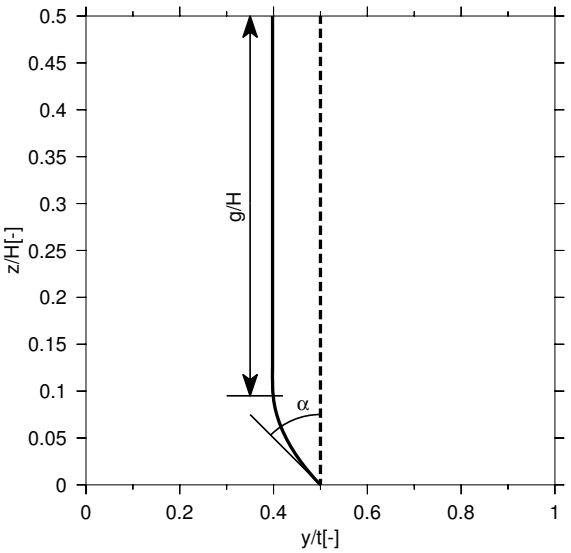

Figure 2. Stacking line of the compound lean blade

3. NUMERICAL APPROACH

3.1 Mesh Generation and Flow Solver

Starting point of the mesh generation process is a two-dimensional mesh at the endwall. This unstructured mesh is bounded by the blade surface, by the inlet plane, by the exit plane and by the periodic boundaries, respectively. The inlet plane and the exit plane are located one chord length upstream respectively downstream of the cascade. Near the blade surface, boundary edges are used to fulfil the near wall requirements of the turbulence model (nondimensional wall distance y^+). To produce a three-dimensional mesh, the two-dimensional mesh at the endwall is shifted along the stacking line, defined by the two parameters α and g/H. This results in a three-dimensional mesh with about 237000 cells which is bounded by the endwall and the plane of symmetry at midspan. The whole mesh generation process is performed using the scripting capabilities of the commercial grid generator GAMBIT2.2.30.

The governing equations for steady, three-dimensional flow are solved numerically using the commercial finite volume solver FLUENT6.2.16. If the conditions at the cascade wind tunnel are taken into account, the flow can be treated as incompressible (Ma < 0.2). A typical blade Reynolds number, defined with the exit velocity and the chord length, is $Re \approx 5 \cdot 10^5$. The turbulent behaviour of the flow is taken into account by the standard k/ε turbulence model with wall functions.

3.2 Boundary Conditions

The inlet boundary conditions are set according to conditions of the cascade wind tunnel. These are the velocity components, the turbulent kinetic energy as well as its dissipation rate. According to the inlet flow angle, the freestream velocity is about 25 *m/s*. The thickness of the endwall boundary layer is 25 *mm* which corresponds to about 17% of the blade height. The velocity distribution inside the endwall boundary layer is approximated by a $1/7^{th}$-power law. The measured freestream turbulence intensity Tu = 5% is used to set the turbulent kinetic energy at the inlet plane. Furthermore, the turbulent dissipation rate is obtained from the assumed turbulent length scale (0.1% of the blade pitch). At the exit plane, a constant static pressure boundary condition is applied. Since only one blade passage is modelled, symmetry boundary conditions are set at midspan and periodic boundary conditions at the periodic boundaries, respectively. Finally, no-slip boundary conditions are set at the blade surface as well as at the endwall.

3.3 Genetic Algorithm

Several calculations were performed before choosing the optimisation algorithm for this work. It turned out that one single solution, which means a computation of one configuration with a certain set of parameters α and g/H, took about one to two hours. Therefore, it was decided to choose a genetic algorithm for the optimisation procedure. Genetic algorithms have, compared with other commonly used algorithms, one big advantage. They do not tend to stop their search when finding a local optimum, as for example gradient methods. On the other hand, they have the big inconvenience that they normally need excessive search time, due to the fact, that they have a random element implemented. However, due to the relatively low computing time for a single solution and the fact that the authors are interested to cover a large

search area without any restrictions, a genetic algorithm proved to be the best optimisation method. Michalewicz [10] proposes several methods for optimising problems, from which a very general approach was selected and used. The first thing to do when using a genetic algorithm is to define the degree of freedom of the investigated system. In the present investigation, this figure is two since two geometrical parameters are varied: α and g/H. The two-dimensional blade section profile is kept constant for all configurations, which means that the profile is rather sheared than tilted. Furthermore, the increments of each parameter have to be defined, in order to calculate the size of the search area in binary numbers. It is decided that α should be varied in steps of 1° and g in steps of 1 *mm*. Since α is chosen in the range ±45° and g between 0 and 75 *mm*, this results in a search area of $2 \cdot 10^7$ times $2 \cdot 10^7 = 16384$ possible solutions. It is taken into account that one has to choose the next higher binary value for each degree of freedom. This number is reduced by 76 + 90 = 166 since every configuration with α = 0° is a cylindrical blade, no matter what value g takes (76 solutions), and each configuration with g = 75 *mm* is a cylindrical blade too, no matter what value α is (90 solutions). Before the algorithm is started, the objective function has to be chosen. A very common and general approach for the optimisation of turbomachinery components is the total pressure loss coefficient [11]. Therefore, the objective function is chosen to

$$\omega = \frac{\overline{\overline{p}}_{t1} - \overline{\overline{p}}_{t2}}{\overline{\overline{p}}_{t2} - \overline{\overline{p}}_{2}}. \qquad (1)$$

The algorithm now needs a starting solution, which can arbitrarily be chosen from the whole search area. Since the population size is set to 10, 10 different configurations are chosen to start. After having performed the necessary grid generations as well as the CFD-calculation, the algorithm sorts the solutions according to the result of their objective function, weights the results relatively to the sum of all 10 results of the whole population and cumulates the results. The binary representations of each configuration are now mated and mutated, if the relative weight of their result is greater than a randomly chosen number between 0 and 1. This gives a new population, which means a new set of 10 configurations which are then calculated and the algorithm starts all over again. Using the above explained algorithm, 1200 solutions are calculated, which represent approximately 7.5% of the whole solution space.

4. RESULTS AND DISCUSSION

4.1 Loss Coefficient

A contour plot of all the results calculated is presented in Figure 3. The region $\alpha > 0°$ represents positive compound lean blades and the region $\alpha < 0°$ negative compound lean blades, respectively. Each dot in the map corresponds to a single geometry and, therefore, to a single solution. The values for the objective function (= loss coefficient) should be compared with the corresponding values for the cylindrical blade (α = 0° or g/H = 0.5, respectively). It can be seen that the objective function increases for negative compound lean blades. On the other hand, there seems to be a region of minimum total pressure losses. This region of nearly constant total pressure losses is characterised by $\alpha \approx 10°$ to 20° at low values of g/H and $g/H \approx 0.4$ at large values of α, respectively.

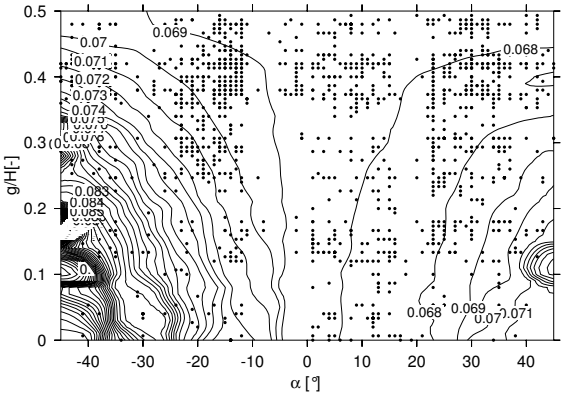

Figure 3. Contour plot of the objective function ω of the calculated solutions

Hence, two configurations (Set 2 and Set 3) of the optimisation process are chosen to be investigated in depth and to be compared with the cylindrical blade (Set 1). Table 2 shows the parameters and the result of the objective function of these configurations. The blade stacking line of Set 2 is a parabolic arc without any straight line at the mid section. On the other hand, the length of the straight line of the Set 3 stacking line is 59 *mm* and the height of the parabolic arc is 16 *mm*. The latter value can be compared with the thickness of the inlet boundary layer (25 *mm*). Set 2 and Set 3 differ considerably according to the values α. On the other hand, Set 2 as well as Set 3 show an improvement of the total pressure loss coefficient of about 1.5% compared with the cylindrical blade (Set 1). However, Set 2 and Set 3 differ according to their performance if local or pitchwise averaged quantities are taken into account. This fact will be presented in the remaining part of the discussion.

Table 2. Geometry parameters and objective functions of the selected configurations

	α	g	g/H	ω	ω/ω_{Set1}
	[°]	[mm]	[-]	[-]	[-]
Set 1	0	75	0.5	0.06864	1.0000
Set 2	15	1	≈ 0	0.06760	0.9848
Set 3	43	59	0.4	0.06756	0.9842

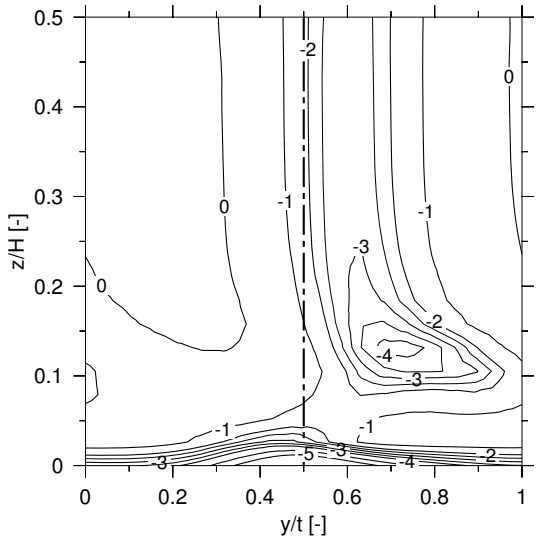

Figure 4. Contour plot of C_{pt2} for Set 1

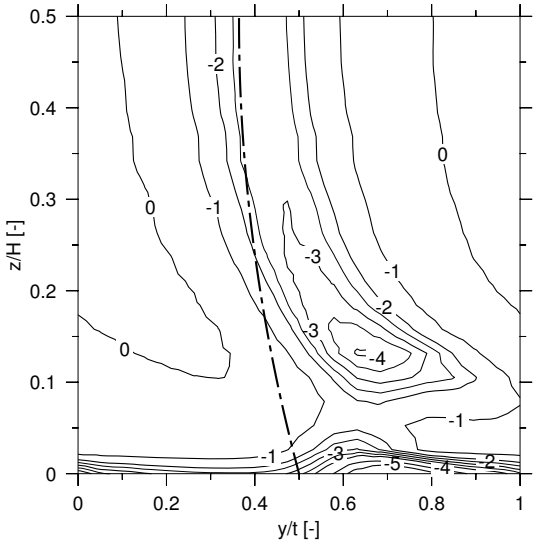

Figure 5. Contour plot of C_{pt2} for Set 2

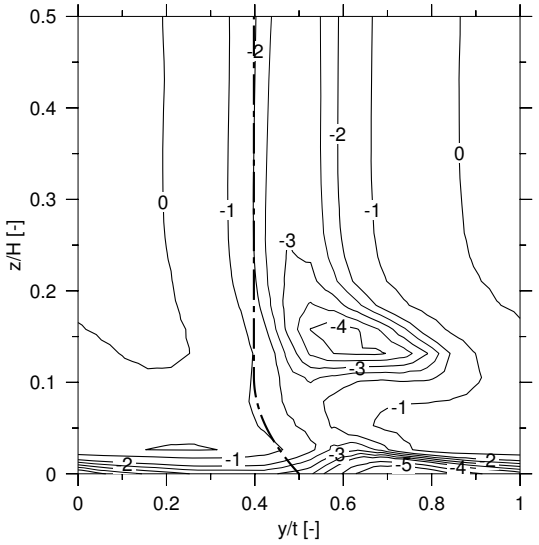

Figure 6. Contour plot of C_{pt2} for Set 3

4.2 Total Pressure Coefficient

The total pressure coefficient C_{pt2} is the difference between the local total pressure p_{t2} and the undisturbed inlet total pressure at midspan p_{t1MS} normalized by the undisturbed inlet dynamic pressure at midspan:

$$C_{pt2} = \frac{p_{t2} - p_{t1MS}}{p_{t1MS} - p_1}. \qquad (2)$$

It is used for the quantification of the total pressure losses in the cascade. The contour plots are given in Figure 4, 5 and 6 for Set 1, Set 2 and Set 3, respectively, at a plane 30% axial chord length downstream of the cascade exit plane. The trace of the blade trailing edge (dash-dotted line) indicates the stacking line of the individual blade. At midspan (z/H = 0.5), the distribution of the total pressure coefficient is a measure for the profile losses. Near midspan, the undisturbed blade wake with the blade pressure side on the left hand side of the trailing edge and the blade suction side on the right hand side of the trailing edge can be seen. The blade wake for Set 2 changes its appearance according to the geometry of the stacking line. The loss core, which can be identified by very low values of C_{pt2} is produced by the passage vortex which convects low momentum fluid from the endwall boundary towards midspan. This loss core seems to get smaller for Set 3, although it even seems to increase for Set 2, compared with Set 1.

4.3 Pitchwise Mass-Averaged Total Pressure Coefficient

The pitchwise mass-averaged total pressure coefficient $\overline{C}_{pt2}$ versus the nondimensional spanwise coordinate z/H is plotted in Figure 7. The respective values at midspan (z/H = 0.5) represent the profile losses and they confirm the fact that Set 2 shows higher profile losses than Set 1 and Set 3. The profile losses are the same for Set 1 and Set 3. Furthermore, the pitchwise mass-averaged total pressure coefficient is rather constant for $z/H > 0.3$. This means that this regoin near midspan is not influenced by three-dimensional flow effects. Near the endwall, Set 2 and Set 3 experience similar pitchwise mass-averaged total pressure coefficients. Both absolute levels are lower than the respective values for Set 1. This means that the losses due to the endwall boundary layer are lower for the compound leaned blades compared with the cylindrical blade. Furthermore, Set 2 shows the lowest absolute pitchwise mass-averaged total pressure coefficient in the peak of the loss core. Following Tab. 2, Set 2 as well as Set 3 show a lower total loss coefficient compared with Set 1. If the endwall losses are taken into account (Fig. 7) Set 2 shows the best performance. However, the lower endwall losses of Set 2 are somewhat balanced out by the increased profile losses.

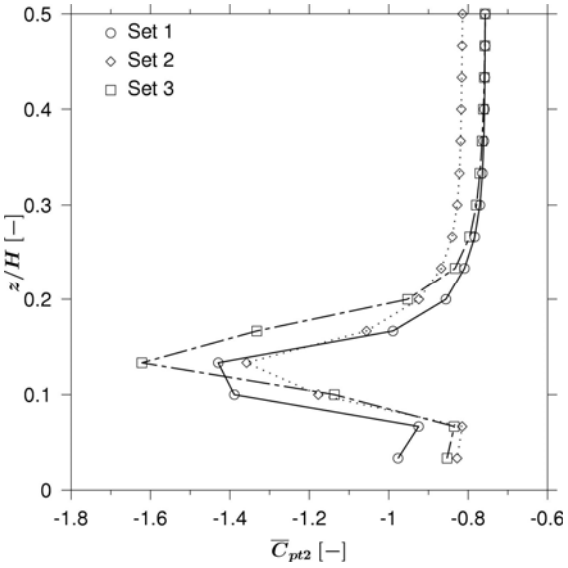

Figure 7. Pitchwise mass-averaged total pressure coefficient $\overline{C}_{pt2}$

4.4 Pitchwise Mass-Averaged Flow Angle

Figure 8 shows the pitchwise mass-averaged flow angle versus the nondimensional spanwise coordinate *z*/*H*. This flow angle indicates the deviation from the blade exit angle β_2'. Therefore, positive values of the pitchwise flow angle indicate an underturning and negative values an overturning, respectively. At midspan (*z*/*H* = 0.5), the flow turning of Set 1 and Set 3 is very similar. Since the inlet flow angle is fixed for all configurations, the flow turning of Set 2 is increased by about 1°. Near the endwall, the flow overturning of Set 2 as well as Set 3 is lower compared with Set 1. This means that the cross flow near the endwall is decreased for both compound lean configurations. Furthermore, Set 3 experiences the lower flow underturning due to three-dimensional effects. A more uniform distributed flow angle in the spanwise direction is in general expected to be favourable for the losses in the downstream rotor blade row. This is due to the decreased incidence losses in the subsequent blade row. Form this point of view, Set 3 shows the best behaviour. On the other hand, it has to be mentioned, that in a real turbine a non-uniformly distributed outflow of a nozzle is not necessarily a disadvantage, since the subsequent rotor blade row can be designed to cope with this fact.

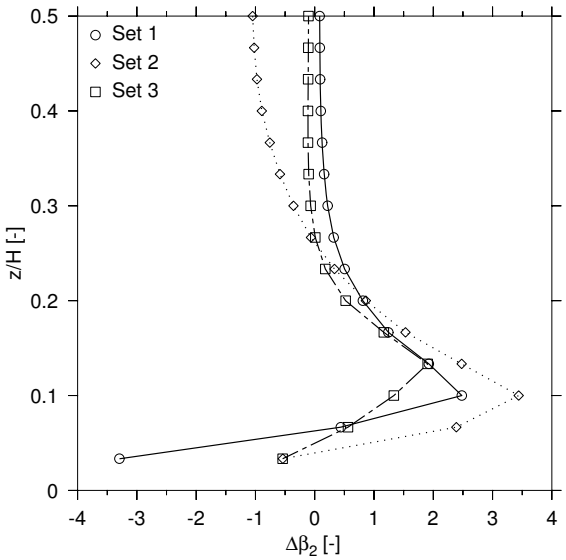

Figure 8. Pitchwise mass-averaged flow angle deviation

4.5 Blade Loading

The behaviour of the various blade designs, which is documented in Fig. 7 and 8 can be explained using the blade loading. This blade loading is quantified by the static pressure coefficient

$$C_p = \frac{p - p_1}{p_{t1MS} - p_1}. \qquad (3)$$

The difference between the local blade pressure p and the static pressure at the inlet plane p_1 is normalized by the undisturbed inlet dynamic pressure at midspan. Figure 9 and Figure 10 show the blade loading at midspan (*z*/*H* = 0.5) and at the endwall (*z*/*H* = 0), respectively, represented by the static pressure coefficient C_p. The pressure side distribution of C_p at midspan (*z*/*H* = 0.5) is the same for all configurations. On the suction side, C_p is lower for Set 2 compared with Set 1 as well as Set 3. This results in an increased blade loading of Set 2 which in turn explains the increased flow turning at midspan as well as the increased profile losses.

A significant unloading of Set 2 and Set 3 compared to Set 1 can be observed at the endwall (*z*/*H* = 0). This results mainly from the various distribution of C_p at the blade suction side. As it was expected, positive compound lean unloads the blade near the endwall. This is due to the blade force in spanwise direction which is induced by the acute angle between the endwall and the blade pressure side. This blade force increases the pressure at the endwall which in turn leads to lower velocities and, therefore, lower endwall losses. Furthermore, the lower pressure difference at the endwall decreases the cross flow and reduces the

intensity of the secondary flow for the positive compound lean configurations.

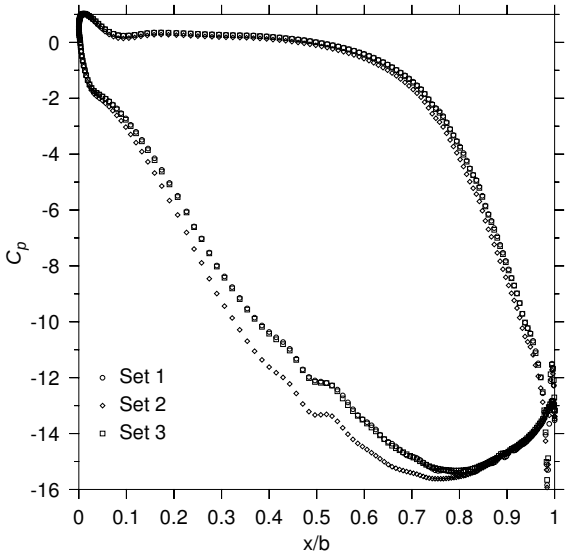

Figure 9. Static pressure coefficients C_p at midspan (z/H = 0.5)

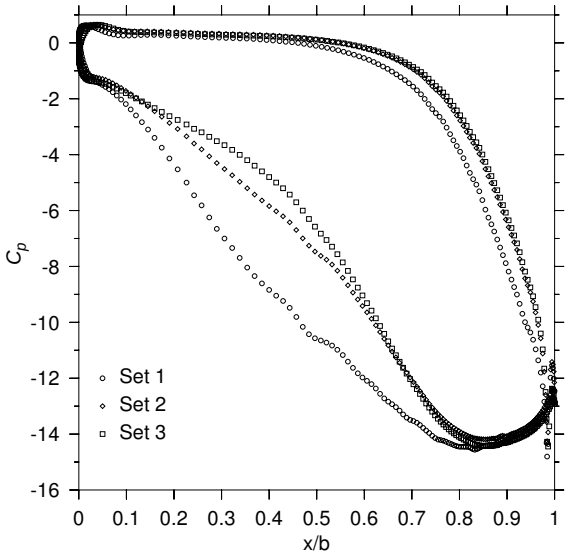

Figure 10. Static pressure coefficients C_p at the endwall (z/H = 0)

5. SUMMARY

A genetic algorithm was used to search a vast space of solutions for an "optimum" compound lean turbine nozzle. Whereas the two-dimensional blade section is kept constant, the blade stacking line is varied during the optimisation approach. The stacking line is characterized by two independent parameters: the lean angle of the parabolic arc near the endwall and the length of the remaining straight piece in the mid section. The total pressure loss coefficient of the individual cascades is used as the objective function. The flow field is computed using a commercial flow solver performing the standard k/ε turbulence model. It turned out that there are configurations that show a more or less constant improvement of the total pressure loss compared with the cascade of cylindrical blades. These "optimum" configurations are defined either by short straight sections and moderate lean angles or by rather long straight sections and higher lean angles. Compared with a cylindrical blade with the same blade profile, the investigated solutions indicate an improvement of about 1.5%, as far as the objective function (total pressure loss coefficient) is concerned. The blade loading is decreased for both compound lean blade sets at the endwall. On the other hand, the blade loading at midspan increased for the compound lean configuration without any straight section near midspan. This results in an increased flow turning as well as increased profile losses for this configuration. The spanwise variation of the pitchwise averaged exit flow angle is lowest for the compound lean configuration with a straight section near midspan.

It is not clear whether compound lean for this HP turbine stator profile and these boundary conditions can lead to an improved efficiency for the turbine stage. This is due to the fact that the results are observed from different point of views, as it was tried in this paper. It seems a promising goal to do the optimisation with other objective functions as well in order to get a better picture of the situation for HP turbine nozzles. The results obtained will be verified by future experiments in order to compare the findings of the calculation with experimental data.

REFERENCES

[1] Denton, J.D., 1993, "Loss Mechanisms in Turbomachines", *ASME J Turbomachinery*, Vol. 115, pp. 621 – 656.

[2] Havakechian, S., and Greim, R., 1999, "Aerodynamic Design of 50 Percent Reaction Steam Turbines", *Proceedings of the Inst. of Mech. Eng., Part C: Journal of Mech. Eng. Science*, Vol. 213, No. 1, pp. 1 – 25.

[3] Sieverding, C.H., 1985, "Recent Progress in the Understanding of Basic Aspects of Secondary Flows in Turbine Blade Passages", *ASME J Engineering Gas Turbines and Power*, Vol 107, pp. 248 – 257.

[4] Langston, L.S., 2001, "Secondary Flows in Axial Turbines – A Review", *Annals of the New York Academy of Sciences*, Vol. 934, pp. 11 – 26.

[5] Harrison, S., 1992, "The Influence of Blade Lean on Turbine Losses", *ASME J Turbomachinery*, Vol. 114, pp. 184 - 190.

[6] Lampart, P., 2003, ”Numerical Optimisation of a High Pressure Steam Turbine Stage”, *Conference on Modelling Fluid Flow (CMFF’03)*, September 3 - 6, Budapest, Hungary.

[7] Wanjin, H., Zhongqi, W., Chunqing, T., Hong, S. and Mochun, Z., 1994, ”Effects of Leaning and Curving of Blades With High Turning Angles on the Aerodynamic Characteristics of Turbine Rectangular Cascades”, *ASME J Turbomachinery*, Vol. 116, pp. 417 – 424.

[8] Bagshaw, D.A., Ingram, G.L., Gregory-Smith, D.G., Stokes, M.R., 2005, ”An Experimental Study of Reverse Compound Lean in a Linear Turbine Cascade”, *6th European Conference on Turbomachinery – Fluid Dynamics and Thermodynamics*, March 7 – 11, Lille, France.

[9] Perdichizzi, A. and Dossena, V., 1993, ”Incidence Angle and Pitch-Chord Effects on Secondary Flows Downstream of a Turbine Cascade”, *ASME J Turbomachinery*, Vol. 115, pp. 383 – 391.

[10] Michalewicz, Z., 1996, ”Genetic Algorithms + Data Structures = Evolution Programs”, Springer Verlag.

[11] Wingelhofer, F., Haselbacher, H., 2004, ”New Optimization Criteria For the Design of Three-Dimensional Bladings Applied to Compound Lean Nozzles of an Axial Turbine”, *ASME Paper GT2004-53830*

Conference on Modelling Fluid Flow (CMFF'06)
The 13th International Conference on Fluid Flow Technologies
Budapest, Hungary, September 6-9, 2006

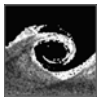

DISORDERS OF VELOCITY PROFILE CALLED OUT EXTRACTION POINT OF STEAM TURBINE

Krzysztof WOSZCZAK[1]

[1] Wroclaw University of Technology, Faculty of Mechanical and Power Engineering, Division of Turbomachines, 50–370 Wroclaw, Wybrzeze Wyspianskiego 27, Tel: +48 71 3723857, Fax: +48 71 3723592, krzysztof.woszczak@pwr.wroc.pl

ABSTRACT

The processes in the steam turbine are usually analysed for an axially symmetric flow. Typical power plant turbines have bleeds (without governing steam pressure) for steam extraction to regenerative feed heaters. The bled steam flows out radially from the space between blade rings significantly changing the flow structure in the steam bleeding zone. The process results in flow disturbances in the turbine's blade system and in a decrease in its efficiency.

The flow of steam through the turbine's bleeds was numerically modelled by CFD (Computational Fluid Dynamics) methods (the typical conservation of mass, momentum and energy equations for a 3D flow, using the k–ε turbulence model). The investigations were carried out for four blade rings (two stages – one before and one after the extraction point). The effect of steam extraction on the efficiency of the stages was studied.

Keywords: steam turbine, axial-flow, steam extraction, flow structure, numerical analysis

NOMENCLATURE

c	[m/s]	absolute velocity
w	[m/s]	relative velocity
u	[m/s]	velocity of transportation
v	[m/s]	velocity
r	[m]	radius
h	[m]	width of diffuser
φ	[$^\circ$]	angle of stage circumference
α	[$^\circ$]	angle of absolute velocity

Subscripts and Superscripts

0, 2	inlet, outlet of stage (cross-section)
1	cross section between stator and rotor blades
a	axial
t	tangential
r	radial
m	absolute
a	axial
‘	velocity of outlet cross-section
A, B, C	cross-section between first and second stage
D÷H	cross-section in diffuser

1. INTRODUCTION

The motion of steam in the turbine is determined assuming that the flow is axially symmetric and that radial equilibrium is maintained [3]. When calculating the individual stages and groups of stages, the circumferential distribution of steam parameters is assumed to be uniform. But in typical condensing turbines bleeds are used to extract steam to the regenerative feed heating system. Between neighbouring groups of stages there is a circumferential gap through which steam flows out to the bypass collector from which (through a blowdown connection) it is fed via a pipeline into a regenerative heat exchanger. Usually one extraction socket is used and it is located at the lowest point of the bypass collector. This design is bound to result in some disturbances in the pressure fields and flow velocities in the space between the group stages situated before and after the extraction point.

Further distortion of the flow field symmetry is caused by the rotating motion of the runner as well as by the tangent component of the velocity vector at the outflow of steam from the stage located before the extraction point. The pressure and velocity fields shift by a certain angle (relative to the extraction socket) and the flow parameters change periodically [1], [2], [4] and [5]. The complexity of the phenomena described increases, especially in the wet steam zone where also liquid phase motion occurs.

2. MODEL

The problem of the influence of the extraction process on the flow structure was solved using the CFD method and the standard k–ε turbulence model. Figures 1, 2 and 3 show the geometry of the measuring chamber model placed between two turbine stages. The distribution of steam parameters at the inlet to the stage located before the extraction chamber was assumed to be uniform. Moreover, the flow was assumed to be adiabatic – the working fluid does not exchange any heat with the chamber walls.

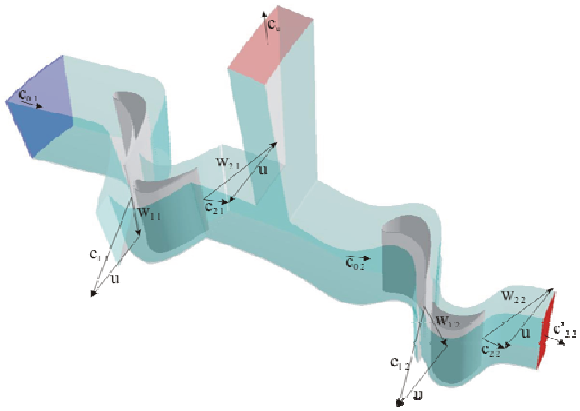

Fig. 1. Individual flow channel

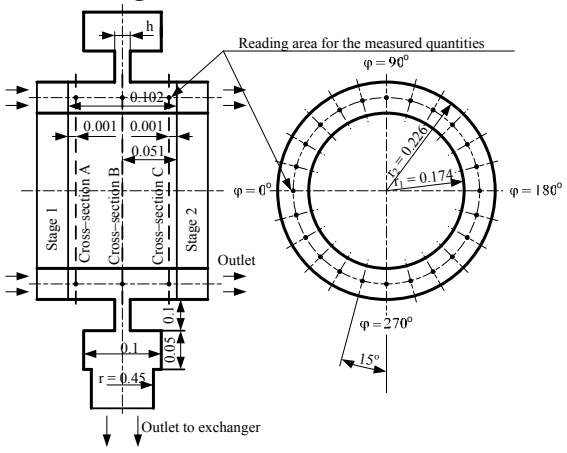

Fig. 2. Scheme of model

The purpose of the investigations was to determine the influence of the extracted steam mass flow rate on the distribution of pressures and velocities within the extraction chamber. Therefore parameter variations in the control cross sections (A, B and C in Fig. 1) of this volume were analysed. In each control cross section, flow parameter values were determined at 24 measuring points equally spaced at every 15° along the circumference (corresponding to the chamber's pitch diameter D = 0.4 m). The location of the extraction socket is defined by angle φ = 270°.

Figures 4÷7 show the geometry of the two

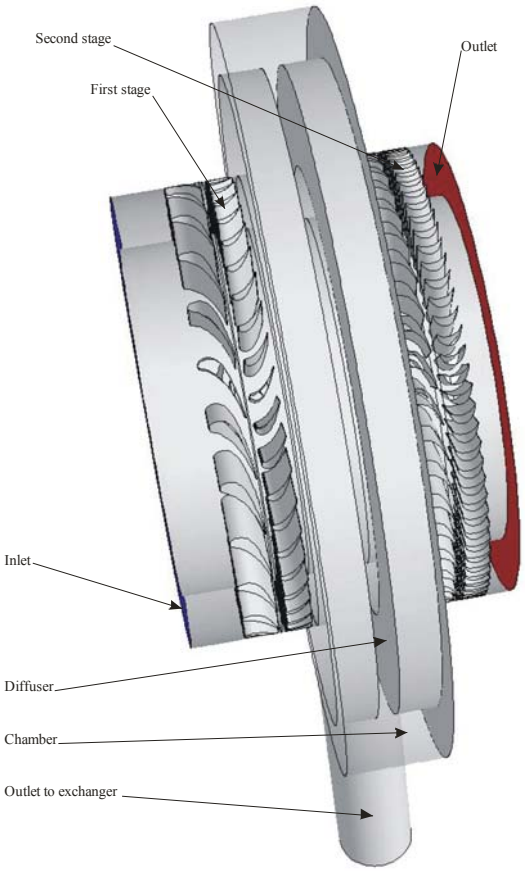

Fig. 3. Geometry of model

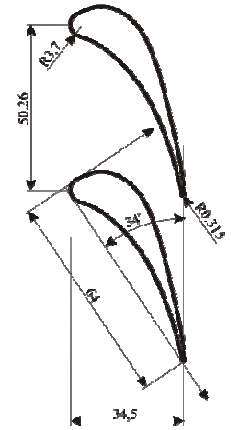

Fig. 4. Geometry of stator blades (1st stage – C9012A)

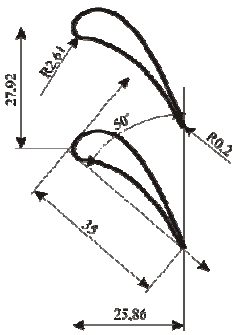

Fig. 5. Geometry of rotor blades (1st stage – C9018A)

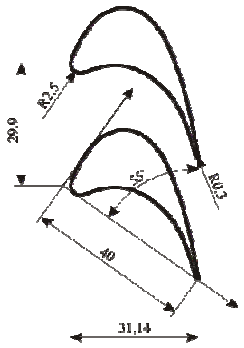

Fig. 6. Geometry of stator blades (2nd stage – C5515A)

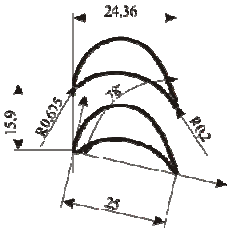

Fig. 7. Geometry of rotor blades (2nd stage – P3525A)

stages' blades. Detailed specifications of the blades are given in table 1.

Table 1. Geometry of blade-ring

Blade profile	Number of blades	Scale	Height of blade [m]
C9012A	25	0.780	0.05
C9018A	45	0.797	0.052
C5515A	42	0.750	0.05
P3525A	79	0.545	0.052

3. RESULTS OF CALCULATION

The flow was modelled for three diffuser widths shown in table 2. The widths are expressed in percentages representing the ratio of the mass flow rate at the extraction point to that at the stage located before the chamber (relative extraction).

Table 2. The comparison of steam q_m/q on outflow with diffuser

h [mm]	Outflow to exchanger			
	I [%]	II [%]	III [%]	IV [%]
10	5.64	11.87	17.2	21.29
20	6.47	13.02	18.58	22.86
30	10.96	13.39	19.07	23.44

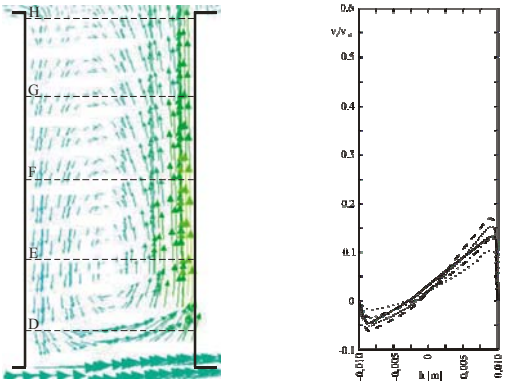

Fig. 8. Flow in diffuser, q_m/q=6.47%, φ=0°, h=0.02m

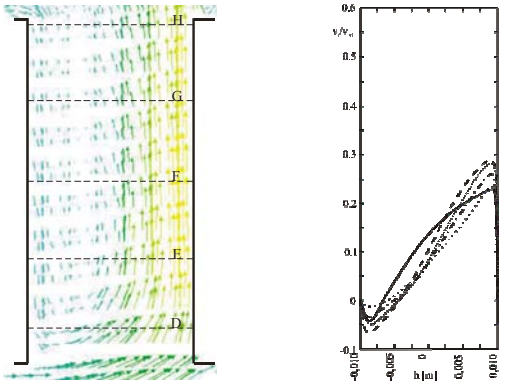

Fig. 9. Flow in diffuser, q_m/q=22.9%, φ=0°, h=0.02m

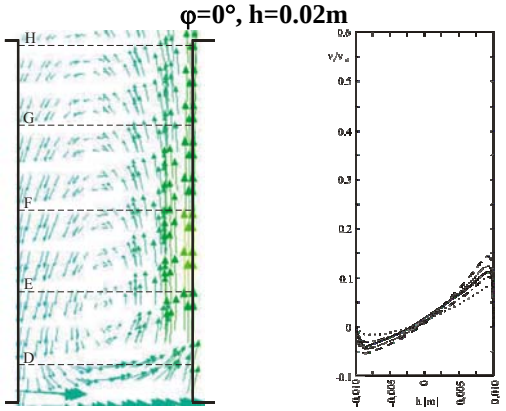

Fig. 10. Flow in diffuser, q_m/q=6.47%, φ=90°, h=0.02m

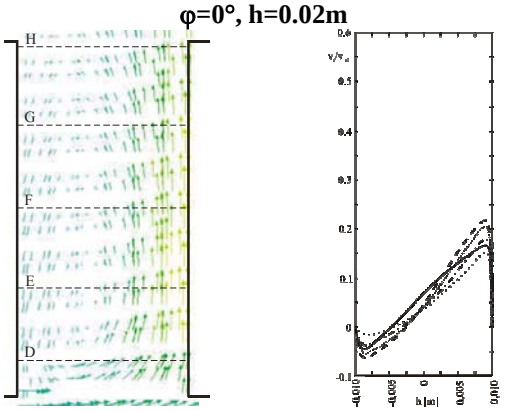

Fig. 11. Flow in diffuser, q_m/q=22.9%, φ=90°, h=0.02m

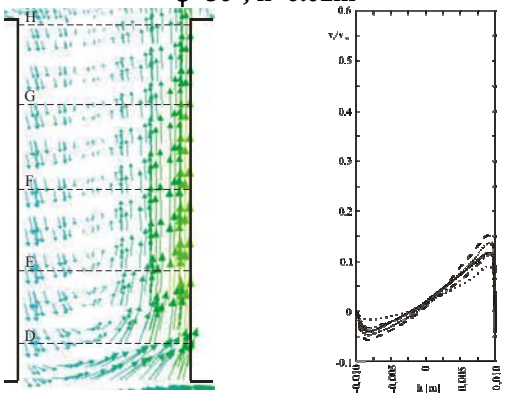

Fig. 12. Flow in diffuser, q_m/q=6.47%, φ=180°, h=0.02m

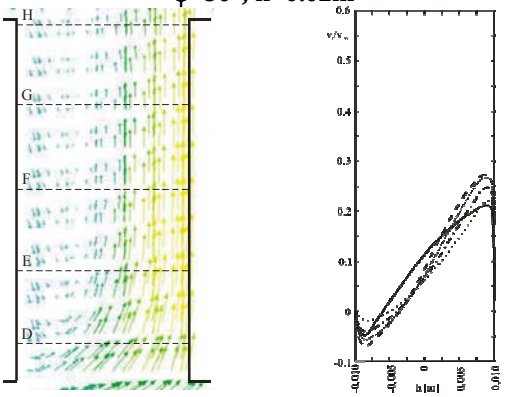

Fig. 13. Flow in diffuser, q_m/q=22.9%, φ=180°, h=0.02m

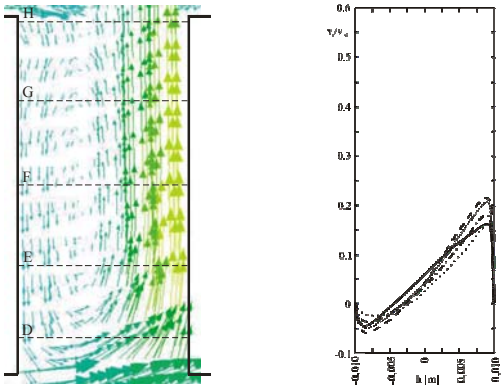

Fig. 14. Flow in diffuser, q_m/q=6.47%, φ=270°, h=0.02m

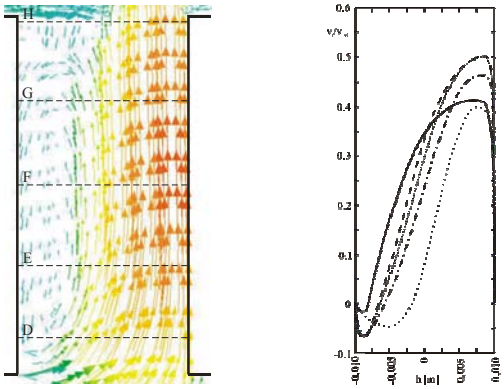

Fig. 15. Flow in diffuser, q_m/q=22.9%, φ=270°, h=0.02m

Legend:

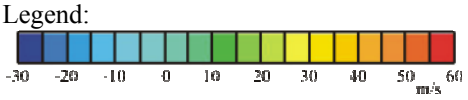

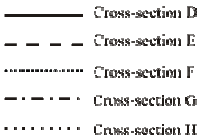

The flow in the diffuser for 12 mass streams (Tab. 2) and the values φ=0, 90, 180 and 270° (Fig. 2) is visualized in Figs 8÷15. The figures on left show the flow in the diffuser while the ones on the right visualize the distribution of the absolute velocity of the stream flowing throught the diffuser (v_{ref}=60 m/s).

The stream flows mainly on the diffuser's right side, some of it returning on the left side to the turbine blade system.

Calculation results for control cross section B and four different extracted mass flows are shown in Figs 16÷30.

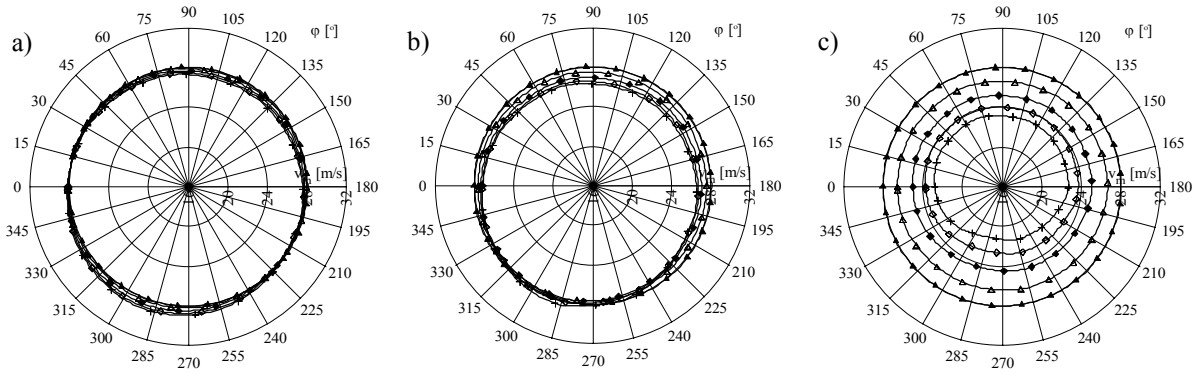

Fig. 16. Distribution of absolute velocity, h=0.01 m, a) cross-section A, b) cross-section B, c) cross-section C

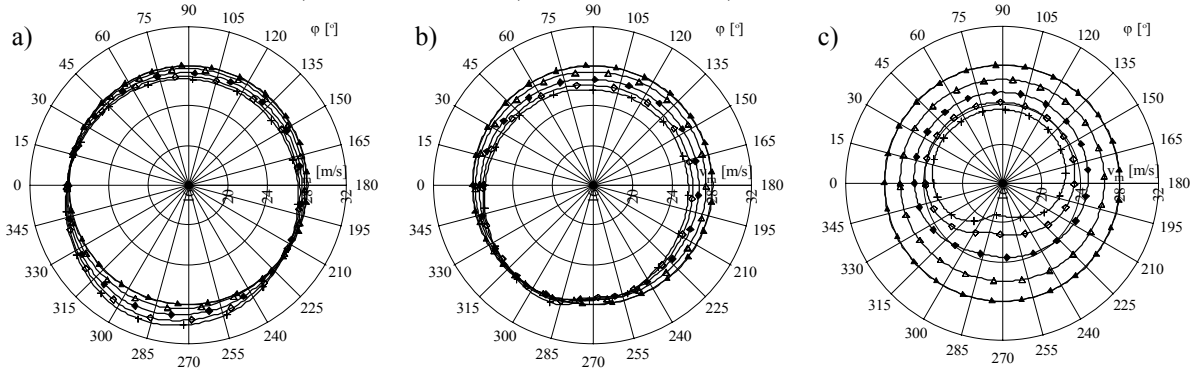

Fig. 17. Distribution of absolute velocity, h=0.02 m, a) cross-section A, b) cross-section B, c) cross-section C

Legend:

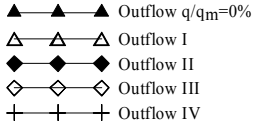

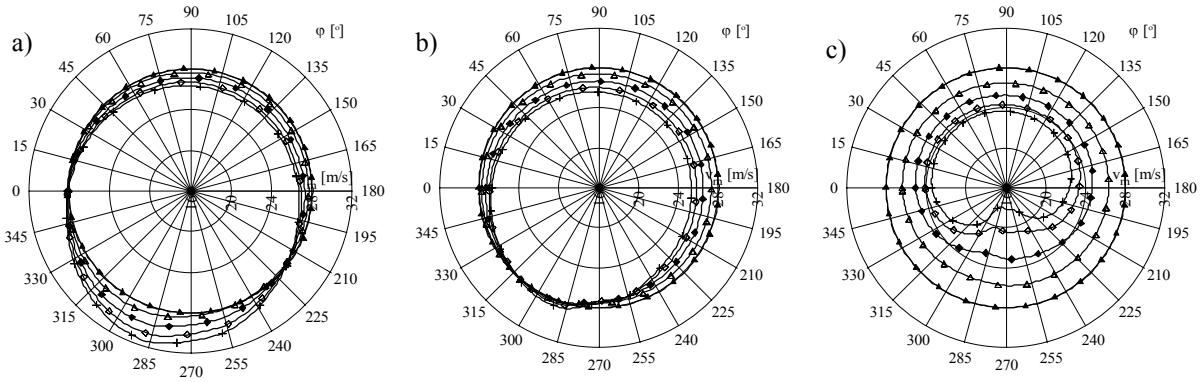

Fig. 18. Distribution of absolute velocity, h=0.03 m,
a) cross-section A, b) cross-section B, c) cross-section C

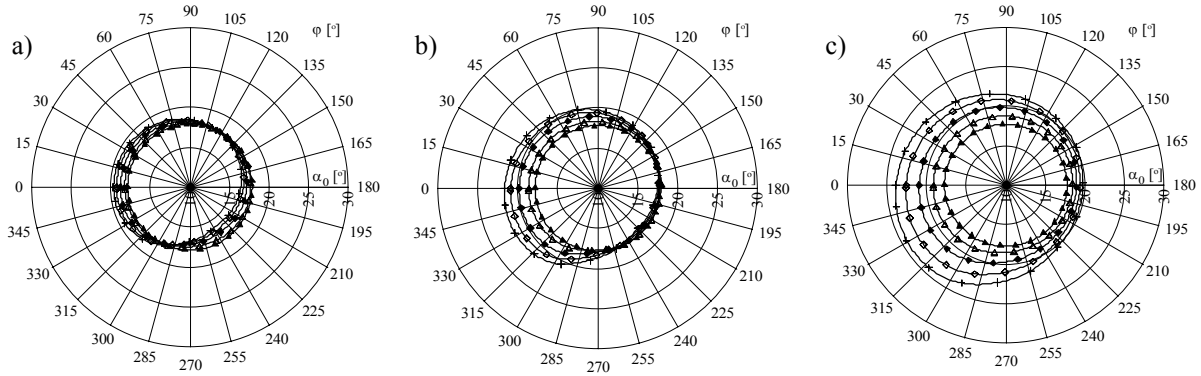

Fig. 19. Distribution of absolute velocity angle, h=0.01 m,
a) cross-section A, b) cross-section B, c) cross-section C

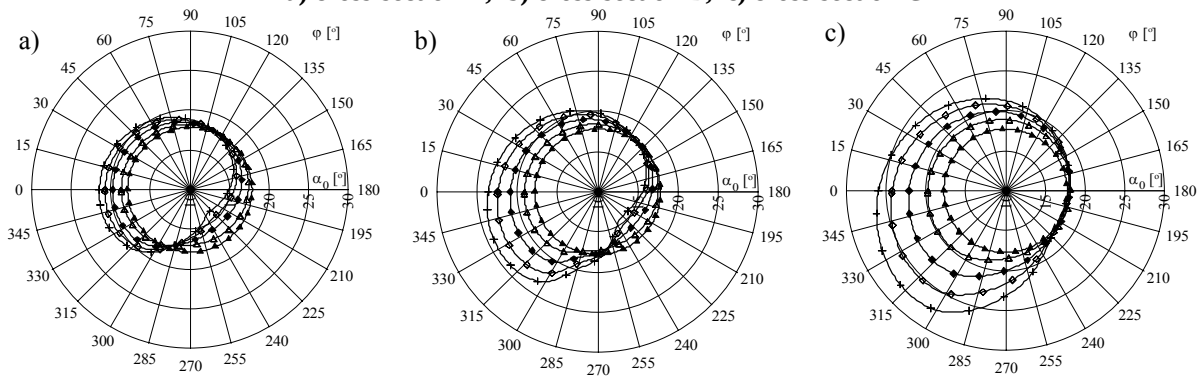

Fig. 20. Distribution of absolute velocity angle, h=0.02 m,
a) cross-section A, b) cross-section B, c) cross-section C

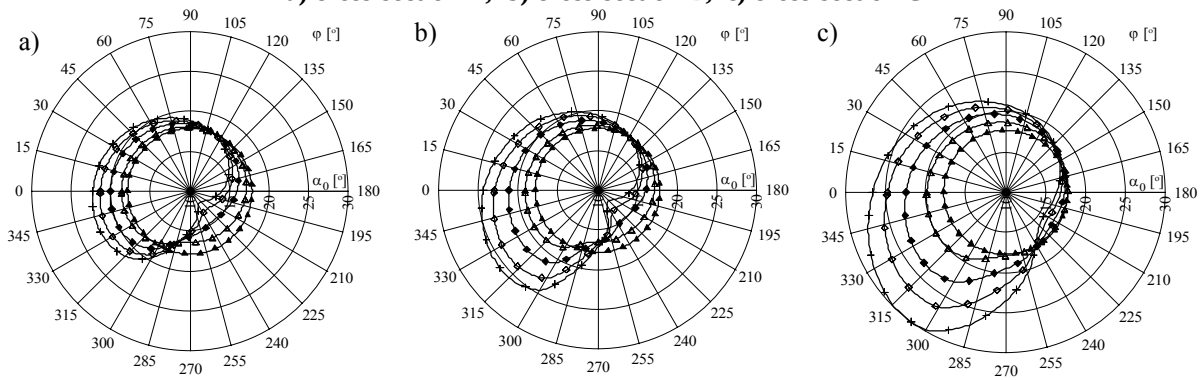

Fig. 21. Distribution of absolute velocity angle, h=0.03 m,
a) cross-section A, b) cross-section B, c) cross-section C

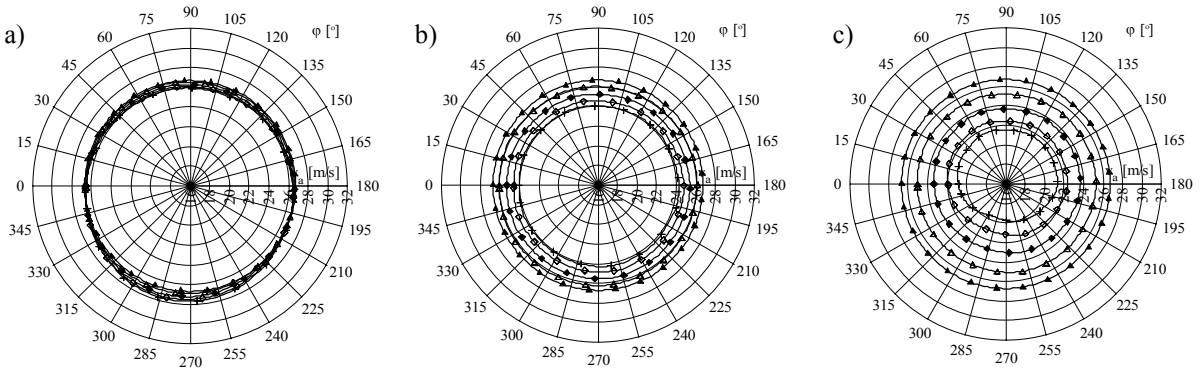

Fig. 22. Distribution of axial velocity, h=0.01 m,
a) cross-section A, b) cross-section B, c) cross-section C

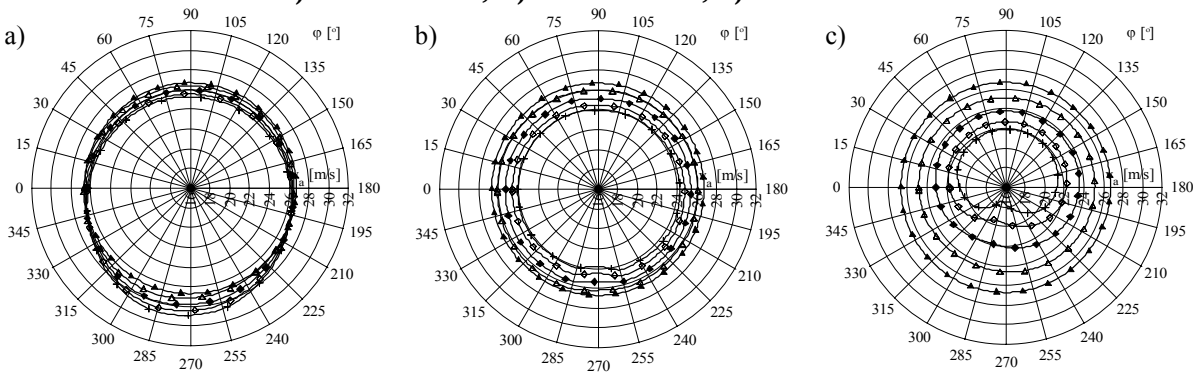

Fig. 23. Distribution of axial velocity, h=0.02 m,
a) cross-section A, b) cross-section B, c) cross-section C

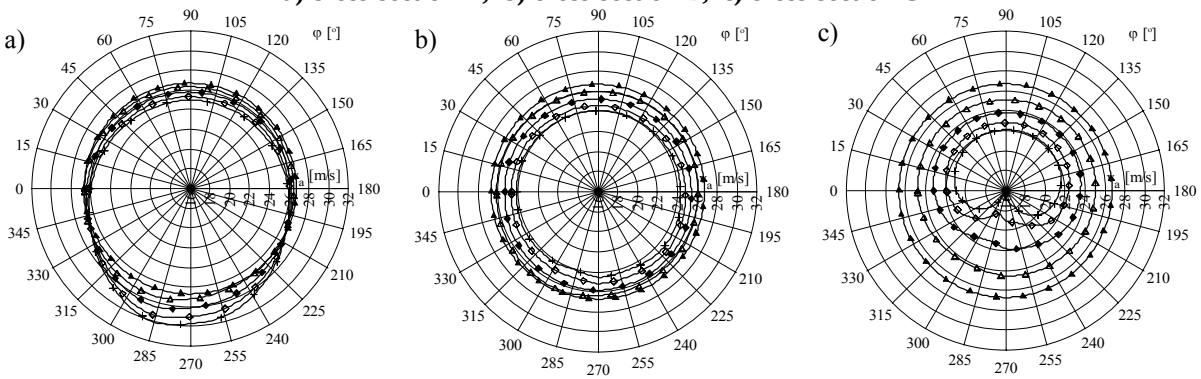

Fig. 24. Distribution of axial velocity, h=0.03 m,
a) cross-section A, b) cross-section B, c) cross-section C

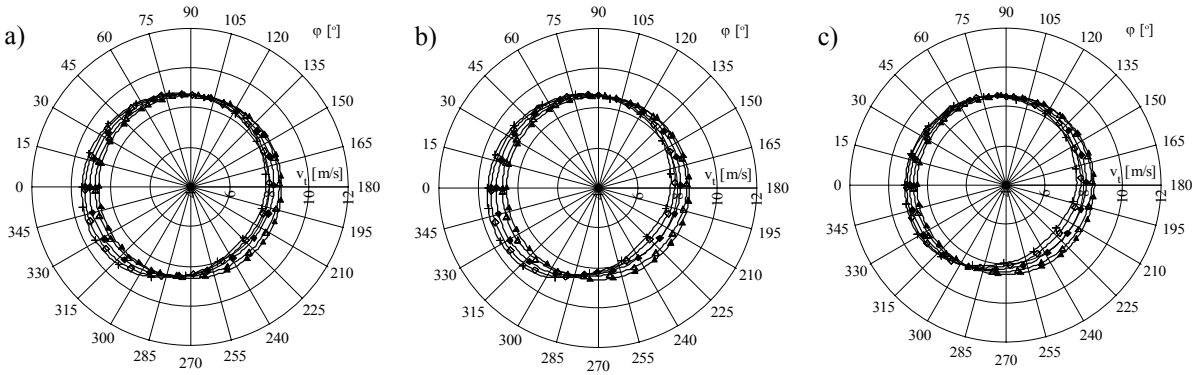

Fig. 25. Distribution of tangential velocity, h=0.01 m,
a) cross-section A, b) cross-section B, c) cross-section C

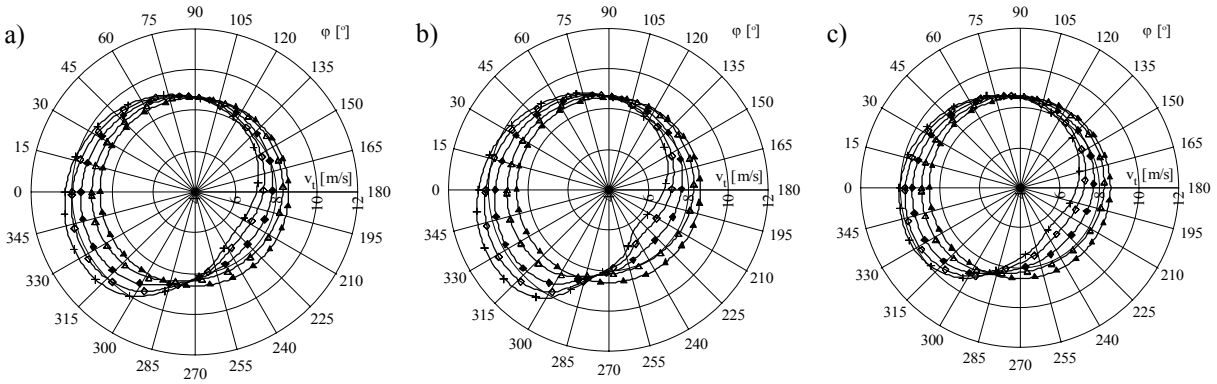

Fig. 26. Distribution of tangential velocity, h=0.02 m,
a) cross-section A, b) cross-section B, c) cross-section C

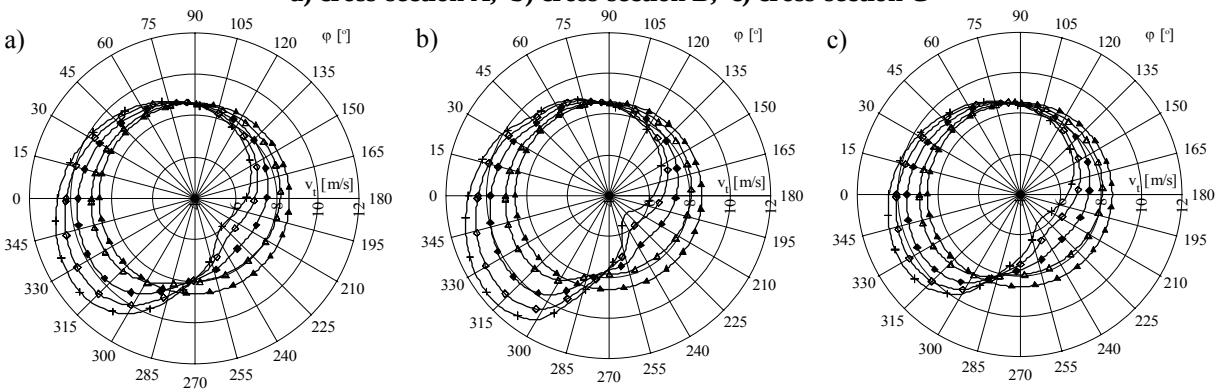

Fig. 27. Distribution of tangential velocity, h=0.03 m,
a) cross-section A, b) cross-section B, c) cross-section C

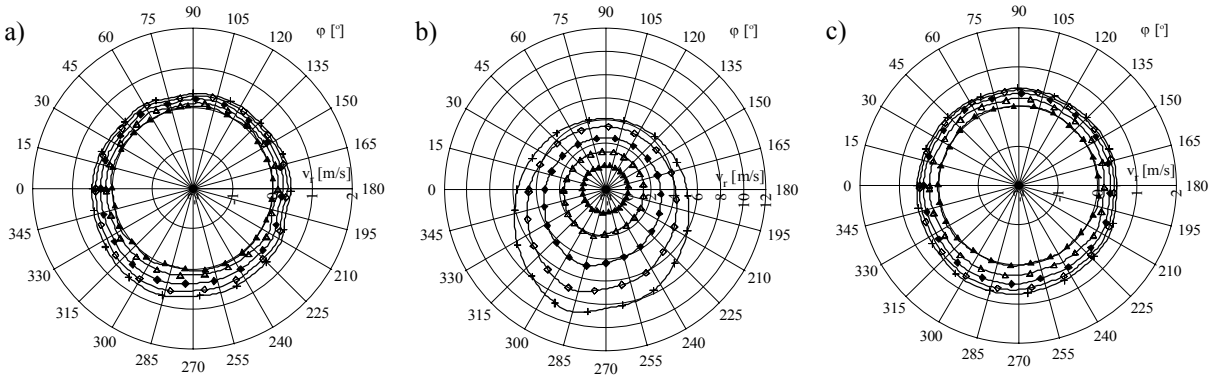

Fig. 28. Distribution of radial velocity, h=0.01 m,
a) cross-section A, b) cross-section B, c) cross-section C

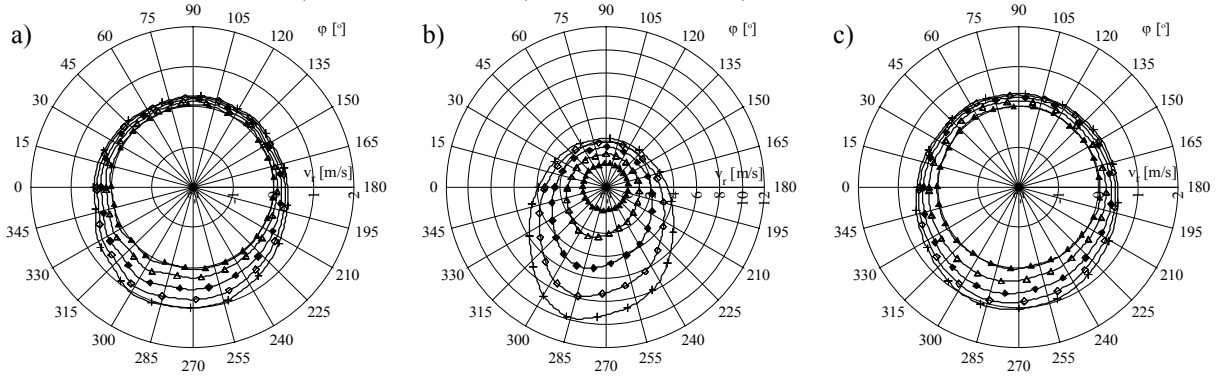

Fig. 29. Distribution of radial velocity, h=0.02 m,
a) cross-section A, b) cross-section B, c) cross-section C

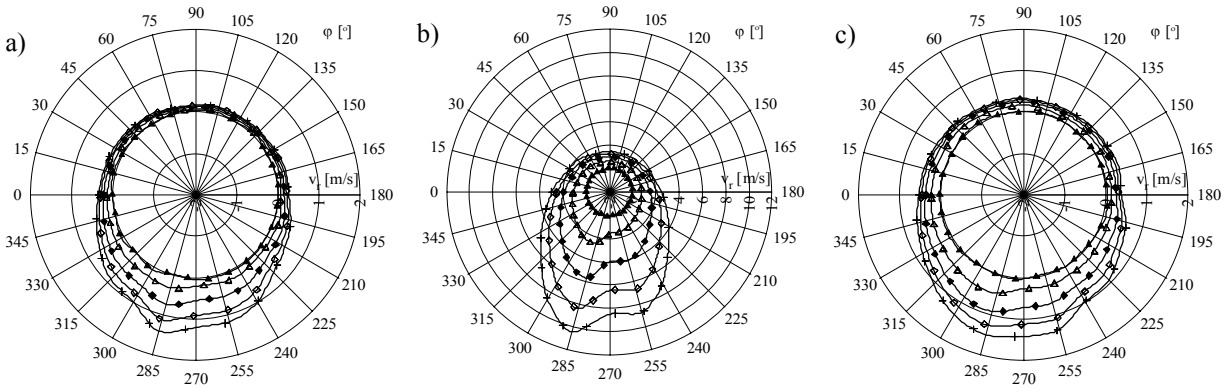

Fig. 30. Distribution of radial velocity, h=0.03 m,
a) cross-section A, b) cross-section B, c) cross-section C

At q=0.0% the extraction socket was shut in order to determine the influence of the extraction collector volume on the flow.

Figures 16÷30 show changes in the steam parameters in control cross sections A, B and C (Fig. 2) along the chamber between the two stages.

4. ANALYSIS

The presented characteristics show that the largest changes in the fluid's parameters occur within an angle range of 180÷30° in cross section B which symmetrically divides the chamber and the extraction gap into two equal parts. Special attention should be drawn to the change in the radial velocity vector which increases from zero (at q = 0.0%) to v_r = 10.8m/s for the largest extraction (q = 23.44%) at φ= 285°. The vector changes similarly, but to a smaller degree, in cross section C.

The vector of tangential velocity v_t is also subject to distortions (Figs 25÷27). When the extracted mass flow is equal to zero, its distortion is negligibly small (similarly as that of the other quantities).

Also important is the characteristic of changes in absolute angular velocity. The initial range of changes in angle α_0 at zero outflow from the bleed is negligibly small but as the extracted stream is gradually increased, the range increases from α_0=18° (constant along the whole circumference – cross section A) to 30.1° (cross section C) and shows an upward trend.

The division of the initial stream into two streams: the extracted one (q) and the one feeding the next turbine stage changes somewhat the steam flow capacity. When at constant inlet parameters steam extraction (bleeding) is increased, the steam flow through the investigated group stage also increases, as is clearly apparent from the characteristics shown in Figs 22÷24 where a distinct upward tendency of the component axial velocity is observed [6].

5. SUMMARY

The presented results show that the extraction of steam for feeding a regenerative heat exchanger causes considerable flow disturbances in the turbine, particularly in control cross section B and to a lesser degree in cross section C. Some parameters, e.g. absolute flow velocity angle α_0, have an increasing tendency.

It should be stressed that changes in pressure and velocity fields may significantly affect the work of the turbine stages situated after the extraction point.

[1] ELSNER, W., WYSOCKI M., 2000, "The Effect of Periodic Disturbances on a Turbine Stage Performance". *Politechnika Łódzka*, Zeszyty Naukowe, No. 117, pp. 167–172.

[2] LAMPART, P., SZYMANIAK, M., KARDAŚ A., 2003, "Unsteady Forces Acting on Rotor Blades of a Large Power Steam Turbine Control Stage at Different Levels of Partial Admission", *Institute of Fluid–Flow Machinery, Polish Academy of Sciences*, No. 114, Gdańsk, pp. 5–17.

[3] PERYCZ, S., 1992, „Turbiny parowe i gazowe", Seria: Maszyny przepływowe t. 10., *Ossolineum*.

[4] PUZYREWSKI, R., BIERNACKI R., 2003, "Volute Scroll as an Alternative to Guide Vanes at Inlet to a Turbine", *Institute of Fluid–Flow Machinery, Polish Academy of Sciences*, No. 114, pp. 99–110.

[5] RZĄDKOWSKI, R., 1998, „Dynamics of Steam Turbine Rotor Blading", Seria: Maszyny Przepływowe t. 22, Part II, *Ossolineum*.

[6] WOSZCZAK, K., 2004, „Badania pracy zintegrowanego układu regeneracji elektrowni cieplnej z wykorzystaniem kondensatora jednej z turbin jako podgrzewacza niskiego ciśnienia", Seria PRE nr 24, *Politechnika Wrocławska.*

Conference on Modelling Fluid Flow (CMFF'06)
The 13th International Conference on Fluid Flow Technologies
Budapest, Hungary, September 6-9, 2006

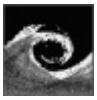

NUMERICAL STUDY OF THE HEAT TRANSFER IN AN AXIAL HELIUM TURBINE

Tom VERSTRAETE[1], Zuheyr ALSALIHI[2], René A. Van den BRAEMBUSSCHE[3]

[1] Corresponding Author. Von Karman Institute for Fluid Dynamics, Waterloose steenweg, 72, 1640 Sint-Genesius Rode, Belgium Tel.: +32 2 359 9611, Fax: +32 2 359 9600, E-mail: verstrae@vki.ac.be
[2 3] Von Karman Institute for Fluid Dynamics, E-mail: alsalihi@vki.ac.be, vdb@vki.ac.be

ABSTRACT

This paper presents a numerical investigation of the conjugate heat transfer in an axial helium turbine. The objective is the prediction of the cooling needed to keep the blade temperature below the allowable material limits. The cooling is applied at the hub by means of internal cooling channels.

A Conjugate Heat Transfer (CHT) solver has been developed for this purpose. It combines a 3D conduction calculation inside the blade with a 3D Navier-Stokes (NS) calculation around the turbine blade. The root casing is approximated by applying a uniform temperature boundary condition at the hub bottom plane.

Various alternative methods to implement the CHT are tested and compared. The results, indicate that the so-called h-method is superior both in terms of accuracy and convergence speed.

Keywords: axial flow turbine, conjugate heat transfer, finite element analysis, h-method, Navier-Stokes, temperature forward flux backward.

NOMENCLATURE

T	$[K]$	Static temperature
h	$[W/(m^2{}^\circ K)]$	heat transfer coefficient
q	$[W/m^2]$	flux

Subscripts and Superscripts

fl	in the flow
W	at the wall
f	from the fluid solver
n	iteration number
s	from the solid solver

1. INTRODUCTION

Conduction in the solid is normally not an important issue in turbomachines except when cooling is applied to high temperature turbines. Most CFD predictions assume adiabatic conditions at the solid boundaries [1]. Others assume a high constant surface temperature. None of these approaches provides a picture of the solid temperature distribution and heat transfer.

The axial helium gas turbine studied in the present work is a typical one for the ones employed in direct cycle Helium cooled nuclear reactors.

The maximum allowable temperature for the turbine disk material is defined from the expected life time of the turbine. An accurate prediction of the heat transfer is critical. A better knowledge of the material temperature is also important since it influences thermal stresses and deformations of the individual components.

Present paper describes a CHT method for the prediction of the temperature distribution in the solids and the heat transfer between fluid flow and the solid.

2. NUMERICAL METHOD

There are two main approaches to the conjugate heat transfer problem in turbomachinery [2-8]. One is by an extension of the CFD code to the solid region, where only the energy equation is solved [4,7,8]. The main advantage is that only one code is needed for the whole domain. However, modifications of the CFD code and grid generator are required.

The other approach is a coupling of two codes: a non-adiabatic Navier-Stokes (NS) solver for the flow in the fluid domain and a Finite Element Analysis (FEA) for the heat conduction in the solid. Continuity of temperature and heat flux at the common boundaries is obtained by an iterative adjustment of the boundary conditions. The advantage of the coupled approach is that one can use standard NS and FEA solvers and grid generators. Those codes have been extensively verified and their limitations and capabilities are well known. A FEA calculation is anyway needed for stress and vibration analysis. These have been

the main arguments for developing the coupled method for present analysis.

Disadvantages of the coupled method are the non-coinciding grids at the common boundary, requiring an interpolation to pass the boundary conditions from one grid to the other and the need for an iterative procedure.

The non-adiabatic flow is calculated by means of TRAF3D [9]. This full 3D compressible Navier-Stokes solver uses a multi-stage Runge-Kutta time integration and central differencing with artificial dissipation applied to finite volumes. Convergence is accelerated by multigrid interpolation and implicit residual smoothing. The overall accuracy is second order at convergence. All calculations are done with the Baldwin-Lomax algebraic eddy-viscosity turbulence model. Despite its simplicity and low computational effort, good agreement with experiments is obtained for conjugate heat transfer as long as the flow is not separated [10]. The steady state computation in the solid domain is predicted by the commercial FEA code SAMCEF [11] using quadratic tetrahedral elements.

2.1 Coupled method

The coupled method uses an iterative approach to obtain the same temperature and heat flux distribution at the boundaries that are common to the NS and FEA calculation domain. Fluid- and solid conduction computations alternate with exchange of boundary conditions in one of the following ways.

In a first method [6], the wall temperature distribution is imposed to the fluid solver and the heat flux distribution, predicted by the fluid computation, is imposed as a boundary condition to the solid conduction solver. This in turn predicts an updated temperature distribution at the fluid solver solid boundaries. This loop is repeated until convergence i.e. when the temperature and heat flux are continuous between both domains. This method is known in literature as the Flux Forward Temperature Back (FFTB) method, as the heat flux is given to the FEA calculation and the temperature is received back. However, imposing the heat flux on the entire boundary of a solid does not result in a unique solution. One must specify the temperature in at least one point of the domain.

Alternatively, one can also impose the heat flux distribution as a boundary condition for the fluid computation and the resulting wall temperature to the solid conduction solver. The updated heat flux is then returned as a boundary condition to the fluid solver. This method has been successfully applied by Heidmann [3] and is known as the Temperature Forward Flux Back (TFFB) method. The advantage of this method is that the temperature is given as a boundary condition to the FEA model. This is a more 'natural' boundary condition for the FEA heat transfer computation.

The third method [5,6,12,13] uses the wall heat transfer Eq. (1) to update the boundary conditions.

$$q_W = h \cdot \left(T_W - T_{fl}\right) \qquad (1)$$

It starts again with an initial temperature distribution T_w at the solid boundary of the flow solver. The results of the NS computation are used to estimate the heat transfer coefficient h and fluid temperature T_{fl}. Substituting them in Eq. (1) provides an implicit relation between T_w and q_w that can be used as a boundary condition for the solid conduction computation. The advantage of using Eq. (1) as boundary condition is an automatic adjustment of q_w as a function of the new T_w. The latter one is then returned to the fluid solver and the loop is repeated until convergence.

The remaining problem is the definition of h and T_{fl} from the NS solution. They also need to satisfy Eq. (1) in which T_w is the imposed boundary condition and q_w is the solution of the fluid solver. However, there is only one equation for two unknowns. One possibility is to make an extra fluid flow calculation with a different wall temperature [6] or even an adiabatic one [5]. Substituting the two solutions of q_w in Eq. (1) and assuming that h and T_{fl} remain unchanged provides Eq. (2) to define h.

$$h = \frac{q^f_{W1} - q^f_{W2}}{T^f_{W1} - T^f_{W2}} \qquad (2)$$

T_{fl} can then be calculated by Eq. (1) in function of the imposed T_w and corresponding q_w. The difficulty is to ensure a positive value of h on the entire solid wall because negative values would make the conduction problem ill-posed [5]. They are likely to occur in regions where the heat flux is changing sign.

A simpler and more stable approach is by imposing a constant positive value of h. This is allowed because the value of h only influences the convergence rate. One can easily show that the choice of h affects only the convergence history and not the final result, [13]. A smaller value of h results in a larger change of the wall temperature between two successive iterations. This leads to a faster convergence but, as confirmed by the numerical experience, also leads to a less stable calculation. The choice of h is a trade off between computational time and stability. A value of 80.000 W/(m^2°K) has been used for all the computations.

The fluid computations between two successive solid calculations are not continued until full convergence. They are stopped after 100 pseudo-time steps to update the wall temperature by a solid conduction calculation. The choice of the number of NS iterations per solid-fluid iteration is driven by a minimization of the total CPU time. The number of pseudo-time steps should be high enough to obtain a modified boundary condition for the FEA code.

Convergence is obtained when q_w and T_w do not change anymore.

The initial guess of the wall temperature at the common boundary can be a uniform temperature, or the local fluid temperature of an adiabatic NS computation.

2.2 Interpolation between grids

Since the appropriate grid generators for both domains are different, the grid points at the common boundaries will not coincide. A NS solver needs small cells at boundaries where the velocity gradients are large. A FEA requires a finer grid distribution in areas of high curvature. Furthermore the NS solver defines the temperature in the cell center, while in the FEA the temperature is stored at the vertices of the elements. Hence two different interpolations are needed on the common wall. The T_{fl}, defined in the center of the NS cells, must be transferred to cell center of the FEA where the boundary condition (eq. 1) is applied. On the other hand, the temperature at the FEA vertices needs to be transferred to the cell center of the CFD cells. A distance-weighted interpolation based on Shapard's method [14] is used in both cases.

2.3 Solid Model

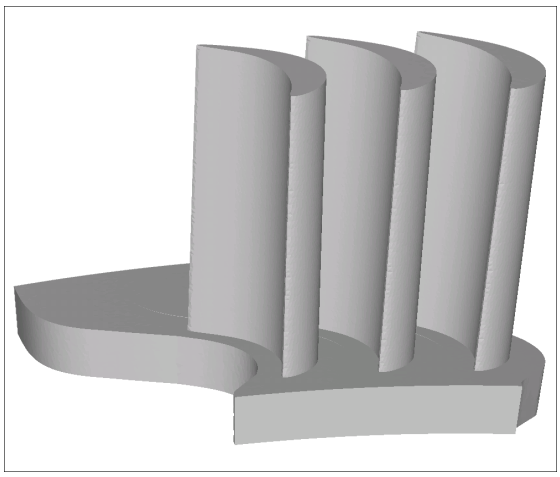

Figure 1. FEA solid model.

The solid model consists of the blade and hub. Periodic boundary conditions are applied at the lateral boundaries of the hub. Three periodic parts of the blade geometry are shown in Figure 1. Manufacturing constraints impose a maximum material temperature of 750 °C at the rotor disk. The cooling needed to fulfil this constraint is calculated by imposing this maximum temperature at the bottom of the hub. The heat flux at the bottom of the hub is the required cooling. This cooling can be applied by cooling holes in the hub, which are not modelled here.

2.4 Geometry and computational details

Shown in Fig. 2 are the Computational Fluid Dynamics (CFD) and Finite Element Method (FEA) solid domains and the boundary conditions.

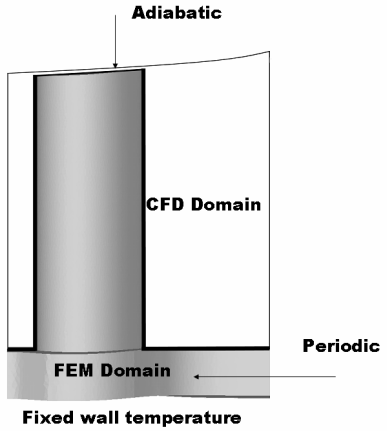

Figure 2. CFD and FEA solid model domains and the boundary conditions in meridional plane.

The axial turbine has 137 blades. Navier-Stokes computations are performed on one blade passage with periodicity boundary conditions in the circumferential direction. Total inlet pressure and temperature are, 65.555 10^5 Pa and 1091.3 °K, respectively. Relative inlet flow angle is 40° measured from axial direction. The inlet flow is uniform in the spanwise direction. At the outflow only the static pressure is set to 0.918 times the inlet total pressure. The shroud is assumed to be adiabatic.

The fluid is Helium which is treated as ideal gas with ideal gas constant R_{gas}=2078 kJ/(kg°K) and specific heat ratio of ?=1.666. The molecular Prandtl number is 0.6. For the turbulent Prandtl number 0.777 is used. The Reynolds number based on the total inlet conditions and axial chord is $11x10^6$. The angular speed is 3000 rpm.

The solid model consists of one blade and the 19.42mm thick hub plate. The turbine is made of Inconel which has a thermal conductivity of 30 W/(m. °K). The only fixed boundary condition used in the solid calculations is the fixed hub wall temperature. Periodicity in the blade-to-blade plane is also imposed in the FEA calculations.

The boundary condition information exchange between the CFD-FEA computations are performed on the domain boundaries shown in full thick line in Fig. 2.

The CFD grid has 120x52x52 cells in the streamwise, blade-to-blade and spanwise directions, respectively. The FEA mesh consists of 330562 nodes and 227583 tetrahedral elements.

3. RESULTS

3.1 CHT using TFFB method

The first CHT results are obtained using the TFFB method. The initial CFD solution is obtained for fully adiabatic flow. The resulting temperature field is used as input to the FEA solver. In the subsequent stages of the CHT, only 10 iterations are performed for each CFD solution for stability reasons. The convergence history of the method in terms of the maximum and rms norms of the temperature difference is shown in Figs. 3a and 3b.

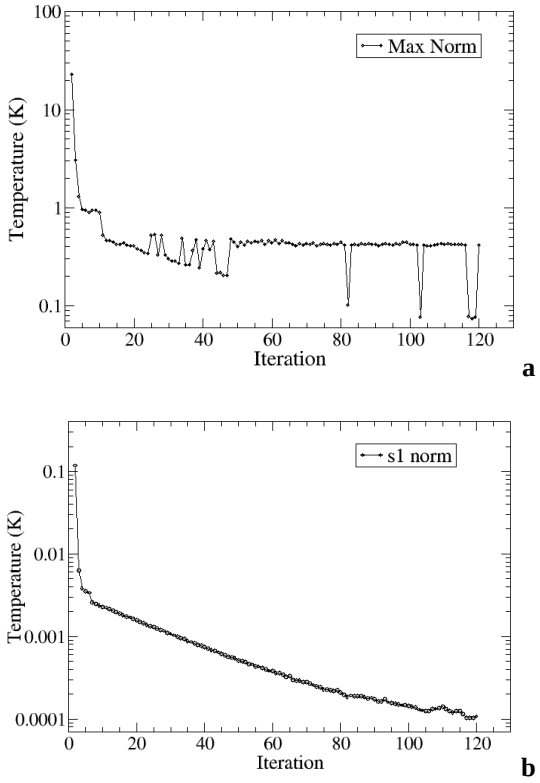

Figure 3. Convergence history of the CHT using the TFFB method: maximum norm (a) and rms norm (b) of the temperature difference between the CFD and FEA methods.

The final maximum temperature difference is 0.4 °K achieved after 120 Solid-Fluid iterations with the average RMS value below 10^{-4} °K. It is interesting to observe the oscillations in the maximum temperature norm, (Fig. 3a). Indeed, the TFFB method shows stability problems and is not very robust. This has triggered the implementation of the h-method.

3.2 CHT using h-method

The initial solution is the same adiabatic CFD solution as in the previous analysis. The convergence history of the h-method is given in Figs 4a and 4b.

The new method, Fig. 4a shows a much faster drop in the maximum norm: about 2 orders of magnitude in the maximum temperature difference. The TFFB method, Fig. 3a, on the other hand, did not even show a 2 order reduction in 120 iterations. The h-method shows a significantly more monotonic maximum residual reduction. The rms norm comparison, (Figs. 3b and 4b) shows about 6 time faster convergence rate for the h-method. The final temperature is already very well estimated after one iteration as can be seen from Fig. 4a.

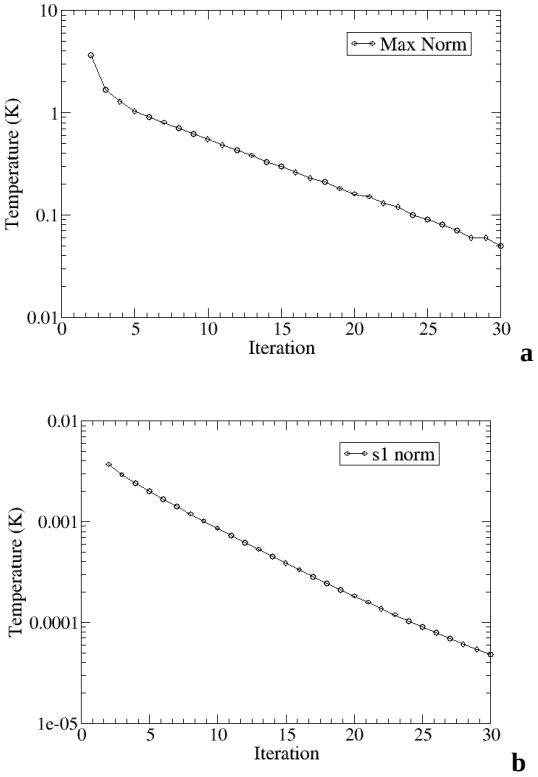

Figure 4. Convergence history of the CHT using the h-method: maximum norm (a) and rms norm (b) of the temperature difference between the CFD and FEA methods.

The solution quality of the h-method is seen in Figs. 5 and 6 where the suction and pressure side surface temperature isolines of both methods are compared. The CFD solutions are compared in the first two figures, 5a and 5b. The temperature fields obtained with the FEA are compared in Fig. 6. The final temperature fields are very close as expected but they are not identical. A smoother temperature variation in the h-method is observed in all three figures.

In the h-method, the wall heat flux is a result of the CFD and FEA calculations. They could be erroneously different even if the wall temperatures are the same. The heat fluxes at the end of the h-method CHT process are compared in Fig. 7. The uncertainity in the calculation of the heat flux is significant for the present Helium calculation where the h coefficient had to be increased to 80,000

W/(m^2°K) to keep the CHT process stable. The value that was previously used for air was 3,000 W/(m^2°K). Consequently only 1 °K temperature difference between the CFD and FEA wall temperature would result in a heat flux difference of 80 kW/m^2 . This is the reason for larger discrepancy between the heat fluxes (Fig. 7) than the temperatures (left-hand side figures of Figs. 5a, 5b and 6).

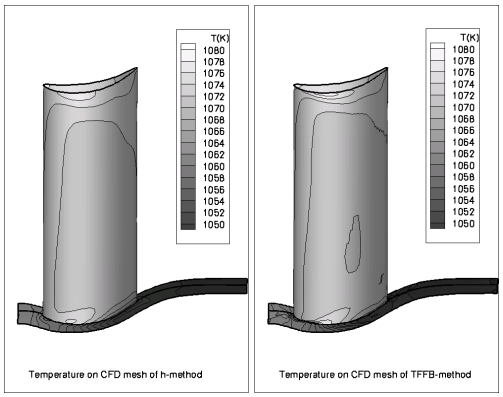

a

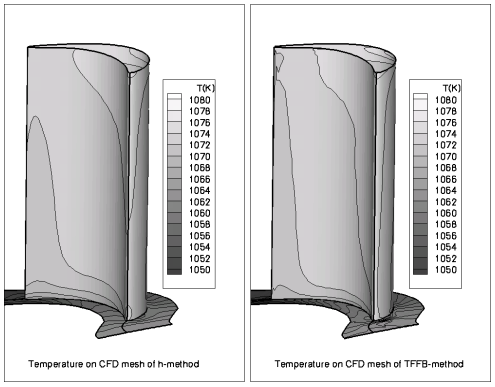

b

Figure 5. Temperature isolines of the final solutions (CFD solution): h-method (left), TFFB method (right): (a) suction side, (b) pressure side

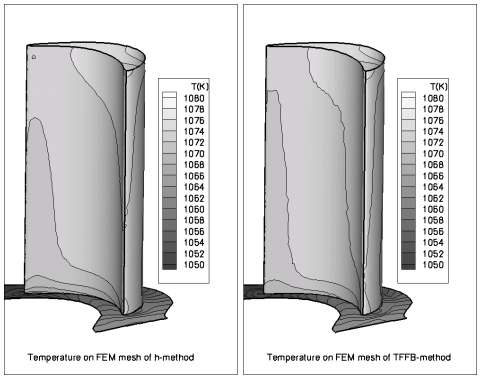

Figure 6 Temperature isolines of the final solutions on the pressure side: FEA solution in combination with h-method (left), TFFB method (right).

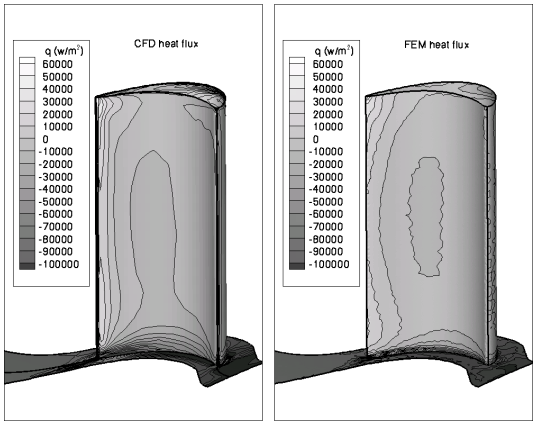

Figure 7. Heat flux isolines of the final solution in the h-method: FEA (left), CFD (right).

The result compares rather well on the blade hub surface. Only a small discrepancy is observed near the blade tip plane. The tip plane is treated as an adiabatic wall by the solid FEA solver.

3.3 Grid refinement studies

Grid dependency is an important aspect of the CFD computations. It is particularly important to ensure that the calculated heat transfer rates are independent of the grid refinement. To investigate the effect of grid refinement, the number of grid cells in the blade-to-blade direction is doubled from 52 to 104. The number of grid points in the other directions is unchanged.

The final temperature field obtained from the previous CHT on the coarser grid using the h-method is used as temperature boundary condition on the finer mesh. The solution computed on the finer mesh is compared with the one obtained on the previous mesh.

Temperature and velocity fields for coarser and finer grids are plotted on k=25 plane (see Figs.8 and 9). This plane is roughly at 30% span. The velocity fields look very comparable.More pronounced differences between the finer and coarser grid solutions are observed in the temperature fields, particularly in the wake region.

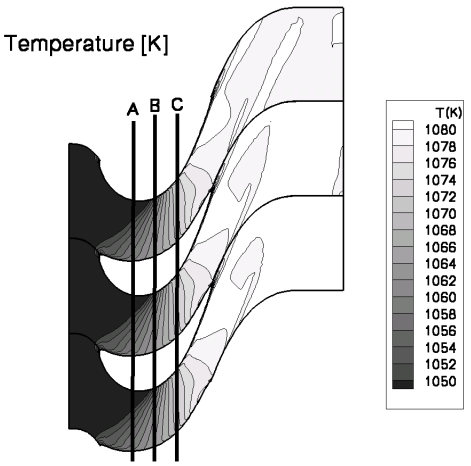

8a

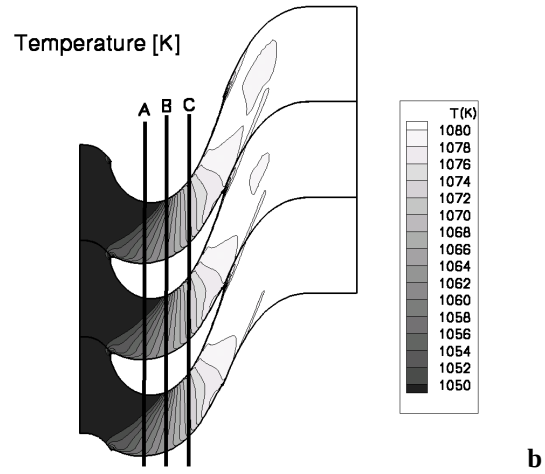

b

Figure 8. Temperature fields at k=25 plane (roughly 30% span from hub). (a) coarser grid 120x52x52, (b) finer grid 120x104x52.

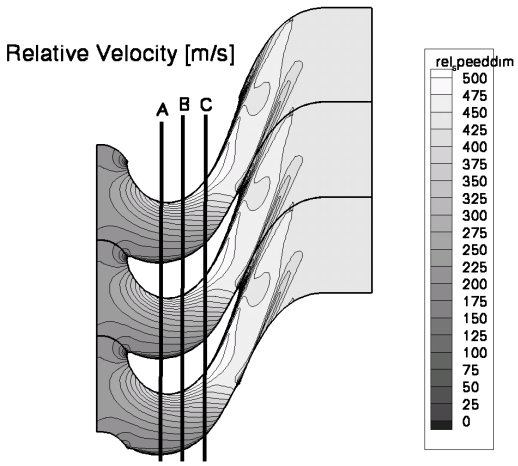

a

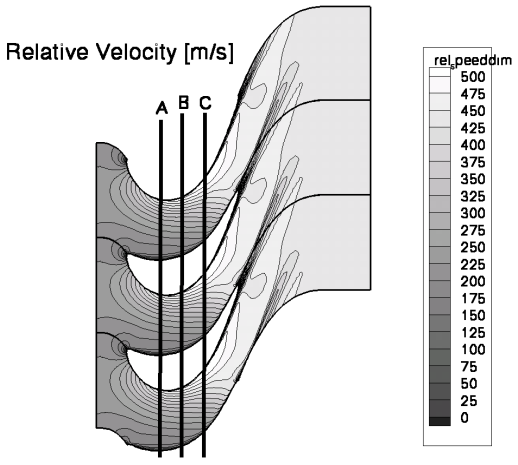

b

Figure 9. Relative velocity fields at k=25 plane (roughly 30% span from hub). (a) coarser grid 120x52x52, (b) finer grid 120x104x52.

A more detailed comparison is shown on Figs. 10 to 12. The temperature and velocity profiles are compared at three different axial positions along the the circle at nearly 30% span measured from hub. The axial positions are approximately 30, 50 and 70% axial chord measured from leading edge, marked with the lines A, B and C in Figs.8 and 9.

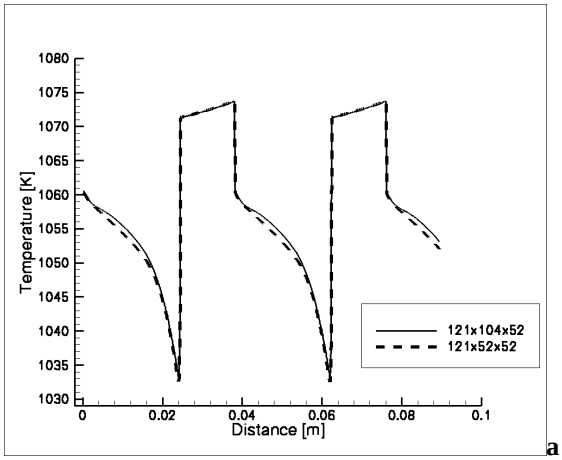

a

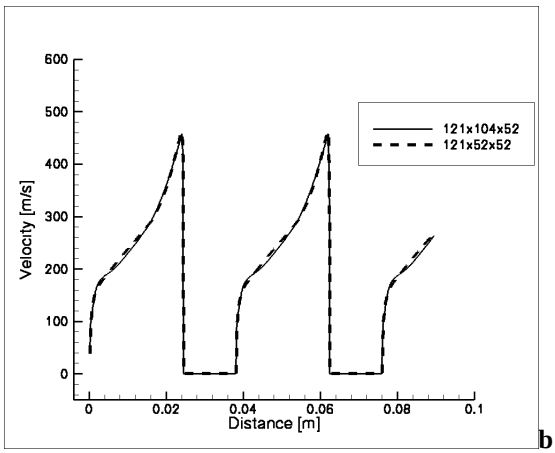

b

Figure 10. Temperature and relative velocity profiles at 30%span from hub and 30% axial chord from leading edge. Coarser grid 120x52x52 (dashed line), finer grid 120x104x52 (solid line): (a) temperature, (b) velocity.

The abscissa of the figures is the distance measured along the circle over 2.5 pitches of the CFD grid. Figures can be interpreted as a signal of a probe flying at constant radius and at constant axial position. The probe crosses the CFD mesh passes through the FEA solid mesh and then crosses again the CFD mesh. It allows seeing also the temperature variation through the blade. It is stressed that the constant axial position is not necessarily perpendicular to the pressure or suction sides, so the profiles are not necessarily boundary layer profiles.

In Figs. 10a and 10b, the temperature and velocity drop as the blade is approached. The temperature at the surface of the suction side of the blade is 1070 °K. The sharp increase from 1035 °K to 1070 °K on the blade surface is achieved in the boundary layer near the suction of the blade. The

pressure side of the blade is approximately 1075 °K. The fluid temperature near the blade region drops to around 1060 °K because of the smaller velocities on the pressure side. It then decreases again to 1035 °K near the suction side of the next blade. It is seen in these figures that the velocity profile is almost unaffected by doubling the grid points in the blade-to-blade direction. The temperature profile in the blade passage is influenced by the refinement, probably due to more adequately resolved mid passage flow, as the grids are strongly stretched near the blade walls.

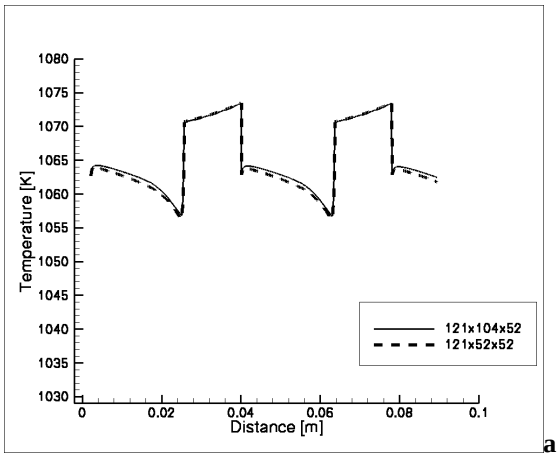

a

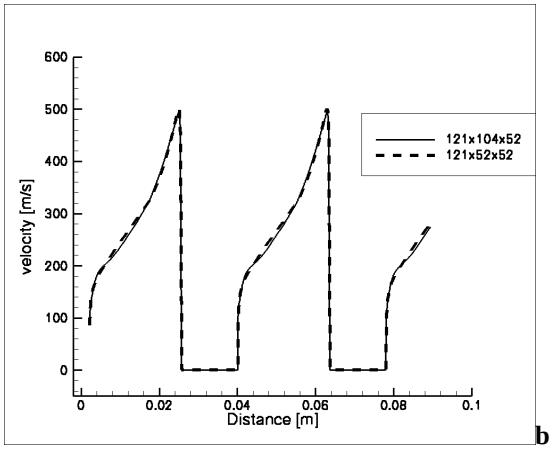

b

Figure 11. Temperature and relative velocity profiles at 30%span from hub and 50% axial chord. Coarser grid 120x52x52 (dashed line), finer grid 120x104x52 (solid line): (a) temperature, (b) velocity.

Temperature and velocity profiles at 50% axial chord from the leading edge are compared in Figs. 11a and 11b. A more uniform temperature profile is observed in the blade passage due to the accelerating flow, but the blade temperature is almost unchanged.

The temperature and velocity profiles at the axial location 70% axial chord are shown in Figs. 12a and 12b. Both at 50% and 70% axial chord cases, a good agreement between the fine and coarse grid calculations is observed for the temperature, this is probably due to better resolution of the reduced flow passage area.

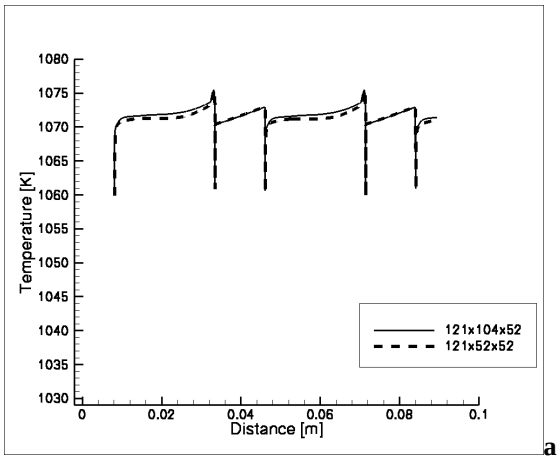

a

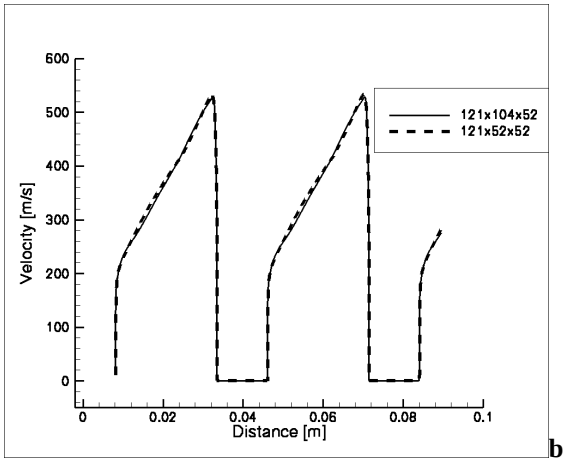

b

Figure 12. Temperature and relative velocity profiles at 30 %span from hub and 70% axial chord from leading edge. Coarser grid 120x52x52 (dashed line), finer grid 120x104x52 (solid line): (a) temperature, (b) velocity

The fluid temperature at 70% axial position in the mid flow passage is almost uniform and higher than the solid temperature (see Fig. 12a).

The velocity plots, Figs 10b, 11b and 12b show a remarkable similarity in all three sections.

4. CONCLUSIONS

Several alternative CHT calculations are evaluated and compared on an axial helium turbine. The h-method proved to be most robust one and faster converging. The influence of CFD grid refinement on the temperature and velocity profiles is also investigated by doubling the number of grid cells in the circumferential direction. The velocity profiles are less sensitive to grid refinement than the temperature profiles. The effect of grid refinement on the temperature is not only restricted to the

boundary layer but also observed in the blade passage main flow.

The computational cost of the h-method CHT is approximately 24 hours on a 3.4 GHz Pentium IV processor. Compared to about 4 hour CPU time required for a single fully converged adiabatic CFD computation the CHT calculations are affordable and cost effective.

5. ACKNOWLEDGEMENTS

This research is sponsored by the IWT, the Institute for the Promotion of Innovation by Science and Technology in Flanders, Belgium, project SBO 030288 "PowerMEMS".

REFERENCES

[1] Meunier, M., 2004, "3D Optimization of a Helium Turbine Stage by Means of Navier-Stokes Calculations, Coupled with an Artificial Neural Network and a Genetic Algorithm", Stagiaire Report 2004-42.

[2] Bohn, D., Bonhoff, B., and Schonenborn, H., 1995, "Combined Aerodynamic and Thermal Analysis of a Turbine Nozzle Guide Vane"' IGTC paper 95-108.

[3] Heidmann, J. D., Kassab, A. J., Divo, E. A., Rodriguez, F. and Steinthorsson, E., 2003. "Conjugate Heat Transfer Effects on a Realistic Film-cooled Turbine Vane", ASME paper No. GT2003-38553.

[4] Han, Z.-X., Dennis, B. H. and Dulikravich, G. S., 2000, "Simultaneous Prediction of External Flow-Field and Temperature in Internally Cooled 3-D Turbine Blade Material", ASME paper No. 2000-GT-253.

[5] Montenay, A., Paté, L. and Duboué, J., 2000, "Conjugate Heat Transfer Analysis of an Engine Internal Cavity", ASME paper No. 2000-GT-282.

[6] Verdicchio, J. A., Chew, J. W. and Hills, N. J., 2001, "Coupled Fluid/Solid Heat Transfer Computation for Turbine Discs", ASME paper No. 2001-GT-0205.

[7] York, W. D. and Leylek, J. H., 2003, "Three-Dimensional Conjugate Heat Transfer Simulation of An Internally-Cooled Gas Turbine Vane", ASME paper No. GT2003-38551.

[8] Bohn, D., Heuer, T. and Kusterer, K., 2003, "Conjugate Flow and Heat Transfer Investigation of a Turbo Gharger: Part I: Numerical Results", ASME paper No. GT2003-38445.

[9] Arnone, A., 1994, "Viscous analysis of Three-Dimensional Rotor Flow Using a Multigrid Method", ASME Journal of Turbomachinery, Vol. 116, pp 435-445.

[10] Grag, V. K., "Heat Transfer Research on Gas Turbine Airfoils at NASA GRC", International Journal of Heat and Fluid Flow 23 (2002), pp 109-136.

[11] SAMCEF FEA code by Samtech Group, www.samcef.com.

[12] Lassaux, G., Daux, S. and Descamps, L., "Conjugate Heat Transfer Analysis of a Tri-Dimensional Turbine Blade Internal Cavity", 24th ICAS 2004.

[13] Verstraete, T., Alsalihi Z., and Van den Braembussche R. V. A., 2006, "Numerical Study of Heat Transfer in Micro Gas Turbines", to be published in Proceedings of GT2006 ASME Turbo Expo 2006: Power for Land, Sea and Air, GT2006-90161, May 8-11, 2006, Barcelona, Spain.

[14] Shepard, D., 1968, "A Two-Dimensional Interpolation Function for Irregularly Spaced Data", Proc. 23rd ACM National Conference (1968) pp 517-524.

Conference on Modelling Fluid Flow (CMFF'06)
The 13th International Conference on Fluid Flow Technologies
Budapest, Hungary, September 6-9, 2006

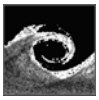

APPLICATION OF INTERMITTENCY BASED MODELS FOR TRANSITION PREDICTION ON A BLADE PROFILE

Witold ELSNER[1], Wladyslaw PIOTROWSKI[2]

[1] Corresponding Author. Department of Mechanical Engineering and Computer Science, Czestochowa University of Technology. Al. Armii Krajowej 21, 42-200 Czestochowa, Poland: Tel. +48 34 32 50 507, Fax: +48 34 32 50 555, E-mail: welsner@imc.pcz.czest.pl
[2] Department of Mechanical Engineering and Computer Science, Czestochowa University of Technology. E-mail: piotrowski@imc.pcz.czest.pl

ABSTRACT

The paper presents the results of numerical investigations aimed to validate two transition modeling approaches i.e. prescribed unsteady intermittency method PUIM, developed at Cambridge University and transport intermittency method developed jointly with Ghent University. The methods were validated against the experimental data collected for N3-60 turbine stator profile both for uniform and unsteady inlet flow conditions. The two tested models solely rely on the intermittency parameter, however in the first framework, the intermittency distribution is obtained based on experimental correlations and in the second it is based on the evolution of intermittency transport equations. For unsteady computations, in both cases the self-similar wake profiles were prescribed at the inlet to the computational domain. Joint validation of PUIM and transport intermittency model versus experimental data showed, that two tested methods, were able to reproduce the periodical evolution of the boundary layer under the influence of impinging wake with adequate quality.

Keywords: boundary layer, transition modelling, by-pass and wake induced transition, turbine blade

NOMENCLATURE

b_s – stator chord
C_p - pressure coefficient
c_1 - outlet velocity
c_∞ - inlet velocity
D_p – pitch diameter
d - bar diameter
f_d – disturbance frequency
g_{tr} - spot formation rate
H – shape factor
p- static pressure
p_{01} – inlet pressure
p_2 – static pressure
S – suction side coordinate
S_g – length of suction side (S_g=369mm)
S_S – reduced length of suction side
St – reduced frequency
T – period
Tu – turbulence intensity
t – time
t_s – stator pitch
U – local velocity
U_∞ - freestream velocity
α_s – blade stagger angle
γ - intermittency factor
λ_θ - Thwaites pressure gradient parameter
σ - spot propagation parameter

Subscripts and Superscripts
p – pressure side
s – stator or suction side

1. INTRODUCTION

The research interest in the modeling of near wall region in turbomachinery is directed towards boundary layers, which due to relatively low Reynolds number are not fully turbulent but laminar and transitional. The problem is important because an efficiency of turbomachinery depends mainly on the boundary layer developing on the blade profile. The additional losses of energy are generated by the interaction of wakes shed by upstream blade cascades and convected downstream the flow. These losses arise primarily from the interaction of wakes with the large regions of laminar and transitional flows, which exist on the suction surface of turbine blades. The correct prediction of transition, especially under the conditions of wake unsteadiness, is therefore a basic requirement in contemporary computations of turbomachinery flows.

For the real turbomachinery conditions, due to the complex aerodynamic interactions of multiple stages, the background turbulence the level attains level of Tu = 2 - 4%, while close to rotor or stator trailing edges the turbulence intensity may be as high as Tu = 13%. As a consequence of high Tu level, turbulent spots in the boundary layer are created as a direct result of turbulence fluctuations of the outer stream, and this type of laminar-turbulent transition is known after Morkovin (1969) as a "by-pass" one. It is necessary to mention that for the modern, heavily loaded blades with a separation bubble on the suction side, the transition due to shear layer instability over the bubble could also occur.

Experimental investigations [1] exhibit various stages of the bypass and wake-induced transition process, such as the formation and growth of a streaky structures, the development of secondary instabilities and than the formation of the incipient spots, which coalescence into fully developed turbulent boundary layer. To obtain a reliable prediction of such type of flow, an accurate physical modeling of all this stages is required. However, it is supposed that transition process could be described with a reasonable degree of accuracy only by the mechanisms of generation, amplification and convection of isolated turbulent spots. These modelling techniques are aimed to determine two basic processes of transition i.e. the location of the region where the generation of turbulent spots is initiated as well as their growth rate, which in turn determines the length of the transition region. The most common approach to model the transition in a proper way is based on the use of the intermittency function. The estimated intermittency factor at the given location and time (for the unsteady calculations) is then used as a multiplication factor of the eddy viscosity in the turbulence model. The paper presents the comparison of two most promising strategies developed recently i.e. the Prescribed Unsteady Intermittency Model (PUIM) elaborated at Cambridge University [2] and transport intermittency method elaborated at Ghent University [3].The methods were validated against the experimental data collected for N3-60 turbine stator profile in the frame of EU project UTAT, both for uniform and unsteady inlet flow conditions.

2. DESCRIPTION OF THE N3-60 TEST CASE

The N3-60 blade profile was experimentally studied at the Institute of Thermal Machinery TU of Czestochowa by Zarzycki and Elsner [4] in the open-circuit wind tunnel equipped with the disturbance (wake) generator As a periodicity generator a wheel of pitch diameter D_p=1950 mm with cylindrical bars rotating in a plane perpendicular to the flow direction is used. The wheel was divided in sections, with different rods mounted spaced by 204 mm in a pitch plane, with section with 4 mm rods, one section with 6 mm rods and one free space section which was used for reference (no wake) measurements were applied. The blade profile N3-60 (see Fig. 4) applied in the research is an industrial one, which was used as a stator vane of the high-pressure part of the TK–200 turbine produced the Polish manufacturer (formerly ZAMECH now ABB ALSTOM). The main geometrical parameters of tested cascade were: the blade chord length b_s=300 mm, the pitch t_s=240 mm, and the blade stagger angle α_s=43˚35'. The axial distance between bars and the leading edge of the blade was equal 70 mm i.e. 0.344 of an axial blade chord b_s. The frequency of incoming wakes was matched to f_d=59 Hz, what corresponded to the reduced frequency $St = f_d \cdot b_s / C_\infty = 1.22$. The exit velocity was kept C_1=30 m/s, which corresponded to a Reynolds number equal to 6×10^5. The application of a movable grid, located upstream of the cascade entrance, enabled to control the freestream turbulence intensity Tu and for the analyzed Test Case its level was set to Tu=3%. Zarzycki and Elsner [4] presented an experimental analysis of the wake parameter influence on the position and the extent of the induced transition zone, in which wakes generated by 4 and 6 mm bars were considered. The case for 4 mm bars was also numerically analysed by Lodefier at al. [5] and Elsner at al. [6]. For the case of the investigations presented in this paper, the unsteady data obtained with 6 mm bars were used.

3. CHARCTERISTIC OF TRANSITION MODELS COMPARED

3.1. PUIM

PUIM procedure developed at Cambridge University calculates a time-distance intermittency distribution as a function of space and time (constant in time in the case of steady flow simulation). The intermittency factor may either be computed using concentrated breakdown concept of Narasimha, or using continuous breakdown hypothesis of Hodson and Shulte [7], taking into account the properties of calmed regions. The intermittency is used as a multiplier of the eddy viscosity in k-ε turbulence model. The PUIM reads the outer flow and boundary layer parameters from main solver and returns the distance-time intermittency field. The communication of the model with the main solver is realized with the use of the exchange files.

PUIM is based on the empirical input. To detect the transition onset it employs Mayle (1991) correlation:

$$\mathrm{Re}_{\theta_{tr}} = 400 \cdot Tu^{-0.625} \qquad (1)$$

Additional criteria for transition onset is the Abu-Ghannam and Shaw correlation modified by Drela (1995), with the critical Reynolds number $Re_{\theta t}$ determined as a function of shape factor H and N_{crit}.

$$\mathrm{Re}_{\theta_{tr}}\left(H, N_{crit}\right) = 155 + 89.0 \cdot {N_{crit}}^{1.25} \cdot \cdot \left(0.25 \cdot \tanh\left(\frac{10}{H-1} - 5.5\right) + 1\right) \quad (2)$$

where

$$N_{crit} = -8.43 - 2.4 \cdot \ln(Tu) \quad (3)$$

Both the transition methods may be activated simultaneously, so the transition is initiated by whichever of the two alternative criteria is satisfied first. The detection of the separation is based on the skin friction and Thwaites criterion. Such a solution ensures that not only attached flow transition onsets but also separated onsets could be identified.

To predict the length of transition zone Gostelow and Walker correlation for spot production rate is used.

$$\frac{g_{tr} \cdot \sigma \cdot \theta_{tr}^3}{\nu} = 0.86 \cdot 10^{-3} \cdot \exp(2.134 \cdot \lambda_\theta \cdot \cdot \ln(Tu) - 59.23 \cdot \lambda_\theta - 0.564 \cdot \ln(Tu)) \quad (4)$$

The spreading of the turbulent spots is prescribed using functions of the edge velocity and the pressure gradient parameter. For separated flow, the other Mayle (1991) correlation gives the spot production rate from the momentum-thickness Reynolds number at separation.

For the unsteady calculations all the inflow and outflow parameters were kept the same as for the steady case and the results from steady calculations were taken as an initial solution.

The PUIM model is coupled with a solution adaptive, unstructured mesh solver 2D unNEWT, while turbulence is modeled with the use of k-ε transport equations of Yang and Shih (1993).

3.2. Intermittency transport model

The intermittency transport model developed at Ghent University [3] denoted later as a Lodefier & Dick model, is based on the SST model with the low Reynolds modifications of Wilcox (Menter, 1993) and two dynamic equations for intermittency: one for near-wall intermittency γ and one for free-stream-intermittency ζ. The near wall intermittency takes into account the fraction of time during which the near-wall velocity fluctuation caused by transition has a turbulent character and tends to zero in the free-stream region. The free-stream factor ζ describes the intermittent behavior of the turbulent eddies coming from the free stream and impacting into the underlying pseudo-laminar boundary layer. Near the wall the eddies are damped and the free-stream factor goes to zero, while in the free-stream it reaches unity.

The intermittency equation of the free-stream factor ζ, which describes the intermittent behaviour of turbulent eddies coming from the free stream is based on the work of Cho and Chung (1992).

$$\frac{\partial(\rho\zeta)}{\partial t} + \frac{\partial(\rho U_i \zeta)}{\partial x_i} = -E_\zeta + \frac{\partial}{\partial x_i}\left[\left(\mu + \frac{\mu_t}{\sigma_\zeta}\right)\frac{\partial \zeta}{\partial x_i}\right] \quad (5)$$

It was extended by the dissipation term E_ζ *w*hich guarantees a zero normal variation of the free-stream factor near the wall. In combination with the boundary condition $\zeta = 0$, this leads to a zero free-stream factor throughout the major part of the boundary layer. The diffusion coefficient μ_ζ included by Steelant and Dick [8] creates an inverse Klebanoff profile for the free-stream factor prior to transition.

The intermittency equation for the near-wall factor γ is a convection-diffusion equation with a source term.

$$\frac{\partial(\rho\gamma)}{\partial t} + \frac{\partial(\rho U_i \gamma)}{\partial x_i} = P_\gamma + \frac{\partial}{\partial x_i}\left[\left(\mu + \frac{\mu_t}{\sigma_\gamma}\right)\frac{\partial \gamma}{\partial x_i}\right] \quad (6)$$

The role of the diffusion term in this equation is to allow a gradual variation of γ towards zero in the free stream. The boundary condition for γ at the wall is a zero value of normal derivative. The damping function f_τ accounts for distributed breakdown of the turbulent spots. During unsteady transition with separation, the starting function takes the value $F_s = 2$ in the production term P_γ. As a consequence, the free stream velocity U_∞, replaces the local velocity U in the production term [3].

For onset detection in case of bypass and turbulence wake induced transition, the model employs Mayle (1991) correlation. For quasi-steady separation transition a criterion proposed for such type of flows by Mayle (1991) is applied. The other criterion is used in the case of wake induced transition over a separation bubble. The intermittency transport model is coupled via User Defined Transport Equations (UDF) with the Fluent NS solver, while turbulence is modeled with the use of already mentioned SST model. This solver is a finite volume (cell centered) solver, used with implicit dual time stepping for convection and with pressure correction.

4. COMPUTATIONAL PROCEDURE

4.1. Geometry and mesh

For both cases the computational domain developed around the tested blade was bounded by inlet plane located 70 mm upstream the leading edge and by outlet plane located 140 mm downstream the trailing edge of the blade. Additionally, the periodical planes have been situated 120 mm above and 120 mm below the blade what corresponds to 1/2 of blade pitch. The meshes in both cases (Fig. 1) were different, because they were created with the use of different mesh generators, even if the same main assumptions were accepted for both cases.
In the domain, far from the wall grids triangular based (for unNEWT) and rectangular based (for FLUENT) have been developed.

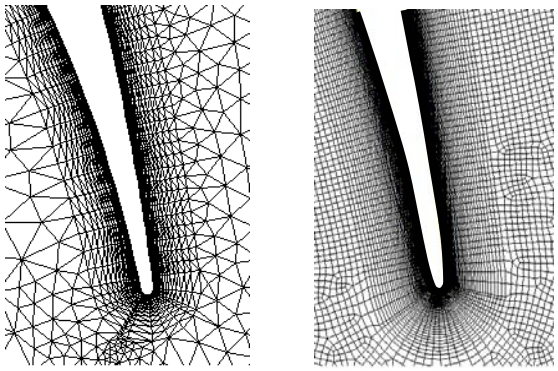

Figure 1. Computational grid around the rear part of the profile, PUIM (left), Lodefier & Dick (right)

To capture the phenomena in the boundary layer the density of the mesh (structured one) has been increased in the direction towards the wall, and the value of stretching factor for the PUIM model was equal 1.2, while for intermittency transport model it was 1.07. The wall adjacent grid cells were located for both cases below the maximum value of $y^+ \approx 0.4$. Compared meshes presented at the Fig. 1 reveal the visible differences in the freestream area. In this region much denser computational mesh for FLUENT in comparison with unNEWT solver was needed. This difference results from the fact that in the unNEWT a multilevel solution-adaptation mesh refinement is possible at the certain regions of the flow (i.e. wakes) what was not possible in FLUENT package. So, for the last case during the unsteady computations such a high density of the grid is necessary to simulate properly the unsteady movement of the wake. The total number of cells for Lodefier & Dick models, both for steady and unsteady cases was equal ~150000. In the case of PUIM model the total number of cells for steady case was equal ~6500, while for unsteady case with local refinement was ~15000.

The number of nodes in the wake region has an important influence on the solution both in the freestream and in the boundary layer. To confirm this observation some tests with the unNEWT solver were performed, and three solutions for three levels of refinement 1, 2 and 3 were compared. Fig. 2 presents the meshes of different resolution for these three cases with the enlargement applied in the wake regions. One may observe the increasing resolution of the mesh, with the number of cells in the wake, at the entrance to the blade channel, equal 16, 26 and 38 respectively.

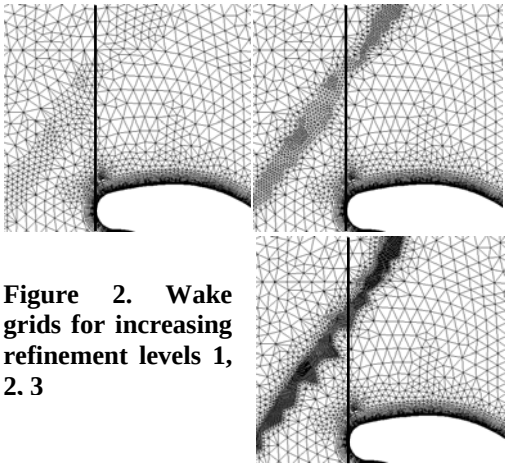

Figure 2. Wake grids for increasing refinement levels 1, 2. 3

To follow the wake evolution, the distributions of turbulence intensity across the wake for two consecutive traverses at the relative distance x/d = 8.9 and 27.0 were analyzed (Fig. 3). To make this analysis easier, the wake was cut in the plane perpendicular to the main flow direction, and figures were scaled in respect of t_s, which is a pitch of the stator cascade. The results of computations were compared with the experimental data gathered in the wake behind the moving bars. As one may notice (see Fig. 3), the number of cells has the significant influence on the wake dissipation, because at the entrance to the cascade (Fig. 3.b) the differences in the turbulence levels Tu between consecutive cases are of several percent. One may also verify that the wake width is dependent on the refinement level, although the influence is less visible as the distance along the flow is increased.

Finally, in the case of both simulations the number of cells at the inlet to the blade cascade was equal to about 50÷60.

4.2. Inlet conditions

The steady calculations were performed for the Reynolds number Re=600,000 and for the inlet stagnation pressure P_s=28800 Pa and inlet stagnation temperature 293.2 °K. The fluctuating properties were defined by the turbulence intensity level Tu=3% and the length scale λ= 3mm (unNEWT) and by the turbulent kinetic energy equal k=0.14 m^2/s^2 and specific rate of dissipation equal ω=924 s^{-1}. In order to have a good comparison with the experimental pressure distribution the inlet angle

was increased by5° The adjustment was necessary to take into account the airflow leakage through the slots located upstream the blade, where the moving bars system is mounted. Such a value of angle was chosen after initial calculations with various inlet flow angles.

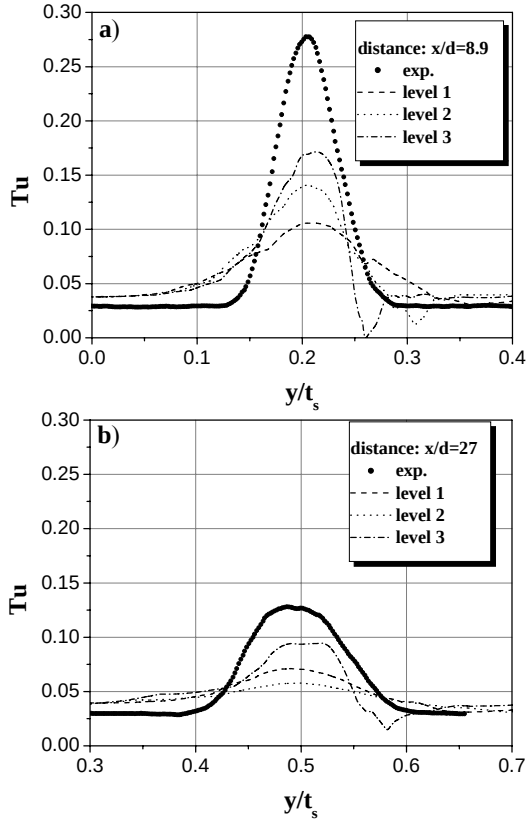

Figure 3. Turbulence intensity profiles across the wake for x/d=8.9, 27 with varying refinement level.

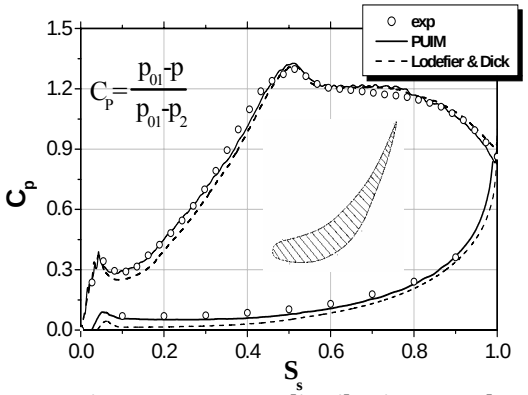

Fig. 4. Pressure distribution on the tested profile

The pressure coefficient C_p distribution around the profile presented in Fig.4 reveals, that on the suction side the flow accelerates sharply and reaches the minimum of pressure for $S_S=S/S_g$ =0.5, then a moderate acceleration is observed. On the pressure side one may observe almost constant velocity of the flow for most of the surface and then the flow gradually accelerates towards the trailing edge. For both pressure and suction sides a good agreement between experimental results and the calculations is obtained. The numerical simulation was even able to confirm the existence of the small deceleration zone close to the leading edge on the suction side, which is due to blade nonlinearity in the region where the circular leading edge matches the further part of the profile.

4.3. Wake definition

The modelling of the flow around moving bars causes serious problems in 2D calculations, due to the absence of spanwise vortex breakup mechanism, and that is why for the unsteady case the self-similar wake profiles were generated and prescribed at the inlet to the computational domain. In the unNEWT framework, the wake profiles were described by the width of the wake, velocity deficit as well as by turbulence intensity profile and turbulence length scale profile calculated from the wake decay correlations. For the FLUENT code, the profiles of velocity, turbulent kinetic energy (k) and specific rate of dissipation of turbulent kinetic energy (ω) were prescribed at the inlet to the computational domain.

For the unsteady calculations 800 time steps per one wake period were needed for the accurate simulation of the unsteady movement of the wake and proper modeling of the wake boundary layer interaction .

5. RESULT AND DISSCUSION

5.1. Steady results

One of the first criteria concerning quality of numerical simulation is the agreement of the pressure distribution around blade profile, what was already discussed within the inlet conditions definition (see Fig.4). The good agreement between experimental and numerical results is also visible in the analysis of Fig. 5, where the mean velocity map is presented.

The more advanced evaluation of the numerical procedures may be performed based on the boundary layer characteristics. Fig. 6 presents distributions of shape factor (6a) and intermittency factor (6b) for the suction side of the blade. When analyzing the shape factor distribution, one may see that numerical data follow the experiment in almost all over the blade surface. After small separation behind the leading edge, the boundary layer remains laminar with small value of shape factor due to the accelerating flow. Then after the minimum pressure peak, the elevated value of shape factor is seen (which is probably due to small separation). The most important region is the rear part of the profile, where the boundary layer development decides about the magnitude of losses. One may see the qualitatively good agreement between simulation

and experiment and only for the intermittency transport model the onset is a bit shifted downstream. The key variable used in describing boundary layer during transition from laminar to turbulent flow is the intermittency factor γ. It is well known, and observed also in other data that some turbulent activity, that the increase of intermittency is observed prior to the change of general flow properties indicated by rise of skin friction and drop of shape factor. The same behaviour of boundary layer is also observed in the analysed case (see Fig. 6b). One can also notice a bit too rapid transition process predicted by the numerics especially visible for Lodefier and Dick model. The delayed onset and the steeper increase of intermittency, is caused by the application of the "sharp" limiter in their model. As it results from recent work performed at Ghent [9] the removal of this limiter leads to better agreement of the intermittency factor with experimental results.

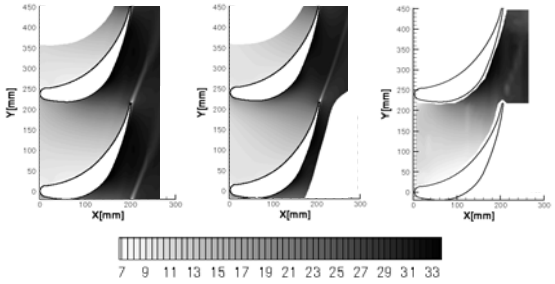

Figure 5. Velocity distributions over the blade passage for PUIM model (left), Lodefier & Dick model (middle), and experimental results (right)

5.2. Unsteady results

Flow unsteadiness strongly affects the location of the laminar-turbulent transition region in boundary layers on the blade surface, that in turn modifies not only the boundary layer structure but also the values of profile loss and heat transfer coefficients on the blade surface. That is why the analysis of the unsteady flow field in turbomachinery is so important. Fig. 7 presents temporal solutions for two compared methods, where the development of the wake inside the blade channel is seen. The picture shows general agreement between both plots, and one can notice only slightly different shape of the wake, which in the second case (Fig. 7b) is less bended.

The most important is however the analysis of boundary layer data. For those purposes two types of parameters are compared, intermittency and shape factor which are both presented on s-t diagrams. The key parameter in both methods is the intermittency factor, which modifies the production of turbulent kinetic energy.

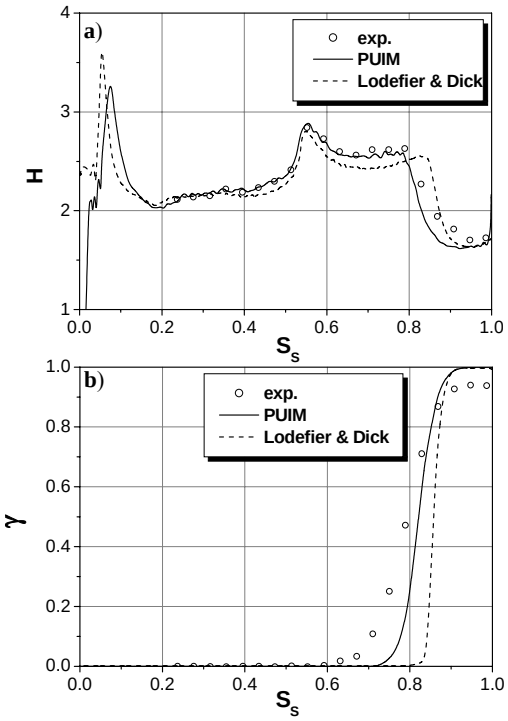

Figure 6. Distribution of shape factorH (a) and intermittency factor γ (b) for Tu=3.0%.

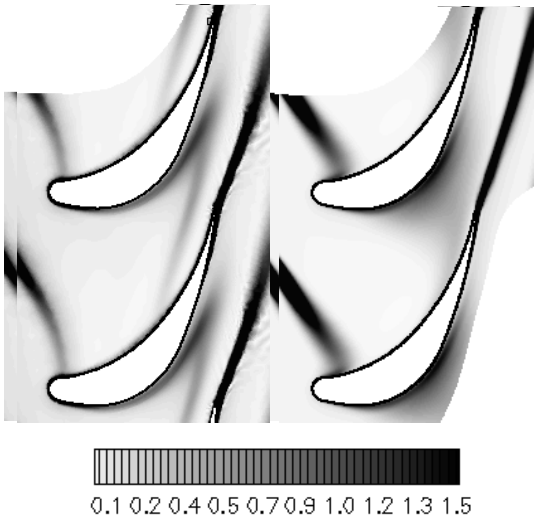

Figure 7. Temporal solutions of turbulence kinetic energy (TKE) for two compared methods, PUIM (left), Lodefier & Dick (right)

Fig. 8 presents the comparison of the numerical results obtained both with the PUIM and intermittency transport models with experimental results. The experimentally obtained intermittency was calculated at a distance 0.2mm from the wall, based on hot-wire measurements. Due to relatively high turbulence level, in both cases the Mayle criterion for transition onset was applied. The start of the transition under the wake was found almost identical (see Fig. 8), even though it was a bit shifted upstream in comparison with the

experimental results (it is more clearly for intermittency transport methodology). After the wake passage, due to lower freestream turbulence intensity and due to the lack of the forcing, the transition was shifted downstream.

It should be noticed, however, that the transition onset was shifted even further than it could be expected based on the steady results. It is due to the becalming effect, which prevents the formation of the spots behind turbulent wedge, due to elevated shear stresses in this region. One may also notice that both simulations show smaller becalming effect than could be noticed from experiment.

Comparison based on shape factor (Fig. 9) leads to similar conclusions. The elevated value of

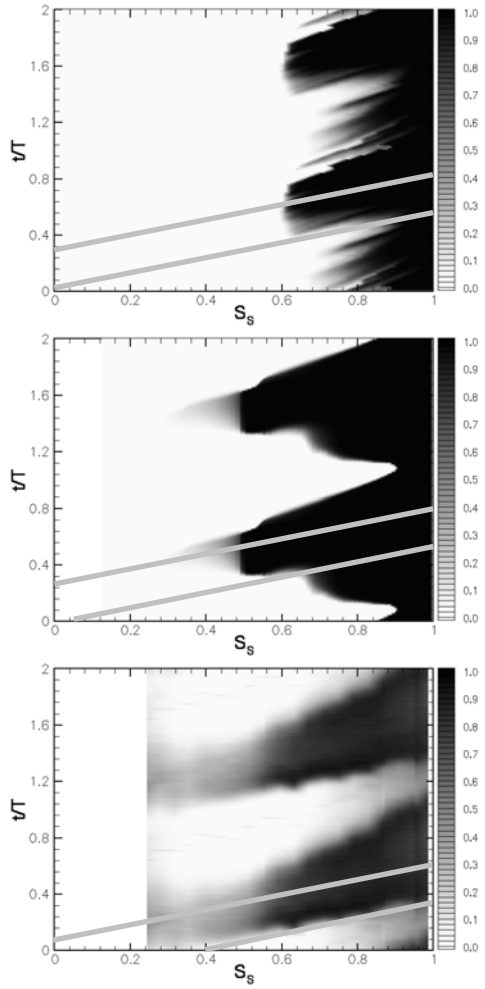

Fig. 8. Space-time diagrams of γ for Tu=3.0% and bar diameter d=6mm obtained with the PUIM model (upper), Lodefier & Dick model (middle), experiment (bottom)

H seen at S_s=0.52-0.58 confirms observation based on steady results. Two solid two lines show the position of the wake based on the local boundary edge velocity. It is evident, that the wake induced transition starts in the center of the wake i.e. in between the two lines, where the turbulence intensity is the highest. This observation, which is in line with experimental findings [5], suggests that transition is initiated not by velocity perturbation, but by the turbulence within the wake. The most encouraging is, however, the evolution of the turbulent wedge (where intermittency attains the unity) under the wake, which in both cases has the similar shape and dimension, what confirms that both models were able to reproduce properly the periodical evolution of the boundary layer. To confirm this observation, the cross-sections of the above s-t diagrams for S_s=0.65 were presented in Fig. 10. One can notice that the character of all curves is similar, not only in the context of the contour but also of the level of H under the wake and in between the wakes.

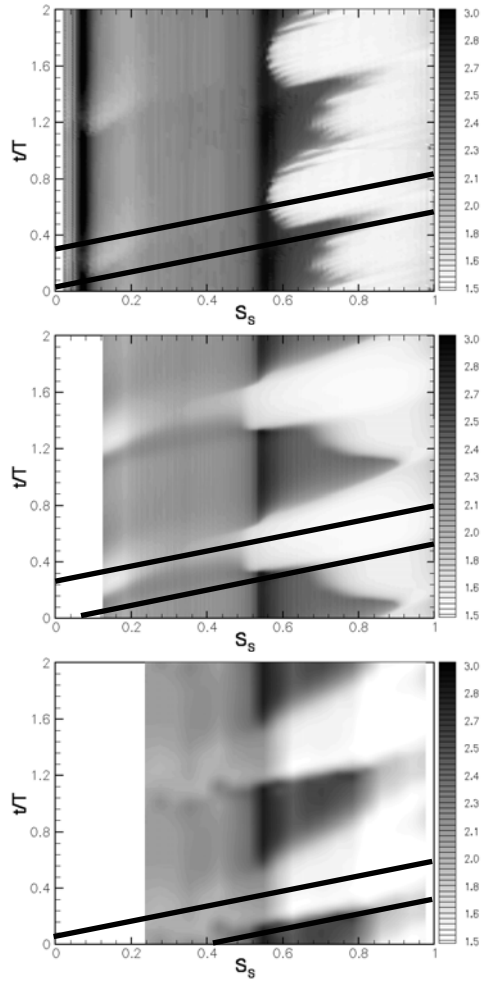

Fig. 9. Space-time diagrams of H for Tu=3.0% and bar diameter d=6mm obtained with the PUIM model (upper), Lodefier & Dick model (middle), experiment (bottom)

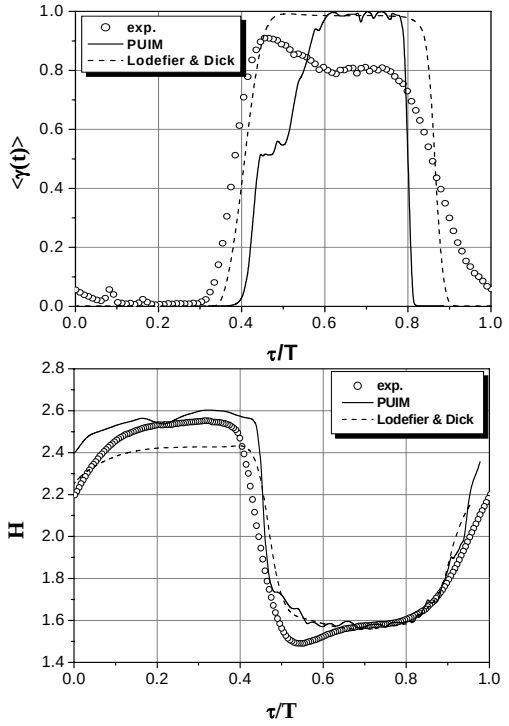

Fig. 10. Time traces of intermittency factor (upper) and shape factor (bottom) at the location S_S=0.65 for two levels of bar diameter

6. CONCLUSIONS

In the paper two different transition models were compared. During the comparison, all the main differences and similar features between the models were pointed out. Joint validation of PUIM and transport intermittency model versus experimental data, showed that two different methods, the first based exclusively on empirical correlations (PUIM), and the second utilizing the transported intermittency quantity (intermittency transport methodology) were able to reproduce the periodical evolution of the boundary layer under the influence of impinging wake with adequate quality.

The results obtained reveal, that the for the adequate numerical prediction of boundary layer it is necessary to select properly and to verify carefully the wake parameters prescribed at the inlet to the computational domain, as well as to adjust sufficiently the number of computational cells across the viscous wake.

ACKNOWLEDGEMENTS

The research was supported by the research project UTAT - "Unsteady Transitional Flows in Axial Turbomachineries", funded by the European Commission under contract number GRD1-2001-40192 as well as by the Polish State Committee for Scientific Research under the research grant No. 3T10B 08426. NEWT code was made available via partnership with Cambridge Flow Solution Ltd.

REFERENCES

[1] Elsner W., 2004, "Influence of nonstationary interactions on laminar-turbulent transition process on a turbine blade profile", CzUT Publishing, Ser. Monographs, vol. 103, Czestochowa

[2] Vilmin, S., Savill, M.A., Hodson, H.P., Dawes, W.N., 2003, "Predicting Wake–Passing Transition In Turbomachinery Using a Intermittency-Conditioned Modelling Approach", 33rd AIAA Fluid Dynamics Conference and Exhibit, Orlando, June

[3] Lodefier K. and Dick E., 2003, "Transition modeling with the SST turbulence model and an intermittency transport equation", ASME GT-2003-38282, Atlanta, USA.

[4] Zarzycki R., Elsner W., 2005, "The effect of wake parameters on the transitional boundary layer on turbine blade" ImechE Part A, J. Power and Energy, vol. 219, s. 471-480.

[5] Lodefier K., Dick E., Piotrowski W., Elsner W., 2005, „Modelling of wake induced transition with dynamic description of intermittency", 6th European Turbomachinery Conference., Paper No. 071_05/66, Lille.

[6] Elsner W., Vilmin S., Drobniak S., Piotrowski W., 2004, "Experimental analysis and prediction of wake-induced transition in turbomachinery", ASME paper no. GT2004-53757, Vienna

[7] Schulte, V., and Hodson, H.P., 1998, "Prediction Of The Becalmed Region for LP Turbine Profile Design", ASME Journal of Turbomachinery, Vol. 120, No. 4, pp. 839-845.

[8] Steelant J., and Dick E., Modeling of laminar-turbulent transition for high freestream turbulence. Journal of Fluids Engineering, 123 (1):22-30, 2001.

[9] Lodefier K. and Dick E., 2006, "RANS modeling of wake induced transition with the dynamic intermittency concept", ASME GT-2006-90044, Barcelona, Spain.

Conference on Modelling Fluid Flow (CMFF'06)
The 13th International Conference on Fluid Flow Technologies
Budapest, Hungary, September 6-9, 2006

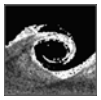

CFD STUDY FOR ASSESSMENT OF AXIAL THRUST BALANCE IN CENTRIFUGAL MULTISTAGE PUMPS

Stefania DELLA GATTA[1], Simone SALVADORI[2], Paolo ADAMI[3], Laura BERTOLAZZI[4]

[1] Corresponding Author. Department of Energetics, University of Florence. Via S.Marta, 3 50139 Florence, Italy. Tel.: +39 055 4796239, Fax: +39 055 4796342, E-mail: stefania.dellagatta@unifi.it
[2] Department of Energetics, University of Florence. E-mail: simone.salvadori@unifi.it
[3] Department of Energetics, University of Florence. E-mail: paolo.adami@unifi.it
[4] Weir Gabbioneta Srl. V.le Casiraghi. 68 20099 Sesto S. Giovanni (MI), Italy. E-mail: laura.bertolazzi@weirgabbioneta.com

ABSTRACT

Present work aims to the numerical investigation of horizontal multistage centrifugal pumps in opposite impeller configuration. Its main target is to apply a three-dimensional CFD based tool to the axial thrust prediction in a multistage industrial machine. A flexible use of CFD is presented to extend the hydraulic behaviour evaluation for the single components to the whole pump characterization. A mixing plane technique has been chosen to study the interaction between rotating and stationary parts. This procedure takes into account the effects of different incidences and inlet velocity distortions.

The 3D CFD investigation on every single component of the multistage pump allows a thorough knowledge of its fluid dynamic fields, but only a correct matching and interpretation of all the components provide a reliable prediction of pump axial thrust as well as its performance curve. Despite the potential high degree of realism allowed by CFD, modelling the whole pump geometry may be quite expensive. In fact, the pump includes a great amount of components and several geometrical details (i.e. inlet and outlet volutes, inter-stage cross-over, leakages through wear rings and balancing drums) that have to be taken into account for a good prediction of the axial thrust. These issues lead to a consistent amount of numerical modelling problems which are considered and discussed.

Keywords: Axial Thrust, CFD, Multistage centrifugal pumps.

NOMENCLATURE

A	$[m^2]$	passage area
BEP	[-]	Best Efficiency Point
d	$[m]$	diameter
g	$[m/s^2]$	gravity
H	$[m]$	head
k,a,b,c	[-]	coefficients
L	$[m]$	passage length
$\vec{n}$	[-]	normal vector
p	$[Pa]$	pressure
Q	$[m^3/s]$	flow rate
r	$[m]$	radial local coordinate
R	$[m]$	impeller radius
Re	[-]	Reynolds number
T	$[N]$	thrust
u	$[m/s]$	blade velocity
v	$[m/s]$	velocity
ω	$[s^{-1}]$	local fluid rotational speed in front and back impeller chambers
Ω	$[s^{-1}]$	rotating speed

Subscripts and Superscripts

ax	axial
ϑ	tangential

1. INTRODUCTION

Residual axial thrust in centrifugal pumps is usually balanced by axial thrust bearings, whose correct and proper design is highly important for the mechanical reliability of the pump itself.

Moreover, a deep knowledge of the components contributing to the axial thrust is of relevant interest. The flow field contribution to the hydraulic axial thrust is mainly realized in the impeller but is also affected by the presence of leakages flows inside the gaps between impeller and casing walls.

Thereby, a numerical investigation of the phenomenon should not be limited to the analysis of the impeller flow field but it has to be extended to the whole machine detailed in its single components.

Present paper is concerned with the investigation of a multistage centrifugal pump designed and produced by Weir Gabbioneta whose section is reported in Figure 1 and whose very complex layout will be described in detail in the next paragraph. As it is evident, the achievement of such a complex task requires the development of a strategy dealing with all the following items:

- The analysis of the single stages, including both rotating and stationary components;
- The study of the flow conditions inside the front and back shroud impeller side chambers and balancing drums and the evaluation of their contribution to the axial thrust;
- The final data collection and processing in order to assess and verify the residual hydraulic axial thrust.

The strategy developed for each single issue will be described in detail and the results of its application to the centrifugal pump in Figure 1 will be presented and discussed here below.

2. MULTISTAGE PUMP GEOMETRY

Present work investigates a five stages horizontal centrifugal pump (Figure 1).

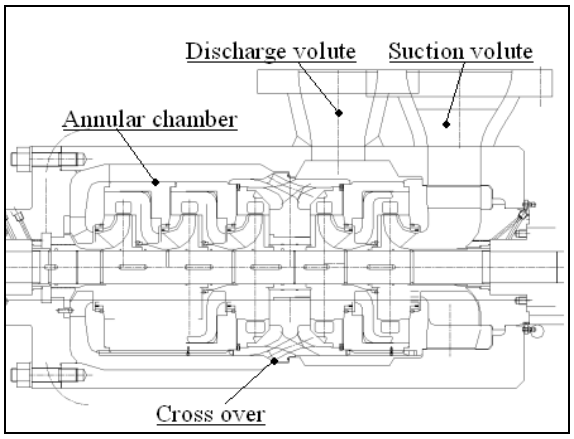

Figure 1. Layout of the investigated multistage centrifugal pump in opposite impellers configuration

Axial thrust balance is primarily obtained thanks to the opposite impeller configuration characterized by the opposite flow direction in the first two stages and in the last three ones. A crossover device leads the flow from the first to the second group of stages through an annular chamber, thus being responsible for the turning of the flow direction. Axial unbalance is evident for the investigated pump due to a different impellers number in the opposite groups of stages, but also in pumps with even impeller number the axial balance is not to be taken for granted due to the presence of leakages flows.

Thrust bearings are then required. To design them correctly, the presence of the impeller side chambers (Figure 2) and balancing drums has to be considered.

The leakage flow in the side chambers can help to reduce the axial thrust, but only penalizing pump efficiency.

In such a complex machine, three kinds of cavities are present: front and back impeller shroud cavities and a central drum. Two of them (the front and the back shroud chambers) are reported in Figure 2.

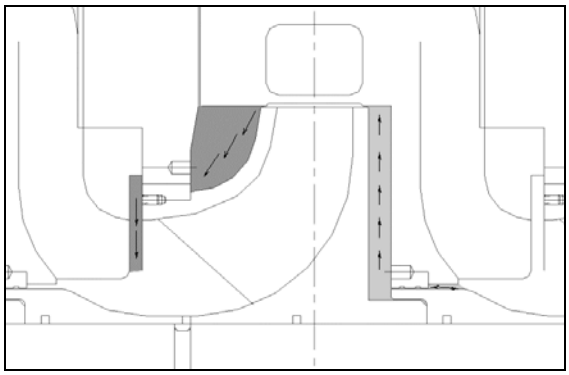

Figure 2. Front and back impeller side chambers for an intermediate stage

While the flow inside the front shroud chamber always radially turns inward, the one inside the back shroud cavity can also radially turn outward depending on different positions. Even if, in this case, mass flow passing through the back shroud chamber has a slight influence on the whole pump performance, its contribution to the axial thrust can not be neglected.

The central balancing drum (Figure 3) is located between the second and the fifth impellers, next to the crossover device. Flow direction is shown in Figure 3.

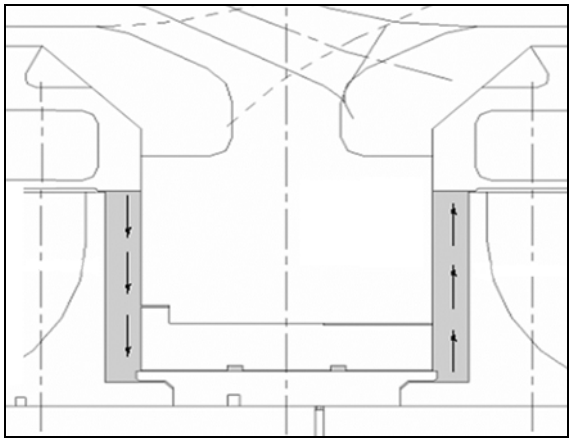

Figure 3. Central balancing drum between the second and the fifth stage

The lateral balancing drum (reported in Figure 4) is located between the first impeller of the second group of stages. A balancing duct connects the drum to the suction nozzle, thus keeping the value

of suction pressure at the external side of the drum itself.

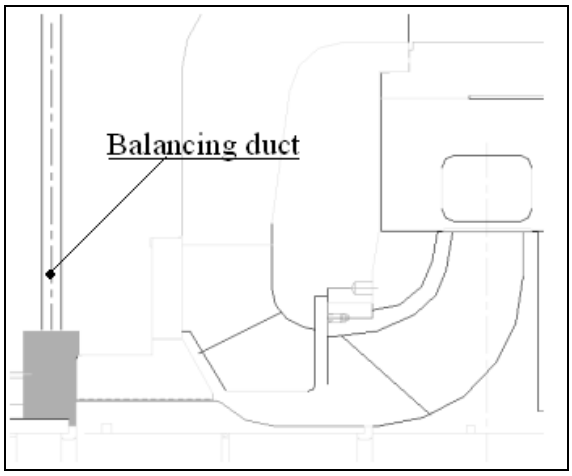

Figure 4. Lateral balancing drum between the first and the second group of stages

All diffusers are characterized by the same vanes except for the second and the fifth which face the crossover. All the impellers are geometrically identical, but have different inlet conditions due to the presence of different static upstream components (i.e. the first impeller follows the suction volute while the third one follows the cross over device annular chamber).

3. NUMERICAL INVESTIGATION FEATURES

Several 3D steady simulations solving RANS (Reynolds Averaged Navier Stokes) equations have been carried out in the fluid domain. Standard techniques have been employed for the numerical computation: a finite-volume pressure-correction procedure for incompressible flow has been employed and a two-equation k-ε turbulence model with standard wall functions has been applied.

Pump main components have been analysed separately in order to reduce computational costs. Even the side chambers flow has been analysed with 2D CFD simulations apart from the main flow inside impeller and diffuser. Furthermore, as stated by Gantar et al. [1] for a geometry which was very similar to the present one, an eventual flow recirculation in impeller exit/diffuser inlet area does not impact on the impeller side chambers. This probably happens because the main impeller passages and the side chambers are sufficiently separated by throttling via a small clearance.

Summarizing, because of their different geometry, the following elements have been modelled:

- Suction volute;
- First impeller;
- Each diffuser not facing the crossover device coupled with its downstream stage impeller,
- Second diffuser and crossover device;
- Third impeller;
- Fifth diffuser and discharge volute;
- Impeller front shroud side chamber;
- Impeller back shroud side chamber;
- Central balancing drum;
- Lateral balancing drum and balancing duct.

Finally, all the results have to be combined in order to obtain the axial thrust of each of the two groups of stages, thus helping to understand their reciprocal balancing effects.

3.1. Stage coupling approach

The hydraulic axial thrust on the machine shaft is due to the pressure integral on the impeller walls. However, simulations of the stationary components are still required to calculate the performance of the whole pump and to provide the correct boundary conditions for the rotating components calculation.

The presence of both rotating (impeller) and stationary (diffuser) parts inside each stage requires a strategy to couple them, namely to deal with the computation of two domains characterised by a different periodic condition because of the different number of blades.

A mixing plane approach has been selected for present study. It allows to solve separately the rotating and the stationary domains in steady conditions. The flow field data from adjacent zones have been imposed as spatially averaged boundary conditions or “mixed” at the mixing plane interface.

This approach removes any unsteadiness deriving from the circumferential variations in the passage-to-passage flow field, thus yielding a steady-state result. However, despite the simplifications, several applications demonstrate that the approximation of the time-averaged results is quite reasonable.

As further hypothesis, the stage kinematic repeatability has been assumed. Therefore, the velocity profile at the impeller exit has been employed to update the diffuser inlet boundary condition.

The whole process can be synthesised in these main steps:

- Solution of the Navier-Stokes equations in both domains;
- Average of the flow in tangential direction;
- Update of the boundary conditions;
- Iteration of the previous steps until convergence is achieved for profiles of velocity and pressure.

The spatial discretisation consists approximately of 500.000 elements both for impeller and diffuser. The surfaces selected for mixing plane and for stage repeatability are reported in Figure 5.

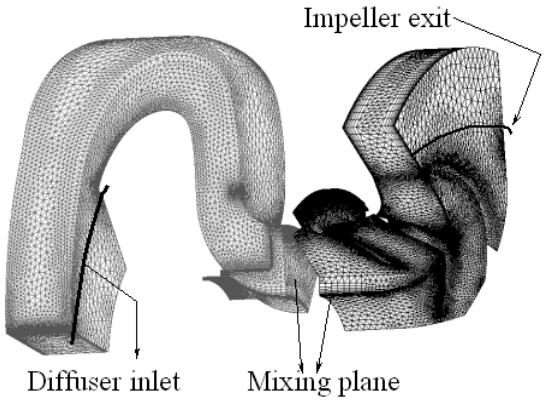

Figure 5. Geometrical domains and surfaces for the stage coupling

Impeller-diffuser interactions is not limited to the main flow, but also involves the leakage flow that considerably affects both the axial thrust and the efficiency of the whole pump.

Leakage flow analysis will be discussed in detail in the next paragraph. To consider the leakage flow entering and exiting from impeller and diffuser, the outward part of the side chamber has been modelled in their geometric domain. For example, the impeller geometric domain has been modelled including the boundary corresponding to the stage interface with the internal leakage flow.

A constant leakage distribution across axial and circumferential extents of the interfaces between main flow and cavities has been assumed Furthermore, it has been verified that the geometries are not sensitive to the direction of the injection velocity, thus confirming leakage mass flow as the most significant parameter.

For this reason, to impose boundary conditions at these interfaces the leakage mass flow dependency on impeller head has to be considered. Then, the boundary conditions need to be uploaded during the computation by checking the actual value of impeller head. This constitutes a further step coupled to the ones previously listed. The procedure is reported in Figure 6.

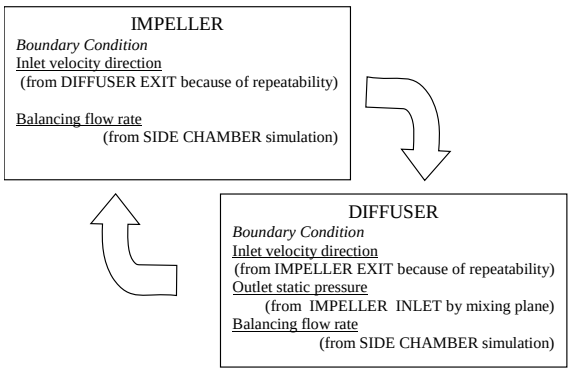

Figure 6. Scheme of the complete coupling procedure

All the CFD analysis have been repeated for different capacities.

Finally, the characteristic curve for the whole pump has been obtained. Its dimensionless version is shown in Figure 7.

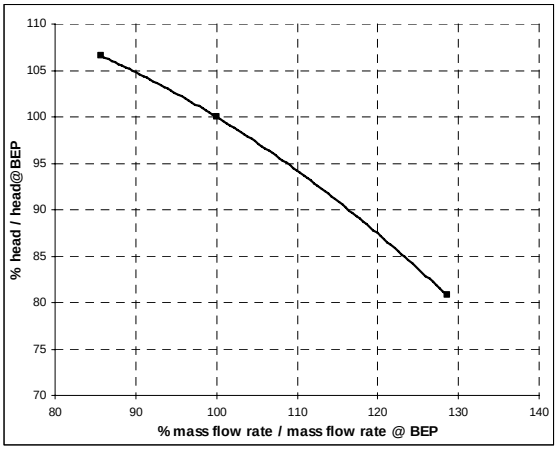

Figure 7. Pump dimensionless characteristic curve

3.2. Impeller side chambers

Impeller side chambers have been studied by means of a 2D-CFD approach. The hypothesis of axial symmetry has been reasonably assumed for this problem.

The flow inside the cavity is radially outward at the rotating wall, while it is radially inwards at the casing wall. The internal flow of the impeller side chamber presents a core zone between the casing-diffuser stationary wall and the impeller rotating one. The central core rotating speed is lower than the impeller one (Batchelor, [2] and Stewartson, [3]).

The rotating velocity inside the chambers depends on peripheral conditions, namely on the impeller rotating speed and on the head across the cavity itself. Due to pump geometry, head across the leakage corresponds to impeller head. Therefore, leakage mass flow and its contribution to the axial thrust depend on pump working conditions.

Results from the front shroud chamber analysis are discussed as exemplification here below and details of the corresponding computational grid (approximately 50.000 elements) are shown in Figure 8.

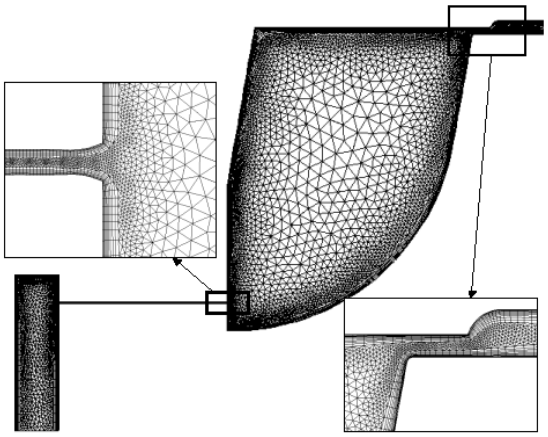

Figure 8. Details of the computational grid of the front shroud impeller chamber

To get an exhaustive leakage characterization, the CFD analysis has been performed for different heads across the cavity and calculating the corresponding leakage mass flow.

These results can be employed to tune some well known correlations from the literature (Traupel [4], Utz [5], Denny [6], Wortster et al. [7]) which allow to update stage analysis boundary conditions in a simple and quick way reaching a good accuracy. By such a way, cavity flow is solved at different operating points in a preliminary phase, but does not require to be calculated at every update of the stage coupling boundary conditions.

As far as leakage mass flow rate is concerned, the correlations take into account wear rings geometrical characteristics, rotational speed and impeller head as follows:

$$Q_p = k\sqrt{2gH}C_d A \qquad (1)$$

$$C_d = \left(\frac{1}{\lambda \frac{L}{d}} + a \right)^{0.5} \qquad (2)$$

$$\lambda = \frac{b}{\mathrm{Re}^{0.25}} \left[1 + 0.5 \left(\frac{u}{v} \right)^2 \right]^c . \qquad (3)$$

Here Q_p is the leakage flow rate, H the head, A the passage area, L the passage length, d the seal diametral clearance, u the blade velocity, v the mean flow speed inside the seal. Coefficients (a, b, c) depend on geometrical characteristics.

The leakage mass flow is obtained as a function of the head across the cavity (Figure 9).

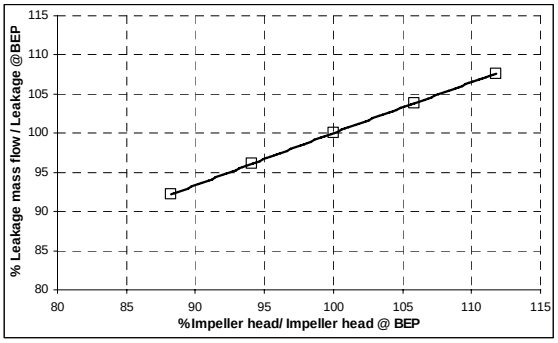

Figure 9. Non-dimensional leakage mass flow rate against non-dimensional impeller head (front shroud impeller chamber)

Head across the cavity results in a centripetal flow with radially inwards structures at the stationary wall and outwards ones at the rotating walls. Local tangential velocity divided by the impeller velocity:

$$\frac{v_\vartheta}{u} = \frac{v_\vartheta}{\Omega r} \qquad (4)$$

has been reported in Figure 10 together with the streamlines inside the cavity.

In the same way, the dimensionless rotating velocity inside the cavity can be defined as follows:

$$\frac{\omega}{\Omega} = \frac{v_\vartheta}{r} \qquad (5)$$

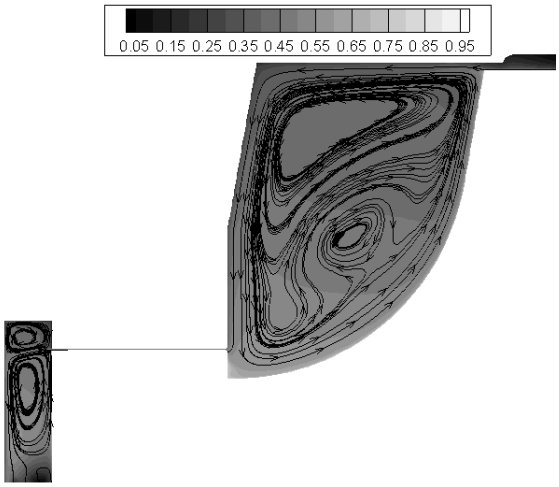

Figure 10. Non-dimensional tangential velocity distribution inside the front shroud impeller chamber

Figure 11 shows the back shroud impeller chamber grid and the corresponding tangential velocity distribution.

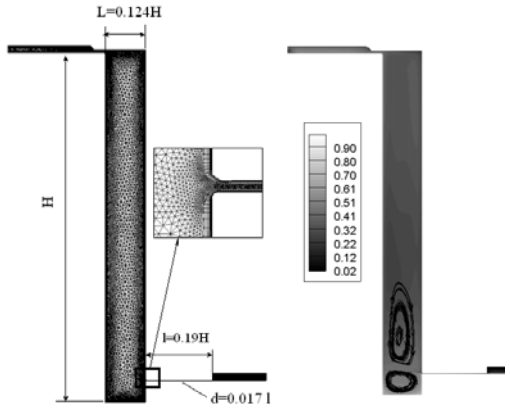

Figure 11. Details of the computational grid and non-dimensional tangential velocity distribution inside the back shroud impeller chamber

Repeating calculations showed that peripheral velocity with respect to the impeller one depends on the mass flow condition through the cavity. The dimensionless rotating velocity distribution in the middle of the cavity is reported in Figure 12 at different flow rates.

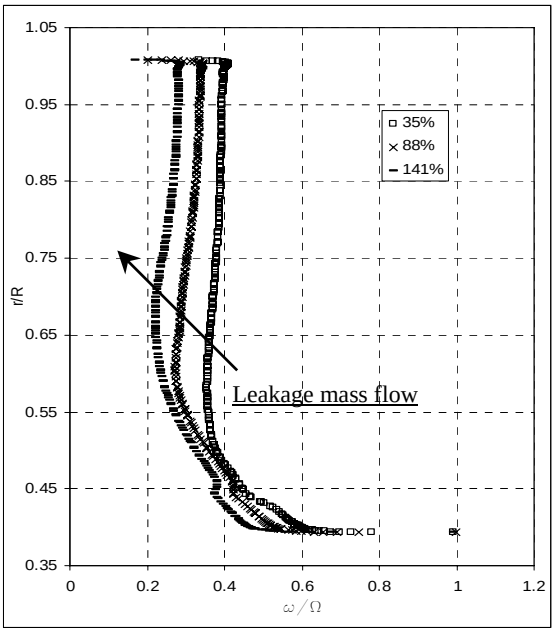

Figure 12. Dimensionless rotating velocity inside the back impeller cavity at different mass flow (referred to the leakage mass flow at BEP)

Fluid rotating speed inside the cavity presents a typical value for dimensionless radius ranging from 0.55 to 1. The typical characteristics of the Batchelor flow (Batchelor, [2]) can be observed, namely, the fluid rotates as a solid body between two boundary layers. For the internal regions, the distribution called as Stewartson flow (Stewartson, [3]) is encountered, with the classic "vortex" distribution.

Increasing the mass flow through the cavity, the presence of the Stewartson distribution is increased, while the value of constant rotating velocity of the core flow is reduced.

This agrees with the results of Debuchy et al. [8]. The conclusion was that the Batchelor type flow can be observed at low mass flow rates, and far from the periphery because of the influence of the inlet conditions. It was also found that the flow structure near the axis is strongly affected by a weak stream, which enhances the level of the core-swirl ratio near the axis.

Pressure distribution on the back and front shroud of the impeller is qualitatively reported in Figure 16, while in Figure 17 the pressure distribution is reported for the second and the fifth impeller back shroud.

The pressure distribution inside the central drum is highly influenced by the flow conditions. The most important parameters are the leakage mass flow rate and the head across the cavity which depend on pump operating conditions, on the main flow rate and on wear rings clearance. Present work has been carried out with fix design values for these clearances. However, during its life, the real pump will undergo a process of wear resulting in wear rings clearance enlargement and consequent increase of leakage flow, global performance worsening and residual axial thrust modifications as far as module and sometimes direction is concerned.

In Figure 13, the radial distribution of static pressure inside the back shroud cavity is reported. A different value of leakage flow rate divided by the leakage flow rate at BEP corresponds to each curve. All the curves are plotted considering the same reference pressure at the impeller exit.

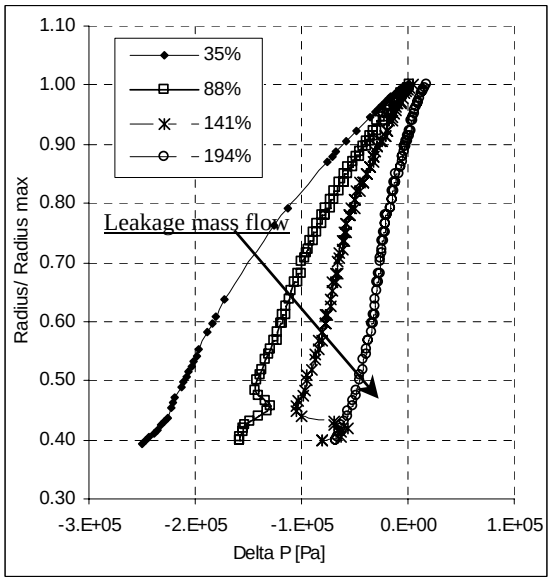

Figure 13. Radial distribution of static pressure inside the back shroud chamber at different mass flow rates

Let consider now the same distribution divided by a term expressing the centrifugal force:

$$\Delta p' = -\frac{\Delta p}{\rho \omega^2 r^2} \qquad (6)$$

as reported for different mass flow in Figure 14.

It should be remember that ω expresses the local fluid rotational speed in front and back impeller chambers and r the local radial coordinate.

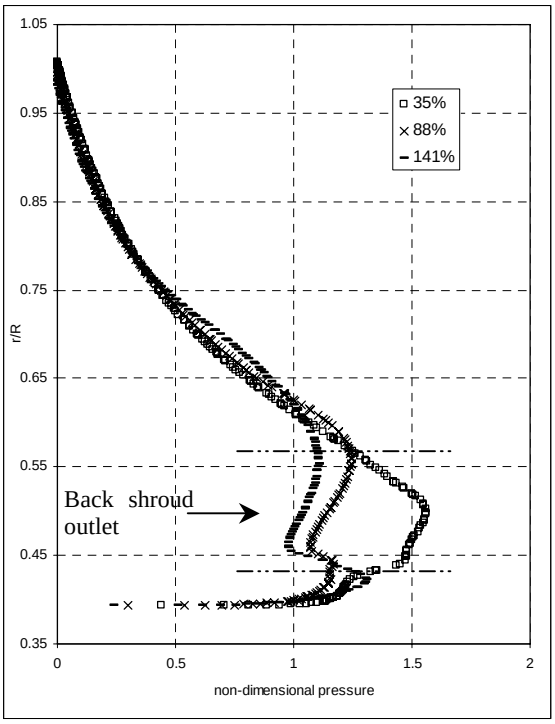

Figure 14. Radial distribution of dimensionless pressure inside the back shroud chamber at different mass flow rates

It should be observed that all curves are coincident except between r/R=0.45 and r/R=0.55, where the outlet of the back shroud chamber is located.

The integral of the pressure distribution is here down plotted as axial thrust against leakage mass flow (Figure 15).

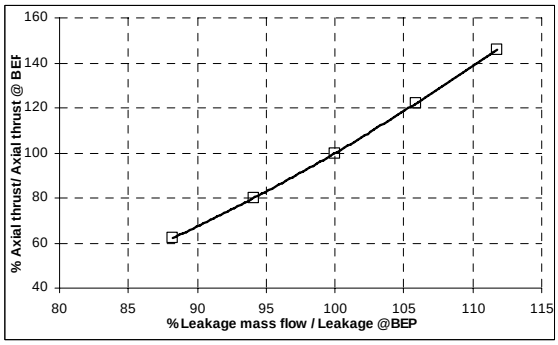

Figure 15. Non-dimensional axial thrust vs. non-dimensional impeller head (back shroud chamber)

The rate of this dependency is quite high. Considering for example a variation of 12% in the back shroud leakage mass flow, a 50% increase in axial thrust is observed. For this reason, the choice of a cavity geometry oriented to reduce leakage mass flow is of relevant importance in balancing the axial thrust.

3.3. Axial thrust calculation

To calculate the axial thrust acting on the whole machine, both the contribution of the main and of the leakage flows have to be considered.

With reference to the single stage, the hydraulic axial thrust acting on the impeller is given by the contribution of the inlet flow and of the front and back shroud leakages flows (Figure 16). The back shroud helps to balance the machine by contrasting the thrust due to impeller and front shroud.

The hydraulic thrust is gathered from the wall pressure distribution obtained by CFD calculations:

$$T_{ax} = \int_A p\,\vec{n}\,dA \qquad (7)$$

As regards the cavities, the axial thrust is calculated adding a constant pressure outlet value and of a term due to the pressure distribution on the rotating wall. Then,

$$T_{ax,cavity} = \int_A p_{exit,impeller}\,\vec{n}\,dA + \int_A p\,\vec{n}\,dA = \\ = p_{exit,impeller} \int_A \vec{n}\,dA + \int_A p\,\vec{n}\,dA \qquad (8)$$

where the area is referred to both the front and back impeller shroud chambers.

Similarly the axial thrust is calculated for central and lateral balancing drums.

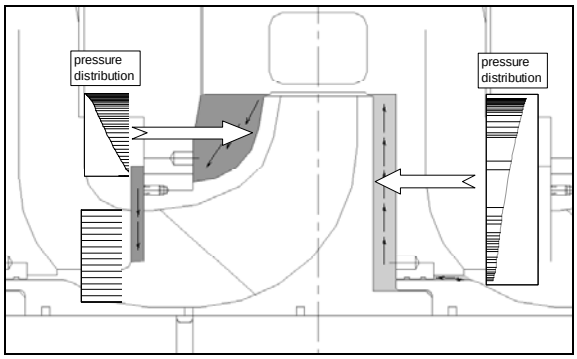

Figure 16. Leakage contributions to the axial thrust

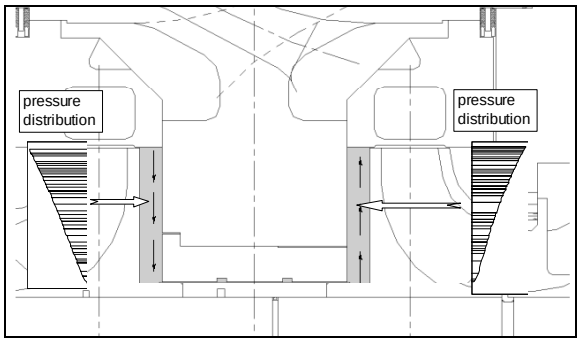

Figure 17. Central balancing drum contributions to the axial thrust

Considering the actual alignment of the stages (shown in Figure 1), these results are extended to the whole machine.

Each component contribution to the axial thrust is reported in Figure 18 and Figure 19.

It can be easily verified that the greater contribution is due to the central balancing drum where the flow is driven by pump head and by wear rings clearances eventually modified by mechanical wear. The sum of all these contributions gives a global thrust estimation.

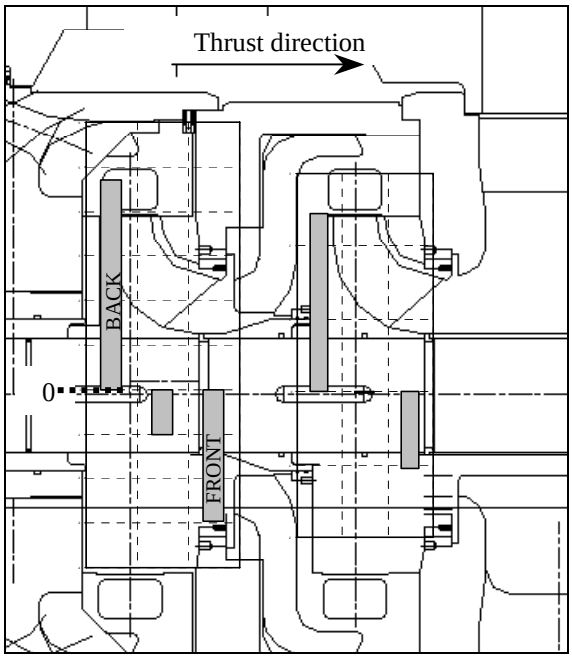

Figure 18 . Effects of the first group of stage on the global axial thrust. The arrow direction refers to the global axial thrust direction.

Although the opposite alignment of the two groups of stages, the global thrust is not null and it is directed as shown by the arrows in Figure 18 and Figure 19.

For a proper design of the thrust bearings, it is still required to know the maximum thrust in pump operating range. Data from manufacturers indicate machine operating conditions between the 80% to the 120% of the BEP flow rate as the preferred operating region. The axial thrust trend in this operating range is reported in Figure 20.

The maximum thrust for the investigated pump is obtained at the lower mass flow, where the total head of the pump is maximum. Really, the machine operating range goes down to the minimum continuous flow. Other analysis have to be carried out to investigate pump behaviour for different range and to verify the increase of residual axial thrust for lower capacity.

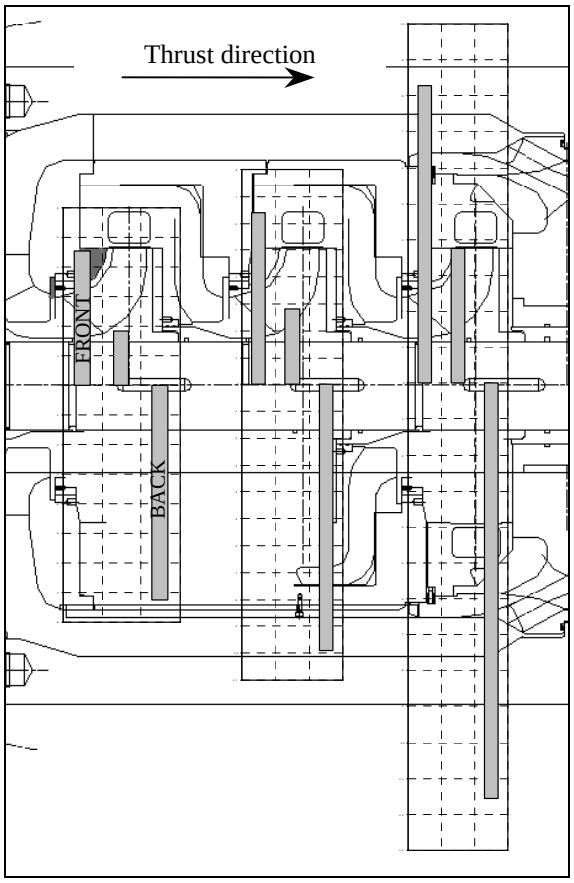

Figure 19. Effects of the second group of stage on the global axial thrust. The arrow direction refers to the global axial thrust direction.

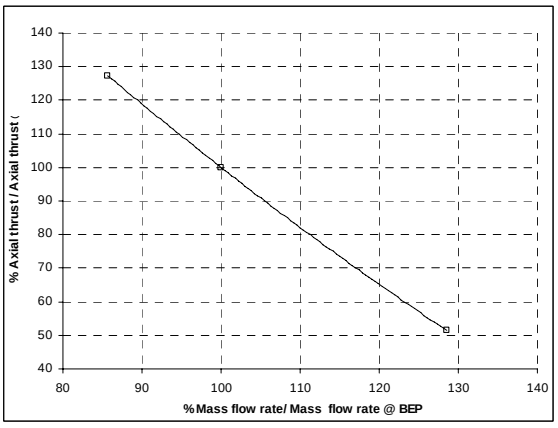

Figure 20. Global dimensionless axial thrust against main flow rate

4. CONCLUSIONS

A numerical investigation of a multistage centrifugal pump has been carried out. Driving the correct design and dimensioning of the axial bearings to balance the hydraulic thrust is the present study main target.

To reach the task, both the main, the impeller chambers and the balancing drums flow have to be considered because of their relevance to the problem of axial load unbalance.

Separated CFD analysis have been carried out for stage (with a mixing plane approach) and side chambers. 2D analysis to characterize the central drum and the lateral balancing drum have been developed.

A methodology to predict the residual axial thrust for a complex machine has been presented and pump sensitivity to the different variables which influence axial thrust have been pointed out.

Actual results show the calculated characteristics maps of the pump and how the axial thrust depends on the operating conditions of the pump as well as its mechanical wear conditions, because of effects on the main flow head and on the pressure distribution inside the side chambers.

Furthermore, it has been highlighted that side chambers give a great contribution to the axial thrust and that their pressure distribution is highly influenced by leakage mass flow and by local rotating speed inside the cavity.

ACKNOWLEDGEMENTS

The authors are grateful to Prof. Ing. F. Martelli of University of Florence, Ing. G. Marenco, Ing. D. Maestri and Ing. A. Piva of Weir Gabbioneta Srl for their valuable suggestions during the development of this work.

REFERENCES

[1] Gantar, M., Florjancic, D., and Sirok, B., 2002, "Hydraulic Axial Thrust in multistage Pumps-Origins and Solutions", *ASME J Fluids Engineering*, Vol. 124, pp. 336-341.

[2] Batchelor, G.K., 1951, "Note on a class of solutions of the Navier–Stokes equations representing steady rotationally-symmetric flow", *quart.J.Mech.Appl.Math.*, Vol.4, pp. 29-41.

[3] Stewartson, K., 1953, "On the flow between two rotating coaxial discs", *Proc.Camb.Phil.Soc.*, Vol. 49, pp. 333-341.

[4] Traupel, W., 1958, *Thermische Turbomaschinen*, Sprinter-Verlag, Berlin.

[5] Utz, C., 1972, „Experimentelle Untersuchung der Strömungveluste in einer mehrstufigen Axialturbine", Mitt.Ins.Therm.Turbomasch. ETH Zurich, Nr.19.

[6] Denny, D.F., 1954, "Leakage flow through centrifugal pump wear rings", *TN460, Beds: BHRA*, Cranfield.

[7] Worster, R.C., and Thorne, E.W., 1959, "Measurement of leakage flow tough the wearing rings of a centrifugal pump and its effect on overall performance", *Beds: RR 619*, Cranfield.

[8] Debuchy, R., Dyment, A., Muhe, H., and Micheau, P., 1998, "Radial inflow between a rotating and a stationary disc", *Eur. J. Mech. B/Fluids*, Vol. 17, N°6, pp. 791-810.

[9] Adami, P., Della Gatta, S., Martelli, F., Bertolazzi, L., Maestri, D., Marenco, G., and Piva, A., 2005, "Multistage turbo-pumps: Assessment of a mixing plane method for CFD analysis", Proc. *60° ATI Conference*, Roma, Italy, ATI60-12-1.

[10] Daily, J.W., and Nece, R.E., 1960, "Chamber dimension effects on induced flow and frictional resistance of enclosed rotating discs", *J. Basic.Eng*, Vol. 82, pp. 217-232.

Conference on Modelling Fluid Flow (CMFF'06)
The 13th International Conference on Fluid Flow Technologies
Budapest, Hungary, September 6-9, 2006

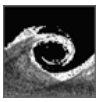

INFLUENCE OF BLADE GEOMETRY ON THE ROTATING STALL IN A RADIAL PUMP IMPELLER

Nico KRAUSE[1], Elemér PAP[2], Dominique THEVENIN[2]

[1] Corresponding Author. Laboratory of Fluid Dynamics and Technical Flows, University of Magdeburg "Otto von Guericke", Universitaetsplatz 2, D-39106 Magdeburg, Germany. Tel.: +49 391 6718194, Fax: +49 391 67 12840, E-mail: nico.krause@vst.uni-magdeburg.de
[2] Laboratory of Fluid Dynamics and Technical Flows, University of Magdeburg "Otto von Guericke".

ABSTRACT

In many applications pumps are used. Often the pipe characteristic is unsatisfactory known and the selected pump has more power than needed. It will thus be throttled or the flow is throttled during operation. In such cases the pump operates under part-load flow and the inflow condition differs from the dimensioning point. In this paper results for three different impeller blade designs are presented. All impeller blades are designed for the same pressure rise over the impeller but using different geometries: one arc of a circle, two arcs of a circle, constant delay. The pump characteristic curves show the resulting modification of the energy transmission and losses. For the investigation of the flow in the impeller Time-resolved Particle Image Velocimetry (TR-PIV) is used. Using TR-PIV it is possible to visualise the vortices in the stall regime. The different characteristics of the impellers and the influence of impeller geometry onto the beginning of stall and rotating stall are presented in the paper.

Keywords: blade design, pump characteristic radial pump, rotating stall, TR-PIV, turbomachinery,

NOMENCLATURE

c	[*m/s*]	absolute velocity
e_u	[*J/kg*]	specific energy transmission
f	[*Hz*]	frequency
n	[min^{-1}]	number of revolutions
n_q	[min^{-1}]	specific number of revolutions
Δp	[*mbar*]	pressure difference
r	[*mm*]	radius
Q	[m^3/h]	flow rate
t	[*s*]	time
u	[*m/s*]	circumferential speed
w	[*m/s*]	relative velocity
X	[*mm*]	cartesian coordinates axis
Y	[*mm*]	cartesian coordinates axis
β	[°]	angle between $\underline{w}$ and $\underline{u}$
ρ	[kg/m^3]	density
$\Re$	[-]	reaction degree

Subscripts and Superscripts

d	design point
kin	kinetic
stat	static
1	inlet of the blade passage
2	outlet of the blade passage

1. INTRODUCTION

In many applications pumps are not used at the design point. Wurm [1] indicates that in head installations over 50% of the time pumps operate at under 25% of the design flow rate. In such cases the pump operates under part-load flow and the inflow condition differs from the dimensioning point.

For turbomachines operating with gases the problem of rotating stall has been known for a long time. The first description was given by Emmons et al. [2]. In turbomachines there exists a velocity triangle with the components $\underline{c}$ (absolute velocity), $\underline{u}$ (peripheral velocity) and $\underline{w}$ (relative velocity) (Eq. 1, Figure 1a).

$$\underline{c} = \underline{u} + \underline{w} \qquad (1)$$

If the flow rate is reduced, the meridian component of the relative velocity w_m also decreases (Figure 1b). For this reduced flow rate the angle of attack rises and the stagnation point is displaced to the pressure side of the blade. When the angle of attack exceeds a certain threshold, the flow on the suction side will detach and stall can appear.

The static pressure inside the stall region is smaller than in the surrounding flow; vortices can therefore appear with the same rotating direction as the impeller. In the outlet of the blade passage a second vortex can be formed with an inverse rotational direction. These vortices can grow until the complete blade passage is blocked. Then, the medium has to pass through the following channel. This leads once more to a displacement of the

stagnation point in the following blade passage, and a new stall cell will be formed in this channel. On the other hand, the flow in the first blade passage will reattach and the flow conditions in this channel will improve. It is furthermore possible that several stall cells exist simultaneously in the impeller.

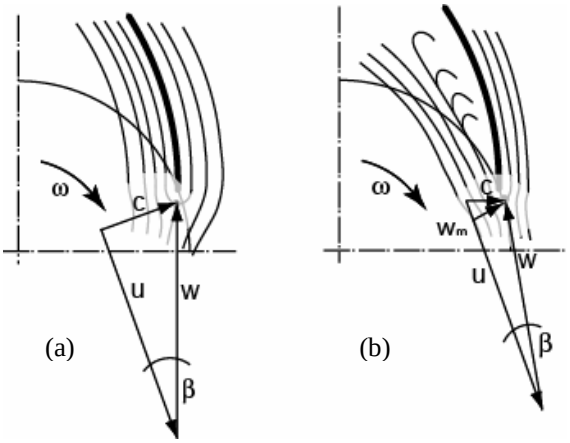

Figure 1a-b. Velocity triangles at design point (a) and for throttled flow (b)

With this mechanism the stall cell(s) can turn around through the impeller. Because the angular velocity of the stall cell is lower than the impeller angular velocity, it turns inside the impeller against the rotational direction.

The main problem is the surge of the system (oscillating forward and backward flow trough the machine). An important parameter is the elasticity for a compressible medium. Rotating stall leads to considerable efficiency losses. Many studies have investigated this phenomenon, mostly in axial compressors [3-5]. Pampreen [6] gives an extensive review of this problem. A limitation of all these studies is that they are based on high frequency single-point measurements of pressure [7-12], temperature or velocity [5,9,13,14], obtained through intrusive diagnostics, or on very low frequency non-intrusive imaging techniques [15]. But, for such instabilities, intrusive measurements can easily falsify the results. A first investigation relying on a high frequency non-intrusive imaging technique was presented by Krause *et al*. [16].

In the present study, velocity fields measured in a centrifugal pump with time-resolved PIV at high frame rates are presented. These measurements concerning instabilities and turbulent processes clearly show rotating stall in a throttled radial water pump with different blade designs.

2. EXPERIMENTAL SET-UP

The set-up used in the experiments consisted in two major parts: the time-resolved PIV system and the rotating machinery installation. Figure 2 shows a sketch of this installation, where the pipes and the acryl model pump can be distinguished.

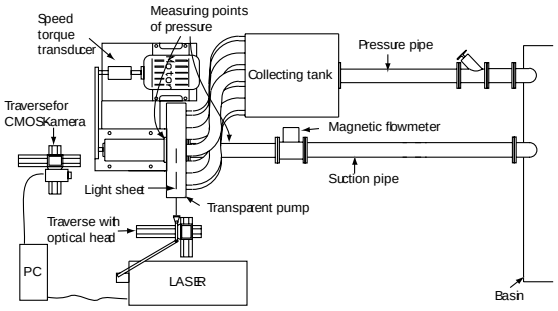

Figure 2. Sketch of the radial transparent pump installation with PIV measurement system.

2.1. Radial pump

For the design of pump blades different concepts are used. The inlet and outlet angles are given by the needed pressure difference and remain the same for all geometries. One simple concept is a blade geometry given by one circular arc with a single radius (later called impeller 1). The advantages are: short length of the mean line, small hydraulic losses and simple structure. The disadvantage is the fast deceleration of the flow in the first third of the blade passage and acceleration near the outlet. Another concept is the constant delay of the relative velocity (later impeller 2). In this case the mean line of the blade is calculated point by point. The advantage is the constant pressure rise in the channel, in opposite stands the higher hydraulic losses, caused by the longer mean line of the blade. To combine these advantages a third concept exists: two circular arcs with different radii (later impeller 3). The mean line of these blades is shorter than the constant delay design and has a slower deceleration than the single circular arc blade. The disadvantage is the discontinuity in the second derivative of the mean line at the junction of the two arcs. The three corresponding geometries are presented in Figure 3 to 5. Figure 6 shows the relative velocity over the mean line for the different blades. Technical parameters are listed in Table 1. A meridian section of the pump is presented in Krause *et al*. [16].

Table 1. Technical parameters of the radial pump

Q_d	47	[m³/h]	Flow rate design point
n	600	[min^{-1}]	Number of revolutions
β_1	19	[°]	Inlet angle
β_2	23	[°]	Outlet angle
r_1	65	[mm]	Inlet radius
r_2	139	[mm]	Outlet radius
n_q	26	[min^{-1}]	Specific speed

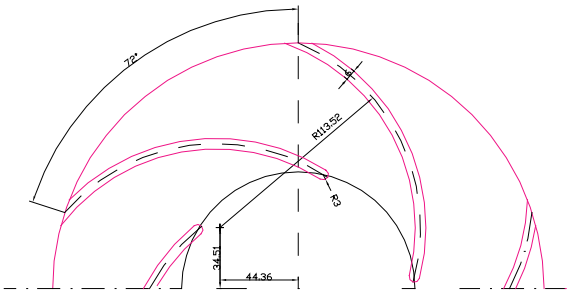

Figure 3. Plane vane as circular arc with a single radius (impeller 1)

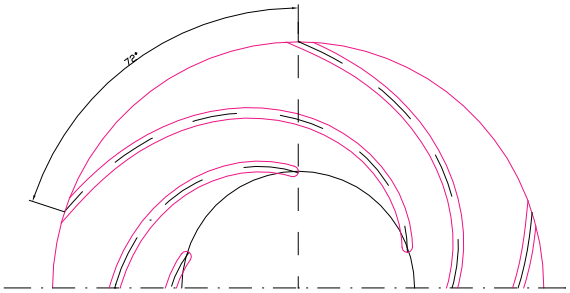

Figure 4. Plane vane with mean line for constant delay of relative velocity (impeller 2)

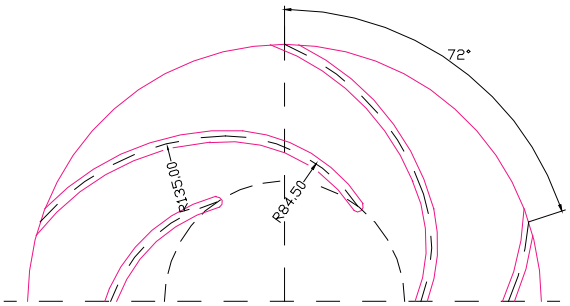

Figure 5. Plane vane composed of two circular arcs with different radii (impeller 3)

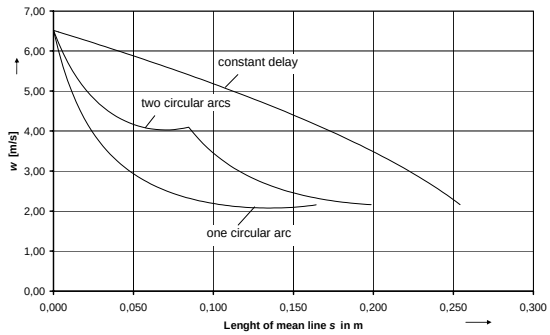

Figure 6. Relative velocity in the impellers over the length of the mean line

2.2. Measuring system

For the velocity measurements a commercial Time-resolved PIV system from DantecDynamics A/S was used. The principles of PIV are described by Willert et al. [17]. The time resolved PIV-system is composed of a Q-switched Nd:YAG laser, a laser-sheet optic, a CMOS double image camera, a synchronisation unit and the control, acquisition and treatment computer. The frequency-doubled, diode-pumped Nd:YAG laser has a variable repetition rate, allowing pulse intervals from 40 to 1000 μs, with a pulse duration of 75-250 *ns*. The pulse energy strongly depends on the repetition rate with a maximum energy of about 22 *mJ* at lower repetition rates. The light sheet optics have been adjusted in order to get a diverging light sheet of 0.5-1 *mm* thickness inside the pump. The PIV images were taken with a 1260x1024 pixel, 10 bit CMOS camera, working with frame rates up to 500 image pairs/s full frame and 800 images pairs/s with 1260x640 pixels. For the investigation frequencies of 50, 500 and 800 *Hz* have been used. The frequency of 50 *Hz* corresponds to a measurement of each blade of the impeller in a fixed position. To follow the vortices within one channel higher frequencies are used, depending on the investigated area. Impellers 1 and 3 with relatively short blades have been measured with a frequency of 800 *Hz* and Impeller 2 with a frequency of 500 *Hz*, for which the full resolution of the camera is still possible. The seeding material consists in Rhodamin-B-doped PMMA-particles with a mean size of 10 μm and a density ρ=1,19 g/cm^3.

To measure the static pressure rise the pressure before the impeller in the suction side and after the impeller at *r*=160 *mm* was recorded.

3. RESULTS

3.1. Pump characteristic

Figure 7 shows the static pressure rise for all three impellers. This is not the complete energy transmission to the fluid because the velocity term is missing.

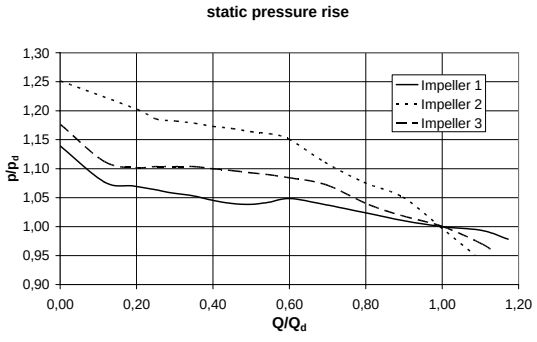

Figure 7. Static pressure rise over the impellers

$$\Re = \frac{e_{u(stat)}}{e_{u(stat)} + e_{u(kin)}} \qquad (2)$$

The reaction degree (Eq. 2) equals $\Re$=0.7 at the design point and depends on the flow rate. The absolute values are Δp_{stat}=312 *mbar* for impeller 1, Δp_{stat}=287 *mbar* for impeller 2 and Δp_{stat}=302 *mbar* for impeller 3.

Figure 7 shows that impeller 1 operates with the best conditions at the design point, but toward lower flow rates the pressure rise is smaller than for impellers 2 and 3. The pressure rise of impeller 2 is better than for impeller 3.

3.1. Part load flow

The measured flow fields are analysed with the Fast-Fourier-Transform (FFT). For this purpose one visible part of the blade passage has been selected, typically the inlet region of a channel. The procedure is similar to that presented in Krause et al. [16]. The examined flow rates are 50% to 20% of the design flow rate in steps of 5%. The onset of rotating stall could be observed for impeller 1 at 35%, for impeller 2 at 25% and for impeller 3 at 30% of the design flow-rate. For all impellers two stall cells have been identified, propagating with a fraction of the impeller speed.

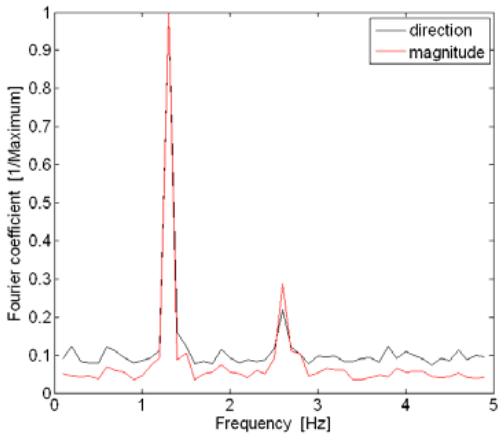

Figure 8. Frequency spectra of impeller 1 at 25% of the design flow rate

3.1.1 Part-load flow of 25% in impeller 1

Figure 9a-h presents the velocity field in two blade passages of the impeller: the outlet of channel 1 and the inlet of channel 2 are observed simultaneously. In this figure the relative velocity vectors and the instantaneous stream lines are represented. In Figure 9a, blade passage 1, two vortices with different rotational directions can be seen, blocking the discharge. Blade passage 2 operates under good conditions. In Figure 9b, channel 1, the inlet vortex moved to the end of the blade on the suction side. In channel 2 the flow stalled on the suction side of the blade at the inlet. From Figure 9c-e, the growing of the inlet vortex is observable. In Figure 9f the flow in blade passage 2 reattached, the vortex is transported to the outlet. At the outlet of blade passage 1 the flow is chaotic. The reattachment in blade passage 2 is finished in Figure 9g and at the outlet of channel 1 the vortex is clearly visible. Figure 9h presents nearly the same conditions as Figure 9a: a stall period is finished. This is confirmed by the FFT. The peak in the frequency spectra is at f=1.3 *Hz* (Figure 8). This corresponds to 7.6 rotations of the impeller. This analysis gives the information that both stall cells rotate with the same fractional speed of the impeller.

3.1.2 Part-load flow of 25% in impeller 2

In the Figure 10a-h a stall period is shown. Parts of three blade passages are visible: the outlet of blade passage 1, the inlet and the middle part of blade passage 2 and the inlet of channel 3. In opposite to impeller 1 the outlet vortex is relatively small (Figure 10f-h). Blade passage 2 (Figure 10d-f) is not completely blocked. On the pressure side the flow is possible through the channel. Another difference with impeller 1 is the separation from the suction side in blade passage 2. It is smaller and consists of more than one single vortex (Figure 10e). The frequency analysis finds also a peak at f=1.3 *Hz*.

3.1.2 Part-load flow of 25% in impeller 3

A stall period in impeller 3 is presented in Figure 11a-h. Here also the outlet of blade passage 1 and the inlet of channel 2 are represented. The vortices behave as an average of impeller 1 and impeller 2. The blockage of blade passage 2 is not as strong as in impeller 1 but the vortex is more intense. The frequency which was computed with the FFT is the same as for the other impellers, f=1.3 *Hz*.

The character of all investigated impellers under rotating stall corresponds to the observed pressure differences.

4. SUMMARY

Time-resolved PIV measurements have been used to determine the velocity fields in rotating radial pump impellers. By the use of this PIV method it was possible to capture unsteady flow phenomena appearing in the impellers at throttled flow rates. Rotating stall cells have been observed in all impellers but the initiation point of rotating stall depends on the impeller geometry. The FFT analysis used to obtain the circumferential speed of the stall cell shows that the speed of the stall cell is independent from the impeller geometry. Nevertheless, the character of the stall cell is different in each impeller. For example, the flow is fully blocked in impeller 1 while the flow can still circulate on the pressure side for impeller 2.

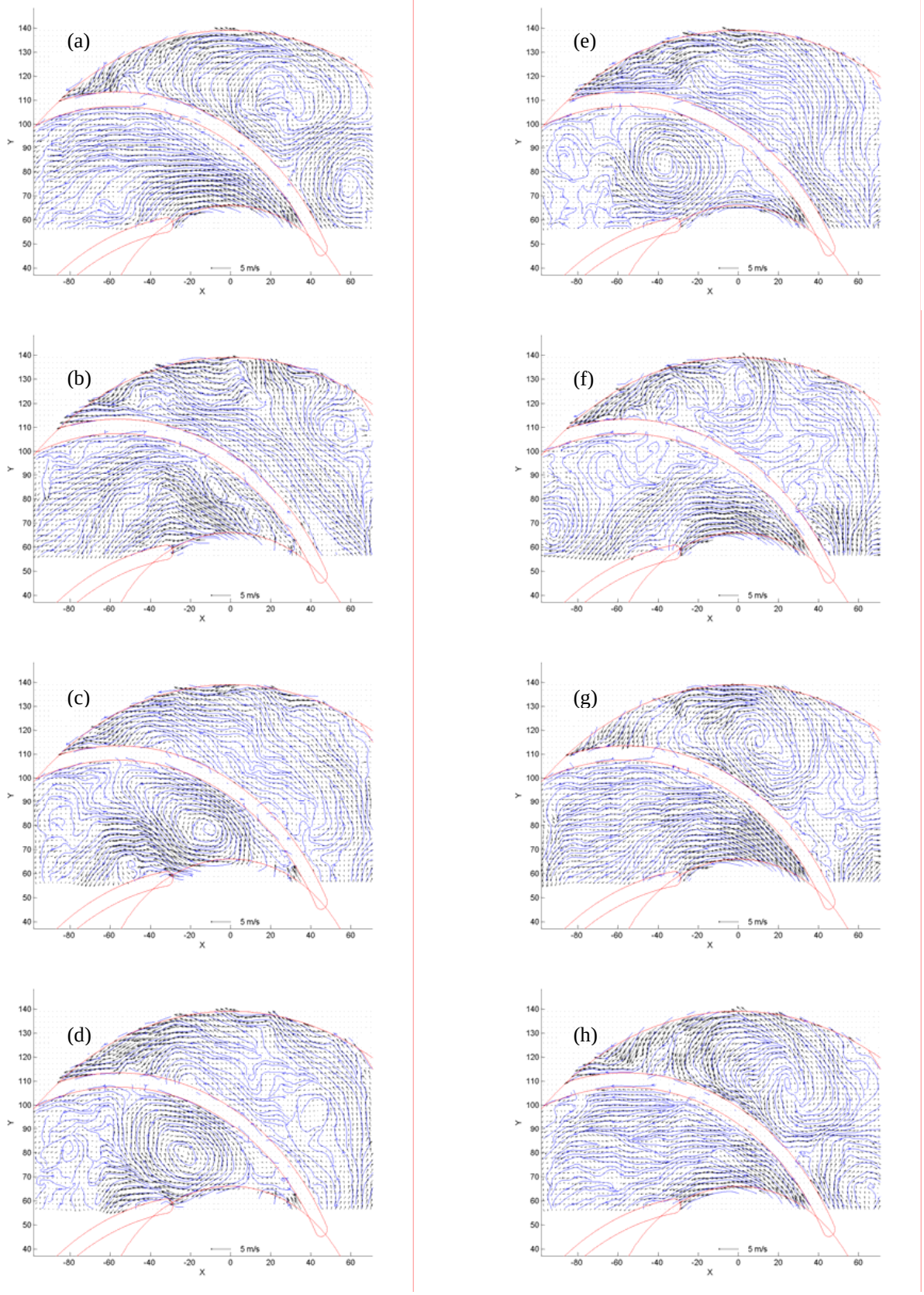

Figure 9a-h. Two blade passages of impeller 1 (t_a=0 ms, t_h=700 ms) from top to bottom, left to right, for Q/Q_d=0,25.

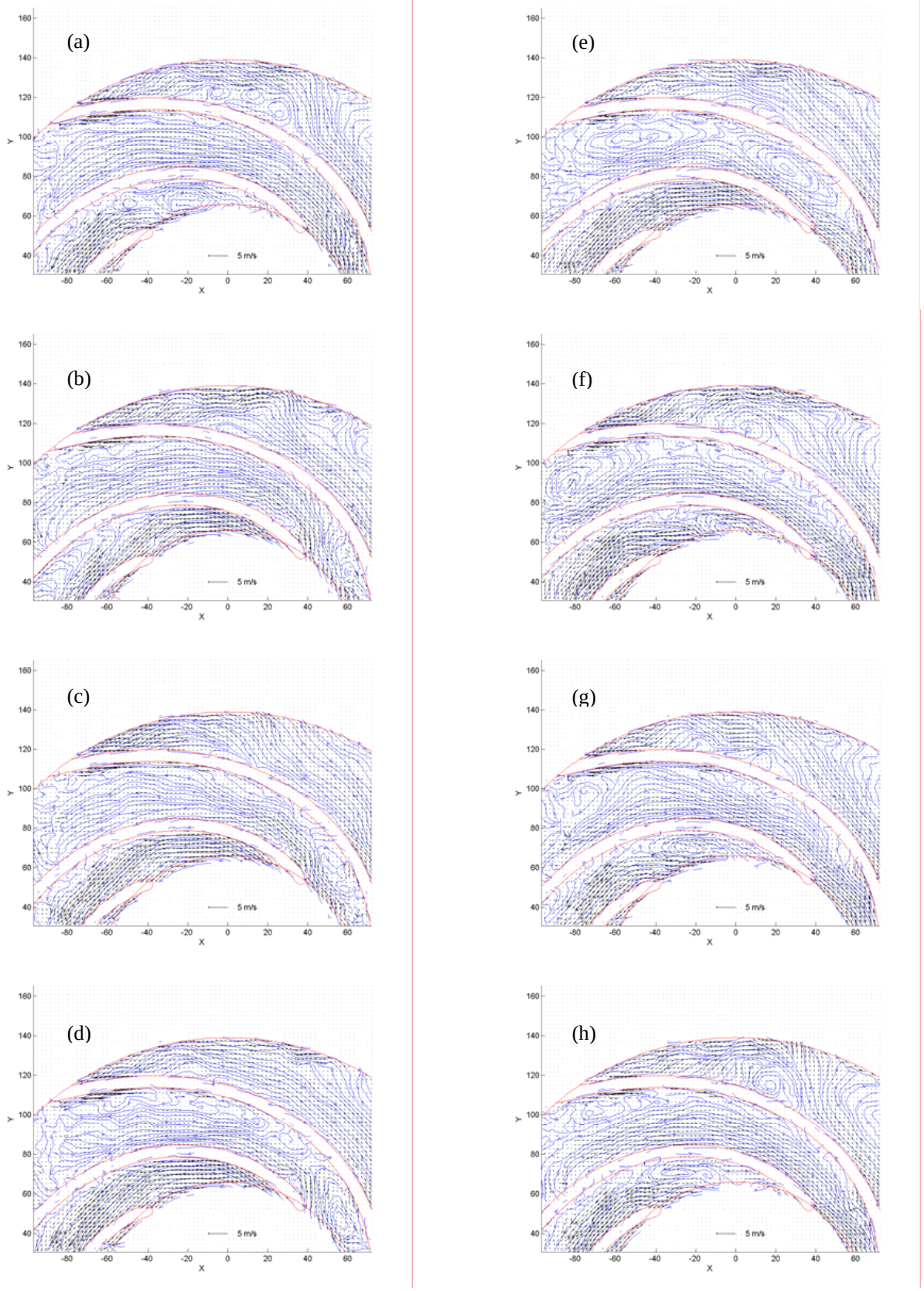

Figure 10a-h Three blade passages of impeller 2 (t_a=0 ms, t_h=700 ms) from top to bottom, left to right, Q/Q_d=0,25.

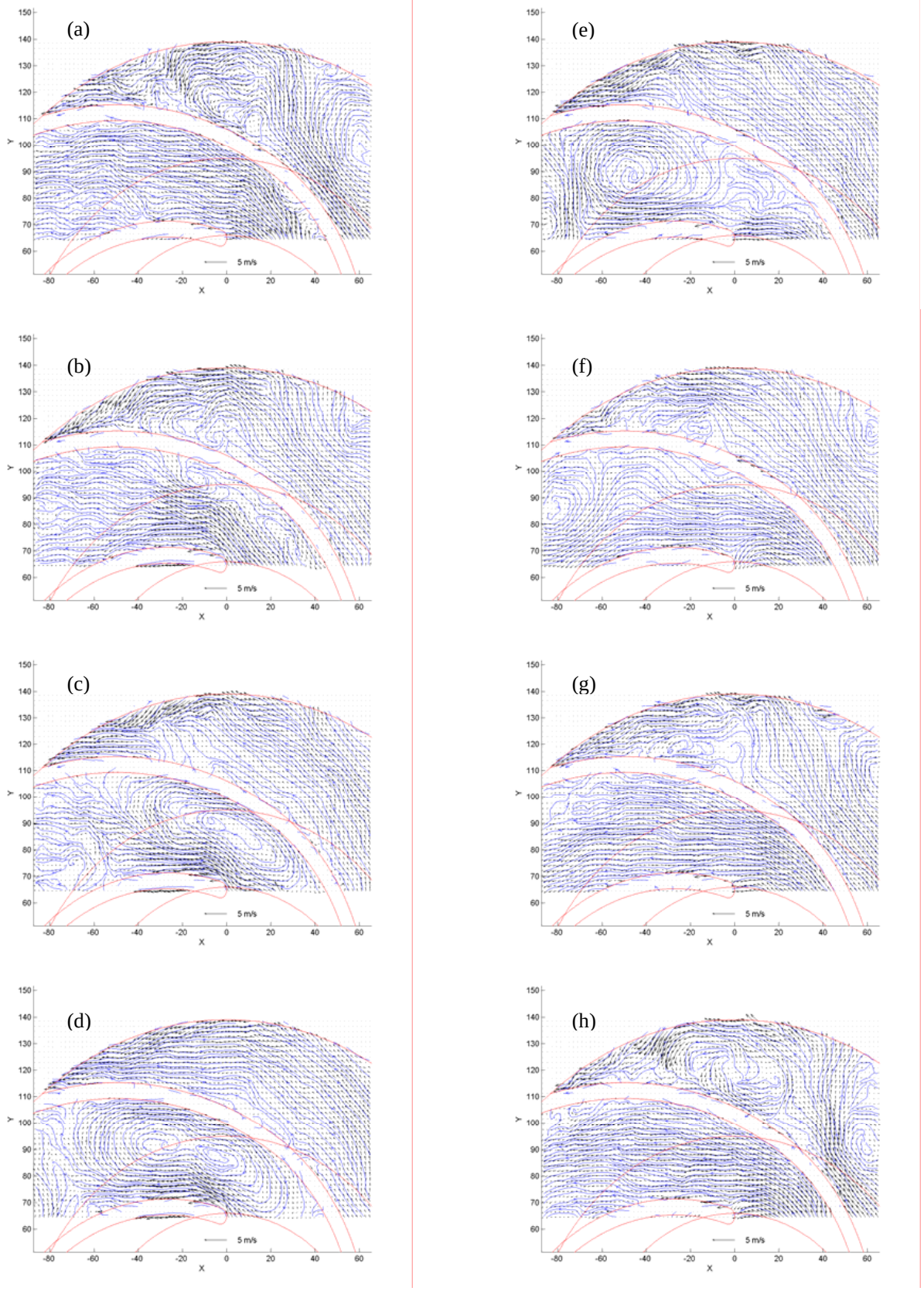

Figure 11a-h Two blade passages of impeller 3 (t_a=0 ms, t_h=700 ms) from top to bottom, left to right, Q/Q_d=0,25.

Further investigations will concentrate on the vortices and their development within the blade passages.

ACKNOWLEDGEMENTS

The authors thank DantecDynamics, Germany for the technical support.

REFERENCES

[1] Wurm, F.-H., 2004, "Systemintegration von Pumpen", Proc. *Pumpentagung Karlsruhe*, Karlsruhe, Germany, 16-3.

[2] Emmons, H. W., Pearson, C. E., and Grant, H. P., 1955, "Compressor surge and stall propagation", *Trans. ASME*, 79, pp. 455-469.

[3] Bently, D. E., Goldman, P., and Yuan, J., 2001, "Rotor Dynamics of Centrifugal Compressors in Rotating Stall", *Orbit*, 22, pp. 40-50.

[4] Inoue, M., Kuroumaru, M., Tanino, T., and Furukawa, M., 2000, "Propagation of multiple short-length-scale stall cells in an axial compressor rotor", *J Turbomachinery*, 122, pp. 45-54.

[5] Walbaum, M., 1999, "*Entstehungs-mechanismen und Erscheinungsformen des Rotating Stall in einem sechsstufigen Axialverdichter mit verstellbaren Leitschaufeln*", Fortschritt-Berichte, VDI Reihe 7, Strömungstechnik, 352, VDI Verl.

[6] Pampreen, R. C., 1993, "*Compressor surge and stall*", Concepts ETI.

[7] Dobat, A., Saathoff, H., and Wulff, D., 2001, "Experimentelle Untersuchungen zur Entstehung von Rotating Stall in Axialventilatoren", Proc. *Ventilatoren: Entwicklung - Planung - Betrieb*, Braunschweig, Germany, pp. 345-360.

[8] Escuret, J. F. and Garnier, V., 1996, "Stall inception measurements in a high-speed multistage compressor", *J Turbomachinery*, 118, pp. 690-696.

[9] Garnier, V. H., Epstein, A. H., and Greitzer, E. M., 1991, "Rotating waves as a stall inception indication in axial compressors", *J Turbomachinery*, 113, pp. 290-302.

[10] Höss, B., Leinhos, D., and Fottner, L., 2000, "Stall inception in the compressor system of a turbofan engine", *J Turbomachinery*, 122, pp. 32-44.

[11] Saxer-Felici, H. M., Saxer, A. P., Inderbitzin, A., and Gyarmathy, G., 1999, "Structure and propagation of rotating stall in a single- and a multi-stage axial compressor", Proc. *International Gas Turbine and Aeroengine Congress and Exhibition*, Indianapolis, Indiana, USA, ASME paper 99-GT-152.

[12] Surek, D., 2001, "Kombination von Radial- und Seitenkanalstufen für Turboverdichter", *Forschung im Ingenieurwesen*, 66, pp. 193-210.

[13] Day, I. J., 1993, "Stall inception in axial flow compressors", *J Turbomachinery*, 115, pp. 1-9.

[14] Place, J. M. M., Howard, M. A., and Cumpsty, N. A., 1996, "Simulating the multistage environment for single-stage compressor experiments", *J Turbomachinery*, 118, pp. 706-716.

[15] Wernet, M. P., Bright, M. M., and Skoch, G. J., 2001, "An investigation of surge in a high-speed centrifugal compressor using digital PIV", *J Turbomachinery*, 123, pp. 418-428.

[16] Krause, N., Zähringer, K., and Pap, E., 2005, "Time-Resolved Particle Imaging Velocimetry for the Investigation of Rotating Stall in a Radial Pump", *Exp. Fluids*, 39, pp. 192 - 201.

[17] Willert, C. E. and Gharib, M., 1991, "Digital Particle Image Velocimetry", *Exp. Fluids*, 10, pp 181-193.

Conference on Modelling Fluid Flow (CMFF'06)
The 13th International Conference on Fluid Flow Technologies
Budapest, Hungary, September 6-9, 2006

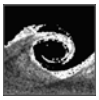

EXPERIMENTAL MEASUREMENTS OF THE EFFECT OF BLADE NUMBER ON A CENTRIFUGAL PUMP IMPELLER

David A. JOHNSON[1], Nicholas PEDERSEN[2], Christian B. JACOBSEN[3]

[1] Corresponding Author. Department of Mechanical Engineering, University of Waterloo, Waterloo, Ontario, Canada, N2L 3G1 Tel.: +1 519 888 4567, Fax: +1 519 885 5862 E-mail: da3johns@uwaterloo.ca
[2]Department of Fluid Mechanics, Research & Technology, Grundfos Management A/S, DK-8850 Bjerringbro, Denmark E-mail: nipedersen@grundfos.com
[3]Department of Fluid Mechanics, Research & Technology, Grundfos Management A/S, DK-8850 Bjerringbro, Denmark

ABSTRACT

Velocity measurements have been obtained in the internal passages of a centrifugal pump with a volute. The measurements have been obtained between the blade passages of a shrouded impeller and in the volute region using laser Doppler velocimetry (LDV). In this study a 3 colour 3 component laser Doppler system in full coincidence mode was utilized to measure three velocities simultaneously. Two impellers were evaluated that were identical with the exception that one contained six blades and the other had seven blades. Both were mounted in the same experimental rig and in the same volute housing. Although the main rotor geometry of each impeller was identical and the measured performance of the impellers was very similar a significant difference was found in the velocity patterns in the internal flow passages for some flow conditions. The velocity through the impeller was measured at both design load and at several off-design conditions. Results show that flow behaviour at design condition Q_d is aligned with the flow passages for both impeller configurations. At reduced flow cases the flow patterns began to differ significantly. For the six blade impeller at reduced flow off-design conditions ($0.25Q_d$) the measured flow pattern was altered significantly showing stable stall in every second passage and through flow in the other passages. In contrast to most previously reported studies significant reverse flow was found in the stalled passages on both the pressure and suction sides of the blade passages at some radial locations. For the seven blade impeller this stable stall phenomena was not observed and the passages were similar to previously reported studies where partially stalled flow passages or rotating stall conditions existed where the stall pattern rotated relative to the impeller with a regular frequency.

Keywords: centrifugal pump, LDV, off-design, stall

NOMENCLATURE

D	[m]	impeller diameter
H	[m]	head
N_s	[-]	specific speed
Q	[m^3/s]	volumetric flow rate
R	[m]	impeller outer radius
Re	[-]	Reynolds number ($\rho Vc/\mu$)
T	[Nm]	shaft torque
U	[m/s]	impeller tip speed
V	[m/s]	absolute fluid velocity
W	[m/s]	relative fluid velocity
c	[m]	blade chord length
g	[m/s^2]	gravitational acceleration
h	[m]	blade height
n	[rpm]	impeller rotation rate
r	[m]	radius
t	[m]	blade thickness
z	[-]	number of blades
β	[°]	blade angle from tangential
η	[-]	pump efficiency ($\rho QgH/T\omega$)
μ	[kg/ms]	fluid dynamic viscosity
ρ	[kg/m^3]	fluid density
ϕ	[-]	flow coefficient (V/U)
θ	[°]	angular position
ψ	[-]	head coefficient (gH_d/U^2)
ω	[rad/s]	impeller angular velocity

Subscripts and Superscripts

d	design value
PS, SS	pressure side, suction side
R	radial direction
T	tangential direction
$1,2$	inlet,outlet

1. INTRODUCTION

Centrifugal impellers have been widely studied in the past and performance of a well-designed machine at its' design point is quite predictable and is possible to model utilizing computational fluid dynamic (CFD) simulations. There is a great deal of interest in the performance of centrifugal machines away from the design point in order to allow a 'flat' efficiency curve (wider operating conditions) and to determine the characteristics. At design conditions flow entry onto the impeller blade surfaces should be aligned with the blade leading edge. Away from the design condition, at reduced flow for example, the fluid flow angles no longer align with the physical blade surfaces. In slight misalignment the stagnation point of the flow onto the blade moves toward the pressure side of the blade and a recirculation area will appear on the adjacent suction side surface. As the flow is reduced this recirculation area grows and will eventually cover the entire passage width. This stalled passage normally becomes stalled and unstalled with time due to factors such as circumferential pressure variation and system dynamics. In this form it is commonly referred to as 'rotating stall'. This type of stall has been documented in both incompressible and compressible flow rotating machinery.

General results of this phenomenon indicate that the propagation speed of a stall cell increases as the flow rate decreases (Shin et al., 1998 [1]). Sinha et al. (2001) [2] found a change in the slope of the performance curve to be indicative of the onset of rotating stall. Using time resolved particle image velocimetry (PIV), Krause et al. (2003) [3], (2005) [4] found rotating stall beginning at 50%Q_d and significant hysteresis in a pump performance curve at the position where rotating stall began. They also briefly discuss the effect of the higher pressure in the diffuser on the low pressure region of a blocked channel leading to inflow to the stalled passage. Studies similar to this have been reported in stationary components such as the vaned diffuser or volute of a centrifugal pump (Sano et al. (2002)[5] and Sinha et al. (2001)[2]) where the stall rotates at a small fraction of the blade passage frequency and the interaction between the diffuser vanes and the impeller is often cited as the cause of this condition (Eisele, 1996 [6]). The results reported here are of a slightly different type of stall condition, although produced under the same general mechanisms, where the stall is stationary with respect to the rotating frame of reference and is a repeatable and consistent condition. Krause et al. (2005)[4] do report a one (of 5) channel stationary stall condition at 0.5Q_d before the initiation of rotating stall. The single channel stall is later attributed to slight variation in manufacturing. The results reported here of a stationary stall condition are not consistent with these previous studies but agree with the results of Pedersen et al. (2003) [7] in a simplified axisymmetric configuration.

This paper will discuss some of the measured differences in the flow field between six and seven blade impeller configurations. For off-design cases the flow field is altered significantly and the measurement of stationary (in the rotating frame) stalled passages on the six blade impeller is discussed.

2. EXPERIMENT

Centrifugal impeller

The impeller under investigation is a shrouded low specific speed centrifugal pump impeller that is used in many applications including multi-stage centrifugal pumps, although it has been designed here as a single stage pump with a volute for these studies (Figure 1). Typical applications of pumps of this type are water transfer and circulation and pressure boosting in industrial process equipment.

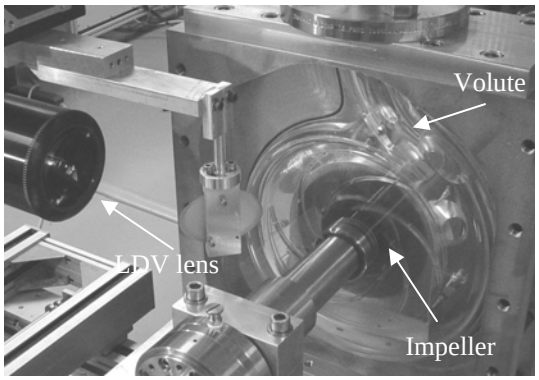

Figure 1: Acrylic centrifugal volute pump model

Figure 2 shows the geometry of one of the impellers, the six blade impeller. It consists of six simple curvature backward swept blades of constant thickness and blunt leading and trailing edges. The impeller has a plane hub and a mildly curved shroud plate such that the axial height of the impeller blade is tapered nearly linearly from 13.8 *mm* at the inlet to 5.8 *mm* at the outlet. Optical access to the impeller passages was accomplished by manufacturing the entire test impeller and volute in acrylic. All measurements were obtained through planar surfaces of acrylic with corrections made for the index of refraction variation (air/acrylic/water/acrylic/water). Table 1 summarizes the main dimensions of the impellers. The seven bladed impeller had identical dimensions and the only difference was the seven equally spaced blades.

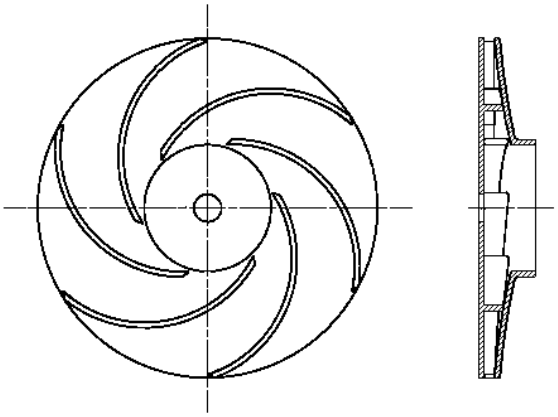

Figure 2: Blade-to-blade (left) and meridional (right) view of the shrouded 6 blade centrifugal pump impeller

Table 1. Impeller Geometries

Inlet diameter	D_1	77	*mm*
Outlet diameter	D_2	190	*mm*
Outlet radius	R	95	*mm*
Inlet height	h_1	13.8	*mm*
Outlet height	h_2	5.8	*mm*
Number of blades	z	6 or 7	-
Blade thickness	t	3	*mm*
Inlet blade angle	β_1	19.7	°
Outlet blade angle	β_2	18.4	°

Operating conditions

The test rig is a closed circuit system comprised of a supply tank, a test section and connecting pipes with the option of providing water temperature control and system pressure (or vacuum) control. The supply tank was continuously circulated to prevent seeding particles from settling. System flow rates were obtained with an Endress+Hauser Promag 30 Electromagnetic Flow Measuring System. Differential pressures were obtained with a Fischer Porter differential pressure transmitter.

The pump was driven by a DC motor. Shaft torque and rotational speed were measured with a calibrated torque meter mounted between the impeller and the motor.

Operating parameters at design are outlined in Table 2. Two test conditions were evaluated, the design condition and a severe off-design condition at 0.25 Q_d. The two test conditions are outlined in Table 3.

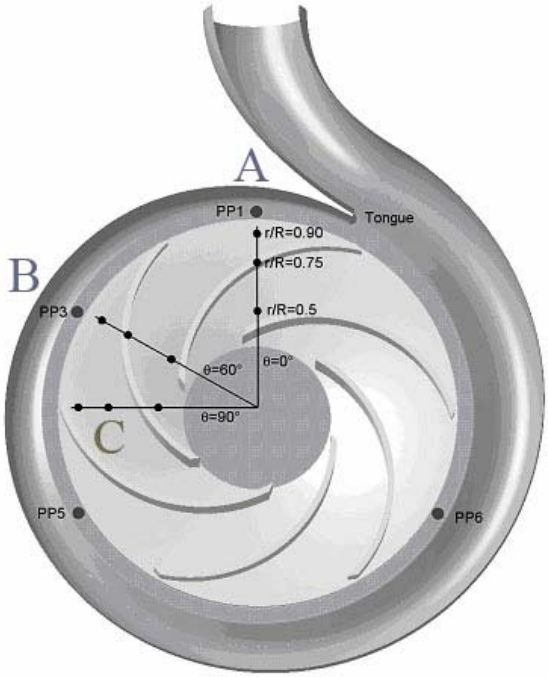

Figure 3: LDV measurement stations along three radial lines (line A θ = 0 deg, line B θ =60 deg and line C θ =90 deg) from the driven shaft side.

Table 2. Operating Conditions at Design

		6 blade	7 blade	
Rotational spd	n	725	725	*rpm*
Specific speed	N_s	0.40	0.39	-
Flow rate	Q_d	10.8	10.8	m^3/h
Head rise	H_d	2.81	2.88	*m*
Head coeff.	ψ_d	0.53	0.54	-
Flow coeff.	ϕ_d	0.12	0.12	-
Reynolds no.	Re	$1.1x10^5$		-
Efficiency	η_d	0.77	0.78	-

LDV System

In this study a 3 colour 3 component laser Doppler system in full coincidence mode was utilized to measure three velocities simultaneously. In this arrangement all 3 separated colour laser beam pairs exit from the same optics in order to facilitate optical access to the rotating impeller. Internal access to the impeller passages was through the planar volute casing on the hub side and through the planar impeller hub. Several optical arrangements using a planar front surface mirror were required (Figure 1). Measured axial velocities

were small relative to the radial and circumferential velocities and will not be discussed in this paper. The flow was seeded with neutrally buoyant polyamide seed particles with a mean diameter of 20 μm.

Table 3. Operating Conditions

6 blade		Design	Off-Design	
Flow rate	Q	10.8	2.7	m^3/h
Head rise	H	2.81	3.29	m
Efficiency	η	0.77	0.44	-
7 blade		Design	Off-Design	
Flow rate	Q	10.8	2.7	m^3/h
Head rise	H	2.88	3.33	m
Efficiency	η	0.78	0.47	-

Data Acquisition

The measurements were obtained in full coincidence mode with a once per revolution pulse reference from an optical transmitter/receiver mounted near the motor shaft. Typical data collection consisted of obtaining 500,000 validated data points at each impeller location with data rates between 50 and 200 Hz. These data were then phase resolved into bins of 360 1-degree bins providing approximately 1400 individual measurements in each bin. Using such small 1-degree bin divisions should allow accurate assessment of turbulence levels (Zhang et al., 1997 [8]). The velocities in each bin were subsequently ensemble averaged to create the bin average. As the volute creates asymmetry in the flow field, measurements were obtained at several angular orientations as shown in Figure 3, including a vertical plane from the centre of the driven shaft to the PP1 pressure tap location (θ = 0 deg, PP1-A), θ = 60 deg (corresponding to PP3 pressure tap location- B) and θ = 90 deg (C). All measurements reported here were all obtained at an axial position corresponding to the mid-height of the impeller exit (h_2/2). The measurements were obtained such that the pressure side (PS) will always be at the lowest angular position, i.e. for the 6 blade impeller 0 deg corresponds to the PS and 60 deg corresponds to the suction side (SS).

Uncertainty

Performance measurements include bias and precision components. Uncertainty in flow measurements are ±0.5% of the reading (±0.054 m^3/h at design) and uncertainty in the measured differential pressure is ±0.05 m water. Uncertainty in torque readings are ±0.2 Nm. Using the root sum square method (RSS) sample uncertainties are outlined in Table 4 (95% confidence).

Table 4. Sample Uncertainty Values

Flow rate	Q_d	10.8±0.054	m^3/h
Head rise	H_d	2.81±.05	m
Head coefficient	ψ_d	0.528±.004	-
Flow coefficient	ϕ_d	0.124±.001	-
Efficiency	η_d	0.77±0.01	-

Errors in LDV measurements are comprised of both bias and precision error components. Bias errors arise from many sources including probe volume positioning, velocity gradients, laser beam geometrical errors and seeding. Probe volume positioning was within 0.2 mm for each axis. Statistical uncertainties in the mean and RMS (root mean square) velocities were estimated to be 1.4% and 4.8% respectively (95% confidence).

RESULTS

The overall performance of the impeller at a speed of 725 *rpm* is shown in Figure 4. At the design flow rate of 10.8 m^3/h, a peak in the efficiency curve occurs. There are only minor variations in the measured head rise between the two blade variations. The 6 blade impeller has somewhat lower (max. 3 %) head rise for some operating points. The figure shows no obvious change in slope of the performance curve as cited by others to be an indicator of stall inception.

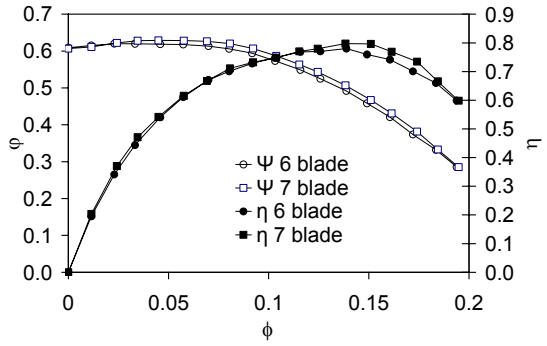

Figure 4: Measured performance curves for the volute pumps under investigation

Design Condition

All vector plots presented are the phase averaged 1 degree bin average velocities or the root

mean square (RMS) of these average values. The flow is well-behaved throughout the passage at the design condition as would be expected. At the inlet higher velocities are measured along the suction surfaces which are reoriented to the pressure side surfaces at the outlet consistent with secondary flow influences.

Design Condition

All vector plots presented are the phase averaged 1 degree bin average velocities or the root mean square (RMS) of these average values. The flow is well-behaved throughout the passage at the design condition as would be expected. At the inlet higher velocities are measured along the suction surfaces which are reoriented to the pressure side surfaces at the outlet consistent with secondary flow influences. A limited data set is shown for the design case due to space limitations.

A plot of the measured radial velocities are shown in Figure 5 for r/R=0.75 at Q=Q_d for the six bladed impeller at (h_2/2) and at all three angular positions (A,B,C) as shown in Figure 3. Each data point represents the bin average of approximately 1400 data points. As there are six impeller passages every 60 deg corresponds to one impeller passage from PS to SS. The similarity between each of the six passages for each radial station (A,B,C) is apparent. There is some variation between the radial stations with the highest velocities at location A and the lowest at location C as would be expected due to the influence of the volute.

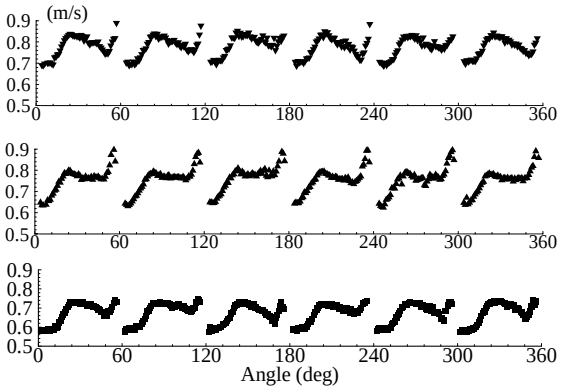

Figure 5: Absolute radial velocity V_R (m/s) for r/R=0.75, at A (θ = 0 deg) (top), B (mid), C (bottom) Design load, 6 blade impeller

Corresponding measurements for the seven bladed impeller are shown in Figure 6. There is less variation in the radial velocities between measurement stations A, B and C although angular position A has consistently higher peak velocities.

The flow behaviour for both impellers is as expected for a low specific speed centrifugal design where the peak radial velocities are highest near the suction side at r/R=0.50 and highest near the pressure side of the blades near the impeller exit at r/R = 0.9 suggesting reorientation near the impeller exit.

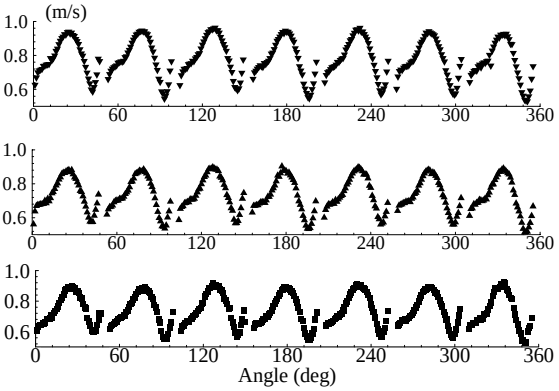

Figure 6: Absolute radial V_R velocity for r/R=0.75, at A (θ = 0 deg) (top), B (mid), C (bottom) Design load, 7 blade impeller

Off-design Condition

A sample complete vector plot for the entire impeller is shown in Figure 7 for the off-design condition measurements obtained along line B (60 deg). In every second passage the flow is well-behaved and the general flow pattern is consistent with the design condition with higher velocities on the suction surfaces at the inlet and reorientation to pressure side surfaces at the outlet. In the alternate passages between the pressure and suction surfaces there is no net flow as the positive through flow balances the reverse flow at each constant radial position. Measurements indicate a 'stall cell' rotating in the passage opposite to the impeller rotation direction. The direction of rotation is consistent with the relative eddy (potential vortex) concept which will occur due to no through flow in the passage and with the rotation direction found in previous studies ([4] and [7]).

A plot of the absolute radial velocities is shown in Figure 8 for the 6 bladed impeller at three radial stations for Q=0.25Q_d. In all radial stations the data shows clear evidence of the repeatability of the measurements between alternating passages. The difference between alternating stalled passages is apparent. The data for this plot would have been collected over a period of approximately 3 hours indicating that the 'stall cell' is not rotating and stable in the blocked passage. Other radial positions indicate similar phenomena. Positive through flow is indicated in every second passage while positive and reverse flow is indicated in the alternate passages. Again, there is some variation between the radial stations with the highest velocities at location A and the lowest at location C as would be expected due to the influence of the volute. RMS velocities, not shown, indicate similar levels to the design condition and do not indicate large velocity fluctuation in any passage.

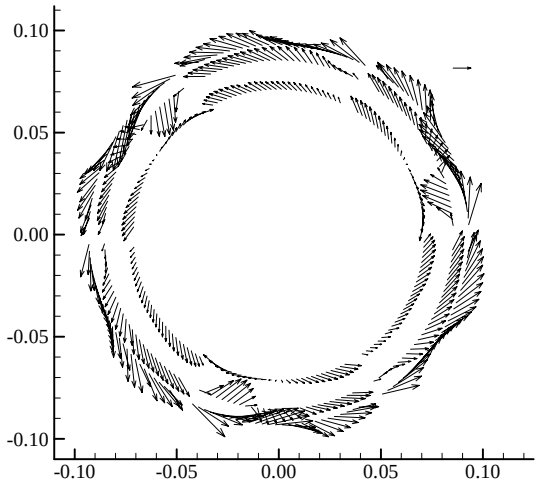

Figure 7: Measured *W* velocity, at θ = 60 deg-B, (Q=0.25Q_d), 6 blade impeller Reference Vector 1m/s Vectors removed for clarity

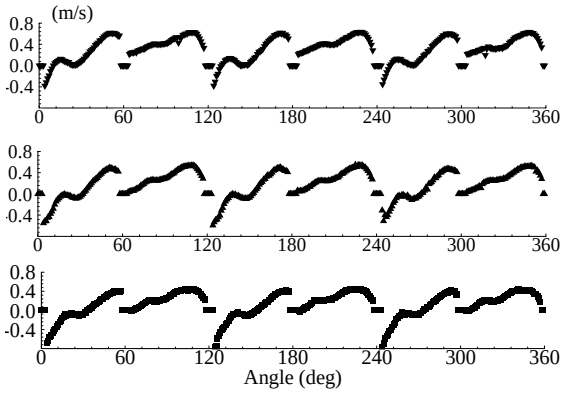

Figure 8: Absolute radial V_R velocity for r/R=0.75, at A (θ = 0 deg) (top), B (mid), C (bottom), Off-Design load Q=0.25Q_d, 6 blade impeller

Figure 9 shows the measured off-design bin average velocities for the 7 blade impeller. The results here are significantly different from those shown in Figure 7 for the 6 blade impeller. There is consistency between all the blade passages. At the inlet the flow is radially outward in the central passage but has slight flow reversal near the suction and pressure surfaces. As the flow progresses through the passage higher velocities are seen on the suction side with flow reversal on the pressure surfaces.

Figure 10 shows the absolute radial velocities for the 7 bladed impeller at three radial stations for Q=0.25Q_d. This plot is significantly different to the previous plot for the 6 blade impeller in that all passages are uniform and there is no variation between passages. Since the volumetric flow rate is the same for both impellers and the geometry, with the exception of the blade number, is the same for both impellers the velocity magnitudes should be very similar. The velocity magnitudes are much lower for the 7 bladed impeller (peak velocity 0.3 m/s) than in the 6 blade impeller. This difference is due to the reverse flow occuring in the 6 blade impeller (peak velocity 0.6 m/s). There is reverse flow indicated on the pressure side of all passages as been found in other low specific speed impellers [7],[10]. The highest velocities are found at location A and the lowest at location C as would be expected due to the influence of the volute.

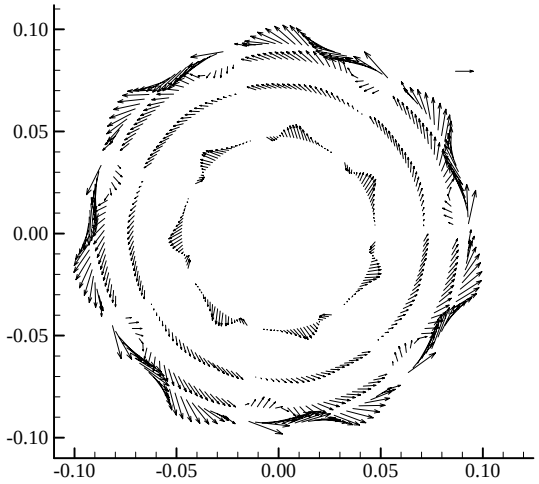

Figure 9: Measured *W* velocity, at θ = 60 deg-B, (Q=0.25Q_d), 7 blade impeller Reference Vector 1m/s Vectors removed for clarity

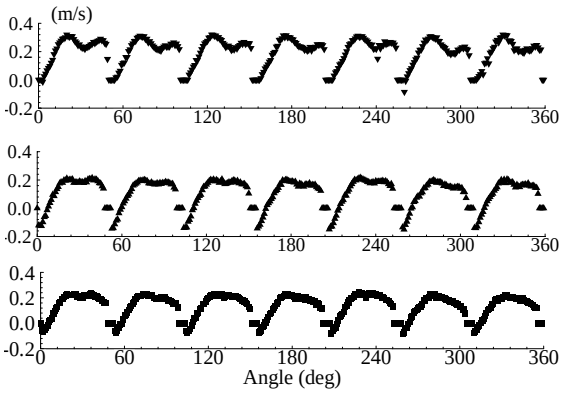

Figure 10: Absolute radial V_R velocity for r/R=0.75, at A (θ = 0 deg) (top), B (mid), C (bottom), Off-Design load Q=0.25Q_d, 7 blade impeller

To further understand the overall flow condition relative tangential velocities are presented for both impellers in Figures 11 and 12 for Q=0.25Q_d. Figure 11 shows that for the six blade impeller in the first passage there is a large velocity range and a sign change indicating that near the r/R = 0.75 location the centre of a rotating cell exists. The following passage (60-120 deg) indicates a standard tangential velocity profile in a passage with low tangential velocity on the pressure side corresponding to small radial velocities (Figure 8).

For the seven blade impeller (Figure 12) tangential velocities are always positive with the exception of near the pressure side.

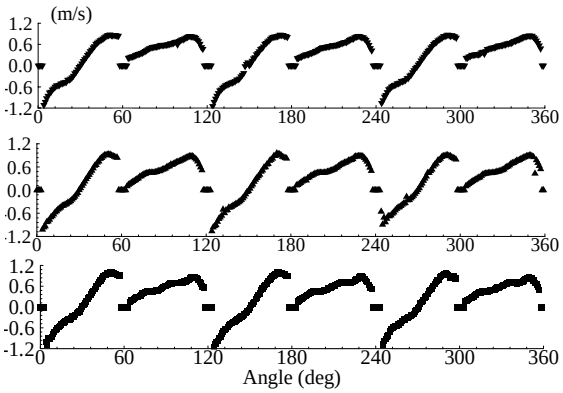

Figure 11: Relative tangential W_T velocity for r/R=0.75, at A (θ = 0 deg) (top), B (mid), C (bottom), Off-Design load Q=0.25Q_d, 6 blade impeller

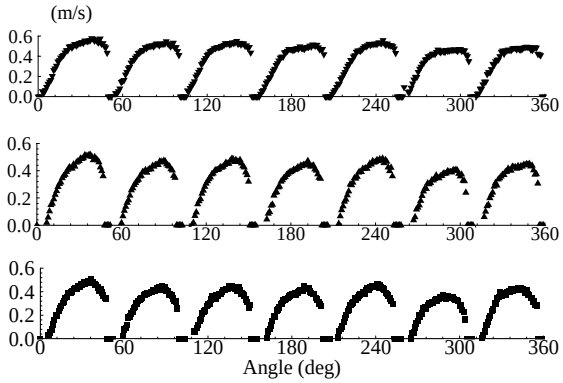

Figure 12: Relative tangential W_T velocity for r/R=0.75, at A (θ = 0 deg) (top), B (mid), C (bottom), Off-Design load Q=0.25Q_d, 7 blade impeller

Six Blade Impeller

For the six blade impeller at r/R = 0.5 the stalled passage has reverse flow over 60% of the passage width flow indicated by the negative radial velocities. The division of this reverse flow is approximately 60/40 suction/pressure side. Integration of the flow between the pressure and suction surfaces at the r/R=0.5 radius indicates a net small positive flow (about 8% of the adjacent passage flow) although it was difficult to measure velocities immediately adjacent to the pressure and suction blade surfaces which, in this case would have been contributions of negative velocity to the integration. At this radial position reverse flow is found on both the suction and pressure surfaces which is quite unusual, the more common finding is reverse flow on the suction surfaces only (see Rothe and Johnston (1976) [9] as an example). These results are more consistent with full stall in a stationary diffuser although the suction side reverse flow is somewhat larger. Reverse flow is never seen in the alternate passage at this radial location.

Near the exit of the impeller (r/R=0.75 and 0.9) there is also significant reverse flow indicated by the negative radial velocities at these positions representing 55% and 33% of the passage width respectively. In contrast to the r/R=0.5 velocity profiles, the reverse flow is apparent only on the pressure side for r/R=0.75 and 0.9. Integration of the flow profiles shows a small net negative or inward flow in the stalled passage. This figure also shows evidence of a small region of reverse flow (6% of passage width at r/R=0.75, 11% of passage width at r/R=0.9) in the unstalled passage on the pressure side of the blade suggesting moderate growth of a recirculating area toward the exit.

For all r/R values the alternate passages that have only directionally positive radial flow are similar in form to the flow profile for the design flow Q_d suggesting that those passages are relatively unaffected by the stall in the adjacent passage.

Seven Blade Impeller

In order to evaluate the flow variation in the seven blade impeller measured rms velocities are shown for the design load and the off-design case in Figures 13 and 14. These measurements are a combination of the effects of turbulence in the flow and the unsteady or fluctuating velocity components due to the relative motion between the measurement volume and the velocity gradients in the flow (Hesse and Howard, 1999 [10]). In all cases passage to passage similarity is very good showing the consistency of the data set and the uniformity of the measured flow. RMS velocity magnitudes are not significantly different between the design case and the off-design case so it is difficult to ascertain if the flow in the off-design case has significant velocity fluctuations that would be indicative of a rotating stall phenomena.

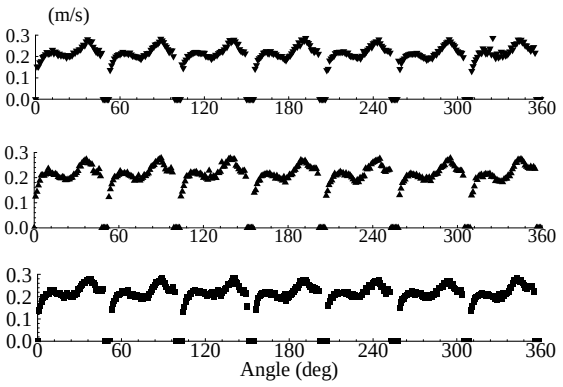

Figure 13: RMS of V_R velocity for r/R=0.75, at A (θ = 0 deg) (top), B (mid), C (bottom), Design load Q=Q_d, 7 blade impeller

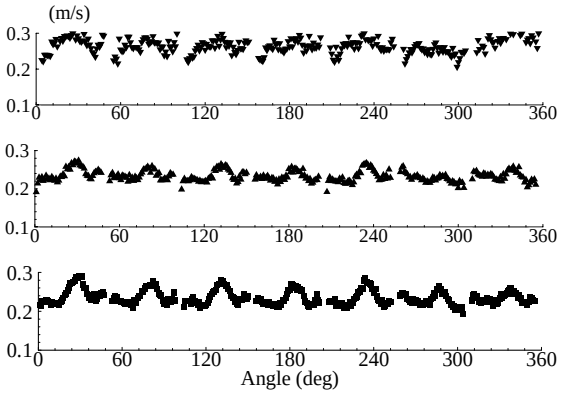

Figure 14: RMS of V_R velocity for r/R=0.75, at A (θ = 0 deg) (top), B (mid), C (bottom), Off-Design load Q=0.25Q_d, 7 blade impeller

CONCLUSIONS

Results of design flow performance measurements for a centrifugal pump are very similar for both six and seven bladed impellers in the same volute housing. Internal impeller passage velocity measurements show a design flow that is aligned with the blade passage for both impellers.

Significant differences were measured at off-design conditions however. The six bladed impeller developed an alternating passage configuration consisting of passages that had a stationary stall cell and passages that indicated aligned through flow.

Typical reported stall studies concentrate on a rotating stall phenomenon that is caused by flow misalignment and appears to rotate at a fraction of the impeller rotational speed. In this study, for the six blade impeller, as the flow is reduced the stalled passage does not become unstalled and remains in this flow pattern with a very stable structure. This phenomenon has been reported with PIV measurements (Pedersen et al., 2003[7]) in an axisymmetric configuration. Pressure variation, due to the volute housing or other mechanisms, that is normally associated with previously reported rotating stall measurements had no measurable influence on the entire passage stall cell. The seven blade impeller velocity measurements at reduced flow show similar flow in all seven passages with flow separation and reverse flow on the pressure surfaces. RMS velocities do not indicate significant variation in the flow passages.

The mechanism for the stable stationary stall cells in the six bladed impeller are not clearly understood but must be linked to the even number of blades in the impeller.

ACKNOWLEDGEMENTS

The first author acknowledges the support of the GRUNDFOS company during his time there.

REFERENCES

[1] Shin Y.H., Kim K.H. and Son B.J (1998). An experimental study on the development of a reverse flow zone in a vaneless diffuser. *Japanese Society of Mech. Eng.* **41**, 546–555.

[2] Sinha M., Pinarbasi A. and Katz J. (2001) The flow structure during onset and developed states of rotating stall within a vaned diffuser of a centrifugal pump. J. Fl. Engng.123, 490–499.

[3] Krause N., Zähringer K. and Pap E. (2003). Rotating stall in a rotating radial pump impeller using time resolved PIV. In Proceedings of CMFF '03, Budapest, Hungary, Sept.3-6, 2003.

[4] Krause N., Zähringer K. and Pap E. (2005). Time resolved particle image velocimetry for the investigation of rotating stall in a radial pump. Exp. Fluids. 39, 192-201.

[5] Sano T., Yoshida Y., Tsujimoto Y., Nakamura Y. and Matsushima T. (2002). Numerical study of rotating stall in a pump vaned diffuser. J. Fluids Engng. 124, 363–370.

[6] Eisele K., Zhang Z. and Muggli F. (1996). Investigation of the unsteady diffuser flow in a radial pump. 8th Int. Symp. Appl. Laser Tech. to Fluid Mechanics, 38.4.1.–38.4.7.

[7] Pedersen N., Larsen P.S. and Jacobsen C.B. (2003). Flow in a Centrifugal Pump Impeller at Design and Off-design Conditions – Part 1: Particle Image Velocimetry (PIV) and Laser Doppler Velocimetry (LDV) Measurements. J. Fluids Engng. 125, 61–72.

[8] Zhang, Z., Eisele K. and Hirt F. (1997). The influence of phase-averaging window size on the determination of turbulence quantities in unsteady turbulent flows. Exp. Fluids. 22, 265-267.

[9] Rothe, P.H. and Johnston, J.P., (1976). Effects of System Rotation on the Performance of Two Dimensional Diffusers. J. Fluids Eng, 98, 422-430.

[10]Hesse, N. and Howard, J.H.G., (1999). Experimental Investigation of Blade Loading Effects at Design Flow in Rotating Passages of Centrifugal Impellers, J. Fluids Eng. 121, 813–823.

Conference on Modelling Fluid Flow (CMFF'06)
The 13th International Conference on Fluid Flow Technologies
Budapest, Hungary, September 6-9, 2006

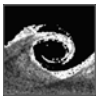

MEASUREMENTS OF UNSTABLE HEADCURVES AND ROTATING STALL IN AXIAL FLOW PUMPS WITH SWEPT BLADES UNDER CAVITATION INFLUENCE BY MEANS OF OSCILLATIONS AND BENDING MOMENTS

Helmut JABERG[1], Gerhart PENNINGER[2]

[1] Corresponding author. Institute for Hydraulic Fluid Machinery, University of Technology, Graz, Austria, E-Mail: helmut.jaberg@tugraz.at
[2] Voith Siemens Hydro Power Generation GmbH & Co. KG, 3100 St. Pölten, Austria, E-Mail: gerhart.penninger@vs-hydro.com

ABSTRACT

Four blade geometries for axial flow pumps were investigated to find out their hydraulic characteristics at the generally well known typical head curve instability. The geometries were a conventional blade with a radial leading edge, two blades with 45° forward , respectively backward, sweep and an blade with a variable forward sweep around 25° optimised with respect to cavitation and efficiency.

Assuming that the cavitational characteristics of axial flow pumps depend on the oscillatory behaviour of the blade, differently to radial blades which are fixed on hub and tip, pressure fluctuations in the flow field as well as blade vibrations were studied in cavitating and also in cavitation free flow. It was found that the incipient cavitation in fact depends on blade vibration but not developed cavitation.

Furthermore it was found that blade vibration indicates earlier than the pressure head the head curve instability, the low system pressure moves the head curve instability to larger flow rates. The head curve instability seems to be caused by suction recirculation rather than by the rotating stall which can be measured both at larger as well as at smaller flow rates than the head curve instability.

Additionally it was found that dynamical blade loading increases strongly in cavitating flow as compared to cavitation free flow.

Keywords: Axial flow pumps, rotating stall, head curve instability, blade sweep, cavitation, pressure fluctuation, blade oscillation

NOMENCLATURE

H	[m]	pressure head
NPSH	[m]	Net pressure suction head
peak	[*N*]	bending force
pressure pulsations	[*Pa*]	band width of pressure fluctuations
pulsations	[*N*]	band width of bending force pulsation
p	[*Pa*]	static pressure
Q	[l/sec]	Flow rate
rel. pressure pulsations	[-]	pressure pulsation non-dimensionalised w.r.t. H

1. INTRODUCTION

Axial flow pumps with forward and backward sweep yield improved cavitation behaviour and especially move the head curve instability with forward sweep to smaller flow rates and with backward sweep to larger flow rates as compared to the conventional un-swept blading. Earlier comprehensive investigations have been performed by Smith and Yeh [1], Beiler, [2], Stark [3], Kuhn [4].

The optimisation of swept bladings was investigated by Glas [5]. Further investigations were performed by Forstner [6] and also by Vad, who compared the fluid dynamical characteristics of swept and un-swept blades with free vortex and none free vortex design [7, 8]. The correlation of the head curve instability to rotating stall is also investigated by Jaberg and Forstner [9] where the results found by Day [10] could be shown to apply also to axial flow pumps and that stall cells and modes exist in this type of turbomachinery in a very similar way.

Cavitation can be influenced by using swept blades instead of conventional blades as is shown by the investigation mentioned above. That cavitation is also influenced by vibrational behaviour and thus it was concluded that the very sensitive cavitation characteristics of axial flow machinery could also be influenced by the vibrational behaviour of its blades which in general are only fixed on the hub and oscillate freely. In fact the vibrational behaviour and its possible subpression by means of an outer liner strongly influences the cavitation onset but not the developed cavitation as could be shown by Penninger [11]. By investigating the vibrational behaviour and pressure pulsations in the flow sys-

tem with swept and un-swept axial pump blades it can be shown that the head curve stability of axial flow pumps is strongly influenced by cavitation and is shifted with low NPSH-values to larger flow rates. The present paper shall give deeper inside in these observations.

2. EXPERIMENTAL SETUP

2.1 Test Rig for Hydraulic Measurements

All experiments were performed of on a cavitation–4-quadrant-test rig always in pump mode. The booster pump is installed as low as possible for cavitational reasons. The model pump and the pressure vessel (to adjust a variable system pressure to allow cavitation free as well as differently strong cavitating flows) are installed in the upper level as shown in figure 1. The model pump as well as the booster pump can be driven by variable speed.

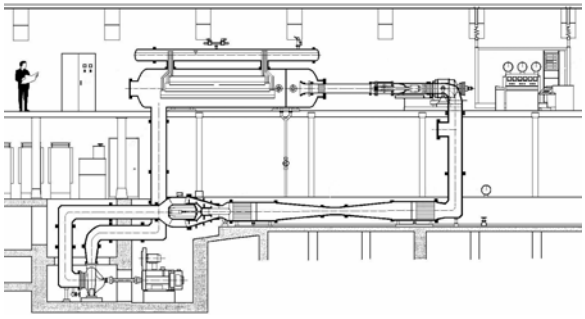

Fig.1: 4-quadrant test rig

The flow rate was as well measured by venturi pipe and differential pressure as well as by inductive flow meter were both were calibrated prior to the measurements. The pressure was measured by electronic differential pressure gauges and the torque by means of a hydrostatic baring and the measurement of the reaction baring force.

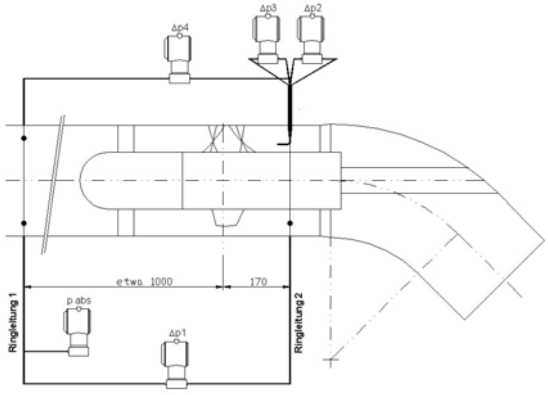

Fig. 2: Pressure measurement

Figure 2 gives an impression of how different pressures and the pump head were estimated.

2.2 Pump Blading

The geometrical data of the unswept pump bladings are given in table 1. The forward and backward swept blades result from this basic blade design by shifting the different profiles on their cylindrical plane in the relative flow direction so that the blade axis is directed 45° towards this flow direction or 45° with it as shown in figure 3 below. No correction of the blade design as recommended by Smith and Yeh [1] was performed.

Tab.1: Blade geometry

position			1	2	3	4	5	6	7
rel. blade height	h_{rel}	[%]	0	5	25	50	75	95	100
inlet angle	$\beta_{1'}$	[°]	37.36	36.06	31.58	27.23	23.87	21.7	21.21
outlet angle	$\beta_{2'}$	[°]	65.64	60.94	46.88	36.22	29.56	25.83	25.04
flow angle	β_{∞}	[°]	48.61	46.03	37.97	31.15	26.44	23.59	22.98
thickness ratio	d/l	[%]	12	11.2	9	7.5	6.5	6.03	6
solidity	t/l	[-]	0.805	0.833	0.946	1.088	1.231	1.355	1.389
profile turning angle	$\gamma=\beta_{2'}-\beta_{1'}$	[°]	38.18	34.26	22.81	15.97	14.02	13.54	13.64
incidence	i	[°]	1.86	1.39	-0.03	-1.64	-3.51	-4.75	-5.07
blade angle	$\beta_1=\beta_{1'}+i$	[°]	39.21	37.45	31.55	25.59	20.36	16.95	16.14
deviation	δ	[°]	11.76	10.77	7.47	5.34	4.82	4.66	4.73
blade angle	$\beta_2=\beta_1+\delta$	[°]	77.39	71.71	54.36	41.56	34.39	30.48	29.77
blade length	l	[mm]	111.9	113.4	118.2	122.8	126.2	127.6	127.6

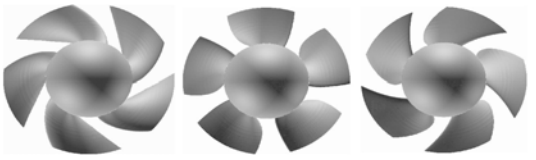

backward sweep wrc 45 | no sweep wuc 00 | forward sweep wvc 45

Fig. 3: Blade geometry

2.3 Measurements of the Bending-Forces in the Rotating System

To measure the blade vibrations the blade were equipped with strain gauges at the hub the orientation of which was chosen in the main stress direction calculated before. The middle strain gauge (fig 4a) served to measure the bending pulsations by means of the force to which it was calibrated [11]. The other two gauges measured the blade torque to which no reference is made in this paper.

The values measured by the strain gauges were led from the rotating to the stationary system by means of collector ring (fig.4b), and to avoid negative influences of electro-magnetic background noise the measurement signals were amplified in the rotating system and the design as a whole took care of electromagnetic compatility.

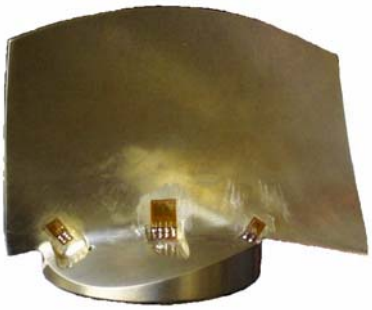

Fig. 4a: Blade with strain gauges

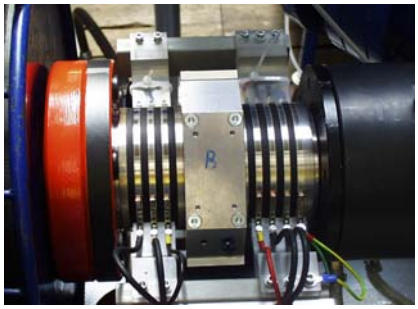

Fig.4b: Collector ring with amplifier

3. PRESSURE PULSATIONS FOR CAVITATING AND CAVITATION-FREE CONDITIONS

The head curves of all 4 pumps were measured as shown in fig. 5, were are the unswept blade and the ones with 45° sweep were published before [4]. All head curves were measured under cavitation free conditions.

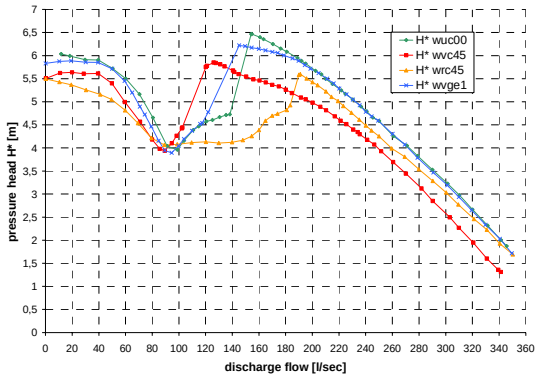

Fig. 5: Head curves with no cavitation

If cavitation of different strength prevails in the flow regime (fig.6) the drop of the head curve is shifted to much larger flow rates. Also visible in fig.6 is the hysteresis which also exists (but is not shown) for cavitation free flow (fig. 5). For large NPSH-values (as given in the box in fig.6) the flow rate where the head curve drops coincides with the one for cavitation free flow (fig. 5) as had to be expected. When throttling from larger to smaller flow rates the head curve drops at or below a flow rate of roughly 150 l/sec and this flow rate increases with decreasing NPSH value. Down to a NPSH value of 7 m no stable working point can be adjusted to the left of the head curve drop as it is shown by the straight line in fig. 6. To the left of a flow rate of 120 l/sec for large NPSH values the stable head curve can be measured again.

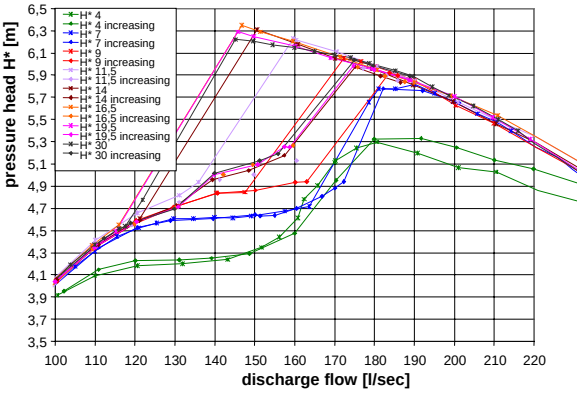

Fig. 6: Head curves with cavitation, NPSH=7 m, optimised forward swept blade wvge1

At a NPSH value of 4.5 m the cavitation is so pronounced that a considerable decrease of pressure head created can be measured and also the unstationary behaviour to the left of the head curve instability disappears – together with the hysteresis.

Thus cavitation obviously has a pronounced influence on the head curve stability even if the head curve does not indicate a presence of cavitation. Also the rotating stall present at flow rates slightly larger than at the instability interferes with cavitation as will be shown in the next paragraph.

When increasing the flow rate from very small values to larger ones, the head curve increases but at a much smaller flow rate then the previously descriped drop of the head curve when throttling the flow. This hysteresis is especially pronounced at large NPSH values (or cavitation free conditions) and it decreases with decreasing NPSH value, i.e. increasing cavitation intensity. For NPSH value of 7 m the head curve instability is still to be observed but practically no hysteresis. For strong cavitation (NPSH = 4,5 m) the hysteresis has disappeared and the drop of the head curve appears in a very stable manner: all operational points to the left of the head curve drop can be run.

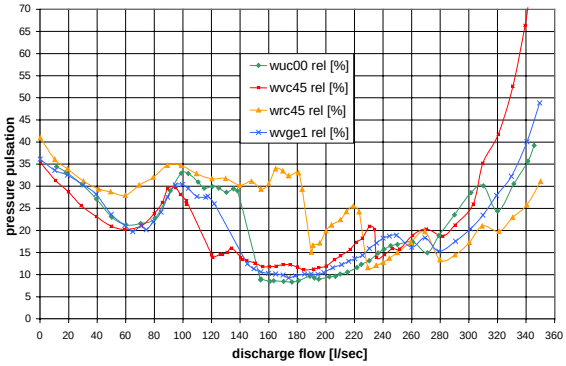

Fig.7: Pressure pulsations in non-cavitating flow

As it was presumed that blade vibrations are related in some way to cavitation the measurements were repeated and the pressure pulsations in the flow were recorded. Measurements of the blade vibrations themselves will be given below. These pressure pulsations are shown in fig. 7 for cavitation free flow, non-dimensionalised by the pressure head created at the appropriate flow rate. To the right of the design flow rate of 292 l/sec very large pulsations can be observed which come from pressure side flow separations at these flow rates. To the left of the design flow rate this pulsations remain at quite low levels (with the exception of the backwards swept blade) until the head curve instability occurs where the vibrational level increases for all 4 blades.

Together with cavitation new effects can be observed (fig.8). Strong pressure pulsations develop which concentrate in the entrance region of the blade as will be shown below. The number and the intensity of these pulsations increases with decreas-

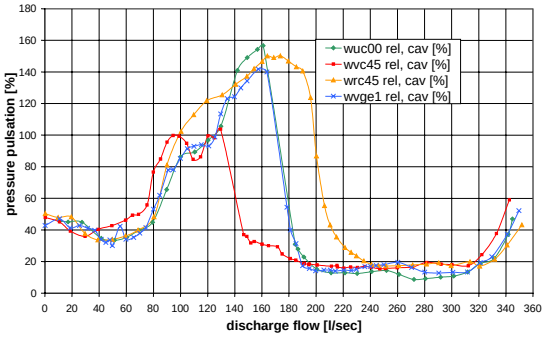

Fig.8: Pressure pulsations in cavitating flow

ing NPSH as had to be expected. Similar observations were made by Dörfler [12]and also Yedidiah [13] who describes that the parabolic pressure distribution in the suction recirculation leads to cavitation along the centreline of the flow shifting the main flow from the centre to the outer diameters which stops the recirculation in these areas and makes the cavitation bubbles implode. As the flow is still low suction recirculation develops anew and also the parabolic pressure distribution restarting the described procedure which goes with strong pressure pulsations and rotates with a frequency of 0.2 to 0.4 of the rotational speed.

If the pressure pulsations are measured (fig. 8) we observe a very similar behaviour at large flow rates above the design point and also at flow rates below the design point, but as soon as the head curve instability is approached the pressure pulsations increase to a much larger value as in the case of cavitation free flow.

It is also remarkable to observe by comparing the values given for the optimised blade in fig. 6 for the head curves and in fig. 8 for the oscillations that the increase of the oscillations commences at flow rates larger than the one where the head curve becomes unstable.

The maximum of the oscillations is observed at a flow rate below the instability thus at flow rates were the suction recirculation has fully developed. The frequencies of the oscillations in this fully developed suction recirculation flow agree with the rotational speed whereas the frequencies to the right (larger flow rates) of the instability point are lower than the rotational speed and thus seem to be correlated to the rotating stall. To look more closely into these correlations the blades were equipped with strain gauges to measure the oscillatory behaviour in the rotating system to get closer insight into the dynamical behaviour of the flow.

4. BLADE OSCILLATIONS IN THE ROTATING SYSTEM

4.1 Bending forces under cavitation influence

Bending forces are predominantly influenced by hydraulic forces lift and drag, the frictional forces in the gap between tip and casing can be shown to be small. Additionally these forces cause a torsion of the impeller blade which is not included here but was discussed by Penninger [11].

Fig. 9 shows the bending forces for the four blades studied without cavitation (bold lines) and under cavitation with NPSH = 7 m (dotted lines). The bending forces are quite different although the pressure head for all blades are roughly the same, for the unswept and the optimised blade they are exactly the same. These differences result from the different geometries of the blades with different radii for the resulting hydraulic forces. As the forward swept blade creates more pressure on the outer radii than the unswept or backward swept blades it creates a higher bending force [4,5].

It is interesting to see that in cavitating flow bending increases at the design point (Q=292 l/sec) for the unswept blade, but it decreases for the optimised blade and remains about unaltered in the case of forward and backward sweep. The unswept blade cavitates strongly at the outer diameters [4] which

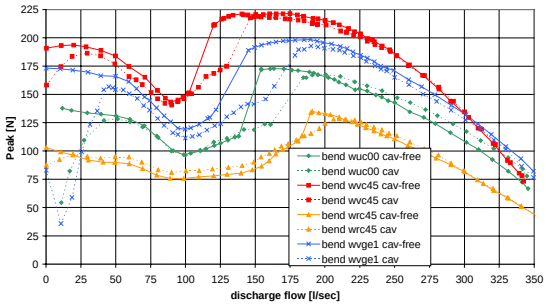

Fig.9: Mean bending forces in cavitating and cavitation free flow

surprisingly enough results in an increased bending force contrarily to what should be expected as the pressure distribution around the blade decreases in cavitating flow. The blade which is optimised with respect to its cavitational behaviour exhibits the

decreased bending force at the design point (and also at larger as well as at lower flow rates) which agrees well with theory as the cavitation is equally distributed from hub to tip causing an equally spread lower pressure distribution around the blade and thus lower bending force.

The forward swept blade cavitates much stronger around the hub and the backward swept blade at the tip [4], the bending forces remain practically constant at the design point, but decrease at partial load and *forward* sweep, and increase at partial load and *backward* sweep. Similar to the unswept blade this is the opposite than what theory tells as in the case of the unswept blade cavitation around the hub should move the blade loading towards the tip and thus increase bending. On the contrary cavitation around the tip (backwards swept blade) should move the blade loading towards the hub and thus decrease bending – always compared to the cavitation free flow.

That bending is much less influenced by cavitation close to zero flow for the swept blades seems to be due to the much better resistance of this blade geometry against developed cavitation as has already be shown by Kuhn [4] as compared to the unswept blade and also to the blade optimised with respect to cavitation which has much lower sweep and seems to loose its improved cavitational behaviour at this extremely low flow rate.

Similar to observations mentioned above the head curve instability is earlier detectable with decreasing flow rate in the case of cavitating flow and the instability itself is shifted to larger flow rates. With the exception of the forward swept blade with its comparatively low unstable flow rate all other head curves alter their shape prior to the instability (i.e. at larger flow rates) and where the backward swept

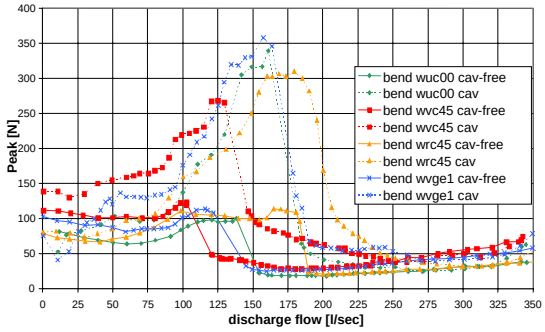

Fig. 10: Pulsations of the bending forces in cavitaing and cavitation free flow

blade looses the instability and simply exhibits a dropping though stable head curve.

If we look at the instationary pulsations of the bending forces (fig. 10) we see comparatively low values around the design point both for cavitating and cavitation free flow. In case of cavitation free flow (bold lines) and decreasing flow rate we see the sudden and steep increase of these pulsations at the head curve instability. But in the case of cavitating flow (NPSH = 7 m, dotted lines) the increase of the bending force pulsations commences at much larger flow rates (around Q=250 l/sec) where the head curve does not at all indicate any influence by the approaching instability.

It is well known that close to head curve instabilities (i.e. at larger flow rates) the rotating stall develops [9,10] correlating with cavitating flow as can be concluded from fig. 10. The interference of the rotating stall with cavitation induces a rotating movement of the cavitation areas [11] increasing at the same time the unstationary loading of the blade. The magnitude of the unstationary forces is lower for forward and backward sweep as compared to the unswept or the optimised blade which also has lower sweep. As the rotating stall develops especially at the casing around the blade tip this interference with cavitation is more pronounced for blades having the cavitation area at the tip (or over the whole blade) than a cavitation area which mainly develops along the hub as is the case for the forward swept blade.

4.2 Blade Loading around the Unstable Part of the Head Curve

Looking more closely at the hydraulic characteristics and the frequencies of instationary blade loading at flow rates slightly above or below the head curve instability gives more insight into their correlation to rotating stall. The following analysis can be made regardless of the blade eigen frequency measured to be 1000 Hz.

Fig.11 shows the vibration amplitudes of the

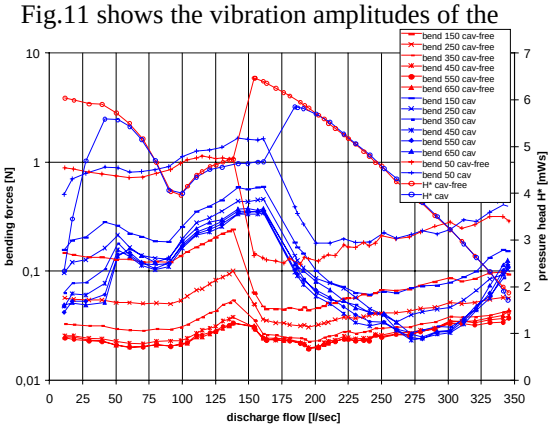

Fig.11: Amplitudes of bending force vibrations for different frequency intervals in cavitating (NPSH = 7 m) and cavitation free flow

bending force on the example of the conventional unswept blade again for cavitating and cavitation free flow. In case of the cavitation free flow and for all frequency intervalls a gradient decreasing with decreasing flow rate can be seen until the design point (292 l/sec) is reached from whereon a slight increase and around instability a sharp increase can be observed.

In case of cavitating flow (NPSH = 7 m) these observations remain almost the same if we look at

low frequency oscillations (50 Hz) but also there it can be shown [11] that it in creases much steeper once the flow rate falls short of the instability point. For larger frequencies a strong increase of the amplitudes of all frequencies is detectable starting at a flow rate of 120 % of the design flow. Fig.11 shows how strongly the bending force vibrations increase in the case of cavitating flow interfering with rotating stall. This is especially pronounced for low freuency vibrations as must be expected from the low rotating stall frequency.

Outside of the existence of rotating stall cavitation influences the blade vibrations in a way which must be caused by the reattachment of the main flow after cavitation areas as the “normal” cavitation frequencies of imploding bubbles are known to be 700 Hz and higher and are not investigated in this context. For larger frequencies than 700 Hz as the ones shown the amplitudes start to fade out (cf. fig.12, 13) and are therefore not of interest.

The rotational speed of the investigated axial pump is 18,33 Hz, further low frequency events are the rotating stall and separation frequencies which dominates around the instability flow rate, separation zones (also the reattaching flow after a cavitation area) and suction recirculation. The interference of the flow with rotaing stall can be seen best when the Fourier analysis of the unstationary blade vibrations (in the rotating system) and also of the pressure pulsations (in the stationary system) are looked at. Fig.12 shows the results on the example of the optimised forward swept blade both for in the

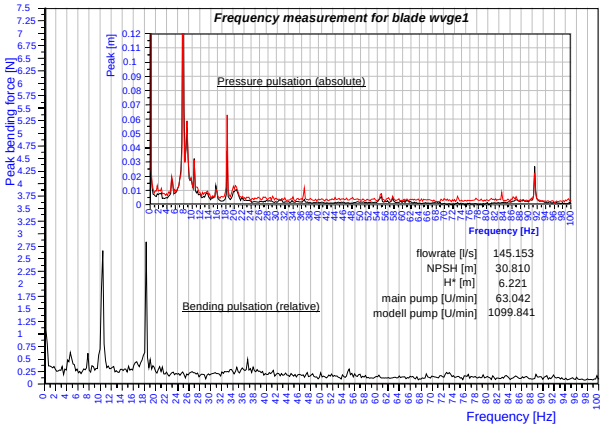

Fig.12: Frequency analysis of vibrational forces, forward swept blade wvge1, cavitation free flow

relative and absolute frame of reference. In both parts of fig.12 the rotational speed of 18.3 Hz is easily seen, also in the stationary system the rotational speed multiplied by the number of blades (5 blades = 91,5 Hz. Other resonances result from interference with the three support vanes in the entrance region or other equipment.

A peak is visible in the rotating system at 10,3 Hz and in the stationary one at 8 Hz. Both indicate the rotating stall the difference between the frequencies in both systems being the rotational speed of 18,3 Hz. It is worth mentioning that the rotating stall is much more pronounced for the unswept blade or the backward swept blade as for the forward swept blade shown.

The Fourier analysis belongs to a certain flow rate, if this measurement is repeated for different flow rates the onset of rotating stall can be detected as shown in fig.13 where its development with decreasing flow rate is shown until the head curve instability where the curves stop.

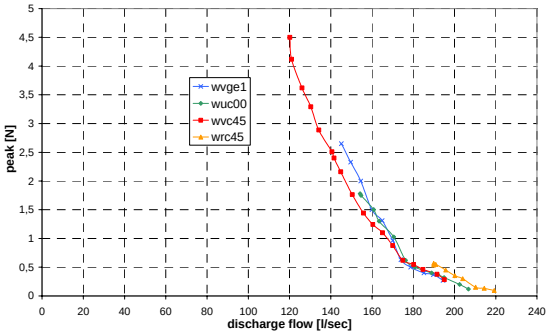

Fig.13: Rotating stall over the flow rate, cavitation free flow

It is interesting to see that all curves for so different blade geometries as forward, backward or unswept bladings coincide from which it must be concluded that the formation of the rotating stall depends on the blade profiles which are the same for all three impellers and differs only slightly for the optimised blade. Vice versa this means that at least for this blade arrangement investigated the rotating stall is a purely two-dimensional phenomenon. As it is known that rotating stall starts at the casing [6,9] it seem not to be dependent on neighbouring profiles or inlet angles.

From fig. 13 the onset of the rotating stall can not be concluded as it was found from blade vibrations and a very weak or small rotating stall could not be differed from the background noise present in fluid systems.

If the Fourier analysis is applied to cavitating flow (NPSH = 5.9 m) of the optimised blade we see

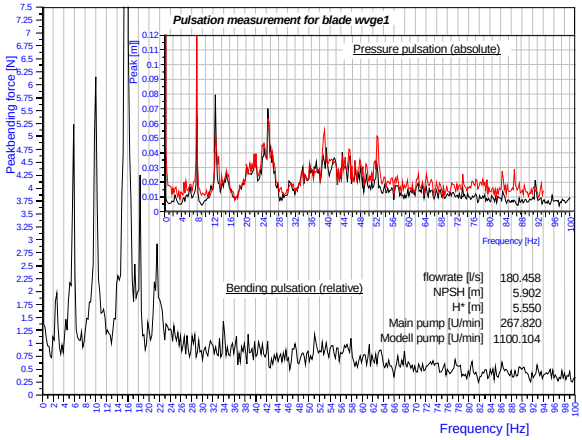

Fig.14: Fourier analysis if cavitating flow, optimised forward swept blade wvge1, NPSH = 5.9 m

first of all that background noise increases rapidly as is usual for cavitating flow (fig.14) and is also found for other blades [11]. But differently to the unswept blade where also in cavitating flow a single stall cell is to be measured we see the remarkable finding of five different resonance frequencies which are concluded to result from a split up of the single stall cell in cavitation free flow into five different cells in case of cavitation. It is also interesting to see that these stall cells obviously rotate with different rotational speeds the fasted of which rotates with more than the rotational speeding in the opposite direction.

In fig. 14 the rotational speed of 18.3 Hz can not be seen in the pressure pulsations in the stationary system due to the large amount of background noise.

In the same manner by measuring the pressure or bending force pulsations (but not shown) it could be seen that a rotating stall is also detectable at flow rates smaller than the instability [11].

5. CONCLUSIONS

From the measurements described above the following conclusions can be drawn, at least for the geometries investigated:

Blade sweep allows to shift the instability flow rate of axial flow pump bladings to smaller flow rates without negative consequences for efficiency or cavitation index.

The instability flow rate depends strongly on the system pressure and is shifted to largely higher flow rates in cavitating flow.

The onset of rotating stall does not depend on blade sweep .

REFERENCES

[1] Smith, L. M., Yeh, H., 1963, Sweep and Dehydral Effects in Axial-Flow Turbomachinery. J. Basic Engineering, 85, 401 – 416.

[2] Beiler, M. G., 1995, Numerical Flow Analysis of Low Pressure Axial Flow Fans with Blade Sweep, 10th Conf. Fluid Mach. Budapest, 58-66.

[3] Stark, U., Bookjans, W., Mauß, M., 1999, Kennlinienberechnung für Axialventilatoren mit gesichelten Schaufeln. VDI Fortschrittsbe-richte, Reihe 7, Nr. 356, VDI-Verlag, Düsseldorf.

[4] Kuhn, K., 2000, Experimentelle Untersuchung einer Axialpumpe und Rohrturbine mit gepfeilten Schaufeln, Diss. TU Graz.

[5] Glas, W., Jaberg, H., 2001, Multi-objective Evolutionary Algorithms for the Optimisation of Swept Pump Impellers. 4th Europ. Conf. Turbo Machinery, Fluid Dynamics and Thermodynamics, Florence.

[6] Forstner, M., Kuhn, K., Glas, W., Jaberg, H., 2001, The Flow Field of Pump Impellers with Forward and Backward Sweep. 4th Europ. Conf. Turbomachinery, Fluid Dynamics, Thermodynamics, Florence, 577 – 588.

[7] Vad, J., Bencze, F., Glas, W., Jaberg, H.: Comparative Investigation on Axial Flow Pump Rotors of Free Vortex and Non-Free Vortex Design.

[8] Vad, J., Kwedikha, A., Jaberg, H., 2004, Influence of Blade Sweep on the Energetic Beha-viour of Axial Flow Turbomachinery Rotors at Design Flow Rate. Proc. 2004 ASME Turbo Expo, Vienna, ASME-Paper GT 2004 – 53544.

[9] Jaberg, H., Forstner, M., 2003, About the Onset of Partload Instability of Swept and Unswept Axial Pump Blades. Conf. Model Fluid Flow (CMFF 03), Budapest.

[10] Day, I. J., 1993, Stall Inception in Axial Flow Compressors, ASME Journal of Turbomachinery, 115, 1 – 9.

[11] Penninger, G., 2004, Schwingungen und mechanische Belastungen von Axialpumpenschaufeln mit und ohne Pfeilung im kavitierenden offdesign Betrieb, Diss. TU Graz.

[12] Dörfler, P., 1982, Schwingungsanregende Strömungsvorgänge in hydraulischen Maschinen, Fachtagung über Schwingungen in Wasserkraftzentralen, Interlaken.

[13] Yedidiah, S., 1974, Oscillations at low NPSH caused by flow conditions in the suction pipe, ASME Cavitation and Multiphase Flow Forum.

Conference on Modelling Fluid Flow (CMFF'06)
The 13th International Conference on Fluid Flow Technologies
Budapest, Hungary, September 6-9, 2006

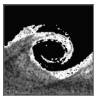

HYDRODYNAMIC FORCES ON THE IMPELLER OF A WATERJET PROPULSION SYSTEM

B.P.M. van Esch[1], N.W.H. Bulten[2]

[1] Corresponding Author. Department of Mechanical Engineering, Technische Universiteit Eindhoven. Postbus 513, 5600 MB Eindhoven, The Netherlands. Tel.: +31 40 2473158, Fax: +31 40 2475399, E-mail: b.p.m.v.esch@tue.nl
[2] Wärtsilä Propulsion Netherlands. E-mail: norbert.bulten@wartsila.com

ABSTRACT

In a waterjet system, a mixed-flow pump is used for ship propulsion. The suction flow to this pump is highly non-uniform due to the boundary layer under the hull of the ship and the shape of the inlet duct. Even at normal operating conditions, variations in axial velocity can be as high as 50 percent of the average value. This paper presents an experimental investigation of the resulting hydrodynamic forces on the impeller.

Measurements are performed on a scale model of a commercial waterjet pump. A newly designed dynamometer is used to measure the instantaneous forces and bending moments. This dynamometer is built between the impeller and the shaft of the pump and co-rotates with the impeller. Various suction flow distributions to the pump are achieved by means of a device situated in the suction pipe.

Results of measurements show the influence of the suction flow and blade interaction on forces. Among the most important observations are a backward whirling motion of the rotor system and a considerable steady radial force with an upward component.

Keywords: fluid-induced forces; hydrodynamics; mixed-flow pump; non-uniform suction flow; rotordynamics.

NOMENCLATURE

D	[m]	impeller outer diameter
N	[rps]	shaft speed
Q	[m^3/s]	flow rate
Re_Ω	[-]	Reynolds number based on shaft speed, $Re_\Omega = \Omega D^2/\nu$
Re_v	[-]	Reynolds number based on pipe velocity, $Re_v = 4Q/(\pi D\nu)$
ν	[m^2/s]	kinematic viscosity
ρ	[kg/m^3]	mass density
Ω	[rad/s]	shaft angular velocity

Subscripts and Superscripts

r	radial direction
X,Y	x- and y-components in lateral direction, in the steady frame of reference

1. INTRODUCTION

Forces on the shaft of a pump can be induced by mechanical causes or by the effect of the working fluid. Mass imbalance or misalignment is a well known cause of mechanical forces. However, fluid induced forces are still not fully understood and subject of ongoing research. Generally, hydraulic unbalance and a non-uniform pressure distribution at the periphery of the impeller are regarded as causes for a lateral force on the impeller. Hydrodynamic excitation forces result from a variety of unsteady flow phenomena such as stall, flow recirculation, cavitation, and interaction between rotor blades and, for example, the tongue of a volute or stator vanes. Hydrodynamic reaction forces on the other hand may result from rotor whirl or precessing motion relative to the casing.

Rotordynamic forces in a centrifugal pump were first measured by Domm and Hergt [1]. They demonstrated that impeller forces depend on rotor eccentricity. Similar investigations were performed by Hergt and Krieger [2], and Chamieh et al. [3].

Investigations by Jerry et al. [4] and Adkins et al. [5] have revealed that rotordynamic forces on the impeller of a radial pump may arise from two causes: firstly, by a non-uniform pressure distribution at the periphery of the impeller and, secondly, by a non-uniform pressure distribution in the leakage flow area between the impeller front shroud and the pump casing.

Jerry et al. [4] measured the reaction forces which resulted from impeller whirl. In these experiments the shaft of the pump was forced to undergo a whirling motion at different frequencies superimposed on the normal rotation of the impeller.

A non-uniform suction flow to a pump has an influence on pump performance (e.g. Toyokura [6], Badowski [7], Del Valle et al. [8]). This type of flow is encountered in many different pump designs, e.g. double suction pumps, sump pumps, in-line radial pumps, and pumps positioned closely to an upstream flow disturbance like a pipe bend. Yet, the effect on hydrodynamic forces has hardly been addressed in literature. Gülich and Egger [9] measured lateral forces on the shaft of a radial pump with different inlet chamber designs. Fujii et al. [10] investigated the blade loading of an inducer under cavitating conditions, with and without inlet flow distortion.

This paper presents an experimental assessment of radial forces on the impeller of a mixed-flow waterjet pump. The pump consists of a 6-bladed impeller and a stator bowl with 7 vanes. It is built into a dedicated test rig in which the forces on the impeller can be measured accurately. A specially designed, co-rotating dynamometer was used to this end. Since the suction pipe to the pump is straight, the axial velocity distribution of the flow is modified by a pipe bundle of a specific geometry. A distribution similar to what is encountered in real waterjet pump installations, is achieved. Results of measurements show the influence of the non-uniformity of the suction flow and the rotor-stator interaction on forces.

2. WATERJET PUMPS

Figure 1 shows a design of a waterjet system as it is encountered in most cases: a mixed-flow pump with an intake duct flush-mounted to the hull of the ship. Water is taken from below the ship and flows through the duct to the pump, is subsequently pressurized and accelerated in the nozzle. The inlet flow distribution in systems like these is inevitably non-uniform, caused by (see Figure 2):

- suction from the boundary layer
- diffusion and/or acceleration in the inlet duct, depending on operating conditions,
- the double bend in the inlet duct, and
- the rotating pump shaft protruding into the inlet duct.

The non-uniform inflow velocity distribution at normal operating condition is a phenomenon which is widely recognized (Seil et al. [11], Verbeek and Bulten [12], Brandner and Walker [13]).

As an example, measured axial velocity distributions are shown in Figure 3. These represent cases with a non-rotating pump shaft (see also Bulten and Van Esch [14]). Two operating conditions are given, representing a fully loaded and an unloaded vessel sailing at maximum power. Operating conditions of waterjet propelled ships are customarily classified according to the inlet velocity ratio *IVR,* which is defined as:

$$IVR = v_s / v_p$$

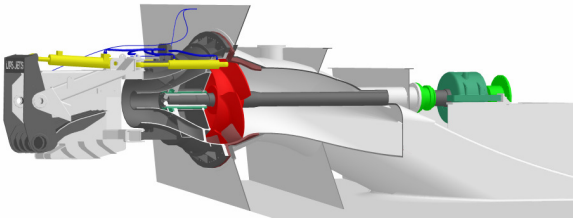

Figure 1. Waterjet propulsion system.

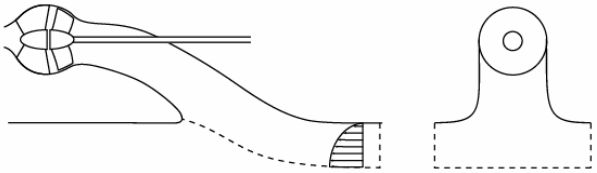

Figure 2. Sketch of a waterjet system showing the stream tube (dashed line) and boundary layer.

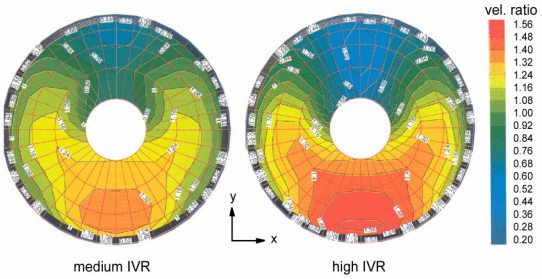

Figure 3. Measured axial velocity distribution in a plane normal to the shaft, just upstream of the impeller. Velocities are normalised with average axial velocity.

with v_s the ship speed and v_p the average axial velocity entering the pump. Thus, a fully loaded ship at maximum velocity has a medium *IVR* value while an unloaded ship at maximum velocity is characterized by a high value of *IVR*. Operating conditions during the start-up phase are characterized by low values of *IVR*.

3. EXPERIMENTAL SETUP

A scale-model version of a waterjet pump manufactured by Wärtsilä Propulsion Netherlands is built into the test facility at the Technische Universiteit Eindhoven (Figure 4). The main characteristics of this setup are: a closed-loop circuit of 18 m, a pipe diameter of 315 mm, an electromagnetic flow meter, a discharge butterfly valve, air release valves, and a pressure tank. The latter is used to pressurize the system in order to prevent cavitation. The pump is of mixed-flow type with a six-bladed impeller and a stator bowl with seven vanes. The impeller outer diameter is 335 mm. Pump characteristics are given in Figure 5. A key feature is the dynamometer. A detailed

description of this force sensing device is given in section 4.

In a normal waterjet pumping unit, the shaft is mounted at the suction side of the pump (Fig. 1). However, in this setup the shaft construction is changed and installed at the discharge (Nyirenda [15]). The reason for this alteration is that it enables a comparison between results obtained at non-uniform suction flow and equivalent results with uniform inlet flow. This is why the straight suction pipe is equipped with a flow redistribution device. Further discussion of this device is postponed till section 5.

Another adaptation to the pump, which is currently not in use however, is the dual shaft system by means of which the rotor can be set into a whirling motion. This feature is included in the design to allow for future measurements of hydrodynamic reaction forces.

Signals of the dynamometer are transmitted by cables which lead to a set of slip rings through a hole in the central shaft. The shaft of the pump is equipped with a pulse per revolution counter from which the instantaneous orientation of the impeller can be determined.

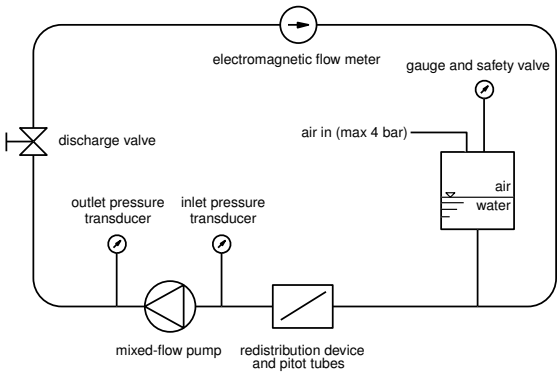

Figure 4. Experimental facility.

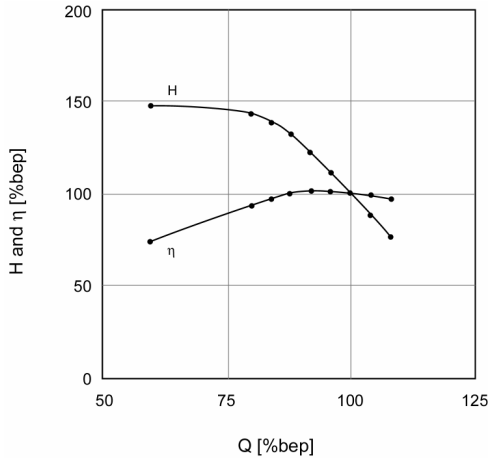

Figure 5. Measured pump characteristics for head H and efficiency η.

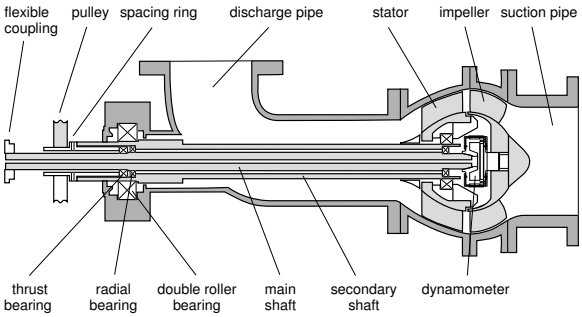

Figure 6. Cross section of the mixed-flow pump indicating the position of the dynamometer.

4. DYNAMOMETER

The dynamometer is a force sensing device which is placed between the shaft of the pump and the impeller (Fig. 6). Forces on the impeller are measured directly, as opposed to using external balances in bearings or pump support structures for which measurements are often hampered by unknown properties of dynamically loaded bearings and seals, or suffer from inaccuracies due to bearing play. The dynamometer has four square posts onto which six full Wheatstone bridges of strain gauges are mounted. This way, six generalized force components can be measured. The capability of the dynamometer to measure radial force as well as its associated bending moment is essential to this investigation, since the point of action of the radial force is not known a priori. The design resembles that of Jerry et al. [4] although positions of strain gauges are different. Electronics for stabilized bridge power supply and signal amplification is built into the dynamometer to minimize noise and prevent loss of signals (Fig. 7).

Calibration of the dynamometer is done both statically and dynamically. Static radial loading consists of a series of measurements with different weights applied at different axial distances from the dynamometer. The accuracy of the calibration is increased further by a dynamic calibration procedure in situ. A disc of known mass is mounted on the shaft at two different axial positions. Bridge signals are sampled while the system is running at the intended shaft speed. From these two measurements and the known mass and axial distances, the response of all six bridges to radial force and associated bending moment can be assessed. Additional runs with a disc of different weight at different positions revealed that the weight and the axial location of its centre of mass are determined with an accuracy of 0.1 and 0.2 percent respectively. The error in instantaneous forces, as calculated from the standard deviation in the ensemble averaged signal, is 3 percent.

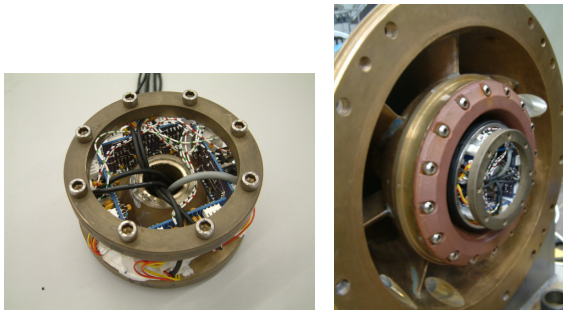

Figure 7. Dynamometer with electronics for bridge power supply and signal conditioning.

5. FLOW REDISTRIBUTION DEVICE

Since the axial velocity profile in the straight suction pipe of the setup is approximately uniform, a flow redistribution device of some sort is required. Its purpose is to modify the velocity distribution into a non-uniform profile as given in Figure 3. A bundle of tubes of small diameter is shaped according to the method of Kotansky [16]. The resulting velocity distribution should be of shear flow type. However, measurements showed that the resulting velocity distribution, though stable and non-uniform, by no means resembles the intended shear profile. Velocity measurements are performed with pitot tubes, in a plane just upstream of the impeller at a distance of 4 pipe diameters downstream of the redistribution device. Measured velocity profiles are given in Figure 8. Velocity profile *B* is obtained after rotation of the pipe bundle over 180 degrees.

Although velocity profile *B* does not closely resemble the situation encountered in waterjet pump installations, the main characteristic of a changing axial velocity in vertical direction is obtained. The resulting variation in velocity is almost in the range of what is normally encountered at medium values of *IVR* (Fig. 9). Therefore, it is concluded that many of the phenomena in waterjet installations related to the non-uniform entrance flow, can be studied in the current setup.

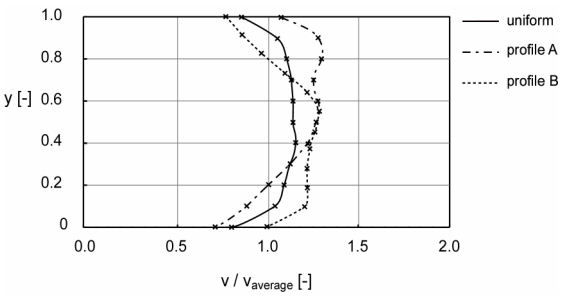

Figure 8. Axial velocity profiles with and without pipe bundle installed, along a vertical traverse.

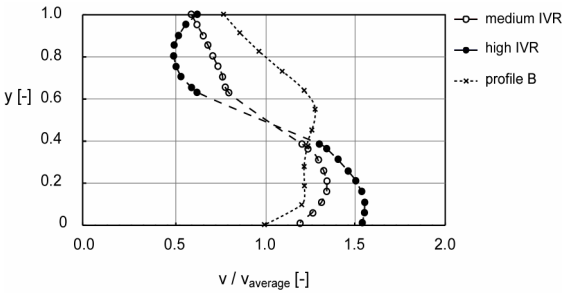

Figure 9. Comparison of velocity profile B with measured profiles in an intake duct (Fig. 3).

6. RESULTS

Experiments are performed with and without velocity redistribution device for different shaft speeds ranging from approx. 450 rpm to 900 rpm. Reynolds numbers are in the range: $Re_\Omega = 5 \cdot 10^6$ - $1.1 \cdot 10^7$, and $Re_v = 6.1 \cdot 10^5$ - $1.2 \cdot 10^6$, based on *BEP* operation. Flow rates are varied between 10% of Q_{BEP} and maximum flow rate (90% Q_{BEP} with pipe bundle installed, 100% Q_{BEP} without pipe bundle). For each run, bridge signals are sampled during approx. 500 shaft revolutions and ensemble averaged. No additional filtering is performed apart from the 50 Hz line frequency.

In section 6.1, results of force measurements are given for a shaft speed of 700 rpm, at maximum flow rate. The influence of the non-uniform suction flow distribution, as well as the blade interaction on radial forces is shown. A detailed study of the influence of flow rate on the steady fluid-induced force is presented in section 6.2. Finally, in section 6.3, the results are compared with values obtained from literature in order to emphasize the practical implications of a non-uniform suction flow in this kind of application.

6.1. Hydrodynamic forces

From the bridge signals, it is clear that the main contributions to the force on the impeller occur at frequencies equal to the shaft frequency and higher harmonics. Of these higher frequencies, the 7th harmonic is dominant. From the ensemble averaged bridge signals, one can calculate radial force components F_X and F_Y in the inertial frame of reference, during one impeller revolution. A typical result is given in Figure 10 for a shaft speed of 700 rpm, at 90% Q_{BEP}, and uniform suction flow profile. Since the geometry is axis-symmetric and the suction flow is uniform, the time-averaged radial force is approximately equal to the weight of the impeller in water.

Instantaneous forces show contributions at different frequencies. This is clearly observed in Figures 11 and 12, where only steady forces and force contributions at shaft frequency are shown.

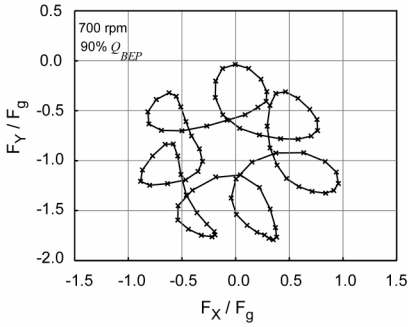

Figure 10. Force vector plot in the inertial frame of reference, normalised with impeller weight F_g in water, for uniform suction flow profile.

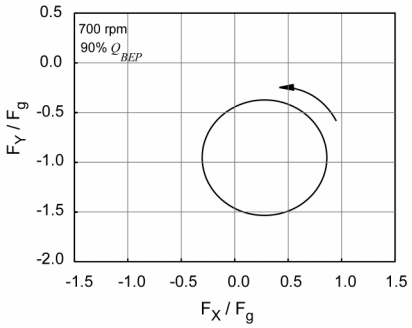

Figure 11. Force vector plot at zero and shaft frequency, for uniform suction flow profile.

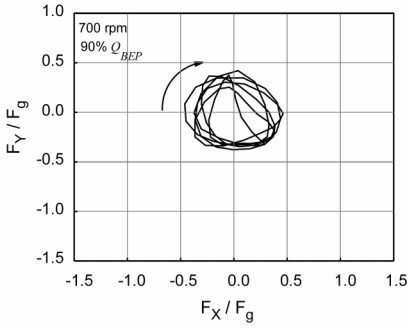

Figure 12. Force vector plot of rotor-stator blade interaction, inducing backward whirl of the impeller.

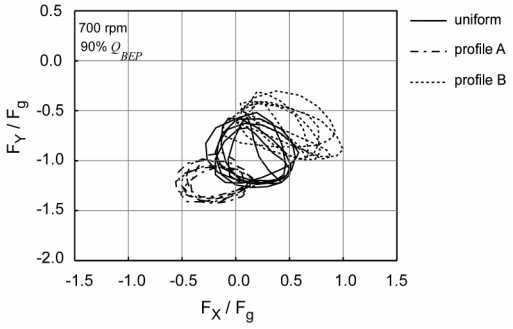

Figure 13. Force vector plot for different suction flow profiles.

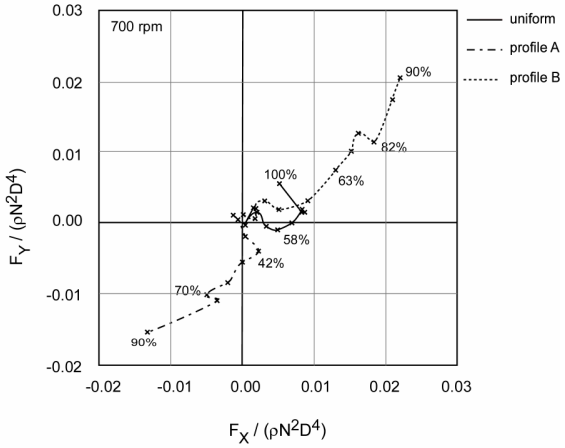

Figure 14. Normalised steady fluid-induced force, for different flow rates and suction flow profiles.

In Figure 11, the influence of impeller weight and centrifugal force is apparent. The latter is caused by mass imbalance and, to a larger extend, hydraulic imbalance. The centrifugal force component rotates in the direction of shaft revolution. Steady hydrodynamic force is small. Rotor-stator blade interaction force is shown in Figure 12, in the inertial frame of reference. Note that this blade excitation force induces a backward whirling motion of the impeller at a frequency of six times shaft frequency. Such motion is normally observed in rotor systems employing non-linear bearings and squeeze film dampers.

In case of a non-uniform suction flow distribution, similar force plots are obtained. However, an additional steady force is observed in a direction which depends on the suction flow profile. Results at 700 rpm and 90% Q_{BEP} are given in Figure 13. This steady force is induced by the working fluid and is directed opposite for velocity profiles *A* and *B*. A detailed analysis is given in the next section.

6.2. Steady fluid forces

Steady hydrodynamic forces have been measured for different combinations of shaft speed and flow rate, and for different suction flow profiles. The resulting fluid-induced force is a result of an unbalanced torque loading of the impeller blades when operating in a shear flow (Bulten and Van Esch [14]). The influence of flow rate on the steady force is given in Figure 14. Apparently, the force magnitude increases with flow rate, which confirms the findings of Gülich [9]. The direction of the force is opposite for the two non-uniform suction flow profiles *A* and *B*, consistent with the two profiles being approximately inversed in *y*-direction.

Measurements for suction profile *B*, which is indicative of the suction flow profile in practical

waterjet applications, are presented in the graphs of Figure 15, for different shaft speeds. Note that the steady fluid-induced force, especially its magnitude, scales with the square of the shaft speed. The direction of the force vector is approx. at 35 to 45 degrees with the horizontal axis for flow rates above 50% Q_{BEP}. For lower flow rate the direction

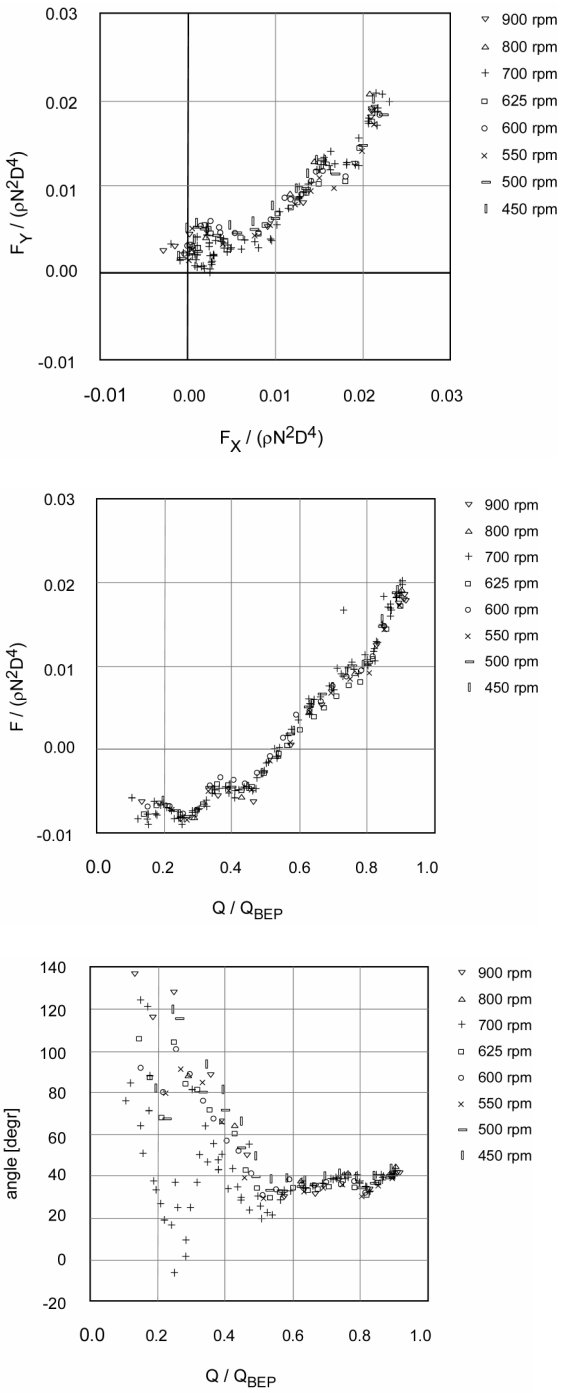

Figure 15. Normalized steady fluid-induced force for different flow rates and shaft speeds and suction velocity profile *B*. Graphs show force vector vectors, magnitude and direction.

deviates presumably due to inlet recirculation which influences the suction velocity profile.

From the results it is concluded that the impeller in a waterjet installation undergoes a lifting force as well as a lateral force component in horizontal direction. If not properly accounted for in the design phase of these pumps, this effect may lead to the bearings being unloaded at times, and thus to high levels of vibration, noise and damage.

6.3. Comparison

It is of interest to compare the magnitude of the forces measured in this investigation to forces mentioned in literature for pumps of the same type. An overview of force measurements on pump shafts can be found in e.g. Gülich [17]. The magnitude of forces is customarily divided in steady and unsteady components (in the inertial frame of reference). Figure 16 presents a comparison of the steady force components, as a function of flow rate. The measured values refer to the steady fluid-induced force caused by the non-uniform suction flow distribution in the experimental setup. Clearly, near design flow rate, the measured force is much higher than the values normally found in these pumps. At overload conditions, this difference only increases. It should be noted that a steady force is potentially harmful to the shaft, since it is experienced by the shaft as a fluctuating force, possibly leading to damage through fatigue failure.

Unsteady CFD calculations performed at Wärtsilä Propulsion indicate that steady fluid-induced forces will be even larger for the suction velocity profiles encountered in practice. Dimensionless radial force may be as high as 0.1 at design flow rate. This means that for the largest installations, the force will exceed the weight of the impeller several times. For smaller sized installations the force can even increase to over 10 times the impeller weight at full power.

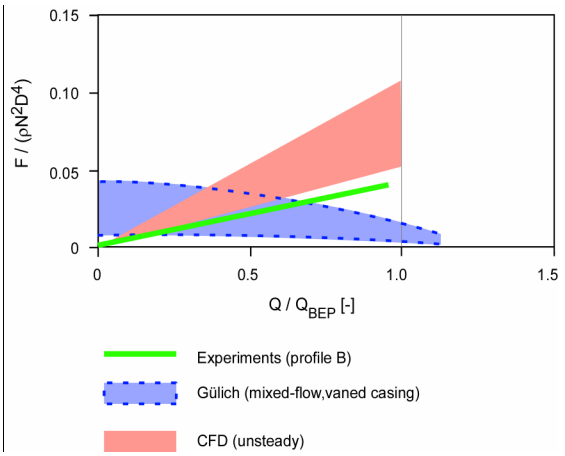

Figure 16. Comparison of radial forces as given in literature with measured values.

7. CONCLUSIONS

Measurements of radial forces are performed on a scale model waterjet pump. A newly designed co-rotating dynamometer is used, which is mounted between the impeller and the shaft. Attention is focused on the effect of a non-uniform suction flow on forces. Main conclusions are:

- Rotor-stator blade interaction generates excitation forces which lead to backward whirling motion of the impeller/shaft system.
- A non-uniform suction velocity profile leads to a steady fluid-induced force, the direction of which depends on the type of suction profile.
- Steady fluid-induced force scales with the shaft speed squared.
- The suction velocity profile as encountered in waterjet installations, generates a steady force with an upward component, essentially lifting the rotor system. In practical situations this may lead to bearings being unloaded.
- The magnitude of the steady fluid-force is much larger than normally anticipated in this type of pump, even for relatively mild suction velocity deviations of +/- 20%.
- For highly distorted suction velocity profiles, like encountered in waterjet applications, the steady force may exceed 10 times the weight of the impeller.

ACKNOWLEDGEMENTS

The authors would like to thank Wärtsilä Propulsion Netherlands for providing the scale model pump and supporting the publication of this paper.

REFERENCES

[1] Domm, U., and Hergt, P., 1970, “Radial forces on impeller of volute casing pumps,”Flow Research on Blading, L.S. Dzung, ed., Elsevier Publ. Co., Netherlands, pp. 305-321.

[2] Hergt, P., and Krieger, P., 1969 - 1970, “Radial forces in centrifugal pumps with guide vanes,” *Proceedings, Institute of Mechanical Engineers*, vol. 184, part 3N, pp. 101-107.

[3] Chamieh, D., Acosta, D.S., Brennen, C.E., and Caughey, T.K., 1985, “Experimental measurements of hydrodynamic radial forces and stiffness matrices for centrifugal pump impeller,” *ASME J Fluids Engineering*, vol. 107, no. 3, pp. 307-315.

[4] Jerry, B., Acosta, A.J., Brennen, C.E., and Caughey, T.K., 1985, “Forces on centrifugal pump impellers,” *Proceedings, 2nd International Pump Symposium*, Houston, TX, April 30- May 2.

[5] Adkins, D.R., and Brennen, C.E., 1988, “Analysis of hydrodynamic radial forces on centrifugal pump impellers,” *ASME J Fluids Engineering*, vol. 110, no. 1, pp. 20-28.

[6] Toyokura, T., 1961, “Studies on the Characteristics of Axial-Flow Pumps,” Parts 1-6, *Bull. JSME,* Vol. 4, pp. 287-340.

[7] Badowski, H. R., 1970, ”Inducers for Centrifugal Pumps,” Internal Report, Worthington Canada, Ltd.

[8] Del Valle, D., Braisted, D. M., and Brennen, C. E., 1992, “The Effects of Inlet Flow Modification on Cavitating Inducer Performance,”ASME *J Fluids Engineering*, Vol. 114, pp. 360-365.

[9] Gülich, J.F., Egger, R., 1992, “Part load flow and hydraulic stability of centrifugal pumps,” EPRI Report TR-100219

[10] Fulii, A., Azuma, S., Yoshida, Y., Tsujimoto, Y, Laffite, S., 2002, "Unsteady stress of 4-bladed inducer blades and the effect of inlet flow distortion," *JSME Int J series B*, vol. 45, pp 47-54.

[11] Seil, G.J., Fletcher, C.A., and Doctors, L.J., 1995, “The application of computational fluid dynamics to practical waterjet propulsion system design and analysis”, *Proceedings FAST’95*, pp. 1379-1389.

[12] Verbeek, R., and Bulten, N.W.H, 1998, “Recent developments in Waterjet Design”, Proceedings *Rina Waterjet Propulsion Conference*, Amsterdam.

[13] Brandner P., and Walker, G.J., 2001, “A waterjet test loop for the Tom Fink cavitation tunnel”, *Proceedings Waterjet Propulsion III Conference*, Gothenburg.

[14] Bulten, N.W.H., and van Esch, B.P.M., 2003, “Calculation of radial forces due to non-uniform entrance flow in a mixed-flow waterjet pump,” *Proceedings, 12th international conference on fluid flow technologies*, Budapest.

[15] Nyirenda, P.J., 2003, “Experimental study of hydrodynamic forces in mixed-flow pumps,” Ph.D. Thesis, Technische Universiteit Eindhoven, Eindhoven, The Netherlands.

[16] Kotansky, D.R., 1966, "the use of honeycomb for shear flow generation," *AIAA J*, vol. 4, pp. 1490-1491.

[17] Gülich, J.F., 1999, “Kreiselpumpen - Ein Handbuch für Entwicklung, Anlageplanung und Betrieb,” Springer-Verlag Berlin

Conference on Modelling Fluid Flow (CMFF'06)
The 13th International Conference on Fluid Flow Technologies
Budapest, Hungary, September 6-9, 2006

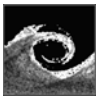

COMBINED ANALYTICAL AND NUMERICAL RADIAL FAN PERFORMANCE OPTIMIZATION

Philipp EPPLE[1], Časlav ILIC[2] and Franz DURST[3]

[1] Corresponding Author. Institute of Fluid Mechanics of the University of Erlangen – Nürnberg. Cauerstraße 4 - 91058 Erlangen – Germany. Telephone ++49-(0)9131-85-29480, Fax ++49-(0)9131-85-29503, Philipp.Epple@lstm.uni-erlangen.de
[2] Institute of Fluid Mechanics of the University of Erlangen – Nürnberg. E-mail: caslav.ilic@gmx.net
[3] Institute of Fluid Mechanics of the University of Erlangen – Nürnberg. E-mail: durst@lstm.uni-erlangen.de

ABSTRACT

In the present work a fully integrated analytical and computational method for radial impeller and fan design is presented, in order to achieve already in design stage the maximum possible efficiency. First the inlet and outlet dimensions for the combined impeller – diffuser – unit are found by a new integrated mean line analysis implemented as software using a steepest gradient method. In this step the system, where the fan has to operate, e.g. a vacuum cleaner, is already considered. After that, the optimum blade shapes for the impeller and the diffuser are computed in a second software module by an inverse method according to a prescribed pressure increase in the blade channels. This method leads to blade shapes with optimised pressure increase in the blade channel and, therefore, to high efficiencies. Looking now to the parameters and characteristic lines relevant for performance, the very best designs only are selected for further CFD computation. The selected designs are simulated with a commercial CFD program. In this step, the results of the design are validated and details are resolved. Finally prototypes were built. These prototypes where measured and the improvements where validated experimentally.

Keywords: CFD, inverse design method, integrated performance optimization, mean line analysis, radial impeller and diffuser, test rig measurements

NOMENCLATURE

Q	[$m^3 s^{-1}$]	flow rate
Re	[-]	Reynolds number
b	[m]	blade height
c	[$m s^{-1}$]	absolute velocity
d	[m]	diameter
n	[min^{-1}]	speed
n_q	[min^{-1}]	specific speed
p	[Pa]	pressure
r	[-]	reaction
r	[m]	radius
s	[m]	blade thickness
u	[$m s^{-1}$]	peripheral velocity
w	[$m s^{-1}$]	relative velocity
z	[-]	number of blades
Δ	[-]	variation of a quantity
Π	[-]	compression rate
α	[rad]	diffuser blade angle, Absolute impeller velocity angle
ß	[rad]	impeller blade angle
δ	[-]	diameter coefficient
φ	[rad]	blade angle
η	[–]	efficiency
ν	[$m^2 s^{-1}$]	kinematic viscosity of air
ρ	[$kg m^{-3}$]	density
σ	[-]	speed coefficient

Subscripts and Superscripts

1	at the impeller inlet
2	at the impeller exit
3	at the diffuser inlet
4	at the diffuser exit
t	total
s	static
d	dynamic
imp	impeller
dif	diffuser
rig	referring to test rig

1. INTRODUCTION

Nowadays the development of turbo-machinery is still performed mostly by improving existing geometries experimentally and/or applying simple design methods and rules out of the text books. The experience of the designer also plays a major role in this process. Increasingly, computational tools for the simulation of the flows in turbomachines are being utilized for turbomachine development. But

the simulation is only as good as the geometry input for simulation. Therefore, this tool is not enough to achieve substantial efficiency improvements.

At the LSTM a method was developed to perform a well directed design of turbomachines, such as centrifugally impellers and impeller-diffuser combinations, with special applications to vacuum cleaner fans, "Figure 1". With this method it is possible to optimise the hydraulic characteristics of turbomachines: flow rate, pressure and efficiency. It is an integrated optimisation strategy combining computer supported advanced design techniques with CFD computations.

The backbone of the method is formed by the classical methods of turbomachinery performance analysis. For the design of fans and centrifugal impellers a full digital mean line design is performed. To compute the blade shapes, an inverse method based on prescribed velocity and pressure distributions is utilized. This method leads to blade shapes with optimised pressure increase in the blade channel and, therefore, to high efficiencies. The numerical computation of these geometries is so fast that one can analyse hundreds of potential 1D designs in quite a short time. Looking now to the parameters and characteristic lines relevant for performance, the very best designs only are selected for further development. This step has more influence on the success of the design than any other part of the design process.

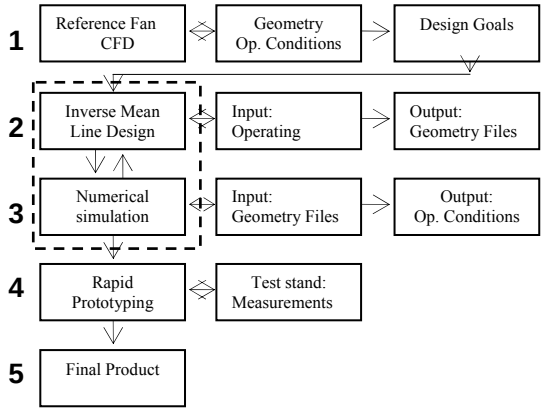

Figure 1. Fan design process

2. PRE-DESIGN CONSIDERATIONS

Vacuum cleaner impellers, diffusers and fans have a specific speed $n_q = 10 - 40$ [min^{-1}], a speed coefficient of about $\sigma = 0.1$ and a diameter coefficient of approximately $\delta = 10$, Bohl [1]. Plotting these numbers in the Cordier diagram, Cordier [2], one can see that one gets a pure radial machine, "Figure 2".

Generally one can say that the compression rate Π of a centrifugal compressor can be classified as follows:

1. Fans: $0 < \Pi < 1.1$
2. Blowers: $1.1 < \Pi < 4$
3. Compressors: $\Pi > 4$

The pressure increase measured in vacuum cleaner fans is of the order of 10.000 [Pa] to 20.000 [Pa]. This means the one has a compression rate of about Π=1.1 – 1.25, Sigloch [5]. This means a density change in the fan of $\Delta\rho$ = 10%-20%. Since this density changes are still small one can perform an incompressible design.

Typical speeds of vacuum cleaner fans are about n=40.000 [min^{-1}], the impeller exit diameter is of the order of $D_2 = 0.1$ [m] and the impeller exit height is of the order of $b_2 = 0.005$ [m]. Computing the Reynolds number Re based on the peripheral speed $U_2 = \pi D n$ of about 200 [m/s] and on the exit height b_2

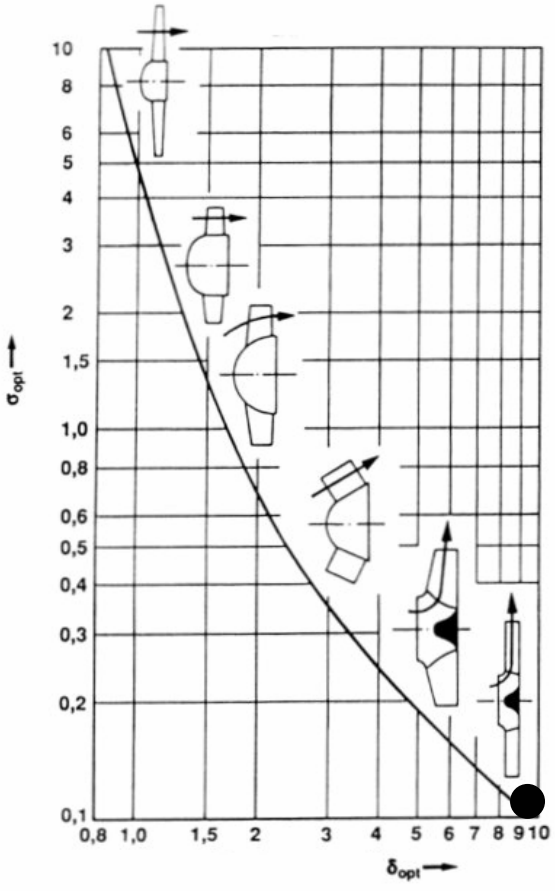

Figure 2. The Cordier diagram (Bohl [1])

$$\mathrm{Re} = \frac{u_2\, b_2}{\nu} = O[10^5] \qquad (1)$$

where ν is the kinematic viscosity of the air. Hence the inertial forces are much greater than the viscous

forces, Batchelor [1], and therefore, for design purposes, the viscous forces may be neglected.

Besides, vacuum cleaner impeller and diffuser blades are single curved. It will be assumed that the flow follows the blade angles and is, for design purposes, essentially one dimensional, Eck [3]. Strictly speaking this condition holds only for an infinite number of blades and for a finite number of blades the flow angle may differ from the blade angle to some extent.

3. INVERSE MEANLINE DESIGN

The present inverse mean line design method is partially based on the method first presented by Pantell [5], only that it is worked out for single twisted blades. Besides, Pantell´s method is a method suited to compute blade shapes only and does not give any information on the proper inlet and outlet parameters. It can be applied to impeller blades as well as to diffuser blades.

3.1 Inlet and outlet parameters

As an input for the blade shape it is first necessary to provide the inlet and outlet geometrical parameters d_1, d_2, b_1, b_2, $ß_1$ and $ß_2$, Figure 3, required by the kinematical form of the Euler turbomachinery equation, Eck [3], as well as the flow rate and the speed, i.e. to fully define the velocity triangles at the inlet and the outlet:

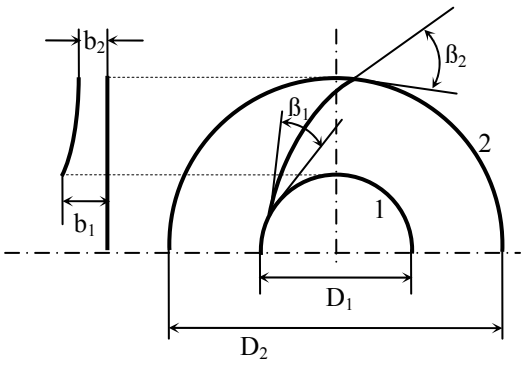

Figure 3. Inlet and outlet geometry parameters

$$\Delta p_{t-imp} = \frac{\rho}{2}\left[\left(c_2^2 - c_1^2\right) + \left(u_2^2 - u_1^2\right) + \left(w_1^2 - w_2^2\right)\right] \quad (2)$$

$$\Delta p_{s-imp} = \frac{\rho}{2}\left[\left(u_2^2 - u_1^2\right) + \left(w_1^2 - w_2^2\right)\right] \quad (3)$$

$$\Delta p_{d-imp} = \frac{\rho}{2}\left(c_2^2 - c_1^2\right) \quad (4)$$

These formulas apply from the inlet to the exit of the impeller. The reaction of the impeller is given by the ratio of the static pressure increase to the total pressure increase, Eck [3]:

$$r = \frac{\Delta p_s}{\Delta p_t} \quad (5)$$

In the literature, e.g. Eck [3] and Enßlinger [4], it is common to read that in order to achieve high efficiencies one should have a reaction as high as possible. The reaction is a measure of the static pressure increase between the inlet and the outlet of the impeller referred to the total pressure between the same points. Since it is a relation between pressure increases the value of the reaction can vary between $0 < r < \infty$. If $c_2 > c_1$ then $r<1$ else $r>1$. Therefore the reaction is not a direct efficiency design parameter, although some authors recommend keeping it high. This can be misleading and a proper efficiency design formula has to be found. For that purpose one has to observe how the pressure, which goes into efficiency, is measured. This can be directly read out of the diagram in Figure 4

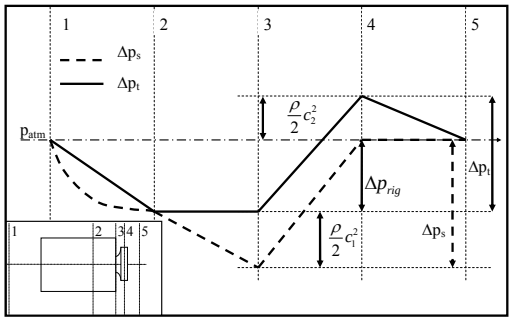

Figure 4. Euler and Rig static pressure increase

$$\Delta p_{s-rig} = \frac{\rho}{2}\left[\left(u_2^2 - u_1^2\right) + \left(w_1^2 - w_2^2\right) - c_1^2\right] \quad (6)$$

$$\Delta p_{d-rig} = \frac{\rho}{2} c_2^2 \quad (7)$$

Also the dynamic pressure is changed properly, delivering the velocity at the exit and total pressure remains the same. Now it can be immediately seen that an ideal efficiency can be defined as

$$\eta_{ideal-imp} = \frac{\Delta p_{s-rig}}{\Delta p_{t-imp}} \quad (8)$$

This is actually what corresponds to a total to static efficiency, Japikse [6]. It can be easily shown and also seen in Figure 4 that it is indeed a total to static efficiency, its value will always lie between 0 and 1. This is the quantity to be optimized in design to set up the Euler parameters d_1, d_2, b_1, b_2, $ß_1$ and $ß_2$. At the same time, as a constrain, one has to keep the relative velocity within a certain range, typically not exceeding 80 to 100 [m s^{-1}]. Furthermore, as a second constrain the rig static pressure computed can not be less than a value prescribed in design, for vacuum cleaner fans typically 30.000 [Pa] at a flow rate of 18 [l/s]. Sweeping the parameter space with a C++ program one can easily find the best configurations satisfying the constrains.

Coupling now the diffuser to the impeller one has to add the terms

$$\Delta p_{t-dif} = 0 \tag{9}$$

$$\Delta p_{s-dif} = \frac{1}{2} \cdot \rho \cdot \left(c_3^2 - c_4^2 \right) \tag{10}$$

$$\Delta p_{d-dif} = \frac{1}{2} \cdot \rho \cdot \left(c_3^2 - c_4^2 \right) \tag{11}$$

where as a first approximation, considering the gap between impeller and diffuser, one can compute

$$c_{3u} = c_{2u} \frac{r_2}{r_3} \tag{12}$$

$$c_{3m} = c_{2m} \frac{b_2 r_2}{b_3 r_3} \tag{13}$$

Hence the efficiency of the coupled impeller-diffuser system can than be written as

$$\eta_{ideal-imp-dif} = \frac{\Delta p_{s-rig} + \Delta p_{s-dif}}{\Delta p_{t-imp}} \tag{14}$$

It is important to note that for ideal flows the total pressure does not change in the diffuser, only the static pressure increases and hence also the efficiency increases. In such a way it is possible to write an equation for the efficiency for the coupled impeller-diffuser unit. Substituting now for the velocities the well known formulas from mean line design, Appendix I and Sigloch [3], one can resolve the velocities as a function of flow rate, rotating speed and inlet and outlet diameter, angle and height. Also the number of blades and the blade thickness has to be considered. In that way it is possible also here, with a parameter sweeping with a proper C++ program, considering also the constraints mentioned above to find the best parameters for the design. It has to be pointed out that in order to get the final best parameters this method has to be coupled with the blade shape computation method described in the next section, otherwise unphysical solutions will be found, leading to huge pressure gradients in the blade channels.

3.2 Blade shape

The blade shape is computed inversely prescribing a proper pressure increase in the impeller as well as a pressure recovery in the diffuser. In order to prescribe these pressure curves it is although necessary to specify the inlet and outlet parameters as described in the previous section. On the other hand, in order to find the proper inlet and outlet dimensions, especially the proper diameters, it is important to verify the velocity or pressure rise in the blade passages, i.e. the blade shapes. Therefore an iterative approach is necessary, i.e. the velocity triangles have to be determined taking into account the blade shapes and the corresponding pressure distribution.

The impeller blade shape is computed from a given velocity distribution, as it is well known from the literature, e.g. Pantell [5] and Sigloch [3], according to the formula

$$\sin ß(r) = \frac{z_{imp}\, s_{imp}}{\pi d} + \frac{Q}{\pi d\, b} \frac{1}{w(r)} \tag{15}$$

(15)

and for the diffuser

$$\sin \alpha(r) = \frac{z_{dif}\, s_{dif}}{\pi d} + \frac{Q}{\pi d\, b} \frac{1}{c(r)} \tag{16}$$

These equations follow directly from the velocity triangle, Figure 5, considering also the blade thickness:

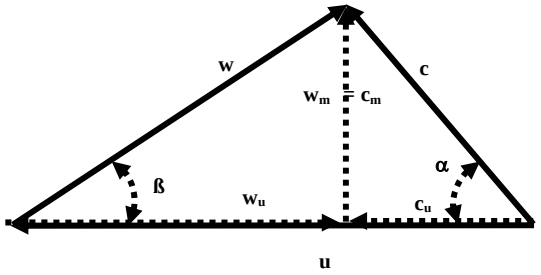

Figure 5. Velocity triangle

$$w(r) = \frac{w_m(r)}{\sin ß(r)} = \frac{Q}{(\pi d \sin ß(r) - z\, s)\, b} \tag{17}$$

Since for design the flow may be treated as incompressible, it is immediate to prescribe a pressure distribution in order to get the blade angles ß and α. Now the blade shape is computed according to the formula, Pantell [5], Figure 6,

$$\varphi(r) = \int_{r_1}^{r} \frac{1}{r \tan ß}\, dr \tag{18}$$

and for the diffuser one hast to substitute the impeller blade angle ß by the diffuser blade angle α. Equation 18 can be solved numerically leading to single twisted blades computed point by point. The hub is assumed to be flat and for the shroud shape b(r) a function is assumed in such a way to result in a proper meridian area and hence a proper meridian velocity distribution.

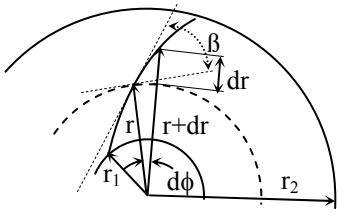

Figure 6. Blade shap representation in polar coordinates

4. CAD MODEL

From the design one gets the blade and shroud shapes which are written out as a text file. In the CAD system the steps for building the model and the fluid domain are, Lamit [7], Köhler [6]:

- reading in of the blade and shroud curves
- generating the blade by protrusion according to the curve read in
- pattern the blade according to the blade number
- cutting off the blade excess according to the shroud curves
- generating the hub and the shroud

An example of an impeller-diffuser unit CAD model is shown in Figure 7. After the model has been generated, the corresponding flow domain, i.e. the blade passages where the flow is taking place has to be models subtracting the flow domain from a volume model enclosed by hub and shroud, Figure 8.

Figure 7. CAD model of impeller-diffuser unit

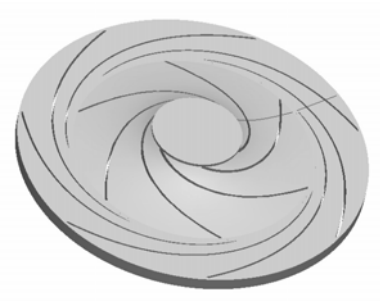

Figure 8. Flow domain of impeller-diffuser unit

Besides, in order to compare the simulation results with measurements, it is necessary to simulate also the test rig measuring section and a region surrounding the impeller diffuser unit, including also the motor, as shown in Figure 9.

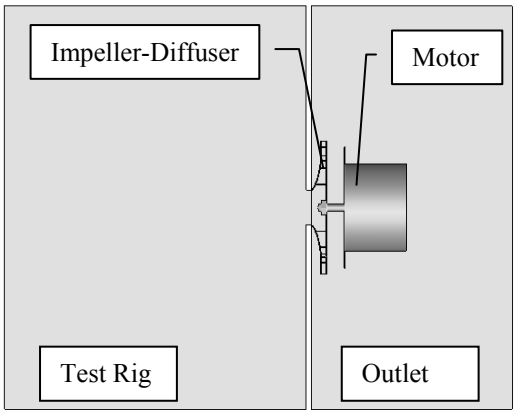

Figure 9. Flow domain including impeller-diffuser unit, test rig and outlet

5. GRID GENERATION

The grid generation is performed using a commercial grid generator, ANSYS ICEM CFD.

When the geometry is complex, this task usually consumes the largest amount of time in the CFD process by far, Ferziger [6]. Due to the amount of impeller-diffuser units run in the iteration loop 2-3 in Figure 1, of the order of 30, and also due to the complexity of the geometry, tetrahedral grid meshing is preferred. Tetrahedral cells are not desirable near walls in the boundary layer needs to be resolved because the first point has to be very close to the wall, Ferziger [7]. For this reason a first layer of prisms is generated near solid boundaries, Figures 10 and 11.

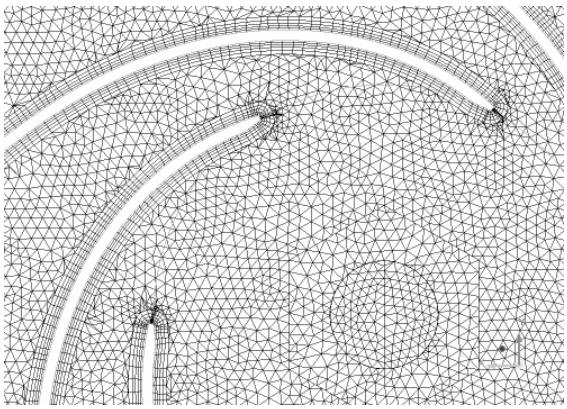

Figure 10. Tetrahedral impeller grid with prism layers

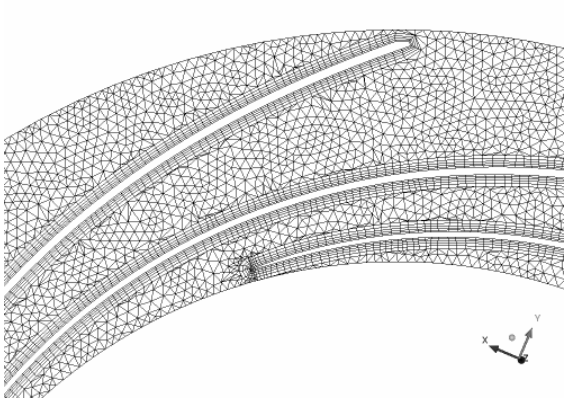

Figure 11. Tetrahedral diffuser grid with prism layers

The total amount of grid elements is around 5 Million, as shown in detail in Table 1

Table 1: Number of grid elements

	Nr. of Elements
Test Rig	278,691
Impeller	2,068,329
Diffuser	1,155,307
Outlet	1,421,749
Total	4,924,076

6. NUMERICAL SIMULATION

The fluid flow is described according to the conservation of mass, momentum and energy. The numerical simulation is performed with a commercial Navier – Stokes solver, ANSYS CFX. As a finite volume solver it satisfies strict global conservation by enforcing local conservation over control volumes which are constructed around each mesh vertex node. Advection fluxes are evaluated using high resolution scheme which is essentially second order accurate.

One of the main problems in turbulence modelling is the accurate prediction of flow separation from a smooth surface. Standard two-equation turbulence models often fail to predict the onset and the amount of flow separation under adverse pressure gradient conditions. Two solve this problem new models have been developed. The model recommended by ANSYS and used in the present computations is the Shear Stress Transport (SST) model of Menter [9]. The model works by solving a turbulence/frequency-based model (k-ω) at the wall and k-ε in the bulk flow. A blending function ensures smooth transition between the two models.

As to the boundary conditions the mass flow was specified at the inlet and atmospheric pressure was specified at the outlet. The rotating speed is dynamically computed according to the torque speed characteristic of the measured reference impeller-diffuser-unit, due to the variable speed of the universal motor drive. A typical torque-speed-curve is shown in Figure 11.

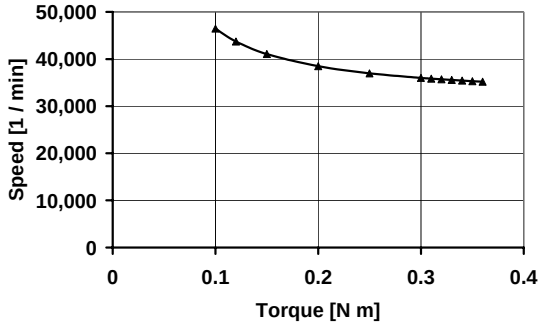

Figure 12. Torque-speed-curve of impeller-diffuser-units

7. NUMERICAL RESULTS

Numerical results for an impeller alone, for a typical impeller-diffuser-unit as well as an LSTM optimized impeller-diffuser-unit are shown in Figure 13.

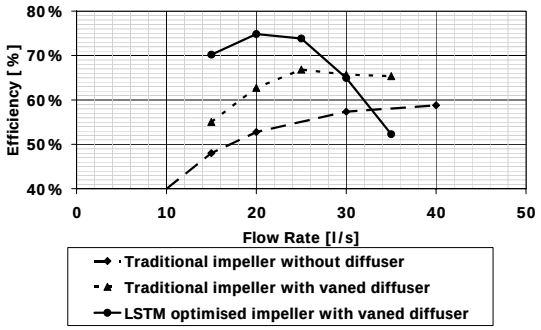

Figure 13. Efficiency curves

It can be seen that considering already in design the impeller and diffuser as one unit much higher efficiencies can be achieved, compared to nowadays industrial impeller-diffuser units, which where designed separately.

8. PROTOTYPES

After finishing the iteration loop 2-3 in Figure 1, prototypes are usually build, as shown in figure 14.

Figure 14. Left: Industrial fan and impeller; Right: corresponding prototypes

These prototypes are built in rapid prototyping process, making it possible to have a fast feedback on the values achieved in simulation. The prototypes are built directly from the CAD data used also for the numerical simulation, ensuring that what is simulated is also precisely measured.

9. MEASUREMENTS

The prototypes are than measured at a test rig built at the LSTM according to DIN 24 163, Figure 15.

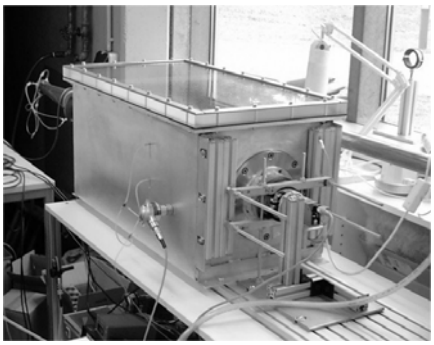

Figure 15. Test rig

Performing a full detail numerical simulation, including the motor details and also the test rig, excellent agreement between simulation and measurement have been achieved, Figure 16.

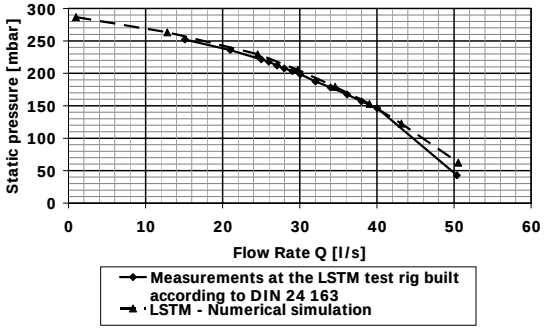

Figure 16. Measurement and CFD results

10 SUMMARY AND CONCLUSIONS

A new analytical approach for the combined design of impeller-diffuser unites was presented. It was shown, that in combination with numerical simulations, the new method is a powerful tool to improve the hydraulic efficiency of such units, improving the efficiency of nowadays impeller-diffuser units in over 10%. Performing a careful and full detail numerical simulation, it is possible also already in the CFD stage of the development to have very accurate prediction of test rig measurements, so that building the prototypes represents almost no risk anymore.

REFERENCES

[1] Batchelor, G.K., 2000, *An Introduction to Fluid Dynamics*, Cambridge University Press, Cambridge.

[2] Bohl, W., 1998, *Strömungsmaschinen 1 – Aufbau und Wirkungsweise*, 7. Auflage, Vogel Buchverlag.

[3] Cordier,O., Oktober 1953, „Ähnlichkeits-bedingungen für Strömungsmaschinen”, *BWK* Bd. 6, Nr. 10.

[4] Eck, B., 1991, *Ventilatoren – Entwurf und Betrieb der Radial-, Axial- und Querstromventilatoren*, 5. Auflage, Springer – Verlag, Berlin.

[5] Enßlinger, J., 1952, „Wirkungsgradsteigerung von Ventilatoren radialer Bauart durch strömungstechnisch richtige Formgebung der Flügelräder”, *M.A.N. Forschungsheft*, S. 59-67.

[6] Ferziger, J.H., Peric, M., 1999, *Computational Methods for Fluid Dynamics*, 2nd Revised Edition, Springer-Verlag, Berlin.

[7] Japikse, D. and Baines, N. C., 1994, *Introduction to Turbomachinery,* Concepts ETI, Inc.

[8] Köhler, P., 2003, *Pro/ENGINEER Praktikum*, VIEWEG Studium Technik, Wiesbaden.

[9] Lamit, L.G., 2004, *Pro/ENGINEER Wildfire*, Thomson Brooks/Cole, Belmont, UK.

[10] Menter, F.R., 1993, "Zonal Two Equation k-ω Turbulence Models for Aerodynamic Flows", *AIAA Paper 93-2906.*

[11] Pantell, K., 1949, „Über die Schaufelausbildung von Turbo-Arbeitsmaschinen", *Konstruktion*, Heft 3, S. 77-82.

[12] Sigloch, H., 1993, *Strömungsmaschinen, Grundlagen und Anwendungen*, 2. Auflage, Carl Hanser Verlag München.

Conference on Modelling Fluid Flow (CMFF'06)
The 13th International Conference on Fluid Flow Technologies
Budapest, Hungary, September 6-9, 2006

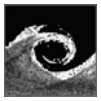

3D UNSTEADY FLOW IN CENTRIFUGAL FAN: IMPELLER – VOLUTE INTERACTION

Mohand YOUNSI[1], Djaafer FEDALA, Farid BAKIR, Smaine KOUIDRI, Robert REY

[1] Corresponding Author. Laboratoire d'Energétique et de Mécanique des Fluides Interne.
151 Boulevard de l'Hôpital 75013 Paris France.
Tel.: +33 (0)1 44 24 64 12, Fax: +33(0)1 44 24 64 11, E-Mail: mohand.younsi@paris.ensam.fr

ABSTRACT

The purpose of this study is to show, using Computational Fluid Dynamics (CFD) analysis, the complex phenomena related to the internal flow in a squirrel-cage centrifugal fan and their impact on the aeroacoustic behaviour. These phenomena are the interactions and unsteadiness induced by the relative motion of the rotating blades compared to the volute. Thus, 3D unsteady calculation using Unsteady Reynolds Averaged Navier-Stokes (URANS) approach was applied on a hybrid mesh grid whose refinement was studied and adapted to the flow morphology. Turbulence was modelled with the k-ω-Shear Stress Transport (SST) model. The computational domain was divided into two zones, a rotating zone including the impeller and a stationary zone including the volute. A sliding mesh technique was applied to the interface in order to allow the unsteady interactions between the two zones. The overall performances measured and predicted by the computations at different flow rates are in good agreement.

The unsteady part allowed locating the noise sources. It is illustrated by the pressure and aerodynamic force fluctuations applied on the blade surfaces, and on different points from the lateral surface of the volute. The analysis of the wake generated by the rotation of the blower shows that the volute tongue is the main zone of unsteadiness and flow perturbations.

Finally, using the pressure fluctuations data acquired upon the surfaces of rotating blades, acoustic pressures were predicted by a hybrid method based on the Ffowcs Williams-Hawking analogy.

Keywords: Aeroacoustics, Centrifugal Fan, CFD, Turbomachinery.

NOMENCLATURE

a_0	[*m/s*]	Far field sound speed
c	[*m/s*]	Sound speed in quiescent medium
$f=0$	[-]	Function that describes the source surface
F	[*Hz*]	Frequency
G	[-]	$= \tau - t + r/c$
$H(f)$	[-]	Heaviside function
n_j	[-]	Unit normal vector
p'	[*Pa*]	Acoustic pressure
P_{ij}	[*Pa*]	Compressive stress tensor
p_{ref}	[*Pa*]	Reference pressure
Psd	[Pa^2]	Power spectral density
t	[*s*]	Observer time
T_{ij}	[*Pa*]	Lightill stress tensor
u_i	[*m/s*]	Fluid velocity in the x_i direction
u_n	[*m/s*]	Fluid velocity in the normal direction
v_i	[*m/s*]	Surface velocity in the x_i direction
v_n	[*m/s*]	Surface velocity in the normal direction
x	[*m*]	Observer position
$\delta(f)$	[-]	Dirac delta function
Δt	[*s*]	Time step
ρ	[Kg/m^3]	Density
τ	[*s*]	Source time

Subscripts

L	Loading noise component
T	Thickness noise component
0	Denotes fluid variable in quiescent medium

1. INTRODUCTION

Squirrel-cage centrifugal fans are widely used in industry. They are used as circulating fans in central heating and air-conditioning systems in buildings, as blowers in automotive heating/cooling units, and in numerous other applications for their large capacity of mass flow, size compactness and low noise.

The recent development of computational fluid dynamics for three dimensional viscous flow fields provides efficient tool for analysis and design, thus flow analysis techniques using URANS approach have made remarkable progress in the applications to turbomachinery.

Recently, more attention has been paid to the study of unsteady phenomena in turbomachines. These phenomena are the interactions and unsteadiness induced by the motion of the rotor relatively to the stator.

As concerns squirrel-cage centrifugal fans, R.J. Kind [1] studied a method for predicting flow behaviour and performance using simulation approach, based on subdividing the fan into a number of zones. Sandra Velarde-Suarez [2] studied the aeroacoustic behaviour based on the theory of vortex sound coupled with experimental data. Siddharth Thakur [3] used three dimensional (3D) CFD approach to analyze fluid flow in a centrifugal fan. Yong Cho and Young J.Moon [4] used the unsteady viscous flow fields of a cross-flow fan computed by solving the two dimensional (2D) incompressible Navier-stokes equations in order to feed the Ffowks Williams Equation, They studied the acoustic benefit of an impeller with uneven blade spacing. Kwang-Yong Kim [5] applied the response surface method using RANS approach to the aerodynamic design of a forward-curved-blade centrifugal fan to optimize the shapes of scroll and blades in order to maximize the flow efficiency.

In this paper, interactions and unsteadiness induced by the motion of rotating blades relatively to the volute were studied using CFD calculation. The computations were validated at different flow rates by comparison with experimental results. The unsteady part of this study is illustrated by the pressure and aerodynamic force fluctuations applied on blade surfaces, and on different points from the lateral surface of the volute. The analysis of the wake generated by the rotation of the blower shows that the volute tongue is the main zone of unsteadiness and flow perturbations.

Finally, based on pressure fluctuations data acquired upon the surfaces of rotating blades, acoustic pressures were predicted by a hybrid method using the Ffowcs Williams-Hawking formalism.

2. NUMERICAL MODELLING

To consider the unsteady interactions between the rotating impeller blades and the stationary fan casing, and to understand the internal flow, a numerical simulation based on the finite volume numerical method using the commercial code *FLUENT 6.2* was carried out. The details of this analysis are presented in the following sections.

2.1. Fan Presentation

The main fan parameters are presented in Table1. These parameters were transformed into complete Computer Aided Design (CAD) model and saved into STL format in order to build prototype using rapid prototyping method which requires that parts are complete and have continuity.

Table 1. Geometrical characteristics of the fan

Impeller	
Description	***Value***
Blade number	39
Impeller width	70 mm
Blade chord length	26.2 mm
Blade thickness	1 mm
Inlet blade angle	5°
Outlet blade angle	70°
Shape blade	circular arc
Rotational speed	3000 rpm
Impeller inlet diameter	120 mm
Impeller outlet diameter	160 mm
Volute casing	
Inlet diameter	120 mm
Outlet size	100 x 76 mm
Volute tongue radius	5 mm
Volute tongue position	Radius 90 mm
Volute shape	Logarithmic law

2.2. Computational Domains and Mesh

The computational domain was divided into two zones, a rotational zone including the impeller and stationary zones elsewhere, taking into account the clearance between the impeller and the volute.

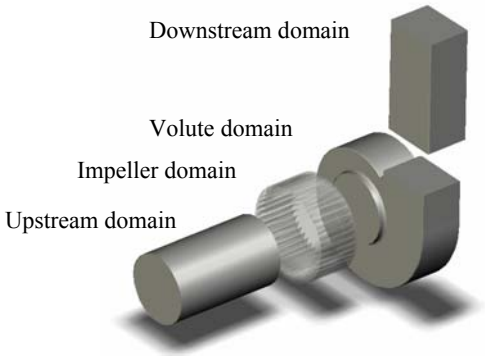

Figure1. Geometry modelling of the flow domains

For numerical stability reasons, and to minimize boundary conditions effects, the computation domain was extended upstream and downstream. The geometry of this configuration is shown in Figure 1.

The resulting geometry was used to build a hybrid mesh. The grid refinement was studied and adapted to the flow morphology, minimizing element distortion and having required resolution in high gradient regions. Figure 2 shows the influence of the mesh refinement on the difference of static pressure between the inlet and the outlet of the fan. According to this figure, the 1.7 x 10^6 cell grid is considered sufficient to ensure mesh independence. Figure 3 shows the resulting mesh. Table 2 gives the details of the retained grid.

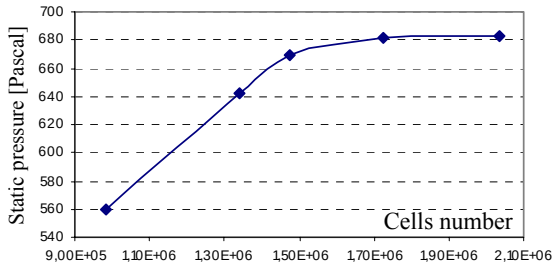

Figure 2. Influence of the grid resolution.

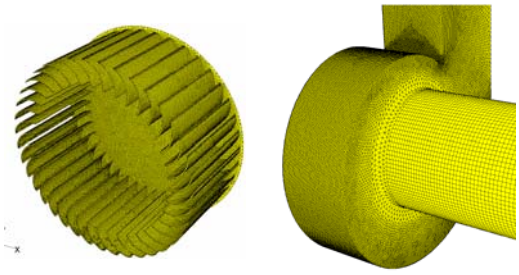

Figure 3. Resulting grid mesh of the fan.

Table 2. Used grid details

Fluid domain	mesh tip	Number of cells
Impeller	Hybrid	999744
Volute	Hybrid	723960
Total		1723704

2.3. Simulation Parameters

Velocity Inlet and Pressure Outlet boundary conditions were applied at the inlet and the outlet respectively. A sliding mesh technique was applied to the interfaces in order to allow the unsteady interactions between the impeller and the volute. Turbulence was modelled with the k-ω-SST model [6]. The k-ω-SST model combines the standard k-ω model with the Standard k-ε and also takes the transport effects of the principal turbulent shear stress into account through a modified turbulent viscosity formulation. It has been shown to perform very well for adverse pressure gradient aerodynamic flows. The stopping criterion for the scaled norm of the residuals is 10^{-4}. The governing equations were solved using the segregated solver and a centred SIMPLE algorithm was used for the pressure velocity coupling. A gauge pressure of 101325 Pascal was applied at the outlet and a suitable value was determined for the inlet. The CFD simulation process began with a steady flow calculation using Multiple Reference Frames (MRF) model. Using the preliminary solution at the operating point whose flow rate is equal to 500m^3/h, an unsteady calculation was then performed using a sliding mesh model (SMM) choosing a time step equal to 5.10^{-5} seconds. This time step is small enough to capture the phenomena due to the impeller rotation.

2.4. Overall Performances Validation

2.4.1. Test Bench

Overall measurements were carried out on the test bench shown in Figure 4a, designed and built at LEMFI-ENSAM according to the ISO 5801 standard. It's composed of an airtight box (1.3 x 1.3 x 1.8 m), witch is placed upstream the centrifugal fan, making possible to vary the flow rate by changing the diameter of an orifice plate (diaphragm). The rotational speed is set by a frequency variator and measured using an optical tachometer of 0.1% accuracy. For each diaphragm of given diameter, the static pressure provided by the centrifugal fan is measured using a micro manometer (precision 1%). The diagram of this test bench is shown in Figure 4b.

Figure 4a. Test bench ISO 5801

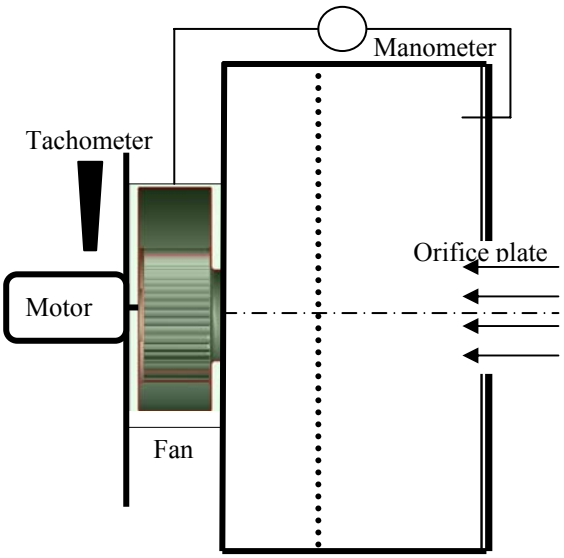

Figure 4b. Diagram of the test bench.

2.4.2. Experimental and Numerical Results Comparison

The CFD calculations were carried at different flow rates, and compared with experimental results. Figure 5 shows that the measured static pressure difference between the inlet and the outlet fan is in good agreement with CFD calculations.

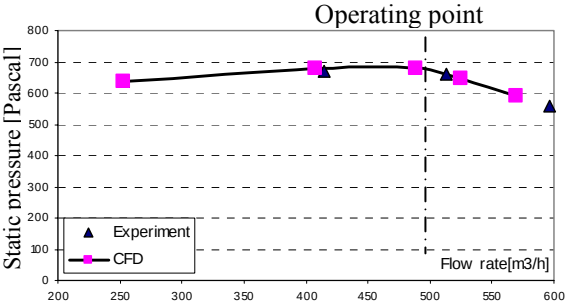

Figure 5. Aerodynamic characteristic of the fan.

2.5. Unsteady Pressures Calculation

Figure 6 shows the different points position around the volute in the middle span (Span 2), where fluctuating static pressures were calculated (Points 1 to 9). The same distribution of points was used in two other parallel spans, Span1 near the inlet of the fan, and Span 3 in the bottom of the volute. For each time step, the data were saved. After the calculation, each recorded sample was Fast Fourier Transform (FFT) processed (reference pressure is set to $2x10^{-5}$ Pa) and then the aerodynamic pressure spectra were finally obtained. These spectra provide a direct measure of the amplitude of the aerodynamic pressure fluctuations at each frequency. The pressure level is given by: $10.\ log_{10}\ (psd\ /\ p^2_{ref})$.

3. ANALYSIS OF NUMERICAL RESULTS

3.1. Pressure and Velocity Fields

Figure 6 shows the instantaneous static pressure field in Span 2 at the nominal flow rate ($500m^3/h$). The conversion of dynamic pressure produced by the impeller rotation into static pressure by the volute casing can be seen, thus the maximum of pressure is obtained in the outlet duct. A non homogenous pressure distribution is observed at the zone around the gap between volute tongue and impeller periphery, characterized by a high gradient of pressure. The volute tongue whose role is to drive the flow towards the fan outlet also presents a singularity for the flow. The shape of the volute casing creates a geometrical asymmetry, this phenomenon influences the pressure distribution and fluctuating efforts on the blades impeller.

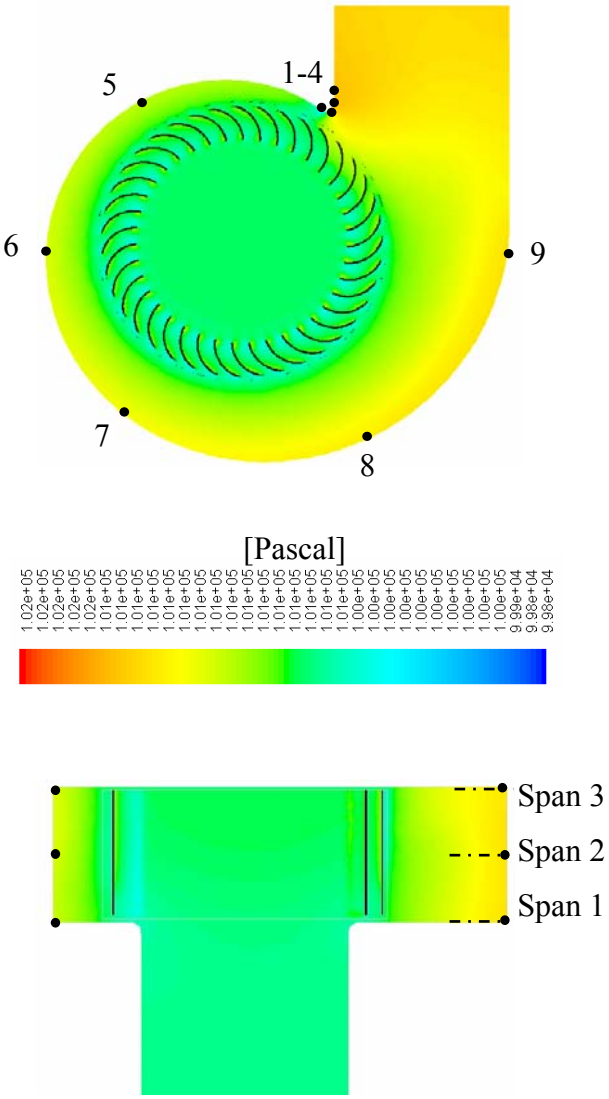

Figure 6. Instantaneous static pressure field: middle surface and meridian surface.

The instantaneous velocity vectors in the fan are plotted in Figure 7. This figure shows, in Span 2, that the volute tongue zone presents a strong recirculation of the fluid particles in the gap between the volute tongue and the impeller periphery.

In the meridian surface, it can be seen that the impeller blades are partially fed by the flow. This non homogenous distribution of the mass flow coupled with the rectangular shape of the volute casing creates strong vortex and recirculation of the fluid at the axial gap, this phenomenon generates aerodynamic losses.

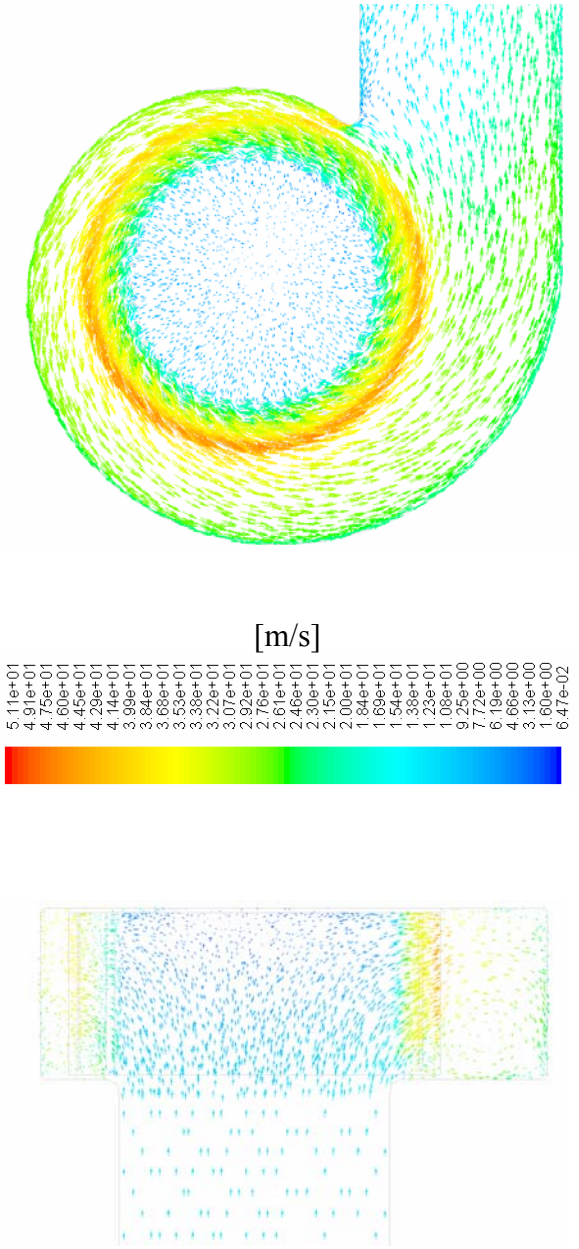

Figure 7. Instantaneous velocity field: middle surface and meridian surface.

3.2. Unsteady Calculation Results

Figure 8 shows two periods of the force fluctuations applied on one blade. The total force component on the blade was computed from the node value by summing the pressure and viscous forces of each cell.

Figure 9 shows the different relative positions of the blade during the calculation. According to this diagram, the influence of the volute tongue on the force variation can be seen between Point 1 and Point 3. A quick fluctuation at Point 2 (two milliseconds between Points 1 and 3) is observed. This fast variation has a significant impact on the loading noise generation defined in section 4.

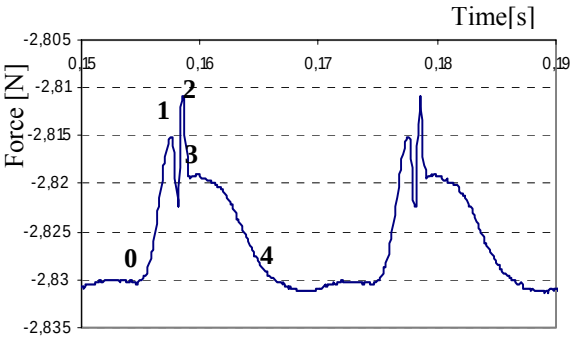

Figure 8. Force fluctuations applied on the blade (2 revolutions)

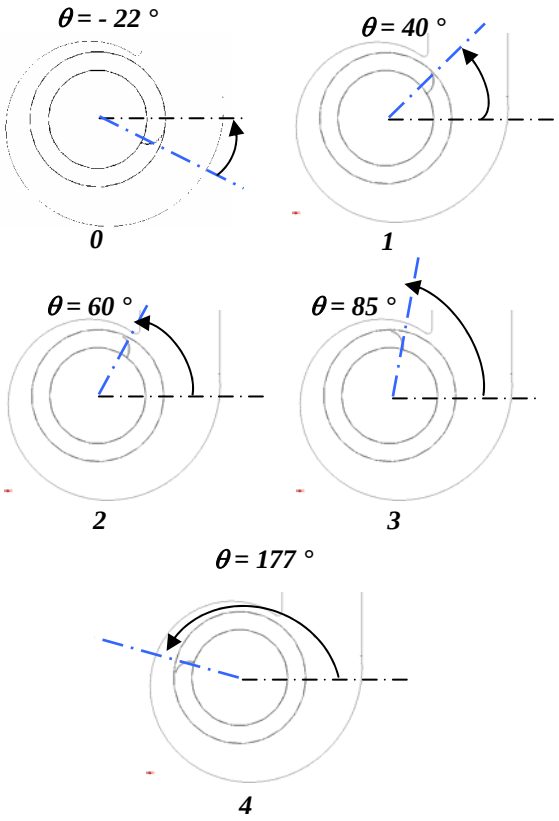

Figure 9. Blade positions during the calculation

Figure 10 shows the spectrum of the aerodynamic pressure calculated at the volute tongue in Span 2. The graph suggests that the dominant mode occurs at 1950 Hz, which corresponds to the blade passing frequency (BPF). A non presence of other peaks in the spectrum at the harmonics frequency is observed. This is due to the nature of the interaction between the impeller and the volute, which does not generate interferences.

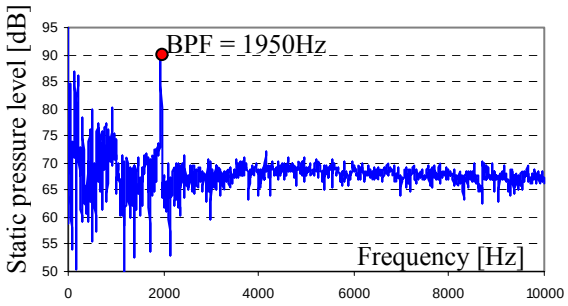

Figure10. Aerodynamic pressure spectrum at the volute tongue.

The Fourier coefficient values at the BPF point, at each computation point, and at the three defined Spans are calculated and reported in the graph shown in figure 11. The graph represents the magnitude of the wake generated by the blades motion around the volute. The shape of the three curves globally matches. The dominant value is observed at the volute tongue point; this result indicates that the volute tongue is the mean zone of unsteadiness and interaction with the rotating impeller. Away from the volute tongue the three curves decrease, thus the minimum value is observed at the zone around the point 7, this is due to the morphology of the flow which becomes stable. The curves increase progressively from the point 7 on. It can be seen that the point 6 is remarkable because of the curve increases, this is due to the flow which becomes disorganized and it can be related to the volute tongue effect.

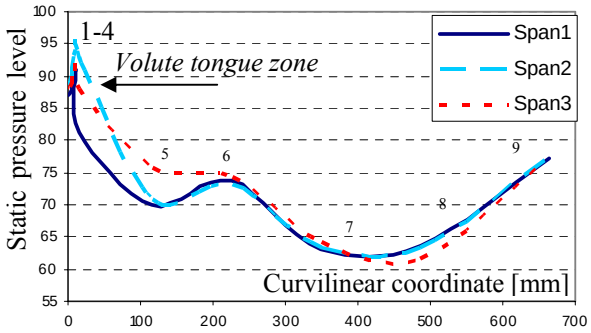

Figure 11. Pressure fluctuation variation around the volute at the BPF (1950Hz).

4. AEROACOUSTIC RESULTS AND DISCUSSION

The Ffowks Williams and Hawkings (FW-H) [7] equation is essentially an inhomogeneous wave equation that can be derived manipulating the continuity equation and the Navier-Stokes equations. The FW-H equation can be written as:

$$\frac{1}{a_0^2}\frac{\partial^2 p'}{\partial t^2}-\nabla^2 p'= \frac{\partial\left[\left[\rho_0 v_n+\rho(u_n-v_n)\right]\delta(f)\right]}{\partial t} - \frac{\partial\left[\left[P_{ij}n_j+\rho u_i(u_n-v_n)\right]\delta(f)\right]}{\partial x_i} + \frac{\partial^2}{\partial x_i \partial x_j}\left[T_{ij}H(f)\right] \quad (1)$$

Where :

$$T_{ij}=\rho u_i u_j + P_{ij} - a_0^2(\rho-\rho_0)\delta_{ij} \quad (2)$$

$$P_{ij}=p\delta_{ij}-\mu\left[\frac{\partial u_i}{\partial x_j}+\frac{\partial u_j}{\partial x_i}+\frac{2\partial u_k}{3\partial x_k}\delta_{ij}\right] \quad (3)$$

The first two source terms in equation (1) are monopole (thickness) and dipole (loading) sources, respectively, based on their mathematical structure. The monopole source term models the noise generated by the displacement of fluid as the body passes. The dipole or loading source term models the noise that results from the unsteady motion of the force distribution on the body surface. Both of these sources are surface sources: i.e., they act only on the surface *f=0* as indicated by the Dirac delta function *δ(f)*. The third source term is a quadripole source term that acts throughout the volume that is exterior to the data surface as indicated by the Heaviside *H(f)*.

Using the free-space Green function (*δ(G)/4πr*), the solution to equation (1) is obtained. Thus the complete solution consists of surface integrals and volume integrals. The surface integrals represent the contribution from monopole and dipole acoustic sources and partially from quadrupole sources if the integration surface is impermeable. The contribution of the volume integrals which represent quadrupole (volume) sources in the region outside the source surface becomes small when flow is subsonic. Thus the volume integrals are neglected.

Finally:

$$p'(\vec{x},t)=p'_T(\vec{x},t)+p'_L(\vec{x},t) \quad (4)$$

The two terms on the right in equation (4), $p'_T(\vec{x},t)$ and $p'_L(\vec{x},t)$, thickness and loading terms respectively are developed in [7].

The fluctuating variables, pressure and velocity upon the impeller surfaces, were obtained for 2000 time steps. Then, sound pressure signals are computed at the receiver location using the source data collected during the aerodynamic calculation. For the time step selected here ($5x10^{-5}$ s), the highest frequency that the acoustic analysis can produce is: $F = \frac{1}{2\Delta t} = 10\,kHz$.

Figure 12 shows the sound pressure level spectrum of the impeller computed one meter away from the axis of the fan.

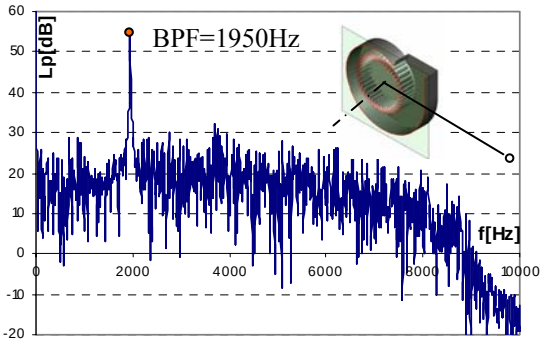

Figure 12. Sound pressure level spectrum of the impeller (x =1m).

It can be seen that there is one dominant peak, this peak occurs at 1950 Hz, which corresponds to the blade passing frequency. The non presence of other harmonics is due to the geometry shape of the volute casing interacting with the rotating blades. Thus, the significant unsteadiness detected by the used calculation models is due only to the presence of the volute tongue in the flow. According to [8], URANS calculations cannot adequately provide the surface pressure fluctuations needed for broadband noise prediction. Thus, the spectrum component, other than the fundamental harmonic peak could be numerical.

5. CONCLUSION

3D unsteady flow in a squirrel cage centrifugal fan was studied in this paper using URANS equations. The used numerical simulation was validated at different flow rate by comparison with experimental results.

The analysis of the flow morphology showed the influence of the geometry design on the aerodynamic performances of the fan.

The analysis of the pressure fluctuations around the lateral surface of the volute, and the force fluctuations indicated that the main source of perturbation and unsteadiness in squirrel cage fan is the volute tongue zone.

The spectral analysis of the sound pressure level computed by the Ffowks Williams equation showed that the main source of tonal noise in the investigated fan is the aerodynamic interactions between the impeller and the volute tongue.

It should be interesting to extend this work by:

- Validating the fluctuating pressures computed on the lateral surface of the volute casing.
- Studying geometry design effect on the tonal noise level generated by the impeller.
- Using Large Eddy Simulation (LES) approach to feed acoustic models.

6. REFERENCES

[1] Kind R. J., 1997, "prediction of Flow Behaviour and Performance of Squirrel Cage Centrifugal Fans Operating at Medium and high Flow rates'', *ASME Journal of Fluid Engeneering*, Vol.119, pp. 639-646.

[2] Sandra Velarde-Suarez, Carlos Santolarya, Rafael Balesteros-Tajadura, 1999, "Experimental Study on the Aeroacoustic Behaviour of a Forward-Curved Blades Centrifugal Fan", *ASME Journal of Fluid Engineering,* Vol.277, pp.276-281.

[3] Siddharth Thakur, Wanlai Lin, and Jeffrey Wright, 2002, "Prediction of Flow in Centrifugal Blower Using Quasi-Steady Rotor-Stator Models", *Journal of Engineering Mechanics*, pp.1039-1049.

[4] Yong Cho, Young J. Moon, 2003, "Discrete Noise Prediction of Variable Pitch Cross-Flow Fans by Unsteady Navier Stokes Computations", *ASME Journal of Fluids Engineering*, Vol.125, pp.543-550.

[5] Kwang-Yong Kim, Seoung-Jin Seo, 2004, "Shape Optimization of Forward-Curved-Blade Centrifugal Fan with Navier-Stokes Analysis", *ASME Journal of Fluids Engineering,* Vol.126, pp.735-742.

[6] Menter, F. R., 1993, "Zonal Two Equations k-ω Turbulence Models for Aerodynamic Flows," AIAA Pap. 93-2906.

[7] Ffowcs Williams, J.E., Hawkings, D.L., 1969, "Sound Generation by Turbulence and Surfaces in Arbitrary Motion", Phi. Trans. Roy. Soc., A264

[8] K.S. Brentner and F. Farassat. 1998, "An analytical Comparison of the Acoustic Analogy and Kirchhoff Formulation for Moving Surfaces", *AIAA Journal, 36(8).*

Conference on Modelling Fluid Flow (CMFF'06)
The 13th International Conference on Fluid Flow Technologies
Budapest, Hungary, September 6-9, 2006

ROTATING STALL IN CENTRIFUGAL COMPRESSOR DIFFUSER

Dragica MILENKOVIC[1], Dragisa NIKODIJEVIC [2], Zivojin STAMENKOVIC[3]

[1] Corresponding Author Department of Fluid Mechanics, Faculty of Mechanical Engineering Nis, Aleksandra Medvedeva 14, 18000 Nis, Serbia and Montenegro, E-mail: dragica@masfak.ni.ac.yu
[2] Department of Fluid Mechanics, Faculty of Mechanical Engineering Nis, Serbia and Montenegro, E-mail: dragisan@masfak.ni.ac.yu
[3] Department of Fluid Mechanics, Faculty of Mechanical Engineering Nis, Serbia and Montenegro. E-mail: zikas@masfak.ni.ac.yu

ABSTRACT

The paper presents the results of the experimental and theoretical investigation of the rotating stall in the centrifugal compressor impeller assembled with the vaned and vaneless diffuser. The study of the phenomenon of the rotating stall in the centrifugal compressor stage has been accomplished by means of automated measuring complex. The objective of the obtained data analyses was determination of the rotating stall appearance. It has been found that two different kinds of stall exist, which points out to two different possibilities of the rotating stall origination.

Keywords: turbo machinery, rotating stall, centrifugal compressor

NOMENCLATURE

C_r	$[m/s]$	absolute radial velocity
C_u	$[m/s]$	absolute circumferential velocity
$\boldsymbol{C_{r2}} = \frac{C_r}{C_{r2}}$	[-]	dimensionless parameter
$\boldsymbol{C_{u2}} = \frac{C_u}{C_{u2}}$	[-]	dimensionless parameter
D	$[m]$	diameter
H	[-]	boundary layer form-parameter
Re	[-]	Reynolds number
U	$[m/s]$	circumferential velocity
V	$[m^3/s]$	volume flow rate
b	$[m]$	width of flow domain
i	$[^o]$	flow attack angle
r	[-]	radial coordinate
t	[-]	radial coordinate
z_3	[-]	number of stalled regions
Π	[-]	compression rate
ψ	[-]	coefficient of unit work
α	$[^o]$	angle between absolute and circumferential velocity
β_{L1}	$[^o]$	blade angle at impeller inlet
β_{L2}	$[^o]$	blade angle at impeller outlet
δ^*	$[m]$	thickness of displacement
δ^{**}	$[m]$	thickness of impulse loss
η	[-]	efficiency rate
ν	$[m^2/s]$	fluid kinematic viscosity
ρ	$[kg/m^3]$	fluid density
τ	$[N/m^2]$	friction stress
$\overline{\omega}$	$[rad/s]$	relative angular velocity of stalled region

Subscripts and Superscripts

0	- cross section at stage inlet
1	- cross section at impeller grid inlet
2	- cross section at impeller grid outlet
3	- cross section at vaned diffuser inlet
4	- cross section at vaned diffuser outlet
iz	- isentropic process

1. INTRODUCTION

It is well known that one or more areas of the opposite flow (which rotate in the direction of the rotor rotation) appear in the annular channel of the compressor during the gradual flow regulation through the compressor. This phenomenon is called the rotating stall and the regions of the opposite flow are called the stalled regions.

In many cases, the transient to the rotating stall can lead to some undesirable consequences. An evident decrease of the pressure and of the flow is possible beyond the compressor, as well as the rapid decrease of the efficiency. The lifetime of the compressor blades is shortened which is caused by the tensions during the compressor operation in the region of the rotating stall. Concerning the above-mentioned special attention has been paid to the rotating stall.

The analyses show that two different types of the stall are present during the decrease of the flow rate in the compressor and they differ in the rapid changes of the disturbance intensity, in the propagation speed and in the number of the stalled regions. The rotating stall consists of several small

stalled regions in the areas of relatively high flow rates, and one or two big stalled regions appear in the areas of the low flow rates. In the first case, the intensity of the disturbance is not so significant, but in the second one, it is greater due to the opposite flow through the regions. These two forms of the rotating stall are called the weak stall and the intensive stall.

The experiments show that during the rotating stall the phenomenon of the hysteresis is present, in addition; a slight difference can be noticed between the point of the rotating stall in the case of the flow decrease and the point of its disappearance in the flow increase. At the transition point there is a difference between the weak and the intensive stall, as well as the difference in the number of the stalled regions during the flow rate increase and decrease.

It is evident that the characteristics of the rotating stall depend on the concrete construction of the compressor [2]. Especially there is a great difference in the number of the stalled regions in the weak rotating stalls. In some compressors the weak stall does not exist at all - the intensive stall is present at the very beginning in such cases.

Considering the dimensions of the regions covered with the stall patches, two forms of the rotating stall can be mentioned: the partial stall - when the smaller stall patches cover only a part of the blade and the full stall - when the stalled region is extended to the full blade.

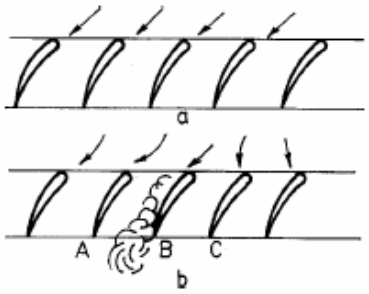

Figure 1. The stalled regions during the flow over the profile lattice

The phenomenon of the rotating stall has been recognized in 1938. by a group of scientists [7] who had been working on the Whittle motor centrifugal compressors. Although the phenomenon had been recognized first in a centrifugal compressor, much more attention has been paid to the axial compressors in the later theoretical and experimental studies. However, all the theories were based on the small disturbances method. Although this method enables the prediction of the rotating stall beginning, it is useless in attempt to describe the uneven flow in the completely developed rotating stall. In the recent years, nonlinear mathematical experiments [9] have been published. However, they are restricted to the discussion of the isolated rotor or a stage, and only 'qualitative ideas' are allowed to be obtained about some characteristics of the stalled regions. Concerning that, it is considered that the medium flow through the annular channel of the compressor remains constant during the process of transition from the flow without stall to the flow with rotating stall. In practice the operation point of the compressor depends on the installed valve and during the transient from the flow without stall to the completely propagated stall, the reduction of the pressure beyond the compressor can lead to a considerable change of the flow rate.

Although the number of the experimental studies is considerable, the studies mainly investigate the number of the stalled regions and the propagation speed. However, regardless to the detailed experimental material, nobody has succeeded in making a clear idea about the physical parameters, which determine the basic flow characteristics with a stall in an axial compressor up to now.

A simple drawing, which can be used to explain the mechanism of the rotating stall, is given in the Figure 1 [6]. The lattice of an axial compressor, which works at great angles of clearance, is considered (Fig. 1a). If any disturbances cause the local increase of the blade B angle of clearance (Fig. 1b), the intensive rotating stall C of this blade will occur. Since the blade gap is narrowed due to the stalled region, the flow is separated from the blade B, which leads to an increase of the angle of clearance on the blade A and a decrease of the angle of clearance on the blade C.

The stall is extended from the right to the left, and in appropriate conditions, it can be developed into fully propagated region extending along the lattice with the velocity V_p (Figure 2).

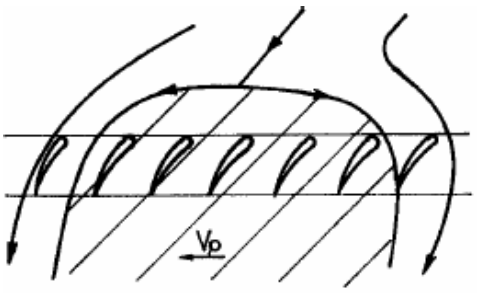

Figure 2. Fully propagated stalled region

Such pattern of rotating stall development is accepted for the centrifugal compressors, too. The difference between axial and centrifugal machines is taken into consideration, and it is emphasized that the investigation of the rotating stall in centrifugal machines is much more complex both from the experimental and theoretical point of view.

The frequency of the rotating stall process is not known in advance. Besides, in the rotating stall the stalled regions are moving (‘rotating’) with angular velocity, which is, as a rule, different from the frequency of rotation. In connection with this, the frequency of the process in the absolute coordinate system (the stationary elements of the flow sector) is different from the one in the relative coordinate system (the impeller).

As can be seen from the detailed investigations of the non-stationary processes in the centrifugal compressor, the measurement of the non-stationary pressures provides for the required idea about the character of the flow in the flow sector, especially when the measuring is done simultaneously on the rotating and stationary elements of the flow sector. According to the shape of the signal, pressure pulses can be divided into following types: constant, slow changing, periodical and random. The periodical oscillation parameters can be easily determined using the procedure of the synchronous accumulation when the beginning phase of the process and the period T are known. The developed informative-mathematical complex has accomplished the algorithm of the synchronous accumulation. The complex consists of an analogue measurement subsystem, synchronization and control subsystem, multi-channel statistic analyzers and a mini computer, static and dynamic calibration subsystem and commutation elements.

An analogue measuring subsystem consists of miniature pressure transducers (frequency of oscillations 70kHz, sensitivity 0.3÷0.9m/kPa on 3V), multi-point electricity governors, differential amplifiers and the amplitude-impulse modulators.

The impeller with $\beta_{L2} = 52^o$, diffuser with vanes ($\overline{D}_3 = D_3 / D_2 = 1.2$) and vaneless diffuser (Figure 3 and Figure 4) have been chosen for the investigation.

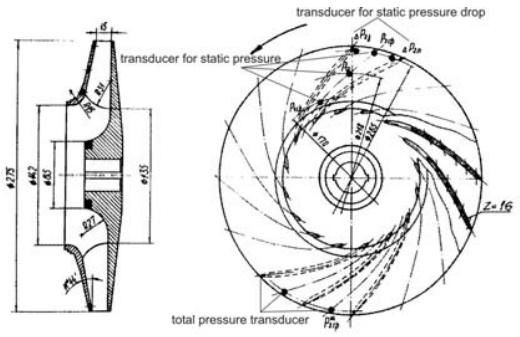

Figure 3. The impeller design

The study of the rotating stall phenomenon in the centrifugal compressor stage has been accomplished by means of automated measuring complex mentioned above. During the non-stationary pressure measurement, the highest attention has been paid to the peripheral part of the impeller. The arrangement of the pressure transducers in the impeller and in the vaned diffuser is shown in the Fig. 3 and Fig. 4.

In all the cases, the receivers of the pressure transducers were arranged so that they could measure the pulsation of the static pressure.

The parameters, which indicate the appearance of the rotating stall, were determined by means of the calculation according to the simultaneous indication of the transducers in the impeller, in the vane diffuser and vaneless diffuser. In addition, the number of the stalled regions z_3 and the relative propagation speed $\overline{\omega}_3$ has been determined as for the axial compressor.

During the aerodynamic measurements performed in order to obtain the integral characteristics of the investigated compressor stage, the averaged total and static pressure, the temperatures and the angles of the stream flows were measured.

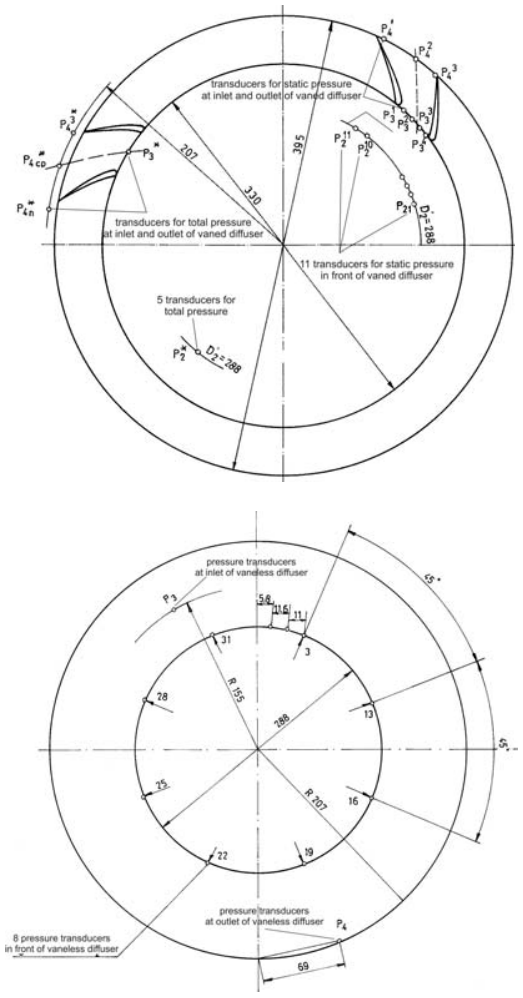

Figure 4. The arrangement of the transducers in a) the vaned diffuser and b) vaneless diffuser

2. THE ANALYSES OF THE VISCOUS GAS FLOW IN A RADIAL VANELESS DIFFUSER

A great number of experimental studies [4] on the centrifugal compressors have been made in order to determine the main initiator of the rotating stall in the centrifugal compressor stage, but without any significant success. All the attempts have been directed to the determination of some characteristic values based on which it has been said that the main initiator was the impeller, vane diffuser or vaneless diffuser, without any theoretical studying.

It is well known that all the studies of the centrifugal machines are complex and they require special mathematical apparatus. Therefore, it is not possible to describe with mathematical models the phenomena in the flow sector of the compressor, no matter how strongly we wish it. The flow of a viscous gas in a radial vaneless diffuser, which is a part of a centrifugal compressor, has been analyzed in this paper. The appropriate analyses have been made in order to determine the initiator of the rotating stall. For analyzing of described problem the system of common differential equations are used:

$$
\begin{aligned}
&-\frac{\alpha}{r^2}\frac{d}{dr}\left[\frac{1}{r}\int_0^\infty\left(1-r^2\boldsymbol{C}_r^2\right)dz\right]+\\
&\qquad+\frac{1}{r^3}\int_0^\infty\left(1-r^2\boldsymbol{C}_u^2\right)dz=-\frac{\tau_{rw}}{\rho C_{u2}^2}\\
&-\frac{\alpha}{r^2}\frac{d}{dr}\left[\int_0^\infty\left(1-r^2\boldsymbol{C}_r\boldsymbol{C}_u\right)dz\right]=-\frac{\tau_{\varepsilon w}}{\rho C_{u2}^2}
\end{aligned}
\tag{1}
$$

For the further work it is necessary to take into account the friction stresses τ_{rw} and $\tau_{\varepsilon w}$ at diffuser walls, and introduce the designations usual in the boundary layer theory:

$$
\begin{aligned}
&\delta_r^*=\int_0^\infty\left(1-\frac{C_r}{\boldsymbol{C}_r}\right)dz\ ;\ \delta_r^{**}=\int_0^\infty\frac{C_r}{\boldsymbol{C}_r}\left(1-\frac{C_r}{\boldsymbol{C}_r}\right)dz\ ;\\
&\delta_\varepsilon^*=\int_0^\infty\left(1-\frac{C_u}{\boldsymbol{C}_u}\right)dz\ ;\ \delta_\varepsilon^{**}=\int_0^\infty\frac{C_u}{\boldsymbol{C}_u}\left(1-\frac{C_u}{\boldsymbol{C}_u}\right)dz\\
&H_r=\frac{\delta_r^*}{\delta_r^{**}}\ ;\ H_\varepsilon=\frac{\delta_\varepsilon^*}{\delta_\varepsilon^{**}}.
\end{aligned}
\tag{2}
$$

Based on experimental data for the velocity profile in the vaneless diffuser it was found that the tangential stresses are:

$$
\begin{aligned}
&\tau_{rw}=\frac{1}{2}\rho\boldsymbol{C}_r^2\,0{,}37\cdot10^{-0{,}85H_r}\,Re_{\delta_r^{**}}^{-0{,}24}\\
&\tau_{\varepsilon w}=\frac{1}{2}\rho\boldsymbol{C}_u^2\,0{,}37\cdot10^{-0{,}85H_\varepsilon}\,\mathrm{Re}_{\delta_r^{**}}^{-0{,}24},
\end{aligned}
\tag{3}
$$

where:

$$
\begin{aligned}
&Re_{\delta_r}^{**}=\frac{R_2\cdot\boldsymbol{C}_r\cdot C_{r2}\cdot\delta_r^{**}}{\nu}\ ;\\
&Re_{\delta_\varepsilon}^{**}=\frac{R_2\cdot\boldsymbol{C}_u\cdot C_{u2}\cdot\delta_\varepsilon^{**}}{\nu}
\end{aligned}
\tag{4}
$$

In the case of turbulent boundary layer on the plain surface ($H=1.4$):

$$
\tau_{\varepsilon w}=\frac{1}{2}\rho\boldsymbol{C}_u^2\cdot0{,}0238\cdot Re_{\delta_\varepsilon^{**}}^{-0{,}24}. \tag{5}
$$

Introducing new variables $u=rC_r$ and $w=rC_u$, the following equations can be written:

$$
\begin{aligned}
&\delta_u^*=\int_0^\infty(1-u)dz\ ;\ \delta_u^{**}=\int_0^\infty u(1-u)dz\ ;\\
&H_u=\frac{\delta_u^*}{\delta_u^{**}}\ ;\ H_v=\frac{\delta_v^*}{\delta_v^{**}}\ ;\ \delta_w^*=\int_0^\infty(1-w)dz\ ;\\
&\delta_w^{**}=\int_0^\infty w(1-w)dz\ ;\ \delta_{uw}^{**}=\int_0^\infty(1-uw)dz\ .
\end{aligned}
\tag{6}
$$

Using the usual methods it can be shown that:

$$
\begin{aligned}
&H_r=H_u\ ,\ H_\varepsilon=H_w\ .\\
&Re_{\delta_r^{**}}=\frac{R_2\cdot C_{u2}}{\nu}\frac{\alpha\delta_w^{**}}{r}\\
&Re_{\delta_\varepsilon^{**}}=\frac{R_2\cdot C_{u2}}{\nu}\frac{\delta_w^{**}}{r}
\end{aligned}
\tag{7}
$$

Substituting the previous expressions into the system (1), it can be reduced to:

$$
\begin{aligned}
&\frac{\alpha^2}{r}\frac{d}{dr}\left[\frac{(1+H_u)}{r}\delta_u^{**}\right]-\frac{2{,}4}{r^3}\delta_w^{**}=\\
&\qquad=0{,}185\cdot10^{-0{,}85H_u}\cdot Re_{\delta_r^{**}}^{-0{,}24}\frac{\alpha^2}{r^2}\\
&\frac{\alpha}{r^2}\frac{d\delta_u^{**}}{dr}=0{,}0119\,Re_{\delta_r^{**}}^{-0{,}24}\frac{1}{r^2}.
\end{aligned}
\tag{8}
$$

Boundary layer does not exist at the vaneless diffuser inlet, so the initial conditions are:

$$
\delta_u^{**}\big|_{r=1}=\delta_w^{**}\big|_{r=1}=0\ . \tag{9}
$$

The equation system (8) is open, unless the connection among δ_{uw}^{**} and the requested values δ_u^{**}, δ_w^{**} and H_u were found. The procedure of recognizing those connections was given in the work [10].

The final form of the solved system is:

$$\frac{d}{dr}\left[\frac{(1+H)}{r}\delta_u^{**}\right]-\frac{2,4}{\alpha^2 r^2}\delta_w^{**}=$$
$$=0,185\cdot 10^{-0,85H}\cdot Re_{\delta_r^{**}}^{-0,24}\frac{1}{r}$$
$$\frac{d\delta_{uw}^{**}}{dr}=0,0119\,Re_{\delta_\varepsilon}^{-0,24}\frac{1}{\alpha} \qquad (10)$$
$$\frac{d}{dr}\left(H_1\delta_u^{**}\right)=F(H)$$

where:

$$H_1=\frac{2H}{H-1};\ Re_{\delta_r^{**}}=\frac{\alpha\delta_u^{**}}{r}\frac{C_{u2}R_2}{\nu}$$
$$Re_{\delta_\varepsilon^{**}}=\frac{C_{u2}R_2}{\nu}\frac{\delta_w^{**}}{r},$$
$$\delta_{uw}^{**}=H\delta_u^{**}+\frac{2}{(H+1)\left[1,2+0,5(H-1)\right]}\cdot \qquad (11)$$
$$\cdot\frac{8,4\delta_w^{**}}{5}\left[\frac{(H-1)}{H(H+1)}\frac{8,4\delta_w^{**}}{\delta_u^{**}}\right]^{0,5(H-1)}$$

The initial conditions are:

$$\delta_u^{**}\Big|_{r=1}=\delta_v^{**}\Big|_{r=1}=0;\ H\Big|_{r=1}=1,5. \qquad (12)$$

The system of the equations was solved using Euler's method with the automatic choosing of the integration rate for small inlet angles to the vaneless diffuser $(\alpha_2=10^o\div 20^o)$ and for $C_{u2}=100\div 200\,m/s$. On this basis, a conclusion can be made that this values correspond to the experimental values. From numerous diagrams only one has been chosen as an illustration (Figure 5) where the stalled limit in a vaneless diffuser was given for different values of the angle α_2 and for three values of C_{u2}.

Practically the 'stalling' in the given case occurs when $\alpha_2<18^o$. These data agree quite well with the results of the experimental determination of the rotating stall limit in the stage with the vaneless diffuser. The obtained results about the stalling of the boundary layer on the walls of the vaneless diffuser and their parameters with the small angles α_2 were established on the idealized image of the flow in the vaneless diffuser; however, they provide the possibility to grasp the physics of the flow process with a stall. It is considered that stalling represents the precursors of the rotating stall in the centrifugal compressor stage with vaneless diffuser.

3. THE EXPERIMENTAL RESULTS

Figures 6 to 11 show the experimental diagrams of the compressor operating regimes for the velocities U_2=100, 150 and 196.4 m/s and the Table 1 shows summary of tested impellers and diffusers and only results for D45 stage operation during the unstable regimes are shown in this paper. Table 2 shows determined parameters of the rotating stall which characterize the D45 stage operation during the unstable regimes.

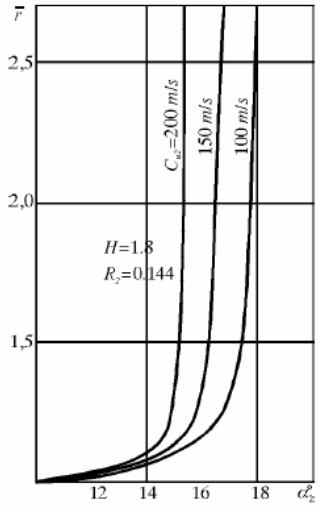

Figure5. The stalled limit in the vaneless diffuser

Table 1. Summary of tested impellers

Impeller	2	1	3	4
Diffuser	β_{L2}=21°	β_{L2}=49°	β_{L2}=21°	β_{L2}=52°
Vaned diffuser $\overline{D}_3=1,09$	B21	B11	B31	
Vaned diffuser $\overline{D}_3=1,2$		B13		B43 (D43)
Vaneless diffuser	K25	T1	B35	D45

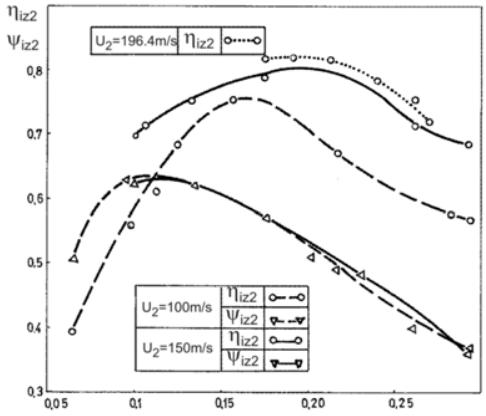

Figure 6. Aerodynamic characteristics of the D43 stage

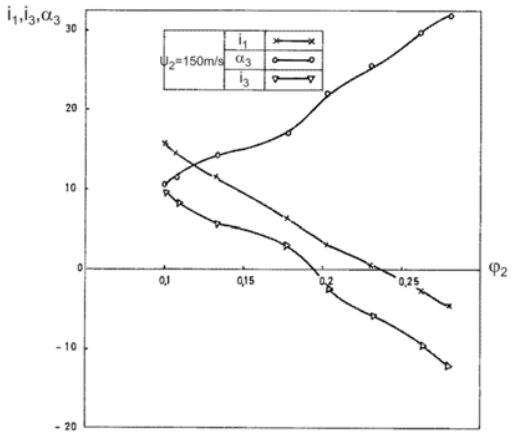

Figure 7. The calculated angles i_1, i_3 and α_3 as a function of angle $\varphi_2 = C_{r2}/U_2$

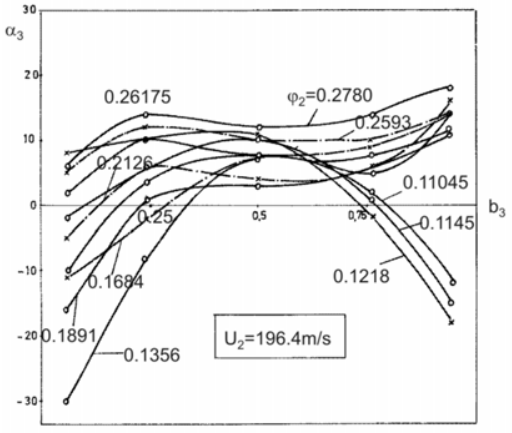

Figure 10. The arrangement of the measured flow angles along the width as a function of φ_2

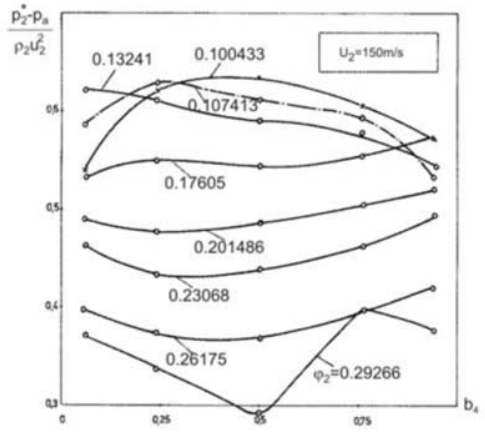

Figure 8. The total pressure p_2^* arrangement along the width as a function of φ_2

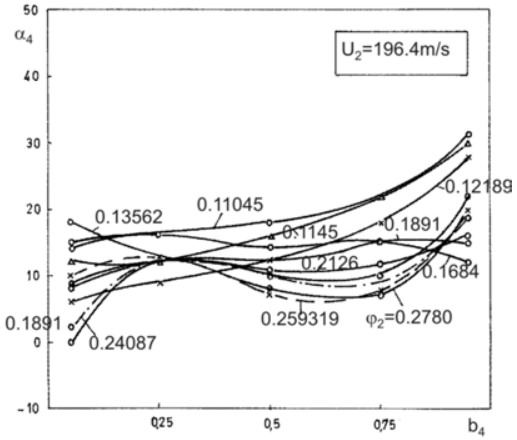

Figure 11. The arrangement of the measured flow angles along the width as a function of φ_2

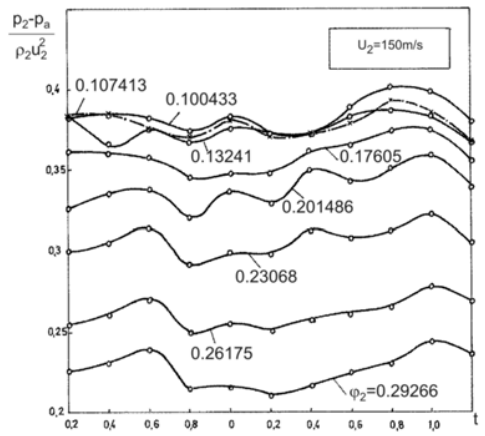

Figure 9. The static pressure in front of vaned diffuser grid (t grid step) at $\overline{D}_3 = 1.05$

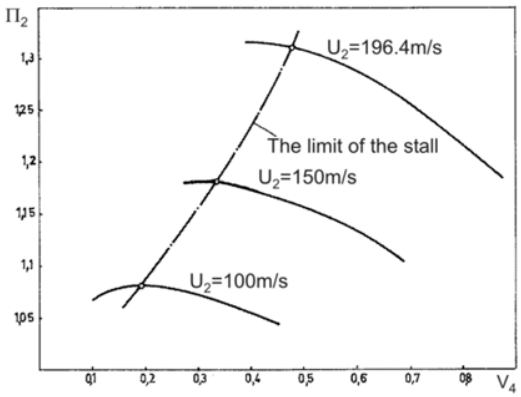

Figure 12. Aerodynamic characteristics of the D43 stage

Table 2. Main parameters which characterize the D45 stage operation during the unstable regimes

		Calculated values		Parameters of the stall		Notes
		φ_0	i_1	α_3	Z_3	ω_3	
U_2=100m/s		0.1417	10.46	13.83	2	0.075	The limit of the stall
		0.1330	11.54	13.11	2	0.077	The stall
		0.1061	13.70	8.98	2	0.078	Chaotic oscillations
		0.0958	16.33	8.62	2	0.080	Stall with triple amplitude
		0.0766	18.89	7.49	2	0.083	Chaotic oscillations
		0.0600	21.12	5.60	2	0.091	The stall
U_2=150m/s	Regime 6	Regimes for which φ_0, i_1, α_3 are not indirectly measured, and only number of stalled regions are determined			2	0.090	The stall
	Regime 7				2	0.083	Chaotic oscillations
	Regime 8				2	0.086	Developed stall
U_2=200m/s	Regime 3				2	0.082	The limit of the stall
	Regime 4				3	0.081	Weak stall
	Regime 5				2	0.080	Dveloped stall

4. SUMMARY

Generalizing given results the following conclusions can be drawn:

1. With an increase of the circumferential velocity, the transitions move in the regions of higher flows.

2. The parameters of the rotating stall significantly depend on the circumferential velocity U_2 which can be seen from the enclosed table.

3. Different values of the angles α_3 and α_4 along the diffuser width correspond to the appearance limit of the rotating stall.

4. The arrangement of the total pressure over the cross section 2-2 along the diffuser width depends on the operating regime of the stage. The character of the pressure arrangement beyond the impeller is uniform along the diffuser width at optimal operating regime.

5. The single-region stall differs from the multi-region stall by the character of forming.

REFERENCES

[1] Акульин Ю Д., Измаилов Р.А. и др., 1980, Использование "ИВК для исследования нестационарных случайных процессов в турбомашинах", Межвузовскй сборник, Ленинград.

[2] Борисов А., Локштанов Е., Ольштейн А., 1962, "Вращающйся срйв в осевом компрессоре", *Примышленая аэрижодинамика,* номер 24, Москва.

[3] Ершов В. Н., 1966, "Неустойчивые режимы турбомашин", Москва

[4] Измаилов Р.А. 1970, "Иследование нестационарных процессов в проточной части центробрежного компрессора" *Дис. на соискание ученой степени канд. Техн. Наук*. Ленинград..

[5] Измаилов Р.А. 1980, "Рауработка и применение информационного – вычисли тельного комплекса для исследования нестационарных течений в центробрежных компрессорах труды", *ЛПИ*, номер 370, Ленинградж.

[6] Стенинг А., 1980, "Вращающийся срыв и помпаж, *Теоретические основы,* номер 1.ж.

[7] Shesire L. J., 1945, "The Design and Development of Centrifugal Compressors for Aircraft Gas Turbines", *Institution of Mechanical Engineers Proceedings*, Vol. 153, War Emergency Issue No12.

[8] Takata N., 1961. "Rotating stall in Multistage Axial Compressors", *Report of Aeronautical Research Institute*, University of Tokio, Vol. 2, No 6.

[9] Таката Н., 1972, "Нелинейный анализ вращающегося срыва", *Энергетичесские машины и установки*, номер 4, Изд-во Мир.

[10] Milenkovic D., 1999, "The Unstable working regimes of the Turbomachines", *Monograph, ,* Faculty of Mechanical Engineering, Univesity of Nis.

Conference on Modelling Fluid Flow (CMFF'06)
The 13th International Conference on Fluid Flow Technologies
Budapest, Hungary, September 6-9, 2006

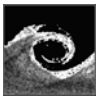

MODELING FOR CENTRIFUGAL COMPRESSOR STABILITY

Yong Sang Yoon[1], Seung Jin Song[2]

[1] Corresponding Author. School of Mechanical and Aerospace Engineering, Seoul National University. San 56-1 Shillim dong, Kwanak gu, Seoul, Korea. Tel.: +82 2 880 1701, Fax: +82 2 883 0179, E-mail: perfect1@snu.ac.kr
[2] School of Mechanical and Aerospace Engineering, Seoul National University. E-mail: sjsong@snu.ac.kr

ABSTRACT

Compared to axial compressors, a model capable of analyzing the flow in centrifugal compressor is lacking because of the complexity in the geometry. Therefore, this paper presents a new model based on Moore-Greitzer methodology to predict the flow field and stability in a centrifugal compressor with a vaneless diffuser. As input parameters, the compressor characteristic and compressor geometry are used. To predict the centrifugal compressor stability, the flow fields obtained from the vorticity equation and stream function at the inlet and exit of the impeller are connected through the compressor characteristic. Thus, the flow coefficient at stall inception and the number and speed of the rotating stall cell can be determined. This model has been applied to the SNU centrifugal compressor with vaneless diffuser. As a result, the rotating stall is initiated with 3 cells at the flow coefficient of 0.297 but its cell number is changed into two at 0.277. The speed of the rotating stall increases as flow coefficient decreases.

Keywords : Centrifugal compressor, vaneless diffuser, asymmetry, stability, analytical model

NOMENCLATURE

Q	[-]	normalized mass flow rate
R	[m]	mean radius
r	[-]	normalized radius
v	[-]	velocity normalized by tip velocity
x	[-]	normalized axial length
Γ	[-]	normalized circulation
α	[rad]	absolute exit angle
β	[rad]	relative exit angle
δ	[-]	perturbation
ε	[m]	eccentricity
γ	[rad]	stagger angle
λ	[r*ad*]	rotor/impeller inertia
ρ	[kg/m^3]	density
τ	[-]	normalized time
ω		vorticity
ψ		pressure rise coefficient, stream function
ζ		vorticity perturbation

Subscripts and Superscripts

imp	impeller
n	n-th harmonic
t	impeller inlet tip
u	unsteady
x	axial direction
θ	circumferential direction
$\overline{0}$	circumferential mean value
$\widetilde{0}$	Fourier spatial coefficient

1. INTRODUCTION

Many analytical and experimental studies have been conducted on the rotating stall and surge inception process in axial compressors. Greitzer [1] has developed a model to explain surge and rotating stall phenomena by introducing the B-parameter. Moore and Greitzer [2] suggested a 2- dimensional unsteady model to explain rotating stall in axial compressors. Based on these models, much research on axial compressor instability has been conducted. Furthermore, Hynes and Greitzer [3] presented an axial compressor stability model to assess the effect of inlet flow distortion. They found that the slope of the compressor characteristic solely determines the stability of the axisymmetric flow fields. Graf et al. [4] examined the effects of tip asymmetry on stability. Gordon [5] further developed Graf's model to account for the solution of the flow in a rotating reference frame.

Less research has been conducted on centrifugal compressor instability. Eckardt [6] experimentally found separation on shround casing on an impeller with no backsweep. Krain [7] also measured separation on shroud casing for an impeller with a 30 degree backsweep. Frigne and Van Den Braembussche [8] suggested an abrupt impeller rotating stall due to a strong interaction between impeller and diffuser and progressive

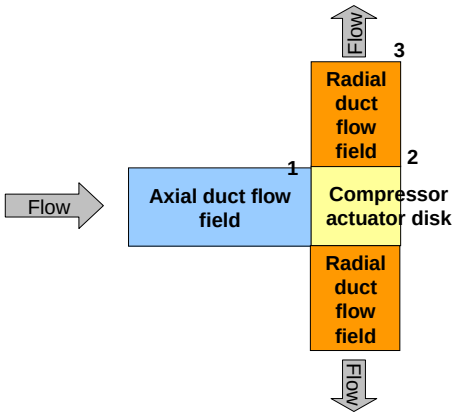

Figure 1. Schematic of modeling component.

impeller rotating stall due to flow separation in the impeller. However, such investigations were focused on the impeller flow field and didn't account for the diffuser effect. In diffusers, Jansen [9], for the first time, found negative radial velocity at stall. Senoo and Kinoshita [10] found the instability criterion for diffuser inlet angles to be between 69 and 81 degrees by using the predicted radial velocity profile across the width of the diffuser. Frigne and Van Den Braembussche [11] suggested a critical diffuser inlet angle of about 76 ~ 85 degrees by modeling. Again, like impeller studies, the diffuser studies were focused solely on the diffuser channel flow.

However, according to Cumpsty [12], the impeller and diffuser are strongly coupled and it is the combined effect which is important. Therefore, stability should be analyzed by considering all of the components. In a recent study, Spakovszky [13] has developed a dynamic instability model by connecting the inlet and exit flow of an impeller with the Euler-turbine equation. Experimentally, Hunziker and Gyarmathy [14] concluded the dynamic instability occurs at the location of the zero slope of the overall centrifugal compressor characteristic, including the influence of both the impeller and the diffuser. Thus, the effect of characteristic slope on statbility in centrifugal compressors is still unclear. Therefore, the objective of this research is to develop a new model to understand the centrifugal compressor stability by considering the compressor characteristic slope and all of the components.

2. MODEL DESCRIPTION

This section introduces a new flow model based on the "Moore-Greitzer" framework for centrifugal compressor stability. A centrifugal compressor system consists of the axial duct, impeller, and radial diffuser. Thus, the model consists of the inlet and exit ducts connected by the compressor characteristic curve. The flow in this system is assumed to be 2-dimensional in the axial and radial ducts. Also, the flow in the impeller is assumed to follow the blades perfectly, and, thus, blockage and deviation are not considered. The impeller is modeled as a semi- actuator disk to connect the flows in the axial duct and radial ducts as shown in Fig. 1.

The flow parameters in the compressor (e.g. stream function, velocity, and pressure) are assumed to be composed of mean and unsteady perturbation components.

$$V(t,\theta) = \overline{V} + \delta v(t,\theta) \tag{1}$$

All of the variables are nondimensionalized with the density, ρ, the impeller tip radius, R, and the impeller inlet tip speed, U. The impeller frequency derived from these values, $\Omega = \frac{U}{R}$ is also frequently used. Therefore, lengths are nondimensionalized as $x = \frac{X}{R}$, velocities as $v = \frac{V}{U_t}$, pressure as $p = \frac{P}{\rho U_t^{\,2}}$, and time as $t = T\Omega$.

2.1. Axial Duct Flow

The flow is assumed as 2-dimensional flow in axial and circumferential directions. The formulation is based on that of Spakovszky [13]. The axial and circumferential velocity perturbations and the pressure perturbation are obtained from the vorticity and the stream function equations. The vorticity equation is shown in Eq. (2)

$$\frac{\partial \delta\omega}{\partial \tau} + \overline{v}_x \frac{\partial \delta\omega}{\partial x} + \overline{v}_\theta \frac{\partial \delta\omega}{\partial \theta} = 0 \tag{2}$$

Also, the vorticity can be described by the stream function as shown in Eq. (5.3).

$$\frac{\partial^2 \delta\Psi}{\partial x^2} + \frac{\partial^2 \delta\Psi}{\partial \theta^2} = -\delta\omega \tag{3}$$

Here, $\overline{v}_x$ and $\overline{v}_\theta$ are the constant mean flow velocities.

Assuming a periodic solution in θ-direction, the vorticity and stream function perturbations can be decomposed into spatial harmonics

$$\delta\omega = \sum_{n=0}^{\infty} \widetilde{\omega}_n(x,t) \cdot e^{jn\theta} \tag{4a}$$

and

$$\delta\Psi = \sum_{n=0}^{\infty} \widetilde{\Psi}_n(x,t) \cdot e^{jn\theta} \tag{4b}$$

In addition, $\widetilde{\omega}_n(x,t)$ is also decomposed into functions of only x and t.

$$\widetilde{\omega}_n(x,t) = \widetilde{\zeta}_n(t) \cdot \chi(x) \tag{5}$$

Thus, the vorticity equation, Eq. (2) can be represented as follows

$$\frac{\dot{\tilde{\zeta}}_n}{\tilde{\zeta}_n} = -\frac{\bar{v}_x \tilde{\chi}_n' + jn\bar{v}_\theta \tilde{\chi}_n}{\tilde{\chi}_n} = \lambda_n \tag{6}$$

and, the vorticity perturbation can be obtained as

$$\tilde{\omega}_n = \tilde{C}_{u,n}\, e^{\lambda_n t} e^{-\left(\frac{\lambda_n}{\bar{v}_x} + jn\frac{\bar{v}_\theta}{\bar{v}_x}\right)x} \tag{7}$$

where λ_n is the eigenvalue which determines stability. Substituting the vorticity perturbation into Eq. (3), the stream function perturbation can be acquired.

$$\tilde{\Psi}_n = \left\{ \tilde{A}_{u,n}\, e^{nx} + \tilde{B}_{u,n} e^{-nx} + \tilde{C}_{u,n} e^{-\left(\frac{\lambda_n}{\bar{v}_x} + jn\frac{\bar{v}_\theta}{\bar{v}_x}\right)x} \right\} e^{\lambda_n t} \tag{8}$$

Subsequently, the axial and tangential velocities are determined from the stream function perturbation as

$$\tilde{v}_{x,n} = \begin{Bmatrix} jn\tilde{A}_{u,n}\, e^{nx} + jn\tilde{B}_{u,n} e^{-nx} \\ + jn\tilde{C}_{u,n} e^{-\left(\frac{\lambda_n}{\bar{v}_x} + jn\frac{\bar{v}_\theta}{\bar{v}_x}\right)x} \end{Bmatrix} e^{\lambda_n t} \tag{9}$$

$$\tilde{v}_{\theta,n} = \begin{Bmatrix} -n\tilde{A}_{u,n}\, e^{nx} + n\tilde{B}_{u,n} e^{-nx} \\ + \left(\frac{\lambda_n}{\bar{v}_x} + jn\frac{\bar{v}_\theta}{\bar{v}_x}\right)\tilde{C}_{u,n} e^{-\left(\frac{\lambda_n}{\bar{v}_x} + jn\frac{\bar{v}_\theta}{\bar{v}_x}\right)x} \end{Bmatrix} e^{\lambda_n t} \tag{10}$$

Finally, the tangential momentum equation gives the pressure perturbation.

$$\begin{aligned} \tilde{p}_n = \{ & \tilde{A}_{u,n}(-j\lambda_n + n\bar{v}_\theta - jn\bar{v}_x) e^{nx} \\ & + \tilde{B}_{u,n}(j\lambda_n - n\bar{v}_\theta - jn\bar{v}_x) e^{-nx} \} e^{\lambda_n t} \end{aligned} \tag{11}$$

Rearranging, the flow field perturbation solution can be denoted with the following transmission matrix and written as

$$\begin{bmatrix} \delta V_x \\ \delta V_\theta \\ \delta P \end{bmatrix} = \sum_{n=1}^{\infty} \left\{ T_{ax,n} \cdot \begin{bmatrix} A_{u,n} \\ B_{u,n} \\ C_{u,n} \end{bmatrix} + \begin{bmatrix} A_{s,n} \\ B_{s,n} \\ C_{s,n} \end{bmatrix} \right\} \cdot e^{\lambda_n t + jn\theta} \tag{12}$$

where

$$T_{ax,n} = \begin{bmatrix} jne^{nx} & jne^{-nx} & jne^{-\left(\frac{\lambda_n}{\bar{v}_x} + jn\frac{\bar{v}_\theta}{\bar{v}_x}\right)x} \\ -ne^{nx} & ne^{-nx} & \left(\frac{\lambda_n}{\bar{v}_x} + jn\frac{\bar{v}_\theta}{\bar{v}_x}\right) e^{-\left(\frac{\lambda_n}{\bar{v}_x} + jn\frac{\bar{v}_\theta}{\bar{v}_x}\right)x} \\ (-j\lambda_n + n\bar{v}_\theta & (j\lambda_n - n\bar{v}_\theta & 0 \\ -jn\bar{v}_x)e^{nx} & -jn\bar{v}_x)e^{-nx} & \end{bmatrix} \tag{13}$$

2.2. Radial Duct Flow

In a centrifugal compressor, the flow enters the impeller axially and exits radially. Therefore, in the radial exit duct, the linearized equations should be solved in cylindrical coordinates and, thus, the flow analysis approach is more complicated than that in the previous section for an axial duct. The procedure to obtain the transmission matrix of the flow in radial duct is similar to that for in Spakovszky [13].

$$\frac{\partial \delta\omega}{\partial t} + \frac{Q}{r}\frac{\partial \delta\omega}{\partial r} + \frac{\Gamma}{r^2}\frac{\partial \delta\omega}{\partial \theta} = 0 \tag{14}$$

where Q and Γ are the mass flow rate and circulation which are defined as $r\bar{v}_r(r)$, $r\bar{v}_\theta(r)$, respectively. In addition, the voriticy and stream function give next equation

$$\frac{\partial^2 \delta\Psi}{\partial r^2} + \frac{1}{r}\frac{\partial \delta\Psi}{\partial r} + \frac{1}{r^2}\frac{\partial^2 \delta\Psi}{\partial \theta^2} = -\delta\omega \tag{15}$$

The vorticity perturbation is obtained from Eq. (14) by separation of variables.

$$\tilde{\omega}_n = \tilde{F}_{3,n}\, e^{\lambda_n t} e^{-\left(jn\frac{\Gamma}{Q}\log r + \frac{\lambda_n}{2Q}r^2\right)} \tag{16}$$

From Eq. (15), the stream function perturbation is as follows.

$$\tilde{\Psi}_n = \left\{ \tilde{D}_{u,n}\, r^n + \tilde{E}_{u,n} r^{-n} + \tilde{F}_{u,n} R_n \right\} e^{\lambda_n t} \tag{17}$$

where

$$R_n = \int_{r_0}^{r} e^{-\left(jn\frac{\Gamma}{Q}\log\xi + \frac{\lambda_n}{2Q}\xi^2\right)} (r^n \xi^{-n+1} - r^{-n}\xi^{n+1}) d\xi \tag{18}$$

Thus, the radial and tangential velocities can be acquired as presented in Eqs. (19) and (20).

$$\tilde{v}_{r,n} = jn\left\{ \tilde{D}_{u,n}\, r^{n-1} + \tilde{E}_{u,n} r^{-n-1} + \tilde{F}_{u,n}\frac{R_n}{r} \right\} e^{\lambda_n t} \tag{19}$$

$$\tilde{v}_{\theta,n} = \begin{Bmatrix} -n\tilde{D}_{u,n}\, r^{n-1} + n\tilde{E}_{u,n} r^{-n-1} \\ -\tilde{F}_{u,n}\dfrac{dR_n}{dr} \end{Bmatrix} e^{\lambda_n t} \tag{20}$$

Also, from the tangential momentum equation, the pressure perturbation in diffuser is obtained.

$$\begin{aligned} \tilde{p}_{\theta,n} = [& \tilde{D}_{u,n}\left\{(-jnQ + n\Gamma) r^{n-2} - j\lambda_n r^n\right\} \\ & + \tilde{E}_{u,n}\left\{(-jnQ - n\Gamma) r^{-n-2} + j\lambda_n r^{-n}\right\} \\ & + \tilde{F}_{u,n} S_n] e^{\lambda_n t} \end{aligned} \tag{21}$$

where $S_n = \frac{Q}{jn}\frac{d^2 R_n}{dr^2} + \left(\frac{\Gamma}{r} + \frac{Q}{jnr} + \frac{\lambda_n r}{jn}\right)\frac{dR_n}{dr}$.

Then, the flow perturbation field is given by the radial transmission matrix as follows.

$$\begin{bmatrix} \delta V_r \\ \delta V_\theta \\ \delta P \end{bmatrix} = \sum_{n=1}^{\infty} \left\{ T_{rad,n} \cdot \begin{bmatrix} D_{u,n}(s) \\ E_{u,n}(s) \\ F_{u,n}(s) \end{bmatrix} \right\} \cdot e^{\lambda_n t} e^{jn\theta} \tag{22}$$

where $T_{rad,n}$ is a 3 by 3 matrix

$$T_{rad,n}(:,1) = \begin{bmatrix} jnr^{n-1} \\ -nr^{n-1} \\ \left\{(-jnQ + n\Gamma) r^{n-2} - j\lambda_n r^n\right\} \end{bmatrix} \tag{23a}$$

$$T_{rad,n}(:,2)=\begin{bmatrix} jnr^{-n-1} \\ nr^{-n-1} \\ \left\{\left(-jnQ-n\Gamma\right)r^{-n-2}+j\lambda_n r^{-n}\right\} \end{bmatrix} \quad (23b)$$

$$T_{rad,n}(:,3)=\begin{bmatrix} jn\dfrac{R_n}{r} \\ -\dfrac{\partial R_n}{\partial r} \\ \left\{\dfrac{Q}{jn}\dfrac{d^2R_n}{dr^2}+\left(\dfrac{\Gamma}{r}+\dfrac{Q}{jnr}+\dfrac{\lambda_n r}{jn}\right)\dfrac{dR_n}{dr}\right\} \end{bmatrix} \quad (23c)$$

2.3. Impeller Actuator Dynamics

In this section, a newly developed semi-actuator disk model is presented for the relation between the impeller exit static pressure and the inlet total pressure as follows.

$$P_2-P_{t1}=\Psi_{ts}-\lambda_{imp}\frac{\partial v_x}{\partial\theta}-\lambda_{imp}\frac{\partial v_x}{\partial\tau} \quad (24)$$

where λ_{imp} presents the inertia of the fluid in the impeller passage and is defined as $\lambda_{imp}=\dfrac{AR_{imp}\cdot\log\left(AR_{imp}\right)}{AR_{imp}-1}\cdot s_{imp}$. Here $AR_{imp}=\dfrac{\rho_2 A_2}{\rho_1 A_1}$ is the impeller area-density ratio and s_{imp} is the mean passage length in the streamwise direction. Eq. (24) shows that the unsteady local pressure difference across the compressor (exit static minus inlet total) is given by the steady local flow compressor pumping characteristic plus a correlation to account for the fact that the flow in the impeller is non-uniform in the circumferential direction since the rotating stall induces the unsteady non-uniform perturbation. In Eq. (24), the utilized compressor characteristic is the axisymmetric total-to-static pressure rise coefficient, Ψ_{ts}, through the impeller as a function of the flow coefficient, ϕ. Linearizing Eq. (24) yields the following equation.

$$\delta P_2-\delta P_{t1}=\frac{\partial\Psi_{ts}}{\partial\phi}\delta v_x-\lambda_{imp}\frac{\partial\delta v_x}{\partial\theta}-\lambda_{imp}\frac{\partial\delta v_x}{\partial\tau} \quad (25)$$

In Eq. (25), $\dfrac{\partial\Psi}{\partial\phi}$ are the derivative of the pressure rise characteristics with respect to axial flow coefficient.

Substituting a spatial harmonic solution into Eq. (25), the relation between the pressure perturbation at the impeller exit and inlet can be obtained, and the radial velocity at the exit of impeller can be obtained from continuity as

$$\boldsymbol{V}_{r2}=\frac{1}{\boldsymbol{AR_{imp}}}\boldsymbol{V}_{x1} \quad (26)$$

The circumferential velocity is obtained with the assumption that the flow follows the blades perfectly.

$$V_{\theta 2}=U_t+V_{r2}\tan\beta_2=V_{r2}\tan\alpha_2 \quad (27)$$

where β_2 and α_2 are a relative exit angle and absolute exit angle, respectively. Eqs. (25), (26) and (27) are linearized and cast into a transmission matrix giving

$$\begin{bmatrix}\delta V_{r2}\\ \delta V_{\theta 2}\\ \delta P_2\end{bmatrix}=\sum_{n=0}^{\infty}\left\{B_{imp,n}\begin{bmatrix}\widetilde{v}_{x1,n}\\ \widetilde{v}_{\theta 1,n}\\ \widetilde{P}_{1,n}\end{bmatrix}\right\}e^{\lambda_n\, jn\theta} \quad (28)$$

Thus, the n-th harmonic transmission matrix for a radial impeller is defined as

$$B_{imp,n}=\begin{bmatrix}\dfrac{1}{AR_{imp}} & 0 & 0\\ \dfrac{\tan\beta_2}{AR_{imp}} & 0 & 0\\ \left(\dfrac{\partial\Psi_{ts}}{\partial\phi}-\left(jn+\lambda_n\right)\lambda_{imp}+\overline{V}_{x1}\right) & \overline{V}_{\theta 1} & 1\end{bmatrix} \quad (29)$$

2.4. Transmission Matrix Stacking

As shown in Fig. 1, the flow passes through the axial duct, the impeller, and the radial diffuser. Thus, from Eqs. (12), (21), and (29), the transmission marices are stacked into 3 different equations.

$$\begin{aligned} &T_{rad,n}(r_2)\cdot\begin{bmatrix}D_{u,n}(s)\\ E_{u,n}(s)\\ F_{u,n}(s)\end{bmatrix}\\ &=B_{imp,n}\cdot\left\{T_{ax,n}\cdot\begin{bmatrix}A_{u,n}(s)\\ B_{u,n}(s)\\ C_{u,n}(s)\end{bmatrix}\right\}\end{aligned} \quad (30)$$

Thus, the spatial harmonic coefficients, ($D_{u,n}$, $E_{u,n}$, and $F_{u,n}$) in the radial diffuser are related to the spatial harmonic coefficients in the inlet duct ($A_{u,n}$, $B_{u,n}$, and $C_{u,n}$).

$$\begin{aligned} &\begin{bmatrix}D_{u,n}(s)\\ E_{u,n}(s)\\ F_{u,n}(s)\end{bmatrix}\\ &=T_{rad,n}(r_2)^{-1}B_{imp,n}T_{ax,n}\cdot\begin{bmatrix}A_{u,n}(s)\\ B_{u,n}(s)\\ C_{u,n}(s)\end{bmatrix}\end{aligned} \quad (31)$$

To connect upstream and downstream flow fields, boundary conditions are needed. In the axial duct, the flow is irrotational. Therefore, $C_{u,n}=0$ in the upstream region (Eq. (32a)). Far upstream of

Table 1. Dimensions for the test centrifugal compressor

Rt1 (Tip radius, m)	0.0317
Rh1 (Hub radius, m)	0.0102
Speed, rpm	30,000
□□impeller exit angle	35
R2 (Impeller exit radius, m)	0.055

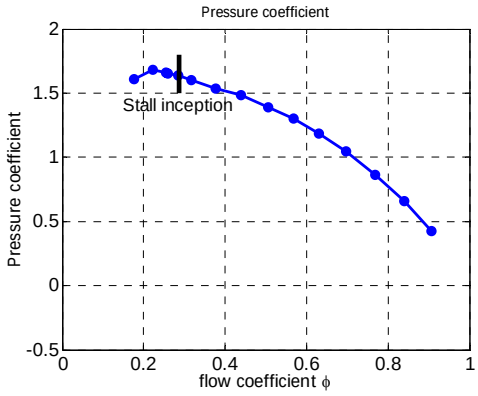

Figure 2. Compressor characteristic used in this model.

compressor, the potential perturbation should be zero since the compressor is the only energy source. Thus, $B_{u,n} = 0$ (Eq. (32b)). Downstream of compressor, the collector dimensions are much larger than compressor diffuser. Therefore, the static pressure perturbation, $\delta P_s(r = r_3)$, is assumed to be zero at the inlet of the plenum (32c).

$$C_{u,n} = 0 \tag{32a}$$

$$B_{u,n} = 0 \tag{32b}$$

$$\left[T_{3rad,n}(3,1)\ T_{3rad,n}(3,2)\ T_{3rad,n}(3,3)\right]\cdot\begin{bmatrix} D_{u,n}(s) \\ E_{u,n}(s) \\ F_{u,n}(s) \end{bmatrix} = 0 \tag{32c}$$

Thus, the 6 unknown spatial harmonic coefficients, $A_{u,n}$, $B_{u,n}$, $C_{u,n}$, $D_{u,n}$, $E_{u,n}$, and $F_{u,n}$ can be obtained from 6 equations (3 boundary conditions and 3 equations in Eq. (31)). Applying the three boundary conditions, Eqs. (32a), (32b), and (32c) to Eq. (31b), the following system of equations can be obtained.

$$T_{3rad,n}(3,:)\cdot T_{rad,n}(r_2)^{-1}\cdot B_{imp,n}\cdot T_{ax,n}\cdot\begin{bmatrix} A_{u,n} \\ 0 \\ 0 \end{bmatrix} = 0 \tag{33}$$

Eq. (33) reproduces the function of only $A_{u,n}$ as shown in Eq. (34).

$$T_{3rad,n}(3,:)\cdot T_{rad,n}(r_2)^{-1}\cdot B_{imp,n}\cdot T_{ax,n}(:,1)\cdot A_{u,n} = 0 \tag{34}$$

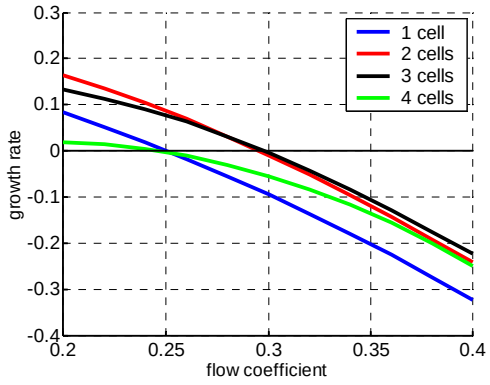

Figure 3. Growth rate versus flow coefficient for each cell number.

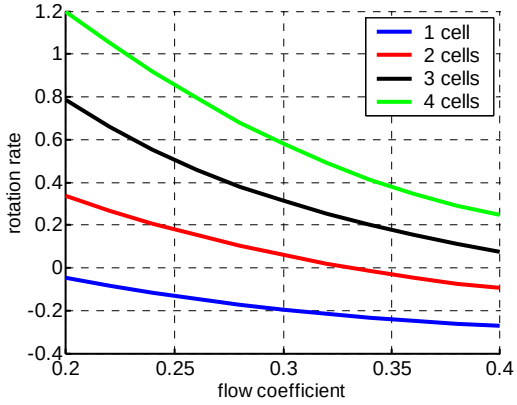

Figure 4. Rotation rate versus flow coefficient for each cell number.

For a non-trivial solution of $A_{u,n}$,

$$T_{3rad,n}(3,:)\cdot T_{rad,n}(r_2)^{-1}\cdot B_{imp,n}\cdot T_{ax,n}(:,1) = 0 \tag{35}$$

Thus, the eigenvalue λ_n can be found independently for each mode. In the $\lambda_n = \sigma_n + j\omega_n$ satisfying Eq. (35), σ_n indicates the growth rate and ω_n the rotation rate. The positive sign of σ_n signifies the onset of rotating stall.

4. RESULTS AND DISCUSSION

In axial compressors, the instability is thought to be initiated at zero slope of the compressor characteristic according to Moore and Greitzer [2], Hynes and Greitzer [3], and Graf [4]. Hunziker and Gyarmathy [14] suggested experimentally that the instability in the centrifugal compressor would also occur at the flow rate giving the maximum overall stage pressure rise characteristic. However, according to the new model, the stability in

centrifugal compressor is determined by (Eq. (35) the characteristic slope, mass flow rate, axial, radial and tangential velocities, circulation, and diffuser geomtry. Here, the axial, radial, and tangential velocities, mass flow rate, and circulation are dependent on flow coefficient according to the diffuser geometry. Therefore, what determines the stability as flow coefficient decreases is the characteristic and diffuser geometry.

Figure 2 shows the compressor characteristic used as a input in this model. This characterisitc was acquired from the Seoul National University centrifugal compressor which has a 64 mm inlet diameter and 30,000 rpm. The details in the facilities are shown in Table. 1. Using these compressor characteristic slope obtained from Fig. 2, the modeling results are presented in Fig. 3. The x-axis in Fig. 3 is the flow coefficient and the y-axis is the growth rate of λ_n which determines the divergence or convergence of the system. From this result, second and third harmonics mainly influence rotating stall dynamics. This centrifugal compressor is predicted to have a stall initiation at ϕ=0.298 due to the third harmonic. At ϕ<0.277, the second harmonic has a higher growth rate so that this centrifugal compressor has a rotating stall with two cells. Figure 4 shows the rotation rate of rotating stall cell versus flow coefficient. The rotation rate has been normalized by the impeller rotation speed. The rotating stall cells' speed increases as flow coefficient decreases. The rotating stall in this compressor has a similiar value in the growth rate for two and three cells near stall inception point.

5. SUMMARY

A new 2-D stability model for centrifugal compressor using compressor characteristic slope has been developed.

1. This model predicts the flow coefficient at rotating stall inception and stall cell speed and number. From the steady compressor characteristic,

2. Contrary to axial compressor stability, the centrifugal compressor stability depends on not only the compressor characteristic but also on the diffuser geometry. Even though it is difficult to define the exact criterion from the eigenvalue problem, this analysis gives the possibility that the centrifugal compressor stability is determined by the relations of the compressor characteristic and flow variables determined by the geometries, not on zero slope of the compressor characteristic.

REFERENCES

[1] Greitzer, E. M., 1976, "Surge and Rotating Stall in Axial Compressors; Part I: Theoretical Compression System Model," ASME Journal of Engineering for Power, Vol. 98, pp. 190-198.

[2] Moore, F. K. and Greitzer, E. M., 1986, "A Theory of Post-Stall Transients in Axial Compressors: Part I – Development of the Equations," ASME Journal of Engineering for Gas Turbines and Power, Vol. 108, pp. 68-76.

[3] Hynes, T. P. and Greitzer, E. M., 1987, "A Method for Assessing Effects of Circumferential Flow Distortion on Compressor Stability," ASME Journal of Turbomachinery, Vol. 109, pp. 371-379.

[4] Graf, M. B., Wong, T. S., Greitzer, E. M., Tan, C. S., Shin. H.-W., and Wisler, D. C., 1998, "Effects of Nonaxisymmetric Tip Clearance on Axial Compressor Performance and Stability," ASME Journal of Turbomachinery, Vol. 120, pp. 648-661.

[5] Gordon, K., 1999, "Three-Dimensional Rotating Stall Inception and Effects of Rotating Tip Clearance Asymmetry in Axial Compressors," PhD thesis, Department of Aeronautics and Astronautics, MIT.

[6] Eckardt, D., 1976, "Detailed Flow Investigations within a High Speed Centrifugal Compressor Impeller," Trans ASME Journal of Engineering for Power, Vol. 97, pp 337-346.

[7] Krain, H, 1987, "Swirling Impeller Flow," 32nd ASME Gas Turbine Conference and Exibit, Anaheim, California, Paper 87-GT-19.

[8] Frigne, P., and Van Den Braembussche, R., 1983,"Distinctioni between Different Types of Impeller and Diffuser Rotating Stall in a Centrifugal Compressor with Vaneless Diffuser," ASME 28th International Gas Turbine Conference and Exhibit, Phoenix Arizona, Paper 83-GT-61.

[9] Jansen, W., 1964, "Rotating Stall in a Radial Vaneless Diffuser," Trans ASME Journal of Basic Engineering, Vol. 86, pp. 750-758.

[10]Senoo, Y. and Kinoshita, Y., 1977, "Influence of Inlet Flow Conditions and Geometries of centrifugal vaneless diffusers on Critical Flow Angle for Reverse Flow," Trans ASME Journal of Fluids Engineering, Vol. 99, pp. 98-103.

[11] Frigne, P., and Van Den Braembussche, R., 1984,"Distinctioni between Different Types of Impeller and Diffuser Rotating Stall in a Centrifugal Compressor with Vaneless Diffuser," Trans ASME Journal of Engineering for Gas Turbines and Power, Vol. 106, pp. 468-474.

[12] Cumpsty, N., 1989, "Compressor Aerodynamics," Longman Scientific & Technical.

[13] Spakovszky. Z. S., 2001, "Applications of Axial and Radial Compressor Dynamic System

Modeling," PhD thesis, Department of Aeronautics and Astronautics, MIT.

[14] Hunziker, R. and Gyarmathy, G., 1994, "The Operational Stability of a Centrifugal Compressor and Its Dependence on the Characteristics of the Subcomponents," Trans ASME Journal of Turbomachinery, Vol. 116, pp. 250-259.

Conference on Modelling Fluid Flow (CMFF'06)
The 13th International Conference on Fluid Flow Technologies
Budapest, Hungary, September 6-9, 2006

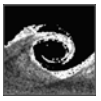

COMBINED EFFECTS OF CONTROLLED VORTEX DESIGN AND FORWARD BLADE SKEW ON THE THREE-DIMENSIONAL FLOW IN AXIAL FLOW ROTORS

János VAD[1], Ali R. A. KWEDIKHA[2], Csaba HORVÁTH[3]

[1] Corresponding Author. Department of Fluid Mechanics, Budapest University of Technology and Economics. Bertalan Lajos u. 4 – 6, H-1111 Budapest, Hungary. Tel.: +36 1 463 2464, Fax: +36 1 463 3464, E-mail: vad@ara.bme.hu
[2] Department of Fluid Mechanics, Budapest University of Technology and Economics. E-mail: kwedikha@ara.bme.hu
[3] Department of Fluid Mechanics, Budapest University of Technology and Economics. E-mail: csaba_h@hotmail.com

ABSTRACT

Comparative studies have been carried out on two axial flow fan rotors at their design flow rate in order to investigate the combined effects of controlled vortex design and circumferential forward skew on blade aerodynamics. The studies were based on Computational Fluid Dynamics, with composition and application of structured hexahedral grids taking up the challenge of the relatively complicated blade geometries due to skew and sweep. The computations indicated that the forward-skewed blade tip modifies the inlet flow field, leading to the rearrangement of spanwise blade load distribution, increase of losses along the dominant part of span, and converting the original non-free vortex spanwise blade circulation distribution toward a free-vortex flow pattern. The radial outward flow on the suction side, being especially significant for non-free vortex rotors, was found to be effectively moderated by forward skew, together with the losses associated. It has been concluded that forward skew is especially recommended for non-free vortex rotors for retardation of tip stalling.

Keywords: axial flow turbomachinery, blade skew, CFD, controlled vortex design

NOMENCLATURE

$C_p = (p-p_\infty)/(\rho u_t^2/2)$ [-] static pressure coefficient
S [-] fraction of span (S = 1: casing)
p [Pa] static pressure
Δp_t [Pa] total pressure rise
u [m/s] circumferential speed
v [m/s] absolute velocity
Φ [-] flow coefficient (annulus area-averaged axial velocity divided by u_t)
Ψ [-] total pressure coefficient (annulus mass-averaged total pressure rise divided by $\rho u_t^2/2$)
$\varphi = v_x / u_t$ [-] local axial flow coefficient
$\varphi_r = v_r / u_t$ [-] local radial flow coefficient
$\psi = \Delta p_t/(\rho u_t^2/2)$ [-] local total pressure coefficient
ρ [kg/m^3] fluid density
$\omega = \psi_{id} - \psi$ [-] total pressure loss coefficient

Subscripts and Superscripts
1 rotor inlet
2 rotor outlet
id ideal (inviscid)
r, x, u radial, axial, tangential
t blade tip
^ pitchwise-averaged
∞ far upstream

1. INTRODUCTION

Rotors of axial flow turbomachines are often of "controlled vortex" design (CVD) [1]. This means that contrarily to the classic free vortex concept prescribing spanwise constant design blade circulation, the circulation – and thus, the Euler work – increases along the dominant part of the blade span in a prescribed manner. CVD guarantees a better utilisation of blade sections at higher radii. By their increased contribution to the rotor performance, rotors of high specific performance can be realised, i.e. relatively high flow rate and total pressure rise can be obtained even with moderate diameter, blade count, and rotor speed [2]. CVD also gives a means for reduction of hub losses by unloading the blade root [3], and offers a potential to avoid highly twisted blades [4]. Furthermore, in multistage machinery, it is a means to realise an appropriate rotor exit flow angle distribution [1].

Blade sweep, dihedral, and skew are known as techniques of non-radial blade stacking. A blade has sweep and/or dihedral if blade sections of a datum blade of radial stacking line are displaced parallel

and/or normal to the chord, respectively [5]. A blade is swept-forward if the sections of a radially stacked datum blade are shifted parallel to their chord in such a way that a blade section under consideration is upstream of the neighbouring blade section at lower radius [2].

A special combination of dihedral and forward sweep is referred to as circumferential forward skew (FSK) [6]. In this case, the datum blade sections are shifted in the circumferential direction, toward the direction of rotation. By this means, the axial extension of the datum blading can be retained, the blade mechanics is expected to be more favourable than in case of forward sweep alone, and the following benefits, dedicated to the incorporated forward sweep, can be utilised. Forward sweep/skew offers a potential for improvement of efficiency [7], increase of pressure peak and extension of stall-free operating range [2][7], and noise reduction [6].

The literature reports extensively on FSK rotors of CVD, e.g. [3][6][7]. In these cases, the CVD design style is documented without further discussion, and the study concentrates on the skew-related effects. However, no special emphasis is given to the combination and interaction of three-dimensional (3D) flow phenomena due to CVD and FSK. This paper aims to contribute to a more comprehensive understanding of such combined effects, in order to aid the designer with guidelines for incorporation of FSK in the CVD technique. To this end, two comparative rotors of CVD, an unskewed (USK) and a FSK one, are studied in the paper at the design flow rate, by means of Computational Fluid Dynamics (CFD).

2. ROTORS OF CASE STUDY

A preliminary study of this work is documented in [8], in which the rotors have been presented in detail. Therefore, only a short account is given here.

The FSK rotor, together with outlet guide vanes, was designed by Vad [8]. It operates in the low-speed wind tunnel facility of the Hungarian Institute of Agricultural Engineering, Gödöllő, Hungary. The main geometrical data and design operational characteristics of the FSK rotor are presented in Table 1.

FSK was originated from the virtual USK rotor of radial stacking line. The blade sections of USK are shifted in circumferential direction toward the direction of rotation in order to obtain FSK, without making any modifications to the blade section geometry. The circular-arc cambered blade sections have C4 (10 %) profiles along the entire span. The trailing edges (TEs) of both USK and FSK fit to planes normal to the axis of rotation.

A virtual image of FSK, obtained from the CFD technique, is shown in Figure 1. The skew angle is defined as the angle between radial lines fitted to the TEs of the datum and to the shifted blade sections at a given radius, and is positive if the skew is applied in the direction of rotation (forward skew). As the figure illustrates, the skew angle is zero at the hub and increases progressively along the span, similarly to the style applied in [7]. By this means, it was intended to avoid any stacking line blend points, for which increased losses may be expected [9]. Geometrical details of the blading are specified in Table 2. The blades have backward sweep of leading edge (LE) near the hub, resulting in positive sweep [5] as a potential means of hub loss reduction.

Table 1. FSK rotor main characteristics

Casing diameter	2000 *mm*	Φ	0.33
Hub-to-tip ratio	0.6	Ψ	0.27
Blade count	12		
Tip clearance (% span)	5 %		

Figure 1. Isometric view of FSK

Table 2. Geometrical details of FSK blading

S	**0 hub**	**0.25**	**0.50 mid**	**0.75**	**1.00 tip**
Solidity	1.38	1.01	0.89	0.80	0.72
Camber angle, deg	20.3	17.3	16.8	15.8	15.3
Stagger angle, deg*	33.9	32.1	30.7	29.9	29.4
Skew angle, deg	0.0	0.0	0.3	1.6	3.5

*Measured from circumferential direction

3. CFD TECHNIQUE

The flow fields in USK and FSK were simulated by means of the commercially available finite-volume CFD code FLUENT [10]. Referring to e.g. [11] reporting on computations regarding swept and leaned compressor rotors, the standard k-ε turbulence model [12] has been used, with enhanced wall treatment of FLUENT. The main feature of this wall treatment is that it is a blended

model between the two-layer model and the logarithmic law of the wall [13].

With consideration of periodicity, the computations regarded one blade pitch only. A typical computational domain is presented in Figure 2. The domains extend to approx. 8 and 3,5 midspan axial chord lengths upstream and downstream of the rotor blading in the axial direction, respectively. The inlet face is a sector of the circular duct with a 30 deg central angle. Downstream of the inlet face, sectors of the steady inlet cone and the rotating hub with one blade in the middle of the domain are included for both types of blading.

At the inlet face, swirl-free uniform axial inlet condition corresponding to the design flow rate has been prescribed. The inlet turbulence intensity has been set to 1 percent, and the casing diameter was taken as the hydraulic diameter for the calculation of the turbulence length scale. Utilising the features of the annular cascade configuration, boundary conditions of periodicity were applied. A zero diffusion flux condition has been used for all flow variables at the outlet boundary (outflow condition in FLUENT [10]).

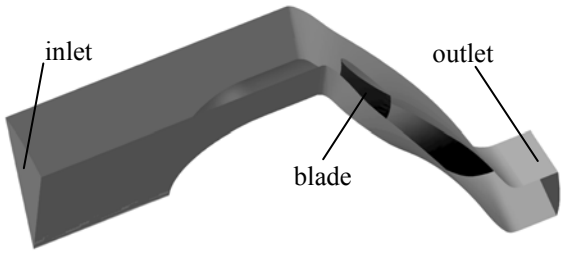

Figure 2. Typical computational domain

Taking e.g. [11] and [14] as preliminary references, a structured fully hexahedral mesh has been developed for the entire computational domain. Following the guidelines in [15] emphasizing the necessity of good grid quality, this meshing technique is felt promising from the viewpoint of computational accuracy. Furthermore, it offers a means to reduce the computational cost by moderating the cell size – although the investment in manpower is significant during mesh composition.

The mesh of the outer domain consists of 202, 26, and 48 grid points in axial, circumferential, and spanwise directions, respectively. The total number of the applied hexahedral cells is approximately 470.000, with about 50 % of cells in the refined domain in the vicinity of the blade. The tip clearance is resolved using 8 grid points, with meshing technique similar to the one applied in [16]. Taking up the challenge of relatively complicated blade geometry due to skew above midspan and LE sweep near the hub, the domain consists of 31 blocks. Figure 3 presents the mesh for FSK near the LE and the TE. An enlarged view of the mesh near the LE at the hub, composed to meet the challenge of LE sweep, is also shown in the figure, from another perspective in order to get better visibility.

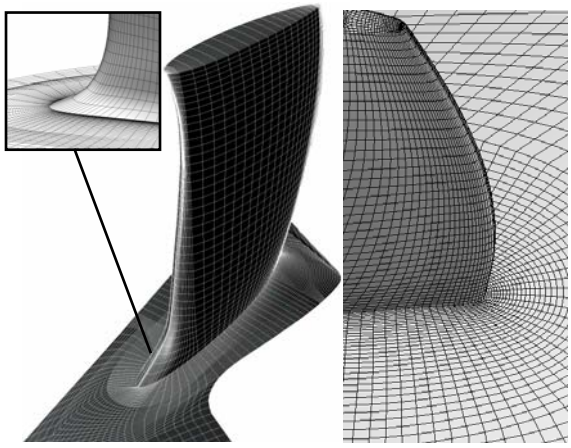

Figure 3. Mesh for FSK near the LE and TE

A C-type mesh topology has been built around the LE and TE, while H-type topology is applied to the entire rotor blade passage. Figure 4 presents an example of the C-type meshing topology, ensuring smooth meshing gradient in the pitchwise direction from blade suction surface towards the periodic boundary.

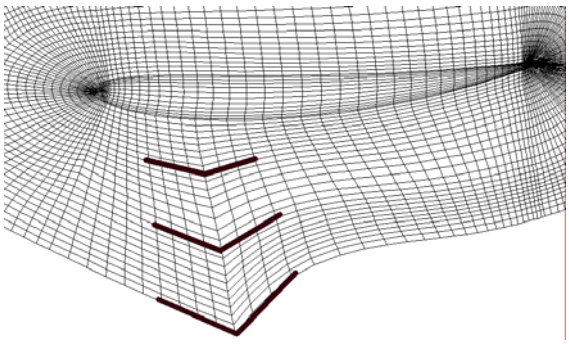

Figure 4. Example for meshing details

The equiangle skewness of a cell is defined as the maximum value of the ratio of actual and possibly highest deviation from the optimum angle, considering each vertex [10]. The grid ensures that 99 % of the cells have equiangle skewness less than 0.7, and the maximum skewness value is 0.82.

During the computations, the majority of y^+ values fell within the range of 15 to 100, fulfilling the requirements of the applied wall law.

The discretisation of the convective momentum and turbulent quantity fluxes were carried out by the Second Order Upwind method. Typical computations required approximately 3000 iterations. The solutions were considered converged

when the residuals of all equations were resolved to levels of order of magnitude of 10^{-6}.

The computations presented here are valid for a rotor speed of 416 RPM. The Reynolds number, calculated with the blade tip speed, the tip chord and the kinematic viscosity of air at 20 °*C* is $1.074 \cdot 10^6$. The Mach number computed with the blade tip velocity and the speed of sound in air at 20 °*C* is 0.13 and therefore, the flow is considered incompressible.

Measurements carried out on FSK available in the Gödöllő wind tunnel facility will serve in the future as a basis for experimental validation of the CFD technique [8]. These experiments regard characteristic curve measurements as well as hot wire anemometer studies upstream and downstream of FSK. The experimental technique and the results will be reported in a later paper. At the time of submission of this paper, no processed and evaluated hot wire measurement data are available.

Characteristic curve measurements were carried out and reported in [8]. At the design point of $\Phi = 0.33$, the measurements resulted in a total pressure rise of $\Psi = 0.27$. The presented computational technique resulted in $\Psi = 0.26$. The preliminary processing of hot wire measurement data on the outlet axial velocity profile showed that the computational technique resolves the hub boundary layer well. The spanwise gradient of outlet axial velocity due to non-free vortex operation and the location of peak axial velocity is also well captured.

4. DISCUSSION OF RESULTS

4.1. Pitchwise-Averaged Data

Figure 5 presents the spanwise distribution of pitchwise averaged values for the dimensionless inlet and outlet axial velocities, outlet radial velocity, outlet ideal total pressure rise, and the total pressure loss coefficient at the outlet. The inlet and outlet planes have the axial position of -0.2 and 1.13 % midspan axial chord, respectively, where the zero axial position indicates the LE at midspan. The ideal total pressure rise has been calculated from the Euler equation of turbomachines, considering swirl-free inlet: $\Delta p_{t\,id} = \rho\, u\, c_{u2}$.

The diagrams suggest the following. The applied blade skew has an influence already on the inlet flow field: the inlet axial velocity for FSK is increased near the tip and is reduced at lower radii. The outlet axial velocity is increased at lower radii for FSK. The difference in radial rearrangement of fluid for USK and FSK is visible on the outlet radial velocity plot. As the ideal total pressure plots suggest, FSK performs also increased Euler work along the dominant part of span. The diagrams show that both the ideal total pressure rise and the outlet axial velocity increase along the dominant part of span, as a consequence of the CVD concept [17]. Although the total pressure loss is reduced near the tip, it is increased over the dominant part of span due to skew. The same tendency was reported in [9] for a rotor with forward sweep at the tip.

The above tendencies will be explained in the following section, by means of analysis of the detailed flow field. Inlet and outlet flow maps will be presented. Furthermore, the flow field will be surveyed at 30 and 90 % span, being two representative locations where significant differences occur in the fluid mechanical behaviour of USK and FSK (see Fig. 5).

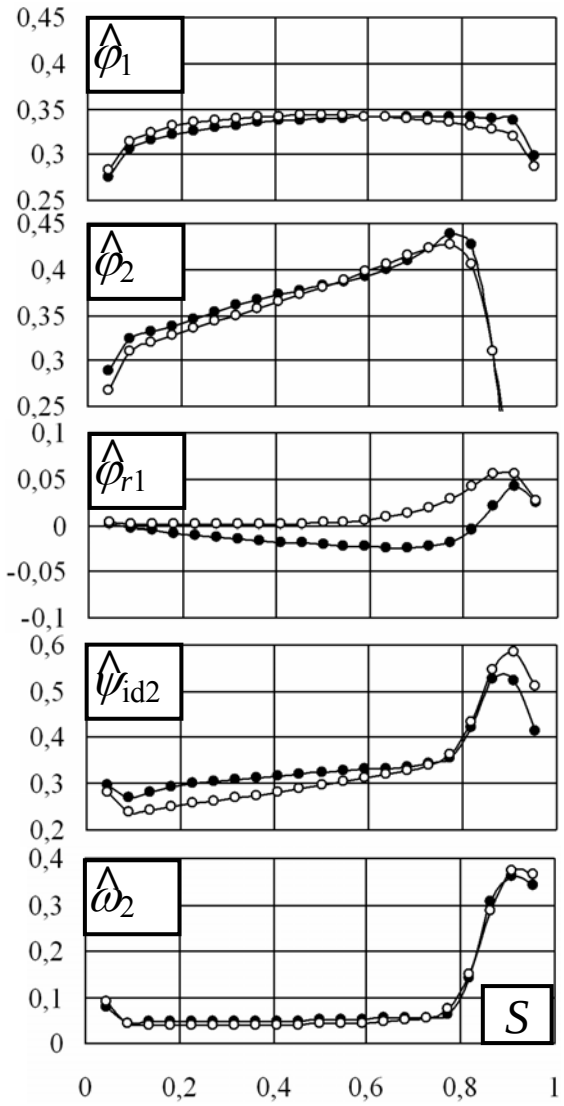

Figure 5. Pitchwise-averaged data. White dots: USK, black dots: FSK

4.2. Flow Details

For the bladings discussed herein, the chordline makes a relatively small angle with the circumferential direction (see Table 2). This suggests that the effect of forward sweep dominates over that of dihedral in the aerodynamics of FSK.

Figure 6 shows the inlet axial velocity maps. A zone of increased inlet axial velocity is observed

near the tip of FSK. The reason is that the near-tip part of the forward skewed blading protrudes into the upstream relative flow field, and carries out work "in advance" compared to the blade sections at lower radii. According to the conservation of mass at the prescribed design flow rate, this results in the reduction of inlet axial velocity at lower radii of FSK, as was already indicated in Fig. 5.

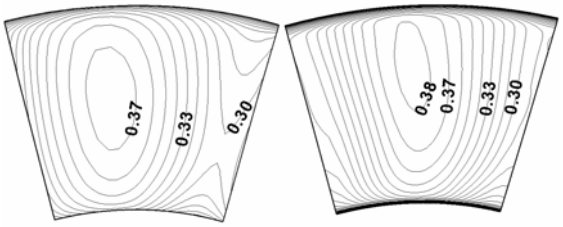

USK, φ_1 **FSK, φ_1**

Figure 6. Inlet axial velocity field

The reduced axial velocity at lower radii of FSK results in increased incidence, manifesting itself in increased lift, i.e. increased depression and overpressure on the suction side (SS) and pressure side (PS), respectively. This is illustrated in the static pressure plots of Figure 7.

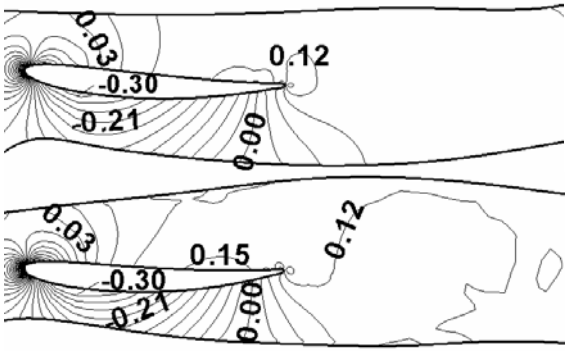

Figure 7. Static pressure coefficient C_p at 30 percent span. Upper: USK, lower: FSK

As [9] also suggests, the higher lift being valid for FSK at lower radii potentially leads to increased Euler work and blade section performance. Indeed, as Figures 8 and 9 indicate, FSK performs higher ideal total pressure rise and axial velocity in the aft-LE region, compared to USK, as was suggested already by Fig. 5.

The increase of axial velocity for FSK in the aft-LE region can be explained by taking a look on the isobar lines on the SS in Figure 10. Due to forward skew, the isobars in the decelerating region are inclined "more forward" for FSK than for USK. Therefore, the local radial outward flow is moderated, the flow is guided "more inward" for FSK on the SS, as also illustrated in Figure 11. The radial flow controlling effect of forward skew has been described qualitatively in [7], with special regard to the flow in the SS boundary layer, but regardless the control of flow in the entire blade passage. According to the conservation of mass, the moderation of radial outflow leads to the increase of the axial velocity at lower radii. The "inward-guiding" effect on the flow due to forward skew, which already appeared in the outlet radial velocity plot of Fig. 5, is observable also on the PS, as Figs. 9 and 11 suggest.

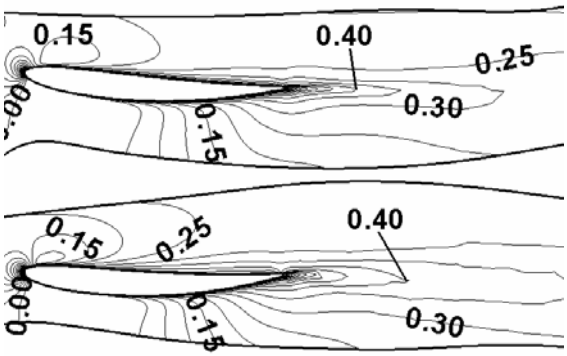

Figure 8. Ideal total pressure rise coefficient ψ_{id} at 30 percent span. Upper: USK, lower: FSK

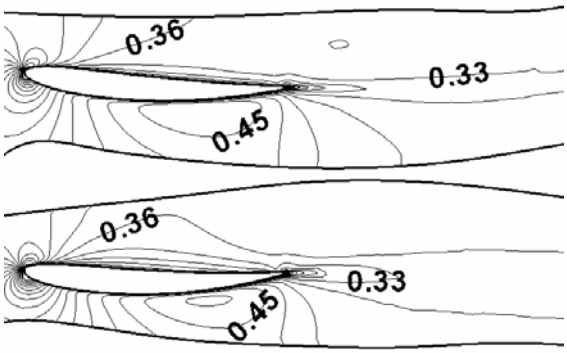

Figure 9. Axial flow coefficient φ at 30 percent span. Upper: USK, lower: FSK

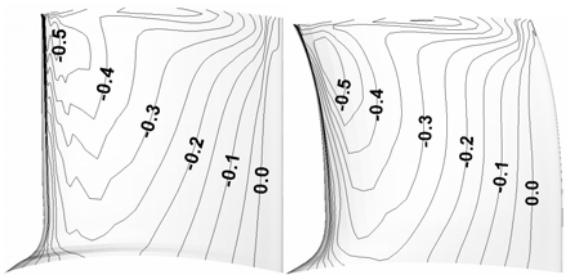

Figure 10. Distribution of static pressure coefficient C_p on the SS. Left: USK, right: FSK

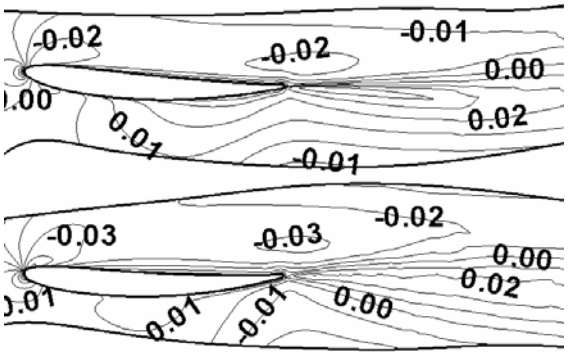

Figure 11. Radial flow coefficient φ_r at 30 percent span. Upper: USK, lower: FSK

As Figure 12 shows, the increased incidence at lower radii of FSK results in higher losses. Such increase of loss due to skew occurs along the dominant part of span, as presented in Fig. 5.

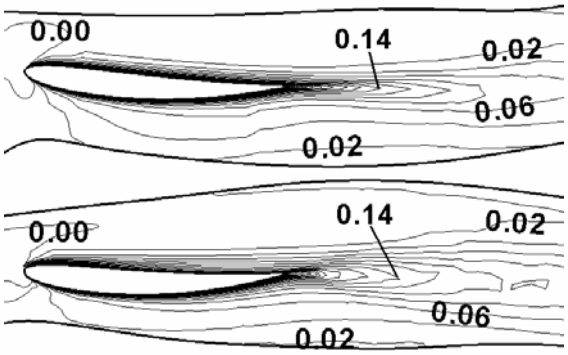

Figure 12. Total pressure loss coefficient ω at 30 percent span. Upper: USK, lower: FSK

In the following, the flow phenomena near the tip are analysed. The loss-reducing effect of forward skew in the near-tip region is apparent in Figure 13, where a "loss trough" of reduced losses and extension can be observed for FSK. Besides this, it must also be noted that not only the losses but also the Euler work has been reduced due to skew near the tip (Fig. 5). Figure 14 shows appropriately selected isosurfaces of radial flow coefficient and total pressure loss coefficient in the near-tip region. It is apparent in the figure that the reduction of radial outward flow due to forward skew leads also to the reduction of loss. Both tendencies can be seen in Fig. 5.

The following comments regard the 3D flow features due to CVD. Fig. 15 presents the maps of flow characteristics at the outlet section. The blade wake is located in the middle, with the PS and SS on the left and right, respectively. The figure demonstrates that the ideal total pressure rise increases along the dominant part of span of USK, in accordance with the CVD concept. However, an inevitable and undesired consequence of CVD is that vortices are shed from the TE, generating a characteristic 3D flow pattern in the blade passage [17]: radial inward and outward flow on the PS and on the SS, respectively. By means of forward skew, the shed vorticity has been moderated along the dominant portion of span. However, as Fig. 5 illustrates, the moderation of shed vorticity acts against the non-free vortex design concept: the spanwise gradient of blade circulation – and that of the related ideal total pressure rise – tends to be reduced toward free vortex operation.

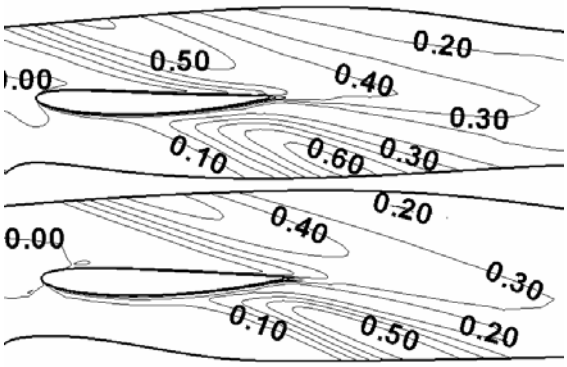

Figure 13. Total pressure loss coefficient ω at 90 percent span. Upper: USK, lower: FSK

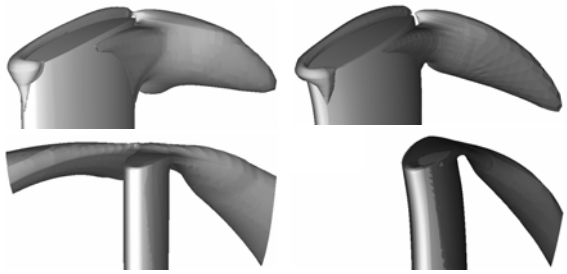

Figure 14. Upper row: φ_r = 0.1 isosurfaces. Lower row: ω = 0.5 isosurfaces. Left: USK, right: FSK

5. REMARKS

5.1. Forward Sweep/Skew vs. Losses

The technical literature reports apparently contradictory results on the loss and performance modifying effects due to forward sweep/skew. In [5], it is pointed out that forward sweep near the tip, i.e. "positive sweep", gives a potential for reduction of near-tip losses. Based on [7], application of near-tip forward skew can be recommended for efficiency improvement over the entire operational range, and for stall margin improvement. [2] and [6] suggest that the application of forward sweep along the entire span is beneficial for loss reduction and performance improvement, and also for extension of stall-free range. However, it has been found in [9] that forward sweep causes the deterioration of efficiency near the design point, although it was

found beneficial at throttled (near-stall) operating points. In [18], the reduction of efficiency was reported for a forward-swept rotor over the dominant part of the entire stall-free operational range.

This paper gives an additional example, together with a detailed explanation, how forward skew may cause the increase of losses at the design flow rate over the dominant portion of span, although it must be acknowledged that the losses are reduced near the tip. It must also be emphasized that in energetic judgment of a skewed rotor, modifications of both the Euler work and losses due to skew, i.e. their balance, must be considered. This can be carried out by CFD-based modern turbomachinery design systems.

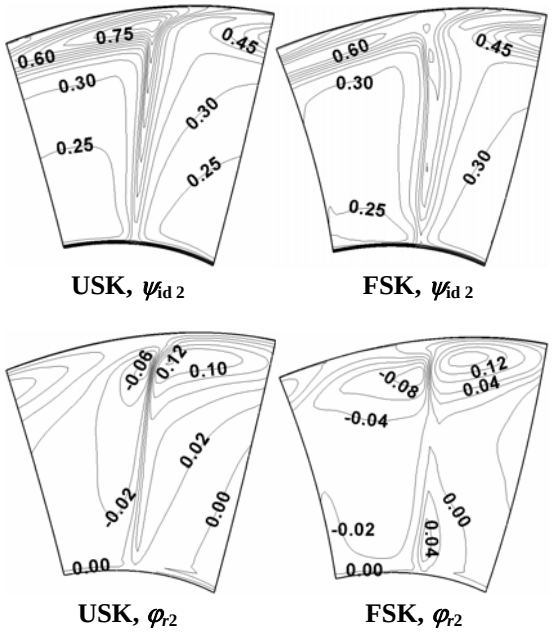

Figure 15. Outlet flow characteristics

5.2. Forward Sweep/Skew vs. Stall

The conclusions of the present paper fit to the former experiences reported in [7] that forward sweep/skew moderates the radial outward migration of the SS boundary layer fluid, and thus, it prevents the near-tip zone from accumulation of stagnating fluid that would lead to tip stalling. Although it was not mentioned in [3][6][7], the applied CVD concept usually intensifies the radial outward flow on the SS, due to shed vorticity. Therefore, the risk of tip stalling is increased for rotors of CVD, and thus, application of forward sweep/skew is especially welcome.

Based on the discussion in [19], it can be concluded that application of forward sweep/skew is especially recommended for CVD rotors to moderate the near-tip stagnating zone.

5.3. Forward Sweep/Skew vs. CVD

As the results presented in the paper indicated, forward sweep/skew reduces the blade load near the tip, and shifts the blade load away from the endwall. This trend is characteristic for near-endwall blade sections with positive sweep [5]. As far as the CVD concept is concerned, this effect acts against it. The results show that the original non-free vortex circulation distribution tends towards that of a free vortex flow pattern (zero spanwise circulation gradient) along the dominant part of span. Therefore, the designer intending to improve the utilisation of blade sections at higher radii (and/or to moderate the load near the blade root for hub loss reduction) by means of CVD must consider the above effect. If no sweep/skew correction is applied to the blade in order to retain the original Euler work distribution, the final result can be a nearly free vortex rotor with reduced efficiency due to off-design incidence.

6. SUMMARY

Comparative CFD studies have been carried out on two rotors in order to investigate the combined effects of CVD and FSK, with use of structured hexahedral meshing. The results are summarised as follows.

1. It has been found that the skewed blade tip protrudes into the upstream relative flow field, and carries out work in advance compared to the blade sections at lower radii. This results in increased and decreased inlet axial velocities near the tip and away from the tip, respectively. The decreased axial velocity at lower radii leads to increased incidence, lift, blade performance, and losses. Forward skew performs an "inward-guiding" effect on the flow in the entire passage. The case study presented herein calls the attention that forward blade skew may cause increased losses along the dominant part of span.

2. It has been pointed out that forward blade skew near the tip moderates the radial outward flow and the losses; although it must be acknowledged that the Euler work near the tip has also been reduced. It was concluded that forward sweep/skew is especially beneficial for CVD rotors in order to reduce the otherwise intensified SS radial outward flow, and thus, to moderate the near-tip stagnating zone.

3. The results showed that forward skew near the tip unloads the near-tip region and uploads the blade at lower radii. This behaviour acts against the CVD concept by reducing the spanwise blade circulation gradient. This fact must be considered in CVD, possibly by correcting the blade in order to retain the original Euler work distribution.

ACKNOWLEDGEMENTS

This work has been supported by the Hungarian National Fund for Science and Research under contracts No. OTKA T 037651and K63704, and, on the behalf of J. Vad, out of the István Széchenyi Fellowship under contract No. SZÖ 271/2003.

REFERENCES

[1] Gallimore, S. J., Bolger, J. J., Cumpsty, N. A., Taylor, M. J., Wright, P. I. and Place, J. M. M., 2002, „The Use of Sweep and Dihedral in Multistage Axial Flow Compressor Blading" – Parts I and II, *ASME J Turbomachinery*, Vol. 124, pp. 521-541.

[2] Corsini, A. and Rispoli, F., 2004, "Using Sweep to Extend the Stall-Free Operational Range in Axial Fan Rotors", *Proc. Instn Mech. Engrs, Part A, J Power and Energy*, Vol. 218, pp. 129-139.

[3] Meixner, H. U., 1995, „Vergleichende LDA-Messungen an ungesichelten und gesichelten Axialventilatoren", *Dissertation Universität Karlsruhe,* VDI-Verlag, Reihe 7, No. 266, Düsseldorf.

[4] Lakshminarayana, B., 1996, *Fluid Dynamics and Heat Transfer of Turbomachinery*, John Wiley & Sons, Inc.

[5] Clemen, C. and Stark, U., 2003, "Compressor Blades with Sweep and Dihedral: a Parameter Study", Proc. *5th European Conference on Turbomachinery Fluid Dynamics and Thermodynamics*, Prague, pp. 129-139.

[6] Beiler, M. G., and Carolus, T.H., 1999, "Computation and Measurement of the Flow in Axial Flow Fans with Skewed Blades", *ASME J Turbomachinery*, Vol. 121, pp. 59-66.

[7] Yamaguchi, N., Tominaga, T., Hattori, S., and Mitsuhashi, T., 1991, "Secondary-Loss Reduction by Forward-Skewing of Axial Compressor Rotor Blading", Proc. *Yokohama International Gas Turbine Congress*, Yokohama, pp. II.61-II.68.

[8] Vad, J., Kwedikha, A. R. A., Kristóf, G., Lohász, M. M., Rábai, G., Rácz, N., 2005, „Effects of Blade Skew in an Axial Flow Rotor of Controlled Vortex Design", Proc. *6th European Conference on Turbomachinery Fluid Dynamics and Thermodynamics*, Lille, pp. 46-55.

[9] Clemen, C., Gümmer, V., Goller, M., Rohkamm, H., Stark, U. and Saathoff, H., 2004, "Tip-Aerodynamics of Forward-Swept Rotor Blades in a Highly-Loaded Single-Stage Axial-Flow Low-Speed Compressor", *Proc. ISROMAC10*, Honolulu, Paper No. 027.

[10] FLUENT 6.2.16 User's Guide, 2004, Fluent Inc., Lebanon, NH, USA.

[11] Benini, E. and Biollo, R., 2006, „On the Aerodynamics of Swept and Leaned Transonic Compressor Rotors", ASME Paper *GT2006-90547*.

[12] Launder, B. E. and Spalding, D. B., 1972, *Lectures in Mathematical Models of Turbulence*, Academic Press, London

[13] Kader, B., 1993, "Temperature and Concentration Profiles in Fully Turbulent Boundary Layers", *Int J Heat Mass Transfer*, Vol. 24, pp. 1541-1544.

[14] Wu, Y., Chu, W., Lu, X. andZhu, J., 2006, "Behavior of Tip Leakage Flow in an Axial Compressor Rotor", *ASME Paper GT2006-90399.*

[15] F.T.Johnson, E.N.Tinoco and N.J.Yu., 2003, „Thirty Years of Development and Application of CFD at Boeing Commercial Airplanes, Seattle", *AIAA paper* 2003-3439.

[16] Benzley, S.E., Borden, M. and Mitchell, S.A., 2001, "A Refinement Technique for All-Hexahedral Adaptive Meshing," *Proc. 1st MIT Conference on Computational Fluid and Solid Mechanics*, Elsevier Science, pp. 1519-1523

[17] Vad, J., and Bencze, F., 1998, "Three-Dimensional Flow in Axial Flow Fans of Non-Free Vortex Design", *Int J Heat Fluid Flow*, Vol. 19, pp. 601-607.

[18] Vad, J., Kwedikha, A. R. A., and Jaberg, H., 2004, "Influence of Blade Sweep on the Energetic Behavior of Axial Flow Turbomachinery Rotors at Design Flow Rate", *ASME Paper GT2004-53544*.

[19] Vad, J., 2006, "Analytical Modeling of Radial Fluid Migration in the Boundary Layer of Axial Flow Turbomachinery Blades", *ASME Paper GT2006-90523*.

Conference on Modelling Fluid Flow (CMFF'06)
The 13th International Conference on Fluid Flow Technologies
Budapest, Hungary, September 6-9, 2006

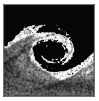

STALL INCEPTION IN AXIAL-FLOW COMPRESSORS WITH AND WITHOUT AN INLET GUIDE VANE

Boris DOBRZYNSKI[1], Horst SAATHOFF[2], Günter KOSYNA[3]

[1] Pfleiderer-Institut für Strömungsmaschinen, Technical University of Braunschweig, Germany.
Tel.: +49 531 391 2922, Fax: +49 531 391 5769, E-mail: b.dobrzynski@tu-bs.de
[2] Institut für Strömungsmechanik, Technical University of Braunschweig, Germany. E-mail: h.saathoff@tu-bs.de
[3] Pfleiderer-Institut für Strömungsmaschinen, Technical University of Braunschweig, Germany. E-mail: g.kosyna@tu-bs.de

ABSTRACT

In the present paper results of an investigation of stall inception phenomena detected in the 1.5-stage low-speed compressor located at the Pfleiderer-Institut, TU Braunschweig, are presented. Two different highly loaded rotor bladings, a conventional 2D and a 3D design, were investigated. The 3D stage employs rotor tip sweep in order to reduce the aerodynamic loading of the blade tip section. This leads to an extended operating range into the region of smaller flow coefficients. In order to understand how the formation of instabilities in the compressor flow field depends on inflow inhomogeneities caused by a blade row upstream of the rotor, both stages mentioned above were also investigated without the inlet guide vane.

Axial compressor, stall inception, spill forward, tip clearance flow, time resolved total pressure measurements

NOMENCLATURE

Re	[-]	Reynolds number
U	[m/s]	circumferential velocity
$\dot{V}$	[Pa]	volume flow rate
h/H	[-]	fractional channel height
l	[m]	chord length
n	[rpm]	speed of rotation
p	[Pa]	static pressure
r, θ, z	[m]	machine coordinate system
s	[m]	tip gap height
t	[m]	pitch
β	[°]	absolute flow angle
φ	[-]	flow coefficient
ν	[-]	hub to tip ratio
ψ	[-]	pressure coefficient

Subscripts and Abbreviations

BPF	blade passing frequency
C	casing
D	design point
H	hub
IGV	inlet guide vane
P	probe
RANS	Reynolds averaged Navier-Stokes
ax	axial
max	maximum
t	total
s	static
0 - 3	measuring planes

1. INTRODUCTION

The stable operation range of axial compressors is limited by emerging instabilities in the region of small flow coefficients. Two characteristic phenomena are known to appear close to compressor stall. Modal waves, which can be described as a long length scale oscillation of the axial inflow velocity. As shown by Moore and Greitzer [1] as well as by Camp and Day [2], modal waves can be detected if the slope of the total-static characteristic at the stall point is positive. For a negative slope, stall inception is caused by short length scale disturbances called spikes. It has been shown theoretically by McDougall [3] and Vo et al. [4] as well as experimentally by Dobat et al. [5] that these disturbances are related to the spillage of endwall flow ahead of the blading (spill forward).

In different experimental investigations on various 1-stage axial compressors, multiple types of rotating stall have been found. Apart from single-cell rotating stall, typical for 1-stage compressors, multi-cell rotating stall or mild stall could also be observed, see Inoue et al. [6]. Hereby the multi-cell rotating stall regime can be described as a stable region of the compressor characteristic where additional throttling of the compressor is required in order to descend to the region of single-cell rotating stall.

This behaviour can also be found at the 1.5-stage low-speed compressor located at the Pfleiderer-Institut, TU Braunschweig, Germany. In the following, the flow phenomena leading to stall inception are described by means of time resolved total pressure measurements up- and downstream of the compressor rotor and an oil flow visualisation technique. Near casing flow patterns are compared to computational results obtained by a commercial RANS solver.

2. TEST RIG

Both compressor stages consist of an IGV (45 blades) a rotor (43 blades) and a stator (45 blades). The 2D stage including the inlet guide vane is shown in Figure 1.

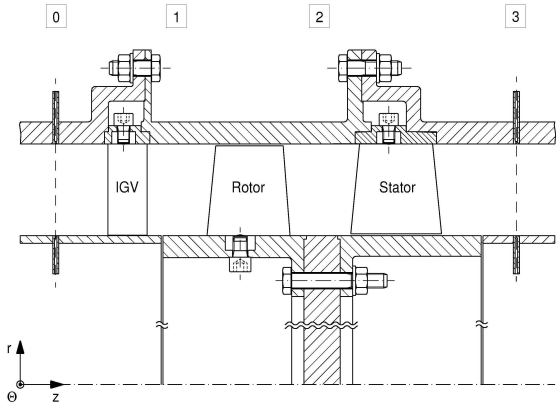

Figure 1: Compressor test stage (2D design)

Table 1: 2D stage design parameters:

flow coefficient	$\varphi_D = 0.52$
pressure coefficient	$\psi_D > 0.45$
hub to tip ratio	$\nu = 0.75$
aspect ratio	$h/l = 1.0$
relative tip gap height	$s/l = 0.01$
casing diameter	$D_C = 0.6$ m
speed of rotation	$n = 2800$ rpm

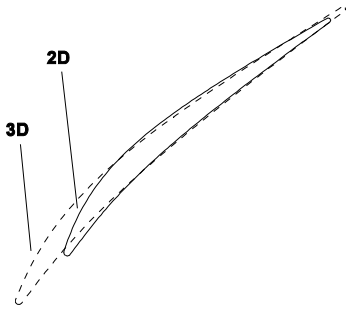

Figure 2: Rotor tip sections

Additional pressure taps, not shown below, were located in plane 1. Based on rotor tip speed and midheight chord length the Reynolds number can be determined to $Re \approx 5 \cdot 10^5$. The main design parameters of the 2D compresssor stage, designed by Gümmer et al. [7] are shown in Table 1. In addition to the 2D stage a 3D stage designed by Goller et al. [8] was investigated. The 3D stage features rotor tip sweep as well as an enlarged tip chord length. The sweep was introduced at h/H = 0.4 while the spanwise distribution of sweep follows an e-type function. At the casing the forward sweep reaches 45° with an increased chord length of 25% (Figure 2). In order to ensure the same spanwise work distribution as for the 2D rotor, the rotor outlet angle distribution of the 3D stage was adjusted, reducing the camber of the rotor tip sections.

As described above, the total-static characteristic (φ, ψ_{ts}) indicates the type of emerging instability prior to the compressor stall. As done in earlier investigations, see Dobrzynski et al. [9], the total-static pressure coefficient was determined by

$$\psi_{ts} = \psi_{ss} - \frac{\varphi^2}{\cos^2 \beta_1}. \qquad (1)$$

The pressure rise was evaluated between planes 1 and 3 as shown in Figure 1.

3. TOTAL-STATIC CHARACTERISTICS

The total-static characteristics of the 2D and the 3D stage with and without IGV are shown in Figure 3. Pressure and flow coefficients are normalised by the design coefficients of the 2D stage.

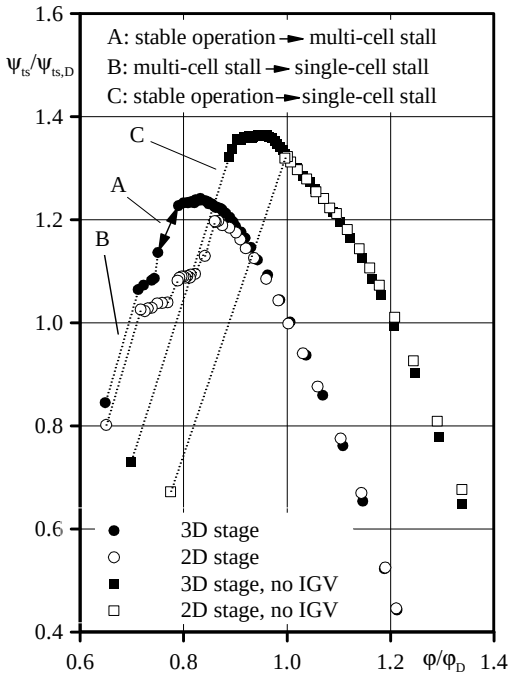

Figure 3: Total-static characteristics

For both stages without IGV a multi-cell rotating stall region can be observed left of the first stall point (transient A). Classical single-cell

rotating stall can only be reached by throttling the compressor to flow coefficients to the left of transient B. For the 2D stage characteristic 3 plateaus can be observed in the multi-cell rotating stall region. As will be shown later on, these plateaus are characterised by the number of rotating stall cells. The 3D stage characteristic shows an extended operating range compared to the 2D stage characteristic. For the 3D stage characteristic only 2 plateaus can be detected in the multi-cell rotating stall regime. For the transient A an unstable behaviour can be observed. Here the operating point and the number of stall cells are continuously changing (double-headed-arrow). In between, also phases of normal operation can be detected. After further throttling a region characterised by a constant number of stall cells is reached. Analysing the slopes at the stall points a negative slope of the 2D and a positive slope of the 3D stage characteristic can be observed. As described in [1] and [2] this indicates the presence of axial velocity oscillations in the area left of the peak of the 3D characteristic.

The total-static characteristics without the IGV are also included in Figure 3. Because of the missing inswirl the characteristics are shifted into the region of higher flow and pressure coefficients. Unlike the configurations with the IGV, no multi-cell rotating stall regimes can be detected here (transient C). However, again a positive sloped branch of the 3D characteristic can be observed.

4. TIME RESOLVED TOTAL PRESSURE MEASUREMENTS

In order to gather information about type and number of the rotating stall cells, time resolved total pressure measurements were carried out up- and downstream of the compressor rotor.

Two cranked total pressure probes (probes 1 & 2), developed by Brodersen and Wulff [10], as well as cylindrical pressure probes (probes 3 & 4) were used. All probes are equipped with high frequency miniature pressure transducers (Kulite XCS-062-5D) inserted into the probe's head. The probes were positioned as shown in Figure 4. All probes were oriented into the main flow direction in order to detect axially backward directed flow. Probe 1 and 2 were turned according to the stagger angle at the casing, because earlier investigations by Deppe et al. [11] indicated spill forward along this direction.

The two cylindrical pressure probes with lateral and downward facing measuring holes were installed just downstream of the rotor. With reference to the 2D pressure distribution of a cylinder, the axis of the lateral measuring holes were aligned with the machine axis in such a way that axially backward directed flow was indicated by a change of sign of the pressure signal.

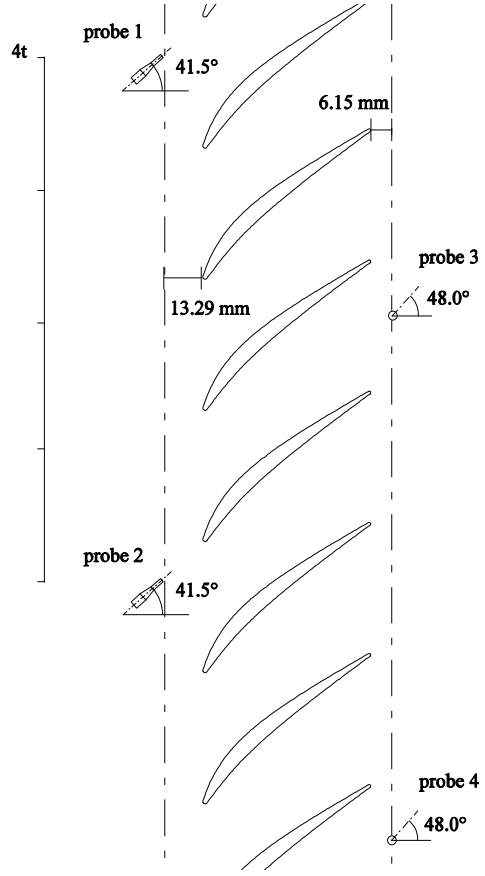

Figure 4: Probe positions

The static pressure obtained by earlier 5-hole probe traverse measurements was used as a reference giving the probe signal $\Delta p = p_P - p_s$. Probes 1,3 and 4 were positioned near the casing at h/H = 0.98, while probe 2 was positioned at midspan. For results related to probe 2 see Dobrzynski et al. [9].The data recording was based on the rotor rotation angle. 1024 data points were recorded per rotor revolution. In order to record data during stall inception, the available data storage was split to save the pre- and post-stall history, using the stall event itself as a trigger. With the rotor at n = 2800 rpm (standard ambient conditions) the sampling rate reaches about 48 kHz, corresponding to 24 samples per blade passage.

The time resolved total pressure signals of probes 1 and 3, 2D stage, are shown in Figure 5. The time shift of the pressure signal due to the different circumferential positions of the probes in the absolute reference system was removed. For probe 3 downstream of the rotor, the baseline is included as well. During stable operation, only the upstream pressure field of the rotor can be identified. The first spike can be detected between rotor revolution 6 and 7. The disturbance, covering about 5-6 passages, moves with about 78% of the rotor speed in the absolute reference system.

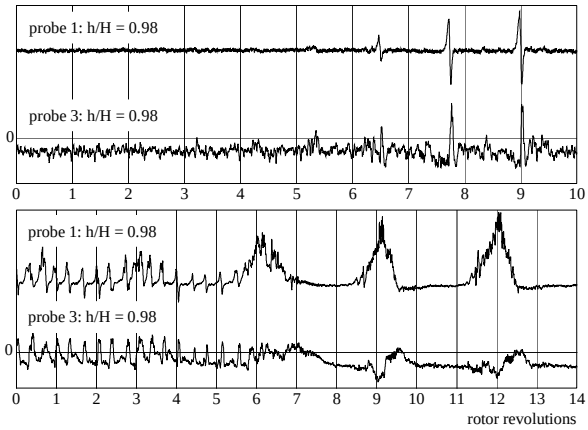

Figure 5: Time resolved total pressure, 2D stage with IGV
Top: Transient A
Bottom: Transient B (Figure 3)

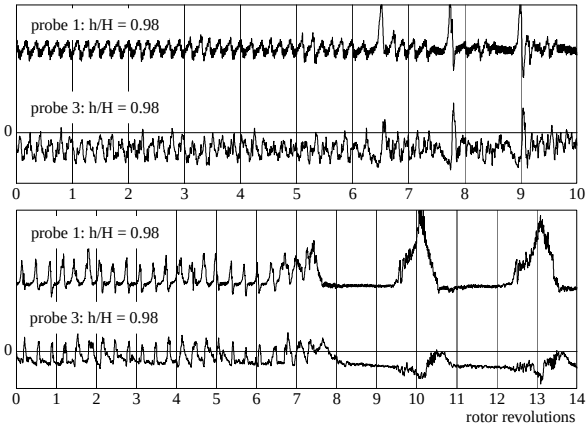

Figure 6: Time resolved total pressure, 3D stage with IGV
Top: Transient A
Bottom: Transient B (Figure 3)

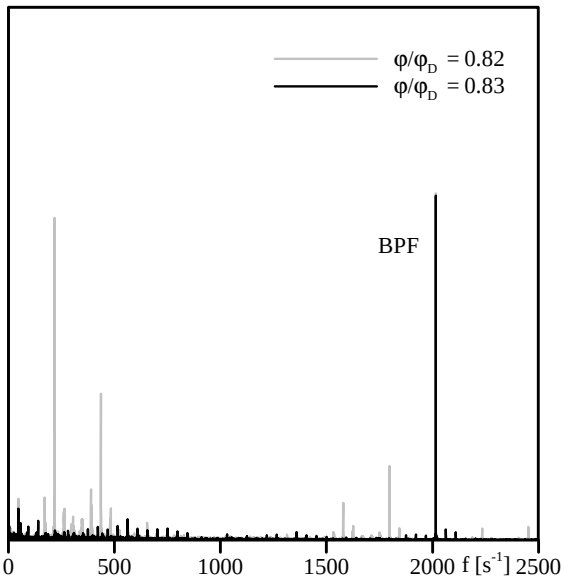

Figure 7: FFT of the total pressure signal close to $\psi_{ts,max}$, 3D stage

The spillage of endwall flow ahead of the blading (spill forward) results in a positive peak (spike) in the time resolved total pressure signal (probe 1). At the same time axially backward directed flow at the rotor trailing edge is indicated by the positive pressure signal at the cylindrical probe 3 (see Vo et al. [4] and Deppe et al. [11]). The details of these near casing flow phenomena can be understood based on results from wall pressure measurements and oil flow visualisations at the compressor casing as well as from cascade tests, see Dobrzynski et al. [9]. It is remarkable that these disturbances do not incept classical single-cell rotating stall after a few rotor revolutions. The amplitude as well as the speed of rotation remain constant in the region between the transients A and B of the 2D stage characteristic (Figure 3). On the characteristic 3 regions can be identified which are characterised by the number of rotating stall cells (2, 3 and 4 cells). After further throttling below $\varphi/\varphi_D = 0.71$ (transient B, Figure 3) a larger single stall cell is formed. The cell rotates with about 34% of the rotor speed in the absolute system. After formation of this cell no more short length scale disturbances can be detected.

As for the 2D stage, the time resolved total pressure signals of the 3D stage indicate the formation of a stable multi-cell stall regime (Figure 6). Compared to the 2D stage characteristic only 2 multi-cell stall regions can be detected. The transient A (Figure 3) is characterised by a continuously changing number of stall cells between 0 and 3. To the left of the transient a stable region with 4 rotating stall cells can be detected. The stall cells' speed of rotation as well as their circumferential extension are similar to the ones recorded for the 2D stage.

Between the peak of the 3D total-static characteristic and the stall limit a short wavelength oscillation of the total pressure signal of all probes can be observed. The frequency spectrum recorded by probe 1 for one operating point slightly to the left ($\varphi/\varphi_D = 0.82$) and one slightly to the right ($\varphi/\varphi_D = 0.83$) of the peak of the 3D characteristic is shown in Figure 7. In the positive sloped branch of the 3D characteristic the frequency of the total pressure oscillation can be determined to $f \approx 220\ s^{-1}$. This frequency decreases slightly with throttling the compressor. Modulations with the blade passing frequency of $f_{BPF} \approx 2000\ s^{-1}$ can also be observed in Figure 7. Similar phenomena have been reported by Mailach et al. [12] for the 4-stage low-speed compressor at the TU Dresden, Germany. Comparing these it can be ascertained that the oscillation reported here is clearly more stable, which is indicated by its narrow peak in the frequency spectrum.

Time resolved total pressure signals during stall inception without the IGV are shown in Figure 8 and 9. As it was already observed in the total-static

characteristic in Figure 3, no multi-cell rotating stall regime can be detected. After the formation of a first spike the compressor descends into the classical single-cell rotating stall within 5-10 rotor revolutions. The speed of rotation of the spike as well as of the fully developed rotating stall cell is the same as for the 1.5-stage configuration. Again short wavelength oscillations of $f \approx 220\ s^{-1}$ can be detected at the positive sloped branch of the 3D total-static characteristic. In addition, an oscillation of longer wavelength can be seen close to the stall limit. This long wavelength oscillation occurs sporadically and can be observed in the time resolved total pressure signals (Figure 9) as well as in the frequency spectrum shown in Figure 10. With a frequency of $f \approx 20\ s^{-1}$, the wavelength of this disturbance can be determined to 43% of the rotor speed and about 1% of the blade passing frequency (BPF). These are typical properties of modal waves reported by other authors, e.g. Camp and Day [2]. However, no increase in amplitude of this disturbance shortly before stall could be detected. Inspecting Figure 9, it can be observed that the formation of the first spike coincides with a pressure maximum of the long length scale oscillation. This can be attributed to the low axial velocity at this location.

5. OIL FLOW VISUALISATION

In the following, the near casing flow patterns shall be visualised by oil flow pictures at the compressor casing as well as by computed near wall flow vectors. The oil flow pictures visualise the circumferentially averaged wall shear stress distribution in the absolute reference frame (time mean portrait of the flow). Results will be presented for both stages with IGV.

To support the experimentally obtained near wall flow patterns, the flow problem was also solved numerically using the commercial flow solver NUMECA Fine/Turbo. Fine/Turbo employs a 3D RANS code using multi-block structured meshes. Because of the fact that these steady calculations are meant to be a basis for later time resolved multi passage computations, the spatial discretisation was limited to about 312000 points per rotor passage. Nevertheless, grid independency of the solution was verified. The flow field of a single passage was calculated presuming circumferential periodicity. Boundary conditions were defined based on experimental data. The massflow determined by the compressor inlet nozzle, as well as the rotor inlet angles based on 5-hole pressure probe traverse data were defined upstream of the rotor. Downstream of the rotor the static pressure was set, considering radial equilibrium.

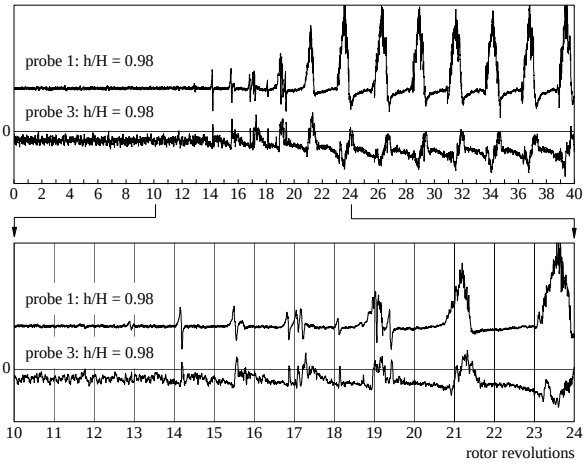

Figure 8: Time resolved total pressure, 2D stage without IGV

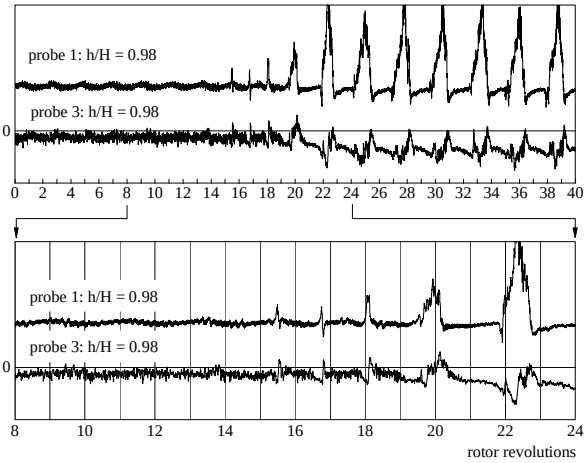

Figure 9: Time resolved total pressure, 3D stage without IGV

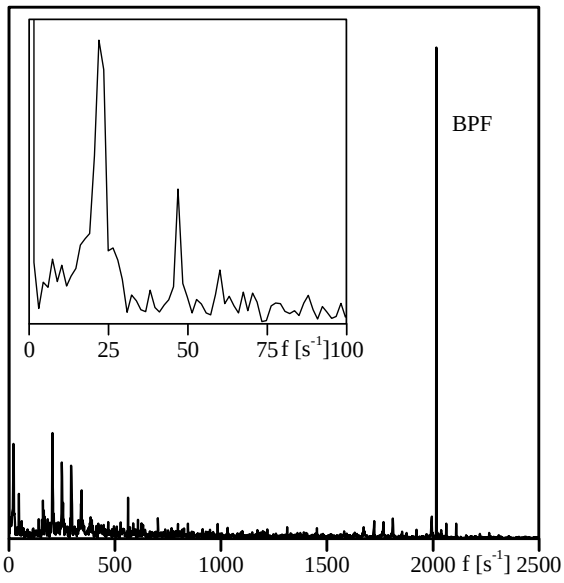

Figure 10: FFT of the total pressure signal φ/φ_D = 0.89, 3D stage without IGV

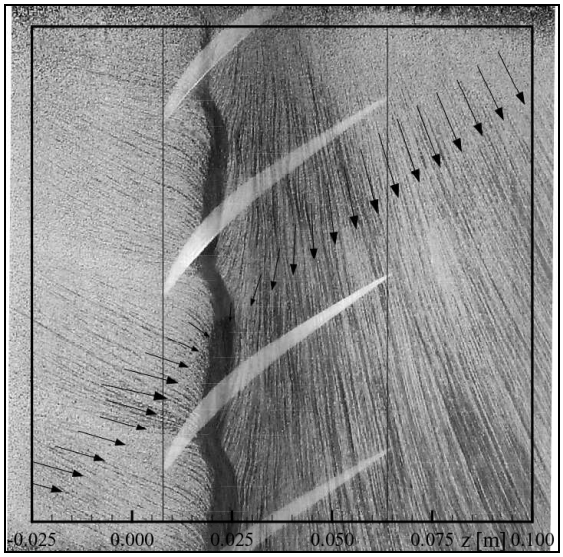

Figure 11: 2D stage, design condition

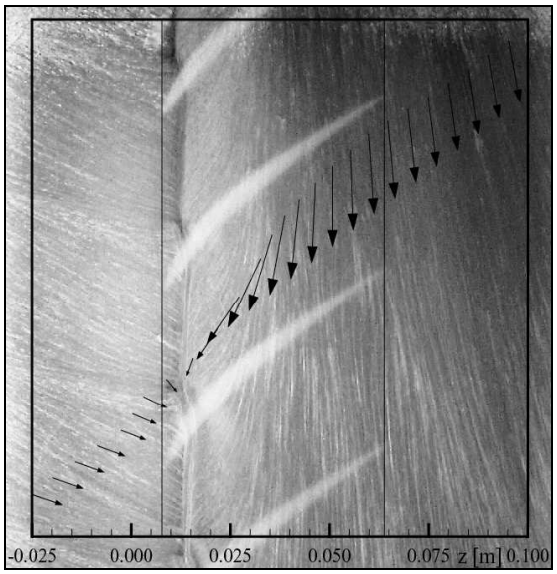

Figure 12: 2D stage, near stall condition

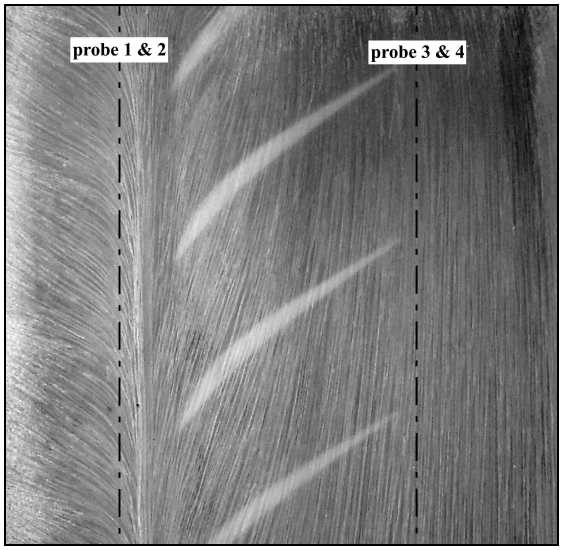

Figure 13: 2D stage, multi-cell stall

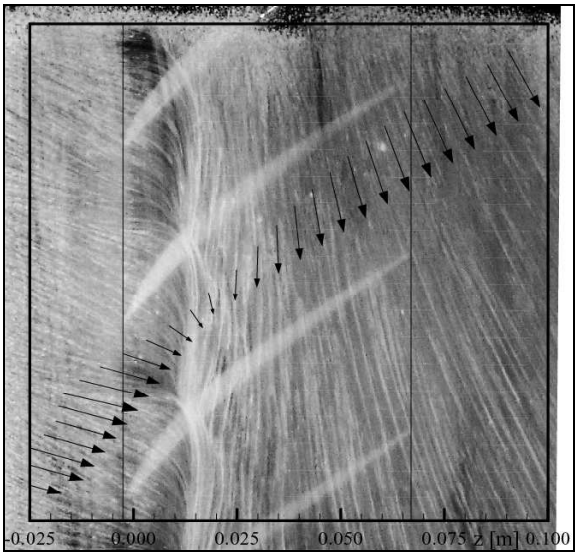

Figure 14: 3D stage, design condition

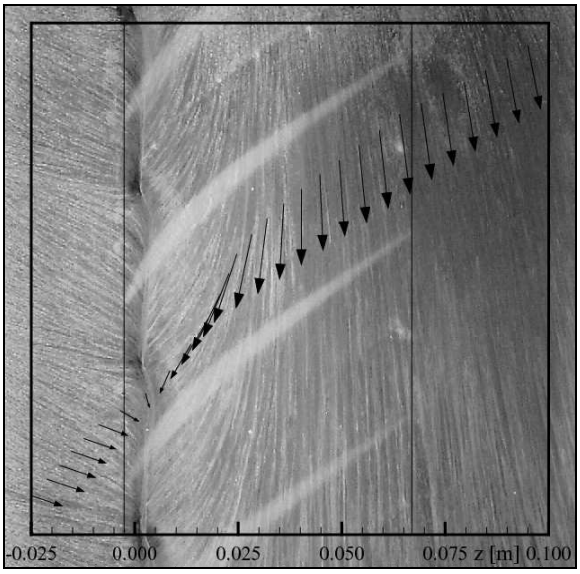

Figure 15: 3D stage, near stall condition

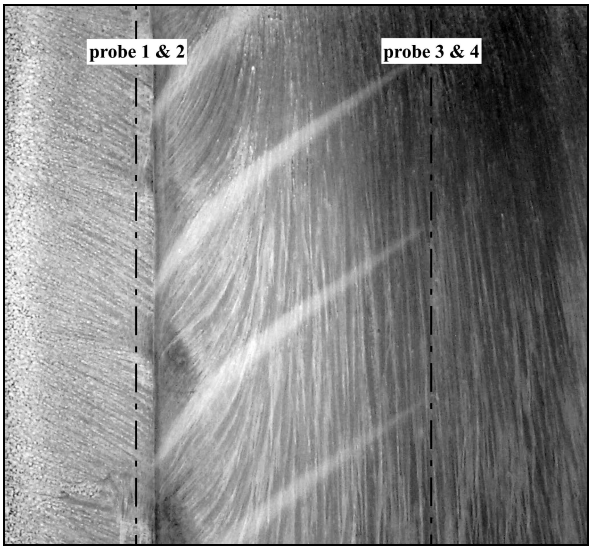

Figure 16: 3D stage, multi-cell stall

Three different turbulence models, a standard high Reynolds k-ε, a low Reynolds k-ε by Yang and Shih as well as the Spalart-Allmaras one equation model were used. In the following, only results obtained with the Spalart-Allmaras turbulence model will be discussed, being closest to the experimental data.

In Figure 11 to 13 oil flow pictures at the casing wall of the 2D stage for 3 different operating points are shown. The main flow is directed from the left to the right. For the stable operating points, the computed circumferentially averaged velocity distributions obtained by evaluating the first gridpoints off the wall are also included (black arrows). The oil flow picture representing design conditions (Figure 11) can be divided into 3 main regions. From the left border of the picture to z = 0.02 m axially forward directed flow can be observed. Due to the IGV outflow, the flow is inclined by about 15°. Within the second region between z = 0.02 m and z = 0.035 m the flow is axially backward directed caused by tip gap and tip vortex related flow phenomena. In between, a separation line, caused by the collision of these two endwall boundary layers can be observed. The wavy form of the separation line results from areas of low axial velocity caused by the IGV wakes. At z = 0.035 m an attachment line followed by a region of axially forward directed flow can be detected. It is noted that the computed positions of the attachment and separation lines as well as the predicted directions of the near casing velocities are in good agreement with the oil flow picture.

When the compressor is throttled to a near stall operating point, the following developments can be observed: The separation line moves upstream towards the rotor leading edge, while the attachment line moves downstream enlarging the region of axially backward directed flow. This is supported by the oil flow picture as well as by the computed near casing flow velocities shown in Figure 12. As described in earlier investigations, see Dobrzynski et al. [9], this development is linked to an upstream movement of the tip clearance vortex exhibiting a more circumferentially directed trajectory. The experimentally obtained as well as the calculated locations of the separation and attachment lines for all stable operating points are summarised in Figure 17. The axial locations are based on the axial chord length of the 2D and 3D blades respectively, see Figure 2. Compared to the separation line positions, the positions of the attachment lines (2D stage) are predicted less well by the CFD solution. Nevertheless, the movement of the attachment line between design and near stall conditions linked to the expansion of the reverse flow region again is in very good agreement with the experimental data.

After throttling the compressor below the stall limit, it descends into multi-cell rotating stall as described above. The separation line jumps in front of the rotor while the attachment line moves far downstream to the right border of Figure 13. In between, an extended region of axially backward directed flow can be observed. During multi-cell rotating stall the separation line is completely straight, indicating that the separation line is merely based on rotating phenomena at the rotor tip and not on the IGV outflow.

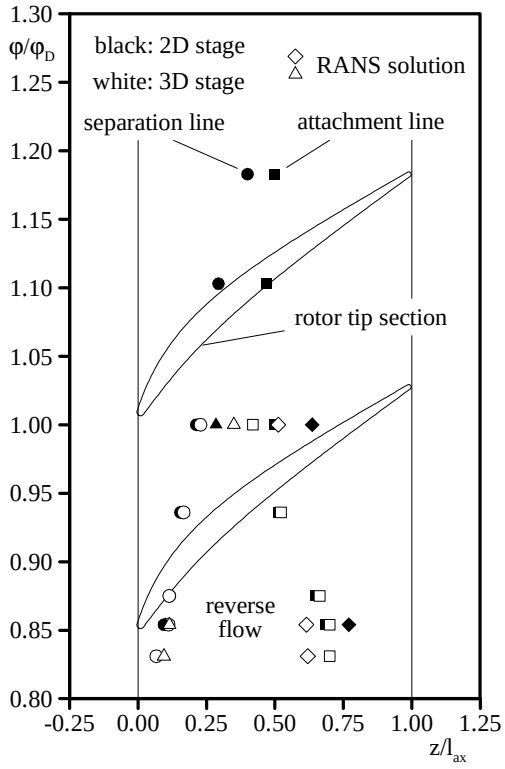

Figure 17: Separation and attachment line positions

The oil flow pictures of the 3D stage configuration are shown in Figure 14 to 16. Due to the reduced aerodynamic loading of the 3D rotor tip section, the intensity of the tip clearance flow is reduced as well. Therefore the separation line is hard to detected in the oil flow picture (Figure 14) as well as in the calculated velocity distributions for the 3D stage at design point conditions. Throttling the compressor, the separation line moves upstream towards the rotor leading edge, while the region of axially backward directed flow expands, see Figure 15 and 17. While the exact positions of the attachment lines are sometimes not well predicted by the numerical flow solution (Figure 17), their movement as well as the size of the reverse flow region is again in very good agreement with the experiments.

During multi-cell rotating stall of the 3D stage (Figure 16) the separation line is located directly at the rotor leading edge, while no decisive increase of the reverse flow region compared to near stall conditions can be observed. Comparing the

positions of the separation lines of the 2D and the 3D stage during multi-cell rotating stall (Figure 13 and 16), it is noted that they are at the same distance from the IGV. This could imply that the IGV may temporarily suppress the development of the classical single-cell rotating stall.

For single-cell rotating stall conditions the separation line can not be detected in the area shown so far. Oil flow pictures and additional time resolved pressure signals recorded at a position upstream of the IGV (not shown here) indicate that the separation line moved to a position just upstream of the IGV.

8. CONCLUSIONS

In the present paper experimental investigations concerning rotating stall inception in an 1.5-stage axial compressor were presented. Two different rotor bladings, a 2D and a 3D blade, were taken into account. In addition, both blading configurations were investigated with and without an IGV. First results of steady RANS calculations were compared to the experimental data at design and partload conditions.

i) For the 2D as well as for the 3D blading configuration a spike induced stall inception can be identified. The spikes are related to local spillage of the endwall flow ahead of the rotor (spill forward).

ii) While the short length scale disturbances (spikes) lead to classical single-cell rotating stall during a few rotor revolutions for the single-stage configuration, a multi-cell rotating stall regime can be observed for the 1.5-stage configuration.

iii) As expected from the positive sloped total-static characteristic of the 3D stage, short and long length scale oscillations can be identified at part load conditions. Stall inception however, is caused by a locally confined spike.

iv) Steady RANS calculations with limited computational expense were able to predict the circumferentially averaged near wall flow features very well. They provide a good basis for future time resolved calculations.

REFERENCES

[1] Moore, F. K.; Greitzer, E. M., 1986, "A theory of post-stall transients in axial compression systems. Parts I & II", *ASME Journal of Engineering for Gas Turbines and Power*, Vol. 108, I: pp.68-76, II: pp. 231-239.

[2] Camp, T. R.; Day, I. J. ,1998, "A study of spike and modal stall phenomena in a low-speed axial compressor", *ASME Journal of Turbo-machinery*, Vol. 120, pp. 393-401.

[3] McDougall, N. M., 1988, "Stall inception in axial compressors", *Ph. D. Dissertation, University of Cambridge*.

[4] Vo, H. D.; Tan, C. S.; Greitzer, M., 2005, „Criteria for spike initiated rotating stall", *Proceedings of the ASME*, GT2005-68374.

[5] Dobat, A.; Saathoff, H.; Wulff, D. "Experimentelle Untersuchungen zur Entstehung von Rotating Stall in Axialventilatoren", *VDI-Berichte* Nr. 1591, S. 345-360.

[6] Inoue, M.; Kuroumaru, M.; Yoshida, S.; Furukawa, M., 2002, "Short and long length-scale disturbances leading to rotating stall in an axial compressor stage with different stator/rotor gaps", *ASME Journal of Turbomachinery*, Vol. 124, pp. 376-384.

[7] Gümmer, V.; Swoboda, M.; Goller, M.; Dobat, A. 2003, "The impact of rotor tip sweep on the three-dimensional flow in a highly-loaded single-stage low speed axial compressor: Part I - Design and numerical analysis", *Proceedings of the ETC 5*, pp. 163-174.

[8] Goller, M.; Gümmer, V.; Clemen, C.; Swoboda, M., 2005, "Enhancement of highly-loaded axial compressor stage performance using rotor blade tip tailoring: Part I - Numerical design studies", *Proceedings of the ETC 6*, pp. 88-99.

[9] Dobrzynski, B.; Saathoff, H.; Kosyna, G., 2005, "Strömungsabriss in Niedergeschwindigkeits-verdichtern mit und ohne Vorleitrad", *Tagungsband der 21. Strömungstechnischen Tagung*, TU Dresden, S. 35-46.

[10] Brodersen, S.; Wulff, D., 1992, "Measurements of the pressure and velocity distribution in low-speed turbomachinery by means of high-frequency pressure transducers", *ASME Journal of Turbomachinery*, Vol. 114, pp. 100-107.

[11] Deppe, A.; Saathoff, H.; Stark, U., 2005, "Spike-type stall inception in axial flow compressors", *Proceedings of the ETC 6*, pp. 178-188.

[12] Mailach, R.; Lehmann, I.; Vogeler, K., 2001 "Rotating instabilities in an axial compressor originating from the fluctuating blade tip vortex", *ASME Journal of Turbomachinery*, Vol. 123, pp. 453-463.

Conference on Modelling Fluid Flow (CMFF'06)
The 13th International Conference on Fluid Flow Technologies
Budapest, Hungary, September 6-9, 2006

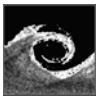

NUMERICAL INVESTIGATION OF ROTOR-STATOR INTERACTIONS IN A 1.5-STAGE LOW-SPEED AXIAL COMPRESSOR

Huixia JIA[1], Konrad VOGELER[2], Lutz MÜLLER[3], Ronald MAILACH[4]

[1] Technische Universität Dresden, Institute of Fluid Mechanics, D-01062 Dresden, Germany. Tel.: +49 351 463 35096, E-mail: jia@tus.mw.tu-dresden.de (School of Energy and Power Engineering, Xi'an Jiaotong University, Xi'an 710049, China. Tel.: +86 29 8266 8783, E-mail: anniejia@mailst.xjtu.edu.cn)
[2] Technische Universität Dresden, Institute of Fluid Mechanics. E-mail: kvogeler@tus.mw.tu-dresden.de
[3] Technische Universität Dresden, Institute of Fluid Mechanics. E-mail: lmueller@tus.mw.tu-dresden.de
[4] Technische Universität Dresden, Institute of Fluid Mechanics. E-mail: mailach@tus.mw.tu-dresden.de

ABSTRACT

The relative motion of rotor and stator leads to viscous and inviscid interactions between the blade rows. This is the reason why the flow in turbomachines is periodically unsteady.

The unsteady flow field of the first stage with inlet guide vane row (IGV) of the Dresden Low-Speed Research Compressor (LSRC) is investigated using a 3D time-accurate, viscous solver. The unsteady profile pressure distribution on the pressure side (PS) and the suction side (SS) of the rotor at midspan (MS) for the design point are presented and analysed. A comparison to experiments performed at the same compressor is drawn [1, 2].

The pressure fluctuation on the rotor depends on the superimposed effect of the wakes of the inlet guide vane and the potential effect of the downstream stator. The time-resolved pressure in the simulation changes nearly simultaneously along the whole chord length like as also observed in the experiment. A phase shift between the pressure fluctuations on the PS and the SS is found.

Furthermore the unsteady blade pressure forces of the rotor blades are calculated from the profile pressure distribution at midspan. The results are compared with the experimental results.

Keywords: axial compressor, periodic unsteady blade pressure fluctuation, unsteady blade pressure force

NOMENCLATURE

A	$[m^2]$	area of blade surface
c_F	[-]	pressure force coefficient
c_M	[-]	moment coefficient
F	$[N]$	pressure force
f	$[Hz]$	frequency
K	[-]	number of time steps
l	$[m]$	chord length
M	$[N{\cdot}m]$	moment
N	[-]	number of time steps
p	$[Pa]$	static pressure
t	$[s]$	time
w	$[m/s]$	relative velocity
x	$[m]$	chordwise position
y	$[m]$	position perpendicular to chord
γ	$[deg]$	angle between resulting force and normal direction
ρ	$[kg/m^3]$	density

Subscripts and Superscripts

–	time-averaged values
∞	average of the velocity vectors of the incoming and outgoing flow
~	fluctuating part
<>	ensemble-averaged value
1	measuring plane upstream of the rotor blade row
cg	centre of gravity
cl	centre of lift
dyn	dynamic
i,j	indices for time traces
x	component in blade chord direction
y	component perpendicular to the blade chord

Abbreviations

BPF	blade passing frequency
IGV	inlet guide vane
LSRC	Low-Speed Research Compressor
MS	midspan
PS	pressure side
RMS	Root Mean Square Value
SS	suction side

1. INTRODUCTION

The flow in turbomachinery is inherently unsteady because of the relative motion between stationary and rotating blade rows. The relative motion between rotor and stator blades induces unsteady aerodynamic interactions which lead to a periodic fluctuation of the profile pressures. The resulting unsteady blade forces have a significant influence on the fatigue behaviour of the blades. Therefore it is necessary to gain a better understanding of the unsteady interaction mechanisms in turbomachines.

Early investigations on rotor-stator interaction were carried out by Kemp et al. [3]. They analysed the unsteady pressure response and the excitation of the unsteady forces theoretically. In recent years several experimental investigations and numerical simulations on this topic were carried out. Hsu and Wo [4] experimentally investigated the unsteady blade row interaction in a large-scale low-speed 1.5-stage axial compressor. Lee and Feng [5] studied the same compressor numerically. Dorney et al. [6, 7] investigated the clocking effect on unsteady force in an axial compressor and a turbine. The pressure fluctuations and the unsteady force changes on the blades were considered for the operating points with maximum and minimum efficiency. Li and He [8] numerically investigated the effect of different stator blade numbers on the unsteady blade loading on the rotor blades and stator blades in a 1.5-stage transonic turbine. Marconcini and Pacciani [9] simulated the effects of clocking on efficiency and unsteady forces in a 1.5-stage high-pressure turbine.

In this paper, the numerical investigation is carried out with the geometry of the Dresden LSRC. The pressure fluctuation and the unsteady blade loading on rotor blades of the first stage are presented and compared with the experimental results from Mailach et al. [1, 2].

2. NUMERICAL METHOD

The Dresden LSRC consists of 4 repeating stages which are preceded by an inlet guide vane row. The blading of the compressor was developed from a typical middle stage of a high pressure compressor of a gas turbine. A detailed description of the Dresden LSRC is given in [10-12].

In this paper, the unsteady flow field of the first stage with IGV of the Dresden LSRC is numerically investigated. The calculations were carried out at MS for design conditions of the compressor.

The 3D time-accurate, viscous flow solver FINE™/Turbo for a compressible ideal gas was used for these investigations. The Baldwin-Lomax algebraic vortex-viscosity model is employed to solve the turbulent flow field. The spatial discretization of the Reynolds-averaged Navier-Stokes equations is based on a cell-centered control volume scheme. The control equations are advanced by a time-marching scheme using an explicit 4-stage Runge-Kutta method. Local time stepping, implicit residual smoothing and multigrids are used to accelerate the computational convergence. A dual time stepping method is used to carry out the unsteady simulation.

The blade number of the IGV, the rotor and the stator blade rows in the experiment are 51, 63 and 83, respectively. In the calculation, the blade number is scaled to 42 inlet guide vanes, 63 rotor blades and 84 stator blades in order to make a compromise between a reasonable precision of the simulation and the cost of the computational time. Thus, with the scaled blade numbers only 2 passages of the IGV, 3 passages of the rotor and 4 passages of the stator have to be simulated in the computational domain.

The complete mesh and the details of the meshes at the leading edge and at the trailing edge of the rotor are shown in Figure 1. To resolve the flow field near the blades O-type grids are used. H-grids are used to resolve the flow field in the blade passages. The total number of grid points is 348,825.

As boundary conditions at the inlet, the stagnation parameters and the flow angle are specified. At the outlet, the pitch-wise mean static pressure is specified. The shroud and hub walls are treated as Euler-wall. The sliding mesh method is employed at the rotor/stator interface. Using this method, the grid of the rotor is rotated in function of the physical time step and the rotor turning speed. Then the flow field is resolved at the given physical time step. In one simulation period, 90 physical timesteps are simulated. One simulation period is the time that one rotor passes two IGV's.

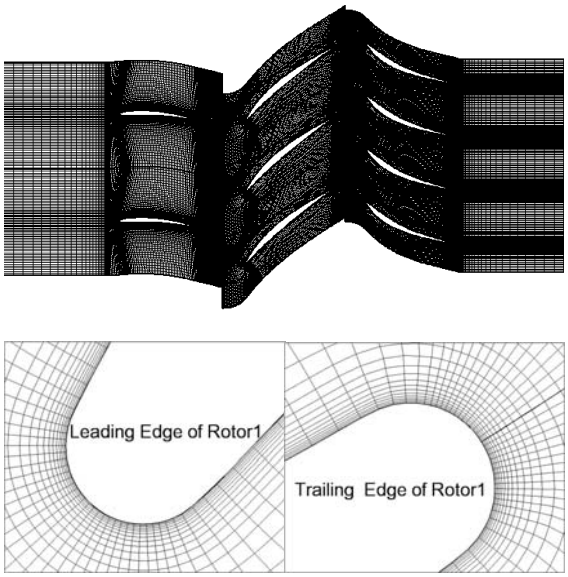

Figure 1. Computational mesh

3. TIME-AVERAGED PRESSURE DISTRIBUTION ON THE ROTOR BLADES

Figure 2 shows the steady distribution of the pressure coefficient for the design condition on the rotor blade at MS. The agreement of the results of the simulation with the experimental data is satisfactory.

It can be observed in Fig. 2 that the flow accelerates to 15% chord on the SS. At 15% chord, the pressure minimum reached. After the pressure minimum, the flow begins to decelerate towards the blade trailing edge. On the PS the flow accelerates to 8% chord where the pressure minimum reached. Then the flow decelerates to 80%. From 80% chord towards the trailing edge the flow accelerates slightly.

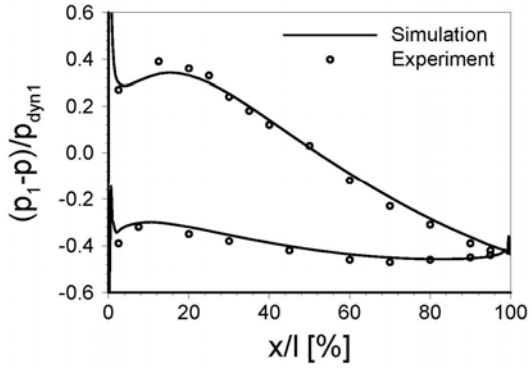

Figure 2. Steady pressure distribution, rotor 1, MS, design point

4. UNSTEADY PRESSURE DISTRIBUTION ON THE ROTOR BLADES

In Figure 3 the time-averaged pressure distribution is given as solid lines for the calculation (Figure 3a) and the experiment (Figure 3b). The pressure coefficient is calculated from the time-averaged values of the unsteady simulation.

The time-averaged Root Mean Square-value (RMS) is calculated as following

$$\overline{\mathrm{RMS}} = \sqrt{\frac{1}{N}\sum_{i=0}^{N-1}(p_i(t)-\overline{p})^2} \qquad (1)$$

which represents information about periodic fluctuation in the simulation. In the experiment, it includes both periodic and stochastic pressure fluctuations.

In Fig. 3 the fluctuations around the time-averaged pressure distributions are shown as dashed lines. It can be seen, that the fluctuations in the experiment are somewhat stronger than that in the simulation. This can also be observed in the space-time-diagrams of the unsteady pressure distribution on the rotor, shown later in this section.

In the simulation, the relative position of the IGV and the stator in every IGV passage is identical, because the stator blade number is twice the blade number of the IGV (42 IGV's and 84 stator blades).

In the experimental setup, the blade numbers of IGV (51) and stator (83) are not multiples. So the relative configuration between the IGV and the stator in every passage is different.

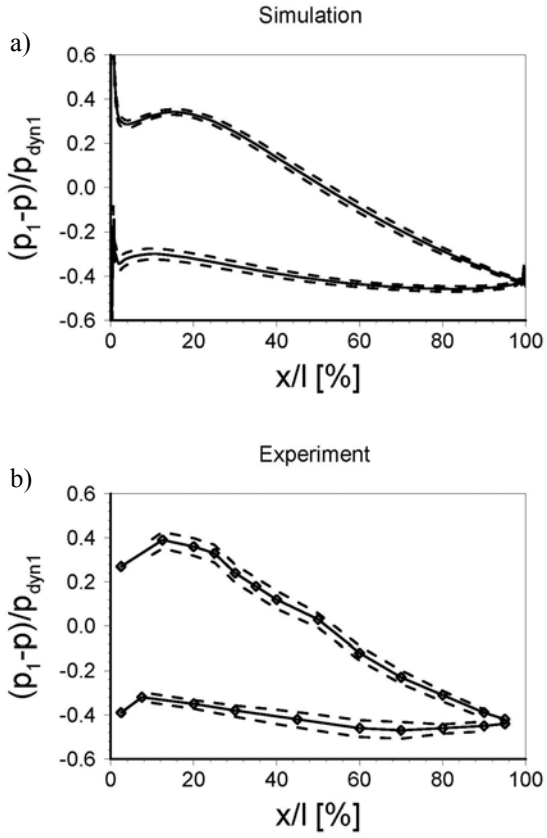

Figure 3. Steady pressure distribution with RMS-values, rotor 1, MS, design point

Therefore the experimental data are considered at a circumferential position of the compressor, where a comparable relative position of IGV and stator blades can be found like in the simulation.

Figure 4a and 4c shows the numerical results for this configuration, whereas the experimental results are shown in Figure 4b and 4d. The time is related to the passing time of the downstream stator t_{stator}. In each case the fluctuating part of the profile pressures is shown. The experimental results are ensemble-averaged using the equation

$$< p(t) >= \frac{1}{K}\sum_{j=0}^{K-1} p_j(t) \qquad (2)$$

It can be observed, that the unsteady profile pressure fluctuation is the superimposed effect of the IGV wake and the potential effect of the downstream stator. For both, the simulation and the experiment, on the PS and the SS the pressure changes nearly instantaneously in time along the chordwise direction.

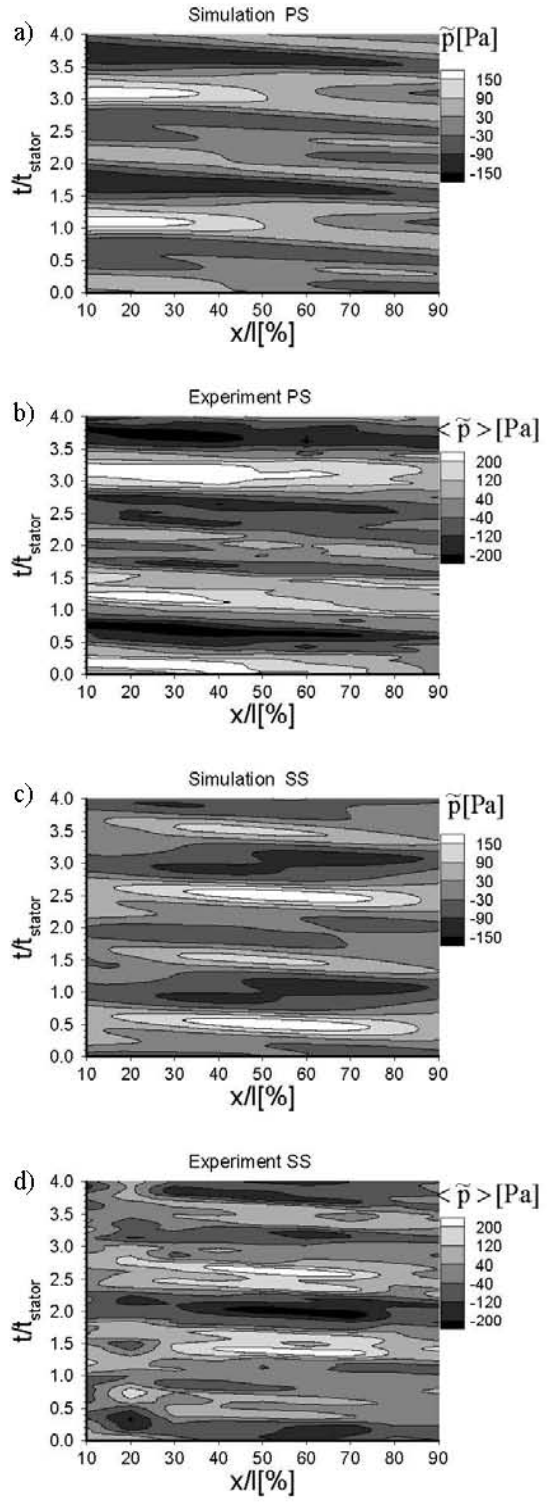

Figure 4. Unsteady pressure distribution on PS and SS of rotor 1, MS, design point

The unsteady profile pressure fluctuation in the simulation appears periodically. In every second stator passing period the pressure fluctuation repeats since the blade number of the stator is twice the IGV number. In the experiments 2 blade passing periods of the stator corresponds to 1.23 periods of the IGV.

If the pressure fluctuation induced by the IGV and the pressure fluctuation due to the downstream stator potential field are superimposed, the pressure fluctuation is intensified (Fig. 4a). This appears at every second blade passing period of the stator. When t/t_{stator} is equal to 1.2 and 3.2, the unsteady pressure fluctuation is intensified on the PS of the rotor. When t/t_{stator} is equal to 0.2 and 2.2, the pressure fluctuation due to the downstream stator is superimposed with a pressure fluctuation of the IGV wake with the opposite sign. As a result resulting pressure fluctuation is reduced.

The same situation can be observed in the experiment (Fig. 4b). If t/t_{stator} is 1.3 and 3.2, respectively, the unsteady pressure amplitude on the PS of the rotor blade reaches a maximum. At t/t_{stator}=2.2 the unsteady pressure amplitude is clearly smaller.

The largest pressure fluctuations on the PS appear between the leading edge and 50% chord. In the simulation the maximum pressure fluctuation amplitude is +/-5% of the dynamic pressure of the incoming flow. Compared to the experimental results, the maximum pressure fluctuations of the simulation are somewhat lower than that from the experiments.

Also on the SS the superposition of the IGV wakes and the potential field of the stator leads to a modulation of the resulting pressure fluctuation amplitudes (Fig. 4c). So the pressure amplitudes at t/t_{stator}=0.6 and 2.6 are somewhat higher than at t/t_{stator}=1.6 and 3.6.

The experimental results on the SS show a comparable pressure distribution concerning the fundamental pattern and the pressure amplitudes (Fig. 4d). However, the increase of the pressure amplitudes for every second passing stator blade does not appear since the ratio of stator blade to IGV number is not equal to two.

On the SS, the largest pressure fluctuations appear in the range of 20-80% chord (Figs. 4c and 4d). In this area, the flow decelerates. Similarly, the maximum pressure fluctuations on the PS appear in the region with decelerated flow (from 10-50% chord, Figs. 4a and 4b).

It can be stated, that a good qualitative consistency of the experiment and the simulation exists. Differences can arise from the fact, that the unsteady pressure fluctuations on rotor 1 are also affected by the potential fields of the stators of the subsequent compressor stages, which are not

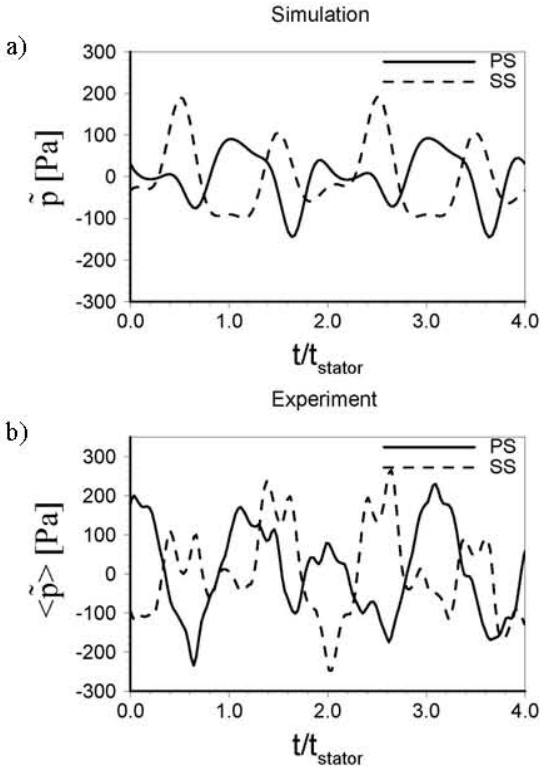

Figure 5. Pressure fluctuations at 50% chord of the rotor blades at MS, design point

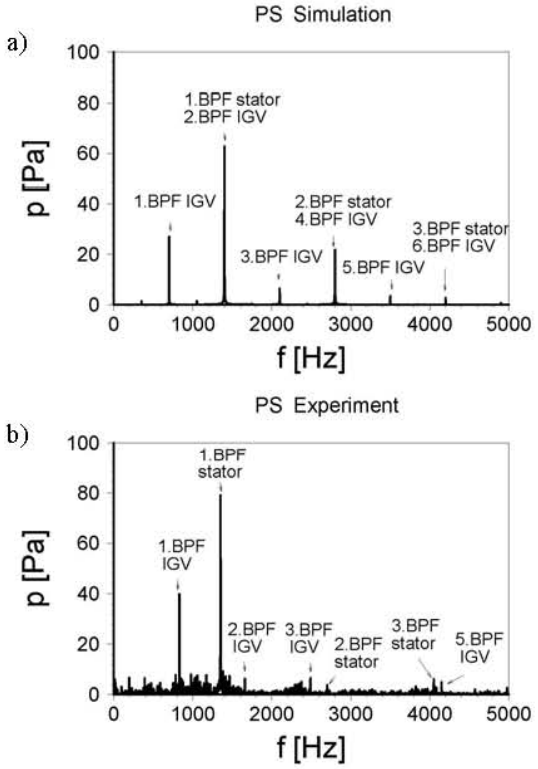

Figure 6. Frequency spectra of pressure on the rotor blades, 50% chord, design point

considered in the simulation. Furthermore the neglected spanwise pressure distribution as well as the not modelled radial gaps of the rotor blades lead to differences between simulation and experiment.

As part of the data of Fig. 4, in Figure 5 the fluctuating part of the profile pressures at the 50% chord positions on PS and SS are presented. Figure 5a shows the time traces of the pressure fluctuation on PS and SS as a result of the calculation. The timescale is again normalised with the passing period of the downstream stator. The 4 passing periods of the downstream stator corresponds to 2 passing periods of the IGV. The pressure fluctuations are caused by the superimposed effect of the IGV wakes and the potential effect of the downstream stator blades. Because of the given blade count ratio the characteristic pattern of pressure fluctuations repeat periodically in every second passing periods of the downstream stator. Between the signals on PS and SS a constant phase shift between the pressure fluctuations on PS and SS of about 180 degrees can be observed.

The corresponding experimental data show more spiky fluctuations with larger amplitudes. The phase shift between the signals on PS and SS is changing in time between 90-180 degrees, depending on the relative position of the IGV wakes and the stator potential effects [1]. This changing phase shift appears because the stator blade number for the experiment is not a multiple of the IGV number.

In Figures 6a and 6b the frequency spectra of the pressure at the 50% chord position on the PS of the rotor are given for the simulation and the experiment. The design rotational speed of the compressor is 1000 revolutions per minute. In the simulation, the blade passing frequencies (BPF) of the IGV and the stator are 700*Hz* and 1400*Hz*, respectively (42 IGV and 84 stator blades). In the experiment the 1. BPF of IGV is 850*Hz* and 1383*Hz* for the stator (51 IGV and 83 stator blades).

In the simulation the dominant periodic influence of the IGV wakes is reflected by the 1. BPF of the IGV. The 2nd BPF of the IGV corresponds to the 1st BPF of the stator blades. Thus for this frequency component the stator potential effect cannot be distinguished from the IGV wake effect. However, in Fig. 4 the dominance of the potential effect of the stator blades versus the IGV wake effect is obvious. According to that, it can be assumed, that the main contribution to the peak at 1.4 *kHz* stems from the potential field of the downstream stator.

This is also confirmed by the experimental data (Fig. 6b). The amplitudes of the potential effect of the downstream stator is about two times of the wake effect of the IGV (1. BPF's of IGV and stator blades). The higher harmonics of the BPF's of the blade rows can be neglected.

In the numerical results the amplitude at the 1. BPF of the IGV is only 43% of that appearing at the 1. BPF of the stator (Fig. 6a). This is the same order of magnitude than observed in the experimental results. At 2.8 *kHz* the pressure amplitude from the simulation is considerably higher than in the experiment. This is due to the superimposed effects of the 2.BPF of the stator and the 4.BPF of the IGV. Other higher harmonics of stator and IGV BPF's are of less importance for the blade excitation.

On the SS (no figure) comparable observations can be made like described for the PS. That means, the amplitude due to the potential effect of the downstream stator (1.BPF stator) is largest and the effect of the IGV wake (1.BPF IGV) amounts to about 50% of the potential effect of the downstream stator (1.BPF stator).

5. UNSTEADY PRESSURE FORCE ON THE ROTOR BLADES

Due to the unsteady profile pressure distribution an unsteady blade pressure force and unsteady moment are generated. The unsteady aerodynamic blade loading significantly influences the blade life cycle. In this section, the unsteady blade pressure forces at MS on the rotor blade in the first stage for the design condition will be discussed. The algorithm used here to calculate the unsteady force, is described by Mailach et al. [2].

Figure 7 shows the force component definitions in blade coordinate system. The components of the force F are denoted as F_x and F_y. These components are directed along the blade chord direction and perpendicular to that, respectively. The moment M_{cg} acts around the centre of gravity of the blade.

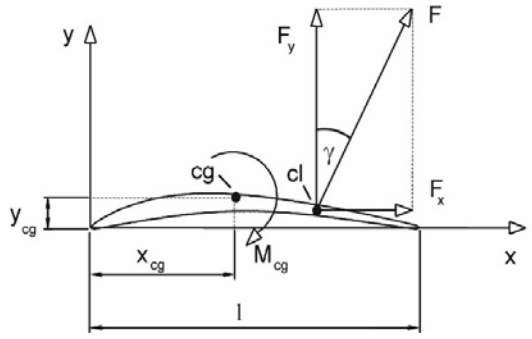

Figure 7. Forces in blade coordinate system

The unsteady pressure force in the experiment is calculated from the pressure distribution, which is measured with piezoresistive pressure transducers [1]. These sensors are arranged at MS on PS and SS each from 10% chord to 90% chord with an equal spacing of 10% chord. At the leading edge and the trailing edge no pressure transducers could be mounted. In the experiment the time traces of the pressure on leading and trailing edge are extrapolated from the transducers mounted at 10% and 90%, respectively.

In the simulation, the force is calculated from the unsteady profile pressure distribution along the whole chord of the rotor blades at MS, including the leading edge and the trailing edge regions.

Because the pressure force is related to the up- and downstream flow field, the force coefficient is calculated with the following relation

$$c_F(t) = \frac{F(t)}{\rho/2 \cdot \overline{w}_\infty^2 \cdot A} \tag{3}$$

while the nondimensional moment is calculated with

$$c_{M,\mathrm{cg}}(t) = \frac{M_{\mathrm{cg}}(t)}{\rho/2 \cdot \overline{w}_\infty^2 \cdot A \cdot l} \tag{4}$$

In Table 1 the time-averaged pressure force coefficient c_F on the rotor, its components $c_{F,x}$ along blade chord direction (x) and $c_{F,y}$ in the perpendicular direction to the blade chord (y) as well as the moment around the center of gravity are given. A good agreement of these time-averaged quantities from the simulation and the experiment is evident. The dominating force component is F_y. Its mean value is about 10 times of F_x. Thus, the force coefficient c_F is nearly equal to the force component coefficient in y direction.

Table 1. Time-averaged pressure force coefficients of the rotor blade for design point

Rotor1	$\overline{c}_F$	$\overline{c}_{F,y}$	$\overline{c}_{F,x}$	$\overline{c}_{M,cg}$	$\overline{\gamma}$ [°]
Simulation	0.566	0.563	-0.05	0.56	-5.2
Experiment	0.55	0.55	-0.06	0.65	-6.7

Time-resolved values from the force calculation are shown in Figure 8. These are the force coefficient, the moment around the centre of gravity and the angle between F_y and F.

As already observed for the unsteady profile pressure distribution, the IGV wakes and the potential effects of the downstream stator blades are the dominating periodic influences.

In the simulation the maximum fluctuation amplitude of the force coefficient c_F is +/-12% of the averaged values. Because of the lower values of $c_{F,x}$, the maximum fluctuation amplitude of the force coefficient $c_{F,y}$ is also +/-12% of the averaged values (no figure). The maximum fluctuation amplitude of the force coefficient in x-direction ($c_{F,x}$) is 8% of the mean values. The maximum fluctuation amplitude of the moment around the

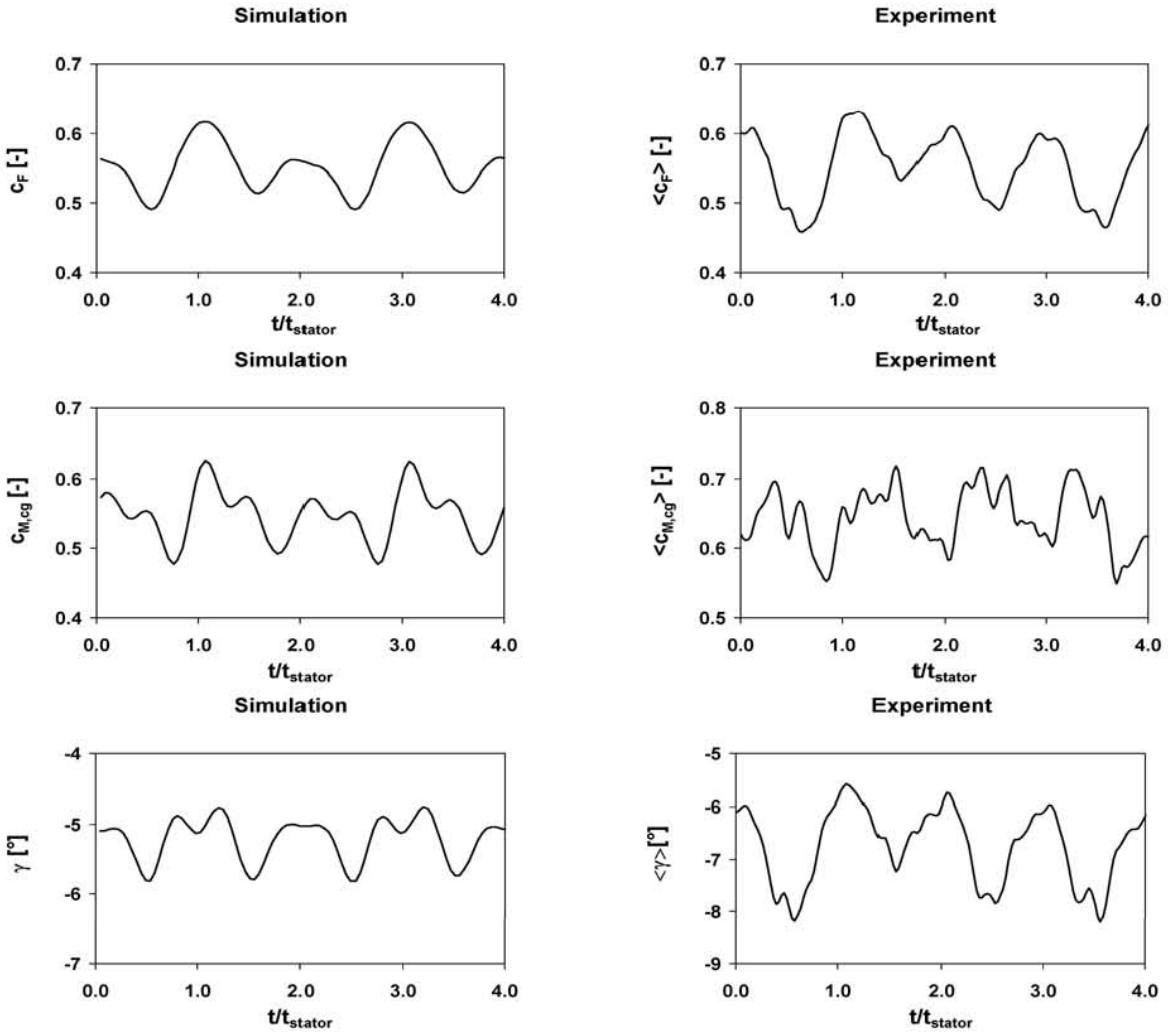

Figure 8. Unsteady pressure force coefficients, momentum coefficient and angle γ on rotor blades, design point

centre of gravity is +/-14% of the mean values. The fluctuation of the angle γ between c_F and $c_{F,x}$ is only +/-0.5 degrees.

Somewhat larger fluctuation amplitudes of the force parameters are observed in the experiments. As reported in [2], the maximum fluctuation amplitudes of the force coefficient are +/-15% of its mean values for the experiment. The fluctuation of the angle γ between c_F and $c_{F,x}$ is about +/-1.0 degrees in the experiment. However, the time-resolved force parameters from the simulation and the experiment show a comparably good agreement. The experimental results are more noisy because the limited spatial resolution and the missing sensors at the leading and trailing edge of the blade.

The frequency spectrum of the force coefficient from the simulation is shown in Figure 9. As already observed for the pressure fluctuation on PS and SS, the potential flow field effect from stator 1 is the dominating periodic influence. In the frequency spectrum of the force the amplitude of the IGV wake effect is 50% of the potential effect of the downstream stator. The distribution of the peaks in the force spectrum is comparable to that of the pressure spectrum (Fig. 6a).

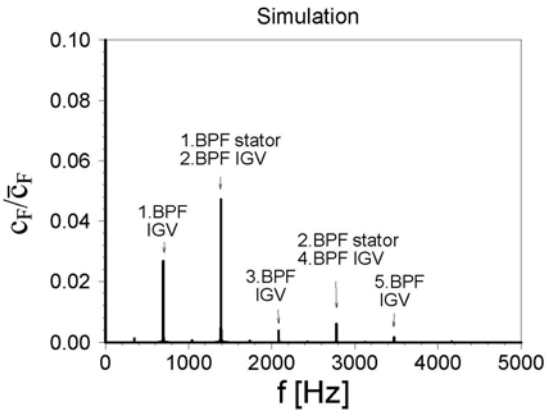

Figure 9. Frequency spectra of force coefficient, MS, design point

6. SUMMARY

The unsteady flow field of a 1.5-stage configuration of the Dresden Low-Speed Research Compressor is investigated using a 3D time-accurate, viscous solver. The numerical results are analysed and compared with the experiments at midspan.

The unsteady profile pressure distributions on PS and SS of the rotor blades in the first stage are presented for the design conditions. The profile pressures are periodically affected by the IGV wakes and the potential effect of the downstream stator blades. The potential effect of the downstream stator dominates the pressure fluctuation. The wakes of the IGV play only a secondary role because of the comparably small velocity deficit of the IGV wakes. The maximum pressure fluctuation is about +/- 5% of the dynamic head of the incoming flow. There is a phase shift of the pressure signals on PS and SS, which amounts to about 180 degrees.

The unsteady blade pressure force parameters of the rotor blades are calculated from the profile pressure distribution. The time traces and frequency contents of the pressure forces are also presented. The mean value of the force coefficient in y-direction is 10-times of that in x-direction. The maximum fluctuation amplitude of the force coefficient c_F is +/- 12% of the mean values.

A detailed comparison of the results from the simulation and the experiments showed a good agreement of both time-averaged and time-resolved flow quantities.

ACKNOWLEDGMENTS

The lead author would like to express her appreciation to DAAD (German Academic Exchange Service) for the scholarship support. The experimental data are from the project: "Unsteady Forces and Boundary Layer Behaviour on the Blades of a Low-Speed Axial Compressor" funded by the DFG (German Research Society).

REFERENCES

[1] Mailach, R., Vogeler, K., 2004, "Rotor-Stator Interactions in a Four-stage Low-speed Axial Compressor – Part I: Unsteady Profile Pressures and the Effect of Clocking", *ASME Journal of Turbomachinery*, Vol. 126, pp. 507–518.

[2] Mailach, R., Müller, L., Vogeler, K., 2004, "Rotor-Stator Interactions in a Four-stage Low-speed Axial Compressor – Part II: Unsteady Aerodynamic Forces of Rotor and Stator Blades", *ASME Journal of Turbomachinery*, Vol. 126, pp. 519–526.

[3] Kemp, R.H., Hirschberg, M.H., and Morgan, W.C., 1958, "Theoretial and Experimental Analysis of the Reduction of Rotor Blade Vibration in Turbomachinery through the Use of Modified Stator Vane Spacing", *NACA, Technical Note* 4373.

[4] Hsu, S.T., Wo, A.M., 1998, "Reduction of Unsteady Blade Loading by Beneficial Use of Vortical and Potential Disturbances in an Axial Compressor With Rotor Clocking", *ASME Journal of Turbomachinery*, Vol. 120, pp. 705-713.

[5] Lee, Y., Feng, J., 2004, "Potential and Viscous Interactions for a Multi-Blade-Row Compressor", *ASME Journal of Turbomachinery*, Vol. 126, No. 4, pp. 464–472.

[6] Dorney, D.J., Sondak, D.L., Cizmas, P.G.A., Saren, V.E., and Savin, N.M., 1999, "Full-Annulus Simulations of Airfoil Clocking in a 1-1/2 Stage Axial Compressor", *International Journal of Turbo and Jet Engines*, Vol. 16, pp. 149-160.

[7] Dorney, D.J., Croft, R.R., Sondak, D.L., Stang, U.E., and Twardochleb, C.Z., 2001, "Computational Study of Clocking in an Embedded Stage in a 4-Stage Industrial Turbine", *ASME* 2001-GT-0509.

[8] Li, H.D., He, L., 2003, "Blade Count and Clocking Effects on Three-Bladerow Interaction in a Transonic Turbine", *ASME Journal of Turbomachinery*, Vol. 125, pp. 632-640.

[9] Marconcini, M., Pacciani, R., 2003, "Numerical Investigation of Wake-Shock Interactions and Clocking in a Transonic HP Turbine", *ASME* GT2003-38401.

[10] Sauer, H., Bernstein, W., Bernhard, H., Biesinger, T., Boos, P., and Möckel, H., 1996, "Konstruktion, Fertigung und Aufbau eines Verdichterprüfstandes und Aufnahme des Versuchsbetriebes an einem Nieder-geschwindigkeits-Axialverdichter in Dresden", *Abschlußbericht zum BMBF-Vorhaben 0326758A, Dresden, Germany*.

[11] Müller, R., Mailach, R., and Lehmann, I., 1997, "The Design and Construction of a Four-Stage Low-Speed Research Compressor", *Proceedings of the IMP 97 Conference on Modelling and Design in Fluid-Flow Machinery*, Gdansk, Poland, pp. 523–530.

[12] Boos, P., Möckel, H., Henne, J.M., Selmeier, R., 1998, "Flow Measurement in a Multistage Large Scale Low Speed Axial Flow Research Compressor", *ASME* 98-GT-432.

Conference on Modelling Fluid Flow (CMFF'06)
The 13th International Conference on Fluid Flow Technologies
Budapest, Hungary, September 6-9, 2006

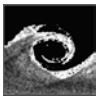

VISCOUS SOLVER DEVELOPMENTS AND CASE STUDY ON THE ROOT OF SEPARATION EXCITED VIBRATION IN REVERSE MODE INSTALLED COMPRESSOR STATOR SEGMENT

Árpád VERESS[1], Tamás GAUSZ[2], János MOLNÁR[3], József ROHÁCS[4]

[1] Corresponding Author. Department of Aircraft and Ships, Budapest University of Technology and Economics. Sztoczek József u. 6. J ép. 426, H-1111 Budapest, Hungary. Tel.: +36 1 463 1992, Fax: +36 1 463 3080, E-mail: veress@rht.bme.hu
[2-4] Department of Aircraft and Ships, Budapest University of Technology and Economics. E-mail: rohacs@rht.bme.hu

ABSTRACT

Numerical modelling and analysis is presented in this paper to model flow field and to recover the origin of HCF (high cycle fatigue) excited by separation in the axial compressor stator at reverse segment installation. In case of incorrect angle of attack the flow separation can oscillate and the flow induced non-linear vibration can lead to the serious problems.

The numerical method is based on the Navier-Stokes equations, which are deduced with using Favre averaging. The convective terms are discretized by Roe approximated Riemann method. Central discretization is applied for diffusive terms. MUSCL (Monotone Upstream Schemes for Conservation Laws) approach is implemented for higher order spatial reconstruction with Mulder limiter for monotonicity preserving. Wilcox k-ω model is implemented for turbulence modelling. The system of equations is solved by the time accurate 4th order Runge-Kutta method to recover unsteadiness of the complex flow field.

As a direct consequence of the non-stationary separated eddies; the oscillated blade forces, the blade pressure distributions and the variation of the reduced blade forces have a significant effect on flow induced non-linear vibration. Hence, following the numerical calculations, detailed analysis has been performed in consideration of the time evolution processes.

Keywords: axial flow turbomachinery, flow induced vibration, Navier-Stokes solver

NOMENCLATURE

c	$[m/s]$	absolute velocity
C	$[m]$	camber length
E	$[J/kg]$	total energy per unit mass
F_B	$[N/m]$	blade force
F,G	[-]	inviscid flux vectors
F_v,G_v	[-]	viscous flux vectors
h^{to}	$[J/kg]$	total enthalpy per unit mass
H_n	[-]	normal flux function
i,j	[-]	spatial variables for indexing
k	$[m^2/s^2]$	turb. kinetic energy per unit mass
L	$[m]$	lenght
n	[-]	normal to the surface
n_x, n_y	$[m]$	components of normal vector
p	$[Pa]$	static pressure
p^*	$[Pa]$	static pressure, turbulent kinetic energy is included
q_i	$[J/m^2/s]$	components of heat flux vector
$r_n^{(i)}$	[-]	right normal eigenvectors
R	$[J/kg/K]$	specific gas constant, residual [-]
S	[-]	vector of source term
t	$[s,-]$	time, unit normal direction to n
u	$[m/s]$	tangential velocity
U	[-]	vector of conservative variables, free stream velocity
u,v	$[m/s]$	components of velocity vector
V_n	$[m/s]$	velocity normal to the surface
w	$[m/s]$	relative velocity
W	[-]	vector of characteristic variables
x, y	$[m]$	Cartesian coordinates in space

Variables (Greek)

α_k	[-]	const. for the Runge-Kutta time it.
$\alpha, \beta_0, \beta_0^*, \xi^*, \sigma, \sigma^*$	[-]	Wilcox model constants
δ	$[m]$	thickness of the boundary layer
Δ	[-]	difference
$\lambda_n^{(i)}$	[-]	eigenvalues
μ	$[Ns/m^2]$	molecular viscosity
μ_t	$[Ns/m^2]$	turbulent viscosity
ρ	$[kg/m^3]$	density
$\tau_{i,j}$	$[N/m^2]$	stress tensor components
ω	$[1/s]$	specific dissipation rate
Ω	$[m^2]$	area of the finite volume

Subscripts and Superscripts

$\bar{}$ vector, time average

~	Favre (mass) average
ˆ	Roe average state space
1,2	inlet and outlet
n	variables normal to the surface
T	turbulent

Abbreviations

DNS	: Direct Numerical Simulation
HCF	: High Cycle Fatigue
L	: left
LES	: Large Eddy Simulation
N_f	: number of faces
R	: right
RANS	: Reynolds Averaged Navier-Stokes
RSM	: Reynolds Stress Model

1. INTRODUCTION

Axial compressors of gas turbines using both aeronautical and industrial applications are designed for operating on optimum or near optimum performance at peak efficiency with high power to weight ratio. Because of guaranteeing design parameters, satisfying constraints come from structural stress and fatigue with respecting optimal power to weight ratio, design of blade geometry leads to compromise and the operation is performed near to fatigue limit. Hence, any kind of fault occurred in manufacturing or maintenance can cause a dramatic change on lifetime curve, which can lead faster fatigue and crash before overhaul.

A gas generator operated in one of the national power plant was tripped due to a surge. According to the failure investigation, a stator blade of stage 7 was crashed probably by fatigue fracture and a cracking was observed in a stator blades at stage 6. The most probable cause of the failures was the aerodynamic induced HCF due to the stage 6 stator blade segment 6 most likely being installed the wrong way around.

There are different possibilities to model fluid dynamics phenomena in the opposite way installed stator segment. Today's intensively developing CFD (Computational Fluid Dynamics) methods such as DNS (direct numerical simulation) [7,9,10,12] and LES (large eddy simulation) [10,11] are confined to low Reynolds number from purely computational consideration. They require a huge amount of computational time and memory comparing to the conventional flow solvers. However, on a physical standpoint, two-equation closure modelling can be properly employed such as to capture the basic mechanisms related to turbulence and separation. Hence, k-ω turbulence model is developed in the structured finite volume framework for modelling fluid flow in the cascade.

Although the application of commercial codes would also have been a possible way for the simulation, the deeper understands of flow physics and the knowledge of program structure allow easier implementation of the expected modifications.

2. NUMERICAL METHOD

The flow in axial compressor cascade belongs to continuum flow regime, because the Knudsen number is less then 0.001. Hence, the Navier-Stokes equation can be used for modelling.

2.1. Governing Equations

The conservative form of the unsteady compressible Navier-Stokes equations in 2 spatial dimensions without body forces and internal heat generation in the Cartesian coordinate system are given by [4]:

$$\frac{\partial U}{\partial t}+\frac{\partial (F-F_v)}{\partial x}+\frac{\partial (G-G_v)}{\partial y}=0\,, \tag{1}$$

where the vector of unknown variables, diffusive and convective terms are next:

$$U=\begin{pmatrix}\rho\\ \rho u\\ \rho v\\ \rho E\end{pmatrix},\ F_v=\begin{pmatrix}0\\ \tau_{xx}\\ \tau_{xy}\\ u\tau_{xx}+v\tau_{xy}-q_x\end{pmatrix}, \tag{2}$$

$$G=\begin{pmatrix}\rho v\\ \rho vu\\ \rho v^2+p\\ \rho vh^{to}\end{pmatrix},\ F=\begin{pmatrix}\rho u\\ \rho u^2+p\\ \rho uv\\ \rho uh^{to}\end{pmatrix} \tag{3}$$

and

$$G_v=\begin{pmatrix}0\\ \tau_{yx}\\ \tau_{yy}\\ u\tau_{yx}+v\tau_{yy}-q_y\end{pmatrix}. \tag{4}$$

2.2. Numerical Discretization

In this project the finite volume discretization is applied, because it tries to combine the geometrical flexibilities of the finite element method with the discretization flexibility of the finite difference method. In order to pass from a continuous to a discrete form, the unknown in a general finite volume of the partitioned computational domain is defined as:

$$U_j=\frac{1}{\Omega_j}\iint_{\Omega} U d\Omega\,. \tag{5}$$

Roe's approximate Riemann solver is used for the discretization of convective terms at the cell interfaces:

$$H_n^{L,R}=\frac{1}{2}\left\{H_n^L+H_n^R-\sum_{i=1}^{N_f}\left|\hat{\lambda}_n^{(i)}\right|\hat{r}_n^{(i)}\Delta W_n^{(i)}\right\} \tag{6}$$

MUSCL (Monotone Upstream Schemes for Conservation Laws) approach is used for higher order spatial extension and MinMod limiter for monotoniticy preserving [13]:

$$\overline{U}^{L,R}_{i\pm\frac{1}{2}} = U_i \pm \frac{1}{4}\left[(1\pm\kappa)\overline{\Delta}_{i+\frac{1}{2}} + (1\mp\kappa)\overline{\Delta}_{i-\frac{1}{2}}\right] \quad (7)$$

where $\kappa = 1/3$,

$$\overline{\Delta}_{i\pm\frac{1}{2}} = MinMod\left(\Delta_{i\pm\frac{1}{2}}, \beta\Delta_{i\mp\frac{1}{2}}\right),\ 1 \le \beta \le \frac{3-\kappa}{1-\kappa} \quad (8)$$

and

$$\Delta_{i+\frac{1}{2}} = U_{i+1} - U_i,\ \Delta_{i-\frac{1}{2}} = U_i - U_{i-1}. \quad (9)$$

Central discretization is applied for diffusive terms.

2.3. Turbulence Modelling

The most widespread turbulence models in the industrial application are the two equations ones. Amongst them, the k-ω models are not as popular as the k-ε, but it shows sophisticated results in many areas, for example in case of handling surface roughness. The Wilcox k-ω two-equation model has been implemented for turbulence modelling [14].

2.4. Time Integration

The final form of the discretized equation is given by:

$$\frac{\partial}{\partial t}[U]_{ij} = -\frac{1}{\Omega_{ij}}\left(\sum_{k=1}^{4}[H_n - H_{vn}]_{ij,k}\Gamma_{ij,k}\right) + [S]_{ij} = \Re \quad (10)$$

where the convective total flux function is next:

$$H_n = \begin{pmatrix} \overline{\rho}V_n \\ \overline{\rho}\widetilde{u}V_n + p^* n_x \\ \overline{\rho}\widetilde{v}V_n + p^* n_y \\ \left(\overline{\rho}\widetilde{E} + p^*\right)V_n \\ \overline{\rho}V_n k \\ \overline{\rho}V_n \omega \end{pmatrix}, \quad (11)$$

the diffusive total flux function is next:

$$H_{vn} = \begin{pmatrix} 0 \\ \left[\tau^{Fk}_{xx} n_x + \tau^{Fk}_{yx} n_y\right] \\ \left[\tau^{Fk}_{xy} n_x + \tau^{Fk}_{yy} n_y\right] \\ \left[\begin{array}{l} \left(\widetilde{u}\,\tau^{Fk}_{xx} + \widetilde{v}\,\tau^{Fk}_{xy} - q_x\right)n_x + \\ \left(\widetilde{u}\,\tau^{Fk}_{yx} + \widetilde{v}\,\tau^{Fk}_{yy} - q_y\right)n_y + \\ + \left(\mu + \sigma^*\mu_t\right)\left[\frac{\partial k}{\partial x}n_x + \frac{\partial k}{\partial y}n_y\right] \end{array}\right] \\ \left[\left(\mu + \sigma^*\mu_t\right)\left[\frac{\partial k}{\partial x}n_x + \frac{\partial k}{\partial y}n_y\right]\right] \\ \left[\left(\mu + \sigma\mu_t\right)\left[\frac{\partial \omega}{\partial x}n_x + \frac{\partial \omega}{\partial y}n_y\right]\right] \end{pmatrix} \quad (12)$$

and the source term is given by:

$$S = \begin{pmatrix} 0 \\ 0 \\ 0 \\ 0 \\ \sum_{i=1}^{3}\sum_{j=1}^{3}\left(\tau^F_{ijT}\frac{\partial \widetilde{u}_i}{\partial x_j}\right) - \beta^*\overline{\rho}k\omega \\ \alpha\frac{\omega}{k}\sum_{i=1}^{3}\sum_{j=1}^{3}\left(\tau^F_{ijT}\frac{\partial \widetilde{u}_i}{\partial x_j}\right) - \beta\overline{\rho}\omega^2 \end{pmatrix}. \quad (13)$$

4th order Runge-Kutta method is used for time stepping:

$$\begin{aligned} U^0_{ij} &= U^n_{ij} \\ U^k_{ij} &= U^0_{ij} + \alpha_k \Delta t \Re^{k-1}_{ij} \\ U^{n+1}_{ij} &= U^k_{ij}, \end{aligned} \quad (14)$$

where $k = 1,2,3,4$ and

$$\alpha_k = \frac{1}{4-k+1}. \quad (15)$$

The conservative variables can be computed at each cell centre for the next time step and only the primitive variables are used from the previous time step.

2.5. Boundary Conditions

In case of information-propagation dominated systems the method of characteristics play a significant role in determining of the number of physical and numerical boundary conditions. Linear extrapolation technique is used for specifying numerical conditions in general and no slip boundary condition is applied at solid surfaces.

2.6. Validation of the Code

In the following sections numerical results are presented for the test problem of transonic channel over circular bump and compression corner.

The first test case is transonic channel over circular bump, in where the flow enters into the channel with Mach number 0.85 and a shockwave develops over the circular bump. The bump has 4.2 % maximum thickness. In the inlet plane the total pressure, total temperature, and flow angles are specified as physical boundary conditions. The static pressure corresponding an isentropic flow at Mach=0.85 is imposed at the outlet. Under these conditions the flow expands in the rear part of the bump up to a Mach number of about 1.2 and ends up into a week shock wave to allow the recovery of the free stream conditions. The results of FLUENT and own code are compared to each other. The Mach number iso-lines show reasonable deflection

in Figure 1, however the present method predicts the shockwave earlier. The shape of the geometry and the thickness of the boundary layer have a dominant effect on the location of the shockwave. Different numerical methods have different inherent mechanism to model boundary layer and shock wave – boundary layer interaction. The boundary layer seems to be thinner at the downstream of the circular bump in case of the commercial code compared to the own one. Hence, the shockwave triggered earlier in case of our model.

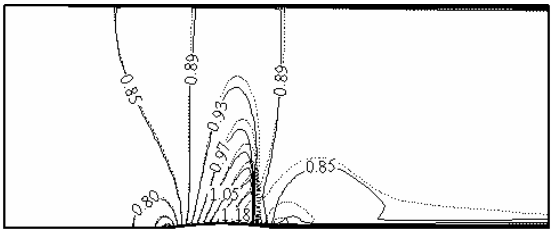

Figure 1. Mach number distribution in transonic channel over circular bump test case (dotted line: FLUENT, continuous line: recent code)

In the second test case a ramp with 20 degrees slope angle is located in the flow channel. The air enters into a channel with Mach number 2.85. Before the ramp an oblique shockwave develops. The geometry and Mach number distribution can be found in Figure 2. The numerical results of the own code and RSM model [1] are compared with each other without significant deviation.

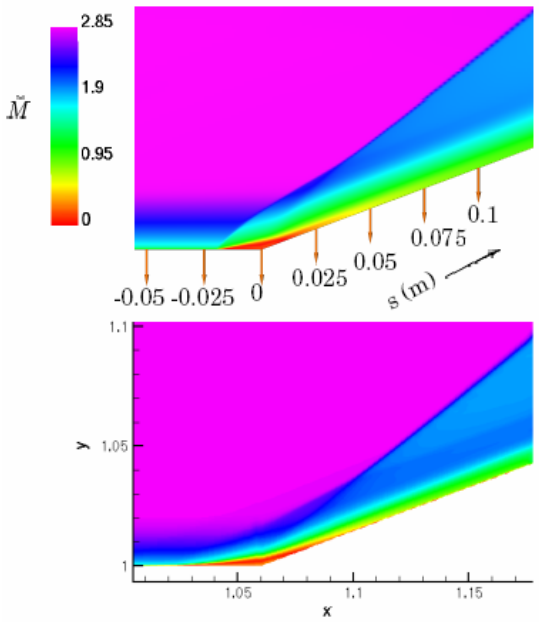

Figure 2. Mach number distribution in compression corner test case (upper figure: RSM model [1], lower figure: recent code)

More information about the numerical method and the validation of the code are available in [6,13].

3. NUMERICAL ANALISYS ON ORIGIN OF FLOW SEPARATION INDUCED VIBRATION

A gas generator operated in one of the national power plants was tripped due to a surge. Borescope inspection revealed damage to the compressor from stage 7 rearwards. According to the failure investigation reported by an inspectorate company, a stator blade of stage 7 was crashed probably by fatigue fracture and a cracking was observed in stator blade stage 6. The most probable cause of the failure of the stage 7 stator blade at this stage was aerodynamic induced HCF cracking due to the stage 6 stator blade segment 6 most likely being installed the wrong way around. The HCF would be originated by the high frequency vortex separation near to the natural frequency of the blade at stator of stage 6. Hence, numerical investigation is presented in this chapter to model flow field in reverse mode installed stator to recover fluid dynamics phenomena.

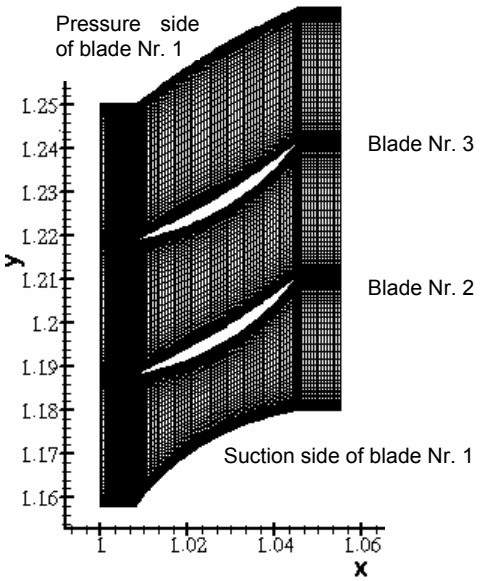

Figure 3. Geometry and meshing of compressor stator segment at stage 6

In reality eight blades belong to a segment of the stator at stage 6, but for the sake of numerical simplification four blades are used in modelling of the cascade. Two of them, which are inserted in reverse mode, are located at the middle part, while the other two ones are over and below of them in correct mode as it can be seen in Figure 3. Structured, stretching based numerical grid generator is also developed for the viscous solver to recover flow structures in the high gradient flow field.

Previous analytical calculation is used to recover physical boundary conditions gives total inlet pressure: 796127 Pa, total inlet temperature: 530.7 K, inlet flow angle: 43°, inlet turbulence intensity: 0.01, static outlet pressure: 654600 Pa. Amongst them, at the blade walls no-slip condition and at the periodic walls periodic boundary condition is used.

Performing numerical calculation huge periodically repeated vortex system is evolved at the suction surface of both blades at reverse installation. An instantaneous plot about the flow

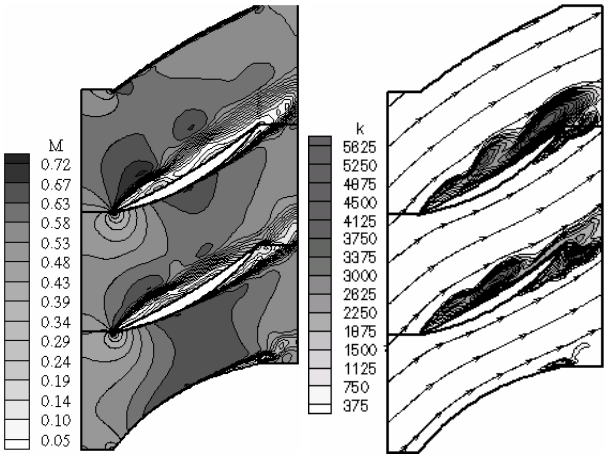

Figure 4. Mach number and turbulent kinetic energy distribution of an instantaneous plot by iso-contours in the investigated blade configuration

field can be found in Figure 4. It has been observed that the separation starts at the leading edge, as a direct consequence of reversing blade segment installation. Vortices are generated and enhance each other by means of co-rotating behaviour and they obtain kinetic energy from the main flow field.

More information can be obtained about the separated flow by focusing only the physical phenomena occurred on the suction and pressure surface of incorrectly placed blades.

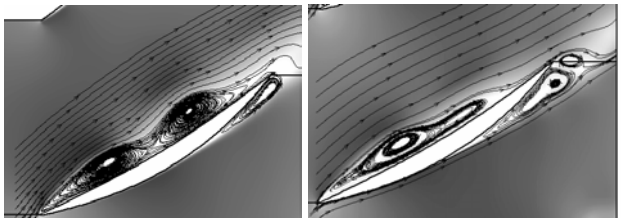

Figure 5. Instantaneous Mach number distribution with stream traces at left: upper and right: lower blade locations

Stream lines in Figure 5 show the vortex systems over the suction side of the upper (blade number 3) and lower (blade number 2). In case of upper blade, the flow channel is tubbier compared to the lower one, hence the effect of the opposite blade to force flow to be reattached is lower. So, the intensity of turbulent kinetic energy at suction surface is higher in the upper located blade. Flow separation also can be observed at the pressure side near to the trailing edge. The adverse pressure gradient is higher between the suction surface of blade 1 and pressure side of blade 2, because the local variation of the cross sectional area is increased more intensively. Strongly separated pulsating flow evolution is amplified by the interaction of separated vortices coming from the suction and pressure side. This pulsation has a certain periodicity, which can play a significant role in the blade excitations and so the vibrations. Hence, the determination of the intensity and frequency of blade forces are devoted to the next paragraph is crucial.

In order to get quantitative information about the oscillating flow field the blade forces are calculated over the profiles:

$$\overline{F}_B = \oint p\bar{n}dA + \oint \mu \frac{dU}{dn}\bar{t}dA \qquad (16)$$

The definition of the boundary layer is used to get an estimate of the velocity gradient near the wall, by which the velocity returns to its free stream condition:

$$\frac{dU}{dn} \approx \frac{U}{\delta} \qquad (17)$$

In this case the wall shear stress – which is approximately constant in the inner layer where $n/\delta \leq 0.1$ – is under estimated, so the turbulent viscosity is included in (16).

The evolution of the magnitude of blade force acting over unit span in the function of time is plotted in Figure 6. The flow instability generates

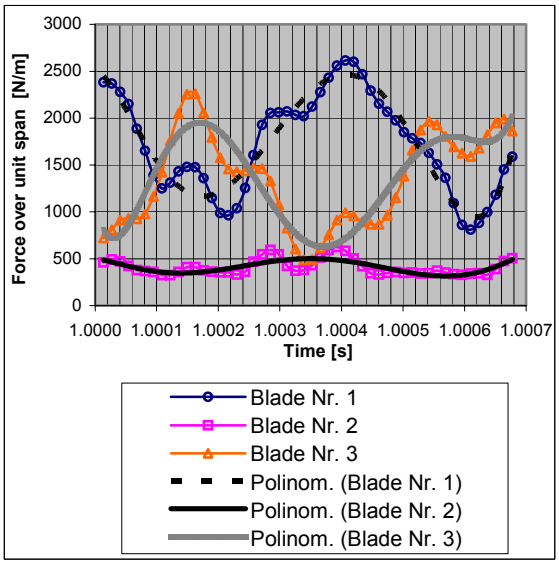

Figure 6. Time evolution of the magnitude of the blade forces acting on profiles

fluctuating blade forces, which has a significant amplitude and frequency. The non-stationary flow separation can be observed in Fig. 4 over blades number 2 and 3, meanwhile the flow around blade number 1 seems to be uniform. The intensities of the forces are not a straightforward consequence of the flow disturbances. Indeed, although the blade number 2 and 3 are inserted in the opposite way, the blade number 3 has much higher amplitude of the oscillation compared to blade number 2. In order to expose the reason of the variance, the pressure distribution is plotted and analysed. The time evolution of the pressure distributions over the given profiles can be found in the same figure in Figure 7 to 9 respectively. The dispersions of the curves are higher in case of blade 1 and 3,

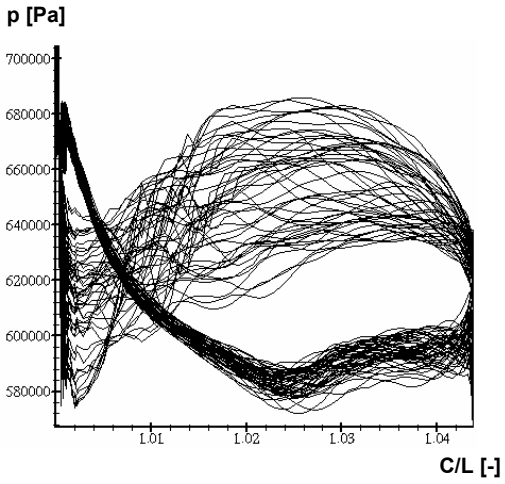

Figure 7. Time evolution of pressure distributions over blade profile number 1

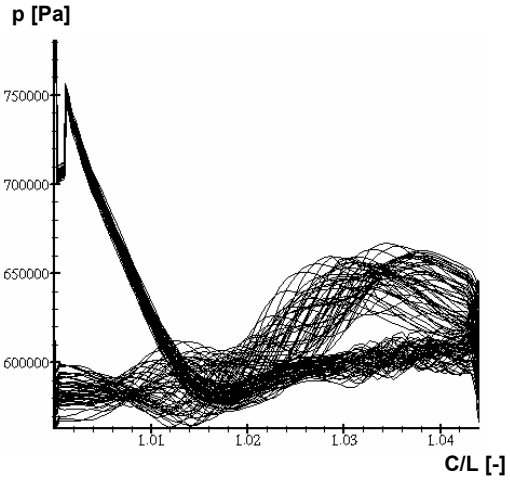

Figure 8. Time evolution of pressure distributions over blade profile number 2

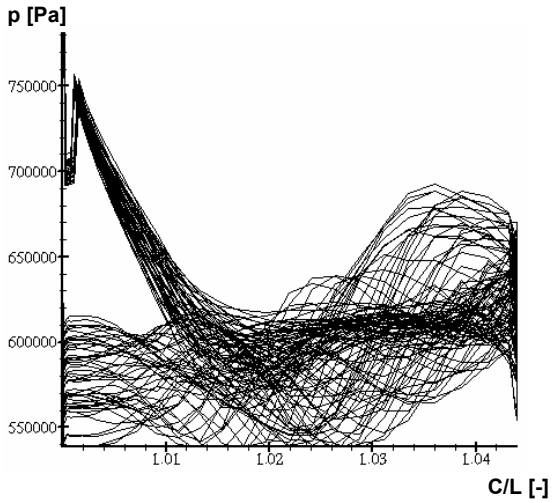

Figure 9. Time evolution of pressure distributions over blade profile number 3

which is the reason of the more intensive force oscillation.

Suction and pressure side of the profiles bound different flow channels. The shape of the channels is in the strong relation of their average pressure. The flow channel between the suction surface of blade 1 and pressure surface of blade 2 has lower pressure level then the other two channels because of narrower flow path. This level of pressure field is the same magnitude as the pressure field near the suction surface of blade 2, which is triggered by the separation. Hence, the average variation of blade loading is less in case of blade 2 compared to the blade 1 and 3. The force component coming from shear stress is not included in the investigation presented above, because its effect is negligible compared to the pressure force.

In combined stress point of view the twisting moment has the same magnitude influence on fatigue then the bending moment. Hence, beside the magnitude, the point of attack of the reduced force is crucial to determine. The twisting moment can be calculated in the function of distance between the point of attack of the reduced force and the centre of twisting of the blade. The time evolutions of the locations of the reduced forces are found in Figure 10 to 12, which belong to blade number 1 to 3 respectively. It can be observed, that the arm of twisting of blade number 2 and 3 can be two times higher compared to blade number 1.

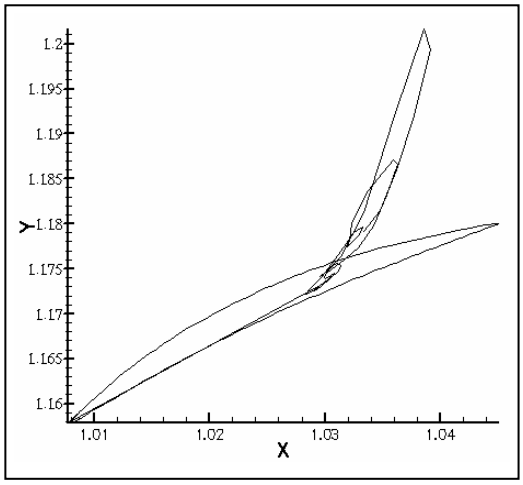

Figure 10. The time evolution of the location of the reduced force at the blade number 1

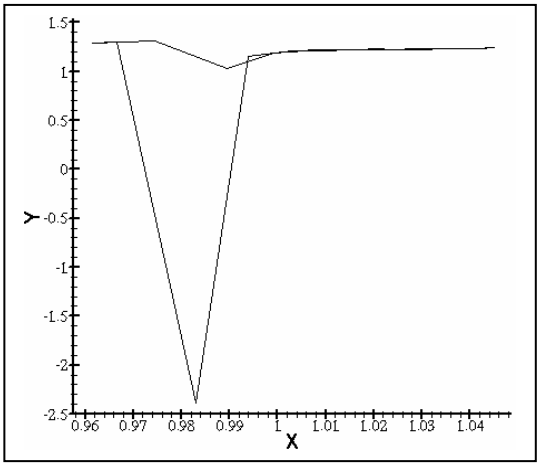

Figure 11. The time evolution of the location of the reduced force at the blade number 2

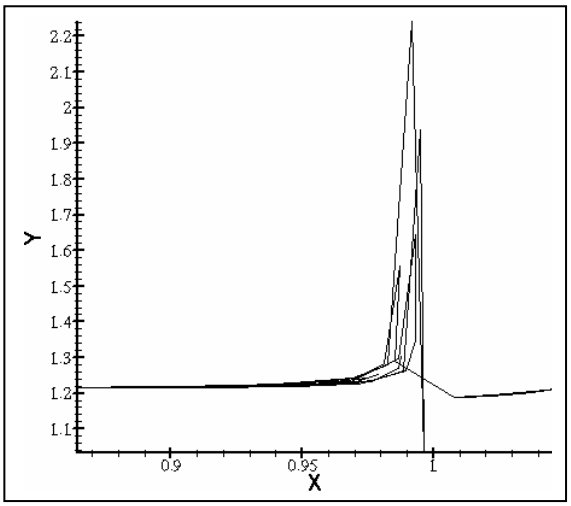

Figure 12. The time evolution of the location of the reduced force at the blade number 3

Taking above consideration, the most critical part of the cascade contains reverse installing blades is the first blade pair, which are shown in Figure 13 with circle. The separated vertices excite blades and the oscillating force can lead to HCF. Moreover, the fluctuating eddies live the cascade can cause serious problems in the later stages, as it can be seen in the domain of influence of separated flow in Figure 13 denoted by hatching.

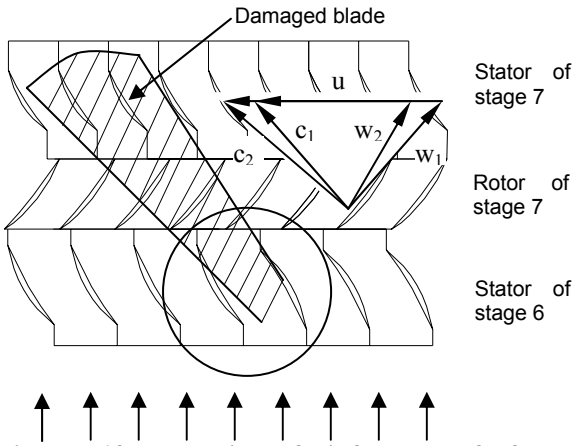

Figure 13. Domain of influence of flow separation (hatched area) with velocity triangle

4. CONCLUSIONS

A 2D Navier-Stokes solver is developed to model flow field and to recover the root of HCF, which is excited by separation in the axial compressor stator at reverse segment installation.

The numerical code is based on structured, cell centered finite volume method. The governing equations in conservative form are deduced with using Favre averaging to filter local fluctuations. The convective terms are discretized by Roe approximated Riemann method. Central discretization is applied for diffusive terms. MUSCL approach is implemented for higher order spatial reconstruction with Mulder limiter for monotonicity preserving. Wilcox k-ω two equations turbulence model is used for turbulence modelling. The system of equation is solved by time accurate 4^{th} order Runge-Kutta method.

Performing numerical analysis, the time accurate computations show an intensive repeated vortex separation originated from the suction surface of the incorrect mode installed blades. Although the frequency of vortices is at about 2.5 kHz, it is difficult to give a correct estimation for the coincidence of the exciting and natural frequency. Three of the most important reasons of that is the complex, deeply stochastic feature of the turbulence, fluid-structure interaction and the complex 3D effect.

The periodicity of the leaving vertices can be changed – mostly based on the effects described before – by which the time interval of HCF can be stretched. So, the crack by HCF can not be occurred within an occasional short time period as usual, but it can be extended in the function of probability rate of the appearance of the separated vertices.

The flow simulation described herein tries to give a possible answer for the separation excited intermittent vibration, which can lead a fatigue crack as it was observed on the specific blades at incorrect blade installation. Based on a report of the inspectorate company, the blade of the stator at the stage 7 is shown in Fig. 13. as "Damaged blade**"** was suffered from fatigue crash by means of metallurgical investigation. Analytical and numerical methods were used in the coupled manner to determine spreading of the intensive vortex shedding from the stator blade row of the stage 6 to the direction of stage 7. It can be concluded that the blade, which was crashed by the fatigue fracture is in the most designated area of the spreading vortices, while the rotor of stage 7 transports them to the direction of stator of stage 7. Hence, the separated flow with stochastic intermittent fluctuation of vortices as described before comes from the stator of stage 6 can cause a serious vibration and HCF, which finally can lead to the crash as it was reported by the inspectorate company. Of course, the intensity and frequency of vortex system are changed across the rotor blades, hence, for determining quantitative parameters a more complex geometrical reconstruction of the computational domain; including 3D stator-rotor-stator interaction using sliding mesh coupling with LES or DNS simulation are indispensable to be made.

As a short summary, it be concluded that the fluctuating separations generate oscillating blade forces, which are mostly caused by pulsating pressure field over the blades. The magnitude of the twisting moment arm is significant and the altering position of the reduced force is responsible for the pulsating twisting moment completing the combined stress. The swirling flow leaves the cascade can cause vibration in the further part of the compressor, too.

REFERENCES

[1] Gerolymos, G. A., Sauret, E., Vallet, I., 2003, "Oblique-Shock-Wave/Boundary-Layer Inter-action using Near-Wall Reynolds-Stress Models", *Université Pierre-et-Marie-Curie*, AIAA 2003-3466.

[2] Hämäläinen, V., 2002, "Implementing an Explicit Algebraic Reynolds Stress Model into the Three-Dimensional FINFLO Flow Solver", *Helsinki University of Technology*.

[3] Hirsch, C., 1988, "Numerical Computation of Internal and External Flows", *John Wiley & Sons*.

[4] Hoffmann, K. A., Steve, T. L., Chiang, M., Siddiqui, S., Papadakis, M., 1996, "Fundamental Equations of Fluid Mechanics", *Engineering Education System*.

[5] Houtmann, E. M., 1996, "Numerical Simulation of Three-Dimensional Compressible Flows", *Faculty of Aerospace Engineering, Delft University of Technology* HSL TM 96381.

[6] Molnár, J., 2005 "Development of k-ω Turbulence Model for Compressible Flow", *MSc. thesis*, Budapest University of Technology and Economics Department of Aircraft and Ships.

[7] Orszag S. A. and Patterson G.S., 1972 "Numerical Simulation of Three-Dimensional Homogeneous Isotropic Turbulence", *Phys. Rev. Lett., 28:76-79*.

[8] Rizzi A. W. and Vivand H., 1981, "Numerical Methods for the Computations of Transonic Flows with Shock Waves" *Notes on Numerical Fluid Mechanics*, 3, Vieweg, Braunschweig.

[9] Rogallo R. S., 1981, "Numerical Experiments in Homogeneous Turbulence", *NASA TM 81315*.

[10] Shen L. and Yue D. K. P., 2001, "Large-Eddy Simulation of Free Surface Turbulence", *J. Fluid Mech., 440, pp. 75-116*.

[11] Smagorinsky J., 1963, "General Circulation Experiments With the Primitive Equations", *Mon. Weather Rev., 93, pp. 99-164*.

[12] Spalart P. R., 1988, "Direct Numerical Simulation of a Turbulent Boundary Layer up to $R_\theta = 1410$", *J. Fluid Mech., 187:61-98*.

[13] Veress, Á., 2004, "Numerical Methods and Application for Flow Calculations in Turbo and Fluid Machines", *PhD thesis,* Budapest University of Technology and Economics Department of Aircraft and Ships.

[14] Wilcox, David C., 1998, "Turbulence Modelling for CFD", *DCW Industries Inc*.

Author's Index

G

H

I

J

K

L

M

N

O

P

R

S

T

U

V